13th IEA HEAT PUMP CONFERENCE
2020 | JEJU KOREA

ISBN 978-91-89385-48-1
http://www.hpc2020.org

13th IEA Heat Pump Conference 2021
Conference Proceedings

- Full Papers

Organized by

Technology Collaboration Programme on Heat Pumping Technologies by International Energy Agency

Co-organized by

The Society of Air-conditioning & Refrigerating Engineers of Korea

Korea National Committee of IIR

Sponsored by

LG Electronics, SAMSUNG, KRAAC, G·ENONE Energy, Carrier 캐리어에어컨, H&C SYSTEM, INTERTECH, KHPA 히트펌프얼라이언스 Korea Heat Pump Alliance, PEB, SWEP, 3S, BOOSTER CO., LTD., KOREA TOURISM ORGANIZATION, Jeju CVB Jeju Convention & Visitors Bureau 제주컨벤션뷰로, KOFST Korean Federation of Science & Technology Societies

MULTI V 5

LG Business Solutions

DESIGNED FOR THE ULTIMATE

CONTINUOUS HEATING



ENHANCED CONTINUOUS HEATING

with Delayed Defrost, Partial Defrost and Smart Oil Management

Delayed Defrost via Dual Sensing Control

By controlling the evaporation temperature considering the humidity, heating operation time is improved.

Partial Defrost

It partially defrosts lower, upper and lower parts of the heat exchanger in order to provide consistent heating for increased heating capacity.

Smart Oil Management

Oil sensor of the Ultimate Inverter Compressor offers enhanced heating operation without periodic oil recovery operation.

SAMSUNG



Free of Wind, Full of Cool

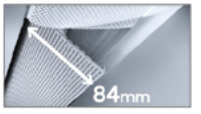
15,700 micro holes keep your space cool without direct wind





Wind-Free™ Cooling

15,700 micro holes allow comfortable cooling without cold drafts.



Big Blades, Long Wind

84mm big blades at wide angles spread cool air farther and evenly.



Motion Detection Sensor

Auto adjusts to optimal modes by detecting movement for energy efficiency.

For more information, visit www.samsung.com/business

Wind-Free™ 4Way Cassette

www.kraac.or.kr

Korea Refrigeration &
Air-conditioning Assessment Center

The Best Partner for HVAC-R Industry

Testing
H/P, AHU, HVAC product

KOLAS/ILAC
ISO/IEC 17025

Inspection
Public Procurement Service

信

CONFIDENCE & RELIABILITY

Certification
RA certification program

Standardization
KS, ISO, Regulation

Education
HVAC training, Technical seminar

KRAAC
KOREA REFRIGERATION & AIR-CONDITIONING ASSESSMENT CENTER

#113 Gyeonggi Technopark, Haean-ro 705,
Ansan-si, Gyeonggi-do, Republic of Korea 15588
Tel. 031-8047-0360 Fax. 031-8047-0393 kraac@kraac.or.kr





Carrier 캐리어에어컨

AUTECH GROUP

'2018 아시아-태평양 지역
고성장 1000대 기업'
(영국 파이낸셜 타임즈 선정)

전 세계의 선택!
시스템 에어컨도 캐리어입니다

세계최고 빌딩 공조 시스템 전문 기업

다양한 실내기 연결 / 에너지 비용 절감 / 강력 냉난방
책임 A/S 시스템 / 호텔, 사무실, 쇼핑몰, 병원에 최적화



인버터 히트펌프 냉동기
USX Edge 칠러

- 한냉지형 실외온도 -15℃에서도 온수 50℃ 출수 가능
- 인버터 펌프 내장 가능

최고의 상업용 멀티에어컨
SMMS-e 시리즈

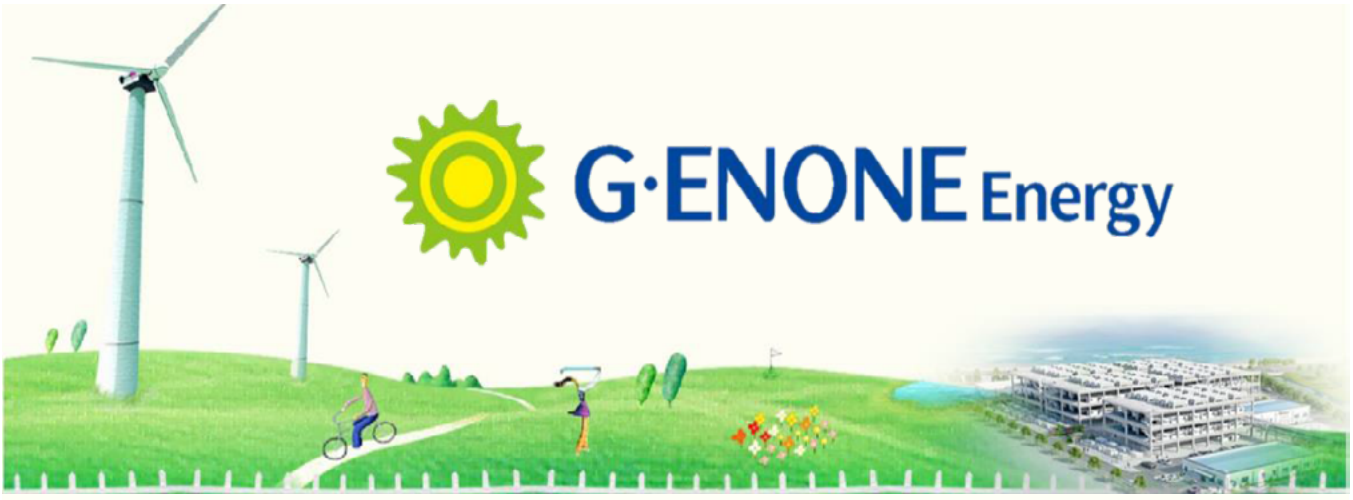
- 강화된 한냉지 난방 (-25℃ 난방 가능)
- 새로운 DC 트윈 로터리 압축기
- 다양한 실내기 연결 (최대 64대)
- 최대 조합 50HP

빌딩 최적 냉난방 멀티에어컨
V6 시리즈

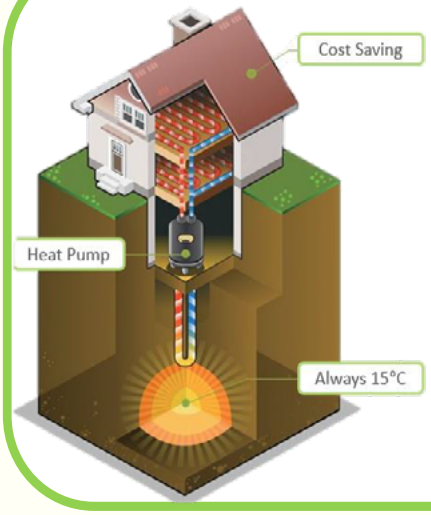
- 32HP의 단일 모델 최대 용량
- 고효율 EVI 인버터 스크롤 압축기
- 강화된 한냉지 난방 (-25℃ 난방 가능)
- 호텔, 사무실, 쇼핑몰, 병원에 최적화

홈페이지 www.carrier.co.kr **쇼핑몰** www.carriermall.co.kr **구입** 1588-8855 **서비스** 1588-8866

에어컨 전문점 개설문의 전국 주요 지역 / 에어컨, 냉난방 공조기기 분야 종사자 및 판매 유 경험자 / 02-3441-8902, 2572 **본사판매원 모집 문의** 02-3416-4801



Geothermal Heating & Cooling System



01 Outstanding Economics
- Minimize energy cost → cost reduction
- Semi-permanent life of major parts (geo-heat exchanger 50 years, heat pump at least 20 years)

02 Geothermal Heating and Cooling System Using Heat Pump
- Next-generation air conditioning system in combination of boiler + air conditioner
- Minimize the area of the machine room to use efficiently

03 Stable Energy Source
- The temperature 200 m underground is consistently at an annual average of 15°C.
- Eco-friendly energy that can be used continuously

04 Safety and Eco-Friendly
- No risk of explosion or fire
- No problems of exhaust gas, pollutant emission or groundwater pollution

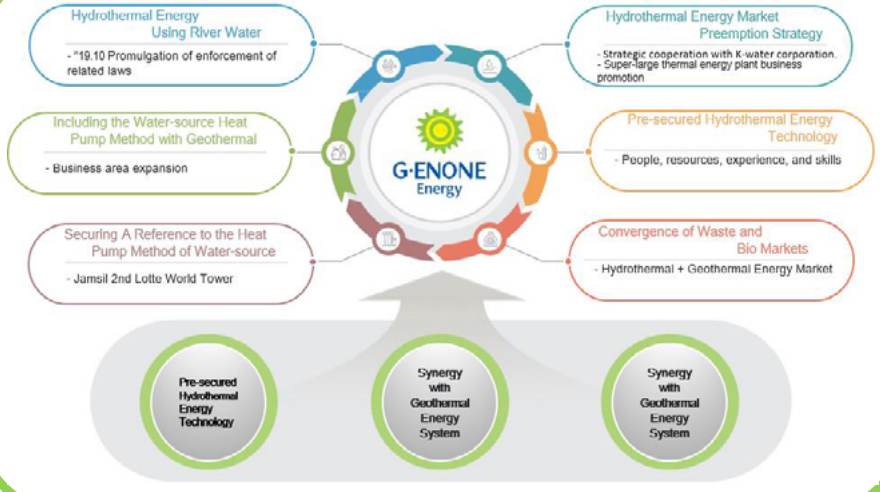


Seoul New office 1100RT



KEPCO New office Building 1350RT

Hydrothermal Heating & Cooling System





Incheon International Airport 2000RT



Lotte World Tower 3000RT

G·ENONE Energy

CEO : Geunhwa Choi
Address : Megavalley 809, 268, Hagui-ro, Dongan-gu, Anyang-si, Gyeonggi-do,Korea
TEL : 031 – 420 – 4677 FAX : 031 -420 – 4678 Email : g.enone@genone.co.kr
Homepage : www.genone.co.kr

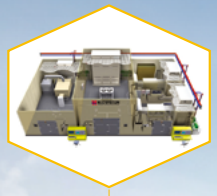
www.hncsystem.co.kr

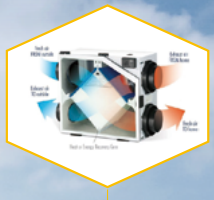
H&C SYSTEM
ACCESS TO INTELLIGENCE

Value Creation For Customers

HEATING & COOLING
SYSTEM PROVIDER

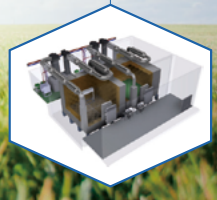
H&C SYSTEM은 최상의 기술 인력 및 경영 시스템을 바탕으로
백색 가전 시험 설비, 산업용 공조기기 시험 설비 전문 제작업체로서
대한민국을 대표하겠습니다.



에어컨 시험 설비 | 주택복합 환경 시험 설비 | 냉장고 시험 설비 | 공기청정기 시험 설비 | 칠러 시험 설비 | 콤프레셔 시험 설비 | 전열교환기 시험 설비 | 무향실 시험 설비



ACCESS TO INTELLIGENCE

H&C HEAD OFFICE
220, Saneop-ro, Gwonseon-gu, Suwon-si, Gyeonggi-do, Korea
TEL : 82-31-419-3916 FAX : 82-31-419-3921
E-MAIL : systemq@hncsystem.co.kr
www.hncsystem.co.kr

H&C INDIA OFFICE
Plot No-37A, udyog vihar Phase VI, Sector-37, Nea Hero Honda Chowk, Gurgaon(122001), Haryana(India)
TEL : +91-9811-02-7692

H&C VIETNAM OFFICE
No. 6, 63/33 Le Duc Tho, Nam Tu Liem, Ha Noi, Viet Nam
TEL : +84-243-996-4086

H&C THAILAND OFFICE
104/71 Moo 12, Soi Rattanachock 12, Tanasit Road,
T.Bangpra,A.Bangplee Samutprakan 10540, Thailand
TEL : (66) 0-2174-6034~5 Fax : 0-2174-6035

경기도 수원시 권선구 산업로 220 **TEL : 031-419-3916** **FAX : 031-419-3921** **E-mail : systemq@hncsystem.co.kr**

KOSDAQ
코스닥상장법인

녹색인증 · 에너지관리공단 고효율인증획득 · 동탑산업훈장 수훈 · 2003 올해의 에너지 히너상 · 가스안전공사 ISO 9001/14001획득 · KAB · 한국환경공단 저녹스버너인정획득 · 고스란디로트 전시장KOSTI획득 · CSEI 인증획득

지열 · 수열 · 공기열 폭넓은 열원의 난방 · 온수급탕 솔루션

부-스타 히트펌프

고효율 NEURON eco

관류보일러 시장 No.1에서 히트펌프 시장 No.1 기업으로 한발 더 앞서갑니다.



고효율 운전 실현!
고효율 운전으로 에너지절약 & 비용절감 실현

친환경 시스템!
CO_2 배출량 삭감, 오존층 파괴하지 않는 냉매 채용

쾌적 공간 실현!
저온에서도 파워풀한 난방과 급탕, 조용한 운전음



ECO 히트펌프(프리미엄 시리즈) 지열 히트펌프 수열 히트펌프

히트펌프
- 신 · 재생에너지설비 인증 획득! (지열 20RT, 지열 30RT, 지열 40RT, 지열50RT)
- 주요 사용처 : 대중시설, 주거시설, 공공시설, 업무시설, 시설재배, 양식장, 축산업, 요식업 등

고객 만족을 추구하는 기업-
(주) 부-스타

www.booster.co.kr
대표전화 02)3665-9600

부스타 콜센터 (AS접수/문의) 1588-3838 [삼팔삼팔]
긴급서비스전화 (032)674-8272 [빨리처리]

Contents

Welcome Message 10

IEA HPT TCP 11

HPC 2020 12

- Introduction
- Organization
- Sponsors
- Endorsed by

Hybrid Conference Model of HPC 2020 15

- How It Works
- Hybrid Operations Overview
- Detailed Formats for All Presentations
- General Information
  - Time Zone
  - Participants Precautions
  - Hybrid Conference Platform
  - Full Papers
  - Opening Ceremony
  - Closing Ceremony
  - Certificate of Participation
  - Session Chair Guideline

Conference Information 23

- Registration
- For Offline Participants
  - Conference Venue
  - Floor Plan
  - Wireless Internet
  - Lunch / Banquet / Coffee Break
- Ritter von Rittinger Award
- Workshop
- Global Student Video Competition

Program Information 35

- Conference Topics
- Program at a Glance
- Session Timetable
  - Oral Session
    Tuesday, April 27, 2021
    Wednesday, April 28, 2021
    Thursday, April 29, 2021
  - Poster Session
- Plenary Lectures
- Keynote Lectures
- Technical Program

Full Paper 79

Author Index 1977

WELCOME MESSAGE

Welcome,

The IEA Technology Collaboration Programme on Heat Pumping Technologies (HPT TCP) operates under the International Energy Agency, as a non-profit organization where member-country participants cooperate in projects in the field of heat pumps and related heat pumping technologies such as air conditioning and refrigeration. Under the management of an Executive Committee representing the member countries, the program carries out a strategy to accelerate heat pump use in all applications where they can reduce energy consumption for the benefit of the environment.

This event is the world's premier event where industry and research experts go to discuss the latest advancements in the field of heat pumps. Focused primarily on technical applications, the event provides a side opportunity for dialogue and the establishment of business and research partnerships.

The Heat Pump Conference is also a key event for policymakers, executives and representatives from industry, utilities and the public sector, R&D managers and technology supporters, energy managers, planners, consultants, etc. This is the place to be for all those who wish to learn about the market trends and the future applications of heat pumps.

The 13th IEA Heat Pump Conference will take place on April 26-29, 2021, a year later than originally scheduled. Due to the corona virus outbreak, the conference is held as online-offline hybrid. The offline conference is held at Ramada Plaza Hotel Jeju in Korea, and the online conference is held along with offline for those who cannot attend the conference physically.

This conference is the perfect forum to learn from and communicate with industry and research experts from all over the world. In spite of the COVID-19, more than 200 high quality papers are ready to be presented. As Chairman of the National Organizing Committee (NOC), it is my pleasure to extend an invitation to showcase your technologies and products as a sponsor.

The Jeju conference will be the 13th in a series of triennial conferences. Previous conferences were held in, Graz, Austria (1984), Orlando, Florida, USA (1987), Tokyo, Japan (1990), Maastricht, the Netherlands (1993), Toronto, Canada (1996), Berlin, Germany (1999), Beijing, China (2002), Las Vegas, USA (2005), Zurich, Switzerland (2008), Tokyo, Japan (2011), Montreal, Canada (2014) and Rotterdam, Netherland (2017).

Although the conference has changed several times, we appreciate your patience, understanding and strong support of the HPC 2020. We hope you stay safe and healthy, and we are looking forward to seeing you at the conference!



Min Soo Kim

Chair
National Organizing Committee of HPC 2020

IEA HPT TCP

Technology Collaboration Programme on Heat Pumping Technologies by International Energy Agency

Every three years the IEA Technology Collaboration Programme on Heat Pumping Technologies, (IEA HPT TCP) stages the IEA Heat Pump Conference. We are members of IEA International Energy Agency (IEA) and the programme was founded in 1978. We have been active in more than 40 years, which is a strength since a lot of knowledge and experiences has been generated during the years.

Only a country's government can participate in a TCP (Technology Collaboration Programme), not separate organisations. This means that all people living in a member country are participants of the programme. We have 16 members in HPT TCP. The current member countries are Austria, Belgium, Canada, Denmark, Finland, France, Italy, Germany, Japan, the Netherlands, Norway, South Korea, Sweden, Switzerland, United Kingdom and the United States.

The HPT TCP is a non-profit organization working in the field of heat pumping technologies, i.e. all technologies where heat is pumped from a lower temperature level to a higher one, such as heat pumps, air conditioning and refrigeration. Under the management of an Executive Committee representing the member countries, the programme carries out a strategy to accelerate the use of heat pumping technologies in all applications where they can reduce energy consumption and increase the use of renewal energy sources for the benefit of the environment.

Chair for HPT TCP is **Mr. Stephan Renz (Switzerland).**

▶ Read more about IEA HPT TCP at our website (http://www.heatpumpingtechnologies.org)

DISCLAIMER

The HPT TCP is part of a network of autonomous collaborative partnerships focused on a wide range of energy technologies known as Technology Collaboration Programmes or TCPs. The TCPs are organized under the auspices of the International Energy Agency (IEA), but the TCPs are functionally and legally autonomous. Views, findings and publications of the HPT TCP do not necessarily represent the views or policies of the IEA Secretariat or its individual member countries.

INTRODUCTION

About the Conference

Energy and the environment – two topics that are always of great concern to human beings. Heating and cooling play a great role in our daily life, we use a tremendous amount of fossil fuels for heating and cooling. When changing temperature levels using substantial energy input, a heat pump is always recommended as promising technologies against climate change.

With this in mind, the 13th IEA Heat Pump Conference will be held in Jeju Island from Monday, April 26st through Thursday, April 29th in 2021. With the theme 'Heat Pumps – Mission for the Green World', we aim to address global climate change and discuss necessary actions.

Considering the varied applications of heat pump systems in the residential, building and industrial fields, this major conference with hundreds of participants will definitely broaden the horizons of our heat pump community. The theme, "Heat Pumps – Mission for the Green World", will make all the researchers proud that we really are creating a Green World together through research and development for a better future.

Conference Goal

Heat pumps, as a reliable and confirmed technology, is the key equipment for energy savings and greenhouse gas reductions with its wide range of application to various energy sources. The upcoming conference will serve as a forum to discuss the latest technologies in heat pumps, and exchange valuable knowledge in market, policy, and standards information on related technologies.

Conference Structure

- Keynote and Plenary lectures by renowned researchers
- Oral and poster presentations on innovative heat pump technology, applications and markets
- Workshops on collaborative projects, connected to annexes in the HPT TCP
- Global Student Video Competition

Previous Conferences

The upcoming conference will be 13th of the series of conferences held by Technology Collaboration Programme on Heat Pumping Technologies by International Energy Agency, (IEA HPT TCP). Preceding conferences were held in Austria (1984), USA (1987, 2005), Japan (1990, 2011), The Netherlands (1993, 2017), Canada (1996, 2014), Germany (1999), China (2002), and Switzerland (2008). After successful histories in Japan and China, it is the fourth Heat Pump Conference to be held in Asia, and the first to be held in the Republic of Korea.

ORGANIZATION

The conference is organized by the International Organizing Committee (IOC) and the National Organizing Committee (NOC) on behalf of the Executive Committee of the IEA HPT TCP.

International Organizing Committee (IOC)

Chair

- Per Jonasson: Swedish Refrigeration & Heat Pump Association, Sweden

Vice-chair

- Sophie Hosatte: CanmetENERGY, Canada
- Hideaki Maeyama: HPTCJ (Heat Pump and Thermal Storage Technology Centre of Japan)

National Organizing Committee (NOC)

Chair

- Min Soo Kim: Seoul National University, South Korea

Vice-chair

- Yong Tae Kang: Korea University, South Korea

Members

- Jae Dong Chung: Sejong University, South Korea
- Young Soo Chang: Kookmin University, South Korea
- Taesung Kim: Sungkyunkwan University, South Korea
- Seong Hyuk Lee: Chung-Ang University, South Korea
- Jun Young Choi: Korea Testing Laboratory, South Korea
- Ji Hwan Jeong: Pusan National University, South Korea
- Jeongsik Seo: Korean Refrigeration and Air Conditioning Assessment Center, South Korea
- Dong Kyu Kim: Chung-Ang University, South Korea
- Youn Cheol Park: Jeju National University, South Korea

Secretary General

- Minsung Kim: Chung-Ang University, South Korea

Conference Secretariat

Enlight PCO

114, Yeoksam-ro, Gangnam-gu, Seoul 06252, South Korea
E-mail : secretariat@hpc2020.org / Tel : + 82-(0)2-6964-8320 / Fax : + 82-(0)2-553-7527

SPONSORS

The Organizing Committee greatly Appreciates the Generous Support of Our Sponsors!

For more information on our sponsors,
please visit the conference website or click on the logo below to connect to the sponsor website.

Diamond

LG Electronics

Gold

SAMSUNG

KRAAC
KOREA REFRIGERATION & AIR-CONDITIONING ASSESSMENT CENTER

Silver

G·ENONE Energy

Carrier 캐리어에어컨

H&C SYSTEM
HEATING & COOLING SYSTEM PROVIDER

INTERTECH

Bronze

KHPA 히트펌프얼라이언스
Korea Heat Pump Alliance

PEB ERC

SWEP
A DOVER COMPANY

3S

BOOSTER CO., LTD.

Endorsed by

ASHRAE

CHPA
中国节能协会热泵专业委员会

ehpa
european heat pump association

HPTCJ

JSRAE

KRAIA
Korea Refrigeration and Air-conditioning Industry Association

REHVA
Federation of European Heating, Ventilation and Air Conditioning Associations

TSHRAE

HYBRID CONFERENCE MODEL OF THE 13TH IEA HEAT PUMP CONFERENCE

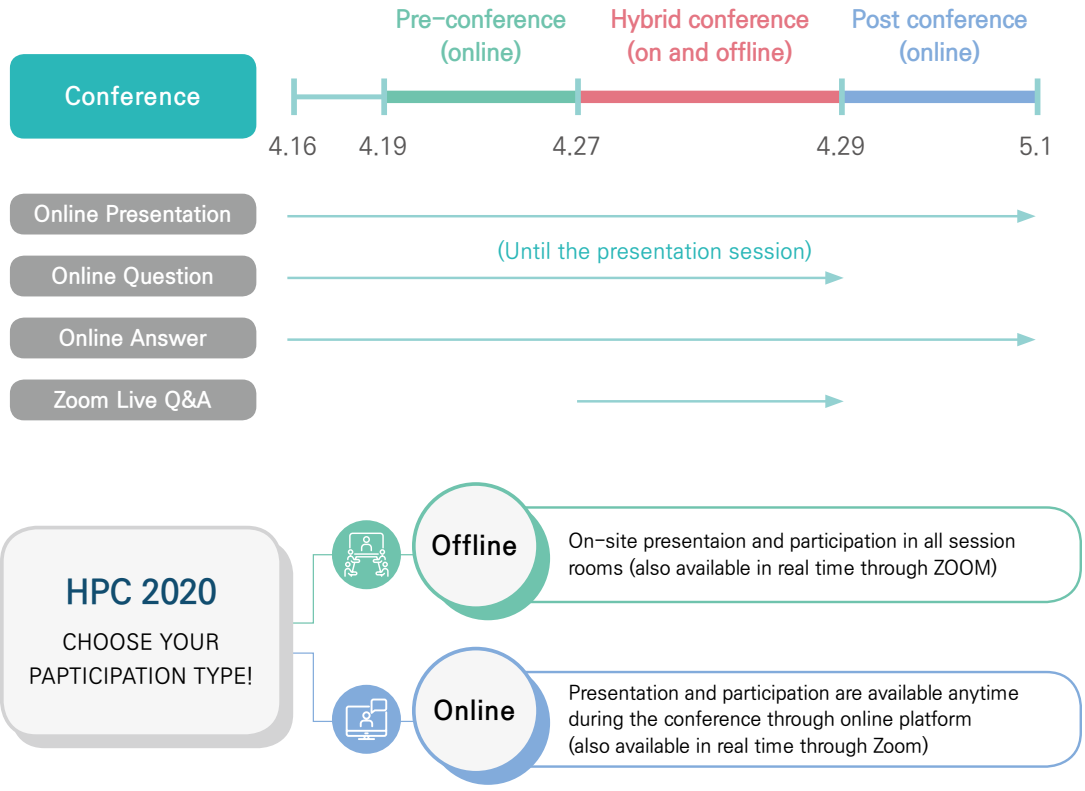
- **How It Works**
- **Hybrid Operations Overview**
- **Detailed Formats for All Presentations**
- **General Information**
  - Time Zone
  - Participants Precautions
  - Hybrid Conference Platform
  - Full Papers
  - Opening Ceremony
  - Closing Ceremony
  - Certificate of Participation
  - Session Chair Guideline

HOW IT WORKS

For the online participants, online conference platform will be provided. The conference program will be a generous online platform, which will give attendees the possibility to take part of the presentations over an extended amount of time. Register now and you will have the opportunity to take part of all the highlights of the 13th IEA Heat Pump Conference between the 18th of April until the 1st of May – on-demand when it suites you.

The Conference will be organized to offer as much value as possible to "offline" (physical) as well as online attendees. The presentations will be pre-recorded, broadcasted online and shown at the conference venue in accordance with the conference program. However, in order to make it possible for the conference attendees to select and take part in as many presentations as possible, it is recommended to watch the pre-recorded presentations on-demand before the conference start. The whole online conference plan in accordance with the scheme is shown in below.

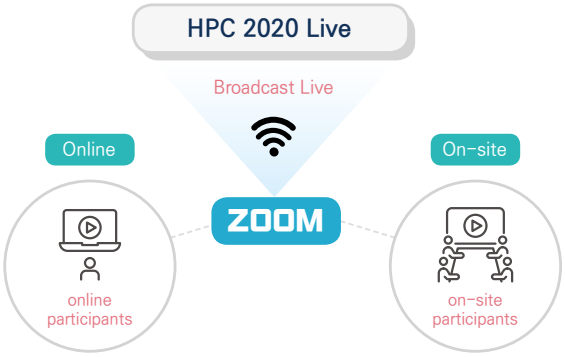
When it comes to questions & answers, there will be two separate schemes for the attendees as well as for the authors. It will be possible for the conference attendees to pose their questions online during the whole pre-conference as well during the conference period. The author is responsible for answering the questions until 1st of May at the latest. During the offline program slot for the presentation, the authors will be encouraged to attend online via Zoom, or physically at the venue, to be able to answer questions from the audience live.



HYBRID OPERATIONS OVERVIEW

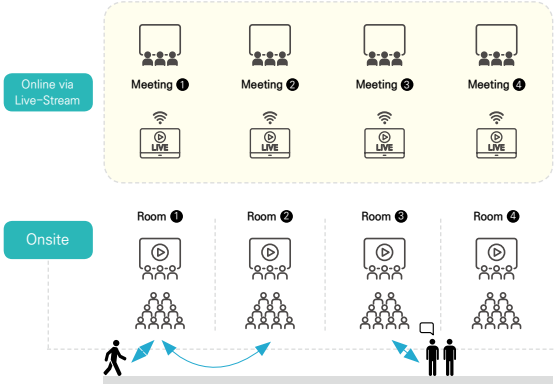
The HPC 2020 Hybrid Model

Onsite-online hybrid model ensures effective interaction between online participants (participants that are not at the venue) and onsite participants (participants that can attend the venue).



Onsite & Online Operations

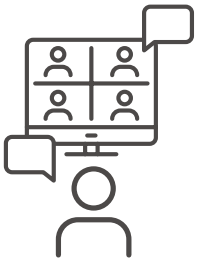
Each room in the conference venue will be equipped with a screen and a microphone, so that participants can join a zoom meeting together and connect with other participants. Whether onsite or online, attendees can freely change room, depending on what presentations are of the most interest. All sessions will be broadcast (live-streamed) to the website on HPC 2020.



Onsite & Online Communication

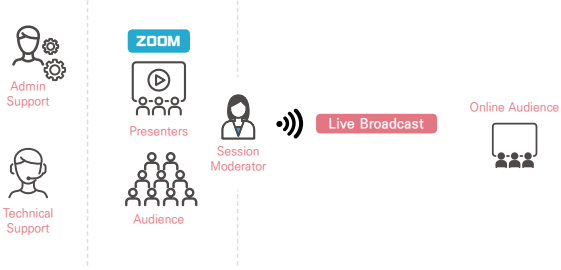
Onsite and Online participants will be able to engage with each other via the Zoom chat interface, leaving questions and comments during pre-conference period on the HPC 2020 website, which the session moderator can navigate through.

Also, The presenters are responsible for answering the questions at the website until 1st of May at the latest.



Room Overview and Roles Involved

Each presentation session will involve the following support roles: Session Chair– moderates the panel; Admin support – hosts the zoom meeting; Technical support – prevents onsite technical issues. (Admin staff and Session Chair do not have to be onsite.)



DETAILED FORMATS FOR ALL PRESENTATIONS

Category		Operation	
		Offline	Online
Plenary	Presentation Video	Pre-recorded presentation must be submitted via website in advance.	
	Q&A	Speakers will participate in real time online or communicate with the participants via chat window of virtual conference platform.	
	Participation	Considering being broadcast on ZOOM, arrive at session room 15 minutes prior to session.	
Keynote /Oral	Presentation Video	Pre-recorded presentation must be submitted via website by Mar. 5, 2021.	
	Q&A	Speakers must participate in real time in the session room.	Speakers must decide whether to participate in live Q&A while submitting their video on website. (Please consider the time difference.)
		All speakers even if who participated in live Q&A is responsible for answering the questions at the website until 1st of May at the latest.	
	Participation	Considering being broadcast on ZOOM, arrive at session room 15 minutes prior to session.	
Poster	Presentation Video	Pre-recorded presentation must be submitted via website by Mar. 5, 2021.	
	Poster File	Submit the poster file via website in advance for online availability by Mar. 5, 2021.	
	Poster Size	A0 (Width 84cm × Height 118cm)	
	Posting	Presenters should put up the poster on your own at the designated place.	The secretariat will print it out and attach it to the assigned spot.
	Q&A	All speakers are responsible for answering the questions at the website until 1st of May at the latest.	
	Participation	Under the social distance policy, direct face-to-face presentation of posters will be omitted.	-
Participants		All participants are able to watch presentation videos or leave questions and comments on the website during Pre-conference (April 18, 2021) to Post-conference (May 1, 2021.) period.	
		Participate in the session room. - If access to the session hall is difficult due to restricted number of people, participate through ZOOM.	Participate in real time through ZOOM.

Time allocation

- **Plenary Lectures** : 25min. (20 min. speech + 5 min. Q&A)
- **Keynote lectures** : 20 min. (15 min. speech + 5 min. Q&A)
- **Oral presentations** : 15 min. (12 min. speech + 3 min. Q&A)
- **Poster presentations** : 5 min. (5 min. speech)

GENERAL INFORMATION

Time Zone

The live stream schedule is based on Korea Standard Time (KST / UTC +9).

Program at a Glance also included Eastern Daylight Time (EDT / UTC-4) and Central European Summer Time (CEST / UTC+2) for international participants.

Participants Precautions

Offline Participants

- All participants are required to have their temperature checked.
- Entry is restricted in case of fever (37.5 °C or higher) and respiratory symptoms (cough, sore throat, etc.).
- Keep a 1-meter distance from each other in the session room. (Photo will be taken in order to keep the room setting.)
- Masks must be worn in all spaces.
- Wash hands often and use hand sanitizer provided.
- Due to social distance policy, it could be difficult to enter the session room if the session room is crowded.

Online Participants

- We recommend you check the network before the session.
- If your security system settings prevent you from accessing through PC, watch it on your mobile device.
- Viewing will be restricted when two or more people enter with the same ID.
- Only one device (PC or mobile) can enter.
- Avoid simultaneous access.
- Use of Chrome/ Safari/ Edge/ Firefox browser is recommended.
- Using Internet Explorer may restrict viewing or access.

Hybrid Conference Platform

- https://www.hpc2020.org
- ID/PW are the same as the HPC 2020 Website.
- It is highly recommended you use only Chrome, Safari, or Firefox to access the platform.
- The platform will be open from April 19, 2021 to May 1, 2021.

Full Papers

- After logging into the Hybrid Conference Platform, you can view the full papers of HPC 2020 by clicking the 'Proceedings' button at the top of the main page or clicking the 'Paper' button next to each presentation video.

GENERAL INFORMATION

Opening Ceremony

Date/Venue	Tuesday, April 27, 2021, 09:00~09:20 (KST/UTC+9) | Room A (Tamna Hall, 8F)
Host	Taesung Kim (Sungkyunkwan University, South Korea)

- **Welcome Address** — Stephan Renz (IEA HPT TCP Chair, Switzerland)
- **Opening Remarks** — Min Soo Kim (President of Society of Air-conditioning and Refrigerating Engineers of Korea, NOC Chair)
- **Congratulatory Remarks** — Won Hee-ryong (Governor of Jeju Province, South Korea)

Closing Ceremony

Date/Venue	Thursday, April 29, 2021, 16:00~17:00 (KST) | Room A(Tamna Hall, 8F)
Host	Minsung Kim (Chung-Ang University, South Korea)

- **Opening Speech** — Per Jonasson (IOC Chair)
- **Award Ceremony** — Per Jonasson (IOC Chair)
  - Ritter von Rittinger Award
  - Global Student Video Competition
- **Conference Report & Closing Speech** — Minsung Kim (Secretary General)
- **The 14th IEA Heat Pump Conference (HPC 2023)** — Brian A. Fricke (Chair of U.S. National Organizing Committee)
- **Closing Remarks** — Minsung Kim (Secretary General)

Session Chair

- **Guideline**

※ **Important Notice**

· We recommend the session chairs to check the **network condition** before the session.
· Use a **high-speed network** for a stable connection to the meeting.
· Use a **headset** to minimize any noise issues.
· Please try to find a **quiet environment** and maintain the environment during a session.
· Please note that **photo taking and video recording are strictly prohibited.**
· Please visit the zoom help center to get more information : https://support.zoom.us/hc/en-us
· **For detailed instructions as follows, please refer to our website.**
- Initial Setup / Before Session / During Session / During Q&A/ After Session

- **List of Session Chairs and Schedule**

  * Time: The live stream schedule is based on Korea Standard Time (KST / UTC +9)

No.	Chair	Affiliation	Country	Date	Time*	Room
1	Akio Miyara	Saga University	JP	Tue., April 27	S 01 : 13:00~14:20	Room C
2	Bamdad Bahar	Xergy	US	Thur., April 29	S 10 : 10:40~12:00	Room B
3	Benjamin Zühlsdorf	Danish Technological Institute	DK	Wed., April 28	S 08 : 16:10~17:30	Room C
4	Bin Hu	Shanghai Jiao Tong University	CN	Tue., April 27	S 01 : 13:00~14:20	Room A
5	Brian Fricke	Oak Ridge National Laboratory	US	Thur., April 29	S 10 : 10:40~12:00	Room A
6	Carsten Wemhöner	HSR University of Applied Sciences Rapperswil	CH	Wed., April 28	S 06 : 13:00~14:20	Room B
7	Christoph Reichl	AIT Austrian Institute of Technology	AT	Tue., April 27	S 02 : 14:40~16:00	Room B
8	Didier Coulumb	IIR Director	FR	Tue., April 27	S 03 : 16:10~17:45	Room A
9	Eckhard Groll	Purdue University	US	Thur., April 29	S 09 : 09:00~10:20	Room C
10	Ed Vineyard	U.S. Department of Energy	US	Thur., April 29	S 09 : 09:00~10:20	Room B
11	Emina Pasic	IEA HPT ExCo Delegate Sweden	SE	Wed., April 28	S 08 : 16:10~17:30	Room B
12	Guoyuan Ma	Beijing University of Technology	CN	Thur., April 29	S 10 : 10:40~12:00	Room C
13	Hideaki Maeyama	Heat pump & Thermal Storage Technology Center of Japan	JP	Wed., April 28	S 05 : 10:40~12:00	Room A
14	Jeffrey Spitler	Oklahoma State University	US	Wed., April 28	S 04 : 09:00~10:20	Room B
15	Ji Hwan Jeong	Pusan National Univ.	KR	Thur., April 29	S 11 : 13:00~14:20	Room B
16	Jun Young Choi	Korea Testing Laboratory	KR	Thur., April 29	S 11 : 13:00~14:20	Room A
17	Jussi Hirvonen	Finnish Heat Pump Association SULPU ry	FI	Tue., April 27	S 02 : 14:40~16:00	Room A
18	Marion Bakker	NL Delegate	NL	Thur., April 29	S 12 : 14:40~16:00	Room A
19	Masafumi Katsuta	Waseda University	JP	Wed., April 28	S 06 : 13:00~14:20	Room C
20	Maurizio Pieve	ENEA	IT	Tue., April 27	S 03 : 16:10~17:45	Room C
21	Michele Mondot	CETIAT	FR	Tue., April 27	S 02 : 14:40~16:00	Room C
22	Mitsuhiro Fukuta	Shizuoka University	JP	Tue., April 27	S 01 : 13:00~14:20	Room B
23	Peter Schossig	Fraunhofer ISE	DE	Wed., April 28	S 07 : 14:40~16:00	Room A
24	Rainer Jacobs	IZW e.V., Information Centre on Heat Pumps and Refrigeration	DE	Wed., April 28	S 07 : 14:40~16:00	Room C
25	Reinhard Radermacher	University of Maryland	US	Wed., April 28	S 04 : 09:00~10:20	Room C
26	Rolf-Iver Hagemoen	EHPA	NO	Thur., April 29	S 12 : 14:40~16:00	Room C
27	Sheng Wang	Gree Electric Appliances, Inc. of Zhuhai	CN	Wed., April 28	S 06 : 13:00~14:20	Room A
28	Signhild Gehlin	Swedish Geoenergi Center	SE	Wed., April 28	S 08 : 16:10~17:30	Room A
29	Sophie Hosatte	Natural Resources Canada - CanmetENERGY	CA	Thur., April 29	S 09 : 09:00~10:20	Room A
30	Stephan Renz/ Carina Alles	Beratung Renz Consulting/Swiss Federal Office of Energy	CH	Thur., April 29	S 12 : 14:40~16:00	Room B
31	Svend Pedersen	Danish Technological Institute	DK	Wed., April 28	S 07 : 14:40~16:00	Room B
32	Tetsushiro Iwatsubo	New Energy and Industorial Technology Development Organaization	JP	Wed., April 28	S 05 : 10:40~12:00	Room B
33	Thomas Fleckl	AIT Austrian Institute of Technology	AT	Tue., April 27	S 03 : 16:10~17:45	Room B
34	Van D. Baxter	Oak Ridge National Laboratory	US	Wed., April 28	S 05 : 10:40~12:00	Room C
35	Veronika Wilks	AIT Austrian Institute of Technology GmbH	AT	Thur., April 29	S 11 : 13:00~14:20	Room C
36	Yunho Hwang	University of Maryland	US	Wed., April 28	S 04 : 09:00~10:20	Room A

CONFERENCE INFORMATION

- **Registration**
- **For Offline Participants**
  - Conference Venue
  - Floor Plan
  - Wireless Internet
  - Lunch / Banquet / Coffee Break
- **Peter Ritter von Rittinger International Heat Pump Award**
- **Global Student Video Competition**

REGISTRATION

※ Offline registration is not accepted for the safety of participants in accordance with the COVID-19 quarantine policy.

※ Participants who have registered in advance should come to the 8th floor, Ramada Plaza Jeju Hotel to receive a name tag, Certificate of participation, program book, and a small gift from HPC 2020 NOC.

Registration Fee

- Considering the current COVID-19 pandemic situation, HPC 2020 will be held as a hybrid event; a combination of "live" face to face event and a "virtual" online component.
- HPC 2020 has decided to reduce registration fees to make the virtual conference widely accessible.

Category		Early Bird (~Jan. 31, 2021)	Regular (~Mar. 15, 2021)	Late (~Mar. 31, 2021)	Last Time (~April 29, 2021)
Offline	Regular	$700	$800	~~$900~~ $800	N/A
	Student	$350	$400	~~$450~~ $400	N/A
Online	Regular	$350	$400	~~$600~~ $400	~~$600~~ $400
	Student	$175	$200	~~$300~~ $200	~~$300~~ $200

※ If you would like to change from offline to online participation, please contact secretariat at secretariat@hpc2020.org no later than April 1, 2021.

Offline Conference Registration

Domestic attendees are recommended to registration for the offline conference. Full registration includes access to all sessions, lunches, banquet, and break refreshments.

Online Conference Registration

International attendees who are not able to come to the conference will give their presentation by the video clip. The registrants can access all the sessions through the online portal.

Requirement of Paper Presentation

- In principle, at least one of the authors must register by January 30, 2021 in order for their papers to be included in the program of HPC 2020
- For authors presenting multiple papers, one registration is valid for rest presentations.

Cancellation and Refund Policy

Before applying for cancellation, please refer to the following policy

Date of Cancellation	Amount to be Refunded
Cancellation before February 28, 2021	Refundable but 75%
Cancellation between March 1 and March 30, 2021	Refundable but 50%
Cancellation after April 1, 2021	Non-refundable

- Note that for administrative reasons, refund will be made after the conference.
- All bank service charges will be deducted from the refunded amount.
- Any phone application will not be accepted, a request letter by email(secretariat@hpc2020.org) is required.

FOR OFFLINE PARTICIPANTS

Conference Venue

About Jeju



Jeju Island is the largest volcanic island in Korea and it has a mild oceanic climate throughout the year with the smallest annual temperature range in South Korea. Officially called Jeju Special Self-Governing Province, this best tourist destination boasts mild weather, as well as scenic beauties of beaches, waterfalls, cliffs and caves. The island is 73km wide and 31km long with a total area of 1,848.85km2. Jeju is the largest island in South Korea.

Mt. Halla rises in the center of Jeju to 1950m above sea level. The rest of the island slopes down from its summit and is covered with dark gray volcanic rocks and volcanic ash soil. Seongsan Ilchulbong Peak with breathtaking views is also one of the most scenic areas, and Manjanggul Cave, the world's longest lava tube has been registered as a UNESCO World Natural Heritage. Meanwhile, Jeju has recently won the Global Geopark certificate, and also has been selected as the New 7 Wonders of Nature.

Ramada Plaza Hotel Jeju

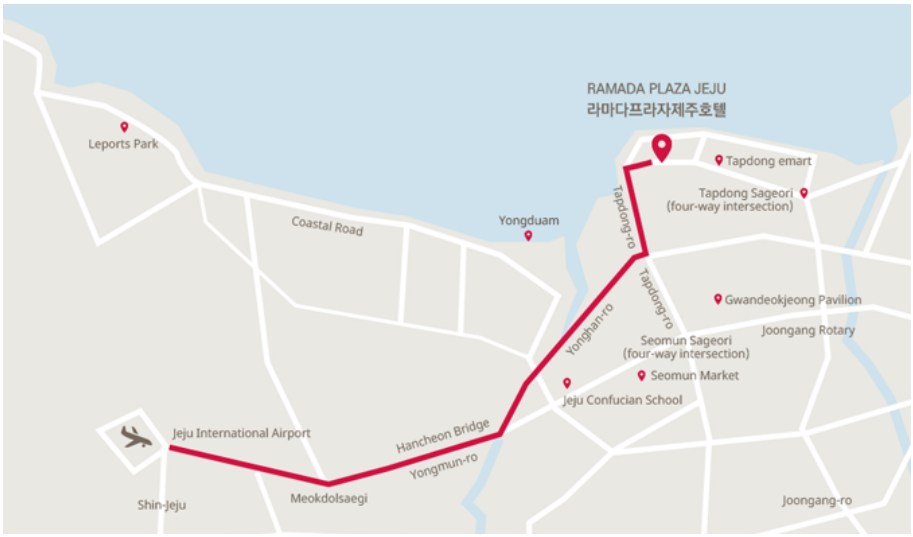


Located near the beautiful ocean at the center of Jeju city

The conference venue is 5 star hotel with 400 guest rooms and suites and a convention room with a meeting capacity of 1200 people. This country's first costal hotel built right on the ocean is located just five minutes away from Jeju International Airport and Jeju Port.

Transportation

The Hotel is located in 3.8 km away from Jeju International Airport. You can reach the hotel in ten minutes by taxi. No shuttle is provided. See the map below:





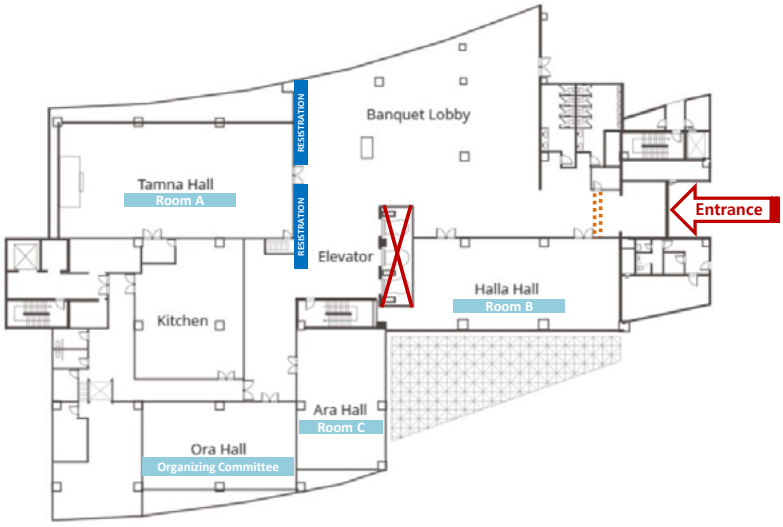
Duration	15 minutes
Fare	About 7,000 KRW(USD 6~7)

Ramada Plaza Jeju Hotel

- Address: 66 Topdong Ro, Jeju, 63165, Korea
- Tel: +82-64-729-8100

FLOOR PLAN

8th Floor,
Ramada Plaza Hotel Jeju



Lobby	• Body Temperature Measurement • Registration/Conference Kit • Poster Session	**Tamna Hall**	• Opening Ceremony • Plenary Sessions • Oral Presentation • Closing Ceremony
Halla Hall	• Oral Presentation	**Ora Hall**	• Organizing Committee (until noon on April 29,2021)
Ara Hall	• Oral Presentation		

Wireless Internet

Wireless internet is available for the participants at the conference venue. ID/PW will be informed on-site.

Lunch / Banquet / Coffee Break

Depending on the COVID-19 situation, Lunches, Banquet, and Coffee Breaks will be provided by applying the local Social Distancing Policy in Jeju at the time of the conference. The NOC is committed to the convenience of offline participants, and the secretariat will inform the details before the conference. We hope for your kind understanding on this matter.

HPC 2020 will do our best to ensure safety of our attendees

1. All participants' body temperature will be checked at the entrance.
2. Hand sanitizer will be provided.
3. All participants must wear a mask.
4. Keep a 1-meter distance from each other in the session room.
5. An attendee list will be made.



RITTER VON RITTINGER AWARD

Peter Ritter von Rittinger International Heat Pump Award

Trittingerhe Peter Ritter von Rittinger International Heat Pump Award is the highest international award in the air conditioning, heat pump and refrigeration field and was introduced at the Las Vegas Conference (8th IEA HP Conference). This award highlights outstanding contributions to the advancement of international collaboration in research, policy development and applications for energy-efficient heat pumping technologies. It is awarded every three years in conjunction with the International Heat Pump Conference.

The Rittinger award is named for Peter Ritter von Rittinger who is credited with the design and installation of the first energy-conserving heat pump system at a salt works in Upper Austria in 1855.

The winners of the Ritter von Rittinger Award 2020 will be announced at the online homepage and closing ceremony.

Previous Awardees

2017	Prof. Eckhard A Groll, Prof. Alberto Cavallini, ORNL Building Equipment Team, Prof. Per Lundqvist
2014	Mr. Frédy Burkhalter, Mr. Daniel Ellis, Dr. Andrew Pearson, Dr. Koichi Watanabe, Dr. Michel Bernier.
2011	Prof. Per-Erling Frivik, Prof. Hermann Halozan, Mr. John D. Ryan.
2008	Prof. Eric Granryd, Prof. Predrag S. Hrnjak, Mr Gerald C. Groff.
2005	Dr Bernard Spinner, Dr Katsuhiko Narita, Mr Nance C. Lovvorn, Research Team GEMINI, Mr. Wayne R. Reedy.





WORKSHOP - ONLINE ONLY

Monday, April 26, 2021

1. Workshop A1 (20:00~22:00 KST/13:00~15:00 CEST/07:00~09:00 EDT)

Title	Annex 42 (HPs in smart grids) and Annex 45 (Hybrid HPs)
Organizer	Peter Wagener (Business Development Holland, wagener@bdho.nl) Maarten Hommelberg (Business Development Holland, hommelberg@bdho.nl)
Theme	What role can hybrid HPs play in the energy transition and how can they contribute to smart grid success? • Introduction into hybrid HPs • The hybrid HP success story in the Netherlands • First results from a hybrid HP monitoring campaign • Hybrid HPs in a smart grid: great results from the Freedom Project (Wales, UK)
Speakers	Peter Wagener (BDH, Netherlands) Oliver Lancaster (Wales & West Utilities, Wales, UK)

2. Workshop A2 (22:00~24:00 KST/15:00~17:00 CEST/09:00~11:00 EDT)

Title	Heat Pumps for Low GWP Refrigerants (Annex 54)
Organizer	Yunho Hwang (University of Maryland, USA)
Theme	Annex 54 aims at promoting the low GWP refrigerant application to accelerate phase down of high GWP HFCs via 1) a comprehensive review of recent R&D progress on component optimization using low-GWP refrigerants, 2) in-depth case studies of component optimization, which can provide design guidelines and real-world experiences.
Program	• *"Introduction of IEA HPT's Annex 54 for Heat Pumps for Low-GWP refrigerants"* by Yunho Hwang (University of Maryland, USA) • *"Experimental evaluation of R410A, R407C and R134a alternative refrigerants in residential heat pumps"* by Pierre Pardo (CETIAT, France) • *"Modular and scalable heat pump models for the design process of heat pump systems"* by Christian Vering (RWTH Aachen University, Germany) • *"Commercialization of R32 in a Window Type Air Conditioner for US Market and Split Air Conditioners for European Market"* by Younghwan Ko (LGE Korea) • *"Comparitive analysis of propane heat pumps - a try to harmonize technical boundary conditions in world-wide projects"* by Thore Oltersdorf, Peter Schossig, Lena Schnabel (ISE Fraunhofer, Germany) • *"Lower GWP Refrigerants for Heap Pump Application"* by Samuel Yana Motta (Honeywell, USA)

3. Workshop B2 (22:00~24:00 KST/15:00~17:00 CEST/09:00~11:00 EDT)

Title	Annex 55 (combined with ECES Annex 34) on Heat Pumps and Storage
Organizer	Peter Wagener (Business Development Holland, wagener@bdho.nl) Maarten Hommelberg (Business Development Holland, hommelberg@bdho.nl)
Theme	Heat pumps and energy storage in smart grids - how can we achieve better results by better integration of HP and storage components? • Introduction to the goal and contents of the annex. • Present status and latest annex results • Recommendations for policy action
Speakers	Peter Wagener (BDH, Netherlands) Caroline Haglund-Stignor (RISE, Sweden) Liu Xiaobing (Oakridge National Laboratories, USA)

4. Workshop C1 (20:00~22:00 KST/13:00~15:00 CEST/07:00~09:00 EDT)

Title	Heat Pumps in Multi-Family Buildings for space heating and DHW (Annex 50)
Organizer	Marek Miara (Fraunhofer ISE, Germany)

Program

Time CEST	Speaker	Topic
13:00-13:20	Odile Cauret EDF – Research & Development	Presentation of the Multi-Family Buildings status in participating countries (results from the Task 1)
13:20-13:40	**Marek Miara** Fraunhofer ISE	Presentation of the "solution matrix" as the main outcome of the Annex 50. From general categorization of solutions to the case studies.
13:40-14:10	**Charles Geelen** Infinitus Energy Solutions Group, **Andreas Zottl** AIT Austrian Institute of Technology GmbH	Presentation of the "solution matrix" as the main outcome of the Annex 50. From general categorization of solutions to the case studies.
14:10-14:30	Nicole Calame CSD INGÉNIEURS SA	Presentation of the case studies, different types of building and dedicated solutions
14:30-14:50	**Marco Simonetti** Politecnico di Torino	New simulation approach – as simple as possible, as precise as required

5. Workshop C2 (22:00~24:00 KST/15:00~17:00 CEST/09:00~11:00 EDT)

Title	Design and integration of heat pumps for nZEB (Annex 49)
Organizer	Prof. Carsten Wemhöner (Professor for Building system technologies Institute partner IET –Institute of Energy Technology, OST – Eastern Switzerland Univ. of Appl. Sciences)
Theme	The workshop presents result of IEA HPT Annex 49 on heat pump application in nearly Zero energy buildings nZEB. Starting from the state of the art of nZEB results of heat pump monitoring in nZEB and simulation-based studies on design and control of heat pumps are presented. The workshop is concluded with developed multifunctional HP prototypes and lessons learned.
Program	**nZEB definition and ambition level** 15:00 – 15:10 Introduction and overview of IEA HPT Annex 49 (C. Wemhoener) 15:10 – 15:20 Swedish nZEB implementation and comparison of heating systems (O. Gustafsson) 15:20 – 15:35 Methodology to compare nZEB ambition level in different countries (F. Ochs) **Case studies and optimisation of heat pumps in nZEB by monitoring/simulation** 15:35 – 15:50 Group of eight buildings with low temperature heating grid (C. Betzold) 15:50 – 16:05 Vögelebichl Innsbruck – Monitoring and simulation of two multi-family houses with heat pump, PV and collectors (F. Ochs) 16:05 – 16:20 Monitoring of Energy plus buildings with different use (F. Bockelmann) **Prototype technologies and heat pump integration options** 16:20 – 16:35 Façade integrated PV-coupled heat pump system for space cooling (A. Heinz) 16:35 – 16:50 Integrated heat pump (IHP) prototypes for NZEB (V. Baxter) **Conclusions** 16:50 – 17:00 Lessons learned (C. Wemhoener)

6. Workshop D1 (20:00~22:00 KST/13:00~15:00 CEST/07:00~09:00 EDT)

Title	Comfort and Climate Box Solutions for warm and humid climates
Organizer	Heat Pump Centre, Oakridge National Laboratory (ORNL) and BDH (in the Netherlands)
Theme	The demand for comfort cooling is growing rapidly in many parts of the world, especially in emerging countries, and stated policies will not be able to curb electricity use for cooling, which is set to grow threefold by 2070 relative to 2019, according to IEA. There are great possibilities to increase the energy efficiency and the share of renewable electricity used for comfort cooling, by combining heat pumping technologies with energy storages and integrated control. The purpose of the workshop is to develop a proposal for a new international collaboration project (i.e. Annex) aiming at speed up deployment of such solutions, so called "Comfort and Climate Boxes" for warm and humid climates – solutions that are efficient, affordable, applicable and scalable.
Program	**Introduction to the theme and challenges - presentations** • General introduction – Monica Axell and Caroline Haglund Stignor, Heat Pump Centre • "Low Carbon and Energy Efficient Cooling in Warm and Humid Areas"– Chiara Delmastro, IEA • "Consumer awareness and use of energy efficient cooling applications in India" – Shika Bhasin, CEEW, India • "Low Carbon and Energy Efficient Cooling in Warm and Humid Areas" - Wang Sheng, GREE, China • "Challenges and opportunities to realize "Comfort and Climate Box solutions" in United States and Beyond" - Kashif Nawaz, ORNL, US **Workshop session** • Presentation of draft Objectives and Scope of a future annex, Kashif Nawaz, ORNL, US • Definition about tasks, means and deliverables from a future annex – group discussion **Summary and next steps**

7. Workshop D2 (22:00~24:00 KST/15:00~17:00 CEST/09:00~11:00 EDT)

Title	Large demonstration project for flexibility by heat pumps (Annex 57)
Organizer	Senior Consultant Svend Pedersen (Danish Technological Institute, Denmark)
Theme	Annex 57 aim is to focus on the implementation of heat pumps in district heating and cooling systems. The main focus areas are 1) the creation of possible flexibility in the thermal network and electrical grids. 2) the possibilities of increasing larger share of renewable energy and excess heat as well as to reduce the CO2 emissions in the heating systems by using heat pumps.
Program	• "Introduction of IEA HPT's Annex 57 Flexibility by implementation of heat pump in multi-vector energy systems and thermal networks" by Svend Pedersen Danish Technological Institute • "Hybrid Energy Networks in a international and national perspective" by Peter Sorknäs Aalborg University • "Experiences from creation of flexibility with heat pumps in district heating grids" by Wibke Messenburg Danish technical University • "Potentials of flexible heat pump operation on a district scale" by Dr.-Ing. Young Jae Yu • Discussion

GLOBAL STUDENT VIDEO COMPETITION

We would like to invite all students who will join our conference to participate in the HPC 2020 Global Student Video Competition. This competition provides an excellent opportunity to create a video that will be awarded at the conference. It aims to exchange creative ideas and relevant knowledge on the topics such as heat pump application, environmental issues, energy, or what students do in the laboratory. The winners, as listed below, will be announced online on the HPC 2020 conference website.

Awards

- Gold Medal (Overall championships) : $300 Award and Certificate
- Silver Medal : $200 Award and Certificate
- Bronze Medal : $100 Award and Certificate

Important Dates

- **March 15, 2021** Open submission for participants
- **March 31, 2021** Closed Submission for participants
- **April 15, 2021** Video Submission deadline (secretariat@hpc2020.org)
- **April 18, 2021** Displayed on the conference homepage
- **April 28, 2021** Announcement of the winners online at the conference website and closing ceremony.

Recommended Categories

- Heat pump applications
- Environmental issues
- Energy
- Research activity in the laboratory
- Etc.

Submission

The competition is open for the students who have finished registration for the HPC 2020.
Students who wish to participate in this competition, please submit the form below through the link below by March 31, 2021.

- Format : Presentation files will be accepted in MP4
- Presentation Time : Less than 3 minutes
- Video Submission : secretariat@hpc2020.org by April 15, 2021.

PROGRAM INFORMATION

- Conference Topics
- Program at a Glance
- Session Timetable
  - Oral Session Tuesday, April 27, 2021
    Wednesday, April 28, 2021
    Thursday, April 29, 2021
  - Poster Session April 27-29, 2021
- Plenary Lectures
- Keynote Lectures
- Technical Program

CONFERENCE TOPICS

Within the conference program, participants will encounter numerous cutting-edge presentations on the following issues:

- Recent Advances on Heat Pumping Technologies
- Environment-friendly Technology
- Systems and Components
- Field Demonstration and Multi-disciplined Applications
- Research and Development
- Policy, Standards, and Market
- International Activities

PROGRAM AT A GLANCE

※ For detailed information about the workshop program on Monday, April 26, 2021, please refer to the page 29.

Date/Time			Mon. April 26	Tuesday, April 27			Wednesday, April 28			Thursday, April 29		
Session Room			Online Workshop	Room A	Room B	Room C	Room A	Room B	Room C	Room A	Room B	Room C
KST (UTC+9)	EDT (UTC-4)	CEST (UTC+2)										
08:30 ~ 09:00				Registration								
09:00 ~ 10:00	(Day -1) 20:00 ~21:00	02:00 ~ 03:00		Opening Ceremony 09:00~09:20 (KST)			Session 4 : 09:00~10:20 (KST)			Session 9 : 09:00~10:20 (KST)		
10:00 ~ 11:00	(Day -1) 21:00 ~22:00	03:00 ~ 04:00		Plenary Lecture 1 (Policy and market) 09:20~10:35 (KST)			Low GWP Refrigerants (3)	Ground Source and Storage	Sorption Heat Pumps (1)	Variable Refrigerant Flow Heat Pumps and Air-conditioners	Heat Exchangers (2)	Food Storage and Display
				Coffee Break and Poster Session 10:35~10:45 (KST)			Coffee Break and Poster Session 10:20~10:40 (KST)					
11:00 ~ 12:00	(Day -1) 22:00 ~23:00	04:00 ~ 05:00		Plenary Lecture 2 (Technology) 10.45~12:00 (KST)			Session 5 : 10:40~12:00 (KST)			Session 10 : 10:40~12:00 (KST)		
							Low GWP Refrigerants (4)	Market and Policy for Heat Pumps (2)	Electrochemical Related	Sorption Heat Pumps (3)	Dehumidifcation Technology	Heat Pump Performance
12:00 ~ 13:00	(Day -1) 23:00 ~24:00	05:00 ~ 06:00		Lunch and Poster Session 12:00~13:00 (KST)								
13:00 ~ 14:00	00:00 ~ 01:00	06:00 ~ 07:00		Session 1 : 13:00~14:20 (KST)			Session 6 : 13:00~14:20 (KST)			Session 11 : 13:00~14:20 (KST)		
				Low GWP Refrigerants (1) - Natural	Air Conditioning and Cooling	Heat Pump Applications	Heat Transfer	Residential Heat Pumps	Heat Exchangers (1)	Industrial Heat Pumps (2)	Heat Pumps in HVAC systems	Advanced Controls and Modelling
14:00 ~ 15:00	01:00 ~ 02:00	07:00 ~ 08:00		Coffee Break and Poster Session 14:20~14:40 (KST)								
15:00 ~ 16:00	02:00 ~ 03:00	08:00 ~ 09:00		Session 2 : 14:40~16:00 (KST)			Session 7 : 14:40~16:00 (KST)			Session 12 : 14:40~15:45 (KST)		
				Market and Policy for Heat Pumps (1)	Acoustics Signatures of Heat Pumps	Space and Hot Water Heat Pumps	Sorption Heat Pumps (2)	Heat Pumps in Smart Grids and District Heating and Cooling Systems (1)	Industrial Heat Pumps (1)	Heat Pumps combined with Thermal Energy Strorage and Recovery	Nearly Zero Energy Buildings	Smart Applications of Heat Pumps
16:00 ~ 17:00	03:00 ~ 04:00	09:00 ~ 10:00		Break 16:00~16:10 (KST)						Break 15:45~16:00 (KST)		
				Session 3 : 16:10~17:30 (KST)			Session 8 : 16:10~17:30 (KST)			Closing Ceremony 16:00~17:00 (KST)		
17:00 ~ 18:00	04:00 ~ 05:00	10:00 ~ 11:00		Low GWP Refrigerants (2)	Heat Pump Analysis - components and cycles	New Heat Pump Technologies	Ground Source Heat Pumps	Heat Pumps in Smart Grids and District Heating and Cooling Systems (2)	High Temperature Heat Pumps			
18:00 ~ 20:00	05:00 ~ 07:00	11:00 ~ 13:00										
20:00 ~ 22:00	07:00 ~ 09:00	13:00 ~ 15:00	Workshop A1/C1/D1									
22:00 ~ 24:00	09:00 ~ 11:00	15:00 ~ 17:00	Workshop A2/B2/C2/D2									

Session color	Presentation time
	EDT (for American)
	EDT/KST (for American and Asian)
	KST/CEST (for Asian and Europian)
	CEST (for Europian)

SESSION TIMETABLE - ORAL SESSION

Date/Time			Tuesday, April 27, 2021		
Session Room			Room A	Room B	Room C
KST (UTC+9)	EDT (UTC-4)	CEST (UTC+2)			
08:30 ~ 09:00			Registration		
09:00 ~ 10:00	(Apr. 26, Mon) 20:00 ~ 21:00	02:00 ~ 03:00	**Opening Ceremony** 09:00~09:20 (KST)		
			Welcome Address (Stephan Renz / IEA HPT TCP Chair) / **Opening Remark** (Min Soo Kim / NOC Chair, President of SAREK / South Korea)		
			Plenary Lecture 1 (Policy and Market) 09:20~10:35 (KST)		
			Plenary Lecture 1-1	**Heat Pumping Technologies in Clean Energy Transitions** (Mechtild Worsdorfer / Director for Sustainability, Technology and Outlooks / IEA)	
10:00 ~ 11:00	(Apr. 26, Mon) 21:00 ~ 22:00	03:00 ~ 04:00	Plenary Lecture 1-2	**The European Legal Framework is Well Set for a Massive Roll-out of Heat Pumps - but More Efforts are Needed!** (Martin Forsen / President of EHPA (European Heat Pump Association))	
			Plenary Lecture 1-3	**Korean Policy for Green World and Heat Pumping Technologies** (Min Soo Kim / NOC Chair, President of SAREK / South Korea)	
			Coffee Break and Poster Session 10:35~10:45 (KST)		
			Plenary Lecture 2 (Technology) 10:45~12:00 (KST)		
			Plenary Lecture 2-1	**Heat Pump System Technology Trend** (Saikee Oh/ Executive Vice President, Center Director of LG Electronics / South Korea)	
11:00 ~ 12:00	(Apr. 26, Mon) 22:00 ~ 23:00	04:00 ~ 05:00	Plenary Lecture 2-2	**Ensuring a Safe Refrigerant Transition** (Xudong Wang/ Vice President of AHRI/US)	
			Plenary Lecture 2-3	**Clean and Safe Air by HVAC systems – Laws and Advanced Technologies in Japan** (Noboru Kagawa / Professor of National Defense Academy / Japan)	
12:00 ~ 13:00	(Apr. 26, Mon 23:00 ~ 24:00	05:00 ~ 06:00	**Lunch and Poster Session** 12:00~13:00 (KST)		
			Session 1 : 13:00~14:20 (KST)		
			Low GWP Refrigerants (1) - Natural	Air Conditioning and Cooling	Heat Pump Applications
			Keynote	Keynote	Keynote
13:00 ~ 14:00	00:00 ~ 01:00	06:00 ~ 07:00	(135) Bin Hu Shanghai Jiao Tong University	(356) J.B.V. Reddy Department of Science and Technology, Government of India	(240) Gilbong Lee Korea Institute of Energy Research
			(297) Takaoki Suzuki Waseda University	(113) Jae Yeon Kim Hyundai Motors / Sungkyunkwan University	(180) Tommy Walfridson RISE AB
			(136) Sergio Maria Capanelli Carel Industries Spa	(035) Myung Sup Yoon Korea Testing Laboratory	(343) Takenobu Kaida Central Reseach Institute of Electric Power Industry
			(170) Valentin Salgado Fuentes Technical University of Denmark	(245) Inguk Hwang Hanonsystems	(117) Yu-Jia He Tongji University
14:00 ~ 15:00	01:00 ~ 02:00	07:00 ~ 08:00	(172) Manuel Verdnik Graz University of Technology	(262) Dae Bok Keon Hanon System	(134) Ivan Malenkovic Fraunhofer Institute for Solar Thermal Systems (ISE)
			Coffee Break and Poster Session 14:20~14:40 (KST)		
			Session 2 : 14:40~16:00 (KST)		
			Market and Policy for Heat Pumps (1)	Acoustic Signatures of Heat Pumps	Space and Hot Water Heat Pumps
			Keynote	Keynote	Keynote
15:00 ~ 16:00	02:00 ~ 03:00	08:00 ~ 09:00	(267) Thomas Nowak European Heat Pump Association aisbl	(192) Gerwin Drexler-Schmid Austrian Institute of Technology	(079) Emilio Navarro-Peris Universidad Politecnica de Valencia
			(150) Cate Lyon Delta Energy & Environment	(068) Christian Vering RWTH Aachen University	(059) Cordin Arpagaus NTB University of Applied Sciences and Technology Buchs
			(238) Martin Forsen International Affairs	(160) Thomas Fleckl AIT Austrian Institute of Technology	(255) Omar Montero Dominguez University of Geneva
			(164) Jussi Hirvonen Finnish Heat Pump Association SULPU ry	(088) Thomas Fleckl AIT Austrian Institute of Technology	(273) Elliot Romano University of Geneva
			(352) Therese Guttmann Austrian Institute of Technology	(184) Ola Gustafsson RISE Research Institutes of Sweden	(270) Carolina Fraga Services Industriels de Geneve
			Break 16:00~16:10 (KST)		
			Session 3 : 16:10~17:30 (KST)		
			Low GWP Refrigerants (2)	Heat Pump Analysis - components and cycles	New Heat Pump Technologies
			Keynote	Keynote	Keynote
16:00 ~ 17:00	03:00 ~ 04:00	09:00 ~ 10:00	(357) Didier Coulomb International Institute of Refrigeration	(067) Constantin Zenz Austrian Institute of Technology	(100) Andreas Längauer ecop Technologies GmbH
			(247) Laure Meljac NIBE	(108) Emilio Navarro-Peris Universidad Politecnica de Valencia	(272) Dominic Zajonc Lucerne University of Applied Sciences and Arts
			(141) Kenneth Hoffmann GEA Refrigeration	(050) Hai Trieu Phan French Atomic Energy and Alternative Energy Commission CEA	(229) Melanie Cop Technische Universität Dresden
17:00 ~ 17:30	04:00 ~ 04:30	10:00 ~ 10:30	(198) Sarah Kim Arkema inc.	(193) Philipp Wagner Graz University of Technology	(163) Ryosuke Suemitsu Mitsubishi Heavy Industries Thermal Systems, Ltd.
			(214) Mahmood Thabaddor Underwriters Laboratories LLC	(179) Laura Maier RWTH Aachen University	(239) Daniel Steger Friedrich-Alexander-Universität Erlangen-Nürnberg

SESSION TIMETABLE - ORAL SESSION

Date/Time			Wednesday, April 28, 2021		
Session Room			Room A	Room B	Room C
KST (UTC+9)	EDT (UTC-4)	CEST (UTC+2)			
08:30 ~ 09:00			**Registration**		
			Session 4 : 09:00~10:20 (KST)		
			Low GWP Refrigerants (3)	Ground Source and Storage	Sorption Heat Pumps (1)
09:00 ~ 10:00	(Apr. 27, Tue) 20:00 ~ 21:00	02:00 ~ 03:00	Keynote (230) Bo Shen Oak Ridge National Lab (055) Xudong Wang Air-Conditioning, Heating, and Refrigeration Institute (017) Bamdad bahar Xergy Inc. (204) Kashif Nawaz ORNL (111) Joshua Hughes The Chemours Company	Keynote (056) Xiaobing Liu Oak Ridge National Laboratory (044) Jeffrey Spitler Oklahoma State University (326) Seama Koohi-Fayegh OntarioTech University (282) Hobyung Chae Hokkaido University (325) Takao Katsura Hokkaido Univerisity	Keynote (023) Bamdad Bahar Xergy Inc. (206) Kyle Gluesenkamp Oak Ridge National Laboratory (016) Bamdad bahar Xergy Inc. (201) Zhiyao Yang Purdue University
10:00 ~ 11:00	(Apr. 27, Tue) 21:00 ~ 22:00	03:00 ~ 04:00	**Coffee Break, Poster Session** 10:20~10:40 (KST)		
			Session 5 : 10:40~12:00 (KST)		
			Low GWP Refrigerants (4)	Market and Policy for Heat Pumps (2)	Electrochemical Related
11:00 ~ 12:00	(Apr. 27, Tue) 22:00 ~ 23:00	04:00 ~ 05:00	Keynote (213) Hidekazu Okamoto AGC Inc. Yokohama Technical Center (139) Jiatong Jiang Shanghai Jiao Tong University (128) Hideyuki Fujimoto Shizuoka University (138) Zhihua Zhang The University of Tokyo (336) Jong-Taek Oh Chonnam National University	Keynote (048) Tetsusiro Iwatsubo New Energy and Industorial Technology Development Organaization (222) Ramanunni Parakkal Menon Concordia University (252) Justin Tamasauskas Natural Resources Canada (010) Melissa Lapsa Oak Ridge National Laboratory	Keynote (021) Bamdad Bahar Xergy Inc. (209) Viral K. Patel Oak Ridge National Laboratory (124) Gabyong Kim Korea University (014) Bamdad bahar Xergy Inc. (350) Joohee Song Chung-Ang University
12:00 ~ 13:00	(Apr. 27, Tue) 23:00 ~ 24:00	05:00 ~ 06:00	**Lunch and Poster Session** 12:00~13:00 (KST)		
			Session 6 : 13:00~14:20 (KST)		
			Heat Transfer	Residential Heat Pumps	Heat Exchangers (1)
13:00 ~ 14:00	00:00 ~ 01:00	06:00 ~ 07:00	Keynote (022) Ji Hwan Jeong Pusan National University (345) Riku Fukuju The University of Electro-Communications (279) Sho Fukuda Kyushu Sangyo University	Keynote (168) Carsten Wemhoener HSR University of Applied Sciences Rapperswil (275) Marek Miara Fraunhofer ISE (047) Minsu Park LG Electronics	Keynote (244) Masafumi Katsuta Waseda University (335) Zhanpeng Liu Tongji University (140) Jin Woo Yoo Korea Institute of Machinery and Materials
14:00 ~ 15:00	02:00 ~ 03:00	08:00 ~ 09:00	(294) Chan Ho Jeong Chung-Ang University (312) Youngsuk Nam Kyung Hee University	(093) Yujin Hwang Hanyang university (127) Xingyu Liang Tongji University	(334) Tiantian Wang Tongji University (316) Andreas Karageorgis ElvalHalcor Company
			Coffee Break and Poster Session 14:20~14:40 (KST)		
			Session 7 : 14:40~16:00 (KST)		
			Sorption Heat Pumps (2)	Heat Pumps in Smart Grids and District Heating and Cooling Systems (1)	Industrial Heat Pumps (1)
15:00 ~ 16:00	02:00 ~ 03:00	08:00 ~ 09:00	Keynote (176) Peter Schossig Fraunhofer Institute Solar Energy Systems ISE (181) Andrea Frazzica Consiglio Nazionale delle Ricerche (133) Ivan Malenkovic Fraunhofer Institute for Solar Thermal Systems (ISE) (341) Hai Trieu Phan French Atomic Energy and Alternative Energy Commission CEA (191) Oliver Ziegler Technische Universität Dresden	Keynote (308) Carlos Infante Ferreira Delft University of Technology (281) Simone Buffa Eurac Research (309) Carlos Infante Ferreira Delft University of Technology (253) Nicky Cowan Star Renwable Energy (151) Cate Lyon Delta Energy & Environment	Keynote (004) Tor-Martin Tveit Olvondo Technology AS (103) Miguel Ramirez Stefanou Tecnalia (156) Andrew Marina TNO (216) Cordin Arpagaus NTB University of Applied Sciences and Technology Buchs (306) Carlos Infante Ferreira Delft University of Technology
			Break 16:00~16:10 (KST)		
			Session 8 : 16:10~17:30 (KST)		
			Ground Source Heat Pumps	Heat Pumps in Smart Grids and District Heating and Cooling Systems (2)	High Temperature Heat Pumps
16:00 ~ 17:00	03:00 ~ 04:00	09:00 ~ 10:00	Keynote (045) Signhild Gehlin Swedish Geoenergi Center (098) Michael Lauermann AIT Austrian Institute of Technology GmbH (243) Franziska Bockelmann Steinbeis-Innovationszentrum energie+ (351) Kamil kwiatkowski Euros Energy	Keynote (072) Thibault Péan IREC (329) Torben Funder-Kristensen Danfoss A/S (043) Stephan Göbel RWTH Aachen University (131) Markus Lindahl RISE Research Institutes of Sweden (301) Wim Boydens boydens engineering	Keynote (104) Miguel Ramirez Stefanou Tecnalia (062) Cordin Arpagaus NTB University of Applied Sciences and Technology Buchs (075) Veronika Wilk AIT Austrian Institute of Technology GmbH (340) Johannes Oehler German Aerospace Center (DLR) (097) Sabrina Dusek Austrian Institute of Technology GmbH
17:00 ~ 18:00	04:00 ~ 05:00	10:00 ~ 11:00			

SESSION TIMETABLE - ORAL SESSION

Date/Time			Thursday, April 29, 2021		
Session Room			Room A	Room B	Room C
KST (UTC+9)	EDT (UTC-4)	CEST (UTC+2)			
08:30 ~ 09:00			**Registration**		
09:00 ~ 10:00	(Apr. 29, Wed) 20:00 ~ 21:00	02:00 ~ 03:00	**Session 9** : 09:00~10:20 (KST)		
			Variable Refrigerant Flow Heat Pumps and Air-conditioners	Heat Exchangers (2)	Food Storage and Display
			Keynote (210) Fatih Meral Purdue University	Keynote (109) Zhenning Li University of Maryland	Keynote (122) Koji Yamashita JRAIA
			(112) Aziz Mbaye Polytechnique Montréal	(332) Haotian Liu Purdue University	(250) Koichi Kitamura Waseda University
			(196) Hanlong Wan University of Maryland	(344) Haruki Mitarai The University of Electro-Communications	(286) Chenghao Wei The University of Tokyo
10:00 ~ 11:00	(Apr. 29, Wed) 21:00 ~ 22:00	03:00 ~ 04:00	(082) Riley Barta Purdue University	(314) Shehryar Ishaque Kyungpook National University	(025) Bamdad Bahar Xergy Inc.
			(283) Ammi Amarnath Electric Power Research Institute	(110) Jiazhen Ling University of Maryland	(027) Bamdad Bahar Xergy Inc.
			Coffee Break and Poster Session 10:20~10:40 (KST)		
			Session 10 : 10:40~12:00 (KST)		
			Sorption Heat Pumps (3)	Dehumidifcation Technology	Heat Pump Performance
11:00 ~ 12:00	(Apr. 29, Wed) 22:00 ~ 23:00	04:00 ~ 05:00	Keynote (086) Jae Dong Chung Sejong University	Keynote (003) Minsung Kim Chung-Ang University	Keynote (130) Katsumi Hashimoto Central Research Institute of Electric Power Industry
			(049) Ding Lu Chinese Academy of Sciences	(026) Bamdad Bahar Xergy Inc.	(346) Parveen Dhillon Purdue University
			(095) Jae-hee Lee Hanyang University	(090) Hyejin Cho Hanyang University	(123) Gulsun Demirezen Ryerson University
			(118) Gawon Lee Korea University	(091) Seong-Yong Cheon Hanyang University	(102) Tyler Shelly Purdue University
			(094) Soo-Jin Lee Hanyang University	(054) Bamdad bahar Xergy Inc.	(101) Jia-Hao Cheng Tongji University
12:00 ~ 13:00	(Apr. 29, Wed) 23:00 ~ 24:00	05:00 ~ 06:00	**Lunch and Poster Session** 12:00~13:00 (KST)		
13:00 ~ 14:00	00:00 ~ 01:00	06:00 ~ 07:00	**Session 11** : 13:00~14:20 (KST)		
			Industrial Heat Pumps (2)	Heat Pumps in HVAC systems	Advanced Controls and Modelling
			Keynote (322) Jongsoo Jeong Waseda University	Keynote (092) Hye-Won Dong Hanyang University	Keynote (096) Yong Hwan Eom Seoul National University
			(232) Soo Kwang Yang Pusan National University	(071) Lei Wang Beijing University of Technology	(339) Myung Sup Yoon Korea Testing Laboratory
			(342) Mehdi Rasti Pusan National University	(175) Mara Magni UIBK	(236) Myung Sup Yoon Korea Testing Laboratory
14:00 ~ 15:00	01:00 ~ 02:00	07:00 ~ 08:00	(241) Dominik Seliger TU Wien	(145) Tzu Wei Yeh Kokushikan University	(032) Xiangfei Liang Gree Electric Appliances, Inc. of Zhuhai
			(271) Raphael Agner Lucerne University of Applied Sciences and Arts	(224) Korbinian Kramer Fraunhofer ISE	(074) Philipp Mehrfeld RWTH Aachen University
			Coffee Break and Poster Session 14:20~14:40 (KST)		
			Session 12 : 14:40~15:45 (KST)		
			Heat Pumps combined with Thermal Energy Strorage and Recovery	Nearly Zero Energy Buildings	Smart Applications of Heat Pumps
15:00 ~ 16:00	02:00 ~ 03:00	08:00 ~ 09:00	Keynote (178) Klemens Marx AIT Austrian Institute of Technology	Keynote (167) Carsten Wemhoener HSR University of Applied Sciences Rapperswil	Keynote (268) Thomas Nowak European Heat Pump Association aisbl
			(307) Carlos Infante Ferreira Delft University of Technology	(066) Fabian Ochs University of Innsbruck	(203) Lena Schnabel Heating and Cooling Technologies
			(008) Franziska Bockelmann Steinbeis-Innovationszentrum energie+	(042) Christina Betzold Technische Hochschule Nuernberg Georg Simon Ohm	(183) Ola Gustafsson RISE Research Institutes of Sweden
			(254) Simon Callegari University of Geneva	(165) Carsten Wemhoener HSR University of Applied Sciences Rapperswil	(310) Aziz Mbaye He-Tech Suisse
16:00 ~ 17:00	03:00 ~ 04:00	09:00 ~ 10:00	**Break** 15:45~16:00 (KST)		
			Closing Ceremony 16:00~17:00 (KST)		

SESSION TIMETABLE - POSTER SESSION

April 27-29, 2021

No.	Paper No.	Name	Affiliation
Track 1: Residential and Building applications			
1	013	Shuxue Xu	Beijing University of Technology
2	069	Christian Vering	RWTH Aachen University
3	258	Jong Min Choi	Hanbat National University
4	260	Yechan Yun	Kookmin University
5	291	Chenxi Ni	Hefei University of Technology
6	311	Jonathan Ore	Purdue University
7	162	Carsten Wemhoener	HSR University of Applied Sciences Rapperswil
8	269	Miwako Fujita	Chubu Electric Power, Co., Inc.
9	331	Nobuhiro Takahashi	Japan Facility Solutions, Inc
10	031	Xiangfei Liang	Gree Electric Appliances, Inc. of Zhuhai
Track 2: Smart Energy Systems and Renewables			
11	039	Euy-Joon Lee	Korea Institute of Energy Research
12	315	Junhyun Cho	Korea Institute of Energy Research
13	348	Rho Kyo Heon	Chung-Ang University
14	285	Lingyan Yang	China Academy of Building Research
15	070	Jussi Alpua	Oilon Oy
Track 3: Air-Conditioning & Industry			
16	147	Hiroshi Nakayama	Chubu Electric Power co.,Inc.
17	148	Hiroyuki Miyazaki	Chubu Electric Power Co.,Inc
18	321	Youngju Joo	SAMSUNG ELECTRONICS
19	353	Sun-Ik Na	Seoul National University
20	354	Gu Hwang Kang	Seoul National University
21	227	Chulwoo Roh	Korea Institute of Energy Research
22	248	Xlaohui Yu	Hebei University of Technology
23	288	Yunchan Shin	Chosun University
24	347	Xiaoning Chen	Emerson Research and Solutions Center
Track 4: Working Fluids and Advances			
25	355	Jinwook Lee	Chung-Ang University
26	349	Minsoo Kim	Chung-Ang University

PLENARY LECTURES 1

Plenary Session 1-1 : Policy and market

- Date/Time : Tuesday, April 27, 2021, 09:20~09:45 (KST/UTC+9)
- Venue : Room A (Tamna Hall, 8F)
- Session Chair : Taesung Kim (Sungkyunkwan University, South Korea)



Heat Pumping Technologies in Clean Energy Transitions

Mechthild Wörsdörfer
IEA Director of Sustainability, Technology and Outlooks, France

Abstract

Heating and cooling in buildings account for almost 15% of total global energy-related CO2 emissions, or 5 gigatons per year. While nearly 60% of global buildings heat provision relies on direct fossil fuel combustion, heat pumps could already supply more than 90% of heat demand with a lower carbon footprint than any fossil alternative. The deployment of heat pumps in new, well-insulated buildings in many places such as the United States or Europe shows that the heat pump market is taking off. Yet, deployment is uneven across market segments. To meet the Paris Agreement, the IEA defined a 3-pillar action plan. First, achieving greater deployment rates across all applications (including in retrofits, district energy systems and industrial processes) would tap into early emissions reduction opportunities. Second, the integration of heat pumps with power systems is essential to ensure their scalability and operability with high shares of variable renewables in the electricity generation mix. Last, enhancing heat pumps is key so that they could become multi-service providers that can operate in a variety of climate contexts (such as hot and humid, cold or multi-seasonal climates) while taking advantage of next generation designs (such as refrigerant-free, evaporative or solid-state applications).

Biography

Heating Mechthild Wörsdörfer (@MWorsdorfer) joined the IEA on 1 October 2018 as Director of Sustainability, Technology and Outlooks (STO). Ms Wörsdörfer plans and co-ordinates the IEA's work on energy sustainability, encompassing clean energy technologies and climate change policy. Previously, Mechthild held several senior management positions in the European Commission, where she coordinated the work on the 2030 Energy and Climate Framework, the Clean Energy Package and the 2050 Energy Roadmap. She had been involved with the IEA for a number of years as IEA Governing Board Representative for the EU, and served in the Cabinet of Commissioners, in charge of industry, competitiveness, trade and digital economy.

PLENARY LECTURES 1

Plenary Session 1-2 : Policy and market

- Date/Time : Tuesday, April 27, 2021, 09:45~10:10 (KST/UTC+9)
- Venue : Room A (Tamna Hall, 8F)
- Session Chair : Taesung Kim (Sungkyunkwan University, South Korea)



The European Legal Framework is Well Set for a Massive Roll-out of Heat Pumps - but More Efforts are Needed!

Martin Forsén
President of European Heat Pump Association, Sweden

Abstract

The present European Commission has, since they entered office in 2019, significantly raised the ambition in policies related to energy and climate actions. The European green deal including a European renovation wave of buildings, circular economy action plan and a strategy for energy system integration are all essential parts of the plan to make Europe the first climate neutral continent by 2050. The aim of the renovation wave is to double the current rate of renovation. Renovations shall be implemented adhering to the energy efficiency first principle as well as the need to decarbonize while increasing the use of renewable energy sources. Electrification of the heating sector will play a central role and in particular by a wide introduction of heat pumps. The energy system integration strategy is expecting an increase of the share of electricity-based heating to double by 2030 and to reach 50-70% by 2050. The tremendous push for decarbonization and electrification will have considerable impact on the revision of existing regulations. This presentation will give an overview of the overarching targets, policies and ongoing revisions of existing regulations as well as the possibilities and challenges faced by the heat pump industry.

Biography

Martin received his Master of Science in mechanical engineering at the Royal Institute of Technology in Stockholm 1997. After a short time at the electric utility company Vattenfall he got back to the university as a researcher, where he stayed until he was hired as President of the Swedish Heat Pump Association 2003. After ten years at the association, Mr Forsén was recruited as Manager International Affairs for NIBE in 2013. Mr Forsén has for the last decade been an active member of the European Heat Pump Association. He has been a member of the board for several years and serves as President for the Association.

PLENARY LECTURES 1

Plenary Session 1-3 : Policy and market

- Date/Time : Tuesday, April 27, 2021, 10:10 ~10:35 (KST/UTC+9)
- Venue : Room A (Tamna Hall, 8F)
- Session Chair : Taesung Kim (Sungkyunkwan University, South Korea)



Korean Policy for Green World and Heat Pumping Technologies

Min Soo Kim
President of Society of Air-conditioning and Refrigerating Engineers of Korea,
NOC Chair, South Korea

Abstract

Responses to climate change have permeated everyday life in the 21st century, as countries are increasingly faced the threat of global warming and natural disasters. Even in the wake of the COVID-19 pandemic, attitudes towards climate change have been mostly unanimous as international cooperation remains tight.

Governments are increasingly implementing green policies in an effort to reduce emissions and to stimulate economic recovery. Recently, U.S. released a climate change plan worth USD1.7 trillion to completely phase out nonrenewable energy and achieve net-zero emissions by 2050. Meanwhile, China pledged to achieve carbon neutrality before 2060, hitting peak emissions before 2030. In Europe, the European Commission announced the European Green Deal as a community-wide policy in December 2019 to make Europe the world's first climate-neutral bloc by 2050.

South Korea also released the New Deal policy in 2020 amid the COVID-19 pandemic situation, outlining targets in renewable energy and ICT infrastructure through the Green New Deal and Digital New Deal. Through the Green New Deal, the Korean government will invest KRW73.4 trillion for transition to a low-carbon, green economy by making additional advancements in mobility, energy, and other supporting climate-friendly technology.

In 2019, renewable energy accounted for 15,791 MW of electricity in Korea, about 13% of total power generation. Out of this, solar energy accounted for 67% of the renewable energy. To accelerate the green transition, the Korean government announced a 3020 renewable energy plan by which it will generate 20% of energy from renewable sources by 2030. In addition, the Korean Hydrogen Roadmap will be used to build a hydrogen economy for the public and private sector by 2040.

To achieve net zero emissions, heating and cooling energy, which accounts for about half of total energy consumption, must be reduced. For this, a heat pump is essential; however, there are many obstacles to adequately supply heat pumps in Korea such as high gas permeability, low energy prices, and sedentary culture. As shown in the examples of geothermal and hydrothermal heat pumps, designation of renewable energy sources can promote the growth of the heat pump industry in Korea. The designation of renewable energy sources for heat pump covering all heat sources will be of paramount help in achieving the net-zero emissions.

Biography

Min Soo KIM received the B.S. (1985), M.S. (1987), and Ph.D. (1991) degrees in mechanical engineering at Seoul National University. He is a Professor of the Department of Mechanical Engineering at Seoul National University since 1994. He serves as chair of the Department of Mechanical Engineering. His major is thermal engineering including refrigeration and air conditioning. He spent three years from 1992 to 1994 at the National Institute of Standards and Technology (NIST) in U.S. as a guest researcher. He has more than 240 journal papers and more than 440 conference papers together with about 40 patents in the field of thermal engineering and refrigeration. He is a member of ASME, ASHRAE, IIR, KSME, and SAREK.

In 2010, he served as Policy Advisor to Minister of the Ministry of Education, Science and Technology, and during 2011-2013, he was a member of Presidential Advisory Council on Education, Science & Technology. He was delegate of Korea to the International Institute of Refrigeration (IIR), and he served as vice president of the Management Committee of IIR and serves now as president of the General Council of IIR.

He got the Outstanding Academic Award from the Society of Air-conditioning and Refrigerating Engineers of Korea (SAREK) in 2006, Asian Academic Award from SAREK/CAR/JSRAE (2012), Outstanding Academic Award from Korean Society of Mechanical Engineers (KSME) (2013), Best Industry-University Cooperation Award from the College of Engineering at SNU (2015), and Minister Award from the Ministry of Land, Infrastructure, and Transport (2016). He was designated as 70 Excellent PhDs of College of Engineering at Seoul National University (2016) and he received Presidential Citation by the Ministry of Public Administration and Security (2017).

PLENARY LECTURES 2

Plenary Session 2-1 : Technology

- Date/Time : Tuesday, April 27, 2021, 10:45 ~11:10 (KST/UTC+9)
- Venue : Room A (Tamna Hall, 8F)
- Session Chair : Taesung Kim (Sungkyunkwan University, South Korea)



Heat Pump System Technology Trend

Saikee Oh
Executive Vice President / Center Director of LG Electronics, South Korea

Abstract

The role of heat pump in reducing greenhouse gases.
Some fundamental bottlenecks of traditional air-source heat pumps.
The cutting-edge heat pump technology to overcome these problems.

Biography

Education

Department of Mechanical Engineering
- Bachelor : Seoul National University (~Fab. 1989)
- Master : KAIST (~Fab. 1991)
- Ph.D. : KAIST (~Fab. 1997)

Professional Activities

LG Electronics
- H&A R&D Center Director (2020~)
- Air Solution R&D Lab. Director (2018 ~ 2019)
- System Air Conditioning Research / Engineering Division Leader (2014 ~ 2017)
- Air Conditioning & Energy Solution Lab. Director (2013)
- Entering LG Electronics (Mar. 1994)

Research Interests

Department of Mechanical Engineering
- Inverter Heat Pump (Air to Air, Air to Water)
- Indoor Air Quality
- Energy Saving HVAC Control

PLENARY LECTURES 2

Plenary Session 2-2 : Technology

- Date/Time : Tuesday, April 27, 2021, 11:10~11:35 (KST/UTC+9)
- Venue : Room A (Tamna Hall, 8F)
- Session Chair : Taesung Kim (Sungkyunkwan University, South Korea)



Ensuring a Safe Refrigerant Transition

Xudong Wang
Vice President of Air-Conditioning, Heating, and Refrigeration Institute, United States

Abstract

The global industry is transitioning to environmentally friendly low global warming potential (GWP) refrigerants. To date, most of promising low GWP refrigerants are flammable. Implementation of these refrigerants in the field requires necessary steps to ensure safety. The presentation will summarize the US industry activities on transitioning to low GWP refrigerants. The content will cover the current status on relevant code and standard development, research and remaining efforts needed in the transition to low-GWP refrigerants in the future.

Biography

Dr. Xudong Wang is the vice president of research at AHRI. He closely works with AHRI Members to develop research programs addressing common issues and challenges that the HVACR industry faces. He has initiated and managed multiple research programs related to assess low GWP refrigerants' performance, compatibility and safety. He holds a Ph.D. in Mechanical Engineering from the University of Maryland at College Park. Dr. Wang is a member of the American Society of Heating, Refrigerating, and Air-Conditioning Engineers ASHRAE.

PLENARY LECTURES 2

Plenary Session 2-3 : Technology

- Date/Time : Tuesday, April 27, 2021, 11:35 ~12:00 (KST/UTC+9)
- Venue : Room A (Tamna Hall, 8F)
- Session Chair : Taesung Kim (Sungkyunkwan University, South Korea)



Clean and Safe Air by HVAC systems
– Laws and Advanced Technologies in Japan

Noboru Kagawa
Professor of National Defense Academy, Japan

Abstract

Experience of health problems and pandemics changes the design of HVAC systems frequently. Accumulated knowledge can improve the HVAC technologies. Related laws and new technologies in Japan will be overviewed.

Biography

Prof. Noboru Kagawa is a Technical adviser and the former president of the Japan Society of Refrigerating and Air Conditioning Engineers, JSRAE, a member of the Executive committee and the Management committee of IIR, and the Leadership councillor of ASHRAE AASA. He works as a professor in Department of Mechanical Systems Engineering of National Defense Academy of Japan. His major fields of study are thermophysical properties of refrigerants, Stirling engine and refrigerator, and refrigerants management. He is also the chair of the 2nd IIR Conference of HFOs and Low GWP Blends, HFO2021 will be held at Osaka in June 2021.

KEYNOTE LECTURES

Tuesday, April 27

- **The Influence of Different Water-injection Methods on Water Vapor High Temperature Heat Pump**

- Bin Hu (Shanghai Jiao Tong University, China)

- **Next Stop: the Mass Market! Heat Pumps on the Verge of Large Scale Deployment in Europe**

- Thomas Nowak (European Heat Pump Association AISBL, Belgium)

- **The low-GWP refrigerant challenge**

- Didier Coulomb (International Institute of Refrigeration, France)

- **Air-Conditioning and Cooling**

- J.B.V. Reddy (Government of India, India)

- **Augmented Reality Acoustics of Air Heat Pumps - APP Development and Methods**

- Gerwin H.S. Drexler-Schmid (AIT - Austrian Institute of Technology, Austria)

- **Numerical Analysis of the Vortex Tube Characteristics Used Within a High Temperature Heat Pump**

- Constantin Zenz (Austrian Institute of Technology, Austria)

- **Development and Implementation of Industrial High Temperature Heat Pumps for Waste Scrubbing Process**

- Gilbong Lee (Korea Institute of Energy Research, South Korea)

- **Design of a Grey Water Heat Recovery System in Order to Satisfy the Domestic Hot Water Demand of a Block of Dwellings**

- Emilio Navarro-Peris (Universidad Politecnica de Valencia, Spain)

- **Test Results of a Rotation Heat Pump and Further Developments**

- Andreas Längauer (ecop Technologies GmbH, CEO, Austria)

Wednesday, April 28

- **Residential Split Heat Pump Using Low GWP Refrigerants**

- Bo Shen (Oak Ridge National Lab, United States)

- **Disproportionation Risk Study for HFO-1123 Compositions as Low-GWP Refrigerants**

- Hidekazu Okamoto (AGC Inc., Japan)

- **Numerical Simulation of Two-phase Flow Distribution in a Vertically Installed Refrigerant Distributor**

- Ji Hwan Jeong (Pusan National University, South Korea)

- **Trends and Recent R&D Activities on Fuel Driven Sorption Heat Pumps**

- Peter Schossig (Fraunhofer Institute Solar Energy Systems ISE, Germany)

- **Half-term Results from IEA HPT Annex 52 - Long-term Performance Monitoring of Large GSHP Systems**

  - Signhild Gehlin (Swedish Geoenergi Center, Sweden)

- **A Novel Geothermal Heat Pump System Integrated with Underground Thermal Storage for Shifting Building Electric Demands**

  - Xiaobing Liu (Oak Ridge National Laboratory, United States)

- **NEDO R&D Project for Innovative Thermal Management**

  - Tetsusiro Iwatsubo (New Energy and Industrial Technology Development Organization (NEDO, Japan)

- **Evaluation of Solar Heat Source and Sink in Multi-functional Heat Pump Operation**

  - Carsten Wemhoener (HSR University of Applied Sciences Rapperswil, Switzerland)

- **Seasonal Thermal Energy Storage for Large Scale District Heating**

  - Carlos Infante Ferreira (Delft University of Technology, Netherlands)

- **Impact of the Weather Forecast on a Predictive Controller Performance : Experimental Studies with a Residential Heat Pump for Space Cooling**

  - Thibault Péan (IREC, UPC, Spain)

- **Membrane-Based Air Dehumidification Using Organic Ionic Liquid Desiccant**

  - Bamdad Bahar (Xergy Inc., United States)

- **An Overview of Hydrogen Compressors for Heat Pump Systems**

  - Bamdad Bahar (Xergy Inc., United States)

- **Study on the Frosting Phenomena between Concavity and Convexity Plate under Forced Convection**
  - The Prediction of Frost Layer Growth using the Observation from the Frost and Defrost Multi-cycle Experiment -

  - Masafumi Katsuta (Waseda University, Japan)

- **Environmentally Friendly Steam Generation Using VHTHPs at a Pharmaceutical Research Facility**

  - Tor-Martin Tveit (Olvondo Technology AS, Norway)

- **Experimental Analysis of a High Temperature Heat Pump Using Stored Heat from a Solar Thermal System.**

  - Miguel Ramirez Stefanou (Tecnalia, Spain)

Thursday, April 29

- **Impact of Variable Speed Components on the Seasonal Performance of a Residential Air-Source Heat Pump**

  - Fatih Meral (Purdue University, Ray W. Herrick Laboratories, United States)

- **Effect of Evaporator and Condenser in the Analysis of Adsorption Chiller**

  - Jae Dong Chung (Sejong University, South Korea)

- **Categorization of Industrial Heat Pump for Integrated Simulation Technology**

  - Jongsoo Jeong (Waseda University, Japan)

- **Dynamic Performance Tests of a Heat Pump Cycle Integrated Latent Heat Thermal Energy Storage for Optimized DHW Generation**

- Klemens Marx (AIT Austrian Institute of Technology, Austria)

- **Refrigerant Circuitry Optimization of Heat Exchangers for Charge Reduction and Robust Performance in Reversible Heat Pump Application**

- Zhenning Li (University of Maryland, United States)

- **Comparison on Vacuum Membrane Dehumidification Systems with Moisture Selective Dense Membrane**

- Minsung Kim (Chung-Ang University, South Korea)

- **Working Fluid Selection of Organic Rankine Cycle for a Liquid Desiccant System**

- Hye-Won Dong (Hanyang University, South Korea)

- **Cost Optimized Design of Ground Probe Fields with Solar Regeneration**

- Carsten Wemhoener (HSR University of Applied Sciences Rapperswil, Switzerland)

- **Risk Assessment of Built-in Refrigerated Display Cabinet Using A3 Refrigerant**

- Koji Yamashita (the Japan Refrigeration and Air Conditioning Industry Association, Japan)

- **Energy Performance Estimation and Verification of an Industrial Waste Heat Recovery Heat Pump**

- Katsumi Hashimoto (Central Research Institute of Electric Power Industry)

- **Deep learning-based Refrigerant Charge Fault Detection Method of Air-source Heat Pump System**

- Yong Hwan Eom (Seoul National University, South Korea)

- **From Smarties, Ice-cream and Flowers**

- Thomas Nowak (European Heat Pump Association AISBL, Belgium)

ORAL SESSION

TUESDAY, APRIL 27, 2021

※ THE LIVE STREAM SCHEDULE IS BASED ON KOREA STANDARD TIME (KST / UTC +9).

Room A (Tamna Hall)

Tuesday, April 27 | Room A (Tamna Hall, 8F)

09:00-09:20	**Opening Ceremony**	Host: Taesung Kim (Sungkyunkwan University, South Korea)
	- Welcome Address (Stephan Renz / IEA HPT TCP Chair, Switzerland) - Opening Remark (Min Soo Kim / NOC Chair, President of Society of Air-conditioning and Refrigerating Engineers of Korea, South Korea) - Congratulatory Remarks (Hee-ryong Won / Governor of Jeju Province, South Korea)	
09:20-10:35	**Plenary Lecture I - Policy and Market**	Session Chair: Taesung Kim (Sungkyunkwan University, South Korea)
09:20-09:45	Plenary Lecture 1-1	**Heat Pumping Technologies in Clean Energy Transitions** Mechtild Worsdorfer, Director for Sustainability, Technology & Outlooks, IEA, France
09:45-10:10	Plenary Lecture 1-2	**The European Legal Framework is Well Set for a Massive Roll-out of Heat Pumps - but More Efforts are Needed!** Martin Forsen, President of European Heat Pump Association, Sweden
10:10-10:35	Plenary Lecture 1-3	**Korean Policy for Green World and Heat Pumping Technologies** Min Soo Kim, NOC Chair of HPC 2020, President of Society of Air-conditioning and Refrigerating Engineers of Korea, South Korea
10:35-10:45	Coffee Break and Poster Session	

Tuesday, April 27 | ROOM A (Tamna Hall, 8F)

10:45-12:00	**Plenary Lecture II - Technology**	Session Chair: Taesung Kim (Sungkyunkwan University, South Korea)
10:45-11:10	Plenary Lecture 2-1	**Heat Pump System Technology Trend** Saikee Oh, Executive Vice President / Center Director of LG Electronics, South Korea
11:10-11:35	Plenary Lecture 2-2	**Ensuring a Safe Refrigerant Transition** Xudong Wang, Vice President of Air-Conditioning, Heating, and Refrigeration Institute, US
11:35-12:00	Plenary Lecture 2-3	**HVAC Systems against COVID-19** Noboru Kagawa, Professor of National Defense Academy, Japan
12:00-13:00	Lunch and Poster Session	

Tuesday, April 27 | Room A (Tamna Hall, 8F)

Session 1A: Low GWP Refrigerants (1) - Natural

Session Chair : Bin Hu (Shanghai Jiao Tong University, China)

13:00-13:20	Keynote	[135]	The Influence of Different Water-injection Methods on Water Vapor High Temperature Heat Pump Di Wu (Shanghai Jiao Tong University), Bin Hu (Shanghai Jiao Tong University) † , R.Z Wang (Shanghai Jiao Tong University)
13:20-13:35		[297]	Annual Performance Assessment of Heat Pump Water Heaters Applying Various Refrigerants Takaoki Suzuki (Waseda University), Zheng Ge (Waseda University), Muhamad Yulianto (Waseda University), Yoichi Miyaoka (Waseda University), Seiichi Yamaguchi (Waseda University), Kiyoshi Saito (Waseda University) †
13:35-13:50		[136]	Benefits and Reliability of Air to Water Heat Pump in Residential Applications, using R290 Refrigerant and Alternative Design Solution to Guarantee High Safety Level with Standard Components Sergio Maria Capanelli (Carel Industries Spa) † , Biagio Lamanna (Carel Industries Spa)
13:50-14:05		[170]	Medium Capacity Low Charge Ammonia Chiller and Heat Pump Valentin Salgado Fuentes (Technical University of Denmark) † , Wiebke Brix Markussen (Technical University of Denmark), Erasmus Damgaard Rothuizen (Technical University of Denmark), Jóhannes Kristófersson (Danish Technological Institute), Claus Madsen (Danish Technological Institute), Brian Elmegaard (Technical University of Denmark)
14:05-14:20		[172]	High-temperature Vapor Compression Heat Pump using Butane (R600) - Development of a Prototype and First Measurements Manuel Verdnik (Graz University of Technology) † , René Rieberer (Graz University of Technology)
14:20-14:40	Coffee Break and Poster Session		

Tuesday, April 27, 2021 | Room A (Tamna Hall, 8F)

Session 2A: Market and Policy for Heat Pumps (1)

Session Chair : Jussi Hirvonen (Finnish Heat Pump Association SULPU ry, Finland)

14:40~15:00	Keynote	[267]	Next Stop: The Mass Market! Heat Pumps on the Verge of Large Scale Deployment in Europe Thomas Nowak (European Heat Pump Association AISBL) †
15:00~15:15		[150]	Disruption to Heat Business Models: From Shifting Boxes to Selling Comfort Cate Lyon (Delta Energy & Environment)) † , Lindsay Sugden (Delta Energy & Environment) † , Roxanne Pieterse (Delta Energy & Environment)
15:15~15:30		[238]	The Role of Heat Pumps in the Decarbonisation of the Heating Sector in Europe Martin Forsen (NIBE Energy Systems), Laure Meljac (NIBE Energy Systems) †
15:30~15:45		[164]	Today's One Million Heat Pumps are Already in Essential Role in Smart Energy Transition Towards Carbon Neutral Finland Jussi Hirvonen (Finnish Heat Pump Association SULPU ry) †
15:45~16:00		[352]	Diffusion Barriers and Strategies for Heat Pump Systems with Integrated Storage and Photovoltaic in Austrian 1-2 Family Dwellings: an Explorative Investigation for the IEA HPT Annex 55/ECES Annex 34 Therese Guttmann (Austrian Institute of Technology) † , Thomas Schoberer (Forschung Burgenland GmbH), Caroline Haglund Stignor (Research Institutes of Sweden), Johann Emhofer (Austrian Institute of Technology)
16:00~16:10	Break		

Tuesday, April 27, 2021 | Room A (Tamna Hall, 8F)

Session 3A: Low GWP Refrigerants (2)

Session Chair: Didier Coulumb (IIR Director, France)

16:10~16:30	Keynote	[357]	The low-GWP Refrigerant Challenge Didier Coulomb (International Institute of Refrigeration)
16:30~16:45		[247]	Increasing Flammable Refrigerant Charge Size without Compromising Safety Laure Meljac (NIBE) † , Martin Forsen (NIBE), Daniel Colbourne (c/o HEAT GmbH)
16:45~17:00		[141]	Is HFO the Last Range of Synthetical Refrigerant? Kenneth Hoffmann (GEA Refrigeration) † , Jan Gerritsen (GEA Refrigeration), Armin Hafner (NTNU)
17:00~17:15		[198]	Very Low GWP Refrigerant for Heat Pump Sarah Kim (Arkema inc) † , Laurent Abbas (Arkema France), Leping Zhang (Danfoss China), Drew Turner (Danfoss LLC)
17:15~17:30		[214]	Improving Risk Assessment of Refrigerant Leakage Hazards: Going beyond Physical Testing Mahmood Thabaddor (Underwriters Laboratories LLC) † , Sangamesh Hosur (UL India Pvt Ltd.) †

Room B (Halla Hall)

Tuesday, April 27 | Room A (Tamna Hall, 8F)

09:00-09:20	**Opening Ceremony**	Host: Taesung Kim (Sungkyunkwan University, South Korea)
09:20-10:35	**Plenary Lecture I - Policy and Market**	Session Chair: Taesung Kim (Sungkyunkwan University, South Korea)
10:35-10:45	Coffee Break and Poster Session	
10:45-12:00	**Plenary Lecture II - Technology**	Session Chair: Taesung Kim (Sungkyunkwan University, South Korea)
12:00-13:00	Lunch and Poster Session	

Tuesday, April 27 | Room B (Halla Hall, 8F)

Session 1B: Air Conditioning and Cooling

Session Chair: Mitsuhiro Fukuta (Shizuoka University, Japan)

13:00~13:20	Keynote	[356]	Air-Conditioning and Cooling J.B.V. Reddy (Department of Science and Technology, Government of India)
13:20~13:35		[113]	Application of Improved Cooling & Heating System to Long-Range Electric Vehicles for Higher Power Efficiency Jae Yeon Kim (Hyundai Motors), Taesung Kim (Sungkyunkwan University) † , Yeon Ho Kim (Hyundai Motors), Jea Wan Kim (Hyundai Motors)
13:35~13:50		[035]	Study on the Smart Operation Approach of an Air Conditioner when Occupants Go Out Myung Sup Yoon (Korea Testing Laboratory) † , Won Sik Yoon (Korea Testing Laboratory)
13:50~14:05		[245]	The Study of Secondary Loop System with Efficient and Flammable Refrigerants in MAC Inguk Hwang (Hanonsystems) † , Haejun Lee (Hanonsystems), Gumbae Choi (Hanonsystems), Jaeyeon Kim (Hyundai Motor Group), Manju Oh (Hyundai Motor Group)
14:05~14:20		[262]	A Development of AHP, the Integrated Climate System Module for EV Dae Bok Keon (Hanon System), Jae Chun Ryu (Hanon System), Ki Young Shin (Hyundai Motor Company), Sung Je Lee (Hanon System), Dong Woo Hwang (Hanon System) †
14:20-14:40	Coffee Break and Poster Session		

Tuesday, April 27, 2021 | Room B (Halla Hall, 8F)

Session 2B: Acoustic Signatures of Heat Pumps

Session Chair: Christoph Reichl (AIT Austrian Institute of Technology, Austria)

14:40~15:00	Keynote	[192]	Augmented Reality Acoustics of Air Heat Pumps - APP Development and Methods Gerwin H.S. Drexler-Schmid (AIT - Austrian Institute of Technology) † , Christian H. Kasess (Austrian Academy of Sciences), Brigitte Blank-Landeshammer (AIT - Austrian Institute of Technology), Christian Köfinger (AIT - Austrian Institute of Technology), Johann Emhofer (AIT - Austrian Institute of Technology), Holger Waubke (Austrian Academy of Sciences), Christoph Reichl (AIT - Austrian Institute of Technology) †

15:00~15:15		[068]	Simultaneous Energy Efficiency and Acoustic Evaluation of Heat Pump Systems Using Dynamic Simulation Models Christian Vering (RWTH Aachen University) † , François Bessac (CETIAT) † , Roberto Fumagalli (Polimi), Henrik Hellgren (RI.SE), Thore Oltersdorf (Fraunhofer ISE), Svend Pedersen (DTI), Christoph Reichl (AIT)
15:15~15:30		[160]	Acoustic Characterisation of an Air-To-Water Heat Pump for Different Operating Conditions: Inter-laboratory Results Thomas Fleckl (AIT), François Bessac (CETIAT) † , Roberto Fumagalli (Polimi), Henrik Hellgren (RI.SE), Thore Oltersdorf (Fraunhofer ISE), Svend Pedersen (DTI), Christoph Reichl (AIT)
15:30~15:45		[088]	Frosting and Defrosting Behavior of Evaporators Thomas Fleckl (Center for Energy, AIT Austrian Institute of Technology), Christoph Reichl (Center for Energy, AIT Austrian Institute of Technology) † , Mirza Popovac (Center for Energy, AIT Austrian Institute of Technology), Felix Hochwallner (Center for Energy, AIT Austrian Institute of Technology), Peter Wimberger (Institute of Applied Physics, Vienna University of Technology), Felix Linhardt (Department of Geography, Kiel University), Johann Emhofer (Center for Energy, AIT Austrian Institute of Technology)
15:45~16:00		[184]	Heat Pump Noise - Seasonal Averaging and Operation Dependence Ola Gustafsson (RISE Research Institutes of Sweden) † , Henrik Hellgren (RISE Research Institutes of Sweden), Caroline Haglund Stignor (RISE Research Institutes of Sweden)
16:00~16:10	Break		

Tuesday, April 27, 2021 | Room B (Halla Hall, 8F)

Session 3B: Heat Pump Analysis - Components and Cycles

Session Chair: Thomas Fleckl (AIT Austrian Institute of Technology, Austria)

16:10~16:30	Keynote	[067]	Numerical Analysis of the Vortex Tube Characteristics used within a High Temperature Heat Pump Michael Lauermann (Austrian Institute of Technology), Constantin Zenz (Austrian Institute of Technology) † , Mirza Popovac (Austrian Institute of Technology)
16:30~16:45		[108]	Analysis of the Refrigerant Maldistribution of Propane Evaporating in Brazed Plate Heat Exchangers as a Function of Operating Conditions Emilio Navarro-Peris (Universitat Politecnica de Valencia) † , Lucas Alvarez (Universitat Politecnica de Valencia), Paloma Albaladejo (Universitat Politecnica de Valencia), Lena Schnabel (Fraunhofer Institute for Solar Energy Systems ISE), Jose Miguel Corberan (Universitat Politecnica de Valencia)
16:45~17:00		[050]	Performance Analysis of a Combined Cooling and Power Cycle Philipp Wagner (Graz University of Technology) † , Rene Rieberer (Graz University of Technology)
17:00~17:15		[193]	Analysis of a Directly Gas-fired Absorption Heat Pump with an Improved Condensing Boiler Technology Philipp Wagner (Graz University of Technology) † , Rene Rieberer (Graz University of Technology)
17:15~17:30		[179]	Simulation-based Eco-economic Assessment of Heat Pump Systems for Refurbishing All-electric Non-residential Buildings with Complex Energy Demand Structures Laura Maier (RWTH Aachen University) † , Xuchao Ying (RWTH Aachen University), Konstantin Finkbeiner (RWTH Aachen University), Sarah Henn (RWTH Aachen University), Jan Richarz (RWTH Aachen University), Markus Nürenberg (RWTH Aachen University), Tanja Osterhage (RWTH Aachen University), Dirk Müller (RWTH Aachen University)

Room C (Ara Hall)

Tuesday, April 27 | Room A (Tamna Hall, 8F)

09:00-09:20	**Opening Ceremony**	Host: Taesung Kim (Sungkyunkwan University, South Korea)
09:20-10:35	**Plenary Lecture I - Policy and Market**	Session Chair: Taesung Kim (Sungkyunkwan University, South Korea)
10:35-10:45	Coffee Break and Poster Session	
10:45-12:00	**Plenary Lecture II - Technology**	Session Chair: Taesung Kim (Sungkyunkwan University, South Korea)
12:00-13:00	Lunch and Poster Session	

Tuesday, April 27 | Room C (Ara Hall, 8F)

Session 1C: Heat Pump Applications

Session Chair: Akio Miyara (Saga University, Japan)

13:00~13:20	Keynote	[240]	Development and Implementation of Industrial High Temperature Heat Pumps for Waste Scrubbing Process Gilbong Lee (Korea Institute of Energy Research), Beomjoon Lee (Korea Institute of Energy Research), Junhyun Cho (Korea Institute of Energy Research), Ho-Sang Ra (Korea Institute of Energy Research), Young-Jin Baik (Korea Institute of Energy Research), Eun Seok Wang (Korea Institute of Energy Research), Hyung-Ki Shin (Korea Institute of Energy Research), Young-Soo Lee (Korea Institute of Energy Research) † , Chulwoo Roh (Korea Institute of Energy Research)
13:20~13:35		[180]	Long-term Evaluation of an Office Building with Large-scale Heat Pump and aquifer System in Southern Sweden Tommy Walfridson (Energy and Circular economy, RISE Research Institutes of Sweden) † , Martin Larsson (Energy and Circular economy, RISE Research Institutes of Sweden), Jessica Benson (Energy and Circular economy, RISE Research Institutes of Sweden), Oskar Räftegård (Energy and Circular economy, RISE Research Institutes of Sweden), Ola Gustafsson (Energy and Circular economy, RISE Research Institutes of Sweden), Caroline Haglund Stignor (Energy and Circular economy, RISE Research Institutes of Sweden), Lovisa Axelsson (Energy and Circular economy, RISE Research Institutes of Sweden), Pia Tiljander (Energy and Circular economy, RISE Research Institutes of Sweden)
13:35~13:50		[343]	Thermodynamic Analysis of Refrigerant Selection for High Temperature Heat Pump Cycles Takenobu Kaida (Central Research Institute of Electric Power Industry (CRIEPI)) †
13:50~14:05		[117]	Approaching Optimal High Pressure by Charge Management in Transcritical CO2 Heat Pump Water Heater Yu-Jia He (Tongji University), Xing-Yu Liang (Tongji University), Jia-Hao Cheng (Tongji University), Liang-Liang Shao (Tongji University) † , Chun-Lu (Tongji University)
14:05~14:20		[134]	Results of an Interlaboratory Comparison on Four Different Heat Pumps: Standards on the Test Stand Ivan Malenkovic (Fraunhofer Institute for Solar Thermal Systems (ISE)) † , Urs Gumbel (Fraunhofer Institute for Solar Thermal Systems (ISE)), Christoph Thoma (Fraunhofer Institute for Solar Thermal Systems (ISE)
14:20-14:40	Coffee Break and Poster Session		

Tuesday, April 27, 2021 | Room C (Ara Hall, 8F)

Session 2C: Space and Hot Water Heat Pumps

Session Chair: Michele Mondot (CETIAT, France)

14:40~15:00	Keynote	[079]	Design of a Grey Water Heat Recovery System in Order to Satisfy the Domestic Hot Water Demand of a Block of Dwellings Emilio Navarro-Peris (Universidad Politecnica de Valencia) † , Estefania Hervas-Blasco (Universitat Politecnica de Valencia), Jose Miguel Corberan (Universitat Politecnica de Valencia), Ximo Masip (Universitat Politecnica de Valencia)
15:00~15:15		[059]	Field Performance of Domestic Heat Pumps for Heating and Hot Water in Switzerland Cordin Arpagaus (NTB University of Applied Sciences and Technology Buchs), Ralph Kuster (NTB University of Applied Sciences and Technology Buchs) † , Manuel Prinzing (NTB University of Applied Sciences and Technology Buchs), Matthias Berthold (NTB University of Applied Sciences and Technology Buchs), Mick Eschmann (NTB University of Applied Sciences and Technology Buchs), Stefan Bertsch (NTB University of Applied Sciences and Technology Buchs)
15:15~15:30		[255]	Air-to-water Heat Pumps as a Substitution of Oil-boiler in a Non-retrofitted Multi-family Building of the 70's. In-situ Monitoring, Actual Energy Balance and Performance Omar Montero Dominguez (University of Geneva), Carolina De Sousa Fraga (University of Geneva), Pierre Hollmuller (University of Geneva), Simon Callegari (University of Geneva) †
15:30~15:45		[273]	CO2 Emission Savings of Heat-pumps in the Residential Sector. Case Study for Multifamily Buildings in Geneva Elliot Romano (University of Geneva) † , Carolina Fraga (University of Geneva), Pierre Hollmuller (University of Geneva)
15:45~16:00		[270]	Which Performance Indicators Should We Provide to Policy Makers to Switch from Gas Boilers to Air to Water Heat Pumps? Carolina Fraga (Services Industriels de Geneve) † , Alisa Freyre (Services Industriels de Geneve), Pierre Hollmuller (Université de Genève), Rodrigo De Pablo (Services Industriels de Geneve), Matthias Rüetschi (Services Industriels de Geneve)
16:00~16:10	Break		

Tuesday, April 27, 2021 | Room C (Ara Hall, 8F)

Session 3C: New Heat Pump Technologies

Session Chair: Maurizio Pieve (ENEA. Italy)

16:10~16:30	Keynote	[100]	Test Results of a Rotation Heat Pump and Further Developments Bernhard Adler (ecop Technologies GmbH), Andreas Längauer (ecop Technologies GmbH) † , Christian Rakusch, (ecop Technologies GmbH)
16:30~16:45		[272]	High Efficiency Low Temperature Lift Heat Pump with Novel Oil-free, Gas-bearing Turbo Compressor Dominic Zajonc (Lucerne University of Applied Sciences and Arts) † , Stefan Flück (Lucerne University of Applied Sciences and Arts), Edward J. Lucas (Lucerne University of Applied Sciences and Arts), Andreas Lehr (Teqtoniq GmbH), Beat Wellig (Lucerne University of Applied Sciences and Arts)
16:45~17:00		[229]	Experimental Investigation of a Rolling Piston Compressor Operated with a Hydrocarbon Refrigerant Mixture Melanie Cop (Technische Universität Dresden) † , Ramona Nosbers (Technische Universität Dresden), Christiane Thomas (Technische Universität Dresden), Ullrich Hesse (Technische Universität Dresden)

17:00~17:15	[163]	Research and Development for 200°C Compressed Water Heat Pump using Exhaust Heat with Low GWP Refrigerant for Industrial Use Ryosuke Suemitsu (Mitsubushi Heavy Industries Thermal Systems, Ltd) † , Masanobu Sakai (Mitsubushi Heavy Industries Thermal Systems, Ltd), Yoshie Togano (Mitsubushi Heavy Industries Thermal Systems, Ltd), Naoki Kobayashi (Mitsubishi Heavy Industries, Ltd), Hiroyuki Yuki (Mitsubushi Heavy Industries Thermal Systems, Ltd), Yasushi Hasegawa (Mitsubushi Heavy Industries Thermal Systems, Ltd), Kazuki Wajima (Mitsubushi Heavy Industries Thermal Systems, Ltd), Kenji Ueda (MHI Bingshan Refrigeration (Dalian) Co., Ltd.)
17:15~17:30	[239]	Lubrication Management of a Reversible Compressor-expander-unit in a Combined HP-ORC-plant Daniel Steger (Institute of Process Machinery and Systems Engineering, Friedrich-Alexander-Universität Erlangen-Nürnberg (FAU)) † , Markus Zwiefler (Institute of Process Machinery and Systems Engineering, Friedrich-Alexander-Universität Erlangen-Nürnberg (FAU)), Eberhard Schlücker (Institute of Process Machinery and Systems Engineering, Friedrich-Alexander-Universität Erlangen-Nürnberg (FAU))

ORAL SESSION

WEDNESDAY, APRIL 28, 2021

※ THE LIVE STREAM SCHEDULE IS BASED ON KOREA STANDARD TIME (KST / UTC +9).

Room A (Tamna Hall)

Wednesday, April 28, 2021 | Room A (Tamna Hall, 8F)

Session 4A: Low GWP Refrigerants (3)

Session Chair: Yunho Hwang (University of Maryland, United States)

09:00~09:20	Keynote	[230]	Residential Split Heat Pump Using Low GWP Refrigerants Bo Shen (Oak Ridge National Lab) † , Moonis Ally (Oak Ridge National Lab)
09:20~09:35		[055]	A3 Refrigerant R290 Leak and Ignition Testing for a Packaged Terminal Air-conditioner (PTAC) Xudong Wang (Air-Conditioning, Heating and Refrigeration Institute) † , George Hunter (UL LLC)
09:35~09:50		[017]	Solid State (Metal Hydride) Refrigerant Based Air Conditioner and Freezer Systems Bamdad Bahar (Xergy Inc.) † , William TomHon (Xergy Inc.), Matt Golben (Xergy Inc.), Jacob Zerby (Xergy Inc.), Mark Golben (Xergy Inc.)
09:50~10:05		[204]	Alternate Refrigerants for Heat Pump Water Heater Applications Kashif Nawaz (Oak Ridge National Laboratory) † , Bo Shen (Oak Ridge National Laboratory), Van Baxter (Oak Ridge National Laboratory), Omar Abdelaziz (Oak Ridge National Laboratory)
10:05~10:20		[111]	Performance Evaluation of Light Commercial Air Conditioning and Heat Pump System Using Low GWP Refrigerants Joshua Hughes (The Chemours Company) † , Minsoo Kim (Air Solution Laboratory, LG Electronics)
10:20~10:40			Coffee Break and Poster Session

Wednesday, April 28, 2021 | Room A (Tamna Hall, 8F)

Session 5A: Low GWP Refrigerants (4)

Session Chair: Hideaki Maeyama (Heat pump & Thermal Storage Technology Center of Japan, Japan)

10:40~11:00	Keynote	[213]	Disproportionation Risk Study for HFO-1123 Compositions as Low-GWP Refrigerants Hidekazu Okamoto (AGC Inc.) † , Hiroki Hayamizu (AGC Inc.), Tetsuo Otsuka (AGC Inc.), Katsuya Ueno (AGC Inc.)
11:00~11:15		[139]	Modeling of Megawatt R1233zd (E) High Temperature Heat Pump System Bin Hu (Shanghai Jiao Tong University) † , R.Z. Wang (Shanghai Jiao Tong University), Hua Liu (Gree Electric Appliances), Zhiping Zhang (GREE Electric Appliances), Hongbo Li (Gree Electric Appliances)
11:15~11:30		[128]	Study on Layer Short Mechanism and Discharge Pattern in Refrigerant Compressor for Refrigerants with Disproportionation Reaction Like HFO-1123 Hideyuki Fujimoto (Shizuoka University), Mitsuhiro Fukuta (Shizuoka University) † , Masaaki Motozawa (Shizuoka University)

11:30~11:45		[138]	Clarification of the Disproportionation Reaction of HFO-1123 and Evaluation of the Reaction Inhibitor Zhihua Zhang (The University of Tokyo) † , Makoto Ito (The University of Tokyo), Chaobin Dang (The University of Tokyo), Eiji Hihara (The University of Tokyo)
11:45~12:00		[336]	Experimental Investigation of Heat Transfer Coefficient of R1234yf During Condensation Inside Multiport Mini-channel Tube Jong-Taek Oh (Chonnam National University) † , Quang Vu Pham (Electric Power University)
12:00-13:00			Lunch and Poster Session

Wednesday, April 28, 2021 | Room A (Tamna Hall, 8F)

Session 6A: Heat Transfer

Session Chair: Sheng Wang (Gree Electric Appliances, Inc. of Zhuhai, China)

13:00~13:20	Keynote	[022]	Numerical Simulation of Two-phase Flow Distribution in a Vertically Installed Refrigerant Distributor Jihwan Jeong (Pusan National University) † , Siyoung Choi (Pusan National University), Hyoin Lee (Pusan National University)
13:20~13:35		[345]	Experimental Investigation of Local Nucleate Boiling Heat Transfer and Mixing Ratio on Copper Surface about Mixture R 32 / R 1234ze (E) Riku Fukuju (The University of Electro-Communications), Koji Enoki (The University of Electro-Communications) † , Kiyoshi Saito (Waseda University)
13:35~13:50		[279]	Effects of Tube Shape on Boiling Heat Transfer of Low-pressure Refrigerant R1233zd (E) Outside Horizontal Tubes Sho Fukuda (Kyushu Sangyo University) † , Yuki Shimizu (Mitsubishi Heavy Industries Thermal Systems, Ltd.), Naoya Miyoshi (Mitsubishi Heavy Industries Thermal Systems, Ltd.), Yasushi Hasegawa (Mitsubishi Heavy Industries Thermal Systems, Ltd.)
13:50~14:05		[294]	High-resolution Surface Plasmon Resonance Imaging of an Evaporating Droplet on the Surface Chan Ho Jeong (Chung-Ang University), Hyung Joo Lee (Chung-Ang University), Seong Hyuk Lee (Chung-Ang University) †
14:05~14:20		[312]	Lubricant-impregnated Surfaces (LIS) Incorporated with the Oil Supply System for Enhanced Durability and Condensation Heat Transfer Performance Youngsuk Nam (Kyung Hee University) † , Donghyun Seo (Kyung Hee University), Jaehwan Shim (Kyung Hee University), Choongyeop Lee (Kyung Hee University) †
14:20-14:40			Coffee Break and Poster Session

Wednesday, April 28, 2021 | Room A (Tamna Hall, 8F)

Session 7A: Sorption Heat Pumps (2)

Session Chair: Peter Schossig (Fraunhofer ISE, Germany)

14:40~15:00	Keynote	[176]	Trends and Recent R&D Activities on Fuel Driven Sorption Heat Pumps Peter Schossig (Fraunhofer Institute Solar Energy Systems ISE), Gerrit Fueldner (Fraunhofer Institute Solar Energy Systems ISE) † , Angeles Rivero Pacho (University of Warwick), Steven Metcalf (University of Warwick), Kyle Gluesenkamp (ORNL), Zhiyao Yang (ORNL), Andrea Frazzica (CNR-ITAE), Marcello Aprile (Politecnico di Milano), Tommaso Toppi (Politecnico di Milano), Mario Motta (Politecnico di Milano), Robert E. Critoph (University of Warwick), Edo Wiemken (Fraunhofer Institute Solar Energy Systems ISE)
15:00~15:15		[181]	Design of a Gas-driven Hybrid Adsorption Heat Pump Coupled to Geothermal Heat Exchangers for Retrofitting Applications Andrea Frazzica (Consiglio Nazionale delle Ricerche) † , Valeria Palomba (Consiglio Nazionale delle Ricerche), Antonino Bonanno (Consiglio Nazionale delle Ricerche), Davide La Rosa (Consiglio Nazionale delle Ricerche), Stefan Löwe (Fahrenheit GmbH), Ralph Herrmann (Fahrenheit GmbH)
15:15~15:30		[133]	Assessment of Standardized Test and Performance Evaluation Methods for Fuel Driven Sorption Heat Pumps Ivan Malenkovic (Fraunhofer Institute for Solar Thermal Systems (ISE)) † , Patrizia Norina Melograno (Politecnico di Milano) † , Peter Schossig (Fraunhofer Institute for Solar Thermal Systems (ISE))
15:30~15:45		[341]	Dynamic Simulations of an Absorption Refrigeration System for Automobile Application Hai Trieu Phan (French Atomic Energy and Alternative Energy Commission CEA) † , Mathilde Wirtz (French Atomic Energy and Alternative Energy Commission CEA), Julien Hergott (Faurecia Clean Mobility), François Boudehenn (French Atomic Energy and Alternative Energy Commission CEA)
15:45~16:00		[191]	CHP-Waste Heat Utilization with Small-scaled Absorption-Resorption Chillers for Supermarket Refrigeration Oliver Ziegler (Technische Universität Dresden) † , Ullrich Hesse (Technische Universität Dresden), Christiane Thomas (Technische Universität Dresden)
16:00~16:10			Break

Wednesday, April 28, 2021 | Room A (Tamna Hall, 8F)

Session 8A: Ground Source Heat Pumps

Session Chair: Signhild Gehlin (Swedish Geoenergi Center, Sweden)

16:10~16:30	Keynote	[045]	Half-term Results from IEA HPT Annex 52 - Long-term Performance Monitoring of Large GSHP Systems Signhild Gehlin (Swedish Geoenergi Center) † , Jeffrey Spitler (Oklahoma State University)
16:30~16:45		[098]	Ground Source Heat Pump Systems for Energy Efficient Building Retrofitting Michael Lauermann (AIT Austrian Institute of Technology GmbH) † , Johann Emhofer (AIT Austrian Institute of Technology GmbH), Karl sen. Ochsner (Ochsner Wärmepumpen GmbH)
16:45~17:00		[243]	It works! - Long-term Performance Measurement of Ground Source Heat Pump Systems Franziska Bockelmann (Steinbeis-Innovationszentrum (SIZ) Energie+) † , Christian Kley (TU Braunschweig)
17:00~17:15		[351]	Initial Stage of Thermal Response Tests Combined with Transient Numerical Model – a Foundation of Short-term Ground Storage of Cold for Effective Cooling of Office Buildings Kamil Kwiatkowski (Euros Energy), Jakub Garbacik (Euros Energy) † , Tomasz Walczak (Euros Energy)

Room B (Halla Hall)

Wednesday, April 28, 2021 | Room B (Halla Hall, 8F)

Session 4B: Ground Source and Storage

Session Chair: Jeffrey Spitler (Oklahoma State University, United States)

09:00~09:20	Keynote	[056]	A Novel Geothermal Heat Pump System Integrated with Underground Thermal Storage for Shifting Building Electric Demands Xiaobing Liu (Oak Ridge National Laboratory) † , Liang Shi (Purdue University), Ming Qu (Purdue University)
09:20~09:35		[044]	Three Years' Performance Monitoring of a Mixed-use Ground Source Heat Pump System in Stockholm Jeffrey Spitler (Oklahoma State University) † , Signhild Gehlin (Swedish Geonergy Center)
09:35~09:50		[326]	Feasibility of Using Ground Source Heat Pumps in Heating and Cooling of Residential Buildings Seama Koohi-Fayegh (OntarioTech University) †
09:50~10:05		[282]	Performance Analysis of Ground Source Heat Pump System with Vertical Borehole Heat Exchangers Affected by Rapid Groundwater Flow Hobyung Chae (Hokkaido University) † , Katsunori Nagano (Hokkaido University), Yoshitaka Sakata (Hokkaido University), Takao Katsura (Hokkaido University), Takeshi Kondo (Nikken Sekkei Research Institute)
10:05~10:20		[325]	Development of LNG Vaporization Systems Applying Hybrid Ground Source Heat Pumps Combined Ground Heat Exchangers with Air-water Heat Exchangers Takao Katsura (Hokkaido University) † , Yutaka Shoji (Hokkaido University), Hitoshi Akai (Hokkaido University), Katsunori Nagano (Hokkaido University), Jun Shishido (Tohoku Electric Power Co., Inc.), Mitsuhiro Ishikawa (Hokkaido Electric Power Co., Inc.), Yuichi Yashima (Tohoku Electric Power Co., Inc.), Koji Tanifuji (Zeneral Heatpump Industry Co., Ltd.)
10:20~10:40	Coffee Break and Poster Session		

Wednesday, April 28, 2021 | Room B (Halla Hall, 8F)

Session 5B: Market and Policy for Heat Pumps (2)

Session Chair: Tetsushiro Iwatsubo (New Energy and Industorial Technology Development Organaization, Japan)

10:40~11:00	Keynote	[048]	NEDO R&D Project for Innovative Thermal Management Tetsusiro Iwatsubo (New Energy and Industrial Technology Development Organization (NEDO)) † , Yuka Ogasawara (New Energy and Industrial Technology Development Organization (NEDO)), Toshihiko Ota (New Energy and Industrial Technology Development Organization (NEDO)), Masanori Kobayashi (New Energy and Industrial Technology Development Organization (NEDO))
11:00~11:15		[036]	Numerical Investigation on PCM-to-refrigerant Heat Exchangers for Thermal Energy Storage Yunho Hwang (University of Maryland) † , Yiyuan Qiao (University of Maryland), Tao Cao (University of Maryland), Jiazhen Ling (University of Maryland), Vikrant Aute (University of Maryland)
11:15~11:30		[222]	Roadblocks to Heat Pump Use in Residential Buildings with Model Predictive Control for Demand Response and Ancillary Markets and Potential Solutions Ramanunni Parakkal Menon (Concordia University) † , Jessen Page (HES-SO Valais/Wallis), Frederic Amblard (HES-SO Valais/EPFL)

11:30~11:45		[252]	A Techno-Economic Assessment of Air-Source Heat Pumping Technologies in the Canadian Residential Sector Justin Tamasauskas (CanmetENERGY/Natural Resources Canada) † , Stephanie Breton (CanmetENERGY/Natural Resources Canada), Martin Kegel (CanmetENERGY/Natural Resources Canada)
11:45~12:00		[010]	US Heat Pump Market Overview–2020 Melissa Lapsa (Oak Ridge National Laboratory) † , Jaewan Joe (Oak Ridge National Laboratory), Mini Malhotra (Oak Ridge National Laboratory), Van Baxter (Oak Ridge National Laboratory)
12:00-13:00	Lunch and Poster Session		

Wednesday, April 28, 2021 | Room B (Halla Hall, 8F)

Session 6B: Residential Heat Pumps

Session Chair: Carsten Wemhöner (HSR University of Applied Sciences Rapperswil, Switzerland)

13:00~13:20	Keynote	[168]	Evaluation of Solar Heat Source and Sink in Multi-functional Heat Pump Operation Carsten Wemhoener (HSR University of Applied Sciences Rapperswil) † , Lukas Rominger (HSR University of Applied Sciences Rapperswil), Simon Büsser (HSR University of Applied Sciences Rapperswil), Roman Schwarz (HSR University of Applied Sciences Rapperswil)
13:20~13:35		[275]	Heat Pumps in Existing Residential Buildings Marek Miara (Fraunhofer ISE) † , Danny Günther (Fraunhofer ISE), Robert Langner (Fraunhofer ISE)
13:35~13:50		[047]	Effectiveness-based Air Flow Rate Optimization for a Residential Heat Pump in Seasonal Performance Conditions Minsu Park (LG Electronics), Min Soo Kim (Seoul National University) †
13:50~14:05		[093]	Energy Saving Potential of an Air Source Heat Pump Heating System Compared with a Radiant Floor Heating System with Ventilation in an Apartment Building Yu-Jin Hwang (Hanyang University), Yong-Kwon Kang (Hanyang University), Beom-Jun Kim (Hanyang University), Jae-Weon Jeong (Hanyang University) †
14:05~14:20		[127]	A Residential Heat Pump System for Cooling, Heating, Dehumidification and Outdoor Air Supply Xingyu Liang (Tongji University), Chen Yang (Tongji University), Jing Zhang (Tongji University), Xiang Cao (Tongji University), Liangliang Shao (Tongji University), Chunlu Zhang (Tongji University), Chun Yang (Emerson Commercial & Residential Solutions), Xiaoning Chen (Emerson Commercial & Residential Solutions), Hongfei Shu (Emerson Commercial & Residential Solutions) †
14:20-14:40	Coffee Break and Poster Session		

Wednesday, April 28, 2021 | Room B (Halla Hall, 8F)

Session 7B: Heat Pumps in Smart Grids and District Heating and Cooling Systems (1)

Session Chair: Svend Pedersen (Danish Technological Institute, Denmark)

14:40~15:00	Keynote	[308]	Seasonal Thermal Energy Storage for Large Scale District Heating Carlos Infante Ferreira (Delft University of Technology) † , Just Remmelts (Delft University of Technology), Sander Tensen (Eneco Industrial & Heat)
15:00~15:15		[281]	Investigation of Model Predictive Control for Fifth Generation District Heating and Cooling (5GDHC) Substations Simone Buffa (Eurac Research, Free University of Bolzano) † , Anton Soppelsa (Eurac Research), Mauro Pipiciello (Eurac Research), Gregor P. Henze (University of Colorado Boulder), Roberto Fedrizzi (Eurac Research)
15:15~15:30		[309]	Low Temperature District Heating based on Low Temperature Geothermal Heat (30oC) Carlos Infante Ferreira (Delft University of Technology) † , Sebastiaan Knepper (Delft University of Technology), Ivo Pothof (Delft University of Technology), Laure Itard (Delft University of Technology)
15:30~15:45		[253]	Replicable Water Source Heat Pumps for a Zero Carbon Future Nicky Jason Cowan (Star Renwable Energy) †
15:45~16:00		[151]	Electrification of Heat and Decarbonisation of the Electricity System: Sector Coupling is Creating Opportunities for Heat Pumps Cate Lyon (Delta Energy & Environment) † , Lindsay Sugden (Delta Energy & Environment) †
16:00~16:10	Break		

Wednesday, April 28, 2021 | Room B (Halla Hall, 8F)

Session 8B: Heat Pumps in Smart Grids and District Heating and Cooling Systems (2)

Session Chair: Emina Pasic (IEA HPT ExCo Delegate Sweden, Sweden)

16:10~16:30	Keynote	[072]	Impact of the Weather Forecast on a Predictive Controller Performance: Experimental Studies with a Residential Heat Pump for Space Cooling Thibault Péan (IREC, UPC) † , Ivan Bellanco (IREC), Jaume Salom (IREC)
16:30~16:45		[329]	Large Heat Pumps for Decarbonized District Heating Torben Funder-Kristensen (Danfoss A/S) † , Drew Turner (Danfoss A/S), Leping Zhang (Danfoss A/S)
16:45~17:00		[043]	Application of the DevOps Methodology on Heat Pump Controllers Stephan Göbel (RWTH Aachen University), Markus Nürenberg (RWTH Aachen University) † , Philipp Mehrfeld (RWTH Aachen University), Dirk Müller (RWTH Aachen University)
17:00~17:15		[131]	Possibilities and Constraints of Grid Flexible Control of Todays and Tomorrows Heat Pumps Markus Lindahl (RISE Research Institutes of Sweden), Tommy Walfridson (RISE Research Institutes of Sweden) † , Jessica Benson (RISE Research Institutes of Sweden) † , Oskar Räftegård (RISE Research Institutes of Sweden), Ola Gustafsson (RISE Research Institutes of Sweden), Caroline Haglund Stignor (RISE Research Institutes of Sweden)
17:15~17:30		[301]	Control Strategy Assessment of a Small GSHP Sourced DH System with End User DHW Booster Heat Pumps Wim Boydens (Ghent University) † , Sigrid Feyaerts (KU Leuven), Annelies Vandermeulen (KU Leuven/VITO/EnergyVille), Lieve Helsen (KU Leuven/EnergyVille) †

Room C (Ara Hall)

Wednesday, April 28, 2021 | Room C (Ara Hall, 8F)

Session 4C: Sorption Heat Pumps (1)

Session Chair: Reinhard Radermacher (University of Maryland, United States)

09:00~09:20	Keynote	[023]	Membrane-Based Air Dehumidification Using Organic Ionic Liquid Desiccant Bamdad Bahar (Xergy Inc.) † , Harish Opradishta (Xergy Inc.), Mark Stutman (Xergy Inc.), Xiaobing Liu (Oakridge National Laboratory), Jason Woods (National Renewable Energy Laboratory)
09:20~09:35		[206]	Semi-open Absorption Water Heater: Experimental Results Kyle R. Gluesenkamp (Oak Ridge National Laboratory) † , Navin Kumar (Oak Ridge National Laboratory), Ahmad Abu-Heiba (Oak Ridge National Laboratory), Viral K. Patel (Oak Ridge National Laboratory), Zhiyao Yang (Purdue University), Saeed Moghaddam (University of Florida), Rohit Bhagwat (University of Florida), Sidharth Sanadhya (University of Florida), Michael Schmid (University of Florida), Richard Rode (University of Florida), Basil Anabtawi (University of Florida)
09:35~09:50		[016]	Water Transmission Mechanisms in Advanced Ionic Membranes for HVAC Applications Bamdad Bahar (Xergy Inc.) † , David McAndrews (Xergy Inc.), Taoli Gu (Xergy Inc.), Abhishek Bandlore (Xergy Inc.)
09:50~10:05		[201]	Dynamic Modelling and Design Optimization of a Heat-Pipe-Integrated Chemisorption Adsorber Zhiyao Yang (Purdue University), Ming Qu (Purdue University), Kyle Gluesenkamp (Oak Ridge National Lab) †
10:05~10:40	Coffee Break and Poster Session		

Wednesday, April 28, 2021 | Room C (Ara Hall, 8F)

Session 5C: Electrochemical Related

Session Chair: Van D. Baxter (Oak Ridge National Laboratory, United States)

10:40~11:00	Keynote	[021]	An Overview of Hydrogen Compressors for Heat Pump Systems Bamdad Bahar (Xergy Inc.) † , Samuel Dorman (Xergy Inc.), Jacob Zergy (Xergy Inc.), Mark Golben (Xergy Inc.), William Tomhon (Xergy Inc.)
11:00~11:15		[209]	Thermoelectric Heat Pump Performance Characterization Viral K. Patel (Oak Ridge National Laboratory) † , Kyle R. Gluesenkamp (Oak Ridge National Laboratory), Philip Boudreaux (Oak Ridge National Laboratory)
11:15~11:30		[124]	Study on a Combined Absorption Heat Pump System Driven by Low Temperature Heat Source Gabyong Kim (Korea University), Han Sol Jung (Korea University), Yong Tae Kang (Korea University) †
11:30~11:45		[014]	Electrochemical Compression of Ammonia/Hydrogen Blends for Heat Pump Applications Bamdad Bahar (Xergy Inc.) † , Ashish Chouhan (University of Delaware), Ajay Prasad (University of Delaware), Premanand Sivakumar (University of Delaware), Utsav Aryal (University of Delaware)
11:45~12:00		[350]	Experimental Study of PEMFC Conditioning Methods Joohee Song (Chung-Ang University), Minsoo Kim (Chung-Ang University), Dongkyu Kim (Chung-Ang University) †
12:00-13:00	Lunch and Poster Session		

Wednesday, April 28, 2021 | Room C (Ara Hall, 8F)

Session 6C: Heat Exchangers (1)

Session Chair: Masafumi Katsuta (Waseda University, Japan)

13:00~13:20	Keynote	[244]	Study on the Frosting Phenomena between Concavity and Convexity Plate under Forced Convection —The Prediction of Frost Layer Growth using the Observation from the Frost and Defrost Multi-cycle Experiment Masafumi Katsuta (Waseda University) † , Shota Ikutaya (Graduate School of Waseda University), Junya Yamagishi (Graduate School of Waseda University), Rio Asakawa (Graduate School of Waseda University), Yuki Terakado (Graduate School of Waseda University), Sangchul Bae (Waseda University)
13:20~13:35		[335]	Investigation on System Performance of Air Source Heat Pump Water Heater with Phase Change Material Zhanpeng Liu (Tongji University), Naiping Gao (Tongji University) † , Tiantian Wang (Tongji University), Hengyi Zhao (International Copper Association), Yifeng Gao (International Copper Association)
13:35~13:50		[140]	A Study on the Determination Method of Defrosting Start Time by Calculation of Frost Volume Jin Woo Yoo (Korea Institute of Machinery and Materials), Yoong Chung (Seoul National University), Dong Ho Kim (Korea Institute of Machinery and Materials), Seok Ho Yoon (Korea Institute of Machinery and Materials), Chan Ho Song (Korea Institute of Machinery and Materials), Kong Hoon Lee (Korea Institute of Machinery and Materials), Ook Joong Kim (Korea Institute of Machinery and Materials), Min Soo Kim (Seoul National University) †
13:50~14:05		[334]	Experimental Investigation of Condenser with Small Diameter Copper Tube in Air Source Heat Pump Water Heater Tiantian Wang (Tongji University), Naiping Gao (Tongji University) † , Zhanpeng Liu (Tongji University), Tingwei Fan (Gomon New Energy Ltd. of Jiangsu Province), Hengyi Zhao (International Copper Association), Yifeng Gao (International Copper Association)
14:05~14:20		[316]	Condensation Heat Transfer and Pressured Drop Characteristics of R-513A as An Alternative Refrigerant of R-134a Andreas Karageorgis (ElvalHalcor Company), George Hinopoulos (ElvalHalcor Company), Man-Hoe Kim (Kyungpook National University) †
14:20-14:40			Coffee Break and Poster Session

Wednesday, April 28, 2021 | Room C (Ara Hall, 8F)

Session 7C: Industrial Heat Pumps (1)

Session Chair: Rainer Jacobs (IZW e.V., Information Centre on Heat Pumps and Refrigeration, Germany)

14:40~15:00	Keynote	[004]	Environmentally Friendly Steam Generation Using VHTHPs at a Pharmaceutical Research Facility Tor-Martin Tveit (Olvondo Technology AS) † , Martin N. Johansson (AstraZeneca), Ron Zevenhoven (Åbo Akademi University)
15:00~15:15		[103]	Development and Lab-scale Performance Evaluation of a High Temperature Heat Pump for integration into a Power-to-Heat-to-Power System Miguel Ramirez (Tecnalia) † , Felipe Trebilcock Kelly (Tecnalia), Xabier Peña (Tecnalia), Asier Martinez-Urrutia (Tecnalia), Abdelrahman Hassan (Universitat Politècnica de València)
15:15~15:30		[156]	Design and Experimental Results of a Two-Stage Steam Producing Industrial Heat Pump Andrew Marina (TNO) † , Simon Smeding (TNO), Anton Wemmers (TNO), Simon Spoelstra (TNO), Peter Kremers (IBK B.V.)
15:30~15:45		[216]	Experimental Comparison of R1224yd (Z) and R1233zd (E) in a High Temperature Heat Pump Cordin Arpagaus (NTB University of Applied Sciences and Technology Buchs) † , Stefan Bertsch (NTB University of Applied Sciences and Technology Buchs)
15:45~16:00		[306]	Heat Pump Assisted Drying of Flower Bulbs Carlos Infante Ferreira (Delft University of Technology) † , Sjors Wagenaar (Delft University of Technology)
16:00~16:10			Break

Wednesday, April 28, 2021 | Room C (Ara Hall, 8F)

Session 8C: High Temperature Heat Pumps

Session Chair: Benjamin Zühlsdorf (Danish Technological Institute, Denmark)

16:10~16:30	Keynote	[104]	Experimental Analysis of a High Temperature Heat Pump Using Stored Heat from a Solar Thermal System Miguel Ramirez Stefanou (Tecnalia) † , Neil J. Hewitt (Ulster University), Asier Martinez-Urrutia (Tecnalia), Nikhilkumar Shah (Ulster University)
16:30~16:45		[062]	Theoretical Investigation of High-temperature Heat Pump Cycles for Steam Generation Cordin Arpagaus (NTB University of Applied Sciences and Technology Buchs), Frédéric Bless (NTB University of Applied Sciences and Technology Buchs) † , Stefan Bertsch (NTB University of Applied Sciences and Technology Buchs)
16:45~17:00		[075]	High Temperature Heat Pumps for Drying – First Results of Operation in Industrial Environment Veronika Wilk (AIT Austrian Institute of Technology GmbH) † , Franz Helminger (AIT Austrian Institute of Technology GmbH), Michael Lauermann (AIT Austrian Institute of Technology GmbH), Bernd Windholz (AIT Austrian Institute of Technology GmbH), Andreas Sporr (AIT Austrian Institute of Technology GmbH)
17:00~17:15		[340]	Part Load Capability of a High Temperature Heat Pump with Reversed Brayton Cycle Johannes Oehler (German Aerospace Center (DLR)) † , Jens Gollasch (German Aerospace Center (DLR)), A. Phong Tran (German Aerospace Center (DLR)), Eberhard Nicke (German Aerospace Center (DLR))
17:15~17:30		[097]	Analysis of a Steam Generating High Temperature Heat Pump for Industrial Waste Heat Recovery Sabrina Dusek (Austrian Institute of Technology GmbH) † , Michael Lauermann (Austrian Institute of Technology GmbH), Franz Helminger (Austrian Institute of Technology GmbH), Veronika Wilk (Austrian Institute of Technology GmbH)

ORAL SESSION

THURSDAY, APRIL 29, 2021

※ THE LIVE STREAM SCHEDULE IS BASED ON KOREA STANDARD TIME (KST / UTC +9).

Room A (Tamna Hall)

Thursday, April 29, 2021 | Room A (Tamna Hall, 8F)

Session 9A: Variable Refrigerant Flow Heat Pumps and Air-conditioners

Session Chair: Sophie Hosatte (Natural Resources Canada – CanmetENERGY, Canada)

09:00~09:20	Keynote	[210]	Impact of Variable Speed Components on the Seasonal Performance of a Residential Air-Source Heat Pump Fatih Meral (Purdue University, Ray W. Herrick Laboratories) † , Oliver Obst (Purdue University, Ray W. Herrick Laboratories), Eckhard Groll (Purdue University, Ray W. Herrick Laboratories), Nicholas P. Salts (Purdue University, Ray W. Herrick Laboratories)
09:20~09:35		[112]	A Parameter-estimation Model for Variable Refrigerant Flow Heat Pump Systems Aziz Mbaye (Polytechnique Montréal) † , Massimo Cimmino (Polytechnique Montréal)
09:35~09:50		[196]	Investigation of VRF System under Cooling Mode through Field Testing and Machine Learning-based Modeling Hanlong Wan (University of Maryland), Tao Cao (University of Maryland), Yunho Hwang (University of Maryland) † , Heunghee Bae (LG Electronics), Saikee Oh (LG Electronics)
09:50~10:05		[082]	Experimental and Mechanistic Numerical Analysis of a Variable Speed Residential Heat Pump Unit with an Expansion Work-Recovery Device Riley B. Barta (Purdue University, Ray W. Herrick Labs) † , Ammar M. Bahman (Purdue University, Kuwait University), Lennart Stania (Purdue University, Ray W. Herrick Labs), Davide Ziviani (Purdue University, Ray W. Herrick Labs), Eckhard A. Groll (Purdue University, Ray W. Herrick Labs)
10:05~10:20		[283]	Next-Generation Residential Space Conditioning System in the United States Ammi Amarnath (Electric Power Research Institute) † , Sara Beaini (Electric Power Research Institute), Aaron Tam (Electric Power Research Institute), Jerine Ahmed (Southern California Edison Company)
10:20~10:40	Coffee Break and Poster Session		

Thursday, April 29, 2021 | Room A (Tamna Hall, 8F)

Session 10A: Sorption Heat Pumps (3)

Session Chair: Brian Fricke (Oak Ridge National Laboratory, United States)

10:40~11:00	Keynote	[086]	Effect of Evaporator and Condenser in the Analysis of Adsorption Chiller Woo Su Lee (Sejong University), Jae Dong Chung (Sejong University) † , Moon Yong Park (Sejong University), Xuan Quang Duong (Sejong University), Ngoc Vi Cao (Sejong University)
11:00~11:15		[049]	Experimental Study on an Absorption Heat Pump Prototype Applied for Rural Residential Heating Ding Lu (Technical Institute of Physics and Chemistry, Chinese Academy of Sciences), Maoqiong Gong (Technical Institute of Physics and Chemistry, Chinese Academy of Sciences) † , Yin Bai (Technical Institute of Physics and Chemistry, Chinese Academy of Sciences), Yanxing Zhao (Technical Institute of Physics and Chemistry, Chinese Academy of Sciences), Xueqiang Dong (Technical Institute of Physics and Chemistry, Chinese Academy of Sciences)
11:15~11:30		[095]	Energy Performance Comparison of Two Different Types of Heat Pump-driven Liquid Desiccant-assisted Air-Conditioning Systems for an Apartment Building Jae-Hee Lee (Hanyang University), Hansol Lim (Hanyang University), Hye-Won Dong (Hanyang University), Jae-Weon Jeong (Hanyang University) †
11:30~11:45		[118]	Experimental Investigation on the Influence of Bubble Pump on the DAR Performance Hyung Won Choi (Korea University), Gawon Lee (Korea University), Jang Seok Lee (LG Electronics Inc.), Byung Ha Kang (Kookmin University), Yong Tae Kang (Korea University) †
11:45~12:00		[094]	Energy Benefits of Ventilation, Dehumidification, and Water Heating System Based on Liquid Desiccant Cycle Soo-Jin Lee (Hanyang University), Hansol Lim (Hanyang University), Yong-Kwon Kang (Hanyang University), Jae-Weon Jeong (Hanyang University) †
12:00-13:00	Lunch and Poster Session		

Thursday, April 29, 2021 | Room A (Tamna Hall, 8F)

Session 11A: Industrial Heat Pumps (2)

Session Chair: Jun Young Choi (Korea Testing Laboratory, Korea)

13:00~13:20	Keynote	[322]	Categorization of Industrial Heat Pump for Integrated Simulation Technology Jongsoo Jeong (Waseda University), Akihiro Ichikawa (Waseda University), Yoichi Miyaoka (Waseda University) † , Takaoki Suzuki (Waseda University), Seiichi Yamaguchi (Waseda University), Kiyoshi Saito (Waseda University)
13:20~13:35		[232]	Experimental Setup and Test of a Desalination System Using a Heat Pump Soo Kwang Yang (Pusan National University), Hae Eun Song (Pusan National University), Young Chull Ahn (Pusan National University) †
13:35~13:50		[342]	Experimental Investigation of Parameters Affecting Drying Time and Power Consumption of a Heat Pump Tumble Dryer Mehdi Rasti (Pusan National University), Su-Il Park (LG Electronics), Geun-Hyung Lee (LG Electronics), Ji Hwan Jeong (Pusan National University) †
13:50~14:05		[241]	Method for a Quick Economic Assessment of Vapor Compression Heat Pumps Dominik Seliger (TU Wien) † , Daniel Lange (TU Wien), Veronika Wilk (AIT), Jürgen Fluch (AEE INTEC), Karl Ponweiser (TU Wien)

14:05~14:20		[271]	Heat Pump and Thermal Energy Storage Integration in Non-continuous Processes – An Application to the Food Industry Raphael Agner (Lucerne University of Applied Sciences and Arts), Edward J. Lucas (Lucerne University of Applied Sciences and Arts) † , Lorenz P. Rast (Lucerne University of Applied Sciences and Arts), Jan A. Stampfli (Lucerne University of Applied Sciences and Arts), Beat Wellig (Lucerne University of Applied Sciences and Arts)
14:20-14:40	Coffee Break and Poster Session		

Thursday, April 29, 2021 | Room A (Tamna Hall, 8F)

Session 12A: Heat Pumps combined with Thermal Energy Storage and Recovery

Session Chair: Marion Bakker (NL Delegate, Netherlands)

14:40~15:00	Keynote	[178]	Dynamic Performance Tests of a Heat Pump Cycle Integrated Latent Heat Thermal Energy Storage for Optimized DHW Generation Klemens Marx (AIT Austrian Institute of Technology) † , Johann Emhofer (AIT Austrian Institute of Technology), Tilman Barz (AIT Austrian Institute of Technology), Johannes Krämer (AIT Austrian Institute of Technology), Philipp Mascherbauer (AIT Austrian Institute of Technology), Luisa F. Cabeza (Universitat de Lleida), Gabriel Zsembinszki (Universitat de Lleida), Andreas Strehlow (AKG Verwaltungsgesellschaft mbH), Birgo Nitsch (AKG Verwaltungsgesellschaft mbH), Michael Wiesflecker (OCHSNER Wärmepumpen GmbH), Raimund Zitzenbacher (OCHSNER Wärmepumpen GmbH)
15:00~15:15		[307]	Heating System based on Heat Recovery from Sewage Carlos Infante Ferreira (Delft University of Technology) † , Maneesh Avadhani (Delft University of Technology), Roland van Rooyen (Gemeente Rotterdam)
15:15~15:30		[008]	Range of Application of Heat Pumps - Implementation of Heat Pumps with Different Heat Sources Franziska Bockelmann (Steinbeis-Innovationszentrum (SIZ) energie+) † , Markus Peter (Steinbeis-Innovationszentrum (SIZ) energie+), Mathias Schlosser (Steinbeis-Innovationszentrum (SIZ) energie+)
15:30~15:45		[254]	In-situ Analysis of a Centralized Wastewater Heat Pump for a Complex of High Energy Standard Buildings Simon Callegari (University of Geneva) † , Fleury De Oliveira Filho (University of Geneva), Pierre Hollmuller (University of Geneva), Carolina De Sousa Fraga (University of Geneva)
15:45~16:00	Break		

Thursday, April 29, 2021 | Room A (Tamna Hall, 8F)

16:00~17:00 Closing Ceremony

Host: Minsung Kim (Chung-Ang University, South Korea)

- Opening Speech (Per Jonasson, IOC Chair, Sweden)
- Award Ceremony (Per Jonasson, IOC Chair, Sweden)
  - Ritter von Rittinger Award
  - Global Student Video Competition
- Conference Report & Closing Speech (Minsung Kim, Secretary General, Korea)
- The 14th IEA Heat Pump Conference (HPC 2023) (Brian A. Fricke, Chair of U.S. National Organizing Committee, U.S.)
- Closing Remarks(Minsung Kim, Secretary General, Korea)

Room B (Halla Hall)

Thursday, April 29, 2021 | Room B (Halla Hall, 8F)

Session 9B: Heat Exchangers (2)

Session Chair: Ed Vineyard (U.S. Department of Energy, United States)

09:00~09:20	Keynote	[109]	Refrigerant Circuitry Optimization of Heat Exchangers for Charge Reduction and Robust Performance in Reversible Heat Pump Application Vikrant Aute (University of Maryland) † , Zhenning Li (University of Maryland), Jiazhen Ling (University of Maryland)
09:20~09:35		[332]	Proof-of-Concept Testing of Adhesive Joints for HVAC&R Applications Haotian Liu (Purdue University) † , Patrick J. Geoghegan (Oak Ridge National Laboratory), Justin A. Weibel (Purdue University), Davide Ziviani (Purdue University), Eckhard A. Groll (Purdue University)
09:35~09:50		[344]	Effect of Shape Change in the Flow Dirction of Mini-channel on the Flow Patterns Haruki Mitarai (The University of Electro-Communications), Tetsuya Kobayashi (The University of Electro-Communications), Koji Enoki (The University of Electro-Communications) † , Kousaku Nishida (MAYEKAWA MFG. Co. Ltd), Ikurou Akada (MAYEKAWA MFG. Co. Ltd)
09:50~10:05		[314]	Refrigerant Circuitry Optimization of an Outdoor Unit Heat Exchanger based on Partial Load Operating Conditions Shehryar Ishaque (Kyungpook National University), Man-Hoe Kim (Kyungpook National University) †
10:05~10:20		[110]	A Dynamic Model for Microchannel Heat Exchanger under Frost Conditions Jiazhen Ling (University of Maryland) † , Lingzhe Wang (University of Maryland), Rohit Dhumane (Modine Manufacturing Company), Vikrant Aute (University of Maryland)
10:20~10:40	Coffee Break and Poster Session		

Thursday, April 29, 2021 | Room B (Halla Hall, 8F)

Session 10B: Dehumidification Technology

Session Chair: Bamdad Bahar (Xergy Inc., United States)

10:40~11:00	Keynote	[003]	Comparison on Vacuum Membrane Dehumidification Systems with Moisture Selective Dense Membrane Hyunjeong Lim (Hyundai Motor Co.), Jinwook Lee(Chung-Ang University), Donik Ku (Chung-Ang University), Sangmi Choi (LG Electronics Inc.), Soyeon Kim (Chung-Ang University), Minkyu Jung (Chung-Ang University), Jihun Lim (Chung-Ang University), Minsung Kim (Chung-Ang University) †
11:00~11:15		[026]	Active Humidity Control for Refrigeration Applications Bamdad Bahar (Xergy Inc.) † , Jacob Zerby (Xergy Inc.)
11:15~11:30		[090]	Theoretical Analysis of Mass Transfer in a Vacuum Membrane Dehumidification System Hye-Jin Cho (Hanyang University), Seong-Yong Cheon (Hanyang University), Su Liu (Hanyang University), Jae-Weon Jeong (Hanyang University) †
11:30~11:45		[091]	Empirical Analysis of Dehumidification Performance of a Hollow-Fiber-Membrane Dehumidifier Seong-Yong Cheon (Hanyang University), Jae-Weon Jeong (Hanyang University) † , Hye-Jin Cho (Hanyang University), Jinyoung Ko (Hanyang University)
11:45~12:00		[054]	Membrane based Pervaporation for Heating and Cooling Bamdad Bahar (Xergy Inc.) † , Harish Opradishta (Xergy Inc.), Mark Stutman (Xergy Inc.), William Tomhon (Xergy Inc.)
12:00-13:00	Lunch and Poster Session		

Thursday, April 29, 2021 | Room B (Halla Hall, 8F)

Session 11B: Heat Pumps in HVAC Systems

Session Chair: Ji Hwan Jeong (Pusan National University, South Korea)

13:00~13:20	Keynote	[092]	Working Fluid Selection of Organic Rankine Cycle for a Liquid Desiccant System Hye-Won Dong (Hanyang University), Beom-Jun Kim (Hanyang University), Li-Hua Lin (Hanyang University), Jae-Weon Jeong (Hanyang University) †
13:20~13:35		[071]	Experimental Investigations of Two Types of the Dual-loop Heat Pump Systems for Ventilation Heat Recovery Lei Wang (Beijing University of Technology), Guoyuan Ma (Beijing University of Technology) † , Anna Ma (Beijing University of Technology), Xiaoya Jia (Beijing University of Technology), Yu Liu (Beijing University of Technology), Feng Zhou (Beijing University of Technology)
13:35~13:50		[175]	Analysis of the Impact of Different HVAC Configurations and Control Strategies on Primary Energy and Cost Savings for an Office Building Mara Magni (Universität Innsbruck) † , Fabian Ochs (Universität Innsbruck)
13:50~14:05		[145]	Fundamental Study on a Green Roof Building Air-conditioning System – Experimental Analysis of Summer Mode using a Reduction Model Apparatus Tzu Wei Yeh (Kokushikan University) † , Toshio Otaka (Kokushikan University) †
14:05~14:20		[224]	Single Source "Solar Thermal" Heat Pump for Residential Heat Supply: Performance with an Array of Unglazed PVT Collectors Korbinian Kramer (Fraunhofer ISE), Christian Schmidt (Fraunhofer ISE), Arim Schäfer (Fraunhofer ISE) †
14:20-14:40	Coffee Break and Poster Session		

Thursday, April 29, 2021 | Room B (Halla Hall, 8F)

Session 12B: Nearly Zero Energy Buildings

Session Chair: Stephan Renz (Beratung Renz Consulting, Switzerland)

14:40~15:00	Keynote	[167]	Cost Optimized Design of Ground Probe Fields with Solar Regeneration Carsten Wemhoener (HSR University of Applied Sciences Rapperswil), Simon Buesser (HSR University of Applied Sciences Rapperswil), Lukas Rominger (HSR University of Applied Sciences Rapperswil)
15:00~15:15		[066]	Control Optimization of a Double Stage Heat Pump with Desuperheater in Multi-family NZEBs Fabian Ochs (University of Innsbruck) † , Nicola Franzoi (University of Innsbruck), William Monteleone (University of Innsbruck), Georgios Dermentzis (University of Innsbruck)
15:15~15:30		[042]	Control Strategies for Modulating Heat Pumps in a Plus Energy Building Christina Betzold (Technische Hochschule Nuernberg Georg Simon Ohm) † , Susanna Bordin (Technische Hochschule Nuernberg Georg Simon Ohm), Arno Dentel (Technische Hochschule Nuernberg Georg Simon Ohm), Gunnar Harhausen (Technische Hochschule Nuernberg Georg Simon Ohm)
15:30~15:45		[165]	Energy Flexibility of Capacity-controlled Air-source Heat Pumps using Rule-based Control in Residential nZEB Carsten Wemhoener (HSR University of Applied Sciences Rapperswil) † , Lukas Rominger (HSR University of Applied Sciences Rapperswil), John Clauß (Norwegian University of Science and Technology, SINTEF Community), Laurent Georges (Norwegian University of Science and Technology)
15:45~16:00	Break		

Thursday, April 29, 2021 | Room A (Tamna Hall, 8F)

16:00~17:00	**Closing Ceremony**	Host: Minsung Kim (Chung-Ang University, South Korea)

Room C (Ara Hall)

Thursday, April 29, 2021 | Room C (Ara Hall, 8F)

Session 9C: Food Storage and Display

Session Chair: Eckhard Groll (Purdue University, United States)

09:00~09:20	Keynote	[122]	Risk Assessment of Built-in Refrigerated Display Cabinet Using A3 Refrigerant Koji Yamashita (the Japan Refrigeration and Air Conditioning Industry Association) †, Yoshihisa Sakamoto (the Japan Refrigeration and Air Conditioning Industry Association), Toshimasa Kato (the Japan Refrigeration and Air Conditioning Industry Association), Shigeki Ishihara (the Japan Refrigeration and Air Conditioning Industry Association), Akira Kobayashi (the Japan Refrigeration and Air Conditioning Industry Association), Hidekazu Kainuma (the Japan Refrigeration and Air Conditioning Industry Association), Takaharu Hasegawa (the Japan Refrigeration and Air Conditioning Industry Association), Katsuyuki Osawa (the Japan Refrigeration and Air Conditioning Industry Association), Hiroshi Nagai (the Japan Refrigeration and Air Conditioning Industry Association), Keiko Hosaka (the Japan Refrigeration and Air Conditioning Industry Association)
09:20~09:35		[250]	Performance Evaluation by Simulation of Refrigerated Display Cabinets Using HFO Refrigerant Koichi Kitamura (Waseda University), Yoichi Miyaoka (Waseda University) †, Takaoki Suzuki (Waseda University), Kosuke Bizen (Waseda University), Seiichi Yamaguchi (Waseda University), Kiyoshi Saito (Waseda University), Tadao Watanabe (Fuji Electric), Takahiro Iwasaki (Fuji Electric), Koji Takiguchi (Fuji Electric)
09:35~09:50		[286]	Evaluation of Interaction between Load of Refrigerated Display Cases and Air Conditioners in a Grocery Store Using CFD Chenghao Wei (Yokohama National University) †, Miwako Fujita (Chubu Electric Power, Co., Inc.), Daisuke Narumi (Yokohama National University)
09:50~10:05		[025]	Electrochemical Inerting (Oxygen Control) for Food Preservation Bamdad Bahar (Xergy Inc.) †, Jacob Zerby (Xergy Inc.)
10:05~10:20		[027]	Pervaporation Membrane for Refrigerator Vegetable Tray Applications Bamdad Bahar (Xergy Inc.) †, Jacob Zerby (Xergy Inc.), Anderson Bortoletto (Sub-zero Group Inc.)
10:20~10:40			Coffee Break and Poster Session

Thursday, April 29, 2021 | Room C (Ara Hall, 8F)

Session 10C: Heat Pump Performance

Session Chair: Guoyuan Ma (Beijing University of Technology, China)

10:40~11:00	Keynote	[130]	Energy Performance Estimation and Verification of an Industrial Waste Heat Recovery Heat Pump Toshihiko Okuno (Science Inc.), Takashi Kuwabara (Science Inc.), Jun Shishido (Tohoku Electric Power Co., Inc.), Katsumi Hashimoto (Central Research Institute of Electric Power Industry) † , Akira Koyama (Science Inc.)
11:00~11:15		[346]	Load-based Testing Methodology for Evaluating Advanced Heat Pump Control Design Parveen Dhillon (Ray W. Herrick Laboratories, Purdue University) † , W. Travis Horton (Ray W. Herrick Laboratories, Purdue University), James E. Braun (Ray W. Herrick Laboratories, Purdue University)
11:15~11:30		[123]	Economical and Environmental Data Analysis of Hybrid HVAC System of Air Source Heat Pump and Natural Gas Furnace for Cold Climate – Canada Gulsun Demirezen (Ryerson University) † , Khalid Ullah (Ryerson University), Amirali Rokn (Ryerson University), Alan S. Fung (Ryerson University)
11:30~11:45		[102]	Dynamic Modeling and Charge Minimization Study of a Packaged Propane Heat Pump with External Flow Reversal for Cold Climates Tyler Shelly (Purdue University), Davide Ziviani (Purdue University) † , Riley Barta (Purdue University), Eckhard Groll (Purdue University)
11:45~12:00		[101]	An Air-water Dual-source Heat Pump System for Shrimp Ponds Jia-Hao Cheng (Tongji University), Peng Gao (Tongji University), Xiang Cao (Tongji University), Peng Shao (Tongji University), Liang-Liang Shao (Tongji University), Chun-Lu Zhang (Tongji University) †
12:00-13:00	Lunch and Poster Session		

Thursday, April 29, 2021 | Room C (Ara Hall, 8F)

Session 11C: Advanced Controls and Modelling

Session Chair: Veronika Wilks (AIT Austrian Institute of Technology GmbH, Austria)

13:00~13:20	Keynote	[096]	Deep Learning-based Refrigerant Charge Fault Detection Method of Air-source Heat Pump System Yong Hwan Eom (Seoul National University), Sung Bin Hong (Seoul National University), Jin Woo Yoo (KIMM), Min Soo Kim (Seoul National University) †
13:20~13:35		[339]	Energy Saving Pre-cooling Pattern Search of an Inverter Air Conditioner Using a Deep Reinforcement Learning Algorithm Myung Sup Yoon (Korea Testing Laboratory) † , Won Sik Yoon (Korea Testing Laboratory)
13:35~13:50		[236]	Application of a Deep Reinforcement Learning Algorithm in Household Inverter Air-conditioner Temperature Control Myung Sup Yoon (Korea Testing Laboratory) † , Won Sik Yoon (Korea Testing Laboratory), Jong-Seok Lee (Yonsei University)
13:50~14:05		[032]	Optimization of Phase Change Thermal Energy Storage Unit based on a New Thermal Resistance Model Lingkun Liu (Gree Electric Appliances, Inc. of Zhuhai), Xiangfei Liang (Gree Electric Appliances, Inc. of Zhuhai) †
14:05~14:20		[074]	Model Calibration of an Air Source Heat Pump System for Transient Simulations in Modelica Philipp Mehrfeld (RWTH Aachen University, E.ON Energy Research Center, Institute for Energy Efficient Buildings and Indoor Climate) † , Markus Nürenberg (RWTH Aachen University, E.ON Energy Research Center, Institute for Energy Efficient Buildings and Indoor Climate), Dirk Müller (RWTH Aachen University, E.ON Energy Research Center, Institute for Energy Efficient Buildings and Indoor Climate)
14:20-14:40	Coffee Break and Poster Session		

Thursday, April 29, 2021 | Room C (Ara Hall, 8F)

Session 12C: Smart Applications of Heat Pumps

Session Chair: Rolf-Iver Hagemoen,(EHPA, Norway)

14:40~15:00	Keynote	[268]	From Smarties, Ice-cream and Flowers Thomas Nowak (European Heat Pump Association AISBL) † , Eirini Litina (European Heat Pump Association)
15:00~15:15		[203]	Evaluation of a Lab Scale Low Charge Heat Pump Circuit Using Propane Lena Schnabel (Heating and Cooling Technologies), Clemens Dankwerth (Heating and Cooling Technologies) † , Timo Methler (Heating and Cooling Technologies), Simon Braungardt (Heating and Cooling Technologies), Thore Oltersdorf (Heating and Cooling Technologies), Christian Sonner (Heating and Cooling Technologies), Marek Miara (Heating and Cooling Technologies), Peter Schossig (Heating and Cooling Technologies)
15:15~15:30		[183]	Heat Pumps for nZEB in a Nordic Climate – Comparison of Field Data with Predicted Performance and LCC Analysis of Different Heat Pump Heating and Ventilation Systems Caroline Haglund Stignor (RISE Research Institutes of Sweden), Ola Gustafsson (RISE Research Institutes of Sweden), Markus Lindahl (RISE Research Institutes of Sweden), Svein Ruud (RISE Research Institutes of Sweden) †
15:30~15:45		[310]	Performance Analysis of a Vapor Extraction Heat Pump System for District Heating/Cooling Applications Aziz Mbaye (He-Tech Suisse), Malick Kane (University of Applied Sciences and Engineering, HES//SO Fribourg) †
15:45~16:00	Break		

Thursday, April 29, 2021 | Room A (Tamna Hall, 8F)

16:00~17:00 **Closing Ceremony**

Host: Minsung Kim (Chung-Ang University, South Korea)

POSTER SESSION

APRIL 27-29, 2021

Lobby (8F)

Track 1: Residential and Building applications

1 [013] Experimental Research on Air-source Heat Pump Using Heat Pipes as Heat Radiator
Shuxue Xu(Beijing University of Technology) † , Guoyuan Ma(Beijing University of Technology),Yueyue Shao(Beijing University of Technology),Yueyue Wang(Beijing University of Technology)

2 [069] Design of Heat Pump Systems Considering Operation Dynamics
Christian Vering (RWTH Aachen University) † , Christoph Höges (RWTH Aachen University), Markus Nürenberg (RWTH Aachen University), Dirk Müller (RWTH Aachen University)

3 [258] Performance Characteristics of Cascade Multi-Functional Heat Pump in Cooling-Hot Water Mode with Variation in Secondary Fluid Temperature Conditions
Selorm Kwaku Anka (Hanbat National University), Jong Min Choi (Hanbat National University) † , Samuel Boahen (Cape Coast Technical University), Kwesi Mensah (Hanbat National University), Won Hee Kang (Korea University), Min Kyeong Park (Korea University), Kwang Ho Lee (Korea University)

4 [260] Development of a Dynamic Model of a Heat Pump System and Fault Detection
Yechan Yun (Kookmin University), Dongwon Han (Korea University), Young Soo Chang (Kookmin University) †

5 [291] Energy Efficiency Research of an Air-source Heat Pump for Floor Heating System in Winter Test
Chenxi Ni (Hefei University of Technology) † , Haihong Huang (Hefei University of Technology) † , Lei Yang (Hefei University of Technology), Tiejun Wang (Hefei University of Technology)

6 [311] Study on Aging of Heat Pump based on Long-term Assessment
Nobuhiro Takahashi (Japan Facility Solutions, Inc),

7 [162] Heat Pump Integration for nZEB – Results of IEA HPT Annex 49
Carsten Wemhoener (HSR University of Applied Sciences Rapperswil) † , Fabian Ochs (University of Innsbruck), Christina Betzold (TH Nürnberg), Arno Dentel (TH Nürnberg Georg Simon Ohm)

8 [269] Research on Energy Saving Calculation Combining Load of Air Conditioner and Load of Refrigerated Display Case in a Grocery Store
Miwako Fujita (Chubu Electric Power, Co., Inc./Yokohama National University) † , Daisuke Narumi (Yokohama National University)

9 [331] Performance Characteristics of Cascade Multi-Functional Heat Pump in Cooling-Hot Water Mode with Variation in Secondary Fluid Temperature Conditions
Nobuhiro Takahashi (Japan Facility Solutions, Inc), Masashi Momota (Tokyo Denki Univ.) † , Masashiko Kumagai (Japan Facility Solutions, Inc) † , Tadahiko Ibamoto (Tokyo Denki Univ.), Takashi Inoue (Tokyo University of Science)

10 [031] Experimental Investigation on One-time Heating R32 Two-stage Air Source Heat Pump Water Heater
Bo Zheng (Gree Electric Appliances, Inc. of Zhuhai), Xiangfei Liang (Gree Electric Appliances, Inc. of Zhuhai) † , Rong Zhuang (Gree Electric Appliances, Inc. of Zhuhai)

Track 2: Smart Energy Systems and Renewables

11 [039] PVT Geo Coupled Air to Water Heat Pump System Twin Test Cell Experimental Study
Euy-Joon Lee (Korea Institute of Energy Research) † , Kwang-Seob Lee (University of Science and Technology), Eun-Chul Kang (Korea Institute of Energy Research), Yu-Jin Kim (University of Science and Technology), Evgueniy Entchev (CanmetENERGY), Libing Yang (CanmetENERGY)

12 [315] Status on the Electric-thermal Energy Storage Technology and Application of a Supercritical Carbon Dioxide Power Cycle
Junhyun Cho (Korea Institute of Energy Research) † , Chulwoo Roh (Korea Institute of Energy Research), Hyungki Shin (Korea Institute of Energy Research), Gilbong Lee (Korea Institute of Energy Research), Bongsu Choi (Korea Institute of Energy Research), Jongjae Cho (Korea Institute of Energy Research), Beomjoon Lee (Korea Institute of Energy Research), Ho-Sang Ra (Korea Institute of Energy Research), Young-Jin Baik (Korea Institute of Energy Research) †

13 [348] Electrochemical Reaction and Fluid Flow Analysis in PEMWE
Kyu Heon Rho (Chung-Ang University), Dong Kyu Kim (Chung-Ang University) †

14 [285] Research and Analysis on Influence Factors of Accuracy of Geotechnical Thermal Response Test
Lingyan Yang (China Academy of Building Research) † , Jintang Li (China Academy of Building Research), Fu Yijun (China Academy of Building Research), Ma Ning (Shandong Yimeike Energy Conservation Service Co., Ltd), Wei Wei (Shandong Yimeike Energy Conservation Service Co., Ltd), Bian Mengmeng (China Academy of Building Research)

15 [070] Combined Heating and Cooling in District Solutions
Jussi Alpua (Industrial heat pumps and Chillers) † , Martti Kukkola (Industrial Heat Pumps and Chillers)

Track 3: Air-Conditioning & Industry

16 [147] Effect of Evaporating Temperature Rising Operation for Multi-Split type Air-Conditioner on Energy Conservation and Thermal Comfort
Hiroshi Nakayama (Chubu Electric Power co.,Inc.) † , Yuji Naka (Chubu Electric Power co., Inc.), Masaaki Miura (Chubu Electric Power co., Inc.), Hideki Tanaka (Nagoya University)

17 [148] Study on Short Circuit of Airflow in Outdoor Unit of Air Conditioner
Hiroyuki Miyazaki (Chubu Electric Power Co., Inc) † , Tsubasa Ito (Mie University), Hiroshi Nakayama (Chubu Electric Power Co., Inc), Masafumi Hirota (Mie University)

18 [321] An Experimental Study on Thermal Comfort Improvement For Residential Air Conditioner Applying a Wind-Free Technology
Youngju Joo (Samsung Electronics), Jun Hwang (Samsung Electronics) † , Hyeongjoon Seo (Samsung Electronics), Byongguk Lim (Samsung Electronics)

19 [353] Performance Simulation of CO2 Transcritical Cooling System with Mechanical Subcooling Cycle Using Low GWP Refrigerants
Sun-Ik Na (Seoul National University), Gu Hwang Kang (Seoul National University), Min Soo Kim (Seoul National University) †

20 [354] A Study on the Performance of Heat Pump by Mixing Ratio of Isobutane/Propane Mixed Refrigerants
Gu Hwang Kang (Seoul National University), Sun Ik Na (Seoul National University), Min Soo Kim (Seoul National University) †

21 [227] A Study on the Heat Pump System for Removing White Plume of Cooling Tower and Recovering Water Vapor
Chulwoo Roh (Korea Institute of Energy Research) † , Gilbong Lee (Korea Institute of Energy Research), Beom Joon Lee (Korea Institute of Energy Research), Eun Seok Wang (Korea Institute of Energy Research), Young Jin Baik (Korea Institute of Energy Research), Hyungki Shin (Korea Institute of Energy Research), Jong Jae Cho (Korea Institute of Energy Research), Jun Hyun Cho (Korea Institute of Energy Research), Bong Soo Choi (Korea Institute of Energy Research)

22 [248] Analysis of the Mixture Refrigerant R600/R245fa Using in High Temperature Heat Pump
Xlaohui Yu (Hebei University of Technology) † , Chang Xu (Hebei University of Technology)

23	[288]	Analytical Study on for Performance of R134a, R404A, and R744 Refrigeration Truck System Honghyun Cho (Chosun University) † , Yunchan Shin (Chosun University), Yeonghun Kim (Chosun University), Minjun Kim (Chosun University)
24	[347]	Novel Cascade Solution of Ultra-temperature Industrial Heat Pump System with Multiple Functions Xiaoning Chen (Emerson Research and Solutions Center) † , Niansheng Han (Emerson Research and Solutions Center)

Track 4: Working Fluids and Advances

25	[355]	Performance Test of Dense Membrane for Vaccum Membrane Dehumidification System Jinwook Lee (Chung-Ang University), Donik Ku (Chung-Ang University), Sangmi Choi (Chung-Ang University), Sanghun Jeong (Chung-Ang University), Sujin Bae (Chung-Ang University), Minsung Kim (Chung-Ang University) †
26	[349]	Analysis of the Operating Characteristics of Electrochemical Hydrogen Compressors through Parametric Study Minsoo Kim (Chung-Ang University), Minsung Kim (Chung-Ang University), Minkyu Jung (Chung-Ang University), Jungchul Kim (Korea Institute of Machinery&Materials), Dongkyu Kim (Chung-Ang University) †

The 13th IEA
Heat Pump Conference
Mission for the Green World

FULL PAPER

13th IEA Heat Pump Conference
April 26-29, 2021 Jeju, Korea

Comparison on Vacuum Membrane Dehumidification Systems with Moisture Selective Dense Membrane

Hyunjeong Lim[1], Jinwook Lee[2], Sangmi Choi[3], Soyeon Kim[4], Minkyu Jung[4], Jihun Lim[4], Minsung Kim[2,4*]

[1]Hyundai Motor Co., 49 Hyundaiyeonguso-ro Namyang-eup, Hwaseong-si, Gyeonggi-do 18278, Republic of Korea
[2]Department of Energy Systems Engineering, Chung-Ang University, 84 Heukseok-ro Dongjak-gu, Seoul 06974, Republic of Korea
[3]LG Electronics Inc., 84 Wanam-ro Seongsan-gu, Changwon-si, Gyeongsangnam-do 51554, Republic of Korea
[4]Department of Intelligent Energy and Industry, Chung-Ang University, 84 Heukseok-ro Dongjak-gu, Seoul 06974, Republic of Korea

Abstract

Membrane heat pump using vacuum membrane dehumidification (VMD) systems have been investigated recently due to the potential of significant enhancement of energy efficiency. The principal of VMD systems lie in the nature of selective transmission of moisture through dense membrane. The driving force of separation is the vapor pressure gradient between feed and permeate side of a membrane, and the vapor is discharged to the atmosphere through a vacuum compressor. In this paper, performance analysis of three different type of VMD systems – a bypass air mixed type, a water vapor discharge type, and a condenser combined type – are compared to evaluate the performance under same temperature and humidity condition. From the simulation, water vapor discharge VMD shows the best dehumidification COP than others. Further, some conditions like ambient air temperature and relative humidity conditions or minimum vapor pressure difference which are assumed in the basic simulation are varied to simulate in depth. Simulation results are discussed at a practical application point of view.

Keywords: Vacuum membrane dehumidification; Dense membrane; Vacuum compressor; Dehumidification COP;

1. Introduction

These days, cooling demand is rapidly increasing due to global warming and globally increased cooling demand [1]. However, conventional vapor compression cycle which has been widely used for cooling leads acceleration of global warming and ozone depletion because of refrigerants it uses. It is necessary to find new technologies from the different point of traditional ones. Most widely used traditional technology for cooling was vapor compression technology. Vapor compression cycles can supply space cooling to maintain a comfortable environment within buildings. Since it was started to use for artificial active cooling, many researchers tried to improve its efficiency and it contributed greatly to energy savings so far. However, it is not enough to satisfy increasing cooling demand due to the improvement of a standard of living. Heating, ventilation and air conditioning (HVAC) system is regarded as an important technology and it accounts for almost 40% of global energy consumption [2]. Moreover, conventional refrigerants used in vapor compression cycles cause global climate change and the ozone layer depletion when they are released to the atmosphere. Some alternative refrigerants have low global warming potential, but they still have issues of toxicity, low efficiency, flammability or high equipment cost. To approach this problem by the new way, alternative systems are considered to replace classical vapor compression cycle.

According to Building Technologies Office in US Department of Energy, non-traditional technologies were evaluated by energy saving potential, installing and operational cost, complexity and realization possibility, etc [3]. From the report, moisture selective membrane was introduced as a key material to reduce energy

* Corresponding author. Tel.: +82-2-820-5973 ; fax: +2-82-3280-5867.
E-mail address: minsungk@cau.ac.kr.

consumption during cooling and dehumidification. So far, its potential of cooling for residential and commercial buildings in all climate regions was studied but yet to be realized as a commercial system.

As a successive study of the technical progress, this study investigated three types of vacuum membrane dehumidification systems by comparing their dehumidification COP. Simulation results were analyzed and compared under several reference conditions.

2. Description of Vacuum Membrane Dehumidification (VMD) System

A membrane is a selective barrier which is used to separate specific species from a mixture. Two sides of the membrane are referred as the feed side and the permeate side. Depending on existence of pores, a membrane can be classified into porous membrane or dense membrane. Porous membrane consists of physical pores sized from micro- to nanoscale. However, dense membrane consists of nanochannels without physical pores, where only a selected gas can pass through with a theoretical background of a solution-diffusion model [4]. When material of the dense membrane is hydrophilic ions, only water vapor can be separated from the air (Fig. 1). In this case, the vapor pressure difference between both sides of the membrane acts as the driving force [5-7]. Therefore, the water vapor can move to the other side by the water vapor pressure gradient. It means that separation can occur even if the absolute pressure of the feed side is lower than the permeate side.

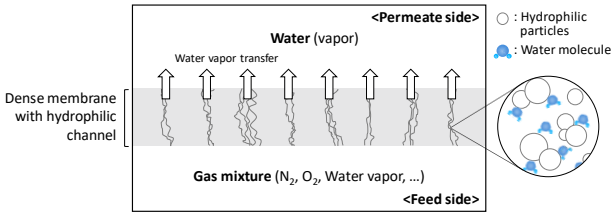


Fig. 1. Structure and vapor separation process of a dense membrane

VMD systems introduced from previous studies consist of a water selective dense membrane and a vacuum compressor [8]. Suction of the vacuum compressor is located at the permeate side of the membrane. Since the vapor pressure at the permeate side is lower than that of humid air, water vapor can be separated through the membrane, and the dehumidified air is supplied to conditioned space. As a simple configuration, direct compression vacuum membrane dehumidification system (D-VMD) is presented in Fig. 2.

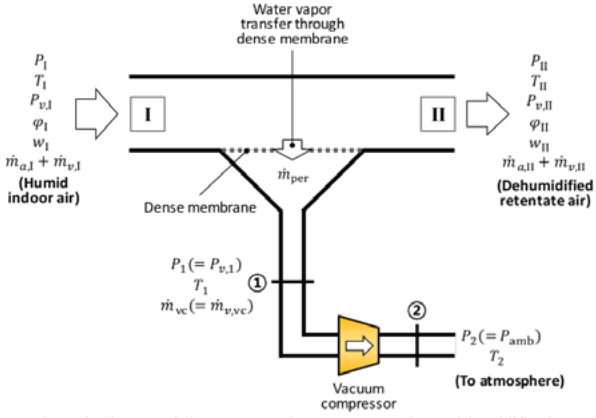


Fig. 2. Schematic diagram of direct compression vacuum membrane dehumidification system

As only water vapor is separated from the humid indoor air by vapor pressure difference, the permeate side pressure of the vacuum compressor inlet can be set below.

$$P_1 = P_{v,II} - \Delta P_{v,min} \quad (1)$$

where $\Delta P_{v,\min}$ is required minimum vapor pressure difference for separation. Since humid air is dehumidified continuously while passing the membrane surface, $\Delta P_{v,\min}$ is obtained based on the exit vapor pressure $P_{v,II}$ where the difference of vapor pressure is the minimized. Thus, $\Delta P_{v,\min}$ can be called pinch point vapor pressure difference which is conceptually the same as pinch point temperature difference in the general heat exchanger.

Since air temperature is kept constant and only absolute humidity (w_I) is decreased during the separation process, the mass flow rate of permeated water vapor can be calculated as below. Assuming that water vapor selectivity of the membrane is infinite, the only water vapor will pass the vacuum compressor.

$$\dot{m}_{vc} = \dot{m}_{per} = (w_I - w_{II})\dot{m}_{a,I} \tag{2}$$

Then the permeated water vapor is compressed to atmospheric pressure (P_{amb}) by the compressor and discharged outwards. However, since vapor pressures ($P_{v,I}$, $P_{v,II}$) are typically very low in a few kilopascals, very high compression ratio (r_{vc}) of 60~100 is required to eject the compressed water vapor, which makes D-VMD system unrealistic. To resolve the high compression ratio issue, several other modified VMD systems like bypass air mixed type, water vapor discharge type, and condenser combined type were proposed.

2.1. Bypass air mixed vacuum membrane dehumidification system (B-VMD)

Figure 3 presents a bypass air mixed VMD (B-VMD) system [9]. As shown in this figure, a portion of dehumidified air is bypassed to the permeate side through a throttling valve.

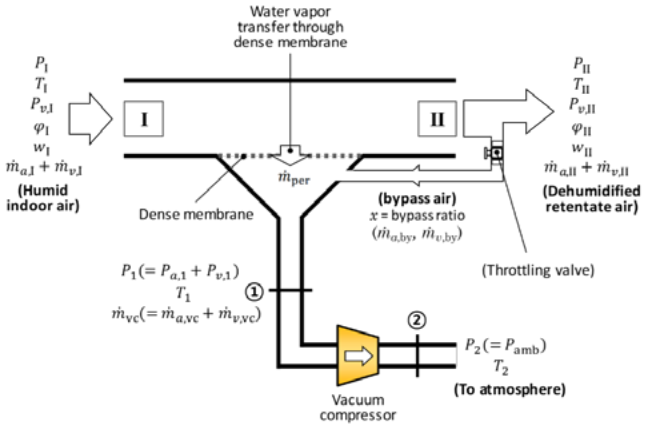


Fig. 3. Schematic diagram of bypass air mixed vacuum membrane dehumidification system

When bypass ratio x is defined by the fraction of bypassed retentate air to the permeate side, the dry air pressure of compressor inlet side ($P_{a,1}$) is multiplication of the bypass ratio and pressure of retentate air ($P_{a,II}$). Therefore, the total pressure of the vacuum compressor inlet side (P_1) becomes higher than the case of D-VMD. Since the vapor pressure of the permeate side is still lower than the feed side like Eq. (1), the vapor can be transferred from the feed side to the permeate side.

$$P_1 = P_{a,1} + P_{v,1} = xP_{a,II} + P_{v,II} - \Delta P_{v,min} \tag{3}$$

When two species are mixed at the same volume, volume flow rates of each material are calculated based on ideal gas law. At the compressor inlet side, the ratio of water vapor volume flow rate to the total flow rate is equal to the ratio of corresponding partial pressure as in Eq. (4).

$$\frac{\dot{V}_{v,1}}{\dot{V}_{a,1}+\dot{V}_{v,1}} = \frac{P_{v,1}}{P_{a,1}+P_{v,1}} \tag{4}$$

By combining Eq. (6) and ideal gas relation, bypass ratio (x) is derived as below.

$$x = \frac{P_{v,II}\dot{n}_{a,II} - P_{a,II}\dot{n}_{per} - \Delta P_{v,min}\dot{n}_{a,II}}{P_{a,II}\dot{n}_{v,II}} \quad (5)$$

Thus, the total mass flow rate through the vacuum compressor is presented as below.

$$\dot{m}_{vc} = \dot{m}_{a,vc} + \dot{m}_{v,vc} = \dot{m}_{a,by} + \dot{m}_{v,by} + \dot{m}_{per} = (x\dot{n}_{a,vc})M_a + (x\dot{n}_{v,vc})M_v + (w_I - w_{II})\dot{m}_{a,I} \quad (6)$$

In B-VMD system, since the mixture of permeated vapor and bypassed air is compressed by the vacuum compressor, compression ratio can be reduced in a reasonable level. However, as the flow rate through the vacuum compressor ($\dot{m}_{vc}$) increases, the vacuum compressor will consume more power.

2.2. Water vapor discharge vacuum membrane dehumidification system (W-VMD)

Figure 8 shows is water vapor discharge VMD (W-VMD) [10]. As seen in the figure, two membrane exchangers are located both at inlet and exit of the vacuum compressor. As in the previous configuration, the water vapor is permeated from the humid air through dense membrane 1. And the vacuum compressor pressurizes the water vapor higher than the vapor pressure of ambient side ($P_{v,III}$, $P_{v,IV}$). Then, the pressurized water vapor passes to the ambient side through dense membrane 2, which enables water vapor separation out of indoor air. As the water vapor is transferred through dense membrane 2, the state IV becomes the highest vapor pressure part of the ambient side. The compressor exit pressure is given as in Eq. (7), where the $P_{v,IV}$ is set slightly higher than $P_{v,III}$ because some permeated water vapor from the vacuum compressor is added to the ambient air stream.

$$P_2 = P_{v,IV} + \Delta P_{v,min} \quad (7)$$

From this concept, compression ratio of the vacuum compressor is lower by 3~5 because water vapor both at the compressor inlet and exit transfers based on partial vapor pressure. Due to the reduced compression ratio, compressor exit temperature is lowered in an acceptable range. Therefore, the flow rate and power consumption is getting much smaller since only water vapor passes the vacuum compressor.

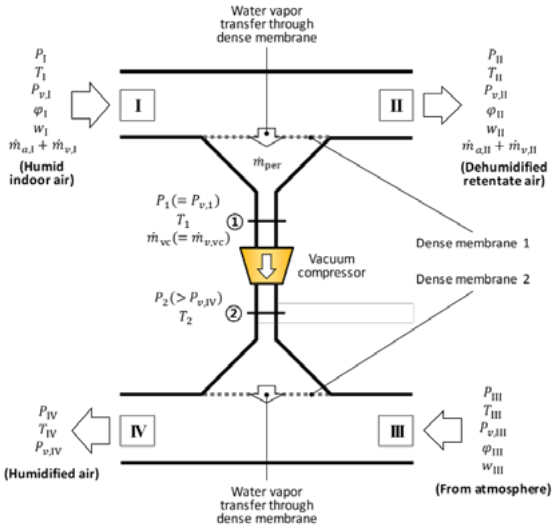


Fig. 4. Schematic diagram of water vapor discharge vacuum membrane dehumidification system

2.3. Condenser combined vacuum membrane dehumidification system (C-VMD)

The modified VMD model is a condenser combined VMD (C-VMD) system which is represented in Fig. 5 [11]. In this system, a condenser cooled by the ambient air is installed at the vacuum compressor exit, where

the compressed water vapor condenses to the liquid state. The condensed water is then rejected to the ambient by a condensed water pump.

In this system, the compressor elevates the vapor pressure to the saturation pressure (P_{cond}) where the condensation temperature (T_{cond}) becomes higher than the ambient air temperature (T_{amb}). Therefore, the compressor exit side pressure is defined as below.

$$P_2 = P_{cond} \tag{8}$$

Since compression ratio is lowered in a practical range for the same reason as the W-VMD system, the C-VMD system can be a potential candidate of the direct VMD systems.

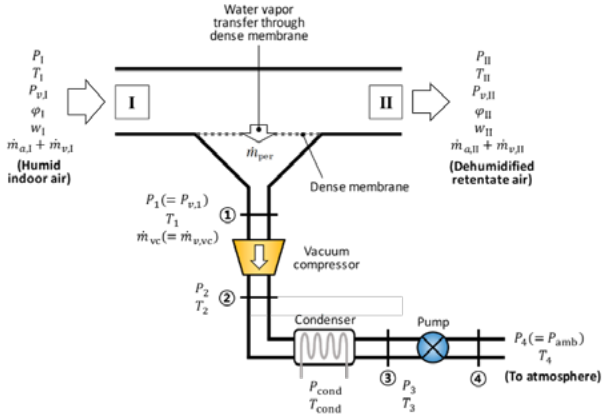


Fig. 5. Schematic diagram of condenser combined vacuum membrane dehumidification system

3. Simulation Methodology

Simulation conditions are set as in Table 1. In the VMD systems, dehumidification process is isothermal so no sensible cooling is considered, where dry bulb temperature of the retentate air and the feed air is the same.

Table 1 Simulation conditions for thermodynamic performance analysis of vacuum membrane dehumidification system

Location	Parameters	Values
Indoor air (Feed air) (I)[1)]	Dry bulb temperature (T_I) [°C]	27
	Relative humidity (φ_I) [%]	46.94
	Absolute humidity (w_I) [kgv/kga]	0.01045
	Mass flow rate ($\dot{m}_I$) [kg/s]	0.05
	Vapor pressure ($P_{v,I}$) [kPa]	1.6749
Retentate air (II)	Dry bulb temperature (T_{II}) [°C]	27
	Relative humidity (φ_{II}) [%]	32.59
	Absolute humidity (w_{II}) [kgv/kga]	0.00722
	Vapor pressure ($P_{v,II}$) [kPa]	1.1632
Ambient air (III)[2)]	Dry bulb temperature (T_{III}) [°C]	27 ~ 39
	Relative humidity (φ_{III}) [%]	40 ~ 90
	Absolute humidity (w_{III}) [kgv/kga]	0.00888 ~ 0.04123
	Vapor pressure ($P_{v,III}$) [kPa]	1.4272 ~ 6.3002
Membrane exchanger	Minimum vapor pressure difference ($\Delta P_{v,min}$) [kPa]	0.2 ~ 1.1
Vacuum compressor/Pump	Isentropic efficiency (η_{pump}, η_{vc}) [-]	0.8
Condenser	Temperature difference (ΔT) [°C]	3 ~ 7

[1)] The condition of indoor air are set based on ISO 5151 standard [12].
[2)] The specific condition of ambient air (35°C, 40.28% RH) is selected from ISO 5151 standard.

From the given total flow rate of feed air, $\dot{m}_I$= 0.05 kg/s, a set of absolute humidity (w) and vapor pressure (P_v) of indoor, retentate, and ambient air are calculated from each dry bulb temperature (T) and relative humidity (φ). The minimum vapor pressure difference ($\Delta P_{v,min}$) between the feed side and the permeate side is varied from 0.2 to 1.1 kPa. Isentropic efficiencies (η) of the compressor and the water pump are set as 0.8. For

the C-VMD model, temperature difference in a condenser (ΔT) is set as 5°C. The permeance of a dense membrane in the VMD systems is referred to σ. The selectivity of air is not considered, which means only water vapor but no air can pass the membrane during the separation. For the simulation, MATLAB software is used for the calculation by combining thermodynamic property database REFPROP 9.0 [13].

To simulate the W-VMD and C-VMD systems, the pressure of membrane permeate side is set equal to P_1 and calculated by Eq. (1) with the assumed minimum vapor pressure difference. Since there is only water vapor at the compressor inlet, it can be said that the total pressure is equal to the vapor pressure ($P_1 = P_{v,1}$). The vacuum compressor exit pressure (P_2) is different for each model. In the B-VMD, the mixture of dry air and water vapor is discharged to the ambient directly, so it is compressed to the atmospheric pressure. On the other hand, the exit pressure of W-VMD is calculated by Eq. (7) based on the vapor pressure of ambient air because there is one more membrane at the compressor exit side. In this case, the vapor pressure difference condition at this additional membrane mass exchanger must be satisfied as well. For C-VMD, P_2 is determined by the condenser temperature which is higher than the ambient air as in Eq. (8). Since the compressed water vapor is condensed by the ambient air, the discharge pressure should be at the saturated pressure of the condenser. Thus, the compression ratio (r_{vc}) of the vacuum compressor in each VMD systems is provided as below.

$$r_{vc} = \frac{P_2}{P_1} = \frac{P_2}{P_{v,II} - \Delta P_{v,min}} \tag{9}$$

Mass flow rates of feed air, retentate air and permeated water vapor are calculated by Eq. (2) and conditions in Table 1. Vacuum compressor mass flow rates for W-VMD and C-VMD are same as that of permeated water vapor, but it is different in B-VMD because the bypassed air is mixed with the permeated water vapor before it enters to the compressor. Therefore, mass flow rate through the vacuum compressor in B-VMD system is determined by Eq. (6). When isentropic efficiency of the vacuum compressor is given by η_{vc}, exit enthalpy is calculated as below.

$$h_2 = \frac{h_{2s} - h_1}{\eta_{vc}} + h_1 \tag{10}$$

From the compressor exit pressure and enthalpy, the exit temperature can be obtained. For the total work of C-VMD, work by the water pump in Eq. (12) is added to that of the vacuum compressor.

$$\dot{W}_{vc} = \dot{m}_{vc}(h_2 - h_1) \tag{11}$$

$$\dot{W}_{pump} = \dot{m}_{vc} \frac{v_{cond}(P_{amb} - P_{cond})}{\eta_{pump}} \tag{12}$$

The latent heat removed by the VMD systems can be calculated as below. For B-VMD system, $\dot{m}_{a,\mathrm{by}} h_{a,\mathrm{II}}$ is subtracted from the Eq. (13) due to feed air reduction by the bypassed air.

$$\dot{Q}_{lh} = (\dot{m}_a h_a + \dot{m}_v h_v)_I - (\dot{m}_a h_a + \dot{m}_v h_v)_{II} \tag{13}$$

COP_{DH} can be calculated by the total work and the total latent heat removed from the humid feed air passing the VMD system as in Eq. (14).

$$COP_{DH} = \frac{\dot{Q}_{total}}{\dot{W}_{total}} = \frac{\dot{Q}_{lh}}{\dot{W}_{vc}} \quad or \quad \frac{\dot{Q}_{lh}}{\dot{W}_{vc} + \dot{W}_{pump}} \tag{14}$$

4. Performance variation by ambient condition

From the above simulation models, the VDM systems are rated from W-VMD, C-VMD, to B-VMD in order of dehumidification performance. In this section, two VMDs of W-VMD and C-VMD which shows applicable performance among the three VMDs are compared as the variation of ambient air condition. For W-VMD, the ambient air is flowing at the permeate side of the membrane 2 at the compressor exit side. The discharged air from the compressor must have higher vapor pressure than that of the permeate side to pass through the membrane. In C-VMD, the vacuum compressor exit pressure (P_2) should be the saturation pressure at the condenser where saturation temperature is set higher by ΔT than ambient temperature. Thus, P_2 is closely related with T_{III}.

Figure 6 shows dehumidification performances simulated under various ambient temperatures. Ambient temperature is changed from 27°C to 39°C under relative humidity (φ_{III}) of 50%, 70%, and 90%. Since compressor exit pressure of the two systems are increased when both temperature and relative humidity increase, the vacuum compressor consumes more work to discharge the permeated vapor to the atmosphere, which results in degradation of COP_{DH}.

Additional simulation of C-VMD is conducted by varying the temperature difference at the condenser (ΔT). When changing the ΔT, the dehumidification performance of C-VMD is also changed because it affects the calculation of saturated vapor pressure. As shown in Fig. 7, when ΔT increases, COP_{DH} is decreased due to the rise of saturated vapor pressure. When we reduce ΔT by 3°C, C-VMD overtakes the performance of W-VMD in some cases of high humid condition in Fig. 7. This is because vacuum compressor exit pressure of W-VMD should be increased due to high vapor pressure of ambient air at the humid conditions. Surely, the larger the condenser size is, the better COP_{DH} becomes by reduced ΔT.

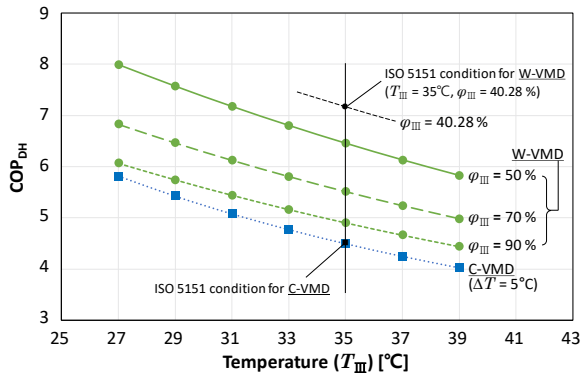


Fig. 6. Simulation results of W-VMD and C-VMD with various ambient temperature (TIII) and relative humidity (φIII) conditions

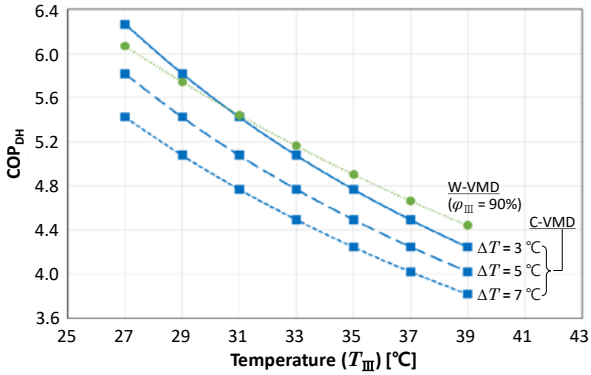


Fig.7. Simulation results of C-VMD with various ambient temperature (TIII) and ΔT conditions

Figure 8 presents a bar chart to compare dehumidification performance of the three VMD systems under selected combinations of ambient temperature and relative humidity. The minimum vapor pressure difference ($\Delta P_{v,min}$), the condenser temperature difference (ΔT), and bypass ratio (x) for B-VMD are fixed as 0.5 kPa, 5°C and 0.1266, respectively. As seen in the chart, the B-VMD system shows the lowest uniform COP_{DH} at all conditions since the performance of B-VMD is affected not by ambient condition but by bypass ratio. COP_{DH} of W-VMD shows a trend to decrease overall as increase of ambient temperature and humidity. As seen in the chart, COP_{DH} shows better performance at low ambient temperature. However, when comparing the humid case (T_{III}=29°C, φ_{III}=90%) and the hot dry condition (T_{III}=35°C, φ_{III}=40.28%), COP_{DH} of W-VMD shows higher value at the hot dry condition due to lower vapor pressure ($P_{v,III}$). Since vacuum compressor work in W-VMD depends on the exit side pressure which is a function of ambient vapor pressure, low ambient vapor pressure

will reduce vacuum compressor work and enhance dehumidification performance. COP_{DH} of C-VMD is continuously decreased as increase of ambient temperature because high ambient temperature requires high condenser temperature. But the performance of C-VMD is only a function of ambient temperature, and not influenced by ambient humidity. The difference between COP_{DH} of W-VMD and C-VMD is reduced in humid condition.

From the mathematical simulation in this study, W-VMD shows the best dehumidification performance among three VMD systems. In terms of COP_{DH}, W-VMD should be used for air conditioning, but there is some problem that must be overcome to use this system in practice. It is known that the vapor passes through the membrane by absolute vapor pressure gradient. However, since the total pressure of membrane 2 permeate side in W-VMD is higher about 30 times than the feed side, the total pressure difference may act as resistance of vapor transportation. Therefore, the membrane should have permeability high enough to transfer the desired mass flow of water vapor and also have durability to withstand the high-pressure difference.

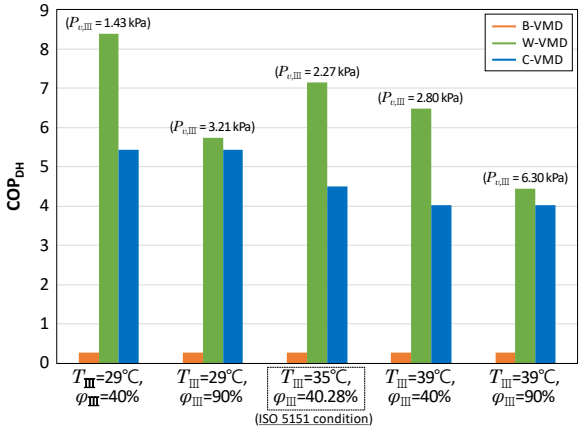


Fig. 8. Dehumidification performance of B-VMD, W-VMD, and C-VMD at selected temperature-humidity conditions of ambient air

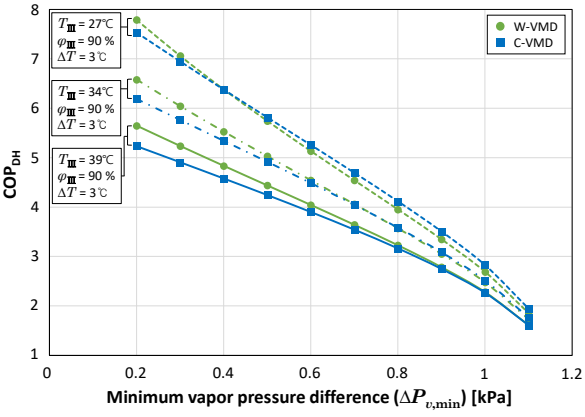


Fig. 9. Dehumidification COP variation by minimum vapor pressure difference

In contrast, C-VMD is practically simpler to implement than W-VMD from a technical point of view since only one membrane exchanger is required for C-VMD. With regard to the performance, C-VMD can compete COP_{DH} with W-VMD in a humid climate once the temperature difference of condenser (ΔT) is designed low. Figure 9 shows COP_{DH} of C-VMD and W-VMD about $\Delta P_{v,min}$ variation at 90% of relative humidity when ΔT is 3°C. In the figure, COP_{DH} of both systems tend to decrease as $\Delta P_{v,min}$ increases, but decline of C-VMD is smaller than that of W-VMD. Especially under low temperature condition, COP_{DH} of C-VMD exceeds W-

VMD partly. Therefore, considering the suitability of implementation, C-VMD can be an option to compete with the W-VMD system in humid climate.

5. Conclusion

Three VMD systems of bypass air mixed type (B-VMD), water vapor discharge type (W-VMD), and condenser combined type (C-VMD) are compared mathematically. In B-VMD system, a part of dehumidified air is bypassed to the vacuum compressor inlet, where the mixture of dry air and water vapor enters to the vacuum compressor. In contrast, since only water vapor exists at the vacuum compressor inlet in W-VMD and C-VMD, mass flow rate through the compressor is much smaller than the B-VMD case. In this manner, B-VMD shows much lower COP_{DH} than W-VMD and C-VMD by the simulation due to a large air flow through the compressor. W-VMD shows the highest dehumidification performance, but requires two membrane mass exchangers. To observe the performance under various climate condition, additional simulation was conducted for W-VMD and C-VMD.

As a recommendation of VMD system, W-VMD shows better performance overall than C-VMD. However, C-VMD shows comparable or better performance than W-VMD under hot and humid climate condition. Considering W-VMD requires two membrane mass exchanger, C-VMD can compete depending on the climate condition. Under the given minimum vapor pressure differences, $\Delta P_{v,\min}$ and compression ratio can be reduced for larger membrane size, which results in COP_{DH} enhancement. From the simulation, we can verify the performance of VMD systems at the design stage. For the experimental validation, the dense membrane having good performance is needed for small membrane size and high durability.

Nomenclature

COP	coefficient of performance [-]	φ	relative humidity [%]
h	enthalpy [kJ/kg]		
$\dot{m}$	mass flow rate [kg/s]	*Subscripts*	
$\dot{n}$	molar flow rate [kmol/s]	a	air
P_a	dry air partial pressure [kPa]	by	bypassed
P_v	vapor partial pressure [kPa]	cond	condenser
r	compression ratio [-]	DH	dehumidification
$\dot{V}$	volume flow rate [m^3/s]	I~IV	location of air flow
v	specific volume [m^3/kg]	lh	latent heat
$\dot{W}$	work [kW]	per	permeated
w	absolute humidity [kgv/kga]	s	isentropic
x	bypass ratio [mol/mol]	v	vapor
η	isentropic efficiency [-]	vc	vacuum compressor

Acknowledgements

This research is jointly supported by National Research Foundation (NRF) (2019R1A2C1088694) funded by Ministry of Science and ICT, Korea Environmental Industry & Technology Institute (KEITI) (2020003060005) funded by Ministry of Environment, and Korea Institute of Energy Technology Evaluation and Planning (KETEP) (20192050100060, 20202020900290) funded by Ministry of Trade, Industry and Energy. Authors sincerely appreciate their supports.

References

[1] International Energy Agency, Energy technology perspectives 2017, June 2017.
[2] B. R. Hughes, H. N. Chaudhry, S. A. Ghani, A review of sustainable cooling technologies in buildings, Renewable and Sustainable Energy Reviews 15 (2011) 3112-3120.
[3] US DOE, Builing Technologies Office, Energy savings potential and RD&D opportunities for non-vapor-compression HVAC technologies, March 2014.
[4] R. S. Murali, T. Sankarshana, S. Sridhar, Air separation by polymer-based membrane technology, Separation and Purification Reviews 42 (2013) 130-186.
[5] M. Qu, O. Abdelaziz, Z. Gao, H. Yin, Isothermal membrane-based air dehumidifiction: A comprehensive review, Reneweable and Sustainable Energy Reviews 82 (2018) 4060-4069.

[6] T. D. Bui, F. Chen, A. Nida, K. J. Chua, K. C. Ng, Experimental and modeling analysis of membrane-based air dehumidification, Separation and Purification Technology 144 (2015) 114-122.
[7] A. Criscuoli, M. C. Carnevale, E. Drioli, Study of the performance of a membrane-based vacuum drying process, Separation and Purification Technology 158 (2016) 259-265.
[8] J. Woods, Membrane processes for heating, ventilation, and air conditioning, Renewable and Sustainable Energy Reviews 33 (2014) 290-304.
[9] P. Scovazzo, A. J. Scovazzo, Isothermal dehumidification or gas drying using vacuum sweep dehumidification, Applied Thermal Engineering (2013) 225-233.
[10] Dais Analytic Corp., Membrane based air conditioning, Building Technologies Office Peer Review, 2017.
[11] D. T. Bui, M. K. Ja, J. M. Gordon, K. C. Ng, K. J. Chua, A thermodynamic perspective to study energy performance of vacuum-based membrane dehumidification, Energy 13 (2017) 106-115.
[12] ISO 5151:2017, Non-ducted air conditioners and heat pumps – Testing and rating for performance, International Organization for Standardization, 2017.
[13] REFPROP 9.0, National institute of standards and technology, 2010.



13th IEA Heat Pump Conference
April 26-29, 2021 Jeju, Korea

Environmentally friendly steam generation using VHTHPs at a pharmaceutical research facility

Tor-Martin Tveit [*a,c], Martin N. Johansson [b], Ron Zevenhoven [ch]

[a] Olvondo Technology AS, Langgata 21 A, NO-3080 Holmestrand, Norway
[b] AstraZeneca R&D, Pepparedsleden 1, SE-431 83 Mölndal, Sweden
[c] Åbo Akademi University, Biskopsgatan 8, FI-20500 Åbo, Finland

Abstract

This paper presents a case study where steam at 1 MPa and 183°C (~140 psi/360°F) is produced using very high temperature heat pumps (VHTHPs) at a pharmaceutical research facility. Steam as an energy carrier has many benefits, and steam systems are also flexible when it comes to the primary source; steam can be generated using heat from combustion of fossil- or renewable fuels, nuclear reactors or directly from electricity. Generating steam using a heat pump can reduce greenhouse gas emissions. At full-scale operation the potential reduction in CO_2-emissions is more than 80%. The heat source for the heat pumps is mainly waste heat from cooling compressors at around 40°C (~100°F). The refrigerant is a natural refrigerant R-704 (Helium). Helium has both global warming potential (GWP) and ozone depletion potential (ODP) equal to zero and the toxicity and flammability classification of Helium is "A1". The working medium stays a gas throughout the cycle, which makes the heat pump process very suitable for use as VHTHPs while the heat pumps are highly adaptive to any changes in the sink or source temperatures.

© HPC2020.
Selection and/or peer-review under responsibility of the organizers of the 13th IEA Heat Pump Conference 2020.

Keywords: VHTHP; steam generation; helium; waste heat; sustainable working medium

1. Introduction

Health is central to a functioning society and connects us all. The pharma industry is a global industry given the possibility to provide health solutions valid to patients all around the globe. Being global in the health sector, one has to address the global issues affecting people's health. AstraZeneca recognises the strong connection between a healthy planet and healthy people and works with environmental protection. AstraZeneca's approach doing this is to follow the science, using science-based targets. The greenhouse gas emission targets are in line with limiting global warming to 1.5 degrees. A big part of lowering CO_2 emissions is to move from the use of fossil fuel to renewable energy. In the pharma industry steam is commonly used to provide the utility needed. Due to the temperature needed, steam is usually produced with fossil fuel, on site, and accounts for a large part of the energy usage at a pharma plant.

AstraZeneca Gothenburg have historically used fossil fuel for steam production with a switch from oil to natural gas in 1997. In 2018 a new switch took palace, this time from fossil natural gas to biogas, to produce steam with a low carbon fuel. A technical part of the upgrade was to pursuing steam production using high lift heat pumps - a more efficient, more robust, less expensive and if possible, even more sustainable solution.

To do this, the site has installed 3 high lift heat pumps. Each with a capacity of 500 kW_{th} at 10 bars steam system pressure and rejected heat from the chillers for the air condition as a heat source. Another one is schedule for 2020 with a capacity of 750 kW_{th}.

* Corresponding author. Tel.: +358 405739890

2. State-of-the-art of high and very high temperature heat pumps

There is no common acceptable definition of high temperature heat pumps (HTHP) or very high temperature heat pumps (VHTP). In their paper Arpagaus et al. [1] present some of the previous definitions and uses the definition as shown in the figure below.

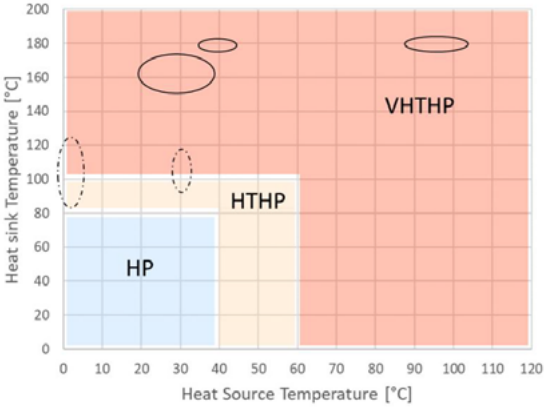


Figure 1. Classification of heat pumps according to the sink and source temperatures. The figure is adapted from Arpagaus et.al. [1]. The temperature range is extended to accommodate the possible temperatures for the HighLift heat pump. The solid line ellipses represent the temperatures for current HighLift installations, where the dotted ellipses represent earlier prototypes that are no longer in operation.

Arpagaus et al. identified more than thirteen manufacturers worldwide working on high temperature heat pumps in 2018. The technology, i.e. heat pump cycle and refrigerants, used in the heat pumps is diverse, though most use a single-stage vapour compressor cycle.

There is a lot of research and development in the field of high temperature heat pumps. For example, in the 12th IEA Heat Pump Conference (2017, Rotterdam), more than 40% of the presentations in the "industry" sessions discussed aspects of high temperature heat pumps. This indicates that there are likely more manufacturers with more mature high temperature heat pumps in the market today.

3. Environmental impact of heat pumps: energy use sustainability and environmental impact

In today's world, the increased availability of electricity from renewable sources may on one hand be intermittent but on the other hand is more predictable than the pricing levels for natural gas. In principle, HPs use a cheap renewable source for both input heat and electricity. System purchases are nonetheless often motivated by an attractive coefficient of performance (COP). Industry is increasingly implementing HP technology that circumvents the production of CO_2 when producing heat, although reaching sufficiently high temperatures may be challenging. A Stirling engine-based heat pump is one approach towards higher output temperatures. A challenge related to the goals of increasing output as well as efficiency, viz. the HighLift concept and its development, is that it conflicts with the thermodynamics that describes heat engines if the goals are simplified to having

- a higher temperature at the hot (water) side of the engine and a larger flow of heat carrier (helium) which can be achieved by raising the pressure of operation, and
- a higher coefficient of performance (COP_h), defined as heat output Q_{out} obtained per input of work (here electricity) W, with energy balance $Q_{out} = W + Q_{in}$, and $COP_h = Q_{out}/W$.

For an ideal, reversible heat engine the highest theoretical (Carnot) efficiency is defined as

$$COP_{Carnot} = \frac{Q_{out,reversible}}{W} = \frac{Q_{out,reversible}}{Q_{out,reversible} - Q_{in,reversible}} = \frac{T_H}{T_H - T_L} = \frac{1}{1 - \frac{T_L}{T_H}} \quad (1)$$

with the higher and lower temperatures of operation T_H and T_L, in K. This shows that raising the output heat temperature T_H with given T_L will inevitably result in a lower efficiency, or COP_h. For an engine that heats water from $T_L \sim 300$ K to $T_H \sim 450$ K the theoretical maximum COP equals $COP_{Carnot} = 3$. Current operation of the HighLift Stirling HP (500 kW per engine, heating water from 30°C to 180°C) gives a COP_h of 1.4 –

1.5: the goal is to raise that to COP_h 1.8 – 1.9 while heating water from 30°C to 200°C at an output of 750 kW. A more general approach of efficiency improvement of real systems involves suppressing irreversibilities that arise from

- friction between moving parts
- heat transfer across large temperature differences
- viscous flow friction in fluid flow lines and flow inlet/outlet section
- compression and expansion losses
- material losses as a result of leakage

Reducing friction between moving parts can achieved by proper design of rigid and flexible parts, and lubricant oils. Heat transfer is impossible without a temperature difference and a trade-off must be made (based on costs) between a large area for heat exchange operating with small temperature difference or vice versa: the first option gives higher losses. Viscous flow losses can be directly related to pressure drop and obviously a leakage of material at elevated pressure and temperature implies an obvious loss of energy. The first three listed will result in a production of entropy at a rate $\dot{S}_{gen}$ which can be used to quantify losses as $\dot{W}_{losses} = T^{\circ} \cdot \dot{S}_{gen}$ (J/s). Here, T° is the temperature of the surroundings, in K (here assumed = 288 K).

These losses imply that a larger work (electricity) input is needed for a given output heat target Q_{out} for a real system:

$$COP_h = \frac{\dot{Q}_{out}}{\dot{W}_{reversible} + \dot{W}_{losses}} = \frac{\dot{Q}_{in} + \dot{W}_{reversible} + \dot{W}_{internal\ losses}\left(1-\frac{T^o}{T}\right)}{\dot{W}_{reversible} + \dot{W}_{losses}} < \frac{\dot{Q}_{out,reversible}}{\dot{W}_{reversible}} \qquad (2)$$

with the (beneficial) complication that viscous friction results in heat that is taken up by a flow that is to be heated, which is not at all a full loss for a Stirling engine heat pump. Therefore, in (2) the internal losses that imply waste heat generation inside the Stirling engine are distinguished from external losses that cross the Stirling engine system boundary. For heat Q at temperature T produced from work W, the losses equate to W·(T°/T). It is clear that a larger electricity input is needed in order to cover for losses. See also Bejan (1997) [2] or Szargut et al. (1989) [3].

With an electrical-to-mechanical energy conversion efficiency η_{elec} = 95% and heat losses $\dot{Q}_{losses}$ to the surroundings found to be of the order of 20-30 kW, i.e. 5% of 500 kW for current operation, equation (2) can be reworked to

$$COP_h = \frac{\dot{Q}_{out}}{\dot{W}_{in}} = \frac{\dot{Q}_{in} - \dot{Q}_{losses} + \dot{W}_{in} - \dot{W}_{losses} + \dot{W}_{losses\ giving\ heat}}{P_{elec} \cdot \eta_{elec}} < \frac{\dot{Q}_{out,reversible}}{\dot{W}_{reversible}} \qquad (3)$$

correcting for input energy not contributing to raising the temperature of the water. Currently P_{elec} ~ 315 kW. Furthermore, heat transfer in the heat exchangers result in entropy production $\dot{S}_{gen} = \dot{Q} \cdot \frac{T_{hot} - T_{cold}}{T_{hot} \cdot T_{cold}}$ (with temperatures in K) giving losses $\dot{W}_{losses} = T^{\circ} \cdot \dot{S}_{gen}$, while pressure drop losses Δp (Pa) for (Helium) volume flow $\dot{V}$ (m^3/s) give additional (viscous friction) losses $\dot{W}_{losses} = \Delta p \cdot \dot{V}$. Following the above, a fraction (1 - T°/T) of the viscous friction losses will add to the useful heat output of the system.

Thus, (3) can be rewritten to give:

$$COP_h = \frac{\dot{Q}_{in} - \dot{Q}_{losses} + \dot{W}_{in} - \dot{W}_{losses} + \sum \Delta p \cdot \dot{V} \cdot \left(1-\frac{T^o}{T}\right)}{P_{elec} \cdot \eta_{elec}} < \frac{\dot{Q}_{out,reversible}}{\dot{W}_{reversible}} \qquad (4)$$

The assessment for the heat exchange applies to the regenerator as well: apart from viscous friction losses the heat transfer involves losses that can be estimated for the cycling heat transfer to/from the helium medium from/to the regenerator material matrix. For the heat transfer, with heat transfer $\dot{Q}$ to/from the helium with a temperature difference ΔT_{He} across the regenerator (here estimated ≈ the average value for average He temperature in the two respective heat exchangers – see also [4]) the entropy production can be estimated using the expression given above with an estimated cycle-average temperature difference $T_{hot} - T_{cold}$ ~ 15 K.

Using Ansys Fluent (v. 19.2) simulations for operation with pressure average 50 bar, amplitude 13 bar, frequency 10 s^{-1} it was found that 500 kW heat output operation will give $\dot{W}_{losses}$ = 30 - 35 kW for the two heat exchangers (being a bit higher for the low temperature heat exchanger than for the high temperature one). On top of this ~15 kW viscous flow losses occur inside the heat exchanger tubes. Pressure drop losses are much larger for the regenerator and inlet/outlet manifolds for that, giving ~ 40 kW viscous friction losses, while losses due to entropy generation in the regenerator add up to ~ 25 kW, with (cycle averaged) $T_{hot} - T_{cold}$ ≈ 15K. (Pressure drop losses are not considered for the side of the water that is heated as the pumping of this

is outside the Stirling engine system boundary.) Examples of calculated results are given in Figure 2, showing velocity intensity and temperature profiles.

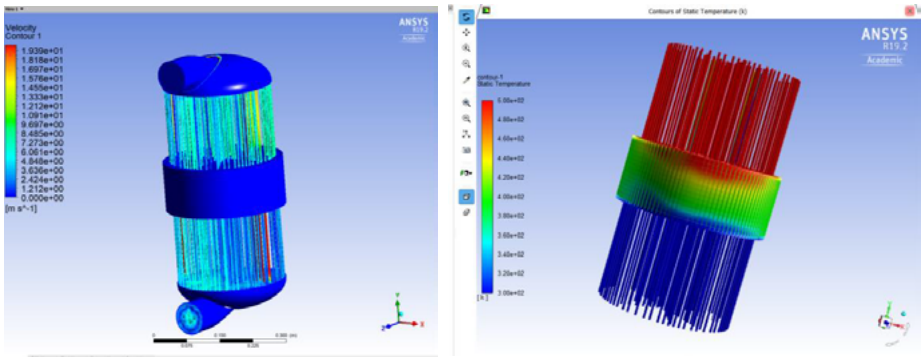


Figure 2. CFD simulated results for (cycle averaged) velocity (left) and temperature (right) for 500 kW heat output operation

A further source of losses are those related to real compression and expansion vs. ideal processes: for He the cycling expansion/compression from 37 to 63 bar gives losses of ~ 100 kW (the expansion stage giving somewhat larger values than the compression) – see [3, p119]. Fortunately these largely (~ 60%) imply generation of heat that stays inside the system (similar to the viscous friction losses), reducing the system losses to ~ 40 kW for this.

Combining all this gives with current operation with 300 kW effective power input that 45-50 kW of this is lost via entropy losses in the heat exchangers, while 55- 65 kW is lost in the regenerator plus ~ 40 kW compression/expansion losses. These add up to ~ 45% of the effective electricity input which, using the expressions for COP_h with heat input $\dot{Q}_{in}$ being of the order of 300 kW explains the value $COP_h = 1.4 – 1.5$. For the heat exchangers, a different design that gives small temperature gradients would be beneficial while for the regenerator the reduction of viscous flow losses is most beneficial. Indeed, such improvements are currently being implemented to the HighLift Stirling engines.

An issue that primarily relates to costs of operation are losses of helium. These are modest yet non-zero but won't give contribution to the enhanced greenhouse effect or ozone layer depleting as values for global warming potential (GWP) and ozone depletion potential are = 0.

4. The HighLift heat pump

The HighLift heat pump process is based on the Stirling cycle. For a more detailed description of the mechanical implementation see the previous work by the authors [5a]. Descriptions of other applications can be found in the papers in previous proceedings [6a, 7a]. Modern Stirling engine development starts with the work done by Philips Electronics BV in the Netherlands in the 1940s. See for instance the book by Finkelstein and Organ [8] for a historical review of the modern Stirling engine. The ideal Stirling cycle is a thermodynamic process that consists of four reversible process in series. A description of the ideal Stirling cycle is available in most introductions to technical thermodynamics, for instance in the book by Moran and Shapiro [9]. Compared to compression and absorption heat pumps, the working medium in a Stirling process is a gas throughout the process. This implies that the process is independent of the evaporation and condensation temperatures of the working medium. A common question from persons not familiar with the Stirling process is related to the choice of working medium. Even though the full story is more complicated, the efficiency of the choice of working medium can easily be seen from the equation below describing the reversible work of an ideal Stirling cycle by an ideal gas.

$$W = -m \cdot R \cdot (T_h - T_c) \cdot ln\left(\frac{V_1}{V_2}\right) \qquad (5)$$

where m is the mass of the working medium, R is the specific gas constant of the working medium, V is the volume, and T is the temperature. Subscripts "1" and "2" refer to initial and final states. As can be seen from the equation, the higher the value of the specific gas constant, the higher the work output from the cycle.

Noting that the specific gas constant for hydrogen, helium and air are approximately 4000, 2100 and 300 J/kgK respectively, it is easily understood why hydrogen and helium are prefered working media to air or nitrogen. The same argument is also valid for the reverse (heat pump) Stirling cycle.

The configuration of the heat pump is a double-acting alpha Stirling engine of the "Franchot" type. "Double-acting" means that the working medium is acting on both sides of the pistons. The Franchot type means in contrast to a "Rinia" or "Siemens" type configuration, one of the cylinders is always containing cold gas and one of the cylinders is hot gas.

5. The heat pump installation at AstraZeneca

The current HighLift heat pump installation at the R&D facility at AstraZeneca in Gothenburg, Sweden, consists of three heat pumps. These heat pumps are designed to deliver 500 kW of steam at full load, and the main motor is a 315 kW nominal power eight poles asynchronous motor. Below, two of the heat pumps in the heat pump room are shown.



Figure 3. Two of the three heat pumps currently installed at AstraZeneca's R&D facility in Gothenburg, Sweden. Heat is transferred to the heat pump from the heat recovery circuit and steam is delivered from the heat pumps' steam generators to the steam distribution system. The third heat pump is installed on the opposite side of the room.

Main components of the installations in addition to the heat pumps are the cold circuits, the hot circuits and the steam generators. The cold circuits are closed water circuits that transfer heat from the heat recovery system at the site to the heat pumps. The hot circuits are closed, pressurised water circuits that transfer heat from the heat pump to the steam generators. The steam generators are shell and plate heat exchangers that get feed water from the site's feed water tanks and generate steam by cooling the hot circuit from the heat pump. Steam thus generated is supplied directly to the steam distribution system at the site. The figure below (Fig 4) shows a simplified P&ID of the installation.

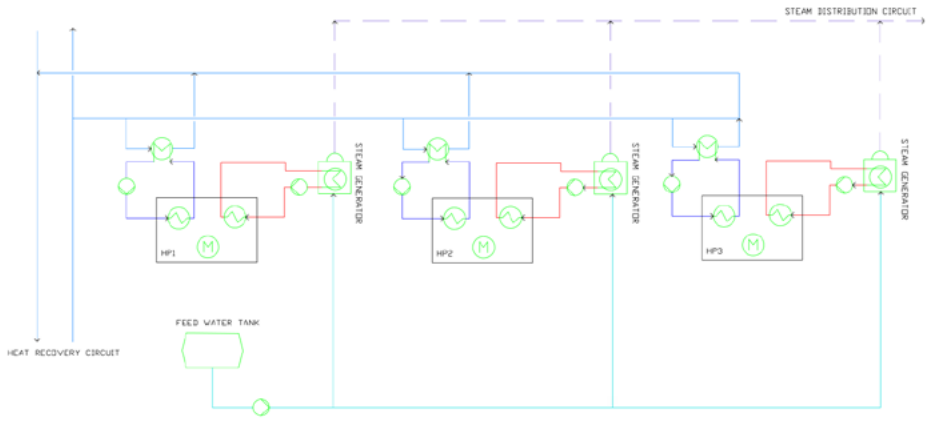


Figure 4. Simplified P&ID for the installation of the three heat pumps at the R&D facility. The cold heat source is a heat recovery circuit that is transferred indirectly to the heat pumps. The heat pump uses this heat to heat a hot circuit that circulates over a steam generator. The steam generator uses this heat to generate steam that is fed to the steam distribution circuit of the plant.

At the time of writing this, the heat pumps have been running for between 5000 and 6800 hours: pump #1 has a running time of 6800 hours, heat pump #2 5000 hours and heat pump #3 6500 hours respectively. The load has been varying, but the temperatures have remained quite constant. In order to present the performance of the heat pump, four cases have been selected from a two months period for heat pump #1. These are selected to have different load. Data for the cases is for a 30 hours period with 1-hour average values. The original data was sampled in 1s intervals except for the temperatures which were sampled in 10s intervals. In the following graphs the values are either based on average for all 30 hours or presented in form of intervals (box and whisker plots). The following figures (Fig. 5) show the average load for each period and the delivered heat as a function of the load for one heat pump.

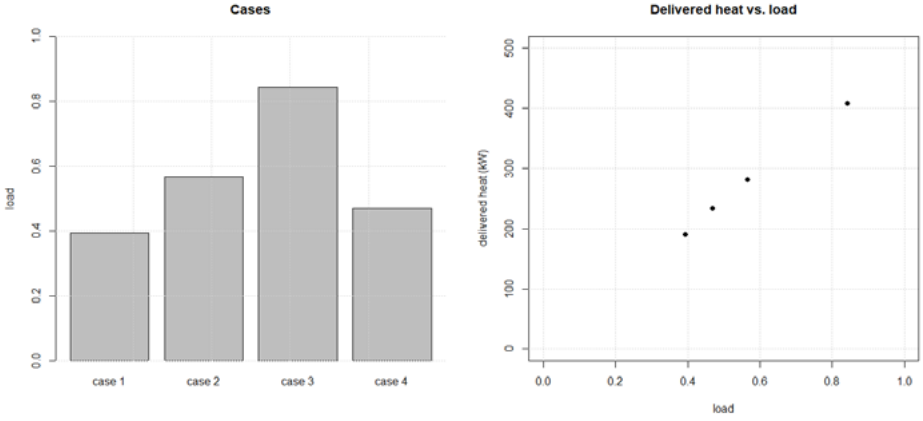


Figure 5. The load for the 4 cases for heat pump #1, where "1" equals full load. The loads and heat duty are average values for each of the cases.

The average temperatures of the external circuits are 183°C (363°F) and 27°C (75°F) on the hot and cold side respectively. The hot and cold side temperatures are presented in the two figures (Fig. 6 and Fig. 7) below.

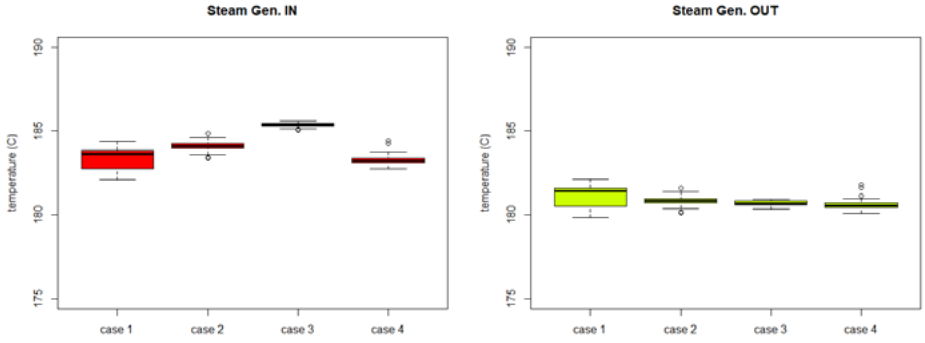


Figure 6. The temperatures of the hot circuit used to transfer heat from the heat pump to the steam generator. The hot water from the heat pump (steam gen. IN) enters the steam generator and heats the feedwater. The colder water is then returned to the heat pump.

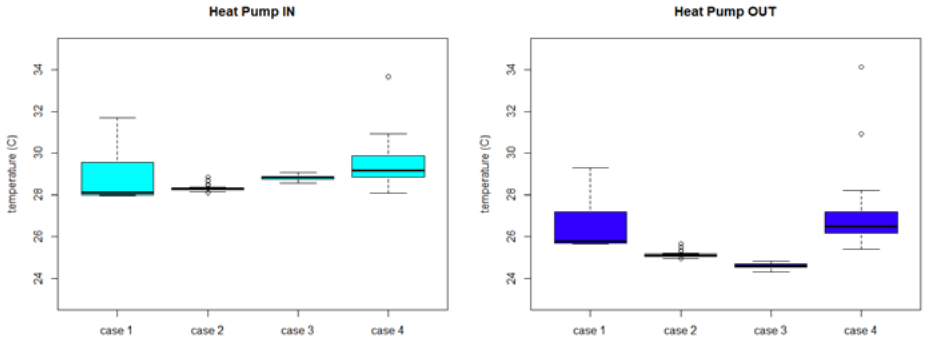


Figure 7. The heat is transferred from the heat recovery circuit to the heat pump via a closed circuit. The water enters the heat pump and is cooled down before returning to the heat exchanger between the closed circuit and the heat recovery circuit.

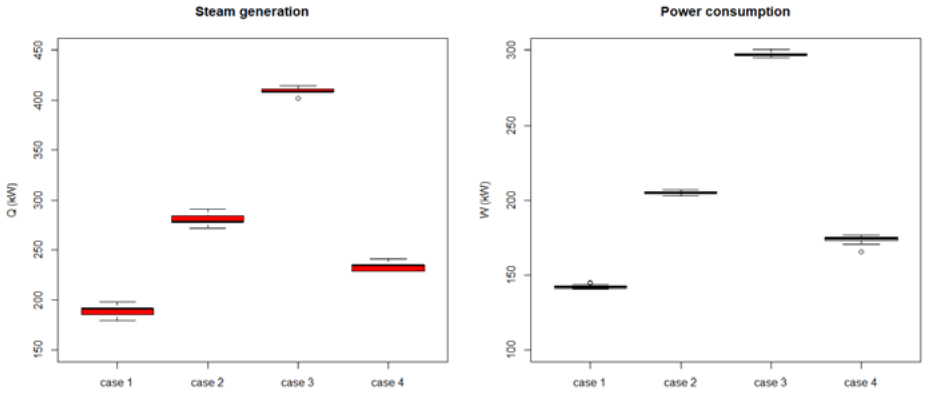


Figure 8. Steam generation and power consumption for the four cases. The steam generation is calculated from the flow of feed water, the feed water temperature and steam pressure. The power consumption is for the main motor and is sampled from the variable frequency drive.

As the conditions on the site are stable, the power consumption and the heat output are linear functions of the load. This can be seen in the figure above (Fig. 8), where the variations in the heat output (steam generation) and power consumptions for the four cases are presented.

The power consumption is only the consumption from the main motor that drives the heat pump measured from the variable frequency drive. In addition, two oil pumps add 1-2 kW of additional power that will not have major impact on the results. The system also has small circulation pumps running at partial load (0.75-2.2 kW full load) for the water circuits, which are not included in the analysis as they are not directly connected to the performance of the heat pump. Based on the power consumption and the steam generation, it is possible to estimate the coefficient of performance of the heat pumps as well as the system efficiency. This is presented in the figure (Fig. 9) below.

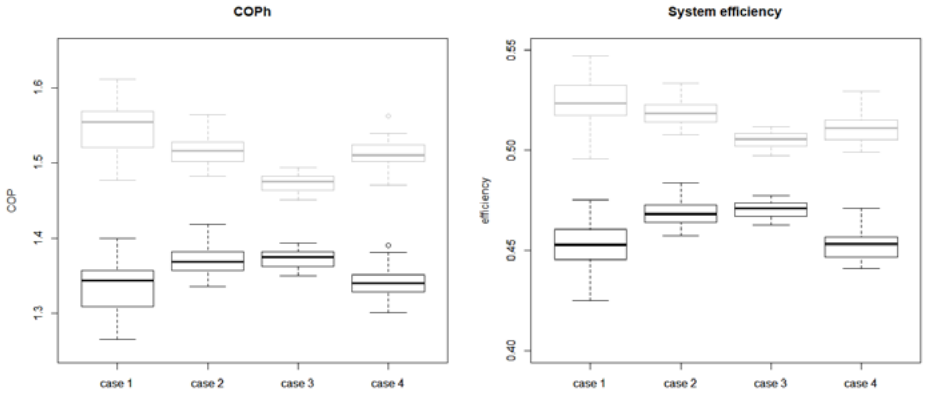


Figure 9. The coefficient of performance is defined as heat used to generated steam divided by the main motor consumption (i.e.$COP_h = Q_h/W$). The system efficiency is defined as the measured COP_h divided by the Carnot COP (i.e. $\eta_{system} = COP_h/COP_{carnot}$). The box and whisker plots in grey are estimated values for a fully thermally insulated heat pump.

During the operation of the heat pump, the heat loss has been higher than standard operation as large parts of the heat pump were not properly insulated. The heat loss has been estimated to approximately 30 kW, and the performance of a fully insulated heat pump is estimated and is shown in grey in the figures (Fig. 9) above.

6. Conclusions

A proven concept is described for a Stirling engine operated as an industrial-scale heat pump, delivering steam at 180°C. A brief assessment of losses and benefits is given, followed by technical performance data on the current installation at AstraZeneca's R&D centre in Sweden. Current activities involve improving system efficiency and reliability while increasing heat output from 500 to 750 kW, at the same time raising the TRL of the heat pump from level 7 to level 9.

Acknowledgements

The work described in this paper is partly financed by the European Commission under the Horizon 2020 Fast Track to Innovation programme, grant agreement number 831062 (2019-2021). Umara Khan at ÅAU is acknowledged for the Ansys Fluent CFD simulations, Mikhail Sinkevich of OT for background information.

References

[1] Arpagaus C, Bless, F, Uhlmann M, Schiffmann J, Bertsch S. High temperature heat pumps: Market overview, state of the art, research status, refrigerants, and application potentials. *Energy* 152 (2018) 985-1010.
[2] Bejan, A. *Advanced Engineering Thermod*ynamics 2nd ed., John Wiley & Sons, 1997
[3] Szargut, J., Morris, D., Steward, F.R. Exergy Analysis of Thermal, Chemical and Metallurgical Processes. Hemisphere Publishing Co, 1988.
[4] Sowale, A., Kolios, A. Thermodynamic performance of heat exchangers in a free piston Stirling engine. Energies 11 (2018) 505 (open source)
[5] Høeg, A, Tveit, T-M, Aase, T, Asphjell T-A. Mechanical Design of the 4-500 kWth Stirling Cycle Heat Pump SPP 4-106. 17th International Stirling Engine Conference, Newcastle upon Tyne, UK; 2016.
[6] Tveit, T-M. Application of an industrial heat pump for steam generation using district heating as heat source.12th IEA Heat Pump Conference HPC 2017; Rotterdam, Netherlands; 2017.
[7] Tveit, T-M, Høeg A. Performance analysis and verification of a novel high temperature difference heat pump. 11th IEA Heat Pump Conference, Montréal, Canada; 2014.
[8] Finkelstein, T., Organ, A.J. Air Engines, ASME Press, 2001
[9] Moran, M.J., and Shapiro, H.N. Fundamentals of Engineering Thermodynamics, 2nd ed., John Wiley & Sons, 1993

13th IEA Heat Pump Conference
April 26-29, 2021 Jeju, Korea

Range of application of heat pumps - Implementation of heat pumps with different heat sources

Franziska Bockelmann*, Markus Peter, Mathias Schlosser*

Steinbeis-Innovationszentrum (SIZ) energie+, Mühlenpfordtstraße 23, 38106 Braunschweig, Germany

Abstract

Through the increasing use of heat pumps, the number of potentially usable low-temperature heat sources and associated heat exchangers on the market is increasing, too. Planners often do not have a sufficient overview of the available technologies and boundary conditions of the individual systems and components. Based on the current results and experiences together with the development of the pre-dimensioning program, further key aspects for the integration and use of heat pumps and various associated components will arise, which will be dealt with in the project “future:heatpump_II”. The following topics will be addressed in this article:

- compatibility of different heat pump technologies, such as absorption, adsorption or power-controlled heat pumps with different low-temperature heat sources and systems.
- consideration of a bivalent operating mode of two heat generators (e.g. heat pump and gas boiler). This is relevant, among other things, for concepts in multi-family and office buildings.
- integration of solar thermal energy for the regeneration of ground-coupled heat pumps.
- energy concepts and their planning with regard to the supply of buildings and districts by heat pumps.

© HPC2020.
Selection and/or peer-review under responsibility of the organizers of the 13th IEA Heat Pump Conference 2020.

Keywords: heat pump; low temperature heat source and heat exchanger system; system design; usage

1. Introduction

Heat pumps are an increasingly applied technology in the energy supply of buildings. This is also reflected in the sales figures and the variety of heat pumps available on the market. In order to maximize the potential of the entire energy supply system, the choice of the low-temperature heat source and the associated heat transfer system and the connection to the building is of crucial importance. In this context, the pre-dimensioning program WPSOURCE (developed as part of the R & D project "future:heatpump" at the Institute for Building Services and Energy Design (IGS) of the Technical University of Braunschweig) is a multifunctional tool that can be used in many areas for project-specific pre-selection and dimensioning of heat sources and heat exchanger systems for heat pumps.

On the basis of the results and experiences from the research project future: heatpump and the development of WPSOURCE, new key aspects arise with regard to the integration and application of heat pumps as well as various additional components that can be coupled with heat pumps. As part of the research project "future:heatpump_II", topics beyond the content of the research project future:heatpump will be dealt with. The processing and analysis of the selected aspects enable an extension of WPSOURCE and contribute to the increased use of heat pumps.

*Corresponding author. Tel.: +49-531-3913557; fax: +49-531-3918125.
E-mail address: franziska.bockelmann@stw.de.

2. Pre-dimensioning program WP$_{SOURCE}$

In order to facilitate the evaluation of suitable heat pump systems together with their low-temperature heat sources (ground, water, air) and heat exchangers, as well as to promote the dissemination of heat pump technology in general, a clear compilation of different technological approaches is helpful. WP$_{SOURCE}$ is designed for the use by a broad range of users and considers different levels of detail and aspects in the planning of buildings and planning of heat pump systems. For this reason, flexibility and versatility is a key feature of WP$_{SOURCE}$ with the adjustments and settings.

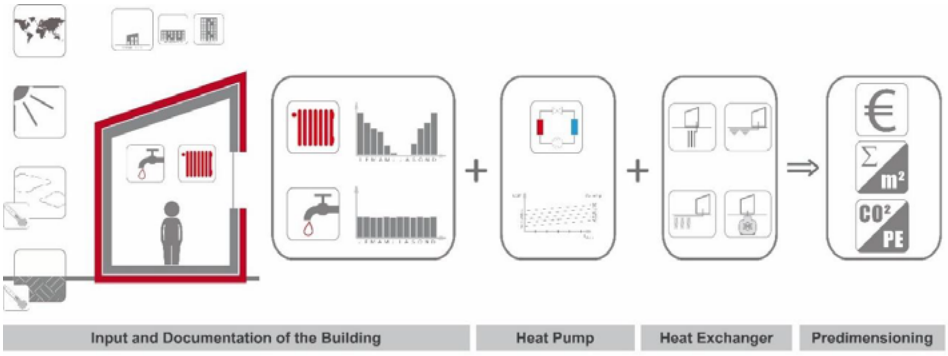


Fig. 1. Scheme for the structure and information flow in WP$_{SOURCE}$

The operation of WP$_{SOURCE}$ (Fig. 1) starts with the documentation and specification of the initial situation and the boundary conditions of the respective project. After entering general project data, the user enters known parameters such as the plot area, the type of building (single-family or multi-family house or office building) and its thermal standard as well as energy demand values, if applicable. In addition, the user specifies the heating and/or cooling system to be designed. From these inputs and other project-specific selection options for the building, the program determines the heating and cooling energy demand (kWh) as well as the heating and cooling capacity (kW).

In principle, a user with detailed knowledge of the basic data and of the heat pump system to be created can benefit from the program, as well as a user with only rough project information can. Depending on the level of information, the user can define the building, e.g. by means of data from an EnEV balance sheet (Energy Saving Regulation (Energieeinsparverordnung - EnEV) presents one of the most fundamental tools of the german federal government's energy and climate policy, it defines requirements and implementation tools for residential, non-residential buildings and refurbishments) [1], according to his own data on heating energy consumption or based on the building's type and year of construction.

Depending on the heating capacity requirement of the defined building, WP$_{SOURCE}$ uses heat pumps with corresponding performance for further calculation. The characteristics of the heat pumps implemented in the program were generated from data from a large number of devices currently on the market. The devices analytically generated for the program represent heat pumps of average quality for the respective output and are used for internal program calculations, e.g. of seasonal performance factor.

The required extraction energy from the low-temperature heat source is calculated using the average monthly coefficient of performance of the heat pump and the monthly heating requirement. This extraction energy forms an essential basis for the selection and (estimated) dimensioning of the low-temperature heat source.

On the basis of the inputs and the functions stored in the program, WP$_{SOURCE}$ derives the sizes required for pre-selection and approximate dimensioning of suitable low-temperature heat sources and associated heat exchangers for an individual application. Ecological (CO_2 emissions, primary energy) and economic factors (investment and operating costs) for the various low-temperature heat source/heat exchanger combinations are also documented.

Figure 2 shows an example of the user interface of WP$_{SOURCE}$. During the development, attention was paid to clarity and user-friendly operation.



Fig. 2: User interface for WPSOURCE (only in German available)

3. Extension of the pre-dimensioning program - additional applications and combinations of or with heat pumps

Today, heat pumps are no longer used exclusively to heat buildings as part of an energy supply concept for buildings. Within the framework of the development of climate-neutral building concepts, heat pumps are seen as a " fundamental element " and are combined with other components to form holistic supply concepts.

With the help of the WPSOURCE program and the extensions currently being implemented, e.g. bivalent systems or the integration of photovoltaics and solar thermal energy, the concept development and planning phase of buildings and systems is to be supported with a focus on sensible integration of regenerative energy sources and various energy producers. Therefore, it can support the dissemination of climate-neutral buildings in praxis.

Within the framework of the research project future:heatpump_II, solutions for additional topics will be developed and analyzed, which will be made available to the planner and user of the systems for practical use in an updated version of WPSOURCE. Different system combinations will be evaluated and meaningful results on their performance will be documented. In the course of the analyses and studies, the concepts under consideration are to be tested for their suitability for practice (meaningfulness and practicability). The results should scientifically prove which concepts are applicable for future buildings and which could possibly be too extensive.

In the following, the first results and work status of the key aspects of future:heatpump_II are summarized. During the project, the presented results for the different key aspects will be implemented in the pre-dimensioning program, so that at the end of the project a new extended version of the program with further energy concept approaches will be available.

3.1. Heat pump typologies and applicable low-temperature heat sources

As far as heat pump technologies are concerned, the current market situation in Germany can be characterised by different types of heat pump. The most common heat pump types can be classified as follows:

- Type of heat source (air, water, brine)
- Type of system to be heated, i.e. the heat sink (water or air)
- Type of driving energy (electric, gas)
- Type of compressor (thermal, electrical)
- Type of capacity control (On-Off, Inverter)

In addition to classic electric compression heat pumps, gas-operated heat pumps are increasingly being offered, although without high market shares yet, as well as different types of sorption heat pumps (thermally compressing absorption and adsorption heat pumps). (Fig. 3)

Gas-operated heat pumps are primarily an alternative to gas condensing boilers in existing buildings. Gas heat pumps and gas-powered sorption systems are based on gas condensing boiler technology, which is well established in Germany, and combine highly efficient gas condensing boiler technology with the use of environmental heat. Sorption heat pumps are currently only of minor importance on the market. Sorption technology is primarily used in refrigeration and is therefore more likely to be found on the market for cooling machines. In sorption technology, high temperatures are used as drive energy, mostly from waste heat from industrial processes (> 50°C or > 75°C). Low-temperature heat sources are therefore not suitable and can only be integrated as a heat source in conjunction with the gas-powered heat pump (driving energy: gas combustion).

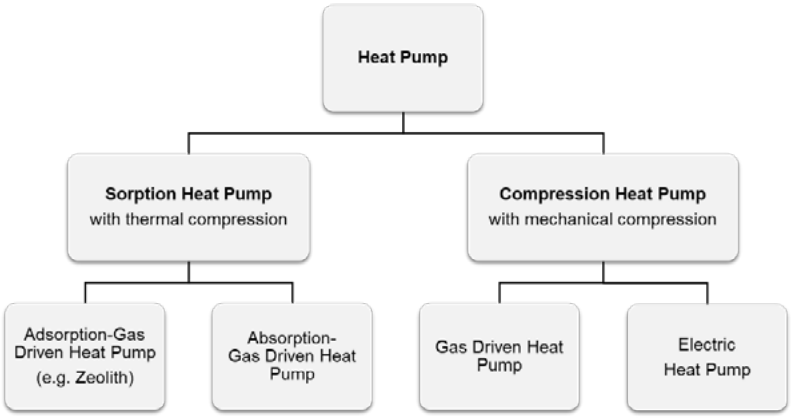


Fig. 3. Classification of heat pump types according to their drive technology

A comparison of the heat pump technologies mentioned shows that the mode of operation and the configuration of the individual designs differ only slightly from each other. All technologies can be used for space heating and domestic hot water production as well as for cooling in reversible operation. The fundamental difference between electric heat pumps and gas motor heat pumps is the type of compressor drive. The thermodynamic cycle is identical for both types. While in an electric compression heat pump an electric motor drives the compressor to compress the working fluid, in a gas heat pump this is done by a gas motor. In contrast to the electric drive, the heat generated by the operation of the gas engine is also used for heating, i.e. as useful heat. In addition to mechanical compressors, there is also so-called thermal compression. Sorption heat pumps use this process. A distinction is made here between absorption and adsorption heat pumps. Thermal compression in sorption heat pumps is based on the physical binding of a gas to a solid (adsorption) or the physical binding of a liquid or gas in a liquid (absorption). Both processes take place with the release of heat. With regard to the usability of different low-temperature heat sources with the heat pump technologies described, it can be seen that, in principle, all heat sources - outdoor air, brine and water - can also be used for gas-operated heat pumps, analogous to the electric heat pump (Fig. 4).

When dimensioning and planning a heat exchanger system, an advantage of gas-operated heat pumps (mechanical as well as thermal) becomes apparent. With this technology, the combustion heat can also be used and thus the source system is less stressed, i.e. less energy is withdrawn from it. For this reason, the heat exchanger system for using environmental heat with gas-operated heat pumps.can be made smaller in size than for conventional electric heat pumps.

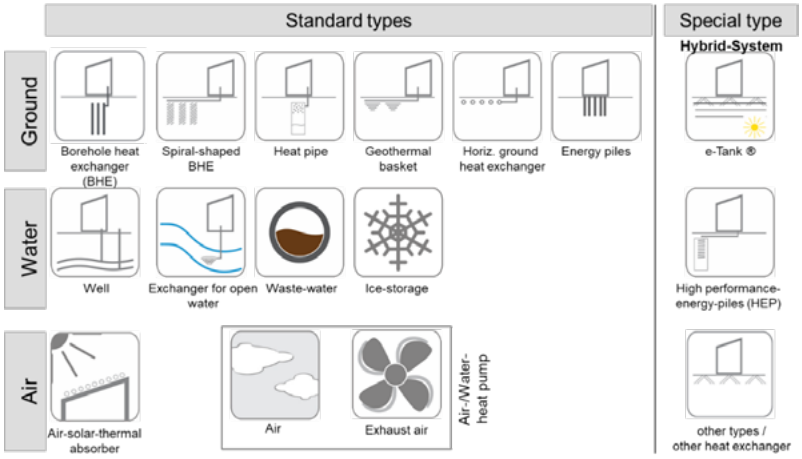


Fig. 4. Low temperature heat sources for heat pumps considered within the framework of future:heatpump and future:heatpump_II

Table 1 summarises the heat pump technologies considered here and presents their advantages and disadvantages. Assessments of the ecological and economic effects of the individual technologies depend, among other things, on current and future electricity and gas prices as well as CO_2 equivalents.

Table 1. Differences and fields of application of different heat pump technologies (main topics / information of the manufacturers)

	Electric heat pump	**Gas driven heat pump**	**Adsorption gas driven heat pump**	**Absorption gas driven heat pump**
Operating mode / medium	mechanical compressor / electrical	mechanical compressor / gas	thermal compressor / gas; (zeolite)	thermal compressor / gas
Temp. level of the source	Depending on source type (air, water, soil) -5 °C to 25°C			
Flow temperature	35 - 55 °C / 65 - 70 °C (heating / domestic hot water)			60 – 70 °C
Thermal capacity range (depending on heat pump, cascades possible)	4 – 300 kW	50 – 200 kW	up to 10 kW (products no longer available on the market)	20 – 45 kW (150 – 5000 kW, for district heating and technical industry)
Application	Residential buildings (single and multi-family houses) to non-residential buildings (office buildings, hospitals, ...) and district heating networks as well as production facilities	Multi-family houses (new construction), commercial and industrial, not residential buildings, existing buildings	single-family house construction	Apartment buildings, industry, commerce, hotels and service companies, existing buildings and for buildings with high water requirements
Advantages	all low-temperature heat sources can be used	for a simple and effective energetic renovation of gas heating systems, since the existing heat distribution and transfer system can largely be reused (existing gas infrastructure mostly usable). Use of combustion heat, therefore up to 40% smaller low-temperature heat source possible. Heat is available at different temperature levels.	hardly any mechanically moving parts, therefore particularly low-noise and low-maintenance	
Disadvantages	Investment costs and space requirements for source system	Gas connection and exhaust system required; mostly only air-water heat pumps on the market		

3.2. Bivalent heating operation mode of heat pump systems

With regard to heat pump systems, bivalent systems or a bivalent mode of operation are heating systems which, for example, combine an electric heat pump with another heat generator (e.g. gas or solid fuel boiler or district heating) and a control system.

The bivalent operation of two heat generators can be a good option for retrofitting existing heating systems. Also, for new office buildings and other non-residential buildings, as well as for new multi-family buildings, a heating system that permits the bivalent operation of a heat pump system is often expedient from both an ecological and an economic point of view. In this context, the heat pump is ideally used to cover a base load. The second heat generator serves to cover the peak load. Due to the low performance requirements, a classical bivalent operation in new single-family houses is rather rare.

The bivalent operation of a heat pump system can be reasonable for various reasons:

- The heat pump cannot provide the temperature required for room heating and/or domestic hot water all year round or can do so only very inefficiently.
- The minimum permissible heat source temperature for the heat pump is not reached during operation.
- The space requirement for the low-temperature heat source is not sufficient for monovalent operation.
- The heat pump cannot provide the heating output required for heating or domestic hot water all year round.
- As part of the energetic modernisation of a building, the existing heating system is supplemented by a heat pump. Renovation of the building shell reduces the heating load so that the existing boiler can be taken out of operation at a later date.
- By using different energy sources, bivalent systems offer a higher security of supply.

Different operating modes result from different applications (Fig. 5). Basically, the operating mode of a heat pump and an additional heat generator can be implemented as follows

- monovalent
  The heat is provided exclusively via the heat pump. A second heat generator is not operated and is not required.
- bivalent parallel
  Above the defined bivalence point (e.g. a defined outdoor temperature (frequently used), CO_2 emissions or the energy prices, etc.), heat is provided exclusively by the heat pump. Below the bivalence point, the second heat generator is operated parallel to the heat pump.
- bivalent partially parallel
  Above the bivalence point, heat is provided exclusively by the heat pump. Below the bivalence point, the second heat generator is operated parallel to the heat pump. If the outside temperature is below an additionally defined switch-off point, the heat pump is switched off and the entire heating heat is provided by the additional heat generator.
- bivalent alternative
  In this operating mode, heat is provided above the bivalence point exclusively by the heat pump. Below the bivalence point, the heat pump is switched off and the entire heating heat is provided by the second heat generator.

Within the framework of the research project and the implementation in the pre-dimensioning program, bivalent parallel operation is considered in addition to monovalent operation. Other modes of operation are named for information purposes, but are not analysed in detail for dimensioning purposes.

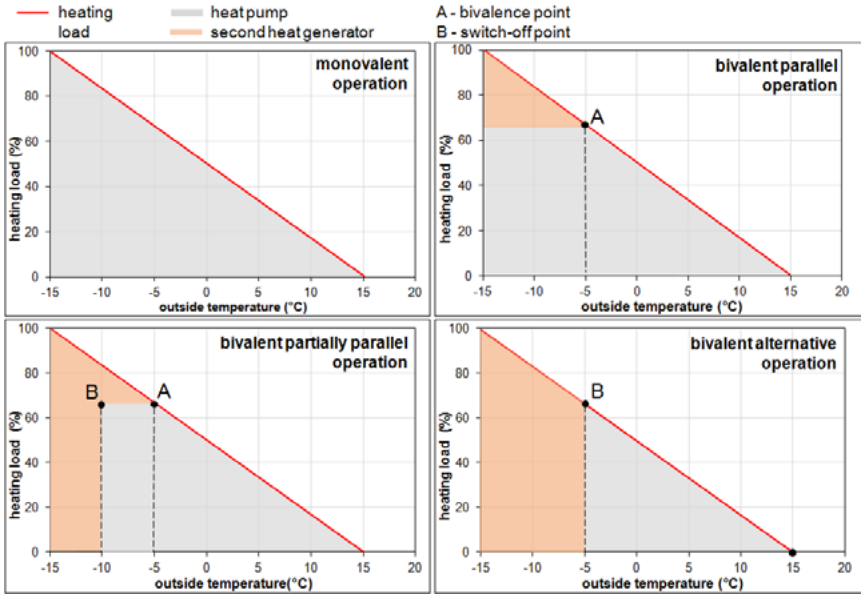


Fig. 5. Operating modes of a heat pump and an additional (second) heat generator

With regard to the integration of a bivalent operation and the associated control as well as the dimensioning of the system components, the expansion of WPsource is initially based on the specifications of DIN V 4701-10 [2] as well as the information sheet no. 57 of the Federal Association of the German Heating Industry (BDH) [3]. The outdoor temperature is used as the numerical value for the bivalence point.

For the dimensioning and the determination of the bivalence point the user has two alternatives at his disposal:

1. Direct determination of the bivalence point, i.e. the switching point of the heat pump to the second heat generator. In addition, the program and the location information are used to determine the share of the total heat requirement and the individual performance data for the generators, as well as the energy quantities that further influence the dimensioning of the low-temperature heat sources and the associated heat exchangers.

2. Determination of the share of the heat pump in the total capacity requirement. On this basis and the location and performance data of the heat pump, the program determines the bivalence point and the amounts of energy that further influence the dimensioning of the low-temperature heat sources and the associated heat exchangers.

Another application for bivalent operation is the integration of solar energy. Building services planners and/or architects are often interested in integrating the thermal use of solar energy not only to support domestic hot water, but also for space heating in the heat supply of single-family and multi-family houses. In addition to a gas condensing boiler or connection to district heating and other heat sources, solar thermal energy can also be used to heat domestic hot water or to support room heating in order to build up a bivalent heat supply. In the context of the extension of WPsource, solar support for domestic hot water and space heating is considered separately. In the project work and in WPsource, the thermal use of solar energy does not fall within the scope of a "classical" bivalent operation.

3.3. Integration of solar thermal energy for the regeneration of geothermal heat sources

The use of solar thermal collectors or absorbers in connection with ground-source heat pump systems has already been investigated in various research projects. For example, the relevance and effects of solar thermal regeneration of the soil were demonstrated in the projects “Terra-Solar-Quelle” and “GeoSolar-WP” [4-6] carried out at the Institute for Solar Energy Research in Hameln (ISFH). The concepts considered are

based on the fact that, starting from a heat pump, a solar system is integrated into the primary circuit (low-temperature heat circuit) of the heat pump. Since the temperature level of the primary circuit is lowered by the heat pump, a larger share of the available solar energy can be used in comparison to the classical installation. The reasons and objectives for the integration and use of thermal solar energy in connection with heat pump systems are based on

- a reduction in the required areas and/or depths of the ground system,
- a reduction in material and/or construction costs,
- the positive influence of regeneration on the operation of the heat pump,
- the achievement of balanced energy and temperature balances and partial compensation of the seasonal shifts between heat supply from the environment and heat demand, as well as
- the cost-benefit ratio of the measure(s).

The use of ground-coupled low-temperature heat sources to provide heat for heat pumps leads to demand-oriented heat extraction from the ground, which cannot always be compensated by natural heat fluxes or active heat input. This leads to long-term cooling effects of the subsurface, especially in geothermal borehole heat exchangers, which causes a negative influence on system efficiency or a larger heat exchanger. With the aid of solar thermal collectors or solar absorbers, regenerative, thermal energy can be injected into the ground in a targeted manner and heat extraction by a heat pump can be compensated. In this way, the soil can be regenerated and a long-term temperature decrease can be avoided. Additonally, the increase in the source temperature for the heat pump results in higher system coefficients of performance.

When dimensioning geothermal heat collectors, the targeted injection of thermal energy into the ground can contribute to reducing the required collector area. By avoiding critical frost and exhaustion conditions as a result of regeneration, a smaller distance between the collector pipes can be achieved. Since the high demand for unsealed surfaces represents a major obstacle to the use of surface collectors, the reduction of the required surface area through regeneration is of particular interest for the application of this technology.

When injecting thermal energy into the brine circuit of a heat exchanger system, the permissible inlet temperatures must be observed. For example, the inlet temperature to a surface collector must generally not exceed 25 °C. For this reason, unglazed collectors, usually solar absorbers, are generally used to regenerate the soil.

Table 2 summarizes key data and applications relevant for the regeneration of ground-coupled low-temperature heat sources.

Table 2. Differences and influences of solar regeneration of geothermal collectors and borehole heat exchangers

	Geothermal heat collectors [4]	**Borehole heat exchangers [5-6]**
The objective of regeneration	Reduction of the collector surface area with constant efficiency	Reduction of borehole length and improvement of system efficiency
Integration of solar thermal technology	Primary side series connection of the solar collectors or absorbers with Geothermal heat collectors	Primary-side series connection of solar collectors or absorbers with borehole heat exchangers
Investigated collector types	Swimming pool absorber, uncovered PVT- and facade collectors	unglazed collector (solar absorber)
Control	Inlet temperature of Geothermal heat collectors max. 25 °C	
Influence of regeneration	Avoidance of critical frost conditions and limitation of exhaustion conditions of the Geothermal heat collectors	Avoiding long-term cooling effects and increasing the annual coefficient of performance (COP)
Effect	Reduction of the collector surface up to 50%. Applicability independent of the type of soil. Good compensation measure for undersized Geothermal heat collectors.	Increase of the COP and increase of the minimum temperatures in the soil. Reduction of the borehole length by up to 30 %. In clearly undersized systems, the influence is significant. Otherwise, efficiency gains are in no economic relation to effort.

3.4. Applicability of heat pumps in local heating networks

Against the background of the energy transition, energy-efficient heat provision for space heating and domestic hot water is essential. Local heating networks with heat pumps will be an important infrastructure element for the heat supply of settlements and quarters in the future. Heat pumps can provide the required heat in comparison to fossil heat generators with low primary energy shares and, if correctly dimensioned, have high efficiency. They offer the possibility of spatial and temporal coordination of heat source, heat generation and heat demand via network design, network temperatures and heat storage. In this way, economically and technically optimised heat supply systems can be created.

The integration of heat pumps in local heating networks can enable the development of previously unused and natural low-temperature heat sources for heat supply. This can reduce primary energy and CO_2 emissions during heat generation.

Based on the basics developed in the project and the example networks considered, different scenarios for a future-oriented local heat supply of quarters with heat pumps can be developed. The concepts differ in the network temperatures, operating modes and usable low-temperature heat sources as well as in the areas of application.

Conventional local heating network with central heat pump

The implementation of conventional local heating networks is primarily of interest for areas with buildings that currently need to be supplied, where heat generation within the building and fuel-based heat generation are available, which require high inflow temperatures. This means that existing quarters with conventional heating systems, which generally also have high heat demand densities, can be considered. Residential and mixed areas with multi-family houses and commercial properties are particularly interesting for conventional local heating supply concepts. Due to the lower density of heat demand, supply areas with single-family housing only (especially new buildings) are less suitable. For consumers, the conversion to conventional local heating involves manageable investments, essentially in new heating technology (replacement of the old heating system with a local heating transfer station).

In conjunction with an environmental heat source, a central heat pump (covering the base load of the heat network) in conjunction with another heat generator provides flow temperatures between 60 °C and 85 °C. This temperature level of the local heating network is usually sufficient for space heating and domestic hot water heating. The return flow temperature is between 50 °C and 35 °C, depending on how much heat is removed. It can be deduced from the networks investigated that route lengths of about one and a half kilometres can be realised.

The potential heat sources for the heat pumps are geothermal borehole heat exchangers, groundwater and solar-thermal long-term heat storages. If the supply area offers the necessary infrastructure, waste water can also be used as a heat source.

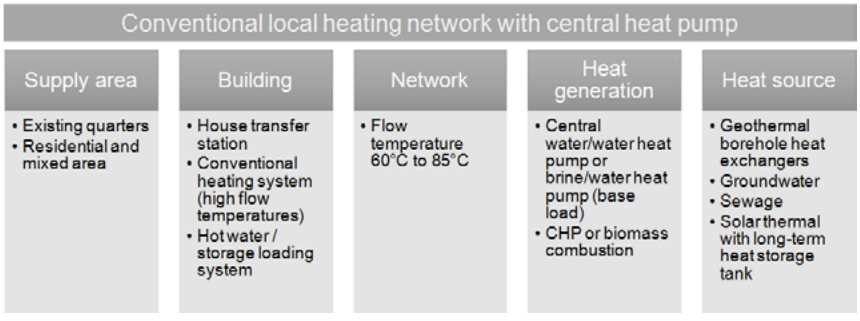


Fig. 6. Overview of a conventional local heating network with central heat pump

Low-temperature network with decentralised heat pumps (Cold local heating network)

A low-temperature network with decentralised heat pumps is particularly suitable for supplying new residential areas. The advantage of cold local heating is not necessarily the heat price, but the fact that the network can be integrated into supply areas characterised by low heat densities, uncertain demand structures

and possible extensions due to further settlements. With brine as the heat transfer medium, the networks usually provide temperatures in the range of 5 °C and around 20 °C. Due to the low heat losses, cold local heating networks can be operated efficiently even with low heat demands. No additional heat generator is required for normal network operation. If eco-electric power is used for the heat pumps, the heat supply can be operated CO_2-neutral. Cold local heating networks are particularly interesting because the heat consumption of buildings decreases due to building insulation and as a result the heat demand density is reduced, too. In order to ensure economic operation of the distribution network, it may be advisable in new housing estates to require a connection to the cold local heat.

The analysis of sample quarters suggests that pipeline lengths of at least one and one and a half kilometres can be achieved. The transport of the heat transfer medium in the distribution network is realised by the individual feed pumps of the decentralised heat pumps in the connected buildings. If there is no heat demand, the heat transfer medium in the distribution network is at a standstill. In order to prevent the temperature level from being lowered by heat exchangers between the heat source and the distribution network, the heat transfer medium from the low-temperature heat source flows directly through the distribution network. Depending on the local conditions, a number of environmental heat sources may be available that are sufficient to cover the required load and do not require an additional heat generator. Common heat sources in this context are geothermal borehole heat exchangers and agrothermal collectors as well as long-term heat storage units such as ice storage units or geothermal storage units.

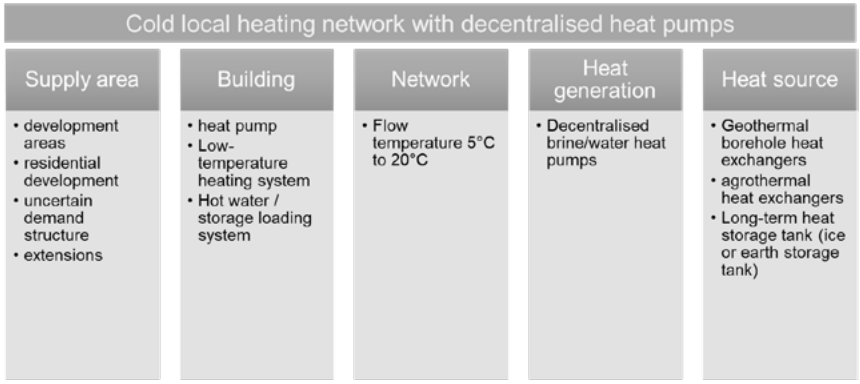


Fig. 7. Overview of a cold local heating network with decentralised heat pumps

Mixed networks

The conversion of an existing (conventional) local heating network to a mixed network with centralised and decentralised heat pumps can improve the efficiency and sustainability of the heat supply. During the winter months, the network is operated as a conventional local heating network with central heat generation and supply flow temperatures in the range of approx. 70 °C to 80 °C. A combined cogeneration unit together with a central heat pump serves as a heat generator. In the summer months, the network temperature is reduced to around 20 °C to 40 °C, and the space heating and domestic hotwater heating is provided by decentralised heat pumps in the connected buildings. The heating system with the cogeneration unit can be switched off during this time. Mixed networks offer the advantage of providing heat at demand-oriented temperature levels. Since the existing local heating routes are used, no work is usually required on the pipelines to convert to a mixed network. For the network operator, investment costs are usually relatively low.

In principle, all environmental heat sources used as heat sources for the heat pump can also be used for heat pump operation in a conventional local heating network. Due to the constant source temperatures of around 10 °C during the winter months, the use of geothermal borehole heat exchangers or groundwater is particularly suitable.

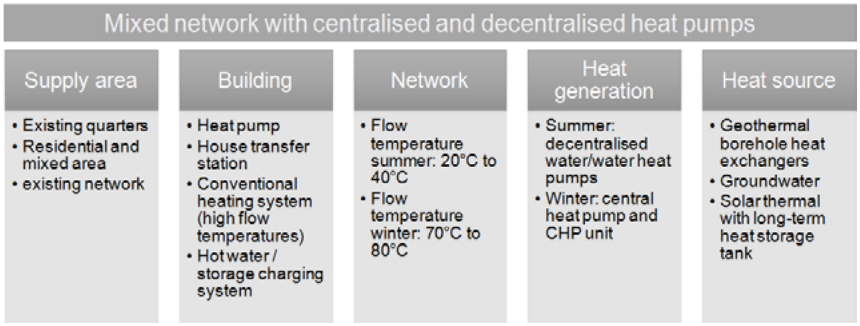


Fig. 8. Overview of a mixed network with centralised and decentralised heat pumps

4. Conclusion

Energy concepts with innovative systems and components such as solar thermal energy, photovoltaics, heat pumps and geothermal energy are increasingly being implemented in building technology. Design aids, such as dynamic simulation, are becoming increasingly important for these systems. The design and dimensioning aids currently available on the market for heat pumps and their low-temperature heat sources and heat exchangers are generally individual solutions that are often provided by manufacturers or suppliers of corresponding products. These design and dimensioning aids usually do not offer planners and architects the possibility of verifying the output results or providing an overview of the alternatives. In particular, the comparison of systems and individual components in different applications and their applicability is a unique characteristic of WPsource.

On the basis of the experiences and results from the research project future:heatpump, the follow-up project "future:heatpump_II" will mainly deal with topics and focal points which on the one hand support the application and expansion of heat pump systems and on the other hand serve the extended use of the WPsource program. The focus will be on other heat exchanger systems, the bivalent operation of heat pump systems, the regeneration of geothermal heat exchangers and the integration of photovoltaics and solutions for districts/quarters. The expansion will enable the programme to present more advanced concepts and approaches with heat pumps.

The current state of work in the area of the new thematic priorities shows that

- different heat pump technologies are available on the market, but the application is primarily focused on electric heat pumps. Gas-operated heat pumps are currently not very important on the market, but can be a sensible solution, e.g. for existing buildings with an existing gas connection.
- the use of bivalent heat pump systems can be a way of resolving the modernisation backlog in existing buildings. They make it easier for the plant operator to decide on future energy sources for heating the building. Bivalent systems can often be installed cost-effectively by extending existing heating systems. Bivalent heat pump systems are also of economic interest in new buildings, especially with high heating loads and different temperature requirements.
- a regeneration or coupling of ground heat exchangers (surface collectors and geothermal borehole heat exchangers) with thermal solar energy leads to a reduction of the collector surface or geothermal borehole heat exchanger length. In addition, the temperatures in the soil rises and the annual performance factors can be increased. Coupling with thermal solar energy has a significant positive influence on undersized systems. In other cases, the efficiency gain is not economically proportional to the effort required to use thermal solar energy to regenerate geothermal heat exchangers.
- a local heating network offers the possibility of a sustainable and economical heat supply with a high flexibility and expandability. In the sense of a future-oriented energy supply, the implementation possibilities of different heat pumps and environmental heat sources in local heating networks should be investigated and, where possible, applied to quarter solutions.

Acknowledgements

The research projects are funded by the German Federal Ministry for Economic Affairs and Energy.

References

[1] EnEV 2014/16, Energieeinsparverordnung. Verordnung über energiesparenden Wärmeschutz und energiesparende Anlagentechnik bei Gebäuden, 2013, Germany
[2] DIN V 4701-10:2003-08 - Energy efficiency of heating and ventilation systems in buildings – Part 10: Heating, domestic hot water supply, ventilation, 08/2003, Beuth Verlag GmbH, Berlin, Germany
[3] Bundesindustrieverband Deutschland Haus-, Energie- und Umwelttechnik e.V.((BDH) Federal Association of the German Heating Industry): Information sheet no. 57, Interessengemeinschaft Energie Umwelt Feuerungen GmbH, 03/2014
[4] HÜSING, F und MERCKER, O. und HIRSCH, H und STEINWEG, J.: Solare Regeneration von Erdwärmekollektoren – Reduzierter Flächenbedarf bei hoher Effizienz, 27. OTTI Symposium Thermische Solarenergie, Bad Staffelstein (2017)
[5] PÄRISCH, P. und BERTRAM, E. und TEPE, R.: Experimente und Modellvalidierung für die Erdsondenregeneration mit Solarwärme, Anwenderforum Oberflächennahe Geothermie, Neumarkt (2013)
[6] TEPE, R., PÄRISCH, P., BERTRAM, E., MERCKER, O., ARNOLD, O. und ROCKENDORF, G.: Hocheffiziente Wärmepumpensysteme mit Geothermie- und Solarthermienutzung - Rückblick auf 3 Jahre Forschung und Entwicklung, 24. OTTI Symposium Thermische Solarenergie, Neumarkt (2014)

13th IEA Heat Pump Conference
April 26-29, 2021 Jeju, Korea

US Heat Pump Market Overview–2020

Jaewan Joe[a], Mini Malhotra[a], Melissa Lapsa[a]*, Van Baxter[a]

[a]Oak Ridge National Laboratory, P.O. Box 2008, Oak Ridge, TN, 37831, USA

Abstract

This paper provides an overview of the US heat pump market in 2020; discusses the key drivers and challenges that have been shaping the market; and discusses the underlying factors that are setting the direction for the research, development, and commercialization of heat pumping technologies in the United States. Following the 2006–2007 housing market collapse, the US heat pump market has shown steady growth since 2010. Air-source heat pump shipments reached nearly 3 million in 2018, a 12.2% increase over 2017 versus the 7.1% estimated growth rate of the global heat pump market. Owing to the recovering economy, growing construction market, relatively stable electricity prices, numerous financial incentives, and technological advancements, the demand for heat pumps has been increasing. The current focus of heat pump research and development in the United States includes development of next-generation systems and components, lower global warming potential refrigerant alternatives, and reduced cost for premium-efficiency technologies. The future heat pump market and technologies will be highly influenced by increasingly stringent minimum efficiency standards, incentive programs, technological innovations, and the national and global economy.

© HPC2020.
Selection and/or peer-review under responsibility of the organizers of the 13th IEA Heat Pump Conference 2020.

Keywords: Heat pumps; shipments; US market; construction market; research and development; efficiency standard

1. Heat Pump Market

1.1. Market trend

The market for heat pumps in the United States has shown healthy growth since 2010 following the 2006–2007 housing market collapse. Figure 1 shows the new single-family heating system market combined annual penetration rate of air-source heat pumps (ASHPs) and ground-source heat pumps (GSHPs). The market share of the ASHP and GSHP systems hovered between 20–30% from 1978 to 2005; since then it has relatively steadily increased to 41% [1]. In the US space heating market, heat pumps primarily compete with natural gas furnaces in addition to other traditional heating appliances like boilers, direct electric heating, etc. Figure 2 shows the annual shipments of ASHPs, gas warm air furnaces, oil warm air furnaces, and unitary air conditioners. ASHP shipments have shown a general increasing trend since 1998. From 2000 to 2006, annual ASHP shipments increased nearly 60% to 2.1 million units, then dropped and leveled off to about 1.7 million units annually between 2007 and 2013 during the housing market crash and recovery. In 2014, annual ASHP shipments surpassed the 2006 peak and have steadily increased in the intervening years, reaching nearly 3 million in 2018, while gas warm air furnaces have yet to fully recover to their 2006 shipment levels. Gas furnace shipments still outnumber ASHP shipments but the gap is much narrower.

* Corresponding author. Tel.: +1-865-576-8620; fax: +1-865-241-4152.
lapsamv@ornl.gov.

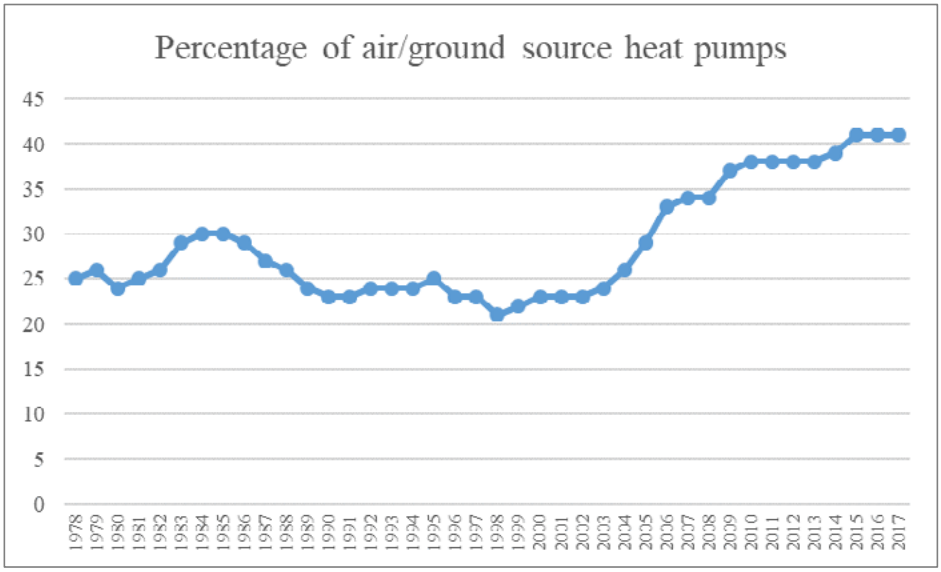


Figure 1 Penetration rate of heat pumps [1]

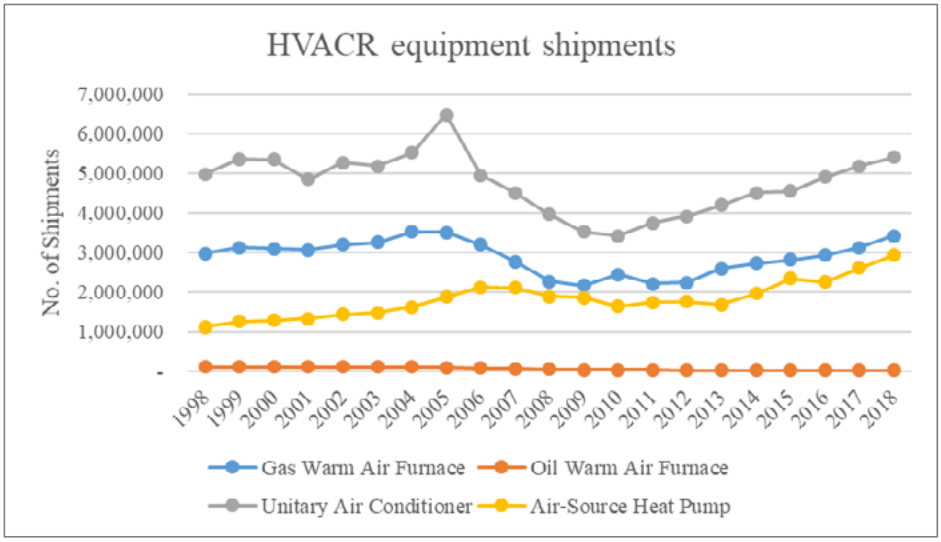


Figure 2 Heating, ventilation, air conditioning, and refrigeration (HVAC&R) equipment shipments [2]

Figure 3 illustrates the trend of annual shipments/installations of GSHPs based on 2003–2009 shipment data from the US Energy Information Administration (EIA) and 2010–2015 shipment estimates based on EnergyStar unit shipment and market penetration reports [3], [4]. Shipments of GSHPs have steadily increased since 2003, partly due to a 30% federal tax credit placed in service after 2008 and lasting through December 31, 2016. The federal tax credit was recently reinstated and will be available until 2021.

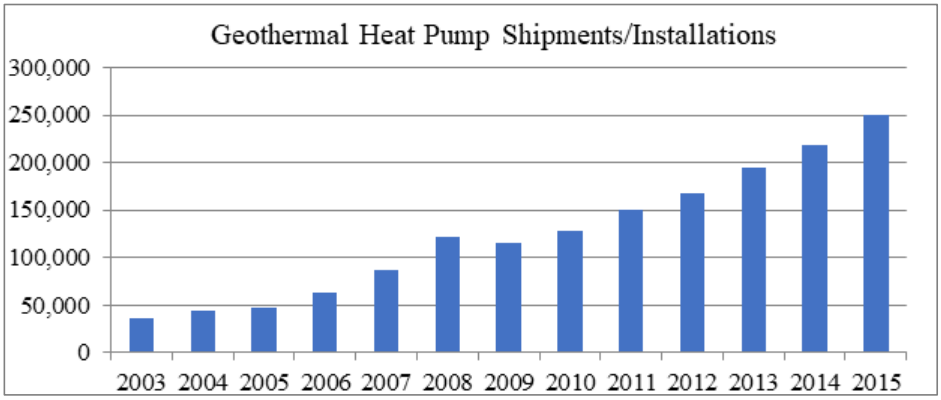


Figure 3 Geothermal heat pump shipments/installations [3], [4]

1.2. Market segments: residential, commercial, and industrial sectors

Despite the US housing market crisis in the late 2000s, heat pumps steadily increased their share of the new home market since 2004, reaching 41% in 2017 compared with only 25% in 1978 for single-family housing, as shown in Figure 1. As for multifamily housing, heat pump share was up to 48% in 2017, whereas competing technologies (forced-air furnace and hot water or steam heating) remained at 37% and 8%, respectively [1].

Similar to the residential market, commercial HP and air conditioner (AC) shipments (above 19.0 kW in capacity) in the United States have experienced some volatility over the past two decades due to economic conditions, fluctuating fuel prices, etc. Since the bottom of the market in 2009, total commercial HP and AC shipments have increased by 49% back up to slightly more than the 2006 level, approximately 312,000 units in 2017 and 2018 [2].

Total industrial HP installations in the United States was estimated at about 2,300 in 1994, growing to a conservatively estimated 5,000–7,000 by 2015/2016. Installations with lumber drying applications were responsible for about 75% of this total. Declining natural gas prices relative to electricity prices is the biggest impediment to this market, along with the 2006–2010 recession.

As mentioned previously, for building comfort cooling and space heating applications of ACs and HPs in the United States, the residential and commercial markets account for 96% and 4% of the total market, respectively; these percentages have varied only slightly (by 2%) over the past 18 years. The percentage distribution by capacity (Figure 4) has also stayed fairly consistent for decades as illustrated in [2].

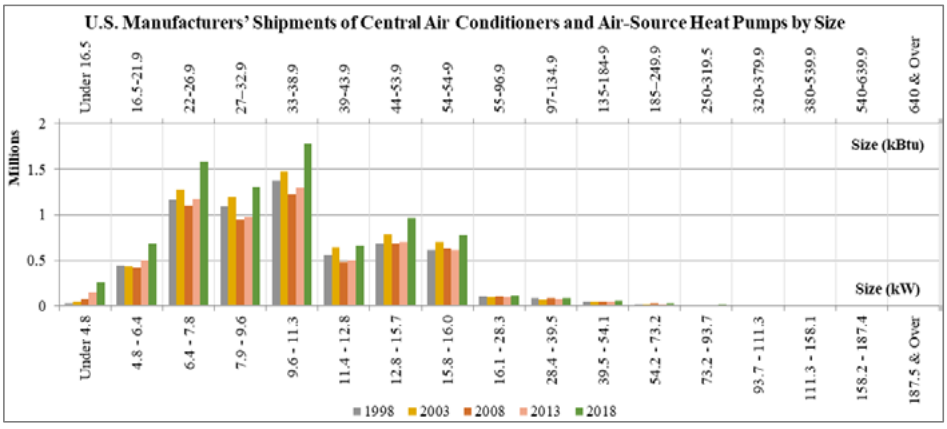


Figure 4 Central AC and ASHP shipment during 1998–2018 by system capacity [2]

2. Market Drivers

The primary appeal of heat pumps in the United States is the increased efficiency, which in turn saves energy and operating costs. Furthermore, it offers both heating and cooling functions, allowing consumers to potentially consolidate their equipment purchases. Also, the heat pump (electric) is the only option for some regions in the United States where natural gas is still not available to some residential and commercial building customers.

2.1. Electricity price

Electricity prices for residential building customers have gradually risen over the 2007–2018 period (Figure 5), whereas prices for other sectors (commercial buildings, transportation, and industry) remain relatively level or even slightly decreased. This trend is a barrier for the penetration of HP in residential sector. However, it drives the research and development (R&D) to improve the performance and efficiency.

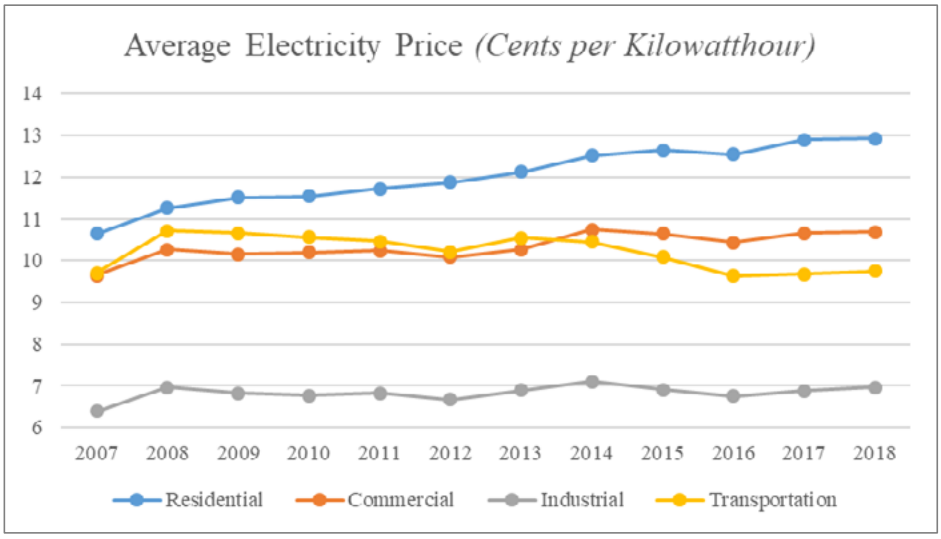


Figure 5 Average electricity price [5]

2.2. Installation cost

Comparisons of retail equipment cost, total installed cost, maintenance cost, and average life of HP technologies with other competing heating technologies for residential and commercial space heating and water heating (WH) are shown in Figure 7, respectively. These are obtained from the EIA's 2018 report on Technology Forecast Updates [6]. The underlying data is based on generic industry products from 2017 including government, R&D organizations, and manufacturers.

The cost comparison plots on the left side axes of the plots in the two figures show the min-max retail equipment cost ranges and total installed cost ranges (plotted along the primary vertical axis) for the typical capacity (plotted along the secondary vertical axis) of each technology type. Installed cost of the heat pump technologies are somewhat higher than those of most of the competing heating technologies. For the ground-source systems, the cost is driven by the drilling, trenching, and other activities required to install the ground loop heat exchanger. One significant advantage for the heat pumping options is that they can provide cooling in the summer as well while other space technologies require separate cooling system, which incur additional cost.



Figure 6 Comparison of heat pump technologies to other technologies: total installed costs with typical capacities and maintenance cost with average life for residential space heating (top) and water heating (bottom) [6].

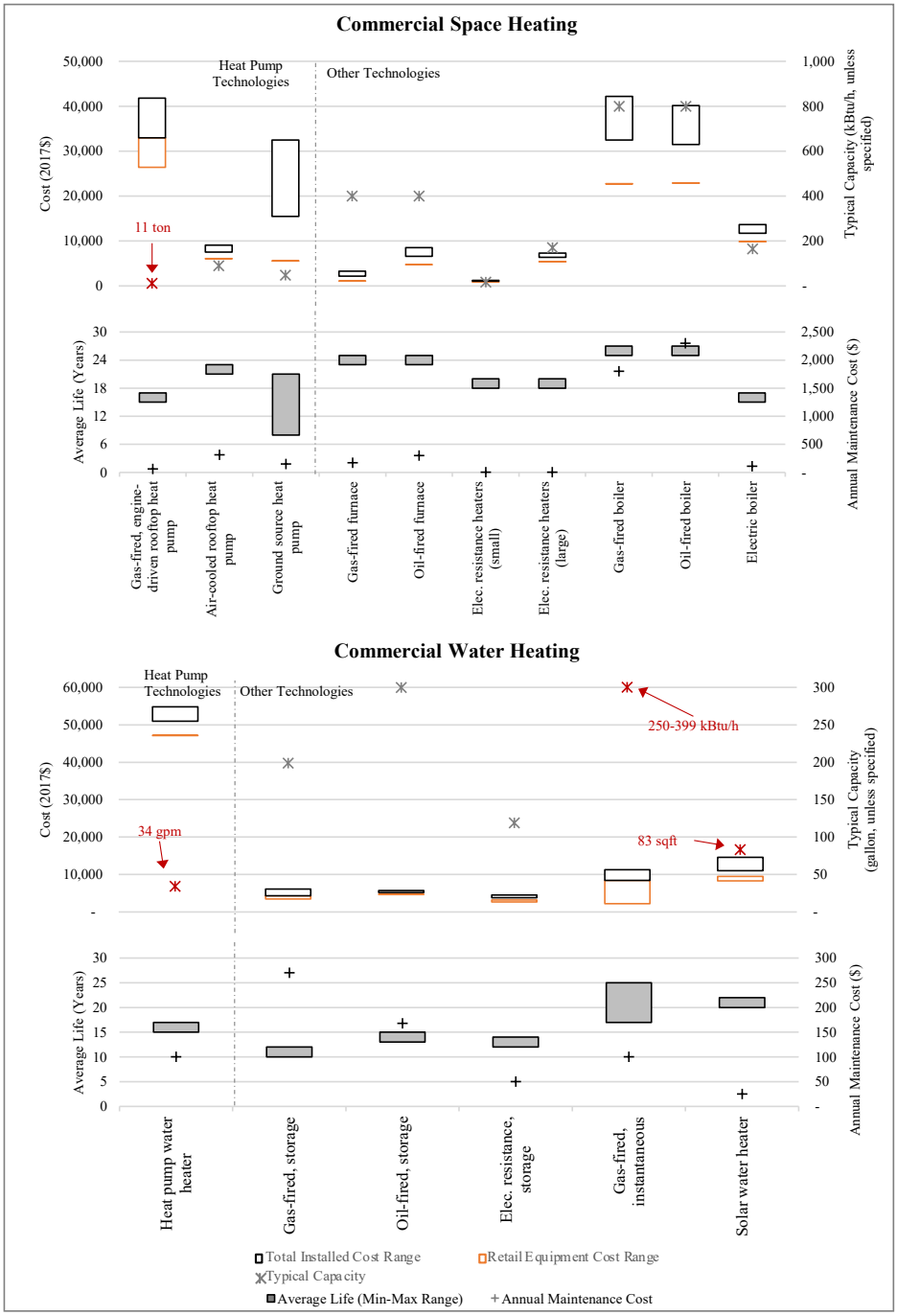


Figure 7 Comparison of heat pump technologies to other technologies: total installed costs with typical capacities and maintenance cost with average life for commercial space heating (top) and water heating (bottom) [6].

The lower plots in each section of the two figures show the min-max ranges of average life (plotted along the primary vertical axis) and average annual maintenance cost (plotted along the secondary vertical axis) for each technology type. Heat pump technologies have average life comparable to other competing technologies and are on the lower maintenance cost regime.

2.3. Financial incentives

HPs have grown in popularity over the past few decades and are now well known to the general public. This increase in awareness was supported by utility and state incentive programs that encouraged deployment of the technologies. Several federal and state-level financial incentives and utility programs for consumers and businesses are available that support HP technologies. Figure 8 shows the total currently active financial incentives and regulatory policies in the United States listed under the Database of State Incentives for Renewables & Efficiency (DSIRE) [7] for HPs including GSHPs. As shown, a large number of rebate and loan programs sponsored by states and utilities exist. Other common mechanisms include tax incentives and tax credits, financing, and grant programs.

Specific to HP technologies, GSHPs qualify for renewable energy tax incentives, whereas no explicit policies or incentives exist for fuel-driven HPs. Numerous appliance and home efficiency programs are in place, which do not specify a technology but support any system, equipment, or appliance that meets the minimum efficiency level (including HP systems). In addition, a few entities provide financial incentives for installers for business development [8].

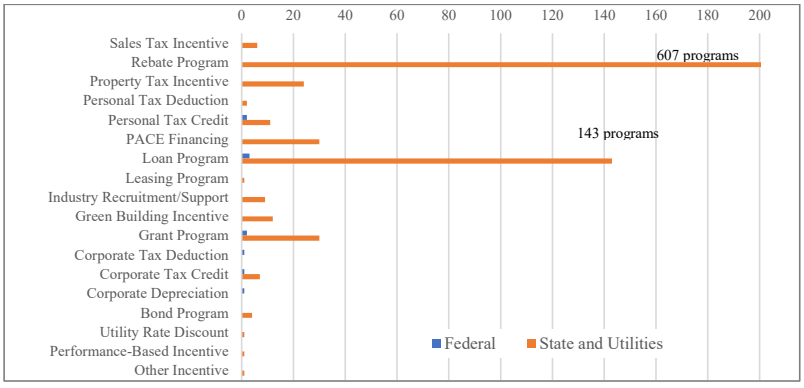


Figure 8 Financial incentives

2.4. Regulatory policy

Figure 9 shows the currently active regulatory policies listed under DSIRE [7] for HP technologies, most of which are enforced by states. On the federal level, the US Department of Energy (DOE) continues to push for elimination of lower efficiency products by implementing more stringent minimum performance regulations, legislation, and standards such as the “Energy Policy Act of 2005 (EPAct 2005)” and the “Energy Independence and Security Act of 2007” (EISA 2007). ENERGY STAR is a voluntary program managed by the US Environmental Protection Agency (EPA) and DOE to promote the eco-friendly industry and cost saving through energy-efficient products. Table 1 summarizes the status of minimum energy performance standards for different HP technologies. The minimum energy performance standards for each technology are provided in the Appendix.

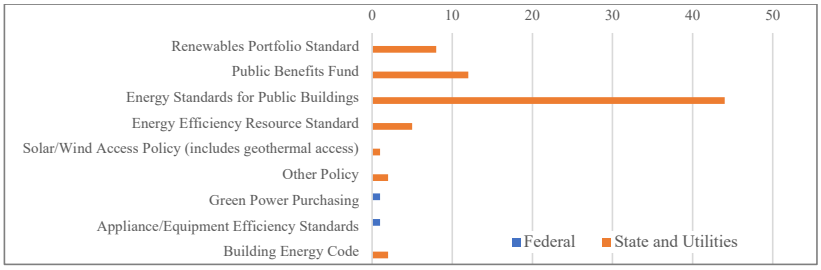


Figure 9 Regulatory policies

Table 1. Status of Minimum Energy Performance Standards for Different HP Technologies [9], [10]

HP Technology		Federal Standard	ENERGY STAR Criteria
Residential	ASHP	Current standards (for central systems) took effect in 2015. See Table A-1	More stringent requirements. See Table A-1
	GSHP	14.1 EER, 3.2 COPh; Current standards (for WSHP[a]) took effect in 2015	See Table A-2
	Air source absorption heat pump	Currently, not covered by NAECA[b]; CEC[c] Title 24 specifies cooling efficiency requirements	
	Heat pump water heater	See Table A-3	See Table A-3
Commercial	Gas-fired, engine-driven rooftop heat pump	Currently, none	
	Air-cooled rooftop heat pump (large ASHPs)	Amended standards in terms of IEER took effect in 2018. More stringent standards will take effect in 2023. See Table A-4	See Table A-4
	GSHP	14.1 EER, 3.2 COPh; Current standards (for WSHP) took effect in 2015	None; Criteria for GSHP apply only to residential applications
	HPWH	Currently, none	Under revision; the public final draft specifies 3.0 COPh

[a]WSHP = Water Source Heat Pump.
[b]NAECA = National Appliance Energy Conservation Act.
[c]CEC = California Energy Commission.

2.5. Technology deployment support

Several trade organizations exist in the United States to promote the deployment of HP technologies with high-quality installations and servicing with industry partners including distributors, vendors, and suppliers. Among these are the Geothermal Exchange Organization [11] and associations in different states, such as Louisiana [12], Minnesota [13], Virginia [14], Colorado, California, and New York [15], and NYSERDA [16]. The California Geothermal Heat Pump Association [17] strives for penetration of the HP into residential and commercial areas while collaborating with the California Energy Commission and the California Public Utility Commission for net zero energy building. There are several regional associations also promoting HP technologies. The Northeast Energy Efficiency Partnerships [18] has programs promoting cold climate ASHPs and HP water heaters (HPWHs) in the northeastern region of the United States. The Northwest Energy Efficiency Alliance has an active program promoting HPWHs [19]. The Electric Power Research Institute has developed an advanced HP specification featuring smart grid response requirements [20].

2.6. Workforce training and education

Some private companies provide classroom and online training for HVAC technicians on HP installation, operation, maintenance and troubleshooting [21][22]. International Ground Source Heat Pump Association (IGSHPA) runs a certification program for GSHP installers and designers [23]. The North American Technician Excellence organization is the largest in the United States for HVAC&R technician certification [24].

3. Overarching R&D in HP Technologies

3.1. Research infrastructure

Within DOE, R&D of HP technologies is supported by the DOE Building Technology Office's (BTO's) HVAC/WH/Appliances Subprogram. This subprogram engages with hundreds of internal and external partners including national laboratories, universities and institutes, industry, small businesses, building owners and operators, other DOE offices and federal agencies, state and local governments, nonprofits, international organizations, and other entities, as well as other subprograms within BTO, to reduce barriers to greater market adoption of premium efficiency technologies (see Figure 10).

DOE's national laboratories provide unique infrastructural support to R&D of HP technologies including modeling capabilities, test beds and simulation platforms, energy system integration facilities, as well as support to regulatory activities. Organizations such as ASHRAE and the Air-Conditioning, Heating, and Refrigeration Technology Institute (AHRTI) also contract R&D to universities, research institutes, and others in the United States and worldwide.

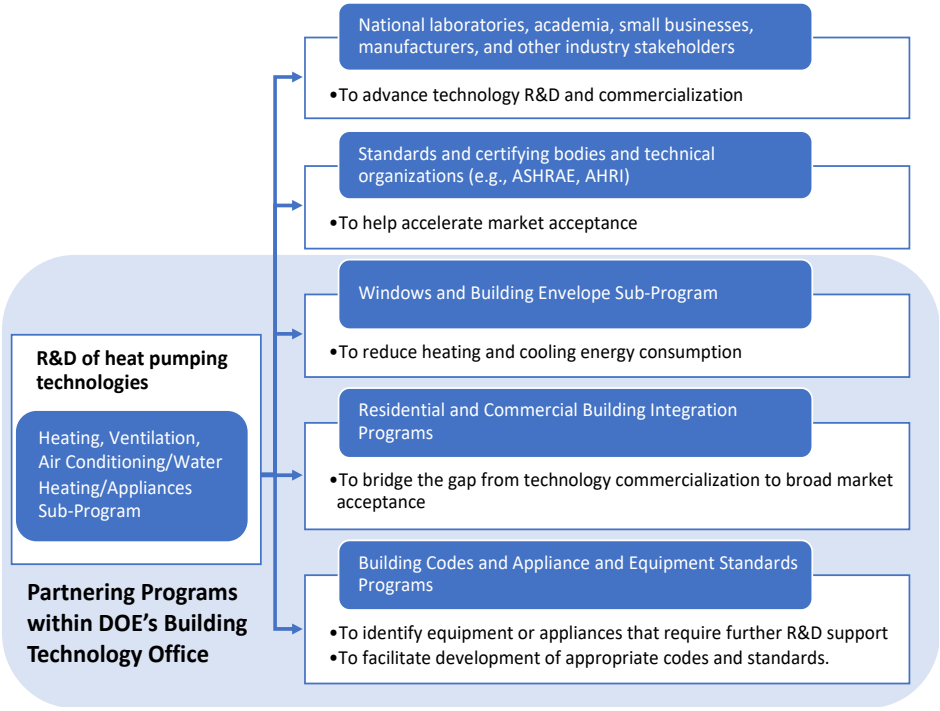


Figure 10 DOE's partners for heat pump R&D [25]

3.2. Research direction

DOE's Multi-Year Program Plan [25] identifies challenges and provides a roadmap for R&D and market simulation. The following are the key challenges for the HP in the R&D, demonstration, and adoption of current and developing HVAC and WH technologies:

- High cost and lack of sustained performance/reliability of high-efficiency systems compared with conventional systems.
- Unrealized design potential of the systems when built out of generic components. Opportunity exists for improved energy and nonenergy performance of many current systems via tailor-made components with advanced materials and designs, though at a higher cost.

- Increasing emphasis on advancing development of nontraditional and advanced vapor compression cycle technologies. Reducing the global environmental impacts of building HVAC&R and WH equipment and systems with advanced technology is extremely challenging.
- High manufacturing costs or lack of manufacturing methods for new components or technologies.

3.3. Research topics

Since 2017, the DOE focus for building energy efficiency R&D, including HPs and HP-related systems, has been increasingly toward advancement of technologies at lower technology readiness levels (TRLs) [25]. So there has been activity on nontraditional cooling and refrigeration technologies (magnetocaloric, elastocaloric, thermoelectric, etc.) and advanced compression technologies (e.g., electrochemical compression). R&D also continues on alternative lower global-warming potential (GWP) refrigerants as well as the low (or zero) GWP alternative technologies. Some work continues in collaboration with manufacturers on maximizing the efficiency of HPWH using lower-GWP refrigerants (moderate to higher TRLs).

The following specific research objectives/topics related to HP technology are being pursued by DOE [25]:

1. Develop and introduce next-generation, transformative technologies for the future such as nontraditional cooling cycles and advanced vapor compression system and component (compressors, heat exchangers, etc.) technologies.
2. Reduce barriers to greater market adoption of premium-efficiency technologies in the near term by refining and reducing the cost of available technologies, including HP technologies for space conditioning and WH.
3. Pursue system-oriented solutions to optimize whole-building energy use. R&D priorities include developing integrated systems that combine end uses, such as energy cascading, as in integrated HP technologies (including ASHPs, GSHPs, and multifunction natural gas–driven HPs).
4. Explore new or different next-generation components to find the best possible cost-effective combinations that have the potential to fully replace or be integrated with conventional technologies, often across end uses.
5. Advance regional solutions to improve the performance of HPs in cold and hot-humid climates (e.g., cold climate heat pump research).
6. Develop advanced vapor compression systems with low- or zero-GWP.
7. Develop HPWH technologies (e.g., electric HPWH with low-GWP; Absorption HPWH; non vapor compression HPWH units, low-GWP solutions).

4. Summary and Outlook

The US HP market has shown steady growth since 2010 following the 2006–2007 housing market collapse. HP shipments have been growing at a faster pace over the past several years relative to competing space heating technologies. The use of ASHPs in cold climates is becoming more feasible through promising R&D and market developments. Current R&D emphases are primarily on advancing development of (1) nontraditional cooling/refrigeration cycles and (2) alternative or advanced compression cycle technologies but also on (3) lower GWP refrigerant alternatives to cope with environmental concerns. Governmental actions, along with public and private-sector incentive programs, promote deploying more efficient HP systems. The future of HP technologies will be highly influenced by the stringent minimum efficiency standards, R&D for advancing nontraditional technologies and alternative lower GWP refrigerants, and tax credits and incentive programs.

Acknowledgments

This research was supported by the DOE Office of Energy Efficiency and Renewable Energy, Building Technologies Office. The authors would like to thank the following individuals and organizations for information and statistical data used in this work: Xudong Wang of AHRI, Xiaobing Liu of ORNL, Jerry Groff of Groff Associates. This manuscript has been authored by UT-Battelle, LLC, under contract DE-AC05-00OR22725 with the US Department of Energy (DOE). The US government retains and the publisher, by accepting the article for publication, acknowledges that the US government retains a nonexclusive, paid-up, irrevocable, worldwide license to publish or reproduce the published form of this manuscript, or allow others to do so, for US government purposes. DOE will provide public access to these results of federally sponsored

research in accordance with the DOE Public Access Plan (http://energy.gov/downloads/doe-public-access-plan).

Appendix

Table A-1. Standard for Residential Air-Source Heat Pump [6]

Residential ASHP Product Class	Current Federal Minimum Efficiency Standards			Current ENERGY STAR Criteria		
	Min.SEER	Min.HSPF	Max. Off Mode Power (W)	Min.SEER	Min.EER	Min.HSPF
Split-System	14	8.2	33	15	12.5	8.5
Single-Package	14	8	33	15	12	8.2
Small-Duct, High Velocity	12	7.2	30	-	-	-
Space-Constrained	12	7.4	33	-	-	-

Note:

- Units for SEER, HSPF and EER are in Btu/Wh (divide by 3.412 to get equivalent dimensionless values).
- For split-system air conditioners (cooling only), the minimum SEER increased to 14 in southern climate regions, while the 13 SEER standard established in 2006 remained effective in the north. Whereas, for split-system ASHPs, the minimum SEER increased to 14 and the minimum HSPF increased to 8.2 in all climate regions.

Table A-2. ENERGY STAR Criteria for Water-to-air Ground Source Heat Pumps

Type	Heating COP	Cooling EER
Closed Loop	3.6	17.1
Open Loop	4.1	21.1
Direct Expansion	3.6	16

Table A-3. Federal Standard and ENERGY STAR Criteria for Residential Electric Storage and Heat Pump Water Heater

Volume Range	Draw Pattern	Federal Standard[1]	Federal minimum UEF for typical sizes	ENERGY STAR
≥ 20 gal and ≤ 55 gal	Very Small	UEF=0.8808-(0.0008*Gal)	No models on the market	2.0
	Low	UEF=0.9254-(0.0003*Gal)	0.91 for a 27-gallon water heater	2.0
	Medium	UEF=0.9307-(0.0002*Gal)	0.92 for a 36-gallon water heater	2.0
	High	UEF=0.9349-(0.0001*Gal)	0.93 for a 45-gallon water heater	2.0
> 55 gal and ≤ 120 gal	Very Small	UEF=1.9236-(0.0011*Gal)	No models on the market	2.2
	Low	UEF=2.0440-(0.0011*Gal)	No models on the market	2.2
	Medium	UEF=2.1171-(0.0011*Gal)	2.03 for a 77-gallon water heater	2.2
	High	UEF=2.2418-(0.0011*Gal)	2.15 for a 82-gallon water heater	2.2

Notes:

- Standards for residential electric storage WH also apply to integrated HPWH.
- Federal standards that came into effect in April 2015 effectively mandate heat pump technology for electric storage water heaters with storage volume > 55 gallons. Thus, the standards for the >55-gallon range and all ENERGY STAR levels are only achievable through heat pump technology.

Table A-4. Federal Standard and ENERGY STAR Criteria for Commercial Air-cooled Packaged Rooftop Heat Pump (large ASHPs) [6]

Cooling Capacity (kBtu/h)	Heating Type	Federal Standard (1/1/2010~)		ENERGY STAR version 2.2 (1/1/2011~)		
		Min. EER	Min. COP at 47°F	Min. EER	Min. IEER	Min. COP at 47°F
Small (≥ 65 and < 135)	Electric resistance or none	11.0	3.3	11.3	11.4	3.35
	Any other type	10.8	3.3	-	-	-
Large (≥ 135 and < 240)	Electric resistance or none	10.6	3.2	10.9	11.0	3.25
	Any other type	10.4	3.2	-	-	-

Note:

- This values in this table are for air-cooled commercial packaged rooftop heat pumps. There are different standards for many other types of commercial heat pumps.
- In 2018, the DOE-regulated metric switched from EER to IEER, and the minimum IEER for ASHPs with electric resistance or no heating system and any other type (e.g., heat pump) are set at 12.2 and 12.0, respectively, for small capacity systems and 11.6 and 11.4 for large capacity systems. They are effective until 2022.

References

[1] US Census, *2017 Characteristics of New Housing*, 2018, https://www.census.gov/construction/chars/pdf/c25ann2017.pdf
[2] AHRI, Historical Data, 2019, http://www.ahrinet.org/Resources/Statistics/Historical-Data, Accessed 7 Jan 2020.
[3] Lapsa, Melissa, G. Khowailed, K. Sikes, and V. Baxter, 2017, "Heat Pumps in North America – 2017 Regional Report," *Proceedings of the 12th IEA Heat Pump Conference*, Rotterdam, Netherlands, May 2017.
[4] EIA, Geothermal Heat Pump Manufacturing Activities, 2010, https://www.eia.gov/renewable/annual/geothermal/archive/geothermalrpt09.pdf
[5] EIA, Electric Power Monthly with Data for November 2018, 2019, https://www.eia.gov/electricity/monthly/current_month/epm.pdf
[6] Navigant Consulting, Inc. Appendix A, EIA - Technology Forecast Updates – Residential and Commercial Building Technologies – Reference Case. Updated Buildings Sector Appliance and Equipment Costs and Efficiency. April 2018, https://www.eia.gov/analysis/studies/buildings/equipcosts/pdf/appendix-a.pdf
[7] DSIRE, Database of State Incentives for Renewables & Efficiency, http://www.dsireusa.org/, Accessed 7 Jan 2020.
[8] New York State Energy Research & Development (NYSERDA) ASHP Program, https://www.nyserda.ny.gov/All-Programs/Programs/Air-Source-Heat-Pump-Program, Accessed 7 Jan 2020.
[9] US Department of Energy, Standards and Test Procedures, https://www.energy.gov/eere/buildings/standards-and-test-procedures, Accessed 7 Jan 2020.
[10] EnergyStar, https://www.energystar.gov/products, Accessed 7 Jan 2020.
[11] Geothermal Exchange Organization, https://www.geoexchange.org/geo/, Accessed 7 Jan 2020.
[12] Louisiana Heat Pump Association, https://www.lhpa.us/about-us/, Accessed 7 Jan 2020.
[13] Minnesota Geothermal Heat Pump Association, https://www.minnesotageothermalheatpumpassociation.com/, Accessed 7 Jan 2020.
[14] Virginia Geothermal Heat Pump Association, http://www.vgshpa.org/, Accessed 7 Jan 2020.
[15] New York Geothermal Energy Organization, https://ny-geo.org/, Accessed 7 Jan 2020.
[16] New York State Energy Research and Development Authority, https://www.nyserda.ny.gov, Accessed 7 Jan 2020.
[17] California Geothermal Heat Pump Association, https://www.californiageo.org/, Accessed 7 Jan 2020.
[18] Northeast Energy Efficiency Partnerships, https://neep.org/, Accessed 7 Jan 2020.
[19] Northwest Energy Efficiency Alliance, https://neea.org/our-work/advanced-water-heater-specification, Accessed 7 Jan 2020.
[20] Electric Power Research Institute, www.epri.com, Accessed 7 Jan 2020.
[21] Carrier University, https://www.carrier.com/carrieruniversity/en/us/, Accessed 7 Jan 2020.
[22] TPC Training, https://www.tpctraining.com/products/heat-pumps, Accessed 7 Jan 2020.
[23] International Ground Source Heat Pump Association, https://igshpa.org/training/, Accessed 7 Jan 2020.
[24] North American Technician Exchange, https://www.natex.org/site/1/Home, Accessed 7 Jan 2020.
[25] DOE, Building Technologies Office Multi-Year Program Plan, Fiscal Years 2016–2020, https://www.energy.gov/sites/prod/files/2016/02/f29/BTO%20Multi-Year%20Program%20Plan%20-%20Final.pdf

13th IEA Heat Pump Conference
April 26-29, 2021 Jeju, Korea

Experimental Research on Air-source Heat Pump Using Heat Pipes as Heat Radiator

Xu Shuxue, Shao Yueyue, Wang Yueyue, Ma Guoyuan*

Beijing University of Technology , Chaoyang district Pingleyuan No 100, Beijing, 100124, China

Abstract

In this study, a concept of air-source heat pump using heat pipes as heat radiator system (ASHPP) for room heating was proposed. The heat pipes radiator was developed to replace the heating terminal equipment used in traditional heat pump plants. All the heat radiators were connected in series. A tested room with artificial load was constructed and an experimental apparatus of ASHPP system was developed. Temperature distribution of each heat radiator has been experimentally investigated. The variations of system heating performance under the condition of different indoor air temperature and outdoor air temperature were researched. The purpose of this study is to provide technique reference for developing new heat pump room heating system.

Keywords: Heat pump;Heat pipe;Compressor;Heating;

1. Introduction

As an efficient technology for energy conservation, air source heat pumps have been widely used in industry and daily life, and are mainly applied for heating water or air. Particularly for household appliances, a heat pump can use water or refrigerant-cooled chillers for cooling in summer and heating in winter. It has the advantages of a high performance coefficient for water-cooled chillers in summer and the ability to function as a heat pump in winter (Willem H et al, 2017 [1] ; Østergaard et al, 2016 [2] ; Chai Qinhu et al,2002 [4]).

Winter heating is of significant concern in northern China, where the requirements for heating quality and thermal comfort have increased. A large amount of energy is consumed in the winter heating period in most of the northern regions of China, and inefficient heating will result in severe environmental pollution. In recent years, the “coal to electricity” program has been applied on a large scale. More than 2 million air source heat pumps were installed in more than 1 million family homes. In some rural areas that cannot be reached by district heating, air source heat pumps are the technology promoted by the government.

The main type of heat pump used in the China “Jing Jin Ji” area is the water loop air source heat pump, and a schematic diagram of the typical form of this common heat pump type is shown in Fig. 1. As shown in Fig. 1, the system consists of an outdoor unit, water pump, water expansion tank, water tank, and indoor radiator. however, they have some disadvantages, including a complex structure and high failure rate, as well as high electrical energy consumption, especially the leak-proof and anti-freeze of the waterway has always caused troubles to heat pump users. (Li Suhua et al, 2014 [5]). In a recent study (Xu et al, 2018 [3]), a new air source heat pump system was proposed. In that system, heat pipes were used as the heat radiator, and a compressor drove the heat pipes to release heat to the room. Based on this research, in order to meet the actual distribution of heating space, a “heat pump with multi-split heat pipe heat radiators” (ASHPP) was proposed for room heating. The heat pipe heat radiators were connected in series, and 9 groups of heat pipe heat radiators were used. At present, there are also many studies at home and abroad for systems that

combine heat pipes and heat pumps. Chen Hongbing et al, 2016 [6] built a heat pipe solar PV/T heat pump system. The test results showed that the average daily power efficiency of the heat pipe mode was 25.7% higher than that of a single photovoltaic power generation system. QU Peipei et al, 2018 [7] established a new dual-evaporator heat pump and separate heat pipe coupling system to investigate the influence of factors such as outdoor temperature and solar radiation intensity on performance parameters under three operating modes.

In this paper, a prototype of the proposed ASHPP heating system was built and an experimental study was performed to analyze the temperature distribution of each radiator. The variation of the heating performance of the system with indoor air temperature and outdoor air temperature were studied. The goal of this research was further improving the energy efficiency level of traditional domestic heat pumps, and developing a new domestic heating technical means.

2. Circulation theory

The ASHPP system is shown in Fig. 1. It consists of a compressor, multiple condensers coupled with heat pipe heat radiators, consists of a compressor, multiple condensers coupled with heat pipe heat radiators, a throttling device, an evaporator, and connecting tubes. The heat pump system operates in servers with the vapour compression circulation. The liquid refrigerant is evaporated in the evaporator and the vapour is absorbed into the compressor. With power consumption in the compressor, the vaporised refrigerant is transformed into a supersaturated vapour at higher temperature/pressure. As shown in Fig. 1, the refrigerant flows out of the compressor through 9 groups of condensers and heat pipes, which combine to function as a heat exchanger. Each piece of equipment releases its embodied thermal energy into a single room, leading to an increase in the in-room air temperature.

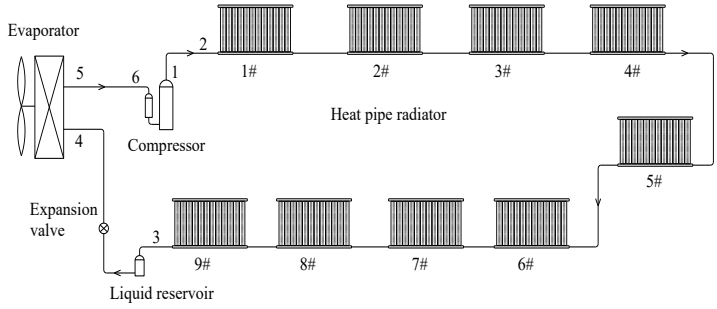


Figure 1: ASHPP system

3. Experimental Study

The heating performance of ASHPP system was mainly affected by indoor and outdoor temperatures. This article built a system and tested it in different indoor and outdoor temperatures. The experimental device mainly included a compressor, finned tube heat exchangers, axial flow fans, etc. The specific models and parameters of the compressor are shown in Table 1.

Table 1 Specific models and parameters of compressors

Model	Frequency	Voltage	LRA I-Block	I-Open max	Volume	Speed
ZW34KSE-PFS-582	50 Hz	220VAC	75.2A	19.75A	8.0 m^3/h	2900/min

The ASHPP system was placed in air enthalpy-type psychrometric rooms, as shown in Fig. 2. A total of 9 indoor units were connected to the outdoor unit in series, and pressure sensors were installed at the inlet and inside each indoor unit. The temperature of both the indoor and outdoor chambers can be controlled from -10 ℃ to 50 ℃.

In the experimental system, the air-side inlet and outlet temperature and humidity could be measured with a temperature transducer (Pt100) and humidity transducer. A hermetic-type compressor with a nominal capacity of 2100 W designed for R410A was installed. Refrigerant pressures in the heat pump and heat pipes were measured using pressure transducers with an uncertainty of ±0.5%. Temperatures were measured using Pt100 temperature transducers with an uncertainty of ±0.15 °C. A mass flow meter was installed to measure the mass flow rate of the refrigerant through the condenser. The power input to the compressor was measured using a power meter with an uncertainty of ±0.5%.

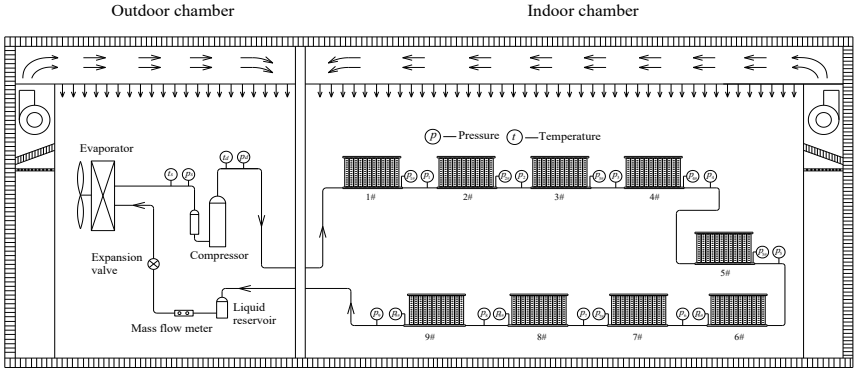


Figure 2: Schematic diagram of the prototype test system

4. Results and discussion

4.1. Radiator surface temperature distribution

Figure 3 shows that, with the exception of the first heat pipe, the surface temperatures of the heat pipes are approximately consistent with each other. For example, the surface temperature of heat pipe 2 is 50 ℃, while it is 49 ℃ at the final heat pipe (#9) when the outdoor temperature t_o=-10 ℃. The surface temperature of first heat pipe (#1), is approximately 18–25 ℃ higher than the other heat pipes. This was because the high-temperature compressor discharge vapor first entered in the first heat pipe (#1), exothermic heat of the first heat pipe contained some sensible heat, so the temperature was high. The surface temperature of heat pipe 2-9 was similar, the final heat pipe (#9) was slightly lower. This indicated that the number of end heat pipe radiators in series matched with the heat pump well, and the refrigerant was fully condensed. Figure 3 also shows that the difference in surface temperature between the first heat pipe and the other heat pipes varies. The lower the outdoor temperature, the larger this surface temperature difference will be. The reason for this is that when the outdoor temperature is lower, the compressor discharge temperature is higher, and the first heat pipe will receive the highest temperature refrigerant from the compressor discharge ports; thus, the surface temperature difference between the first heat pipe and the other heat pipes is increased.

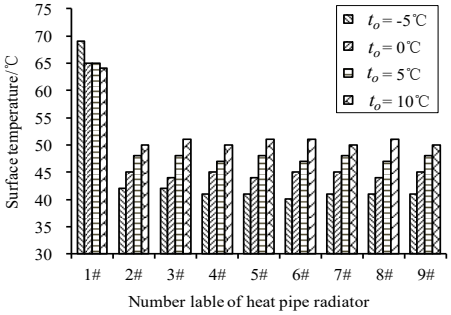


Figure 3: Surface temperature of ASHPP system

4.2. Heating performance of the ASHPP system

According to the experimental results, the heating performance of the system is analyzed. The unit heating capacity formulas are calculated as follows:

$$Q = m(h_1 - h_2) \tag{1}$$

In the formula:
Q——Heating capacity, kW;
m——Mass ratio of refrigerant to mixed liquid in mixed liquid of refrigerant and lubricating oil, kg/s;
h_1——Specific enthalpy of refrigerant at the inlet of heat exchanger, kJ/kg;
h_2——Specific enthalpy of refrigerant at the outlet of heat exchanger, kJ/kg;

The system power consumption was analyzed with the power data recorded by the power meter when the system reached at a stable operating state under a given working condition. The COP was calculated by the power meter and the heating value was calculated by the enthalpy difference during the system reaches at a stable operating state:

$$Q = m(h_2 - h_3) \tag{2}$$

According to calculation, the variation in heating performance with different refrigerants is shown in Fig. 4. Four different refrigerants (R134a, R410A, R32, and R718) were considered, with outdoor temperatures of -10 ℃, -5 ℃, and 0 ℃; the indoor temperature was 20 ℃. Figure 5 indicates that the selection of refrigerant g has an effect on the heating capacity and heating COP of the system. R32 and R410A yield the highest heating capacity and heating COP. Among the four types of refrigerants, the heating COP value with R32 is approximately 1.3%–2.2% higher than that with R134a. For example, the heating COP value of R32 can reach 2.8 for an outdoor temperature of -10 ℃ and indoor temperature of 20 ℃. R718 can also be used as a heat pipe working fluid for room heating, but its heating COP is relatively low, about 8% less than that of R410A.

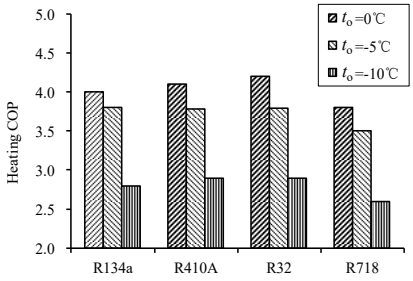


Figure 4: Heating COP for different refrigerant

5. Conclusion

An air-source heat pump with multi-split heat pipe heat radiators (ASHPP) system for room heating was proposed. Heat pipe radiators were connected in series and driven by a compressor and condenser. A test room with an artificial load was constructed, and an experimental ASHPP system was developed. The pressure and temperature distribution were investigated experimentally. Variations in the system heating performance with different numbers of heat pipes were investigated, and the most important conclusions of this study are as follows:

1) Except for the first heat pipe, the surfaces of the other heat pipes were approximately consistent with each other. The surface temperature of the first heat pipe was about 18–25 ℃ higher than that of the other heat pipes.

2) R32 and R410A yield the highest heating capacity and heating COP. Among the four types of refrigerants tested, the heating COP value of R32 was about 1.3%–2.2% higher than that of R134a. R718 can

also be used as the heat pipe working fluid for room heating, but its heating COP was relatively small, about 8% less than that of R410A.

3) When the ASHPP system was run with an outdoor temperature of -10 ℃ and indoor temperature of 20 ℃, the heating COP can reach 2.8.

6. Acknowledgements

This project was supported by the General project of science and technology program of Beijing Education Committee (Grant No. SQKM201810005011). Young Top-Notch Talents Team Program of Beijing Excellent Talents Funding (2017000026833TD02)

7. References

[1] Willem H, Lin Y, Lekov A. Review of energy efficiency and system performance of residential heat pump water heaters, Energy and Buildings. 2017, 143: 191-201
[2] Østergaard, PA, Andersen, AN. Booster heat pumps and central heat pumps in district heating, Int J Refrig. 2016,184: 1374-1388
[3] Xu SX, Ding RC, Niu JH, Ma GY. Investigation of air-source heat pump using heat pipes as heat radiator, Int J Refrig. 2018, 90: 91-98
[4] Chai QH, Ma GY. Status and progress of research on low temperature adaptability of air source heat pumps, Energy Engineering (in Chinese), 2002 (5): 25-31
[5] LI SH, DAI BM, MA YT. The development and situation analysis of air source heat pump, Refrigeration Technology (in Chinese), 2014, 34(1): 42-48
[6] Chen HB, Zhang L, Chu S, et al. Research on performance of heat pipe solar PV/T heat pump system, Renewable Energy, 2016, 34 (5): 639-644
[7] Qu PP. Performance analysis of coupled system of double evaporator heat pump and separate heat pipe, Nanjing Normal University (in Chinese), 2018

13th IEA Heat Pump Conference
April 26-29, 2021 Jeju, Korea

ELECTROCHEMICAL COMPRESSION OF AMMONIA/ HYDROGEN BLENDS FOR HEAT PUMP APPLICATION

Ashish Chouhan[a], Utsav R. Aryal[a], Premanand O. Sivakumar[b], Bamdad Bahar[c*], Ajay K. Prasad[a]

[a]Department of Mechanical Engineering, University of Delaware, Newark DE 19716, USA
[b]Department of Chemical Engineering, University of Delaware, Newark DE 19716, USA
[c]Xergy Inc., 299A Cluckey Dr., Harrington DE 19952, USA

Abstract

Ammonia is widely used as a refrigerant in air conditioning, food preservation and for fuel storage purposes. Ammonia is an attractive candidate for electrochemical compression (ECC). Electrochemical compressors can be an ideal replacement for mechanical compressors because of noiseless operation, higher efficiencies at lower voltages and the ability to operate without the use of Global Warming Potential (GWP) working fluids. This paper explores the electrochemical compression of ammonia with hydrogen as a carrier gas, using fuel cell type hardware. A perfluorosulfonic acid (PFSA) membrane allows the transfer of ammonia, using hydrogen as a carrier gas, by the conduction of NH_4^+ ions from anode to cathode. The ECC performance was evaluated using electrochemical methods using a single cell at STP. The effects of back-diffusion in the compression process are highlighted and suggestions to improve the ECC of ammonia-hydrogen blends are proposed.

Keywords: Ammonia; Hydrogen; Electrochemical compression; Nernst voltage; Diffusion; Compression Ratio

1. Introduction

Global energy demand is rising rapidly as we face the depletion of conventional sources of energy. There is a need to look for sustainable alternatives to traditional mechanical energy conversion devices such as heat pumps that account for a large and growing portion of the global demand for energy. The developments in fuel cell technology to generate electricity in a clean and environment-friendly manner has placed hydrogen as an important energy vector to meet both stationery and automobile power generation applications. Ammonia is a rich source of hydrogen and could also play a significant role as an energy vector in a hydrogen economy. Moreover, ammonia itself is widely used as a refrigerant in large scale industrial heat pump applications particularly in applications involving the food chain. Electrochemical compression of ammonia therefore can be used for conveying ammonia when used as a bulk energy vector but could also be an alternative to mechanical compressors for heat pump applications.

Electrochemical compression is superior to mechanical compression as it offers the potential to compress a working fluid at higher efficiency, noiseless operation, usage of green refrigerants, and greater reliability due to a lack of moving parts.

The first validation of the concept of an electrochemical compressor based on hydrogen was done by Sedlak et al. [1], who applied a potential difference to transfer protons across a proton exchange membrane and

* Corresponding author. Tel.: +1-302-218-4279.
E-mail address: Bamdad.bahar@xergyinc.com

achieved higher pressures. Rohland et al. [2] and Strobel et al. [3] carried the idea forward to electrochemically transfer and purify hydrogen. All these studies were only focused on hydrogen compression until 2009, when the general idea of using electrochemical compression for heat pump applications was pioneered by Bahar et al. [4]. Bahar et al. [5] then proposed the use of ammonia in electrochemical compressors (ECC) using hydrogen as the carrier gas by engaging perfluorosulfonic acid (PFSA) membranes to electrochemically compress ammonia under a potential difference. An overall system analysis was favorably reported by Tao et al. [6] in 2017.

Ammonia is a well-established contaminant for PFSA membranes in fuel cell applications and is actively scrubbed out of reformed hydrogen gas streams used for fuel cells. Our challenge in this project was to understand and then develop transportation mechanisms for ammonium ions in ion-exchange membranes.

The hardware of an ECC is similar to that of a fuel cell and consists of a membrane-electrode-assembly (MEA) sandwiched between two graphite plates with flow fields for gas distribution, held together by end plates on either side. The entire assembly is held together by eight bolts, all maintained at a same torque (Figure 1).

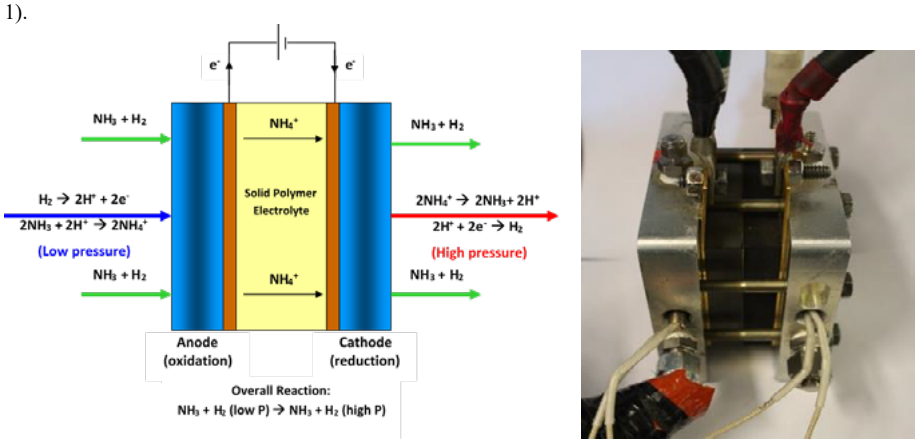


Fig. 1. Schematic of an electrochemical ammonia compressor (left); ECC hardware (right)

A mixture of ammonia and hydrogen gases is fed to the anode, where, by applying a DC voltage, hydrogen gets oxidized to protons (H^+), which combine with ammonia to form ammonium ions ($NH_4{}^+$), as in Equations 1 and 2.

$$H_2 \rightarrow 2H^+ + 2e^- \tag{1}$$

$$2NH_3 + 2H^+ \rightarrow 2NH_4{}^+ \tag{2}$$

The ammonium ions get transferred across the membrane to the cathode. Two electrons are required for this reaction to take place, as per Equation 1. The ammonium ions are reduced at the cathode to regenerate ammonia and hydrogen gases at a higher pressure, as shown in Equations 3 and 4.

$$2NH_4{}^+ \rightarrow 2NH_3 + 2H^+ \tag{3}$$

$$2H^+ + 2e^- \rightarrow H_2 \tag{4}$$

The overall electrochemical reaction can be written as:

$$2NH_3 + H_2\,(low\ pressure) \rightarrow 2NH_3 + H_2\,(high\ pressure) \tag{5}$$

The production of protons facilitates the formation of ammonium ions which is the species conducted by the PFSA membrane. The membrane needs to be functionalized by soaking in aqueous ammonia solution overnight. In this paper, the use of ammonia as a working fluid in an electrochemical compressor (ECC) is

reviewed. The performance of the ECC is presented in the form of output pressures reached within the phase conversion pressure limits of gaseous ammonia at room temperature; cathode pressures and current densities are also plotted for all voltages tested.

The membrane used for experiments was a sulfonated tetrafluoroethylene-based fluoropolymer-copolymer membrane, 50 µm thick. The platinum (Pt) catalyst loading on the electrodes was 0.3 mg/cm^2. The membranes were functionalized for ion exchange from H^+ to $NH_4{}^+$ by soaking in ammonia solution overnight, after which, they were thoroughly rinsed with deionized water and dried gently using paper towels. The membrane surface has residual ammonia and does not readily stick to the electrodes, so the membrane and electrodes were stacked together inside the ECC and assembled by tightening the bolts. The ECC was assembled with 25 cm^2 hardware.

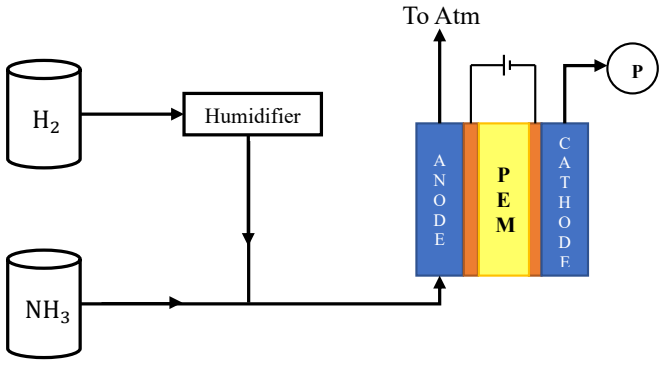


Fig. 2. Experimental setup of the electrochemical ammonia compressor

The ECC was tested at room temperature (22°C) and pressure (1 atm). The PFSA membranes used for experiments only function when properly hydrated [7, 8]. Hence, it is important to maintain adequate humidity in the system. The inlet gas stream at the anode consisted of a 50-50 mixture of fully hydrated hydrogen (100% RH at a flow rate of 100 cm^3/min) and dry ammonia (0% RH at a flow rate of 100 cm^3/min), resulting in an overall humidity around 50%, whereas, the cathode port terminated with a pressure transducer. A schematic of the experimental setup is shown in Figure 2. The ammonia inlet stream was kept dry as ammonia reacts with water to form ammonium hydroxide, which can precipitate inside the humidifier chamber. The anode outlet was open to the environment, hence the anode pressure was fixed at 1 atm. The ECC cell was tested using the fuel cell test station (FCTS) from Arbin Instruments. The experiments were performed at four different operating voltages: 0.025, 0.05, 0.075 and 0.1 V.

2. Results and Discussion

Before preparing the MEA, the membranes were soaked in ammonia solution, which makes them alkaline in nature implying that the contribution of H^+ to the generated current can be neglected, which is also evident by the almost zero current when the ECC was tested with only hydrogen at the anode. Also, the total amount of ammonia and hydrogen gases generated at the cathode can be expressed in terms of total current I:

$$\dot{n}_{H_2} = \frac{I}{2F} \tag{6}$$

$$\dot{n}_{NH_3} = \frac{I}{F} \tag{7}$$

where $\dot{n}_{H2}$ is the mol/s of hydrogen transferred across the membrane according to Faraday's law [9], $\dot{n}_{NH3}$ is the mol/s of ammonia transferred, and F is Faraday's constant.

The applied cell voltage E_{cell} is the sum of the Nernst potential, the activation overpotential, and ohmic (IR), mass transport and back diffusion losses [10]:

$$E_{cell} = E_{Nernst} + \Delta E_{Activation} + \Delta E_{Ohmic} + \Delta E_{Transport} + \Delta E_{Back\ Diffusion} \tag{8}$$

The activation overpotential $\Delta E_{Activation}$ is a sum of the overpotentials at the anode and the cathode. The ohmic losses ΔE_{Ohmic} arise mainly due to the membrane resistance and contact resistance between difference components of the ECC. At high current densities, mass transport losses denoted by $\Delta E_{Transport}$ could become significant due to the inability to maintain adequate reactant gas supply to the anode catalytic sites; however this loss term is not expected to be significant in the case of ammonia compression due to the small operating currents. $\Delta E_{Back\ Diffusion}$ represents losses due to back diffusion of ammonia and hydrogen from the pressurized cathode to the anode through the membrane. All of these losses cause the required voltage to exceed the Nernst voltage for a given compression ratio. The Nernst potential E_{Nernst} defined by the Nernst equation, Equation 9, depends logarithmically on the pressure ratio between the cathode (high) and anode (low). The total pressure at the anode and cathode can be expressed in terms of the partial pressures of hydrogen and ammonia.

$$E_{Nernst} = \frac{RT}{F} ln\left\{\left(\frac{P_{H_2,out}}{P_{H_2,in}}\right)^{\frac{1}{2}}\left(\frac{P_{NH_3,out}}{P_{NH_3,in}}\right)\right\} \tag{9}$$

where R is the universal gas constant, and T is the cell temperature in K.

The ECC performance at different operating voltages is presented in Figure 3. For each applied voltage, the current density (red curve) is the highest at the start of the operation and declines rapidly at first before gradually reaching an equilibrium value after a few hours. Concurrently, the cathode pressure (blue curve) rises rapidly at the start and eventually plateaus to an equilibrium value. Both the initial and equilibrium current densities increase with the applied voltage as shown in Figure 3. Similarly, the equilibrium pressures also increase with the applied voltage. The fact that the current is non-zero although the cathode pressure has equilibrated indicates that back-diffusion is occurring.

The backward diffusive flux $(\dot{n}_b)$ as given by Fick's law is directly proportional to the difference in the concentration of individual species (ΔC) across the membrane and inversely proportional to the membrane thickness (d):

$$\dot{n}_{b,NH_3} = \mathcal{D}_{NH_3} A \frac{\Delta C_{NH_3}}{d}, \quad \dot{n}_{b,H_2} = \mathcal{D}_{NH_3} A \frac{\Delta C_{H_2}}{d} \tag{10}$$

where $\dot{n}_{b,NH_3}$ and $\dot{n}_{b,H_2}$ are the backward diffusive fluxes for ammonia and hydrogen, respectively. $\mathcal{D}_{NH_3}$ and $\mathcal{D}_{NH_3}$ are the diffusivities of ammonia and hydrogen, respectively, in the membrane. The concentration of ammonia and hydrogen at either face of the membrane is directly related to their partial pressures through Henry's law. Henry's constant (H) depends on the type of membrane and the gas in contact with the membrane [10].

$$C = HP \tag{11}$$

Combining Equations 10 and 11, we can express the diffusive fluxes as a function of cathode and anode pressures as:

$$\dot{n}_{b,NH_3} = (\mathcal{D}H)_{NH_3} A \frac{(P_c - P_a)_{NH_3}}{d} \tag{12}$$

$$\dot{n}_{b,H_2} = (\mathcal{D}H)_{H_2} A \frac{(P_c - P_a)_{H_2}}{d} \tag{13}$$

where $\mathcal{D}H$ is the permeability constant and depends on the nature of the gas and membrane. Denoting $\dot{n}_n$ as the net molar flow rate to the cathode (= forward flux – back diffusive flux), and assuming that both ammonia and hydrogen follow the ideal gas law, we can write:

$$(\dot{n}_n)_{NH_3} = \dot{n}_{f,NH_3} - \dot{n}_{b,NH_3} = \frac{\dot{P}_{c,NH_3} V_c}{RT} \tag{14}$$

$$(\dot{n}_n)_{H_2} = \dot{n}_{f,H_2} - \dot{n}_{b,H_2} = \frac{\dot{P}_{c,H_2} V_c}{RT} \tag{15}$$

where $\dot{P}_c$ is the rate of cathode pressure rise (Pa/s), and V_c is the pressurized volume on the cathode side (m^3). Substituting the expressions for forward and backward fluxes in Equations (14) and (15), the compression equations can be written as:

$$\text{Ammonia: } \frac{I}{F} - (\mathcal{D}H)_{NH_3} A \frac{\left(P_{NH_3,c} - P_{NH_3,a}\right)}{d} = \frac{\dot{P}_{NH_3,c} V_c}{RT} \tag{16}$$

$$\text{Hydrogen: } \frac{I}{2F} - (\mathcal{D}H)_{H_2} A \frac{\left(P_{H_2,c}(t) - P_{H_2,a}\right)}{d} = \frac{\dot{P}_{H_2,c} V_c}{RT} \tag{17}$$

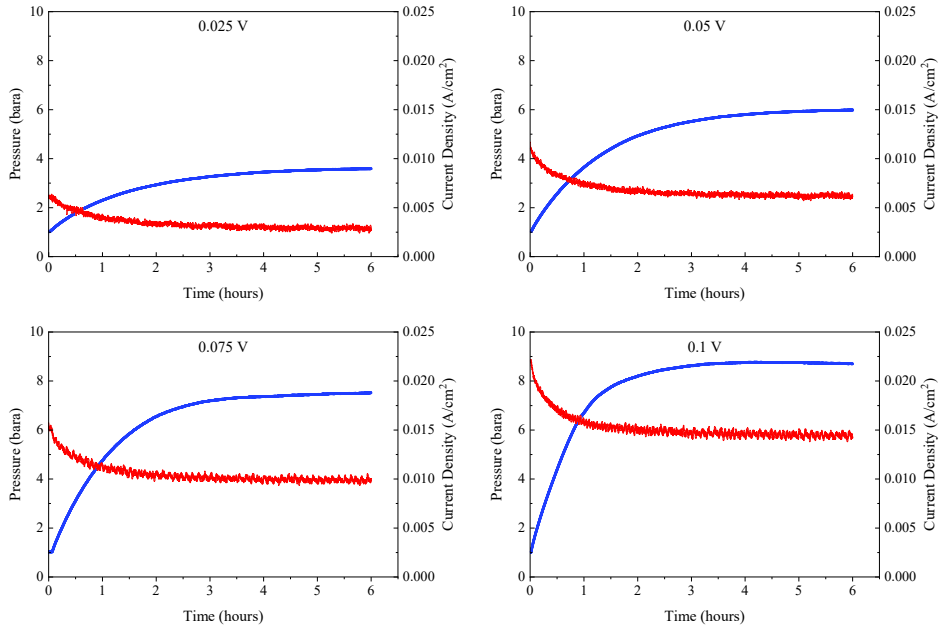


Fig. 3. Pressure (blue) and current density (red) vs. time for Nafion 212 at different applied voltages

Since ammonium is a much bulkier ion than a proton, the current density observed in this case is much less than in the case of a pure hydrogen compressor [7].

When the pressure reaches its equilibrium value, $\dot{P}_c = 0$, in an ideal scenario without back-diffusion, the equilibrium current would also reduce to zero. However, in reality, the forward flux equals the backward flux at steady state, and hence, there is an equilibrium current which maintains the cathode at equilibrium pressure $\left(P_{c,eq}\right)$given by Equations (18) and (19).

$$\frac{I_{eq}}{F} = \frac{(\mathcal{D}H)_{NH_3} A \left(P_{c,eq} - P_a\right)_{NH_3}}{d} \tag{18}$$

$$\frac{I_{eq}}{2F} = \frac{(\mathcal{D}H)_{H_2} A \left(P_{c,eq} - P_a\right)_{H_2}}{d} \tag{19}$$

As the pressure builds at the cathode, with the anode still at atmospheric pressure, it creates a pressure difference across the membrane, which in turn forces ammonia to permeate back through the membrane to the anode by back-diffusion. This poses a barrier in achieving higher pressures. The back-diffusion losses increase

as the pressure difference across the membrane increases, hence lowering the ECC efficiency at higher pressures.

The composition of the ammonia-hydrogen gas mixture at the cathode side was measured using the Nesslerization method at two different stages of compression – (i) cathode open and (ii) cathode closed. The cathode outlet stream containing the ammonia-hydrogen mixture was passed into a graduated cylinder (250 mL) which was completely filled with and held inverted in a 1250 mL beaker containing Nessler's reagent. Ammonia in the outlet stream immediately and completely reacts with Nessler's reagent to change its color from pale yellow to yellowish-brown [11,12], which was analyzed using a spectrophotometer (Vernier SpectroVis Plus). The hydrogen in the mixture is inert with respect to Nessler's reagent and was collected in the graduated cylinder using the downward displacement method.

First, the quantification of the cathode outlet stream was carried out when the cathode was open to the atmosphere. At this stage, both anode and cathode were maintained at the same pressure $(P_a = P_c)$ and hence, back-diffusion losses were zero. In this case, the ratio of ammonia to hydrogen measured was 2, which is also the stoichiometric ratio of NH_3 and H_2 at the cathode as per Equations 1-4.

Next, the cathode outlet was closed and ECC was allowed to pressurize. After the pressure attained equilibrium, the quantification of the cathode outlet stream was carried out by slowly opening the outlet valve and passing the constituents to the Nessler's reagent solution. The ammonia-hydrogen ratio obtained in this case is plotted along with the results from the cathode open case for all four operating voltages in Figure 4.

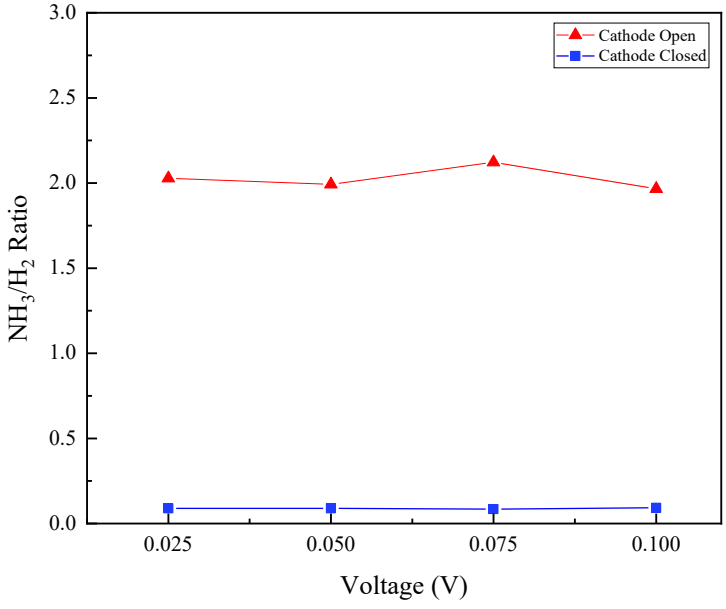


Figure 4. $NH_3{:}H_2$ volumetric ratios for 'cathode open' and 'cathode closed' cases for the four voltages tested

The $NH_3{:}H_2$ for cathode open case was measured to be 2. However, the ratio obtained in the 'cathode closed' case is only about 0.085. This means that the cathode chamber is predominantly composed of hydrogen in the 'cathode closed' case. Thus, one can conclude ammonia diffuses back to the anode at a significantly faster rate than hydrogen.

Furthermore, separate depressurization experiments were carried out to evaluate the permeability coefficients of both hydrogen and ammonia through the Nafion membrane. The cathode was initially pressurized by directly connecting it to the respective gas cylinders. The applied voltage was set to zero and the cathode was allowed to depressurize. The gas diffusing back from cathode to anode was detected by the formation of gas bubbles when the anode outlet tube was immersed in oil.

The rates of depressurization can be determined by setting $I = 0$, $P_{NH_3,a} = 0$, and $P_{H_2,a} = 0$ in Equations (16) and (17), which gives exponential expressions for the rates of depressurization:

$$P_{NH_3,c}(t) = P_{NH_3,c,i}\exp\left(-\frac{(\mathcal{D}H)_{NH_3}ART}{dV_c}t\right) \quad (20)$$

$$P_{H_2,c}(t) = P_{H_2,c,i}\exp\left(-\frac{(\mathcal{D}H)_{H_2}ART}{dV_c}t\right) \quad (21)$$

where $P_{NH_3,c,i}$ and $P_{H_2,c,i}$ are the initial cathode pressures of ammonia and hydrogen, respectively, at the start of depressurization.

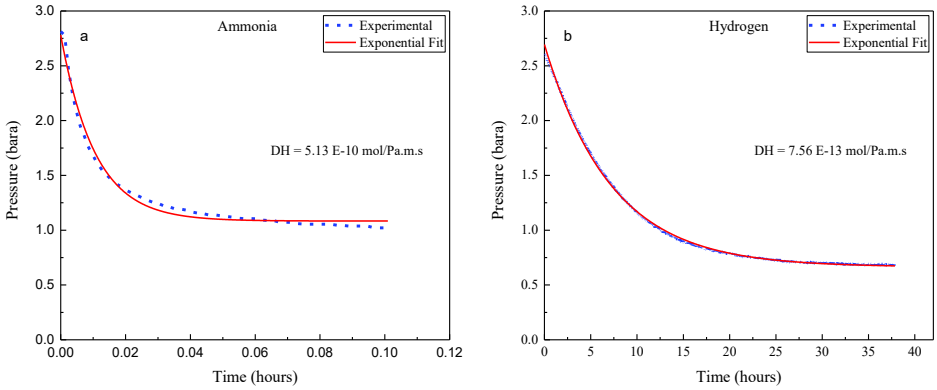


Figure 5. Cathode depressurization profiles for (a) ammonia, and (b) hydrogen

Figure 5 shows the measured depressurization curves (blue) obtained for both ammonia and hydrogen. The exponential curve fits (red) closely match the experimental curves for both gases as shown in Figure 5. Using the curve fits and substituting the known values of $\boldsymbol{A}, \boldsymbol{R}, \boldsymbol{T}, \boldsymbol{d}$, and $\boldsymbol{V_c}$, into Equations (20) and (21), the values of the two permeability coefficients are obtained as:

$$(\mathcal{D}H)_{NH_3} = 5.13\,E-10\ \mathrm{molPa^{-1}m^{-1}s^{-1}}$$

$$(\mathcal{D}H)_{H_2} = 7.56\,E-13\ \mathrm{molPa^{-1}m^{-1}s^{-1}}$$

The permeability coefficients obtained here are similar to the values found for Nafion membranes for ammonia ($\sim 9E-10\ \mathrm{molPa^{-1}m^{-1}s^{-1}}$) in Refs. [12-14] and hydrogen ($\sim 3.5\,E-14\ \mathrm{molPa^{-1}m^{-1}s^{-1}}$) in Refs. [15–17]. Figure 5 shows that when $(\mathcal{D}H)_{NH_3} \gg (\mathcal{D}H)_{H_2}$, then the cathode chamber is mostly composed of hydrogen and ammonia is only present in trace quantities. The Nafion membrane functionalized in ammonia solution is highly permeable to molecular ammonia and hence, it is very difficult to pressurize ammonia using an ECC with the given set of materials and conditions. Nafion being a PFSA membrane, requires moisture to function properly. However, higher hydration levels also exacerbate back-diffusion. Therefore, a better candidate for ammonia compression could be a membrane that can operate at low humidity levels. Also, membrane chemistry could be optimized to enhance the conduction of ammonium ions while mitigating the diffusion of molecular ammonia. A thicker membrane could also reduce the rate of back-diffusion and improve the working process of compression.

3. Conclusion

This work discusses the advantages of an electrochemical ammonia compressor over a conventional mechanical compressor. Electrochemical compression hardware was used for the ECC of an ammonia-hydrogen blend; hydrogen was used as the carrier gas, which facilitates the generation of ammonium ions. The ECC was operated at various voltages using a single cell setup. When the cathode outlet is open, the amount of ammonia produced at the cathode is twice that of hydrogen. When the cathode is closed, the pressure rises rapidly and eventually plateaus to an equilibrium value. Similarly, the current is maximum at the start of the compression and drops to attain an equilibrium value. The quantification of cathode constituents during

equilibrium resulted in an ammonia:hydrogen ratio to be around 0.085, which is much smaller than the ideal value of 2. Separately conducted depressurization experiments for ammonia and hydrogen showed that the permeability coefficient of ammonia is about three orders of magnitude larger than that of hydrogen. This implies that ammonia back-diffuses much faster than hydrogen and hence, hydrogen contributes almost the entire cathode pressure. Successful ECC of ammonia would require an alternate membrane formulation that allows the forward transfer of ammonium ions while simultaneously reducing the back diffusion of molecular ammonia.

Acknowledgements

This work was supported by a research award DE-EE-0008218 funded by the U.S. Department of Energy, Building Technologies Office.

References

[1] J. M. Sedlak, J. F. Austin, and A. B. Lacont, “Hydrogen recovery and purification using the solid polymer electrolyte electrolysis cell,” International Journal of Hydrogen Energy, Vol. 6, pp. 45-51, 1981.

[2] B. Rohland, K. Eberle, R. Ströbel, J. Scholta, and J. Garche, "Electrochemical Hydrogen Compressor," Electrochimica Acta, vol. 43, pp. 3841-3846, 1998.

[3] R. Ströbel, M. Oszcipok, M. Fasil, B. Rohland, L. Jörissen, and J. Garche, "The Compression of Hydrogen in an Electrochemical Cell Based on a PE Fuel Cell Design," Journal of Power Sources, vol. 105, pp. 208-215, 2002.

[4] B. Bahar, US Pat., 8,769,972 2009; 8,627,671 2010; 9,464,822 2011.

[5] B. Bahar, US Pat., 9,909,224 2016.

[6] Y. Tao, W. Gibbons, Y. Hwang, R. Radermacher, and C. Wang, “Electrochemical ammonia compression,” Chem. Commun., 2017,53, 5637-5640.

[7] A.V. Anantaraman, CL, Gardner, “Studies on ion-exchange membranes. Part 1. Effect of humidity on the conductivity of Nafion®”, Journal of Electroanalytical Chemistry, vol. 414, pp 115-120, 1996.

[8] J. Zhang, Y. Tang, C. Song, Z. Xia, H. Li, H. Wang, and J. Zhang, “PEM fuel cell relative humidity (RH) and its effect on performance at high temperatures,” Electrochimica Acta, vol 53, pp 5315-5321, 2008.

[9] J. Larminie, and A. Dicks, "Fuel cell systems explained", John Wiley & Sons LTD, 2001.

[10] Chouhan A, Bahar B, Prasad AK. Effect of back-diffusion on the performance of an electrochemical hydrogen compressor. International Journal of Hydrogen Energy, 45(2020), pp. 10991-99. https://doi.org/10.1016/j.ijhydene.2020.02.048.

[11] Jeong H, Park J, Kim H. Determination of NH 4 + in Environmental Water with Interfering Substances Using the Modified Nessler Method. Journal of Chemistry 2013;2013. https://doi.org/10.1155/2013/359217

[12] Koch FC, McMeekin TL. A new direct nesslerization micro-kjeldahl method and a modification of the nessler-folin reagent for ammonia. Journal of the American Chemical Society 1924;46:2066–9. https://doi.org/10.1021/ja01674a013.

[13] He Y, Cussler EL. Ammonia permeabilities of perfluorosulfonic membranes in various ionic forms. Journal of Membrane Science 1992;68:43–52. https://doi.org/10.1016/0376-7388(92)80148-D.

[14] Lee YT, Iwamoto K, Seno M. Gas permeabilities of perfluorocarboxylate membranes in various ionic forms. Journal of Membrane Science 1990;49:85–93. https://doi.org/10.1016/S0376-7388(00)80779-6.

[15] Sakai T, Takenaka H, Torikai E. Gas Diffusion in the Dried and Hydrated Nafions. Journal of The Electrochemical Society 2019;133:88–92. https://doi.org/10.1149/1.2108551.

[16] Broka K, Ekdunge P. Oxygen and hydrogen permeation properties and water uptake of Nafion® 117 membrane and recast film for PEM fuel cell. Journal of Applied Electrochemistry 1997;27:117–23. https://doi.org/10.1023/A:1018469520562.

[17] Bessarabov D, Millet P. PEM Water Electrolysis, Volume 2. Academic Press; 2018. https://doi.org/10.1016/c2018-0-02127-1.

13th IEA Heat Pump Conference
April 26-29, 2021 Jeju, Korea

Water Transmission Mechanisms in Advanced Ionic Membranes for HVAC Applications

David McAndrews[a], Taoli Gu[a], Abhishek Bandlore[a], Bamdad Bahar[a*]

[a]Xergy Inc., 299A Cluckey Dr, Harrington DE 19952, USA

Abstract

Ionic membranes are widely used in the electrochemical applications such as electrolysis and fuel cells. Recent advances in these membranes have led to new markets for ionic membranes, that can provide high water permeability in heating, ventilation, and air conditioning (HVAC) applications. These materials can be useful in many applications to help provide more efficient building technologies and higher indoor air quality through devices such as ionic liquid heat pumps (ILHPs), ionic liquid desiccants (ILDs), and energy recovery ventilators (ERVs) and water-based evaporators (WBEs). Water transmission mechanisms behind the water transport is not well understood, since different functional membranes provide transmission in different ways. Water transportation can be a function of ionomer structure via the building blocks of the backbone, or from the functional groups on the side chains or from subtle features in membrane design and composition. In this work, we studied the permeation properties of different advanced ionic membranes. Membranes that show high water selectivity, and permeances exceeding $4x10^5$ g/(day*m^2*Pa) are presented. Principal mechanisms driving the water transmission such as sorption, diffusion, and pervaporation (permeation/evaporation) are described and identified for different classes of membranes. High performance membranes are identified for optimum applications for different HVAC systems.

© HPC2020.
Selection and/or peer-review under responsibility of the organizers of the 13th IEA Heat Pump Conference 2020.

Keywords: Moisture Transmission; Membranes; Ionomer; ERV; Ionic Liquid

1. Introduction

The number of air conditioning units employed globally will increase from approximately 1.2 billion units to at least 4.5 billion by 2050. Developing countries will see a fivefold increase in demand over the same period. This increased demand will place a massive new burden on electricity grids that are already straining under current demand. When combined with the atmospheric impact of the refrigerants utilized by air conditioners, the energy consumption associated with mechanical cooling represents one of the largest end-use risks to our climate. Hence heating and cooling for buildings is accounts for a good portion of the resource demand in the developed world. Sustainable and high efficiency technology for heating and cooling applications is critical global need.

Water transporting membranes can be useful in many HVAC applications that reduce the total energy load for buildings. In one application, this is done by reducing the relative humidity in the air to be treated (and reduction in latent heat requirements in HVAC systems). Ionic liquids, as the name implies, are ionic salts that remain liquid under normal operating conditions. These fluids are mainly useful for their desiccation properties as concentrated ionic liquids (ILD's), as they can adsorb or desorb water vapor to help control the relative humidity of the air in its container. With membranes, they are mainly utilized in flat sheet or shell and tube contactors that utilize fluid flows of air and desiccant in crossflow patterns. These systems can dehumidify gas streams with high efficiency. Additionally, these contactors can be paired with a heat pump system to

* * Corresponding author. Tel.: +1 (302)-629-5768.
E-mail address: bamdad.bahar@xergyinc.com

regenerate the desiccant so that the system can be operated in a loop. In Energy recover ventilator (ERV) applications, an assembly of membranes allows exchange of heat between a cool and warm airstream (incoming and outgoing streams required to make up fresh air in buildings). In yet another application, membranes are used to enable heated water from heat pump systems to evaporate. Membranes in all these applications allow water vapor to transport from one side to the other. Interestingly, these classes of membranes are also being used to control humidity in vegetable trays in refrigerators. There are many other critical applications like for example sea water desalination membranes where water transmitting membranes have utility. Thus, the transport rate of water in membranes is clearly a critical issue in the performance of these systems. This paper provides basic insight into water transmission across functional (non-porous) membranes.

Figure 1 & 2. Applications for Advanced Ionic Membranes





It should be noted that there are two classes of membranes used for these applications, porous and non-porous membranes. Porous membranes are typically microporous structures with 'open' pores which allow for gas flow across the membranes; while non-porous membranes typically involve impervious polymer films that do not allow any bulk (gas) flow across them. There are significant differences in how these two classes of membranes perform. Micro-porous membranes generally offer higher water transmission rates, but also allow bulk flow (i.e. contaminants) to also cross the membranes. Impervious (non-porous) membranes offer much higher selectivity, however with some reduction in water transmission rates. This paper only reviews impervious non-porous membranes, which are targeted at applications that require no, or low cross contamination; and usually very long operating life. These applications include ERV's where contamination of incoming air into a building is a critical issue, and in ILD's where salt carryover, and salt crystallization in micro-porous membranes is also a critical issue in operation.

Polymeric, non-porous reinforced membranes made from (ionically) functionalized polymer materials that transmit water were originally developed as solid polymer electrolytes for electrochemical applications [1]. These materials were originally developed as solid polymer electrolytes for electrochemical applications. These materials typically have ionically conductive groups embedded in the repeating unit of the polymer. These functional groups aid in the transport of water through the membrane.

Water mass transfer mechanisms are reviewed, different transport mechanisms are discussed, and performance data is provided for reference.

2. Water Transmission Mechanisms

Water transmission mechanisms behind the water transport is not well understood, since different functional membranes provide transmission in different ways. Water transportation can be a function of

ionomer structure via the building blocks of the backbone, or from the functional groups on the side chains or from subtle features in membrane design and composition.

2.1. Electro-Osmotic Drag

When a voltage is applied across the polymer electrolyte membrane, water is mainly transported inside the membrane by electroosmotic drag. Fig. 3 is a schematic of the water transport in a fuel cell membrane. The two main water transport processes in the membrane are electro-osmotic drag and back diffusion. Electro-osmotic drag refers to the phenomenon of water molecules being dragged by the current-carrier protons from the anode to the cathode. The electro-osmotic coefficient is the transport number of water molecules that are carried with each proton moved from the anode to the cathode. The electro-osmotic coefficient mainly depends on the temperature and water content.

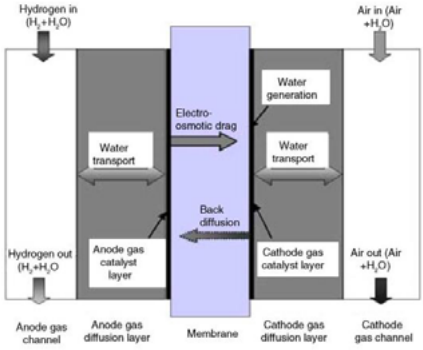


Figure 3: Schematic of water transport in a proton exchange membrane (PEM) fuel cell

2.2. Solution-Diffusion Theory

Solution-diffusion is the generally accepted mechanism of mass transport through non-porous membranes, which was first proposed by Graham [1] based on his extensive research on gas permeation through homogeneous membranes. It is held that gas permeation through a homogeneous membrane consists of three fundamental processes: (1) solution of gas molecules in the upstream surface of the membrane. (2) Diffusion of the dissolved species across the membrane matrix. (3) Desorption of the dissolved species in the downstream face of the membrane. These three fundamental processes also govern the mass transport across pervaporation membranes [2]. A schematic of the solution-diffusion theory is as shown in Fig. 4.

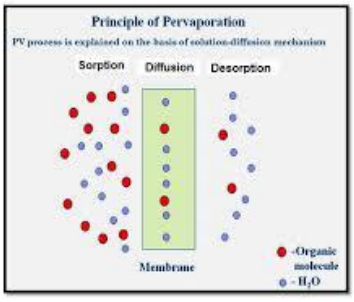


Fig. 4. Schematic of Solution-Diffusion in Pervaporation

It is to be noted that the solution-diffusion theory is only valid for governing permeation through non-swollen membranes. If membranes are swollen or plasticized by transporting species, the interactions between polymer chains tend to be diminished, and the membrane matrix will therefore experience an increase in the free volume. Hence, to reflect the permeation the solution-diffusion must be modified to account for the increase in the free volume. In the next section we discuss the results obtained from ASTM E96 and MDM testing.

2.3. Pervaporation

Pervaporation (permeative evaporation) is a mass transport phenomenon present in dense non-porous membranes. Pervaporation occurs in a gas-liquid separation system that is separated by the membrane, as the liquid contacts the membrane surface it permeates and undergoes a liquid to vapor phase change to end up in the gas stream. This can be done in reverse to remove a gas vapor to the liquid phase, as would be done in an ILD system. There are two main models that are used to describe the transport process: Free Volume and Diffusion; the latter being the more common. However, both models are important to understand and may describe the systems better in cases discussed below.

The free volume model describes a system where vapor passes through a membrane from a high concentration feed to a low concentration permeate stream. This low concentration can be established by using a vacuum line or a condenser, but the driving force is established by the difference in partial pressures between the two feeds. The mass flux is established through corresponding adsorption-desorption processes on the corresponding faces of the membrane. This flux can be established by using a condenser downstream on the permeate side, and it can be increased by adding a heater to the feed stream. These units would create the pervaporation process in the combination of the adsorption and corresponding desorption of the liquid within the membrane, and the evaporation of the liquid from the surface of the membrane with partial pressure differential. This model for membrane flow is more useful in porous materials such fiberglass or expanded polytetrafluoroethylene membranes like those commonly used in air conditioners [3], [4].

For non-porous membranes the model must include a mechanism for the diffusion of the pervaporate through the solid structure of the polymer. The solution-diffusion is defined by Fick's laws of diffusion. Fick's first law defines the flux of the system to be proportional to the concentration gradient of the fluid. This law is represented mathematically as Equation 1, where J is the flux of the system, D is the diffusion coefficient, φ is the concentration of the molecule to be dissolved, and x is the one-dimensional distance. This law describes the molecular movement of molecules from areas of high concentration to low. Fick's second law describes the diffusion dependence of the concentration gradient with respect to time. This law is derived from the first law's interaction with the law of mass conversation. The equation can be written as Equation 2. This is useful for non-steady state systems such as the air conditioning cycle. The diffusion coefficient will change based on the conditions of the system. The predominant variables are temperature, viscosity, and density. For polymer systems the diffusion coefficient can also be dependent on the primary on the concentration of the molecule within the membrane itself. This permeate in polymer is known as swelling and can have both positive and negative effects on the pervaporate and mechanical performance of the membrane [5]. Additionally, this can make real systems significantly more complicated as the change in concentration can create a change in membrane thickness [1], [3-5], [6].

$$J = -D\frac{d\varphi}{dx} \tag{1}$$

$$\frac{\partial\varphi}{\partial t} = D\frac{\partial^2\varphi}{\partial x^2} \tag{2}$$

The driving force for transport of different components is provided by a chemical potential difference between the liquid feed/retentate and vapor permeate at each side of the membrane. The retentate is the remainder of the feed leaving the membrane feed chamber, which is not permeated through the membrane. The chemical potential can be expressed in terms of fugacity, given by Raoult's law for a liquid and by Dalton's law for (an ideal) gas. During operation, due to removal of the vapor-phase permeate, the actual fugacity of the vapor is lower than anticipated on basis of the collected (condensed) permeate.

For many systems, ionically functionalized polymers are proving to be the most exciting developments. These systems are made from standard polymer backbones that could be functionalized with sidechains capped with an ionic group. These chains can be of varying length and the caps are of strong acids or bases. The most well-known of these is perfluorosulfonic acid (PFSA), which consists of a backbone of polytetrafluoroethylene with an end capped with a sulfonic acid group. This ionomer is both temperature and chemically stable. Other ionomers are functionalized with trimethylammonium, pyridine, or imidazole groups as well. The ionic groups significantly aid these materials in their water transport properties due to their hydrophilic nature. However, research in recent years indicates that the ionic groups form ionic channels formed my areas of clustered functional groups. These channels form ordered pathways for the water to more easily transfer from one surface

of the membrane to the other that are more thermodynamically favorable than the simpler diffusion seen a homopolymer with a hydrophilic backbone. These micro- or nanostructures can be aided with the addition of a surfactant or a scavenger [2], [7], [8].

Pervaporation was mainly studied and used for organic solvent dehydration. Several hydrophilic and hydrophobic membranes have been used for this application. However, hydrophobic membranes work for these purposes by selectively allowing organic compound to pass through while rejecting water and they cannot be used for HVAC applications since the membranes need to permit water movement at high flux rates. There are several available commercial polymer membranes such as polyurethanes (PU), polyvinyl alcohol (PVA), polyimides (PI), Sulfonic Acid functionalized polymer (Perfluoro and Polystyrene i.e. PFSA's and PSSA's) and polyacrylonitrile (PAN) [9].

Water transport in PFSA membranes has been studied extensively in relation to their use in electrochemical devices (such as fuel cells and electrolysis applications). In PFSA's water transport proceeds through a combination of diffusion through void spaces in the membrane, along with protons through the pores in the membrane due to electro-osmotic drag and hydraulic permeation due to pressure gradient [10]. Sulfonated styrene/ethylene – butylene/styrene (S-SEBS) triblock polymer is another low-cost proton conducting material. The sulfonic acid functional group is connected to the backbone via a fluorocarbon sidechain in PFSAs and via a benzene ring in S-SEBS [11]. The hydrophilic and hydrophobic regions in both these materials show microphase separation as seen in Figure 5, forming narrow channels through which proton and water transport takes place. In the left of Figure 5, the hydrophobic sulfonated "heads" form the outer ring of the channel with the hydrophilic fluorocarbon "tails" inside of the electron transport channels. To the right, the fluorocarbon tails face outwards, creating a proton channel within the ring.

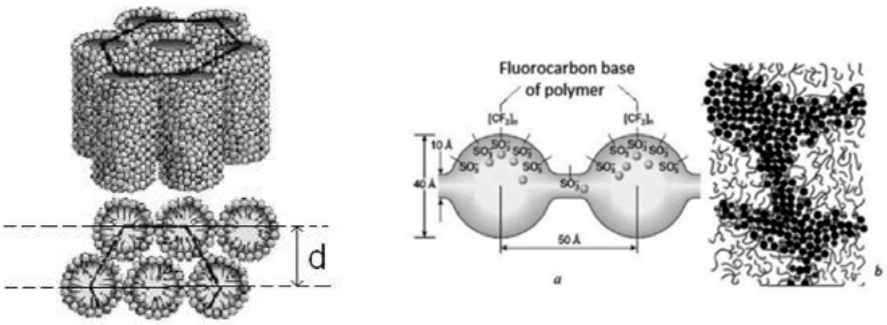


Fig. 5. (Left) Packing structure of PFSA channels; (Right) Microphase separation and channels in PFSA

2.4. Composite Membranes

High Performance Ionomers for water transport require water adsorption in order to function. However, water channels in the Ionomer make the polymer structure weak (gel like). High water content increases the water transmission rate but decreases the mechanical strength. The ideal membrane system is thin (shortest transport path), strong (durable and easily installed), and utilizes highest functionality polymer (i.e. highest water adsorption). In order to address the competing requirements of high-water transmission (i.e. thinness) and mechanical strength, membranes are typically made by reinforcing the functional polymer with a mechanically strong structural element – i.e. composited.

Therefore, composite membranes consist of at least two structural elements made from different materials, as shown in Figure 2. A single-layer composite membrane consists of a thin, selective layer atop a microporous support. The support provides mechanical strength, whereas the water transmission is performed by the thin top-layer. A multi-layer composite membrane can consist of a porous support and many layers of different materials, each performing a specific function. Thin-film composite membranes are typical for pervaporation applications.

The selective layer can be applied by lamination, solution coating, interfacial polymerization, or plasma polymerization methods. Compared to integrally-skinned asymmetric membranes, composite membranes offer several significant advantages: (i) independent selection of materials from which the separating layer and the porous support are formed, (ii) independent preparation of the separating layer and the porous support membrane, thereby making it possible to optimize each structural element, and (iii) very expensive membrane materials (>1000 $/lb) can be used because only a very small amount of polymer is required for the formation of the thin separation layer (~1 g polymer/m^2 of membrane for a 1-µm-thick selective layer).

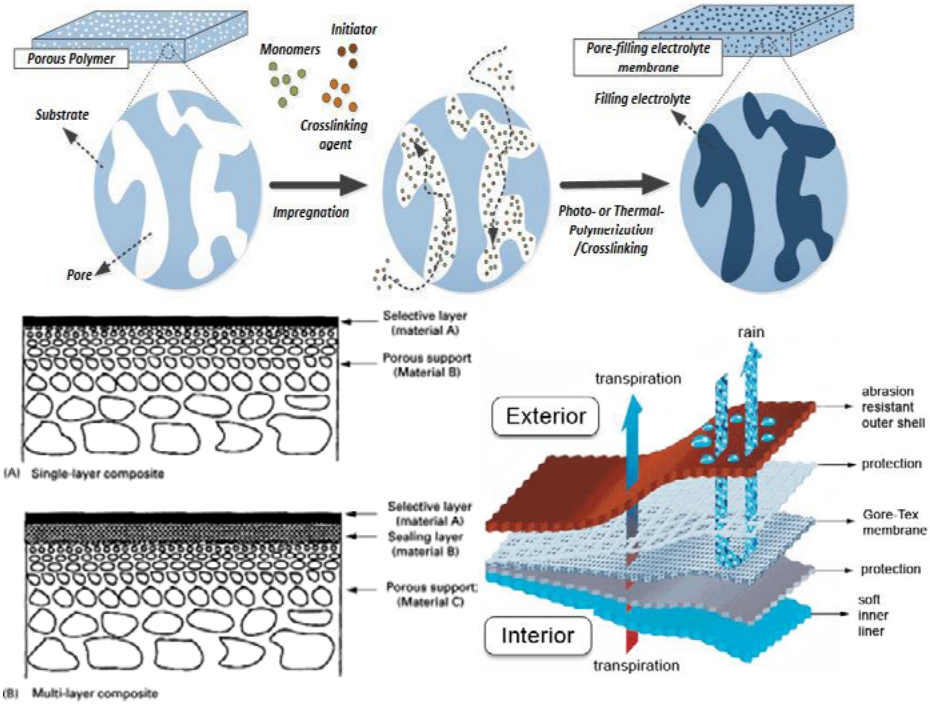


Figure 6: (Top & bottom left) Graphics showing functional polymer combined with porous reinforcement to form a reinforced non-porous composite membrane; (bottom right) composite structures in clothing industry

Composite structures are very common in the clothing industry. Beyond ionic polymers, other polymers that provide water transmission can be found in fabric outerwear. For example, the simplest sort of rain wear is a two-layer sandwich. The outer layer is typically nylon or polyester and provides strength. The inner one is polyurethane (PU), and provides water resistance, at the cost of breathability. Polyether Block Amide are also now increasingly used for footwear applications. This schematic (Figure 6, bottom) describes a composite structure developed by W.L. Gore and Associates for the fabrics industry.

3. Experiment & Results

3.1. Description of Test Conditions

Reinforced and unreinforced membranes were tested using a modified method based on ASTM E96 standards developed to determine the moisture vapor transmission rate (MVTR) of highly permeable materials [12]. The test consists of a cup filled with saturated NaCl solution and sealed with ePTFE (expanded Polytetrafluoroethylene). A layer of ePTFE is attached to a support and set to float in a freshwater bath. The membrane to be tested is placed on the ePTFE film and the saltwater cup is inverted on it. The saturated NaCl solution in the cup acts as a desiccant and provides a driving force for the movement of water from the tub to the cup. The cup is weighed after 10 minutes and the increase in weight represents water transport through the

membrane. The average moisture vapor transfer rate was calculated from this weight change and was then normalized by the area of the membrane and the pressure differential across the membrane. The room and bath temperatures were controlled at 20˚C. The saturated NaCl solution provides a RH of 75%. At 20˚C, the saturation vapor pressure is 2.33 kPa and the pressure differential, the driving force of the mass transfer, is 0.5825 kPa.

Table 1. Different reinforcements and their properties

Support	Construction	Thickness (μm)	Porosity
R1	ePE	5	60%
R2	ePTFE	3	80%
R3	ePTFE	10	80%

As seen in Table 1, two different reinforcement constructions were investigated: expanded polyethylene (ePE) and expanded polytetrafluorethylene (ePTFE). The expanded polytetrafluorethylene support was tested at two different thicknesses. As seen in Table 2, these reinforcements were coupled with three different ionomers to make a reinforced membrane: two cationic ionomers, a long perfluorosulfonic acid (PFSA) (ionomer A) and a garment membrane (ionomer B); and an anion exchange ionomer (ionomer C). In addition to reinforced ionomers, unreinforced membranes were made using ionomers B and C.

Table 2. Membrane permeabilities

MVTR Test Index	Ionomer	Reinforcement	Thickness (um)	Permeance (g/m^2*day*kPa)
1	A	R3	25	$2.51x10^5$
2	B	R1	10	$4.67x10^5$
3	C	R2	5	$2.15x10^5$
4	B	-	25	$6.90x10^5$
5	C	-	15	$6.82x10^5$

3.2. Results & Analysis

As seen in Figure 7, membranes without reinforcement outperformed membranes with reinforcement, due to the increased channel distance and the hydrophobicity of the reinforcement. Of the unreinforced membranes, the garment membrane shows the greatest potential for further research. It outperformed the PFSA and AEM, despite being a thicker membrane. The potential of the water vapor transmission of ionomer B becomes even more apparent when the permeance was normalized to the thickness (Figure 7b). While these unreinforced membranes had sufficient mechanical strength for the 0.5824 kPa driving pressure differential, in an HVAC application the driving pressure can easily exceed 5 kPa, and even 100 kPa, depending on the design of the system. These high pressures will increase the crossover and possibly even burst the unreinforced membrane. Furthermore, because the unreinforced membranes gain their mechanical stability from their thickness, they tend to be significantly more expensive, requiring more ionomer resin than a reinforced membrane.

Of the reinforced membranes, sample 2, the garment membrane supported by ePE, performed the best. This is particularly significant as ePE was not the thinnest membrane and exhibited the lowest porosity, both key factors in water transport through porous membranes. However, by imbibing the material with garment ionomer, the material outperforms thinner membranes with higher porosity.

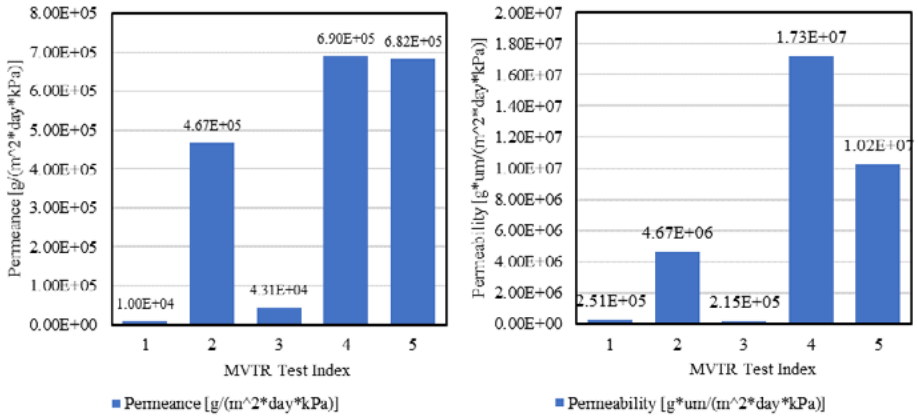


Fig. 7. Comparison of permeance of different membranes (left) and comparison of permeability (permeance normalized to membrane thickness) (right)

Conclusions

The HVAC industry has been relatively slow to adopt the use of water transmission membranes for its applications. Until relatively recently, most ERV modules for example, used paper media as the interfacial layer between incoming and outgoing air streams. In ILD systems, porous structures that allow for bulk flow across them are also very common.

These results confirm that thinner non-porous membrane layer does exhibit the highest water permeation rate – consistent with theoretical expectations. While transmission rates (normalized for thickness) are generally lower in the 'bulk polymers' compared to porous membranes, by reducing the thickness of the polymer layer you can more than compensate for the rate reduction, and obtain water transmission rates (permeability) that are comparable – or indeed better than porous membranes. While at the same time, also take advantage of the greater selectivity (i.e. reduction in cross stream contamination). This remains true for both polymers and all supports. Also, crucially, the thinnest (highest performance) membrane is also the lowest cost system.

This outcome is disruptive and transformational, because it enables entry into many historically 'cost' sensitive applications – where impervious membranes have always been an attractive but also prohibitively expensive engineering option.

To move this membrane technology to the market, larger scale application testing must be performed. In the theoretical application to a subtropical monsoon climate similar to that of New Delhi, the average daily latent cooling load of a 90 m^2 apartment is about $2.67x10^4$ kJ or about 11 kg of water per day. Assuming the same pressure drop through the air conditioner would provide a similar driving pressure as in the MVTR testing (0.5825 kPa), the air conditioner would require about 4 m^2 of the best performing reinforced membrane or about 2.8 m^2 of the unreinforced membrane. Further research into the design of such a system can be made to determine and improve the driving pressure differential. This research would also help to determine the coefficient of performance of the system – which is directly related to the fan speed and driving pressure differential.

This is especially true for reinforced (composite) membranes since very thin non-reinforced membranes are simply too weak for engineering integration. Typically, a decrease in thickness corresponds to a decrease in mechanical properties. By combining a reinforcement with the functional polymer, a new class of high-water transmission membrane is now available to the HVAC industry.

4. Nomenclature

Table 2. Acronyms and abbreviations, defined

Term	Definition	Term	Definition

ePE	Expanded polyethylene	PFSA	Perfluorosulfonic acid
ePTFE	Expanded polytetrafluoroethylene	PI	Polyimides
ERV	Energy recovery ventilator	PSSA	Polystyrenesulfonic acid
HVAC	Heating, ventilation and air conditioning	PU	Polyurethanes
ILD	Ionic liquid desiccant	PVA	Polyvinyl alcohol
ILHP	Ionic liquid desiccant	S-SEBS	Sulfonated styrene/ethylene-butylene/styrene
MVTR	Moisture vapor transmission	WBE	Water-based evaporator
PAN	Polyacrylonitrile		

Acknowledgements

This work was supported by a research award DE-EE-0008218 funded by the U.S. Department of Energy, Building Technologies Office. The technologies disclosed in this paper are protected under US patents [13]. This publication is a part of a 10-paper series to commemorate Xergy's 10-year anniversary, bringing advanced membrane technology to the global HVAC industry. This series includes papers providing further insight into membrane based pervaporative heating and cooling, and ionic liquid desiccant heat pumps.

References

[1] Bahar, B. "Electrochemical compressor and refrigeration system," 2009. US8769972B2
[2] Acharya, H.r., et al. "Separation of Liquid Benzene/Cyclohexane Mixtures by Perstraction and Pervaporation." Journal of Membrane Science, vol. 37, no. 3, 1988, pp. 205–232., doi:10.1016/s0376-7388(00)82430-8.
[2] Berrod, Quentin, et al. "Nanostructure and Transport Properties of Proton Conducting Self-Assembled Perfluorinated Surfactants: A Bottom-Up Approach toward PFSA Fuel Cell Membranes." Macromolecules, vol. 48, no. 17, 2015, pp. 6166–6176., doi:10.1021/acs.macromol.5b00770.
[3] Binning, Robert, et al. "Separation of Liquid Mixtures by Permeation." Industrial & Engineering Chemistry, vol. 53, no. 1, 1961, pp. 45–50., doi:10.1021/ie50613a030.
[4] Mafi, Amirhossein, et al. "A Comparative Study on the Free Volume Theories for Diffusivity through Polymeric Membrane in Pervaporation Process." Journal of Applied Polymer Science, vol. 131, no. 15, 2014, doi:10.1002/app.40581.
[5] Kappert, Emiel J., et al. "Swelling of 9 Polymers Commonly Employed for Solvent-Resistant Nanofiltration Membranes: A Comprehensive Dataset." Journal of Membrane Science, vol. 569, 2019, pp. 177–199., doi:10.1016/j.memsci.2018.09.059.
[6] Ye, Yun-Sheng, et al. "Water Soluble Polymers as Proton Exchange Membranes for Fuel Cells." Polymers, vol. 4, no. 2, 2012, pp. 913–963., doi:10.3390/polym4020913.
[7] Saito, Morihiro, et al. "Mechanisms of Ion and Water Transport in Perfluorosulfonated Ionomer Membranes for Fuel Cells." The Journal of Physical Chemistry B, vol. 108, no. 41, 2004, pp. 16064–16070., doi:10.1021/jp0482565.
[8] Zhang, Lingling, et al. "High CO2 Permeation Flux Enabled by Highly Interconnected Three-Dimensional Ionic Channels in Selective CO2 Separation Membranes." Energy & Environmental Science, vol. 5, no. 8, 2012, p. 8310., doi:10.1039/c2ee22045h.
[9] G. Jyoti, A. Keshav and J. Anandkumar, "Review on Pervaporation: Theory, Membrane Performance, and Application to Intensification of Esterification Reaction", Journal of Engineering, vol. 2015, pp. 1-24, 2015. Available: 10.1155/2015/927068.
[10] Jiao, K., & Li, X. (2011). Water transport in polymer electrolyte membrane fuel cells. Progress in Energy and Combustion Science, 37(3), 221–291. doi:10.1016/j.pecs.2010.06.002
[11] Edmondson, C. (2002). Free volume and percolation in S-SEBS and fluorocarbon proton conducting membranes. Solid State Ionics, 152-153, 355–361. doi:10.1016/s0167-2738(02)00336-3
[12] Crosby, Philip M. (Northeast, MD)1989, Test method for determination of moisture vapor transmission rate, United States, W. L. Gore & Associates, Inc. (Newark, DE), 4862730
[13] US Patents: 10,202,292 and Applications: 20190291054, 20190256384, 20190226703, 20180251616, 20180187906, 20180093905, 20170284685

13th IEA Heat Pump Conference
April 26-29, 2021 Jeju, Korea

Solid State (Metal Hydride) Refrigerant Based Air Conditioner and Freezer Systems

Bamdad Bahar[a*], William TomHon[a], Matt Golben[a], Jacob Zerby[a], Mark Golben[a]

[a]*Xergy Inc., 299A Cluckey Dr., Harrington DE 19952, USA*

Abstract

Chlorine and Fluorine containing refrigerant based heat pumps currently consumes over 2,000 Trillion-Watt hours per year of electric power [1]. Current refrigerants used in these devices have climate harming "Global Warming Potentials" (GWP) that are thousands of times higher than that of CO_2 gas. This paper explores a novel heat pump technology based on solid-state (metal hydride based) refrigerant employing hydrogen compression. This paper provides performance data for solid state refrigerant heat pumps for air conditioning (AC) and Ultra Low Temperature (ULT) freezer systems. Operational data, lessons learnt, and optimal practices needed to deploy these systems are reviewed. Key components in the system are analyzed, including the metal hydride heat exchangers, (electrochemical and other) Hydrogen compressors, and system controls.

© HPC2020.
Selection and/or peer-review under responsibility of the organizers of the 13th IEA Heat Pump Conference 2020.

Keywords: Metal Hydride; Solid State Refrigerant; Electrochemical Compression; Hydrogen; Air Conditioner; Ultra-Low Temperature Freezer

1. Introduction to Solid-State refrigerant (Metal-Hydrogen Sorption Systems)

A refrigerant is a substance used in a heat pump or refrigeration cycle that typically undergoes phase transition with favorable thermodynamic properties that enables heat absorption or rejection upon phase transition. Chlorine and Fluorine containing refrigerant based heat pumps currently consumes over 2000 Trillion-Watt hours per year of electric power [1]. Current refrigerants used in these devices have climate harming "Global Warming Potentials" (GWP) that are thousands of times higher than that of CO_2 gas. Therefore, alternatives to current refrigerants are critically needed to address the shortcomings of current refrigerants.

Solid state refrigerants hold the potential to provide a highly efficient, low cost, recyclable, environmentally friendly alternative to traditional refrigerants. Metal hydrides (MH) are a class of solid-state refrigerants. Metal hydrides are metallic compounds, in which one or more hydrogen centers have nucleophilic, reducing, or basic properties. For heat pumps, we utilize the reversible heat-driven reaction of a hydride-forming metal/alloy, or intermetallic compound (IMC) with hydrogen gas. Hydrogen changes phase from a gas to a solid metal alloy with very favorable thermodynamic properties.

$$M(s) + xH_2(S) \rightleftharpoons MH_x(s) + Q \quad (1)$$

In Eq.1, M is a metal or alloy (e.g., vanadium (V) or a body-centred cubic (BCC) solid solution based upon it), or an IMC (typically with linear (AB_2) or trigonal bipyramidal (AB_5) molecular geometries); (s) and (g) relate to solid and gas phases, respectively, and Q is the reaction enthalpy. The overall process performance is strongly dependent on the intrinsic features of metal hydride reaction including its thermodynamic and kinetic

* Corresponding author. Tel. +1 (302)-629-5768.
E-mail address: bamdad.bahar@xergyinc.com

characteristics, as well as composition, structure and morphology of the solid phases (M, MH_x) involved in the process. These features are mainly related to fundamental aspects of hydride materials.

Equilibrium of the metal-hydrogen reaction is characterized by an interrelation between hydrogen pressure (P), concentration of hydrogen in the solid phase (C) and temperature (T). PCT diagrams can be generated to characterize specific hydride-forming materials. These provide the thermodynamics of its interaction with gaseous hydrogen. At low hydrogen concentrations ($0 \leq C < a$) hydrogen atoms form an interstitial solid solution in the matrix per Henry–Sieverts law. When the value of C exceeds concentration of the saturated solid solution, precipitation of the hydride (β-phase with hydrogen concentration) occurs. The system then exhibits a first order phase transition at a constant hydrogen pressure, $P = P_P$ ($a \leq C \leq b$). This pressure is called the plateau pressure (P_P) in the metal–hydrogen systems. The process is almost exactly (100%) reversible, with slight differences as the concentration changes. This is termed hysteresis and is a source of efficiency loss (<5%).

Depending on the type and composition of the hydride-forming material, the equilibrium hydrogen pressures vary in a very broad range, from below 1 bar to exceeding 1 kbar at room temperature. Most of the lower pressure compression alloys (P_H < 200 bar at T_H < 150 °C) belong to the AB_5-type intermetallic compounds while significantly higher, >1 kbar, hydrogen pressures can be generated using AB_2-type compounds. Current prototype systems have been built using a wide variety of commercial AB_5 compounds, although in the future, the high thermal exchange capacity of AB_2 could lead to smaller heat exchangers.

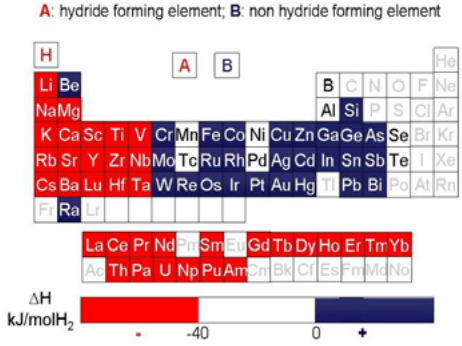
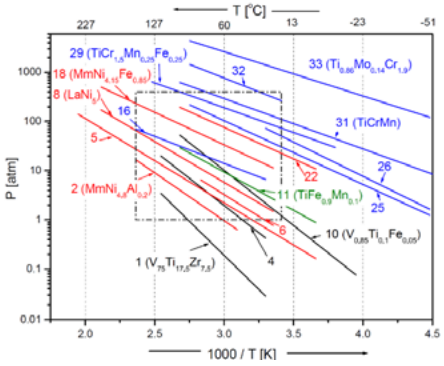


Fig. 1. Hydride and non-hydride forming elements in the periodic system of elements [2].

Proper hydride selection is critical to designing useful metal hydride heat exchangers. Figure 2 (right) provides equilibrium characteristics of the interaction of hydride-forming alloys suitable for Hydrogen. The data is sorted in the ascending order for desorption plateau pressure. Figure 2 (left) provides Van't Hoff plots for selected hydride-forming alloys suitable for hydrogen.



Index	Formula	SR Designation	-ΔS° (J/(mol-H_2*K))	-ΔH° (J/(mol-H_2))
1	$V_{75}Ti_{17.5}Zr_{7.5}$	R-2120	145.1	52.98
2	$MmNi_{4.6}Al_{0.2}$	R-2410A	111.3	37.20
4	$V_{75}Ti_{10}Zr_{7.5}Cr_{7.5}$	R-2300	132.3	42.23
5	$LaNi_{4.8}Sn_{0.2}$	R-2560B	104.3	32.83
6	$Mm_{0.7}La_{0.3}Ni_{4.7}Sn_{0.3}$	R-2660	111.2	32.80
8	$LaNi_5$	R-2500	110.0	31.80
10	$V_{0.85}Ti_{0.1}Fe_{0.05}$	R-2310	148.0	42.90
11	$TiFe_{0.8}Mn_{0.1}$	R-2700	107.7	29.70
16	$Zr_{0.7}Ti_{0.3}Mn_2$	R-2860	85.0	21.00
18	$MmNi_{4.15}Fe_{0.85}$	R-2440B	105.4	25.00
22	$Ca_{0.2}Mm_{0.8}Ni_5$	R-2420	109.5	24.50
25	$TiCr_{1.8}Mo_{0.01}$	R-2816B	113.0	24.80
26	$TiCr_{1.9}$	R-2810	122.0	24.80
29	$TiCr_{1.6}Mn_{0.25}Fe_{0.3}$	R-2843A	101.6	19.32
31	TiCrMn	R-2840	106.0	19.60
32	$ZrFe_{1.8}Ni_{0.2}$	R-2904	119.7	21.50
33	$Ti_{0.86}Mo_{0.14}Cr_{1.8}$	R-2816A	117.0	17.20

Fig. 2. Van't Hoff plot and enthalpy and entropy of formation of hydride complex for selected sorbent refrigerants (SRs) [2]

Hydrogen compression is critical for a metal hydride refrigerant based heat pump cycle. Hydrogen can be compressed using mechanically driven, electrochemically driven or metal hydride (heat driven) compressors. For durable performance, hydride systems must remain dry and hydrogen gas streams must be pure and free of contaminants. Much like other refrigerant systems, the type of compression employed must be mated with the specific type of hydride selected and the overall requirements of a specific heat pump application. One of the first modern metal hydride heat pumps (MHHPs) was built in 2014 (Figure 3). Hydrogen compression ratio (P_H/P_L) for hydrides can vary in the range 10–50.

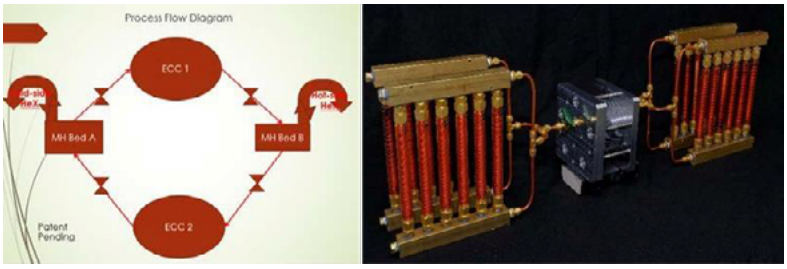


Fig. 3. (a) A schematic for a potential ECC-based MHHP. (b) Picture of prototype ECC-based MHHP

Initial development of the electrochemical compressor-based metal hydride system was conducted with commercially available hydride cylinders with heat exchanger capability. Two designs differing in the placement of the heat exchanger coil and the aspect ratio of the units were tested: exterior-wrapped tubes brazed to the high aspect-ratio hydride containing cylinder (Figure 4a), and a coiled tube placed inside a lower aspect ratio hydride cylinder (Figure 4b). Both designs showed significant deficiencies in heat exchange capability.

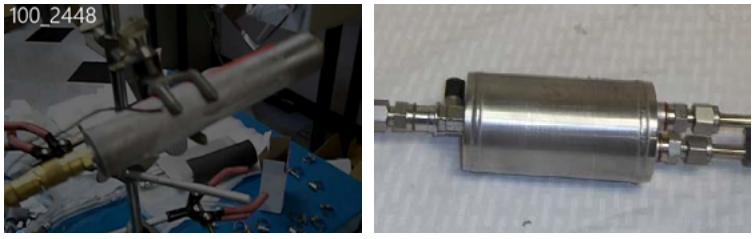


Fig. 4. Hydride cylinders with heat exchanger capability (a) high aspect-ratio hydride with potential for exterior wrap-around coil and (b) (b) a coiled tube placed inside a lower aspect ratio hydride cylinder.

Figure 5 shows results for COP vs operating voltage. While low voltages (<0.1 V) provide the greatest benefit to COP, low voltage systems have a lower current and H_2 flow and thus require larger, more expensive systems to maintain a constant temperature. Conversely, faster heating can be achieved with smaller systems by operating at higher voltages represented (>0.2 V).

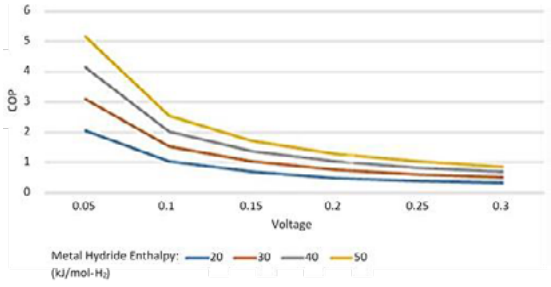
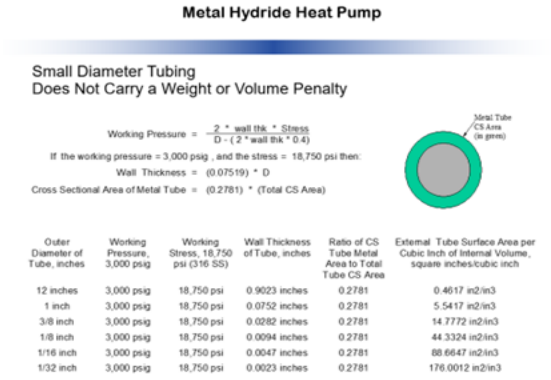


Fig. 5. ECC-MHHX Heat Pump Water Heater COP (heating COP) as a function of voltage for metal hydrides with different enthalpies.



Outer Diameter of Tube, inches	Working Pressure, 3,000 psig	Working Stress, 18,750 psi (316 SS)	Wall Thickness of Tube, inches	Ratio of CS Tube Metal Area to Total Tube CS Area	External Tube Surface Area per Cubic Inch of Internal Volume, square inches/cubic inch
12 inches	3,000 psig	18,750 psi	0.9023 inches	0.2781	0.4617 in2/in3
1 inch	3,000 psig	18,750 psi	0.0752 inches	0.2781	5.5417 in2/in3
3/8 inch	3,000 psig	18,750 psi	0.0282 inches	0.2781	14.7772 in2/in3
1/8 inch	3,000 psig	18,750 psi	0.0094 inches	0.2781	44.3324 in2/in3
1/16 inch	3,000 psig	18,750 psi	0.0047 inches	0.2781	88.6647 in2/in3
1/32 inch	3,000 psig	18,750 psi	0.0023 inches	0.2781	176.0012 in2/in3

Fig. 6. Working pressure and surface per internal volume of various diameters of metal hydride tubing

As seen in Figure 6, microtube heat exchangers provide practical benefits including: the ability to hold very high pressures within tubes, flexible tubes which can be coiled, and highly configurable tube patterns which allow precise thermal performance. Furthermore, microtubes take advantage of fundamental design principles as decreasing the diameter increases the surface area per unit volume. As the convective heat transfer rate (Q) is proportional to the surface area, per Equation 2, small diameter tubes increase the heat transfer rate as well.

$$Q = Time \times h \times External\ Surface\ Area \times \left(T_{surface} - T_{external}\right) \quad (2)$$

In most heat exchangers, the technical design limitation to tube diameter is pressure drop. However, the small molecular size and high velocity of hydrogen enables it to travel through very small diameter tubes with very little pressure loss. Microtubes tubes have allowed for over a 10X decrease in sorption time. In lab testing (Figure 7), 100% of the MHHX hydrogen capacity is absorbed in under 40 seconds, compared to 1600 seconds with the previous generation of MHHX.

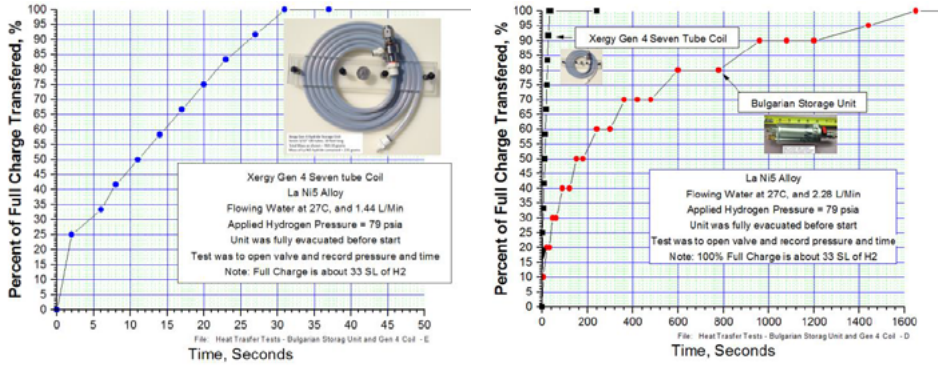


Fig. 7. Comparison of mass flow rate of hydrogen into metal hydride microtubes (left) and into a typical tank-type metal hydride cannister (right).

2. Environmental and Commercial Analysis of Room Air Conditioners Employing Metal Hydride Solid-State Refrigerant Technology

2.1. Introduction

Air conditioning solutions utilizing heat exchangers with metal hydride refrigerant show a very strong potential to provide a novel cooling solution with low energy consumption and zero GWP. Like a vapor compression air conditioner, a MHHX uses a compressor to generate its cooling power, however the cooling is generated via ionic sorption of hydrogen gas rather than through the incumbent vapor-compression refrigeration. The compression can be provided by a typical mechanical compressor or an electrochemical compressor (ECC) – like a proton exchange membrane (PEM) ECC or a nickel hydrogen (Ni-H) ECC. While a mechanical compressor's efficiency is thermodynamically limited to the Carnot cycle, an electrochemical compressor is electrochemically limited by the materials in the system.

The refrigeration efficiency of a metal hydride heat pump (MHHP) system using a PEM ECC, Ni-H ECC, or mechanical compression was explored. The energy use and economic viability of the systems was explored for the current technology with a target payback period of 3 years on the premium over an incumbent room air conditioner (RAC). As the energy use of such a system is very dependent on the climate conditions, this analysis uses climate data for a 90 m^2 apartment in New Delhi, India, a climate reflective of the median cooling requirements of the emerging middle class. The benchmark unit operates with a seasonal COP of 3.5 and a GWP of 17601 [3].

2.2. System Overview

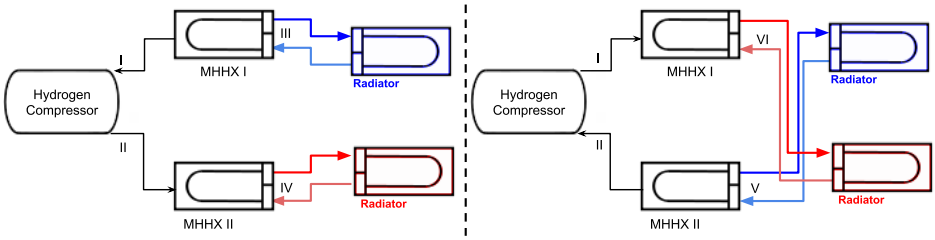


Fig. 8. MHHP RAC system half-cycles with H_2 flows (I, II) and heat transfer fluid flows (III-VI). Left: First half-cycle; Right: Second half-cycle.

Regardless of the hydrogen compressor in the system, a MHHP RAC system functions the same. During the first half of a cycle (Figure 8, left), high pressure hydrogen flows out of the compressor (II) and adsorbs onto MHHX II, while low pressure hydrogen is desorbed from MHHX I and flows into the compressor (I). The coil under low pressure adsorbs heat from the cooling fluid (III) to generate cooling power on the cold radiator, while the coil under high pressure releases heat in the waste heat exchange fluid (IV) to the hot radiator. During the second half of a cycle (Figure 8, right), the hydrogen flow is reversed. High pressure hydrogen flows out of the compressor (I) into MHHX I and low-pressure hydrogen flows out of the MHHX II and into the compressor (I). MHHX II now generates the cooling power (V) for the cold radiator and MHHX II (VI) now rejects waste heat to the hot radiator.

2.3. Benchtop Prototype PEM-ECC-MHHP System

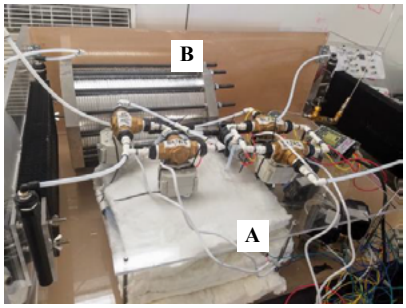


Fig. 9. Benchtop prototype air conditioner with a pair of MHHX in insulation (A) and PEM-ECC (B).

A benchtop prototype AC (Figure 9) was designed and built using 250 W PEM ECC and MHHX technology as a proof of concept. The initial run of the system (Figure 10) showed that the average temperature drop across a MHHP under low pressure is about 3.56 C and provided a 174 W cooling load (of the expected 250 W). After "breaking-in" the PEM ECC, a process that takes about 50 minutes, the PEM ECC performed as expected for about 20 minutes, until the humidifier ran out of water and the performance of the system dropped. During the time that the PEM ECC performed as expected, its average power consumption was 163 W. Although the COP of this run (~1) is less than that of the incumbent technology, the benchtop prototype provided a standard system design for the RAC systems.

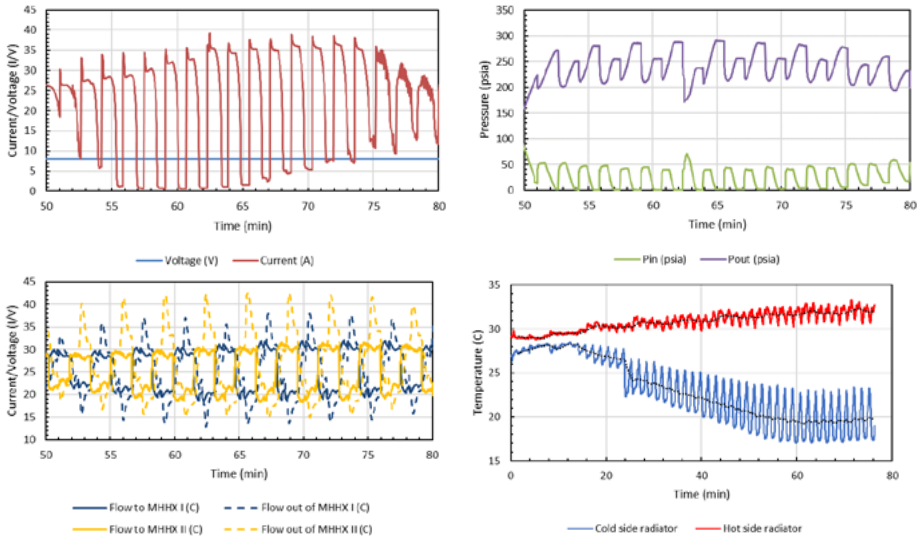


Fig. 10. (Clockwise, from top left) Compressor power, compressor pressure, and MHHX performance of benchtop prototype after first run start-up procedure, heat pump temperature throughout a run of the prototype

This analysis identified the first key engineering challenge in designing a MHHP RAC – reducing the required hydrogen flow rate. Substituting the R-2006, an AB_5 metal hydride, with R-2042, a Vanadium-BCC metal hydride, increased the hydrogen to sorption enthalpy ratio by 1.4, decreasing the required hydrogen flow by about 28%. The required hydrogen flow was further reduced by increasing the cycle time from 2 minutes to 4 minutes – reducing the required hydrogen flow by 50% but increasing the required metal hydride mass by a factor of 2.

With these modifications, the 250 W system was scaled up to a residential RAC system. An analysis of the cooling requirements of a New Delhi apartment showed that a MHHP system would require 2.5 kW of sensible cooling power to maintain a comfortable room temperature. Both PEM ECC-MHHP RAC and Ni-H ECC-MHHP systems were designed with an ILD subsystem to meet these conditions.

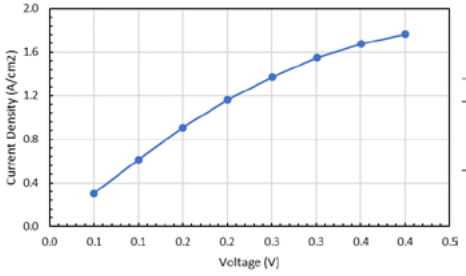
2.4. Overview of 2.5 kW MHHX Subsystem for Residential RAC

Regardless of the type of compressor used, every system has the same fundamental 2.5 kW MHHX subsystem design. The system requires 4 MHHX coils using R-2042X solid state refrigerant. Two coils make up each metal hydride heat exchanger (i.e. MHHX I and MHHX II seen in Figure 1) to provide a constant output of sensible cooling. The total subsystem material cost of the metal hydride heat exchangers is about $22.10, although this is largely due to the cost of the heat exchangers – the R-2042X solid state refrigerant would only cost an estimated $4.00. The refrigerant required for a comparable conventional air conditioner, using R-410A is about 6 lbs. Estimating from its cost on business-to-business (B2B) ecommerce sites, R-410A costs about $1.25 per pound, the total cost of conventional refrigerant is $7.50.

2.5. Residential RAC PEM-ECC-MHHP

A residential room air conditioner (RAC) with a metal hydride heat pump using a proton exchange membrane electrochemical compressor (PEM-ECC-MHHP) was designed to meet the cooling requirements of a typical New Delhi apartment. Given the modifications outlined in the previous section, the design requirements (Figure 11) of the ECC were calculated.

The key design variable in a PEM electrochemical compressor is the voltage applied to each cell. Changing the voltage applied to a cell changes the current density of the cell as dictated by the polarization curve, as seen in Figure 11. As the ECC requires a total 6,150 amps, the voltage determines both the number of cells the ECC requires as well as its power consumption and coefficient of performance.



Parameter	Requirement
Hydrogen Flow Rate (SLM)	42.9
Total Amperage (A)	6,150
Active Area (cm^2)	150

Fig.11. Polarization Curve of selected 25.4 μm PEM and design requirements of PEM-ECC for a 2.5 kW MHHP

As seen in Figure 14, the optimal COP design of the system is about 6.67. This system would require 57 cells with a voltage and current density of 0.12 V and 0.73 A/cm^2. With the current technology, the bill of materials (BOM) of the system totals to about $490.

The PEM-ECC was, again, identified as the cost critical component, equal to 62% of the total BOM. To achieve the target payback period of 3 years, the system must be improved. The membrane component of the system showed the strongest potential for improvement. The current density of a membrane can be improved at a given voltage by decreasing the thickness of the membrane. A general analysis of current membranes shows that at any given voltage the current density improves with the thickness by about 0.7-0.8 (A/cm2)/μm. As seen in Figure 12, the system requires about a 1.86X improvement to its current density to achieve a payback period of 3 years. This system would require membranes about 10μm thick and would operate at a voltage of 0.12 V with a current density of 1.36 A/cm2. The BOM of this system would be about $343. The system would have a 1.83X decrease in energy consumption and a 2.3X decrease on overall climate impact from the benchmark technology [3].

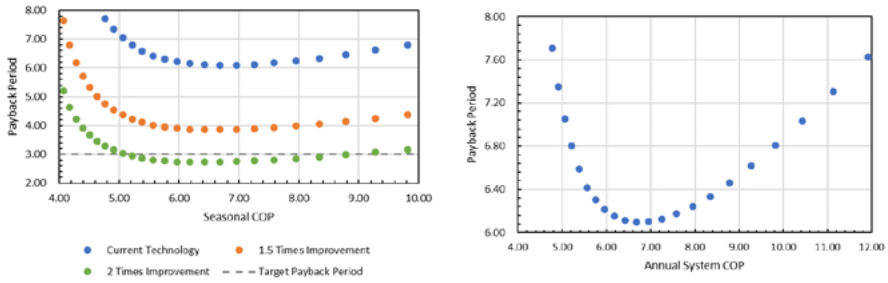


Fig. 12. Required improvement to current density of PEM ECC to achieve target payback period of 3 years (left) and payback period analysis of current PEM ECC to find optimum design COP (right)

2.6. Residential RAC Ni-H-ECC-MHHP

A Nickle Metal Hydride Electrochemical Compressor has the same design requirements as the PEM ECC. However, because the Ni-H ECC functions in a "batch" mode, compressing a batch of hydrogen to the appropriate pressure and then discharging it, two Ni-H ECC subsystems would be required to provide a continuous flow of hydrogen to the metal hydride coils. Like the PEM ECC, the key Ni-H ECC design variable is the cell voltage. However, for a Ni-H ECC, the relation between the cell voltage and the current density is considerably more linear and was assumed to be linear for the purpose of this investigation.

As seen in Figure 13, the optimum COP of the system is 5.25, achieving a payback period of 2.6 years. The given a 3-year restraint on the payback period the maximum COP of the system is 7.7. A system designed for a COP of 7.7 would require 0.044 volts per cell, resulting in a current density of 0.11 A/cm^2. The BOM of this system would be about $374 when produced at 100,000 units/year. This system would have a 2.21X reduction in power consumption from the benchmark unit and a 2.76X decrease in overall climate impact.

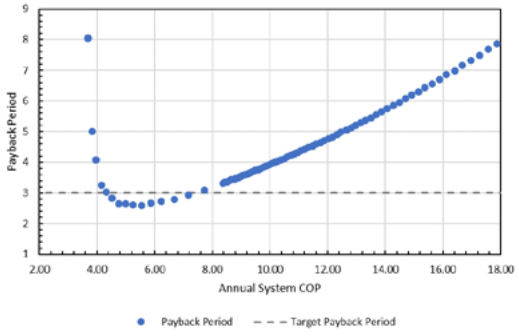


Fig. 13. Payback period analysis of Ni-H ECC to find Optimum Design COP

2.7. Residential RAC Using Rotary Compression MHHP with Integrated ILD System

While electrochemical compressors have the potential to greatly increase the COP of a MHHP RAC, conventional RAC rotary and scroll compressors can also provide the required hydrogen flow. A rotary mechanical compressor designed for a 6000 BTU/hr., R-22 RAC was substituted for the PEM-ECC in the R-2008 benchtop prototype. This mechanical compressor provided a hydrogen flow rate of 30 SLPM-H2 – 5X the required hydrogen flow for the 250 W unit. Therefore, the RAC providing 2.5 kW of sensible cooling would require 8,600 BTU/hr. mechanical compressor to provide ~42.9 SLPM-H2.

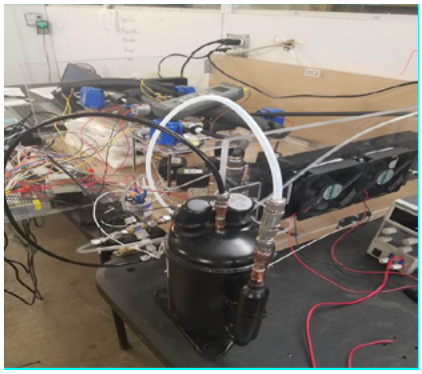


Fig. 14. Benchtop RAC prototype (250 W, R-2008) using a rotary compressor designed for a 6000 BTU/hr. (1758 W) RAC using R-22

An analysis of the compressors rotary and scroll compressor products product found that the average COP of these compressors, when using R-22 is 3.17 [4]. The average COP of these compressors in a R-2042 MHHP subsystem would be 4.52, with a power consumption of 550 W. While these systems were not designed nor optimized for hydrogen flow, they still show strong potential for a high efficiency cooling solution. The MHHX component costs of the RAC is comparable to the non-compressor components of a conventional RAC. Therefore, a RAC utilizing a conventional compressor shows strong potential for an early, low cost MHHP-RAC.

2.8. Comparative Cost Analysis

With the current technology, the Ni-H ECC was found to be a much more effective system than the PEM ECC. The main cost difference between the Ni-H ECC and PEM ECC is the cost of the electrochemical cells. As seen in Table 1, although the Ni-H ECC requires considerably more cells, the cost per cell is far lower. This is largely due to the decreased material cost of the Ni-H bipolar plates and electrode. The Ni-H uses 1% platinum carbon rather than the more costly pure platinum coating of the PEM cells. The PEM plates are over 10x thicker than the Ni-H plates, requiring much more material.

Table 1. Cost Comparison between the Ni-H ECC (0.068 V, 0.17 A/cm2) and PEM ECC (0.125 V, 0.761 A/cm2) Designed for a Minimum Payback Period Using Current Technology

Component	Ni-H Cost per Cell	PEM Cost per Cell
Electrode	$0.323	$2.833
Metal Support	$0.029	$0.05
Gasket & Sealing	$0.098	$0.756
Bipolar Plate	$0.049	$2.00
Total Cost per Cell	**$0.0490**	**$0.5639**
Optimal Number of Cells	296	54
Cost of Cells	$145.04	$304.51
Cost of other Components	$50.00	$58.28
Optimal COP	5.25	6.67
Minimum Payback Period (yrs.)	2.6	6.11

3. ULT Freezer Application

A ULT freezer is freezer that operates between -40 and -86°C. Modern ULT freezers typically use up to 20 times the energy footprint of household fridges. One approach to building these units involves employing hydrofluorocarbon R-508B. Alternatively, Dichlorodifluoromethane (R-12) and Chlorodifluoromethane (R-22) are also used for this application as a refrigerant, although recently their use has been banned under the

Montreal Protocol. These units are used for many sensitive applications (such as storage of medical samples) and operate 24-7 consuming significant energy; and operate with very poor efficiency (COP < 0.5).

One feature of solid-state refrigerant heat pump systems is their ability to provide significantly higher efficiencies at ultra-low temperatures. Changes of temperatures of almost -100°C are being demonstrated (Figure 15) with very small diameter tubing possessing extremely high surface areas per unit mass and unit volume.

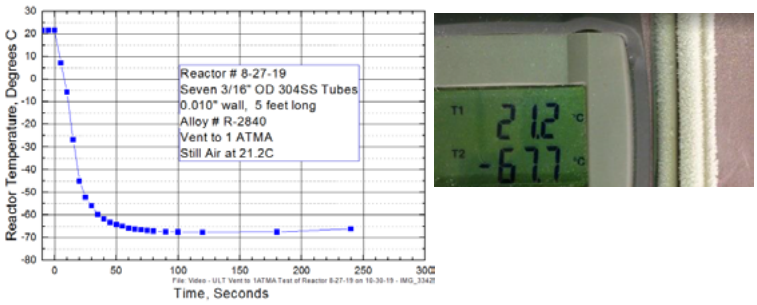


Fig. 15. Reactor temperature of ultra-low temperature (ULT) prototype run (left) and prototype reactor showing frost on surface (right)

An additional advantage of metal hydride air conditioners, refrigerators and ULT freezers is their ability to run on low grade thermal energy (such a solar thermal or geothermal energy). Even heat source temperatures as low as 70°C can be used for any application because the metal hydride alloys can be "staged" to produce any pressure needed to operate the metal hydride device.

Figure 16 below demonstrates this unique ability where only 70°C hot water can be used to compress Hydrogen gas from 21 psia up to over 5000 psig using only five stages of metal hydride alloys. This is possible because each hydride alloy will generate a threefold pressure rise (via the 70°C heat) during its compression stage, thus increasing the hydrogen outlet pressure to over three times the inlet pressure coming into the hydride stage. Each following hydride "stage" has been alloyed engineered to accept the "high pressure" hydrogen gas exiting the previous hydride stage as it's "low pressure' inlet hydrogen. Additionally, multi-staged metal hydrides can be applied beyond heat pump applications to high pressure hydrogen gas generation.

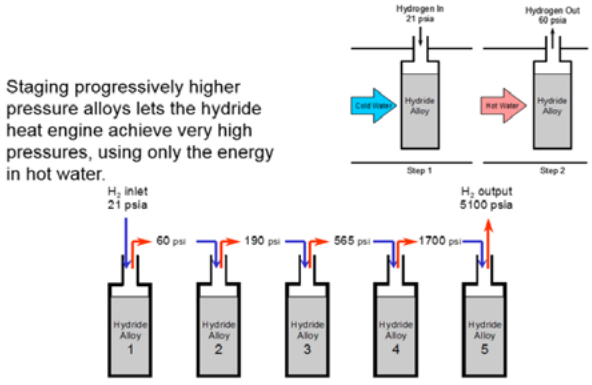


Fig. 16. Low-cost solar thermal energy can be used as the energy source to power (top right); Multi-staged MH Alloys to produce cooling, gas liquefaction and high-pressure hydrogen gas generation.

4. Conclusions & Further Applications

The comparably low cost of solid-state refrigerant per ton of cooling, as well as the removal of materials with global warming potential, is very promising for its use to reduce the carbon footprint of residential air

conditioners. Metal hydride technology utilizes the exceptional heat transfer ability of metal hydride alloys - housed in very small diameter tubes - to create extremely large external surface areas per unit volume, mass and cost. This new heat transfer technology is a new technology platform that represents a paradigm shift in the reduction of energy use, and the cost of, many of our cooling, heating and power generation products, and will greatly speed up our transition to a solar energy economy.

5. Nomenclature

Table 2. Acronyms and abbreviations, defined

Term	Definition	Term	Definition
AB2	Linear molecular geometry	MHHX	Metal hydride heat exchanger
AB5	Trigonal bipyramidal geometry	Mm	Mischmetal
B2B	Business-to-business	Ni-H	Nickel-hydrogen
BCC	Body-centered cubic	PCT	Pressure-concentration-temperature
BOM	Bill of materials	PEM	Proton exchange membrane
COP	Coefficient of performance	P_H	Pressure (high)
ECC	Electrochemical compressor	P_L	Pressure (low)
GWP	Global-warming potential	P_P	Pressure (plateau)
IMC	Intermetallic compound	RAC	Room air-conditioner
MH	Metal hydride	SR	Sorbent refrigerant
MHHP	Metal hydride heat pump (a system containing 2+ MHHX)	ULT	Ultra-low temperature

Acknowledgements

This work was supported by a research award DE-EE-0008218 funded by the U.S. Department of Energy, Building Technologies Office. The technologies outlined in this paper are protected by US Patents referenced [5].

References

[1] Lototskyy, M.V., Yartys, V.A., Pollet, B.G., Bowman, R.C. "A review of Metal hydride hydrogen compressors", *International Journal of Hydrogen Energy* 2014. 39: 5818-5851. https://doi.org/10.1016/j.ijhydene.2014.01.158
[2] Dorheim, M., "Thermodynamics of Metal Hydrides: Tailoring Reaction Enthalpies of Hydrogen Storage Materials." *Thermodynamics: Interaction Studies – Solids, Liquids, and Gases*. doi: 10.5772/21662.
[3] "Prize Criteria," *Global Cooling Prize*, https://globalcoolingprize.org/prize-details/criteria/. Accessed: 05 Nov 2019.
[4] LG. "Rotary & Scroll Compressor," *Compressor Technology for Air-Conditioning*. https://www.lg.com/global/business/compressor-motor/rotary
[5] US Patents: 10,294,930; 10,228,161; 10,087,532; 10,024,590; 9,909,224; 9,738,981; 9,599,364; 9,464,822; 9,457,324; 9,005,411; 8,769,972; 8,640,492; 8,627,671; and US Patent Applications: 20190293324; 20190212072; 20170350024; 20170198947

6. Appendix I: Proposed Nomenclature for Sorbent Refrigerants

6.1. Appendix I.A: Nomenclature for Metal Hydride Solid State Refrigerants

Below is the proposed nomenclature for metal hydride based, solid state refrigerants (the R-2000 series refrigerants). The R-2100 to R-2300 series refrigerants are Vanadium-BCC metal hydrides. The R-2400 to R-2600 series refrigerants are AB5-type intermetallics. The R-2700 series refrigerants are TiFe based, AB-type intermetallics. The R-2800 to R-2900 series refrigerants are AB2-type intermetallics. The R-20XX series refrigerants have been left as a place holder for miscellaneous, novel, and proprietary metal hydride refrigerants.

Table 3. Metal Hydride Solid State Refrigerants

Metal Hydride Solid State Refrigerant	**Metal Hydride Class**	**SR Designation**
V(75)Ti(17.5)Zr(7.5)	V-BCC	R-2120

V(75)Ti(10)Zr(7.5)Cr(7.5)	V-BCC	R-2300
V(0.85)Ti(0.1)Fe(0.05)	V-BCC	R-2310
V(92.5)Zr(7.5)	V-BCC	R-2220
MmNi(4.8)Al(0.2)	AB_5	R-2410A
LaNi(4.7)Sn(0.3)	AB_5	R-2560A
LaNi(4.8)Sn(0.2)	AB_5	R-2560B
LaNi(4.8)Sn(0.2)	AB_5	R-2560C
Mm(0.5)La(0.5)Ni(4.7)Sn(0.3)	AB_5	R-2660
LaNi(4.8)Al(0.2)	AB_5	R-2510
LaNi(5)	AB_5	R-2500
MmNi(4.7)Fe(0.3)	AB_5	R-2440A
La(0.85)Ce(0.15)Ni(5)	AB_5	R-2570
MmNi(4.7)Al(0.3)	AB_5	R-2410B
La(0.2)Y(0.8)Ni(4.6)Mn(0.4)	AB_5	R-2535
MmNi(4.15)Fe(0.85)	AB_5	R-2440B
La(0.4)Ce(0.4)Ca(0.2)Ni(5)	AB_5	R-2527
Mm(1-x)Ca(x)Ni(5-y)Al(y)	AB_5	R-2412
Ca(0.2)Mm(0.8)Ni(5)	AB_5	R-2420
TiFe(0.9)Mn(0.1)	AB	R-2700
Zr(0.7)Ti(0.3)Mn(2)	AB_2	R-2860
Ti(0.9)Zr(0.1)Mn(1.4)Cr(0.35)V(0.2)Fe(0.05)	AB_2	R-2871
Ti(0.8)Zr(0.2)CrMn	AB_2	R-2870A
Zr(0.8)Ti(0.2)FeNi(0.8)V(0.2)	AB_2	R-2832
Ti(0.77)Zr(0.3)Cr(0.85)Fe(0.7)Mn(0.25)Ni(0.2)Cu(0.03)	AB_2	R-2875
TiCr(1.9)Mo(0.01)	AB_2	R-2816B
TiCr(1.9)	AB_2	R-2810
ZrFe(1.8)Cr(0.2)	AB_2	R-2913
[Ti(0.97)Zr(0.03)](1.1)Cr(1.6)Mn(0.4)	AB_2	R-2870B
TiCr(1.5)Mn(0.25)Fe(0.25)	AB_2	R-2843A
TiCr(1.5)Mn(0.2)Fe(0.3)	AB_2	R-2843B
TiCrMn	AB_2	R-2840
ZrFe(1.8)Ni(0.2)	AB_2	R-2904
Ti(0.86)Mo(0.14)Cr(1.9)	AB_2	R-2816A
Xergy ULT Refrigerant	AB_2	R-2028X
Xergy A/C Refrigerant	AB_5	R-2006X
Xergy A/C Refrigerant	V-BCC	R-2042X

6.2. Appendix I.B: Nomenclature for other Sorbent Refrigerants

Other sorbent refrigerants include Metal Organic Framework (MOF) solid state refrigerants (R-3000s) and liquid desiccant (LD) sorbent liquid refrigerants (R-4000s). The proposed general nomenclature for these refrigerants can be found in the table below.

Table 2. Metal Organic Framework Solid State Refrigerants

Metal Organic Framework Classification	Dimension of Organic/Inorganic	SR Series
Molecular Complexes	0/0	R-30XX

Chain Coordination Polymers	1/0	R-31XX
Layered Coordination Polymer	2/0	R-32XX
3-D Coordination Polymer	3/0	R-33XX
Hybrid Inorganic Chains	0/1	R-34XX
Mixed Inorganic-Organic Layers	1/1	R-35XX
Mixed Inorganic-Organic 3-D Framework	2/1	R-36XX
Hybrid Inorganic Layers	0/2	R-37XX
Mixed Inorganic-Organic 3-D Framework	1/2	R-38XX
3-D Inorganic Hybrids	0/3	R-39XX

Table 3. Liquid Desiccant Sorbent Liquid Refrigerants

Liquid Desiccant Classification	**SR Series**
Room Temperature Ionic Liquid Desiccant	R-41XX
Alkali Metal Liquid Desiccant	R-42XX
Alkali Earth Metal Liquid Desiccant	R-43XX
Organic Liquid Desiccant	R-44XX

13th IEA Heat Pump Conference
April 26-29, 2021 Jeju, Korea

An overview of hydrogen compressors for heat pump systems

Jacob Zerby[a], Bamdad Bahar[a*], Mark Golben[a], Sam Dorman[a], William TomHon[a]

[a]*Xergy, Inc., 299A Cluckey Dr., Harrington DE 19952, USA*

Abstract

Metal hydrides present an alternative heat pump approach to efficiently achieving extreme temperatures, without high GWP refrigerants. These materials work by complexing with hydrogen in order to generate incredible thermal lifts; an alloy of TiCrMn, complexes hydrogen at 90°C and exhausts at approximately -60°C, for example. A drawback of this class of materials is that greater temperature lifts require higher pressure hydrogen. This paper analyzes four methods of producing pressurized hydrogen: two electrochemical systems, one system employing metal hydride compression, and one using conventional mechanical compression. Electrochemical compression makes use of ion selective electrolytes that provide pressurized hydrogen when a potential gradient is applied. Metal hydride compressors operate by reversing the principle behind the metal hydride heat exchangers used in these heat pumps – i.e. releasing hydrogen at pressure when the metal hydride is heated. Mechanical compressors use various designs to move a mass of gas and shrink the volume it occupies, thereby compressing the gas. This paper provides operational data for these four different compression strategies. Heat pump cycles employing these systems are analyzed for critical performance parameters.

© HPC2020.

Selection and/or peer-review under responsibility of the organizers of the 13th IEA Heat Pump Conference 2020.

Keywords: metal hydride heat pump; metal hydride compressor; electrochemical compressor; nickel hydrogen battery; hydrogen compressor; metal hydride heat exchanger

1. Background

1.1. Metal Hydride Heat Pump

Metal hydride heat pumps (MHHP) operate using pair(s) of metal hydride heat exchangers (MHHX) to generate heating and cooling. Any compression technology that pumps hydrogen can be utilized to adsorb and desorb hydrogen from the MHHX. Adsorption of hydrogen on to the metal hydride is an exothermic reaction that produces heat, and desorption of hydrogen from the metal hydride is an endothermic reaction and pulls heat from the surroundings.

During the first half of a cycle, high pressure hydrogen flows out of the compressor (I) and adsorbs onto the metal hydride of MHHX A, while low pressure hydrogen is desorbed from the metal hydride of MHHX B and flows into the compressor (II). The coil under low pressure pulls heat from the cooling liquid (III) to generate cooling power on the cold radiator (C), while the coil under high pressure releases heat in the waste heat liquid (IV) to the hot radiator (D). During the second half of a cycle, the hydrogen flow is reversed. High pressure hydrogen flows out of the compressor (II) and MHHX B and low-pressure hydrogen flows out of the MHHX A and into the compressor (I). MHHX A now generates the cooling power (V) for the cold radiator (C) and MHHX B (VI) now rejects waste heat to the hot radiator (D).

* Corresponding author. Tel.: +1-302-629-5768
E-mail address: Bamdad.bahar@xergyinc.com.

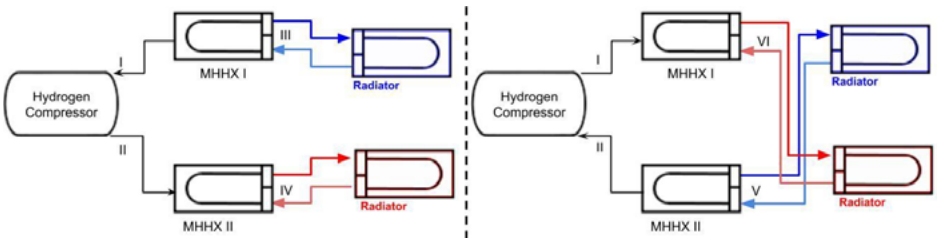


Fig. 1. MHHP configuration and flows during first half-cycle (top) and second half-cycle (bottom)

Different forms of compression were analyzed assuming a room air conditioner (RAC) with a capacity of 2.5 kW of cooling. To improve the economics of the MHHP from the benchtop testing the cycle time was doubled (decreasing the hydrogen flow rate and increasing the mass of the MHHX), and a different metal hydride was selected with a greater heat of formation. This allows for smaller compressors, the most cost critical component in the system. Based on the selected metal hydride, the cycle time, and cooling capacity, the estimated hydrogen flow rate for all systems was 43 SLM.

1.2. Proton Exchange Membrane (PEM) Based Electrochemical Compression

Proton exchange membrane (PEM) electrochemical compression (ECC) is a method of hydrogen compression that is a derivative of fuel cell technology. It is a solid-state compression technology that offers the benefits of no moving parts, no noise, and high efficiencies. Pressure lifts are generated by transporting hydrogen in its ionic form as protons.

A PEM, depicted in Figure 2, is sandwiched on either side by a catalyst and a gas diffusion layer. A voltage is applied to the membrane electrode assembly (MEA) to drive the hydrogen compression reaction. Hydrogen contacts the catalyst/membrane interface at the anode of the system and reacts to form protons and electrons. The protons transport across the membrane, as the membrane is ion-selective and allows cations to transport across. The protons recombine with the electrons at the catalyst/membrane interface of the cathode to form hydrogen. The method of applying a potential to the MEA allows for high pressure hydrogen to be generated from a low-pressure hydrogen feed.

The overall standard potential for the system is 0.00 V, however this assumes an ideal case with no pressure differential and perfectly balanced half cells. The overpotential, or additional energy, that must be applied due to the pressure differential is given below.

$$V = \frac{RT}{2F} * ln\left(\frac{P_{cathode}}{P_{anode}}\right);\ Anode: H_2 \rightarrow 2H^+ + 2e^-, E° = 0.00\ V;$$
$$Cathode: 2H^+ + 2e^- \rightarrow H_2, E° = 0.00\ V;\ Overall: H_{2,low} \rightarrow H_{2,high},\ E°_{total} = 0.00\ V$$

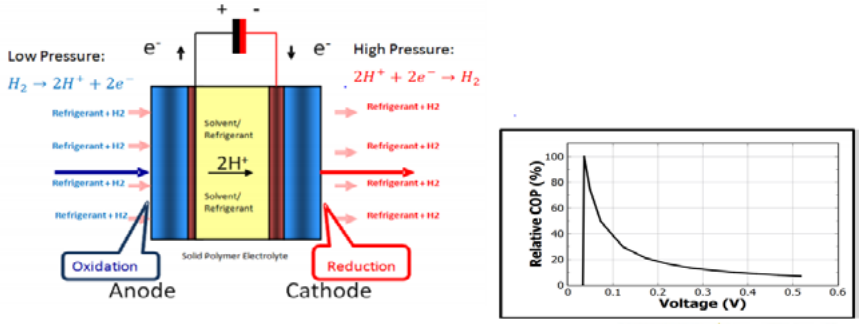


Fig. 2. Proton exchange membrane electrochemical compressor proton flow diagram (left) and COP curve (right)

When operating the cell at low pressure differentials the voltage required is very close to 0.00 V, i.e. the system efficiency is very high. However, some heat pump applications require pressure ratios of >10x, decreasing the overall efficiency of the PEM ECC. From Figure, the COP of an ECC system exponentially increases at cell voltages <0.1 V. In order to make PEM ECC-MHHP systems viable, the current density (proportional to the hydrogen flow per unit area) must be increased at low voltages.

The development of PEM ECCs has been focused on decreasing the weight and volume and increasing the current density, to improve the economic viability and the energy efficiency of the system. Additionally, combined PEM ECC-MHHP systems have been successfully run for initial analysis.

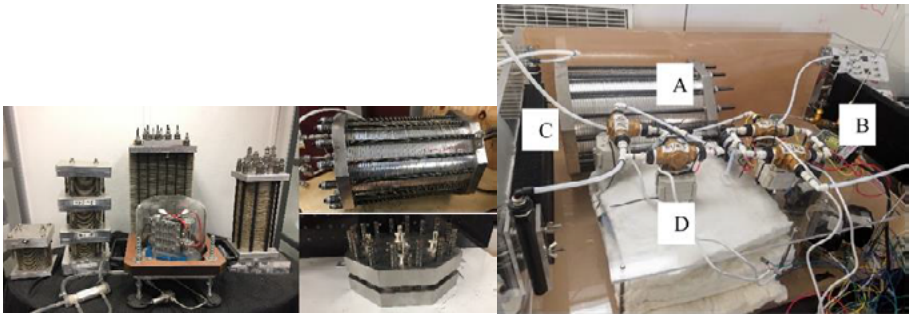


Fig. 3. Left: A selection of PEM-ECCs; Right: Proof-of-concept 250 W PEM ECC-MHHX

A benchtop prototype AC unit was designed and built using a nominal 250 W MHHX as a proof of concept. The main system components are (a) PEM ECC, (b) cold-side radiator, (c) hot-side radiator, (d) pair of MHHX, heat exchange fluid line (the white plastic tubing in Figure 3), and hydrogen line (the metal piping). The heat exchange fluid line is designed to transfer the heating and cooling from the MHHXs to the appropriate radiators. The cold side radiator cools down the space, while the hot side radiator dumps heat to the ambient air. The hydrogen line has valving to change which MHHX is feeding to the inlet and outlet based on the cycle.

During testing the outlet pressure of the compressor ranged from 13.8-20.7 bar (200-300 psia), and the inlet ranged from 3.44 (50 psia) to near vacuum. The average temperature drop across a MHHX under low pressure was about 3.56°C, providing a cooling load of 174 W (of the expected 250 W). After “breaking-in” the PEM ECC, a process that took about 50 minutes, the PEM ECC performed as expected for about 20 minutes, until the humidifier ran out of water and the performance of the system dropped. During the time that the PEM ECC performed as expected, its average power consumption was 163 W. Although the COP of this run, ~1, is less than that of the incumbent technology, the benchtop prototype provided a standard system design for the RAC systems, and there are many variables to optimize to improve system efficiency. The system run also provided a basis for hydrogen compression analysis of the other compressors.

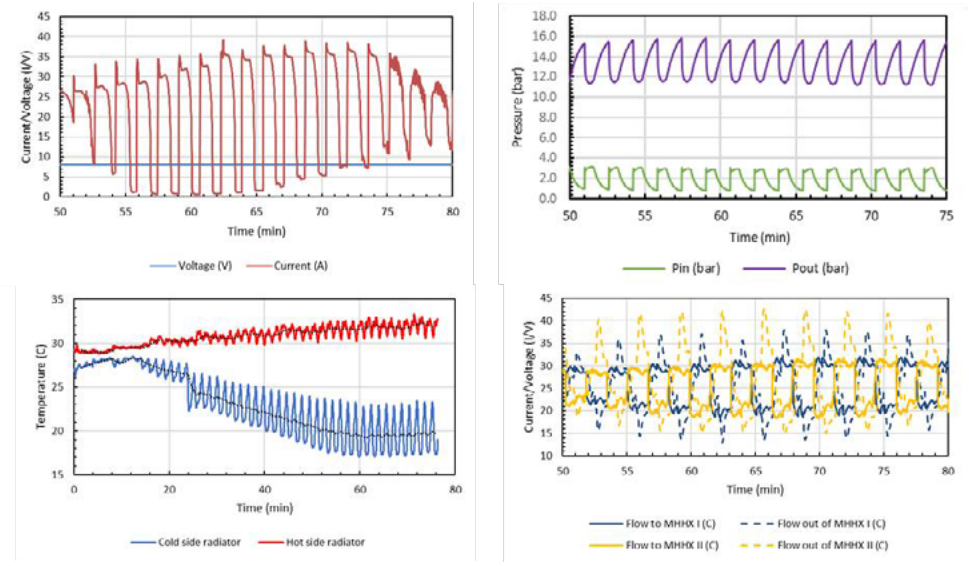


Fig. 4. (Clockwise from top left) Power consumption; ECC pressure differential; MHHXs' temperature; and Cooling during proof-of-concept runs

Based on current testing data, utilizing 25.4 µm membranes would require a total number of 57 cells with an active area of 150 cm^2 to meet a 3-year payback period (on a premium over a conventional, mini-split ductless RAC) for a 2.5 kW air conditioner, operating at 0.12 V per cell and 0.71 A/cm^2. The estimated total power consumption for the compressor is 730 W with a system cost of $380. The weight, dimensions, and volume of the PEM ECC are 149.7 kg, 25.4 cm x 25.4 cm x 29 cm, and 18.7 L (330 lbs, 10"x10"x11.4", and 1,140 in^2), respectively. Future improvements with the membrane and bipolar plate are required to improve the economics of the system. Extrapolating from the information in Figure 5, with a decrease in thickness to about 10 µm, 0.12 V could provide 1.36 A/cm^2 (capturing 75% of the improved ionic conductivity). The number of cells decreases to 30, with an estimated energy consumption of 730 W and costing $230. The weight, dimensions, and volume decrease to 65.8 kg, 25.4 cm x 25.4 cm x 12.7 cm, and 8.20 L (145 lbs, 10"x10"x5", and 500 in^3). Further improvements can be made to the system overall to reduce the voltage at the required current level, which would lead to improvements in COP.

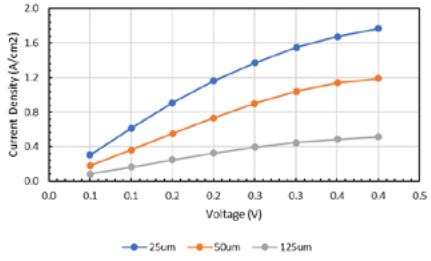


Fig. 5. Potential of improvement to PEM ECC due to membrane thickness

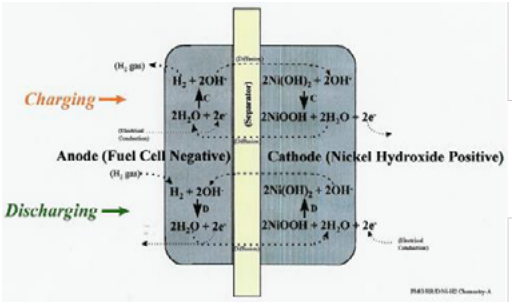
1.3. Alkaline Electrochemical Compression

The anionic electrochemical compression technology analyzed for use in a MHHP is based on well-established nickel hydrogen (Ni-H) battery technology. Going from a cationic to anionic systems greatly reduces the cost of the system. The expensive metal plates in the cationic systems, stainless steel and titanium,

can be replaced with cheaper metals like nickel, and the expensive platinum group metals (PGM) can either be replaced entirely with non-PGM catalysts, or reduced in quantity.

The battery technology is used in reverse, where power is put in to compress hydrogen instead of hydrogen expanding to produce power. While the energy density is only about one third as that of a lithium battery, the Ni-H battery has a long life, with cells capable of operating for 15 years at 80% depth of discharge (DOD) in satellite applications [1]. The cells can be designed to operate up to 82.74 bar (1200 psi), so this technology is applicable to MHHPs [2].

The nickel-hydrogen battery combines the positive nickel electrode of a nickel-cadmium battery with the negative electrode of a fuel cell. During charging, water is reduced at the anode to form hydroxyl ions and hydrogen gas. The hydroxyl ions transport through the alkaline electrolyte, typically KOH, and oxidize the nickel hydroxide ($Ni(OH)_2$) to form nickel oxyhydroxide (NiOOH). During discharging the reverse reactions occur, where the NiOOH is reduced back to $Ni(OH)_2$ and hydrogen gas is oxidized to reform water. There are three main architectures for designing a Ni-H battery: individual pressure vessel, common pressure vessel, and bipolar design. For this application we analyzed the bipolar plate design, with a positive electrode made up of porous nickel structure, which is packed with the nickel hydroxide, and a negative electrode like that of a fuel cell, which contains a platinum group metal catalyst with a gas diffusion layer.



$$Negative: H_2O + e^- \leftrightarrow \frac{1}{2}H_2 + OH^-$$
$$Positive: Ni(OH)_2 + OH^- \leftrightarrow NiOOH + H_2O + e^-$$
$$Overall: Ni(OH)_2 \leftrightarrow NiOOH + \frac{1}{2}H_2$$

Fig. 6. Alkaline exchange membrane electrochemical compressor electron flow diagram (left) and equations on electrodes (right)

In our proposed system a pair of Ni-H batteries work in tandem, i.e. one is charging while the other one is discharging. This allows for one to provide compressed hydrogen gas to the adsorbing MHHX, while the other is pulling hydrogen gas from the desorbing MHHX. The discharging battery provides most of the electrical power for the charging battery through a step-up converter, and the net difference is provided by an external source. The pair cycles back and forth like the MHHXs, and the discharging battery becomes the charging battery. Therefore, the power consumption of the system is the external voltage at the operational current of the battery providing high pressure hydrogen.

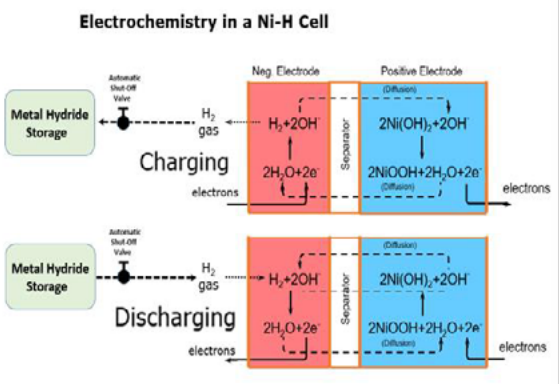




Fig. 7. Electrochemistry in a Ni-H cell (left) and prototype AEM ECC (right)

To meet the demands of a 2.5 kW air conditioner and achieve a payback period of 3 years, each battery will comprise of 228 cells at an active area of 490 cm^2. The discharging battery will operate at a voltage of about 1.25 V/cell at 11 mA/cm^2, and the charging battery will operate at 1.206 V/cell at 11 mA/cm^2, such that the input voltage is 0.044 V/cell. The input power to the system would be 540W with a system cost of $270. The weight, dimensions, and volume of the Ni-H battery system are 40.8 kg, 61 cm x 30.5 cm x 11.43 cm, and 21.23 L (90lbs, 24”x12”x4.5”, and 1,296 in^3), respectively.

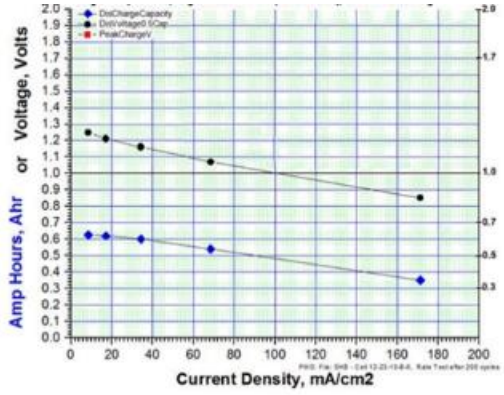


Fig. 8. Performance of NiMH compressor with respect to current density

1.4. Metal Hydride Compression

Metal hydrides (MH) are metallic compounds or alloys that adsorb and desorb hydrogen based on the temperature and hydrogen pressure conditions experienced by the MH. Based on the characteristics of the MH, it will adsorb a certain mass of low-pressure hydrogen at a specific low temperature. Once saturated with hydrogen the hydride is then heated causing the plateau pressure of the hydride to increase (as it is temperature dependent). This increase in plateau pressure causes the hydrogen to desorb from the hydride, allowing for compression of hydrogen gas by the metal hydride compressor (MHC) The temperature of the hydride and the mass of the hydride determines the flow rate, and the output pressure is controlled by the final temperature and the heating rate. Once the hydrogen is completely desorbed the hydride is cooled and then refilled with low pressure hydrogen to start the cycle over again. Figure 9 shows the basic cycle in action.

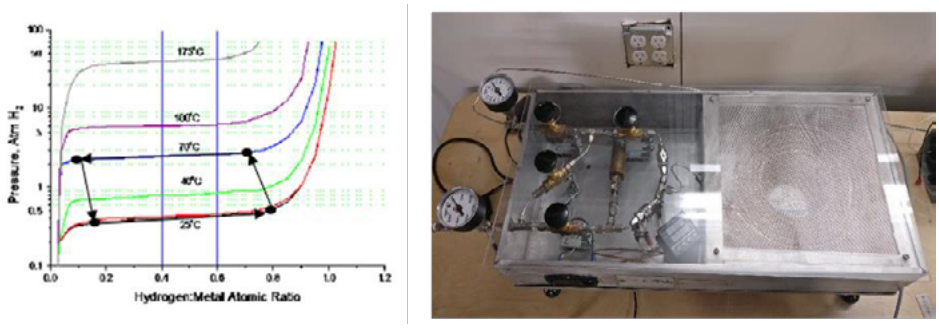


Fig. 9. Metal hydrogen compressor pressure cycle (left) and example compressor (right)

In our proposed system a series of MHCs work in tandem, i.e. some will be adsorbing hydrogen while the others will be desorbing hydrogen. The MHCs that is desorbing hydrogen is heated using a nichrome resistive heating wire, and the MHCs that is adsorbing is cooled down by a fan.

To meet the demands of a 2.5 kW air conditioner, the MHC system will comprise of 20 MHC coils of 1.524 m (5 ft) in length, with 10 producing hydrogen at any time. To achieve the desired pressure and hydrogen output each will need to be heated to 200°C, resulting in a power consumption of ~500 W per coil, or 5000W total. The coils cooling down will be running on a fan system that draws an average 70 W, for a total system power draw of 5500W, at a system cost of $456. The weight, dimensions, and volume of the MHC system are 22.7 kg, 30.5 cm x 61 cm x 25.4 cm (50lbs, 12”x24”x10”, and 2880 in^3), respectively.

1.5. Mechanical Compression

The final method of compression analyzed for the MHHP was a standard mechanical compressor that is already mass manufactured. The type of mechanical compressor selected for testing was an R-22 compressor for a vapor compression (VC) heat pump with a rated cooling capacity of 6,330 kJ/hr (6,000 BTU/hr). This type of compressor is a scroll compressor, with two interleaving scrolls to pump, compress or pressurize fluids such as liquids and gases. Often, one of the scrolls is fixed, while the other orbits eccentrically without rotating, thereby trapping and pumping or compressing pockets of fluid between the scrolls. Another method for producing the compression motion is co-rotating the scrolls, in synchronous motion, but with offset centers of rotation. The relative motion is the same as if one were orbiting.



Fig. 10. R-22 compressor (left) and MHHP employing the same (right)

Connecting the compressor to a hydrogen tank provided a flow rate of ~30 SLPM of hydrogen at a current of 2.4 A and a voltage of 110 VAC. When only connected to a tank the compressor was able to achieve a 12.4 bar (180 psi) maximum from atmospheric pressure. Once it was turned off, a large internal leak caused the sharp increases of the inlet pressure of Figure 11. The compressor was also hooked up to imitate the pressure swings of the MHHP and maintain the 13.8 bar (200 psi) necessary to provide heating and cooling from the MHHXs.

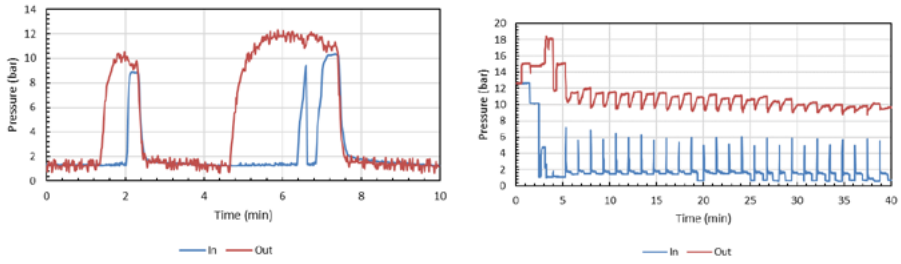


Fig. 11. Compressor when connected to a tank (left) and compressor imitating pressure swings of MHHP (right)

Because the 2.5 kW cooling system requires ~43 SLM of hydrogen and the 6330.4 kJ/hr (6,000 BTU/hr) compressor provided 30 SLM, a compressor sized for ~9074 kJ/hr (8,600 BTU/hr) should provide the requisite flow rate. The power consumption for a mechanical compressor in a MHHP system was estimated from the power consumption of rotary scroll compressors that met or exceeded (by less than 1055 kJ/hr (1000 BTU/hr)) the cooling load requirement. Assuming the power consumption is linear to the output cooling load, the power consumption of the compressors was proportionally decreased by the amount their cooling load exceeded 9073.5 kJ/hr (8600 BTU/hr). The average COP of typical systems employing R-22 is 3.17 [3]. With an average power consumption of 550 W, the average COP of employing a mechanical compressor in the MHHP is 4.52, with a system cost estimated in the range of $50-100. The weight, dimensions, and volume of the Ni-H battery system are 15.4 kg, 22.9 cm x 15.24 cm x 22.9 cm, and 7.96 L (34 lbs, 9”x6”x9”, and 486 in^3), respectively. While these systems were not designed nor optimized for hydrogen flow, they still show strong potential for a high efficiency cooling solution. The MHHX component costs of the RAC is comparable to the non-compressor components of a conventional RAC. Therefore, a RAC utilizing a conventional compressor shows strong potential for an early, low cost MHHX-RAC.

2. Conclusion

Experimental and theoretical data shows that hydrogen compression systems coupled with MHHP technology provides a realistic alternative to standard freon based heat pump systems.

From performance data and techno-economic analysis it is evident that PEM Compressors are highly efficient for low to medium pressure application but require more initial cost. At higher pressures the cost increases even further, limiting the technology to low temperature lift applications. Ni-H compressors provide a better electrochemical alternative with lower cost and higher efficiency than PEM for low to medium pressure application. This is a relatively low TRL technology for hydrogen compression, but with more development, this technology can overcome PEM compressor technology. MHC is the most expensive and least efficient of all the technologies. However, it does allow for much higher-pressure applications. One such application is in extreme temperature systems, such as ultra-low temperature freezers. Because the temperature drop is to -85°C, MHHXs designed for this application require very high pressures (>2000 psi). Mechanical compression of hydrogen offers the most near-term solution to implementation of a MHHP but will not see the advancements that the electrochemical systems will see, in terms of cost reduction and improvements in power consumption, with future development in the electrochemical compression technology.

The Table 1, below, provides a comparison of different hydrogen compression technologies.

Table 1. Summary of hydrogen compression technologies

Compression Technology	System Cost ($)	System Power Consumption (W)	Weight (lb)	Volume (in^3)
PEM ECC	380	730	330	1140
Ni-H	270	540	90	1296
MHC	456	5500	70	2880
Mechanical	50-100	550	34	486

3. Nomenclature

Table 2. Acronyms and abbreviations, defined

Term	Definition	Term	Definition
AEM	Anion Exchange Membrane	MHHP	Metal Hydride Heat Pump
COP	Coefficient of Performance (Wh/Wh)	MHHX	Metal Hydride Heat Exchanger
DOD	Depth of Discharge	PEM	Proton Exchange Membrane
ECC	Electrochemical Compressor	PGM	Platinum Group Metal
MEA	Membrane Electrode Assembly	RAC	Room Air-Conditioner
MH	Metal Hydride	SLM	Standard-Liter per Minute (0°C, 1 bar)
MHC	Metal Hydride Compressor	VC	Vapor Compression

Acknowledgements

This work was supported by a research award DE-EE-0008218 funded by the U.S. Department of Energy, Building Technologies Office. The technology outlined in this paper is covered by a US Patents referenced [4]. This publication is a part of a 10-paper series to commemorate Xergy's 10-year anniversary, bringing advanced membrane technology to the global HVAC industry.

References

[1] Shen, Bo; Fackler, Scott; and Bamdad, Bahar, "Experimental Study to Characterize Performance of a Prototype Electrochemical Compressor" (2018). *International Compressor Engineering Conference*. Paper 2524

[2] Ye Tao, Hoseong Lee, Yunho Hwang, Reinhard Radermacher, Chunsheng Wang. "Electrochemical compressor driven metal hydride heat pump," *International Journal of Refrigeration*, Volume 60, 2015, Pages 278-288, ISSN 0140-7007

[3] LG. "Rotary & Scroll Compressor," *Compressor Technology for Air-Conditioning*. https://www.lg.com/global/business/compressor-motor/rotary

[4] US Patents: 10,294,930; 10,228,161; 10,087,532; 10,024,590; 9,909,224; 9,738,981; 9,599,364; 9,464,822; 9,457,324; 9,005,411; 8,769,972; 8,640,492; 8,627,671; and US Patent Applications: 20190293324; 20190212072; 20170350024; 20170198947

13th IEA Heat Pump Conference
April 26-29, 2021 Jeju, Korea

Numerical simuation of two-phase flow distribution in a vertically installed refrigerant distributor

Siyoung Choi[a], Hyoin Lee[a], Jihwan Jeong[a]*

[a] School of Mechanical Engineering, Pusan Nat'l Univ, 2, Busandaehak-ro 63beon-gil, Geumjeong-gu, Busan, 46241, Republic of Korea

Abstract

If two-phase flow occurs in the Variable Refrigerant Flow (VRF) system air conditioner, the distribution characteristic may be changed, and uneven distribution problem will occur. In addition, changing the orientation of the refrigerant distributor from horizontal to vertical in order to reduce the installation space, this uneven distribution becomes even worse. In this study, computational fluid dynamics (CFD) simulation is used to calculate uneven distribution of two-phase flow in a vertically installed distributor and to analyze the factors affecting the uneven distribution by analyzing the internal flow. CFD results are validated by the previous experimental results. Due to the momentum difference, liquid phase flows toward the end of the header and the gas phase flows near the inlet. Uneven distribution is exacerbated as the void fraction increased. The geometry of the header is modified to improve the non-uniform distribution and the result are compared with the existing data.

© HPC2020.
Selection and/or peer-review under responsibility of the organizers of the 13th IEA Heat Pump Conference 2020.

Keywords: computational fluid dynamics (CFD), distribution, two-phase

1. Introduction

Variable Refrigerant Flow (VRF) system is an air conditioning system that supplies refrigerant to several indoor units using one outdoor unit. VRF system has high efficiency because it can control the cooling and heating depending on thermal loads of each indoor space. Due to its convenience and efficiency, demand is increasing in commercial and residential buildings. VRF system supplies the refrigerant to each indoor unit by using a refrigerant distributor, and the refrigerant distributor can also be connected to other refrigerant distributors. As the height of a building increases, the height difference criteria of the refrigerant distributor also increase. In a vertical pipe connecting the distributor, the refrigerant flowing in the liquid state can be vaporized into a two-phase state due to the static pressure loss caused by the height difference. When a two-phase flow is supplied to the refrigerant distributor, unlike the distribution tendency of a single phase flow, uneven distribution occurs. In addition, in order to reduce the installation space, there is a demand to change the direction of the refrigerant distributor from horizontal to vertical. If the refrigerant is distributed to each indoor unit through a vertically installed distributor, the uneven distribution can be worse than the horizontal installation. If uneven distribution occurs inside the refrigerant distributor for the influence of such supply conditions, some of the indoor units do not receive sufficient refrigerant mass flow rates to meet their thermal demand. Then, the outdoor unit will have additional operation to supply the required mass flow rate in the indoor space, and it will be a negative impact on the energy efficiency of the system. Therefore, it is necessary to investigate the distribution characteristics when the two-phase flow is supplied to the vertically installed refrigerant distributor.

The refrigerant distributor is a manifold shape. The flow distribution problem in the manifold shape has been mainly dealt with in the research of parallel-flow heat exchangers. Many researchers [1-6] have conducted experimental and numerical studies on the flow distribution in parallel-flow heat exchangers. Dario et al. [1] reviewed the study of two-phase flow distribution in parallel channels and summarized the factors that influence the two-phase flow distribution. The factors affecting the distribution are divided into geometrical

factors, fluid properties, and operating conditions. Kim et al. [2] experimentally investigated the two-phase flow distribution of R-134a in a downward flow mini-channel heat exchanger varying the operating conditions (mass flux, quality), geometrical factor (inlet position) and compared with the data conducted with R-410A. Vist and Pettersen [3] experimentally investigated the two-phase distribution varying geometrical factors (header diameter, flow direction) and operating conditions (mass flow rate, quality, heat load). Lee and Lee [4] experimentally investigated the two-phase distribution tendency varying the geometrical factor (intrusion depth) and operating conditions (mass flux, quality). Zhou et al. [5] numerically investigated the flow distribution in a central-type parallel heat exchanger. Flow distribution by changing the geometrical factor (dividing and combining header ratio, header and tube diameter ratio) was mainly considered. Said et al. [6] numerically investigated reducing mal-distribution at heat exchanger by installing orifice and nozzle between header and branch tubes.

In the previous study, many researchers conducted experimental and numerical study on flow distribution in heat exchangers. As a result, geometric factors and flow conditions affected the flow distribution in the manifold. In the case of experimental study, however, there are limitations in the analysis of the internal flow characteristic of header by installing the measurement device inside the distributor. In the numerical study, the flow characteristic in the header by the change of geometrical factor was performed by 3-D simulation, but the analysis was mainly dealt with in single phase flow.

In this study, computational fluid dynamics (CFD) simulation is conducted to investigate the two-phase flow distribution characteristics in a vertically installed distributor used in the VRF system. The distributor shape is modeled by simulating the refrigerant distributor used in the VRF system, and the two-phase flow distribution is calculated by changing the inlet tube position and void fraction. Two-phase flow inside the header are analyzed through quantitative values such as the void fraction of the cross-section and the superficial velocity. Based on the analysis, the geometry of the distributor is modified to improve the flow distribution. Then distribution characteristics of the modified distributor are compared with those of the existing distributor.

2. Numerical Method

2.1. Geometry

The VRF system consists of three pipes, two of them are gas pipe and the other is a liquid pipe. The two-phase flow due to height difference occur in the liquid pipe of refrigerant distributor. The modelling of refrigerant distributor is shown in Fig. 1. The header is installed vertically, and the shape of the header is a double pipe through which a circular tube passes in the center. Then four circular branch tubes for supplying the refrigerant to each indoor unit are installed having the 3mm of intrusion depth. The number of each branch tube is named from channel #1 to channel #4 according to the installed location from the top to the bottom. The direction of inlet tube is horizontal and is perpendicular to the installation direction of the branch tube. The position of the inlet tube varies depending on the analysis conditions.

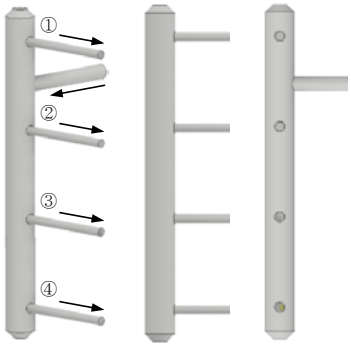


Fig. 1. Modelling of Refrigerant Distributor

2.2. Governing Equation

Transient analysis is conducted to calculate two-phase flow distribution in the distributor modelled in chapter 2.1. The commercial CFD code STAR-CCM+ is used for the numerical computations. A second order upwind scheme is used to discretize the velocity convective term and SIMPLE (Semi-Implicit Method for Pressure-Linked Equations) algorithm is adopted for the velocity-pressure coupling in STAR-CCM+

The flow pattern of two-phase flow inside the header was bubbly flow [7]. Therefore, Eulerian-Eulerian model is adopted to solve the governing equation. In Eulerian-Eulerian approach, each phase is treated mathematically inter-penetrating continua and mixed in each control volume. Then, governing equations are solved for each phase. Assuming adiabatic and incompressible flow, continuity and momentum equation of each phase is given as follows:

$$\frac{\partial}{\partial t}(\rho_k \alpha_k) + \frac{\partial}{\partial x_i}(\rho_k \alpha_k U_{i,k}) = 0 \tag{1}$$

$$\frac{\partial}{\partial t}(\rho_k \alpha_k U_{i,k}) + \frac{\partial}{\partial x_j}(\rho_k \alpha_k U_{i,k} U_{j,k}) = -\alpha_k \frac{\partial p}{\partial x_i} + \alpha_k \rho_k g_i + \frac{\partial}{\partial x_j} \mu \alpha_k \left[\left(\frac{\partial U_j}{\partial x_i} + \frac{\partial U_i}{\partial x_j} \right) - \frac{2}{3} \frac{\partial U_j}{\partial x_j} \delta_{ij} \right] + M_{i,k} \tag{2}$$

where α_k and $M_{i,k}$ represent the volume fraction of phase k and interfacial momentum transfer. In this study, Inlet tube, manifold, branch tubes have different flow directions each other. To model the momentum transfer of interface, dispersed phases are assumed spherical particle and only the drag force is considered in this study. Drag is interfacial force that disturbs the flow of bubbles by the surrounding liquid. For drag coefficient C_D, Schiller and Naumann drag coefficient [8] is chosen. Drag force and drag coefficient are given as follows:

$$F_d = \frac{3}{4} \frac{C_D}{d_b} \alpha \rho_c |U_r| U_r \tag{3}$$

$$C_D = \begin{cases} \frac{24}{Re_d}\left(1 + 0.15 Re_d^{0.687}\right) & 0 < Re_D \le 1000 \\ 0.44 & Re_D > 1000 \end{cases} \tag{4}$$

Where Re_d and ρ_c represent the Reynolds number of dispersed phase and density of continuous phase. To calculate turbulence, RANS model is used, which is calculated by dividing the average component and the variation component. Since the Eulerian-Eulerian model is used, the turbulence model of each phase is also calculated separately. In the case of continuous phase, the Realizable K-epsilon model is used, which modify the standard k-e model to calculate the Reynolds stress [9]. The equations for turbulence kinetic energy k and turbulence dissipation rate ε are as follows:

$$\frac{\partial \alpha_c \mathrm{k_c}}{\partial \mathrm{t}} + \frac{\partial (\alpha_c \mathrm{k_c} U_{i,c})}{\partial x_j} = \frac{1}{\rho_c} \frac{\partial}{\partial x_j} \left[\alpha_c \left(\mu_c + \frac{\mu_{T,c}}{\sigma_k} \right) \frac{\partial \mathrm{k_c}}{\partial x_j} \right] + \alpha_c \frac{\mu_{T,c}}{\rho_c} \left(\frac{\partial \mathrm{U_{i,c}}}{\partial \mathrm{x_j}} + \frac{\partial \mathrm{U_{j,c}}}{\partial \mathrm{x_i}} \right) \frac{\partial \mathrm{U_{i,c}}}{\partial \mathrm{x_j}} - \alpha_c \varepsilon_c \tag{5}$$

$$\frac{\partial \alpha_c \varepsilon_c}{\partial \mathrm{t}} + \frac{\partial (\alpha_c \varepsilon_c U_{i,c})}{\partial x_j} = \frac{1}{\rho_c} \frac{\partial}{\partial x_i} \left[\alpha_c \left(\mu_c + \frac{\mu_{T,c}}{\sigma_\varepsilon} \right) \frac{\partial \varepsilon_c}{\partial x_j} \right] + \alpha_c C_1 \frac{\varepsilon_c}{2} \left(\frac{\partial \mathrm{U_{i,c}}}{\partial \mathrm{x_j}} + \frac{\partial \mathrm{U_{j,c}}}{\partial \mathrm{x_i}} \right) \frac{\partial \mathrm{U_{i,c}}}{\partial \mathrm{x_j}} - \alpha_c C_2 \frac{\varepsilon_c^2}{k_c + \sqrt{(\mu_c/\rho_c)\varepsilon_c}} \tag{6}$$

where α_c represents volume fraction of continuous phase.

Turbulence response model is used to calculate the turbulence of the dispersed phase. The turbulence of dispersed phase is correlated from the turbulence of the continuous phase by using the correlation derived from the response coefficient. In this study, the Issa response coefficient which is a function of void fraction is used [10].

2.3. Grid

To generate the mesh in fluid domain, polyhedral mesh and prism layer mesh are applied. In order to calculate the turbulence, the area identified by the law of wall should be generated in a compact grid and calculated for each area. In this study, the prism layer thickness is generated to satisfy $y^+ < 5$ condition to calculate the turbulence from the viscous sublayer. To determine the base size of polyhedral mesh, grid

independence test is performed by comparing the y-axis velocity distribution in the branch tube and the base size is determined to be 8,200,000 cells.

2.4. Boundary Condition

The working fluid in this study is an air-water mixture. The void fraction is calculated by assuming a slip ratio of 1 when the quality of the refrigerant is varied from 0 to 0.1. The mass flow rate of air and water are determined by using the same void fraction. The wall is assumed an adiabatic wall and no-slip condition. Inlet boundary condition is set to mass flow boundary condition. The mass flow rate of water is $0.26\ \mathrm{kg/s}$, and the mass flow rate of air is varied in the range of $1.16 \times 10^{-4} \sim 9.70 \times 10^{-4}\ \mathrm{kg/s}$ depending on the void fraction. The outlet boundary condition is selected as the pressure boundary condition and set to 0 Pa based on the atmospheric pressure. The inlet boundary conditions used in the analysis are shown in Table 1.

Table 1. Inlet boundary condition of air and water

Material	Volume flow rate [kg/s]
Water	0.26
Air at $\alpha = 0.17$	1.16×10^{-4}
Air at $\alpha = 0.39$	4.43×10^{-4}
Air at $\alpha = 0.53$	9.70×10^{-4}

3. RESULT AND DISCUSSION

3.1. Simulation Results and Validation

CFD simulation is used to calculate the two-phase flow distribution in the header according to the inlet position and the void fraction change. The void fraction has been changed from 0.17 to 0.53 and the inlet position is located at the top or bottom of the header and is called the upper inlet and bottom inlet in each case. The calculated mass flow results show fluctuations, and time-averaged values are used. The mass flow rate distributed to each branch tube is represented by Liquid Fraction which is the ratio of the mass flow rate distributed to each branch tube to the total mass flow rate. The distribution tendency calculated by CFD are compared with the experimental data conducted by Ham [7]. A comparison of results is shown in Fig. 2.

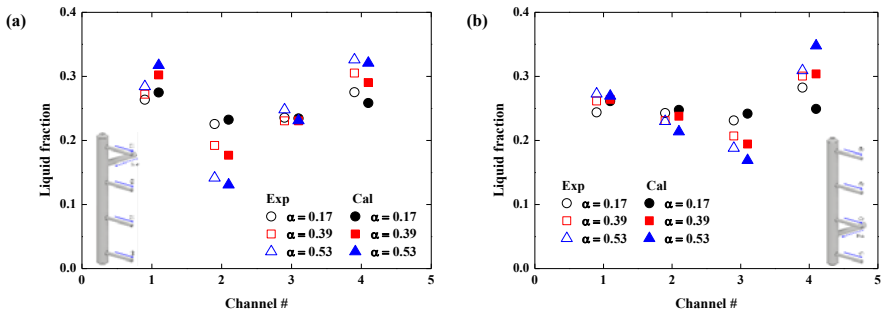


Fig. 2. Validation with The Experimental Data by Ham[7]: (a) Upper Inlet, (b) Bottom Inlet

Fig. 2. (a) shows the distribution tendency at the upper inlet condition. The analysis result shows that the gas fraction tends to be high in channel #2 near the header inlet tube. In contrast, liquid fraction of channel #1 and #4 located at both ends of the header is high and liquid fraction flowing into channel #2 is low. The maximum difference of 3.30%p is observed in the channel #1 when the void fraction is 0.53, and the distribution of CFD follows the experimental results.

The distribution tendency at the bottom inlet conditions is shown in Fig. 2. (b). The analysis result shows that liquid fraction flow into channel #4 at the bottom of the header is high. And liquid fraction liquid fraction

flowing into channel #2, #3 is low due to gas fraction inflow. The liquid fraction shows a maximum difference of 3.85%p at channel #4 when the void fraction is 0.53. Therefore, the bottom inlet case also follows the experimental distribution tendency of liquid phase.

3.2. Effects of inlet position and void fraction

Two-phase flow characteristics according to the void fraction change at each inlet location are analyzed by internal flow. When the two-phase flow develops from the inlet tube, phase separation occurs due to density difference between the liquid phase and the gas phase. As the two-phase flow flows into the header, it collides with the double pipe installed inside the header, and two-phase flow is divided into two branches and flow to the wall of the header. Then the incoming flow creates two vortices. First, since the diameter of the header is larger than that of the inlet tube, vortices and flow separation are generated at the part where the inlet tube and the header are connected. When the flow is passing through the double pipe, like external flow, the second vortices are generated causing separation at the rear end of the double pipe. In the region where the flow separation is generated, the gas phase with small momentum rotates and flows toward the axis direction of header. Fig. 3 shows the cross-sectional contours of volume fraction and velocity vector distribution in the cross-section (yz plane) at the header adjacent to the inlet. In the figure, gas fraction is concentrated in the region close to the inlet tube and in the rear part of the double pipe. As the void fraction increased, the size of the vortex increased.

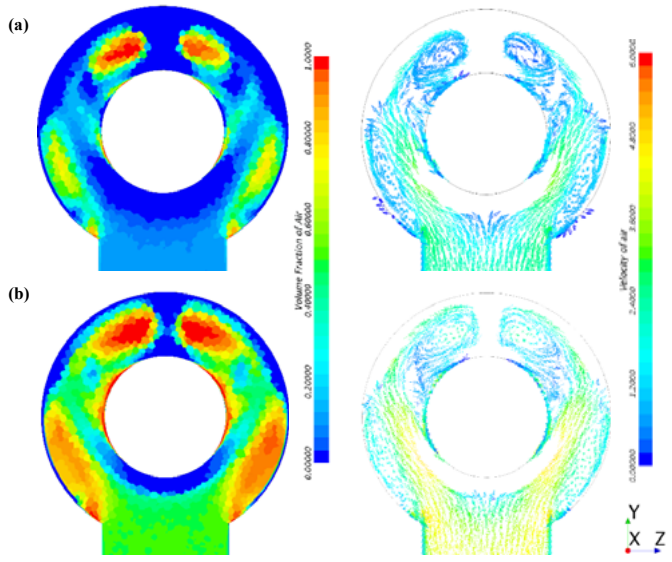


Fig. 3. Cross-Sectional Contours of Void Fraction and Velocity Vector of Header Adjacent to The Inlet: (a) $\alpha = 0.17$, (b) $\alpha = 0.53$

Flow developed at the inlet splits in both directions of the header, while generating a vortex. Volume fraction contours of the header cross-section are shown in Fig. 4.

In the upper inlet case, flows are split two ways that upward direction to channel #1 and downward direction to channel #2, #3, and #4. In each direction, the flow develops while maintaining the vortex and then flows toward the branch tube. Since the liquid phase has a greater momentum than the gas phase, the liquid phase flows toward both ends of the header due to the inertia force. The gas phase tends to flow to the channel located at the center of header. Therefore, the gas phase flowing in the upper part of the inlet cross-section due to phase separation, is directed downward. In the downward section contains channels #2, #3, and #4, due to the momentum difference, the gas phase flows to channels #2 and #3 close to the inlet and the liquid phase flows to channel #4 located at the end of header. The direction of flow and the buoyancy are inconsistent, then the gas phase lose momentum while flowing between channels #2, and #3 and flow back to channels #2.

In the bottom inlet case, the two-phase flow from the inlet generates vortices and develops and is divided into downward direction to channel #4 and the upward direction to channel #1, #2, and #3. The downward

flow to the channel #4 has less gas phase than the upward flow due to the phase separation at the inlet. In addition, because the flow direction is downward, the gas phase flows back to upward due to the buoyancy effect. Therefore, in the case of void fraction 0.17, no gas phase flow to the channel #4, and some gas phase is distributed as the void fraction increased. The upward flow is similar with the downward at upper inlet case. Due to the momentum difference, much of gas phase flow to the channel close to the header. Although little amount of gas phase flows to the channel #4 at the bottom end of header, gas phase flowing upward is distributed more uniform than the upper inlet condition. In order to compare quantitatively to the distribution tendency according to the inlet position, standard deviation of distribution is compared. Table 2 shows the standard deviation of the liquid fraction at upper and bottom inlet case according to the change of void fraction. The distribution tendency of the bottom inlet case is more uniform than the upper inlet case in all void fraction conditions.

Table 2. Standard deviation of liquid fraction according to inlet position

	Upper inlet	Bottom inlet
α=0.17	0.018	0.007
α=0.39	0.050	0.034
α=0.53	0.078	0.067

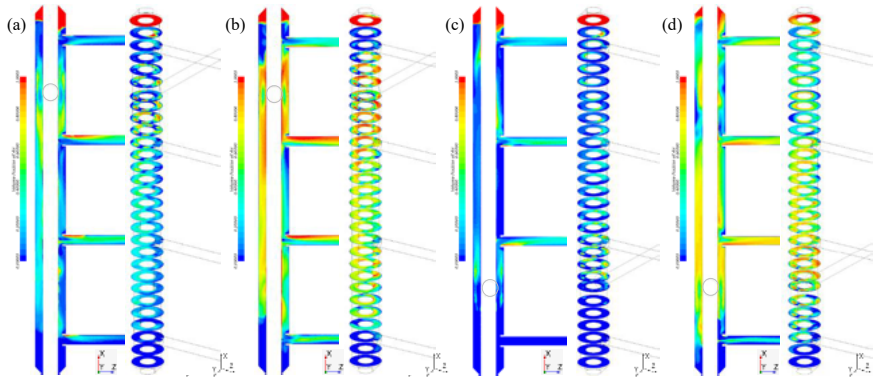


Fig. 4. Contour of Volume Fraction: Upper Inlet (a) $\alpha = 0.17$, (b) $\alpha = 0.53$; Bottom Inlet (c) $\alpha = 0.17$, (d) $\alpha = 0.53$

To compare the velocity of the gas phase and liquid phase and to analyze the change in the magnitude of the momentum in each section, the superficial velocity is compared. The superficial velocity is defined as follows:

$$U_{s,k} = \alpha_k U_k \tag{7}$$

where α_k and U_k represents volume fraction and velocity of the phase k. Fig. 5 is a graph of the axial cross-sectional mean magnitude of superficial velocity inside the header for gas phase and liquid phase at a void fraction of 0.53. The x axis represents the position in the axial direction of the header and the y axis represents the cross-sectional mean superficial velocity. Fig. 5. (a) and (b) are the upper and lower inlet cases, respectively.

The superficial velocity distribution of the liquid phase is the highest at the x=-0.078 m cross-section where the inlet tube is located due to the influence of the mass flow rate from the inlet tube to the header. The liquid flow collides on the rear wall of the header and flows axially in two directions. At the inlet of the header where the liquid flow splits from the wall into bifurcation, creating a vortex, the superficial velocity decreases significantly. As the flow splits in two directions at the inlet of the header, the superficial velocity gradually decreases. Branches are located at the cross-sections at x=0.12 m, 0.04 m, -0.04 m, and -0.12 m, respectively. However, the liquid phase maintains superficial velocity up to channel #1, #4 (x=0.14 m, -0.14 m) at both ends of the header. Comparing the two inlet conditions, the superficial velocity of the liquid phases tended to be the same. But in the bottom inlet case, liquid phase is less distributed to the channel #4 located downwards due to

the influence of gravity. Therefore, the superficial velocity is higher than that of channel #1 in the upper inflow condition.

The gas flow shows different tendency in two cases compared to the liquid phase. Since the phase separation of the gas phase in the inlet tube, most of the gas phase flows in the upper part of the inlet cross-section. In the upper inflow condition, however, most of the gas flowed to downward. Therefore, the highest superficial velocity value is obtained in the cross-section of x=-0.078 m.

However, the bottom inlet case shows the highest superficial velocity at the cross-section of x=-0.07 m rather than x=-0.078 m because the gas phase located at the top of the inlet flows directly to the top of the header. In addition, the upper inlet case is due to the buoyancy, the gas phase flows backward, and most of the flow rate flows into the channel #2. Then the superficial velocity decreases significantly after channel #2 (x=0.04 m). In Fig. 5. (a), the superficial velocity of x=-0.04 m to x=0.04 m is 0.3 m/s. However, the bottom inlet case shows that the superficial velocity decreases relatively uniformly in channels 2 and 3. In Fig. 5. (b), the superficial velocity of the same section is 0.5 m/s, which is relatively high. And in both cases, there is a region filled with gas phase on top of header (x=0.14 m), so the velocity of the liquid phase is zero, but the velocity of the gas phase is not zero.

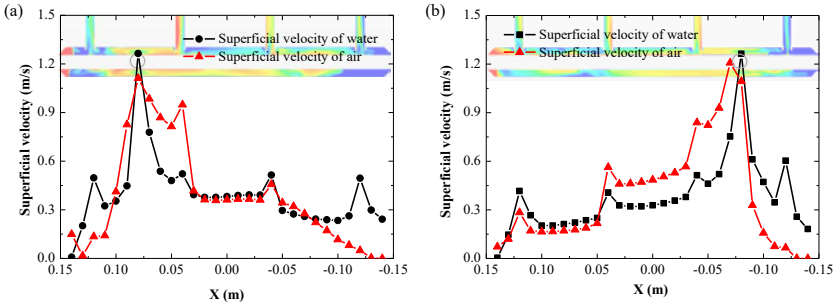


Fig. 5. Cross-Sectional Superficial Velocity Magnitude of Header: (a) Upper Inlet, (b) Bottom Inlet

3.3. Geometry Modification

It is confirmed that uneven distribution occurs when two-phase flow flows into the vertically installed header. Under every condition, most of gas phase flow into the channel #2 and #3, which are close to the header inlet, and most of liquid phase flow into the channel #1 and #4 located at both ends of the header. As the void fraction of the two-phase flow increased, this uneven distribution became more exacerbated.

The factor that most influences the uneven distribution inside the header is the density difference between the two fluids. Due to the difference in the density, phase separation and buoyancy occur, and despite homogeneous flow, the difference in momentum occurs and each phase has a different distribution tendency. The distribution characteristic of two-phase flow is shown in Table 2. The bottom inlet case shows a relatively uniform distribution than upper inlet case because the effect of buoyancy is reduced. Therefore, in this study, the header is modified under the bottom inlet case. In the bottom inlet case, the gas phase mostly flows upward, and the liquid phase is distributed at both ends of the header. To improve distribution, the gas phase flowing through channels # 2 and # 3 must be distributed along with the liquid phase to the end of header. In particular, the # 4 channel has little gas phase due to the buoyancy effect, so it needs to be improved through geometry modification.

Various researchers have tried to improve the distribution by modifying the header design. Webb and Chung [11] attempted to improve the distribution by inserting obstacles such as baffles or weirs inside the header or by inserting inlet tubes. When inserting the obstacle, the incoming two-phase flow created a jet through the obstacle, and each phase were mixed well, then it improved distribution characteristics. However, obstacles depended on the internal geometry of the header. If the part of the geometry changed, the design must be changed accordingly. Mahvi and Garimella [12] and Pistoresi [13] tried to improve the distribution by reducing the cross-section area of the headers instead of inserting obstacles. The header is designed that the cross-section is narrowed from the header inlet to the end, then the mixing of the gas and the liquid phase is improved to have the uniform distribution.

In the case of the header used in this study, since direction of the inlet tube is horizontal and the header is installed vertically and the double pipe is inserted the center of header, the method of reducing the outer diameter of the double pipe header is used. Under the bottom inlet case, it is expected that if the diameter of the header heading toward channel #4 is reduced, the momentum of the gas phase heading to channel #4 is increased, and the liquid fraction of channel #4 is reduced and flow to the upper part of header.

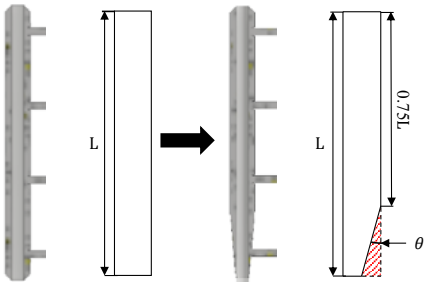


Fig. 6. Schematic of header plane-section modification: (a) Modification Channel #4, (b) Modification Channel #1 and #4

Schematic of the geometry modification of the header is shown in Fig. 6. The diameter of the cross-section from the header inlet to channel #4 is adjusted through the modification angle θ. The modification angle of the header can be converted from 1° to 5°.

The CFD simulation is performed with the void fraction 0.53 condition as a default, which has the largest uneven distribution in the bottom inlet case. The distribution tendency according to the modification angle of the header simulated by CFD is shown in Fig. 7. In the distribution tendency shown in Fig. 7, the distribution is improved as the modification angle increases. Unlike the effect of changing the void fraction, the amount of change in the liquid and gas phases due to the change in modification angle is relatively small. At the bottom of the header, the liquid fraction gradually decreases, but the gas fraction gradually increases. The increasing liquid mass flow rate to the upper side of the header does not change the liquid fraction in channels # 2 and # 3 when the modification angle is changed to 3°. As the angle increases to 5°, the volume fraction change affects to the channel #1, so that the liquid fraction distribution is improved in the upper part of header.

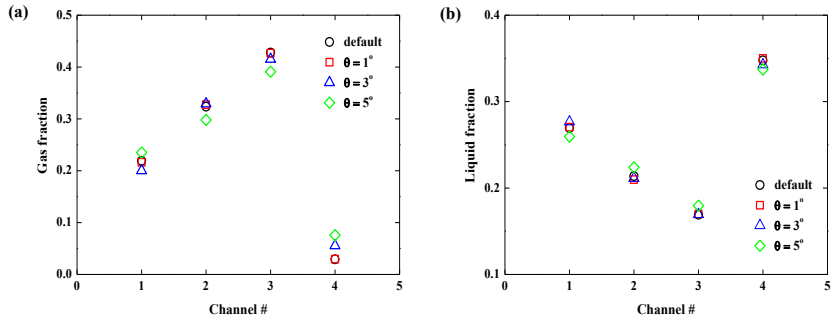


Fig. 7. Effect of header modification angle on flow distribution: (a) Gas Fraction, (b) Liquid Fraction

Table 3. Standard deviation of liquid fraction according to inlet position

Modification angle	Air	Water
Default	0.147	0.067
1°	0.146	0.067
3°	0.136	0.066
5°	0.115	0.058

Table 3 shows standard deviation according to the modification angle. The distribution tendency according to the modification angle is shown through the standard deviation. As the modification angle is increased, the distribution is gradually improved.

4. Conclusion

In this study, the two-phase distribution characteristics of the refrigerant distributor used in the VRF system is investigated by CFD simulation. Internal flow of the header is analyzed by CFD simulation and the factor that affects the uneven distribution of two-phase flow is investigated. The analysis conditions are divided into upper inlet condition and bottom inlet condition according to the header inlet position. For each condition, the flow characteristics in the header are analyzed according to the change of void fraction. Based on the analysis, the geometry of the header is modified to evaluate the two-phase flow distribution characteristics. Some major conclusions are as follows:

- The two-phase flow distribution results simulated by CFD are following the tendency as those measured by the previous experimental study.
- Most of the gas phase flows into the channel close to the inlet tube both the upper inlet and the bottom inlet cases, and the liquid phase flows to the both rear part of the header.
- As the void fraction is increased, uneven distribution is exacerbated.
- When the inlet position is located at the upper part of the header, the buoyancy force acts on the gas phase flowing downward then the gas phase flows counter currently.
- When the inlet is located at the bottom part of the header, a small amount of gas phase is distributed to channel #4, but the overall flow distribution shows less uneven compared to the upper inlet conditions.
- The geometry is modified to narrow the diameter of the headers towards branch 4 to improve the non-uniform distribution.
- As the modification angle is increased, the liquid phase distributed to branch 4 decreases while gas fraction increases.
- Standard deviation results show that the distribution is and improved as the modification angle increased.

References

[1] Dario, E. R., Tadrist, L., Passos, J. C., 2013. Review on two-phase flow distribution in parallel channels with macro and micro hydraulic diameters: Main reults, analyses, tendency. Applied Thermal Engineering. 59, 316-335.
[2] Kim, N. H., Lee, E. J., Byun, H. W., 2012. Two-phase refrigerant distribution in a parallel flow minichannel heat exchanger having horizontal headers. International Joural of Heat and Mass Transfer. 55, 7747-7759.
[3] Vist, S. and Pettersen, J, 2004. Two-Phase Flow Distribution in Compact Heat Exchanger Manifolds. Experimental Thermal and Fluid Science. 28, 209-215.
[4] Lee, J. K. and Lee, S. Y., 2004. Distribution of Two-Phase Annular Flow at Header- Channel Junctions. Experimental Thermal Fluid Science. 28, 217-222.
[5] Zian, J., Ding, M., Bian, H., Zhang, Y., Sun, Z., 2018. CFD simulation for the effect of the header match on the flow distribution in a central-type parallel heat exchanger. Chemical Engineering Research and Design. 136, 144-153.
[6] Said, S. A. M, Ben-Mansour, R., Habib, M. A., Siddiqui, M. U., 2015. Reducing the flow mal-distribution in a heat exchanger. Computer & Fluids. 107, 1-10.
[7] Ham, S. K. and Jeong, J. H., 2018. Two-phase flow distribution according to variation of flow resistance and flow path in manifold shaped distributor. Trans. Korean Soc. Mech. Eng. B, Vol. 2018 No.4, 98~99
[8] Naumann, Z., Schiller, L., 1935. A drag coefficient correlation. Z Ver Deutsch Ing. 77-318.
[9] Shih, T.-H., Zhu, J., Lumbly, J. L., 1995. A new Reynolds stress algebraic equation model. Computor Methods in Applied Mechanics and Engineering. 125, 287-302.
[10] Behzadi, A., Issa, R. I., Rusche, H., 2004. Modelling of dispersed bubble and droplet flow at high phase fractions. Chemical Engineering Science. 59, 759-770.
[11] Webb, R. L., Chung, K, 2005. Two-phase flow distribution to tubes of parallel flow air-cooled heat exchangers. Heat Transfer Engieering. 26, 3-18.
[12] Mahvi, M., Garimella, S., 2017. Visualization of flow distribution in rectangular and triangular header geometries. International Journal of Refrigeration. 76, 170-183.
[13] Pistoresi, C., Fan, Y., Luo, L., 2015. Numerical study on the improvement of flow distribution uniformity among parallel mini-channels. Chemical Engineering and Processing: Process Intensification. 95, 63-71.

13th IEA Heat Pump Conference
May 11-14, 2020 Jeju, Korea

Membrane-based air dehumidification using organic ionic liquid desiccant

Bamdad Bahar[a*], Harish Opadristha[a], Mark Stutman[a], Xaiobing Liu[b], Jason Woods[c]

[a]*Xergy Inc., 299A Cluckey Dr., Harrington DE 19952, USA*
[b]*Oak Ridge National Laboratory, Oak Ridge TN 37830, USA*
[c]*National Renewable Energy Laboratory, Lakewood CO 80401, USA*

Abstract

Membrane Ionic Liquid Desiccant Air Dehumidification (MILDAD) is a promising alternative to conventional dehumidification systems that employ mechanical compressors and refrigerant-based cooling with evaporator and condensing coils. However, its application has been limited due to high manufacturing and installation cost, durability issues, concerns with corrosion due to leakage and salt carry over into the downstream air and onto surfaces. This paper reviews substantial progress made with new systems based on combining advanced ionic membranes that are pressure resistant, thin walled with high water permeability, and non-porous with synthetic organic, non-crystalline ionic liquid desiccants. Alternative design configurations are discussed comparing cross flow shell-and-tube membrane contactors employing ionic membrane tubes through which ionic liquid desiccant air flows. Performance data for MILDAD prototypes is provided. Dehumidification of the incoming supply airstream and regeneration into exhausted building air is demonstrated. The latent effectiveness of the MILDAD system will be discussed along with some future steps to improve performance of the system.

© HPC2020.
Selection and/or peer-review under responsibility of the organizers of the 13th IEA Heat Pump Conference 2020.

Keywords: Ionic Liquid Desiccants; Pervaporation; Membrane;

1. Introduction

According to U.S. Energy Information Administration [1], the world's energy consumption grew 54% between 1990 and 2015. Buildings accounted for 20% of the total energy consumption in the world, and 40% in the United States. About 55% of the energy consumed in U.S. buildings is to keep the indoor environment thermally comfortable [2]. Humidity level is one of the important indicators of the quality of the indoor environmental quality (IEQ), which directly affect people's productivity and health. ASHRAE standard 55-2013 and 62.1-2016 request that HVAC system must be able to maintain a humidity ratio of below 0.012, and the relative humidity should be controlled below 65% to keep a good IEQ. Previous studies have observed that water provides a major breeding ground for the growth of bacteria and fungi in buildings, thus, affecting people's health [3][4]. In many regions, air dehumidification is necessary to reduce the moisture level in the indoor environment.

Conventional air dehumidification methods include mechanical cooling and sorption (adsorption with solid desiccant or absorption with liquid desiccant). With mechanical cooling, air is cooled down to its dew point temperature and water vapor in the air is condensed. To provide acceptable air temperature for air-conditioning or ventilation, the cold air usually needs to be warmed (reheat), which wastes energy. Sorption method uses solid or liquid desiccant to absorb water vapor in the air [5]. In a conventional Liquid Desiccant Air Dehumidification (LDAD) system, the liquid desiccant is in direct contact with the wet air to be treated and absorbs water vapor in the wet air. With LDAD, the air temperature and humidity can be independently

*Corresponding author. Tel.: +1 (302)-629-5768. *E-mail address:* bamdad.bahar@xergyinc.com

regulated, and the cooling system can work more energy efficiently with higher evaporating temperature. However, since air flow directly contacts with liquid desiccant in conventional LDAD systems, small solution droplets can be carried over by the air flow and spread into ductwork or the conditioned space. It not only negatively impacts the health of occupants, but also results in corrosion of the air supply ductwork. In addition, dehumidification performance of the liquid desiccant could degrade due to exposure to the pollutants in the ambient environment.

A liquid-to-air membrane energy exchanger can be used to eliminate the carry-out or entrainment of tiny desiccant droplets. The study reported here investigates the new membrane-based ionic liquid desiccant air dehumidification (MILDAD) system by using the aqueous solution of an ionic liquid as the desiccant. The first innovation of the system is using membrane-based mass-heat exchanger to eliminate the carry-over problem of the typical LDAD. The second innovation of the MILDAD is the use of ionic liquid as desiccant. Ionic liquid is synthesized liquid salts which are in the liquid phase when exposed to room temperature and atmospheric pressure. They have high thermal stability, negligible or no vapor pressure, high solubility in water, low or no corrosion to metals, and low driving temperatures to release water vapor (for regeneration). Ionic liquid, therefore, are ideal substitutes for traditional desiccant liquids because they can reduce or eliminate the corrosion and save the liquid desiccant used in the operation. Using ionic liquids has potential to remarkably reduce the operation and maintenance cost, as well as improve system performance.

2. Technology Description

2.1. Membrane Contactors

A MILDAD system uses semi-permeable membranes to separate the liquid desiccant and the air so that the problem of carryover is avoided [6]. A porous membrane is a thin material with pores in it that allow some substances to penetrate through it while preventing others from entering. A non-porous membrane is a thin material that incorporates (typically a polymer) material that transmits water. The driving force between the air and the liquid desiccant is the difference in water vapor pressure on either side of the membrane. There are two main parameters to describe a membrane: water transmission rate and selectivity. The water transmission rate (sometimes referred to as “Permeability”) is the rate at which vapor permeates through a membrane per unit area or per unit driving force; selectivity is the ratio of the permeability coefficient of vapor and the others in the humid air through the membrane [5]. The degree of selectivity is largely based on the membrane properties. There are some technical challenges to using MILDAD, such as biological fouling on the membrane; low moisture permeability, poor strength, and high cost of the membrane [7]. Yang et al. (2015) reported that the uneven distribution of liquid desiccant mainly caused by membrane deflection will significantly reduce performance [8]. In this work, we report data for non-porous i.e. gas impervious membranes [9]. In order to minimize membrane deflection and leakage issues (which is typical of systems incorporating flat sheet membranes) a tubular construct was developed. This also reduces the uneven distribution of desiccant. It should be noted that while porous membranes show higher initial rates of moisture permeability compared to non-porous (i.e. impervious or dense or composite membranes), non-porous membranes provide much better selectivity and eliminate cross-contamination and biological fouling; thus even at a lower permeation rates, they maintain stable performance and exceed the moisture permeation rates of porous membranes over time.

2.2. Ionic Liquid Desiccant

The most frequently used liquid desiccants are lithium chloride, triethylene glycol, and calcium chloride [10]. However, the traditional desiccant liquids have problems of corrosion, high cost and so on. Thus, alternative liquid desiccant is highly desirable. Ionic liquids are salts comprised of organic cations and inorganic anions or organic anions. In this study, the aqueous solution of an ionic liquid [EMIM][OAc] (1-Ethyl-3-methylimiadazolium acetate) is used as the liquid desiccant. It has high thermal stability and with low or no corrosion to metals [11]. Moreover, it does not have any crystallization problem. Fig. 1(a) shows the constant [EMIM][OAc] concentration lines in a psychrometric chart, which indicate the equilibrium conditions for air in contact with an [EMIM][OAc] solution at the specified concentrations. Fig. 1(b) shows the commonly used concentration ranges of various liquid desiccants at 20 ºC for typical air dehumidification operation, which is indicated by the blue band of equilibrium vapor pressure.

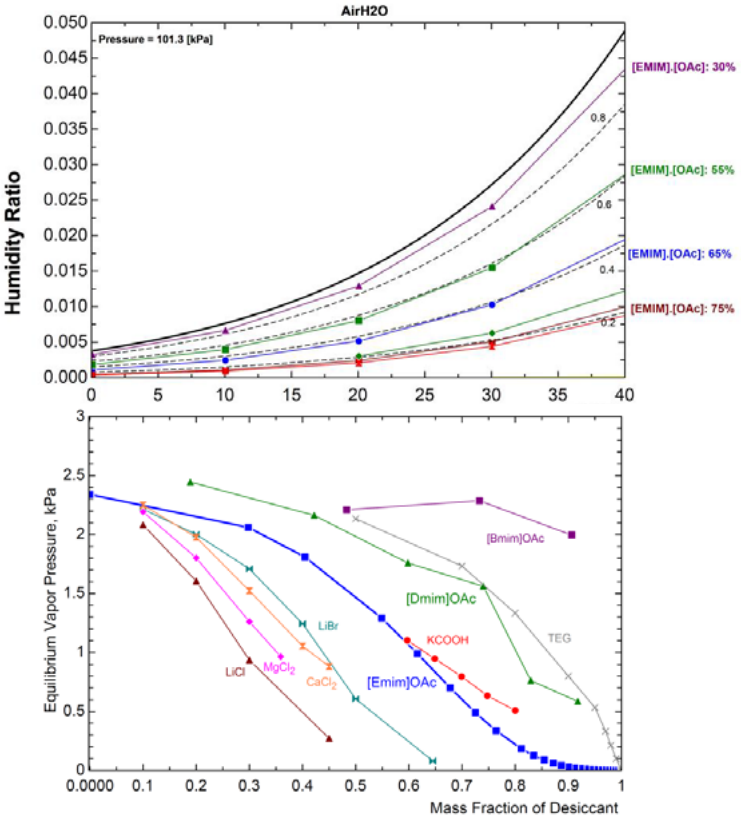


Fig. 1: Properties of [EMIM][OAc] dehumidification capacities at different concentrations (top), (b) commonly used concentration ranges of different desiccants (bottom)

2.3. Membrane-based Liquid Desiccant System

Fig. 2 shows the construction of a counter-flow membrane-based liquid desiccant air dehumidification system. A MILDAD is generally comprised of two supply air streams and two modules—a dehumidifier and a regenerator. A liquid desiccant solution is pumped through the permeate side channels, and an air stream is drawn to the feed side channels at the same time. Because of the difference between the temperature and humidity of the solution stream and air stream, heat and mass are exchanged through the membrane. In this process, the concentration of the solution is reduced by absorbing water vapor. Meanwhile, the solution absorbs heat generated by phase transformation of water vapor and then its temperature rises. The water vapor pressure on the surface of the solution increases with the decrease of the concentration of liquid desiccant and the increase of temperature, and the moisture absorption capacity of the solution decreases. The hot dilute solution is pumped into the regenerator to exchange heat and mass with a hot and dry air stream to evaporate the moisture. After that, the solution becomes concentrated again, and the vapor pressure becomes lower as well. It will be sent to the dehumidification module to keep continuous operation of the MILDAD.

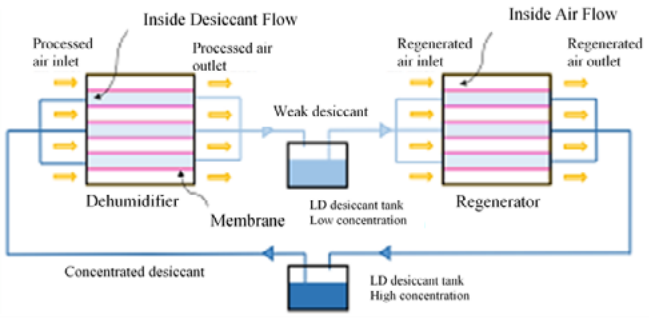


Fig. 2: Schematic diagram of basic procedure of membrane-based liquid desiccant system

3. Design of a Small-Scale Prototype MILDAD

A small-scale prototype MILDAD was developed. It uses a bundle of membrane tubes made with an ionic (nonporous) membrane instead of multiple membrane plates as in the referenced studies. The membrane tubes have better mechanical strength than the membrane plates and thus are expected to work at higher flow rates on both the air and solution sides of the membrane without any leakage. The schematic of the new prototype is shown in Figure 3.

The small-scale MILDAD prototype is shown in Figure 4. It measures 2.5 inches (64 mm) long, 4 inches (102 mm) wide, 4 inches (102 mm) high. It has 26 tubes made with an ionic (nonporous) membrane. The tubes are laid out in a staggered arrangement. Each tube has an outer diameter of 0.13 inch (3.3 mm) and an inner diameter of 1/8 inch (3.2 mm). The distance between two adjacent tubes is 1/4 inch (6.4 mm). The staggered arrangement could provide better convection heat and mass transfer but could also result in a higher air-side pressure drop. The end of each tube is connected to a header containing ILD solution. The ILD solution flows inside the tubes from the top header to the bottom header, while air is drawn through the outer surface of the tubes perpendicularly to the solution flow to exchange heat and water vapor with the ILD solution, forming a crossflow pattern.

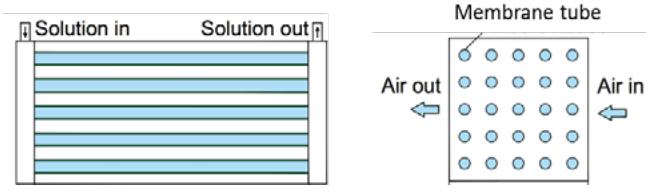


Fig. 3. Concept design of a MILDAD using membrane tubes: a side view (left) and a section view (right).

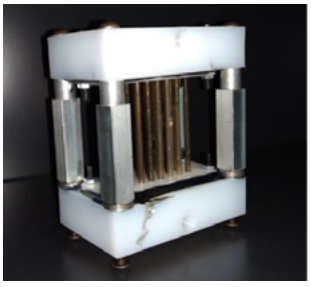


Fig. 4. A small-scale prototype of the MILDAD.

4. Experiments

The performance of both the dehumidification and humidification (regeneration) of the small-scale prototype MILDAD was evaluated under various operating conditions, including inlet air temperature and humidity, air and ILD solution flow rate, and ILD solution temperature.

Several performance metrics are evaluated based on the measured data, including moisture removal rate (m_v), specific vapor transportation rate (J), effective permeance (P), latent cooling (Q), and latent effectiveness (ε_L).

The moisture removal rate (m_V) is the product of the absolute humidity difference (ΔAH) and the mass flow rate of air (m_{air}), which represents the quantity of water vapor removed within a unit time, as expressed in Eq. (1).

$$\dot{m}_v = \Delta AH \cdot \dot{m}_{air} \tag{1}$$

The specific vapor transportation rate (J) is expressed with Eq. (2):

$$J = \frac{\dot{m}_v}{A_{eff}} \tag{2}$$

where m_v is the moisture removal rate, and A_{eff} is the effective contact area.

The effective permeance of the MILDAD (P) is calculated with Eq. (3).

$$P = \frac{J}{\Delta P_v} \tag{3}$$

where ΔP_v is the vapor pressure difference between two surfaces of the membrane.

The latent cooling capacity of the MILDAD (Q) is calculated with Eq. (4):

$$Q = \dot{m}_v \times L \tag{4}$$

where L is the latent heat of vaporization of water, 2260 J/g at 20 °C.

The latent effectiveness (ε_{lat}) is the ratio of the actual to the maximum possible water vapor transfer rates of the MILDAD, as expressed with Eq. (5):

$$\varepsilon_{lat} = \frac{w_{air,in} - w_{air,out}}{w_{air,in} - w_{sol,in}}, \tag{5}$$

where w is the humidity ratio referring to the moisture content in the air (i.e., grams of water vapor in each kilogram of dry air), and for liquid desiccant, w_{sol} represents the equilibrium humidity ratio of the liquid desiccant solution, which is determined by the temperature and concentration of a given liquid desiccant solution.

4.1. Experimental Apparatus

Figure 5 shows the experimental apparatus for the tests, which were performed in a national lab climate chamber. The prototype was placed in the middle of an Omega WT4401-D wind tunnel, which measures the airflow rate going through the prototype based on the measured pressure drop across the prototype. The airflow rate can be adjusted by regulating the wind tunnel's variable speed fan. The wind tunnel was in a climate chamber, in which the air temperature and relative humidity could be maintained within a small range (±0.5ºC temperature and ±1% relative humidity) of specific conditions. During a test, room air in the precisely controlled climate chamber was drawn through the small-scale prototype MILDAD. The air pressure, temperature, and relative humidity at the inlet and outlet of the MILDAD were measured by individual sensors. The ILD solution was circulated through the prototype at a fixed flow rate by a solution pump. A small reservoir was placed in the solution loop. The solution temperature in the reservoir was maintained at a specified setpoint by a refrigerated/heated circulating water bath. A high solution electronic scale was applied to weigh the solution reservoir in order to calculate the vapor absorbed by the ILD solution. A data acquisition

system was used to collect and save data from the sensors during each test. The measurement devices and corresponding accuracies are shown in Table 1.

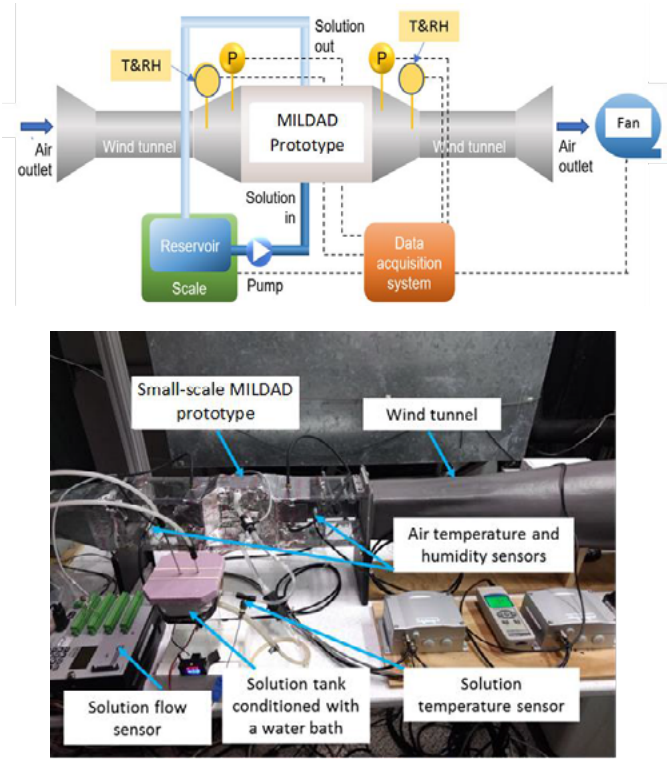


Fig. 5. The experimental apparatus for testing a small-scale MILDAD prototype: schematic diagram (top); and actual setup (bottom)

Table 1. Sensor Specifications

Target parameters	Measurement devices	Corresponding accuracies	Range
Temperature	Vaisala HMT330	± 0.25 C	-15~ +40 C
Relative humidity	Vaisala HMT330	± (1.0 + 0.008 X reading) %	0 – 95%
Differential air pressure	Omega PX02K1-16A5T	0.25%	0 – 32 in. Hg
Scale	Torbal AG4000	0.01 gram	4,000 grams

4.2. Test Results of the small-scale prototype

The tests were separated into the following five groups based on the conditions of the solution in the membrane tubes and the room air in the climate chamber. Each group included two to three tests with different airflow rates. Test results are summarized in the Table 2. The results of test group 5 were not included because leakage of the ILD solution was observed during the tests.

- **Case 1**: Humidification (membrane tubes filled with pure water) at 35°C and 20% relative humidity (RH) chamber condition, with 0.49 liters per minute (LPM) solution flow rate
- **Case 2**: Humidification (membrane tubes filled with pure water) at 25°C and 80% RH chamber condition, with 0.49 LPM solution flow rate
- **Case 3**: Humidification (membrane tubes filled with pure water) at 25°C and 80% RH chamber condition with lower water flow, with 0.30 LPM solution flow rate

- **Case 4**: Dehumidification (membrane tubes filled with EMIMOAc solution with 75% concentration) at 25°C and 80% RH chamber condition, with 0.15 LPM solution flow rate
- **Case 5**: Regeneration (membrane tubes filled with EMIMOAc solution with 75% concentration) at 35°C and 20% RH chamber condition, with 0.30 LPM solution flow rate

The test results indicate that the small-scale prototype MILDAD can humidify (Cases 1 through 3) and dehumidify (Case 4) air. The specific vapor transportation rate ranged from 53 to 105 g/(h-m^2) for humidification, and it was between 32 to 47 g/(h-m^2) for dehumidification. Figure 6 shows that the specific vapor transportation rate of the MILDAD was affected by the airflow rates, but the trend was determined by other factors, including chamber condition and solution flow rate. For humidification, when the chamber condition was very dry (Case 1), increasing the airflow resulted in a decrease in the specific vapor transportation rate. However, when the chamber condition was humid (Cases 2 and 3), the specific vapor transportation rate was not as sensitive to the airflow rate as it was under dry condition. Furthermore, under the same chamber condition and with the same airflow rate, lowering the solution flow rate decreased the specific vapor transportation rate. For dehumidification (Case 4), increasing the airflow from 4.6 to 10.6 m^3/h increased the vapor transportation rate, but further increases in the airflow rate resulted in a decrease in the vapor transportation rate.

The measured overall permeance of the small-scale prototype MILDAD ranged from 0.4 to 0.6 E-8 kg/(m^2-s-Pa) in dehumidification mode and from 0.4 to 2.9 E-8 kg/(m^2-s-Pa) in humidification mode.

Table 2. Test conditions and results

Case	Test Conditions (Measured Data)								Measured Performance	
	$T_{Air,in}$	$T_{Air,out}$	$RH_{Air,in}$	$RH_{Air,out}$	Air Flow Rate	T_{Sol}	Con_{Sol}	Solution Flow Rate	Permeance	Specific Vapor transportation Rate
	C	C	%	%	CFM	C	%	GPM	kg/(m^2-s-Pa)	g/(hr-m^2)
Case 1-1	35.22	35.15	19.37	19.81	4.8	35	0	0.13	4.3E-09	74.4
Case 1-2	35.25	35.12	19.57	20.27	3.3	35	0	0.13	4.5E-09	77.8
Case 1-3	35.27	35.11	19.52	21.04	1.8	35	0	0.13	6.1E-09	105.1
Case 2-1	25.14	25.10	79.21	80.28	2.9	25	0	0.13	2.6E-08	63.4
Case 2-2	25.14	25.09	79.84	80.51	6.0	25	0	0.13	2.7E-08	64.2
Case 2-3	25.20	25.16	80.21	80.71	8.7	25	0	0.13	2.9E-08	66.5
Case 3-1	25.13	25.09	80.07	80.55	8.6	25	0	0.08	2.3E-08	53.4
Case 3-2	25.07	25.03	80.02	80.66	5.9	25	0	0.08	2.6E-08	62.9
Case 4-1	25.07	25.51	79.81	77.21	2.7	25	75	0.04	4.8E-09	36.1
Case 4-2	25.6	25.36	79.49	78.26	6.3	25	75	0.04	6.2E-09	46.7
Case 4-3	25.20	25.44	79.92	78.65	8.5	25	75	0.04	4.2E-09	32.2

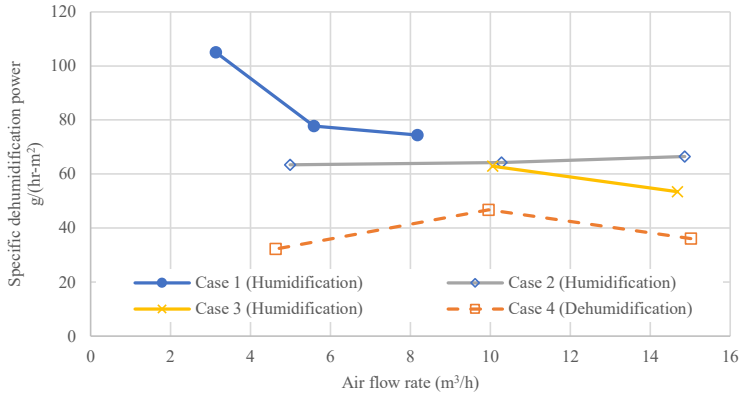


Figure 6. Measured specific vapor transportation rate of the small-scale MLDAD prototype in dehumidification and humidification operation at various airflow rates.

4.3. Test results of a medium-scale prototype

A medium-scale MILDAD prototype is tested in a wind tunnel, as shown in Fig. 7. The air velocity; and temperature, relative humidity at the inlet and outlet of the MILDAD are measured. A data acquisition system is used to collect and save data from all sensors during each test. The measurement devices and corresponding accuracies are shown in Table 3. The volumetric flow rate of the system is calculated by multiplying the cross-sectional area of the air channel with the air velocity. To smooth the air circulation in the test chamber, louvers are added at the air-side inlet and outlet of the MILDAD. The air circulation inside the wind tunnel is maintained at a rate of 10 CFM (0.28 m^3/min) with a fan. Humidity was measured both upstream and downstream of the MILDAD prototype.



Figure 7: Experimental Apparatus for characterizing the performance a medium-scale MILDAD prototype

Table 3. The measurement devices and corresponding accuracies

Target parameters	Measurement devices	Corresponding accuracies	Range
Temperature	Vaisala HMT330	± 0.25°F	-15 … +40°F
Relative humidity	Vaisala HMT330	± (1.0 + 0.008 X reading) %	0 – 95%
Flow Rate	PerfectPrime WD9829, Precise Sensitive Hotwire Thermal Anemometer Probe	Resolution: 0.01 m/s ± (0.05 X reading)	0.1 ∽ 25.0 m/s

The results of the dehumidification test are as shown in Table 4. The relative humidity upstream and downstream of the MILDAD prototype are plotted with respect to time as shown in Fig. 8. The specific vapor transportation rate of the medium-scale prototype, 111 g/(m^2-hr), is about 3 time higher than that of the small-scale prototype. It is thought to be due to higher flow rate and the longer tube length, which increase the contacting time for heat and mass exchange between ILD and air.

Table 4. Results from dehumidification test

Total testing time*	79.33	minutes
Air Flow Rate	0.28	m^3/min
Total Volume of Air Processed	22.5	m^3
Average ΔAH	1.3	g/m^3
Total Moisture Removed*	29.68	g
Specific Water Removal Rate	0.03	g/m^2/s
Cumulative latent cooling	72,843	J
Latent cooling power	15.3	W
Power consumption of fan and pump	14.4	W
Estimated COP of latent cooling	1.06	W/W

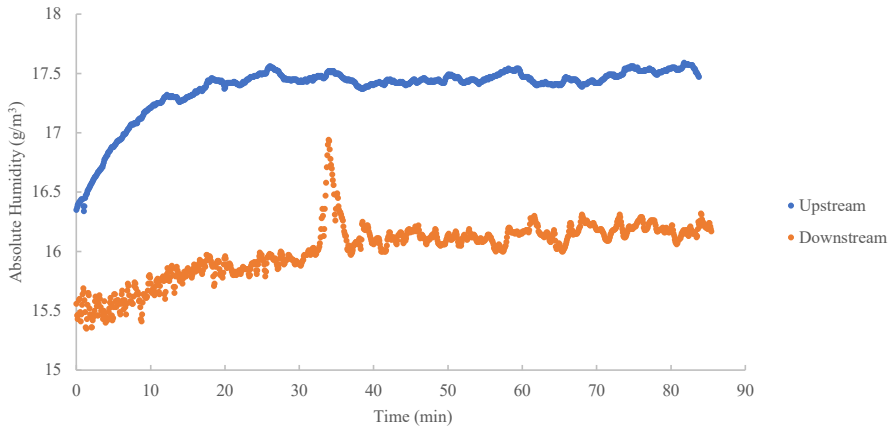


Figure 8: Dehumidification performance of dehumidifier module at 0.28 m^3/min. *Note that the spike in AH between 30 and 40 min was caused by a leak in the system. This leak was resolved during the test and these data points were disregarded in the analysis.

5. Design and Expected Performance of a Full-sized MILDAD

It is calculated that 1,371 membrane tubes are needed to have the same latent cooling capacity of a conventional 5,000 Btu (1.5 kW) air-conditioner—0.3 kW latent cooling capacity, or 0.12 g/s water vapor removal rate. Dimensions of a MILDAD with 0.3 kW latent cooling capacity are listed in Table 5.

The humidity ratio of typical entering air, $w_{air,in}$, of a room air-conditioner is 10.95 g/kg (26.7ºC and 50% relative humidity). The airflow rate of a 5,000 Btu (1.5 kW) air-conditioner is 170 CFM, or 0.095 kg/s. With a 0.12 g/s water vapor removal rate, the humidity ratio of the exiting air ($w_{air,out}$) will be reduced to 9.69 g/kg. The equilibrium humidity ratio of an ILD solution ($w_{sol,in}$) at 68% concentration and 26ºC is 6.53 g/kg. Based on these values, the latent effectiveness of the full-size MILDAD is calculated as 0.3.

Table 5. Dimensions of a MILDAD with 0.3 kW latent cooling capacity

Overall permeance	0.000027	g/(m^2-s-Pa)
Vapor pressure difference	700	Pa
Water removal rate	0.0189	g/(m^2-s)
Total membrane surface area	6.5	m^2

Tube diameter	0.003	m
Tube length	0.457	m
Surface area per tube	0.005	m^2
Total number of tubes	1371	[-]
Tube length	0.457	m
Tube spacing (2× dia.)	0.007	m
MILDAD width	0.762	m
MILDAD height	0.076	m

6. Conclusions

Small- and medium-scale prototypes of MILDAD using hollow tubes made with nonporous membranes and an ILD was successfully built. The small-scale prototype was evaluated for both dehumidification and humidification (regeneration) performance under various operating conditions. The test results provided a proof of concept of the nonporous MILDAD system to effectively humidify and dehumidify air. The specific vapor transportation rate ranged from 53 to 105 g/(h-m^2) for humidification, and it was between 32 to 47 g/(h-m^2) for dehumidification, depending on operating conditions. The measured permeance of the prototype ranged from 0.4 to 0.6 E-8 kg/(m^2-s-Pa) in dehumidification mode and from 0.4 to 2.9 E-8 kg/(m^2-s-Pa) in humidification mode. The technology was found to scale well, as the specific vapor transportation rate of the medium-scale prototype, 144 g/(h-m^2), is about 3 times higher than that of the small-scale prototype. It is thought to be due to higher flow rate and the longer tube length, which increase the contacting time for more heat and mass exchange between ILD and air.

Based on the measured permeance, a full-size MILDAD unit would require 1,371 membrane tubes to meet the latent cooling load of a 5,000 Btu (1.5 kW) air-conditioner with a 0.3 latent effectiveness. Coordinating with a commercial air conditioner manufacturer will be key to the development of a full-sized MILDAD.

Acknowledgements

This work was supported by a research award DE-EE-0008218 funded by the U.S. Department of Energy, Building Technologies Office. The technologies disclosed in this paper are protected under US Patents referenced [12]. This publication is a part of a 10-paper series to commemorate Xergy's 10-year anniversary, bringing advanced membrane technology to the global HVAC industry. This series includes papers providing further insight into water transmission mechanisms in advanced membranes and membrane based pervaporative heating and cooling.

References

[1] U.S. Energy Information Administration, International Energy Outlook 2017. *Federal Statistical System of the United States*. September 14, 2017.

[2] Abdel-Salam, M.R.H., Ge, G., Fauchoux, M., Besant, R., Simonson, C. (2014), State-of-the-art in liquid-to-air membrane energe exchangers (LAMEEs): A comprehensive review. *Renewable and sustainable Energy Reviews*, 39: 700-728. doi:10.1016/j.rser.2014.07.022

[3] Dannemiller, K. C., Weschler, C. J. and Peccia, J. (2017), Fungal and bacterial growth in floor dust at elevated relative humidity levels. *Indoor Air*, 27: 354-363. doi:10.1111/ina.12313

[4] Frankel M., Bekö G., Timm M., Gustavsen S., Hansen E.W., Madsen A.M. Seasonal variations of indoor microbial exposures and their relation to temperature, relative humidity, and air exchange rate. *Appl. Environ. Microbiol*. 2012;78:8289–8297. doi: 10.1128/AEM.02069-12.

[5] Qu, M., Abdelaziz, O., Gao, Z., & Yin, H. (2018). Isothermal membrane-based air dehumidification: a comprehensive review. *Renewable & Sustainable Energy Reviews*, 82

[6] Mohamed, A. S. A., Ahmed, M. S., Hassan, A. A. M., & Hassan, M. S. (2016). Performance evaluation of gauze packing for liquid desiccant dehumidification system. *Case Studies in Thermal Engineering*, 8, 260-276.

[7] Wang, W., Wu, L., Li, Z., Fang, Y., Ding, J., & Xiao, J.. (2013). An overview of adsorbents in the rotary desiccant dehumidifier for air dehumidification. *Drying Technology*, 31(12), 1334-1345

[8] Yang, B., Yuan, W., Gao, F., & Guo, B. (2015). A review of membrane-based air dehumidification. *Indoor & Built Environment*, 24(1).

[9] US Patents, Bahar et al: 10,386,084, Applications 20190291054, 20180187906

[10] Sahlot, M., & Riffat, S. B. (2016). Desiccant cooling systems: a review. *International Journal of Low-Carbon Technologies*, ctv032
[11] Qu, M., Abdelaziz, O., Sun, X. G., & Yin, H. (2017). Aqueous solution of [emim][oac]: property formulations for use in air conditioning equipment design. *Applied Thermal Engineering*, 124, 271-278.
[12] US Patents: 10,202,292 and Applications: 20190291054, 20190256384, 20190226703, 20180251616, 20180187906, 20180093905, 20170284685

13th IEA Heat Pump Conference 2020

13th IEA Heat Pump Conference
April 26-29, 2021 Jeju, Korea

Electrochemical inerting (oxygen control) for food preservation

Jacob Zerby[a], Bamdad Bahar[a]*

[a]*Xergy, Inc., 299A Cluckey Dr, Harrington DE 19954, USA*

Abstract

One of the primary applications for heat pumps is for refrigeration as part of the food chain. Despite widescale adoption, approximately 1.3 billion tons of food is wasted per year around the world [1], leading to excess energy requirements and greenhouse gas emissions. An alternate approach to food preservation is to decrease the oxygen levels in a container to deter spoilage. Decreasing the oxygen levels by merely 3% improves the shelf life of meats and other foods from several days to upwards of weeks. In this paper we describe a solid-state method of oxygen control based on an electrolysis cell, a derivative technology of fuel cells. This technology is quiet, requires no maintenance, and takes up very little space in a refrigerator, making it superior to current pressure/membrane swing adsorption (PSA/MSA) systems employing compressors. This low energy system can be used in conjunction with heat pumps for refrigeration, and in some cases replace heat pumps completely. This paper provides real life, in situ operational data.

© HPC2020.
Selection and/or peer-review under responsibility of the organizers of the 13th IEA Heat Pump Conference 2020.

Keywords: Inerting; Electrolysis; Food Preservation;

1. Introduction

Creating an inert environment through electrochemical means is a disruptive method for food preservation that can reduce, and in some cases replace, the energy footprint required by heat pump technology to maintain reduced temperatures in a refrigerator.

Currently, inerting systems utilize PSA systems in which a gas stream is fed to a reactor bed by means of a compressor. Certain gas molecules preferentially absorb onto the reactor bed, while others pass through unreacted. The system then undergoes a pressure swing, or change in pressure, to remove the reacted molecules and regenerate the reactor bed. Because there is a regeneration phase the system operates in batch mode, typically requiring multiple beds out of phase This method is very noisy, due to the use of a compressor, bulky, due to the batch method of operation, and energy intensive. The purpose for developing an alternative method of oxygen removal is to reduce the noise, size, and energy requirement of the traditional PSA system.

Several years have been devoted to the development of these systems to assist standard refrigeration in the preservation of food. As depicted in Figure 1, 5 Generations of systems have been manufactured and implemented, each with increases in performance and decreases in cost from the previous generation [2].

* Corresponding author. Tel.:1-302-218-4279 *E-mail address:* bamdad.bahar@xergyinc.com

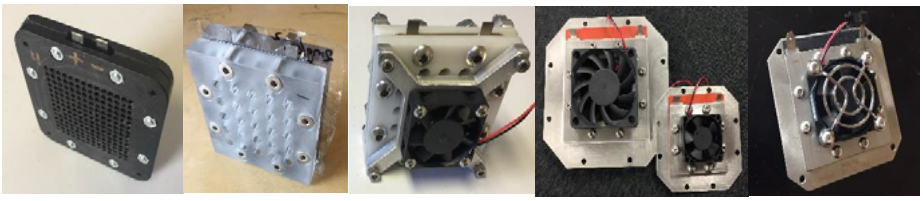


Fig. 1. The 5 generations of oxygen control devices

For an electrochemical inerting system, half of the electrochemical cell operates like the anode of a proton exchange membrane (PEM) water electrolyzer (PEMWE), and the other half of the cell operates like the cathode of a PEM fuel cell (PEMFC). Below, Figure 2 details the operation of all three systems.

The PEM is coated with catalyst on both the anode and cathodes, and then sandwiched by gas diffusion layers (GDL) to assist in electrical conductivity and gas/liquid diffusion to and from the membrane. In PEMWE, water is introduced at the anode side of the system and broken down to oxygen and protons. The protons transport across the membrane to the cathode and react to form hydrogen. In PEMFC, hydrogen is introduced at the anode and reacted to form protons. The protons transport across the membrane and react with oxygen at the cathode to form water and energy.

The PEM inerting system takes moisture out of the air and reacts that moisture at the anode to generate protons and oxygen. The protons transport across the PEM to the cathode and react with oxygen to reform water. The formation of water depletes oxygen in the environment making it rich with nitrogen. The additional water can back diffuse across the PEM or be removed via another dehumidification technology.

Table 1. PEM water electrolysis technology reaction pathways

PEMWE	PEMFC
$Anode: H_2O \rightarrow 2H^+ + \frac{1}{2}O_2 + 2e^-, E^0 = 1.23V$	$Anode: H_2 \rightarrow 2H^+ + 2e^-, E^0 = 0.00V$
$Cathode: 2H^+ + 2e^- \rightarrow H_2, E^0 = 0.00V$	$Cathode: 2H^+ + \frac{1}{2}O_2 + 2e^- \rightarrow H_2O, E^0 = -1.23V$
$Total: H_2O \rightarrow \frac{1}{2}O_2 + H_2, E^{0,total} = 1.23V$	$Total: H_2 + \frac{1}{2}O_2 \rightarrow H_2O, E^{0,total} = -1.23V$
PEM Inerting	
$Anode: H_2O \rightarrow 2H^+ + \frac{1}{2}O_2 + 2e^-, E^0 = 1.23V$	
$Cathode: 2H^+ + \frac{1}{2}O_2 + 2e^- \rightarrow H_2O, E^0 = -1.23V$	
$Total: Oxygen\ Depletion, E^{0,total} = 0.00V$	

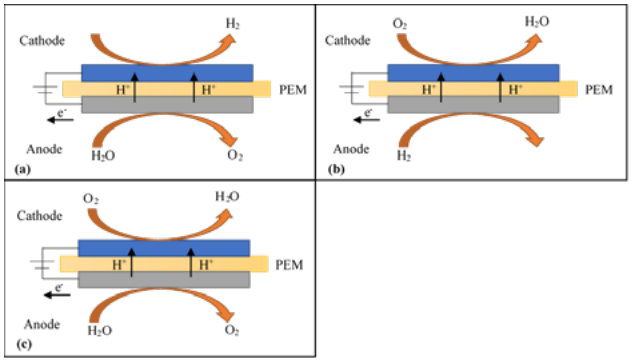


Fig. 2. Operation of (a) a PEMWE for hydrogen generation, (b) a PEMFC for power generation, and (c) a PEM inerting system for oxygen removal

2. Testing and Results

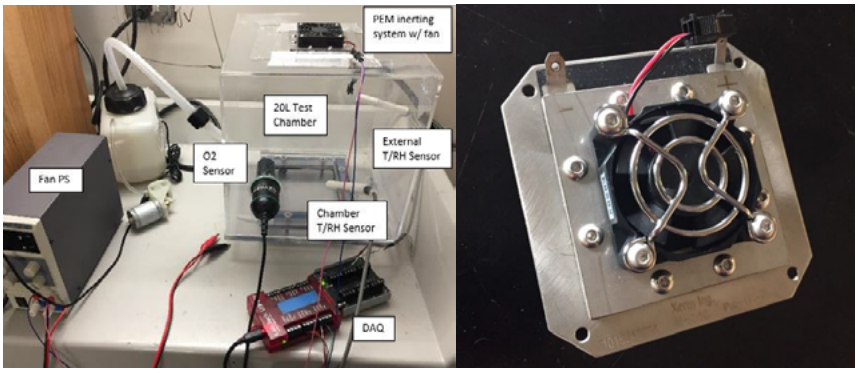


Fig. 3. Oxygen control chamber test set up (left); Sample oxygen cell (right)

The oxygen control chamber test was set up as depicted in Figure 3. Single cell membrane electrode assemblies (MEAs) were sandwiched between current collectors and housings to conduct performance testing. Several membranes were then tested to characterize the performance and determine feasibility of an air-based oxygen depletion system, including commercially produced perfluorosulfonic acid/PTFE copolymer membranes and in-house developed composite membranes. Testing was carried out in a 20 L container, while monitoring cell performance (voltage and current), temperature, humidity, and chamber oxygen levels. All cells were equipped with fans to improve mass flow of moisture to the membrane surface. The room RH was maintained between 45-55% and the room temperature was maintained between 22-23C. A constant 2 V was applied to each cell to carry out inerting.

Three composites of varying thickness (<50 µm) and ionomer composition were assembled into housings and testing against commercially produced 50.8 µm (212) and 127 µm (115) membranes. All systems achieved 75% efficiency for oxygen removal. The composite membranes all gave equivalent performance of around 1 g/hr. while NR212 and N115 achieved oxygen removal rates of 0.58 g/hr. and 0.23 g/hr. respectively. Composites A and B had the highest levels of back diffusion, leading to the lowest humidity increase of all the systems during the inerting process. This is desirable as an environment below 100% RH is preferred for food preservation. The difference in moisture addition to the box for the various membranes highlights the ability to adjust the internal conditions of the chamber through membrane customization.

The results of this testing (Figure 4) shows a power consumption of approximately 10.7 W (membrane - 4.75A @ 2V, fan – 12V @ 0.1A) for the membrane system used in testing. It took approximately 0.64 hours to drop the oxygen from 20.8% to 17.8%, giving the energy consumption of the system to be approximately 6.8 Wh or 9.5 Wh/g-O_2. This system would typically cycle three times a day, for three hours each cycle, putting

its average daily energy consumption at about 61 Wh/day. Large-scale PSA systems, the energy consumption is around 500 kWh/tonne-O_2 (0.0005 Wh/g-O_2) [3]. Figure 5 provides an image of a refrigerator equipped with a commercial PSA-type oxygen control system now available in China. While the electrochemical system requires water vapor to operate, the bulk humidity in empty refrigerators is sufficient. Refrigerators to tend to have a bulk relative humidity in the range of 20%-50%, and only increase as food is added.

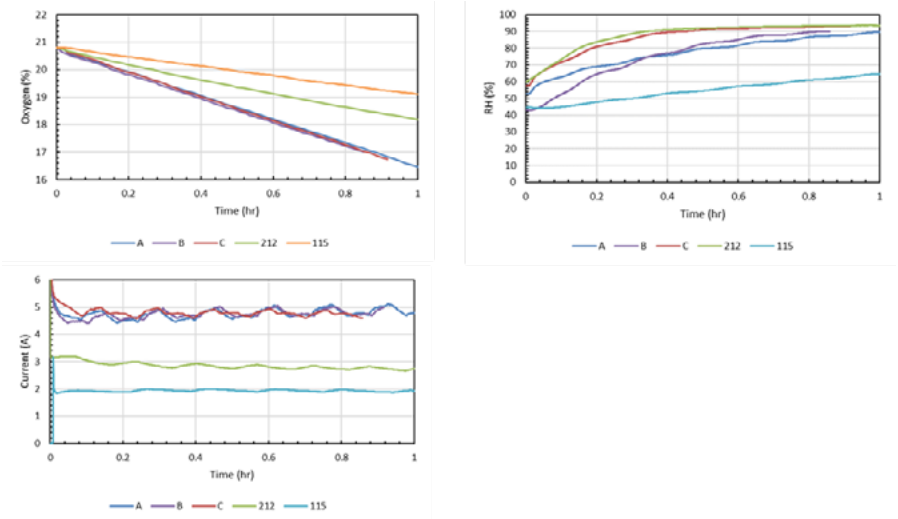


Fig. 4. Test results (in clockwise order, starting with the top left), Oxygen control results; Relative humidity change during oxygen control; Current draw during testing.



Fig. 5. Commercial Refrigerator with PSA type Oxygen control system

The fan system of the electrochemical system emits a faint noise of 20 dBa and is the only component significantly contributing to the noise of the system. As seen in Figure 6, this noise is quieter than a bedroom at night. Micro-compressors in PSA-type systems have noise levels upwards of 65 dBa [4]. This is as loud as normal conversation. In fact, 60 dBa is the threshold of possible permanent damage, thus this noise level is not appropriate for consumers [5].

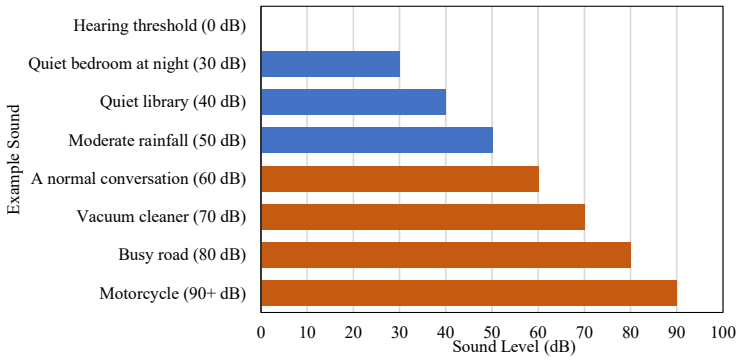


Fig. 6. Decibel levels of common sounds (sound levels at which long-term exposure can lead to hearing damage in orange) [4]

3. Conclusion

An electrochemical inerting system provides a much simpler, sleek, less complex, and lower noise alternative to PSA systems. The largest downside to the novel system is the greater energy consumption. Despite this increased energy consumption, the daily energy consumption of the system is still minimal; its daily power consumption is less than 4% of a typical 2 kWh/day refrigerator [6]. This system still has the potential for further development, exploring new membranes and decreasing the catalyst loading to improve its efficiency and decrease the system cost.

Thin composite membranes achieve the oxygen depletion rates in an electrochemical device, which is required for food preservation, whereas conventional free-standing membranes in the same devices do not [3]. This is a unique aspect of this technology and has resulted in dramatic performance improvements in food preservation applications.

4. Nomenclature

Table 2. Acronyms and abbreviations, defined

Term	Definition	Term	Definition
GDL	Gas Diffusion Layers	PEMWE	Proton Exchange Membrane Water Electrolyzer
MEA	Membrane Electrode Assembly	PSA	Pressure Swing Adsorption
PEM	Proton Exchange Membrane	PTFE	Polytetrafluoroethylene
PEMFC	Proton Exchange Membrane Fuel Cell	RH	Relative Humidity

Acknowledgements

The technologies outlined in this paper are protected by US Patents referenced [2]. Certain aspects of this technology were originally developed under US DOE SBIR funding sponsored by the Building Technologies Office. This publication is a part of a 10-paper series to commemorate Xergy's 10-year anniversary, bringing advanced membrane technology to the global HVAC industry.

References

[1] Food and Agriculture Organization of the United Nations. "Key facts on food loss and waste you should know!" *Save Food: Global Initiative on Food Loss and Waste Reduction.* http://www.fao.org/save-food/resources/keyfindings/en/. Accessed: 6 May 2019.

[2] US Patent Applications: 20190192806, 20190100844

[3] T. Banaszkiewicz, M. Chorowski, W. Gizicki. "Comparative analysis of cryogenic and PTSA technologies for systems of oxygen production," *AIP Conference Proceedings*. 1573, 1373 (2014): https://doi.org/10.1063/1.4860866
[4] DEWIN. "Air Pump – DC 12V Micro Vacuum Pump," *Amazon*. https://www.amazon.com/Air-Pump-Electric-Treatment Instrument/dp/B07FGFPKNS/ref=sr_1_7?keywords=micro+air+compressor+vacuum+pump&qid=1573518624&sr=8-7 Accessed: 12 Aug. 2019
[5] "Noise Level Chart: Decibel Levels of Common Sounds with Examples," *Boomspeaker*. https://boomspeaker.com/noise-level-chart-db-level-chart/. Accessed: 19 Dec. 2019.
[6] "Energy Use of Some Typical Home Appliances," *Consumer Energy Information: EREC Reference Briefs*. Merrifield, VA: DOE Energy Efficiency and Renewable Energy Clearing House. http://physics.oregonstate.edu/~hetheriw/energy/quick/eff/EREC_Brief_Energy_Use_of_Some_Typical_Home_Appliances.htm Accessed: 19 Dec. 2019

13th IEA Heat Pump Conference 2020

13th IEA Heat Pump Conference
April 26-29, 2021 Jeju, Korea

Active humidity control for refrigeration applications

Jacob Zerby[a], Bamdad Bahar[a*]

[a]*Xergy, Inc., 299A Cluckey Dr., Harrington DE 19952, USA*

Abstract

According to the Food and Agriculture Organization of the UN, approximately 1.3 billion tonnes of food is wasted per year around the world [1], leading to excess energy requirements and greenhouse gas emissions. It is important to control all aspects of spoilage, including food storage during refrigeration. Maintaining adequate humidity levels during the storage of foods is essential to increasing their shelf life. In this paper we describe a solid-state method of humidity control based on an electrolysis cell, a derivative technology of fuel cells. The technology operates by interacting with moisture in the air, leading to a novel method of simple and accurate control of humidity levels inside an enclosure such as a refrigerator. It requires no maintenance, is quiet, and takes up very little space in a refrigerator. Current technology is limited to one-way operation, either as a humidifier or dehumidifier, and requires either a drain of liquid water for dehumidification or a source of water for humidification. The system can work in conjunction with a heat pump to manage moisture levels inside a refrigerator. Real life, in-situ performance data is provided.

© HPC2020.
Selection and/or peer-review under responsibility of the organizers of the 13th IEA Heat Pump Conference 2020.

Keywords: Active Humidity Control; Electrolysis; Refrigeration;

1. Introduction

There are many foods stored in a refrigerator that require different levels of humidity to increase their shelf life. In some instances, like vegetables, the foods may off-gas moisture during storage, which can lead to saturated environments. These saturated environments lead to pooling off water and subsequent rotting of food.

Current methods to avoid this issue include vents that allow the moisture to be pulled out of the container and the use of pervaporative membranes, which only allow moisture to pass through based on a humidity gradient. These are methods of passive control and their effectiveness depends on the food and conditions within the refrigerator. An electrochemical humidity control device allows for both humidification and dehumidification at precise levels, something no other technology can do.

Several years have been devoted to the development of these systems to assist standard refrigeration in the preservation of food. As depicted in Figure 1, 5 Generations of systems have been manufactured and implemented, each with increases in performance and decreases in cost from the previous generation [5].

* Corresponding author. Tel.: +1 (302)-629-5768. *E-mail address:* bamdad.bahar@xergyinc.com

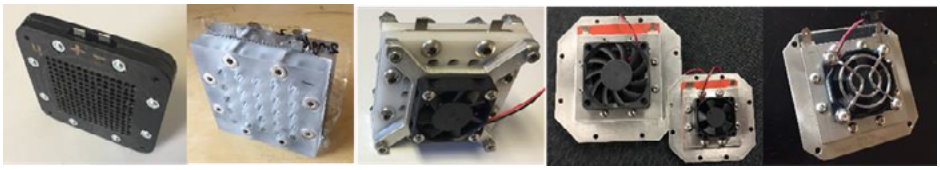


Fig. 1. The development of electrochemical humidity control systems over five generations

For the humidity control system, half of the electrochemical cell operates like the anode of a proton exchange membrane (PEM) water electrolyzer (PEMWE), and the other half of the cell operates like the cathode of a PEM fuel cell (PEMFC). Figure 2 details the operation of all three systems.

The PEM is coated with catalyst on both the anode and cathodes, and then sandwiched by gas diffusion layers (GDL) to assist in electrical conductivity and gas/liquid diffusion to and from the membrane. In PEMWE, water is introduced at the anode side of the system and broken down to oxygen and protons. The protons transport across the membrane to the cathode and react to form hydrogen. In PEMFC, hydrogen is introduced at the anode and reacted to form protons. The protons transport across the membrane and react with oxygen at the cathode to form water and energy.

The PEM humidity control system takes moisture out of the air and reacts that moisture at the anode to generate protons and oxygen. The protons transport across the PEM to the cathode and react with oxygen to reform water. If the anode is interfaced with the chamber then dehumidification is performed, if the cathode is interfaced with the chamber then humidification is performed.

Table 1. PEM water electrolysis technology reaction pathways

PEMWE	PEMFC
$Anode: H_2O \rightarrow 2H^+ + \frac{1}{2}O_2 + 2e^-, E^0 = 1.23V$	$Anode: H_2 \rightarrow 2H^+ + 2e^-, E^0 = 0.00V$
$Cathode: 2H^+ + 2e^- \rightarrow H_2, E^0 = 0.00V$	$Cathode: 2H^+ + \frac{1}{2}O_2 + 2e^- \rightarrow H_2O, E^0 = -1.23V$
$Total: H_2O \rightarrow \frac{1}{2}O_2 + H_2, E^{0,total} = 1.23V$	$Total: H_2 + \frac{1}{2}O_2 \rightarrow H_2O, E^{0,total} = -1.23V$
PEM Humidity Control	
$Anode: H_2O \rightarrow 2H^+ + \frac{1}{2}O_2 + 2e^-, E^0 = 1.23V$	
$Cathode: 2H^+ + \frac{1}{2}O_2 + 2e^- \rightarrow H_2O, E^0 = -1.23V$	
$Total: Moisture\ Transfer, E^{0,total} = 0.00V$	

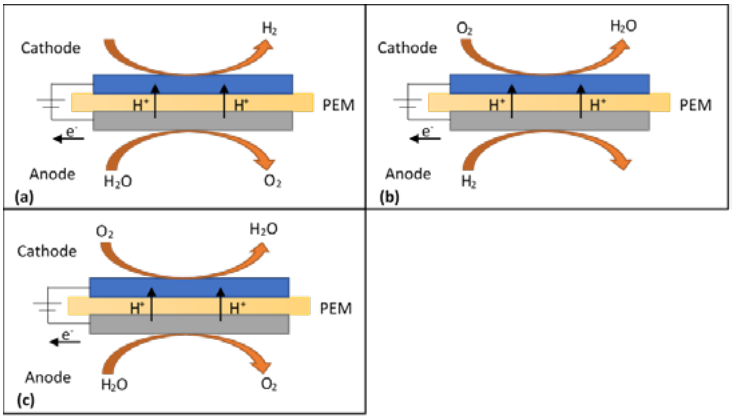


Fig. 2. Operation of (a) a PEMWE for hydrogen generation, (b) a PEMFC for power generation, and (c) a PEM humidity control system for oxygen removal

2. Testing and Results

Single cell MEAs were sandwiched between current collectors and housings to conduct performance testing. Several membranes were then tested to characterize the performance and determine feasibility of a water-vapor-based humidity control system. Testing was carried out in a 20 L container, while monitoring cell current, temperature, and humidity.

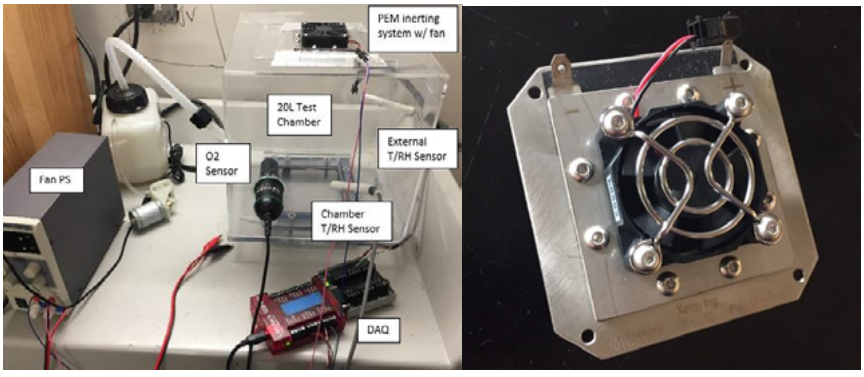


Fig. 3. Humidification testing set up (left); Sample commercial humidity control cell (right)

Membranes of various thicknesses were tested to determine the effect of thickness on moisture transfer rate. The test was terminated when the target relative humidity level, 15% RH, was reached. Membrane A was the thinnest membrane, while membrane C was the thickest membrane. As, as seen in Figure 4, membrane thickness increases the moisture transfer rate increase. However, the increase in thickness comes with an increase in cost, so it is essential to balance the two variables for a commercially viable moisture control system. Although membrane C reached the target relative humidity the fastest, its thickness left it cost prohibitively expensive and membrane B was selected for further testing and production.

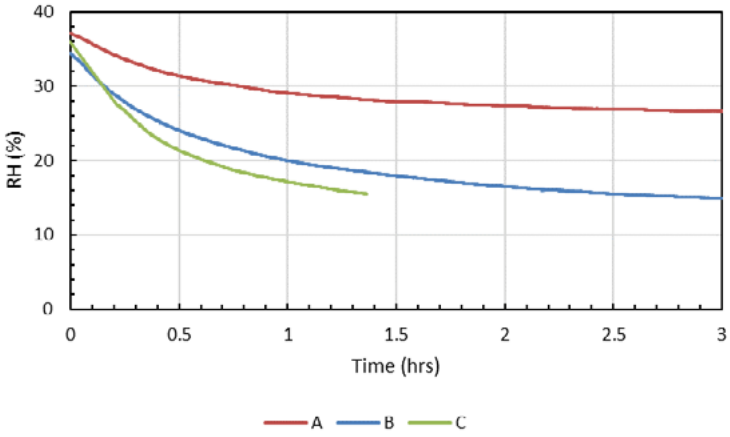


Fig. 4. Humidity control performance of membranes A, B, and C

A cell was run with and without a fan system to determine the improvement to the overall system (Figure 5) [2]. At the low external humidity conditions during testing, 30% RH at 18°C, the moisture transfer rate was 1.65 g/day and 8.5 g/day for the system without a fan and with a fan, respectively. Running solely on moisture available in the air makes this technology simple and compact but does limit the capacity to humidify and dehumidify. Improving the mass transfer of water molecules to the system has shown to improve rates by upwards of 5 times. Any increase in performance equates to a decrease in size, so the improved fan system allows for a 5 times reduction in size, leading to less catalyst and membrane, and makes the electrochemical humidity control system commercially viable.

A similar test was conducted for the humidification at low external humidity conditions, 22% RH at 18°C, and the moisture transfer rates were 1.2 g/day and 1.7 g/day for the system without a fan and with a fan, respectively. Note: at higher humidity conditions the membrane will exhibit a higher conductivity and the moisture transfer rate increases. The increase in humidification is less than that for dehumidification at these reduced moisture levels due to an overall decrease in membrane conductivity; the fan system only improves the performance by around 1.5 times.

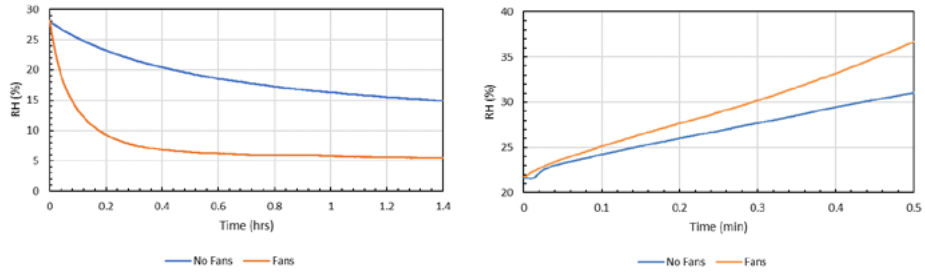


Fig. 5. Results of humidity test

After selecting the appropriate membrane thickness and fan system, the modules were tested in a fridge. Typically, temperature has a negative impact on chemical reactions, so it is essential to prove feasibility at the temperatures experienced in a fridge. As seen in Figure 6, the system was able to both humidify and dehumidify around the humidity level inside the fridge at temperatures between 8°C and -1°C.

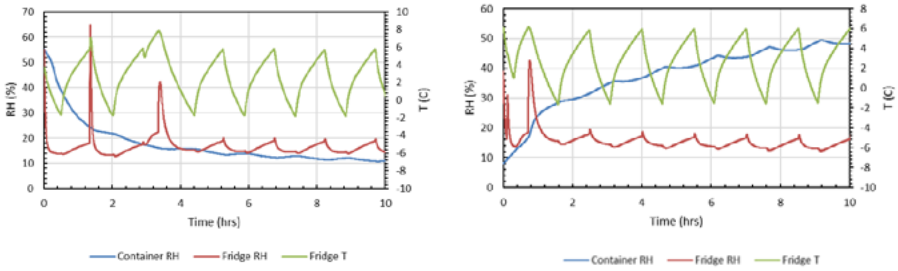


Fig. 6. Dehumidification (left) and humidification (right) testing in a refrigerator

3. Conclusions

Electrochemical cells have successfully been developed and demonstrated to provide both humidification and dehumidification, with the target of improving food preservation and aiding in refrigeration. Performance and cost targets have been met to make this product commercially viable for appliances and reduce the burden for heat pumps used in refrigeration. The proposed system is able to humidify a 35 L enclosure from 30% to 80% RH in less than 3 hrs or dehumidify the same enclosure from 80% to 30% RH in the same amount of time. There are many other applications for this technology including in controlling humidity in museum displays, and moisture/condensation sensitive optics and electronics applications.

4. Nomenclature

Table 2. Acronyms and abbreviations, defined

Term	Definition	Term	Definition
GDL	Gas Diffusion Layers	PEMFC	Proton Exchange Membrane Fuel Cell
MEA	Membrane Electrode Assembly	PEMWE	Proton Exchange Membrane Water Electrolyzer
PEM	Proton Exchange Membrane	RH	Relative Humidity

Acknowledgements

The technologies outlined in this paper are protected by US Patents referenced [2]. Certain aspects of this technology were originally developed under US DOE SBIR funding sponsored by the Building Technologies Office. This publication is a part of a 10-paper series to commemorate Xergy's 10-year anniversary, bringing advanced membrane technology to the global HVAC industry.

References

[1] Food and Agriculture Organization of the United Nations. "Key facts on food loss and waste you should know!" *Save Food: Global Initiative on Food Loss and Waste Reduction.* http://www.fao.org/save-food/resources/keyfindings/en/. Accessed 6 May 2019.

[2] US Patent Applications: 20190192806, 20190100844

13th IEA Heat Pump Conference
April 26-29, 2021 Jeju, Korea

Pervaporation Membrane for Refrigerator Vegetable Tray Applications

Jacob Zerby[a], Bamdad Bahar[a*], Anderson Bortoletto[b]

[a] *Xergy Inc. 299 A Cluckey Drive, Harrington, DE 19952*
[b] *Sub-Zero Group, Inc. 4717 Hammersley Road, Madison, WI 53711*

Abstract

Many vegetables produce moisture and need moisture for preservation. Higher relative humidity in the vegetable trays or crisper drawers helps to keep vegetables sturdy and fresh. However, cold surfaces can result in condensation and the presence of liquid water inside the unit. One disadvantage of using heat pumps in refrigerators, it the propensity to develop condensation inside vegetable trays. Approximately 1.3 billion tonnes of food is wasted per year around the world [1], leading to excess energy requirements and greenhouse gas emissions. It is important to control all aspects of spoilage, including food storage during refrigeration. One method to increase the storage time of vegetables is to control moisture inside these trays and reduce dehydration, while preventing condensation, or pooling of water. In this paper we describe a pervaporation method, utilizing advanced composite ionic membranes, to control the humidity levels of a sealed box. The system involves an ultra-thin, ultra-strong, ultra-high-water permeability ionic membrane, with a circulation system for enhanced pervaporation. The system improvements allow for a sealed box, Air Exchange Rate (AER) <0.5/hr, with a large reduction in membrane area and reduced dehydration of food illustrated by reduced fluctuations of the internal relative humidity. Membrane properties, chemistry selection and methods of operation for optimal design of a vegetable tray preservation system with heads of lettuce as the source of moisture. Real life, in-situ performance data is provided.

© HPC2020.
Selection and/or peer-review under responsibility of the organizers of the 13th IEA Heat Pump Conference 2020.

Keywords: Membrane; Humidity Control; Vegetable Tray; Refrigerator;

1. Main text

1.1. Introduction

During storage of vegetables in vegetable trays, water vapor is released from the vegetables and must be removed at a specified, preferably variable, rate to eliminate condensation and rotting of the produce. Currently, the main method for reducing condensation in a vegetable tray is through an opening that can be manually adjusted to let out water vapor as needed. This requires the customer to adjust the opening on the food being stored and is prone to user error. A smarter, more elegant solution with adaptive moisture transfer rates is required to meet the growing demands of food preservation.

The proposed pervaporative solution, portrayed in Figure 1, allows a pathway for high levels of moisture to diffuse to an environment with less moisture, while cutting off the transport of other gaseous species. Pervaporation through a membrane is the process of a liquid or gas-sorbing onto the feed side of a membrane, permeating through the membrane, and subsequently evaporating off at the permeate side of the membrane. The driving force across the membrane is the concentration gradient, with high humidity inside the tray transferring to the low humidity environment in the refrigerator. The dense membrane only allows the transport

* Corresponding author. Tel.: 1-302-629-5768
E-mail address: bamdad.bahar@xergyinc.com

of polar species through, i.e. water, and acts as a barrier to nitrogen and oxygen. High moisture levels are desirable to maintain the freshness of the vegetable and extend the shelf life, whereas allowing too much water vapor to leave the tray causes the vegetable to dry out and be thrown away. There is a need to remove just enough moisture to prevent condensation, without drying out the vegetables.

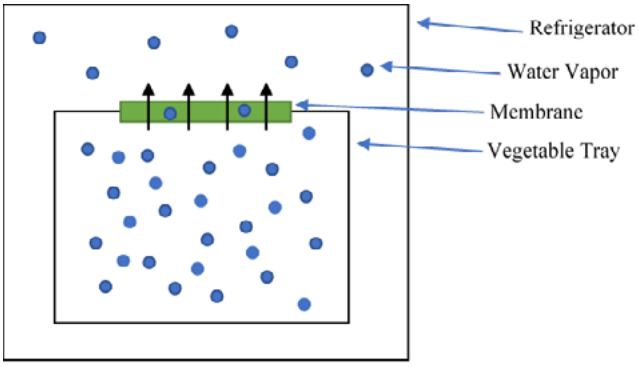


Fig. 1. Diagram of Pervaporative Solution for Humidity Control for Vegetable Trays

1.2. Testing

Initial testing and down selection of membranes was conducting at ambient conditions in the 20 L enclosure, depicted in Figure 2. The room was held around 50% RH and 20°C for all tests. An ultrasonic humidifier was placed in a water bath and plumbed to the box. An air compressor was hooked up to the humidification setup to increase the amount of water vapor entering the box. The humidification system was turned on until the humidity inside the box reached ~90% RH. The test ran until the box hit below 75% RH.

Tests were conducted with and without a fan system to quantify the enhancement to pervaporation.

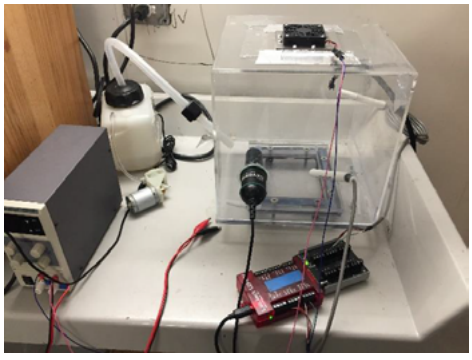


Fig. 2. Membrane Testing Enclosure

1.3. Results and Discussion

The slope of the change in absolute humidity over time was calculated between the range of 85-75% RH and multiplied by the volume of the box, giving the estimated flux rate of the membrane with a box RH of 80% and a room RH of 50%. The following equation was used to calculate the permeance of the membrane:

$$Permeance = \frac{Flux}{(Active\ Area) * (VP_{box} - VP_{ambient})}$$

where the Active Area is the open area of the membrane, VP_{box} is the vapor pressure inside the box (at ~80% RH and ~20°C), and $VP_{ambient}$ is the ambient vapor pressure. Note that the testing methods differ from the ASTM E96; the test method was modified to more closely resemble the actual in application use of the membrane [2]. Instead of maintaining a constant RH in the test chamber, as in the ASTM method, the chamber was charged with an initial 80% RH, which was then allowed to decrease over the period of the test. This batch-like test is reflective of the actual vegetable tray application.

The permeance of the membranes increased with decreasing thickness as expected, as there is less material for the moisture to permeate through. While small changes where not found to have a statistically significant effect on the permeance, as in the range of thickness of membranes B in Figure 3, the permeance of membranes significantly increases with large decreases in thickness, as in membrane A. The best two performing membranes, A and C, are derived from fluorinated ionomers, while membrane B is a non-fluorinated ionomer.

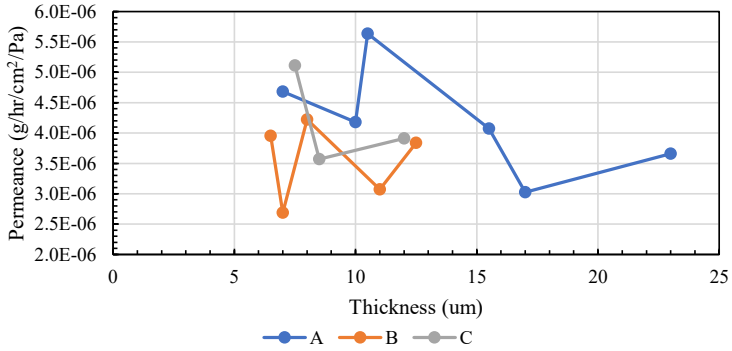


Fig. 3. Permeance of membranes without fan systems

The same test was carried out to analyses various fan systems. As depicted in Figure 4, using a single fan on the inside or outside of the membrane led to a minimal increase in moisture removal rate. However, using a fan on both sides improved the pervaporation by 25x. This suggests that the rate limiting steps are the sorption onto the membrane surface and evaporation from the permeate side, and that they are around the same magnitude and must be addressed simultaneously, as seen in Figure 5. Having such a large increase in performance from the fan system allows for a smarter humidity control system to be used. The fan speeds can be adjusted to adjust the moisture transfer rate based on a sensor in the enclosure; the slower the fan the slower the moisture transfer rate. Employing the fan system is essentially employing a “switch”. By sizing the membrane appropriately, the membrane acts as a poor transmitter of moisture when the fans are off, or a moisture barrier, and rapidly removes humidity when the fans are on the and the membrane is “switched” on.

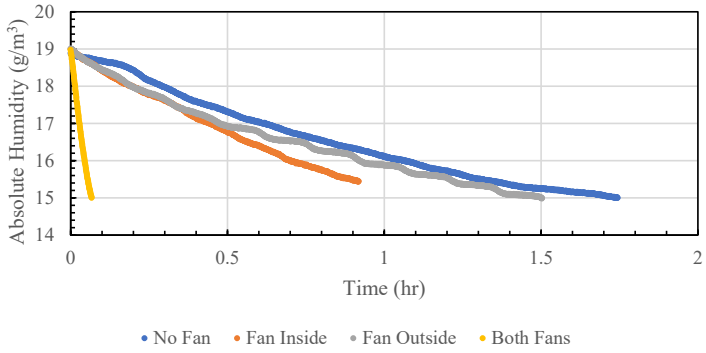


Fig. 4. Results of Fan Configuration Testing

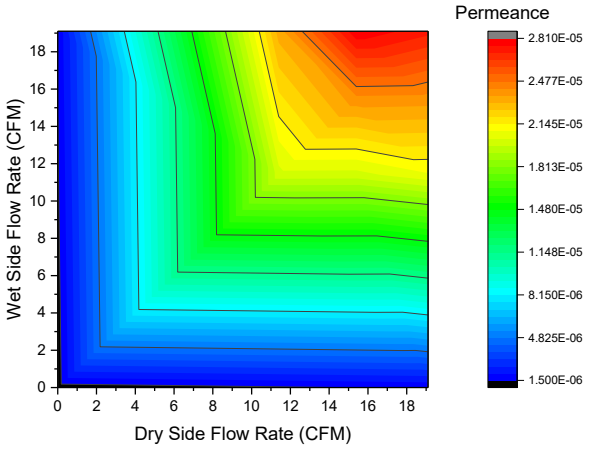


Fig. 5. Results of Flow Rate Analysis

All membranes tested were composite structures, with a base polymer imbibed into a porous support layer. The composite structure allowed for membranes almost 5 µm thick to be evaluated, allowing for high moisture permeance, without sacrificing on the mechanical properties of the membrane. In Table 1, the various support structure-polymer architectures were analyzed, and several (containing Support 1 and 2) were found to have enough mechanical strength for use in a vegetable tray.

Table 1. Mechanical strength of various combinations of base polymer and support material

Architecture	Support 1 – Chemistry 1	Support 1 – Chemistry 2	Support 2 – Chemistry 1	Support 2 – Chemistry 2	Support 3 – Chemistry 2	Support 4 – Chemistry 1
Force (N)	24.76	12.48	6.11	5.57	3.60	1.16
Ultimate Tensile Strength (MPa)	247.6	124.8	58.2	50.6	36.0	11.6

Figures 6 illustrate prototype membrane systems for humidity control for a vegetable tray inside a refrigerator.



Fig. 6. Vegetable Tray with Prototype Membrane System and a fan system (left) and without a fan system (right) Installed for Testing

2. Conclusions

The high permeability and tensile strength of the tested membranes shows strong potential for their application in vegetable trays and crisper drawers. During in-refrigerator application testing, the bulk refrigerated space was found to cycle between 20% and 50% RH. Without a pervaporative membrane the loaded vegetable tray tended have a very high relative humidity, condensing and pooling water. In application, the pervaporative membrane was able to maintain the optimal RH of over 90% without condensation. This system does not have a significant power requirement. The fan system draws 12 V at 0.1 A and the remainder of the system does not draw any power. The fan system can be set to a timer or humidity sensor as a method of controlling the humidity of the tray. Even if the fans ran 24 hours a day, would increase the total daily energy consumption of a typical refrigerator by less than 2%. In the future, thinner membranes and new materials can continued to be explored for higher performance, strength, and permeability.

Acknowledgements

Aspects of this technology were developed under US DOE SBIR funding programs. The technology is patented as referenced [4]. This publication is a part of a 10-paper series to commemorate Xergy's 10-year anniversary, bringing advanced membrane technology to the global HVAC industry.

References

[1] T. Banaszkiewicz, M. Chorowski, W. Gizicki. Comparative analysis of cryogenic and PTSA technologies for systems of oxygen production. AIP Conference Proceedings. 1573, 1373 (2014): https://doi.org/10.1063/1.4860866

[2] ASTM E96 / E96M-16, Standard Test Methods for Water Vapor Transmission of Materials, ASTM International, West Conshohocken, PA, 2016, www.astm.org

[3] G. Paltrinieri. Handling of Fresh Fruits, Vegetables, and Root Crops: A Training Manual for Grenada. Food and Agriculture Association of the United Nations. (1989): http://www.fao.org/3/T0073E/T0073E00.htm

[4] US Patent Applications: 20190192806, 20190100844

Appendix: The Food and Agriculture Organization of the United Nations' suggested storage conditions for selected produce

Table 2. Storage requirements of humidity sensitive produce [3]

Produce	Storage Temperature (°C)	Relative Humidity (%)
Asparagus	0-2	95
Green Beans	5-7	90-95
Carrots	0	90-95
Cauliflowers	0	90-95
Cucumbers	7-10	90-95
Cabbage	0	90-95
Peppers	7-10	90-95
Ceuregettes	0-10	90-95

13th IEA Heat Pump Conference
April 26-29, 2021 Jeju, Korea

Experimental Investigation on One-time Heating R32 Two-stage Air Source Heat Pump Water Heater

Bo Zheng[a,b], Xiangfei Liang[a,b,*], Rong Zhuang[a]

[a]Gree Electric Appliances, Inc.of Zhuhai, Zhuhai 519070, China
[b]National Engineering Research Center of Green Refrigeration Equipment, Zhuhai 519070, China

Abstract

A one-time heating R32 two-stage air source heat pump water heater was experimentally studied under various working conditions, and compared with a static heating type. The tested results show that when the inlet water temperature and the outlet water temperature are fixed, the heating COP is almost unchanged with the increase of the heating capacity; when the heating capacity is fixed, the heating COP decreases with the increase of the inlet water temperature or the outlet water temperature; the condensation temperature of one-time heating type is much lower than that of the static heating type, and also lower than the outlet water temperature. A one-time heating two-stage compression cycle can effectively reduce the discharge temperature and broaden the operating range of the R32 air source heat pump water heater, and improve the reliability of R32 compressor under low ambient temperature and high outlet water temperature conditions.

© HPC2020.
Selection and/or peer-review under responsibility of the organizers of the 13th IEA Heat Pump Conference 2020.

Keywords: R32; heat pump water heater; one-time heating; static heating

1. Introduction

With the improvement of living standards, the water heater has become an indispensable living facility in people's lives. Air source heat pump water heater (HPWH) is increasingly popular for its energy saving and environmental protection. At present, most of refrigerants for use in the domestic HPWHs are R22 and R134a, and a few R410A. R22 is listed as a phased-out refrigerant for its ODP (ozone depletion potential) above zero, while R134a and R410A acting as transitional refrigerants will be phased out for their relatively high GWP (greenhouse effect potential). R32 is one of components of R410A and is classified as A2L safety class according to the standard ANSI/ASHRAE 34-2013[1]. ODP and GWP of R32 is zero and 675, respectively. A large number of experimental researches and theoretical analyses on R32 and its system have been carried out [2~5]. The results show that R32 is a good alternative refrigerant in terms of climate impact and safety use. Theoretical analysis [2~3] shows that the energy efficiency ratio (EER) of R32 compression cycle is improved by 5.3% and the cooling capacity is improved by 12.7% compared with R410A. Tu et al [4] carried out a drop-in test to compare R32 with R410A in a fixed speed room air conditioner. The results show that the cooling capacity and EER are improved by 8.04% and 3.27%, respectively, under rated cooling condition, while the charge of R32 is reduced by 24%. Mei et al [5] carried out a comparative experimental study on the cycle characteristics of R32 and R410A in air-cooled chillers. The results show that the cooling capacity of R32 is about 10% higher than that of R410A, and EER is slightly increased. Huang et al [6] pointed out that R32 is more suitable for one-time heating HPWH than R410A.

However, the discharge temperature of R32 is about 10~25℃ higher than that of R410A. The high discharge temperature problem is more prominent on R32 HPWH due to its high condensation temperature. The high discharge temperature can cause a series of reliability issues, including accelerating the

* Corresponding author. Tel.: +86-756-8589554; fax: +86-756-8668982.
E-mail address: liangxf@cn.gree.com.

decomposition of lubricant oils, the deterioration of various non-metallic materials in compressor, and the reduction of viscosity of lubricant oil. According to theoretical analysis, when the evaporation temperature is -20℃ and the condensation temperature is 45℃, the discharge temperature can be kept below 135℃ as long as the suction vapor quality of compressor is controlled to 0.93 [7]. That is, the high discharge temperature problem can be solved by reducing the suction vapor quality of the compressor. For two-stage air source HPWH with vapor injection system [8], the high discharge temperature problem can be solved by vapor injection under low ambient temperature.

Reducing the suction vapor quality of the compressor can reduce the discharge temperature effectively. However, the capacity and EER decrease with the decrease of the suction vapor quality of the compressor [9]. If the discharge temperature can be reduced by reducing the condensation temperature, then the high discharge temperature problem of R32 can be solved, moreover the system energy efficiency can be improved.

According to the national standard on HPWH [10-11], the HPWH has three types based on the heating mode, which are the static heating type, the circulating heating type and the one-time heating type. The one-time heating type means that the initial cold water reaches the target water temperature through the heat exchanger of the HPWH once. In this paper, the characteristics of the one-time heating R32 HPWH are researched to provide guidance for design.

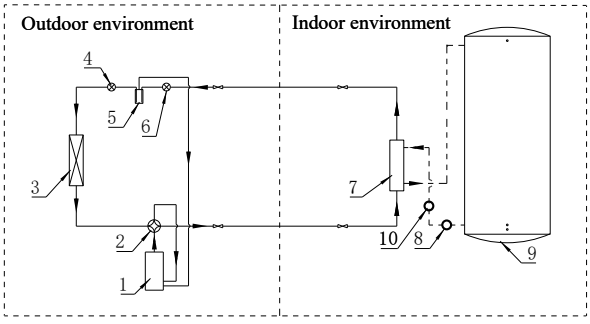
2. Experiment and data analysis

2.1. Experiment

The one-time heating R32 HPWH experimental system is shown in Fig.1, which consists of the heat pump system and the water system. The detailed information is shown in Table 1. The heat pump consists of a two-stage rotary compressor, a tube-in-tube condenser, an electronic expansion valve, an evaporator and a flash tank. The water system consists of a water tank, a water pump and the tube-in-tube condenser. Fig.2 shows a cross-sectional view of the tube-in-tube condenser, which is a counterflow heat exchanger and optimized based on the characteristics of one-time heating HPWH and R32 heat transfer characteristics.

The experiment was carried out on the water-enthalpy laboratory, which includes a indoor chamber and an outdoor chamber. The compressor, the evaporator, the electronic expansion valve and the flash tank of the heat pump system were placed in the outdoor chamber, and the water system was placed in the indoor chamber. The tested conditions and water temperature are listed in Table 2.

In the experiment, the inlet water temperature and the outlet water temperature of the tube-in-tube condenser were measured by Pt100, the circulating water flow rate was measured by a magnetic flowmeter, and the pressure and the temperature of the heat pump system were measured by the pressure sensor and T-type thermocouple respectively. The uncertainties of the instruments are listed in Table 3.



1—Compressor，2—Four-way valve，3—Evaporator，4、6—Electronic expansion valve，5—Flash tank，7—Tube-in-tube condenser，8—Water pump，9—Water tank，10—Magnetic flow meter

Fig. 1. The one-time heating R32 HPWH experimental system

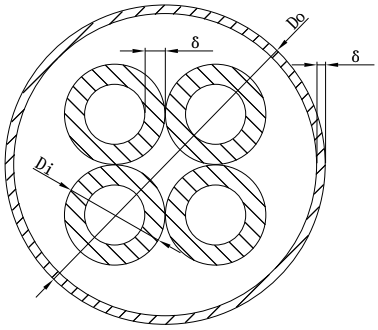


Fig. 2. The cross-sectional view of the tube-in-tube condenser

Table 1. Information of one-time heating R32 HPWH

Compressor	Two-stage compressor with a displacement of 12cm^3/rev
Condenser	Tube-in-tube, Do=12.7mm, δo=0.34mm, Di=4mm, δi=0.8mm
Evaporator	Fin-and-tube heat exchanger with the tube diameter of 7mm
Electronic expansion valve	DPF(T01)1.6 with a diameter of 1.6mm
Flash tank	Self made
Refrigerant	R32
Water tank	200L
Water pump	LX-0.36/10-A with a rated flow of 0.36m^3/h and a rated input power of 10W

Table 2. Test conditions

Conditions	Outdoor Chamber	Indoor Chamber	Inlet Water Temperature (IWT)	Outlet Water Temperature (OWT)
	℃	℃	℃	℃
Condition 1	20	20	15~39	45~65
Condition 2	7	20	9~39	45~65
Condition 3	-20	20	9~39	45~65

Table 3. Uncertainties of instruments

Instruments	Range	Uncertainty
Pt100	0~60℃	±0.1℃
Flowmeter	0~30L/min	±0.35%
Pressure sensor	0~5MPa	±0.5%
T-type thermocouple	-50~150℃	±0.5℃

2.2. Data analysis

The heating capacity and the heating COP are calculated based on the parameters of the water, the equations are as follows.

$$Q_w = \rho_w V_w C_{P,w}\left(T_{w,out} - T_{w,in}\right) \quad (1)$$

$$COP = Q_w / W_{input} \quad (2)$$

Where, Q_w is the heating capacity, ρ_w is the density of water, V_w is the water volume flow rate, $C_{P,w}$ is the specific heat of water, $T_{w,in}$ is the inlet water temperature of tube-in-tube condenser, $T_{w,out}$ is the outlet water temperature of tube-in-tube condenser, W_{input} is the input power(including the power of the heat pump system and the power of water pump).

3. Result and discussion

3.1. Characteristics under different conditions

Fig.3 shows the curves that the COP changes with the heating capacity. Under different conditions, the heating capacity has little effect on the COP. Analyses are as follows. The increase of the heating capacity is achieved by increasing the rotary speed of the compressor. As the increase of the rotary speed of the compressor, the refrigerant mass flow rate increases, the heat exchange capacity of the evaporator and the condenser increase. The heat transfer of the refrigerant in both evaporator and condenser enhance due to the increase of the refrigerant mass flow rate increases. The heat exchange temperature difference in both evaporator and condenser increase due to the increase of the heat exchange capacity. Because the inlet water temperature and the outlet water temperature keep constantly, so the condensation temperature increases and the evaporation temperature decreases. But the enhancement of the heat transfer weakens the increase of the condensation temperature. Meanwhile, because the inlet water temperature and the outlet water temperature are fixed, the water flow rate increases with the increase of the heating capacity, which enhances the heat transfer on the water side of the condenser, further suppresses the increase of the condensation temperature. Therefore, the change of the condensation temperature is not obvious. The enhancement of the heat transfer of the refrigerant in the evaporator weakens the decrease of the evaporation temperature, so the change of the evaporation temperature is not obvious. Thus, the change of the pressure ratio is not obvious (Fig.4) and the increase of the specific compression work is not obvious. The change of the temperature and the pressure of the refrigerant at the inlet and the outlet of the condenser are not obvious, so the change of the refrigerant specific enthalpy difference between the inlet and the outlet of the condenser is not obvious. Therefore, the input power of the compressor increases with a definite proportion with the increase of the heating capacity. Because the input power of the water pump is very small in comparison with the compressor, so the change of the COP is not obvious.

Fig.5 and Fig.6 show the curves that the COP changes with inlet water temperature and outlet water temperature. In Fig.5, the COPs decrease with the increase of the inlet water temperature when the outlet water temperature is fixed. Analyses are as follows. The heat exchange temperature difference between the refrigerant and the water of the condenser keeps constantly when the heating capacity is fixed, the average temperature on the water side of the condenser increases with the increase of the inlet water temperature, then the condensation temperature increases (Fig.7), and the COP decreases. In Fig.6, under the same condition, when the inlet water temperature is fixed, the higher the outlet water temperature is, the lower the COP is. For the same reason, the condensation temperature increases (Fig.8) with the increase of the average temperature on the water side of the condenser, then the COP decreases. At the same time, it can be seen that when the outdoor ambient temperature decreases, the influence of the inlet water temperature or the outlet water temperature on the COP becomes smaller.

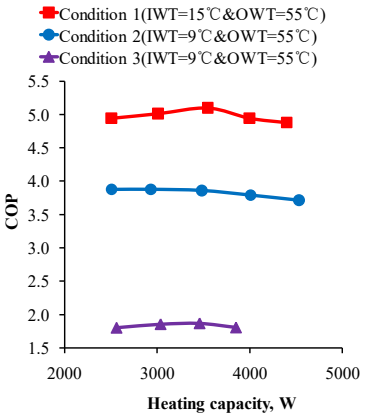


Fig. 3. Curves of the COP with the heating capacity

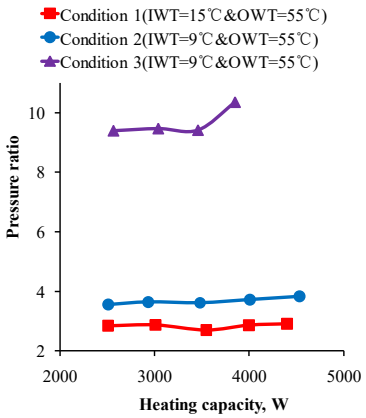


Fig. 4. Curves of the pressure ratio with the heating capacity

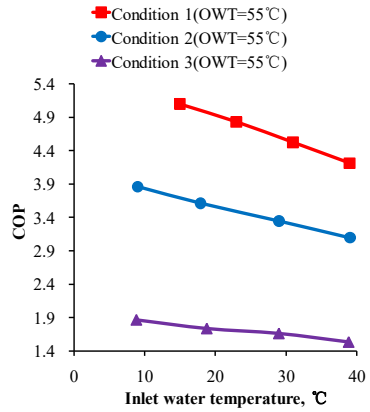


Fig. 5. Curves of the COP with the inlet water temperature

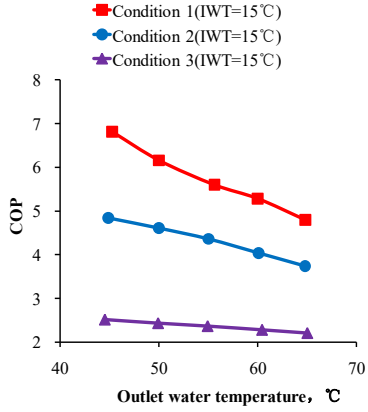


Fig. 6. Curves of the COP with the outlet water temperature

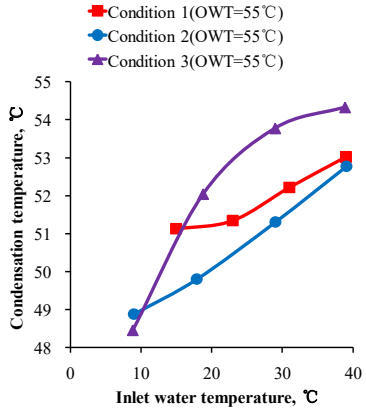


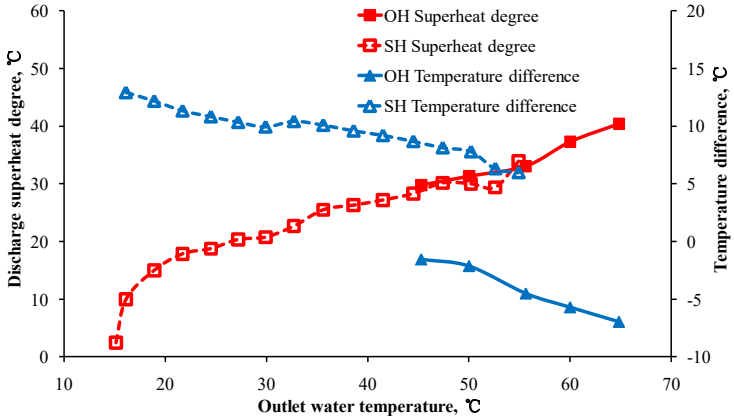
Fig. 7. Curves of the condensation temperature with the water temperature

3.2. Characteristics of system parameters

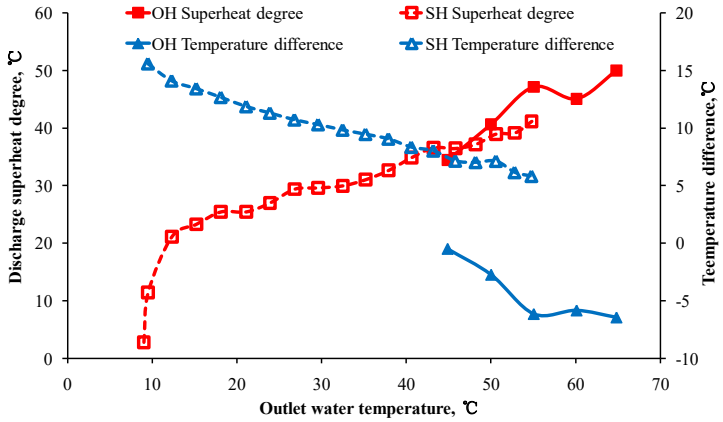
Fig.8 shows the discharge superheat degree (the temperature difference between the discharge temperature and the condensation temperature) and the temperature difference between the condensation temperature and the outlet water temperature changing along with the outlet water temperature under different conditions for the one-time heating(OH in figure) R32 HPWH, and the static heating(SH in figure) R32 HPWH is added for comparison, the discharge temperature curves are shown in Fig.9. For the static heating type, the inlet water temperature means the initial water temperature and the outlet water temperature means the final water temperature. It can be seen as follows.

When the discharge superheat degrees are equivalent, the temperature differences between the condensation temperature and the outlet water temperature of the one-time heating R32 HPWH are always less than the static heating type and also less than zero. This indicates that, the condensation temperature of the one-time heating R32 HPWH is much lower than the static heating type and lower than the outlet water temperature. Taking Fig.8(c) as an example, the condensation temperature of the one-time heating R32 HPWH is 10℃ lower than the static heating type, but the discharge superheat degrees of the two types are comparative, that is, the discharge temperature of the one-time heating R32 HPWH is about 10℃ lower than the static heating type. Analyses are as follows. The tube-in-tube condenser is a counter flow heat exchanger, which is helpful to fully utilize the heat of the superheated refrigerant gas to heat the water, so that the target water temperature can be achieved at a condensation temperature lower than the target water temperature. This is very beneficial to reduce the discharge temperature of R32, broaden the operating temperature range, and also increase the COP.

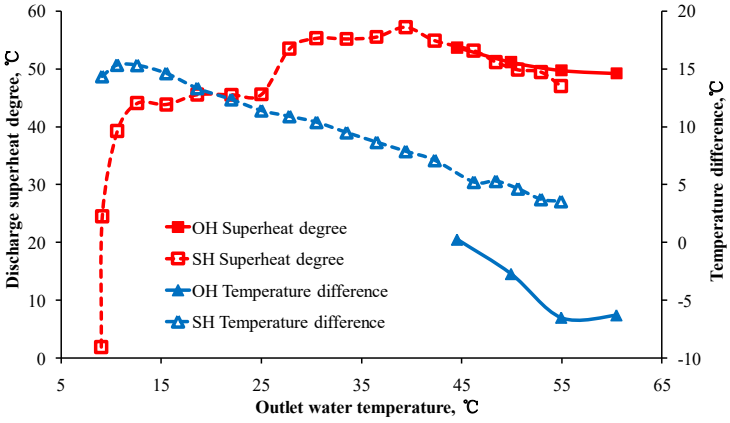
For the one-time heating R32 HPWH under condition 1, as the outlet water temperature increases, the discharge temperature increases, the discharge superheat degree increases and the absolute value of the temperature difference between the condensation temperature and the outlet water temperature increases. This can be explained that, when the outlet water temperature is relatively lower, the condensation temperature is relatively lower, the discharge temperature is relatively lower and the discharge superheat degree is relatively smaller, the heat of the superheated refrigerant gas is not enough to achieve the target water temperature under a relatively lower condensation temperature, so the absolute value of the difference between the condensation temperature and the outlet water temperature is relatively smaller. Along with the increase of the outlet water temperature, the condensation temperature increases, the discharge temperature increases and the discharge superheat degree becomes larger, the heat of the superheated refrigerant gas increases, and so the absolute value of the temperature difference between the condensation temperature and the outlet water temperature increases.



(a) Condition 1 (Inlet water Temperature =15℃)



(b) Condition 2 (Inlet water Temperature = 9℃)



(c) Condition 3 (Inlet water Temperature =9℃)

Fig. 8. Temperature curves of the heating process

For the one-time heating R32 HPWH under condition 3, with the increase of the outlet water temperature, the discharge temperature increases, the discharge superheat degree decreases, and the absolute value of the temperature difference between the condensation temperature and the outlet water temperature increases firstly and then keeps constantly. This can be explained that, the evaporation temperature is very lower and the discharge temperature is very high under low outdoor ambient temperature, when the discharge temperature exceeds the allowable limit value(in this paper, the allowable limit value is 100℃), specific measures must be taken to reduce the discharge temperature, the discharge superheat degree decreases accordingly and the heat of the superheated refrigerant gas decreases. For this reason, no other than to rise the condensation temperature, the target water temperature can be achieved. Thus, the condensation temperature increases with an equivalent value with the increase of the outlet water temperature, and the absolute value of the temperature difference between the condensation temperature and the outlet water temperature keeps constantly.

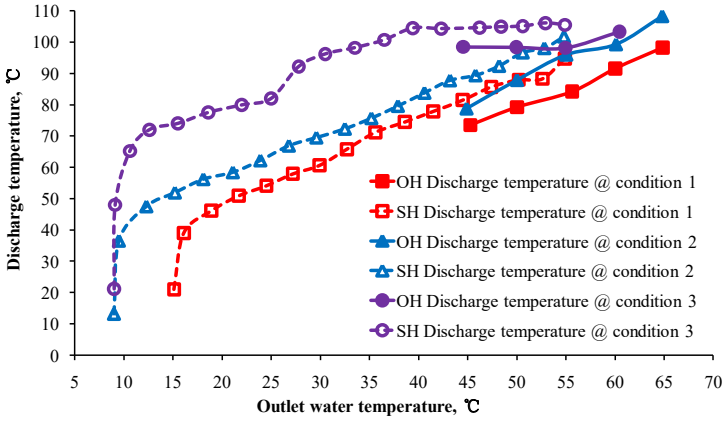


Fig. 9. Curves of the discharge temperature

4. Conclusions

A one-time heating R32 two-stage air source HPWH was experimentally studied under various working conditions, and compared with a static heating type. Conclusions are as follows. For the one-time heating R32 HPWH, the COP is almost unchanged when the inlet water temperature and the outlet water temperature are fixed and the heating capacity increases with the increase of the rotary speed of the compressor; when the heating capacity is fixed, the COP decreases with the increase of the inlet water temperature or the outlet water temperature; when the outlet water temperature is fixed and the discharge superheat degree is comparative, the condensation temperature of the one-time heating R32 HPWH is about 10℃ lower than the static heating type and also lower than the outlet water temperature; under normal temperature conditions, the absolute value of the temperature difference between the condensation temperature and the outlet water temperature increases with the increase of the outlet water temperature; under low temperature conditions, the absolute value of the temperature difference between the condensation temperature and the outlet water temperature increases firstly and then keeps constantly with the increase of the outlet water temperature.

The characteristic of the one-time heating R32 HPWH that the condensation temperature is lower than the outlet water temperature can be fully utilized to reduce the discharge temperature, broaden the operating temperature range and improve the compressor reliability under low ambient temperature and high outlet water temperature.

References

[1] ANSI/ASHRAE Standard 34-2013, Designation and safety classification of refrigerants.
[2] Zhu M S, Shi L. Exploration of using R32 to substitute for R22 in household/commercial air-conditioning. Refrigeration and Air-conditioning (in Chinese) 2009; **9(6)**: 31-34
[3] Shi L, Zhu M S. Re-analysis on using R32 to substitute for R22 in household/commercial air-conditioning. Journal of Refrigeration (in Chinese) 2010; **31(1)**:1-5
[4] Tu X P, Liang X F, Zhuang R., 2011.Study of R32 refrigerant for residential air-conditioning applications, The 23th IIR International Congress of Refrigeration, Beijing, China, paper #259.
[5] Mei K, Li M, Liang L J. Comparative research on the cycle performance of R32 & R410A. Refrigeration and Air-conditioning (in Chinese) 2011; **11(2)**:56-59
[6] Huang Y Y, Wang J, Yin Q, et al. Experimental study of R32 air source heat pump water heater. Refrigeration and Air-conditioning (in Chinese) 2011; **11(2)**: 69~72
[7] Yajima R, Yoshimi A, Piao C C. Measures to reduce the discharge temperature of R32 compressor. Refrigeration and Air-conditioning (in Chinese) 2011; **11(2)**:60-64.
[8] Wang T, Wang F, Chen H Q, et al. Feasibility of R32 Using in enhanced Vapor Injection Heat Pump Water Heater. Building Energy Efficiency (in Chinese) 2017; **45(1)**:139~144
[9] Zheng B, Liang X F, Wu Y W, et al. Study on the influence of wet compression on R32 system performance. Refrigeration and Air-conditioning (in Chinese) 2014; **14(2)**:45-49
[10]GB/T 23137-2008, Heat pump water heater for household and similar application.

[11] GB/T 21362-2008, Heat pump water heater for commercial & industrial and similar application.

13th IEA Heat Pump Conference
April 26-29, 2021 Jeju, Korea

Optimization of Phase Change Thermal Energy Storage Unit Based on a New Thermal Resistance Model

Lingkun Liu[a], Xiangfei Liang[a,b,*]

[a]Refrigeration Institute of Gree Electric Appliances, Inc.of Zhuhai, Zhuhai 519070, China
[b]National Engineering Research Center of Green Refrigeration Equipment, Zhuhai 519070, China

Abstract

Considering the lack of the heat transfer behavior calculation methods of the phase change thermal energy storage (PCTES) unit, a new comprehensive model based on the effective thermal resistance coupled with heat transfer temperature difference is established and validated by CFD results. The effects of relative physical properties of the phase change material (PCM) and all the configuration parameters of the PCTES unit have been implemented into the model. It is proved that the average heat transfer rate and time duration for the PCM to be fully melt/solidified can be well predicted. To achieve better heat transfer behavior and larger heat storage density with acceptable cost, the optimization of fin-and-tube PCTES unit is established. Based on the average heat transfer rate per unit cost, the recommended structural parameters and PCM properties for PCTES unit are given.

© HPC2020.
Selection and/or peer-review under responsibility of the organizers of the 13th IEA Heat Pump Conference 2020.

Keywords: Phase change material; Thermal energy storage; Thermal resistance model; Parameters optimization

NOMENCLATURE

c_p	Specific heat ($Jkg^{-1}K^{-1}$)	**Greek symbols**	
F_p	Fin pitch (m)	δ	Thickness (m)
h	Heat transfer coefficient ($Wm^{-2}K^{-1}$)	γ	Phase change fraction
L	Tube length (m)	λ	Thermal conductivity ($Wm^{-1}K^{-1}$)
M	Mass (kg)	μ	Dynamic viscosity (Pas)
P	Heat transfer rate (W)	ρ	Density (kgm^{-3})
P_t	Transversal tube pitch (m)		
P_l	Longitudinal tube pitch (m)	**Subscripts**	
Q	Heat (J)	ave	Average value
r	Radius (m)	fluid	Heat transfer fluid inside tube
r_e	Characteristic radius (m)	mush	Mushy zone
R	Thermal resistance (KW^{-1})	in	Tube inner wall
t	Time-consuming of phase change (s)	out	Tube outer wall
T	Temperature (K)	out2	Fin collar outer wall
y	Coordinate in gravity direction (m)	pci	Phase change interface
m,n,l	Empirical constant in the model	PCM	Phase change material

1. Introduction

As a new thermal energy storage medium, phase change material (PCM) has been widely used in energy peak-to-valley transfer, building energy conservation, industrial waste heat recovery, electronic device heat dissipation, etc [1]. Phase change materials are generally classified into low temperature phase change

* Corresponding author. Tel.: +86-756-8589554; fax: +86-756-8668982.
E-mail address: liangxf@cn.gree.com.

materials (less than 80℃), medium temperature phase change materials (80-200℃) and high temperature phase change materials (above 200℃). Medium and low temperature PCMs have been widely used in various thermal energy storage systems [2]. In applications, the thermal performance of thermal energy storage systems is limited by the low thermal conductivity, subcooling and phase separation of PCMs. Fan and Khodadadi [3] summarized the experimental and theoretical approaches of enhancing the thermal conductivity of PCM in past studies. Safari et al. [4] summarized the effects of subcooling on the thermal performance of phase-change energy storage systems, analyzed various methods to improve or control the degree of subcooling, and conducted a method for optimizing the phase-change energy storage system with subcooling. Gunasekara et al. [5] analyzed the phase change properties of PCMs from the perspective of phase diagram based on phase equilibrium theory, and summarized the causes of instability of phase change systems and methods to solve them. In addition to directly improving the performance of the PCM, the optimization of the thermal energy storage device, such as the addition of fins and the improvement of its structure, has also become a research aspect [6]. Chang et al. [7] studied the variation of the heat transfer coefficient outside the small-diameter light tube with different structural arrangements.

For the theoretical and numerical study of the phase change process of PCMs, Neumann [8] obtained the analytical solution of the semi-infinite large plane case by the mathematical method. Subsequent studies have been applied to more complex situations. With the development of numerical methods, various physical models have emerged to replace mathematical analytical solutions, which can be applied to any complex geometric conditions. Voller [9] proposed a melting/solidification model based on a fixed grid method. The energy equation is expressed by enthalpy, and a mushy zone constant is used to solve the momentum transfer near the phase change interface. Further, Chen et al. [10] studied the effect of this mushy zone constant on melting/solidification characteristics and overall heat transfer performance. Meanwhile, various simplified phase-change thermal models have also been applied by various building energy analysis software [11].

When studying a specific type of TES device filled with PCM, the thermal resistance model based on the heat flow is also proposed and improved due to its simplicity and good reliability. Tay et al. [12] proposed a thermal resistance model of a flat fin-and-tube PCTES unit, which splits the heat flow into an isothermal heat flow and a parallel heat flow, and correspondingly establishes the corresponding thermal resistance network. An empirical constant P factor is used to calculate the ratio of the two heat fluxes. The model can be used for thermal resistance analysis and evaluate the efficiency of the heat transfer unit using the Effectiveness-NTU method. Similarly for the flat fin-and-tube PCTES unit, Chen et al. [13] proposed a more concise parallel thermal resistance network model, which approximates the total transferred heat to the heat passing through the solid-liquid interface. This method does not require the P factor, and still possesses small deviations.

The effectiveness of the PCTES unit based on the above thermal resistance model is the integral average of thermal resistance with respect to coordinates. However, due to the complexity of the phase change interface migration, the method of calculating the thermal resistance is not very accurate, and whether its effectiveness can accurately reflect its thermal performance is still a problem [14]. Moreover, the model can not calculate the phase change time and heat transfer rate of the specific TES unit under specific working conditions. In this situation, for the common PCTES unit filled with PCM outside the tube, this work proposes a method for establishing the effective thermal resistance based on Chen's phase interface thermal resistance model, and cooperates with a PCM temperature distribution hypothesis.

2. Physical model

2.1. Basic thermal resistance model of fin-and-tube PCTES unit

The schematic diagram of the structure of the fin-and-tube heat exchanger arranged in a regular triangular cross row is shown in Fig.1(a). Considering the heat flow flowing through a heat storage unit, it can be divided into two paths as shown in Fig.1(b). A part of heat flows from the in-tube heat transfer fluid through the tube wall and the flanged fins into the PCM, and the rest flows through the tube wall and the protruding fins into the PCM [13]. The equivalent thermal resistance network is shown in Fig.2. The expressions of the thermal resistance of each part in a PCTES unit are as follows

$$R_{fluid}=\frac{1}{2\pi r_{in}Lh_{fluid}},\quad R_{tube}=\frac{ln(r_{out}/r_{in})}{2\pi L\lambda_{tube}},\quad R_{collar}=\frac{ln(r_{out2}/r_{out})}{2\pi L\lambda_{collar}},\quad R_{fin}=\frac{ln(r_e/r_{out})}{2\pi\delta_{fin}\lambda_{fin}} \tag{1}$$

$$R_{PCM,1} = \frac{(r_{pci} - r_{out2})/(r_e - r_{out2}) \cdot (F_p - \delta_{fin})/2}{\pi(r_e^{\,2} - r_{out2}^{\,2})\lambda_{PCM}} \tag{2}$$

$$R_{PCM,2} = \frac{ln(r_{pci}/r_{out2})}{2\pi(F_p - \delta_{fin})\lambda_{PCM}} \tag{3}$$

$$R_{PCM\&fin} = \left(\frac{1}{R_{fin} + R_{PCM,1}/2} + \frac{1}{R_{PCM,2}} \right)^{-1} \tag{4}$$

$$R_{total} = R_{fluid} + R_{tube} + R_{collar} + R_{PCM\&fin} \tag{5}$$

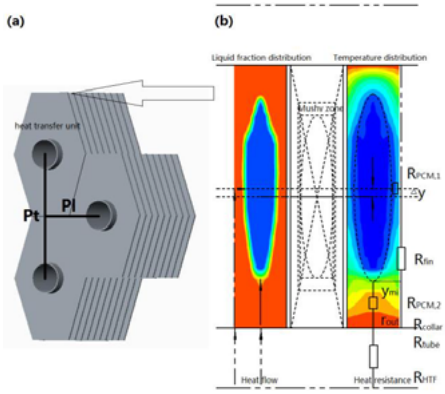


Figure 1 (a) Fin-and-tube heat exchanger structure (b) Fin-parallel cross section between two neighboring tubes of PCTES unit: heat flow paths (left), thermal resistance (right), liquid fraction distribution (left), solid-liquid interface approximation rectangular (middle) and temperature distribution (right)

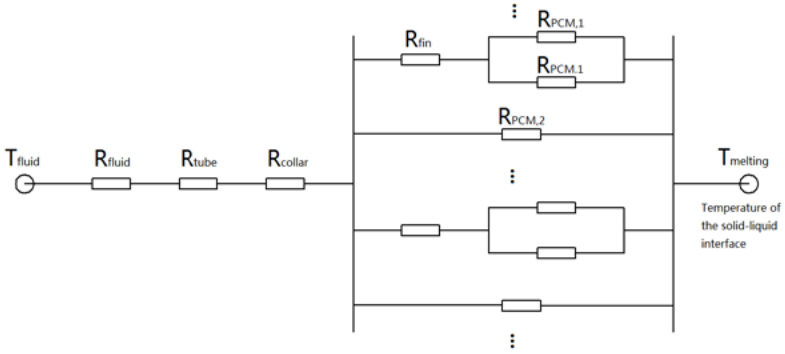


Figure 2 Schematic diagram of the thermal resistance network

In order to calculate the instantaneous heat transfer rate in the whole phase change process, it is also necessary to define the heat transfer temperature difference between the in-tube fluid and the PCM corresponding to the total thermal resistance of the network. The PCM temperature distribution assumption is brought out, where the PCM average temperature in the specific region is used as the PCM side characterization temperature, and the semi-theoretical semi-empirical corrections based on the CFD simulation results are carried out to obtain the outside-tube thermal resistance $R_{PCM\&fin.}$ For the sake of brevity, the following discussion is based on a single PCTES unit, ignoring the finless zone in the TES container.

2.2. Heat transfer temperature difference distribution assumption

The temperature distribution assumptions of the PCM depending on time and space are presented as follows.

(1) As shown in Fig.3(a), the phase change process is artificially divided into two periods noted as p1 and p2, the PCM enthalpy increment in the p1 period includes all sensible heat from the initial temperature to the melting point and partial latent heat. A rough approximation is used for the p1 period: when integrating time, the PCM average temperature and the phase change fraction are assumed to vary linearly with time, and the ratio of their variation rate is set to a constant value.

(2) Fig.1(b) shows the liquid fraction distribution (left side) and temperature distribution (right side) of the intermediate surface between the adjacent fins in the TES unit presented by the CFD simulation result. It is assumed that the temperature distribution law along the tube radial and fin normal direction of the PCM is the same.

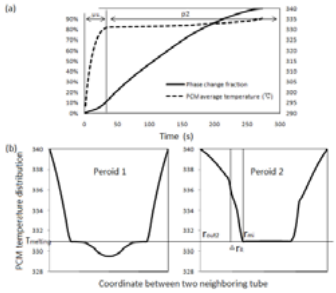


Figure 3 Schematic diagram of the (a) segmentation during a phase change process (b) PCM temperature distribution between neighboring heat transfer unit

(3) As shown in Fig.3(b), it indicates that during the p2 period, the temperature of the non-phase-change region has reached a constant value of $T_{melting}$. And in the already-phase-change region, it suggests that the equivalent PCM thermal resistance layer is thinned due to the temperature of the near-tube region has approached the fluid temperature. The thickness of the effective thermal resistance layer is approximated by an empirical formula:

$$\Delta r_R = m(r_{mi} - r_{out2}) \tag{6}$$

Where r_{mi} is the coordinate of the mushy zone inner interface, r_{out2} is the coordinate of outer wall of the fin flange and m is an empirical constant. In the region of r_{out2} to r_{mi}–Δr_R, the temperature is assumed to be equal to the fluid temperature T_f, and in the region *of* r_{mi}–Δr_R, the temperature distribution is

$$T(r) = (T_f - T_{melting})\frac{r - r_{mi}}{m(r_{out2} - r_{mi})} + T_{melting} \tag{7}$$

From the assumption (2), the average PCM temperature of the region corresponding to the effective thermal resistance is the expression of r_{mi}, denoted as $T_{eff}(r_{mi})$. Record the heat transfer temperature difference as $\Delta T_{eff}(r_{mi}) = T_f - T_{eff}(r_{mi})$, expressed by

$$\Delta T_{eff}(r_{mi}) = \frac{T_{melting} \cdot \pi(r_e^{\,2} - r_{mi}^{\,2}) + \int_{r_{mi}-\Delta r_R}^{r_{mi}} T(r) \cdot 2\pi r dr}{\pi[r_e^{\,2} - (r_{mi} - \Delta r_R)^2]} \tag{8}$$

2.3. Correction of thermal resistance outside the tube

The correction of the outer side thermal resistance from Eq.(4) includes these aspects: mushy zone correction; effective PCM thermal resistance layer correction; effective fin thermal resistance correction; TES unit shape correction; phase interface migration correction.

(1) Mushy zone correction

As shown in Fig.1(b), due to the amorphous nature of the specific PCM, resulting in a thin-layer solid-liquid interface instead of a sharp interface. In a common used solid-liquid phase enthalpy model [9], a mushy zone constant A_{mush} is used to reflect its amorphous nature. To describe this feature, a mushy zone shaped as a thin layer with the linearly distributed liquid fraction is established. The thickness of the mushy zone is described by the following correlation:

$$\Delta r_{mush} = n(r_{mi} - r_{out2}) \tag{9}$$

n is mainly affected by the mushy zone constant (which can be considered as a PCM inherent physical property) and viscosity. The data is fitted to the following relationship by CFD simulation results.

$$n = 0.5\left(A_{mush}^{\,1/3} \cdot \mu\right)^{-0.5} \tag{10}$$

Thus, the expression of the total phase change fraction of the PCM with respect to the interface coordinates r_{mi} in the mushy region can be obtained as $\gamma(r_{mi})$. Note that when the mushy zone advances to the boundary of the TES unit, the expression changes.

(2) Effective PCM thermal resistance layer correction

This correction has been described in Section 2.2. The two local thermal resistances corrected are

$$R_{eff,PCM,1}(r_{mi}) = \frac{\Delta r_R/(r_e - r_{out2}) \cdot (F_p - \delta_{fin})/2}{\pi(r_e^{\,2} - r_{out2}^{\,2})\lambda_{PCM}} \tag{11}$$

$$R_{eff,PCM,2}(r_{mi}) = \frac{ln[r_{mi}/(r_{mi} - \Delta r_R)]}{2\pi(F_p - \delta_{fin})\lambda_{PCM}} \tag{12}$$

(3) Effective fin thermal resistance correction

The fin thermal resistance calculated from Eq.(1) is the annular thermal resistance from the fin base to the fin tip, but the heat flow is through the side face of the fin. Thus the fin thermal resistance needs to be corrected. Assuming that the fin temperature distribution is linearly distributed in the radial direction, find the radial coordinate where the fin temperature is the mass average fin temperature. The annular thermal resistance from the fin base to the calculated coordinate is considered as the effective fin thermal resistance. Simplified expression is

$$R_{fin}=\frac{ln(r_e/r_{out2})}{2\pi\delta_{fin}\lambda_{fin}}\left(\frac{r_e^2}{r_e^2-r_{out2}^2}-\frac{1}{2ln(r_e/r_{out2})}\right) \quad (13)$$

(4) PCTES unit shape correction

As shown in Fig.4, the PCTES unit is divided into hexagons, since there is no analytical expression for the irregular hexagon shape factor, it is convenient to use the approximate ellipse to characterize the shape of PCTES unit. Its long and short axes are of a=2/3P$_l$ (horizontal direction) and b=1/2P$_t$ (gravity direction). It is assumed that the phase interface is from the outer wall of the tube at the beginning of the phase change, and gradually migrates to the end of the ellipse shown in Fig.4.

(5) Phase interface migration correction

As shown in Fig.4, due to the difference between solid and liquid density and natural convection, the low-density phase moves upward and the high-density phase moves downward, causing the overall migration Δy of the phase interface in the direction of gravity, mainly affected by the difference in solid-liquid density and PCM liquid viscosity. Fitting the CFD simulation results into a correlation:

$$\Delta y=(y_{mi}-y_{out2})[1-exp(-l\frac{\Delta\rho}{\mu})] \quad (14)$$

Where $\Delta\rho$ is the PCM density difference between solid and liquid phases in unit of kg/m^3, μ is the PCM liquid dynamic viscosity in unit of kg/m.s and l is an empirical constant.

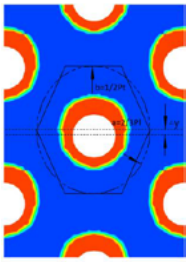


Fig.4 Schematic diagram of PCTES unit shape correction

So far, the total thermal resistance based on the effective PCM thermal resistance layer is obtained with respect to the boundary coordinate r of the mushy zone, and is denoted as $R_{eff,total}(r_{mi})$. The calculation of the instantaneous heat transfer rate can be done with the help of the previously obtained $\Delta T_{eff}(r_{mi})$ and $\gamma(r_{mi})$.

First, the total time of the phase change process is calculated by integration. The total enthalpy change of the PCM in each infinitesimal element period is equal to the total heat it receives:

$$t=\int_{t1|\gamma=\gamma1}^{t2|\gamma=\gamma2}dt=M_{PCM}\int_{\gamma=\gamma1}^{\gamma=\gamma2}\frac{C_p\cdot d\Delta T+LH\cdot d\gamma}{\Delta T_{eff}/R_{eff}}=M_{PCM}\int_{y_{mi2}|\gamma=\gamma1}^{y_{mi1}|\gamma=\gamma2}\frac{C_p\frac{\partial\Delta T}{\partial y_{mi}}+LH\frac{\partial\gamma}{\partial y_{mi}}}{\Delta T_{eff}/R_{eff}}dy_{mi} \quad (15)$$

Where y_{mi1} and y_{mi2} are interface coordinates in the y-direction mushy region corresponding to the phase change fractions γ1 and γ2 based on the expression of $\gamma(r_{mi})$. Similarly, the PCM average temperatures T1 and T2 corresponding to the phase change fractions γ1 and γ2 can be calculated from $T(r_{mi})$. Then the total transferred heat and average heat transfer rate of the considered process are

$$Q_{total}=M_{PCM}[C_p(T2-T1)+LH(\gamma2-\gamma1)] \quad (16)$$

$$P_{ave} = Q_{total} / t \tag{17}$$

Similarly, the time average of the effective heat transfer temperature difference and the effective thermal resistance can be integrated.

$$R_{eff,ave} = \int_{t1|\gamma=\gamma1}^{t2|\gamma=\gamma2} R_{eff}(y_{mi})dt \Big/ t \tag{18}$$

$$\Delta T_{eff,ave} = \int_{t1|\gamma=\gamma1}^{t2|\gamma=\gamma2} \Delta T_{eff}(y_{mi})dt \Big/ t \tag{19}$$

2.4. Model Validation

The CFD simulation on the fin-and-tube PCTES unit is as shown in Fig.6, the calculation domain includes the solid fin region and the solid-liquid PCM phase change region. The two regions are thermally coupled to each other, the upper and lower boundaries are periodic, and the left and right boundaries are symmetrical. Melting/solidification model is adopted and UDFs are used to set the changeable physical parameters. A series of non-steady-state phase change processes are simulated to fit the required empirical coefficients and relationships in this paper. After that, simulation results under arbitrary parameters and working conditions are used for the validation. The deviation between the CFD simulation and the model is shown in Table 1.

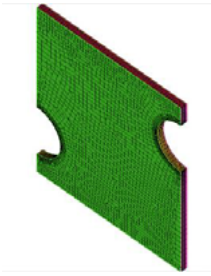


Fig.5 Mesh grid diagram of PCTES unit for CFD simulation

Table 1. Deviation between calculation model and CFD simulation results

		φ7 tube		φ6 tube	
		$\Delta T_{heating}$= 9K	$\Delta T_{heating}$= 6K	SAT	Paraffin
Phase change completed time-consuming (s)	CFD results	191	273	100	52.7
	Model results	198.42	279.53	100.21	51.20
	Deviation	3.88%	2.39%	0.21%	-2.85%
Average heat transfer rate (W/m^3)	CFD results	2.474E+06	1.700E+06	4.619E+06	3.662E+06
	Model results	2.468E+06	1.724E+06	4.781E+06	3.752E+06
	Deviation	-0.24%	1.41%	3.51%	2.46%

It can be seen that the model can accurately predict the heat transfer performance for different heat transfer conditions with variable structure parameters and PCM types. The deviation of the average heat transfer rate between the model results and CFD results is below 4%. It can be considered that the performance of the fin-and-tube PCTES calculated by this model is with enough accuracy and versatility.

3. PCTES unit structure parameters optimization

The thermal performances of the PCTES unit for the fin-and-tube under a constant wall temperature boundary condition are investigated. The focused performances are as follows: the PCTES unit cost C (RMB/m^3), the latent heat storage density (MJ/m^3) of the TES unit, and the average heat transfer rate P_{ave} (W/m^3) during the whole phase change process.

The latent heat storage density = PCM density × PCM volume fraction in the PCTES unit × PCM melting enthalpy

The PCTES unit cost = Tube cost + Fin cost + PCM cost

The average heat transfer rate = Total amount of transferred heat / Time-consuming during the whole phase change process

The latter two are combined to form a new performance that reflects the unit cost performance of the TES unit: heat transfer rate per unit cost = P_{ave}/C (W/RMB).

Table 2 shows the fixed parameters, the reference structure parameters and heat transfer conditions for the discussed fin-and-tube PCTES unit.

Table 2. Parameters set for the fin-and-tube PCTES unit calculation

Copper tube specifications	φ7(54g/m)	φ5(34.2g/m)	φ4(24.6g/m)
Reference structure parameters (mm)	Pt=22, Pl=19.05	Pt=19.05, Pl=16.5	Pt=14.7, Pl=13.8
	Fp=1.7, δ_{fin}=0.105	Fp=1.4, δ_{fin}=0.105	Fp=1.3, δ_{fin}=0.105
Working conditions	PCM initial temperature 15℃, $\Delta T_{heating}$= 9℃		
Material price (RMB/kg)	Copper (tube material): 50; Aluminum (fin material): 16;		
	PCM: Sodium acetate trihydrate (SAT): 5; Paraffin: 4；		

For the fin-and-tube, the change of structural parameters has much greater influence on the heat transfer rate than the energy storage density. Therefore, the influence on heat storage density is ignored. The heat transfer rate per unit cost under various structural parameters of different tube diameters is shown in Fig.6-8. The x, y, and z axes respectively represent the change of the transversal tube pitch, the longitudinal tube pitch, and the fin pitch of the PCTES unit structure, the pentagonal point is a commonly used structure. Each colored surface represents structural parameter combinations that possess the equal heat transfer rate per unit cost. The right side box compares the heat transfer rate per unit cost when the two PCMs are used under the reference structure at pentagonal point.

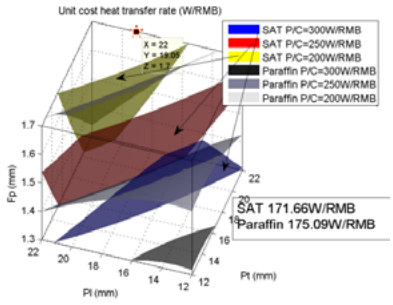


Figure 6 φ7 fin-and-tube PCTES unit cost performance with structural parameters

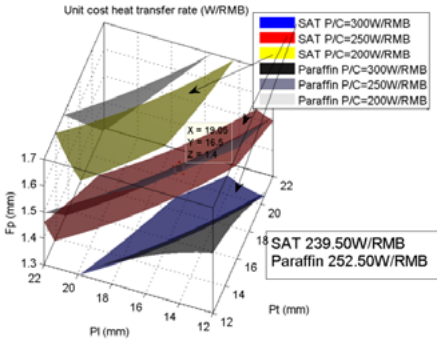


Figure 7 φ5 fin-and-tube PCTES unit cost performance with structural parameters

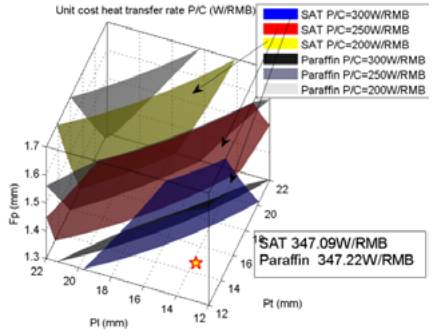


Figure 8 φ4 fin-and-tube PCTES unit cost performance with structural parameters

It can be seen that, the smaller the tube pitch and the fin pitch, the higher the heat transfer rate per unit cost. The influence of the transversal and longitudinal tube pitch is similar, and simultaneously reducing the transversal and longitudinal tube pitch is better than reducing only one of them. In the case of a large tube pitch, the fin pitch variation within the range of the figure has little effect on the heat transfer rate per unit cost, which is due to the effective fin thermal resistance expression of the annular fin thermal resistance in the equation (13). As the heat transfer unit characteristic radius re increases, it increases sharply and will dominate the thermal resistance outside the tube.

It can be seen that for paraffin and SAT used as PCM, the heat transfer rate per unit cost is very close to each other under the PCTES structure at pentagonal point. The decline in performance due to the low thermal conductivity and high viscosity of paraffin is compensated by its low mushy zone constant and low cost. But it should be noted that in terms of heat storage density, SAT is about (264*1300)/(168*830)=2.46 times of paraffin. Generally, the higher the thermal conductivity of PCM, the lower the viscosity, the stronger the amorphous and the larger the ratio of latent-sensible heat, the better the average heat transfer rate of the PCTES unit.

It can also be seen from the figure that the dependency of heat transfer rate per unit cost on the fin pitch is more obvious for paraffin than SAT. When the fin pitch is greater than 1.5 mm, the P/C=300 surface shrinks sharply inward, that is, with the increase in film distance, the heat transfer rate per unit cost drops dramatically. It can be explained that when the PCM thermal conductivity is low, and the $R_{PCM,1}$ and $R_{PCM,2}$ in the outside-tube thermal resistance of Eq.(4) occupy a larger proportion. After the fin pitch increases to a certain extent, the outside-tube thermal resistance increases sharply, causing the overall performance deteriorates drastically.

When the PCM is SAT, the heat transfer rate per unit cost of the φ7, φ5 and φ4 fin-and-tube PCTES units is 172W/RMB, 239W/RMB and 330W/RMB, respectively. It indicates that the unit cost performance will increase with the decrease of the tube diameter. And there is a similar increase when the PCM is paraffin.

Therefore, in the currently used size range of fin-and-tube heat exchangers, when used as a PCTES container, smaller diameter should be selected.

4. Conclusion

A physical model based on the thermal resistance network that can be used for the non-steady state heat transfer calculation of the PCTES unit is established. The model can predict average heat transfer rate under different structural parameters, heat transfer conditions and PCM types with high accuracy. The following conclusions can be summarized:

(1) The model extends the conventional thermal resistance analysis methods of PCTES unit, making the model available for the calculation of actual heat transfer rate. Further, it has small deviation from CFD simulation results and high computational efficiency, and can be used for multi-dimensional multi-objective optimization of PCTES unit.

(2) In the structural parameters range of fin-and-tube PCTES unit currently used, the smaller the tube pitch and the fin pitch, the higher the heat transfer rate per unit cost. The heat transfer rate per unit cost of φ4, φ5 and φ7 fin-and-tube PCTES unit is 172W/RMB, 239W/RMB and 330W/RMB, respectively. Therefore, for the 4-10 mm tube diameter range of fin-and-tube heat exchangers, when used as a PCTES container, structure parameters with smaller diameter should be selected.

(3) In the case of a large tube pitch, the fin pitch variation within the range of 1.3-1.7mm has little effect on the heat transfer rate per unit cost. And its dependency on the fin pitch is more sensitive for the PCM with low thermal conductivity than that with high thermal conductivity. For paraffin and SAT used as PCM, the heat transfer rate per unit cost is coincidentally very close to each other under several commonly used PCTES structure.

References

[1] Tao YB, He YL. A review of phase change material and performance enhancement method for latent heat storage system. Renewable and Sustainable Energy Reviews 2018;93:245–259.
[2] Sharma A, Tyagi VV, Chen CR, Buddhi D. Review on thermal energy storage with hase change materials and applications. Renewable and Sustainable Energy Reviews 2009;13:318–45.
[3] Fan L, Khodadadi JM. Thermal conductivity enhancement of phase change materials for thermal energy storage: a review. Renewable and Sustainable Energy Reviews 2011;15:24–46.
[4] Safari A, Saidur R, Sulaiman FA, Xua Y, Dong J. A review on subcooling of Phase Change Materials in thermal energy storage systems. Renewable and Sustainable Energy Reviews 2017;70:905–919.
[5] Saman Nimali Gunasekara, Viktoria Martin, Justin Ningwei Chiu. Phase equilibrium in the design of phase change materials for thermal energy storage: State-of-the-art. Renewable and Sustainable Energy Reviews 2017;73:558–581.
[6] Merlin K, Delaunay D, Soto J, Traonvouez L. Heat transfer enhancement in latent heat thermal storage systems: Comparative study of different solutions and thermal contact investigation between the exchanger and the PCM. Applied Energy 2016;166:107–116.
[7] Chang NC, Li CJ, Wang CC. Performance of bare-tube bundle having small diameter tube: with and without partial bypass. International Communications in Heat and Mass Transfer 2015;67:73–80.
[8] Weker P, Mineur JM. A performance index for thermostatic radiator valves. Applied Energy 1980;6:203–215.
[9] Voller VR. A fixed grid numerical modeling methodology for convection-diffusion mushy region phase-change problems. International Journal of heat Mass Transfer 1987;30(8):1709–1719.
[10] Chen YL, Peng CH, Guo Y. Experimental and numerical study on melting process of paraffin in a vertical annular cylinder. Thermal Science 2019;23(2A):525–535.
[11] Sole CA. An overview on design methodologies for liquid-solid PCM storage systems. Renewable and Sustainable Energy Reviews 2015;52:289–307.
[12] Tay NHS, Belusko M, Castell A, Cabeza LF, Bruno F. An effectiveness-NTU technique for characterising a fin-and-tubes PCM. Applied Energy 2014;131:377–385.
[13] Chen H, Liang XF, Wu YW. Thermal resistance analysis for fin-and-tube phase change thermal energy storage unit. Proceedings of the 25th IIR International Congress of Refrigeration; ID:1440.
[14] Groulx D. The rate problem in solid-liquid phase change heat transfer: efforts and questions toward heat exchanger design rules. Proceedings of the 16th International Heat Transfer Conference 2018;IHTC–16:KN23.

13th IEA Heat Pump Conference
April 26-29, 2021 Jeju, Korea

Study on the smart operation approach of an air conditioner when occupants go out

Myung Sup YOON[a,*], Won Sik YOON[a]

[a]Energy Technology Center, Korea Testing Laboratory, 87 Digital-ro 26-gil, Guro-gu, Seoul, 08389, Republic of Korea

Abstract

This study demonstrates how to use an inverter air conditioner more effectively when a room is not occupied for a relatively short period of time (2 ~ 3 hours). We directly employed environmental changes (outdoor temperature, indoor building load) during daytime in a qualified test room with specific dimensions. The energy consumption of three behavioral cases was compared under several experimental simulation conditions. The first case involved turning on the air conditioner steadily using the same setting temperature without touching even if no occupants. The second involved turning off the air conditioner while occupants were out and restoring the set temperature rapidly after their return. The third case involved an artificial set temperature adjustment while occupants were out. Using several climate and building load data of Korea and the Middle East, the three air conditioner operation approaches were analyzed while occupants were out. Results showed that the first and third operating cases were energy saving depending on the environmental conditions. These results can be used for the design of smart air conditioners or policy guides for nationwide energy saving.

Keywords: Inverter air conditioner; Smart operation; Going out time operation; Energy saving; Smart home appliances

1. Introduction

According to IEA data [1], the number of air conditioners per population in homes is close to 90% in Japan, the United States, and Korea. Unexpectedly, however, the air conditioner penetration rate is presently low in many hot parts of the world (Saudi Arabia (~ 60%), China (~ 60%), Brazil (~ 15%), Mexico (~ 15%), Indonesia (~ 10%), South Africa (~ 10%), and India (~ 5%)). Therefore, this report predicts that energy consumption for space cooling will increase to nearly 40% by 2050 if no action is taken, due to the increase of air conditioners in the above developing countries.

In order to reduce the use of electricity caused by the increase of air conditioners, it is important for manufacturers to develop high-efficiency air conditioner products and for consumers to operate them efficiently. For some time, a lot of research has been undertaken to increase the efficiency of air conditioners. In particular, the efficiency of each component (e.g., compressor, heat exchanger, fan, valve, etc.) constituting an air conditioner can be improved to increase the efficiency of the final product [2,3]. Over the past 20 years, inverter compressors and vapor injection technology have been used to improve product efficiency [3,4]. In the future, technologies such as high-efficiency refrigerants, multi-stage cycles, and human recognition sensors are expected to be used widely [5–7].

Consumers are also required to take action to save air conditioner energy, such as by purchasing high-efficiency products referring to energy labels, refraining from open-door cooling, and maintaining proper room temperature. One of the important questions related to the third area is how to operate an air conditioner while occupants are out. Is it good to turn off an air conditioner when occupants go out? If the going out time is long enough, such as one day, cooling supply energy is not necessary, but if the going out time is short, as in a few

* Corresponding author. Tel.: +82-2-860-1555 ; Fax: +82-2-860-1559
E-mail address: msyun95@ktl.re.kr

hours, we need to worry about what to do with the air conditioner. This was not a problem in the past when air conditioner control technology was not very sophisticated and the thermal insulation of a typical home was poor. However, if it is possible to precisely control the part-load of the cooling capacity of an air conditioner and offer good insulation conditions such as in a zero-energy building, careful research on the approach to air conditioner operation is necessary. When operating an inverter compressor, in order to save energy by the efficient low-speed driven compressor, it may be better to set the temperature slightly higher than the ordinary set temperature while an occupant is out, rather than turning it off when going out and turning it on again rapidly after returning home. In particular, if IoT or AI technology is further developed, it will be driven automatically by using real-time weather status, weather forecast, and occupant status information without worrying about energy saving.

With this in mind, the present study experimented with various operation conditions to discover the energy saving effect of an inverter air conditioner according to the operation approach of an air conditioner during occupants' absence.

2. Experimental Approach

2.1. Preliminary work

It is well known that inverter air conditioners have a higher operating efficiency than constant speed air conditioners. However, even if an air conditioner uses inverter compressor technology, an efficiency difference between inverter products may occur due to the performance difference in an inverter compressor and control technology depending on the manufacturer and model of the product. Figure 1 shows the operation of three different inverter air conditioner models when the remote controller's set temperature is maintained at 26°C. Under the same time-dependent outdoor temperature and indoor building load condition during the day, the change in room temperature and power input shows different patterns.

If it is an ideally designed product, the room temperature should remain constant at a set temperature of 26°C, and the instantaneous power input should have a smooth, cubic function curve with a peak at 16:00 and a minimum at 06:00, following the same building load or outdoor temperature variation patterns. The exact design specifications and technology of the products are unknown, but Fig. 1 shows the desirable control pattern toward the right in the order of (a), (b), and (c). In the case of (a), the power input and room temperature vary largely in all regions of the graph. In (b), there are large deviations of power input and room temperature under large building load and high outdoor temperature (12:00 – 14:00) regions. A near ideal product case is (c), which has a small variation in room temperature and the smoothest change in power consumption among the three cases.

Although it is difficult to state directly what the quantitative energy saving effects between the products are because of the different product specifications (such as the rated capacity and rated power consumption of the three products), it can be reckoned that case (c) is the most energy efficient case judging by the simple insight. Therefore, the product corresponding to Fig. 1(c), which allows precise control, was selected and experimented with throughout this paper. Details of the specifications are in Table 1.

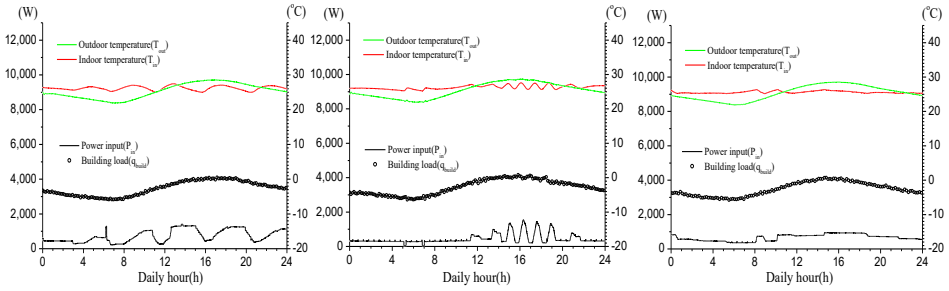


Fig. 1. Improvements in the control aspects of an inverter air conditioner ((b) is reproduced from Yoon et al [8,9])

Table 1 Specifications of the tested inverter product

Contents	Specification
Electricity	220 V, 60 Hz
Rated cooling capacity	7 000 W
Rated power input	2 010 W
Middle cooling capacity	4 700 W
Middle power input	1 250 W
Minimum cooling capacity	1 600 W
Minimum power input	330 W
Refrigerant	R410a
Product type	Floor stand split type

2.2. Problem set up

In this study, three behavior cases of air conditioner operation while occupants were out were experimentally set up, as shown in Fig. 2. In the first case, the air conditioner was operated without being turned off regardless of occupants' going out for a few hours. In the second case, the air conditioner was turned off when occupants went out and was turned back on to the target temperature immediately after returning home. In the third case, the air conditioner's compressor ran at low speed at a slightly higher set temperature and was activated again to reach the target temperature just before occupants returned.

If we go out for a day or for a few days, turning off air conditioners in uninhabited spaces is a good thing. However, if we need to go out for a short time (a few hours), we should consider whether to turn on (case 1) an air conditioner or not (case 2). And if an air conditioner can automatically adjust the temperature, it is also possible to raise the set temperature slightly while occupants are absent and return the temperature before they come back (case 3). These three behavioral cases were experimented with under the various climate environments of Table 2.

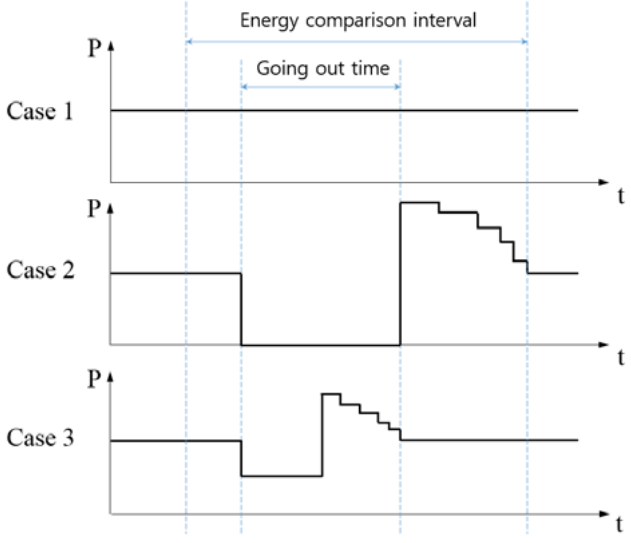


Fig. 2. Energy consumption comparison concept

Table 2 Comparison environments

	Climate condition	Behavioral case	Going out time	Total test time	Energy comparison interval	Remarks (Case 3 artificial T_{set} operation)
Env. 1	Middle East (October)	Case 1	12:00 ~ 14:30	10:00 ~ 23:00	12:00 ~ 22:00	~ 12:00 (T_{set} = 26°C)
		Case 2				12:00 ~ 14:00 (T_{set} =27°C)
		Case 3				14:00 ~ (T_{set} =26°C)
Env. 2	Seoul (August)	Case 1	12:00 ~ 15:30	Same as above	Same as above	~ 12:00 (T_{set} = 26°C)
		Case 2				12:00 ~ 14:30 (T_{set} =28°C)
		Case 3				14:30 ~ (T_{set} =26°C)
Env. 3	Seoul (August)	Case 1	12:00 ~ 15:30	Same as above	Same as above	~ 12:00 (T_{set} = 26°C)
		Case 2				12:00 ~ 15:00 (T_{set} =27°C)
		Case 3				15:00 ~ (T_{set} =26°C)
Env. 4	Middle East (April)	Case 1	12:00 ~ 15:30	Same as above	Same as above	~ 12:00 (T_{set} = 26°C)
		Case 2				12:00 ~ 15:00 (T_{set} =27°C)
		Case 3				15:00 ~ (T_{set} =26°C)
Env. 5	Middle East (October)	Case 1	14:00 ~ 16:30	Same as above	Same as above	~ 14:00 (T_{set} = 26°C)
		Case 2				14:00 ~ 16:00 (T_{set} =27°C)
		Case 3				16:00 ~ (T_{set} =26°C)

The going out time started at midday, except for Environment 5 (14:00), and the duration of the going out time was set to 2.5 (Env. 1 and 5) or 3.5 hours (Env. 2 ~ 4). Three climate conditions were used for the outdoor temperature and indoor building load, as in Fig. 3. The total test time during the day was 13 hours from 10 to 23 h, but the power consumption from 12 to 22 h was calculated to compare at the same room temperature conditions (26°C) of the start and the end between cases 1, 2, and 3 (energy comparison interval of Fig. 2).

Inverter air conditioner compressors improve efficiency at minimum operation [4], so it is important to identify what the effect is of increasing the remote control set temperature slightly during a short period of non-occupancy, as long as it has the 26°C room temperature again at the moment of occupants' return. Throughout the test environments of case 3, T_{set} was raised to 27 or 28°C during the going out period, and the T_{set} was adjusted again to 26°C a few minutes before occupants returned home (remarks of Table 3).

TRNSYS simulation was used to generate the test environments of the outdoor side temperature ($T_{out}(t)$) and indoor side building load ($q_{build}(t)$). The same methodology was used as previous studies [8,9]. In previous studies, the building load ($q_{build}(t)$) was determined under the condition that the interior room temperature was constant at 26°C. Although this hypothesis does not exactly fit behaviors 2 and 3 in this study, behavior 3 would not have a significant effect because the difference between the indoor target temperature and the instantaneous temperature is within 2°C.

Table 3 TRNSYS simulation conditions in Seoul and the Middle East [8,9]

Input variable	Seoul	Middle East
Space size (single zone)	10m × 8m × 2.5m	10m × 8m × 2.5m
Window	60% of the southern wall area – 15m^2	30% of the southern wall area – 7.5m^2
Floor of space	Located between floors – up and down insulations	Located between floors – up and down insulations
Glass	1.20 W/m^{2}K	1.720 W/m^{2}K
Wall	0.21 W/m^{2}K	0.345 W/m^{2}K
Room temperature & humidity	26°C & 60 %R.H.	26°C & 60 %R.H.
Heating & light element	25 W/m^2	25 W/m^2
Persons	4	4
Infiltration	0.4 (1/h)	0.4 (1/h)
Ventilation	0.6 (1/h)	0.6 (1/h)

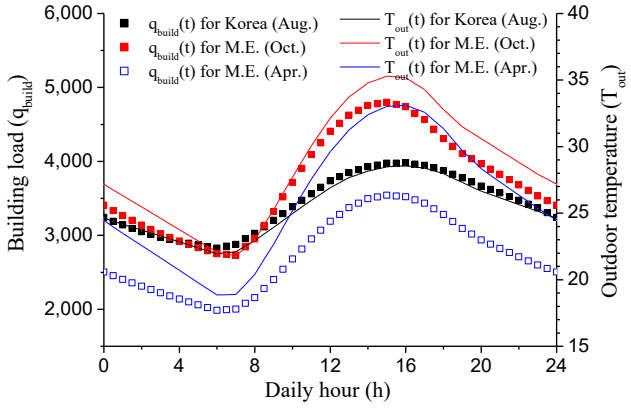


Fig. 3. Simulated building load and outdoor temperature

3. Results and Discussions

3.1. Environment 1 results

This is the climate case of October in the Middle East. For case 3, T_{set} was adjusted to 26 → 27 → 26 °C, as in the remarks of Table 2. For case 1 in Fig. 4, even if T_{set} is kept at 26°C, the power consumption of case 1 shows a parabolic shape from 12 h to 22 h with a maximum value at the vicinity of 16 h. This power input variation is due to the variations of the T_{out}(t) and q_{build}(t) during the day. In general, the instantaneous power input of the air conditioner is proportional to the compressor operation rate according to the outdoor side temperature and the internal building load (Figs. 1(c) and 4(a)). In case 2, the power input is zero during the going out time because the air conditioner is turned off, and the indoor temperature soars due to the heat of the building load. Even though the external outdoor temperature reaches up to 35°C (Fig. 3), the internal indoor temperature rise to close to 45°C is somewhat unrealistic and seems to be overestimated even when explained by radiative heat transfer through windows. This is due to the assumption of a constant indoor temperature of 26°C when simulating TRNSYS (Table 3). Because the heat intrusion from the outside of the building is qualitatively proportional to the temperature difference between the outside and the indoor temperature, that is, $q_{build} \sim (T_{out} - T_{in})$, the q_{build}(t) graph of Fig. 3 is overestimated when it assumes constant indoor temperature of 26°C. For accurate quantitative assessments in the future, instantaneous TRNSYS simulations are required to take into account changes in the indoor room temperature (T_{in}(t)) caused by the air conditioner test sample.

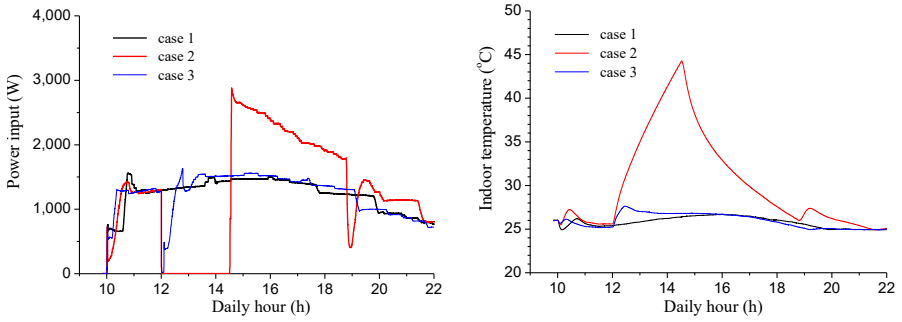


Fig. 4. Power consumption and indoor temperature variation (Environment 1)

In case 3 (blue line), during the non-occupancy period, less power is consumed than case 1 (black line), and the total final power consumption for the energy comparison interval is lowest in case 3 (12 474 Wh), as shown in Table 4. Considering the actual room temperature of 27 to 28°C, not 26°C when occupants are out, the power input of case 3 was also slightly overestimated. Therefore, an operation similar to case 3 seems to be more energy saving in practice (less than 12 474 Wh).

3.2. Environment 2 results

In order to increase the energy saving, the test conditions were changed by allowing the compressor to be in minimum load operation while occupants were out. The climate condition was set as August in Korean, which has a lower heat load than the Middle East, and T_{set} was adjusted to 26 → 28 → 26 °C for the behavior 3 case. In addition, in order to observe the energy saving effect over a longer period, we increased the going out time (total 3.5 hours).

Contrary to expectations, however, case 3 consumed more electricity energy (7 814 Wh) than case 1 (7 258 Wh) in Environment 2. This is evident in the case 3 graph of Fig. 5(a). When returning the set temperature from 28°C to 26°C in advance in preparation for an occupant returning at 15:30, it consumes more electricity than case 1 as a side effect. In other words, raising and lowering the temperature by 2°C may consume more electricity than adjusting by 1°C.

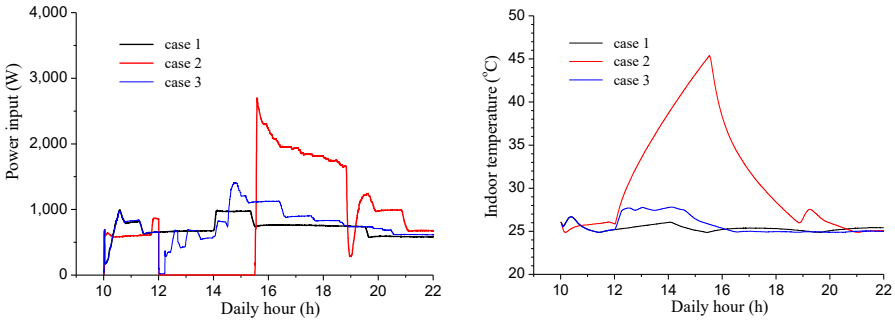


Fig. 5. Power consumption and indoor temperature variation (Environment 2)

3.3. Environment 3 results

This time, to eliminate the adverse effect of the suspect 2°C adjustment in Environment 2 – case 3, the temperature adjustment in Environment 3 – case 3 was limited to 1°C, and it was restored to 26°C, 30 minutes before the occupants' return.

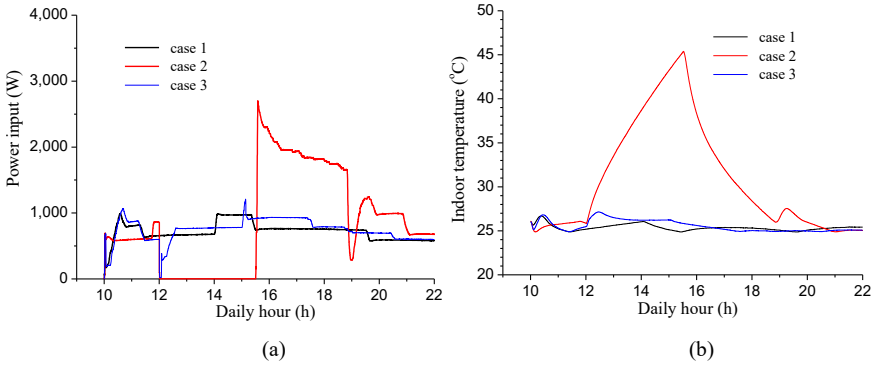


Fig. 6. Power consumption and indoor temperature variation (Environment 3)

Environment 3 – case 3 recorded energy consumption of 7 562 Wh, which is less than Environment 2 – case 3 of 7 814 Wh, but still more than the energy consumption of case 1 (7 258 Wh). This shows that 1°C of temperature adjustment is somewhat effective, but not the main point of the energy saving as in Environment 1 – case 3. Environments 4 and 5 impose Middle East climate conditions where energy saving in case 3 occurred (Environment 1).

3.4. Environments 4 and 5 results

Figures 7 (Env. 4) and 8 (Env. 5) show the test results for the April and October climate and building load conditions in the Middle East, respectively. Because the Middle East's April condition (Env. 4) is similar to Seoul's August condition, the energy saving aspect is similar to Environments 2 or 3. In the case of Environment 5, the test conditions of Environment 1 were slightly modified to change the going out time from 14:00 to 16:30 when the $T_{out}(t)$ and $q_{build}(t)$ are relatively higher than the going out time of Environment 1 – case 3 (from 12:00 to 14:30). Then, the energy consumption of Environment 3 – case 3 (11 735 Wh) becomes smaller than Environment 1 – case 3 (12 474 Wh). These results indirectly show that in order for inverter air conditioners to achieve energy saving with minimal operation, the product must be operated in a partial cooling load range where inverter compressor efficiency can be achieved to some extent.

The part-load operation rate of Environment 5 – case 3 is approximately 67% (= building load, 4 700 W / product rating, 7 000 W). As future work, it will be necessary to further verify the energy saving effect under various conditions in terms of part-load operation rate.

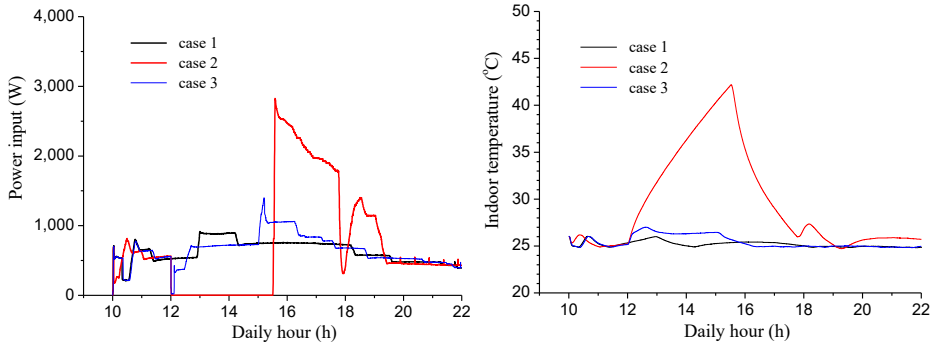


Fig. 7. Power consumption and indoor temperature variation (Environment 4)

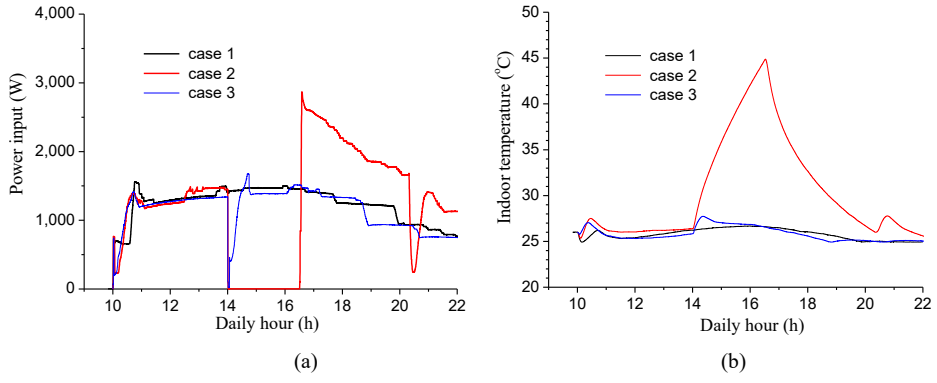


Fig. 8. Power consumption and indoor temperature variation (Environment 5)

3.5. Summary

The summarized energy consumptions (Wh) for the energy comparison interval (12:00 ~ 22:00) are shown in Table 4. There exist obviously smart operational approaches of an air conditioner that can save energy for a short period of non-occupancy of 2.5 or 3.5 hours at special environment conditions. Environments 1 and 5 could reduce the energy consumption when occupants were out by 139 Wh and 878 Wh, respectively, during 2.5 hours without occupancy. This amount is replaced by 56 W and 351 W per hour, respectively.

Table 4 Summary of the energy consumption for each test case

	Climate condition	Behavioral case	Energy consumption (Wh) between 12:00 ~ 22:00
Env. 1	Middle East (October)	Case 1	12 613
		Case 2	12 963
		Case 3	12 474
Env. 2	Seoul (August)	Case 1	7 258
		Case 2	9 118
		Case 3	7 814
Env. 3	Seoul (August)	Case 1	7 258
		Case 2	9 118
		Case 3	7 562
Env. 4	Middle East (April)	Case 1	6 521
		Case 2	7 592
		Case 3	6 770
Env. 5	Middle East (October)	Case 1	12 613
		Case 2	12 557
		Case 3	11 735

4. Conclusion and Future Work

Considering that inverter air conditioners are highly efficient at low-speed operation, energy consumption was compared for three behavioral cases: turned on (behavior case 1), turned off (behavior case 2), or the set temperature was adjusted to minimal operation (behavior case 3) while occupants were out for a short time. If air conditioner technology is further improved, it will be developed to save energy by inputting the outdoor condition, building load condition, and a user's usage pattern by combining with IoT and AI technology. In order to evolve in this direction, it is necessary to pre-study under what conditions an inverter air conditioner can be operated in an energy saving manner and whether current products have the hardware capability to perform such selective operation. With several arbitrary environmental conditions, we found that inverter air conditioners can save electricity by adjusting the set temperature when occupants go out. Assuming 2.5 or 3.5 hours of going out time in Korea and the Middle East climates, three air conditioner operational behaviors during non-occupancy were examined. Under certain conditions when the part-load operation rate was near 65%, the electrical energy consumption order was case 3 < case 1 < case 2, and under some conditions the order was case 1 < case 3 < case 2 when the part-load operation rate had small values under 65%.

In future work, however, TRNSYS analysis is needed to reflect the temperature change ($T_{in}(t)$) inside a building by the test product instead of assuming constant T_{in} (= 26°C). This will yield more accurate and realistic results for case 2. In addition, a wider investigation of the part-load operation rate and going out time environmental conditions is required for various types of inverter air conditioners.

Acknowledgements

The authors highly appreciate the financial support from Korea Testing Laboratory (Project No. CBS1826).

References

[1] Slade M. The future of cooling–Opportunities for energy-efficient air conditioning. Energy efficiency division of IEA; 2018.
[2] Goetzler W, Guernsey M, Young J, Fuhrman J, Abdelaziz O. The future of air conditioning for buildings. U.S. Department of Energy; 2016.
[3] EECJ. Final reports on the Top Runner target prodcut standards–Air conditioners. Quality Stadards of Japan; 2006.
[4] Hamad AJ, Khalifa AHN, Khalaf DZ. The effect of compressor speed variation and vapor injection on the performance of modified refrigeration system. IREME; 2018, vol. 12, p. 285–292.
[5] Saito K. Latest heat pump technologies in Japan. In Proceedings of the 12th IEA Heat Pump Conference; 2017, K.4.7.1.
[6] Cheng CC, Lee D. Smart sensors enable smart air conditioning control. Sensors; 2014, vol. 14, p. 11179–11203.
[7] Cheng CC, Lee D. Enabling smart air conditioing by sensor development: A review. Sensors; 2016, vol. 16, p. 2028.
[8] Yoon MS, Lim J, Qahtani TS, Nam Y. Experimental study on comparision of energy consumption between constant and variable speed air-conditioners in two different climates. In Proceedings of the 9th Asian Conference on Refrigeration and Air-conditioning; 2018, E342.
[9] Lim J, Yoon MS, Qahtani TS, Nam Y. Feasibility study on variable-speed air conditioner under hot climate based on real-scale experiment and energy simulation. Energies; 2019, vol. 12, p. 1489.

13th IEA Heat Pump Conference
April 26-29, 2021 Jeju, Korea

Numerical investigation on PCM-to-refrigerant heat exchangers for thermal energy storage

Yiyuan Qiao[a], Tao Cao[a], Yunho Hwang[a,*], Jiazhen Ling[a], Vikrant Aute[a]

[a] Center for Environmental Energy Engineering, Department of Mechanical Engineering, University of Maryland, 4164 Glenn Martin Hall Bldg., College Park, MD 20742, United States

Abstract

Recently, the application of thermal energy storage systems using phase change materials (PCM) is expanding in many fields due to the high energy storage density of PCMs and the narrow phase-change temperature range. In this paper, we conducted a numerical investigation on a shell-and-tube configured PCM-to-refrigerant heat exchanger (PCMHX) coupled in a vapor compression cycle for personal cooling. The enthalpy method was applied to the phase change analysis. The finite-volume method was employed to address the two-dimensional PCMHX numerical solution. Different from most of the previous studies on PCM-to-water heat exchangers, the proposed PCMHX works as a condenser. We validated the simulation results against the experiment data, including condenser pressure, capacity, and PCM temperature profiles. Since the refrigerant-side heat transfer coefficient changes along the condenser length, the heat transfer flux is not uniform across the PCM. Therefore, we analyzed the uneven PCM melting and its effects on the condensing temperature. Results show that PCM near the condenser outlet melts slower than other sections because of the low heat transfer coefficient and small temperature difference in a subcooled liquid region. The developed PCMHX model can reasonably predict the time-dependent heat transfer performance and the PCM melting process.

© HPC2020.
Selection and/or peer-review under responsibility of the organizers of the 13th IEA Heat Pump Conference 2020.

Keywords: Modeling; Phase change; PCM-to-refrigerant heat exchanger; Thermal energy storage; Enthalpy method

Nomenclature			
A, A'	heat transfer area (mm^2)	cond	condenser
C	specific heat ($kJ \cdot kg^{-1} \cdot K^{-1}$)	dia	diaphragm of TXV
C_v	flow coefficient (--)	evap	evaporator
h	enthalpy ($kJ \cdot kg^{-1}$)	fin	fin
H	latent heat ($kJ \cdot kg^{-1}$)	i	inner
i, j	segment number	in	inlet
k	thermal conductivity ($W \cdot m^{-1} \cdot K^{-1}$)	ini	initial
K	spring constant ($N \cdot m^{-1}$)	isen	isentropic
L	length of the PCM cylinder (mm)	l	liquid phase
Le	Lewis number (--)	m	melting, motor
m	mass (kg)	o	outer
$\dot{m}$	mass flow rate ($g \cdot s^{-1}$)	out	outlet
N	rotational speed (rpm)	p	PCM
P	pressure (kPa)	r	radial direction
r, R	radius (mm)	ref	refrigerant
t	time (s)	s	solid phase

* Corresponding author. Tel.: +1-301-405-5247.
E-mail address: yhhwang@umd.edu.

T	temperature (°C)	t	tube
W	power consumption (W)	top	top
y	deflection of spring in TXV (m)	th	throttle of TXV
z	length in z direction (mm)	vol	volumetric
		w	wall
Greek symbols		z	axial direction
α	heat transfer coefficient ($W \cdot m^{-2} \cdot K^{-1}$)		
η	efficiency	Abbreviations	
ρ	density ($kg \cdot m^{-3}$)	CENG	compressed expanded natural graphite
λ	liquid fraction (--)	COP	coefficient of performance
δ	thickness of wall (mm)	MCHX	micro-channel heat exchanger
ω	humidity ratio ($kg \cdot kg^{-1}$)	MFM	mass flow meter
		PCM	phase change material
Subscripts		PCMHX	PCM heat exchanger
A	ambient	TXV	thermostatic expansion valve
b	bulb sensor of TXV	VCC	vapor compression cycle
comp	compressor		

1. Introduction

Phase change material (PCM) coupled heat exchangers are attracting more attention recently since PCM can absorb or release heat within a narrow temperature range. Most PCMHX (PCM heat exchangers) models were developed by commercial CFD software and only a few through self-developed programming [1]. The two most common numerical methods can be used to build the PCM numerical heat transfer model: (1) enthalpy method, (2) effective heat capacity method [1,2]. In the enthalpy method, by introducing enthalpy, the phase change process can be much more straightforward. Latent heat and sensible heat are combined as the enthalpy in the energy equation to avoid nonlinearity in the heat conduction problem [3]. The governing equation is the same for the liquid phase, mushy phase, and solid phase. The melting interface conditions are automatically achieved by evaluating the PCM enthalpy [2,4]. Most PCMs are not pure, and thus phase change occurs over a range of temperatures rather than at a constant temperature. In this paper, a vapor compression cycle (VCC) coupled with PCM through PCMHX was proposed and modeled. The proposed system could be used as a personal cooling system [5,6], in which PCMHX worked as a condenser to store the waste heat to avoid dumping heat to the ambient and reducing human comfort. The enthalpy method was applied to develop the transient model of the refrigerant-to-PCM heat exchanger. We validated the transient VCC system model and PCMHX model against the experimental results, and PCMHX heat transfer characteristics and system performance were also analyzed and discussed in this study.

2. System description

The PCM coupled VCC system can be used as a personal cooling system. Using the personal cooling system, the thermal state setting of the building can be higher to reduce the building energy consumption, and meanwhile, occupants can feel comfortable with the localized cooling. The schematic diagram of VCC coupled with PCM through PCMHX is illustrated in Fig. 1(a), in which PCMHX works as a condenser in the VCC system to store the waste heat from refrigerant condensation. So that the heat is not to the ambient and cannot reduce the human comfort. Therefore, the whole system including the PCMHX can be assembled together on a robotic base and powered by an electric battery to achieve the movability in buildings. The air-to-refrigerant evaporator is used for providing personal cooling in the VCC-based system. A more comprehensive system experimental investigation could be found in [5]. PCMHX was designed with multiple parallel tubes with the refrigerant flowing inside tubes and PCM was filled in the annular space between PCM container and tubes as illustrated in Fig. 1(b). R134a worked as a refrigerant flowing vertically downward. Paraffin/graphite was selected as the PCM composite, in which paraffin was immersed inside the compressed, expanded natural graphite (CENG) matrix. A refrigerant distribution header and collection header were installed at the top and bottom of PCMHX, respectively, in which the refrigerant was assumed to be uniformly distributed to eight copper branch tubes. PCMHX specifications are listed in Table 1.

3. PCM condenser model

A segment-by-segment condenser model was developed for the PCMHX. Assumptions of the PCMHX model used were: (1) radiation heat to the surrounding was neglected, (2) refrigerant conduction, viscous dissipation, kinetic energy, and potential energy were neglected, (3) only thermal conduction in the CENG matrix was considered, and the effective thermal conductivity was different in the axial and radial directions, (4) the specific heat of PCM was different for the solid and liquid phases, and (5) a unit of a single tube and PCM cylinder can represent the heat transfer performance of original eight-tube PCMHX design. Fig. 1(c) is the single tube unit. To keep the same mass of PCM per tube, the cross-section of the single-tube unit was 1/8 of the original cross-section. To maintain the same heat transfer area per tube, the tube length of the single unit (L) was the same as the eight-tube design. Paraffin wax, PureTemp37, was selected as the PCM with a melting temperature of 37°C. The thermal properties of PureTemp37 are listed in Table 2.

Table 1: PCMHX design properties

Parameters	Unit	Value
PCM container diameter	mm	265
PCM composite height	mm	280
Tube length	mm	300
Tube without PCM length	mm	20
Numbers of tubes	--	8
Tube inside diameter	mm	4.8
Tube outside diameter	mm	6.4
Header length	mm	51.8
Header inside diameter	mm	7.9
Header outside diameter	mm	9.5

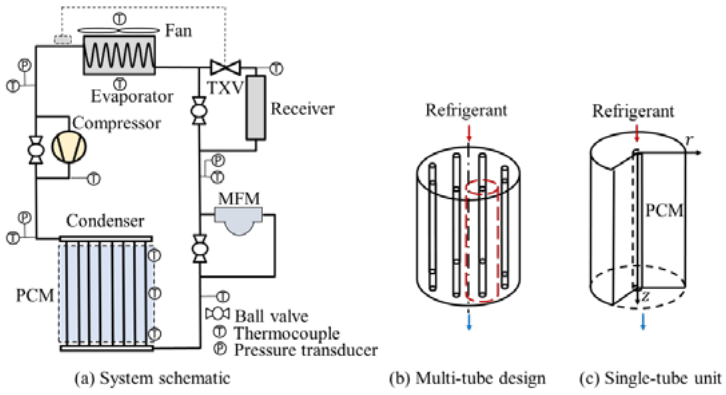


Fig. 1. PCMHX design and modeling unit (TXV: thermostatic expansion valve. MFM: mass flow meter).

Table 2. Properties of PureTemp37

Properties	Unit	Value
Melting temperature	°C	36.5~37.5
Latent heat	kJ·kg^{-1}	210
Thermal conductivity	W·m^{-1}·K^{-1}	0.15 (liquid), 0.25 (solid)
Density	kg·m^{-3}	840 (liquid), 920 (solid)
Specific heat	kJ·kg^{-1}·K^{-1}	2.63 (liquid), 2.21 (solid)

3.1. PCM side model

Under the cylindrical coordinate system, there is a rotation symmetric heat transfer to PCM with respect to the longitudinal axis (see Fig. 1(c)). Therefore, a transient two-dimensional (2D) numerical model was used to simulate heat transfer and PCM melting process in the PCM condenser. The enthalpy method was adopted for the 2-D PCM modeling. The energy equation is given by Eq. (1). T_p and h_p are PCM temperature and enthalpy, respectively. h_p is a function of PCM temperature. $k_{p,r}$ and $k_{p,z}$ are PCM effective thermal conductivity in radial direction and axial direction, respectively. PCM enthalpy and effective thermal conductivity are two crucial parameters that need to be determined to solve this energy equation.

$$\rho_p \frac{\partial h_p}{\partial t} = k_{p,r} \frac{1}{r} \frac{\partial}{\partial r}\left(r \frac{\partial T_p}{\partial r}\right) + k_{p,z} \frac{\partial^2 T_p}{\partial z^2} \tag{1}$$

PCM liquid fraction is given by Eq. (2) to evaluate the PCM melting process. T_s and T_l are PCM temperatures at the beginning and the end of the phase change process, respectively.

$$\lambda(T_p) = \begin{cases} 0 & h \le h_s \\ \dfrac{T_p - T_s}{T_l - T_s} & h(T_s) < h < h(T_l) \\ 1 & h \ge h_l \end{cases} \tag{2}$$

The PCM effective thermal conductivity in the radial direction, $k_{p,r}$, and that in the axial direction, $k_{p,z}$ are significant parameters to address this numerical problem as in Eq. (1). $k_{p,r}$ and $k_{p,z}$ are different due to the manufacturing process of PCM/CENG composite [7]. The thermal conductivity of the CENG matrix in the compression force direction is less than the perpendicular direction. The correlations used for effective conductivities $k_{p,r}$ and $k_{p,z}$ are proposed by Py et al. [8].

Boundary conditions for PCM temperature are given in Eqs. (3) to (6). R_i is the inner radius of the PCM cylinder, which is the same as the tube outer radius. R_o and L are the outer radius of the single-tube unit and the cylinder length, respectively. A_i and A_{top} is the heat transfer area contacted tube walls and the top area of the PCM cylinder, respectively. A_o is the equivalent outer heat transfer area for the single-tube unit to the surrounding. $A_o = A_o'/8$, in which A_o is the outer surface area of the original multi-tube design. α_1, α_2 and α_3 are the natural convection heat transfer coefficient at the outer, top and bottom boundary, which are calculated by the correlation proposed by [9]. T_a and T_w are the surrounding and wall temperatures, respectively.

$$k_{p,r} \frac{\partial T_p(r,z,t)}{\partial r} = A_i \frac{2k_w}{\delta}\left(T_w(z,t) - T_p(r,z,t)\right) \quad r = R_i \tag{3}$$

$$k_{p,r} \frac{\partial T_p(r,z,t)}{\partial r} = \alpha_1 A_o\left(T_p(r,z,t) - T_a\right) \quad r = R_o \tag{4}$$

$$k_{p,z} \frac{\partial T_p(r,z,t)}{\partial r} = \alpha_2 A_{top}\left(T_p(r,z,t) - T_a\right) \quad z = 0 \tag{5}$$

$$k_{p,z} \frac{\partial T_p(r,z,t)}{\partial r} = \alpha_3 A_{top}\left(T_p(r,z,t) - T_a\right) \quad z = L \tag{6}$$

The initial condition for PCM temperature is as follows:

$$T_p(r,z,t) = T_{ini} \quad t = 0 \tag{7}$$

A finite-volume method was adopted to solve the aforementioned governing equations for PCM. As illustrated in Fig. 2, uniform segments were applied for the discretization along with axial and radial directions in the PCM domain. Control volumes in the axial and radial directions are designated by *i* and *j*. Each PCM control volume is an annular space. The discretized energy equation for PCM heat transfer using the enthalpy method is given in Eq. (8). $A_{p,r}$ and $A_{p,z}$ are the heat transfer areas of each control volume in the radial direction and axial direction, respectively.

$$m_{p_{(i,j)}}\frac{h_{p_{(i,j)}}}{\partial t}=\frac{k_{p,r}}{dr}A_{p,r_{(j)}}\left(T_{p_{(i,j-1)}}-T_{p_{(i,j)}}\right)-\frac{k_{p,r}}{dr}A_{p,r_{(j+1)}}\left(T_{p_{(i,j)}}-T_{p_{(i,j+1)}}\right)+\frac{k_{p,z}}{dz}A_{p,z_{(j)}}\left(T_{p_{(i-1,j)}}-T_{p_{(i,j)}}\right)-\frac{k_{p,z}}{dz}A_{p,z_{(j)}}\left(T_{p_{(i,j)}}-T_{p_{(i+1,j)}}\right) \quad (8)$$

3.2. Refrigerant side model

The refrigerant flow was one-dimensional, and the conduction term was neglected. The energy equation and continuity equations of the refrigerant flow are given in Eqs. (9) and (10), respectively. Pressure (P) and specific enthalpy (h) were selected as state variables [10,11]. Refrigerant properties including density, ρ, the partial derivative of density with respect to enthalpy, $(d\rho/dh)|_p$, and that with respect to pressure, $(d\rho/dP)|_h$, were obtained by refrigerant property functions proposed in [12].

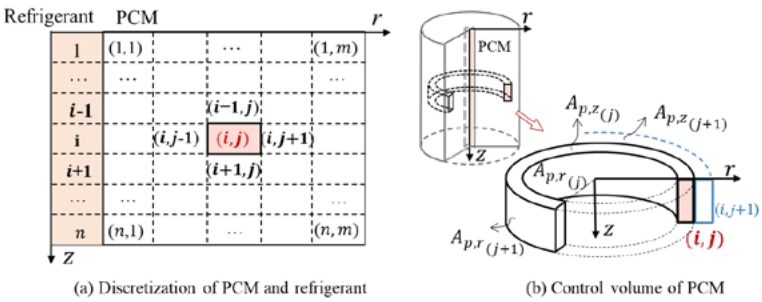
$$\frac{dU}{dt}=\mathrm{V}\left[\left(h\left.\frac{d\rho}{dP}\right|_h-1\right)\frac{dP}{dt}+\left(h\left.\frac{d\rho}{dh}\right|_p+\rho\right)\frac{dh}{dt}\right] \quad (9)$$

$$\frac{dm}{dt}=\mathrm{V}\left(\left.\frac{d\rho}{dP}\right|_h\frac{dP}{dt}+\left.\frac{d\rho}{dh}\right|_p\frac{dh}{dt}\right) \quad (10)$$

As shown in Fig. 2, spatial discretization along the axial direction was adopted for the refrigerant flow as well. Discretized energy and continuity equations for the refrigerant are given in Eqs. (11) and (12), respectively. h_{in} and h_{out} are refrigerant enthalpy flowing into and out of the selected cross section. $\dot{m}_{in}$ and $\dot{m}_{out}$ are refrigerant mass flow rate flowing into and out of the selected section. α_{ref} is the convective heat transfer coefficient. For single-phase flow, α_{ref} is calculated from correlations proposed in [13]. For two-phase flow, α_{ref} calculation was based on the correlation in [14]. α_{ref} of two-phase flow changes with quality x, and the smooth function was used at $x < 0.05$ and $x > 0.95$ to prevent discontinuities of the heat transfer coefficient at the phase transition point.

$$V_{(i)}\left(\left.\frac{d\rho}{dP}\right|_{h_{(i)}}\frac{dP}{dt}_{(i)}+\left.\frac{d\rho}{dh}\right|_{p_{(i)}}\frac{dh}{dt}_{(i)}\right)=\dot{m}_{(i)}-\dot{m}_{(i+1)} \quad (11)$$

$$V_{(i)}\left[\left(h(i)\left.\frac{d\rho}{dP}\right|_{h_{(i)}}-1\right)\frac{dP}{dt}_{(i)}+\left(h(i)\left.\frac{d\rho}{dh}\right|_{p_{(i)}}+\rho_{(i)}\right)\frac{dh}{dt}_{(i)}\right]=\dot{m}_{(i)}h_{(i)}-\dot{m}_{(i+1)}h_{(i+1)}+\alpha_{ref(i)}A_{p,r_{(1)}}(T_{HTF\,(i)}-T_{w(i)}) \quad (12)$$



(a) Discretization of PCM and refrigerant (b) Control volume of PCM

Fig. 2. Discretization of PCMHX

4. Other component models

Different from most of the previous studies on water-to-PCM heat exchangers, in this paper, the refrigerant flowing inside PCM tubes is the refrigerant. Since PCM temperature profiles vary during the melting process, and affect the PCMHX performance, and thus for the VCC the refrigerant inlet states and heat transfer coefficient along the flow direction vary with time in the PCMHX. This variation can also be reflected by Eq. (3), showing that the PCM boundary condition at R_i is neither the constant heat flux nor the constant wall temperature. Therefore, to simulate the PCMHX performance, the VCC system should be modeled. Components include an evaporator, thermostatic expansion valve (TXV), compressor, receiver, and pipes.

4.1. Evaporator model

A fin-and-tube heat exchanger was selected as the evaporator design. Discretized governing equations of refrigerant in evaporator are the same as those in the PCM condenser, as described in Eqs. (11) and (12). Heat transfer coefficient of refrigerant, α_{ref}, was calculated using correlations propose by [15] for two-phase flow and by [13] for single-phase flow. For tube wall and fins, the energy equation is given by Eq. (13).

$$\begin{aligned}\left(M_w C_{p,w} + M_{fin} C_{p,fin}\right)\frac{dT_w}{dt} \\ = \alpha_{ref} A_{ref}\left(T_w - T_{ref}\right) + \dot{m}_a C_{p,a}\left(T_{a,in} - T_{a,out}\right) + \dot{m}_a H_a(\omega_{a,in} - \omega_{a,out})\end{aligned} \tag{13}$$

In Eq. (13), the first term at the right-hand side is the heat transfer between tube walls and refrigerant, the second term means sensible heat released from air to tube walls, and the third term is the latent heat from the air. $\dot{m}_a$, $C_{p,a}$ and H_a are air mass flow rate, air specific heat, and water vaporization heat, respectively. $T_{a,in}$, $T_{a,out}$, $\omega_{a,in}$ and $\omega_{a,out}$ are air inlet temperature, outlet temperature, inlet humidity ratio and outlet humidity ratio, respectively. $T_{a,in}$ and $\omega_{a,in}$ are known. $T_{a,out}$ and $\omega_{a,out}$ can be solved by Eqs. (14) and (15), yielding air side governing equations as described by [10].

$$T_{a,out} = T_{a,in} + (T_w - T_{a,in})\left\{1 - exp\left[-\frac{\alpha_a\left(A_t + \eta_{fin}A_{fin}\right)}{\dot{m}_a C_{p,a}}\right]\right\} \tag{14}$$

$$\omega_{a,out} = \omega_{a,in} + \left\{1 - exp\left[-\frac{\alpha_a\left(A_t + \eta_{fin}A_{fin}\right)}{\dot{m}_a C_{p,a} Le^{2/3}}\right]\right\} min\left(0, \omega_{a,sat} - \omega_{a,in}\right) \tag{15}$$

A_t and A_{fin} are heat transfer area of tube-side and fin-side, respectively. Fin efficiency, η_{fin} was calculated using correlations proposed by [16]. Airside heat transfer is enhanced by plate wavy-herringbone fins with a staggered tube layout. Thus, the air-side heat transfer coefficient, α_a, was obtained from the correlations proposed by [17]. *Le* is the Lewis number yielding $Le^{2/3}$=0.9 [18].

4.2. TXV model

The TXV model is described in [10] and [19]. TXV was assumed to be adiabatic. The expansion of the refrigerant was assumed to be isenthalpic. The refrigerant mass flow rate controlled by the TXV is given by Eq. (16), in which C_v is the flow coefficient, A_t is the flow area of the throttle, Δp is the pressure drop across the valve.

$$\dot{m} = C_v A_t (\rho_{in} \Delta p)^{1/2} \tag{16}$$

The refrigerant flow area was controlled by a needle movement, which reflects the superheat degree at the evaporator outlet. Valve geometry and a function to obtain the TXV bulb temperature are presented in [10]. The force balance on the diaphragm is given in Eq. (17). The sensor provides a force on the one side of the diaphragm, $P_b A_{dia}$, which is the same with the total forces on the other side supplied by evaporator pressure and the spring. k_{sp}, y_{sp} and $F_{sp,ini}$ are the spring constant, deflection and the initial force, respectively.

$$k_{sp} y_{sp} + F_{sp,ini} + P_{evap} A_{dia} = P_b A_{dia} \tag{17}$$

4.3. Compressor model

The compressor provides a refrigerant mass flow throughout the VCC. The efficiency-based compressor model was applied in this study. Volumetric efficiency, η_{vol}, isentropic efficiency, η_{isen} and motor efficiency, η_m, were used to calculate the compressor power consumption, W_{comp}, as given in Eqs. (18) to (20). $\dot{m}$ and N are the mass flow rate and compressor speed, respectively. ρ_{in} is the refrigerant density at the inlet of the compressor.

$$h_{out} = h_{in} + \frac{h_{out,s} - h_{in}}{\eta_{isen}} \tag{18}$$

$$\dot{m} = \frac{\eta_{vol}\rho_{in}V_{comp}N}{60} \tag{19}$$

$$W_{comp} = \dot{m}\frac{h_{out} - h_{in}}{\eta_m} \tag{20}$$

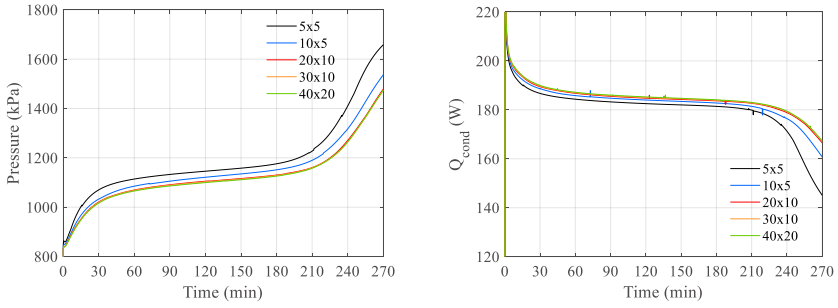
4.4. Receiver and pipe models

The receiver model and connecting pipe model are essentially the same as the evaporator model. As described before, the refrigerant side can be solved by discretized equations as in Eqs. (11) and (12). The air-side heat transfer was based on natural convection.

5. Results

5.1. Grid sensitivity

Sensitivities to grid size and aspect ratio were investigated. The model was simulated under different grid sizes and aspect ratios as follows: 40x20, 30x10, 20x10, 10x5, and 5x5. Results are shown in Fig. 3. The deviation of both pressure and capacity between grids 40x20 and 30x10 is less than 1.0%. Therefore, the grid of 30x10 was good enough to be adopted in the simulation.



(a) Condenser pressure

(b) PCM condenser capacity

Fig. 3. Grid independence of numerical solution.

The PCMHX model and system model were developed in Dymola®. The algorithm of Lsodar was adopted, which is an implicit multi-step method. The backward differentiation formula was applied in the algorithm to solve differential equations. Time step size was determined on every step with a tolerance of $1e^{-6}$.

5.2. Simulation results

Fig. 4 (a)-(e) show the comparison of the experimental and numerical results on system operating pressures, condenser outlet subcooling and evaporator outlet superheat, mass flow rate, COP, and heat exchanger capacities indicating that numerical results match well with the experimental results. The good agreements illustrate that the numerical model is reliable. Fig. 4(f) shows the PCM temperatures at 1/3 from the top and bottom of the PCMHX for both numerical and experimental results. From Fig. 4(a), evaporating pressure was

almost constant due to the steady surrounding temperature. The condenser pressure increased with the cooling time due to the process of PCM melting. As the PCM absorbed heat from the condenser tube, its average temperature increased (Fig. 4(f)) and thus the condensing temperature was increased, leading to the increased of subcooling at the condenser outlet as well. Fig. 4(c) indicates mass flow rate decreased gradually, which is because the higher condensing pressure led to lower volumetric efficiency. Fig. 4(d) and (e) show the slightly decreased COP and capacity due to the increase of the condensing pressure. As can be seen from Fig. 4(f), the proposed PCMHX model can predict the PCM melting process well.

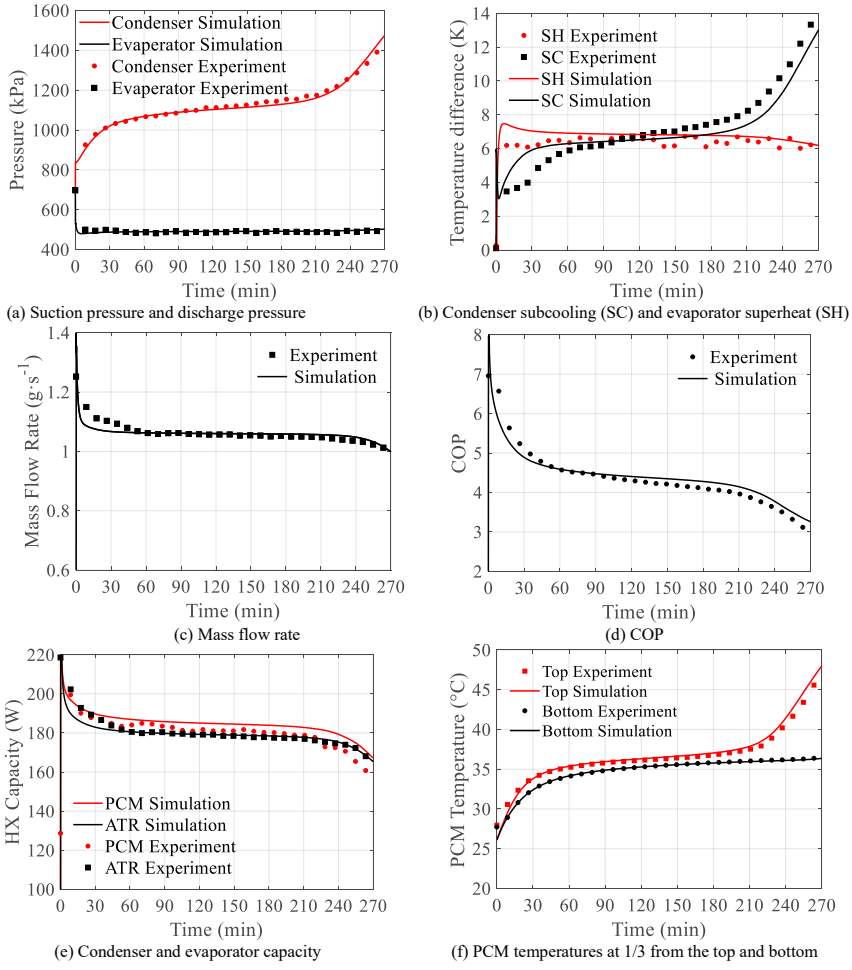


Fig. 4. Numerical results compared with experimental results.

Fig. 5 and Fig. 6 shows the numerical solution of the PCM temperature and melting fraction of the single-tube unit. The vertical direction means the condenser length direction, and the horizontal direction represents the radial direction. Refrigerant flowed downward from the top to the bottom. It can be found that the PCM melting rate decreased along the condenser length direction. The bottom PCM temperature was lower than the top and middle sections, which can also be verified by Fig. 4(f). The PCM temperature gradient in the radial direction was smaller than the axial direction. Besides, the heat transfer area of subcooled-liquid refrigerant increased with the cooling time. The refrigerant liquid zone at the bottom was greater than the vapor zone at the top near the condenser inlet. From Fig. 6, at 270 minutes, liquid fractions at the top 1/3 were higher than 0.9, while at the bottom 1/3 PCM liquid fractions were less than 0.4. This uneven PCM melting is due to the

uneven refrigerant heat transfer coefficient. At the top and middle section, the refrigerant-side heat transfer coefficient is much higher than that at the bottom because the refrigerant is in two-phase at the top and middle, while it becomes sub-cooled liquid at the bottom. It can be concluded that the utilization ratio of the PCM latent heat needs to be improved.

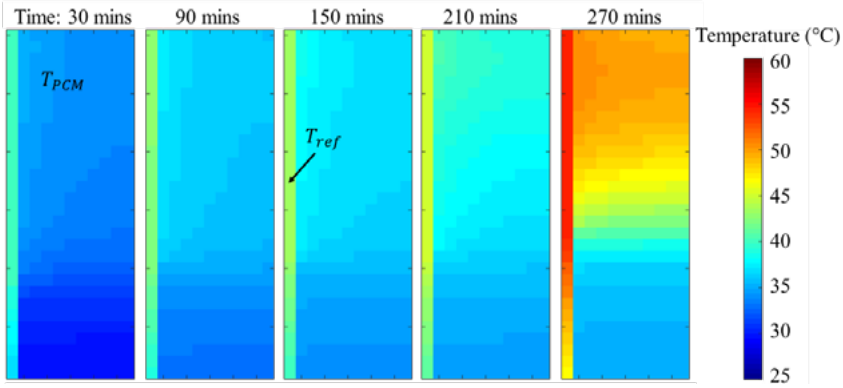


Fig. 5 PCM and refrigerant temperatures

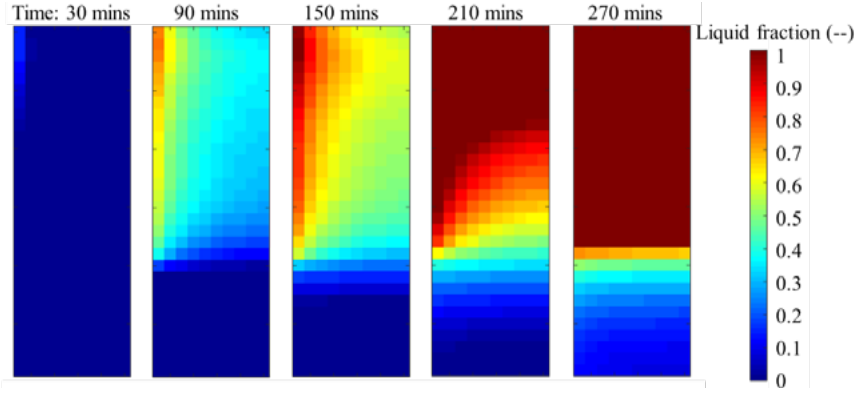


Fig. 6. PCM liquid fractions

Conclusions

In this paper, we developed the two-dimensional PCM-to-refrigerant heat exchanger model and transient system model of the VCC coupled with PCMHX in a personal cooling system. PCMHX works as a condenser of the VCC system and interface for thermal energy storage. Grid size sensitivity was checked, and numerical results were compared with the experimental results. It shows good agreements between simulation and experiment for both system performance and PCM heat transfer characteristics. Uneven PCM melting was also observed and reasoned due to the uneven heat transfer rate from the refrigerant to PCM along the condenser length. Therefore, a better PCMHX design should be further investigated to fully utilize the advantage of all the latent heat.

Acknowledgments

This research was supported by the Advanced Research Projects Agency - Energy (ARPA-E) under Award DE-AR0000530 and the Center for Environmental Energy Engineering (CEEE).

References

[1] Al-Abidi AA, Bin Mat S, Sopian K, Sulaiman MY, Mohammed AT. CFD applications for latent heat thermal energy storage: a review. Renew Sustain Energy Rev 2013;20:353–63. doi:10.1016/j.rser.2012.11.079.

[2] Jin X, Hu H, Shi X, Zhou X, Zhang X. Comparison of two numerical heat transfer models for phase change material board. Appl Therm Eng 2018;128:1331–9. doi:10.1016/j.applthermaleng.2017.09.015.

[3] Eyres NR, Hartree DR, Ingham J, Jackson R, Sarjant RJ, Wagstaff JB. The Calculation of Variable Heat Flow in Solids. Philos Trans R Soc A Math Phys Eng Sci 1946;240:1–57. doi:10.1098/rsta.1946.0002.

[4] Dutil Y, Rousse DR, Salah N Ben, Lassue S, Zalewski L. A review on phase-change materials: Mathematical modeling and simulations. Renew Sustain Energy Rev 2011;15:112–30. doi:10.1016/j.rser.2010.06.011.

[5] Qiao Y, Du Y, Muehlbauer J, Hwang Y, Radermacher R. Experimental study of enhanced PCM exchangers applied in a thermal energy storage system for personal cooling. Int J Refrig 2019;102:22–34. doi:10.1016/J.IJREFRIG.2019.03.006.

[6] Dhumane R, Qiao Y, Muehlbauer J, Ling J, Aute V. Evaluating Recharge Options for Phase Change Material Storage of a Personal Conditioning System. Int. Refrig. Air Cond. Conf. Purdue. Purdue Univ. West Lafayette., 2018, p. 1–10.

[7] Merlin K, Delaunay D, Soto J, Traonvouez L. Heat transfer enhancement in latent heat thermal storage systems: Comparative study of different solutions and thermal contact investigation between the exchanger and the PCM. Appl Energy 2016;166:107–16. doi:10.1016/j.apenergy.2016.01.012.

[8] Py X, Olives R, Mauran S. paraffin/porous-graphite-matrix composite as high and constant power thermal storage material. Int J Heat Mass Transf 2001;44:2727–37.

[9] Churchill SW, Chu HHS. Correlating equations for laminar and turbulent free convection from a vertical plate. Int J Heat Mass Transf 1975;18:1323–9. doi:10.1016/0017-9310(75)90243-4.

[10] Qiao H, Aute V, Radermacher R. Transient modeling of a flash tank vapor injection heat pump system - Part I: Model development. Int J Refrig 2015;49:169–82. doi:10.1016/j.ijrefrig.2014.06.019.

[11] Laughman CR, Qiao H. On the influence of state selection on mass conservation in dynamic vapour compression cycle models. Math Comput Model Dyn Syst 2017;23:262–83. doi:10.1080/13873954.2017.1298625.

[12] Aute V, Radermacher R. Standardized Polynomials for Fast Evaluation of Refrigerant Thermophysical Properties. Int. Compress. Eng. Refrig. Air Cond. High Perform. Build. Conf., 2014, p. 1–10.

[13] Gnielinski V. On heat transfer in tubes. Int J Heat Mass Transf 2013;63:134–40. doi:10.1016/j.ijheatmasstransfer.2013.04.015.

[14] Shah MM. An improved and extended general correlation for heat transfer during condensation in plain tubes. HVAC&R Res Sept 2009;15.

[15] Jung DS, Radermacher R. Prediction of pressure drop during horizontal annular flow boiling of pure and mixed refrigerants. Int J Heat Mass Transf 1989;32:2435–46. doi:10.1016/0017-9310(89)90203-2.

[16] Hong KT, Webb RL. Calculation of Fin Efficiency for Wet and Dry Fins. HVAC&R Res 1996;2:27–41.

[17] Kim N-H, Yun J-H, Webb RL. Heat Transfer and Friction Correlations for Wavy Plate Fin-and-Tube Heat Exchangers. J Heat Transfer 1997;119:560–7. doi:10.1115/1.2824141.

[18] Thomas H. Kuehn, James W. Ramsey JLT. Thermal Environmental Engineering. vol. 188. 1998.

[19] Wang F, Maidment G, Missenden J, Tozer R. The novel use of phase change materials in refrigeration plant. Part 2: Dynamic simulation model for the combined system. Appl Therm Eng 2007;27:2902–10. doi:10.1016/j.applthermaleng.2005.06.009.

13th IEA Heat Pump Conference
April 26-29, 2021 Jeju, Korea

PVT Geo Coupled Air to Water Heat Pump System Twin Test Cell Experimental Study

Euy-Joon Lee[a,b,*], Kwang-Seob Lee[a,b], Eun-Chul Kang[b], Yu-Jin Kim[a,b], Entchev Evgueniy[c], Libing Yang[c]

[a]Korea Institute of Energy Research, 152 Gajeong-ro, Yusung-gu, Daejeon 34129, Korea
[b]University of Science and Technology, Korea, 217 Gajeong-ro, Yusung-gu, Daejeon 34113, Korea
[c]CanmetENERGY Research Centre, Ottawa, ON K1A 1M1, Canada

Abstract

A new PVT (Photovoltaic-Thermal) and ground coupled AWHP (Air to Water Heat Pump) system has been developed and verified with a TTC (Twin Test Cell) in Korea. This renewable energy hybrid system technology could support Korea government's energy policies about RE3020(20% by renewable energy in 2030) and the zero energy building policy for the public sector in 2020 and the private sector in 2030. In this paper, a photovoltaic-thermal and ground air heat exchanger hybrid technology will be introduced for local and global energy issues. SET (Separate Effect Test) models have been developed to verify PVT, GAHX and AWHP units performance. And also IET (Integral Effect Test) model with TTC has been developed to validate PVT-GAHX hybrid system performance. Initial commissioning of TTC both were matched in 99%. Seasonal test of heating and cooling weeks will be performed and introduced in terms of primary energy savings.

© HPC2020.
Selection and/or peer-review under responsibility of the organizers of the 13th IEA Heat Pump Conference 2020.

Keywords: Photovoltaic-Thermal(PVT), Ground Air Heat Exchanger(GAHX), AWHP hybrid, Twin Test Cell(TTC), Demonstration, Primary Energy Saving

1. Introduction

Photovoltaic-thermal (PVT) and ground air heat exchanger (GAHX) hybrid system is a combined one with photovoltaic, solar thermal and geothermal technologies. The dual functions of the PVT system result in a higher overall solar conversion rate than that of solely photovoltaic or solar collectors and thus enable a more effective use of solar energy. GAHX system takes advantage of constant ground temperatures to precondition incoming fresh air hence reducing the heating and cooling loads. In this study, PVT and GAHX hybrid system were combined with air to water heat pump (AWHP). The concept and the TTC site of hybrid system are shown as Fig. 1.

* Corresponding author. Tel.: +82-42-860-3514;
E-mail address: ejlee@kier.re.kr

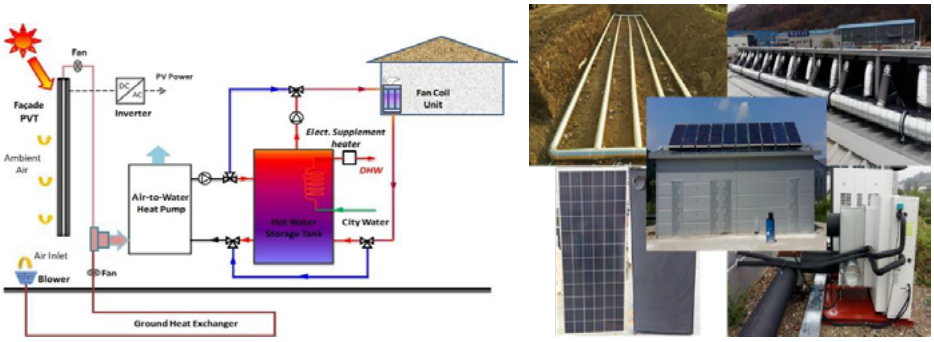


Fig. 1. PVT and ground coupled AWHP system (left) / IET TTC test site (right)

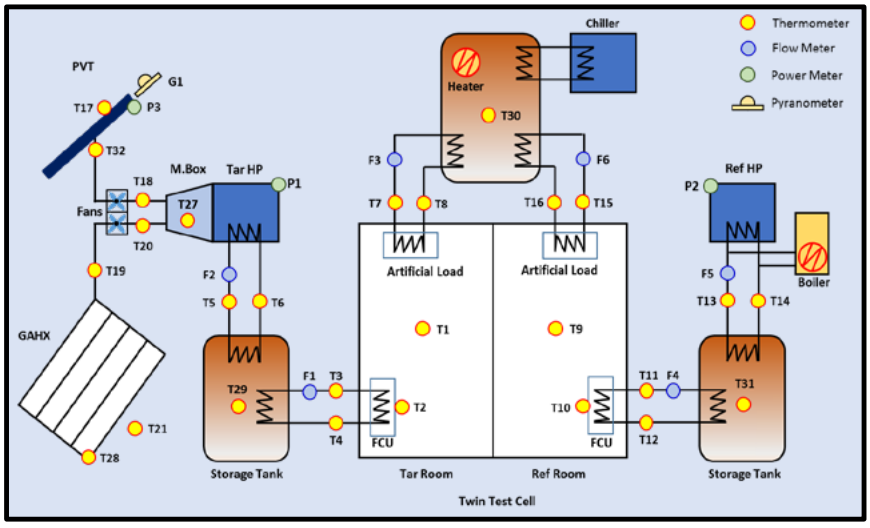


Fig. 2. TTC demonstration system schematic

2. PVT-GAHX Hybrid System TTC Study

The Twin-Test-Cell (TTC) facility (shown as Fig. 1) in Korea has been used as a testbed for HVAC components and systems testing and evaluation under real-life conditions. The Twin-Test-Cell consists of two identical rectangular-shaped rooms each with a dimension of 4m by 5m. Between the two test cells, there is a engineering room (3m by 5m) for locating the HVAC systems to be tested and compared. The horizontal ground-to-air heat exchanger is buried around the perimeter of the twin-test-cell and PVT panels are installed on the roof of the twin-cell.

The hybrid system to be installed at TTC is designed for an average detached house with the peak heating and cooling demand of 9 kW and 6 kW respectively. 10 PVT panels with a system power of 3.1 kW total have been installed power capacity and 40% of thermal efficiency and 200 m GAHX duct were installed in the ground and it is steel spiral type duct of 250 mm diameter. As the TTC (shown as Fig. 2) has the area of just 20 m2 and a volume of 54 m3 and 32 temperature sensors, 6 flow meters, 3 power meters and 1 pyranometer.

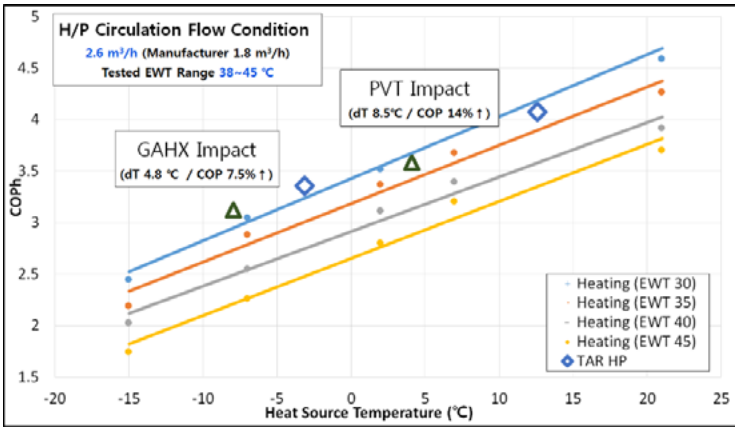


Fig. 3. AWHP SET/IET performance data mapping

The AWHP has 9.5 kWt heating capacity and its performance data are presented shown as Fig 3. PVT and GAHX's contribution are described on Fig.3. Heating week test (2018.02.15~2018.02.22) was conducted target system (PVT-GAHX hybrid H.P.) and reference system (conventional H.P.) at the same time for a week. The target AWHP COP was 4.0 while the reference was 3.4. The hybrid system's COP increase due to source temperature increase (Shown in Fig. 3) and it is about 15% performance improvement from the coupling of the PVT and ground heat exchanger system.

3. Conclusion

PVT and ground coupled TTC system has been introduced and developed to justify the IET model by comparing the reference and the target system with the solar and geothermal component. Twin test cell with the hybrid system was installed in a local actual site and initial commissioning test has been performed with a good accuracy more than 99%. The hybrid system's COP increase due to the source temperature advantage was consistent and justified with IET and SET. GAHX impact 4.8℃ on source temperature, contributed 7.5% COP and PVT impact 8.5℃ on source temperature, contributed 14% COP improve. For the heating season week performance comparison test, the target system with PVT-GAHX hybrid system showed a 15% energy saving of the target system in the location and the test cell conditions. In addition, the system achieves lower primary energy consumption in comparison to the Reference boiler-chiller system. The annual primary energy saving expected as 45% in Korea by yearly simulation methodology. The system components' contributions to these saving vary during the seasons but in general are due to the multipurpose renewable utilization and high heat pump COP. For the future work, a shoulder month week and cooling month week test will be conducted for a seasonal and yearly performance data improved justification.

Acknowledgements

This work was supported by the Korea Institute of Energy Technology Evaluation and Planning(KETEP) and the Ministry of Trade, Industry & Energy(MOTIE) of the Republic of Korea (No. 20188550000430).

References

[1] Eugeni Entchev., et. al., 2017, "CO2 free heating, cooling and power trigeneration system joint research 2nd year report"
[2] E. J. Lee, et. al., 2017, "Smart Hybrid Renewable Microgeneration System for Residential Applications", Int. J. of Global Warming. https://doi.org/10.1504/IJGW.2017.087212
[3] Anil Kumar, Prashant Baredar, Uzma Qureshi, 2015. "Historical and recent development of photovoltaic thermal (PVT) technologies", Renewable and Sustainable Energy Reviews 42, 1428-1436. DOI: 10.1016/j.rser.2014.11.044

[4] Chow T.T., 2010. “A review on photovoltaic/thermal hybrid solar technology”, Applied Energy 87, 365-379. DOI : 10.1016
[5] Abdeen Mustafa Omer, 2008. “Ground-source heat pumps systems and applications”, Renew Sustain Energy Rev 12 344-371. DOI: 10.1016

13th IEA Heat Pump Conference
April 26-29, 2021 Jeju, Korea

Control strategies for modulating heat pumps in a plus energy building

Christina Betzold*, Susanna Bordin, Arno Dentel, Gunnar Harhausen

Technische Hochschule Nürnberg Georg Simon Ohm, 90429 Nuremberg, Germany

Abstract

Since the feed-in tariff of photovoltaics (PV) decreases [1], PV self-consumption becomes more profitable. Especially heat pumps, which are able to modulate the compressor speed, open up more flexibility for consuming fluctuating PV power. For exploiting the full potential of PV self-consumption smart control strategies for modulating heat pumps (MHPs) are needed. In this research, the development and the real application of optimized control strategies for MHPs in plus energy terraced houses, built in 2017, are realized. Two control strategies, a PV rule based (PVC) and a model predictive control (MPC) are tested and compared in simulation. Results for the MPC of a 12 months simulation show potential for a moderate increasing PV self-consumption up to 2.1 % and significant reducing operating costs up to 36.1 %. In real application in the terraced houses, the PVC offers an increase of PV self-consumption by 4.1 % for a monitored week, compared to a heat controlled operation.

© HPC2020.
Selection and/or peer-review under responsibility of the organizers of the 13th IEA Heat Pump Conference 2020.

Keywords: PV self-consumption;operating costs; modulating heat pumps; control strategies

1. Introduction

Since the feed-in tariff decreased and the electricity price of energy supply companies is increasing in Germany, PV self-consumption is becoming economically interesting for building owners. Smart control strategies in combination with thermal storage tanks have the potential to reduce operating costs by converting the PV surplus into thermal power. Battaglia, M. et al. [2] show, how control strategies can reduce costs for electricity by overheating thermal storage tanks. Psimopoulos et al. [3] investigate control algorithms and their contribution to final energy, solar fraction, self-consumption and seasonal performance factor in the simulation software TRNSYS. Results show an increase of PV self-consumption to 50.5 % by using control strategies in combination with thermal and electrical storage units.

High potential for reducing energy costs is expected by MPC as it uses numerical optimization algorithms and price or weather prediction. Fischer, D. et al. [4] shows in his research work that in a multi-family house MPC increases annual PV self-consumption from 56 % - 58 % up to 64 % - 71 % and decreases energy costs by 6 % - 16 % in the case of variable electricity prices. In his research work, Pichler, M. et al. [5] investigates the direct consumption of PV energy by controlling a heat pump with a MPC in an annual simulation. The MPC increased the direct consumption of PV energy from 20 % to 50 % in a single-family house.

In a previous simulation study, a control strategy, the Demand Side Management System (DMS), for the energy system of eight terraced houses was developed in TRNSYS [6] and is described by Dentel, A. et al. [7]. The DMS was changed during the implementation due to different configuration input parameters from the manufacturers. PV optimized control (PVC) was developed and is implemented in the building automation of the terraced houses since October 2018. The PVC includes the controlling of heat pumps and a battery in the energy system. The energy concept of the terraced houses consists of two shared MHPs, connected to a two storage cascade, eight decentralized domestic hot water heat pumps (DHW-HPs) with a 200 liter storage each and a shared battery of 40 kWh capacity. The first buffer storage has a size of 800 liters and is charged during

* Corresponding author. Tel.: +49-911-5880-3123; fax: +49-911-5880-7120.
E-mail address: christina.betzold@th-nuernberg.de.

grid and PV consumption. The second surplus storage in the storage cascade has a volume of 2000 liters and is charged only during PV production. The terraced houses represent a total energy system that includes thermal energy for heating and DHW as well as household electricity. Another control strategy, the Model Predictive Control (MPC), is developed in MATLAB [8] and will be implemented in the energy system as well.

In this research, two advanced control strategies, PVC and MPC, are compared to heat controlled strategies in a simulation environment in order to evaluate the potential for increasing PV self-consumption and reducing operating costs. All models and control strategies are developed and tested in MATLAB [8]. Furthermore, the PVC, realized in the terraced houses in October 2018, is compared to a heat controlled strategy by analyzing measurement data from the monitored terraced houses.

2. Method

2.1. PV optimized control (PVC)

The PVC is a rule-based control strategy and aims to increase the PV self-consumption by operating the heat pumps during PV production. As real application and simulation offer different implementation and parameter options, the PVC differs in the real application and simulation. A detailed description of the PVC and the implementation is published by Betzold, C. et al. [9].

In real application four different modes for the heat pump operation are defined:

1. Grid Mode: This mode is active, when PV production is off or already fully consumed by household electricity. The 800 liter buffer storage is charged to maximal 35 °C by the MHPs. The DHW storage tanks are charged up to 50 °C.
2. PV Mode: This mode is active, when there is PV production and a PV surplus is left after fulfilling the energy needs of the household electricity. The 800 liter buffer storage and the 2000 liter surplus storage are charged to 35 °C by the MHPs. The DHW storage tanks are charged up to 60 °C.
3. Load Management: The Load Management aims to avoid electrical load peaks of the terraced houses. The PVC switches all heat pumps off for 15 minutes, if a load peak of 16 kW is reached.
4. Priority Mode: This mode ensures that the thermal comfort in the terraced houses is fulfilled at all times. The Priority Mode starts, when the temperature falls under 27 °C in the 800 liter buffer storage, and ends, when the temperature reaches 32 °C. The DHW storage tanks are charged from 40 °C to 45 °C.

In simulation the energy system is simplified to a model that bases on energy flows coupled in an energy node. The energy node for the MHP system is shown in Equa. 1, where Q_{MHP} is the thermal energy of the MHP, $Q_{st,cap}$ is the thermal storage capacity, $Q_{st,loss}$ is the constant loss of the thermal storage and Q_{th} is the thermal load of the building. In Equa. 2 the DHW-HP system (i = 1-8) is shown, where $Q_{DHW\text{-}HP,i}$ is the thermal energy of each DHW_HP, $Q_{DHW\text{-}st,cap,i}$ is the thermal storage capacity of each DHW storage, $Q_{st,loss}$ is the constant loss of the DWH storage and $Q_{th\text{-}DHW,i}$ is the DWH load of each terraced house. Equa. 3 describes the battery system where P_{PV} is the PV surplus, $C_{bat,cap}$ is the electrical storage capacity, P_{MHP} is the electrical energy of the MHP and $P_{DHW\text{-}HP}$ is the electrical energy of the DHW-HP. The investigated control strategies use the same models to ensure comparability.

$$Q_{MHP1} + Q_{MHP2} + Q_{st,cap} = Q_{st,loss} + Q_{th} \quad (1)$$

$$Q_{DHW-HP,i} + Q_{DHW-st,cap,i} = Q_{DHW-st,loss} + Q_{th-DHW,i} \quad (2)$$

$$P_{PV} * n_{loss} + C_{bat,cap} = P_{MHP1} + P_{MHP2} + \sum_{n=1}^{8} P_{DHW-HP,n} \quad (3)$$

Mode 3, the Load Management and Mode 4, the Priority Mode are not integrated for this investigation of different control strategies. Thus, there are two modes in the PVC simulation:

1. Grid Mode: The MHPs only deliver as much thermal energy as necessary to cover the thermal load. If the DHW storage reaches the minimal storage capacity, the DHW-HP starts to charge the DHW storage with a constant thermal energy until the maximal storage capacity is reached.
2. PV Mode: The MHPs adapt to the available PV surplus power and deliver as much thermal energy as corresponds to the compressor speed. If the thermal load can not be covered during PV adaption, then the MHPs adapt the thermal energy to the thermal load as in the grid mode. The storage is charged to

its maximal capacity for 2800 liters. As soon as there is PV power left after the MHPs, the DHW-HPs start in row to charge the DHW storages tanks with a constant thermal energy until the maximal storage capacity is reached.

2.2. Model predictive control (MPC)

The MPC bases on the same simplified energy models of the heat pumps and storage tanks as shown in Equa. 1 - 3. In this research, a mixed-integer linear programming (MILP) optimization algorithm is used. The MPC is realized in MATLAB [8] with the additional software GUROBI [10], for using the Special Ordered Set (SOS) option. The SOS option enables an interpolation between defined operation points of the MHP in order to describe the MHP polynomial at every modulation step for B5 °C/W35 °C. Thus, the thermal power of the MHPs can be between 4.8 kW and 18.1 kW and the electrical power can be between 1.0 kW and 4.7 kW. The DHW-HPs have a thermal power of 2.2 kW and an electrical power of 0.5 kW. Each storage tank is modeled as an energy node that balances in- and output energy flows. Operating limits are defined by the minimal and maximal storage capacities and by the complete cover of the thermal and electrical load. The cost function bases on operating costs (c) for the household electricity ($P_{el,household}$), the MHPs ($P_{el,MHP,n}$) and the DHW-HPs ($P_{el,DHW\text{-}HP,n}$) depending on the consumption of grid, PV or battery as well as a bonus for grid feed-in (see Equa. 4 and Equa. 5).

$$min\,J = \sum_{t=1}^{t_{end}} P_{el,PV,t} * c_{PV} + \sum_{t=1}^{t_{end}} P_{el,Bat,t} * c_{Bat} + \cdots$$
$$\sum_{t=1}^{t_{end}} P_{el,Grid,t} * c_{Grid} - \sum_{t=1}^{t_{end}} P_{el,Feedin,t} * c_{Feedin} \quad (4)$$

$$P_{el} = P_{el,household} + \sum_{n=1}^{2} P_{el,MHP,n} + \sum_{n=1}^{8} P_{el,DHW-HP,n} \quad (5)$$

In this research work, the MPC has a 15 minute timestep and a 48 hours optimization horizon. After 24 hours the MPC is restarted with the boundary conditions at the end of the previous optimization at time 24 hours. The PV, thermal and electrical load prediction is ideal.

3. Simulation and comparison of PVC and MPC

For analyzing the potential of the MPC, regarding PV self-consumption (see Equa. 6) and operating costs, the MPC is compared to PVC and a heat controlled strategy (HC) for heat pumps for a 12 months period. The HC bases on the grid mode of the PVC and the two heat pumps are on/off heat pumps (no modulation). The PVC enables to adapt the MHPs to the thermal load or the available PV power. As first results have shown that the HC has higher energy consumption due to low COP at on/off HP operation (up to 11.8 %), a second HC variant with modulation option is introduced. The heat controlled modulation strategy (HCmod) operates like the grid mode of the PVC with the ability to adapt to the thermal load. Table 1 shows the four control strategies with the different heat pump models and the operation modes.

Table 1: Heat pump model and operation modes according to the control strategies

Control strategy	On/off HP	MHP	Grid Mode	PV Mode	Free Mode
HC	x		x		
HCmod		x	x		
PVC		x	x	x	
MPC		x			x

Real monitored measurement data of the energy system of the terraced houses is used for the comparison. For offering an overview of the potential a whole period of 12 months from October 2018 until September 2019 is chosen. The measured PV power as well as measured thermal and electrical load are used as ideal prediction for the MPC. For the HC, HCmod and PVC simulation the measurements serve as actual PV production and loads. The operation and comparison are implemented in MATLAB [8]. Boundary and start conditions are the same in the four cases. The energy consumption and production for the period of 12 months are shown in Table 2.

Table 2: Boundary conditions for the 12 month period from October 2018 until September 2019

Energy consumption	
Thermal load in MWh	39.60
DHW load in MWh	25.60
Electrical load in MWh	28.90
PV production in MWh	85.85

This research work is focused on the operation of the control strategies and its contribution to PV self-consumption and operating costs for the 12 months period. Economic efficiency and price increases are not observed in this analysis. Thus, the electricity prices for PV and battery do not include repayments of investments. The price for the PV self-consumption contains fees and taxes. The feed-in tariff depends on the year of commissioning and the PV plant size and is introduced for the terraced houses in 2017. Especially in MPC operation the usage of the battery is avoided due to battery prices that can not compete with grid electricity price and feed-in tariff. In this price scenario, the battery price has to be below 0.147 €/kWh (including battery losses of 30 %) to be cheaper than using the grid as an electricity storage, that costs 0.21 €/kWh. The prices for electricity are shown in Table 3.

Table 3: Energy prices for electricity consumption and PV feed-in

Energy prices	
Grid electricity	0.32 €/kWh
PV electricity	0.12 €/kWh
Battery electricity	0.14 €/kWh
PV feed-in electricity	0.11 €/kWh

The results of the simulation for the 12 months period from October 2018 until September 2019 are shown in Fig. 1 and Fig. 2. The end capacities of the storage tanks are taken into account for the cost calculation. Higher or lower end capacity is added as a bonus or substracted as an extra fee and is calculated by the average price of 0.19 €/kWh. The electricity consumption is calculated by a COP of 4.8 for the buffer storage and by a COP of 4.3 for the DHW storage tanks.

The results of the PV self-consumption and the self-sufficiency of the comparison are shown in Fig. 1. The definition of PV self-consumption and the self-sufficiency are explained in Equa. 6 and Equa. 7. In general, the results do not vary significantly between the different control strategies. Regarding the PV self-consumption the maximal variation for direct PV is up to 2.1 % and for grid feed-in is 6.0 %. Regarding the self-sufficiency, there is an increase of direct PV up to 9.5 % and a decrease of grid consumption up to 8.7 %.

$$PV\ self-consumption = \frac{\sum Direct\ PV}{\sum PV\ production} \tag{6}$$

$$Self-sufficiency = \frac{\sum Direct\ PV}{\sum Total\ energy\ consumption} \tag{7}$$

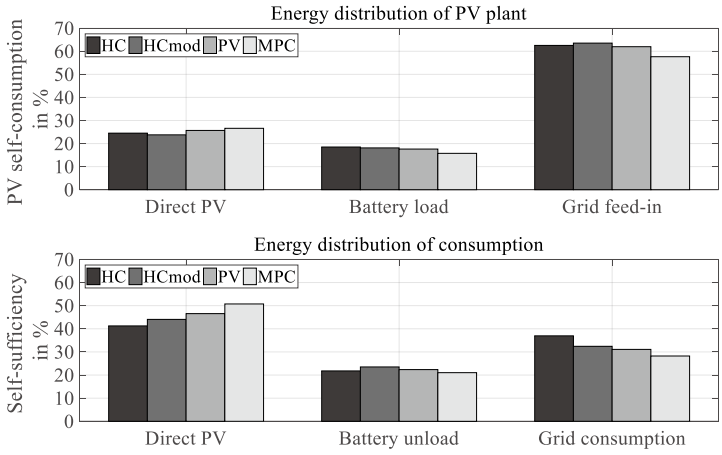


Fig. 1: Energy distribution regarding PV self-consumption and self-sufficiency

The results in Fig. 2 give an overview of operating costs and total energy consumption. Regarding the operating costs, the HC variant is the most expensive and the MPC is the cheapest strategy. However, comparing the HC and the HCmod, both operating in grid mode only, significant cost savings occur in the HCmod, which includes the ability of modulation. The HC also has the highest total energy consumption, which results from the on/off heat pump operation with lower COP. HCmod and MPC have quite similar total energy consumption, while PVC has a higher result for adapting the MHPs to the available PV power and thus, operating in lower COP.

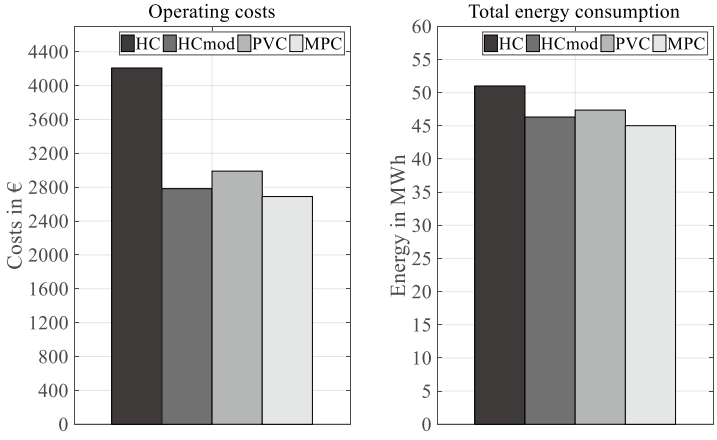


Fig. 2: Operating costs and total energy consumption of 12 months period

4. Comparison of measured operation of HCmod and PVC

The PVC is implemented in the energy system of the eight terraced houses since October 2018. For analyzing the influence of the PVC on the PV self-consumption two time periods are compared. The first time period is a week in December 2018 with low PV production, in which the MHPs operated only in grid mode (HCmod). The second time period is a week in February 2019 with higher PV production, in which the MHPs operated every day in PV mode. Both selected weeks start on Monday and end on Sunday.

For comparing the influence of the PVC on the PV self-consumption and the operating costs, the low PV production of the December week is replaced by the high PV production of the February week. The operation of the MHPs, DHW-HPs and the total energy consumption stays the same. As the operation of the battery is different due to higher load and unload, the battery is modelled as an energy node (see Equa. 3) with battery losses of 25 % from the February week. In contrast to the analysis of the HCmod in December and the PVC in February whose results are only measured, the HCmod with PV from February (HCmodPV) is a combined measured and simulated variant.

Fig. 3 shows the course of the PV production and the total energy consumption in the February week as well as the total energy consumption in the December week. The total energy consumption includes household electricity, MHPs and DHW-HPs electricity. In general, the course of the total energy consumption is quite similar in the two compared weeks, but in February there are higher load peaks. Table 4 gives an overview of the compared variants with the sum of measured energy consumption for both weeks.

Table 4: Overview of variants with measured energy consumption in one week in December 2018 and February 2019

Description	HCmod	PVC	HCmodPV
Time period	Week in December	Week in February	mixed
Control strategy	HCmod	PVC	HCmod
Thermal load in kWh	1.502	1.462	1.502
DHW load in kWh	543	675	543
Electrical load in kWh	480	483	480
PV production in kWh	255	1.191	1.191

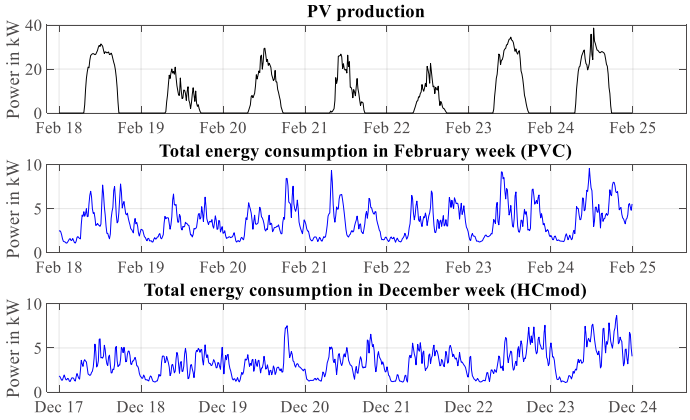


Fig. 3: Course of PV production in February week, total energy consumption of February and December week

The results of the comparison are shown in Fig. 4 and Fig. 5. In general, the total energy consumption of the PVC in February is higher (see Fig. 5 right) and a clear comparison of the variants, regarding operating costs, is not possible. Comparing the PV self-consumption of the variants PVC and HCmodPV, the PVC can increase the PV self-consumption up to moderate 4.1 %. On the other hand a higher grid feed-in of 6.7 % is visible in variant HCmodPV. The results for direct PV, battery load and unload and grid consumption do not vary a lot between the two variants.

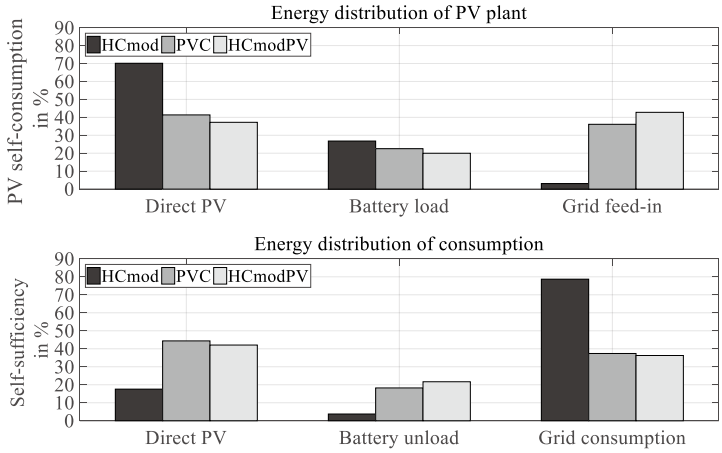


Fig. 4: Energy distribution regarding PV self-consumption and self-sufficiency, measured in variant HCmod and PVC and as well as combined measured and simulated in variant HCmodPV

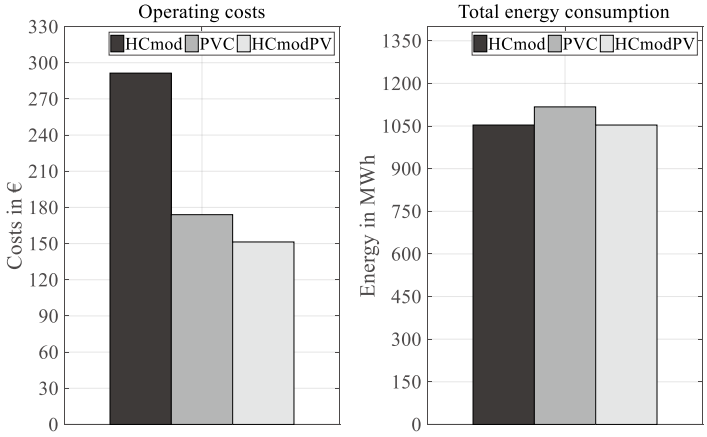


Fig. 5: Operating costs and total energy consumption, measured in variant HCmod and PVC and as well as combined measured and simulated in variant HCmodPV

Conclusion

In this research, two advanced control strategies, a PV rule based (PVC) and a model predictive control (MPC) are developed and compared in simulation with two different heat controlled strategies. Furthermore, the PVC was implemented in real application in eight terraced houses and was compared to a heat controlled operation.

In the simulation study, the control strategies of PVC and MPC increase PV self-consumption with low effect up to 2.1 % and reduce operating costs up to 36.1 % compared to a heat controlled strategy (HC) with on/off heat pumps. However the cost savings mainly result from less energy consumption of a more efficient operation of modulating HPs in part load. Table 5 shows the relative reduction of total energy consumption and cost savings and the relative increase of PV self-consumption and of the Seasonal Performance Factor (SPF) compared to the HC. A heat controlled strategy with the ability to modulate the HPs (HCmod) can easily compete with the advanced control strategies, and even gets partly better results as the PVC.

The influence of the advanced control strategies, PVC and MPC, on PV self-consumption and operating costs is limited. The actual PV and battery prices can not compete to reduce the energy costs significantly because the electricity price for grid and the feed-in tariff offer the economically attractive option to use the public grid as an electricity storage. An energy efficient operation in part load operation of the MHP, as shown in the HCmod, has higher influence than advanced control strategies, increasing PV self-consumption. In further research work, electricity prices are investigated to give an economically attractive solution for PVC and MPC.

Table 5: Relative energy reduction of total energy consumption and cost savings as well as relative increase of PV self-consumption and SPF compared to HC

	Energy reduction	Cost savings	PV self-consumption (without battery)	SPF
HCmod	-9.2 %	-33.9 %	-0.7 %	26.9 %
PVC	-7.1 %	-29.0 %	1.2 %	19.7 %
MPC	-11.8 %	-36.1 %	2.1 %	37.2 %

For comparing the operation of HCmod and PVC regarding PV self-consumption and operating costs in real operation, two periods are analyzed in the monitored terraced houses. The first time period is a week in December 2018 with low PV production, in which the MHPs operated only in grid mode (HCmod). The second time period is a week in February 2019 with higher PV production, in which the MHPs operated every day in PV mode (PVC). To compare the influence of the PVC on the PV self-consumption and the operating costs, the PV production of the December week is replaced by the PV production of the February week (HCmodPV). In general, this method represents a possibility to approximately compare HCmod and PVC mainly with measurements without using detailed simulation tools. The results of PVC show an increase of PV self-consumption of moderate 4.1 % compared to the HCmodPV. As well, the relative parts of battery load and unload and grid consumption do not vary a lot between PVC and HCmodPV. The influence of the PVC is also limited as the course of the total energy consumption in the December and February week are quite similar. In both weeks higher energy consumption occurs during the day and fits to periods of PV production.

In general, the total energy consumption of the variant PVC in February is higher and a clear comparison of the variants, regarding operating costs, is not possible. However under unfavorable assumption, that the additional consumption of the PVC was consumed by grid electricity and thus the highest price is taken into account, the operating costs of the PVC are still 1.5 % higher than the operating costs of the HCmodPV.

As shown in the simulation study and in the comparison of real operation, advanced control strategies increase PV self-consumption in a moderate amount. Furthermore, regarding the operating costs with the assumed electricity prices, it becomes clear, that an energy efficient operation of (modulating) heat pumps has higher influence on operating costs than the increase of PV self-consumption. Under these conditions PV or MPC driven control strategies are not able to compensate an inefficient operation during PV production by cost savings due to higher PV self-consumption.

Acknowledgements

This paper represents results from the project ”Herzo Opt – Monitoring der Gebäudehülle, des thermischen Raumkomforts und der Anlagentechnik mit Betriebsoptimierung“ (FKZ 03ET1641A). The project is supported by the Federal Ministry for Economic Affairs and Energy on the basis of a decision by the German Bundestag.

References

[1] Wirth, H., 2018. Recent Facts about Photovoltaics in Germany. Fraunhofer ISE.
[2] Battaglia, M., Haberl, R., Bamberger, E. and Haller, M., 2017. Increased self-consumption and grid flexibility of PV and heat pump systems with thermal and electrical storage. Energy Procedia 135, 358-366.
[3] Psimopoulos, E., Leppin, L., Luthander, R. and Bales, C., 2016. Control algorithms for PV and Heat Pump system using thermal and electrical storage. ISES International Solar Energy.
[4] Fischer, D., Bernhardt, J., Madani, H., Wittwer, C., 2017. Comparison of control approaches for variable speed air source heat pumps considering time variable electricity prices and PV. Applied Energy.
[5] Pichler, M., Heinz, A., Rieberer, R., 2017. Model predictive heat pump- and building control to maximize PV-power on site use. 12th IEA Heat Pump Conference 2017.
[6] TRNSYS (2017). TRaNsient SYstems Simulation, Solar Energy Laboratory, University of Madison-Wisconsin. Version 17.2
[7] Dentel, A. and Betzold, C., 2017. Control Strategies for Geothermal Heat Pump Systems in Combination with Thermal and Electrical Storage Units. Building Simulation 2017.
[8] The MathWorks, Inc., MATLAB Version: 9.0.0.341360 (R2016a)
[9] Betzold, C. and Dentel, A., 2019. PV Optimized Control of Modulating Heat Pumps regarding PV Self-Consumption. Building Simulation 2019.
[10] Gurobi Optimization, LLC., Gurobi Version 8

13th IEA Heat Pump Conference
April 26-29, 2021 Jeju, Korea

Application of the DevOps methodology on heat pump controllers

Markus Nürenberg[a], Stephan Göbel[a], Philipp Mehrfeld[a], Dirk Müller[a]

[a] RWTH Aachen University, E.ON Energy Research Center, Institute for Energy Efficient Buildings and Indoor Climate, Mathieustrasse 10, 52074 Aachen, mnuerenberg@eonerc.rwth-aachen.de

Abstract

In the work, we show how the DevOps methodology supports the development of heat pump (HP) systems. Modern software development and operation control uses the DevOps method to roll out quickly new software, while keeping an overview of the effects and changes. These features are also applicable for HP controller software. Since rolling out new software to customers is a risky task, the deployment stage of the DevOps cycle runs additional hardware-in-the-loop (HiL) experiments first. If the result is sufficient, the next stage is carried out. Evidently, this requires a high level of automation. On the software side, we use the GitLab CI/CD infrastructure to validate software under static and dynamic measures. Once the HP software is ready to run on a real refrigerant circuit, it is automatically deployed to one. The HP within the HiL setup continues to run with the new software. Since the HiL experiments perform in real time, a continuous observation is necessary to abort the experiment once it fails. Thus, the HiL test bench requires a complex data handling and processing infrastructure.

© HPC2020.
Selection and/or peer-review under responsibility of the organizers of the 13th IEA Heat Pump Conference 2020.

Keywords: DevOps; heat pump; controller; software development; hardware-in-the-loop

1. Introduction

In this paper, we propose the use of the DevOps methodology to build the next generation of HP controllers. Various work (e.g. [1] and [2]) shows that more sophisticated HP controllers will achieve a major step towards more efficient HP systems. HP manufactures are bound be the obligation that their products shall work for several years, which implies a robust system. Within the software development domain, a uniformly and automatic testing of algorithms is state of the art [3]. Thus, controller software should also be designed and tested according to these standards. However, in the domain of HP software development we often find manually tested software. Especially, when software is applied on machines (like a HP) we have to assume a curtain amount of complexity. This even increases, when we add more components to a HP system and couple the on a data a hydraulic level. Disturbances permute thou the system and the controller work against that. The developer is not aware of all disturbances in advance, therefore, laboratory and field tests have to be conducted. Especially the dynamic behavior of the HP system is still not completely described by simulation. Therefore, HiL experiments are powerful method to gather a useful amount of data from a system under realistic conditions.

2. The DevOps mythology

The DevOps mythology is a relatively new concept within the agile work methods. The name “DevOps” consists of the two words “Development” and “Operations”. Development represents the whole process of factoring software code until the deployment phase. Once software is deployed, operations takes over. Typical

services are technical support, distribution of software, collecting user and technical feedback. In the best-case scenario these information then find a way back to the development department. The DevOps approach now forces these units together into a continuous workflow. However, this usually applies for software produces and services, but for hardware products. Especially for those who have a live span of a decade. The following graphic illustrates the DevOps concept. Starting in blue with the "Plan" phase of the development branch. In the next two phases, software is created and tested. After various successful tests the software is prepared for the deployment. In the "Release" and "Config." phase, the software is rolled out and databases and servers are reconfigured to match new requirements. During the "Monitoring" phase, the operations team gather data regarding the penetration of the update but also the feedback from costumers and their systems. These information lay the basis for further feature or fix development, which closes the cycle.

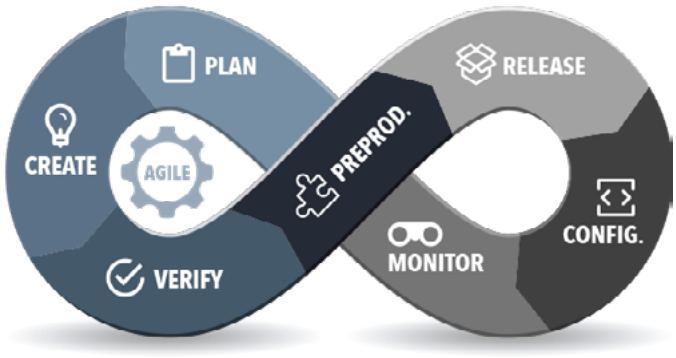


Fig. 1. The DevOps cycle [4]

3. DevOps for HP controller development

We will now propose the application of this DevOps methodology onto the development of a HP controller. Hereby, the controller could just be controlling the refrigerant cycle or the whole HP system, which consists of more other actors and sensors (e.g. pumps, storage temperature, etc.).

The start of our DevOps cycle is again the plan phase. Here, features are pronounced or derived from a requirements engineering process. Zia Babar [5] describes the process in his work. From a market research, customer surveys and user input a product backlog derives. After a grooming of the product backlog this merges into a planning release. However, smaller changes, parameter studies or design of experiments (DoE) studies, such as Mehrfeld [6] used to determine the influences on the seasonal performance of HP systems, can also be set up. If the changes is not based on a simple technical solution but more a holistic request such as "better system performance" or "faster defrost cycle", we will need to translate this into a technical problem first. One of the challenges during this process is the use of different languages, which are brought by the experts of different domains. For example has the word "faster" a different meaning in the field of thermal building processes than on an electrical scope. Therefore, a clear description of the changes and the expected is necessary and can be achieved by creating a specific "definition of done". In addition, the use of issue temples supports this process and ensures that all information, necessary to the task, are available. In fact, there are several platform tools available to support one in this task. We use GitLab as it supports the whole DevOps cycle and is hosted by the university.

After the planning, the coding process starts. Whether it is done in a high-level language such as C/C++ or with an interpreted language such as Python or Java, the source code needs to be available on the platform to run the next steps fully automated. Usually, for each issue a new branch of the project is created in order to separate contributions to different issues. All changes in the software code are committed and pushed to the platform. An ".yml" configuration file (depending on the platform) than leads through the following phases. In case of a parameter study or DoE automated code generation performs this step multiple times. Hereby, we use the CI capability of GitLab to start multiple tests sequences. These sequences are labeled pipeline and can

be tagged with various attributes to route their further way. The following graphic (Fig.2) illustrates the transition from the creating phase to the testing or verifying phase.

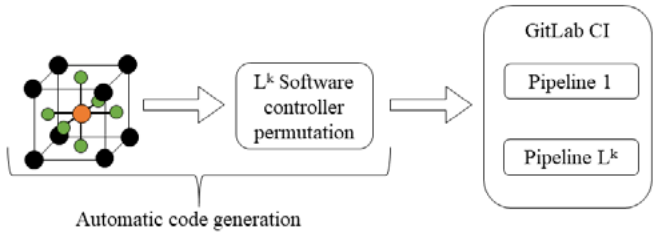


Fig. 2. DoE process as part of DevOps phase. L = Levels, k = number of factors

In this example automatic code generation sets up L^k permutation of the controller. For k being the number factors we want to change and L the number of levels each factor is set to. For a parameter study with no changes to the functionality or structure of the code, the first step of testing would be a simple unit test. When other changes are made, it is wise to run some static code tests first. Figure 3 illustrates a series of test, which can be performed to make sure the controller code matches the company standards towards naming and avoids security issues and common errors. Since errors are recognized before detecting them in expensive hardware tests that even might break the device under test money can be saved.

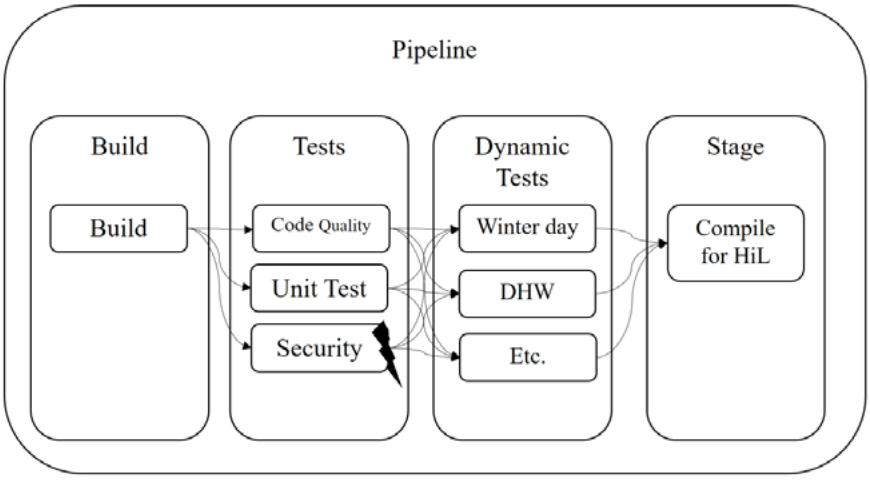


Fig. 3. Pipeline with four stages. Some of the tests are parallel, in order to skip them if necessary. In this case the security test fails but the process continues anyway. After dynamic performance tests a release candidate is compiled to run on the HP controller. The process chain ends with this stage. A HiL experiment toolchain is now able to pull the controller.

These static tests can run in sequel, parallel or as a combination. This depends on the usage of the test result. If the failure of a test represents an abort criteria, there is no need in pursuing any further test. In the example, a security test fails because of a hard coded ip address. This would not be acceptable for production, since the test is tagged accordingly for development, the testing continuous anyway. After the completion of all static tests, the unit testing starts. In a test driven development unit tests are written beforehand. This means, that any code that satisfies the test is consider acceptable. Therefore, the creation of unit tests should be done thoroughly. When focusing on the HP controller the following unit tests should be considered:

- Test for faulty input
    - This tests checks whether the controller reacts correctly to faulty sensor input (e.g. cable break) and if the HP then goes into the correct save or failure mode.

- Test for refrigerant cycle working envelop
  - The refrigerant cycle is bound by the chemical properties (decomposition risk) of the refrigerant and physical properties of the components (burst or vacuum limitations). Here, the temperature and the pressure of the refrigerant are to be handled by the controller within a working envelop.
- Test for correct state switches
  - When working with a state machine the transient conditions allow a step from one to the other state. This test should check if the conditions allow a correct operation or if a deadlock occurred.
- Test for critical comfort conditions
  - This test checks if comfort conditions like domestic hot water and space heating temperatures are met.
- Etc.

Most of these tests can be designed as a rule based sequence. If time constants or timers are involved in the controller function the test framework needs to be able to speed up the internal time, since tests would take too long to finish in real time. This quality is fundamental for any dynamic testing. With these kind of tests we do not only want to determine if a controller works, but how good according to several KPIs.

We use Modelica as modeling language and the ”Functional Mockup Interface” (FMI) [7] to connect the controller to a virtual environment. The FMI standard would allow us to use different modeling approaches as well. The models can vary from simple weather input to tapping profiles to building simulation with the duration from hours to months. If possible, a time clustering should be applied to shorten the simulation time, as Schütz et al [8] described.

If all tests are positive, the software candidate is passed to the next phase. This one is called preproduction and marks, in our case, the link between the virtual testing and hardware testing. The platform builds the controller software for the target HP platform. Thus, all libraries and additional software must be present or the process takes a detour to a manufacture’s building process. This might be necessary when third party intellectual property is involved. Figure 4 illustrates the building phase with known e.g. open source software and company owned closed source software.

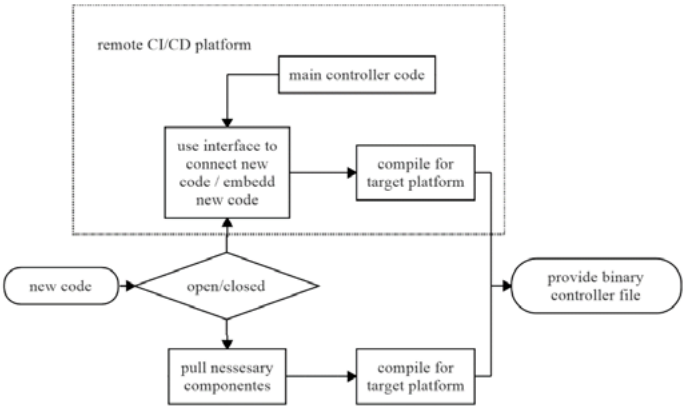


Fig. 4. Process of new code being added to the main controller code. Lower path for known e.g. open code. All necessary components such as libraries or the main code are pulled from registers and compiled according to the target systems’ specifications. The upper path couples a remote CI/CD platform or runner to the process. The main code or any library is unknown. The new code is either embedded into a function or uses an interface to connect to the main code. The code is then compiled by the remote system and a binary file of the controller is provided.

At this point we take the testing to our laboratory, which is equipped with a hardware-in-the-loop infrastructure. There, a HP system is set up according to the release plan. This marks the next phase of the DevOps cycle. This phase determines who will when get which update. When distributing updates to multiple

devices, it might be helpful to do so in waves. Hereby, occurring issues will not affect all devices at one time. Since we are focusing on one HP the HiL infrastructure will run one test at a time. The following figure 5 illustrates the digital setup of the HiL infrastructure. The config phase of the DevOps cycle stets up the production environment, in our case the HiL experiment. A service runner configures all software entities according to a predefined test plan.

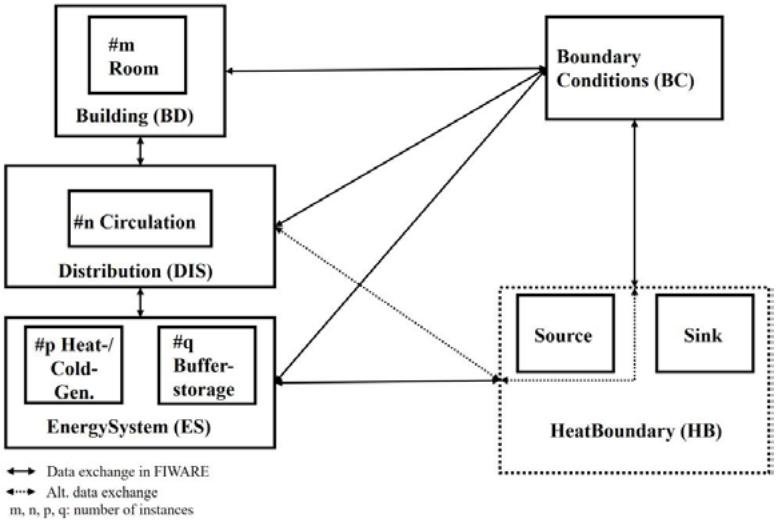


Fig. 5. HiL digital infrastructure. Each component is capsulated and is represented by hardware measurements or a simulation. The entities communicate via MQTT [9] within the FIWARE [10] platform. The installed HP is operated in a climate chamber (HB Source) and connected to a hydraulic test bench (DIS). The digital image of the HP is located in one ES instance. The building simulation BD operates as virtual sink for the HP system. Where the BC instance provides further conditions such as weather or user occupancy.

After the experiment is set up, the compiled controller is flashed onto the HP. The HP is then configured via automated procedure or manually (e.g. heating curve, etc.). From there on the monitoring phase begins. By gathering various data the experiment is evaluated in real time. Watchdog entities hook themselves onto the data streams and calculate various KPIs. In addition, they monitor the test bench behavior. Is either the test bench out of its limitations or a KPI is outside its acceptance, the experiment can be aborted early. The data is stored in a time series database and available for debugging. From there a decision can be made is the experiment and therefore the controller function or parameter set is an improvement and worth to be pursued. From here the DevOps cycle starts again with the planning phase.

4. Conclusion

In this paper we shine a spotlight on the possibilities of the DevOps for HP controller development. We start off with the general introduction of the DevOps methodology in the software development domain. Followed by a use case in the field of HP development. Hereby, we suggest an automated code generation for parameter studies, with creates a full factorial set of controllers, which have to be evaluated. Since the controller software is hosted on a CI/CD platform the following phases of the DevOps cycle are driven by the platform. After a series of tests and evaluations of the code, its performance or even feasibility is tested by dynamic simulations. Candidates, which outperform predefined KPIs are staged for a HiL infrastructure to be tested. A semi-automated process sets up the HiL experiment, while an extensive monitoring evaluates the experiment in real time. This data can then be used to measure the success of the implementation or be the basis for further work.

References

[1] J. A. Candanedo, V. R. Dehkordi and J. Tamasauskas, "IMPACT OF HEAT PUMPS AND PREDICTIVE CONTROL ON RESIDENTIAL ENERGY USE, LOAD AND GRID INTERACTION: A CANADIAN PERSPECTIVE," Hyderabad, India, 2015.

[2] D. Fischer, J. Bernhardt, H. Madani and C. Wittwe, "Comparison of control approaches for variable speed air source heat pumps considering time variable electricity prices and PV," 2017.

[3] I. J. 1. 7. I. J. 1. 7. ISO/IEC JTC 1/SC 7 Software and Systems Engineering, *Software and systems engineering - Software testing,* International Organization for Standardization, 2018.

[4] Perforce Software, "https://www.perforce.com/," Perforce Software , 14 11 2019. [Online]. Available: https://www.perforce.com/solutions/devops.

[5] B. Z., L. A. and Y. E., Modeling DevOps Deployment Choices Using Process Architecture Design Dimensions, Springer, 2015.

[6] P. Mehrfeld, M. Nürenberg, K. Huchtemann and D. Müller, "Influences on the Seasonal Performance of Heat Pump Systems Investigated Via Dynamic Simulations," Portorož, Slovenia, 2016.

[7] Modelica Association, "fmi-standard," 14 11 2019. [Online]. Available: https://fmi-standard.org/.

[8] T. S. (CA), M. H. Schraven, H. Harb, M. Fuchs and D. Müller, "Clustering algorithms for the selection of typical demand days for the optimal design of building energy systems," PORTOROŽ, SLOVENIA, 2016.

[9] OASIS Open, "OASIS Open MQTT Version 5.0," 14 11 2019. [Online]. Available: https://docs.oasis-open.org/mqtt/mqtt/v5.0/mqtt-v5.0.html.

[10] FIWARE Foundation, "FIWARE," 14 11 2019. [Online]. Available: https://www.fiware.org/.

13th IEA Heat Pump Conference
April 26-29, 2021 Jeju, Korea

Three Years' Performance Monitoring of a Mixed-Use Ground Source Heat Pump System in Stockholm

Jeffrey D. Spitler[a, *], Signhild Gehlin[b]

[a]School of Mechanical and Aerospace Engineering, Oklahoma State University, Stillwater, Oklahoma, USA
[b]The Swedish Geoenergy Center, Box 1127, 22104 Lund, Sweden

Abstract

The student center, Studenthuset, at Stockholm University in Stockholm, completed in the fall of 2013, is a thoroughly instrumented mixed-use 6300 m^2 four-story building. Space heating and hot water are provided by a ground source heat pump (GSHP) system consisting of five 40 kW off-the-shelf water-to-water heat pumps connected to 20 boreholes in hard rock, drilled to a depth of 200 m. Space cooling is provided by direct cooling from the boreholes. The Studenthuset building monitoring project is part of the IEA HPT Annex 52 – *Long-term performance measurement of GSHP systems serving commercial, institutional and multi-family buildings*. This paper presents results from three years of measured performance data to calculate the long-term performance of the Studenthuset GSHP system. A number of performance indices are calculated and presented to describe the short-term and long-term system performance for selected system boundaries. Seasonal, monthly and binned performance coefficients for both heating and cooling operation are presented and discussed. The Legionella protection system, hot water continuous circulation system, and internal heating/cooling distribution system reduce the system energy performance.

© HPC2020.
Selection and/or peer-review under responsibility of the organizers of the 13th IEA Heat Pump Conference 2020.

Keywords: Ground source heat pumps; performance monitoring; COP; SPF; system effects

1. Introduction

It is well known that many building heating and cooling systems consume excess energy due to errors in design and installation, as well as non-optimal operating and control settings. Such problems may not be detected and mitigated for months or years, unless performance measurements are made. Despite the obvious need for better knowledge and means to secure optimal energy performance in buildings, published results from long-term performance monitoring of building energy systems are scarce.

Gleeson and Lowe [1] reviewed field measurements of heat pump systems for residential buildings, mainly single-family buildings, comprising 600 heat pump systems in six European countries. Of these 216 were ground source heat pump (GSHP) systems. There are few published long-term performance measurements of larger, non-residential GSHP systems. Spitler and Gehlin [2] give an overview of published long-term ($\geq$ 1 year) measured SPF and COP values reported in the literature for 55 GSHP systems worldwide. Such systems are necessarily more complex than GSHP systems for small residential buildings, and often include both heating and cooling as well as supplementary heating and cooling sources and heat recovery. With this in mind, a four-year international collaboration project IEA HPT Annex 52, *Long-term performance measurement of GSHP systems for commercial, institutional and multi-family buildings* [3] was initiated in 2018 with the aim to monitor and analyze the long-term performance of a large number of ground source heat pump systems in several countries. The emphasis is on heat pump and system performance, e.g. determining coefficients of performance, seasonal performance factors and other system efficiency indices.

* Corresponding author. Tel.: +1 405 744 6578.
E-mail address: spitler@okstate.edu.

One of these long-term performance monitoring projects within IEA HPT Annex 52 is the GSHP system at the student union building Studenthuset at Stockholm University in Sweden. Gehlin et al [4] and Spitler and Gehlin [2] analyze performance data for one year of operation (April 2016-March 2017) at Studenthuset including a detailed uncertainty analysis. The analyses include seasonal performance factors and monthly, daily, and binned average values of coefficients of performance. This paper aims to extend the analysis to include 45 months of monitoring (January 2016 through September 2019) and further investigate the correlation between performance factors and load provided.

1.1. Studenthuset building and GSHP system

The student union building Studenthuset is located within the large campus area of Stockholm University in central Stockholm, Sweden. The 6300 m^2 four-story building was completed in the fall of 2013 and contains office area, meeting rooms, study-booths for students and a café. The building services are thoroughly instrumented and maintained by highly skilled staff.

Space heating and hot water are provided by a ground source heat pump (GSHP) system consisting of five 40 kW off-the-shelf water-to-water heat pumps connected to a borehole field. Space cooling is provided by direct cooling from the boreholes; with the maximum fluid temperature leaving the boreholes not to exceed 16°C. Heat distribution inside the building is provided by radiators with a larger-than-usual surface area so that the distribution temperature is 40°C instead of 55°C, which is more common in Sweden. Cooling distribution is done by a combination of VAV-system (variable air volume) and CAV-system (constant air volume) with chilled beams for ventilation and cooling. The system also includes heat recovery from the kitchen cooling circuit. No auxiliary heating or cooling is installed, except for an electric resistance heater that boosts the hot water temperature to protect against Legionella.

The borefield consists of 20 groundwater-filled boreholes in hard rock, drilled to a depth of 200 m, and fitted with single u-tubes filled with an ethanol/water mixture. The borefield is located below a landscaped courtyard. The boreholes are drilled at an angle so that they reach under the surrounding building (Figure 1).



Fig. 1. Studenthuset in Stockholm, front view (left) and top view with borehole field (right). Photo: Jeffrey D. Spitler.

1.2. System performance indicators

Performance of a GSHP system and its individual parts may be indicated in various ways depending on the purpose of the performance analysis, e.g. energy performance, technical performance and economic performance. The overall system performance is affected by the performance of the source side ground circuit, as well as the heat pump (HP) unit performance and the load side circuit performance, including supplementary heating and cooling. Energy use intensity (EUI), often expressed in kWh/m^2, is an example of a commonly used performance indicator for building heating and cooling systems. However, it does not differentiate between the effects of the building envelope, its usage, and the performance of the heating and cooling system. Therefore, it gives little information about GSHP system performance. For GSHP systems, system coefficients of performance (COP and SCOP), energy efficiency ratio (EER and SEER) and seasonal performance factors (SPF) with various boundaries are used, however not in a consistent way [2]. Gehlin and Spitler [5] discuss target groups for GSHP system performance and indicators at various system levels identified by the IEA HPT Annex 52 workgroup. Such indicators, some of which we will use in this paper, are performance factors (PF) with a clear indicator of the time period (seasonal, monthly, weekly, daily, or binned – SPF, MPF, WPF, DPF, BPF) and with subscripts that correspond to the boundary conditions, e.g. H1, C4. Another type of performance indicator is the building energy signature, which shows the building heating and cooling loads at various

outdoor air temperatures. The ground heat exchanger pressure drop and exiting fluid temperature (GHE ExFT) variation over time (seasons and multiple years) give indications such as of possible ground source circulation failure and ground heat balance.

1.3. System boundaries

One reason of the confusion in GSHP performance literature, pointed out by Spitler and Gehlin [2], is the inconsistent or non-existent declaration of chosen system boundaries for performance evaluation. Within HPT Annex 52 the system boundary schema developed within the EU project SEPEMO [6] was used for calculation of COP and SPF as a starting point. The SEPEMO boundary schema was therefore used in the performance calculations of the Studenthuset operation in 2016 by Gehlin et al. [4] and Spitler and Gehlin [2]. The SEPEMO boundary schema was aimed at small monovalent or bivalent heat pump systems and has limitations when accounting for the complexity of larger GHSP systems such as Studenthuset. HPT Annex 52 has therefore proposed a new system boundary schema [5], consisting of six defined boundaries and an indicator for use of supplemental heating or cooling. This system boundary schema is used in this paper for the evaluation of the Studenthuset operation over the period January 2016-September 2019 (Figure 2). The Annex 52 boundary schema and its relation to the SEPEMO boundaries is shown in Table 1.

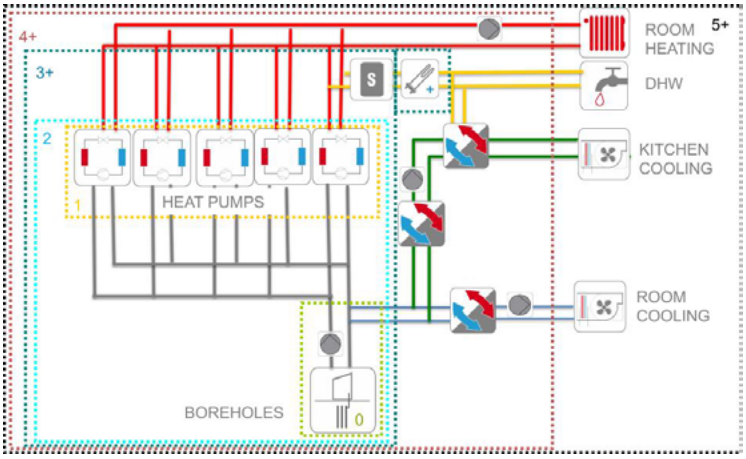


Fig. 2. Schematic and Annex 52 system boundaries for Studenthuset.
Pictograms in drawing used with permission from TU Braunschweig IGS.

Table 1: System boundaries according to the HPT Annex 52 schema and comparison with the SEPEMO boundaries. From [5].

Boundary description	HPT Annex 52 Boundary levels											
	0	0+	1	1+	2	2+	3	3+	4	4+	5	5+
Ground Source (circulation pumps+ ground source)	X	X			X	X	X	X	X	X	X	X
Heat pump unit including internal energy use, excluding internal circulation pump			X	X	X	X	X	X	X	X	X	X
Buffer tank (including circulation pumps between heat pump and buffer tank)							X	X	X	X	X	X
Circulation pump on load-side (between buffer tank & building H/C distribution system)									X	X	X	X
Building H/C distribution system											X	X
Auxiliary heating or cooling		X		X		X		X		X		X
Equivalent in the SEPEMO boundary schema			H1/C1		H2/C2	H3					C3	H4/C4

For Studenthuset the following performance factor levels exist and can theoretically be determined for the heating system; H0, H1, H2, H3+, H4+ and H5+. However, the available measurement data only allows for

H1 (approximately), H2, H3+ and H4+ to be calculated. For the cooling system C0, C2, C3, C4 and C5 exist, but only C2, C3 (C2 and C3 are the same for this system) and C4 are possible to calculate from the available measurement data with a sufficient degree of accuracy. There is no cooling machine in the cooling system and no supplementary cooling.

2. Measurements and Analysis

2.1. Instrumentation

Compared to many buildings, the Studenthuset GSHP system is extensively instrumented. There are, unfortunately, no measurements made of airflow rates, so it is not possible to estimate either the heating or cooling provided to the ventilation air or the building by the heat recovery systems, which means that level 5 performance factors cannot be determined. The level 1 boundary for heating cannot be calculated without also including internal electricity use in the heat pump unit, i.e. internal circulation pump and control board. We therefore denote the performance factors for level 1, included its internal electricity use, with an asterisk. With the existing measurements, it is possible to estimate performance factors for the Annex 52 boundary levels 1*, 2, 3+ and 4+ for heating, and levels 2 (= 3) and 4 for the cooling.

A full description of the instrumentation is given in [2]. Briefly, heat transfer rates from the heat pumps to the building heat distribution system are measured with an energy meter that determines the heat transfer rate calorimetrically. The heat provided by the heat pumps to the DHW is determined using the volume flow rate measured with a flow meter, the controlled temperature provided by the heat pumps (55°C) and the estimated incoming temperature from the Stockholm water supply based on measurements made at seven different buildings in Stockholm [7,8]. Heating provided by the Legionella protection system is estimated based on a steady consumption of 3 kW of electricity due to the recirculation pump and dissipated energy from the hot water that was continuously circulated around the building, and energy provided by the electric resistance heater to heat the DHW from 55°C to 60°C. The cooling provided by the system is measured with the same type of instrumentation as used for measuring the building heating provided.

The system electrical energy consumption is monitored continuously and recorded on an hourly basis. Electricity use for the five heat pumps including the heat pump that is dedicated to DHW heating and the electricity consumed by the Legionella protection system are measured by one electricity meter. Electrical energy consumed by the heat pumps for boundary H2 is estimated by subtracting the energy consumed by the Legionella protection system.

Electrical energy consumed by the source-side circulation pump was metered along with the electrical energy for fans used for air conditioning, circulation pumps on the load side (distribution), and circulation pumps on the source side (boreholes), as well as electricity used for running the rotary exhaust air heat exchangers in the kitchen and building. A separate set of measurements over a two-week period was made to allow estimation of the electricity used by the source-side circulation pump as a function of flow rate. The electricity used for heating and cooling respectively during those many hours of operation when both heating and cooling are being provided by the system, was allocated based on the amount of heating and cooling provided at each hour.

2.2. Analysis and uncertainty analysis

Estimation of the uncertainty of the performance factors is highly desirable to understand the significance of the results as well as to shed light on design and specification of instrumentation for future monitoring projects. The uncertainty analysis in this study is described in detail in [2]. It involves calculation of the propagation of uncertainties from the physical measurements to the final quantities of interest, and follows the general procedures described by Taylor [9]. The uncertainty in the performance factor calculations are represented with error bars in Figures 4-6 and 8-11.

3. Results

This paper uses measured performance data to characterize the actual thermal performance of the GSHP system over 45 months of operation. Measured data from the period January 1 2016 through October 15 2019, are used.

3.1. Heating and cooling loads

The annual energy loads for space heating (excluding heat recovery), space cooling and domestic hot water (DHW) including the Legionella protection system (LPS) over the measured period are shown in Table 2. The heating load for each of these years is around 200 MWh, which is in accordance with the design heating load. The cooling load for 2018 is nearly 50% higher than the other years due to an exceptionally warm summer in 2018.

Table 2. Annual energy loads 2016-2019

Year	2016	2017	2018	2019 Through Oct. 15th
Cooling (MWh)	111	114	161	107
Heating (MWh)	201	198	214	144
DHW including LPS	16	17	19	17

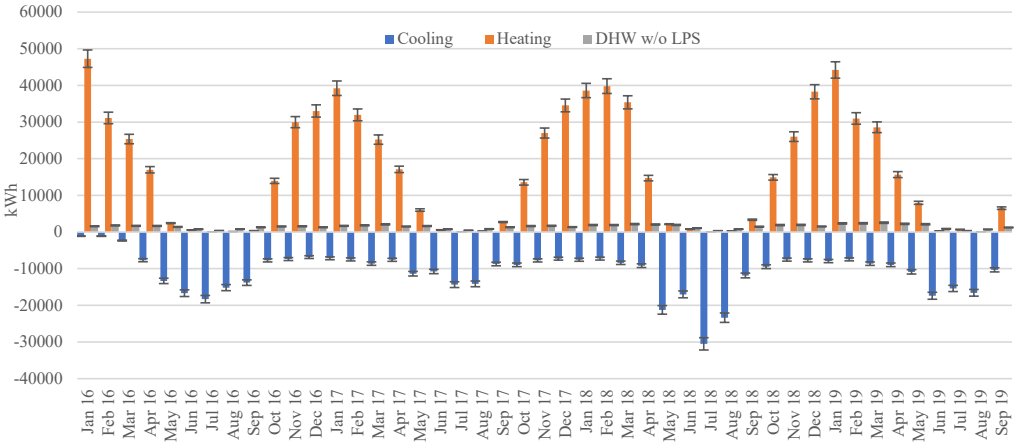


Fig. 3. Measured monthly heating and cooling loads for Studenthuset January 2016-September 2019.
(DHW w/o LPS refers to domestic hot water heating, not including Legionella protection system energy use)

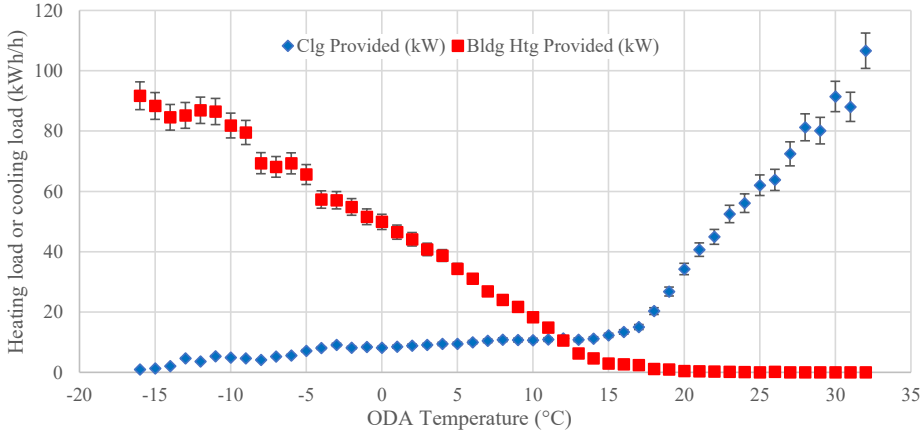


Fig. 4. Measured building energy signature for Studenthuset 2016-2019 with error bars.

Monthly energy loads for the measurement period are shown in Figure 3. Figure 4 shows the building energy signature for Studenthuset, i.e. the heating and cooling load respectively versus outdoor air temperature (ODA). As can be inferred from Figure 3 and 4, heating and cooling is provided simultaneously over a substantial part of the year. The cafeteria in the building requires kitchen cooling throughout the year.

3.2. Monthly Performance

Monthly heating performance factors are presented in Figure 5. In order to keep the figure readable, only sample error bars are shown for January-February and July-August each year. Accuracy is generally good when heating loads are high or when boundaries H3+ and H4+ are used. One notable feature of Figure 5 is that the monthly performance factors are highest in the winter months and lowest in the summer months. This is counter to the expectation that the heating performance factors will be higher when the heat pump entering fluid temperatures are higher.

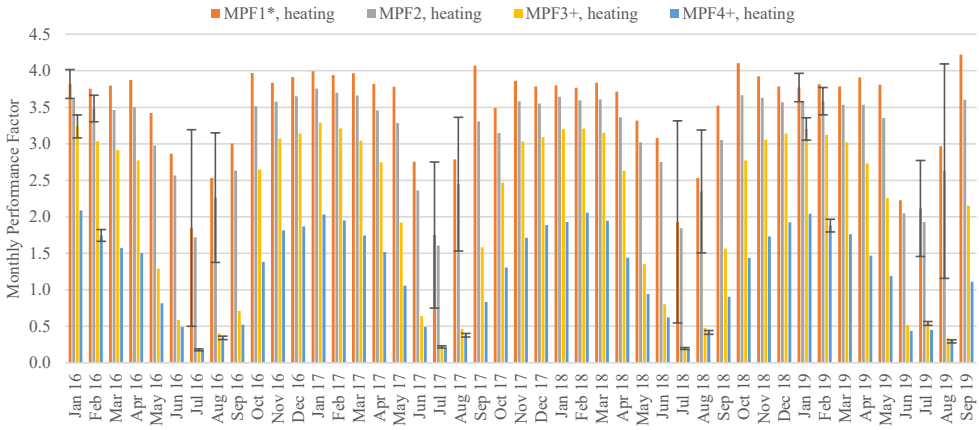


Fig. 5. Monthly heating performance factors with sample error bars, January 2016-September 2019. (The asterisk in MPF1* means that the heat pump internal electricity use is included).

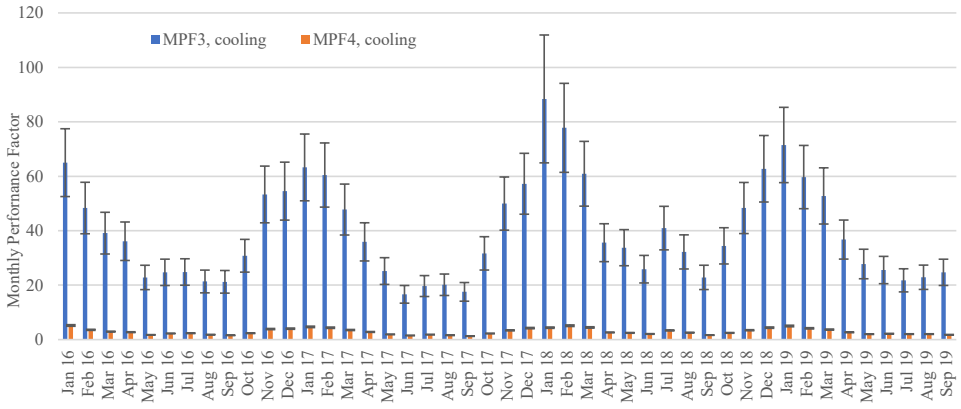


Fig. 6. Monthly cooling performance factors, January 2016-September 2019

Figure 6 shows very high MPFC3, which, in this system, is the same as MPFC2. Because the cooling is provided directly without a heat pump, the only power used at levels C2 and C3 is the source-side circulating pump. Furthermore, because the source-side circulating pump provides both cooling and the source fluid for

heating with heat pumps, its energy consumption is allocated between cooling and heating, thus further lowering the required input energy, and increasing the cooling MPFC3. However, the energy required to distribute the chilled water to the air handling units, accounted for in boundary C4, substantially reduces the cooling performance factors. It may also be noted that the cooling MPFs are higher in the winter months when the ground loop fluid temperatures are lower.

3.3. Seasonal performance

Table 3 summarizes the seasonal performance factors for each boundary. In addition to those presented above, combined SPF for heating and cooling taken together are presented in the last two rows. This avoids the problem of having to allocate pumping power between heating and cooling and, for more complex systems, may make more sense than attempting to determine heating and cooling SPF separately. The SPF calculated for each year are fairly similar, though the unusually hot summer of 2018 significantly increased the cooling load and also increased the cooling and combined SPF values.

One notable feature is the significant reduction in SPF going from boundary level 3 to 4. The only difference is the inclusion of pumping power to distribute chilled water and hot water to air handlers and panel radiators. An interesting, but inconclusive comparison can be made between this system and the ASHRAE Headquarters building GSHP system in Atlanta. [10, 11] This system is a distributed system with reversible water-to-air heat pumps. The reported system heating and cooling COPs for a 2 year-period [10] are roughly equivalent to SPFH4 and SPFC4 and are 3.6±0.3 and 4.2±0.6, respectively. (The ASHRAE system includes the fan energy to deliver the heating and cooling to the space. But, like the Studenthuset system, the ventilation fan energy is not included.) The Studenthuset GSHP system serves about four times the area of the ASHRAE GSHP system; the building energy signatures are significantly different, and the ground temperatures in Atlanta are warmer than in Stockholm. Yet, the ASHRAE system SPFH4 and SPFC4 are both considerably higher than the Studenthuset system. At the very least, this suggests that the pumping power used to distribute heating and cooling in the Studenthuset building is quite high. Whether it could be reduced by modifying the controls settings, or whether the high pumping power is “baked in” by the hydronic design is an open question at this point.

Table 3. Seasonal performance factors 2016-2019. The asterisk denotes that the heat pump internal electricity use is included.

Year	2016	2017	2018	2019 until Oct 15th
SPFH1*	3.8±0.2	3.8±0.2	3.8±0.2	3.8±0.2
SPFH2	3.4±0.2	3.5±0.2	3.5±0.2	3.5±0.2
SPFH3+	2.6±0.1	2.7±0.1	2.7±0.1	2.6±0.1
SPFH4+	1.5±0.1	1.5±0.1	1.6±0.1	1.5±0.1
SPFC2(3)	37±7	37±7	46±9	38±7
SPFC4	2.9±0.2	2.8±0.2	3.3±0.2	2.9±0.2
SPFCH2	5.0±0.2	5.1±0.2	5.6±0.2	5.5±0.2
SPFCH4+	1.8±0.3	1.7±0.3	2.0±0.3	1.8±0.3

3.4. Factors influencing performance

As discussed in Spitler and Gehlin [2] the system performance for both heating and cooling was more dependent on the heating and cooling provided than the ground heat exchanger exiting fluid temperature. This was demonstrated somewhat indirectly by plotting the overall daily performance factor vs. the total daily heating and cooling loads. Here, we have refined the analysis to calculate performance factors that are binned by the amount of heating and cooling provided.

First, Figure 7 shows the monthly average temperature exiting the ground heat exchanger and entering the heat pump, along with the monthly average air temperature. As expected, the fluid temperatures are relatively moderate compared to the air temperatures. The GHE exiting fluid temperatures are slightly higher in the summer of 2018 than other summers due to the increased cooling loads; but, otherwise, the temperature cycle is fairly stable.

Figure 8 shows the binned heating performance factors relative to the ground heat exchanger (GHE) exiting fluid temperature (ExFT). The general trend is that the heating performance factors decrease as the GHE ExFT increases, contrary to expectations based on thermodynamic considerations for the heat pump. BPFH3+ shows

a marked decrease between 10°C and 11.5°C. In this range, the building heating and cooling loads are low; the building heating loads go to zero at 12°C, and so the system heating performance becomes dominated by the domestic hot water heating. As can be seen, at 11°C and above, BPFH3+ and BPFH4+ are below one. This is due to the Legionella protection system, which consumes electricity to heat the water from 55°C to 62°C, and continuously circulates the water, dissipating about 3 kW heat to the building year-round. During the summer months, when there is little or no building heating needed, this energy is wasted, leading to performance factors less than one.

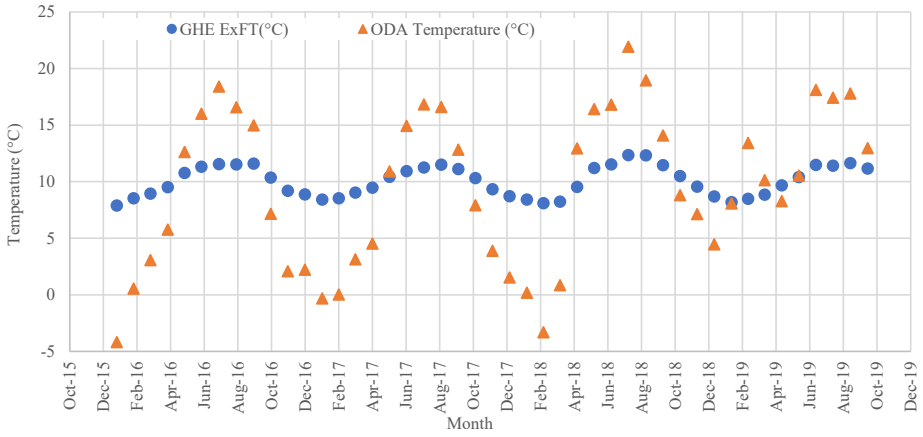


Fig. 7. Monthly average outdoor air temperatures (ODA) and borehole exiting temperatures January 2016 - September 2019

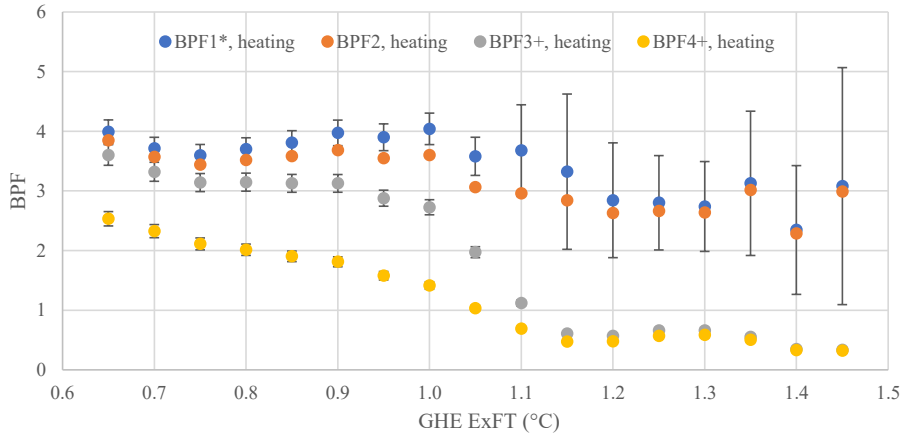


Fig. 8. Heating performance vs GHE Exiting fluid temperature (Error bars have been omitted on BPF2; they are similar, but between 5% and 35% lower than those shown for BPF1* (the asterisk denotes that the heat pump internal electricity use is included). 2016-2019.

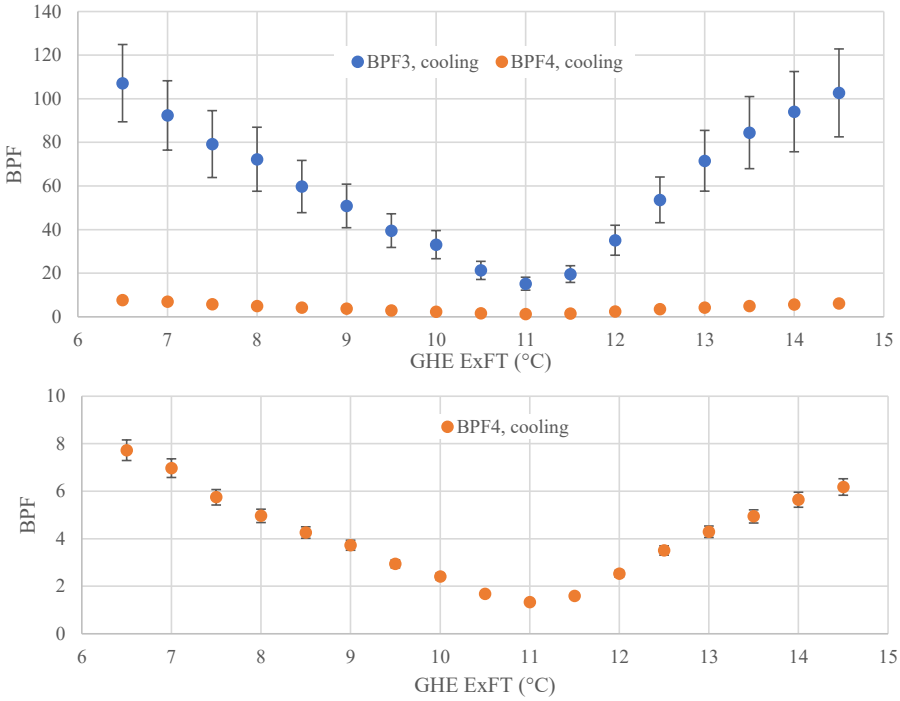


Fig. 9. Cooling performance vs GHE Exiting fluid temperature (°C). 2016-2019.

Figure 9 shows BPFC3 and BPFC4; the V-shaped trend is rather interesting. It is caused by a combination of effects. The cooling load is quite small below 11°C, and most of the pumping power is allocated to heating. Above 11°C, the cooling loads increase significantly. The pumping power also follows a V-shaped trend with a maximum of about 17 kW at both low and high GHE ExFT, and a minimum at 11°C of 11.5 kW. However, when plotted against the GHE ExFT, the pumping does not decrease near as much as the load and the result is the V-shaped profiles shown in Figure 9.

In Figure 10, the heating performance factors have been binned against the heating load. Likewise, in Figure 11, the cooling performance factors have been binned against the cooling load. With the exception of a slight wiggle at 30 kW of cooling provided, the performance factors increase monotonically with the load, demonstrating that the system performance is highly driven by the load. The decrease in the performance with decreasing load has been attributed [2] to cycling losses in the heat pump, parasitic losses within the heat pump (e.g. control hardware), pumping energy, and the use of electric resistance heating. For this system, there is a particularly strong influence of the Legionella protection and DHW recirculation systems, which use 3 kW continuously year-round to circulate hot water around the building.

Another factor is the source-side circulating pump. It is variable-speed, but the lower limit of flow is kept at 8 L/s and the pump uses about 1 kW. This relatively high lower limit often results in a very low temperature difference across the ground loop and continuous power consumption of 1 kW, even when the load is very low.

This sensitivity of the load is not unique to the Studenthuset building. Other systems with measured performance data, including a distributed GSHP system in the US [10, 11] and a central GSHP system in the UK [12] show similar trends.

Possible improvements to the system include lowering the minimum flow on the variable speed control and scheduling the operation of the Legionella protection system and DHW recirculation system. These actions should significantly decrease the energy consumption at low heating and cooling loads.

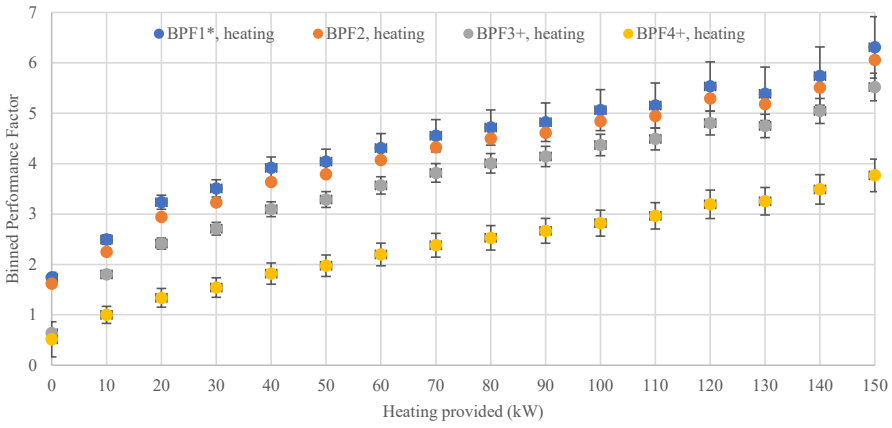


Fig. 10. Binned Performance Factors vs heating load, 2016-2019.
(The asterisk in BPF1* means that the heat pump internal electricity use is included).

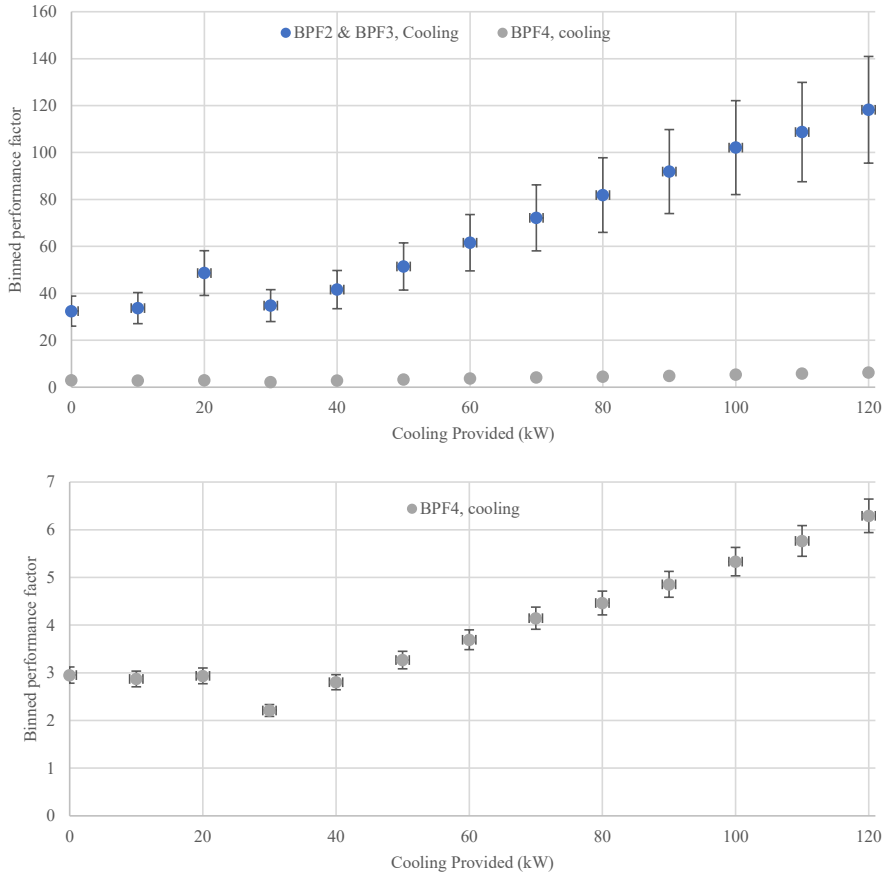


Fig. 11. Binned Performance Factor vs cooling load, 2016-2019

4. Conclusions

This paper has extended the previous one-year analysis [2] of the Studenthuset ground-source heat pump system to nearly four years. For the most part, the trends observed in the first year are still present. The system performance is now more clearly shown to be strongly related to the load – as the load increases, the system performance increases. This also means that the system has relatively poor performance at times when there is little heating or cooling load. A particularly warm summer in 2018 significantly increased the seasonal cooling load, but also increased the cooling performance.

It appears that reducing the minimum flow rate on the source-side (ground loop) circulation pump could improve the system performance at low loads. However, the distribution system that circulates hot water and chilled water from the heat pumps or ground loop to the air handlers and panel radiators consumes much more energy. Improvement of the distribution system could significantly improve the overall system performance. Design engineers, building owners and maintenance staff should take care to minimize energy usage by the distribution system.

Acknowledgements

Thanks to Anders Larsson at Akademiska Hus for his help and support, and for providing measurement data and information about the monitored building. The support from the authors' employers and the Swedish Energy Agency (TERMO research program Grant 45979-1) is gratefully acknowledged. This work is part of the IEA HPT Annex 52, *Long-term performance measurement of GSHP systems serving commercial, institutional and multi-family buildings.* [3].

References

[1] Gleeson, C.P.; Lowe, R. Meta-analysis of European heat pump field trial e_ciencies. Energy Build. 2013, 66, 637–647.
[2] Spitler, J.D. and S.E.A. Gehlin.: Measured performance of a mixed-use commercial-building ground source heat pump system in Sweden. *Energies* 2019, **12**, 2020; doi:10.3390/en12102020. Open access at: https://www.mdpi.com/1996-1073/12/10/2020 (2019).
[3] IEA HPC.: Annex 52 - Long term performance measurement of GSHP Systems serving commercial, institutional and multi-family buildings . Retrieved Nov. 7, from https://heatpumpingtechnologies.org/annex52/ (2019).
[4] Gehlin, S., Spitler, J.D., Larsson, A. & Annsberg, Å.: Measured performance of the University of Stockholm Studenthuset ground source heat pump system. 14th International Conference on Energy Storage-EnerSTOCK2018, Adana, Turkey. (2018).
[5] Gehlin, S. and Spitler, J.D.: Half-term Results from IEA HPT Annex 52 - Long-term Performance Monitoring of Large GSHP Systems. Proceedings of the 13th IEA Heat Pump Conference, May 11-14, 2020 Jeju, Korea. (2020).
[6] Nordman, R.: Seasonal Performance factor and Monitoring for heat pump systems in the building sector, SEPEMO-Build, Final Report. Intelligent Energy Europe. (2012).
[7] Bergkvist, B. *Kartläggning av VVC-förluster i flerbostadshus - mätningar i 12 fastigheter - slutrapport*. BeBo. (2015*).* Available online at http://www.bebostad.se/library/1893/slutrapport-kartlaeggning-av-vvc-foerluster.pdf
[8] Bergqvist, B. *VVC-förluster i kontor och lokaler - mätningar i 11 byggnader - Slutrapport.* Bebo. (2016). Available online at: http://www.energi-miljo.se/sites/default/files/vvc_lokaler_slutrapport_20161129.pdf
[9] Taylor, J.R. An Introduction to Error Analysis—The Study of Uncertainties in Physical Measurements, 2nd ed.; University Science Books: Sausalito, CA, USA. (1997).
[10] Southard, L. E., X. Liu and J. D. Spitler. 2014. Performance of HVAC Systems at ASHRAE HQ – Part 2. ASHRAE Journal 56(12): 12-23.
[11] Spitler, J. D., L. E. Southard and X. Liu 2017. Ground-source and air-source heat pump system performance at the ASHRAE headquarters building. 12th IEA Heat Pump Conference. Rotterdam, Netherlands.
[12] Naicker, S. S. and S. J. Rees. 2018. Performance analysis of a large geothermal heating and cooling system. Renewable Energy 122: 429-442.



13th IEA Heat Pump Conference
April 26-29, 2021 Jeju, Korea

Half-term Results from IEA HPT Annex 52 - Long-term Performance Monitoring of Large GSHP Systems

Signhild Gehlin[a*], Jeffrey D. Spitler[b]

[a]The Swedish Geoenergy Center, Box 1127, 22104 Lund, Sweden
[b]School of Mechanical and Aerospace Engineering, Oklahoma State University, Stillwater, Oklahoma, USA

Abstract

IEA HPT Annex 52, *Long-term performance measurement of GSHP systems serving commercial, institutional and multi-family buildings*, started in January 2018 and will close in December 2021. Within the annex, a large number of larger ground source heat pump (GSHP) systems in seven countries are monitored and analyzed from a long-term performance perspective. By the end of 2019, 40 GSHP performance-monitoring case studies, located in Sweden, the Netherlands, the UK, Finland, Germany, Norway and the USA, form part of the Annex 52 work. These case studies cover a range of building types, system applications and ground sources. Annex 52 offers unique experience and information on GSHP system performance, which will result in guidance on instrumentation, monitoring, uncertainty analysis, data analytics, performance analysis and suitable performance indices based on international experience. This paper gives an overview of Annex 52, including the active monitoring projects and the work and findings so far.

© HPC2020.
Selection and/or peer-review under responsibility of the organizers of the 13th IEA Heat Pump Conference 2020.

Keywords: Ground source; GSHP; performance; monitoring; HPT Annex 52

1. Introduction

The four-year international collaboration project IEA HPT Annex 52, *Long-term performance measurement of GSHP systems for commercial, institutional and multi-family buildings*, has now reached its midway point. As of the end of 2019, seven countries are participating in this annex (Sweden, the USA, Finland, Norway, Germany, the UK and the Netherlands). The aim of this IEA Annex is to monitor and analyze a large number of ground source heat pump systems in several countries from a long-term performance perspective. The emphasis is on heat pump and system performance, e.g. determining coefficients of performance, seasonal performance factors and other system efficiency indices. The results and experience from the many monitoring projects will be used in three annex subtasks. Within the first subtask, an annotated bibliography of previously published long-term monitoring projects reported will be compiled, together with a case study report summarizing all the included Annex 52 monitoring projects. The second and third subtasks will provide guideline documents on instrumentation, monitoring, analysis and key metrics for long-term performance of large ground source heat pump (GSHP) systems.

It is a well-known fact that many building heating and cooling systems consume excess energy due to problems that are only discovered after months or years, and that design decisions and control settings can have significant deleterious impacts on energy efficiency, and yet are poorly understood. Unless performance measurements are made, such problems may never be detected. Table 1 lists possible questions that may be answered by performance monitoring. This Annex is taking steps to standardize methods and analyses that will support widespread performance monitoring of ground-source heat pump systems.

* Corresponding author. Tel.: +46-75-700 88 20
E-mail address: signhild.gehlin@geoenergicentrum.se

Table 1: Possible questions to be answered by performance monitoring

Possible users	Questions to be answered
Prospective building owners	Is a GSHP system worth the extra investment?
Building owners	Is my system saving me the money that I expected?
Building owners	How does my system compare to other systems in the area serving similar buildings?
Building owners	How well does my system meet environmental criteria and building certification requirements?
Code-writing and regulatory bodies	How can we make informed decisions for energy policy, codes, and regulations?
Consulting (HVAC design) engineers	Do the systems I designed work as well as I expected? What should I do differently next time?
Consulting (HVAC design) engineers	How have other GSHP systems for similar applications in my area worked?
Building maintenance staff	Does my system need attention? Are there any failing components? Has the performance increased or decreased since last year? Is it likely to fail in the coming year?
Building energy managers	Is there room for further improvement in the system, or do we need to address other areas?
Controls engineers	How can setpoints be optimized? What are optimal setpoint values?
Commissioning agents	How does the system work compare to the intended design? Is the system constructed according to design documents?
Equipment manufacturers	How well do my products perform in the field? What market opportunities are there for new products and new features on existing projects?
Environmental Certification and Building Performance Certification Authorities	How can certification programs reward real energy efficient systems and not just planned efficiency or low building energy consumption, which may be due to low occupancy?
Handbook authors	What are best practices leading to highly efficient systems?
Researchers	How can simulation models be validated?

1.1. Performance indicators

The over-all performance of a GSHP system is affected by the performance of the source side ground circuit, as well as the heat pump (HP) unit performance and the load side circuit performance, including supplementary heating and cooling. Within Annex 52 we aim to identify and recommend performance indicators that will allow evaluation on all three levels, from a commissioning point of view as well as for fault detection, system optimization and future system development. Table 2 gives an overview of GSHP system performance indicators at various system levels.

A commonly used performance indicator for building heating and cooling systems is energy use intensity (EUI), typically expressed as annual energy usage of the building per unit area, e.g. kWh/m^2. EUI does not differentiate between the effects of the building envelope, its usage, and the performance of the heating and cooling system. Hence it gives little information about GSHP system performance. For GSHP systems, system coefficients of performance (COP) and seasonal performance factors (SPF) with various boundaries have occasionally been reported in the literature. Such measurements, whether termed COP or SPF, have the advantage of being able to focus solely on the actual system performance without comingling the effects of the building envelope and usage. Within the heat pump industry, certain terms (COP, SCOP, EER, SEER) are commonly used to refer to indices that are calculated based on physical testing of a heat pump unit under one or more conditions in a laboratory. Although these indices often have implications for codes and regulations, some researchers [1-3] have used “COP” or “SCOP” to refer to field measurements. The term “performance factor” is used more widely when referring to field measurements, but it has also been used [4] to refer to calculated values based on testing of heat pumps under multiple conditions in a laboratory. SPF (Seasonal Performance Factor) has also been used to refer to periods shorter than a year, e.g. Wemhoener et al. [5] present a graph with monthly SPF. Given the confusing situation, we plan to use the term “performance factor” with an indicator of the time period (seasonal, monthly, weekly, daily, or binned – SPF, MPF, WPF, DPF, BPF) with subscripts that correspond to the boundary conditions, e.g. H1, C4.

Table 2: GSHP system performance indicator matrix

	Is it as designed? (Commissioning)	Does it work well? (Fault detection)	Could it work better? (Optimization)	Could future systems work better?
Ground source	Do measured ground heat exchanger loads, flow rates and temperatures match design values?	What are the measured ground circuit (level 0) performance factors over seasons, months, days? Temperatures and pressure drop?	Could ground circuit pumps and pump control strategies be adjusted? Are there delay times in on-off mode? Are set-points optimal?	Can borehole thermal resistance be decreased? Could better hydraulic design and lower pressure drop be obtained?
Heat pump unit	Do measured HP entering fluid temperatures and flow rates, match design values?	What are the measured HP unit (level 1) performance factors over seasons, months, days? System Efficiency Index (SEI)? Temperatures and pressure drop?	Could HP unit controls be changed (e.g. control curves and set points) Could the HP be changed?	Could sizing be better? Could internal control be improved?
System level	Do measured temperatures, flow rates, energy signatures, seasonal heating and cooling loads and supplemental heating and cooling match design values?	What are the measured system (level 2-5) performance factors over seasons, months, days? Temperatures and pressure drop? Simultaneous heating and cooling?	Are operation schedules and control set-points for supplementary heating and cooling optimal?	Could better hydraulic design and lower pressure drop be obtained? Could components be improved?

2. Annex 52 achievements

In its first two years, Annex 52 has gathered more than 60 international experts from research institutions and industry at four international experts' meetings and a number of national workshops. The focus has been on selecting and setting up GSHP monitoring case studies in all participating countries and surveying previously published large-scale GSHP long-term performance studies and performance indicators. Based on this work, guideline documents and recommendations are under way. A summary of the Annex 52 outcomes so far follows.

2.1. Bibliography

In partial fulfillment of Annex 52 subtask 1, the participants have compiled an annotated bibliography containing 65 publications describing 55 buildings where long-term performance monitoring of larger GSHP systems has been performed and that contain some form of SPF measurement. A further 18 references describe monitoring of larger GSHP systems that do not go as far as determining any SPF. Spitler and Gehlin [6] present a comprehensive review of this performance measurement literature for large GSHP systems. The authors conclude that nomenclature for performance indicators used by different authors is inconsistent, reflecting a lack of consensus on how to evaluate, express and present performance for complex large-scale GSHP systems. Another conclusion is that existing performance data is far too limited to be useful in setting performance expectations.

2.2. System boundary schema

As a starting point for Annex 52 the system boundary schema developed within the EU project SEPEMO [7] has been used for calculation of COP and SPF. The SEPEMO schema is used for SPF calculations of ground, air and water source heat pumps in the EU renewable energy directive. However, several other similar schemas have been published in the literature. Spitler and Gehlin [6] identified five other system boundary schemas different from the SEPEMO schema. For the most part, these schemas are aimed at small monovalent or bivalent heat pump systems and have limitations when accounting for the complexity of larger GHSP systems used in commercial, institutional and multi-family residential buildings. Though performance

evaluation for most of the case studies included in Annex 52 is still in the beginning stages, it is evident that the SEPEMO boundary schema used for SPF calculation is insufficient for covering the complex nature of large-scale GSHP systems.

Therefore, as part of subtask 3 the Annex 52 group has proposed a new system boundary schema, consisting of six defined boundaries and an indicator for use of supplemental heating or cooling (Figure 1). This system boundary schema is better suited for large and complex GSHP systems of the kind that are the focus of Annex 52. The system boundary schema may be used for seasonal performance factors (SPF), shorter time intervals, e.g. daily, monthly (DPF, MPF), or binned performance factors (BPF). The system boundary schema is an extension of the SEPEMO schema, such that every SEPEMO boundary matches one of the Annex 52 boundaries (Table 3). The proposed schema is now being tested on the 40 included case studies within Annex 52.

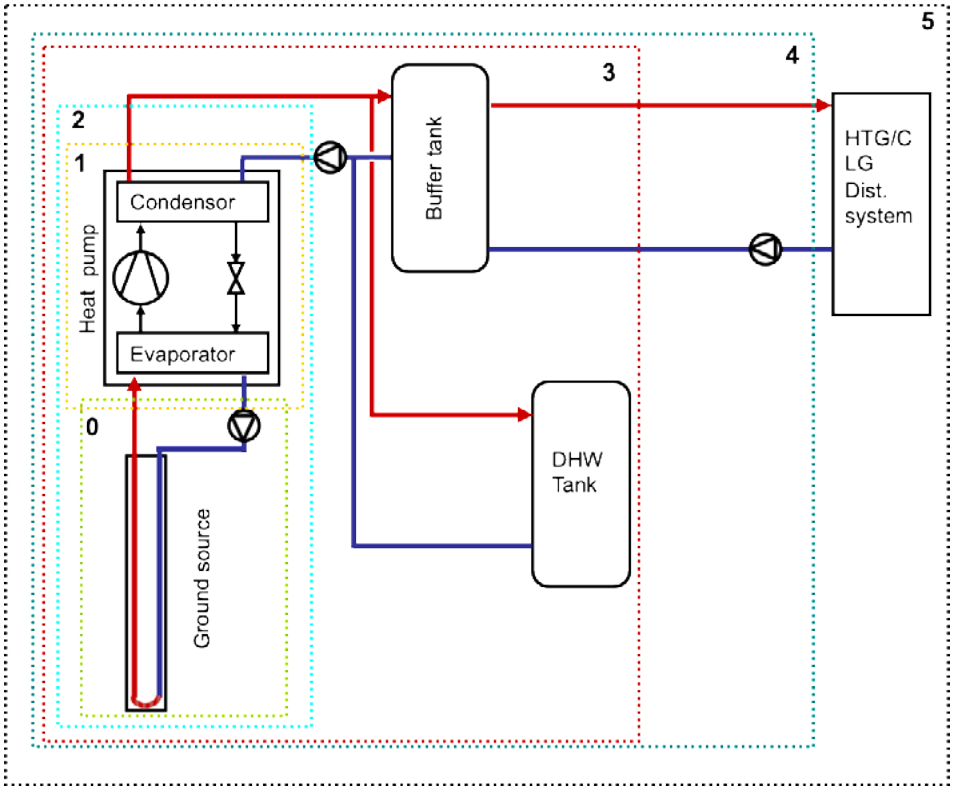


Fig. 1. Proposed Annex 52 system boundary schema. Auxiliary heating and cooling could be added at any boundary level, which will then be indicated with a "+" superscript.

Table 3: System boundary schema comparison of the SEPEMO scheme and the proposed Annex 52 schema for SPF and COP. (Mapping corresponds with having auxiliary heating (H) or cooling (C) only at the same levels as SEPEMO. For the proposed schema, the "+" superscript indicates auxiliary heating/cooling within the boundary).

Boundary description	Boundary levels											
	0	0+	1	1+	2	2+	3	3+	4	4+	5	5+
Ground Source (CP + GHE)	X	X			X	X	X	X	X	X	X	X
Heat pump unit including internal energy use, excluding internal CP			X	X	X	X	X	X	X	X	X	X
Buffer tank (including CPs between HP and BT)							X	X	X	X	X	X
CP on load-side (between BT & building H/C distr. system)									X	X	X	X
Building H/C distribution system											X	X
Auxiliary heating or cooling		X		X		X		X		X		X
Equivalent in the SEPEMO boundary schema			H1/C1		H2/C2	H3					C3	H4/C4

2.3. Case studies

As part of Annex 52 subtask 1, 40 GSHP monitoring case studies, covering a range of applications, located in seven countries, are included in the annex work. Locations and types of ground sources for the 40 case studies are summarized in Figure 2 and Table 4. These case studies, in various stages of completion, will be reported with consistently defined performance indicators in a comprehensive case study report at the closing of Annex 52. Results from several of the Annex 52 case studies have already been published in reports, conference papers and journal papers. These are indicated with an asterisk in Table 4.

Naicker and Rees [8-9] present seasonal system performance factors for the GSHP system serving the Hugh Aston building in Leicester in the UK. Seasonal performance factors are presented for SEPEMO levels C1 and H1, and combined cooling and heating SPF, referred to as SPF1, SPF2, and SPF4, are also defined corresponding to SEPEMO levels H1, H2 and H4. The authors show that cycling losses increase with decreasing cycle time, and that SPF2 and SPF4 are affected by the pumping controls that start the circulating pumps three minutes before the compressors. Several approaches to improving the system performance are identified.

Spitler and Gehlin [6] analyze one year of monitoring data for the mixed-use commercial GSHP system for the student union building Studenthuset at the university of Stockholm in Sweden. SPF values for SEPEMO boundaries H2, H3 and C2 are calculated. The authors show that the system provides space heating consistent with the design values, and that the cooling provided is about four times higher than anticipated in the design. Measured COPs are more affected by the amount of heating and cooling provided than by the entering fluid temperature to the heat pumps. Heating COPs are higher at lower entering fluid temperatures, which correspond to higher run-time fractions for equipment and less influence of “parasitic” loads such as pumps and unit control boards. The Legionella protection system and domestic hot water (DHW) recirculation system run all the time, causing the COP to approach 1 at times in the summer. In addition, the minimum flow rate set point in the borehole circuit leads to excess flow and excess energy consumption by the circulating pump.

The journal papers by Naicker and Rees [8-9] and Spitler and Gehlin [6] provide two sets of high-quality open access measurement data, which may be used by researchers and developers in their future work. Providing at least one set of open access reference monitoring data for a large commercial GSHP system has been one of the important goals of HPT Annex 52.

Results from long-term performance monitoring of two distributed heat pump systems at the ASHRAE Headquarters building in Atlanta in the USA were published by Southard et al. [10, 2] and Spitler et al. [11]. An air-source variable-refrigerant flow heat pump system and a ground-source heat pump system were analyzed and seasonal heating and cooling system coefficients of performance were calculated for the two systems. Because the distributed heat pumps delivered heating and cooling with fans integrated in the heat pump units, and the electrical energy was measured for all heat pumps and the source-side circulating pump together, the coefficients of performance correspond to SEPEMO levels H4 and C4.

The industrial high-temperature borehole storage in Emmaboda in Sweden was operated without heat pumps over several years [12-13]. In 2018 heat pumps were installed. This will improve the possibilities to cool industrial processes and provide improved thermal comfort in the facility. System performance before and after heat pump installation will now be compared.

Boon et al. [14] describe a retrofitted groundwater loop heat pump system at Grangetown nursery school in Cardiff, UK, and its three years of field monitoring. Seasonal performance factors corresponding to SEPEMO level H4 were calculated to be 4.5 over the measurement period.

A first performance evaluation of the early operation of the Rosenborg groundwater heat pump system in Stockholm, mainly focused on the ground source performance, is presented by Abuasbeh and Acuña [15].

Two GSHP systems for multi-family buildings in Stockholm were analysed by Börjesson [16]. One of the buildings was built in 1939 and has been retrofitted with a GSHP system in two steps in 1970 and 2011. This building has supplementary heating with district heating. The other building and its GSHP system were built in 2011 and has supplementary heating from electric heating. Seasonal performance factors over 8 years of operation, corresponding to SEPEMO level H2 and H3 were calculated for the first building and level H2, H3 and H4 were calculated for the second building.

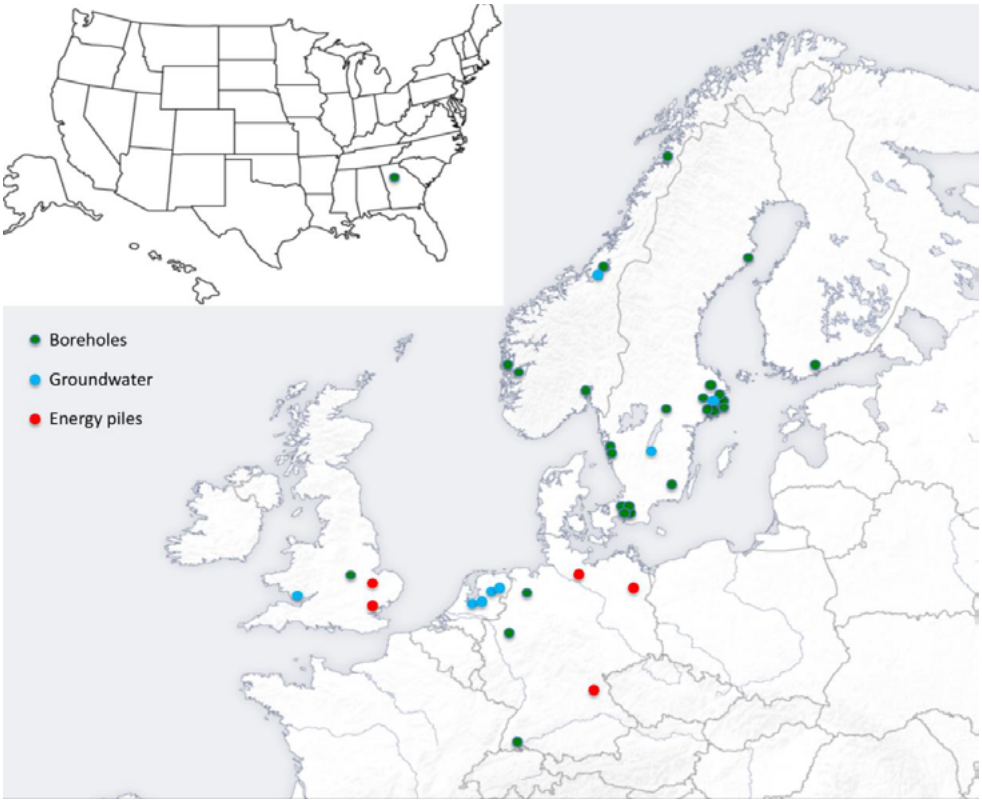


Fig. 2. GSHP case studies included in IEA HPT Annex 52 by the end of 2019.

Table 4: The GSHP monitoring projects included in IEA HPT Annex 52 by the end of 2019. *) Publication available.

#	Country	Location	Building name	Building type	Ground source
1	Finland	Espoo	Aalto University	University	Boreholes
2	Germany	Vechta	AOV	Office	Boreholes
3	Germany	Geisenkirchen	GEW	Office	Boreholes
4	Germany	Konstanz	KON	Residential	Boreholes
5	Germany	Berlin	EFB	Office	Energy Piles
6	Germany	Lüneburg	VGH	Office	Energy Piles
7	Germany	Neumarkt	WGG	School	Energy Piles
8	Netherlands	Utrecht	SKU OVT	Office/train station	Aquifer
9	Netherlands	Drente	Provinciehuis	Office	Aquifer
10	Netherlands	Amsterdam	DeLaMar Theatre	Theatre	Aquifer
11	Netherlands	Meppel	The Schiphorst	Care home	Aquifer
12	Norway	Bergen	Scandic Flesland	Conference hotel	Boreholes
13	Norway	Drammen	Fjell skole	School	High temperature Boreholes
14	Norway	Saltdal	Vensmoen Eiendom	Assembly building	Boreholes
15	Norway	Trondheim	Otte Nielsens vei 12E	Office	Boreholes
16	Norway	Melhus	Lena Terasse	Residential	Aquifer
17	Norway	Bergen	Sweco office building	Office	Boreholes
18*	Sweden	Stockholm	Studenthuset	Office	Boreholes
19*	Sweden	Emmaboda	Xylem	Industry	High temperature Boreholes
20	Sweden	Lund	Traktorn	Residential	Boreholes + District heating
21	Sweden	Lund	Briljanten	Residential	Boreholes + District heating
22	Sweden	Jönköping	Domstolen	Office	Aquifer
23	Sweden	Gothenburg	Backadalen	Residential	Boreholes + District heating
24	Sweden	Uppsala	IKEA	Warehouse	Boreholes
25	Sweden	Umeå	NUS	Hospital campus	Boreholes in thermal grid
26	Sweden	Stockholm	KTH Rocks	Residential	Boreholes
27	Sweden	Stockholm	NPQ	University campus	Boreholes in thermal grid
28*	Sweden	Stockholm	Rosenborg	Office	Aquifer
29	Sweden	Malmö	Polishuset	Office	DGC Boreholes
30	Sweden	Malmö	Klipporna	Office	Boreholes
31	Sweden	Gothenburg	Frölunda Club	Club house	Boreholes
32	Sweden	Stockholm	Lindhagen	Office	DGC Boreholes
33	Sweden	Stockholm	Beckomberga	Residential	Boreholes + Sewage
34*	Sweden	Stockholm	011-Stockholm	Residential	Boreholes + District heating
35*	Sweden	Stockholm	249-Stockholm	Residential	Boreholes + Electric heating
36*	UK	Leicester	Hugh Aston Building	University	Boreholes
37*	UK	Cardiff	Grangetown	Nursery school	Aquifer
38	UK	London	The Crystal	Office	Boreholes/Energy piles
39	UK	Cambridge	22 Station Road	Office	Energy Piles
40*	USA	Atlanta	ASHRAE HQ	Office	Boreholes

2.4. On-going guideline preparation

Within the Annex 52 subtask 2, instrumentation and measurement guidelines are currently in preparation. The instrumentation guideline document will cover GSHP system-related instrumentation hardware and its installation and associated error and uncertainty, as well as data management with recommendations on measurement intervals and data storage. A draft document has been compiled and discussed; an updated version will be presented in the spring of 2020. Another related useful tool for quantitative evaluation of

monitoring data from GSHP systems is a guide to uncertainty analysis that has been prepared as an aid to the Annex 52 case studies and future performance monitoring studies. This document will be an integrated part of the final instrumentation guideline.

In parallel with the instrumentation guideline, there is on-going work on defining recommended key performance indicators for various system boundaries and performance objectives (Tables 1 and 2). These recommended performance indicators will affect the instrumentation guideline recommendations on instrumentation points.

3. Conclusions

Annex 52, *Long-term performance measurement of GSHP systems for commercial, institutional and multi-family buildings,* aims to provide tools to improve the state of the art, based on wide international experience from 40 case studies evaluated as part of the annex. These tools include an improved boundary schema with complementary performance indicators, guidelines on instrumentation and monitoring, guidelines on analysis and key metrics, a thorough bibliography and a unique case study report with long-term performance evaluation of 40 GSHP systems worldwide, using a harmonized evaluation scheme. The results from Annex 52 will contribute significantly to harmonization and system development of such tools. With these new tools, we hope to prepare the way for widespread long-term performance monitoring to become a useful tool for a variety of end users in the GSHP market, such as the audiences listed in Table 1.

At half-term, Annex 52 has already fulfilled two of its goals – the annotated bibliography of previously published large-scale GSHP performance measurements, and two sets of open access reference data. Updates on the Annex 52 work and results are continuously posted on the Annex web site [17].

Acknowledgements

The support from the authors' employers and the Swedish Energy Agency (TERMO research program Grant 45979-1) is gratefully acknowledged. This work is part of the IEA HPT Annex 52, *Long-term performance measurement of GSHP systems serving commercial, institutional and multi-family buildings.* [17].

References

[1] Zhai, X. Q. and Yang, Y.: Experience on the application of a ground source heat pump system in an archives building. Energy and Buildings 43(11): 3263-3270. (2011).
[2] Southard, L.E., Liu, X., Spitler, J. D.: Performance of HVAC Systems at ASHRAE HQ, Part 2. ASHRAE Journal, December 2014, 12-23. (2014b).
[3] Liu, X., Malhotra, M., Im, P.: Performance Analysis of Ground Source Heat Pump Demonstration Projects in the United States. Proceedings of the 12th IEA Heat Pump Conference, May 2017, Rotterdam, the Netherlands. (2017).
[4] IEA HPT TCP: Annex 39. A Common Method for Testing and Rating of Residential HP and AC Annual/Seasonal Performance. Final Report. HPT-AN39-1. (2016)
[5] Wemhoener, C., Hässig, W., Wyss, S., and Staubli, J.: Heat pump application in nearly zero energy buildings. Science and Technology for the Built Environment 23(4): 637-650. (2017).
[6] Spitler, J.D. and S.E.A. Gehlin.: Measured performance of a mixed-use commercial-building ground source heat pump system in Sweden. *Energies* 2019, **12**, 2020; doi:10.3390/en12102020. Open access at: https://www.mdpi.com/1996-1073/12/10/2020 (2019).
[7] Nordman, R.: Seasonal Performance factor and Monitoring for heat pump systems in the building sector, SEPEMO-Build, Final Report. Intelligent Energy Europe. (2012).
[8] Naicker, S. S. and S. J. Rees.: Performance Analysis of a Large Geothermal Heating and Cooling System. *Renewable Energy* **122**:429–42. https://doi.org/10.1016/j.renene.2018.01.099 (*Measurement data available as open access at* ***http://archive.researchdata.leeds.ac.uk/272/***). (2018).
[9] Naicker, S. S. and S. J. Rees.: Long-term high frequency monitoring of a large borehole heat exchanger array. *Renewable Energy,* **145**:1528-1542. https://doi.org/10.1016/j.renene.2019.07.008 (*Measurement data available as open access at* ***http://archive.researchdata.leeds.ac.uk/272/***). (2020).
[10] Southard, L.E., Liu, X., Spitler, J. D.: Performance of HVAC Systems at ASHRAE HQ, Part 1. ASHRAE Journal, September 2014, 14-24. (2014a).
[11] Spitler, J. D., Southard, L. E., Liu, X.: Ground-source and air-source heat pump system performance at the ASHRAE headquarters building. Proceedings of the 12th IEA Heat Pump Conference 2017, Rotterdam, The Netherlands, May 15-17, 2017. 12 pp. (2017).

[12] Nordell, B., Liuzzo Scorpo, A., Andersson, O., Rydell, L., Carlsson, B.: The HT BTES plant in Emmaboda. Operation and Experiences 2010-2015. Water Resources Engineering. Luleå University of Technology, Research Report. (2016).
[13] Andersson, O., Rydell, L.: The HT-BTES in Emmaboda, Sweden – Lessons learned and Further Actions. Enerstock 2018, Adana, Turkey, April 2018. (2018).
[14] Boon, D.P., Farr, G.J., Abesser, C., Patton, A.M., James, D.R., Schofield, D.I., Tucker, D.G.: Groundwater heat pump feasibility in shallow urban aquifers: Experience from Cardiff, UK. *Science of the Total Environment* **697** (2019) 133847. 11 pp. (2019).
[15] Abuasbeh, M., Acuña, J.: ATES System Monitoring Project, First Measurement and Performance Evaluation: case study in Sweden. IGSHPA Research Track 2018, Stockholm, Sweden, September 18th 2018. (2018).
[16] Börjesson, M.: Performance evaluation of ground source heat pump heating systems in Stockholm. Master Thesis, KTH The Royal institute of technology, Stockholm, Sweden. To be published in autumn 2019 at http://kth.diva-portal.org. (2019).
[17] IEA HPC.: Annex 52 - Long term performance measurement of GSHP Systems serving commercial, institutional and multi-family buildings. Retrieved Nov. 29, from https://heatpumpingtechnologies.org/annex52/ (2019).

13th IEA Heat Pump Conference
April 26-29, 2021 Jeju, Korea

Effectiveness-based air flow rate optimization for a residential heat pump in seasonal performance conditions

Minsu Park[a], Min Soo Kim[b*]

[a]LG Electronics Corp., 128 Yeouidae-ro, Yeongdeungpo-gu, Seoul 07736, Republic of Korea
[b]Seoul National University, 1 Gwanak-ro, Gwanak-gu, Seoul 08826, Republic of Korea

Abstract

The conventional rating performance of a residential heat pump system is being replaced by the seasonal performance due to increased demands for the energy saving. In order to achieve the satisfactory seasonal performance, the current system should be modified according to the part load characteristics. Moreover, operating conditions of actuators must be optimized for each test condition to acquire the utmost system efficiency. Fan speeds of both indoor and outdoor units are one of the most significant variable since they are individually controllable and the operating ranges of them are broad. Hence, in this study, effectiveness-based simulation model is introduced to accurately predict the optimum air flow of the system for each seasonal performance condition. The heat exchanger performance is predicted by the modified effectiveness, which can be obtained from the developed non-dimensional correlation. The compressor performance is estimated by the semi-empirical efficiency models. From the verification result, the developed model can estimate the optimum air flow rate within an error of 10% for seasonal performance conditions.

© HPC2020.
Selection and/or peer-review under responsibility of the organizers of the 13th IEA Heat Pump Conference 2020.

Keywords: Residential heat pump; Seasonal energy efficiency ratio (SEER); Seasonal coefficient of performance (SCOP); Modified effectiveness; Air flow rate;

1. Introduction

The amount of energy consumed by HVAC system is the large part of total power supply and thus demands for the high efficiency system have been constantly increased. Heat pump is considered as one of the most efficient device so many researches have been conducted for the performance improvement. Conventional researches have concentrated on the rating performance but seasonal performance is being more important due to the rising usage of an inverter compressor. Therefore, new performance index is required to represent the overall performance in various part load conditions, so European Union introduced the new energy label for SEER and SCOP [1]. As a result, consumers are not interested in the rating efficiency any more but consider the energy grade for seasonal efficiency and thus manufacturers are now focusing on improving seasonal performance. Regarding SEER and SCOP, part load efficiency is significant for seasonal performance so it is inevitable to optimize current system according to part load characteristics [2].

Regarding a compressor, it is required to secure better performance in part load conditions, so the accurate estimation of the efficiency is essential for various operating conditions. For this reason, many researchers tried to estimate compressor efficiencies with various methods. Ishii et al. numerically examined the net efficiency for various geometry [3] and Yang et al. established a model for volumetric and isentropic efficiency with neural network method [4]. Dutra and Deshamps developed an induction motor model for motor efficiency [5]. However, stated models are not appropriate to be applied for any compressor since they are only

* Corresponding author. Tel.: +82-2-880-8362; fax:.
E-mail address: minskim@snu.ac.kr.

valid for the certain compressor. Therefore, semi-empirical efficiency models are developed for the compressor installed in the reference system shown in Table 1.

Regarding a heat exchanger, it is essential to reduce air side thermal resistance for better performance but this enhancement generally augments air side pressure drop [6]. As a result, COP can be deteriorated due to the increased fan power consumption, especially at the low load conditions. Thus, it is required to consider both air side hA and pressure drop for each part load condition. In other words, the optimum air flow rate of each heat transfer condition should be defined to maximize the heat exchanger performance. Lee et al. introduced the simulation-based solution with utilizing genetic algorithm and identified the big difference between the optimized and non-optimized air flow rate under seasonal performance conditions [7]. However, new dataset will be required if specifications of the system are changed. Thus, the author established the simulation model to easily obtain required performance data but it still takes considerable time since iteration processes are included. The calculation time can be drastically increased as iteration loops should be repeatedly conducted for various indoor and outdoor air flow rates. Furthermore, correction factors should be appropriately selected for each correlation to accurately calculate the heat exchanger performance if geometries are changed. The model that has many iteration loops or needs updates for changeable specifications will not be appropriate for a commercial system considering the practical capability of a MiCom in the system.

Hence, this study investigates the non-iterative and universal solution to optimize both indoor and outdoor air flow rates for seasonal performance conditions. The developed model can instantly predict the optimum air flow rate and its accuracy is validated by experiments.

2. Model description

2.1. Heat exchanger model

The modified effectiveness is newly proposed to calculate both sensible and latent heat transfer rate for various heat exchanger geometries. In case of a heat exchanger of the refrigerant cycle, the actual and the maximum heat transfer rate can be expressed as the following Eqs. (1) and (2) [8]. Only two-phase heat transfer is considered for the refrigerant side since the heat transfer mainly occurs at that region. The temperature at the halfway point of a single path is considered as the $T_{ref,sat}$ and the effectiveness for dry condition can be expressed as Eq. (3) for dry condition.

$$Q_{actual} = C_c\left|T_{c,i} - T_{c,o}\right| = \dot{m}_{a,ID} C_{p,a,ID}\left|T_{a,ID,i} - T_{a,ID,o}\right| \tag{1}$$

$$Q_{max} = C_{min}\left|T_{h,i} - T_{c,o}\right| = \dot{m}_{a,ID} C_{p,a,ID}\left|T_{ref,sat} - T_{a,ID,i}\right| \tag{2}$$

$$\varepsilon_{dry} = \frac{Q_{actual}}{Q_{max}} = \frac{\Delta T_a}{\left|T_{ref,sat} - T_{a,i}\right|} \tag{3}$$

Table 1. Specifications of the reference system

Model		AS-W126M, LG Electronics
Performance	Rating capacity [kW]	3.5 for cooling, 4.0 for heating
	Rating COP	4.22 for cooling, 5.19 for heating
	Pdesign [kW]	3.5 for cooling, 3.8 for heating
	SEER	8.5 (A+++)
	SCOP	5.1 (A+++)
Outdoor Unit	Compressor	12.8 cc Twin Rotary
		DA128A1FA-20F, Toshiba
	Heat exchanger	Fin and tube, Φ7, 2 Rows, 814 mm
	Fan	Axial, BLDC motor
	EEV	Φ 1.65 mm orifice, Sanhua
Indoor Unit	Heat exchanger	Fin and tube, Φ7, 3 Rows, 680 mm
	Fan	Cross flow, BLDC motor
Refrigerant		R410A, 1.0 kg

Table 2. Specifications of heat exchangers

	#1	#2	#3
Fin type	Slit	Slit	Corrugated
Number of rows	3	3	2
Number of steps	16	24	24
FPI	21	22	18
D_o [mm]	7.35	5.20	7.35
L [mm]	680	740	814
P_R [mm]	12.7	10.0	18.2
P_S [mm]	21	14	21

In case of wet condition, the effectiveness cannot be acquired by the temperature difference due to the latent heat, so the effectiveness is defined as the ratio of the actual to the maximum enthalpy difference of air [9]. In order to obtain h_{max}, the enthalpy of the outlet air is assumed to be the smallest when the air wet bulb temperature is equal to the evaporating temperature. The effectiveness can be expressed as Eq. (4) for wet condition.

$$\varepsilon_{wet} = \frac{h_{actual}}{h_{max}} = \frac{\Delta h_a}{h_{a,i} - h_{a,min}} \tag{4}$$

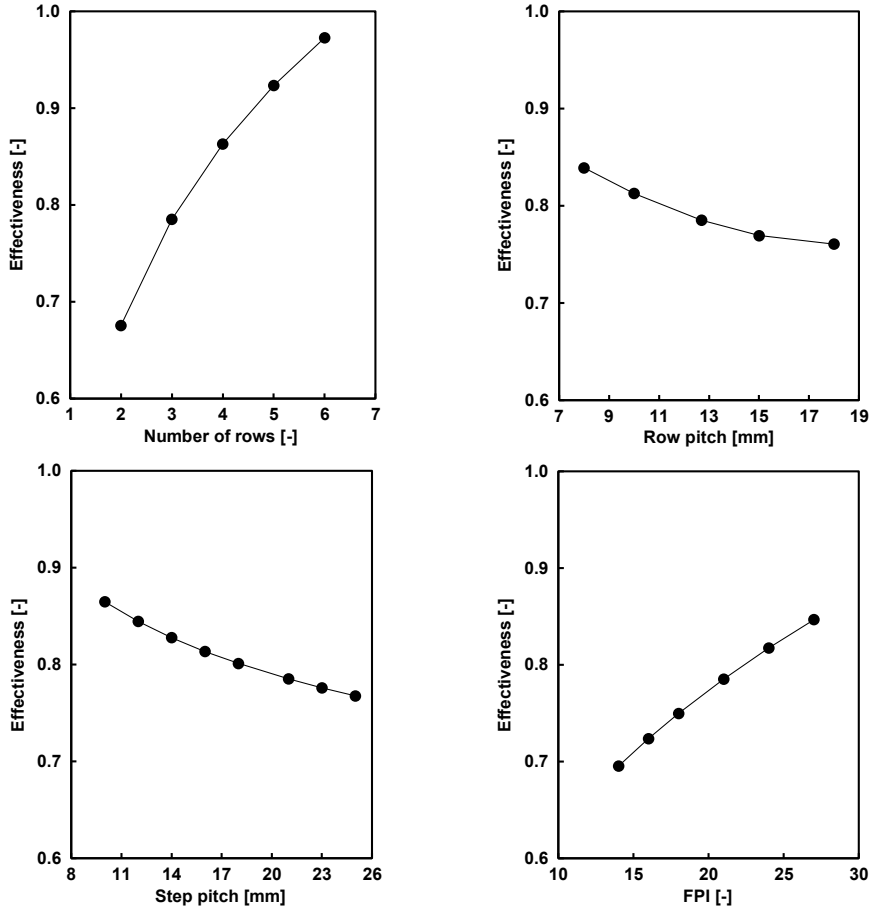


Fig. 1. Variation of the modified effectiveness for various heat exchanger geometry

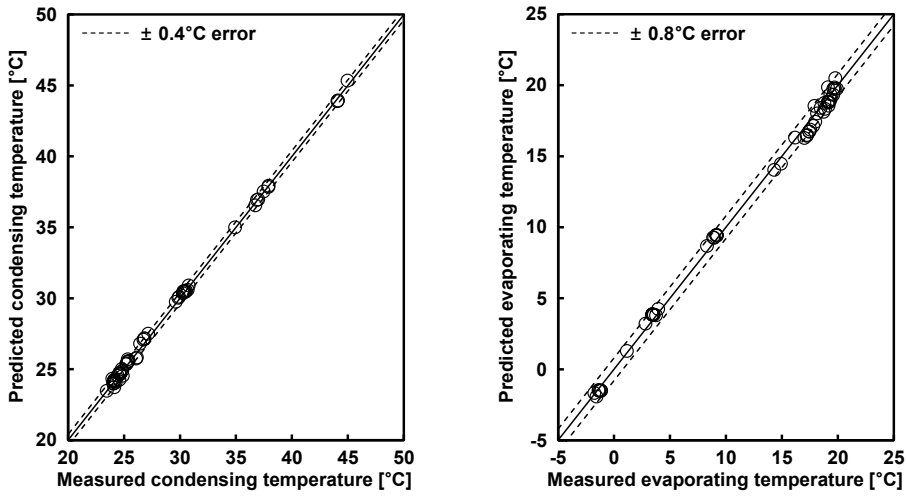


Fig. 2. Validation for saturation temperatures

Heat exchangers were selected as described in Table 2 and experimental data were obtained for each heat exchanger to establish the correlation between the effectiveness and various geometries of the heat exchanger. Key factors are selected by data analysis and the effect on the effectiveness is examined for each factor. Consequently, a non-dimensional correlation for the modified effectiveness which represents both ε_{dry} and ε_{wet} is developed as Eq. (5). α is 1.00 for the corrugated fin and 1.06 for the slit and louvered fin, while β is -0.02 for condensation and 0.02 for evaporation. The root mean square (RMS) error of the developed model is 2.7% for condensation and 5.3% for evaporation. Hence, this correlation can accurately predict the modified effectiveness for heat exchangers which have various geometries. Fig. 1 shows the variation of the effectiveness for number of rows, row pitch, step pitch and FPI, respectively.

$$\varepsilon = 0.43\alpha(0.2644\ln R + 0.4761)\left(\frac{P_r}{P_f}\right)^{0.3}\left(\frac{P_r}{P^*}\right)^{-0.35}\left(\frac{P^*}{P_s}\right)^{0.02\left(\frac{P_r}{D_c}\right)^{3.6}} PLR^{\beta}(1-0.00025\mathrm{Re_D}) \quad (5)$$

Capacity can be fixed for each seasonal performance condition since the inverter compressor will be operated to match the part load. Thus, heat transfer rate of the indoor heat exchanger can be the input and the heat transfer rate of the outdoor heat exchanger can be calculated by Eqs. (6) and (7). Temperature and enthalpy difference of air side can be acquired by Eqs. (1) and (8), respectively. As a result, saturation temperatures of the refrigerant can be attained without an iteration process from the modified effectiveness. The RMS error of the predicted condensing temperature is only 0.19°C while 0.41°C for evaporating temperature as shown in Fig. 2.

$$Q_{OD,c} = Q_{ID}(1 + 0.18PLR^{1.3}) \quad (6)$$

$$Q_{OD,h} = Q_{ID}/(1 + 0.08PLR^{1.16}) \quad (7)$$

$$Q_e = \dot{m}_a(h_{a,i} - h_{a,o}) \quad (8)$$

In addition, in order to estimate the power consumption of both indoor and outdoor fans, the empirical polynomial equations are established from the pressure to volume flow rate data provided by the manufacturer.

Table 3. Compressor coefficients

V_0	V_1	V_2	V_3	V_4	M_0	M_1	M_2	M_3	M_4
1.1160	-0.0764	0.2934	0.0006	-0.0351	0.6944	-0.0001	0.0171	-0.1619	-0.0010

2.2. Compressor model

In order to determine the optimum air flow rate, compressor power should be accurately calculated since it is the largest part of the power consumption. If experimental data is attainable for the whole operating range, map-based model will be effective. However, it is unavailable to conduct the experiment when rotational speed of a compressor is very low. Furthermore, the excessive DSH should be maintained at the compressor suction according to the compressor performance standards. Hence, map-based model is inapposite for part load conditions and thus efficiency-based model is applied for the compressor. Semi-empirical correlations are developed as the following Eqs. (9) to (13) for isentropic, volumetric and mechanical efficiency. Regarding Eqs. (12) and (13), several coefficients are applied to reflect various specifications of a compressor and coefficients for the reference system are indicated in Table 3. RMS error of the developed correlation is 5.6% for η_{isen}, 3.1% for η_{vol} and 6.3% for η_{mech} including motor and drive efficiencies.

$$\eta_{isen,c} = -0.0782\Theta^2 + 0.4121\Theta + 0.3297 \tag{9}$$

$$\eta_{isen,h} = -0.0261\Theta^2 + 0.2060\Theta + 0.5905 \tag{10}$$

where

$$\Theta = \frac{T_{dis,ideal} - T_{a,OD,i}}{2\pi N \cdot 3600 \cdot V_{disp} \cdot PR} \tag{11}$$

$$\eta_{vol} = V_0 + V_1 PR^2 + V_2 PR + V_3 \rho_{suc}^2 + V_4 \rho_{suc} \tag{12}$$

$$\eta_{mech} = M_0 + M_1 N^2 + M_2 N + M_3 PR + M_4 T_{a,OD,i} \tag{13}$$

3. Experiments

3.1. Experimental setup

Experiments are conducted in the calorimeter consists of the indoor and the outdoor chambers to verify the established simulation model. The wind tunnel is installed in the indoor chamber to measure the capacity of the indoor unit by air-enthalpy method. Temperature and humidity are steadily maintained by air handling units, so that deviations of every air temperature are less than ± 0.1°C from each set value. The air flow rate of the indoor unit is acquired by the differential pressure sensor at the nozzle.

Table 4 shows test conditions of EN 14825 and SCOP A, E and F are excluded since these conditions are insignificant on SCOP. Experiments are carried out with various indoor air flow rates and outdoor fan speeds for each test condition to determine the optimum air flow rate. Compressor speed is controlled to make the capacity correspond to the part load for each condition and EEV is adjusted to maintain DSH at the evaporator outlet as 1°C for all conditions. In D conditions of both SEER and SCOP, COP will be degraded by the following Eq. (14) since the capacity substantially exceeds the part load even though the compressor operates at the lowest rotational speed [1].

Table 4. Test conditions

		PLR [%]	Outdoor DBT / WBT [°C]	Indoor DBT / WBT [°C]
SEER	A	100	35 / 24	27 / 19
	B	74	30 / 20	27 / 19
	C	47	25 / 16	27 / 19
	D	21	20 / 12	27 / 19
Heating	Rating	100	7 / 6	20 / 15
SCOP	B	54	2 / 1	20 / 15
	C	35	7 / 6	20 / 15
	D	15	12 / 11	20 / 15

$$COP_d = COP(1 - C_d(1 - Q_{rating}/Q_{measured})) \quad (14)$$

3.2. Data reduction

The measurement data is obtained at the complete steady-state according to the standard [10] and both capacity and COP are calculated by the following Eqs. (15) to (18). The latent heat is not considered if the air speed is significantly high since condensation does not occur in the evaporator.

$$Q_{a,c} = \dot{m}_{a,ID}(h_{a,ID,i} - h_{a,ID,o}) + KA_{WT,surf}(T_{a,ID,i} - T_{a,ID,o}) \quad (15)$$

$$Q_{a,c,SH} = \dot{m}_{a,ID}\, C_{p,a,ID}(T_{a,ID,i} - T_{a,ID,o}) + KA_{WT,surf}(T_{a,ID,i} - T_{a,ID,o}) \quad (16)$$

$$Q_{a,h} = \dot{m}_{a,ID}\, C_{p,a,ID}(T_{a,ID,o} - T_{a,ID,i}) + KA_{WT,surf}(T_{a,ID,o} - T_{a,ID,i}) \quad (17)$$

$$COP = Q_a/W \quad (18)$$

3.3. Uncertainty analysis

Uncertainty of the acquired data is shown in Table 5 and its propagation is indicated in Table 6. In order to analyze the uncertainty of the cooling capacity and COP, the uncertainty of the air enthalpy should be examined. However, it cannot be directly measured by sensors but can be calculated by temperatures or humidity. Generally, it can be obtained by measured dry bulb and wet bulb temperature through the complicated calculating process which is not appropriated for the uncertainty analysis. Therefore a linear formula is developed as Eq. (19) within the measurable range, so the propagated error of the cooling capacity and COP can be calculated as the following Eqs. (20) to (22) for every test condition [11]. If the condensation does not occur, it is recommended to only consider sensible heat to reduce the error since the uncertainty of the air enthalpy difference is crucially larger than that of the temperature difference. As a result, the uncertainty is 2.0 ~ 4.3% for cooling COP and 1.8 ~ 2.6% for heating COP which are deserved to be reliable.

$$h_a = -0.0437\, T_{DB} + 3.160 T_{WB} - 4.508 \quad (19)$$

$$\frac{U_{h_a}}{h_a} = \sqrt{\left(\frac{\partial h_a}{\partial T_{DB}}\right)^2 + \left(\frac{\partial h_a}{\partial T_{WB}}\right)^2} \quad (20)$$

$$\frac{U_{COP_c}}{COP_c} = \sqrt{\left(\frac{U_{\dot{m}_a}}{\dot{m}_a}\right)^2 + \left(\frac{U_{\Delta h_a}}{\Delta h_a}\right)^2 + \left(\frac{U_W}{W}\right)^2} \quad (21)$$

$$\frac{U_{COP_h}}{COP_h} = \sqrt{\left(\frac{U_{\dot{m}_a}}{\dot{m}_a}\right)^2 + \left(\frac{U_{\Delta T}}{\Delta T}\right)^2 + \left(\frac{U_W}{W}\right)^2} \quad (22)$$

Table 5. Uncertainty analysis

Measurable value		Uncertainty
Indoor air inlet dry bulb temperature	[°C]	0.04
Indoor air inlet wet bulb temperature	[°C]	0.08
Indoor air outlet dry bulb temperature	[°C]	0.05
Indoor air outlet wet bulb temperature	[°C]	0.07
Outdoor air inlet dry bulb temperature	[°C]	0.03
Outdoor air inlet wet bulb temperature	[°C]	0.06
Indoor air outlet Nozzle ΔP	[%]	0.10
Power consumption	[%]	0.20

Table 6. Error propagation analysis

For cooling condition		A	B	C	D
Air mass flow rate	[%]	1.67	1.67	1.67	1.67
Inlet air enthalpy	[kJ kg^{-1}]	0.25	0.25	0.25	0.25
Outlet air enthalpy	[kJ kg^{-1}]	0.22	0.22	0.22	0.22
Enthalpy difference	[%]	2.95	3.92	4.95	5.55
Temperature difference	[%]	-	-	0.91	1.07
Capacity	[%]	3.39	4.26	1.90	1.98
COP	[%]	3.43	4.29	2.21	2.03
For heating condition			B	C	D
Air mass flow rate	[%]		1.67	1.67	1.67
Temperature difference	[%]		1.07	1.28	1.60
Capacity	[%]		1.98	2.10	2.31
COP	[%]		2.08	2.58	2.35

4. Result analysis

The optimum indoor and outdoor air speeds of each seasonal performance condition are obtained by the established simulation model and validated by measured data. In order to obtain the optimum air flow rate via simulation, wide range of air speed is given and then COP is promptly calculated for each air speed without any iteration process. The optimum air speed can be ascertained for each seasonal performance condition from the results. Detailed simulation results for both indoor and outdoor heat exchangers are indicated in Table 7 and it is obvious that each operating condition has its own optimum air speed that can achieve the best performance. The optimum air speed has a positive correlation with the capacity but the tendency is slightly different for indoor and outdoor heat exchanger. The indoor heat exchanger is more influenced by the cooling capacity while the outdoor heat exchanger is more affected by the heating capacity, which identifies that the air flow rate of the evaporator is less influential for the performance.

In order to examine the stated correlation between the optimum air speed and the capacity, distribution of the power consumption should be firstly considered. The power consumption of the compressor is more than 80% of the total at the full load condition, so it can be advantageous to increase the air flow rate to reduce the pressure ratio of the compressor. However, at the low load condition, it will be reduced under 60% and hence the power consumption of both fans is about 30% instead. Therefore, COP can be significantly decreased when the air speed is not well optimized. For instance, COP will be deteriorated by 10% in SEER D condition if the indoor air flow rate is 75% of the optimum value but it will decline by only 1% in SEER A condition. In fact, in order to achieve the remarkable seasonal performance, it is essential to operate the system at the optimum air speed. Secondly, the suitable air side temperature difference should be secured for the thermal comfort of occupants, so UA of the indoor heat exchanger is generally smaller than that of the outdoor heat exchanger. In addition, both sensible and latent heat exist at the evaporator, the air flow rate can be less influential since the

Table 7. Verification results

Test condition		Optimum indoor air flow rate [CMM]			Optimum outdoor air flow rate [CMM]		
		Predicted	Measured	Error	Predicted	Measured	Error
SEER	A	24.0*	15.5	+ 54.8%	39.4*	32.6	+ 20.9%
	B	18.5*	15.5	+ 19.4%	32.0	32.2	- 0.6%
	C	13.0	12.5	+ 4.0%	24.6	25.9	- 5.0%
	D	10.3	10.0	+ 3.0%	20.9	19.5	+ 7.2%
SCOP	B	14.4	14.5	- 0.7%	23.4	23.7	- 1.3%
	C	11.7	11.5	+ 1.7%	16.0	17.2	- 7.0%
	D	10.3	10.0	+ 3.0%	13.5	15.0	- 10.0%

* Above the permissible sound pressure level

reduced temperature difference between the fin surface and the moist air will decrease the latent heat which has the exceedingly large enthalpy difference. Consequently, the decreasing tendency of the optimum air flow rate according to the capacity is differently observed for indoor and outdoor heat exchanger as well as cooling and heating operation. Therefore, the optimum air flow rate should be separately investigated by considering the heat transfer circumstance of the heat exchanger.

Simulation results are validated by the experimental results and described in Table 7. In some cases, the air flow rate cannot reach the predicted optimum value even though fan motor is operated at its maximum speed. Practically, the air flow rate should be regulated to satisfy the noise regulation, so maximum speed of the motor is designed around the limit value. Thus, results cannot be obtained for the air flow rate which exceeds the maximum speed nevertheless the optimum COP is not identified within the experimental data. As a result, the modeling shows an unusual large error for those test conditions. However, it can precisely predict the optimum air flow rate with the RMS error of 4.9%, 2.7% for the indoor air flow rate and 6.2% for the outdoor air flow rate. Furthermore, if the real-time capacity can be secured during heat pump operation, the optimum air flow rate of both indoor and outdoor units will be instantly obtained for the current operating condition. In fact, the system can be operated with the optimum air flow rate all the time, which implies the most practical energy saving.

5. Conclusion

In this study, effectiveness-based simulation model is established to accurately predict the optimum air flow rate for various operating conditions. The non-dimensional correlation which can reflect various heat exchanger geometries is introduced for the modified effectiveness, so COP can be ascertained for various air flow rate and load conditions. The correlation can predict the condensing and evaporating temperature within the RMS error of 2.7% and 5.3%, respectively. Furthermore, the optimum air flow rate of various seasonal performance test conditions can be predicted within the RMS error of 4.9% for the permissible operation range of both fans. If the system is available to calculate its real-time capacity, the utmost COP can be always secured by predicting the optimum air flow rate for the calculated capacity.

Acknowledgements

This research is supported by the Institute of Advanced Machinery and Design (IAMD) and Institute of Engineering Research (IER) of Seoul National University. Supports from the Brain Korea 21 Plus Project (F14SN02D1310) of the Ministry of Education and the Basic Science Research Program through the National Research Foundation (NRF) of the Ministry of Science, ICT & Future Planning (2016R1A2A1A05005510) are appreciated. The program of the Korea Institute of Energy Technology Evaluation and Planning (KETEP) from the Ministry of Trade, Industry & Energy of Korea (No. 20173010032150) is also appreciated. Support from the R&D Center for reduction of Non-CO2 Greenhouse gases (2017002430001) funded by Korea Ministry of Environment (MOE) as Global Top Environment R&D Program is sincerely recognized.

References

[1] EN 14825, 2013. Air conditioners, liquid chilling packages and heat pumps, with electrically driven compressors, for space heating and cooling – Testing and rating at part load conditions and calculation of seasonal performance. British Standards Institution, London, U.K.

[2] Kinab, E., Marchio, D., Reviere, P., 2010. Reversible heat pump model for seasonal performance optimization. Energy and Buildings 42, p. 2269-2280.

[3] Ishii, N., Morita, N., Ono, M., Yamamoto, S., Sano, K., 2000. Net efficiency simulations of compact rotary compressors for its optimal performance. International Compressor Engineering Conference 1424, p. 475-482.

[4] Yang, L., Zhao, L., Zhang, C., Gu, B., 2009. Loss-efficiency model of single and variable-speed compressors using neural networks. International Journal of Refrigeration 32, p. 1423-1432.

[5] Dutra, T., Deschamps, C. J., 2015. A simulation approach for hermetic reciprocating compressors including electrical motor modeling. International Journal of Refrigeration 59, p. 168-181.

[6] Fischer, S.K., Rice, C.K., 1983. The Oak Ridge heat pump models: I. A Steady-state computer design model for air-to-air heat pumps. Oak Ridge National Laboratory, Tennessee.

[7] Lee, S., Jeon, Y., Chung, H., Cho, W., Kim, Y., 2018. Simulation-based optimization of heating and cooling seasonal performances of an air-to-air heat pump considering operating and design parameters using genetic algorithm. Applied Thermal Engineering 144, 362-370.
[8] Incropera, F. P., DeWitt, D., 2002. Fundamentals of Heat and Mass Transfer, 5th ed. Wiley, New York.
[9] Mansour, M. K., 2016. Practical effectiveness-NTU model for cooling and dehumidifying coil with non-unit Lewis Factor. Applied Thermal Engineering 100, p. 1111~1118
[10] EN 14511-3, 2013. Air conditioners, liquid chilling packages and heat pumps with electrically driven compressors for space heating and cooling – Part 3: Test methods. British Standards Institution, London, U.K.
[11] ASHRAE Guideline 2-2010, 2014. Engineering analysis for experimental data. ASHRAE, Atlanta, GA.

Nomenclature

$A_{WT,\,surf}$	surface area of the wind tunnel [m^2]
C_p	specific heat [kJ kg^{-1} K^{-1}]
C_d	degradation coefficient
COP	coefficient of performance
Dc	fin collar diameter [mm]
DSH	degree of superheat [°C]
ε	effectiveness of a heat exchanger
h	enthalpy [kJ kg^{-1}]
K	heat transmission coefficient [W m^{-2} K^{-1}]
$\dot{m}$	mass flow rate [kg h^{-1}]
N	rotational speed of a compressor [Hz]
P	pitch [mm]
*P**	reference pitch, 25.4 [mm]
PLR	part load ratio
PR	pressure ratio
Q	transferred heat [kW]
R	number of rows
Re_D	Reynolds number based on fin collar diameter
SCOP	seasonal coefficient of performance
SEER	seasonal energy efficiency ratio
T	temperature [°C]
U	uncertainty
$\dot{V}$	volume flow rate [m^3 min^{-1}]
V_{disp}	compressor displacement [cc]
W	work [W]
Δh	enthalpy difference [kJ kg^{-1}]
ΔT	temperature difference [°C]
η	compressor efficiency
ρ	density [kg m^{-3}]

Subscripts

a	air side
c	cooling
DB	dry bulb
dis	discharge
e	evaporating
f	fin
h	heating
i	inlet
ID	indoor unit
isen	isentropic
max	maximum
mech	mechanical
min	minimum
o	outlet
OD	outdoor unit
r	row
ref	refrigerant
s	step
sat	saturation
SH	sensible heat
suc	suction
vol	volumetric
WB	wet bulb

13th IEA Heat Pump Conference
April 26-29, 2021 Jeju, Korea

NEDO R&D Project for Innovative Thermal Management

Tetsushiro Iwatsubo[a*], Yuka Ogasawara[a], Toshihiko Ota[a], Masanori Kobayashi[a]

[a]New Energy and Industrial Technology Development Organization (NEDO), 212-8554 Japan

Abstract

A national R&D project "Research and Development Project for Innovative Thermal Management Materials and Technologies" in NEDO is introduced in this paper. In this project, technology developments are conducted to Reduce (which technologies for reducing heat usage; thermal insulation, heat shield and thermal energy storage), Reuse (which technologies for reusing heat; heat pump technologies) and Recycle (which technologies for reusing heat by converting it; thermoelectric energy conversion, waste heat power generation) unutilized thermal energy effectively, including total thermal management based on the combination of these technologies, and realize a future energy-efficient society. This paper focuses on high temperature heat pumps and its new refrigerants.

© HPC2020.
Selection and/or peer-review under responsibility of the organizers of the 13th IEA Heat Pump Conference 2020.

Keywords: R&D Project; Thermal Management; Unutilized Thermal Energy; Industrial Heatpumps; New Refrigerant;

1. Introduction

In July 2018, the Cabinet of Japan approved the new Strategic Energy Plan, and the new plan emphasizes the strengthening of efforts to ensure continued, concrete results towards 2030. Towards 2050, the new plan seeks to achieve energy transitions and decarbonization, in light of the global momentum in this direction and in enforcement of the Paris Agreement, and to pursue all tenable options toward this end.

In Japan, about 30% of primary energy, mainly fossil resources such as oil, coal and natural gas, are lost when they are converted into electricity and fuel [1], and at the final consumption, it is used only a small portion, so most of primary energy is considered not to be used effectively but discarded as heat. NEDO refers to such artificially discharged heat as "unutilized thermal energy", and it is the key for realizing thorough energy efficiency to effectively reduce, reuse and recycle this huge amount of unutilized thermal energy discharged into this environment, and it can be said to be a frontier.

In this paper, it is introduced that an overview of a national R&D project "Research and Development Project for Innovative Thermal Management Materials and Technologies", which aims to realize thorough energy efficiency promoted by New Energy and Industrial Technology Development Organization (NEDO). Above all they focus on R&Ds of new high-temperature heat pumps and their refrigerants that make use of heat efficient in industrial fields by reusing unused thermal energy for process heating instead of boilers.

2. Surveys of actual exhaust heat and R&D target

Although it is expected that unutilized thermal energy will be used for thorough energy efficiency, the temperature zone, amount, and location vary. Therefore, in order to grasp the actual state of unutilized thermal energy, NEDO conducted a large-scale questionnaire survey and estimated exhaust heat in industrial field, in "Research and Development Project for Innovative Thermal Management Materials and Technologies" [2]. It is believed that such data on temperature and quantity of exhaust heat are valuable for introduction

* Tetsushiro Iwatsubo. Tel.: +81-44-520-5281; fax: +81-44-520-5187.
E-mail address: thermal-energy@nedo.go.jp.

consideration not only on high temperature heat pumps introduced below, but also on applications of relatively low temperature industrial heat pumps and absorption chillers that have already been established technically. However, such large-scale surveys of actual exhaust heat in industrial fields had not been conducted since the survey conducted from 1997 to 2000 [3]. Figure 1 shows the estimated amounts of nationwide unutilized thermal energy, by sector and temperature based on the survey result from 1,273 factories of 15 industries. The nationwide estimation of the amount of unutilized thermal energy (exhausted as gas) was based on results of questionnaires, approximation calculated by the correlation between energy inputs to factories and unutilized thermal energy as exhaust gas by industry, and FY2015 energy consumption statistics of manufacturing industries.

The total amount of exhaust gas heat in these 15 industries was 743 PJ / year, and the 76% (565 PJ / year) was occupied by exhaust gas heat of less than 200 ° C. As shown in Fig. 1(a), it can be seen that a lot of exhaust gas from steel industry, non-ferrous metal industry, and transportation equipment industry, with melting and heat treatment processes, is in high-temperature of 500 ° C or higher, and exhaust gas from clean-up industry and other manufacturing industries, with incineration processes, is concentrated from 150 ° C to 249 ° C. On the other hand, when comparing exhaust gas calorific value of 15 industries estimated in 2015 with the result of 2000, as shown in Figure 1(b), it decreased by about 14% from 2000, and it was speculated about 10% energy efficiency was achieved for 15 years.

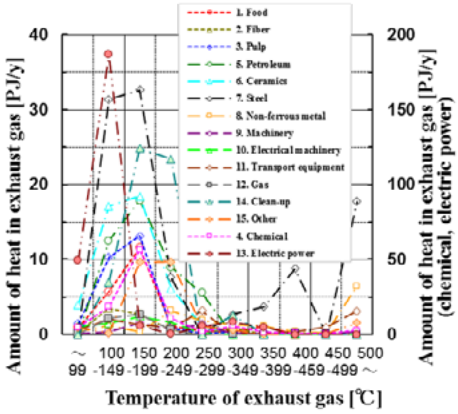


Fig. 1(a). Estimation of amount of heat in exhaust gas from industry by temperature range

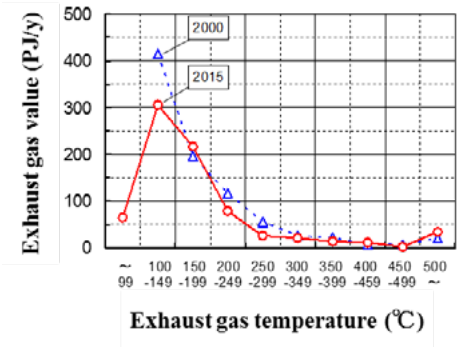


Fig. 1(b). Comparison with survey results between 2000 and 2015

Based on the above, NEDO is promoting an R&D project to effectively reduce (heat insulation, heat shield and thermal storage), reuse (heat pumps) and recycle (thermoelectric generation abd heat power generation) of unutilized thermal energy mainly below 200 ° C or above 500 ° C, with thermal management technologies, led by Dr. Haruhiko Ohara, the project leader, who also serves as the Deputy Director-General of the Planning Headquarters of the National Institute of Advanced Industrial Science and Technology (AIST),

with industry-academia collaboration of the Thermal Management Materials and Technology Research Association (TherMAT) described in Fig. 2. As the oucomet of this R&D and penetration of these technologies, NEDO and they aim to achieve domestic fossil fuel reduction effect of about 6 million kL per year or more in crude oil equivalent and CO_2 reduction effect of over 17 million t-CO_2 per year in 2030 alone. In order to NEDO also aims to realize these effects by reducing or utilizing unutilized waste heat, which is above 500 ° C, mainly with heat insulation and thermoelectric generation technologies, and which is below 200 ° C, mainly with heat pumps, thermal storage and heat power generation technologies. In this way, this R&D project is intended for a wide range, but here it is introduced that an R&D on high temperature heat pumps and its refrigerant, which are the core of this R&D project and can show high energy efficiency effect.

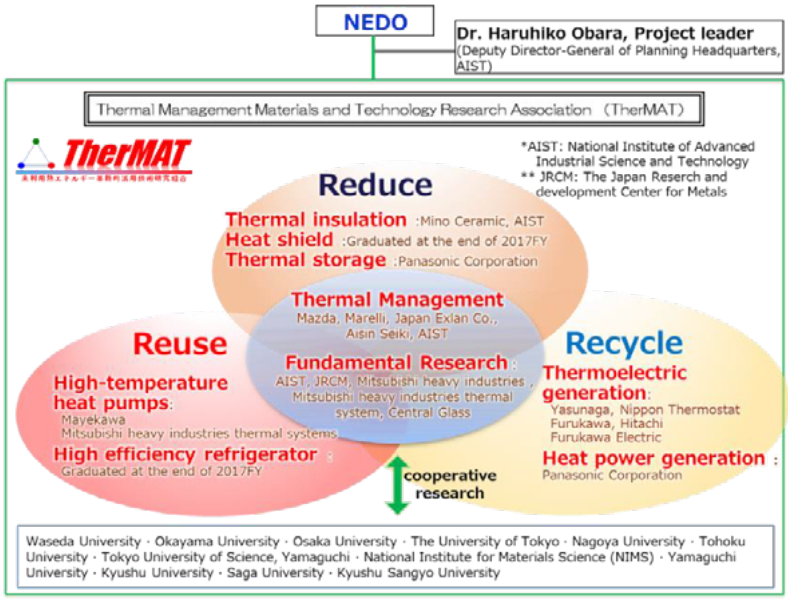


Fig. 2. Organizational chart of "Research and Development Project for Innovative Thermal Management Materials and Technologies"

3. R&D of high temperature heat pumps and refrigerants in NEDO

Currently, boilers using fossil resources are often used as heat sources for industrial heating applications, and a large amount of unutilized thermal energy is discharged from each heating process. By reusing this waste heat as a heat source, it is expected to regenerate it to a higher temperature and replace the heat sources from conventional boilers with high temperature heat pumps, for which NEDO has been promoting the R&D of that. In this project, it aims to develop high temperature heat pumps which can supply high-temperature heat about from 160 ° C to 200 ° C with high efficiency (e.g. COP: 3.5 or higher), recovering from waste heat of 80 ° C or 100 ° C which is discarded from industrial manufacturing processes, and as the result of penetrating them as alternatives to steam boilers, can contribute to use primary energy efficiently and reduce CO_2 emissions. In addition, refrigerants used in the heat pumps are selected, developed and evaluated as compounds which have small GWP (Global Warming Potential) and are suitable for high-temperature applications, in this project.

3.1. Development of industrial high-efficiency and high-temperature heat pump capable of supplying maximum 200 ° C

In this project, Mayekawa Mfg. Co., Ltd. and Mitsubishi Heavy Industries Thermal Systems, Ltd., who are the members of TherMAT, are developing heat pump systems with having the goal that can meet the supply temperature range up to 200 ° C, and achieve COP: 3.5 or higher by heating from 100 ° C to 200 ° C at the end of 2022.

Mayekawa Mfg. Co., Ltd. got the analysis based prospect of achieving COP4.10 by heating from 80 ° C to 160 ° C and the intermediate target (COP3.5) using the developed integrated analysis simulator. Also the ultrahigh-speed turbo compressor was developed, and results by fluid analysis and structural analysis showed achieving the adiabatic efficiency target of 70% or more. In addition, the correlation model necessary for the design was created by the trial model tests of the high-temperature and high-pressure heat exchanger, and the basic design of the heat pump prototype was completed. Based on these, they designed and manufactured a prototype heat pump using R600 refrigerant with a maximum heating temperature of 200 ° C and a heating

capacity of 300kW, and started performance verification tests. (Fig. 3) For the purpose of further improving efficiency, they evaluated HFO refrigerants as working media, and they clarified that it was non-flammable, and low GWP, and the rotation speed of the compressor was expected to be lower than that of R600 refrigerants. Based on the above, they have started the development of an oil-free turbo compressor with this working medium.



Fig. 3(a). High temperature heat pump prototype unit



Fig. 3(b). Developed oil-free and ultra-high speed turbo compressor

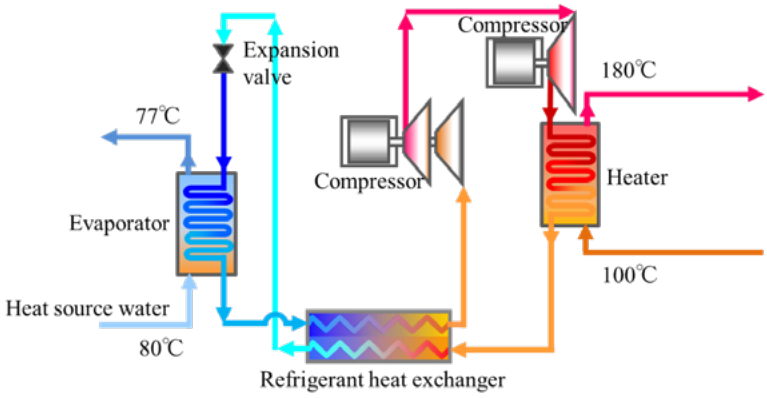


Fig. 3(c). Primary prototype testing machine flow chart of the high temperature heat pump

Mitsubishi Heavy Industries Thermal Systems, Ltd. selected the optimum heat pump cycle as the result of basic heat pump analyses at 160 ° C and 200 ° C. They also decided the refrigerant adopted for the 160 ° C hot water output heat pump, completed their basic plan, and got the prospect for realizing over COP 4.0. In addition, drop-in operation tests using refrigerant candidates in high temperature ranges were performed on an element verification test machine modified an existing product, and the validity of elemental technologies was evaluated. (Fig. 4) At the same time of these R&Ds, they extracted industrial processes that are expected to have high effect including energy efficiency with introduction of high-temperature hot water output heat

pumps, and grasped the actual operating conditions including heat balance and energy consumption in each process.



Fig. 4. Drop-in test with low GWP refrigerant

3.2. R&D of refrigerants suitable for high-temperature heat supply heat pumps

In order to be applied to turbo heat pumps with 500kW or more that can be introduced into industries such as machinery and chemical industries, Mitsubishi Heavy Industries, Ltd., Mitsubishi Heavy Industries Thermal Systems, Ltd., Central Glass Co., Ltd. and AIST, who are the members of TherMAT, in collaboration with Kyushu University, Saga University and Kyushu Sangyo University, have been exploring, developing, evaluating physically and selecting several low GWP refrigerants, that meet the requirements for the temperature zone when industrial heat pumps will be used.

By FY2017, they selected refrigerants that were promising for using at 160 ° C hot water output heat pumps. Specifically, among the compounds for which some thermophysical property data are known, three compounds were selected as new refrigerant candidates, and their performance (normal boiling point and critical temperature), thermal stability, safety (toxicity and flammability), environmental impact (GWP <20) were evaluated, and also thermodynamic properties and transport properties data (PVT properties, thermal conductivity and viscosity) were obtained. In addition, they conducted synthesis studies using cheaper catalysts, confirmed the high selectivity and long life of the catalyst and revealed the low toxicity as the result of subacute toxicity tests.

New refrigerant candidates suitable for use for 200 ° C hot water output heat pump have not been studied yet, including other applications, and had no REFPROP FLD files. Therefore, they have developed a method for preliminary toxicity test and synthetic method with high yield for new refrigerants candidate corresponding to 200 ° C, and they evaluated five screened candidate refrigerants from points of view of thermal stability, basic thermophysical properties, safety and environmental impacts, and as the result of that candidate refrigerants were narrowed down to two. They developed equation of state based on sound of speed in gas phase, PVT property measurements and vapor pressure measurement for the refrigerant candidate, and confirmed that it was almost the same as the actual measurement value of physical property. Also, they have also found a catalyst with high selectivity, high conversion and long life in the synthesis process.

3.3. Next steps

Based on above R&D, materials can be selected by analyzing thermodynamic characteristics and heat exchange characteristics of the 200 ° C output heat pump cycle using new refrigerant candidates, and evaluating elastomer compatibility suitable for the refrigerant candidate. Then, toward the final goal, they will conduct element verification tests of high temperature heat pumps using new refrigerant candidates suitable for 200 ° C output machines, confirm the each component performance of heat pump cycles, together with evaluation of the soundness, evaluate overall performance of the heat pumps, and determine basic specifications.

On the other hand, toward introduction of the heat pumps after the end of R&D, it can be difficult to see the effect or value when they apply to actual heat utilization equipment in factories. Especially it will be even more

difficult to conduct verification to grasp the energy efficiency effect in the actual environment using the existing systems. Therefore, it will be proceed with activities of model cases studies, assumed actual heat utilization facilities, and based on the results of this studies, calculation and quantitatively evaluation of the effect or value including energy efficiency, cost merit and heat pump system configuration post introduction. As the result of the activities, "visualization" of introduction effect will be progressed and it will be possible to share the installation image of heat pumps in industrial heating processes with customers, which will be able to lead to acceleration of the introduction. It is planned to construct equipment utilizing systems with high temperature heat pumps including attached facilities, proceed with model case verifications that examine optimal applied processes and clarify economic effects, and studies on "visualization" of introduction effect with TherMAT and all Japan in this R&D project. Through these activities, the newly developed industrial high-efficiency and high-temperature heat pumps will be properly arranged and used for process heating instead of boilers, thereby promoting energy efficiency in factories and contributing to solving energy and environmental problems in the future.

4. Conclusion

"Energy efficiency" is the primary expectation for the realization of "3E + S" (simultaneously achieving Energy Security, Economic Efficiency and Environment, with coming Safety always at first) in Japan and global long-term decarbonization, but most of primary energy is still discharged as unutilized thermal energy without being effectively used, even though various measures have been taken so far. Among energy forms such as fuel, electricity, and hydrogen that are expected to be used in the future, the last remaining form is heat, and decarbonization of all sectors that use this heat can be the key to construct the sustainable recycling society. Now all the relevant people are required to promote to implement technologies for effectively reducing or recovering a large amount of unutilized thermal energy discharged into the environment including high-temperature heat pumps, to the society with economic rationality, realize significant energy efficiency of the entire society and a "circular economy", and there can be no doubt that this R&D project has been a driving force for it.

References

[1] Agency for Natural Resources and Energy, *FY2017 Energy Supply and Demand Report*, (2019) (in Japanese)
[2] NEDO, TherMAT, *Industrial Waste Heat Survey Report*, (2019) (in Japanese)
[3] Energy Conservation Center, Japan, Research on Energy Systems in Factories, Wide-area Energy-utilization Nnetwork System (Eco-energy City), (2000) (in Japanese)

13th IEA Heat Pump Conference
April 26-29, 2021 Jeju, Korea

Experimental study on an absorption heat pump prototype applied for rural residential heating

Ding Lu[a,b], Maoqiong Gong[a,b,*], Yin Bai[a,b], Yanxing Zhao[a,b], Xueqiang Dong[a,b]

[a] Key Laboratory of Cryogenics, Technical Institute of Physics and Chemistry, Chinese Academy of Sciences, Beijing 100190, China
[b] University of Chinese Academy of Sciences, Beijing 100049, China

Abstract

In order to replace the inefficient and polluting boilers, an ammonia-water absorption heat pump prototype is proposed for rural residential heating. The prototype can be driven by the combustion of biogas that is widely available in rural areas. Experimental investigations are carried out to analyze its performance under different working conditions. During the experiment, the prototype works with an electric oil heater which simulates the biogas burner in real applications, and uses conduction oil as the heating medium. Experimental results indicate that at the ambient temperature of -5 °C, the prototype can provide 25 kW heating capacity and the supply water temperature is 50 °C, with the coefficient of performance and primary energy efficiency of 1.37 and 1.14, respectively. By introducing the intermediate process, 2.39 kW exhaust heat is recovered, and the exhaust heat temperature is reduced to 41.3 °C. Moreover, the primary energy efficiency of the proposed system is still greater than 1 even when the ambient temperature is reduced to -10 °C, showing an obviously better performance than that of the conventional boiler.

© HPC2020.
Selection and/or peer-review under responsibility of the organizers of the 13th IEA Heat Pump Conference 2020.

Keywords: absorption heat pump; residential heating; biomass energy; exhaust heat recovery; experimental study.

1. Introduction

In China, buildings consume a large amount of energy, which occupies about 24% of the total energy consumption [1], and this number is expected to gain further enhancement considering the improving living standard [2], especially in rural areas where over 40% of the nation's whole population live in. Among the building energy consumption, residential heating systems account for over 20% [3]. At present, most of these heating systems are coal-fired boilers in rural areas of China, which produce a huge amount of aerosol and contaminant that is the main source of air pollution. Even worse, the primary energy efficiencies (PEEs) of the boilers are very low, ranging from 0.8 to 0.9. In order to meet the demand of energy conservation, emission reduction and environmental protection, more efficient and environmental friendly heating technologies haven been proposed to replace the boiler systems. Among these, absorption heat pump (AHP) is outstanding because of its higher primary energy efficiency. Conventional AHP systems use high-grade combustion heat of fossil fuels or waste heat of the industrial areas as the driving force, recover additional low-grade heat from the ambient (mainly including air and ground), and produce intermediate-grade heat for water heating, ranging from 40 °C to 100 °C.

The single-effect AHP systems applied for residential heating have been studied extensively. Some articles analyzed systems that are driven by the heat network, and a ground-source AHP [4] was analyzed for residential heating. The results showed that it was more efficient than the compression heat pump (CHP). Further studies [5] demonstrated that the AHP system has an energy efficiency that is 54% higher than that of the conventional

* *Corresponding author. Tel.: +86-010-82543728; fax: +86-010-82543728.*
E-mail address: gongmq@mail.ipc.ac.cn.

heating systems based on boilers. Wu et al. [6] proposed a water-source AHP system to provide 45 °C water for district heating. Experimental study indicated that as the evaporation temperature is -10 °C, the COP is 1.2. Nitkiewicz et al. [7] compared the performance of a CHP, an AHP, and a gas-fired boiler. Results showed that the heating plant using ground-source AHP system had a much lower eco-indicator and environmental impact than those of the CHP and boiler. Li et al. [8] used an AHP to utilize heat from a heat network, and found that both the heating capacity and PEE were enhanced by recovering the low-grade renewable energy. Besides, the coal and power consumption was reduced significantly, and thus the operating cost became relatively lower. Other papers focused on directly gas-fired systems, and an AHP system that could provide hot water above 57 °C was proposed [9], and theoretical studies showed that the COP was 1.74 as the ambient temperature was about 20 °C. At the similar ambient temperature, an AHP prototype [10] could provide 45 °C hot water and the COP was 1.63. Baig et. al. [11] tested the performance of an AHP prototype. It was shown that when the ambient temperature was -5 °C, the PEE was above 1, which was higher than that of the conventional boiler. However, as the ambient temperature went down to -5 °C, the PEE decreased sharply below 1.

Although the traditional single effect AHP system is an efficient district heating method, its performance decreases obviously under low ambient temperature, which limits its application in cold areas [12]. Besides, no matter it is directly gas-fired or utilizes heat from the heating network based on gas boiler (combustor), there is no effective recovery method of flue gas waste heat.

In this paper, an ammonia-water absorption heat pump prototype is proposed for rural residential heating. The prototype can be driven by the combustion of biogas that is widely available in rural areas. Experimental investigations are carried out to analyse its performance under different working conditions. During the experiment, the prototype works with an electric oil heater which simulates the biomass burner in real applications, and uses conduction oil as the heating medium. Intermediate process is introduced, and the prototype can utilize both the low-grade ambient heat and waste heat from biomass combustion through the evaporator and intermediate evaporator, respectively.

2. System Structure

The rural residential heating network based on the proposed AHP system is shown in Fig. 1. The driving heat is generated by the combustion of biogas that comes from the biogas digester, and heat conduction oil is used as the heating medium to transform heat from the combustor to the generator. Return water from the heat consumer is heated in sequence through the rectifier, condenser and absorber, with its temperature increases gradually, and then the heated water is supplied to the heat consumer. A higher PEE is obtained because of the ambient heat, including air- and ground-source, recovered in the evaporator, and waste heat of exhaust gas recovered in the intermediate evaporator [13].

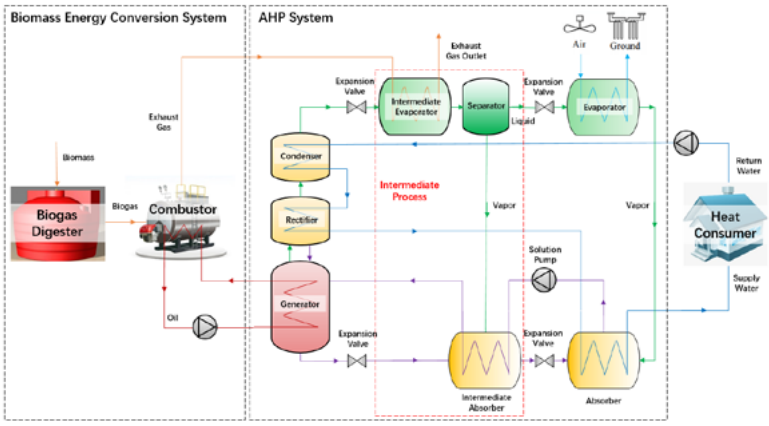
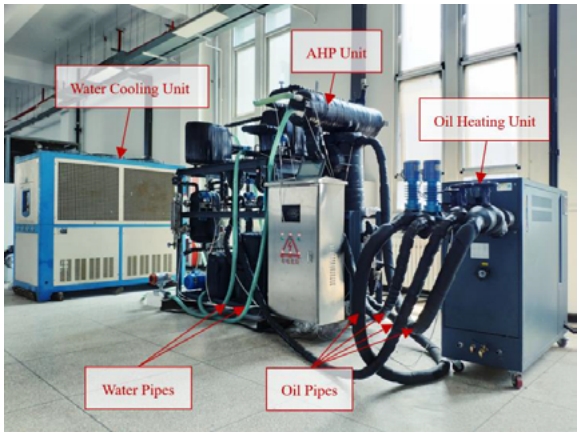


Fig. 1. Residential heating network based on AHP system.

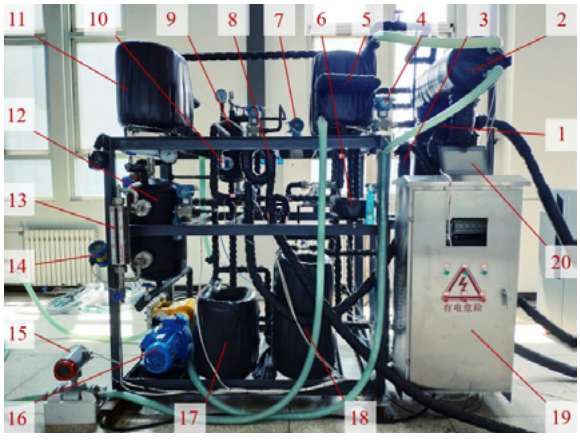
The proposed AHP system has the intermediate process. Exhaust gas from the biomass combustor enters the intermediate evaporator and the waste heat is recovered in the intermediate evaporator, where partial ammonia evaporation happens. The ammonia two-phase flow enters the separator, and the liquid and vapour

flows to the evaporator and intermediate absorber, respectively. The vapour is absorbed by the weak solution from the generator, and the heat from the intermediate absorption process is recovered by the pressurized strong solution. The above process occurs at the intermediate pressure between the system high pressure and low pressure. The additional intermediate pressure can reduce the degradation of system performance due to the large pressure difference at the low ambient temperature. In addition, the introduction of intermediate processes has two additional benefits: lower waste heat discharge temperature and improved internal heat recovery.

Based on the previous simulation studies [40], an experimental prototype system of residential heating is designed and built, as is shown in Fig. 2(a). The system contains three units: the oil heating unit, the water cooling unit and the AHP unit. The oil heating unit is an electric oil heater (simulating the biogas combustor), which heats the oil to the target temperature and delivers it to the generator of the AHP unit through the oil pipes; the water cooling unit is a water chiller (simulating the heat consumer), which cools the supply water down to the target return water temperature and delivers it to the AHP unit through the water pipes. The structure of the AHP unit is shown in Fig. 2(b).



(a) Three units of the experimental prototype system.



(b) Structure of the AHP unit.

1-Generator, 2-Rectifier, 3-Solution preheater, 4-Pressure transmitter, 5-Condenser, 6-Subcooler, 7-Mass flowmeter, 8-Intermediate evaporator, 9-Separater, 10-Temperature transmitter, 11-Evaporator, 12-Solution tank, 13-Content gauge, 14-Concentration meter, 15-Volume flowmeter, 16-Solution pump, 17-Absorber, 18-Intermediate absorber, 19- Electric control cabinet, 20-Display panel.

Fig. 2. Experimental prototype system of residential heating.

3. Calculation Method

3.1. Calculation of the generation heat Q_G

The generation heat Q_G is defined as the enthalpy difference between heat conduction oil inlet and outlet of the generator. It is calculated based on Eq. (1):

$$Q_G = m_{OG} \cdot c_{p,O} \cdot \Delta T_{OG} = \rho_O \cdot V_{OG} \cdot c_{p,O} \cdot \left(T_{OG,in} - T_{OG,out}\right) \tag{1}$$

where m_{OG} and V_{OG} are the mass and volume flow rates of the heat conduction oil through the generator; ρ_O and $c_{p,O}$ are the linear mean values of its density and specific heat, considering that they both change with temperature.

3.2. Calculation of the recovered exhaust heat Q_{WH}

The recovered exhaust heat Q_{EH} consists of two parts: waste heat recovered in the solution preheater Q_{SP} and waste heat recovered in the intermediate evaporator Q_{IE}. They are calculated based on Eqs. (2) ~ (4):

$$Q_{SP} = m_{OIE} \cdot c_{p,O} \cdot \Delta T_{OSP} = \rho_O \cdot V_{OIE} \cdot c_{p,O} \cdot \left(T_{OSP,in} - T_{OSP,out}\right) \tag{2}$$

$$Q_{IE} = m_{OIE} \cdot c_{p,O} \cdot \Delta T_{OIE} = \rho_O \cdot V_{OIE} \cdot c_{p,O} \cdot \left(T_{OIE,in} - T_{OIE,out}\right) \tag{3}$$

$$Q_{EH} = Q_{SP} + Q_{IE} = \rho_O \cdot V_{OIE} \cdot c_{p,O} \cdot \left(T_{WH,in} - T_{WH,out}\right) \tag{4}$$

where m_{OIE} and V_{OIE} are the mass and volume flow rates of the heat conduction oil through the intermediate evaporator; $T_{OSP,in}$ and $T_{OSP,out}$ are the oil inlet and outlet temperatures of the solution preheater, and $T_{OSP,in}$ is equal to $T_{WH,in}$; $T_{OIE,in}$ and $T_{OIE,out}$ are the oil inlet and outlet temperatures of the intermediate evaporator, and $T_{OIE,out}$ is equal to $T_{WH,out}$.

3.3. Calculation of the heating capacity Q_{HC}

In the experimental prototype, the return water passes through the condenser, rectifier and absorber, and are heated to the target temperature. Therefore, the heating capacity Q_{HC} consists of three parts: condensation heat Q_C, rectification heat Q_R and absorption heat Q_A. They are calculated based on Eqs. (5) ~ (8) [14]:

$$Q_C = m_W \cdot c_{p,W} \cdot \Delta T_{WC} = \rho_W \cdot V_W \cdot c_{p,W} \cdot \left(T_{WC,out} - T_{WC,in}\right) \tag{5}$$

$$Q_R = m_W \cdot c_{p,W} \cdot \Delta T_{WR} = \rho_W \cdot V_W \cdot c_{p,W} \cdot \left(T_{WR,out} - T_{WR,in}\right) \tag{6}$$

$$Q_A = m_W \cdot c_{p,W} \cdot \Delta T_{WA} = \rho_W \cdot V_W \cdot c_{p,W} \cdot \left(T_{WA,out} - T_{WA,in}\right) \tag{7}$$

$$Q_{HC} = Q_C + Q_R + Q_A = \rho_W \cdot V_W \cdot c_{p,W} \cdot \left(T_{SW} - T_{RW}\right) \tag{8}$$

where m_W and V_W are the mass and volume flow rates of the circulating water; ρ_W and $c_{p,W}$ are its density and specific heat; $T_{WC,in}$ and $T_{WC,out}$ are the water inlet and outlet temperatures of the condenser; $T_{WR,in}$ and $T_{WR,out}$ are the water inlet and outlet temperatures of the rectifier; $T_{WA,in}$ and $T_{WA,out}$ are the water inlet and outlet temperatures of the absorber; T_{SW} and T_{RW} are the supply water and return water temperatures, T_{SW} is equal to $T_{WA,out}$, and T_{RW} is equal to $T_{WC,in}$.

3.4. Calculation of the heating efficiency COP and PEE

The experimental prototype has two heating efficiency indexes: the coefficient of performance COP and the primary energy efficiency PEE, which are calculated based on Eq. (9) and (10):

$$\mathrm{COP} = \frac{Q_{HC}}{Q_G + W_P} \tag{9}$$

$$\mathrm{PEE} = \frac{Q_{HC}}{Q_G / \eta_C + W_P / \eta_E} \approx \frac{Q_{HC}}{Q_G + Q_{EH} + W_P / \eta_E} \tag{10}$$

where W_P is the pump work; η_C is the efficiency of the combustor; η_E is the efficiency of electricity generation, which is around 33% [2]; Q_G / η_C is the calorific value of the natural gas, and is approximately

equal to the combustion heat plus flue gas waste heat: $Q_G / \eta_C \approx Q_G + Q_{EH}$ [13].

4. Results and Discussion

4.1. Performance under basic working condition

The performance of the experimental prototype system is studied under the basic working condition: the ambient temperature is about -5 °C, the oil inlet temperature is 180 °C, and the return water temperatures is 35 °C. Summary of experimental performance under the basic working condition is shown in Table 1. In the basic working condition, the return water passes in sequence through the condenser, rectifier and absorber, and its temperature increases to 40.0, 46.2 and 50.6 °C, respectively, when the flow rate is kept at 1.4 m^3/h. It is also shown that by introducing the intermediate process, 2.39 kW exhaust heat is recovered, and the exhaust heat temperature is reduced to 41.3 °C, which is lower than the dew point of the exhaust gas, indicating that the exhaust heat recovery is improved. Besides, the pressurized strong solution of 46.5 °C is first heated to 127.6 °C by recovering the intermediate absorption heat, and then it is further heated in the solution preheater into the two-phase flow, indicating that the internal heat recovery is improved. Moreover, the energy input and output of the AHP unit are 26.59 and 25.43 kW, respectively. Therefore, the heat loss is about 1.16 kW that is only 4.4% of the total energy input, indicating that the experimental prototype is in good energy balance. It is shown that when the evaporation temperature is -5 °C, the experimental prototype system can provide 25 kW heating capacity to heat the water from 35 °C to above 50 °C, and the COP and PEE are 1.37 and 1.14, respectively.

Table 1. Summary of experimental performance under basic working condition

	Components	Energy input (kW)		Energy output (kW)	
		Value	Uncertainty	Value	Uncertainty
Energy Transfer	Generator	18.13	±0.41	/	/
	Rectifier	/	/	6.45	±0.31
	Condenser	/	/	10.14	±0.47
	Evaporator	5.57	±0.35	/	/
	Intermediate Evaporator	1.54	±0.21	/	/
	Absorber	/	/	8.84	±0.42
	Solution Preheater	0.85	±0.05	/	/
	Solution Pump	0.50	±0.03	/	/
	Total	26.59	±0.57	25.43	±0.69
Performance Parameters	Parameters	Value		Uncertainty	
	Heating Capacity	25.43 kW		±0.69 kW	
	Recovered Exhaust Heat	2.39 kW		±0.07 kW	
	Supply Water Temperature	50.6 °C		±0.3	
	Exhaust Heat Temperature	41.3 °C		±0.3	
	COP	1.37		±0.05	
	PEE	1.14		±0.03	

4.2. Influence of the oil inlet temperature

The oil inlet temperature T_{OI} is an important working condition parameter of the absorption heat pump system, because of its effects on the generation process and system performance. Low T_{OI} cannot provide sufficient driving force for system operation, while high T_{OI} will cause huge exergy destruction in the heat transfer process. Some research shows that there is an optimal T_{OI}, and when the value continue goes up, the system performance will not improve or even degrade. This is also observed in this study, as is shown in Fig. 3. When T_{OI} increases from 165 to 186 °C, both COP and PEE increase rapidly at first till reach 1.61 and 1.32, respectively, and then remain nearly constant. The turning point happens when T_{OI} is about 175 °C.

For the exhaust heat temperature, it raises along with T_{OI}, but basically keeps between 39 and 42 °C. Moreover, the supply water temperature increases linearly from 54 to 59 °C when T_{OI} increases from 165 to 186 °C, and is expected to continue to raise when T_G further increases. Therefore, in order to obtain the target supply water temperature, the oil inlet temperature can be appropriately increased above the optimal value, at the cost of slightly reducing the COP.

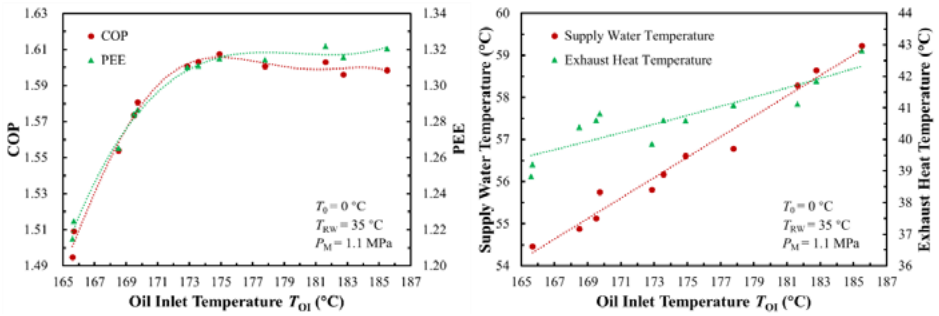


Fig. 3. Influence of the oil inlet temperature on the system performance

4.3. Influence of the ambient temperature

The ambient temperature T_0 has a huge influence on the evaporation process and thus the system performance. It is shown in Fig. 4 that as T_0 decreases from 5 °C to -10 °C, the heating capacity reduces from 30 kW to 22 kW, and the COP decreases from 1.60 to 1.25. The proposed system has a much higher primary energy efficiency than that of the conventional boiler, and it is higher than 1 even when the ambient temperature T_0 is reduced to -10 °C.

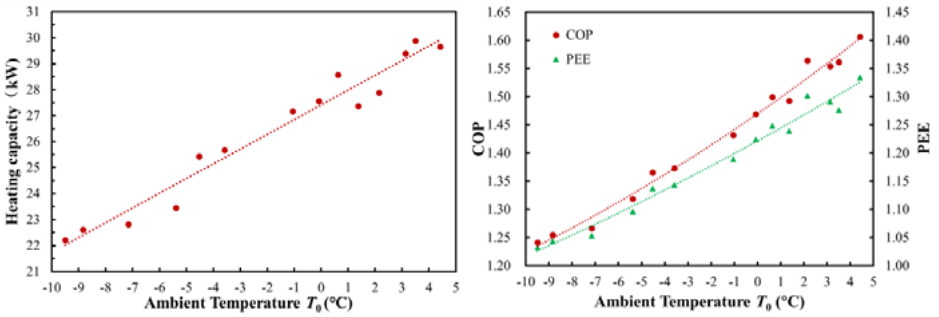


Fig. 4. Influence of the ambient temperature on the system performance

4.4. Influence of the return water temperature and water flow rate

The return water temperature T_{RW} has effects on almost all the processes of the AHP system, including the condensation, rectification, generation and absorption processes. If T_{RW} is high, the ammonia vapour becomes difficult to condense in the condenser and rectifier, and the system high pressure will increase, which has a negative effect on the generation process. Even worse, it also obstructs the absorption process since the absorption heat is hard to carry away. In the previous analysis, T_{RW} is fixed at 35 °C, which is a common return water temperature for most residential heating systems. However, it changes as the working condition deviates from the set state, such as the ambient temperature suddenly drops. Fig. 5 indicates that the system is quite sensitive to the return water temperature when the water flow rate V_W is fixed. It is shown that the COP drops linearly from 1.57 to 1.27, as T_{RW} increases from 30 to 40 °C. At the same time the supply water temperature T_{SW} raises from 46.6 to 52.3 °C. On the other hand, if the return water temperature T_{RW} is fixed, the COP will increase and the supply water temperature T_{SW} will decrease, as the water flow rate V_W raises, as is shown in Fig. 6. Therefore, if T_{RW} deviates from the set value, V_W can be adjusted accordingly to stabilize the system performance. More specifically, enlarge V_W if T_{RW} increases, and reduce V_W if T_{RW} decreases.

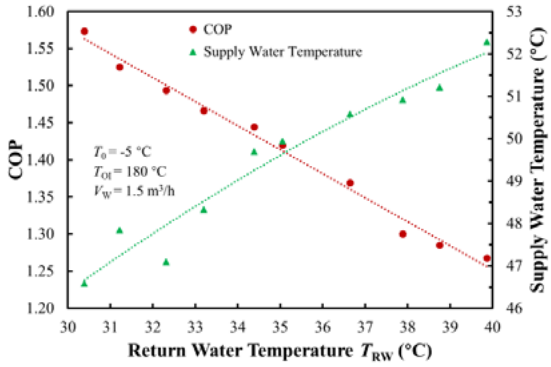


Fig. 5. Influence of the return water temperature on the system performance

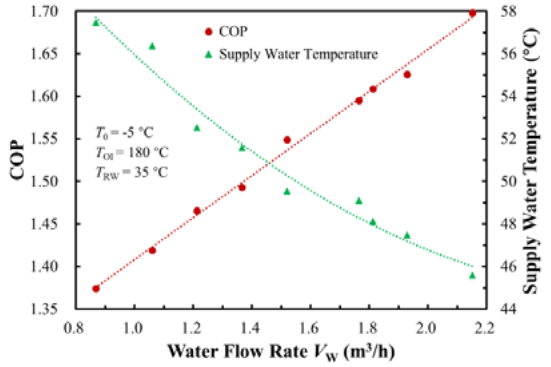


Fig. 6. Influence of the water flow rate on the system performance

4.5. Influence of the return water temperature and water flow rate

The intermediate pressure P_M is a key parameter of the proposed system, and its value influences both the waste heat recovery of the intermediate evaporator and the solution heat recovery of the intermediate absorber. Fig. 7 shows that as the intermediate pressure increases, the waste heat outlet temperature raises from 39 °C to 45 °C, indicating that the waste heat recovery is limited. It is probably because the enhanced intermediate pressure raises the intermediate evaporation temperature and thus increases the waste heat outlet temperature. On the other hand, a higher intermediate pressure causes a higher solution heat recovery outlet temperature of the intermediate absorber, indicating that the internal heat recovery is improved.

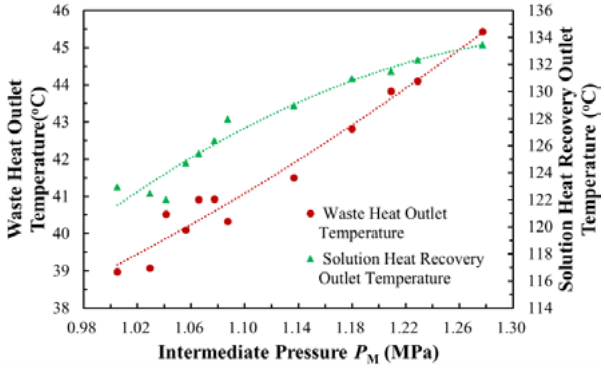


Fig. 7. Influence of the intermediate pressure on the system performance

5. Conclusions

In order to replace the inefficient and polluting boilers, an ammonia-water absorption heat pump prototype is proposed for rural residential heating. The prototype can be driven by the combustion of biogas that is widely available in rural areas. Experimental investigations are carried out to analyse its performance under different working conditions. During the experiment, the prototype works with an electric oil heater which simulates the biomass burner in real applications, and uses conduction oil as the heating medium. Several conclusions are drawn as following.

- When the ambient temperature is -5 °C and the oil inlet temperature is 180 °C, the experimental prototype system can provide 25 kW heating capacity to heat the water from 35 °C to above 50 °C, and the COP and PEE are 1.37 and 1.14, respectively.
- By introducing the intermediate process, 2.39 kW exhaust heat is recovered, and the exhaust heat temperature is reduced to 41.3 °C, which is lower than the dew point of the exhaust gas, indicating that the exhaust heat recovery is improved.
- When the oil inlet temperature increases, both COP and PEE increase rapidly at first, and then remain nearly constant. The turning point happens when the oil inlet temperature is about 175 °C.
- As the ambient temperature decreases from 5 °C to -10 °C, the heating capacity reduces from 30 kW to 22 kW, and the COP decreases from 1.60 to 1.25. The proposed system has a much higher primary energy efficiency PEE than the conventional boilers, and it is higher than 1 even when the ambient temperature is reduced to -10 °C.
- The COP drops and the supply water temperature raises as the return water temperature increases. On the other hand, the COP increases and the supply water temperature decreases as the water flow rate raises. Therefore, if the return water temperature deviates from the set value, the water flow rate can be adjusted accordingly to stabilize the system performance.
- As the intermediate pressure increases, the waste heat outlet temperature raises from 39 °C to 45 °C, indicating that the waste heat recovery is limited. On the other hand, a higher intermediate pressure causes a higher solution heat recovery outlet temperature of the intermediate absorber, indicating that the internal heat recovery is improved.

Acknowledgements

The authors would like to thank the support of the National Science Fund for Distinguished Young Scholars (No. 51625603) and the International Partnership Program of Chinese Academy of Sciences (No. GJHZ1876).

References

[1] Tsinghua University Building Energy Saving Research Center. Annual Report on China Building Energy Efficiency. Beijing: *China Architecture and Building Press*; 2013 [in Chinese].
[2] Yang L, Yan H, Lam J C. Thermal comfort and building energy consumption implications – A review. *Applied Energy* 2014; 115(Supplement C): 164-73.
[3] Tsinghua University Building Energy Saving Research Center. Annual Report on China Building Energy Efficiency. Beijing: China *Architecture and Building Press*; 2017 [in Chinese].
[4] Qunli Z, Mingkai C, Qiuyue Z, et al. Research on a new district heating method combined with hot water driven ground source AHP. *Energy Procedia* 2015; 75: 1242-1248.
[5] Zhang Q, Zhang X, Sun D, et al. Municipal space heating using a ground source absorption heat pump driven by an urban heating system. *Geothermics* 2019; 78: 224-232.
[6] Wu W, Ran S, Shi W, et al. NH_3-H_2O water source AHP (WSAHP) for low temperature heating: Experimental investigation on the off-design performance. *Energy* 2016; 115: 697-710.
[7] Nitkiewicz A, Sekret R. Comparison of LCA results of low temperature heat plant using electric heat pump, absorption heat pump and gas-fired boiler. *Energy Conversion and Management* 2014; 87: 647-652.
[8] Li Y, Fu L, Zhang S, et al. A new type of district heating system based on distributed absorption heat pumps. *Energy* 2011; 36(7): 4570-4576.
[9] Keinath C M, Garimella S, Garrabrant M A. Modeling of an ammonia–water AHP water heater for

residential applications. *International Journal of Refrigeration* 2017; 83: 39-50.
[10] Garrabrant M, Stout R, Glanville P, et al. Development and Validation of a Gas-Fired Residential Heat Pump Water Heater-Final Report. *Stone Mountain Technologies, Inc.*; 2013.
[11] Baig A A, Ethirveerasingham K, Fung A. Development of a Monitoring System for a Gas-Fired Absorption Heat Pump and Results for Testing in Heating and Cooling Mode. *Energy Procedia* 2019; 158: 2202-2209.
[12] Wang J, Wang B, Wu W, et al. Performance analysis of an absorption-compression hybrid refrigeration system recovering condensation heat for generation. *Applied Thermal Engineering* 2016; 108: 54-65.
[13] Lu D, Chen G, Gong M, et al. Thermodynamic and economic analysis of a gas-fired absorption heat pump for district heating with cascade recovery of flue gas waste heat. *Energy Conversion and Management* 2019; 185: 87-100.
[14] Wu W, Shi W, Wang J, et al. Experimental investigation on NH3–H2O compression-assisted absorption heat pump (CAHP) for low temperature heating under lower driving sources. *Applied Energy* 2016; 176: 258-271.

13th IEA Heat Pump Conference
April 26-29, 2021 Jeju, Korea

Performance analysis of a Combined Cooling and Power Cycle

N. Voeltzel[a], H.T. Phan[a,*], N. Tauveron[a], Q. Blondel[a] and B. Gonzalez[a]

[a]Univ. Grenoble Alpes, CEA, LITEN, DTBH. F-38000 Grenoble, France

Abstract

Absorption cycles cogenerating cooling and power are flexible systems able to adapt to the irregularity of the user's needs. To facilitate their integration in industrial processes and mobility applications, this work investigates the performance and control of a water-ammonia based cogeneration system operating at low-grade heat (< 200 °C). Through a complete model of a cogeneration cycle implementing an accurate description of an expander, the optimal performance of power and/or cooling production are explored according to the needs and the available temperature sources. Simulations show that power and cooling productions can respectively reach the performances of Kalina and absorption cycles for determined operating conditions. They also highlight the critical features of an expander in a combined production cycle. The model is then imported in a dynamic solver to investigate the transient behavior of a cogenerating system. Such complex systems present significant inertia when starting or switching from one production mode to another (between cooling and power). This study provides some insight on the most critical elements of the cycle.

© HPC2020.
Selection and/or peer-review under responsibility of the organizers of the 13th IEA Heat Pump Conference 2020.

Keywords: Combined cooling - power; Absorption cycle; Transient study

1. Introduction

Quantity	Symbol	Unit
Area	A	mm^2
Exchanged Heat	Q	J
Overall heat transfer coefficient	U	$W\ m^{-2}\ K^{-1}$
Temperature	T	°C
Efficiency	η	
Expander generated power	$\dot{W}$	kW
Mass flow rate	$\dot{m}$	$kg.s^{-1}$
Specific enthalpy	h	$kJ.kg^{-1}$
Friction coefficient	τ_{loss}	N
Split ratio	r_s	
Valve switching time	t_v	s

Quantity	Subscript
Expander	*expa*
Experimental	*exp*
Numerical	*U*
Expander inlet	*in*
Expander outlet	*Out*
Critical	*c*
Coefficient of Performance	COP
Combined Cooling and power	CCP
Organic Rankine Cycle	ORC
Hydrofluorocarbons	HFC
Built-in Volume Ratio	BVR

The literature depicts various architectures of combined cooling and power (CCP) production. A first overview of the systems studied was proposed by Ayou *et al.* (2013). Two main families stand out: the cogeneration architectures in series [2]–[4] and those in parallel [5]–[7]. The architectures in series are generally more efficient for simultaneous co-generation of cold and electricity while the architectures in parallel enable more flexibility in term of production. Parallel architectures are also easier to implement

* Corresponding author. Tel.: +33 4 79 79 23 72; fax: +33 4 38 78 53 96.
E-mail address: haitrieu.phan@cea.fr.

because only two levels of pressure are present. Independently of the architectures, the cold can be produced using the principle of the absorption chillers [3], [5], [6] or that of the ejectors [2]. The combination of both technologies was also considered in several studies [7], [8]. Electricity is produced by the expansion of the working fluid in an expander (volumetric type or turbine) coupled to a generator. The development of expanders notably benefits from the recent study of organic fluid Rankine cycles (ORC) [9].

As cogeneration systems are quite complex cycles, only a few experimental investigations have been conducted so far and they usually simulate hard-provisioning components with simplified equivalents [5]. In return, the numerical approach is widely used to explore the performance of innovative architectures. Concerning cooling production, the physical models that describe the various components of thermodynamic cycles have already been well investigated and have led to numerous numerical studies of both absorption and compression machines [10]. Concerning power production, expander models need further investigation due to complex phenomena and a wide range of existing technologies.

Lemort *et al.* (2009) developed a first scroll expander model. This semi-empirical model considers the physics related to the transformation of the fluid from the inlet to the outlet of a scroll. In CCP systems coupling an absorption cycle with an expander, the expanded gas in the expander is most often ammonia containing traces of water. Hence, there is a real interest in adapting this model to work with ammonia. Based on experimental data, Mendoza et al. (2014) developed a simplified version of Lemort's model with ammonia as working fluid. The model is later included into a CCP cycle (Mendoza et al., 2014) and the performance of a scroll expander is then calculated for three different working fluids.

As a continuous of the literature work, the present study aims to optimize the performance of CCP cycles. A parallel architecture of the expander integrated into an ammonia-water absorption chiller has been studied. Numerical models of the cycle were developed with a detailed model of a scroll-type expander. Tests were also conducted on an ORC system and an absorption-chiller machine, giving experimental data for calibration of the model parameters and boundaries. The simulation results were then analyzed, giving us information about the key factors affecting the cycle performance. Finally, the transient behavior of the cogenerating system has been investigated through dynamic simulations. This illustrates the stability of the system and gives insights on typical response times to control the operation of the cycle.

2. Cycle description

The CCP cycle considered in the present study is shown in Figure 1. It consists of a water-ammonia absorption cycle in parallel with an ORC cycle, the one using part of the desorbed ammonia as a working fluid and a scroll expander for power production.

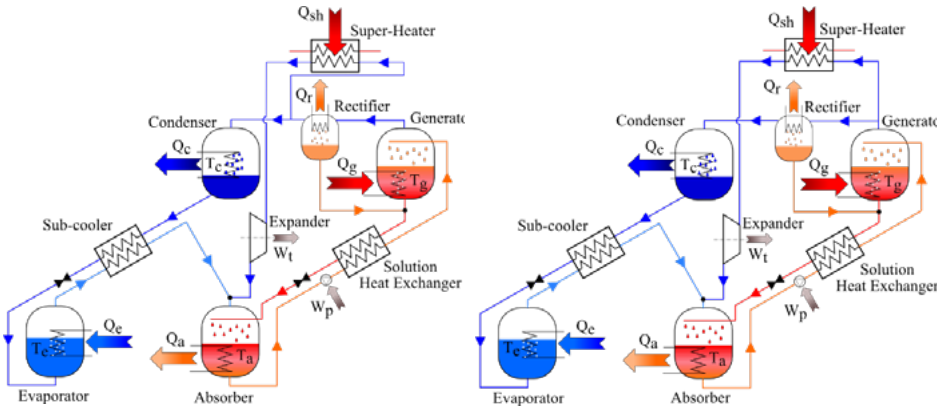


Fig.1. Scheme of the CCP cycle with two different configurations

On the solution circuit loop, a first line of ammonia-rich solution flows from the absorber to the generator through pressurization by a pump. A second line with an expansion valve brings the poor solution back to the absorber. An economizer preheats the rich solution with the poor solution coming out of the generator.

Upstream of the production lines, a rectifier maximizes the ammonia content of the gas produced at the generator in order to obtain better performance for cooling production. In Configuration A (Figure 1), the rectification is effective for both the cooling and the power production lines, while in Configuration B the ammonia expended to produce power is not rectified as the switch valve directing the flow between the two production lines is positioned before the rectifier. The two variations of the cycle exist in different architectures founded in the literature [5], [6].

To produce power, a superheater raises the temperature of the fluid to ensure that it remains in a gaseous state throughout the expansion. In the scroll expander, the fluid is then trapped and expanded in expansion chambers. By deforming, the chambers cause the rotation of a shaft that is coupled to a generator to produce electricity.

To produce cooling, a heat exchange with an intermediate temperature source (usually the ambient) condenses the ammonia flowing from the generator. A valve expands the ammonia to low temperature so it can take calories at the evaporator for cooling production. Finally, a sub-cooler allows the ammonia to be pre-cooled before it is expanded, by using the ammonia coming out of the evaporator.

The flows from the two production lines mix and are finally absorbed into the poor solution through cooling by a source of intermediate temperature (the same as the one used in the condenser).

3. Experimental devices

Two different devices provide data to setup the following numerical models: the scroll expander model is parametrized according to tests performed on an ORC test rig, and an absorption cycle is characterized to setup the other components in the model of the complete CCP cycle.

3.1 Organic Rankine Cycle

Scroll expanders ensure the continuous expansion of a fluid in closed chambers. This solution is therefore very relevant for small power applications with moderate flow rates [12]. A 1 kW Air Squared® scroll expander (model E15H022A-SH) was mounted on an existing ORC test rig [13]. A preheater has also been added to the initial device to increase the range of test conditions. In detail, a Hydra-Cell pump ensures the circulation and pressure elevation of the fluid. A preheater and an evaporator transfer up to 18 kW of thermal energy to it. Then the gaseous fluid expands in the scroll expander by driving a generator. Finally, a series of three condensers, fed by the same cold source, liquefy the fluid before it returns to the pump.

As ammonia cannot be directly tested in the installation, another pure fluid serves to characterize the scroll expander. The choice is an HFC commonly used in the heat pump industry: R245fa. This refrigerant have already demonstrated its ability to produce energy by expansion in an expander [14], [15]. Thanks to adaptation laws between fluids described by [14], the characterization completed with R245fa allows to project the scroll behavior when operating with ammonia.

3.2 Absorption chiller

To characterize the other components in the studied CCP cycle, tests are performed on an existing water/ammonia absorption chiller device. This experimental cycle produces up to 5 kW of cold (at temperature from -10°C to 20°C) from a heat source at low-grade temperature (70°C to 130°C) and a source at intermediate temperature (15°C to 45°C). The operating pressures vary between 8 and 20 bar on the high-pressure side and from 2 to 6 bar on the low-pressure side. Details of the design of the device and its detailed description were the subject of a previous paper [16]. In short, the operation of the device is identical to that of the CCP cycle studied and presented above, without the electricity production line parallel to the cooling production. The tests carried out on the device make it possible to estimate the pinches of temperature, pressure drops, and efficiencies associated with the various components presented in the CCP cycle.

The two following models were implemented in the ‘Engineering Equation Solver’ (EES) environment to be solved. The calculated values of specified thermodynamic states come from EES’s database for pure ammonia and water/ammonia mixtures.

4. Numerical models

4.1 Expander scroll modelling

Lemort's semi-empirical model [11] has been used in many studies to explore the different operating conditions of a scroll expander [14], [17]. It quantitatively estimates the performance of an expander with a

limited number of operating conditions (flow rates, pressures and temperatures) at the inlet. In detail, the model decomposes the flow of fluid through the scroll into seven distinct thermodynamic transformations. It also considers the mechanical and thermal exchanges of the scroll with its environment. The equations specific to each transformation and balance are detailed in the reference publication [11].

Table. 1: Scroll properties determined from experimental data with R245fa.
The bold values identify the corrections for operation with ammonia.

	A_{in} (mm²)	$AU_{in,n}$ (W/K)	$AU_{out,n}$ (W/K)	AU_{amb} (W/K)	BVR	A_{leak} (mm²)	τ_{loss} (N.m)
R245fa	28	12	31,4	7,5	2,7	5,7	0,2
Ammonia	28	**6**	**14,7**	7,5	**1,9**	**1**	0,2

The design of the expander, the working fluids and the operating conditions are inputs of the model Table.1 lists the parameters related to the nature of the expander. A_{in} is the flow cross-section of the fluid at the expansion inlet. $AU_{in,n}$, $AU_{out,n}$ and AU_{amb} are the heat exchange coefficients of a fictitious isothermal wall with, respectively, the fluid before expansion, the fluid after expansion and the ambient. The Built-in Volume Ratio (BVR) characterizes the volume expansion rate. A_{leak} represents the total leakage area related to the flow of fluid through the expander that does not produce work. Finally, τ_{loss} is a mechanical friction coefficient. All these parameters are determined by minimizing the differences between experimental measurements and model calculations. The scroll response (power generation, output temperature and flow rate) was experimentally measured through 30 tests performed on the previously introduced ORC test bench for different temperature and flow rate conditions over the operating range of the expander. The same tests were simulated with the model by imposing four input parameters: the scroll speed, the temperature of the inlet fluid and the pressures upstream and downstream of the expander. The difference between the numerical and experimental results is quantified by the error:

$$\varepsilon = \sum \left[\left(\frac{T_{out,exp} - T_{out,num}}{\overline{T_{out,exp}}} \right)^2 + \left(\frac{\dot{W}_{exp} - \dot{W}_{num}}{\overline{\dot{W}_{exp}}} \right)^2 + \left(\frac{\dot{m}_{exp} - \dot{m}_{num}}{\overline{\dot{m}_{exp}}} \right)^2 \right] \quad (1)$$

T_{out}, $\dot{W}$ and $\dot{m}$ are respectively the expansion outlet temperature, the power output and the fluid mass flow rate. The *exp* and *num* indices distinguish experimental quantities from numerically calculated quantities. A genetic algorithm is used to minimize the error ε and determine the value of the parameters listed in Table 1. To assess the accuracy of the model, a comparison is made between the experimental measurements and the recalculated numerical values based on the newly determined parameters (see Figure 2). It shows that the differences are less than 10% for 26 of the 30 configurations studied, what tends to validate the numerical approach.

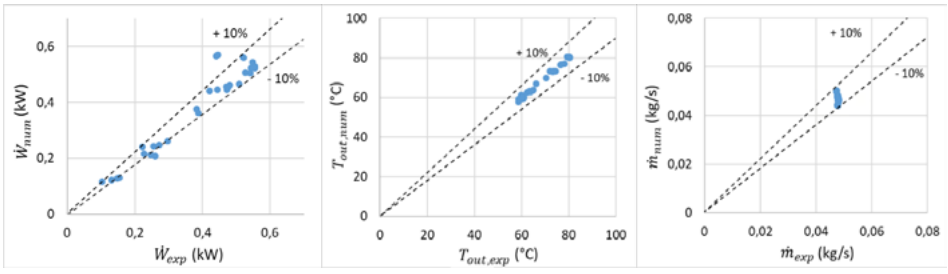


Fig.2. Comparison of numerical (vertical axis) and experimental (horizontal axis) results of $\dot{W}$, T_{out} and $\dot{m}$

The heat exchange coefficients of the model depend on both the properties of the scroll and the working fluid. In order to preserve the validity of a model calibrated on a type of scroll expander for different fluids, [14] uses the intrinsic properties of the fluids to recalculate the heat exchange coefficients. Thus, the values of the exchange coefficients $AU_{in,n}$ and $AU_{out,n}$ determined for R245fa take the values of 6 W/K and 15.7 W/K

respectively with ammonia. The study of an expander designed to operate with ammonia also requires adapting its geometry to be compatible with the properties of the fluid. Thus, since the expansion rate of ammonia is significantly higher than that of R245fa, the BVR is reduced to 1.9 in the scroll expander model.

To evaluate the performance of the expander, its efficiency is defined as follows:

$$\eta_{expa} = \frac{\dot{W}}{\dot{m} . \Delta h_{is}} \quad (2)$$

With Δh_{is} the enthalpy variation of the fluid in the scroll in the case of an isentropic transformation (ideal).

4.2 Modelling of the combined cooling and power cycle

A numerical model was developed based on the prototype of absorption cycle presented previously [16]. For each component, the energy and mass conservation equations were formalized. The experimentally set values of pinch, pressure drop, and efficiency configure the heat exchanger model. Finally, it is assumed that the fluids are saturated at the outlet of each exchanger (except for an imposed superheating of 5 °C at the evaporator outlet). From this configuration, the model predicts the performance and thermodynamic states of the system for given operating conditions (temperature or power of the sources and solution mass flow rate).

To complete the development of the CCP cycle, the scroll expander model is integrated into the parallel absorption chiller model of the cold production circuit (see Figure 1). In addition, a superheater modelled as an adjustable power supply to the fluid precedes the scroll. In order to control the share of cold and electricity production, the split ratio r_s divides the refrigerant flow between the two production lines. It is equal to the ratio of the mass flow rate of ammonia passing through the evaporator to the mass flow rate of ammonia produced at the generator.

To estimate the cold production efficiency of the CCP cycle, the COP is defined as follows:

$$COP = \frac{Q_{evap}}{Q_{gen} . r_s} \quad (3)$$

With Q_{evap} the thermal power exchanged at the evaporator and Q_{gen} that at the generator.

5. Results and analysis

A first analysis focuses on the operation of the scroll expander under the operating conditions of the CCP cycle and define a newly criteria to assess the quality of expanders. We then explore the performance of the complete cycle and carry out a comparative study between the two configurations of the cycle presented in Figure 1. Finally, a transient study of the cycle introduces the dynamical behavior of this complex system.

5.1 Scroll performance under operating conditions of the CCP cycle

In a conventional absorption cycle, the flow of ammonia produced at the generator matches 20-30% of the flow of rich solution [10]. Tests on the absorption chiller device estimate a maximum flow rate of fluid through the expander of about 0.01 kg/s. Figure 3 shows the power production of the scroll with ammonia as a function of flow rate. In order to highlight the sensitivity of the scroll performance to the low flow rate imposed by the CCP cycle (~ 0.01 kg/s), the study focuses on the influence of the following sensitive parameters: the pressure variation in the expander ΔP and the leakage area A_{leak}. We note that for a leakage area equivalent to that determined for the expander installed on the ORC test rig (solid curves), energy production is nil or very low for flows below 0.01 kg/s. Indeed, in this configuration, the internal leakages are too large compared to the ammonia flow and the scroll is not being driven. This effect is even more important as the pressure differential in the scroll is high (bold curves).

With a leakage area reduced to 1 mm², the critical flow rate required to produce power is reduced to about 0.003 kg/s (dotted curves). As the leakage area is directly related to the volume efficiency of scroll expanders, this result illustrates the need to design highly efficient expanders for the development of small capacity CCP cycles. The reduced leakage area is retained for the rest of the study (A_{leak}= 1 mm²).

The characterization of leaks in expanders operating with ammonia is of major concerns as there are essential in the development of CCP cycle, Kalina cycle [18] or ORC operating with ammonia. Considering a critical leakage area being the limit for A_{leak} above the one there is no power generation, it is relevant for expander constructors to evaluate this critical area easily from the foreseen operating conditions. The equations that governs the leaks in Lemort's model involve numerous parameters [11].

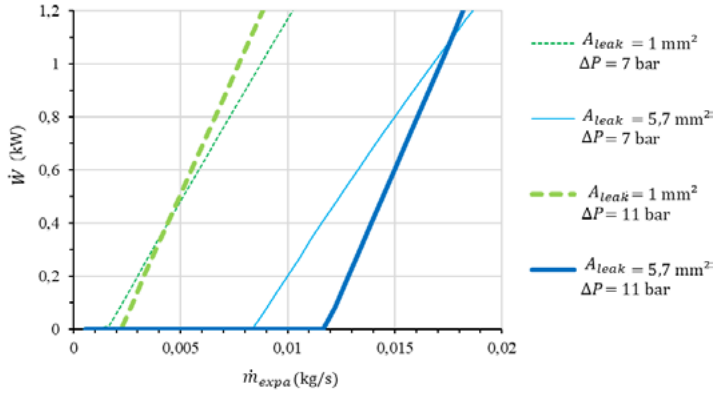


Fig. 3. Power produced by the scroll expander as a function of the leakage area and the pressure variation in the expander

A sensitivity analysis stated that mostly the leakage area, the upstream pressure and the fluid nature influence the leakage mass flow rate. Considering ammonia as operating fluid, an evaluation of the leaks evolution, with variations of the two remaining parameters, enable to identify an analytical law to predict the critical mass flow rate:

$$A_{leak,c} = k\frac{\dot{m}_{expa}}{P_{in}} \tag{4}$$

With k a constant consistent with speed unit and proper to the fluid. A regression of the mean square deviation between the law and the numerical prediction gives a value of k = 612.3 m/s for ammonia as working fluid. Finally, the prediction of the analytical law (equation 4) fits with the numerical calculation of a critical leakage area with less than 3.7 % of relative error (see Figure 4).

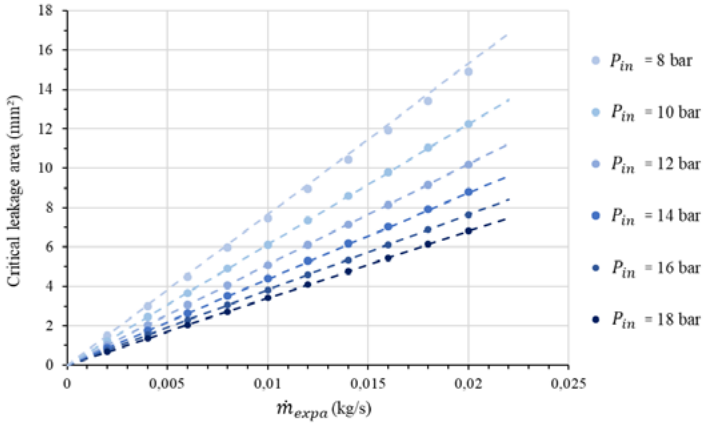


Fig.4. Numerical and analytical calculations of the critical leakage area of a scroll expander as a function of the ammonia mass flow rate and the pressure differential through the scroll.

The numerical data are computed for an inlet temperature of the fluid in the turbine of 110 °C and an outlet pressure of 4 bar. Nonetheless, sensitivity calculations show that the leakage mass flow rate varies less than 11 % for an input temperature between 90° and 160°C, with a slight leakage decrease when the temperature increases. Moreover, the outlet pressure doesn't act on the leakage numerical calculation unless it is greater than about 53 % of the inlet pressure, what is very rarely the case in ammonia absorption chiller. Thus, the

scope of validity of the analytical law to estimate a critical leakage area (equation 3) cover a large range of CCP cycles empowered by low-grade temperature source (90°C to 160°C).

5.2 Impact of the rectification of ammonia for power production

To compare the two configurations of cycles previously introduced, this study analyses the action of the rectifier on the cycle performance. By lowering the temperature of the gas produced at the generator, the rectifier will condense the remaining traces of water in the ammonia and redirect them to the poor solution. Thus, the rectifier limits the water content in the ammonia, but also reduces the flow rate in the downstream production lines. To quantify the overall influence of the rectification on cycle efficiencies, Figure 5 shows, for both configurations, the expander efficiency (equation 2) and the COP (equation 3) of the cold production as a function of the mass fraction of ammonia in the evaporator. For the comparison, the cycle inputs are set as follow: the sources of hot, intermediate and cold temperatures are set respectively to 110°C, 27°C and 18°C; the rich solution flow rate is set at 0.028 kg/s; the superheater imposes an increase of temperature of 15°C between the generated ammonia and the inlet of the scroll.

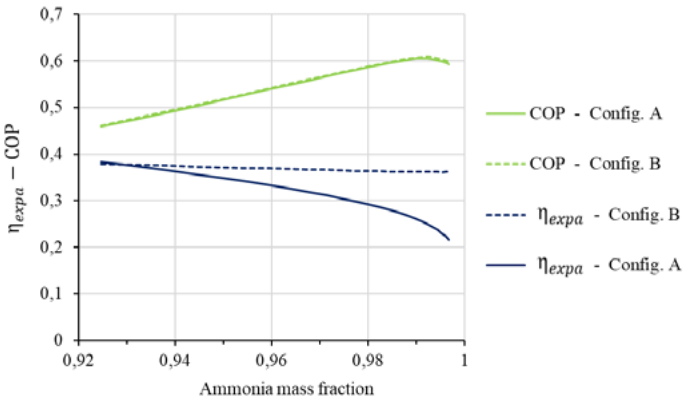


Fig.5. Expander efficiency and COP of the cooling production as a function of the mass fraction of ammonia at the evaporator

The results confirm the relevance of the rectifier to improve the performance of cooling production as the COP increases to an optimum corresponding to an ammonia content of 99.2%. In addition, it can be observed that the COP is logically relatively unaffected by the cycle configuration since in both configurations the rectifier is always upstream of the cold production line.

Focusing on power production, the rectification of ammonia before it passes through the expander (configuration A) results in a significant decrease of the expander efficiency. For instance, an optimal rectification for cooling production (99.2% ammonia content) leads to a 34% reduction of the efficiency. This trend does not occur when the ammonia entering the expander is not rectified (configuration B). The decrease of the expander efficiency is then limited to 5% and is due to the reduction of the high pressure of the cycle, which is related to the rectification rate occurring on the cooling production line. Finally, this result makes it possible to establish that the loss of performance attributable to the presence of water vapor in the working fluid is less significant than that due to the reduction in flow rate caused by the rectification.

Note that other constraints (serial CCP cycle, combined generator-rectifier, etc.) may favor the choice of a less optimal configuration (type configuration A). Then the quantified comparison presented in this study can be used as a reference to arbitrate between different architectural options.

5.3 Transient analysis of varying production of power and cooling

A dynamic model of the CCP cycle based on the previously used steady one is developed in the dynamic solver Dymola®. The objective is to foresee typical response times and potential instability of the cycle when changing the operation mode to adapt the production of cooling and power to the user needs. Those data would latter benefit to configure an efficient predictive control of the system. Some simplifications were made to the dynamic model to accelerate the calculation time of the simulations and to gives the possibility to explore various scenarios. Hence, the rectification and the sub-cooler system are not present in the dynamic modelling

and the expander is modelled via an isentropic efficiency and an imposed rotational speed of 60 Hz as if connected to a national electrical grid.

Figure 6 illustrates for two transient scenarios the typical response times of the power and cooling productions to a change of control of the three-way valve dividing the ammonia flux in the production lines. In the first setup, the split ratio r_s starts at a steady value of 0.5, corresponding to a simultaneous production of cooling and power. From $t = 0$, the operating control changes to reach $r_s = 0$ (i.e. power production alone). In the second setup, the split ratio r_s starts at a steady value of 0 and from $t = 0$, the operating control changes to reach $r_s = 1$ (i.e. cooling production alone). To match the behavior of classic automated valves, the valve switching time t_v is set to 20 seconds in the first scenario and 30 seconds in the second one.

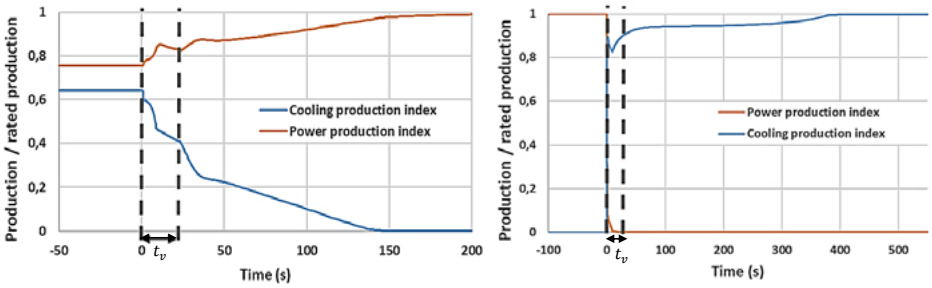


Fig.6. Evolution of the productions of cooling and power after a change of the controlling inputs. From a mix of both productions to power production alone (left) and from a power production alone to cooling production alone (right)

The first important observation is that there is no important instability of the system when switching from a production mode to another. The dynamic simulations predict that the transitions are not systematically instant, but they are always smooth enough to guarantee the stability of the system.

When switching from a mix production mode to a power alone production mode, a transient phase occurs before the cooling production stops and the power production reaches its nominal value. This is mainly the consequence of the condenser and evaporator inertia. Both heat exchangers partly contain liquid ammonia when cooling production is operating, so when the valve closes before the condenser, this ammonia will take time to evaporate as the system low pressure decreases. The symmetrical increase of power production is a consequence of the lowering low pressure that implies an increase of the pressure ratio at the expander ends. In the present simulation, this transient state last about two minutes and this time will be directly correlated to the volumes of the heat exchangers.

In the second scenario, when switching to power production alone to cooling production alone, the power production stops instantaneously as there is no storage of ammonia before the expander and the flow is immediately null. The initialization of cooling production is instant too, but it takes about 6 minutes to reach the optimal cooling production as the heat exchangers takes time to reach their liquid/vapor equilibrium.

6. Conclusion

Among the CCP cycle architectures under development, those in parallel are the most versatile and easiest to implement but they have not been widely investigated. To contribute to the development of these systems, a complete numerical model of the parallel CCP cycle was developed and configured through the characterization of two experimental devices: an ORC test rig to characterize a scroll expander and an absorption cycle to evaluate the rest of the system.

Early results highlighted the importance of using a detailed expander model to quantify the intrinsic physics of the flows in the scroll. Indeed, under the operating conditions of a small capacity machine, low flow rates require the use of expanders of high volume efficiency. Moreover, an analysis focusing on the role and position of the rectifier in the cycle highlights its influence on the performance of power production. This result introduces a new criterion for cycle architecture optimization. Finally, dynamic simulations of a combined cooling and power cogeneration system predict that the transition between production modes are quite stable and the transition times are longer when stopping cooling production than when stopping power one.

Acknowledgements

The French Alternative Energies and Atomic Energy Commission (CEA) and Carnot Energies du Futur supported this work.

References

[1] D. S. Ayou, J. C. Bruno, R. Saravanan, and A. Coronas, "An overview of combined absorption power and cooling cycles," *Renewable and Sustainable Energy Reviews*, vol. 21. Elsevier, pp. 728–748, 2013.
[2] A. Khaliq, "Energetic and exergetic performance investigation of a solar based integrated system for cogeneration of power and cooling," *Appl. Therm. Eng.*, vol. 112, pp. 1305–1316, 2017.
[3] J. Muye, D. S. Ayou, R. Saravanan, and A. Coronas, "Performance study of a solar absorption power-cooling system," *Appl. Therm. Eng.*, vol. 97, pp. 59–67, 2016.
[4] F. Xu, D. Yogi Goswami, and S. S. Bhagwat, "A combined power/cooling cycle," *Energy*, vol. 25, no. 3, pp. 233–246, 2000.
[5] G. P. Kumar, R. Saravanan, and A. Coronas, "Experimental studies on combined cooling and power system driven by low-grade heat sources," *Energy*, vol. 128, pp. 801–812, 2017.
[6] L. C. Mendoza, D. S. Ayou, J. Navarro-Esbrí, J. C. Bruno, and A. Coronas, "Small capacity absorption systems for cooling and power with a scroll expander and ammonia based working fluids," *Appl. Therm. Eng.*, vol. 72, no. 2, pp. 258–265, 2014.
[7] J. Wang, Y. Dai, T. Zhang, and S. Ma, "Parametric analysis for a new combined power and ejector-absorption refrigeration cycle," *Energy*, vol. 34, no. 10, pp. 1587–1593, 2009.
[8] G. K. Alexis, "Performance parameters for the design of a combined refrigeration and electrical power cogeneration system," *Int. J. Refrig.*, vol. 30, no. 6, pp. 1097–1103, 2007.
[9] N. Tauveron, S. Colasson, and J. A. Gruss, "Available systems for the conversion of waste heat to electricity," in *Proceedings of the ASME 2014 International Mechanical Engineering Congress & Exposition*, 2014, pp. 1–12.
[10] K. Herold, R. Radermacher, and S. Klein, "Absorption Chillers and Heat Pumps, Second Edition," 2016.
[11] V. Lemort, S. Quoilin, C. Cuevas, and J. Lebrun, "Testing and modeling a scroll expander integrated into an Organic Rankine Cycle," *Appl. Therm. Eng.*, vol. 29, no. 14–15, pp. 3094–3102, 2009.
[12] O. Dumont, R. Dickes, and V. Lemort, "Experimental investigation of four volumetric expanders," *Energy Procedia*, vol. 129, pp. 859–866, 2017.
[13] A. Landelle, N. Tauveron, R. Revellin, P. Haberschill, S. Colasson, and V. Roussel, "Performance investigation of reciprocating pump running with organic fluid for organic Rankine cycle," *Appl. Therm. Eng.*, vol. 113, pp. 962–969, 2017.
[14] A. Giuffrida, "Modelling the performance of a scroll expander for small organic Rankine cycles when changing the working fluid," *Appl. Therm. Eng.*, vol. 70, no. 1, pp. 1040–1049, 2014.
[15] S. Declaye, S. Quoilin, L. Guillaume, and V. Lemort, "Experimental study on an open-drive scroll expander integrated into an ORC (Organic Rankine Cycle) system with R245fa as working fluid," *Energy*, vol. 55, pp. 173–183, 2013.
[16] F. Boudéhenn, H. Demasles, J. Wyttenbach, X. Jobard, D. Chèze, and P. Papillon, "Development of a 5 kW cooling capacity ammonia-water absorption chiller for solar cooling applications," *Energy Procedia*, vol. 30, pp. 35–43, 2012.
[17] L. C. Mendoza, J. Navarro-Esbrí, J. C. Bruno, V. Lemort, and A. Coronas, "Characterization and modeling of a scroll expander with air and ammonia as working fluid," *Appl. Therm. Eng.*, vol. 70, no. 1, pp. 630–640, 2014.
[18] P. K. Nag and A. V. S. S. K. S. Gupta, "Exergy analysis of the kalina cycle," *Appl. Therm. Eng.*, vol. 18, no. 6, pp. 427–439, 1998.

13th IEA Heat Pump Conference
April 26-29, 2021 Jeju, Korea

Membrane Based Pervaporation for Heating and Cooling

Bamdad Bahar[a*], Harish Opadrishta[a], Mark Stutman[a], William TomHon[a]

[a]*Xergy, Inc., 299A Cluckey Dr., Harrington DE 19952, USA*

Abstract

Recent advances have introduced ionic membranes that can provide high water permeability in heating, ventilation, and air conditioning (HVAC) applications. These materials can be useful in many applications to help provide more efficient building technologies and higher indoor air quality through devices such as ionic liquid heat pumps (ILHPs), ionic liquid desiccants (ILDs), and energy recovery ventilators (ERVs). Water transmission mechanisms behind the water transport is not well understood, since different ionic membranes provide transmission in different ways. Water transportation can be a function of ionomer structure via the building blocks of the backbone, or from the functional groups on the side chains or from subtle features in membrane design and composition. In this work, we studied the permeation properties of different advanced ionic membranes. Membranes that show high water selectivity, and permeabilities exceeding 2*10-5 g/(s*m^2*Pa) are presented. High performance membranes are identified for optimum applications for different HVAC systems.

© HPC2020.

Selection and/or peer-review under responsibility of the organizers of the 13th IEA Heat Pump Conference 2020.

Keywords: Pervaporation; Membranes; Ionic Liquid Dessicants; Evaporative Cooling;

1. Introduction

Building operation consumes more than 40 percent of the total energy used in the United States and building heating and cooling loads comprise the largest fraction [1]. Demand for cooling energy is exacerbated in hot and humid climates. High humidity poses a serious limitation to the design and operation of buildings, promoting mold and dust mites and often associated with increased disease transmission. Consequently, dehumidifying air in building ventilation systems is normally a requirement to mitigate the effects of high humidity, improve indoor thermal comfort, and meet indoor design conditions.

For over a century, the vapor-compression system (VCS) has been the de facto technology of choice in heating, ventilation, and air conditioning (HVAC), especially for dehumidification and cooling. Despite its success, research, policy, and economics all encourage change considering its many inherent shortcomings. From an energy standpoint, the inability of the VCS system to decouple latent and sensible loads leaves condensation, an energy intensive process, as the only means for dehumidification. The heart of the VCS system lies in the refrigerant, whose chemistry has evolved in response to policy and environmental concerns. From chlorofluorocarbons (CFCs) and hydrochlorofluorocarbons (HCFCs), banned under the Montreal Protocol in 1987, to hydrofluorocarbons (HFCs), such as R-134a with a global warming potential (GWP) 1430 times that of carbon dioxide (CO_2), environmental concerns associated with VCS can no longer be overlooked [2]. These concerns, coupled with potential excess greenhouse gas (GHG) emissions resulting from the inefficiencies inherent in the system, place research on future HVAC technologies at the cornerstone of any effort aimed at mitigating climate change.

* Corresponding author. Tel.: +1 (302)-629-5768. *E-mail address:* bamdad.bahar@xergyinc.com

Researchers are pursuing alternatives to these conventional practices, especially for cooling and dehumidification. Advancements in artificial membranes enable new possibilities in this area. While traditionally used for industrial separations, such as reverse osmosis and gas separation, membranes provide a means to selectively transfer water vapor from one fluid to another [3], [4]. Polymeric, non-porous reinforced membranes are made from ionically functionalized polymer materials. These materials have ionically conductive groups embedded in the repeating unit of the polymer that aid in the transportation of water through the membrane. The methods for this mass transfer are being researched, and a few of the HVAC applications and transport methods are discussed in the following section.

2. Technology Description

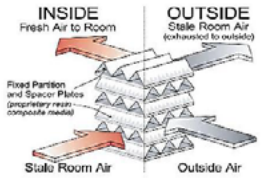


Fig. 1. Schematic of an ERV

In this paper, we explain the importance of pervaporation in heating, ventilation and air conditioning. The term ‘pervaporation’ is derived from a three-step process: (a) Sorption of permeating components at the feed side into a membrane, (b) Transport of components across a membrane by diffusion according to Fick’s law and (c) Evaporation or desorption at the permeate side into vapor phase. The driving force for transport of different components is provided by a chemical potential difference between the liquid feed/retentate and vapor permeate at each side of the membrane. The main advantage of a pervaporation technique versus conventional approaches in a heat and mass exchange application is its fundamental capacity to save energy and water. Pervaporation systems eliminate aerosols or air contamination by liquid water and therefore avoid any entrained contaminants evolved from dissolved solids in the feed water stream carried over to air streams. Pervaporation systems are modular, scalable, simple to operate and can be started up and shut down rapidly. The objective for these pervaporative systems and membranes are to reduce the total energy load for the systems. This is done by latent cooling i.e. reducing the relative humidity in the air to be treated. Energy recovery ventilators (ERV) and pervaporative cooling of water are also discussed.

Ionic liquids, as the name implies, are synthetic ionic salts that remain liquid under normal operating conditions. These fluids are mainly useful for their water desiccation properties, as they can adsorb or desorb water vapor to help control the relative humidity of the air in its container. With membranes, they are mainly utilized in flat sheet or shell and tube contactors that utilize fluid flows of air and desiccant in crossflow patterns. These systems can dehumidify gas streams with relatively high efficiency. Additionally, these contactors can be paired with a heat pump system to regenerate the desiccant so that the system can be operated in a loop. The synthetic ionic liquids can be engineered such that the waste heat from the heat pumps can be utilized to regenerate them.

ERVs will use an assembly of corrugated sheet membranes to allow heat and mass transfer between the outgoing exhaust air stream and incoming makeup air. A schematic of an ERV is shown in Fig. 1. In this figure “outside” makeup air is contacted with “inside” exhaust air and heat and moisture are exchanged. This passively conditions the air before entering the air-conditioner and reduces energy load of the HVAC system.

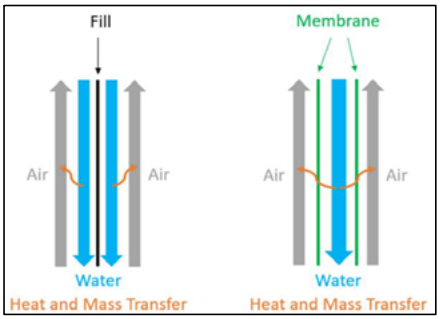


Fig. 2. Schematic of a cooling tower fill and our proposed membrane based evaporative condenser

Pervaporation can also be used as a substitute to evaporative cooling. Unlike conventional cooling tower fills (shown in the left side of Fig. 2), in which the cooling water and the ambient air are in direct contact, in the proposed concept, (shown in right side of Fig. 2) the membrane acts as a selective barrier between the two phases: the liquid-phase feed and the vapor-phase permeate. It allows the desired component(s) of the liquid feed to permeate (transfer) through it by vaporization. The driving force for the separation is the difference in the partial pressures of the components on the two sides and not the volatility difference of the components in the feed.

3. Experiment & Results

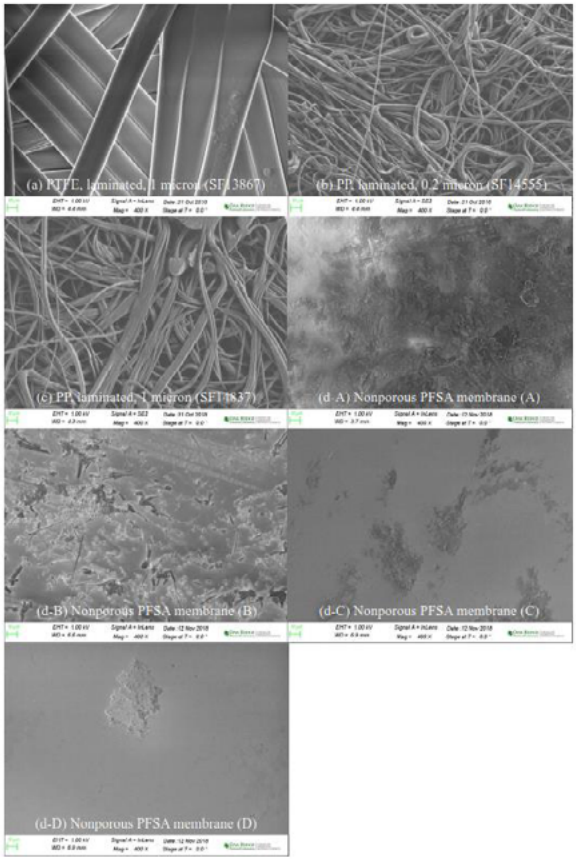


Fig. 3. Microstructures of membranes tested

In this section we discuss moisture vapor transmission results of four PFSA (perfluoronated sulfonic acid) nonporous membranes with different acidity and three commonly used porous membranes. The four PFSA nonporous membranes are the acid form of the perfluorinated sulfonic ionomer membrane (PFSA), which is an ion-conductive polymer, with an electrically neutral semi-crystalline polymer backbone (hydrophobic polytetrafluroethylene) and a randomly tethered sidechain with a pendant ionic group (hydrophilic), SO_3^-, that is associated with a specific counterion (e.g., $SO_3^- + H^+ \rightarrow SO_3H$). Two of porous membranes are unlaminated polypropylene membranes with the pore size of 0.2 μm (model number: SF14555) and 1.0 μm (model number: SF14837), respectively. They have a thickness of 150~250 μm and a porosity of 60% approximately. Another is a laminated PTFE membrane with the polypropylene (PP) support (model number: SF13867). It has a pore size of 1.0 μm, a thickness of 150~220 μm, and a porosity of 80~90% approximately [5], [6]. The test index, type, and properties of the investigated membranes are listed in Table 1. Moreover, the microstructures of the tested membranes are photographed using the transmission electron microcopy technology, as shown in Figure 5.

Table 1. Properties of the tested membranes.

Model Number	A	B	C	D	SF13867	SF14555	SF14837
Membrane Test Index	1	2	3	4	5	6	7
Dense/Porous	Non-Porous	Non-Porous	Non-Porous	Non-Porous	Porous	Porous	Porous
Wettability	Hydrophilic	Hydrophilic	Hydrophilic	Hydrophilic	Hydrophobic	Hydrophobic	Hydrophobic
Pore size (μm)	N/A	N/A	N/A	N/A	1.0	0.2	1.0
Porosity (%)	N/A	N/A	N/A	N/A	80-90%	60%	60%
Thickness (μm)	~25	~25	~25	~25	150-220	150-250	150-250

The water vapor transmission rate (WVTR) of the membranes were measured with the wet cup and dry cup method described by ASTM E96 (ASTM 1995), as well as some modified methods such as upright wet cup fulfilled with water, reversed wet cup, and upright wet cup filled with liquid desiccant. The basic procedure of the test is sealing a tested membrane to the open mouth of a permeability cup which contains a certain amount of water or desiccant inside. During the test, the permeability cup is placed on the top of a scale in an air-conditioned chamber with controlled air temperature and humidity. Periodic weighing is documented by the data acquisition system to determine the rate of water vapor movement through the membrane from the cup inside to the controlled chamber or vice versa.



Figure 4: Cup configurations: (a) wet cup with air gap, (b) dry cup using solid desiccant, (c) wet cup without air gap, and (d) reversed wet cup

The first method we used is wet cup method. The wet cup is shown in Figure 4(a), with distilled water inside, and an air gap existing between the membrane and distilled water. The second method is the dry cup method containing a certain amount of anhydrous calcium chloride ($CaCl_2$) as shown in Figure 4(b). The membrane and the solid desiccant do not contact with each other. The wet cup method is typically used to simulate regions of high humidity and the dry cup is more reflective of drier climates. The third method is the wet cup without air gap method. This method is very similar to the conventional wet cup method. The only difference is that the distilled water is filled in the permeability cup and the membrane is bonded and contacted with the water tightly without any air gap, as shown in Figure 4(c). The fourth one is the reversed wet-cup method. This method is also very similar to the wet cup method. The only difference is that the permeability cup is reversely placed in the chamber so that the distilled water inside the cup contacts with the membrane directly as shown in Figure 4(d). By inverting the cup, there is a greater pressure driving force across the membrane making the test more reflective of conditions with a signifigant pressure driving force.The last two methods we used are the liquid desiccant methods (not pictured), which use an aqueous solution of calcium

chloride ($CaCl_2$) with a mass concentration of 40% with air gap (e) or without any air gap (f). The test conditions are listed in Table 2.

Table 2. Summary of test conditions

Cup method	B	A	C	D	E	F
Membrane Test Index	1-7	1-7	2,3,4	1-7	1-7	1-7
Air gap	Yes	Yes	No	No	Yes	No
$T_{chamber}$ (°C)	24.5	24.5	24.5	24.5	24.5	24.5
$RH_{chamber}$ (%)	80.8%	80.8%	80.8%	80.8%	80.8%	80.8%
$Pv_{chamber}$ (Pa)	2495	2495	2495	2495	2495	2495
Materials inside cup	$CaCl_2$	Distilled water	Distilled water	Distilled Water	$CaCl_2$ Solution	$CaCl_2$ Solution
Pv_{cup} (Pa)	0	3076	3076	3076	1260.5	1260.5
Pv_{diff} (Pa)	2495	581	581	581	1234.5	1234.5

With the above experimental apparatus, the water vapor permeance of the seven membranes were tested at several different conditions, including wet cup with air gap, wet cup without air gap, reversed wet cup and dry cup (using solid desiccant) with air gap. These experiments were used to generate weight change data, with respect to time. Figures 5 and 6 provide examples of the results of these experiments.

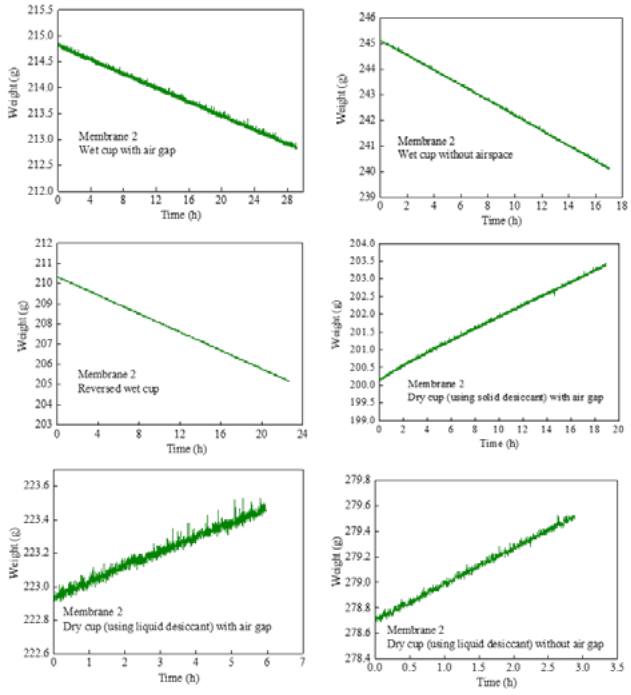


Fig. 5. Example weight change with time for a non-porous membrane (membrane 2)

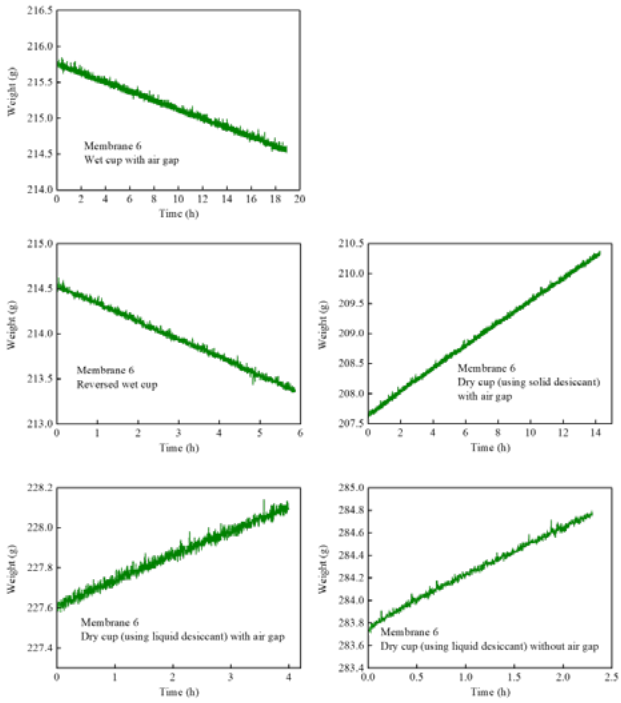


Fig. 6. Example weight change with time for a porous membrane (membrane 6)

The water vapor transmission rates of the membranes were derived for each membrane using figures similar to Figure 5 and 6. These rates were normalized to the surface area of the membrane and the pressure difference across the membrane (the driving force of permeation) to calculate the water vapor permeance, as reported in Table 3.

Table 3. Measured water vapor permeance of seven membranes (10^{-5} g/m^2-s-Pa)

Cup Test Method	Non-Porous Membrane				Porous Membrane		
	1	2	3	4	5	6	7
A	0.8474	1.080	1.118	1.118	0.9810	1.010	0.9684
C	N/A	4.689	4.465	4.396	N/A	N/A	N/A
D	3.150	3.638	3.482	3.654	3.155	3.168	3.133
B	0.5796	0.6138	0.7546	0.6589	0.8110	0.6993	0.7773
E	0.7899	0.6594	0.8163	0.8372	0.9047	0.9267	0.8412
F	2.696	2.090	2.944	2.767	2.824	3.259	3.267

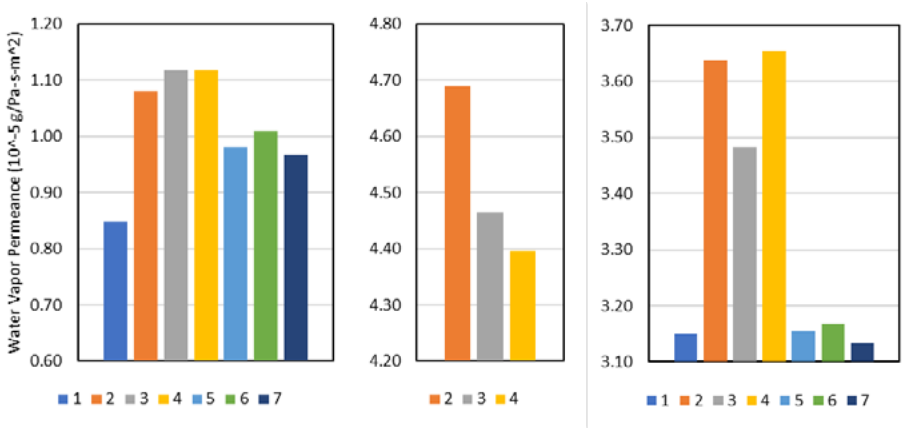


Fig. 7. Water vapor permeance of different membranes measured with (left to right) wet cup with air gap, wet cup without air gap, and reversed wet cup methods

The wet cup testing methods are the most reflective of the conditions seen in ERVs, evaporative cooling towers, and ILD modules. As seen in Fig. 7, Membrane 2 had on average the best performance during the wet cup tests. Membrane 4 was a close second, however, taking economic considerations into account, (Membrane 2 is commercially produced while Membrane 4 is currently only produced for R&D purposes), Membrane 2 was selected as the transport element in the experimental heating and cooling devices. While Cup Test Methods E and F could have provided insight into the interaction between the membranes and a liquid desiccant, the tests did not produce conclusive results. The results of Cup Test Method B, which is more commonly used with low permeation materials [7], was not analyzed further in this study.

4. Pervaporative HVAC Devices using Membrane 2

4.1. Ionic Liquid Desiccant based dehumidifier

A new membrane-based liquid desiccant air dehumidification (MLDAD) technology utilizes the membrane technology and ionic liquid desiccants (ILDs) to prevent carryover and corrosion in LDAD [8]. The semi-permeable membrane separates the air and liquid desiccant but allows a good mass transfer between them. Therefore, solution droplets cannot enter the air stream to corrode the metal ductwork and degrade the air quality. The ILDs are synthesized salts in the liquid phase. They are non-corrosive to metal and non-crystallizable so that the solution side corrosion issues can be avoided and the reliability of the MLDAD system can be improved. The performance of the dehumidifier at different conditions are as shown in Figures 8 through 10.

The high humidity upstream air was dehumidified by the MLDAD to the decreased humidity downstream. The analysis of these figures was only performed at steady-state, roughly 5 minutes after the test began and after the inlet (upstream) humidity stabilized. Startup conditions varied, depending on the air flow rate. The primary variable effecting the dehumidification power of the system was found to be the ambient (upstream) relative humidity. When comparing Figures 9 and 10, the high inlet humidity (94.0% RH, Figure 9) increased the absolute humidity drop across the module to over twice the absolute humidity drop under the inlet conditions of Figure 10. At low upstream absolute humidities and low airflow, as in Figure 8, the MLDAD module does not provide significant latent cooling – the average absolute humidity drop across the membrane is about 1 g/m^3.

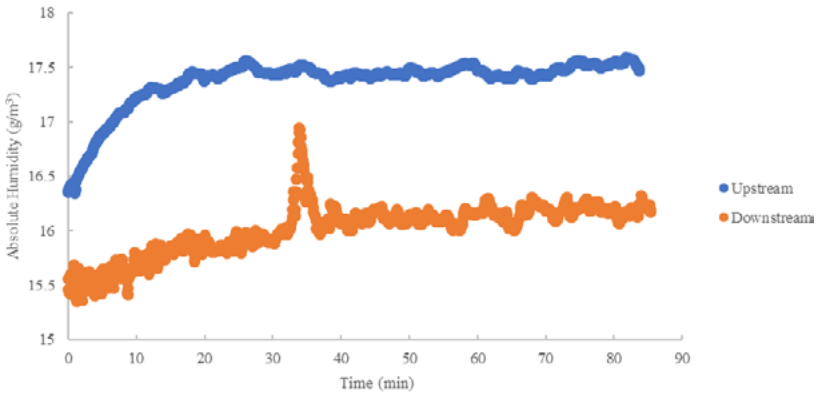


Fig. 8. Dehumidification of air at 0.28 m³/min (10 CFM), average inlet (upstream) RH of 53.0% and an average outlet (downstream) of 50.0% RH (30.5°C). Note that the spike in AH between 30 and 40 min was caused by a leak in the system. This leak was resolved during the test and these data points were disregarded in the analysis.

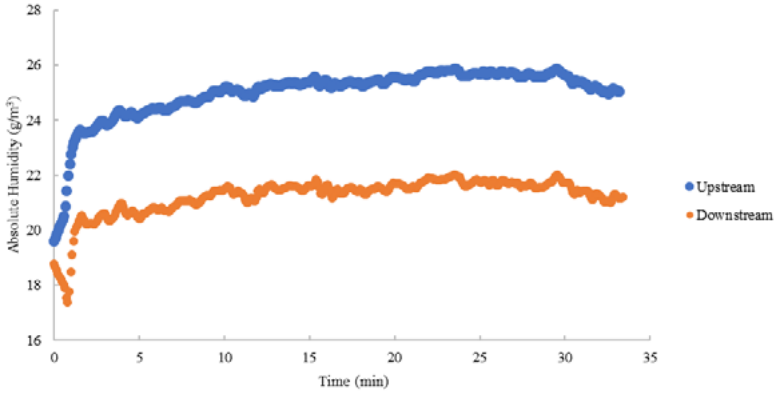


Fig. 9. Dehumidification of air at 0.85 m³/min (30 CFM), average inlet (upstream) RH of 94.0% and an average outlet (downstream) RH of 78.5% (26.8°C)

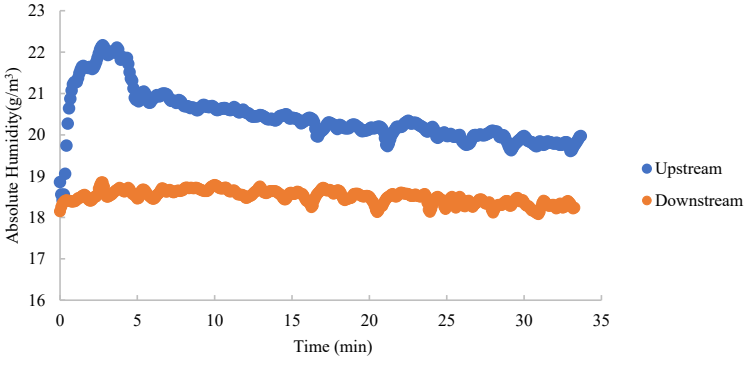


Fig. 10. Dehumidification of air at 0.85 m³/min (30 CFM), average inlet (upstream) RH of 70.3% and an average outlet (downstream) RH of 63.3% (28.8°C)

4.2. Membrane based cooling towers

Pervaporative membrane tubes or flat sheets can also be used in manufacturing advanced evaporative cooling devices. These devices can be used to provide cooling to water downstream of the condenser side of chiller. They can also be used to cool large datacenters and other electronics cooling applications. In Figure 11, we show an evaporative cooling prototype made of pervaporative membranes. It is 40.6 cm (16") in height, 30.5 cm (12") in width and 15.2 cm (6") in depth. The small scale evaporative cooling device made of pervaporative membranes was tested using inlet water at 35°C (95°F) and water flow rate between 9.5 and 37.9 LPM (2.5 and 10 GPM). Figure 12 compares the heat transfer capacity of pervaporative cooling device at different flow rates of water. The test data shows a significant enhancement of pervaporation cooling performance due to an increase in water flow rate; the heat rejection is nearly directly proportional to the flow rate. This shows that advanced pervaporative cooling towers are feasible and scalable, especially when coupled with energy efficient water pumps.



Figure 11. Membrane Evaporative Cooling Module

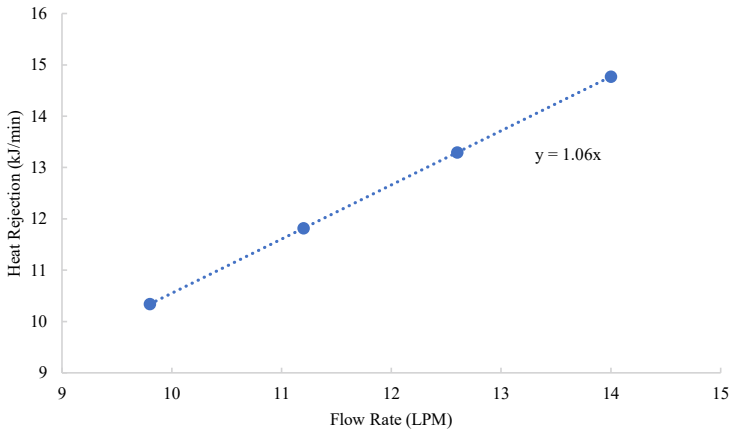


Figure 12. Heat rejection characteristics of membrane evaporative cooling module & linear fit where "y" is the heat rejection in kJ per min and "x" is the flow rate in liters of water per minute

5. Conclusions

Pervaporative membranes show strong potential for energy efficient heating and cooling. As presented in this paper, proof-of-concept laboratory protoypes have been developed for membrane based liquid desiccant air dehumidification and pervaporative membrane heating and cooling towers. The MLDAD system was able to provide dehumidification while preventing the potential for corrosion, seen in previous systems. Membrane based cooling towers were found to be a scalable source of evaporative cooling. However, as HVAC membrane

technology is considerably young, when compared to traditional vapor compression air conditioning, there is still significant research and development to be made in the field. In order to be competive with conventional technology, the next steps to commercialization is cost and longevity research. However, the technologies described in this paper are at different stages and have their own research needs.

Specifically, measured performance is needed on commercial products for a range of inlet temperatures and humidities. In-the-field monitoring can also show how performance varies with inlet condition, and also how it deteriorates with time. Membrane liquid desiccant dehumidifiers require manufacturing methods that ensure leak-free modules, which can be checked with accelerated life testing of the conditioner and regenerator. Membrane prototypes for evaporative cooling and humidification have shown the feasibility of this process. It is also unclear whether membranes, with their added cost, will be preferred to wicked surfaces. Across all systems membrane fouling may present a problem. However, using lessons learned from the fouling issues in industrial membrane processes, the magnitude of this problem can be mitigated. The HVAC applications are also expected to see fewer contaminants than traditional industrial membrane processes, further decreasing the significance of this issue.

The outlook for these membrane devices is uncertain. Advances in membrane technology over the previous few decades have enabled these unique devices for HVAC applications, which could potentially lead to more energy efficient products. But more research and development are needed if these products are to compete against the inexpensive and established air conditioning technologies.

6. Nomenclature

Table 4. Acronyms and abbreviations, defined.

Term	Definition	Term	Definition
AH	Absolute humidity (g/m^3)	ILD	Ionic liquid desiccant
CFC	Chlorofluorocarbons	ILHP	Ionic liquid heat pump
CFM	Cubic feet per minute	LDAD	Liquid desiccant air dehumidifier
ERV	Energy recovery ventilation	LPM	Liters per minute
GHG	Greenhouse gas	PFSA	Perfluorosulfonic acid
GPM	Gallons per minute	PP	Polypropylene
GWP	Global warming potential	PTFE	Polytetrafluoroethylene
HCFC	Hydrochloroflurocarbon	RH	Relative humidity
HFC	Hydroflurocarbon	VCS	Vapor compression system
HVAC	Heating, ventilation, and Air Conditioning	WVTR	Water vapor transmission rate

Acknowledgements

This work was supported by a research award DE-EE-0008218 funded by the U.S. Department of Energy, Building Technologies Office. The technologies disclosed in this paper are protected under US patents [9]. This publication is a part of a 10-paper series to commemorate Xergy's 10-year anniversary, bringing advanced membrane technology to the global HVAC industry. This series includes papers providing further insight into water transmission mechanisms in advanced membranes and ionic liquid desiccant heat pumps.

References

[1] Abdel-Salam, M.R.H., Ge, G., Fauchoux, M., Besant, R., Simonson, C. (2014), State-of-the-art in liquid-to-air membrane energe exchangers (LAMEEs): A comprehensive review. *Renewable and sustainable Energy Reviews*, 39: 700-728. doi:10.1016/j.rser.2014.07.022

[2] "The Montreal Protocol on Substances that Depleate the Ozone Layer." *United Nations Environment Programme* (1987).

[3] Lonsdale, H.K. The growth of membrane and technology, J. Membr. Sci. 10 (1982) 81

[4] Binning, R.C., Lee, R.J., Jenning, J.F., Martin, E.C. Separation of liquid mixtures by permeation, Ind. Eng. Chem. 53 (45) (1961) 6–50.

[5] Adachi, M., Navessin, T., Xie, Z., Frisken, B., Holdcroft, S. "Correlation of in situ and ex situ measurments of water permeation through Nafion NRE211 proton exchange membranes. *J. Electrochem. Soc.* (2009). 156 (6): 782-790.

[6] Kusoglu, A., Weber, A.Z. "New Insights into Perfluroninated Sulfonic Acid Ionomers" *Chem. Rev.* 2017, 117, 3, 987-1104. doi: https://doi.org/10.1021/acs.chemrev.6b00159

[7] ASTM D1653-13, Standard Test Methods for Water Vapor Transmission of Organic Coating Films, ASTM International, West Conshohocken, PA, 2013, www.astm.org. doi: 10.1520/D1653-13
[8] Abdelaziz, O.A., Qu, M., Sun, X., Bahar, B., Parmelee, W., Fackler, S., Sherrer, R., Zerby, J., Chouhan, A. "Developent of Separate Sensible and Latent Cooling System Using Electrochemical Compressor," *12th IEA Heat Pump Conference* (2017).
[9] US Patents: 10,202,292 and Applications: 20190291054, 20190256384, 20190226703, 20180251616, 20180187906, 20180093905, 20170284685

13th IEA Heat Pump Conference
April 26-29, 2021 Jeju, Korea

A3 Refrigerant R290 Leak and Ignition Testing for a Packaged Terminal Air-conditioner (PTAC)

Xudong Wang[a, *], George Hunter[b]

[a]Air-Conditioning, Heating, and Refrigeration Institute, 2311 Wilson Blvd, Suite 500, Arlington, VA 22201, USA
[b]UL LLC, 333 Pfingsten Rd, Northbrook, IL 60062

Abstract

R290 (propane) is a flammable refrigerant having an A3 classification according to the ASHRAE Standard 34. Because of its extremely low Global Warming Potential (GWP), several regions around the world use or consider using it for air-conditioning and refrigeration applications. On the other hand, the R290 application is currently limited to small charged self-contained air-conditioning and refrigeration products in most of the world due to its high flammability and safety implications. The possibility of increasing R290 charge limits set by relevant safety standards (IEC/UL-60335-2-40 and IEC/UL-60335-2-89) is being evaluated in the working groups of these standards.

To properly address A3 refrigerants in safety standards, the Air-Conditioning, Heating, and Refrigeration Technology Institute (AHRTI) undertook a research project to investigate R290, specifically to carry-out leak and ignition testing under whole room scale conditions.

This paper summarizes the results of A3 refrigerant R290 leak and ignition tests for a packaged terminal air-conditioner (PTAC). A mock-up full scale motel room was built with a wall mounted PTAC installed. The testing simulated refrigerant leaks from the evaporator with ignition sources present. Two different R290 charge levels (114g and 217g) were tested. The tests also included using the PTAC circulation fan to disperse leaked refrigerant in the test room as a mitigation method. The tests demonstrated that the ignition severity depended on the charge level and the fan operating state. In all ignition events observed, the highest temperatures were recorded close to floor level indicating flames were low in height. The results were also compared to existing test results of A2L refrigerants R32 and R452B under the same test setup.

© HPC2020.
Selection and/or peer-review under responsibility of the organizers of the 13th IEA Heat Pump Conference 2020.

Keywords: Low GWP, refrigerant, flammability

1. Introduction

The global industry is transitioning to environmentally friendly low global warming potential (GWP) refrigerants. To date, most of promising low GWP refrigerants are flammable. Implementation of these refrigerants in the field requires revisions of relevant safety standards and codes. To advance the understanding of flammable refrigerants safety, AHRTI launched a research project to conduct whole room scale testing. The objective was to conduct refrigerant leak and ignition testing under whole room conditions to understand the potential ignition and event severity associated with the use of A2L and A3 refrigerants [1, 2]. The whole room testing was conducted by AHRTI's contractor UL at its test facility in Northbrook, IL.

The overall testing consisted of scenarios that represented refrigeration and air conditioning applications. The refrigeration applications included reach-in coolers testing. Air conditioning scenarios included (i) motel

* Corresponding author. Tel.: +1-703-600-0305.
E-mail address: xwang@ahrinet.org.

room with PTAC unit; (ii) motel room with mini-split unit. For simplicity, this paper provides a high-level summary of the PTAC tests. More detailed information is contained in the project final reports [1, 2].

2. Test Setup and Procedures

Refrigerants R290, R32 and R452B were tested for the PTAC. Their information is listed in Table 1. One can observe that R290 has significantly lower LFL than the two. Therefore, its allowable charge amount is much less than A2Ls.

Table 1. Refrigerant properties

Parameter	R290	R32	R452B
Safety Classification per ASHRAE Standard 34 [3]	A3	A2L	A2L
Lower Flammability Limit (LFL, % volume)	2.1%	14.4%	11.9%
Lower Flammability Limit (LFL) kg/m³ at 101.3 kPa	0.038	0.307	0.310
Upper Flammability Limit (UFL, % volume)	9.5%	29.3%	22%
Laminar Burning Velocity (cm/s)	44	6.7	<4.0
Composition (% mass)	R290 (100%)	R32 (100%)	R32/R1234yf/R125 (67%/26%/7%)

A full scale motel room was built to simulate real application. To avoid over-pressure and damage to the test room from ignition events, six deflagration vents were created at the top section of two walls. Four of them had dimensions of 0.6m x 1.2m (2ft. x 4ft.), and two had dimensions of 0.6m x 0.9m (2ft. x 3ft.). They were covered by plastic sheets. The plastic sheets provided air seal environment inside the test room and could be blown or melted open due to pressure/temperature rise should an ignition event occur.

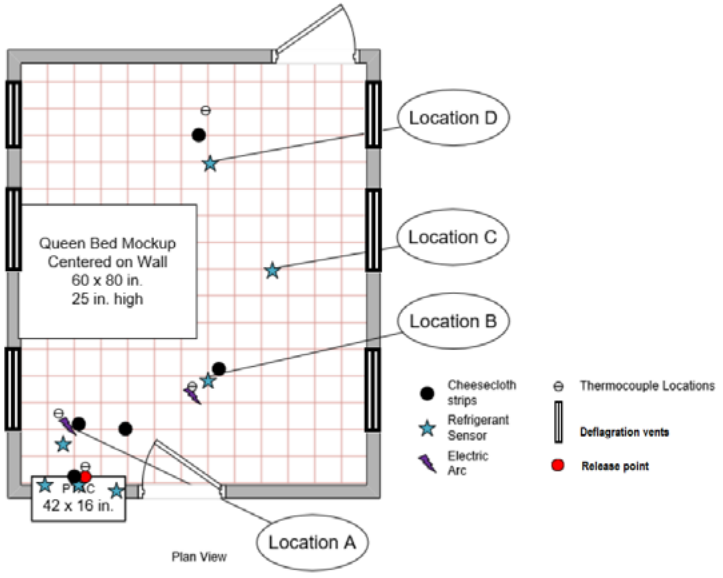


Fig. 1. Schematic of test room setup and instrumentation plan [2]

The plan view of the test setup is shown in Figure 1. The room dimensions were 3.95m x 4.81m x 2.42m (13ft. x 15ft. 9in. x 7ft. 11in.). The enclosed volume was 46.0 m³ (1620 ft³). The floor area was 19.0 m² (205 ft²). A mockup bed was located in the room. A PTAC was mounted such that the base of the unit was 0.4 m (16 inches) above the floor at the minimum distance from the side wall. An 8mm (¼ inch) O.D. copper tube

was placed in the center of the evaporator coil at 0.6 m (24 inches) above the floor. The tube was angled directly out from the face of the evaporator towards the front grill as shown in Figure 2. When used, the unit fan was operated on low speed. The fan volume flow rate was determined to be 5.7 m³/min (200 CFM). The measurements were made with a calibrated vane anemometer at several locations across the exhaust outlet and integrated with area to determine volume flow rate.

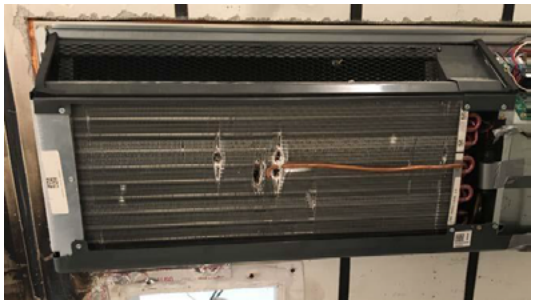


Fig. 2. PTAC discharge tube location [2]

The locations of the instrumentation, and ignition sources were located in clusters at locations A, B, C and D shown in Figure 1. These locations were chosen according to the expected refrigerant flow path. The leaked refrigerant gas concentration in the test room was measured by oxygen sensors (Apogee SO-220 electrochemical sensor). High speed video cameras installed at different angles to document the test events. Cheesecloth strips were used to indicate whether the refrigerant ignition would cause a secondary fire. A total of 32 Type K thermocouples were used to measure the temperature at different locations and heights within the room. The thermocouple response time was approximately 3 seconds. Their readings do not reflect actual flame temperatures. The instantaneous temperatures of the flames are higher than what the thermocouples recorded because thermocouples have response time delay, and the flames have fast movements.

During the test, the refrigerant in liquid phase was released into test room with several viable ignition sources present. The refrigerant release system is illustrated in Figure 3. Its two main components are a pressurizer tank and a release tank that are equipped with accessories such as control valves and temperature and pressure measurement. Both tanks contained R290 and were submerged in heated water tanks to achieve desired pressure and temperature conditions. The pressurizer tank ensures the release tank to release liquid refrigerant to the test room at a constant rate. The refrigerant release rate was controlled by a control valve that continuously adjusts its opening according to the feedback from the mass flow meter. The solenoid valve was used to start and stop the refrigerant flow during testing.

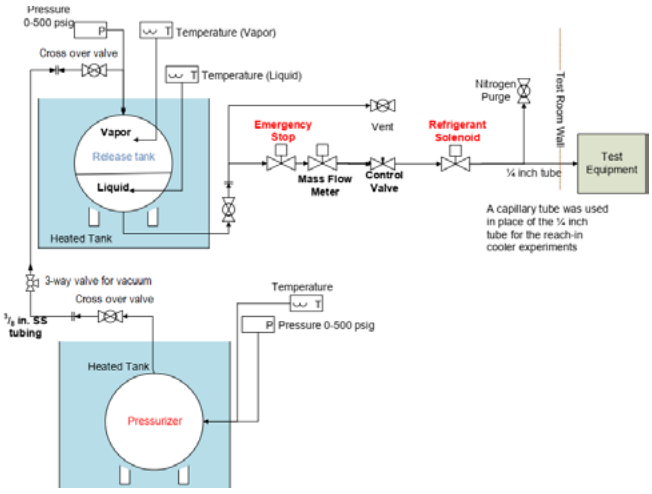


Fig. 3. Schematic of the refrigerant release mechanism setup [2]

The ignition sources used in the scenario tests are electric arcs. The electric arcs were created by a step-up gas tube transformer. The electric arc transformer was continuously energized for several minutes during the tests. The energy of the electric arc in one-half 60 Hz cycle was 0.147 joules (147 mJ). This ignition energy is nearly 300 times the commonly accepted minimum ignition energy of propane/air mixtures at 0.46 mJ [2].

The general procedure for testing was to get the refrigerant release system ready, initiate the data acquisition prior to release of the refrigerant, discharge the target quantity of refrigerant at the target flow rate, and energize the electric arcs at 5 seconds after the completion of the discharge.

The R290 test matrix is shown in Table 2. Two tests were conducted with the circulating fan off. One test was planned with the fan running before the discharge began.

Table 2. R290 test matrix

Fan State	Planned Discharge (g)	Planned Discharge Rate (g/s)
Off	114g	21.4
Off	217g	21.4
On	217g	21.4

The R290 charge levels used in the testing had their bases in either existing or proposed limits for A3 refrigerants. In the absence of recommended limits for A3 refrigerants, the formulas for A2L refrigerants were used on the assumption that limits for A3's would follow the same formula. This approach allowed the project to assess safety factors for refrigerant charge quantity and mitigation criteria including mitigation response time and airflow rate for mixing and threshold for performing a certain safety test for commercial refrigerators. Table 3 and the notes below the table contain the determination of the charge limits used in this test series. The R290 discharge rate was based on the finding that the mass flow rate of liquid propane is 49% of the R-32 liquid mass flow rate at the same saturation temperature and orifice size [2]. The value was selected so that comparisons are possible between the A2L and propane refrigerant tests in the 9007-01 [1] and 9007-02 [2] programs.

Table 3. PTAC Charge Limit Determination [2]

Charge Limit	A3 (R290)	A2Ls	Mitigation Requirement
m_1 per UL 60335 2-40 Nov 2017	$3 \times LFL$ (114g)	$6 \times LFL$ (R-32: 1.81kg, R-452B: 1.85kg)	No mitigation required
m_1 per IEC 60335 2-40 Edition 6	$4 \times LFL$ (152g)		
m_{max} per UL 60335 2-40 Nov 2017	217g (notes 1,3)	$0.5 \times LFL \times h_a \times A$	Air circulation
m_{max} per IEC 60335 2-40 Edition 6	325g (notes 2, 3, 4)	$0.75 \times LFL \times h_a \times A$	Air circulation

Notes:
1. Nov. 2017 draft of UL 60335-2-40 [4]: $m_{max} = 0.5 \cdot LFL \cdot h_a \cdot A = 217g$
2. IEC 60335-2-40 Edition 6 [5]: $m_{max} = 0.75 \cdot LFL \cdot h_a \cdot A = 325g$
3. Using A2L equations for A3. A3 equations in development.
4. 325g not tested because 217g ignited with air circulation

3. Test Results [1, 2]

The PTAC ignition tests are summarized in Table 4. Three ignition tests (PTAC_14, 16 and 17) were performed following the plan outlined in Table 2. In PTAC_15 test, the electric arcs were energized ~1 s instead of planned 5 s after completion of the discharge. This test was repeated as PTAC_16. While PTAC_15 was incorrect in its procedure, the largest number of deflagration vents were burst in this test due to the higher concentrations existing immediately after completion of the discharge.

R290 tests all resulted in ignition even in the case that the fan was running continuously before the start of the discharge of 217g R290. The severity depended on the charge level. Without fan running, the highest temperatures were recorded close to floor level indicating flames were low in height (C-08, 8 inch above floor at location C). With the fan running, the highest temperature was measured at 60 inches above the floor at location B (B-60). Temperatures at the ceiling level were due to buoyant transport and not direct flame impingement. Temperatures and refrigerant concentrations over time at measured locations were not presented in this paper for simplicity. Readers are encouraged to read the report for details. Since all three planned tests resulted in ignition, testing at higher charge level was terminated.

Table 4. PTAC R290 ignition test results

Test Code	Fan State	Measured Discharge (g)	Measured Discharge Rate (g/s)	Max Temp (°C)	Max Temp Location	Max Ceiling Temp (°C)	Number of Vents Burst /Melted	Arc Delay Time (s)
PTAC_14	Off	214	18.3	463	C-08	216	3/3	4.3
PTAC_15	Off	111	20.9	534	C-08	277	4/1	0.9
PTAC_16	Off	110	20.4	371	C-08	99	2/1	5.7
PTAC_17	On (200cfm)	215	20.4	383	B-60	117	3/1	5.7

Estimates for the maximum flame size were made from the videos and are shown in Figure 4. The photos demonstrate the effect of timing the electric arcs. PTAC_15 was an invalid test and the comparison to PTAC_16 shows the effect of early ignition before the propane was able to mix and diffuse. PTAC_15 is considered an invalid test because its igniter timing was too short compared to the test plan, but still contains informative data about ignition timing. Comparison of PTAC_14 (Fan off) and PTAC_17 (Fan ON) both with 217 g discharges shows a small effect from the action of the fan in reducing the size of the flames. PTAC_17 (Fan on) resulted in bursting three deflagration vents compared to two bursts in the PTAC_14 test (Fan off)

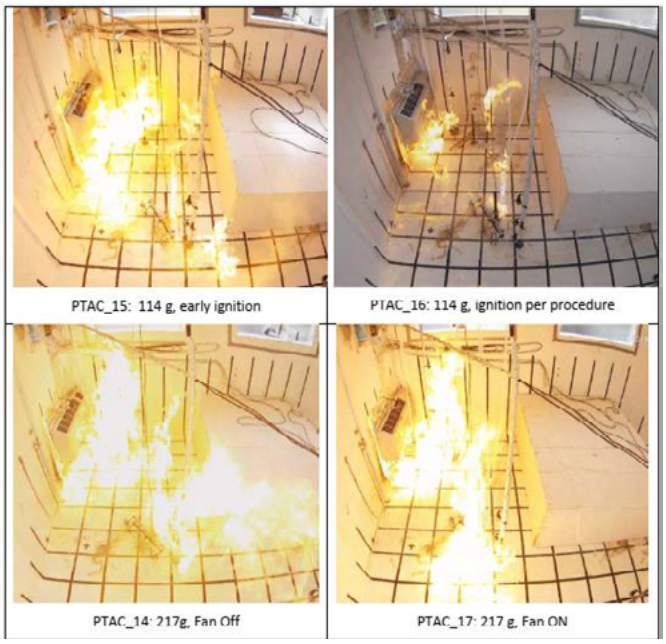
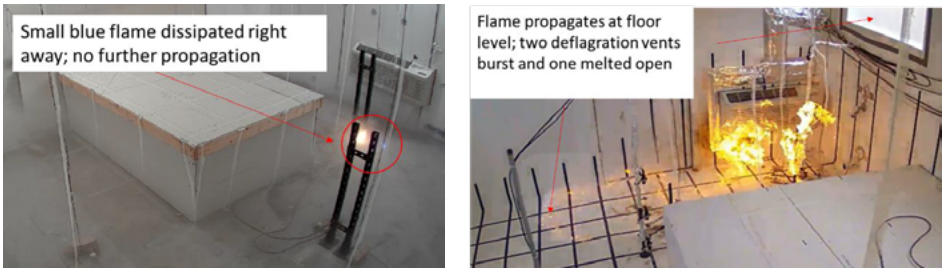


Fig. 4. PTAC Estimated maximum flame sizes

For comparison purpose, Figure 5 shows test results for both A2L refrigerant R452B and A3 refrigerant R290 using UL-60335-2-40 m1 charge level specified in Table 3. The R290 test parameters were listed as PTAC_16 in Table 4. The R452B test was conducted under the same room dimension and similar test procedure. 1.9 kg of R452B was actually released during the test (the target amount was 1.85kg). The R452B release rate was ~47g/s due to the density difference from R290 as noted before. The ignition source and ignition timing used for R452B test were also different from the R290 test. The ignition sources were electric arcs (same as R290 tests) with tea candles.

For R452B test, the ignition sources were energized approximately 27 second after the completion of the release. A small refrigerant flame was observed near location A (in front of the PTAC). The flame was quickly distinguished with no further propagation. The total flaming time for the refrigerant flame was 3 seconds. The cheesecloth was not ignited. The same test was performed using A2L refrigerant R32 at around 1.8kg with same release rate as R452B. The ignition sources were energized approximately 15 second after the completion of the R32 release. No ignition was observed. For R290 PTAC_16 test, the flame propagated along the floor indicating a flammable region had formed at the floor level.



(a)R452B, 1.9 kg, 47.4 g/s, no mitigation (b)R290, 110 grams, 21 g/s, no mitigation

Fig. 5. PTAC Test R452B vs R290

4. Discussion

The PTAC testing was designed to assess the R290 charge levels according to the then current proposed "Preliminary Comment Draft" of 3rd Edition UL 60335-2-40 (dated Nov 22, 2017) which was based on the 6th Edition of IEC 60335-2-40. According to the draft UL 60335-2-40, the charge limit for R290 is 114g regardless the room size for direct systems; however, the IEC standard 60335-2-40 Edition 6.0 allows higher charge. The IEC standard allows R290 charge up to 152g without room size restriction. Charge higher than 152g is correlated to the room area and equipment installation height for an unventilated room.

The PTAC AC tests indicated that the flammable cloud can form at floor level and be ignited at the current charge limit of 114g without room size restriction defined in UL 60335-2-40. The testing also demonstrated that the maximum allowable charge (325g) per the test room area (19m2) calculated using IEC 60335-2-40 would have caused R290 to build up flammable region around the unit vicinity at floor level and caused ignition when the ignition sources were present.

Both IEC and UL 60335-2-40 specify requirements for equipment using A2L refrigerants with incorporated circulation airflow which includes an incorporated fan to be either continuously operated or initiated by a refrigerant detection system. This concept is to ensure circulation airflow prevents refrigerant stagnation so that the equipment can use higher refrigerant charge than those without this feature. At present, neither the IEC nor UL 60335-2-40 has specified such requirements for A3 refrigerants that would allow higher A3 refrigerant charge quantity. IEC has established a WG (SC61D/WG16) to develop additional requirements for A3 refrigerants including the incorporated airflow concept. This project used the existing requirements for A2Ls in terms of determining charge quantity, minimum airflow rate for R290 tests to assess these requirements applicability to A3 refrigerants. The PTAC testing demonstrated that ignition can even happen while the PTAC fan is kept constantly on at low speed setting during the refrigerant release. This indicates that 1) the safety factor in the calculation of refrigerant quantity may not be enough; and 2) the mitigation using air flow may require a higher air flow rate than the A2L refrigerants to mitigate A3 refrigerants for floor mounted products.

The test results demonstrated that R290 was much easier to be ignited, and the ignition events were more severe compared to A2L refrigerants R32 and R452B at m1 charge level.

It should be stressed that testing scenarios were designed according to the existing requirements or proposed requirements in the IEC Standards 60335-2-40 and its equivalent North American version UL 60335-2-40. However, the R290 discharge rates were based on the finding that the mass flow rate of liquid propane is 49% of the R-32 liquid mass flow rate at the same saturation temperature and orifice size [2]. These values were selected so that comparisons are possible between the A2L and propane refrigerant tests in the 9007-01 [1] and 9007-02 [2] programs. As with the 9007-01 program, leak rates were almost always higher than the rate corresponding to total loss of charge in four minutes that was generally considered by the IEC/UL 60335-2-40. Generally speaking, this means the scenarios are more severe than they would have been with four minute leaks.

5. Summary

The PTAC testing generated a set of R290 dispersion and ignition data at different release amounts. The results provide useful information to product safety standard IEC/UL 60335-2-40. According to the testing, the following findings are recommended to the IEC/UL 60335-2-40 committee for consideration:

- Raising the current m1 (114g for R290) charge limit per UL 60335-2-40 should be carefully considered especially for floor or near floor mounted products.
- Any potential ignition sources should be avoided underneath installed units and near the projected area at floor level
- Air flow requirements as a mitigation method should be carefully considered in relation to the amount of refrigerant, and perhaps type of refrigerant (A2L's vs A3's).

The testing was more focused on understanding the ignition event severity, rather than the probability of the refrigerant ignition event. The future work should include characterization of refrigerant leak scenarios with actual equipment in "on" and "off" states, and real world ignition sources in terms of ignition energy, quantity, spatial location throughout the room, and activation frequency.

Acknowledgements

The project was strongly desired and supported by the HVACR industry. A group of industry experts provide technical guidance and products for testing. AHRTI is grateful to all of them for contributing their expertise and resources to the project.

References

[1] Gandhi, P, Hunter, G., Haseman, R. and Rodgers, B., Benchmarking Risk by Whole Room Scale Leaks and Ignitions Testing of A2L Refrigerants, AHRTI Project 9007 Final Report, 2017
[2] Hunter, G., Benchmarking Risk by Whole Room Scale Leaks and Ignitions Testing of A3 Refrigerants, AHRTI Project 9007-02 Final Report, 2019
[3] ASHRAE, ASHRAE Standard 34: Designation and Safety Classification of Refrigerants, 2016
[4] UL, Preliminary Comment Draft 3rd Edition of UL 60335-2-40, November 22, 2017
[5] IEC, IEC 60335-2-40: Household and similar electrical appliances- Safety - Part 2-40: Particular requirements for electrical heat pumps, air-conditioners and dehumidifiers, 2018

13th IEA Heat Pump Conference
April 26-29, 2021 Jeju, Korea

A novel geothermal heat pump system integrated with underground thermal storage for shifting building electric demands

Liang Shi[a], Ming Qu[a], Xiaobing Liu[b*]

[a]Purdue University, School of Civil Engineering, West Lafayette, IN 47906, USA
[b]Oak Ridge National Laboratory, Oak Ridge, TN 37831, USA

Abstract

The intermittent supply of renewable power and the continuous increase of electric demands pose challenges to the stability of existing electric grids and utilization efficiency of renewable power. The thermal energy storage applied to buildings is capable of utilizing the overproduced renewable power to store thermal energy, which is later discharged to meet thermal demands of buildings when renewable power production decreases. A novel geothermal heat pump system incorporated with underground thermal energy storage was investigated through a case study of applying the proposed system to a residential building in Baltimore, Maryland. A transient one-dimensional heat transfer model of the proposed dual-purpose underground thermal battery (DPUTB) was developed and integrated with simulation models of a dual source heat pump (DSHP) and a typical residential building to form a quasi-steady-state model of the proposed system. Simulation results indicate that the proposed system can shift the building electric demand from peak hours to other times when electricity is cheap. In a cooling season, the electricity consumption during peak hours is reduced by 40% and the associated electricity cost is reduced by 20%.

© HPC2020.
Selection and/or peer-review under responsibility of the organizers of the 13th IEA Heat Pump Conference 2020.

Keywords: underground thermal energy storage; geothermal heat pump; electric load shifting

1. Introduction

In the U.S., the penetration of renewable power generation has increased to reduce greenhouse gas emissions. However, the intermittent outputs of renewable energy pose challenges to the existing electric grid. The grid operators curtail renewable power when the power production is greater than the demand from the consumer. Thus, it reduces the economic and environmental benefits of renewable power [1]. When renewable energy is not available (sunsets, cloudy, etc.), the power demand from the existing grid increases dramatically. It requires the electricity generators ramp up their production rate quickly, resulting in low operating efficiency and high power production cost.

Buildings consume 73% of all U.S. electricity according to Energy Information Administrator [2]. The electricity consumed for space heating and cooling counts 22% and 14% of the total electricity consumption in residential and commercial buildings, respectively, on an annual basis [3]. It means that space heating and cooling for buildings is responsible for 13% of the total electricity consumption each year in the U.S.

Thermal energy storage (TES) is a promising technology that allows storing heat (or cooling energy) generated with overproduced renewable power, or electricity from the grid during off-peak hours, and using them to meet the thermal demands of buildings during peak hours. One promising technology is the integration of TES with heat pump systems [4]. Heat pump technologies utilize electricity to provide space cooling and/or space heating, as well as domestic water heating. The TES integrated heat pump systems provide valuable load

* Corresponding author. Tel.: +1-865-574-2593
E-mail address: liux2@ornl.gov

shifting resources to utility companies for reducing its operation cost while meeting the demands for electricity, without increasing power generation capacity [5].

TES can be integrated into a building's thermal system in passive or active ways. The passive applications usually utilize the existing thermal mass of the building. However, it is difficult to control the charging and discharging rate in passive applications, and normally more energy is consumed due to high thermal loss to the ambient. On the other hand, the active applications utilize a dedicated TES and associated heating/cooling system to charge and discharge the TES with more precise control.

Stratified water tanks are widely used for demand side management (DSM) due to its availability and low cost [5-7]. Stratified water tanks integrated with air source heat pump (ASHP) for heating application in residential buildings are investigated before. Renaldi et al. [6] proposed an optimization method to minimize the total operating cost of the system. The simulation result indicated that 6% energy cost reduction can be achieved with the proposed system compared with a conventional gas boiler system when a time-of-use electricity rate is available. Arteconi et al. [5] applied a DSM strategy to shift electric load during 3-hour peak hours to off-peak hours. They concluded that by adding a water tank to the heat pump system, the load shifting effect can be realized without influencing the indoor thermal comfort. However, 4% more electricity was consumed compared to the baseline heat pump system (without TES). Stratified water tanks are also applied for DSM in cooling applications. Yan et al. [7] proposed an active TES using chilled water tank in an office building in Hong Kong. The simulation results showed that the proposed system was able to reduce the capacity of the chiller by 24%. However, 2.6% more electricity was consumed due to additional pumping and thermal loss from the TES tank.

Besides water tanks, phase change material (PCM) tanks [8,9] are also applied to heat pump systems for DSM because of the high energy storage density of PCMs during phase change process. Most previous studies for PCM tank integrated thermal systems are for heating application only. Lizana et al. [8] integrated a stratified PCM tank with an air-water heat pump (AWHP) in a residential building in UK and proposed a DSM strategy to minimize the electric cost by utilizing a time-of-use (TOU) electric rate tariff. The simulation results indicate a 20% electricity cost reduction, while the total electricity consumption increased by 8%. Hirmiz et al. [9] customized a hybrid PCM water tank and integrated it with a ground source heat pump (GSHP) in a residential building in Canada. The system could shift the peak electric demand during 6-hour to off-peak hours. In addition, by applying PCM, the tank volume was reduced by 3 folds compared with using water tanks.

Previous studies concluded that TES integrated heat pump systems could make the electric demand of a building more flexible. With appropriate sizing, the system can shift electric demand from peak period (3 to 6 hours) to off-peak period. If time-of-use electricity rate is available, the load shifting can lead to significant (up to 20%) electricity cost savings. In addition, by applying TES, capacity of the heat pump can be smaller. However, the TES integrated systems always consume more energy (3% - 8% increase) than conventional systems due to the heat loss from the TES tank and the additional pumping power. Moreover, most studies used ASHPs due to their low cost and easy installation. However, the efficiency of an ASHP is usually lower than a GSHP, especially in cold climates. TES tanks in previous studies are installed above the ground, which not only occupy floor area, but also be heavily insulated to reduce heat loss. Besides, neglected by most previous studies, the cost of the TES integrated system is high due to additional component for TES. As a result, its applications is limited despite of its potential benefits to both the building owners and the grid operators.

The current study proposes a novel geothermal heat pump system integrated with an underground thermal energy storage to make the electricity demand of buildings flexible. The proposed system includes a state-of-art design for a dual-purpose underground thermal battery (DPUTB), which combines TES and ground heat exchanger (GHE) into one tank to reduce the initial cost and does not occupy any floor space and roof area for installation. A dual-source heat pump (DSHP) as the second main component of the proposed system can not only achieve higher efficiency than ASHPs, but also reduce the needed size of GHEs. Because the DPUTB is installed underground and any heat loss from the TES can be recovered though the GSHP operation, there is little heat loss to the ambient. This paper presents a preliminary study of the load shifting capability, thermal performance, and associated operating costs of the proposed system.

2. System Description

The proposed system consists of a DSHP and a DPUTB as depicted in Fig. 1. The DSHP is an electricity-driven heat pump using vapor compression refrigeration cycle, which utilizes either the ambient air or the ground as its heat source/sink. A refrigerant-to-air heat exchanger is used in the source side of the DSHP when

the ambient temperature is suitable for achieving a relatively high COP of the heat pump. When the ambient air temperature is too high in summer (or too low in winter) to be used as a heat source/sink, the heat pump switches to utilize the DPUTB as its heat source/sink (through a refrigerant-to-water heat exchanger) for a better COP. The DSHP can reduce the seasonal imbalance of the thermal loads of the GHE and thus reduce the needed size of the GHE.

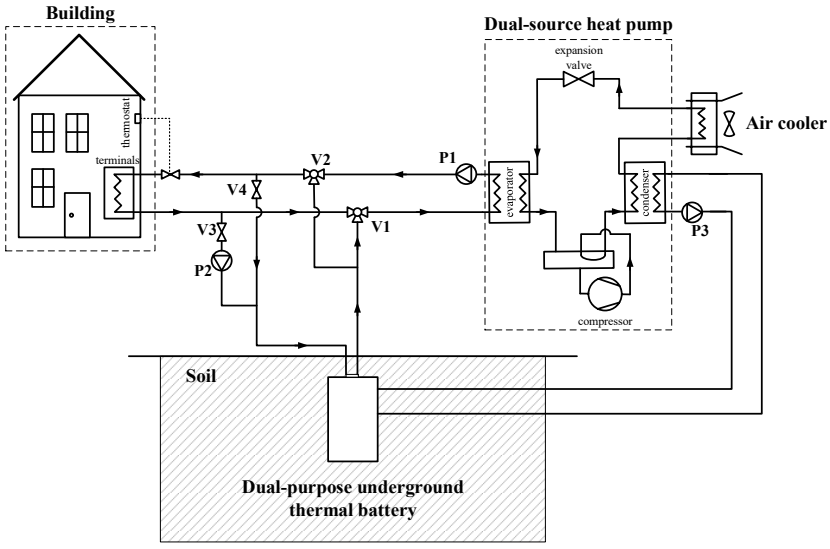


Fig. 1. System configuration diagram (cooling mode, DPUTB charging)

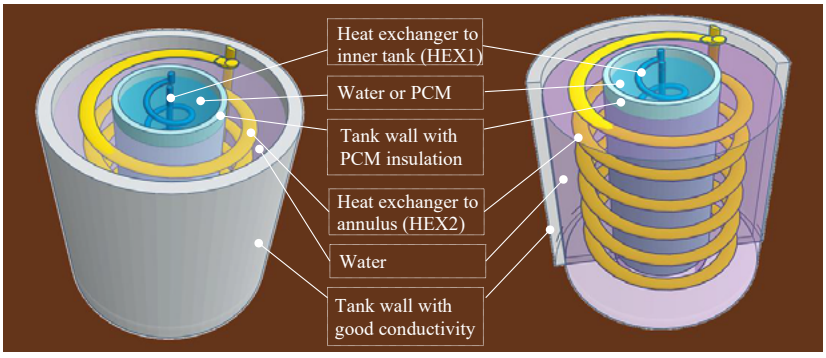


Fig. 2. Schematic of the DPUTB

The schematic of the DPUTB is shown in Fig. 2, it consists of an enclosed inner tank within a larger water tank. The inner tank works as a TES while the outer tank works as a GHE. A low-cost PCM encapsulated in a thin plastic panel is wrapped around the outer surface of the inner tank. Due to the low thermal conductivity and high latent heat of the PCM, it reduces the heat exchange between the inner and outer tanks. Another type of PCM with a different melting temperature is supplied in the inner tank for storing the thermal energy. Two coil heat exchangers are installed in the inner and outer tanks, respectively, to exchange heat with the HVAC system of the building. This design allows for storing thermal energy in the inner tank and later for providing direct heating or cooling to eliminate or reduce the electricity consumption for space heating or space cooling during peak hours of the electric grid. The outer tank of the DPUTB not only exchanges heat with the surrounding soil but also recovers energy losses from the inner tank for more efficient heat pump operation.

3. Component Modeling

3.1. DSHP

The DSHP is modelled as a combination of two conventional heat pumps: an air-water heat pump (AWHP) for air source and a water-water heat pump (WWHP) for ground source. The curve fitting models for the AWHP and the WWHP are developed based on the heat pump models (type 927 and type 941) of TRNSYS [10]. These heat pump models use performance curves of typical AWHP and WWHP units to predict their heating and cooling outputs and associated power consumption based on the inlet conditions from the condenser and evaporator. The rated COPs for AWHP and WWHP are 4.0 and 5.0, respectively.

3.2. DPUTB

A simplified one-dimensional transient model of the DPUTB has been developed in MATLAB [11] based on following assumptions and simplifications:

1. The PCM in the inner tank and the water at the outer tank are both well mixed. They are individual bulks with homogeneous properties within their domains.
2. The DPUTB is cylindrical symmetric and heat transfer occurs only along the radial direction.
3. The convection heat transfer within PCMs is neglected; only the conduction heat transfer is modeled.
4. The PCM's freezing point is identical to its melting point.

The model accounts for the following heat transfer phenomena:

1. Heat transfer between the heat exchanger in the inner tank (HEX1) and the inner tank PCM
2. Heat transfer between the heat exchanger in the outer tank (HEX2) and the outer tank water
3. Heat transfer between the inner tank PCM/water and the outer tank water through the inner tank wall and the PCM wrapped around the inner tank
4. Heat transfer between the DPUTB shell and the surrounding soil
5. Phase change process within the wrapping PCM and the inner tank PCM

3.2.1 Heat Exchanger

HEX1 and HEX2 are heat exchangers that direct contact with the inner and outer tank fluids. The input thermal energy to the tank fluid can be determined using equation (1):

$$q = UA \cdot \Delta T_{lm}, \tag{1}$$

where UA is the product of the overall heat transfer coefficient and the heat transfer area of a heat exchanger; ΔT_{lm} is the logarithm mean temperature difference between the fluid in the heat exchanger and the fluid in the tank at a given time step, which is expressed with equation (2):

$$\Delta T_{lm} = \frac{(T_{HEX,in} - T_{tank}) - (T_{HEX,out} - T_{tank})}{\ln \frac{T_{HEX,in} - T_{tank}}{T_{HEX,out} - T_{tank}}}, \tag{2}$$

where $T_{HEX,in}$ and $T_{HEX,out}$ are the heat transfer fluid temperatures at the inlet and outlet of the heat exchanger, respectively; T_{tank} is the average tank water temperature.

For the current case, the UA value of the heat exchanger is proportional to the mass flow rate of the heat exchange fluid, and it can be determined through experimental data regression.

At steady state, the heat exchange rate is also equal to the enthalpy change of the fluid in the heat exchanger, which can be determined using Eq. (3):

$$q = \dot{m}_{HEX} \cdot c_p \cdot \left(T_{HEX,in} - T_{HEX,out}\right), \tag{3}$$

where $\dot{m}_{HEX}$ is the mass flow rate of the heat transfer fluid; c_p is the specific heat of the heat transfer fluid.

The above equations are solved to determine the heat exchanger outlet temperature at a given time step with known inlet fluid temperature, thus the heat transfer rate can be calculated. The heat transfer rates from HEX1 and HEX2 are used as boundary conditions of the DPUTB model.

3.2.2 Natural convection

The empirical correlations describe the convection heat transfer coefficient between the tank fluid and its surrounding solid surfaces. The Rayleigh number and the Nusselt number can be determined using equation (4) and (5), respectively:

$$\mathrm{Ra} = \frac{g \cdot \beta \cdot |T_s - T_\infty| \cdot L^3}{\nu \cdot \alpha}, \tag{4}$$

where g is the gravitation; β is the thermal expansion coefficient; T_s is the temperature at the surface; T_∞ is the temperature of the fluid at bulk; L is the characteristic length; ν is the kinematic viscosity; and α is the thermal diffusivity.

$$\mathrm{Nu} = \left\{ 0.825 + \frac{0.387 \cdot \mathrm{Ra}^{\frac{1}{6}}}{\left[1 + (0.492/Pr)^{\frac{9}{16}}\right]^{\frac{8}{27}}} \right\}^2, \tag{5}$$

where Pr is the Prandtl number.

Thus the convective heat transfer coefficient can be determined using equation (6):

$$h_{conv} = \mathrm{Nu} \cdot \frac{k}{L}, \tag{6}$$

where k is the thermal conductivity of the fluid in the tank.

The surface temperature of the solid wall in contact with the liquid can be calculated based on the energy balance at the surface:

$$h_{conv} \cdot (T_\infty - T_s) = \frac{k_{wall}}{\Delta x} \cdot (T_s - T_{wall}), \tag{7}$$

where k_{wall} is the thermal conductivity of the solid wall; Δx is the thickness of the wall; T_{wall} is the surface temperature at the other side of the wall.

Equations (4) to (7) are solved to determine the convection heat transfer at the solid surface at a given time step.

3.2.3 Conduction heat transfer

Heat conduction is considered in the tank wall, the surrounding soil, and the wrapping PCM. For 1D heat conduction in the cylindrical coordinate, the conduction heat transfer equation can be expressed as:

$$\frac{1}{r}\frac{\partial}{\partial r}\left(r \cdot k \frac{\partial T}{\partial r}\right) = \rho \cdot c_p \frac{\partial T}{\partial t}, \tag{8}$$

where r is the position in the radial direction; ρ is the density; t is the time step.

Due to the complexity of the whole simulation domain, the explicit method is applied for the numerical calculation. Therefore, the conduction heat transfer equation is discretized into the form expressed in equation (9), subscript i represents the position along the radial direction:

$$\frac{1}{r_i} \cdot \frac{r_{i+\frac{1}{2}} \cdot k_{i+\frac{1}{2}} \frac{T_{i+1} - T_i}{\Delta r} - r_{i-\frac{1}{2}} \cdot k_{i-\frac{1}{2}} \frac{T_i - T_{i-1}}{\Delta r}}{\Delta r} = \rho \cdot c_p \frac{T_i^{new} - T_i}{\Delta t}, \tag{9}$$

The temperatures in the tank wall, the surrounding soil, and the wrapping PCM are determined at each time step with the above numerical method and given boundary conditions at each simulation domain.

3.2.4 Phase change

The latent heat accumulation method [12] is applied to simulate the phase change process within the wrapping PCM and the inner tank PCM. For a certain amount of PCM, the maximum latent heat it can store/release can be determined as:

$$Q_{latent,max} = m \cdot \Delta H, \tag{10}$$

where m is the mass of the PCM; ΔH is the specific latent heat of the PCM.

It is assumed in this model that the temperature of a PCM is kept intact when it is undergoing phase change process. The phase change process is indicated with a 'solid fraction' factor. The 'solid fraction' factor during the melting process of a PCM is quantified using following equation:

$$\theta = 1 - \frac{Q_{latent,acc}}{Q_{latent,max}}, \tag{11}$$

where $Q_{latent,acc}$ is the accumulated latent heat in the PCM during phase change; $Q_{latent,max}$ is the maximum latent heat the PCM can store.

In this model, the PCM wrapping around the inner tank is modeled as a series of coaxial hollow cylinders and each hollow cylinder has uniform temperature and phase status. The temperature and phase status of each hollow cylinder is updated at the end of each time step after calculating the heat transfer within the PCM domain. The inner tank PCM is modeled as one volume with uniform temperature and phase status, which is updated at each time step based on the heat transferred from the heat exchanger and through the wall of the inner tank.

3.3. Control Strategy

The integrated DSHP and DPUTB system can be operated in ten different modes, as listed in table 1. To achieve specific goals (e.g., energy cost reduction, load leveling, etc.), different control strategies can be developed to determine the operation mode at a given time of a day. In this study, a rule-based control strategy is developed to shift the electric demand of the building from peak hours to off-peak hours so that it can take advantage of the time-of-use (TOU) electric tariff to reduce the energy cost of the building. The logic flow chart of this control strategy is shown in Fig. 3.

Table 1. System operation mode description

Mode #	Building Load	Heat Pump Status	TES Status
1	no	off	off
2	yes	off	discharge
3	yes	air-source	off
4	yes	ground-source	off
5	yes	air-source	charge
6	yes	ground-source	charge
7	yes	air-source	discharge
8	yes	ground-source	discharge
9	no	air-source	charge
10	no	ground-source	charge

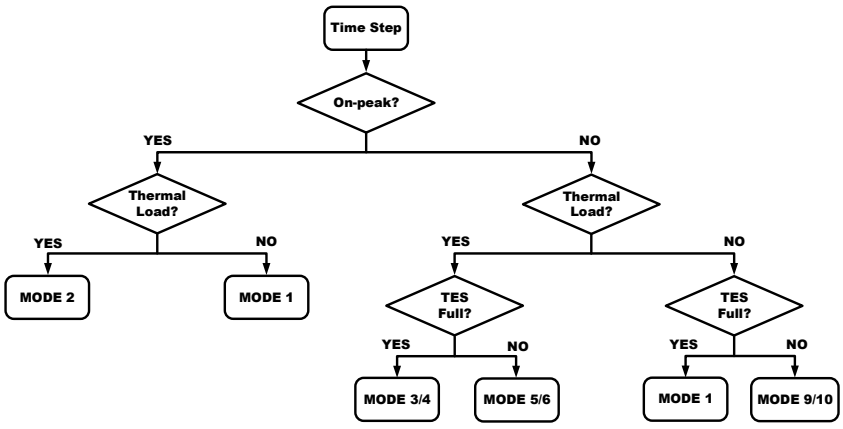


Fig. 3. Control strategy for reducing energy cost

4. Case Study

4.1. Building Information and Equipment Sizing

A typical U.S. residential building [13] in Baltimore, Maryland is chosen for a case study. It is a single-family detached house located with 223 m^2 air-conditioned floor space. The air-conditioning system is a centralized constant volume air system with on/off control to maintain the room temperature within 22.2 to 23.9 °C. The nominal cooling capacity of the air-conditioner used in the building is 2-ton (7 kW) and its nominal COP is 3.97. This air-conditioner is used as a baseline in this study to be compared against the integrated DSHP and DPUTB system.

A pilot TOU electric tariff is used in this study. This TOU electric tariff named 'Schedule RD' was introduced by the Baltimore Gas and Electricity Company for residential customers who have installed smart meters. According to this tariff, during the summer of 2019, the electricity retail price is 0.339 $/kWh between 14:00 and 19:00 on weekdays, which is defined as on-peak hours, and it is 0.064 $/kWh during other time (off-peak hours) [14].

The sizes of the DSHP and the DPUTB are determined based on the thermal load of the building and the control strategy described in Section 3.3. The thermal energy storage capacity of the DPUTB should be no less than the total thermal load during on-peak hours of the design day. It ensures that the stored thermal energy is adequate for providing space cooling during the on-peak period, and thus the heat pump can be turned off to reduce electric demand. The capacity of the heat pump could be smaller than the peak cooling load of the building during a cooling season, but it should be larger than the maximum cooling load during the off-peak period so that it can simultaneously cools the inner tank for storing sufficient cooling energy while providing space cooling during the off-peak hours. To meet the cooling load of the residential building, two identical DPUTBs are needed, and the nominal cooling capacity of the DSHP is 1.75-ton (6.125 kW), which is 12.5% smaller than the baseline air-conditioner. The key parameters of the DPUTB are listed in table 2.

Table 2. Key parameters of the system components

Property	Value	Unit
DPUTB dimensions		
Inner tank diameter	39	cm
Inner PVC shell thickness	0.55	cm
PCM blanket thickness	2.54	cm
Outer tank diameter	101.37	cm
Outer PVC shell thickness	0.82	cm
Height of the inner tank	609.60	cm
Height of the outer tank	609.60	cm
Inner shell thermo-physical properties		
Material	PVC	–
Thermal conductivity	0.19	W/m K
Density	1380	kg/m^3
Specific heat	1000	J/kg K
Outer shell thermo-physical properties		
Material	HDPE	–
Thermal conductivity	0.50	W/m K
Density	950	kg/m^3
Specific heat	1900	J/kg K
Inner tank PCM thermo-physical properties		
Melting point	13	°C
Heat of fusion	160	kJ/kg
Density (solid)	917.5	kg/m^3
Density (liquid)	998	kg/m^3
Thermal conductivity (solid)	2.25	W/m K
Thermal conductivity (liquid)	0.6	W/m K
Specific heat (solid)	2027	J/kg K
Specific heat (liquid)	4182	J/kg K

Annulus PCM thermo-physical properties		
Melting point	15	°C
Heat of fusion	160	kJ/kg
Density	1118	kg/m^3
Thermal conductivity (solid)	0.1489	W/m K
Thermal conductivity (liquid)	0.1596	W/m K
Specific heat (solid)	3000	J/kg K
Specific heat (liquid)	2740	J/kg K
Soil thermos-physical properties		
Thermal conductivity	1.70	W/m K
Density	1602	kg/m^3
Specific heat	2100	J/kg K
Undisturbed ground temperature	14.4	°C
Heat exchanger properties		
UA value	5000	W/°C

4.2. System Simulation

Numerical models of DPUTB and DSHP, as well as the control strategy, are implemented in MATLAB and integrated together to simulate the performance of the integrated DPUTB and DSHP system at each time step (60 seconds).

The hourly cooling load and electricity consumption of the building resulting from using the baseline air-conditioner during the entire cooling season is obtained from computer simulation of the residential building using typical meteorological year (TMY3) weather data [15]. The simulation-predicted hourly cooling load is used as the inputs to the simulation model of the integrated DPUTB and DSHP system.

4.3. Design-Day Simulation Results

Some featured results for a design-day (July 21) simulation of the integrated DPUTB and DSHP system with the rule-based control strategy are shown in Fig. 4. The first sub-figure clearly shows that a considerable amount of electricity demand has been shifted from on-peak (14:00 – 19:00) to off-peak hours.

From 0:00 to 8:00, due to the relatively low ambient temperature, the DSHP operates as an ASHP to supply space cooling to the building as well as to charge the DPUTB. The operating COP of the ASHP is stabilized at around 5 (4th subplot). The solid fraction of the inner tank PCM keeps increasing until it is fully charged (i.e., when the average temperature of the PCM is 3ºC lower than its melting temperature) at around 6:00 (3rd subplot). As long as the inner tank is fully charged, the heat pump solely operates to satisfy the cooling demand of the building. Otherwise, the heat pump works to charge the inner tank and to meet the thermal load of the building simultaneously. During this period, there is no heat rejection to the outer tank of the DPUTB. Thus, the temperature of the outer tank water is slightly cooled down by the inner tank and the surrounding soil, as can be observed from the 2nd subplot.

From 8:00 to 14:00, while it is still in the off-peak period, the ambient temperature is higher than 26.7 ºC, which is the threshold for switching from ASHP to GSHP. Therefore, instead of rejecting condensing heat to the ambient air via the refrigerant-to-air heat exchanger, the DSHP rejects condensing heat to the soil via the heat exchanger in the outer tank of the DPUTB. It can be observed from the 2nd subplot that the outer tank water temperature increases and the heat transfer rate from the tank to the soil also increases (5th subplot). The average operating COP of the GSHP is around 5.5 (4th subplot), and it decreases with the increase of the outer tank temperature.

The on-peak period begins at 14:00 and ends at 19:00. During this period, the heat pump is completely turned off (5th subplot), and the cooling energy stored in the inner tank of the DPUTB is used to meet the thermal load of the building. A significant reduction of the stored cooling energy can be observed from the decreasing trend of the solid factor of the PCM as shown in the 3rd subplot. Since the heat pump is turned off, there is no heat rejected to the outer tank of the DPUTB, and its temperature is cooled down by the surrounding soil, as depicted in the 2nd subplots. After 19:00 (the end of the peak hours), the heat pump is turned on to simultaneously cool the building and the inner tank of the DPUTB. It can be observed that right after 19:00, the electric demand of the integrated DPUTB and DSHP system is higher than the baseline, this is because that

the DSHP operates at its full capacity to meet the building thermal load and to charge the DPUTB at the same time, while for the baseline case, the air conditioner only works partially to meet the building thermal demand.

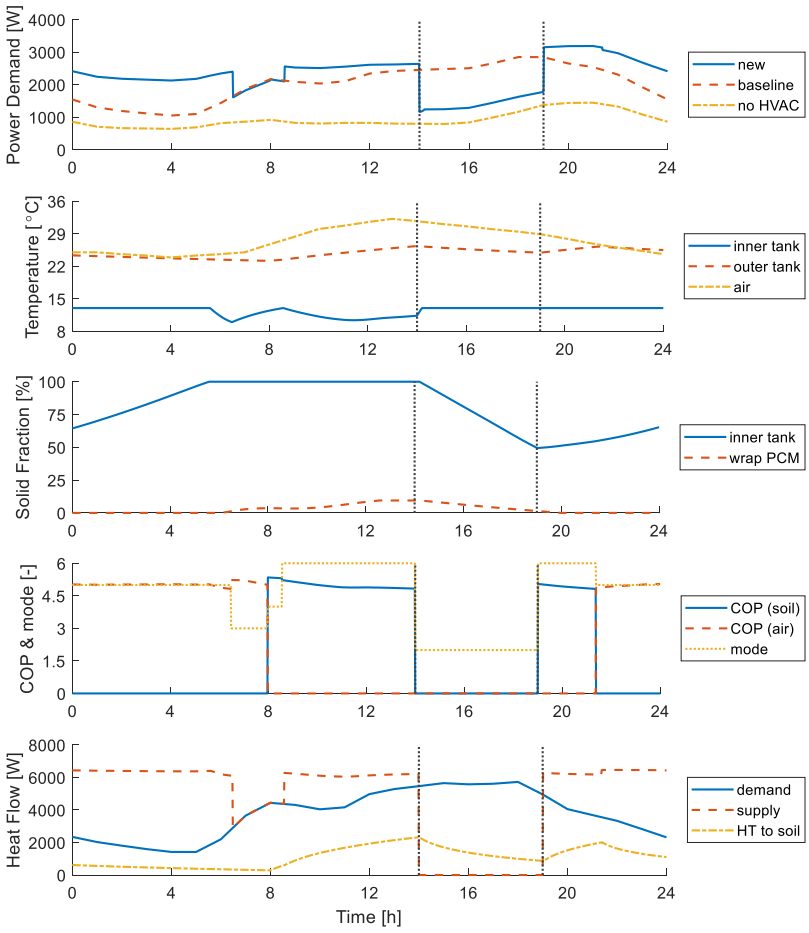


Fig. 4. Featured simulation results of the integrated DPUTB and DSHP system on the design-day (July 21)

The power consumption and the electricity cost of the design day are summarized in Table 3. The result shows that by applying the novel system with the rule-based control strategy, the daily electricity consumption is increased by 11%. However, the on-peak electricity consumption contribution (on-peak electricity consumption divided by total daily electricity consumption) is reduced from 26.9% to 13.1%. The electricity cost is reduced by 19.5%. It indicates that the novel system with the proposed control strategy can effectively shift the electric load from on-peak to off-peak period, but more electricity is consumed during the whole day.

Table 3. Energy consumption and cost for design-day simulation with rule-based control

System	Control	Total electricity consumption [kWh]	On-peak electricity consumption [kWh]	Cost [$]
Baseline	conventional on/off	49.06	13.21	6.77
Novel	rule-based control	54.43	7.14	5.45

4.4. Simulation Results of a Cooling Season

A seasonal simulation (June 1 to September 30) is conducted to investigate the long-term performance of the integrated DPUTB and DSHP system. Fig. 5 shows some of the simulation results. The 1st subplot of Fig. 5 indicates that, with the cost-reduction oriented control strategy, the hourly electric demand of the integrated DPUTB and DSHP system fluctuates within 640 – 3500W in each day. Overall, this control strategy cannot flatten the electric demand profile of the building. To achieve load leveling with the integrated system, a different control strategy needs to be used. During the entire cooling season simulation, the outer tank water temperature ranges from 15 ºC to 30 ºC (2nd subplot), which ensures the DSHP operate at a relatively high COP when it switches to ground source. The air source operation of the DSHP (when the ambient temperature is relatively low) gives more time to the outer tank for dissipating heat to the surrounding soil and thus cools down the outer tank water temperature. As shown in the 2nd subplot, the outer tank water temperature recovers to its original level after the entire cooling season operation. The 3rd subplot shows the solid fraction profile of the inner tank PCM and wrapping PCM. The stored latent cooling energy of the inner tank PCM never exhausted, which indicates that the sizing of the DPUTB is reasonable. The wrapping PCM is solid at the beginning of the cooling season because its melting temperature (15 °C) is higher than the surrounding soil temperature (14.4 °C). The wrapping PCM is melted gradually after cooling season starts, as indicated by the decrease of its solid fraction. The wrapping PCM cycles between melting and solidification on a daily basis (i.e., melting when heat from the GSHP is rejected into the outer tank, and re-solidifying when releasing heat to the surrounding soil and the inner tank). The simulation result indicates that the DPUTB maintains a significant temperature difference between the inner and outer tank every day.

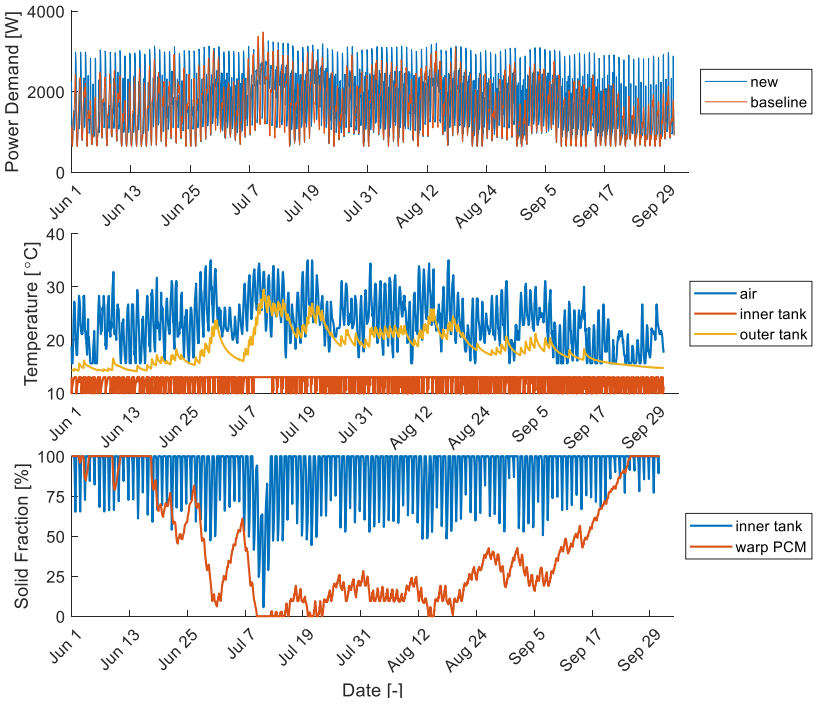


Fig. 5. Featured simulation results of the integrated DPUTB and DSHP system during a cooling season

The electricity consumption and the associated cost during the entire cooling season are listed in Table 4. These data show that although the electricity consumption of the entire building (including both HVAC and non-HVAC electric consumption) is increased by 4.5%, the on-peak electricity consumption of the building is

reduced by 40% compared with that resulting from using the baseline air-conditioner, and the electricity cost is reduced by 19.5% over the entire cooling season.

Table 4. Energy consumption and cost for seasonal simulation with rule-based control

System	Control	Total electricity consumption [kWh]	On-peak electricity consumption [kWh]	Cost [$]
Baseline	conventional on/off	4764	1333	671
Novel	rule-based control	4978	805	540

5. Conclusions

This study conducts a preliminary evaluation of a novel dual-source heat pump (DSHP) integrated with an underground thermal energy storage system (DPUTB) for shifting the electric demand of a residential building in the United States during a cooling season. A simplified numerical model has been developed for the DPUTB. A computer simulation of the integrated DPUTB and DSHP system is conduced to evaluate its load shifting performance and resulting energy cost. Following conclusions can be drawn from the simulation results:

- The system shifts 5-hour on-peak electricity consumption for space cooling to off-peak period, which results in a 40% reduction in the peak electricity consumption of the building over the entire cooling season
- The associated electricity cost reduction is around 20%, which is higher than other active TES systems reported in existing literature
- The heat pump capacity is reduced by 12.5% compared with the baseline air-conditioner, which does not have any TES
- The COP of the DSHP remains high (around 5) during the cooling season
- Total electricity consumption increases by 4.5% over the cooling season due to additional pumping

Further work includes optimizing the charging control of the inner tank and applying better thermal insulation to reduce heat transfer between the inner tank and the outer tank. It is also planned to investigate the heating season performance of the integrated system. More advanced controls, such as model-based control or artificial intelligence, will also be investigated for improving the capability of the integrated system for effectively reshape the electric demand profile in response to the demand side management signal of the electric grid while satisfying all the thermal demands of the building.

Acknowledgements

The authors thank the Low-Temperature Geothermal Program of the Geothermal Technologies Office at the U.S. Department of Energy for funding this research project.

References

[1] NREL (2015). Overgeneration from Solar Energy in California: A Field Guide to the Duck Chart. https://www.nrel.gov/docs/fy16osti/65023.pdf.
[2] EIA (2019), Electric Power Monthly with Data for August 2019. https://www.eia.gov/electricity/monthly/current_month/epm.pdf.
[3] Schwartz, L. et al. (2017). Electricity end uses, energy efficiency, and distributed energy resources baseline.
[4] Lizana, J., Chacartegui, R., Barrios-Padura, A., & Ortiz, C. (2018). Advanced low-carbon energy measures based on thermal energy storage in buildings: A review. *Renewable and Sustainable Energy Reviews*, *82*, 3705-3749.
[5] Arteconi, A., Hewitt, N. J., & Polonara, F. (2013). Domestic demand-side management (DSM): Role of heat pumps and thermal energy storage (TES) systems. *Applied thermal engineering*, *51*(1-2), 155-165.
[6] Renaldi, R., Kiprakis, A., & Friedrich, D. (2017). An optimisation framework for thermal energy storage integration in a residential heat pump heating system. *Applied energy*, *186*, 520-529.
[7] Yan, C., Xue, X., Wang, S., & Cui, B. (2015). A novel air-conditioning system for proactive power demand response to smart grid. *Energy conversion and management*, *102*, 239-246.

[8] Lizana, J., Friedrich, D., Renaldi, R., & Chacartegui, R. (2018). Energy flexible building through smart demand-side management and latent heat storage. *Applied energy*, *230*, 471-485.
[9] Hirmiz, R., Teamah, H. M., Lightstone, M. F., & Cotton, J. S. (2019). Performance of heat pump integrated phase change material thermal storage for electric load shifting in building demand side management. *Energy and Buildings*, *190*, 103-118.
[10] Klein, S. A. et al. (2017). "TRNSYS 18: A Transient System Simulation Program." Solar Energy Laboratory, University of Wisconsin, Madison. http://sel.me.wisc.edu/trnsys.
[11] MATLAB version 9.4 (2018). Natick, Massachusetts: The MathWorks Inc.
[12] Muhieddine, M., Canot, E., and March, R. (2009). Various approaches for solving problems in heat conduction with phase change. *International Journal on Finite Volumes*, 19.
[13] DOE, Residential Prototype Building Models. https://www.energycodes.gov/development/residential/iecc_models
[14] Baltimore Gas and Electricity Company (2018). Residential delivery and energy time-of-use pilot – electric schedule RD. https://www.bge.com/MyAccount/MyBillUsage/Documents/Electric/Schedule_RD.pdf
[15] Wilcox, S. and W. Marion. (2008). User's Manual for TMY3 Data Sets, NREL/TP-581-43156. April 2008. Golden, Colorado: National Renewable Energy Laboratory.

13th IEA Heat Pump Conference
April 26-29, 2021 Jeju, Korea

Field Performance of Domestic Heat Pumps for Heating and Hot Water in Switzerland

Ralph Kuster*, Manuel Prinzing, Matthias Berthold, Cordin Arpagaus, Mick Eschmann, Stefan S. Bertsch
NTB University of Applied Sciences of Technology, Institute for Energy Systems, Werdenbergstrasse 4, CH-9471 Buchs, Switzerland

Abstract

This study presents the development, the methods, and the state of the art of heat pump field tests as they are currently carried out by the Heat Pump Test Center (WPZ) in Buchs. Since 2016, heat pumps for hydronic heating systems in single-family houses in Switzerland have been investigated. So far, nearly 20 air-source and geothermal heat pumps, primarily located in the lowlands have been added to this governmental quality assurance program. For each heat pump system, calibrated sensors record approximately 50 data points at 10 seconds intervals, which ensures very low measurement uncertainty.
The aim of this field study is to record the efficiency of the real systems in operation and to draw comparisons with characteristic parameters from laboratory measurements and manufacturer data. Further goals are the identification and optimization of possible deficiencies in planning and installation as well as in the controls of the heat pump devices. The results of field measurements show the importance of careful design and installation of these systems. The optimal integration in retrofit systems (building renovations) is also a major challenge.
Heat pumps installed in new and refurbished buildings have been investigated with different system boundaries. The results show significant differences between the systems as well as typical installation faults. After a year of baseline performance evaluation, the systems are optimized to determine the potential of such measures and better define guidelines for planners and installers. An overview of such measures is also presented.

© HPC2020.
Selection and/or peer-review under responsibility of the organizers of the 13th IEA Heat Pump Conference 2020.

Keywords: heat pump field tests; seasonal performance factors; annual coefficient of performance; domestic hot water, state of the art

1. Introduction

The use of domestic heat pumps (DHP) in Swiss households for heating and domestic hot water production is advancing. The number of heat pumps sold in Switzerland in 2018 increased by almost 10 % compared to 2017 and almost 19 % compared to 2016 [1]. 70 % of the heat pumps are air/water heat pumps (AWHP), 28 % brine/water heat pumps (BWHP) and 2 % are groundwater heat pumps (GWHP).

Along with increasing DHP sales, the estimation of the field performance of such heat pump systems is gaining importance since the efficiency of heat pumps reacts sensitively to their integration into the heating system and the settings of the heat pump controller. Such performance gaps cannot be determined by measuring the system in the laboratory, but only by taking measurements at the actual place of use. Therefore, 25 years ago, a comprehensive field study of DHP in Switzerland, called FAWA (field analysis of heat pump installations) was launched [2], which was commissioned by the Swiss Federal Office of Energy (SFOE) and carried out with the support of industrial and academic partners.

Between 1996 and 2003, a total of 221 heat pumps with a maximum heating capacity of 20 kWth were measured, mainly in new single-family houses. According to the defined system boundary (Seasonal performance factor SPF (JAZ)) [2] an average coefficient of performance (COP) of 2.7 for AWHP-systems

* Corresponding author. Tel.: +41 81 755 31 82
E-mail address: ralph.kuster@ntb.ch

and 3.5 for BWHP-systems were recorded. At that time, data was still recorded manually, at best once a week.

Outside of Switzerland, DHP-field studies were performed in several other countries starting in 2005 with the Frauenhofer (ISE) studies [3] [4]. The first ISE study showed average seasonal performance factors (SPFH3) of 2.7/3.5 (AWHP/BWHP) whereas the second study in 2009 revealed slightly increased factors for both AWHP (2.9) and BWHP (3.9) systems.

In contrast to the SPF definitions used in Switzerland, many European studies are based on the harmonized systems boundary definitions (SPFH1 to SPFH4) introduced during the SEPEMO project (SEasonal PErformance factor and MOnitoring for heat pump systems in the building sector) in 2011 [5] [6].

Gleeson et al. [7] investigated eight different European studies and the respective system boundaries or key figures used (Table 1).

Table 1. Overview of key figures in European field studies [7]

Field study	No. of units	*SPF1 (JAZ1)*	*SPF2 (JAZ2)*	SPF_{hps}	SPF_{H1}	SPF_{H2}	SPF_{H3}	SPF_{H4}	DHW share
FAWA [2]	221	-	221	-	-	-	-	-	50%
Frauenhofer 2009 [3] [4]	74	-	-	-	74	74	74	74	100%
Frauenhofer 2005 [3] [4]	70	-	-	-	-	-	70	-	100%
DTI	150	-	-	-	-	-	-	150	100%
LAHR [8]	25	25	25	-	-	-	-	-	unknown
SPTRI 2007	5	-	-	5	-	-	-	5	100%
SPTRI 2010	6	-	-	-	6	-	6	-	86%
EST	71	-	-	-	-	-	-	-	77%
Total	622	25	246	5	80	74	150	229	

Apart from the FAWA study, only the Lahr field trials (2006 to 2014) [8] performed in Germany used the SPF definitions, which makes direct comparison difficult. In fact, performance figures of field test studies are only meaningful in combination with their respective boundary conditions. All further results presented in this work will use the performance figures and the system boundaries defined by the Swiss Federal Office of Energy (SFOE).

The heat pump test center WPZ at the University of Applied Sciences of Technology in Buchs, CH is an EN 17025 and EN14511 certified inspection authority [9]. It offers comprehensive testing service in the field of heat pump and refrigeration technology. Field measurements from the extended monitoring period between 2015 and 2019, which were commissioned by the SFOE, are currently being evaluated.

The main objective of the monitoring study was to identify suitable indicators based on the data measured and evaluated over the period of two years. Subsequently, comparisons should show optimization potentials of the systems, which can then be implemented. Each year, approximately five new heat pumps are included in the series of measurements.

The current heat pump field study at the Heat Pump Test Center (WPZ) in Buchs is carried out in cooperation with the Swiss Federal Office of Energy (SFOE) and pursues the following strategy:

- Investigation of the real-life performance of heat pump systems.
- Identification of optimization potential.
- Annual addition of five heat pumps to the campaign.
- Reliable measuring data through pre-calibration of the field measuring system.
- Meaningful measuring data thanks to high sampling rate and accurate measuring devices.
- Implementation of suggested optimizations after two years of recording and evaluation.

The ongoing study currently comprises nearly 20 heat-pump systems mainly located in the German speaking lowlands of Switzerland.

2. Technology, boundaries and methods of the field tests

Compared to the earlier studies in the 1990s, the measurement methodology and data acquisition technology have changed considerably. Nowadays, thanks to digitalization, much more data is available. Short recording intervals (10 s) can be used to describe temporal processes in heat pump systems in detail, enabling an easier detection of defects such as heat losses and unwanted circulation. Based on the collected data series, it is also possible to investigate the following processes deeper, which was not feasible with manual readings [9]:

- starting behavior,
- defrosting,
- on/off cycling,
- detailed breakdown by different levels of utilization,
- measurement at the different system boundaries,
- value of the building/structural condition, and
- effect of auxiliary devices on efficiency (circulating pump, heating elements, etc.).

Due to the short sampling time and the high-resolution data, processes can be viewed not only energetically but also in terms of performance over time. Thus, the measured values can be assigned to a clear chronological sequence. For example, the efficiency of domestic hot water generation and heating water charging can be considered separately.

It is also possible to categorize processes in which the compressor is switched off and only the auxiliary heater is active (standby power consumption analysis) [9]. Such temporal differentiation is becoming increasingly important for the calculation of meaningful key figures. Another advantage of having high-resolution data is the ability to distinguish between the heating and cooling modes of a heat pump. This is particularly interesting for BWHP systems, as no reversible compressor and cycle is required and the excess heat can be fed into the ground. Due to global warming and the resulting hot summers, the demand for heat pump systems with cooling function has significantly increased already in Switzerland.

As mentioned, the SFOE sets its own guidelines for key figures and system boundaries. In terms of energy figures, they are defined as follows [9]:

$$SPF = \frac{Q_{SH}+Q_{DHW}}{E_{tot}-E_{CP,Sink}-E_{ext,HE}} \quad (1) \qquad HUR = \frac{Q_{SH}+Q_{DHW}}{E} \quad (2)$$

$$SUR_{DHW} = \frac{Q_{DHWU}}{E_{DHW}} \quad (3) \qquad Q_{HD} = \frac{Q_{SH}}{E_{RA}} \quad (4)$$

$$THR = \frac{Q_{SH}+Q_{DHW}}{E_{RA}} \quad (5) \qquad HR_{DHW} = \frac{Q_{DHW}}{E_{RA}} \quad (6)$$

$$\eta_{DHW} = \frac{Q_{DHWU}}{Q_{DHW}} \quad (7)$$

The annual performance factor *SPF* mainly determines the efficiency of the heat pump. Only the electrical energy of the compressor, fan (AWHP), source pump (BWHP) and the control electronics of the heat pump are considered in this indicator. The heat utilization ratio *HUR* also includes the electrical energies of the heat sink circulating pump and all auxiliary heating elements. This way the efficiency of the complete heating integration is illustrated and made comparable to other heating systems. The third parameter, the SUR_{DHW} (system efficiency of domestic hot water use), shows the hot water efficiency with respect to usage, including all storage and distribution losses. In addition, this key figure can also be used to assess domestic hot water heat pumps (DHWHP).

Fig. 1 shows the corresponding system boundaries [9]. It can be seen, that the SEPEMO boundaries SPF_{H1} and SPF_{H2} match with *COP, SPF* according to the SFOE [7] [9]. However, the SPF_{H3} does not include the circulation pump and the auxiliary heating of the DHW tank like *HUR* does. In contrast to the outermost boundary SUR_{DHW} the SPF_{H4} does include the entire HP-System with both DHW and space heating buffer tank and is therefore not included in the schematic below.

In order to assess the influence of the building itself or the user behavior and its location, the characteristic values Q_{HD} and *THR* are determined and displayed. However, since the interior temperature is not recorded for any of the 13 measurement the determination of user influences is limited. The heating degree days $HGT_{20,12}$ are determined by a heating limit temperature of 12 °C and a target internal temperature of 20 °C. The $HGT_{20,12}$ is then calculated from the difference between the average daytime temperature and 20 °C. The $HGT_{20,12}$ are only counted if the average daytime temperature is lower than the heating limit (here 12 °C) [9].

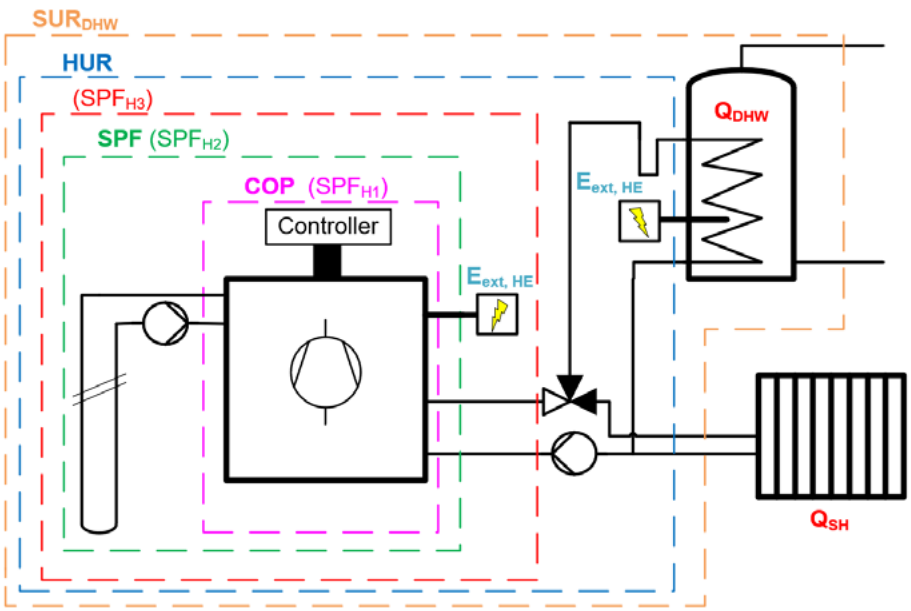


Fig. 1. System boundaries and key figures (*SUR*, *HUR*, *SPF*, *COP*) based on the SFOE [9] and SEPEMO definition [7]

Thermal and electrical energy numbers are measured as numerical integration of several power sensors with a sampling interval of 100 ms. With this approach low sensor costs were combined with high accuracy and the ability to gather rapid changes in the system. The values are then recorded every 10 s, leading to an averaging of 100 datapoints and a small statistical error.

Of course, a discretization error cannot be avoided. This can cause problems if the measured variable changes abruptly. However, it has been shown that for the majority of measurement series a recording interval of 30 s would already be sufficient, since thermodynamic systems tend to change at a slow pace.

The performance values themselves are formed from the effective measured variables according to the established methodology.

By using a volume flow sensor and temperature measurements, the mass flow is determined via the density, where $\rho_w = f(T)$. The heat output for example is then calculated as follows:

$$\dot{Q}_{heat,i} = \dot{m}_w \cdot c_{p,w} \cdot \Delta T = \dot{V}_w \cdot \rho_w(T_{supply}) \cdot c_{p,w}(T_{supply}) \cdot (T_{supply} - T_{return}) \quad (8)$$

The volume flow is measured in the supply pipe. The temperature difference between supply and return flow is determined from two temperature measurements. The formula (9) shows that the temperature measurements are included several times in the calculation. This means that the measurement error of the temperatures has a strong effect on the overall measurement uncertainty of the heat output. For this reason, great importance is attached to temperature measurement that is as accurate as possible. The aim is an overall uncertainty of the target values of <10 %. To reliably achieve this goal, a measurement uncertainty of the temperature measurement (absolute) of ± 0.02 K has to be met. Calibrated PT-100 sensors with four-wire technology are immersed in the flow and thermally decoupled. For redundancy reasons, important temperatures points are measured twice and the sensors are calibrated and immersed in the flow. The basic placement of the sensors in the system can be seen in Fig. 2. However, the real positioning can be slightly different for each case depending on the type of HP-system or building.

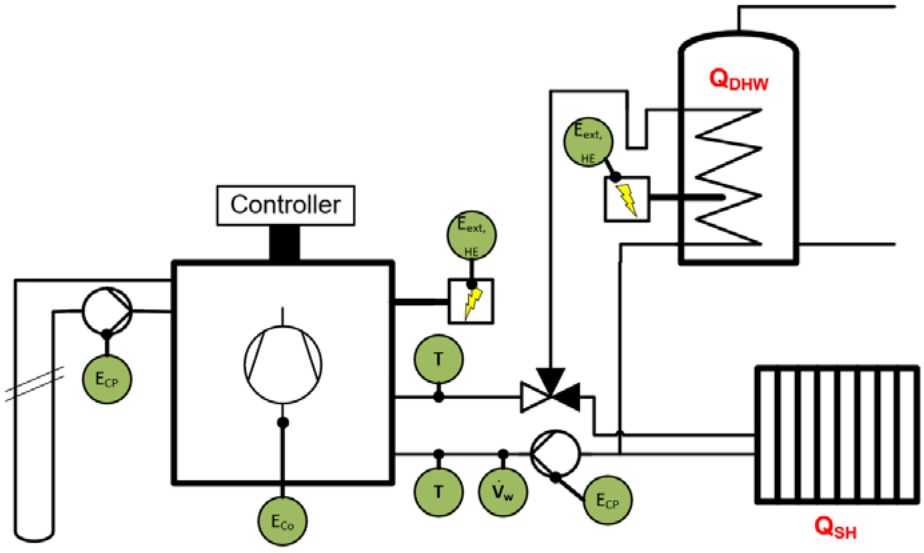


Fig. 2. Basic placement of sensors in a typical heat pump system according to the WPZ [10]

After measurement, the data is automatically read and stored daily on a server in Switzerland for further processing. The storage structure includes 5 different databases and is relational. That means each piece of information is only stored once in one of the five databases. This makes it very easy to keep the data up-to-date and consistent [10].

For data protection reasons, the link to the personal data is made via specially generated ID's, whereby the personal data are stored in the other databases and not apparent in plain language. Furthermore, the database system is also designed to evaluate external measurement data.

As mentioned, every year approximately five new installed heat pump systems are added to the ongoing field study. Arpagaus et al. [10] explained the sequence of a complete measurement and evaluation cycle for a new installation of a system:

1. Application of a customer (who wants to install a heat pump system privately).
2. Calibration of the heat pump with field measuring equipment at the WPZ in Buchs under laboratory conditions.
3. Comparison of laboratory measurements with manufacturer's specifications.
4. Installation of the heat pump system on site, whereby the intended field measuring equipment is also installed.
5. Commissioning of the heat pump system in the presence of an employee of the WPZ.
6. Ongoing measurement of the heat pump system.
7. Comparison and analysis of measured data with laboratory and field test data.
8. Recommendations for optimization and improvements after one year of data collection.
9. Implementation of the proposed optimization in coordination with the customer.
10. Control measurement to record improvements of the heat pump system.
11. Field measuring equipment remains on site with the customer, and data recording is continued.

Inadmissible defects and weaknesses of the heat pump itself are usually detected during laboratory measurements. On the construction site of the building, it should be noted that the installation of the heat pump system as well as its commissioning and handover to the customer is the responsibility of the planning office and the heating installer. The WPZ staff only coordinate the installation of the necessary sensors and data acquisition. Possible errors or defects of the HP systems caused by the installation or commissioning are detected with the help of the data during the measurement phase. Suitable improvement measures or optimizations are suggested to the customer, which then can be carried out under the responsibility of the HP installer.

3. Results, analysis and optimization of current field studies

The results presented in this section include measurements taken in the heating period of 2017/18 and 2018/19 (two years) respectively. In total 13 heat pump devices have been analyzed and compared within the current study, out of which 7 are Air/Water heat pumps (AWHP) and 6 are Brine/Water heat pumps (BWHP) with vertical boreholes. Overall 9 out of 13 devices are operated as variable speed compressors. The data was evaluated from standard heat pump devices that have not yet been optimized based on these field studies.

Fig. 3 shows the connection between the annual coefficient of performance (SPF) and different design temperatures [9].

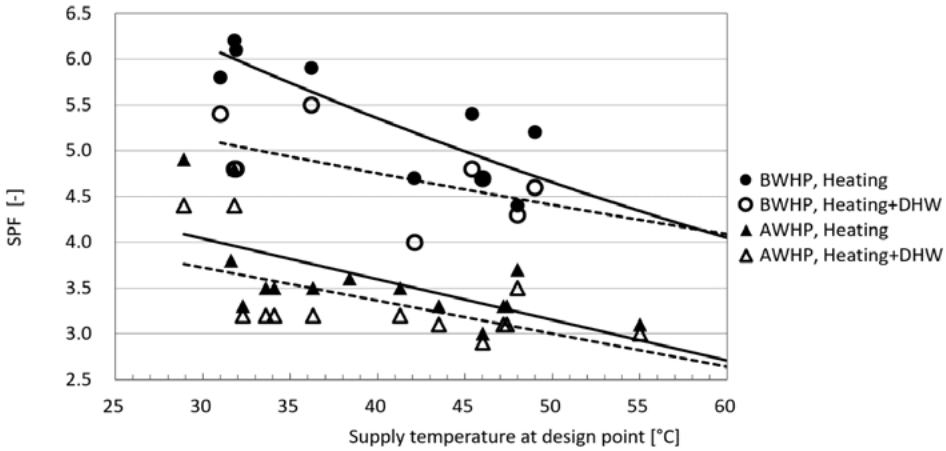


Fig. 3. Efficiency (*SPF*) of Air/Water heat pumps (AWHP) and Brine/Water heat pumps (BWHP) depending on predefined heating and heating+DHW curves.

The data is displayed as a function of the heating curve pre-set on the heat pump. It can be seen that Brine/Water heat pumps in new buildings (supply temperature of approx. 30 °C at the design point) achieve an annual efficiency (*SPF)* of more than 6 in pure heating operation. In combination with domestic hot water (DHW) production, the *SPF* drops to approx. 5.2. In contrast, Air/Water heat pumps achieve an efficiency of about 4.0 for heating, and 3.7 for heating+DHW production.

As expected, the efficiency decreases with higher supply temperatures. Especially refurbished buildings need higher supply temperatures due to their radiator heating system. However, with a *SPF* of over 4.0, BWHP systems are still very suitable for such renovated buildings. Even compared to new variable-speed AWHP, BWHP still show a significant efficiency advantage of approximately 30 %.

Table 2 provides a more detailed overview of the evaluated performance of AWHP and BWHP by heating and heating+DHW application.

Table 2. Annual Coefficient of Performance (SPF) for different AWHP and BWHP applications [9]

Supply temperature at design point	35 to 30°C (New building)	45 to 40°C (Renovation)	55 to 55°C (Old building)
Heating AWHP	3.7	3.3	2.9
Heating BWHP	5.7	5.0	4.4
Heating + DHW AWHP	3.5	3.1	2.8
Heating + DHW BWHP	4.9	4.6	4.3

As already mentioned, it is essential to use comparable system boundaries in practice when matching systems. Significant differences can be identified between the efficiency of heat production and the heat actually used especially when it comes to DHW production. This is partly caused by the use of electric heating elements (e.g. Legionella circuit), but mainly due to storage losses. Fig. 4 shows a comparison of the average annual coefficient of performance *(SPF)*, heat utilisation ratio *(HUR)* and system utilization ratio *(SUR_{DHW})* for AWHP and BWHP systems [9].

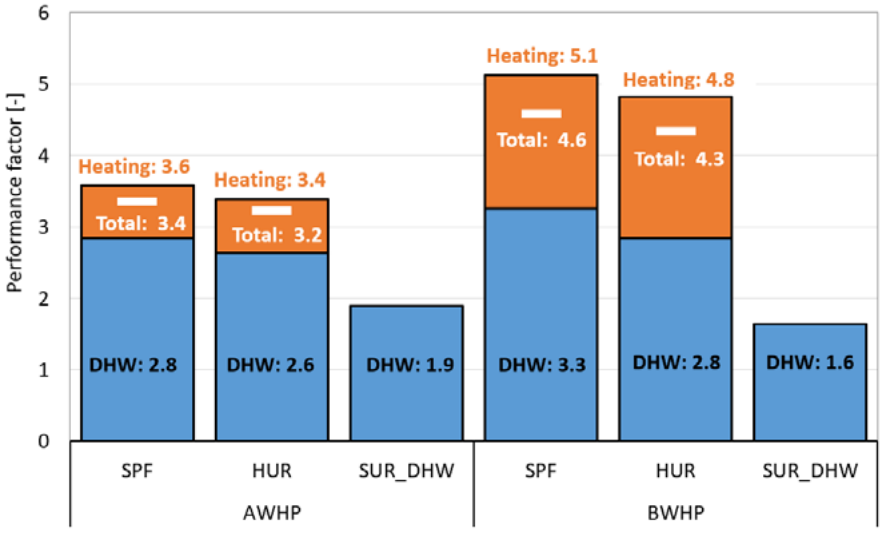


Fig. 4. Comparison of averaged *SPF*, *HUR* and SUR_{DHW}

As expected, the efficiency of DHW production is 17.5 % to 19 % lower than the overall efficiency for heating+DHW production due to the higher sink temperatures.

For BWHP this difference is much bigger (28 % to 35 %) because of lower source temperatures compared with AWHP in summertime. It is also remarkable that the *HUR* is 0.1 or 0.3 points lower than the *SPF*. This is mainly due to the electric heating elements for Legionella control and the circulation pumps. No electric heating element had to be used to support the heating system of any heat pump investigated during the period under consideration. This also applies to the cold periods at the end of February, beginning of March 2018 which showed outside average temperatures between -6 to -9 °C and up to 2 K below the design temperature.

For conceptional reasons, the system utilization ratio *(SUR_{DHW})* can only be determined for DHW production and it is considerably lower than the *HUR*. This is primarily caused by storage losses, especially for buildings with a low DHW demand. When it comes to single-family houses the overall system efficiency suffers particularly when a DHW circulation is used to keep the distribution lines warm. Therefore, hot water circulation is clearly not recommended for such applications from an energetical point of view.

The detailed data recording of several measured variables during more than one heating period offer the determination of various optimization possibilities and the comparison of different objects with regard to the heating settings.

An important optimization scope of heat pump systems is the proper adjustment of the heating curve and the heating limit respectively. Considerable differences were found between properties within the same building standard. New buildings in particular, were found to have a heating curve that is too high with respect to the outside temperature. Nevertheless, only three heating curves out of 13 monitored objects were adjusted downwards whereas two were increased. This is because many residents were satisfied with the current setting and no adjustment was desired. By integrating an intelligent heating curve with averaged outside temperatures, the annual heating energy demand can be reduced distinctly. One of the monitored new buildings shows theoretical potential savings of 6 % of the annual energy demand by solely adapting the upper heating limit without affecting comfort [9]. The upper heating limit is defined as the ooutside temperature at which heating is automatically turned off.

In a concrete example of an implemented heating curve adjustment, a rather low *SPF* of 2.6 at a daily mean temperature of 7 °C in the period from 10/01/2017-12/17/2017 was successfully increased to *SPF*=3.7 (42 %) in the second recording period until 10/31/2018.

A considerable optimization potential can also be found in DHW production. AWHPs benefit greatly from a larger charging timeframe at midday with a previous charging delay that leads to a reduced set temperature. Since temperatures at noon can be over 10 K higher than in the morning, charging efficiency can be increased by 10 to 20 % [9]. Although this optimization measure seems obvious, only in one HP-system controller out of 13 this measure was implemented to make use of a smaller temperature-lift at noon.

Around 50 % of the investigated heat pump systems use only electric auxiliary heating (heating rod) to perform their weekly Legionella program by heating up the water tank to over 60 °C. Three systems first make use of the compressor to support charging, which would be an obvious method to reduce the electric energy demand. In a typical example, 180 kWh electric energy can be saved annually by implementing this simple software modification to always preheat the domestic hot water using the compressor before switching to auxiliary heating, with no further costs.

4. Conclusions

Between 1996 and 2017 more than 600 heat pump systems, mainly in single-family houses, were investigated in the field in Europe. On average, slightly more (approx. 60 %) brine/water heat pump (BWHP) systems were recorded than air/water heat pump (AWHP) systems. Although the amount of data collected over these years is important, it can only be used in part for comparison, due to different definitions of key figures and system boundaries or long sampling intervals.

Detailed analyses of temporal processes are possible by recording power values instead of energy values. This requires short sampling intervals (<30 s) in order to adequately map dynamic processes.

Great importance is attached to the measurement of temperature because of its major influence on the overall uncertainty. Therefore, the supply and return temperatures are measured with an uncertainty of ± 0.02 K (absolute) using PT-100 sensors and four-wire technology. Together with the prior calibration of the whole field measuring equipment in the laboratory, an overall uncertainty of the target values (*COP, SPF*) of <10 % was achieved. Of course, these measurement accuracies require relatively complex and expensive measurement equipment.

However, such precision is not always required or necessary. In the field of building performance estimation, cheaper and simpler solutions can be found recently.

Frei et al. [11] described a concept that combines a variety of different sensors for temperatures, humidity, heat flux, CO_2 etc. embedded as a wireless sensor network (WSN) with open source software platform for communication and data analysis. Although the field of application showed is different, there is common ground and some ideas may be useful for future solutions. Such an installation would help to identify major errors in the applications.

The current study, which now includes almost 20 heat pump systems in the field, clearly shows strong dependence of the annual performance factor *(SPF)* on the supply temperature and the selected heat source. Therefore, AWHPs in new buildings reach an average *SPF* of 3.7 for floor heating (35 °C) whereas BWHPs attain a *SPF* of 5.7. With higher supply temperatures of around 50°C found in old buildings average SPF values of around 2.9 for AWHP and 4.4 for BWHP were measured, respectively.

Combined systems for heating and domestic hot water (DHW) production show 3 to 9 % lower coefficients of performance (e.g. SPF) values due to the increased supply temperatures.

After investigation of the monitored heat pump systems for more than one heating period, various optimization potentials were identified, such as intelligent heating curves or Legionella routines. By implementing these simple software updates, the charging efficiency of DHW could be increased by 10 to 20 %. Typical optimization measures are:

- Adjustment of the heating curve and heating limit.
- Increased charging timeframe at midday.
- Preheating of DHW with the compressor.

In the field of refurbished buildings BWHPs are recommended. For drawing the correct conclusions when comparing heat pump systems, it is crucial to use the correct system limits and boundaries. The current field study shows, that the investigated heat pumps work well overall, but there is still potential of improvement, especially when it comes to DHW production.

Acknowledgements

The results published in this report were funded and obtained in close cooperation with the Swiss Federal Office of Energy (SFOE). The content and conclusions of this report are sole responsibility of the authors.

Nomenclature

AWHP	Air/water heat pump	
BWHP	Brine/water heat pump	
$c_{p,w}$	Specific heat capacity of water	[J/kg-K]
COP	Coefficient of performance	[-]
DHW	Domestic hot water	
E_{Co}	Electrical energy of the heat pump compressor	[kWh]
$E_{CP,Sink}$	Electrical energy of the circulating pump at the heat sink	[kWh]
E_{DHW}	Electrical energy of the HP in DHW operation	[kWh]
$E_{ext,HE}$	Electrical energy of the external heating elements	[kWh]
E_{RA}	Energy reference area of the building	[m^2]
E_{tot}	Electrical energy input of the entire heat pump system	[kWh]
FAWA	Field analysis of heat pump installations	
GWHP	Groundwater/water heat pump	
$HGT_{20,12}$	Heating degree days for 20, 12 °C (heating limit)	[°C]
HP	Heat pump	
HUR	(WNG) Heat utilization ratio according to definition of SFOE	
ISE	Frauenhofer Institute for Solar Energy Systems	
NTB	University of Applied Sciences of Technology Buchs	
Q_{DHW}	Thermal energy of the HP in DHW operation	[kWh]
Q_{DHWU}	Thermal energy of domestic hot water usage (DHWU)	[kWh]
Q_{HD}	Specific heating demand	[kWh/m^2]
Q_{SH}	Thermal energy of the HP in space heating operation	[kWh]
HR_{DHW}	Specific domestic hot water heat requirement	[kWh/m^2]
SEPEMO	SEasonal PErformance factor and Monitoring	
SFOE	Swiss Federal Office of Energy (BFE)	
SPF	(JAZ) Seasonal performance factor according to definition of SFOE	[-]
SPF1-2	(JAZ1-2) Seasonal performance factors according to FAWA bound	[-]
$SPF_{H1\text{-}H4}$	Seasonal performance factors according to SEPEMO boundaries	[-]
SPF_{hps}	Seasonal performance factors according to SPTRI 2007 boundaries	[-]
SUR_{DHW}	System utilization ratio according to SFOE	[-]
THR	Total specific heat requirement (Heating and DHW)	[kWh/m^2]
T_{return}	Return temperature	[°C]
T_{supply}	Supply temperature	[°C]
WPZ	Heat pump test center (Buchs, CH)	
η_{DHW}	Thermal efficiency of domestic hot water usage	[-]
$\dot{m}_w$	Water mass flow	[kg/s]
$\dot{Q}_{heat,i}$	Thermal output power i	[kW_{th}]
$\dot{V}_w$	Water volume flow	[m^3/s]
$\rho_w(T)$	Density of water	[kg/m^3]
ΔT	Temperature difference	[K]

References

[1] Fachvereinigung Wärmepumpen FWS, «Statistik 2018,» FWS, Bern, 2019.

[2] M. Erb, P. Hubacher und M. Ehrbar, «FAWA Feldanalyse von Wärmepumenanlagen,» BFE, Bundesamt für Energie, 2004.

[3] M. Miara, D. Günther, T. Kramer, T. Oltersdorf und J. Wapler, «Wärmepumpen Effizienz, Messtechnische Untersuchung von Wärmepumpenanlagen zur Analyse und Bewertung der Effizienz im realen Betrieb,» ISE, Fraunehofer Institut für Solare Energiesysteme, Freiburg, 2011.

[4] M. Miara, D. Günther, R. Langner, S. Helmling und J. Wapler, «WP Monitor, Feldmessung von Wärmepumpenanlagen,» ISE, Frauenhofer Institut für Solare Energiesysteme , Freiburg, 2014.

[5] R. Nordman, K. Andersson, M. Axell und M. Lindahl, «Calculation methods for SPF for heat pump systems for comparison, system choice and dimensioning,» Technical Research Institute of Sweden, Sweden, 2010.

[6] "SEPEMO-Build.," SEPEMO, 31 May 2012. [Online]. Available: http://sepemo.ehpa.org/. [Accessed 30 September 2019].

[7] C. P. Gleeson und R. Lowe, «Meta-analysis of European heat pump field trial efficiencies,» Elsevier, London, 2013.

[8] F. Auer und H. Schote, «Schlussbericht Zweijähriger Feldtest Elektro – Wärmepumpen am Oberrhein: Nicht jede Wärmepumpe trägt zum Klimaschutz bei zumKlimaschutz bei Erdreich-Wärmepumpen mit positiver Ökobilanz Kritis-che Bewertung von Luft-Wärmepumpen.,» Lahr, 2012.

[9] M. Prinzing, M. Berthold und M. Eschmann, «Jahresbericht WP-Feldmessung 2018,» BFE, Bundesamt für Energie Schweiz, Bern, 2019.

[10] C. Arpagaus, M. Berthold und M. Eschmann , «Jahresbericht WP-Feldmessung 2017,» BFE, Bundesamt für Energie Schweiz, Bern, 2018.

[11] M. Frei, C. Deb, R. Stadler, Z. Nagy und A. Schlueter, «Wireless sensor network for estimating building performance,» Elsevier, Zürich, 2020.

13th IEA Heat Pump Conference
April 26-29, 2021 Jeju, Korea

Theoretical investigation of high-temperature heat pump cycles for steam generation

Frédéric Bless*, Cordin Arpagaus, Stefan Bertsch

NTB University of Applied Sciences of Technology Buchs, Werdenbergstrasse 4, 9471 Buchs, Switzerland

Abstract

This paper presents a thermodynamic analysis of different heat pump cycles that are capable of delivering 150 °C (4.8 bar) saturated steam from 80 °C recovered waste heat. A detailed comparison of the advantages and disadvantages of the following cycles is presented:

1. Transcritical cycle using butane (R600),
2. Classical closed-cycle using low GWP hydrofluoroolefin (HFO) refrigerant (e.g. R1233zd),
3. Reversed Brayton cycle using carbon dioxide (R744) or argon (R740),
4. Closed-cycle using R600 or R1234ze(Z) with flash tank and additional steam compressors for mechanical vapor recompression, and
5. Open-cycle using water (R718) as working fluid and multiple steam compression stages.

Performance parameters such as COP, compressor efficiency, pressure ratio, steam generation rate, cycle controllability, safety, running and investment costs, and component availability are evaluated and discussed. Under the assumed operating conditions (e.g. temperature lift of approx. 70 K), the theoretically calculated COPs of these cycles range between 1.3 and 3.1. In the transcritical R600 cycle, only a small part of the heat can be used to generate steam, limiting the COP to about 1.3. However, the efficiency can be increased by parallel hot water generation in a second gas cooler. Decisive for a system with a classical closed-cycle heat pump (COP of 1.8) are the use of an environmentally friendly refrigerant (e.g. HFO) and a temperature-resistant compressor with cooling function and stable lubrication. The Reversed Brayton cycle (COP of 2.3) requires a compressor with very high isentropic efficiency (> 0.9) in order to achieve reasonable efficiencies. Depending on the application, a temperature glide on the heat source can be advantageous to transfer more heat. The availability of oil-free compressors is crucial for open steam compression cycles (COP of 3.1). Their achievable pressure ratio determines the number of compression stages. Overall, the study contributes to a better understanding of steam generating heat pump cycles for industrial heating processes and it highlights the current research and technological gaps.

© HPC2020.
Selection and/or peer-review under responsibility of the organizers of the 13th IEA Heat Pump Conference 2020.

Keywords: high-temperature heat pump; heat pump; steam generation; cycle analysis, transcritical heat pump

1. Introduction

1.1. Steam generation heat pumps (SGHP)

Electrification of heat generation in the industrial sector is a trend, which is continuously growing. Heating with fossil fuel has a higher environmental impact. Furthermore, due to the decreasing cost of renewable electricity and the introduction of a carbon tax in some countries, heating by fossil fuel is not always the cheapest solution anymore [1]. Heat pump technology using energy from waste heat, ground heat or air, offers

* Corresponding author. Tel.: +41 81 755 31 48
E-mail address: frederic.bless@ntb.ch

an efficiency that is much higher than a heating system based on combustion [2]. However, heat pump systems are limited in the maximal achievable supply temperature. Thus, high-pressure steam (e.g. 15 bar and higher) cannot easily be generated efficiently by heat pump systems, but low-pressure steam (e.g. < 6 bar) can be produced by heat pump processes, especially if a heat source with a high temperature (e.g. waste heat of 60 °C to 80 °C) is available. The advantages of steam compared to hot water are especially the much better heat transfer due to the latent heat release during condensation and the easier temperature control [3].

Mechanically driven vapor compression heat pump systems for steam generation is an evolving technology that is becoming more widespread in the coming years to reduce primary energy consumption and greenhouse effect gas emission [4]. A characteristic constructive difference to a conventional heat pump is the condensing part. The generated steam is either used directly or further recompressed by mechanical vapor recompression (MVR) [5]. A flash tank is normally used as a reservoir for the two-phase water.

The advantages of a steam generation heat pump (SGHP) are in particular the recovery of industrial waste heat in the range of approx. 60 °C to 100 °C and the conversion into low-pressure steam (e.g. < 6 bar) for many potential application fields, e.g. distillation of alcohol, condensation, disinfection, sterilization of food and beverages, concentration of liquids and juices, humidification, or drying processes [4, 6, 7, 8]. Steam generation takes place at a relatively low temperature when using waste heat, thus avoiding exergy losses compared to the combustion of fossil fuels at high temperatures [6, 7]. Moreover, a SGHP can generate more heat from the same primary energy source than a fossil-fueled boiler [9].

1.2. Literature review on SGHP

Several authors investigated the suitability of SGHP by thermodynamic simulations [2, 10, 11, 12]. Experimental investigations are rather rare. Table 1 summarizes a selection of experimental research studies on SGHP categorised by organization, heating capacity, heat source and steam temperature, heat pump cycle, compressor, refrigerant, and COP.

Table 1. Selection of experimental research studies of steam generation heat pumps (SGHP)

Organization, country	Heating capacity (kW)	Heat source temperature (°C)	Steam temperature (°C) (flow rate kg/h)	Heat pump cycle, compressor	Refrigerant	COP (source/sink temperature °C)	Reference (year)
Korea Institute of Energy Research (KIER)	300	60	128 (422)	HTHP + flash tank, piston	R245fa	n.a.	Chang et al. (2016) [13]
	100	70	120	HTHP + flash tank, open screw	R245fa	3.05 (70/120)	Wang et al. (2018) [14]
	25	60	104 - 123	HTHP + IHX + flash tank + valve	R245fa	~ 3.5 (60/105)	Lee et al. (2017) [15]
Seoul National University, Korea	6 - 8	60 - 70	115 - 125 (10.8)	HTHP, piston	R245fa	2.95 (60/125) 3.59 (60/115)	Kang et al. (2019) [9]
	6 - 12	60 - 80	115 - 125	HTHP + steam reservoir + MVR	R245fa	3.39 (80/125) 2.72 (60/115)	Yoo et al. (2017) [3]
Tokyo Electric Power, Mayekawa, Japan	400	80 - 90	130	HTHP, screw	R601 (pentane)	4.5 (80/130)	Yamazaki and Kubo (1986) [16]
Kobe Steel, Ltd., CRIEPI, and electric companies, Japan	660	35 - 70	165 (890)	HTHP + MVR, screw	R134a/R245fa (SGH165)	2.5 (70/165)	Kaida et al. (2015) [4]
	380	25 - 65	120 (20)		R245fa (SGH120)	3.2 (65/120)	Kuromaki (2012) [8]
Mayekawa, Waseda University, Japan	300	80	100 - 180 (thermal oil)	Transcritical HTHP, centrifugal	R600 (butane)	3.5 (80/180) calculated	Kimura et al. (2018) [17]
Shanghai Jiao Tong University, China	285	75 - 85 (evaporation)	111 - 150 (condensation)	VHTHP + flash tank, twin-screw	R718 (water)	6.10 (85/117) 1.96 (85/150)	Wu et al. (2020) [18]
ECN, IBK, Bronswerk, Smurfit-Kappa, Netherlands	160	60	125 (2.4)	HTHP + IHX + subcooler, piston	R600 (butane)	1.9 (60/125)	Wemmers et al. (2017) [19]
Olvondo Technology, TINE dairy, Norway	449	80 - 90	184 (10)	HTHP (reversed Stirling cycle), piston	R704 (helium)	2.1 (85/183)	Tveit (2017) [20]
NTNU, SINTEF, Norway	20	25 - 35	115	HTHP cascade + IHX	R290/R600 (propane/butane)	2.1 (25/115)	Bamigbetan et al. (2019) [21]
AlterECO project, EDF, France	200	35 - 60	80 -140 (condensation)	HTHP + IHX + subcooler, two scroll	ECO3 containing R245fa	2 - 3 (50-60/125) (evap/cond)	Bobelin et al. (2012) [22]
PACO project, Uni Lyon, EDF, France	380	85 - 95	130 -140 (condensation)	HTHP + flash tank, twin-screw	R718 (water)	~5.5 (94/121)	Chamoun et al. (2012) [23, 24]
National Research Council Canada	45	55 - 80	103.5 - 135.5	HTHP + IHX, piston	R113 & R123 (ozone depleting)	2.7 (75/135, R113) 3.6 (60/120, R123)	Linton (1990, 1993) [25, 26]

The Korea Institute of Energy Research (KIER) has researched on SGHP since about 2013. Lee et al. [15] investigated a 25 kW HTHP for the production of low-pressure steam in a suitable cycle configuration. An internal heat exchanger (IHX) was implemented in the HTHP cycle to ensure superheating of the refrigerant R245fa. The generated heat from the HTHP was transferred in the condenser to a circulating pressurized water circuit. By reducing the pressure, part of the water was converted into steam (flashing method). A steam reservoir separated the steam and the water. In an open circuit configuration, additional water is supplied to the flash tank. With this configuration, steam temperatures of 104 to 123 °C (1.2 to 2.2 bar) were reached. At 60 °C heat source and 105 °C steam temperature a COP of about 3.5 was achieved.

Wang et al. [14] developed a larger SGHP that recovered waste process heat and generated steam at 120 °C. A flash tank served as phase separator. By optimizing the experimental setup, a heating capacity of 101.4 kW and a COP of 3.05 was achieved at 70 °C heat source temperature.

Chang et al. [13] studied the design of a high-temperature condenser for a SGHP with R245fa and 300 kW capacity. For saturated steam of 128 °C (2.3 bar) a steam production rate of 0.422 t/h was evaluated.

Yoo et al. [3] from the Seoul National University designed a laboratory-scale SGHP system and observed a 25% and 80% increase in COP and heating capacity, respectively, with increasing heat source temperature from 60 to 80 °C. The SGHP showed a much better performance compared to a steam boiler.

From the same research group, Kang et al. [6] reviewed recent research studies on SGHP systems. More recently, Kang et al. [9] conducted an experimental study on the performance of a laboratory-scale SGHP with IHX for performance increase. The system consists of an HTHP with a second stage using a flash tank and MVR. The COP was 2.95 at 125 °C, 3.24 at 120 °C and 3.59 at 115 °C steam temperature. Up to 10.8 kg/h steam was generated. The integration of an IHX could increase the amount of steam by 22%.

In Japan, already in 1985, the researchers Yamazaki and Kubo [16] presented a 400 kW heat pump operated with pentane (R601) providing condensation temperatures of up to 135 °C. The heat pump generated low-pressure steam of 130 °C using waste heat of 90 °C as heat source. A variable-capacity screw compressor was used with a motor power of 75 kW. A COP of 4.5 was reached at 80 °C evaporation and 135 °C condensation.

In 2011, Kobe Steel Ltd., CRIEPI (Central Research Institute of Electric Power Industry), and Japanese electric companies have jointly developed and commercialized the KOBELCO Steam Glow Heat Pump (SGH) SGH120 and SGH165, which enable steam temperatures of 120 °C and 165 °C (6 bar). The rated performance of SGH120 is 520 kg/h of steam with a COP of 3.5 at 65 °C heat source [8]. The SGH165 uses an additional water flash tank and MVR to achieve a higher temperature and steam pressure. About 890 kg/h of steam at 165 °C is generated with a COP of 2.5 when using waste heat of 70 °C. Kaida et al. [4] from CRIEPI investigated experimentally the steam generation rate, energy efficiency and controlled performance of the SGH165 under various operating conditions. More recently, Kaida et al. [27] also presented first experimental results of R1224yd(Z) as an environmentally friendly alternative to R245fa, which is to be phased out in the foreseeable future due to high Global Warming Potential (GWP) of 858. At operating point W50/W95, R1224yd(Z) exhibited a 3% higher heating capacity and 12% higher COP compared to R245fa.

Latest developments in heat pump technology in Japan include a transcritical butane (R600) heat pump with a target maximum temperature of 200 °C and a calculated COP above 3.5 at 80 °C heat source (i.e. waste heat). In a joint project with Mayekawa and Waseda University, Kimura et al. [17] developed such a prototype for heating thermal oil from 100 ˚C to 180 ˚C. The experimental setup consists of two oil-free centrifugal compressors with active magnetic bearings. The gas cooler has a capacity of 300 kW. Due to the flammability of the refrigerant, the test apparatus is explosion-proof and enclosed in a housing with active ventilation. Experimental performance evaluation of the system is ongoing.

For condensation temperatures beyond 140 °C to 150 °C, water (R718) is becoming increasingly efficient and very attractive compared to other refrigerants. There are a few studies on HTHPs using water as refrigerant, as summarized by Bertsch et al. [28]. Bless et al. [2] theoretically analyzed different steam generation methods with open cycles. Results showed that water vapor compression methods using water injection require about three times less energy than direct heating systems (i.e. gas-fired boilers or electrical heating).

Shibata et al. [7] from Hitachi proposed an SGHP with water as refrigerant and a four-stage centrifugal compressor with water spray intercooling. The proposed system generates 5'000 kg/h of steam at 130 °C by recovering the waste heat from 60 °C hot water. A test apparatus was developed to validate the first stage of the steam compressor at sub-atmospheric pressure, i.e. compression from 0.2 bar (65 °C) to 0.4 bar (148 °C).

In China, Wu et al. [18] from Shanghai Jiao Tong University investigated the performance of a very high temperature heat pump (VHTHP) prototype using water as refrigerant. An oil-free twin-screw water vapor compressor with water injection was developed. With condensing temperature rising from 117 °C to 150 °C and constant evaporating temperature of 85 °C, the COP decreased from 6.10 to 1.96. The heating capacity decreased from 285 kW to 162 kW, respectively.

In France, Bobelin et al. [22] from EDF (Électricité de France) were among the first to build a 200 kW VHTHP pilot plant in 2012, which can supply hot water of up to 140°C, or low-pressure steam. The heat pump operates with IHX, subcooler, and two parallel scroll compressors. ECO3, a refrigerant mixture containing R245fa, was used. COPs of 2 to 3 were achieved at 125 °C condensation and 50 °C to 60 °C evaporation temperature. Chamoun et al. [23, 24] presented experimental investigations of a water (R718) vapor HTHP pilot plant in 2012 for industrial heat recovery. After condensation, the water was collected in an accumulator and was expanded to low pressure in a flash tank. The main technical feasibility was demonstrated attaining a condensation temperautre of up to 145 °C. Waste heat of 85 °C to 95 °C was used as source providing a heat output of more than 380 kW. At 94 °C source and 121 °C sink temperature, a COP of about 5.5 was measured.

In the Netherlands, Wemmers et al. [19] designed a pilot R600 heat pump able to deliver low-pressure steam of up to 2.4 bar (125 °C) from 60 °C waste heat at a COP of 1.9. The HTHP was developed from commercially available components to ensure quick market introduction. The heat pump configuration also includes a subcooler in order to heat process water at 70 °C.

In Norway, in a cooperation project between NTNU and SINTEF, Bamigbetan et al. [21] reported on the experimental performance of a 20 kW cascade HTHP with propane (R290) in the low-stage and butane (R600) in the high-stage for high temperature heating up to 115 °C. The heat pump was found to have an average COP of 2.1 for a temperature lift of 98 to 101 K and 3.1 for 58 to 72 K, which makes it a better alternative to gas boilers at current carbon emissions and electricity cost rates.

Tveit [20] from Olvondo Technology AS presented an industrial HTHP capable of producing steam up to 10 bar (184 °C) using 80 °C to 90 °C from district heating as the heat source. The so-called SPP HighLift heat pump is based on a reversed Stirling cycle with helium (R704) as working medium, which is continuously in the gas phase. A closed hot water circuit heats the feed water to the saturated steam temperature. In a case study in a dairy plant, the heat pump generates steam for sterilizing UHT milk (for long-life products) at 135 °C to 150 °C for a few seconds. Simulated data showed a heat capacity of 449 kW and a COP of 2.1 at 183 °C heat sink and 85 °C heat source temperature.

Finally, it is worth mentioning the works of Linton [25, 26] from the National Research Council Canada from 1990, who presented a 45 kW steam generating HTHP test facility running with R113 (ozone depletion potential ODP of 0.85) and R123 (ODP of 0.03). This was before the Montreal Protocol entered into force, which banned ozone-depleting substances. The heat pump contained an IHX and a piston compressor with a water-cooled oil cooler. The test stand operated with 55 °C to 80 °C hot water as heat source and produced saturated steam from 103.5 °C to 135.5 °C. The COP with R113 was 2.7 at 75 °C/135 °C and 3.2 with R123 at 65 °C/135 °C.

In summary, the above literature review shows that experimental research on SGHP has intensified worldwide in recent years. Most studies are based on laboratory and prototype tests with heating capacities in the range of a few 100 kW. The majority of pilot plants generate steam temperatures of 130 ± 20 °C. Often a multi-stage configuration with one HTHP and one condenser with pressurized water circuit, flash tank and MVR is used. The average COP is around 3.2 at a temperature lift of 60 K using 70 °C waste heat.

As can be seen, R245fa is predominantly used in SGHP as refrigerant as it offers a suitable temperature range. For subcritical processes, a high critical point for two-phase heat exchange at the steam generation temperature is crucial. However, because of its high GWP of 858 researchers turned to the use of natural refrigerants like hydrocarbons (R600) or water (R718). New synthetic hydrofluoroolefins (HFO) and hydrochlorofluoroolefins (HCFO) with very low GWP such as R1233zd(E), R1224yd(Z) and R1336mzz(Z) are also preferred and investigated. More details on HTHP can be found in Arpagaus et al. [29, 30].

Beside mechanically driven vapor compression heat pumps, thermally driven absorption cycles are also an option for waste recovery and steam generation. As these cycles are not the focus of this study, reference is made to relevant review literature for further details [31, 32].

1.3. Goals of this study

The goal of this study is to analyze different heat pump cycles in order to produce saturated steam at 150 °C (4.76 bar). The influence of various refrigerants, heat source temperatures, and isentropic efficiency of the compressor(s) on their efficiency, cost, and complexity are investigated theoretically. This study compares the following five different heat pump cycles:

(1) ***Transcritical cycle:*** A transcritical cycle is when the heat sink temperature is above the critical temperature of the refrigerant. The heat is suppled via a gas cooler (not a condenser) with a temperature glide. The glide can be an asset in terms of efficiency for certain applications. However, when it comes

to evaporating a fluid, a temperature glide is a disadvantage. In this study, the natural refrigerant butane (R600) is used to generate heat above 155 °C, making the cycle transcritical.

(2) ***Classical closed-cycle HTHP:*** A HTHP is simulated using the common subcritical closed-loop cycle. The condensation temperature was fixed at 155 °C. At this temperature there are only a few refrigerants available, which can be used below their critical temperature. R1233zd(E) was used in this simulation as is it one of the few low GWP HCFO refrigerants with a critical temperature higher than 150 °C.

(3) ***Reversed Brayton cycle:*** A reversed Brayton cycle, also known as gas refrigeration cycle or Bell Coleman cycle, was simulated as well. In a reversed Brayton cycle, the refrigerant stays in gaseous state. In order to use refrigerants that are in the gas state at the low temperature of the heat source, the refrigerants used in the simulation were R744 (CO_2) and R740 (argon).

(4) ***Closed-cycle heat pump with mechanical vapor recompression:*** As only a few refrigerants are subcritical up to 155 °C a combined cycle was simulated, consisting of a low-stage HTHP creating steam at temperatures between 90 °C to 130 °C and a second-stage steam recompression system. This temperature was then fixed to 110 °C in order to optimize the COP while keeping the number of compression stages to two. Depending on the pressure ratio of the steam compressor, multiple compression steps are necessary to reach the desired high pressure. The refrigerants used in the HTHP simulations were R600, R1234ze(Z), and R1233zd(E). The cycle is called high temperature heat pump with mechanical vapor recompression (HTHP with MVR).

(5) ***Open-loop water heat pump:*** This cycle first expands the water to the necessary low pressure in order to evaporate it directly by the heat source. The steam is then re-compressed to reach the desired temperature at the saturation state. Depending on the evaporating pressure and the pressure ratio of the steam compressor, multiple compression stages and inter-cooling sections are needed.

1.4. Refrigerants

The refrigerants studied need to be compatible with the future standards otherwise this study will contain information which will be quickly irrelevant. The European directive on mobile air conditioning systems (MACs) (Directive 2006/40/EC) will prohibit the use of F-gases with a global warming potential (GWP) more than 150 times greater than carbon dioxide [33]. The refrigerants used in the simulations are R1233zd(E), R1234ze(Z), R600 (butane), R718 (water), and R744 (CO_2) with a GWP of less than 10. Some refrigerants like R600a (isobutane) were not simulated because they have very similar properties to the ones mentioned above. Table 2 shows some properties of these refrigerants.

Table 2. Properties of the refrigerants used in this simulation study. ODP = Ozone Depletion Potential (R11 is the ODP reference of 1), GWP = Global Warming Potential (CO_2 is the GWP reference of 1), ASHRAE Standard 34 ranks the toxicity (A, B) and the flammability (1, 2L, 2, 3) of a refrigerant.

Refrigerant	ODP	GWP	Safety group
R1233zd(E)	0.00034	1	A1
R1234ze(Z)	0	6	A2L (slightly flammable)
R600 (butane)	0	4	A3 (flammable)
R718 (water)	0	0.2	A1
R744 (CO_2)	0	1	A1

2. Methodology

To compare the cycles, saturated steam is generated at 150 °C (4.762 bar), and the initial water state is assumed to be 10 °C at 1 bar. The generation of steam is split into two heat exchangers. First, the water is compressed to its evaporating pressure, then the first heat exchanger preheats the water to the evaporating temperature, and finally the second heat exchanger evaporates the water.
Some cycles use steam compression, which compresses the steam to the final state. For example, the open-loop water cycle is different, it first expands the water to a lower pressure, evaporates it, and then compresses it. An IHX is used in some cycles to recover some energy from the subcooling to superheat the refrigerant. The superheating at the compressor inlet is fixed at 10 K for the HTHP and the HTHP with MVR cycles and to 14 K for the transcritical cycle using R600, to avoid wet compression.

The COP of a cycle corresponds to the ratio of the enthalpy difference between the final water state (saturated steam at 150 °C, 4.76 bar) and the initial water state (10 °C, 1 bar) and the work needed by the compressor(s). Each compressor work is calculated by the enthalpy difference between the enthalpy h_1 at the outlet of the compressor and the enthalpy h_0 at the inlet (compressor work = $(h_1 - h_0)$). The outlet enthalpy depends on the isentropic efficiency of the compressor (η_{is}).

EES (Engineering Equation Solver, from F-Chart) is used to simulate the different cycles. However, code for the Reversed Brayton could not converge, thus a self-made Python code using the Coolprop library for the refrigerant data was used instead. The following assumptions are made:

- Pinch point of 5 K in every heat exchanger
- Isentropic efficiency of 0.75 (if not otherwise specified)
- No heat losses in the system (e.g. pipes, heat exchanger, etc.) and no pressure losses
- No energy consumption of water pump(s) (negligible compared to the compressor power)
- Constant temperature glide of 20 K on the heat source
- In the case where heat is delivered at higher and lower temperature than 155 °C, only heat to create the steam is considered (5 K pinch point) and the rest of the energy is used to warm the water from the initial temperature to the final temperature before the evaporation.
- The fresh water is first pumped to its final pressure for all cycles except for the HTHP with MVR cycles and for the open loop R718 cycle (see Figure 1 for more details on the cycles).
- Fixed pressure ratios for steam compressors with a maximum of 2.5. In case of steam compression, the number of compressor stages is thus depending on the pressure ratio of each compressor.
- Between each compression stage, intercooling is added by injecting liquid water at the same pressure to cool the overheated steam to its saturated state.
- Controllability: The heat pump cycles are assumed to be regulated to keep the generated steam constant while the heat source varies.
- Safety and emissions depend on the refrigerant used. The safety concerns may origin from the high pressure needed in the heat pump cycle or from the toxicity or flammability of the refrigerant. The environmental impacts only occur if there is a leakage of the refrigerant. Each refrigerant has a certain GWP summarized in Table 2.

Operating costs are directly dependent on the COP and capital costs vary by cycle. A cost estimation of each component is made to compare the investments costs of the cycles. Using the COP of the cycle, the total cost of the systems is estimated over a period of 15 years. For the reversed Brayton cycle, the expander price is estimated to be the same as a compressor. Equation (1) is used to estimate the price (see Chapter 2 in [34]):

$$C_e = C_b \left({}^{Q}/_{Q_b} \right)^M \cdot f_m \cdot f_p \cdot f_t \tag{1}$$

where C_e is the equipment cost, C_b the known base cost for a capacity of Q_b, M the constant depending of the equipment, and the f's are correction factors for the material of construction, pressure, and temperature. The correction factors where fixed for all components at 1, 1, and 1.6 respectively. C_b, Q_b, and M are given in Table 2.1 of reference [34]. The capacity Q is calculated as function of the cycle for a particular condition.

For the cost analysis, the heating capacity of the heat pump is fixed at 200 kW, which corresponds to about 266 kg/h of saturated steam at 150 °C (4.762 bar). General investment costs are hard to determine and the results have to be taken with care. The yearly electricity consumption cost is calculated using the following equation:

$$Yearly\ electricity\ cost = 7'000\ [\mathrm{h}] \cdot cost_{elec}\ \left[{}^{\$}/_{\mathrm{kWh}} \right] \cdot \frac{200}{COP}\ [\mathrm{kW}] \tag{2}$$

The cost of electricity ($cost_{elec}$) is 0.13 $/kWh with taxes, which is approximatively the EU-28 weighted average retail electricity price for industry for the last couple of years (Figure 4 in reference [35]). The yearly maintenance cost was fixed to 6% of the capital cost according to Table 5 from Wang and Zhang [36]. The capital cost of the cycle is an estimation of all the component costs according to equation (3), and the two formulae for the cost of the expansion valve and the piping and instrumentation coming from Table 3 of reference [36].

$$C_{\text{expansion valve}} = 114.5 \cdot \dot{m} \tag{3}$$

where $\dot{m}$ is the mass flow of the refrigerant. The piping and instrumentation costs are assumed to be 28% of the sum of all the components cost (except the steam compressors), as described in [36].

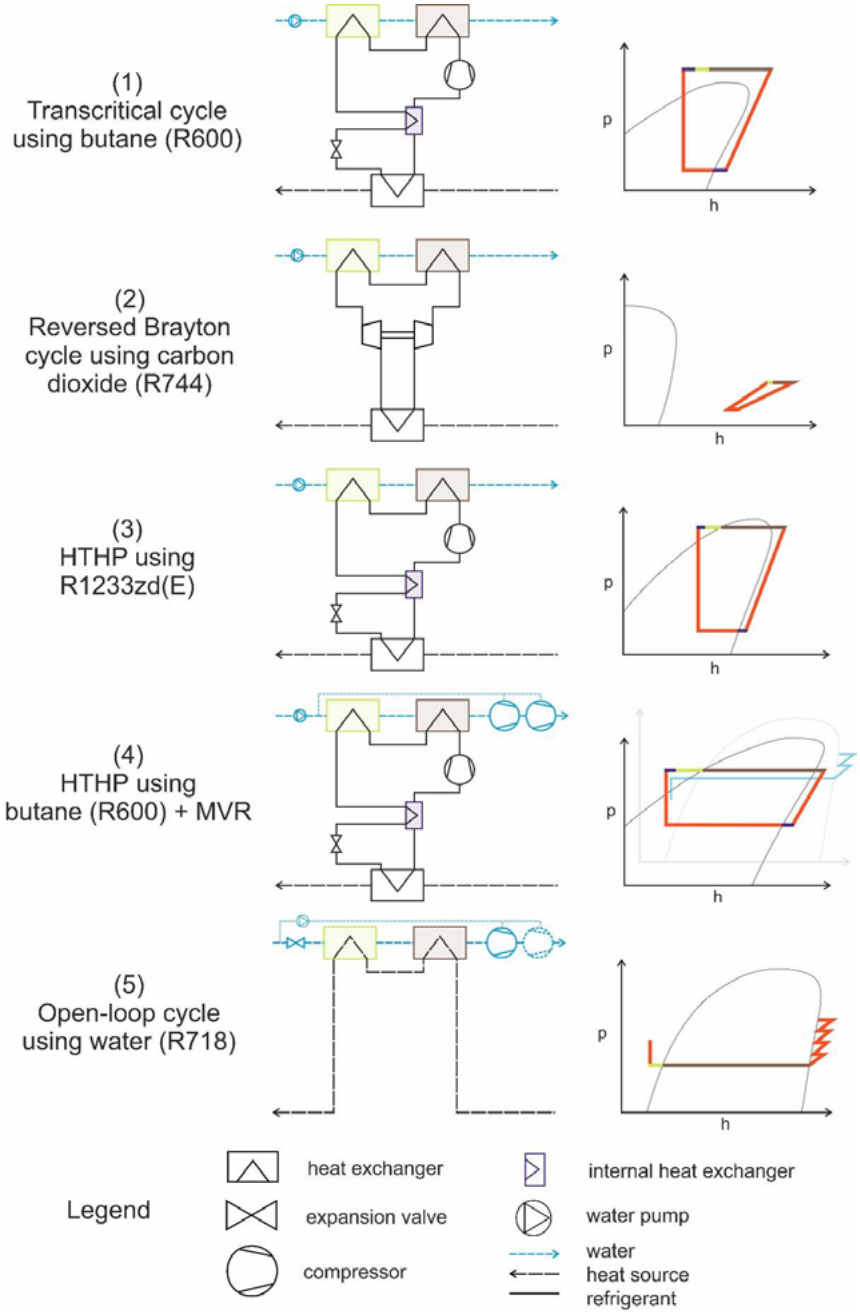


Fig. 1. Schematics and p-h diagrams of the five investigated heat pump cycles. (1) Transcritical R600 cycle, (2) Reversed Brayton cycle with R744 (CO_2) or R740 (Argon). (3) Classical closed-cycle HTHP using R1233zd(E), (4) Closed-cycle HTHP with mechanical vapor recompression (MVR), and (5) Open-loop cycle with R718 (water).

3. Results

3.1. COP simulations

The COP is simulated with different heat source temperatures and different isentropic efficiencies of the compressor(s). Figure 2 shows the COP for the different heat pump cycles generating steam of 150 °C (4.76 bar) as a function of the heat source outlet temperature (with constant temperature glide of 20 K on heat source) with an isentropic efficiency of 75%. As expected, the COP of each cycle increases with higher heat source temperature. The reversed Brayton cycle is the cycle least affected by the increase in source temperature. For the open-loop R718 heat pump cycle, the number of compressions stages varies as follows: six stages for temperatures below 40 °C, five for temperatures between 40 and 50 °C, four for temperatures between 50 and 70 °C, and three for temperatures above 70 °C. Since the steam compressor is not perfect, each compression step leads to a loss in process performance. This explains the lower COP of the open-loop cycle with water at lower source temperature compared to the HTHP with MVR cycles. For heat source temperatures of 75 °C and above the cycle's efficiencies are comparable. The transcritical cycle and the reversed Brayton cycle are not as efficient due to their temperature glides in their heat sink whereas the other cycles have a constant temperature.

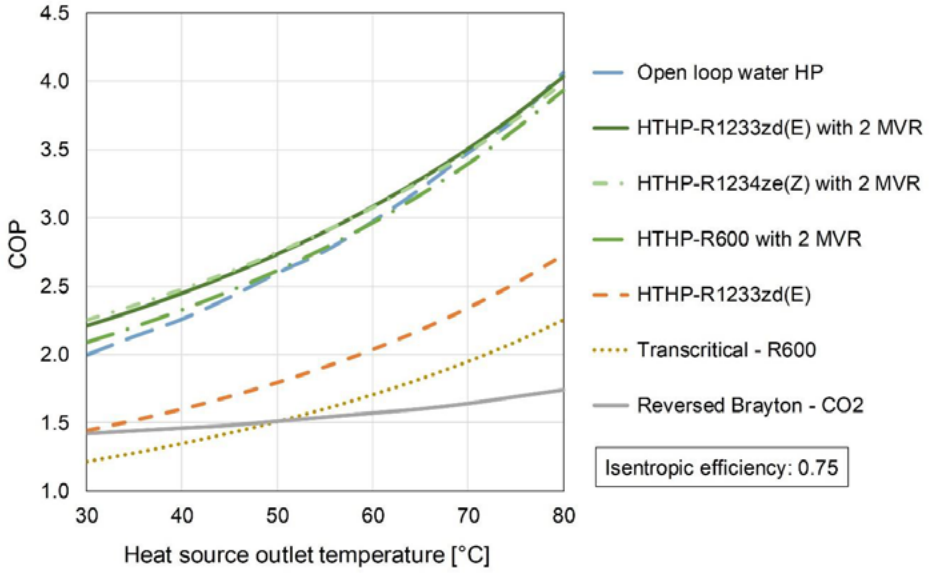


Fig. 2. COP for the different heat pump cycles generating steam of 150 °C (4.76 bar) as a function of the heat source outlet temperature (heat source temperature glide: 20 K, heat sink water inlet: 10 °C, isentropic compressor efficiency: 0.75)

Figure 3 shows the COPs as a function of the isentropic efficiency of the compressor(s) using a heat source inlet/outlet temperature of 80/60 °C. The increase of the COPs is linear except for the reversed Brayton cycle where the relation is much stronger than linear. The reversed Brayton cycle becomes most efficient for steam generation if it is operated with a compressor with a very high efficiency. The HTHP+MVR cycles and the open-loop water HP are still more efficient up to η_{is} of 95%, only with 98.5% and above the reversed Brayton cycle is above all the other cycles.

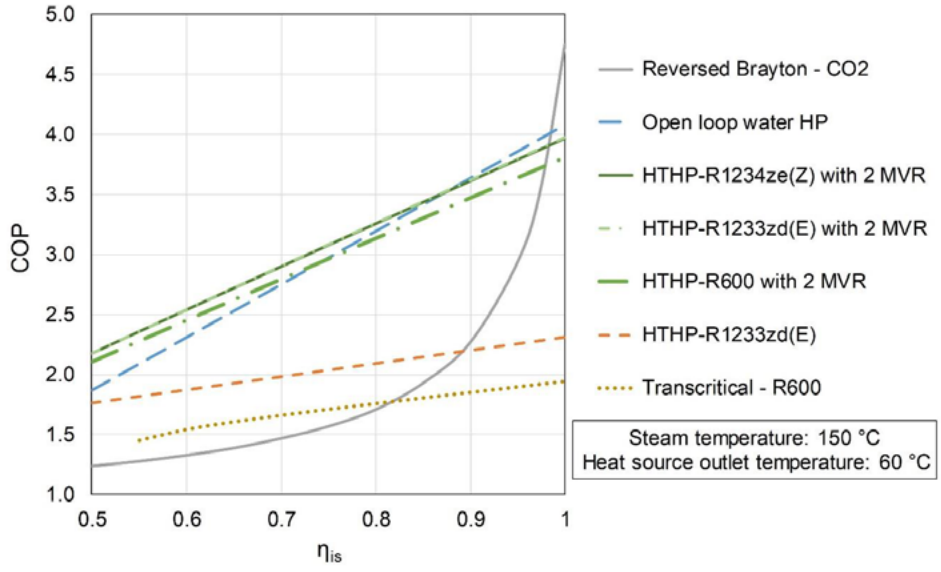


Fig. 3. COP for different heat pump cycles generating steam of 150 °C (4.76 bar) at 60 °C heat source outlet temperature (20 K temperature glide) as a function of the isentropic efficiency of their compressor(s) (η_{is}).

3.2. Cost analysis

Table 3 shows some estimated cost for the representative cycles at 60 °C heat source outlet temperature and η_{is} 75 %. The HTHP-R600 with 2MVR is simulated with a HTHP having a condensation temperature of 110 °C. The HTHP and the transcritical cycles have roughly the same capital cost due to their similarity. The open loop cycle with R718, as seen in Table 3, has a price similar to the previous cycles even though it needs 4 compressors; the reason is this cycle needs less heat exchangers. The reversed Brayton cycle shows the highest cost of all cycles. The main reason is that its compressor needs around twice the power compared to the other cycles. This can be schematically seen in the p-h diagram of the cycle in Figure 1 (2), where the ratio of the enthalpy difference of the compressing step over the heating step is small. Furthermore, the expander also costs much more than the expansion valve used in the other cycles.

Table 3. Estimation of the capital costs, the maintenance, and the electricity costs for a particular condition (60 °C heat source outlet temperature, η_{is} = 75 %) for each cycle. The HTHP-R600 with 2MVR cycle is simulated with a condensation temperature of 110 °C.

Cycle	Capital cost (CC) [$]	Yearly maintenance cost (6% of CC) [$]	Yearly electricity consumption cost [$]
(1) Transcritical R600 cycle	174'054	10'443	106'433
(2) Reversed Brayton with R744	516'697	31'002	115'924
(2) Reversed Brayton with R744 with η_{is} = 95%	640'451	38'427	59'477
(3) HTHP with R1233zd(E)	182'258	10'935	89'216
(4) HTHP with R600 with 2 MVR	217'388	13'043	61'279
(5) Open loop cycle with R718 (4 MVR)	181'868	10'912	61'279

Figure 4 shows an estimation of the total costs (i.e. investment and operating costs) as a function of the year according to the costs displayed in Table 3. The graph shows, which cycles are the most interesting in terms of cost depending on its usage. The transcritical R600 has the lowest capital cost, however, after only one year of operation (by the conditions assumed), the standard HTHP-R1233zd(E) and the open loop R718 HP are cheaper. One year later, the HTHP-R600 with 2 MVR also becomes a cheaper option.

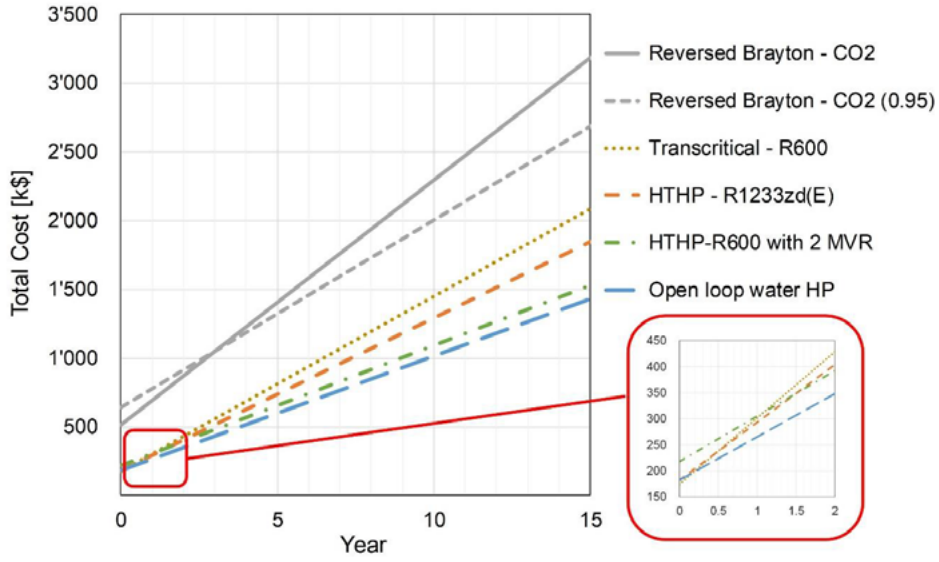


Fig. 4. Total cost (capital cost, maintenance cost, and operating cost) for the different heat pump cycles for 15 years with the following conditions: heat source inlet temperature: 80 °C, isentropic efficiency: 0.75 (except for the second reversed Brayton where it is 0.95), k$ corresponds to 1'000 $.

The maintenance costs were estimated simply by estimating a percentage of the capital cost, but do not consider the simplicity of the maintenance. To get an overview of the complexity of the different cycles, Table 4 summaries the number of components included in each cycle.

Table 4. Components of the five heat pump cycles.

Cycle	Heat exchanger (evaporator, condenser, gas HEX, or IHX)	Compressor	Steam compressor	Expander
(1) Transcritical	4	1		
(2) Reversed Brayton	4	1		1
(3) HTHP	4	1		
(4) HTHP with MVR	4	1	2	
(5) Open loop	2		4	

Table 4 shows that the first three cycles are very similar in terms of components. The reversed Brayton cycle has an additional expander, which is linked to the compressor. Such a system can be achieved with a turbo compressor and an expander on the same shaft [37]. The cycle with the additional steam compressor(s) has to deal with more compressors and more control. The open loop R718 cycle has only half the number of heat exchangers, which reduces the need for cleaning depending on the fluid used, but the high number of steam compressors makes this cycle particularly difficult to control and the complexity makes it more difficult to optimize and operate at its best efficiency.

4. Discussions

No combination of cycles was analyzed in this study, which could increase the COP by using different refrigerants with lower temperature lifts, instead of having one refrigerant with a high temperature lift. The cycle combining the transcritical heat pump as low stage with the reversed Brayton cycle as high temperature stage was nevertheless analyzed, as it seemed like a good combination due to the temperature glide in the heat sink of the former cycle and in the heat source of the latter. Although this system shows a 28% higher COP compared to the transcritical R600 cycle and has similar costs (the system has more components but with lower

unit prices), this combination is much more complex to control and offers no increased performance over the HTHP cycle in terms of efficiency.

The reversed Brayton cycle is interesting when the isentropic efficiency of the compressor is very high. When η_{is} of the compressor(s) are above 90%, the cycle is a good alternative for HTHP especially when the temperature lift is higher than 100 °C. However, the only heat pump compressor with isentropic efficiency higher than 90% found nowadays is the Rotational Heat Pump from ECOP [38]. This near market-ready machine is using an original idea: a rotational heat pump where the entire system (i.e. heat exchangers, expansion) is located inside a rotating cylinder that acts as a compressor [38].

The availability of heat pump components for temperatures higher than 120 °C is limited. Although components exist, they are far more expensive than standard low-temperature components for conventional heat pumps. This issue should dissipate in the future as soon as HTHP become more common. For the two cycles, which recompress the steam, an oil-free compressor is mandatory depending on the usage of the steam in order to avoid contamination. Oil-free steam compressors are not common in the market for low- to mid-range power (e.g. tens of kW to hundreds of kW). Steam compressors are more often used in the high-power range for MVR in order to recover the steam, which hasn't condensed [39].

The number of case studies of HTHPs in industry producing steam is very scarce [12, 15, 20, 40]. There are some articles that propose closed-cycle R718 heat pumps [23, 24, 41], and many articles on HTHPs [30, 42, 43]. As described in the literature review at the beginning of this paper, there are also some publications on experimental studies producing steam by heat pumps from Korea [3, 9, 13, 14, 15], Japan [4, 8, 16, 17, 27], China [18], Europe [19, 20, 21, 22, 23, 24], and Canada [25, 26], as well as theoretical works [2, 10, 11, 12].

Validation of this theoretical work is important to gain the trust of industries in order to build pilot projects.

In terms of technical readiness level, the five cycles analyzed can be put into three categories. The transcritical HP and HTHP are at the production level, the reversed Brayton cycle with high isentropic efficiency is according to [38] at the validation level, and the low- to mid-range HTHP with MVR and the open-loop R718 HP are considered to be at the development level.

5. Conclusions

Different heat pump cycles were simulated in order to generate saturated steam at 150 °C (4.76 bar) using only low GWP refrigerants that are future-proof according to the F-gas regulations. They show different COP trends depending on the heat source temperature and the isentropic compressor efficiency. A transcritical heat pump or a reversed Brayton cycle can be very efficient to generate heat at different temperatures thanks to the temperature glide in their heat sink. However, these cycles are not as efficient when used to generate steam at constant heat sink temperature. The heat pump cycles using steam recompression offer higher efficiency and are cheaper after a few years, taking into account maintenance and operating costs.

The authors hope that this study will promote further research into heat pump cycles for steam generation and, above all, motivate the realization of prototypes and pilot projects. The validation of such a study is crucial to rapidly increase the technical readiness level of heat pump cycle for low-pressure steam generation.

Acknowledgements

This research project is part of the Swiss Competence Center for Energy Research SCCER EIP of the Swiss Innovation Agency Innosuisse.

References

[1] C. Bernath, G. Deac et F. Sensfuss, «Influence of heat pumps on renewable electricity integration: Germany in a European context,» *Energy Strategy Reviews,* vol. 26, 2019.

[2] F. Bless, C. Arpagaus, S. S. Bertsch et J. Schiffmann, «Theoretical analsis of steam generation methods - Energy, CO2, emission, and cost analysis,» *Energy,* vol. 129, pp. 114-121, 2017.

[3] J. W. Yoo, D. H. Kang et M. S. Kim, «Experimental study on lab-scale steam generation heat pump with waste heat recovery,» *12th IEA Heat Pump Conference, 15-18 May, 2017, Rotterdam, The Netherlands,* pp. 1-7, 2017.

[4] T. Kaida, I. Sakuraba, K. Hashimoto et H. Hasegawa, «Experimental performance evaluation of heat pump-based steam supply system,» *9th International Conference on Compressors and their Systems, IOP Conf. Series: Materials Science and Engineering,* vol. 90, pp. 1-9, 2015.

[5] B. Hu, D. Wu et R. Wang, «Water vapor compression and its various applications,» *Renewable and Sustainable Energy Reviews,* vol. 98, pp. 92-107, 2018.

[6] D. H. Kang, S.-I. Na and M. S. Kim, "Recent Researches on Steam Generation Heat Pump System," *International Journal of Air-Conditioning and Refrigeration,* vol. 25, no. 4, pp. 1-8, 2017.

[7] T. Shibata, S. Hatamiya et H. Kusumoto, «Steam-Generating Heat Pumps using Multi-Stage Centrifugal Compressors for Industrial Applications,» *9th International IEA Heat Pump Conference, 20-22 May 2008, Zurich, Switzerland,* pp. 1-11, 2008.

[8] Y. Kuromaki, «Industrial Heat Pump Reduce Cost and Save Energy in Actual Case Studies,» *Chillventa Conference, Nuremberg, October 15, 2012,* pp. 1-57, 2012.

[9] D. H. Kang, S.-I. Na, J. W. Yoo, J. H. Lee et M. S. Kim, «Experimental study on the performance of a steam generation heat pump with the internal heat exchanging effect,» *International Journal of Refrigeration,* vol. 108, pp. 154-162, 2019.

[10] B. Zühlsdorf, F. Bühler, M. Bantle et B. Elmegaard, «Analysis of technologies and potentials for heat pump-based process heat supply above 150 °C,» *Energy Conversion and Management,* vol. 2, 2019.

[11] R. Bergamini, J. K. Jensen et B. Elmegaard, «Thermodynamic competitiveness of high temperature vapor compression heat pumps for boiler substitution,» *Energy,* vol. 182, pp. 110-121, 2019.

[12] A. Meroni, B. Zühlsdorf, B. Elmegaard et F. Haglind, «Design of centrifugal compressors for heat pump systems,» *Applied Energy,* vol. 232, pp. 139-156, 2018.

[13] K. Chang, S. Kim et K. Kim, «A Study on the Performance Characteristics and Design of a High-Temperature Condenser for a Steam Heat Pump with R245fa,» *Vth International Symposium on Fusion of Science & Technology, New Delhi, India, January 18-22, 2016,* pp. 1-4, 2016.

[14] E. Wang, S.-I. Na, G. Lee, Y.-J. Baik, Y.-S. Lee et B. Lee, «Experimental Study on Heating Performance Characteristic of 100 kW Heat Pump to generate 120 °C Steam,» *Korean Journal of Air-Conditioning and Refrigeration Engineering,* vol. 30, n° %12, pp. 100-106, 2018.

[15] G. Lee, L. Bomjoon, C. Junhyun, R. Ho-Sang, B. Young_Jin, S. Hyung-Ki et L. Young-Soo, «Development of steam generation heat pump through refrigerant replacement approach,» *12th IEA Heat Pump Conference, 15-18 May, 2017, Rotterdam, The Netherlands,* pp. 1-10, 2017.

[16] T. Yamazaki et Y. Kubo, «Development of a High-Temperature Heat Pump,» *IEA Heat Pump Centre, Newsletter, Vol. 3, No. 4,* pp. 18-21, 1985.

[17] T. Kimura, H. Fuchikami, K. Nishida, M. Kudo, A. Machida, K. Saito, Y. Ohta et M. Katsuta, «Development of a high temperature heat pump using reusable heat as the heat source,» *JRAIA International Symposium 2018,* pp. 1-8, 2018.

[18] D. Wu, J. Jiang, B. Hu et R. Wang, «Experimental investigation on the performance of a very high temperature heat pump with water refrigerant,» *Energy,* vol. 190, p. 116427, 2020.

[19] A. Wemmers, A. v. Haasteren et P. K. J. v. d. Kremers, «Test results R600 pilot heat pump,» *12th IEA Heat pump conference, Rotterdam, May 14-17, 2017,* pp. 1-9, 2017.

[20] T.-M. Tveit, «Application of an industrial heat pump for steam generation using district heating as a heat source,» *12th IEA Heat Pump Conference, 15-18 May, 2017, Rotterdam, The Netherlands,* pp. 1-7, 2017.

[21] O. Bamigbetan, T. Eikevik, P. Neksa, M. Bantle et C. Schlemminger, «The development of a hydrocarbon high temperature heat pump for waste heat recovery,» *Energy,* vol. 173, pp. 1141-1153, 2019.

[22] D. Bobelin, A. Bourig et J.-L. Peureux, «Experimental Results of a Newly Developed Very high temperature industrial heat pump (140 °C) equipped with scroll compressors and working with a new blend refrigerant,» *International Refrigeration and Air Conditioning Conference, July 16-19, 2012, Purdue, Paper 1299,* pp. 1-10, 2012.

[23] M. Chamoun, R. Rulliere, P. Haberschill et J.-L. Peureux, «Experimental and numerical investigations of a new high temperature heat pump for industrial heat recovery using water as refrigerant,» *International Journal of Refrigeration,* vol. 44, pp. 177-188, 2014.

[24] M. Chamoun, R. Rulliere, P. Haberschill et J.-L. Peureux, «Experimental Investigation of a New High

Temperature Heat Pump Using Water as Refrigerant for Industrial Heat Recovery,» *International Refrigeration and Air Conditioning Conference, Purdue Conference, 2012, Paper 1165,* pp. 1-9, 2012.

[25] J. Linton, «Description and Test Results of a High Temperature Heat Pump Test Facility,» *Heat Pumps, Solving Energy and Environmental Challenges, 3rd IEA Heat Pump Conference, 12-15 March 1990, Tokyo, Japan,* pp. 455-465, 1990.

[26] J. Linton et W. Snelson, «An Overview of Current High Temperature Heat Pump Technology,» *Heat Pumps for Energy Efficiency and Environmental Progress,* pp. 217-227, 1993.

[27] T. Kaida, M. Fukushima et K. Iizuka, «Application of R1224yd(Z) as R245fa alternative for high temperature heat pump,» *CR 2019, The 25th IIR International Congress of Refrigeration, August 24-30, Montréal, Québec, Canada,* pp. 1-8, 2019.

[28] S. Bertsch, C. Arpagaus, F. Bless, A. Weickgenannt et J. Schiffmann, «Theoretical Investigation of a High Temperature Heat Pump using a Micro Turbo Compressor and Water as a Refrigerant,» *13th IIR-Gustav Lorentzen Conference on Natural Refrigerants, 18-20 June 2018, Valencia, Spain,* pp. 1-9, 2018.

[29] C. Arpagaus et S. Bertsch, «Experimental results of HFO/HCFO refrigerants in a laboratory scale HTHP with up to 150 °C supply temperature,» *2nd Conference on High Temperature Heat Pumps (HTHP), 9 September 2019, Copenhagen, Denmark,* pp. 1-9, 2019.

[30] C. Arpagaus, F. Bless, M. Uhlmann, J. Schiffmann et S. S. Bertsch, «High temperature heat pumps: Market overview, state of the art, research status, refrigerants, and application potentials,» *Energy,* vol. 152, pp. 985-1010, 2018.

[31] W. Rivera, R. Best, M. Cardoso et R. Romero, «A review of absorption heat transformers,» *Applied Thermal Engineering,* vol. 91, pp. 654-670, 205.

[32] Z. Xu et R. Wang, «Absorption heat pump for waste heat reuse: current states and future development,» *Front. Energy,* vol. 11, n° %14, pp. 414-436, 2017.

[33] European Commission, «EU legistlation to control F-gase,» [En ligne]. Available: https://ec.europa.eu/clima/policies/f-gas/legislation_en. [Accès le October 2019].

[34] R. Smith, Chemical Process design and integration, second éd., Wiley, 2017, pp. 1-896.

[35] European commission, «Report from the commission to the european parliament, the council, the european economic and social committee and the committee of the regions Energy prices and costs in Europe,» [En ligne]. Available: https://eur-lex.europa.eu/legal-content/AUTO/?uri=CELEX:52019DC0001&qid=1571060005520&rid=4. [Accès le October 2019].

[36] G.-B. Wang et X.-R. Zhang, «Thermoeconomic analysis of optimization potential for CO2 vapor compression cycle: From transcritical to supercritical operation for waste heat recovery from the steam condenser,» *International Journal of Energy Research,* vol. 43, 2018.

[37] J. Demierre, D. Favrat, J. Schiffmann et J. Wegele, «Experimental investigation of a Thermally Driven Heat Pump based on a double Organic Rankine Cycle and an oil-free Compressor-Turbine Unit,» *International Journal of Refrigeration,* vol. 44, pp. 91-100, 2014.

[38] A. Längauer, B. Adler, C. Rakusch et K. Ponweiser, «COP tests of a rotation heat pump,» chez *25th IIR International Congress of Refrigeration*, Montreal, 2019.

[39] GEA Wiegand Gmbh, «Evaporation Technology using Mechanival Vapour Recompression,» Ettlingen - Germany.

[40] Hokkaido Bioethanol Co., Ltd, Tokachi Shimizu Factory, «Introduction of high efficiency steam supply heat pump innovates energy saving in the distillation process, which introduces cutting running cost and reduction of CO2 emissions,» Heat Pump & Thermal Storage Technology Center of Japan, Japan, 2014.

[41] D. Wu, H. Yan, H. Bin et W. R.Z., «Modeling and simulation on a water vapor high temperature heat pump system,» *Energy,* vol. 168, pp. 1063-1072, 2019.

[42] G. Kosmadakis, «Estimating the potential of industrial (high-temperature) heat pumps for exploiting waste heat in EU industries,» *Applied Thermal Engineering,* vol. 156, pp. 287-298, 2019.

[43] D. Mikielewicz et J. Wajs, «Performance of the very high-temperature heat pump with low GWP working fluids,» *Energy,* vol. 182, pp. 460-470, 2019.

13th IEA Heat Pump Conference
April 26-29, 2021 Jeju, Korea

Control optimization of a double stage heat pump with desuperheater in multi-family NZEBs

Fabian Ochs[a*], William Monteleone[a], Nicola Franzoi[a], Georgios Dermentzis[a]

[a]University of Innsbruck, Innsbruck, 6020, Austria

Abstract

Two multi-family buildings (MFB) with together 26 flats were designed to achieve a net Zero Energy (NZE) balance for heating, domestic hot water (DHW) preparation and all auxiliary energies. The roof of one of the MFB is covered by PV, the other is partly used for PV and partly for solar thermal (ST). A double-stage ground water heat pump (HP) with hot gas desuperheating (DSH) provides the remaining energy for heating and DHW. The system was designed with a low temperature distribution system (floor heating) and separate decentral fresh water preparation (DHW plate heat exchanger) for low thermal losses and optimal efficiency.
Detailed performance maps of the double-stage HP pump with DSH were generated analyzing the monitoring data and by means of refrigerant cycle simulation. Simulation based optimization was performed with the aim to operate the HVAC system with improved performance. Different system configurations (i.e. with or without ST, with different buffer storage sizes, with different control strategies and set points) can be compared and evaluated also considering (seasonal) variations of the share of renewables in the electricity mix.

© HPC2020.
Selection and/or peer-review under responsibility of the organizers of the 13th IEA Heat Pump Conference 2020.

Keywords: NZEB; Multi-family buildings; double stage heat pump; desuperheater; building and HVAC simulation

1. Introduction

In order to reach the ambitious targets of a sustainable energy system, strong efforts in improving energy efficiency in the building sector are required, see [1]. Only with a combination of passive (i.e. building envelope) and active (i.e. HVAC system) measures as well as integrating renewable energies (RE) these targets can be reached. System solutions, i.e. well designed and matching components with a robust control scheme and the possibility of easy quality control, are required.

While there is a discussion among experts about the most economic building energy standard (e.g. whether it is Passive House standard or less ambitious), it is undiscussed that heat pumps (HP) will play a major role in heating (and cooling) of buildings. HPs exist in a large variety with respect to the source (air, water, ground, waste heat) and the sink (air, water; low temperature heating, DHW etc.) and in almost any size (from some 100 W to several 100 kW). Even though there is experience with HPs since several decades and a strong development of HPs within at least the last 20 years, there is still a lack of knowledge of HP operation and optimal system design for nZEB [2,3]and in particular nZE multi-family buildings [4, 5]. In [6, 7, 8, 9] increasing performance of installed HP systems within the recent years is reported. However, the market and its players lack experience and guidelines for HP system for nZEB are still missing (see also e.g. IEA HPT Annex 49).

In this paper, a case study of two NZE multi-family buildings in Passive House standard is presented with an innovative HVAC system. In this work, it is presented, how by means of simulation with models that were parameterized using detailed monitoring data (refrigerant cycle as well as building and HVAC simulations), failures could be detected and how the performance could be improved. The results can be used to derive guidelines for HP system design and failure detection and quality control.

* Corresponding author. Tel.: + 43 512 507 63603;
E-mail address: Fabian-ochs@uibk.ac.at.

Nomenclature

Abbreviation	Description	Abbreviation	Description
BMS	Building management system	HW	Hot water
BS	Buffer storage	HX	Heat exchanger
CW	Cold water	HVAC	Heating ventilation air conditioning
comp	Compressor	LEH	Low energy house
cond	Condenser	MFB	Multi-family building
DHW	Domestic hot water	NZE(B)	Net Zero energy (building)
DSH	Desuperheater	nZEB	Nearly Zero energy building
el	Electric	PH	Passive house
evap	Evaporator	PM	Performance map
FH	Floor heating	PV	Photovoltaic
GW	Ground water	RE	Renewable energy
H	Heating	SFH	Single-family house
HD	Heating demand	SC	Solar collector
HP	Heat pump	ST	Solar thermal

Symbol	Description	Unit	Symbol	Description	Unit
A	area	m²	Q	Heat	kWh
Cp	Specific heat	kJ/(kg K)	SPF	Seasonal Performance Factor	-
COP	Coefficient of Performance	-	T	Absolute Temperature	K
D	Compressor Displacement	m³	U	Heat transfer coefficient	W/(m² K)
f_{DSH}	Share of DSH to DHW preparation	-	η_C	Carnot performance factor	-
h	Specific enthalpy of refrigerant	kJ/kg	η_{vol}	Volumetric efficiency	-
$\dot{m}$	Mass flow	Kg/s	η_{is}	Isentropic efficiency	-
N_{min}	Rotational speed of compressor	min^{-1}	ρ_{suc}	Refrigerant vapour density	kg/m³
P	Pressure	Pa	ϑ	Temperature	°C
P	Power	W	τ	Compression Ratio	-

2. Case Study

In Innsbruck Vögelebichl, two multi-family buildings (MFB) were designed to achieve a net Zero Energy (NZE) balance for heating, domestic hot water (DHW) preparation and auxiliary energies. The roof of one of the MFB is covered by PV, the roof of the other MFB is partly used for PV and partly for solar thermal (ST). A double-stage ground water (GW) heat pump with hot gas de-superheating provides the remaining energy for heating and DHW.

2.1. Buildings

The two buildings with together 26 flats and together 2149 m² of treated area (see Fig. 1) were already described in detail in [10, 11, 12, 13]. The buildings were designed to reach Passive House Standard (Heating Demand HD ≤ 15 kWh/(m² a)). One roof of the MFB is covered by PV (99.8 m²), the other is partly used for PV (52.5 m²) and partly for ST (73.6 m²).

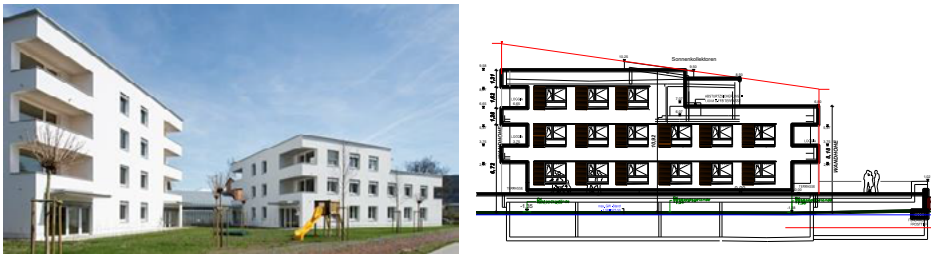


Fig. 1. (left) two multi-family buildings in Passive House standard (NHT, Innsbruck Vögelebichl), (right) west view on south building with 10 flats

2.2. Heat Pump System and Hydraulic Scheme

A ground water (GW) heat pump (HP) (with two stages, i.e. two parallel compressors) and solar thermal collector (SC) field charge the buffer store which provides heat with a low temperature heat distribution and the separate decentral fresh water preparation (DHW plate HX) to the buildings, see Fig. 2. The double-stage HP is equipped with hot gas (HG) de-superheating. Depending on the operation mode (heating or DHW preparation), the flow of the HP enters the buffer store (BS) at the top or at 1/3 of the height from the top. The combined return of the heating and DHW loop enters the large 6 m³ buffer store depending on the temperature level either at the bottom or at about 1/3 of the height of the tank in order to enhance stratification. The electric backup heater (BH) is currently not in use.

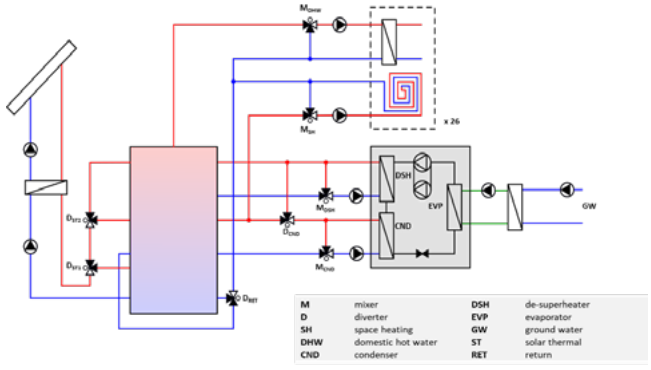


Fig. 2. Simplified hydraulic scheme with Solar Collectors (SC), Buffer Store (BS), 2-stage ground water heat pump (HP) with hot gas HG) desuperheating (DSH) in heating mode with floor heating (FH) and decentral heat exchanger (HX) for domestic hot water (DHW) preparation

2.3. Heat Pump

The heat pump has a nominal capacity of 52 kW (at W55, see Table 1). The performance map (PM) data of the HP according to the manufacturer is available only for double-stage operation and without DSH loop. PM data is available for other source temperatures, but no data is available for single-stage operation and for operation with desuperheating loop. Hence, the required performance maps have to be generated using dynamic monitoring data, which will be described shortly in the next section.

According to the EN 14511 measurements (compare table 1) there is not DSH or the DSH is in series to the condenser.

Table 1. Performance map (PM) of the double-stage HP with R410A according to data sheet (EN 14511)

(data sheet) EN 14511	W35	W45	W55
Heating Power at W10 / [kW]	58	55	52
COP at W10 / [-]	6	4.6	3.7
El. Power at W10 / [kW]	9.7	11.8	13.9
Cooling Power at W10 / [kW]	49	43	38

2.4. Double stage heat pump

Double-stage HPs are on the market already for several years. Double-stage HPs feature higher investment costs but have potentially lower operation costs. A double-stage compressor has a low capacity, which is 50% or about 70% in most models, and high capacity (100%). Variable-speed or modulating compressors vary capacity from about 40% to 100% in increments of less than 1% and are the most efficient. They have the highest advantage if either the source (e.g. air) and or the sink have variable temperature or power level (e.g. for heating).

With a single-stage HP, the compressor runs only at full load capacity, i.e. once the required temperature level is satisfied, the compressor turns off. A double-stage compressor can operate at part load or full load

capacity. The two-stage HP compressors turn on and run until stage two of the thermostat is satisfied, then one compressor continues to run at a lower level, stage one. If the HP is connected directly to the heating system, this would allow to avoid swings, i.e. for a more even room temperature.

Potentially, the double-stage HP consumes less energy and does not have to work as hard to adjust to swings in room temperature. This could result in a lower operating cost while keeping occupants at the same comfort level. In [14] it was found that such a coupling process improved energy efficiency ratio by 20 % compared to a purely air source HP.

2.5. Heat Pump with Desuperheater

One possibility to improve the performance of a HP in residential applications is a desuperheater (DSH). The additional heat exchanger between the compressor and the condenser of the HP transfers the heat of the superheated refrigerant to a secondary circuit. It is suited for DHW preparation (directly or indirectly via a storage tank) because of the relative high temperature level that can be reached (e.g. 55 °C to 60 °C). The condensation of the de-superheated refrigerant takes place in the condenser of the HP at lower temperature level, e.g. at 35 °C in case of floor heating system and the heat is transferred to the heating system directly or via a separate buffer storage tank.

An energetic advantage is obtained as a part of the heat for DHW preparation that has to be provided at high temperature with usually relative low performance in “DHW preparation mode” is provided at higher efficiency at low condensing temperature in “heating mode”. During this simultaneous operation (heating and DHW preparation), the HP operates at a lower condensing pressure compared to DHW preparation only. The amount of high temperature heat that can be provided and that reduces operation hours at low efficiency depends on the heating load and heating demand of the building (load duration curve). An extensive investigation for a single family home can be found in [15] and in [16]. In [13] the theoretical upper limit of performance increase by use of a DSH was shown as a function of the ratio of heating and DHW demand.

2.6. Buffer Tank

A scheme of the buffer tank is shown in Fig. 3 with inlets and outlets for (left) the heat generation part and (right) for the load. The dots indicate the position of the temperature sensors. The tank was modelled with the storage model of the Carnot Blockset in Matlab/Simulink.

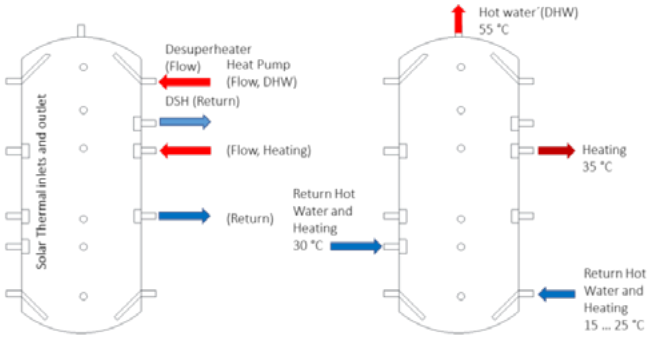


Fig. 3. Hot water tank (6 m³) with (left) heat generation (ST, HP DHW, HP Heating and desuperheating and (right) outlets for hot water preparation and heating and common return inlets

2.7. Hydraulic integration of desuperheater

The sizing and integration of the desuperheater is a nontrivial problem. Generally, the desuperheater can be connected in a parallel loop, as currently implemented in this system (Fig. 4), or it can be connected with a controlled diverter valve and can be operated in mixed parallel/series operation (Fig. 5). In parallel operation, either speed controlled circulation pumps or flow temperature control mixing loops are required to achieve the appropriate flow temperature. The latter is implemented in this system.

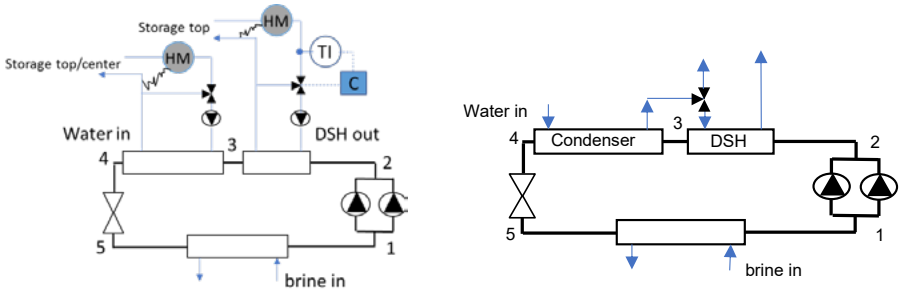


Fig. 4. (a) Parallel operation of condenser and desuperheater with flow temperature control of condenser and DSH with heat meter (HM), temperature indicator (TI) and controller (C) (TI and C of the condenser loop are not shown for better visibility); (b) Flow temperature control of condenser and DSH (mixed parallel / series operation)

2.8. Control

Theoretically, only for the heat pump eight different operation modes exist as shown in the following figure. The current implementation of the system does not allow operating the desuperheater in series, a slight change of the hydraulic scheme would be necessary. Currently, the HP is operated either in DHW mode (if the top third of the storage tank is below 48 °C, set point temperature of storage top temperature = 52 °C) in stage II or in heating mode in stage I or II depending on the outdoor temperature. An improved system concept is shown in the discussion section.

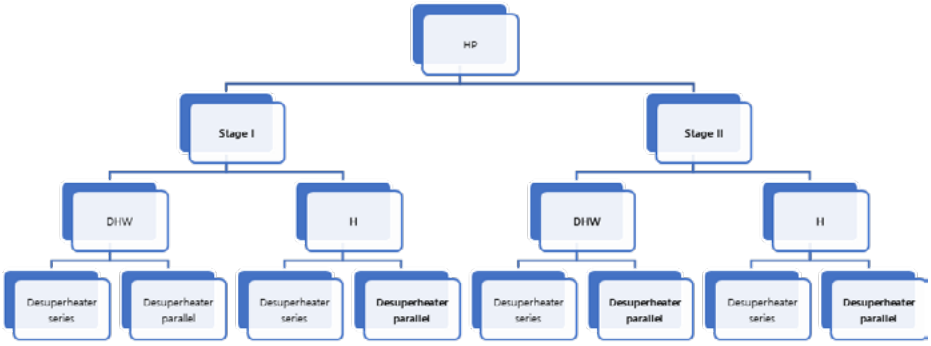


Fig. 5. Theoretical control options of a double stage heat pump with desuperheater and current control implementation in bold (stage I, and stage II heating mode, stage II DHW mode; DSH always in parallel operation)

2.9. Monitoring System

Detailed monitoring of the buildings (all flats in one of the two MFB), the HVAC system including thermal losses and the performance of PV and ST allowed to study the behavior of NZEBs in practice. The simulation-assisted analysis of the monitoring data allowed to identify problems and faults of the installation and of the operation. By means of simulation, influences of climate and of the user behavior (set points, etc.) could be considered and the monitoring results could be normalized to standard conditions.

The measurement system consists of Pt100 (1/3 DIN), heat meters and electricity meters. The measurement system is connected to the BMS and readings are stored with a 1 min. time step. Data is post-processed and average or integrated values are reported.

Detailed monitoring results were collected for a period of three years, analyzed by means of dynamic simulation and the performance of the buildings was evaluated with respect to the aim of achieving the NZE balance. The dynamic building and HVAC simulation was performed with Matlab/Simulink.

3. Research Questions

The following research questions can be defined:

- Does a double-stage outperform a single-stage HP?
- Is there a cost benefit and is there a benefit with respect to service life (i.e. can excessive on/off cycles be avoided)?
- What is the optimum control strategy for a double stage HP?
    - for heating and for DHW preparation
    - in combination with a buffer storage
- What is the theoretical and real benefit of the DSH?
- Does a 2 + 2-pipe system outperform the 3 pipe system (with common return of heating and DHW loop)?
- By how much can the storage stratification and the system performance be improved by variable input heights of the return flow to the tank?

The particular question in this project is whether the performance of a HP can be improved in these MFBs with very high energy standard (PH Standard) with relative low heating demand (15 kWh/(m² a) and relative high DHW demand (ca. 25 kWh/(m² a)) and by how much? And can the goal of NZEB be achieved?

4. Method

Firstly, based on the analysis of monitoring results, conclusions on the actual performance are derived and typical operation conditions of the heat pump are identified. Secondly, refrigerant cycle simulations are performed in order to identify the performance map for the different operation modes. Finally, dynamic simulations are performed in order to detect faults in the current system and to identify possible improvements with respect to the control strategy and set points but also regarding improved system design.

5. Monitoring Results

5.1. Heating Load and DHW demand

The heating load is 24 kW for both buildings according to the design (PHPP, max. daily average). DHW load adds approx. further 12 kW with a buffer tank acc. to the standard recommendations. For the south building detailed data of each flat is available. The maximum daily heating load is 7 W/m² (see Fig. 6). There is a clear trend of heating load vs. ambient temperature, which is not typical for passive houses. The heating capacity of the heat pump in stage I is always sufficient to cover the heating load of the building. However, in stage II higher share of desuperheater can be expected.

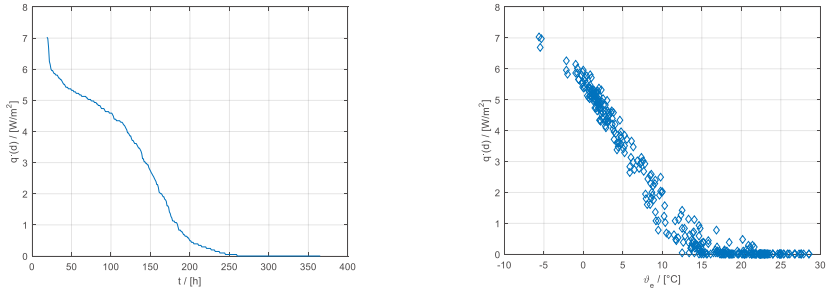


Fig. 6. (a) Load duration curve of the south building and (b) daily heating load vs. ambient temperature

Domestic hot water demand is not monitored in detail. The total delivered DHW from the storage is measured and includes distribution losses. In 2018 it was 26 kWh/(m² a) and in the range of the predictions. The flow temperature to the decentral fresh water heat exchangers is in the range of 52 °C and always sufficient to provide hot water with sufficient comfort.

5.2. Electricity Energy Demand and Net Zero Energy Balance

In 2018, the electricity consumption of the HP was 21 MWh and auxiliary energies were responsible for 14 MWh. The PV field produced in average around 27 MWh. Fig. 7 reports the electric energy balance for the years 2016 to 2018. In spite of the reduced total energy demand in 2018 (mainly because of the decreased heating demand), the NZE balance was not achieved. (Remark: Actually, the PV production was 24.5 MWh in 2018 because of a technical failure of the inverter of the north building PV field. A yield between 26.6 MWh and 27.2 MWh can be predicted based on data of 2016 and 2017 for the case without the failure).

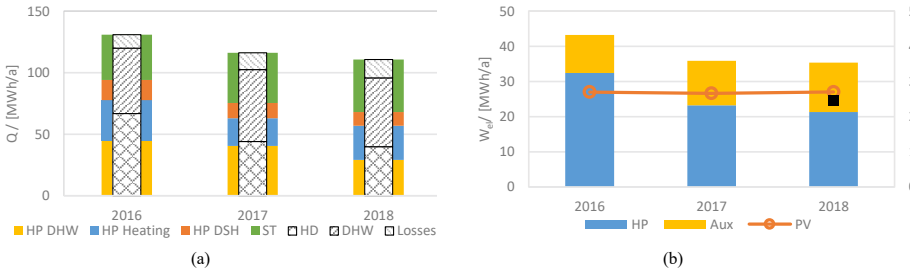


Fig. 7. Thermal (a) and electric (b) balance with HP, auxiliary energies (aux) and photovoltaic (PV)

5.3. HP Operation

A series of typical HP operation modes is shown in Fig. 8. The HP operates with full capacity (stage II) in DHW mode. Also the DSH delivers around 11 kW. The condenser power is 28 kW. With the electric power of the compressor of 14 kW, the COP is 2.8. In heating mode (with single compressor operation) the heating power is 25 kW. No useful desuperheating can be measured. The COP under these conditions is 6.25 (4 kW of electric power). There is one short period with heating mode at stage II with a small contribution by the DSH. It has to be mentioned here, that the heat meters measure the heat that is delivered to the storage tank. In order to deliver the energy at the required temperature level, flow temperature control is implemented, as shown in Fig. 4, above. Furthermore, it is important to remark that the presented operation of the HP does not represent the optimum configuration but is the one implemented and is used to identify the HP operation and generate the PMs.

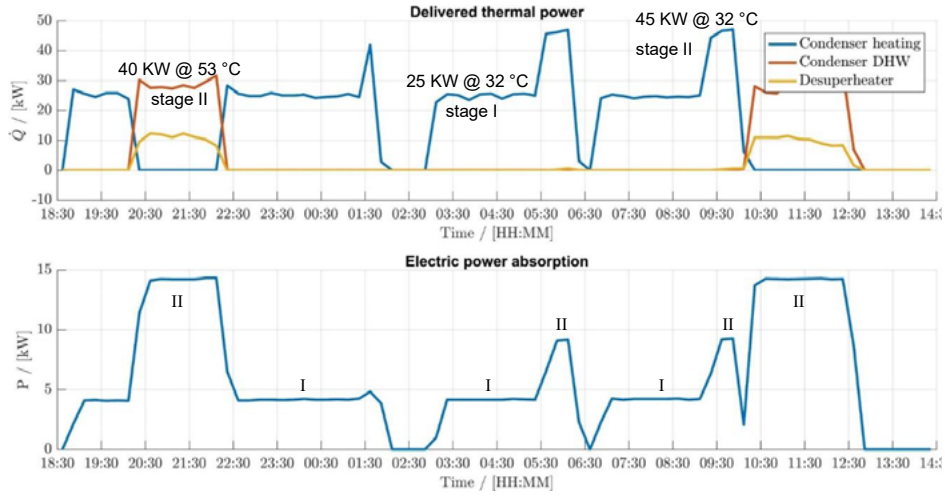


Fig. 8. Heat Pump operation with different operation modes (stage I and stage II, DHW and Heating with and without DSH)

6. Component and System Modelling

6.1. Refrigerant Cycle

A simplified scheme of the refrigerant cycle of a double-stage HP with DSH is shown in Fig. 5. In order to predict the performance of the HP under various conditions, a simplified physical vapour cycle model was developed in Matlab using the CoolProp database for refrigerants [17]. Pressure losses in and between the components are disregarded with the exception of the pressure loss in the condenser, which can be considered by a given pressure difference Δp_{cond}. Subcooling and superheating are considered in a simplified way with given temperature differences ΔT_{sub} and ΔT_{super}, respectively.

The evaporator is divided in three sections (film evaporation, evaporation and superheating). The heat transfer coefficients are assumed to be constant in each section. The following equations are applied.

$$\dot{Q}_{evap} = \dot{m}_b \cdot \Delta h_b = \dot{m}_{ref} \cdot (h_1 - h_5) \quad (6)$$

$$\dot{Q}_{evap} = \sum UA_{evap,i} \cdot \Delta\vartheta_{log,evap,i} \quad (7)$$

Correspondingly, the condenser is divided in desuperheating, condensation and sub-cooling sections with constant (i.e. given) heat transfer coefficients.

$$\dot{Q}_{cond} = \dot{m}_w \cdot c_w \cdot \Delta T_w = \dot{m}_{ref} \cdot (h_3 - h_4) \quad (8)$$

$$\dot{Q}_{cond} = \sum UA_{cond,i} \cdot \Delta\vartheta_{log,cond,i} \quad (9)$$

Then for the DSH it applies that

$$\dot{Q}_{DSH} = \dot{m}_{w,DSH} \cdot c_{p,w} \cdot \Delta T_{w,DSH} = \dot{m}_{ref} \cdot (h_2 - h_3) \quad (10)$$

$$\dot{Q}_{DSH} = UA_{DSH} \cdot \Delta\vartheta_{log,DSH} \quad (11)$$

The mass flow of the refrigerant

$$\dot{m}_{ref} = D \frac{N_{min}}{60\ \mathrm{s/min}} \cdot \rho_{suc} \cdot \eta_{vol} \quad (12)$$

is a function of the displacement and of the volumetric efficiency. The compressor power in the refrigerant cycle is calculated based on the isentropic efficiency η_{is}.

$$P_{comp} = \dot{m}_{ref} \cdot \frac{h_{2s} - h_1}{\eta_{is}} \quad (13)$$

where $h_{2s} = h(p_{dis}, s_1)$ is the enthalpy of superheated gas at isentropic compression. The isentropic efficiency η_{is} depends on the compression ratio, which is a function of the compressor discharge p_{dis} and suction p_{suc} pressure.

$$\tau = \frac{p_{dis}}{p_{suc}} \quad (14)$$

Both, the volumetric and the isentropic efficiency can be approximated based on literature data by a polynomial or a 2D-lookup table.

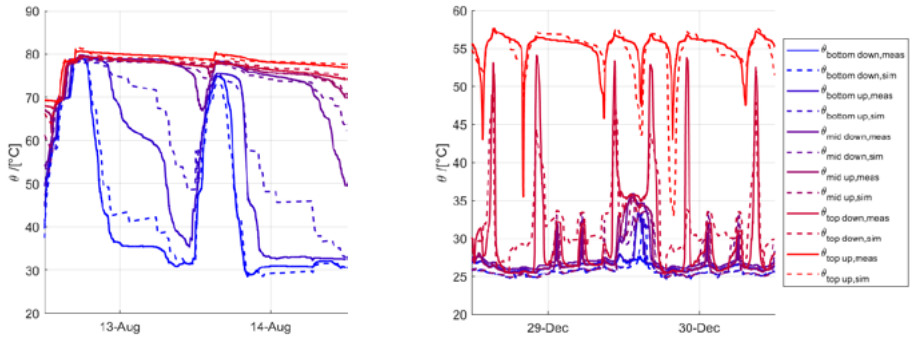
The electrical efficiency of the compressor η_{el} is approximated with a linear function depending on the compressor temperature. Then the performance of the HP can be calculated as follows

$$COP_{HP} = \frac{\dot{Q}_{cond} + \dot{Q}_{DSH}}{P_{\mathrm{el,comp}}} \quad (15)$$

7. Results

7.1. Buffer Storage

The measured and simulated storage temperatures for a period in winter and in summer (with ST operation) are shown in Fig. 9. Overall, the agreement is acceptable. In detail, there are some deviations in the dynamic behavior during some days for some sensors, but with respect to the research question discussed in this paper, the deviations are acceptable.



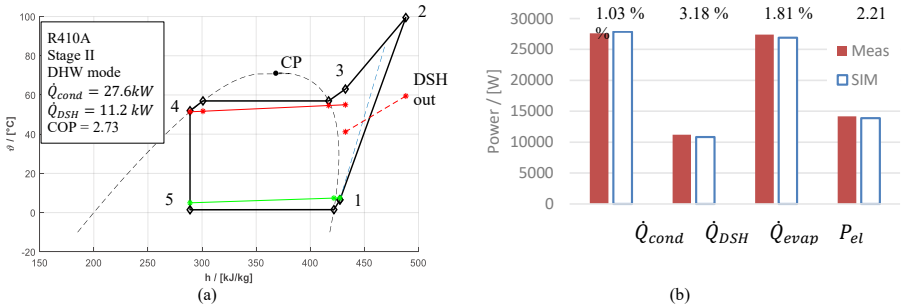
(a) (b)

Fig. 9. Measured (meas) and simulated (sim) storage temperatures for a period in summer (a) and in winter 2018 (b)

The measured thermal losses are within an average factor of about 10 times higher than the predicted ones (for a tank of that size and with that insulation level, corresponding to a ErP class C tank, EU efficiency classes for storage losses). One main reason is that losses from pipes, valves and pumps between the tank and the heat meters are included in the energy balance. Unwanted buoyancy flows could be excluded by analyzing the monitoring data for all hydraulic loops except for the cooling loop (in summer the ground water can be used with a heat exchanger to do some cooling with the floor heating system.) This is still under investigation.

7.2. HP Model Parameterization

The simplified physical HP model, described above, was parameterized using measured data from monitoring. The source temperature showed little variation between around 8 °C and 12 °C over the course of the year. Two typical operation modes were identified: DHW operation with desuperheating at double-stage and heating mode at single-stage without significant desuperheating. The resulting refrigerant cycle is shown on the following Fig. The corresponding heating power (condenser, DSH and evaporator) and electric power (compressor) are shown in Fig. 10. The deviations are highest for the DSH with 3.2 %.



(a) (b)

Fig. 10. (a) Refrigerant Cycle at DHW operation mode with DSH, stage II; (b) Comparison of measured and simulated heating powers and electric powers and relative deviations (remark: the presented operation of the HP does not represent the optimum configuration)

7.3. PM of Heat Pump Model DSH

With the parameterized HP model, performance maps for the different operation modes were generated. These include

- Stage I or stage II
- DSH in series (i.e. without separate DSH loop) or separate DSH loop
- DSH inlet temperature

$$\dot{Q}_{cond}, \dot{Q}_{DSH}, P_{el} = \mathrm{f}(\vartheta_{src}, \vartheta_{snk,} \vartheta_{DSH}, stage, DSH) \qquad (16)$$

Fig. 11 (left) reports the heating power of the HP. The uncertainty of the model is indicated by the error bars and is in the range of 6 kW. Fig. 11 (right) shows the corresponding COP. It is significantly lower than the COP according to the data sheet. One reason for lower performance is the lower volume flows on the source and sink side compared to the measurement acc. to the standards. Furthermore, a slight degradation of the heating capacity of the HP could be identified within the first three years of operation, which could be explained by some refrigerant leakage. Further detailed investigations will be carried out to identify the reason for the deviation of the measured data and the data sheet.

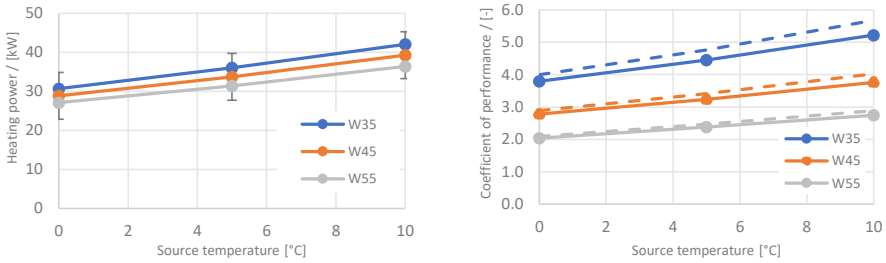


Fig. 11. Heating power for stage 2 (left) and COP for stage I and stage II (right) for the configuration with DSH in series to the condenser as in Fig. 5 (series configuration)

7.4. Dynamic Heat Pump Model DSH

The comparison of measured and simulated thermal power in condenser and desuperheater as well as electric power of the compressor(s) (bottom) is shown in Fig. 12 for a typical day in winter. The agreement is overall acceptable for all the three operation modes (heating stage I and II, DHW preparation stage II).

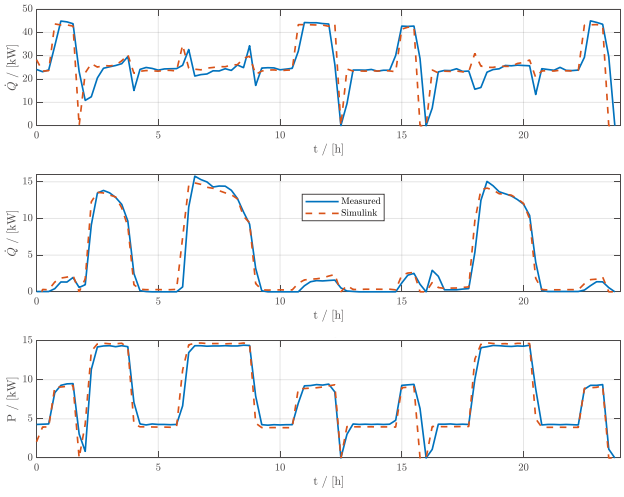


Fig. 12. Comparison of measured and simulated thermal power in condenser (top) and desuperheater (center) as well as electric power of the compressor(s) (bottom) for a typical day in winter

8. Discussion

The simulation assisted analysis of the monitoring results of the two buildings and of the HVAC system (including distribution losses, heat pump performance factors, auxiliary electricity demand, solar thermal and PV yield) allows to identify and solve problems that frequently occur during commissioning of the system. With the help of the simulation study, the control of the system can be optimized in order to reach the anticipated performance.

The net zero energy balance (for heating and DHW and auxiliary energies) could not be achieved during the first three years of monitoring. The implementation of first optimization measures shows a reduction of the demand. The performance of the HP is significantly lower than expected based on data sheet PM. There is a potential improvement of the performance by using the DSH loop, however, due to the high COP in heating mode in stage I that mode should be preferred. the following control scheme is recommended see Fig. 13. Optimal switching between single and double stage operation in heating mode is subject of current investigations.

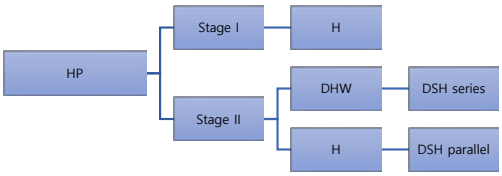


Fig. 13. Recommended operation modes: stage II in winter, stage I in intermediate season; (DSH in series in heating mode stage I)

Predictions based on results after introduction of improvements show that Net Zero could be achieved, see Fig. 14. In future projects more care should be taken in the appropriate dimensioning of the components (in particular heat pump capacity and storage volume) Passive House (PH) standard is key for achieving NZEB level for heating, DHW and aux. energies. If appliances was included in the energy balance, additional PV on the south façade would be required.

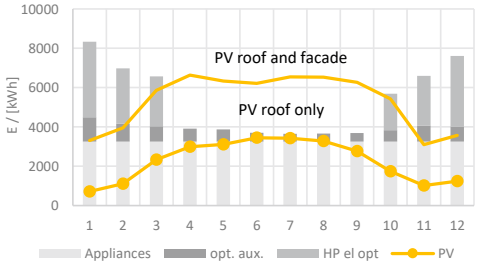


Fig. 14. Predicted monthly electric energy balance after improvements with appliances and with additional PV on the façade

A Simulink model of the HP was developed. The multi-dimensional PM model allows to simulate different HP operation strategies with and without DSH as well as single and double-stage operation. The optimization of both, the control strategy and of the components, is performed with the aim to operate the HVAC system with improved performance. Predictions show that the NZE can be achieved with improved control strategy and when the auxiliary energies are reduced.

9. Conclusions

Two multi-family buildings (MFB) with together 26 flats were designed to achieve a net Zero Energy (NZE) balance for heating, domestic hot water (DHW) preparation and all auxiliary energies. The roof of one of the MFB is covered by PV, the other is partly used for PV and partly for solar thermal (ST). A double-stage ground water heat pump (HP) with hot gas desuperheating (DSH) provides the remaining energy for heating and DHW. The system was designed with a low temperature distribution system (floor heating) and separate decentral fresh water preparation (DHW plate heat exchanger) for low thermal losses and optimal efficiency.
Detailed monitoring of the buildings, the HVAC system including thermal losses and the performance of the

HP, PV and ST allowed to study the behavior of NZEBs in practice. The simulation-assisted analysis of the monitoring data allowed to identify problems and faults of the installation and of the operation (i.e. control). Detailed performance maps of the double-stage HP pump with DSH were generated analyzing the monitoring data and by means of refrigerant cycle simulation. Simulation based optimization was performed with the aim to operate the HVAC system with improved performance. Different system configurations (i.e. with or without ST, with different buffer storage sizes, with different control strategies and set points) can be compared and evaluated also considering (seasonal) variations of the share of renewables (RE) in the electricity mix. Recommendations for the design and for the operation of the HP system (including control optimization) for MFB and blocks of buildings can be derived from the simulation results. It is evident that basic monitoring of the performance of the HVAC system is required to detect faults and to be able to guarantee efficient operation (quality control).

Acknowledgements

The financial supports from the Austrian Ministry for Transport, Innovation and Technology and the Austrian Research Promotion Agency (**FFG**) through the IEA Research Cooperation to this work are gratefully acknowledged.

References

[1] BPIE (2015). Nearly Zero Energy Building definitions Across Europe, Factsheet. Brussels.
[2] European Parliament (2010). Directive 2010/31/EU of the European Parliament and Council of May 19, 2010 on the energy performance of buildings (recast), Journal of the European Union, p. L 153/13.
[3] Garcia J. F., Kranzl L. (2018). Ambition Levels of Nearly Zero Energy Buildings (nZEB) Definitions: An Approach for Cross-Country Comparison. *Buildings 8(10), 143.*
[4] Ahmed, K., Carlier, M., Feldmann, C., Kurnitski, J. (2018). A New Method for Contrasting Energy Performance and Near-Zero Energy Building Requirements in Different Climates and Countries. *Energies 11(6), 1-22.*
[5] Bernier M., Ferron Y., Biaou A. L., Simulation of zero net energy homes, Journée thématique du, 2006 - simurex.ibpsa.fr
[6] Miara M., Günther D., Langner R., Helmling S. (2014). Efficiency of Heat Pumps in Real Operating Conditions - Comparison of three Monitoring Campaigns in Germany. REHVA Journal 5/2014, 7-12.
[7] Miara M., Günther D., Langner R., Helmling S., Wapler J. (2017). 10 years of heat pumps monitoring in Germany. Outcomes of several monitoring campaigns. From low-energy houses to un-retrofitted single-family dwellings. IEA HPC 2017, Montral, Canada.
[8] FHG ISE Pressemitteilung (2017). Gestiegene Effizienz: Feldtests Bestätigen Potenzial von Wärmepumpen als wichtigster Heiztechnik der Zukunft.
[9] Chua K.J., .Chou S.K, Yang W.M. (2010). Advances in heat pump systems: A review. *Applied Energy 87(12), 3611-3624.*
[10] Ochs F., Dermentzis G., Feist W. (2014). Minimization of the Residual Energy Demand of Multi-storey Passive Houses – Energetic and Economic Analysis of Solar Thermal and PV in Combination with a Heat Pump. *Energy Procedia 48, 1124-1133.*
[11] Ochs F., Dermentzis G., Ksiezyk A. (2018), Simulation and Monitoring Results of two MFHs in PH Standard with Heat Pump, Solar Thermal and PV, Solar World Congress, 2018, Abu Dhabi, UAE.
[12] Ochs F., Dermentzis G. (2018), Evaluation of Efficiency and Renewable Energy Measures Considering the Future Energy Mix, IBPC, Syracuse, USA.
[13] Ochs F., Dermentzis G., Monteleone W., Simulation-assisted Optimization of the HVAC system of NZE Multi-family Buildings, IBPSA 2019, Rome, Italy.
[14] Wang W., Ma Z., Jiang Y., Yang Y., Xu S., Yang Z. (2005). Field test investigation of a double-stage coupled heat pumps heating system for cold regions. *International Journal of Refrigeration 28(5), 672-679.*
[15] Hengel F., Heinz A., Rieberer R. (2016). Performance analysis of a heat pump with desuperheater for Residential buildings using different control and implementation strategies. *Applied Thermal Engineering 105, 256-265.*
[16] Lee A. H.W., Jones J. W. (1996). Thermal performance of a residential desuperheater/water heater system. *Energy Conversion and Management 37(4), 389-397.*
[17] www.coolprop.org.
[18] EN ISO 14511, Air conditioners, liquid chilling packages and heat pumps with electrically driven compressors for space heating and cooling — Part 1: Terms and definitions.

13th IEA Heat Pump Conference
April 26-29, 2021 Jeju, Korea

Numerical analysis of the vortex tube characteristics used within a high temperature heat pump

Constantin Zenz[a,*], Michael Lauermann[a], Mirza Popovac[a]

[a]Austrian Institute of Technology, Giefinggasse 2, 1210 Vienna, Austria

Abstract

The application of heat pumps in high temperature processes bears a high potential with respect to energy savings and reductions of greenhouse gas emissions. As heat pumps operating at high temperatures typically involve high refrigerant pressure levels, followed by high expansion work in the refrigerant cycle, an increase in energy efficiency can be achieved by recovering a part of that expansion energy. This paper investigates the applicability of vortex tubes as expansion devices in heat pumps. A vortex tube separates an incoming high-pressure stream into a cold and hot low-pressure stream, respectively. The flow field characteristics inside a vortex tube are investigated using state-of-the-art CFD tools. Two possible heat pump cycles utilizing a vortex tube are presented and evaluated using a one-dimensional model of a heat pump. It is shown that the applicability of a vortex tube as expansion device in a heat pump is limited due to several restricting factors. One promising configuration and application is identified and presented in detail, where the use of a vortex tube improves the COP by 19% over a standard heat pump.

© HPC2020.
Selection and/or peer-review under responsibility of the organizers of the 13th IEA Heat Pump Conference 2020.

Keywords: Ranque-Hilsch effect; Expansion work; Energy efficiency; CFD; 1D system simulation.

1. Introduction

In standard heat pumps, the expansion process takes place in an isenthalpic throttle valve. Replacing the throttle valve by a so-called Ranque-Hilsch vortex tube has been previously proposed e.g. by Nellis and Klein [1] and Sarkar [2]. A vortex tube, originally invented by Ranque in 1933 [3] and further refined by Hilsch [4], is a simple device with no moving parts, consisting of a tube, where a high-pressure fluid is injected tangentially through nozzles. The fluid develops a swirling flow pattern of high angular velocity, separating the fluid into a stream of high temperature fluid exiting on one axial end near the outer radius of the tube, and a stream of low temperature fluid exiting on the other axial end near the center of the tube. By controlling a valve at the hot end, the fraction of mass flow exiting at the cold side, $\gamma = \dot{m}_c/\dot{m}_i$, called the cold fraction, can be adjusted. In general, if γ increases, T_h increases, and T_c decreases for decreasing γ. At $\gamma = 0.5$, both the hot and cold temperature separation are equal.

Until today, this unique temperature separation effect, called the Ranque-Hilsch effect, is not entirely physically explained, although numerous investigations have been conducted. Hilsch [4] suggested that kinetic energy is transferred from the center to the outer part of the tube through internal friction, with shear work being the underlying mechanism of the temperature separation. Reynolds [5] identified heat and energy fluxes due to turbulent mixing as result of radial pressure and temperature gradients, buoyancy forces and Reynolds shear stresses as underlying physical processes. Ahlborn and Gordon [6] analyzed the vortex tube as a classical refrigeration cycle, identifying a primary loop at the outer radius of the tube as the coolant loop and a secondary

* Corresponding author.
E-mail address: constantin.zenz@ait.ac.at

loop close to the center of the tube as refrigerant loop which performs heat rejection at the outer radius and energy absorption at the center.

Throughout the many investigations that have been conducted both experimentally and numerically on the vortex tube, the working fluid was mostly air. Very little research has been conducted on working fluids other than air. Balmer [7] experimentally analyzed the expansion of liquid water inside a vortex tube, concluding that for inlet pressures of 20 to 50 MPa, a temperature separation of 10 to 20 K is obtainable, notably with both outlet temperatures being higher than the inlet temperature. Although the necessary pressure lies two orders of magnitude above the pressures usually employed in a vortex tube operated with air, Balmer [7] concluded that the working fluid does not necessarily need to be compressible for a temperature separation to occur. Collins and Lovelace [8] performed experiments with two-phase propane inside a vortex tube. This study is especially interesting for the use of vortex tubes in refrigeration cycles, as propane is a common refrigerant and the expansion process in a standard heat pump occurs within the two-phase region. It was concluded in [8] that for inlet vapor qualities above 80%, a significant temperature separation can be obtained, but when the inlet vapor quality is further lowered, the Ranque-Hilsch effect vanishes rapidly.

Based on the research that has been done on the Ranque-Hilsch effect, it does not seem reasonable to replace the throttle valve of a heat pump cycle with a vortex tube, although this has been proposed earlier. The refrigerant entering the throttle valve is usually fully condensed liquid, and pressure levels in heat pumps are by far not sufficient for the Ranque-Hilsch effect to occur with a liquid as working fluid. Also, when two-phase refrigerant enters the vortex tube, e.g. by not fully condensing the fluid, the vapor quality would need to be very high. Therefore, it is concluded that when using a vortex tube inside a heat pump cycle, it must be assured that it is always operated with a fluid in fully gaseous (i.e. superheated) state. This has similarly been concluded previously by Mohiuddin and Elbel [9].

In order to assess different heat pump cycles and analyze possible COP-improvements, a CFD model of the vortex tube has been developed. In this way, the characteristics of the vortex tube under different refrigerants, geometries and operating conditions could be obtained and used for 1D-simulations of different heat pump configurations.

2. CFD Model

The flow inside the vortex tube is modeled as steady, three-dimensional, turbulent and compressible. Therefore, the three-dimensional Favre-averaged Navier-Stokes equations and continuity equation, together with an equation for the conservation of energy are used. The Reynolds stress tensor that comes up when time- (or Favre-) averaging the equations is modeled through the Boussinesq Assumption employing the Standard k-ε turbulence model, which was shown to predict the flow inside a vortex tube with sufficient accuracy, e.g. by Dutta et al. [10]. The model was used with scalable wall functions, making the solver always set $y^* \geq 11.225$ to ensure the first grid point is placed within the fully turbulent sub-layer even if the near-wall mesh is too fine. Viscous heating, i.e. the thermal energy created by viscous shear was included as previous research suggests this mechanism is important in vortex tube flows. Also, a compressibility correction in terms of a dilatation dissipation was included in the k-equation. The density of the fluid was modeled with the ideal gas law, with all material properties being constant except for the specific heat when performing simulations with refrigerants, where c_p was given linear temperature-dependency. To solve this set of equations, a pressure-based coupled solver was used, employing second-order upwind schemes for density, momentum and energy equations, first order upwind schemes for k- and ε-equations, and a second order scheme for pressure. Simulations have also been performed using the third-order MUSCL scheme, but did not show significant changes in the solution, and were therefore omitted for enhancing convergence.

A mesh consisting of tetrahedral cells, with refinements near walls, was used. A purely hexahedral mesh was also created but did not show changes in the solution. Mesh independence was ensured by running numerous simulations with meshes of different cell numbers, using the value of $\Delta T_{h,c} = T_{h,c} - T_i$ for judging mesh independence.

The inlets and outlets were defined as pressure-inlets and pressure-outlets. All walls were treated with a no-slip condition. To judge convergence, besides monitoring the scaled residuals, mass-averaged values of total temperature at both outlets of the vortex tube, T_h and T_c, and the cold fraction, γ, were monitored.

3. Flow pattern

3.1. Air

At first, the geometry used in the study of Skye et al. [11] was used, which is given in Table 1. The exact geometry could not be reproduced, as the dimensions of the hot outlet are unknown, as is the exact geometry of the inlet. The CFD model of [11] was two-dimensional, with a radial exit and a continuous annular inlet, and exhibited discrepancies between experimental and numerical pressure values. Hence also the experimental and CFD results of [11] differ.

Table 1. Vortex tube geometry:

symbol	description	value
L	working length	106 mm
D	tube diameter	11.4 mm
r_c	cold outlet radius	3.1 mm
A_i	total inlet area (6 nozzles)	8.2 mm^2

The working fluid was air, the inlet total pressure was kept at 483 kPa and the inlet total temperature was kept at 294 K. The cold outlet static pressure was kept at ambient pressure and the hot outlet pressure was varied to adjust γ. The results of these simulations are given in Figure 1, where the separation of the hot and cold exit temperatures from the inlet temperature, ΔT_h and ΔT_c, are plotted for varying cold fractions γ. Also, the results of [11] are plotted in Figure 1 for comparison. The obtained results match the CFD results of [11] quite well. It is noted that both the CFD model of this study and that of [11] underpredict the experimental values of ΔT_c. Nevertheless, the qualitative results are identical, exhibiting the same steepness of T-γ-dependency, with $\Delta T_h = \Delta T_c$ at $\gamma \approx 0.5$ and a larger overall temperature separation towards very high values of γ.

Figure 2 shows the profiles of tangential and axial velocity over the radius of the vortex tube at different axial locations. Figure 3 shows the radial profiles of total and static temperature at different axial locations. Both Figures match the velocity- and temperature-profiles produced by Behera et al. [12], suggesting that the physical processes inside the vortex tube are accurately modeled in the underlying CFD-model. In Figure 4, a contour plot of total temperature distribution over the vortex tube is given. Figure 5 shows a contour plot of density.

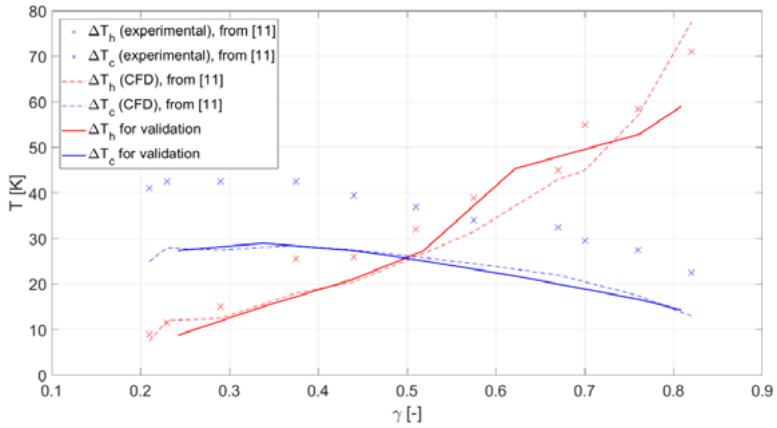


Fig. 1. Total temperature separation at hot and cold outlet as function of γ plotted against CFD and experimental results of [11]

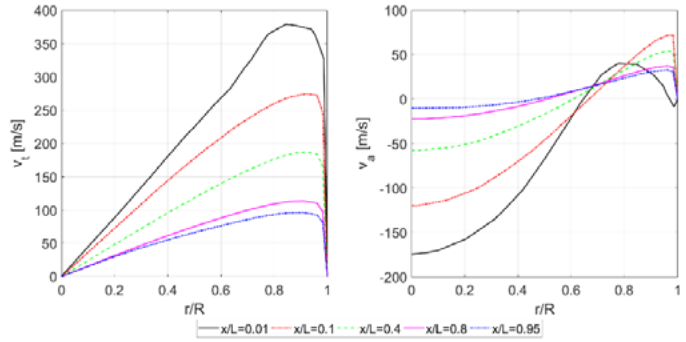


Fig. 2. Tangential (left) and axial (right) velocity profiles at different x/L-locations (air, $\gamma = 0.6$)

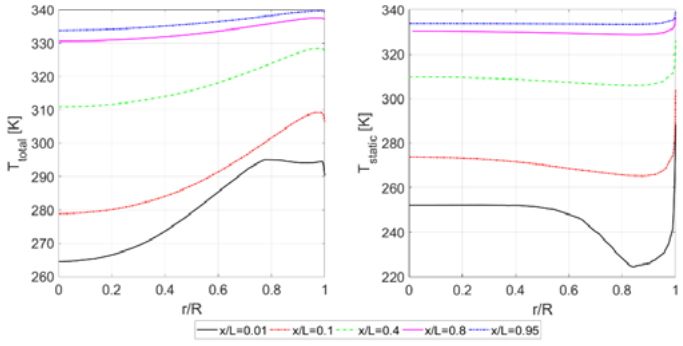


Fig. 3. Total (left) and static (right) temperature profiles at different x/L-locations (air, $\gamma = 0.6$)

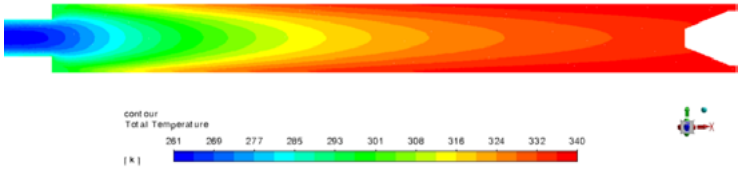


Fig. 4. Contour plot of total temperature throughout the vortex tube (air, $\gamma = 0.6$)

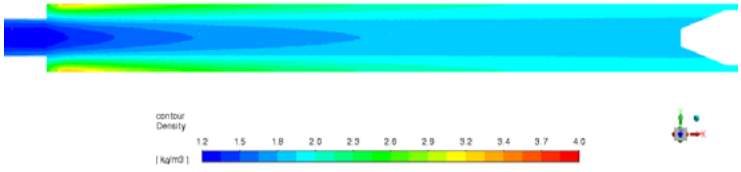


Fig. 5. Contour plot of density throughout the vortex tube (air, $\gamma = 0.6$)

3.2. Water

In order to investigate the flow of an incompressible fluid inside a vortex tube, simulations using liquid water as working fluid have been conducted. The same geometry was used as in the above simulation with air. The geometry is in its overall size comparable to that used by Balmer [7] for experiments with water, although the exact geometric specifications of [7] were not provided. The overall temperature separation obtained for an inlet pressure of 50 MPa was, depending on the cold fraction, around 10 K, with both T_h and T_c being above inlet temperature, which is congruent with the results of [7]. A contour plot of total temperature distribution throughout the vortex tube is provided in Figure 6. It is notable that with water as working fluid, the radial temperature gradient seems to be significantly lower than with air (compared to Figure 5), the temperature variation seems to be almost purely axial. Figure 7 shows tangential and axial velocity profiles and Figure 8 shows total and static temperature profiles at the same axial locations as in the above simulation with air. While the tangential velocity profiles exhibit a similar behavior, the maximum axial velocity at the center is, in contrast to the case with air, not found at $x/L = 0.01$, but at $x/L = 0.1$. Also, the axial velocities at the outer radius exhibit a sharper peak. For the temperature profiles shown in Figure 7 it is notable that while the static temperature profiles seem to be resembling that of the case with air, the total temperature profiles show much less change over the radius compared to Figure 3.

Generally, the flow patterns in terms of velocity and temperature distribution differ from the usual ones observed in vortex tubes operated with gaseous fluids. Another interesting observation is, that when viscous heating is excluded from the CFD model, a lower, yet still significant temperature separation occurs with air. Excluding the viscous heating term from the CFD model for calculations with water, however causes the temperature dissipation to fully vanish, i.e. no temperature gradient over the entire domain of the vortex tube can be observed. This shows that at least in the numerical model, thermal energy created by viscous shear is the only underlying physical process causing the temperature separation. As the results of the numerical analysis deliver similar results to the experimental study of Balmer [7], it is questionable if the Ranque-Hilsch effect is the reason for the temperature separation observed in [7]. The fact that with water both outlet temperatures are higher than the inlet temperature supports the theory that viscous shear is the main reason for this temperature separation.

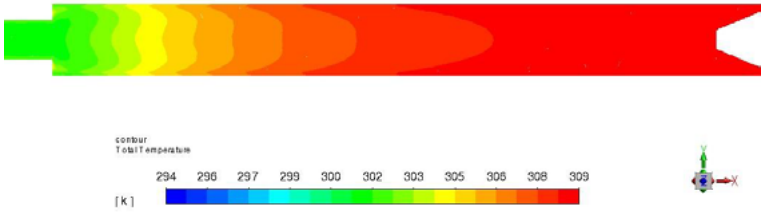


Fig. 6. Contour plot of total temperature throughout the vortex tube (water, $\gamma = 0.54$)

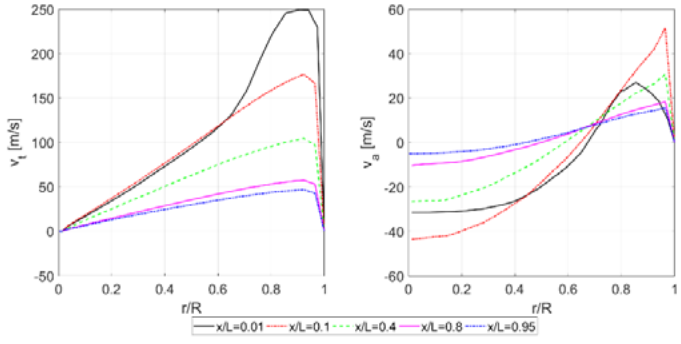


Fig. 7. Tangential (left) and axial (right) velocity profiles at different x/L-locations (water, $\gamma = 0.54$)

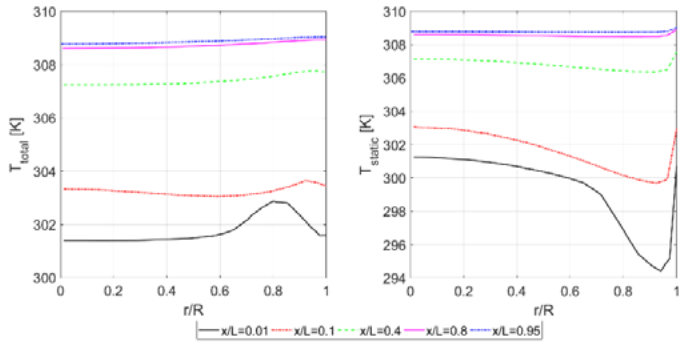


Fig. 8. Total (left) and static (right) temperature profiles at different x/L-locations (water, $\gamma = 0.54$)

3.3. Other Fluids

Simulations with other fluids, mainly natural and synthetic refrigerants, and helium have been conducted. It was noted that in general, the Ranque-Hilsch effect decreases with an increasing molar mass of the fluid. Therefore, helium, being the second lightest element, showed the largest temperature separation. For refrigerants, which generally have a higher molar mass than air, a smaller temperature separation was observed. Using helium as working fluid in a vapor compression cycle is however not feasible as even isentropic compression of helium involves very high temperature rises.

Apart from the molar mass, also thermal conductivity, viscosity and heat capacity ratio of a fluid have been reported to have a significant influence on the Ranque-Hilsch effect [13,14].

As the geometric specifications of the used vortex tube were derived from vortex tubes usually used with air, it is unclear whether a fundamentally different design could substantially improve the Ranque-Hilsch effect when employing a refrigerant. Also, as detailed studies of vortex tubes with refrigerants as working fluids where all geometric specifications and boundary conditions are given were unavailable, a validation of the CFD model for the use of other fluids than air was not possible. Hence, CFD results have to be treated with caution and should merely be used as initial probing to identify possible applications where further experimental investigations seem reasonable.

Figure 9 shows simulation results in terms of hot and cold exit total temperature separation from inlet total temperature for two different vortex tube geometries (different length-to-diameter ratio). The working fluid is R1336MZZ(Z), with an inlet pressure of 10 bar and a cold outlet pressure of 1.978 bar. It can be seen that a change in length-to-diameter ratio has a negligible effect on the temperature separation, and while the pressure ratio between inlet and cold outlet is comparable to that of the case with air (Figure 1), the magnitude of the temperature separation is significantly lower with R1336MZZ(Z) as working fluid.

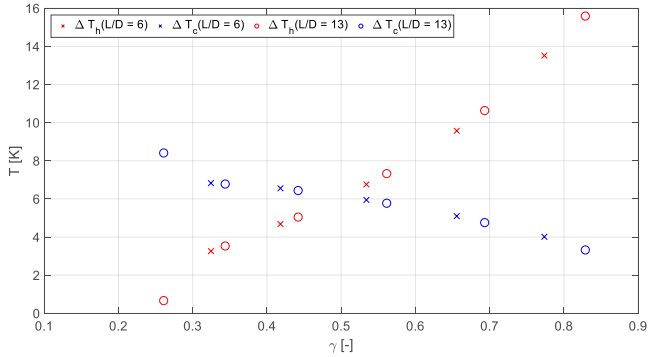


Fig. 9. Total temperature separation at hot and cold outlet as function of γ for two different geometries (R1336MZZ(Z))

4. Applications

Although vortex tubes have been investigated for almost one century by now, and find some specialized applications, there are still no heat pump or refrigeration cycles that make use of the Ranque-Hilsch effect. The focus of this investigation is set on high temperature applications as they are found in industrial steam generation. In Austria, steam generation accounts for 29 % of usable energy in industrial applications, with the majority of that energy being sourced from natural gas, bearing a large potential for the reduction of CO2 emissions [15]. However, to initiate a shift towards the use of (regeneratively sourced) electrical energy for steam generation calls for efficient means of heating. Two possible heat pump cycles for such applications making use of the Ranque-Hilsch effect are presented and discussed here.

4.1. Intermediate Expansion Heat Pump Cycle

When using a vortex tube for expansion in a heat pump cycle, the most promising cycle layout seems to be one introduced similarly by Mohiuddin and Elbel [9]. The schematic layout and log(p)-H-diagram is given in Figure 10. From state 1 to 3, the cycle is identical to that of a conventional heat pump. From state 3 to 4 the refrigerant is expanded to an intermediate pressure level, between that of condenser and evaporator, inside a throttle valve. Then, liquid (5a) and vapor (5b) are separated, with the vapor being fully expanded to evaporator pressure inside a vortex tube (6b/6c). The hot stream (6c) can then be used for further heating purposes, depending on the absolute temperature. The cold stream (6b) is internally recuperated and then mixed with the fully expanded (7a) and evaporated (8) remaining refrigerant.

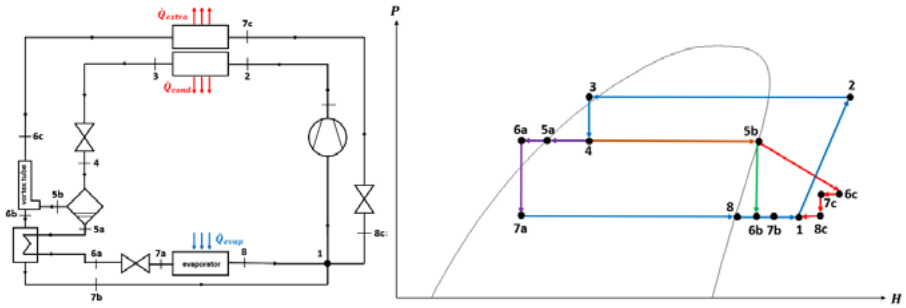


Fig. 10. Schematic cycle layout and theoretical log(p)-H-diagram (based on [9]) of a heat pump with vortex tube expansion

The COP-improvement of such a configuration when compared to a traditional heat pump is estimated by Mohiuddin and Elbel [9] to be around 5 to 10% over a conventional heat pump cycle. Choosing an adequate intermediate pressure level, p_{int}, is crucial for such a configuration, as with p_{int} decreasing, a greater amount of vapor can be utilized inside the vortex tube, but at the same time, the temperature separation effect inside the vortex tube decreases with decreasing inlet pressure. It seems intuitive that there must be an optimum. To estimate the location of this optimum for a given refrigerant, the analytical formulae for calculating the temperature separation inside a vortex tube that were developed by Ahlborn and Gordon [6] were used. These read:

$$\Pi_T = \frac{T_h}{T_c} \approx 1 + \frac{(\kappa-1)\zeta(\gamma+1)}{\kappa} \tag{1}$$

$$\zeta = \frac{p_i - p_c}{p_i + 2p_c} \tag{2}$$

where κ is the heat capacity ratio and p_i and p_c are inlet and cold outlet pressure, respectively. The temperature separation estimated by Eq. (1) is only a very rough estimate, derived using many assumptions, and not taking into account any geometric considerations. Nevertheless, even if the absolute value of Π_T is

far off the reality, its relative change with respect to pressure ratio is believed to show a qualitatively similar behavior to that of a real vortex tube, therefore not influencing the location of that optimum. Using the fact that at $\gamma = 0.5$ the hot and cold temperature separation are equal, absolute temperature values can be obtained:

$$T_h|_{\gamma=0.5} - T_i|_{\gamma=0.5} = T_i|_{\gamma=0.5} - T_c|_{\gamma=0.5} \quad (3)$$

$$T_h|_{\gamma=0.5} = \frac{2T_i|_{\gamma=0.5}}{1+1/\Pi_T} \quad (4)$$

Now, the quantity to be maximized is the difference of enthalpy flow rate between hot and cold outlet, as this quantity includes both the temperature separation, ΔT, that increases with increasing intermediate pressure level and the mass flow rate inside the vortex tube, $\dot{m}$, which decreases with increasing intermediate pressure:

$$\Delta\dot{H} = c_p \dot{m} \Delta T \rightarrow max \quad (5)$$

In Figure 11, $\Delta\dot{H}$ is plotted for a heat pump cycle with R600 as refrigerant, with a condenser pressure $p_{cond} = 26.63$ bar and evaporator pressure $p_{evap} = 6.864$ bar. It can be seen, that there is a clear optimum, below which the inlet pressure of the vortex tube is not high enough, and above which the vapor fraction entering the vortex tube is too low. In this case, the optimum intermediate pressure level is found at $p_{int} = 20$ bar. Any classical heat pump configuration can theoretically be modified in this way. The important question is in each case, if T_h is high enough to be usable with γ being low enough to for the hot end mass flow to be of significant amount.

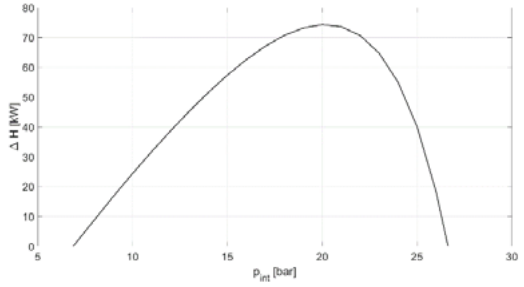


Fig. 11. $\Delta\dot{H}$ as function of p_{int} for R600 in a high temperature heat pump, calculated according to Eqs. (1)-(5)

Apart from maximizing the output of usable energy of the vortex tube itself via Eq. (5), it is at least equally important to tune T_h to a value at which the additional heat provided at the vortex tube's hot exit can be used.

4.2. Heat Boost Cycle

Another way to operate a vortex tube while ensuring the fluid entering the vortex tube remains purely gaseous is a heat boost cycle, which has also previously been suggested by Mohiuddin and Elbel [9]. A schematic layout of such a cycle is given in Figure 12. From state 1 to 2 liquid refrigerant is pumped to a high pressure, where it is then fully evaporated (state 3). From state 3 to 4a/4b, the gaseous refrigerant is expanded inside a vortex tube, using the superheated vapor at state 4a for steam generation.

The advantage of the combined vortex tube heat boost cycle is that the temperature level can be lifted without an increase in pressure. Also, for a given heat source at an already high temperature level, where

otherwise exergetically expensive resistive heating is employed for heat boosting, this configuration seems to be a reasonable alternative. On the other hand, only a small fraction of the overall refrigerant mass flow can be used for steam generation, as high hot end temperatures inside a vortex tube occur at high cold fractions.

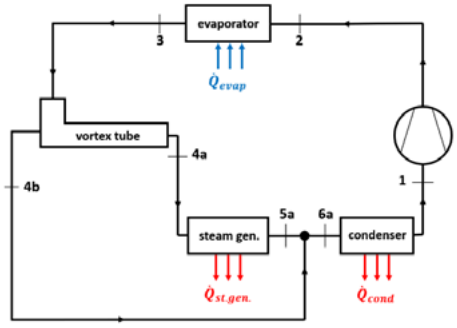


Fig. 12. Schematic cycle layout of a standard vortex tube heat boost cycle with vortex tube

5. Results

A one-dimensional system simulation model for the intermediate expansion cycle (based on the schematic layout presented in Figure 10) was developed as shown in Figure 13. By using the results generated from the CFD model of the vortex tube for different operating conditions and refrigerants to model the vortex tube within these 1D-system simulations, different applications in terms of temperature- and pressure levels, refrigerants and mass flow rates were evaluated. The CFD results of the vortex tube were incorporated in the 1D-model as a lookup-table containing data for several operating conditions. The aim of these system simulations was to identify applications and refrigerants for which the use of vortex tube expansion is promising in terms of COP-improvement.

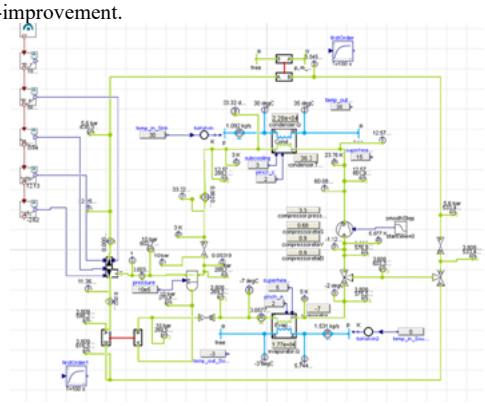


Fig. 13. System simulation model of an intermediate expansion heat pump cycle

As presumed from the findings in Section 4, the intermediate expansion cycle was found to outperform a conventional heat pump cycle in the presence of the following two circumstances:

- A high difference in condenser and evaporator pressure is present, allowing for a relatively low level of intermediate expansion pressure while still maintaining a high enough inlet pressure at the vortex tube.

- The refrigerant exhibits a relatively flat saturation line, yielding a high vapor quality at intermediate expansion pressure level.

Of the conducted simulations, the most promising in terms of COP – improvement was a heat pump cycle aimed at industrial applications where a waste heat source at 70 °C was used to provide heat for steam generation at 160 °C with R1336MZZ(Z) as refrigerant. As a high temperature lift is needed, the difference in condenser and evaporator pressure is high, which in combination with the properties of the refrigerant leads to a significant vapor quality after intermediate expansion. In Figure 14, the log(p)-H-diagrams of both the conventional heat pump cycle and the corresponding intermediate expansion cycle are given, with the hot exit stream of the vortex tube marked in red and the cold exit stream of the vortex tube marked in orange. As can be seen, the separation at intermediate pressure level, combined with the non-isenthalpic expansion in a vortex tube leads to an increased condenser and evaporator heat flow. The COP of the intermediate expansion heat pump cycle was shown to be 19 % higher than that of a conventional heat pump for the same application. The additional heat provided by the hot exhaust of the vortex tube was not used for COP calculations as it is highly case-dependent whether a heat sink exists where this heat can be utilized. Therefore, if demand for additional heat at the temperature level of the vortex tube's hot exit is needed, the COP might increase further.

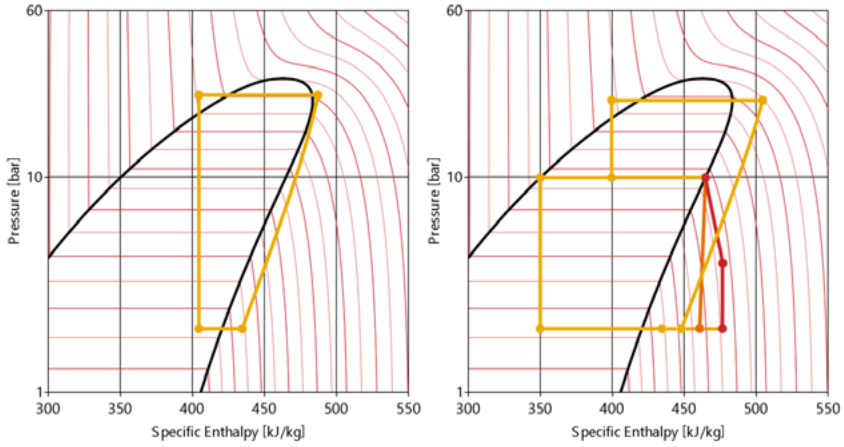


Fig. 14. Log(p)-H-diagrams of conventional (left) and intermediate expansion (right) heat pump cycle for steam generation with R1336MZZ(Z) (result of one-dimensional simulation using results of CFD simulations of a vortex tube)

6. Conclusions

- Although vortex tubes can be operated with liquid working fluids at sufficient inlet pressure, it is not obvious that the underlying physical processes are the same as within vortex tubes operated with gas. The numerical analysis presented here strongly suggests that it is not the same effect that causes energy separation within a vortex tube when operated with liquid as with gas.
- When designing heat pump configurations that involve expansion inside a vortex tube, it is concluded crucial that the fluid remains in gaseous state inside the vortex tube. Two such cycle layouts are presented.
- From the results of CFD simulations it is observed that the Ranque-Hilsch effect decreases when using refrigerants as working fluids. This is believed to partly stem from the higher molecular weight of refrigerants compared to air.
- One of the two presented heat pump configurations, the intermediate expansion heat pump cycle, was simulated and compared to a conventional heat pump cycle. It was found that while for many applications the COP-improvement is negligible, there are cases where vortex tube expansion from an intermediate pressure level can significantly improve the COP. One such cycle aimed at

industrial steam generation using R1336MZZ(Z) as refrigerant is presented and shows a COP improvement of 19 % over a conventional heat pump.
- By identifying promising cases for further investigation using the tools presented in this study - namely a detailed three-dimensional CFD simulation of the vortex tube, combined with a one-dimensional analysis of the heat pump cycle - a foundation for further experimental investigations can be established.

Acknowledgements

The financial support for the work presented in this paper has been provided by FFG – Österreichische Forschungsförderungsgesellschaft mbH (project "VWE", project number 871723).

References

[1] G.F. Nellis & S.A. Klein (2002): The application of vortex tubes to refrigeration cycles. *International Refrigeration and Air Conditioning Conference*, Paper 537.
[2] J. Sarkar (2008): Use of vortex tube as expansion device in isobutane based refrigeration system. *ICRDME*, January 23-25 2008, SUS College of enfineering & Technology Tangori, Mohali (Punjab) India.
[3] G.J. Ranque (1933): Experiments on Expansion in a Vortex with Simultaneous Exhaust of Hot and Cold Air. *Le Journal De Physique et le Radium (Paris)*, Vol. 4, pp. 112-114.
[4] R. Hilsch (1946): Die Expansion von Gasen im Zentrifugalfeld als Kaelteprozess. *Zeitschrift fuer Naturforschung A*, Vol. 1(4), pp. 208-214.
[5] A.J. Reynolds (1961): Energy Flows in a Vortex Tube. *Zeitschrift fuer angewandte Mathematik und Physik ZAMP*, Vol. 12(4), pp. 342-357.
[6] B.K. Ahlborn & J.M. Gordon (2000): The Vortex Tube as Classical Refrigeration Cycle. *Journal of Applied Physics*, Vol. 88(6), pp. 3645-3653.
[7] R.T. Balmer (1988): Pressure-driven Ranque-Hilsch Temperature Separation in Liquids. *Journal of Fluids Engineering*, Vol. 110(2), pp. 161-164.
[8] R.L. Collins & R.B. Lovelace (1979): Experimental Study of Two-Phase Propane Expanded Through the Ranque-Hilsch Tube. *Journal of Heat Transfer*, Vol. 101(2), pp. 300-305.
[9] M. Mohiuddin & S. Elbel (2014): A Fresh Look at Vortex Tubes Used as Expansion Device in Vapor Compression Systems. *International Refrigeration and Air Conditioning Conference*, Paper 1393.
[10] T. Dutta, K.P. Sinhamahapatra, S.S. Bandyopdhyay (2010): Comparison of Different Turbulence Models in Predicting the Temperature Separation in a Ranque-Hilsch Vortex Tube. *International Journal of Refrigeration*, Vol. 33(4), pp. 783-792.
[11] H.M. Skye, G.F. Nellis, S.A. Klein (2006): Comparison of CFD Analysis to Empirical Data in a Commercial Vortex Tube. *International Journal of Refrigeration*, Vol. 29(1), pp. 71-80.
[12] U. Behera, P.J. Paul & S. Jacob (2008): Numerical Investigations on Flow Behaviour and Energy Separation in Ranque-Hilsch Votex Tube. *International Journal of Heat and Mass Transfer*, Vol. 51(25), pp. 6077-6089.
[13] N. Li, Z. Wang, X. Han, G. Chen (2014): Experimental Study of the Coupling Characteristics Between Vortex Tube and Refrigerants. *International Refrigeration and Air Conditioning Conference*, Paper 1518.
[14] X. Han, N. Li, K. Wu, Z. Wang, L. Tang, G. Chen, X. Xu (2013): The Influence of Working Gas Characteristics on Energy Separation of Vortex Tube. *Applied Thermal Engineering*, Vol. 61, pp. 171-177.
[15] Statistik Austria. *Nutzenergieanalyse Oesterreich 2017*. URL: http://www.statistik.at/web_de/statistiken/energie_umwelt_innovation_mobilitaet/energie_und_umwelt/energie/nutzenergieanalyse/index.html (accessed: 14.11.2019).

13th IEA Heat Pump Conference
April 26-29, 2021 Jeju, Korea

Simultaneous energy efficiency and acoustic evaluation of heat pump systems using dynamic simulation models

Christian Vering[a*], Jonas Klingebiel[a], Christoph Reichl[b], Johann Emhofer[b], Markus Nürenberg[a], Dirk Müller[a]

[a]Institute for Energy Efficient Buildings and Indoor Climate, RWTH Aachen University, Mathieustraße 10, 52074 Aachen, Germany
[b]AIT Austrian Institute of Technology GmbH, Center for Energy, Giefinggasse 2, 1210 Wien, Österreich

Abstract

Heat pumps are a key technology in Germany's energy system transformation process for achieving the federal government's environmental goals. A crucial factor, increasing heat pump's comfort, is its acoustics. Air-to-water-heat pumps need a compressor and a fan to operate efficiently. Both components have sound emissions that can be disturbing regarding humans' psychoacoustics. Thus, it is necessary to develop energy efficient and quiet heat pumps.

Within this work, we show that it is possible to estimate energetic and acoustic performance of heat pumps in dynamic simulation models simultaneously. Therefore, we link the Sound Source Extension Library to a dynamic heat pump simulation model, designed using the AixLib. The acoustic signatures of compressor and fan are coupled to their corresponding rotational speeds. Furthermore, we apply an Extremum Seeking Controller to operate the heat pump in an energy-acoustic optimum mode, which is specified by a predefined target function. By consequently optimizing the evaporator fan speed, we are able to reduce overall acoustic emission of the simulated heat pump by about 8 dB(A) while increasing its energy efficiency by about 4 %.

© HPC2020.
Selection and/or peer-review under responsibility of the organizers of the 13th IEA Heat Pump Conference 2020.

Keywords: heat pump; dynamic simulation model; acoustic emission; noise; extremum seeking control

1. Introduction

Within Germany's energy transition process, air-to-water heat pumps are a promising technology in order to replace conventional heating systems in the building stock. To accelerate the replacement process, there is an urgent need to improve their energy efficiency and user comfort. The coefficient of performance (*COP*) is a common measure to estimate heat pump's energy efficiency. Many studies investigate the influence of used refrigerant and building's temperature levels on the *COP*. Almost all of these studies aim for a *COP* maximization by optimizing either design or operation. Simultaneously, an increasing issue related to user comfort is heat pump's noise emissions. With regard to the A-weighted acoustic emissions, the fan and compressor of an air-to-water heat pump are the main sources of noise. According to Graf [1], the evaporator fan causes 90% of the noise perceived in the neighborhood. Reducing fan's noise emission by optimal design and operation implies a great potential to increase heat pump's user comfort. Apparently, both measures depend on component design and operation. However, energy efficient design and noise emission reduced design are contrary. The same applies for energy efficient and noise emission reduced operation. Since many design studies already exist, we focus on operation optimization within this work.

On the one hand, energy efficient operation studies discuss different heat pump control approaches. These commonly differ between rule-based-control (RBC), extremum seeking control (ESC) and model predictive control (MPC). Compared to conventional control approaches, MPC shows greatest potentials in order to

* Corresponding author. Tel.: +49 241 80 49 786; fax: +49 241 80 49 769.

increase energy efficiency. Nonetheless, expert system understanding is necessary to set up a MPC. ESC, in contrary, is easy to implement, as it is a model-free method.

On the other hand, there are two approaches reducing noise emissions. The primary measures include the acoustic optimization of the components or the acoustic optimization of the operating point. Secondary measures decrease sound radiation indirectly through silencers and sound insulation capsules. This work focuses on the acoustic optimization of the operating point. Manufacturers have implemented measures, to reduce the sound emission of the heat pump during night, by changing speeds of fan and/or compressor. This procedure is normally done solely based on time of day, which is set by the installer or user. The mode is called differently ranging from "silent" to "quiet" mode of operation.

However, a simultaneous operation optimization of energy efficiency and noise emission reduction was not identified in the literature, yet. Therefore, we introduce an approach that concurrently takes energetic and acoustic optimal operation (EAO) into account. According to Burns and Laughman [2], it is possible to provide a constant cooling capacity at different compressor and fan speeds. These combinations imply different energy efficiencies as well as noise emissions. Using multi-objective optimization, we can determine the trade-off between energetic and acoustic optimal operation.

Therefore, this work contributes to the EAO operation of heat pumps:

- Chapter 2 gives an overview on the literature regarding energy efficient operation as well as acoustic signatures of heat pumps. Furthermore, we introduce the basics of ESC.
- In Chapter 3 we describe the energetic simulation model. In addition, we show the acoustic data and how it was measured. Lastly, we describe the coupling approach of both models and apply it to ESC.
- We apply ESC to our model in order to simultaneously optimize acoustic emission and energetic efficiency in Chapter 4.
- Chapter 5 discusses results conducted before.
- We summarize our findings and give an outlook in Chapter 6.

2. State of the Art

In order to replace conventional heating technologies such as gas- or oil-fired boilers heat pumps need to be improved economically, ecologically and user-friendly. Therefore, increasing their energy efficiency and decreasing their noise emissions have an integrated potential to accelerate the replacement process.

2.1. Energetic assessment of heat pump systems

A common instantaneous thermodynamic measure for heat pump's energy efficiency is its *COP*. The *COP* is described as the quotient of heat extracted from the condenser $\dot{Q}_{\mathrm{Cond}}$ divided by the power to drive the compressor P_{Comp}:

$$COP = \frac{\dot{Q}_{\mathrm{Cond}}}{P_{\mathrm{Comp}}}. \tag{1}$$

Different studies use the *COP* as target function to determine the heat pump with highest efficiency according to different refrigerants or operating points. Using this target function an optimization program maximizes the condenser heat $\dot{Q}_{\mathrm{Cond}}$ and minimizes the compressor power P_{Comp}.

In order to introduce a simultaneous approach to optimize energetics and acoustics, the fan power has to be taken into account as well. Therefore, we introduce the system's coefficient of performance:

$$COP_{Sys} = \frac{\dot{Q}_{\mathrm{Cond}}}{P_{\mathrm{Comp}}+P_{\mathrm{Fan}}}, \tag{2}$$

which sums up the power consumption of the fan P_{Fan} in the denominator. This consideration allows an energetic assessment of both noise sources.

Considering the heat pump as a heat supply system, however, implies that the building's heat demand is fixed. As consequence, a heat pump system has to deliver a fixed amount of heat at a minimized sum of compressor power and fan power. Since we have no heat pump prototype yet, we assess the potential of EAO in a realistic simulation study. Conducting simulation studies requires an energetic heat pump model.

In the literature, many modelling approaches of heat pumps are widely discussed. Typically, approaches distinguish between black box, grey box and white box modelling. On the one hand, black box approaches allow a fast calculation of heat pump's behavior within a certain validated scope. Results from physical extrapolations, however, are restricted applicable.

On the other hand, white box models emulate real physical system with its geometrics. Therefore, complete understanding of the system is necessary. This modelling approach reveals the advantage of perfect system behavior estimation. In contrary, calculation speed is often very low.

A trade-off between both black box and white box approach is called grey box approach. It bases on physical equations to estimate its behavior and simplifies equations at some points by mathematical descriptions. Hence, we apply a grey box approach to estimate the physical behavior of the heat pump at reasonable simulation speed. In addition, we need information about the component's acoustic signature itself in order to determine their acoustic behavior.

2.2. Acoustic signature of heat pumps

Acoustic emissions of heat pumps can be retrieved using a variety of methods. For certification purposes – depending on the acoustic characteristics of the climate chamber - sound intensity measurements using scanning techniques or sound power measurements with a number of microphones distributed in the climate chamber are performed. According to the standards – in the end – one value for the sound power level will be given on the label for the standard operating point. This also means, that the transient behavior of the sound emission, the directivity of the sound emission and the effect of operating the heat pump at different conditions is not covered. For the measurements, which are the base for the simulations presented here, an acoustic dome with 61 microphones was used to record the acoustic sound pressure level at positions surrounding the heat pump as a function of time (see Figure 1). The data can then be used to calculate the transient A-weighted sound power level.

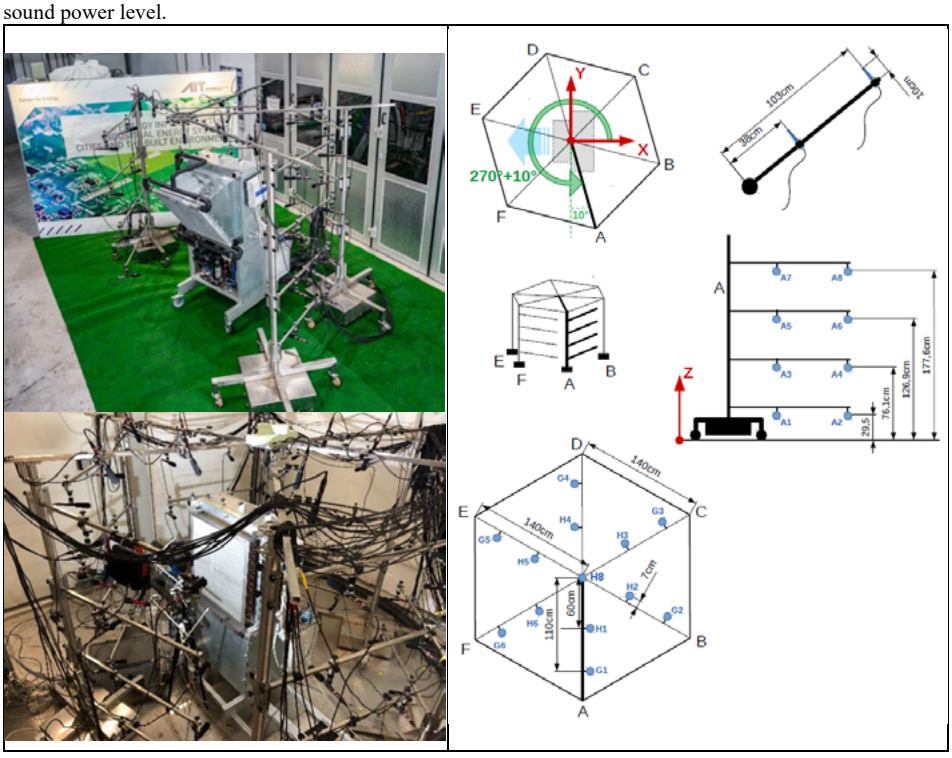


Fig. 1: Presentation image of a part of the acoustic dome around the SilentAirHP (top, left), which has been used to generate the data and SilentAirHP (bottom) in the climate chamber at AIT surrounded by the acoustic dome during frosting experiments; Geometrical setup of the acoustic dome. 48 microphones are placed on the sides, 13 microphones above the heat pump (right).

In order to simultaneously optimize heat pump's energetics and its acoustics, an optimization procedure is necessary. In this work, we therefore apply a model-free, adaptive Extremum Seeking Controller.

2.3. Extremum Seeking Control (ESC) applied to heat pumps

Common adaptive control methods, the two linear and non-linear, aim to control the output of a process to a known set point or a reference trajectory. The aim of ESC, however, is to find a manipulated variable, so that the variable to be controlled is kept at a minimum or maximum [3]. The manipulated variable is therefore disturbed periodically by a perturbation signal. This results in an oscillation of the system output. By determining the gradient between the manipulated variable and the system output, the manipulated variable can be modified so that the system output is optimized. Applying ESC, in addition to a target function t an amplification factor K and the parameters of the gradient estimator, must be determined.

In contrast to MPC, this is a model-free procedure. For the application of ESC in real processes, no model of the controlled system must exist. The method was already used in the 1950s [4] and has gained in importance due to the stability proofs of Krstic and Wang [5] in 2000. In the last 10 years, ESC has established itself as a promising control strategy for energy optimization of HVAC devices [6, 7]. In the Literature, simulation studies exist in which ESCs are tested on simulation models as well as studies in which it was implemented on test benches.

Burns and Laughman [2] applied ESC with conventional gradient estimation for the first time to a chiller in 2012. They investigated the fan's influence on the electrical power consumption of the entire plant. The temperature was kept constant by controlling the compressor speed. They were able to determine that at a constant cooling capacity different, equivalent combinations of compressor speed and fan speed exist. The electrical power consumption of the system was reduced from 700 W to 450 W by ESC. This corresponds to an improvement in the COP from 2.9 to 4.4. In their experiment, the nominal fan speed was almost doubled, and the compressor speed was reduced to the minimum frequency of 35 Hz. After activation, the algorithm took about two hours to reach the optimum.

Koeln and Alleyne [8] implemented ESC with classical gradient estimation in 2014. They investigated the influence of the expansion valve opening on subcooling. For cost reasons, the installation of a pressure sensor at the compressor outlet often is renounced. Subcooling is therefore unknown and cannot be controlled. The authors used ESC to find an optimal expansion valve opening for COP-optimal subcooling. They improved the COP by 9 %. The algorithm took three hours to reach the optimum.

The work of Xiao et al [9] deals with a multivariable ESC. By simultaneously optimizing the speeds of the evaporator's and condenser's fan of an air-to-air heat pump, the power consumption was reduced from 625 W to 325 W.

Burns et al. [10] developed a gradient estimator based on a recursive-least-square estimator. Thereby they were able to reduce convergence time by a time scale. They investigated the influence of the temperature at the compressor outlet on the electrical power consumption. By using ESC to determine the optimum target value for the outlet temperature, they were able to reduce the power consumption from 535 W to 450 W. This corresponds to a 14% improvement in COP. In subsequent work by Burns et al. [11] in 2018, the performance of ESC was further improved and the convergence time was reduced to 50 minutes in an experiment.

The literature review shows that a great potential exists to optimize HVAC systems using ESC. A contribution that simultaneously optimizes energetics and acoustics of heat pumps was not identified, yet. Therefore, we show in Chapter 3 the methodology to apply ESC in order to optimize heat pump's energy efficiency and its acoustics during operation.

3. Dynamic modeling of a vapor compression system

Since we have no prototype of a heat pump at our institute, yet, we firstly set up two heat pump models: one for its energetic and one for its acoustic behavior. In a second step, we connect both models. Therefore, we link the compressor's and fan's noise emissions according to their rotational speeds. Lastly, we define the target function and apply ESC to our simulative prototype.

3.1. Energetic Modeling of Vapor Compression System

Regarding the trade-off between accuracy and simulation speed, we choose a grey box approach to model our system's components. The used components are taken from the Aixlib [12], an open-source Modelica library. Therefore, we use following approaches to model all components.

Based on efficiency correlations, the compressor model is validated against measurement data. We use energy and mass balances according to state changes based on these efficiency correlations. We apply the same approach to model the expansion valve. The heat exchangers are modeled using the Epsilon-NTU method. At

the evaporator air-side, we implemented an additional Nusselt correlation to model the behavior of heat transfer as a function of air velocity. Applying energy conversion and mass continuity, air velocity is cubic proportional to the fan power.
A simple PI-controller controls heat pump's supply temperature by adjusting compressor's speed. Another one keeps a constant level of superheated vapor at the evaporator outlet by controlling expansion valve's opening.

3.2. Coupling acoustic measurement data to dynamic energetic simulation model

Using a highly symmetric hexagonal setup, 61 microphones are surrounding the heat pump (see Figure 1, right). The microphones are calibrated with a 94 dB calibrator operating at 1000 Hz. Sound pressure levels are continuously recorded and later analyzed using Fast Fourier Transformation FFT techniques to be able to access the A-weighted sound power levels as a function of time.

The SilentAirHP is an experimental air-to-water heat pump which was designed to provide a heating power of 5 kW at a heating water temperature of 35 °C at an ambient air temperature of 2 °C. The refrigerant R410A was used and the entire heat pump was located inside the AIT climatic chambers during the measurements. Inside the chamber, the temperature and the humidity could be defined and kept constant. The heating water was cooled with the in-house chilled water reservoir guaranteeing a sufficient heat transfer from the condenser, whereby the back flow of the heating water was regulated to 30 °C. The compressor was operated with a controllable rotational speed (a speed of 98Hz corresponds to a 5 kW heating power at 2 °C outdoor temperature and 35 °C warm-water temperature). An internal controller, which uses the superheating of the refrigerant as reference variable controlled the degree of opening of the expansion valve. The superheating was always set to 7 °C during the experiments.

Typical experiments at a given operating point yield the transient sound power level together with the transient thermodynamic parameters of the climate chamber and the heat pump (see Figure 2).

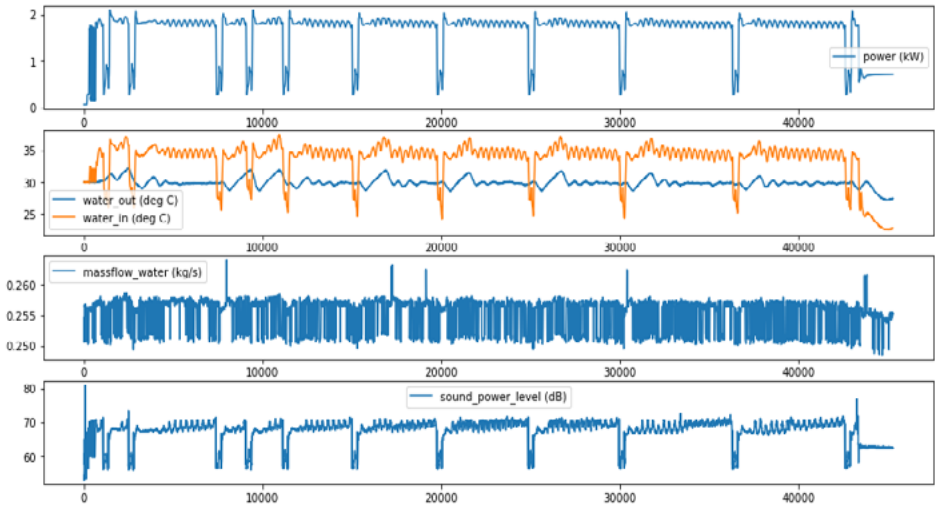


Fig. 2: Transient thermodynamic and acoustic data during a typical experiment. These measurements results are the basis of the following implementation.

In order to use these experimental sound power level results as basis for ESC, we re-write them according to their dependency of fan speed and index of third octave band. This allows us to couple the presented energetic model to its acoustic signature at a rotational speed. Additionally, increasing simulation speed, we use a fitting procedure to describe the dependency of sound power level on the rotational speed at a certain octave band. The fitting procedure increases calculation speed at an accuracy of $RMSE = 0.66$, which is within measurement uncertainty.

Using the AIT's Sound Source Extension Library (SSELib) [13], the energetic model can be extended by an acoustic interface. The library has components that can be used to determine the propagation of sound in air, the effects of silencers and the location. In addition, several sound sources can be superimposed. In order

to couple acoustic measurement data with an energetic simulation model, the acoustic signature is correlated with the rotational speed of the respective component.

This coupling of energetics and acoustics enables us to underline the conflict between energy efficiency and sound emissions. Regarding a common operating point at an air temperature of 7 °C and a water temperature of 50 °C (short: A7W50), our model is now able to calculate its energetic and acoustic performance, which are shown in Figure 3. According to a fixed heat demand as discussed in Chapter 2 and in Burns and Laughman [2], there are many combinations of compressor speed and fan speed to match the demand. By increasing the fan speed at a constant heat demand, the heat transfered from the ambient to the refrigerant increases so that compressor speed can decrease. In addition, this causes an increase in *COP* (blue dashed line). Applying systems *COP* (blue line) one can observe an increase to a certain maximum. After that the system *COP* decreases again. This means up to this maximum the power consumption of the fan increases more than the power consumption of the compressor decreases. The maximum is the energetic maximum in this operating point.

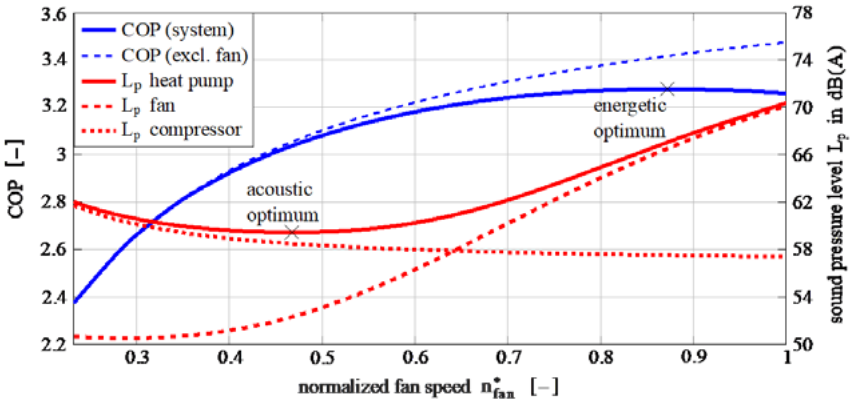


Fig. 3: The conflict of objectives between energetic efficiency and acoustic emissions of an air-to-water heat pump. The heat pump control provides constant heating output and a superheat of 5K. Above a threshold value, the increase in electrical power of the fan is greater than the resulting decrease in electrical power of the compressor. This point represents the energetic optimum of the system. The varying speeds of compressor and fan result in different acoustic emissions of the components. The noise level of a heat pump (compact design) is determined by the logarithmic addition of the compressor and fan emissions. For this operating point (A7W50), the acoustic optimum is at lower fan speeds compared to the energetic optimum.

The varying speeds of compressor and fan lead to different acoustic emissions of the heat pump as well. An increase in the fan speed leads to an increase in the sound pressure level caused by the fan. The effect of the compressor is the opposite: as the fan speed increases, the compressor speed and thus, also the emitted noise decreases. Both sound sources were added logarithmically. Since the components were measured individually and under the same structural conditions, this is permissible. Due to the acoustic dominance of the fan, the acoustic optimum lies at lower fan speeds. The simulation study shows that the operating points for the acoustic and energetic optimum do not coincide, resulting in a conflict of objectives.

Furthermore, the Figure shows a Pareto effect between energy efficiency and acoustic emission: A comparatively small deviation from the energetic optimum results in a disproportionately reduction of sound emission. For a normalized speed of n^*_{Fan} = 0.7, the coefficient of performance of the system is reduced from $COP_{Sys,energ.}$ = 3.27 to COP_{Sys} = 3.23. This means a reduction in energy efficiency by 1.22 %. The acoustic emission drops from $L_{p,energ.}$ = 67.24 dB(A) to L_p = 62.2 dB(A). Thus, by reducing the system efficiency by 1.22 %, the noise level emission can be reduced by ΔL_p = 5.04 dB(A). This Pareto effect is used in the following sections to achieve EAO.

The respective optima are strongly dependent on the ambient temperature and the heat demand. This results in the optima shifting during heat pump operation. In order to solve the conflict of objectives, a real-time-capable, adaptive optimization algorithm must therefore be selected. In addition, the procedure should be easy to implement and operate without complex measurement technology in order to enable economical application in new heat pump systems. One possibility is MPC. However, this technology has very high requirements on model accuracy and model speed, which makes practical implementation more difficult [14]. For this reason, research on model-free adaptive optimizers has intensified in recent years. This includes ESC, the suitability of which to solve the described conflict of objectives is examined in the following.

3.3. Extremum Seeking Control Design

In order to apply ESC, it is important to define a gradient estimator and an objective function. In our case, we use a simple benchmark model to identify the gradient estimator that fits best. Common gradient estimators are a combination of high-pass and low-pass filter (simple perturbation PB), a recursive-least-square method (RLS) and a Kalman filter (Kalman).

Former researches showed the functionality of a gradient estimator using a simple so called Hammerschmidt model [10]. Using this model, they were able to benchmark different gradient estimators.

The results of the three ESCs are shown in Figure 4. Models are started with a constant value of u = 2. After 100 s, ESC is activated and all ESCs converge to the optimum at y* = 1. The curves of the RLS-ESC and PB-ESC correspond to the literature [10]. The control signal u of the PB-ESC oscillates strongly according to its parameterization. This results in the oscillation of the output signal y. The control signals of the RLS-ESC and the Kalman-ESC also oscillate. Due to the lower magnitude of their amplitudes, this is not visible in the Figure. The PB-ESC converges after 470 s (not shown in the Figure), whereas RLS-ESC and Kalman-ESC show similar convergence times about 35 s. Concluding this test, we use the Kalman filter as the gradient estimator in the following simulation studies.

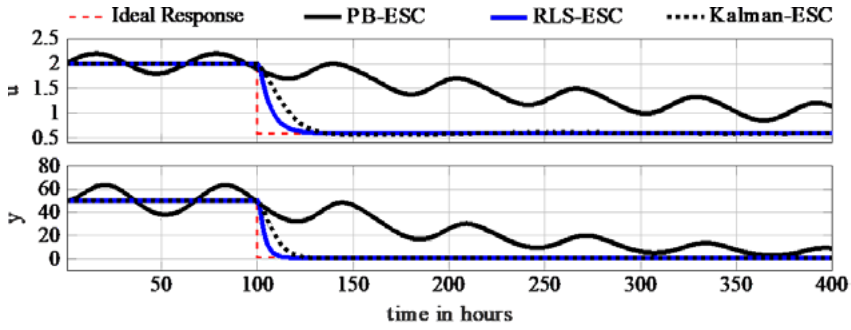


Fig. 1 Graph of the manipulated variable u and output variable y with ESC on a Hammerstein model. PB-ESC has a significantly slower convergence time than RLS-ESC and Kalman-ESC. RLS-ESC and Kalman-ESC show simuliar performances with convergence times about 35 s.

Additionally, ESC requires an objective function to be implemented. In order to consider the compromise between energetic efficiency and acoustic emission in the simulation model, a corresponding objective function is defined (Equation 3). The *COP* is not suitable to evaluate the energetic efficiency of the heat pump, as the transferred heat output at the condenser must be determined for this purpose. The flow temperatures and the mass flow of water must be known (or alternatively the condensation temperature and the mass flow of the refrigerant) respectively. Measuring the mass flow is particularly complex and therefore expensive. With respect to our optimization problem, electrical power data of compressor and fan, on the other hand, have the same informational content to implement the target function. In addition, the electrical power of both can easily be measured or recorded without great effort, which makes this approach favourable. Therefore, the minimization of compressor's and fan's power consumption defines the first part of the objective function. The acoustic emission of the heat pump is specified by the sound pressure level and depends on the design. We distinguish design between compact and split design as it is common in air-to-water heat pumps. Regarding both, the target function (TF) is defined as follows:

$$TF = \min a \underbrace{\frac{\sum_i P_{\mathrm{el,i}}}{\sum_i P_{\mathrm{el,max,i}}}}_{\text{Energetic}} + (1-a) \underbrace{\frac{\sum_i L_{\mathrm{p,i}}}{\sum_i L_{\mathrm{p,max,i}}}}_{\text{Acoustic}} \tag{3}$$

The left term contains the energetic evaluation of the current operating point and the right term contains the acoustic information. The terms are normalized with their maximum values for comparability. With the parameter a, which assumes values between zero and one, the operating point to be controlled can now be specified:

- a = 1: Energy-optimal operating point
- a = 0: Acoustically optimal operating point

Setting a = 1, the ESC will converge to the energy-optimal solution, while for a = 0, the quietest operating point is set. For values 0 < a < 1, a continuous weighting between energy-optimal and acoustically-optimal operating point is possible.

In general, objective functions for ESC need to be convex to ensure optimization. Figure 5 shows the objective functions for split and compact design. Compact design (left) is composed of the acoustic emission of compressor and fan. The acoustic emissions of the split design (right) are determined solely by the fan. Obviously, both are convex, since the terms used to describe energetics and acoustics are convex as well.

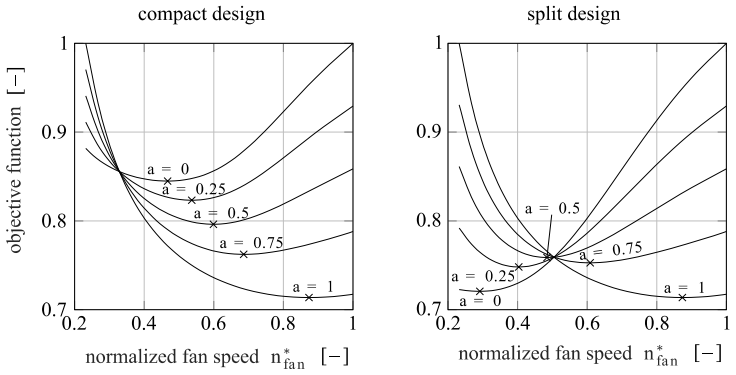


Fig. 5 The target function of the ESC at A7W50. With parameter “a”, a continuous trade-off between energy-optimal (a = 1) and acoustically-optimal operation (a=0) can be achieved.

4. **Simulation Study**

Applying ESC to our heat pump model, we use two setups. First use a fixed condition setup to evaluate the functionality of ESC. Therefore, we choose the operating point A7W50 as it was discussed in Chapter 3 as well. After proving functionality, we discuss a use case with realistic and highly dynamic boundary conditions.

4.1. Fixed Condition

First, the general functionality of the ESC is to be tested using Kalman-filter as a gradient estimator. For a constant operating point (A7W50), the models are initialized with constant fan speed. After 200 s ESC is activated with different values of EAO factor “a”. In addition, the manipulated variable n^*_{Fan} is perturbed with a square wave oscillation with an amplitude of A = 0.02 and a frequency of f = 0.06. The frequency of the oscillation is set to 0.06. The frequency of the square wave oscillation is set to 0.02. The amplification factor K is set to K = -0.0075.

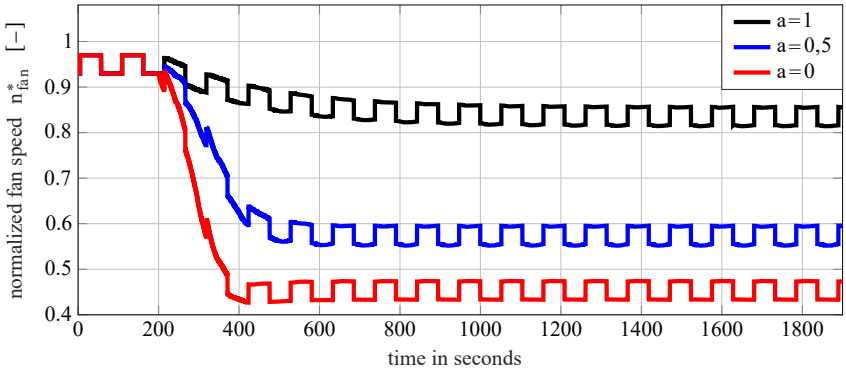


Fig. 6 Kalman-ESC with different values for parameter “a” at A7W50 and compact design. ESC is activated after 200 seconds and the steady-state values correspond to the optima in Figure 5.

According to Figure 6 energetic optimal control (a=1) fits to the corresponding energetic optimum at $n^*_{Fan} = 0.873$ resulting in a *COP* =3.27 and L_p=67.1 dB(A). Setting a=0 (acoustic optimal control), ESC finds the acoustic optimum at $n^*_{Fan} = 0.467$ with *COP*=3.04 and L_p=59.46 dB(A). In between, setting a=0.5, EAO is determined by ESC to be at $n^*_{Fan} = 0.598$ resulting in a *COP* = 3.19 and L_p=60.2 dB(A). All in all, this Figure shows a successful implementation of ESC to enable EAO.

4.2. Realistic Condition

After the basic functionality of ESC has been demonstrated, the acoustic and energetic effects for a realistic 24-hour operation will be quantified. The heat demand which is to be covered by the heat pump is shown in the Figure below (Figure 7). The ambient temperature varies between 2°C and 6°C. The maximum flow temperature is 58 °C.

Three scenarios are compared with each other for this purpose. First, the ESC is deactivated and the fan speed is set to nominal fan speed (1000 rpm). For the other two scenarios, the ESC is activated and the parameter "a" is set to constant a=1 in one scenario. This results in energy-optimal operating points. At last, the parameter "a" is varied depending on the time of day. Therefore, this day is split in three parts. At night (10 pm to 6 am), we define a silent mode at a=0.4. In the morning (6 am to 8 am) and in the evening (8 pm to 10 pm) we increase energy efficiency by setting a=0.8. At the rest of the day (8 am – 8 pm) we set a=1. The results of ESC are shown in Figure 7.

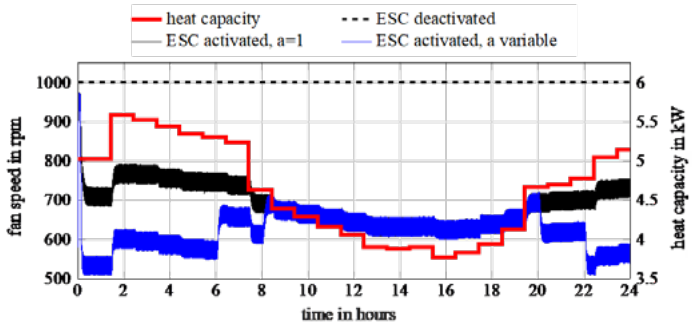


Fig. 7 ESC at variable operating conditions (24-hour heat demand profile). Fan speed curves for three different scenarios: Constant nominal fan speed (black, dashed), active ESC with constant a = 1 (blue), active ESC with daytime-dependent values for parameter "a".

When ESC is active, the fan speed is always significantly lower than the nominal speed. For scenario 3, the fan speed is lower in the morning, in the evening and at night than in the energy-optimal scenario. During the day (8 am to 8 pm), the rated speeds of scenario 2 and 3 are identical, as both are approaching energy-optimal operating points. For the scenario with constant fan speed, the compressor power is consistently lowest and the electrical consumption of the fan is constant at 200 W. If the heat output is provided in an energy-optimal way, a higher compressor output is required than in scenario 1, but therefore the fan power can be reduced significantly. For example at 4 am, the compressor power differs from scenario 1 to 2 by $\Delta P_{el,comp.}$ = 71 W, while the fan power decreases by $\Delta P_{el,Vent.}$ = 115.5 W. The comparatively high difference between the fan outputs of the two scenarios is based on the cubic relationship between fan output and fan speed. The maximum saving is 98 W. Over the entire period 1.63 kWh can be saved, which corresponds to a reduction in electrical energy consumption of 3.75 %.

In nominal operation (scenario 1) the sound emissions vary between 70.6 dB(A) and 70.9 dB(A) and are dominated by fan emissions. While the fan emissions are constant, the compressor emissions fluctuate with the heat demand. In energy-optimized operation, less noise is emitted due to the reduced fan speed. The sound pressure level varies between 65.1 dB(A) and 60 dB(A), which represents a volume reduction between 5.8 dB(A) and 10.9 dB(A). This leads to a reduction of the subjectively perceived volume by up to half. The acoustic emissions can thus be significantly reduced without the acoustics having any weight in the target function of the ESC. In this scenario, the fan is the dominant component for noise emissions. In scenario 3, noise emissions can be further reduced compared to energy-optimal operation. The sound pressure level fluctuates between 62.6 dB(A) and 59.7 dB(A). In periods where the parameter "a" does not assume the value one (0-8 h and 20-24 h), the compressor is the dominant component in noise emission.

5. Discussion

The challenges of the presented procedure lie in the implementation and parameterisation of ESC in a real heat pump. Since heat pumps have time delays due to the thermal intertia of the heat exchangers, the convergence time of the algorithm is limited. The achieved convergence times are not yet representative due to the simplified dynamic modelling of the heat exchangers. In the experiment, it has to be shown that the convergence time of the algorithm is fast enough to ensure economic use.

Experiments from the literature show convergence times between one and three hours. However, a comparison is difficult because these are largely dependent on the distance between the initial manipulated variable and the optimum manipulated variable. If it can be excluded that ESC changes the manipulated variable against the optimization direction due to measurement errors or incorrect parameterization, ESC leads to an improvement of the current state, even if the algorithm has not yet converged to the optimum.

In addition to the convergence time, the parameterisation of the gradient estimator on a real heat pump is also challenging since the dynamics of the heat exchangers slow down the parameterisation process. Because these dynamics are not yet realistically represented by the simulation model, the parameters of the gradient estimator used in this paper probably deviate from test bench parameters. It is expected that the frequency must be reduced in order to counteract the slow dynamics and a possibly poor controller design. Due to loss mechanisms, interference influences and measurement uncertainties, the course of the system output cannot be attributed exclusively to the perturbation of the manipulated variable. In order to quantify the influence of perturbation, the amplitude of the perturbation must therefore be increased if necessary.

Depending on the heat pumps surrounding's, further improvements of factor "a" estimation can additionally be deduced. Therefore, we suggest installing an internal heat pump microphone. This microphone is on the one hand able to measure the heat pump's acoustic environment. The factor "a" can be set to a reasonable value depending on environment's acoustics. On the other hand, a high frequent microphone yields to applications of predictive maintenance because high frequency changes can indicate aging effects.

6. Conclusion and further work

In this work, the conflict of objectives between energetic efficiency and acoustic emission is addressed. The analysis is based on the fact that a constant heat demand at the condenser can be realized by a multitude of combinations between fan power and compressor power. A simulation study shows that the acoustically optimal combination of compressor and fan power does not correspond to the energetic optimum, thus creating a conflict of objectives. A comparatively small deviation from the energetic optimum can reduce the noise emission disproportionately. This Pareto effect is used to achieve optimal energetic-acoustic operation. With the help of the adaptive, model-free Extremum Seeking Control, any states between energetic and acoustic optimum can be realized by means of an objective function. For the first time, acoustics is implemented as a variable to be optimized. The energetic and acoustic effects are quantified based on a realistic 24 h heat demand profile. Compared to nominal operation, the energy efficiency of the system can be increased by 3.75 % with ESC, while at the same time the noise emission decreases by up to 10.9 dB(A). This means that the subjectively perceived volume is halved.

This procedure increases the two system efficiency and user comfort. This work, thus, contributes to the development of new control concepts, which, in addition to energy efficiency, can also optimize and evaluate the sound emission of heat pumps. No additional measurement technology needs to be installed on the heat pump to apply the presented method. However, an experimental evidence is necessary to take heat exchanger dynamics into account.

For the next steps, a microphone can be attached to the heat pump to improve the assessment of acoustic emissions. This allows location-dependent factors, such as the installation location, to be considered within the optimization process. High-frequent microphones can also be suitable for predictive maintenance.

Acknowledgements

This publication has been developed in the framework of IEA HPT TCP Annex 51 "Acoustic Signatures of Heat Pumps". We thank the IEA for continuously supporting this topic.

The Austrian Research Promotion Agency (FFG) and the Austrian Climate and Energy Fund (KLIEN) is gratefully acknowledged for funding this work under Grant No. 848891 (program line 'Energieforschung e!Mission 1st call', project 'SilentAirHP'). We also want to thank the Federal Ministry of the Republic of

Austria for Transport, Innovation and Technology for supporting IEA HPT Annex 51 in Austria in the framework of the IEA Research Cooperation.

References

[1] Graf, H. R. Lärmreduktion bei Luft/Wasser-Wärmepumpenanlagen. 2002.
[2] Burns, D. J., Laughman, C. R. Extremum Seeking Control for Energy Optimization of Vapor Compression Systems. *International Refrigeration and Air Conditioning Conference* (2012).
[3] Skafte, A. An Introduction to Extremum-Seeking Control, 2017.
[4] Morosanov, I. Method of extremum control. Automation and Remote Control (1957), Nr. 18, S. 1077–1092.
[5] Krstic, M.,Wang, H. Stability of extremum seeking feedback for general nonlinear dynamic systems. *Automatica 36* (2000), Nr. 4, S. 595–601. – DOI 10.1016/S0005– 1098(99)00183–1.
[6] Tan, Y., Moase, W. H., Manzie, C., Nešic, D., Mareels, I. M. Y. Extremum seeking from 1922 to 2010. *Proceedings of the 29th Chinese Control Conference*, 2010, S. 14–26.
[7] Keating, B. D., Alleyne, A. Combining self-optimizing control and extremum seeking for online optimization with application to Vapor Compression cycles. In: *2016 American Control Conference (ACC)*. Piscataway, NJ : IEEE, 2016. – ISBN 978–1–4673–8682–1, S. 6085–6090.
[8] Koeln, J. P., Alleyne, A. G. Optimal subcooling in vapor compression systems via extremum seeking control: Theory and experiments. *International Journal of Refrigeration 43* (2014), S. 14–25. – DOI 10.1016/j.ijrefrig.2014.03.012.
[9] Xiao, Y., Li, Y., Seem, J. E. Multi-variable Extremum Seeking Control for Mini-split Air-conditioning System. *International Refrigeration and Air Conditioning* (2014).
[10] Burns, D. J., Weiss, W. K., Guay, M. Realtime Setpoint Optimization with Time- Varying Extremum Seeking for Vapor Compression Systems. *American Control Conference (ACC)* 2015, S. 974–979. – DOI 10.1109/ACC.2015.7170860.
[11] Burns, D. J., Laughman, C. R., Guay, M. Proportional-Integral Extremum Seeking for Vapor Compression Systems. *IEEE Transactions on Control Systems Technology* (2018), S. 1–10. – DOI 10.1109/TCST.2018.2882772.
[12] Müller D., Lauster M., Constantin A., Fuchs M., Remmen P. AixLib - An Open-Source Modelica Library within the IEA-EBC Annex 60 Framework. *BauSIM* (2016), S. 3–9.
[13] Emhofer, J., Zitzenbacher, R., Reichl, C. Sound Source Extension Library for Modelica. *Proceedings of the 12th International Modelica Conference* (2017).
[14] Péan, T. Q., Salom, J., Costa-Castelló, R. Review of control strategies for improving the energy flexibility provided by heat pump systems in buildings. *Journal of Process Control 74* (2018), S. 35–49. – DOI 10.1016/j.jprocont.2018.03.006.

13th IEA Heat Pump Conference
April 26-29, 2021 Jeju, Korea

Design of Heat Pump Systems Considering Operation Dynamics

Christian Vering[a*], Christoph Höges[a], Markus Nürenberg[a], Dirk Müller[a]

[a]*Institute for Energy Efficient Buildings and Indoor Climate, RWTH Aachen University, Mathieustraße 10, 52074 Aachen, Germany*

Abstract

Decreasing carbon dioxide emissions in heat supply of buildings, heat pump systems (HPS) allow the replacement of conventional technologies that utilize fossil-based energy sources. Increasing HPS market penetration, investment and operational costs need to be reduced significantly.
Recent studies show cost reductions by solving optimization problems and considering operation already in the design process. However, many studies assume systems linear in order to simplify optimization procedures. Therefore, we investigate the applicability of a hybrid approach to design simultaneously heat pump, heating rod, space heating and domestic hot water tank considering their nonlinear interactions introduced by operation. We achieve this by combining dynamic simulation models with a multi-objective genetic algorithm using annualized costs and annual emissions as target functions.
Optimal designed systems reduce annualized costs by installation of smaller heat pumps and larger storage tanks compared to normative design standards. In addition, a reasonable larger heating rod ensures annual reliable supply. Thus, total annualized costs can be reduced by up to 12 %. The design highly depends on heat pump modelling and input weather data though.

© HPC2020.
Selection and/or peer-review under responsibility of the organizers of the 13th IEA Heat Pump Conference 2020.

Keywords: Heat pump design; design optimization; genetic algorithm; multi-objective optimization

1. Introduction

The building energy sector requires significant ecological improvements to meet political goals until 2050. Within this sector, the main contributor to its emissions is the supply of space heating and domestic hot water. Typically, conventional technologies like gas-fired or oil-fired boilers are used to meet the demand. Exchanging boilers with heat pump systems (HPS) can reduce heat supply related emissions. In general, however, HPS have higher costs than conventional systems. Hence, HPS need a cost reduction.
Costs mainly consist of investments and operating costs. Investment costs relate to system's component sizes whereas operational costs belong to the electricity costs to operate the system. Investments and operational costs are mutually depend and their interdependencies are nonlinear. Nevertheless, conventional design processes do the component design first and regard operation by designing the controller afterwards. Therefore, transient interdependencies of design and operation are neglected. Thus, in order to reduce total costs, there is a potential for advanced design processes that simultaneously take component design and operation into account.

In this study, HPS consists of a heat pump, an electric backup heater and two thermal storages: one for space heating and one for domestic hot water. In the literature, we mainly found two approaches that describe the design processes of these components. On the one hand, there are conventional design processes that design component sizes for steady-state operating points. This procedure is either traditional by applying standardized rules or more advanced by using optimization functions in order to define component sizes. On the other hand, first approaches dealing with simultaneous design of component sizes and controller exist. These use optimization procedures to organize the design process. In order to apply deterministic optimization procedures,

*Corresponding author. Tel.: +49 241 80 49786; fax: +49 241 80 49769.

systems often are linearized. Therefore, nonlinear interactions are neglected as a compensation to determine an optimal solution. However, Dongellini et al. [1] and Naldi et al. [2] show that interactions between component size and control influence considerably each other. In addition, Maier et al. [3] prove that interactions are nonlinear as well. Within this work we, therefore, contribute to the establishment of design procedures that consider nonlinear interactions between components. This design procedure introduces a simulation-based optimization method in order to design component sizes simultaneously including operation:

- In Chapter 2, we give an overview about design methodologies regarding conventional design standards as well as improved procedures.
- Our simulation-based optimization approach is introduced in Chapter 3. We distinguish between three steps. First, we show our data processing procedure to generate the algorithm's input data. Afterwards, we describe our system model and highlight nonlinearities introduced by dynamic simulation models. Lastly, we explain the optimization process.
- We show optimization results in Chapter 4. On the one hand, we compare our results with a German normative design standard. On the other hand, we discuss the influence of different boundary conditions.
- A detailed discussion of all results is done in Chapter 5.
- Finally, in Chapter 6, we conclude our work and give an outlook for further investigations.

2. Literature review

Replacing gas-fired or oil-fired heating systems by HPS, there is an urgent need to reduce heat pump system's costs. Costs depend on component design and operation, which again are mutually dependent. Common design procedures, however, are either conventional, sequential ones or linearly simplified to ensure optimal solutions.

Within this work, we define a heat pump system as a heat pump, an electric backup heater, a space-heating tank and a domestic hot water tank according to [3]. These components need to be designed and operated related to a building demand.

In Germany, there is a normative design standard DIN EN 15450 that describes the design process of HPS. It uses simple design rules to successively define the component's sizes. Applying these rules, a heat pump system is specified that ensures reliability of supply [4]. On the one hand, this procedure has the advantages of simple application as well as a repeatable methodology. On the other hand, it is obvious that these rules design all sizes very conservative to ensure system's reliability.

Dongellini et al. [1] and Naldi et al. [2] introduce and discuss advanced design procedures, which take interdependencies of components and operational aspects into account. While Dongellini et al. prove in [1] the dependency between heat pump sizing and its consequence on system performance, Naldi et al. show in [2] that system's efficiency is closely linked to considered climate and heat pump type. Therefore, it is promising to apply simulation-based approaches in order to design HPS considering system interdependencies as well as different climate conditions.

Designing HPS using simulation-based approaches is straight forward, respectively. However, if boundary conditions are insufficiently chosen, this approach will not lead to mathematical optimal designs. Therefore, Wolisz et al. [5], Schütz et al. [6] and Bischi et al. [7] introduce mixed integer linear programs (MILP) as deterministic optimization design procedure. This leads to optimal design results for mathematical linearized systems. According to Maier et al. [3], however, some nonlinear interactions exist. Concluding these insights, MILP procedures demonstrate design trends accurately. Deducing conclusions is hardly possible regarding reasonable system dynamics. Therefore, combined approaches, which find optimal solutions considering system dynamics are necessary.

Solving nonlinear problems, a trade-off between solution's optimality and dynamics accuracy leads to further design approaches. Therefore, Nguyen et al. present in [8] a review on simulation-based optimization methods. They suggest genetics algorithms (GA) to optimize the design of building energy systems stochastically. Additionally, they show that multi-objective optimization leads to reasonable designs that take costs and for example thermal comfort into account. Fazlollahi et al. confirm in [9] using combined approaches is promising.

The literature review shows great potential to optimize the design process of HPS by simultaneously considering dynamic operation. A contribution that optimizes component sizes at minimal costs and emissions was not identified, yet. Therefore, we show in Chapter 3 the methodology to apply our simulation-based optimization algorithm in order to minimize total costs and emissions.

3. Simulation-based optimization algorithm

Within this work, we introduce a simulation-based optimization algorithm, which includes a multi-objective genetic algorithm (MO-GA). In order to design heat pump heating systems, we need three calculation procedures according to Fig. 1. These three steps are data processing, simulation and optimization. Executing the data processing step, external inputs of location and building characteristics are necessary. Regarding the optimization part, user settings are additionally required. Developing an efficient optimization procedure, all models need to be both fast and accurate.

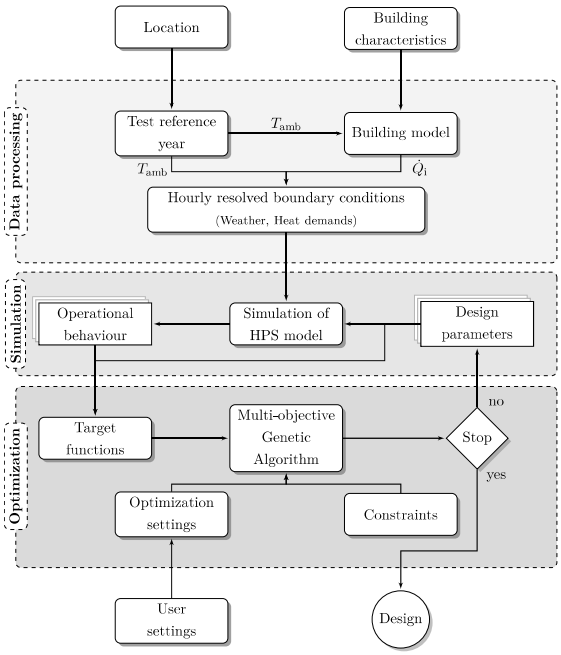


Fig. 1. Superstructure of developed simulation-based optimization algorithm. The algorithm is divided in three parts. Within data processing, the simulation model inputs are prepared. During the simulation, different designs are used to calculate operation behavior. The optimization part improves systems design regarding annual emissions and annualized costs.

3.1. Data processing

Within the data processing, we accumulate few input data in order to estimate the building's energy demand. Based on location, weather data of German weather service (DWD) will be used providing hourly resolved weather conditions in shape of different test reference years (TRY) [11]. Weather data serves as input for thermal building model simulation as well as for HPS model simulation.

Using a high-order building model from the open-source AixLib Library [10], building's demand is calculated hourly resolved. Both time series, weather data and energy demand, are simulation inputs. By taking this step, we neglect the interaction of heat supply system and building's hydraulics in order to increase simulation speed significantly. Simultaneously, we consider hourly resolved system dynamics regarding heat demand, which is reasonable because of large time constants in buildings. For the presented study, we exemplarily use a building located in Aachen, Germany, with a net area of 150 m², year of construction about 1960, insulation standard according to WSchV1984 at normal and cold TRY.

Regarding short time constants, profiles for domestic hot water (DHW) supply are applied according to the German normative standard DIN EN 16147. Within our study, we calculate profile XL, which is common in the heat pump system design process.

In Aachen, normal and cold TRY are summarized in Table 1. In the normal TRY, operating hours below 0 °C arise 313 hours a year, which is only about 4 % of the year. By reducing this temperature by another 2 K, the operating hours decrease to 80 h, which are about 1 %, respectively. The overall mean temperature is 11.48 °C at a lowest temperature of -5.7 °C. This temperature distribution results in a building heat demand of about 63.2 GJ.

In the cold TRY, operating hours below 0 °C are almost doubled with 863 h, which is about 10 % of a year. Operating hours between -2 °C now take 5 % of a year, which means 490 h, respectively. As consequence, the annual mean temperature decreases to 10.66 °C and the lowest temperature is -7.5 °C. With respect to the normal TRY, the building's heat demand increases by about 50 % to 93.4 GJ.

Table 1: Properties of different TRY. Data is proved by DWD. The normal TRY represents the last 20 years best for one region, whereas the cold TRY offers extreme conditions.

Studied year	Hours below 0 °C	Hours below -2 °C	Mean temperature in °C	Coldest temperature in °C	Resulting heat demand in GJ
Normal TRY	313	80	11.48	-5.7	63.2
Cold TRY	863	490	10.66	-7.5	93.4

Comparing both TRYs, the difference of temperatures and heat demands becomes clear. According to Naldi et al. [6], these differences will lead to different system designs as well as system efficiencies and emissions. Both TRYs and hourly resolved building energy demands serve as input for subsequent HPS simulation.

3.2. Heat pump system simulation

As already introduced, HPS consist of a heat pump, a heating rod, which generate heat (Fig. 2). Additionally, there are two storage tanks: one for space heating (Thermal Energy Storage: TES) and one for DHW, which are interconnected by a hydraulic system. These build the distribution system. In combination with a controller, the generation system and the distribution system match the consumer's heat demand.

For the simulation of the HPS, simulation models need to meet different requirements: simulation speed, simulation stability, simulation accuracy. Therefore, we assume reasonable simplifications.

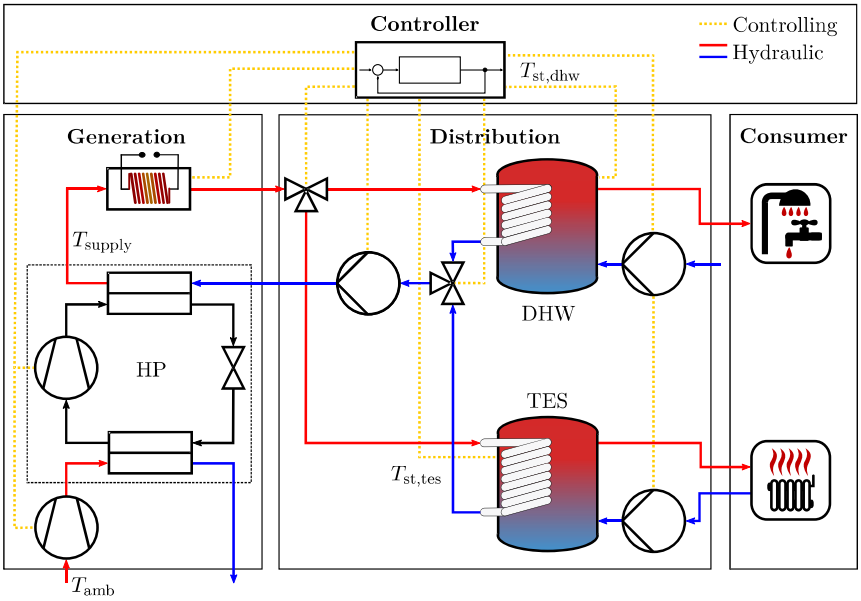


Fig. 2. Schematic structure of used heat pump system models. The system is divided into four subsystems: generation, distribution, consumption and controlling. Generation consists of a heat pump and a heating rod. Within the distribution subsystem storages and the hydraulic system are located. Consumer regard demands for space and hot water heating.

Heat generation:

Instead of using a physical heat pump model with its four components, we summarize its behavior in a characteristic map according to Fig. 3. Using this map, we neglect time delays between two operating points, which means quasi steady-state operation. Therefore, the heat pump is assumed speed controlled between 50 % and 120 % of nominal load according to [12]. We consider start-up losses according to Maier et al. [3] while neglecting defrosting due to missing data. The heating rod has a thermal efficiency of 0.97.

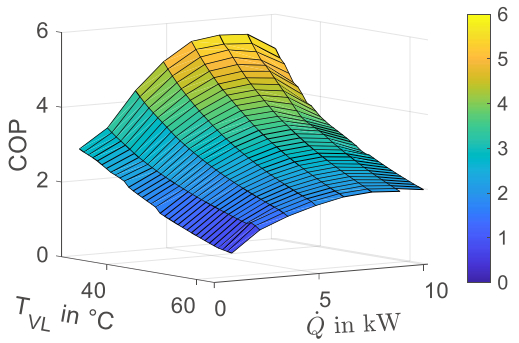


Figure 3: Efficiency map of the heat pump for an ambient air temperature of 0 °C. Within simulations, a three dimensional performance map summarizes dependency of ambient air temperature, supply temperature and condenser heat flow rate.

Distribution system and consumer:

The use of storage tanks is crucial for overall system performance. With respect to implemented models, two target quantities are addressed in the simulation. On the one hand, we define the capacity of a storage by its volume. Both volumes are optimized by the implemented MO-GA. Simplifying the geometry, we assume both storages a cylinder with constant height (h) to diameter (d) ratio of $h/d = 2$. On the other hand, heat losses scale with the surface of the storage tank and heat transition coefficients. Heat transition is calculated assuming free convection on the inner ($\alpha_i = 100\ W/m^2$) and outer side ($\alpha_o = 10\ W/m^2$). In between, heat conduction through insulation is taken into account by $k = 0.045\ W/mK$ and a thickness of $s = 0.12\ m$.

Simple pumps with constant isentropic efficiency are modelled and stratified storages with indirect loading procedure are used in order to match the heat demand of the consumer. As discussed before, the consumer is described by an hourly-resolved data set. Hence, user comfort cannot be measured, yet.

Controller:

Within the scope of this work, we demonstrate that design optimization considering operational dynamics is possible and promising. Therefore, we do not optimize the controller settings for different designs, yet. The controller is a simple heating curve function, which is state of the art. We implement a hysteresis band in order to decrease on/off switches. In addition, DHW has charging priority to increase user's comfort. We do not define a bivalence temperature but use the heating rod, if the lower hysteresis temperature is hurt for more than 20 min. Using this simulation model, the optimization method can be introduced.

3.3. Optimization method

Within this work, we apply a multi-objective genetic algorithm (MO-GA) based on Deb's NSGA-II [13]. In order to adapt it to our design procedure, two further extensions are implemented: The first one is local search in order to improve optimization performance around pareto-optimal solutions [14]; secondly, we use death penalty to deal with constraint hurting solutions [15].

Regarding very extreme demands at normative ambient temperature, thermal power of heat pump and heating rod have to meet normative heat demand according to DIN EN 12831-1, which is 9.7 kW at -12 °C in our use case.

The target functions are annual costs defined by annuity method and annual emissions: costs are defined by the combination of investment costs (according to [3]) investment specific maintenance costs and electric costs (constant specific value of 0.3048 €/kWh in Germany); emissions: specific emissions of German electricity grid (473 g/kWh).

4. Optimal design results

Using the simulation-based optimization approach, we design different systems. In Chapter 4.1 we show the difference between optimized designs compared to normative design standards. Afterwards, we study the effect of different boundary conditions that serve as input for the data processing procedure.

4.1. Comparison of normative and optimized design

When applying the simulation-based optimization algorithm, a pareto front according to annual costs and annual emissions will be calculated. The results are shown in Fig. 4. We discuss three highlighted ones compared to the normative design standard.

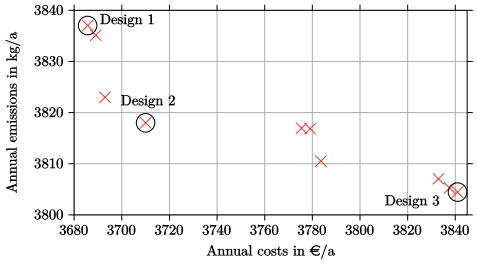


Figure 4: Resulting optimization pareto front using normal TRY. Three designs will be studied more thorough. Design 1 represents the cost optimal solution, design 3 the emission optimal solution and design 2 shows a trade-off between both targets.

Design 1 represents the cost-optimal, design 3 the emission-optimal and design 2 the solution that provides the best trade-off between the two target functions. Table 2 shows the component dimensions of the three optimizations. In addition, the design in accordance with DIN EN 15450 is shown. The corresponding values of the target functions were determined with the aid of an annual simulation in order to allow comparison.

Table 2: Design and performance parameters of optimization and normative designs. Design 1 represents the cost optimal solution, design 3 the emission optimal solution and design shows a trade-off between both targets.

Design label	Heat pump size in kW	Heating rod power in kW	TES volume in l	DHW storage volume in l	Costs in €/a	Emissions in kg/a	SCOP
Cost Optimal	3.95	7.83	578	269	3841	3804	2.76
Cost and Emission	4.03	7.77	412	77	3710	3818	2.74
Emission Optimal	4.18	7.76	257	50	3688	3837	2.72
Normative design	8.25	6.64	193	100	4206	4551	2.39

The three optimised designs show only minor differences in the heat generators' thermal performance. The heat pump thermal power is rated at approximately 4 kW and the heating rod at about 7.8 kW. The cost-optimized solution provides a heat pump's thermal power that is about 5 % greater. In the case of storage tanks, on the other hand, the differences are greater. With a TES of 257 l and a DHW of 50 l, the cost-optimal solution delivers the smallest and the emission-optimal solution the largest storage tanks with 578 l and 269 l, respectively. It is noticeable that the dimensions of the other pareto-dominant optimization solutions for each component lie between the two optimal solutions for a target function. Overall, the different interpretations lead to a difference of 4 % in cost function and about 1 % in annual emissions.

Compared to the normative design, larger differences are identified. This results in a cost savings potential of up to 12 % and a savings potential for emissions of up to 16 %. This is also accompanied by larger differences in the components' sizes. The normative standard designs the heat pump up to 50 % larger. Ensuring reliable supply, the thermal power of the heating rod can be decreased by about 20 %. In addition, an up to three times smaller TES is installed, whereas the dimensioning of the DHW, apart from the emission-optimal solution, lies between the interpretations of the normative standard. Overall, smaller design leads to a reduction in investment costs.

Due to the illustrated design changes, system behaviour varies overall. The efficiency of the system can be illustrated using the seasonal coefficient of performance (*SCOP*). It represents the ratio of the heat provided over the year and the electrical energy required. The *SCOP* of the overall system is 2.39 for the normative design, whereas the *SCOP* varies between 2.72 and 2.76 when using the optimization results. Consequently, *SCOP* can be increased by up to 15 % when using the simulation-based optimized design.

Main contributors to the improved overall efficiency are the changes of TES volume and heat pump capacity. Due to a reduced capacity, the heat pump can be operated more frequently and for longer periods. Therefore, losses related to switching can be decreased by up to 50 % since heat pump starts are reduced. Furthermore, increased full load operation due to larger TES volume is possible, so that efficiency losses in partial load operation are reduced.

In addition, the heating rod provides about 4 % of total heat. Within the scope of reference values according to DIN EN 15450, this result is reasonable, because the use of heating rods should not exceed 5 % of total heat. Hence, it is conspicuous that the heating rod is almost not used during system simulation of normative designed system. The share of the heat supply is below 1 %. Several possible reasons exist for this finding. Either the heat pump is oversized in the normative design or the normal TRY represents a comparatively warm year with a high mean temperature. In order to investigate the influence of different weather data sets, the cold TRY is applied to the algorithm.

4.2. Influences of different weather data sets

We distinguish between optimized design 1 (Opt.1), optimized design 2 (Opt. 2) and normative design (Norm). Case Opt. 1 is the optimized design already presented in Chapter 4.1. Regarding the normal TRY (Fig. 5, red bars), this case shows the optimal solution compared to the other design as expected. In Opt. 2 the design is optimized according to the cold TRY (blue bars). Obviously, Opt. 2 shows the best design compared to the others for both costs and emissions.

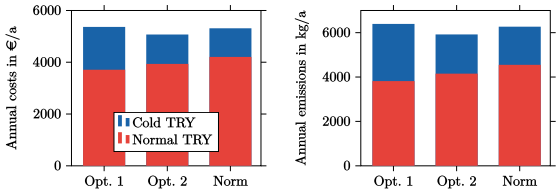


Figure 5: Target functions for the trade-off solutions of optimizations using different TRY as well as the normative design. Opt.1 represent optimization using the normal TRY and Opt.2 represent optimization using cold TRY.

With respect to the normal TRY, normative design rules perform worse. In case of the cold TRY, the normative design procedure nearly obtains the results compared to Opt.1. In Table 3, the component sizes of all design procedures are shown.

Due to the increased heat demand during the cold TRY, the heat pump within Opt. 2 is designed about 60 % larger than in Opt. 1. At the same time, heating rod power can be reduced by around 14 % while satisfying used boundary conditions. In addition, TES is designed at half the volume, whereas the DHW is increased by 10 %. Overall, significantly smaller deviations of the individual components from the normative design procedure can be detected compared to Opt. 1, which reduces potential savings. Nevertheless, the optimized annual costs are about 5 % below the normative design.

Table 3: Optimal designed systems regarding a normal TRY (Opt. 1) and a cold TRY (Opt. 2) compared to a normative designed system. Opt. 2 designs a heat pump with a 60 % higher thermal power and therefore with a reasonable smaller heating rod. Both storage tank volumes are in between Opt. 1 and normative design.

Design label	HP size in kW	HR size in kW	BS volume in l	DHW volume in l	SCOP (standard year)	SCOP (cold year)
Opt. 1 (normal TRY)	4.03	7.77	412	77	2.74	2.24
Opt. 2 (cold TRY)	6.45	6.60	224	93	2.58	2.48
Normative design (Norm)	8.25	6.64	193	100	2.39	2.37

Increasing comparability between the results, operation of all designs is calculated for both weather conditions. For this purpose, annual simulations with both TRYs as boundary conditions are created. Table 3 provides the *SCOP* of the respective simulation and Fig.5 displays each target function.

Opt.1 shows the greatest potential for savings in terms of both costs and emissions compared to normative design. Best results can be observed when using the normal TRY, which leads to a *SCOP* of 2.74. The same design, however, also leads to the lowest *SCOP* during a cold winter. Main reason is the increased operation of the heating rod. When using cold TRY, the heating rod provides about 8 % of the heat demand which requires 20 % of the total primary energy due to its low efficiency. Therefore, both costs and emissions increase significantly.

Opt. 2, on the other hand, provides a lower overall savings potential, but improves target functions by up to 9 % under both TRYs. Consequently, the choice of weather data during the design process has a direct influence on the dimensioning of the components.

Furthermore, Figure 5 shows similar trends for both target functions investigated. This suggests a correlation between the two target functions and can be explained by the predominant influence of operational costs and emissions as a function of power consumption. The operational electricity costs account for between 60 % and 80 % of the total costs. The share of emissions is even higher with up to 90 %. As a result, subsequent work should revise target functions and make it possible to decouple the two goals.

5. Discussion

In contrast to the normative designs, HPS is designed that it ensures just reliable supply when normative heat demand is needed, which reduces heat pump's thermal power and increases the TES volume for space heating. The ecological optimum of the optimization delivers in each case the design with the smallest heat pump and the largest thermal storage. This coincides with the findings according to [3] where an bigger sized TES leads to a continuous improvement in the final energy consumption which is equivalent to a reduction in indirect emissions.

Due to downsizing heat pump's capacity, the optimized designs include an increased heating rod power, so the reliability of supply is ensured even at very low ambient temperatures. Accordingly, the heating rod must be operated earlier, whereby the bivalence temperature shifts towards warmer temperatures. Since the bivalence temperature is dependent on the installed heat pump power, it should be optimized in further studies.

The optimized designs highly depend on the boundary conditions and used models. In particular, changing the weather data by using an extreme year instead of an average one with a 50 % increase in heat demand shows large differences in the design. Due to the increased heat demand, heat pump capacity is increased by 60 % compared to other optimization calculations. There are two major reasons for the different heat pump size. Firstly, the general share of total costs accounted by operation increases when using a higher heat demand. Within the normal year, investment costs account for 34 % of the total annual costs, which drops to only 20 % when using the cold TRY. As a result, operational improvements are weighted more strongly than investment costs accompanied by increasing heat pump capacity. Secondly, the inefficient operation of the heating rod is reduced, which improves the overall operation.

When designing HPS under normal weather conditions, the overall efficiency of the system can drop below the efficiency of a system designed using normative design procedure in years with lower mean outdoor temperatures. In contrast, designing for cold boundary conditions shows an economic and ecological improvement compared to normative design at both low and high mean annual temperatures. Consequently, the cold TRY should first be used during the design process. However, further work should investigate to what extent the extreme TRY is necessary when designing HPS and if a trade-off between the two investigated designs can be made. For this purpose, the optimization should be carried out for different locations.

6. Conclusions

In this work, we investigate a simulation-based optimization algorithm to design HPS. The introduced approach improves the component dimensioning of HPS. As a basis for comparison, the design according to the German standard DIN EN 15450 is used. In order to estimate the improvement potential, an optimization algorithm is developed. It consists of a MO-GA, which optimizes HPS models regarding annualized costs and annual emissions. Optimization results are compared with the normative method by using annual system simulation. A potential for improvement regarding the annual costs of up to 12 % and with regard to emissions of up to 16 % is shown. The results of the optimization are influenced by several factors. Among other things, the weather conditions have great influence on the designed system.

If a year with a cold winter is used instead of the normal TRY of the DWD, where heat demand is about 50 % greater, the heat pump capacity increases by up to 60 %. A comparison of system simulations of both designs under different weather conditions shows that the design using the normal TRY is less efficient than the normative design at low annual mean temperatures. Only the cold TRY optimized system guarantees improved operation regardless of weather conditions. Consequently, it must be investigated which weather conditions are required for the design in order to ensure an optimal design. For this purpose, further locations should be included in the comparison in order to validate the statements.

References

[1] M. Dongellini, Abbenante, Massimiliano, Morini, Gian Luca, A strategy for the optimal control logic of heat pump systems: impact on the energy consumptions of a residential buidling, 12th IEA Heat Pump Conference 2017 (2017).
[2] C. Naldi, M. Dongellini, G.L. Morini, Climate Influence on Seasonal Performances of Air-to-water Heat Pumps for Heating, Energy Procedia 81 (2015) 100–107.
[3] L. Maier, C. Vering, K. Brinkmann, M. Lauster, D. Müller, Economic assessment of air-to-water heat pumps in the German building stock considering heating system design and dynamic operation, Proceedings of ECOS 2019, 2019.
[4] C. Vering, K. Brinkmann, L. Meier, M. Lauster, D. Müller, Vergleich der Jahresarbeitszahlen normativ ausgelegter Wärmepumpensysteme - Teil 1, HLH Lüftung/Klima, Heizung/Sanitär, Gebäudetechnik (2019).
[5] H. Wolisz, T. Schütz, T. Blanke, M. Hagenkamp, M. Kohrn, M. Wesseling et al., Cost optimal sizing of smart buildings' energy system components considering changing end-consumer electricity markets, Energy 137 (2017) 715–728.
[6] T. Schütz, X. Hu, M. Fuchs, D. Müller, Optimal design of decentralized energy conversion systems for smart microgrids using decomposition methods, Energy 156 (2018) 250–263.
[7] A. Bischi, L. Taccari, E. Martelli, E. Amaldi, G. Manzolini, P. Silva, S. Campanari, E. Macchi, A detailed MILP optimization model for combined cooling, heat and power system operation planning, Energy 74 (2014) 12-26.
[8] A. Ngyuyen, et al., A review on simulation-based optimization methods applied to building performance analysis, Applied Energy 113 (2014) 1043-1058.
[9] S. Fazlollahi, et al., Methods for multi-objective investment and operating optimization of complex energy systems, Energy 45 (2012) 12-22.
[10] D. Müller, M. Lauster, A. Constantin, M. Fuchs, P. Remmen, AixLib - An Open-Source Modelica Library within the IEA-EBC Annex 60 Framework, BauSIM 2016, p.3–9, September 2016 (2016).
[11] Deutscher Wetterdienst, Handbuch: Ortsgenaue Testreferenzjahre von Deutschland für mittlere, extreme und zukünftige Wetterverhältnisse, [September 07, 2019], https://www.bbsr.bund.de/BBSR/DE/FP/ZB/Auftragsforschung/5EnergieKlimaBauen/2013/.
[12] B. Filliard, A. Guiavarch, B. Peuportier, Performance evaluation of an air-to-air heat pump coupled with temperate air-sources integrated into a dwelling, Eleventh International IBPSA Conference (2009).
[13] K. Deb, A. Pratap, S. Agarwal, T. Meyarivan, A fast and elitist multi objective genetic algorithm: NSGA-II, IEEE Trans. Evol. Computat. 6 (2002) 182–197.
[14] A. Konak, D.W. Coit, A.E. Smith, Multi-objective optimization using genetic algorithms: A tutorial, Reliability Engineering & System Safety 91 (2006) 992–1007.
[15] C.A.C. Coello, Theoretical and numerical constraint-handling techniques used with evolutionary algorithms: a survey of the state of the art, Computer Methods in Applied Mechanics and Engineering 191 (2002) 1245–1287.

13th IEA Heat Pump Conference
April 26-29, 2021 Jeju, Korea

Combined Heating and Cooling in District solutions

Jussi Alpua*, Martti Kukkola

Oilon Oy, Niittytie 25 A, Vantaa 01300, Finland

Abstract

Energy companies can now produce energy efficient cooling with heat pumps outside of the traditional district cooling network. Property-specific heat pumps can be used to provide cooling services to customers within the energy company's district heating network. This concept makes it possible to offer energy efficient cooling services to customers without having to build a district cooling network. In property-specific cooling, the heat pumps are installed in the customer's property produces cooling and transfer the generated heat into the district heating network. The cooling service offered to the customer acts as decentralized heat source for the district heating network. In this Combined Heating and Cooling (CHC) concept, energy is not wasted. In many commercial and office buildings, hospital, datacenter as well as apartment buildings can be changed environment friendly cooling in future.

© HPC2020.
Selection and/or peer-review under responsibility of the organizers of the 13th IEA Heat Pump Conference 2020.

Keywords: heat pump; district cooling; district heating; combined heating and cooling; CHC

1. Introduction

The low carbon roadmap published by the European Commission in December 2011 aims at a near-zero emission energy system by 2050. For example, Finland's long-term goal is to reduce greenhouse gas emissions by 80 % by 2050. These more stringent political climate goals, increasingly volatile and lower wholesale electricity prices, and customer awareness of the need for renewable energy production forms to combat climate change are driving district heating companies to look for new energy sources and heat production forms. The use of heat pumps in a district heating system enables the utilization of a wide variety of different heat sources and increases the flexibility of the district heating system and the share of renewable energy production. According to the study, heat pumps could produce between 3 to 4 terawatt hours (TWh) of district heat per year, which would represent 9-13 percent of the annual sales of district heat in Finland. Current district heat production from heat pumps in Finland is about 0.6 TWh, which is around 1.7 percent of the total district heat production. In Sweden, for example, about 7.4 % (4.0 TWh) of district heat is generated by heat pumps [1].

This article looks at property cooling solutions implemented with heat pumps. In the implemented solutions, the cooling energy (cold water) required by the property is produced by heat pumps and the condensate energy generated in the production of cooling energy is transferred to the district heating network for further utilization of thermal energy. Typically, the cooling of the real estates is implemented with a cooling solution, in which the condensate energy generated during the cooling is not utilized and condensate energy is lost through outdoor condensers to the air.

* Corresponding author. Tel.: +358-44-337-4475; fax: +358-3-857-6239.
E-mail address: jussi.alpua@oilon.com .

The implemented solution can be applied and is sensible to apply to large properties that require cooling and are not able to be connected to the district cooling network and have been connected or will be connected to the district heating network. A large property here refers to a property with a design cooling power greater than ~ 30 kW.

2. The principle of cooling the property by heat pump

Figure 1 presents a cooling solution to a property, in which the condensate heat generated during cooling is transferred to the district heating network by use of a heat pump (lower example). Figure 1 also shows a conventional cooling solution in which condensate energy generated during cooling is transferred to the outdoor air via a heat transfer fluid (upper example). Heat pump and water chiller unit share similar operation principles. The temperature level of the water/liquid leaving from heat pump is high enough to utilize the condensate energy to the heat sink. For example in this figure 1 only adding 100 kW of electricity, there can be heat recover 600 kW high temperature water, instead of losing 500 kW to the air with chiller.

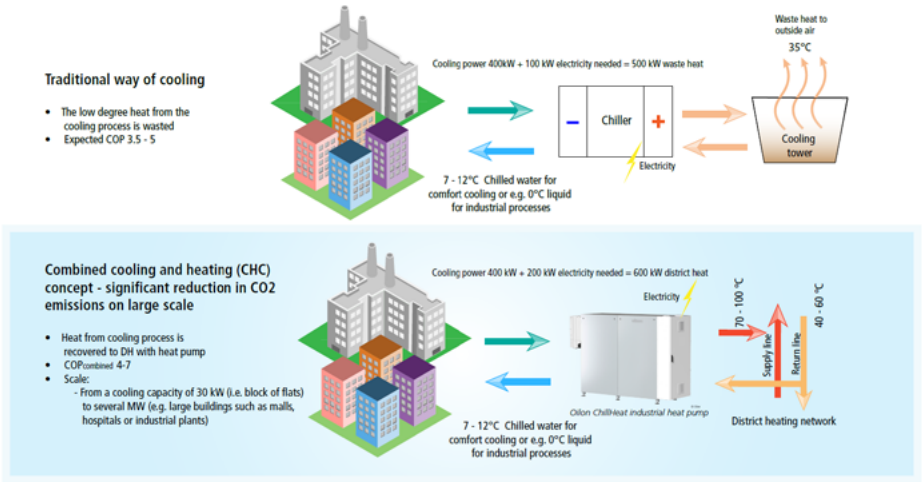


Fig. 1. Above is a traditional cooling solution in which condensate energy produced by cooling is transferred to the outdoor air via a heat transfer fluid. Below is a real estate cooling solution with a heat pump, where the condensate heat generated during cooling is transferred to the district heating network

The combined heating and cooling (CHC) system is not tied to any specific constant temperature like district cooling networks are. For example, the system can produce cooling liquid of -5 ˚C while recovering heat to the district heating network. In addition, the system can be installed in a small space. This is an advantage when operating normally on the client's existing premises.

Heat pump energy balance is:

$$Q_H = Q_c + P_e - Q_q \quad (1)$$

where Qc = cooling energy of the heat pump (kWh)
Pe = electric energy consumed by the heat pump compressor(s) (kWh)
QH = condensate energy of the heat pump (kWh)
Qq = heat losses of the heat pump to the environment (kWh)

The heat losses of the heat pump to the environment (engine room) are typically about 3 % of the electric energy with compressors equipped with semi-hermetic frequency converters.

The energy efficiency of cooling processes can be examined with the so called cooling efficiency factor (ε), defined by the formula:

$$\varepsilon = \frac{Q_c}{P_e} \tag{2}$$

The cooling efficiency of the cooling process depends on the temperature of the water (liquid) leaving the evaporator and condenser. The larger this temperature difference, the worse the cooling efficiency of the cooling process. The so called overall efficiency of the process can be determined to the cooling process, in which the condensate energy can be utilized:

$$\varphi_{tot} = \frac{Q_c + Q_H}{P_e} \tag{3}$$

If all the condensate energy generated by the cooling process is utilized, the overall efficiency as a function of the cooling efficiency is:

$$\varphi_{tot} = 2\varepsilon + 1 \tag{4}$$

3. The cooling solution for the property with a heat pump implemented in 2017

In 2017, a heat pump system was delivered for cooling the property, in which the condensate energy generated during cooling is transferred to the district heating network for further utilization according to the principle shown in the figure 1 (lower example). The design cooling capacity of the property to be cooled was calculated to be approximately 500 kW. Cooling water is utilized for cooling the property during warm periods and for condensate heat recovery of the year-round commercial refrigeration.

Two serial connected Oilon ChillHeat heat pumps were selected, based on the design cooling capacity of the property. Figure 2 shows the performance of the selected heat pump. Cooling water outlet is 10 ˚C and heating side outlet is 80 ˚C. Calculated total COP is 5,4. The heat pump performance is calculated using the Oilon Selection Tool program developed by Oilon Oy.

The selected heat pumps each have three piston compressors. In one heat pump two compressors are equipped with frequency drives (VFDx2). The six compressors in total achieve stepless cooling capacity control in the range of 8 %...100 %. Due to the control method of the heat pump, the efficiency of the heat pump remains almost constant throughout the power control range. In the implemented project, the heat pump and the cooling system require good adjustability, since the need for the cooling capacity of the property varies greatly e.g. depending on the outdoor temperature.

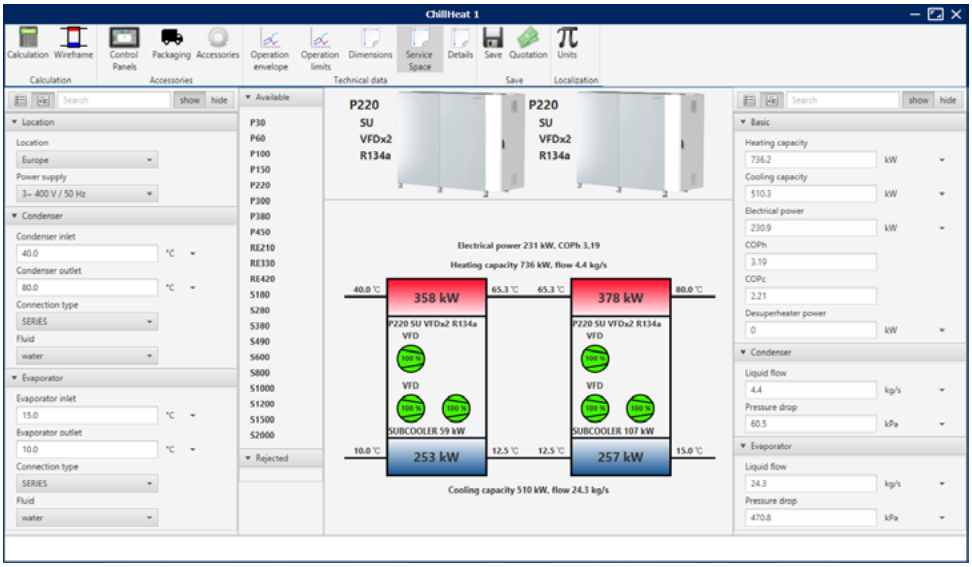


Fig. 2. Design information for the heat pump. The heat pump performance is calculated using the Oilon Selection Tool program

3.1. System description

The principle PI diagram of the system is presented in the figure 3. The system consists of the following main components:

- heat pump and automation (1)
- storage tank for the cooling circuit (2)
- cooling circuit circulation pump with a frequency converter (3)
- energy metering of the cooling circuit (4)
- district heating circuit pump with a frequency converter (5)
- district heating energy metering (6)
- district heating circuit 2-way control valve (7)
- district heating circuit check valve (8)
- filters (9)
- Electrical cabinet (10)

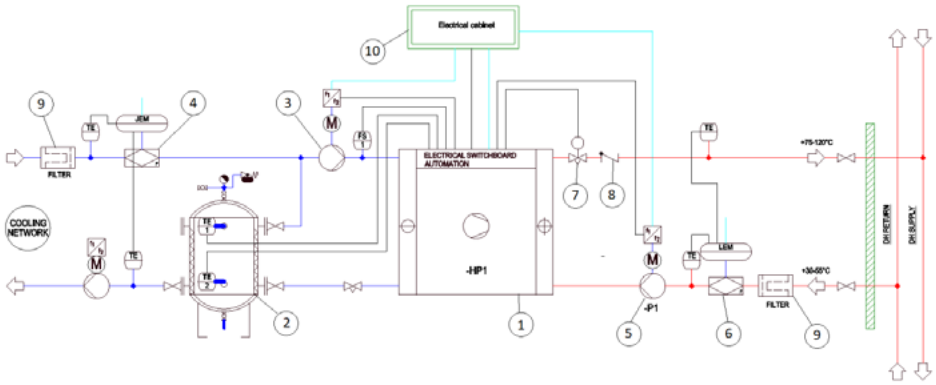


Fig. 3. Principal PI diagram for combined heating and cooling solution

The system does not need external control or automation to operate. The heat pump receives a running permission according to the lower temperature of the cooling accumulator. First, the circulation pumps (3 & 5) are started, both in the cooling and heating circuit. The cooling circuit is equipped with a flow switch (FS1) which detects the flow. When the flow is detected, the heat pump (1) can start.

The cooling power is controlled by adjusting the heat pump power, (1) and the temperature to the cooling network is controlled by changing the flow rate of the circulation pump (3). A set value for the outgoing water in the heating circuit is also set to the heat pump automation. This temperature is controlled by changing the flow rate with the frequency controlled pump (5) and the control valve (7). The control valve control is used when the circulation pump control range runs out. This ensures that the water entering the network is at the set point temperature. The heat pump will shut down after a delay when the power requirement is so low that it does not correspond to the minimum load on the unit.

3.2. Implemented system running in year 2019

This implemented solution was producing cooling approximately 850 MWh in year 2019. Heat pumps were consuming electricity 373,8 MWh and 80 ˚C hot water were produced 1 224 MWh. Total COP was 5,55. So the COP is higher than calculated COP. Note that this COP doesn't include circulation pumps electric consumption.

The system is owned by an energy company. Energy company is responsible for the running costs electricity and maintenance. Customer pays for the cooling energy. They also receive a compensation for the recovered heat. The energy company has not announced the price of sold cooling energy. Electricity price in Finland is typically 80-100 €/MWh without taxation. This size CHC solution installation costs are typically 450-480 €/kW (cooling). This price doesn't include pipe work from district heating network to machine room.

4. CHC in the future

The future looks pride for the CHC solutions. Last two years Oilon has supplied more than 20 CHC solutions in Nordic countries. This is just a start. For example energy companies in Finland have begun to open district heating networks, so that third party can access networks if the agreements can be settle.

Moving to 4th generation district heating networks give also more advance to CHC solution. In 4th generation district heating networks supplied water temperature will be low as 70 ˚C and even lower. Decentralized large scale heat pump systems are named one of the heat sources to the 4th generation district heating networks. Heat pumps can produce heating to the buildings as well as they can be used for 2-way district heating as CHC is. [2]

Lower network temperature will increase the CHC system efficiency and decrease the capital costs. Also lower temperature gives better possibility to use CHC solution storage tanks as heat storage when cooling is not needed. This of course needs some modification for the current system piping.

Maybe the best efficient way to use CHC is 5th generation district heat networks. This generation is using heat sharing networks where the temperature is near ambient ground temperature. Heat pumps are installed in customer buildings, as in CHC concept. Heat sharing networks can be used as heat source for the heating as well as for rejecting the heat to the network when a building needs cooling. This increases the CHC efficient, because the heat pump condensing temperature can be much lower. [3]

5. Summary

The low carbon roadmap published by the European Commission in December 2011 aims at a near-zero emission energy system by 2050. Finland's long-term target is to reduce greenhouse gas emissions by 80% by 2050. Cooling large buildings with heat pumps enables the condensate energy generated by cooling to be utilized in the district heating network, which reduces the amount of district heat produced by fossil fuels in the district heating network.

Combined Heating and Cooling solution (CHC) is simple, functional and effective system. Heat pump total COP can be over 5,5 when producing 10 ˚C cooling and 80 ˚C hot water. These systems can be implemented in new and existing properties.

CHC potential can be seen to increase in future. District heating companies are more and more opening the networks to third parties. Also moving forward to use 4th and 5th generation district heating networks increases the use of CHC's. Lower network temperature, decentralized sources and 2-way network will increase the benefits of using heat pump systems like CHC.

References

[1] Passi, Pekka et al. 2016. Suuret lämpöpumput kaukolämpöjärjestelmässä. The final report on August 29, 2016. Finnish Energy. PDF publication of 50 pages. Available: http://energia.fi/files/993/Suuret_lampopumput_kaukolampojarjestelmassa_Loppuraportti_290816_paivitetty.pdf

[2] H. Lund et al., "4th Generation District Heating (4GDH) Integrating smart thermal grids into future sustainable energy systems," Energy, vol. 68, pp. 1–11, Apr. 2014.

[3] S. Buffa, M. Cozzini, M. D'Antoni, M. Baratieri, and R. Fedrizzi, "5th generation district heating and cooling systems: A review of existing cases in Europe," Renew. Sustain. Energy Rev., vol. 104, pp. 504–522, 2019;

13th IEA Heat Pump Conference
April 26-29, 2021Jeju, Korea

Experimental investigations of two types of the dual-loop heat pump systems for ventilation heat recovery

Guoyuan MA*, Lei WANG, Anna MA, Xiaoya JIA, Yu LIU, Feng ZHOU

College of Environmental and Energy Engineering, Beijing University of Technology, Beijing 100124, China

Abstract

Heat recovery capability of ventilation system can be effectively improved by using multiple loop independent heat pump cycles. This paper focus on how to further improve the performance in the heat pump system under constant loop number and compressor displacement. The heat recovery performance differences between two types of the dual-loop heat pump system were compared through experimental testing. Results show that COP of the system in which the displacement in the low-pressure loop is twice of that in the high-pressure loop can be increased by 14.78% comparing with the system in which the displacement in the low-pressure loop is half of that in the high-pressure loop. Especially, the COP of the former system is even higher than that of the triplex loop heat pump system under some operating conditions. Therefore, in multi-loop heat pump system for ventilation heat recovery, it is more significant to increase the circulating flow rate of the working fluid in low-pressure loop.

© HPC2020.
Selection and/or peer-review under responsibility of the organizers of the 13th IEA Heat Pump Conference 2020.

Keywords: heat pump ; ventilation heat recovery ; dual loop; displacement ratio

1. Introduction

According to statistics, the energy consumption of buildings accounts for more than 40% of the total energy consumption in the European Union [1]. As the largest developing country in the world, the energy consumption of civil buildings accounts for about 25% of the total energy consumption in China [2]. Reducing the building energy consumption caused by ventilation system is an effective way to reduce building energy consumption [3-4]. Relevant studies have also confirmed that heat recovery from indoor exhaust air can greatly reduce the energy consumption of buildings [5-6].

The recovery efficiency of heat pump heat recovery system can reach 100% [7]. Some scholars have analyzed the energy-saving buildings using heat pump for ventilation heat recovery, and considered that the heat pump system has excellent performance, and the heat pump system has a better application prospect for ventilation heat recovery [8-9]. However, with the decrease of outdoor temperature in cold climate, the circulating mass flow rate of refrigerant will gradually decline in the heat pump system, and the excessive attenuation of circulating mass flow rate is not conducive to the heat recovery of exhaust air. Therefore, in order to improve the performance of the system at low outdoor temperature, some scholars have proposed a solution of multi-loop compression cycle [10].

The multi-loop heat pump ventilation heat recovery system proposed in reference [10] has excellent heat recovery performance with the same compressor displacement in each loop. Whether the displacement distribution of loops has influence on the performance of the system has not been studied. Therefore, this paper proposed two kinds of dual-loop heat recovery system. The total displacement of the compressors in the two systems is the same, but the displacement ratio in the high- and low-pressure loop is different. The performance

* Corresponding author. Tel.: +86-010-67391613.
E-mail address: magy@bjut.edu.cn.

of different dual-loop systems is analyzed by experiments, and the difference of displacement ratio for influence the performance of system is summarized and analyzed.

2. Method

2.1. System principle

Compressors A, B and C with the same specifications were used for experiments. Dual-loop system I represents a dual-loop system with a displacement ratio of 2 between high- and low-pressure loop, the system scheme is shown in Fig. 1. Compressors A and B were connected in parallel in the original experimental platform, so that the displacement in the high-pressure loop was twice as large as that in the low-pressure loop. At the same time, heat exchanger # 1 and # 2 were paralleled used as the condenser of high pressure-loop, heat exchanger # 4 and # 5 were used as the evaporator of high-pressure loop. Low-pressure loop was driven by compressor C. Heat exchanger # 3 and # 6 were used as condenser and evaporator of low-pressure loop, respectively. The low-temperature outdoor fresh air first passed through the low-pressure loop composed of compressor C, and then heated by the high-pressure loop composed of compressor A and B in parallel, finally sent into the indoor.

Dual-loop system II represents a dual-loop system with a displacement ratio of 0.5 between high- and low-pressure loop, the system scheme is shown in Fig. 2. The low-pressure loop was driven in parallel by the compressors B and C. At the same time, the heat exchangers # 2 and # 3 were used as the condenser of the low-pressure loop, the heat exchangers # 5 and # 6 were used as the evaporator of the low-pressure loop. High-pressure loop was driven by compressor A. Heat exchangers #1 and # 4 were used as condenser and evaporator of high-pressure loop, respectively. The low-temperature outdoor fresh air first passes through the low-pressure loop composed of compressors B and C, and then heated by the high-pressure loop composed of compressor A, finally sent into the indoor.

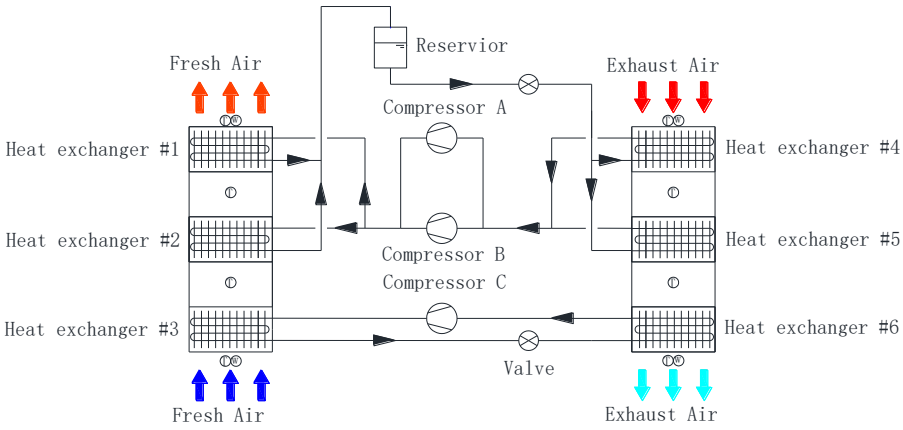


Fig. 1. Dual-loop system I: Displacement ratio between high-pressure loop and low-pressure loop is 2.

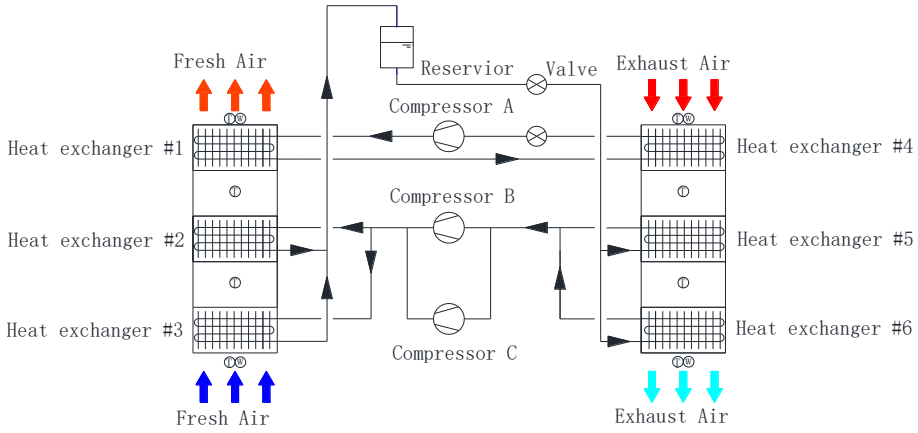


Fig. 2. Dual-loop system II: Displacement ratio between high-pressure loop and low-pressure loop is 0.5.

Fig. 3 is the representation of dual-loop heat pump ventilation heat recovery system on P-h diagram. The dual-loop system on the P-h diagram is composed of two independent cycles. A1-A2-A3-A4-A1 stands for low-pressure cycle, B1-B2-B3-B4-B1 stands for high-pressure cycle. There is no heat or mass exchange between the two cycles.

When the relatively low-temperature fresh air first enters the condenser of the low-pressure loop, the condensing pressure of the loop is lower because of the low air temperature. The air is gradually heated when flowing through the condensers. When fresh air entering the condenser of the next loop, the air temperature is already high. So the condensing pressure of this loop is higher than that of the low-pressure loop. When the exhaust air with high temperature enters the evaporators, the evaporating pressure of the loop which contact exhaust air first will relatively high, and then the evaporating temperature and evaporation pressure of the next loop are lower because the air has been cooled. This is the principle of the formation of high-pressure loop and low-pressure loop in dual-loop system. The two loops are combined in a step by step way to recover heat from exhaust air. C1-C2-C3-C4-C1 represents the system cycle in which the traditional heat pump ventilation heat recovery system works in a large temperature and pressure range.

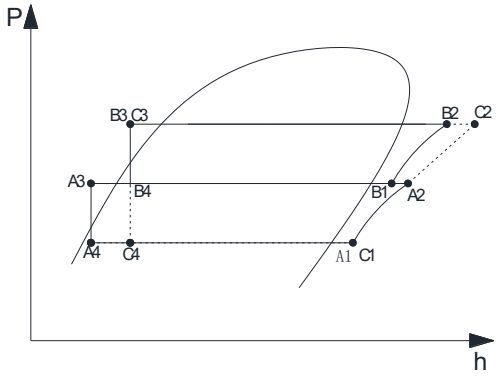


Fig. 3. P-h diagram of the dual-loop system cycle

2.2. Experimental procedure

Fig. 4 shows the photo of the experimental platform. The compressors used in the experiment are three GMCC rotary compressors of the same specification, the frequency is 50Hz, and the refrigerant used is R410A.

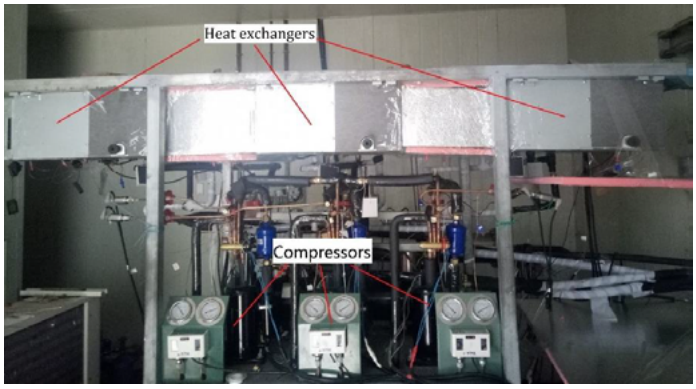


Fig. 4. Photo of the experimental platform

The fresh air heat exchangers (condensers) and the exhaust air heat exchangers (evaporators) of the experimental platform are respectively arranged in the outdoor environment simulation room and the indoor environment simulation room. The working environment of the ventilation heat recovery device can be realized by adjusting the temperature of the simulation rooms. The experimental test conditions are shown in Table 1.

Table 1. Test conditions

Test conditions	Indoor temperature (℃)	Outdoor temperature (℃)
Winter	20	15,10,5,0,-5,-10,-15,

3. Results and discussion

Fig. 5 shows the heating capacity changes for fresh air in different systems. From the point of view of the heating capacity to the fresh air, with the decrease of outdoor temperature, the heat obtained by the fresh air also increases gradually. The heating capacity of dual-loop system II is higher than that of dual-loop system I, which the growth amount can be up to 11.21%. That is, the heat recovery ability of dual-loop system II is higher than that of dual-loop system I. With the decrease of outdoor temperature, the fresh air temperature entering each heat exchanger is gradually declined. The temperature difference between the discharge temperature of the compressor and the fresh air temperature at the inlet of the condenser corresponding to the loop is gradually increased. The increase of the temperature difference between the refrigerant and the air will increase the heat transfer capacity of the heat exchanger to a certain extent. Therefore, with the decrease of outdoor temperature, the heating capacity of systems will gradually increase.

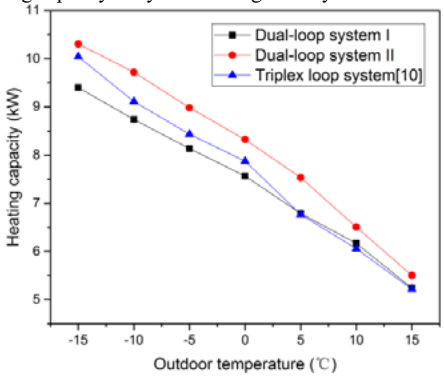


Fig. 5. Heating capacities of heat pump systems.

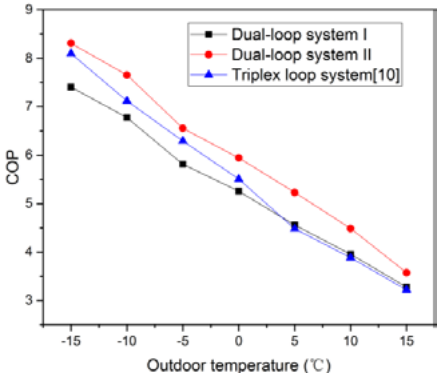


Fig. 6. COP of the heat pump systems.

The changes of system COP under each test condition is shown in Fig. 6. With the decrease of the outdoor temperature, the COP of the various systems are gradually increasing. The COP of dual-loop system II is higher than that of dual-loop system I at all test conditions, and the improvement can reach a maximum of 14.78%. The COP of the dual-loop system II is 2.61%~16.69% higher than that of triplex loop system as well. This is mainly because that the higher heating capacity and lower power input has been attained in dual-loop system II. This method to enlarge the displacement in the low-pressure loop can significantly improve the system performance while reducing the loop numbers and simplifying the composing for multiple loop heat recovery system as much as possible.

In general, heating capacity and COP of heat pump increase with increase of outdoor temperature, but the results of this study are opposite. This is actually the difference caused by the application of heat pump system in different occasions. When the heat pump system absorbs the heat from the low temperature outdoor air and then releases it to the high temperature indoor air, the heat source temperature in this condition is lower than the heat sink temperature. So the heating capacity and COP increase with the increase of the outdoor temperature. When the heat pump system is used for ventilation heat recovery, the system absorbs heat from the exhaust air（heat source） and then releases heat into fresh air（heat sink）. In this application, the temperature of the heat source is higher than that of the heat sink in winter. Operating condition is just opposite to an ordinal heating condition, so the heating capacity and COP decrease with the increase of the outdoor temperature. Of course, this trend will change with the heat transfer limit of the device and the deterioration of the operating environment.

4. Conclusion

In this paper, based on the theory of multiple loop heat pump ventilation heat recovery system, the influences of two dual-loop systems with different displacement ratio on heat recovery performance were analyzed and compared by experiments, and the following conclusions were drawn:

(1) COP of dual-loop system with a displacement ratio of 0.5 in high- and low-pressure loop can be 14.78% higher than the dual-loop system with a displacement ratio of 2, and the heating capacity can be 11.21% higher.

(2) Compared with dual-loop system with a displacement ratio of 2 in high- and low-pressure loop, system performance in dual-loop system with a displacement ratio of 0.5 is better in system performance, which indicates that increasing the displacement ratio of the low-pressure loop is more beneficial to the performance improvement of the multiple loop system.

Acknowledgements

We gratefully acknowledge funding support from the National Natural Science Foundation of China (51776004) and the General Project of Science and Technology Program of the Beijing Municipal Education Commission (KM201910005017).

References

[1] Herrando M, Cambra D, Navarro M, et al. Energy Performance Certification of Faculty Buildings in Spain: The gap between estimated and real energy consumption. Energy Conversion and Management, 2016, 125: 141-153.

[2] Zhang Y, He C Q, Tang B J, et al. China's energy consumption in the building sector: a life cycle approach. Energy and Buildings, 2015, 94: 240-251.

[3] Gilles F, Bernard S, Ioannis A, et al. Decision-making based on network visualization applied to building life cycle optimization. Sustainable cities and society, 2017, 35: 565-573.

[4] Li B, Wild P, Rowe A. Performance of a heat recovery ventilator coupled with an air-to-air heat pump for residential suites in Canadian cities. Journal of Building Engineering, 2019, 21: 343-354.

[5] Fehrm M, Reiners W, Ungemach M. Exhaust air heat recovery in buildings. International Journal of Refrigeration 2002;(25):439–49.

[6] Mardiana-Idayu A, Riffat S B. Review on heat recovery technologies for building applications. Renew Sustain Energy Rev 2012;16:1241e55.

[7] Alonso M J, Liu P, Mathisen H M, et al. Review of heat/energy recovery exchangers for use in ZEBs in cold climate countries[J]. Building and Environment, 2015, 84: 228-237.

[8] Fracastoro G V, Serraino M. Energy analyses of buildings equipped with exhaust air heat pumps (EAHP). Energy and Buildings, 2010, 42(8): 1283-1289.

[9] Kuusk K, Kalamees T, Maivel M. Cost effectiveness of energy performance improvements in Estonian brick apartment buildings. Energy and Buildings, 2014, 77: 313-322.

[10] Wang L, Ma G, Ma A, et al. Experimental study on the characteristics of triplex loop heat pump for exhaust air heat recovery in winter. Energy Conversion and Management, 2018, 176: 384-392.

13th IEA Heat Pump Conference
April 26-29, 2021 Jeju, Korea

Impact of the weather forecast on a predictive controller performance: experimental studies with a residential heat pump for space cooling

Thibault Péan[a,b,*], Ivan Bellanco[a,c], Jaume Salom[a]

[a]Catalonia Institute for Energy Research (IREC), 08930 Sant Adrià de Besòs (Barcelona), Spain
[b]Universitat Politècnica de Catalunya (UPC), 08028 Barcelona, Spain
[c]Universitat Rovira i Virgili (URV), 43007 Tarragona, Spain

Abstract

Heat pumps represent ideal systems to exploit the energy flexibility potential of buildings and their embedded thermal storage possibilities, particularly when they are operated by intelligent management systems such as model predictive controllers (MPC). The present study proposes to evaluate in an experimental setup the performance of an MPC controller used to control an air-to-water, variable speed heat pump for a residential building. In particular, the impact of the forecast quality is investigated, since MPC relies on the access to forecasts of the disturbances (weather, price, occupancy…) to perform its optimization. Two experiments of three days were thus repeated, the first one with a real weather forecast retrieved periodically from a commercial service, while the second one considered a perfect forecast. In cooling mode, the case with imperfect forecast resulted in an increase of the electrical energy use of the heat pump of 5.8%, corresponding to a cost increase of 11.2%, compared to the case with perfect forecast. These experimental results highlight the importance of the forecast quality on the performance of model predictive controllers for heat pumps.

Keywords: model predictive control; weather forecast; experimental study; residential applications; space cooling.

1. Introduction

With the growing penetration of wind and solar plants in our energy mix, the need for demand-side flexibility is becoming more and more relevant to maintain a proper operation of the power grids. In particular, the heating and cooling loads of buildings can be regarded as flexible demand, since they can be shifted in time to a certain extent, by exploiting their embedded mass as thermal storage. Heat pump systems enable firstly to electrify this demand, and secondly to make it more flexible, if operated by smart controllers.

In this regard, model predictive controllers (MPC) have shown a growing interest in recent years to exploit the energy flexibility of buildings [1]. Such control strategies rely on an optimization problem solved periodically, making use of a forecast of the external disturbances and a model of the dynamic systems to project their behavior over a certain finite horizon in the future, and thus find the optimal control sequence. MPC usually provides greater benefits in terms of savings, comfort or energy flexibility (depending on the chosen objective), than simpler strategies such as rule-based controls, even though its development costs are higher. The performance of MPC depends highly on its formulation, the reliability of the model used, and the accuracy of the disturbances forecast, which most commonly consists of weather predictions. About this last point, little literature was found about the influence of the forecast quality on the performance of MPC used in building climate control. A summary of existing articles and their learnings is presented hereafter.

The literature on the subject often uses a “performance-bound MPC”, sometimes also called “perfect MPC”, “optimal MPC” or “optimal policy”, as a benchmark for other control strategies [2]. It is an “idealized” MPC, which creates a perfect agreement between predictions and reality. Such studies are possible in computer

simulations where the future evolution of the exogenous parameters can be known beforehand, but could not be applied to field tests. It enables to see the upper limit of the benefits that MPC could ideally provide, if it had a perfect knowledge of the future. Mendoza-Serrano et al. [3] compared for instance different configurations, with the MPC provided either with a perfect forecast (full future information), either with zero future information. The first case lead to savings of 31% compared to a standard reference case, while the second one lead to savings of only 27%. The authors highlighted the fact that the savings strongly depend upon the level of information provided to the MPC algorithm. Similarly, Allen et al. [4] reported savings of -13% on the total energy costs with a perfect forecast, and -11% with an imperfect forecast. Rolando et al. [5] developed a predictive rule-based control, and found that the system energy consumption was reduced of about 15% when the control logic utilized the information of the perfect solar radiation forecast, over the entire heating season. Lazos et al. [6] also commented that weather variables are significant components of the evolution of building energy systems and minimizing the uncertainty in predicting their evolution can lead to significant savings, usually in the range of 15–30% compared to a deterministic and non-weather sensitive control approach. Lohr et al. [7] compared a controller when fed with a perfect forecast, or with the data of the previous day used as predictions for the next day (yesterday-based predictions). They found that the performance decreased only slightly, if historical data is chosen as forecast for the upcoming day, but the proposed controller performed well in both cases.

Most of the reviewed literature agrees on a significant influence of the forecast quality over the MPC performance. However, it remains unclear how much better the MPC can perform with a perfect knowledge of the future, compared to other imperfect methods used to predict the future evolution of the disturbances. In fact, a complete absence of knowledge of the future is as unrealistic as a perfect knowledge: since weather parameters have a certain inertia, and repeat daily and seasonal patterns, a certain approximation of the next day weather can always be estimated. Furthermore, most of the reviewed articles resorted to simulation work, and did not consider the application on real systems like heat pumps operated in a realistic setup. The present work intends to fill this gap by proposing a comparative study which shows the performance of an MPC controller on a real heat pump operated in a semi-virtual laboratory setup. The experimental nature of the study considers all practical aspects related to applying MPC as a heat pump supervisory control, and enables to obtain more realistic results than previous simulation-only work. In this study, the MPC was run firstly in real time, using weather forecasts updated every hour from a commercial service, while the current weather was also measured in parallel. In a second experiment, the recorded weather conditions were reproduced in a climate chamber where the heat pump outdoor unit is placed, also providing this information as a perfect forecast to the MPC controller. In this way, the performance of the MPC with a perfect or with an imperfect, but real-life forecast could be compared with the same boundary conditions.

2. Methods

2.1. Experimental setup: semi-virtual environment and heat pump system

The tests were performed in a semi-virtual environment setup in a laboratory, according to the schematic of Figure 1. The real heat pump is an air-to-water, reversible model of 11 kW capacity, able to regulate the speed of its compressor (variable speed). Its outdoor unit is placed in a climate chamber where the air temperature and relative humidity can be accurately controlled to reproduce the desired climatic conditions in a dynamic manner. Two thermal benches emulate the thermal loads from the building according to the simulation made in real time with the TRNSYS software: the first thermal bench emulates the space cooling load, by controlling the return temperature from the emission system that goes back to the heat pump. The other thermal bench schedules the tapping of DHW from the storage tank, according to a fixed and predefined schedule.

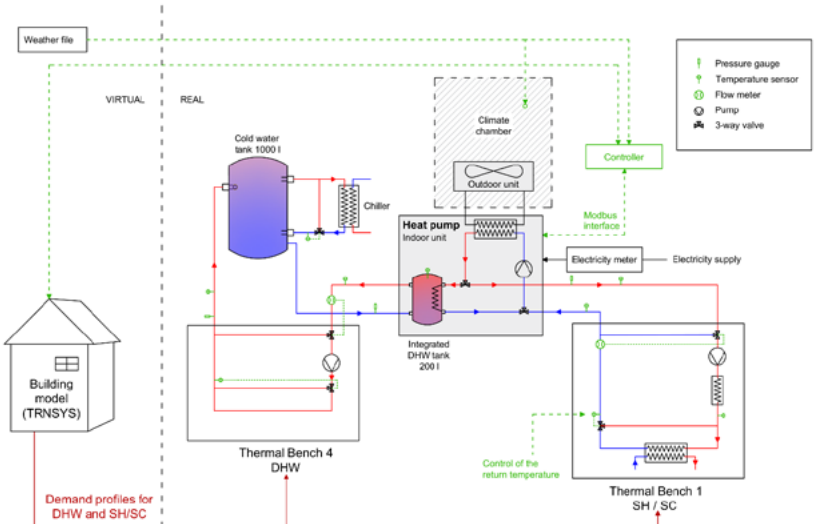


Figure 1. Schematic of the laboratory setup, applying the concepts of semi-virtual environment and hardware-in-the-loop.

2.2. Study case and utilized models

The control configurations have been tested on a building study case representative of the climate of the Catalonia region in Spain. It is a flat of 110 m^2 with 3 bedrooms, occupied by a family of 4 and conditioned by a circuit of eight Fan-Coil Units (FCU) supplied by the air-to-water heat pump. The flat is modelled in TRNSYS as a detailed white-box model. The occupation of the apartment is modelled stochastically, with a profile of the heat gains from people and equipment. The climate files used for the tests originate from a weather station situated in Tarragona (Spain), see also next section 2.4 about the forecasts on this matter.

In the present case, only a period of the cooling season was chosen for the tests. In this configuration, the heat pump functions in cooling mode to provide space cooling (SC), and in heating mode to produce Domestic Hot Water (DHW) stored in an integrated tank. Only one mode is allowed at any time, with DHW having priority over SC. The experiments carried out cover three days of September 2018, from the 13th to the 15th included, with a sufficiently high cooling load.

2.3. Model predictive controller

The controller tested in this study is a model predictive controller whose formulation is presented hereafter. The MPC formulation is summarized in this section; for any doubt or for further details, the reader is referred to previous publications [8], [9], and to the nomenclature at the end of this paper.

Objective: $\min_{u,\delta} J = [\alpha_\varepsilon J_\varepsilon + \alpha_{\Delta u} J_{\Delta u} + (1 - \alpha_\varepsilon - \alpha_{\Delta u}) J_{cost}]$

Subject to, $\forall k \in [\![1, N]\!]$:

Model:

$$\begin{cases} \boldsymbol{x}(k+1) = \boldsymbol{A} \cdot \boldsymbol{x}(k) + \boldsymbol{B_u} \cdot \boldsymbol{u}(k) + \boldsymbol{B_e} \cdot \boldsymbol{e}(k) \\ \boldsymbol{y}(k+1) = \boldsymbol{C} \cdot \boldsymbol{x}(k) \end{cases}$$

Constraints on the inputs:

$$\begin{cases} \delta_{SC}(k) \cdot \underline{Q_{SC}} \leq Q_{SC}(k) \leq \delta_{SC}(k) \cdot \overline{Q_{SC}} \\ \delta_{TES}(k) \cdot \underline{Q_{TES}} \leq Q_{TES}(k) \leq \delta_{TES}(k) \cdot \overline{Q_{TES}} \\ \delta_{SC}(k) + \delta_{TES}(k) \leq 1 \end{cases}$$

Constraints on the outputs:

$$\begin{cases} T_{int}(k) \leq \overline{T_{int}}(k) + \varepsilon(k) \\ \underline{T_{TES}} - \varepsilon(k) \leq T_{TES}(k) \end{cases} \qquad (\varepsilon \geq 0)$$

The cost function is multi-objective: it combines a comfort objective J_ε, a smoothing objective $J_{\Delta u}$ (which aims at avoiding too frequent changes in the frequent actions), and a cost reduction objective J_{cost}. These conflicting objectives have been balanced by choosing appropriate values for the weighting coefficients α_ε and $\alpha_{\Delta u}$.

The MPC controller projects the behavior of the systems on a horizon of 24 hours in the future (denominated N), using a simplified model of the building. This model is a resistance-capacitance grey-box model which represents the building envelope and the capacity of the thermal mass of the building to store energy. The model is expressed here in a state-space format (matrices A, B_u, B_e and C), using two different kinds of inputs: the vector $u(k) = [Q_{SC}\ Q_{TES}]^T$ contains the thermal powers of the heat pump for either space cooling or DHW production operation. These are the decision variables of the MPC. The vector $e(k) = [T_{amb}\ I_H\ Q_{occ}\ Q_{DHW}]^T$ contains the exogenous, non-controllable variables (also called disturbances), that must be forecasted for the MPC to be able to make its projections in the future. The ambient temperature T_{amb} and the solar irradiation I_H represent the weather forecast: this is where different forecast strategies have been tested in the present work. The heat gains from occupants and equipment Q_{occ} and the DHW tapping profile Q_{DHW} represent the other disturbances.

The constraints on the inputs ensure that the thermal power chosen by the MPC stays within the operation limits of the chosen heat pump system, between the minimum $\underline{Q}$ and the maximum $\overline{Q}$. The binary variables δ_{SC} and δ_{TES} allow the MPC to decide whether to operate the heat pump in SC or in DHW mode, and the last input constraint guarantees that only one mode is activated at a time. The output constraints ensure the provision of comfortable conditions to the occupants. The indoor temperature T_{int} is thus limited below the limit of $\overline{T_{int}} = 25℃$ and the tank temperature T_{TES} above the limit of $\underline{T_{TES}} = 50℃$. These constraints are softened by the slack variable ε, which is included in the objective J_ε. In this way, the constraints can sometimes be violated, but at a certain cost reflected in the objective function.

Finally, the cost objective is formulated as shown in Equation (2). A simplified model of the heat pump enables to estimate its power consumption P_{el} in function of the thermal power Q, the ambient temperature T_{amb} and the supply temperature T_{sup}. This power consumption is then multiplied at every time step by the price of electricity c_{el} which varies hourly but still presents two distinct periods with high and low tariffs.

$$J_{cost} = P_{el}(Q, T_{amb}, T_{sup}) \cdot c_{el} \tag{1}$$

The MPC controller is called every hour, and only the first control actions are sent to the real heat pump, before another instance of the MPC is formulated and solved.

2.4. Forecasts

In this study, the forecasts used within the MPC controller play an important role. Two configurations have been developed and tested: with perfect or imperfect forecast. During the days of September 13th to 16th of 2018, the outdoor temperature and solar irradiation were measured from a weather station situated in Tarragona (Spain). In parallel, every hour a forecast of these two weather parameters for the next 24 hours was retrieved from an external service and stored. It is a commercial service available online through an API [10], which enables the automatic download of the weather forecast periodically. This information was then used as input for the MPC.

The case with perfect forecast uses the actual measurements as forecasts, therefore it has a perfect knowledge of the future. It should be noted that the forecasts used are in fact a resampled version of the real measurements, to fit with the discretization time step of the MPC optimization problem (12 minutes). For this reason, the forecasts are slightly smoothed but have a very similar shape than the measurements.

The case with imperfect forecast uses the successive forecasts, as it would happen in a real operation on site with an actual building. The MPC runs its optimization every hour, therefore it updates with the best forecast information that it can have at the present moment.

The measurements and forecasts are presented in Figure 2. In the case of solar radiation, it appears that the forecasts did not take into account the cloud coverage, and only offered an estimation of the solar irradiation based on the location and hour of the day. This forecast matches well with the reality in the first day, as the sky was cloud-free, however it produces an important error on the third day, where the day was cloudier. The irradiation forecast does not actually change from one forecast to the next retrieved one hour later, for this reason all the curves are superposed. It should be noted that the weather forecast chosen was a free service, for this reason it is of poor quality, but it represents an actual service available on the market, for this reason it is interesting to investigate how the MPC would perform with such input.

In the case of the ambient temperature, the forecasts are shown on the bottom of Figure 2, and they provide a better estimation of the future evolution of the outdoor temperature, compared to the measurements carried out afterwards. The forecast is updated regularly, for this reason we observe a stack of curves. The forecast is relatively good although for instance in the third day it shows more uncertainty, probably due to the more irregular weather of that day.

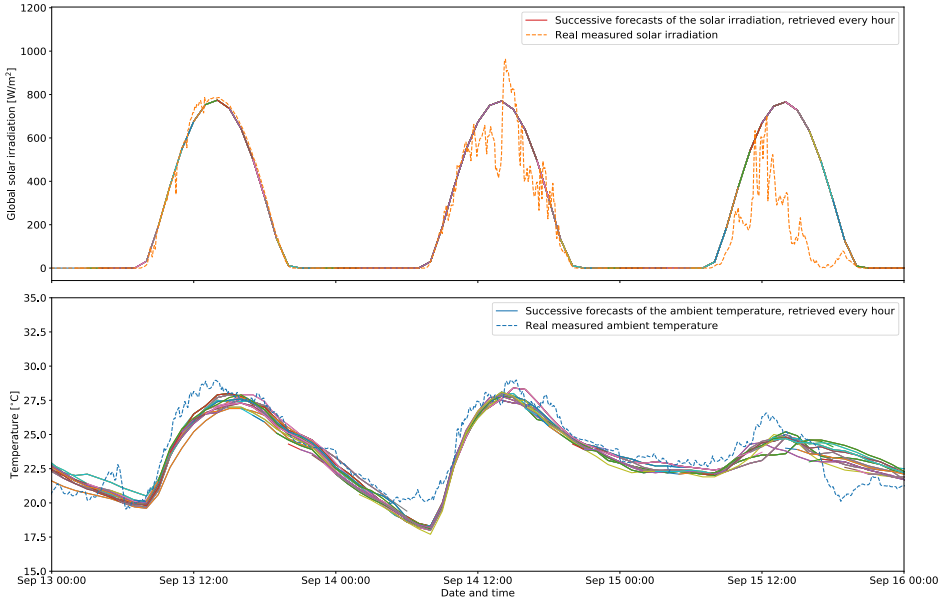


Figure 2. Measurements and successive forecasts of the solar irradiation and the ambient temperature in Tarragona (Spain) during three days of September 2018.

2.5. Performance indicators

The performed tests are analyzed in the view of different performance indicators. The summed energy values constitute the first series of indicators: the thermal energy produced by the heat pump, and the electrical energy that it used, over the three days of experiment. It should be noted that the thermal energy is always counted positive, whereas it is cooling energy like in space cooling operation, or heating energy like during DHW production (both of them are then summed to obtain the total thermal energy). The ratio of these two quantities (thermal and electrical energy) represents the efficiency of the heat pump, also called coefficient of performance (COP). Next, the costs incurred by the use of the heat pump are computed: the calculation consists in an integration of the electrical energy over the three days, weighted at each time step by the price of electricity in EUR/kWh at that time step, using for this purpose an hourly price profile available for small consumers in Spain (PVPC) [11]. This electricity tariff has a higher price period in the afternoon, therefore the economic MPC strategy tends to avoid the heat pump operation during these hours.

To evaluate the comfort conditions in the building, the average indoor temperature is calculated, as well as the percentage of time spent in Category I according to standard EN15251 [12], the category of highest comfort. Finally, an indicator able to estimate if the control strategy is able to shift the loads towards low-price periods is chosen. The flexibility factor is a performance indicator that reveals if the heat pump has used more energy during low price hours (up to a value of 1) or during high price hours (down to a value of -1) [13]. Its formula is indicated in Equation (2), where P_{el} represents the electrical power of the heat pump, and lp and hp the low and high price periods respectively.

$$FF = \frac{\int_{lp} P_{el} dt - \int_{hp} P_{el} dt}{\int_{lp} P_{el} dt + \int_{hp} P_{el} dt} \quad (2)$$

3. Results

The main results of the two experimental cases are presented in Table 1, in terms of summed energy values, average COP and comfort conditions, as well as with the chosen flexibility indicator.

Table 1. Summed or average values of several performance indicators over the three days of experiment in the two cases. The variation of the imperfect forecast case with respect to the perfect forecast case is indicated in absolute and/or relative terms.

Parameter	Unit	PERFECT	IMPERFECT
Thermal energy	**[kWh]**	**94.4**	**99.9**
Absolute variation	*[kWh]*		*+5.5*
Percentage variation	*[%]*		*+5.8%*
Electrical energy	**[kWh]**	**40.4**	**42.8**
Absolute variation	*[kWh]*		*+2.3*
Percentage variation	*[%]*		*+5.8%*
COP	**[-]**	**2.3**	**2.3**
Absolute variation	*[-]*		*+0.0*
Cost	**[EUR]**	**4.1**	**4.6**
Absolute variation	*[EUR]*		*+0.5*
Percentage variation	*[%]*		*+11.2%*
Average zone temperature	**[°C]**	**24.7**	**24.7**
Absolute variation	*[°C]*		*+0.0*
Time in Comfort Category I	**[%]**	**91.5%**	**95.0%**
Absolute variation	*[%]*		*+3.5%*
Flexibility factor cost FF	**[-]**	**0.5**	**0.3**
Absolute variation	*[-]*		*-0.2*

To evaluate the performance of the two configurations comparatively, the energy costs constitute the most interesting indicator, since this is the declared objective of the MPC controller. In this regard, the case with imperfect forecast performs worse than the case with perfect forecast, resulting in an increase of 11% of the costs. It thus appears that knowing an accurate forecast of the weather conditions in advance constitutes an important advantage for the controller. The thermal energy delivered and the electrical energy used by the heat pump both also increase when the forecast is imperfect, but in a less important manner, by 5.8%.

Next, the impact of the control configurations on the load shifting towards low price periods is investigated. Although the price forecast is equal in both cases, the case with perfect forecast managed to shift a greater proportion of the loads towards the periods of low price, reaching a value of $FF = 0.5$, while with imperfect forecast it stayed at a value of $FF = 0.3$.

The different strategies had little impact on the comfort of the occupants: the average temperature within the inhabitable zone is equal in both configurations, with a value 24.7°C. The percentage of time spent in comfort category I (i.e. with temperatures below 25.5°C in cooling mode for residential buildings) increased a little in the case of imperfect forecast, with 95%, while the case of perfect forecast only had 91.5% of the time in Cat. I, which is still entirely satisfactory, given that Cat. I represents the highest level of expectation. The extra energy spent thus enables to slightly improve the comfort conditions.

To understand better the dynamic behavior of the two configurations of the MPC controller, the time series of Figure 3 are plotted. The two versions of the controller behave in general similarly, for instance they tend to precool the building before the price increase happening every day, so as to limit the energy expenditure during the period of expensive electricity. However, some discrepancies are also observed, which explain the different results previously presented. For instance, on the third and last day, the imperfect forecast anticipated a large solar irradiation during the afternoon, while in fact the sky happened to be cloudy with low incoming solar radiation. Because of its overestimation, the MPC with imperfect forecast decided to cool the building in the early afternoon, anticipating an incoming solar radiation that never actually occurred, and so as to stay within the imposed comfort boundaries. On the other hand, the MPC with perfect forecast knew that the solar radiation would stay at a low level, and that active cooling would not be necessary to stay within the comfort zone. Since this difference in behavior occurred during a high price period, it had an important impact on the final energy costs, as can be seen in the end of the cumulative cost curves (third graph from the top). This

illustrates perfectly the importance of an accurate forecast for an MPC controller, and explains why the MPC with perfect forecast performed significantly better.

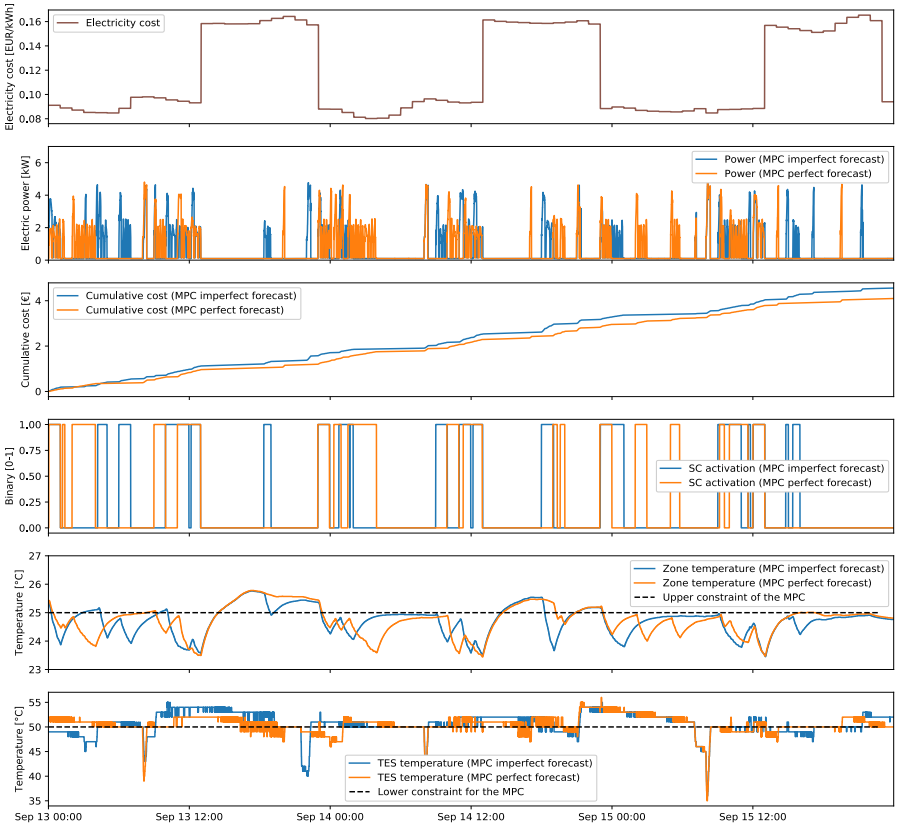


Figure 3. Time series comparing the dynamics of both studied configurations along the three days of the experiments.

4. Conclusions

In this study, an MPC controller was tested on a real heat pump system in an experimental laboratory setup, following the hardware-in-the-loop principles. Two experiments of three days duration were performed, one where the MPC controller was provided with a perfect forecast of the weather conditions for the next day, and the other where it used an imperfect forecast retrieved from an external service. When operated by the MPC with perfect forecast, the heat pump used 6% less electricity, which resulted in 11% savings on the energy costs, compared to the case with imperfect forecast. In the two experiments, the weather in the climate chamber where the heat pump is placed was identical, only the weather forecasts for the MPC was changed, which enabled to perform a thorough comparison on the MPC performance, when provided with a different forecast input. The results corroborate the learnings of the existing literature, highlighting the influence of the forecast accuracy on the savings achieved by the MPC. Additionally, the experimental nature of the work gives further reliability to the presented results, since few experimental studies on this topic had been carried out so far. From the obtained results, it can be concluded that a special care should be given to the choice of the weather forecast service when designing and implementing MPC in real buildings for climate control.

The weather forecasts used in this study originated from a commercial API available online, which gave a real-life example of service that could be connected to an MPC. However, it proved to be significantly inaccurate, especially regarding the solar irradiation. Better forecast service could have been used and would probably have reduced the difference with the perfect forecast case. Another idea for further research could be

to study separately the influence of the forecast of the ambient temperature and the solar irradiation, to understand if there exists any difference in their impact, or if one of those parameters could be forecasted more loosely than the other without significant loss of performance. Finally, the presented study only presented real-life cases of three days duration in cooling mode: these results could be extrapolated by performing longer experiments or simulations, also considering heating mode to find out whether the impact of the disturbance forecast changes seasonally. For instance, it appears that it was particularly important to forecast well the solar irradiation in cooling mode, since it is responsible for important heat gains and thus of the cooling demand, but on the other hand in heating mode, the ambient temperature might be the most important parameter to forecast accurately. These constitute interesting topics for further research.

Nomenclature

$J, J_{\Delta u}, J_{\varepsilon}, J_{cost}$	Global objective function, and subobjective terms, respectively for smoothing, comfort and cost reduction.
$\alpha_{\varepsilon}, \alpha_{\Delta u}$	Weighting coefficients of the sub-objectives
A, B_u, B_e, C	Matrices of the state-space building model (parameterized with resistance and capacitance values)
x, y, u, e	Vectors of the states, outputs, controllable inputs, and exogenous inputs
$T_{amb}, I_H, Q_{occ}, Q_{DHW}$	Exogenous inputs: ambient temperature, solar irradiation, heat gains from occupants/equipment, heat losses from DHW tapping
$\delta_{SC}, \delta_{TES}$	Binary variables for the activation of SC or DHW
Q_{SC}, Q_{TES}	Thermal power for SC or DHW operation of the heat pump
$\underline{Q_{SC}}, \overline{Q_{SC}}, \underline{Q_{TES}}, \overline{Q_{TES}}$	Lower and upper limits of thermal power in SC or DHW modes respectively
$\overline{T_{int}}, \underline{T_{TES}}$	Comfort constraints (upper constraint for the room temperature and lower constraint for the DHW storage tank temperature)
ε	Slack variable to relax the comfort constraints
T_{sup}, T_{int}	Supply temperature of the heat pump, indoor temperature of the building
P_{el}	Electrical power use of the heat pump
FF	Flexibility factor

Acknowledgements

This project has received funding from the European Union's Horizon 2020 research and innovation programme under the Marie Skłodowska-Curie grant agreement No 675318 (INCITE). Part of this work stems from the activities carried out in the framework of the IEA-EBC Annex 67 (International Energy Agency – Energy in Buildings and Communities program) about Energy Flexibility in Buildings.

References

[1] T. Péan, J. Salom, and R. Costa-Castelló, "Review of control strategies for improving the energy flexibility provided by heat pump systems in buildings," *J. Process Control*, vol. 74C, no. Special Issue on Efficient Energy Management, pp. 35–49, Apr. 2019.

[2] H. Thieblemont, F. Haghighat, R. Ooka, and A. Moreau, "Predictive control strategies based on weather forecast in buildings with energy storage system: A review of the state-of-the art," *Energy Build.*, vol. 153, pp. 485–500, 2017.

[3] D. I. Mendoza-Serrano and D. J. Chmielewski, "Smart grid coordination in building HVAC systems: EMPC and the impact of forecasting," *J. Process Control*, vol. 24, no. 8, pp. 1301–1310, 2014.

[4] J. Allen, A. Halberstadt, J. Powers, and N. H. El-Farra, "Supervisory Model Predictive Control of Flexible Building Loads with On-site Solar Generation," *Proc. Am. Control Conf.*, vol. 2018-June, pp. 4622–4627, 2018.

[5] D. Rolando, H. Madani, G. Braida, and R. Tomasetig, "Heat pump system control : the potential

improvement based on perfect prediction of weather forecast and user occupancy," in *12th IEA Heat Pump Conference 2017*, 2017, pp. 1–9.

[6] D. Lazos, A. B. Sproul, and M. Kay, "Optimisation of energy management in commercial buildings with weather forecasting inputs: A review," *Renew. Sustain. Energy Rev.*, vol. 39, pp. 587–603, 2014.

[7] Y. Lohr and M. Mönnigmann, "Receding horizon heat flow control in domestic buildings-Yesterday-based disturbance predictions," *2018 Eur. Control Conf. ECC 2018*, pp. 404–409, 2018.

[8] T. Péan, R. Costa-Castello, E. Fuentes, and J. Salom, "Experimental testing of variable speed heat pump control strategies for enhancing energy flexibility in buildings," *IEEE Access*, vol. 7, no. 1, pp. 37071–37087, 2019.

[9] T. Péan, R. Costa-Castelló, and J. Salom, "Price and carbon-based energy flexibility of residential heating and cooling loads using model predictive control," *Sustain. Cities Soc.*, vol. 50, Oct. 2019.

[10] Weatherbit, "Weatherbit API Documentation," 2019. [Online]. Available: https://www.weatherbit.io/api. [Accessed: 30-Oct-2019].

[11] Red Electrica de España, "ESIOS – Sistema de información del operador del sistema.," 2018. [Online]. Available: https://www.esios.ree.es/en (accessed 07/03/2018). [Accessed: 04-Apr-2017].

[12] CEN, "EN 15251: Indoor environmental input parameters for design and assessment of energy performance of buildings addressing indoor quality, thermal environment, lighting and acoustic." European Committee for Standardization, Brussels, Belgium, 2007.

[13] J. Le Dréau and P. Heiselberg, "Energy flexibility of residential buildings using short term heat storage in the thermal mass," *Energy*, vol. 111, no. 1, pp. 1–5, 2016.

13th IEA Heat Pump Conference
April 26-29, 2021 Jeju, Korea

Model Calibration of an Air Source Heat Pump System for Transient Simulations in Modelica

Philipp Mehrfeld[a,*], Markus Nürenberg[a], Dirk Müller[a]

RWTH Aachen University, E.ON Energy Research Center, Institute for Energy Efficient Buildings and Indoor Climate, Mathieustrasse 10, 52074 Aachen, Germany

Abstract

Within the scope of HVAC and building performance simulations, 74 % perform manual calibrations whilst the remaining 26 % aim for a fully automated process. Nonetheless, with focus on detailed grey-box simulation models for complex HVAC systems, such as a heat pumps (HP), a full automation might lead to several assumptions and, thus, to inaccuracies regarding the calibration results in terms of its misfit measures. Therefore, we define clear requirement specifications for an experimental design in combination with a semi-automated calibration procedure for an electrically driven air source HP system. The device under test is located in a climatic chamber and coupled to a hydraulic test bench, representing the source and sink of HP, respectively. As software toolchain, we use a combination of Python-based framework and Modelica-based simulation model library. We define the objective function as a chained and weighted KPI consisting of the normalized misfit measure CV(RMSE) of supply temperature and consumed electrical power. In a three-day long test with realistic dynamic boundary conditions, covering a comprehensive spectrum of inputs, we validate the calibrated models. The validation misfit measures show a deviation of 1.6 %.

© HPC2020.
Selection and/or peer-review under responsibility of the organizers of the 13th IEA Heat Pump Conference 2020.

Keywords: Type your keywords here, separated by semicolons ;

1. Introduction

Electrically driven heat pumps (HPs) are a main rising technology in the building energy sector. With a growing share of renewable energy sources in the current mixture of electricity, HPs are the most promising energy conversion system to convert electricity efficiently into thermal power. This work will focus mainly on air source heat pumps as they have a higher market share than ground source HP [1].

As the computing power has massively increased over time, HVAC plant simulation models represent an ever-increasing approach to predicting system performance using transient simulation. There are different approaches, ranging from white-box to grey-box to black-box modelling. Anyway, in every case adequate parameterization is necessary so that the simulation model is able to represent a real plant. In addition to parameterization with the aid of manufacturer data sheets, a semi-automatic calibration of a grey-box air-source HP (ASHP) model is used in this paper. Semi-automatic in this case means that besides a manual aggregation of existing model classes in the modelling language Modelica, an individual preprocessing of used input time series data takes place. The rest of the calibration process is fully automatic.

A well calibrated model of the HVAC system is necessary, for example, to:

- predict system performance for e.g. one year using a simulation with a suitable sink model (building + e.g. underfloor heating and dynamic user boundary conditions)
- derive a model for inclusion in an MPC algorithm [2, 3]

* Corresponding author. Tel.: +49 241 80 49776; fax: +49 241 80 49779.
E-mail address: pmehrfeld@eonerc.rwth-aachen.de.

- test functionalities of the system and the controller virtually (model in the loop) and thus save cost-intensive hardware tests

For this reason, measurement data is extracted from a 3-day dynamic test for an ASHP. About 60 % of the time series data is used for training and 40 % for validation purposes.

This paper deals with a developed framework consisting of a python-based and a modelica-based part. Figure 2 shows an overview of the process. The use case applied represents the calibration of an ASHP from existing time series data. In order to keep further influences to a minimum, the domestic hot water preparation and the control system are left out, although both were part of the experiment that provides the measurement data.

2. State of the art and initial condition

2.1. Calibration

Calibration is the variation of model parameters so that the difference between simulated and measured data is as small as possible [4]. A challenge in the field of modelling is the divergence between simulated and practical behavior [5]. In order to make building energy simulations a reliable tool for analyses regarding energy saving potentials or operational optimizations, there is a great interest in a correspondence between simulated and measured values of technical systems [6].

Within this framework, a model calibration in its core describes the parameterization of a model so that generated simulation results fit the measurement results of real systems. Before this, sensitive model parameters can be identified by sensitivity or uncertainty analyses and afterwards applied to the calibration process. [6]. However, we skip this step in the context of this work, since we know the model sufficiently well to determine the tuner parameters ourselves.

The mathematical methods differentiated Coakley et al. [7] in optimization methods and alternative modeling techniques. The optimization procedures are based on an objective function that evaluates the difference between measured and simulated data in the form of a statistical indicator or misfit measure. The optimization problem is formulated as a minimization problem, since this difference has to be reduced. The practical implementation typically takes place via the coupling of a simulation software with an optimization algorithm.

2.2. Measurement Data

To calibrate a model, it is vital to have extensive measurement data. In the scope of our case study, we obtained the dataset from a hardware-in-the-loop experiment [8, 9]. Figure 1 shows test bench arrangement of the ASHP system mentioned above and locations where the monitoring equipment are mounted. The HP is inverter controlled. While the outdoor unit of the split HP was positioned in a climatic chamber, the indoor unit was connected to a hydraulic test bench in order to emulate the outside air conditions and heat sink, respectively. With heat sink it is meant that simulation models of the hydronic network, the radiator heat transfer system and the building shell of a single family house were running during the experiment and values were interchanged online. Since a feedback of the simulation influences the hardware setup and vice versa, this explains the origin of the term hardware-in-the-loop. Tests with a monitoring frequency of 1 s represent the measurement database for the later performed calibration.

Uncertainties of measurements are evaluated for the supplied thermal energy and electrical energy consumption from a set of 11 reproducibility tests [10]. Results show a maximum uncertainty of 1.85 % for the thermal and 0.87 % for the electric energy.

Furthermore, we apply highly dynamic user profiles to the building model during the hardware-in-the-loop experiment. In terms of user profile we mean internal Gains up to 700 W, air change rates up to 0.8 1/h and room set temperatures up to 24 °C in the bathroom. The combination of all these boundary conditions and general heat losses of HVAC components like the buffer storage lead to a certain heat demand even during warmer days.

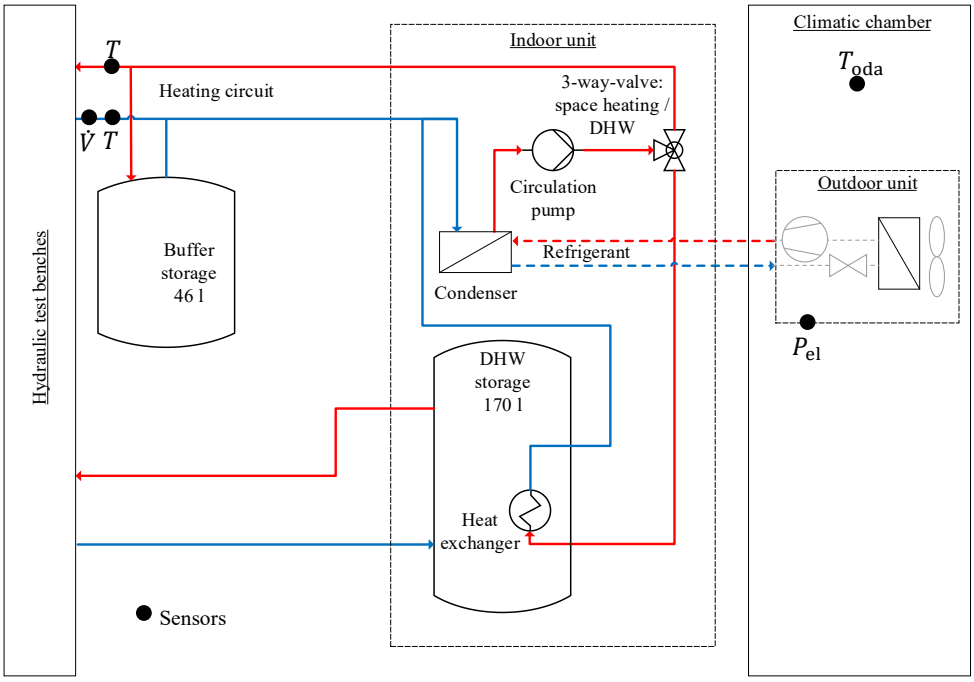


Figure 1: Experimental setup of hardware-in-the-loop experiment

2.3. Models

Throughout this work, we use the open-source and object-oriented language Modelica to model and run building performance and HVAC simulations. Modelica is specially designed for modeling physical systems [11]. To perform the required simulations for this work we use the freely model library AixLib [12] [13], which is a part of the IBPSA Project 1 [14] (former IEA EBC Annex 60 [15], therefore some models will be found as well in the main library IBPSA [14]. The HP model depends on tabulated data as stated by EN 14511 [16]. The model uses both black-box and grey-box modeling approaches. The first is used for the refrigerant circuit, whilst the latter is used for the remaining model parts. This means that thermal capacities, heat losses and pressure drops of the heat exchangers at both sides of the heat pump, condenser (con) and evaporator (eva), are implemented as grey-box approach in the model. A variable compressor speed signal represents one mandatory and time variable input to the model. A PT1 element of the model characterizes the dynamic behavior of start-up and shut-off phases of the compressor. The heat losses at the condenser to the atmosphere is parametrized by the combination of a thermal resistance-capacity model. Furthermore, in order to be able to model the temperature change due to heat losses in connected piping – even when there is no circulating fluid – a time constant in the temperature sensor can be defined in the corresponding Modelica model.

Furthermore, the simulation setup, consists of the HP model and the following three main components. The models are a 46 l buffer tank for hydraulic decoupling between the loading and the heating circuit (HC), a loading pump that allows the heating water to flow through the condenser, and a fan on the evaporator side. The storage model is discretized into three volumes.

2.4. Framework

As described above, this work is primarily concerned with structuring a calibration process based on Modelica models. For this reason, a two-part internal institute framework consisting of a Python-based and a

Modelica-based part was set up. The Python part is called AixCaliBuHA and stands for "**Aix** (from French Aix-la-Chapelle) **Cali**bration for **Bu**ilding and **H**VA**C** Systems". The Modelica part is a library of templates called MoCaTe and stands for "**Mo**delica **Ca**libration **Te**mplates". The template models of the library allow to be filled with arbitrary models, but designate certain inputs and outputs, which are needed for each calibration procedure (compare Figure 2). In the general pre-processing phase e.g. low pass filters or moving averages can be applied to the time series data. In terms of variable declaration, a fixed naming specifies the following three vectors, which contain the variables necessary for calibration and occur in every calibration: „Measured inputs" (mi), „Target values measured" (tv_{meas}) und „Target values simulated" (tv_{sim}). The latter two are compared in the objective function to be minimized and a misfit measure is formed. AixCaliBuHA allows the following misfit measures by default: Mean-absolute error (MAE), mean-square error (MSE), root-mean-square error (RMSE), coefficient of variation of the RMSE (CV(RMSE)), normalized RMSE, coefficient of determination (R^2). In the case of the present work it is the weighted chaining of CV(RMSE) [17]. The CV(RMSE) is defined as follows:

$$CV(RMSE) = \frac{\sqrt{1/n \cdot \sum_{j=1}^{n} (tv_{meas} - tv_{sim})^2}}{\overline{tv}_{meas}} \tag{1}$$

With n as the number of data points in the time series and $\overline{tv}_{\mathrm{meas}}$ as the arithmetic mean of the measured time series.

The parameterization of AixCaliBuHA provides for the definition of time segments and the definition of tuner parameters for these time classes with associated constraints in the form of minimal and maximal values. Start values can also be assigned. The core of the framework is the optimization of an objective function under consideration of the mentioned constraints. This objective function always calls the simulation necessary for the aimed period, extracts the simulated target values and compares them with the measured target values as calculation of an integral misfit measure. In the scope of this work this is the CV(RMSE).

The currently implemented optimization algorithms are dlib.find_min_global [18] and scipy.optimize.minimize [19], which in turn allows multiple algorithms. The non-linear optimizer dlib was used in the work. It is important to note that the optimizer cannot only optimize linear problems, since the behavior of the models used is usually non-linear.

In order to describe the dlib library, which provides a Python application programming interface, I quote the description from the website [18]: "Dlib is a modern C++ toolkit containing machine learning algorithms and tools for creating complex software in C++ to solve real world problems. It is used in both industry and academia in a wide range of domains including robotics, embedded devices, mobile phones, and large high performance computing environments. Dlib's open source licensing allows you to use it in any application, free of charge."

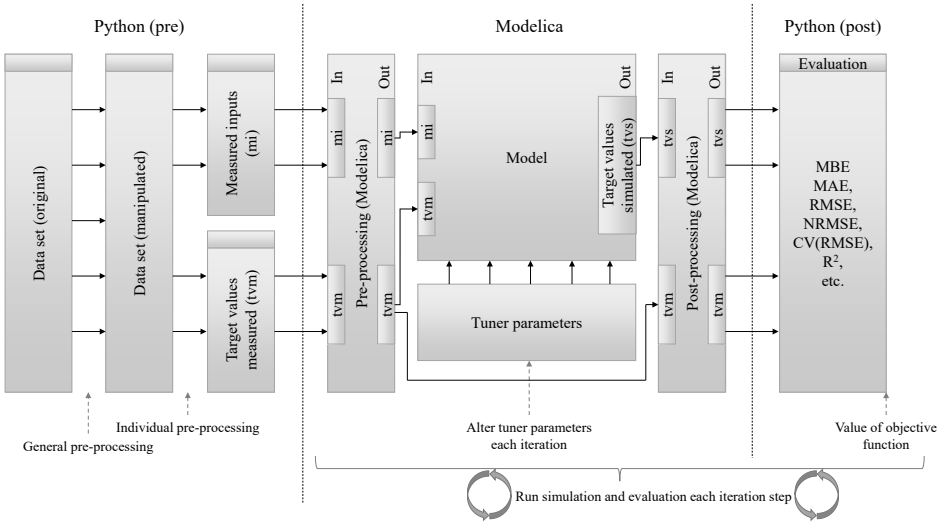


Figure 2: Overview and temporal representation of toolchain

In Modelica, the explicit statement "Evaluate=false" must be in the annotation of all tuner parameters. This ensures that the compiler excludes the parameter from the symbolic pre-processing. In some cases, however, this is not possible, namely when so-called structural parameters are involved which change the system of equations in a structural way. In these cases, the entire model must be recompiled each time in each iteration step of the optimization, which results in a significantly greater expenditure of time. The framework checks if all tuner parameters can be excluded from the symbolic pre-processing of the compilation and informs the user if this is not possible.

Finally, it should be said that the partial framework AixCaliBuHA can be fed with arbitrary forms of models. The use of Modelica models is only the choice during this work. It is therefore conceivable to use Functional Mock-Up Units [20] or models written in other programming languages that can be placed in the AixCaliBuHA framework via defined inputs and outputs.

3. Carrying out the calibration

The target values (tv) are on the one hand the **heating circuit flow temperature** $\boldsymbol{T_{HC,flow}}$ and on the other hand the total **electrical power consumption** $\boldsymbol{P_{el}}$ of the system including powers consumed by fan, pump, controller unit and compressor. The total objective function to be minimized is composed of the chain approach:

$$min \sum f_{tv_i} \cdot CV(RMSE)(tv_i) \;\forall\; tv_i \in \{T_{HC,flow}, P_{el}\} \tag{2}$$

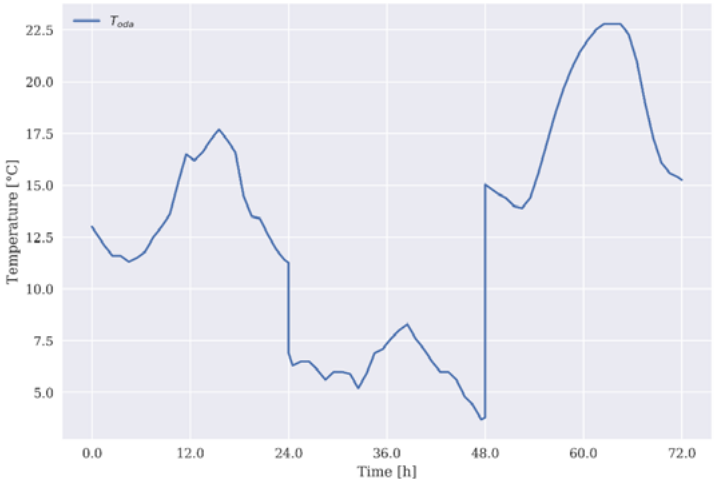


Figure 3: Outdoor air temperature T_{oda} that was emulated by the climatic chamber

Under the premise that the sum of all f_{tv_i} equals 1. The aim is to weight the two targets equally. For this reason, both terms must be in the same order of magnitude, for which a sensible choice of the factors f_{tv_i} is done. For this purpose, we conducted a preliminary investigation that the order of magnitude of $\mathrm{CV(RMSE)}(T_{\mathrm{HC,flow}})$ lies at approximately 0.01 and that of $\mathrm{CV(RMSE)}(P_{\mathrm{el}})$ is about 0.2. Therefore, the factors are $f_{T_{\mathrm{HC,flow}}} = 19/20$ and $f_{P_{\mathrm{el}}} = 1/20$, in order to ensure approximately equal weighting.

The time series data refer to three experimental days in the hardware-in-the-loop test mentioned above. Figure 3 displays the curves of the outside temperature, emulated by the climatic chamber. The test days come from an autumn, winter and summer day and are representative and realistic.

The following variables represent time series variables as „Measured inputs“ given with a brief description each:

- `nSpeedFanEva_1_0`: Relative fan speed (either 0 or 1)
- `TEva_K`: Outdoor air temperature emulated and measured in climatic chamber
- `THCRet_K`: Return temperature of heating circuit measured at hydraulic test bench
- `nSpeedPumpCon_1_0`: Relative pump speed of supply / loading pump near condenser (either 0 or 1)
- `m_flowHC_kg_s`: Mass flow rate through heating circuit measured by hydraulic test bench
- `nSpeedHP_invCtrld_0_1`: Relative and variable compressor speed with a minimum threshold of 25 %

The following variables represent the „Tuner parameters“:

- `scaleHPQCon_nominal`: Scaling factor for tabulated data of default thermal powers for the HP model
- `scaleHPPEl_nominal`: Scaling factor for tabulated data of default electrical powers for the HP model
- `mCon_flow_nominal`: Nominal mass flow rate on water side of the condenser (condenser model derives nominal pressure drop and heat transfer capabilities from this value)
- `mHC_flow_nominal`: Nominal mass flow rate on air side of the evaporator (evaporator model derives nominal pressure drop and heat transfer capabilities from this value)
- `fQWarm`: Additional scaling factor for thermal powers in the range of $T_{\mathrm{oda}} \geq 12\ °\mathrm{C}$
- `fQMed`: Additional scaling factor for thermal powers in the range of $2\ °\mathrm{C} < T_{\mathrm{oda}} < 12\ °\mathrm{C}$
- `fQCold`: Additional scaling factor for thermal powers in the range of $T_{\mathrm{oda}} \leq 2\ °\mathrm{C}$
- `fPWarm`: Additional scaling factor for electrical powers in the range of $T_{\mathrm{oda}} \geq 12\ °\mathrm{C}$
- `fPMed`: Additional scaling factor for electrical powers in the range of $2\ °\mathrm{C} < T_{\mathrm{oda}} < 12\ °\mathrm{C}$
- `fPCold`: Additional scaling factor for electrical powers in the range of $T_{\mathrm{oda}} \leq 2\ °\mathrm{C}$

- `T_fixAmbTestHall`: Assumed temperature in the test hall, wo which indoor unit, most piping and sensors were exposed to and transferred heat to as losses
- `lambdaIns`: Thermal conductivity of buffer storage envelope
- `tauVolCon`: Time constant that scales the assumed condenser volume of the HP model

In terms of the measured inputs, we conduct chosen individual pre-processing like in the step in Figure 2 states. This is necessary since we do not have all the necessary knowledge of all operational states of the HP For example, we derive the fan speed `nSpeedFanEva_1_0` as well as the pump speed `nSpeedPumpCon_1_0` from one phase of the monitored electrical power consumption. This means the fan and pump is enabled when the power consumption exceeds a threshold of 0.5 % of maximal power. Furthermore, we gain the relative and modulating compressor speed `nSpeedHP_invCtrld_0_1` by normalizing the total electrical power between its maximum and minimum for each day. It is necessary to distinguish between the days and, thus, in a certain way between the outdoor temperature since this mainly determines the level of power consumption.

4. Results

4.1. Training

The plot of the objective function's values in Figure 4 shows that already from approximately iteration 50 onwards the deviation mainly lies below 0.02.

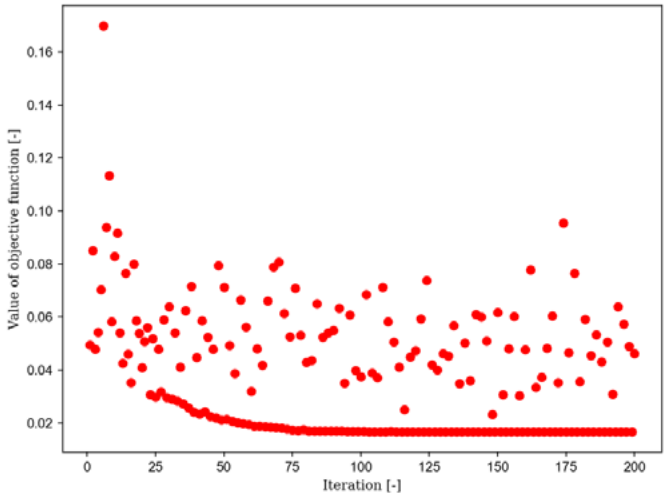


Figure 4: Progress of the objective function's values over iteration steps (training phase)

Figure 5 shows the measured and simulated target values for the 1.5 day-long training phase. The behavior of the dynamics fits predominantly well. In particular with regard to $T_{\mathrm{HC,flow}}$, in some places deviations become apparent, which can be explained with a high degree of probability by the control that was not transferred from real experiment into the simulation domain. In contrast, during the experiments the control of the HP system was active, including pump's pre- and post-run times, heating rod control, partial DHW tank charging. For the calibration, a speed control for the inverter-controlled compressor was derived from the power consumption only. The following target value function results from a quantitative point of view:

$$\left[f_{T_{HC,flow}} \cdot CV(RMSE)\left(T_{HC,flow}\right) + f_{P_{el}} \cdot CV(RMSE)(P_{el})\right]_{Training} \tag{3}$$

$$= \frac{19}{20} \cdot 0.0090 + \frac{1}{20} \cdot 0.1463 = \mathbf{0.0158} \tag{4}$$

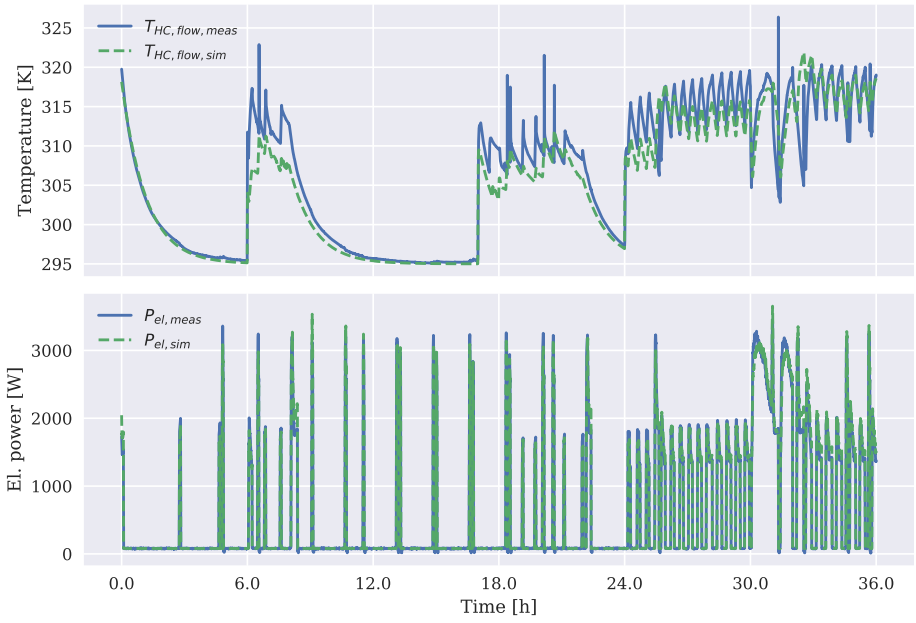


Figure 5: Curves of target values plotted for training data (day 1 and first half of day 2)

Table 1 shows the finally selected tuner parameters' values that the optimization algorithm found. The development of the tuner parameters' value search displays Figure 6.

Table 1: Final values of optimized tuner parameters

scaleHPQCon_nominal [-]	**scaleHPPEl_nominal [-]**	**fQWarm [-]**	**fQMed [-]**	**fQCold [-]**	**T_fixAmbTestHall [K]**	
0.82	0.70	0.77	1.31	1.76	295.45	
mCon_flow_nominal [kg/s]	**mHC_flow_nominal [kg/s]**	**fPWarm [-]**	**fPMed [-]**	**fPCold [-]**	**lambdaIns [W/m/K]**	**tauVolCon [s]**
0.34	0.49	1.97	1.77	1.94	0.15	150.00

4.2. Validation

The data set for the validation consists of two partial days. On the one hand from the second half of the winter day (day 2) and on the other hand a part from the summer day (day 3), since this has a similar behavior to the transition day (day 1). However, the first 25 % of the summer day were excluded from the validation data as there is an incomprehensible discrepancy between measured and simulated values of the target values. This probably stems from a control strategy such as the use of the heating rod, which we could no longer clearly prove from the experimental documentation at the time of calibration. The hardware-in-the-loop tests were performed several months before calibration and the system was already dismantled. The experiments were selected because of their very high measurement resolution of 1 s, as they provide a good basis for calibrating transient models. However, we did not conduct the experiments with this aim in mind.

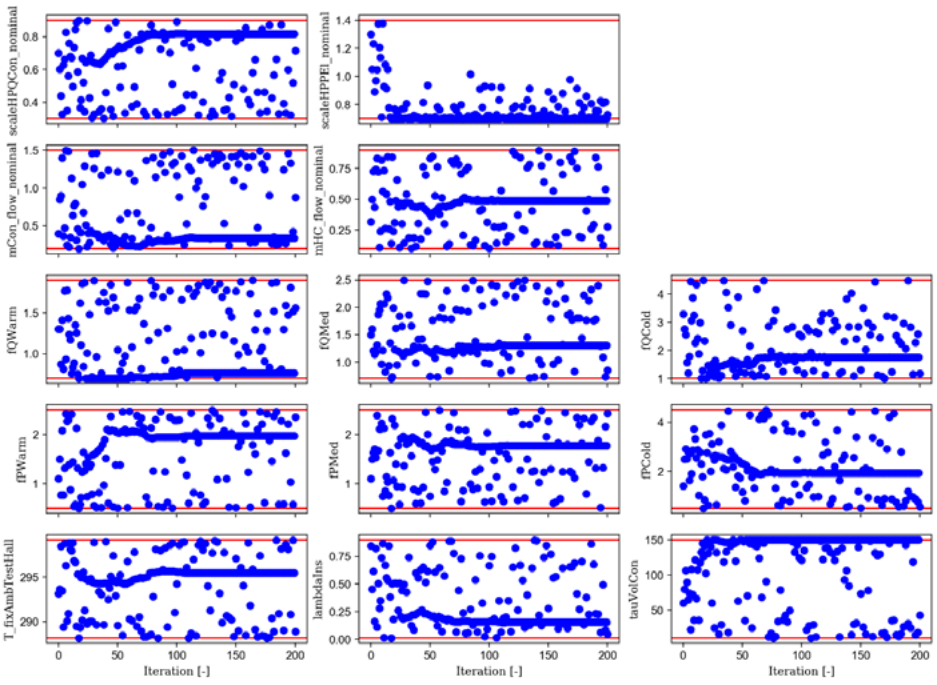


Figure 6: Process of the tuner parameters' value during optimization (red lines: minimal and maximal boundaries)

Figure 7 shows the measured and simulated target values for the two periods mentioned above. Hereby, the time series parts of day 2 and day 3 are concatenated.

The calculation of the value of the combined objective function looks as follows:

$$\left[f_{T_{HC,flow}} \cdot CV(RMSE)\left(T_{HC,flow}\right) + f_{P_{el}} \cdot CV(RMSE)(P_{el})\right]_{Validation} \tag{5}$$

$$= \frac{19}{20} \cdot 0.0085 + \frac{1}{20} \cdot 0.1343 = \mathbf{0.0148} \tag{6}$$

5. Conclusions

In the scope of this work, we develop and present a toolchain to calibrate transient simulation models of HVAC plants. This framework is preliminary based on the programming language and can be interfaced to a sub-framework of the simulation model. In the case of this work this is the open-source and object-oriented modelling language Modelica. The calibration framework provides general as well as individual pre-processing possibilities and multiple evaluation strategies with focus on time series data. These evaluation strategies create key performance indicators by comparing the measured to the simulated time series of defined target values. These key performance indicators are meant to be minimized by one of the implemented optimizers.

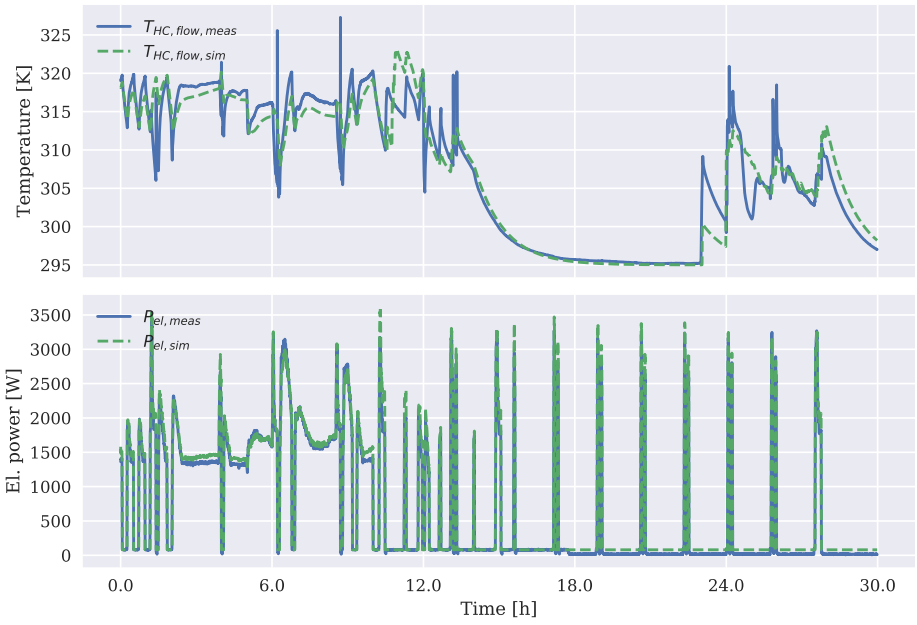


Figure 7: Curves of target values plotted for validation data (part of day 2 and 3 concatenated)

The use case is the calibration of an air-to-water heat pump, of which we gained high-frequent measurement data of a hardware-in-the-loop test that we conducted in our institute's laboratory. Since the boundary conditions of this 3-day long experiment are volatile and covering a broad range, e.g. in terms of outdoor air temperature, the data suits well for the application in a calibration process.

To calibrate the air-source heat pump we split the measurement time series into 60 % training and 40 % validation data. With 200 Iterations for calibrating the model on the basis of the chosen training set, we achieve a coefficient of variation of the root-mean-square error CV(RMSE) = 0.0158. For this purpose, we use 13 tuner parameters. The validation reaches an even better value of CV(RMSE) = 0.0148. Whilst the target value P_{el} (electrical power consumption) shows a satisfying congruence in terms of dynamics and level of the values, the other target value $T_{HC,flow}$ (heating circuit's flow temperature) displays in the time series plot solely in terms of dynamics good results. Offsets within certain time spans are probably due to neglecting control phenomena during the calibration process.

Especially the latter mentioned effect asks for further improvement of the process. The suggestion is to have individual calibrations for individual components like the heat pump unit itself, the hot water storages and the controller. For this reason, monitoring equipment must be installed with focus for a feasible calibration. Furthermore, the calibration of a controller is a challenging task due to lots of binary states like mode for domestic hot water or space heating.

Acknowledgements

We gratefully acknowledge the financial support by Federal Ministry for Economic Affairs and Energy (BMWi), promotional reference 03ET1595A.

References

[1] T. Nowak und P. Westring, *European Heat Pump Market and Statistics Report 2018,* v1.6 Hrsg., The European Heat Pump Association AISBL, Hrsg., Brussels, Belgium, 2018.

[2] R. W. Wimmer, „Regelung einer Wärmepumpenanlage mit Model Predictive Control," Eidgenössiche Technische Hochschule, Zürich, 2004.

[3] T. Storek, A. Esmailzadeh, P. Mehrfeld, M. Schumacher, M. Baranski und D. Müller, „Applying Machine Learning to Automate Calibration for Model Predictive Control of Building Energy Systems," *Building Simulation 2019: 16th Conference of IBPSA,* 2019.

[4] T. G. Trucano, L. P. Swiler, T. Igusa, W. L. Oberkampf und M. Pilch, „Calibration, validation, and sensitivity analysis: What's what," *Reliability Engineering & System Safety,* Bd. 91, Nr. 10-11, p. 1331–1357, 2006.

[5] G. Dall'O', L. Sarto, N. Sanna und A. Martucci, „Comparison between predicted and actual energy performance for summer cooling in high-performance residential buildings in the Lombardy region (Italy)," *Energy and Buildings,* Bd. 54, p. 234–242, 2012.

[6] E. Fabrizio und V. Monetti, „Methodologies and Advancements in the Calibration of Building Energy Models," *Energies,* Bd. 8, Nr. 4, p. 2548–2574, 2015.

[7] D. Coakley, P. Raftery und M. Keane, „A review of methods to match building energy simulation models to measured data," *Renewable and Sustainable Energy Reviews,* Bd. 37, p. 123–141, 2014.

[8] M. Nürenberg, P. Mehrfeld, K. Huchtemann und D. Müller, „Hardware-in-the-Loop test bench setup and its application to determine seasonal performance of heat pump systems," 2017.

[9] P. Mehrfeld, M. Nürenberg, M. Knorr, L. Schinke, M. Beyer, M. Grimm, M. Lauster, D. Müller, J. Seifert und K. Stergiaropoulos, „Dynamic evaluations of heat pump and micro combined heat and power systems using the hardware-in-the-loop approach," *Journal of Building Engineering,* Bd. 28, p. 101032, 2020.

[10] A. Miehlich, „Studies on the repeatability of Hardware-in-the-loop experiments," RWTH Aachen University, Aachen, 2017.

[11] Modelica Association, „Modelica," 2019. [Online]. Available: https://modelica.org/.

[12] AixLib, *AixLib - A Modelica model library for building performance simulations,* 2018.

[13] D. Müller, M. Lauster, A. Constantin, M. Fuchs und P. Remmen, „AixLib - An Open-Source Library within the IEA-EBC Annex60 Framework," 2016, p. 3–9.

[14] IBPSA, *IBPSA Project 1: BIM/GIS and Modelica Framework for building and community energy system design and operation,* 2018.

[15] International Energy Agency, *IEA EBC Annex 60: New generation computational tools for building and community energy systems based on the Modelica and Functional Mockup Interface standards,* 2018.

[16] DIN EN 14511-3, *Air conditioners, liquid chilling packages and heat pumps for space heating and cooling and process chillers, with electrically driven compressors - Part 3: Test methods; EN 14511-3:2018,* Bd. 27.080; 91.140.30, 2018.

[17] R. J. Hyndman und A. B. Koehler, „Another look at measures of forecast accuracy," *International Journal of Forecasting,* Bd. 22, Nr. 4, p. 679–688, 2006.

[18] D. E. King, „Dlib," 2019. [Online]. Available: http://dlib.net/.

[19] Scipy, „SciPy: Scientific Library for Python (Function: optimize.minimize)," 2019. [Online]. Available: https://docs.scipy.org/doc/scipy/reference/generated/scipy.optimize.minimize.html.

[20] T. Blockwitz, M. Otter, J. Akesson, M. Arnold, C. Clauss, H. Elmqvist, M. Friedrich, A. Junghanns, J. Mauss, D. Neumerkel, H. Olsson und A. Viel, „Functional Mockup Interface 2.0: The Standard for Tool independent Exchange of Simulation Models," Linköping University Electronic Press, 2012, p. 173–184.

13th IEA Heat Pump Conference
April 26-29, 2021 Jeju, Korea

High temperature heat pumps for drying – first results of operation in industrial environment

Veronika Wilk[a*], Franz Helminger[a], Michael Lauermann[a], Andreas Sporr[a], Bernd Windholz[a]

[a]AIT Austrian Institute of Technology GmbH, Giefinggasse 2, 1210 Vienna, Austria

Abstract

Heat pumps make an important contribution to increasing the efficiency of industrial processes and avoiding CO_2 emissions and therefore are considered as an important element for industrial heat supply by valorizing waste heat. Heat utilisation temperatures above 120°C will significantly expand the field of application for heat pumps in industry. This article presents the first results of operation of the H2020 project DryFiciency. Closed loop high temperature heat pumps with a heating capacity of 400 kW and heat supply temperatures up to 160°C are being developed, built and operated. The heat pumps are integrated in industrial drying processes recovering waste heat available on site. In this article, a first assessment of the operation of the heat pump for brick drying at Wienerberger AG in Uttendorf (Austria) is presented.

© HPC2020.
Selection and/or peer-review under responsibility of the organizers of the 13th IEA Heat Pump Conference 2020.

Keywords: High temperature heat pumps; industrial application; drying; HFO refrigerant; demonstation

1. Introduction

Decarbonization of industrial production is a key element to achieve the climate goals of the European Union. This requires drastic reduction of energy consumption and CO_2 emissions, as well as the transition to renewable energy supply. Increasing energy efficiency of industrial processes will contribute significantly to achieve these goals, however, new processes are also needed, such as electrification to replace fossil energy supply. Industrial heat pumps enable both, efficiency increase and electrification and will therefore play a major role in the future energy system.

Although heat pumps are an established technology for domestic heating and hot water preparation, integration of heat pumps into industrial processes is still in an early diffusion phase. Currently, there is no statistical data available on how many heat pumps are already applied in industry. In the framework of the collaborative IEA HPT Annex 48 project, more than 300 application examples for industrial heat pumps were collected from 7 countries. [1] These heat pumps are applied in many different industrial sectors. For example, in Austria a large number of examples is reported for the food industry, utilities and metal processing industry. The heat supply temperatures of the heat pumps in the examples are in the range of 45-95 °C, which corresponds to the products available on the market. Heat pumps supplying that temperature range have been available on the market for many years. [2]

In the last years, new developments have raised the heat supply temperature to more than 100 °C. With heat pumps that deliver high temperature heat up to 160 °C, a larger range of applications in industry can be covered. However, there are some barriers that still slow down the diffusion of heat pumps in industry despite the great application potential. Arpagaus [3] summarized the findings of several studies on market barriers for industrial heat pumps: There are important economic barriers, such as stringent expectations of short payback periods

* Corresponding author. Tel.: +43 664 6207794; fax: +43 50550-6679.
E-mail address: veronika.wilk@ait.ac.at

by industry and competing heating technologies based on fossil fuels at low energy prices. But there are also barriers related to knowledge and trust in a new technology: low level of awareness of the technical possibilities due to further development, lack of knowledge about the integration into industrial processes and lack of pilot and demonstration systems. [3]

Industrial demonstration projects are an important step to address the knowledge-related barriers. Within DryFiciency, an H2020 project, heat pumps for drying processes are developed, constructed and operated in a real industrial environment. Drying processes are among the most energy intense processes; they are wide spread in industry and mostly fired with fossil fuels. The heat pumps are used to recover waste heat that is available at the industrial sites and upgrade it to process heat for drying at temperatures up to 160 °C. In the project, different types of heat pumps are developed: heat pumps for air drying processes based on a closed loop vapor compression system and heat pumps for steam drying based on an open loop mechanical vapor recompression system. The heat pumps for air drying are demonstrated in a starch drying process of Agrana Stärke GmbH, an Austrian company specialized in processing and refining of agricultural raw materials such as corn, wheat and potatoes; and in a brick dryer of Wienerberger AG, the world's largest brick producer. The open loop heat pump for steam drying is demonstrated in a batch dryer for sludge of Scanship Holding AS in Drammen/Norway. First, the industrial drying processes were analyzed in detail, then, the heat pumps and their system integration were designed. A special focus was placed on the selection of materials and compounds to ensure stability and reliability at the demanding conditions of the high temperature applications. The heat pumps were constructed and integrated at the industrial sites. Commissioning of the heat pumps started in November 2019. In this work, a first assessment of the operation of one of the DryFiciency heat pumps are presented: the closed loop heat pump for brick drying at Wienerberger.

2. Brick drying process with heat pump

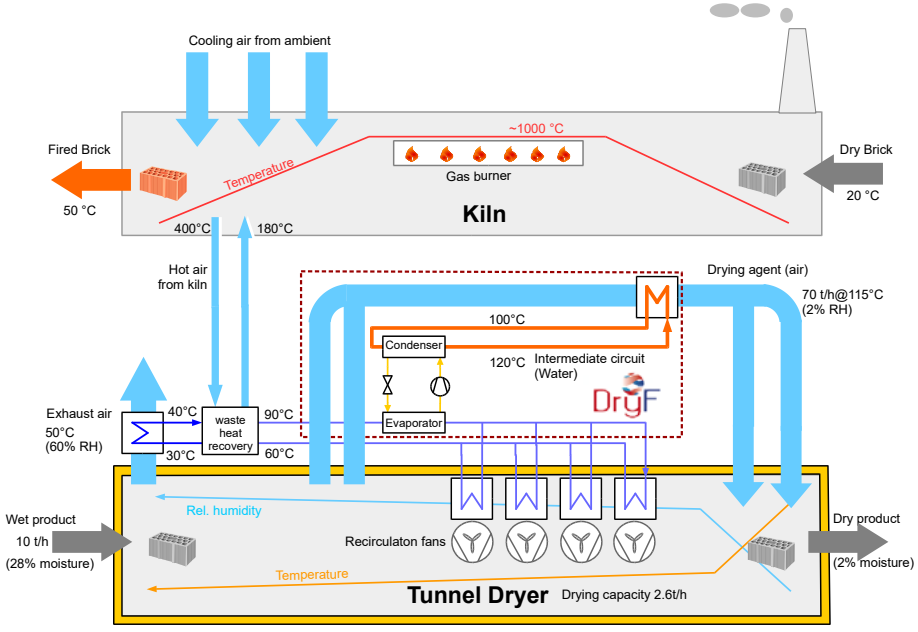


Fig. 1. Illustration of brick drying process at Wienerberger with the DryFiciency heat pump, the indicated temperatures values of the intermediate circuit and the drying agent show the design operating point for the DryFiciency heat pump, the thin red line in the kiln indicates the temperature profile in the kiln, the thin blue and orange lines the temperature and moisture profile in the tunnel dryer.

Wienerberger operates approx. 200 brick dryers in its manufacturing units worldwide. The DryFiciency heat pump was integrated at the production site in Uttendorf in Austria.

In general, the production of bricks and other clay products can be divided into several steps: preparation of the raw materials, shaping of the bricks, drying and firing. The drying process prepares the bricks for firing by extracting moisture from the soft shaped bricks. The shaped bricks (so-called "green" bricks) with a

moisture content of around 28 % are dried to a moisture content of 2 % required at the entrance of the kiln. Drying is the most energy intensive step in the brick production process.

The dryer, the kiln and the heat pump are illustrated in Fig. 1. It is a continuous drying process in a tunnel dryer using air as drying agent flowing counter-currently to the bricks. Drying air is heated by internal heat exchanger surfaces in the tunnel, which are supplied with water with 90 °C by a heat recovery cycle. The heat pump also uses the heat recovery cycle as the heat source. The evaporator of the heat pump is installed before the heat exchangers. The heat pump provides hot air via an intermediate circuit, heat supply temperatures up to 160 °C can be reached there. The hot air is fed into the outlet zone of the tunnel dryer, where the highest temperatures are required. The heat pump acts as a booster for the heat recovery cycle. It replaces a natural gas burner, that was used for that purpose.

2.1. Heat pump and integration infrastructure

The heat pump is designed as a closed loop compression heat pump with a heating capacity of up to 400 kW. R-1336-mzz(Z) by Chemours is used as refrigerant, it is based on HFO (hydrofluoro-olefins). The refrigerant has been already successfully tested at AIT in a lab-scale heat pump prototype for high temperature applications up to 160 °C. [4]. It has a low GWP value of 2 (global warming potential) and is non-flammable, non-toxic and not subject to the F-gas regulation.

The piston compressors integrated in the demonstrator were developed and supplied by Viking Heat Engines AS. The compressor design is based on an ORC (Organic Rankine Cycle) expander used for heat recovery applications with an overall design temperature of 215 °C. The expander has already been extensively tested at high temperatures and achieves high efficiencies. The compressor designed is 90 % the same as the ORC expander and built on the same piston bottom-end, only the cylinder head is different. Over the past five years the piston expander has undergone a comprehensive development program to achieve a long service life and high durability at very high temperatures. Today, this piston machine technology is equally capable of operating in organic Rankine cycles (ORC) as well as vapor compression heat pump systems. The compressor is designed for use with R-1336-mzz(Z). A single piston compressor has a swept volume of 55 m^3/h at 1800 rpm. A total of eight compressors arranged in two modules of four are used. Fuchs Schmierstoffe GmbH has developed a suitable lubricant for the compressors, which fulfils all necessary requirements regarding lubrication, viscosity, and thermal and chemical stability together with the refrigerant.

The heat pump is designed as a twin cycle system consisting of two refrigerant cycles (see also Fig. 5). The condensers of the two cycles are connected in series. Thus, the temperature lift from the heat source to the heat sink is reduced to a certain extend for one of the two cycles and about one half of the heating capacity is provided at a higher COP (coefficient of performance). In each refrigerant cycle there is one compressor module with four compressors. Due to the thermodynamic properties of the refrigerant, an internal suction gas heat exchanger is used to ensure dry compression.

The heat pump is placed in a container with approximately 8 m in length and 3 m in height and width. It is equipped with eight doors to enable easy access and if necessary, replacement of components of the heat pump. It contains all piping and other connections that are needed to connect the heat pump with the integration infrastructure at the brick dryer. Fig. 2 and Fig. 3 show the heat pump container from the outside and with open doors. The heat pump itself consists of hundreds of single parts of the following main component categories:

- Components for the refrigerant cycles such as piston compressors, condensers, evaporators, etc.
- Components for water distribution for the heat source and heat sink including control and safety valves, metal bellows compensator, etc.
- Housing including refrigeration machinery room equipment like ventilation, leakage detection system and warning devices
- Control system including cabinet, programmable controller, frequency converters, electrical fuses, control transformer, visualization, data logging and data transfer equipment to allow profound monitoring activities
- Measurement devices



Fig. 2: Heat Pump Container (outside)



Fig. 3: Heat Pump Container (inside, before insulation)

As illustrated in Fig. 1, the heat pump is integrated into the drying process by an intermediate water circuit. The water circuit allows testing a wide range of heat supply temperatures from 110 – 160 °C. In the intermediate circuit, a pressure holding device including a circulation pump and a water-to-air heat exchanger (air register) are installed.

2.2. Measurement equipment

Monitoring, data logging and data transfer are separated into two parts, one with the existing process control system of Wienerberger, where also the integration infrastructure (intermediate water circuit, air register and heat source) belongs to, and the other one of the DryFiciency heat pump. Both process control systems have their own measurement points and separate data transfer to AIT.

The heat pump is equipped with numerous sensors for data monitoring. Temperature sensors are integrated at all important parts of the refrigerant cycles, for example at the condensers, the internal heat exchanger, the expansion valve, the evaporators and the compressors. Pressure sensors are located among others before and after the compressors, at the inlet of the condensers and before the expansion valves. Electricity consumption of the motors is measured in terms of power, energy, voltage, current and power factor. In addition, heat meters to monitor the heat source and the heat sink are integrated.

Numerous parameters of the drying process from the existing process control system are used to determine the impact of the heat pump on the brick production process. The following parameters from the tunnel dryer are used: Volume flow of drying air into the dryer, inlet and outlet conditions of the air in the dryer, inlet and outlet temperature and mass flow of hot water used in the heat exchanger to heat the tunnel dryer, mass flow of wet bricks, mass reduction of bricks from inlet to outlet of the dryer.

3. Results

During commissioning, a trial operation of the heat pump system is carried out to provide proof of operational safety and functional capability. Also, the quality of the heat pump system is assessed based on fundamental functional tests according to predefined operating conditions to test the control algorithms, compressor lubrication, oil separation, operating temperatures of the compressors the suction gas super heating and part load conditions. The successful completion of the trial operation is the end of the commissioning and an important prerequisite for the subsequent long-term monitoring. Four different operation conditions are described in more detail that are characterized by different heat supply temperatures: 120, 140, 150 and 160 °C (Table 1).

Table 1: Operation points during trial operation

Operation point	Heat sink inlet temp., °C	Heat sink outlet temp., °C
1	95	120
2	110	140
3	120	150
4	130	160

Fig. 4 illustrates the heat source and heat sink inlet and outlet temperatures for the four operation points. The yellow area indicates the preparation phase, the green area stationary operation. For OP1, 2 and 3, stationary operation lasted more than three hours and did not show any fluctuations in the heat source and heat sink. For OP4, operation was shorter and lasted about one hour. The heat source inlet temperature was 88 °C for all operation points. The complete heat source mass flow was used for the heat pump without flow regulation, as a result, the heat source was cooled by 3 – 6 K.

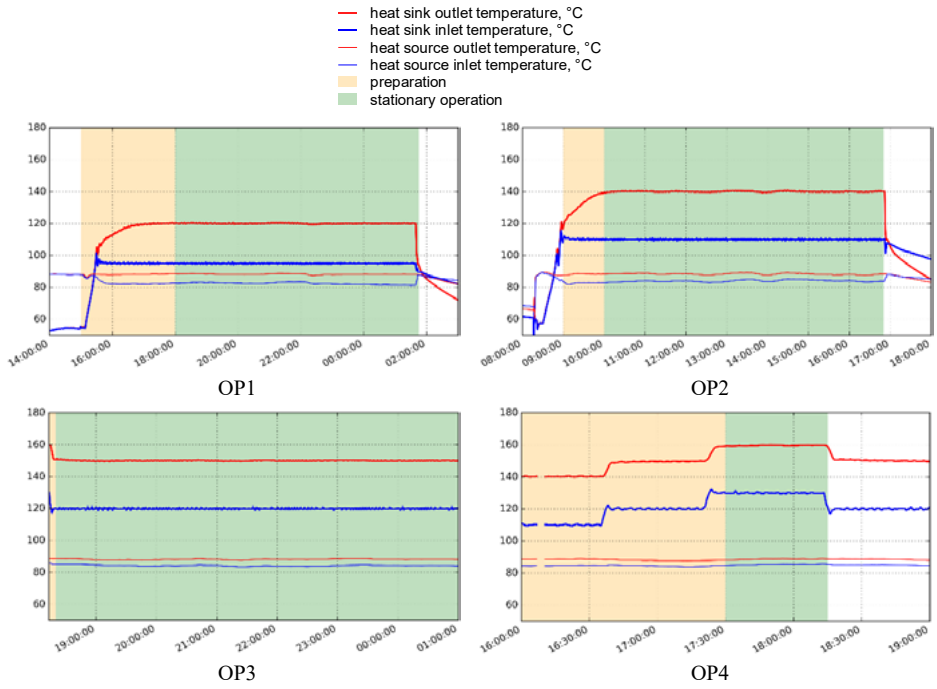


Fig. 4: Time series diagrams for four different operation points (120, 140, 150 and 160 °C)

As previously mentioned, the DryFiciency heat pump is designed as a twin cycle system consisting of two refrigerant cycles. The layout is shown in Fig. 5. The condensers of the two cycles are connected in series, therefore the condensation temperature of cycle 1 (yellow) is lower than the condensation temperature of cycle 2 (orange). The evaporators can be either operated in series or parallel. For the trial operation, they were operated in parallel. Fig. 6 shows the log(p)-h diagram for both cycles for OP1 (120 °C). The section 1-2 takes place in the compressor, 2-3 in the condenser, 3-4 in the sub-cooler, 4-5 at the hot side of the internal heat exchanger (IHX), 5-6 in the expansion valve, 6-7 in the evaporator and 7-1at the cold side of the internal heat exchanger. Due to the sub-cooler, more heat can be supplied to the industrial process. The sub-cooler is integrated between the condenser and the internal heat exchanger (not illustrated in Fig. 5). In cycle 2, more heat is provided in the sub-cooler than in cycle 1. For both cycles, the evaporation temperature amounted to 78 °C. As indicated by point 7, the refrigerant leaves the evaporator with super heat. The internal heat exchanger increases the efficiency by transferring heat from the high pressure side to the low pressure side of the heat pump. Point 1 and 2 indicate the satisfying function of the super heat control to ensure dry compression. The difference in condensation temperature between cycle 1 and cycle 2 was 10 K.

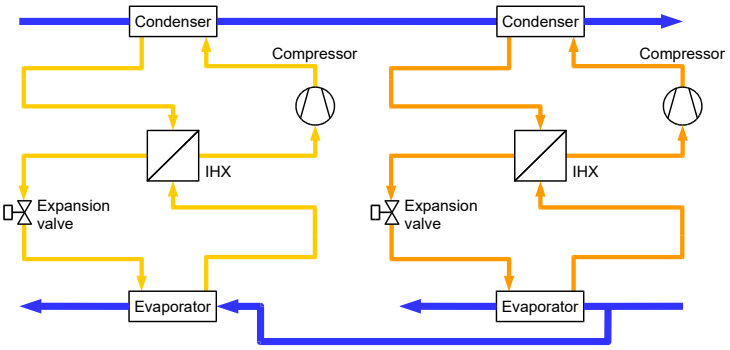


Fig. 5: Layout of the DryFiciency heat pump (yellow = cycle 1, orange = cycle 2)

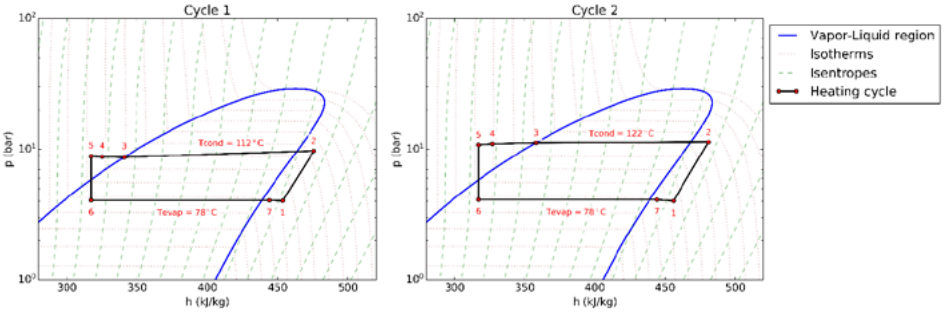


Fig. 6: Log(p)-h diagram for cycle 1 and 2 of the heat pump, OP1 (120 °C)

OP2, OP3 and OP4 show similar behavior as illustrated in Fig. 7, Fig. 9 and Fig. 10. With increasing temperature lift, more compressor work is needed to achieve higher discharge pressures. At a heat supply temperature of 160 °C, condensation takes place at the upper end of the vapor dome close to the critical point. With increase in supply temperature, the beneficial effect of the internal heat exchanger becomes more apparent. More superheat is needed at higher temperatures because of the shape of the vapor dome of R-1336mzz(Z).

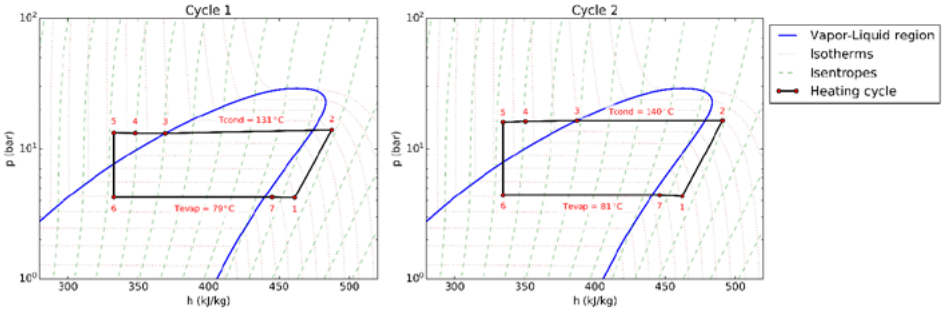


Fig. 7: Log(p)-h diagram for cycle 1 and 2 of the heat pump, OP2 (140 °C)

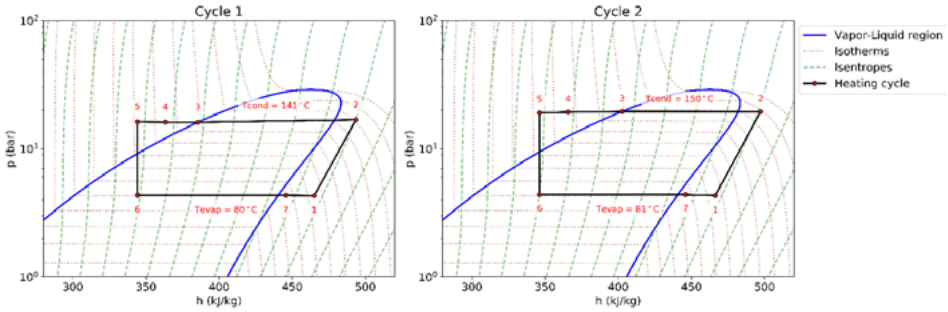


Fig. 8: Log(p)-h diagram for cycle 1 and 2 of the heat pump, OP3 (150 °C)

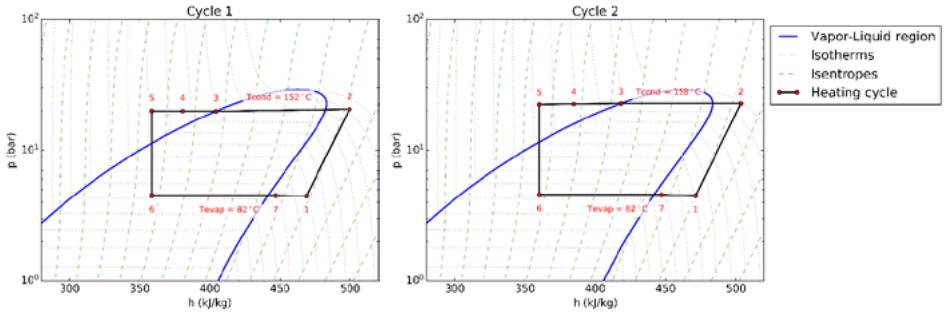


Fig. 9: Log(p)-h diagram for cycle 1 and 2 of the heat pump, OP3 (160 °C)

In Table 2, energy flows, mass flows and temperatures are compiled for the trial operation. The compressors were operated at 1500 rpm. Q_{heat} is the sum of the heat transferred to the industrial process in the condenser and in the sub-cooler, ranging from 200 – 300 kW for the trial operation. Q_{cool} is the heat extracted from the heat source in the evaporator, ranging from 150 – 240 kW. For OP1, the COP is the highest due to the smallest temperature lift of 40 K. It amounted to 4.65. At OP4 (heat sink outlet temperature of 160°C), the COP was 2.66.

In Fig. 9, the DryFiciency heat pump is compared with various other industrial high temperature heat pumps that were compiled by Arpagaus [3]. Data comprises heat pumps by different manufacturers, such as Kobelco, Viking Heat Engines, Ochsner, Friotherm, Combitherm, GEA, Star Refrigeration, etc. All these heat pumps have heat supply temperatures exceeding 90 °C covering the whole range of heating capacities from 30 kW to more than 10 MW. The lines in Fig. 10 indicate the COP of a heat pump with heat supply temperatures of 120 °C and 160 °C that reaches 50 % of the COP of the ideal Carnot process (Second law efficiency). The COP of the DryFiciency heat pump is in good agreement with efficiency data from the other industrial heat pumps and ranges among the higher values that were reported. The second law efficiency of the DryFiciency heat pump is in the range of 50 %. The comparison shows that the trial operation of the DryFiciency heat pump was highly satisfactory.

Table 2: Operation points during trial operation

OP	Qheat, kW	Qcool, kW	Pel, kW	COP	Vsink, m³/h	Vsource, m³/h	Tsink_in, °C	Tsink_out, °C	Tsource_in, °C	dTsource, K
1	281.7	239.0	60.6	4.65	9.9	33.3	95.8	120.9	88.3	6.5
2	254.0	208.5	68.5	3.71	7.5	45.5	110.7	140.9	88.4	4.2
3	221.2	174.3	69.6	3.18	6.5	37.6	120.7	150.9	88.4	4.3
4	195.9	148.4	73.8	2.66	5.9	42.3	130.7	160.7	88.6	3.3

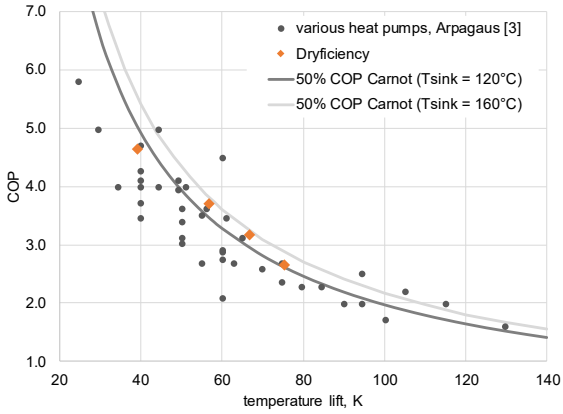


Fig. 10: Comparison of the COP of the DryFiciency heat pump and other industrial heat pumps, based on data from Arpagaus [3]

4. Conclusion

In this article, a first assessment of the operation of the DryFiciency heat pump for brick drying at Wienerberger AG in Uttendorf (Austria) is presented. It was commissioned in November 2019 recovering waste heat at around 90 °C and providing hot air for the brick dryer. It is the first demonstration of a high temperature heat pump in real industrial environment providing up to 160 °C. During trial operation, the basic functionality of the heat pump was assessed. Four different operation points with varying heat supply temperatures were analyzed in more detail. Trial operation proved that the heat pump is working in stationary conditions without any fluctuations of the heat source or heat sink covering the whole range of 120 – 160 °C. Due to the twin cycle layout of the refrigerant cycle, the condensers are arranged in series with a temperature difference of 10 K in condensing temperature. Suction gas and discharge gas super heat are important to ensure dry compression because of the thermodynamic properties of the refrigerant. An internal heat exchanger provides the super heat and increases the efficiency of the refrigerant cycle. A comparison of the COP of the DryFiciency heat pump and various other industrial high temperature heat pumps confirms that the DryFiciency heat pump is among the most efficient devices. The results of the trial operation prove that brick drying is more efficient when using a high temperature heat pump, because it decreases energy consumption and provides a higher drying air temperature in the final drying zone in the brick dryer. Future work focuses on long term stability of the heat pump and its components such as refrigerant, lubricant and compressors.

5. Acknowledgement

The project has received funding from the European Union's Horizon 2020 programme for energy efficiency and innovation action under grant agreement No. 723576.

6. References

[1] Jakobs R, Successful Applications of Industrial Heat Pumps, Workshop WS4, 25th IIR International Congress of Refrigeration, Montreal, 2019.

[2] Wilk, V, Fleckl, T, Arnitz, A, Rieberer, R. Industriewärmepumpen in Österreich: Status Quo und Potentiale, 11. Internationale Energiwirtschaftstagung, Vienna, 2019.

[3] Arpagaus C, Bless F, Uhlmann M, Schiffmann J, Bertsch S, High temperature heat pumps: Market overview, state of the art, research status, refrigerants, and application potentials, Energy (152), p.985-1010, 2018.

[4] Helminger F, Kontomaris K, Pfaffl J, Hartl M, Fleckl T, Measured Performance of a High Temperature Heat Pump with HFO-1336mzz-Z as the working fluid, ASHRAE 2016 Annual Conference, St. Louis, Missouri, 2016.

13th IEA Heat Pump Conference
April 26-29, 2021 Jeju, Korea

Design of a grey water heat recovery system in order to satisfy the domestic hot water demand of a block of dwellings

Estefania Hervas-Blasco, Ximo Masip, Emilio Navarro-Peris*, Jose Miguel Corberán

Instituto Universitario de Investigación en Ingenieria Energetica, Universitat Politecnica de Valencia, Camino de Vera s/n, 46022, Valencia, Spain.

Abstract

Passive houses linked to more efficient heating and cooling technologies have been one of the focus in last years. However, to close the loop of the building sector, there is still one open source: wasted heat from grey water. This paper addresses the potentiality of the wasted heat from grey water to produce domestic hot water (DHW) based on a heat pump system. A heat pump designed specifically for that application, a heat recovery heat exchanger and two variable volume storages tanks compose the system. The main objective of this work is to determine the potential of recovering this waste heat source in order to minimize the house energy consumption. An optimization of the size of the different elements and of the operation algorithm of the system has been performed in order to minimize the CO2 emissions and evaluate the maximum potential of the proposed strategy. The potential of using this type of waste heat as a source for heat pump system is demonstrated and could imply a recovery of available energy of up to 60%.

© HPC2020.
Selection and/or peer-review under responsibility of the organizers of the 13th IEA Heat Pump Conference 2020.

Keywords: Energy efficiency; Heat Recovery; Heat Pump; Domestic Hot Water;

1. Introduction

In recent years, there has been a great effort in order to reduce the energy consumption in buildings. The main actions have been focused on both, the reduction of heating demand and on the improvement of the technologies used for heating and cooling ends. However, little attention has been paid to the reduction of the energy demand related to DHW production even though, in developed countries, accounts for approximately 15% [1].

Furthermore, 85-90% of the total energy dedicated to hot water production [2] is wasted to the ambient after its use and the recuperation of it has not been explored in depth.

Based on that, the use of high efficient technologies for water heating applications as well as the heat recuperation from warm wastewater can significantly contribute to the reduction of the energy consumption and the GHG emissions associated to the building sector. Heat pumps are the most suitable technology dealing with the mentioned two aspects: high efficiency and the use of medium-low temperature water flows as a heat source.

The main characteristic of this kind of systems are:

a. The heat sink has a high water temperature lift and a high demand variability.

* Corresponding author. Tel.: +34963879123
E-mail address: emilio.navarro@iie.upv.es

b. The heat source has slightly higher temperature than the water from the net (and stable through the year) and high variability.

In order to deal efficiently with the characteristics of the heat sink of this kind of system transcritical CO2 systems or subcritical with subcooling control systems has been used and usually they work against a tank which could absorb the variability. Regarding the other point, it is not so widely analysed in the litreature, heat pumps are able to work properly with the temperatures of the heat source and also a tank could respond to the variability of this source but based on the temperature level to include in the system a heat exchanger recuperator will increase the efficiency of the system. Considering all these factors, at this point, the most critical point about this part of the system is related with the amount of energy available and the optimum way to use it in order to satisfy the demand.

The control strategy plays a key role on the system efficiency. Most works dealing with HPs use pre-defined schedules function of electric tariffs and base their design on that, hiding the real potential of a HP system or even deteriorating the performance by simply avoiding energy aspects[3]. Furthermore, the solutions obtained in that way may be specific just for a specific case. For instance, in [4] the operation of the heat pump is directly driven by the off-peak electricity period or in [5] the majority of the production also takes place in these periods. In [6], the authors analyze under an energy and economic point of view the impact of the operation control of a HP-photovoltaic system concluding that the optimization of energy factors results in a degradation of the economic factor and viceversa. An approach to maximize the energy efficiency and then couple it with specific economic aspects may be more interesting.

The aim of this work is to analyze the influence of the available waste energy in the energy consumption of a DHW system based on heat pumps. To do so, a thermodynamic analysis of the most suitable system able to produce hot water depending on the heat source characteristics is done. As a proof of concept, 20 dwells have been used as an example to develop the proposed methodology. The study considers first an infinite availability of heat source. Thereafter, a finite but constant profile of grey water has been taken into account and finally, profiles based on the grey water produced by the dwells are studied and compared to previous cases.

The considered systems are composed of a heat exchanger regenerator, two water tanks and a heat pump using the control of subcooling to optimize the efficiency working with high water temperature lift in the condenser. The study includes the sizing of the different components (heat pump, recuperator, tanks) and the definition of the optimum control strategy of the system. The obtained results allow quantifying irreversibility added to the system by the use of low-grade heat sources, gives some guidance about its potential that could be used in other works and supplies an estimation about the expected differences in energy consumption associated to the system design and waste heat availability.

2. Methodology

2.1 Heat sink and heat source characterization

This study focuses on DHW production for residential sector. Thus, the heat sink is the end-user hot water demand. A yearly profile for 20 dwellings generated with the stochastic model, DHWcalc [7], has been used. The selected time step has been of 1 minute. This profile includes an estimation of socioeconomic factors and it has been validated with SynPro[8]. The profile is the same as the one used in [9]. The reader is referred to it for further details.

The daily DHW demand is 54.1 l. of water at 45ºC per person and per day. This represents an annual average energy consumption of 576kWh (for a net water temperature of 10ºC). That is, an average water consumption at 45ºC of 105.5 litre per apartment and a total mean water consumption of 2110 litre/day (for 20 dwells).The profile for the water inlet temperature has been determined following the methodology proposed in [10] and used in [8] based on Eq. 1.

$$T_{net} = \overline{T_{amb}} - 3 \cdot \cos\left(\frac{2\pi}{365}\left(n_{day} - n_{days,offset}\right)\right) \quad (1)$$

Where T_{amb} is the mean ambient temperature (10ºC), n_{day} is the day of the year and $n_{daus,offset}$ is the offset, set according to the coldest day of the year.

Regarding the heat source, the grey water production from 20 dwellings has been considered. Grey water includes all water consumptions in a house except that from toilets (black-water) collected before the general sewage system. Due to the scarce information about grey water in the litreature, the estimation of the profiles and its characteristics have been done based on the total average water consumption, the end-use, the typical

temperatures according to its use, the characterization of the DHW load profile and data found in literature.

Germany has been considered as the reference country for the grey load profile used. Furthermore, as the consumption in this country is rather conservative compared to other developed countries, for the potential estimation of heat recovery, which will imply that the obtained results would be conservative. According to [11], the average drinking water consumption in Germany is 123 litre per day and person (240 litre per day and apartment). The final end-mix for the grey water is based on [12]: 15% to shower, 25% to bath, 30% to flush the toilet, 13% to the clothes washing machine, 7% to dishwasher, 6% to hand wash, cleaning and gardening and 4% destined to cook. That is, grey water represents 70% of the total drinking water consumption (168litre per day and apartment).

Furthermore, both streams, DHW and drinking consumption, are related in terms that all DHW mass flow would be part of the grey water. Hence, as the daily average DHW consumption per household is 105.5 litre at 45ºC, the rest would come from the other uses except, toilets.

On the one hand, the grey water from DHW water has been considered to follow the same profile as the DHW but one-minute delayed (time considered between the hot water consumption and its availability as a grey source). These flows have been increased with drinking water (net water) up to the user final temperature demanded (45 ºC).

On the other hand, a profile representing the use of clothes and dish washing machines has been generated with DHWcalc software. Average flow rates, frequency and temperatures have been estimated according to the work presented in [13] and the mentioned drink water consumption.

Table 1 collects the main inputs used in DHWcalc software for the characterization load profile of the clothes and dish machines. An average consumption of 960litre/day, 20 dwells with a daily probability function based on a step function for weekends and weekdays, a 120% probability weekday/weekend and seasonal variations are accounted by means of sinusoidal function have been considered.

Table 1: Drink water use in appliances that do not require DHW inputs for DHWcalc.

Draw-off type	End-use temperature [ºC]	Mass flow [lpm]	Duration [min]	Probability [%]
Dishwasher	65	4.8	1	11
Hot rinse	50	4.2	1.5	15
Cold rinse	45	3.6	1	9
Cloth washer	37	10.2	3	65

From the available data, the authors consider as good estimation the values of the hot water temperature used in the work presented in [13] which have been obtained from a wide literature review and experimental measurements. Table 2 collects the temperature of the end-user used in this work for both types of streams.

Regarding to the temperature of the grey water at the drain, a drop of 7K from the end-user temperature has been estimated regardless the nature of the consumption. This value is based on the most conservative study performed [14].

The grey water load profile is obtained aggregating the DHW profile with one-minute delay, the profiles of the clothes and dish washing machines with a thirty-minutes delay generated with DHWcalc and mixed with cold water until the end-use temperature for an annual time-frame and one-minute step time. An average daily grey water availability of 3360litre (168litre/apartment) and an average grey water temperature of 32.8ºC is obtained out of that mix.

2.2 Model description

Figure.1 shows a scheme of the main components, water flows and average temperatures of the system.

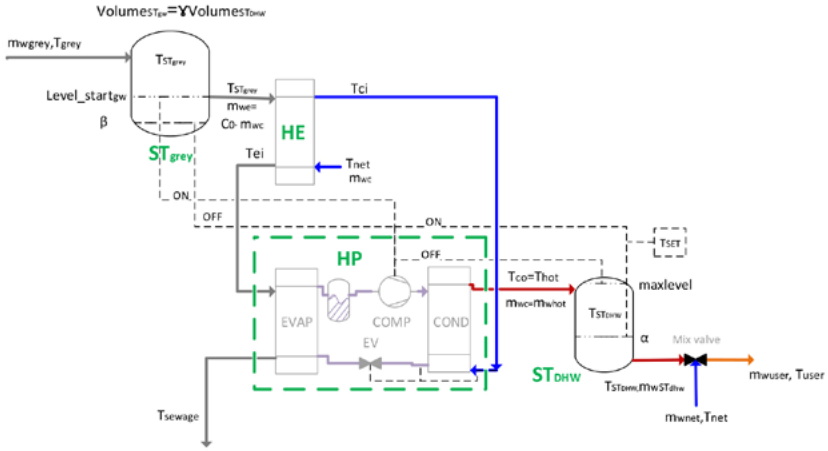


Figure.1: Lay-out of the system and average temperature conditions.

The main components of the system modelled are:

- Grey water storage tank (ST_{gw}): The variable volume storage tank modelled in Type 39 has been used. The size of the tank (Vol_{grey}) is one of the optimization parameters to minimize CO2 emissions.
  As conservative case, a geometric configuration that favours stratification has been used, that is H/D=4. The heat loss coefficient has been set to the one required by the Spanish legislation for DHW production, *RITE 07 IT 1.2.4.2.1.2,* that is 0.8W/m2K. An ambient temperature of 20ºC is set for all the simulations, as it is a typical value inside the houses through the year.
- Heat recovery heat exchanger (HE): Heat exchanger with an efficiency of 0.75 (type 5b). This heat exchanger will allow a first energy recovery.
- Water to water subcooled heat pump (SHP): This type contains a validated model of the subcooled heat pump [12].Due to its especial characteristics, a common HP type does not represent its behaviour properly and a new type was required. For further details about the developed type, the reader is referred to [15].
- DHW Storage tank (ST_{DHW}): For DHW Type 39 has also been used. As it is the case in $ST_{gw,}$ the size of the tank (Vol_{DHW}) is one of the optimization parameters to minimize emissions. The same insulation, geometry and characteristics used in the storage tank for grey water have been set in this case.
- Auxiliary water pumps and circuits: Types 742 with an efficiency of 0.3. Only the pressure drop of the heat exchangers were considered in order to evaluate their consumption.

Figure.2 represents the main inputs, outputs and optimization parameters of the model. In that scheme, scale is the size of the SHP, Volume is the size of the ST_{DHW}, γ indicates the proportion of the ST_{DHW} size and it is used for the ST_{gw} size ($Volume_{gw}$= γ·$Volume_{DHW}$). α is the ST_{DHW} level when the heat pump switches on, Tset is the ST_{DHW} temperature, Tco is the condenser outlet temperature and C_0 is related to the grey water mass flow rate (evaporator water mass flow rate) as a proportional value of the condenser water mass flow rate.

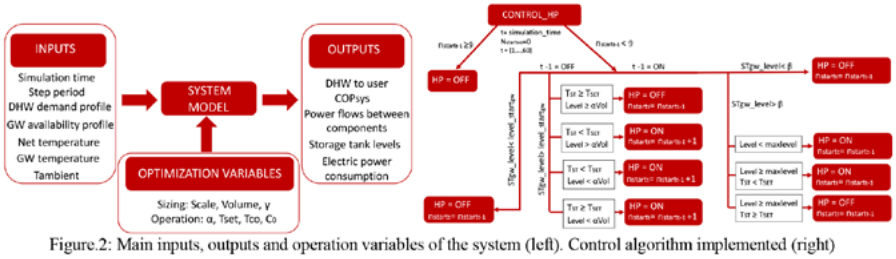


Figure.2: Main inputs, outputs and operation variables of the system (left). Control algorithm implemented (right)

The performance of the system (COP_{system}) is calculated according to Eq. 2

$$COP_{system} = Energy/Electric = \int_{t=0}^{t=simulationtime} (Q_{ST_{DHW_out}})/(W_{c_corr} + \sum W_{pumps}) \quad (2)$$

One should notice that the "useful energy" supplied by the system is the result of the heat exchanged in the HE and the heating capacity of the HP after the ST losses.

The scheme of the used control algorithm is presented in figure 5 (right) and it is based in the minimization of the time that the water is stored in the tank.In that figure *t* is the minute simulation time within each hour, T_{ST}, *Level*, *α*, *Vol*, T_{SET} and *maxlevel* refer to the DHW storage tank while subscript *gw* is used for conditions related to the grey water storage tank. It should be pointed out that once the HP is operating and while there is enough availability on the grey water storage tank, it keeps in the ON mode until the maximum level of the tank is reached or, in case it was already at that level, it keeps recirculating until the set point temperature (Tset) is reached. The used comfort criteria are based in two conditions, satisfy the demand 99% of the time and do not allow more than one-minute shortage at the same hour daily.

3. Performed Studies

Three cases based on the grey water conditions have been investigated and compared:

a) Infinite availability of grey water.
b) Finite availability of grey water and constant in time
c) Finite availability of grey water and no constant in time

According to [9], there is a set of system combination (size of the system componets and control) resulting in similar performances. Taking this point into account, the conditions b) and c) will be analysed in more detail for the solution corresponding to the smaller heat pump size (scale) and the solution with the smaller ST sizes (ST_{DHW}). Grey water energy available along the year is the same for the case 2 and 3 (the only change is when this energy is available). Table 2 shows the main inputs, variables used for limited m_{wgrey} availability based on the profiles of T_{net}, T_{grey} and m_{wgrey} presented in the methodology section.

Table 2: Main inputs used in each case

		T_{net} [ºC]	T_{gw} [ºC]	GW_{avail}	C_0 [-]
1	Infinite grey	10	33	∞	10
2a	Finite, $Scale_{min}$	10	33	Constant	2.27
2b	Finite, ST_{dhwmin}	10	33	Constant	2.27
3a	Design cond. $Scale_{min}$	7	25	Constant	2.33
3b	Design cond. ST_{dhwmin}	7	25	Constant	2.33
3c	Real cond. $Scale_{min}$	Profile	Profile	Profile	Opt.
3d	Real cond. ST_{dhwmin}	Profile	Profile	Profile	Opt.

a) Case 1: Infinite availability of grey water

This case will define the base case in order to evaluate the constrains imposed by limitations in the heat availability for the rest of the analysis. The methodology followed in [9] has been used. Notice that infinite availability of the heat source leads to the absence of the ST_{grey} and its derived variables.

Parametric studies have been done in order to obtain the map of possible solutions and the set of optimal combinations (heat pump size, Tank of DHW, alpha) that lead to minimum CO2 emissions satisfying the DHW demand under the comfort levels and operating constrains.

Figure 3 shows the parametric studies performed over the different design alternatives (heat pump size, storage tank size and control algorithm) for the available grey heat source (optimal m_{wevap}). This matrix comprises more than 4000 simulations

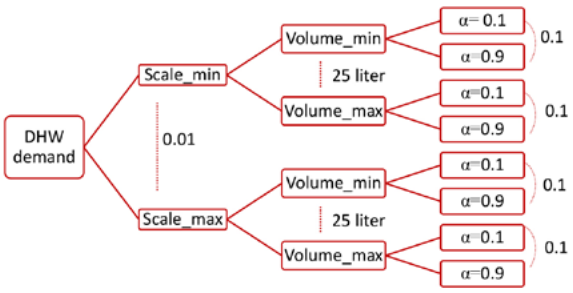


Figure 3: Parametric studies performed for available grey heat source based on variations of 0.01 in the scale of heating capacity, of 25litre in the ST_{DHW} tank and of 0.1 in α.

Where:

- *Scale* variation range: it has been expressed in terms of heating capacity (Q_{cond}) in the results section.
- *Volume* variation range: for each heating capacity, the maximum and minimum ST size that meet discomfort levels are investigated.
- *Alpha (α)* variation range: for each ST size, the variation of the control level in terms of a volume percentage.

b) Case 2: Finite availability of grey water and constant in time

The same parametric studies shown in Figure 3 have been performed. In order to compare this case with the case 1, two situations have been analysed quantitatively:

1. Case 2a: Solution with minimum heat pump size (scale factor).
2. Case 2b: Solution with minimum ST_{dhw}.

c) Case 3: Finite and not constant availability of grey water

Real applications introduce variability in three ways: time, temperature and quantity. These variables add complexity to the system and require the use of a ST_{gw}.

The main target of this study consists of analysing, on the one hand, the impact on efficiency of these limitations in the available energy compared to the previous cases and, on the other hand, the coupling of all the system components considering dynamic and real conditions from the system point of view. Hence, the use of a ST_{gw} and the definition of a proper operating strategy to integrate it in the system is necessary. In addition, this will help to get an estimation of the influence in the efficiency of the system design. Two subcases will be analysed in this part:

1. *System design based on a constant profile of waste water*

The size of the system is performed following the same methodology of case 2 but for T_{net}=7ºC and Tgrey=25ºC. These temperatures correspond to the worst expected conditions along the year. The available m_{gw} is the mean value of the grey water produced along the day.

The tandem HP-ST_{DHW} is sized according to these conditions. In this conditions, it is necessary to include in the design the ST_{gw} in order to accumulate the produced grey water when the system is not on. This component is dimensioned as: $Volume_{STgw}=\gamma \cdot Volume_{STDHW}$. Two solutions are analysed for this case:

Case 3a: Solution with minimum heat pump size (scale factor).
Case 3b: Solution with minimum ST_{dhw}.

2. *System design based on a real profile of waste water*

The system has been optimized in order to satisfy the real profiles of the wastewater and of the net water temperature. This optimization is based mainly in:

- C_0 control: This parameter is optimized when using the highest available m_{wgrey} To maximize its use, the control is based on the maximum available m_{wgrey}.

- α control:The minimum α capable to satisfy the demand is the one that ensures the shortest water stored time (for a given size of the components).

Finally, and following the same procedure as before, the two cases were analyzed:

Case 3.2.a: Minimum heating capacity
Case 3.2.b: Minimum ST_{dhw} .

4. Results

This section shows the results obtained from the previous cases. First, the feasible set of combinations are detailed by case. Second, the most representative results are collected in Table 4 in order to compare them. Third, a detailed analysis of the obtained results from CASE 3 is presented.

Case 1: Infinite availability of grey water

Figure 4 depicts the possible sizes combinations for the optimal α that meet the discomfort standards described in the methodology section. Figure 4a refers to the operating hours, Figure 4b to the COP of the system and Figure 4c to the associated CO2 emissions.

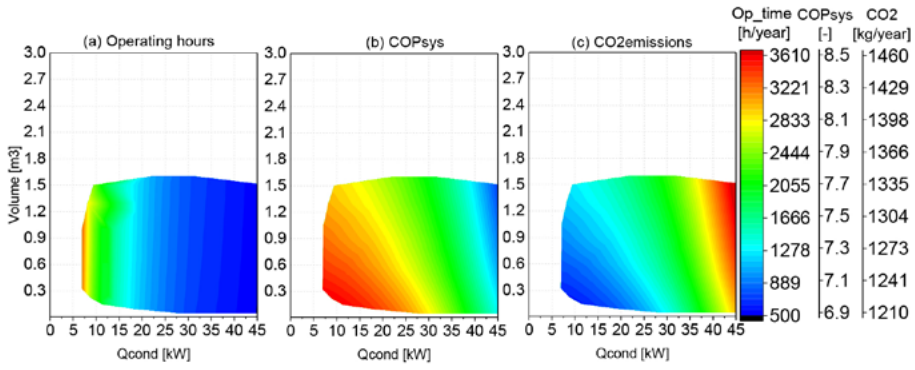


Figure 4: Annual operating hours, COP of the system and CO2 emissions associated to an infinite available grey water heat source and the optimal alpha.

According to Figure , low-temperature heat source recuperation has a great potential in DHW production applications. There is a wide range of combinations HP-ST_{DHW} that result in similar CO2 emissions (around 1230kg/year) and that are capable to operate under COPs up to 8.5 with operating hours around 2200 hours (6h/day). From all these combinations, the minimum CO2 emissions value is obtained for α=0.5, Scale=0.15 (heating capacity of 9.42Kw) and a ST_{DHW}=250litre.

To be able to compare directly results, that case has been taken as an example or base case out of all the possible best combinations. These results are presented in table 4.

Case 2: Finite availability of grey water

Figure 5 shows the possible ST-HP combinations for the optimal α that meet the discomfort standards described in the methodology section when limiting grey water to the considered availability. Figure 5a refers to the operating hours, Figure 5b to the COP of the system and Figure 5c to the associated CO2 emissions.

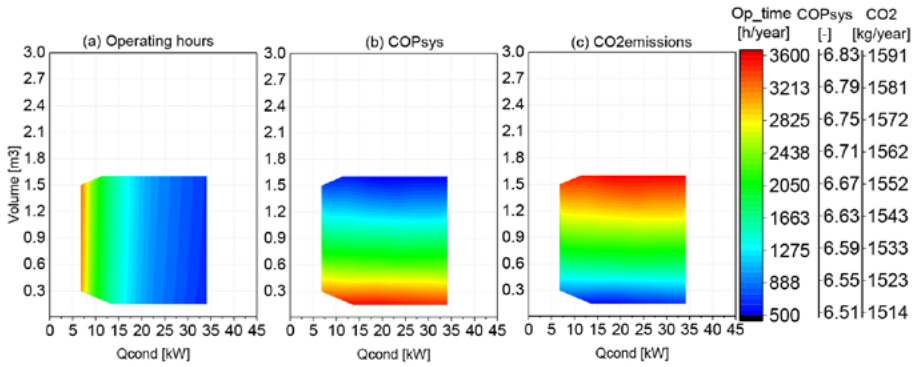


Figure 5: Annual operating hours, COP of the system and CO2 emissions associated to a finite available grey water heat source and the optimal alpha.

In this case, the reference combination obtained with optimal m_{wgrey} does not meet comfort standards. Hence, higher ST and/or heating capacities are required. Furthermore, the limitation of m_{wgrey}, lead to small COP variations with the increase of the heating capacity of the heat pump (for a given ST_{DHW} size). The ST_{DHW} size the most influent variable on the performance.

According to Figure and Figure 5, from the comparison of the optimal solutions in both systems (the combination with minimum CO2 strictly), the limitation of the available grey water results in a reduction in the COP of the system up to 20%.

In order to compare from a quantitative point of view the obtained results. Table 4 presents the numerical values for case 2a (solution with the minimum heat pump size) and case 2b (solution with the minimum ST size). In this table, it can be seen that for the case 2a the heating capacity is reduced due to a COP_{hp} loss and the solution results in higher ST_{DHW} as well as CO2 emissions. For the case 2b, the heating capacity required is significantly greater and 23% increase of CO2 emissions is obtained.

Case 3: Finite and variable availability of grey water

Similar results to the ones shown Figure 5 were obtained from the parametric studies performed in case 3 to design the components of the system. From all the possible combinations, two have been highlighted: the combination with minimum Scale (case 3. a) and the combination with minimums ST_{DHW} and ST_{gw} (case 3. b). The same situation is found once the system is adapted to the real profiles and results considering the adaptation to the profiles for the minimum HP size (case 3.c) and the minimum ST_{DHW} and ST_{gw} sizes (case 3.d) are highlighted Table 4 collects the most important results of each case.

Table 3: STgw-HP-STdhw optimal combinations for infinite availability of the heat source, finite availability but constant, and finite and variable availability.

		Scale [-]	Heating capacity [kW]	ST_{DHW} [l]	ST_{gw} [l]	α [-]	COPsys [-]	Annual Op.g hours [h]	Annual emissions [kgCO2]
1	Infinite grey	0.15	9.42	250	-	0.5	8.49	2310	1219.4
2a	Finite, $Scale_{min}$	0.15	6.9	300	-	0.9	6.85	3100	1510.9
2b	Finite, ST_{dhwmin}	0.2	9.08	250	-	0.9	6.8	2351	1522.6
3a	Design cond. $Scale_{min}$	0.15	6.06	500	1250	0.9	5.68	4261	1970.6
3b	Design cond. ST_{dhwmin}	0.25	10.09	350	875	0.9	5.73	2541	1959.6
3c	Real	0.15	6.81	500	1250	0.9	6.67	3175	1540.3

3d	cond. $Scale_{min}$ Real cond. ST_{dhwmin}	0.25	11.38	350	875	0.5	6.72	1890	1529.1

According to Table 3, the consideration of real profiles (demand, temperatures and grey water availability) with a design based on extreme constant conditions, cases 3.a-3.b leads to a solution with higher sizes of the main components and the performance of the system decreases in more than 30% compared to case 1 and 20 compared to case 2. However, once the design is dynamically adapted to the variable conditions (cases 3.c-3.d)., the loss of efficiency diminishes to 2% compared to Case 2. High values of optimal α allow the reduction of the ST_{gw} γ_{min} parameter, while low-medium values require the design condition of γ_{min}.

Figure 6 contains the main characteristics of the grey water heat source. Figure 6a represents the monthly grey water energy extracted by the HP (grey column) and by the HE (line-filled column), the grey energy available in light brown and the percentage of energy extracted from the total available. Figure 6b shows the temperature of the grey water at the outlet of the evaporator (grey water temperature to the sewage) through the year.

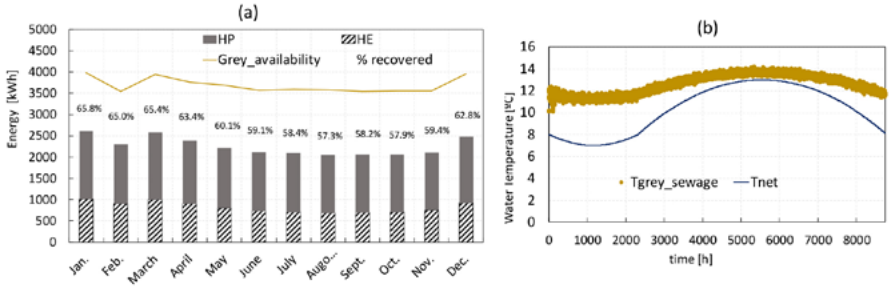


Figure 6: Monthly grey energy recovered and available and final annual grey water outlet temperature (to the sewage).

As it can be seen in Figure 6, a significant heat extraction is done by the HE with slightly seasonal fluctuations. From the available energy to extract (considering the minimum water temperature of the sewage as 2ºC), an average extraction of 60% has been enough for the DHW supply. In addition, figure 6b represents the net water temperature and the temperature of the grey water at the outlet of the SHP, it can be seen that always the Tgrey_sewage >Tnet, therefore the system is able to satisfy the DHW demand only with recovered energy from the dwellings, in addition figure 6b also shows that the energy recovery system is more effective during the colder months.

Results highlight the great potential of grey water heat recovery as a heat source for DHW production based on a HE (recuperator) and a HP.

5. Conclusions

In this work, the influence of having a limited (and variable) availability of heat source at a given temperature in order to satisfy the demand of DHW has been addressed. The obtained results have been systematically compared with the results obtained when this restriction is not present and an optimum system configuration (HE (recuperator)+SHP+STdhw+STgw) have been proposed.

This analysis has allowed estimating the variations in energy consumption that could be expected from different design criteria. Finally, a system in order to satisfy the DHW demand of 20 dwellings using their grey water production as a heat source has been analysed in detail.

Regarding to the obtained results, the main conclusions can be summarized as:

- A decrease of 20% in the efficiency could be derived when there is a limitation of the available grey water in terms of average quantity compared with a system in which that availability of heat source water is not limited.
- When there is a not constant availability of grey water, and the system is sized according to the most critical conditions, the energy efficiency of the system could be reduced up to 17%.
- In the previous situation, significantly larger sizes of the components are required in order to satisfy the user comfort levels (for instance, double ST_{DHW} capacities for the minimum HPsize).

- The systems with a variable grey water availability could increase significantly their efficiency if the design conditions are based on the real profiles instead of the most critical conditions. With that design criteria, the decrease on the performance is only 2% compared to the case with a constant availability of grey water (case 2).
- The system is can work only with energy recovered from the heat pump, and the advantage of this type of system is higher when the ambient temperatures are lower.

Finally, a great potential of grey water used as a heat source for DHW production based on SHP has been demonstrated. When the system is properly designed and adapted to real availability and demand profiles, it is able to supply the required energy for water heating purpose only using only the grey water produced by the dwelling with high efficiency. In fact, only with the extraction of 60% of the available energy all the production can be satisfied for the example analysed in this work and all the used energy is energy recovered from the grey water source. Comparing this case with the case in which this energy is extracted from a heat pump of the same characteristics but using the air as a heat source, the potential savings derived from using the grey water are higher than 40%.

Nomenclature

DHW: domestic hot water
ST: storage tank
HE: pre-heating heat exchanger (recuperator)
SHP: subcooled heat pump
Tei: water inlet temperature at the evaporator [ºC]
Teo: water outlet temperature at the evaporator [ºC]
Tci: water inlet temperature at the condenser [ºC]
Tco: water outlet temperature at the condenser [ºC]
Tnet: water mains/net temperature [ºC]
Tgrey: water heat recovery temperature [ºC]
Tsewage: grey water temperature after its recovery (to the sewage) [ºC]
T_{ST}: water stored temperature in the respective tank [ºC]
Thot= water temperature at the system conditions [ºC]
Tuser= water temperature supplied to the user [ºC]
Tdemanded=water demand temperature [ºC]
Tset= temperature control [ºC]
Tamb= ambient temperature [ºC]
Qcond=Heat pump heating capacity [kW]
Qevap=Heat Pump cooling capacity [kW]
COP_{hp}: Heat pump Coefficient of Performance, [-]
COP_{sys}: System Coefficient of Performance, [-]
COP_{Lorenz}: Lorenz Coefficient of Performance, [-]
m_{wgr}: grey water mass flow rate [kg/s]
mw_{user}= water mass flow rate to the user [kg/s]
m_{wc}:condenser water mass flow rate [kg/s]
m_{we}:evaporator water mass flow rate [kg/s]
Wc: Heat pump electric consumption [kW]
Scale: Relative size of the heat pump compared to the reference value
Volume: capacity of the respective tank [litre]
ρ: Water density [kg/m3]
α: Control level rate in the DHW tank[-]
β: Control level rate in the grey water tank[-]
λ: Ratio between the hot water mass flow and the grey water mass flow [-]
γ: proportion of the DHW storage tank capacity [-]
C_0: proportion of the condenser water mass flow rate [-]
Subscripts
ST: storage tank
HP: Heat pump
gw: grey water
DHW: domestic hot water
hot: hot water (at production temperature, 64ºC)

Acknowledgements

Part of the work presented was carried out by Estefanía Hervás Blasco with the financial support of a PhD scholarship from the Spanish government SFPI1500X074478XV0. The authors would like also to acknowledge the Spanish 'MINISTERIO DE ECONOMIA Y COMPETITIVIDAD', through the project "MAXIMIZACION DE LA EFICIENCIA Y MINIMIZACION DEL IMPACTO AMBIENTAL DE BOMBAS DE CALOR PARA LA DESCARBONIZACION DE LA CALEFACCION/ACS EN LOS EDIFICIOS DECONSUMO CASI NULO" with the reference ENE2017-83665-C2-1-P and the Universitat Politecnica deValencia program "ayuda a primeros Proyecto de investigación" through the project with reference SP20180039 for the given support.

References

[1] Energy consumption in households - Statistics Explained 2018. http://ec.europa.eu/eurostat/statistics-explained/index.php/Energy_consumption_in_households (accessed August 1, 2018).

[2] Technical | Passive House energy reduction and efficiency 2017. http://recoupwwhrs.co.uk/technical/passive-house/ (accessed August 1, 2018).

[3] Hervas, Estefania, et al. "Design of a System for the Production of Domestic Hot Water from Wastewater Heat Recovery Based on a Heat Pump Optimized to Work at High Water Temperature Lift." Purdue Conference (2018). 2018:1–10.

[4] Wong LT, Mui KW, Guan Y. Shower water heat recovery in high-rise residential buildings of Hong Kong. Appl Energy 2010;87:703–9. doi:10.1016/J.APENERGY.2009.08.008.

[5] Spriet J, McNabola A. Decentralized drain water heat recovery: A probabilistic method for prediction of wastewater and heating system interaction. Energy & Buildings. 2019.183; 684-696. doi:10.1016/j.enbuild.2018.11.036

[6] Postrioti L, Baldinelli G, Bianchi F, Buitoni G, Maria F Di, Asdrubali F. An experimental setup for the analysis of an energy recovery system from wastewater for heat pumps in civil buildings. Appl Therm Eng 2016;102:961–71. doi:10.1016/J.APPLTHERMALENG.2016.04.016.

[7] Baek NC, Shin UC, Yoon JH. A study on the design and analysis of a heat pump heating system using wastewater as a heat source. Sol Energy 2005;78:427–40. doi:10.1016/j.solener.2004.07.009.

[8] Dar UI, Sartori I, Georges L, Novakovic V. Advanced control of heat pumps for improved flexibility of Net-ZEB towards the grid. Energy Build 2014;69:74–84. doi:10.1016/J.ENBUILD.2013.10.019.

[9] Hervás-Blasco E, Navarro-Peris E, Corberán JM. Optimal design and operation of a central domestic hot water heat pump system for a group of dwellings employing low temperature waste heat as a source. Energy 2019;In Press.

[10] Jordan U, Vajen K. Realistic Domestic Hot-Water Profiles in Different Time Scales 2001.

[11] TRNSYS 17. 2009.

[12] Fischer D, Wolf T, Scherer J, Wille-Haussmann B. A stochastic bottom-up model for space heating and domestic hot water load profiles for German households. Energy Build 2016;124:120–8. doi:10.1016/J.ENBUILD.2016.04.069.

[13] Bertrand A, Aggoune R, Maréchal F. In-building waste water heat recovery: An urban-scale method for the characterisation of water streams and the assessment of energy savings and costs. Appl Energy 2017;192:110–25. doi:10.1016/J.APENERGY.2017.01.096.

[14] Nehm G, Nehme G, Palandre L, Clodic D. Purdue e-Pubs High Efficiency Heat Pump for Domestic Hot Water Generation 2008.

[15] Hervás-Blasco E, Navarro-Peris E, Barceló-Ruescas F, Corberán JM. Improved water to water heat pump design for low-temperature waste heat recovery based on subcooling control. Int J Refrig 2019. doi:10.1016/J.IJREFRIG.2019.06.030.

13th IEA Heat Pump Conference 2020



13th IEA Heat Pump Conference
April 26-29, 2021 Jeju, Korea

Experimental and Mechanistic Numerical Analysis of a Variable Speed Residential Heat Pump Unit with an Expansion Work-Recovery Device

Riley B. Barta[a,*], Ammar M. Bahman[a,b], Lennart Stania[a], Davide Ziviani[a], Eckhard A. Groll[a]

[a]Ray W. Herrick Laboratories, School of Mechanical Engineering, Purdue University
West Lafayette, 47907-2099, USA
bartar@purdue.edu; abahman@purdue.edu; stania@tfd.uni-hannover.de; dziviani@purdue.edu; groll@purdue.edu
[b]Mechanical Engineering Department, College of Engineering and Petroleum, Kuwait University
P.O. Box 5969, Safat 13060, Kuwait
a.bahman@ku.edu.kw

Abstract

In recent years, variable-speed heat pump systems for residential applications have gained significant attention in order to improve the part-load operations during heating and cooling seasons. A single-stage 5-ton (17.58 kW) heat pump unit with R-410A as a working fluid has been considered as a test case to assess the performance of a variable-speed rolling piston compressor. Moreover, the heat pump has been retrofitted with a prototype expansion work-recovery device to replace the conventional expansion valve for cooling mode. The heat pump performance has been tested extensively in a pair of psychrometric chambers. In order to facilitate future optimization of the system, a fully-mechanistic steady-state cycle model of the heat pump has been developed. In particular, the system model is based on a charge-sensitive approach with semi-empirical models for the compressor and the work-recovery device as well as detailed heat exchanger models. The cycle model has been validated and tuned with the experimental data collected. Future work is to utilize the validated mechanistic model for cycle optimization and charge sensitivity studies.

© HPC2020.
Selection and/or peer-review under responsibility of the organizers of the 13th IEA Heat Pump Conference 2020.

Keywords: Variable speed; Expansion work recovery; Mechanistic model; Charge sensitive

1. Introduction

Growing concerns over climate change are driving innovation in almost every industry. However, given that in 2017, 38% of US energy consumption was in buildings [1], much of which is attributable to heating, ventilation, air conditioning, and refrigeration (HVAC&R), innovation in this industry is particularly vital. To this end, both academia and industry have been investigating different ways to increase the efficiency of the vapor compression cycle (VCC). Most of the optimization efforts focused on three of the four primary components in a VCC, being the compressor, the condenser, and the evaporator. Within these efforts, the use of variable-speed compressors represents a significant performance benefit without any fundamental changes to the cycle. The fourth component of a VCC enables the expansion from condensing to evaporating pressure and is generally achieved with a thermostatic expansion valve (TXV) or an electronic expansion valve (EXV). When modeling these devices an isenthalpic assumption is generally made, meaning that any potentially recoverable work from the expansion process is wasted. In response to this, researchers have investigated

* Corresponding author. Tel. +1-720-933-1211.
E-mail address: bartar@purdue.edu.

several ways to recover the expansion work. The two most common methods for expansion work recovery in VCCs are ejectors and expanders. The former has been proven to be more reliable and is by far the most common technique used in industry. Two of the most common techniques for controlling an ejector are actively-varying geometry of a single ejector [2-4] or the use of a multiple fixed-geometry ejectors in parallel [5-7]. While expanders have been theoretically shown to have greater potential for increased coefficient of performance (COP) benefits relative to ejectors, designing these devices for application in HVAC&R with a high enough isentropic efficiency to realize this gain has proven to be challenging, before even considering how to control them. To reduce overall development costs, high-fidelity VCC system models have been extensively researched as well. Both dynamic and steady-state models have been researched, but within those categories there is still a lack of charge-sensitive mechanistic models. Consideration of the charge inventory within a VCC and its optimization are essential to overall cycle performance. Experimentally-validated charge-sensitive mechanistic models utilizing charge tuning methods proposed by Shen et al. [8] have been developed by Bahman et al. for a 4-component VCC [9] as well as a VCC with economization and compressor vapor-injection [10].

This study focuses on the development of a detailed mechanistic model for an R-410A residential heat pump system that utilizes an expansion work recovery device with phase separation and an evaporator vapor bypass previously investigated by Czapla et al. [11] and Barta et al. [12]. Cycle performance was predicted with imposition of charge inventory with estimation using both one- and two-point tuning methods. Individual component efficiencies within the expander were modeled and experimentally-validated to isolate losses within the component.

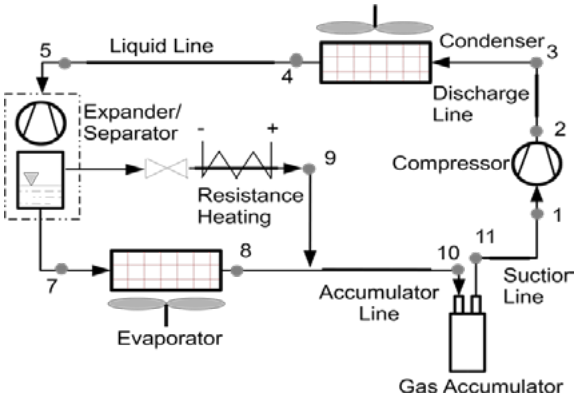


Fig. 1. Schematic of mechanistic cycle model that shows the main system components

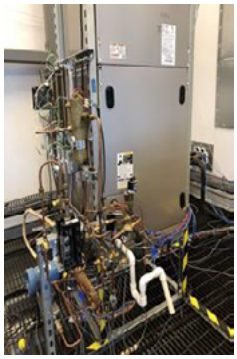


Fig. 2. View of the indoor unit showing the expander



Fig. 3. View of the variable-speed rolling piston compressor

2. Model Description

Fig. 1 shows the schematic of the variable-speed heat pump system to be modeled, with a photo of the indoor unit shown in Fig. 2. The primary difference between this cycle and a standard four-component VCC is the inclusion of the expander/separator, which simultaneously recovers expansion energy and separates vapor and liquid phases from the turbine outlet. The liquid exits the bottom of the expander housing to enter the evaporator, while the vapor exits the top before passing through a resistive heater to ensure superheat and mixing with the evaporator outlet upstream of the accumulator. The cycle components are simulated in an object-oriented fashion by using the programming language Python [13]. The thermo-physical properties of the working fluid (R-410A) were obtained from Bell et al. [14].

2.1. Compressor model

A variable speed reciprocating compressor model proposed by Mendoza-Miranda et al. [15] was used which is based on dimensionless volumetric, isentropic, and overall efficiencies. This model has also been shown to be applicable to scroll and rotary rolling piston compressors. The model characterized the compressor efficiencies in terms of certain groups of dimensionless parameters. Specific experimental data from a 5-ton (17.58 kW) Hitachi variable speed rotary rolling piston compressor (Fig. 3) were used to determine the values of the dimensionless parameters (*i.e.,* a_i coefficient values). Furthermore, the model was capable of accounting for different working fluids. In particular, Mendoza-Miranda et al. [15] employed the model to analyze the performance of a variable speed reciprocating compressor using R-1234yf, R-1234ze(E), and R-450A as alternatives to R-134a. Bahman et al. [9] validated the model for variable speed rolling-piston compressor using R-410A. The correlations for the dimensionless efficiencies were expressed as a power law function of the remaining π groups and given in Eqs. 1 to 3. The dimensionless groups for volumetric, isentropic, and overall efficiency can be found in Bahman et al. [9].

$$\eta_v = \pi_2^{0.1257}\pi_4^{0.0958}\pi_5^{0.4158} \quad (1)$$

$$\eta_s = \pi_2^{0.2166}\pi_3^{0.34781}\pi_4^{0.0773}\pi_6^{-0.03923} \quad (2)$$

$$\eta_{oa} = \pi_2^{-0.3632}\pi_3^{-0.30562}\pi_6^{0.02766}\pi_7^{0.76003} \quad (3)$$

The comparisons between measured and predicted values of the compressor mass flow rate, discharge temperature, and electric power input can be found in Bahman et al. [9].

2.2. Heat exchanger models

The heat exchanger models from Bell [16] were modified to be used in this work. The condenser model

was constructed using a moving boundary method, which divides the heat exchangers according to the phases of refrigerant flow. Each section of the heat exchanger models was simulated using the ε-NTU method as separate crossflow fin-and-tube heat exchangers with louvered fins [17], assuming constant refrigerant pressure equal to the saturation pressure.

To accurately estimate the behavior of the heat transfer from the air to the refrigerant side of the evaporator, the partially-wet and partially-dry method by Braun [18] is utilized in predicting the air side sensible and latent heat transfer when the surface temperature of the coil falls below the dew-point of air at the inlet of the evaporator. The evaporator model was solved by separating the heat exchanger into two sections. The section with surface temperatures higher than the dew-point was solved by a completely dry analysis, while the other section was solved assuming a completely wet analysis. Both heat exchanger models included Zivi slip flow model [19] to improve the refrigerant charge estimation in the two-phase region. The correlations used to estimate the heat transfer coefficients and friction factors in the condenser and evaporator models are summarized in Table 1, while the geometrical parameters used are listed in Table 2.

Both evaporator and condenser fans were modeled by using experimental data for steady-state operation conditions. The average airflow rate and power consumption for the evaporator fan were equal to 0.826 m^3/s and 0.4 kW, respectively, while the airflow across the condenser fan was equal to 1.91 m^3/s corresponding to an average measured power consumption of 0.25 kW.

Table 1. Heat transfer and pressure drop correlations in heat exchanger models

		Single-Phase	Two-Phase
Refrigerant-Side	Heat Transfer	Gnielinski [20]	Condensation: Shah [21], Evaporation: Shah [22]
	Pressure Drop	Churchill [23]	Lockhart and Martinelli [24]
Air-Side	Heat Transfer	Wang et al. [25]	
	Pressure Drop	Wang et al. [25]	
	Fin Efficiency	Schmidt [26] modified by Hong and Webb [27]	

Table 2. Geometrical parameters in heat exchanger models

Parameter	Condenser	Evaporator	Parameter	Condenser	Evaporator
Number of tubes per bank	24	60	Transverse distance of tubes [mm]	25.4	25.4
Number of banks	2	3	Fins per inch	20	14.5
Number of circuits	8	8	Fin waviness [mm]	1.0	1.0
Length of tubes [mm]	2252	452	Half-wavelength of fin wave [mm]	1.0	1.0
Outer diameter of tubes [mm]	9.13	9.13	Fin thickness [mm]	0.11	0.11
Inner diameter of tubes [mm]	8.49	8.49	Conductivity of fins [W/m-K]	237	117
Longitudinal distance of tubes [mm]	19.1	19.1			

2.3. Expander and separator model

The expander model consisted of a series of sub-models whose efficiencies were experimentally validated. A schematic showing the sub-models is provided in Fig. 4. The thermo-physical properties of the inlet state were measured, and the electrical power $\dot{W}_{elec}$ output was also measured. Generator efficiency η_{elec} was assumed to be 88% per manufacturer recommendation and mechanical efficiency η_{mech} was assumed to be 90%.

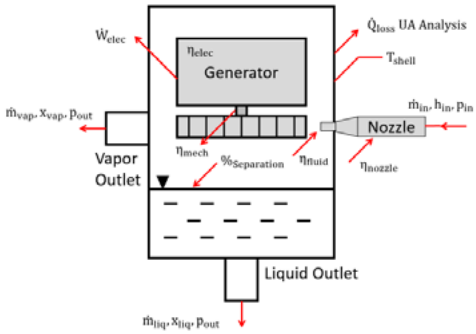


Fig. 4. Expander schematic with sub-model efficiencies

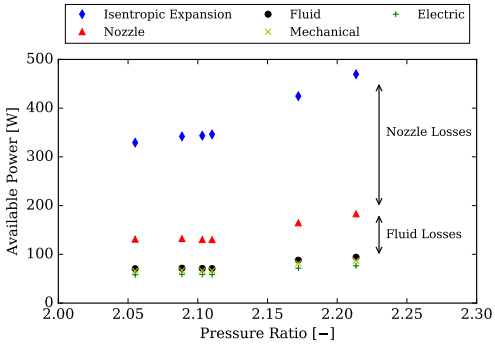


Fig. 5. Expander sub-model power availability visualization

An experimentally-validated nozzle model from Stania [28] was utilized to determine the nozzle isentropic efficiency η_{nozzle}. The nozzle model was developed for converging nozzles and includes modifications to Elliot and Weinberg [29] such as the inclusion of inter-phase drag within the vapor dome and the Smith [30] slip flow model, among others. These calculations left only the fluid efficiency, which represents losses between the outlet of the nozzle and turbine, as well as when the flow impacts the turbine. Using six experimental data points, a polynomial of this efficiency was developed as a function of expander pressure ratio. The assessed power extracted from each sub-model is shown in Fig. 5. Additionally, a natural convection heat transfer analysis was conducted to estimate the heat loss. The heat transfer rates were on the order of 2 to 5 W, but this transfer was important for completeness of the energy balance. Finally, ideal separation of phases was not achieved experimentally. As such, the liquid outlet quality was estimated as 0.025 from experimental data.

2.4. Linesets model

The pressure drop of refrigerant flow in the system linesets was calculated using ACHP model Bell [31] with the Churchill [23] correlation to estimate the pressure drop friction factor. The ε-NTU method from Bergman et al. [17] was used to estimate the amount of heat loss, if any, in all the linesets. Note that the volume of the linesets was considered for the purpose of refrigerant charge calculation. The geometry of the pipelines was measured from the experimental setup and is summarized in Table 3.

Table 3. Geometrical parameters of the system linesets

	Suction line	Discharge line	Liquid line	Accumulator line

Length [mm]	7600	300	7600	571
Outer diameter of tubes [mm]	28.58	28.58	9.53	22.23
Inner diameter of tubes [mm]	26.04	26.04	6.35	19.05
Insulation thickness [mm]	20	-	20	-
Conductivity of tubes [W/m-K]	0.19	0.19	0.19	0.19
Conductivity of insulation [W/m-K]	0.036	-	0.036	-

2.5. Accumulator model

A suction gas accumulator was modeled as a cylindrical vapor-only container. This implies that natural heat transfer occurred between the surfaces of the accumulator and the surroundings. The natural convection correlations from Bergman et al. [17] was used to account for the heat transfer across the circumference of the accumulator. The volume of the accumulator was considered for the purpose of refrigerant charge estimation. The accumulator has a height of 274 mm with inner and outer diameters of 115 mm and 123.6 mm, respectively.

2.6. Charge model

Due to the inaccurate estimation of the system volumes, ambiguous flow patterns under two-phase flow conditions, and amount of refrigerant dissolved in the compressor lubricant, both a single-point and a two-point charge tuning procedure were implemented based on the methodology proposed and validated by Shen et al. [8]. The total refrigerant charge of the system is given by the sum of the mass calculated by the cycle model and a contribution fitted onto the experimental data, which can be expressed as

$$m_{\text{charge}} = m_{\text{pred}} + \Delta m_{\text{liq}} \tag{4}$$

$$\Delta m_{\text{liq}} = C + K\left(w_{\text{liq,pred}} - w_{\text{ref}}\right) \tag{5}$$

where C, K, and w_{ref} are the coefficients to be determined through only two experimental data points to calibrate the model. The tuning coefficients are listed in Table 4. Note that for the one-point regression model, Eq. 5 results with the coefficient C only.

Table 4. Charge model tuning coefficients

C [kg]	0.987
K	-1.059
w_{ref}	0.0466

2.7. Pre-conditioner model

In order to obtain good initial guesses and reduce computational time for the main cycle solver, a pre-conditioner model from Bell [31] was modified to estimate values for refrigerant evaporation and condensation temperatures. The pre-conditioner model duplicates the main cycle to be solved with simplified models for condenser and evaporator, as shown in Fig. 6. The independent variables (*i.e.,* T_{evap} and T_{cond}) are iterated to minimize the residual vector (Eq. 6) by means of *fsolve* function [32] until convergence. Note that the superheat degree T_{sh} is deterministically evaluated in the main cycle. However, in the pre-conditioner model a targeted value was used as an input to ensure continuity.

$$\vec{\Delta} = \begin{bmatrix} \dot{W}_{\text{comp}} + \dot{Q}_{\text{evap}} - \dot{Q}_{\text{cond}} - \dot{W}_{\text{exp}} + \dot{Q}_{\text{heater}} \\ \dot{Q}_{\text{cond,a}} - \dot{Q}_{\text{cond,r}} \\ \dot{Q}_{\text{evap,a}} - \dot{Q}_{\text{econ,r}} \end{bmatrix} \tag{6}$$

2.8. Overall system model

The flow chart in Fig. 7 shows the algorithm used in the system-level solver. The components in the system-level model were simulated consecutively as shown in Fig. 7. The independent variables (*i.e.,* T_{evap}, T_{cond}, and T_{sh}) are iterated by means of the Broyden [33] method to drive the residual vector (Eq. 7) to zero.

$$\vec{\Delta} = \begin{bmatrix} m_{charge} - m_{charge,target} \\ h_{mix,out} - h_{accum.in} \\ \dot{Q}_{heater} - \dot{Q}_{target} \end{bmatrix} \tag{7}$$

The model checks for the pressure drop residual (Eq. 8) after the residual vector (Eq. 7) converges. The pressure drops in the high- and low-pressure linesets are considered after the cycle iteration completed to avoid numerical difficulties. Hence, new effective saturation temperatures (*i.e.,* T^*_{cond} and T^*_{evap}) are calculated and iterated in the cycle model until the updated effective pressure drops (*i.e.,* P^*_{high} and P^*_{low}) are equal to the pressure drop terms calculated from the converged cycle model (*i.e.,* P_{high} and P_{low}). The solver converges when the pressure drop residual (Eq. 8) is less than 1 Pa.

$$\vec{\Delta} = \begin{bmatrix} P^*_{high} - P_{high} \\ P^*_{low} - P_{low} \end{bmatrix} \tag{8}$$

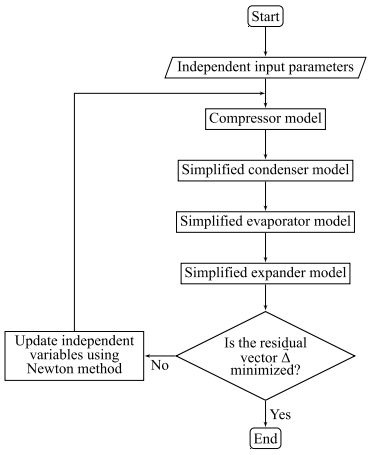


Fig. 6. Flowchart of pre-conditioner solver

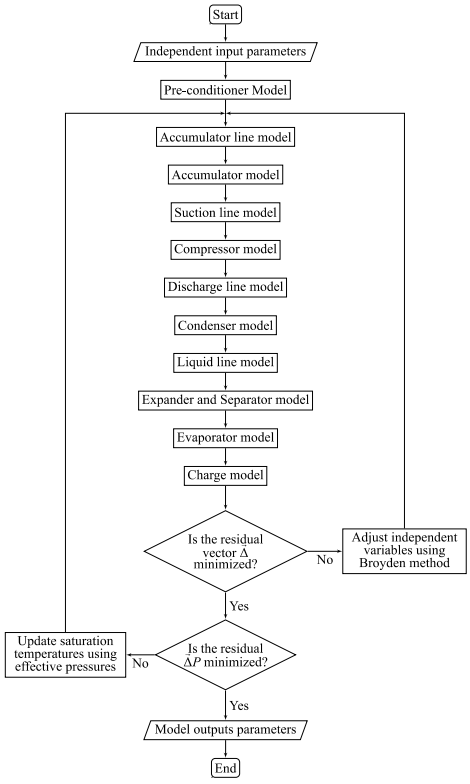


Fig. 7. Flowchart of mechanistic cycle solver

Table 5. Testing conditions for heat pump system with expander

Test	Outdoor condition		Indoor condition	
	Dry-bulb [°C]	Wet-bulb [°C]	Dry-bulb [°C]	Wet-bulb [°C]
1	35.1	23.3	25	17.7
2	40.0	27.3	25.1	17.8
3	42.0	28.9	25	17.7
4	35.0	23.4	26.8	19.2
5	35.0	23.4	23.5	16.5
6	35.0	23.4	24.0	16.9

3. Results and Discussion

3.1. Experimental methodologies

A 5-ton (17.58 kW) single-stage split-type heat pump with R-410A as the working fluid was installed inside a pair of psychrometric chambers at the Herrick Laboratories. A variable-speed rolling piston compressor was installed to replace the original scroll compressor, and the expander device was installed to replace the original TXV. The unit was tested at six points according to the test matrix in Table 5. All test conditions were performed according to AHRI Standard 210/240 [34] conditions using refrigerant-side data. The unit was charged with 4.81 kg (10.6 lb) to ensure consistent subcooling in the liquid line. Experimental cooling capacity, $\dot{Q}_{\text{evap}}$, and COP values for these test conditions are provided in Fig. 8. Cooling capacity and COP were defined based on AHRI Standard 210/240 [34] as shown in Eq. 9 and Eq. 10, respectively.

$$\dot{Q}_{\text{evap}} = \dot{m}_{\text{ref}}\left(h_{\text{evap,out}} - h_{\text{evap,in}}\right) \tag{9}$$

$$\text{COP} = \frac{\dot{Q}_{\text{evap}}}{\dot{W}_{\text{tot}}} \tag{10}$$

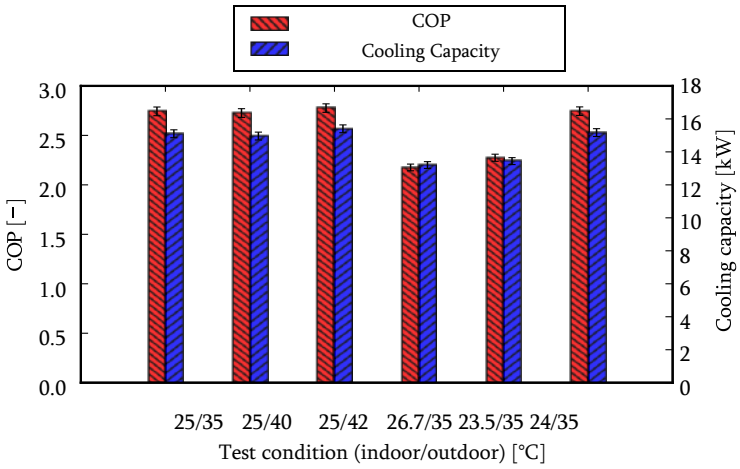


Fig. 8. Experimental COP and cooling capacities

Table 6. Tuning multipliers for expander heat pump cycle model

Compressor displacement scale factor	1.002
Condenser air-side convection heat transfer coefficient	1.289
Condenser refrigerant-side convection coefficient	0.973
Condenser refrigerant-side pressure drop correlation	1.077
Evaporator air-side convection heat transfer coefficient	1.302
Evaporator refrigerant-side convection coefficient	1.6
Evaporator refrigerant-side pressure drop correlation	0.998
Expander and separator vapor mass fraction	0.058

3.2. Model tuning

There was a systematic bias between the simulation and experimental results due to simplifications and imperfect information related to the heat pump system components. To minimize the bias, eight tuning multipliers were introduced to adjust mass flow rates, heat transfer coefficients and pressure drop on both air-side and refrigerant-side for the condenser and evaporator model as well as the separation fraction in the expander. The estimation of the multipliers was conducted by means of an iterative scheme to eliminate the discrepancy between the experimental results and the estimations of the mass flow rates, the condenser and evaporator heat transfer rates, the compressor power consumption, and the expander power generation. The optimization problem was solved with a bounded differential evolutionary (DE) method [35] and the resulting tuning factors are summarized in Table 6. It can be noticed from Table 6 that the air-side multipliers for the evaporator and the condenser are relatively high (approximately equal to 1.3) due to the influence of the air leakage around the heat exchangers in the experimental measurements.

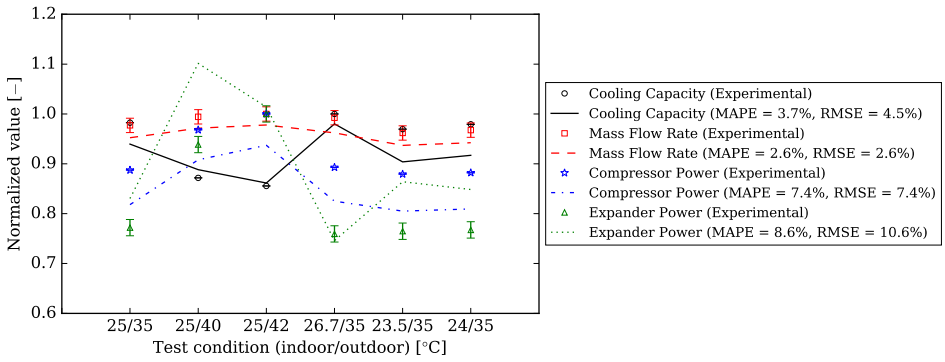


Fig. 9. Comparison of estimated model performance parameters with experimental data (normalized with maximum experimental value)

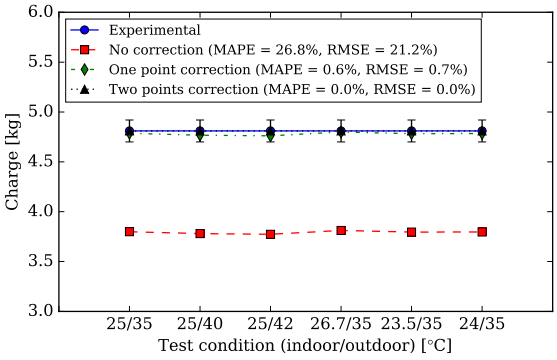


Fig. 10. Comparison of charge prediction with experimental data using one- and two-point regression charge model

3.3. Model validation

The validation was carried out with the six test conditions which were experimentally conducted on the retrofitted heat pump unit with expander device and variable-speed rolling piston compressor. The comparisons of the refrigerant mass flow rate, the condenser and evaporator capacities as well as the compressor power consumption and expander power generation between the model simulations and the experimental results are illustrated in Fig. 9. The error between the predicted and experimental values is calculated by the mean absolute percentage error (MAPE) and the root mean square deviation error (RMSE). Fig. 9 shows that the model, after tuning, captured the system and component performances within a reasonable margin of error. The minimum MAPE and RMSE of 2.6% and 2.6% corresponded to the total mass flow rate, while the maximum MAPE and RMSE of 8.6% and 10.6% were associated with the predictions of the expander power generation, respectively.

Using the charge model coefficients (Table 4) and the system tuning factors (Table 6), as well as by imposing the system charge inventory, the cycle was simulated at the same experimental test conditions to assess the charge estimation as shown in Fig. 10. Fig. 10 compares the charge predictions for the cases without any correction with one-point regression charge model, and with two-point model. It can be seen that the one-point charge model eliminates all the biases and predicts the charge inventory with MAPE and RMSE less than approximately 1%, while the two-point charge model [8] perfectly estimates the system charge with no errors.

4. Conclusions and Recommendations

This paper aimed to develop a detailed mechanistic and charge-sensitive model for an expander heat pump system to accurately estimate the system performance. The developed system model was tuned and validated with experimental data from a 5-ton (17.58 kW) single-stage split-type heat pump tested at different operating conditions in the Herrick Laboratories. The results yielded the following conclusions. First, the mechanistic expander heat pump system model predicted the performance parameters (*i.e.,* mass flow rates, compressor and expander power, and heat exchanger capacities) with a reasonable margin of MAPE and RMSE less than approximately 9% and 11%, respectively. Second, the charge imposed model with one- and two-point correction methods accounted for the discrepancy in refrigerant charge estimation with MAPE and RMSE less than approximately 1%. Finally, the detailed charge inventory model allows the analyses of drop-in working fluid replacements and their effects on the system sizing. Furthermore, the model also allows to optimize the charge level to take advantage of variable-speed compressors and power generation expanders. Future work entails the use of the system model for system, charge, drop-in fluid assessment, and multi-objective economic optimization. Additionally, the sub-models will be utilized to prioritize expander component re-design and further experimental analysis.

Acknowledgements

The authors would like to acknowledge the support from the Center for High Performance Buildings (CHPB) at the Ray W. Herrick Laboratories as well as the Research Section at Kuwait University for the financial and technical support.

References

[1] USEIA. U.S. Energy Information Agency Monthly Energy Review - April 2018. 2018.
[2] Elbel, S., Hrnjak, P. Experimental validation of a prototype ejector designed to reduce throttling losses encountered in transcritical R744 system operation. *Int. J. Refrig.* 2008;**31(3)**:411–422.
[3] Carel. EmJ - Carel electronic modulating ejector. Carel.com. 2019.
[4] Bodys, J., Smolka, J., Palacz, M., Haida, M., Banasiak, K., Nowak, A., Hafner, A. Performance of fixed geometry ejectors with a swirl motion installed in a multi-ejector module of a CO2 refrigeration system. *Energy*. 2016;**117**:620-631.
[5] Hafner, A., Försterling, S., Banasiak, K.. Multi-ejector concept for R-744 supermarket refrigeration. *Int. J. Refrig. 2014;***43**:1–13.
[6] Hafner, A., Schönenberger, J., Banasiak, K., Girotto, S., 2014. "R744 ejector supported parallel vapour compression system," Proc. of the 3rd IIR International Conference on Sustainability and Cold Chain. London, UK. p. 23–25.
[7] Pardiñas, Á. Á., Hafner, A., Banasiak, K. Novel integrated CO2 vapour compression racks for supermarkets. Thermodynamic analysis of possible system configurations and influence of operational conditions. *Appl. Therm. Eng.* 2018;**131**:1008–1025.
[8] Shen, B., Braun, J. E., Groll, E. A. Improved methodologies for simulating unitary air conditioners at off-design conditions. *Int. J. Refrig.* 2009;**32(7)**:1837–1849.
[9] Bahman, A. M., Ziviani, D., Groll, E. A., 2018. "Development and validation of a mechanistic vapor-compression cycle model," Proc. of the 17th Int. Refrig. and Air Cond. Conf. at Purdue. West Lafayette, Indiana, USA. Paper #2444.
[10] Bahman, A. M., Ziviani, D., Groll, E. A., 2018. "Validation of a charge-sensitive vapor-injected compression cycle model with economization," Proc. of the 17th Int. Refrig. and Air Cond. Conf. at Purdue. West Lafayette, Indiana, USA, Paper #2445.
[11] Czapla, N., Inamdar, H., Salts, N., Groll, E. A., 2016. “Performance testing of unitary split-system heat pump with an energy recovery expansion device,” Proc. of the 16th Int. Refrig. and Air Cond. Conf. at Purdue. West Lafayette, Indiana, USA. Paper #2549.
[12] Barta, R. B., Simon, F., Groll, E. A., 2018. “Experimental analysis and design improvements on combined viper expansion work recovery turbine and flow phase separation device applied in R410A heat pump,” Proc. of the 17th Int. Refrig. and Air Cond. Conf. at Purdue. West Lafayette, Indiana, USA. Paper #2251.
[13] Python, “Python Language Reference, Version 2.7.13,” 2016.
[14] Bell, I. H., Wronski, J., Quoilin, S., Lemort, V. Pure and pseudo-pure fluid thermophysical property evaluation and the open-source thermophysical property library CoolProp. *Ind. Eng. Chem. Res.* 2014;**53(6)**:2498–2508.
[15] Mendoza-Miranda, J. M., Mota-Babiloni, A., Ramírez-Minguela, J. J., Munoz-Carpio, V. D., Carrera-Rodriguez, M., Navarro-Esbri, J., Salazar-Hernandez, C. Comparative evaluation of R1234yf , R1234ze (E) and R450A as alternatives to R134a in a variable speed reciprocating compressor. *Energy*. 2016;**114**:753-766.
[16] Bell, I. H., Quoilin, S., Georges, E., Braun, J. E., Groll, E. A., Hortung, W. T., Lemort, V. A generalized moving-boundary algorithm to predict the heat transfer rate of counterflow heat exchangers for any phase configuration. *Appl. Therm. Eng.* 2015;**79**:192–201.
[17] Bergman, T. L., Incropera, F. P., DeWitt, D. P., Lavine, A. S. *Fundamentals of heat and mass transfer, 7th edition*, John Wiley & Sons; 2011.
[18] Braun, J. E., 1988. “Methodologies for the Design and Control of Central Cooling Plants,” PhD Thesis.
[19] Zivi, S. M. Estimation of steady-state steam void-fraction by means of the principle of minimum entropy production. *J. Heat Transf.* 1964;**86(2)**:247-251.
[20] Gnielinski, V. New equations for heat and mass transfer in turbulent pipe and channel flow. *Int. Chem. Eng.* 1976;**16(2):**359–368:.
[21] Shah, M. M. A general correlation for heat transfer during film condensation inside pipes. *Int. J. Heat Mass Transf.* 1979;**22(4):**547–556.
[22] Shah, M. M. A new correlation for heat transfer during boiling flow through pipes. *ASHRAE Trans.* 1976;**82**:66–86.

[23] Churchill, S. W. Friction-factor equation spans all fluid-flow regimes. *Chem. Eng.* 1976;**84(24)**:91–92.
[24] Lockhart, R., Martinelli, R. Proposed correlation of data for isothermal two-phase, two-component flow in pipes. *Chem. Eng. Prog.* 1949;**45(1)**:39–48.
[25] Wang, C. C., Tsai, Y. -M., Lu, D. -C. Comprehensive study of convex-louver and wavy fin-and-tube heat exchangers. *J. Thermophys. Heat Transf.* 1998;**12(3)**:423–430.
[26] Schmidt, T. E. La production calorifique des surfaces munies d'ailettes. *Annex. Du Bull. L'Institut Int. Du Froid, Annex* 1945;**G-5**.
[27] Hong, K. T., Webb, R. L. Calculation of fin efficiency for wet and dry fins. *HVAC&R Res.* 1996;**2(1)**:27–41.
[28] Stania, L., 2019. "Experimental Analysis of a Viper Expansion Turbine for Work Recovery and its Factors Influencing Cycle Stability within a R410A Residential Heat Pump," Ray W. Herrick Labs Final Report.
[29] Elliott, D. G., Weinberg, E., 1968. "Acceleration of liquids in two-phase nozzles," Jet Propuls. Lab., Tech. Rep. 32-987.
[30] Smith, S. L., 1969, "Void fractions in two-phase flow: A correlation based upon an equal velocity head model," Proc. Inst. Mech. Eng. **184(1)**, p. 647–664.
[31] Bell, I. H., "Air conditioning and heat pump mpdel (ACHP) source code version 1.5," 2015.
[32] More, J., Garbow, B., Hillstrom, K., "User guide for MINPACK-1," 1980.
[33] Broyden, C. G. A class of methods for solving nonlinear simultaneous equations. *Math. Comput.* 1965;**19(92)**:577–593.
[34] ANSI/AHRI, "Performance rating of unitary A/C and air-source heat pump equipment 210/240," 2008.
[35] Storn, R., Price, K. Differential evolution - a simple and efficient heuristic for global optimization over continuous spaces. *J. Glob. Optim.* 1997;**11(4)**:341–359.

Nomenclature

A	Dimensionless coefficient	-
C	Charge tuning coefficient	kg
h	Specific enthalpy	$\frac{kJ}{kg}$
K	Charge tuning coefficient	-
k	Thermal conductivity	$\frac{W}{m-K}$
L	Length	mm
m	Mass	kg
M	Molar mass	$\frac{kg}{kmol}$
$\dot{m}$	Mass flow rate	$\frac{kg}{s}$
N	Speed	$\frac{1}{min}$
P	Pressure	kPa
$\dot{Q}$	Heat transfer rate	kW
T	Temperature	°C
UA	Overall heat transfer	$\frac{W}{K}$
V	Volume	m^3
$\dot{V}$	Volumetric flow rate	$\frac{m^3}{s}$
W	Charge tuning coefficient	-
$\dot{W}$	Power	kW
X	Quality	-

Greek Symbols

Δ	Change	-
$\vec{\Delta}$	Residual vector	Multiple

Acronyms

ACHP	Air Conditioning Heat Pump Software
COP	Coefficient of Performance
DE	Differential Evolutionary
EXV	Electronic Expansion Valve
HVAC&R	Heating, Ventilation, Air Conditioning and Refrigeration
MAPE	Mean Absolute Percentage Error
NTU	Number of Transfer Unit
RMSE	Root Mean Square Deviation Error
TXV	Thermostatic Expansion Valve
VCC	Vapor-Compression Cycle

Subscript

a	Air
accum	Accumulator
amb	Ambient
comp	Compressor
cond	Condenser
dis	Discharge
disp	Displacement
elec	Electric
evap	Evaporator
exp	Expander

ε	Effectiveness	-	gen	Generator
η	Efficiency	-	I	Coefficient
π	Dimensionless coefficient	-	liq	Liquid
ρ	Density	$\frac{kg}{m^3}$	mech	Mechanical
			oa	Overall isentropic
			pred	Predicted
			R	Refrigerant
			ref	Reference
			S	Isentropic
			suc	Suction
			sh	Superheat
			V	Volumetric
			*	Effective

13th IEA Heat Pump Conference
April 26-29, 2021 Jeju, Korea

Effect of Evaporator and Condenser in the Analsis of Adsorption Chiller

Woo Su Lee[a], Moon Yong Park[a], Xuan Quang Duong[a], Ngoc Vi Cao[a], Jae Dong Chung[a]* *

[a]Department of Mechanical Engineering, Sejong University, Seoul 05006, Korea

Abstract

In many studies, numerical analysis in adsorption chillers has focused on analyzing adsorption bed, which is the most important part, and evaporator and condenser are ideally assumed. It is doubtful whether this analysis properly evaluated the performance of the adsorption chillers. Although there have been some studies involving evaporators and condensers, it is questionable whether this is a quantitative result because the adsorption bed which has the greatest effect on performance, is analyzed by a lumped parameter model (LPM). In this study, an adsorption chiller including an evaporator and a condenser is analyzed and the results are compared with the result of a previous study that assumes an ideal evaporator and a condenser. As a result of analyzing in terms of coefficient of performance and specific cooling power, the analysis including the evaporator and condenser showed 16.12% and 24.64% overestimation compared. Also, LPM analysis including evaporator and condenser showed that COP and SCP were 22.82% and 11.28% larger than our model, respectively

© HPC2020.
Selection and/or peer-review under responsibility of the organizers of the 13th IEA Heat Pump Conference 2020.

Keywords: adsorption chiller; numerical analysis, evaporator, condenser

1. introduction

Because of global warming and economic development, cooling demand has rapidly increased. There are many kinds of refrigerator types. The vapor compression refrigerator has been most commonly used, however, it suffers from a negative impact on the environment and an excessive electric power requirement. Therefore, many researchers have focused on developments of eco-friendly refrigeration systems, and heat driven refrigerators have been highly attracted such as absorption, desiccant, and adsorption cooling system.

The adsorption refrigerator operates reversible adsorption and desorption processes, in a cycle of preheating, heating, pre-cooling, and cooling. The size of adsorption chiller is large and cycle time is too long. For this reason, the experimental study is highly time-consuming and expensive, a numerical study has been widely used, to understand the process in adsorption refrigerator.

Niazmand et al [1] focused on the issue of bed geometry and found the difference in performance caused by heat and mass transfer ability. The performance of refrigerator was improved by changing fin height and fin space. Mahdavikhah et al. [2] investigated the pressure distribution of the bed in isosteric phase to understand the complex mechanism of heat and mass transfer in the square finned adsorption bed. They found the optimized shape which evenly distributed the heat energy.

* Corresponding author. Tel.: +0-000-000-0000 ;
E-mail address: jdchung@sejong.edu.

From the literature survey, even though adsorption bed is one of the crucial components in adsorption refrigerator, the research target was mainly confined to the adsorption bed. The effect of its integration with evaporator and condenser has not been closely examined till now. A few works have focused on this issue. Khan et al. [3] numerically analyzed reheat-2stage adsorption refrigerator using LPM (lumped parameter model). They performed a case study with the parameters of silica gel mass and its surface area. Zhang et al. [4] analyzed an adsorption refrigerator driven by solar power with Simulink. They found the cooling capacity by assuming day-time solar radiation and showed that the COP was different depending on the initial temperature. Ng et al. [5] researched a desalination cycle driven by waste heat and suggested an optimal condition.

A few works have focused on the analysis including not only adsorption bed but also additionally including evaporator and condenser. Therefore, in this study, we focus on refined CFD simulation for adsorption bed with evaporator and condenser which is the more realistic model.

2. Numerical method

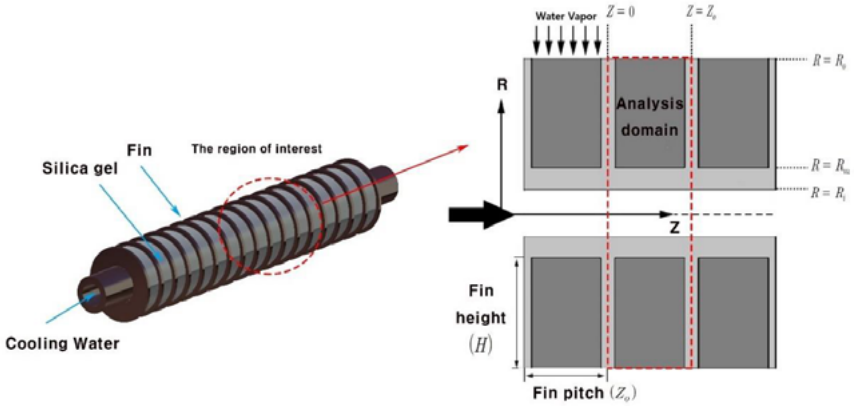


Fig. 1. numerical model of the circular fin – tube

Fig. 1 describe numerical model of fin-tube type adsorption chiller. The numerical model includes the following assumptions.

(1) 2-D axisymmetric model is assumed.
(2) No heat loss through the wall and effect of radiation is negligible.
(3) Vapor is an ideal gas and silica gel is liquid phase.
(4) Particle has uniform size and same porosity.

The detailed properties such as isotherm of adsorbent, bed analysis model, and numerical model verification were described in our recent studies (Hong et al. [6]), so it is not discussed further.

Another model, which contains evaporator and condenser, use same equation with previous model for analysis of adsorption bed. We use equations for evaporator and condenser which can be found in some existing paper (Khan et al. [3]).

3. Result

Fig. 2 describes the Clapyron diagram of an adsorption refrigerator that reaches quasi-equilibrium state. As indicated by the dotted line, the idealized model does not follow the actual pressure, but rather has constant saturation pressure corresponding 15℃ and 30℃, which are evaporator and condenser temperature. On the other hand, a realistic model indicated by the solid line follows the pressure corresponded with actual evaporation or condensation temperature. The existence of the pressure gradient finally affects the adsorption/desorption isotherm. Fig. 3 shows difference in water uptake amount.

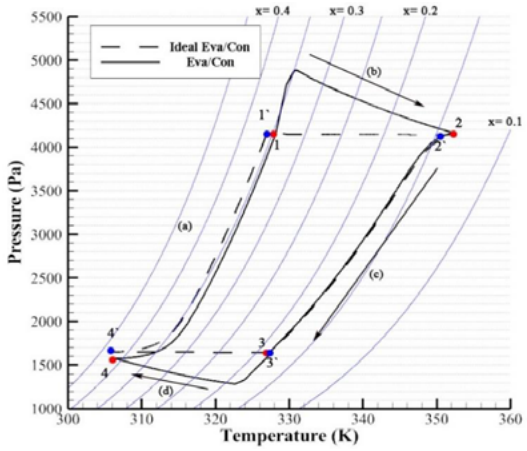


Fig. 2. P-T diagram in adsorption bed of two models

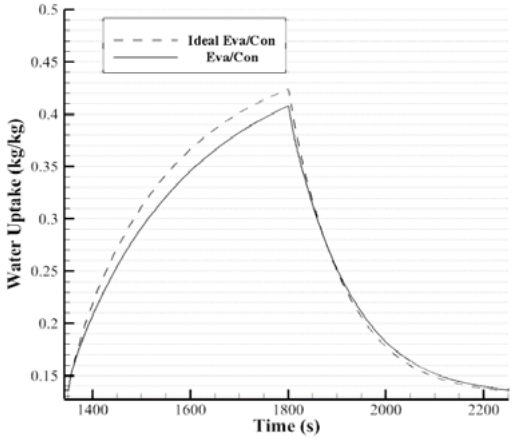


Fig. 3. Difference in water uptake between two model

For this reason, when evaporator and condenser was ideally designed, COP was overvalued up to 16.12%. Furthermore, SCP was overvalued up to 24.64%. So, it is better to use the analysis which cover evaporator and condenser to avoid distorting the result.

Acknowledgements

This research was supported by Basic Science Research Program through the National Research Foundation of Korea (NRF) funded by the Ministry of Education (No. 2017R1D1A1B05030422)

References

[1] Niazmand H., Talebian H., Mahdavikhah M., 2012, Bed geometrical specifications effects on the performance of silica/water adsorption chillers, International Journal of Refrigeration 2261–2274.
[2] Mahdavikhah M., Niazmand H., 2013, Effects of plate finned heat exchanger parameters on the adsorption chiller performance, Applied Thermal Engineering 50 939–949.
[3] Khan M.Z.I., Alam K.C.A., Saha B.B., Hamamoto Y., Akisawa A., Kashiwagi T., 2006, Parametric study

of a two-stage adsorption chiller using re-heat—The effect of overall thermal conductance and adsorbent mass on system performance, International Journal of Thermal Sciences 45 511–519.

[4] Zhang, G., Wang, D.C., Zhang, J.P., Han, Y.P., Sun, W., 2011, Simulation of operating characteristics of the silica gel–water adsorption chiller powered by solar energy, Solar Energy 85, 1469–1478.

[5] Ng, K.C., Thu, K., Saha, B.B., Chakraborty, A., 2012, Study on a waste heat-driven adsorption cooling cum desalination cycle, International Journal of Refrigeration 35 685–693.

[6] Hong S.W., Ahn S.H., Kwon O.K., Chung J.D., 2014, Validity of intra-particle models of mass transfer kinetics in the analysis of a fin-tube type adsorption bed, Journal of Mechanical Science and Technology 28 (5) 1985–1993.

13th IEA Heat Pump Conference
April 26-29, 2021 Jeju, Korea

Effect of Evaporator and Condenser in the Analsis of Adsorption Chiller

Woo Su Lee[a], Moon Yong Park[a], Xuan Quang Duong[a], Ngoc Vi Cao[a], Jae Dong Chung[a]* *

[a]Department of Mechanical Engineering, Sejong University, Seoul 05006, Korea

Abstract

In many studies, numerical analysis in adsorption chillers has focused on analyzing adsorption bed, which is the most important part, and evaporator and condenser are ideally assumed. It is doubtful whether this analysis properly evaluated the performance of the adsorption chillers. Although there have been some studies involving evaporators and condensers, it is questionable whether this is a quantitative result because the adsorption bed which has the greatest effect on performance, is analyzed by a lumped parameter model (LPM). In this study, an adsorption chiller including an evaporator and a condenser is analyzed and the results are compared with the result of a previous study that assumes an ideal evaporator and a condenser. As a result of analyzing in terms of coefficient of performance and specific cooling power, the analysis including the evaporator and condenser showed 16.12% and 24.64% overestimation compared. Also, LPM analysis including evaporator and condenser showed that COP and SCP were 22.82% and 11.28% larger than our model, respectively

© HPC2020.
Selection and/or peer-review under responsibility of the organizers of the 13th IEA Heat Pump Conference 2020.

Keywords: adsorption chiller; numerical analysis, evaporator, condenser

1. introduction

Because of global warming and economic development, cooling demand has rapidly increased. There are many kinds of refrigerator types. The vapor compression refrigerator has been most commonly used, however, it suffers from a negative impact on the environment and an excessive electric power requirement. Therefore, many researchers have focused on developments of eco-friendly refrigeration systems, and heat driven refrigerators have been highly attracted such as absorption, desiccant, and adsorption cooling system.

The adsorption refrigerator operates reversible adsorption and desorption processes, in a cycle of preheating, heating, pre-cooling, and cooling. The size of adsorption chiller is large and cycle time is too long. For this reason, the experimental study is highly time-consuming and expensive, a numerical study has been widely used, to understand the process in adsorption refrigerator.

Niazmand et al [1] focused on the issue of bed geometry and found the difference in performance caused by heat and mass transfer ability. The performance of refrigerator was improved by changing fin height and fin space. Mahdavikhah et al. [2] investigated the pressure distribution of the bed in isosteric phase to understand the complex mechanism of heat and mass transfer in the square finned adsorption bed. They found the optimized shape which evenly distributed the heat energy.

* Corresponding author. Tel.: +0-000-000-0000 ;
E-mail address: jdchung@sejong.edu.

From the literature survey, even though adsorption bed is one of the crucial components in adsorption refrigerator, the research target was mainly confined to the adsorption bed. The effect of its integration with evaporator and condenser has not been closely examined till now. A few works have focused on this issue. Khan et al. [3] numerically analyzed reheat-2stage adsorption refrigerator using LPM (lumped parameter model). They performed a case study with the parameters of silica gel mass and its surface area. Zhang et al. [4] analyzed an adsorption refrigerator driven by solar power with Simulink. They found the cooling capacity by assuming day-time solar radiation and showed that the COP was different depending on the initial temperature. Ng et al. [5] researched a desalination cycle driven by waste heat and suggested an optimal condition.

A few works have focused on the analysis including not only adsorption bed but also additionally including evaporator and condenser. Therefore, in this study, we focus on refined CFD simulation for adsorption bed with evaporator and condenser which is the more realistic model.

2. Numerical method

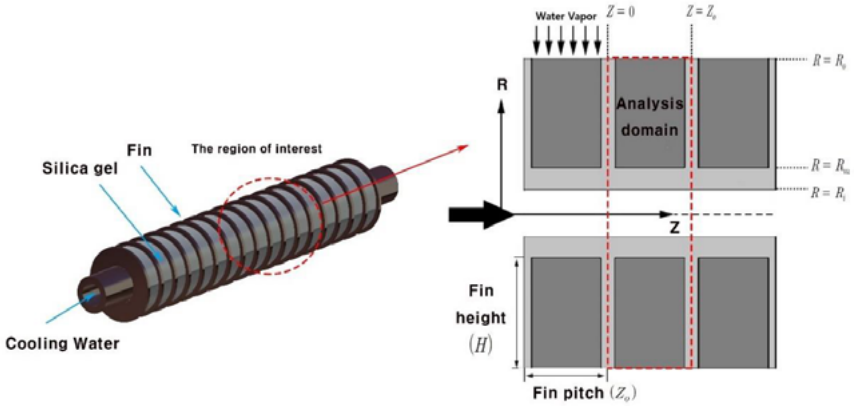


Fig. 1. numerical model of the circular fin – tube

Fig. 1 describe numerical model of fin-tube type adsorption chiller. The numerical model includes the following assumptions.

(1) 2-D axisymmetric model is assumed.
(2) No heat loss through the wall and effect of radiation is negligible.
(3) Vapor is an ideal gas and silica gel is liquid phase.
(4) Particle has uniform size and same porosity.

The detailed properties such as isotherm of adsorbent, bed analysis model, and numerical model verification were described in our recent studies (Hong et al. [6]), so it is not discussed further.

Another model, which contains evaporator and condenser, use same equation with previous model for analysis of adsorption bed. We use equations for evaporator and condenser which can be found in some existing paper (Khan et al. [3]).

3. Result

Fig. 2 describes the Clapyron diagram of an adsorption refrigerator that reaches quasi-equilibrium state. As indicated by the dotted line, the idealized model does not follow the actual pressure, but rather has constant saturation pressure corresponding 15℃ and 30℃, which are evaporator and condenser temperature. On the other hand, a realistic model indicated by the solid line follows the pressure corresponded with actual evaporation or condensation temperature. The existence of the pressure gradient finally affects the adsorption/desorption isotherm. Fig. 3 shows difference in water uptake amount.

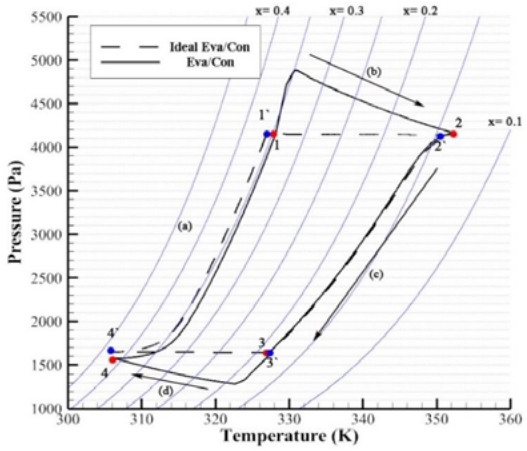


Fig. 2. P-T diagram in adsorption bed of two models

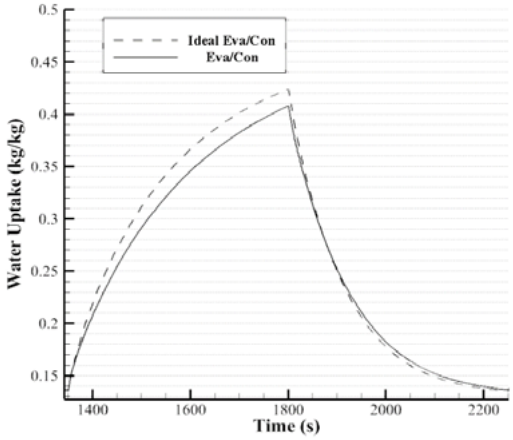


Fig. 3. Difference in water uptake between two model

For this reason, when evaporator and condenser was ideally designed, COP was overvalued up to 16.12%. Furthermore, SCP was overvalued up to 24.64%. So, it is better to use the analysis which cover evaporator and condenser to avoid distorting the result.

Acknowledgements

This research was supported by Basic Science Research Program through the National Research Foundation of Korea (NRF) funded by the Ministry of Education (No. 2017R1D1A1B05030422)

References

[1] Niazmand H., Talebian H., Mahdavikhah M., 2012, Bed geometrical specifications effects on the performance of silica/water adsorption chillers, International Journal of Refrigeration 2261–2274.
[2] Mahdavikhah M., Niazmand H., 2013, Effects of plate finned heat exchanger parameters on the adsorption chiller performance, Applied Thermal Engineering 50 939–949.
[3] Khan M.Z.I., Alam K.C.A., Saha B.B., Hamamoto Y., Akisawa A., Kashiwagi T., 2006, Parametric study

of a two-stage adsorption chiller using re-heat—The effect of overall thermal conductance and adsorbent mass on system performance, International Journal of Thermal Sciences 45 511–519.

[4] Zhang, G., Wang, D.C., Zhang, J.P., Han, Y.P., Sun, W., 2011, Simulation of operating characteristics of the silica gel–water adsorption chiller powered by solar energy, Solar Energy 85, 1469–1478.

[5] Ng, K.C., Thu, K., Saha, B.B., Chakraborty, A., 2012, Study on a waste heat-driven adsorption cooling cum desalination cycle, International Journal of Refrigeration 35 685–693.

[6] Hong S.W., Ahn S.H., Kwon O.K., Chung J.D., 2014, Validity of intra-particle models of mass transfer kinetics in the analysis of a fin-tube type adsorption bed, Journal of Mechanical Science and Technology 28 (5) 1985–1993.

13th IEA Heat Pump Conference
April 26-29, 2021 Jeju, Korea

Frosting and Defrosting Behavior of Evaporators

Christoph Reichl[a,*], Mirza Popovac[a], Felix Hochwallner[a], Peter Wimberger[b], Felix Linhardt[a,b], Thomas Fleckl[a], Johann Emhofer[a]

[a]Austrian Institute of Technology GmbH, Center for Energy, Vienna 1210, Austria
[b]Vienna University of Technology, Institute of Applied Physics, Vienna 1040, Austria

Abstract

Air-to-water heat pumps - being essential to reach the ambitious climate goals – don't come without challenges: Evaporators of air-to-water heat pumps are prone to severe frosting in humid climatic during late fall, winter and spring. To sustain a reasonable CoP, de-frosting strategies are employed to remove the frost layer and restore normal operation. De-frosting, however, also reduces efficiency due to downtimes and heat loss due to reverse operation. Frosting and de-frosting of evaporators is characterized using overview and detailed image capturing. The frost growth is additionally quantitatively assessed using a digital high-resolution scale. Together with the thermodynamic data of the heat pump and the control parameters of the climatic chamber a full transient data set is available and analysed deriving frosting and de-frosting correlations. The extensive data set is an important base for numerical simulation: Frost growth and weight increase can be used to validate three-dimensional frosting models necessary to simulate and - in a second stage - optimize evaporator designs. Furthermore, the thermodynamic behaviour during frosting and de-frosting is an important input to one-dimensional system models of heat pumps.

© HPC2020.
Selection and/or peer-review under responsibility of the organizers of the 13th IEA Heat Pump Conference 2020.

Keywords: frosting; de-frosting; evaporator; image processing

1. Introduction

The frosting of heat exchangers is typically undesired in heat pump operation, given that in most of the cases it implies a deterioration of the equipment performance or even critical safety problems. In that view, the understanding of the factors affecting the frosting process is of high practical relevance, and a large research community is involved in the investigation of the frosting behaviour.

Empirical correlations for the relevant frost characteristics (respectively, frost density and conductivity, mass diffusivity and latent heat of sublimation) have been presented by [1], [2] and [3], among others. This is accompanied by comprehensive numerical work to provide the theoretical background: In a series of studies, Na and Webb [4], [5] presented their work on the frost formation over simple geometrical configurations, successfully reproducing the experimental frosting results. Focusing on the reduction of the computational cost, [6] proposed an algebraic approach for the frost growth and densification. [7] advanced the psychometric and surface conditions under which the frost formation occurs.

Comprehensive reviews are available on frosting of air-to-air heat exchangers (see [8], [9]) and the frost deposition on flat surfaces [10]. Different surface structures have been investigated [11], [12]. Heat transfer characteristics under frosting and defrosting are discussed in [13] and have been put in the general context of building applications by [14].

* Corresponding author. Tel.: +43-50550-6605; fax: +43-50550-6649
E-mail address: christoph.reichl@ait.ac.at

In this paper time dependent frosting of the heat exchanger has been observed in the SilentAirHP heat pump assembly by measuring the mass increase and using postprocessing of captured images of the heat exchanger during frosting for different environmental conditions. In section 2 we will describe the experimental heat pump setup. This is followed by a discussion of the experimental methods used to characterize frosting on the evaporator in section 3. In section 4 we are going to present and discuss the experimental results. We will conclude this work by summarizing our experimental approaches and presenting an overview of planned future work.

2. Experimental Heat Pump and Evaporator Component

For our measurements we used an experimental air-source heat pump (see Figure 1) which was designed to provide a heating power of 5 kW at a heating water temperature of 35°C and at an ambient air temperature of 2°C. The refrigerant R410A was used and the entire heat pump was located inside the AIT climatic chambers during the measurements. Inside the chamber, the air temperature and humidity could be controlled. The heating water was cooled with an in-house chilled water reservoir with the back flow of the heating water regulated to 30°C. The compressor was operated at a fixed rotational speed of 98Hz. The superheating was always set to 7°C during the experiments. The fan operated at a constant rotational speed what corresponds to an average velocity of 2 m/s at the fin and tube evaporator. The dimensions of the evaporator are 630 mm x 560 mm with a depth of 120 mm. The fins are made of corrugated aluminium and placed in a distance of 4 mm. 78 horizontal tubes made of smooth copper are organized in 4 columns in air flow direction. The overall pressure drop of the evaporator is about 54 Pa, if dry. The condenser has been realized as a plate condenser designed for a heating capacity of 5 kW at an outside air temperature of 2°C and a supply temperature of 35°C and a condensation temperature of 40°C.

3. Measurement methods

Alongside the acquisition of thermodynamic data of both the heat pump and climatic chamber, transient weight measurements and image capturing techniques have been used.

3.1. Heat Pump and Climatic Chamber Thermodynamics

The temperatures at the refrigerant inlet and outlet of the evaporator were measured with calibrated PT100-class A temperature sensors. The sensors were mounted with heat-conductive paste on the outside of the copper pipes as close to the inlet as possible. Furthermore, the sensors were insulated to reduce heat exchange with the ambient air. The climatic conditions in the chamber are measured with several combined temperature and humidity sensors placed at the suction side of the heat exchanger according to the standards normally used for heat pump certification tests (EN14511-3:2018) [15]. An additional temperature and humidity sensor is placed at the suction side for climate chamber control.

3.2. Transient Weight Measurements

The heat pump assembly has been placed on a scale capable of measuring the weight as a function of time. By calculating the difference between the increasing weight and the initial weight, the amount of frost on the heat exchanger can be extracted. As the weight of the heat pump assembly was by a factor of 1.5 higher than the maximum detectable load of the scales, a balance construction was put in place and the system was calibrated by subsequently placing known weights on the dry heat exchanger and recording a calibration curve before starting the frosting experiments.

We selected a setup with an air inflow temperature of 2°C with quite small defrosting cycle times for better visualization of the procedure. Figure 3 shows the measured mass signal on the left side. As a next step each frosting cycle is identified (shown in Figure 3 right side marked with a unique colour). As the final step, the mass signals of the different frosting cycles are superimposed (see Figure 4) and a mean mass signal is derived which can then be used for comparison to numerical data (see also Figure 11).

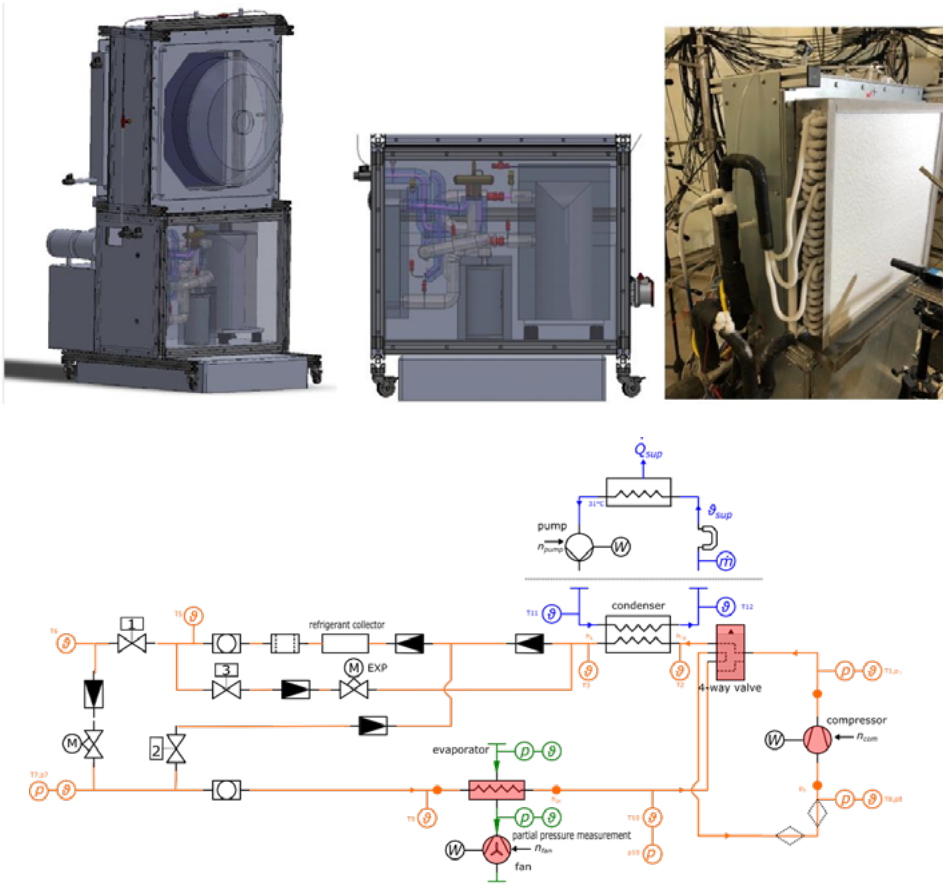


Fig. 1. (top left) Sketch of the experimental SilentAirHP heat pump showing the major components; (top middle) lower part of the SilentAirHP with compressor, condenser, expansion valve and duct network; (top right) SilentAirHP evaporator fully covered with ice in the climatic chamber of AIT. (bottom): sketch of the heat pump design with sensor positions.

3.3. Image Capturing and Highlight Event Extraction

Two cameras have been used to capture the frosting of the heat exchanger. A thermal-camera capable of recording thermographic stills and standard image stills at the same time and a macro camera recording a detailed view of a part of the heat exchanger used for highlight event extraction. For the standard images both, a normal view and a differential view between the actual image and an image recorded in the initial state (without frost) is shown: an example of the detailed view is given in Figure 2 on the right side; the total view is given on the left side. The setup of the cameras can also be seen in Figure 5.

In order to quantify the frost accumulation, the scale signal and the amount of pixel exceeding a certain brightness threshold in the pictures may be used. A pixel exceeds the brightness threshold if the mean of the red, green and blue value is higher than 200. At the beginning only the pixels displaying the metallic surface of the fins will exceed this brightness threshold. But as soon as frost is accumulating, additional pixel will exceed this threshold. Pixels exceeding the stated threshold (“white” pixels) are from now flagged as highlight events for additional processing.

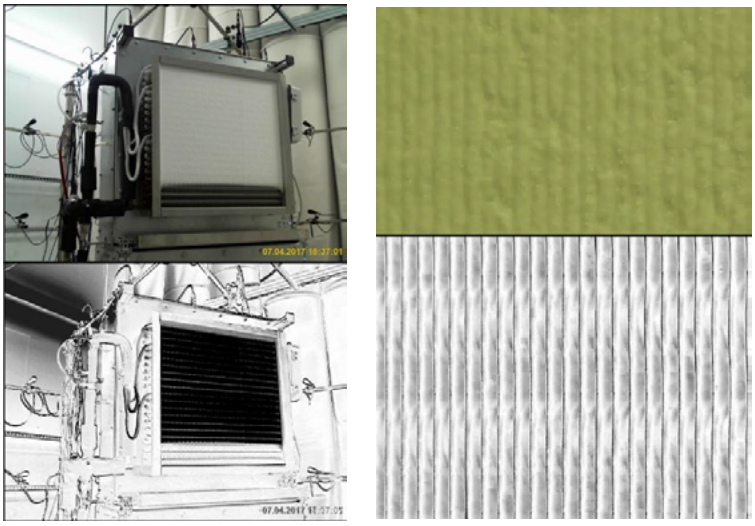


Fig. 2. Measurement overview with full frosting. The humidity in the climatic chamber has been increased to its maximum reachable value to reach full frost state. Left side: full image of the heat pump showing severe frosting on the top and a differential image of the heat exchanger showing frost only on the bottom; Right side: detailed view on the heat exchanger fins with full frosting on top and differential image of detailed view on the frosting heat exchanger showing frost only on the bottom.

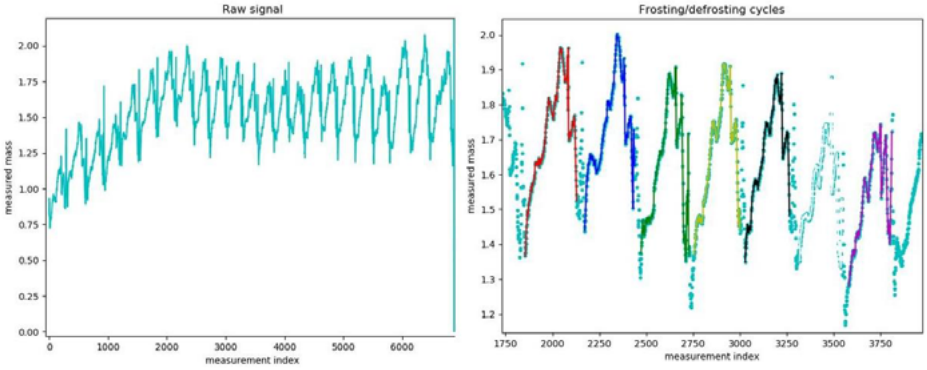


Fig. 3. (left) Measured mass given in kg shown as function of the measurement index for an inflow air temperature of 2°C; (right) Frost mass versus measurement index for a section of the whole measurement period (shown on left side). Each frosting cycle is identified by visual inspection and marked with a unique colour for visualization.

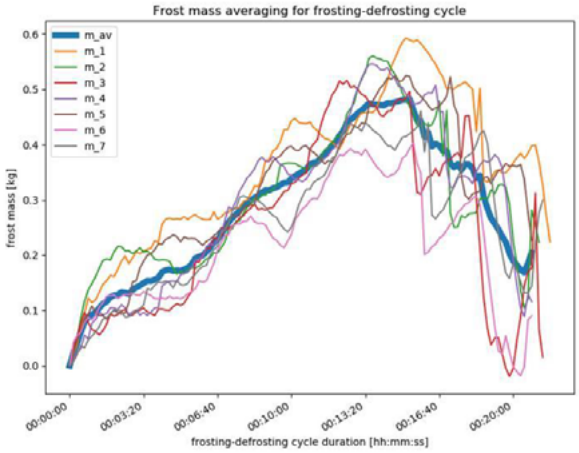


Fig. 4. Frost mass given in kg as a function of frosting-defrosting duration. The single repetitive events shown in Fig. 3 right are now superimposed to allow for the generation of a mean average frosting cycle and presented via the time duration.

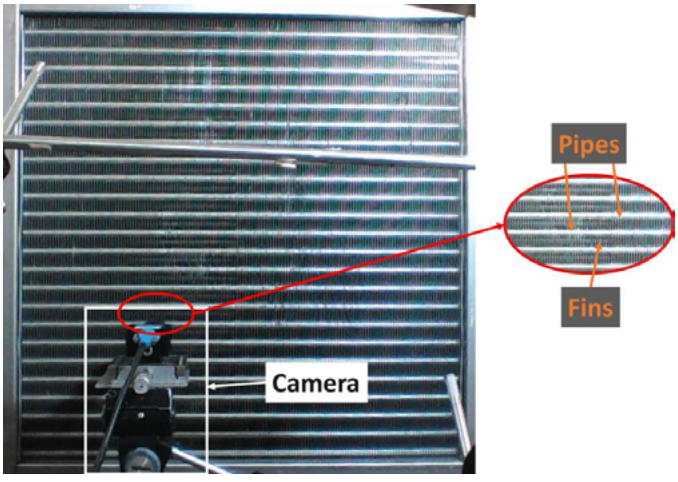


Fig. 5. Surface of the SilentAirHP heat exchanger and macro camera used to visualize the frost accumulation on the heat exchanger fins.

4. Experimental Results and Discussion

A common webcam can also be used to visualize the nonuniform frost accumulation on the heat exchanger surface (see Figure 6). It can be seen, that the frost is not forming uniformly on the whole heat exchanger surface, but rather patchy. The camera with the macro lenses used to visualize the frost growth between two fins is located at a representative area, where the frost growth is clearly visible. The rod looming over the pictures is a humidity sensor.

The macro camera was used to give a detailed view of the frost accumulation and dissipation on one or two fins of the heat exchanger. In Figure 5 the surface of the SilentAirHP heat exchanger and the macro camera used to visualize the frost accumulation on the heat exchanger fins is shown. The boundary conditions for the frosting behaviour analysis of the SilentAirHP are listed in Table 1. The pictures of the frost accumulation

between two fins can be seen in Figure 7. In Figure 8 the scale measurements and the amount of highlight events is shown over time.

Table 1. Operation and ambient conditions for the analysis of the frosting behaviour of the SilentAirHP.

θ_{amb}	RH_{amb}	η_{comp}	η_{fan}	Refrigerant	Fin type	Coating	Fin area
6.3°C	71.8%	94 Hz	99 Hz	R410A	Straight flat fins	Clearcoat U-Sil 120 GL	11.44 m^2

Legend:
θ_{amb} … Ambient temperature // RH_{amb} … Relative Humidty // η_{comp} … Rotational frequency of the compressor
η_{fan} … Rotational frequency of the fan // Refrigerant … Used refrigerant // Fin type … Fin type used for the reported measurement
Coating … Coating used for surface treatment of the fins // Fin area … Total area of the fins

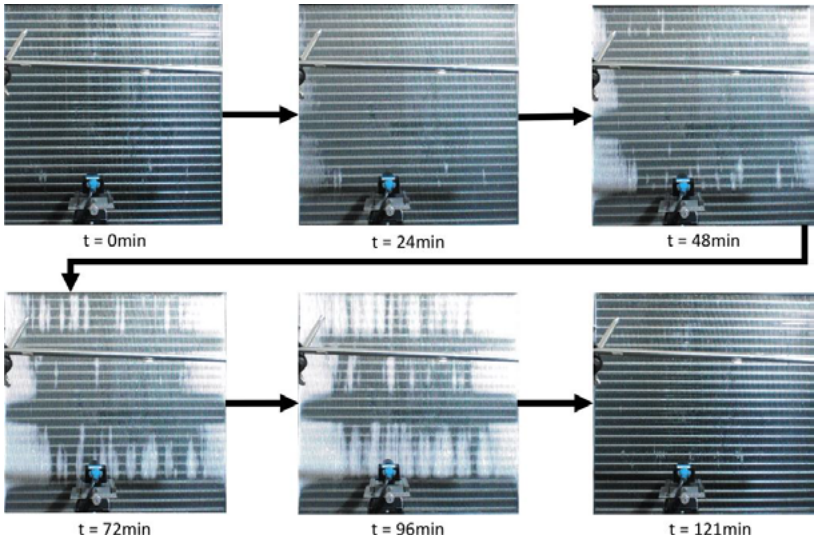


Fig. 6. Nonuniform frost formation on the heat exchanger surface of the SilentAirHP.

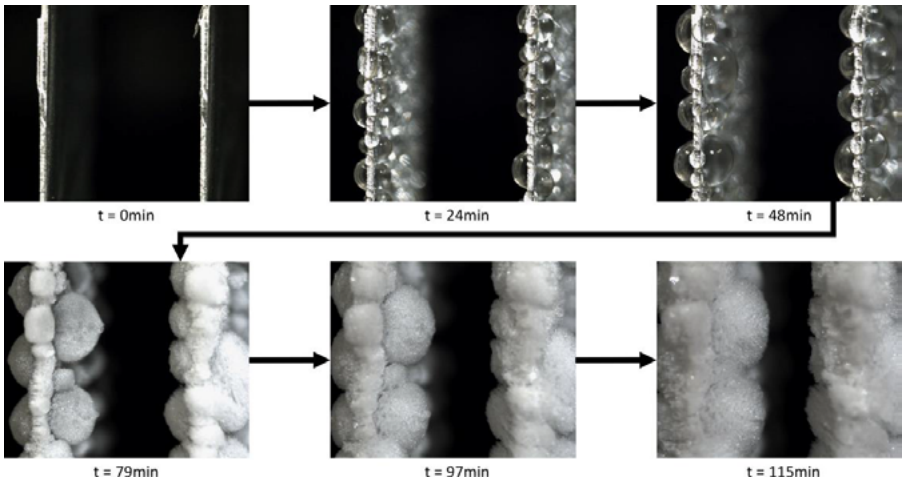


Fig. 7. Frost accumulation on two fins of the coated evaporator of the SilentAirHP for operation and ambient conditions as defined in Table 1.

Frosting of the SilentAirHP starts with small water drops condensing on the surface of the vertical fins. The water drops start fusing together forming bigger water drops. These bigger water drops start to freeze, building frost globes on the fins of the heat exchanger. Advancing in time, the frost globes start fusing together and the frost continues to densify. When the frost layer is too thick, the SilentAirHP starts to defrost, in order to assure continues stable operation. This defrosting is done by reversing the cycle via a four-way valve.

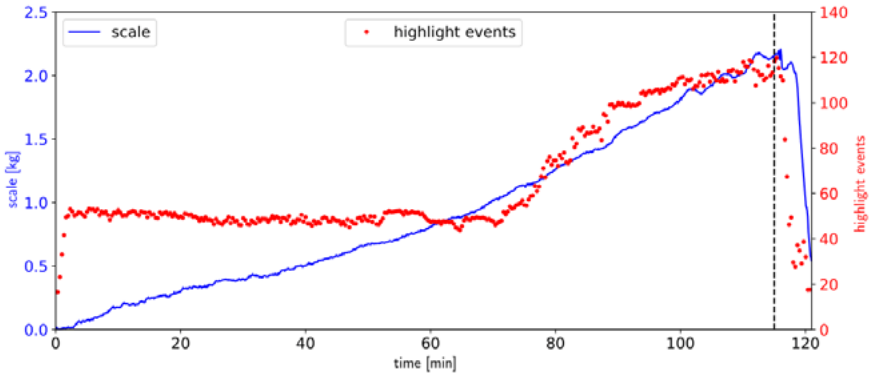


Fig. 8. Scale measurement and amount of highlight events in pictures of the SilentAirHP during frosting conditions and defrosting operation. The time when defrosting is initiated is marked with a dotted line.

After reversing the cycle, the frosted heat exchanger, which acted as the evaporator for the refrigerant, afterwards works as the condenser for the refrigerant, transferring heat to the outlet air and to the frost on its fins. Defrosting of the heat exchanger is done in a very short period of time. The defrosting of the SilentAirHP can be seen in Figure 9.

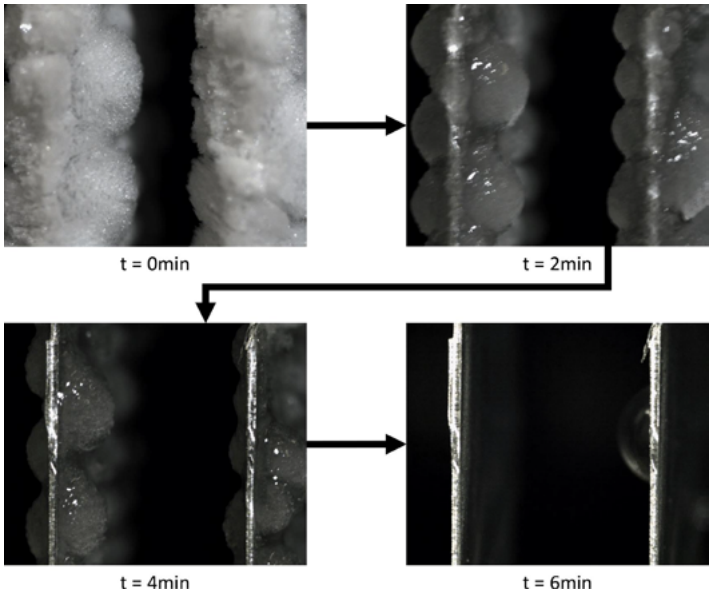


Fig. 9. Defrosting of the coated evaporator of the SilentAirHP for operation and ambient conditions as defined in Table 1.

Defrosting of the SilentAirHP takes only 6 min, while the operation at frosting conditions was able to be operated in an almost stable manner for 115 minutes for the settings given in Table 1. Therefore, the heat pump can be operated in regular heating mode for approximately 95% of the time at these conditions. When the ice layer is formed on the evaporator surface, however, the heat pump performance begins to decrease slightly. This can also be seen in the temperature sensors placed inside the heat pump (see Fig. 12). When the frost layer grows starting around 70 minutes (see Fig. 8), the valve, compressor and condenser temperatures both on the discharge and suction side begin to fall slightly indicating this decrease in performance.

During the remaining 5% of the time the heat exchanger has to be defrosted. When defrosting is started, the fins rapidly take the hot temperature of the refrigerant. Therefore, the frost is melted from its surface, forming liquid water which flows down the vertical fins. This water flows down the heat exchanger until it reaches the ground it stands on. In Figure 8 the scale measurements and the amount of highlight events in the pictures during frosting and defrosting operation of the SilentAirHP is shown. The mass on the heat exchanger is constantly rising, due to condensing water on the heat exchanger fins and afterwards frosting of the water drops and densifying of the frost. During the first 70 minutes nearly no change in highlight events is visible, as the condensed water drops do not count as highlight events, but only frost does. After 70 minutes the amount of highlight events is increasing. Just after beginning of defrost operation, which is marked with a dotted line in the plot, the amount of highlight events and the mass of the scale is decreasing rapidly, as the frost is melting, and the water drains off. It is interesting to compare the close-up view (Figure 7) with the global view (Figure 6): On the first and last picture in the global view, where the close up camera suggests complete termination of the defrosting operation, falling water drops are still visible on the webcam pictures.

Frosting cycles have been measured for several environmental conditions defined by the evaporator air inflow temperature. The climate chamber was set to a sustain a defined relative humidity. This can only be achieved with some fluctuations especially in the vicinity of defrosting. For and outdoor air temperature of 2°C, 4.5°C and 7°C, a relative humidity of 87.3%, 86.4% and 78%, respectively was measured. During defrosting, however, the relative humidity in the chamber cannot be sustained by the climate chamber control and deviates from this number. After defrosting the humidity control of the climate chamber is able to bring the conditions back. The relative mass signals are shown in Figure 10 for air inflow temperatures of 2.0°C, 4.5°C and 7.0°C. The average frost mass for these different air inflow temperatures is shown in Figure 11. It can clearly be seen, that the implemented control algorithm acts differently for the different situations. Cycle times for the 7°C air inflow temperature are - with around 120 min - longer than those for an air inflow temperature of 4.5°C which lie around 80 minutes. Not only the amount of accumulated frost is different – also the shape of the weight increase curves shows a different behaviour – not only in curvature but also in their repetitiveness. The employed control algorithm leads to very frequent defrosting for the 2°C air inflow temperature setting.

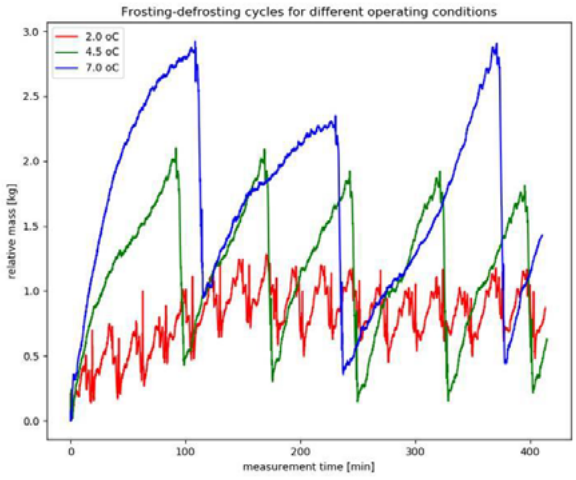


Fig. 10. Frost mass given as a function of the measurement time for three different temperatures (given in °C) of the inflow air. In all cases, several frosting/defrosting cycles are shown.

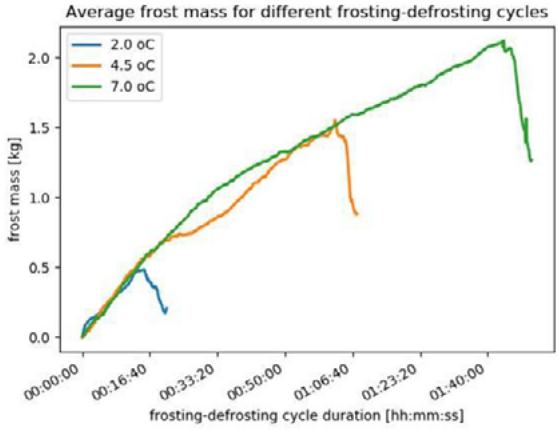


Fig. 11. Average frost mass given as a function of the measurement time for three different temperatures (given in °C) of the inflow air.

Defrosting of the heat pump was triggered once the evaporator pressure (which is equivalent to an evaporation temperature) has fallen below a certain lower limit. This is an indication for a decreased heat transfer through the evaporator what goes hand in hand with an increased frost thickness and a lower COP. Since, the defrost condition was not corelated to the outdoor temperature condition in our experiments, the time before defrosting increases for higher outdoor temperatures. This fact is also reflected in the differences in frost aggregation (mass uptake, see Figure 11).

The refrigerant temperatures during operation are shown in Figure 12 for the settings given in Table 1. During operation of the heat pump at frosting conditions most refrigerant temperatures fluctuate but the mean of most temperatures stay approximately constant. However, about thirty minutes before defrosting the mean of some refrigerant temperatures, as well as the compressor suction and discharge temperatures, decrease slightly. When defrosting is initiated the compressor discharge temperature, the valve suction temperature, the condenser suction temperature and the condenser discharge temperature fall significantly. Meanwhile, the compressor suction and the valve discharge temperature rise. This operation mode is maintained only for a very short time and the temperatures are fluctuating heavily during this mode.

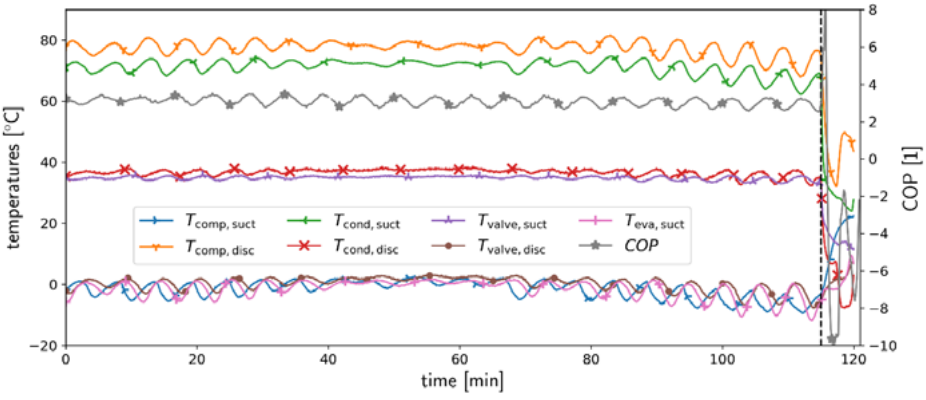


Fig. 12. Development of the refrigerant temperatures over time during operation of the SilentAirHP at frosting conditions. The time when defrosting is initiated is marked with a black dotted line. The CoP is added as a grey curve.

5. Conclusions and Outlook

Frosting of evaporators is commonly observed especially in mild climates and a defrosting procedure has to be put in place allow for a continuous operation of the heat pump. The evaporator, however, is only one part of the complete setup: Frosting of the fins and tubes and hence subsequent blocking of the evaporator leads to an increased pressure drop over the evaporator which could force the fan to run in a different operating point. Furthermore, the frost layer changes the heat transfer characteristics of the evaporator.

In this paper we introduced methods for measuring the weight increase using scales and visualizing ice accretion using postprocessing of images captured from the evaporator surface during heat pump operation. We could show, that there is a good correlation between the weight increase and the number of highlight events present in the images captured. Furthermore, the formation of droplets on the fin structures and subsequently freezing eventually building up an ice layer between the fins could be shown with a macro camera providing very detailed images. It should be noted, that selecting the right spot for the macro camera is important to achieve representative ice accretion data.

The experimental characterization methodologies built around the experimental heat pump "SilentAirHP" proved to be a robust testbed for identification of efficient ways to detect frosting states, which will be used to derive soft sensors in the framework of the IoT (Internet of Things) heat pump initiative. The test-rig using full control capabilities of the self-made heat pump is further capable of comparing different evaporators and/or evaporators with different coatings.

Finally, the data base available through the frosting and defrosting experiments is key to validate numerical simulations performed to simulate the frosting process either on full evaporator geometries or smaller symmetric elements used to reconstruct the behaviour of the full evaporator setups. The images from the macro camera visualize the frosting process and can be used to compare to very high detailed simulation results. The numerical approaches allow for assisting in evaporator design and development.

Acknowledgements

The Austrian Research Promotion Agency (FFG) and the Austrian Climate and Energy Fund (KLIEN) is gratefully acknowledged for funding this work under Grant No. 848891 (program line 'Energieforschung e!Mission 1st call', project 'SilentAirHP'). Part of the work has been performed within the 7th Framework Programme (FP7) European Commission grant agreement No FP7-Energy-2012-308816.

References

[1] Y. Hayashi, A. Aoki, S. Adashi, K. Hori, Study of frost properties correlating with frost formation types, *ASME J. Heat Transfer* **99** (1977) 239245.

[2] H. R. Pruppacher, J. D. Klett, Microphysics of Clouds and Precipitation, Reidel, Dordrecht, 1978.

[3] P. G. Mago, S. A. Sheriff, Frost formation and heat transfer on a cold surface in ice fog, *AIAA-2004-164*.

[4] B. Na, R. Webb, A fundamental understanding of factors affecting frost nucleation, *Int. J. Heat Mass Transfe*r **46** (2003) 3797 3808.

[5] B. Na, R. Webb, Mass transfer on and within a frost layer, *Int. J. Heat Mass Transfer* **47** (2004) 899911.

[6] C. J. L. Hermes, R. O. Piucco, J. R. B. Jr., C. Melo, A study of frost growth and densification on flat surfaces, *Experimental Thermal and Fluid Science* **33** (2009) 371-379.

[7] R. O. Piucco, C. J. L. Hermes, C. Melo, J. R. B. Jr., A study of frost nucleation on at surfaces, *Experimental Thermal and Fluid Science* **32** (2008) 17101715.

[8] M. R. Nasr, M. Fauchoux, R. W. Besant, C. J. Simonson, A review of frosting in air-to-air energy exchangers, *Renewable and Sustainable Energy Reviews* **30** (2014) 538-554. doi:https://doi.org/10.1016/j.rser.2013.10.038. URL http://www.sciencedirect.com/science/article/pii/S1364032113007375

[9] Z. Qi, Water retention and drainage on air side of heat exchangers - a review, Renewable and Sustainable *Energy Reviews* **28** (2013) 1-10. doi:https://doi.org/10.1016/j.rser.2013.07.014. URL http://www.sciencedirect.com/science/article/pii/S1364032113004590

[10] A. Loni, M. Mondot, F. Durier, R. Revellin, P. Haberschill, State-of-the-art review of frost deposition on flat surfaces, *International Journal of Refrigeration* **68** (2016) 198-217. doi:https://doi.org/10.1016/j.ijrefrig.2016.04.004.

URL http://www.sciencedirect.com/science/article/pii/S0140700716300457

[11] P. Ganesan, S. Vanaki, K. Thoo, W. Chin, Air-side heat transfer characteristics of hydrophobic and super-hydrophobic fin surfaces in heat exchangers: A review, *International Communications in Heat and Mass Transfer* **74** (2016) 27-35.doi:https://doi.org/10.1016/j.icheatmasstransfer.2016.02.017.
URL http://www.sciencedirect.com/science/article/pii/S0735193316300549

[12] M.-H. Kim, H. Kim, K.-S. Lee, D. R. Kim, Frosting characteristics on hydrophobic and superhydrophobic surfaces: A review, *Energy Conversion and Management* **138** (2017) 1-11.
doi:https://doi.org/10.1016/j.enconman.2017.01.067.
URL http://www.sciencedirect.com/science/article/pii/S0196890417300833

[13] M. S. Patil, J.-H. Seo, M.-Y. Lee, Heat transfer characteristics of the heat exchangers for refrigeration, air conditioning and heat pump systems under frosting, defrosting and dry/wet conditions - a review, *Applied Thermal Engineering* **113** (2017) 1071-1087.
doi:https://doi.org/10.1016/j.applthermaleng.2016.11.107.
URL http://www.sciencedirect.com/science/article/pii/S1359431116332847

[14] C. Zeng, S. Liu, A. Shukla, A review on the air-to-air heat and mass exchanger technologies for building applications, *Renewable and Sustainable Energy Reviews* **75** (2017) 753-774.
doi:https://doi.org/10.1016/j.rser.2016.11.052.
URL http://www.sciencedirect.com/science/article/pii/S1364032116308127

[15] EN14511-3:2018, Air conditioners, liquid chilling packages and heat pumps for space heating and cooling and process chillers, with electrically driven compressors Part 3: Test methods

13th IEA Heat Pump Conference
April 26-29, 2021 Jeju, Korea

Theoretical Analysis of Mass Transfer in a Vacuum Membrane Dehumidification System

Hye-Jin Cho[a], Seong-Yong Cheon[a], Su Liu[a], Jae-Weon Jeong[a*]

[a]Department of Architectural Engineering, College of Engineering, Hanyang University, Seoul, 04763, Republic of Seoul

Abstract

This paper theoretically investigated the dehumidification performance of a vacuum membrane dehumidification system. Dehumidification effectiveness and the coefficient of performance (COP) were adopted as measures of performance. A one-dimensional numerical model was developed to analyze the mass transfer in a membrane dehumidifier module as a function of variation of four operating parameters: the inlet air temperature, humidity ratio, velocity, and the pressure in the vacuum side. Parametric analysis of the proposed model demonstrated that the inlet air velocity and the pressure in the vacuum side significantly affected dehumidification performance. When the pressure in the vacuum side decreased from 101.3 to 1.0 kPa, the dehumidification effectiveness increased from 2.1 to 54.1 %, while the COP decreased from 23.9 to 1.7. Similarly, the dehumidification effectiveness decreased from 73.9 to 15.8 % and the COP increased from 1.9 to 2.5 with an increase in air velocity from 0.1 to 2.0 m/s. In addition, the energy performance of the proposed vacuum membrane dehumidification system in building application was evaluated by comparing with a conventional cooling coil system.

© HPC2020.
Selection and/or peer-review under responsibility of the organizers of the 13th IEA Heat Pump Conference 2020.

Keywords: vacuum membrane dehumidification; isothermal dehumidification; numerical simulation; air conditioning;

1. Introduction

To provide a suitable indoor environment to building occupants, the temperature and humidity of air inducted from the outside into buildings should be controlled. For decades, vapor compression-based air conditioning systems have been widely adopted in air conditioning systems since they are highly effective and convenient in operation. However, vapor compression air conditioning systems may have energy penalty because of the overcooling and reheating of the process air [1]. Desiccant-assisted systems have been suggested as an alternative option for dehumidification in air conditioning applications [2]. A desiccant absorbs moisture when a water vapor pressure difference exists between the process air and desiccant. Consequently, the desiccant system does not require the supply of overcooling and reheating energy. However, regeneration of the desiccant material results in considerable energy consumption if there are no free-heat sources.

Vacuum membrane-based dehumidification systems have been suggested in recent years as an alternative to vapor compression and desiccant-based dehumidification systems [3,4]. The membrane is made of hydrophilic and polymeric materials for transferring water vapor across the membrane. In a vacuum membrane dehumidification system, the main driving force for the transfer of moisture is the pressure difference across the membrane. Water vapor in the humid process air is absorbed and diffuses through the membrane owing to the pressure difference, which is generated by a vacuum pump depressurizing the permeate side. Water vapor that has penetrated to the permeate side is exhausted externally. Accordingly, the vacuum membrane dehumidification system can isothermally remove the latent load in the process air, and does not require heating or cooling during dehumidification.

* Corresponding author. Tel.: +82-2-2220-2370; fax: +82-2-2220-1945.
E-mail address: jjwarc@hanyang.ac.kr (J.-W. Jeong).

Several studies have investigated the potential of vacuum membrane dehumidification systems as a function of the membrane's material and configuration under various operating conditions [5–7]. However, research that addresses the operating conditions and workable design of a vacuum membrane dehumidifier remain very rare.

This study suggested the operating conditions and configuration of a vacuum membrane dehumidifier based on the results of a theoretical analysis. A one-dimensional numerical model for a vacuum membrane dehumidifier is derived, and the sensitivity of dehumidification performance to each operating parameter was analyzed by using the proposed model. The dehumidification and energy performance of the proposed system were evaluated by comparing it with a conventional vapor compression-based dehumidification system.

2. Vacuum membrane dehumidification system

2.1. System overview

In a vacuum membrane-based dehumidification system, dehumidification occurs by the vapor pressure difference between the feed side (or primary air side) and the permeate side (or secondary air side), which is separated by a dense hydrophilic membrane (Fig. 1). During dehumidification, water vapor in the feed side diffuses on the membrane and is transferred to the permeate side, and is then exhausted to the outside by a vacuum pump. The key function of the membrane is selective gas separation. In membrane-based gas separation, a membrane is characterized by its permeance, that is, the amount of a species passing through the membrane per unit area and unit pressure difference, and by its selectivity, the ratio of the amount of a species passing through membrane to that of other species [7]. Therefore, the permeability and the selectivity of the membrane to water vapor have significant impacts on the performance of the vacuum membrane dehumidification system.

In this study, a hollow fiber polyamide membrane coated with carboxylated titanium dioxide (C-TiO_2) nanoparticles dehumidifier was adopted. This membrane has a water vapour permeance of 4.68×10^{-7} mol/s m^2Pa and a selectivity of 510 for water vapor/dry air [3]. The thickness of membrane was 150 μm, and the inner and outer diameters of the hollow fiber were 480 μm and 685 μm, respectively. The outer diameter of the membrane module was 0.2 m. The number of hollow fibers in the membrane modules was set at 30,000.

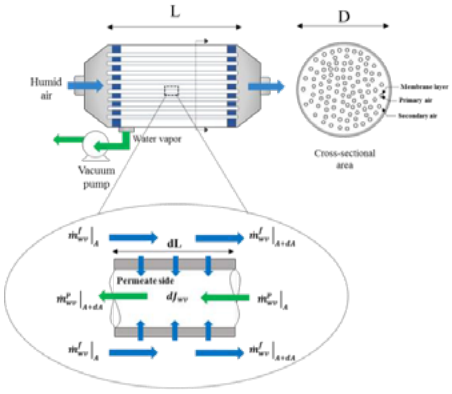


Fig. 1. Schematic of a vacuum membrane dehumidification system.

2.2. Numerical model derivation

In this study, it was assumed that mass transfer occurred along the direction of air flow (i.e. x-axis), from *x=0 to x=L*, and the water vapor transferred to the permeate side was exhausted in the opposite direction, from *x=L to x=0*, by the vacuum pump (Fig. 1). Other assumptions are as follow:

1. Dehumidification occurs under ideal gas conditions.
2. Dehumidification occurs in a steady state.
3. The permeability and selectivity are constant.
4. The process air only consists of water vapor and dry air.
5. The total air pressure from feed and permeate sides remain constant.
6. The initial water vapor pressure in permeate side is zero, the initial dry air pressure in permeate side is equal to the total vacuum side pressure.

2.3. Overall mass transfer coefficient

The simulation model in this work mainly consists of an overall mass transfer coefficient model and the mass balance equations between the air in feed side and permeate sides. In the overall mass transfer coefficient model, the convection-based mass transfer of the boundary layer of feed/permeate sides, and the permeance of the membrane to water vapor was considered. In addition, the overall mass resistance of the dry air should be considered in the performance of a vacuum membrane dehumidification system. Therefore, the overall mass transfer resistance of water vapor ($R_{t,wv}$) and dry air ($R_{t,da}$) can be estimated by the mass transfer resistance of water vapor ($R_{diff,wv}$) and dry air ($R_{diff,da}$), the mass resistance of the boundary layer in the feed side (R_{bl}^{f}) and permeate sides (R_{bl}^{p}) (Eqs. 1 and 2):

$$R_{t,wv} = R_{diff,wv} + R_{bl}^{f} + R_{bl}^{p} \tag{1}$$

$$R_{t,da} = R_{diff,da} + R_{bl}^{f} + R_{bl}^{p} \tag{2}$$

The overall mass resistance of the boundary layer can be estimated by Eq.3 with the molar density (ρ), and the mass transfer coefficient at the boundary layer (k_{bl}), which is defined by Eq. 4:

$$R_{bl} = \frac{1}{\rho k_{bl}} \tag{3}$$

$$k_{bl} = \frac{D_w \cdot Sh}{D_h} \tag{4}$$

where D_w is the diffusivity of water vapor in air, *Sh* is the Sherwood dimensionless number, and D_h is the hydraulic diameter of the fiber module. In this study, the *Sh* is defined by an empirical model, including the Reynolds (*Re*) and Schmidt (*Sc*) numbers (Eq.5), as suggested by Wang et al. [8]:

$$Sh = 0.3 + (0.62 Re_a^{0.5} \frac{Sc_a^{\frac{1}{3}}}{(1+(\frac{0.4}{Sc_a})^{\frac{2}{3}})^{\frac{1}{4}}} \cdot (1 + \frac{(\frac{Re_a}{282000})^5}{8})^{4/5} \tag{5}$$

In terms of the mass transfer coefficient of the dense membrane, the overall mass transfer resistance can be calculated from the membrane's thickness (δ_m) and water vapor permeance (Per_{wv}) (Eq. 6):

$$R_{diff,wv} = \frac{1}{Per_{wv}} \tag{6}$$

In addition, the overall mass transfer resistance of the dry air can be obtained if the water vapor permeance and the water vapor/dry air selectivity are known (Eq. 7):

$$Per_{da} = \frac{Per_{wv}}{Sel} \tag{7}$$

2.4. Mass balance equations

The mass balance of the water vapor in the feed/permeate sides can be written by the governing equations for the mass flux of water vapor (Eqs. 8 and 9):

$$\frac{dJ_{wv}}{dA} = \frac{(P^f_{wv} - P^p_{wv})}{R_{t,wv}} \tag{8}$$

$$dA = n_{fiber} \cdot \pi \cdot d_{i,f} \cdot dx \tag{9}$$

Where dJ_{wv}/dA indicate the mass flux of water vapor for the superficial surface area of each fiber module (dA), which can be obtained from the number of hollow fibers, the inner fiber diameter and fiber length. The total water vapor mass flow rate in feed/permeate sides after passing through the membrane can be estimated from the calculated mass flux for water vapor for each module (Eqs. 10 and 11):

$$\dot{m}^f_{wv}\big|_{A+dA} = \dot{m}^f_{wv}\big|_A - dJ_{wv} \tag{10}$$

$$\dot{m}^p_{wv}\big|_{A+dA} = \dot{m}^p_{wv}\big|_A + dJ_{wv} \tag{11}$$

Where $\dot{m}^f_{wv}$ and $\dot{m}^p_{wv}$ is the mass flow rate of water vapor of the feed/permeate sides and the pressure of the water vapor in feed/permeate sides can be obtained from Dalton's law of partial pressures for an ideal gas. The total dry air vapor mas flow rate in feed/permeate sides can also be obtained with the same method (Eqs. 12 and 13):

$$\dot{m}^f_{da}\big|_{A+dA} = \dot{m}^f_{da}\big|_A - dJ_{da} \tag{12}$$

$$\dot{m}^p_{da}\big|_{A+dA} = \dot{m}^p_{da}\big|_A + dJ_{da} \tag{13}$$

Then, the outlet air humidity ratio can be obtained from the pressure of the water vapor and dry air of the feed side (Eq. 14).

$$\omega_{a,out} = 0.622 \frac{P^f_{wv,out}}{P^f_{da,out}} \tag{14}$$

The differential elements of the computational domain can be expressed as *dx=L/N* when the domain is discretized by dividing the module length *L* (*x-axis*) into N segments. In this work, the domain was divided into 20 along the *x-axis*. Therefore, the governing equations for calculating the mass flux of the water vapor can be expressed the following discretized form (Eqs. 15–18):

$$J_{wv}[i+1] - J_{wv}[i] = \frac{\left(P^f_{wv}[i] - P^p_{wv}[i]\right)}{R_{t,wv}} \left(n_{fiber} \cdot \pi \cdot D_{i,f} \cdot \frac{L}{N}\right) \tag{15}$$

$$\dot{m}^f_{wv}[i+1] = \dot{m}^f_{wv}[i] - (J_{wv}[i+1] - J_{wv}[i]) \tag{16}$$

$$\dot{m}^p_{wv}[i+1] = \dot{m}^p_{wv}[i] + (J_{wv}[i+1] - J_{wv}[i]) \tag{17}$$

$$\omega_a[i+1] = 0.622 \frac{P^f_{wv}[i+1]}{P^f_{da}[i+1]} \tag{18}$$

The mass flux of dry air also can be calculated the same way. The gradients of humidity ratio in feed side in each segment can be estimated when the following boundary conditions are given: the initial water vapor/dry air pressure in the feed side, calculated from the inlet air temperature and humidity ratio, the mass resistance in the feed side boundary layer, calculated from the inlet velocity, and the vacuum side total pressure.

3. Simulation results

Dehumidification effectiveness (ε_{deh}), defined as the ratio of the humidity ratio difference between the inlet and outlet air to the inlet air humidity ratio (Eq. 19), was used as a measure of performance:

$$\varepsilon_{deh} = \frac{\omega_{a,in} - \omega_{a,out}}{\omega_{a,in}} \tag{19}$$

In gas separation-based dehumidification the vacuum pump is used to compress the water vapor pressure of the feed side to equal that of the permeate side. The dehumidification COP was calculated as Eq. 20.

$$COP = \frac{\dot{Q}_{lat}}{W_{pump}} \tag{20}$$

Where $\dot{Q}_{lat}$ is the latent load removed by the vacuum membrane dehumidification system (Eq. 21), and W_{pump} is the vacuum pump's workload, obtained by Eq. 22.

$$\dot{Q}_{lat} = \dot{m}_a h_{fg} (\omega_{a,in} - \omega_{a,out}) \tag{21}$$

$$W_{pump} = \frac{\left(\frac{\dot{dm}_{mv}}{MW_{wv}} + \frac{\dot{dm}_{da}}{MW_{da}}\right) RT_k}{\varepsilon_{pump}} ln \frac{P_{atm}}{P_{vac}} \tag{22}$$

Where $\dot{dm}_{mv}$ and $\dot{dm}_{da}$ indicate the total mass flux of water vapor and dry air pumped by the vacuum pump, and the MW_{wv} and MW_{da} are the molar mass of water vapor and dry air, respectively. R is the ideal gas constant, and T_k is the absolute temperature of the inlet air. P_{atm} and P_{vac} indicate atmospheric and vacuum pressures, respectively and ε_{pump} is the vacuum pump's efficiency. In this study, vacuum pump efficiency was assumed to be 0.6.

3.1. Model validation

To validate the reliability of the proposed model, simulation results from the numerical model were compared with the experimental data from a previous study [7]. The operating ranges of the simulation conditions were set based on the valid range of each operating parameter: the inlet air temperature was varied from 25 to 33 ºC, the inlet air humidity ratio ranged from 0.012 to 0.026 kg/kg. The air flow rate was 0.067 kg/s. The permeability, selectivity, and the physical configuration of membrane dehumidifier were identical to those of the simulation model.

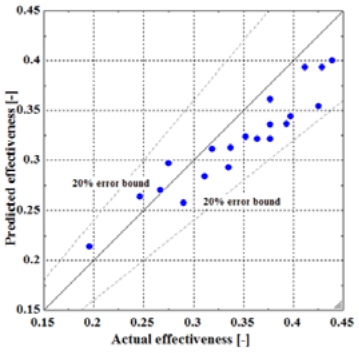


Fig. 2. Comparison of dehumidification effectiveness value with measurement data.

Figure 2 compares the dehumidification effectiveness values predicted by the proposed simulation model with the measurement data, which shows that the predicted values generally agreed well with the measurement data within 20 % error bounds. Therefore, the proposed model can be used to predict the dehumidification performance of a vacuum membrane dehumidification system.

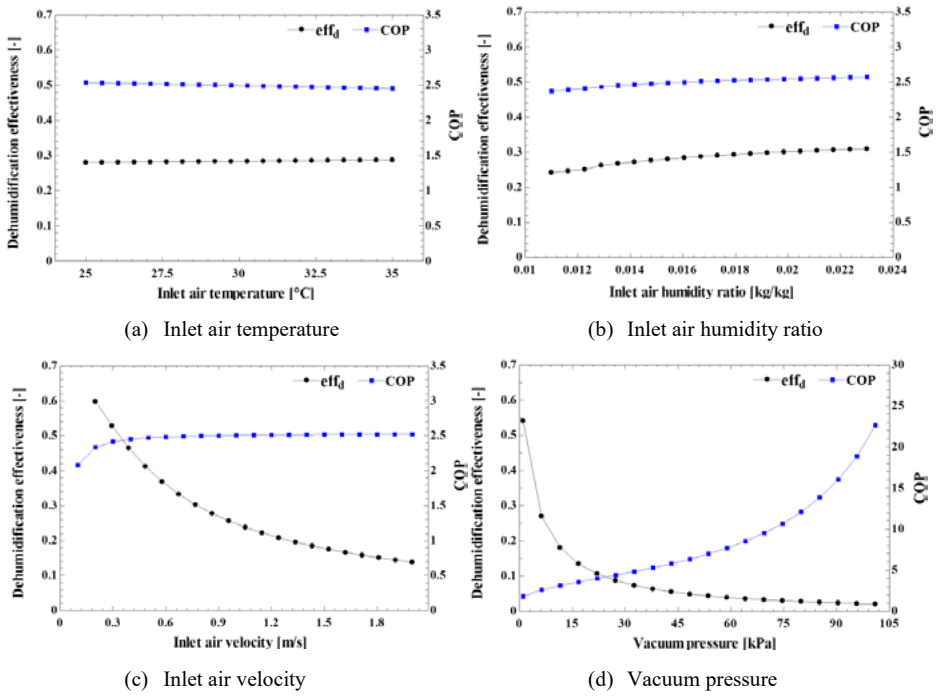
3.2. Parametric analysis

In this section, parametric analysis was conducted to analyze the effects of variation in operating parameters on dehumidification performance of a vacuum membrane dehumidification system. The initial conditions of the four operating parameters were set as the average value in the valid range. Simulations were performed by sequentially varying each of operating parameters within the valid range, while the remaining parameters were fixed to their initial conditions. Table 1 shows the simulation conditions of each operating parameter.

Table 1. Simulation conditions of operating parameters.

Operating parameter	Range		
	Min.	Ave.	Max.
Inlet air temperature ($T_{a,in}$) [ºC]	25	30	35
Inlet air humidity ratio ($\omega_{a,in}$) [kg/kg]	0.011	0.017	0.023
Air velocity (V_a) [m/s]	0.1	1.0	2.0
Vacuum pressure (P_{vac}) [kPa]	1	5	100

Figure 3 shows the effect of each operating parameter on the dehumidification performance of a vacuum membrane dehumidification system. Air velocity (Fig. 3c) and the vacuum side pressure (Fig. 3d) significantly affected the dehumidification effectiveness and dehumidification COP, while the inlet air temperature and inlet air humidity ratio exerted minimal effect. When the vacuum side pressure increased from 1–100 kPa, the dehumidification effectiveness decreased from 55.5–2.1 % while the dehumidification COP increased from 2.15 to 23. This is because decreasing the permeate side pressure from atmospheric pressure to almost a complete vacuum can increase the water vapor difference between the feed and permeate sides, thereby increasing the driving force to remove water vapor in feed side. In terms of dehumidification COP, decreasing the vacuum side pressure had a negative effect because decreasing permeate side pressure to an almost complete vacuum imposes a large workload on the pump. Similarly, an increase in air velocity decreased the dehumidification effectiveness from 73.9 % to 15.8 %, and increased the dehumidification COP from 2.1 to 2.5. This is because the higher air velocity results in a shorter air-membrane contact time. Nevertheless, the higher air velocity increased the latent load removed by the membrane dehumidification system, which resulted in an increase of the dehumidification COP. Consequently, both dehumidification performance and COP of the vacuum membrane dehumidification system was highly affected by vacuum side pressure and inlet air velocity.



(a) Inlet air temperature (b) Inlet air humidity ratio

(c) Inlet air velocity (d) Vacuum pressure

Fig. 3. Effect of changes in operating parameters on dehumidification performance.

4. Application and discussion

In this section, energy and dehumidification performances were simulated to evaluate the operating performance of the vacuum membrane dehumidification system in HVAC applications. The design supply air flow rate was set at 200 m^3/h, which is a minimum ventilation rate for a single-story office building, located in Seoul, with 150 m^2 of floor area and eight occupants [9]. International weather for energy calculation (IWEC) data was adopted to perform the simulation for the cooling seasons in Seoul. The latent load in a model space was calculated using the TRNSYS 18 program, using the physical information of the model building (Table 2) and an office occupant and HVAC schedule addressed in ASHRAE 90.1 [10]. To maintain the supply air humidity ratio at a target point (i.e. 0.0085 kg/kg) during cooling seasons, the vacuum pump was operated to maintain the vacuum side pressure to a water vapor pressure of a target supply air (i.e. 1.19 kPa). A membrane dehumidifier with a module diameter in 0.6 m and a module length in 0.8 m was selected in order to accommodate the peak latent load during simulations.

Table 2. Physical information of the simulated building model.

Location	Seoul, Republic of Korea	
Building	15 × 10 × 3 m^3	
Heat gain	Occupants	5 persons /100 m^2
	Lights	13 W/m^2
	Computers	230 W/persons
U-value (insulation)	Exterior wall	0.524 W/m^2K

	Window	5.68 W/m^{2}K
	Roof	0.152 W/m^{2}K

4.1. Dehumidification performance

Figure 6 shows the supply air humidity ratio of the vacuum membrane dehumidification system. The performance of the dehumidifier was highly affected by the outdoor air humidity ratio. As shown in Figure 4, the supply air humidity ratio varied from 0.004 kg/kg to 0.0086 kg/kg, which demonstrated that the vacuum membrane dehumidification system can sufficiently dehumidify the outdoor air to meet the target point throughout most of the cooling seasons.

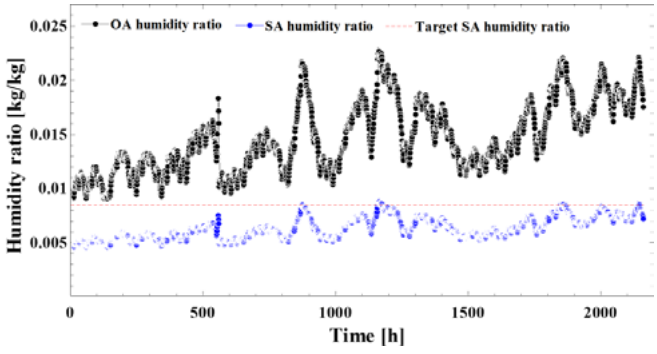


Fig. 4. Hourly supply air humidity ratio in a vacuum membrane dehumidification system.

A cooling coil was chosen as a reference system to evaluate the energy performance of the vacuum membrane dehumidification system in HVAC applications. It was assumed that the cooling coil removed the latent load to meet the supply air humidity ratio, which was the same as that of the vacuum membrane dehumidification system. Figure 5 shows the dehumidification process of a vacuum membrane dehumidification system and a conventional condensation-based dehumidification system. The vacuum membrane dehumidification system can isothermally dehumidify the outdoor air (Eq. 23), while the vapor compression system cools the outdoor air to the dew point temperature, which causes unnecessary sensible cooling (Eq. 24). Therefore, the latent cooling load for a vacuum membrane dehumidification system requires about 47 % less thermal load than that in a reference system (Fig. 6).

$$\dot{Q}_{VMD} = \dot{m}_{oa} h_{fg} (\omega_{oa} - \omega_{sa}) \tag{23}$$

$$\dot{Q}_{CC} = \dot{m}_{oa} (h_{oa} - h_{sa,dp}) \tag{24}$$

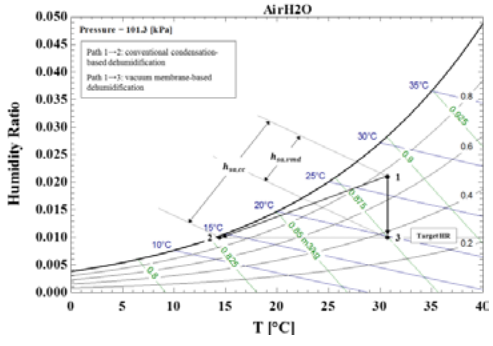


Fig. 5. Dehumidification of the proposed and reference case, presented in a psychrometric chart.

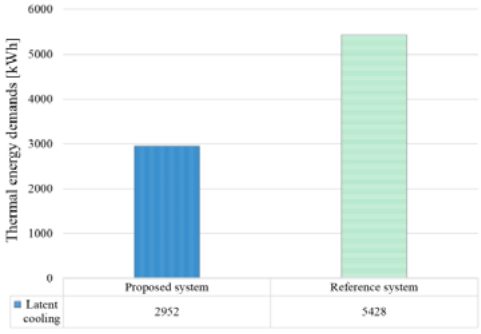


Fig. 6. Comparison of dehumidification loads.

4.2. Energy performance

Figure 8 shows that the vacuum membrane dehumidification system can reduce 47 % of the latent cooling load compared with a reference system. To evaluate the energy performance of the vacuum membrane dehumidification system, the primary energy consumption of both cases was calculated. The primary energy consumption of a vacuum membrane dehumidification system was estimated by calculating the vacuum pump operating energy with Eq. 22. The primary energy consumption of a reference system was obtained by using a chiller energy prediction model [11].

Figure 7 shows the primary energy consumption of the proposed system and reference case in cooling seasons. In contrast to the latent cooling load, the vacuum membrane dehumidification system could save only 5 % of primary energy compared to that of the reference system. This is because the dehumidification COP of a vacuum membrane dehumidifier is lower than that of the chiller. The COP of the vacuum membrane dehumidification system was maintained between 2.1 and 2.3, while that of the chiller ranged from 4.1 to 5.4. The vacuum pump should maintain the permeate side pressure to almost a complete vacuum to achieve satisfactory dehumidification, which leads to the high energy requirements of the vacuum pump. Therefore, one can conclude that the COP of the vacuum membrane dehumidification system should be improved by enhancing the dehumidification performance through a lower vacuum pump operating load.

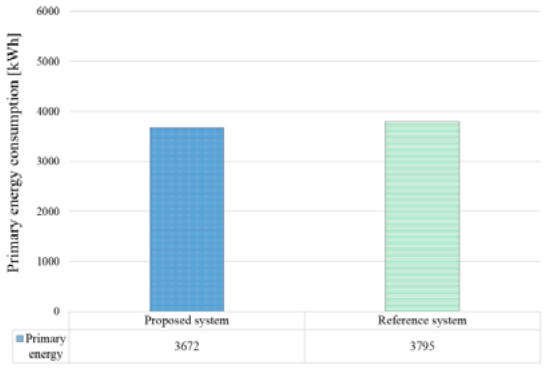


Fig. 7. Comparison of the primary energy consumption in VMD and CC

5. Conclusions

This study theoretically analyzed the dehumidification performance of a vacuum membrane dehumidification system. The governing equations for the mass flux of water vapor and dry air were derived based on the mass balance between the water vapor and dry air in the feed/permeate sides. The sensitivity of dehumidification performance on changes in operating parameters was analyzed using the proposed model. The vacuum side pressure and inlet air velocity were the most critical factors determining both dehumidification and energy performance. In particular, the dehumidification performance of a vacuum membrane dehumidification system significantly increased when the vacuum pump compressed the vacuum side pressure to equal the water vapor pressure in the inlet air.

The energy and operating performance of a vacuum membrane dehumidification system was also evaluated by comparing it with a conventional vapor compression system. The vacuum membrane dehumidification system decreased the latent cooling load by 47 % compared with a conventional cooling coil system. However, there was little energy saving potential because of the lower dehumidification COP compared to that of a reference system. Consequently, further study should consider the optimization of the vacuum pump operation strategy so that satisfactory dehumidification performance can be achieved with lower vacuum pump working loads.

Acknowledgements

This work was supported by the National Research Foundation of Korea (NRF) grant (No. 2019R1A2C2002514), the Korean Institute of Energy Technology Evaluation and Planning (KETEP) (No. 20184010201710), and the Technology development Program(S2782284) funded by the Ministry of SMEs and Startups(MSS, Korea).

References

[1] Ling, J., Hwang, Y., Radermacher, R. Theoretical study on separate sensible and latent cooling air-conditioning system, Int. J. Refrig. 2010; 33:510–520.
[2] Misha, S., Mat, S., Ruslan, M.H., Sopian, K. Review of solid/liquid desiccant in the drying applications and its regeneration methods, *Renew. Sustain. Energy Rev.* 2012; **16**:4686–4707.
[3] Woods, J. Membrane processes for heating, ventilation, and air conditioning, *Renew. Sustain. Energy Rev.* 2014; **33**:290–304.
[4] Qu, M., Abdelaziz, O., Gao, Z., Yin, H. Isothermal membrane-based air dehumidification: A comprehensive review, *Renew. Sustain. Energy Rev.* 2018; **82**:4060–4069.
[5] Bui, T.D., Wong, Y., Islam, M.R., Chua, K.J. On the theoretical and experimental energy efficiency analyses of a vacuum-based dehumidification membrane, *J. Memb. Sci.* 2017; **539**:76–87.
[6] Bui, T.D., Nida, A., Ng, K.C., Chua, K.J. Water vapor permeation and dehumidification performance of poly(vinyl alcohol)/lithium chloride composite membranes, *J. Memb. Sci.* 2016; **498**:254–262.
[7] Jang, J., Kang, E.C., Lee, H.K., Jeong, S., Park S.R. Energy demand comparison between hollow fiber membrane based dehumidification and evaporative cooling dehumidification using TRNSYS, *Energies.* 2018;**11**:1181-1196.
[8] Wang, K.L., McCray, S.H., Newbold, D.D., Cussler, E.L. Hollow fiber air drying*, J. Memb. Sci.* 1992; **72**:231–244.
[9] ASHRAE 62.1-2016 Ventilation for Acceptable Indoor Air Quality. Atlanta; 2016.
[10] ASHRAE Standard 90.1-2016. Energy standard for buildings except low-rise residential buildings. Atlanta; 2016.

13th IEA Heat Pump Conference
April 26-29, 2021 Jeju, Korea

Empirical Analysis of Dehumidification Performance of Hollow-Fiber-Membrane Dehumidifier

Seong-Yong Cheon[a], Hye-Jin Cho[a], Jinyoung Ko[a], Jae-Weon Jeong[a,*]

[a]Department of Architectural Engineering, College of Engineering, Hanyang University,
222 Wangsimni-Ro, Seongdong-Gu, Seoul 04763, Republic of Korea

Abstract

Membrane dehumidifiers dry air via an isothermal process, which is why they can potentially yield a better dehumidification performance than conventional dehumidification systems. In this research, the dehumidification performance of a hollow-fiber-membrane dehumidifier was estimated by means of a series of experiments. The membrane dehumidifier consists of a hollow-fiber-membrane unit and an air pump. As the prototype unit used a sweep-gas, the use of dehumidified air was a drawback on the permeate side. Five operating parameters were considered as effective dehumidification variables: inlet air temperature, inlet air relative humidity, intake air flow rate, sweep gas ratio, and inlet air pressure. The dehumidification performance of the membrane dehumidifier was quantified as the difference in the humidity ratio and amount of dehumidification. The experimental data were analyzed by means of a parametric study involving the five independent operating parameters. Consequently, we found that the dehumidification performance was significantly impacted by the inlet air pressure that formed the driving force, and the inlet air conditions also exhibited a positive correlation with performance. When the sweep-gas ratio ranged from 0.4 to 0.6, a high value of dehumidification was achieved under balanced flow conditions.

© HPC2020.
Selection and/or peer-review under responsibility of the organizers of the 13th IEA Heat Pump Conference 2020.

Keywords: Membrane dehumidifier, Dehumidification performance, Empirical analysis;

1. Introduction

Desiccant-based air-conditioning technologies have recently been proposed for decoupling dehumidification and sensible cooling as an alternative to conventional cooling and dehumidification systems [1,2]. Desiccant-material-based systems pre-condition the intake outdoor air, and subsequently, the dehumidified air is controlled by a mechanical and evaporative cooling system to achieve the target temperature. Decoupled air-conditioning systems can afford high energy savings when the significant amount of heat consumed for regenerating the desiccant material is supplied by free energy [3–5].

Recently, membrane-based dehumidification systems have been suggested as an alternative system of vapor compression and desiccant-based dehumidification [6,7]. There is no requirement for a cooling and heating source as isothermal processes in such systems, compared with conventional dehumidification systems. In a membrane dehumidification system, the intake air is dehumidified via transferring water vapor between hydrophilic membrane layers by the application of a partial vapor gradient [6]. When a vapor pressure gradient is generated between membrane layers, the water vapor in the process air soaks and diffuses to the membrane layer, and subsequently, the layer is desorbed by another air stream. In this regard, several studies have investigated the dehumidification performance of membrane driers made of various materials under several design conditions [8,9]. Bui et al. [8] theoretically investigated a membrane dehumidification system with a flat plate. The membrane materials were assumed to consist of ceramic and polymeric layers with high

* Corresponding author. Tel.: +82-2-2220-2370; fax:+82-2-2220-1945.
E-mail address: jjwarc@hanyang.ac.kr (J.-W. Jeong).

permeability and selectivity of water vapor. The study results showed that the factors affecting the dehumidification performance included air velocity, permeability and selectivity of the membrane, pressure, and humidity of the processed air. Here, we note that membrane selectivity and pressure significantly affect a membrane drier's performance. Moreover, some studies have considered the use of membrane dehumidification systems for the air-conditioning of buildings; El-Dessouky et al. [10] proposed a membrane-dehumidifier-integrated air-cooling system, which has a vacuum-based membrane drier for dehumidification and evaporative coolers for sensible cooling. The authors showed that membrane-dehumidification-based air-conditioning systems can reduce the energy consumption by up to 86% when compared with conventional air-conditioning systems.

In this context, several studies have focused on membrane dehumidification systems to evaluate their energy and dehumidification performance for various membrane materials and system configurations. However, very few studies have experimentally evaluated the dehumidification performance of membrane dehumidification systems as applied to building heating, ventilation, and air-conditioning (HVAC). In this study, we developed a hollow-fiber-type membrane dehumidifier and evaluated its dehumidification performance under various operating conditions.

2. Hollow-fiber-membrane dehumidifier

In this section, we describe the general principle underlying membrane dehumidification along with the theoretical dehumidification process. Furthermore, we present our prototype hollow-fiber-membrane dehumidifier.

2.1 Hollow-fiber-membrane dehumidifier

The membrane dehumidifier dries the intake air via an isothermal process, which is hard to realize in conventional dehumidifiers. The membrane dehumidifier has two main parts: membrane modules and air compressor, as shown in Figure 1. The membrane module for dehumidification uses permeated water vapor, and the air compressor generates a partial vapor pressure gradient between the membrane layers. When the partial vapor pressure gradient between the membrane layers is created by the air compressor, the water vapor permeates from the feed side to the permeate side. The dehumidification performance is dependent on the membrane material, particularly its permeability and selectivity to water vapor. When the membrane affords a high level of permeability and selectivity, the dehumidification performance and energy efficiency of the membrane unit is correspondingly higher. In this study, the type of membrane used is a hollow-fiber membrane, which is easy to manufacture structurally, and the air compressor is used to pressurize the inlet air for creating the vapor pressure gradient between membrane layers. To maintain the dehumidification performance, a part of the intake air is "swept" out to the permeate side, thereby removing the water vapor.

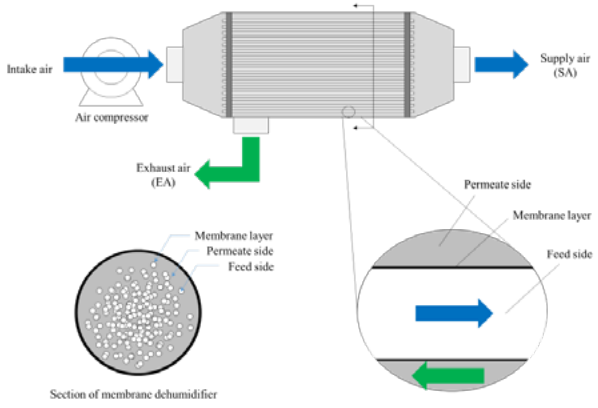


Fig. 1. Configuration of hollow-fiber-membrane dehumidifier

When the intake gas is assumed to be an ideal mixture of two gases, dry air and water vapor, the dehumidification process of the membrane dehumidifier can be represented by a solution–diffusion process between the feed side and the permeate side with a partial pressure gradient, as shown in Figure 2. When the feed-side air of the unit is pressurized for dehumidification, water vapor and dry air permeate through the membrane layer. The molar mass flow rates of water vapor and dry air (i.e., $\dot{M}'_w$ and $\dot{M}'_d$) through the membrane layer are estimated by means of the classical solution–diffusion model as represented by Equations (1) and (2), respectively. To estimate the partial pressure gradient, which acts as the force driving the dehumidification, we represent the partial pressure of each gas on the permeate side as the ratio of the molar mass flow rate through the membrane layer (i.e., y_1 and y_2) in Equations (3) and (4). The values of permeability (Per), selectivity (S), membrane area (A_{mem}), and membrane thickness (z) are determined according to the performance of the membrane materials, and these values affect the dehumidification performance along with energy consumption of the air compressor. Each molar mass flow rate is dependent on the membrane material and sweep gas used to remove the water vapor on the permeate side.

$$\dot{M}'_w = \frac{\mathrm{Per}_v A_{mem}}{z}\left(P_{f,v} - y_1 P_{p,tot}\right) \tag{1}$$

$$\dot{M}'_d = \frac{\mathrm{Per}_d A_{mem}}{z}\left(P_{f,d} - y_2 P_{p,tot}\right) = \frac{\mathrm{Per}_v}{S}\frac{A_{mem}}{z}\left(P_{f,v} - y_2 P_{p,tot}\right) \tag{2}$$

$$y_1 = \frac{\dot{M}'_v + \dot{M}'_{sweep,v}}{\dot{M}'_d + \dot{M}'_v + \dot{M}'_{sweep,d} + \dot{M}'_{sweep,v}} \tag{3}$$

$$y_2 = \frac{\dot{M}'_d + \dot{M}'_{sweep,d}}{\dot{M}'_d + \dot{M}'_v + \dot{M}'_{sweep,d} + \dot{M}'_{sweep,v}} \tag{4}$$

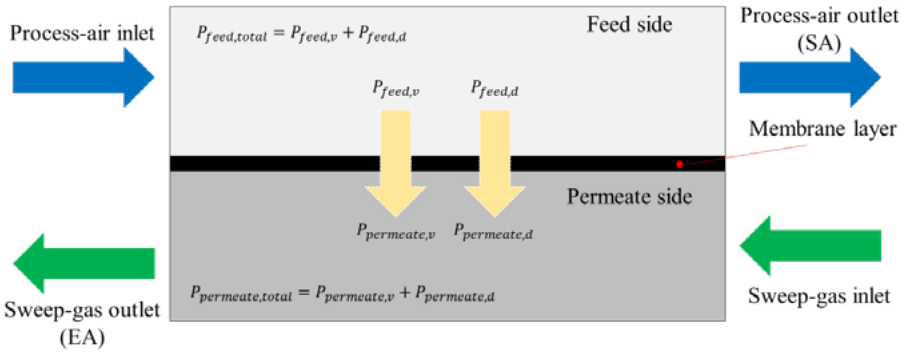


Fig. 2. Schematic of dehumidification process in membrane dehumidifier

2.2 Prototype of hollow-fiber-membrane dehumidifier

When the basic theoretical model does not consider the membrane type and configuration, it is not easy to estimate the dehumidification performance of the membrane dehumidifier under various operating conditions. Therefore, we developed a prototype hollow-fiber-membrane dehumidifier and estimated its dehumidification performance under various conditions. The configuration of the prototype unit is shown in Figure 3. The prototype unit has an inlet air channel on the feed side and sweep-gas air channel on the permeate side. In the study, the membrane module of our proposed dehumidifier was of the cylinder type, and the length of the module was 0.3 m, with the module diameter being 0.08 m. The module contained 170 hollow-fiber membranes each with a fiber inlet diameter of 1.6 mm, corresponding to a packing fraction ratio of 0.11. The hollow-fiber length was 0.23 m, and its total effective contacting area was 0.282 m^2. The specifications of our prototype module are listed in Table 1.

Table 1: Specifications of prototype unit

Design parameters	Values	Design parameters	Values
Module diameter [mm]	80	Fiber thickness [mm]	0.35
Module length [mm]	300	Contacting area of membrane [m^2]	0.282
Fiber inlet diameter [mm]	1.6	Number of fibers [-]	170
Fiber outlet diameter [mm]	2.3	Packing fraction [-]	0.11
Fiber length [mm]	230		



Fig. 3. Prototype configuration of hollow-fiber-membrane dehumidifier

3. Test setup and dehumidification performance

3.1 Experimental setup of prototype

To analyze the dehumidification performance of our prototype unit, we varied five independent parameters: air temperature, relative humidity, airflow rate, inlet air pressure, and sweep-gas ratio. The experimental setup for controlling these five independent parameters is shown in Figure 4. In the setup, the environmental chamber is used to maintain the experimental air conditions, and the air compressor maintains the airflow ratio of the conditioned air to the prototype unit. The rotation speed of the air compressor is controlled by means of a switched-mode power supply (SMPS) that controls the electric current and voltage. The pressure of the feed side is controlled by open-to-close ratio of the inlet valves to generate the partial pressure gradient. Moreover, the sweep-gas ratio, which corresponds to the ratio of the intake supply airflow rate to the sweep-gas flow rate, is controlled by the outlet valve as an adjustable open-to-close ratio. The measured data to estimate the dehumidification performance of the prototype unit are collected and saved in the data logger.

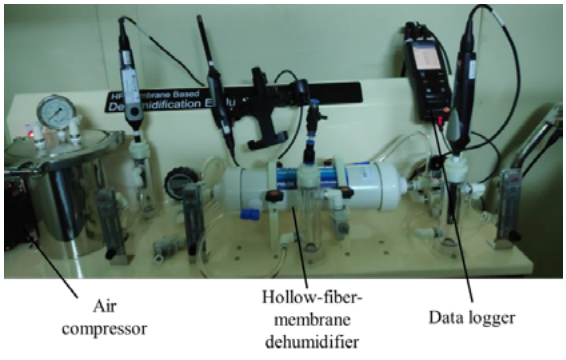


Fig. 4. Schematic of experimental setup of hollow-fiber-membrane dehumidifier

3.2 Operation conditions

In this study, we conducted 24 sets of experiments for analyzing the dehumidification performance of the hollow-fiber-membrane dehumidifier unit. The dehumidification performance of the prototype unit was estimated as the differential of the humidity ratio and amount of dehumidification, as expressed by Equations (5) and (6), respectively. The humidity ratio differential is representative of the driving force of the vapor pressure gradient, and the amount of dehumidification represents the dehumidification per unit time as a function of the latent cooling capacity.

$$\Delta w = w_{in} - w_{out} \quad (5)$$

$$\dot{m}_d = \dot{m}_{sa}\Delta w = (\dot{m}_{intake} - \dot{m}_{sweep})\Delta w \quad (6)$$

To analyze the dehumidification performance under various conditions, we acquired the performance data for various values of the five operating parameters: air temperature, relative humidity, airflow rate, sweep-gas ratio, and inlet air pressure. As the sweep-gas ratio is the airflow ratio of the intake air to the sweep-out air, a high level of sweep gas implies that the supply airflow rate is reduced for a given intake air flow rate. To estimate the differential of the humidity ratio and amount of dehumidification, each parameter was suitably varied. As the air temperature and humidity ratio were set to reflect humid and mild air conditions, these were maintained in the range of 15 to 30 ℃ and 40 to 80%, respectively. The detailed operational range is listed in Table 2. To estimate the dehumidification performance of the prototype unit, we did parametric study from the experimental results, which were based on the base case, and subsequently, only a single parameter was modulated in the operation range when all other parameters were fixed.

Table 2: Operating ranges of experimental conditions

Parameter	Symbol	Input values		
		Low	Base	High
Inlet air temperature [℃]	$T_{a,in}$	15	27	30
Inlet relative humidity [%]	$RH_{a,in}$	40	60	80
Inlet air flow rate [l/min]	$\dot{V}_{a,in}$	20	25	30
Sweep-gas ratio [−]	x	0.18	0.5	0.82
Inlet pressure [kPa]	p_{air}	101.3	101.3	260

The measurement sensors in our setup included high-precision humidity/temperature, differential pressure, and absolute pressure sensors. The high-precision humidity/temperature sensor measures the inlet and outlet temperatures and relative humidity. The airflow rate is measured by the differential pressure sensor in conjunction with a digital flow meter. The measurement points corresponding to airflow rate measurements include the inlet, outlet, and exhaust sides. The inlet air pressure is measured by the absolute pressure sensor, where the inlet air pressure is controlled by the air compressor by means of valves. To quantify the dehumidification performance, the measurement data were converted into the humidity ratio, which is affected by the air temperature, relative humidity, and pressure.

Table 3: Specifications of measuring instruments

Variable	Device	Characteristics		
Dry-bulb temperature and relative humidity of air	High-precision humidity/temperature probe	Range	Temperature	−20 ℃ to +55 ℃
			Relative humidity	0%–100%
		Accuracy	Temperature	±0.4 ℃
			Relative humidity	±2%RH
Air flow rate	Differential pressure sensor	Range	Pressure	0–1250 Pa
		Accuracy		±0.30%
Inlet air pressure	Absolute pressure sensor	Range	Pressure	0–1250 Pa
		Accuracy		±0.30%

4. Experimental results and discussion

We experimentally investigated the performance of the prototype unit considering the influences of the five air inlet parameters: inlet air temperature, relative humidity, air pressure, inlet air flow rate, and sweep-gas ratio. The influence of each of the five parameters considered was analyzed via the differential of the humidity ratio and amount of dehumidification; the results are shown in Figure 5.

We note from the figure that the air temperature and relative humidity exhibit a positive correlation with the differential of the humidity ratio and amount of dehumidification. We note that higher levels of inlet temperature and relative humidity correspond to a higher partial vapor gradient between the membrane layers. In addition, as the inlet air pressure increases, the partial vapor pressure gradient between membrane layer was increased , and the dehumidification performance improves. The sweep-gas ratio and intake airflow rate exhibit no positive correspondence with the dehumidification performance. When the sweep-gas ratio ranges from 0.4 to 0.6, the differential of the humidity ratio and the amount of dehumidification are maximal because the mass transfer between the feed and permeate sides increases as a balanced flow. When the intake air flow rate decreases, the face velocity on the feed side also decreases with increase in the contact time of the unit. The differential of the humidity ratio is strongly affected, but the amount of dehumidification is only relatively impacted by the airflow rate.

The main parameters that significantly affect the dehumidification performance of the prototype unit are the inlet air pressure and sweep-gas ratio. To increase the dehumidification performance, the inlet air pressure should be sufficiently high, and the sweep-gas ratio must be maintained around 0.5 for balanced flow. Here, we note that to control the outlet humidity ratio, a suitable rotation speed modulation strategy of the air compressor or sweep-gas ratio should be estimated.

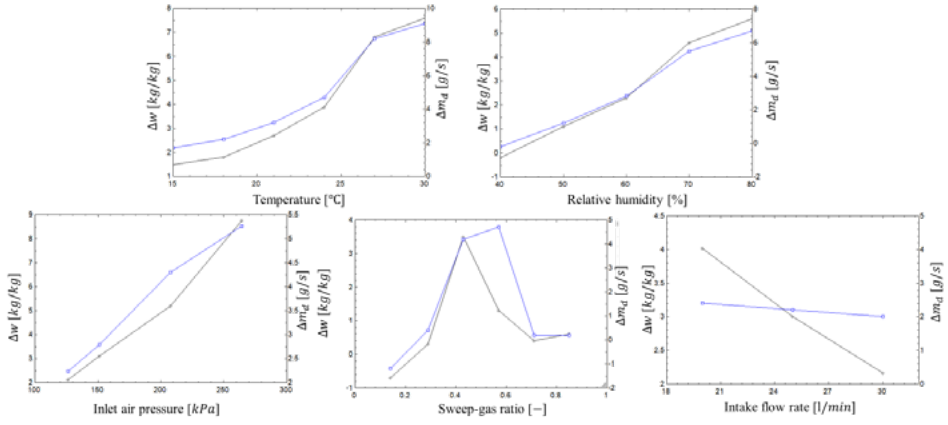


Fig. 5. Parametric analysis of hollow-fiber-membrane dehumidifier

5. Conclusions

In this study, we experimentally investigated the dehumidification performance of a hollow-fiber-membrane dehumidification unit. Our prototype unit was composed of a membrane module containing a bundle of hollow membranes and an air compressor to pressurize the inlet pressure, which forms the driving force underlying the process. Experiments were conducted using the prototype unit to estimate the differential of the humidity ratio and amount of dehumidification, and the relevant performance data were collected. The input parameters that influence the dehumidification performance are the air temperature, relative humidity, inlet air pressure, sweep-gas ratio, and intake air flow rate. The air temperature and relative humidity exhibited a positive correlation with the performance, which indicates that a larger amount of air with water vapor affords increased dehumidification performance. The inlet air pressure also positively affects the performance via increasing the driving force of the vapor pressure drop. The dehumidification performance was maximal when the sweep-gas ratio was in the range of 0.4 to 0.6 under balanced flow conditions. When the intake air flow rate was decreased, the dehumidification performance increased because of the increased contacting time of air with the prototype unit.

In future study, we plan to analyze the dehumidification efficiency under various operation conditions. In addition, the data collected in the study can be applied to extend the utilization of the control logic of the hollow-fiber-membrane dehumidifier.

Acknowledgements

This work was supported by the National Research Foundation of Korea (NRF) grant (No. 2019R1A2C2002514), the Korean Institute of Energy Technology Evaluation and Planning (KETEP) (No. 20184010201710), and the Technology development Program(S2782284) funded by the Ministry of SMEs and Startups(MSS, Korea).

References

[1] Rafique MM, Gandhidasan P, Bahaidarah HMS. Liquid desiccant materials and dehumidifiers - A review, *Renew. Sustain. Energy Rev* 2016;56:179–195.
[2] Ling J, Hwang Y, Radermacher R. Theoretical study on separate sensible and latent cooling air-conditioning system, *Int. J. Refrig* 2010;33:510–520.
[3] Yang Z, Lian Z, Li X, Zhang K. Concept of dehumidification perfectness and its potential applications, *Energy* 2015; 91:176–191.
[4] Gommed K, Grossman G. Experimental investigation of a liquid desiccant system for solar cooling and dehumidification, *Sol. Energy* 2007;81:131–138.
[5] Misha S, Mat S, Ruslan MH, Sopian K. Review of solid/liquid desiccant in the drying applications and its regeneration methods, *Renew. Sustain. Energy Rev* 2012;16:4686–4707.
[6] Woods J. Membrane processes for heating, ventilation, and air conditioning, *Renew. Sustain. Energy Rev* 2014;33:290–304.
[7] Labban O, Chen T, Ghoniem AF, Lienhard JH, Norford LK. Next-generation HVAC: Prospects for and limitations of desiccant and membrane-based dehumidification and cooling, *Appl. Energy* 2017;200:330–346.
[8] Bui DT, Nida A, Ng KC, Chua KJ. Water vapor permeation and dehumidification performance of poly(vinyl alcohol)/lithium chloride composite membranes, *J. Memb. Sci* 2016;498:254–262.
[9] Bui DT, Wong Y, Islam MR, Chua KJ. On the theoretical and experimental energy efficiency analyses of a vacuum-based dehumidification membrane, *J. Memb. Sci* 2017;539:76–87.
[10] El-Dessouky HT, Ettouney HM, Bouhamra W. A novel air conditioning system: membrane air drying and evaporative cooling, *Chem Eng Res Des* 2002;78:999–1009.

13th IEA Heat Pump Conference
April 26-29, 2021 Jeju, Korea

Empirical Analysis of Dehumidification Performance of Hollow-Fiber-Membrane Dehumidifier

Seong-Yong Cheon[a], Hye-Jin Cho[a], Jinyoung Ko[a], Jae-Weon Jeong[a,*]

[a]Department of Architectural Engineering, College of Engineering, Hanyang University,
222 Wangsimni-Ro, Seongdong-Gu, Seoul 04763, Republic of Korea

Abstract

Membrane dehumidifiers dry air via an isothermal process, which is why they can potentially yield a better dehumidification performance than conventional dehumidification systems. In this research, the dehumidification performance of a hollow-fiber-membrane dehumidifier was estimated by means of a series of experiments. The membrane dehumidifier consists of a hollow-fiber-membrane unit and an air pump. As the prototype unit used a sweep-gas, the use of dehumidified air was a drawback on the permeate side. Five operating parameters were considered as effective dehumidification variables: inlet air temperature, inlet air relative humidity, intake air flow rate, sweep gas ratio, and inlet air pressure. The dehumidification performance of the membrane dehumidifier was quantified as the difference in the humidity ratio and amount of dehumidification. The experimental data were analyzed by means of a parametric study involving the five independent operating parameters. Consequently, we found that the dehumidification performance was significantly impacted by the inlet air pressure that formed the driving force, and the inlet air conditions also exhibited a positive correlation with performance. When the sweep-gas ratio ranged from 0.4 to 0.6, a high value of dehumidification was achieved under balanced flow conditions.

© HPC2020.
Selection and/or peer-review under responsibility of the organizers of the 13th IEA Heat Pump Conference 2020.

Keywords: Membrane dehumidifier, Dehumidification performance, Empirical analysis;

1. Introduction

Desiccant-based air-conditioning technologies have recently been proposed for decoupling dehumidification and sensible cooling as an alternative to conventional cooling and dehumidification systems [1,2]. Desiccant-material-based systems pre-condition the intake outdoor air, and subsequently, the dehumidified air is controlled by a mechanical and evaporative cooling system to achieve the target temperature. Decoupled air-conditioning systems can afford high energy savings when the significant amount of heat consumed for regenerating the desiccant material is supplied by free energy [3–5].

Recently, membrane-based dehumidification systems have been suggested as an alternative system of vapor compression and desiccant-based dehumidification [6,7]. There is no requirement for a cooling and heating source as isothermal processes in such systems, compared with conventional dehumidification systems. In a membrane dehumidification system, the intake air is dehumidified via transferring water vapor between hydrophilic membrane layers by the application of a partial vapor gradient [6]. When a vapor pressure gradient is generated between membrane layers, the water vapor in the process air soaks and diffuses to the membrane layer, and subsequently, the layer is desorbed by another air stream. In this regard, several studies have investigated the dehumidification performance of membrane driers made of various materials under several design conditions [8,9]. Bui et al. [8] theoretically investigated a membrane dehumidification system with a flat plate. The membrane materials were assumed to consist of ceramic and polymeric layers with high

* Corresponding author. Tel.: +82-2-2220-2370; fax:+82-2-2220-1945.
E-mail address: jjwarc@hanyang.ac.kr (J.-W. Jeong).

permeability and selectivity of water vapor. The study results showed that the factors affecting the dehumidification performance included air velocity, permeability and selectivity of the membrane, pressure, and humidity of the processed air. Here, we note that membrane selectivity and pressure significantly affect a membrane drier's performance. Moreover, some studies have considered the use of membrane dehumidification systems for the air-conditioning of buildings; El-Dessouky et al. [10] proposed a membrane-dehumidifier-integrated air-cooling system, which has a vacuum-based membrane drier for dehumidification and evaporative coolers for sensible cooling. The authors showed that membrane-dehumidification-based air-conditioning systems can reduce the energy consumption by up to 86% when compared with conventional air-conditioning systems.

In this context, several studies have focused on membrane dehumidification systems to evaluate their energy and dehumidification performance for various membrane materials and system configurations. However, very few studies have experimentally evaluated the dehumidification performance of membrane dehumidification systems as applied to building heating, ventilation, and air-conditioning (HVAC). In this study, we developed a hollow-fiber-type membrane dehumidifier and evaluated its dehumidification performance under various operating conditions.

2. Hollow-fiber-membrane dehumidifier

In this section, we describe the general principle underlying membrane dehumidification along with the theoretical dehumidification process. Furthermore, we present our prototype hollow-fiber-membrane dehumidifier.

2.1 Hollow-fiber-membrane dehumidifier

The membrane dehumidifier dries the intake air via an isothermal process, which is hard to realize in conventional dehumidifiers. The membrane dehumidifier has two main parts: membrane modules and air compressor, as shown in Figure 1. The membrane module for dehumidification uses permeated water vapor, and the air compressor generates a partial vapor pressure gradient between the membrane layers. When the partial vapor pressure gradient between the membrane layers is created by the air compressor, the water vapor permeates from the feed side to the permeate side. The dehumidification performance is dependent on the membrane material, particularly its permeability and selectivity to water vapor. When the membrane affords a high level of permeability and selectivity, the dehumidification performance and energy efficiency of the membrane unit is correspondingly higher. In this study, the type of membrane used is a hollow-fiber membrane, which is easy to manufacture structurally, and the air compressor is used to pressurize the inlet air for creating the vapor pressure gradient between membrane layers. To maintain the dehumidification performance, a part of the intake air is "swept" out to the permeate side, thereby removing the water vapor.

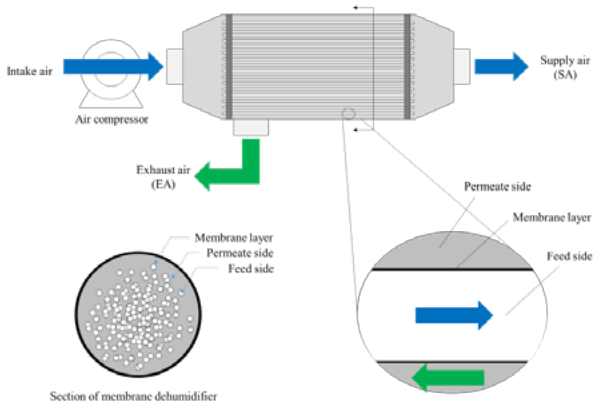


Fig. 1. Configuration of hollow-fiber-membrane dehumidifier

When the intake gas is assumed to be an ideal mixture of two gases, dry air and water vapor, the dehumidification process of the membrane dehumidifier can be represented by a solution–diffusion process between the feed side and the permeate side with a partial pressure gradient, as shown in Figure 2. When the feed-side air of the unit is pressurized for dehumidification, water vapor and dry air permeate through the membrane layer. The molar mass flow rates of water vapor and dry air (i.e., $\dot{M}'_w$ and $\dot{M}'_d$) through the membrane layer are estimated by means of the classical solution–diffusion model as represented by Equations (1) and (2), respectively. To estimate the partial pressure gradient, which acts as the force driving the dehumidification, we represent the partial pressure of each gas on the permeate side as the ratio of the molar mass flow rate through the membrane layer (i.e., y_1 and y_2) in Equations (3) and (4). The values of permeability (Per), selectivity (S), membrane area (A_{mem}), and membrane thickness (z) are determined according to the performance of the membrane materials, and these values affect the dehumidification performance along with energy consumption of the air compressor. Each molar mass flow rate is dependent on the membrane material and sweep gas used to remove the water vapor on the permeate side.

$$\dot{M}'_w = \frac{\mathrm{Per}_v A_{mem}}{z}\left(P_{f,v} - y_1 P_{p,tot}\right) \tag{1}$$

$$\dot{M}'_d = \frac{\mathrm{Per}_d A_{mem}}{z}\left(P_{f,d} - y_2 P_{p,tot}\right) = \frac{\mathrm{Per}_v}{S}\frac{A_{mem}}{z}\left(P_{f,v} - y_2 P_{p,tot}\right) \tag{2}$$

$$y_1 = \frac{\dot{M}'_v + \dot{M}'_{sweep,v}}{\dot{M}'_d + \dot{M}'_v + \dot{M}'_{sweep,d} + \dot{M}'_{sweep,v}} \tag{3}$$

$$y_2 = \frac{\dot{M}'_d + \dot{M}'_{sweep,d}}{\dot{M}'_d + \dot{M}'_v + \dot{M}'_{sweep,d} + \dot{M}'_{sweep,v}} \tag{4}$$

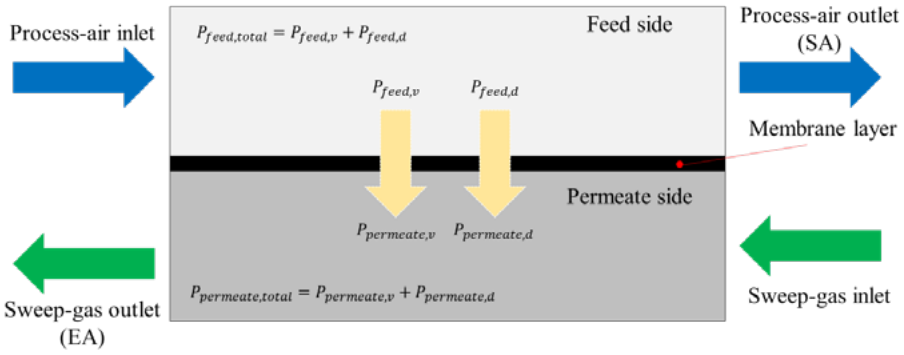


Fig. 2. Schematic of dehumidification process in membrane dehumidifier

2.2 Prototype of hollow-fiber-membrane dehumidifier

When the basic theoretical model does not consider the membrane type and configuration, it is not easy to estimate the dehumidification performance of the membrane dehumidifier under various operating conditions. Therefore, we developed a prototype hollow-fiber-membrane dehumidifier and estimated its dehumidification performance under various conditions. The configuration of the prototype unit is shown in Figure 3. The prototype unit has an inlet air channel on the feed side and sweep-gas air channel on the permeate side. In the study, the membrane module of our proposed dehumidifier was of the cylinder type, and the length of the module was 0.3 m, with the module diameter being 0.08 m. The module contained 170 hollow-fiber membranes each with a fiber inlet diameter of 1.6 mm, corresponding to a packing fraction ratio of 0.11. The hollow-fiber length was 0.23 m, and its total effective contacting area was 0.282 m^2. The specifications of our prototype module are listed in Table 1.

Table 1: Specifications of prototype unit

Design parameters	Values	Design parameters	Values
Module diameter [mm]	80	Fiber thickness [mm]	0.35
Module length [mm]	300	Contacting area of membrane [m^2]	0.282
Fiber inlet diameter [mm]	1.6	Number of fibers [-]	170
Fiber outlet diameter [mm]	2.3	Packing fraction [-]	0.11
Fiber length [mm]	230		



Fig. 3. Prototype configuration of hollow-fiber-membrane dehumidifier

3. Test setup and dehumidification performance

3.1 Experimental setup of prototype

To analyze the dehumidification performance of our prototype unit, we varied five independent parameters: air temperature, relative humidity, airflow rate, inlet air pressure, and sweep-gas ratio. The experimental setup for controlling these five independent parameters is shown in Figure 4. In the setup, the environmental chamber is used to maintain the experimental air conditions, and the air compressor maintains the airflow ratio of the conditioned air to the prototype unit. The rotation speed of the air compressor is controlled by means of a switched-mode power supply (SMPS) that controls the electric current and voltage. The pressure of the feed side is controlled by open-to-close ratio of the inlet valves to generate the partial pressure gradient. Moreover, the sweep-gas ratio, which corresponds to the ratio of the intake supply airflow rate to the sweep-gas flow rate, is controlled by the outlet valve as an adjustable open-to-close ratio. The measured data to estimate the dehumidification performance of the prototype unit are collected and saved in the data logger.

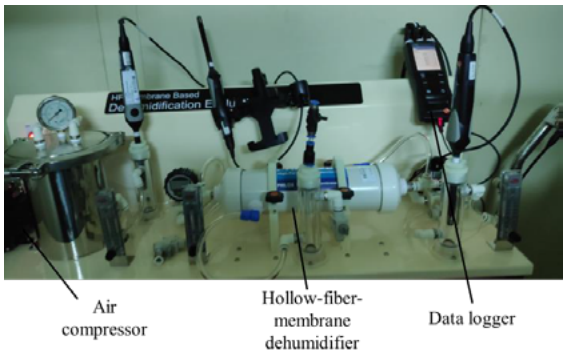


Fig. 4. Schematic of experimental setup of hollow-fiber-membrane dehumidifier

3.2 Operation conditions

In this study, we conducted 24 sets of experiments for analyzing the dehumidification performance of the hollow-fiber-membrane dehumidifier unit. The dehumidification performance of the prototype unit was estimated as the differential of the humidity ratio and amount of dehumidification, as expressed by Equations (5) and (6), respectively. The humidity ratio differential is representative of the driving force of the vapor pressure gradient, and the amount of dehumidification represents the dehumidification per unit time as a function of the latent cooling capacity.

$$\Delta w = w_{in} - w_{out} \quad (5)$$

$$\dot{m}_d = \dot{m}_{sa}\Delta w = (\dot{m}_{intake} - \dot{m}_{sweep})\Delta w \quad (6)$$

To analyze the dehumidification performance under various conditions, we acquired the performance data for various values of the five operating parameters: air temperature, relative humidity, airflow rate, sweep-gas ratio, and inlet air pressure. As the sweep-gas ratio is the airflow ratio of the intake air to the sweep-out air, a high level of sweep gas implies that the supply airflow rate is reduced for a given intake air flow rate. To estimate the differential of the humidity ratio and amount of dehumidification, each parameter was suitably varied. As the air temperature and humidity ratio were set to reflect humid and mild air conditions, these were maintained in the range of 15 to 30 ℃ and 40 to 80%, respectively. The detailed operational range is listed in Table 2. To estimate the dehumidification performance of the prototype unit, we did parametric study from the experimental results, which were based on the base case, and subsequently, only a single parameter was modulated in the operation range when all other parameters were fixed.

Table 2: Operating ranges of experimental conditions

Parameter	**Symbol**	**Input values**		
		Low	Base	High
Inlet air temperature [℃]	$T_{a,in}$	15	27	30
Inlet relative humidity [%]	$RH_{a,in}$	40	60	80
Inlet air flow rate [l/min]	$\dot{V}_{a,in}$	20	25	30
Sweep-gas ratio [−]	x	0.18	0.5	0.82
Inlet pressure [kPa]	p_{air}	101.3	101.3	260

The measurement sensors in our setup included high-precision humidity/temperature, differential pressure, and absolute pressure sensors. The high-precision humidity/temperature sensor measures the inlet and outlet temperatures and relative humidity. The airflow rate is measured by the differential pressure sensor in conjunction with a digital flow meter. The measurement points corresponding to airflow rate measurements include the inlet, outlet, and exhaust sides. The inlet air pressure is measured by the absolute pressure sensor, where the inlet air pressure is controlled by the air compressor by means of valves. To quantify the dehumidification performance, the measurement data were converted into the humidity ratio, which is affected by the air temperature, relative humidity, and pressure.

Table 3: Specifications of measuring instruments

Variable	**Device**	**Characteristics**		
Dry-bulb temperature and relative humidity of air	High-precision humidity/temperature probe	Range	Temperature	−20 ℃ to +55 ℃
			Relative humidity	0%–100%
		Accuracy	Temperature	±0.4 ℃
			Relative humidity	±2%RH
Air flow rate	Differential pressure sensor	Range	Pressure	0–1250 Pa
		Accuracy		±0.30%
Inlet air pressure	Absolute pressure sensor	Range	Pressure	0–1250 Pa
		Accuracy		±0.30%

4. Experimental results and discussion

We experimentally investigated the performance of the prototype unit considering the influences of the five air inlet parameters: inlet air temperature, relative humidity, air pressure, inlet air flow rate, and sweep-gas ratio. The influence of each of the five parameters considered was analyzed via the differential of the humidity ratio and amount of dehumidification; the results are shown in Figure 5.

We note from the figure that the air temperature and relative humidity exhibit a positive correlation with the differential of the humidity ratio and amount of dehumidification. We note that higher levels of inlet temperature and relative humidity correspond to a higher partial vapor gradient between the membrane layers. In addition, as the inlet air pressure increases, the partial vapor pressure gradient between membrane layer was increased , and the dehumidification performance improves. The sweep-gas ratio and intake airflow rate exhibit no positive correspondence with the dehumidification performance. When the sweep-gas ratio ranges from 0.4 to 0.6, the differential of the humidity ratio and the amount of dehumidification are maximal because the mass transfer between the feed and permeate sides increases as a balanced flow. When the intake air flow rate decreases, the face velocity on the feed side also decreases with increase in the contact time of the unit. The differential of the humidity ratio is strongly affected, but the amount of dehumidification is only relatively impacted by the airflow rate.

The main parameters that significantly affect the dehumidification performance of the prototype unit are the inlet air pressure and sweep-gas ratio. To increase the dehumidification performance, the inlet air pressure should be sufficiently high, and the sweep-gas ratio must be maintained around 0.5 for balanced flow. Here, we note that to control the outlet humidity ratio, a suitable rotation speed modulation strategy of the air compressor or sweep-gas ratio should be estimated.

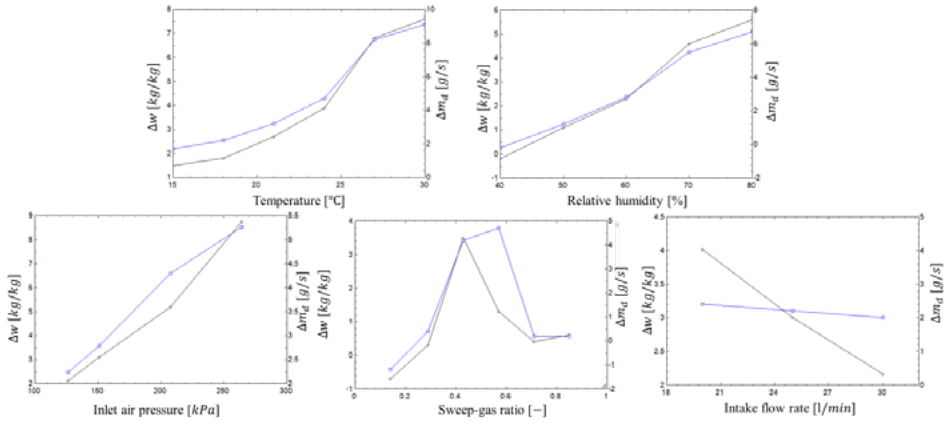


Fig. 5. Parametric analysis of hollow-fiber-membrane dehumidifier

5. Conclusions

In this study, we experimentally investigated the dehumidification performance of a hollow-fiber-membrane dehumidification unit. Our prototype unit was composed of a membrane module containing a bundle of hollow membranes and an air compressor to pressurize the inlet pressure, which forms the driving force underlying the process. Experiments were conducted using the prototype unit to estimate the differential of the humidity ratio and amount of dehumidification, and the relevant performance data were collected. The input parameters that influence the dehumidification performance are the air temperature, relative humidity, inlet air pressure, sweep-gas ratio, and intake air flow rate. The air temperature and relative humidity exhibited a positive correlation with the performance, which indicates that a larger amount of air with water vapor affords increased dehumidification performance. The inlet air pressure also positively affects the performance via increasing the driving force of the vapor pressure drop. The dehumidification performance was maximal when the sweep-gas ratio was in the range of 0.4 to 0.6 under balanced flow conditions. When the intake air flow rate was decreased, the dehumidification performance increased because of the increased contacting time of air with the prototype unit.

In future study, we plan to analyze the dehumidification efficiency under various operation conditions. In addition, the data collected in the study can be applied to extend the utilization of the control logic of the hollow-fiber-membrane dehumidifier.

Acknowledgements

This work was supported by the National Research Foundation of Korea (NRF) grant (No. 2019R1A2C2002514), the Korean Institute of Energy Technology Evaluation and Planning (KETEP) (No. 20184010201710), and the Technology development Program(S2782284) funded by the Ministry of SMEs and Startups(MSS, Korea).

References

[1] Rafique MM, Gandhidasan P, Bahaidarah HMS. Liquid desiccant materials and dehumidifiers - A review, *Renew. Sustain. Energy Rev* 2016;56:179–195.
[2] Ling J, Hwang Y, Radermacher R. Theoretical study on separate sensible and latent cooling air-conditioning system, *Int. J. Refrig* 2010;33:510–520.
[3] Yang Z, Lian Z, Li X, Zhang K. Concept of dehumidification perfectness and its potential applications, *Energy* 2015; 91:176–191.
[4] Gommed K, Grossman G. Experimental investigation of a liquid desiccant system for solar cooling and dehumidification, *Sol. Energy* 2007;81:131–138.
[5] Misha S, Mat S, Ruslan MH, Sopian K. Review of solid/liquid desiccant in the drying applications and its regeneration methods, *Renew. Sustain. Energy Rev* 2012;16:4686–4707.
[6] Woods J. Membrane processes for heating, ventilation, and air conditioning, *Renew. Sustain. Energy Rev* 2014;33:290–304.
[7] Labban O, Chen T, Ghoniem AF, Lienhard JH, Norford LK. Next-generation HVAC: Prospects for and limitations of desiccant and membrane-based dehumidification and cooling, *Appl. Energy* 2017;200:330–346.
[8] Bui DT, Nida A, Ng KC, Chua KJ. Water vapor permeation and dehumidification performance of poly(vinyl alcohol)/lithium chloride composite membranes, *J. Memb. Sci* 2016;498:254–262.
[9] Bui DT, Wong Y, Islam MR, Chua KJ. On the theoretical and experimental energy efficiency analyses of a vacuum-based dehumidification membrane, *J. Memb. Sci* 2017;539:76–87.
[10] El-Dessouky HT, Ettouney HM, Bouhamra W. A novel air conditioning system: membrane air drying and evaporative cooling, *Chem Eng Res Des* 2002;78:999–1009.

13th IEA Heat Pump Conference
May 11-14, 2020 Jeju, Korea

Working Fluid Selection of Organic Rankine Cycle for a Liquid Desiccant System

Hye-Won Dong[a], Beom-Jun Kim[a], Li-Hua Lin [a], Jae-Weon Jeong[a,*]

[a]Department of Architectural Engineering, College of Engineering, Hanyang University, Seoul, 04763, Republic of Korea

Abstract

In this study, a working fluid selection was conducted for an organic Rankine cycle (ORC). The ORC used in this study adopted the district heat source, which is rarely utilized in the cooling season. The power and heat generated from the ORC was used for a liquid desiccant system. Considering the environmental impact, n-Pentane, R1233zd(E), and Novec649 were utilized and compared with R245fa, which is one of the hydrofluorocarbons. Thermodynamic analyses of all the fluids were conducted, and Novec649 was selected owing to the high total net power and heat output. The testbed for ORC driven liquid desiccant system was developed using Novec649, and it can provide the desiccant solution at over 50°C to enter the regenerator of liquid desiccant system without requiring an auxiliary heater.

© HPC2020.
Selection and/or peer-review under responsibility of the organizers of the 13th IEA Heat Pump Conference 2020.

Keywords: Organic Rankine cycle; Working fluid; Liquid desiccant; District heating

Nomenclature

h	Enthalpy (J/kg)
$\dot{m}$	Mass flow rate (kg/s)
η	Efficiency (-)
P	Power (kW)
$\dot{Q}$	Load (kW)
T	Temperature (℃)
s	Temperature (℃)
$\dot{W}$	Work (kW)

1. Introduction

In recent years, the applications of distributed power generation systems using small-scale combined heat and power (CHP) systems have increased in commercial buildings and apartment complexes. However, the heat generated from CHP systems, which is a relatively low-temperature heat source, is insufficiently utilized in the cooling season due to the decrease in the heat demand. Integrating the CHP system with a thermally driven cooling system can be a good alternative to increase the heat demand in the cooling season [1-3].

An organic Rankine cycle (ORC), which is one of the commercial CHP systems, uses a relatively low grade heat source to produce the heat and power upon employing organic fluid, when compared with the conventional Rankine cycle. The performance of the ORC depends mainly on the working fluid; therefore, the selection of the working fluid considering the operating temperature range is important for the ORC.

* Corresponding author. Tel.: +82-2-2220-2370; fax: +82-2-2220-1945.
E-mail address: jjwarc@hanyang.ac.kr

Cho and Cho [4] recommended R245fa as the working fluid of ORC for the heat source temperature below 60°C when considering the efficiency of cycle and power generation. Darvish et al. [5] selected R134a, considering both exergy and cost at the heat source at 120°C. Gao et al. [6] selected R152a and R143a, which represent the maximum power output and minimum cost as the working fluid of ORC, respectively, using industrial waste heat.

Previous studies primarily performed the working fluid selection when using low-temperature heat sources (i.e., solar heat, industrial waste heat), but research addressing the heat produced by ORC was rare. Although employing the same heat source, various working fluids may be applied depending on the purpose of the heat from the ORC. Therefore, the selection of working fluid is required while considering the heat source, heat demand, power generation of the ORC when designing the ORC, and the environmental impact of working fluid. This study addresses the selection of low global warming potential (GWP) and ozone depletion potential (ODP) working fluid of the ORC using a district heat source for liquid desiccant (LD) system, which is one of the thermally driven cooling systems.

2. System Overview

ORCLD

The ORC used in this study consist of an evaporator, expander, condenser, and pump. Figure 1 shows the small-scale (<100 kW) ORC-driven LD (ORCLD) system as a distributed power generation system for commercial buildings and apartment complexes. The ORCLD receives the heat from the district heat source, and the heat reclaimed from the condenser is used for heating the desiccant solution in the regenerator of LD.

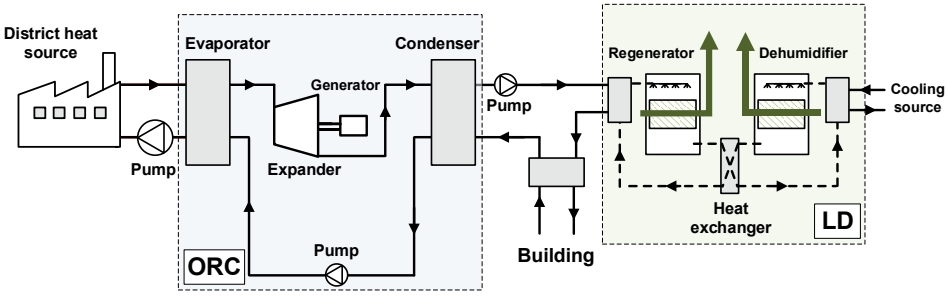


Fig. 1. Schematic of ORCLD

The district heat source was selected as a heat source for ORC operation. The hot water used for district heating, supplied at approximately 120°C, is relatively hot for direct use in apartment buildings, so hot water can be supplied upon lowering its temperature via a central heat exchanger in the apartment building. If the ORC is used instead of heat exchanger, it is possible to simultaneously supply hot water at the temperature required by the heat demand (i.e., regenerator, building) and generate electricity.

Meanwhile, the LD is a representative thermally driven cooling technology to improve the utilization of heat produced in the CHP system during summer season. The LD is mainly composed of a dehumidifier and a regenerator, with a desiccant solution circulating between them. A strong solution is required to dehumidify the process air, and it is also necessary to cool the desiccant solution for effective dehumidification. However, once the desiccant solution is used in the dehumidifier, it becomes weak; hence, a heat source is required to regenerate it.

The heat reclaimed from the condenser is preferentially utilized as the heat source for heating the desiccant solution entering the regenerator, and the remaining heat is consumed in the building. For stable ORC operation, a closed-loop system using water was applied for the heat recovery in the condenser, so the temperature of the water supplied to the condenser by the ORC was constant. The electricity produced by the ORC will be provided to run common appliances (i.e., lighting, elevator) in the building and operating pumps and fans for LD.

Working fluid selection

There are many organics that can be used as a working fluid of the ORC, and new fluids are also being developed. Because each fluid has different thermodynamic and environmental properties, the determination

of a suitable working fluid for the ORC can be an issue, and recommendations for working fluids vary among researchers. Therefore, a suitable working fluid under the given conditions should be selected. In this study, considering the environmental impact, the working fluid of ORC is recommended to heat the desiccant solution without an auxiliary heater when using the district heat source as the heat source of the ORC. The conditions for selecting a working fluid are as follows.

- Isentropic or dry fluid
- Stability
- Low flammability and toxicity
- Low cost

This work, which is built in an Engineering Equation Solver (EES) program, considered three environmentally friendly working fluids as possible alternatives to hydrofluorocarbons (HFCs). The characteristics of three working fluids are compared with those of R245fa, which is one of the representative HFCs. The characteristics of the four working fluids are listed in Table 1. All of the working fluids reviewed have zero ODP and a low GWP, except for R245fa.

Table 1. Properties of each working fluid

	R245fa	n-Pentane	Novec649	R1233zd(E)
Boiling point [°C]	15.3	36	49	18
Molecular weight [g/mol]	134	72.15	316	130.5
Critical pressure [MPa]	3.6	3.369	1.88	3.623
Critical point [°C]	154	196.7	169	165.6
Liquid density [kg/m^3]	1,339	1,321.3	1,600	1,321.3
Heat of vaporization [kJ/kg]	190	366	95	192
Specific heat [kJ/kgK]	0.92	2.32	1.10	0.82
global warming potential [-]	1030	11	1	1
ozone depletion potential [-]	0	0	0	0

Considering the operating range of the ORCLD to select the working fluids available for the given design conditions, the previous researches showed that a desiccant solution with a temperature of at least 40°C is required to sufficiently regenerate the solution in the regenerator of LD using an aqueous lithium chloride (LiCl) solution [7,8]. In the ORC evaporator, it was assumed that a heat source at 120°C, the normal maximum temperature of district heating, is supplied. The cycle efficiency and thermodynamic characteristics of working fluids were evaluated under the design conditions of ORCLD as shown in Table 2.

Table 2. Design conditions of ORCLD

Design parameter	Value
Thermodynamic power [W]	100
ORC pump efficiency [%]	70
Expander efficiency [%]	70
Cooling source (water) inlet temperature [°C]	40
Heat source (water) inlet temperature [°C]	120
Temperature difference between heat and cooling source [°C]	15
Expander inlet temperature [°C]	115
Pressure ratio [-]	3

Thermodynamic analysis

The thermodynamic properties of all the fluids were calculated using the EES program considering the thermodynamic cycle of the ORC under the design conditions. It was assumed that power output, expander and pump efficiency, district heating and cooling water supply temperature, pressure ratio ($P_{exp,in}/P_{exp,\ out}$), and pinch point were all constant. Among the design conditions shown in Table 2, the flow rates of heating, cooling, and working fluids; cycle efficiency; expander pressures; pump power consumption; and duty of evaporator and condenser for working fluids were compared. The thermodynamic equations for analyzing the ORC performance are as follows (Equations 1-4).

$$\eta_{exp} = (h_{exp,in} - h_{exp,out})/(h_{exp,in} - h_{exp,out,s}) \quad (1)$$

$$\eta_{pump} = (h_{pump,out,s} - h_{pump,in})/(h_{pump,out} - h_{pump,in}) \quad (2)$$

$$\dot{Q}_{evap} = \dot{m}_{orc}(h_{evap,in} - h_{evap,out}) \quad (3)$$

$$\eta_{orc} = (\dot{W}_{exp} - \dot{W}_{pump})/\dot{Q}_{evap} \quad (4)$$

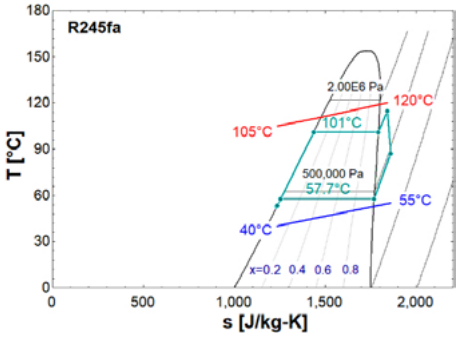
The energy inputs and outputs of the four major components of the ORC are obtained as the product of the working fluid flow rate and the inlet and outlet enthalpy differences. The enthalpy values can be obtained using the isentropic efficiency values of the expander and pump shown in Table 2 and Equations 1 and 2. Because the power generated by the expander was assumed to be 100 W, the enthalpy of each component was calculated, and the required flow rate of the working fluid could be obtained.

The heat supply in the evaporator is shown in Equation 3. Since the inlet and outlet temperature difference of heating fluid was assumed to be 15°C, the required water flow rate could be obtained. The same applied to the condenser; finally, the thermal efficiency of the cycle was calculated using Equation 4.

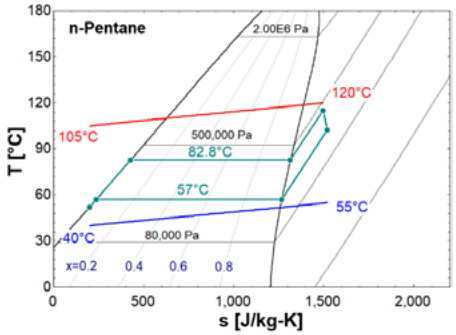
3. Results

The thermodynamic characteristics of the T-s diagram of the four working fluids are shown in Figure 2, and the performance characteristics of ORCLD for the working fluids are summarized in Table 3.

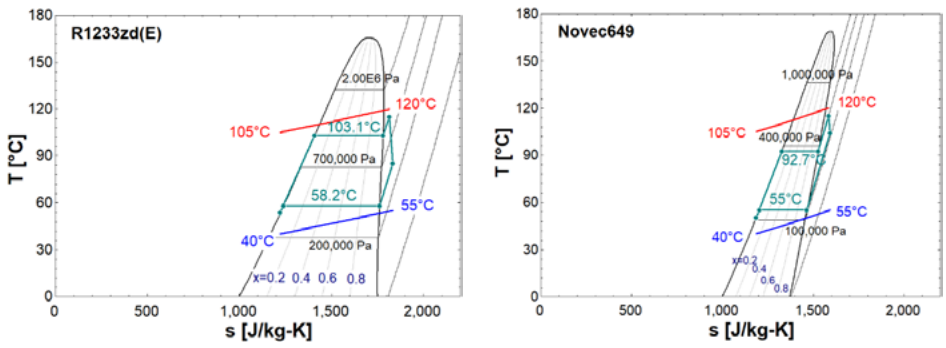
To produce an output of 100 W under the design conditions of Table 2, wherein 1,460 W of heat energy is shown to be required, and R245fa exhibited 6.41% of thermal efficiency. To satisfy the given design conditions, for n-Pentane, either the pressure ratio or cooling water supply temperature had to be lowered, so the pressure ratio of n-Pentane was set as 2. Although n-Pentane has the highest critical temperature and exhibits the lowest efficiency, its power output is the highest. However, n-Pentane was excluded from the final working fluid selection because it is a flammable fluid and is difficult to operate under the design conditions. The cycle efficiency was the highest in R1233zd (E), but it was determined that the actual power output was more meaningful than the cycle efficiency when utilizing wasted energy during the summer. Additionally, R245fa and R1233zd (E) operate at a relatively higher pressure to supply heat to the LD system, and it will be difficult to recover the higher temperature of water. Novec649 exhibited a relatively low efficiency due to its high molecular weight, but its actual power output was the highest, except for n-Pentane, and it was possible to obtain hotter water by increasing the pressure. It can be recommended as a suitable working fluid to be applied to the proposed system, which focuses on heat recovery.



(a) R245fa



(b) n-Pentane



(c) R1233zd(E) (d) Novec649

Fig. 2. T-s diagram of the working fluids

Table 3. Performance characteristics of the working fluids

	R245fa	n-Pentane	Novec649	R1233zd(E)
Efficiency [%]	6.41	4.22	4.78	6.74
Hot water flow rate [kg/s]	0.02301	0.03647	0.03192	0.02204
Cooling water flow rate [kg/s]	0.02179	0.03536	0.03076	0.02079
Working fluid flow rate [kg/s]	0.006577	0.005023	0.01407	0.0064
High pressure [kPa]	1298	394	373	1115
Low pressure [kPa]	433	197	124	372
Pressure ratio[-]	3	2	3	3
Total net power [W]	93.54	97.62	96.72	94.3
Heat input [W]	1460	2315	2026	1398
Heat generation [W]	1366	2217	1929	1304

4. Discussion

In this study, the ORCLD system was designed and developed using Novec649, which was determined to be the most suitable working fluid, and an experiment was conducted to verify the performance of the proposed system. The desired temperature of district heating was realized through the electric heater, the ORC (Figure 3) was installed at the LD part of the existing desiccant, and an evaporative cooling system called LD-IDECOAS [9] was adopted to monitor the temperature of the desiccant solution supplied to the regenerator. Therminol 55, which is a thermal fluid that attain temperatures of up to 300°C without causing toxicity to humans and the environment, was used instead of water.

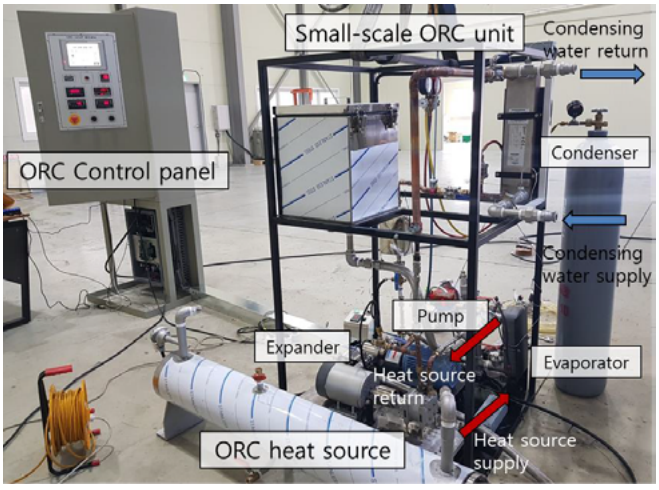


Fig. 3. Experimental setup of ORC

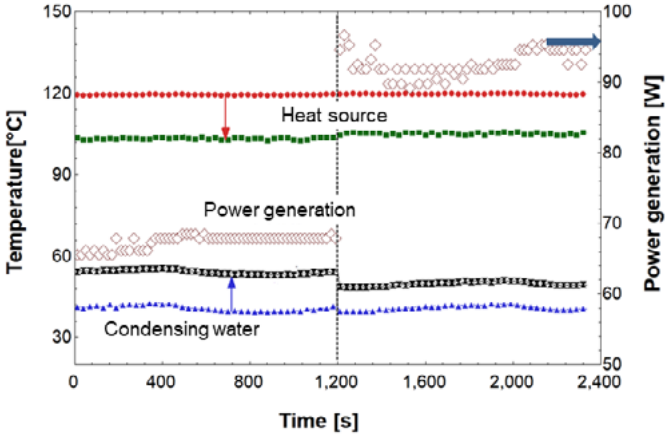


Fig. 4. Test results

The experiment result showed that the power output was 67 W, which is lower than that of the simulation condition (100 W). Moreover, the pressure ratio was 2.37 when the ORC operated with the maximum flow rate of the working fluid and heating fluid (Figure 4). In that case, the desiccant solution entering the regenerator could be supplied at a temperature of approximately 51°C. When the flow rates of the heating and working fluids were decreased while maintaining the temperature of heating fluid at 120°C, the pressure ratio was increased to 2.72, so the power output also increased to approximately 93 W. The output power in the second case was larger than that in the first case; however, in the case with higher pressure ratio, the heat transfer rate of the condenser decreased. The temperature of cooling water exiting the condenser was 50°C, which is insufficient to supply heat for regeneration in the LD regenerator.

Conclusion

In this study, the working fluid for the ORC CHP system was determined considering the environmental impact and effective utilization of the district heating, while supplying the required heat for the liquid desiccant system in the cooling season. R245fa (HFCs) and environmentally friendly working fluids such as R514A, n-

Pentane, R1233zd (E), and Nove649 were considered. When the district heat source is at 120°C, and cooling water at 40°C is supplied to the ORC, which produces 100 W of output power, Novec649 was selected as the working fluid applicable to the ORCLD. Novec649 can transfer significant heat energy to the regeneration part with the largest actual power generation, except for n-Pentane, which is a flammable fluid.

Using Novec649, a testbed for the ORCLD system was developed, and the performance of the system was investigated. The ORCLD with Novec649 could supply sufficient heat energy for the solution regeneration without requiring additional heat, and the solution inlet temperature of the regenerator was over 50°C.

Increasing the ORC power generation may also reduce the heat transfer rate that can be recovered in the condenser, so further studies must be conducted to determine an optimal operating method for the ORC to minimize the energy consumption of the LD system.

Acknowledgments

This work was supported by the National Research Foundation of Korea (NRF) grant (No. 2019R1A2C2002514), the Korean Institute of Energy Technology Evaluation and Planning (KETEP) (No. 20184010201710), and the Technology development Program(S2782284) funded by the Ministry of SMEs and Startups(MSS, Korea).

References

[1] Badami, M., Portoraro, A., & Ruscica, G. (2012). Analysis of trigeneration plants: engine with liquid desiccant cooling and micro gas turbine with absorption chiller. International Journal of Energy Research, 36(5), 579 – 589. https://doi.org/10.1002/er.1817

[2] Cho, H., Smith, A. D., & Mago, P. (2014). Combined cooling, heating and power: A review o f performance improvement and optimization. Applied Energy, 136, 168 – 185. https://doi.org/10. 1016/j.apenergy.2014.08.107

[3] Wu, D. W., & Wang, R. Z. (2006). Combined cooling, heating and power: A review. Progress in Energy and Combustion Science, 32, 459 – 495. https://doi.org/10.1016/j.pecs.2006.02.001

[4] Cho, S.Y. & Cho, C. H., 2014, Selection of Working fluid for the Organic Rankine Cycle to Utilize Low-Temperature Waste Heat, New&Renerable Energy, 10(4), 36-46.

[5] Darvish, K., Ehyaei, M., Atabi, F., & Rosen, M. (2015). Selection of optimum working fluid f or organic Rankine cycles by exergy and exergy-economic analyses. Sustainability, 7(11), 15362 –15383.

[6] Gao, H., Liu, C., He, C., Xu, X., Wu, S., & Li, Y. (2012). Performance analysis and working fluid selection of a supercritical organic Rankine cycle for low grade waste heat recovery. Ener gies, 5(9), 3233-3247.

[7] Katejanekarn, T., Chirarattananon, S., & Kumar, S. (2009). Performance of a solar-regenerated l iquid desiccant ventilation pre-conditioning system. Solar Energy, 83, 920 – 933. https://doi.org/1 0.1016/j.solener.2008.12.006

[8] Dong, H. W., Cho, H. J., Park, J. Y., & Jeong, J. W. (2019). Optimum regeneration temperatu re of a desiccant solution in a packaged liquid desiccant-assisted air conditioning unit. Internati onal Journal of Refrigeration, 101, 155–166.

[9] Kim, M.H., Park, J.S., Jeong, J.W. (2013). Energy saving potential of liquid desiccant in evapo rative-cooling-assisted 100% outdoor air system, Energy, 59, 726–736. doi:10.1016/j.energy.2013. 07.018.

13th IEA Heat Pump Conference
April 26-29, 2021 Jeju, Korea

Energy Saving Potential of an Air Source Heat Pump Heating System Compared with a Radiant Floor Heating System with Ventilation in an Apartment Building

Yu-Jin Hwang[a], Yong-Kwon Kang[a], Beom-Jun Kim[a], Jae-Weon Jeong[a,*]

[a]Department of Architectural Engineering, College of Engineering, Hanyang University,
222 Wangsimni-Ro, Seongdong-Gu, Seoul, 04763, Republic of Korea

Abstract

This study aims to investigate and compare the energy performance of an air source heat pump heating system and a radiant floor heating system with an energy recovery ventilator in an apartment building. The thermal load for a conditioned zone was derived using simulation tool TRNSYS 18, and the total energy consumption of the systems was calculated using an engineering-equation-solver (EES) for each component model. The coefficient of performance (COP) of the heat pump was calculated as 3.16, and the efficiency of the boiler in a radiant floor system was established as 0.9. The results indicate that the proposed system reduces energy consumption by 21.8% compared with the conventional floor heating system. The primary reason for this result is because the COP of the heat pump is dominant, even though the primary energy factor of electricity is 2.75.

© HPC2020.
Selection and/or peer-review under responsibility of the organizers of the 13th IEA Heat Pump Conference 2020.

Keywords: Air source heat pump, radiant floor heating system, enthalpy recovery ventilator, energy savings;

1. Introduction

Radiant floor heating systems have been developed and used in Korea for residential buildings for over 500 years. The traditional radiant floor heating system is called Ondol, and it is very efficient because the floor is heated using waste heat leftover from kitchen use in the past [1]. Furthermore, the system provides abundant thermal comfort for a sedentary lifestyle [2]. In modern times, people have applied radiant heating systems by laying water pipes under the floor, instead of using waste heat.

It is recent knowledge that energy consumption in buildings accounts for a significant portion of total energy use, and therefore, various methods to minimize building loads have been suggested. One system that can minimize load is the heat pump, which has been adapted to numerous HVAC systems and is classified as a renewable energy source in Europe [3]. Worldwide, there has been considerable research undertaken regarding the heat pump and how to improve its performance under various operation conditions [4,5]. However, in Korea, heat pumps are only installed in commercial buildings and office buildings [6,7], because radiant floor heating systems have traditionally been used in Korea and are heavily preferred for residential buildings.

In addition, apartments recently built in Korea are equipped with built-in air conditioners for cooling the air during the summer. Although a single heat pump can be used for both cooling and heating, the heat pump-based air conditioners in Korea are used for cooling in the summer; however, they are not used for heating in the winter. Instead, the space is heated by radiant floor heating in the winter. By separating the cooling and heating systems, the construction and management costs and time are increased.

* Corresponding author. Tel.: +82-2-2220-2370; fax: +82-2-2220-1945.
E-mail address: jjwarc@hanyang.ac.kr (J.-W. Jeong).

In this study, the potential of integrating cooling and heating into a single heat pump system was investigated. This would eliminate the need for two different systems. Additionally, the energy use of a radiant floor heating system was compared with a heat pump air heating system.

2. System Overview

2.1. Air heating system

Figure 1 shows an air heating system with an air-source heat pump and an enthalpy recovery ventilator. Explained briefly, a heat pump used in the reverse cycle (to the vapor compression cycle) will result in the pump pulling up low heat from the source to the high heat storage. A heat pump consists of a compressor, a condenser, an evaporator, and an expansion valve. Refrigerant absorbs heat in the evaporator and releases it out to the heat sink in the condenser, using input power. The released heat is then used to heat the conditioned zone by supply air.

For this research, the type of air source was selected so that the heat pump obtained heat from the outside air. This was because the system was already installed for cooling in the summer, as is common in Korean apartments, and thus was available for both heating and cooling. Simply driving the vapor-compression cycle in the reverse direction, the air conditioner functioned as a heat pump cycle. However, it could not be used for heating due to the differences in the ambient and supply air temperatures of summer and winter. Because the amount of heat absorption and dissipation depends on the operating conditions, the design for the existing air conditioner had to be redesigned for heating use. The detailed temperature setting and design process for each component is covered in the simulation overview below. In the case that the air supply cannot reach the desired target point (due to insufficient capacity), a heating coil was added before supply to be achieved through as an auxiliary heater.

The air heating system was separated from the ventilation system, which is different from conventional heating, ventilation, and air conditioning (HVAC) systems. Thus, the heat pump only recirculates the indoor air, and effectively handles the building load.

In an enthalpy recovery ventilator (also called an energy recovery ventilator (ERV)), an enthalpy exchanger can be used to transfer the energy, including sensible and latent heat. During the heating season, the system takes heat from the return air and uses it to heat the outdoor air and supply fresh air into the room. Generally, an enthalpy recovery ventilator is used to pre-cool, or pre-heat, before air-conditioning. This process not only reduces system loads, but also satisfies ventilation requirements. For this study, the enthalpy recovery ventilator was separated from the heating systems.

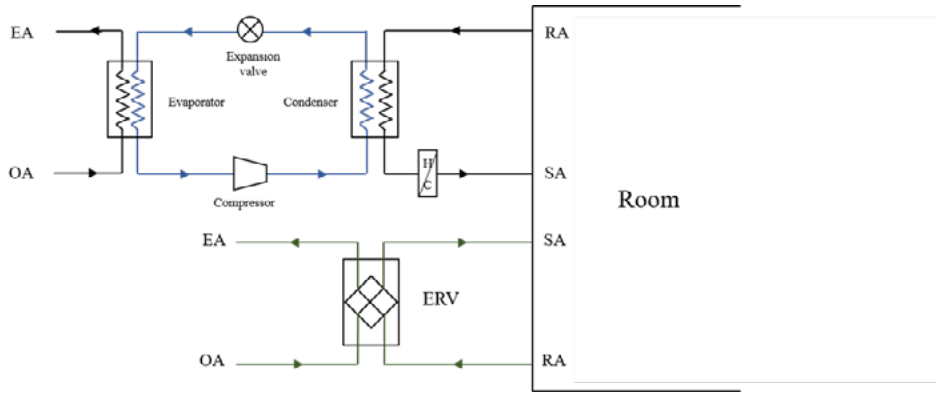


Fig. 1. Schematic of Air Heating System with an Air Source Heat Pump and an Enthalpy Recovery Ventilator (ERV)

2.2. Floor heating system

Figure 2 shows a floor heating system with a radiant floor and enthalpy recovery ventilator. Radiant floor heating system have water pipes buried in the floor. As hot water flows through the pipes, the heat is absorbed by the floor, and released to the room above.

The heat is transferred by conduction from the water pipes to the concrete layers, then by convection from the flooring to the air through natural stratification, and by radiance between the heated floor and other walls according to temperature differences. The heating capacity of the radiant floor depends on the spacing of the pipes, diameter of the pipe, heat conductivity of the pipe, heat resistance of the concrete layer and floor structures, water temperature, and the mass flow rate through the pipes. Because the process of heat transfer is complex and relies on several variables, it is difficult to calculate the heating capacity of radiant floor heating systems.

Radiant floor heating systems make structures (such as floors) warm first, and then use the structures to heat the room. This is different from heat pump heating systems that heat the air and supply directly. In terms of the energy used for heating, indirect heating systems use more energy than direct heating systems.

Similar to the air heating system described above, the floor heating system was separated from the ventilation system. Thus, the radiant floor only handles the building load and ventilation load of the space by itself. An enthalpy ventilator in the proposed floor heating system was operated in the same way addressed previously for the air heating system.

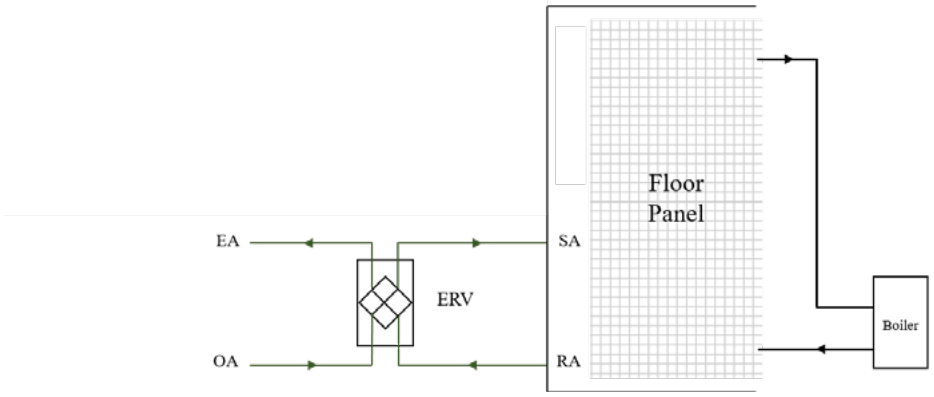


Fig. 2. Schematic of Floor Heating System with a Radiant Floor and an Enthalpy Recovery Ventilator

3. Energy Simulation

3.1. Simulation overview

The energy simulation to calculate the performance of the air heating system and the floor heating system was conducted using engineering-equation-solver (EES). The heating loads to be handled by the systems were derived through an energy simulation tool TRNSYS 18. The model space was designed to have a floor area of $100\ \mathrm{m}^2$ with $3\ \mathrm{m}$-height, located in Seoul, South Korea. Structures such as walls, floors, ceilings, and windows, were designed to satisfy the U-values of domestic legal standard. There were five occupants in the space and the room temperature was maintained at 22 ℃. For both systems, the simulation was set to turn on only when residents occupied the space. Additional physical information for the model is described in Table 1.

Table 1. Model building parameters

Location	Seoul, South Korea	
Volume	$10\ \mathrm{m} \times 10\ \mathrm{m} \times 3\ \mathrm{m}, 300\ \mathrm{m}^3$	
Window-to-Wall Ratio	0.25	
U-value	Ceiling	$0.117\ \mathrm{W/m^2}K$
	Wall	$0.117\ \mathrm{W/m^2K}$
	Window	$0.95\ \mathrm{W/m^2K}$
	Floor	$0.132\ \mathrm{W/m^2K}$

Schedule	20:00 – 8:00 on weekdays, all day on weekends

The ventilation load (Q_{vent}) was acquired by calculating the temperature of the air passing through the enthalpy recovery ventilator (T_{erv}), and the airflow rate of ventilation requirements ($\dot{V}_{vent}$) through Eq. (1). The airflow rate of ventilation to fulfill the requirements for five residents was set to follow the ASHRAE standard 62.1 [8]. The temperature passing through the enthalpy recovery ventilator was calculated for sensible and latent heat exchange efficiencies. The efficiency was set to 70%, and 50% for the sensible heat exchange and for the latent heat exchange, respectively [9]. As shown in Figs. 1 and 2, an energy recovery ventilator was included in both systems. Thus, an equal ventilation load was added to the building load for both systems. For an enthalpy recovery ventilator, the heat exchange takes place between the outdoor air and return air from the conditioned zone. The outdoor air takes heat from the return air and supplies fresh air to conditioned room.

$$\dot{Q}_{vent} = \rho \cdot \dot{V}_{vent} \cdot c_p \cdot (T_{ra} - T_{erv}) \quad (1)$$

3.2. Air heating system

In order to design the optimal heat pump size for the residential place, it was important to make the compressor small, so that the temperature to be pumped up from the heat source was reduced. The design flow rate of the supply air (V_{sa}) was set to 1000 m^3/h, adequate for residential spaces, and the design temperature of the supply air (T_{sa}) was set to 34 ℃ to manage the derived heating load. Thus, the design temperature of the condenser was set to 40 ℃. The flow rate of the supply air ($\dot{V}_{sa}$) was variable and determined by the loads to be managed, as described in Eq. (2). The design temperature of the evaporator was set to −20 ℃ because it had to absorb sufficient heat from the cold outdoor air. Assuming that the evaporator exchanges sufficient heat with outdoor air by a large enough flow rate. The flow rate of the exhaust air ($\dot{V}_{ea}$) was controlled by the amount necessary at the condenser, calculated using Eq. (3) within 1000 m^3/h, that is the design flowrate of exhaust air. The load to be absorbed from the outdoor air was acquired by multiplying the cooling capacity at the evaporator ($Q_{hp,evap}$) and circulated amount of refrigerant (G). The coefficient of performance (COP) of the heat pump was considered as a fixed value, because the inverter control of the compressor in the heat pump was adapted by calculating the amount of refrigerant circulated (G) required every hour [10]. Hence, when the amount of heat from 1000 m^3/h of outside air at the evaporator was lacking compared with the amount required at the condenser for the heating load, the heating coil was turned on to heat up the supply air. The heat exchange efficiency between the outside air and the evaporator was assumed as 70%, and the heat exchange efficiency between the return air and condenser was also assumed as 70%. The compressive efficiency of the compressor was also 70% (used commonly) and the actual enthalpy of compressor was derived using the compressor efficiency. The design parameters of the heat pump are organized below in Table 2.

$$\dot{V}_{sa} = \frac{Q_{heating\ load} + Q_{ventilation\ load}}{\rho_{sa} \cdot cp_a \cdot (T_{sa} - T_{ra})} \quad (2)$$

$$\dot{V}_{ea} = \frac{Q_{hp,evap} * G}{\rho_{ea} \cdot cp_a \cdot (T_{oa} - T_{ea})} \quad (3)$$

Table 2. Designed specifications of the heat pump

Specifications	Values
Heating capacity	4 kW
COP	3.16
Circulating refrigerant	70 kg/h
Nominal horse power	2.5 PS

As explained in the details above, the heating coil was turned on only when the supply air did not reach its desired value. The primary energy consumption of the electric heating coil was multiplied by the primary energy factor of electricity.

The power of the variable flow fans was estimated using the general variable-air-volume fan power equation stated by ASHRAE 90.1 [11]. The part load ratio of the variable flow fan is the ratio of the present airflow rate

to the design airflow rate. The efficiency of each fan was assumed to 50%. The design pressure drop of each fan was referred from previous studies [12]. In particular, for the supply fan and exhaust fan, the pressure drop was used by referring to the value from the variable air volume (VAV) system.

3.3. Floor heating system

Similar to the way we calculated the performance of the heat pump system with the inverter control, the performance of the floor heating system was also calculated using the boiler by part load ratio. The performance of floor heating systems has been evaluated by several previous studies [13].

To manage the required heating load for the floor heating system, a conventional gas boiler was used to supply hot water to the pipes buried under the floor. The boiler was operated using the modulated part load ratio, depending on the heating load to be administered. The part load ratio of the boiler is the ratio of the present heating load to the design heating capacity of the boiler. It was set to 0.4 as referred to from previous studies [14].

The boiler energy ($\dot{Q}_{boiler}$) was calculated using the simple hot water boiler Eq. (4) suggested by Energy Plus, which takes into account the efficiency of boiler ($\varepsilon_{\text{boiler}}$) and the boiler efficiency performance curve (BEC). The efficiency of the boiler was set to 90% for this research.

$$Boiler\ Efficiency\ Curve = f(PLR_{boiler}) \tag{5}$$

$$\dot{Q}_{boiler} = \dot{Q}_{heating}/(\varepsilon_{boiler} \cdot Boiler\ Efficiency\ Curve) \tag{6}$$

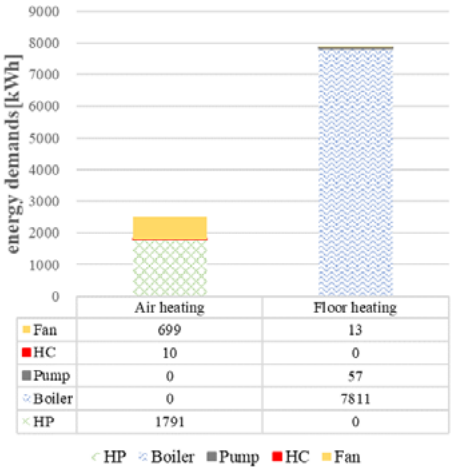
There was only one pump in the floor heating system supplying hot water. The power calculation of the pump was estimated by the fan power equation, suggested from Energy Plus, and the efficiency of the pump was assumed to be 60%.

4. Simulation Results

The energy performance evaluation of the air heating system and the floor heating system was conducted for four months, during the heating season from December to March. Figure 3 shows the total energy demands of each system, and also the demands of each component.

In the air heating system, the heat pump was only used to heat the room, and for managing the heating load and ventilation load as indicated in the simulation overview section. As shown in Fig. 4, fan power comprised a significant amount of energy needed for the heat pump heating system. This was because the equation used was a function of the part load ratio and pressure drop of the fan. Because the fans used in the air heating system were designed to have 1000 m^3/h, a significant pressure drop was applied.

In the floor heating system, the energy consumption was calculated assuming that a boiler produces hot water for traveling through the pipes to satisfy the heating and ventilation load. Thus, a gas boiler was controlled to modulate as required to reduce energy consumption. As a result, the air heating system requires 68.3% less energy than the floor heating system.

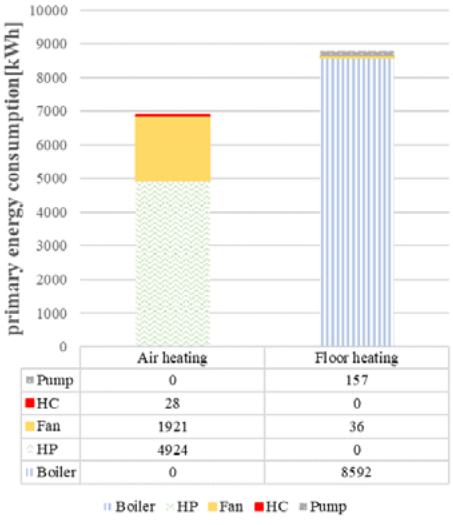


	Air heating	Floor heating
Fan	699	13
HC	10	0
Pump	0	57
Boiler	0	7811
HP	1791	0

Fig. 3. Energy Demands of Air Heating Mode and Floor System during Heating Season (Dec, Jan, Feb, Mar)

To compare the equivalent energy performance of both systems, and because the two systems have different energy sources, primary energy factors adequate for each system were applied. For the air heating system, the heat pump, fan, and auxiliary heater (electric heating coil) all use electricity. For the floor heating system, the boiler uses natural gas, however, the fan and pump both use electricity. The applied local primary energy factors are 2.75 for electricity, and 1.1 for natural gas. Because both systems process equivalent sensible loads, including ventilation load, the energy consumption of an energy recovery ventilator (ERV) fan was applied for both systems. As seen in Fig. 4, the primary energy consumption of the air heating system became larger than energy demands for it, and yet the air heating system still consumes less energy than the floor heating system.

In conclusion, it was observed that the air heating system consumed a total of 21.8% less primary energy when compared with the floor heating system using a conventional gas boiler in total.



	Air heating	Floor heating
Pump	0	157
HC	28	0
Fan	1921	36
HP	4924	0
Boiler	0	8592

Fig. 4. Primary Energy Consumption of Air Heating Mode and Floor System in Heating Season (Dec, Jan, Feb, Mar)

5. Conclusion

For this research, an air heating system with a heat pump and floor heating system with radiant floors were compared from the view of total energy consumption. The air heating system required 68.3% less energy than the floor heating system to handle total loads. Furthermore, the air heating system consumed 21.8% less energy than the floor heating system, even though a significant energy factor was observed because electricity was adapted for the system. If a gas heat pump was to be applied, instead of an electricity heat pump, it is calculated that an additional reduction of approximately 55% or more of reduced energy will be seen.

While floor heating systems are poor choices in view of the high energy consumption they require, they still are a strong preference among building occupants in regard to thermal comfort. Further studies in terms of occupant thermal comfort are required in the future. If further studies establish that floor heating systems are preferred for thermal comfort, combined heating systems using radiant floor heating and a heat pump can be adapted to apartments in Korea.

Acknowledgements

This work was supported by the National Research Foundation of Korea (NRF) grant (No. 2019R1A2C2002514) and the Korean Institute of Energy Technology Evaluation and Planning (KETEP) (No. 20184010201710).

References

[1] H.-W.L. Gook-sup Song, Bong-Ku Jeon, A study on the thermal comfort comparison between wooden floor and concrete floor based on seating life style, (2000).

[2] K.S. Chung, A study on the suggestion of thermal comfort range in radiant floor Ondol heating system, (2004).

[3] N.J. Hewitt, M.J. Huang, M. Anderson, M. Quinn, Advanced air source heat pumps for UK and European domestic buildings, Appl. Therm. Eng. 31 (2011) 3713–3719. https://doi.org/10.1016/j.applthermaleng.2011.02.005.

[4] B. Li, P. Wild, A. Rowe, Performance of a heat recovery ventilator coupled with an air-to-air heat pump for residential suites in Canadian cities, J. Build. Eng. 21 (2019) 343–354. https://doi.org/10.1016/j.jobe.2018.10.025.

[5] S.S. Bertsch, E.A. Groll, Two-stage air-source heat pump for residential heating and cooling applications in northern U.S. climates, Int. J. Refrig. 31 (2008) 1282–1292. https://doi.org/10.1016/j.ijrefrig.2008.01.006.

[6] B. Sohn, H.S. Kwon, Performance prediction on the application of a ground-source heat pump (GSHP) system in an office building, Korean J. Air-Conditioning Refrig. Eng. 26 (2014) 409–415. https://doi.org/10.6110/kjacr.2014.26.9.409.

[7] Y. Nam, R. Ooka, S. Hwang, Development of a numerical model to predict heat exchange rates for a ground-source heat pump system, Energy Build. 40 (2008) 2133–2140. https://doi.org/10.1016/j.enbuild.2008.06.004.

[8] D.T. Stevens, P. Francisco, S.J. Emmerich, D.A. Baylon, T.M. Brennan, R.R. Crawford, D.C. Delaquila, L.L. Delaura, S.C. Drumheller, P.W. Fairey, D.H. Heberer, R.L. Hedrick, T.P. Heidel, M.C. Jackson, D.E. Jacobs, G.P. Langan, J.W. Lstiburek, J. Malone, S.I. Mason, J.C. Moore, A.B. Musser, J.P. Proctor, P.H. Raymer, M.H. Sherman, I.S. Walker, E.D. Werling, C.S. Barnaby, ANSI/ASHRAE Standard 62.1-2013 - ventilation and acceptable indoor air quality in low-rise residential buildings ASHRAE staff liaison: Mark Weber, Ashrae. 2013 (2013) 58.

[9] Y. Hee Choi, D. Song, D. Seo, J. Kim, Analysis of the variable heat exchange efficiency of heat recovery ventilators and the associated heating energy demand, Energy Build. 172 (2018) 152–158. https://doi.org/10.1016/j.enbuild.2018.04.066.

[10] B.J. Dechesne, F.M. Tello-Oquendo, S. Gendebien, V. Lemort, Residential air-source heat pump with refrigerant injection and variable speed compressor: experimental investigation and compressor modeling, Int. J. Refrig. (2019). https://doi.org/10.1016/j.ijrefrig.2019.08.034.

[11] R. and A.-C.E. American Society of Heating, ANSI/ASHRAE/IES Standard 90.1-2013 (S-I edition): Energy standard for buildings except low-rise residential buildings, Am. Soc. Heating, Refrig. Air-

Conditioning Eng. Inc. 2013 (2013) 404–636. https://doi.org/http://dx.doi.org/10.1108/17506200710779521.

[12] S.J. Lee, H.J. Kim, H.W. Dong, J.W. Jeong, Energy saving assessment of a desiccant-enhanced evaporative cooling system in variable air volume applications, Appl. Therm. Eng. 117 (2017) 94–108. https://doi.org/10.1016/j.applthermaleng.2017.02.007.

[13] S.H. Park, W.J. Chung, M.S. Yeo, K.W. Kim, Evaluation of the thermal performance of a Thermally Activated Building System (TABS) according to the thermal load in a residential building, Energy Build. 73 (2014) 69–82. https://doi.org/10.1016/j.enbuild.2014.01.008.

[14] G.J.J.† Kyu Nam Rhee, Analysis of heating energy saving performance in low-energy residential buildings considering boiler part load efficiency, (2019) 736–739.

13th IEA Heat Pump Conference
April 26-29, 2021 Jeju, Korea

Energy benefits of ventilation, dehumidification, and water heating system based on liquid desiccant cycle

Soo-Jin Lee[a], Hansol Lim[a], Yong-Kwon Kang[a], Jae-Weon Jeong[a,*]

[a]Department of Architectural Engineering, College of Engineering, Hanyang University, Seoul, 04763, Republic of Korea

Abstract

This study aims to propose a liquid desiccant ventilation system and investigate the energy benefits of this system in comparison with a conventional variable air volume system. The proposed system is operated to achieve ventilation, dehumidification, and water heating. An energy simulation is performed via a series using TRNSYS 18 and the Engineering Equation Solver program. The simulation results demonstrate that the proposed system can save 27% of the primary energy in comparison with the reference system. The use of tap water for solution cooling instead of a cooling device is the main reason behind the significant energy savings. The heat exchanger used to provide hot water for the building with the aid of the scavenger air also reduces the overall operating energy of the proposed system.

© HPC2020.
Selection and/or peer-review under responsibility of the organizers of the 13th IEA Heat Pump Conference 2020.

Keywords: Ventilation, dehumidification, evaporative cooling, water heating, liquid desiccant ;

1. Introduction

Recently, an alternative energy saving air-conditioning method has been introduced, which involves a liquid desiccant system. In a liquid desiccant system, a solution absorbs water vapor from the air in the absorber, thereby dehumidifying the air and reducing the concentration of the solution. The solution is then re-concentrated in a regenerator using solar, waste, or district heat to desorb the water vapor to the air. Previous studies have reported upon the operation of liquid desiccant systems to achieve dehumidification using variable heat sources [1-5]. Such liquid desiccant systems can significantly reduce primary energy consumption because the liquid desiccant system is a decoupled system, which can be summarized as a decoupling of the sensible and latent load functions. Dong et al. [3] suggested a desiccant-enhanced evaporative (DEVap) cooling system, and the system involving a district heat source consumed 46% less primary energy compared with the system using a conventional gas boiler. Kim et al. [6] investigated the annual operating energy performance of a desiccant- and evaporative cooling-assisted 100% outdoor air system. The proposed system showed an 82% energy saving potential over the conventional variable air volume (VAV) system during the summer. Kim et al. [7] suggested the integration of a liquid desiccant system into an evaporative cooling-assisted 100% outdoor air system. The solar water heating system used to regenerate the desiccant solution contributed to the reduction of the required operation energy. Ham et al. [8] developed a liquid desiccant and dew point evaporative cooling-assisted 100% outdoor air system (LDEOAS) and evaluated its energy saving potential. Simulation results showed that LDEOAS could save 12% of the primary energy consumption compared with a conventional VAV system.

A liquid desiccant system requires a heat source for cooling the absorber inlet solution, as well as for providing heat for regeneration. Although a cooling tower (instead of a chiller) is used to provide energy savings associated with the cooling process, chilled water is not stably produced from the cooling tower in hot and humid climates.

* Corresponding author. Tel.: +82-2-2220-2370; fax: +82-2-2220-1945.
E-mail address: jjwarc@hanyang.ac.kr.

In this study, tap water is used for solution cooling as the water recovered the heat from the solution. After undergoing auxiliary heating to achieve a target temperature, the water is supplied into the building as hot water. Consequently, a liquid desiccant ventilation system, which can provide both ventilation and water heating, is proposed. This system consists of several components based on the liquid desiccant system and it is operated to achieve ventilation, dehumidification, and water heating. The energy saving potential of the proposed system over the conventional VAV system is estimated by conducting an energy simulation using a dynamic simulation program (i.e., TRNSYS 18 and the Engineering Equation Solver (EES)).

2. System Overview

2.1. Liquid desiccant ventilation system

The liquid desiccant ventilation system was proposed to accommodate the ventilation, dehumidification, and water heating processes that are essential for buildings in hot and humid climates. Fig. 1 illustrates the proposed system, which consists of an absorber, a regenerator, three heat exchangers, a heating coil, and an indirect evaporative cooler.

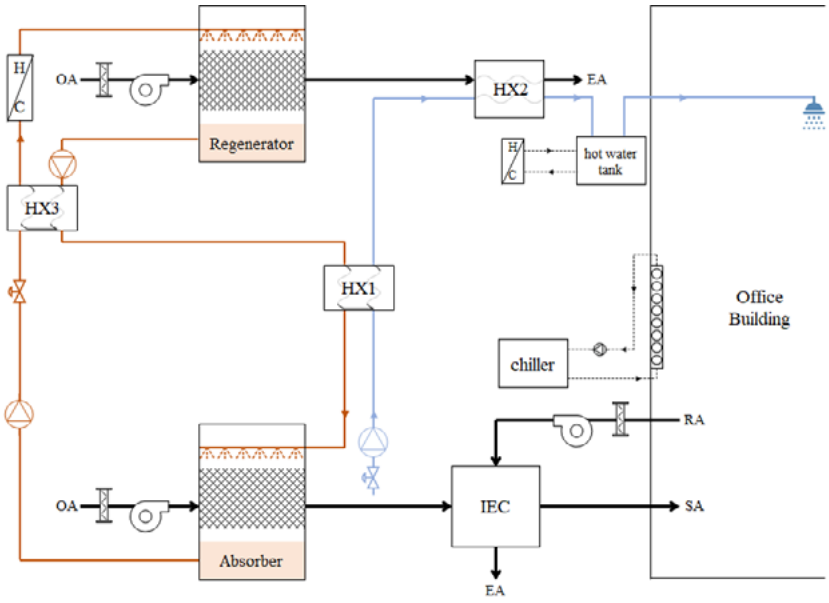


Fig. 1. Schematic of the liquid desiccant ventilation system

The process air is dehumidified by an absorber in a hot and humid climate. The air at the outlet of the absorber is dry and hot, and it must therefore be cooled to maintain the indoor air temperature. An indirect evaporative cooler is used to cool the process air. Room air is used as secondary source of air in the indirect evaporative cooler. The process air is cooled in the indirect evaporative cooler to a temperature below the average room temperature.

The process water flows into a liquid-to-liquid heat exchanger from tap water. The tap water recovers the sensible heat of the solution while the solution is cooled to available for absorber. Next, the process water passes into an air-to-liquid heat exchanger, wherein the sensible heat of the air leaving the regenerator is recovered. If the process water does not reach a set temperature, it is supplied to the building after undergoing the auxiliary heating process.

The proposed liquid desiccant system was operated for the dehumidification of the process air. A strong solution absorbs the water vapor from the process air in the absorber. Following this, a weak solution desorbs the water vapor to the scavenger air in the regenerator. These processes occur simultaneously, and the liquid desiccant system can be used continuously.

2.2. Variable air volume system

In a hot and humid climate, the supply air volume flow rate of a VAV system is determined based on the sensible and latent loads of the building. As shown in Fig. 2, outdoor air is mixed with the return air. The mixed air is cooled by a cooling coil. The cooling coil is activated to achieve dehumidification as well as cooling. The process air is then reheated after encountering the cooling coil to achieve the desired supply air conditions (i.e., 15°C, 80%).

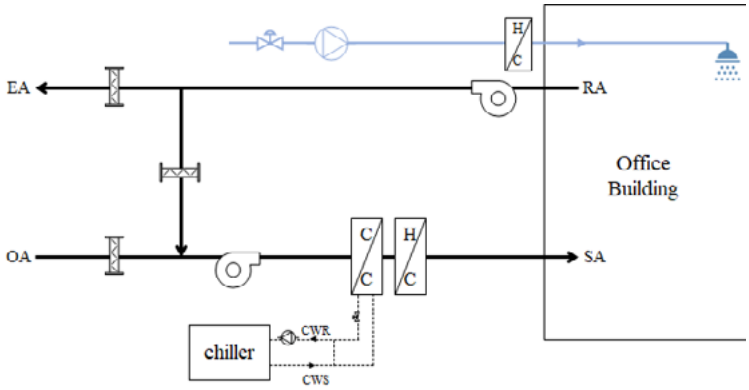


Fig. 2. Schematic of a VAV system

3. Simulation Overview

In this study, the hourly load profile of the model building was obtained by using energy simulation software (i.e., TRNSYS 18). The operating energy consumptions of both the systems required to meet the thermal load of the building were estimated using a commercial equation solver program (i.e., EES) by integrating both the system component models.

3.1. Model space

The model space was a $1{,}000\ \mathrm{m}^2$ office space with a $3\ \mathrm{m}$ ceiling height. Two $30\ \mathrm{m}^2$ windows were located on the south and north exterior walls, and the window-to-wall ratio was 0.16. The heat generation from the occupants and light were $115\ \mathrm{W/person}$ and $6\ \mathrm{W/m}^2$, respectively, and the occupancy and system schedules recommended by ASHRAE Standard 90.1 [9] for an office building were used to obtain the thermal loads by using TRNSYS 18. The room set conditions were a 26°C dry-bulb temperature and 60% relative humidity for cooling. The physical conditions of the model space are summarized in Table 1.

Table 1. Physical parameters of the model space

Location	Seoul, South Korea	
Weather data	TMY2	
Building type	Open plan office	
Geometry	31.62 m (W) × 31.62 m (L) × 3 m (H)	
U-Values	Ceiling	$0.297\ \mathrm{W/m^2K}$
	Wall	$0.252\ \mathrm{W/m^2K}$
	Windows	$1.4\ \mathrm{W/m^2K}$
Internal heat gain	Occupants	$115\ \mathrm{W/person}$ [10]
	Light	$6\ \mathrm{W/m^2}$
Room set points	Temperature	26°C
	Relative humidity	60%

3.2. Liquid desiccant unit

An empirical model for predicting the effectiveness of an absorber to absorb moisture was found in literature [11]. The effectiveness values of the absorber to affect the moisture and temperature of the input air indicate the degree of heat and mass transfer. The temperature differences between the air and desiccant solution allows for the exchange of thermal energy due to heat and mass transfer. The difference in the moisture contents between the air and desiccant solution permits mass transfer between the air and solution. In addition, the mass flow rates of the fluids and the system design parameters are also important factors in determining the effectiveness of the absorber. The initial mass flow rate and concentration of the desiccant solution are 0.5 kg/s and 42%, respectively. The absorber inlet temperature of the solution is 20-25°C. The process air that flows into the absorber is outdoor air. The equilibrium humidity ratio and enthalpy of the desiccant solution were calculated using previous studies [12,13].

The regenerator model was suggested by Martin and Goswami [13]. The equation for this model is a function of several variables. These variables are combined to form non-dimensional parameters, and this model can predict the effectiveness of the regenerator using these non-dimensional parameters. The liquid-to-gas ratio is set at 4.0, and the temperature effectiveness of the regenerator is same as the mass effectiveness [7]. The equilibrium humidity ratio of the regenerator is calculated using the same study that the absorber was based upon [12]. The inlet temperature of the solution is set at 60°C. The effectiveness of the dehumidification and regenerator were determined using Eq. 1 and 2. The absorber and regenerator outlet conditions of the process air were determined using Eq. 3.

$$\varepsilon_{abs} = \frac{\left(1 - \frac{0.024\left(\frac{\dot{m}_a}{\dot{m}_s}\right)^{0.6} exp\left(1.507\frac{T_{a,in}}{T_{s,in}}\right)}{(aH)^{-0.185}\pi^{0.638}}\right)}{\left(1 - \frac{0.192\, exp\left(0.615\frac{T_{a,in}}{T_{s,in}}\right)}{\pi^{-21.498}}\right)} \quad (1)$$

$$\varepsilon_{reg} = 1 - 48.3\left(\frac{\dot{m}_s}{\dot{m}_a}\right)^{0.396\left(\frac{\gamma_L}{\gamma_C}\right)-1.57}\left(\frac{h_{a,in}}{h_{s,in}}\right)^{-0.751}(aH)^{0.0331\left(\frac{\gamma_L}{\gamma_C}\right)-0.906} \quad (2)$$

$$\varepsilon_{abs,reg} = \frac{w_{a,in}-w_{a,out}}{w_{a,in}-w_{eq}} = \frac{T_{a,in}-T_{a,out}}{T_{a,in}-T_{s,in}} \quad (3)$$

3.3. Indirect evaporative cooler

The dry-bulb temperature at the outlet of the indirect evaporative cooler (IEC) can be estimated using Eq. 4 when the IEC effectiveness is provided. In the proposed system, the humidity ratio of the process air that leaves the IEC is identical to that of the exiting liquid desiccant because condensation and dehumidification does not occur in the IEC. The IEC effectiveness was assumed to be 0.7.

$$\varepsilon_{IEC} = \frac{T_{pri,in}-T_{pri,out}}{T_{pri,in}-WBT_{sec,in}} \quad (4)$$

3.4. Heat exchanger

Two different types of heat exchangers were used in this study for the heat recovery processes. One is a liquid-to-liquid type and the other is liquid-to-air type. The liquid-to-liquid type heat exchanger was used to transfer the heat from the solution leaving the regenerator to the solution leaving the absorber. The other liquid-to-liquid type heat exchanger was used to transfer the heat from the solution leaving heat exchanger 3 to the tap water. The liquid-to-air type heat exchanger was used to transfer the heat from the scavenger air to the process water. The outlet conditions of each exchanger were estimated using Eqs. 5 to 7 and the efficiency of each heat exchanger was assumed to be 0.8, in accordance with literature [5].

$$C^* = MIN(\dot{m}_{hot}C_{p,hot}, \dot{m}_{cold}C_{p,cold}) \quad (5)$$

$$\dot{Q}_{ideal} = C^*(T_{hot,in} - T_{cold,in}) \quad (6)$$

$$\dot{Q}_{real} = \varepsilon\dot{Q}_{ideal} = \dot{m}_{hot}C_{p,hot}\left(T_{hot,in} - T_{hot,out}\right) = \dot{m}_{cold}C_{p,cold}\left(T_{cold,out} - T_{cold,in}\right) \quad (7)$$

3.5. Supply air flow rate

In the VAV system, the supply air flow rate was determined based on the sensible and latent loads using Eq. 8. The return air flow rate was calculated using the supply air flow rate and the minimum required outdoor air ventilation rate, as recommended by the ASHRAE Standard 62.1. On the other hand, in the liquid desiccant ventilation system, the supply air flow rate was same as the minimum required outdoor air ventilation rate. The required outdoor air flow rates per person and per unit area are $2.5\,\mathrm{L/(s\,person)}$, and $0.3\,\mathrm{L/(s\,m^2)}$, respectively, based on the ASHRAE guidelines for an office space. Thus, the minimum required outdoor air ventilation rate for the both systems was $0.51\,\mathrm{kg/s}$, and the maximum supply air flow rate for the VAV system was determined to be $1.265\,\mathrm{kg/s}$.

$$\dot{m}_{sa} = \frac{\dot{Q}_{sen}+\dot{Q}_{lat}}{h_{ra}-h_{sa}} \quad (8)$$

3.6. Cooling and heating coil

A cooling coil is activated to achieve dehumidification and cooling of the process air in the VAV system. This coil performs dehumidification via condensation, as well as cooling of the process air, to satisfy the target humidity ratio of the process air. The cooling load of the coil was calculated using the difference between the inlet and outlet enthalpies. The inlet condition of the cooling coil is same the mixed air condition and the outlet condition is set to be the dew point.

A heating coil heated the solution in the regenerator of the liquid desiccant ventilation system. In the VAV system, the process air is reheated by a heating coil. The outlet temperature of the cooling coil is low such that reheating is necessary to satisfy the set point conditions. Additionally, a heating coil is used for water heating in both systems.

3.7. Parallel unit

In the proposed system, the supply air did not remove the sensible load of the conditioned zone, whereas the supply air of the reference system sufficiently removed the sensible load. Therefore, a fan coil unit was used as a parallel system in the proposed system, in which the remaining sensible load of the conditioned zone was removed. The load of the parallel unit was determined by Eq. 9.

$$\dot{Q}_{parallel} = \dot{Q}_{sen} - \dot{m}_{sa}(h_{ra} - h_{sa}) \quad (9)$$

3.8. Chiller and boiler

Energy derived from a chiller was consumed in both systems. In the proposed system, it is used as a parallel unit that is located in the building. In the reference system, it is used as a cooling coil. The air-cooled chiller model provided be EnergyPlus [14] was used for estimating the chiller energy consumption.

A conventional gas boiler was used for the reheating coil of the VAV system, heating coil of the liquid desiccant ventilation system, and water heater for both systems. The boiler was operated to achieve the heating loads required by the reheating coil, heating coil, and water heaters. The boiler was modeled using a function of boiler efficiency and the efficiency performance curve. The efficiency curve is a cubic efficiency curve of the part load ratio that was provided by EnergyPlus [14]. The part load ratio is the ratio of the current heating load to the boiler capacity. The theoretical boiler efficiency was set at 82% in this study [3].

3.9. Fan and pump

The design of the fan powers in both systems were calculated using a fan efficiency of 0.5 and Eq. 10. The maximum air flow rate was used as the volume flow rate of this design. The simulation of the proposed system was constructed using three fans: variable volume supply, return, and constant volume liquid desiccant (LD). The reference system was designed with variable volume supply and return fans. The fan power at the variable volume flow rate was estimated using Eq. 11 based on the generic fan power curve.

$$P_{fan,design} = \frac{\dot{V}_{design} \times \Delta P}{\eta} \tag{10}$$

$$P_{fan} = (0.0013 + 0.0447PLR + 0.9506PLR^2 - 0.0998PLR^3) \times P_{fan,design} \tag{11}$$

The pump powers for both systems were calculated using Eq. 12 with a pump efficiency of 0.6. In the proposed system, the constant speed pump supplies the liquid desiccant circulation, hot water, and the chilled water for the cooling coil and fan coil unit (FCU). In the reference system, the pump supplies the chilled water for the cooling coil and the hot water.

$$P_{pump} = \frac{\dot{m} \times H \times g}{\eta} \tag{12}$$

4. Simulation Results

4.1. Thermal behavior of the air

The conditions of the process air over the course of a day are depicted in Fig. 3. The hot and humid outdoor air was dehumidified to the required humidity ratio in the liquid desiccant unit and cooled to below the set temperature of the room in the liquid desiccant unit and indirect evaporative cooler. The temperature gradient of the process air was greatest in the indirect evaporative cooler. Finally, the supply air possessed approximately a 0.007 kg/kg humidity ratio and 22°C dry-bulb temperature.

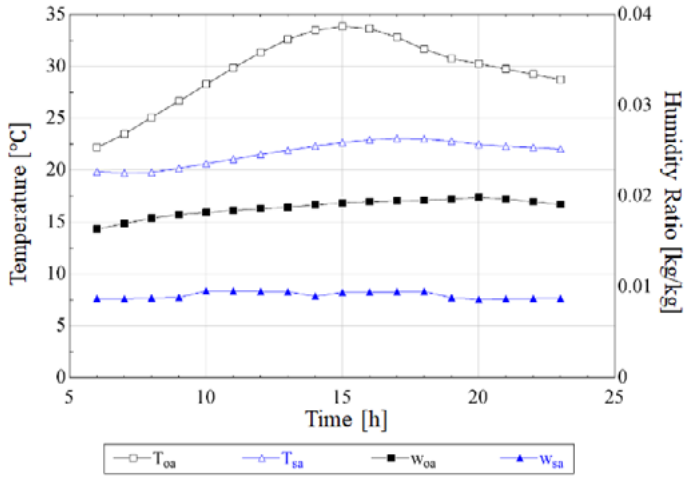
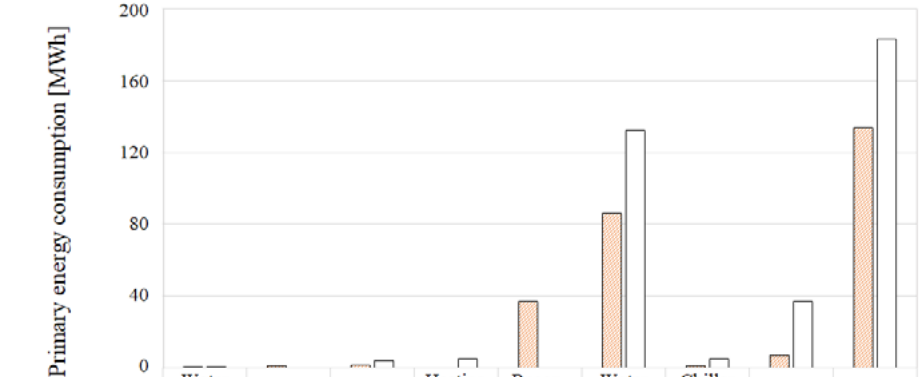


Fig. 3. Temperature and humidity ratio profile of the process air

4.2. Primary energy consumption

To compare the overall energy performances of the proposed and reference systems, the operating energy consumption was converted into the primary energy consumption for each heat source.

Fig. 4. shows the comparison of the primary energy consumptions in the proposed and reference systems. The water-heating energy is lessened in the proposed system as heat from the two heat exchangers is recovered by the process water, while the reference system consumed this heat. Although the proposed system consumed the heat for the regenerator, the total heating energy of the proposed system is less than that of the reference system because the recovered heat from the solution was used for water heating in the proposed system. The proposed system also demonstrated the requirement of a lower amount of cooling energy for the solution because tap water is used for solution cooling. Additionally, the indirect evaporative cooler was used to supply air cooling. The fans consumed energy in the supply, return, and liquid desiccant cycle processes in the proposed system. The fans in the reference system consumed energy for only the supply and return processes. The proposed system consumed less fan energy than the reference system because the air flow rate was equal to the minimum ventilation rate. In contrast, the reference system air flow rate was much greater than the minimum ventilation rate. Although the proposed system used more pump energy than the reference system because of the liquid desiccant circulation, the pump energy of the proposed system is less than that of the reference system. The chiller pump of the reference system consumed more energy than that required liquid desiccant circulation in the proposed system. Consequently, the proposed system consumed 27.0% less primary energy compared with the reference system, as shown in Fig. 4.



	Water pump	LD pump	Air fan	Heating coil	Regen-erator	Water heating	Chiller pump	Chiller	Total
Proposed system	0.5	1.0	1.3	0.0	37.0	85.9	1.0	7.1	133.8
Reference system	0.5	0.0	4.1	4.9	0.0	132.0	4.7	37.1	183.3

Fig. 4. Comparison of the primary energy consumptions of the two systems

5. Conclusion

This study proposed a liquid desiccant ventilation system that can provide both ventilation and water heating. The energy savings associated with the operation of the proposed system was quantitatively analyzed through comparison with a VAV reference system using a TRNSYS 18 and EES simulation. The integration of the liquid desiccant and water heating cycles was proposed to recover the heat required for water heating and reduce the cooling energy required for dehumidification. The possibility of maintaining the required supply-air conditions using an indirect evaporative cooler was investigated through a detailed energy simulation.

The operating energy consumption of the liquid desiccant ventilation system revealed that the proposed system can provide operating energy savings of 27.0% during the summer in comparison with the reference system. The potential for such significant energy savings is mainly due to the heat transferred from the liquid desiccant to the water heating cycle. This strategy also contributes to reducing the cooling energy required for the solution.

Considering the proposed system for use as a ventilation system, energy benefits were achieved in a hot and humid climate. Heat may be recovered from the solution to the water when the liquid desiccant and water heating cycles are operated simultaneously. This system should next be tested for use in dry and cold climates.

Acknowledgements

This work was supported by the National Research Foundation of Korea (NRF) grant (No. 2019R1A2C2002514) and the Korean Institute of Energy Technology Evaluation and Planning (KETEP) (No. 20184010201710).

References

[1] Gommed K, Grossman G. Experimental investigation of a liquid desiccant system for solar cooling and dehumidification. *Sol. Energy* 2007;**81**:131–138.
[2] Zhang L, Hihara E, Saikawa M. Combination of air-source heat pumps with liquid desiccant dehumidification of air. *Energy Convers. Manag.* 2012;**57**:107–116.
[3] Dong HW, Lee SJ, Yoon DS, Park JY, Jeong JW. Impact of district heat source on primary energy savings of a desiccant-enhanced evaporative cooling system. *Energy* 2017;**123**:432–444.
[4] Lim H, Jeong JW. Energy saving potential of thermoelectric modules integrated into liquid desiccant system for solution heating and cooling. Appl. Therm. Eng. 2018;136:49–62.
[5] Shin JH, Park JY, Jo MS, Jeong JW. Impact of heat pump-driven liquid desiccant dehumidification on the energy performance of an evaporative cooling-assisted air conditioning system. *Energies* 2018;**11**:345.
[6] Kim MH, Park JY, Sung MK, Choi AS, Jeong JW. Annual operating energy savings of liquid desiccant and evaporative-cooling-assisted 100% outdoor air system. *Energy Build.* 2014;**76**:538–550.
[7] Kim MH, Park JS, Jeong JW. Energy saving potential of liquid desiccant in evaporative-cooling-assisted 100% outdoor air system. Energy 2013;59:726–736.
[8] Ham SW, Lee SJ, Jeong JW. Operating energy savings in a liquid desiccant and dew point evaporative cooling-assisted 100% outdoor air system. *Energy Build.* 2016;**116**:535–552.
[9] Ferguson SC. ASHRAE Standing Standard Project Committee 90.1 Cognizant TC: TC 7.6., Systems Energy Utilization SPLS Liaison: Mark Modera ASHRAE Staff Liaison, 2013
[10] ASHRAE, Handbook HVAC Fundamentals, 2009.
[11] Chung TW, Luo CM. Vapor pressures of the aqueous desiccants. *J. Chem. Eng. Data* 1999;**44**:1024–1027.
[12] Fumo N, Goswami DY. Study of an aqueous lithium chloride desiccant system: air dehumidification and desiccant regeneration. *Sol. Energy* 2002;**72**:351–361.
[13] Martin V, Goswami DY. Effectiveness of heat and mass transfer processes in a packed bed liquid desiccant dehumidifier/regenerator. *Hvac&R Research* 2010;**6**:21–39.
[14] EnergyPlus. Energyplus engineering reference. U.S. Department of Energy, Building Technologies Program 2013.

13th IEA Heat Pump Conference
April 26-29, 2021 Jeju, Korea

Energy Performance Comparison of Two Different Types of Heat Pump-Driven Liquid Desiccant-Assisted Air-Conditioning Systems for an Apartment Building

Jae-Hee Lee[a], Hansol Lim[a], Hye-Won Dong[a], Jae-Weon Jeong[a,*]

[a]Department of Architectural Engineering, College of Engineering, Hanyang University, Seoul, 04763, Republic of Korea

Abstract

The purpose of this study is to compare the energy performance of two heat pump-driven liquid desiccant (HPLD) systems that use different mechanisms for solution pre-conditioning. The design and operating logic of the HPLD systems were proposed for an apartment building. The HPLD system comprises a liquid desiccant (LD) unit for dehumidifying the process air, and a heat pump (HP) unit for cooling and heating the LD solution and cooling the process air. In Case A, the temperature and concentration of the solution can be controlled simultaneously in the HPLD system using a single sump, whereas in Case B, they are controlled separately using a dual sump that uses an additional simple device. The load of the target zone and energy performance of the HPLD system were analyzed using TRNSYS 18 and commercial engineering equation solver (EES), respectively. The results showed that the method used in Case B saved 77 % of the operating energy. The mean system COP in Case B was three times higher compared to that in Case A owing to the decrease in the solution cooling and heating loads.

© HPC2020.
Selection and/or peer-review under responsibility of the organizers of the 13th IEA Heat Pump Conference 2020.

Keywords: Heat pump system; Liquid desiccant system; Energy consumption; Apartment building;

1. Introduction

Recently, a liquid desiccant air conditioning (LDAC) system has emerged as an interesting system among independent handling devices for latent and sensible loads of air conditioning in terms of energy saving potential and improvement in indoor air quality [1,2]. The desiccant solution should be pre-cooled before entering the absorber and preheated before entering the regenerator to widen the difference in vapor pressure between the solution and air for enhanced dehumidification and regeneration effectiveness [3]. This process is the major factor for operating energy consumption in LDAC, and it can be realized by using low-grade heat sources [4] Heat pump systems have drawn attention because it can cover the solution cooling and heating loads simultaneously by the heat absorption process of the evaporator and heat release process of the condenser [5]. Hence, a heat pump-driven liquid desiccant (HPLD) system is considered as an efficient LDAC application owing to its ability of independent temperature and humidity conditioning and energy efficiency [6]. Additionally, a capacity matching of the HPLD system between the solution cooling and heating loads of the LD unit and the evaporator and condenser loads of the HP unit was considered [7].

On the other hand, LDAC applications have the drawbacks of large scale production and high initial cost, which hinder its potential for widespread utilization. Hence, LDAC applications were initially targeted toward commercial buildings and not residential buildings despite the distinct advantages of independent temperature and humidity control. To make LDAC applications attractive for the residential market, the LDAC applications should be improved through products focusing on the simplicity and compactness of the system [8,9]. The

* Corresponding author. Tel.: +82-2-2220-2370; fax: +82-2-2220-1945.
E-mail address: jjwarc@hanyang.ac.kr (J.-W. Jeong).

HPLD system has been recognized as a compact one among the LDAC applications. However, there is a lack of research regarding its applicability in an apartment building [10].

In this research, two HPLD systems that used different mechanisms for pre-conditioning the solution temperature and concentration were designed for an apartment building, and the overall operation strategies were explained. Energy simulation for air conditioning during the summer operation period was performed using the commercial engineering equation solver (EES) program and TRNSYS 18. The applicability of the two HPLD systems in an apartment building was compared based on their performance in terms of energy saving potential and system coefficient of performance (COP).

2. System Overview

The system consists of a heat pump (HP) unit and a liquid desiccant (LD) unit. The LD unit dehumidifies the process air to remove the indoor latent load. The HP unit pre-cools or preheats the desiccant solution and cools the dried process air to remove the indoor sensible load. To cool the solution and air simultaneously, the refrigerant from the HP unit is driven in parallel to two evaporators. Thus, the system can operate as a dehumidifying and cooling device in summer without a separate air handling device.

2.1. Heat pump unit

The heat pump (HP) unit consists of a solution-side evaporator to pre-cool the solution before entering the absorber, an air-side evaporator to cool the dried air returning from the absorber to meet the design target temperature of the supply air, a compressor using a frequency inverter for part-load operation, a solution-side condenser to preheat the solution before entering the regenerator, and an electric expansion valve (EEV) for controlling the refrigerant flow rate. The refrigerant absorbs heat from the heat sources of the evaporators (i.e., cooling capacity) and releases the heat to the heat sink of the condenser (i.e., heating capacity) through the phase change process. Considering the part-load operation mode to cover the variation of cooling loads of the desiccant solution and air, the compressor with inverter control and EEV are used. Then, a required electrical input power of the compressor by the load control can be estimated [11].

2.2. Liquid desiccant unit

The LD unit consists of an absorber (ABS) that operates as a dehumidifying device in summer, and a regenerator (REG) that makes strong solution. The outdoor air and return air are mixed and passed through the absorber to discharge its moisture to the cooled desiccant solution. The temperature of the dried absorber outlet air can be separately controlled by the air-side evaporator of the HP unit. After the dehumidification process, the absorber outlet solution becomes diluted and heated compared to the inlet state because the cooled absorber inlet solution is in contact with the hot and humid air that releases exothermic heat as the solution absorbs the moisture from the air [12]. The scavenging air that adopts the outdoor air, passes through the regenerator and absorbs the moisture from the heated desiccant solution. After the regeneration process, the regenerator outlet solution becomes strong and cool compared to the inlet state; because the heated regenerator inlet solution is in contact with the relatively cold air.

2.3. Heat pump driven liquid desiccant system

In this research, two HPLD systems are discussed: an HPLD system using a single sump i.e., Case A, (Fig. 1), and an HPLD system using dual sump i.e., Case B, (Fig. 2). In Case A, the cold and dilute absorber outlet solution, and the hot and strong regenerator outlet solution are mixed in a single sump. Hence, the concentration and temperature of the outlet solutions can be pre-conditioned simultaneously in the single sump by the mixing process that replaces the function of a conventional heat exchanger between the absorber and regenerator outlet solutions.

In Case B, the outlet solutions from the absorber and regenerator flow toward the respective sump and then circulate to each packed bed. The solution is cooled and diluted in the absorber sump. Whereas, the solution is heated and concentrated in the regenerator sump. An additional condenser is required for releasing the remaining heat to the regenerator outlet air considering the capacity matching between the HP unit (evaporator and condenser loads) and the LD unit (cooling and heating loads of the desiccant solution and air). Moreover, an additional simple device is required for exchanging the solutions between the absorber and regenerator sumps to maintain the solution concentration of each sump constant. Hence, two pipes are placed between the

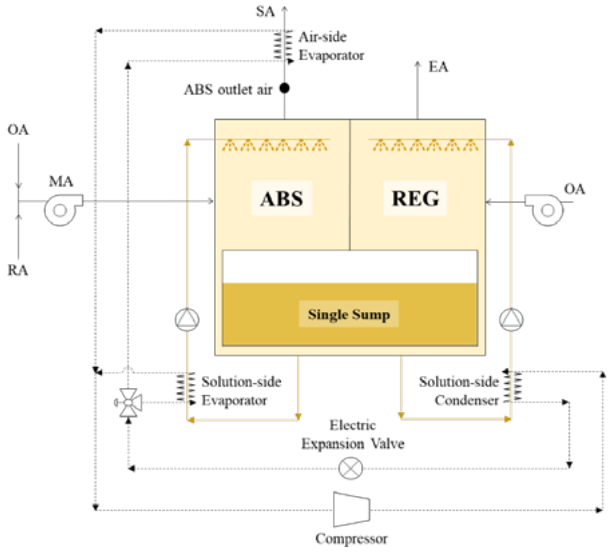


Fig. 1. Schematic diagram of a single sump HPLD system (Case A)

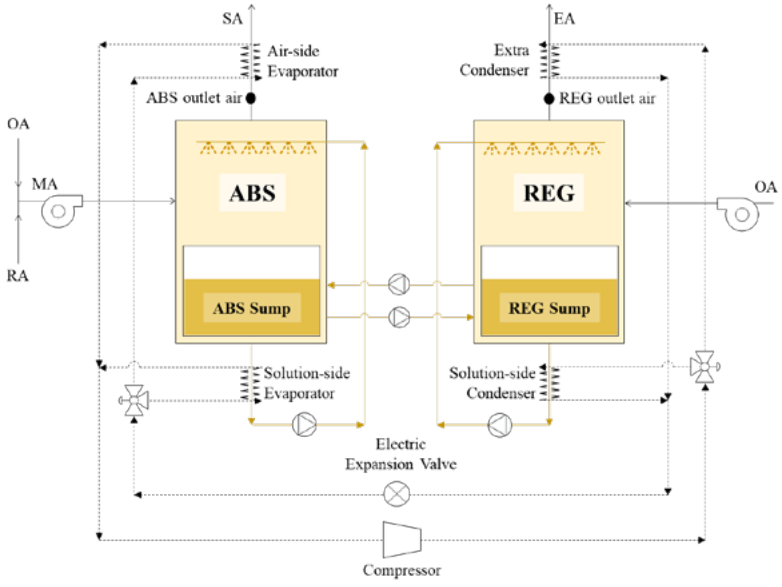


Fig. 2. Schematic diagram of a dual sump HPLD system (Case B)

dual sump for solution exchange after the dehumidification and regeneration process. The temperature and concentration of the outlet solutions can be pre-conditioned separately using the additional device. Then, it can be predicted that the compressor will work in the part-load operation mode deriving the energy consumption saving owing to the decrease in the solution cooling and heating loads.

3. Simulation Overview

3.1. Model building

A single-storey household with 4 occupants in an apartment building located in Seoul, South Korea was selected as the model building for the simulation. Table 1 summarizes the detailed information of the model building that was based on passive house design standards. The indoor target condition was set at 26 °C (T_{ra}) with 50 % relative humidity (RH_{ra}) as per the comfort zone of ASHRAE standard 55. TRNSYS 18 was used for obtaining the hourly thermal load profile of the model during the summer operation period (i.e., June–September). Considering the system compactness for the apartment building, the design flow rate of the supply air ($\dot{V}_{sa,design}$) was assumed as 800 m^3/h and the real time flow rate was variable according to the hourly thermal load. The design target condition of the supply air was determined as 15 °C ($T_{sa,design}$) with 10 g/kg humidity ratio ($\omega_{sa,design}$) based on the peak sensible load and peak latent load. The overall energy simulation was conducted using EES.

Table 1. Model building parameters

Parameters	Conducted values
Simulation period	Cooling season (June-September)
Location	Seoul, South Korea
Occupant/Schedule	4 people/ HVAC schedule addressed in ASHRAE standard 90.1
Volume	192 m^3 (10 m (W) × 8 m (D) × 2.4 m (H), a household on one floor in an apartment building)
Window-to-wall ratio	South: 0.44, North: 0.05
U-value	Floor: 0.39 W/m^2·K, Exterior wall: 0.15 W/m^2·K
Internal heat gains	Lights: 2.7 W/m^2, Equipment: 8 W/m^2, People: 70 W/person of sensible heat, 45 W/person latent heat
Indoor air set conditions	26°C dry-bulb temperature, 50% relative humidity
Supply air target conditions	800 m^3/h, 15°C dry-bulb temperature, 10 g/kg humidity ratio

3.2. Liquid desiccant unit model

Lithium chloride (LiCl) was the solution selected in this research. The absorber and regenerator solution were circulated at a constant mass flow rate of ($\dot{m}_s$) 0.26 kg/s to meet the target condition of the supply air in the proposed system. The regenerator inlet air was blown at a constant rate of 1000 m^3/h to achieve a satisfactory regeneration rate and treat the extra condensing load.

The dehumidification effectiveness (ε_{abs}) in the absorber and regeneration effectiveness (ε_{reg}) in the regenerator are defined as the ratio of the humidity ratio change between the packed bed inlet and outlet air to the maximum change with respect to the equilibrium humidity ratio ($\omega_{eq,s}$) of the inlet solution (Eq. (1) and (2)). Additionally, the dehumidification and regeneration effectiveness can be defined as the temperature change in the inlet and outlet air with the inlet solution temperature (Eq. (1) and (2)). The equilibrium humidity ratio ($\omega_{eq,s}$) of the inlet solution can be estimated with its equilibrium vapor pressure (p_s) (Eq. (3)), which is expressed as a second-order polynomial function established by Fumo and Goswami [13].

$$\varepsilon_{abs} = \frac{\omega_{abs,i,a}-\omega_{abs,o,a}}{\omega_{abs,i,a}-\omega_{abs,eq,s}} = \frac{T_{abs,i,a}-T_{abs,o,a}}{T_{abs,i,a}-T_{abs,i,s}} \quad (1)$$

$$\varepsilon_{reg} = \frac{\omega_{reg,o,a}-\omega_{reg,i,a}}{\omega_{reg,eq,s}-\omega_{reg,i,a}} = \frac{T_{reg,o,a}-T_{reg,i,a}}{T_{reg,i,s}-T_{reg,i,a}} \quad (2)$$

$$\omega_{eq,s} = 0.622 \times \frac{p_s}{101.325-p_s} \quad (3)$$

When the conditions of the packed bed inlet solution ($T_{i,s}$, $\chi_{i,s}$) and air ($T_{i,a}$, $\omega_{i,a}$) are given, the dehumidification effectiveness (ε_{abs}) and regeneration effectiveness (ε_{reg}) can be predicted, and the temperature and humidity ratio of the outlet air ($T_{o,a}$, $\omega_{o,a}$) can be estimated using Eq. (1) and Eq. (2). To

predict the dehumidification effectiveness (ε_{abs}), the model derived by Chung and Luo was used [14]. The regeneration effectiveness (ε_{reg}) was fixed at 0.3 because its experimental value in the previous literature slightly fluctuated from 0.3 to 0.4 under variable operating conditions [15].

The dehumidified moisture rate ($\dot{m}_{dehum}$) from the humid air in the absorber can be calculated by multiplying the mass flow rate of the inlet air and the humidity ratio change before and after passing through the absorber. Similarly, the regeneration rate ($\dot{m}_{regen}$) in the regenerator can be calculated by multiplying the mass flow rate of the scavenging air and its humidity ratio change. The conditions of the absorber and regenerator outlet solution can be estimated based on the mass balance and energy balance.

Considering the compactness of the system, the volume of the dual sump was set at 20 L and that of the single sump at 40 L. It was assumed that the initial conditions of the desiccant solution in the sump can be affected by the indoor set conditions. Therefore, the initial temperature ($T_{sump,old}$) and concentration ($\chi_{sump,old}$) of the solution in the sump was set to 26 °C and 30 %, and initial solution weight of the sump was set to 26 kg ($W_{sump,old}$) based on the LiCl density. It was assumed that the real-time state of the single sump can be constant at 26 °C with 30 % concentration and 26 kg of weight because the opposite outlet solutions were mixed in the single sump. On the other hand, the conditions such as temperature, concentration, and weight of the dual sump changes whenever the system operates. Hence, the conditions were calculated with transient analysis using EES. Additionally, the appropriate rate for the solution exchange was estimated to be 4 L/h, which is sufficient to cover both the dehumidification and regeneration rate.

3.3. Heat pump unit model

The refrigerant type selected in this research was R410A. To analyze each component of the heat pump (HP) unit, several assumptions were made as follows: 1) the evaporating temperature (T_{evap}) and condensing temperature (T_{cond}) of the refrigerant are constant during its phase change. 2) The effectiveness of the heat exchange of the evaporator (ε_{evap}) and condenser (ε_{cond}) is constant at 0.7, and the isentropic efficiency (η_{comp}) of the compressor is 0.75. 3) The superheating and subcooling degree can be neglected.

The evaporating and condensing temperature were determined as 12 °C and 55 °C based on several requirements as follows: 1) the estimated temperature and humidity ratio of the supply air should approach the target conditions of 15 °C and 10 g/kg. 2) The estimated temperature of the solution before entering the regenerator should be above 40 °C. 3) The required input power of the compressor should be below 4 horsepower for an apartment building. 4) After compression, the refrigerant should completely release its heat to the heat sink to avoid extra condensing load.

The thermodynamic properties of R410A of each state in the HP cycle were acquired by intrinsic function of the EES based on the determination of the evaporating and condensing temperature. The actual compressor outlet enthalpy ($h_{act,comp,o}$) can be calculated by Eq. (4), with the compressor isentropic efficiency (η_{comp}).

$$h_{act,comp,o} = \frac{h_{ideal,comp,o} - h_{evap,o}}{\eta_{comp}} + h_{evap,o} \tag{4}$$

Figure 3 shows the calculation process of the cooling capacity of the evaporator, required input power of the compressor, and the heating capacity of the condenser. The actual cooling capacity of the solution-side evaporator ($\dot{Q}_{act,evap,s}$) and air-side evaporator ($\dot{Q}_{act,evap,a}$) can be calculated using Eq. (5) and (6), based on the evaporating temperature (T_{evap}) and heat exchange effectiveness (ε_{evap}). Then, the actual cooled temperature of the absorber inlet solution ($T_{abs,i,s}$) and supply air (T_{sa}) can be obtained by Eq. (7) and (8).

$$\dot{Q}_{act,evap,s} = \varepsilon_{evap}\left(\dot{m}C_p\right)_{abs,i,s}\left(T_{abs,sump,old} - T_{evap}\right) \tag{5}$$

$$\dot{Q}_{act,evap,a} = \varepsilon_{evap}\left(\dot{m}C_p\right)_{abs,o,a}\left(T_{abs,o,a} - T_{evap}\right) \tag{6}$$

$$\dot{Q}_{act,evap,s} = \left(\dot{m}C_p\right)_{abs,i,s}\left(T_{abs,sump,old} - T_{abs,i,s}\right) \tag{7}$$

$$\dot{Q}_{act,evap,a} = \left(\dot{m}C_p\right)_{abs,o,a}\left(T_{abs,o,a} - T_{sa}\right) \tag{8}$$

The total cooling capacity ($\dot{Q}_{act,evap,tot}$) of the evaporator can be expressed as the sum of the actual cooling capacity of the solution-side evaporator and air-side evaporator. The refrigerant flow rate ($\dot{m}_{ref}$) required to treat the cooling capacity can be calculated by Eq. (9), using the enthalpy change before and after passing

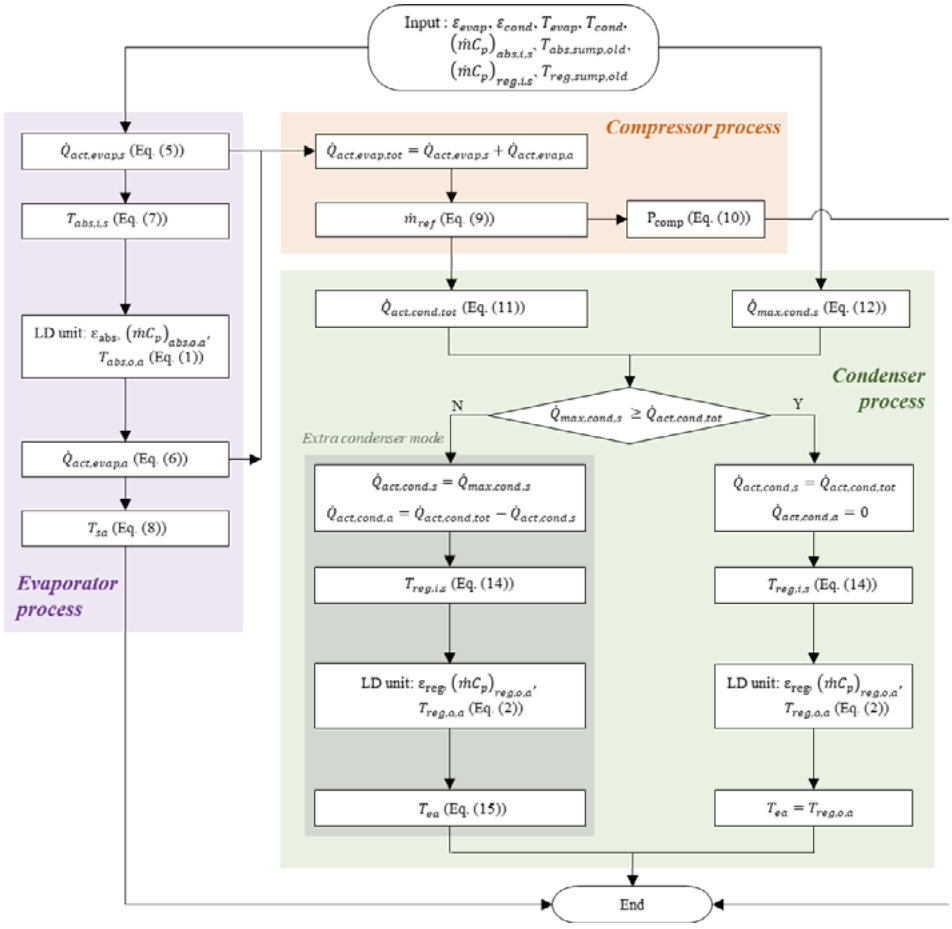


Fig. 3. Flow chart of the calculation process of the heat pump unit

through the evaporator. Then, the required input power (P_{comp}) to the compressor can be assessed by Eq. (10) with the calculated refrigerant rate.

$$\dot{Q}_{act,evap,tot} = \dot{m}_{ref}(h_{evap,o} - h_{evap,i}) \tag{9}$$

$$P_{comp} = \dot{m}_{ref}(h_{act,comp,o} - h_{evap,o}) \tag{10}$$

The total heat that should be completely released to the heat sink ($\dot{Q}_{act,cond,tot}$) can be estimated by Eq. (11) using the calculated refrigerant rate and the enthalpy change before and after passing through the condenser. The maximum heat transfer rate of the solution-side condenser ($\dot{Q}_{max,cond,s}$) and air-side condenser ($\dot{Q}_{max,cond,a}$) can be estimated by Eq. (12) and (13) based on the condensing temperature (T_{cond}) and heat exchange effectiveness (ε_{cond}). When the total heat to be released ($\dot{Q}_{act,cond,tot}$) is higher than the maximum heat transfer rate of the solution-side condenser ($\dot{Q}_{max,cond,s}$), extra condensing load occurs, which should be released to the air-side condenser. Otherwise, the solution-side condenser releases all the heat to the solution. According to the decision of the actual heating capacity of each condenser ($\dot{Q}_{act,cond,s}$,$\dot{Q}_{act,cond,a}$), the heated regenerator inlet solution ($T_{reg,i,s}$) and exhaust air (T_{ea}) can be obtained by Eq. (14) and (15).

$$\dot{Q}_{act,cond,tot} = \dot{m}_{ref}(h_{act,comp,o} - h_{cond,o}) \tag{11}$$

$$\dot{Q}_{max,cond,s} = \varepsilon_{cond}\left(\dot{m}C_p\right)_{reg,i,s}\left(T_{cond} - T_{reg,sump,old}\right) \quad (12)$$

$$\dot{Q}_{max,cond,a} = \varepsilon_{cond}\left(\dot{m}C_p\right)_{reg,o,a}\left(T_{cond} - T_{reg,o,a}\right) \quad (13)$$

$$\dot{Q}_{act,cond,s} = \left(\dot{m}C_p\right)_{reg,i,s}\left(T_{reg,i,s} - T_{reg,sump,old}\right) \quad (14)$$

$$\dot{Q}_{act,cond,a} = \left(\dot{m}C_p\right)_{reg,o,a}\left(T_{ea} - T_{reg,o,a}\right) \quad (15)$$

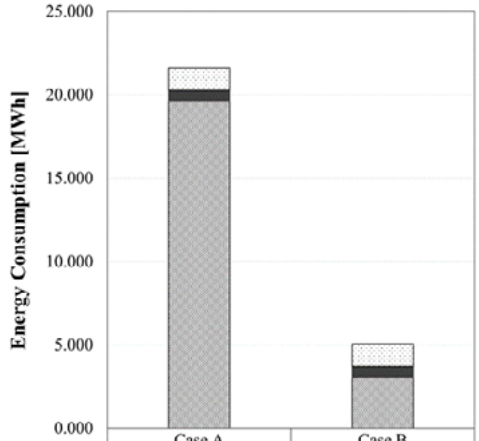
The system COP was defined as the ratio of the heat capacity of the supply air to the total electric energy consumption, as shown in Eq. (16). The total electric energy consumption was derived by the compressor, fans, and pumps. The energy consumption of the fans and pumps was predicted by an empirical model from open literature.

$$COP_{sys} = \frac{\dot{m}_{sa}(h_{ra} - h_{sa})}{P_{comp} + P_{fan} + P_{pump}} \quad (16)$$

4. Simulation Results

4.1. Energy consumption comparison

Figure 4 shows the total energy consumption converted to primary energy for the two HPLD systems using the local conversion factor of 2.75 for electricity. Case A consumed 21.6 MWh of total energy, whereas Case B consumed 5.06 MWh of total energy. The energy consumption of the fan was same for the two systems because the air flow rate of the absorber and regenerator was the same for the two systems. The pump energy consumption was 4 kWh higher in Case B due to the need for solution exchange at 4 L/h. In Case A, the temperature of the solution in the single sump can be constant at 26°C by mixing the cold absorber outlet solution and the hot regenerator outlet solution. Then, the compressor should work in full-load to cool the solution in the single sump of 26°C and heat the solution in the single sump of 26°C. In Case B, the solution in the absorber sump becomes cooled below 26°C (i.e., 15°C) and the solution in the regenerator sump becomes heated above 26°C (i.e., 45°C). Then, the compressor can work in part-load to cool the solution in the absorber sump of 15°C and heat the solution in the regenerator sump of 45°C. The compressor energy consumption saved 16.6 MWh in Case B because the compressor can work in part-load operation mode owing to the decrease in solution cooling and heating loads. Hence, Case B saved 77 % of the total energy consumption than Case A and the key factor of this result is the energy consumption of the compressor.



	Case A	Case B
Pumps	1.368	1.372
Fans	0.608	0.608
Compressor	19.662	3.083

Fig. 4. Energy consumption comparison

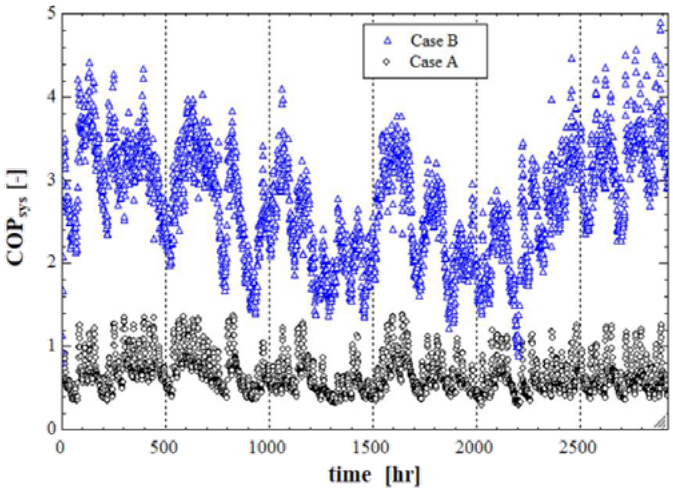


Fig. 5. System COP comparison

4.2. System COP comparison

Figure 5 shows the system COP comparison of the two HPLD systems. In all cases, Case B had a higher system COP than Case A. The mean system COP was 0.7 for Case A and 2.7 for Case B. The reason for this tendency is that both the systems satisfy the target temperature and humidity ratio of the supply air similarly. However, Case B can save operating energy consumption compared to Case A. According to the result, if the heat capacity matching between the HP unit and LD unit is achieved and the solution concentration of each sump is constant, Case B can generate the desired supply air by consuming less operating energy.

5. Conclusion

In this study, two HPLD systems, one using a single sump and another using a dual sump were suggested for an apartment building. The two systems have different mechanisms for pre-conditioning the temperature and concentration of the desiccant solution. The energy consumption and system COP for cooling and dehumidifying were compared between the two systems to analyze the applicability. The results showed that Case B reduced 77 % of the total operating energy consumption. Its system COP was always higher than that of Case A, (mean value of 2.7 against 0.7). The greatest energy-saving component was the compressor that operated in the part-load mode. Therefore, Case B can be an appropriate HPLD system for an apartment building in terms of its productivity and energy efficiency by satisfying the capacity matching and constant solution concentration.

Although, the performance comparison during the summer operation period was conducted in this study, the HPLD system can be reversible and annually operated. Therefore, additional performance comparison during the intermediate and winter season should be conducted and an optimal sequence for annual operation should be considered. In addition, an experimental verification of the simulation results in this study should be conducted in the future.

Acknowledgements

This work was supported by the National Research Foundation of Korea (NRF) grant (No. 2019R1A2C2002514), the Korean Institute of Energy Technology Evaluation and Planning (KETEP) (No. 20184010201710), and the Technology development Program(S2782284) funded by the Ministry of SMEs and Startups (MSS, Korea).

References

[1] Daou, K., 2006. Desiccant cooling air conditioning a review. Renewable and Sustainable Energy Reviews 10, p. 72.
[2] Liu, X., 2006. Annual performance of liquid desiccant based independent humidity control HVAC system. Applied Thermal Engineering 26, p. 1198.
[3] Dong, H., 2019. Optimum regeneration temperature of a desiccant solution in a packaged liquid desiccant-assisted air conditioning unit. International Journal of Refrigeration 101, p. 155.
[4] Gurubalan, A., 2019. A comprehensive review of liquid desiccant air conditioning system. Applied Energy 254, p. 5.
[5] Zhang, T., 2012. Performance optimization of heat pump driven liquid desiccant dehumidification systems. Energy and Buildings 52, p. 133.
[6] Zhang, L., 2010. Performance analysis of a no-frost hybrid air conditioning system with integrated liquid desiccant dehumidification. International Journal of Refrigeration 33, p. 122.
[7] Niu, X., 2012. Investigation on capacity matching in liquid desiccant and heat pump hybrid air-conditioning systems. International Journal of Refrigeration 35, p. 161.
[8] Mei, L., 2008. A technical review on use of liquid-desiccant dehumidification for air-conditioning application. Renewable and Sustainable Energy Reviews 12, p. 686.
[9] Rafique, M., 2016. Liquid desiccant materials and dehumidifiers – A review. Renewable and Sustainable Energy Reviews 56, p. 192.
[10] Xie, Y., 2016. Performance investigation of a counter-flow heat pump driven liquid desiccant dehumidification system. Energy 115, p. 447.
[11] Shin, J., 2018. Impact of Heat Pump-Driven Liquid Desiccant Dehumidification on the Energy Performance of an Evaporative Cooling-Assisted Air Conditioning System. Energies 11, p. 5.
[12] Nóbrega CEL, Brum NCL. *Desiccant-Assisted Cooling: Fundamentals and applications.* Springer; 2014.
[13] Fumo, N., 2002. Study of an aqueous lithium chloride desiccant system: air dehumidification and desiccant regeneration. Solar Energy 72, p. 355.
[14] Chung, T., 1999. Vapor Pressures of the Aqueous Desiccants. Journal of Chemical and Engineering Data 44, p. 1026.
[15] Longo, G., 2005. Experimental and theoretical analysis of heat and mass transfer in a packed column dehumidifier/regenerator with liquid desiccant. International Journal of Heat and Mass Transfer 48, p.5250.

13th IEA Heat Pump Conference
April 26-29, 2021 Jeju, Korea

Deep learning-based refrigerant charge fault detection method of air-source heat pump system

Yong Hwan Eom[a], Sung Bin Hong[a], Jin Woo Yoo[b], Min Soo Kim[a*]

[a] Department of Mechanical and Aerospace Engineering, Seoul National University, Seoul 08826, Republic of Korea
[b] KOREA INSTITUTE OF MACHINERY & MATERIALS

Abstract

Energy demands grow every year, and a significant amount of energy consumption is used for buildings cooling and heating. Since heat pump systems have high efficiency and can be utilized for buildings cooling and heating, they are commonly used around the world. Many studies show heat pumps have the best COP at the optimal refrigerant charge. Therefore, it is imperative to monitor the current refrigerant charge of the system and maintain it optimally in view of energy saving. However, some researches show that many heat pumps in the field have refrigerant leakage fault or overcharge fault. The refrigerant charge error can cause energy waste and thermal discomfort. Hence, many researchers have conducted studies for refrigerant charge fault detection (RCFD) method. In recent years, RCFD methods based on deep learning technology have been developed actively. This paper suggests a novel and efficient RCFD strategy using convolutional neural network (CNN). The CNN based multiple outputs regression model shows excellent results for predicting power consumption, cooling capacity (heating capacity), and the refrigerant charge amount simultaneously with a single model.

© HPC2020.
Selection and/or peer-review under responsibility of the organizers of the 13th IEA Heat Pump Conference 2020.

Keywords: heat pump; refrigerant charge fault detection; deep learning;multiple outputs regression; energy saving;

1. Introduction

The US Energy Information Administration presented that 39.7% of US total energy consumption in 2015 was used in commercial and residential buildings, and about 40% of it was spent on buildings heating and cooling [1]. Since heat pumps have high efficiency and can be utilized for buildings cooling and heating, heat pump systems are widely used all over the world. Therefore, many researchers have conducted studies to increase the efficiency of heat pump systems for energy saving.

Optimum refrigerant charge is essential in vapor compression systems [2-4]. However, Jacob et al. [5] found that 46% of HVAC systems installed in 75 buildings in California did not have an appropriate refrigerant amount, reducing performance and consuming unnecessary energy. Therefore, in terms of energy, a technique for detecting undercharge or overcharge of refrigerant is essential, and many studies for RCFD methods have been conducted so far [6-8]. Recently, due to the improved computational power of computers and big data, data-driven researches such as an artificial neural network (ANN) are trendy in refrigerant charge prediction techniques [9-12].

However, there are some limitations to the conventional ANN-based RCFD method. First, due to simple classification such as undercharge and overcharge, it was not possible to provide a quantitative refrigerant amount. Second, many conventional ANN-based RCFD methods only took one operation mode (cooling or heating mode) into consideration. Finally, many ANN-based RCFD articles provided only information on the refrigerant charge amount. However, the essential things that we want to know are the cooling or heating capacity and the efficiency of the heat pump systems according to the change of the refrigerant charge amount.

* Corresponding author.
E-mail address: minskim@snu.ac.kr (M.S. Kim).

The predictive ability for these three attributes can help determine the urgency of whether or not current refrigerant fault needs repairing right now.

In order to improve these limitations, this paper proposes a novel RCFD technique using CNN based multiple outputs regression model. Since the refrigerant charge amount, power consumption, and cooling capacity (heating capacity) of the heat pump system are substantially real numbers, the prediction for the three targets is a multiple outputs regression task [13-14]. The contributions of this proposed method are as follows. First, it provides quantitative information about the current amount of refrigerant in the heat pump system. Second, it also predicts the current heating capacity (cooling capacity) and the power consumption of the heat pump quantitatively. Thus, the current COP of the system can be calculated. In addition, the prediction for these three attributes can give information on the severity of the refrigerant charge fault. Third, both heating and cooling modes were considered, and a single model was used.

Briefly describing the results, including both cooling and heating mode, the refrigerant amount prediction error is within RMS error of 4.9%, the power consumption prediction error is within RMS error of 3.8%, and the cooling capacity (heating capacity) is below RMS error of 3.4% with a single model.

2. Methodology

2.1. Convolutional neural network (CNN)

The basic structure of CNN, one of the deep learning technologies, is composed of a convolutional layer, a pooling layer, and a fully-connected layer.

The convolutional layers and the pooling layers extract the features from the original raw data together [15]. After the input images and several filters perform a convolutional operation, the convolutional layer extracts a feature map by applying an activation function.

The pooling layer plays a role to reduce the size of the extracted feature map and to alleviate the sensitivity according to the location. Among the pixel values in the region of interest of the feature map, acquiring the largest value is called max-pooling, and calculating the average value is called average-pooling. Generally, max-pooling is widely used for CNN. Therefore, it is used for the RCFD model in this study.

The convolutional layers and the hidden layers of the fully-connected layers require a nonlinear function as the activation function. Mainly the rectified linear unit (ReLU) function is used.

The fully-connected layers have a similar structure to the existing ANN. All pixel values of the feature map after the pooling layer are connected to the input nodes of the fully-connected layer. After going through several hidden layers, the predicted value for each output node in the output layer is calculated using a linear activation function instead of the softmax function. In this study, the output layer has three output nodes to predict power consumption, cooling capacity (heating capacity), and the refrigerant charge amount.

The architecture of the CNN-based RCFD regression model used in this article is described in Table 1.

Table 1. The architecture of CNN-based RCFD multiple outputs regression model

Layer name	Input size	Filter size	Filter number	Stride	Output size	Activation function
Input	29×30×1	-	-	-	-	-
Convolutional 1	29×30×1	3×3	8	1	27×28×8	ReLU
Convolutional 2	27×28×8	3×3	8	1	25×26×8	ReLU
Max-pooling 1	25×26×8	2×2	-	2	12×13×8	-
Convolutional 3	12×13×8	3×3	8	1	10×11×8	ReLU
Convolutional 4	10×11×8	3×3	8	1	8×9×8	ReLU
Max-pooling 2	8×9×8	2×2	-	2	4×4×8	-
Flatten 1	4×4×8	-	-	-	128×1	-
Fully-connected 1	128×1	-	-	-	50×1	ReLU
Output	50×1	-	-	-	3×1	Linear

Since the proposed model was a CNN-based regression model, we used a linear activation function instead of the softmax function at the output layer and a mean squared error as a loss function. A loss function using a mean squared error is depicted as follows.

$$E(\boldsymbol{w}) = \frac{1}{2N}\sum_{n=1}^{N}\sum_{k=1}^{K}(y_{nk} - d_{nk})^2 \qquad (1)$$

where $\boldsymbol{w}$ is the weight of a neural network, N is the total number of samples, K is the total number of output nodes, d_{nk} is the correct answer of the k_{th} output node in the n_{th} sample, and y_{nk} is the output value of the k_{th} output node in the n_{th} sample.

The learning process is to update the weights of each layer so that the value of the loss function is minimized. Stochastic gradient descent and backpropagation methods are widely used. We shuffled the training data randomly, and the shuffled data for learning was divided by mini-batch size. Since early stopping is widely utilized to prevent overfitting that deteriorates the generalization of a learned model [16], the early stopping algorithm was considered in this research.

2.2. Time-domain data to 2-D image data conversion method

Generally, CNN uses 2-D image data as input. Therefore, It is needed a process of converting time-series data of various sensors installed in the heat pump into 2-D image data. Although there are many conversion methods, in this study, the values of multiple sensors measured at fixed time intervals were stacked in chronological order and were converted to the 2-D image data [17]. Twenty-nine features were collected at two-second intervals and converted to one image data using the dataset obtained for 60 seconds. Therefore, one 2-D data sample size is 29×30.

Data normalization is essential for convergence and performance in neural network methods. In general, the min-max scaling method and the standardization method are used widely. In this study, training, validation, and test data were preprocessed with the min-max scaling method.

3. Experimental setup

3.1. Experimental setup and conditions

Experiments were carried out using a commercial 30 kW heat pump system with two indoor units and one outdoor unit. The heat pump is equipped with a variable-speed scroll compressor, three inverter fans, multiple EEVs, and a 4-way valve. Fig. 1 shows a schematic of the experimental setup [18].

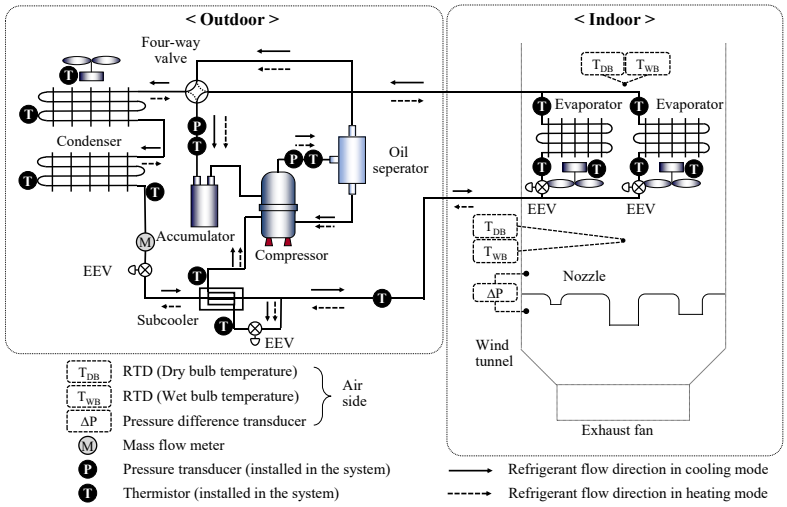


Fig. 1. Schematic of an experimental setup [18]

The sensors in black circles are initially installed sensors by the manufacturer. A pressure difference transducer, mass flow sensor, and RTD sensors are installed additionally for this research. However, it was noted that the measured values acquired from the additional sensors were not utilized for learning the CNN-based models. The nominal charge amount of refrigerant is 6 kg in heating mode and 9 kg in cooling mode. The outdoor unit was installed in the chamber to simulate the outdoor temperature and humidity conditions, and the two indoor units were installed in the chamber to create the indoor temperature and humidity conditions.

The experiments were carried out in both the cooling and heating mode. In the heating mode, the experiments started with 3 kg of refrigerant charge. After obtaining experimental data while changing the DSH for at least two hours in each refrigerant charge, an additional 1 kg of refrigerant charge was added. This process was repeated until the final refrigerant amount reached 8 kg. In cooling mode experiments, the refrigerant charge was added step by step from 6 to 11 kg, as mentioned above. When the target DSH was changed, or the refrigerant of 1 kg was added, the heat pump system became a transient state for about five minutes. This transient-state data was included in the training and test data with the steady-state data together.

The operation mode, various air conditions, compressor rotating speed, and target DSH were variables for the validation of this new RCFD method under various experimental conditions. The fan RPM in the outdoor unit was fixed at all experimental conditions, and two indoor units were always operated. In heating mode, the EEVs of both indoor units were fully opened, and the EEV of the outdoor unit was activated with the manufacturer's control logic.

In contrast, in cooling mode, the EEVs of the two indoor units were controlled, and the EEV of the outdoor unit was fully opened. Considering ANSI / AHRI standard 1230 [19], four air temperature conditions for cooling mode, and two air temperature conditions for heating mode were chosen. The experiment test conditions are described in detail in Table 2.

Table 2. Experimental conditions for cooling and heating mode

Variables	Value					
Refrigerant	R410A					
Lubricant	Polyvinyl ether(PVE) type					
Lubricant charge amount (kg)	3					
Operation mode	Cooling mode				Heating mode	
Refrigerant charge amount (kg)	6 - 11 (Δ=1)				3 - 8 (Δ=1)	
Target DSH (K)	5, 10, 15 (or maximum EEV opening)				5, 10 (or maximum EEV opening)	
Air condition (ANSI/AHRI 1230)	Rating	Low temp.	Condensate	Max load	Rating (low temp.)	Rating (high temp.)
ID inlet DB (˚C)	26.7	19.4	26.7	26.7	21.1	21.1
ID inlet WB (˚C)	19.4	13.9	23.9	19.4	15.6 (max)	15.6 (max)
OD inlet DB (˚C)	35.0	19.4	26.7	46.1	-8.3	8.3
OD inlet WB (˚C)	23.9	13.9	23.9	23.9	-9.4	6.1
Compressor speed (Hz)	60, 100	60	60, 100	60, 100	60, 100	60

The 29 features were selected based on previous studies [6-8], experimental conditions, and the attributes required to analyze the thermodynamic properties of the heat pump system. All the features utilized in the development of the model in this research can be acquired from the monitoring variables that the manufacturer provides.

3.2. Splitting of training, validation, and test data

In general, three datasets, such as the training data, the validation data, and the test data are required to improve the prediction performance of machine learning-based models. The total number of two-second interval data in this study is 223,590. To estimate the generalization error of this proposed model, experimental data, including refrigerant charges of 8 kg and 9 kg at condensation condition in cooling mode, were previously

separated into test data. Besides, experimental data with the refrigerant charge of 4.5 kg, 5.5 kg, 6.5 kg, and 7.5 kg at rating conditions (high temperatures) under heating mode were added into test data in advance. The number of previously prepared test data mentioned above is 31,140. The number of rest data is 192,450. The rest of the data were split into three groups as 7 vs. 2 vs. 1. So, there were 134,700 for training data, 38,670 for validation data, and 19,080 for testing. Therefore, the number of training data is 134,700, the number of validation data is 38,670, and the number of final test data is 50,220. Finally, the number of 2-D converted training data is 4,490, the number of 2-D validation data is 1,289, and the amount of 2-D test data 1,674.

4. Results and discussion

The quantitative prediction of refrigerant levels is essential for proper monitoring and management of heat pump systems. Besides, if the power consumption and cooling capacity of the system can be predicted, it is possible to know the effect of the refrigerant charge fault on the heat pump system. This prediction can help determine the urgency of repairing a refrigerant fault. In this paper, we suggest a novel method that can predict power consumption, cooling capacity (heating capacity), and the refrigerant charge amount quantitatively and simultaneously using a single model.

Fig. 2 shows the prediction results for the power consumption values and cooling capacity (heating capacity), and the refrigerant charge amount of the heat pump systems. From Fig. 2 (a), the performance of power consumption prediction is within an RMS error of 3.8%. The error in the prediction of cooling capacity and heating capacity is an RMS error of 3.4% from Fig. 2 (b). Fig. 2 (c) shows that the CNN-based model achieved the predictive performance on the refrigerant charge amount with an RMS error of 4.9%.

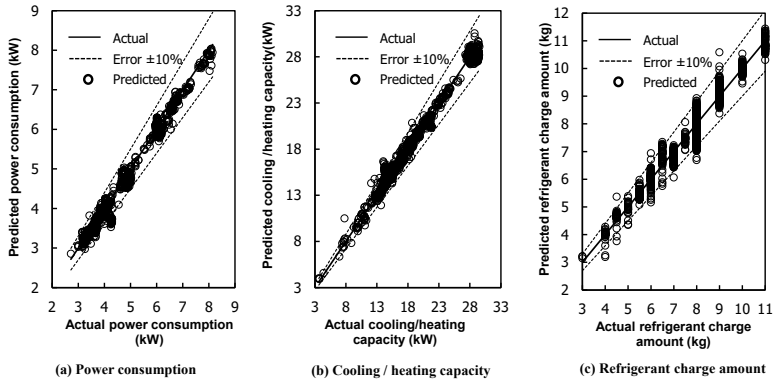


Fig. 2. Actual and predicted power consumption, cooling/heating capacity, and refrigerant charge in CNN-based regression model

The COP of a heat pump can be calculated because power consumption and cooling capacity are predicted according to the refrigerant amount change.

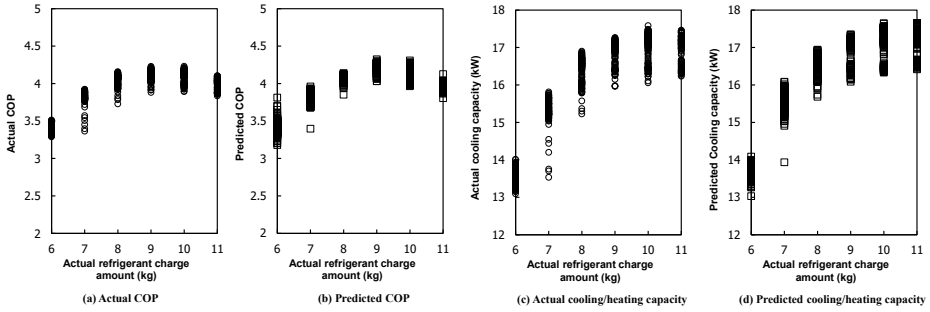


Fig. 3. Actual and predicted COP and cooling/heating capacity at the rating condition in the cooling mode

Fig. 3 (a) and (b) show the COP change of the system according to the amount of refrigerant at the rating condition in the cooling mode. They show that the predicted COP is similar to the actual COP. From Fig. 3 (c) and (d), it can be known that the cooling capacity of the heat pump with the refrigerant charge amount of 8 kg is reduced by about 2.4% compared to the nominal refrigerant charge amount of 9 kg. However, the cooling capacity in the refrigerant charge amount of 7 kg is reduced by about 8.8%. In this case, consumers may feel thermal discomfort due to reduced cooling capacity. When the refrigerant charge is 7 kg, the urgency of repairing the fault is much higher than 8 kg.

5. Conclusions

This research proposes a novel CNN-based RCFD multiple outputs regression method which has excellent quantitative prediction accuracy. This multiple outputs regression model can predict power consumption, cooling or heating capacity, and the refrigerant charge amount with a single model quantitatively. Therefore, it can provide helpful information for the severity of the refrigerant charge fault to the manufacturer or the service engineer. This comprehensive information can help manufacturers or maintenance engineers decide whether to fix a refrigerant charge defect urgently. In addition, this suggested model can predict three target variables in both the cooling and heating mode. The prediction errors for power consumption, cooling or heating capacity, and refrigerant charge amount are RMS errors of 3.8%, 3.4%, and 4.9%, respectively.

Acknowledgements

This work was supported by the Brain Korea 21 Plus Project (F14SN02D1310) of Seoul National University. Additional support by Basic Science Research Program through the National Research Foundation of Korea (NRF) funded by the Ministry of Science, ICT & Future Planning (2016R1A2A1A05005510) is much appreciated. This project was also supported by the R&D Center for reduction of Non-CO2 Greenhouse gases (2017002430001) funded by Korea Ministry of Environment (MOE) as Global Top Environment R&D Program. Support from Korea Institute of Energy Technology Evaluation and Planning (KETEP) from the Ministry of Trade, Industry & Energy of Korea (No. 20173010032150) is also much appreciated.

References

[1] U.S. Energy Information Administration. Annual energy outlook 2017. US Energy Information Administration. 2017.
[2] Kim DH, Park HS, Kim MS. The effect of the refrigerant charge amount on single and cascade cycle heat pump systems. International Journal of Refrigeration. 2014;40:254-68.
[3] Kim JH, Cho JM, Kim MS. Cooling performance of several CO2/propane mixtures and glide matching with secondary heat transfer fluid. International Journal of Refrigeration. 2008;31(5):800-6.
[4] Kim JH, Cho JM, Lee IH, Lee JS, Kim MS. Circulation concentration of CO2/propane mixtures and the effect of their charge on the cooling performance in an air-conditioning system. International Journal of Refrigeration. 2007;30(1):43-9.
[5] Jacobs P, Smith V, Higgins C, Brost M. Small commercial rooftops: Field problems, solutions and the role of manufacturers. In: National Conference on Building Commissioning; 2003. p. 7-8.
[6] Grace IN, Datta D, Tassou SA. Sensitivity of refrigeration system performance to charge levels and parameters for on-line leak detection. Applied Thermal Engineering. 2005;25(4):557-66.
[7] Li H, Braun JE. Development, Evaluation, and Demonstration of a Virtual Refrigerant Charge Sensor. HVAC&R Research. 2009;15(1):117-36.
[8] Hong SB, Yoo JW, Kim MS. A theoretical refrigerant charge prediction equation for air source heat pump system based on sensor information. International Journal of Refrigeration. 2019.
[9] Tassou SA, Grace IN. Fault diagnosis and refrigerant leak detection in vapour compression refrigeration systems. International Journal of Refrigeration. 2005;28(5):680-8.
[10] Kocyigit N. Fault and sensor error diagnostic strategies for a vapor compression refrigeration system by using fuzzy inference systems and artificial neural network. International Journal of Refrigeration. 2015;50:69-79.
[11] Shi S, Li G, Chen H, Liu J, Hu Y, Xing L, et al. Refrigerant charge fault diagnosis in the VRF system using Bayesian artificial neural network combined with ReliefF filter. Applied Thermal Engineering. 2017;112:698-706.
[12] Guo Y, Li G, Chen H, Wang J, Guo M, Sun S, et al. Optimized neural network-based fault diagnosis strategy for VRF system in heating mode using data mining. Applied Thermal Engineering. 2017;125:1402-13.
[13] Murphy KP. *Machine learning: a probabilistic perspective*: MIT press, 2012.
[14] Bishop CM. *Pattern recognition and machine learning*: springer, 2006.

[15] LeCun Y, Bengio Y, Hinton G. Deep learning. Nature. 2015;521(7553):436-44.
[16] Prechelt L. Automatic early stopping using cross validation: quantifying the criteria. Neural Networks. 1998;11(4):761-7.
[17] Xia M, Li T, Xu L, Liu L, De Silva CW. Fault diagnosis for rotating machinery using multiple sensors and convolutional neural networks. IEEE/ASME Transactions on Mechatronics. 2018;23(1):101-10.
[18] Eom YH, Yoo JW, Hong SB, Kim MS. Refrigerant charge fault detection method of air source heat pump system using convolutional neural network for energy saving. Energy. 2019;187:115877.
[19] ANSI/AHRI Standard 1230. Performance Rating of Variable Refrigerant Flow (VRF) Multi-Split Air-Conditioning and Heat Pump Equipment. 2010.

13th IEA Heat Pump Conference 2020



13th IEA Heat Pump Conference
April 26-29, 2021 Jeju, Korea

Analysis of a steam generating high temperature heat pump for industrial waste heat recovery

Sabrina Dusek[a,*], Michael Lauermann[a], Franz Helminger[a], Veronika Wilk[a]

[a]AIT Austrian Institute of Technology GmbH, Giefinggasse 2, 1210 Vienna, Austria

Abstract

Steam is one of the most important energy carriers in industrial processes. For example, steam is used for sterilization, cooking and drying processes and as a heat transfer medium for various processes. Fossil fuels are often used to generate steam, but the use of fossil fuels, especially in industry, must be reduced in the future to reduce CO_2 emissions and to achieve climate targets. Heat pumps are already being used successfully in industrial applications, valorizing waste heat. With a high temperature heat pump, waste heat can be used to generate steam. This extension of the application range of heat pumps will provide a further contribution to achieving climate targets. A model of a steam generating high temperature heat pump was elaborated to study the technology under different operating conditions. This contribution shows the simulation results of a steam generating high temperature heat pump system with different refrigerants. The results are compared in terms of COP and compressor displacement. The goal is to identify the most appropriate refrigerant for a specific steam pressure.

© HPC2020.
Selection and/or peer-review under responsibility of the organizers of the 13th IEA Heat Pump Conference 2020.

Keywords: High temperature heat pump; Industrial waste heat recovery; Steam generation; Modeling;

1. Introduction

All over the world, industrial processes are rejecting large amounts of low temperature waste heat in the form of exhaust gases and waste water. According to an analysis of Forman et al [1], a total of 29 539 TWh of energy was supplied to industrial processes worldwide in 2012, but only 49% were actually used. The remaining 51% were identified as losses in the form of waste water and hot off gases (about two thirds of the losses) and other losses such as radiation, friction, resistance, etc. Due to the low temperature level, these waste heat streams can no longer be used in an efficient way and are released unused into the environment. High temperature heat pumps allow for using these waste heat streams because they provide process heat at a higher temperature level. Heat pumps that provide steam are of particular interest to the industry because steam generation has a significant share in process heat. For example, steam generation accounts for 27% of the useful energy in industry in Austria (92 PJ). A total of 45% of the steam was generated by combustion of natural gas (41 PJ). [2] If heat pumps are used for low pressure steam generation instead of steam generators operated with fossil fuels, significant reductions in primary energy and CO_2 emissions are achieved.

For steam production, high temperature heat pumps are required with supply temperatures up to 150°C, which are mainly determined by the choice of the refrigerant. Conventional industrial heat pumps can reach temperatures up to 90-100ºC, but new developments have raised the working temperature to above 100ºC in the last years (e.g. CO_2 based heat pumps from Engie Refrigeration [3] and Mayekawa (Japan) [4], R245fa heat pumps for the supply of hot water at 130°C by Ochsner Energietechnik GmbH (Austria) [5], heat pumps from Viking Heat Engines AS (Norway) with supply temperatures above 150ºC).

* Corresponding author. Tel.: +43-664-825-1411; fax: +43-505-506-679.
E-mail address: Sabrina.Dusek@ait.ac.at.

Nomenclature

Abbreviations

COP	coefficient of performance
GWP	global warming potential
NBP	boiling point at nominal pressure
ODP	ozone depletion potential
SPHE	shell and plate heat exchanger

Roman symbols

a	pattern amplitude, m
A	heat transfer area, m^2
d	plate diameter, m
h	specific enthalpy, Jkg^{-1}
h"	specific enthalpy of dry saturated steam, Jkg^{-1}
m	mass, kg
$\dot{m}$	mass flow, kgs^{-1}
n	number of plates
l	length of the plate pack, m
p	pressure, bar_a
P_{el}	electrical power, W
$\dot{Q}_H$	heating capacity, W
$\dot{Q}$	heat flow, W
s	plate thickness, m
t	time, s
V	volume, m^3
X	wave number

Greek symbols

Λ_P	wave length, m
Φ	area extension factor

Subscripts

in	incoming
out	outgoing

Heat pumps for steam generation are still very rarely used in industrial processes. A 200 kW pilot plant was integrated into the Smurfit Kappa Roermond paper mill in the Netherlands by TNO (former ECN), which proved the ability to deliver steam at 120°C from a waste heat source at 60°C with R600 (critical temperature 152°C) as refrigerant. Based on the results of this project a roadmap for industrial heat pumps was created. [6-7] In 2011, a heat pump with R245fa was launched on the Japanese market under the brand name Kobelco, which supplies steam at 120°C and has a heating capacity of around 370 kW. The critical temperature of R245fa is 154°C. To achieve higher steam temperatures of 165°C, a vapour compressor can be connected downstream (SGH 165) [8]. Recently, Kaida published an overview on industrial applications of SGH heat pumps in Japan, reporting end user satisfaction and positive effects of the heat pump integration. The heat pump steam generators are applied in the chemical industry for distillation of ethanol (5 units supplying 2t/h of 120°C steam), sterilization of chemical containers (1 unit, 165°C steam) and for sewage sludge drying (1 unit, 165°C steam). [9] Those heat pumps are currently only available in Japan.

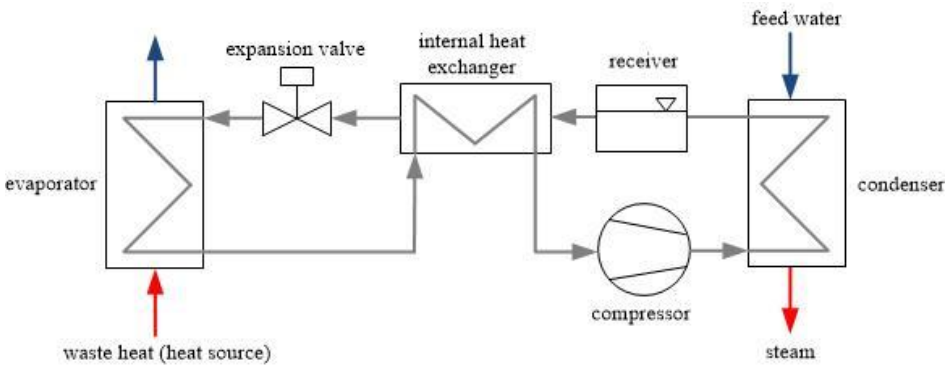


Fig. 1. Schematic representation of the steam generating heat pump cycle

In the BAMBOO project, the prototype of a heat pump is developed, which provides low-pressure steam with up to 5 bar_a (152°C) for industrial steam networks. A novel HFO-refrigerant, R1336mzz(Z) is applied that has no negative impact on the environment. It is well suited for high supply temperatures of up to 160°C, thus for the production of saturated steam at up to 5 bar_a. A novel type of piston compresssor is selected as the compressor, which is already operating successfully on R1336mzz(Z). An innovative condenser is developed, where steam is generated directly on the secondary side. Thereby the heat pump becomes more efficient, compact and cost-effective. The heat pump prototype has a nominal heating capacity of 200 kW and can be easily scaled up to higher heating capacities. The heat pump will be thoroughly tested in the lab and then implemented in real industrial environment to demonstrate functionality at TRL7.

All the above-mentioned examples for steam generating heat pumps are subcritical processes. Subcritical processes are well suited for steam generation because the majority of heat is transferred at constant temperature. In this work a simulation model for a subcritical steam generating heat pump cycle is discussed. Fig. 1 illustrates the layout of the heat pump cycle. A shell and plate heat exchanger (SPHE) is used as the condenser and it is also the steam generator. The simulation model was used to compare different refrigerants, in terms of coefficient of performance (COP) and compressor displacement, using the same heat pump cycle. The analysis was carried out for three different steam pressures. The aim of this investigation was to find the most suitable refrigerant for a specific steam pressure.

2. Steam generating heat pump model

The steam generating heat pump cycle was modeled in the simulation environment Dymola/Modelica [10]. The TIL-Library [11] was used to model the components in the cycle. For the evaporator, the internal heat exchanger, receiver and the expansion valve standard components from this library were used. The condenser and the compressor were modeled in a custom way. The models of the individual components are described in more detail in the following chapters. A receiver after the condenser (see Fig. 1) enables the lowest possible condensation temperature for a wide range of operating conditions. For determining the required thermal-physical properties of the involved media (Refrigerants, Water) the TILMedia-Library [11] was used. Both thermal and pressure losses were neglected in this model. In addition, constant values were assumed for the heat transfer coefficients between the media and the heat transfer area of the heat exchangers.

2.1. Shell and Plate heat exchanger model

As mentioned before, in the steam generating heat pump a SPHE is used as condenser. This particular type of heat exchanger is a combination of a shell and tube and a plate heat exchanger [12]. In this heat exchanger arrangement, the rounded corrugated plate pack is surrounded by a cylindrical shell filled with the secondary fluid as it is shown in Fig. 2. The plate pack is welded so that the primary and secondary fluid streams flowing through the channels do not come into contact. [12–14] The welded construction has the advantage that significantly higher operating temperatures and pressure levels are possible [13-14]. However, the disadvantage is the limited accessibility which makes cleaning more difficult [14].

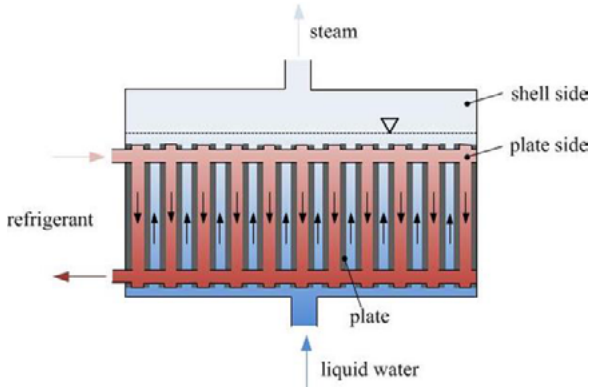


Fig. 2. Schematic representation of the modelled plate-and-shell heat exchanger

In the steam generating heat pump the steam is produced with the SPHE, therefore the shell side of the heat exchanger contains a two-phase fluid of liquid water and steam. The condensing refrigerant is located at the plate side (see Fig. 2). The following assumptions for modelling the SPHE were made:

- Heat exchange between the refrigerant and the water was entirely done via the plates
- Only the vertical flow of the refrigerant between the plates was considered
- In each refrigerant channel the same mass flow with the same temperature enters
- In each refrigerant channel the same mass flow with the same temperature exits
- Thermodynamic equilibrium between the two water phases on the shell side
- Plates are not contact with the steam phase

The length of the plate pack l, which is equal to the length of the cylindrical shell was calculated as shown in equation (1), where the number of plates n, the plate thickness s and the pattern amplitude a are needed.

$$l = (n-1) \cdot 2a + n \cdot s \tag{1}$$

The heat transfer area A between water and refrigerant can be calculate with equation (2).

$$A = (n-2)\frac{d^2}{4}\pi \cdot \Phi \tag{2}$$

The calculation of the area extension factor Φ (equation (3)), which occurs in equation (2), was done as it is presented in the VDI Heat Atlas [15]. The area extension factor describes the ratio between the wavy plate surface and the plane surface projection. For the calculation a sinusoidal corrugation of the plates was assumed. For the calculation of the area extension factor the wave number X is needed, which depends on the plate amplitude and the wavelength Λ_P (equation (4)).

$$\Phi = \frac{1}{6}\left(1 + \sqrt{1+X^2} + 4\sqrt{1+\frac{X^2}{2}}\right) \tag{3}$$

$$X = \frac{2\pi a}{\Lambda_P} \tag{4}$$

In Fig. 2 horizontal feedthroughs of the refrigerant, which are arranged at the plate side of the SHPE, are shown, which reduce the surface area. This reduction is neglected in equation (2). The shell side contains a two-phase fluid of liquid water and steam. The incoming mass flow of liquid water $\dot{m}_{in}$ enters the liquid water

volume and the outgoing steam mass flow $\dot{m}_{out}$ exits the steam volume. A thermodynamic equilibrium between the two phases is assumed. Therefore, only one energy and mass balance equation according to equation (5) and equation (6) must be fulfilled. Both phases on the shell side have the same pressure and are connected by an evaporating mass and energy flow. The evaporating mass flow has the specific enthalpy of dry saturated steam.

$$\frac{dm}{dt} = \dot{m}_{in} + \dot{m}_{out} \tag{5}$$

$$m\frac{dh}{dt} = \dot{m}_{in}(h_{in} - h) + \dot{m}_{out}(h_{out} - h) + \dot{Q} + V\frac{dp}{dt} \tag{6}$$

2.2. Plate heat exchanger model

For modeling the internal heat exchanger and the evaporator, the standard plate heat exchanger model from TIL-Library was used. This model is based on the geometry of the heat exchanger described by the number of plates, length and width of the plate and other properties, and two heat transferring fluids. In addition to that, the heat transfer model and pressure drop model can be chosen for both heat transferring fluids separately. Different correlations to describe the heat transfer and the pressure drop are available. In order to describe the heat conduction mechanism within the plate, it can be chosen as a constant heat resistance value or the heat conduction is calculated based on the given plate geometry and material. In this work the geometry based method was used.

2.3. Compressor and expansion valve model

In order to reduce the complexity of the steam generating heat pump model, the compressor was modelled based on isentropic and volumetric efficiency instead of using a physical approach as in the positive displacement compressor model from the TIL-Library. Therefore, the efficiencies are given as a function of pressure ratio. Furthermore, an electrical efficiency must be defined in the model. The pressure difference between discharge and suction side are given by the evaporator and the condenser model. Therefore, the electric power is calculated in the compressor model with a given swept volume and the actual efficiencies.

For the expansion valve an orifice valve component based on the equation of Bernoulli from the TIL-Library was used. An effective flow area of the valve must be given in this component.

3. Numerical simulations

The aim of the investigation was to assess the suitability of different refrigerants for three different steam pressures provided by the steam generating heat pump. Table 1 presents the properties of the considered refrigerants in terms of critical temperature, critical pressure, global warming potential (GWP), ozone depletion potential (ODP) and boiling point at nominal pressure (NBP).

The refrigerants listed in Table 1 are not all suitable for each studied steam pressure. Therefore, Fig. 3 illustrates the estimated possible steam temperatures for each of the selected refrigerants. Moreover, the saturation temperature for each studied pressure is shown by the vertical dashed lines. The diagram starts at 100°C, because this is equal to the saturation temperature for steam at atmospheric pressure. Only subcritical processes are considered in this work, therefore the upper limit is defined based on the critical temperature of the refrigerant and the assumption of a minimum temperature difference between refrigerant and steam temperature of 10 K. R601, R601a and R1336mzz(Z) are suitable for all steam pressures. R1233zd(E) and R1224yd(Z) are suitable for 2 and 4 bar_a steam. R600, R1234ze(Z) and R600a can only be used for 2 bar_a steam.

Table 1. Properties of the used refrigerants

Refrigerant	Critical temperature, °C	Critical pressure, bara	GWP	ODP	NBP °C	Reference
R601	196.6	33.7	5	0	36.1	[16]
R601a	187.3	33.8	5	0	27.9	[17-18]
R1336mzz(Z)	171.3	29	2	0	33.4	[16]
R1233zd(E)	166.5	36.2	1	0.00034	18	[16]
R1224yd(Z)	155.5	33.3	<1	0.00012	14	[16]
R600	152	38	4	0	-0.5	[16]
R1234ZE(Z)	150.1	35.3	<1	0	9.8	[16]
R600a	134.7	36.3	3	0	-11.8	[16]

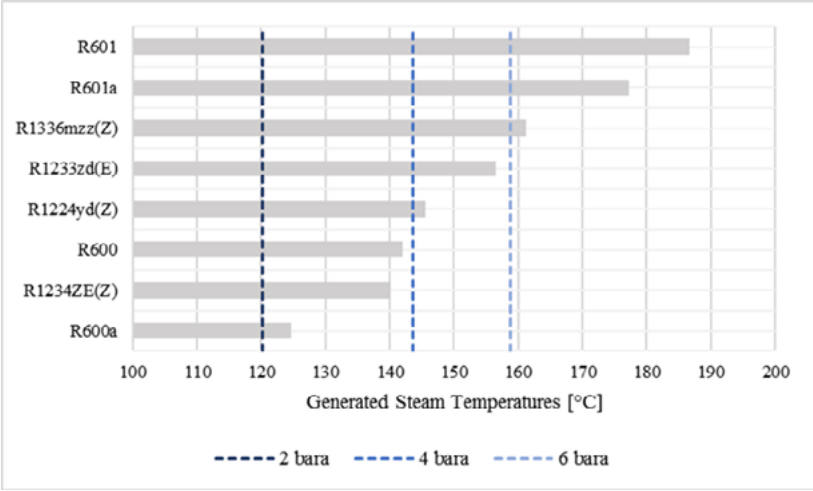


Fig. 3. Possible generated steam temperatures for the used refrigerants

3.1. Boundary conditions and control strategy

For all refrigerants and steam pressures the same model settings were used for geometry, heat transfer coefficients, liquid feed water temperature (85°C), heat source temperature (85°C) and generated steam mass flow (200kgh^{-1}). Only the heat transfer area of the internal heat exchanger has been adapted to achieve a superheating of approximately 15 K after the compressor, which is exemplarily shown in the log(p), h-diagram of R601 in Fig. 4.

Moreover, the mass flow of the source fluid was controlled in such a way that the heat source will be cooled down by 5 K in the evaporator, under the restriction of a heat source mass flow higher than 0.4 t/h. The expansion valve is regulated so that saturated vapour is present at the outlet of the evaporator. The compressor displacement is controlled according to the desired steam pressure at the outlet of the condenser, it is equal to the pressure on the shell side of the SPHE. The liquid feed water mass flow is set to a constant value for the filling level in the SPHE. The liquid filling level is the ratio between the liquid water volume and the total shell side volume of the SPHE. It is assumed that the plate pack of the SPHE is only in contact with the liquid water phase for the chosen liquid filling level. All the control mechanisms explained before are realized as continuous control with PI controllers from the TIL-Library.

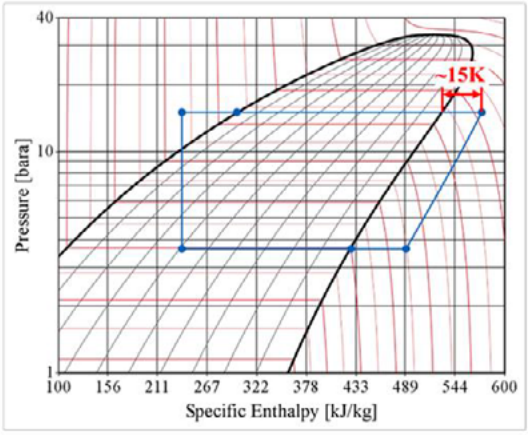


Fig. 4. Log(p), h diagram of R601 and refrigeration cycle for 4 bara generated steam pressure

3.2. Results

The different refrigerants are compared in terms of COP and compressor displacement, the corresponding results are shown in Fig. 5 and Fig. 6. The COP is calculated as it is presented in equation (9), where the heating capacity $\dot{Q}_H$ and the electrical power of the compressor P_{el} are needed.

$$COP = \frac{\dot{Q}_H}{P_{el}} \tag{9}$$

If 2 bar_a steam is produced, the COP is in the range of 3.26 and 4.3. For a steam pressure of 4 bar_a the COP is in the range of 2.28 and 2.89. A COP in the range of 1.93 and 2.29 is reached for a steam pressure of 6 bar_a. R601 has the highest critical temperature and provides the highest COP for all steam pressures (see Fig. 5).

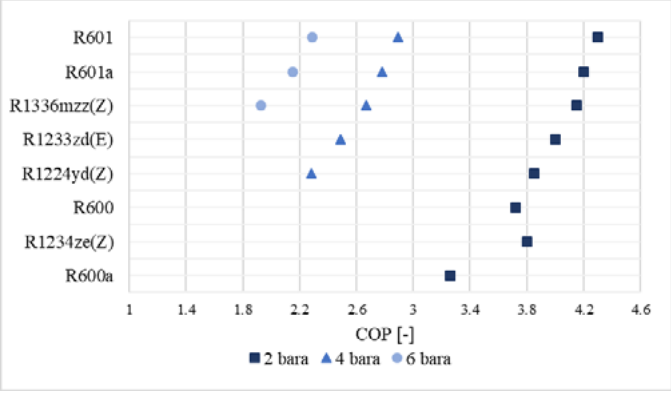


Fig. 5. COP for different refrigerants and steam pressures

The choice of refrigerant influences the COP to large extent. For example, using R1233zd(E) instead of R1224yd(Z) for a steam pressure of 4 bar_a results in an increase in COP of 9%. Comparing R600a and R601 for the production of 2 bar_a steam, the difference in COP amounts to about 24%. These differences can hardly be overcome only by adjusting the design of the refrigeration cycle.

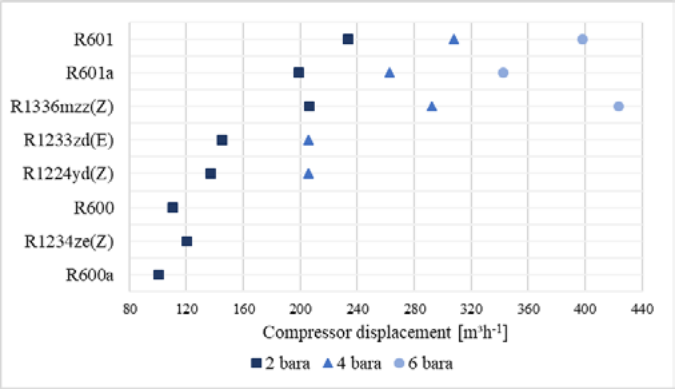


Fig. 6. Compressor displacement for different refrigerants and stem pressures

Furthermore, the results in terms of compressor displacement (Fig. 6) shows that R601 has the highest compressor displacement for all steam pressures except at a steam pressure of 6 bar_a. For this steam pressure the compressor displacement of R1336mzz(Z) is higher than for R601. In Fig. 5 it can be seen that the COP significantly decreases for higher steam pressures and the compressor displacement increases more or less with increasing steam pressure as it can be seen in Fig. 6.

Generally, it is easy to see that the choice of refrigerant is a trade-off between COP and compressor displacement, which leads to larger compressors. For example, for a steam pressure of 2 bar_a the COP of R1233zd(E) is 7% smaller than the COP of R601, but the compressor displacement of R1233zd(E) is 38% smaller than the compressor displacement of R601. This leads to a significant smaller compressor, where the COP is not decreasing that significantly. For the steam pressure of 6 bar_a R1336mzz(Z) shows the lowest COP but the highest compressor displacement.

In Fig. 7 the condensation enthalpy as a function of suction gas density for a steam pressure of 2 bar_a and all tested refrigerants are presented. The condensation enthalpy is equal to the width of the two-phase area in loq(p),h-diagram at condensation pressure. As it can be seen, R601 and R601a have the highest condensation enthalpy but also the lowest suction gas density. The high COP of R601 can among others be explained by the high condensation enthalpy. For R600 and R1336mzz(Z) the suction gas density is similar, but the condensation enthalpy of R600 is significantly higher than that of R1336mzz(Z). The suction gas densities of R600a and R1233zd(E) and the condensation enthalpies are very similar to each other. Fig. 7 illustrates the differences in material properties of the refrigerants, that have an important impact on the performance in a heat pump.

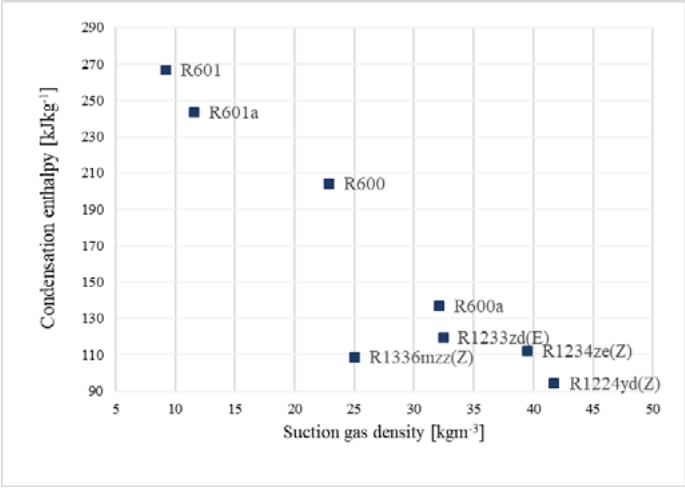


Fig. 7. Condensation enthalpy as a function of suction gas density for all investigated refrigerants and a steam pressure of 2 bar_a

4. Conclusion

In this work a model for a steam generating heat pump is presented. Simulations are an important tool for the design of heat pump systems and help to optimize the refrigeration cycle in an efficient way. This model was used for studying the suitability of different refrigerants for different generated steam pressures in a specified steam generating heat pump. The investigation has proven that the model is well suited to design the steam generating heat pump for different applications or requirements.

Furthermore, the simulation results show for the different preselected refrigerants and steam pressures, a range of 1.93-4.3 in terms of COP and a range of 101-424 m^3h^{-1} in terms of compressor displacement. R601 has the highest COP of 4.3, 2.89 and 2.29 for the three chosen steam pressures of 2 bar_a, 4 bar_a and 6 bar_a. This refrigerant shows also the highest compressor displacement for a steam pressure of 2 bar_a and 4 bar_a, which results in the largest required compressor volume. The choice of refrigerant is a trade-off between COP and compressor displacement. The choice of refrigerant also has an important influence on both investment and operation cost. The COP mainly determines the operation costs, the compressor displacement is an indicator of the size of the heat pump and therefore impacts on the investment costs. However, when selecting the refrigerant for a real implementation, attention must be paid to the fact that market-ready components are not available for all refrigerants. For example, R1336mzz(Z) and R600 are refrigerants which are already used in heat pump cycles and therefore all components are available. In contrast to R600, which is only suitable for a steam pressure of 2 bar_a, R1336mzz(Z) is suitable for all three investigated steam pressures. Therefore, in the project BAMBOO R1336mzz(Z) is used in the refrigeration cycle to generate steam at 5 bar_a. In the next step a prototype will be realized in the project BAMBOO which will be tested in a laboratory environment as well as in a real industrial process. Moreover, different heat pump cycle configurations and further operating conditions will be investigated in future investigations.

As an outlook for future technological developments, it should not go unmentioned that further industrial users can be gained by expanding the range of available industrial heat pumps. The investment decisions of industrial users are ultimately influenced by economic aspects. Therefore, optimized design of the industrial heat pumps and the use of standard components to lower the costs are important. Current technical limitations, such as maximum possible steam pressures, should be overcome by further efforts.

Acknowledgements

The project has received funding from the European Union's Horizon 2020 programme for energy efficiency and innovation action under grant agreement No. 820771.

References

[1] Forman C, Muritala I K, Pardemann R, and Meyer B. Estimating the global waste heat potential. *Renewable and Sustainable Energy Reviews* 2016; **57**: 1568–1579.
[2] Statistik Austria, STATcube- Statistical database of Statistik Austria. Useful energy analysis 2016 (in German), accessed on March 23 2018.
[3] ENGIE Refrigeration GmbH, CO_2-chillers and CO_2-high temperature heat pumps (in German). https://www.engie-refrigeration.de/export/sites/cofelyrefrigeration/content/documents/DE/Broschueren/thermeco2/DE_Folder_thermeco_W%C3%A4rmepumpen_web.pdf, accessed on October 29 2019.
[4] Davis T W. Introduction of Mayekawa's ECO cute water source hot water heat pump at Torres De Alba Hotel: Using the Natural Refrigerant CO_2. In*: Atmosphere America Business Case Natural Refrigerants* 2014, June 18-19, San Francisco, http://www.atmo.org/presentations/files/460_4_Mayekawa_Davis.pdf, accessed on January 01 2020.
[5] OCHSNER Energie Technik GmbH, Highest temperature series (IWWDS, ISWDS, IWWDSS) (in German), http://ochsner-energietechnik.com/hoechsttemperatur-waermepumpen/, accessed on October 29 2019.
[6] Wemmers A K, Van Haasteren A W M B, Kremers P, Van der Kamp J. Test results R600 pilot heat pump. In: *12th IEA Heat Pump Conference 2017*, May 15-18, Rotterdam, Netherlands.
[7] De Boer R. Industrial heat pumps in the Netherlands-developments and demonstrations. In: Zühlsdorf B, Bantle M, Elmegaard B, editors. *Book of presentations of the 2nd Symposium on High-Temperature Heat Pumps* 2019, September 09, Copenhagen, Denmark.
[8] Kaida T, Sakuraba I, Hashimoto K, Hasegawa H. Experimental performance evaluation of heat pump-based steam supply system . *IOP Conference Series: Materials Science and Engineering* 2015; **90**: 012076.
[9] Kaida T. High-temperature heat pumps in Japan- Potential, development trends and case studies. In: Zühlsdorf B, Bantle M, Elmegaard B, editors. *Book of presentations of the 2nd Symposium on High-Temperature Heat Pumps* 2019, September 09, Copenhagen, Denmark.
[10] Dassault Systèmes, https://www.3ds.com/de/produkte-und-services/catia/produkte/dymola/, accessed on November 01 2019.
[11] TLK-Thermo GmbH, https://www.tlk-thermo.com, accessed on November 01 2019.
[12] Ayub ZH. Plate heat exchanger literature survey and new heat transfer and pressure drop correlations for refrigerant evaporators. *Heat Transfer Engineering* 2003; **24**(5): 3–16,.
[13] Arsenyeva OP, Tovazhnyanskyy LL, Kapustenko PO, Khavin GL, Yuzbashyan AP, Arsenyev PY. Two types of welded plate heat exchangers for efficient heat recovery in industry. *Applied Thermal Engineering* 2016; **105**: 763–773.
[14] Lim J, Song KS, Kim D, Lee DC, and Kim Y. Condensation heat transfer characteristics of R245fa in a shell and plate heat exchanger for high-temperature heat pumps. *International Journal of Heat and Mass Transfer* 2018; **127**(A): 730–739.
[15] *VDI Heat Atlas*. VDI-Gesellschaft Verfahrenstechnik und Chemieingenieurwesen, editor. Springer-Verlag Berlin Heidelberg 2010, 2nd edition, Germany.
[16] Arpagaus C. *High temperature heat pumps: Market overview, state of the art and potential applications* (in German). VDE Verlag GmbH 2019, Berlin, Germany.
[17] Umweltbundesamt. Global Warming Potential (Global Warmin Potential, GWP) of selected compounds and their mixtures according to IPCC Fourth Assessment Report over a period of 100 years (in German), https://www.umweltbundesamt.de/sites/default/files/medien/2503/dokumente/treibhauspotentiale_ausgewaehlter_verbindungen_und_deren_gemische.pdf, accessed on November 01 2019.
[18] Ge Z, Li J, Duan Y, Yang Z, Xie Z. Thermodynamic performance analyses and optimization of dual-loop organic rankine cycles for internal combustion engine waste heat recovery. *Applied Sciences* 2019; **9**(4):680.

13th IEA Heat Pump Conference
April 26-29, 2021 Jeju, Korea

Ground source heat pump systems for energy efficient building retrofitting

Michael Lauermann[a*], Johann Emhofer[a], Karl Ochsner sen.[b]

[a]AIT Austrian Institute of Technology GmbH, Center for Energy,
Giefinggasse 2, 1210 Wien, Austria
[b]Ochsner Wärmepumpen GmbH
Krackowizerstraße 4, 4020 Linz Austria

Abstract

In the case of building retrofitting, the integration of ground source systems with heating/cooling solutions and heat pumps to achieve maximum performance is a great challenge that demands a solution. In order to find a suitable solution for a given building retrofit scenario, two different heat pump configurations are numerically analysed and compared to each other in terms of heating capacity and coefficient of performance (COP). As working fluid, the Low Global Warming Potential (GWP) refrigerant R1234ze(E) with a GWP smaller than 10 will be used to meet with the current F-Gas regulation by reducing the GWP of fluorinated refrigerants. One favourable heat pump configuration is a twin-cycle system. Alternatively, a single-stage configuration which uses a significantly larger condenser for enhanced subcooling in the refrigeration circuit is also analysed. Both systems allow a more efficient operation compared to state-of-the-art heat pump systems in the case of building retrofitting. In that way, the COP increase in relation to a standard heat pump cycle with typical subcooling is in the range of 10-15% depending on the operating point.

© HPC2020.
Selection and/or peer-review under responsibility of the organizers of the 13th IEA Heat Pump Conference 2020.

Keywords: Geothermal systems; building retrofitting; ground source heat pumps; twin-cycle configuration; enhanced subcooling

1. Introduction

In Europe, the building sector is responsible for 40 % of the total energy consumption and represents about a third of Europe's CO_2 emissions. This is a huge socioeconomic and environmental problem, more if we consider that almost half of the EU buildings have boilers installed before 1992, with an efficiency rate of below 60 % [1]. Although energy renovation of existing buildings could help to achieve the EU climate and energy tar-gets, the refurbishment rate is currently below 1 % and renewables are not widely used in the building sector. Within the H2020 project GEOFIT, easy-to-install, economical and enhanced geothermal systems for energy efficient building retrofitting are going to be implemented and demonstrated at five dedicated pilot sites across Europe - a historical building (ITA), a primary school (ESP), an indoor swimming pool (IRL), an office building (FRA) and a single-family house (IRL).

2. Low GWP refrigerants

Component providers and heat pump manufacturers are currently facing new challenges with the so-called F-Gas regulation, which provides for a gradual reduction in emissions of fluorinated greenhouse gases by 2030. Since beginning of 2018, the number of refrigerants that can still be used in the medium term has been drastically reduced, which has led to a significant increase in the price of fluorinated refrigerants.

The GEOFIT heat pump concept is generally foreseen for retrofitting the heating system of existing buildings. The working medium or refrigerant has a major influence on the area of application and the desired

temperature levels. The prohibition of chlorofluorocarbon (CFCs) and hydrochlorofluorocarbons (HCFCs) has severely restricted the availability of suitable working media. According to the EU Regulation No. 517/2014 on F-gas reduction (which came into force throughout the EU on 1.1.2015) [2] to reduce greenhouse gas emissions, a drastic multi-stage phase-down of HFCs (hydrofluorocarbons) applies until 2030, with the first significant stage already coming into force at the beginning of 2018. This will exacerbate the shortage of available working media and refrigerants.

For this reason, more and more companies and consumers are looking for alternatives. One option is based on natural refrigerants. Natural refrigerants include hydrocarbons, CO_2, ammonia and water. The most common hydrocarbons are isobutane and propane. However, propane is highly flammable and can form an ignitable and explosive gas mixture with the ambient air. A third generation of synthetic refrigerants, hydrofluoroolefin (HFOs), has recently launched on the market. A candidate would be the low-GWP refrigerant R1234ze(E) with a GWP smaller than 10. However, the core component in a heat pump system – the compressor – lacks approval from the manufacturers for these new refrigerants, e.g. due to technological barriers regarding the long term long-term stability of the seals.

3. Heat pump systems – the different technologies

A technology comparison in Table 1 provides an excerpt and overview of the state of the art for the relevant heat pump technologies, where brine/water and air/water heat pumps are compared with each other. The advantages and disadvantages of brine/water or air/water systems as well as the requirements of the various heat sources are shown. The annual performance factor (SCOP) is the benchmark for the efficiency of a heat pump system over a whole year. It indicates how much heating energy is delivered by the heat pump in relation to the electrical energy used over the course of a whole year. The so-called COP indicates a snapshot of the ratio of heating power to electrical power used. Modern heat pumps achieve COP values of 4 to 5 under standardized test conditions for supply temperature in the range of 35 °C for space heating. For hot water production the COP drops down to values below 3 at a temperature level of 55 °C.

Table 1: Comparison of the relevant technologies and state of the art of ground source and air-based heat pump systems in Austria, adapted from [3].

Heat source	Boreholes	Ambient air
General requirements	• Suitable ground • Required depth: 25 m/kW	• Sufficient distance between supply and exhaust air duct • Split-device: Ensure sound insulation, frost-proof condensate drain
Space requirements (outside the technical room)	• Borehole distance: approx. 10 m • 2.5 m Distance to property boundary • 1.5 m distance to supply and disposal lines (sewer, water, etc.)	• Split device: manufacturer-specific • Indoor installation: none
SCOP	3.5 – 5	2.5 – 3.5
Advantages/Disadvantages	+ high, stable source temperature throughout the year, high efficiency, low space requirement - higher investment costs	+ Low additional installation effort - strongly dependent on temperature level and amount of exhaust air - Sound emissions

The dimensioning of the heat pump in the case of retrofitting depends, among other things, on the previous oil or gas consumption. These values can be used to determine the effective heating energy required. The flow temperature plays an important role in the operation of the heat pump. For well renovated apartments with underfloor heating 35 °C is sufficient. If the heat transfer area of existing radiators is large enough, the temperature should be 50 °C, and in the case of an older building standard 65 °C can be regarded as a guide value. However, the efficiency of the heat pump deteriorates with increasing flow temperature. At this point, the GEOFIT solution comes in.

4. Description of the heat pump system

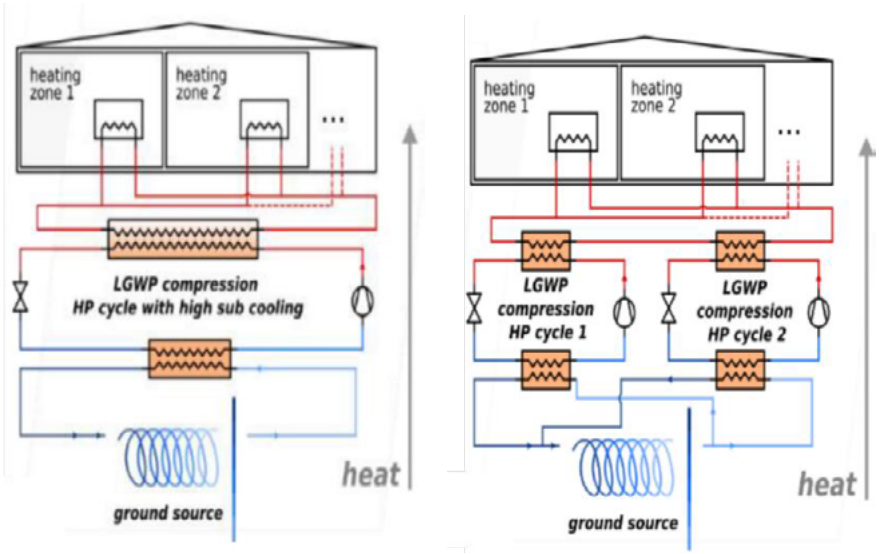
The GEOFIT heat pump system uses a low GWP refrigerant R1234ze(E) with a GWP<10 instead of state-of-the art refrigerants like R134a which has for example a GWP of 1430. The system makes uses of cost effective heat exchangers (e.g. heat exchangers made of Aluminum) that due to the lower raw material costs

of Aluminum compared to Copper (about of a third), represent a potential to lower the costs of the heat pumps without performance loss. Since, high temperature differences can be required for retrofit heating systems; we investigate two alternatives to provide them within the project. (1) One solution is based on using two heat pumps with different condensation temperatures but with the same evaporation temperature (see Figure 1 right). (2) The other solution uses a significantly larger condenser compared to a state-of-the art heat pump condenser to make use increase the sensible subcooling of the refrigerant (see Figure 1 left).

The general idea behind the first mentioned configuration is to split up a single refrigeration cycle into two cycles. In that way, one of the two refrigerant cycles does need not to overcome the entire temperature lift. Hydraulically, the two condensers are connected in series, whereas the two evaporators are connected in parallel. Assuming a similar compressor scale on both cycles, roughly half of the total heating capacity can be delivered at a higher COP than the other. This configuration is referred as "Twin-cycle" heat pump configuration depicted in Figure 4. The second configuration is a "Single-Stage" heat pump configuration. In contrary to the Single-Stage heat pump configuration, the Twin-cycle heat pump configuration shows considerable advantages regarding safety, start-up time and legal requirements, as the refrigerant charge for each cycle is only half compared to the Single-Stage configuration. Those advantages and disadvantages are summarized in Table 2.

Table 2: Advantages and disadvantages of the considered heat pump configurations.

Configuration	Advantages	Disadvantages
Single-Stage	• Simplest refrigeration cycle → Low invest costs • Good overall performance in terms of COP and energy cost savings from very low to medium temperature lifts	• Higher refrigerant charge per cycle • Start-up time • Legal requirements due to refrigerant charge • Lower efficiency at high temperature lifts • No part load possible without speed control
Twin-cycle	• Lower refrigerant charge per cycle • Best overall performance from very low to medium temperature lifts • Without speed control, still 50% part load possible	• More complex refrigeration cycle →Higher invest costs



Single-Stage Twin-cycle

Figure 1: GEOFIT concepts for the heat pump systems.

5. Operating modes

When talking about operation of a heat pump, its actual heating capacity in the design point[1] plays a significant role. There is a certain degree of flexibility regarding heat pump sizing. According to that, the following two operating modes will be discussed:

- Monovalent
- Bivalent

5.1 Monovalent operation

A heat pump is usually sized to at least 100% heat demand of the heating season for any given house, meaning that the heat pump should be able to entirely heat the house without electric or other back up system except under the most extreme conditions. In practice, this translates to systems being designed to a target external design temperature[2], depending where the property is located. This type of application should therefore be preferred as far as possible. Brine/water or water/water heat pumps in a state of the art building standard are usually operated monovalently. Monovalent operation of air/water heat pumps is also possible, but not always feasible.

5.2 Bivalent operation

The heat pump covers most of the heat demand on its own. At very low outside temperatures, the heat pump and the supplemental heat generator, work together. This temperature is known as the bivalent point (BP). This operating mode is used when renovating existing buildings while retaining the installed gas boiler. If the heat pump could not cover all the heat load and is also restricted to its maximum supply temperature at extreme outdoor conditions, the additional heating system will pick up the shortfall in terms of increased capacity and increased supply temperature. In the case of building retrofitting, it is usually the existing gas boiler. Figure 2 shows an overview of the different operating modes.

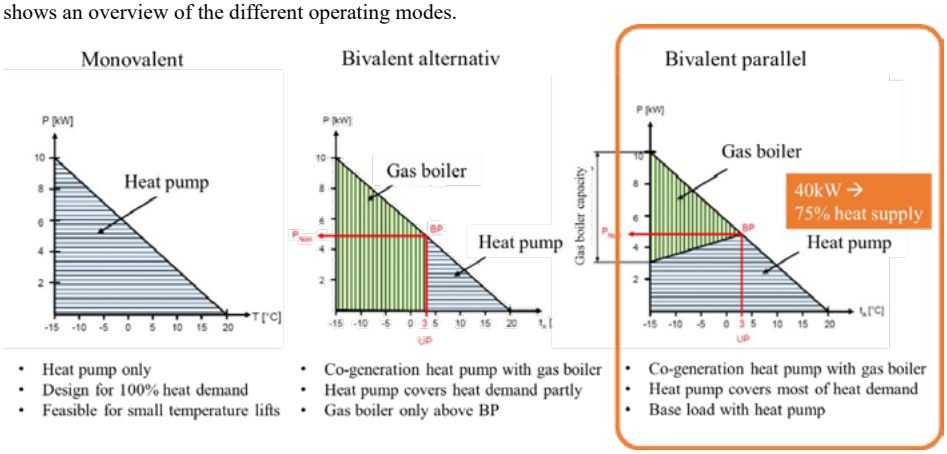


Figure 2: Heat pump operating modes. Monovalent, Bivalent alternative and Bivalent parallel. For the GEOFIT case, a heat pump with 40kW heating capacity is able to deliver 75% heat demand.

If gas boilers are already installed, the bivalent parallel is a favorable option, where the heat pump acts as base load system and the existing gas boilers are switched on below the bivalent point as discussed in [4]. With such operating control, the maximum operating hours of the heat pump can be achieved, having the most economical solution for retrofitting. However, this operating mode poses a great challenge regarding the hydraulic integration and the control of the two coupled systems in order to avoid derogating the heat pump efficiency when the gas boiler turns on. Though, the hydraulic integration is not part of this work as we address the refrigeration circuit layout assuming a correct integration and operating control.

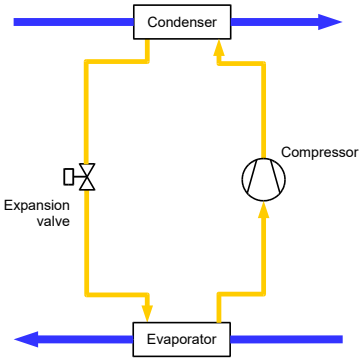
[1] The design point for a heat pump system is usually given by the most extreme operating condition, i.e. coldest day of the year.
[2] This is the target minimum low external temperature as established according to National Building Codes or based upon statistical or historical meteorological data available for each location.

6. Simulation environment

The numerical simulations are performed in Dymola. Dymola is a commercially available simulation environment to solve actual problems written in the modelling language Modelica. It is suited for multi-domain modelling, (e.g. thermal, mechanical, electrical and hydraulic). Modelica is an equation-based object-oriented modelling language, which allows reproducing complex physical systems and solving time-dependent problems in mechanical, electrical, hydraulic, thermal, fluid and control fields, with the help of algebraic, differential and discrete equations [5].

The heat pump modelling in general takes place in the thermo-hydraulic domain. A heat pump system is built up by standard components, such as heat exchangers, compressors, expansion valves, control systems, sensors, etc. These components can be custom written or selected from either free or commercial libraries written in Modelica. Within the GEOFIT project, we use the TIL-Library [6] for the thermal component modelling as it is widely used and proven by the refrigeration industry. The specific modelling approach allows for a detailed representation of the physics and parameterization of each heat pump component from the compressor to the heat exchangers up to the entire piping of the refrigerant cycle, if necessary. Furthermore, an extensive database of refrigerants is available in TIL libraries. Figure 3, Figure 4 show the different heat pump configurations as simple schematic view and model representations in Dymola.

Schematic view of a Single-Stage cycle



Graphical view of the Modelica model in Dymola

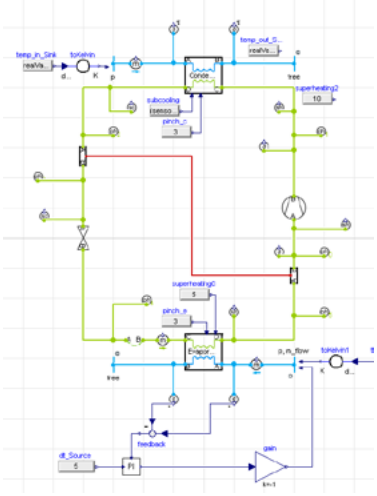


Figure 3: Schematic view (left) and Modelica model in Dymola (right) of a single-stage heat pump.

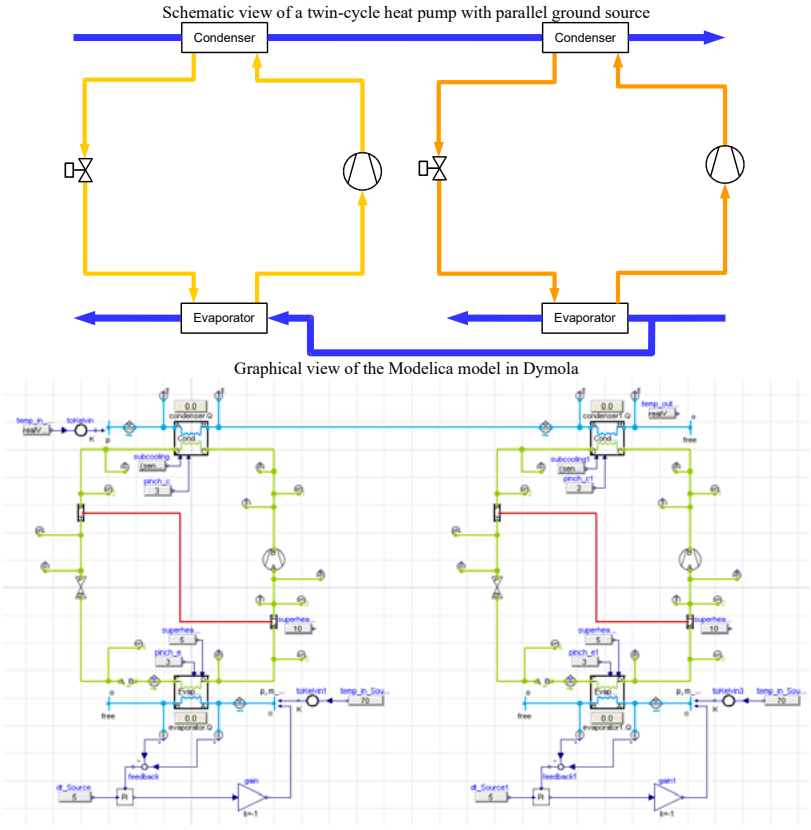


Figure 4: Schematic view (top) and Modelica model in Dymola (bottom) of a twin-cycle heat pump cycle with parallel source.

7. Methodology

The methodology for the layout and design of heat pump system is roughly depicted in Figure 5. After the implementation and model setup phase, the model parameters are set to manufacturer data. A critical role is played by the compressor characteristics, which are usually given for a standard refrigerant with high-GWP values (e.g. R134a). At present, efficiency data for low-GWP refrigerants, such as R1234ze(E) is not yet available for the chosen compressor type. The Bitzer refrigerant report states [7], that operating experiences gained from laboratory and field trials to date allow a positive performance assessment on the efficiency behavior compared to R134a. For the usual operation range, the COP is within a range of 5 %. Therefore, it is expected that simple system modifications will provide the same efficiency as with R134a. However, R1234ze(E) is sometimes called an R134a substitute, the resulting heating capacity is the range of 20 % below that of R134a. With this information and the proper heat pump configuration, we changed the refrigerant from R134a to R1234ze(E) in our models keeping the efficiency values from R134a. We are aware that an accurate quantitative assessment is not possible with this methodology but a qualitative comparison of different heat pump configurations.

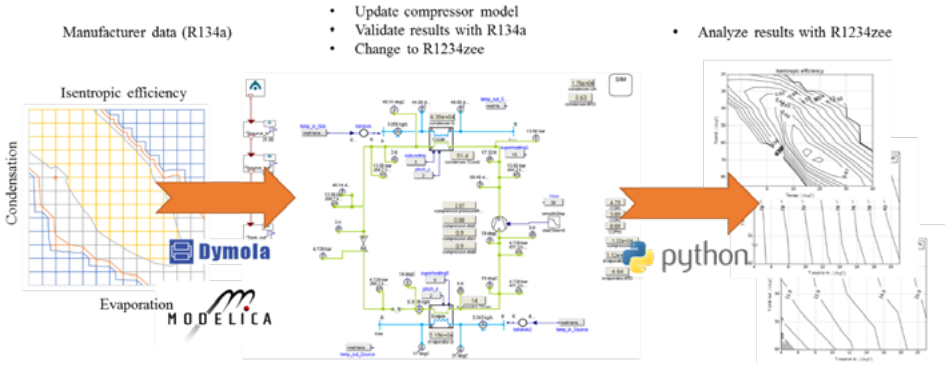


Figure 5: Methodology for the evaluation of the heat pump system.

Six typical operating states were simulated and the parameters such as heating capacity of the heat pump ($\dot{Q}_{heat}$), electricity consumption of the compressor (P_{el}) and COP were used to compare to each other. Those operating states are given in the Table 3. The temperature conditions on the source and on the sink – assuming a proper control strategy and hydraulic integration for the retrofit case - are the inputs for the numerical models.

Table 3: Temperature boundary conditions for the typical reftofit case.

Operating point	T_{source_in}	T_{source_out}	T_{sink_in}	T_{sink_out}
-		degC		
1	4	2	35	40
2	4	2	45	50
3	11	7	35	40
4	11	7	45	50
5	21	17	35	40
6	21	17	45	50

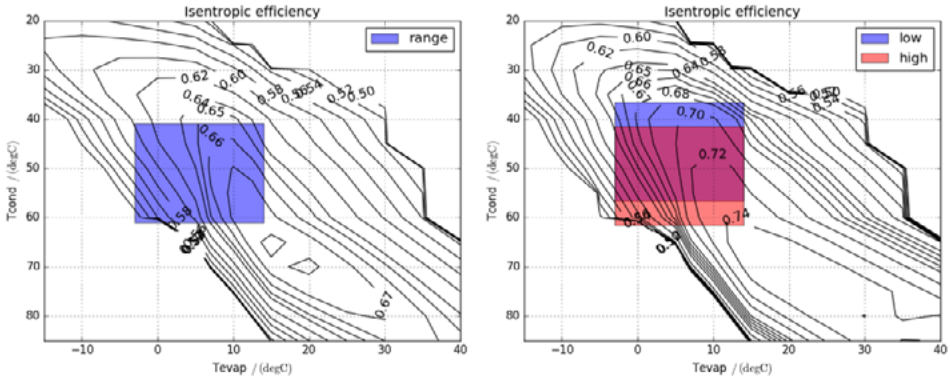
In GEOFIT, the compressor type of the electrical driven heat pump system is chosen to be a scroll compressor. This specific compressor type is a positive displacement compressor. We chose to follow the efficiency-based modeling approach. In order to describe the compression cycle, the isentropic and the volumetric efficiency are prescribed. They are usually given as a function of pressure ratio and condensing or evaporating temperature. An ideal isentropic compression is complemented by different physical effects:

- pressure drop suction side
- pressure drop discharge side
- internal leakage
- re-expansion of the compressed fluid
- mechanical friction
- heat losses

The volumetric efficiency gives the relation between the geometrical mass flow and the actual mass flow over the compressor. The geometrical mass flow can be calculated with the known refrigerant properties on the suction side and the swept volume. For the specific scroll compressor in GEOFIT, the manufacturer provides efficiency curves for R134a. While the isentropic efficiency is used to calculate the discharge enthalpy of the refrigerant, the effective isentropic efficiency represents the electric power consumption of the motor. Usually, it's the effective isentropic efficiency which is experimentally identified, as the measurement of electric power is more accurate, than the measurement of the discharge temperature. However, for the sake of simplicity, both efficiencies are considered equal for the considerations in this work.

Figure 6 shows the compressor characteristics based on manufacturer data for the two heat pump configurations. The blue region for the Single Stage system (left) show the resulting operating window based on the values in Table 3 for a single compressor. For the Twin-cycle system (right), the blue region reflects the lower cycle and the red region the higher cycle. Both compressor types are from the same compressor series, but only differ in displacement. The compressor for the Single-stage system has approx. twice the displacement than one of the two compressors for the Twin-cycle system. Even though the compressors belong

to the same compressor series, when comparing the isentropic efficiencies in Figure 6, it can be seen, that the qualitative behavior is similar but the peak value for the Twin-cycle compressors is at 0.74 while for the Single-stage compressor it is at 0.67. This difference is directly affecting the resulting COP as it can be seen in the next section.



Single Stage Twin-cycle

Figure 6: Compressor characteristics for the Single-stage system (left) and the Twin-cycle system (right).

8. Results

Before comparing the two heat pump configurations, a general remark on operating a heat pump in building retrofitting. The lower the return flow temperature, the higher the efficiency of the heat pump. Together with an existing gas boiler, the interaction between those two heating elements must be even more carefully considered in order to avoid high return flow temperatures when operating in bivalent parallel mode. In GEOFIT a top-level control for the two heating systems will be implemented to ensure an energy efficient operation.

Figure 7 shows the results for the Single-stage system and Figure 8 the results for the Twin-cycle system. The contour plots with the isolines allow for a quick assessment of the characteristics at different operating points. For both systems, the heating capacity depends almost only on the source temperature. The sink temperature has a minor impact where the heating capacity slightly decreases with increasing sink temperature. Comparing the different configurations, the Twin-cycle shows the best results in terms of COP. Due to reduced temperature lift on the low cycle, less electricity is consumed by the compressors compared to the Single-Stage configuration. For both configurations, the overall heating capacity varies from roughly 42 kW down to 26 kW depending on the source temperature level with slightly higher values for the Twin-cycle configuration. The COP values are in the range of 2.2 to 5.8 for the Single-stage system and 2.5 to 6.5 for the Twin-cycle system. Therefore, the COP increase for the Twin-Cycle is approx. 5 to 15% according to the operating point, which is a significant improvement considering long term operation and energy costs. In Figure 9, the increase is depicted for all operating points.

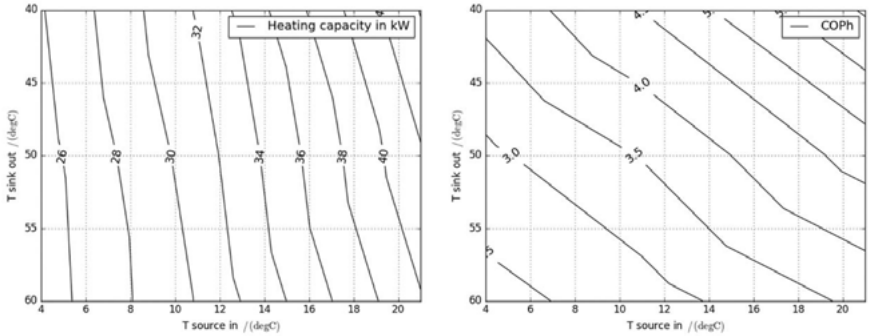


Figure 7: Results for the Single-Stage system.

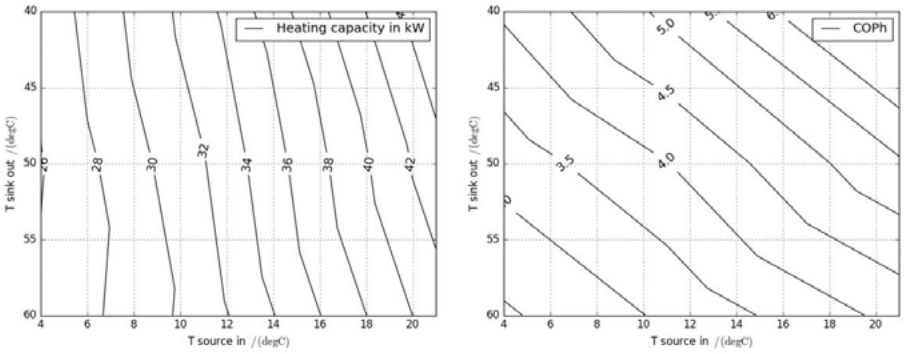


Figure 8: Results for the Twin-cycle system.

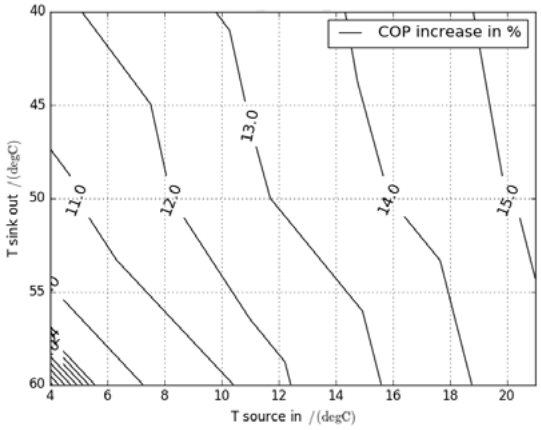


Figure 9: COP increase of the Twin-cycle system compared to a Single-stage system.

9. Conclusion

This paper presents a numerical comparison of two different heat pump configurations for a specific building retrofitting case in the framework of the H2020 project GEOFIT. The compressor characteristics were taken from manufacturer data for R134a and transferred for the use of the low-GWP refrigerant R1234ze(E). The results show a significant COP increase in the range of up to 15% for a Twin-cycle configuration compared to a Single-stage heat pump with enhanced subcooling.

The results are based on a given temperature spread on the supply side of 5K by preserving the installed radiators in the building. Increasing the heat transfer area of the heat distribution system in the building by either changing the radiators or upgrading them with a ventilation system, can lower return temperatures significantly. This has a positive effect on the heat pump efficiency by lowering the mean supply temperature between flow and return side.

In this work we outline a possible way to increase the heat pump efficiency by a twin-cycle system. There are also other ways for an improved heat pump cycle, e.g. a two-stage with EVI-injection. But all those enhancements come along with increased investment costs compared to a Single-Stage system. These additional costs need to be contrasted with the efficiency gain and is part of the future work within the GEOFIT project. In the case of building retrofitting, a parallel operation with an existing gas boiler is the most economical solution. A great challenge is the hydraulic integration and the control of the coupled systems in order to avoid derogating the heat pump efficiency when the gas boiler turns on.

A successful integration of ground source heat pumps systems in existing buildings needs an integral approach where the ground source, the heat pump and the hydraulics in the building receive equal attention. In that way it is possible to increase the commercial attractiveness of geothermal energy in combination with ground source heat pumps and therefore increase the penetration of this renewable source in building retrofitting.

Acknowledgements

The projects have received funding from the European Union's Horizon 2020 programme for energy efficiency and innovation action under grant agreement No.792210.

References

[1] European Comission, *Towards a smart, efficient and sustainable heating and cooling sector*, 2016.
[2] *Regulation (EU) No 517/2014 of the European Parliament and of the Council of 16 April 2014 on fluorinated greenhouse gases and repealing Regulation (EC) No 842/2006 Text with EEA relevance*, 2014.
[3] H. Huber, P. Schöfmann, and A. Zottl, "Wärme!pumpen zur energieeffizienten Wärmeversorgung: Technologieleitfaden Wärmepumpen," 2014.
[4] K. Ochsner, *Geothermal heat pumps: A guide for planning and installing*. London: Earthscan, 2008.
[5] P. A. Fritzson, *Introduction to modeling and simulation of technical and physical systems with Modelica*. Hoboken, N.J.: Wiley; IEEE Press, 2011.
[6] W. Tegethoff, R. Kossel, and C. Richter, *Objektorientierte Modellierung und Simulation thermischer Systeme*. Kursunterlagen zur Modelica Schulung (de).
[7] BITZER Kühlmaschinenbau GmbH, "Refrigerant Report 19," 2019.

13th IEA Heat Pump Conference
April 26-29, 2021 Jeju, Korea

Test results of a Rotation Heat Pump and further developments

Andreas Längauer[a*], Bernhard Adler[a], Christian Rakusch[a]

[a]ecop Technologies GmbH, Perfektastraße 73/Top A1, 1230 Vienna, Austria

Abstract

Strict regulations for refrigerants in terms of global warming potential (GWP) force industries and suppliers to develop new compressors, working fluids and lubrication systems. In contrast of solving these challenges, the Rotation Heat Pump (RHP) is based on a completely new principle and design which eliminate them via a fully integrated system. The compression in a RHP, which uses a nontoxic, ecologically friendly and not flammable working fluid, is based on centrifugal forces. This results in a very high compression efficiency of more than 99% and furthermore in a high coefficient of performance (COP). The process itself relies on a Joule cycle where the heat transfer is sensible and the working fluid is always gaseous. As a consequence, the process is not depending on the critical point of the fluid. A Rotation Heat Pump K7, developed during the last few years, was installed in January 2019 at the customers site and performance data has been collected since then. These results will be shown additionally to further examples of tests which have been done at a test rig. The advantage of flexibility in terms of temperature as well as the performance (COP) are shown in different charts. The next step of engineering is the development of a RHP-M2, which will provide a maximal thermal power at the sink of 2 MW. Additionally, some new arrangements will allow a temperature spread between sink and source of about 100 K. Another new feature will be special heat exchangers which will enable advanced operation modes. A further possibility for a new design is the downscaling to a 10 kW RHP, which would be possible to use in a standard household.

© HPC2020.
Selection and/or peer-review under responsibility of the organizers of the 13th IEA Heat Pump Conference 2020.

Keywords: Rotation Heat Pump, High Temperature, COP, Energy Efficiency

1. Introduction

Reducing CO_2-Emissions has to be the main target to keep the global warming in a bearable range for mankind to save biodiversity and human well-being. Many different aspects have to be accounted, processes have to be optimized and new technologies need to be applied to use renewable energy. Knowing that heat takes a major part of emitting CO_2, it is essential that heat pumps find their way not only further to space heating but also to industries and district heating. Additionally, it is necessary that heat pumps are using refrigerants with a very low Global Warming Potential (GWP) to ensure an environmentally friendly implementation. During the last years a lot of engineering has led to different low-GWP working fluids which may have some kind of disadvantage in terms of flammability and toxicity. In contrast to those fluids a Rotation Heat Pump (RHP) is using a mixture of noble gases, which GWP is zero and is neither flammable nor toxic. This is possible due to the used counterclockwise thermodynamic cycle, based on the Joule process. It means that the working fluid is always gaseous and is not condensing or evaporating in the heat exchangers. The big challenge to ensure an efficient system is, as for commercial heat pumps as well, the efficiency of the compression. In a RHP this challenge has been overcome by using centrifugal forces in a rotating domain to compress the gas. A short introduction how this compression has been realized and how it works will be given in the next section, details about that can also be found in [1], [2], [3] and [4].

* Corresponding author. Tel.: +43 -1-865-10-62-27
E-mail address: andreas.laengauer@ecop.at

This paper deals mainly with measured results, gained at a test rig as well as in a final application, to demonstrate the function and advantages of this principle.

2. Function and Design

A Rotation Heat Pump is based on two main components which are the rotor and the housing. The rotor is the essential part for the realization of the thermodynamic cycle because it provides through the rotation the compression and expansion of the working fluid. Also, the heat exchangers are mounted on the rotor which means that they are in motion during the process. The housing and additional components ensure the electrical supply, encapsulate the rotor and transfer the process fluids of sink and source into the rotating domain. In Figure 1 the design of a RHP is shown, on the left hand side the entire machine with the upper case removed and on the right hand side a pair of heat exchangers and the pipe system.

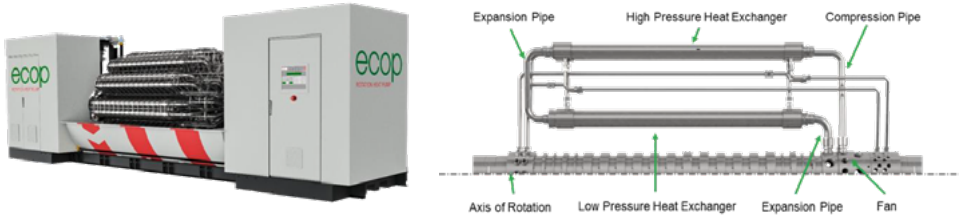


Figure 1: Design of a Rotation Heat Pump

In addition to the mechanical design, the following Figure 2 shows the Temperature-Entropy diagram (left) corresponding to the design and presents the thermodynamic cycle of the working fluid in the rotor (right) based on CFD (Computational Fluid Dynamics) calculations. The shown temperatures are just an example, the process can be shifted to different temperature levels easily, while the Coefficient of Performance (COP) remains almost constant. The temperature increase (5.2 to 2) is caused by the compression based on the centrifugal forces and vice versa the expansion (3 to 4 and 5 to 5.1). Heat is transferred from the working fluid to the sink (2 to 3) and from the source to the working fluid (4 to 5). A fan ensures the mass flow in the system and provides the exergy to the process via an electrical motor. The rotational speed of the fan can be controlled independently of the speed of the main rotor by using a separate frequency converter for this engine. The fan basically acts like a commercial compressor but consists of special designed blades. More details about the function and design are represented in [2] and [4].

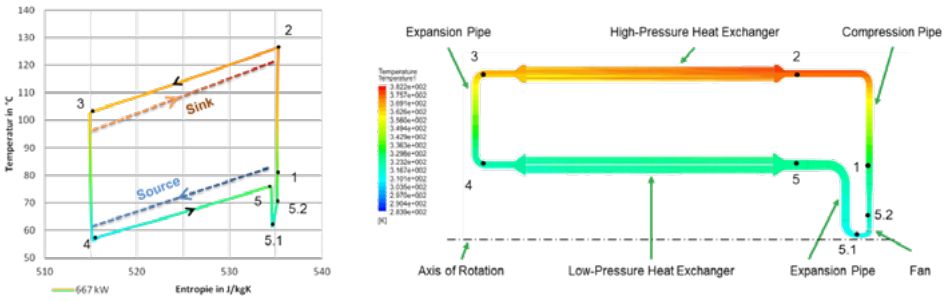


Figure 2: Joule cycle (left) and corresponding design (right) of a Rotation Heat Pump

2.1. Calculation of the Coefficient of Performance (COP) for a RHP

A common used, representative parameter for characterizing the efficiency of a heat pump is the Coefficient of Performance (COP). Also, for the Rotation Heat Pump the COP can be calculated by using the thermal power at the output and the electrical power consumption. The ratio of those values represents how many times thermal power is provided at the output (sink) compared to the input of electrical power. The electrical power consumption of a RHP is mainly caused by the engines of the fan and the rotor. Since they are measured

separately, a COP of the thermodynamic process itself can be calculated as well when considering only the power of the fan. The used expression for calculating the COP is

$$COP = \frac{\dot{Q}_{sink}}{P_{electric}} \quad (1)$$

where $\dot{Q}_{sink}$ is the thermal power at the sink and $P_{electric}$ is the electrical power consumption, all given in W. If only the fan is used for the power consumption and calculation the efficiency is named $COP_{Process}$.

3. Testing

To test the Rotation Heat Pump two different ways are presented, first the combination with a test rig to show short term tests and second the results of an operation period of three days in the final application at the customer site. The data of the test rig arrangement should give an initial impression about how the system responses to planned changes while the second data set points out possible boundary conditions in the field application and how a RHP can deal with them.

3.1. Test rig

As already presented in [5], the test rig and Rotation Heat Pump are installed like shown in Figure 3 for testing and evaluating data. Different sensors to measure mass flow, temperature, pressure, rotation speed, electrical power and so on, are installed and values are stored on a flash device. Since for the evaluation and testing of specific design points it was not necessary to run the system for long time at constant parameters. Those tests are therefore considered as short-term tests in contrast to the following section about the installation at the customer site where data of the RHP over 72 hours is shown.

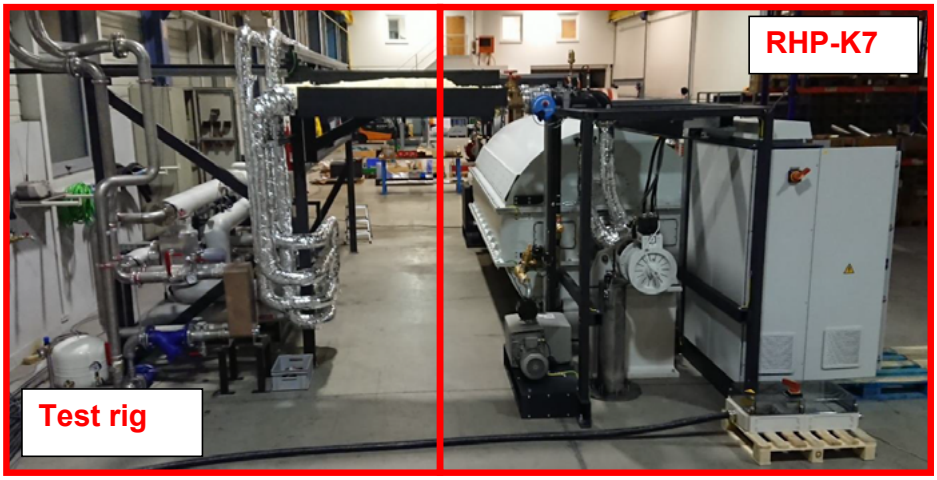


Figure 3: Overview test rig and RHP-K7 [5]

The test setup shown in Figure 3 can be represented as a scheme including sensors and hydraulic connections as well. The scheme (Figure 4) also includes all heat exchangers and pumps which are used for heat recovering/transferring and providing fluid flow. To adjust temperatures and thermal power of the system to a certain design point, the valves V1 and V2 can be controlled via remote control or the touch panel. The positions of the mentioned sensors are shown as well as the engines. For evaluating the electrical power consumption, the frequency converters have been used. Details about the test rig can be found in [5].

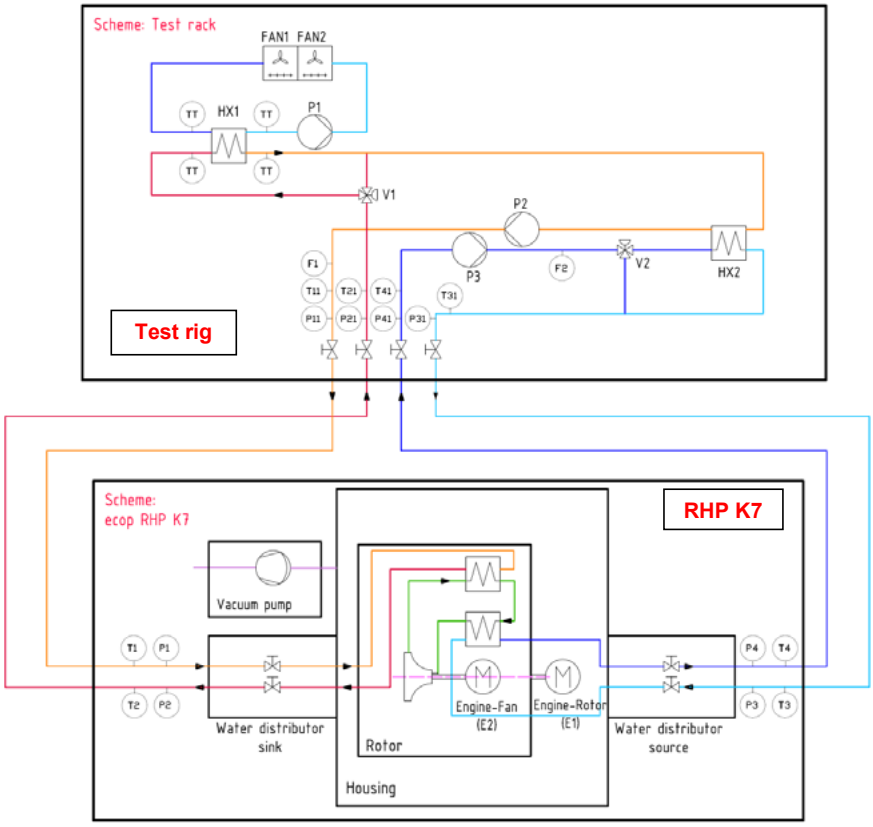


Figure 4: Simplified scheme of the test rig and RHP-K7

The collected measurement data was used to evaluate the COP corresponding to the temperature of sink and source and the rotational speed. The temporal development of temperatures, speed, mass flow, power and COP are stated in the following diagrams.

The first arrangement of measurement curves shows the response of the system to slow changes in temperature, see Figure 5 and Figure 6. Due to the fact, that the temperature spread between sink and source is constant as well as the mass flow and the rotational speed, the COP is remaining almost constant. The temperature level as displayed is changing to some of 15K at sink and source which is representative for changing conditions due to a day-night cycle for example. Further information about the dependence of the COP to the thermal power and the temperature lift will be discussed later with respect to the results of the field application. The results of the test rig demonstrate mainly the flexibility in terms of temperature level and the possibility to reach high temperatures.

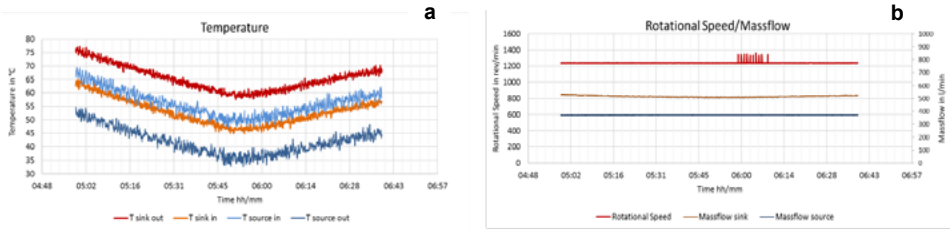


Figure 5: Temperature of sink and source (a), mass flow and rotational speed (b)

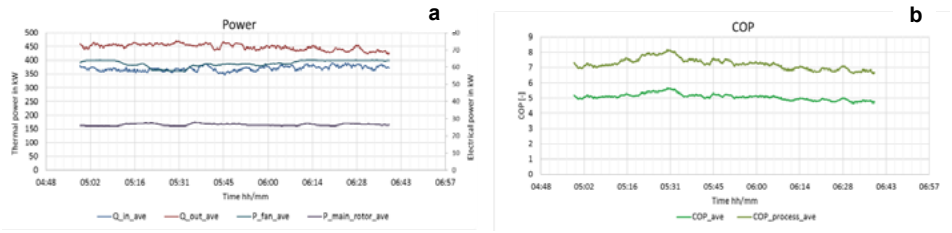


Figure 6: Thermal and electrical power (a), COP (b)

To demonstrate the possibility of switching from a lower temperature level to a higher one, the following figures show the temperature drift from around 65°C to about 90°C output temperature at the sink. The spread between sink and source is again kept constant and so the COP is at an almost constant level. The reason for differing to the constant operation mode (04:19h to 05:02h, Figure 7 and Figure 8) is caused by the fact, that the system is not balanced in terms of energy. To increase the temperature level more energy input is necessary than at the output appears. Thus, the power at the output is less than at constant conditions and also the COP is affected. However, when reaching a steady state, the power and COP are at the same level as before the dynamic increase. Figure 7 and Figure 8 show the described behavior.

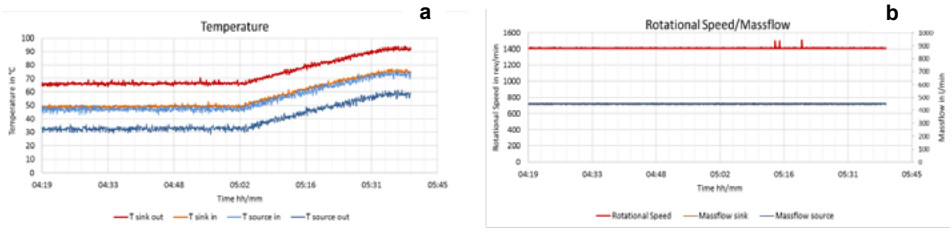


Figure 7: Temperature of sink and source (a), mass flow and rotational speed (b)

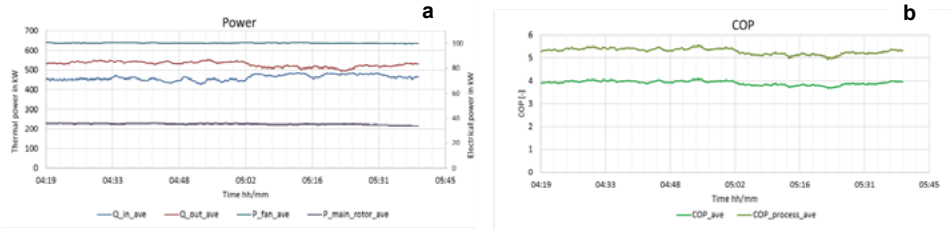


Figure 8: Thermal and electrical power (a), COP (b)

Further data of tests from the test rig are mentioned in [5] where some representative test cases have been analysed additionally.

3.2. Field application

After the previous described tests in combination with a test rig, the RHP has been installed at the customers site where further tests have been performed. Of course, it is not possible to provide boundary conditions as flexible as at the test rig but it is also essential to validate the function in field applications. In the following Figure 9 the field installation of the first RHP-K7 is shown. On the left-hand side the control cabinet for power supply including frequency converters is represented while on the right-hand side the control cabinet for the programmable logic controller is installed. The closed main housing including the rotor is located in between. The data of the following paragraphs show measured values of three consecutive days.



Figure 9: RHP-K7, field installation

Results in terms of measured data of the field installation show the daily variation of temperatures and also, since the mass flow was kept almost constant, the variation of power and COP. This is based on the fact, that the RHP has not been run in optimization mode. To ensure a maximum COP the mass flow as well as the rotational speed can be dynamically adjusted by a programmable logic controller. This feature has not been used during the measurement period and so the COP is sometimes dropping to a lower level and also rising to a higher one. Another fact which should be mentioned, is the general operation at an off-design point. The designated thermal power of the RHP-K7 is 700 kW at the sink, for this power all components are designed and optimized for. Since during the time of testing only 100-600 kW have been needed at the sink, the optimal operation point has not been reached.

The following figures show always a measuring duration of 24h, each day is constituted by a set of 4 diagrams including same measurands and calculated values as in the test scenario described in the previous section. Each figure states out, that the temperature of the source is increasing after appr. 07:00h until it remains almost constant after approximately 13:00h. The decreasing of the source temperature begins at around 17:00h on day two and three while on the first demonstrated day it starts more spontaneous at around 14:00h. The drop of source temperature at 14:24h is caused by switching on an internal fan of the CHP plant, where the RHP is integrated, for cooling the source. Thus, it is a change of boundary conditions due to external circumstances which results in this stairstep for the supply temperature. But, as the diagram shows as well, it is not a problem to keep the thermodynamic process ongoing.

The peak of thermal power always corresponds with an increased electrical power consumption of the fan while the power for the main rotation is always almost constant. The reason for this behavior of power consumption of the fan engine is the divergence of the isobars. If more heat is transferred from the working fluid to the process fluid, it is necessary that the fan overcomes the increased pressure difference caused by this divergence. This can be seen in Figure 2 where the pressure increase by the fan is shown from point 5.1 to 5.2 in the T-s-diagram. It is the same effect as it is used in turbines for power transformation based on the clockwise Joule-cycle. For the Rotation Heat Pump, it means, that the more thermal power is transferred, the more electrical power is necessary. Furthermore, this divergence also depends on the temperature lift between the source and the sink provided by the rotational speed of the main rotor. It can be stated, that the higher the temperature lift and the more heat transferred, the higher is the necessary pressure increase and the electrical power consumption of the fan. The power consumption of the main rotor in turn is always constant at a certain rotational speed. This value mainly depends on the friction of sealings and bearings.

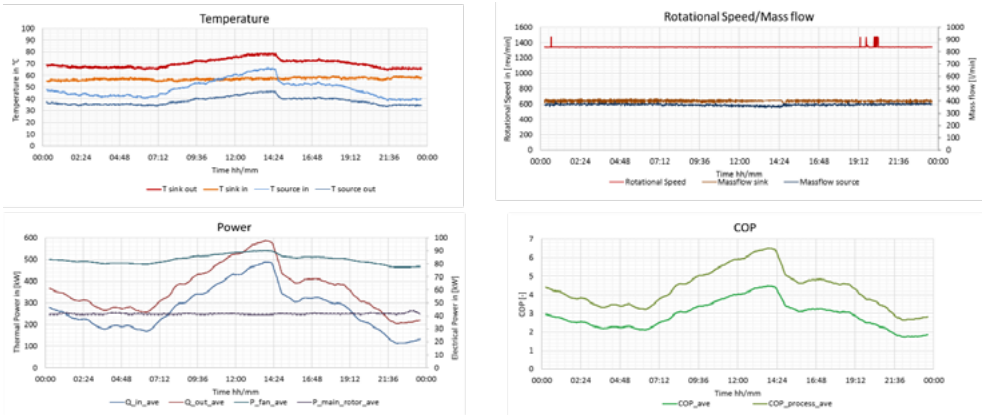


Figure 10: Test data, 1st day

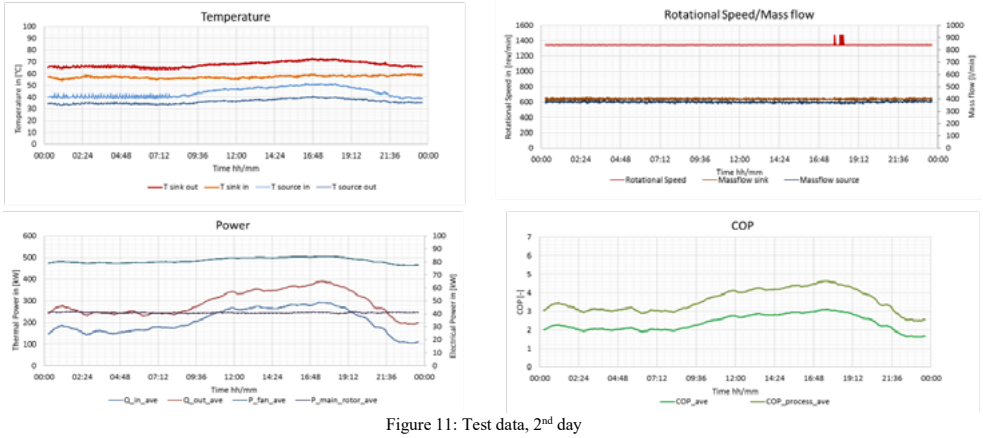


Figure 11: Test data, 2nd day

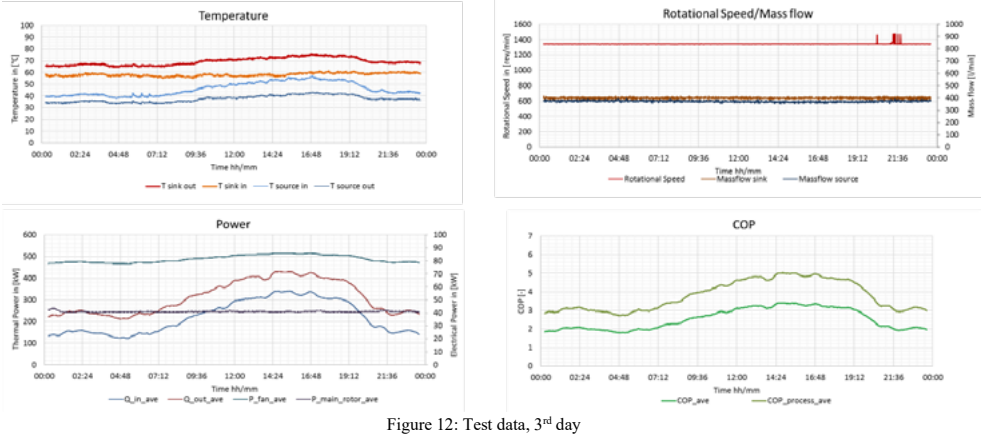


Figure 12: Test data, 3rd day

4. Further developments

To show the potential of a rotation heat pump and the joule-cycle based on centrifugal compression, some further developments will be shown. Right now, the focus is based on industrial applications, which make sense because there is a huge potential to reduce CO_2 emissions in this area. This fact is targeted by the development of a RHP-M2 which will provide 2 MW of thermal power at the sink. This type of machine will also allow a temperature lift of appr. 100K because internally there are two separated gas-cycles which can be switched from parallel to serial operation mode. Therefore, the mass flows of sink and source are split up and an intermediate circuit of process water is used. This operation mode allows a high lift but, in this case, the thermal power output at the sink is reduced to 1 MW.

However, the aim is also to reduce refrigerants with a high GWP in the field of space heating and refrigeration. Compared to the design of actual Rotation Heat Pumps, supplying 700 kW thermal power, it needs just some adaptions for downscaling to smaller machines of around 1- 10 kW. This power range is fitting good for household installations. The main principle, the compression via centrifugal forces, will not change but in terms of size those machines will be quite smaller. Another promising approach would be the development of a “Rotation Chiller” for supplying cold in refrigeration systems in combination with an environmentally friendly working fluid. In Figure 13 the actual designs are shown as well as the planned developments corresponding to the temperature level at the sink and the thermal output.

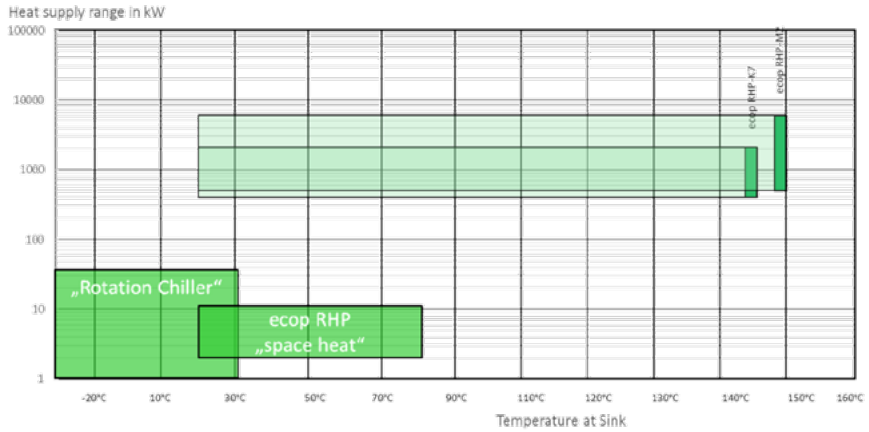


Figure 13: Actual designs and further developments

One further advantage is the design flexibility concerning the arrangement of heat exchangers. Right now, they are installed in parallel to the axis of rotation which makes sense for transferring sensible heat with an optimal temperature spread of sink and source according to the mass flow of the working fluid. But, since the incline of the heat exchangers can be seen as a degree of freedom to adjust the process, the thermodynamic cycle can be optimised for many different operating conditions (Table 1). It is a big advantage, that the heat capacity rates need not to be equal for minimizing exergy losses of the heat exchangers. The drawback of this layout is finally, that the design is more complex compared to the standard layout.

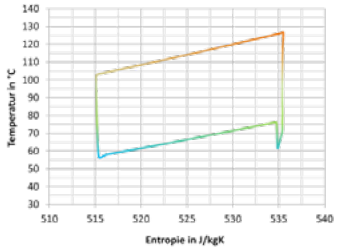
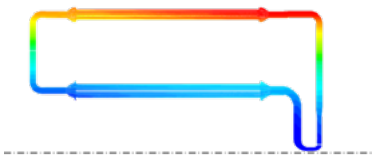
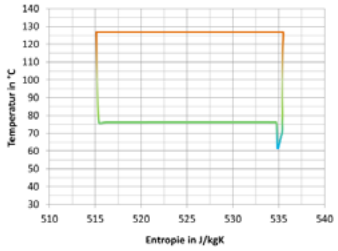
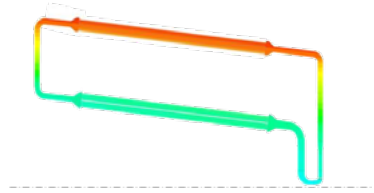
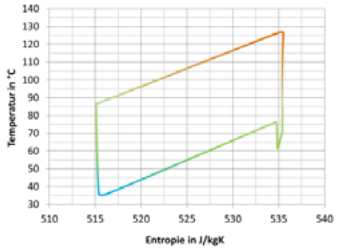
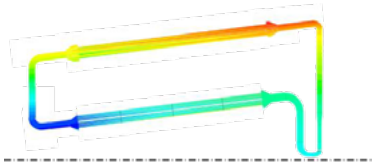
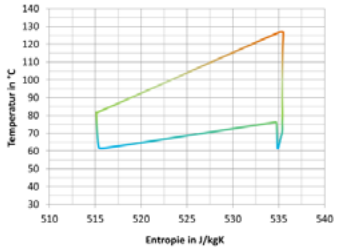
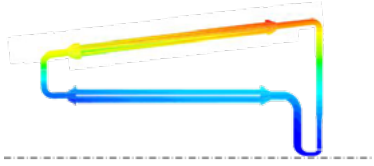
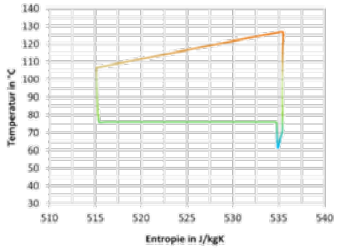
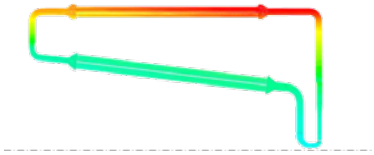
A positive incline of both, the low-pressure and high-pressure heat exchanger, enables the possibility to realize a thermodynamic process quite close to the Carnot-cycle. The reason therefore is the heat transfer during the working fluid is further compressed in the heat exchanger. That arrangement would fit perfect for high mass flows at sink and source while the temperature spread is quite low for a certain power output.

The opposite, the negative incline of the heat exchangers uses the cooling based on the expansion of the working fluid during the flow to a lower diameter of the rotor. The transferring of heat during this expansion allows further cooling and therefore a high temperature spread of sink and source is possible. So, the thermal power can be provided by having a low mass flow but high spread in terms of temperature.

The last two examples shown in Table 1 demonstrate the possibility to incline only one heat exchanger. This may be an advantage if there is a sink with low mass flow and high temperature spread in combination with a moderate cool down of the source, demonstrated by the negative incline of only the source. The last

case presents the positive incline of the source-heat exchanger, this would be most efficient if the mass flow of the source is high and the temperature spread is low. The sink in this case is not adjusted.

Table 1: Possible arrangements of the heat exchangers and corresponding T-s-Diagrams (schematic)

	T-s-Diagram	Heat exchanger arrangement
Standard design		
Positive incline (small spread of sink and source)		
Negative incline (large spread of sink and source)		
Positive incline at sink (large spread of sink)		
Negative incline at source (small spread of source)		

5. Conclusions

After different studies about the principle and function of a Rotation Heat Pump (RHP) have been published, test results are now available. In addition to the measurement data, gained at a test rig and a field installation, also a short introduction about the main principle and design of a RHP is given in this paper.

The first reference plant of a RHP-K7 has been manufactured and assembled as well as been tested. For simulating various operation modes by providing different boundary conditions in terms of temperature and mass flow of sink and source, a custom test rig was used. All necessary sensors have been installed while by using different heat exchangers, pumps and control valves the system was controlled and measurement data was collected. A scheme of the test rig and RHP present the setup and allow to comprehend the system. The focus of this installation was put on showing the flexibility in terms of temperature but also to verify the achievement of high temperatures at the output. Both cases are visualized via measurement data in diagrams and confirm these functions. Further, it is demonstrated, that at constant mass flow and rotational speed the temperature level can be easily adjusted without affecting the efficiency.

Beside the test application, the field installation was used to gain data of three consecutive days of operation. Relevant sensors have been logged again and measurement values have been analyzed in each case to calculate the Coefficient of Performance as a representative value for the efficiency. Since the system was not run in an optimization mode, the mass flow was kept constant and also the rotational speed. The input temperatures have been varying as they where depending on the operation of a CHP-plant where the RHP is implemented. In contrast to the boundary conditions at the test rig, the input temperature of sink and source have been changing not in a uniform way but much more irregular. Thus, the supplied thermal power and also the electrical power consumption where affected. The relation of those values to the temperature is analyzed and discussed where the divergence of the isobars plays a key role.

To give an outlook for further development possibilities, new fields of application are listed as well as design studies to optimize the thermodynamic process. Because the principle of centrifugal compression is also efficient in small scales, besides the upscaling of the RHP-K7 (700 kW) to the RHP-M2 (2 MW) the downscaling for space heating is of major interest. The changing of design parameters like the incline of the heat exchangers is a new degree of freedom for a heat pump and is introduced. Because of this option, it is possible to adjust the thermodynamic process exactly for individual implementations. These research projects are discussed in a last section where advantages and disadvantages are mentioned.

Acknowledgements

This project has received funding from the European Union's Horizon 2020 research and innovation programme under grant agreement No 823463.

References

[1] Adler, B., et al., Centrifugal compression turbo heat pump made by ECOP, 10th IEA Heat Pump Conference, Tokyo, Japan, 2011
[2] Adler B., Riepl, S., Heat pump for process industry, 11th IEA Heat Pump Conference, Montreal, Canada, 2014
[3] Adler, B., et al., Industrieller Einsatz einer Rotationswärmepumpe, DKV-Tagung, Bremen, Germany, 2017
[4] Adler, B., Mauthner, R., Rotation Heat Pump (RHP), 12th IEA Heat Pump Conference, Rotterdam, Netherlands, 2017
[5] Adler, B., et al., COP tests of a Rotation Heat Pump, 25th IIR International Congress of Refrigeration, Montreal, Canada, 2019

13th IEA Heat Pump Conference
April 26-29, 2021 Jeju, Korea

An air-water dual-source heat pump system for shrimp ponds

Jia-Hao Cheng, Peng Gao, Xiang Cao, Peng Shao, Liang-Liang Shao*, Chun-Lu Zhang*

School of Mechanical Engineering, Tongji University, Shanghai 201804, China

Abstract

Ponds in farmland have been widely used for shrimp culture in eastern coastal regions of China. To maintain the pond water temperature in winter, an environment-friendly, energy-saving and low-cost heating system is urgently needed. This paper proposed a new air-water dual-source heat pump system (AWDSHPS), which is equipped with two parallel evaporators, one taking heat from air and the other from water in idle ponds. The two heat sources can be used separately or simultaneously, based on ambient conditions and heating demand. A validated load model is built to calculate heating demand accurately. Another simulation model is applied to fulfill system design and performance prediction. Furthermore, operational strategy of full growing season is optimized. The results showed that, compared with the same system in which only air source is used, the AWDSHPS has higher evaporating temperature. That increases from -7.7°C to -3.2°C at ambient temperature of 0°C, resulting in 7% increase in energy efficiency and 27% increase in heating capacity. Therefore, system energy performance becomes more stable, reducing the heat pump size to lower both initial investment and operating costs.

Keywords: heat pump; shrimp pond; dual heat sources; energy saving

1. Introduction

To meet the growing market demand, a vast quantity of whiteleg shrimp, *Litopenaeus vannamei*, is farmed in humid and cold eastern coastal regions of China. In there, thousands of farming ponds have been excavated in farmland. There are three growing seasons every year. Two are in winter, one from November to January and the other from February to April. To maintain the normal growth of shrimp, an acceptable pond water temperature range is 20°C~32°C [1]. This range is much higher than local average ambient temperature of 5° C in winter. Thus, additional heat input is urgently needed.

Thanks to inexpensive investment and low operating costs, the coil-fired boilers were popular among local farmers in the past few years. However, given the serious pollution to the environment, regional authorities banned coil-fired boilers for shrimp culture. Therefore, an alternative heating system is urgent to be designed. It should be environment-friendly, energy-saving and low-cost.

Among the existing heating technologies, heat pump is the first choice. Depending on the heat source, traditional heat pump technologies are divided into various types, among which ground source heat pump (GSHP) and air source heat pump (ASHP) is most popular. The former takes ground, groundwater, or surface water as heat source and sink. It is widely used owing to high thermal-efficiency and relatively low operating costs [2, 3]. However, inappropriate application of GSHP may cause environment risks, including thermal pollution and groundwater contaminations [4]. Other potential risks also have been pointed out by many researchers [5-7]. As for ASHP, which takes air as heat source, is also favorable for its simple structure, low initial cost and high energy efficiency [8]. But in practical applications, energy performance of ASHP is often unsatisfactory [9]. The sensitivity to environmental temperature and heating capacity attenuation caused by frosting are two main problems [10, 11]. Besides, some dual-source heat pump (DSHP) systems have been proposed, mainly for producing domestic hot water, space heating and cooling for buildings [12-14].

* Corresponding author. Tel.: +86-136-71825-133.
E-mail address: shaollpaper@gmail.com (L.-L. Shao), chunlu.zhang@gmail.com (C.-L. Zhang).

However, the various traditional heat pump system mentioned above is not suitable for local shrimp culture. If GSHP is used, thermal imbalance will be a problem because there is no heat injected back to ground in summer. The shrimp pond needn't be cooled at that time. Groundwater contamination is another concern. Regional authorities have banned groundwater heat pumps. As for ASHP, oversize scale is needed as a result of its unstable poor performance under low temperature conditions, which brings about a higher initial investment.

To solve the above problems, in this paper, we proposed a new air-water dual-source heat pump system (AWDSHPS) according to local practices. It can absorb heat from air and water in idle ponds separately or simultaneously, based on weather condition and heating demand. With water as additional heat source, the system benefits from more stable energy performance, lower investment and operating costs. In order to achieve these, a load model of shrimp pond was built and validated first, as shown in section 2. In section 3, with the help of load model, heating demand was calculated accurately. Then the new AWDSHP system was designed and optimized using GREATLAB. In section 4, the system energy performance was analyzed in different modes under various working conditions. Based on that, in section 5, the operational strategy of full growing season in winter was optimized to minimize power consumption. Lastly, the conclusions were provided in section 6.

2. Load model

In this section, based on the principles of thermodynamics and heat transfer, load model of shrimp pond was built first, and then validated with experimental data. This model will be used to calculate heating demand for system design, as shown in section 3.2. Moreover, in section 5, it will be used to simulate pond water temperature of full growing season.

2.1. Modeling

The typical ponds we studied here are of uniform size, about 40m long, 9m wide and 1m deep. At the top, the pond is covered with one or two layers of transparent plastic film for insulation. The bottom is directly the soil. The real picture is shown in Fig. 1.



Fig. 1. Picture of shrimp pond in farmland

The energy balance of the shrimp pond is made up of multiple heat transfer processes. Heat input is mainly from solar radiation and external equipment, while heat loss from conduction through soil, heat transfer between water and inner cover (convection, radiation, evaporation and condensation), convection with air outside, and sky radiation.

Fig. 2 demonstrates the energy fluxes in the water volume and at the covering surface. Note that the heat capacity of plastic surface is ignored because of its small thickness (about 1×10^{-4}m) and negligible heat mass. Considering the energy balance, we have,

$$Q_{r,w,f} + Q_{a,w,i} + Q_{c,w,g} + Q_{l,w} - Q_{sr,w} - H = c_w m_w \frac{dT_w}{d\tau} \quad (1)$$

$$Q_{r,w,f} + Q_{a,i,f} + Q_{l,f} + Q_{sr,f} - Q_{r,f,o} - Q_{a,f,o} = 0 \quad (2)$$

where every term of equation represents a kind of heat transfer. $Q_{r,w,f}$, for example, is the radiation between water and film. All symbols can be found in Nomenclature.

Each of heat transfer processes, listed in Eq.1. and Eq.2. above, can be defined by a mathematical expression. Since this paper mainly focuses on the performance of the new proposed system, specific methods are not introduced here. Relative information can be easily found in professional books and papers [15, 16].

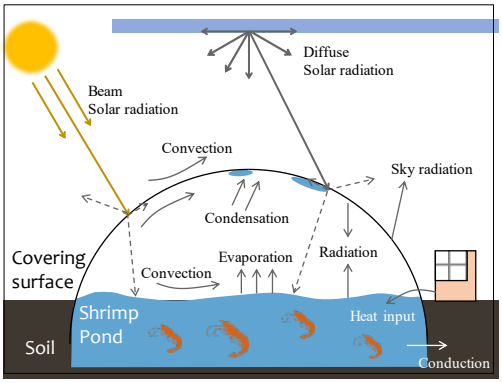


Fig. 2. Energy fluxes in the water volume and at the covering surface

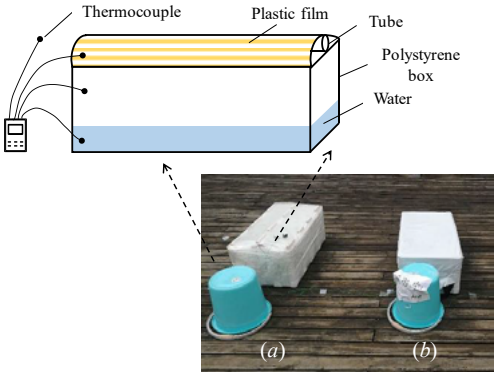


Fig. 3. Shrimp pond model (a-covered with 2 layers transparent PE film, b-covered with 1 layer)

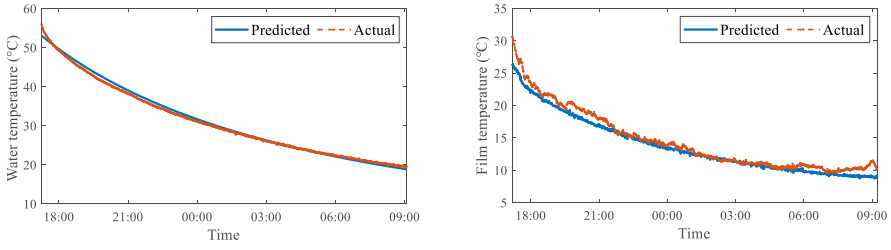


Fig. 4. Comparison of simulation and test data

2.2. Model validation

In order to validate the accuracy and reliability of load model, an experiment was conducted. We first made a simple shrimp pond model, as shown in Fig. 3. The open polystyrene box is used to simulate the pond. Some water is stored inside. Plastic film covers it on top, supported by a horizontal tube. The film material is the same as the actual use. To acquire data for further validation, temperatures of stored water, covering film, internal and external air were measured once a minute. A simple digital thermometer, coupled with K-type thermocouples, was used. Measurement uncertainty of ±1°C is acceptable here. Besides, this experimental model can be employed to compare effect of various insulation schemes, such as covering different layers of film.

By modifying relative geometric parameters and boundary conditions of the original load model, we achieved a suitable model for the polystyrene box. Then above experimental data were used to calibrate the property parameters of film, including thermal conductivity, radiation transmittance and so on. The model after calibration can well predict the water and film temperature, as shown in Fig. 4. Later, these calibrated parameters will be substituted into the original load model.

3. System design

In this section, the working principle for the new AWDSHPS is first introduced, and its simulation model is developed later using GREATLAB [17]. This simulation model can predict system performance, as shown in later sections 4 and 5.

3.1. System description

Fig. 5 is the schematic diagram of the new AWDSHPS. The heat pump unit is composed of two parallel evaporators (fin-tube type for air-cooled one and brazed plate type for water-cooled one), a rotary compressor, a brazed plate condenser, two expansion valves, a reserving valve, etc. Unlike the traditional system, another evaporator is adopted to absorb heat from water in heat storage ponds. These ponds are idle in winter because less shrimp are farmed to reduce risk and achieve higher market price. Having heat taken from the heat storage ponds, the water temperature should not be below 0°C. They keep energy balance by absorbing solar energy at daytime. Heat absorbed, together with the power input, is then transferred to the secondary refrigerant (25% ethylene glycol solution with a freezing point of -10°C) in the condenser. The heated secondary refrigerant flows through the bottom pipes to provide heat, keeping shrimp pond water temperature above 20°C. In addition, the shrimp pond is covered with one film more than the heat storage pond to achieve a balance between energy-saving and investment.

By closing and opening the expansion valves, the unit can take heat from air and water separately or simultaneously. Thus, three heating modes can be fulfilled: (a) air source heating mode, ASHM; (b) water source heating mode, WSHM; (c) air-water source heating mode, AWSHM. With water as additional heat source, the heating system benefits from higher surrounding temperature, therefore, better system performance would be obtained from higher evaporating temperature. Moreover, the heating capacity attenuation caused by defrosting, which is common in air source heat pump system, can be mitigated.

3.2. System modeling

Based on the validated load model in section 2 and meteorological data from the past 5 years, we accurately calculate heating demand of shrimp pond. The result shows, with heat input at a constant level of 16kW, the water temperature of shrimp pond can be maintained in the range of 20°C~31°C during full growing season. Fig. 6 is the simulation result of the typical growing season in 2017. Consequently, the heating capacity of heat pump is designed at 16kW.

As to design conditions, extremely serious ones that possibly encountered in future operation, are usually adopted. Design conditions in this case are listed in Table 1. For heat sink, the water temperature of shrimp pond is set to 20°C. For heat source, both air and water of heat storage pond should be considered. For one thing, in the worst case, water temperature of heat storage pond is the freezing point, 0°C. For another, although the lowest ambient temperature is roughly -10°C in farming region, the water in heat storage pond can be alternative heat source in the cold winter. Given the days of ambient temperature below 0°C is no more than 7% in recent five years, ambient temperature is set to dry bulb temperature of 0°C and web bulb temperature of -1°C.

Table 1. Design conditions of the AWDSHPS

Water temperature of shrimp pond	Ambient temperature (DB/WB)	Water temperature of heat storage pond
20°C	0/-1°C	0°C

According to design requirements mentioned above and engineering practice, we developed the system simulation model in GREATLAB, which is a well-validated vapor-compression system modeling and analysis tool. Since this paper focused on the proposed AWDSHPS and its operating performance during full growing season, modeling methods are not described here. Detailed information can be found in the references [17, 18]. Fig. 7 is the system model of the novel AWDSHPS using GREATLAB, of which the operating principle is in accordance with that shown in Fig. 5.

Based on the design conditions (Table 1), component performance got from manufacturers and size limitations, we carried out the system optimum design with simulations. Specifications are listed in Table 2. On this basis, we can analyze system performance at design and off-design conditions in later section.

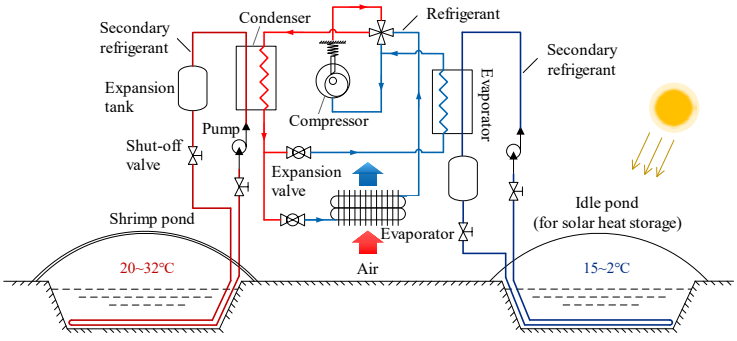


Fig. 5. Schematic diagram of the AWDSHPS

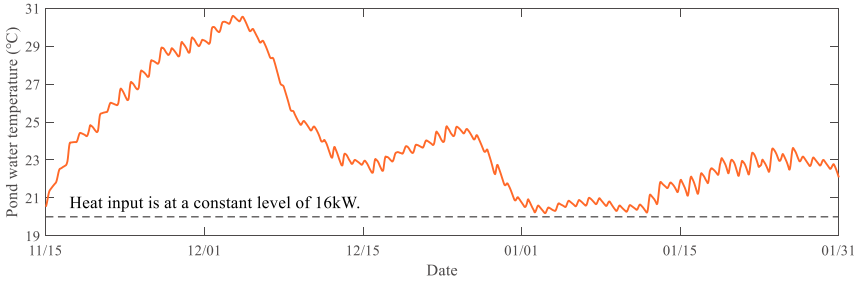


Fig. 6. Pond water temperature of full growing season (2017/11~2018/1)

Table 2. Specifications of the optimum system design

Name	Specification	Simulation model type
Refrigerant	R410A	REFPROP 9.0
Compressor	Rotary	Curve-fitting model
Condenser	Brazed plate	1D incremental model
Air-cooled evaporator	Finned-tube, three rows, 1300mm×914.4mm×50mm	Incremental tube-by-tube model
Water-cooled evaporator	Brazed plate	1D incremental model
Expansion device	EXV	Curve-fitting model
Fan	Axial Fan, variable speed	Curve-fitting model
Pump	Centrifugal pump, variable speed	Curve-fitting model

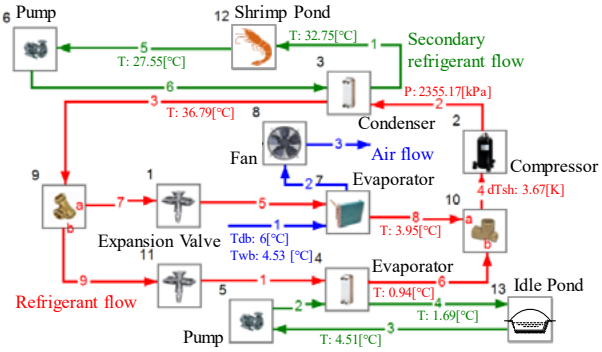


Fig. 7. Screenshot of system model in GREATLAB

4. System performance analysis

In this section, system performance at design and off-design conditions were numerically analyzed. Ambient temperature varies in the range of -5°C to 15°C. For simplicity, water temperature of heat storage pond is always 5°C higher than the ambient. As shown in Fig. 8, with the increment of ambient temperature, system COP and heating capacity increase almost linearly as well. For the three heating modes, system in WSHM has the highest COP with an average of 3.7, followed by 5% decrease in AWSHM and 10% in ASHM. As to the heating capacity, system in all three modes can meet the desired value of 16kW when ambient temperature is above 2°C. Even at serious conditions that ambient temperature drops to -5°C, the WSHM and AWSHM can still satisfy this requirement.

Above comparison of COP and heating capacity in three modes partly demonstrates the advantages of additional heat source of water. That of evaporating temperature in Fig. 9 further reveals this. In comparison to very low ambient temperature at night or cold winter, water temperature of heat storage pond is about 5°C higher owing to its huge heat capacity. Therefore, taking heat from water or air and water together will lead to an increase in evaporating temperature. The system performance benefits from it. For example, the evaporating temperature increases from -7.7°C in ASHM to -3.2°C in AWSHM at ambient temperature of 0°C, resulting in 7% increase in energy efficiency and 27% increase in heating capacity. Furthermore, higher evaporating temperature mitigates the influence of frosting. The air-cooled fin-tube evaporator is easy to frost in winter due to relatively lower evaporating temperature and higher humidity ratio. For conventional air source heat pump system, frosting often occurs at the working condition that ambient temperature is below 7/6°C according to Chinese standard [19]. Under that working condition, the relative evaporating temperature in ASHM of this system is about -3°C. By comparison, the same evaporating temperature (-3°C)

in AWSHM of this system appears at ambient temperature of 0°C. That means frosting can only happen on the most severe days with proper heating mode switch, thus the heating capacity attenuation is much smaller than that of air source heat pump system. That's why the new system can be downsized, which lower both initial investment and operating costs.

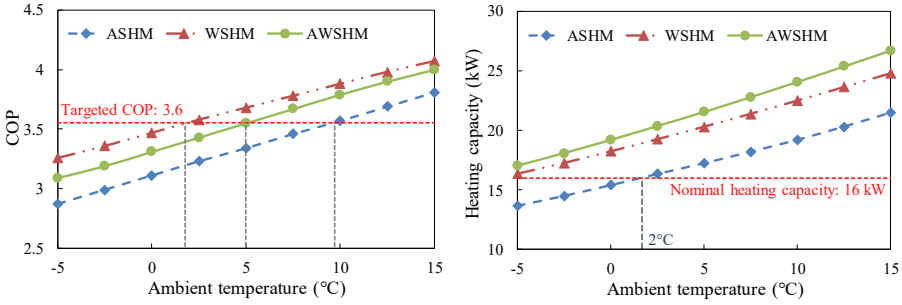


Fig. 8. System performance versus ambient temperature

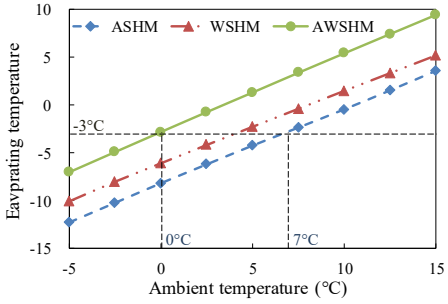


Fig. 9. Evaporating temperature versus ambient temperature

5. Operational strategy of full growing season in winter

The proposed AWDSHPS will be applied to heat shrimp pond for the whole growing season, nearly 3 months. To generate better operational strategy, two aspects should be considered. Firstly, timely heating mode switch. According to comparison and analysis in section 4, at severe conditions, system performance in ASHM is very poor. Although the other two modes perform better, they cannot always enable because the heat absorbed from heat storage pond is limited. Otherwise, excessive heat loss will lead to icing. Thus, WSHM or AWSHM should be adopted at severe conditions while ASHM at better ones. Secondly, proper on-off operation. In the early days when ambient temperature is above 15°C, system efficiency is high but additional heat input is unnecessary. With time going on, the ambient temperature gradually decreases, resulting in growing heating demand. Meanwhile, the energy performance gets worse and worse. However, shrimp pond water temperature can fluctuate in a large range of 20°C~32°C. Thus, a certain amount of heat can be stored. At the beginning of growing season, we can turn on heat pump unit to store oversupply of heat, keeping pond water temperature at a high level. So, shrimp pond requires less heat in cold winter when system is underperforming. More power is saved to compensate for early input.

Based on load model and system model, we optimized the operational strategy. Fig. 10 is the overall logic diagram. With historical meteorological data and strategy mode as input, AWDSHPS model calculates heat input to shrimp pond and heat absorbed from heat storage pond. The two outputs are then given to subsequent load models, from which water temperature of full growing season is finally obtained. According to this procedure, operational strategy is optimized with minimum power consumption as objective and water temperature as constraints.

For ease of application, we introduce a simple optimized operational strategy here. The principles are,

- If water temperature of shrimp pond is below 23°C, turn on machine. Select ASHM, WSHM or AWSHM at ambient temperature of greater than 10°C, 5~10°C, or less than 5°C, respectively.
- If water temperature of shrimp pond exceeds 23°C, turn off machine.

The following command of mode switch is shown in Fig. 11.

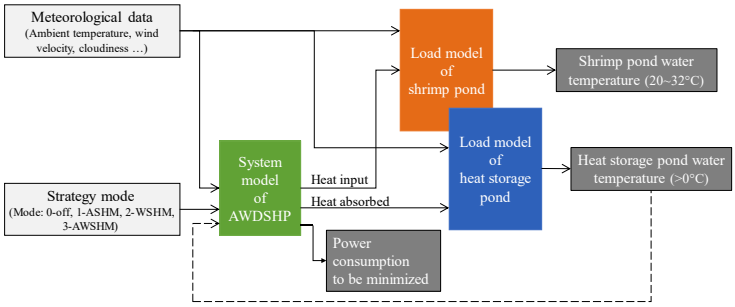


Fig. 10. Block diagram showing the optimization logic

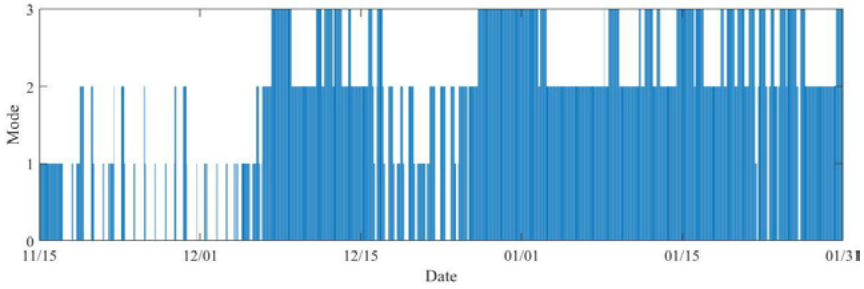
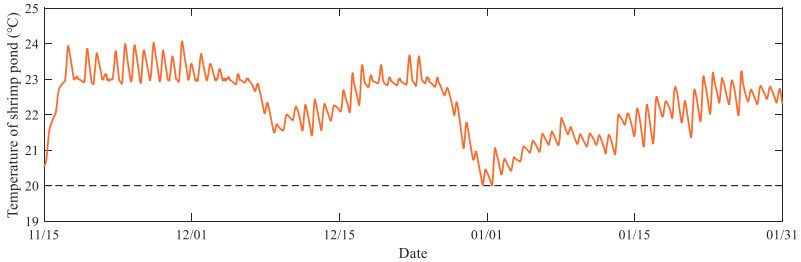
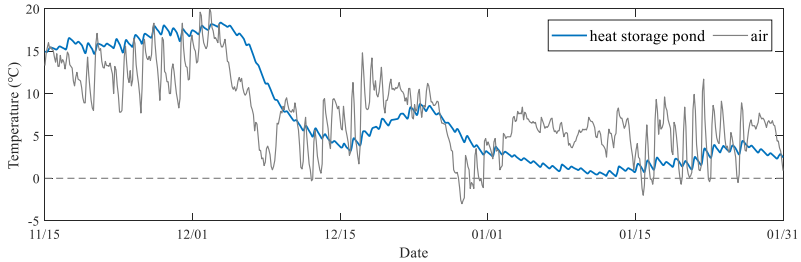


Fig. 11. Mode switch during full growing season (0-off, 1-ASHM, 2-WSHM, 3-AWSHM)



(*a*)



(*b*)

By substituting above strategy into the model, the results obtained are shown in Fig. 12. Water temperature of shrimp pond fluctuated from 20°C to 24°C, which is suitable for shrimp culture. That of heat storage pond always keeps above 0°C, which ensures the heat absorption in WSHM and AWSHM. Besides, the fluctuation of shrimp pond water temperature is less than that in Fig. 6, resulting in lower power consumption.

Consequently, we reduced the total power consumption to 8372kWh. Multiplied by local average electricity price of 0.55CNY per kWh, total operating costs were 4600CNY. The initial investment of our new AWDSHPS is approximately 16000CNY, of which heat storage pond is not included. Since all heat storage ponds have been excavated before. They are used for shrimp farming in summer but idle in winter. By comparison, coil-fired boiler with shrimp pond covered 1-layer film was common in the past. According to calculation by load model and on-site investigation, total coal consumption was about 11360kg and corresponding costs were 10220CNY. As a result, approximately 55% of energy costs can be saved with our new AWDSHPS.

6. Conclusions

In this study, a new AWDSHPS was proposed for shrimp culture. The load model of shrimp pond was built, experimentally validated, and then used for heating demand calculation. Furthermore, system design and modelling were fulfilled using GREATLAB and system energy performance was analyzed. At last, operational strategy of full growing season was optimized and a simple but effective one was adopted for practical use. All in all, main conclusions can be drawn as follows.

The proposed AWDSHPS is proven to have more stable energy performance, lower investment and operating costs than traditional heat pump systems. It is more suitable to replace original coil-fired boilers. This type of system can also be considered for other aquaculture applications, especially where two suitable heat sources are available.

With water in idle pond as additional heat source, the AWDSHPS has shorter defrost cycle and better energy performance. At ambient temperature of 0°C, for example, the evaporating temperature increases from -7.7°C to -3.2°C, resulting in 7% increase in energy efficiency and 27% increase in heating capacity.

For multiple heat source systems, the characteristics of different heat sources should be deeply understood. In this case, heat storage capacity of water source and performance attenuation of air source are comprehensively considered. With optimized operational strategy in full growing season, the total costs reduced by 55% relative to that of boiler heating. This value could be bigger by adopting better strategy, which is expected to be further discovered.

Nomenclature

AWDSHPS	air-water dual-source heat pump system	*Greeks*	
		τ	time (s)
ASHM	air source heating mode		
ASHP	air source heat pump	*Subscripts*	
AWSHM	air water source heating mode	a	convection
c	specific heat (kJ kg-1 K-1)	c	conduction
COP	coefficient of performance	f	film
GSHP	ground source heat pump	g	ground
H	heat input (kW)	i	inner
m	mass (kg)	l	latent
Q	heat transfer (kW)	o	outside
T	temperature (°C)	r	radiation
WSHM	water source heating mode	sr	solar radiation
		w	water

References

[1] H.A. Abdelrahman, A. Abebe, C.E. Boyd, Influence of variation in water temperature on survival, growth and yield of Pacific white shrimp Litopenaeus vannamei in inland ponds for low-salinity culture, Aquaculture Research, 50 (2019) 658-672.
[2] I. Sarbu, C. Sebarchievici, General review of ground-source heat pump systems for heating and cooling of buildings, Energy and Buildings, 70 (2014) 441-454.
[3] X.B. Liu, S.L. Lu, P. Hughes, Z. Cai, A comparative study of the status of GSHP applications in the United States and China, Renewable & Sustainable Energy Reviews, 48 (2015) 558-570.
[4] K. Zhu, L. Fang, N.R. Diao, Z.H. Fang, Potential underground environmental risk caused by GSHP systems, 10th International Symposium on Heating, Ventilation and Air Conditioning, Ishvac2017, 205 (2017) 1477-1483.
[5] M. Saaly, P. Maghoul, Thermal imbalance due to application of geothermal energy piles and mitigation strategies for sustainable development in cold regions: a review, Innovative Infrastructure Solutions, 4 (2019).
[6] P. Majuri, Technologies and environmental impacts of ground heat exchangers in Finland, Geothermics, 73 (2018) 124-132.
[7] S. Lacombe, E.A. Sudicky, S.K. Frape, A.J.A. Unger, Influence of Leaky Boreholes on Cross-Formational Groundwater-Flow and Contaminant Transport, Water Resources Research, 31 (1995) 1871-1882.
[8] L. Zhang, Y.Q. Jiang, J.K. Dong, Y. Yao, Advances in vapor compression air source heat pump system in cold regions: A review, Renewable & Sustainable Energy Reviews, 81 (2018) 353-365.
[9] X.Y. Liang, J.H. Cheng, Y.J. He, L. Wang, H. Li, L.L. Shao, C.L. Zhang, Study on annual energy performance of transcritical CO2 heat pump water heating systems in Shanghai, Int. J. Refrig., 107 (2019) 174-182.
[10] M.S. Patil, J.H. Seo, M.Y. Lee, Heat transfer characteristics of the heat exchangers for refrigeration, air conditioning and heat pump systems under frosting, defrosting and dry/wet conditions-A review, Applied Thermal Engineering, 113 (2017) 1071-1087.
[11] Y. Zhang, G.M. Zhang, A.Q. Zhang, Y.H. Jin, R.R. Ru, M.C. Tian, Frosting Phenomenon and Frost-Free Technology of Outdoor Air Heat Exchanger for an Air-Source Heat Pump System in China: An Analysis and Review, Energies, 11 (2018).
[12] I. Grossi, M. Dongellini, A. Piazzi, G.L. Morini, Dynamic modelling and energy performance analysis of an innovative dual-source heat pump system, Applied Thermal Engineering, 142 (2018) 745-759.
[13] J.M. Corberan, A. Cazorla-Marin, J. Marchante-Avellaneda, C. Montagud, Dual source heat pump, a high efficiency and cost-effective alternative for heating, cooling and DHW production, International Journal of Low-Carbon Technologies, 13 (2018) 161-176.
[14] X. Gou, S. Liu, Y. Fu, Q.Y. Zhang, S.M. Iram, Y.F. Liu, Experimental Study on the Performance of a Household Dual-Source Heat Pump Water Heater, Energies, 11 (2018).
[15] K.V. Garzoli, J. Blackwell, An analysis of the nocturnal heat loss from a single skin plastic greenhouse, J. agric. Engng Res., (1981).
[16] A. Baille, J.C. López, S. Bonachela, M.M. González-Real, J.I. Montero, Night energy balance in a heated low-cost plastic greenhouse, Agricultural and Forest Meteorology, 137 (2006) 107-118.
[17] C.L. Zhang, L. Yang, L.L. Shao, Refrigeration and air-conditioning system modeling and analysis using GREATLAB, Chemical Industry Press, 2015.
[18] C.L. Zhang, Fundamentals of vapor-compression refrigeration and air-conditioning system modeling, Chemical Industry Press, 2012.
[19] GB/T-23137, Heat pump water heater for household and similar application, Standards Press of China, Peking, 2008 (in Chinese).

13th IEA Heat Pump Conference
April 26-29, 2021 Jeju, Korea

Dynamic modeling and charge minimization study of a packaged propane heat pump with external flow reversal for cold climates

Tyler J. SHELLY[a] , Riley B. BARTA[a] , Davide ZIVIANI[a,*], Eckhard A. GROLL[a]

[a]Ray W. Herrick Laboratories, School of Mechanical Engineering, Purdue University
West Lafayette, 47907-2099, USA
tshelly@purdue.edu; bartar@purdue.edu; dziviani@purdue.edu; groll@purdue.edu

Abstract

Buildings consume approximately 40% of the primary energy used in the U.S. The energy-independence challenge is particularly acute for buildings in colder U.S. climates that have a longer heating season. Heating is by far the biggest consumer of energy, accounting for at least 30%, and in some cases as much as 60%, of total energy use. In addition, the gradually phase-down of current refrigerants requires further research to identify suitable low-global warming potential (GWP) replacements. Hydrocarbons represent a possible solution, but their flammability yields to a number of challenges towards the actual commercialization in the residential sector. In this paper, a packaged air-source heat pump with external flow reversible is proposed as a viable solution to safely utilizing flammable refrigerants, such as propane (R-290). The proposed system can also be adapted to serve as a cold-climate heat pump that provides heating, cooling, and domestic hot water. A detailed dynamic model has been developed to evaluate the performance benefits of the proposed system architecture. Moreover, the use of propane as the working fluid reduces the total charge required by the system, which yields to possible down-sizing of the equipment. To this end, a charge minimization study has been carried out to further investigate the trade-off between reduced charge inventory and performance.

© HPC2020.
Selection and/or peer-review under responsibility of the organizers of the 13th IEA Heat Pump Conference 2020.

Keywords: Cold-Climate Heat Pump, Seasonal Modeling, Propane, Charge Sensitivity

1. Introduction

As the adverse environmental effects of using hydrofluoricarbon (HFC) refrigerants become more and more apparent, the efforts towards developing technology to efficiently utilize alternative refrigerants has grown significantly. Specifically, R-290 (propane) is being considered due to its negligible global warming potential (GWP) and ozone depletion potential (ODP). However, propane inside a residential heat pump needs to be combined with a secondary loop due to its flammability. Commonly, R-290 heat pumps are paired with Ethylene Glycol/water (EG) secondary loops that can travel through the home. Application of this technology in northern regions of the US presents several challenges, with the largest being the broad range of both heating and cooling ranges necessary in this region. The components selected need to strike a balance between efficiency and being able to meet requirements over large operating conditions. According to a 2014 Northeast/Mid-Atlantic Air-Source Heat Pump Marketing Strategies Report [1], the adoption of air-source heat pumps in homes that currently use electricity, oil, or Propane furnaces for heating in the Northeast/Mid-Atlantic region could result in an annual savings of $1.2 Billion and over 7 million metric tons of annual carbon emissions. Additionally, the report found that the average heat pump capacity in the Massachusets market is 2.3 tons. According to the Department of Energy [2], the minimum required seasonal performance for these

* Corresponding author. Tel.: +1-619-496-9011.
E-mail address: dziviani@purdue.edu.

heat pumps is an 8.2 heating seasonal performance factor (HSPF) and a 14 seasonal energy efficiency ratio (SEER).

Wang et al. [3] performed a comprehensive literature review on the advantages of using hydrocarbon refrigerants in secondary loop heat pumping systems. In addition to increased safety, lower charge levels, and potentially reduced operating costs, it was found that hydrocarbons saw an average of 9.6% improvement in performance over fluoronated refrigerants while in heat pumping applications. Palm [4] concluded that the Coefficient of Performance (COP) of systems using hydrocarbon refrigerants would be equal to or greater than those of systems using R-134a or R-22, and also found that the majority of components for HFC systems can be used in R-290 sytems. Some disadvantages listed by this paper are the smaller number of compressors available in high-capacity ranges, as well as the danger of flammability. Park and Jung [5] experimentally compared R-290 and other hydrocarbons in air conditioning application and found that R-290 achieved a 1.9% higher COP but had 11.5% smaller cooling capacity. However, the paper found that this result was achieved with less than 50% mass of charge. Fernando et al. [6] experimentally validated the temperature profile through an evaporator that legitimizes the decision to use glycol as a seondary loop fluid, as shown in Fig. 1. Additionally, Fernando found that small propane charges in heat pump applications both increase the safety of the system, and also still result in similar COP to HFC systems under similar operating conditions.

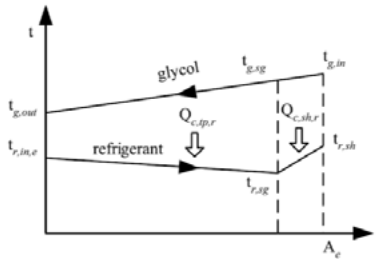


Fig. 1. Evaporator temperature profile [6].

A 50/50 combination of EG will reduce the freezing temperature of the secondary loop fluid to below -33℃, making it safe for use during the coldest temperatures measured in the Boston area, and is non-toxic. Ginies et al. [7] studied the effects of low-solubility oils in R-290 refrigeration systems in an effort to allow end users to utilize larger capacity units while staying within safety standards set by EN378, ISO5149, and the like. The study focused on Polyalkylene Glycol (PAG) and Polyolester (POE) oils, and found that when the correct oil is chosen for a 0.1 kg R-290/kW in a 60 kW system, the charge could be reduced by 18-30% without compromising capacity.

While many technologies aimed at increasing vapor compression cycle (VCC) have been investigated, there is often difficulty justifying increased completixty to obtain performance benefits. As such, generally only solutions that are both simple and efficient are widely accepted. One of these methods is known as economization, which comes in two forms. First, a flash tank can be placed in the expansion process to separate phases in a two-phase flow, allowing saturated liquid to enter the evaporator and bypassing the vapor to the compressor. This strategy has been proven to be controllable without compromising compressor suction superheat by Xu et al. [8]. The second form of economization is known as closed economization and achieved with an internal heat exchanger (IHX), which can be effectively controlled with an electronic expansion valve (EXV) [9]. Economization also allows vapor injection into the compressor at specific points, with increased precision on the superheat control. In theory, an infinite number of injection ports can be used to achieve saturated-vapor compession and can result in up to 51% COP improvement in an R-404A cycle. However, 75% of this performance benefit can be achieved with only three injection ports, which is considered to be the practical limit by Mathison et al. [10].

Multi-stage compression technology applied in a cold climate heat pump (CCHP) has been investigated via simulation by Caskey [11]. In this work, a gas heating system was compared to a two-stage heat pump in US Army barracks located in the central and northern US. The analysis resulted in a predicted CO_2 reduction by 33.5% while simultaneously reducing the heating cost by 25%. Gschwend et al. [12] further analyzed

possibilities to reduce power consumption of barrack buildings for the U.S. Army. The researchers concluded that the use of a two-stage heat pump lead to a seasonal COP of approximately 3.0, along with potential energy savings of 20% – 35% in the existing buildings.

This work presents the design and modeling of a packaged vapor-injected (VI) two-stage R-290 VCC featuring two EG/Water secondary loops and external flow reversal for hydronic heating and cooling of a residential home. The design focuses on cold climates, thus designating this work a CCHP. A 5-ton system design is proposed, annual data is analyzed for Boston, USA, and the system is assessed for performance in both weather datasets at two design temperatures. A dynamic and detailed model of the system has been developed and utilized to assess the impact of charge inventory.

2. System Design and Approach

2.1. System overview

The proposed R-290 – EG heat pump schematic is shown in Fig. 2. The VCC uses 2-stage compression with VI in the intermediate stage. An IHX is utilized to facilitate closed economization with the dual purpose of further sub-cooling the flow from the condenser outlet and superheating the economized vapor to be injected into the compressor. All three system heat exchangers will be plate heat exchangers (PHX). The IHX used for economization will be the smaller capacity heat exchanger (HX), while the condenser and evaporator will be larger PHXs that transfer heat between R-290 and the EG secondary loop. There is no 4-way valve associated with the VCC because the EG loop enters a multi-input multi-output (MIMO) valve which enables transition between heating and cooling modes to the home. Additional components in the VCC include an oil separator located at the second stage discharge that returns the oil to the suction of the first stage of compression, as well as a suction-line accumulator to ensure no 2-phase flow enters the compressor suction port. A filter-drier is located at the outlet of the condenser to remove potential contaminants from the R-290, and there is also a liquid receiver placed at the inlet to the sub-cooler for charge modulation.

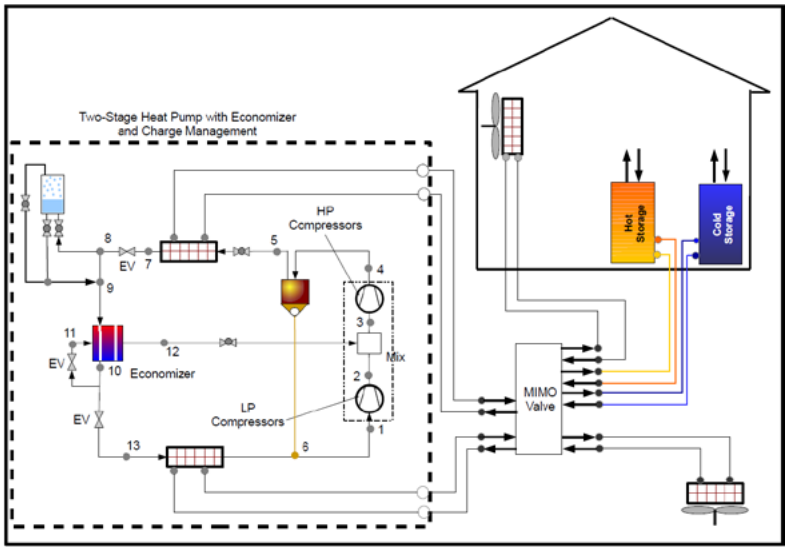


Fig. 2. Concept schematic of the packaged R-290 CCHP with secondary loops, external flow reversal, and possible coupling with cold and hot storage tanks.

The EG MIMO valve is used to direct flow into the home and has four sets of inputs and outputs. One set directs flow to an air-source heat exchanger exposed to the ambient to provide capacity modulation. The other three lead to the home, with one leading to an air-source heat exchanger to control the indoor environment and the other two leading to a hot and cold storage tank. This enables the system to utilize nearly 100% of the heat

pumped by the VCC, either at that moment or later on via thermal storage. This also enables grid-interaction with the system, as thermal storage can be used to eliminate the need to run the VCC during peak hours.

2.2. Seasonal weather and load calculations

The system design was based off of weather data from Typical Meteorological Year 3 (TMY3) [13], for the Boston Logan airport. This data contains, among other things, average dry bulb temperatures and relative humidity for every day in a typical year. This allowed the calculation of how many hours the heat pump system would need to run at the given operating conditions over the course of one year. Data from Boston is shown in **오류! 참조 원본을 찾을 수 없습니다.**. The design internal environment was 50% relative humidity with a dry bulb temperature of 21.1 ℃. Therefore, at 21.1 ℃ there was zero load, designating this temperature as the chosen balance point. A heat pump capacity of 5 tons was the design target, motivating a design capacity of 17.58 kW at -20 ℃. The target load profile is shown in Fig. 4. On the cooling side, a design temperature of 30 ℃ was chosen, and a sensible heat ratio (SHR) across the evaporator was assumed to be 0.7. This resulted in a design total cooling load of 7.3 kW after the consideration of occupants and other heat sources. It is assumed that each occupant creates 100 W of heat and that four occupants are in the home. Additionally, the lighting and appliance heat loads are assumed to be 750 W each. The complete cooling load calculation can be seen in Eqs. 1 through 5.

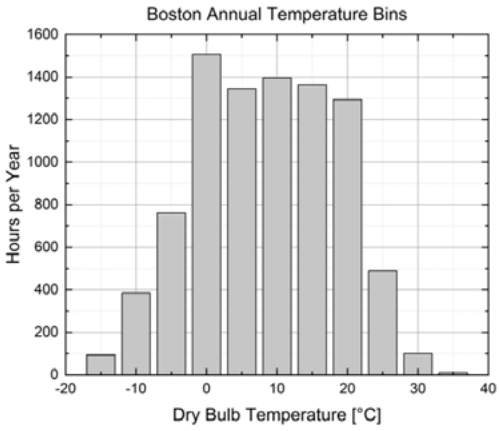


Fig. 3. Dry-bulb temperature bins for Boston over 1 year.

$$\dot{Q}_{\text{cool,sens}} = \frac{(T_{\text{amb,cooling}} - T_{\text{indoor}}) \cdot \dot{Q}_{\text{heat,design}}}{(T_{\text{indoor}} - T_{\text{amb,heat,design}})} \tag{1}$$

$$\dot{Q}_{\text{cool,sens}} = \dot{Q}_{\text{cool,base}} \cdot SHR \tag{2}$$

$$\dot{Q}_{\text{cool,base}} = \dot{Q}_{\text{cool,sens}} + \dot{Q}_{\text{cool,lat}} \tag{3}$$

$$\dot{Q}_{\text{int}} = \dot{Q}_{\text{occupant}} \cdot N_{\text{occupant}} + \dot{Q}_{\text{lighting}} + \dot{Q}_{\text{appliance}} \tag{4}$$

$$\dot{Q}_{\text{cool}} = \dot{Q}_{\text{cool,base}} + \dot{Q}_{\text{int}} \tag{5}$$

After these two capacities were specified along with the balance point, linearization was conducted for both heating and cooling mode to provide design capacities at individual ambient temperatures across the design range. These functions are shown in the load profile shown in Fig. 4.

When these loads are multiplied by the hours at which the heat pump needs to operate at these conditions (**오류! 참조 원본을 찾을 수 없습니다.**), the overall energy requirement for both heating and cooling can be calculated, in kWhr. These plots for heating are shown in Fig. 5, while cooling mode demand is shown in Fig. 6.

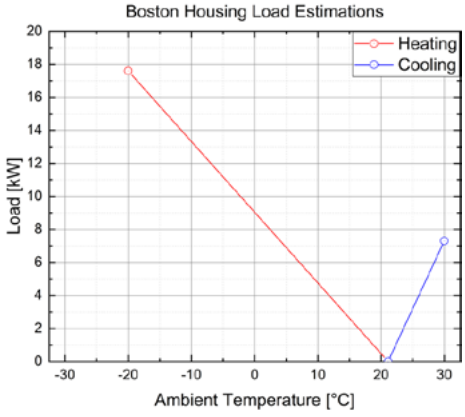


Fig. 4. Heat-pump design loads for Boston with balance point fixed at dry bulb temperature of 21.1 ℃ and 50% relative humidity.

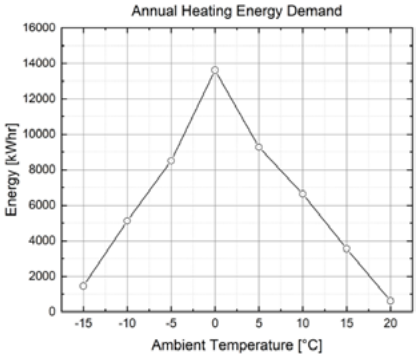


Fig. 5. Boston annual heating energy demand.

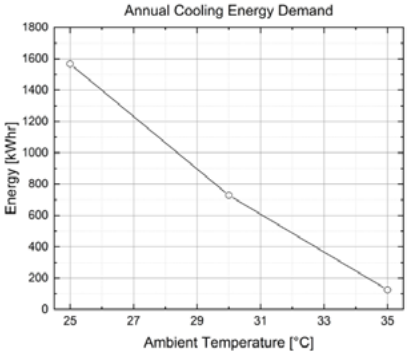


Fig. 6: Boston annual cooling energy demand.

2.3. Modeling overview

Once the loads are determined, a dynamic model was developed using the Modelica language [14] in a Dymola environment [15] utilizing the TIL Suite [16]. This form of modelling was chosen to enable both pseudo-steady state modelling, as will be conducted with the seasonal analysis herein, but also dynamic modelling for charge sensitivity and control strategy studies. The system within Dymola is shown in cooling mode in Fig. 7.

For a given operating condition, defined by the ambient temperature, indoor temperature, and required capacity, the primary method of performance quantification is the COP. The COP is the ratio of delivered capacity to power input, including only compressor power. The delivered capacity is defined as heat absorbed via the evaporator in cooling mode heat rejected via the condenser in heating mode and, shown in Eqs. 6 and 7, respectively.

$$COP_{\text{cool}} = \frac{\dot{Q}_{\text{evap}}}{\dot{W}_{\text{in}}} \tag{6}$$

$$COP_{\text{heat}} = \frac{\dot{Q}_{\text{cond}}}{\dot{W}_{\text{in}}} \tag{7}$$

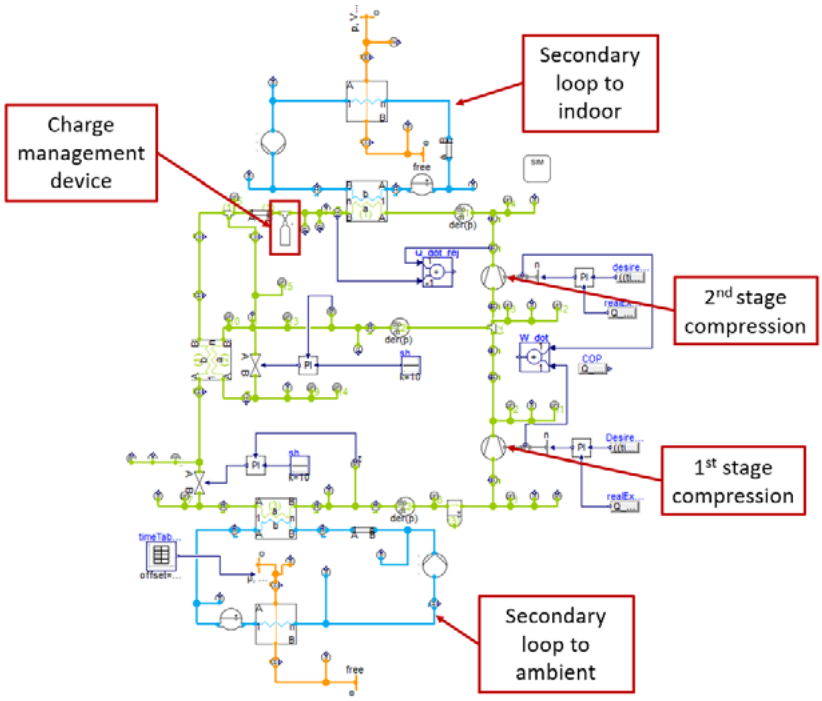


Fig. 7. View of the complete CCHP model within Dymola including secondary loops and charge management system.

Once the COP of the system is calculated it can be converted into two metrics that are more commonly used in industry for quantifying the performance of a system. These metrics are SEER and HSPF for cooling and heating modes, respectively. Both metrics are the ratio of desired heat transfer over the work input, which is the same as COP except for being seasonal averages. This means that each HSPF and SEER rating at an operating condition is weighted by how many hours the system operates at that condition, resulting in an assessment of seasonal performance. Additionally, COP takes both the numerator and denominator to have the same units, resulting in a dimensionless value. Both HSPF and SEER take the heating or cooling capacity in BTU, with the power input in Watt-hrs., resulting in a factor of 3.412 to convert from COP to the units for SEER and HSPF. The calculation of SEER and HSPF are shown in Eqs. 8 and 9.

$$SEER = \frac{\sum_{i=1}^{N} COP_i \cdot N_{\text{hours,i}}}{\text{Total Cooling Hours}} \tag{8}$$

$$HSPF = \frac{\sum_{i=1}^{N} COP_i \cdot N_{\text{hours,i}}}{\text{Total Heating Hours}} \tag{9}$$

The second shared component model is for the compressor, which follows a standard AHRI 10-Coefficient map that outputs mass flow rate as $\dot{m}_{\text{map}}$ and power consumption as $\dot{W}_{\text{in}}$ for a given condensation and evaporation temperature. The format for the map is shown in Eq. 10.

$$C_1 + C_2 \cdot T_{\text{evap}} + C_3 \cdot T_{\text{cond}} + C_4 \cdot T_{\text{evap}}^2 + C_5 \cdot T_{\text{evap}} \cdot T_{\text{cond}} + C_6 \cdot T_{\text{cond}}^2 + C_7 \cdot T_{\text{evap}}^3 + C_8 \cdot T_{\text{evap}}^2 \cdot T_{\text{cond}} + C_9 \cdot T_{\text{cond}}^2 \cdot T_{\text{evap}} + C_{10} \cdot T_{\text{cond}}^3 \quad (10)$$

The compressor is assumed to be variable speed, and the required speed is determined as a ratio of the mass flow rate given by the compressor map, $\dot{m}_{\text{map}}$, and the required flow rate across a given heat exchanger, $\dot{m}_{\text{Req'd}}$, determined from the simplified system model. As the authors were unable to obtain an experimental map for a variable speed R-290 compressor of this capacity, a map for a smaller variable speed R-290 scroll compressor was utilized and scaled up via speed as well as by the number of compressors in tandem for both the first and second stages to provide the desired capacity. This ratio is shown by Eq. 11, and the operation frequency is calculated by Eq. 12 for 60 Hz operation. The overall isentropic efficiency of the compressor is then calculated by Eq. 13.

$$Frac_{\text{speed}} = \frac{\dot{m}_{\text{req'd}}}{\dot{m}_{\text{map}}} \quad (11)$$

$$f_{60} = \text{Frac}_{\text{speed}} \cdot 60 \quad (12)$$

$$\eta_{\text{is,o}} = \frac{Frac_{\text{Speed}} \cdot \dot{m} \cdot (h_{2,\text{s}} - h_1)}{\dot{W}_{\text{in}}} \quad (13)$$

where

$$h_{2\text{s}} = f(p_2, s_1) \quad (14)$$

and

$$\dot{W}_{\text{in}} = Frac_{\text{Speed}} \cdot (h_2 - h_1) + \dot{Q}_{\text{comp}} \quad (15)$$

where

$$\dot{Q}_{\text{comp}} = 0.05 \cdot \dot{W}_{\text{in}} \quad (16)$$

Because the compressor map from Eq. 10 was calculated with a fixed suction superheat of 10 K, superheat correction was added to ensure an accurate prediction of compressor performance. Mass flow rate with a correction factor F of 0.75 and power consumption are corrected using Eqs. 17 and 18, respectively.

$$\frac{\dot{m}_{new}}{\dot{m}_{data}} = 1 + F \cdot \left(\frac{\rho_{suc,new}}{\rho_{suc,data}} - 1 \right) \quad (17)$$

$$\frac{\dot{W}_{new}}{\dot{W}_{data}} = \frac{\dot{m}_{new}}{\dot{m}_{data}} \cdot \frac{\Delta h_{s,new}}{\Delta h_{s,data}} \quad (18)$$

Table 1. Heat exchanger pressure drop and heat transfer correlations.

Heat Exchanger	Heat Transfer	Pressure Drop
Fin-and-Tube, R-290 Side	Gnielinski [18]; Dittus, and Boelter [19]	Konakov for Smooth Pipes [20]
Fin-and-Tube, Air Side	Haaf [21], constant η [22] (Assumed to be 0.9)	Haaf [21]
Plate IHX	Evaporation: Shah [23] Chen [24] / Condensation: Shah [25] / 1-Phase: Gnielinski [18], Dittus, and Boelter [19]	Konakov for Smooth Pipes [20]
Plate HX, R-290 Side	Evaporation: Longo [26] Condensation: Longo [27]/ Gnielinski, Dittus, and Boelter	Quadratic Mass Flow Dependent [28]
Plate HX, EG Side	VDI Plate Alpha [29]	VDI Single-Phase [29]

This CCHP utilizes two types of heat exchangers, and both models assumed homoegenous equilibrium flow. The EG to air are fin-and-tube heat exchangers, while the R-290 to EG transfer utilizes plate heat exchangers.

The dimension of these heat exchangers were obtained through a separate modeling effort using a tool from Bell et al. [17] known as ACHP. Additionally, to conservatively estimate secondary loop losses, an extra 20% load was placed on the R-290 side of the cycle. A summary of heat transfer and pressure drop correlations utilized is provided in Table 1.

3. Results and Discussion

A full piping and instrumentation diagram (P&ID) is provided in Fig. 8 to offer a detailed schematic of the VCC aspect of this work. To simulate the TMY3 data, both ambient temperature and the required capacity for that temperature needed to be actively called into the model. This was completed by utilizing an externally-defined table that drove conditions assessed in the model. Fig. 9 shows the ability of the model to import TMY data as an air-temperature inlet value over the course of a year, and Fig. 10 shows the P-h diagram ability of the model, following the nomenclature from Fig. 8. Capacity modulation is to be achieved through control of the compressor speeds along with active modulation of the EXVs via proportional-integral (PI) control.

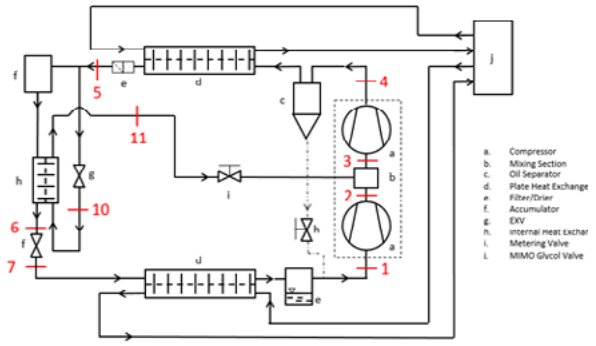


Fig. 8. P&ID of the proposed VCC.

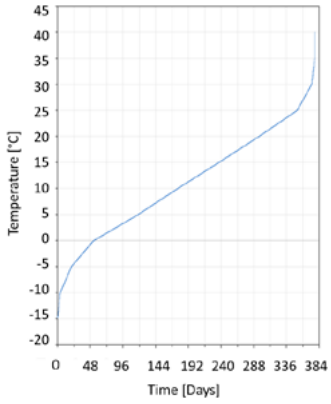


Fig. 9. 1 Year of TMY data for Boston in Dymola.

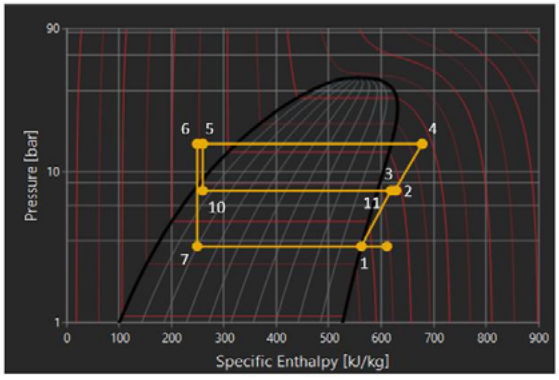


Fig. 10. P-h diagram of R-290 system in Dymola.

Preliminary results were achieved with a steady-state model of similar fidelity, which are presented in this section. These results include supplementary electrical heating to achieve the desired heating capacity. To identify the amount of supplementary capacity, the sources of heating capacity is differentiated between compressors and supplementary electric heating in Fig. 11. COP calculation with supplementary resistive heating is calculated using Eq. 19, where the COP of the electric heating is assumed to be the ideal value of 1.

$$COP_{\text{weighted}} = \frac{COP_{\text{VCC}} \cdot \dot{Q}_{\text{VCC}} + (1) \cdot \dot{Q}_{\text{elec}}}{\dot{Q}_{\text{total}}} \quad (19)$$

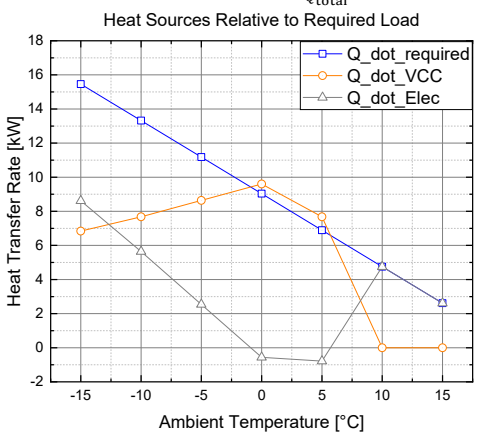


Fig. 11. Heat source variation with ambient temperature and associated load.

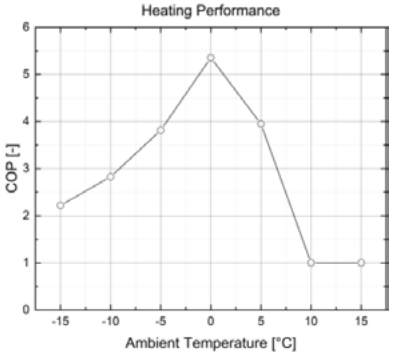


Fig. 12. Seasonal COP in heating mode.

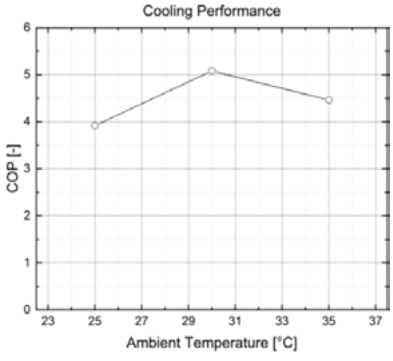


Fig. 13. Seasonal COP in cooling mode.

Tandem compressors were utilized, and variable speed inputs were used to simulate engaging and disengaging compressors to provide as much capacity as possible. This system achieved a SEER rating of 14.1 and an HSPF of 10.1. Seasonal COP results from the model are provided for heating and cooling modes in Fig. 12 and Fig. 13, respectively.

Being R-290 an A3 refrigerant, charge minimization while guaranteeing system performance throughout the season is a very important aspect to be investigated. The dynamic model was utilized to simulate performance of the system in heating mode, including dependence of the charge of the system. This was accomplished through a parametric study which used time dependent ambient and heating load conditions across a range of imposed system charges. The charge modulation has been accomplished by including a charge filling station on liquid line after the condenser, as shown in Fig.7. These conditions are embodied in Fig. 14 for the ambient condition in dependence of time during the dynamic simulation.

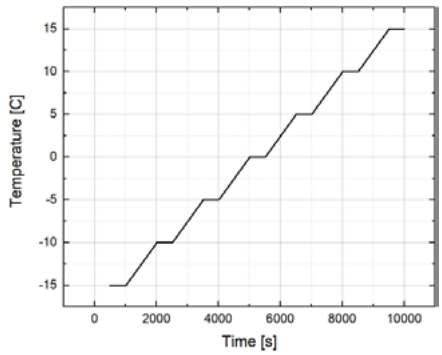


Fig. 14 Simulated heating season across a range of -15 ℃ to 15 ℃

The periods of steady temperature are taken from Fig. 4 in increments of 5 ℃. These were simulated across a range from -15 ℃ to 15 ℃ via a time dependent table interpolation. A curve fit of the heating load data from Fig. 4 allowed the calculation of the heating load at each point in time according to the ambient temperature. Finally, a total charge was imposed upon the system across each simulated heating season to find an optimal minimal charge that ensures system performance across the heating season while minimizing hazards of excessive charge inside the system. This study was conducted across a range of system charge from 0.1 kg to 0.6 kg.

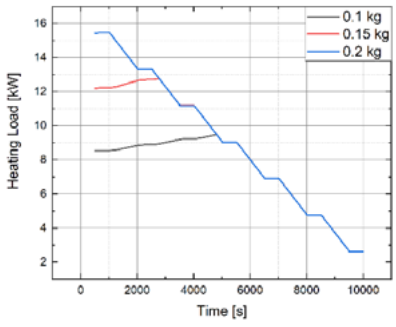


Fig. 15 Simulated heating performance in dependence of total system charge

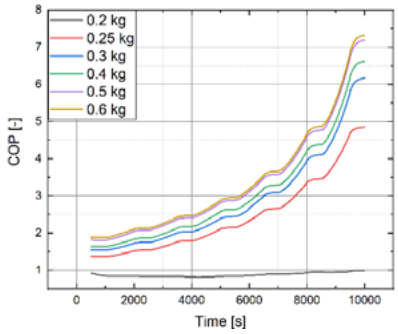


Fig. 16 Simulated heating COP in dependence of total system charge

The first criteria for the minimum charge required was to achieve the heating load determined by the ambient condition. As seen in **오류! 참조 원본을 찾을 수 없습니다.**, the system began to meet the heating demand at a system charge of 0.2 kg. This was taken as an absolute minimum charge, but the system COP, as shown in **오류! 참조 원본을 찾을 수 없습니다.**, indicated poor system performance at this charge amount. As expected, the system COP increased with increasing charge until diminishing returns were observed at higher amounts of system charge, serving as a maximum realistic amount of charge within the system. A system charge between 0.4 kg and 0.5 kg is clearly indicated as the optimal charge in the system, as an increase to 0.6 kg provided little benefit in system performance.

4. Conclusions and Recommendations

A multi-stage VI CCHP architecture using R-290 as the refrigerant has been proposed and was coupled to a novel EG secondary loop connected to a residential home. The target environment is the northern US, so TMY3 data from Boston, USA was utilized, and dry bulb temperature bins were developed for one year. A target heating capacity of 5 tons (17.58 kW) at -20 ℃ was chosen with a suggested balance point of 21.1 ℃

and 50% relative humidity indoor condition to provide a seasonal load profile. A dynamic modeling structure was developed and described, and the TMY temperatures were input. However, COP calculations using seasonal loads and temperatures were performed using a steady-state model with similar assumptions. These calculations were then used to provide both seasonal performance calculations for the proposed architecture as well as a reference parameters and results for further dynamic modeling development. The proposed cycle was able to achieve a SEER value of 14.1 and an HSPF of 10.1. Finally, charge minimization was performed with respect to system performance in terms of heating load demand and system COP to ensure both the performance and safety of the system to be constructed. A preliminary charge estimation of 0.45 kg to meet heating demand and moderate system COP was calculated. Future work is to repeat the seasonal calculations with the proposed dynamic model and further assess control algorithms and active charge management to leverage the dynamic modeling abilities. Furthermore, a potential prototype system is being developed for experimental validation.

5. Acknowledgements

The authors would like to thank IMBY Energy for financial support and the faculty and staff of the Ray W. Herrick Laboratories for technical and financial support.

Nomenclature

C	Compressor map coefficient	-
E	Energy	kWhr
F	Frequency	Hz
Frac	Fraction	-
h	Specific enthalpy	kJ/kg
m	Mass	kg
$\dot{m}$	Mass flow rate	kg/s
N	Number	-
$\dot{Q}$	Heat transfer rate	kW
T	Temperature	℃
$\dot{W}$	Power	kW

Greek Symbols

η	Efficiency	-
Δ	Change	-
ρ	Density	kg/m^3

Subscript

amb	Ambient
base	Base load
comp	Compressor
cond	Condenser
cool	Cooling
data	Data
elec	Electric
evap	Evaporator
heat	Heating
i	Index
in	Inlet
int	Internal
is,o	Overall isentropic
lat	Latent
map	Map
new	New
s	Isentropic
sens	Sensible

Acronyms

CCHP	Cold-Climate Heat Pump
COP	Coefficient of Performance
EG	Ethylene-Glycol
ELLA	Electronic Liquid Level Actuator
EXV	Electronic Expansion Valve
GWP	Global Warming Potential
HFC	Hydrofluorocarbon
HP	High Pressure
HSPF	Heating Seasonal Performance Factor
HX	Heat Exchanger
IHX	Internal Heat Exchanger
MIMO	LP
MIMO	Multi-Input Multi-Output
ODP	Ozone Depletion Potential
PAG	Polyalkylene Glycol
PHX	Plate Heat Exchanger
PI	Proportional Integral
POE	Polyolester
P&ID	Piping and Instrumentation Diagram
SEER	Seasonal Energy Efficiency Ratio
SHR	Sensible Heat Ratio
TMY3	Typical Meteorological Year
VCC	Vapor-Compression Cycle
VI	Vapor Injected

References

[1] NEEP, "Northeast / Mid-Atlantic Air-Source Heat Pump Market Strategies Report," 2014.

[2] USDOE and EERE, "Minimum Efficiency Requirements for Air-Source and Geothermal Heat Pumps," 2019.

[3] K. Wang, M. Eisele, Y. Hwang, and R. Radermacher, "Review of secondary loop refrigeration systems," *Int. J. Refrig.*, vol. 33, no. 2, pp. 212–234, 2017.

[4] B. Palm, "Hydrocarbons as refrigerants in small heat pump and refrigeration systems – A review," vol. 31, pp. 552–563, 2008.

[5] K. Park and D. Jung, "Thermodynamic performance of HCFC22 alternative refrigerants for residential air-conditioning applications," vol. 39, pp. 675–680, 2007.

[6] P. Fernando, B. Palm, P. Lundqvist, and E. Granryd, "Propane heat pump with low refrigerant charge : design and laboratory tests," vol. 27, pp. 761–773, 2004.

[7] P. Ginies, P. Dewitte, M. F. Terrier, and M. Charni, "Low GWP Refrigerant and Partial Miscible Lubricant," *Proc. 23rd Int. Compress. Eng. Conf. Purdue*, p. Paper 2700, 2014.

[8] X. Xu, Y. Hwang, and R. Radermacher, "Transient and steady-state experimental investigation of flash tank vapor injection heat pump cycle control strategy," *Int. J. Refrig.*, vol. 34, no. 8, pp. 1922–1933, Dec. 2011.

[9] S. S. Bertsch and E. A. Groll, "Two-stage air-source heat pump for residential heating and cooling applications in northern U.S. climates," *Int. J. Refrig.*, vol. 31, no. 7, pp. 1282–1292, Nov. 2008.

[10] M. M. Mathison, J. E. Braun, and E. A. Groll, "Performance limit for economized cycles with continuous refrigerant injection," *Int. J. Refrig.*, vol. 34, no. 1, pp. 234–242, 2010.

[11] S. L. Caskey and D. Kultgen, "Simulation of an Air-Source Heat Pump with Two- Stage Compression and Economizing for Cold Climates," 2012.

[12] A. Gschwend, T. Menzi, S. Caskey, E. A. Groll, and S. S. Bertsch, "Energy consumption of cold climate heat pumps in different climates – Comparison of single-stage and two-stage systems," *Int. J. Refrig.*, vol. 62, pp. 193–206, 2016.

[13] NREL, "Typical Meteorological Year Data (TMY)," *1991-2005 Update*, 2019. [Online]. Available: https://rredc.nrel.gov/solar/old_data/nsrdb/1991-2005/tmy3/.

[14] S. E. Mattson, H. Elmqvist, and J. F. Broenink, "Modelica: An international effort to design the next generation modelling language," *J. A, Benelux Q. J. Autom. Control*, vol. 38, no. 3, pp. 16–19, 1998.

[15] "Dassault Systems - DYMOLA Systems Engineering," 2019.

[16] TLK-thermo, "TIL Suite simulates Thermal Systems." 2018.

[17] I. H. Bell, "Air conditioning and heat pump mpdel (ACHP) source code version 1.5." p. Online; accessed 10-Sept-2019, 2015.

[18] V. Gnielinski, "New equations for heat and mass transfer in turbulent pipe and channel flow," *Int. Chem. Eng.*, vol. 16, no. 2, pp. 359–368, 1976.

[19] H. D. Baehr and K. Stephan, *Waerme-und Stoffuebertragung, 2 Auflage*. Springer, 1996.

[20] P. K. Konakov, "A new correlation for the friction coefficient in smooth tubes," *Berichte der Akad. der Wissenschaften der UDSSR*, vol. 51, p. 51, 1946.

[21] S. Steimle, *Handbuch der Kaeltetechnik, Waermeuebertragung in Luftkuehlern*. Springer, 1988.

[22] Schmidt, "Heat transfer calculations for extended surfaces," *Refrig. Eng.*, vol. 57, pp. 251–357, 1949.

[23] M. M. Shah, "A new correlation for heat transfer during boiling flow through pipes," *ASHRAE Trans.*, vol. 82, pp. 66–86, 1976.

[24] J. C. Chen, "A correlation for boiling heat transfer to saturated fluids in convective flow," *Ind. Eng. Chem. Process Des. Dev.*, vol. 5, no. 3, pp. 322–329, 1966.

[25] M. M. Shah, "A general correlation for heat transfer during film condensation inside pipes," *Int. J. Heat Mass Transf.*, vol. 22, no. 4, pp. 547–556, 1979.

[26] G. A. Longo, S. Mancin, G. Righetti, and C. Zilio, "International Journal of Heat and Mass Transfer A new model for refrigerant boiling inside Brazed Plate Heat Exchangers (BPHEs)," *Int. J. Heat Mass Transf.*, vol. 91, pp. 144–149, 2015.

[27] G. A. Longo, G. Righetti, and C. Zilio, "International Journal of Heat and Mass Transfer A new computational procedure for refrigerant condensation inside herringbone-type Brazed Plate Heat Exchangers," *Int. J. Heat Mass Transf.*, vol. 82, pp. 530–536, 2015.

[28] W. Wagner, *Stroemung und Druckverlust*. Vogel, 2008.

[29] H. Martin and T. Kit, "VDI Heat Atlas," *VDI Heat Atlas*, 2010.

13th IEA Heat Pump Conference
April 26-29, 2021 Jeju, Korea

Development and Lab-scale Performance Evaluation of a High Temperature Heat Pump for Integration into a Power-to-Heat to-Power System

Miguel Ramirez[a*], Felipe Trebilcock[a], Xabier Peña[a], Asier Martinez-Urrutia[a], Abdelrahman H. Hassan[b,c]

[a]Tecnalia Research & Innovation, Energy and Environment Division, Area Anardi 5, Azpeitia, Guipuzkoa 20730, Spain.
[b]Instituto Universitario de Investigación en Ingeniería Energética, Universitat Politècnica de València, 46022, Valencia, Spain.
[c]Mechanical Power Engineering Department, Faculty of Engineering, Zagazig University, Zagazig 44519, Egypt.

Abstract

Power-to-heat-to-power systems are an interesting approach to deal with the intermittent power generation from renewable energy sources. However, storing heat requires large storage volume and associated heat losses decrease the system performance. High Temperature Heat Pump (HTHP) systems can operate during surplus power generation periods storing heat in a latent heat storage and discharge it to drive a heat engine for electricity generation. The presented work has been performed under the frame of the EU funded CHESTER project (www.chester-project.eu) in which the performance of this technology is assessed. This paper presents the experimental study of a HTHP which will be integrated into a Compressed Heat Energy STorage (CHEST) system. A Low Global Warming Potential (GWP) working fluid is implemented and the configuration cycle is selected to optimize the charging conditions of a latent heat storage. The operating temperatures of the HTHP are set from 72°C to 105°C in the heat source side. The heat sink temperature is set at 133°C that corresponds to the melting point of the phase change material.

© HPC2020.
Selection and/or peer-review under responsibility of the organizers of the 13th IEA Heat Pump Conference 2020.

Keywords: High Temperature Heat Pump; Compressed Heat Energy Storage; Reciprocating Compressor; Low Global Warming Potential fluids; R1233zd(E);

1. Introduction

The amount of electricity produced by renewable energy systems in the EU reached 30% of the total gross electricity consumption in 2016. Hydro and wind power play a key role in the renewable power market contributing with 36.9% and 31.8% respectively of the total renewable power consumed [1]. However, the intermittent nature of renewable energy sources poses a challenge to overcome the successful coverage of the electricity network. Electricity storage systems are expensive and the existing technologies cannot satisfy the demand requirements of the grid at an affordable cost [2].

Other concepts of large-scale power storage systems are pumped hydro storage (PHS), compressed air energy storage (CAES), and pumped thermal electricity storage (PTES). PHS dominates the electricity storage market with 96% of the total stored capacity worldwide. It requires large water reservoirs and high height of elevation between the reservoirs. CAES is also depending on geographical characteristics of the area since it requires underground reservoirs [3]. PTES systems have been implemented in solar power systems being the second larger electricity storage technology [4]. Thermal storage presents lower cost than electricity storage systems and with an attractive life expectancy that can reach 10,000 cycles of operation [5].

* Corresponding author. Tel.:+34-946-430-850; fax: +34-946-430-850.
E-mail address: Miguel.ramirez@tecnalia.com

PTES systems can present different configurations and various combination of systems have been proposed in the literature. A combination of heat pump, thermal storage and organic Rankine cycle (ORC) can results in high roundtrip efficiency when the heat source temperature of the heat pump is higher than the condensing temperature of the ORC. Roundtrip efficiencies can reach values equivalent to 1.3 for heat source temperatures from 80° to 110°C and using R-1233zd(E) as working fluid [6]. Another similar concept the called Compressed Heat Energy STorage (CHEST) system has presented power ratio values of 1.25 operating with 100°C heat source temperature and 15°C of heat sink in the ORC side [7].

Nomenclature

COP	Coefficient of performance, [-]
cp	Specific heat capacity, [kJ/kg°C]
f	Frequency, (Hz)
h	Enthalpy, [kJ/kg]
m	Mass flow rate, [kg/s]
n	Number of pistons
P	Power, [kW]
Q	Heat capacity, [kW]
T	Temperature, [°C]
W_{in}	Electric power consumption, [kW]

Greek letters

Δ	Difference, [-]
η	Efficiency, [%]

Subscripts

dis	Discharge
displ	Displacement
el	Electric
in	Inlet
is	Isentropic
out	Output
r	Refrigerant
su	Suction
vol	Volumetric
w	Water

Abbreviations

CAES	Compressed air energy storage
CHEST	Compressed Heat Energy Storage
GWP	Global Warming Potential
HCFO	Hydrochlorofluoro-olefin
HFO	Hydrofluoro-olefin
HTHP	High Temperature Heat Pump
LH-TES	Latent Heat Thermal Storage
SH-TES	Sensible Heat Thermal Storage
ORC	Organic Rankine Cycle
PHS	Pumped hydro storage
PTES	Pumped thermal electricity storage

2. The CHESTER project

The CHEST system of this study is a combination of Rankine cycles and a latent heat storage unit that can use either water or organic media as working fluid [5]. The system is activated via high temperature heat generated from low temperature heat via a thermal cycle (heat pump). The high temperature heat generated charges the latent heat thermal energy storage (LH-TES). Sensible heat could be also stored in a sensible heat thermal energy storage (SH-TES) to optimize the cycle. Then during power demand periods heat from both the LH-TES and SH-TES storages is discharged to drive a heat engine cycle, in this case is an organic Rankine cycle (ORC), to generate electricity. This is an attractive concept to operate when cheap electricity and low temperature heat is available to cover power demand during high demand periods.

The aim of the CHESTER project is to develop and validate via a small-scale CHEST system of 10kWe the possibility to store power in heat and to deliver it as power minimizing losses. This system is destinated to store excess power from the generation of RES into thermal storage systems and to deliver it as electricity when demanded. The four main sub-systems developed for the CHEST system are the HTHP, the LH-TES along with the SH-TES, the ORC, and an isobaric expansion engine that will minimize the power consumption of the ORC system. The schematic diagram presented in Fig. 1 shows the basic configuration of the system and heat and power flows.

The heat source temperature of the CHEST prototype ranges from 60 to 100°C and the LH-TES charging temperature is in the range of 133-145°C. Therefore, these temperatures are considered as the heat source and heat sink of the HTHP, respectively. For these high temperature operating conditions, specialized components must be implemented such as compressor, refrigerant, lubricant, expansion device and others.

On the ORC side the heat source temperature is designed to be 133-145°C. In the in the dissipation side the temperature of the sink is in the range between 10 to 40°C. The operation of the ORC cycle is not analyzed in this study.

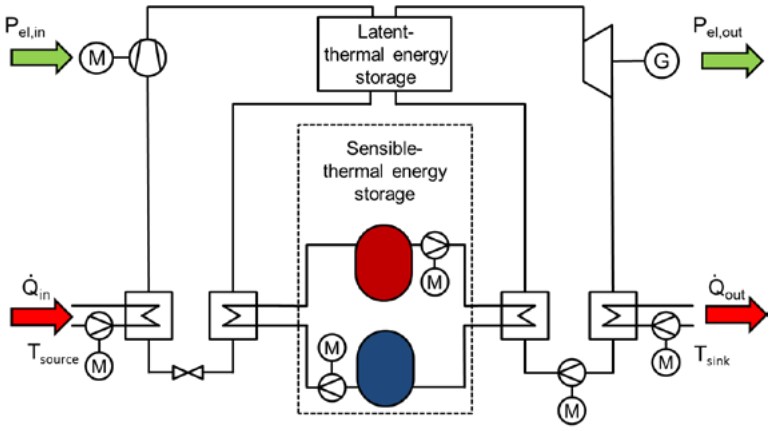


Fig. 1. Schematic diagram representing the CHEST system concept [8].

3. Testing method

For this study a water-to-water heat pump has been considered. Water flow temperatures can be controlled to simulate the operating conditions of the Chester project prototype. The water temperature is controlled in the source and both sink sides, the latent and the sensible.

The testing conditions and periods are selected according to the objectives of this study and the very high operating temperatures. Heat source water temperatures from 70° to 105°C are selected to obtain the performance curves at different temperature conditions of the source. In the sink side the water outlet temperature is maintained steady at approximately the melting point of the phase change material (133°C) and with the minimum experimentally possible temperature difference between inlet and outlet. In this way it is possible to simulate the operation of the HTHP during the charging of the LH-TES. In the subcooler the ΔT between the fluid inlet and outlet is maintained between 50 to 70 K by controlling the water inlet temperature. All water flow rates in the secondary circuits were maintained stable during each test.

During charging of the LH-TES the heat transfer coefficient will drop decreasing the capacity needed at the condensing. To match the heat pump´s heating capacity with the charging capacity of the LH-TES partial load can be applied. This is achieved via a speed drive (inverter) which controls the compressor speed and can drop the heating capacity of the heat pump. To measure the compressor capacity at part load conditions three compressor speeds were chosen for the testing campaign between 1000 to 1500 rpm.

It is also considered that the maximum operating temperature of some components in the liquid line is 80°C. Therefore, a secondary function of the subcooler was to cool the liquid leaving the condenser to protect the components in the liquid line. The subcooled water inlet temperature was controlled and set according to the subcooler refrigerant outlet temperature. The range of operating conditions are presented in Table 1.

Table 1. List of main components of the HTHP.

Parameters	Setpoint values
Compressor speed	1000, 1230, 1500rpm
Heat source inlet temperature	72, 82, 92, 105°C
Heat sink temperature	133-135°C
Superheating degree setpoint	8-10 K
ΔT Subcooler	50–70 K

4. Experimental setup

The characterization of the HTHP for the Chester project system has been performed in a water-to-water heat pump testing rig in TECNALIA's thermal energy laboratory facilities. This testing rig is used to test heat pump components for high temperature applications (up to 160°C) and heating capacities up to 300kW. The prototype has been manufactured according to safety regulations 2014/68/EU, EN 16084:2011 and EN 378:2016.

The HTHP prototype mainly comprises a compressor, a condenser, a subcooler, an expansion device, and a rack of evaporators. Additional auxiliary components are included in the refrigerant circuit in order to protect the main components and to operate the heat pump safely.

In the suction line, a suction separator is installed to ensure only refrigerant in vapor state is entering the compressor. At the discharge line, a muffler is installed to minimize pressure pulsations. After the condenser a liquid receiver is positioned to accumulate the liquid refrigerant during partial load operation. In the liquid line, a filter/drier is used to protect the expansion device from debris and to maintain the fluid dry. A solenoid valve is mounted to stop liquid migration into the evaporator during off-cycles. Finally, sight glasses are installed in both the suction and liquid lines to control visually the state of the fluid.

The working fluid charged in the circuit is the R-1233zd(E) which is a low GWP fluid and its critical temperature is 165.6°C [9], [10]. A compressor able to operate at very high temperatures has been selected. The compressor is the HBC511 model, manufactured by Viking Heat Engines and can operate at temperatures up to 215°C [11]. There is available study in the literature about the performance of the HBC511 compressor operating with other fluids such as HFO-1336mzz(Z) and R-245fa [12], but none with HCFO-1233zd(E).

Part of the pipelines of the refrigeration cycle and the heat exchangers were kept uninsulated or with removable insulation for visual control, thermography and material monitoring. This causes drop of the global performance of the system, however, the equipment and personnel safety are prioritized.

The list of the main components including the model and manufacturer is presented in Table 2 and the configuration of the proposed HTHP is presented in Fig. 3.

Table 2. List of main components of the HTHP.

Component	Manufacturer	Model
Compressor	Viking Heat Engine	HBC511
Inverter	Siemens	G120
Lubricant	Fuchs	SEZ320
Evaporator #1	SWEP	B80Hx30
Evaporator #2	SWEP	B120Tx30
Condenser	SWEP	B25THx50
Subcooler	SWEP	B86Hx57
Expansion device	Danfoss	ETS12.5
Liquid receiver	Bitzer	FS152
Suction accumulator	Emerson	A17
Discharge muffler	ESK	GDX
Filter/dryer	SANHUA	DTG/L

The secondary fluid circuits consist of four different closed water loops, for the condenser, the subcooler, the evaporators and for the compressor cooling system. The water loop of the condenser is connected to the laboratory cooling system which consists of a buffer tank of 1 m^3 volume, a water cooler, a three-way valve and a water pump driven by an inverter. The subcooler is connected to the medium temperature water loop of the laboratory which is cooled by a geothermal system. The water to the evaporators is heated by a gas boiler and the control is achieved via a secondary loop and a three-way valve. The water loop of the compressor cooling circuit is pumped via a small water pump of 35 W and the water is cooled in a copper pipe coil.

4.1. Monitoring and data logging

Temperature, pressure and flow rates values are measured by sensors in the refrigerant circuit and the four water loops. All data is logged every 1 second by the acquisition system of the laboratory and recorded in a

computer. The datalogging period is considered when the temperature, pressure and flow rate values have been in steady state for a minimum period of time of 10 minutes. The data stored in these periods is averaged and used for the data analysis.

The temperature values in the refrigerant circuit are measured with 4-wire RTD PT100 1/3 DIN sensors custom made by TC-direct. The sensors are positioned in stainless steel thermowells in a counter-current position at the inlet and outlet of each of the main components. Pressure is measured with pressure transducers SPKT*D made by Carel. Two different measure ranges are used depending on the location of measurement whether to be in low- or high-pressure side. Refrigerant mass flow rate is monitored by the Coriolis meter SITRANS FC410 made by SIEMENS.

The temperature in the water loop is measured by six 4-wire PT100 class 1/10 DIN sensors. They are inserted in thermowells at the water inlet and outlet lines of the heat exchangers. Flow rate of the water in the evaporator, condenser and subcooler is measured via three electromagnetic flow meters Sitrans MAG3100 sensors made by SIEMENS. The range of measurements of the sensors and their uncertainties are presented in Table 2.

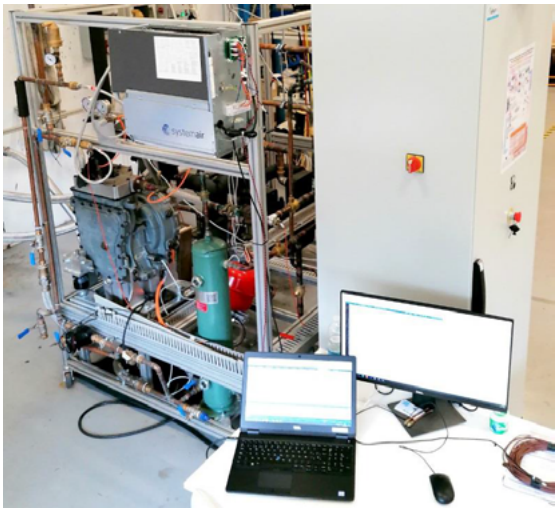


Fig. 2. View of the HTHP testing rig, control panel and datalogging equipment.

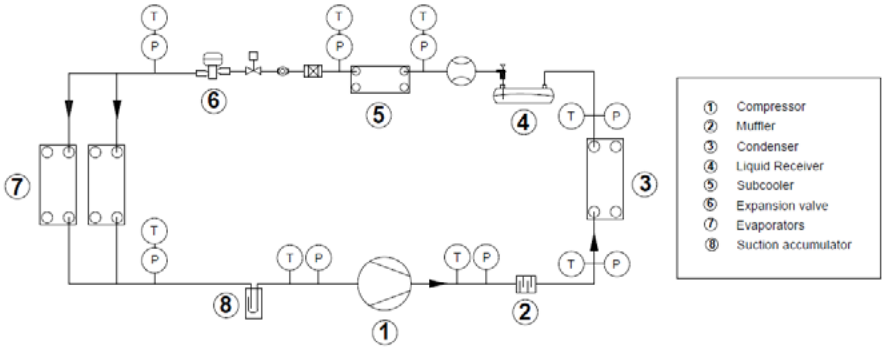


Fig. 3. Schematic diagram of the refrigerant cycle of the HTHP test bench.

Table 2. List of measurement ranges and uncertainties of the monitoring devices.

Measurement	Type	Range	Uncertainty
Temperature - water	PT100, 1/10 DIN	-50 +200°C	±(0.03 °C+0.5%)
Temperature - refrigerant	PT100, Class A	-50 +200°C	±(0.15 °C+0.2%)
Pressure	Transducer	-0.5 to 7 bar / 0 to 30 bar	±0.24% FS
Mass flow – water	Electromagnetic	5-100 l/min	±1.5% FS
Mass flow - refrigerant	Coriolis	20 to 6400 kg/h	0.1% FS
Power	Analyzer	10 to 520 VAC / 40 to 70 Hz	±1% FS

5. Experimental results

The results of the testing campaign are used to study the performance of the HTHP under the Chester system operating conditions and to evaluate the compressor´s performance. The obtained results are considered for the optimization of the HTHP prototype for its integration with the LH-TES and the SH-TES in a CHEST system.

The cooling capacity of the HTHP was calculated for both evaporators considering a single water inlet and outlet. The capacity of both in-parallel connected evaporators ranged from 27.5 to 68.6 kW. The superheating degree was set through the controlled at 8 K and the actual value measured ranged from 7.5 to 8.7 K. Water inlet and outlet temperatures in the evaporator ranged from 72 to 105°C and from 66 to 95°C respectively.

The function of the condenser in the CHEST system will be delivered by the phase change material within the LH-TES. The heating capacities values calculated in this study are used for the sizing of the storage systems. The heating capacity delivered to the condenser´s water loop was calculated between 12.1 kW and 42.3 kW. Water temperatures ranged from 123 to 128°C and 130 to 133.5 °C in the condenser inlet and outlet respectively. The average water temperature difference was approximately 5.5 K. The water pumps used limited the further drop of the temperature difference, therefore they will be substituted for the next testing campaign. In the refrigerant side the condenser inlet and outlet temperatures were measured between 143 to 133 °C and 135 to 132 °C, respectively. The subcooling at the condenser was calculated from 1 to 1.6 K.

The heat transferred to the water in the subcooler ranged from 10.8 to 29.2 kW at water outlet temperatures from 75.8 to 114.6 °C. The subcooling degree measured in the subcooler ranged from 50 to 68 K. The liquid refrigerant leaving the subcooler was maintained below 80 °C due to components' temperature limitations.

Water flow rate and pressure were maintained steady in all loops at 1.32, 0.93, and 0.19 kg/s in the evaporator, condenser and subcooler, respectively. The pressure in the water loops was maintained above 3 bar-g.

The evaporating temperatures and pressures for all tests ranged from 64.1 to 93.6 °C and 4.4 to 9.1 bar-a, respectively. Since the condensing temperature was fixed above 133 °C, the condensing pressure was very stable at approximately 20.4 bar-a.

It should be mentioned that the heat losses in the refrigeration cycle were very high due to poor insulation at the main sections of the piping, specially in the high-pressure side. The existing insulation material in the test bench had to be removed because it presented some irregularities due to high temperature operation such as outgassing and hardening. Furthermore, the vibrations coming from the compressor caused failure in the soldering and some parts of the pipeline were maintained uncovered for material monitoring purposes. This have caused considerable heat losses which are calculated to be between 10 to 26% of the heat produced. The heat transferred to the cooling water of the compressor crankcase is also included in the mentioned percentage and it has to be further evaluated.

In Fig. 4 the COP of the HTHP and power consumption are presented over the temperature lift which is the difference between the condensing and evaporating temperature. As expected, the highest COP value of 7.2 is seen during 1000 rpm speed and at low temperature lift. For 1230 and 1500 rpm the maximum values resulted in 6 and 5.4, respectively, under temperature lifts of approximately 30 K. The lowest COP values for the three compressor speeds were between 3.8 and 4.1 and are observed at temperature lift of 60 K, approximately.

According to the Chester prototype site requirements the compressor must operate consuming below 15 kWe of power (W_{in}). The results presented in Fig. 4 show that the power consumption of the HTHP, which consists of the compressor and inverter consumption, ranged from 5.5 to 13.2 kW. Therefore, the HTHP can run at any speed up to 1500rpm when integrated to the CHEST system.

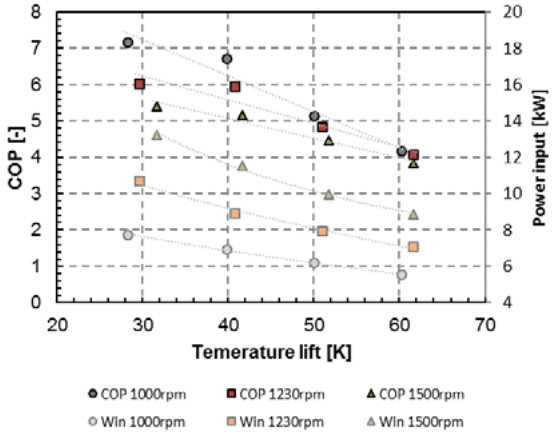


Fig. 4. Performance of the heat pump (COP) and the power consumed (W_{in}) by the compressor and inverter versus the temperature lift.

5.1. Compressor performance

The compressor suction and discharge temperatures ranged from 71.2 to 101.2 °C, and from 136.6 to 149.4 °C, respectively. The suction and discharge pressures ranged from 4.2 to 8.7 bar-a, and 20 to 21.9 bar-a, respectively. Fig. 5 presents the measured mass flow rates for each compressor speed over the evaporating temperature. The lowest mass flow rate was 0.14kg/s, which was measured at compressor speed of 1000 rpm. The mass flow rate increased with the compressor speed to 0.17 and 0.19 kg/s for 1230 and 1500 rpm, respectively. For speed of 1230 rpm the mass flow rate ranged from 0.17 to 0.36 kg/s and for compressor speeds of 1500 rpm the mass flow rate ranged from 0.19 to 0.40 kg/s.

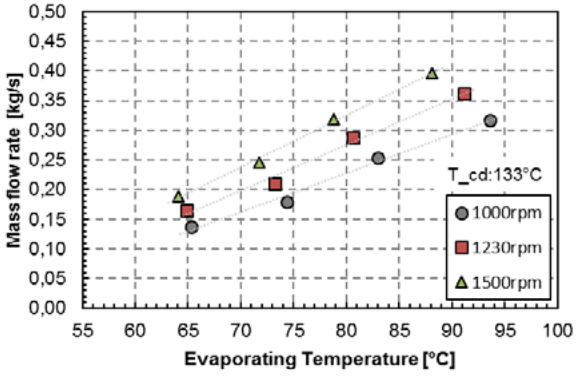


Fig. 5. Refrigerant mass flow rate values at condensing temperature 133°C.

The lowest pressure ratio was calculated at compressor speed of 1000 rpm and heat source of 72 °C. The maximum pressure ratio recorded was 4.9 at 1500 rpm and heat source temperature of 105 °C. The performance of the compressor is further evaluated through the isentropic and volumetric efficiencies. In Fig. 6 both the isentropic and volumetric efficiencies are presented over the pressure ratio. The isentropic efficiency was calculated by Equation 4. The highest value of the isentropic efficiency was 82.4% which corresponds to compressor speed of 1000 rpm and pressure ratio of 4.5. The lowest value is calculated for operation at 1500 rpm speed and pressure ratio of 2.9.

The volumetric efficiency was calculated by Equation 5 and the results ranged from 70.9 to 85.4%. The calculated points show a pattern that splits the values depending on the evaporating temperature and therefore on the mass flow rate.

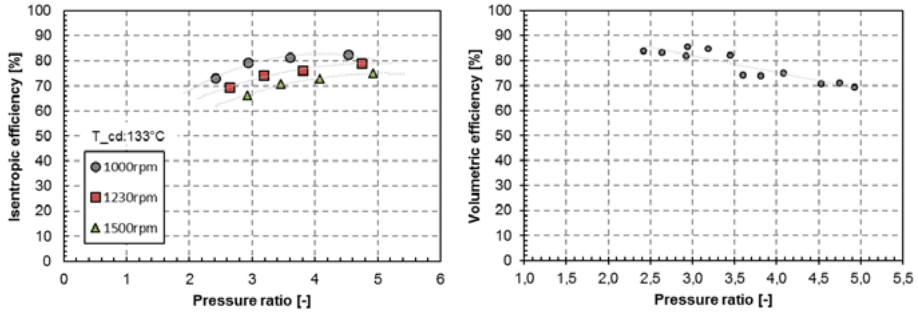


Fig. 6. The isentropic efficiency of the compression phase at different compression speeds (left); and the volumetric efficiency of the compressor (right).

In this study the main objective is to evaluate the performance of the compressor working with R-1233zd(E) to facilitate the selection of the main components of the CHEST system's HTHP. The COP of the HTHP was calculated using Equation 3 but the results are not used for characterization purposes of the testing bench due to the low quality of insulation used. Moreover, the evaporators have not been sized for this specific compressor, therefore, are not optimum for this configuration. However, the results of performance are promising, and they can be used for comparison purposes with future tests.

6. Data reduction and simulations

The presented results have been calculated using equations and calculation software packages such as Microsoft Excel and REFPROP [13]. Both the cooling and heating capacities of the HTHP were calculated using the Equations 1 and 2 described below.

$$Q_w = m_w \cdot c_{p,w} \cdot \Delta T_w \quad (1)$$

$$Q_r = m_r \cdot \Delta h_r \quad (2)$$

Where the heating/cooling capacity of the heat pump (Q_w) is the result of the water mass flow rate (m_w) by the specific heat capacity ($c_{p,w}$) by the temperature difference between the water inlet and outlet of the heat exchanger (ΔT_w). The heating/cooling capacity in the refrigerant side (Q_r) is the refrigerant mass flow rate (m_r) by the enthalpic difference (Δh_r) of the fluid between the inlet and outlet of the refrigerant in the heat exchangers.

The COP is calculated from the ratio of the sum of heating capacities in the condenser and subcooler (Q_{out}) over the power consumed (W_{in}). by both the compressor and the inverter (Equation 3)

$$COP = \frac{Q_{out}}{W_{in}} \quad (3)$$

The isentropic efficiency is calculated from the ratio of the enthalpy difference in the compression process assuming an isentropic compression to the experimental enthalpy difference of the compression stage as presented in Equation 4. The isentropic compression enthalpy is calculated from the difference between the isentropic enthalpy at the discharge ($h_{dis,is}$) and the enthalpy at the suction (h_{su}). The actual compression enthalpy is calculated by the difference between the actual enthalpy at the discharge (h_{dis}) and the enthalpy at the suction of the compressor.

$$\eta_{is} = \frac{h_{dis,is} - h_{su}}{h_{dis} - h_{su}} \quad (4)$$

The volumetric efficiency is calculated by Equation 5, and is the ratio of the refrigerant mass flow rate (m_r) by the specific volume at the suction (V_{su}), over the theoretical volume of gas displaced by the piston (V_{displ}) multiplied by the frequency per second and by the number of pistons (n). The volumetric displacement of the single piston compressor considered for this study is 511cm^3. The specific volume of the gas at the suction line is calculated using REFPROP [13].

$$\eta_{vol} = \frac{m_r . V_{su}}{V_{displ} \cdot (f/60) \cdot n} \quad (5)$$

7. Conclusions

The performance of a HTHP working with a low-GWP working fluid has been investigated. The HTHP is designed to be part of a CHEST system where its function is to charge a LH-TES at temperatures above 133°C. Additional sensible heat from the subcooler charges a SH-TES system resulting in a subcooling degree between 50-68 K.

Water was used as secondary fluid and the mass flow rates were maintained steady during the testing campaign. The water inlet temperatures set for the testing campaign ranged from 72°C to 105°C, and the condenser water outlet temperature ranged from 133 to 135°C. For each testing condition three compressor speeds were tested, 1000, 1230, and 1500rpm.

The capacity of both evaporators in parallel configuration was measured as a sum and ranged from 27.5 to 68.6 kW. The heating capacity delivered to the water in the condenser was estimated from 12.1 to 42.3 kW. The subcooler's heating capacity was calculated from 10.8 to 29.2 kW with a temperature difference in the water-side from 13 to 35 K.

Evaporating and condensing temperatures ranged from 64 to 94°C and 133 to 125.8 °C, respectively. The compressor suction temperatures ranged from 71.2 to 101.2 °C, and the discharge temperatures from 136.6 to 149.4 °C, respectively. The suction pressures ranged from 4.2 to 8.7 bar-a and the discharge pressures remained stable as expected between 20 to 21.9 bar-a. The superheating degree value resulted from 7.5 to 8.7 K and the total subcooling degree achieved in both the condenser and subcooler resulted from 50.7 to 69.4 K. Using the subcooler was crucial to protect the components in the liquid line and maintain them below their maximum operating temperatures (80°C).

The operating pressure ratios of the compressor were calculated from 2.4 to 4.9. The lowest compressor speed presented higher isentropic efficiency ranging from 73 to 82%. While for 1500 rpm, the isentropic efficiency ranged from 66 to 75%. The highest volumetric efficiency was 85% and was recorded under the 1000 rpm compressor speed at high pressure ratio conditions. However, the volumetric efficiency was weakly influenced by the compressor speed since the difference between the volumetric efficiency values resulted from 0.5-1.4% at each operating condition.

The COP of the HTHP tested resulted in values from 3.8 to 7.2. The maximum values were recorded as expected at the lower compressor speeds, 1000 rpm and 105 °C heat source temperature. The lowest performance values resulted under heat source temperature of 72 °C and temperature lift of 60 K.

Power consumption of the HTHP that consisted of the consumption of the compressor and the inverter was measured in the range of 5.5 to 13.2 kW. Since the power supply in the Chester prototype site is limited to 15kWe the results show that there is no limitation for any of the compressor speeds tested.

Finally, actualization of the control algorithm is necessary to control the operation range of the HTHP coupled to the CHEST system. Different operating modes will be implemented into the control and will be tested individually. In addition, further optimization of the thermal insulation of the refrigerant pipeline must be conducted to increase the efficiency of the cycle.

Acknowledgements

The authors would like to express their gratitude to Viking Heat Engines for their technical support and to Fuchs Petrolub SE for the lubricant supplied for this specific application. This work is part of the European Union's Horizon 2020 research and innovation program CHESTER (Grant agreement No. 764042).

References

[1] Eurostat. (2016). Eurostat. Retrieved October 10, 2019, from https://ec.europa.eu/eurostat/web/products-eurostat-news/-/DDN-20180921-1

[2] Zhang, C., Wei, Y. L., Cao, P. F., & Lin, M. C. (2018). Energy storage system: Current studies on batteries and power condition system. Renewable and Sustainable Energy Reviews, 82(July 2017), 3091–3106.

[3] Irena, International Renewable Energy Agency. (2012). IRENA-IEA-ETSAP Technology Brief 5: Electricity Storage, (April).

[4] Irena, International Renewable Energy Agency. (2017). Electricity storage and renewables: Costs and markets to 2030.

[5] Steinmann, W. D. (2014). The CHEST (Compressed Heat Energy STorage) concept for facility scale thermo mechanical energy storage. Energy, 69, 543–552.

[6] Frate, G. F., Antonelli, M., & Desideri, U. (2017). A novel Pumped Thermal Electricity Storage (PTES) system with thermal integration. Applied Thermal Engineering, 121, 1051–1058.

[7] Jockenhöfer, H., Steinmann, W. D., & Bauer, D. (2018). Detailed numerical investigation of a pumped thermal energy storage with low temperature heat integration. Energy, 145, 665–676.

[8] Weller T., Jockenhöfer H., Fiss M., B. D. (2019). Detailed design of the high temperature TES laboratory prototype. Retrieved from https://www.chester-project.eu/public-documents/

[9] Honeywell Brochure. (2013). Honeywell Refrigerants Improving the Uptake of Heat Recovery Technologies. Honeywell Brochure, 53(9), 1689–1699.

[10] Gil, B., & Kasperski, J. (2018). Efficiency evaluation of the ejector cooling cycle using a new generation of HFO/HCFO refrigerant as a R134a replacement. Energies, 11(8), 1–18.

[11] Viking Heat Engines. (2018). HBC 511 - Data Sheet 1.1. Retrieved May 10, 2018, from www.vikingheatengines.com/upl/files/144869

[12] Nilsson, M., Nes, H., & Kontomaris, K. (2017). Measured performance of a novel high temperature heat pump with HFO-1336mzz(Z) as the working fluid. In 12th Heat Pump Conference. Rotterdam: IEA Heat Pump Conference.

[13] Lemmon, E. W., Bell, I. H., Huber, M. L., & McLinden, M. O. (2018). NIST Standard Reference Database 23: Reference Fluid Thermodynamic and Transport Properties-REFPROP. Gaithersburg: National Institute of Standards and Technology.

13th IEA Heat Pump Conference
April 26-29, 2021 Jeju, Korea

Experimental Analysis of a Hight Temperature Heat Pump Using Stored Heat from a Solar Thermal System

Miguel Ramirez[a*], Asier Martinez-Urrutia[a], Neil J. Hewitt[b], Nikhhilkumar Shah[b]

[a]Tecnalia Research & Innovation, Energy and Environment Division, Area Anardi 5, Azpeitia, Guipuzkoa 20730, Spain.
[b]Centre for Sustainable Technologies, Ulster University, Newtownabbey, Co. Antrim, BT37 0QB, Northern Ireland, UK.

Abstract

Thermal storage systems use for district heating can improve their efficiency by decreasing their storage temperature and therefore minimizing heat losses and cost. A high temperature heat pump (HTHP) operating with heat source temperature between 30 °C to 50 °C can further optimize the performance of the system and deliver hot water above 70 °C at demand. In this study a HTHP that uses thermal energy produced by a solar thermal system and stored in a seasonal thermal storage has been developed, installed and experimentally investigated under real conditions. An additional challenge of the present work was to build the heat pump using off-the shelf components without further modifications. During two years of operation the water source temperatures measured were from 31 °C to 40 °C and the heating capacity resulted from 35 kW to 43.7 kW. The COP calculated resulted in values from 5.3 to 6 for pressure ratios between 2.3 to 2.8. The results demonstrated that HTHPs are an attractive approach to use low grade heat sources specially when produced by renewable energy sources.

© HPC2020.
Selection and/or peer-review under responsibility of the organizers of the 13th IEA Heat Pump Conference 2020.

Keywords: Seasonal Thermal Storage; High Temperature Heat Pump; Vapour Compression; Space Heating; Hot Water Supply;

1. Introduction

Seasonal thermal energy storage systems charged by solar thermal energy present a potential to provide heating for domestic applications. Large solar collector surfaces and large volume of storage accumulators can balance the seasonal mismatch during the year [1]. For thermal storage specially during the season, low temperature storage is preferable to minimize the heat losses during the year. Heat pumps are systems that can use low temperature heat source to produce high temperature water for space heating applications. In addition, heat pumps help the stratification of the storage tank by returning the source water colder [2]. In previous studies on heat pumps combined with seasonal thermal storage and gas boilers, results showed that heat pumps can provide between 49 to 67 % of the heating demand, while the direct discharge of the storage can cover between 33 to 39 % [3].

The performance of a heat pump as part of a combination of heating systems is maximized when is correctly integrated considering the thermal behavior of the system. The correct integration of the heat pump in the system has a greater impact on its performance than the COP of the heat pump itself [4]. Systems such as seasonal thermal storage charged by a solar thermal system present high temperature fluctuations during the year. For high fluctuation profiles between heat source and heat demand temperatures the capacity of the heat pump is recommended to be 60 % of the maximum hourly peak demand [5].

* Corresponding author. Tel.: +34-946-430-850; fax: +34-946-430-850.
E-mail address: Miguel.ramirez@tecnalia.com

Nomenclature

COP	Coefficient of performance, [-]
cp	Specific heat capacity, [kJ/kg°C]
f	Frequency, (Hz)
h	Enthalpy, [kJ/kg]
m	Mass flow rate, [kg/s]
n	Number of pistons
Q	Heat capacity, [kW]
T	Temperature, [°C]
W_{in}	Electric power consumption, [kW]

Greek letters

Δ	Difference, [-]
η	Efficiency, [%]

Subscripts

cd	Condenser
dis	Discharge
displ	Displacement
ev	Evaporator
i	Inlet
is	Isentropic
out	Output
r	Refrigerant
su	Suction
vol	Volumetric
w	Water

Abbreviations

CAES	Compressed Air Energy Storage
EEV	Electronic Expansion Valve
GWP	Global Warming Potential
HFC	Hydrofluoro-carbon
HTHP	High Temperature Heat Pump
STES	Seasonal Thermal Energy Storage
SEER	Seasonal Energy Efficiency Ratio

2. Description of the site

The heat pump prototype of this study is part of a seasonal thermal storage demonstration plant installed in Warsaw, Poland. The installation consists of a solar thermal collector field, a seasonal thermal energy storage tank (STES), a gas boiler, the heat pump and the heating load (building) as presented in Fig. 1. The solar thermal collector field's total area is 151 m^2 of flat plate collectors positioned on the ground. The thermal storage tank consists of a heavily insulated water tank with a total internal volume of 800 m^3. The building is part of a hospital with a total surface area of 793 m^2 in two-floors. The building´s heating system consists of a gas boiler of 92 kW heating capacity. Finally, the high temperature heat pump (HTHP) is a prototype that has been developed for this specific application. It is designed for nominal operating conditions of 30 °C evaporation and 75 °C condensing temperatures and a maximum heating capacity of 63 kW.

The solar collectors' field is located near the storage tank and heat is transferred using glycol as a medium. The HTHP is located in the underground floor of the building to heat. Heat from the STES tank is transferred to the building via underground insulated water pipes.

The operation of the system starts when the STES is charged with thermal energy via the solar collectors during high solar radiation periods. Thermal energy can then be stored in the seasonal thermal energy storage for long periods during the year, in order to be used to heat the building during the heating period (April – September).

In the heating season heat from the storage tank is directed to the building heating system by demand. Hot water from the storage tank is directed to the building via the underground piping and heat is transferred to the building´s heating water loop via heat exchangers. When the temperature of the hot water coming from the STES is below the temperature set by the heating system the water is directed to the heat pump. If the supply water temperature is below 45 °C then the HTHP is activated. The hot water produced by the heat pump is driven into a 1m^3 buffer to moderate its cycle periods. When the hot water temperature coming from the storage tank is not high enough for space heating neither for the heat pump operation (< 30 °C), then the gas boiler is activated to cover the heating demand.

The heating water supply temperature and flow conditions are set by the control algorithm of the building´s heating system and gas boiler. The mass flow rate in the sink side is set at 1.08 lt/s, which is the maximum flow rate that the gas boiler can operate. The building heating requirements is 82.8 kW with a maximum supply and return water temperatures of 75 °C and 56 °C.

The operation of the heat pump prototype during the testing campaign is fully dependent on the environmental conditions, the heat stored in the storage tank and the heating demand. The water supply temperature is defined by the control algorithm of the building´s heating system. Therefore, the ON/OFF cycles of the heat pump are conditioned to the heating capacity stored into the buffer tank and the heating demand.

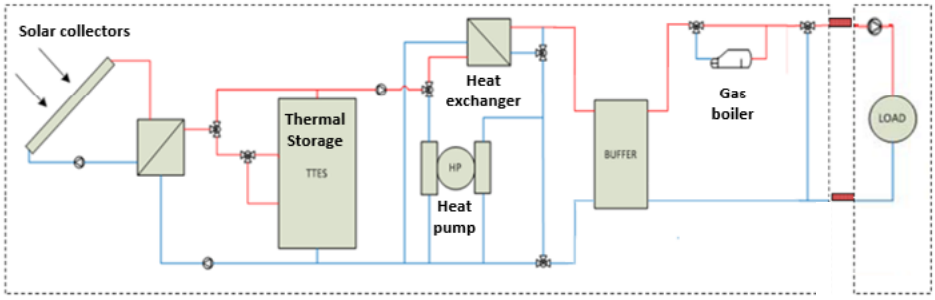


Fig. 1. Schematic diagram of the demo site in which the HTHP is installed, showing the configuration between the solar thermal field, the STES, the HTHP, the buffer tank, the gas boiler and the load.

3. Heat pump description

The HTHP prototype is a single loop water-to-water heat pump equipped a reciprocating compressor. The main components of the refrigeration cycle consist of the compressor, the condenser, a liquid receiver, the expansion device, and the evaporator as shown in Fig. 2. The safety equipment and auxiliary components consists of a suction accumulator, an oil separator, a filter/drier, two sight-glasses and block valves. The suction accumulator and the oil separator are positioned in the suction and discharge line respectively. The liquid receiver is installed between the condenser and the expansion device.

The compressor used in this prototype is the semi-hermetic reciprocating compressor 6MU-40X made by Copeland. It is a six cylinders compressor with bore 80.6mm, stroke 57.5 mm and 153 m^3/h volumetric displacement. The maximum suction and discharge pressures are 22.5 bar-g and 32.5 bar-g. The compressor is charged with 3.3 lt of POE ISO46 lubricant. The expansion device installed is an electronic expansion valve (EEV) ETS25 made by Danfoss. It is equipped with a stepper motor of 160 steps and it is controlled via an electronic control (EKD316). The evaporator is the brazed plate heat exchanger B120Tx90 made by SWEP and it has a heat transfer surface area of 6.19 m^2. The condenser is the V200Tx50 also a brazed plate heat exchanger made by SWEP with a surface area of 11.6 m^2.

The working fluid used in this prototype is the 1,1,1,3,3-pentafluoropropane (R-245fa). This fluid is a non-flammable HFC normally used for organic Rankine cycle applications. It has a boiling point of 15.3 °C and critical point of 153,8 °C [6]. It belongs to B1 category of ASHRAE 34-2013 [7]. It has a global warming potential (GWP) of 1030. [8]

3.1. Methodology and data monitoring

The data collected and used for this work belongs to a period of 12 months of operation. During the datalogging period the HTHP operated for a total of 9934 minutes which consisted in 209 operation cycles. The duration of the cycles ranged from 13 minutes to 10 hours and 40 minutes of continuous operation. All monitored values are measured and recorded every 30 seconds for 24 hours per day.

For the data analysis the data logged is filtered and only operation cycles with steady source and supply water temperatures are considered. Data belonging to the start-up period of approximately 5 minutes and the last 1 minute of every cycle is not considered in this analysis. In addition, cycles lower than 20 minutes of duration are not considered in this study due to their unstable performance. Average values of temperature, pressure, power and flow measurements are calculated and analyzed.

Fig. 2 shows the location of the sensors in both the refrigerant and water cycles. Temperature in both the refrigerant and water circuits are measured using 4-wire PT100 type “A” sensors. The temperature sensors in the water side are intrusive type inserted within the water pipes at the inlet and outlet ports of the heat exchangers. The temperature sensors of the refrigerant cycle are mounted on the surface of the copper pipeline at the inlet and outlet of the main components. The refrigerant pressure is measured by pressure transducers mounted at the inlet and outlet of the main components via Schrader access ports. The sensors output signal is 4-20 mA and require a supply voltage of 24 Vdc. There are two models of sensors mounted on the circuit of

different measurement range, the PT5-07 and PT5-18 both made by ALCO Emerson, both have a measurement error of ≤±1 % FS.

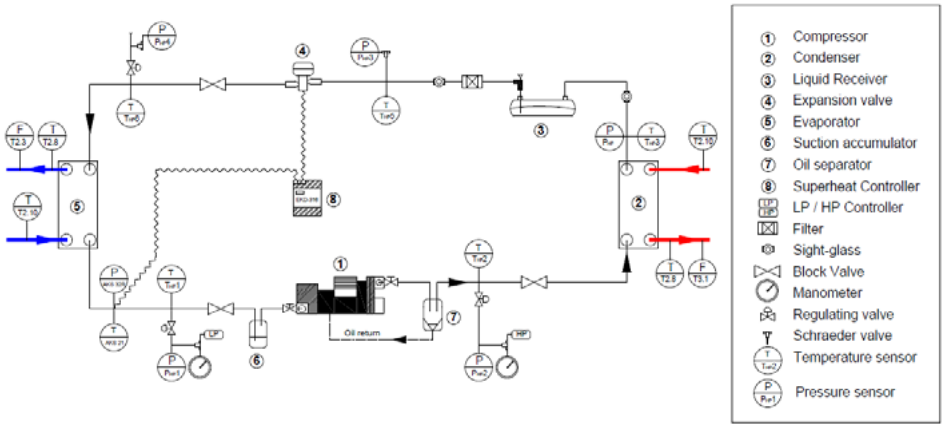


Fig. 2. Schematic diagram of the heat pump prototype presenting the configuration, the main components and the data measuring points.

The water flow rate in both the heat source and heat sink is measured by two electromagnetic ENDRESS HAUSER flow meters. The output signal is 4-20 mA and the maximum operating temperature is 225 °C with an accuracy of ±0.5 % of reading. The energy consumed by the compressor is measured by an energy meter connected to the power supply within the electrical power box. In addition, voltage and current of the compressor power supply are also measured in all three phases.

4. Experimental results

During the 12 months of monitoring the seasonal storage tank temperature ranged from 60 °C at the beginning of September to 25 °C in January. From January to April the temperature of the water in the tank remained low and was not used. After April the solar radiation increased and the charging of the storage tank continued.

In Fig. 1 are presented the water source and sink temperatures during the heat pump operation. The water source temperature variated between 31.2 °C to 39.9 °C and the water outlet in the condenser from 46.2 °C to 54.5 °C. The temperature difference between the water inlet and outlet of the evaporator and condenser was calculated from 5.2 K to 7.1 K and 5.4 K to 6.8 K respectively. Both water pumps in the evaporator and condenser loop were maintained at steady speed. However, the flow rate fluctuated slightly during the monitoring period, from 1.25 to 1.33 kg/s in the evaporator and from 1.52 to 1.56 kg/s in the condenser.

The cooling and heating capacity were calculated from the measurements of mass flow rate and temperature in the water cycles as presented in Equation 1.

$$Q_w = m_w \cdot c_{p,w} \cdot \Delta T_w \quad (1)$$

In the evaporator the capacity transferred from the storage tank water to the refrigerant ranged between 29 up to 37.1 kW as presented in Fig 3. On the condenser side the minimum and maximum heating capacity was calculated 34.9 and 43.7 kW respectively.

The variation of the water source and sink side temperatures was approximately between 8.3-8.7 K, which resulted in a small range of operation conditions. Three points were selected to present the lowest and highest performance values. In Table 1 are presented three operating cycles that correspond to minimum and maximum source temperatures recorded (31.2 and 39.9 °C). The data from the operation during the maximum temperature lift (31.3 K) is also presented, which is calculated from the difference between the condensing and evaporating temperature.

Table 1. Experimental results from selected operating cycles.

			Tw,ev,i		ΔT_lift
			Min	Max	Max
Evaporator	Water inlet	°C	31,24	39,93	36,03
	Water outlet	°C	26,02	32,81	30,12
	Water flow	kg/s	1,33	1,25	1,31
	Evaporating temp.	°C	18,94	25,82	22,07
	Evaporating press.	bar-a	1,18	1,53	1,33
Condenser	Water outlet	°C	47,60	54,53	52,39
	Water inlet	°C	42,24	47,75	46,42
	Water flow	Kg/s	1,56	1,54	1,52
	Condensing temp.	°C	48,6	55,64	54,44
	Condensing press.	bar-a	3,19	3,9	3,7
Temperature lift		K	29,7	29,9	31,4

The refrigerant evaporating and condensing temperatures were calculated via REFPROP software [9] using as input values the low and high side pressures. The evaporating temperature and pressure ranged from 18.9 °C to 25.8 °C and 1.18 bar-a to 1.53 bar-a respectively. The condensing temperature and pressure resulted from 47.3 °C to 55.64 °C and 3.05 bar-a to 3.9 bar-a respectively. The pressure ratio calculated from the ratio of the absolute evaporating and condensing pressures resulted between 2.3 to 2.8.

The superheating degree at the suction line was controlled by the superheat controller of the EEV. It was set at higher value than in conventional systems due to the risk of saturation in the compressor´s suction port. The superheating and subcooling degree values ranged from 7.7 to 13 K and 7 to 9 K respectively.

Figure 4, shows the pressure enthalpy diagram of the cycles presented in Table 1. The green and red lines correspond to the operation during minimum and maximum source temperature. The blue line corresponds to the highest temperature lift recorded.

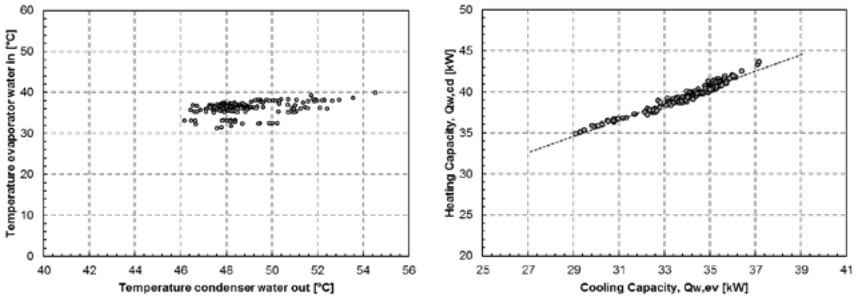


Fig. 3. Graphs of the temperatures of heat source and heat sink (left) and the heating capacity over the cooling capacity (right).

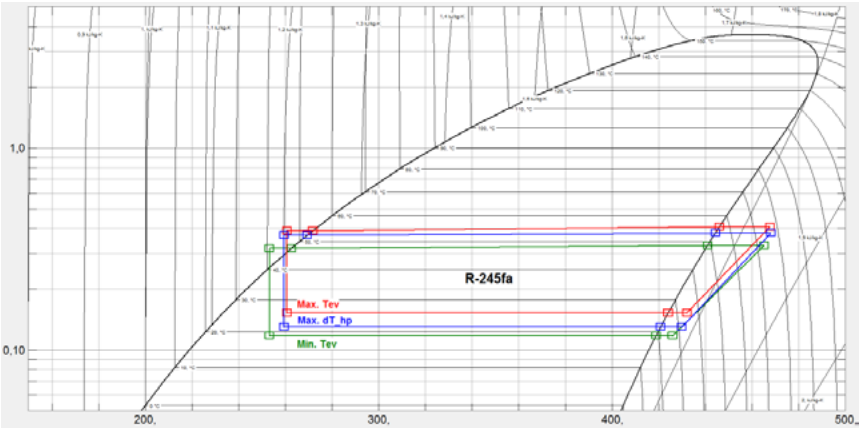


Fig. 4. Pressure and enthalpy diagram of R-245fa showing the operation of the HTHP under the conditions presented in Table 1.

During the monitoring campaign the speed of the compressor was maintained steady at 1500 rpm. The minimum and maximum suction and discharge temperatures recorded ranged from 26.8 °C and 35.3 °C to 72.2 °C to 77.3 °C respectively. The suction and discharge pressure ranged from 1.2 bar-a to 1.5 bar-a and 3.2 bar-a to 4.1 bar-a respectively. The power consumed by the compressor was measured in the range from 6.3 kW to 7.8 kW.

To evaluate the compressor performance the isentropic and volumetric efficiencies were calculated using Equations 1 and 2. The isentropic efficiency presents the ireversibilities during compression. The volumetric efficiency is the ratio of the volumetric flow rate over the volumetric displacement of the compressor. The volume in the suction (V_{su}) is calculated by REFPROP. The mass flow rate (m_r) is calculated from the ratio of the heating capacity at the condenser over the enthalpy difference between the refrigerant inlet and outlet in the condenser (Equation 3). The volumetric displacement (V_{displ}) is provided by the compressor manufacturer, the frequency (f) is 1500 rpm and the number of pistons (n) is six.

The minimum and maximum isentropic efficiency resulted from 45 % to 51 %. The volumetric efficiency was almost stable and ranged from 56 % to 58 % as shown in Figure 4 (left) in which are presented both efficiencies over the pressure ratio.

$$\eta_{is} = \frac{h_{dis,is} - h_{su}}{h_{dis} - h_{su}} \quad (1)$$

$$\eta_{vol} = \frac{m_r . V_{su}}{V_{displ} \cdot (f/60) \cdot n} \quad (2)$$

$$\dot{m}_r = \frac{Q_{w,cd}}{\Delta h_{cd}} \quad (3)$$

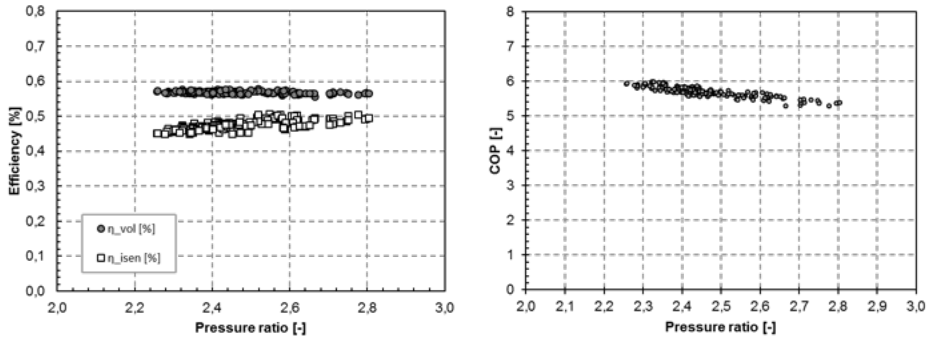


Fig. 4. Diagram of the isentropic and volumetric efficiencies over the pressure ratio (left) and the COP values of the HTHP over the pressure ratio (right).

The low isentropic efficiency values show that ireversibilities and losses are considerable under these operating conditions. Low temperature lift and overheating of the compressor could also be the causes of this inefficiencies. It is also observed that the volumetric efficiency is low. The low evaporating temperature and pressure conditions reduce the density of the fluid, reducing also the volumetric flow rate.

The COP of the heat pump was calculated by the ratio of the heating capacity by the power consumed by the heat pump (Equation 4). The results present a short range of values due to the also small range of operating conditions. The minimum and maximum calculated COP values resulted in 5.3 and 6 respectively. The power consumed by the compressor resulted from 6.3 kW to 7.8 kW. In Figure 4 (right) are presented the COP values over the pressure ratio of the heat pump.

$$COP = \frac{Heating\ Cap}{Power\ input} = \frac{Q_{out}}{W_{in}} \quad (4)$$

The total amount of energy stored in the seasonal storage during the datalogging period was 55.44MWh from which 34 % were lost through heat losses. The total amount of thermal energy delivered from the storage to the HTHP was 18.23 MWh and to the building 18.46 MWh. The total amount of energy consumed by the building for heating was 112.32 MWh in one year, from which 16.4 % was covered by the heat directly supplied from the seasonal thermal storage, 19 % was covered by the HTHP and 64.6 % was produced by the gas boiler. The total amount of electricity consumed by the compressor resulted in 3.73 MWh.

From the ratio of the total energy supplied to the building to the total energy consumption the Seasonal Energy Efficiency Ratio (SEER) was calculated 5.73.

According to the European Environment Agency from data of 2016, the emissions related to electricity generation are equivalent to 0.773 grams of CO_2eq per kWh [10]. The heat pump´s electricity consumption is equivalent to 2.88 tonnes CO_2eq per year. The emissions that have been saved by the heat pump considering a gas boiler instead would be 4.3 tCO_2eq per year. Therefore, total emissions of 1.42 tCO_2eq are saved by the HTHP during the year of operation. On the other hand, the emissions that saved from the heat provided by the seasonal thermal storage to the building are 3.72 tCO_2eq considering that gas boiler would be the heat source. In total the saved emissions of the full installation are 5.14 tCO_2eq in one year of operation.

5. Conclusions

The experimental data of one year of operation of a water-to-water high temperature heat pump which used heat from a STES tank to provide heat to a hospital has been presented. The HTHP was designed and manufactured using off-the-shelf components. The design operating temperatures are between 30-45 °C in the heat source side and up to 75 °C in the sink side. The working fluid used is R-245fa and the secondary fluid in both loops, the evaporator and condenser is water. The hot water produced by the heat pump is directed to a buffer tank of 1 m^3 internal volume and then delivered to the heating water grid.

Data was collected for a period of 12 months of the system´s operation. During this period the heat pump operated for a total of 9934 minutes which consisted in 209 operation cycles. The monitored values were measured and recorded every 30 seconds for 24 hours per day.

The water source temperature variated between 31.2°C to 39.9°C and the water outlet in the condenser from 46.2°C to 54.5°C. Both water pumps in the evaporator and condenser loop were maintained at steady speed and presented flow rates between 1.25 to 1.33 kg/s in the evaporator and from 1.52 to 1.56 kg/s in the condenser. The heating capacity of the heat pump variated between 34.9 kW and 43.7 kW.

The evaporating temperature and pressure ranged from 18.9°C to 25.8°C and 1.18 bar-a to 1.53 bar-a respectively. The condensing temperature and pressure resulted from 47.3°C to 55.64°C and 3.05 bar-a to 3.9 bar-a respectively. The pressure ratio calculated variated between 2.3 to 2.8.

The compressor´s isentropic efficiency resulted in values between 45 % and 51 %. The volumetric efficiency presented stable values that ranged from 56 % to 58 %. The compressor presented low performance due to the losses related to the high temperature operation. In addition, the fluid conditions at the suction line present low density which could be improved by increasing the evaporation temperature. The power consumption of he compressor resulted from 6.3 to 7.8 kW and the COP of the heat pump variated between 5.3 and 6.

In terms of the demo system, the total amount of energy stored in the seasonal storage during resulted in 55.44 MWh from which 34 % were lost through heat losses. The heat delivered by the seasonal thermal storage to the building corresponded to the 50.3 % and to the heat pump the 49.7 % of the total heat delivered. The total heat demand of the building was 112.32 MWh in one year, from which 16.4 % was covered by the heat directly supplied from the seasonal thermal storage, 19 % by the HTHP and 64.6 % was delivered by the gas boiler.

The total saved emissions from the heat pump operation comparing to a gas boiler operation in Poland are 1.42 tCO_2eq. The combined emissions saved from the heat delivered by both the heat pump and the thermal storage are 5.14 tCO_2eq in one year.

It is concluded that improvements on the control algorithm will certainly increase the seasonal performance of the heat pump and of the installation. During the operation cycles the heating water outlet temperature was controlled by the building´s control algorithm. The temperature of the buffer tank could not exceed the temperature set by the control causing short cycling of the heat pump.

The experimental results have demonstrated that HTHP systems are an attractive approach to use when low temperature heat source is available. In cases where the heat source is produced by renewable energy sources it could further improve the efficiency and the carbon footprint of the system.

Acknowledgements

This work has been conducted using data from a demonstration plant developed by the FP7 project EINSTEIN (Effective INtegration of Seasonal Thermal Energy storage systems IN existing buildings) with Grant agreement number 284932.

References

[1] Bauer, D., Marx, R., Nußbicker-Lux, J., Ochs, F., Heidemann, W., and Müller-Steinhagen, H., "German central solar heating plants with seasonal heat storage," *Sol. Energy*, vol. 84, no. 4, pp. 612–623, 2010.

[2] Hesaraki, A., Holmberg, S., and Haghighat, F., "Seasonal thermal energy storage with heat pumps and low temperatures in building projects - A comparative review," *Renew. Sustain. Energy Rev.*, vol. 43, pp. 1199–1213, 2015.

[3] Marx, R., Bauer, D., and Drueck, H., "Energy efficient integration of heat pumps into solar district heating systems with seasonal thermal energy storage," *Energy Procedia*, vol. 57, pp. 2706–2715, 2014.

[4] Franck, T., Wallin, P.A., Berntsson, E., "Process integration of various types of heat pump" in *Applications and efficiency of heat pump systems*, Springer-Verlag Berlin Heidelberg GmbH, Ed. 1990.

[5] Pieper, H., Ommen, T., Elmegaard, B., and Brix Markussen, W., "Assessment of a combination of three heat sources for heat pumps to supply district heating," *Energy*, vol. 176, pp. 156–170, 2019.

[6] Honeywell, "Genetron 245fa," 2010.

[7] Wilson, D.P., *et al.*, "ANSI/ASHRAE Standard 34-2013," 2013.

[8] UmweltBundesamt, "Global Warming Potential (GWP) of certain substances and mixtures that

contain such substances, based on the Fourth Assessment Report of the Intergovernmental Panel on Climate Change and a hundred years time period", 2017.
[9] Lemmon, M.O., Bell, E.W., Huber, I.H., McLinden, M.L., "NIST Standard Reference Database 23: Reference Fluid Thermodynamic and Transport Properties-REFPROP." National Institute of Standards and Technology, Gaithersburg, 2018.
[10] European Environment Agency, "CO2 emission intensity," 2018. [Online]. Available: https://www.eea.europa.eu.

13th IEA Heat Pump Conference
April 26-29, 2021 Jeju, Korea

Analysis of the refrigerant maldistribution of propane evaporating in brazed plate heat exchangers as a function of operating conditions

Lucas Alvarez[a], Paloma Albaladejo[a], Emilio Navarro-Peris[a*], Lena Schnabel[b], Jose Miguel Corberan[a]

[a]Instituto de Ingenieria Energetica, Universitat Politecnica de Valencia, Camino de vera s/n 46022, Valencia, Spain
[b] Fraunhofer ISE, Heidenhofstr. 2, 79110, Freiburg, Germany

Abstract

One of the most common factors affecting the performance of brazed plate heat exchangers (BPHE) is the not uniform distribution of the refrigerant. This problem is especially important in the evaporator as the refrigerant enters in it in two phase flow and usually the distribution of liquid and vapor is not uniform over all the channels. This problem is very well known in the literature, and manufacturers have implemented some technical solutions like introducing distributors in the inlet port in order to minimize this effect. Nevertheless, the applied solutions usually are developed only for nominal conditions and the deviations in other conditions are normally not known. In this contribution, an experimental analysis of the refrigerant distribution in an evaporator BPHE as a function of the inlet and outlet conditions will be presented. BPHE has been tested and evaluated working at several inlet conditions (quality) and outlet conditions, the refrigerant distribution inside the BPHE has been registered using thermography. From this analysis an estimation of the influence of the refrigerant maldistribution in the system performance has been obtained.
© HPC2020.
Selection and/or peer-review under responsibility of the organizers of the 13th IEA Heat Pump Conference 2020.

Keywords: Evaporator,maldistribution, efficiency, natural refrigerant ;

1. Introduction

The use of braze plate heat exchangers (BPHEs) for two-phase flow boiling was increasingly investigated within the last 10-15 years with the intention of using the high compactness and efficiency. Maldistribution was quickly observed as higher demands and bigger heat exchangers were needed. In that sense, BPHE evaporators are very sensitive to uneven distribution of the refrigerant among the different plates because of the fact of having two phase flow in their inlet port. As a consequence of that, the heat transfer can be highly degraded affecting significantly to the global system performance.

The precise determination of the real refrigerant mass flow in each plate is difficult but some research has been done in the qualitative estimation of it based on infrared thermography. This technic can be applied because of the fact that the refrigerant/water temperature in each plate would have a different profile depending on the vapor/liquid refrigerant distribution in each channel.

From the early literature on the plates arrangements on flow distribution is presented by boasiouny et al [1, 2] where results indicate that manifold diameter and number of channels have great influence in maldistribution. Maldistribution causes higher or lower thermal performance degradation depending on if it is a U-type or Z-type heat exchanger. Z-type plate arrangement have more tendency to suffer maldistribution, see Tonon et al. [3].

The quality distribution in heat exchanger manifolds were investigated by Vist et al. [4] and thermal performance can be reduced due to liquid/vapor maldistribution. From their observations, vapor is taken out

in the first channels when the inlet quality was low (x=0.11) but distributes evenly in the first channels when quality increased. However, no mention about the superheat in the evaporator is made.

Mass flow, flow pattern and inlet quality are variables to take into account to have mass flow evenly distributed within the channels. For high mass flow and low inlet quality, better distribution is mentioned by many researchers [5,6]. However, depending on the flow pattern better or less distribution is observed. Flow visualization before entering the evaporator recognized two patterns: churn and separated flow. Churn flow is recommended as liquid and vapor phase are homogeneously mixed whereas in separated flow, the different layers of vapor and liquid, according to Zou et al., are perfectly separated [7].

For microchannel heat exchangers, Elbel et al. [8] proposed an improvement for achieving better refrigerant distribution. The solution consisted in remove flash gas; vapor phase is separated from liquid phase after the expansion valve. In this way, only liquid is flowing within the microchannel heat exchanger while the vapor phase is being bypassed. Thermography pictures showed clear more uniformly distributed superheat with this flash gas removal system. Furthermore, better system performance was observed when using the separation device. Although quality maldistribution can be reduced in some cases introducing some modifications in the inlet, Tou et al. [9] reported that the outlet header pressure drop can have an influence in the mass flow rate maldistribution from tube to tube.

As mentioned before, infrared thermography has been used in order to study this phenomenon. It has the advantadge of being non-intrusive and non-contacting, which makes this technic easy to apply. In the works of Bowers et al, or Longo [10, 11] used thermography in microchannel heat exchangers to visualize the two-phase flow region for different outlet vapour qualities and superheats of 5 and 10 K and to outline a methodology to quantify both refrigerant maldistribution and effective usage of the heat exchanger respectively.

Regarding BPHE, although the problem is known [6] and some solutions has been adopted by the main manufacturers in order to achieve a better refrigerant distribution, see for instance [12] where a system that feeds homogenously with refrigerant all channels has been developed or the introduction of what is call equalancer distributor in order to improve the refrigerant distribution [13], from the practical point of view, there is not a final totally satisfactory solution for this problem. In fact, the intrinsic design characteristics of this type heat exchanger made that the analysis of the refrigerant distribution more difficult to carry on and the detailed examination of the maldistribution from the experimental point of view is challenging. This has made that the amount of information in the open literature of this kind of phenomena for this type of heat exchanger is significantly less than for other heat exchangers like tube and fin or microchannel heat exchangers.

In this paper, the refrigerant maldistribution problem in BPHEs is going to be analyzed as a function of different operation parameters like evaporator inlet quality, evaporator superheat and water temperature difference. The analysis has included a wide test campaign in which the refrigerant distribution in the evaporator has been characterized at different working conditions using infrared thermography. Later on the influence of the refrigerant maldistribution in the system performance has been evaluated in such a way that the influence of this type of problem can be quantified.

2. Experimental Set-up

The test bench for the characterization of water to water heat pumps was used. The test bench was able to control the water mass flow through the evaporator and the condenser in such a way that it allows maintaining a constant water temperature difference at a constant inlet water temperature in both heat exchangers. In this test bench a heat pump able to control its operational subcooling and superheat has been installed. The scheme of the heat pump is shown in figure 1. Between the condenser and the liquid receiver there is throttling valve, this valve allows the control of the subcooling at the outlet of the condenser. Its operation principle is shown in figure 1b, in steady state conditions, the liquid receiver must be in saturated conditions, this fact produces that changing the pressure drop introduced by the throttling valve, the system is able to control the amount of refrigerant inside the liquid receiver and the heat pump subcooling. In order to measure the subcooling, it was made measuring the temperature and the pressure at the outlet of the condenser. Between the liquid receiver and the evaporator there is an electronic expansion valve which allow the control of superheat. In a similar way the determination of superheat was done measuring the temperature and the pressure at the compressor inlet, it was assumed that the pipe from the evaporator to the compressor was short enough in order to assume that these conditions would be the conditions at the evaporator outlet. This experimental set up allows the stable control of the vapor quality at the evaporator inlet (subcooling at a condensing temperature) and the superheat at the evaporator outlet.

The system topology shown in figure 1 only allows working in stable conditions at superheats higher than 5K. In order to work in saturated conditions, the heat pump shown in Figure 1 has been modified.

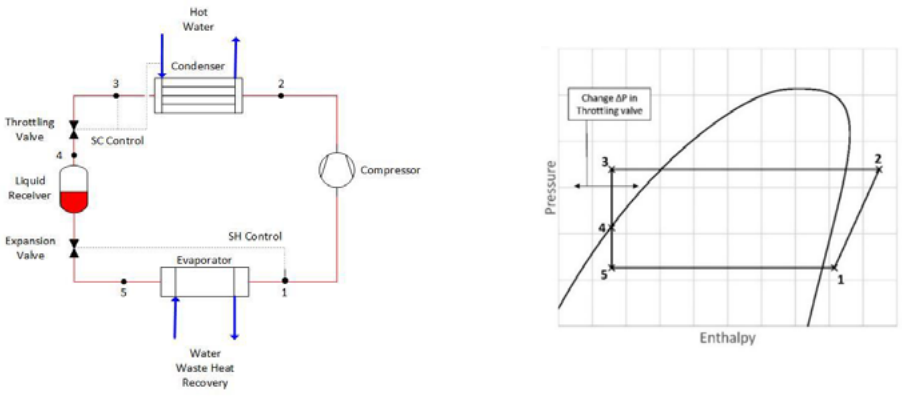


Figure 1. Mode 1 configuration system lay-out and refrigerant cycle

Figure 2 shows the other working alternative which allows working with 0 K superheat. In this configuration, a by pass system has been installed in the heat pump in such a way that the liquid receiver is placed at the outlet of the evaporator

the expansion valve is dedicated to control the subcooling at the expense of losing the superheat control which is fixed to 0 K. In this sense, the liquid receiver is placed at the outlet of the evaporator (point 5) ensuring saturated vapor conditions at compressor inlet (zero superheat). The expansion valve is removed from the system and therefore the superheat will be not controlled and the only heat pump control is related to the subcooling.

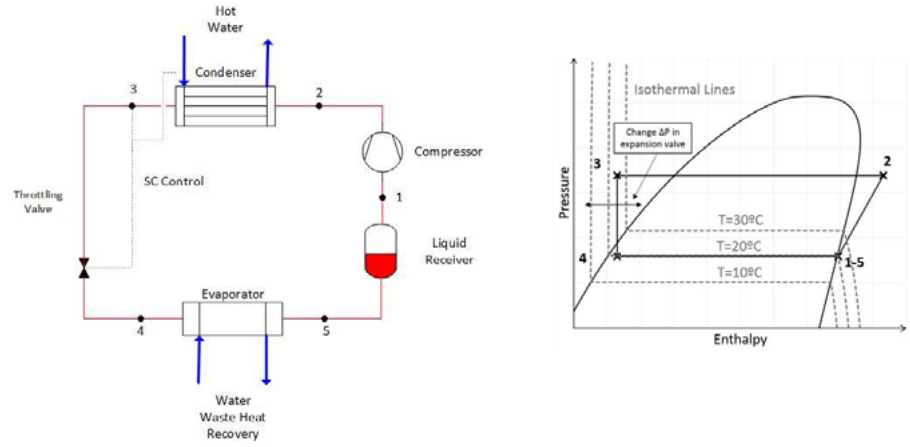


Figure 2. Mode 2 configuration: system lay-out and refrigerant cycle

Figure 3 shows a scheme of the test unit with all the instrumentation used. The green box corresponds to the BHPE evaporator. The main characteristic of it are 120 plates, capacity of 40 kW capacity at the nominal point, a horizontal port distance and vertical port distance of 50 mm and 466 mm respectively resulting a 6 m^2 heat transfer area.

There is a water loop in the condenser and in the evaporator, each water loop has a temperature sensor at the inlet and outler of the water side and have a Coriolis mass flow meter to measure the water mass flow rate. The water pumps of each circuit are equipped with an inverter which adjusts the water mass flowrate in such a way that the water temperature difference can be maintained as constant. These two water loops are connected to a third one which allows to control the water temperature inlet in both heat exchangers. More detailed information about this system can be found in [14].

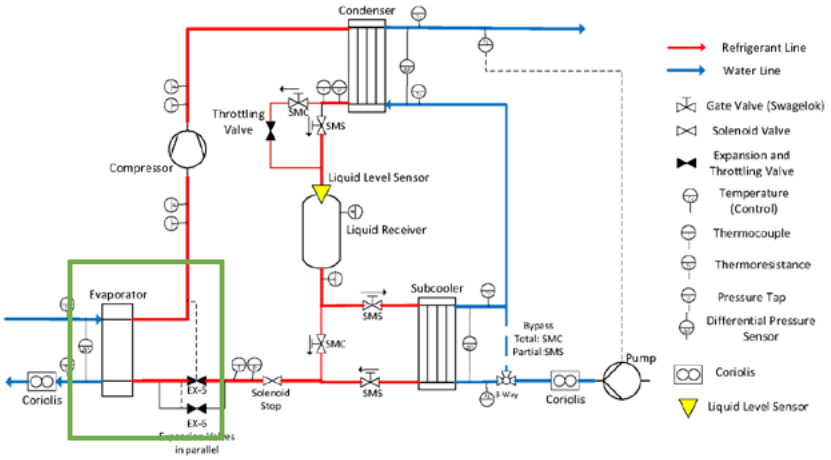


Figure 3. Propane Water-to-water heat pump in which the refrigerant distribution in the evaporator has been tested.

Regarding the refrigerant circuit, two temperature sensors are placed in each inlet and outlet of both heat exchangers. Three Rosemount sensors are installed in the refrigerant side, at the compressor inlet and outlet and in the liquid receiver. The last pressure sensor constitutes a way to verify the subcooling value. The mass flow rate in the refrigerant side is determined by means of a heat balance between the water side and the refrigerant side. In order to monitor and measure the parameters on the BHPE, all the sensors were connected to a data acquisition system "Agilent 34970A", where all parameters were monitored. The relative and absolute accuracy of each device are shown table 1.

Table 1. Instrumentation used in the test rig

	Model	Relative accuracy	Absolute accuracy
Pressure	P 1151 Smart GP7 Rosemount	0.12 % of Span	0.03
	P 1151 Smart GP8 Rosemount	0.15 % of Span	0.08
	P 3051 TG3 Rosemount	0.14 % of Span	0.04
Temperature	RTD Class 1/10 DIN		0.06
Mass Flow	Coriolis SITRANS F C MASS 2100	0.3 % of Reading	
Thermography Cam	FLIR P640	0.3%	2ºC

To register the refrigerant distribution, the surface of the evaporator is been photographed using the camera FLIR P640 infrared camera. The accuracy of the camera is shown in table 1, it should be also commented that although the estimation of the exact temperature has a higher error than an RTD, the sensibility of the camera is of 30mK, therefore although quantitative test could present significative deviations from the reality, under the proper, the camera would be able to supply a qualitative representation of the heat transfer process in the BPHE. The IR camera was set to a measuring range of -40 to 120ºC.

Figure 3 shows a transversal picture of the evaporator installed in the system and a frontal view with the location of the refrigerant and water inlet/outlet ports. As it can be seen in the picture, the transversal side of the evaporator was covered with a non-reflective painting in order avoid any possible dispersion derived from undesired environmental radiation reflections.

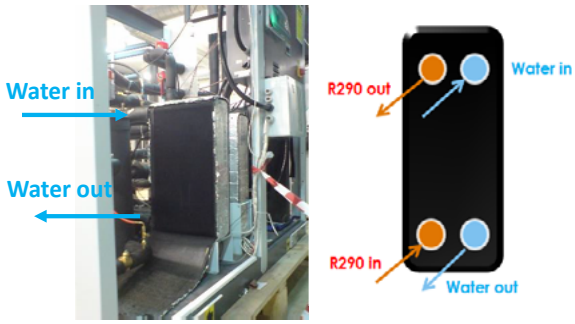


Figure 3. Picture of a frontal view of the evaporator and a transversal view with the location of the inlet/outlet ports

With this experimental setup and after the pre-evaluation and literature research on the relevant aspects that could affect the refrigerant distribution in the evaporator, the points represented in the test matrix shown in figure 4 where measured. The refrigerant distribution in the evaporator was evaluated for evaporator outlet superheat (SH) from 0 K to 15 K and the evaporator inlet quality (x) for a water temperature difference in the evaporator of dT_water=5 K and dT_water=13 K with a water inlet temperature of 20ºC.

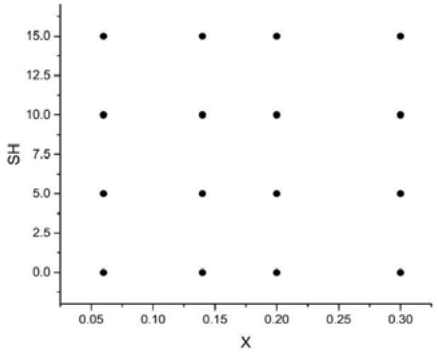


Figure 4. Experimental measures points for dTwater= 5 K and dTwater= 13 K

3. Obtained Results

Table 2 and table 3 shows the corresponding IR thermographies for a water temperature difference of 5 K and 15 K respectively. They are given in tables in the corresponding order of superheats. The minimum temperature of the scale is set to -6ºC and the maximum to 20ºC. The same scale is maintained for both sets of data in order to be able to stablish comparisons among them.

The values shown in the different columns represents different superheats and the values represented in the different files represents different evaporator inlet qualities.

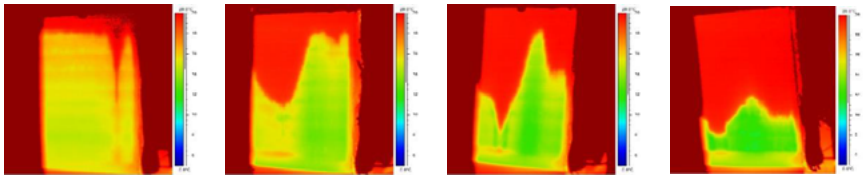
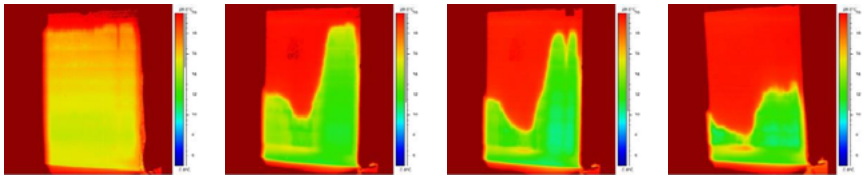
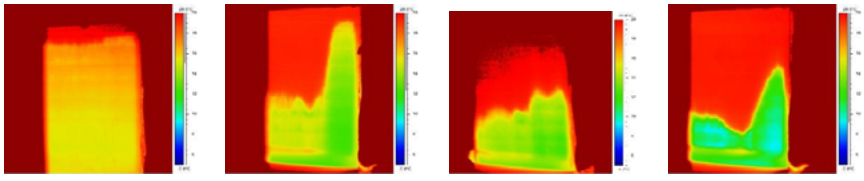
In order to evaluate the maldistribution influence in the system performance, the evaporation temperature (T_evap) has been selected as the basic indicator parameter.

The points can be observed in the thermography pictures presented in table 2 and table 3:

- The two-phase flow region can be identified by a sharp change in color from yellow/green to red.
- The minimum temperature in table 3 are smaller than in table 2.

- The measured evaporation temperature is approximately 2 K lower than the minimum surface temperature registered by the camera.
- In the points with superheat, the two-phase flow region is not even distributed, indicating a maldistribution of the refrigerant mass flow. The right or the central part of the heat exchanger has a a larger fraction of the heat exchanger at lower temperature. This indicates a larger amount of liquid refrigerant in passing through this part of the heat exchanger.
- The points with 0 K superheat show a quite similar evaporation temperature independently of the refrigerant inlet quality.
- The inlet quality influences the distribution in a complex way. For qualities close to 0 and qualities about 0.3 the degradation of the system performance with the superheat is smaller than for the quality values the between them. The possible explanation could be related to the distribution system, which probably is optimized for vapor qualities of 0.3, then as we go further from these values the refrigerant distribution will be worst. The improvement at low vapor qualities could be related to the fact that at these conditions all the refrigerant is almost in liquid phase. In fact, in these conditions the observed pattern is different to the rest.
- For higher superheats the two-phase flow area is smaller than for lower superheats.
- Comparing both tables, the degradation of the BPHE performance is higher at higher water temperature differences.

Table 2. Thermographies for dT_{water}= 5 K with variation of inlet quality and superheat

	SH=0	SH=5	SH=10	SH=15
	Tevap=12.34ºC	Tevap= 10.34 º C	Tevap= 9.00 º C	Tevap= 4.61 º C
x=0,07				
	Tevap= 12.81 º C	Tevap= 8.37 º C	Tevap= 7.39 º C	Tevap= 4.61 º C
x=0,14				
	Tevap= 13.38 º C	Tevap= 10.01 º C	Tevap= 8.17º C	Tevap= 4.81 º C
x=0,20				
	Tevap= 13.34 º C	Tevap= 12.71 º C	Tevap= 9.50º C	Tevap= 4.92 º C

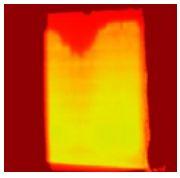
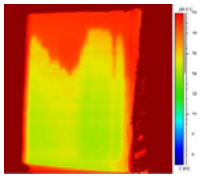
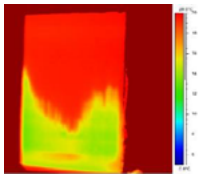
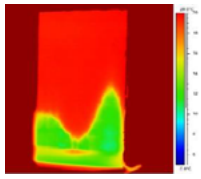
x=0,30				

Table 2. Thermographies for dT_{water}= 13 K with variation of inlet quality and superheat

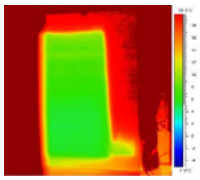
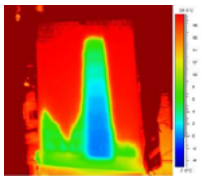
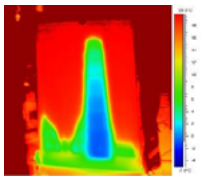
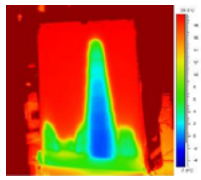
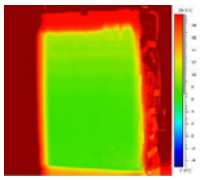
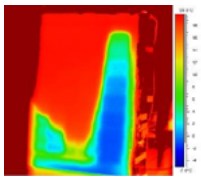
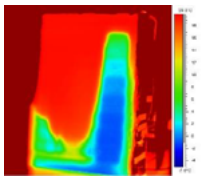
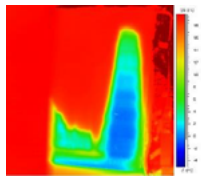
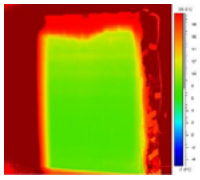
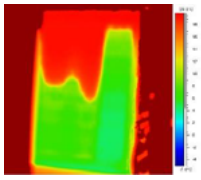
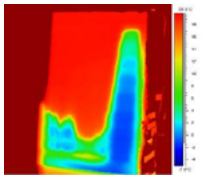
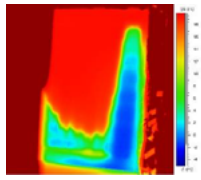
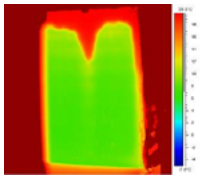
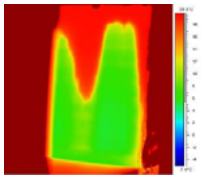
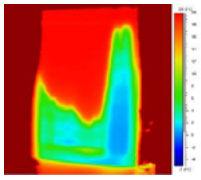
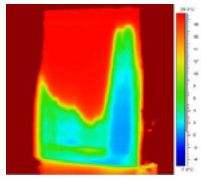
	SH=0	SH=5	SH=10	SH=15
x=0,07	Tevap= 4.04 ºC 	Tevap= -1.02 ºC 	Tevap= -1.82 ºC 	Tevap= -1.88 ºC 
x=0,14	Tevap= 5.97 ºC 	Tevap= -2.02 º C 	Tevap= -2.46 º C 	Tevap= -1.88 ºC 
x=0,20	Tevap= 6.20 ºC 	Tevap= 3.52 ºC 	Tevap= -2.45 ºC 	Tevap= -2.31 ºC 
x=0,30	Tevap= 6.04 ºC 	Tevap= 4.81 ºC 	Tevap= 3.67 ºC 	Tevap= -0.46 ºC 

Figure 5 represents the evaporation temperature as a function of the vapor quality and superheat for both sets of experiments. In that figure 5 (left) can be observed that evaporation temperature is almost independent of vapor quality except when superheat have a value comparable or lower than the water temperature difference. If the maldistribution of the refrigerant depends on the refrigerant quality at the evaporator inlet and it is

independent of the water side, the information obtained from figure 5 (left) points to the fact that, although there is a maldistribution it do not have a direct influence on the heat exchanger performance as the evaporating temperature do not change significantly. In figure 5 (right) the results are not so clear, but it can be stated that the obtained results depend in all the working map on the superheat and on the vapor quality.

A possible explanation could be related to the fact that in figure 5 (right) water temperature lift is similar or higher than the superheat in all the cases. Based on that hypothesis, the performance of the heat exchanger will be affected by the maldistribution problem when water temperature lift is higher than superheat, and in these cases the vapor quality at the inlet will have influence on the heat exchanger performance.

Based on that explanation for the obtained results, it can be determined that refrigerant maldistribution could increase its effects in the degradation of the heat exchanger performance in applications where the temperature difference in the secondary fluid side could be high like when the heat pump evaporator is used in heat recovery applications with a finite source of low temperature heat in order to produce heat at high temperature.

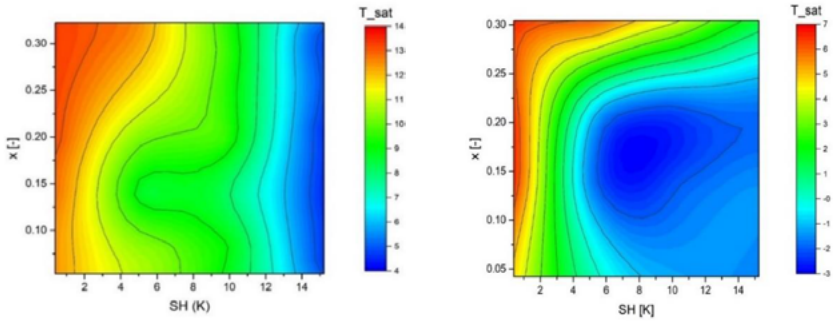


Figure 5. Saturation temperature for dT_{water}= 5 K (left). Saturation temperature for dT_{water}= 13 K (right)

4. Conclusions

Maldistribution in a brazed plate heat exchanger has been experimentally observed with infrared thermography. When maldistribution occurs, evaporator surface temperature is distributed unevenly and can be registered with thermography as it is non-intrusive and non-contacting, having no influence in the evaporator. Inlet quality and superheat has been changed during the tests for a given water temperature difference to observe this phenomenon.

As observed in the thermography pictures (figures 2 and 3), inlet quality has an influence in maldistribution at first sight. For high inlet quality, better refrigerant distribution is observed. However, superheat is observed to have a minor effect. The higher the superheat, better distribution is shown in the thermography for a 5 K water temperature difference Most homogeneous temperature map distribution is achieved when no superheat is performed.

Evaporation temperature has a great impact in system efficiency. Were the evaporator forced to work with a high level of superheat, less area is available for evaporation thus, evaporation temperature decreases. As expected, higher evaporation temperature is achieved when both low superheat and high inlet quality refrigerant is flowing. Although maldistribution is observed in thermography, underperformance is not inherited to all the cases. Related to that it is crucial to be able to determine how the maldistribution influence the performance of a BPHE as in some applications it could be higher than expected. In fact maldistribution have a higher influence in system performance when water temperature differences are equal or higher than superheat. This could be a relevant factor to take into account in applications where there is a high temperature difference on the secondary fluid like heat pumps used for energy recovery applications based on waste heat sources of finite availability.

Acknowledgements

Part of the work presented was carried out by Estefanía Hervás Blasco with the financial support of a PhD scholarship from the Spanish government SFPI1500X074478XV0. The authors would like also to

acknowledge the Spanish 'MINISTERIO DE ECONOMIA Y COMPETITIVIDAD', through the project "MAXIMIZACION DE LA EFICIENCIA Y MINIMIZACION DEL IMPACTO AMBIENTAL DE BOMBAS DE CALOR PARA LA DESCARBONIZACION DE LA CALEFACCION/ACS EN LOS EDIFICIOS DECONSUMO CASI NULO" with the reference ENE2017-83665-C2-1-P and the Universitat Politecnica deValencia program "ayuda a primeros Proyecto de investigación" through the project with reference SP20180039 for the given support.

References

[1] Bassiouny, M K; Martin, H. *Flow distribution and pressure drop in plate heat exchangers—I U-type arrangement*. *Chemical Engineering Science* [online]. 1984, **39**(4), 693–700

[2] Bassiouny, M K; Martin, H. *Flow distribution and pressure drop in plate heat exchangers—II Z-type arrangement*. *Chemical Engineering Science* [online]. 1984, **39**(4), 701–704

[3] Thonon, B; Mercier, P. *Les échangeurs à plaques: dix ans de recherche au GREEth: Partie 2. Dimensionnement et mauvaise distribution*. *Revue Générale de Thermique* [online]. 1996, **35**(416), 561–568

[4] Vist, S; Pettersen, J. *Two-phase flow distribution in compact heat exchanger manifolds*. *Experimental Thermal and Fluid Science* [online]. 2004, **28**(2–3), 209–215

[5] Brix, W; Kaern, M R; Elmegaard, B. *Modelling refrigerant distribution in microchannel evaporators*. *International Journal of Refrigeration* [online]. 2009, **32**(7), 1736–1743

[6] Jensen, J K; Kaern, M R; Ommen, T; Markussen, W B; Reinholt, L; Elmegaard, B. *Effect of liquid/vapour maldistribution on the performance of plate heat exchanger evaporators*. In: *Refrigeration Science and Technology* [online]. 2015, s. 2007–2014

[7] Zou, Y; Hrnjak, P S. *Refrigerant distribution in the vertical header of the microchannel heat exchanger – Measurement and visualization of R410A flow*. *International Journal of Refrigeration* [online]. 2013, **36**(8), 2196–2208

[8] Elbel, S; Hrnjak, P. *Flash gas bypass for improving the performance of transcritical R744 systems that use microchannel evaporators*. *International Journal of Refrigeration* [online]. 2004, **27**(7), 724–735

[9] Tuo, H; Hrnjak, P. *Effect of the header pressure drop induced flow maldistribution on the microchannel evaporator performance*. *International Journal of Refrigeration* [online]. 2013, **36**(8), 2176–2186

[10] Bowers, C D; Wujek, S S; Hrnjak, P. *Quantification of Refrigerant Distribution and Effectiveness in Microchannel Heat Exchangers Using Infrared Thermography*. *Refrigeration And Air Conditioning*. 2010, (2006), 1–8.

[11] Longo, G A. *Heat transfer and pressure drop during HFC refrigerant saturated vapour condensation inside a brazed plate heat exchanger*. *International Journal of Heat and Mass Transfer* [online]. 2010, **53**(5–6), 1079–1087

[12] Swep. SWEP distribution system. *SWEP Refirgerant handbook* [online]. [vid. 2019-01-17]. Dostupné z: https://www.swep.net/refrigerant-handbook/6.-evaporators/asas5/

[13] Alfa laval manual. https://www.energyrent.no/ViewFile.aspx?ItemID=576

[14] Pitarch, M; HERVAS-BLASCOrvas-Blasco, E; Navarro-Peris, E; Gonzalvez-Macia, J; Corberan, J M. *Evaluation of optimal subcooling in subcritical heat pump systems*. *International Journal of Refrigeration* [online]. 2017, **78**, 18–31

13th IEA Heat Pump Conference
April 26-29, 2021 Jeju, Korea

Refrigerant Circuitry Optimization of Heat Exchangers for Charge Reduction and Robust Performance in Reversible Heat Pump Application

Zhenning LI[a], Vikrant Aute[a,*], Jiazhen LING[a]

[a]Center for Environmental Energy Engineering
Department of Mechanical Engineering, University of Maryland
College Park, MD 20742 USA

Abstract

Heat pumps are becoming more and more desirable around the world as an efficient mean of space conditioning for both cooling and heating requirements. Heat exchangers (HXs) are the key components in these devices and pose some unique design challenges because the same HX has to operate as an evaporator in one mode and as a condenser in the other. Studies have proved that by optimizing the refrigerant circuitry, the performance of HXs can be significantly improved. In a reversible heat pump application, the optimal circuitry obtained under the air conditioning (AC) mode cannot guarantee optimal performance if it is used in the heat pump (HP) mode. Our study shows that the single objective optimal design obtained under AC mode yields 11.4% capacity degradation when it is used in HP mode. This paper presents a multi-objective refrigerant circuitry optimization approach to achieve robust heat exchanger performance in both cooling and heating modes. This work builds on a newly developed Integer Permutation based Genetic Algorithm (IPGA), which can guarantee good manufacturability of optimal circuitry designs. The enhanced IPGA extends the capabilities to generate designs with splitting and merging circuits, thus exploring the design space thoroughly. Two multi-objective problem formulation is proposed. One formulation aims at minimizing refrigerant charge, and the other formulation aims at maximizing HX capacity. The optimal HX designs are analyzed at the system level as a part of a reversible heat pump simulation. A case study using an A-type indoor unit shows that the optimal design obtained using the formulation to minimize charge can yield charge reduction by 19.2% under AC mode and 21.6% under HP mode. The optimal design using the formulation to maximize capacity improves the cooling capacity by 2.3% and system COP by 2.5% under AC mode and meanwhile, improves the heating capacity by 3.0% and system COP by 2.8% under HP mode. Considering the performance degradation of the single objective optimal, the effective capacity improvement of the bi-objective optimal is 14.4%.

© HPC2020.
Selection and/or peer-review under responsibility of the organizers of the 13th IEA Heat Pump Conference 2020.

Keywords: Heat exchanger; Circuitry optimization; Genetic Algorithm, Charge reduction, Reversible heat pump

1. Introduction

Tube-fin heat exchangers (TFHXs) are prominent components in air conditioning and heat pump systems. This type of heat exchanger consists of a bundle of tubes with fin sheets. The performance of TFHXs is greatly affected by a large number of structural parameters (tube diameter, tube length, fin type, fin thickness, etc.) and therefore, conducting optimization on such parameters can significantly improve its performance [1]. In addition to those parameters, the configuration of tube connections, i.e. refrigerant circuitry, determines the refrigerant flow path, and also significantly impacts the heat exchanger performance [2-8]. For an existing

* Corresponding author. Tel.: +1-301-405-8726
E-mail address: vikrant@umd.edu

TFHX design with a given geometry, performing optimization on refrigerant circuitry is more convenient and cost effective than varying other structural parameters. For example, changing the circuitry is a matter of changing U-bend length and locations, whereas changing tube-spacing can require new fin dies, which is costly and has much longer lead time.

Researchers have tried to use different tube-fin HX circuitry optimization approaches to obtain the best circuitry under a specific operating condition. Domanski et al. [2] developed an optimization tool called ISHED (Intelligent System of Heat Exchanger Design). This optimization scheme switches between Evolutionary learning and Symbolic learning. They performed comprehensive studies to optimize circuitry of TFHXs as evaporators or condensers [9-11]. Their maximum reported HX capacity improvement from optimization runs and experimental validations are 13% from CO_2 gas cooler [12] and 2.2% from a R410A evaporator [13], respectively. Wu et al. [14; 15] developed another optimization approach, which switches between knowledge-based GA and Simulated Annealing. Moreover, the group created effective operators (greedy crossover and greedy mutation) to improve the convergence. They performed circuitry optimization on 3 evaporators and 1 condenser, and the maximum predicted capacity improvement in their study is 7.4%. Ploskas et al. [16] represented circuitry using an adjacency matrix and constrained the hairpins to be on one side of the HX. By comparing five different derivative-free optimization algorithms, they concluded that TOMLAB/glcDirect and TOMLAB/glcSolve can efficiently find optimal or near-optimal circuitries. In their study, the TFHXs are also optimized under specific operating conditions either as an evaporator or as a condenser.

For a reversible heat pump system, the same TFHX operates as a condenser in one mode and as an evaporator in the other mode. In literature [17], various performance metrics have been used as objectives for the TFHX circuitry optimization studies, however, all reported circuitry optimization are performed under specific refrigerant operating condition. Taking an indoor unit as an example, the optimal circuitry obtained by optimizing the HX as an evaporator in air conditioning mode does not necessarily guarantee desirable performance when the refrigerant flow is reversed, and it operates as a condenser under heat pump mode. It is thus clear that circuitry optimization for HX in reversible heat pump application has not been explored. This paper aims at tackling this challenge.

The remainder of the paper is organized as follows. Section 2 details an enhanced heat exchanger circuitry optimization algorithm. Section 3 presents two multi-objective problem formulations to achieve robust heat exchanger performance in a reversible heat pump. Section 4 presents a case study to demonstrates the efficacy of the proposed circuitry optimization algorithm and compare the bi-objective problem formulations with a single objective problem formulation. Section 5 analyses the optimization results and presents system level simulation results. Section 6 presents the conclusions of this study.

2. Enhanced Integer Permutation based Genetic Algorithm

2.1. Chromosome representation

To conduct optimization using Genetic Algorithm, the first step is to find a mathematical representation of the circuitry. A good individual representation (chromosome) can not only reduce the searching space, but can also simulate the nature of the problem [18]. In our previous research, an Integer Permutation based Genetic Algorithm (IPGA) [17] was developed to obtain the optimal circuitry designs. IPGA represents tubes as a sequence of integers (i.e. integer permutation). For an integer permutation, each integer (i.e., tube number) appears exactly once, thus, any chromosome generated by the Genetic Algorithm can be mapped to a valid circuitry and the size of the search space is dramatically reduced by the elimination of redundant designs. Li and Aute [19] have shown that IPGA demonstrates superior capability to obtain better refrigerant circuitries with lower computational cost than the other methods in literature. Readers are referred to the original paper [19] for more details of the IPGA developed in our previous research.

However, the previous IPGA cannot generate designs with splitting and merging of circuits. In order to remedy this limitation, a new chromosome representation called ‘Split Branch Chromosome’ (Fig. 1(a)) is developed and implemented in the enhanced IPGA. The new chromosome representation uses the concept of jagged arrays, with each element of this array representing a branch of tubes. Each branch contains 3 parts. The 1st part of the branch represents the tube sequence. The 2nd part of the branch represents the upstream tube. The 3rd part of the branch represents the downstream tube. Dummy tube number ‘0’ is used as the place holder in the 2nd part, if the 1st tube of the branch is an inlet tube of a circuit. And dummy tube number ‘-1’ is used as the place holder in the 3rd part, if the last tube of the branch is an outlet tube of a circuit.

Fig. 1(b) shows the chromosome representation of the 24-tube heat exchanger in Fig. 1(a). This sample heat exchanger has one splitting tube (tube # 3) and one merging tube (tube #20). With the ‘Split Branch

Chromosome', number of circuits is flexible, i.e., the optimal number of circuits is also an output from optimization and it can represent circuitry designs with splitting and merging circuits.

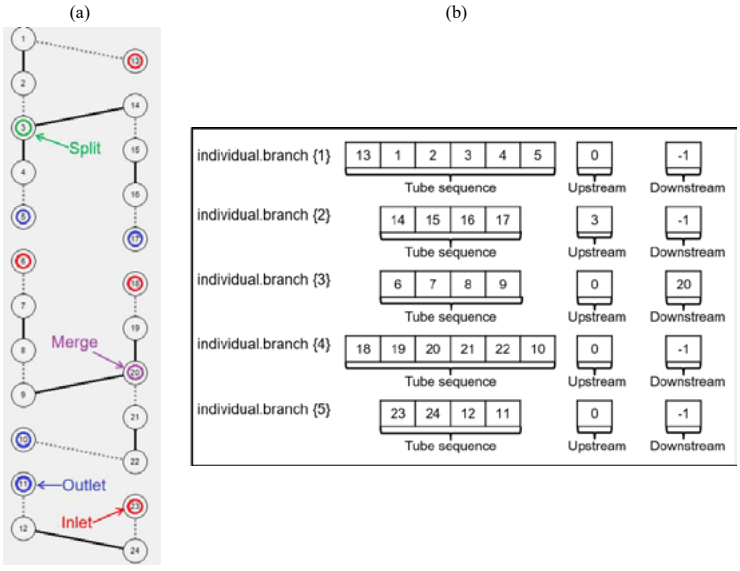


Fig. 1. Chromosome Representation: (a) 24-tube heat exchanger sample; (b) Split branch chromosome

2.2. GA Operators

In Genetic Algorithm, the creation of new individuals relies on the genetic operators. By transforming the selected individual to a new individual with potentially better fitness, the genetic operators direct the search and drive the optimization process.

To adapt the new chromosome representation and extend IPGA's capability to generate designs with splitting and merging circuits, the enhanced IPGA requires new genetic operators. Therefore, two novel genetic operators (Fig. 2) are developed. In order to generate circuit splitting, the split operator in Fig. 2 (a) randomly determine one tube as the splitting tube and make a sub-section of tubes to form a new branch, thus creates a split. Oppositely, the merge operator in Fig. 2 (b) randomly determines one tube as the merging tube and makes a sub-section of tubes to form a new branch, thus creates a merging of circuits.

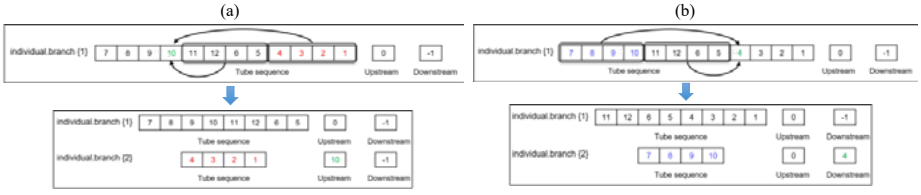


Fig. 2. (a) Split operator; (b) Merge operator

In order to adapt to the change of the chromosome representation, the six GA operators from previous IPGA [17] are modified to form six new GA operators (Fig. 3). The 'gene sequence inversion' operator in Fig. 3(a) chooses a random subsection of a branch and inverts the order of the tubes. The 'gene insertion' operator in Fig. 3(b) puts a randomly selected tube into a random position. The 'in-branch transposition' operator in Fig. 3(c) reverses two randomly chosen tubes inside a single branch, while the 'cross-branch transposition' operator in Fig. 3(d) reverses two randomly selected tubes between different branches. The 'branch detachment' operator in Fig. 3(e) splits a randomly selected branch into two branches. The 'branch union' operator in Fig. 3(f) chooses two branches and unites them into one branch. With the 'branch union' and 'branch detachment' operators, the number of circuits can be varied and optimized in a generic fashion.



Fig. 3. GA Operators: (a) Gene sequence inversion; (b) Gene insertion; (c) In-branch transposition; (d) Cross-branch transposition; (e) Branch detachment; (f) Branch union

3. Problem Formulations

To achieve stable heat exchanger performance in reversible heat pump, two problem formulations are explored. The 1st formulation in Equation (1) aims at maximizing the heat exchanger capacity under different operating conditions. One of the objectives is to maximize the HX capacity when it is operated as an evaporator under cooling mode, and the other objective is to maximize the capacity when it is operated as a condenser under heating mode. The 2nd formulation in Equation (2) aims at minimizing refrigerant charge. One objective is to minimize charge under cooling mode and the other objective is to minimize charge under heating mode. It should be noted that real heat pump systems may use a charge reservoir (e.g., accumulator or receiver) to store charge, but such reservoir is not considered here as the focus is to minimize the charge in the heat exchangers only.

Both problem formulations implement 8 constraints. The first 5 operating constraints limit capacity, refrigerant pressure drop, refrigerant charge, outlet refrigerant saturation ΔT and sensible heat ratio in acceptable ranges as compared with the baseline. The remaining 3 constraints are manufacturability constraints. Specifically, the 6th constraint ensures the inlet and the outlet tubes on the same side of HX. The 7th constraint avoids long U-bends spanning over 2 tube rows. The last constraint avoids partially overlapped U-bends crossing. The manufacturability constraints and the constraint handling scheme are detailed in Li et al. [17].

It is worthwhile to mention that in order to evaluate the performance of the HX under both operating modes, the HX performance under AC mode is first evaluated, then the refrigerant flow direction is reversed (i.e. the inlets and outlets tubes are swapped), and the HX performance under HP mode is evaluated. In addition to the reversion of refrigerant flow direction, the air and refrigerant inlet conditions and the empirical correlations to predict in-tube heat transfer coefficient and pressure drop are also changed to accommodate the switch between AC mode and HP mode.

$$
\begin{aligned}
&\textit{Objective}-1:\ \textit{Maximize}(\mathrm{Q}_{\mathrm{AC\ mode}})\\
&\textit{Objective}-2:\ \textit{Maximize}(\mathrm{Q}_{\mathrm{HP\ mode}})\\
&\textit{Subject to}:\\
&\quad \mathrm{Q} \geq \mathrm{Q}_{\mathrm{baseline}}\\
&\quad \Delta\mathrm{P}_{\mathrm{refrigerant}} \leq \Delta\mathrm{P}_{\mathrm{refrigerant,baseline}}\\
&\quad \mathrm{Charge} \leq \mathrm{Charge}_{\mathrm{baseline}}\\
&\quad \left|\Delta T_{\mathrm{sat}} - \Delta T_{\mathrm{sat,baseline}}\right| \leq 1K\\
&\quad \left|SHR - SHR_{\mathrm{baseline}}\right| \leq 3\%\\
&\quad \text{Inlets and outlets on the same side of HX}\\
&\quad \text{No long U-bend spanning over 2 tube rows}\\
&\quad \text{No overlapped U-bend crossing}
\end{aligned}
\qquad (1)
$$

$$
\begin{aligned}
&\textit{Objective}-1:\ \textit{Minimize}(\text{Refrigerant charge}_{\mathrm{AC\ mode}})\\
&\textit{Objective}-2:\ \textit{Minimize}(\text{Refrigerant charge}_{\mathrm{HP\ mode}})\\
&\textit{Subject to}:\\
&\quad \mathrm{Q} \geq \mathrm{Q}_{\mathrm{baseline}}\\
&\quad \Delta\mathrm{P}_{\mathrm{refrigerant}} \leq \Delta\mathrm{P}_{\mathrm{refrigerant,baseline}}\\
&\quad \mathrm{Charge} \leq \mathrm{Charge}_{\mathrm{baseline}}\\
&\quad \left|\Delta T_{\mathrm{sat}} - \Delta T_{\mathrm{sat,baseline}}\right| \leq 1\ K\\
&\quad \left|SHR - SHR_{\mathrm{baseline}}\right| \leq 3\%\\
&\quad \text{Inlets and outlets on the same side of HX}\\
&\quad \text{No long U-bend spanning over 2 tube rows}\\
&\quad \text{No overlapped U-bend crossing}
\end{aligned}
\qquad (2)
$$

4. Case Studies

An evaporator from an A-type indoor unit (Fig. 4(a)) is used as the baseline for circuitry optimization, because it is experimentally validated in our laboratory. Table 1 shows the structural parameters for the baseline indoor coil. Table 2 shows the operating conditions for the baseline coil working in cooling mode and heating mode. The air side conditions are adopted from ASHRAE Test Standard [20]. The air velocity flow maldistribution at the frontal face of the A-type indoor unit is simulated using an OpenFOAM® based CFD model (Fig. 4(b)), and the air maldistribution profile is imposed on the air side to improve the HX performance prediction. Table 3 lists the empirical correlations used for local heat transfer and pressure drop calculations during the performance evaluation of the HX as an evaporator or a condenser.

Table 1: Structural Parameters and Operating Conditions of Baseline Evaporator

Structural Parameters	Unit	Value
Tube Outer Diameter	mm	9.5
Fins Per Inch	FPI	15
Fin Type	-	Wavy Louver
Tube Length	m	0.503 m
Vertical Spacing	mm	20.0 mm
Horizontal Spacing	mm	25.0 mm
Number of Tube Banks		4
Number of Tubes Per Bank		22

Table 2: Operating Conditions of Baseline Working as an Evaporator and a Condenser

Operating Parameters	Unit	Baseline as Evaporator	Baseline as Condenser
Refrigerant	-	R410A	R410A
Pressure	kPa	1154.55	2432.44
Temperature	◦C	12.03	65.07
Refrigerant Quality	-	0.22	-
Refrigerant Mass Flow Rate	kg/s	0.0312	0.0275
Air Volume Flow Rate	ft^3/min	600	617
Air Pressure	kPa	101.325	101.325
Air Temperature	◦C	26.42	21.23
Air Relative Humidity	%	50.97	58.80

Table 3: Correlations Adopted in HX Simulation

Operating Mode	Heat Transfer Correlations	Pressure Drop Correlations
Refrigerant - Liquid Phase	Dittus and Boelter [21]	Blasius [22]
Refrigerant - Two Phase Boiling (Evaporator)	Jung *et al.* [23]	Jung and Radermacher [24]
Refrigerant - Two Phase Condensation (Condenser)	Cavallini et al. [25]	Lockhart and Martinelli [26]
Refrigerant - Vapor Phase	Dittus and Boelter [21]	Blasius [22]
Air	Wang *et al.* [27]	Wang *et al.* [27]

At the fitness evaluation stage, a finite volume heat exchanger model [28] is used to simulate the performance of the heat exchanger with different circuitries. The model can account for the refrigerant flow maldistribution among different circuits by iterating on the pressure residual at the outlet of each circuit. This

HX model was validated with measured data [29] for the same baseline HX under AC and HP modes, and the deviation between simulations and experiments are below 5% as shown Fig. 4(c).

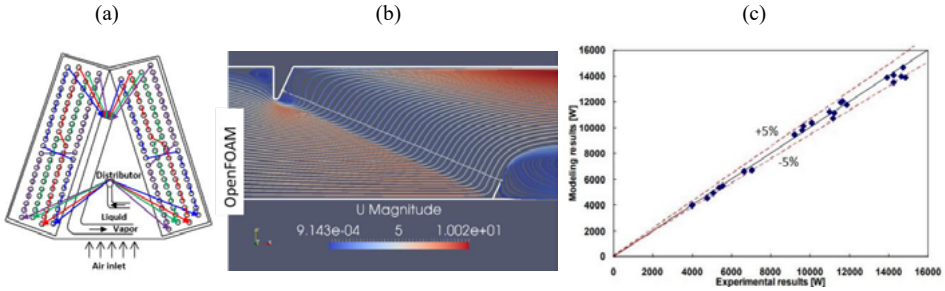


Fig. 4. (a) Baseline Circuitry; (b) Air Maldistribution in A-type Unit Simulated by CFD Model; (c) Experiment Tests vs Simulations

5. Results

5.1. Bi-objective optimization result

In this case study, the GA population size is set to 200, the number of generations is set to 500 and the population replacement ratio is 20% (i.e. the elitism reservation ratio is 80%). Fig. 5(a) shows the Pareto front for Formulation (1) plotted in the objective space. The Pareto front consists of 23 optimal designs. Fig. 5(b) shows the Pareto front using Formulation (2). The X-axis and Y-axis are the refrigerant charge under AC and HP mode. This Pareto front consists 36 optimal designs. Among the optimal designs in two Pareto fronts, the designs whose capacity/charge ranks at the median of the all designs in the Pareto front are sampled for further analysis, since it is expected to exhibit balanced performance under AC and HP modes.

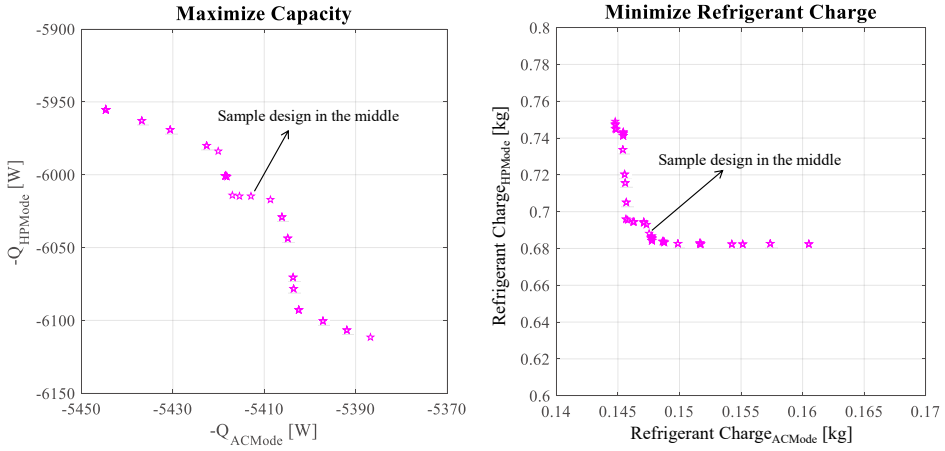


Fig. 5. (a) Pareto Front for Maximizing Capacity; (b) Pareto Front for Minimizing Refrigerant Charge

5.2. Single objective optimization result

To emphasize the necessity to use the multi-objective problem formulation to optimize heat exchangers in reversible heat pumps, the same baseline heat exchanger is optimized solely under air-conditioning mode using a single objective problem formulation. The only objective is to maximize the evaporator cooling capacity under AC mode. The operating constraints and the manufacturability constraints are kept the same as those in Section 3. And the GA settings (the population size, the number of generations and population replacement ratio) are also the same as in the previous practice. Fig. 6(a) shows the GA evolution progress of the single objective optimization. The single objective optimal yields 2.4% capacity improvement under AC mode.

Fig. 6(b) shows the performance comparison between the single objective optimal with the bi-objective optimal to maximize capacity under both AC and HP modes. The bi-objective optimal yields 2.3% capacity increase under AC mode, which is a little less than the improvement of the single objective optimal under AC mode (2.4%). However, if the single objective optimal is used as a condenser in a reversible heat pump, the capacity degrades from 5845 W to 5177 W by 11.4% compared to the baseline. In contrast, the bi-objective optimal still improves condenser capacity by 3.0% under HP mode, it indicates that the effective capacity improvement of bi-objective optimal under HP mode is 14.4% (i.e., 11.4%+3.0%) considering the performance degradation of the single objective optimal under HP mode.

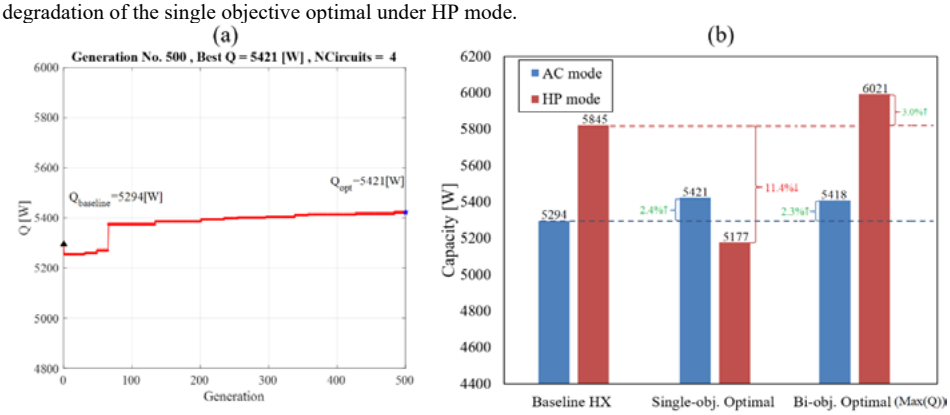


Fig. 6. (a) Single objective optimization GA progress; (b) Comparison of single-obj. with bi-obj. optimal

Table 4 presents the detailed performance of the baseline, the single objective optimal and the bi-objective optimal designs sampled from above Pareto fronts. Compared with the baseline, the optimal design from bi-objective Formulation (1) yields a capacity increase of 2.3% when it is used as an evaporator under AC mode and it yields the capacity increase of 3.0% when it is used as a condenser under HP mode. This indicates that its circuitry design is resilient to variation in operating conditions. Both refrigerant charge and the pressure drop are less than or equal to the baseline under the corresponding modes.

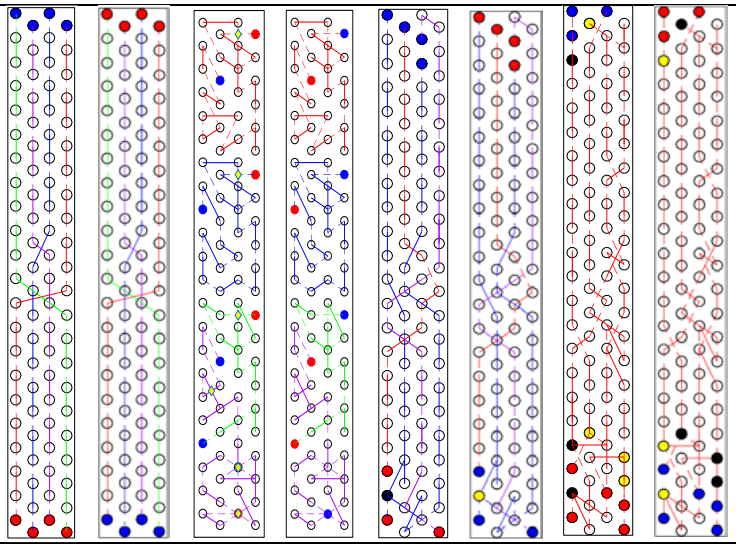
As a result of optimization using Formulation (2), the optimal design by minimizing refrigerant charge yields a charge reduction of 19.2% under AC mode and the charge reduction by 21.6% under HP mode. Meanwhile its capacity is slightly higher than the baseline under the corresponding operating modes.

Table 4: Summary of Optimization Results

Case	**Baseline**		**Single-obj. Optimal (Maximize Q)**		**Bi-objective Optimal (Maximize Q)**		**Bi-objective Optimal (Minimize Charge)**	
Mode	AC	HP	AC	HP	AC	HP	AC	HP
Capacity [W]	5294	5845	5421 (2.4%↑)	5177 (11.4%↓)	5418 (2.3%↑)	6021 (3.0%↑)	5305 (0.2%↑)	5918 (1.2%↓)
Ref. DP [kPa]	11.9	7.3	11.7 (1.7%↓)	7.3 (-)	11.9 (-)	6.5 (11.0%↓)	11.7 (1.6%↓)	6.6 (9.6%↓)
Sensible Heat Ratio	79.9%	100%	80.6%	100%	79.8%	100%	79.5%	100%
Outlet Saturation ΔT [K] (+ superheat, - subcooling)	+8.4	-9.48	+9.4	-8.5	+8.7	-10.13	+8.85	-10.02
Refrigerant Charge [g]	182.5	877.8	168.9 (7.5%↓)	828.5 (5.6%↓)	161.0 (11.8%↓)	877.8 (-)	147.5 (19.2%↓)	688.3 (21.6%↓)

Table 5 presents the circuitry of the baseline, the single objective optimal design and the bi-objective optimal designs from problem Formulation (1) and Formulation (2). In the circuitry plots, a solid line represents a U-bend on the near end of the heat exchanger, while a dotted line represents a U-bend on the far end. The red tubes are the inlets, while the blue ones are outlets. Merging tubes and splitting tubes are represented by yellow and black circles, respectively. In terms of manufacturability, the baseline has 2 long U-bends spanning over 3 tube rows, while all U-bends from the optimal designs are shorter than 3 tube rows.

Table 5: Circuitry of Baseline and Optimal Designs

Case	Baseline		Single-obj. Optimal (Maximize Q)		Bi-objective Optimal (Maximize Q)		Bi-objective Optimal (Minimize Charge)	
Mode	AC	HP	AC	HP	AC	HP	AC	HP
Circuitry								
U-bends (Length ≤ 2 tube rows)	82	82	84	84	85	85	87	87
U-bends (Length > 2 tube rows)	2	2	0	0	0	0	0	0

5.3. System level result

In order to test the system performance of the optimal designs and the baseline, a component-based vapor compression simulation tool [30] is used to simulate a realistic reversible heat pump cycle which is experimentally validated [29] using the baseline HX as the indoor coil. Fig. 7(a) and Fig. 7(b) show the schematic of the reversible heat pump system under cooling mode and heating mode, respectively. The information of other components (outdoor HX, compressor, expansion device) is detailed in the original paper [29]. The test condition is the ANSI/AHRI Standard 210/240 A cooling and heating conditions [31].

In Fig. 7(a) and Fig. 7(b), the air flow maldistribution profile simulated using an OpenFOAM® based CFD model ([32]) can be observed at the frontal face of A-type indoor unit. The air velocity at the apex is largest and the air velocity decreases from top to bottom of the coil.

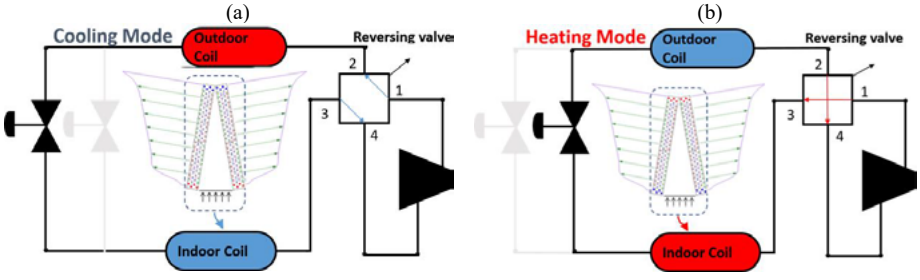


Fig. 7. Schematic of Reversible Heat Pump System: (a) Cooling (i.e. AC) Mode Operation; (b) Heating (i.e. HP) Mode Operation

Fig. 8 shows the system performance of the reversible heat pump system using the baseline or the optimal circuitry designs as indoor coil. Under cooling mode (Fig. 8(a)), the optimal design by maximizing capacity gains COP improvement from 3.54 to 3.63 by 2.5%, but the optimal design by minimizing refrigerant charge

only leads to COP improvement from 3.54 to 3.55 by 0.3%. Meanwhile, under heating mode (Fig. 8(b)), the optimal design by maximizing capacity gains COP improvement from 4.61 to 4.74 by 2.8%, but the optimal design by minimizing refrigerant charge only leads to COP improvement from 4.61 to 4.65 by 0.8%.

From the P-h diagrams, when the optimal design by maximizing capacity (red line in Fig. 8) operates as an evaporator in AC mode, it induces higher evaporating temperature. When it operates as a condenser in HP mode, it induces lower condensing temperature. Thus, the system efficiency is improved.

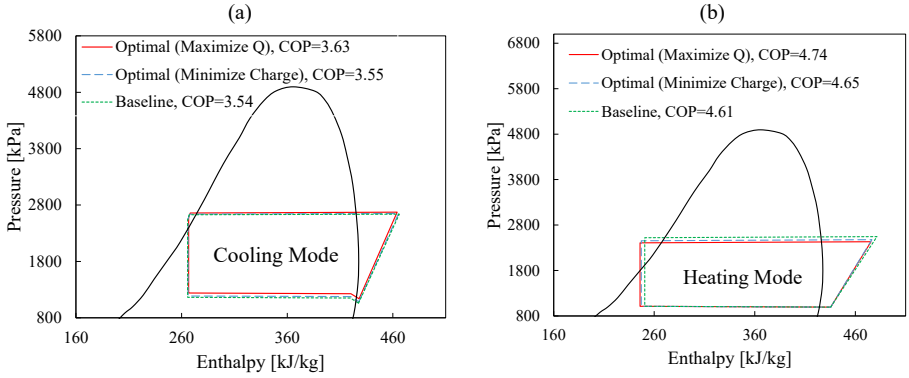


Fig. 8. R410A P-h diagram using Different Circuitry Designs in Indoor Unit: (a) Cooling mode; (b) Heating mode

6. Conclusion

This paper presents a newly developed tube-fin heat exchanger circuitry optimization algorithm. A new chromosome representation and eight GA operators are developed to extend the capability of Integer Permutation based Genetic Algorithm. In order to obtain optimal circuitries with improved performance under both air conditioning and heat pump modes for reversible heat pump system, two multi-objective problem formulations are explored. Case studies using an A-type indoor unit from a reversible heat pump system shows that the optimal design using the formulation with the objective to maximize heat exchanger capacity leads to 2.3% (AC mode) and 3.0% (HP mode) capacity improvement. In addition, it yields COP improvement by 2.5% (AC mode) and 2.8% (HP mode). Considering the single-objective optimal design obtained under solely AC mode induces 11.4% capacity degradation if it is used in HP mode, the effective capacity improvement of the bi-objective optimal is 14.4%. The optimal design obtained using the formulation with the objective to minimize refrigerant charge effectively reduce heat exchanger refrigerant charge by 19.2% (AC mode) and 21.6% (HP mode), meanwhile maintaining the heat exchanger capacity and COP to be the similar amount as the baseline. Use of the proposed circuitry optimization approach in early design stages can help assure a certain minimum robust performance of heat exchangers in heat pumps during both cooling and heating mode usage as well as assist in redesign of existing heat exchangers for new lower-GWP refrigerants.

Acknowledgements

This work was supported by the Modeling and Optimization Consortium of the Center for Environmental Energy Engineering at the University of Maryland.

References

[1] L. Huang, V. Aute, and R. Radermacher. A Survey of Optimization Formulations and Techniques for the Design of Heat Exchangers Using Lower Gwp Refrigerants. ASHRAE Winter Conference. (2015)

[2] M. Chwalowski, D. Didion, and P. Domanski. Verification of Evaporator Computer Models and Analysis of Performance of an Evaporator Coil. ASHRAE Transactions 95 (1989): 1229-36.

[3] C. C. Wang, et al. Effect of Circuit Arrangement on the Performance of Air-Cooled Condensers. International Journal of Refrigeration 22.4 (1999): 275-82.

[4] G. Bigot, L. Palandre, and D. Clodic. Optimized Design of Heat Exchangers for" Reversible" Heat Pump Using R-407C. International Refrigeration and Air Conditioning Conference. Purdue, USA. (2000).

[5] S. Liang, T. Wong, and G. Nathan. Numerical and Experimental Studies of Refrigerant Circuitry of Evaporator Coils. International Journal of Refrigeration 24.8 (2001): 823-33.
[6] W. Ding, et al. A General Simulation Model for Performance Prediction of Plate Fin-and-Tube Heat Exchanger with Complex Circuit Configuration. Applied Thermal Engineering 31.16 (2011): 3106-16.
[7] H.Y. Ye, and K.S. Lee. Refrigerant Circuitry Design of Fin-and-Tube Condenser Based on Entropy Generation Minimization. International Journal of Refrigeration 35.5 (2012): 1430-38.
[8] C. M. Joppolo, L. Molinaroli, and A. Pasini. Numerical Analysis of the Influence of Circuit Arrangement on a Fin-and-Tube Condenser Performance. Case Studies in Thermal Engineering 6 (2015): 136-46.
[9] D. A. Yashar, et al. A Dual-Mode Evolutionary Algorithm for Designing Optimized Refrigerant Circuitries for Finned-Tube Heat Exchangers. HVAC&R Research 18.5 (2012): 834-44.
[10] P. A. Domanski, and D. Yashar. Application of an Evolution Program for Refrigerant Circuitry Optimization, Proceedings of ACRE Conference, New Delhi, India (2007).
[11] P. A. Domanski, and D. Yashar. Optimization of Finned-Tube Condensers Using an Intelligent System. International Journal of Refrigeration 30.3 (2007a): 482-88.
[12] H. Cho, and P. A. Domanski. Optimized Air-to-Refrigerant Heat Exchanger with Low-GWP Refrigerants. 12th IIR Gustav Lorentzen Natural Working Fluids Conference, UK, Edinburgh (2016).
[13] D. A. Yashar, S. Lee, and P. A. Domanski. Rooftop Air-Conditioning Unit Performance Improvement Using Refrigerant Circuitry Optimization. Applied Thermal Engineering 83 (2015): 81-87.
[14] Z. Wu, et al. Application of a Genetic Algorithm to Optimize the Refrigerant Circuit of Fin-and-Tube Heat Exchangers for Maximum Heat Transfer or Shortest Tube. International Journal of Thermal Sciences 47.8 (2008b): 985-97.
[15] Z. Wu, et al. Knowledge-Based Evolution Method for Optimizing Refrigerant Circuitry of Fin-and-Tube Heat Exchangers. HVAC&R Research 14.3 (2008a): 435-52.
[16] N. Ploskas, et al. Optimization of Circuitry Arrangements for Heat Exchangers Using Derivative-Free Optimization. Chemical Engineering Research and Design 131 (2018): 16-28.
[17] Z. Li, J. Ling, and V. Aute. Tube-fin Heat Exchanger Circuitry Optimization Using Integer Permutation Based Genetic Algorithm. International Journal of Refrigeration. 103 (2019): 135-144.
[18] K. Deb. Optimization for Engineering Design: Algorithms and Examples. PHI Learning Pvt. Ltd., 2012.
[19] Z. Li, and V. Aute. Optimization of Heat Exchanger Flow Paths Using a Novel Integer Permutation Based Genetic Algorithm. EngOpt 2018 Proceedings of the 6th International Conference on Engineering Optimization, Lisboa, Portugal (2018).
[20] ASHRAE. Methods of Testing for Rating Seasonal Efficiency of Unitary Air Conditioners and Heat Pumps. ANSI/ASHRAE Standard (2010): Atlanta, GA, USA.
[21] F. Dittus, and L. Boelter. Heat Transfer in Automobile Radiators of the Tubular Type. International Communications in Heat and Mass Transfer 12.1 (1985): 3-22.
[22] H. Blasius. Grenzschichten in Flüssigkeiten Mit Kleiner Reibung. Druck von BG Teubner, 1907.
[23] D. Jung, et al. A Study of Flow Boiling Heat Transfer with Refrigerant Mixtures. International Journal of Heat and Mass Transfer 32.9 (1989): 1751-64.
[24] D. Jung, and R. Radermacher. Prediction of Pressure Drop During Horizontal Annular Flow Boiling of Pure and Mixed Refrigerants. International Journal of Heat and Mass Transfer 32.12 (1989): 2435-46.
[25] A. Cavallini, et al. Condensation in Horizontal Smooth Tubes: A New Heat Transfer Model for Heat Exchanger Design. Heat Transfer Engineering 27.8 (2006): 31-38.
[26] R. Lockhart, and R. Martinelli. Proposed Correlation of Data for Isothermal Two-Phase, Two-Component Flow in Pipes. Chem. Eng. Prog 45.1 (1949): 39-48.
[27] C. C. Wang, et al. Heat Transfer and Friction Correlation for Compact Louvered Fin-and-Tube Heat Exchangers. International journal of heat and mass transfer 42.11 (1999): 1945-56.
[28] H. Jiang, V. Aute, and R. Radermacher. Coildesigner: A General-Purpose Simulation and Design Tool for Air-to-Refrigerant Heat Exchangers. International Journal of Refrigeration 29.4 (2006): 601-10.
[29] A. Alabdulkarem, et al. Testing, Simulation and Soft-Optimization of R410a Low-GWP

Alternatives in Heat Pump System. International Journal of Refrigeration 60 (2015): 106-17.
[30] J. Winkler, V. Aute, and R. Radermacher. Component-Based Vapor Compression Simulation Tool with Integrated Multi-Objective Optimization Routines. International Refrigeration and Air Conditioning Conference. Purdue Univ. (2006).
[31] AHRI. Standard 210/240-2008. Performance Rating of Unitary Air Conditioning and Air-Source Heat Pump Equipment. AHRI (2008)
[32] M. S. Lee, et al. A CFD Assisted Segmented Control Volume Based Heat Exchanger Model for Simulation of Air-to-Refrigerant Heat Exchanger with Air Flow Mal-Distribution. Applied Thermal Engineering 131 (2018): 230-43.

13th IEA Heat Pump Conference
April 26-29, 2021 Jeju, Korea

A Dynamic Model for Microchannel Heat Exchanger under Frost Conditions

Jiazhen Ling[a,*], Lingzhe Wang[b], Rohit Dhumane[c], Vikrant Aute[a]

[a]Center for Environmental Energy Engineering, Univresity of Maryland, College Park, Maryland, 20742, USA
[b]Center for Sustainability in the Built Environment, University of Maryland, College Park, Maryland, 20740, USA
[c]Modine Manufacturing Company, 1500 Dekoven Ave, Racine, Wisconsin, 53403, USA

Abstract

Heat pump manufacturers gradually adopt microchannel heat exchangers (MCHX) as the outdoor coils due to the compactness and lower cost. The relatively small hydraulic diameter of MCHX also enhances the heat transfer compared to traditional tube and fin coils. However, such benefits may turn to a challenge when heat pumps operate under the frost condition. Air flow is easily blocked when frost builds up in the smaller flow channels formed by the fins and microchannel tubes. To study the MCHX performance under frost condition, we developed a Modelica-based dynamic model that accounts for the performance degradation under frost conditions. The MCHX is modeled using the finite volume method and the sensible and latent heat transfer between refrigerant and moist air is solved using both heat and mass conservation equations. Regarding the frost accumulation, the model considers both the frost densification and thickness growth which will reduce the conductivity of the tube surface and the minimum free flow area, leading to poor air-side heat transfer. The model can also be applied on a heat pump system along with other in-house developed Modelica component models to assist the understanding of heat pump COP degradation during frost.

© HPC2020.
Selection and/or peer-review under responsibility of the organizers of the 13th IEA Heat Pump Conference 2020.

Keywords: Heat pump; microchannel heat exchangers; frost simulation; transient/dynamic modeling

1. Introduction

In winter, heat pump systems are typically more energy efficient in providing heating than electric heaters or gas fired furnaces. Following the principle of the Carnot Cycle, heat pumps can transform the low-grade ambient heat to higher-grade space heat, making the cycle Coefficient of Performance (COP) higher than one. The popularity of heat pumps in many places of the world has been motivating researchers and engineers to further improve the system efficiency and reduce the cost. To that end, microchannel heat exchangers (MCHX) gain momentum in heat pump installations. MCHX, being widely used in the automotive AC industry, has a typical hydraulic diameter of 1 mm which is much smaller than the ones of tube-and-fin heat exchangers (TFHX). The small hydraulic diameter leads to compactness since the increase of heat transfer area-to-volume ratio is accompanied by the decrease of hydraulic diameter. Khan and Fartaj [1] conducted a literature review on MCHX in which the MCHX's compactness was corroborated by the example that a state-of-the-art multi-port flat tube heat exchanger registered a capacity per volume in the range of 2-3 MW/m^3. Although, it goes without saying that using MCHX in heat pumps is advantageous, there are still challenges faced by the traditional TFHXs, that MCHXs cannot address better. One such challenge is the frost-induced performance degradation during winter operations. As the outdoor unit becomes evaporator during a heat pump operation, its surface temperature may be lower than both the freezing point and the dewpoint of ambient air. Frost can therefore accumulate on the evaporator and as a result, the thermal resistance of the evaporator increases, eventually deteriorating the heat pump efficiency.

* Corresponding author. Tel: 1-301-405-8270
Email: jiazhen@umd.edu

To mitigate the frost built-up and its negative impact on cycle performance, we need to understand how frost first appears and distributes on the evaporator; how the increased thermal resistance due to frost built-up alters the operation of vapor compression cycle; lastly how the altered VCC operation reciprocates on the frost accumulation. Those questions can be answered either through experimental or numerical studies. Henry Barrow [2] was among the first to register his concern over frost accumulation in heat pumps. Through his fin model, he concluded the increased thermal resistance due to frost were majorly caused by air flow blockage, and the impact from lower thermal conductivity of frost was secondary. Moallem et al. [3] experimentally measured both the frost thickness and weight accumulated over two evaporators used in air source heat pumps. They used a digital scale to measure the frost weight and a CCD camera to capture the frost thickness growth over time. They concluded the frost onset was highly dependent on local fin temperature and the frost grew faster when the water vapor content of incoming air is higher. The same group of researchers [4] later developed a semi-empirical model that predicts non-uniform frost growth on heat exchangers. The model adopts a quasi-steady state, heat and mass balance-based segment-by-segment approach.

This paper introduces a Modelica-based full dynamic microchannel heat exchanger model with frost prediction capability, as opposed to a quasi-steady state approach, and further applies the model on a vapor compression cycle model, so that the impact from frost accumulation on cycle operation can be quantified. As suggested in the above literature, a comprehensive frost model should consider both the frost densification process which impacts the fin surface thermal conductivity and the frost thickness growth which blocks air passage through the heat exchanger. By exercising the model, we would like to demonstrate that it is a helpful tool when conducting research on: how frost first appears and distributes on the evaporator? How the increased thermal resistance due to frost built-up alters the operation of vapor compression cycle?

2. Modeling Methodology

The modeling methodology includes two main pieces: a segment-by-segment based microchannel model and a frost model that serves as an add-on to the first one. The microchannel model further includes three control volumes: the air-side control volume, the refrigerant-side control volume and the fin and flat-tube wall control volume. The frost model is applied to air-side control volume only so that the frost simulation will not be constrained to particular geometries of the MCHX as well as the refrigerant flowing inside the MCHX flat tube.

2.1 Segment-by-segment based microchannel heat exchanger model

The above-mentioned control volumes are better visualized in Figure 1. In the direction of flat tubes, the heat exchanger is divided into a number of segments which comprise the three control volumes. The structure of the control volumes enables the reusability of each control volume for other types of heat exchangers. The green ports and red ports are Fluidports and Heatports, respectively. They both act as connectors and by connecting those ports to each other, a set of conservation equations are established (Eq. 1 – 4). Eqn. 2 and 3 also carry the information of flow direction through the positive and negative signs.

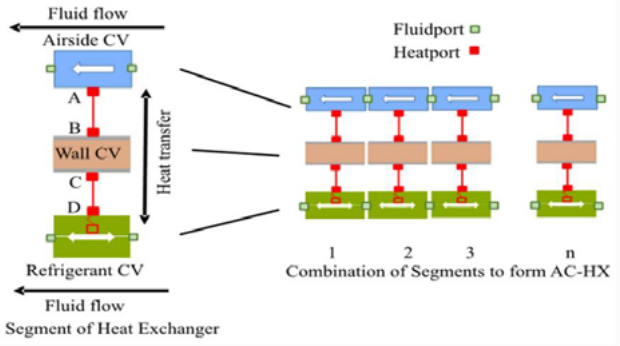


Figure 1 Subcomponent structure for MCHX model

Fluidports: $P_1 = P_2$ (1)

$$\dot{m}_1 + \dot{m}_2 = 0 \quad (2)$$

$$\dot{m}_1 h_1 + \dot{m}_2 h_2 = 0 \quad (3)$$

Heatports: $\dot{q}_1 + \dot{q}_2 = 0$ (4)

The refrigerant-side control volume is a lumped model which merges the multiple MCHX ports into a single tube (see Figure). The implicit assumptions here are that the refrigerant maldistribution among the ports are neglected and consequently there is a single temperature along the width of the tube (width here means length along the airflow direction). According to Li et al. [5], such an assumption tends to neglect the refrigerant maldistribution in each port which could lead to a heat exchanger level capacity degradation of 3.6%.

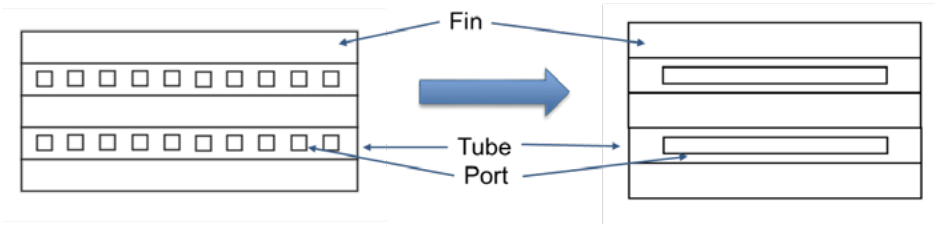


Figure 2: Refrigerant-side port-level simplification for MCHX model

The tube temperature for the lumped port profile of the model MCHX is evaluated as discussed below. The thickness δ_t is evaluated from Equation 5, using the tube height (H_t) and port height (H_p). The tube mass (m_t) is obtained from Equation 6, where n_t is number of tubes and ρ_t is the tube material density. The fin mass (m_f) of MCHX is evaluated from Eqn. 7, where A_s is surface area, t_f is fin thickness and ρ_f is fin material density. Weighted averages of specific heat capacity (c) and mass (m) from Equations 8 and 9 are used in the energy equation for the tube control volume to evaluate the dynamic temperature profile in Equation 10. Q_a and Q_r are heat flows to air-side and refrigerant-side respectively.

$$\delta_t = \frac{H_t - H_p}{2} \quad (5)$$

$$m_t = n_t \rho_t L_t (H_t W_t - A_c) \quad (6)$$

$$m_f = \frac{A_s}{2} t_f \rho_f \quad (7)$$

$$c = \frac{m_t c_t + m_f c_f}{m_t + m_f} \quad (8)$$

$$m = m_t + m_f \quad (9)$$

$$mc \frac{dT}{dt} = \dot{Q}_a + Q_r \quad (10)$$

The Q_a term is evaluated in the airside control volume. Fin efficiency η is used to combine primary and secondary heat transfer areas into a single effective heat transfer area (Eqn. 11). The primary and secondary areas for heat transfer are evaluated from Eqns. 12 and 13. The number of fins per unit length (called fin density) is represented by ξ. Pt is the tube pitch (distance between consecutive tubes).

$$A_e = A_p + \eta A_f \quad (11)$$

$$A_p = 2L_t(W_t + H_t - \xi t_f W_t) \quad (12)$$

$$A_s = 2L_t \xi \left[W_t (P_t - H_t) + P_t (W_f - W_t) \right] \quad (13)$$

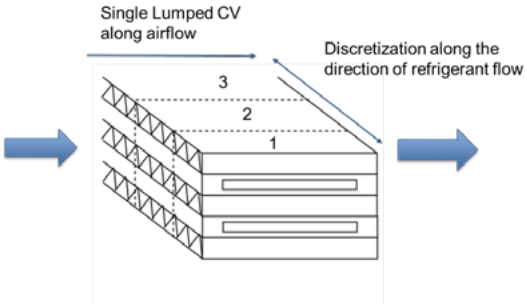


Figure 3: Discretization of airside control volume

The heat transfer coefficient for airside is critical for accurate evaluation for heat transfers. A linear correlation developed from experimental data is fed into the model for improved accuracy. The face area (A_f) is evaluated from geometrical parameters by Eqn. 14.

$$A_f = (n_t - 1)P_t + L_t \tag{14}$$

$$u = \frac{\dot{V}}{A_f} \tag{15}$$

$$\alpha = min\left(\left(\frac{\tilde{\alpha}}{\tilde{u}}\right)u, \alpha_0\right) \tag{16}$$

Face velocity (u) is obtained from volume flow rate ($\dot{V}$) using Eqn. 15 and is used as independent parameter for heat transfer coefficient (α) evaluation from the empirical Eqn. 16, obtained from manufacturing data. To model natural convection at zero flow rate, a condition happens during cycle shut down or mode switch, a minimal volume flow rate can be provided to get non-zero heat transfer coefficient values for zero flow case. The correlating terms $\tilde{\alpha}$and $\tilde{u}$are obtained from the linear trend line passing through origin. Epsilon-NTU method is used to evaluate air outlet temperature and airside heat transfer capacity (Q_a) can be now evaluated using the values of total heat transfer area, heat transfer coefficient and air temperatures.

The refrigerant-side control volume contains dynamic mass and energy conservation equations. Pressure and enthalpy are the state variables used for evaluating other thermo-physical quantities and for the progress in time. Homogenous model of void fraction is used in the model for faster simulation time because the refrigerant charge distribution is not critical parameter for evaluation.

2.2 Frost model

As discussed earlier, a complete frost model should consider both the frost thickness and the frost densification. Figure 4 describes the modeling approach that captures basic frost phenomenon [6].

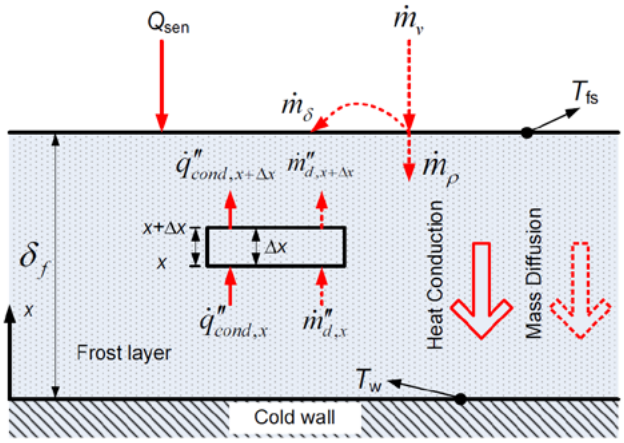


Figure 4: Schematic for frost modeling [6]

In Figure 4, the MCHX fin surface is generalized as a cold surface and the dotted shades represent the frost layer. The x direction points to the frost growth direction. As cold and moist air flows on the top of the cold surface at T_w, moisture deposits on the surface at a rate of $\dot{m}_v$, and turns to frost. The air stream rejects both sensible heat, Q_{sen}, and latent heat, in the condensate rate of $\dot{m}_v$, to the MCHX surface covered by frost. The condensate, $\dot{m}_v$, may either deposit on top of the fresh frost or, through the gap of topmost frost, deposit in the middle of the frost layer, resulting both the frost thickness growth, in the rate of $\dot{m}_\delta$, and the frost densification, in the rate of $\dot{m}_\rho$, respectively. As a result, the frost thickness, δ_f, and the frost density increases, the latter of which further affects the frost layer thermal conductivity. The basic frost accumulation phenomenon embodies a heat and mass transfer process, so the governing equations applied to the control volume are shown in Eqns. 17 and 18.

Mass Balance:

$$\dot{m}''_{d,x} - \dot{m}''_{d,x+\Delta x} = -\frac{\partial \dot{m}''_{d,x}}{\partial x}\Delta x = \frac{\partial}{\partial t}(\rho_f \Delta x) \tag{17}$$

Energy Balance:

$$\Delta x\left[-\frac{\partial q''_{cond,x}}{\partial x} - \frac{\partial}{\partial x}\left(\dot{m}''_d h_v\right)\right] = \frac{\partial}{\partial t}(\rho_f h_f \Delta x) \tag{18}$$

For the sake of simplicity, the paper omits the detailed mathematical deduction which can be found in [6] and only presents the solutions to the above governing equations. In addition, an empirical equation is used to connect the frost densification to the change of frost thermal conductivity.

Water vapor absorbed by the frost layer:

$$\dot{m}''_\rho = \frac{\zeta p_{v,sat}(T_w)}{R_v T_w \varphi}\sinh(\varphi \delta_f) \tag{19}$$

Where

$$\zeta = D_{eff}\{\frac{1}{\delta_f}cosh^{-1}[\frac{T_w}{T_{fs}}\frac{p_{v,sat}(T_{fs})}{p_{v,sat}(T_w)}]\}^2 \tag{20}$$

$$\varphi = \sqrt{\frac{\zeta}{D_{eff}}} \tag{21}$$

The average density of frost for the next time step:

$$\bar{\rho}_{f,t+\Delta t} = \bar{\rho}_{f,t} + \frac{\dot{m}_{\rho}^{"}}{\delta_f}\Delta t \tag{22}$$

The frost thickness for the next time step:

$$\delta_{f,t+\Delta t} = \delta_{f,t} + \frac{\dot{m}_{v}^{"} - \dot{m}_{\rho}^{"}}{\bar{\rho}_{f,t}}\Delta t \tag{23}$$

The thermal conductivity of the frost layer [7]:

$$k_f = 0.132 + 3.13 \times 10^{-4}\bar{\rho}_f + 1.6 \times 10^{-6}{\bar{\rho}_f}^2 (50 < \bar{\rho}_f < 400 \frac{kg}{m^3}) \tag{24}$$

3. Case study: Frost accumulation prediction on MCHX in a heat pump

With the help of the model described above, we can now analyze the frost accumulation by reviewing the air-side control volume of each segment. In the scope of this paper, the focus is to explore the frost thickness growth, the increase of frost density as well as the related frost thermal conductivity change on different locations of a MCHX. Furthermore, we want to compare the heat pump frost performance over two MCHX pass configurations: one pass and two-pass.

3.1 Heat pump system

The details of the system, a 3-ton R410A heat pump using a scroll compressor and thermal expansion valve (TXV), are described in [8] with only one replacement to the outdoor unit. A microchannel HX replaced the original tube-and-fin heat exchanger. Table 1 shows the dimensions of the microchannel heat exchanger.

Table 1: The one pass MCHX parameters

Refrigerant pass configuration	1 pass
Total number of flat tubes	48
Tube length (mm)	50
Tube pitch (mm)	2.54
Number of ports in a tube	10
Port height/width (mm/mm)	1/1
Fin type	Flat fin
Fins per inch	12

The operating condition of the heat pump follows the frost accumulation condition pursuant to ASHRAE Standard 116 (1995) [9]: the outdoor air condition is 1.7°C/0.7°C (dry bulb/wet bulb) and the indoor air condition is 21.1°C/13.2°C (dry bulb/wet bulb).

3.2 Prediction of frost growth, densification of MCHX

Since dynamic simulations require initial values to determine the solutions for the future time steps, the surface temperature, as shown in Figure 5, of MCHX is assumed to be 3K warmer than the incoming air at time 0. As vapor compression cycle starts, the refrigerant flowing inside the evaporator gradually cools the fin surface and in about 80 seconds, the fin surface temperature drops below the freezing point. It has to be noted that the system uses TXV to regulate the outlet superheat and thus, there will be an initial time region in which refrigerant temperature fluctuates, responding to the superheat adjustment by the TXV. This fluctuation is reflected on the surface temperature profile which rises and drops shortly after reaching sub-freezing temperature region. The surface temperature eventually stabilizes, and the last two segments are in superheated region. It needs to be noted that we only showed four out of ten segments' results for all plots in this section. This is because all simulation results show Segments 1 through 6, and Segments 7 and 8 have very similar predicted values. So, to clearly show the results and avoid putting a line on top of each other, we only reported the four segments that can best represent the trend of frost distribution. Figure 6 shows the frost growth in each MCHX segment. Segment 1 is the section closest to the inlet and Segment 10 is the section closest to the outlet, and the other segments fall in places in between. The frost starts to grow at about 80 seconds which coincides with the time at which surface temperature of the heat exchanger falls below the freezing point. The frost growth rate is very close to linear and its slope is determined by the frost surface temperature, and it is intuitive that the superheat region of the heat exchanger has the least amount of frost covered.

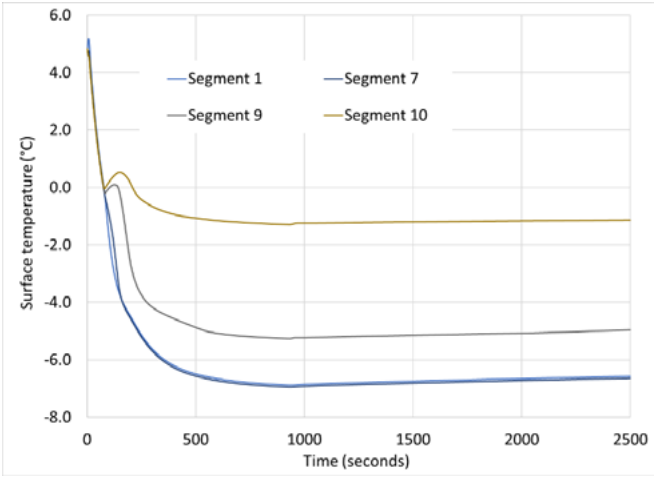


Figure 5: The surface temperature distribution over MCHX

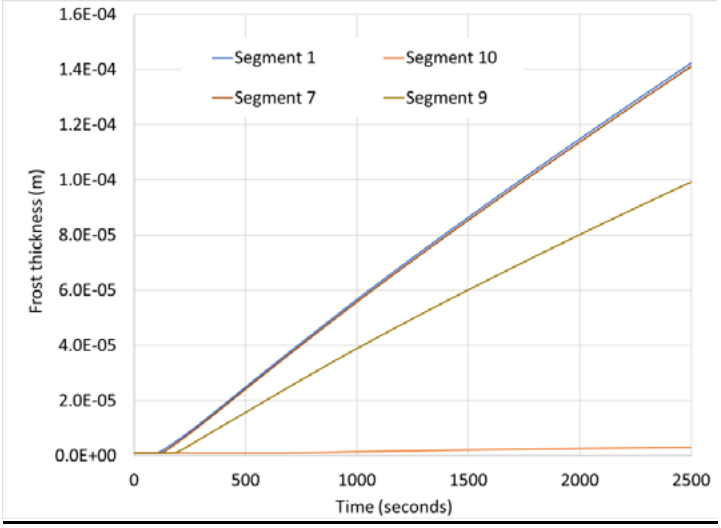


Figure 6: The frost thickness distribution over MCHX

Regarding the second aspect of frost accumulation, we use Figure 7 to examine the frost density distribution over the MCHX. To avoid any singularities, the initial frost density is assumed to be 30 kg/m^3 or 0.03 g/cm^3 [6,10]. Unlike the frost thickness growth, the frost densification process is non-linear and those segments closer to the evaporator outlet have slightly denser frost which are caused by the significantly smaller frost thickness. As shown in Figure 7, the densification of frost increases the frost thermal conductivity but such a level of increase is shadowed by the growth of frost thickness and, as as a result, the change of overall thermal resistance is dominant by the frost thickness growth.

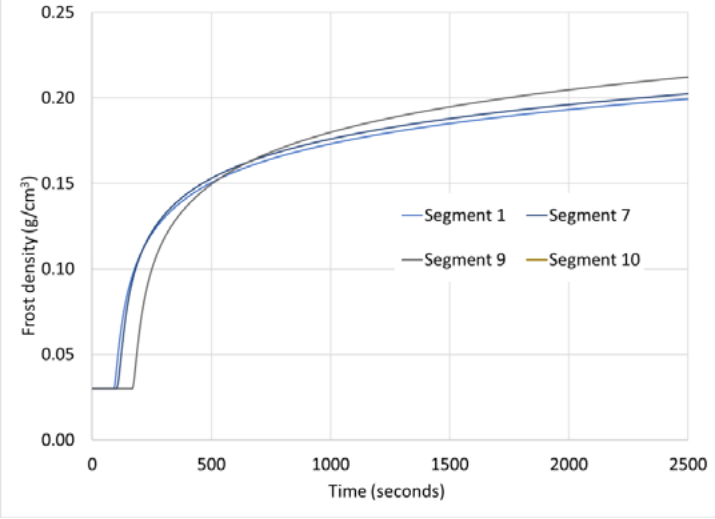


Figure 7: The frost density distribution over MCHX

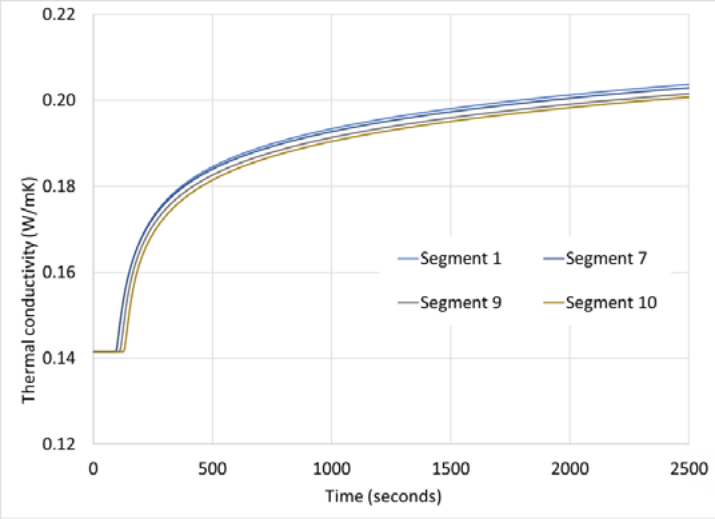


Figure 8: The frost thermal conductivity distribution over MCHX

To summarize, the increase in frost thickness will increase the thermal resistance between air and the refrigerant. The change in thermal conductivity due to frost densification plays a minor role in the change of thermal resistance. This can be observed by the fact that the change of thermal conductivity in Figure 8 is on relatively a smaller scale compared to the frost thickness growth. The net impact from both, the increase of frost thickness and frost density, is the increase of thermal resistance that impedes the heat transfer of air to refrigerant in the outdoor unit. The reduction of thermal conductive resistance is not the only reason for the cycle performance deterioration under frost conditions. As pointed out by Henry Barrow, there is yet another important factor contributing to the heat pump frost operation: air flow blockage. As frost grows among tubes and fins, the effective air flow passage becomes smaller, increasing the air-side pressure drop. Figure 8 depicts such a phenomenon. The air-side pressure drop doubles the amount than the non-frost value when assuming the air flow through the evaporator maintains constant. This also doubles the power of the fan in order to overcome the flow resistance. It has to be pointed out that in reality, the fan power usually remains constant and as a result, the air flow rate will decrease due to the increase of air side pressure drop. This further impairs the cycle capacity and COP. In the future, the current model will be improved by considering the air flow reduction during frost accumulation.

3.3 MCHX flow pass configuration to heat pump operation under frost condition

MCHXs are typically one or more passes as shown in Figure 9 [11]. By using a buffer (separator), refrigerant is restricted to flow into part of the tubes comprising the first pass, as opposed to flow into all tubes in the case of one pass. The refrigerant then turns 180° and flows into the rest of tubes comprised of the second pass. For an evaporator, the two-pass design expands the refrigerant as it turns into vapor, causing higher mass flux in tubes which may lead to better heat transfer and potentially higher pressure drop. However, since the air-side heat transfer remains dominant and such dominance is further amplified in the frost condition, the benefits of using two-pass over one-pass in heat transfer could be further depreciated. To make a closer examination, we established a two-pass MCHX that maintains all specifications of the one-pass design with the only modification that the flat tubes are divided into two passes: 8 tubes in the first pass and 40 tubes in the second pass.

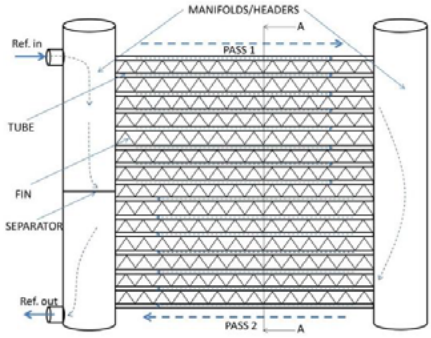


Figure 9: A sample view of Mircochannel Heat Exchanger

Figure 10 compares the pressure levels of the same heat pump system using one pass MCHX and two-pass MCHX. The two systems show almost identical pressure levels and only to compare the second digit after the decimal, one concluded that one-pass MCHX leads to both higher evaporating and condensing pressure levels. If we further compare the heat pump COP, which is demonstrated in Figure 11, we notice the COP is also similar and we have to compare the third digit after the decimal to conclude the two-pass MCHX leads a slightly larger heat pump performance. Such a close result is anticipated because the air-side condition is identical to the two evaporators and frost intensifies the air-side heat resistance dominance, meanwhile reduces the impact of better refrigerant-side heat transfer. In fact, at time when frost is yet to accumulate (t <80 seconds), we can notice the two pass MCHX cycle has a clearer edge in COP which disappears as frost builds up.

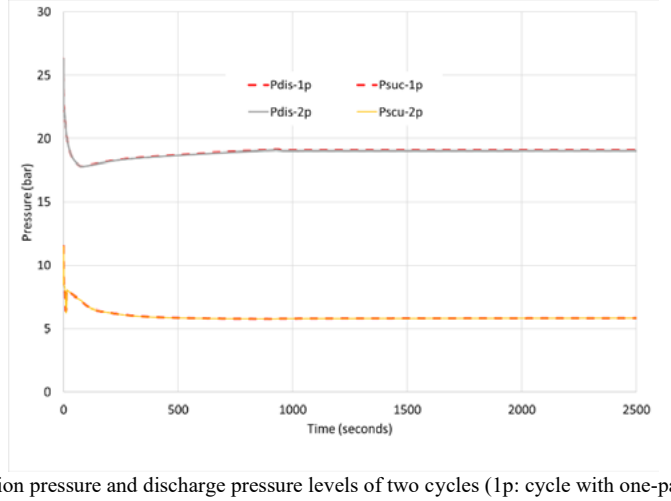


Figure 10: Suction pressure and discharge pressure levels of two cycles (1p: cycle with one-pass MCHX; 2p: cycle with two-pass MCHX)

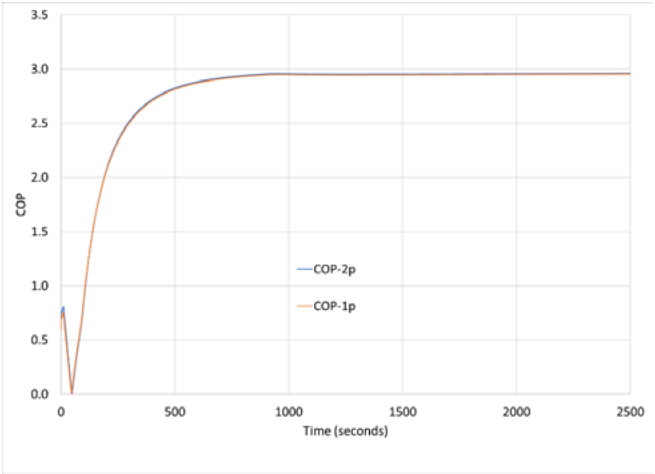


Figure 11: Coefficient of Performance (COP) of two cycles (1p: cycle with one-pass MCHX; 2p: cycle with two-pass MCHX)

4. Conclusions

The paper presents a numerical study on the operation of heat pump system with microchannel heat exchanger during frost accumulation. We modeled the microchannel heat exchanger using a segment-by-segment approach and lumped the multiple ports in the flat tube into one flow channel. The frost model is applied to the air-side control volume of the heat exchanger model so that it can be extended to other types of heat exchanger. We modeled the basic frost phenomena including frost densification and thickness growth. Through a set of case studies, we determined the frost growth on a heat exchanger depended mostly on the heat exchanger surface temperature. Regarding the heat transfer resistance due to frost accumulation, the thermal conductivity change due to the frost densification is apparently a secondary factor shadowed by the frost thickness growth. On a cycle-level comparison, we did not find significant performance enhancement by using a two-pass microchannel heat exchanger. We believe the dominance of air-side heat transfer resistance is further intensified by frost accumulation and as a result, the COP improvement from the two-pass MCHX is very much limited.

Acknowledgements

This work was supported by the Modeling and Optimization Consortium (MOC) at the University of Maryland.

References

[1] Khan M. G. and Fartaj A., 2011, A review on microchannel heat exchangers and potential applications.
[2] *Int. J. Energy Res.*, 35: 553–582
[3] Barrow H., 1985, A note on frosting of heat pump evaporator surfaces, *J. of Heat Recovery sys.*,
[4] 5 (3), 1985, 195-201
[5] Moallem E., Padhmanabhan S., Cremaschi L., Fisher D.E., 2010, Experimental study of onset and growth of rost on outdoor coils of air-srouce heat pump systems, *ASME-ATI-UIT 2010 Conference on Thermal and Environmental Issues in Energy Systems, 16-19 May, 2010, Sorrento, Italy*
[6] Padhmanabhan S., Fisher D.E., Cremaschi L., Moallem E., Modeling non-uniform frost growth on a fin-and-tube heat exchanger, *Int. J. of Ref.,* 34 (8), 2011, 2018-2030

[7] Li Z., Ling J., Aute V., Radermacher R., 2017, Investigation of Port Level refrigerant flow maldistribution in microchannel heat exchanger, 12th IEA Heat Pump Conference, Rotterdam, Netherland
[8] Qiao H., 2014, Transient modeling of two-stage and Variable Refrigerant Flow Vapor Compression Sytems with Frosting and Defrosting, PhD dissertation, University of Maryland, College Park
[9] Lee, J., Byun J.S., 2009, Experiment on the performance improvement of air-to-air heat pump adopting the hot gas bypss method by outdoor fan speed, Journal of Mechanical Science and Technology 23, 2009, 3407-3415
[10] Alabdulkarem Abdullah, Yunho Hwang, Reinhard Radermacher, 2013, System Drop-In Tests of Refrigerants R-32, D2Y-60, and L-41a in Air Source Heat Pump, *Air-Conditioning, Heating, and Refrigeration Institute Low-GWP Alternative Refrigerants Evaluation Program, Test report #20*, University of Maryland, College Park
[11] ASHRAE Standard 116 (1995) Methods of Testing for Rating Seasonal Efficiency of Unitary Air Conditioners and Heat Pumps
[12] Le Gall R., Grillot J.M., Jallut C., 1997, Modeling of frost growth and densification, International Journal of Heat Mass Transfer, Vol. 40, No. 13, pp. 3177-3187
[13] Mehendale S., Aute V., Radermacher R., Principles of refrigerant circuit optimization in single row microchannel condensers, 2014 Purdue Conference-Compressor short course, July 13, 2014

13th IEA Heat Pump Conference
April 26-29, 2021 Jeju, Korea

Performance evaluation of light commercial air conditioning and heat pump system using low GWP refrigerants

Hughes Joshua[a*], Minsoo Kim[b]

[a]The Chemours Company, 1007 Market Street P.O. Box 2047, Wilmington, Delaware 19899, USA
[b]LG Electronics, LG Electronics 2nd factory Seongsan-dong Seongsan-gu, Changwon-si 51554, KOREA

Abstract

Concerns about global climate change and potential legislation that may impact the use of refrigerants with high global warming potential (GWP) have accelerated the development of new refrigerants with reduced impact on climate change. Along with the Kigali amendment to the Montreal Protocol to phase down use of HFCs, there are regulations around the world with specific GWP limits for air conditioning and heat pump applications. The most common refrigerant used globally in residential and light commercial air conditioning systems and heat pumps is R410A, with a GWP of 2088. Regulations are already in place to limit the GWP to below 750 in many regions globally, and there may be further reductions needed in the future. This paper discusses alternative fluids that have been developed to most nearly meet the most often cited requirements for environmental, physical, and performance properties for air conditioning and heat pump applications. R454B, with a GWP of 466 and both performance and properties similar to R410A, is a potential alternative to meet these requirements while maintaining compatibility with systems similar to those of existing R410A designs to enable an orderly transition to lower GWP. Performance will be evaluated in a light commercial air conditioning and heat pump system and compared with R410A at both standard air conditioning and heating operating conditions. These refrigerants are shown to provide useful options to help maintain the quality of life and health benefits from air conditioning and refrigeration, but in an energy efficient, cost-effective, and environmentally sustainable manner.

© HPC2020.
Selection and/or peer-review under responsibility of the organizers of the 13th IEA Heat Pump Conference 2020.

Keywords: GWP; R454B; refrigerant; air conditioning; heat pump; DR-5A; XL41; R32

Nomenclature

GWP Global warming potential
C_v Isochoric specific heat, kJ/kg-K
EEV Electric expansion valve
DB Dry bulb temperature, ºC
SEER Seasonal energy efficiency ratio, Wh/Wh
COP Coefficient of performance
C_p Isobaric specific heat, kJ/kg-K
EER Energy efficiency ratio, W/W
ErP Energy-related Products Directive
WB Wet bulb temperature, ºC
SCOP Seasonal coefficient of performance, Wh/Wh

1. Introduction

The current generation refrigerant for residential air conditioning and heat pumps, R410A, has a global warming potential (GWP) of 2088 [1] and is subject to regulations in many regions globally. R-410A is a

* Hughes, Joshua Tel.: +1-302-683-8275; fax: +1-302-683-8255.
E-mail address: joshua.hughes@chemours.com

non-flammable mixture of 50 wt% R32 and 50 wt% R125. R32 has been proposed for many years as an alternative refrigerant which has about 70% lower GWP than R410A and high cooling capacity. Therefore, many manufacturers have optimized some air conditioning products for the adoption of R32, with millions of air conditioning units using R32 as a refrigerant sold throughout Asia, New Zealand, Australia, US and Europe. However due to the Kigali amendment and F-gas regulation, as shown in Fig. 1, CO_2 emissions would need to be reduced significantly over time from previous baseline emissions. Therefore, R32 is likely not an ultimate solution to meet regulations for the future.

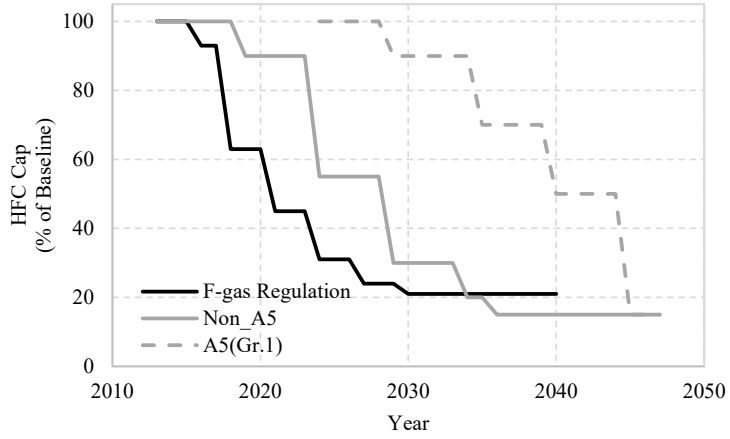


Fig. 1. HFC Phase-Down Steps of EU and Kigali Amendment (2016)

The HVAC&R industry has been searching for alternative refrigerants to help meet these new and anticipated future regulations. R454B, also known as DR-5A or XL41, is a low GWP replacement for R410A which provides similar capacity and energy efficiency to R410A. R454B is a mixture containing 68.9 wt% R32 and 31.1 wt% of HFO-1234yf. As shown in Table 1, R454B has a 100-year GWP (AR4) of 466 which could allow it to become a longer term solution to meet CO_2 reduction targets than other higher GWP candidates. Pressure of R454B is slightly lower than that of R410A and R32 at the same operating temperatures. Also, its lower liquid density contributes to the mass of refrigerant charge of R454B in an equivalent air conditioning or heat pump system that would be lower than that of R410A.

R454B is a mildly flammable refrigerant and has a received a safety classification of A2L under ASHRAE SSPC 34 [2]. The specific heat ratio is slightly higher for R454B compared to R410A, contributing to compressor discharge temperature of R454B that is slightly higher than that of R410A but well below the discharge temperatures of R32. Therefore, R454B is a potential alternative to meet environmental, physical and performance requirements while maintaining compatibility with systems similar to existing R410A designs.

Previous research of R454B has shown that R454B is a design-compatible replacement candidate for R410A. Schultz et al. [3] performed tests on a 4 RT (14 kW) rooftop heat pump to evaluate the performance of lower GWP refrigerants as alternatives to R410A in unitary air-conditioning and heat pump equipment. Minamida et al. [4] evaluated the system performance using R454B for VRF and mini-split air conditioner and observed R454B to have better COP than R410A. Also, previous testing by Hughes et al. [5] in a unitary ducted split air conditioning and heat pump system designed for R-410A has shown has similar cooling capacity and energy efficiency to R-410A.

Table 1. Property and performance comparison of refrigerants (ASHRAE-T condition, isentropic efficiency = 0.75)

Refrigerant	R410A	R32	R454B
GWP(AR4)	2088	675	466
Safety classification	A1	A2L	A2L
Condensing pressure [kPa]	3393	3473	3204
Evaporating pressure [kPa]	998	1018	913
Latent heat [kJ/kg]	159 (100%)	242 (152%)	194 (122%)
Volumetric capacity [kJ/m^3]	5646 (100%)	6236 (110%)	5378 (95%)
Discharge temperature [°C]	94	115	102
Cp/Cv (specific heat ratio)	1.412	1.514	1.414
Density suction [kg/m^3]	35.5	25.7	27.7
Density condenser [kg/m^3]	870.8 (100%)	812.2 (93%)	830.5 (95%)
Displacement volume [cm^3/rev]	31.6	31.6	31.6
Mass flow rate [kg/s]	0.065 (100%)	0.047 (72%)	0.050 (78%)
Cooling capacity [kW]	10.26 (100%)	11.33 (110%)	9.77 (95%)
Work [kW]	3.09 (100%)	3.33 (108%)	2.96 (96%)
EER [W/W]	3.32 (100%)	3.40 (102%)	3.30 (100%

2. Details of test setup

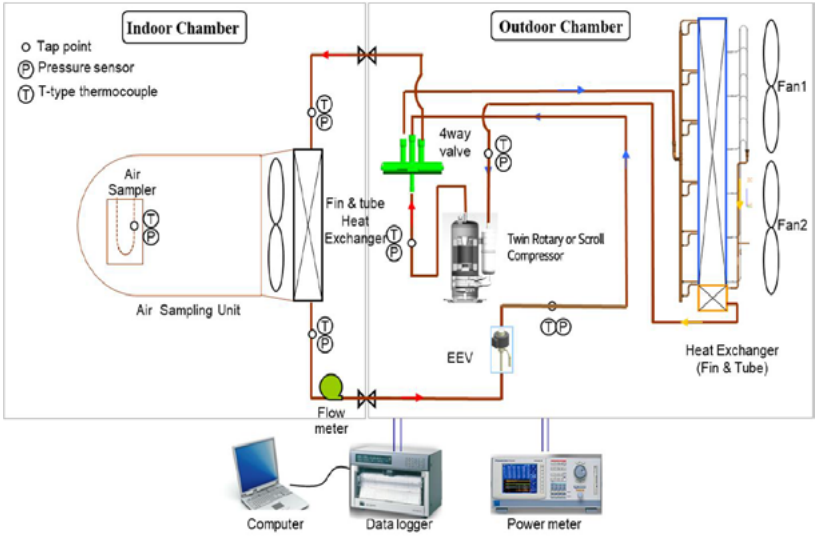


Fig. 2. Calorimeter layout for ceiling-mounted system (arrows show direction of refrigerant flow in space heating operation)

The wall-mounted type and ceiling-mounted type air conditioners commonly used in non-ducted air conditioning and heat pump systems were used to compare the performance of R410A replacement candidates. The specifications of each of the products are detailed in Table 2. The wall-mounted type air conditioner consists of an inverter rotary compressor for a conventional system and inverter twin rotary compressor for the modified system. Both the conventional and modified systems have two fin-tube type heat exchangers, one indoor fan, one outdoor fan, a 4-way reversing valve and EEV. The ceiling-mounted type air conditioner consists of inverter twin rotary compressor for the conventional system and an inverter scroll compressor for the modified system. Both systems have two fin-tube type heat exchangers, one indoor fan, two outdoor fans, a 4-way reversing valve and EEV.

Table 2. Specification of products

Product	Wall-mounted type	Ceiling-mounted type
Capacity	12kBtu/hr	48kBtu/hr
Compressor	Inverter Twin Rotary	Inverter Scroll
	10.6cm^3/rev	31.6cm^3/rev
Indoor heat exchanger	Φ7 2R 15C 21FPI	Φ7 2R 12C 21FPI Louver L2084mm
	S-Fin(Half) L616.8mm	+ Φ7 1R 10C 21FPI Louver L1930mm
Outdoor heat exchanger	Φ7 2R 22C 18FPI Louver fin L667mm	Φ7 2R 64C 14FPI Wide Louver L950mm
EEV orifice inner diameter [mm]	Φ1.65	Φ2.0

The baseline R410A test, R32 test and R454B tests have been completed as per ISO 13253 in a psychrometric calorimeter chamber at the conditions shown in Table 3 with the layout of the test apparatus detailed in Fig. 2 (ceiling-mounted schematic shown; wall-mounted system layout was similar). Each experimental parameter was recorded using a data acquisition system after the system reached a quasi-steady state. It was determined that the system is in the quasi-steady state when the measured parameters of the cycle do not change for 15 minutes after the change of the experimental conditions, such as the change of the compressor frequency. Then experimental data were recorded for 35 minutes at intervals of 5 seconds. The temperatures of the indoor chamber and the outdoor chamber were controlled in the range of -35-60ºC and 0-50ºC, respectively. Dry and wet bulb temperatures of the two chambers were controlled within the range of ±0.1ºC. All temperatures in the system are monitored using T-type thermocouples. The accuracy of the temperature measurements is estimated to be ± 0.2ºC.

Table 3. ErP test conditions and extra test conditions (EN14511 – Rated conditions, EN14825 – Part load conditions)

Conditions		Indoor		Outdoor	
		DB[ºC]	WB[ºC]	DB[ºC]	WB[ºC]
Cooling mode at rated condition		27	19	35	24
Heating mode at rated condition		20	15	7	6
SEER	Cooling A	27	19	35	24
	Cooling B			30	20
	Cooling C			25	16
	Cooling D			20	12
SCOP	Heating A	20	15	-7	-8
	Heating B			2	1
	Heating C			7	6
	Heating D			12	11
	Heating E			-10	-11
	Heating F			-8	-9
Cooling overload		32	23	48	29
		32	19	54	32
Heating low temperature		20	15	-5~-25	-

SEER is seasonal efficiency of a unit calculated for the reference annual cooling demand, which is determined from mandatory conditions given in this European Standard and used for marking, comparison and certification purposes. SCOP is seasonal efficiency of a unit calculated for the reference annual heating demand(s), which is determined from mandatory conditions given in this European Standard and used for marking, comparison and certification purposes.

The heating D condition is the lowest part load ratio condition. Therefore, to meet the part load of heating D condition, the frequency (Hz) of the compressor should be very low. It can miss the operational range of the compressor so the efficiency of the product may decrease despite having lower power consumption.

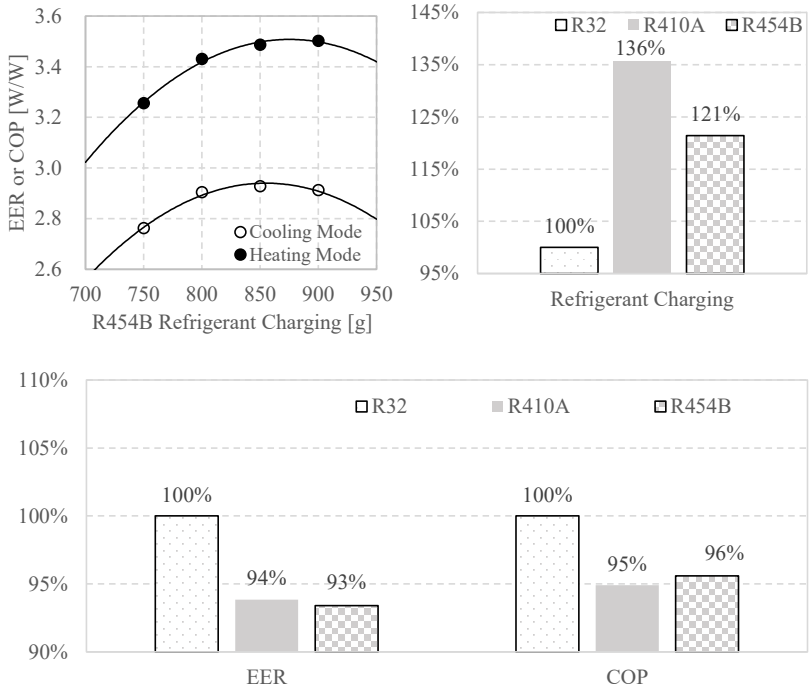
3. Results and discussions

3.1. Wall-mounted type air conditioner with inverter rotary compressor

As shown in Table 4 and Fig.3, R454B refrigerant charge size is 11% lower than the R410A charge. The R32 refrigerant charge size is 26% lower than R410A charge. The EER and COP of R454B are almost same with those of R410A. The EER and COP is 7% and 5% higher respectively for R32 compared to R410A. The discharge temperature of R454B is 5ºC higher than that of R410A in cooling standard condition and 4ºC higher than that of R410A in heating standard condition. The discharge temperature of R32 is 12ºC higher than that of R410A in cooling standard condition and 11ºC higher than that of R410A in heating standard condition.

Table 4. Comparison of performance (wall-mounted type)

Refrigerant	Refrigerant Charging [g]	Cooling mode (3.5kW at rated condition) EER [W/W]	Discharge Temperature [ºC]	Heating mode (4.0kW at rated condition) COP [W/W]	Discharge Temperature [ºC]
R410A	950	2.94	73	3.46	76
R32	700	3.14	85	3.65	87
R454B	850	2.93	78	3.49	80



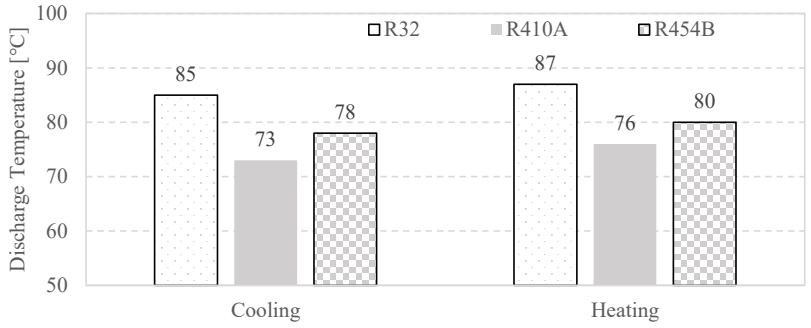


Fig. 3. Performance test results at rated conditions (wall-mounted type)

As shown in Fig. 4, as the ambient temperature increases in cooling condition and decreases in heating condition, R454B shows higher reduction of cooling capacity than R410A because of the higher discharge temperature. At high ambient temperature in cooling mode and cold climate condition in heating mode, buildings require high cooling and heating demand. So, in those conditions, it may be desired for the air conditioning system to increase the compressor frequency of an inverter compressor. When the inverter system is used in those conditions, the compressor frequency is limited by discharge temperature. The discharge temperature of compressor is affected by specific heat ratio (C_p/C_v) and the specific heat ratio of R454B is higher than that of R410A. Also, the molar mass of R454B is smaller than that of R410A, so the effect of refrigerant leakage in the compressor is larger for a R454B system compared to a R410A system. This could cause the reduction of volumetric efficiency of the compressor and higher discharge temperature. Thus, the capacity of R454B system decreases more abruptly than that of R410A in those conditions because of the higher discharge temperature.

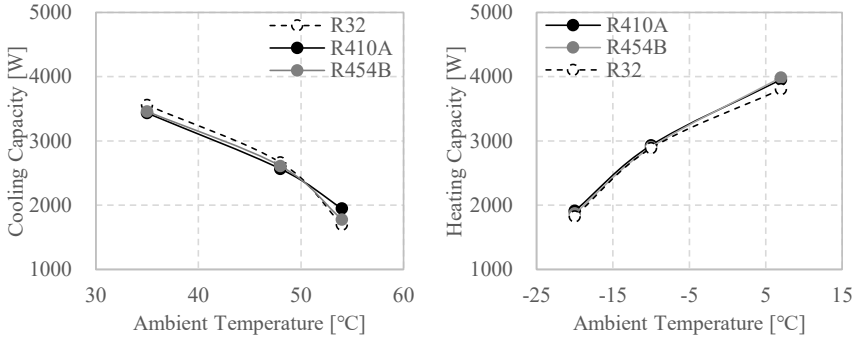


Fig. 4. The capacity comparison at high ambient temperature in cooling mode and cold climate condition in heating mode (wall-mounted type)

As shown in Fig. 5, The SEER is 2% higher and SCOP is almost equal for R454B compared to R410A. The SEER is 6% higher and SCOP is almost equal for R32 compared to R410A.

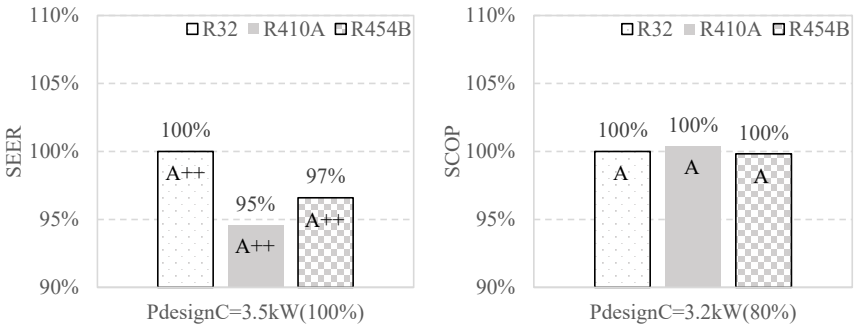


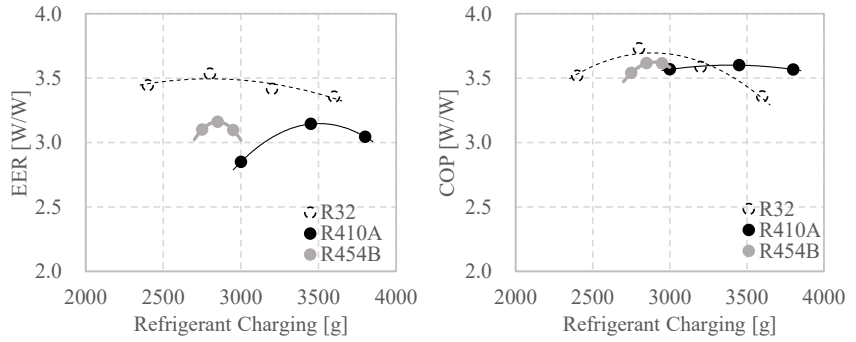
Fig. 5. Cooling and heating seasonal performance (wall-mounted type)

3.2. Ceiling-mounted type air conditioner with inverter scroll compressor

As shown in Table 5 and Fig. 6, R454B refrigerant charge size is 14% lower than the R410A charge and R32 refrigerant charge size is 19% lower than R410A charge. The EER and COP is 1% and 4% higher respectively for R454B compared to R410A. The EER and COP is 12% and 7% higher respectively for R32 compared to R410A. The discharge temperature of R454B is 6°C higher than that of R410A in cooling standard condition and 7°C higher than that of R410A in heating standard condition. The discharge temperature of R32 is 10°C higher than that of R410A in cooling standard condition and 20°C higher than that of R410A in heating standard condition.

Table 5. Comparison of performance (ceiling-mounted type)

Refrigerant	Refrigerant Charging [g]	Cooling mode (14.0kW at rated condition) EER [W/W]	Discharge Temperature [°C]	Heating mode (16.0kW at rated condition) COP [W/W]	Discharge Temperature [°C]
R410A	3450	3.14	66	3.50	73
R32	2800	3.53	86	3.73	83
R454B	3950	3.19	81	3.62	79



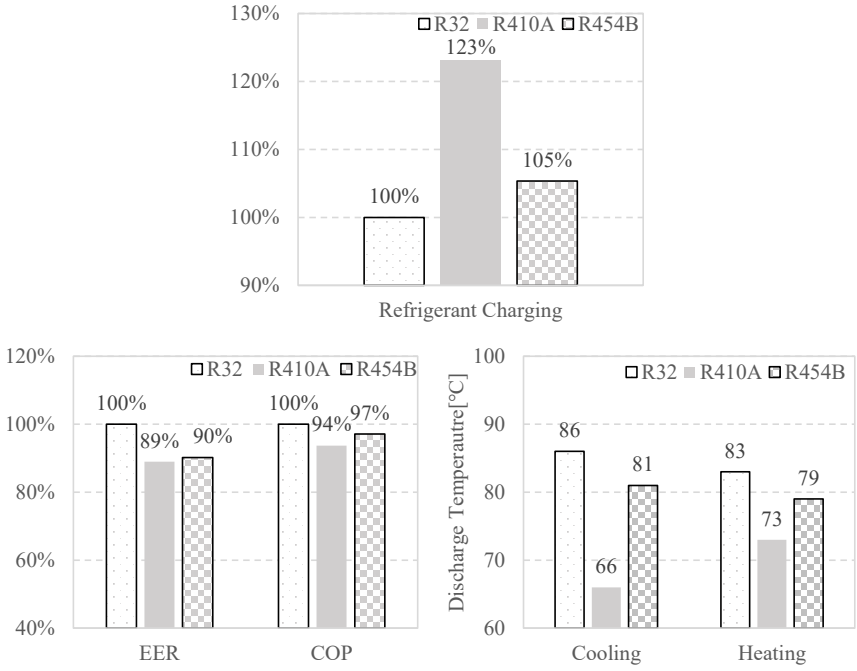


Fig. 6. Performance test results at rated conditions (ceiling-mounted type)

As shown in Fig. 7, as the ambient temperature increases in cooling condition and decreases in heating condition, R454B again shows higher reduction of cooling capacity than R410A because of the higher discharge temperature. Because of compressor current limitations, the maximum heating capacity of R32 is lower than that of R410A and R454B at the ambient temperature of 7°C.

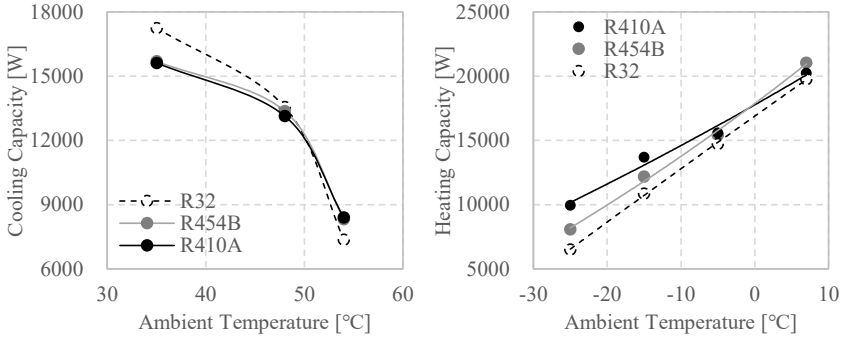


Fig. 7. The capacity comparison at high ambient temperature in cooling mode and cold climate condition in heating mode (ceiling-mounted type)

As shown in Fig. 8, the SEER and SCOP are 1% higher for R454B compared to R410A. The SEER and SCOP is 7% and 2% higher respectively for R32 compared to R410A.

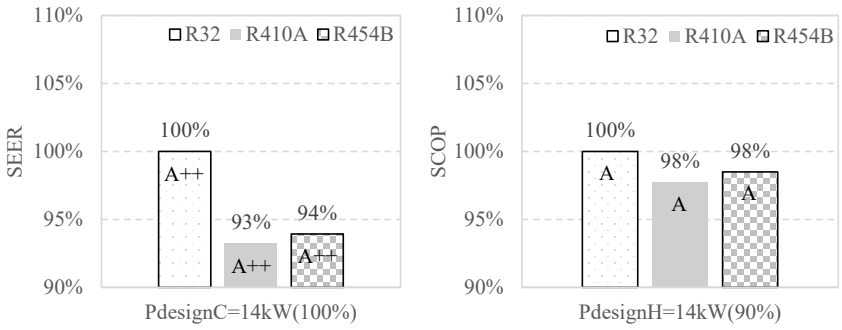


Fig. 8. Cooling and heating seasonal performance (ceiling-mounted type)

4. Conclusions

The performance of low GWP refrigerant alternatives for R410A was evaluated in light commercial air conditioning and heat pump systems and compared with R410A. Performance was tested in both wall-mounted and ceiling-mounted air conditioning and heat pump equipment. The energy efficiency and discharge temperature of R454B are slightly higher than R410A. The capacity of R32 was also higher in conjunction with higher discharge temperature, primarily because of the high value of specific heat ratio and small molar mass. As the ambient temperature increases in cooling condition and decreases in heating condition, the capacity of R32 system abruptly decreases because of the high discharge temperature.

The performance of R32 and R454B suggest they could be lower GWP alternatives to R410A in air conditioning and heat pump systems. Because of its similar properties and performance characteristics to R410A, R454B could be compatible in new system designs that are similar to R410A equipment. As research to develop replacement refrigerants for R410A has been on-going for several years, many small air conditioning and heat pump systems in Asia and Europe using R410A are being transitioned to R32. However the GWP of R32 may be too high to meet phasedowns being proposed around the world to reduce global warming over the long term. R454B is well-positioned to replace R410A with both good energy performance and with a lower GWP that could enable it to be a viable option further into the future. The lower GWP of R454B could enable it to be a promising long-term solution to help meet global CO_2 emissions goals and reduce the potential impact on the environment.

Acknowledgements

The authors gratefully acknowledge Chemours Refrigerants and LGE for their contributions and support this research and development work.

References

[1] IPCC. Jallow, B.P., L. Kajfez-Bogataj, R. Bojaru, D. Hawkins, S. Diaz, H. Lee, A. Allali, I. Elgizouli, D. Wratt, O. Hohmeyer, D. Griggs, and N. Leary (eds.). Intergovernmental Panel on Climate Change Fourth Assessment Report – Climate Change 2007: Synthesis Report. <http://www.ipcc.ch/ipccreports/ar4-syr.htm>.

[2] ANSI/ASHRAE Standard 34-2016. Designation and Safety Classification of Refrigerants. American Society of Heating, Refrigerating and Air-Conditioning Engineers (ASHRAE), Atlanta, GA, 2016.

[3] Schultz K, Perez-Blanco M, Kujak S. System Soft-optimization Tests of Refrigerant R-32, DR-5A, and DR-55 in a R-410A 4-ton Unitary Rooftop Heat Pump-Cooling Mode Performance. AHRI AREP, test report # 56, 2015.

[4] Minamida T, Iwata I, Kumakura E, Furusho K, Haikawa T, Taira S. Evaluation and Optimization of System Performance using HFO-mix Refrigerants for VRF and Mini-Split Air-Conditioner. 17th International Refrigeration and Air Conditioning Conference at Purdue; 2018.

[5] Hughes J, Shah S. Testing of Low GWP Replacements for R-410A in Stationary Air Conditioning. 16th International Refrigeration and Air Conditioning Conference at Purdue; 2016.

Disclaimer

The information set forth herein is furnished free of charge and based on technical data that Chemours believes to be reliable. It is intended for use by persons having technical skill, at their own risk. Since conditions of use are outside our control, we make no warranties, expressed or implied and assume no liability in connection with any use of this information. Nothing herein is to be taken as a license to operate under, or a recommendation to infringe any patents or patent applications.

13th IEA Heat Pump Conference
April 26-29, 2021 Jeju, Korea

A parameter-estimation model for variable refrigerant flow heat pump systems

Aziz Mbaye[a*], Massimo Cimmino[a]

[a]Department of Mechanical Engineering, Polytechnique Montréal, 2900 Edouard Montpetit Blvd, Montreal H3T 1J4, Canada

Abstract

A variable refrigerant flow (VRF) model based on a simplified vapor compression cycle is presented. The outdoor unit and the indoor units are modelled separately. An optimization procedure is used to identify their parameters by minimizing the differences between the model predicted capacities and power input and manufacturer data. Calibration results show a root mean square error (RMSE) in range of 4%, 8.8% and 7.3% for the indoor unit total capacity, the outdoor unit capacity and power consumption respectively. Three configurations of VRF heat pump are evaluated using previously calibrated indoor unit and outdoor unit models. The results show that the model-predicted cooling capacity and power input are close to the manufacturer data with an average RMSE of 2.2% for both the power input and the cooling capacity.
Keywords: Variable refrigerant flow; Modelling and simulation, Model calibration

1. Introduction

Variable refrigerant flow (VRF) heat pump systems are growing in popularity for heating and cooling applications in buildings. When equipped with a heat recovery unit, VRF systems can provide simultaneous heating and cooling, with high efficiency, to different zones of the same building. To support their development, facilitate their design and evaluate their performance, simulation tools that model their behavior are necessary.

Lin et al. [1] gave a substantial review of recent development in modelling VRF heat pumps. VRF models range from detailed physics-based models to equation-fit models with varying levels of accuracy. Yan et al [2] developed a physical-based model for dual-evaporator air conditioning systems, including the effects of the pressure drop and the refrigerant piping length in the system performance. The model was developed by adding a second evaporator to an existing single-evaporator air conditioning system model. Hong et al. [3] developed a physical-based VRF model in EnergyPlus. The model validation using field test results of an instrumented house showed that the error associated with the VRF power demand is in range of 10%. Zhu et al. [4] implemented a modular transient VRF model in TRNSYS. Results showed an average deviation between simulation results and experimental data of 7.9%, 12.5% and 6.2% for the capacity, the power input and the coefficient of performance (COP), respectively. Cheung and Braun [5] proposed a component based gray box model for ductless multi-split systems with a variable frequency compressor. Parameters are first tuned using experimental data and then applied to the model. Comparisons between experimental data and simulation results after parameter tuning showed that the error in the power consumption is in range of 8%. More recently, Sun et al. [6] developed a general VRF model using graph theory. The model can simulate systems with arbitrary layouts and under various operating conditions including partial load operation. The model is validated using experimental data and the results showed deviations of 3% and 3°C for the capacity and the indoor unit (IU) temperature, respectively. While physical-based models have been shown to predict VRF behavior with acceptable accuracy, they are not widely used in energy simulation software such as EnergyPlus. They require inputs that are not readily provided in manufacturer literature and are typically computationally expensive. Some authors have proposed empirical equation-fit models using performance curves based on manufacturer data. Raustad [7] developed an equation-fit model implemented in EnergyPlus. A comparison of the model predicted energy use against field test results showed that the error is in range of 25% overall [8].

* Corresponding author. Tel.: +1-514-340-4711.
E-mail address: aziz.mbaye@polymtl.ca.

Kim et al. [9] showed that a proper calibration of Raustad's model can improve its accuracy. Experiments in an office building showed that the error decreased from 32.3% to 15.7% for the non-calibrated and calibrated models, respectively. Torregrosa-Jaime et al. [10] have developed an improved equation fit-model based on Raustad's model that adjusts better to the manufacturer data. They proposed to evaluate the VRF power consumption directly as a function of the operating temperatures and the partial load ratio (PLR) while the original model uses intermediate parameters that are inferred from the manufacturer data (i.e. energy input ratio as function of the temperature, energy input ratio as function of the PLR). For partial load operation, the model still loses accuracy and shows considerable variations with the manufacturer's data.

This paper presents the development of a model for the simulation of VRF heat pump systems based on a simplified thermodynamic cycle. The indoor units (IU) and the outdoor units (OU) that form the VRF heat pump are modelled independently so that various VRF configurations with multiple IUs can be evaluated. Model parameters are inferred from a parameter-estimation procedure on available manufacturer data to minimize the error between the model-predicted performance metrics (e.g. capacity, power input) and the performance data from the manufacturer. Calibrated OU an IU models are then assembled into various VRF system configurations.

2. Methodology

The VRF model is based on a simplified vapor compression cycle as proposed by Jin [11]. The benefit in such cycle is to reduce the number of the model parameters in order to facilitate the calibration process and to reduce the computational time since only few refrigerant states are required. Here, the Martin-Hou equation of state for R410A is used to evaluate the thermodynamic parameters of the refrigerant [12]. Figure 1 presents a pressure-enthalpy diagram of the simplified vapor compression cycle that relies on the following assumptions:

- There is no subcooling in the condenser; the refrigerant leaves the condenser (point B) in a saturated liquid state.
- The refrigerant leaving the evaporator (point C) is in a superheated vapor state with a constant degree of superheating.
- The sensible heat transfer (from point A to point C) in the evaporator is neglected, as it is small compared to the latent heat transfer.
- The expansion process through the electronic expansion valve (EEV) is isenthalpic.
- The pressure drops within the heat exchangers as well as those in the refrigerant pipes are neglected.

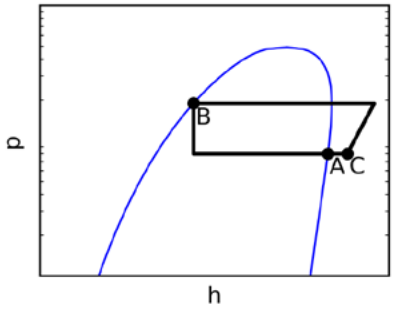


Fig. 1. P-h diagram of the simplified vapor compression cycle

3. Variable refrigerant flow heat pump model

3.1. Indoor unit model

The IU is likened to an air-refrigerant heat exchanger operating at a constant refrigerant temperature. The model parameters are the inside and the outside surface heat transfer coefficients (UA_{in} and $h_c A_{out}$). As shown in Figure 2, the model requires as inputs the air mass flow rate ($\dot{m}_{IU}$), dry bulb temperature ($T_{DB,IU}$), wet bulb temperature ($T_{WB,IU}$) and the total capacity ($\dot{q}_{IU}$). The outputs of the model are the sensible and latent capacities ($\dot{q}_{sen,IU}$ and $\dot{q}_{lat,IU}$) and the refrigerant evaporating (in cooling mode) or condensing (in heating mode) temperature (T_{ref}).

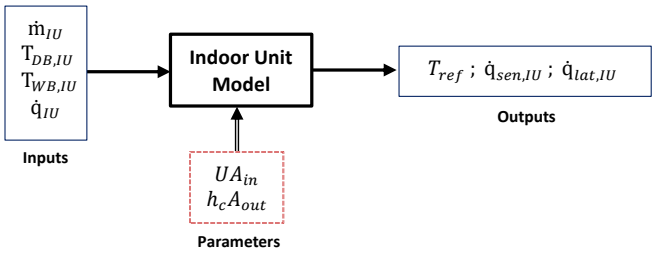


Fig. 2. Indoor unit model: parameters, inputs and outputs

The heat exchanger efficiency is calculated by the ε-NTU method:

$$UA = \frac{1}{\frac{1}{h_c A_{out}} + \frac{1}{UA_{in}}} \tag{1}$$

$$\text{NTU} = UA/\dot{m}_{IU} c_{p,a} \tag{2}$$

$$\varepsilon = 1 - e^{(-NTU)} \tag{3}$$

where NTU is the number of transfer units, UA is the global heat transfer coefficient, ε is the heat exchanger efficiency, and $c_{p,a}$ is the specific isobaric heat capacity of the moist air.

When the indoor unit operates as an evaporator (i.e., in cooling mode), condensation may occur at the outside surface of the cooling coil. Depending on the operating conditions, the cooling coil may be fully dry, fully wet or partially wet, and each case will affect the heat transfer coefficient. Therefore, the model of the IU should take account of whether it operates as an evaporator or condenser. In heating mode, there is no condensation and the IU operates as a sensible heat exchanger. The heat transfer rate is given by:

$$\dot{q}_{IU} = \varepsilon \cdot \dot{m}_{IU} c_{p,a} \left(T_{DB,IU} - T_{ref}\right) \tag{4}$$

In cooling mode, the outside surface of the coil is considered to be fully wet as proposed by Jin [11]. The heat exchanger behavior follows the enthalpy potential method. The total heat transfer from the air stream to the coil surface is a combination of sensible heat transfer ($\dot{q}_{sen,IU}$) and latent heat transfer ($\dot{q}_{lat,IU}$):

$$\dot{q}_{IU} = \dot{q}_{sen,IU} + \dot{q}_{lat} \tag{5}$$

$$\dot{q}_{IU} = \varepsilon_{eff} \dot{m}_{IU} \left(h_a - h_{a,e}\right) \tag{6}$$

$$\varepsilon_{eff} = 1 - e^{(-NTU_{eff})} \tag{7}$$

$$\text{NTU}_{eff} = UA_{eff}/\dot{m}_a c_{p,a} \tag{8}$$

where UA_{eff} is the effective heat transfer coefficient for the total (i.e. sensible and latent) heat transfer, h_a is the enthalpy of the moist air evaluated at the inlet air dry bulb and wet bulb temperature ($T_{DB,IU}$ and $T_{WB,IU}$), $h_{a,e}$ is the enthalpy of the moist air at the refrigerant evaporating temperature (T_{ref}), ε_{eff} and NTU_{eff} are the corresponding heat exchanger effectiveness and number of transfer units, respectively.

The effective heat transfer coefficient UA_{eff} is given by:

$$UA_{eff} = \frac{1}{\frac{1}{h_c A_{out}} + \frac{c_{p,a,s}}{c_{p,a}} \frac{1}{UA_{in}}} \tag{9}$$

where $c_{p,a,s}$ is the specific isobaric heat capacity of saturated air evaluated at the coil effective surface temperature.

The sensible heat transfer rate is evaluated analogically to a sensible heat exchanger from the outside surface heat transfer coefficient, considering a uniform coil surface temperature:

$$\dot{q}_{sen,IU} = \varepsilon' \dot{m}_{IU} c_{p,a} \left(T_{DB,IU} - T_{surf}\right) \quad (10)$$

$$\varepsilon' = 1 - e^{(-NTU_a)} \quad (11)$$

$$\mathrm{NTU}_a = h_c A_{out} / \dot{m}_{IU} c_{p,a} \quad (12)$$

where NTU_a is the number of air side transfer units, ε' is the air side effectiveness and T_{surf} is the effective surface temperature of the coil, which corresponds to the moist air dry bulb temperature at the coil.

The effective surface temperature is inferred from the corresponding enthalpy of saturated air $h_{a,s}$:

$$h_{a,s} = h_a - \dot{q}_{IU} / \dot{m}_{IU} \varepsilon' \quad (13)$$

3.2. Outdoor unit model

The OU model is based on the simplified heat pump cycle previously presented in Figure 1. It consists of two components: a compressor and a heat exchanger. The heat exchanger model is the same as presented in section 3.1 for the indoor units. Depending on the operation mode, it is considered as a sensible heat exchanger (i.e., condenser in cooling mode) or as a latent/sensible heat exchanger (i.e., evaporator in heating mode). Frost accumulation is not considered in the model. Figure 3 shows a schematic chart of the OU model with its parameters, inputs and outputs.

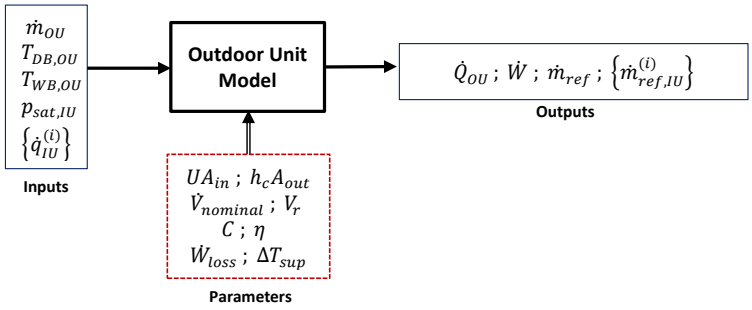


Fig. 3. Outdoor unit model: parameters, inputs and outputs

The scroll compressor is modelled according to Jin [11]. The compressor work is a result of isentropic compression at the built-in volume ratio followed by isochoric compression to the discharge pressure as described by Winandy et al. [13]:

$$\dot{W}_t = \frac{\gamma}{\gamma - 1} p_{eva} \dot{V}_{nominal} \left(\frac{\gamma}{\gamma - 1} \frac{p_{con}}{p_{eva} V_r} + \frac{1}{\gamma} p_r^{\frac{\gamma}{\gamma - 1}} - 1 \right) \quad (14)$$

where $\dot{W}_t$ is the theoretical compressor work, p_{eva} and p_{con} are the evaporating and condensing pressure, γ is the isentropic exponent of the refrigerant at the suction of the compressor, $\dot{V}_{nominal}$ is the nominal refrigerant volume flow rate, V_r is the built-in volume ratio between the discharge and the suction of the compressor and $p_r = V_r^{\gamma}$ is the built-in pressure ratio. In cooling mode, p_{con} is the refrigerant pressure in the OU heat exchanger and $p_{eva} = p_{sat,IU}$ is the pressure in the IU. In heating mode, $p_{con} = p_{sat,IU}$ is the refrigerant pressure in the IU and p_{eva} is the pressure in the OU heat exchanger.

The power input of the compressor is given by:

$$\dot{W} = \frac{\dot{W}_t}{\eta} + \dot{W}_{loss} \tag{15}$$

where η is the electromechanical efficiency of the compressor and $\dot{W}_{loss}$ are constant power losses.

Since the sensible heat transfer to the refrigerant is neglected in the evaporator, the evaporator heat transfer rate is evaluated from the enthalpy difference between points A and B of Figure 1:

$$\dot{Q}_{eva} = \left(\frac{\dot{V}_{nominal}}{v_{suc}} - \dot{m}_{leak}\right)(h_A - h_B) \tag{16}$$

where $\dot{Q}_{eva}$ is the total evaporator heat transfer rate, v_{suc} is the specific volume at the suction of the compressor, $\dot{m}_{leak}$ is the leakage mass flow rate in the compressor. Based on Chen et al. [14], the leakage mass flow rate can be estimated as a function of the condensing and evaporating pressures:

$$\dot{m}_{leak} = C\, p_{con}/p_{eva} \tag{17}$$

where C is the leakage coefficient. The total condenser heat transfer rate, $\dot{Q}_{con}$, can then be obtained by an energy balance:

$$\dot{Q}_{con} = -\left(\dot{Q}_{eva} + \dot{W}\right) \tag{18}$$

In cooling mode, $\dot{Q}_{con}$ and $\dot{Q}_{eva}$ are the OU heat rejection ($\dot{Q}_{OU}$) and the sum of the IU capacities $\left\{\dot{q}_{IU}^{(i)}\right\}$ respectively. In heating mode $\dot{Q}_{eva}$ is the OU heat absorption ($\dot{Q}_{OU}$) and $\dot{Q}_{con}$ is the sum of the IU capacities $\left\{\dot{q}_{IU}^{(i)}\right\}$.

3.3. Assembled VRF model

For the assembled VRF model, it is important to ensure that the refrigerant is always at the same pressure in each IU since many IUs with different operating conditions can be involved. The operating conditions are then evaluated by iteration. The refrigerant mass flow rate in the IUs is adapted to meet the required capacity. Figure 4 presents the calculation procedure for the VRF model in cooling mode that follows this sequence:

1. Initialize the IU and the OU operating conditions using the nominal values of the IU capacity, dry bulb temperature and wet bulb temperature and the OU capacity, power consumption dry bulb temperature and wet bulb temperature. These nominal values correspond to the rated conditions and performances in accordance to the ANSI/AHRI standard 1230. They can be found in the product datasheets.
2. Evaluate each IU refrigerant temperature ($T_{ref,IU}^{(i)}$) using Eq. 4.
3. Evaluate the minimum IU refrigerant evaporating temperature:

$$T_{sat,IU} = \min\left[T_{ref,IU}^{(i)}\right] \tag{19}$$

4. Evaluate the IU capacities $\dot{q}_{IU}^{(i)}$ using Eq. 4 and the minimum evaporating temperature.
5. Evaluate the refrigerant condensing temperature at the OU using Eq. 4.
6. Evaluate the evaporating pressure p_{eva}, the condensing pressure p_{con} and the enthalpies (h_A and h_B) from the refrigerant equation of state.
7. Evaluate the capacity ($\dot{Q}_{eva}$), the heat rejection ($\dot{Q}_{con}$) and the power consumption ($\dot{W}$) using Eqs. 14 – 18.

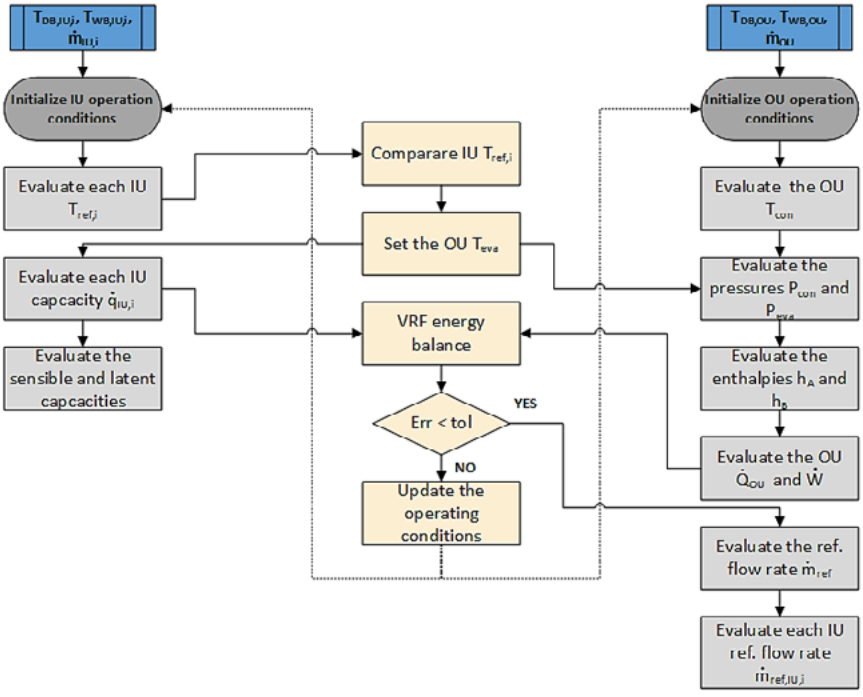


Fig. 4. Layout of the VRF heat pump model in cooling mode

8. Evaluate the errors in the VFR energy balance:

$$\Delta\dot{Q}_{eva} = \dot{Q}_{eva} - \Sigma_i \dot{q}_{IU}^{(i)} \tag{20}$$

$$\Delta\dot{W} = \dot{W} - \dot{W}^{-} \tag{21}$$

$$\Delta\dot{Q}_{con} = \dot{W} - \dot{Q}_{eva} - \dot{Q}_{con} \tag{22}$$

where $\dot{W}^{-}$ is the power consumption at the previous iteration.

9. Evaluate the sum of the heat rejection and power consumption absolute relative errors:

$$Err = \left|\Delta\dot{Q}_{con}/\dot{Q}_{con}\right| + \left|\Delta\dot{W}/W\right| \tag{23}$$

10. If Err is above the tolerance, update the VRF state for the next iteration:

$$\dot{Q}_{eva}{}^{+} = \dot{Q}_{eva} + \delta\Delta\dot{Q}_{eva} \tag{24}$$

$$\dot{Q}_{con}{}^{+} = \dot{Q}_{con} + \delta\Delta\dot{Q}_{con} \tag{25}$$

$$\dot{W}^{+} = \dot{W} + \delta\Delta\dot{W} \tag{26}$$

$$\dot{q}_{IU}^{(i)+} = \dot{Q}_{eva}{}^{+}\frac{\dot{q}_{IU}^{(i)}}{\Sigma_i \dot{q}_{IU}^{(i)}} \tag{27}$$

where δ is a relaxation coefficient. A relaxation coefficient of 0.7 and a tolerance of 10^{-8} are used in this study. The new VRF state is then used to reinitialize the IU and OU before the next iteration, starting from step 2.

11. If Err below the tolerance, evaluate the refrigerant mass flow rate for each IU using the refrigerant routines and Eq. 17:

$$\dot{m}_{ref} = \frac{\dot{V}_{nominal}}{v_{suc}} - \dot{m}_{leak} \tag{28}$$

$$\dot{m}_{ref,IU}^{(i)} = \dot{m}_{ref} \frac{\dot{q}_{IU}^{(i)}}{\sum_i \dot{q}_{IU}^{(i)}} \tag{29}$$

4. Calibration procedure

Parameters to the models are unknown, as manufacturers do not typically provide values of the VRF heat pump parameters. Here, parameters are estimated by calibration of the models over the published manufacturer performance data. The IU model has two parameters (UA_{in} and $h_c A_{out}$), while the OU model has 8 (UA_{in}, $h_c A_{out}$, $\dot{V}_{nominal}$, V_r, C, η, $\dot{W}_{loss}$ and ΔT_{sup}). For IUs, manufacturers usually provide data of latent and sensible capacities at different airflow temperatures (dry bulb and wet bulb) and flow rates. For OU, manufacturers provide the power consumption in addition to latent and sensible capacities at different airflow temperatures. Regarding IU, sometimes the air flow rate is given as a set of two or three values (corresponding to the fan speed control, e.g., Low, Med, Hi) and it is not clearly indicated which value is used to generate the data. In such case, the calibration is performed successively with the different values of air flow rate. The air flow rate that leads to the minimal error between the model and the data is retained.

4.1. Indoor unit

Component models for IUs as well as calibration routines are implemented in Python. The parameters that minimize the sum of squared errors between the model and the manufacturer data are identified using the Sequential Least Squares Programing method (SLSQP) from the Python SciPy library:

$$SSE_{IU} = \sum_j \left[\left(\frac{\dot{q}_{sen,IU}^{(j)} - \dot{q}_{sen,data}^{(j)}}{\dot{q}_{sen,data}^{(j)}} \right)^2 + \left(\frac{\dot{q}_{lat,IU}^{(j)} - \dot{q}_{lat,data}^{(j)}}{\dot{q}_{lat,data}^{(j)}} \right)^2 \right] \tag{30}$$

where for the set of data points (j): $\dot{q}_{sen,IU}^{(j)}$ and $\dot{q}_{lat,IU}^{(j)}$ are the IU model sensible and latent capacities, $\dot{q}_{sen,data}^{(j)}$ et $\dot{q}_{lat,data}^{(j)}$ are the latent and the sensible capacities form the IU manufacturer data

For the calibration procedure, it is important to choose proper guess values for the parameters to ensure that the result converges in any case. Cimmino et al. [12] proposed a procedure based on the nominal values of the capacity and power input to evaluate the guess parameters. This approach was implemented assuming a pinch value of 5K in the heat exchanger. The initialization of the IU parameters follows this sequence:

1. Set the refrigerant temperature difference : $\Delta T = 5\,°C$ (31)
2. Evaluate the IU heat transfer coefficients: $h_c A_{out} = UA_{in} = 2\dot{Q}_{nominal}/\Delta T$ (32)

4.2. Outdoor unit

While an OU embodies only a compressor and a single heat exchanger, a second heat exchanger is included in the calibration model to complete the cycle and evaluate the OU capacity and power input. The heat transfer of this heat exchanger is not taken into account in the cost function but its heat transfer coefficient is still calibrated. Moreover, the exchanger is assumed to operate in sensible heat transfer mode in the air side and the air mass flow rate is set to the same value as the one given by the manufacturer for the outdoor unit heat exchanger. The same method as for the IU is used to minimize the sum of squared errors between the model and the manufacturer data for the OU:

$$SSE_{OU} = \sum_j \left[\left(\frac{\dot{Q}_{OU}^{(j)} - \dot{Q}_{data}^{(j)}}{\dot{Q}_{data}^{(j)}} \right)^2 + \left(\frac{\dot{W}^{(j)} - \dot{W}_{data}^{(j)}}{\dot{W}_{data}^{(j)}} \right)^2 \right] \tag{33}$$

where for the set of data points (j): $\dot{Q}_{OU}^{(j)}$ and $\dot{W}^{(j)}$ are the OU model heat rejection and power consumption respectively and $\dot{Q}_{data}^{(j)}$ and $\dot{W}_{data}^{(j)}$ are the heat rejection and power consumption from the OU manufacturer data.

For the calibration procedure, the guess values assume a pinch value of 5K in the IU and OU heat exchangers. The heat transfer coefficient of the inside and the outside surface are set at the same initial value. The leakage mass flow rate is set at 1% of the refrigerant mass flow rate. The guess value of the electro-mechanical efficiency is chosen to be η = 0.95 and the superheating, ΔT_{sup} = 5K. The nominal values of the temperatures are the one at the rated condition.

The guess values of the OU parameters are evaluated with this following sequence in cooling mode:

1. Evaluate the refrigerant temperature:

$$T_{eva} = T_{DB,in,eva,nominal} - 5°C \tag{34}$$

$$T_{con} = T_{DB,in,con,nominal} + 5°C \tag{35}$$

2. Evaluate the evaporator heat transfer rate at nominal conditions:

$$\dot{Q}_{eva,nominal} = \dot{W}_{nominal} - \dot{Q}_{con,nominal} \tag{36}$$

3. Evaluate the evaporating pressure p_{eva} and condensing pressure p_{con} from the refrigerant equation of state.
4. Evaluate the specific volume and isentropic exponent at the compressor suction from the refrigerant equation of state using the condensing pressure p_{con} and the suction temperature $T = T_{eva} + \Delta T_{sup}$
5. Evaluate the volume ratio:

$$V_r = (p_{con}/p_{eva})^{\frac{1}{\gamma}} \tag{37}$$

6. Evaluate the nominal refrigerant volume flow rate:

$$\dot{V}_{nominal} = (\dot{m}_{ref} + \dot{m}_{leak})v_{suc} \tag{38}$$

$$\dot{m}_{ref} = \dot{Q}_{eva,nominal}/(h_A - h_B) \tag{39}$$

$$\dot{m}_{leak} = 0.01\dot{m}_{ref} \tag{40}$$

7. Evaluate the leakage coefficient:

$$C = \dot{m}_{leak}/(p_{con}/p_{eva}) \tag{41}$$

8. Evaluate the constant part of the power losses with the previously evaluated parameters and the theoretical power (Eq. 14):

$$\dot{W}_{loss} = \max(0, \eta\dot{W}_{nominal} - \dot{W}_t) \tag{42}$$

9. Evaluate the condenser and evaporator heat transfer coefficients:

$$\{UA_{eva}, UA_{con}\} = \dot{Q}_{eva,nominal}/5°C \tag{43}$$

10. Evaluate the evaporator internal and external heat transfer coefficients:

$$h_c A_{out,eva} = UA_{in,eva} = 2UA_{eva} \tag{44}$$

5. Results

5.1. Indoor unit calibration results

A commercial IU of 3.5 kW nominal capacity is used to verify the model and the calibration procedure in cooling mode. Values of sensible and latent heat transfer rates are given for different sets of dry bulb and wet bulb temperature. The temperature range goes from 22.7°C to 31.1°C for a total of 24 data points. Two air mass flow rates (0.104 kg/s and 0.168 kg/s), corresponding to two fan speeds, are given in the data. The calibration is performed with each of the two air mass flow rates and the best result is retained. The guess values and the calibration result of each parameter are shown in Table 1. Figure 5 shows the comparison between the model predicted and the manufacturer provided values of the IU sensible, latent and total capacities.

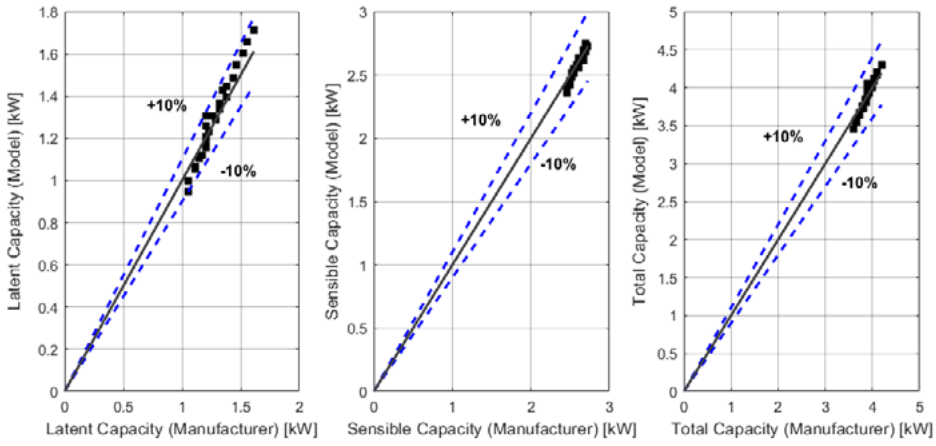


Fig. 5. Comparison of manufacturers and calibrated IU capacities

Table 1. IU parameters calibrated with manufacturer data

Parameters	Guess values	Calibrated values
UA_{in} $[W/K]$	1406.4	1543.1
$h_c A_{out}$ $[W/K]$	1406.4	1567.6

The root mean square error (RMSE) is 4.9%, 1.5% and 1.9% for the latent, sensible and total capacities, respectively. The maximum difference between values from the model and the manufacturer data is 10.3%, 4% and 4% for the latent, sensible and total capacities, respectively. The error on the latent capacity is caused by the assumption of a coil that is completely wet. The results are acceptable in the context of energy simulation, considering that the total capacity is the most relevant performance metric in this case. Various IU sizes from different manufacturers have been also verified and similar results have been obtained.

5.2. Outdoor unit calibration results

The OU model and calibration method is also verified against manufacturer data. Data from a 10.5 kW nominal capacity outdoor unit is used to calibrate the model in cooling mode. The nominal coefficient of performance (COP) of the OU is 3.37. As the OU heat exchanger operates as a condenser, only the external heat transfer coefficient ($h_c A_{out}$) is calibrated. Table 2 shows the guess values and the calibration result of each parameter and Figure 6 shows the comparison between the model and the manufacturer data of power and capacity.

An RMSE of 2.1% and 2.3% is obtained for the power input and the capacity, respectively. The maximum differences are 8.8% and 7.3% for the power input and the capacity, respectively. Similar results have been obtained with OUs of different capacities and from different manufacturers.

Table 2. OU parameters calibrated with manufacturer data.

Parameters	Guess values	Calibrated values
UA_{in} $[W/K]$	-	-
$h_c A_{out}$ $[W/K]$	2491	1016.1
$\dot{V}_{nominal}$ $[m^3/s]$	0.001	0.0026
V_r $[-]$	2.16	2.45
C $[kg/s]$	0.0091	0.0
η $[-]$	0.95	0.99
$\dot{W}_{loss}$ $[W]$	358.7	0.0
ΔT_{sup} $[°C]$	5.0	0.5

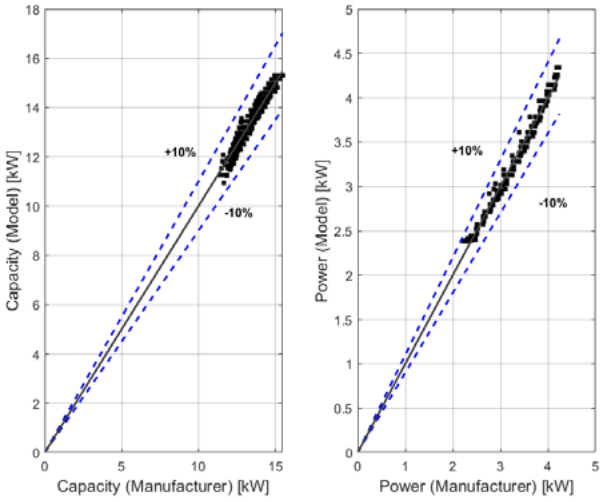


Fig. 6. Comparison of manufacturers and calibrated power and capacity of the OU

5.3. VRF model results

The VRF model is verified by assembling an OU and several IUs. Since manufacturers do not communicate data of assembled VRF units, the performance metrics of the model are compared to the available manufacturer data for the corresponding OU. Previously calibrated OU and IUs are used to build different configurations of VRF units. Table 3 and Table 4 show the parameters of the IUs and OU considered. The parameters are obtained by calibration, while the air mass flow rates are the values given by the manufacturer and used during the calibration process. Three cases corresponding to three VRF configurations are evaluated.

Table 3. Calibrated indoor units used to build VRF configurations.

Indoor unit	Capacity $[kW]$	$h_c A_{out}$ $[W/K]$	UA_{in} $[W/K]$	$\dot{m}_a$ $[kg/s]$
A	2.6	1192	506	0.162
B	3.5	1567	1543	0.168
C	5.3	4312	3211	0.231
D	7	5723	3630	0.272

The units are assembled to maintain a capacity ratio between OU and IUs equal to one. In case 1, the OU is paired to 3 IUs (2A + 1C). In case 2, 3 IUs of same capacity (3B) are connected to the OU. In case 3, the OU is paired to 2 IUs (1B + 1D). Comparisons of the VRF input power and capacity between the calibrated model and the OU manufacturer data are shown on Figure 7. Table 5 shows that the RMSE is in range of 1.8% to 3.5% for the power input and 1.9% to 5.1% for the capacity.

Table 4. Calibrated outdoor unit used to build VRF configurations.

Parameters	Values
UA_{in} $[W/K]$	1834
$h_c A_{out}$ $[W/K]$	-
$\dot{V}_{nominal}$ $[m^3/s]$	0.002325
V_r $[-]$	2.807
C $[kg/s]$	0.0
η $[-]$	0.81
$\dot{W}_{loss}$ $[W]$	0.0
ΔT_{sup} $[°C]$	1
$\dot{m}_a$ $[kg/s]$	2.162

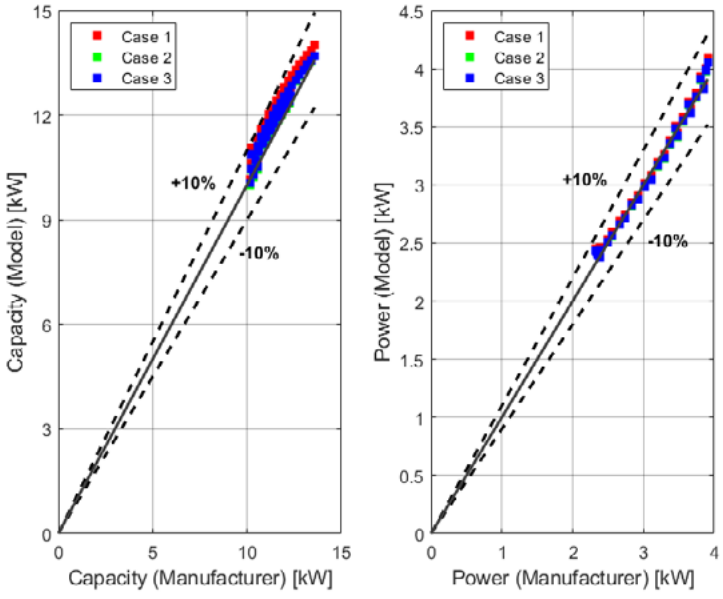


Fig. 7. Comparison of assembled VRF and manufacturer power and capacity

Table 5. VRF configurations and RMSE values compared to manufacturer data

Case	Configuration	Error on the Power		Error on the Capacity	
		Maximum	RMSE	Maximum	RMSE
1	OU + IUs {A, A, C}	5.2%	2.1%	8.3%	5.1%
2	OU + IUs {B, B, B}	4.4%	3.5%	6.3%	1.9%
3	OU + IUs {B, D}	4.4%	1.8%	6.2%	3.3%

6. Conclusions

A model for an air source variable refrigerant flow heat pump is presented. The model is based on a simplified vapor compression cycle to reduce the number of thermodynamic properties evaluation and maintain a low computational time. The IUs and OU are modelled separately so that various VRF configurations with multiple IUs can be considered. Models for the units and a calibration procedure were implemented in Python. The parameters of the models are calibrated by using manufacturer data and by minimizing the differences between the model's performance metrics and those given in manufacturer data.

Different configurations of VRF heat pumps were evaluated by using previously calibrated IUs and OU. Comparison with manufacturer data showed that the model predicts very closely the input power and the capacity of the outdoor unit. A maximum root mean square error of 2.9% and 2.8% were observed respectively for the capacity and the power input. Future work will be devoted to the implementation of a partially wet coil in the heat exchanger model, defrosting in heating mode, the extension of the model for partial load operation and heat recovery.

Acknowledgements

The authors acknowledge the support of the Natural Sciences and Engineering Research Council of Canada (NSERC), [funding reference number RGPIN-2018-04471]. The authors also acknowledge the support of the Trottier Energy Institute and Hydro-Québec for a scholarship awarded to the first author.

References

[1] Lin, X., et al., *A review of recent development in variable refrigerant flow systems.* Science and Technology for the Built Environment, 2015. **21**(7): p. 917-933.

[2] Yan, P., et al., *A modeling study on the effects of refrigerant pipeline length on the operational performance of a dual-evaporator air conditioning system.* Applied Thermal Engineering, 2012. **39**: p. 15-25.

[3] Hong, T., et al., *Development and validation of a new variable refrigerant flow system model in EnergyPlus.* Energy and Buildings, 2016. **117**: p. 399-411.

[4] Zhu, Y., et al., *Simulation of variable refrigerant flow air conditioning system in heating mode combined with outdoor air processing unit.* Energy and Buildings, 2014. **68**: p. 571-579.

[5] Cheung, H. and J.E. Braun, *Component-based, gray-box modeling of ductless multi-split heat pump systems.* International Journal of Refrigeration, 2014. **38**: p. 30-45.

[6] Sun, H., et al., *A general simulation model for variable refrigerant flow multi-split air conditioning system based on graph theory.* International Journal of Refrigeration, 2017. **82**: p. 22-35.

[7] Raustad, R., *A Variable Refrigerant Flow Heat Pump Computer Model in EnergyPlus.* Ashrae Transactions 2013, Vol 119, Pt 1, 2013. **119**: p. 299-308.

[8] Sharma, C. and R. Raustad, *Compare Energy Use in Variable Refrigerant Flow Heat Pumps Field Demonstration and Computer Model.* Ashrae Journal, 2013.

[9] Kim, D., et al., *Model calibration of a variable refrigerant flow system with a dedicated outdoor air system: A case study.* Energy and Buildings, 2018. **158**: p. 884-896.

[10] Torregrosa-Jaime, B., et al., *Modelling of a variable refrigerant flow system in energyplus for building energy simulation in an open building information modelling environment.* Energies, 2019. **12**(1).

[11] Jin, H. *Parameter estimation based models of water source heat pumps*. Ph.D. Thesis. (2002) Oklahoma State University, Stillwater, OK, USA.

[12] Cimmino, M., and Wetter, M., *Modelling of Heat Pumps with Calibrated Parameters Based on Manufacturer Data*, in 12th International Modelica Conference, 2017, Prague, Czech Republic.

[13] Winandy, E., C. Saavedra, J. Lebrun. 2002. *Experimental Analysis and Simplified Modeling of a Hermetic Scroll Refrigeration Compressor*. Applied Thermal Engineering, Vol. **22**, n. 2, pp. 107-120.

[14] Chen Y., N. Halm, E. A. Groll, J. E. Braun. 2000. *A Comprehensive Model of Scroll Compressors, Part II: Overall Scroll Compressor Modeling*. Proceedings of the 2000 International Compressor Engineering Conference at Purdue. Purdue University, West Lafayette, IN., pp. 725-734.

13th IEA Heat Pump Conference
April 26-29, 2021 Jeju, Korea

Application of Improved Cooling & Heating System to Long-Range Electric Vehicles for Higher Power Efficiency

Jae Yeon Kim[a], Yeon Ho Kim[b], Jea Wan Kim[c], Taesung Kim[d]*

[abc]Hyundai Motors, 150, hyundaiyonguso-ro, Namyang-eup, Hwaseong-si,Gyeonggi-do,18280, Korea
[d]School of Mechanical Engineering and SAINT, Sungkyunkwan University, 300 Cheoncheon-dong, Jangan-gu, Suwon-si,, Gyeonggi-do, 440-746, Korea

Abstract

The challenge for long-range electric vehicles is to increase the driving distance by maintaining the highest battery energy density level and by managing energy efficiently. An effective battery thermal management system is required to control the operating temperature of the battery for optimal battery energy density. For efficient energy management, more efficient cabin heating system is needed because they consume a lot of energy during winter. In this paper, the performance of the dual coolant-cooled battery cooling system was studied. In addition, the heat pump system that utilizes battery waste heat was studied to further improve the energy efficiency of the existing heat pump using the ambient air heat and power electric module waste heat. The results showed that a dual coolant-cooled battery cooling system combined with a radiator and Air Conditioning (AC) system can reduce power consumption by 75% at the ambient temperature of 15°C compared to using the AC system only. In addition, the use of battery waste heat in the heat pump system increased mileage by up to 9% at the low ambient temperature of -7°C.

© HPC2020.
Selection and/or peer-review under responsibility of the organizers of the 13th IEA Heat Pump Conference 2020.

Keywords: Cooling system, Air-conditioning system ,.Battery thermal management, Heat pump system ;

1. Introduction

As environmental regulations on greenhouse gas emissions tighten, interest in Electric Vehicles (EVs) has increased [1]. The main issues for the development of EVs are to select an appropriate energy storage system and to use the battery energy efficiently to improve mileage [2]. Lithium-ion (Li-ion) batteries are considered to be the most suitable energy storage devices for EVs because they have a higher energy density, higher power, lighter, lower self-discharge rate, and a longer lifespan than other rechargeable batteries such as nickel-cadmium [3]. However, since the performance of the Li-ion batteries is sensitive to varying temperature, the driving distance of the EVs will be reduced if the battery temperature is not controlled properly [4]. Therefore, the Battery Thermal Management System (BTMS) is needed to increase the mileage of EVs. Pesaran [5] suggested that the Li-ion battery operating temperature range should be maintained between 15°C and 35°C and the maximum temperature difference should be kept below 5°C.

Hyundai Motor Company (HMC) defines “short-range EVs” as the vehicles with below 200 miles/one full charge represented by Ionic EV and “long-range EVs” as vehicles with over 200 miles/one full charge represented by Kona EV. For long-range EVs, high current is used to reduce charging time, thus the heat generation inside the battery and On Board Charger (OBC) can be more increased [6]. This additional battery waste heat requires a more powerful battery cooling system, but on second thought, it can be used as cabin heating for EVs. For Mitsubishi I-MIEV, the driving distance is reduced by up to 45% during heating operation and up to 27% during indoor AC operation [7]. By utilizing the waste heat of the battery in addition to the

* Corresponding author. Tel.:+82-31-290-7466; fax:+82-31-290-5889.
E-mail address: tkim@skku.edu.

waste heat of the power electric (PE) module, it is possible to improve the heating performance to minimize the reduction of the EVs mileage. Therefore, in order to improve the mileage, a cooling system is needed to maintain the battery temperature properly, and its waste heat is effectively utilized for cabin heating.

In this paper, a dual coolant-cooled battery cooling system that can use both radiator and AC system was studied as a way to relieve the self-heating of high energy density batteries and high-efficiency heat pump system that utilizes battery waste heat as well as conventional PE waste heat was studied.

2. Main subject

2.1. Application of dual coolant-cooled battery cooling system

2.1.1. Importance of battery thermal management

The performance of Li-ion batteries is closely related to temperature, so it is important to understand the heat generation inside the battery. According to Thomas and Newman [8], Li-ion cells are known to generate heat by reversible entropy, resistive dissipation, a concentration gradient of cells and relaxation of chemical reactions, as expressed by Gu et al. [9] in Eqn. (1). Q is the heat generation rate, I is the current through the cell, U is the battery open-circuit voltage, and V is the cell voltage.

$$\dot{Q} = I(U - V) - I(T\frac{dU}{dT}) \quad (1)$$

The relationship of battery lifespan to temperature is shown in Fig. 1 [10], which shows that the battery life will be drastically reduced when the temperature is out of the proper level. In addition, the relationship between the performance of the battery and the temperature has been studied extensively. Amine et al. [11] showed a capacity reduction of 72% as a result of repeating 140 charge and discharge cycles with a C/2 discharge rate at 55°C. Ehrlich [12] studied the performance decrease after 500 iterations at 1C discharge rate at 45°C. Therefore, battery performance is directly related to the driving distance of the EVs, requiring a suitable cooling system to dissipate battery heat.

2.1.2. Cooling system for battery thermal management

The battery cooling system was reviewed by Kim et al. [13] in terms of cycles. According to them, the independent use of air-cooled cooling system and system without vapor compression cycle (VCC) for long-range EVs battery cooling are difficult due to the efficiency and performance limitations of the system. Mahle [14] also compared each system using the VCC as shown in Table 1 and found that the liquid (coolant) cooling system is superior in terms of cooling performance and efficiency. The air-cooled cooling system utilizes cabin air for the battery cooling, and only needs some additive parts such as fans and ducts, so it is advantageous in terms of weight and price. However, due to the low heat capacity (Cp) of the air, as shown in Eqn. (2), a large amount of an air flow rate ($\dot{m}$) is required to remove heat (Q) generated from the battery, resulting in larger fan power consumption and bulky ducts and manifolds. Therefore, it is difficult to accumulate a large number of cells in a limited pack because the spacing between the battery cells must be wide, which makes it difficult to apply to long-distance EVs. Liquid cooling systems, on the other hand, are suitable for long-distance EVs as they use liquid coolant with higher heat capacity and higher heat transfer rates than air, which allows the battery to be cooled more effectively with less mass flow rate.

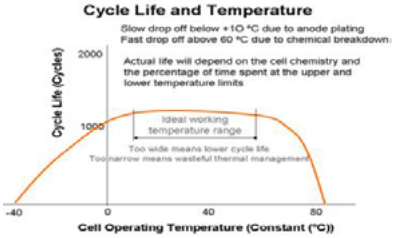


Fig. 1. Battery life graph according to battery temperature [10]

Table 1. Comparison of Battery Cooling Systems (Mahle [14])

- Bad, O Normal, + Good	Air		Coolant	Refrigerant
	Extra HVAC unit	Cabin air used		
System Weight	-	+	-	+
System Package	-	O	O	+
System Costs	-	+	-	O
Energy Efficiency	O	+	+	O
Availability (Winter)	-	+	+	-
Applicant Effort	O	+	+	O/-
Cooling Power	O	-	+	+

$$\dot{Q} = \dot{m} C_p \Delta T \tag{2}$$

2.1.3. Dual coolant-cooled battery cooling system

In the case of Kona EV, HMC's long-range EVs, the heat generation of the PE module and battery increased more than twice compared to Ionic EV under HMC cooling test conditions as shown in Fig. 3. The Kona EV is limited to existing air-cooled battery cooling systems in order to keep the battery temperature at an appropriate level. Therefore, a liquid-cooled cooling system has been developed and applied. According to the battery cooling method, the structure of the battery is different as shown in Fig. 4, and the research of the dual coolant-cooled battery cooling system for cooling the coolant has been conducted.

A dual coolant-cooled battery cooling system is used to cool the battery with the radiator and AC system by constructing the battery cooling system circuit as shown in Fig. 5 (a). The battery coolant line is connected to the cooling circuit for the PE module and OBC so that the battery can be cooled through the existing radiator without any additional parts. On the side of the refrigerant circuit, the system consists of the evaporator for cabin cooling and the battery chiller for the battery cooling. Therefore, the dual coolant-cooled battery cooling system can be installed by the addition of minimal parts to the existing cooling system and AC systems. The cooling mode of this system is operated as follows. First, if the battery cell temperature is lower than the coolant temperature passing through the radiator, the battery cooling line is disconnected from the PE module cooling line and the coolant flows into the battery chiller, where the cold refrigerant flows. Second, if the battery cell temperature is higher than the coolant temperature through the radiator, the AC is not activated to cool the coolant while the battery cooling line is connected to the PE module cooling line to cool the battery with coolant cooled by ambient air temperature in the radiator as shown in Fig. 5 (c). By adding a 3way valve to the coolant circuit, the two modes described above can be operated.

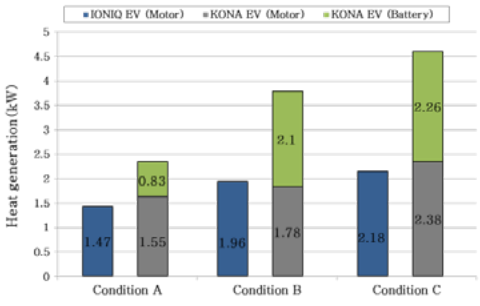


Fig. 3. Ionic EV and Kona EV Heat generation value

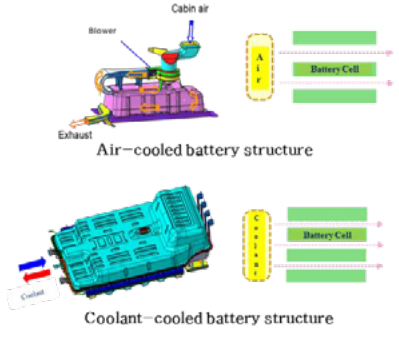


Fig. 4. Comparison of battery structures by cooling method

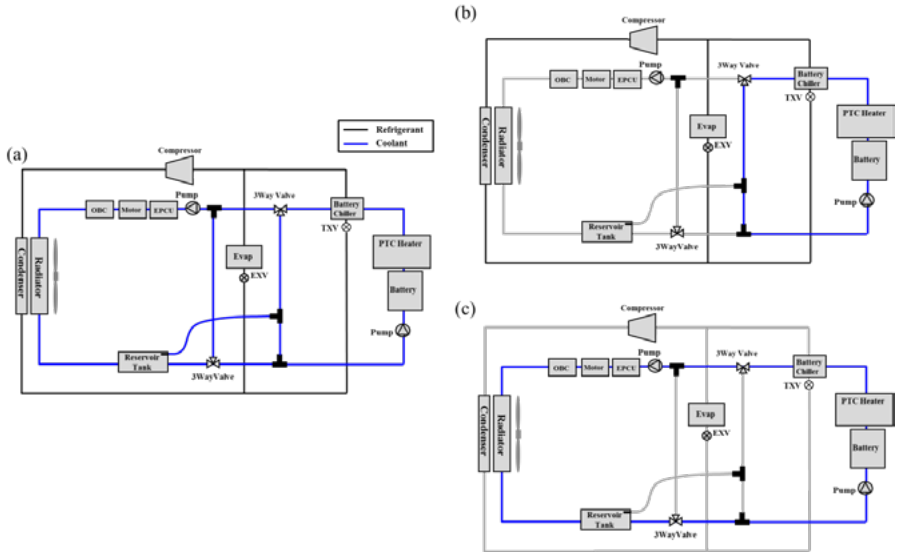


Fig. 5. (a) Dual coolant-cooled battery cooling system circuit diagram, (b) battery cooling mode utilizing AC system, (c) battery cooling mode utilizing radiator

The specifications of the main components of the dual coolant-cooled battery cooling system applied to Kona EV are shown in Table 2. Existing Ionic EV components were basically used, and the newly added battery chiller was evaluated for the different number of plates in consideration of the heat generated from the HMC cooling evaluation condition to look for the optimum capacity. The battery chiller test results are shown in Fig. 6. As the number of plates increased, the cooling performance was improved by an enlarged heat transfer area, but the pressure drop of the coolant decreased. In this study, 20 plates were selected in consideration of the HMC target for the chiller heat dissipation.

Table 2. Main component specifications of the system

Component	Type	Specification	Unit
Compressor	Scroll	33	cm3
Condenser	Micro channel HX	572.6x365x20	mm
Evaporator	Micro channel HX	215x256.5x45	mm
Radiator	Micro channel HX	610x411.5x14	mm
Chiller	Dimple	102x64x62	mm

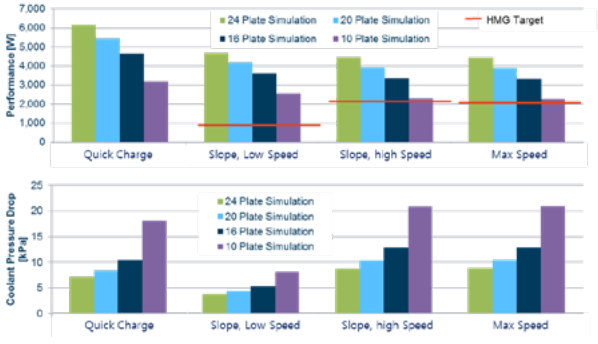


Fig. 6. Battery chiller performance test results

2.1.4. Effect of dual coolant-cooled battery cooling system

The two modes of the dual coolant-cooled battery cooling system proposed in this paper were evaluated by comparing the cooling mode using the AC system and the cooling mode using the radiator. The system bench test for each mode under the same conditions at an ambient air temperature of 15°C showed that AC utilization mode increased cooling performance by 1.57% compared to radiator utilization mode, but consumption power increased by 75%, resulting in a 58.3% reduction in COP (Fig. 7 (a).). In addition, the comparison of the two modes with the initial temperature conditions of 30°C, 110km/h and three-hour continuous driving conditions at ambient air temperature of 25°C showed improvement of up to 4% in terms of vehicle power consumption by reducing cooling power consumption when using the radiator compared to cooling using the AC system (Fig. 7 (b).). In other words, the use of a radiator was advantageous in terms of efficiency compared to using an AC system to cool the battery at low outside temperatures. This is because the compressor consumes a lot of electricity to operate the AC system. If the ambient temperature is high, the cooling mode utilizing the AC system will only operate because the battery cannot be cooled by utilizing the radiator.

2.1.5. Optimal control of battery cooling and cabin cooling

The biggest problem with the application of the battery cooling system using AC is the temporary rise in indoor discharge temperature due to increased cooling load when the battery cooling system is operated. In such a case, a sudden hot wind occurs during the operation of the AC, which may cause customer dissatisfaction such as unpleasantness and odor in terms of AC productivity. The conventional thermal expansion valve allows only passive expansion in proportion to the temperature and pressure of the vapor phase refrigerant passing through the chiller. There was a problem of instantaneous flow of refrigerant to the chiller side during operation of the battery cooling system and during indoor cooling, resulting in a rapid increase of the indoor discharge temperature. In order to solve this problem, an electronic expansion valve that can actively control the opening amount is applied to the battery side, and the superheat degree is controlled after stabilizing the evaporator temperature. As a result, the cooling performance was stabilized by preventing an initially large flow rate to the chiller side. The solenoid thermal expansion valve is applied to the evaporator side for the cabin cooling to realize the battery cooling on mode when the AC is off and the battery cooperative control point of view.

2.2. Cabin heating using battery waste heat

2.2.1. Importance of battery waste heat

EVs without engine waste heat sources use electric heaters with an efficiency of 0.8 to 0.9 when heater operation is required, such as spring and autumn comfort temperature control and winter heating. However, when the electric heater is used, the driving distance of the vehicle is excessively reduced because the power consumption is large. Therefore, in order to maintain the driving distance during heating, it is advantageous to use a heat pump system with high efficiency (COP of 2 to 3) by utilizing an external heat source. However, this system has a problem that it is difficult to secure the heat source as the outside air temperature is lower in winter so that the operating condition is limited at a low temperature below -10°C. The existing Ionic EV heat pump system utilizes the PE module waste heat as well as the outside air heat to increase efficiency. In

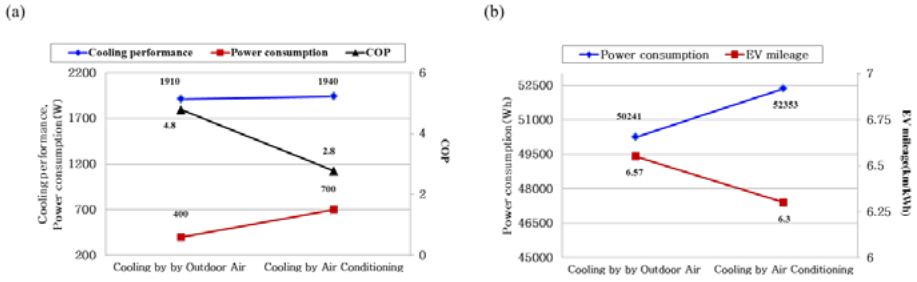


Fig. 7. Comparison of Battery Cooling Mode with Ambient Temperature and Battery Cooling Mode with A ((a) ambient air temperature 15°C conditions, (b) ambient air temperature 25°C and 110 km/h driving conditions)

long-range EVs, battery generated heat is greatly increased in addition to the PE module, numerous studies have been conducted on heat pump systems utilizing battery waste heat [14]. However, as shown in Table 3, there were very few EVs using heat pump system utilizing battery waste heat. Therefore, research on the heat pump system utilizing battery waste heat as well as the outdoor heat source and waste heat of the PE module is needed to minimize the reduction of driving distance.

Table 3. Heat Pump Operating Modes of Global EVs

Application Mode	HYUNDAI IONIQ EV	TESLA	GM BOLT EV	NISSAN LEAF	HYUNDAI KONA EV (This Paper)
Heating of waste heat recovery in PE module	O	X	X	△	O
Heating of waste heat recovery in PE module and batteries	X	X	X	X	O
Heating and Dehumidification of waste heat recovery in PE module	O	X	X	△	O
Heating and Dehumidification of waste heat recovery in PE module and batteries	X	X	X	X	O
Heating of waste heat recovery in PE module (Recognition of frost formation)	O	X	X	X	O
Heating of waste heat recovery in PE module and batteries(Recognition of frost formation)	X	X	X	X	O

2.2.2. Utilization of battery waste heat

In the existing short-range EVs, as shown in Fig. 8 (a), the heat pump was operated using only waste heat from the PE module, and the battery heat was thrown into the air. In this paper, to improve the performance of the heat pump system, the system that utilizes the waste heat from the battery, OBC and PE module is constructed by using the dual coolant-cooled battery cooling system as shown in Fig. 8 (b). A more specific schematic of this system is shown in Fig. 9. This system circulates coolant through PE module, OBC, and battery, and recovers waste heat through heat exchange with refrigerant in waste heat recovery chiller and uses it for heat pump heating.

2.2.3. Performance and efficiency impact of increasing battery waste heat

To analyze the heat pump performance according to the amount of waste heat, the proposed system was evaluated while increasing the waste heat to 0.55kW, 1kW, and 2kW under the condition of -20°C and 50km/h. The refrigerant pressure-enthalpy diagram to the evaluation of the system is shown in Fig. 10 (a). As the waste heat is increased, the evaporative pressure and temperature and condensation pressure and condensation are increased, and the heating performance is improved, but the refrigerant flow rate is increased by increasing the density of refrigerant entering the compressor. This is because the refrigerant does not have to be expanded to lower pressure in order to recover waste heat. More specific performance results are shown in Fig. 10 (b). Increasing the waste heat by 1.45 kW, the heating capacity is increased by 0.6 kW, but the compression work is increased by 0.15 kW, and the heating efficiency is increased from 2.33 to 2.57.

Table 4. Power consumption of cabin heating according to the use of battery waste heat

Application mode	Compressor power consumption (kWh)	PTC power consumption (kWh)	Heating power consumption (kWh)	Heating power savings (%)
Battery waste heat not used	0.574	0.5	1.074	Base
Battery waste heat used	0.52	0.354	0.874	18.6

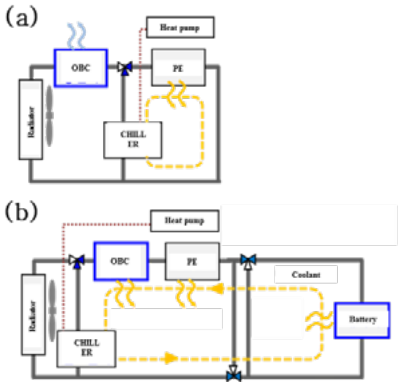


Fig. 8. Electric vehicle heat pump system ((a) utilization of waste heat from PE module, (b) utilizes waste heat from PE module, OBC and battery)

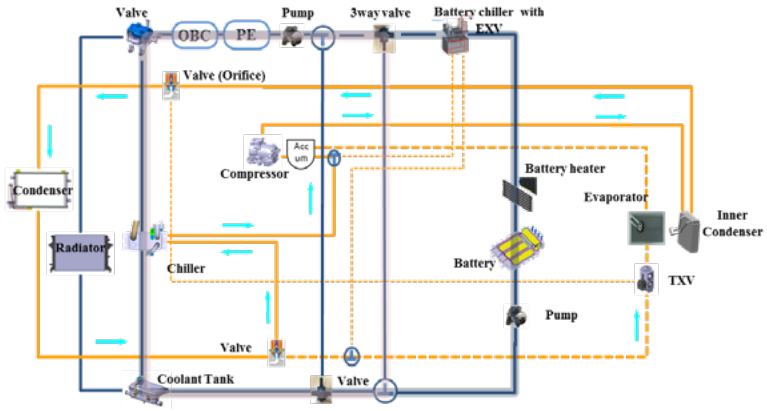


Fig. 9. Heat pump system circuit diagram using battery waste heat

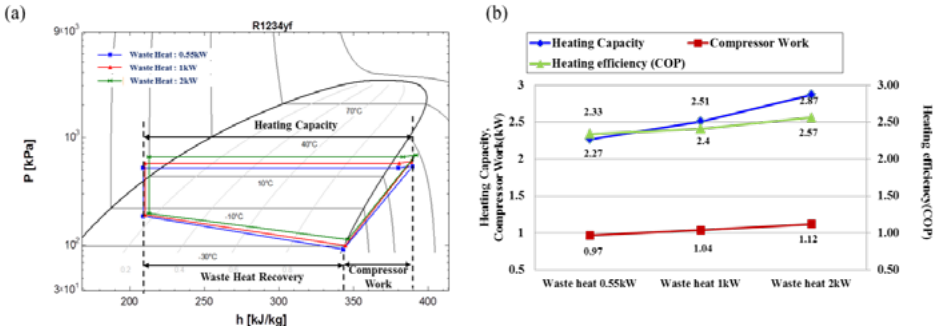


Fig. 10. (a) System refrigerant pressure-enthalpy diagram according to waste heat, (b). Evaluation result of heating performance according to waste heat

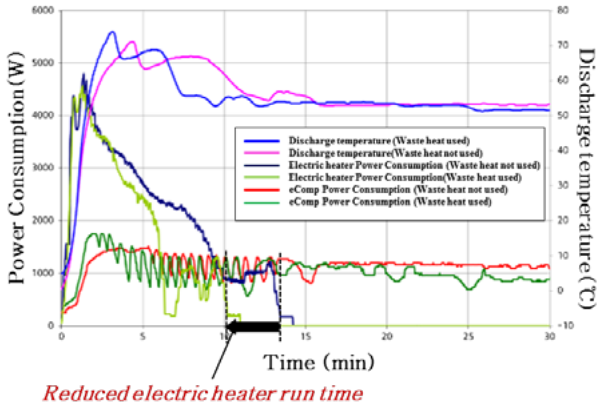


Fig. 11. Evaluation result of heating performance with or without battery waste heat

In order to confirm the effect of the heat pump system using the battery waste heat, the use of the waste heat during the cabin heating at normal temperature 0°C, FATC (Full Auto Temperature Control) 23°C and vehicle speed 50km/h after charging was compared and evaluated. The results of the performance assessment based on the availability of waste heat for 30 minutes are shown in Fig. 11. More simply, the numerical results are shown in Table 4. The reduction of electric heater consumption by improving the efficiency of the heat pump system reduced the heating power consumption by 0.2kWh, resulting in 18.6% reduction in heating power consumption. Calculating these effects as mileage improvements is estimated to be 6.8%. According to the real vehicle assessment, the Ionic EV had a 19% difference in driving distance when heating on / off, but the Kona EV reduced the difference by 9% due to the improved efficiency of the cooling AC system due to the increase of available waste heat source.

3. Conclusion

In this paper, the following conclusions were obtained through the study of the dual coolant-cooled battery cooling system and the heat pump system utilizing battery waste heat.

(1) A dual coolant-cooled battery cooling system is to supply low-temperature cooling coolant to the battery. It is possible to supply low-temperature coolant by heat exchange through AC system in chiller or heat exchange through outdoor air temperature in the radiator.

(2) When using the AC system to cool the battery, the cooling performance increased by 1.57% compared to the radiator utilization mode under ambient air temperature of 15°C, but the power consumption increased by 75%, resulting in a 58.3% reduction in overall efficiency (COP). In other words, if the ambient temperature is low, it is better to use the radiator to cool the coolant than the AC system.

(3) With 1.45 kW waste heat, heating capacity is increased by 0.6 kW, but compression work is increased by 0.15 kW. Therefore, it is advantageous to recover waste heat since heating efficiency is increased from 2.33 to 2.57.

(4) Utilizing waste heat generated when charging batteries, heating consumption power was reduced by 0.2 kWh due to reduced use of electric heater when operating heat pumps, resulting in an 18.6% reduction in AC consumption power, improving driving fuel economy by 6.8%.

(5) As a result of the evaluation of low-temperature, full-charging driving distance certification, Ionic EV had a 19% difference in driving distance when heating was turned on / off. On the other hand, Kona EV narrowed the gap by 9% due to the improved efficiency of the cooling AC system as the available heat source and waste heat increased.

Reference

[1] De Wilde HPJ, Kroon P. Policy options to reduce passenger cars CO2 emissions after 2020.ECN. ECNE13005 2013

[2] Lukic SM, Cao J, Bansal RC, Rodriguez F, Emadi A. Energy storage systems for automotive applications. IEEE Transactions on industrial electronics 2008;55:2258-67

[3] Lowe M, Tokuoka S, Trigg T, Gereffi G. Lithium-ion batteries for electric vehicles. Duke University Center on Globalization, Governance and Competitiveness, Tech. Rep., 2010

[4] Bandhauer TM, Garimella S, Fuller TF. A critical review of thermal issues in lithium-ion batteries. Electrochemical Society 2011;158:R1-25

[5] Pesaran AA. Battery thermal models for hybrid vehicle simulations. power sources 2002;110:377-82

[6] Wang Q, Jiang, B, Li B, Yan Y. A critical review of thermal management models and solutions of lithium-ion batteries for the development of pure electric vehicles. Renewable and Sustainable Energy Reviews 2016;64:106-28

[7] K. Umezu, H. Noyana, "Air Conditioning System for Electric Vehicles, i-MiEV", JSAE 2010 annual conference, 2010

[8] Thomas KE, Newman J. Thermal modeling of porous insertion electrodes. Electrochemical Society 2003;150:A176-92.

[9] Gu WB, Wang CY. Thermal-electrochemical modeling of battery systems. Electrochemical Society 2000;147:2910-22.

[10] SAMADANI, Ehsan, et al. Impact of temperature on the A123 Li-ion battery performance and hybrid electric vehicle range. SAE Technical Paper, 2013.

[11] Amine, K, Liu J, Belharouak I. High-temperature storage and cycling of C-LiFePO 4/graphite Li-ion cells. Electrochemistry communications 2005;7:669-73.

[12] Ehrlich, G. M. Lithium-ion batteries. Handbook of batteries, 2002.35-53.

[13] Jaewan Kim, Jinwoo Oh, Hoseong Lee, Review on Battery Thermal Management System for Electric Vehicles, ATE, 149, 192-212

[14] Markus Wawzyniak (mahle), Battery thermal managment architectures and components, 2015

13th IEA Heat Pump Conference
April 26-29, 2021 Jeju, Korea

Approaching optimal high pressure by charge management in transcritical CO_2 heat pump water heater

Yu-Jia He, Xing-Yu Liang, Jia-Hao Cheng, Liang-Liang Shao*, Chun-Lu Zhang*

School of Mechanical Engineering, Tongji University, Shanghai 201804, China

Abstract

Transcritical CO_2 cycle has been widely applied in heat pump systems. Optimal high pressure is crucial to the performance of transcritical CO_2 heat pump water heater (HPWH). However, current techniques for high pressure control cannot meet the requirements of easy-to-implement and low COP loss simultaneously. From the perspective of charge management, this work aims to approach optimal high pressure in CO_2 HPWH without high pressure control.

By modeling a running CO_2 HPWH, we in-depth investigated the relationship between optimal high pressure and refrigerant charge. It was found that for practical systems, the essence of optimal high pressure control is to manage optimum refrigerant charge of the system. If the optimum charge of the system remains constant under any working conditions, the system can be guaranteed at optimal high pressure with fixed refrigerant charge. Then the influence of water inlet temperature, water outlet temperature and ambient temperature on optimum refrigerant charge was analyzed. Two system design methods with the aim of minimizing the change of optimum charge under different working conditions are presented, which are re-sizing heat exchangers and adding additional refrigerant reservoir. The minimum average COP loss of the redesigned system can be reduced to only 2.82% and 0.67%, respectively.

Keywords: Heat pump water heater; Transcritical CO_2 cycle; Optimal high pressure; Refrigerant charge management

Nomenclature

A	cross-sectional area in pipe (m^3)	V	volume (m^3)
COP	coefficient of performance (-)	v	specific volume ($m^3 \cdot kg^{-1}$)
DB	dry bulb	WB	wet bulb
EXV	electronic expansion valve	x	flowing vapor mass quality (-)
HPWH	heat pump water heater	$\dot{m}$	mass flow rate (kg s^{-1})
L	length (m)	p	pressure (kPa)
M	refrigerant charge (kg)	T	temperature (°C)
S	slip ratio		
Greek symbol			
α	void fraction	ρ	density ($kg \cdot m^{-3}$)
Subscripts			
c	condensing	GC	gas cooler
COMP	compressor	L	liquid
e	evaporator, evaporating	RES	reservoir
EVAP	evaporator	SH	superheat
G	gas	TP	two phase

* Corresponding author. Tel.: +86-136-71825-133.
E-mail address: shaollpaper@gmail.com (L.-L. Shao), chunlu.zhang@gmail.com (C.-L. Zhang).

1. Introduction

With the increasing awareness of environmental protection around the world, natural refrigerants, as carbon dioxide, have received extensive attention. Since transcritical CO_2 cycle was first proposed by Lorentzen [1, 2] in the 1990s, it has been successfully applied in heat pump systems [3-5]. The heat transfer process (gas cooling) of transcritical CO_2 cycle is in the supercritical region, which leads to high discharge temperature and large temperature glide. Therefore, CO_2 heat pump water heater (HPWH) is capable of matching water temperature profile, and supply high temperature water with rather high efficiency [6].

In supercritical region, temperature of CO_2 is independent of pressure. The change of discharge pressure will affect cooling capacity and power consumption simultaneously. Consequently, optimization of discharge pressure is crucial to system efficiency. In open literature, two main methods can be concluded for high pressure control: offline method and online method.

The offline method is primarily proposed and then thoroughly investigated. It is to fit the correlations of optimal high pressure and other parameters of the system based on thermodynamic model or experimental data. Kauf [7] first proposed a linear equation of optimal high pressure with a single variable. On this basis, Liao, Zhao [8] analyzed the influence of gas cooler outlet temperature, the evaporating temperature and compressor performance on optimal high pressure. Regressions were made to various forms of correlations. Sarkar, Bhattacharyya [9] conducted energetic and exergetic analyses for optimization, and developed correlations of optimal high pressure with gas cooler outlet temperature and the evaporating temperature. Later, many researchers have in-depth investigated different forms of optimal high pressure correlations in transcritical CO_2 cycle [10-14].

Although the offline method is simple and easy to implement, the coefficients of correlations are closely related to the structure of the system. Meanwhile, it was found by Cecchinato, Corradi [15] that the direct use of pressure control correlations might cause huge performance deterioration up to -30% in HPWHs. Furthermore, the research of Liang, He [16] indicates that for CO_2 HPWH, multiple factors will influence the optimal high pressure, resulting in complexity of control correlations.

Given the drawbacks of offline correlations, researchers recently explored a more effective way, called online method. Cecchinato, Corradi [15] proposed that a real-time algorithm is a more effective and robust solution for determining the optimal high pressure. Minetto [17] took the lead in using real-time control algorithm in a CO_2 HPWH. Zhang and Zhang [18] used the steepest descent method to update the set value of the high pressure, and realized the real-time control of the single-stage transcritical CO_2 system by using the PI controller. Later, more comprehensive work has been conducted by researchers on real-time control problems [19-23].

However, the real-time optimization algorithm of on-line method is rather complex, with long time of optimization and high cost of hardware implementation. In a word, there are still many problems unsolved in control of optimal high pressure in transcritical CO_2 system. How to achieve the optimal performance rapidly while ensuring the stability of the system still has not been fundamentally solved.

In this work, a new approach for system optimization of CO_2 HPWH is proposed. From the perspective of charge management, this work aims to approach optimal high pressure in CO_2 HPWH and spare the traditional high pressure control methods. In section 2, a simulation model based on a running CO_2 HPWH was established. In section 3, we quantitively analyzed the relationship between optimal high pressure and refrigerant charge, then proposed charge management approach. In section 4, main factors affecting optimum charge are analyzed. In section 5, two system design methods with the aim of minimizing the change of optimal charge are presented.

2. Modeling and validation

In this section, we tested a running CO_2 HPWH and established its simulation model using GREATLAB [24].

2.1. Test unit

The test unit was officially put into operation in May 2018, and the external influences such as fouling of heat exchangers are negligible. Therefore, the practical characteristics of the CO_2 HPWH can be truly reflected. The nominal heating capacity of this unit is 140kW, with water entering temperature 15°C and water supply temperature 55°C. Fig. 1 shows the schematic of the unit. Tap water is directly heated in the CO_2 HPWH, and then stored in high temperature water tank for further use.

Field test on the unit was conducted in April 2019. Refrigerant parameters and water temperatures were manually collected from the machine's control panel. Besides, in order to gain more information on the evaporator, measurement of evaporator tube wall temperatures was conducted, as shown in Fig. 2. is a summarization of the data collection.

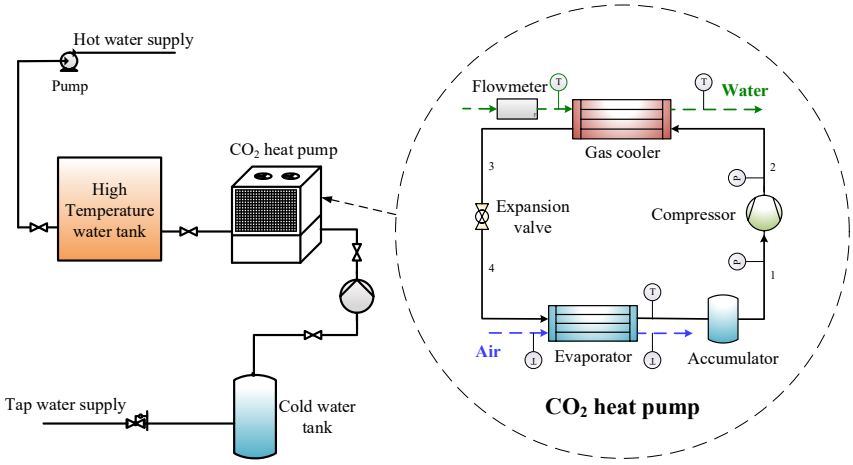


Fig. 1 Schematic of the tested CO_2 HPWH

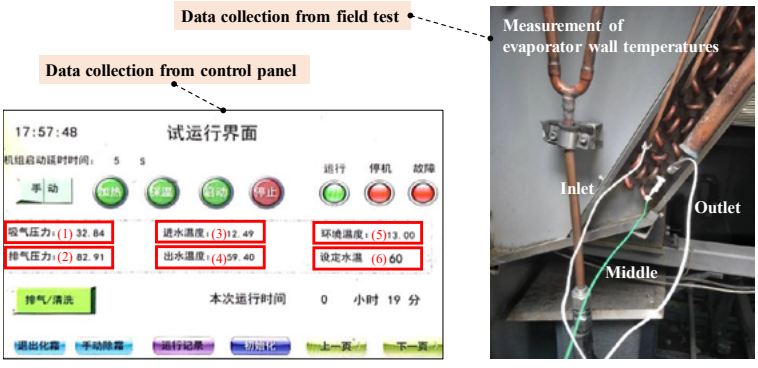


Fig. 2 Field data collection

(1) Suction gauge pressure, 32.84bar. (2) Discharge gauge pressure, 82.91bar. (3) Water entering temperature, 12.49°C. (4) Water leaving temperature, 59.40°C. (5) Ambient temperature, 13.00°C. (6) Set supply water temperature, 60°C.

Table 1 Information of data collection

Parameters	Measurement	Uncertainty
Refrigerant pressures	Panel readings	± 0.5%
Refrigerant /water temperatures		± 0.5°C
Air velocity	Air flow anemometer	± 3%
Dry bulb temperature of air	Humidity & temperature meter	± 1°C
Relative humidity of air		± 3%
Evaporator wall temperatures	Temperature meters	± 0.5°C
Hot water supply	Flow meter	± 3%

2.2. System modeling

2.2.1. Components models

According to the known information, we established a simulation model of the test unit using GREATLAB. GREATLAB is a series of in-house developed software, which focuses on refrigeration, heat pump, and air-conditioning systems modeling and analysis. Detailed information on modeling can be found in the GREATLAB references [24, 25]. Specification of the unit and component models used for system simulation are listed in **오류! 참조 원본을 찾을 수 없습니다.**.

Tube-by-tube incremental model is adopted for air-cooled finned-tube evaporator modeling. Incremental model can take detailed geometric parameters of evaporator into account, as well as air maldistribution and refrigeration distribution of the coil. Fig. 3 shows the screenshot of finned-tube heat exchangers modeling tool in GREATLAB. The geometric and other operating parameters of the actual heat exchanger are input into the modeling tool to predict the performance of the heat exchangers, including refrigeration or heating capacity, refrigerant and air temperature profiles, refrigerant and airside pressure drops, etc.

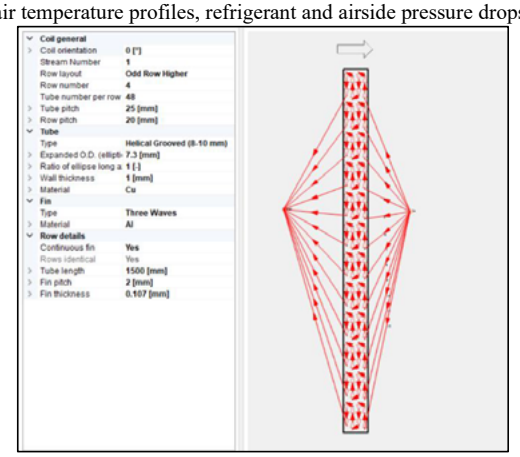


Fig. 3 Screenshot of finned-tube heat exchangers modeling tool

Table 2 Specification of the test unit

Name	Specification	Simulation model type
Refrigerant	CO_2	REFPROP 9.0[26]
Compressor	Reciprocating, single-speed	Curve-fitting model
Evaporator	Finned-tube; 4 rows; 1700mm × 914.4mm × 56mm	Incremental tube-by-tube model
Gas cooler	Brazed plate	1D incremental model
Expansion device	EXV	Curve-fitting model
Fan	4 axial fans for evaporator, single speed	Curve-fitting model

A curve-fitting model was used to describe the performance of single-speed reciprocating compressor. Namely [27],

$$y = c_1 + c_2 p_e + c_3 p_c + c_4 p_e^2 + c_5 p_e p_c + c_6 p_c^2 + c_7 p_e^3 + c_8 p_e^2 T_c + c_9 p_e p_c^2 + c_{10} p_c^3 \quad (1)$$

where y represents power consumption or refrigerant mass flow rate of the compressor. p_e and p_c stand for the suction pressure and discharge pressure for transcritical compression cycles, respectively. Coefficients c_1 - c_{10} are curve-fitted with relevant data of the compressor from manufacturer.

The Electronic expansion valve and fan were modeled using performance curves provided by the manufacturer.

Finally, with all component models in place, we developed the system model in GREATLAB [24], as shown in Fig. 4. The system solver is based on the Newton-Raphson algorithm.

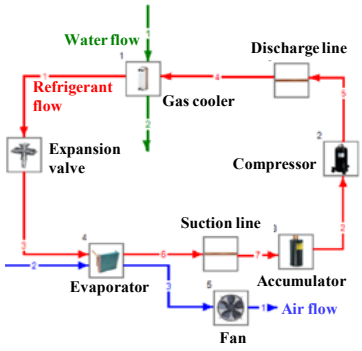


Fig. 4 Screenshot of CO_2 HPWH model in GREATLAB

2.2.2. System charge model

The total refrigerant charge of system is calculated by adding up the charge present in each component and connecting tubes, as described by

$$M = M_{\mathrm{EVAP}} + M_{\mathrm{GC}} + M_{\mathrm{COMP}} + M_{\mathrm{other}} \tag{2}$$

The evaporator is divided into two-phase section and superheat section based on the state of refrigerant. Total charge of the evaporator is calculated by summing up the charge in each discrete element:

$$M_{\mathrm{EVAP}} = M_{\mathrm{TP,e}} + \int_0^{V_{\mathrm{SH,e}}} \rho \mathrm{d}V \tag{3}$$

The total mass in two-phase section can be obtained by

$$M_{\mathrm{TP,e}} = \int_0^{L_{\mathrm{TP}}} \rho_{\mathrm{TP}} A \mathrm{d}L = \int_0^{L_{\mathrm{TP}}} [\alpha\rho_{\mathrm{G}} + (1-\alpha)\rho_{\mathrm{L}}] A \mathrm{d}L \tag{4}$$

where α represents void fraction. ρ_{G} and ρ_{L} are the density of gas and liquid, respectively. A stands for the cross-sectional area in pipe.

Therefore, the accuracy of calculated refrigerant charge is closely related to average density in two-phase section, which is determined by void fraction. Void fraction represents the cross-sectional area occupied by vapor,

$$\alpha = A_{\mathrm{G}}/A \tag{5}$$

It is assumed that the liquid and vapor phases are separated into two streams that flow through the tubes with different velocities, u_{G}, u_{L} [28]. The void fraction is generally represented as a function of various types of properties. As for refrigerant in-tube flow, it can be described as

$$\alpha = \frac{1}{1+s\left(\frac{1}{x}-1\right)\frac{\rho_{\mathrm{G}}}{\rho_{\mathrm{L}}}} \tag{6}$$

where x represents flowing vapor mass quality, namely,

$$x = \frac{\dot{m}_{\mathrm{G}}}{\dot{m}_{\mathrm{L}}+\dot{m}_{\mathrm{G}}} = \frac{\dot{m}_{\mathrm{G}}}{\dot{m}} \tag{7}$$

S is the slip ratio, estimated differently by various investigators. The zivi method [29] is mostly recommended on the basis of simplicity, where S is given by

$$S = \left(\frac{\rho_G}{\rho_L}\right)^{-\frac{1}{3}} \tag{8}$$

Due to the fluid properties of CO_2, transcritical CO_2 cycle is under high working pressures. The density ratio of gas and liquid is much smaller than traditional refrigerants. Given this, the slip ratio S is considered as a constant value of 1 during the calculations and the model is reduced to a homogeneous one.

In gas cooler, the refrigerant is supercritical single-phase fluid. Thus, the charge is calculated by the 1D incremental model:

$$M_{GC} = \int_0^{V_{GC}} \rho dV \tag{9}$$

As for the compressor, refrigerant in compressor contains single-phase vapor inside the cylinder and refrigerant dissolved in lubricant oil.

$$M_{COMP} = \rho_{COMP} V_{COMP} + M_{oil} \tag{10}$$

Finally, the refrigerant charges in the connecting tubes are calculated assuming the tubes to be adiabatic.

2.3. Model validation

In order to validate the accuracy and reliability of the simulation model, we conducted a comparison of simulation results and test data under same operating condition. The tap water entering temperature is 12.5°C, water supply temperature is 59.4°C and ambient temperature is DB 11.6°C / WB 9.0°C.

The comparison results are shown in **오류! 참조 원본을 찾을 수 없습니다.**. The error between simulation results and test data is less than 5%, which indicates desirable accuracy and reliability of the simulation model.

Table 3 Comparison of simulation results and test data

Parameter / unit	Test	Simulation	Error
Suction pressure / bar	34.4	33.8	-1.8%
Discharge pressure / bar	84.9	83.9	-1.2%
Evaporator entering temperature / °C	4.5	4.7	0.2
Evaporator leaving temperature / °C	10.3	9.6	-0.7
Dry bulb temperature of outlet air / °C	7.2	6.9	-0.3
Hot water supply / L s^{-1}	0.67	0.70	4.3%

On the other hand, the simulation model of CO_2 HPWH built in GREATLAB has also been well validated in our previous work [30]. The model was established to predict monthly power consumption of CO_2 HPWHs, as illustrated in Fig. 5. The predicted results were in good agreement with actual data, with only 0.6% deviation in sum.

Therefore, the simulation model can well predict the performance of CO_2 HPWH and be used for in-depth analysis of the system.

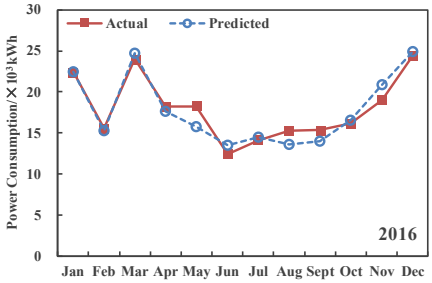


Fig. 5 Comparison between predicted and actual monthly power consumption in 2016 [30]

3. Optimal high pressure and refrigerant charge

In this section, we quantitively investigated the relation of compressor discharge pressure and overall refrigerant charge of system. Then from the perspective of charge management, a new approach for system optimization is proposed.

Based on previous research, the pressure in the high side of transcritical CO_2 cycle is determined by refrigerant charge, inside volume and temperature, as described by [31]

$$p = p(v, T) = p\left(\frac{V}{m}, T\right) \tag{11}$$

As a result, three basic approaches to controlling high pressure can be found in practical transcritical CO_2 systems. However, in most cases, inside volume of high side is fixed and temperature/pressure relation will be influenced by leakage. Thus, high-side charge control is mostly adopted pressure control method.

In systems with high-side charge control, a refrigerant buffer must be provided to ensure the evaporator won't be flooded or dried out. High-side pressure is controlled by adjusting the expansion valve, which will change the balance between mass flow rate of compressor and valve flow rate, thereby changing refrigerant mass in high side. Therefore, controlling high pressure is essentially regulating the amount of refrigerant charge actually running in the system.

Based on this deduction, we made some calculations to investigate the relation of refrigerant charge (charge in accumulator is not counted) and discharge pressure. The results are shown in Fig. 6. As the discharge pressure changes, the COP will reach the maximum value, and the corresponding pressure is the optimal high pressure. Meanwhile, with the increase of discharge pressure, the refrigerant charge of the system increases monotonously. It is indicated that the discharge pressure is in a one-to-one correspondence with refrigerant charge. Therefore, the change in discharge pressure can be truly reflected by the change in the charge amount. Furthermore, the optimal high pressure also corresponds to the optimum charge of the system. That is to say, when the refrigerant charge in the system is optimum, the system is under optimal high pressure.

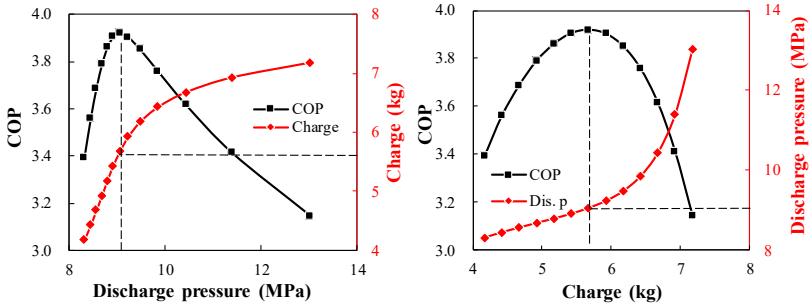


Fig. 6 The relation of optimal high pressure and optimum refrigerant charge

In a word, it was found that for practical systems, optimal high pressure control is fundamentally to manage optimum refrigerant charge of the system. Based on this conclusion, we propose that: if the optimum charge of the system remains constant under any working conditions, then the system can be guaranteed at optimal high pressure with fixed refrigerant charge. In this situation, the control objective of expansion valve switches to superheat rather than discharge pressure, which is the same as subcritical systems. Therefore, if reasonable system design methods are carried out with the aim of keeping optimum charge fixed, then the traditional high pressure control methods can be replaced by superheat control with fixed system charge.

4. Parametric analysis of optimum charge

In this section, parametric study of main factors affecting optimum charge of CO_2 HPWH and their effects is carried out. For a running CO_2 HPWH, ambient temperature, water entering and leaving temperatures are

main external factors affecting optimal high pressure. Since frosting has a significant influence on system performance, ambient wet bulb temperature is selected for further analysis. Relevant calculation conditions are shown in **오류! 참조 원본을 찾을 수 없습니다.**. At each working condition, optimum charge of system under which COP reaches maximum value is calculated. To further demonstrate the root cause of the change in optimum charge, schematic diagrams of the change of charge in each component are drawn.

Table 4 Calculation conditions

Group	Ambient temperature (wet bulb) /℃	Relative humidity	Water entering temperature /℃	Water leaving temperature /℃
A	[-25, 25]	0.6	15	55
B	15	0.6	[1, 30]	55
C	15	0.6	15	[40, 90]

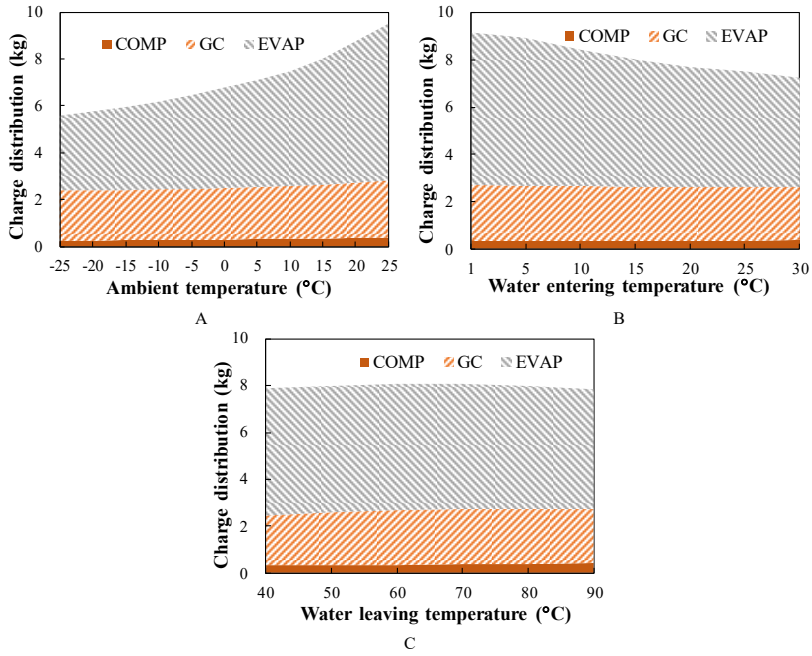


Fig. 7 The change of refrigerant charge in each component

As shown in Fig. 7A, with the increase of ambient temperature, the optimum charge of system increases by 69.6%. The change in evaporator is the main influencing factor, which accounts for 90% of the total increase. The contribution from gas cooler and compressor is 7.8% and 1.8%, respectively. The main cause is that rise of ambient temperature will lead to an increase in the evaporating temperature, resulting in significant density change in evaporator. However, the density change at high pressure side is relatively small, so that charge in gas cooler is almost unchanged.

Similarly, Fig. 7B illustrates the influence of water entering temperature on optimum charge. The optimum charge decreases by 27.9% with the increase of water entering temperature. The contribution of the change in evaporator is 97%, while of gas cooler and compressor is 4.0% and 0.5%, respectively. Since the gas cooler in HPWH is counterflow heat exchanger, an increase in water entering temperature will cause the rise of refrigerant temperature leaving gas cooler. Consequently, vapor quality of CO_2 entering evaporator will increase, resulting in mass decrease in evaporator.

The water leaving temperature has little influence on optimum charge, as shown in Fig. 7C.

In a word, ambient temperature and water entering temperature will both lead to significant change in optimum charge of CO_2 HPWH. Among all components, change in evaporator has the leading effect, while change in gas cooler and compressor have limited influence.

5. System charge management methods

According to the parametric analysis in section 4, the optimum charge of CO_2 HPWH will be influenced by working conditions, of which change in evaporator has major influence. As proposed in section 3, if optimum charge remains constant under any working condition, high pressure control in CO_2 HPWH can be replaced by traditional superheat control with fixed system charge. Therefore, in this section, two system charge management methods with the aim of restraining the change of optimum charge are proposed. Comparison with optimal high pressure system is also conducted.

5.1. Heat exchangers resizing

In the test unit, the evaporator is finned-tube heat exchanger, while gas cooler is compact brazed-plate heat exchanger. Refrigerant stored in evaporator is much more than in gas cooler. Therefore, re-sizing heat exchangers is proposed to improve the distribution of refrigerant in each component, so that the influence of change in evaporator can be restrained. Re-sized heat exchangers should also meet the nominal heating capacity requirement of the CO_2 HPWH.

Two approaches are adopted for re-sizing heat exchangers. On the one hand, reduce the inside volume of evaporator. The evaporator of the test unit is equipped with conventional 7mm heat exchange tube, which is now changed into 5mm tubes. The use of small diameter tubes can reduce charge by 30~40% in heat exchangers. Meanwhile, the capacity is ensured by increasing the number of tubes. Geometric parameters of the original and resized evaporators are listed in **오류! 참조 원본을 찾을 수 없습니다.**.

On the other hand, increase the inside volume of gas cooler. Considering the cost constraints and heat transfer capacity requirements, the number of gas cooler plates is increased by 20%.

Table 5 Geometric parameters of evaporator

Parameters	Original	Resized
Row number	4	5
Tube number	48	60
Outer diameter	7.45 mm	5.25mm
Tube pinch	25mm	19.05mm
Row pinch	20mm	11.4mm
Length between tube sheets	1.5 m	1.5m
Circuit number	12	30
Flow configuration	Cross-counter flow	Cross-counter flow
Fin pitch	1.4 mm	1.4 mm
Fin thickness	0.115 mm	0.115 mm
Fin type	Wavy	Wavy

Based on the simulation model built in section 2, we established a new system model with superheat control instead of high pressure control. In new model, the overall system charge is fixed and the accumulator is eliminated, thus referred as fixed-charge system. In the following analysis, we quantitively compared the system performance of optimum system (with optimal high pressure control) and fixed-charge system.

Considering that for air-source CO_2 HPWH, ambient temperature varies in a larger range than water entering temperature, it is chosen as independent variable for further analysis. The charge of fixed-charge system is the optimum charge when ambient temperature is 0°C.

Fig. 8 illustrates the impact of ambient temperature on charge distribution after re-sizing heat exchangers. The relative change of optimum charge is 55.9%, 13.7% less than original system. The comparison of COP is shown in Fig. 9A. When ambient temperature varies from -25-10°C, COP of optimum system and fixed-charge system is very close. However, when ambient temperature is above 10°C, the COP of fixed-charge system drops significantly. Because in fixed-charge system, the evaporator occupies more refrigerant when ambient temperature increasing. It will cause charge in gas cooler far below the optimal value, thus resulting in COP attenuation. In this situation, the average COP loss of fixed-charge system compared with optimum system is 3.51%.

Besides, COP loss could be further restrained by optimizing the charge of fixed-charge system. As shown in Fig. 9B, optimal charge exists for fixed-charge system, where average COP loss is only 2.82%.

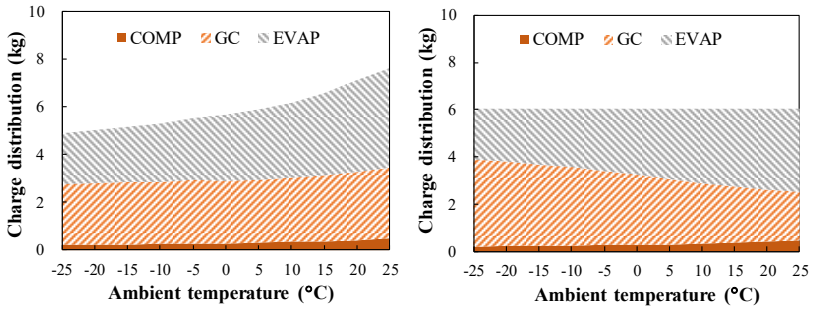


Fig. 8 Impact of ambient temperature on charge distribution after re-sizing heat exchangers

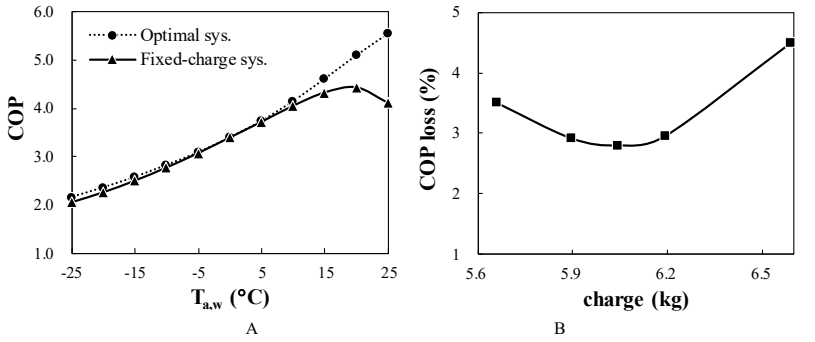


Fig. 9 COP comparison between optimum system and fixed-charge system / Impact of refrigerant charge on COP Loss in fixed-charge system

5.2. Additional refrigerant reservoir

However, the performance improvement achieved by re-sizing heat exchangers is limited for fixed-charge system. As analyzed in Section 4, change in evaporator is the predominant factor affecting optimum charge of system. If change in evaporator can be restrained, the optimum charge will remain constant in most situations. Accordingly, adding additional refrigerant reservoir is proposed in this work to make up for the change in evaporator.

Similarly, ambient temperature is chosen as independent variable. The root cause of change in evaporator is the density change affected by the evaporating temperature. Based on parametric analysis, with the increase of ambient temperature, the charge in evaporator will also increase. To offset the change in evaporator, the possible location for an additional component is the inlet and outlet of gas cooler. **오류! 참조 원본을 찾을 수 없습니다.** displays the impact of ambient temperature on density at different locations. With the increase of ambient temperature, the refrigerant density at the inlet of gas cooler and evaporator both increase. However, at the outlet of gas cooler, refrigerant density is rather large and slightly decreases. Therefore, if a reservoir is added at the outlet of gas cooler, overall charge of system will increase that change in evaporator will be weakened. Moreover, the slight decrease of density can make up for the increase in evaporator.

Table 6 Impact of ambient temperature on refrigerant density at different locations

Ambient temperature /°C	Density of CO_2 /kg·m^{-3}		
	Evaporator	GC inlet	GC outlet
-25	37.9	121.9	864.7
-15	50.5	142.2	863.5
-5	66.8	164.4	861.0

5	88.2	189.0	857.8
15	119.7	219.5	853.5
25	171.5	265.0	856.6

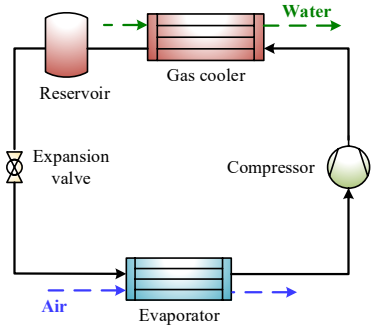


Fig. 10 CO_2 HPWH with additional reservoir at the outlet of gas cooler

Therefore, we added a reservoir at the outlet of gas cooler, as shown in Fig. 10. By changing the volume of the reservoir, we compared the system performance of optimum system and fixed-charge system. As shown in Fig. 11, when volume of high-pressure reservoir increases, the relative change of optimum charge decreases from 72% to 11%, and the average COP loss of fixed-charge system decreases from 6.35% to 0.76%. This also proved that with the decrease of the change of optimum charge, optimal system performance can be ensured by fixing refrigerant charge.

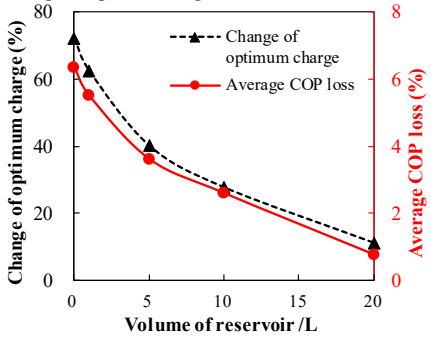


Fig. 11 Impact of reservoir volume on COP Loss and change of optimum charge

Fig. 12 illustrates when the volume of reservoir is 20L, the change of refrigerant charge in optimum system and fixed-charge system. In optimum system, with the increase of ambient temperature, charge in evaporator increases while charge in refrigerant reservoir is in decline. Therefore, the relative change of total charge decreases significantly to only 11.0%. In fixed-charge system, the change in evaporator will be offset by refrigerant reservoir, thus reducing its impact on gas cooler. In this situation, the average COP loss of fixed-charge system is only 0.76%. Moreover, with the increase of volume of reservoir, the average COP loss will be further reduced.

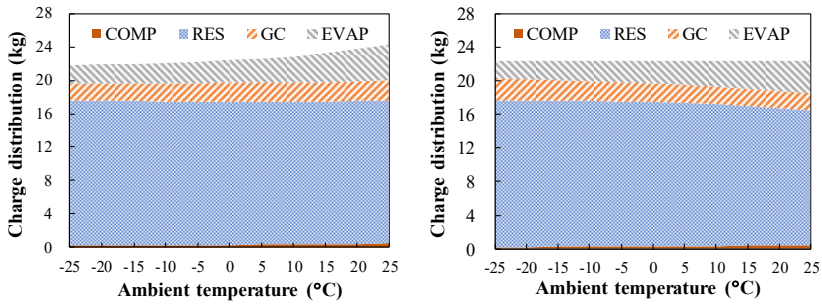


Fig. 12 The change of refrigerant charge after adding additional opponent

In summary, with reasonable charge management methods, the change of optimum charge can be effectively restrained. Then traditional high-pressure control methods can be replaced by fixing charge for robust and efficient control.

6. Conclusions

In this work, new charge management method is proposed to approach optimal high pressure rather than pressure control in CO_2 HPWH. By developing simulation model on a running CO_2 HPWH, the relation of discharge high pressure and refrigerant charge is thoroughly investigated. At last, two charge management methods are presented. Main conclusions can be drawn as follows.

The high pressure control in practical systems is fundamentally to manage refrigerant charge optimum. If optimum charge remains constant under any working condition, then the system can be guaranteed at optimal high pressure with fixed refrigerant charge.

Ambient temperature and water entering temperature both have noteworthy influence on optimum charge. Among all components, the change in evaporator has decisive effect on the change of optimum charge, accounting for 90% and 97%, respectively.

Two system charge management methods aimed at restraining the variation of optimum charge are proposed. After re-sizing heat exchangers, the change of optimum charge is 13.7% less than original system. The minimum average COP loss of fixed-charge system verses optimum system is 2.82%. After adding a high-pressure reservoir at the outlet of gas cooler, the change of optimum charge is 58.6% less than original system. The minimum average COP loss is only 0.76%.

References

[1] Lorentzen, G. and J. Pettersen, A new, effcient and environmentally benign system for car air-conditioning. International Journal of Refrigeration, 1993. 16(1): p. 4-12.
[2] Lorentzen, G., Revival of carbon-dioxide as a refrigerant. International Journal of Refrigeration, 1994. 17(5): p. 292-301.
[3] Austin, B.T. and K. Sumathy, Transcritical carbon dioxide heat pump systems: A review. Renewable and Sustainable Energy Reviews, 2011. 15(8): p. 4013-4029.
[4] Ma, Y., Z. Liu, and H. Tian, A review of transcritical carbon dioxide heat pump and refrigeration cycles. Energy, 2013. 55: p. 156-172.
[5] Cao, F., Y.L. Song, and M.J. Li, Review on development of air source transcritical CO2 heat pump systems using direct-heated type and recirculating-heated type. International Journal of Refrigeration, 2019. 104: p. 455-475.
[6] Cecchinato, L., et al., Carbon dioxide as refrigerant for tap water heat pumps: A comparison with the traditional solution. International Journal of Refrigeration, 2005. 28(8): p. 1250-1258.
[7] Kauf, F., Determination of the optimum high pressure for transcritical CO2-refrigeration cycles. International Journal of Thermal Sciences, 1999. 38(4): p. 325-330.
[8] Liao, S.M., T.S. Zhao;, and A. Jakobsenb, A correlation of optimal heat rejection pressures in

transcritical carbon dioxide cycles. Applied Thermal Engineering, 1999. 20(9): p. 831-842.
[9] Sarkar, J., S. Bhattacharyya, and M.R. Gopal, Optimization of a transcritical CO2 heat pump cycle for simultaneous cooling and heating applications. International Journal of Refrigeration, 2004. 27(8): p. 830-838.
[10] Chen, Y. and J. Gu, The optimum high pressure for CO2 transcritical refrigeration systems with internal heat exchangers. International Journal of Refrigeration, 2005. 28(8): p. 1238-1249.
[11] Agrawal, N., S. Bhattacharyya, and J. Sarkar, Optimization of two-stage transcritical carbon dioxide heat pump cycles. International Journal of Thermal Sciences, 2007. 46(2): p. 180-187.
[12] Wang, S., et al., Experimental investigation on air-source transcritical CO2 heat pump water heater system at a fixed water inlet temperature. International Journal of Refrigeration, 2013. 36(3): p. 701-716.
[13] Yang, L., et al., Minimizing COP loss from optimal high pressure correlation for transcritical CO2 cycle. Applied Thermal Engineering, 2015. 89: p. 656-662.
[14] Qi, P.C., et al., Experimental investigation of the optimal heat rejection pressure for a transcritical CO2 heat pump water heater. Applied Thermal Engineering, 2013. 56(1-2): p. 120-125.
[15] Cecchinato, L., M. Corradi, and S. Minetto, A critical approach to the determination of optimal heat rejection pressure in transcritical systems. Applied Thermal Engineering, 2010. 30(13): p. 1812-1823.
[16] Liang, X.Y., et al., Difference analysis on optimal high pressure of transcritical CO2 cycle in different applications. International Journal of Refrigeration, 2019. 106: p. 384-391.
[17] Minetto, S., Theoretical and experimental analysis of a CO2 heat pump for domestic hot water. International Journal of Refrigeration, 2011. 34(3): p. 742-751.
[18] Zhang, W.J. and C.L. Zhang, A correlation-free on-line optimal control method of heat rejection pressures in CO2 transcritical systems. International Journal of Refrigeration, 2011. 34(4): p. 844-850.
[19] Cecchinato, L., et al., A real-time algorithm for the determination of R744 systems optimal high pressure. International Journal of Refrigeration, 2012. 35(4): p. 817-826.
[20] Penarrocha, I., et al., A new approach to optimize the energy efficiency of CO2 transcritical refrigeration plants. Applied Thermal Engineering, 2014. 67(1-2): p. 137-146.
[21] He, Y., et al., Performance optimization of a transcritical CO2 refrigeration system using a controlled ejector. International Journal of Refrigeration, 2017. 75: p. 250-261.
[22] Hu, B., et al., Real-time minimization of power consumption for air-source transcritical CO 2 heat pump water heater system. International Journal of Refrigeration, 2018. 85: p. 395-408.
[23] Yin, X., F. Cao, and X.L. Wang, Investigation on the real-time control of the optimal discharge pressure in a transcritical CO2 system with data-handling and neural network method. 2nd International Conference on Energy and Power (Icep2018), 2019. 160: p. 451-458.
[24] Zhang, C.L., L. Yang, and L.L. Shao, Refrigeration and Air-Conditioning System Modeling and Analysis Using GREATLAB. Refrigeration and Air-conditioning System Modeling and Analysis using GREATLAB, 2015.
[25] Zhang, C.L., Fundamentals of Vapor-Compression Refrigeration and Air-Conditioning System Modeling. Fundamentals of Vapor-Compression Refrigeration and Air-Conditioning System Modeling, 2012.
[26] Lemmon, E.W., M.L. Huber, and M.O. McLinden, NIST Standard Reference Database 23: Reference Fluid Thermodynamic and Transport Properties-REFPROP, 2010.
[27] AHRI, AHRI Standard 571-Performance Rating of Positive Displacement Carbon Dioxide Refrigerant Compressors and Compressor Units. 2012, AHRI: Air-Conditioning, Heating, and Refrigeration Institute,Arlington,VA, USA.
[28] Rice, C.K., The effect of void fraction correlation and heat flux assumption on refrigerant charge inventory predictions. ASHRAE transactions, 1987. 93(1): p. 341-367.
[29] Zivi, S.M., Estimation of steady-state steam void-fraction by means of the principle of minimum entropy production. Journal of heat transfer, 1964. 86(2): p. 247-251.
[30] Liang, X.Y., et al., Study on annual energy performance of transcritical CO2 heat pump water heating systems in Shanghai. International Journal of Refrigeration, 2019. 107: p. 174-182.
[31] Kim, M.H., J. Pettersen, and C.W. Bullard, Fundamental process and system design issues in CO2 vapor compression systems. Progress in Energy and Combustion Science, 2004. 30(2): p. 119-174.

13th IEA Heat Pump Conference
April 26-29, 2021 Jeju, Korea

Experimental investigation on the influence of bubble pump on the DAR performance

Gawon Lee[a], Hyung Won Choi[a], Jang Seok Lee[b], Byung Ha Kang[c], Yong Tae Kang[a*]

[a]School of Mechanical Engineering, Korea University, 145 Anam-ro, Seongbuk-gu, Seoul 02841, Republic of Korea
[b]L&A Center, LG Electronics Inc., Seoul 08592, Republic of Korea
[c]School of Mechanical Engineering, Kookmin University, 77 Jungrung-ro, Seongbuk-gu, Seoul 02707, Republic of Korea

Abstract

Diffusion absorption refrigeration (DAR) system is driven by thermal energy supplied to the bubble pump. The refrigerant is heated and regenerated while flowing through the bubble pump. For this reason, the operating characteristics of the DAR cycle significantly depend on the bubble pump performance. This study focuses on the influence of the bubble pump on the operation of DAR cycle on the aspects of the cross-sectional area and the heat input. The DAR cycle uses a mixture of low GWP refrigerant and organic absorbent as the working fluids: R1234ze(E) and N,N-dimethylacetamide(DMAC). Experiments are conducted with various conditions to estimate the operating performance. The results show that the evaporation temperature tends to decrease as the cross-sectional area of the bubble pump increases, though it increases when the cross-sectional area exceeds a certain optimum level. It also turns out that the increased heat input lowers the evaporation temperature in the overall cross-sectional area range of 7.917mm^2 – 17.814mm^2.

Keywords: DAR, Refrigeration cycle, Absorption, Bubble pump, Measurement

1. Introduction

A diffusion absorption refrigeration(DAR) cycle is used for creating a cooling effect only with a heat supply. Conventional working fluids used in this system are ammonia and water which are used as refrigerant and absorbent, respectively. However, without compressor nor electric pump, this cycle has relatively a low coefficient of performance(COP). Besides, the toxicity of ammonia and high system pressure are other unfavorable characteristics.

Derived from these practical problems, there have been numerous studies focusing on enhancing COP and substituting ammonia with new refrigerants. Zohar et al. [1] announced improvements in COP when using a partially detached bubble pump compared to the one with integrated structure. Zohar et al. [2] also numerically simulated the DAR cycle operation using five different refrigerants (R22, R32, R124, R125 and R134a) and DMAC as a common absorbent, then compared the results to the ammonia/water system. Wang et al. [3] performed a numerical investigation on the DAR cycle performance operating with a binary refrigerant, R23/R134a, and an organic absorbent, DMF. Koyfman et al. [4] conducted experiments using R22 and DMAC as working fluids and analyzed the results with respect to heat input.

However, due to the serious global warming problems, adopting the low GWP refrigerants instead of the conventional refrigerants with high GWPs is taken as an important concern. And there is still a need for further research to apply such refrigerants to the DAR system. Motivated from these issues, this study focuses on experimental investigation on the operation characteristics of a low GWP refrigerant based DAR cycle. R1234ze(E) is used as refrigerant and N,N-dimethylacetamide(DMAC) is used as absorbent. Helium is chosen as auxiliary gas. After constructing the refrigeration cycle with bubble pumps with various cross-sectional

* Corresponding author. Tel.: 82-2-3290-5952; fax: 82-2-922-3260.
E-mail address: ytkang@korea.ac.kr.

areas, the evaporation temperature is measured for each case. Heat input is also varied in order to find its influence on the evaporation temperature.

2. Experiments

2.1. Experimental setup and procedure

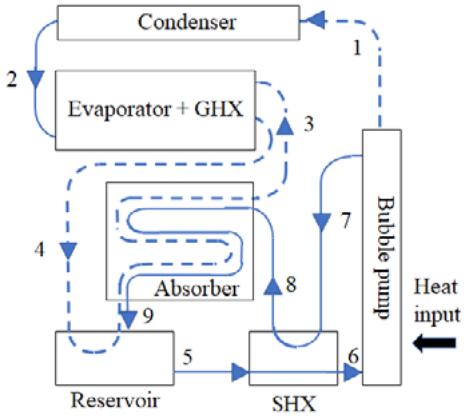


Fig. 1. Schematics diagram of the DAR cycle

Fig. 1 shows the schematic diagram of the DAR cycle. The insulated bubble pump is placed on the right side, in which the refrigerant vapor is generated(1). The condenser is installed at the top where the saturated liquid refrigerant comes out and enters the evaporator(2). The auxiliary gas and the unabsorbed refrigerant vapor also join at the evaporator(3), and evaporation takes place due to the low partial pressure. After the evaporation process, the gas mixture flows to the absorber(4) through the gas heat exchanger. Flowing upward inside the absorber, the refrigerant vapor is absorbed to the solution and the strong solution drips into the reservoir(9). The strong solution is supplied to the bubble pump after flowing through the solution heat exchanger(5, 6). After the refrigeration vapor generation, the remaining weak solution returns to the absorber(8, 8) from the top of the bubble pump(7).

The experiment is conducted by the following procedure:

(1) Separate the bubble pump from the system and set it with a new bubble pump of desired cross-sectional area.
(2) Prepare a mixture of absorbent and refrigerant to make up the concentration of experiment condition.
(3) Make the experimental setup to a vacuum state and inject the working fluid.
(4) Charge helium gas so that the internal system pressure reaches 4.5bar.
(5) Supply heat to the bubble pump with an electric heater.
(6) Measure the temperature of the evaporator using thermocouples attached to the wall.

2.2. Cross-sectional area of bubble pump

A set of experiments are conducted in order to investigate the influence of cross-sectional area on the operating temperature characteristics of DAR cycle, especially the evaporation temperature. For each test, bubble pump is replaced with a new one with different cross-sectional area. The rest of the system components and experiment conditions are maintained. The detailed experimental conditions are summarized in Table 1.

Table 1 Experiment conditions for comparisons of different cross-sectional areas

Cross-sectional area [mm^2]	Pressure [bar]	Heat input [W]	Concentration [wt%]
7.9	4.5	70	35
17.8	4.5	70	35
31.7	4.5	70	35

2.3. Heat input

Another set of experiments are performed to see the effect of heat input to the bubble pump on the cycle operation. Maintaining the basic experimental conditions of Experiment 2.2, different values of heat input are given for every type of bubble pump. The detailed conditions are given in Table 2.

Table 2 Experiment conditions for comparison of different heat inputs

Heat input [W]	Pressure [bar]	Cross-sectional area [mm^2]	Concentration [wt%]
50	4.5	7.9, 17.8, 31.7	35
70	4.5	7.9, 17.8, 31.7	35

3. Results and discussion

3.1. Cross-sectional area of bubble pump

Fig. 2 presents the evaporation temperature versus the cross-sectional area of bubble pump. Three different cross-sectional areas were tested, and the evaporation temperature was measured after the system reached a steady state. From the experimental results, it turns out that the evaporation temperature initially decreases when the cross-sectional area increases. But continuous area increase eventually leads to the increment in the evaporation temperature. Provided with the heat input of 70W, the evaporation temperatures are measured as -2.1°C, -5.2°C and 1.1°C when the cross-sectional area changes from 7.9mm^2 to 31.7mm^2. As the bubble pump gets larger, the pressure drop along the bubble pump decreases. It results in the bubble pump efficiency enhancement and more refrigerant vapor is generated, thus reducing the evaporation temperature. However, with further increasing area, the solution can only be heated up to lower the temperature under same heat input condition, causing the reduction in the refrigerant vapor generation. Also, the large cross-sectional area disrupts the formation of slug flow inside the bubble pump, which is essential in order to pump up and circulate the solution through the vertical pipe. These factors together contribute to lower refrigerant generation and higher evaporation temperature at 31.7mm^2.

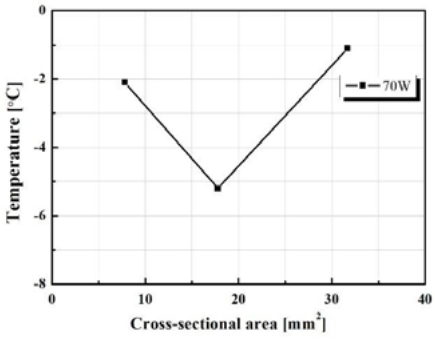


Fig. 2. Measured evaporation temperature with bubble pumps of different cross-sectional areas

3.2. Heat input

Maintaining the fundamental experimental conditions, a decreased amount of heat input is given to evaluate the influence of heat input on the evaporation temperature. The heat input value is initially set as 50W. Generally, with the increased heat input, the evaporation temperature shows a meaningfully decreasing tendency. Fig. 3 shows the evaporation temperature change when the bubble pump has a cross-sectional area of 7.9mm^2. The temperature is measured to be 0.99℃ with 50W of heat input. But it reaches a lower temperature of -2.1℃ when 70W of heat is supplied. This behavior is also observed when the cross-sectional area is increased to 17.8mm^2, as depicted in Fig. 4. As more heat is given to the bubble pump, the evaporation temperature decreases from -1.08℃ to -5.2℃. However, as seen in Fig. 5, an exceptional temperature change is observed when using a bubble pump with a larger cross-sectional area of 31.7mm^2. It turns out that the system fails to operate as a refrigerator when only 50W of heat is provided. Moreover, the system is incapable of reaching a steady state during the test time. The system shows a normal operational behavior when a larger heat input, 70W, is given. The evaporation temperature is measured as 1.1℃. Regarding the COP, the growing temperature difference between the evaporator and the surrounding leads to the increase of heat transfer. Therefore, for both heat inputs, 50W and 70W, highest COPs were obtained at lowest evaporation temperature and the values were 0.1356 and 0.1157 respectively.

The consequential temperature drop by the increased heat input is due to the increased generation of refrigerant vapor. As more thermal energy is consumed, the refrigerant mass flow rate increases, thus lowering evaporation temperature. However, when the cross-sectional area is enlarged too far, minimum value of heat needed to generate enough amount of refrigerant vapor also grows. For this reason, it is not able to obtain the cooling effect with a heat input of 50W when the cross-sectional area is 31.7mm^2.

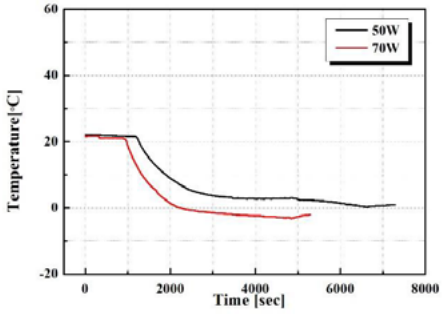


Fig. 3. Measured evaporation temperature with different heat inputs to 7.9mm^2 bubble pump

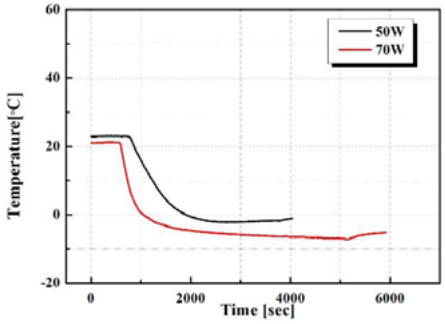


Fig. 4. Measured evaporation temperature with different heat inputs to 17. 8mm^2 bubble pump

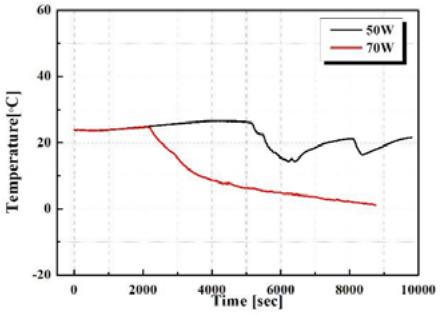


Fig. 5. Measured evaporation temperature with different heat inputs to 31.7mm^2 bubble pump

4. Conclusions

In this study, the evaporation temperatures of the DAR system using R1234ze(E) and DMAC are measured depending on the variations of cross-sectional area of bubble pump and heat inputs. The tested cross-sectional areas are 7.9mm^2, 17.8mm^2 and 31.7mm^2. Both 50W and 70W of heat inputs are given to all types of bubble pumps for comparisons. The following conclusions are drawn from the present study.

- The optimum cross-sectional area for 70W of heat input is 17.8mm^2 and the achieved evaporation temperature is -5.2℃.
- Using the bubble pump with the cross-sectional area of 7.9mm^2, the evaporation temperature decreases from 0.99℃ to -2.1℃ as heat supply increases from 50W to 70W.
- Using the bubble pump with the cross-sectional area of 17.8mm^2, the evaporation temperature decreases from -1.08℃ to -5.2℃ as heat supply increases from 50W to 70W.
- Enlarged cross-sectional area requires a higher heat supply for normal operation of the system. The system is unable to reach a steady low temperature when only 50W is given to the bubble pump with the cross-sectional area of 31.7mm^2.

Acknowledgements

This work was supported by Korea Institute of Energy Technology Evaluation and Planning(KETEP) grant funded by the Korea government(MOTIE) (No. 10060218, The development of cooling capacity 200RT class triple effect gas fired absorption chiller).

References

[1] Zohar, A., Jeluinek, M., Levy, A., Borde, I. The influence of the generator and bubble pump configuration on the performance of diffusion absorption refrigeration (DAR) system. International Journal of Refrigeration 2008;31:962-969.
[2] Zohar, A., Jelinek, M., Levy, A., Borde, I. Performance of diffusion absorption refrigeration cycle with organic working fluids. International Journal of Refrigeration 2009;32:1241-1246.
[3] Wang, Q., Gong, L., Wang, J.P., K. Cui, Sun, Chen, G.M. A numerical investigation of a diffusion absorption refrigerator operating with the binary refrigerant for low temperature applications. Applied Thermal Engineering 2011;31:1763-1769.
[4] Koyfman, A., Jelinek, M., Levy, A., Borde, I. An experimental investigation of bubble pump performance for diffusion absorption refrigeration system with organic working fluids. Applied Thermal Engineering 2003;32:1881-1894.

13th IEA Heat Pump Conference
April 26-29, 2021 Jeju, Korea

Risk assessment of built-in refrigerated display cabinet using A3 refrigerant

Koji Yamashita[a,*], Yoshihisa Sakamoto[a], Toshimasa Kato[a], Shigeki Ishihara[a], Akira Kobayashi[a], Hidekazu Kainuma[a], Takaharu Hasegawa[a], Katsuyuki Osawa[a], Hiroshi Nagai[a], Keiko Hosaka[a]

[a]The Japan Refrigeration and Air Conditioning Industry Association, 3-5-8, Shibakoen, Minato-ku,Tokyo, 105-0011, Japan

Abstract

In Japan, from 2011 to 2016, risk assessment of each type of equipment using A2L refrigerants was carried out and JRAIA standards which prescribed safe operating method were created, resulting in the relaxation of law was realized. In order to respond to demand in recent years to further lower GWP, risk assessment of built-in refrigerated display cabinet using A3 refrigerants was carried out. CFD analyses on refrigerant leakage from inside or outside the refrigerated space of each refrigerated display cabinet was carried out, the flammable volume was calculated, the ignition sources were investigated, and the ignition probability was calculated. Risk assessments were carried out at each stage of transportation, storage, installation, usage, service, and disposal. In this paper, the contents of the study and safe operating method created as a result are summarized.

Keywords: CFD analysis; Flammable volume; Ignition source; Risk assessment; Display Cabinet

1. Introduction

The use of A2L refrigerants for HVAC&R products was investigated in Japan from 2011 to 2016. Risk assessments of the products have been carried out[1], to establish methods for ensuring the safe use of the products using A2L refrigerants, resulting in the relaxation of relevant regulation and followed by product launches in Japanese market. However, further reduction of GWP are expected in response to the Kigali Amendment to the Montreal Protocol, and the Japan Refrigeration and Air Conditioning Industry Association (JRAIA) has been carrying out the risk assessment for built-in refrigerated display cabinets using A3 refrigerants.

In this paper, the duration and the mean volume of flammable region obtained by CFD analysis for each refrigerated display cabinet were formulated. The investigative findings on the characteristic ignition sources in the stages of usage and working are shown, and the methods for ensuring safe operation are explained.

2. Method of Risk assessment

Ignition probability is calculated by multiplying the temporal encounter probability representing the time rate of contacting between the ignition source and the flammable region, the spatial encounter probability representing the spatial distribution of the flammable region and the refrigerant leakage probability. Flammable region is the area where refrigerant concentration is between the lower flammability limit (LFL) and the upper flammability limit (UFL). Flammable volume is the volume of the flammable region, the time when flammable region exists is the duration of the flammable region, and the flammable volume-time integration is obtained by multiplying the duration of the flammable region and the mean flammable volume. Temporal encounter probability is calculated by using the duration of the flammable region, the duration of the ignition source and the frequency of occurrence of ignition source. Spatial encounter probability is calculated by dividing the mean

* Corresponding author. Tel.: +81-3-3432-1671; fax: +81-3-3438-0308.
E-mail address: Yamashita.Koji@aj.MitsubishiElectric.co.jp.

flammable volume by the volume of the target space. The duration of the flammable region and the mean flammable volume are obtained by CFD analyses. The ignition probability is obtained by calculating the average of the ignition probabilities weighted by operating rate for both the operation and stoppage (e.g. due to system failure) of the air circulating fan.

3. CFD Analysis of Refrigerant Leakage

CFD analysis was carried out with STAR CCM+ using the Realizable k-ε model. The subject refrigerant is R290, and the values at 25 °C in atmospheric pressure calculated by REFPROP Ver. 8.0 are used as its physical properties. The value 1.12×10^{-5} (m^2/s) calculated from the molecular diffusion equation is used as the diffusion coefficient of R290, 2.1 (vol%) and 9.5 (vol%) are used as LFL and UFL values, respectively. Leakage analysis was carried out for reach-in, horizontal and vertical open refrigerated display cabinets. Analysis models and calculation results of the reach-in refrigerated display cabinet and the horizontal refrigerated display cabinet are shown below. Validity of the results of CFD analysis has been verified by simulation of R32 leak from an indoor unit of the residential air conditioner. In addition, CFD analysis when the refrigerant was R170 (molecular weight is 30.0, LFL is 3.1 (vol%)), R1270 (molecular weight is 42.1, LFL is 2.7 (vol%)) or R600a (molecular weight is 58.1, LFL is 1.8 (vol%)) was carried out. When the refrigerant is R170 or R1270, the duration of the flammable region and the mean flammable volume are smaller than the value of R290. As a result, when the refrigerant is R600a, the mean flammable volume was almost the same as the value of R290 and the duration of the flammable region was 10 to 20 % longer than the value of R290.

3.1. Analysis of refrigerant leakage from the reach-in refrigerated display cabinet

3.1.1. Analysis model of refrigerant leakage

Because the flammable region in the shop becomes the largest when the door is fully opened rapidly after refrigerant leakage inside the refrigerated space of the reach-in refrigerated display cabinet, CFD analyses were carried out for this case. The CFD model of the reach-in refrigerated display cabinet installed in the shop with an area of 24.01 m^2 is shown in Fig. 1. The display cabinet has 1.08 m^3 of refrigerated volume, and its external dimensions are 2.0 m in height, 1.542 m in width, 0.7 m in depth. The condensing unit consists of a compressor, a condenser and a fan installed in the lower part of the display cabinet. The air is sucked from the front of the condensing unit, passes through the rear side and is exhausted from the top of the display cabinet. Area of the

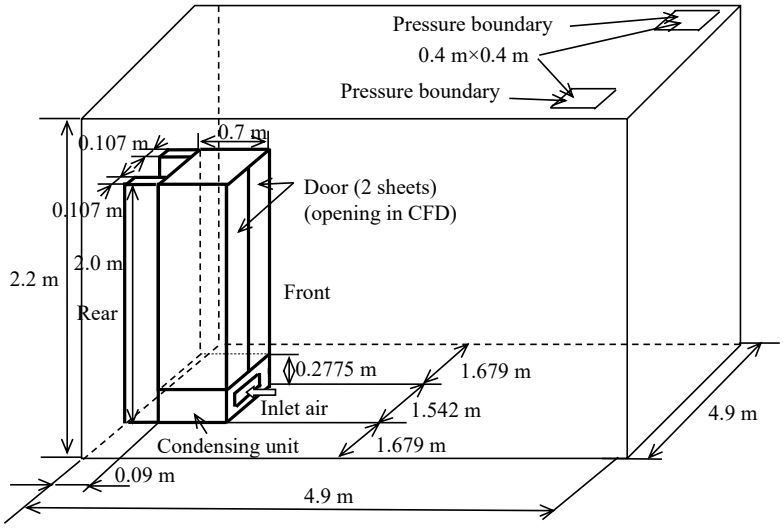


Fig. 1. CFD model of reach-in refrigerated display cabinet installed in the shop area with an area of 24.01 m^2

air inlet opening is set to 8.3×10^{-2} m^2 and the air flow rate is varied from 0 to 0.249 m^3/s, which corresponds to air velocity of 0 to 3 m/s. The display cabinet is assumed to be installed at the center of a wall of a shop with square-shaped floor, and the both corners of the ceiling opposite the display cabinet has the pressure boundaries

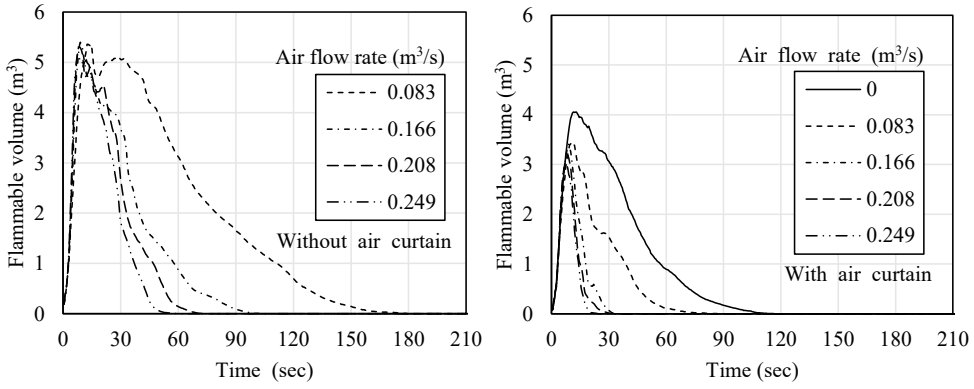
with a size of 0.4 m × 0.4 m. Both with and without the down flow air curtain from the top-front of the refrigerated space have been considered in this study. As an initial condition, the refrigerant concentration was set to be uniform in the refrigerated space. Then, the calculation was started from the state, and the refrigerant was assumed to fall naturally from the front of the display cabinet assuming that there was no door. These analyses assume the situation of the display cabinet with sliding doors. The air velocity of the air curtain is set to 2.08 m/s and the air flow rate is 0.137 m^3/s. CFD analyses were carried out for cases with the floor area of 17.14 m^2, 24.01 m^2, 36.00 m^2, 64.00 m^2 and 100.00 m^2 while the refrigerant amount was set to 0.358 kg and 0.5 kg. The dimensions of the shop were set to 4.14 m×4.14 m, 4.9 m×4.9 m, 6.0 m×6.0 m, 8.0 m×8.0 m and 10.0 m×10.0 m, respectively. The ceiling height of the shop was set to 2.2 m.

3.1.2. Calculation results of refrigerant leakage from inside of the refrigerated space

Fig. 2 shows the change with time in the flammable volume when the air flow rate of the condensing unit is varied when the floor area is 24.01 m^2 and the refrigerant amount is 0.5 kg. Fig. 2 (a) is the calculation results without the air curtain, (b) is the results with the air curtain. With the air curtain, the duration of the flammable region is shortened and the flammable volume is reduced, but the difference in values with and without the air curtain is not so great. In addition, when the air flow rate of the condensing unit is increased, the duration of the flammable region is reduced both with and without the air curtain, but the maximum value of the flammable volume is hardly reduced. Therefore, it is found when the door of the reach-in refrigerated display cabinet is suddenly opened that the large flammable volume is always generated outside the refrigerated space, although for a short time.

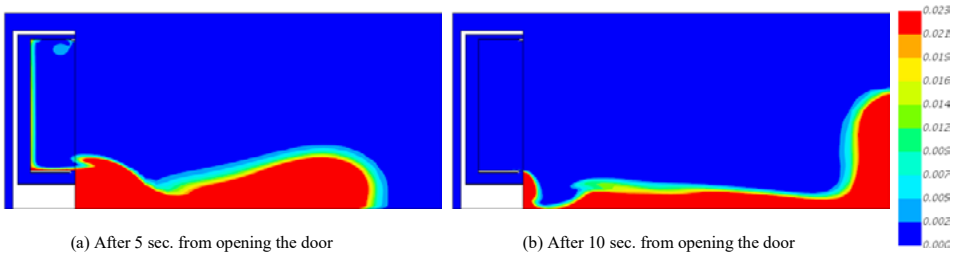
Next, the refrigerant concentration distribution at the center of the display cabinet in the store after 5 sec. and 10 sec. from opening the door are shown. Fig. 3 and Fig. 4 are figures when the floor area is 24.01 m^2, refrigerant amount is 0.5 kg, without the air curtain and the air flow rate of the condensing unit is 0 m^3/s and 0.166 m^3/s, respectively. In both cases, flammable region spreads over the entire floor surface or entire ceiling surface in a short time. As for A3 refrigerant, a relay or a thermostat of electrical equipment in the shop, a lighting switch, plugging/unplugging of power outlet and hot surfaces such as heaters are also ignition sources, and there is a risk of ignition even if the flammable region is generated for several seconds. The calculation results with the air curtain were almost the same as those without the air curtain

Since there are several types of the reach-in refrigerated display cabinet with different air flow pattern in the refrigerated space, e.g. top-face-forward discharge and bottom-front suction type refrigerated cabinet (air curtain type system), and top-rear discharge and upper-front suction type refrigerated cabinet, risk assessment by JRAIA is based on the worst-case scenario of having no air curtain, and the values with and without the air flow rate of the condensing unit are used as operating and stopping value, respectively. Fig. 5 and Fig. 6 show the calculation results of the mean flammable volume and the duration of the flammable region without the air curtain. The figures show the case with the air flow rates of 0 m^3/s and 0.166 m^3/s (air velocity of 2.0 m/s), respectively. In the figures, the horizontal axis shows the value obtained by dividing the refrigerant amount (M) by the floor area (A) inside the shop. Both the mean flammable volume (V_v) and the duration of the



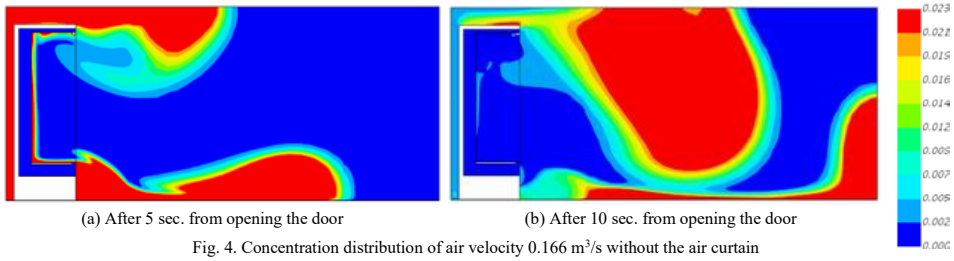
(a) Flammable volume without the air curtain (b) Flammable volume with the air curtain

Fig. 2. Change of flammable volume with time when the air flow rate of the condensing unit is varied



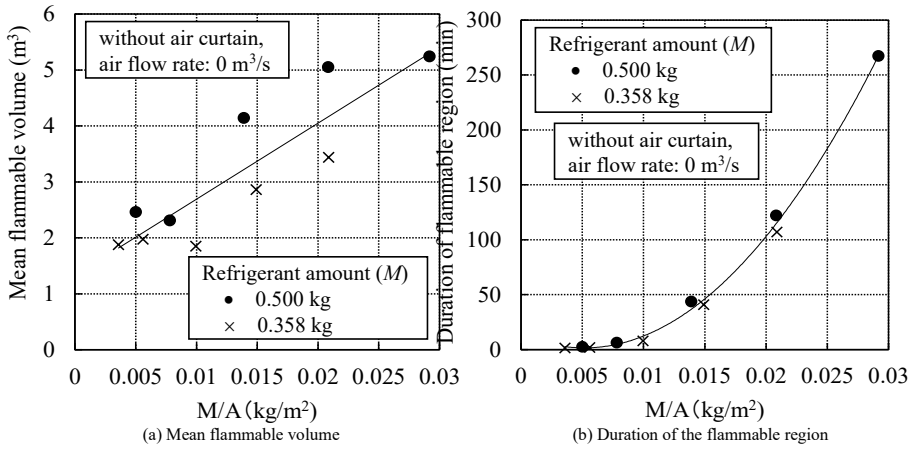
(a) After 5 sec. from opening the door (b) After 10 sec. from opening the door

Fig. 3. Concentration distribution of air velocity 0 m^3/s without the air curtain



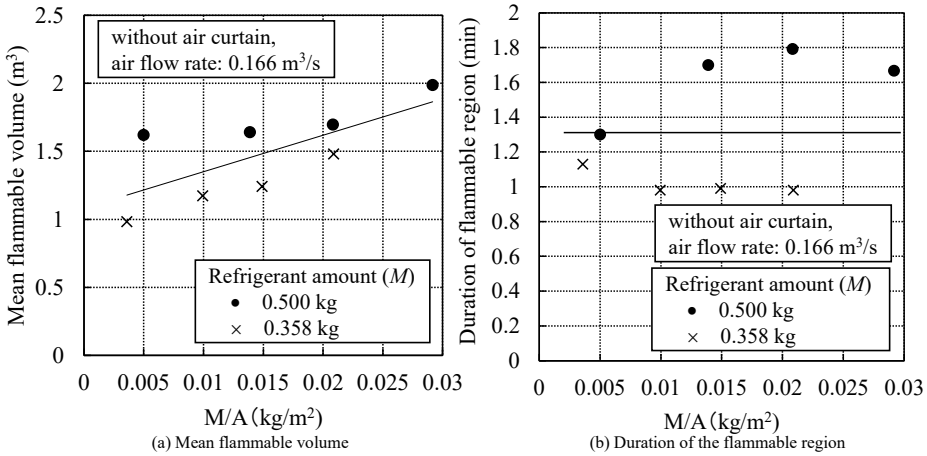
(a) After 5 sec. from opening the door (b) After 10 sec. from opening the door

Fig. 4. Concentration distribution of air velocity 0.166 m^3/s without the air curtain



(a) Mean flammable volume (b) Duration of the flammable region

Fig. 5. Duration and volume of flammable region of air flow rate 0 m^3/s without the air curtain



(a) Mean flammable volume (b) Duration of the flammable region

Fig. 6. Duration and volume of flammable region of air flow rate 0.166 m^3/s without the air curtain

flammable region (T_v) can be expressed as a function of the value M/A. The obtained least squares approximate equations are expressed by Eq. (1) to Eq. (3), and at the air flow rate of 0.166 m^3/s, the duration of the flammable region does not change so much and is expressed as an average value as shown in Eq. (4). These equations are shown as solid lines in Fig. 5 and Fig. 6, respectively. In the case of leakage inside the reach-in refrigerated display cabinet, the flammable region outside the refrigerated space did not disappear even when the air flow rate of the condensing unit was increased. This is the same even when there is the air curtain in front of the refrigerated space.

$V_v=1.36\times10^2\times(M/A)+1.34$ (air flow rate ; 0 m^3/s) (1)

$T_v=4.61\times10^5\times(M/A)^2-4.76\times10^3\times(M/A)+1.38\times10^1$ (air flow rate ; 0 m^3/s) (2)

$V_v=2.68\times10^1\times(M/A)+1.08$ (air flow rate ; 0.166 m^3/s) (3)

$T_v=1.32$ (air flow rate ; 0.166 m^3/s) (4)

3.1.3. Refrigerant leakage from the condensing unit

As a result of CFD analyses of refrigerant leakage from the condensing unit at the bottom of reach-in refrigerated display cabinet, the duration of the flammable region was almost the same as the value of the horizontal refrigerated display cabinet described in section 3.2.2 and the mean flammable volume was about half of the value of horizontal refrigerated display cabinet, when the air flow rate of the condensing unit was 0 m^3/s. CFD analysis showed that the influence of the difference in the leak rate on the generation of the flammable region was small when the refrigerant leaked from the condensing unit at the bottom of the refrigerated display cabinet. Since the lower opening area of the condensing unit of the reach-in refrigerated display cabinet was half of that of the horizontal refrigerated display cabinet, the mean flammable volume was likewise halved. And, regardless of the kind of refrigerant, if the airflow rate of the condensing unit was increased, the flammable region was not generated outside the refrigerated display cabinet in the case of refrigerant leakage from the condensing unit.

3.2. Analysis of refrigerant leakage of the open refrigerated display cabinet

3.2.1. Analysis model of refrigerant leakage from the condensing unit of the horizontal display cabinet

CFD analyses were carried out for refrigerant leakage from the condensing unit at the bottom of the horizontal refrigerated display cabinet. The CFD model is shown in Fig. 7. The external dimensions of the display cabinet are 0.81 m in height, 1.8 m in width and 1.09 m in depth. The condensing unit consists of a compressor, a condenser and a fan installed in the lower part of the display cabinet. Air is sucked from one side of the condensing unit and exhausted from another side. Area for both air inlet and outlet openings were set to 6.89×10^{-2} m^2 (0.733 m×0.094 m), and the air flow rate was varied from 0 to 0.207 m^3/s, which corresponds to air velocity of 0 to 3 m/s. The display cabinet is assumed to be installed at the center of a square-shaped shop floor. At the opening of the condensing unit, the value k and ε were set to 1×10^{-4}, the refrigerant concentration was set to 100% when the air flow rate was 0 m^3/s, and the concentration when the air flow rate exceeded 0 m^3/s was set to calculated value. When the air flow rate was 0 m^3/s, the refrigerant was leaked evenly from both air inlet opening and air outlet opening. The refrigerant was leaked from the air outlet opening when the air flow rate was over 0 m^3/s. CFD analyses were carried out for the cases with the floor area of 15.21

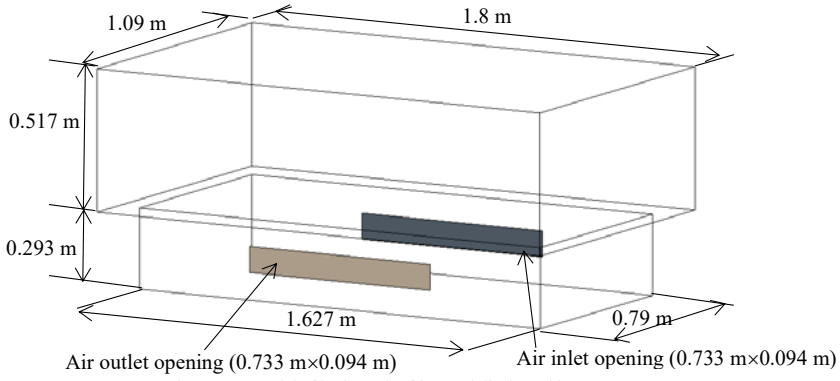


Fig. 7. CFD model of horizontal refrigerated display cabinet

m^2, 24.01 m^2, 36.00 m^2, 64.00 m^2 and 100.00 m^2 while refrigerant amount was 0.5 kg. The dimensions of the shop were set to 3.9 m×3.9 m, 4.9 m×4.9 m, 6.0 m×6.0 m, 8.0 m×8.0 m and 10.0 m×10.0 m, respectively. The ceiling height of the shop was set to 2.2 m.

3.2.2. Calculation results of refrigerant leakage from the condensing unit of the horizontal display cabinet

At the first, the calculations were performed when the leak rate was set to the value at which the total refrigerant amount was leaked in 4 minutes. The leak rate was 7.5 kg/h for 0.5 kg, and 5.37 kg/h for 0.357 kg. Fig. 8 shows the calculation results of the mean flammable volume and the duration of the flammable region when air flow rate of the condensing unit of the horizontal refrigerated display cabinet is 0 m^3/s. Its horizontal axis shows the value obtained by dividing the refrigerant amount (M) by the area (A) inside the shop. Both the mean flammable volume (V_v) and the duration of the flammable region (T_v) can be expressed as a function of the value M/A. The obtained least squares approximate equations are expressed by Eq. (5) and Eq. (6) and as solid lines in Fig. 8, respectively. If the airflow rate of the condensing unit was increased, flammable region was not generated outside of the refrigerated display cabinet at the time of refrigerant leakage from the condensing unit.

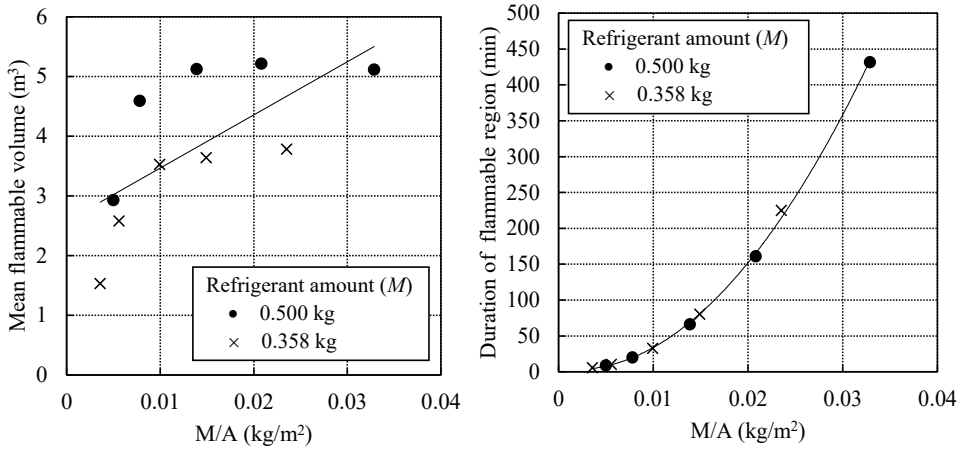
$$V_v=8.90\times10^{1}\times(M/A)+2.58 \quad \text{(air flow rate ; 0 } m^3/s) \tag{5}$$

$$T_v=4.41\times10^{5}\times(M/A)^2-1.42\times10^{3}\times(M/A)+3.94 \quad \text{(air flow rate ; 0 } m^3/s) \tag{6}$$

As for the leakage from the condensing unit, when the air flow rate of the condensing unit was set to 0.150 m^3/s calculated by Eq. (7) proposed by Colbourne et al. [2], no flammable region was generated outside the display cabinet. Similar results were obtained when the refrigerant was changed to R170, R1270, or R600a.

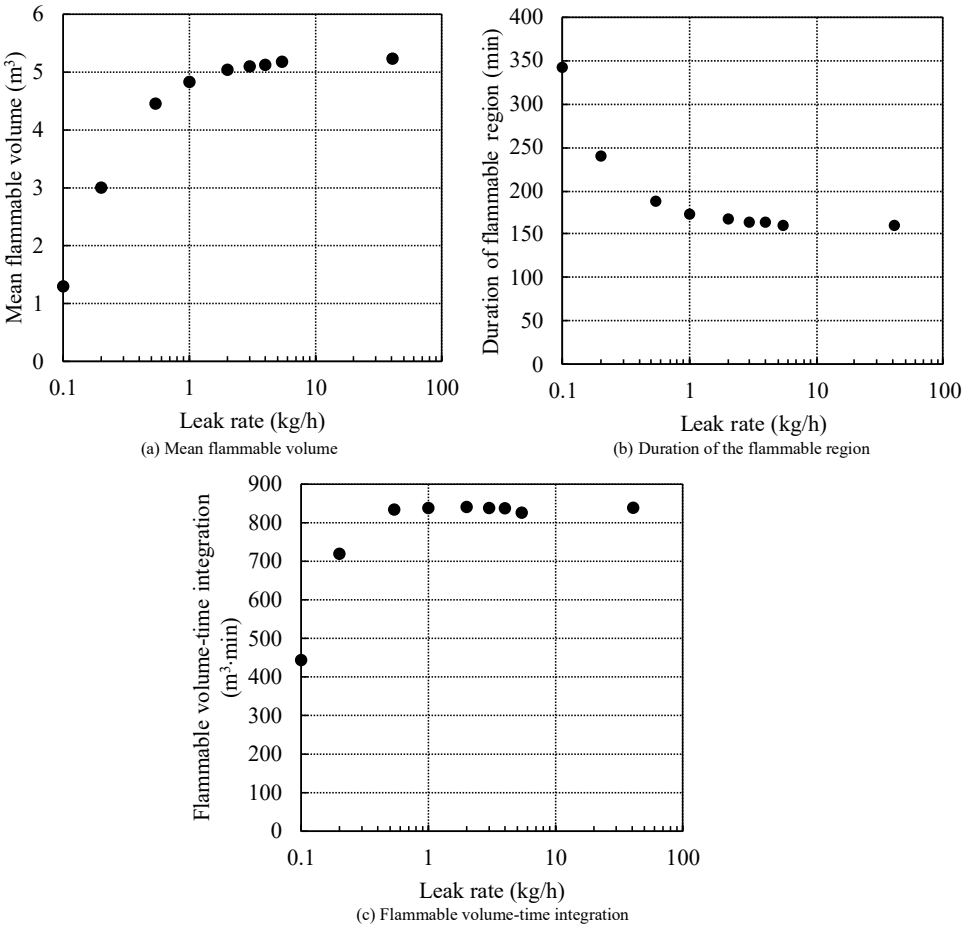
$$Q \geqq \frac{5\times\sqrt{A_0}\times w^{3/4}}{h_0^{1/8}\times\{G\times(1-F)\}^{5/8}} \tag{7}$$

Next, the calculations were performed when the leak rate was varied from 40.71 to 0.1 kg/h when the shop area of 24.01 m^2, the refrigerant amount of 0.5 kg, and the condenser air flow rate of 0 m^3/s. The calculation results of the mean flammable volume, the duration of the flammable region and the flammable volume-time integration are shown in Fig. 9. The mean flammable volume is almost the same when the leak rate is 2 kg/h or faster, and begins to decrease when the leak rate becomes slower than that, and the value at the leak rate of 0.2 kg/h was about 60% of that at 2 kg/h and the value at 0.1 kg/h was about 25%. The duration of the flammable region increases when the leak rate is decreased because the time from the start to the end of the refrigerant leakage becomes long. The flammable volume-time integration was almost the same at leak rate of 0.54 kg/h or faster, and begins to decrease when the leak rate becomes slower than that, but the value at 0.1 kg/h is about 50% of that at 0.54 kg/h. Therefore, the refrigerant leak from the condensing unit at the bottom of the display cabinet generates a sufficiently large flammable region even of the slow leak rate, and it is necessary to calculate the ignition probability considering all leaks including slow leak in the risk assessment. The slow leak rate is 1 kg/h for R32 and 0.54 kg/h when converted to R290.



(a) Mean flammable volume (b) Duration of the flammable region

Fig. 8. Calculation results for a horizontal refrigerated display cabinet at air flow rate of 0 m^3/s



(a) Mean flammable volume

(b) Duration of the flammable region

(c) Flammable volume-time integration

Fig. 9. Calculation results when leak rate varies

3.2.3. Refrigerant leakage from inside the refrigerated space of the open refrigerated display cabinet

Since the air curtain is formed in the upper opening of the horizontal refrigerated display cabinet and built-in refrigerated display cabinet has a small refrigerant amount, almost of the refrigerant leaked inside of the refrigerated space does not leak outside the refrigerated space.

As a result of CFD analysis for refrigerant leakage from inside of the vertical refrigerated display cabinet, a slight flammable region was generated outside the refrigerated display cabinet when there was no airflow outside the refrigerated display cabinet. However, there was nearly no generation of the flammable region outside the display cabinet, even with little airflow, when there was the condensing unit at the bottom.

3.2.4. Refrigerant leakage from the condensing unit of the vertical refrigerated display cabinet

Behavior at the time of refrigerant leakage from the condensing unit at the bottom of the vertical refrigerated display cabinet is the same as the condensing unit of the reach-in refrigerated display cabinet.

4. Calculation of Ignition Probability and Safety Measures

4.1. Equations for calculating ignition probability

Temporal encounter probability (P_t) representing the time rate of contacting between the ignition source and the flammable region is calculated by using Eq. (8), based on the theory of geometric probability[3], using

the total time of the target stage (T_a), the duration of the flammable region (T_v), the duration of the ignition source (T_I) and the frequency of occurrence of ignition source (n). Here, the frequency of occurrence of ignition source (n) is the number of times that the ignition source is ignited within the total time of the target stage (T_a). The coefficient k is a coefficient representing the abundance ratio of the ignition source, dissemination rate of the electric equipment, or the degree of concentration when operation of the ignition source concentrates in a certain time zone. Spatial encounter probability (P_s) is calculated by Eq. (9), using the mean flammable volume (V_v) and the volume of the target space (V_a). Ignition probability (P) is calculated by Eq. (10), using the temporal encounter probability (P_t), the spatial encounter probability (P_s) and the refrigerant leak probability (P_R).

$$P_t=k\times[1-\{1-(T_I+T_v)/T_a\}^n] \quad (8)$$

$$P_s=V_v/V_a \quad (9)$$

$$P=P_t\times P_s\times P_R \quad (10)$$

Assuming the allowable value of ignition probability is on the level of a serious accident occurring once every 100 years, the allowable value was set to 5.26×10^{-9} by using 1.9 million units which is the number in operation in the market. Also, since the work is carried out by experts, the allowable value at the time of work was set to 5.26×10^{-8} which is 10 times the value for usage.

4.2. Calculation of ignition probability at usage stage and safety measures

Ignition probability for convenience stores in Tokyo, Japan was investigated. Table 1 shows the main ignition sources assumed at the usage stage. Static electricity is assumed to occur at a humidity of 30% or less, the occurrence probability was set to 18.7 % at the shop temperature and the discharge time was set to 1 μsec. It is assumed that ignition does not occur if air is flowing around the brush motor at velocity sufficiently higher than the burning velocity of the refrigerant, and ignition occur only when the brush motor turns on. The electric spark discharge time was set to 5 msec. Additionally, ignition accidents involving electrical equipment were also taken into consideration, based on survey data of the National Institute of Technology and Evaluation (NITE). The air flow rate of the condensing unit of the display cabinet was assumed to be set at the air flow rate at which flammable region does not generate. Regarding leakage from the condensing unit, it is assumed

Table 1 Ignition sources assumed at the usage stage

Name	Type	T_i (sec.)	n	k	Note
Coffee machine	Electric spark	5×10^{-3}	186	1	Relay operates when selling
Switch of deep frying machine	Electric spark	5×10^{-3}	10	1	Cooking every 4 hrs in a span of 20 hrs
Chinese-style buns steamer	Electric spark	5×10^{-3}	10	1	Cooking every 4 hrs in a span of 20 hrs
Heating appliance for “Oden”	Electric spark	5×10^{-3}	10	1	Cooking every 4 hts in a span of 20 hrs
Power outlet	Electric spark	5×10^{-3}	4	0.5	Unplugging twice a day for cleaning; occurrence ratio: 50 %
Light switch	Electric spark	5×10^{-3}	4	1	Switch on/off twice a day
Copier	Electric spark	180	50	1	50 times in a day, usage time 3 min. per time
Brush motors of other equipment	Electric spark	5×10^{-3}	144	0.01	Turn on 6 times in a hour. dissemination rate: 1 %
Static electricity (door of reach-in refrigerated display cabinet)	Electrostatic spark	1×10^{-6}	434	0.187	Taking out iced coffee
Static electricity (exterior of open refrigerated display cabinet)	Electrostatic spark	1×10^{-6}	22	0.187	Shoppers touch metallic parts
Static electricity (other doors)	Electrostatic spark	1×10^{-6}	22	0.187	Assumed to share the same value as above
Electronic lighter	Open flame	5	5	1	Five people trying ignition in a day
Combustion type boiler	Open flame	3.6×10^{4}	1	0.0001	Use 10 hrs in a day, Dissemination rate: 0.01%

Table 2 Safety measures for usage stage

Safety measures
1. The fan of the condensing unit is operating even while defrosting.
2. The air flow rate of the condensing unit is set to a specified value or higher
3. Equipped with the function of detecting refrigerant leakage into the refrigerated space of reach-in refrigerated display cabinet, and function of shutting off the refrigerant leakage into the refrigerated space in case of refrigerant leakage.

that no flammable region is generated during operation, but flammable region is generated during stoppage such as defrosting or system failure. The mean flammable volume and the duration of the flammable region were calculated by Eq. (5) and Eq. (6), respectively. As for the refrigerant leakage from inside the refrigerated space of the reach-in refrigerated display cabinet, Eq. (3) and Eq. (4) were used to calculate the mean flammable volume and the duration of the flammable region at operation, and Eq. (1) and Eq. (2) were used for cases of stoppage. The effective area in the shop where the leaked refrigerant can diffuse is set to 84.7 m^2, and the refrigerant amount of each refrigerated display cabinet is set to 0.5 kg. M/A was set to 0.0059 in Eq. (1) through Eq. (6). It is assumed that no flammable region is generated outside the refrigerated space at the time of refrigerant leakage from inside of the refrigerated space of the open refrigerated display cabinet. It is necessary to also consider the slow leak rate in the risk assessment for A3 refrigerants, shown in Fig. 9, though only the rapid leak rate, 10 kg/h for R32 (5.4 kg/h when converted to R290), or higher was considered in the risk assessment for A2L refrigerants. Refrigerant leakage probability in usage was calculated based on the survey results of refrigerant leak accidents in the market involving built-in refrigerated display cabinets manufactured by JRAIA member companies. The refrigerant leak probability was set to 1.00×10^{-3}.
As a result, the ignition probability exceeded the allowable value, and fell to the allowable value or less by taking the safety measures shown in Table 2. In the reach-in refrigerated display cabinet, the ignition probability exceeds the allowable value even if only a slight flammable region is generated outside the refrigerated space when the door is suddenly opened after the refrigerant leak in the refrigerated space. It was possible to prevent the generation of the flammable region outside the refrigerated space at the time of opening the door suddenly by detecting the refrigerant leakage in the refrigerated space in the reach-in refrigerated display cabinet and shutting off the refrigerant circuit. As a result, the ignition probability was reduced to be not higher than the allowable value. It was also confirmed that the ignition probability became not more than the allowable value even if the duration of flammable region was set to the value of R600a.

4.3. Calculation of ignition probability at various working stage and safety measures

In the various working stages, such as transportation, storage, installation, repair and disposal, ignition sources were assumed and the ignition probabilities were calculated. Table 3 shows the main ignition sources assumed at each stage. Transportation on a minivan with an internal volume of 2.9 m^3 was assumed as the transportation stage. Storage was assumed to be in a medium-sized warehouse of 1000 m^2 or a small-sized warehouse of 15 m^2 in storage stage. For installation, repair and disposal, ignition sources described in Table 1 were considered in addition to the ignition sources at the time of work since such work is carried out while using the equipment in the shop. Static electricity is assumed to occur at a humidity of 30% or less, and the occurrence probability was set to 18.7 % annually at shop temperature, 54.5% in winter at shop temperature, 3.2% at outdoor temperature, and the discharge time was set to 1 μsec. As for the refrigerant leakage probability, the value was calculated for each stage by using the value of human error or similar value. The mean flammable volume and the duration of the flammable region were calculated by Eq. (3) and Eq. (4) for the value at the

Table 3 Ignition sources assumed at each working stage

Name	Type	T_i (s)	n	k	Note
Common; Smoking by workers	Open flame	4.5×10^{1}	1/hour	0.282	Cigarette smoked: 1 stick/person/hrs; ignition time with lighter: 5 sec.; duration of high cigarette temperature: 40 sec.; smoking rate: 28.2%
Transportation (minivan)					2 hrs, 2 workers
Static electricity when the key contacts	Electrostatic spark	1.0×10^{-6}	2	0.04675	2 times, discharge ration: 25 %
Static electricity when undressing	Electrostatic spark	1.0×10^{-6}	1/person	0.1362	Acrylic sweater: 1 time per person; discharge ratio: 12.5 %
Storage (small-sized warehouse)					2 hrs, 2 workers, 15 m^2
Static electricity	Electrostatic spark	1.0×10^{-6}	1/person	0.064	Contact with worker (reuse, without cover)
Heater	Open flame	7.2×10^{2}	1	0.082	Usage of 120 days per year; usage rate: 25%
Install, repair or disposal					1 to 4 hrs, 1 to 2 workers
Ignition source in usage-					See Table 1
Power outlet	Electric spark	5.0×10^{-3}	2	0.25	Unplugging; occurrence rate: 25%
Electric screwdriver	Brush motor	3.0	10	0.05	Opening/closing screws; occurrence rate: 5%
Static electricity	Electrostatic spark	1.0×10^{-6}	10	0.187 /person	Contact with display cabinet
Burner for brazing	Open flame	1.2×10^{2}	4	1	2 min × 2 places

Table 4 Safety measures for working stage

Stage	Safety measures
Transportation (for minivan transportation only)	1. Marking of warning of risk of fire on the product 2. Using a portable leak detector and ventilating after detection of leakage
Storage	1. Use of work gloves to prevent electrostatic discharge 2. Marking of warning of risk of fire on the product and packing
Installation	1. Use of work gloves to prevent electrostatic discharge 2. Marking of warning of risk of fire on the product 3. Using a portable leak detector and stopping the working at the time of leakage
Repair	1. Use of work gloves to prevent electrostatic discharge 2. Using a portable leak detector and diffusing refrigerant to the surroundings at the time of leakage (e.g. electric fan, paper fan)
Disposal	1. Use of work gloves to prevent electrostatic discharge 2. Using a portable leak detector and stopping the working at the time of leakage

time of leakage inside the refrigerated space, and Eq. (5) and Eq. (6) for the value at the time of leakage from the condensing unit.

As a result, the ignition probability exceeded the allowable value at all stages, and fell to the allowable value or less by taking the safety measures for each stage shown in Table 4. It was also confirmed that the ignition probability became not more than the allowable value even if the duration of flammable region was set to the value of R600a.

5. Conclusion

For built-in refrigerated display cabinet using A3 refrigerant, CFD analysis of refrigerant leakage from inside the refrigerated space and from the condensing unit of each display cabinet were carried out, and risk assessments at the stages of usage and working were carried out by using the CFD results. This led to the clarification of methods to ensure safe operation of the equipment.

(1) Flammable region was generated outside of the refrigerated space when the door was opened suddenly after all refrigerant leaked in the reach-in refrigerated display cabinet. Approximate equations using R290 were introduced to calculate the mean flammable volume and the duration of the flammable region without the air curtain and with or without the airflow of the condensing unit.

(2) Equations were introduced to calculate the mean flammable volume and the duration of the flammable region with or without the airflow of the condensing unit in case of refrigerant leakage of R290 from the condensing unit of the horizontal refrigerated display cabinet.

(3) Flammable region was not generated when the air flow rate was set to a specified value or higher at the time of refrigerant leakage from condensing unit.

(4) Risk assessments were carried out by identifying the ignition sources at the stages of usage and working for a convenience store. The ignition probability using A3 refrigerants such as R290 or R600a at the usage stage did not exceed the allowable value by taking safety measures, such as the product function enabling the fan of the condensing unit to keep operating even while defrosting, the function of detecting refrigerant leakage into the refrigerated space of reach-in refrigerated display cabinet and the function of shutting off the refrigerant leakage into the refrigerated space at the time of refrigerant leakage. The safety measures at each stage of working were also clarified.

Acknowledgements

This study was carried out by member companies of JRAIA, Mitsubishi Electric and its affiliate, Sanden Retail Systems, Okamura, Toshiba Carrier, Nakano Refrigerators, Panasonic, Fukushima Industries, Fuji Electric, and Hoshizaki. Observers from each company are Hiroichi Yamaguchi, Makoto Handa, Takeshi Shinmyou, Masahiro Onoguchi, and Akio Oki, who cooperated with this study. The authors would like to deeply appreciate these members support.

Nomenclature

A	shop area (m^2)
A_0	area of air outlet (m^2)
F	coefficient (safety factor), equal to 0.25
G	LFL (kg/m^3)
h_0	height of centerline of air outlet (m)
k	coefficient
M	refrigerant amount (kg)
n	frequency of occurrence of ignition source
P	ignition probability
P_R	refrigerant leak probability
P_s	spatial encounter probability
P_t	temporal encounter probability
Q	air flow rate of outlet air (m^3/s)
T_a	total time of target stage (s)
T_i	duration of the ignition source (s)
T_v	duration of the flammable region (s)
V_a	volume of target space (m^3)
V_v	mean flammable volume (m^3)
w	refrigerant leak rate (kg/s)

References

[1] Yajima, R., Kiguchi, Y., Sekine, T., Sasaki, S., Ito, S., Yamashita. K., Kannon, T., 2016. Risk Assessment for VRF System with Mildly Flammable Refrigerants. Trans. JSRAE 33(1), 23-39. (in Japanese).

[2] Colbourne, D., Suen, K. O., 2018. “Minimum Airflow Rates to Dilute R290 Concentrations Arising from Leaks in Room Air Conditioners”. Proc. 13th IIR Gustav Lorentzen Conference. Valencia, Spain, paper 1104.

[3] Okabe, Y., 2010. Probability and Statistics. Asakura Publishing, Tokyo, 131-133. (in Japanese)

13th IEA Heat Pump Conference
April 26-29, 2021 Jeju, Korea

Economical and environmental data analysis of hybrid HVAC system of air source heat pump and natural gas furnace for cold climate - Canada

Gulsun Demirezen[a,*], Khalid Ullah[a], Amirali Rokn[a], Dr. Alan S. Fung[a]

[a]Department of Mechanical and Industrial Engineering, Ryerson University, Toronto, M5B 2K3, Ontario, Canada

Abstract

This preliminary study is part of a bigger cloud-based Smart Dual Fuel Switching System (SDFSS) for hybrid heating, ventilation and air conditioning (HVAC) systems. The SDFSS being developed enables flexible and cost-optimized control between the natural gas furnace and air source heat pump (ASHP), allowing simultaneous reduction in energy costs and greenhouse gas (GHG) emissions. To meet the optimal energy consumption requirements and satisfaction of the residents, the employment of smart sensors and software are broadly used. By using experimental data retrieved from an actual near net-zero energy house (nNZEH), this study investigates the GHG emissions as well as the energy costs from the combined electricity consumption of the ASHP and the natural gas consumption from the furnace. The results demonstrate the potentials for large-scale implementation and deployment of such smart control strategy for hybrid residential HVAC system of natural gas furnace and air source heat pump in reducing overall GHG emission in a cost-effective manner in cold climate of province of Ontario, Canada where relatively expensive but clean source of electricity is available. These results demonstrate the potential for large-scale implementation and deployment of a SDFSS in colder climates such as in Canada.

© HPC2020.
Selection and/or peer-review under responsibility of the organizers of the 13th IEA Heat Pump Conference 2020.

Keywords: ASHP;greenhouse gas emissions; hybrid HVAC system; natural gas furnace; data analytics

1. Introduction

To minimize the negative impacts of climate change, the United Nations Framework Convention on Climate Change (UNFCCC) developed the Paris Agreement [1]. This Agreement aimed to unite all countries to mitigate the impacts of and to adapt to climate change and find ways to reduce greenhouse gas (GHG) emissions. After signing this Agreement, Canada also introduced the Pan-Canadian Framework on Clean Growth and Climate Change (the Pan-Canadian Framework) to help address the impacts of climate change nationwide. Similar to the Paris Agreement, the Pan-Canadian Framework encourages innovation and the development of technology to find efficient energy solutions to help minimize climate change impacts. Additionally, the Federal Government of Canada has recently introduced taxes for carbon pollution. Moreover, the Pan-Canadian Framework has set an ambitious target to reduce GHG emissions by 30% by 2030 and by 80% by 2050, relative to 1990 levels [2].

A breakdown of Canadian GHG emissions by sector is shown in Figure 1, demonstrating that the residential sector produces a significant portion of GHG emissions. Moreover, Canada Green Building Council (CaGBC) established a building code to reduce energy use by 50% for one million homes in Toronto while working to meet Canada's 2030 goals of constructing net-zero energy buildings (NZEB)s. To achieve this goal, one of

* Corresponding author.
E-mail address: gulsun.demirezen@ryerson.ca

Canada's strategic plans for promoting systems and technologies that minimize natural gas and fossil fuel usage while increasing the use of clean electricity.

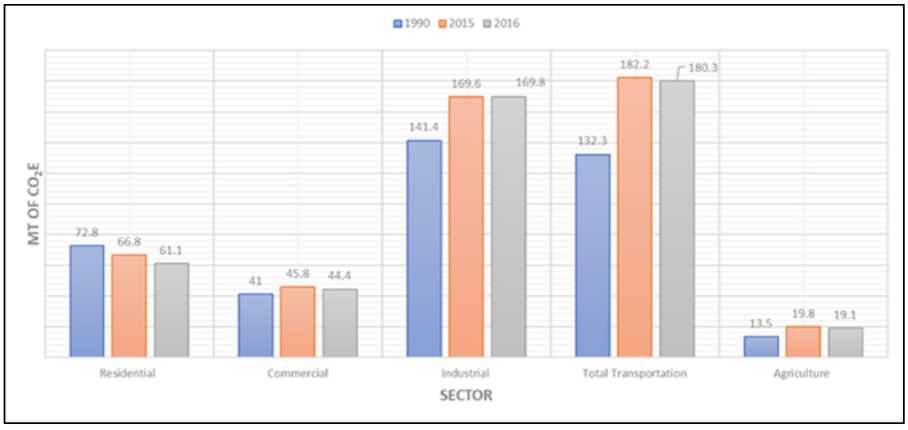


Fig. 1. Breakdown of Canadian GHG emissions by sectors [3]

Buildings are Ontario's third-largest source of emissions, representing about 19% of the province's total GHG emissions. Additionally, the residential sector's heating demand contributes to 80% of the total household energy consumption [3]. This suggests that energy consumption in buildings is a key contributor to GHG emissions. Regardless of the type of fuel that is being used for space heating, energy demands are increasing in the Canadian residential sector. Meanwhile, the combination of North America's cold climate condition and outdated HVAC control systems is contributing to higher energy consumption and increasing GHG emissions.

Even though most governments and scientists agree on being fossil-free as soon as possible, there is still room for greater technological innovation to help achieve their goal of reducing GHG emissions and energy costs. Therefore, it is important to introduce a technology that addresses this transition period before Canada becomes 100% carbon neutral.

For Canada to meet its energy reduction commitments by 2030 and 2050, low fossil fuel energy sources such as an ASHP could be considered an alternative to help reduce natural gas usage in residential buildings. However, only using electricity to meet residential buildings' heating/cooling demands is not feasible technically and economically as electricity is more expensive than natural gas in Canada [citation]. With this being said, hybrid electric ASHPs and natural as (NG) furnace systems are viewed as a lower-cost option that is better for the environment [4, 5, 6].

Although numerous research work has been conducted for managing the energy demand, smart dual fuel switching systems (SDFSS) are rarely found in the literature. The studies mentioned in [7] and [8] discussed three strategies for operating the energy demand of an archetype house through the optimal utilization of an electric air-source heat pump (ASHP) and a natural gas-fired mini-boiler using a predictive controller. To address this, a working cloud- based SDFSS prototype was implemented and tested for a one-year period in 2018 to account for the entire heating and cooling seasons. The house is located in the town of Strathroy, Ontario, Canada and is a near net-zero energy house (nNZEH). This paper studies the effects of the newly developed SDFSS system and its ability to reduce GHG emissions while considering the economic impacts of electricity and NG consumption from the HVAC equipment.

2. Case Study Description

The developed SDFSS system was implemented in a newly constructed house with 2586 sqft of conditioned living space (combined main floor and basement) and is owned and occupied by a retired couple with two dogs. A photograph of the house is presented in Figure 2. The house has a rooftop mounted PV (photovoltaic) array with a total capacity of 8.745 kWp and uses a hybrid electric ASHP, a NG furnace, and an electric enthalpy recovery ventilation (ERV) for its heating, cooling, and ventilation needs. The house uses NG for its domestic hot water production, cooking range and fireplace. The ASHP is used for both the heating and cooling needs of the house depending on the season.

Additionally, the ASHP defrost was taken into account. Hence, the ASHP was disabled to operate below the balance point temperature [13]. In this case, the NG furnace was used as an auxiliary system. The cloud-based SDFSS implemented operates based on the temporal thermal demand of the house and optimizes its HVAC operation using short-term weather forecast information to minimize the operating cost for a few hours on the cloud server. The SDFSS then communicates with the house's HVAC system via a connected smart thermostat to operate either the ASHP or the supplementary heater, and in this case, an NG furnace [9]. The ASHP operates as an air-conditioning system during the cooling season. A computer platform and a physical communication interface board were developed to mimic and observe the behaviour of the SDFSS. The developed system iterates an algorithm consisting of various temporal parameters such as time of day, TOU price of electricity, outdoor temperature, ASHP performance/capacity, NG furnace performance and thermal demand of the house to select the most cost-effective fuel source for the given hour. The TOU electricity pricing scheme is demonstrated in Figure 3. As an added benefit, this system also reduces GHG emissions since the NG furnace is optimally substituted by an ASHP powered by a relatively clean source of electricity to meet the space heating demand of the house dynamically on an hourly basis.



Fig. 2. Exterior photographs of the house

The cloud based SDFSS implemented operates based on the temporal thermal demand of the house and optimizes its HVAC operation, using short-term weather forecast information, to minimize the operating cost for the next few hours on the cloud server. It then communicates with the house's HVAC system, via a connected smart thermostat, to operate either the ASHP or the supplementary heater, in this case a NG furnace [9]. The ASHP operates as an air-conditioning system during the cooling season. In addition to computer platform developed to mimic and observe the behavior of SDFSS, the physical communication interface board was developed to test the actual system. The developed system iterates an algorithm consisting of various temporal parameters such as time and day, TOU price of electricity, outdoor temperature, air-source heat pump performance/capacity, natural gas furnace performance and thermal demand of the house to select the most cost-effective fuel source for the given hour. TOU electricity pricing scheme is demonstrated in Figure 3. As an added benefit, this system also reduces the GHG emission since the NG furnace is optimally substituted by an ASHP powered by the relatively clean source of electricity to meet the space heating demand dynamically on an hourly basis.

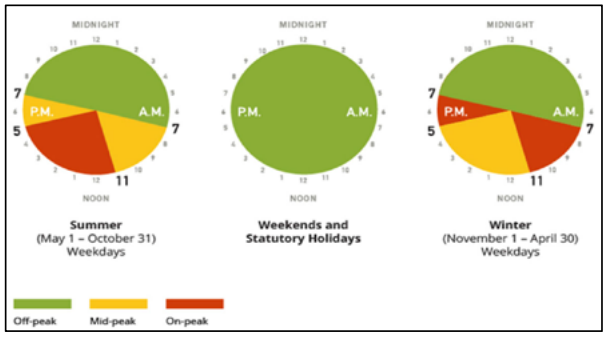


Fig. 3. TOU electricity pricing scheme [12]

The main focus of this study is to examine the environmental and economic impacts of implementing a cloud-based SDFSS for hybrid residential HVAC systems. By using experimental data retrieved from an actual near net-zero energy house, this study aims to investigate the reduction of GHG emissions as well as the energy costs associated with the electricity consumption of the ASHP and the NG consumption from the furnace. Therefore, a net zero energy building (NZEB) in Ontario, Canada was studied to investigate the viability of the SDFSS. The preliminary analysis demonstrated that the implemented SDFSS is a cost-effective and environmentally-friendly alternative to conventional HVAC equipment used in North American cold climates.

3. Methodology

The SDFSS modelled, developed, and implemented at the studied house accounts for the following factors in deciding whether the NG furnace or the ASHP should be operated at a specific time to meet space heating demand (HD) of the house [4]:

- π_{TOU}: TOU electricity price which changes based on hour of the day such as off-peak, mid-peak, on-peak hours [10]
- π_{NG}: Natural gas price (which is constant during the day)
- COP_{ASHP}: Coefficient of performance of the ASHP which is derived from the manufacturer's data and then calibrated with experimental data [5, 10]
- $\eta_{FURNACE}$: Efficiency of the NG furnace (89% with multiple measurements on site)
- NG energy density: 10.395 kWh/m^3 [R]
- T_{amb}: Ambient outdoor dry bulb temperature

To estimate HD of the house, a TRNSYS model was developed. This model is depicted in [10]. The curve for the COP_{ASHP} formulated from manufacturer's data and then calibrated with the experimental data is as follows:

$$COP_{ASHP} = 0.0053T_{amb}^2 + 0.0.0834T_{amb} + 2.8545 \quad (1)$$

Hourly space heating demand (HD) of the house is expressed in terms of COP_{ASHP}, $\eta_{FURNACE}$, consumption from ASHP (D_{elec}), consumption from NG furnace (D_{NG}) as the following equations:

$$D_{elec} = HD/COP_{ASHP},\ D_{NG} = HD/\eta_{FURNACE} \quad (2)$$

Based on the consumption of the equipment calculated, the total cost from ASHP operation (C_{ASHP}) and the total cost from NG furnace (C_{NG}) are defined as follows:

$$C_{ASAP} = D_{elec} * \pi_{TOU},\ C_{NG} = D_{NG} * \pi_{NG} \quad (3)$$

The SDFSS decides whether ASAP or NG furnace should be in operation based on the cheapest total cost amongst C_{ASAP} and C_{NG}. The data-driven SDFSS model consisted of an optimization algorithm which was ran hourly.

4. Results

From Equation 1, 2, and 3; CASAP, CNG, DNG, Delec are calculated for the period where the SDFSS was in operation. The first day of the data retrieval was on the 16th of February 2018. The first day of activating the SDFSS was on the 7th of November 2018, and the final day of the SDFSS experimentation was on the 6th of December 2018. The broader study also concluded on December 6th, 2018.

The average hourly GHG emission factors (in gCO_2eq/kWh) from the Ontario grid were taken from [11]. Along with the TOU dependency based on heating and cooling season, the weekends and statutory holidays are considered as the off-peak hours for the operation of the ASHP. Therefore, the day of the week and these holidays are also included in the analysis.

A detailed analysis of the outcomes of the SDFSS in terms of cost (in CAD) and GHG emissions released (in $kgCO_2/day$) from the HVAC equipment used during this period is depicted in Table 1. It is observed that on some days, only one type of the HVAC equipment was active. On other days, the switching happened during the day. So, there was both electricity and NG consumption from HVAC equipment. GHG emissions occurred from both HVAC systems. The results demonstrate that the NG furnace releases relatively more GHG emissions, but it is cost-effective. Similarly, the ASHP releases relatively less GHG emissions, but it is more expensive than NG.

Table 1. A detailed analysis on ambient temperature, cost, GHG emission, and loads from the HVAC equipment when the SDFSS in operation (from 7th of November to 6th of December 2018)

	SDFSS in OPERATION OUTDOOR TEMPERATURE (°C)				HP_COST	FURNACE_COST	TOTALCOST	HP_LOAD	Furnace_LOAD		HP_GHG	Furnace_GHG	Total GHG
DAYS	AvgTemp	MinTemp	MaxTemp	SpreadingTemp	CAD	CAD	CAD	kWh	kWh	DayoftheWeek	$kgCO_2$/day	$kgCO_2$/day	$kgCO_2$/day
7	0.35	-0.70	1.90	2.60	0.78	0.26	1.04	23.19	9.47	Wednesday	0.28	1.86	2.14
8	7.85	1.20	17.20	16.00	1.47	0.21	1.68	44.39	7.58	Thursday	0.51	1.49	1.99
9	3.08	0.30	10.40	10.10	0.00	0.93	0.93	0.00	33.62	Friday	0.00	6.60	6.60
10	-0.26	-1.10	2.20	3.30	0.00	1.51	1.51	0.01	54.45	Saturday	0.00	10.70	10.70
11	-1.10	-4.60	4.20	8.80	0.32	1.01	1.33	9.82	36.46	Sunday	0.11	7.16	7.28
12	-1.53	-2.80	-0.20	2.60	0.27	0.88	1.14	8.50	31.72	Monday	0.14	6.23	6.37
13	5.64	3.40	7.10	3.70	0.04	0.62	0.65	1.11	22.25	Tuesday	0.01	4.37	4.38
14	3.32	2.30	4.80	2.50	0.00	1.40	1.40	0.00	50.66	Wednesday	0.00	9.95	9.95
15	1.77	0.30	2.90	2.60	0.00	1.37	1.37	0.00	49.72	Thursday	0.00	9.77	9.77
16	-1.55	-4.80	1.50	6.30	1.00	0.59	1.59	31.29	21.31	Friday	0.41	4.19	4.60
17	0.13	-2.20	2.70	4.90	0.74	0.03	0.76	24.17	0.95	Saturday	0.37	0.19	0.56
18	1.60	-3.20	6.30	9.50	0.16	0.98	1.14	5.09	35.51	Sunday	0.07	6.98	7.05
19	0.52	-1.90	2.70	4.60	0.00	1.18	1.18	0.02	42.61	Monday	0.00	8.37	8.37
20	-2.73	-5.60	3.80	9.40	0.59	1.02	1.61	18.52	36.93	Tuesday	0.25	7.25	7.51
21	-2.28	-4.50	-0.10	4.40	0.00	1.43	1.43	0.00	51.61	Wednesday	0.00	10.14	10.14
22	0.10	-0.60	0.50	1.10	0.02	1.87	1.89	0.51	67.71	Thursday	0.01	13.30	13.31
23	1.13	-0.10	2.40	2.50	0.28	1.13	1.41	8.50	40.72	Friday	0.18	8.00	8.18
24	-0.50	-1.80	1.30	3.10	1.15	0.01	1.16	40.78	0.47	Saturday	0.62	0.09	0.71
25	-0.83	-6.70	7.40	14.10	0.72	0.00	0.72	27.40	0.00	Sunday	0.38	0.00	0.38
26	-0.85	-5.80	2.10	7.90	1.14	0.00	1.14	28.47	0.00	Monday	0.43	0.00	0.43
27	-1.94	-5.60	0.10	5.70	0.40	1.34	1.74	12.53	48.77	Tuesday	0.15	9.58	9.73
28	-7.19	-10.70	1.30	12.00	0.00	1.58	1.58	0.02	57.76	Wednesday	0.00	11.35	11.35
29	-0.28	-6.20	8.20	14.40	0.00	1.54	1.54	0.01	56.34	Thursday	0.00	11.07	11.07
30	4.65	2.40	7.50	5.10	0.36	0.97	1.33	8.73	35.51	Friday	0.16	6.98	7.13
1	5.55	3.70	7.60	3.90	0.73	0.75	1.49	22.79	27.46	Saturday	0.37	5.39	5.76
2	2.46	1.00	3.40	2.40	0.45	0.00	0.45	19.34	0.00	Sunday	0.17	0.00	0.17
3	-1.36	-2.40	1.70	4.10	0.95	0.00	0.95	27.49	0.00	Monday	0.50	0.00	0.50
4	-1.86	-2.60	-0.90	1.70	1.03	1.05	2.08	21.55	38.35	Tuesday	0.47	7.53	8.00
5	-2.24	-3.40	-0.50	2.90	0.00	1.29	1.30	0.03	47.35	Wednesday	0.00	9.30	9.30
6	-0.38	-1.80	1.70	3.50	0.00	1.05	1.05	0.01	38.35	Thursday	0.00	7.53	7.53

To further analyse the outcomes of the SDFSS introduced, the actual loads of the HVAC equipment were analysed along with the average outdoor temperature, the average minimum temperature, and the average maximum temperature on the days when the SDFSS was in operation. This analysis is demonstrated in Figure 4. It should be noted that spreading temperature is the absolute difference of the maximum and minimum outdoor temperature of a specific day. Additionally, Figure 5 depicts the GHG emissions from the HVAC equipment when the SDFSS was in operation.

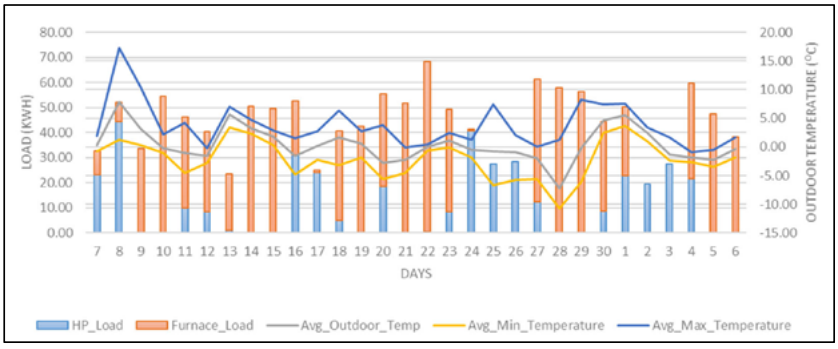


Fig 4. Ambient temperature and loads from the HVAC equipment when the SDFSS in operation (from 7th of November to 6th of December 2018)

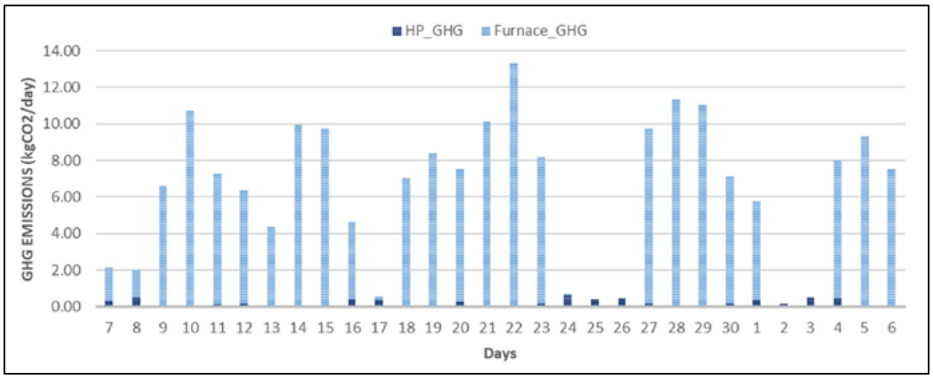


Fig 5. GHG emissions from the HVAC equipment when the SDFSS in operation (from 7th of November to 6th of December 2018)

The COP and capacity of the ASHP depend on the ambient outdoor temperature, which has led HVAC manufacturers to have a built-in temperature sensor on their ASHP. The ambient outdoor temperature of the specific location of the house is required in defining and meeting the thermal demand of the house. Therefore, the ambient outdoor temperature is a pivotal factor in this analysis to observe the smart switching optimal temperatures based on the introduced algorithm of the SDFSS. Table 2 depicts the marginal TOU electricity pricing based on TOU tiers such as off-peak, mid-peak, and on-peak hours [12]. The electricity prices from the consumption of electricity from ASHP are calculated based on the criteria given in Table 2. However, NG marginal price is \$0.3038/m^3 and has been fixed.

Table 2. Marginal TOU electricity pricing

Off-peak	\$0.092/kWh
Mid-peak	\$0.124/kWh
On-peak	\$0.163/kWh

Moreover, the costs and GHG emissions released from the electricity and NG consumption by the hybrid HVAC equipment when SDFSS is active and inactive were compared. For instance, when the thermostat switching setting was fixed at 0°C, the days with almost the same outdoor temperature conditions were analyzed. Table 3 demonstrates the analysis considered the entire month of February 2018. When the SDFSS was inactive, a fixed fuel switching temperature was introduced at 0°C, where ASHP operated when the outdoor temperature was above 0°C. Otherwise, when the outdoor temperature was below 0°C, the NG furnace was operated. For the SDFSS, the ASHP was in operation during the off-peak TOU hours and when the ambient temperature was above the optimal switching points. When on-peak and mid-peak TOU hours and the ambient temperature was below the optimal switching points, the NG furnace was in operation.

Table 3. A detailed analysis on ambient temperature, cost, GHG, and loads from the HVAC equipment when the switching point was at 0°C (from 16th of February to 28th of February 2018)

FEBRUARY	OUTDOOR TEMPERATURE (°C)				HP_COST	FURNACE_COST	TOTALCOST	HP_LOAD	Furnace_LOAD		HP_GHG	Furnace_GHG	Total GHG
DAYS	AvgTemp	MinTemp	MaxTemp	SpreadingTemp	CAD	CAD	CAD	kWh	kWh	DayoftheWeek	$kgCO_2$/day	$kgCO_2$/day	$kgCO_2$/day
16	-8.93	-9.60	-8.40	1.20	0.00	1.58	1.58	0.00	57.29	Friday	0.00	11.25	11.25
17	-4.50	-10.80	-0.10	10.70	0.00	1.92	1.92	0.00	69.60	Saturday	0.00	13.67	13.67
18	-0.41	-3.60	5.10	8.70	0.00	1.47	1.47	0.00	53.03	Sunday	0.00	10.42	10.42
19	4.68	-0.60	12.20	12.80	0.00	1.16	1.16	0.00	42.14	Monday	0.00	8.28	8.28
20	13.23	10.50	15.70	5.20	0.00	0.51	0.51	0.00	18.47	Tuesday	0.00	3.63	3.63
21	2.63	-2.20	12.30	14.50	0.00	0.99	0.99	0.00	35.98	Wednesday	0.00	7.07	7.07
22	0.17	-2.30	8.30	10.60	1.05	0.82	1.88	20.53	29.83	Thursday	0.36	5.86	6.22
23	3.90	0.10	8.30	8.20	1.33	0.03	1.36	41.88	0.95	Friday	0.51	0.19	0.69
24	2.38	1.00	4.20	3.20	0.67	0.00	0.67	19.24	0.00	Saturday	0.24	0.00	0.24
25	4.65	0.40	9.70	9.30	1.13	0.00	1.13	35.12	0.00	Sunday	0.35	0.00	0.35
26	3.10	-1.80	9.30	11.10	0.75	0.01	0.77	22.04	0.47	Monday	0.29	0.09	0.38
27	6.47	-0.70	13.60	14.30	0.00	0.59	0.59	0.01	21.31	Tuesday	0.00	4.19	4.19
28	8.44	3.60	16.40	12.80	0.92	0.00	0.92	34.16	0.00	Wednesday	0.34	0.00	0.34

After analysing the cost and GHG emission values for the days that had similar ambient temperature values, it is observed that the SDFSS cost less while preserving lower GHG emissions. For instance, on the 16th and

17th of November 2018, the SDFSS was active and on the 22nd of February 2018, the SDFSS was inactive, and the switching was at a fixed temperature of 0°C. The days that had similar conditions were defined based on maximum difference in ambient temperatures. The overall costs and GHG emissions released these days are a significant depiction of the SDFSS better than the conventional HVAC equipment in terms of these criteria.

As previously mentioned, the electricity prices are more costly than natural gas prices in Ontario, Canada. Therefore, a supplementary analysis was conducted to exhibit the overall applicability of the SDFSS on operating ASHP. Figure 6 shows the overall cost from operating ASHP, when the SDFSS is active and inactive. Following the methodology defined above, the associated ambient temperatures were taken into account to compare them with the days when the SDFSS was operating. The operational costs from the ASHP were mapped against the days in November 2018. It is seen that when the SDFSS was in operation, the electricity cost from the ASHP was more economical than the conventional testing period. When the SDFSS was active, the cost did not exceed $1.50.

In contrast, when the SDFSS was inactive, the costs reached up to $4. The ASHP was less expensive during the operation of the SDFSS because when the extreme outdoor temperatures and the on-peak hours of electricity pricing occurred, the NG furnace was turned on for operation to meet the space heating demand. As NG furnace was not operated consistently, the SDFSS switched between the NG furnace and the ASHP. The GHG emissions were not higher than the conventional periods, where there was a fixed switching temperature at 0°C.

The comparison of GHG emissions obtained from the operation of the ASHP between the days, when the SDFSS was in operation (in November 2018) and other days in the heating season are demonstrated in Figure 7. This comparison was performed while considering the mean difference in ambient temperatures between the days with similar weather conditions and the days when SDFSS was in operation. Based on these differences, the GHG emissions from the consumption of the HVAC equipment were compared. It is observed that in November 2018 as the SDFSS was active, the GHG emissions were relatively lower than the period, where the fixed switching temperature was in operation.

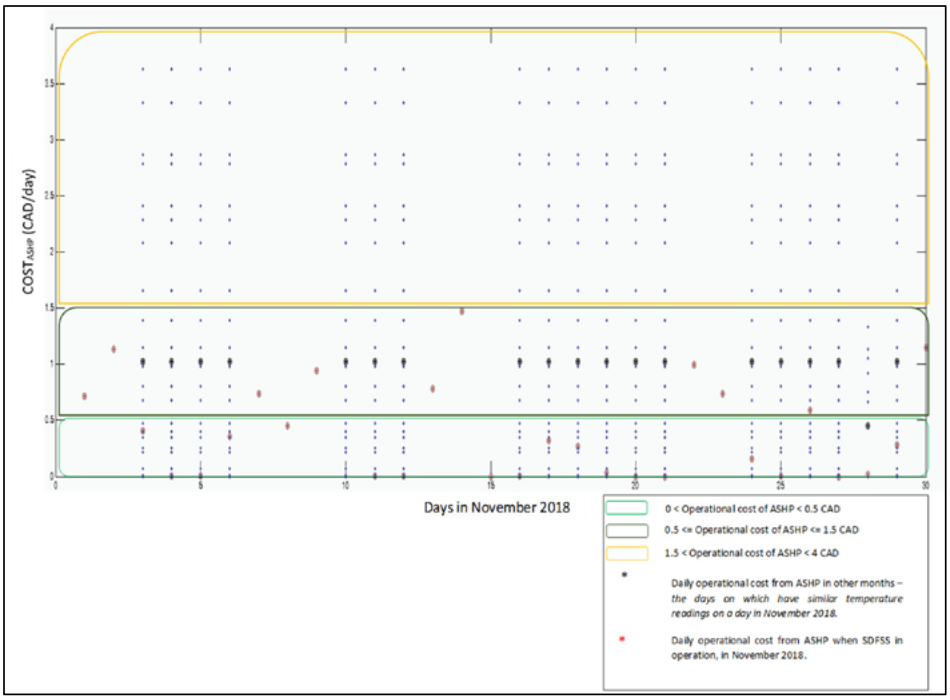


Fig. 6. Comparison of operational cost of ASHP between the days when SDFSS in operation (in November 2018) and other days in the heating season

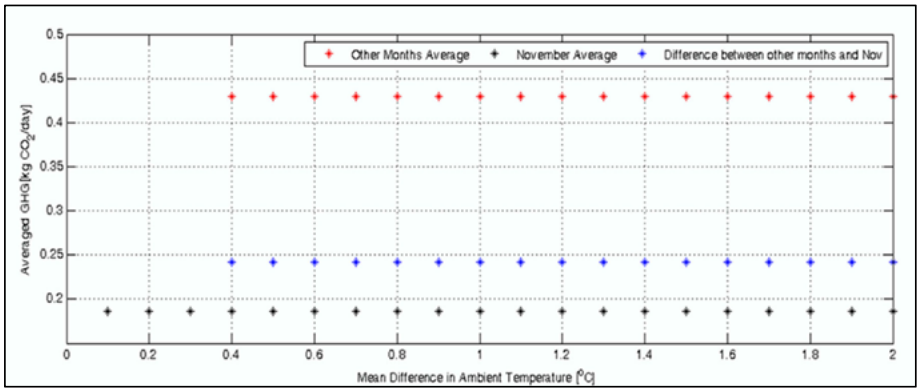


Fig. 7. Comparison of GHG emissions obtained from the operation of ASHP between the days when SDFSS in operation (in November 2018) and other days in the heating season

5. Conclusion

This study introduced a unique and innovative approach to account for the balance between economic and environmental impacts of the residential space heating in cold climates by proposing a flexible, cost effective, and clean energy solution. The technology, called the SDFSS, was developed, installed, and implemented at a Net Zero Energy House in Strathroy, Ontario, Canada. The SDFSS estimates the optimal switching point temperatures by considering various temporal factors such as TOU electricity prices, the efficiency of the NG furnace, the COP and capacity of the ASHP, and NG prices. Using Internet of Things (IoT) technologies and cloud servers, the data from the heating of the house when the SDFSS was in and out of operation were retrieved and analyzed in detail. This study focused on the environmental and economic impact of implementing these alternative technologies, called cloud based SDFSS for hybrid residential HVAC systems, in the transitioning period of prior being completely fossil-fuel free. The preliminary analysis demonstrated that the implemented SDFSS is a cost-effective, flexible, and environmentally friendly alternative to conventional HVAC equipment used in the North American cold climate.

Future work will examine the potential benefits, in terms of reduction of operating cost and GHG emissions of such cloud-based SDFSS for hybrid residential HVAC system in meeting different GHG emission reduction targets by 2030 and 2050 with the recently introduced federal carbon taxes of $20/tonne, $30/tonne, $40/tonne, and $50/tonne of CO_2 from 2019 to 2022.

Acknowledgements

Authors would like to thank Union Gas Limited, Ontario Centres of Excellence (OCE) and MITACS for the support.

References

[1] UNFCC, United Nations Framework Convention on Climate Change, https://unfccc.int/ (Retrieved on 1 January 2019)
[2] PCFCGCC, https://www.canada.ca/en/services/environment/weather/climatechange/pan-canadian-framework.html (Retrieved on 10 October 2019).
[3] Natural Resources Canada, “Canada’s GHG Emissions by Sector, End Use and Subsector – Including Electricity-Related Emissions,” 2017, http://oee.nrcan.gc.ca/corporate/statistics/neud/dpa/showTable.cfm?type=HB&sector=aaa&juris=ca&rn=3&page=0. (Retrieved on 16 November 2018).
[4] Yu, D., Tung, K. Y., Ekrami, N., Demirezen, G., Fung, A., Mohammadi, F., & Raahemifar, K. (2019, December). Proof of Concept of a Cloud-Based Smart Dual-Fuel Switching System to Control the Operation of a Hybrid Residential HVAC System. In 2019 IEEE PES Asia-Pacific Power and Energy Engineering Conference (APPEEC) (pp. 1-5). IEEE.

[5] Tung, K., Yu, D., Ekrami, N., & Fung, A. S. (2019, February). Experimental and sensitivity analysis of a smart dual fuel system in a net-zero energy home. In IOP Conference Series: Earth and Environmental Science (Vol. 238, No. 1, p. 012018). IOP Publishing.
[6] Demirezen, G., Ekrami, N., & Fung, A. S. (2019, September). Monitoring and Evaluation of Nearly-Zero Energy House (NZEH) with Hybrid HVAC for Cold Climate–Canada. In IOP Conference Series: Materials Science and Engineering (Vol. 609, No. 6, p. 062001). IOP Publishing.
[7] Alibabaei, N., Fung, A. S., Raahemifar, K., & Moghimi, A. (2017). Effects of intelligent strategy planning models on residential HVAC system energy demand and cost during the heating and cooling seasons. Applied Energy, 185, 29-43.
[8] Alibabaei, N., Fung, A. S., & Raahemifar, K. (2016). Development of Matlab-TRNSYS co-simulator for applying predictive strategy planning models on residential house HVAC system. Energy and Buildings, 128, 81-98.
[9] Demirezen, G., & Fung, A. S. (2019). Application of artificial neural network in the prediction of ambient temperature for a cloud-based smart dual fuel switching system. *Energy Procedia*, *158*, 3070-3075.
[10] Demirezen, G., Fung, A. S., & Deprez, M. (2020). Development and optimization of artificial neural network algorithms for the prediction of building specific local temperature for HVAC control. *International Journal of Energy Research*, *44*(11), 8513-8531.
[11] Greenhouse Gas Ontario Grid Emission Summary Statistics, 2016, Retrieved by contacting IESO.
[12] Ontario Energy Board: Rates and your bill. https://www.oeb.ca/rates-and-your-bill/electricity-rates (Retrieved on November 2018)
[13] Ye, K. K., Demirezen, G., Fung, A. S., & Janssen, E. (2020, March). The use of artificial neural networks (ANN) in the prediction of energy consumption of air-source heat pump in retrofit residential housing. In *IOP Conference Series: Earth and Environmental Science* (Vol. 463, No. 1, p. 012165). IOP Publishing.
[14] Enbridge - Union Gas, "Conversion Factors - Business - Union Gas." [Online]. Available: https://www.uniongas.com/business/save-money-and-energy/analyze-your-energy/energy-insights-information/conversion-factors.

13th IEA Heat Pump Conference
April 26-29, 2021 Jeju, Korea

Study on a combined absorption heat pump system driven by low temperature heat source

Gabyong Kim[a], Han Sol Jung[a], Yong Tae Kang[b*]

[a] Graduate School of Mechanical Engineering, Korea University, Seoul, 02841, Republic of Korea
[b]Department of Mechanical Engineering, Korea University, Seoul, 02841, Republic of Korea

Abstract

In this study, type 1 and type 2 combined absorption heat pump system using R32/DMAC is developed for heating and cooling applications. Waste heat from the heat with low temperature (below 90℃) is utilized as the heat source. R32 and an organic fluid of DMAC(Dimethylacetamide) are used as refrigerant and absorbent, respectively. Additionally, the combined heat pump system has two splitters placed after the generator outlet and condenser outlet. Cooling, heating and system coefficient of performance (COP) are calculated according to the change of generator temperature. The maximum cooling COP is estimated as 0.400, the maximum heating COPs with and without superheat are 0.196 and 0.161, respectively. Maximum system COP is estimated as 0.596. It is found that the heating performance of the system is more sensitive to the generator temperature than the cooling performance.

Keywords: 1st and 2nd Type Combined Absorption heat pump, COP, Low temperature heat source, R32

1. Introduction

Research and development on low GWP refrigerants have been actively proceeded. In addition, fossil fuels are the main cause of micro dust that directly affects the respiratory diseases, and regulations on the use of fossil fuel are being tightened. International efforts are being made in response to these environmental regulations. After the Fukushima nuclear accident in 2011, Japan declared its de-nuclearization policy and halted the nuclear power plant sequentially, causing the problems in energy supply and demand. To solve this problem, they have introduced Ene-farm that uses hydrogen as an alternative energy. The Ene-farm is a combined fuel cell system that generates 0.7kW of auxiliary power in consideration of economic feasibility, and the waste heat from the electricity production process is used for heating. The amount of waste heat generated in the process in fuel cells takes about 50% of total chemical energy and the operating temperature ranges from 80 to 1300℃ depending on electrolyte type of each fuel cell. Waste heat from Ene-farm is only used as a hot water supply device, so its use is limited. In addition, as the operating temperature of the PEMFC is only 70-80℃ [1], the waste heat from this is more limited. Furthermore, although research on energy recovery system using solar energy is being actively conducted, its use is also limited because it generates 60 to 70℃ when solar energy is collected.

Regarding the development of absorption cycles, working fluid pairs(refrigerant/absorbent) are as important as all the components of absorption cycles. H_2O/LiBr and NH_3/H_2O are most widely used at present. Despite the outstanding performance of the existing pairs, as shown in Table 1, these pairs have some critical disadvantages. H_2O/LiBr doesn't work under the generator temperature of 90℃ and it has the freezing problem under 0℃. To deal with these problems, the use of an alternative refrigerant and absorbent as a working pair for the absorption refrigeration cycle has been proposed. Therefore, in this study, a sorption heat pump that uses waste heat from the low temperature heat source(which is lower than the temperature of 90℃)

* Corresponding author. Tel.: 82-2-3290-5952; fax: 82-2-922-3260.
E-mail address: ytkang@korea.ac.kr.

is proposed. The sorption heat pump system uses alternative refrigerant and organic liquid as absorbent, which can solve the problems mentioned above at the same time.

Table 1 Characteristics of representative refrigerants for absorption refrigeration system

	NH_3/H_2O	**$H_2O/LiBr$**
Absorbent	H_2O	LiBr
Refrigerant	NH_3	H_2O
Crystallization	N	Y
Toxicity	Y	N
Flammability	Y	N
Disadvantages	1. Flammable, Explosive, Toxic 2. Regulated by national regulations	1. Frozen/refrigeration system: Not applicable 2. Difficulty in air cooling due to high boiling point of refrigeration

2. Simulation Methodology

2.1. Description of Type 1 and Type 2 combined sorption heat pump

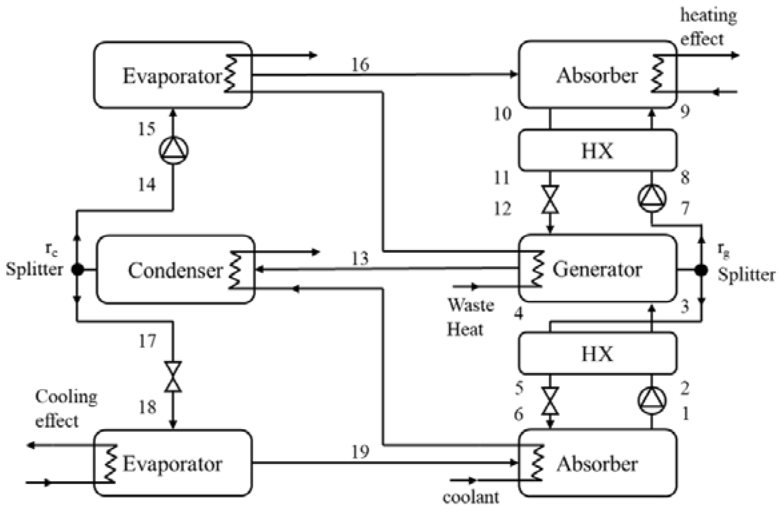


Figure 1. Schematic diagram of type 1 and type 2 combined sorption heat pump cycle

Figure 1 is a schematic diagram of Type 1 and Type 2 combined sorption heat pump system. The refrigerant and absorbent mixed solution is transferred from the low temperature absorber to the generator through the pump and the generated refrigerant which is recovered at the generator by absorbing the waste heat from the low temperature heat source moves to the condenser. Splitter attached to the generator splits the solution to be transferred to the high and low temperature absorbers. The refrigerant transferred to the condenser is fully condensed in the condenser. The liquid refrigerant is transferred to the high temperature evaporator and the low temperature evaporator through a splitter attached to the condenser. The refrigerant transferred to the high temperature evaporator is compressed by a pump, and the refrigerant transferred to the low temperature evaporator is expanded in the expansion valve. In the high temperature evaporator, the residual heat which already supplied to the generator is absorbed by the refrigerant.

The evaporated refrigerant from the high temperature evaporator is absorbed in the high temperature absorber, raises the temperature of the high temperature absorber outlet solution, and transfers heat to the heating target. Whereas, the refrigerant transferred to the low temperature evaporator is evaporated while cooling the target system in the low temperature evaporator and is retrieved to the low temperature absorber.

2.2. Selection of refrigerant and absorbent pair

After considering toxicity, safety, stability, flammability and corrosivity problems, R32 which is an alternative refrigerant for R410A and R407C has received much attention in recent years. R32 has about one third lower GWP than that of R410a and has an ODP of zero. Furthermore, R32 requires less charge as it has a 20% higher volumetric capacity. By considering the critical-point which is higher than R410A's, heat capacity and saturation pressure difference, R32 is finally selected. Due to the negligible vapor pressure, good thermal and chemical stability and solubility with many refrigerants, DMAC is considered as a promising absorbent for the combined sorption cycles.

2.3. Cycle modelling of the sorption cycle

During the cycle simulation process, the following assumptions are made.
(1) Steady state.
(2) The pressure drop is negligible.
(3) Condensation and evaporation occur completely in condenser and evaporator, respectively.
(4) The effectiveness of the solution heat exchanger is assumed 0.8. [2]
The entire simulation of the sorption heat pump is carried out using the Engineering Equation Solver (EES).

2.3.1. Mass and species conservations

Principles of mass and energy conservations are considered for each component of the system as follows.

- Mass balance

$$0 = \sum \dot{m}_i - \sum \dot{m}_o \tag{1}$$

$$0 = \sum \dot{m}_i(1 - x_i) - \sum \dot{m}_o(1 - x_o) \tag{2}$$

- Energy balance

$$0 = \sum \dot{m}_i h_i - \sum \dot{m}_o h_o + \sum \dot{Q}_i - \sum \dot{Q}_o + \dot{W} \tag{3}$$

- Solution pump

$$h_o = h_i + \frac{\dot{W}_p}{\dot{m}_i} \tag{5}$$

- Expansion valve

For refrigerant and solution pump expansion valves, the isenthalpic processes are assumed.

$$h_o = h_i \tag{6}$$

2.3.2. COP

The heat recovered by the high temperature evaporator was excluded from the calculation. This is because the remaining heat is used instead of the heat source for operation.

$$COP_{cooling} = \frac{\dot{Q}_{evap}}{\dot{Q}_{gen} + \dot{W}_{pump}} \tag{7}$$

$$COP_{heating} = \frac{\dot{Q}_{abs,high}}{\dot{Q}_{gen} + \dot{W}_{pump}} \tag{8}$$

$$COP_{system} = \frac{\dot{Q}_{abs,high}+\dot{Q}_{evap}}{\dot{Q}_{gen}+\dot{W}_{pump}} \quad (9)$$

3. Results and discussion

The condenser outlet temperature(T_{cond}) and the low temperature absorber outlet temperature($T[1]$) are set to 30℃, respectively. The low temperature absorber outlet mass flow rate is set to 0.1(kg/s), and the split ratios of generator and condenser are 0.5, respectively as the base lines as summarized in Table 2.

Table 1 Characteristics of representative refrigerants for absorption refrigeration system

T_{gen}(℃)	T_{cond}(℃)	$T[1]$(℃)	$T[10]$(℃)	$m[1](kg/s)$	T_{16}(℃)	$r_g r_c$
66~70	30	30	75	0.1	45~50	0.5

3.1. Effect of the generator temperature on the cooling and heating performances

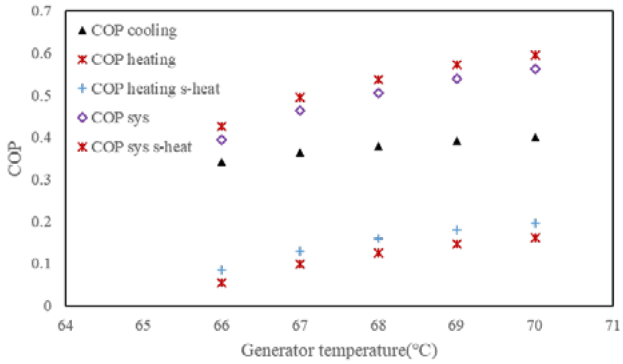


Figure. 2. Effect of generator temperature on COP

Figure 2 shows the COPs according to the generator temperature change. As the generator temperature increases, cooling COP($COP_{cooling}$) and heating COP($COP_{heating}$) increases. The maximum cooling COP and heating COP are calculated 0.400 and 0.161, respectively, at the generator temperature of 70℃. When heat is recycled in the high temperature evaporator, i.e., when the refrigerant passing through the high temperature evaporator is heated to 50℃, it always shows a higher performance and the maximum heating COP with superheat($COP_{heating\ s-heat}$) is calculated 0.196 which is 0.035 higher than the heating COP without superheat because the heat recycled in the high temperature evaporator is directly used to increase the heat capacity in the high temperature absorber. Maximum system COP without superheat consideration(COP_{sys}) is calculated 0.561 and COP with superheat consideration ($COP_{sys\ s-heat}$) is calculated 0.596 at the temperature of 70℃. When the generator temperature increases 4℃ from 66℃, cooling COP, heating COP, and heating COP with superheat increase 17.4%, 197.9%, and 134.0%, respectively. From this result, the heating COPs are more sensitive to the generator temperature than the cooling COP because as the generator temperature increases, the amount of heat delivered to the high temperature absorber by solution increases.

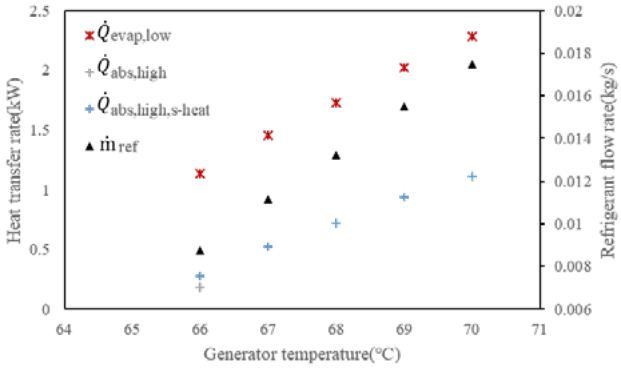


Figure 3. Effect of generator temperature on heat transfer rate and refrigerant generation

Figure 3 shows the heat transfer rate and refrigerant mass flow rate according to the generator temperature. As the generator temperature increases, the total generated refrigerant flow rate($\dot{m}_{ref}$) and heat transfer rate in low temperature evaporator and high temperature absorber increase. Maximum heat transfer rate of low temperature evaporator ($\dot{Q}_{evap,low}$), high temperature absorber ($\dot{Q}_{evap,low}$) without superheat and high temperature absorber with superheat($\dot{Q}_{abs,high,s-heat}$) are calculated 2.280kW, 0.9157kW and 1.114kW, respectively. Maximum generated refrigerant flow rate is calculated 0.0175kg/s. When the generator temperature increases from 66(℃) to 70(℃), the generator refrigerant flow rate increases 100.2% at the temperature of 70(℃). It is found that the heat transfer rates are improved, as the generator temperature increases, which makes refrigerant flow rate increase. The results for each state point are summarized in Table 3.

Table 3 Results for the state points of the cycle($T_e = 5℃, T_c = 30℃$)

	T(℃)	$P(kPa)$	$h(kJ/kg)$	$\dot{m}$(kg/s)	Concentration	Quality
[1]	30.0	951.5	212.2	0.1	0.386	
[2]	30.0	1928.0	212.2	0.1	0.386	
[3]	59.8	1928.0	286.0	0.1	0.386	
[4]	70.0	1928.0	305.8	0.09126	0.327	
[5]	38.0	1928.0	225.0	0.09126	0.327	
[6]	37.1	951.5	225.0	0.09126	0.327	
[7]	70.0	1928.0	305.8	0.09126	0.327	
[8]	70.0	2254.0	305.8	0.09126	0.327	
[9]	74.6	2254.0	319.0	0.09126	0.327	
[10]	75.0	2254.0	326.9	0.1	0.386	
[11]	71.0	2254.0	314.8	0.1	0.386	
[12]	65.6	1928.0	314.8	0.1	0.386	
[13]	70.0	1928.0	570.0	0.01749		1.000
[14]	30.0	1928.0	255.3	0.008743		0.000
[15]	30.1	2254.0	255.3	0.008743		0.000
[16]	36.2	2254.0	514.1	0.008743		1.000
[17]	30.0	1928.0	255.3	0.008743		0.000
[18]	5.0	951.5	255.3	0.008743		0.151
[19]	5.0	951.5	516.1	0.008743		1.000

4. Conclusions

The performance of the type 1 and type 2 combined sorption heat pump using the waste heat from the low temperature heat sources according to the change of generator outlet concentration and the split ratio at the

generator is analyzed. The working fluid pair is selected for the sorption heat pump using an alternative refrigerant R32 as refrigerant and organic liquid DMAC as absorbent. The following conclusions are drawn from the present study.

1. Between the generator temperature of 66℃ and 70℃, the maximum cooling COP, maximum heating COPs with and without superheat are calculated 0.400, 0.196, and 0.161, respectively when the generator temperature is 70℃. Heating COP is more sensitive to the generator temperature because as the temperature of the generator increases, heat supplied to the refrigerant of the high temperature absorber increases.

2. Heat transfer rate at the low temperature evaporator and high temperature absorber increases as the generator temperature increases because as the generator temperature increases, refrigerant flow rate increases due to the P-T-X equilibrium. Maximum heat transfer rates of low temperature evaporator, high temperature absorbers without and with superheat are calculated 2.280kW, 0.9157kW and 1.114kW, respectively.

Acknowledgements

This work was supported by Korea Institute of Energy Technology Evaluation and Planning(KETEP) grant funded by the Korea government(MOTIE) (No. 10060218, The development of cooling capacity 200RT class triple effect gas fired absorption chiller).

References

[1] Fly, A, Thring, R, H. Temperature regulation in an evaporatively cooled proton exchange membrane fuel cell stack. International Journal of Hydrogen Energy 2015; 40:11976-82.

[2] Wu, W., You, T., Zhang, H., Li, X. Comparisons of different ionic liquids combined with trans-1, 3, 3, 3-tetrafluoropropene (R1234ze (E)) as absorption working fluids. International Journal of Refrigeration 2018; 88:45-7.

[3] Li, X., Zheng, D., Shen, Y., Meng, X., Li, B. Vapor–liquid equilibria of difluoromethane+ N, N-dimethylacetamide, difluoromethane+ dimethylether diethylene glycol and 1, 1-difluoroethane+ dimethylether diethylene glycol systems. Fluid Phase Equilibria 2013; 347:15-21.

13th IEA Heat Pump Conference
April 26-29, 2021 Jeju, Korea

A residential heat pump system for cooling, heating, dehumidification and outdoor air supply

Xing-Yu Liang[a], Chen Yang[a], Jing Zhang[a], Xiang Cao[a], Liang-Liang Shao[a], Chun-Lu Zhang[a,*], Chun Yang[b], Xiao-Ning Chen[b], Hong-Fei Shu[b,*]

[a]School of Mechanical Engineering, Tongji University, Shanghai 201804, China
[b]Emerson Commercial & Residential Solutions, Suzhou 215021, China

Abstract

With growing demands of indoor air quality and thermal comfort, dedicated outdoor air system with dehumidification function is becoming more popular for residential use. However, due to limited air volume of outdoor air, dedicated outdoor air system often needs to supply air at very low humidity ratio for dehumidification, which decreases the system energy efficiency. In this work, by combining dedicated outdoor air system and small air-cooled chiller, a heat pump system for cooling, heating, dehumidification and outdoor air supply is proposed. In the system, a high temperature water coil is applied to precool the outdoor air for decreasing the energy consumption of dehumidification. Besides, dehumidification capacity of outdoor air system with precooling is enough to handle overall latent load. In the meantime, without the demand of dehumidification, the water supplying temperature of chiller can rise to 15°C or above, which is not only beneficial to energy efficiency improvement, but also available for dry terminal. Modeling results of the system indicate that the annual power consumption of the new system can be reduced by 16.9% relative to the combined operation of a dedicated outdoor air system and an individual small chiller.

Keywords: heat pump; air conditioning; chiller; outdoor air system; dehumidification

Nomenclature

A	area (m^2)	SA	supply air
APF	annual performance factor	*T*	temperature (°C)
c	specific heat($kJ \cdot kg^{-1} \cdot K^{-1}$)	TMY	typical meteorological year
COP	coefficient of performance	*v*	specific volume ($m^3 \cdot kg^{-1}$)
D	diameter (m)	WB	wet bulb
DB	dry bulb		
DOAS	dedicated outdoor air system	*Greeks*	
EXV	electronic expansion valve	η	efficiency
f	friction factor; frequency (Hz)		
G	mass flux ($kg \cdot s^{-1} \cdot m^{-2}$)	*Subscripts*	
h	specific enthalpy ($kJ \cdot kg^{-1}$)	a	air
Le	Lewis number	c	condensing; cooling season
m	mass flow rate ($kg \cdot s^{-1}$)	e	evaporating
OA	outdoor air	h	heating season
p	pressure (kPa)	r	refrigerant
Q	cooling/heating capacity(kW)	s	surface
RA	return air		

* Corresponding author. Tel.: +86-136-71825-133.
E-mail address:, chunlu.zhang@gmail.com (C.-L. Zhang). Speed.Shu@Emerson.com (H.-F. Shu).

1. Introduction

Since people pay more attention to indoor air quality today, residential dedicated outdoor air system (DOAS) become more popular in the market, and different types of DOAS have been widely researched, too. The basic type of DOAS is just in charge of fresh air supplying and purification. But considering energy saving and indoor thermal comfort, now DOAS usually has an additional dehumidification unit and can deal with partial or overall latent load.

For dehumidification DOAS, desiccant dehumidification and mechanical dehumidification are the two main approaches[1]. Desiccant dehumidification method transfers water from air to solid or liquid desiccant by adsorption or absorption process. It usually has better dehumidification efficiency, but it also has the problem of high cost, large volume and regeneration[2]. On the contrary, mechanical dehumidification method, which has relative lower dehumidification efficiency but lower cost and small volume, is more popular in residential DOAS market. Up to now, most of improved DOAS types were developed for better performance. Mumma et al. developed a novel DOAS to reduce humidification and reheating load, including a preheat coil, an enthalpy wheel, a deep cooling coil and a sensible heat exchanger[3]. Zhang et al. proposed a novel DOAS with total heat exchanger[4, 5]. Li et al. proposed a novel DOAS with multi-stage direct expansion coil and zero-energy heat pipe[6]. This system could reduce about 15.6% annual energy consumption according to the simulation results. Zhang et al. designed a frost-free exhaust air heat recovery DOAS[7]. Zhang et al. proposed a novel DOAS with two-stage direct-expansion dehumidification, subcooled reheating, and exhaust air heat recovery[8]. Coefficient of performance (COP) of this novel DOAS can reach 5.42 and 26% higher than the conventional one.

With the development of DOAS technology itself, the issue about how DOAS help air conditioning system save energy is also drawing much attention. A conventional solution is DOAS with the sensible heat load handling device. In this solution, a dehumidification DOAS deals with overall latent load, and the indoor terminal only deal with partial sensible load. This solution is a way to achieve temperature and humidity independent control, which can improve indoor thermal comfort effectively. Mumma et al. has shown that the combination of DOAS and radiant cooling system can reduce about 29% energy consumption compared to conventional variable air volume systems[9]. Saber et al. evaluated the performance of a decentralized DOAS with a radiant cooling system in the tropical climate[10]. Yin et al. analyze the energy saving potential of DOAS with radiant cooling system under different climate conditions in China[11]. Zhang et al. discussed the adaptability of the combined system with DOAS and radiant cooling panels in summer moist heat regions[12]. Li et al. developed a radiant air conditioning system with outdoor air dehumidifier for temperature and humidity independent control, and tested the performance of this system under variable operating conditions[13]. Lim et al. compared the performance of DOAS with thermoelectric module radiant cooling panel or hydraulic ceiling radiant cooling panels via a detailed energy simulation[14]. However, although the COP of chiller in this combination solution can be improved due to the high temperature of chilled water, COP of dehumidification DOAS in such solution is still relatively low. COP of the common mechanical dehumidification DOAS in the market is at most 3.5[6]. Due to the limited air volume of outdoor air, dehumidification DOAS often needs to supply air with very low humidity ratio and low temperature, which lead to low evaporating temperature and increase the energy consumption for dehumidification. Therefore, a higher efficiency solution for dehumidification DOAS is still needed to be explored.

In this work, we proposed a novel multi-function residential heat pump system, which included chiller subsystem and outdoor air subsystem. In the system, a high temperature water coil is applied to precool the outdoor air for decreasing the energy consumption of dehumidification. With an ingenious iterative design of two subsystems, the new system can achieve better performance than direct combination of chiller and DOAS. This paper is composed of five sections. Section 2 gives a system description of this new system. Section 3 presents a system model of the new system for performance analysis, and introduces the method of system modeling. Section 4 discusses the performance of new system under variable operating conditions, according to the simulation results. And section 5 gives some brief conclusions of this work.

2. System description

The new system is an integration of conventional chiller system and DOAS. Fig. 1 is the schematic of new system. It has 2 subsystems: chiller subsystems and outdoor air subsystem (OA subsystem), and the two subsystems are connected with each other by water pipes.

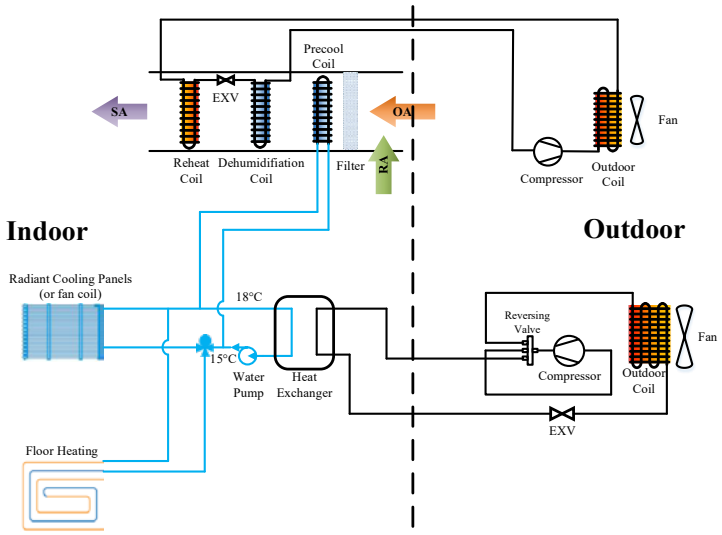


Fig. 1. Schematic of the new system

The chiller subsystem(below) is similar to a conventional residential chiller system. The difference is that water temperature of chilled water is 15°C in cooling season. And types of terminals are radiant cooling panels or dry fan coil. High temperature chilled water means better performance and less energy consumption of the chiller subsystem. But the chiller subsystem only deals with sensible load due to high temperature of chilled water.

The OA subsystem deal with the overall latent load and part of sensible load of rooms in cooling season. In order to increase the air volume, return air is mixed with outdoor air. Then the mixed air flow through three coils: precool coil, dehumidification coil and reheat coil. Precool coil is a water-air coil and water are from chiller subsystem. Dehumidification coil and reheat coil belong to a dedicated refrigeration cycle, driven by a dedicated compressor and an outdoor coil of OA subsystem. The mixed air is cooled, dehumidified and reheated by these three coils and sent to indoor finally.

In terms of the control strategy, temperature and humidity independent control is an important control target of this system. Therefore, compressors in both chiller subsystem and OA subsystem are variable speed compressor. The desired indoor dry bulb temperature is controlled by compressor of chiller subsystem, and the desired absolute humidity of supply air (SA) is controlled by compressor of OA subsystem. The suction superheat of these two refrigeration cycles is controlled by the EXV in respective cycle.

In heat pump mode, the dedicated refrigeration cycle of OA subsystem is turned off, and the precool coil change to preheat coil. To avoid unnecessary energy waste of mixing process, the RA inlet is turned off by an air valve in heat pump mode. Since there is no latent load in heating season, the overall load of OA subsystem is less than in cooling season. Therefore, the heating capacity of preheat coil is enough to heat the outdoor air to about 42°C.

There are three main advantages of this new system:

1) High chilled water temperature of chiller. Performance of chiller and thermal comfort of terminals are improved.
2) Outdoor air precooled by chilled water from chiller. Precooling process can reduce the cooling load of the dedicated refrigeration cycle, which means less energy consumption, smaller compressor and smaller outdoor unit of OA subsystem.
3) In heat pump mode, outdoor air can be effectively heated without dedicated heat pump cycle for OA subsystem.

3. System modeling

In order to analyze the performance of new system, a simulation model is developed using GREATLAB[15, 16]. GREATLAB is a general simulation software of refrigeration and air-conditioning system. The main methods of component and system simulation are briefly introduced below. More details about this model could be found in the references[15, 16].

Fin-tube coil is the main type of heat exchangers in this system. A tube-in-tube incremental model, which can account refrigerant and air distribution of the coil, is applied for fin-tube coil modeling. This model includes four levels: element level, tube level, circuit level and heat exchanger level. And the model is solved from inside to outside. First the equations at element level are solved. Then every tube is calculated by results at element level, and every circuit is calculated by results at tube level. Finally, all circuits are calculated and the mass flow rate is adjusted to balance pressure drop between circuits.

The equations at element level are as follows.

Refrigerant energy equation.

$$Q_{\mathrm{r}} = m_{\mathrm{r,in}} \left(h_{\mathrm{r,in}} - h_{\mathrm{r,out}} \right) \tag{1}$$

Refrigerant mass conservation equation:

$$m_{\mathrm{r,in}} = m_{\mathrm{r,out}} \tag{2}$$

Refrigerant momentum equation.

$$p_{\mathrm{r,in}} - p_{\mathrm{r,out}} = G^2 \left(v_{\mathrm{r,out}} - v_{\mathrm{r,in}} \right) + f \frac{G^2 v_{\mathrm{m}}}{2D} \tag{3}$$

Air energy equation.

$$Q_{\mathrm{a}} = m_{\mathrm{a}} \left(h_{\mathrm{a,in}} - h_{\mathrm{a,out}} \right) \tag{4}$$

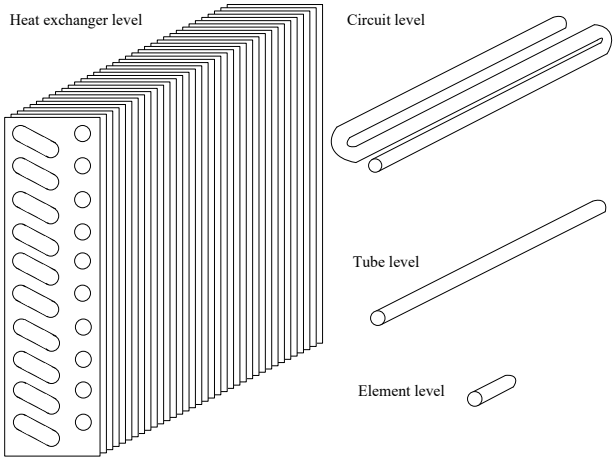


Fig. 2. Structure of the finned-tube heat exchanger model.

Where,

$$Q_{\mathrm{a,sens}} = \frac{A_{\mathrm{s}}}{1/\left(k_{\mathrm{a}}\eta_{\mathrm{s}}\right)+\left(R_{\mathrm{m}}+R_{\mathrm{fr}}\right)+\left(A_{\mathrm{s}}/A_{\mathrm{r}}\right)/k_{\mathrm{a}}}\left(T_{\mathrm{a}}-T_{\mathrm{r}}\right) \tag{5}$$

$$Q_{\mathrm{a,latent}} = m_{\mathrm{a,d}}\left(W_{\mathrm{a,in}}-W_{\mathrm{a,out}}\right)h_{\mathrm{latent}} \tag{6}$$

Air humidity equation

$$-m_{\mathrm{a}}\,\mathrm{d}W_{\mathrm{a}} = k_{\mathrm{d}}\left(W_{\mathrm{a}}-W_{\mathrm{w}}\right)\mathrm{d}\,A_{\mathrm{a}} \tag{7}$$

where,

$$k_{\mathrm{d}} = \frac{k_{\mathrm{a}}}{Le\cdot c_{\mathrm{p,a}}} \tag{8}$$

The correlations chosen for heat transfer coefficient and pressure drop are shown in **오류! 참조 원본을 찾을 수 없습니다.**.

Table 1 Correlations of heat transfer coefficients and friction factors

Air	**Heat transfer**	**Wang et al.**[17]
	Pressure drop	**Wang et al.**[17]
Refrigerant single phase	Heat transfer	Gnielinski[18]
	Pressure drop	Blasius
Refrigerant evaporation	Heat transfer	Gungor and Winterton[19]
	Pressure drop	Choi et al.[20]
Refrigerant condensation	Heat transfer	Cavallini et al.[21]
	Pressure drop	Choi et al.[20]

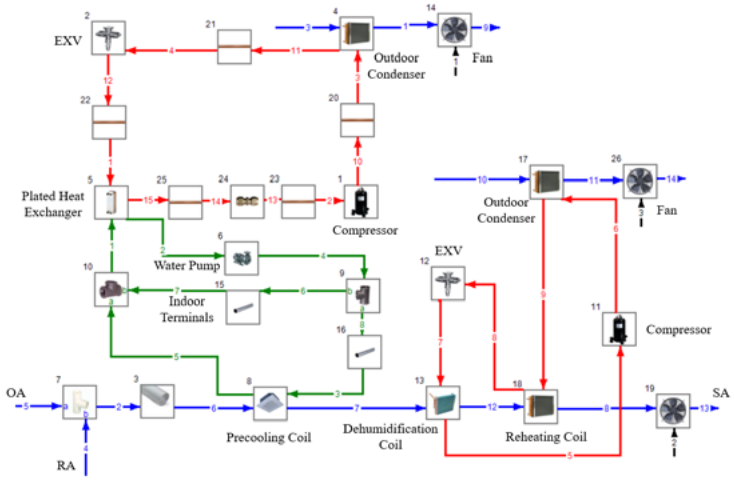


Fig. 3. System model of the new system in GREATLAB (cooling season).

Since the two compressors in this system are both variable-speed compressor, a multi-variable polynomial model[15] is applied for compressor simulation.

$$y = c_1 + c_2 T_e + c_3 T_c + c_4 f_r + c_5 T_e^2 + c_6 T_c^2 + c_7 f_r^2 + c_8 T_e T_c + c_9 T_e f_r + c_{10} T_c f_r + c_{11} T_e^2 f_r + c_{12} T_e f_r^2 + c_{13} T_c^2 f_r + c_{14} T_c f_r^2 + c_{15} T_e T_c f_r \quad (9)$$

where y can represent mass flow rate or power consumption of compressor. T_e and T_c represent evaporating temperature and condensing temperature, respectively. f_r represents compressor frequency. Coefficients c_1-c_{10} are curve-fitted according to compressor manufacturer's data.

Performance of expansion valves and fans are calculated according to the performance curves from manufacturers.

Based on all these component models, simulation model of the new system can be set up in GREATLAB, as shown in Fig. 3. System solver of this model is based on the Newton-Raphson algorithm. All fluid properties are calculated by REFPROP 9.0[22]. With the simulation model, we can analyze the performance of the new system under variable operating conditions. And the advantages of this new system will be discussed in detail in the next section.

4. System performance analysis and discussions

In this section, performance of the new system is numerically analyzed under different operating conditions. Firstly, a suitable baseline and some typical operating conditions are chosen in subsection 4.1. Then, an annual performance factor method is developed to analyze the annual performance of the new system in subsection 4.2. Finally, the results are presented and discussed in subsection 4.3.

4.1. Baseline and typical operating conditions.

To analyze performance of the new system, a comparison between the new system and conventional residential air-conditioning solution is necessary. In this study, a combination of chiller system and basic DOAS is chosen as the baseline of comparison and analysis. Schematic of baseline system is shown in Fig. 4.

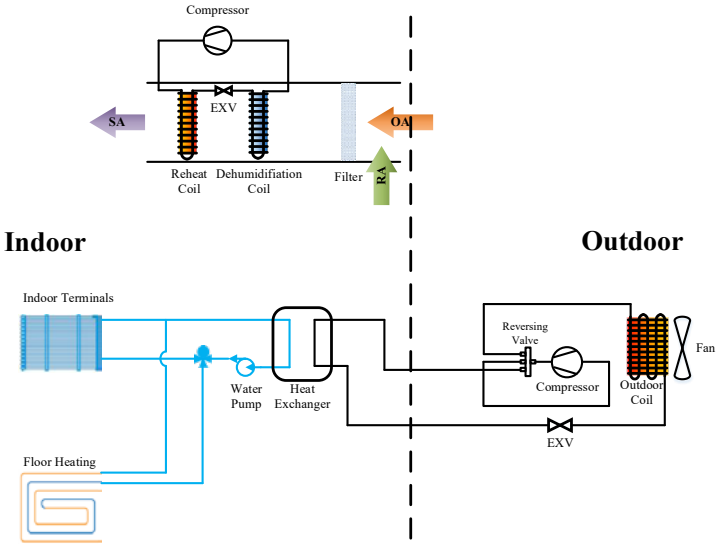


Fig. 4. Schematic of baseline system.

The chiller in both baseline system and improved new system is a practical chiller prototype, which has about 15kW design cooling capacity and is designed for about 150m^2 room. Some important design information of this chiller is shown in **오류! 참조 원본을 찾을 수 없습니다.**. And following the modeling method introduced in section 2, the simulation model of chiller was set up and well validated by experimental data. The comparison of some key performance parameters between simulation data and experimental data is presented in **오류! 참조 원본을 찾을 수 없습니다.**.

Table 2 Specifications of chiller

Name	Specification	Name	Specification
Refrigerant	R410A	Condenser	Fin-tube coil, 2 rows, 108 tubes, Tube length: 1000mm.
Design Cooling Capacity	15kW	Evaporator	Plated heat exchanger
Compressor	Rotary, variable-speed	Fan	Double axial fans, variable speed
Expansion device	EXV		

Table 3 Validation of chiller simulation model

Operating conditions	Cooling(heating) capacity/kW			Power/kW			Mass flow rate (water)/L·s^{-1}		
	Simulation	Test	Error	Simulation	Test	Error	Simulation	Test	Error
Cooling 100% load	15.11	14.93	**1.2%**	5.21	5.20	**0.2%**	0.69	0.68	**1.5%**
Cooling 75% load	11.20	11.29	**0.8%**	3.02	2.90	**4.1%**	0.68	0.68	**0.3%**
Cooling 50% load	8.02	7.58	**5.7%**	1.88	1.89	**0.5%**	0.71	0.68	**4.4%**
Cooling 25% load	5.52	5.29	**4.2%**	1.25	1.19	**5.0%**	0.70	0.68	**2.9%**
Heating 100% load	17.12	17.68	**3.2%**	5.84	5.80	**0.7%**	0.69	0.70	**1.4%**

The DOAS in baseline system is also a typical type of residential DOAS, prototype of this DOAS is shown in Fig. 5. The key design information of this DOAS is shown in Fig. 6. In this study, considering the demand of fresh air supplying and dehumidification for about 150m^2 room, one chiller needs to match 3 DOAS in the baseline system.

Table 4 Specification of DOAS

Name	Specification	Name	Specification
Refrigerant	R407C	Evaporator	Fin-tube coil, 4 rows, 36 tubes, Tube length: 420mm.
Design Dehumidification Capacity	26L/Day	Condenser	Fin-tube coil, 4 rows, 36 tubes, Tube length: 420mm.
Rotary	Rotary, constant speed	Fan	Single centrifugal fans, constant speed
Expansion device	Capillary tube		

As a multi-function heat pump system, it is necessary to analyze its system performance under variable operating conditions in cooling season, heating season and transitional season. Therefore, a variable operating conditions analysis is necessary for the new system. In this section, some typical operating conditions are chosen according to the typical meteorological year (TMY) data of Shanghai, as shown in Fig. 6. The TMY data are from DeST[23].

Fig. 6 shows the chosen 7 typical cooling operating conditions and 4 typical heating operating conditions. Point A is the rated cooling operating conditions (T_{DB}=35°C, T_{WB}=28°C). Point B and C are two 40°C+ extreme cooling operating conditions. Point D-F are three low temperature cooling operating conditions. Point G represents dehumidification operating conditions in transitional season. Point H-J are three different heating operating conditions. And point K represents heating operating conditions in transitional season.



Fig. 5. Photo of DOAS in baseline system.

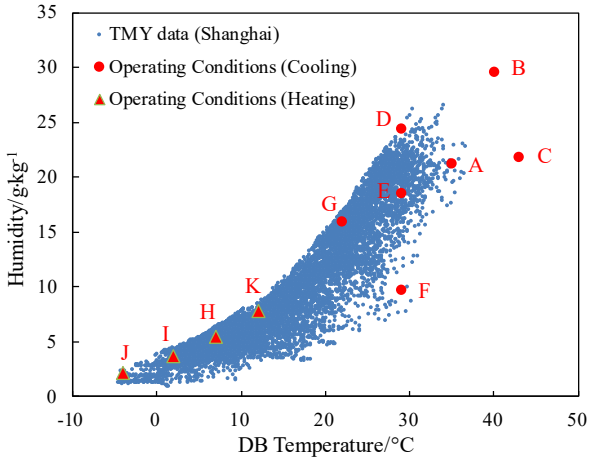


Fig. 6. Typical operating conditions in Shanghai.

4.2. Annual performance factor analysis

For further analysis, the annual performance factor (APF) of the new system is applied. In this study, APF is defined as:

$$\mathrm{APF} = \frac{Q_c + Q_h}{W_c + W_h} \tag{10}$$

where Q_c represents the total cooling capacity in cooling season and Q_h represents the total heating capacity in heating season. W_c and W_h represent the total power consumption in cooling season and heating season respectively.

APF is also calculated with TMY data of Shanghai, which is a typical region with hot moist summer and cold winter. In this work, APF is calculated as follows. Firstly, cooling season and heating season is divided into several temperature zones. The temperature and humidity interval of each zone is 1°C and 1g/kg respectively. Secondly the annual occurred time of each temperature zone is counted according to the TMY data. Then the energy consumption and cooling or heating capacity of system is calculated in every temperature zone, based on the simulation model. Finally, APF can be calculated in terms of the statistics of total energy consumption and total cooling or heating capacity within a year.

4.3. Results and discussions.

Based on the simulation model, performance of baseline system and the improved new system is calculated and compared with each other under variable operating conditions. The results in cooling season are shown in **오류! 참조 원본을 찾을 수 없습니다.**. Under rated operating conditions (A), COP of the new system is 3.94 and 46.5% higher than baseline system. Under the operating conditions B-F, the new system has about 23.7%-45% COP improvement compared to baseline system. Under the operating conditions G, which is a typical dehumidification operating conditions in transitional season, the new system has about 96.2% COP improvement compared to the baseline system. These results indicate better performance of the new system over the common combination of chiller and DOAS, especially under the operating conditions with large latent load.

Table 5 Performance comparison in cooling season

Operating Conditions	Outdoor Temperature (DB/WB)	Cooling Capacity /W	Latent Cooling Capacity /W	COP (Baseline)	COP (New System)	COP Improvement
A	35°C/28°C	14772	2275	2.69	3.94	**46.5%**
B	43°C/30°C	22162	2324	2.04	2.56	**25.5%**
C	40°C/33°C	20738	3654	2.15	3.01	**40.0%**
D	29°C/19°C	7525	522	3.76	4.65	**23.7%**
E	29°C/25°C	8799	1824	3.80	4.78	**25.8%**
F	29°C/28°C	9823	2848	3.31	4.80	**45.0%**
G	22°C/21°C	1898	1388	2.66	5.22	**96.2%**

Table 6 Contribution of different aspects to system performance improvement

System	Operating Conditions A		Operating Conditions F	
	COP	COP Improvement	COP	COP Improvement
Baseline	2.69	-	3.31	-
+ Outdoor Unit of DOAS	3.46	**28.6%**	3.81	**15.1%**
+ Precool coil	3.94	**46.5%**	4.80	**45.0%**

Performance improvement for the new system is mainly from two aspects: precooling process and heat rejecting to outdoor ambient. **오류! 참조 원본을 찾을 수 없습니다.** shows the contribution of different technology under operating conditions A and F. Both two aspects are important to the overall system performance improvement, and these two feature technology have different performance effect under different operating conditions. Under operating conditions A (T_{DB}=35°C, T_{WB}=28°C), adding outdoor unit of DOAS can bring 28.6% COP improvement, and adding precool coil can further increase COP improvement to 46.5%. But under operating conditions F (T_{DB}=29°C, T_{WB}=28°C), which is a low temperature dehumidification operating conditions, COP improvement from outdoor unit of DOAS is merely 15.1% while the overall COP improvement is nearly same to operating conditions A. The results indicate that precooling process is more effective for dehumidification operating conditions while heat rejecting is more important for those operating conditions with high cooling load.

Fig. 7 shows the detailed dehumidification process in OA subsystem under rated operating conditions according to the simulation results. It shows why the precool coil can reduce energy consumption of dehumidification. The precool coil, which handles about half cooling capacity, works with high temperature chilled water. Namely, half of cooling load for dehumidification process can be taken away in a more efficient way. And with this stepped cooling and dehumidification process, the uniformity of temperature difference in the whole duct is improved. Therefore, the overall COP of this system is higher than a conventional combined solution. Moreover, due to the cooling load of the dedicated cycle in OA subsystem is less than conventional DOAS, a smaller outdoor unit can be applied in OA subsystem of this multi-function system.

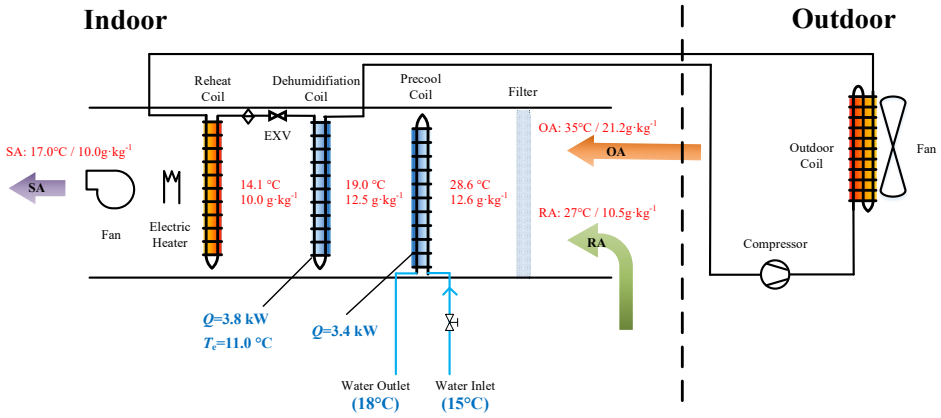


Fig. 7. Detailed schematic of dehumidification process in OA subsystem

The results in heating season are shown in 오류! 참조 원본을 찾을 수 없습니다.. In heat pump mode, compressor of OA subsystem is turned off in both baseline system and the new system. Since the improvement of the new system is mainly for cooling and dehumidification process, COP of the new system has little improvement compared to baseline system.

Fig. 8 shows the supply air temperature of OA subsystem under different heating operating conditions. This system can effectively heat outdoor air without dedicated heat pump cycle for OA subsystem. And the supply air temperature of OA subsystem can keep steadily under different operating conditions. In heat pump mode, the compressor of dedicated cycle in OA subsystem is turned off, only the water coil still works in OA subsystem. Even so, with the 45°C hot water supplied from chiller, the outdoor air can also be stably heated to about 42°C without mixing return air. And the indoor thermal comfort can be easily ensured under different operating conditions in winter.

Table 7 Performance comparison in heating season

Operating Conditions	Outdoor Temperature (DB/WB)	COP (Baseline)	COP (New System)	COP Improvement
H	7°C/6°C	2.82	2.76	**-2.1%**
I	2°C/1°C	2.06	2.06	**0.0%**
J	-4°C/-5°C	1.87	1.85	**-0.1%**
K	12°C/11°C	3.21	3.15	**-1.9%**

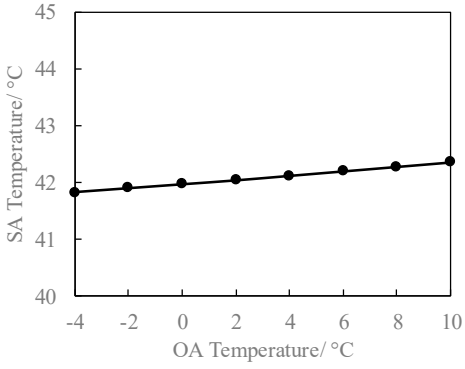


Fig. 8. Supply air temperature under different operating conditions in heating season

Table 8 APF of different system

Baseline	New System	APF Improvement
2.84	3.32	**16.9%**

Results of APF analysis are shown in **오류! 참조 원본을 찾을 수 없습니다.**. According to the simulation results, APF of the new system is 3.32 and 16.9% higher than baseline under the meteorological conditions of Shanghai. The results indicate that the new system has better performance and can reduce considerable energy consumption in annual operation especially in hot moist summer and cold winter region.

5. Conclusions

In this study, a novel multi-function residential heat pump system for cooling, heating, dehumidification and outdoor air supply is proposed. This system is composed by two subsystems: chiller subsystem and OA subsystem. In cooling season, the chiller subsystem only deals with sensible load and supply 15°C high temperature chilled water to sensible heat terminals. The OA subsystem has a dedicated refrigeration cycle and deals with overall latent load and partial sensible load. In order to decreasing the energy consumption of dehumidification and improve the performance of dehumidification, a precool water coil is added to precool outdoor air by high temperature chilled water. In heat pump mode, the outdoor air can be heated to over 40°C only by the water coil in OA subsystem.

A simulation model is developed and performance of this system is numerically analyzed based on modeling results. The overall COP of the new system can reach 3.94 under rated operating conditions, which is 46.5% higher than a conventional residential air-conditioning solution. And in terms of annual performance, APF of the new system is 3.32 and 16.9% higher than the conventional solution, under the meteorological conditions of Shanghai. Since the structure of this new system is complex and interactive, performance analysis in this work mainly focuses on the overall performance of whole system. In order to research the specific sources of energy conservation in this system, some other suitable analysis methods, such as uniformity analysis or second law analysis, are still worth to be applied for further analysis in future works.

References

[1] Mazzei P., Minichiello F., Palma D. HVAC dehumidification systems for thermal comfort: a critical review. Applied Thermal Engineering, 2005; 25(5-6): 677-707.
[2] Angrisani G., Sasso M. Experimental assessment of the energy performance of a hybrid desiccant cooling system and comparison with other air-conditioning technologies. Applied Energy, 2015; 138(C): 533-545.
[3] Mumma S. A., Shank K. M. Achieving Dry Outside Air in an Energy-Efficient Manner. ASHRAE Transactions, 2001; 107: 553-561.
[4] Zhang L. Z., Zhu D. S., Deng X. H., et al. Thermodynamic modeling of a novel air dehumidification system. Energy & Buildings, 2005; 37(3): 279-286.
[5] Zhang L. Z. Energy performance of independent air dehumidification systems with energy recovery measures. Energy, 2006; 31(8): 1228-1242.
[6] Li H., Lee W. L., Jia J. Applying a novel extra-low temperature dedicated outdoor air system in office buildings for energy efficiency and thermal comfort. Energy Conversion and Management, 2016; 121: 162-173.
[7] Zhang Z.-Y., Zhang C.-L., Ge M.-C., et al. A frost-free dedicated outdoor air system with exhaust air heat recovery. Applied Thermal Engineering, 2018; 128: 1041-1050.
[8] Zhang Z.-Y., Cao X., Yang Z., et al. Modeling and experimental investigation of an advanced direct-expansion outdoor air dehumidification system. Applied Energy, 2019; 242: 1600-1612.
[9] Mumma S. A. Ceiling Panel Cooling Systems. Ashrae Journal, 2001; 43(11): 28-32.
[10] Saber E. M., Iyengar R., Mast M., et al. Thermal comfort and IAQ analysis of a decentralized DOAS system coupled with radiant cooling for the tropics. Building & Environment, 2014; 82: 361-370.
[11] Yin X. L., Tian Z., Liu K. X., et al. Study on Energy Saving Potential of Radiant Cooling System in China. Advanced Materials Research, 2012; 433-440: 1458-1464.

[12] Zhang X. H., Li N. P., Yang J. G. Adaptability Analysis of New Ceiling Radiant Cooling Panels with Dedicated Outdoor Air Systems Used in Summer Moist Heat Regions. Key Engineering Materials, 2012; 517: 864-869.
[13] Zhao L., Jianbo C., Haizhao Y., et al. The development and experimental performance evaluation on a novel household variable refrigerant flow based temperature humidity independently controlled radiant air conditioning system. Applied Thermal Engineering, 2017; 122: 245-252.
[14] Lim H., Jeong J. W. Energy saving potential of thermoelectric radiant cooling panels with a dedicated outdoor air system. Energy & Buildings, 2018; 169:
[15] Zhang C. L. Fundamentals of vapor-compression refrigeration and air-conditioning system modeling. Bejing: Chemical Industry Press. 2012.
[16] Zhang C. L., Yang L., Shao L. L. Refrigeration and air-conditioning system modeling and analysis using GREATLAB. Bejing: Chemical Industry Press, 2015.
[17] Wang C. C., Jang J. Y., Chiou N. F. A heat transfer and friction correlation for wavy fin-and-tube heat exchangers. International Journal of Heat and Mass Transfer, 1999; 42(10): 1919-1924.
[18] Gnielinski V. New equations for heat and mass transfer in turbulent pipe and channel flow. International Chemical Engineering, 1976; 16: 359-368.
[19] Gungor K. E., Winterton R. H. S. A general correlation for flow boiling in tubes and annuli. International Journal of Heat and Mass Transfer, 1986; 29(3): 351-358.
[20] Choi J. Y., Kedzierski, M.A., Domanski, P.A. A generalized pressure drop correlation for evaporation and condensation of alternative refrigerants in smooth and micro-fin tubes. NIST 6333, 1999:
[21] Cavallini A., Col D. D., Doretti L., et al. Heat transfer and pressure drop during condensation of refrigerants inside horizontal enhanced tubes. International Journal of Refrigeration, 2000; 23(1): 4-25.
[22] Lemmon E. W., Huber M. L., McLinden M. O. NIST Reference fluid thermodynamic and transport properties-REFPROP version 9.0. 2010.
[23] Jiang Y. Building environmental system simulation and analysis: DeST. Beijing: China Architecture & Building Press 2006.

13th IEA Heat Pump Conference
April 26-29, 2021 Jeju, Korea

Study on layer short mechanism and discharge pattern in refrigerant compressor for refrigerants with disproportionation reaction like HFO-1123

Mitsuhiro Fukuta[a,*], Hideyuki Fujimoto[b], Masaaki Motozawa[a]

[a]Shizuoka university, 3-5-1 Johoku, Naka-ku, Hamamatsu, 432-8561, Japan
[b]Shizuoka university, Graduate school of Integrated Science and Technology, 3-5-1 Johoku, Naka-ku, Hamamatsu, 432-8561, Japan

Abstract

HFO-1123, one of the low GWP refrigerants, will be decomposed with receiving large amounts of energy under high temperature and pressure condition. Short-circuit between motor winding wires caused by an insulation breakdown, i.e. layer short, in refrigerant compressors could be a trigger of the disproportionation reaction of HFO-1123.

In this study, the layer short mechanism and the electric energy discharged by the layer short of winding wire in the refrigerant compressor were investigated. A compressor equipped with a short-circuit generation mechanism in a compressor shell was used to measure the electric energy by the layer short during the compressor operation. Experiments were carried out mainly with the short-circuit between both ends of a main-winding as the worst case. There were several short-circuit patterns and the maximum current was observed to be 700 - 900 A and the electric energy was about 160 J. When the short-circuit occurred between terminals of the main-winding and an auxiliary-winding, the motor stopped while the electricity was continuously supplied, and temperature of the winding wire increased approximately 2.5℃/s.

Keywords: HFO1123, Disproportionation reaction, Compressor, Motor, Layer short, Electric energy

1. Introduction

From the viewpoint of preventing the global warming, the Kigali amendment to the Montreal protocol entered into force to phase-down the production and consumption of HFCs, and the use of the low GWP refrigerant is eagerly desired. HFO refrigerants have the low GWP, and application of the HFOs has been investigated in recent years. HFO-1123 is one of the low GWP refrigerants whose GWP is less than one and a mixture of HFO-1123 is considered as an alternative of R410A and R32. Although the GWP of the HFO-based mixed refrigerant can be reduced by increasing the mixing ratio of HFO-1123, a disproportionation reaction of HFO-1123 may occur when HFO-1123 gets high ignition energy under pressurized condition in refrigerant compressors [1,2]. If the disproportionation reaction occurs in the refrigerant compressor, the temperature and pressure in the compressor will rise steeply, and the refrigerant compressor might be destroyed. Since short-circuit between motor winding wires caused by an insulation breakdown, i.e. layer short, in the refrigerant compressors could be a trigger of the disproportionation reaction of HFO-1123, layer short mechanism and an electric energy caused by the layer short should be clarified [3].

In this study, the layer short mechanism and the electric energy discharged by the layer short of winding wire in the refrigerant compressor were investigated. A compressor equipped with a short-circuit generation mechanism in a compressor shell was used to measure the electric energy by the layer short during the compressor operation. The short-circuit between any two lead wires of the motor could be produced in the compressor with the short-circuit mechanism. As the first step of the study, experiments were carried out mainly with the short-circuit between both ends of a main-winding as the worst case. Current, voltage and

* Corresponding author. Tel.: +81-53-478-1054; fax: +81-53-478-1054
E-mail address: fukuta.mitsuhiro@shizuoka.ac.jp

electric power when the short-circuit occurred were measured.

2. Experiment

Figure 1 shows a schematic diagram of the compressor for generating a layer short in the refrigerant compressor. A compression mechanism and a motor were assembled into a shell having a large space above the motor element. The short-circuit generation mechanism (Fig.1, right) was mounted at the upper space in the shell, and it could generate the short-circuit with two enamel wires in the motor winding by operating an external screw head during compressor operation. In addition, a glass window was installed on the shell, and the short-circuit generation could be observed from the outside.

Figure 2 shows a schematic diagram of the refrigeration cycle with the compressor shown in Fig.1.The refrigeration cycle was a gas cycle consisting of the compressor, a radiator, an expansion valve. The pressure condition was adjusted with the throttle valve and charge amount of refrigerant controlled using a small refrigerant cylinder connected to the cycle. The suction pressure and the discharge pressure were measured by Bourdon tube gauges. The temperature was measured by T-type thermocouple at suction and discharge pipe of the compressor, and before and after the throttle valve. Beside those, the temperature of stator windings inside the compressor were measured by the thermocouples at two points. The refrigerant used was R410A instead of HFO-1123 because of safety, and the oil used was PVE (VG68).

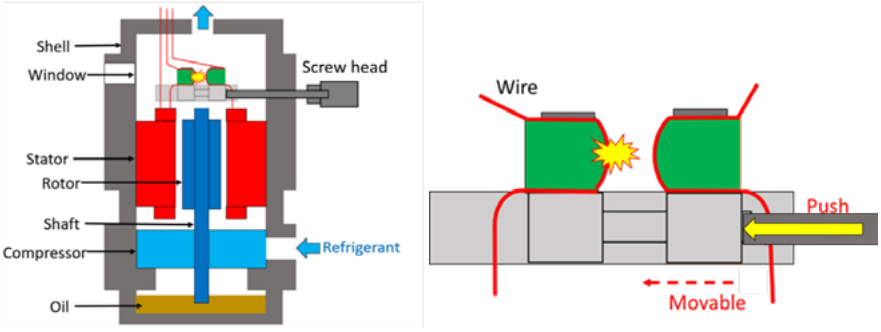


Fig. 1. Compressor for short-circuit experiment

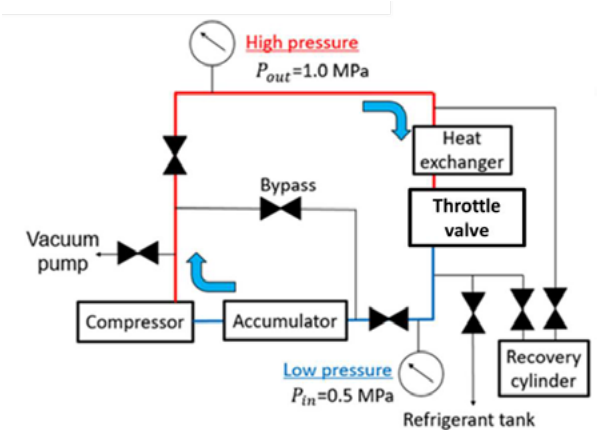


Fig. 2. Experimental gas cycle

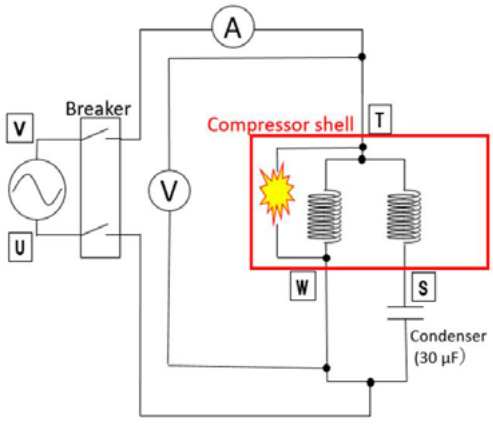


Fig. 3. Electric circuit (W-T short)

Figure 3 shows the motor driving circuit diagram. The motor was a 200 V single-phase permanent split type induction motor (rated output power is 750 W, outer diameter of motor stator is 112 mm, diameter of winding is 0.8 mm, resistance of winding is 35 Ω/km). A red square in Fig. 3 is the compressor shell and coils in the shell are the main-winding and the auxiliary-winding of the motor, respectively.

A breaker rated at 20 A was installed between the power source and the compressor. Over Load Protector (OLP) was not used at this time. Symbols W, T, and S represent the terminals of a glass terminal connected to the motor in the compressor. The short-circuit between W and T (W-T short) in the compressor shell is shown in Fig. 3. Enameled wires whose enamel coating was partially removed were inserted to lead wires of W and T, and these enameled wires were set at the layer short-circuit mechanism. When the short-circuit was produced, the voltage between the short-circuited terminals and the current flowing through the short-circuited enameled wire were measured using a high-voltage differential probe and a Rogowski coil, respectively. In addition to the W-T short, the short-circuit between W and S (W-S short) was conducted in this study.

After turning on the compressor, when the suction pressure and the discharge pressure reached 0.5 MPa (g) and 1.0 MPa (g), respectively, and became steady state, the short-circuit between two wires set at the short-circuit generation mechanism was yielded intentionally. The instantaneous electric power was calculated by the production of the current and the voltage. The electric energy due to the short-circuit was obtained by integrating the electric power with the time during which a large current was generated (short-circuit time). In addition, a high-speed camera was used to observe the sparks that occurred by the short-circuit generation.

3. Experimental result

3.1. Short-circuit at both ends of main-winding (W-T short)

The W-T short is shot-circuit between the both ends of the main-winding. Since it is equivalent to the short-circuit of the power source, this short-circuit is considered as the worst case discharging the maximum electric energy. When the W-T short occurred, a big spark rose, and the breaker was activated at that moment. Figure 4 shows the spark taken by the high-speed camera. The enamelled wire at the contact point after the short-circuit was fused as shown in Fig. 5 or welded. Figure 6 shows changes in current, voltage, and electric power against the time when the W-T short occurs. The zero point of the time on the horizontal axis is the time when the short-circuit occurred. Until the short- circuit occurred, the voltage waveform shows a sinusoidal one with an amplitude of 283 V. Although the current before the short-circuit is difficult to read from the figure because the full scale for the current is very large, it shows a sinusoidal wave with an amplitude of about 4 A. When the short-circuit occurred, the voltage between the W-T dropped to 0 V, and an instantaneous large current (maximum value of 784 A) flowed. The short-circuit time was 6 ms, and the electric energy due to the W-T short was 219 J.

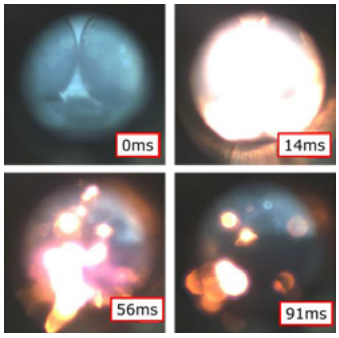


Fig. 4. Observation of the W-T short

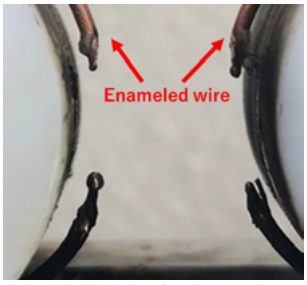


Fig. 5. Winding wire after the W-T short

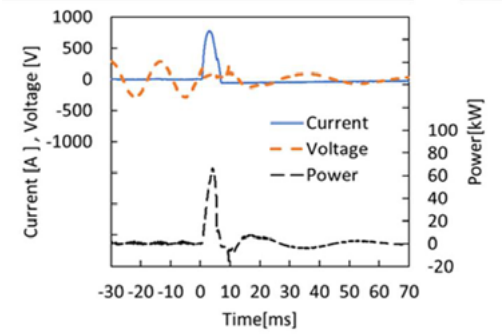


Fig. 6. Current, voltage, power (W-T short No.1)

Figure 7 shows another result when the W-T short generated under the same condition. As can be seen in Fig.7, once the voltage dropped to 0 V by the short-circuit, then increased and became 0 again. The instantaneous large current due to the short-circuit shows two peaks according to the voltage change. The short-circuit time was 6 ms in total for the two peaks. Electric energy generated was 168 J. In the case shown in Fig. 7, the two peaks were explained as that when the short-circuit occurred, only the contact part of the two enamel wires melted, the circuit temporarily recovered from the short-circuit to the normal state, and then the short-circuit occurred again.

In order to compare the results with the W-T short generated inside the compressor, W and T terminals were short-circuited at the outside of the compressor shell. No significant differences were observed in the current and voltage waveforms between them. Results for the W-T short generated both inside and outside of the compressor are summarized in Fig. 8 against phase angle θ of the voltage at the instant of the short-circuit generation.

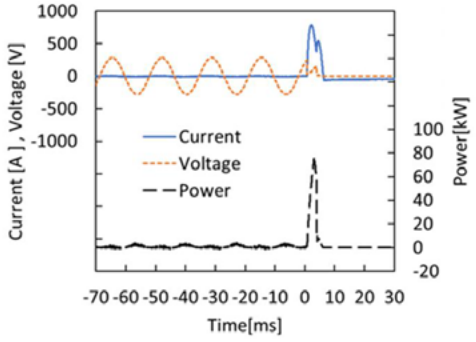


Fig. 7. Current, voltage, power (W-T short No.2)

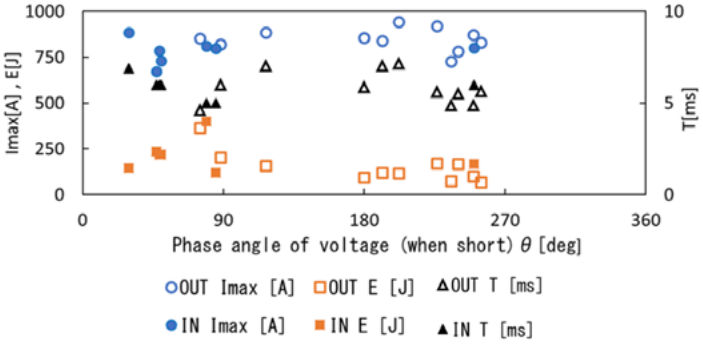


Fig. 8. Maximum current, short circuit time, and electric energy

The vertical axes of Fig. 8 represent the maximum current I_{max}, the electric energy E, and short-circuit time T. IN and OUT in Fig. 8 express the position where inside or outside of the compressor the short-circuit was generated. There was no significant influence of the voltage phase angle on the peak current, the electric energy, and short-circuit time. It can also be seen that the short-circuit often occurred at the range of phase angle 0-90°and 180 - 270°.The peak current was about 850 A, the electric energy was about 160 J, and the short-circuit time was about 7 ms. Since there was no difference between the short-circuit generated the inside and the outside of the compressor, the electric energy caused by the W-T short can be evaluated by the short-circuit between the W and T terminals outside the compressor. However, the layer short of the motor windings in the compressor accompanied by electric discharge should be examined in the compressor shell under the refrigerant atmosphere since the electric discharge is strongly affected by the refrigerant pressure [4], and an insulation of enamel deteriorates by high temperature [5].

3.2. Short-circuit between ends of the main-winding and auxiliary-winding (W-S short)

The W-S short is a short-circuit across the capacitor and makes the electric circuit of the motor into parallel two coils. When the W-S short occurred, the rotation of the motor stopped while the electricity was continuously supplied, and the motor temperature started to increase. Figure 9 shows the changes in the temperature of two positions of the upper coil end and the discharge pipe temperature when the W-S short occurred. When the motor temperature reached 150°C, the power was intentionally turned off to protect the motor. The temperature of Coil end (1) increased at 2.5°C/s after the short-circuit. If the temperature of the winding wire becomes so high that the enamel wire coating will deteriorate, the layer short may happen. This kind of risk is expected to be prevented by applying an over load protector in a power supply circuit.

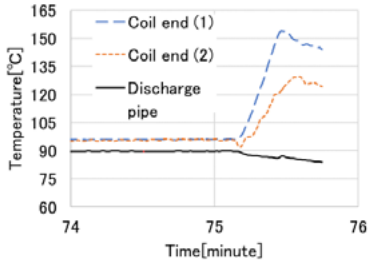


Fig. 9. Temperature change when the W-S short occurs

4. Future works

The following issues will be done to clarify the layer short mechanism and the discharge energy by the short-circuit in compressors.

1. Current and voltage measurement during the temperature rise by the W-S short
2. Investigation of the effect of over load protector
3. Short-circuit between both ends of auxiliary winding (T-S short)
4. Current, voltage and energy measurement in the case that the discharge occurs between wires with a certain minute gap.
5. Examination of degradation of enamelled wire due to short-circuit which occurs locally in the motor windings

5. Conclusion

Electric energy discharged by the short-circuit of winding wire in refrigerant compressors was investigated with a compressor equipped with a short-circuit generation mechanism in a compressor shell. The short-circuit between both ends of a main-winding (W-T short) was considered as the worst case. The maximum current was observed to be 700 - 900 A for about 7 ms, and the electric energy was about 160 J. When the short-circuit between both ends of a capacitor (W-S short), the motor stopped while the electricity was continuously supplied, and temperature of the winding wire increased approximately 2.5℃/s. Further study is needed to clarify the layer short mechanism in the refrigerant compressors.

Acknowledgement

This study was supported by the New Energy and Industrial Technology Development Organization (NEDO) in Japan. We would like to express our deep appreciation to NEDO.

References

[1] Tetsuo Otsuka, Hidekazu Okamoto, Katsuya Ueno, Masamichi Ippommatsu and Ritsu Dobashi, 2018, Development of control method of HFO-1123 disproportionation and investigation of probability of HFO1123 disproportionation . AGC Research Report, Vol. 68; pp.1-7. (in Japanese)

[2] Makoto Ito, Naoya Kurokawa, Chaobin Dang, Eiji Hihara, 2018, Disproportionation Reaction of HFO-1123 Refrigerant, International Refrigeration and Air Conditioning Conference.Paper 2069; pp.1-9.

[3] Hisahide Nakamura, 2015, Proposal for a New Means of Identifying Slot Inserted Coils with Short-circuit Faults in Stator Winding Based on Changes in Magnetic Field, Trans. of The Society of Instrument and Control Engineers, Vol.51, No.4 ; pp. 260-266. (in Japanese)

[4] Mitsuhiro Fukuta, Masaaki Motozawa, 2017, Separation of Oil Droplet by Coulomb Force, Refrigeration , 92,1074; pp.261-265. (in Japanese)

[5] S. Grzybowski, E. A. Feilat, P. Knight, 1999, Accelerated aging tests on magnet wires under high frequency pulsating voltage and high temperature, 1999 Annual Report Conference on Electrical Insulation and Dielectric Phenomena; pp.555-558.

13th IEA Heat Pump Conference
April 26-29, 2021 Jeju, Korea

Energy Performance Estimation and Verification of an Industrial Waste Heat Recovery Heat Pump

Toshihiko OKUNO [a], Takashi KUWABARA [a], Akira KOYAMA [a], Jun SHISHIDO [b] and Katsumi HASHIMOTO [c*]

[a] Sales Dept., Science Inc., Saitama-Shi, Saitama, 331-0812, Japan
[b] Research and Development Center, Tohoku Electric Power Co., Inc., Sendai-shi, Miyagi, 981-0952, Japan
[c] Energy Innovation Center, Central Research Institute of Electric Ppower Industry, Yokosuka-shi, Kanagawa, 240-0196, Japan

Abstract

Aiming to save primary energy, reduce greenhouse gas, and save running cost, it is important to construct systems in industrial factories more efficient by utilizing heat from warm wastewater. To realize more efficient water heating system, it is essential to develop and evaluate affordable direct heat-recoverable heat pump which has direct recoverable evaporator. An experimental performance evaluation and an estimation based on the results have been conducted. According to the evaluation, developed heat pump achieved a COP of 4 or more, with an warm wastewater temperature of 35°C. Verification of the estimation was conducted by the field measurement. A problem, performance degradation according to fouling of the evaporator. A solution was developed, and availability was validated through the field measurement.

Keywords: wastet heat recovery, heat pump, direct recoverable evaporator, experimental performance evaluation, verification

1. Introduction

Heat pumps are expected to penetrate significantly due to their high energy conservation and greenhouse gas mitigation effects and have already established themselves as key components in air-conditioning equipment for residential and commercial buildings. Conversely, although penetration into the industrial sector is also now developing, due to exceptional energy conservation and greenhouse gas mitigation potential [1], some hindrances remain, for example, the high initial cost and the lack of awareness.

Heat recovery water-heating heat pumps capable of heating water up to high temperatures efficiently powered by waste heat from industrial processes are expected to spread because they use renewable energy (it is waste heat) efficiently, reduce primary energy input and offer high generality. Most conventional systems, however, were inefficient and involved high running costs because of their indirect construction, which meant an extra circulation loop was needed to recover heat from waste heat. Accordingly, commercialization of a “direct heat-recoverable heat pump”, capable of recovering heat directly in the evaporator (“direct heat-recoverable evaporator”) from waste heat, has been expected, which could conserve primary energy, reduce greenhouse gas, save on initial and running costs and reduce footprint. Many issues, however, remain when it comes to developing the “direct heat-recoverable evaporator”, for example, separating it from the heat pump, its ability to withstand various chemical species and impurities, anti-fouling performance and so on. Kuwabara et al. [2] reported the shell-and-coil type heat exchanger as a possible solution and a direct heat-recoverable heat pump is also being developed.

In this report, the direct heat-recoverable heat pump using a shell-and-coil type evaporator is evaluated in a performance evaluating facility and through field measurement. Degradation of heating capacity due to fouling accumulation and its fixing using self-cleaning found on the field measurement are also reported.

* Corresponding author. Tel.: +81-70-65-68-94-48;
E-mail address: hashimo@criepi.denken.or.jp.

2. Experimental performance evaluation and modeling of efficiency

2.1. Heat pump to be tested

The direct heat-recoverable heat pump water heater is selected for testing, with specifications as in Table 1 and the following features [2]: (1) The evaporator can be settled separately from the main body (see Figure 1) and the maximum separation distance is 10 m, (2) it has a fixed speed compressor and (3) the outlet temperature can be controlled using a water-control valve.

Table 1. Specifications of heat pump to be tested

Heating capacity	50 kW
Refrigerant	R410A
Output temperature	50 – 65 °C
Upper limit of heat source temperature	53 °C
Maximum distance to evaporator	10 m

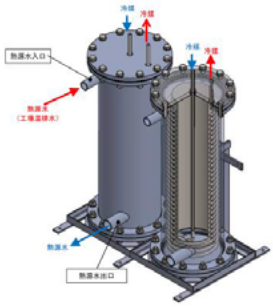


Figure 1 Schematic diagram of direct recoverable evaporator in the heat pump [2]

2.2. Performance evaluating facility

The performance evaluation facility is in the Central Research Institute of Electric Power Industry and Hashimoto et al. [3] reported on the design and performance of the facility, within which the heat pump to be tested is installed (see Figure 2). To measure performance, the hot water volumetric flow rate, hot water inlet and outlet temperature, heat source water volumetric flow rate, heat source water inlet and outlet temperatures and electricity consumption were measured highly accurate, with particular focus on ensuring accurate temperature measurement. A highly accurate resistance thermometer and highly accurate logger (NETSUSHIN NX1000) were used.

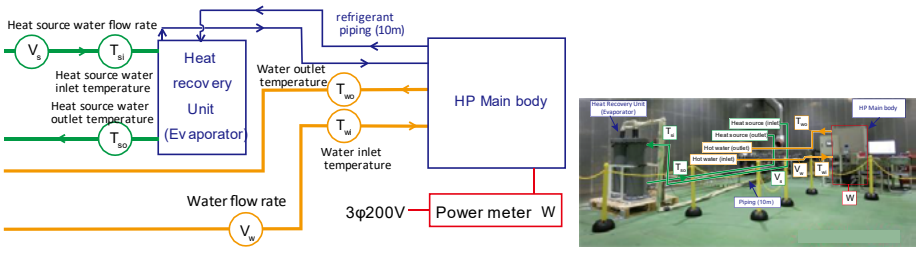


Figure 2 Photograph of the heat pump in the evaluating facility

2.3. Definitions of evaluation indexes

Water heating capacity, or Q_w, is defined as the following equation:

$$Q_w = \frac{60\, V_w (T_{wo} - T_{wi})}{860} \quad (1)$$

Here, V_w, T_{wi} and T_{wo} constitute the hot water volumetric flow rate (L/min), hot water inlet temperature (ºC) and hot water outlet temperature (ºC), respectively. And density of water assumed to be 1kg/L.

Coefficient of performance of water heating, or COP_w, is defined as the following equation:

$$COP_w = \frac{Q_w}{W} \quad (2)$$

Here, W is electricity consumption (kW).

2.4. Result of evaluation

(a)Rating condition

Table 2 shows the result of the performance in terms of the rating condition. Assuming that the heat pump is used for preheating boiler feedwater, that is inlet temperature T_{wi} is 17 ºC and target outlet temperature T_{wo} is 65 ºC, and using warm waste water as a heat source, that is heat sink inlet temperature T_{si} is 30 ºC, the conditions shown in the notation were used as rated conditions. As a result of the measurement, A was 64.89 ºC, that is almost equal to the target of 65 ºC, and the heating capacity was 53.59kW and COP_w was 3.84.

Table 2 Performance in rating condition. (Run 65-1-1)

Title	Setpoint	Title	Results
T_{wi} (ºC)	17	Q_w (kW)	53.59
T_{si} (ºC)	30	V_w (L/min)	16.09
		W (kW)	13.95
		COP_w (-)	3.84
T_{wo} (°C)	65	T_{wo} (°C)	64.89

(b)Performance map

The water-heating capacity map (Figure 3) is obtained using the hot water inlet temperature and the heat source water inlet temperature as parameters.

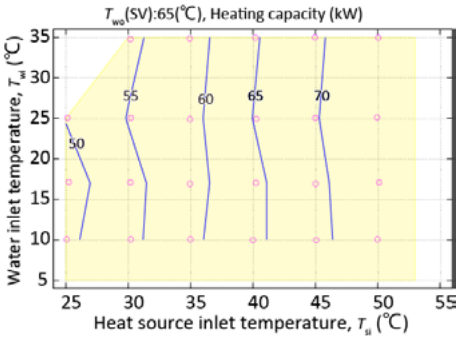


Figure 3 Performance map (T_{wo} (SV) =: 65 ºC)

2.5. Modeling of efficiency

Performance measurements are used to obtain a modeling equation. Assuming a hot water outlet temperature of 65 ºC, the water heating COP is modeled as per Equation (3).

$$COP_w = 0.065\,T_{si} + 1.95 \quad (3)$$

Here, T_{si} is heat source water inlet temperature. Since the influence of T_{wi} is very weak, it is ignored.

3. Verification by field measurement

3.1. Outline of the field measurement

A field measurement is conducted in a cleaning factory located near Sendai City, Miyagi prefecture (in the Tohoku region of Japan). Figure 4 shows a schematic diagram of the field measurement. This factory uses about 70 tons of steam per day, and all of which is supplied by a steam boiler fueled with A-type heavy oil.

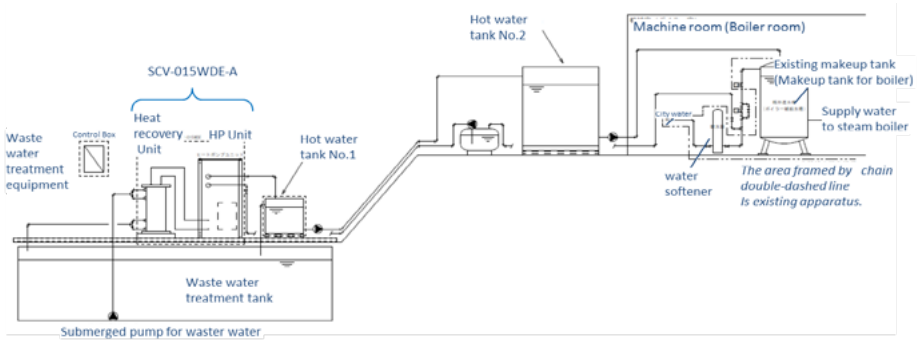


Figure 4 Schematic diagram of the field performance evaluation.

The overall amount of warm effluent wasted from all the cleaning processes in the factory constitutes about 300 tons per day, which is collected in a waste water treatment tank and then discarded as sewage after purification and pH adjustment. The warm wastewater contains fiber waste, dust, detergent components, soap scum and so on.

The heat pump to be tested is installed on top of the wastewater treatment tank and the warm wastewater is propelled to the heat pump by the pump, whereupon heat is recovered from the same and the wastewater is returned to the wastewater treatment tank.

The standard specification of the evaporator shell is made of PVC, but was made of acrylic for the field measurement to visualize the fouling inside the evaporator. The distance between the heat pump main body ("HP Unit") and the heat-recoverable evaporator ("Heat Recovery Unit") is set at 5 m.

There are two hot water tanks. Tank 1, volume of $2m^3$, is located on the wastewater treatment tank, while Tank 2 is located near the steam supplying boiler in the mechanical room. The distance between the two tanks is 140m and they are connected by well-insulated hot water piping. The existing replenishing tank (makeup tank) and Tank 2 are also connected by piping.

In the field measurement, the following two type of tests are conducted:

1. Non-load test:
   Heat is recovered from warm wastewater to generate hot water, and the hot water is discharged into a wastewater treatment tank.
2. Full-scale load test:
   Hot water generated by recovering heat from warm wastewater is supplied to the replenishing tank to be used for preheating replenishing water.

Field measurements are conducted from July 2017 to February 2018. The no-load test lasted for about 6 months from July 2017 to January 2018, while the full-scale load test lasted for two weeks from February 5 to 16, 2018. The factory does not operate at weekends.

Well water (temperature 12 - 16 ºC) is used as a heated medium to generate hot water, and the target hot water outlet temperature was set to 65 ºC.

3.2. Field measurement result and the verification of the modeling

The heating capacity is degraded due to cumulative fouling in the field measurement, which is mitigated by daily self-cleaning. Details will be described in Section 4 and the following description is based on the result after conducting self-cleaning.

Figure 5 shows the daily average heating COP by field measurement (hereinafter referred to as heating COP (field), indicated as "Field test" in figure 5) from February 5 to 16 and heating COP (lab) calculated from Equation (3). The heated COP (field) on February 5 is about 10% higher than the heated COP (lab), which is presumably attributable to the length of the refrigerant pipe between the evaporator and main body.

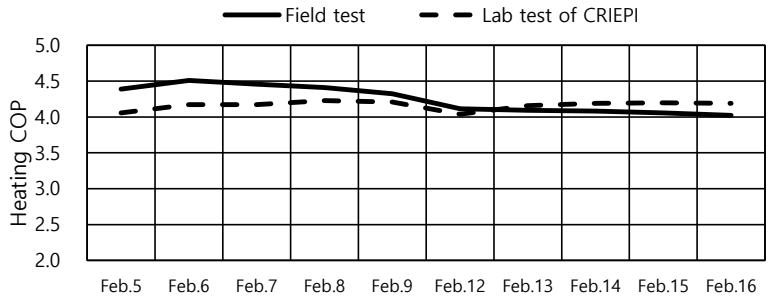


Figure 5 Performance comparison between field measurement and modeling by lab evaluation

From February 6 to 12, the heating COP (field) is on a downward trend, which implies that daily self-cleaning cannot completely remove the fouling from the coil surface of the evaporator. Conversely, since the decreasing trend of heated COP (field) after February 12 has been alleviated, self-cleaning is considered effective in preventing any reduction in heated COP.

3.3. Estimation of the installation effect

Figure 6 shows the estimated reduction in daily A-type heavy oil and increase in daily electricity consumption based on the field measurement. The average reduction in A-type heavy oil was about 88L, and the average increase in electricity was about 194kWh.

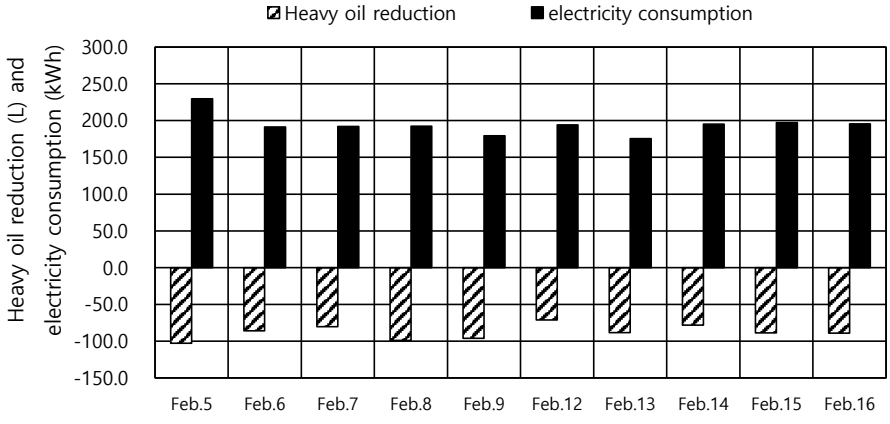


Figure 6 Daily variation of estimated electricity consumption and A-type heavy oil reduction effects.

The annual introduction effect is estimated based on this result. Assuming 262 working days per year, a primary energy reduction effect of 395 GJ and a CO_2 emission-reduction effect of 36 ton- CO_2 can be expected. Here, the grid power primary energy conversion factor, A-type heavy oil calorific value, grid power CO_2 emission intensity (2015) and A-type heavy oil CO_2 emission intensity are assumed at 9.97 MJ / kWh, 39.1 MJ / L, 0.53 kg- CO_2 / kWh and 2.71 kg- CO_2 / L, respectively.

With regard to the CO_2 emission-reduction effect, further intensification can be expected as the decarbonization of grid power progresses.

4. The cumulative fouling on the coil of evaporator and the effect of self-cleaning

Figure 7 shows the water-heating-capacity and heat source temperature at the inlet of the evaporator (denoted as “draining temp”) under operation. A decline in heating capacity is observed as shown in the graph denoted as “no cleaning” (from February 14 to 16), at a rate estimated at 094 MJ/h. Based on the virtually constant heat source temperature and the accumulation of cotton-lint fouling observed, it was suggested that the latter fouling may explain the deterioration, something supported by the significant fouling adhesion on the first day and the concurrent significant decline.

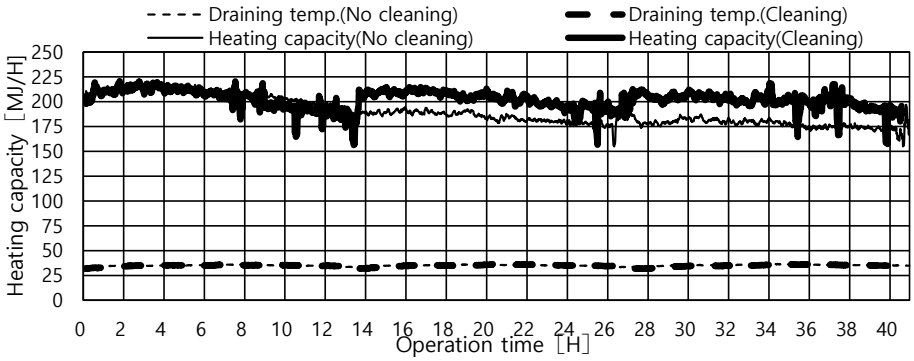


Figure 7 Decreasing heating capacity with adherence onto coil surface and recovery by the self-cleaning

There has been concern about the decline in the evaporator heating capacity due to cumulative fouling on the evaporator coil surface since the project started. Annual chemical cleaning and disassembly cleaning (once every two to three years) are being considered and urgent measure to counter daily performance degradation are required due to cumulative fouling beyond expectations.

Self-cleaning using discharge heat source water from the evaporator is carried out as an urgent measure. To realize the self-cleaning, a discharge valve is installed on the piping on the evaporator outlet. Random bubbling from the discharge valve helps to clean more effectively.

Figure 7 also shows the heating capacity and heat source temperature at the evaporator inlet after self-cleaning, the results of which are shown as “cleaning” (from February 14 to 16). The self-cleaning is conducted daily just after stopping operation. It is confirmed that the visual impact of the cumulative fouling was eased and the heating capacity recovered after the self-cleaning.

5. Conclusion

A heat-recoverable water heating heat pump is evaluated in two ways, via a performance measurement facility and field measurements and its high performance due to a direct heat-recoverable evaporator was confirmed, despite being designed as an affordable heat pump.

In addition, a problem of fouling on the surface of the evaporator coil is solved by using a new heat exchanger cleaning method (daily self-cleaning) and it was confirmed that performance recovered after this cleaning. It is also understood that the length of the separation pipe between the main body and evaporator impacted on performance.

Aiming to conserve more primary energy in the industrial sector, it is important not only to improve heat pump efficiency but also to improve the total design of the hot water supply system and system operation. We will continue to challenge these improvements.

Nomenclature

COP	: Coefficient of Performance, -	W	: Electricity consumption, kJ・s^{-1}
Q	: Heating capacity, kJ・s^{-1}	w	: (subscript) hot water (heat sink)
T	: Temperature, °C	s	: (subscript) heat source water
V	: Volumetric flow rate, L・min^{-1}	i,o	: (subscript) inlet, outlet

References

[1] Heat pump and thermal storage center of Japan, Primary energy saving and CO2 reduction effect by increasing diffusion of Heat Pump, News release, 4th Aug. 2017
[2] Kuwabara T. and Shishido J., Development of Hot Water Supplying System by Direct Expansion-type Water Source Heat Pump for Exhaust Heat Recovery, Electro-Heat, 213 (2017), pp. 66-69. (in Japanese)
[3] Hashimoto K. et al., kkkkDevelopment of Large-Capacity Heat Pump Performance Evaluationg Apparatus, Proceedings of the 11th Heat Pump Conference, (2019), P.4.7



13th IEA Heat Pump Conference
May 11-14, 2020 Jeju, Korea

Possibilities and constraints of grid flexible control of todays and tomorrows heat pumps

Markus Lindahl[a], Tommy Walfridson[a], Jessica Benson[a], Oskar Räftegård[a], Ola Gustafsson[a], Caroline Haglund Stignor[a]

[a]Energy and Circular economy, RISE Reseach Institutes of Sweden, Box 857, SE-501 15 BORÅS, Sweden

Abstract

In this article possibilities and constraints of grid flexible control of heat pumps for domestic heating are investigated. By creating dynamic coalitions of heat pumps and control their power consumption, demand response can be offered to the power grid. For a functional power grid, the heat pumps electrical power consumption needs to follow the electrical grids needs accurately.

Possibilities to externally control the power consumption of a ground source heat pump has been investigated. Both direct control, where the compressor speed is set directly, and indirect control, achieved with outdoor temperature sensor override, has been evaluated. For the evaluation a test cycle for laboratory testing of a heat pumps grid flexibility has been developed.

Based on the test cycle, the heat pumps possibilities to follow the load profile using both direct and indirect control was tested in laboratory. Both control methods were possible to use, with the direct control being significantly more accurate. Using direct control, the power consumption of the compressor managed to be within ±10% of the stated power consumption for 97% of the time.

© HPC2020.
Selection and/or peer-review under responsibility of the organizers of the 13th IEA Heat Pump Conference 2020.

Keywords: Grid flexible heat pump; Heat Pump control; Smart grid; Demand response; Heat Pump

1. Introduction

The European power system undergoes a major transformation driven by a steadily increasing share of power from renewable intermittent energy sources, such as wind power and solar energy. When the production of electric power from intermittent sources increases, the need to control the variations in the power system increases as well [1][2]. Heat pumps, with their possibility to convert power to heat, can support the transformation of the power system. Making use of the building's thermal inertia in combination with controlling the heat pump´s power consumption makes it possible to use the heat pump to provide demand response [1]. Historically heat pump design has focused on providing a good indoor climate and domestic hot water (DHW) with as high efficiency as possible. In the future with more and more variable power production it will likely be of greater importance to provide comfort with low impact on global warming rather than with as high efficiency as possibility.

By external control of the heat pumps and their power consumption, demand response can be offered to the power grid. The term "demand response" includes controlling the power consumption to better match the consumption with the power supply. Demand response can be used to avoid power peaks, balance the power consumption, avoiding curtailment of power production from intermittent renewable sources etc. One way to

offer a larger flexibility in electric power is to make dynamic clusters of heat pumps, giving higher flexibility when controlled together [1][3].

1.1. Scope

The objective with the article is to evaluate different strategies for indirect and direct control of a grid flexible heat pump and give recommendation of the best way to externally control a heat pump with variable speed compressor for offering grid flexibility. A grid flexible heat pump is defined as a heat pump that can adjust its electrical power use to external demands.

1.2. Method

Two different strategies for heat pump control have been evaluated by laboratory tests of a ground source heat pump with a variable speed compressor. The strategies evaluated are indirect control via temperature sensor override and direct control of the heat pumps compressor speed. In addition, other possibilities and constrains of heat pump control have been evaluated using a literature survey and a questionnaire sent out to four Swedish heat pump manufacturers.

1.3. Delimitations

The article focuses on how to control the heat pumps power consumption externally. How the power profile for offering demand response is calculated and distributed to the individual heat pumps are out of the scope of the article and only briefly described. The article studies the control of the heat pumps power consumption and heat production related to space heating, production of domestic hot water is not included.

1.4. Background

The benefit with heat pumps, when it comes to demand response, is their possibility to transform power to heat. In combination with the thermal inertia in buildings, or thermal storages, it gives a possibility to control, within certain limits, when the building needs to be heated and still keep a good indoor climate. By controlling the power consumption of the heat pump, it is possible to help balancing the power systems variations in supply and demand. But controlling the power output from a single heat pump gives low flexibility to the grid, in order to provide a useful size of power to use for demand response a coalition of heat pumps needs to be controlled together. In the EU project Flexible Heat and Power (FHP) [4], which work the article is based on, this is done in several steps. First the available thermal flexibility from the individual buildings is calculated, followed by aggregating the flexibility from all individual buildings for a neighborhood or a community. Then the aggregated plan can be used to offer balancing services to the local distribution system operator (DSO) or the balance responsible party (BRP). Finally, the decided control of the heat pump coalition will be disaggregated and dispatched to the individual heat pumps, where each heat pump is given a power profile to follow. This article focuses on the last step, how to control the heat pumps power consumption and follow a decided power profile given by an external party.

1.4.1. Heat pump control

There have been other projects during the last years investigating the use of heat pumps to offer demand response in different ways. How the heat pumps power consumption is controlled varies. In some projects an off-signal is sent to the heat pump. One example is the EU project EcoGrid [5], the project demonstrated the operation of a power system with high amount of renewable and variable energy resources on the Danish island of Bornholm. The operating tools for heat pumps developed in the project had the possibility to send an off signal to the heat pump for a certain time period.

Another way to control the heat pump is based on the German “Smart grid ready” or “SG ready” standard. It is a standard for smart control defined by the German Bundesverband Wärmepumpe e.V. [6]. The standard makes it possible to send a signal to the heat pump that activates one of the four defined modes. The activation of each mode is done based on how two terminals are open (0) or closed (1). The setting of the terminals activates different setting of the heat pump control. When one of the modes is activated, the heat pump is programmed to respond in a certain way. The exact response for each mode is not defined by the standard and can vary from one heat pump model to another.

The four defined heat pump working modes are [7]:

1. Blocking mode: HP is switched off, until storage reaches its lower allowed temperature level. (1:0)
2. Normal mode: HP operates with normal set-points. (0:0)
3. Low price mode: HP is switched on. (0:1)
4. Over capacity mode: HP is switched on, storage temperatures increased to the maximum temperature allowed by the HP. (1:1)

2. Strategies for heat pump control

One important step in the chain to provide demand response is to be able to control the heat pump based on external signals in order to make the heat pump consume the amount of electricity asked for. Both sending an off signal to the heat pump or using the SG ready standard gives a very rough control of the heat pumps power consumption. In order to make the heat pump follow a defined power profile a method with higher accuracy is needed. Two alternative methods are evaluated in order to find a way with higher accuracy. External control of a heat pump can be divided into two main categories, direct- and indirect control.

2.1. Indirect control

The heating demand of a building is dependent on the outdoor temperature and a heat pump is programmed to adjust its heat production based on the outdoor temperature. Most heat pumps are equipped with an outdoor temperature sensor, giving information about actual temperate, used to estimate the heating demand of the building. At low winter temperatures the auxiliary heater may need to start to cover the total heating demand of the building. Manipulating the temperature sensor and sending a fake outdoor temperature to the heat pump is a possible way to indirect control the heat pumps heat production and power demand. An alternative way to control the heat pump indirect is to adjust the heat pumps heating curve. In the tests related to this project the outdoor temperature sensor was replaced with an adjustable precision potentiometer making it possible to manually set the outdoor temperature wanted.

2.2. Direct control

At direct control the heat pumps ordinary, internal control to set the compressor speed and switch between space heating and production of DHW is bypassed and the compressor is controlled directly. This makes it possible to control the heat pumps power consumption fast and with higher accuracy. To make this work it is necessary that the heat pumps is prepared for external control and that it is possible to communicate with it. No heat pump on the market has this functionality today.

During the laboratory tests with direct control a software developed by the heat pump manufacturer of the tested heat pump was used. The software is normally used for internal testing by the manufacturer. Via a computer connected to the heat pump, the software made it possible to set the compressor frequency directly. As a complement to the software an add-on was created. The add-on makes it possible to set the frequency profile asked for via a csv-file. This made it possible to create a test sequence that automatically changes the compressor speed at desired times, making it easier to test longer sequences with changing compressor speed or to make fast changes.

2.3. Constrains in compressor speed change

The heat pumps on the market today are developed to give high comfort with as high efficiency as possible. But in order to be flexible, the heat pump needs to handle fast changes in compressor speed. A survey sent out to four Swedish heat pump manufacturers showed that different manufacturers have different approaches, comparing the time inverter heat pumps took from off mode to maximal heat production or from the lowest compressor speed to the highest. Figure 1 shows large differences in time going from minimum to maximum speed depending on the choice of heat pump model. Note that for the laboratory test presented in this article “HP A” has been used.

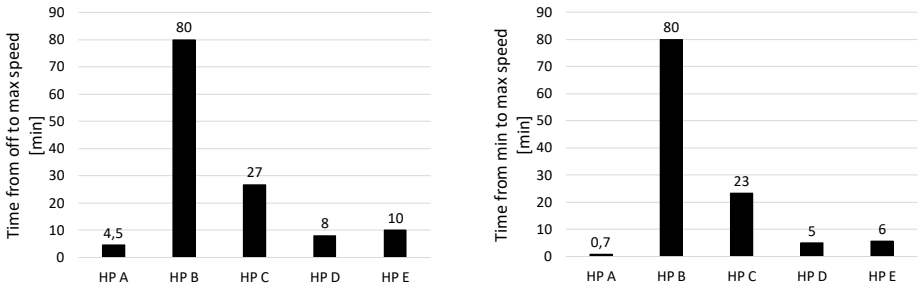


Figure 1. Time from compressor off to full speed (left) and from running at lowest compressor speed to highest compressor speed (right).

Another constraint is the start-up phase, where the compressor typically needs to run at a fixed, midrange speed for minutes, to secure lubrication before the speed asked for can be set. The speed control also varies between different manufacturers, not all use stepless speed control, but instead use fixed speed in steps to alter between. The reason is to have better control of the performance, as stepwise means most operation modes can be tested and optimised, and since the heating system and building has high inertia, there is little point of controlling speed exactly.

3. Test method

The performance using both indirect and direct control of a ground source heat pump was tested in laboratory based on a standardized test cycle for evaluating the possibilities to control a grid flexible heat pump. In addition, a number of 24h test profiles were developed and tested using direct control.

3.1. Test cycle

In order to standardise testing and evaluation of the control of a grid flexible heat pump an eight-hour long test cycle for laboratory testing was developed. The purpose with the test cycle is partly to evaluate how close the heat pump in combination with the external control manage to follow the specified test profile. Partly to test if the heat pump control manages a number of functions, such as start and stop of the compressor, changing the compressor speed and start and stop the auxiliary heater, se Figure 2.

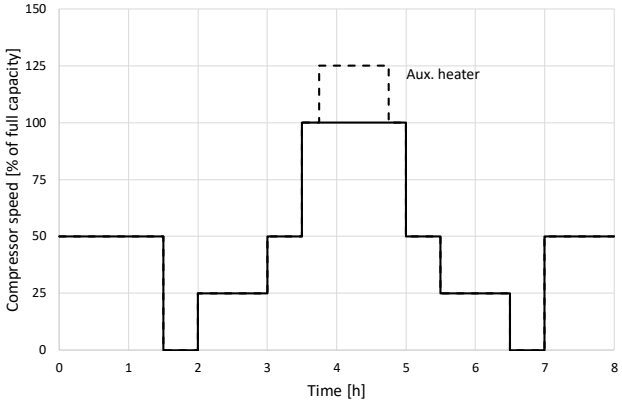


Figure 2. Test cycle for laboratory testing of a grid flexible heat pump

3.2. Key performance indicators

Four key performance indicators (KPI) for the flex function was identified in order to evaluate the results. KPI_1 - KPI_3 expresses how well the heat pump can follow the test cycle, while KPI_4 expresses how the flex function affects the heat pumps coefficient of performance, COP. In Table 1 below each KPI is defined:

Table 1. Definition of key performance indicators for evaluation of grid flexible heat pump control

Key Performance Indicators	
$KPI_{1, a \text{ and } b}$	Average deviation between the measured compressor speed, heat production or power consumption compared to stated value by the test cycle. The result for KPI_1 is expressed in revolutions per second (rps) or in watt (W). With a: auxiliary heater included and b: auxiliary heater excluded.
$KPI_{2, a \text{ and } b}$	Percentage of the time the compressor speed, heat production or power consumption is within ±3% of the value given by the test cycle, where the interval, ±3%, is defined at maximum compressor speed. With a: auxiliary heater included and b: auxiliary heater excluded.
$KPI_{3, a \text{ and } b}$	Percentage of the time the compressor speed, heat production or power consumption is within ±10% of the value given by the test cycle, where the interval, ±10%, is defined at maximum compressor speed. With a: auxiliary heater included and b: auxiliary heater excluded.
$KPI_{4, a \text{ and } b}$	KPI_4 gives the impact on the heat pump efficiency, COP, related to making the heat pump follow the test cycles variations instead of working on stable conditions. KPI_4 is calculated as the average COP during the whole test cycle (time 0h to 8h) divided by average COP during test time 0.5h to 1.25h (when the compressor is working on stable conditions at 50% of maximum speed). With a: auxiliary heater included and b: auxiliary heater excluded.

4. Results

The results from the laboratory tests with indirect and direct control are presented below, followed by a comparison of the results from the two tests.

4.1. Test cycle, indirect control

During the test a manipulated outdoor temperature was sent to the heat pump making the heat pump change the compressor speed in order to follow the test sequence in Figure 2. This was done manually using a potentiometer. The results from the test is presented in Figure 3 below. The figure shows that the test cycle is followed relatively well, but not perfect. It also shows that the compressor follows the test cycle better than the auxiliary heater does. An additional outcome from the test was that it is easier to follow the profile going up in compressor speed than going down with high accuracy.

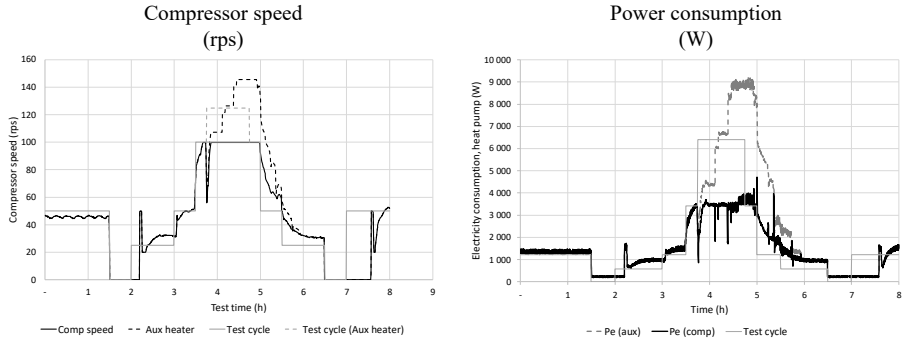


Figure 3. Results indirect control of compressor speed and auxiliary heater via temperature sensor override. Compressor speed (left) and power consumption (right)

The outdoor temperature corresponding to a specific compressor speed and thus a specific heating capacity and electricity consumption is individual for each heat pump, depending on the heat pump model, the heating demand of the building and the heat curve chosen.

4.2. Test cycle, direct control

During the test with direct control, changes to the compressor speed were made manually by a test engineer using the software described in chapter 2.2 and following the test sequence in Figure 2. The results from the test is presented in Figure 4 below. The figure shows that the heat pump compressor follows the test cycle with high accuracy, but it was not possible to activate the auxiliary heater using this version of the program for direct control. The largest deviation of the compressor speed compared to the test cycle occurs after two hours, when the compressor needs to start at 50% before it can reduce the speed to 25% to follow the test cycle. Otherwise the compressor speed follows the test sequence very well.

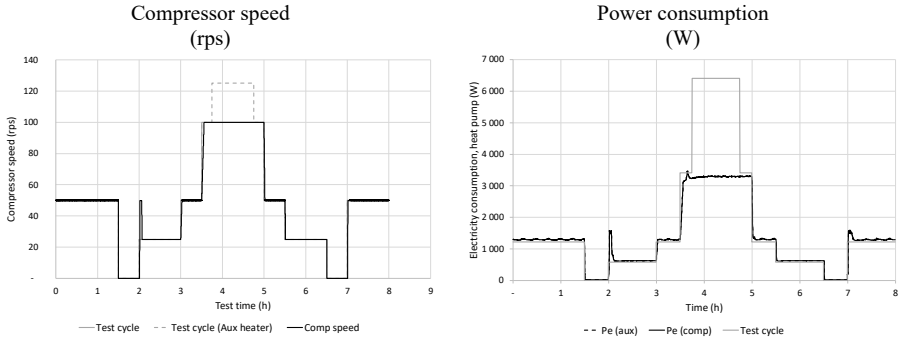


Figure 4. Results for direct control of compressor speed and auxiliary heater. Compressor speed (left) and power consumption (right)

4.3. Comparison results indirect and direct control

Comparing the results from the two laboratory tests shows that the direct control follows the test cycle much better. Looking at the compressor only, the direct control is in average 1rps from the set value compared to 9rps for indirect control. For the total, also including the auxiliary heater, the direct control is approximately 10rps better, even though the direct control function couldn't start the auxiliary heater.

Table 2. Summary of test results, results for KPI_{1-3} based on compressor speed.

	Total (Auxiliary heater included)		**Compressor only** (Auxiliary heater excluded)	
	Indirect control	Direct control	Indirect control	Direct control
KPI_1 Average deviation from test cycle	14rps	4rps	9rps	1rps
KPI_2 Time share within ±3% of the test cycle	24%	85%	36%	97%
KPI_3 Time share within ±10% of the test cycle	62%	85%	75%	98%
KPI_4 Decrease COP			-13%	-11%

Looking at KPI_2, the time within ±3% of the set value, there is a large difference between direct and indirect control, but looking at KPI_3, the time within ±10% of the set value, the differences has decreased. This indicates that the indirect control can follow the cycle roughly, but if high accuracy is needed direct control is much better. KPI_4 shows how COP is affected by using the heat pump for flexibility services following the test cycle in Figure 2. In this test COP decreased with approximately 10-15% following the flexible test cycle instead of running the heat pump at stable condition with a compressor speed at 50rps. Additional tests show that the impact on COP depends on the shape of the power profile asked for, see chapter 4.4. Since neither the direct control nor the indirect control managed to start the auxiliary heater correctly, the results on how COP is affected for the total is not included in the results but starting the auxiliary heater will make COP decrease further.

Table 3. Summary of test results, results for KPI_{1-3} based on power consumption.

	Total (Auxiliary heater included)		**Compressor only** (Auxiliary heater excluded)	
	Indirect control	Direct control	Indirect control	Direct control
KPI_1 Average deviation from test cycle	900W	470W	370W	100W
KPI_2 Time share within ±3% of the test cycle	12%	76%	19%	76%
KPI_3 Time share within ±10% of the test cycle	54%	85%	64%	97%
KPI_4 Decrease COP			-13%	-11%

The heat pump power consumption can be followed within ±100W with direct control, roughly four times better than with indirect control. Comparing $KPI_{2 \text{ and } 3}$ in Table 2 and Table 3 shows that with the control methods used in the test it is easier to set the correct compressor speed, translating the compressor speed to power consumption will make the accuracy decrees.

4.4. 24 h test profiles with direct control

In order to further evaluate direct control of the heat pump a number of 24h test profiles were developed and tested in laboratory as a complement to the test cycle. The profiles were based on different scenarios and the purpose with the test was to evaluate how well a heat pump can follow a specified profile using direct control and how the heat pump´s COP, will be affected by following an external profile instead of working in more stable conditions. Below two examples of profiles are presented.

For each test profile a csv-file was created including information about time and compressor speed for every change in speed. Data for the conversion was based on performance tests in the laboratory. The general settings of the heat pump are based on test condition B in table 14 in the test standard for heat pumps, EN14825:2018 [8], representing the conditions at an outdoor temperature of +2°C, for a medium temperature application (typical radiator system) in cold climate.

4.4.1. Profile for peak shaving

A 24h profile for peak shaving has been developed for a theoretic model house with radiator heating. The outdoor temperature is assumed to be +3°C all day, in this case leading to a constant heating demand of 5kW. In the profile the heat pump is assumed to be switched off from 07:00 to 10:00 and from 17:00 to 20:00, it is also assumed that the building has an thermal inertia that makes it possible to switch off the heat pump for three hours and still keep a good indoor climate. To compensate for the period when it is switched off the heat pump produces more heat during other hours. In this case it is assumed that the heat pump will compensate by producing the heat needed at maximum capacity. In the morning this is done before the heat pump is switched of and in the afternoon, it is done after. The result from the test is presented in Figure 5.

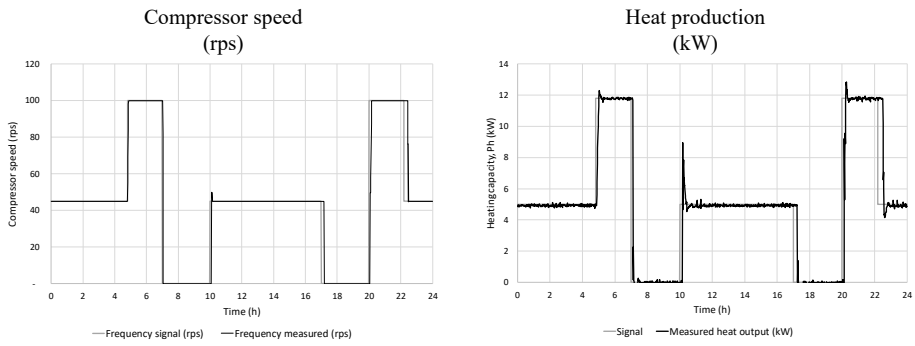


Figure 5. Control signal vs. measured compressor speed (left) and vs. measured heat production (right), profile from peak shaving at +3°C.

The average deviation in heat production between the profile and the measured values from the heat pump test is about 460W. Using a peak shaving profile, as described in Figure 5, instead of working in stable conditions at 5kW heating will decrease COP with 8%, based on data from the laboratory test. Note that the test cannot fully simulate a real installation. In the laboratory tests the return temperature to the heat pump as well as the brine inlet temperature is kept constant independent on how the heat pumps is operated. In a real installation it is a risk that COP will decrease further.

4.4.2. Profile for cost minimization, Aahus Nov 26th

The purpose with the cost minimization profile used for testing is to make a test profile with hourly changes of the heat pumps power consumption in order to minimize the heating cost. For this a simple cost minimization algorithm has been developed for a theoretical model house, based on Excels solver function, with focus on the creation of a relevant test profile. The cost minimization is based on historical climate data in Aarhus, Denmark in combination with historically hourly electricity prices. Nord Pool [9] and DMI [10] are used as a data sources. Aarhus, Denmark November 26th, 2018 was chosen as an example of a day due to its large variations in the hourly electricity prices. This was a day with large changes in electricity prices and a moderate variation in outdoor temperature, from -4°C to +2°C, see Figure 6 below.

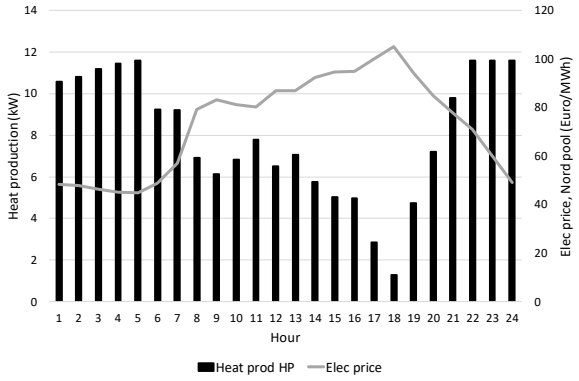


Figure 6. Load profile for heating 26 Nov. 2018 in Aarhus, based on cost minimization in relation to hourly variations in electricity price from Nord Pool [9]

The results from the test is summarized in Figure 7. The average deviation in heat production between the profile and the measured values from the heat pump test is about 380W. Despite a lower COP (-4%) the heating costs decreases with 6%, following the cost minimization profile instead of producing heat based on the actual outdoor temeprature (based on Nord Pool prices, no other costs included).

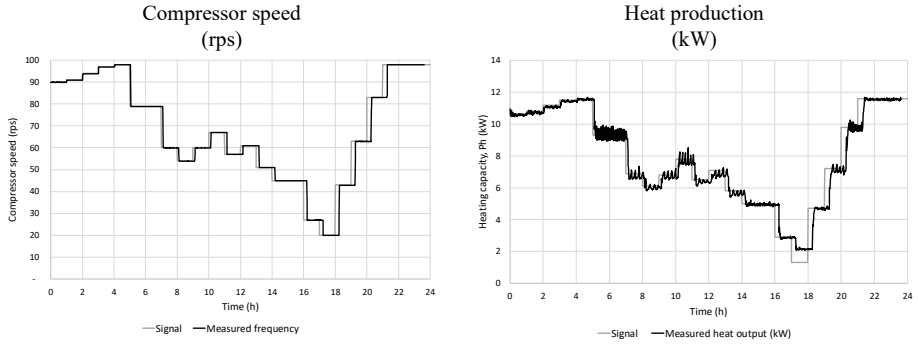


Figure 7. Control signal vs. measured compressor frequency (left) and vs. measured heating capacity (right), profile from cost minimization in Aarhus Nov. 26th, 2018.

5. Discussion

The overall aim with controlling the heat pump performance is to be able to externally control the power consumption and thereby be able to offer demand response. The electricity consumption can be controlled in different ways, which can be divided into two main groups; via indirect or direct control of the heat pump.

The results from laboratory tests with indirect control shows that it is possible to follow changes in a test cycle by using indirect control via temperature sensor override. The heat pump cannot follow the cycle in detail, but the general trend is followed relatively well. A benefit with using outdoor temperature sensor override is that the same software and equipment will work on most heat pump models. The disadvantage is that the equipment must be physically installed at the heat pump and the temperature sensor must be replaced.

A direct control of the heat pump compressor speed or its electricity consumption gives better possibilities to control the heat pump performance with high accuracy. At present day an individual software, overriding manufacturers internal control circuits, will be needed for each heat pump model to use direct control. To make this solution come true, the option needs to be part of manufacturers standardized protocol for controlling the heat pump as a complement to today´s temperature control.

The results from the different 24h-profiles tested in the heat pump laboratory shows that in general the profiles can be followed with high accuracy using direct control. The compressor speed in the profile can be followed with ±1-2rps and the heat pumps total power consumption with approximately ±100W. The evaluation of the results from the laboratory tests show that COP decreases with 0-10% depending on the shape of the profile, if the auxiliary heater is started COP decreases further. In real installations COP might decrease further, since the test rig cannot fully simulate a real heat pump installation. In the laboratory the return temperature to the heat pump is kept at a constant temperature, independent on how the heat pumps is operated. How the return temperature in a building will be affected depending on how the heat pump is controlled is hard to simulate in lab. This can lead to both higher and lower COP. In the same way, as for the return temperature, the brine inlet temperature to the heat pump is kept constant in the laboratory tests. In a real installation the brine inlet temperature will drop if the heat pump works on high compressor speed for a while. This will cause a decrease in COP.

6. Conclusions

Recommendations for external control of the heat pumps electricity consumption can be summarized as:

1. For older heat pumps or non-premium heat pumps sold today:
   Outdoor temperature sensor override: This is a solution that will work on more or less all heat pumps, but the accuracy of the heat pumps electricity consumption is not as good as for other alternatives. There is also a need for a physical installation on the heat pump which is costly.
2. For premium heat pumps sold today and future heat pumps:
   Indirect control of the temperature settings by adjustments of the heating curve or similar via web-API. Many premium heat pumps sold today are connected to the internet and a web interface or an app makes it possible for the owner to make changes related to the heat pump settings at a distance.
3. For future heat pumps:
   Direct control of the heat pump will give the fastest control of the power consumption and have the best accuracy. To make this happening it needs to be part of the manufacturers standardized protocol for controlling the heat pump.
4. Chose a heat pump with a fast response variable speed compressor. A survey to a few manufacturers shows a built-in limit between 4.5 and 80 minutes to go from compressor off to maximum capacity for heat pumps with variable speed compressors.

Acknowledgements

This article is based on research done within the EU-project Flexible Heat and Power (FHP). The FHP-project has received funding from the European Union's Horizon 2020 research and innovation program under grant agreement No 731231 and includes the following partners: Vito (project leader), Tecnalia, Noda, Honeywell, Ecovat, RISE and Karlshamn Energi.

References

[1] Fisher, D. and Madani, H. (2017) On heat pumps in smart grids: A review. Renewable and Sustainable Energy Reviews 70 (2017) 342-357.
[2] Paterakis et al. (2017) An Overview of Demand Response: Key-elements and international experience. Renewable and Sustainable Energy Reviews 69 (2017) 871-891.
[3] Sweco. (2016) Elkunders möjlighet till flexibel elanvändning: En underlagsrapport till Energimarknasinspektionen. (In Swedish)
[4] Flexible Heat and Power, (2019-10-31) http://fhp-h2020.eu/.
[5] Lund, Per & Nyeng, Preben & Grandal, Rune & Sørensen, Stig & Bendtsen, Maja & Ray, Guillaume & Larsen, Emil & Mastop, Jessanne & Judex, Florian & Leimgruber, Fabian & Kok, Koen & MacDougall, Pamela. (2016) EcoGrid EU Deliverable 6.7: overall evaluations and conclusions.
[6] BWP Bundesverband Wärmepumpe e.V. (2013) Regularium für das Label "SG Ready" für elektrische Heizungs- und Warmwasserwärmepumpen. s.l. : BWP Marketing & Service GmbH. (In German)
[7] Fischer, David. (2017) Integrating Heat Pumps into Smart Grids -A study on system design, controls and operation. Stockholm : KTH, ISSN 1102-0245.
[8] CEN, EN14825:2018. (2018). Air conditioners, liquid chilling packages and heat pumps, with electrically driven compressors, for space heating and cooling – Testing and rating at part load conditions and calculation of seasonal performance, Brussels.
[9] Nord Pool. (2018-08-07). https://www.nordpoolgroup.com/.
[10] Danmarks Meteorologiske Institut. (2019-02-21). DMI Vejrarkive, https://www.dmi.dk/vejrarkiv/.

13th IEA Heat Pump Conference
April 26-29, 2021 Jeju, Korea

Assessment of Standardised Test and Performance Evaluation Methods for Fuel Driven Sorption Heat Pumps

Patrizia N. Melograno[a*], Ivan Malenković[b*], Peter Schossig[b]

[a]Politecnico di Milano, via Lambruschini 4, 20156 Milano, Italy
[b]Fraunhofer Institute for Solar Energy Systems ISE, Heidenhofstr. 2, 79110 Freiburg, Germany

Abstract

Space and DHW heating appliances play a major role in increasing energy efficiency and reducing greenhouse gas emissions. A number of recent publications identified fuel driven sorption heat pumps (FSHP) as a promising technology which can considerably contribute to these goals, compared with current state-of-the-art gas appliances. The EU Ecodesign Regulation and the Implementing Regulations for different groups of energy-related products have highlighted the need for unbiased and transparent testing and performance evaluation methods. Although the technology is not new, the market is still developing and the current standards have yet to be evaluated regarding their applicability, unambiguousness and comprehensiveness. Within the IEA HPT Annex 43 and the EcoTest Projects round robin tests on gas driven sorption heat pumps have been performed based on the current European standards. In this paper, the results of the test will be presented with an emphasis on the assessment of the test and evaluation methods and their comparison. As one of the results, shortcomings of the methods and possible improvements have been detected and provided to the relevant CEN Technical Committees for further consideration.

Keywords: gas heat pump; test methods; quality assurance; energy label

1. Introduction

A proclaimed goal of the EU energy policy is to reduce the greenhouse emissions to 80-95 % below the levels of 1990 by 2050. As around 40 % of the final energy consumption in the EU countries can be attributed to the building sector (85 % thereof for space heating and domestic hot water (DHW) preparation), a fast deployment of energy-efficient solutions is crucial to reach this target. The EU addressed this issue in a number of directives regulations, most notably within the Ecodesign and EPBD directives, in which the standards for the energy efficiency of the buildings and HVAC equipment are defined.

The energy consumption for space heating per square meter heated area has been decreasing steadily in the EU countries since 2000. As new dwellings are being built at a rate of about 1,1 % of the total dwelling stock annually, the main contribution to the decrease of specific energy consumption can be attributed to the boiler retrofit and energy efficiency measurements on building envelope. This shows that the retrofit market is the main key to reaching the goals in the given time frames under current market development in the building sector. Therefore, efficient and affordable technologies targeting this market are needed to meet the proclaimed targets of the environmental policy. A number of recent publications (e.g. [1], [2]) on future energy market see fuel driven sorption heat pumps (FSHP) as a promising technology in that respect. The technology is seen by many as the next step in the development of fossil fuel heating systems. It can considerably increase the energy efficiency and usage of renewable energy sources while decreasing greenhouse gas emissions, compared with current state-of-the-art fossil fuel boilers. With expected net decarbonisation of gas grid by increasing biogas

* Patrizia N. Melograno. Tel.: +39-02-2399-8502; fax: +39-02-2399-3868.
E-mail address: patrizia.melograno@polimi.it.
* Ivan Malenković. Tel.: +49-761-4588-5533; fax: +49-761-4588-9533.
E-mail address: ivan.malenkovic@ise.fraunhofer.de

production, development of power-to-gas concepts and evolution towards the usage of hydrogen, the FSHP, especially gas-fired heat pumps, may further gain in importance.

Calculations to identify the optimal technology mixtures both on the energy production and demand sides in terms of overall annual costs until 2050 were reported in [1]. The simulations were based on a comprehensive model of the overall German energy sector which takes into account the geographical, political, social, economic and technological characteristics of the location and forecasts their development in the upcoming decades. Having the minimum cumulative cost of the transition from the current energy system to an energy system with a substantial reduction of CO_2 emissions as the target function, the simulations yielded the optimal technology mix for a number of different target values.

Figure 1 shows the projected development of the share of heating systems for the buildings by 2050 for the assumed 85 % CO_2 emission reduction compared to 1990 values. This scenario seems to be slightly optimistic since the proclaimed policy of the German government sees an emission reduction of 80 % for the same time period. However, it shows the potential of the heat pump not only as a highly efficient technology, but also as the most cost-effective one in the decades to come. According to the scenario, most of the electricity will be produced by solar and wind power plants by 2050. Fluctuating electricity production will require considerable storage capacities to ensure a reliable energy supply. In that context, production of combustibles by power-to-gas processes and usage of current gas grid and its storage potentials will play a very important role in the future. This means that, even in an electricity-dominated energy system, the need for efficient gas fired energy conversion appliances using existing gas infrastructure will most probably exist.

The scenario sees a domination of heat pumps as heating systems in buildings by 2035 and a complete takeover by late 2040s. GHPs would reach a share of around a quarter of the total market. The technology should experience its first major break-through around 2026-2027 when a threshold of 1 million installed units should be reached. Although this estimation seems to be rather enthusiastic considering just a couple of thousands of currently installed units and not more than a handful of products available on the market, it shows the potential of the technology if the presumed cost and efficiency targets are met and a decarbonisation of energy system is pushed at projected pace. Needless to say, this estimation is highly dependable on a number of factors, including further technology development and acceptance, future energy system configuration, development of energy prices, incentive policy and development of competing technologies, among many others.

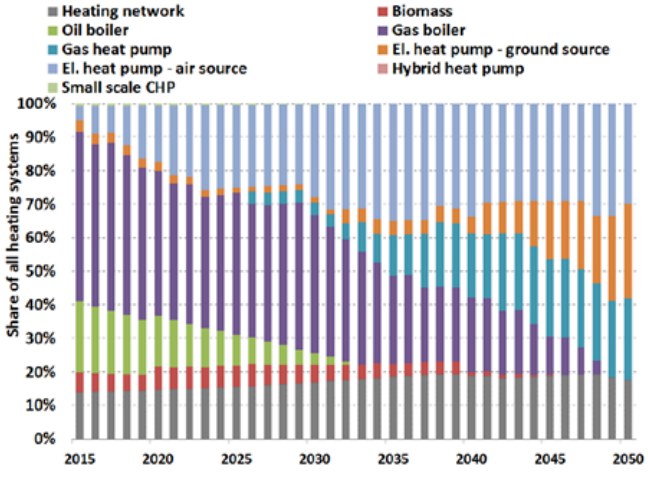


Figure 1. Development of heat supply technologies in buildings until 2050. Source: [1]

2. Market and appliances

Since its market entry in the mid-2000s and until 2010, only one manufacturer (Robur S.p.A.) of gas driven heat pumps was active on the European market. With heating capacities of around 40 kW the appliances were used mainly in small commercial installations. From 2010 onwards, a number of products aiming at single

family house market – both new and retrofit – were introduced by major heating equipment manufacturers. All available products were built using sorption technologies. However, almost all these products have been removed from the market in the last 2-3 years leaving Robur to be the sole provider of this technology once again.

Two main concepts were being pursued by the manufacturers: bivalent appliances with an adsorption heat pump using water as refrigerant supported by a modulating condensing boiler. These units need a heat source above 0 °C to avoid freezing – a ground heat source or solar collectors are needed. The adsorption heat pumps were sized to cover only one part of the nominal load up to ca. 4-5 kW. The concept did not prove to be interesting for the market and these appliances were withdrawn by the manufacturers. Absorption appliances are monovalent machines and run with ammonia-water working pair. Due to a lower freezing point of ammonia, they can operate with ambient air as heat source at temperatures well below 0 °C. These units can modulate their output capacities in the range of ca. 30 to 100 % of nominal thermal power.







Manufacturer	Viessmann		Vaillant		Robur			Bosch Thermotechnik	BoostHeat
Model	Vitosorp 200-F D2RA 001|002	Vitosorp 200-F D2RA 003|004	zeoTHERM VAS 106/4	zeoTHERM VAS 156/4	GAHP - GS | WS [5]	GAHP - A [6]	K18	Junkers Supraeco 9000i-G Buderus Logatherm GWPS(L)192-18 i	BOOSTHEAT.20
Nom. Capacity [kW] [1]	11.00	16.70	10.20	15.00	42.61 | 43.90	41.00	17.6	18.00 [3]	20 kW
Technology	adsorption		adsorption		absorption			absorption	mechanical compression
Working pair	water/zeolite		water/zeolite		ammonia/water			ammonia/water	carbon dioxide
Heat source	geothermal | solar		solar		borehole | ground water	air	air	borehole | air	air | borehole | ground water
Aux. heat source	condensing gas boiler		condensing gas boiler		-	-	-	-	condensing gas boiler
Annual GUE [%] [1]	1.38 | 1.39	1.31 | 1.35	1.31	1.22	1.58 | 1.53	1.36	-	>1,25	1.95 | 1.65 [7]
Nominal GUE [%]							1.69 [2]	1.70 [4]	2.29 [8]
Market entry	2013	2013	2010	2012	2004	2004	2016	2016 (planned)	2019
Not available since	2017	2017	2016	2016	-	-	-	2018 (abandoned)	-

[1] According to VDI4650-2 for supply and return temperatures 35-28°C, except values for Robur K18 and Bosch Thermotechnik. Source: www.bafa.de
[2] According to EN12309-2 for air inlet temperature 7 °C and water supply temperature 35 °C. Source: www.robur.it
[3] According to the manufacturer for brine inlet temperature at heat source 0 °C and supply temperature of 65 °C. Source: www.junkers.com
[4] Test conditions not known. Source: www.junkers.com
[5] Products with same specifications available from Bosch Thermotechnik (Logatherm GWPS/GWPW 41), and OERTLI-ROHLEDER (GAWP 40 SW)
[6] Products with same specifications available from Bosch Thermotechnik (Logatherm GWPL 41), OERTLI-ROHLEDER (GAWP 35 LW) and Remeha (GAS HP 35 A)
[7] According to VDI4650-2 for supply and return temperatures 35-28°C
[8] According to VDI4650-2 for supply and return temperatures 55-45°C

Figure 2. Overview of available and withdrawn GHPs in the European market with main characteristics

In 2019, a start-up company BOOSTHEAT SA brought up their heat pump to the market after eight years of development. Unlike all other gas driven appliances for heating, it is not based on sorption technology but uses an own-developed mechanical compression system.

It is expected that the main market, due to its size, availability of gas mains and technology characteristics will be boiler replacement, especially in countries which are traditionally dominated by this fuel. Figure 2 gives an overview of currently available and withdrawn products with their main characteristics.

Despite a rather slow market development, a number of development activities have been reported in the recent years, both in the EU and in the USA. The main driver in Europe is to find an efficient solution for retrofit for heating in countries with well-developed gas grid. In the USA, the legislation on the minimum efficiency of sanitary water heaters created a need for more efficient gas-fired appliances. Figure 3 gives an overview of some of the reported appliances / concepts under development.

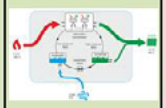
					
Manufacturer	Sorption Energy	Cooll	ClimateWell	ThermoLift	SMTI
Model	-	-	HeatBoost	TCHP	-
Nom. Capacity [kW]	7.00	?	?	?	40.00
Technology	adsorption	adsorption	absorption	Vuilleumier	absorption
Working pair/fluid	ammonia/active carbon	ammonia/active carbon	water/salt	helium (?)	ammonia/water
Heat source	air	air	-	-	air
Aux. heat source	-	-	-	-	-
Status	laboratory tests	laboratory tests	halted	laboratory tests	field testing

Figure 3. A non-exhaustive selection of reported GHP appliances / concepts under development

3. Standardised test methods and quality assurance

The Ecodesign Regulation and the corresponding Implementing Regulations for different groups of energy-related products have highlighted the need for unbiased and transparent testing and performance evaluation methods for all technologies. In the Communication of the European Commission 2014/C 207/02 [3], a list of harmonised standards for testing and performance evaluation of different heating appliances is provided. For gas fired sorption heat pumps EN 12309 [4] is referred to as the reference document for space heating application. The current version of EN 12309, Parts 1 and 3 to 7 have been published in December 2014. Part 2 "Safety" was published a year later in April 2016. The standard has been developed to be compatible with the corresponding methodologies used for electrically driven heat pumps in EN 14511 [5] and EN 14825 [6] and, thus, uses the same basic methodology for the testing and calculation of the seasonal performance figures. A basic description of the methodology can be found e.g. in [7]. For non-sorption units, no standards are currently available on the European level.

Table 1. Main features and differences between EN 12309-7 and VDI 4650-2

EN 12309	VDI 4650-2
Part load conditions related to the declared heating/cooling load	Part load conditions related to the declared HP capacity
Electrical and thermal energies are consequently separated, PER is used for an overall energy consumption	Electrical and thermal energies are put together in some figures; electrical efficiency not provided as a separate figure
Data for three different climates available, adaption to other climates possible	Part load data based on only one climate, adaption to other climates rather difficult
Performance evaluation for bivalent (hybrid) units possible (gas boiler and solar thermal)	Calculation of bivalent operation possible (only solar)
Heating and cooling considered, DHW is missing	Cooling not considered
Electrical power input during idle time considered for the calculation of seasonal performance	Electrical power input in standby mode not considered in performance figures

Due to a lack of suitable EN standards at the time, a VDI guideline for calculation of the seasonal efficiency of gas driven heat pumps was developed – the VDI 4650-2 [8] for the purpose of granting subsidies for the appliances in Germany. Similarly to the corresponding EN standards, the calculation method is strongly based on the VDI 4650-1 [9] which applies to electrically driven units. It inherited the operating conditions, including the part load rations, but was extended with new features to suit the needs of the products. These extensions include solar thermal collectors as heat source, direct solar DHW production, a performance figure to take into account dual driving energy and so forth. An overview of the main features of both standards is given in Table 1. Despite the availability of the EN 12309 and its current harmonisation with the EU Ecodesign and Energy

label Directives, the VDI 4650-2 is still used for product assessment within the German federal subsidy program for heating with renewable energies.

In 2018, a new standard (EN 13203-6 [10]) for the energy consumption evaluation of sorption gas heat pumps for sanitary hot water production was introduced as part of a series of similar standards for a variety of gas driven appliances, including hybrid heat pumps (combination of a gas boiler and an electrically driven heat pump).

Both the EN 12309 and the EN 13203-6 have been scrutinised in round robin tests organised within the IEA HPT Annex 43 [11] and the EcoTest [12] projects. The findings have been reported to the relevant Technical Committees (TCs) and will be considered within the current revision processes which aim to harmonise these standards with the Ecodesign and Energy Labelling Directives.

The main European independent and voluntary certification mark, the Heat Pump Keymark, has added gas driven heat pumps to its scope in 2019.

4. Round Robin Test on a hybrid adsorption heat pump (IEA HPT Annex 43)

The project IEA HPP Annex 43, among other objectives, aimed at investigating the applicability, unambiguousness and comprehensiveness of the relevant existing standards used for assessing fuel sorption heat pumps. For the purpose, a round robin test on a gas-driven hybrid heat pump was carried out according to the standard EN 12309:2014.

The choice to test this kind of appliance was dictated mainly by its operational complexity. In hybrid heat pumps, the combination of two technologies in one appliance, such as a condensing boiler for the peak load and a sorption module for the base load, generates a discontinuous operation of the appliance.

In this specific case, the tested machine was a geothermal hybrid heat pump consisting of a condensing boiler and a zeolite (adsorption) heat pump module. The presence of the adsorption module caused a cyclical machine's operation.

The tests were carried out at two different temperature applications: low temperature application (28 °C - 35 °C) and medium temperature application (35°C – 45 °C), both for "average" climate conditions. The method used was the "inlet temperature method" while, for results' reproducibility reasons, water was employed as heat transfer medium at the outdoor heat exchanger.

Analysing an operation cycle (see Figure 4), it's possible to distinguish four different phases: adsorption phase, during which only the sorption module is working; adsorption plus boiler phase, where both the condensing boiler and the sorption module are working; boiler phase, where only the condensing boiler is working and, finally, desorption phase, where only the sorption module is working and no heating energy is delivered.

These four phases and their alternation affect the applicability of several requirements of the analysed test procedure such as the limits on the permissible deviations of the quantities of interest. For example, the evaporator (i.e. the "outdoor" heat exchanger) and the internal circulation liquid pump, responsible for the circulation of the heat transfer medium between the machine and the geothermal probes, work only when the sorption module is adsorbing. This means that the monitored quantities at this component such as the inlet and outlet temperatures, flow rate and the differential external static pressure will have an unsteady behaviour (see Figure 5). It's easy to understand that it's not possible to respect the limits on permissible deviations prescribed in Table 4 of the standard EN 12309:2014, Part4.

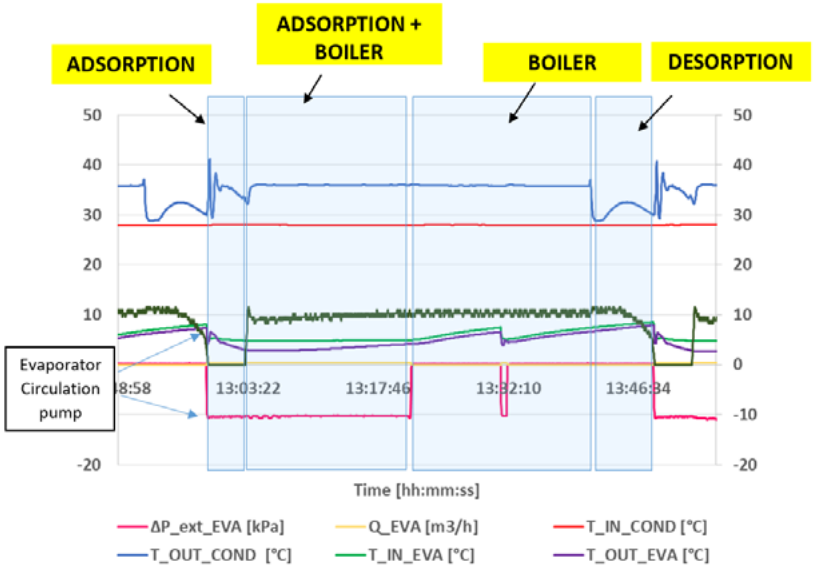


Figure 4. Operation cycle of the hybrid heat pump under test (ΔP_ext_EVA – external pressure difference over the evaporator; T_OUT_COND – outlet water temperature from the condenser; Q_EVA – water volume flow rate through the evaporator; T_IN_EVA – inlet water temperature to the evaporator; T_IN_COND – inlet water temperature to the condenser; T_OUT_EVA – outlet water temperature from the evaporator)

The same can be said for the condenser (i.e. the "indoor" heat exchanger), where the only two parameters that can respect the limits of permissible deviations are the inlet temperature (red line in Figure 5) and the flow rate since, after a certain time, their behaviour depend only on the control of the test rig. The only parameter that, in this case, is influenced by the hybrid heat pump's operation and, therefore, has an unsteady behaviour, is the outlet temperature (see Figure 5, dark blue line). Nevertheless, no requirements are foreseen on this parameter even if it is crucial for the distribution system. With this regard, it could be useful to have a requirement (a permissible deviation) on that.

Concerning the permissible deviations of the inlet temperatures, they vary (the amplitude) based on machine's load: i.e. as the load decreases, the deviation increases. This is not necessary since the fluctuation of the inlet temperatures depend only on the test rig control and not on the machine.

Another remark concerns the duration of the test (equilibrium phase plus data collection phase): From the executed tests, it emerged that some "special" cycles occur (see Figure 5, light red rectangles). This means that the choice of the test duration shall be done in order to consider all operational peculiarities of the hybrid heat pump under test. According to the prescription given in the paragraph 4.5.2.1 of EN 12309-4:2014, the equilibrium period and the data collection period shall be at least 40 minutes and 30 minutes, respectively.

It's clear that, for this kind of machines, the definition of these periods in terms of minutes is not representative but it shall be done in terms of complete operational cycles instead. From the tests carried out, it was concluded that minimum appropriate number of operational cycles that can also allowed to collect a significant number of samples could be eight. This number is also high enough to include all possible strange or peculiar cycles.

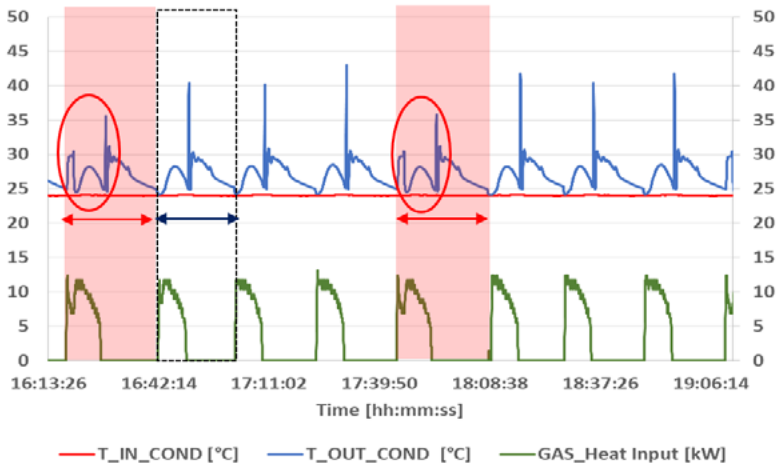


Figure 5. Operational cycles: definition of test duration (T_IN_COND – inlet water temperature to the condenser; T_OUT_COND – outlet water temperature from the condenser; GAS_Heat Input – energy input from the gas calculated with the lower heating value)

A final remark concerning the reduced capacity tests: according to the standard, when the minimum heating capacity provided by the machine is higher than the required part load ("target"), on-off tests shall be performed, i.e. tests where periods when the machine is "on" and works at the minimum allowed capacity alternate with periods when the machine is "off". The duration of these periods are calculated using a given formula. From the round robin test it emerged that these tests are not only being far away from the real operation conditions, but they are also quite time consuming.

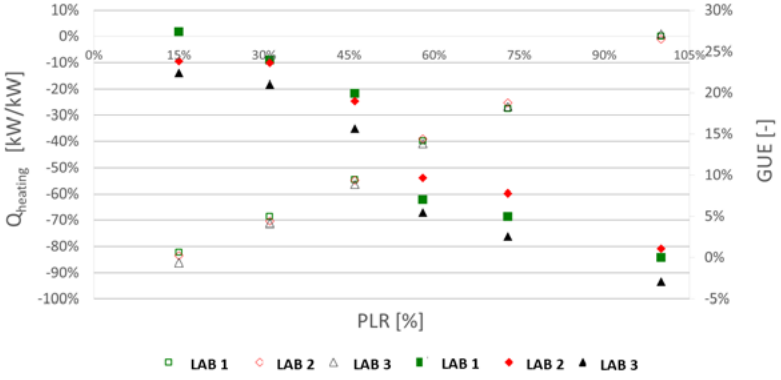


Figure 6. Dimensionless test results: measured heating capacities (left axis, filled marks) and GUE for each laboratory (right axis, hollow marks)

The round robin test involved three laboratories, two of them being also in the consortium of the EcoTest Project for performing round robin tests on fuel absorption heat pumps, as described in the next chapter.

Figure 6 shows the (dimensionless) results obtained during the round robin test. As it is possible to observe, even if there is the necessity to revise some parts of the test procedure, the achieved results showed a high grade of consistency among them especially in terms of Gas Utilisation Efficiency (GUE).

While concerning the heating capacity, due to a wrong flow rate at source side used by the laboratory 3, the difference between the highest and the lowest value on the average vary from 3 % to 7 %.

5. Round Robin Test on a water-to-water absorption heat pump (EcoTest)

Within the EcoTest project, a water-to-water absorption heat pump was tested according to EN 12309 and EN 13203-6. The aim of the project was to assess the inter-laboratory reproducibility, intra-laboratory repeatability and variability required to be used for the application of the regulations by evaluating the standards implementing those regulations. The work also aimed at commenting on the applicability and understandability of the relevant standards and their applicability in the light of market surveillance, minimise the room for different interpretations and to suggest improvements to the CEN/TCs.

5.1. Space heating efficiency according to EN 12309

The measurements according to EN 12309 were conducted by four participating laboratories. The appliance was tested for high temperature application (supply temperature of 55 °C), constant water volume flow rates at both the heat source and the heat sink. The appliance was a continuously operated water-to-water absorption unit with a nominal capacity of 40 kW.

The laboratories showed an overall high level of common understanding regarding the testing and test data evaluation methodology. Only a small number of questions in this regard were raised during the test cycle.

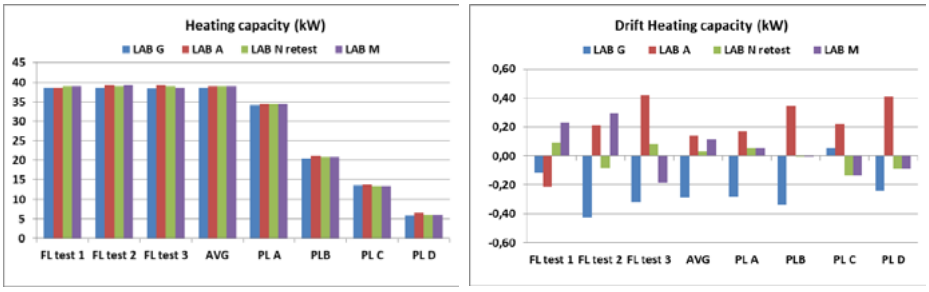


Figure 7. Measured heating capacities (left) and absolute deviation from the average value for each laboratory (right)

As shown in Figure 7, the measured heating capacities by each of the laboratory were very close to each other with a highest absolute deviation from the arithmetic mean value of 400 W or about 1 % of the nominal heating load for full load test (FL) or around 7 % for part load (PL) D (6 kW).

The test at full load was performed three times at each lab to assess the intra-laboratory repeatability of the measurement. The arithmetic average values from all three tests are shown in column “AVG”. It can be seen from Figure 7 that the intra-laboratory repeatability of the measurements did not differ in its magnitude from the inter-laboratory reproducibility, which is a positive indication for the robustness of the methodology as well as for the high level of the measurement quality by the participating laboratories.

In Figure 8, the calculated seasonal space heating efficiency η_s (left) and the deviations of the results for each laboratory from the arithmetic mean value of the round robin test (right) are shown. The difference between the highest and the lowest reported value is 3,5 %, as can be seen also in Table 2. The maximum deviation from any single reported value from the overall average is less than 2 %. Taking into account the complexity of the method and the characteristics of the appliance under test, these results can be considered to be very good and show that the provisions of the methodology described in EN 12309 are in line with the requirements of the Ecodesign and Eco Labelling Regulations in this respect. However, as only four laboratories took part in the testing, a final conclusion based on a full statistical evaluation cannot be drawn.

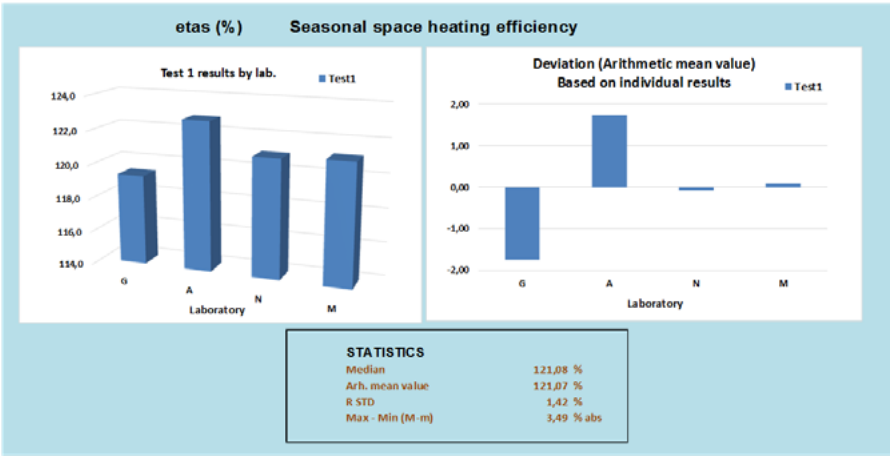


Figure 8. Calculated η_s (left) and absolute deviation from the average value for each laboratory(right)

Other reported significant efficiency parameters such as Seasonal Auxiliary Energy Factor (SAEF) and Seasonal Gas Utilisation Efficiency (SGUE) also showed very good agreement among the laboratories. In Table 2, the median, arithmetic mean, standard deviation, difference between the maximum and the minimum reported values (max-min) and its relative difference ((max-min/avg) are shown for SAEF, SGUE and seasonal space heating efficiency η_s.

Table 2. Statistical values obtained for the seasonal performance parameters for space heating

Parameter	Median	Arithmetic average	Standard deviation (σ_R)	max-min	(max-min) / avg [%]
SAEF	20,73	20,62	0,83	1,87	**9,0**
SGUE	1,48	1,48	0,02	0,04	**2,7**
η_s	121,08	121,07	1,42	3,49	**2,9**

5.2. Energy consumption for the domestic hot water production according to EN 13203-6

At the time of the testing, the EN 13203-6 was still not officially published. While scrutinising the final draft, some inconsistencies of the method compared to the methodology described in the EU Regulations and in a methodologically similar standard for electrically driven heat pumps (EN 16147:2017) were detected. Therefore, it was decided to adapt the methodology and to perform two tapping cycles for comparison: one according to EN 13203-6 and one according to EN 16147. The resulting overall test protocol is shown in Figure 9.

After the common heating-up and standby measurements, the EN 16147 tapping cycle was initiated right after the end of the standby period with the first draw-off at 07:00. After the 24 hours' cycle and after the heat pump was switched off by the controls when the set hot water tank temperature was reached, the two tapping cycles of EN 13203-6 starting with the first draw off at 21:30 were performed.

The system used consisted of the appliance described in Chapter 5.1 with an additional 1000 l tank. As the unit is not declared by the manufacturer for the DHW production, hydraulic connections and controls had to be adapted to enable the laboratories to perform the tests. Thus, the results were used only to discuss the applicability of the standard itself and not to conclude on the reproducibility or repeatability of the methodology. Already while preparing the measurement and discussing the methodology, a number of remarks on EN 13203-6 was made. Obvious mistakes and inconsistencies were fixed for the test protocol and were reported to the relevant CEN Technical Committee.

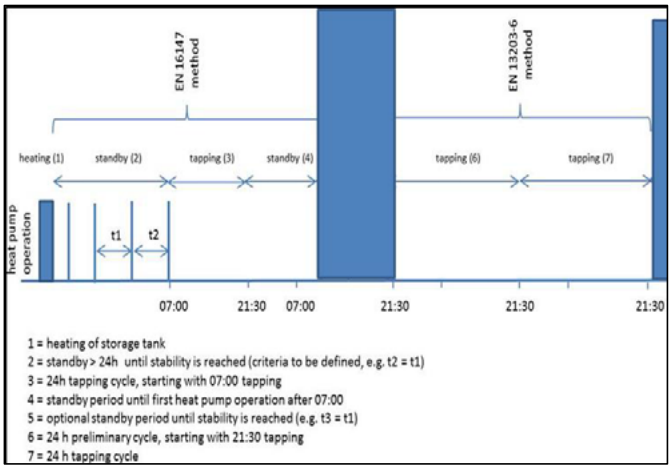


Figure 9. Test protocol for the evaluation of EN 13203-6

Table 3 shows the results for gas (Q_{gas}) and electricity (Q_{elec}) consumptions, as well as for the seasonal water heating efficiency (η_{wh}). Compared to the results for space heating, the variability of the reported results is much higher for all parameters. This lies partly in the lack of the experience with the newly developed standard, partly in the methodology description itself, but partly also in the tested system itself, since it was only adapted to the water heating function. Therefore, as stated before, the results below cannot be taken for any final conclusion regarding the measurement quality or the methodology itself.

Table 3. Statistical values obtained for the seasonal performance parameters for domestic hot water

Parameter	Arithmetic average	Standard deviation (σ_R)	max-min	(max-min) / avg [%]
Q_{gas}	24,80	2,71	5,42	**21,85**
Q_{elec}	1,32	0,12	0,12	**9,09**
η_{wh}	68,70	8,11	15,87	**23,10**

6. Conclusions

Even though there are only a few products on the market for residential heating and sanitary hot water application, a considerable amount of R&D activity is reported from many countries. The current EU legislative, including the Ecodesign and the Energy Labelling Regulations include the technology, which is a very important market drive. Further, gas heat pumps are explicitly eligible to obtain the Heat Pump Keymark, the main voluntary quality scheme in Europe – also a very important signal for the end consumers, as well as governmental subsidies, which are available for gas heat pumps in most of the principal European markets. There are testing and performance standards available – both on the CEN and national levels. The CEN standards are currently in the process of harmonisation with the Energy Labelling directive. Within two recent projects, the CEN standards EN 12309 and EN 13203 were evaluated in round robin tests. The results showed that the methodology is yielding very good results regarding applicability, repeatability and reproducibility. For the continuously operated absorption heat pump the reported seasonal efficiency values lie within 3,5 percent points for the heating application. For the water heating application, the reported values were not homogenous, mainly due to the novelty and some shortcomings of the described methodology in the standard, as well as due to the system used for the test. Further, a more in-depth analysis by the expert community pointed out some weak points of both standards and proposed improvements which will be considered by the relevant technical committees.

It has to be pointed out that the results shown above were obtained on only two products (one of which has been removed from the market) and by a rather small number of participating laboratories. As the market

develops and more products enter the market, similar trials will have to be performed in order to ensure that the testing and evaluation methodology is transparent and fair for all stakeholders.

With current primary energy efficiencies, gas heat pumps can deliver heat with 30 % higher efficiency than condensing gas boilers. If applied on a large scale as a replacement product for the gas boiler, they can considerably reduce the CO_2 emissions in short time period without the need of further investments in supply grids or building envelopes.

A large scale monitoring campaign to investigate the full potential of the technology and supply reliable information for the policy and customers would be needed. It would also send a message to hesitant manufacturers, that the investment in the technology can pay off in the future.

Acknowledgements

The project EcoTest was financed by the EU, agreement number A/CEN/GROW/EFTA/534/535/2015-14

References

[1] Henning, H.-M., Palzer, A.What will the energy transformation cost? Pathways for transforming the German energy system by 2050. Publication by Fraunhofer ISE, 2015. Accessed on 30.10.2016 from https://www.ise.fraunhofer.de/en/publications/veroeffentlichungen-pdf-dateien-en/studien-und-konzeptpapiere/study-what-will-the-energy-transformation-cost.pdf

[2] Bakker, E.-J., Van der Garde, J., Jansen, K., Travesari, R., Wagener, P., Gas Heat Pumps – Efficient heating and cooling with natural gas. ISBN 978-90-79147-12-0. GasTerra / Castel International Publishers. Accessed on 03.11.2019 from www.gasterra.nl

[3] CEN, Commission communication in the framework of the implementation of Commission Regulation (EU) No 813/2013 implementing Directive 2009/125/EC of the European Parliament and of the Council with regard to ecodesign requirements for space heaters and combination heaters and of Commission Delegated Regulation (EU) No 811/2013 supplementing Directive 2010/30/EU of the European Parliament and of the Council with regard to the energy labelling of space heaters, combination heaters, packages of space heater, temperature control and solar device and packages of combination heater, temperature control and solar device. CEN, 2014

[4] CEN, EN12309, Parts 1 to 7, Air conditioners, liquid chilling packages and heat pumps for space heating and cooling and process chillers, with electricylly driven compressors. CEN, 2014/2016

[5] CEN, EN14511:2018, Parts 1 to 4, Air conditioners, liquid chilling packages and heat pumps for space heating and cooling and process chillers, with electricylly driven compressors. CEN, 2018

[6] CEN, EN14825:2018, Heat pumps, air conditioners and chilling liquid packages – testing and rating at part load conditions. CEN, 2018

[7] Wemhöner, C., Afjei, T., IEA HPP Annex 28 – A uniform energy-related characterisation of heat pump systems. Article from the 5th IEA Heat Pump Conference 2005 in Las Vegas, USA. Accessed on 03.11.2019 from https://heatpumpingtechnologies.org/publications/iea-hpp-annex-28-a-uniform-energy-relatedcharacterisation-of-heat-pump-systems/

[8] VDI, VDI 4650-2, Simplified method for the calculation of the annual heating energy ratio and the annual gas utilisation efficiency of sorption heat pumps – gas heat pumps for space heating and domestic hot water. VDI, 2013

[9] VDI, VDI 4650-1, Calculation of the seasonal coefficient of performance of heat pumps - Electric heat pumps for space heating and domestic hot water. VDI, 2019

[10] CEN, EN 13203-6, Gas-fired domestic appliances producing hot water – Part 6: Assessment of energy consumption of adsorption and absorption heat pumps. CEN, 2019

[11] www.annex43.org

[12] www.ecotest.dgc.eu



13th IEA Heat Pump Conference
April 26-29, 2021 Jeju, Korea

Results of an Interlaboratory Comparison on Four Different Heat Pumps: Standards on the Test Stand

Ivan Malenković[a,*], Urs Gumbel[a], Christoph Thoma[a]

[a] Fraunhofer Institute of Solar Energy Systems ISE, Heidenhofstrasse 2, 79110 Freiburg, Germany

Abstract

As a part of the review process of the EU Ecodesign and Eco Labelling Regulations, project EcoTest was carried out in order to evaluate the standards used for assessing the efficiency of space, combination and sanitary hot water heaters and to issue recommendations to the relevant CEN Technical Committees. Within the project, all technologies with their respective standards covered by the Regulations for the aforementioned products, including some emerging technologies, were assessed in a series of round robin tests performed by accredited laboratories Europe wide. Heat pumps, as one of the acknowledged key technologies in the process of decarbonisation of heat generation in buildings, had a prominent place within the project. Four different electrically driven heat pumps were tested in a series of round robin tests following the latest versions of the relevant standards. In the present paper, selected findings of the project regarding the methodology of the standards, the reproducibility itself and influence of different parameters on the reproducibility of the methods are shown and discussed.

Keywords: Ecodesign; standards; heat pumps; comparison; round robin test

1. Introduction

In order to reduce the greenhouse gas emissions from space, combination and domestic hot water (DHW) heaters, which are responsible for 82 % of the overall final energy consumption in the residential sector within the EU [1], the European Commission introduced requirements for the energy efficiency and labelling of these products with Regulations 813/2013 and 814/2013 and Delegated Regulations 811/2013 and 812/2013 [2-5]. The regulations aim at setting minimum efficiency requirements regarding the seasonal efficiency of the products and obligatory information for the end users on the product efficiency with a labelling system using standardized, reproducible testing and efficiency evaluation methods. The described test and evaluation methods were mostly based on relevant EN standards, with some differences, which were taken into account by issuing mandates to the relevant EN technical committees to harmonise the standards with the regulations [6-7]. The implementation of these regulations started on September 26th, 2015.

Following Article 7 of the aforementioned Commission Regulation and Commission Delegated Regulation, these documents are currently in the process of revision taking into account the advancements in the market products and the applicability of the current testing methodology. In order to evaluate the applicability of the test standards, which are the basis for the performance evaluation of the products covered by the Regulations, the European Commission in cooperation with CEN asked for an action to evaluate and improve, if necessary, the relevant standards.

A group of 22 accredited laboratories gathered in a consortium won an open tender with their proposal for the project EcoTest with the aim to evaluate the standards and formulate recommendation for the CEN TCs regarding possible improvements.

* Corresponding author. Tel.: +49 761 4588-5533; fax: +49 761 4588-9533.
E-mail address: ivan.malenkokvic@ise.fraunhofer.de

2. Project EcoTest

Project EcoTest started in October 2017 and finished in July 2019. It gathered 22 accredited laboratories covering all technologies in the scope of the Ecodesign and Eco Labelling Regulations for space, combination and DHW heaters. The aim was to assess the inter-laboratory reproducibility, intra-laboratory repeatability and variability by evaluating the testing and evaluation methodology used for the implementation of those regulations. The work also aimed at commenting on the applicability and understandability of the relevant standards and their applicability in the light of market surveillance, minimise the room for different interpretations and to suggest improvements to the CEN/TCs. The structure of the project is shown in Figure 1 (left).

The work programme consisted in a series of round robin tests based on the latest versions of the relevant standards that were followed by a detailed analysis of the results for each of the technologies (product groups) in scope, **오류! 참조 원본을 찾을 수 없습니다.** (right).

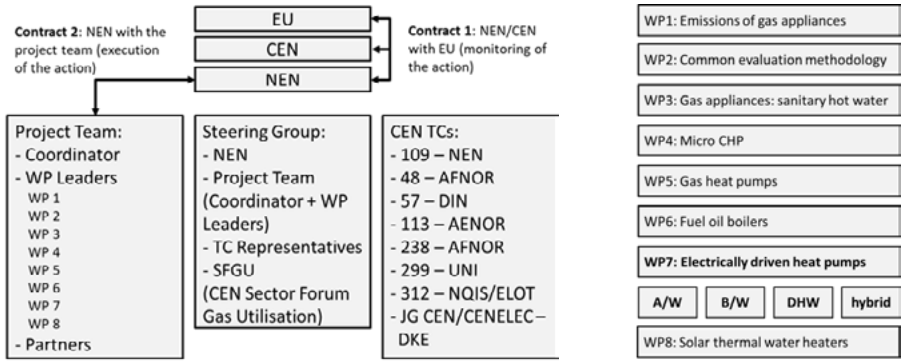


Figure 1: Structure of the EcoTest Project (left) and technologies covered within the Work Packages (right)

Besides the execution of the test and analysis of the results, the participating experts were scrutinising and commenting all applied standards. CEN/TCs were directly involved in the project work through liaisons, which facilitated a first-hand, continuous communication between the project and the CEN experts.

The outcome of the project was put into a series of reports. The main findings were collated in the Project Report. All documents were sent to the EC for approval. The publication is expected by the end of 2019.

3. Execution of the tests on electrically driven heat pumps and methodology evaluation

Within the Work Package 7 for electrically driven heat pumps, four round robin tests (RRTs) on four different appliances were executed. An overview of the main appliance data, applied test conditions and standards used is given in Table 1. A total of 8 laboratories took part in the testing. However, not all laboratories participated in all RRTs which negatively influenced the possibilities for statistical evaluation of the results in some cases.

As three out of four standards were in the process of revision at the beginning of the project, CEN/TC 113 provided the final versions of the revised standards, which had some differences in comparison to the versions in use at the time. This ensured the up-to-dateness of the results and comments, but also imposed a challenge for the participating laboratories, since some of the procedures were new (e.g. for hybrid heat pumps) and executed for the first time by most of the laboratories. This had as a consequence that the focus of RRT4 (hybrid) was rather on providing feedback on the applicability of the newly developed method and the understandability of the method description than on the repeatability or reproducibility.

All laboratories reported their values using templates which were created and distributed for each of the round robin test. A generic template for all appliances within the EcoTest project was common to ensure comparability of the results. However, this document had to be adapted to the specific needs and features of each of the appliances.

Table 1: Overview of the main appliance data, applied test conditions and standards for all four round robin tests

	RRT1	RRT2	RRT3	RRT4
Main appliance data				
HP type (source/sink)	outdoor air / water	water / water	indoor air / DHW	outdoor air / water
Capacity control	inverter	staged (2)	no	only gas burner
Indoor liquid pump	integrated	integrated	-	integrated
Outdoor liquid pump	-	not integrated	-	-
$P_{designh}$ [kW]	12	32.2	-	7 (whole unit)
Installation	outdoor	indoor	indoor	indoor
Water tank capacity [l]	-	-	300	-
DHW set temperature	-	-	55 °C	-
Profile / smart control	-	-	XL / no	-
Acoustic tests	yes	no	no	no
Test conditions and standards used				
Climate	average, "A"	average, "A"	average, "A"	average, "A"
Water flow indoor HX	fixed	fixed	-	fixed
Temperature indoor HX	variable outlet	variable outlet	-	variable outlet
Water flow outdoor HX	-	fixed	-	-
Temperature application	low (35 °C)	medium (55 °C)	-	medium (55 °C)
Liquid pump indoor	integrated	-	-	-
Standards implemented	EN 14511 [8], EN14825 [9], EN 12102-1 [10]	EN 14511, EN14825	EN 16147 [11]	EN 14511, EN14825

After completing a test, a laboratory first sent preliminary data to the work package leader (WPL) who checked them and gave his consent to the reporting lab to send the appliance to the next laboratory. Final results and selected measurement data were reported to the WPL using the templates, as described above. The WPL processed the received data in the following steps:

1. All received data were first checked for plausibility and reporting errors like signs, units, syntax errors etc. Obvious errors were corrected by the WPL.
2. The data sets were compared to each other and outliers and stragglers were detected using a common analysis procedure, as described below.
3. The key performance values were recalculated from the provided data in order to detect inconsistencies and errors in the calculations.
4. A check of the compliance of relevant values with the permissible deviations defined in the standard was carried out.

All deviations, inconsistencies – obvious or assumed – were protocolled for all round robin tests. The reported data and the found inconsistencies were discussed within the group or in telephone calls or emails between the WPL and the respective laboratory in order to find the cause and to decide whether the whole test or a part of it needed to be repeated or a calculation procedure used revised.

A number of corrections were made in the course of the data evaluation. All corrections have been added to the protocols and the most important ones – influencing the final result – were reported in the Final Report which gives a detailed analysis of the specific results from each of the round robin tests.

4. Main results for electrically driven heat pumps

4.1. Compliance with the procedures

In general, all the laboratories showed a very high level of knowledge regarding the implementation of standardised test methods to different kinds off appliances. Some deviations from the described methodology

or the common practice in some laboratories were detected but they could be attributed mostly to the imprecise formulation within the standards and also to translation issues. In this respect, a number of comments to the TC113 consider clarification in the methodology description.

Most issues regarding the compliance with the procedures were observed during the testing of the hybrid appliance since the methods were used for the first time by all laboratories except one. Discussions prior to, during and after the measurements delivered valuable input to the TC 113 and ad hoc JWG TC 113/WG7 – TC 109/WG1 which has the mandate to develop testing procedures for this type of appliances.

4.2. Compliance with the requirements regarding permissible deviations

The laboratories showed a very high level of maintaining the operating conditions within the permissible deviation ranges throughout the measurements. However, some laboratories did exceed the limits in a small number of cases, both for mean as well as for single measured values.

Table 2 shows the deviations of measured values to the operation conditions' target values for RRT1 and Table 3 the same quantities for RRT2. The biggest problem for the laboratories, as expected, was to reach and maintain the relative humidity of the outdoor air within the required tolerances (RRT1, Table 2). Interestingly, all laboratories managed to keep the single measured vales within the tolerance band of ± 1 K. However, the maximum allowed deviation of the mean from the target value was in one case (one laboratory, one operating condition) outside the tolerance band of ± 0.4 K.

Table 2: Deviations of measured to the operation conditions' target values for RRT1 (impermissible deviations marked in bold)

RRT1: A/W Heat Pump					
		deviation of mean values		*deviation of single measured values*	
		permissible deviation	*max*	*permissible deviation*	*max*
Outdoor heat exchanger					
Inlet air temperature (dry bulb)	*°C*	±0.3	0.19	±1.0	0.71
Inlet air temperature (wet bulb)	*°C*	±0.4	**-0.43**	±1.0	-0.83
Temperature difference (db-wb), deviation from 1 K	*K*	±0.3	**-0.41**	-	0.49
Indoor heat exchanger					
Outlet temperature	*°C*	±0.3	0.11	±0.6	0.40
Inlet temperature	*°C*	±0.2	-0.12	±0.5	-0.37
Mass flow	*%*	±1.0	**-1.03**	±2.5	-1.53
Voltage	*%*	±4.0	2.34	±4.0	3.49

All water temperatures, both at the inlet and at the outlet of the appliances, could be kept well within the respective permissible deviation bands, as well as the voltage. Keeping the mass flow rate constant seems to be a challenge for some laboratories. In RRT2, one laboratory exceeded permissible deviation for the mass flow rate mean value by far in case of one operating condition, which, however, did not significantly influence the final result of the measurement.

Table 3: Deviations of measured to the operation conditions' target values for RRT2 (impermissible deviations marked in bold)

RRT2: W/W Heat Pump				
	deviation of mean values		*deviation of single measured values*	
	permissible deviation	*max*	*permissible deviation*	*max*

Outdoor heat exchanger					
Outdoor HX inlet temperature	*°C*	±0.2	0.1	±0.5	-0.3
Outdoor HX outlet temperature	*°C*	±0.3	0.09	±0.6	0.21
Indoor heat exchanger					
Indoor HX inlet temperature	*°C*	±0.2	0.1	±0.5	0.35
Indoor HX outlet temperature	*°C*	±0.3	0.15	±0.6	0.39
Mass flow rate indoor HX	*%*	±1.0	**-1.08**	±2.5	1.99
Mass flow rate outdoor HX	*%*	±1.0	**1.99**	±2.5	**-4.21**
Voltage	*%*	±4.0	2.24	±4.0	2.79

In Table 4, the deviations of measured to the operation conditions' target values for the indoor-air DHW heat pump during the draw-off test are shown. The provided values are considering only the periods with draw-offs and not the entire 24 h test. Even though the arithmetic mean values were very well within the permissible deviation range, the single measured values of the indoor air were well outside the range at one laboratory. The temperature of the cold water at the inlet was not always within the permissible ±1 K at two laboratories.

Table 4: Deviations of measured to the operation conditions' target values for RRT3 during Stage E (EN 16147). Impermissible deviations marked in bold

RRT3: DHW Heat Pump (draw-offs)						
			arithmetic mean values for the entire tapping cycle		*individually measured values*	
			deviation of mean values		*deviation from target*	
		target value	*permissible deviation*	*max*	*permissible deviation*	*max*
$T_{air,dry\ bulb}$	*°C*	20	±0.6	0.27	max. ±1.5	**2.49**
$T_{air,wet\ bulb}$	*°C*	15	±0.4	0.18	max. ±1.0	**3.45**
$T_{cold\ water,inlet}$	*°C*	10	±1.0	-0.72	±1.0	**1.74**

4.3. Reproducibility of the methods

One of the key aims of the project was to evaluate the reproducibility of the standardised test methods and to investigate possible improvements, especially regarding the key performance factors such as seasonal efficiency $\eta_{s,h}$ for heating appliances and η_{wh} for DHW appliances.

After the initial inspection of the data received from the participating laboratories, a number of errors was discovered. In order to evaluate their influence on the final result ($\eta_{s,h}$ or η_{wh}), all errors were divided into five categories:

1. Syntax error or wrong units, no influence on the final result;
2. Problem with the measurement or data acquisition / post processing, no correction possible but no influence on the final result;
3. Problem with the measurement / data post processing, influence on the final result. Corrected by the laboratory;
4. Problem with the measurement or data acquisition / post processing, no correction possible, influence on the final result;
5. Procedure not followed, influence on the final result.

Many small errors occurred in the course of transferring data into the provided templates. These errors were mostly corrected by the work package leader and were not further considered since they are not likely to happen in circumstances outside of this project (category 1). Some errors were attributed to e.g. the wrong setting of the measurement equipment, but did not influence the result such as setting of the voltmeter for one instead of three phase measurement (category 2). In quite a number of cases, the laboratory reported a wrong value or made a mistake in the calculation. These values were then corrected by the laboratory itself and put into protocol (category 3). In a small number of cases, the laboratories did not comply with the procedures or acquired wrong measurement values which did influence the final result (categories 4 and 5). These errors were, however, rather isolated and could be attributed to the novelty of the method (as for hybrid units) or alternative understanding of the procedure. In cases where errors of categories 4 or 5 happened and the measurement could not be repeated, the results were mostly not taken into account for statistical evaluation (if very obvious) or detected as outliers / stragglers during the statistical analysis.

Table 5: Analysis of the error types encountered in the analysis of the reported data

	RRT1	RRT2	RRT3	RRT4
Category 1	47%	31%	60%	48%
Category 2	0%	0%	0%	14%
Category 3	51%	29%	40%	21%
Category 4	1%	0%	0%	4%
Category 5	0%	40%	0%	12%
# Errors	78	48	10	188

Table 5 shows the number of different error types found in the reported data from the four RRTs. The number of errors is taking into account each single value that was affected, including error propagation up to the final figure. It can be seen that most errors were found in RRT4 for the test on the hybrid appliance. That was expected, since the test methods applied were new and the staff performing the tests had no previous experience. Also interesting, that quite a number of errors of category 5 (procedure not followed) were found in RRT2 for the test of a staged water-to-water heat pump. The reason was the same as for RRT4 – these appliances are not so commonly tested in most laboratories.

Quite a large absolute number of errors of category 3 found, especially in RRT1 and RRT2, could be attributed to the issues connected to the measurement of the electricity consumption in non-active operation modes and calculation errors in the data post-processing. These issues were specifically addressed in the recommendations to the TC 113.

The impact of the detected errors in the initially reported values can be seen from Table 6. It shows the differences between the highest and the lowest reported values by all laboratories for $\eta_{s,h}$ and η_{wh} (RRT3) before and after all corrections have been made. In case of RRT1, the difference slightly increased, in most cases, however, it could be considerably reduced.

Table 6: Difference between the maximum and minimum reported values for $\eta_{s,h}$ or η_{wh} from initially reported values and after corrections

max-min	RRT1	RRT2	RRT3	RRT4 separated	RRT4 combined
initial	24.10	33.30	8.09	51.70	19.27
final, after corrections	25.20	14.10 (2.00)	8.09	2.30	7.20

High difference for RRT1 can be explained with different behavior patterns of the unit in some of the laboratories. In one case, the unit performed a defrost cycle at 7 °C outdoor air temperature, which considerably lowered the calculated seasonal efficiency. If these results are removed from the analysis, the max-min value drops from 25.2 to 16.8. Another factor which had a considerable influence on the results in RRT1 and RRT2 was the measurement of the electricity consumption in non-active operation modes. It was found, that the if

the standby mode was reached by lowering the thermostat on one hand or by setting the operation mode to "summer" on the other, substantially different electricity consumptions were measured. This influence can be seen in

Table 6: Difference between the maximum and minimum reported values for $\eta_{s,h}$ or η_{wh} from initially reported values and after corrections

in the RRT2 column. In the first case, the final value for max-min is 14.10, in the second it drops to 2.00.

In Table 7, the statistics on the main parameters from all RRTs are shown. The main quantities shown in the table are the following:

- median: median value from all reported values;
- average: arithmetic mean value from all reported values;
- sR: standard deviation;
- minmax: difference between the highest and the lowest reported value for the parameter;
- **minmax/avg**: difference between the highest and the lowest reported value for the parameter, divided by the arithmetic mean value in %. **This quantity was chosen as the main parameter to conclude on the reproducibility**;
- R1 (abs): reproducibility calculated by multiplying the standard deviation by a factor of 2.83;
- R2 (abs): reproducibility calculated by multiplying the standard deviation by a factor of 4.00;
- R1 (%avg) and R2 (%avg): reproducibility calculated as a percentage of the average;
- N test-lab: the number of reported, valid test results. For each laboratory only one result is considered;
- stragglers and outliers: indication whether there are stragglers (an unusual data point which, when examined using e.g. Grubbs' test, Cochran's test or KSD has the probability between 1 % and 5 % of being valid) and outliers (an unusual data point which, when examined using e.g. Grubbs' test, Cochran's test or KSD has the probability of less than 1 % of being valid) and how many.

However, the number of reported values, i.e. participating laboratories in the RRTs was in the context of statistic evaluation relatively low. Thus, the statistic evaluation of the results can be taken rather as a guide to address some of the issues that were found during the tests than as a hard fact in order to finally conclude on the reproducibility of the methods or to provide recommendations for e.g. adjustment of the market surveillance tolerances.

For a number of parameters taken into account a straggler or an outlier were found. The data were then evaluated again without the straggler or the outlier. These values are indicated with (w/o straggler) or (w/o outlier). In presented data sets, not more than one straggler or one outlier per parameter were found, if any. When excluded, the reproducibility improved significantly. However, in some cases a new straggler or outlier have been detected (indicated with "one new straggler / outlier"). The data were not repeatedly evaluated without the indicated straggler or outlier.

The variation of the reported efficiency figures for the air-to-water capacity controlled heat pump (RRT1) was rather high. The main reason for that was the difference in the appliance behaviour during the testing and presumably influence of the control setting during the measurements of electricity consumption during non-active operation modes as well as different possibilities to account for the efficiency losses during on-off operation of the heat pump (C_d factor). If excluded from the analysis, the reproducibility of the results increases considerably. The same observations were made for the water-to-water two-stage heat pump (RRT2).

Table 7: Statistics on main parameters from all four RRTs

	median	*average*	*sR*	*minmax*	*minmax/avg*	*R1(abs.)*	*R2(abs.)*	*R1(%avg)*	*R2(%avg)*	*N test-lab*	*stragglers and outliers*
RRT1: A/W Heat Pump											
$\eta_{s,h}$ *(%)*	157.60	157.46	7.84	25.21	**16%**	22.17	31.34	14.10%	19.90%	7	(*)
$SCOP_{on}$	4.12	4.08	0.19	0.61	**15%**	0.55	0.78	13.50%	19.00%	7	one straggler
$SCOP_{on}$ *(w/o straggler)*	4.13	4.14	0.13	0.35	**9%**	0.36	0.51	8.80%	12.40%	6	(*)

Sound power (dB) @ 20%	66.80	66.88	1.20	3.10	log scale	3.38	4.78	log scale	log scale	5	one straggler
Sound power (dB) @ 20% (w/o straggler)	66.45	66.41	0.61	1.32	log scale	1.74	2.45	log scale	log scale	4	(*)
RRT2: W/W Heat Pump											
$\eta_{s,h}$ *(%)*	185.70	185.50	5.49	14.10	**8%**	15.54	21.96	8.40%	11.80%	5	(*)
$SCOP_{on}$	4.94	4.94	0.10	0.27	**5%**	0.28	0.39	5.60%	8.00%	5	(*)
SCOP	4.84	4.76	0.24	0.60	**13%**	0.69	0.98	14.50%	20.50%	5	(*)
RRT3: DHW Heat Pump											
η_{wh}	138.50	138.07	2.69	8.09	**6%**	7.61	10.75	5.50%	7.80%	8	one straggler
η_{wh} *(w/o straggler)*	138.70	138.77	1.97	4.97	**4%**	5.57	7.88	4.00%	5.70%	7	(*)
θ'_{wh} *(°C)*	53.05	52.98	0.59	1.97	**4%**	1.66	2.35	3.10%	4.40%	8	one straggler
θ'_{wh}*(w/o straggler)*	53.09	53.15	0.35	1.03	**2%**	1.00	1.42	1.90%	2.70%	7	(*)
V_{40} *(l)*	405.12	398.32	16.31	47.97	**12%**	46.17	65.25	11.60%	16.40%	8	one outlier
V_{40} *(w/o outlier)*	406.23	403.51	7.72	23.20	**6%**	21.85	30.89	5.40%	7.70%	7	one new outlier
RRT4: Hybrid Heat Pump - separated method											
$\eta_{s,h}$ *(%)*	97.80	97.54	0.86	2.30	**2.4%**	2.43	3.44	2.50%	3.50%	5	(*)
$SCOP_{on}$	2.52	2.52	0.02	0.06	**2.3%**	0.06	0.08	2.40%	3.30%	5	(*)
SCOP	2.52	2.51	0.02	0.06	**2.3%**	0.06	0.09	2.40%	3.40%	5	(*)
RRT4: Hybrid Heat Pump - combined method											
$\eta_{s,h}$ *(%)*	98.70	100.80	5.84	15.60	**15.5%**	16.54	23.38	16.40%	23.20%	5	one straggler
$\eta_{s,h}$ *(%) (w/o straggler)*	98.70	98.45	2.95	7.20	**7.3%**	8.36	11.81	8.50%	12.00%	4	(*)
$SCOP_{on}$	2.54	2.61	0.17	0.45	**17.2%**	0.48	0.68	18.50%	26.10%	5	one straggler
$SCOP_{on}$ *(w/o straggler)*	2.54	2.54	0.07	0.18	**7.1%**	0.21	0.30	8.20%	11.60%	4	(*)

The sound power measurements showed relatively good agreement of the results among the laboratories. However, the variability of the results is higher than the market surveillance verification tolerance defined by the European Commission of 2 dB. However, if a straggler is removed, the difference between the highest and the lowest reported values drops down to 1.32 dB. Also here, some differences in the appliance behaviour could be observed regarding the fan speed, which has the largest single influence on the overall sound power level. No direct correlation between the applied measurement methods and the obtained sound power could be observed.

A considerably lower variability in the reported efficiencies was observed for the DHW heat pump. The minmax/avg value was 4 % after removing a straggler. Also the values for the reference hot water temperature θ'_{wh} showed a very good agreement for all laboratories. The reported volumes of mixed water (V_{40}), however, showed much higher deviations. One laboratory reported a volume smaller by 36 l or around 10 % from the arithmetic mean of the whole measurement series, which was detected as an outlier. The reason for such a measurement outcome could not be found during the discussion of the results with the laboratory. If removed from the statistical evaluation, the minmax/avg value drops to the same level as for other reported parameters.

The two newly developed test methods for hybrid heat pumps (RRT4) showed a very good agreement of calculated efficiencies among themselves. For the separated method, being the simpler one between the two, the difference between the maximum and the minimum reported efficiency figures was very low – around 2 %. Results from the combined method show a much higher variability, at levels comparable to RRT1 and RRT2. These relatively high values could be reduced by half after removing a straggler.

4.4. Brainstorming on standards

The standards used in Work Package 7 have been repeatedly discussed and revised in the past years. At the time when the round robin tests began, all but one standard were under revision and new versions just about

to be published. Meanwhile, all versions of the standards used in the project have been published but most of them are already in a new revision process which will consider the outcome of the EcoTest project.

The cause for an almost on-going revision process is that the heat pump market is developing very fast and the emerging products are increasingly complex with more sophisticated controls and rising application diversity. Therefore, many features of the newly published standards were applied by most of the laboratories for the first time and the comments were collected until the end of the testing period. This gave the group less time to discuss the issues reported and search for possible solutions or investigate them within the round robin tests. A considerable number of comments was handed over to TC113 for further discussion.

5. Conclusions and further steps

There are many different types of heat pump appliances on the market win a variety of different configurations using different heat sources. Not all could be covered by the project. Through the choice of the appliances for the round robin tests, an attempt was made to cover as much features of the standards as possible.

From the analysis of the reported data, certain conclusions, some of which can be generally applied to all conducted round robin tests, can be made. In the WP7 Final Report, a more detailed analysis is provided for each of the tested appliances and used test procedures.

- Very good general understanding of the rather complicated test methods by the laboratories, even for appliances which were not easy to test. However, in certain points the reading of the standards differs among the laboratories. As the complexity of the appliances increases, as well as the type of applications covered, it gets harder to follow all the requirements of the standards.
- The specifications for some procedures in certain measurement cases are quite scattered around the standards and can be hard to understand and to follow by laboratories / engineers with less experience. This is especially the case if in a new, revised standard some changes in formulae, coefficients etc. are made.
- All laboratories have shown a high level of accuracy regarding reaching and keeping all test conditions constant throughout the measurements. In just a few cases, minor deviations outside of the permissible range have been found which in most cases did not significantly influence the final result. The parameters, for which outliers could be found, are in areas which are quite well controllable. A better real-time control of these parameters could be implemented to avoid exceeding the permissible deviations.
- In general, the settings on the appliance may quite vary from one laboratory to the other if no or insufficient information from the manufacturer is available. As the controls get more complicated, the variety of possibilities to reach a certain test condition rises. Thus, with current test methods, the support from the manufacturer has an influence on the reproducibility of the results.
- Differences in the measured values for the electricity consumptions in non-active operation modes have been observed. It has not been completely clarified in all cases whether the laboratories used different settings to reach the operation mode or the appliances behaved differently. It was shown that with alternative settings on the controller different values were measured by the same laboratory, which had a considerable influence on the seasonal efficiency (RRT2: 16 % for $\eta_{s,h}$).
- Quite large reported differences between the highest and the lowest values for seasonal efficiencies ($\eta_{s,h}$) for air-to-water capacity controlled (25.2 %) and water-to-water staged (14.1 %) unit. However, the difference could be diminished by:

    a. calculative elimination of the appliance behaviour influence, influence of the freedoms in calculation of seasonal efficiencies;
    b. using an alternative method for the measurement of the electricity consumption in non-active operation mode (influence of the manufacturer's support).

Even though valuable conclusions and recommendations for the improvement of the relevant standards could be made from the project, many issues – some of which were found in the course of testing and discussions – still remain unsolved. In order to solve some of these issues, further experimental investigation on a broader basis is needed. Therefore, a clear commitment regarding the importance of the standardisation work, followed by financial support for similar joint actions, from both the industry and the policy is needed.

Acknowledgements

The project EcoTest was financed by the EU, agreement number A/CEN/GROW/EFTA/534/535/2015-14

The authors would like to thank all participants of the EcoTest Project for good cooperation and commitment without which this publication would not have been possible.

References

[1] Fleiter, T., Steinbach, J., Ragwitz, M. et al., Mapping and analysis of the current and future (2020-20130) heating/cooling fuel deployment (fossil/renewables). European Commission, Directorate General for Energy, Brussels, Belgium

[2] Commission Delegated Regulation (EU) No 811/2013 of 18 February 2013 supplementing Directive 2010/30/EU with regard to energy labelling of space heaters, combination heaters, packages of space heater, temperature control and solar device and packages of combination heater, temperature control and solar device

[3] Commission Delegated Regulation (EU) No 812/2013 of 18 February 2013 supplementing Directive 2010/30/EU with regard to energy labelling of water heaters, hot water storage tanks and packages of water heater and solar device

[4] Commission Regulation (EU) No 813/2013 of 2 August 2013 implementing Directive 2009/125/EC with regard to ecodesign requirements for space heaters and combination heaters

[5] Commission Regulation (EU) No 814/2013 of 2 August 2013 implementing Directive 2009/125/EC with regard to ecodesign requirements for water heaters and hot water storage tanks

[6] COMMISSION IMPLEMENTING DECISION M/535 of 27.4.2015 on a standardisation request to the European standardisation organisations pursuant to Article 10(1) of Regulation (EU) No 1025/2012 of the European Parliament and of the Council in support of implementation of Commission Regulation (EU) No 813/2013 of 2 August 2013 implementing Directive 2009/125/EC of the European Parliament and of the Council with regard to ecodesign requirements for space heaters and combination heaters and Commission Delegated Regulation (EU) No 811/2013 of 18 February 2013 supplementing Directive 2010/30/EU of the European Parliament and of the Council with regard to the energy labelling of space heaters, combination heaters, packages of space heaters, temperature control and solar device and packages of combination heater, temperature control and solar device.

[7] COMMISSION IMPLEMENTING DECISION M/534 of 27.4.2015 on a standardisation request to the European standardisation organisations pursuant to Article 10(1) of Regulation (EU) No 1025/2012 of the European Parliament and of the Council in support of implementation of Commission Regulation (EU) No 814/2013 of 2 August 2013 implementing Directive 2009/125/EC of the European Parliament and of the Council with regard to ecodesign requirements for water heaters and hot water storage tanks and Commission Delegated Regulation (EU) No 812/2013 of 18 February 2013 supplementing Directive 2010/30/EU of the European Parliament and of the Council with regard to the energy labelling of water heaters, hot water storage tanks and packages of water heater and solar device.

[8] CEN, FprEN14511, Parts 1 to 4, Air conditioners, liquid chilling packages and heat pumps for space heating and cooling and process chillers, with electricylly driven compressors, October 2017, CEN, Belgium

[9] CEN, prEN14825-draft-2017-12-31-final, Heat pumps, air conditioners and chilling liquid packages – testing and rating at part load conditions. January 2018, CEN, Belgium

[10] CEN, FprEN12102-1, Air conditioners, liquid chilling packages, heat pumps and dehumidifiers with electricylly driven compressors – Determination of the sound power level – Part 1: Air conditioners, liquid chilling packages, heat pumps for space heating and cooling, dehumidifiers and process chillers, July 2017, CEN, Belgium

[11] CEN, EN16147, Heat pumps with electrically driven compressors – Testing, performance rating and requirements for marking of domestic hot water units, January 2017, CEN, Belgium

13th IEA Heat Pump Conference
April 26-29, 2021 Jeju, Korea

The influence of different water-injection methods on water vapor high temperature heat pump

Di Wu[a], Bin Hu[a*], R.Z. Wang[a]

[a]Institute of Refrigeration and Cryogenics, Shanghai Jiao Tong University, Shanghai 200240, China

Abstract

To yield higher temperature output and better performance, a high temperature heat pump with water refrigerant is developed and the corresponding prototype is established. Water-injection is adopted to reduce the discharge superheat. The theoretical results show that compared with HFO and HC refrigerants and traditional HFC refrigerant, water has better performance when the condensation temperature is above 100°C. With the increase of the condensation temperature, the simulation performance of water vapor heat pump is better, which means water is more suitable for higher temperature application fields. Based on the experimental investigation, the system performance with different injection lines and ports are compared. Its start-up and dynamic performance present that this heat pump reaches steady-state in 10 minutes and water-injection can effectively decrease the discharge temperature. The internal injection line can realize the self-adjustment of injected-water and discharge temperature. The coefficient of performance of this heat pump with internal water-injection is better than that of external.

Keywords: Water refrigerant; High temperature heat pump; COP; Internal water-injection;

1. Introduction

Global warming has always been a major environmental issue of concern to the whole world, which has brought a huge and disastrous impact on global biodiversity and the stability of the ecological environment. In order to curb global warming, effective methods must be adopted to reduce the consumption of fossil fuels and the emission of greenhouse gases. Heat pumps are an energy-saving technology with significant potential for industrial applications. Especially, vapor compression heat pumps are the most widely used and are available in a wide variety of sizes for different applications [1].

As shown in Fig. 1, the heat pumps can be classified as low-temperature heat pumps (LTHPs), medium-temperature heat pumps (MTHPs), high-temperature heat pumps (HTHPs), and ultra-high-temperature heat pumps (UHTHPs). In this classification, the different kinds of heat pumps are strictly defined by the output temperature and loosely defined by the heat source temperature. Based on the above classification, the vapor compression heat pump with output temperature ranging from 100℃ to 160℃ is regarded as the HTHP. Many researchers are studying the HTHP with different working fluids, including natural refrigerants [2, 3], HCs [4, 5] and HFOs [6, 7]. Bamigbetan O et al. [8, 9] experimentally investigated an R600 HTHP with a prototype compressor for industrial waste heat recovery from 50℃ to heat delivery at 115℃. Kondou C et al. [10] designed different cycle configurations with R1234ze(Z) refrigerant to supply the output temperature of 160℃ as the waste heat was 80℃. Arpagaus C et al. [11] examined the experimental performance of R1336mzz(Z) in a laboratory single-stage HTHP with 5~10 kW heating capacity using a variable speed piston compressor. When the heat source is 60℃ and output is 110℃, the coefficient of performance (COP) of this R1336mzz(Z) heat pump with an internal heat exchanger is 3.0 with a 24% increment compared with

* Bin Hu. Tel.: +86 15021685354.
E-mail address: hb1223@sjtu.edu.cn.

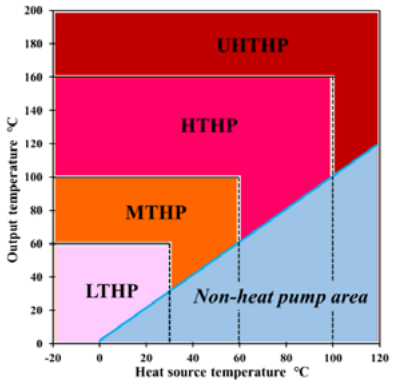


Fig. 1. The classification of vapor compression heat pump

it. By comparing with other HFO and HCFO refrigerants theoretically, they also found that R1336mzz(Z) achieves the highest COP in the temperature range from 120℃ to 10℃ [12]. Wu D et al. [13, 14] presented a novel water vapor HTHP system with 80~90℃ waste heat recovery and above 100℃ hot water supply. When the evaporation temperature was 85℃, the COP decreased from 6.10 to 1.96 with condensation temperature increasing from 110℃ to 150℃.

In this work, based on the existing experimental investigation on water vapor HTHP, preliminary experimental investigation of the water vapor HTHP system performance with different injection lines and injection ports is carried out to find the effect of different injection methods on the heat pump performance.

2. Working fluid

Nowadays, the selection principle of refrigerant takes ozone depletion potential (ODP) and global warming potential (GWP) into consideration and considers them as the main indexes on environmental protection, which limits that ODP is 0 and GWP is below 150 [15]. In Table.1, five kinds of refrigerants (GWP<150)-R718, R600, R601, R1234ze(Z) and R1336mzz(Z)-are chosen to be used in HTHP systems as working fluids. A high GWP HFC refrigerant, R245fa, is added as the representative of traditional HTHP refrigerants.

Table.1 The properties of HTHP refrigerants [1, 16]

Refrigerant	Chemical formula	T_{crit} /℃	P_{crit} /bar	ODP	GWP	SG	NBP/℃
R718	H_2O	373.9	220.6	0	0	A1	100.0
R600	$CH_3CH_2CH_2CH_3$	152.0	38.0	0	20	A3	-0.5
R601	$CH_3CH_2CH_2CH_2CH_3$	196.6	33.7	0	20	A3	36.1
R1234ze(Z)	$CHF=CHCF_3$	150.1	35.3	0	1	A2	9.8
R1336mzz(Z)	$CF_3CH=CHCF_3$	171.3	29.0	0	2	A1	33.4
R245fa	$CHF_2CH_2CF_3$	154.0	36.5	0	858	B1	14.9

The theoretical performance of HTHPs with these selected refrigerants are calculated in an idealized single-stage heat pump cycle with the following assumptions: (1). the condensation and evaporation processes are isobaric; (2). the expansion process is isenthalpic; (3). the suction temperature of the compressor has 20℃ superheat for R601 and R1336mzz(Z) and has 5℃ superheat for the left refrigerants; (4). compression process with a constant isentropic efficiency of 0.7; (5). the condensation temperature increases from 100℃ to the critical temperature with a constant 40℃ temperature lift.

The calculation results and comparison at 40℃ temperature differences are illustrated in the following pictures, including the COP (Fig. 2), the compression ratio (Fig. 3) and the volumetric heating capacity (Fig. 4).

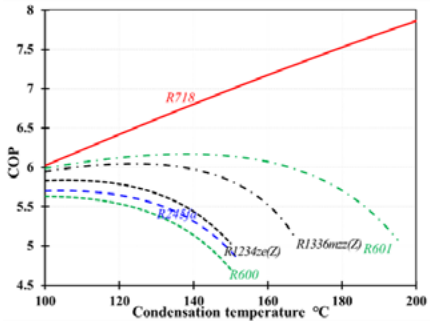


Fig. 2. The COP of the HTHPs with selected refrigerants

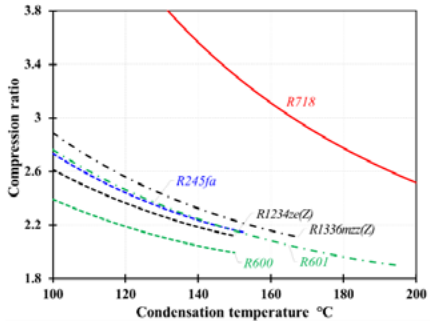


Fig. 3. The compression ratio of the HTHPs with selected refrigerants

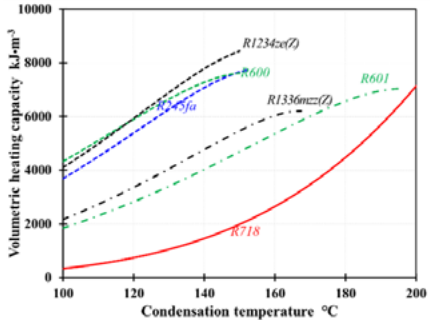


Fig. 4. The volumetric heating capacity of the HTHPs with selected refrigerants

Based on the above table and calculation results, compared with the other five refrigerants, water has many advantages in HTHP applications, especially in ultra-high-temperature output fields. Water has the highest critical temperature, the best environmental protection performance, and the safest property. The calculation COP, shown in Fig.2, also presented that water has the best theoretical performance when the condensation temperature is above 100℃. However, Fig.3 and 4 also illustrated the disadvantages of water refrigerant in heat pump systems. Compared with the other kind of refrigerants, water has the biggest compression ratio and the smallest volumetric heating capacity in the simulation conditions. So the application of water in the HTHP field needs an appropriate compressor with a bigger compression ratio to satisfy high temperature lift and a bigger volume flow rate to overcome its small volumetric heating capacity.

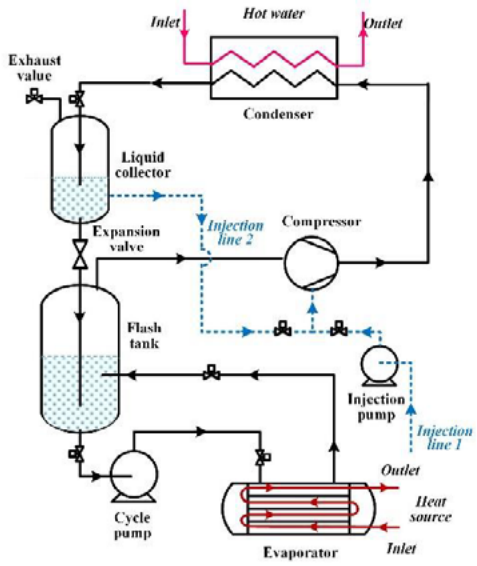


Fig. 5. The schematic diagram of the R718 HTHP with two injection lines

Furthermore, the big compression ratio of water will also lead greatly high discharge superheat and temperature in the heat pump system. So the discharge superheat and temperature must be lowed to promise the safety application of water in HTHP systems. What's more, with the increasing of the condensation temperature, the simulation COP and volumetric heating capacity of water vapor HTHP increases and the compression ratio of the heat pump decreases, which means water vapor HTHP has better performance in higher temperature application fields.

3. Water vapor HTHP

As shown in Fig.5, the schematic diagram of the water vapor HTHP has two different injection lines: external injection line (injection line 1) and the internal injection line (injection line 2). The external injection line is used to inject water from the outside with constant pressure and low temperature, and the internal injection line is used to inject condensed water from the liquid collector with various pressure and high temperature. There are also two injection ports in the water vapor HTHP prototype: the suction side injection port and the compression chamber injection port. These different injection lines and ports may have different effects on the performance of the water vapor HTHP.

4. Experimental results

Based on the schematic diagram of the water vapor HTHP, a prototype of this heat pump with two different injection lines and two different injection ports were set up. Experimental investigations were carried out to study the performance of the water vapor HTHP, including the start-up and dynamic performance, the influence of different injection ports and the injection lines.

4.1. Start-up and dynamic performance

As shown in Fig. 6(a), (b), and (c), the start-up and dynamic performance of the water vapor HTHP is presented with internal water injection in the compression chamber. With the rotate speed increasing from 0 to 5000 rpm in 8 minutes, the system reached steady-state in 10 minutes as the evaporation pressure was uncharged near 0.4 bar and other working properties were steady. In the start-up process, with the increase of the rotate speed, more water vapor was suctioned from the evaporator and the evaporation pressure decreased directly. At first, the condensation pressure increased and then decreased with the increase of the rotate speed,

which is mainly due to the accumulation of the discharge steam and the flow rate of the condensation water. With the increase of the rotate speed, the discharge temperature and superheat temperature increased rapidly as the rotate speed was above 2400 rpm. In order to control the discharge temperature in the start-up process, the injected-water was injected into the compressor with a much higher flow rate when the rotate speed was 2400 rpm. After the rotate speed reaching the highest value, 5000 rpm, the flow rate of the injected-water was adjusted to control the discharge temperature near the saturation temperature.

After the start-up process, by adjusting the opening of the expansion valve to control the condensation temperature, the dynamic performance of the water vapor HTHP was illustrated as the rotate speed and the evaporation pressure were invariant. With the increase of the condensation temperature, more power consumption was demanded to protect the larger compression ratio and enthalpy lift in the compression process. Larger compression ratio and enthalpy lift mean higher discharge temperature and more injected-water, so the flow rate of the injected-water also increased. However, the flow rate of the injected-water is not only controlled by the opening of the injection valve but also adjusted by the pressure of liquid collector. As shown in Fig. 6(c), when the opening of the injection valve is fixed, with the increasing of the condensation pressure, the flow rate of injected-water also increased to control the discharge temperature. When the pressure adjustment of the injected-water was failure and the discharge temperature was higher than the saturation temperature, the opening of injection valve will permit more injected-water to control the discharge temperature.

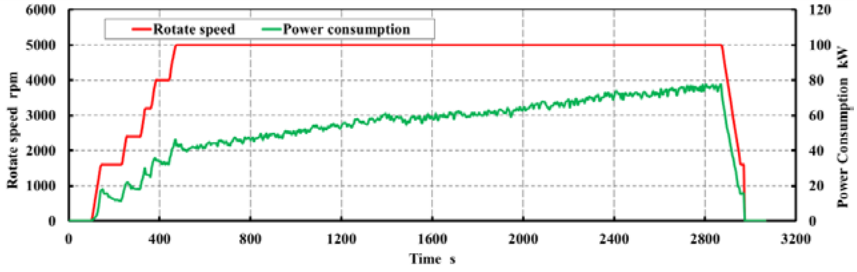


Fig. 6(a). The start-up and dynamic performance of rotate speed and power consumption

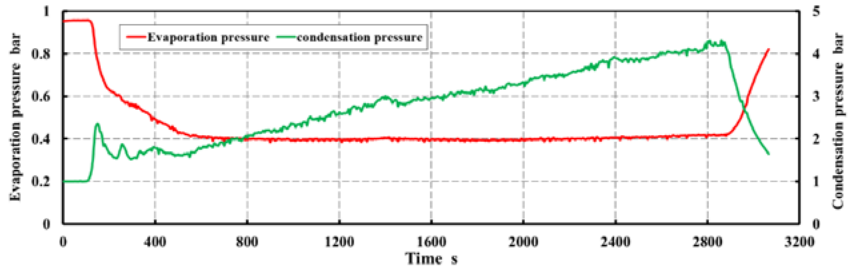


Fig. 6(b). The start-up and dynamic performance of evaporation and condensation pressure

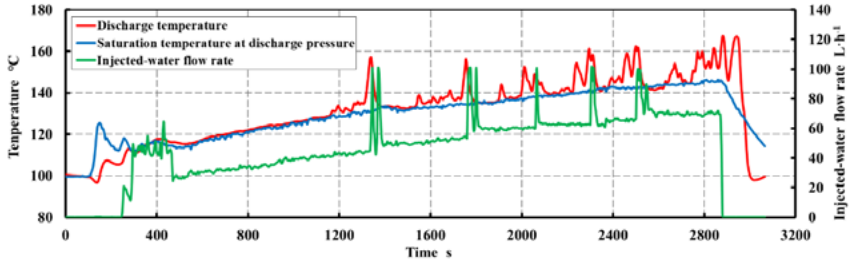


Fig. 6(c). The start-up and dynamic performance of discharge temperature and injected-water flow rate

4.2. The influence of injection ports

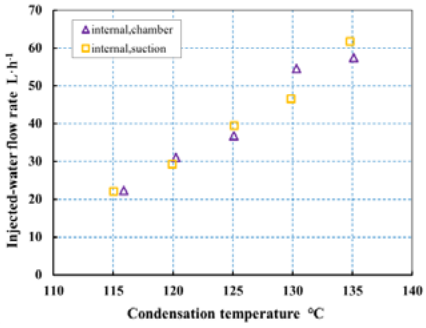


Fig. 7(a) Injected-water flow rate comparison

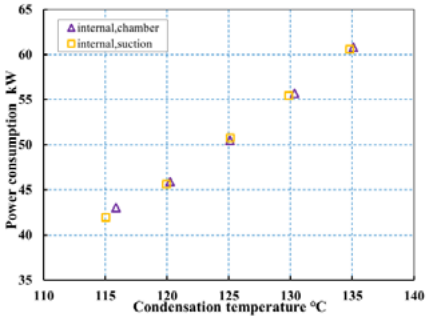


Fig. 7(b) Power consumption comparison

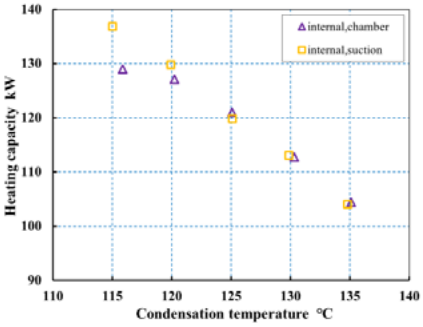


Fig. 7(c) Heating capacity comparison

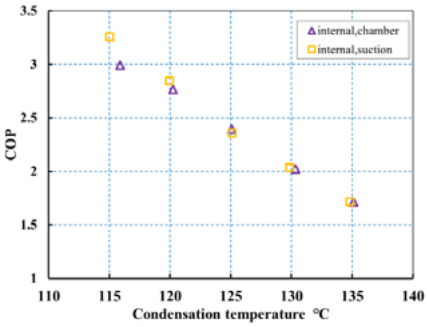


Fig. 7(d) COP comparison

Fig. 7. The performance comparison of the water vapor HTHP with different injection ports

There are two different injection ports designed in the water vapor HTHP. One is in the compressor chamber with water directly injected into the compression process to lower the discharge temperature. The other is in the suction side with water injected into the suction side of the compressor and then mixed with water vapor and suctioned into the compression chamber. When the water is injected into the system, different injection ports may have different effects on the system performance, especially on the control of the discharge temperature. When the water is injected into the compressor chamber, it can directly absorb the superheat of the compressed water vapor and lower the temperature timely. However, when the water is injected into the suction side, it can separate and mix uniformly with the water vapor, which is better for absorbing heat in the compression process. The control of the discharge temperature has a delay as the water is injected into the suction side.

To compare the influence of different injection ports, an experimental investigation is carried out with internal water injection at 73°C evaporation temperature. The result comparison is shown in Fig. 7(a) to (d), including the injected-water flow rate, power consumption, heating capacity, and COP. The result presented that the difference in system performance with different injection ports is not obvious and the injection ports have little influence on the system performance. This may due to that the compression process is faster than the heat transfer in the compression chamber, and most of the injected-water has not evaporated into steam when it was discharged from the compressor. So the separate and fogging degree of the injected-water has little influence, and the flow rate of the injected-water plays the most important role. However, more experimental investigations are needed to prove the results.

4.3. The influence of injection channels

To provide the steady of the injected water and keep the mass conversation of the water in the system, two injection lines are designed in the water vapor HTHP, external water injection from the outside and internal

water injection from the liquid collector. When the injected-water is from the outside, the temperature, pressure

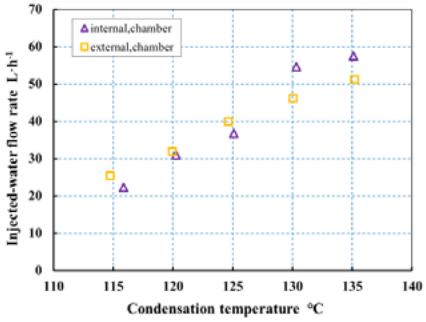


Fig. 8(a) Injected-water flow rate comparison

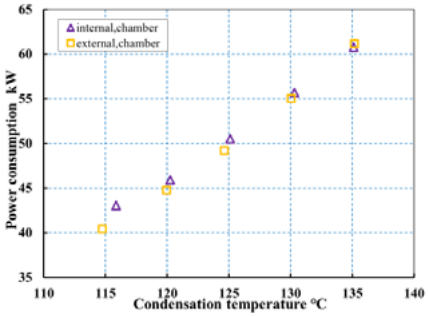


Fig. 8(b) Power consumption comparison

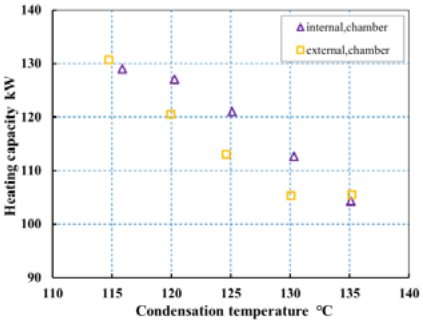


Fig. 8(c) Heating capacity comparison

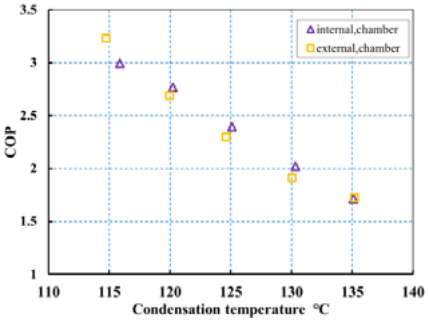


Fig. 8(d) COP comparison

Fig. 8. The performance comparison of the water vapor HTHP with different injection channels

and flow rate of the injected-water are controlled easily, which is good for the steady operation of the heat pump. However, external water injection will lead to an increase in the working fluid in the system, and destroy the balance of long-time operation. In this experimental investigation, to keep the balance of the water refrigerant in the system with the external water injection, some water will be discharged from the liquid collector. When the injected-water is from the liquid collector, the system working fluid is conversation and the flow rate of injected-water will increase simultaneously with the increase of the condensation temperature. It can realize the self-adjustment of injected-water and discharge temperature of the system. However, the temperature and pressure of the injected-water are changed with the condensation temperature.

The experimental investigation is carried out with different injection channel at 73℃ evaporation temperature. The result comparison is shown in Fig. 8(a) to (d), including the injected-water flow rate, power consumption, heating capacity, and COP. The result presented that the difference of injected-water flow rate and power consumption with different injection lines is not obvious. However, the heating capacity and COP of the two injection line systems are different. The internal injection system has better heating capacity and COP, which may due to the higher temperature of the injected-water.

5. Conclusions

Water vapor HTHP is a significant vapor compression heat pump with a high output temperature. The theoretical simulation results show that compared with new HFO and HC refrigerant and traditional HFC refrigerant, R718 has better performance when the condensation temperature is above 100oC. What's more, with the increasing of the condensation temperature, the simulation COP and volumetric heating capacity of water vapor HTHP increases and the compression ratio of the heat pump decreases, which means water vapor HTHP is more suitable for higher temperature application fields. Its start-up and dynamic performance

present that this heat pump can reach steady-state in 10 minutes and water injection can effectively decrease the discharge temperature. The internal injection line can realize the self-adjustment of injected-water and discharge temperature. When the opening of the injection valve is fixed, with the increasing of the condensation pressure, the flow rate of injected-water also increased to control the discharge temperature. When the pressure adjustment of the injected-water was failure and the discharge temperature was higher than the saturation temperature, the opening of the injection valve will permit more injected-water to control the discharge temperature. Different injection ports have little influence on heat pump performance. However, the different injection channels have influence on the heat pump performance, especially on the heating capacity. So it is very significant to design a suitable water vapor heat pump cycle with the best injection method.

6. Copyright

By submittal of his or her full paper to the Agency for the 13th Heat Pump Conference, the author(s) assumes full responsibility for ensuring that his or her paper does not infringe on another party's intellectual property rights, which include copyright and agree that the paper has not previously been submitted for publication elsewhere. Furthermore, the author, by submittal of his or her conference paper to the conference, grants publishing rights of that paper to the Agency for the 13th Heat Pump Conference, which may:

1. Publish or arrange to publish the paper as part of the Conference proceedings,
2. Copy and distribute the paper in its entirety in print and electronic form, and
3. Copy and distribute excerpts from the paper.

Acknowledgments

This research was supported by the National Natural Science Foundation of China (51706131), the National Key R&D Program of China (2016YFB0601200) and Fundamental Research Funds for the Central Universities (18X100040029). The authors gratefully acknowledge the financial support from the Research Council of Norway and user partners of HighEFF (Centre for an Energy Efficient and Competitive Industry for the Future, an 8-year Research Centre under the FME-scheme)

References

[1] Arpagaus C, Bless F, Uhlmann M, Schiffmann J, Bertsch SS. High temperature heat pumps: Market overview, state of the art, research status, refrigerants, and application potentials. Energy 2018;152:985-1010.
[2] Chamoun M, Rulliere R, Haberschill P, Berail JF. Water vapour as refrigerant for a new high temperature heat pump. Japanese Journal of Radiological Technology 2011;49:1879-87.
[3] Larminat PD, Arnou D, Le Sausse P, Clunet F, Peureux JL. A high temperature heat pump using water vapor as working fluid. 11th IIR Gustav Lorentzen Conference on Natural Refrigerants. China: Hang Zhou, 2014, p.857-64.
[4] Bamigbetan O, Eikevik TM, Nekså P, Bantle M, Schlemminger C. Theoretical analysis of suitable fluids for high temperature heat pumps up to 125 °C heat delivery. International Journal of Refrigeration 2018;92:185-95.
[5] Schlemminger C, Starheim Svendsen E, Steffanussen Foslie S, Bantle M, Bamigbetan O, Neksa P. Performance of high temperature heat pump for simultaneous and efficient production of ice water and process heat. The 25th IIR International Congress of Refrigeration. Montreal, Canada 2019.
[6] Hu B, Wu D, Wang LW, Wang RZ. Exergy analysis of R1234ze(Z) as high temperature heat pump working fluid with multi-stage compression. Frontiers in Energy 2017;11:493-502.
[7] Helminger F, Hartl M, Fleckl T, Kontomaris K, Pfaffl J. Hochtemperatur Wärmepumpen Messergebnisse einer Laboranlage mit HFO-1336MZZ-Z bis 160°C Kondensationstemperatur. 14th Symposium Energieinnovation. TU Graz 2016. p.1-20.
[8] Bamigbetan O, Eikevik TM, Nekså P, Bantle M, Schlemminger C. Experimental investigation of a prototype R-600 compressor for high temperature heat pump. Energy 2019;169:730-8.
[9] Bamigbetan O, Eikevik TM, Nekså P, Bantle M, Schlemminger C, Dallai M. Experimental investigation of a hydrocarbon piston compressor for high temperature heat pumps. 24th international compressor engineering conference. West Lafayette 2018. p.S0140700718301750.

[10] Kondou C, Koyama S. Thermodynamic assessment of high-temperature heat pumps using Low-GWP HFO refrigerants for heat recovery. International Journal of Refrigeration 2015;53:126-41.
[11] Arpagaus C, Kuster R, Prinzing M, Bless F, Uhlmann M, Buchel E, et al. High temperature heat pump using HFO and HCFO refrigerants - system design and experimental results. The 25th IIR International Congress of Refrigeration. Montreal, Canada 2019.
[12] Arpagaus C, Prinzing M, Kuster R, Bless F, Uhlmann M, Schiffmann J, et al. High temperature heat pumps - Theoretical study on low GWP HFO and HCFO refrigerants. The 25th IIR International Congress of Refrigeration. Montreal, Canada 2019.
[13] Wu D, Hu B, Yan H, Wang RZ. Modeling and simulation on a water vapor high temperature heat pump system. Energy 2019;168:1063-72.
[14] Wu D, Hu B, Wang RZ. Theoretical and experimental investigation on a very high temperature heat pump with water refrigerant. The 25th IIR International Congress of Refrigeration. Montreal, Canada 2019.
[15] European Commission. Regulation (EU) No 517/2014 of the European Parliament and of the Council of 16 April 2014 on fluorinated greenhouse gases and repealing Regulation (EC) No 842/2006. In: Union TEPaTCotE, editor. Europe: European; 2014.
[16] Mclinden MO, Kazakov AF, Brown JS, Domanski PA. A thermodynamic analysis of refrigerants: Possibilities and tradeoffs for Low-GWP refrigerants International Journal of Refrigeration 2014;38:80-92.

13th IEA Heat Pump Conference
April 26-29, 2021 Jeju, Korea

The influence of different water-injection methods on water vapor high temperature heat pump

Di Wu[a], Bin Hu[a*], R.Z. Wang[a]

[a]Institute of Refrigeration and Cryogenics, Shanghai Jiao Tong University, Shanghai 200240, China

Abstract

To yield higher temperature output and better performance, a high temperature heat pump with water refrigerant is developed and the corresponding prototype is established. Water-injection is adopted to reduce the discharge superheat. The theoretical results show that compared with HFO and HC refrigerants and traditional HFC refrigerant, water has better performance when the condensation temperature is above 100°C. With the increase of the condensation temperature, the simulation performance of water vapor heat pump is better, which means water is more suitable for higher temperature application fields. Based on the experimental investigation, the system performance with different injection lines and ports are compared. Its start-up and dynamic performance present that this heat pump reaches steady-state in 10 minutes and water-injection can effectively decrease the discharge temperature. The internal injection line can realize the self-adjustment of injected-water and discharge temperature. The coefficient of performance of this heat pump with internal water-injection is better than that of external.

Keywords: Water refrigerant; High temperature heat pump; COP; Internal water-injection;

1. Introduction

Global warming has always been a major environmental issue of concern to the whole world, which has brought a huge and disastrous impact on global biodiversity and the stability of the ecological environment. In order to curb global warming, effective methods must be adopted to reduce the consumption of fossil fuels and the emission of greenhouse gases. Heat pumps are an energy-saving technology with significant potential for industrial applications. Especially, vapor compression heat pumps are the most widely used and are available in a wide variety of sizes for different applications [1].

As shown in Fig. 1, the heat pumps can be classified as low-temperature heat pumps (LTHPs), medium-temperature heat pumps (MTHPs), high-temperature heat pumps (HTHPs), and ultra-high-temperature heat pumps (UHTHPs). In this classification, the different kinds of heat pumps are strictly defined by the output temperature and loosely defined by the heat source temperature. Based on the above classification, the vapor compression heat pump with output temperature ranging from 100℃ to 160℃ is regarded as the HTHP. Many researchers are studying the HTHP with different working fluids, including natural refrigerants [2, 3], HCs [4, 5] and HFOs [6, 7]. Bamigbetan O et al. [8, 9] experimentally investigated an R600 HTHP with a prototype compressor for industrial waste heat recovery from 50℃ to heat delivery at 115℃. Kondou C et al. [10] designed different cycle configurations with R1234ze(Z) refrigerant to supply the output temperature of 160℃ as the waste heat was 80℃. Arpagaus C et al. [11] examined the experimental performance of R1336mzz(Z) in a laboratory single-stage HTHP with 5~10 kW heating capacity using a variable speed piston compressor. When the heat source is 60℃ and output is 110℃, the coefficient of performance (COP) of this R1336mzz(Z) heat pump with an internal heat exchanger is 3.0 with a 24% increment compared with

* Bin Hu. Tel.: +86 15021685354.
E-mail address: hb1223@sjtu.edu.cn.

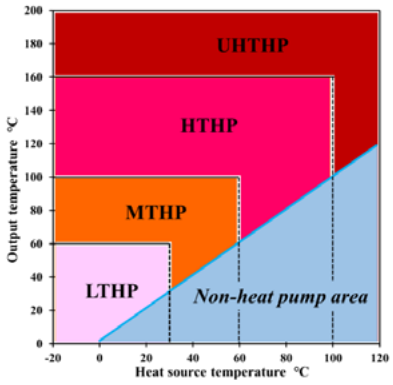


Fig. 1. The classification of vapor compression heat pump

it. By comparing with other HFO and HCFO refrigerants theoretically, they also found that R1336mzz(Z) achieves the highest COP in the temperature range from 120℃ to 10℃ [12]. Wu D et al. [13, 14] presented a novel water vapor HTHP system with 80~90℃ waste heat recovery and above 100℃ hot water supply. When the evaporation temperature was 85℃, the COP decreased from 6.10 to 1.96 with condensation temperature increasing from 110℃ to 150℃.

In this work, based on the existing experimental investigation on water vapor HTHP, preliminary experimental investigation of the water vapor HTHP system performance with different injection lines and injection ports is carried out to find the effect of different injection methods on the heat pump performance.

2. Working fluid

Nowadays, the selection principle of refrigerant takes ozone depletion potential (ODP) and global warming potential (GWP) into consideration and considers them as the main indexes on environmental protection, which limits that ODP is 0 and GWP is below 150 [15]. In Table.1, five kinds of refrigerants (GWP<150)-R718, R600, R601, R1234ze(Z) and R1336mzz(Z)-are chosen to be used in HTHP systems as working fluids. A high GWP HFC refrigerant, R245fa, is added as the representative of traditional HTHP refrigerants.

Table.1 The properties of HTHP refrigerants [1, 16]

Refrigerant	Chemical formula	T_{crit} /℃	P_{crit} /bar	ODP	GWP	SG	NBP/℃
R718	H_2O	373.9	220.6	0	0	A1	100.0
R600	$CH_3CH_2CH_2CH_3$	152.0	38.0	0	20	A3	-0.5
R601	$CH_3CH_2CH_2CH_2CH_3$	196.6	33.7	0	20	A3	36.1
R1234ze(Z)	$CHF=CHCF_3$	150.1	35.3	0	1	A2	9.8
R1336mzz(Z)	$CF_3CH=CHCF_3$	171.3	29.0	0	2	A1	33.4
R245fa	$CHF_2CH_2CF_3$	154.0	36.5	0	858	B1	14.9

The theoretical performance of HTHPs with these selected refrigerants are calculated in an idealized single-stage heat pump cycle with the following assumptions: (1). the condensation and evaporation processes are isobaric; (2). the expansion process is isenthalpic; (3). the suction temperature of the compressor has 20℃ superheat for R601 and R1336mzz(Z) and has 5℃ superheat for the left refrigerants; (4). compression process with a constant isentropic efficiency of 0.7; (5). the condensation temperature increases from 100℃ to the critical temperature with a constant 40℃ temperature lift.

The calculation results and comparison at 40℃ temperature differences are illustrated in the following pictures, including the COP (Fig. 2), the compression ratio (Fig. 3) and the volumetric heating capacity (Fig. 4).

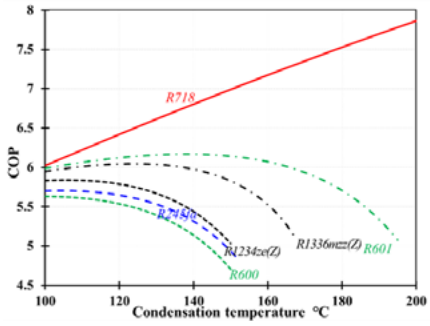


Fig. 2. The COP of the HTHPs with selected refrigerants

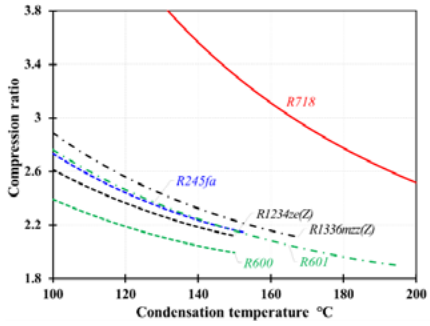


Fig. 3. The compression ratio of the HTHPs with selected refrigerants

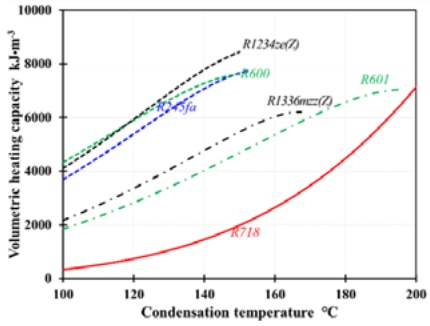


Fig. 4. The volumetric heating capacity of the HTHPs with selected refrigerants

Based on the above table and calculation results, compared with the other five refrigerants, water has many advantages in HTHP applications, especially in ultra-high-temperature output fields. Water has the highest critical temperature, the best environmental protection performance, and the safest property. The calculation COP, shown in Fig.2, also presented that water has the best theoretical performance when the condensation temperature is above 100℃. However, Fig.3 and 4 also illustrated the disadvantages of water refrigerant in heat pump systems. Compared with the other kind of refrigerants, water has the biggest compression ratio and the smallest volumetric heating capacity in the simulation conditions. So the application of water in the HTHP field needs an appropriate compressor with a bigger compression ratio to satisfy high temperature lift and a bigger volume flow rate to overcome its small volumetric heating capacity.

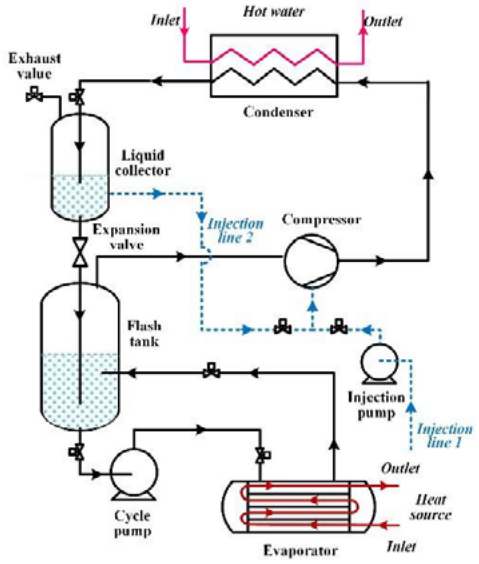


Fig. 5. The schematic diagram of the R718 HTHP with two injection lines

Furthermore, the big compression ratio of water will also lead greatly high discharge superheat and temperature in the heat pump system. So the discharge superheat and temperature must be lowed to promise the safety application of water in HTHP systems. What's more, with the increasing of the condensation temperature, the simulation COP and volumetric heating capacity of water vapor HTHP increases and the compression ratio of the heat pump decreases, which means water vapor HTHP has better performance in higher temperature application fields.

3. Water vapor HTHP

As shown in Fig.5, the schematic diagram of the water vapor HTHP has two different injection lines: external injection line (injection line 1) and the internal injection line (injection line 2). The external injection line is used to inject water from the outside with constant pressure and low temperature, and the internal injection line is used to inject condensed water from the liquid collector with various pressure and high temperature. There are also two injection ports in the water vapor HTHP prototype: the suction side injection port and the compression chamber injection port. These different injection lines and ports may have different effects on the performance of the water vapor HTHP.

4. Experimental results

Based on the schematic diagram of the water vapor HTHP, a prototype of this heat pump with two different injection lines and two different injection ports were set up. Experimental investigations were carried out to study the performance of the water vapor HTHP, including the start-up and dynamic performance, the influence of different injection ports and the injection lines.

4.1. Start-up and dynamic performance

As shown in Fig. 6(a), (b), and (c), the start-up and dynamic performance of the water vapor HTHP is presented with internal water injection in the compression chamber. With the rotate speed increasing from 0 to 5000 rpm in 8 minutes, the system reached steady-state in 10 minutes as the evaporation pressure was uncharged near 0.4 bar and other working properties were steady. In the start-up process, with the increase of the rotate speed, more water vapor was suctioned from the evaporator and the evaporation pressure decreased directly. At first, the condensation pressure increased and then decreased with the increase of the rotate speed,

which is mainly due to the accumulation of the discharge steam and the flow rate of the condensation water. With the increase of the rotate speed, the discharge temperature and superheat temperature increased rapidly as the rotate speed was above 2400 rpm. In order to control the discharge temperature in the start-up process, the injected-water was injected into the compressor with a much higher flow rate when the rotate speed was 2400 rpm. After the rotate speed reaching the highest value, 5000 rpm, the flow rate of the injected-water was adjusted to control the discharge temperature near the saturation temperature.

After the start-up process, by adjusting the opening of the expansion valve to control the condensation temperature, the dynamic performance of the water vapor HTHP was illustrated as the rotate speed and the evaporation pressure were invariant. With the increase of the condensation temperature, more power consumption was demanded to protect the larger compression ratio and enthalpy lift in the compression process. Larger compression ratio and enthalpy lift mean higher discharge temperature and more injected-water, so the flow rate of the injected-water also increased. However, the flow rate of the injected-water is not only controlled by the opening of the injection valve but also adjusted by the pressure of liquid collector. As shown in Fig. 6(c), when the opening of the injection valve is fixed, with the increasing of the condensation pressure, the flow rate of injected-water also increased to control the discharge temperature. When the pressure adjustment of the injected-water was failure and the discharge temperature was higher than the saturation temperature, the opening of injection valve will permit more injected-water to control the discharge temperature.

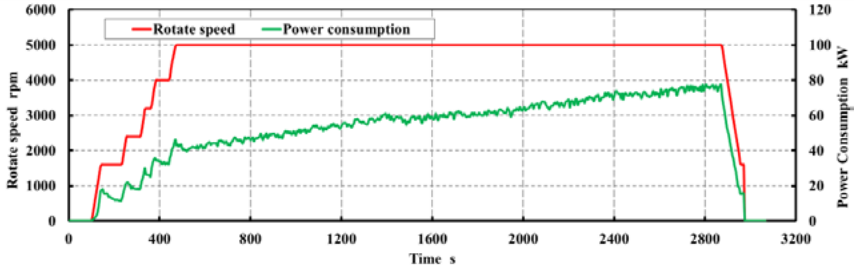


Fig. 6(a). The start-up and dynamic performance of rotate speed and power consumption

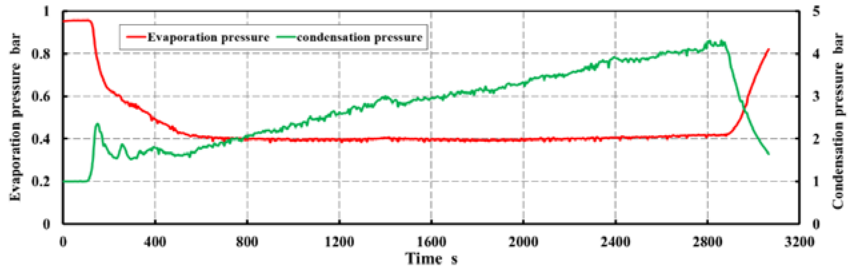


Fig. 6(b). The start-up and dynamic performance of evaporation and condensation pressure

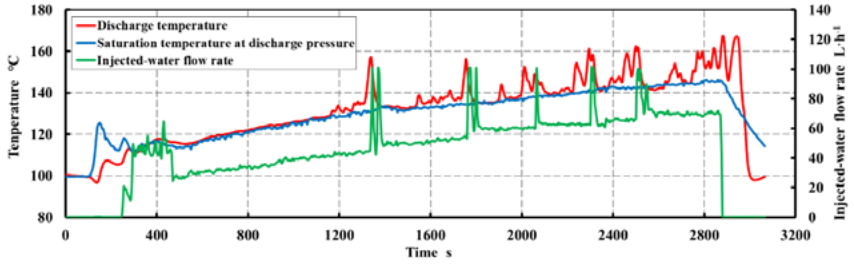


Fig. 6(c). The start-up and dynamic performance of discharge temperature and injected-water flow rate

4.2. The influence of injection ports

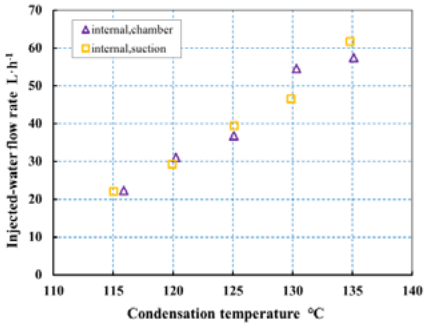


Fig. 7(a) Injected-water flow rate comparison

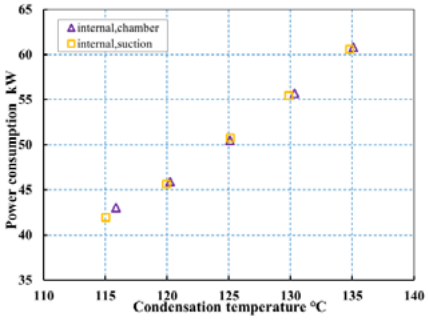


Fig. 7(b) Power consumption comparison

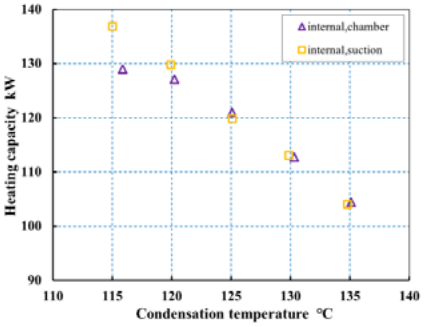


Fig. 7(c) Heating capacity comparison

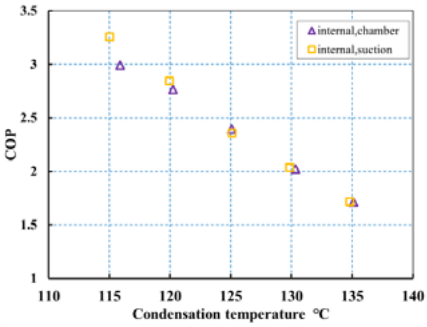


Fig. 7(d) COP comparison

Fig. 7. The performance comparison of the water vapor HTHP with different injection ports

There are two different injection ports designed in the water vapor HTHP. One is in the compressor chamber with water directly injected into the compression process to lower the discharge temperature. The other is in the suction side with water injected into the suction side of the compressor and then mixed with water vapor and suctioned into the compression chamber. When the water is injected into the system, different injection ports may have different effects on the system performance, especially on the control of the discharge temperature. When the water is injected into the compressor chamber, it can directly absorb the superheat of the compressed water vapor and lower the temperature timely. However, when the water is injected into the suction side, it can separate and mix uniformly with the water vapor, which is better for absorbing heat in the compression process. The control of the discharge temperature has a delay as the water is injected into the suction side.

To compare the influence of different injection ports, an experimental investigation is carried out with internal water injection at 73℃ evaporation temperature. The result comparison is shown in Fig. 7(a) to (d), including the injected-water flow rate, power consumption, heating capacity, and COP. The result presented that the difference in system performance with different injection ports is not obvious and the injection ports have little influence on the system performance. This may due to that the compression process is faster than the heat transfer in the compression chamber, and most of the injected-water has not evaporated into steam when it was discharged from the compressor. So the separate and fogging degree of the injected-water has little influence, and the flow rate of the injected-water plays the most important role. However, more experimental investigations are needed to prove the results.

4.3. The influence of injection channels

To provide the steady of the injected water and keep the mass conversation of the water in the system, two injection lines are designed in the water vapor HTHP, external water injection from the outside and internal

water injection from the liquid collector. When the injected-water is from the outside, the temperature, pressure

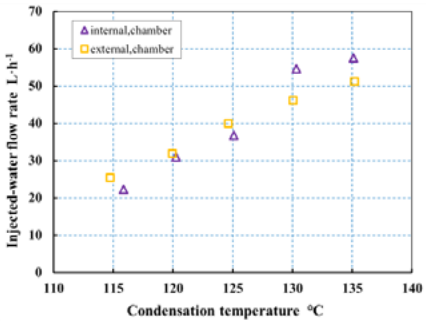


Fig. 8(a) Injected-water flow rate comparison

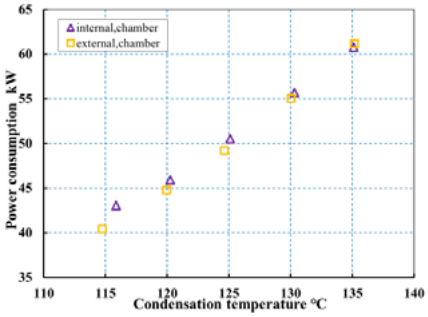


Fig. 8(b) Power consumption comparison

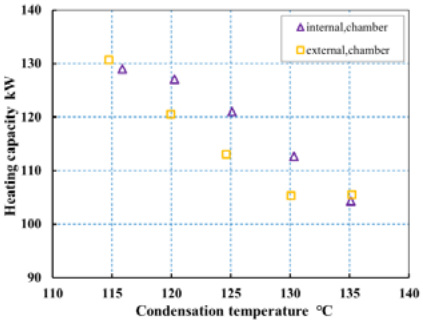


Fig. 8(c) Heating capacity comparison

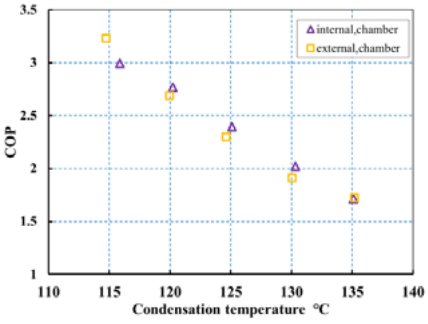


Fig. 8(d) COP comparison

Fig. 8. The performance comparison of the water vapor HTHP with different injection channels

and flow rate of the injected-water are controlled easily, which is good for the steady operation of the heat pump. However, external water injection will lead to an increase in the working fluid in the system, and destroy the balance of long-time operation. In this experimental investigation, to keep the balance of the water refrigerant in the system with the external water injection, some water will be discharged from the liquid collector. When the injected-water is from the liquid collector, the system working fluid is conversation and the flow rate of injected-water will increase simultaneously with the increase of the condensation temperature. It can realize the self-adjustment of injected-water and discharge temperature of the system. However, the temperature and pressure of the injected-water are changed with the condensation temperature.

The experimental investigation is carried out with different injection channel at 73℃ evaporation temperature. The result comparison is shown in Fig. 8(a) to (d), including the injected-water flow rate, power consumption, heating capacity, and COP. The result presented that the difference of injected-water flow rate and power consumption with different injection lines is not obvious. However, the heating capacity and COP of the two injection line systems are different. The internal injection system has better heating capacity and COP, which may due to the higher temperature of the injected-water.

5. Conclusions

Water vapor HTHP is a significant vapor compression heat pump with a high output temperature. The theoretical simulation results show that compared with new HFO and HC refrigerant and traditional HFC refrigerant, R718 has better performance when the condensation temperature is above 100oC. What's more, with the increasing of the condensation temperature, the simulation COP and volumetric heating capacity of water vapor HTHP increases and the compression ratio of the heat pump decreases, which means water vapor HTHP is more suitable for higher temperature application fields. Its start-up and dynamic performance

present that this heat pump can reach steady-state in 10 minutes and water injection can effectively decrease the discharge temperature. The internal injection line can realize the self-adjustment of injected-water and discharge temperature. When the opening of the injection valve is fixed, with the increasing of the condensation pressure, the flow rate of injected-water also increased to control the discharge temperature. When the pressure adjustment of the injected-water was failure and the discharge temperature was higher than the saturation temperature, the opening of the injection valve will permit more injected-water to control the discharge temperature. Different injection ports have little influence on heat pump performance. However, the different injection channels have influence on the heat pump performance, especially on the heating capacity. So it is very significant to design a suitable water vapor heat pump cycle with the best injection method.

6. Copyright

By submittal of his or her full paper to the Agency for the 13th Heat Pump Conference, the author(s) assumes full responsibility for ensuring that his or her paper does not infringe on another party's intellectual property rights, which include copyright and agree that the paper has not previously been submitted for publication elsewhere. Furthermore, the author, by submittal of his or her conference paper to the conference, grants publishing rights of that paper to the Agency for the 13th Heat Pump Conference, which may:

1. Publish or arrange to publish the paper as part of the Conference proceedings,
2. Copy and distribute the paper in its entirety in print and electronic form, and
3. Copy and distribute excerpts from the paper.

Acknowledgments

This research was supported by the National Natural Science Foundation of China (51706131), the National Key R&D Program of China (2016YFB0601200) and Fundamental Research Funds for the Central Universities (18X100040029). The authors gratefully acknowledge the financial support from the Research Council of Norway and user partners of HighEFF (Centre for an Energy Efficient and Competitive Industry for the Future, an 8-year Research Centre under the FME-scheme)

References

[1] Arpagaus C, Bless F, Uhlmann M, Schiffmann J, Bertsch SS. High temperature heat pumps: Market overview, state of the art, research status, refrigerants, and application potentials. Energy 2018;152:985-1010.
[2] Chamoun M, Rulliere R, Haberschill P, Berail JF. Water vapour as refrigerant for a new high temperature heat pump. Japanese Journal of Radiological Technology 2011;49:1879-87.
[3] Larminat PD, Arnou D, Le Sausse P, Clunet F, Peureux JL. A high temperature heat pump using water vapor as working fluid. 11th IIR Gustav Lorentzen Conference on Natural Refrigerants. China: Hang Zhou, 2014, p.857-64.
[4] Bamigbetan O, Eikevik TM, Nekså P, Bantle M, Schlemminger C. Theoretical analysis of suitable fluids for high temperature heat pumps up to 125 °C heat delivery. International Journal of Refrigeration 2018;92:185-95.
[5] Schlemminger C, Starheim Svendsen E, Steffanussen Foslie S, Bantle M, Bamigbetan O, Neksa P. Performance of high temperature heat pump for simultaneous and efficient production of ice water and process heat. The 25th IIR International Congress of Refrigeration. Montreal, Canada 2019.
[6] Hu B, Wu D, Wang LW, Wang RZ. Exergy analysis of R1234ze(Z) as high temperature heat pump working fluid with multi-stage compression. Frontiers in Energy 2017;11:493-502.
[7] Helminger F, Hartl M, Fleckl T, Kontomaris K, Pfaffl J. Hochtemperatur Wärmepumpen Messergebnisse einer Laboranlage mit HFO-1336MZZ-Z bis 160°C Kondensationstemperatur. 14th Symposium Energieinnovation. TU Graz 2016. p.1-20.
[8] Bamigbetan O, Eikevik TM, Nekså P, Bantle M, Schlemminger C. Experimental investigation of a prototype R-600 compressor for high temperature heat pump. Energy 2019;169:730-8.
[9] Bamigbetan O, Eikevik TM, Nekså P, Bantle M, Schlemminger C, Dallai M. Experimental investigation of a hydrocarbon piston compressor for high temperature heat pumps. 24th international compressor engineering conference. West Lafayette 2018. p.S0140700718301750.

[10] Kondou C, Koyama S. Thermodynamic assessment of high-temperature heat pumps using Low-GWP HFO refrigerants for heat recovery. International Journal of Refrigeration 2015;53:126-41.
[11] Arpagaus C, Kuster R, Prinzing M, Bless F, Uhlmann M, Buchel E, et al. High temperature heat pump using HFO and HCFO refrigerants - system design and experimental results. The 25th IIR International Congress of Refrigeration. Montreal, Canada 2019.
[12] Arpagaus C, Prinzing M, Kuster R, Bless F, Uhlmann M, Schiffmann J, et al. High temperature heat pumps - Theoretical study on low GWP HFO and HCFO refrigerants. The 25th IIR International Congress of Refrigeration. Montreal, Canada 2019.
[13] Wu D, Hu B, Yan H, Wang RZ. Modeling and simulation on a water vapor high temperature heat pump system. Energy 2019;168:1063-72.
[14] Wu D, Hu B, Wang RZ. Theoretical and experimental investigation on a very high temperature heat pump with water refrigerant. The 25th IIR International Congress of Refrigeration. Montreal, Canada 2019.
[15] European Commission. Regulation (EU) No 517/2014 of the European Parliament and of the Council of 16 April 2014 on fluorinated greenhouse gases and repealing Regulation (EC) No 842/2006. In: Union TEPaTCotE, editor. Europe: European; 2014.
[16] Mclinden MO, Kazakov AF, Brown JS, Domanski PA. A thermodynamic analysis of refrigerants: Possibilities and tradeoffs for Low-GWP refrigerants International Journal of Refrigeration 2014;38:80-92.

13th IEA Heat Pump Conference
April 26-29, 2021 Jeju, Korea

Benefits and reliability of air-to-water heat pumps in residential applications, using R-290 refrigerant and an alternative design solution to guarantee high safety with standard components.

Sergio Maria Capanelli*

Carel Industries S.p.A., Via dell'Industria 11, 35020 Brugine (PD), Italy

Abstract

The optimisation of energy consumption, the search for higher system efficiency and the need to reduce CO_2 emissions are driving the heat pump market, especially in residential applications. In EMEA especially, the need to switch to alternative refrigerants is changing the criteria for selecting components and developing projects. Most of the market trends have already identified flammable refrigerants as the way to solve compliance issues, while at the same time raising new issues regarding usability and reliability of potentially explosive devices in residential systems. Unit and component manufacturers are starting to work together in order to develop affordable and reliable solutions, not only improving component technologies and their mounting in the unit, but working closely together right from the start of the project.
Here below we describe an example of a fruitful collaboration for the development of an R-290 air-to-water heat pump, where accurate unit design, experience as HVAC component and heat pump manufacturers, have led to the development of a product with the highest performance in terms of efficiency and reliability, meeting all the standards for the use of flammable refrigerants on the European residential heating market.

Keywords: heat pumps; R-290; safety; DC; EEV;efficiency

1. Introduction

The Kigali amendment to the Montreal Protocol [1] entered into force on 1 January 2019, and was aimed at phasing down hydrofluorocarbons (HFCs) by cutting their production and consumption, so as to reduce so-called direct CO_2 emissions. However, actions to reduce the use of HFC refrigerants had already started in most developed countries. In the European Union, F-gas regulations [2] were published in 2014, establishing restrictions to the use of HFC refrigerants according to their global warming potential (GWP) and introducing the concept of quota, which refers to a reduction in the admissible production and import of HFCs in Europe over time. This has already led to an increase in prices and a decrease in the availability of high GWP refrigerants such as R-410A, driving the use of alternatives with a much lower GWP.

Lower GWP alternatives to R-410A for heat pumps include R-290 (propane), a high efficiency natural refrigerant with very a low GWP and zero ODP. The only drawback is its flammability, being in group A3 in accordance with ASHRAE Standard 34 [3]. IEC 60335-2-40 [4] specifies particular requirements for electrical heat pumps when using flammable refrigerants, updated on April 2018, with different requirements for systems depending on the propane charge. For instance, additional mechanical ventilation is compulsory for systems with between 1 kg and 5 kg of propane.

Efficiency is currently another important subject in standards, which impact both the reduction of indirect CO_2 emissions and the electricity bill. Ecodesign and Energy Labelling Directives in Europe are very active in the definition of new regulations for energy-using and energy-related products. There are two Ecodesign regulations that include the requirements for different types of heat pumps: ENER Lot 1 [5] and ENER Lot 21[6]. Both of these, in line with regulations for other HVAC/R applications, establish seasonal energy

* Author's contact tel.: +39 049 971 6616
E-mail address: sergio.capanelli@carel.com.

efficiency limits, thus taking into account the variations in outside air temperature over the year. This brings more precision to the procedure and more advantages from the use of variable speed technology, which is able to adapt energy consumption to the needs of the application. The Energy Labelling regulation for heat pumps [7] includes space heaters, combination heaters, packages of space heater, temperature control and solar device, as well as packages of combination heater, temperature control and solar device. The second stage of this Energy Labelling regulation came into force on 26 September 2019, when new energy labels for classes A+++ to D were required.

In this context, accurate unit design and choice of components plays an essential role when developing a heat pump, in order to optimise energy consumption and reduce total CO_2 emissions, while ensuring safety. The aim of this project was to develop an R-290 air-to-water residential heat pump with high performance, meeting all the required safety and usability goals for the use of flammable refrigerants on the European residential heating/cooling market.

2. Description of the project

This project was completed by our company in collaboration with a European customer, and lasted almost three years, including component selection, unit design, performance testing, certification, field testing and start of production. The field tests and most of the data taken outside of the laboratory referred to an area in central Germany area, with an annual average temperature of 9°C.

The unit described is an air-to-water heat pump, comprising a packaged outdoor unit, connected via fluid piping to an indoor unit equipped with a distribution system for space heating and cooling, and a water tank for domestic hot water storage.

The outdoor unit includes a refrigerant circuit equipped with variable-speed DC scroll compressor and electronic expansion valve.

Table 1 shows the other main characteristics of the unit:

Table 1. Summary of heat pump characteristics

Heat pump characteristic	Value
Refrigerant	R-290
Power supply	400V 3-phase
Heating capacity (A2/W35)	1.9 - 7 kW
Cooling capacity (A35/W18)	2.3 - 7 kW

The unit is also equipped with an electric heater for auxiliary use, for example to reach a water temperature of 70°C in the event of system request, or for use as backup, to guarantee continuous heating service for the end user even in the event of a unit fault. This heater was not activated during the comparison tests.

3. Test results

3.1. Comparison with R-410A unit

To perform this comparison test, an existing unit equipped with R-410A refrigerant and with the same nominal heating capacity as the heat pump studied (7 kW) was used as reference. The sample is a standard unit already available on the market, coupled with an indoor unit for fluid management and distribution. The scheme can be seen in Fig.1. In this section, for brevity, the R-290 unit is called “Unit A” and the one with R-410A “Unit B”. To perform the tests, we used the same indoor unit for both Unit A and Unit B. The data used for this comparison between the two units was acquired by certification testing laboratories. The characteristics are summarised in Table 2.

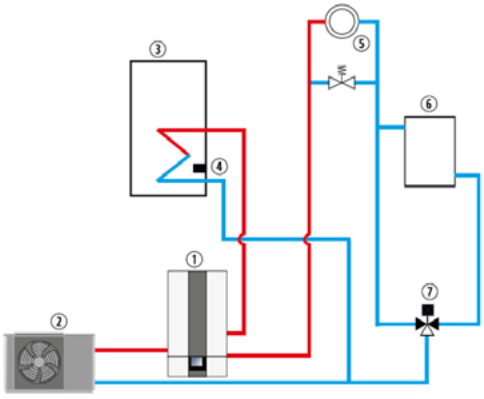


Fig. 1. Diagram of the fluid and distribution system used for the comparison test
1.Indoor unit | 2.Outdoor unit | 3.Hot water tank | 4.Storage tank sensor | 5.Heating circuit | 6.Intermediate water tank | 7.Three-way heating / cooling switching valve

Table 2. Summary of heat pump Unit A and Unit B characteristics

Heat pump characteristic	Unit A	Unit B
Refrigerant type / GWP	R-290 / 3	R-410A / 2088
Refrigerant charge	3.1 kg	2.15 kg
CO_2 equivalent	0.009 t	4.49 t
Heating operating limits (water)	+20°C to +70°C	+20°C to +55°C
Heating operating limits (air)	-22°C to +40°C	-20°C to +35°C
Cooling operating limits (water)	+7°C to +30°C	+7°C to +20°C
Cooling operating limits (air)	+10°C to +45°C	+10°C to +45°C

The most striking difference is the GWP value, i.e. the quantity of CO_2 that can be emitted into the environment. Considering that the two units have comparable power consumption (at -7°C air temperature, with a heating capacity of 6 kW, consumption of Unit A is 2.15 kW, and consumption of Unit B is 2.28 kW), the much lower GWP value makes Unit A the best solution to meet the emissions reduction requirements of the international agreements and regulations mentioned above.

Fig.2, Fig.3 and Fig. 4 show a comparison between the different efficiency levels in different test conditions.

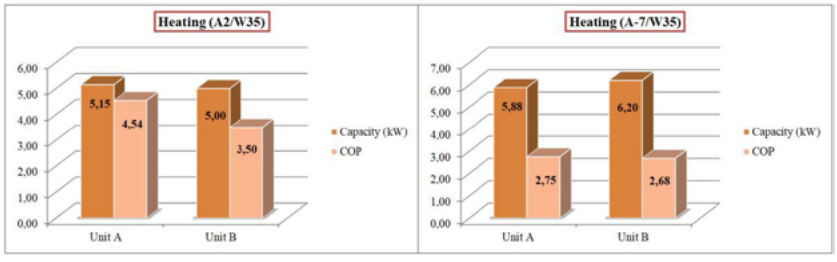


Fig. 2. Comparison test in heating mode. Nominal performance according to EN14511.

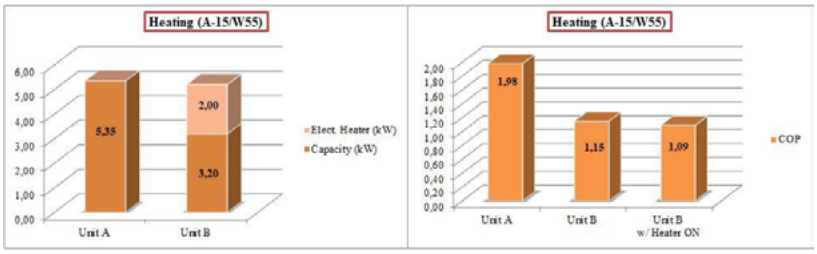


Fig. 3. Comparison test in heating mode with low air temperature.

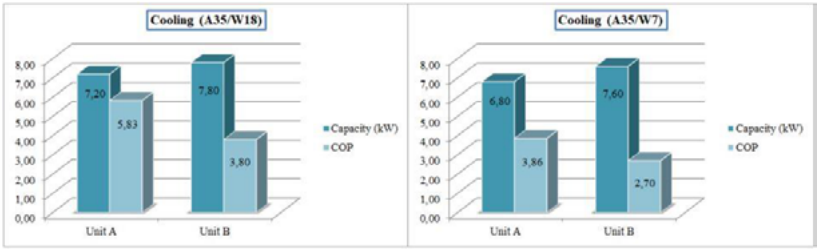


Fig. 4. Comparison test in cooling mode. Nominal performance according to EN14511.

The results shown in Fig. 2 indicate that, in both test conditions, the two units have a virtually identical heating capacity. The efficiency value is higher in Unit A, both with air at -7°C (+ 3%) and above all at + 2°C (+ 30%).

A significant difference is seen in working conditions with a low outside temperature, specifically -15°C: the characteristics of the refrigerant and compressor on Unit A allow a higher heating capacity and better efficiency than Unit B, as shown in Fig.3.

The results shown in Fig. 2 indicate that in both test conditions the two units have a comparable heating capacity: a difference of 1.5% with A2/W35, and 2.5% with A-7/W35. The COP value is higher for Unit A in both cases: +3% with A-7, +30% with A2.

An additional test was performed with lower outside temperature conditions, in order to highlight how the use of R-290, compared with R-410A, can avoid an excessive reduction in unit heating capacity.

The results are shown in Fig. 3. In test conditions A-15/W55 (high supply water temperature in cold climate conditions), Unit A has a capacity of 5.35 kW, with a COP value of 1.98, while Unit B has a capacity of 3.2 kW (40% lower than Unit A) with a COP value of 1.15. The electric heater on Unit B needs to be switched on (2 kW) in order to reach a comparable heating capacity between the two units, reducing the difference in capacity to 3%. However, this leads to a further reduction in the COP of unit B, which drops from 1.15 to 1.09.

The results shown in Fig.4 are related to cooling mode.

The comparison tests show that cooling capacity is a little bit higher in Unit B, +3.8% with W18 and +5.2% with W7. On the other hand, the COP coefficient measured is significantly higher in Unit A, +35% with W18 and +29% with W7 There are two important factors to consider when evaluating the results:

- The air heat exchangers on Unit A and Unit B are different in terms of size, design and plastic or polypropylene components used to guide the air flow inside the unit. We can assume by looking at the nominal performance data for the two heat exchangers that the one used on Unit A is +14% more efficient than the one used on Unit B;
- Unit B is equipped with a single EEV, used in two-way flow configuration so as to support both heating and cooling mode. In fact, the EEV is sized to assist operation in heating mode, in order to have the necessary flow control precision in the most extreme environmental conditions, such as high water temperature production with a low outside air temperature.
  Unit A is equipped with 2 EEVs: one is used in heating mode, the other in cooling mode. The EEV

for cooling mode can ensure an increase of 30% in the maximum allowable refrigerant flow rate, but at the same time a loss in control precision at low opening: each step of movement can increasingly affect the amount of refrigerant in the evaporator.
In this way, the modulation range for each EEV can be sized for the specific operating mode: this is especially useful in cooling mode, when performance is often not fully optimised in order to favour heating mode, considered the main operating mode.

3.2. Considerations about the use of R-290

Thanks to the operating envelope of the R-290 compressor, the two most significant values of extended operating range concern heating mode. A higher outside air temperature limit allows the production of domestic hot water even in the most severe summer conditions.

The most significant value concerns the higher hot water supply temperature, which has three main benefits:

- Production of hot water can also be used for systems with high temperature distribution systems, such as radiators. This allows the use of the unit in installations where the use of R-410A is difficult due to problems with high condensing pressure.

- It is possible to produce hot water with a temperature higher than 50°C even with an outside temperature below -15°C, with better efficiency than with the currently used refrigerants.

- The possibility to reach an outlet water temperature of 65-70°C, when conditions are favourable, to perform anti-legionella treatment on the domestic hot water without activating the electric heater: this means high energy savings for the system and therefore a considerable increase in COP.

4. Safety measures

One of most challenging issues of this project was the safe use of the electronic controls, devices and components normally used in HVAC applications, but not certified for compliance with EN 60079:15 [8] and EN 60335-2:40.

Appliances shall be constructed so that any leaked refrigerant will not flow or stagnate so as cause a fire or explosion hazard in areas within the appliance and connected ducts where electrical components, which could be a source of ignition and which could function normal conditions or in the event of a leak, are fitted.

These components shall comply with one of the following conditions:

- Components should be placed inside an enclosure which complies with Clause 20 of IEC 60079:15-2010;
- A test of Annex FF of EN 60335-2:40 must be performed with a leak simulation test: with this method must be demonstrated that a potentially flammable gas mixture will not accumulate;
- Components are compliant with Clause 16 to 22 of IEC 60079-15:2010.

The most critical components were the electronic control board and the compressor speed drive: both components are certified and fully eligible to be used for general HVAC residential applications. However, the presence of components that could be identified as possible spark sources, for example the relay, does not permit the use of these devices in the open air in this kind of application.

The solution selected follows the first of the conditions listed above: create a dedicated metal enclosure of dimensions and features compatible with its positioning within the outdoor unit. The most critical points of the panel design, construction and component selection are described as follows.

4.1. Panel tightness

First, it was necessary to guarantee tight closing of the panel, in order to avoid hazardous amounts of gas accumulated in critical concentrations inside. This is an issue that may occur in the event of malfunctions and leakages.



Fig. 5. Details of fixing system for the panel enclosure.

Fig.5 shows the details of the panel enclosure. The cover is equipped with an inner gasket, positioned around the entire inside perimeter. When the cover is positioned, the inner gasket is aligned exactly with the edge of the panel (see image on the left in Fig. 5), and after placement and fixing by the screws inserted in the side brackets (image on the right in Fig. 5), the gasket is pressed down by 3 mm, around 50% of its thickness. The position of soldered bracket guarantees the correct pressure of the bottom part of the enclosure against the cover gasket without any specific screw torque value: this makes it possible to guarantee panel tightness with a faster industrialised process, and only a visual check is performed on the presence of all 8 screws.

Furthermore, the size of the different cables needed for control of the unit may be the source of holes or openings that compromise insulation of the enclosure, creating a possible pathway that flammable gas can pass through and accumulate inside the enclosure: communication cables, sensors, driver cooling fan, compressor connection and panel power supply in general.



Fig. 6. Details of the connection kits for cable glands.

All cables connecting components inside the panel with the outside devices pass through specific cable glands, as shown in Fig. 6. The image on the left shows the outer part of the kit, while on the right is the inside view. The large rectangular gland with 8 subsections is a specific custom part, created to satisfy the specific combination of cables needed for these units. However, the gland comprises a main black part and inner grey parts: these are all standard components. This solution guarantees compliance of the enclosure with Clause 20 of IEC 60079:15-2010: the required degree of insulation is a subset of requirements for IP54 protection.

Except for the screw holes used for this gland and other holes made for compressor drive pass-through mounting or another specific cable glands, no other drilling operations are performed when manufacturing the enclosure: all of the screws present are welded directly onto the inside surface of the enclosure, in order to avoid further possible causes of loss of tightness.

At the end of enclosure manufacturing process, a negative pressure test is performed. During this test, automatic equipment is connected via a silicone pipe to the inside of the enclosure: the enclosure is de-pressurised until reaching a “pressure test setting”. The equipment then stops taking in air and starts checking the inside pressure value, so as to measure the volume of air that flows into the enclosure to rebalance the pressure. To guarantee compliance, the volume should be lower than 1.8 l/min, a value defined in relation to the size of the enclosure.

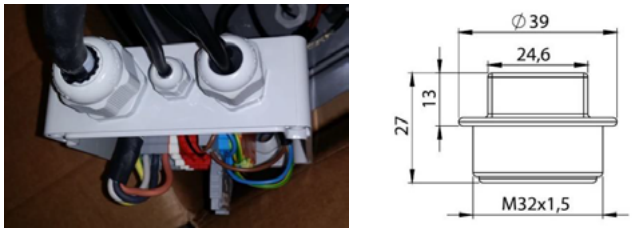


Fig. 7. Example of cable gland usage and selected model to satisfy requirements for correct enclosure usage in a residential heat pump.

Fig. 7 shows the junction box for power supply and serial communication connections. This box has been made separately from the main electrical panel as it must be guaranteed that installers or untrained personnel cannot open the enclosure in the field, especially during installation. This junction box is the connection point when placing the unit, in order to allow power connection to the supply line and serial connection for communication between the outdoor unit, where the enclosure is placed, and the indoor unit for fluid management, equipped with the control display.

For the junction box, the designers also selected a specific electrical box and cable glands compatible with this application, but at the same time easily purchasable on the market.

Table 3 shows some details of the connectors.

Table 3. Connector specifications.

Material	Polycarbonate (PC)
Flame class	UL94-V0, self-extinguishing
IP rating	IP54, with gasket and correct selection of the cable grommets
Temperature range	-30°C to +100°C
Properties	Halogen-free, silicone-free

4.2. Panel cooling

As the panel is sealed, it is necessary to guarantee correct heat dissipation from the panel in order to keep the contained devices in safe conditions. The compressor driver, due to its power consumption when operating, is the “hottest” critical point. The solution adopted was to use a driver equipped with pass-through ventilated heat sink system. In order to guarantee the air flow across the finned heat sink, two small fans are mounted on the front. The fan motors are insulated and compliant with the required clauses of the standards, so as to be used outside of the panel.

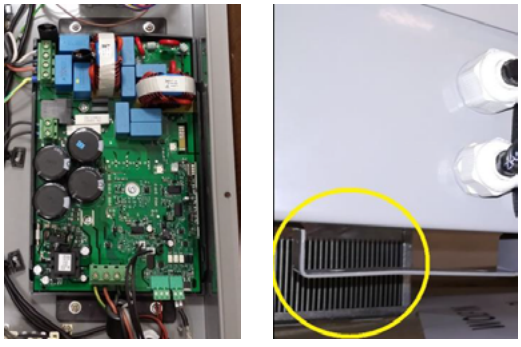


Fig. 8. Inverter drive placement in the panel and detail of pass-through heat sink.

To obtain this configuration, we used a standard device already equipped with a gasket underneath the moulded plastic base, which ensures tightness after fixing the drive to the panel using the special brackets. The only significant change was to use a plastic moulding for the base without holes for the cooling fan cables: the cables were passed through dedicated cable glands, of the type described above.

Using this specific base without holes and mounting the driver with correct positioning of the gasket around the hole, the tightness of the enclosure and IP54 protection were guaranteed when testing the complete panel solution.

With this equipment, the unit was tested up to the maximum outside air temperature allowed for operation (cooling mode): at 40°C the air surrounding electronic components does not exceed the limit threshold of 65°C. These values are compatible with the temperature operating range of the electronic components placed inside the enclosure.

5. Conclusions

The results of these tests, carried out in the field and in the laboratory, have shown how the use of R-290 refrigerant in heat pumps with packaged outdoor units is a fully usable, industrialised, efficient and safe solution. The high efficiency, low GWP and high energy yield values compared to traditional refrigerants, make these units optimal devices to reduce power consumption, increase system efficiency and contribute to a reduction in CO_2 emissions.

The goal for the near future is to expand the range of units in order to cover a greater variety of needs, maintaining the same structure presented above. At the same time, we are working, by mutual agreement with our customers and certification bodies, on further certification of standard components that can be used in specific HVAC applications in the presence of flammable refrigerants.

Acknowledgements

This project was carried out in partnership between WOLF Gmbh and Carel Industries S.p.A. The author wold like to thank WOLF Gmbh (in particular Mr. Siegmund) for information on the unit and for allowing publication of some of the research results.

Nomenclature

COP:	Coefficient Of Performance
EEV:	Electronic Expansion Valve
GWP:	Global Warming Potential
HFC:	HydroFluoroCarbon
HVAC:	Heating Ventilation Air Conditioning
IEC:	International Electrotechnical Commission
IP:	International Protection
ODP:	Ozone Depletion Potential

References

[1] Handbook for the Montreal Protocol on Substances that Deplete the Ozone Layer, Thirteenth edition (2019): 898-909.

[2] Regulation (EU) No 517/2014 of the European Parliament and of the Council of 16 April 2014 on fluorinated greenhouse gases and repealing Regulation (EC) No 842/2006; Official Journal of the European Union; 150-195.

[3] Standard 15-2019 (packaged w/ Standard 34-2019) -- Safety Standard for Refrigeration Systems and Designation and Classification of Refrigerants (ANSI Approved).

[4] International Standard 60335-2-40, Household and similar electrical appliances- Safety- Part 2-40: Particular requirements for electrical heat pumps, air-conditioners and dehumidifiers; Edition 6.0; 2018-01.

[5] Commission Regulation (EU) 2015/1095 of 5 May 2015 implementing Directive 2009/125/EC of the European Parliament and of the Council with regard to ecodesign requirements for professional refrigerated storage cabinets, blast cabinets, condensing units and process chillers; Official Journal of the European Union; 177-19.
[6] Commission Regulation (EU) 2016/2281 of 30 November 2016 implementing Directive 2009/125/EC of the European Parliament and of the Council establishing a framework for the setting of ecodesign requirements for energy-related products, with regard to ecodesign requirements for air heating products, cooling products, high temperature process chillers and fan coil units; Official Journal of the European Union; 346-1.
[7] Commission Delegated Regulation (EU) No 811/2013 of 18 February 2013 supplementing Directive 2010/30/EU of the European Parliament and of the Council with regard to the energy labelling of space heaters, combination heaters, packages of space heater, temperature control and solar device and packages of combination heater, temperature control and solar device; Official Journal of the European Union; 239-1.
[8] IEC 60079-15:2017, Requirements for the construction, testing and marking for Group II electrical equipment with type of protection “n” which includes; sealed devices “nC”, hermetically sealed devices “nC”, non-incendive components “nC” and restricted breathing enclosures “nR” intended for use in explosive gas atmospheres; Edition 5.0; 2017-12-08

13th IEA Heat Pump Conference
April 26-29, 2021 Jeju, Korea

Clarification of the disproportionation reaction of HFO-1123 and evaluation of the reaction inhibitor

Zhihua Zhang, Makoto Ito, Chaobin Dang, Eiji Hihara *

Dept. of Human & Engineered Environmental Studies, University of Tokyo
Kashiwa, 277-0882, Japan

Abstract

The hydrofluoroolefin (HFO) refrigerant 1,1,2-trifluoroethene (HFO-1123) has a very low global warming potential (GWP) and ozone depletion potential (ODP); thus, it is proposed as a next-generation refrigerant. However, a short circuit of the motor under high-temperature and high-pressure conditions may cause a disproportionation reaction of HFO-1123. Therefore, to enable commercialization of HFO-1123 in split air conditioners, it is necessary to develop a technology to suppress the disproportionation reaction. In this study, disproportionation experiments were performed under various temperature and pressure conditions and changes due to these different pressure, temperature, and input energy were recorded. Conventionally, fusing and discharge methods are employed for ignition in experiments. Using the two ignition methods, we experimentally determined the threshold pressure of the disproportionation reaction and compared the differences in the reaction limits of the ignition methods. The disproportionation reaction was photographed with a high-speed camera, and the flame temperature was measured using the two-color temperature radiometry method (H & B method). The experiment was performed using difluoromethane (R32) and trifluoroiodomethane (R13I1) as disproportionation reaction inhibitors, and the suppression effect of the disproportionation reaction was evaluated.

Keywords: Refrigeration; HFO-1123; Reaction inhibitor; Disproportionation reaction.;

1. Introduction

In the fields of refrigeration and air conditioning, the development of alternative refrigerants such as hydrofluorocarbons (HFCs) has been promoted to prevent the depletion of the stratospheric ozone layer by chlorofluorocarbon (CFC) and hydrochlorofluorocarbon (HCFC) refrigerants. However, although the HFC refrigerant has a low ozone depletion potential (ODP), it has been regulated by the Global Change Framework Convention as a causative material for global warming due to its high global warming potential (GWP). Later, the Kigali amendment to the Montreal Protocol calling for the phase-down of HFC refrigerants was adopted in 2016; subsequently, UN member states were required to switch to low-GWP refrigerants, such as hydrofluoroolefins (HFOs) and natural refrigerants.

Trifluoroethene (HFO-1123, CF_2CHF) has a very low GWP, as shown in Table 1, because it has a short lifespan in the atmosphere. Therefore, it is expected to be a next-generation refrigerant in the fields of refrigeration and air conditioning. However, HFO-1123 is known to cause a disproportionation reaction under high-temperature and high-pressure conditions, as shown in Eq. (1). When energy is applied due to equipment failure, the generated flame propagates, and the pressure and temperature may increase significantly due to the generated heat. This is not a combustion reaction that requires oxygen, but a self-decomposition reaction.

Table 1. GWP and ODP of typical refrigerants (HFC-410A, HFC-32, and HFO-1123)

	HFC-410A	HFC-32	HFO-1123
ODP	0	0	0
GWP	2090	675	0.3

$$2CF_2=CHF \rightarrow CF_4+3C+2HF+500kJ \quad (1)$$

To put HFO-1123 to practical use, it is necessary to clarify the conditions under which the disproportionation reaction occurs and to suppress the reaction because the occurrence of a disproportionation reaction is dangerous. It is also effective to add a reaction inhibitor. There are two possible mechanisms for inhibiting the disproportionation reaction of HFO-1123 by the addition of substances.

(1) The thermal dilution effect of mixing inactive gases.

(2) The suppression of disproportionation reaction propagation by trapping radicals of the reaction intermediate products.

In this study, the conditions for the disproportionation reaction were investigated experimentally for the composition of HFO-1123 mixed with two types of inhibitors, as shown in the triangular diagram in Fig. 1. Table 2 summarizes the test gas composition, where R32 stands for difluoromethane and R13I1 denotes trifluoroiodomethane. The mixed composition of R32 was selected such that the GWP of the gas mixtures was 150 or 200. The initial temperature of the test gas was fixed at 150 °C, and the initial pressure was changed to determine whether the disproportionation reaction propagated. When the initial pressure is low, the flame does not propagate, but when it exceeds a certain pressure, it propagates. As the pressure increases and the density of the HFO-1123 molecules increases, the reaction continues, and the flame propagates. The pressure at the boundary where the flame propagates was examined. To investigate the mechanism of the reaction inhibitor, the flame temperature was measured, and a qualitative analysis of the reaction gas was performed using gas chromatography–mass spectrometry (GC–MS).

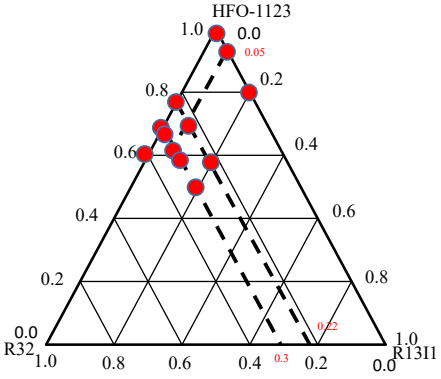


Fig. 1. Ternary plot of the compositions of the test gas mixtures

Table 2. Compositions of the test gas mixtures

No.	GWP of mixture	HFO-1123 (mass%)	R32 (mass%)	R13I1 (mass%)
1-1		100		0
1-2	< 10	95	0	5
1-3		80		20
2-1		78		0
2-2	150	72.4	22	5.6
2-3		58		20
3-1		70		0
3-2		68		2
3-3	200	65	30	5
3-4		60		10
3-5		50		20
4-1	270	60	40	0

i

2. Experimental method

Figure 2 shows the experimental apparatus used for observing the disproportionation reaction of HFO-1123 and for investigating the pressure boundary where the disproportionation reaction was propagated. The experimental equipment consists of a stainless-steel pressure vessel, an ignition source, a vacuum pump, a refrigerant vessel, and a safety valve. After the pressure and temperature of the gas supplied to the pressure vessel were set at certain values and stabilized, energy was applied, and the disproportionation reaction was initiated. Subsequently, it was determined from the pressure change whether the reaction propagated or not. At the same time, the movement of the flame was observed from the two upper and lower observation windows installed in the pressure vessel.

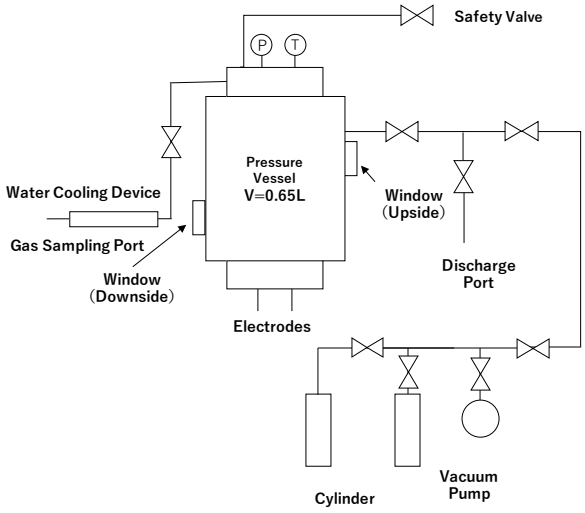


Fig. 2. Outline of the experimental apparatus

In previous studies, energy was introduced into the pressure vessel by fusing thin molybdenum wires; however, in this study, we switched to the arc discharge method. This is because the arc discharge is similar to a short circuit that may occur in the compressor motor of air conditioners. The arc discharge is a continuous large current generated between the electrodes at a low voltage, unlike a spark discharge, which is a discontinuous discharge generated between the electrodes at a high voltage.

In this experiment, a part of two copper spiral electrodes partially overlapped, and a 220 V DC was applied between the electrodes for 1.5 ms to generate an arc discharge between the spiral electrodes, and energy was supplied into the pressure vessel. The input energy was calculated from the results of the time-integrated changes in the voltage and current.

Figure 3 shows the current–voltage (I–V) curve of an ideal discharge that occurs in air. Because the high insulation resistance of the refrigerant gas hindered the discharge, the I–V curve is as shown in Fig. 4. The input energy during the discharge in air was in the range of 16–18 J, and it was in the range of 20–24 J during the discharge in the refrigerant after heating.

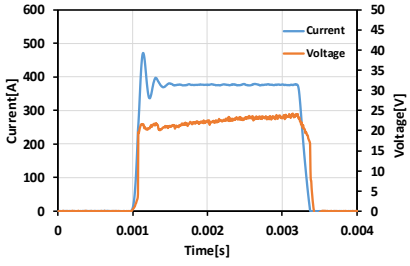


Fig. 3. I–V curve of the ideal discharge in air

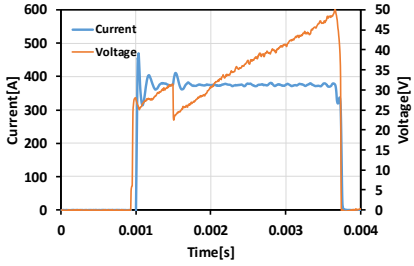


Fig. 4. I–V curve of the discharge in refrigerant

3. Experimental results

3.1 Ignition by fusing method

When the fusing method was employed for ignition, it was determined that the disproportionation reaction had propagated when a large pressure increase was measured; when the pressure increase was not measured, it was determined that the disproportionation reaction did not propagate. Figure 5 shows the results of the pressure boundary where the reaction propagates when the gas temperatures before the reaction were 100, 130, 150, and 170 °C. Although the disproportionation reaction was considered to propagate at a pressure above the solid line in Fig. 5, the boundary was stochastic and not deterministic.

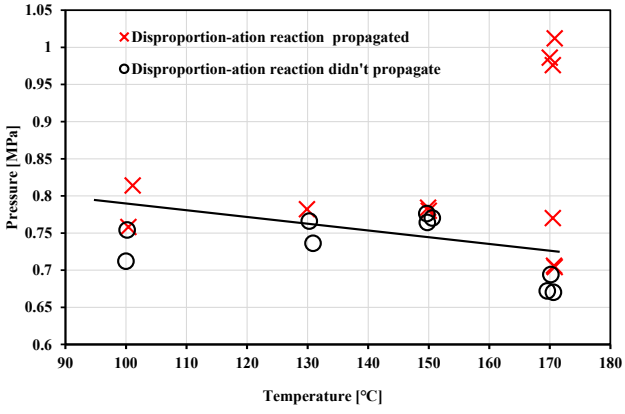


Fig. 5. Result of disproportionation reaction of HFO-1123 by fusing method

3.2 Ignition by discharge method

Compared with the fusing method, the discharge method could not easily determine whether the disproportionation reaction propagated as a result of the increase in pressure. In some cases, the pressure did

not increase even when a flame was observed, and the relationship between the flame propagation and pressure increase was unclear. In this study, we considered two criteria for determining the propagation of the disproportionation reaction of HFO-1123.

Judgment condition (1): When there is a sharp peak in the pressure change, as shown in Fig. 6, it is determined that the disproportionation reaction has propagated. If this condition is not satisfied, it is determined that the disproportionation reaction has not propagated even if a flame is observed from the observation window.

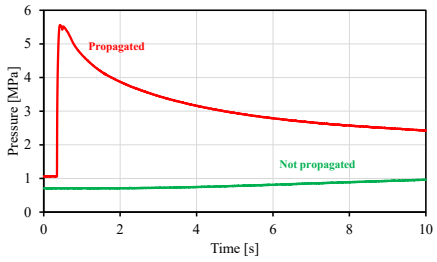


Fig. 6. Examples of the propagated and not propagated cases using judgment condition (1)

Judgment condition (2): Determine whether the reaction has propagated based on the pressure convergence value 10 s after ignition. When the pressure after 10 s exceeds the initial pressure by 1.5 times, it is determined that the disproportionation reaction has propagated.

Based on the judgment conditions described above, the pressure boundary at which the disproportionation reaction of HFO-1123 and gas mixtures propagate at a temperature of 150 °C was investigated.

3.3 Pure refrigerant HFO-1123

For the HFO-1123 refrigerant, the pressure boundary at which the disproportionation reaction propagated was investigated experimentally while maintaining a temperature of 150 °C. The pressure boundary was investigated based on the two judgment conditions described in Section 3.2. Figure 7 shows the pressure change after the voltage application. By observing the pressure change, it was found that the pressure waveform was divided into two cases: a sudden increase and a gradual increase. Even when the disproportionation reaction was considered not to have propagated when the fusing method was used (e.g., 150 °C and 0.70–0.76 MPa), an increase in the pressure was observed in the discharge method.

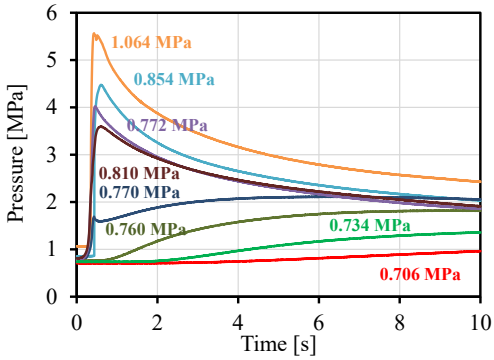


Fig. 7. Pressure curve of HFO-1123 after ignition

Figures 8 and 9 show the results of comparing the pressure boundary using the two judgment conditions and the pressure boundary using the fusing method. Based on the results of judgment condition 1, when the initial pressure is 0.772 MPa, the pressure increases stochastically with a peak, and when the initial pressure is 0.770 MPa, it increases stochastically gradually. The pressure condition at which the reaction propagated

was approximately 0.770 MPa. This is close to 0.780 MPa, which is the pressure boundary of the fusing method. Conversely, using judgment condition 2, the pressure boundary was approximately 0.75 MPa, which was slightly different from that of the fusing method. From the perspective of risk assessment, it is possible to prevent accidents due to compressor explosions by utilizing a pressure-relief valve if the pressure increases slowly. Hence, we considered that the speed of the pressure increase was more significant than the converging pressure and decided to use only judgment condition 1 to determine the pressure boundary.

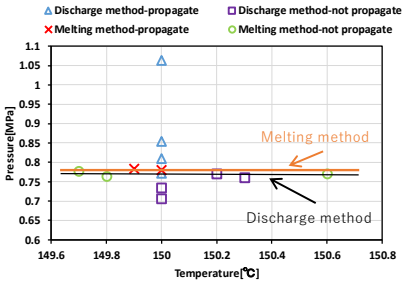


Fig. 8. Result using judgment condition (1)

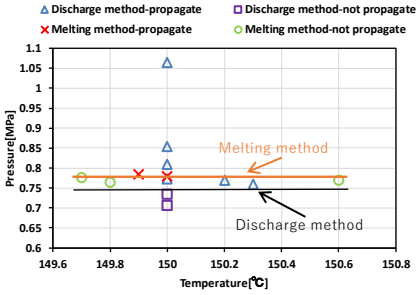


Fig. 9. Result using judgment condition (2)

3.4 Binary mixtures of HFO-1123 + R32 or R13I1

Experiments to determine the pressure boundary of the disproportionation reaction of gas mixtures containing HFO-1123, R32, and R13I1 were conducted using the discharge method at an initial temperature of 150 °C.

(1) Binary mixtures of HFO-1123 + R32

Mixing the R32 refrigerant with HFO-1123 is expected to lower the partial pressure of HFO-1123 and dilute the heat of the disproportionation reaction. The GWP of the mixed gases was set to 150 and 200 by mixing 22 mass% and 30 mass% of R32 (GWP 675), respectively. The test mixtures of HFO-1123 + R32 were named No. 2-1, No. 3-1, and No. 4-1 (Table 2).

Figure 10 shows the relationship between the initial pressure and the pressure increase of No. 2-1. The pressure boundary is between 0.82 and 1.05 MPa. When the concentration of R32 is 30 mass%, as shown in Figure 11, the pressure boundary of No. 3-1 is 1.54 MPa. When the concentration of R32 is increased to 40 mass% (No. 4-1), the pressure boundary is considered to be over 2.0 MPa.

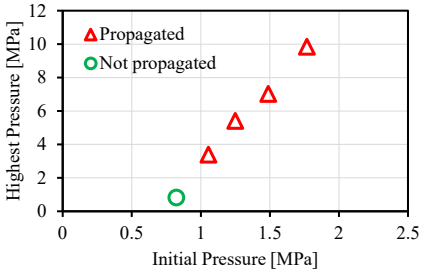


Fig. 10. Judgment map of reaction propagation for the gas mixture of HFO-1123 + 22 mass% R32 (No. 2-1)

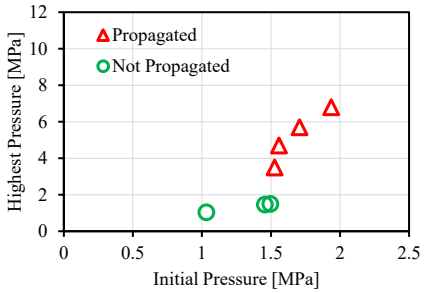


Fig. 11. Judgment map of reaction propagation for the gas mixture of HFO-1123 + 30 mass% R32 (No. 3-1)

(2) Binary mixtures of HFO-1123 + R13I1

R13I1 is a typical flame retardant and is often used as a fire extinguisher. It is also used in the non-flammable refrigerant R466A, developed by Honeywell. It is expected that iodine in the R13I1 molecule will trap the radicals generated during the disproportionation reaction. Because a small amount of addition is expected to have an inhibitory effect, mixed compositions of 5 and 20 mass% were used. The pressure boundary of the No. 1-2 results is shown in Fig. 12. The results show that when R13I1 is mixed at 5 mass%, the pressure boundary is approximately 0.92 MPa, and there is no dramatic reaction suppression effect. When the concentration of R13I1 was increased to 20%, as shown in Fig. 13, the pressure boundary of No. 1-3 decreased instead.

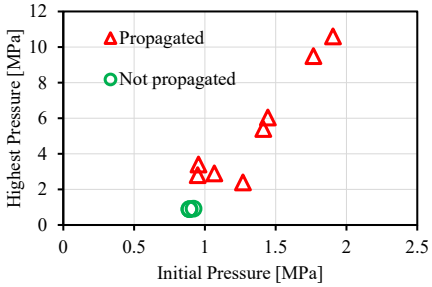


Fig. 12. Judgment map of reaction propagation for the gas mixture of HFO-1123 + 5 mass% R13I1 (No. 1-2)

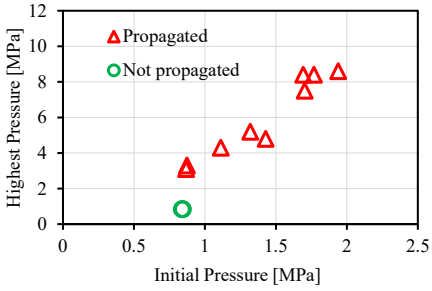


Fig. 13. Judgment map of reaction propagation for the gas mixture of HFO-1123 + 20 mass% R13I1 (No. 1-3)

3.5 Ternary mixtures of HFO-1123 + R32 + R13I1

As a result of the experiments with binary gas mixtures, in which R32 or R13I1 was mixed with HFO-1123, the suppression effect was not as great as expected. Therefore, experiments were conducted with ternary gas mixtures in which two types of inhibitors were mixed simultaneously. Figure 14 shows the results of the determination of gas mixture No. 3-3. The pressure boundary was between 1.54 MPa and 1.61 MPa. These results indicate that a synergistic effect can be obtained when the inhibitors with two types of inhibition mechanisms are mixed at the same time. In Fig. 15, when the concentration of R32 was 30 mass%, the pressure boundary increased to 2.36 MPa.

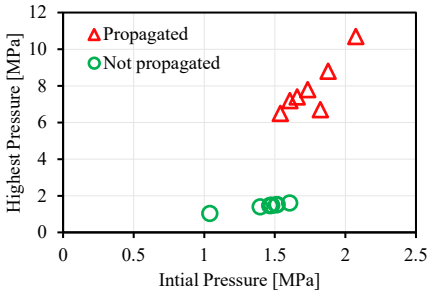


Fig. 14. Judgment map of reaction propagation for the gas mixture of HFO-1123 + 5.6 mass% R13I1 + 22 mass% R32 (No. 2-2)

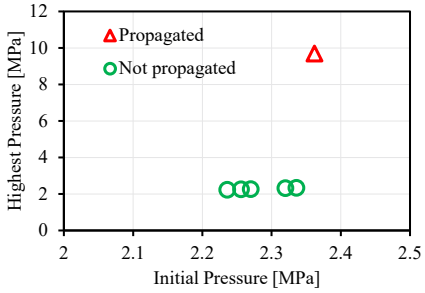


Fig. 15. Judgment map of reaction propagation for the gas mixture of HFO-1123 + 5 mass% R13I1 + 30 mass% R32 (No. 3-3)

3.6 Flame temperature measurement by the two-color method

Flame temperature is an important parameter when analyzing combustion phenomena using a thermal model. The disproportionation reaction is similar to the combustion reaction from the viewpoint of flame propagation. Thus, it would be beneficial to measure the flame temperature. Therefore, in this study, the flames caused by the disproportionation reaction were photographed with a high-speed camera from two observation windows installed at the top and bottom of the pressure vessel, and the flame temperature was analyzed using the two-color method. The flame of HFO-1123 taken from the upper window is shown in Fig. 16. The generated soot appears black, and the flame shines brightly. The shooting speed is 3000 f/s, and the exposure time is 100 μs.

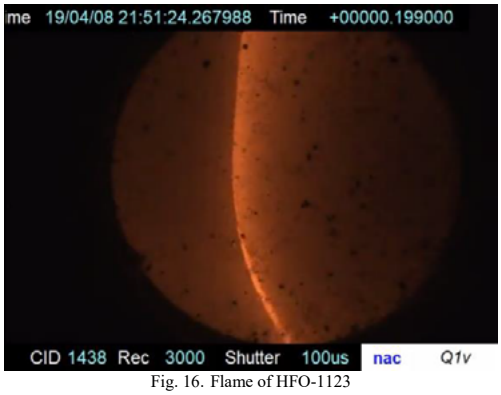
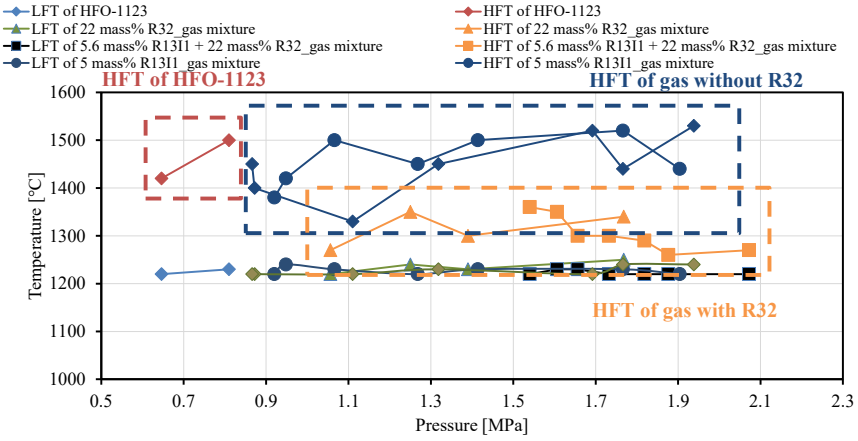


Fig. 16. Flame of HFO-1123

The flame temperature varies with a large distribution in place and time. In this study, the mode temperature of the flame was defined as the flame temperature, and the maximum and minimum values were analyzed. The results for pure HFO-1123 and the three types of gas mixtures are shown in Fig. 17.

The results of the flame temperature measurement show that the minimum flame temperature remains almost unchanged between 1200 and 1250 °C; however, the maximum flame temperature is divided into two groups, depending on whether or not R32 is included in the mixture. The maximum flame temperatures of HFO-1123 and the HFO-1123 + R13I1 mixture were 1400–1500 °C, whereas the maximum flame temperatures of the gas mixed with R32 were 1250–1350 °C. It is assumed that the decrease in the maximum flame temperature results from the thermal dilution effect of R32.



LFT: Lowest Flame Temperature HFT: Highest Flame Temperature

Fig. 17. Results of flame temperature analysis of the test gas mixtures

3.7 Qualitative analysis of the disproportionated reaction gas by GC–MS

In this study, when the disproportionation reaction propagated, the reaction gas was collected after water cooling, and a qualitative analysis of the gas composition was performed using GC–MS. Fig. 18 shows the composition analysis results of the reaction gas of HFO-1123. The reaction gas composition of the 22 mass% R32 gas mixture was almost the same as that of HFO-1123.

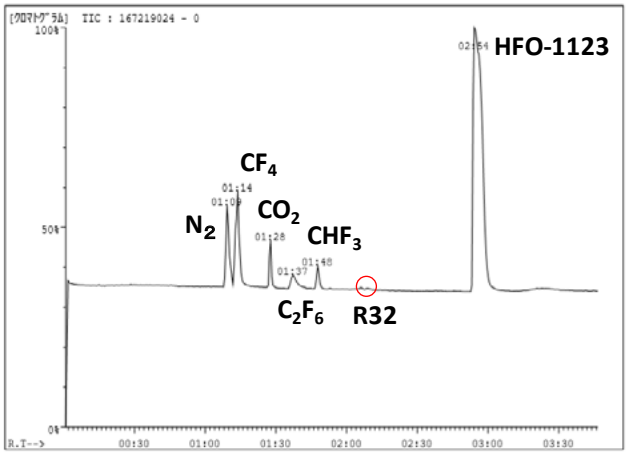


Fig. 18. Results of qualitative analysis of reaction gas of HFO-1123

The results of the qualitative analysis of the 5.6 mass% R13I1 + 22 mass% R32 + 72.4 mass% HFO-1123 gas mixture are shown in Fig. 19. A plurality of intermediate products could be detected in the reaction gas. This is presumed to be the result of the change in the disproportionation pathway caused by R13I1.

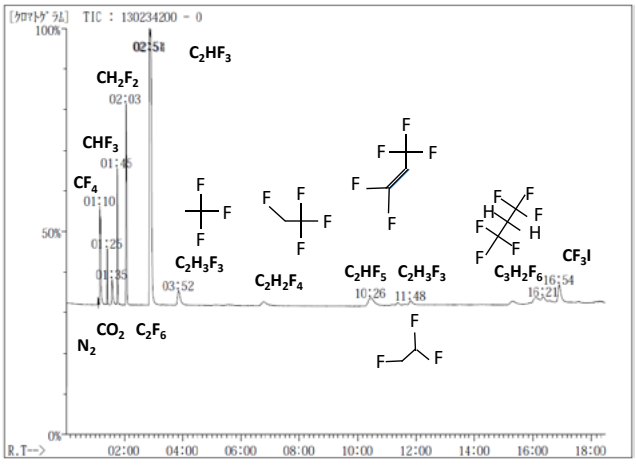


Fig. 19. Results of qualitative analysis of reaction gas of 5.6 mass% R13I1 + 22 mass% R32 + 72.4 mass% HFO-1123 mixture

4. Conclusion

In this study, the initial temperature was fixed at 150 °C, and the boundary was investigated of the initial pressure at which the disproportionation reaction of HFO-1123 and the gas mixtures was propagated. The pressure boundary of each gas mixture is illustrated in Fig. 20. The pressure boundary increased from 0.77 MPa to over 2.0 MPa by mixing with 40 mass% R32, which is expected to be suppressed by thermal dilution, and the pressure boundary increased to 0.92 MPa by mixing with 5 mass% R13I1, which is expected to be suppressed by radical trapping. The suppression effect of mixing only one type of inhibitor was not significant. However, in the case of the ternary gas mixed with inhibitors having two types of inhibition mechanisms simultaneously, an enhanced suppression effect could be obtained, and the pressure boundary increased to over 2.4 MPa (No. 3-5). In addition, to evaluate the suppression effect, the maximum and minimum values of the mode temperature of the flame were obtained using the two-color method, and the composition analysis of the reaction gas was also investigated using GC–MS. Consequently, it was found that R32 exerts a thermal dilution effect and R13I1 changes the reaction pathway.

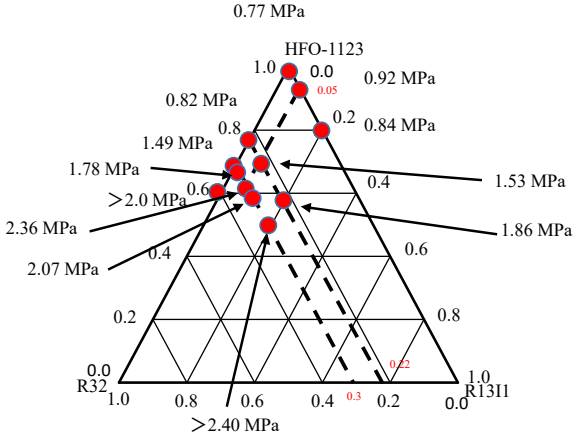


Fig. 20. Pressure boundary of each of the gas mixtures

Acknowledgments

The authors wish to express their gratitude to the New Energy and Industrial Technology Development Organization (NEDO) for the financial support of this study.

References

[1] Ito, M., Kurokawa, N., Dang, C., Hihara, E., 2018. Disproportionation reaction of HFO-1123 refrigerant. 17th International Refrigerant and Air Conditioning Conference at Purdue, July 9-12,2018
[2] Fukaya, H., Hayakawa, Y., Okamoto, H., Ueno, K., Otsuka, T., Theoretical study of disproportionation reaction of fluorinated ethylenes. Journal of Fluorine Chemistry, 200(2017), 133-141
[3] Otsuka, T., Ueno, K., Okamoto, H., Ippommatsu, M., and Dobashi, R., 2018. Analysis of disproportionation process of trifluoroethylene using high power spark ignitions over 5 J. Journal of Loss Prevention in the Process Industries, 51(2018), 36-41
[4] Otsuka, T., Ueno, K., Okamoto, H., Ippommatsu, M., and Dobashi, R. (2018). Analysis of disproportionation process of trifluoroethylene mixtures. Journal of Loss Prevention in the Process Industries, 54(2017), 179-182.
[5] Munkhbayar B., James B.B. Rate coefficient for the gas-phase OH+CHF=CF2 reaction between 212 and 375 K. International Journal of Chemical Kinetics, 48(2016), 714-723. DOI 10.1002/kin.21027(2016)
[6] Otsuka, T., Okamoto, H., Ueno, K., Ippommatsu, M., and Dobashi, R., Development of control method of HFO-1123 disproportionation and investigation of probability of HFO-1123 disproportionation. AGC Research Report, 68(2018)

13th IEA Heat Pump Conference
April 26-29, 2021 Jeju, Korea

Modeling of Megawatt R1233zd(E) High Temperature Heat Pump System

JiaTong Jiang[a], Bin Hu[a,*], R.Z. Wang[a], Hua Liu[a,b], Zhiping Zhang[b], Hongbo Li[b]

[a]Institute of Refrigeration and Cryogenics, Shanghai Jiao Tong University, Shanghai 200240, China
[b] SKL of Air-Conditioning Equipment and System Energy Conservation, GREE Electric Appliances, INC. Zhuhai 519070, China

Abstract

With the enactment of the Kigali amendment, the HFCs are falling into disuse and HFOs are proposed to be studied for replacement. R1233zd(E) as a new HTHP working fluid with low GWP has yet to be further developed. The HTHP is an ideal replacement of boiler to supply heat in industry. However, the construction of megawatt unit usually has a huge investment and may not achieve the desired results. Therefore, a mathematical model is imperative to conduct the performance prediction. This paper proposed a model and it can effectively verify the feasibility of the megawatt R1233zd(E) HTHP system, which recovers 60-80℃ waste heat and outputs 100-160℃ pressured water. The conditions of condensation temperature from 90-160℃ with temperature lift of 50K, were calculated and the COP changed in 3.0-3.8. When evaporating at 60℃ and condensing at 110℃, the heat capacity was up to 1.95MW with COP over 3.8. From the results, R1233zd(E) is a reliable refrigerant for both high temperature output and high system efficiency, which will be a direction for future experiments.

Keywords: Dynamic mathematical model; R1233zd(E); High temperature heat pump; Megawatt; COP.

Nomenclature (usually used with subscript)

c	specific heat (J/(kg·K))	α	void fraction
c_p	specific heat (isobaric) (J/(kg·K))	**Subscripts**	
c_v	specific heat (isovolumetric) (J/(kg·K))	*cu*	copper
h	convective heat transfer coefficient (W/(m^2·K))	*C*	condenser
i	specific enthalpy (W/K)	*crit*	critical condition
m	mass flow rate (kg/s)	*COM*	compressor
N	rotation frequency (HZ)	*d*	porous desiccant coating (including pores)
p	pressure (Pa)	*E*	Evaporator
P	electricity consumption (W)	*f*	falling fill area
t	time (s)	*l*	full liquid area
T	temperature (℃)	*r*	refrigerant
u	x component of velocity (m/s)	*TP*	the two-phase refrigerant
v	y component of velocity (m/s)	*rg*	saturated gas of the two-phase refrigerant

* Corresponding author. Tel.: 15021685354; fax: 021-34206548.
E-mail address: hb1223@sjtu.edu.cn.

V	volume (m^3)	rl	saturated liquid of the two-phase refrigerant
λ	conductivity (W/(m·K))	t	tube
ρ	density (kg/m^3)	W	water
l	Characteristic length (m)	TV	throttling valve

1. Introduction

Heat pump is an effective technology for improving grade of thermal energy, especially applied in absorbing heat from air or industrial waste source. In terms of high temperature heat pump (HTHP), it is mainly utilized in industry field to replace boiler [1] (e.g. coal combustion boiler, natural gas boiler, electrical boiler), which can enhance utilization of energy significantly and decrease the consumption of fossil fuels. R245fa has been recognized as the relative appropriate refrigerant for HTHP, which can achieve both high heat sink temperature and COP [2]. In France, there is an R245fa HTHP unit achieves COP of 2.3 at 60℃ heat source and 100℃ output temperature [3], and another large capacity unit (900-1200kW) can reaches 120℃ sink temperature [4]. But with the promulgation of Kigali amendment in the 28th conference of Montreal Protocol, HFCs with high GWP (Global Warming Potential) need to be cut down gradually [5]. To control the emissions of green-house gases, it is necessary and urgent to find better substitutes. HFOs with GWP only 1 has been recommended as potential candidate for both HTHP [6] and Organic Rankine Cycle (ORC) [7]. R1233zd(E), one kind of HFOs, has been studied widely in ORC to replace R245fa with satisfactory result [7, 8]. For HTHP, Kondou and Koyama [9] has achieved huge temperature lift of 80K (70/150℃) with remarkable COP of 5.3, similarly to that of R245fa. There is insufficient study of R1233zd(E) used in HTHP, especially theoretical study. Therefore, it is essential to have careful theoretical research of R1233zd(E) HTHP system for the optimization.

For theoretical research of heat pump, mathematical model is generally the basic key theory. There are some mature methods shown in Fig.1 [10], ranging from simplified lumped parameter model to detailed discretized model. This study mainly bases on the physics modeling methods and not takes black- and grey-box models into account. Lumped parameter model is a common and class physics-based models for heat pump system simulation. Typically, the temperature distribution in the heat exchanger is independent of the coordinates and can be considered as averaged during the heat transformation. This approach effectively simplifies the computation and leads to dimensionality reduction. Yao et al [11] proposed a lumped parameter model for vapor compression system and the prediction models met with experiments within 10% by converting the governing equations of conservation equations to state-space notation. Moving boundary method [12] is generally cooperated with lumped parameter model. Heat exchanger is divided into separate control volumes according single- and two-phase and properties are averaged in each phase. Moving boundary method can reduce computational cost while providing details of phase boundaries, with relative lower accuracy.

The detailed discretized models use finite volume and finite difference to divide the system component into multiple control volumes. From the discretion of governing equations and solving equations simultaneously, the time response of properties can be simulated. Therefore, the discretized models can predict property change over smaller spatial scale. Compared with moving boundary method, finite volume method was fond to be more robust [12]. But as a result of high accuracy, the calculation is more complex and huger [10]. To simplify the formulation, most models neglect the momentum conservation equation. The earliest dynamic research of vapor compression heat pump system can date back to 1985, Gruhle et al [13] proposed an evaporator model (including momentum conservation) and a method for the control of expansion valve. Mac Arthur et al [14] also proposed a discretized model of evaporator but neglecting momentum conservation and verified by experiments. Hermes et al [15] reviewed the modeling methods and simulated the response of a household refrigerator. Bendapudi et al reviewed the dynamic models of vapor compression equipment [16] and proposed a discretized finite volume model (not including momentum conservation) of a vapor compression system and validated with experiments [17]. They also discussed the detailed model formulation and approaches for numerical solution.

For refrigerant, the space for flow is huge inside the shell and the distance between inlet and outlet is relatively short. The pressure drop of refrigerant can be ignored. Therefore, discretized finite volume model (without momentum conservation) is the approach of this study to better simulate the operation of a

megawatt R1233zd(E) HTHP unit.

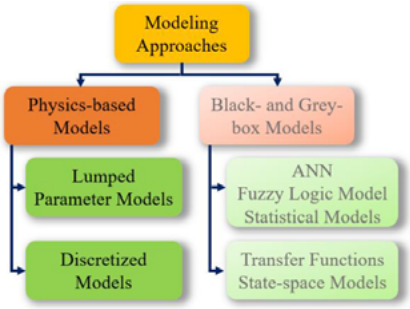


Fig. 1. Classification of modeling approaches for heat pump.

2. Model description

The studied unit is mainly composed of falling film evaporator, double-stage centrifugal compressor, shell-and-tube condenser, electronic expansion valve and flash tank, shown as Fig.2. The double-stage centrifugal compressor is divided into two independent compressors to show the intermediate vapor injection process more clearly.

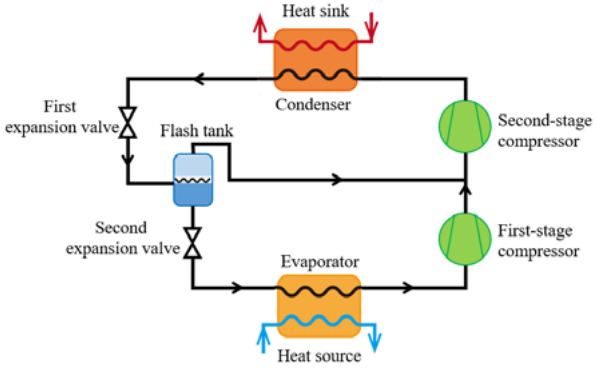


Fig. 2. Schematic of heat pump system cycle

2.1 Compressor model

The type of the compressor is double-stage centrifugal, of which the frequency N_{COM} is 50r/s, the adiabatic efficiency (η_s) is 75%, mechanical efficiency (η_{me}) is 98% and the motor efficiency (η_{mo}) is 97%. Actually, the capacity of centrifugal compressor is controlled by variable inlet guide vanes. In this study, to simplify model the compressor is simulated to operate under wide-open vanes with maximum flow rate. The basic governing equations are shown as equation 1, the mass flow rate $m_{r,COM}$ can be obtained, and given the $i_{r,COMint}$ (enthalpy of refrigerant from evaporator inlet) can get the $i_{r,COMout}$ (enthalpy of condenser outlet). Finally, the power consumption of compressor can be calculated.

$$\begin{cases} m_{r,COM} = N_{COM} V_{COM} \rho_{r,COMin} \\ i_{r,COMout} = \frac{(i_{r,iso-entropy} - i_{r,COMin})}{\eta_s} + i_{r,COMin}, \quad \eta_s = 0.75 \\ P_{COM} = \frac{m_{r,CM}(i_{r,COMout} - i_{r,COMin})}{\eta_{me}\eta_{mo}}, \qquad \eta_{me} = 0.98, \eta_{mo} = 0.97 \end{cases} \tag{1}$$

2.2 Expansion valve

The function of expansion valve is to expand the refrigerant from high pressure and temperature to low pressure and temperature meeting the evaporation condition. At the same time, the expansion can adjust the flow rate of refrigerant by controlling the opening degree of valve to response to the load change. According to equation 2, the mass flow rate $m_{r,TV}$ of the expansion valve is determined by the pressure difference ($p_{r,TVin}$-$p_{r,TVout}$), and the inlet enthalpy $i_{r,TVin}$ is considered to be the same with outlet enthalpy $i_{r,TVout}$ because of the ideal iso-enthalpy throttling process.

$$\begin{cases} m_{r,TV} = K\sqrt{(p_{r,TVin} - p_{r,TVout})\rho_{r,TVin}} \\ i_{r,TVin} = i_{r,TVout} \end{cases} \tag{2}$$

2.3 Evaporator

In this model, the four tube-passes falling film evaporator is applied, with the arrangement of tubes inside the evaporator approximately displayed in Fig. 3 and detailed number of tubes listed in Table 1. The outer and inner diameter of tube (light tube) inside evaporator and condenser are all 19.05mm and 16.2mm respectively. The general flow patterns of a falling film evaporator can be divided into film shape, column shape and dry shape from top to bottom. There will be pluges of heat trasfer coefficent when drop spot occurs, so the heat transfer process needs to be discussed seperatelly. The heat transfer coefficient inside tube of evaporator and condenser is the same, calculated as equation 7. The coefficient of refrigerant outside the evaporator in the falling film area is estimated as equation 8 [18]. When the liquide film evaporates to dry out, the coefficent of heat transfer follows equation 10. In full liquid area, pool boiling heat tansfer coefficient is calculated as the Cooper formula (equation 10) [19].

$$h_W = \frac{\lambda Nu}{Di} = \frac{\lambda_w * 0.023 * Re_w^{0.8} Pr_w^{0.4}}{Di} \tag{7}$$

$$\begin{cases} h_{r,f} = Kh_p \\ K_f = (1 - 0.335\frac{d_t}{d_{t,sta}})[2.059 + 2.37\frac{q_{i,j}}{q_{crit}} + 7.793(\frac{q_{i,j}}{q_{crit}})^2] \end{cases} \tag{8}$$

$$\begin{cases} h_{r,f} = Kh_p \\ K_d = \frac{K_{f,crit}}{Re_{crit}} Re_r, \qquad Re_r = \frac{4m_r}{\mu_r} \\ \frac{Re_r}{Re_{crit}} = (\frac{q_{i,j}}{q_{crit}})^2, \qquad Re_{crit} = 2(0.00339 * q_{crit} + 82.3) \end{cases} \tag{9}$$

$$\begin{cases} h_{r,l} = 55 * q_{i,j}^{0.67} M_r^{-0.5} p_r^m (-lgp_r)^{-0.55} \\ m = 0.12 - 0.21gR_p, \qquad R_p = 0.3 - 0.4\mu m \end{cases} \tag{10}$$

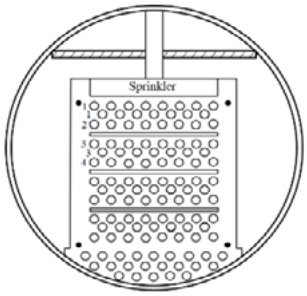


Fig. 3. Inner structure of falling film evaporato

Table 1. Number of tubes of heat exchanger

Tube Row	No. of tubes	
	Evaporator	Condenser
1	19	12
2	19	23
3	19	24
4	10	23
5	19	24
6	19	24
7	19	25
8	10	24
9	19	25
10	19	23
11	9	24
12	10	23
13	24	22
14	21	21
15	18	18
16	15	13
17	10	8
Total	279	356

2.4 Condenser

A horizontal shell-and-tube condenser with one shell process and two tube processes, shown as Fig. 4. The tubes of condenser adopted an equilateral triangle arrangement with total 356 tubes and the number of every row is listed at Table 1. Because of the staggered arrangement, condensate may not fall directly on the tube beneath as Fig. 5 shown, but falls on the slanted and middle tubes, which is defined as lateral drainage. since the condensate drains over intermediate tube, the rows number of tubes should be adopted as Fig.5 reflected. From some ideal simplification, almost half of one tube volume is flooded. Above the analysis, Eissenberg et al [20] proposed the heat transfer coefficient of condensation according different rows (equation 11). From the equation, hn is set to the valve of h1 which is the first row of condensation.

$$\begin{cases} \frac{h_n}{h_1} = 0.7974 + 0.2327n^{-1/5} \\ \frac{h_1}{\lambda_1}[\frac{\mu_l^2}{g\,\rho_l^2}]^{1/3} = 1.523(\frac{4m_1}{\mu_l})^{-1/3} \end{cases} \tag{11}$$

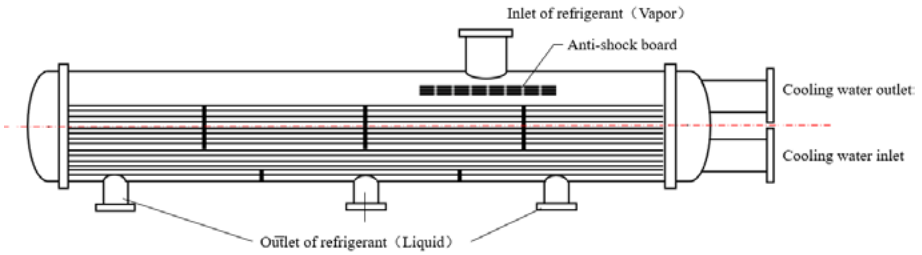


Fig. 4. Structure diagram of horizontal shell-and-tube condenser<1-2>

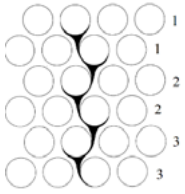


Fig. 5. Pure lateral drains and tube rows.

Here, the methods for control volume division and finite difference of condenser are described carefully, and they are similar to evaporator. With the method of finite volume, heat exchanger is divided into limited control volume according to the inner node method, shown in Fig.6. In condenser, superheated vapor enters

from top and passes through the anti-shock plate, then it flows downward more uniformly. The vapor condenses on the surface of the heat exchange tube, and the condensation liquid gradually flows downward due to gravity. Cooling water flows into heat exchanger from low tubes and out of heat exchanger from up tubes. When cooling water is out of low tubes ($i_{9\text{-}N}j_{M+1}$ side), there is a mixed process of tubes of i_9-i_N which is assumed as well mixed to T_{wmid} and the inlet temperature of i_1-i_8 is also T_{wmid}. The results of discretized equations (3-7) are in appendix, and it should be noted that the boundary of the model like nodes i_0j_1, i_1j_{M+1}, $i_{N+1}j_1$ and $i_{N+1}j_M$, using Taylor expansion method to discretize. Because of the flow direction of refrigerant and water, second-order upwind difference scheme is used as discretization method of governing equations. Second-order center difference is called for discretization of tube wall governing equations due to no fluid flowing and only energy conservation.

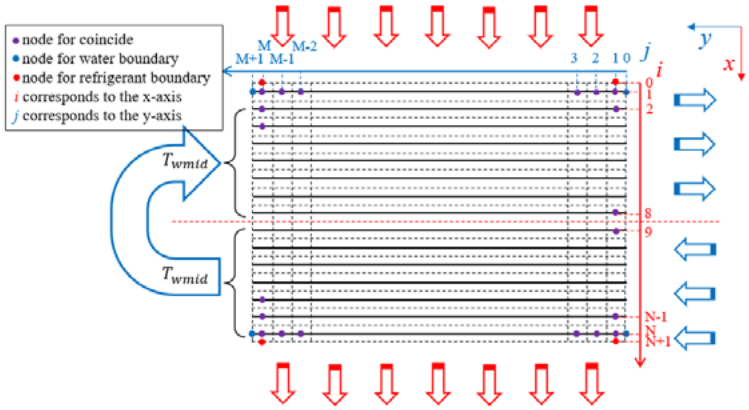


Fig. 6. Schematic of discretized finite volume of condenser.

2.5 *Flash tank model*

The flash tank mainly works to adjust the mass flow rate of vapor injection. The pressure inside flash tank is same with outlet of first expansion valve and first-stage compressor. The saturated vapor is injected to the middle of compressor and mix with the superheated vapor of outlet first-stage compressor to a moderate superheat temperature. At the same time, the mass flow rate of main stream (evaporator) contains constant.

3. Calculation algorithm

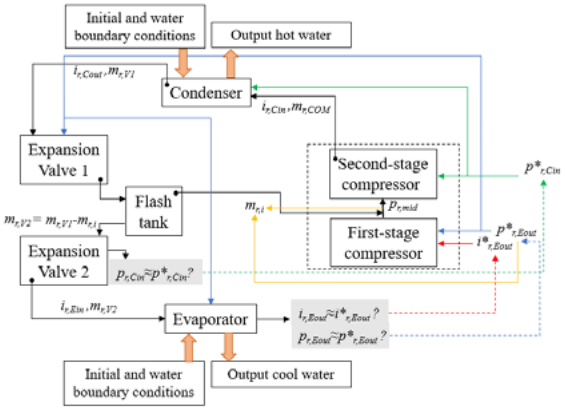


Fig. 7. Framework of the system simulation of the HTHP

The calculation algorithm of double-stage compression with intermediate vapor injection heat pump system is shown in Fig.7. First, the evaporation pressure ($p^*_{r,Eout}$), enthalpy of evaporator outlet ($i^*_{r,Eout}$) and condensation pressure ($p^*_{r,Cin}$) are assumed and the pressure between two-stage compressor is set, then the mass flow rate of intermediate vapor injection can be determined. Refrigerant flows through compressor, condenser and expansion valves, with current pressure of condensation ($p_{r,Cin}$) calculated. With current $p_{r,Cin}$ as initial input $p^*_{r,Cin}$, iterate $p_{r,Cin}$ until $p_{r,Cin}$ is equal to $p^*_{r,Cin}$. Similarly, $i_{r,Eout}$ and $p_{r,Eout}$ can be updated after calculating the properties of evaporator and set $i_{r,Eout}$ and $p_{r,Eout}$ as assumed value of initial input until they are equal. Transient properties of refrigerant, tube and water during the operation can be estimated by the repeated calculation of iteration. The calculation is finished by C++ program.

4. Results and discussion

The simulated system is equipped with intermediate vapor injection system, in which saturated vapor from flash tank was injected to the suction port of Second-stage compressor. Therefore, there will be an optimum mid-pressure injection. Fig. 8-11 shows the system performances varying with the increasing of mid-pressure, and the calculated working condition is evaporating at 55℃, condensing at 80℃, 2℃ subcooling at the outlet of condenser and mass flow rate of First-stage compressor constant at 15kg/s. In Fig.8, the vapor injected mass flow rate shows a downward trend. When the open degree of first-stage throttle remains unchanged, the pressure difference between inlet and outlet of throttle shrinks, and mass flow rate decreases (according equation 2). Further, the superheat of Second-stage compressor discharge decreases slightly, which is mainly due to the physical properties of R1233zd(E) that the slope of isentropic line is larger than saturated gas line and the distance between them is closer in higher temperature area. Therefore, the refrigerant compressed from mid-pressure to Second-stage will get the state closer to saturated gas line when mid-pressure higher. The heating capacity is larger than 2 MW, and decreases with the mid-pressure increasing, which is mainly due to the decreasing of mass flow rate in condenser (shown as Fig. 9). In Fig. 10, the power consumption of First-stage and Second-stage compressor are compared and the consumption of Second-stage compressor decreases with the increasing of mi-pressure. The decline is mainly because of the decrease of injected vapor mass flow rate and enthalpy difference. The increasing enthalpy difference with mi-pressure increasing is the reason of power consumption of First-stage compressor increase. Last, the system COP is calculated, shown in Fig. 11. There is a peak value with the increasing of mid-pressure, therefore, an optimum mid-pressure exists. The COP is calculated according to the definition that ratio of heating capacity to power consumption. Actually, the heating capacity and total power consumption are both decreasing, so, the changing trend of COP is owing to the relative changing trend of them.

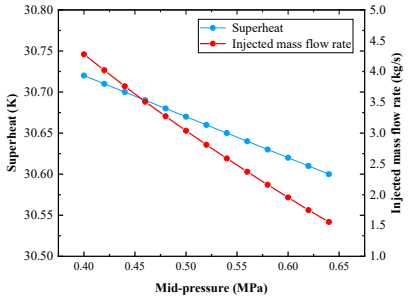


Fig. 8. Variation of superheat of compressor and injected vapour mass flow rate with mid-pressure increasing

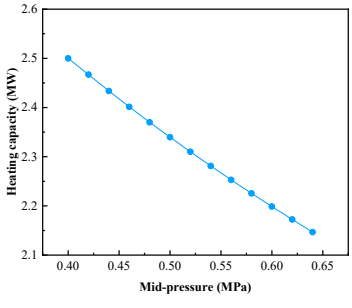


Fig. 9. Variation of heating capacity with mid-pressure increasing

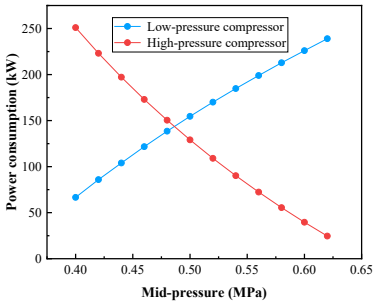


Fig. 10. Variation of power consumptions of First-stage and Second-stage compressor with mid-pressure increasing

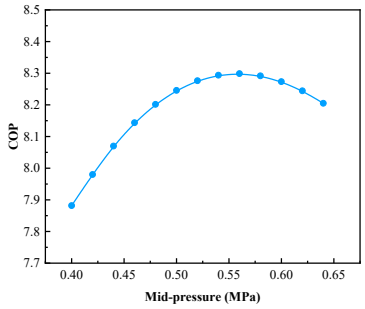


Fig. 11. Variation of COP with mid-pressure increasing

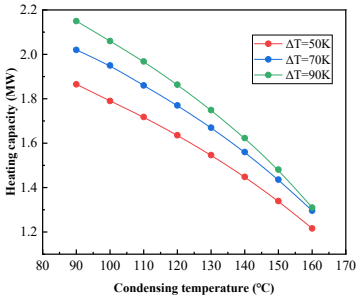


Fig. 12. Variation of heating capacity with condensing temperature increasing (in different ΔT)

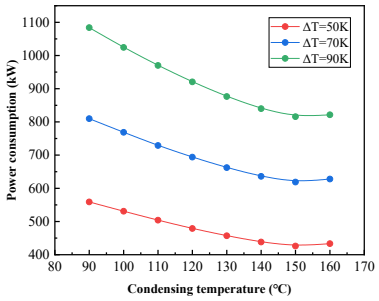


Fig. 13. Variation of power consumption with condensing temperature increasing (in different ΔT)

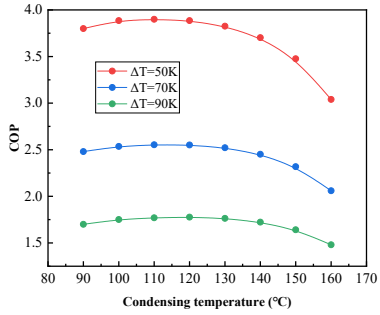


Fig. 14. Variation of COP with condensing temperature increasing (in different ΔT)

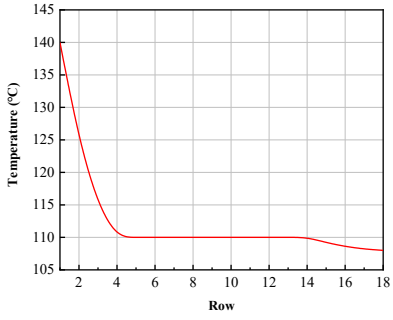


Fig. 15. The temperature distribution of refrigerant inside shell-tube condenser according to the tube row

Further, the system performance in different working conditions are simulated at fixed temperature lift and optimum mid-pressure injection (evaluated as equation12 [21]), shown as Fig12-14. Heating capacity reduces with the condensing temperature increasing (Fig.12), which is mainly attributed to the enthalpy difference decreasing in higher temperature area. At the same time, the heating capacity decreases with the temperature lift dropping, which is owing to that higher evaporation temperature leads to higher optimum mid-pressure and less injected mass flow rate. In Fig. 13, the total power consumption decreases with the absolute slope smaller. The power consumption increases with the temperature lift larger. Even the heating capacity of condition ΔT=90K higher than other, the higher power consumption decides the COP of ΔT=90K is the smallest. And from the comprehensive consideration of heating capacity and power consumption, the COP also has a fluctuating change with the increasing of condensing temperature (shown as Fig. 14). The change is also because of the different reduced rate of heating capacity and power consumption.

$$p_{opt} = \sqrt{p_e p_c} \tag{12}$$

To reveal the inner detailed heat transfer process, temperature distribution of refrigerant inside shell according to the tube row is reflected as Fig. 15. Initially, cooling water (100℃, 115kPa) is pumped to heat

exchange tube of condenser with 32L/s, and the vapor refrigerant (110℃ and 1.28MPa), with about 30℃ superheated. In the first three rows, the superheated refrigerant vapor exchange sensible heat with tube. In the 4-14th row, refrigerant condenses to liquid gradually and exchange latent heat with tube. During the condensation process, the condensate flows from top to full liquid area, therefore, some single-phase heat transfer also appears in two-phase heat transfer area. In the bottom of condenser, there is full liquid area, with saturated liquid cooling to subcooled liquid. The outlet temperature of refrigerant in condenser is about 108℃, with about 2℃ subcooled.

5. Conclusion

In this paper, a mathematical model of megawatt HTHP system adopting R1233zd(E) refrigerant is built. From the discretization of governing equations and the division of limited finite volume, parameters at each control volume can be obtained. The optimum injection mid-pressure is estimated, and due to the physical properties of R1233zd(E), the injected mass flow rate dropping with the increasing of mid-pressure. To predict the operation performance of megawatt R1233zd(E) HTHP, the conditions of condensation temperature from 90-160℃ with temperature lift of 50K, 70K and 90K were calculated. In the condition of 50K temperature lift, he COP changed in 3.0-3.8, and there is a peak value in the range. When evaporated at 60℃ and condensed at 110℃, the heat capacity of this heat pump system was up to 1.9MW with COP above 3.8 during stable operating. From the results of model, R1233zd(E) is kind of a reliable refrigerant for both high temperature output and high system efficiency, which will be a direction for future experiments.

6. Copyright

By submittal of his or her full paper to the Agency for the 13th Heat Pump Conference, the author(s) assumes full responsibility for ensuring that his or her paper does not infringe on another party's intellectual property rights, which include copyright and agree that the paper has not previously been submitted for publication elsewhere. Furthermore, the author, by submittal of his or her conference paper to the conference, grants publishing rights of that paper to the Agency for the 13th Heat Pump Conference, which may:

1. Publish or arrange to publish the paper as part of the Conference proceedings,
2. Copy and distribute the paper in its entirety in print and electronic form, and
3. Copy and distribute excerpts from the paper.

Acknowledgements

This research work was founded by State Key Laboratory of State Key Laboratory of Air-conditioning Equipment and System Energy Conservation (ACSKL2018KT1204) and Fundamental Research Funds for the Central Universities (18X100040029). The authors gratefully acknowledge the financial support from the Research Council of Norway and user partners of HighEFF (Centre for an Energy Efficient and Competitive Industry for the Future, an 8-year Research Centre under the FME-scheme).

References

[1] Zhang J, Zhang H H, He Y L, et al. A comprehensive review on advances and applications of industrial heat pumps based on the practices in China. Applied Energy, 2016, 178:800-825.
[2] Annex 35 IEA. Application of Industrial Heat Pumps, Final report, Part 1. Report No. HPP-AN35e1. 2014.
[3] Lee G, Lee B, Cho J, Ra H-S, Baik Y, Shin HK, et al. Development of steam generation heat pump through refrigerant replacement approach. In: 12th IEA Heat Pump Conference, Rotterdam; 14-17 May, 2017. p. 1-10.
[4] Peureux JL, Sicard F, Bobelin D. French industrial heat pump developments applied to heat recovery. In: 11th IEA Heat Pump Conference, Montreal, Canada; May 12, 2014.
[5] http://conf.montreal-protocol.org/meeting/mop/mop-28/final_report/English/MOP28-Dec1.docx (Ozone Sec Secretariat Conference Portal).
[6] Honeywell. Solstice refrigerants roadmap: The future of refrigerants. Brochure FPR-004-2016-09-EN.

2016. p. 1e2.
[7] Eyerer S, Wieland C, Vandersickel A, et al. Experimental study of an ORC (Organic Rankine Cycle) and analysis of R1233zd-E as a drop-in replacement for R245fa for low temperature heat utilization. Energy, 2016, 103(12):660-671.
[8] Yang J, Ye Z, Yu B, et al. Simultaneous experimental comparison of low-GWP refrigerants as drop-in replacements to R245fa for Organic Rankine cycle application: R1234ze(Z), R1233zd(E), and R1336mzz(E). Energy, 2019, 173:721-731.
[9] Kondou C, Koyama S. Thermodynamic assessment of high-temperature heat pumps using low-GWP HFO refrigerants for heat recovery. Int J Refrig 2015;53:126e41.
[10] Anurag Goyal, Srinivas Garimella. Generalized transient simulation of two-phase heat exchangers using zeotropic fluid mixtures. Int J Refrig 2019:105:120-134.
[11] Yao, Y., Huang, M., Chen, J. State-space model for dynamic behavior of vapor compression liquid chiller. Int. J. Refrig, 2013, 36 (8), 2128–2147.
[12] Bendapudi S, Braun J E, Groll E A . A comparison of moving-boundary and finite-volume formulations for transients in centrifugal chillers. Int. J. Refrig, 2008, 31(8):1437-1452.
[13] Gruhle, W.D., Isermann, R., 1985. Modeling and control of a refrigerant evaporator. J. Dyn. Syst. Measurem. Control 107 (4), 235–240.
[14] MacArthur, J.W., Grald, E.W., 1989. Unsteady compressible two-phase flow model for predicting cyclic heat pump performance and a comparison with experimental data. Int. J. Refrig. 12 (1), 29–41.
[15] Hermes, C.J., Melo, C., 2008. A first-principles simulation model for the start-up and cycling transients of household refrigerators. Int. J. Refriger. 31 (8), 1341–1357.
[16] Bendapudi, S., Braun, J.E., 2002. A Review of Literature on Dynamic Models of Vapor Compression Equipment. ASHRAE, Atlanta, Gap.
[17] Bendapudi, S., Braun, J.E., Groll, E.A., 2005. Dynamic model of a centrifugal chiller system–model development, numerical study, and validation. ASHRAE Trans. 111 (1).
[18] Roques JF, Thome JR. Falling films on arrays of horizontal tubes with R-134a, Part II: flow visualization, onset of dryout, and heat transfer predictions. Heat Transfer Eng 2007;28(5):415–34.
[19] Cooper MG. Saturation nucleate pool boiling - a simple correlation. Int Chem Eng Symp Ser 1984;86:785–92.
[20] Eissenberg, David Martin, Noritake, H.M., 1970. Computer model and correlations for prediction of horizontal-tube condenser performance in sea water distillation plants. Technical report, Oak Ridge National Laboratory.
[21] S. M. Zubair, M. Yaqub and S. H. Khan, 1996. Secondlaw-based thermodynamic analysis of two-stage and mechanical-subcooling refrigeration cycles, Int. J. Refrig. 19:506

13th IEA Heat Pump Conference
April 26-29, 2021 Jeju, Korea

A study on the determination method of defrosting start time by calculation of frost volume

Jin Woo Yoo[a,*], Yoong Chung[b], Dong Ho Kim[a], Seok Ho Yoon[a], Chan Ho Song[a], Kong Hoon Lee[a], Ook Joong Kim[a], Min Soo Kim[b]

[a]Korea Institute of Machinery and Materials, 156 Gajeongbuk-Ro, Yuseong-Gu, Daejeon, 34103, Republic of Korea
[b]Department of Mechanical and Aerospace Engineering, Seoul National University, 1 Gwanak-Ro, Gwanak-Gu, Seoul, 08826, Republic of Korea

Abstract

In cold winter season, most air heat pumps suffer from the frost formed on the surface of the outdoor heat exchanger. This frost must be removed, otherwise the heat pump performance will keep degrading and deviate from the design conditions, causing severe damage to the components. For this reason, it is necessary to determine the appropriate defrost start time. Several methods have been suggested, however, most of them are either based on empirical studies that require large number of experiments or less practical because they use expensive sensors. In this study, a new method is proposed to determine the defrost start time and verified with experiment. Three steps are required. First, calculate the frost mass that is generated per unit time using the heat and mass transfer analogy. Second, obtain the volume by dividing the frost mass with the density of frost. Third, the frost volume generated per unit time is accumulated and compared with the heat exchanger volume to determine the defrost start timing. With this method, the defrosting operation can be appropriately initiated.

Keywords: heat pump, heat exchanger, frost, defrost start time, frost volume, blocking ratio;

1. Introduction

In cold winter season, most air heat pumps in humid region suffer from the frost. It forms naturally due to the sublimation from air to the surface of the outdoor heat exchanger when the surface temperature becomes lower than the freezing temperature of water and the dew point temperature of the ambient air. This frost disturbs the air flow in the outdoor heat exchanger and lowers the heat exchange rate, thus reduce the overall performance of the heat pump system. In the experiment from Yan et al. [1], heat transfer rate and overall heat transfer coefficient drop while pressure drop of the heat exchanger rises under frosting conditions. In addition, Shao et al. [2] showed the decline of both heating capacity and COP in fin-tube microchannel heat exchangers during frost formation process. The frost on the surface must be removed, otherwise the heat pump performance will keep degrading and cause significant energy loss. Moreover, heat pump operation might deviate from the design conditions. Thereby determining the proper defrosting start time to prevent severe damage to the components is one of the important issue in heat pumps

Up to now, several methods have been suggested to judge defrosting start time. For direct frost detection methods, photoelectric sensors with emitter and receiver that measure the intensity of infrared ray between the inlet and outlet of air flow at the outdoor heat exchanger is proposed by Byun et al. [3]. Similarly, from the study of Chung et al. [4], the differential pressure can be measured to monitor the frost formation. The direct detection method measures a certain spot of the heat exchanger and let us know whether there is frost in that spot or not. This approach generally raises the issue of representativeness as to whether the point can represent the whole. For indirect frost detection methods, Kim and Lee [5] proposed the effective mass flow fraction (EMF) that follows the trend heating capacity. Zhu et al. [6] suggested temperature–humidity–time (T-H-T) method that utilizes a frosting map which is evolved from simple temperature-time (T-T) method. In this

* Corresponding author. Tel.: +82-42-868-7359; fax: +82-42-868-7338.
E-mail address: jwyoo@kimm.re.kr

method, a concept of accumulated time is introduced to determine the defrost start time. However, it only considered outdoor air condition and not the conditions of heat pump itself. The indirect detection methods generally describe overall system performance change but proposed methods are either hard to implement or limited on certain cases.

In this study, a new indirect frost detection method is proposed to determine the defrost start time and verified with experiment. The accumulated frost volume is calculated and compared with the volume of heat exchanger. The concept of accumulation is important because the state of the heat pump continues to change during its operation. This method also considers both factors of outdoor air (temperature and humidity) and heat pump itself (speed of compressor, the temperature of heat exchanger).

2. The calculation of frost volume and blocking ratio

Yoo et el. [7] explains the frost formation depends on the air temperature, humidity, and surface temperature of heat exchanger and heat exchange rate at evaporator. To form frosts two conditions must be met. The evaporator temperature should be lower than 0°C and the humidity ratio of outdoor air needs to be higher than that of air at the saturated condition at surface temperature of heat exchanger. The point 1 in Fig. 1 explains this condition. Otherwise, frost will not form. (point 2)

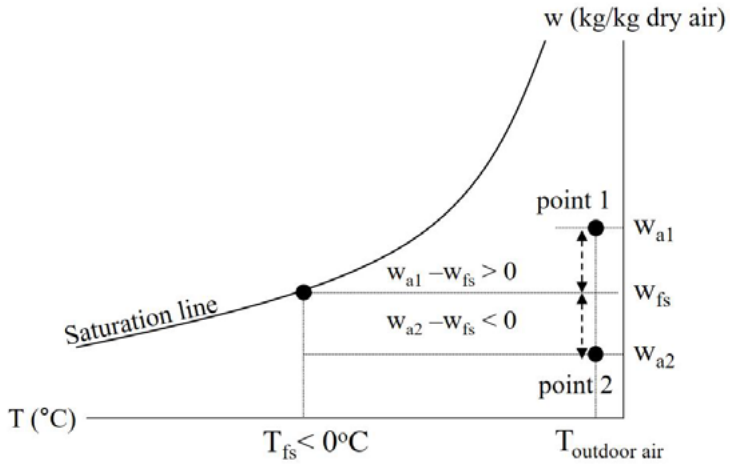


Fig. 1. Humidity ratio in psychrometric chart [7]

For the calculation of accumulated frost volume, three steps are required. First, we calculated the frost mass that is generated per unit time (Eq. (2)) by using the heat and mass transfer analogy in Eq. (1). Detailed derivation is represented in the study of Yoo et al. [7]

$$h_m = \frac{h_a}{C_{p,a}\rho_a Le^{2/3}} \tag{1}$$

$$\Delta m_f(t) = \frac{\dot{m}_{ref}\left(h_{comp,in} - h_{cond,out}\right) \times (w_a - w_{fs})\Delta t}{C_{p,a}Le^{2/3}(T_a - T_{fs}) + (w_a - w_{fs})L_{ig}} \tag{2}$$

Second, we obtained the frost volume per unit time by dividing the frost mass with the density which is Eq. (3).

$$\Delta V_f(t) = \frac{\Delta m_f(t)}{\rho_a(t)} \tag{3}$$

The equations of frost density were developed over time. We used the equation (Eq. (4)) that has the same form from Hayashi *et al*. [8]

$$\rho_f = f(T_{fs}) = C_1 \exp(C_2 T_{fs}) \tag{4}$$

Third, the frost volume generated per unit time is accumulated (Eq. (5)) and compared with the heat exchanger volume to determine the defrost start timing. In Eq. (6), blocking ratio (BR) is defined to evaluate the ratio between two volumes.

$$V_{f,accum}(t) = \sum_{\tau=0}^{t} \Delta V_f(\tau) \tag{5}$$

$$BR = V_{f,accum}/V_{heat\ exchanger} \tag{6}$$

With the BR, which is an index of the ratio of frost volume and heat exchanger size, the time of defrost can be determined. In this work, the defrost process starts at the timing when BR becomes 1.

3. Experiment setup and test condition

In order to calculate the frost volume and blocking ratio that were presented in section 2, several sensor data are needed which are dry bulb temperature and relative humidity of outdoor air inlet, the evaporator inlet temperature, the pressure and temperature at the inlet of compressor and the outlet of condenser. Heat pump data are also required which are outdoor heat exchanger size, compressor displacement, current compressor rotational speed. Fig. 2 provides the measurement information of heat pump experiment. The properties of air such as density, enthalpy, specific heat and humidity ratio, were calculated by the equations from ASHRAE Handbook [9]. The air flow rate of the indoor units was obtained according to the ANSI/AMCA 210 [10].

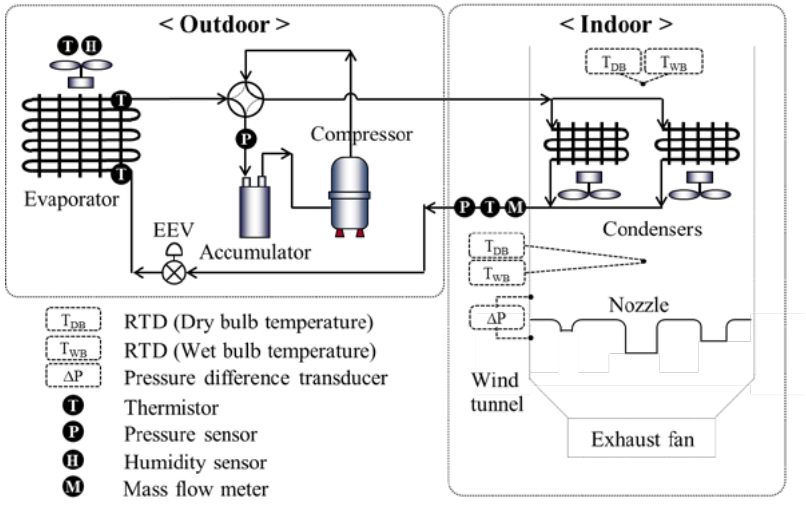


Fig. 2. The schematic of the heat pump system for experiment [7]

Table 1 gives the specification of the heat pump. It has variable speed compressor and fin-tube type heat exchangers, electronic expansion valve and uses refrigerant R410A.

Table 1. Specifications of heat pump system

Component	Specifications
Compressor	Inverter-driven scroll compressor / Stroke volume : 62.1 cm^3
Condenser side (2 Indoor units)	Fin-tube heat exchangers Tube inner / outer diameter (mm): 6.3 / 7.7 Row / Step: 2 / 10 Width / length / height (mm): 3000 / 40 / 200 Fin pitch (mm): 1.5
Evaporator side (1 Outdoor unit)	Fin-tube heat exchanger Tube inner / outer diameter (mm): 6.3 / 7.7 Row / Step: 3 / 45 Width / length / height (mm): 1650 / 60 / 1220 Fin pitch (mm): 1.7
Expansion device	Electronic expansion valve
Refrigerant	R410A

In Table 2, experiment conditions and results are presented. To verify the proposed frost volume calculation method, total 7 experiments were conducted. In case 1, 2 and 3, outdoor dry bulb temperature is set at 2, -4, -10˚C and all the other variables were fixed. Likewise, in case 1, 4 and 5, outdoor relative humidity changed from 68 to 83.8 %, in case 1, 6 and 7, compressor rotational speed was varied from 60 to 100 Hz.

Table 2. Experiment conditions and results

Experimental case	1	2	3	4	5	6	7
Indoor inlet T_{DB} (˚C)				20			
Indoor inlet T_{WB} (˚C)				15			
Outdoor inlet T_{DB} (˚C)	2	-4	-10	2	2	2	2
Outdoor inlet RH (%)	83.8	83.8	83.8	75	68	83.8	83.8
Compressor speed (Hz)	100	100	100	100	100	80	60
Q drop at the defrosting start time at BR=1 (%)	12.8	17.1	16.6	17.3	13.3	12.8	15.4
COP drop at the defrosting start time at BR=1 (%)	8.3	12.3	12.2	10.7	10.0	9.6	14.2
Time from start of operation to BR=1 (minutes)	72.0	70.0	65.2	96.5	135.1	82	108.6

The uncertainty analysis was done with respect to each cases, according to ASHRAE Guideline 2 [11]. At 95% confidential level, the maximum uncertainty of heating capacity and COP were 5.43% and 5.49% respectively.

4. Results

4.1. Determination of the defrost start time with the calculated blocking ratio

With the calculated BR derived from section 2, the defrost starts at the timing of BR equals 1 in all 7 experiment cases. The change of heating capacity, COP and BR for every cases is shown in Fig. 3. In Case 1 (Fig.3 (a)), when heat pump starts to operate the heating capacity and COP increases until 15 minutes. After that, heating capacity and COP does not show as drastic change between 15 and 60 minutes. However, after 60 minutes, the performance drop becomes noticeable. 72 minutes later, BR reaches 1 and at that time, the heating capacity and COP are dropped 12.8 % and 8.3% respectively. On the other hand, BR continues to grow from the beginning of operation because the value of humidity ratio difference in Eq. (2) is positive during operation and increases the value of frost volume in Eq. (5). All the other cases show similar trend which is divided into three stages. After heat pump is on, the performance value increases at first, shows only minor change at certain amount of time and begins to drop prominently. At the condition of BR =1, the defrost start timing for all cases lies at the 3rd stage where performance drop occurs and the specific percentage at that time is shown in Table. 2. Heating capacity drop is between 12.8 and 17.3 % while COP drop is between 8.3 and 14.2 %. With the proposed volume calculation method, it properly judges the defrost start time.

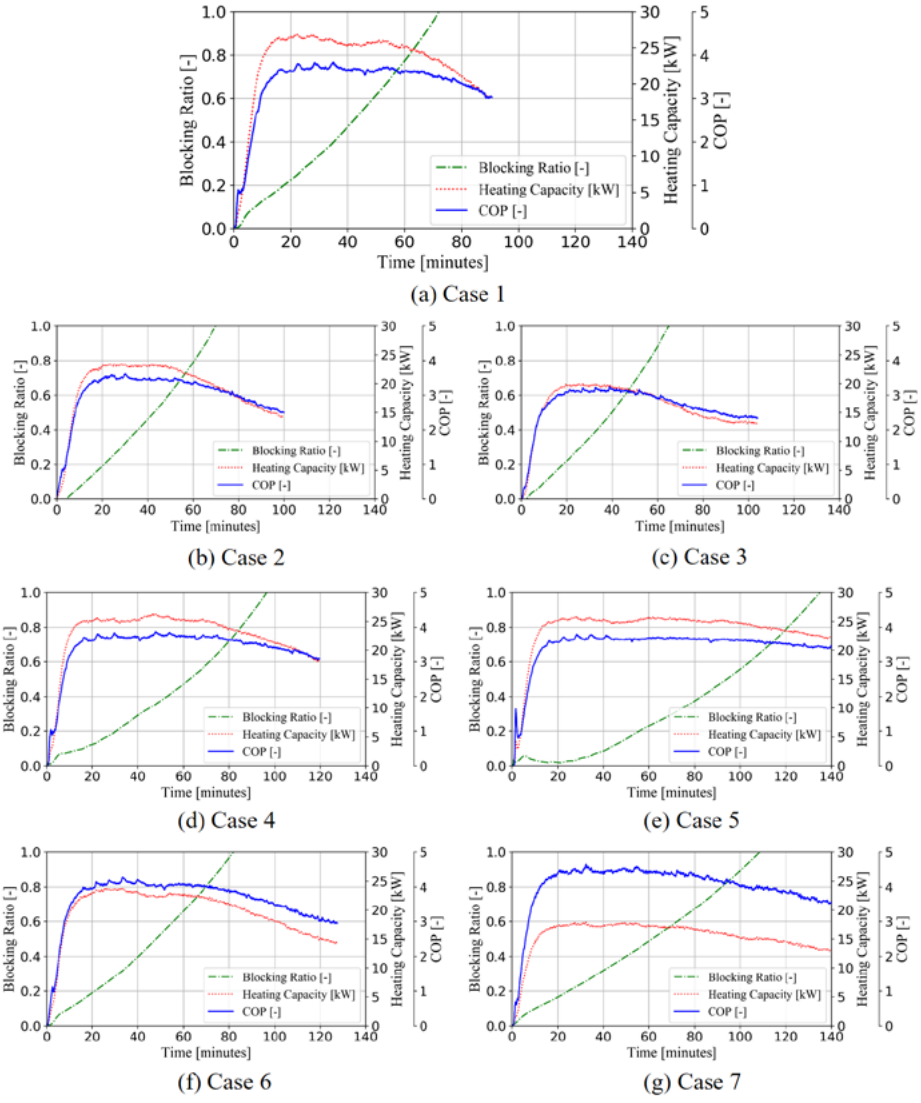


Fig. 3. Time vs. locking ratio, Heating capacity and COP at each cases

To support usefulness of the volume calculation method, the pictures of both front and right side of the outdoor heat exchanger were taken for every cases in Fig.4. At the defrosting start time, the majority of the area is covered with frost. No experimental cases show any mal-defrost.

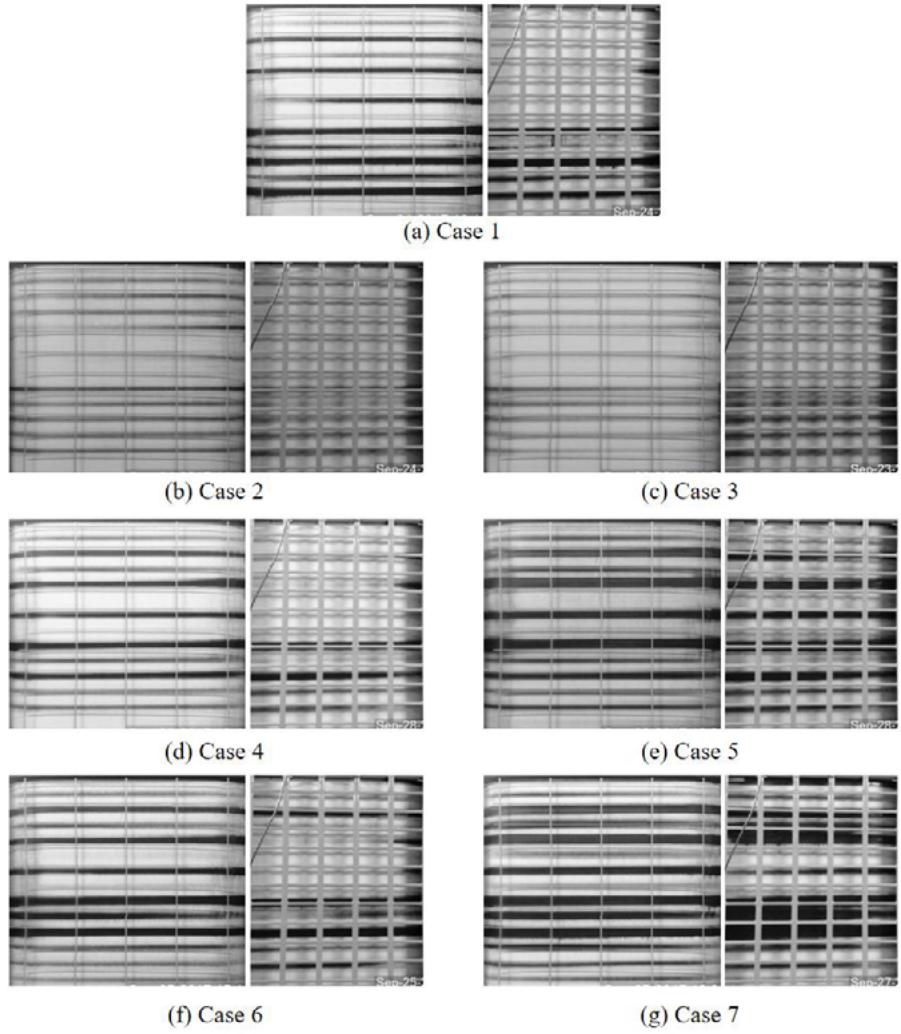


Fig. 4. The picture of outdoor heat exchanger at the defrost start time (front and right side)

4.2. The effect of outdoor dry bulb temperature, relative humidity and compressor rotational speed

With the 7 experiments in Table 2, the effect of outdoor dry bulb temperature, relative humidity and compressor rotational speed can be found. In case 1-3, all the other conditions are the same except outdoor dry bulb temperature. As the dry bulb temperature decreases, the start timing becomes shorter because the frost covers heat exchanger faster due to the lower frost density. (larger specific volume) When comparing case 1, 4 and 5, only the outdoor relative humidity is different. The relative humidity drop causes longer time from start of operation to BR=1. This is because the difference in humidity ratio ((w_a-w_{fs}) in Fig.1) decreases and forms less frost mass from Eq.(2).The effect of compressor rotational speed can be compared from case 1, 6 and 7. As the speed gets slower the mass flow rate of the refrigerant gets lower thereby creates less frost from Eq.(2).

5. Conclusion

In this study, a frost volume and blocking ratio calculation method is suggested in order to determine the defrosting start time. Detail calculation of BR and experiment setup is presented in section 2. To verify the method at various operating conditions, total 7 experiment were done at different outdoor dry bulb temperature, relative humidity and compressor rotational speed. In all cases, the defrosting start time (when BR becomes 1) were properly predicted at the performance decrease stage. The performance drop of heating capacity and COP is between 12.8 and 17.3 %, 8.3 and 14.2 % respectively at the defrost start time.

Acknowledgements

This work was supported by Korea Institute of Energy Technology Evaluation and Planning(KETEP) grant funded by the Korea government(MOTIE) (10052919, Development of Core Technologies for Low GWP Refrigeration System) (20192010107020, Development of hybrid adsorption chiller using unutilized heat source of low temperature)

References

[1] Yan W, Li HY, Wu YJ, Lin JY, Chang WR. Performance of finned tube heat exchangers operating under frosting conditions. Int J Heat and Mass Transfer 2003;46:871–877.
[2] Shao LL, Yang L, Zhang CL. Comparison of heat pump performance using fin-and-tube and microchannel heat exchangers under frost conditions. Applied Energy 2010;87:1187–1197.
[3] Byun JS, Jeon CD, Jung JH, Lee J. The application of photo-coupler for frost detecting in an air-source heat pump. Int J Refrig 2006;29: 191–198.
[4] Chung Y, Na SI, Choi J, Kim MS. Feasibility and optimization of defrosting control method with differential pressure sensor for air source heat pump systems. Applied Thermal Engineering 2019;155: 461–469.
[5] Kim MH, Lee KS. Determination method of defrosting start-time based on temperature measurements. Applied Energy 2015;146: 263–269.
[6] Zhu J, Sun Y, Wang W, Ge Y, Li L, Liu J. A novel Temperature-Humidity-Time defrosting control method based on a frosting map for air-source heat pumps. Int J Refrig 2015;54: 45–54.
[7] Yoo JW, Chung Y, Kim GT, Song CW, Yoon PH, Sa YC, Kim MS. Study of frost properties correlating with frost formation types. J Heat transfer 1977;92(2): 239–245.
[8] Hayashi Y, Aoki A, Adachi S, Hori K. Determination of defrosting start time in an air-to-air heat pump system by frost volume calculation method. Int J Refrig 2018;96: 169–178.
[9] ASHRAE Handbook Fundamentals. Atlanta, GA: ASHRAE; 2009.
[10] ANSI/AMCA 210 Laboratory methods of testing fans for certified aerodynamic performance rating, Arlington, IL: Air Movement and Control Association International, Inc.; 2007
[11] ASHRAE Guideline 2 Engineering analysis of experimental data. Atlanta, GA: ASHRAE; 2010.

13th IEA Heat Pump Conference
April 26-29, 2021 Jeju, Korea

Is HFO the last generation of synthetical refrigerants?

Kenneth Hoffmann[a], Jan Gerritsen[a], Armin Hafner[b]

[a]GEA Refrigeration, De Beverspijken 7c, 5221 EE `s-Hertogenbosch, Netherlands
[b]NTNU, Trondheim, Norway

Abstract

Since 1920 many different synthetical refrigerant have been introduced onto the market. The latest so-called 4th generation synthetical refrigerant is the unsaturated HFC or HFO (Hydrofluoroolefins). They introduced to combat an environmental issue, i.a. the global warming potential of HFC refrigerant, however, they are creating a new challenge. Recent research has shown that there is a build-up of fluoride substances as Trifluoroacetic acid (TFA) in drinking water globally. Some of the HFO molecule are breaking down 100% into trifluoroacetic acid, which can lead to large health cost in the future, due to this environmental pollution. Whereas the heat pump industry working with natural refrigerant are focusing on low charge and no leakages solutions, due to the flammability and toxicity of some of the natural refrigerant, there is very little effort by the industry working with synthetical refrigerant to create similar safe and low charge solutions. Research have shown that all current HFO based system solutions could be replaced by units applying natural refrigerants without significant cost implication.

Keywords: HFO; R1234yf; TFA; global warming; heat pumps; toxicity; natural refrigerant.

1. Introduction

The market of refrigeration and heat pump is growing each year, however, also the concern for the global environment and humans' impact on Earth's climate. We all want to keep the Earth healthy for the next generations to come. This paper has collected some of the recent research into the effect of introducing HFO as a refrigerant in large scale. Most of the research have been made on R-1234yf which is the main refrigerant discussed in this paper, although many other HFO refrigerants with similar properties have been introduced into the marked lately.

2. The history of refrigerants

Humans learned already from the primitive times that keeping food cold helped to extend their shelf life. In Egypt and Greek time there where, widespread use of storage pits to keep products cool. In the 1740's the first scientific results of creating cold by creating pressure change was proven by William Cullen. It took however another 60 years before Thomas Moore invented commercial refrigeration by taking energy from an ice storage into a dairy plant. This was the start of refrigeration as we know it today. Up through the 19th hundred mechanical compression refrigeration was introduced using CO_2, Ammonia or SO_4 as refrigerants. Due to lack of knowledge, training and material quality there where several accidents with these first refrigeration system, with several of them being fatal. By 1930 the first synthetical refrigerants, chlorofluorocarbons also known as CFC's, where commercialised by Thomas Midgley[1]. The CFC's where introduced as safe refrigerants as they are not flammable. This led to a large increase in use of refrigeration, in new areas where the end user's knowledge of refrigeration was limited like home appliances, supermarket- and HVAC units.

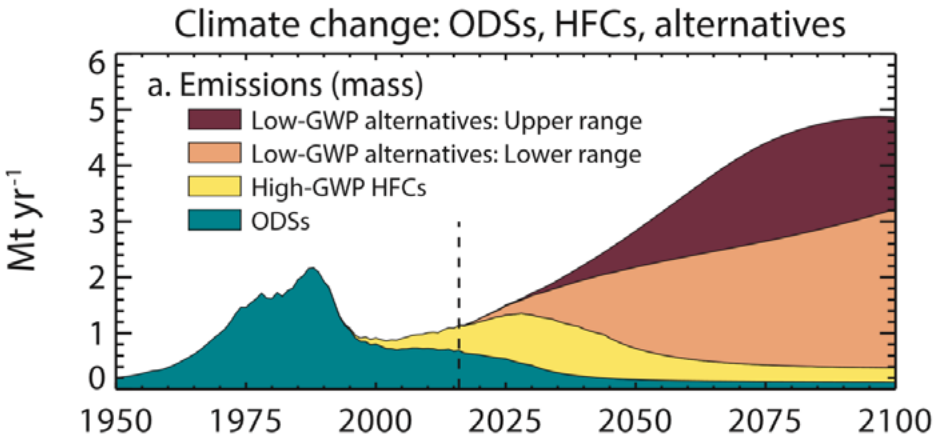


Figure 1: The figure shows the emission of refrigerant gas in Mt per year[4]. After 2016 it is a forecast based on current global development and legislation. By 2040 the release of low GWP refrigerants (HFOs) will exceed the peak release of ODS refrigerants (CFCs).

In the 1980's it was realised that the CFC refrigerants was causing a hole in the ozone layer in the stratosphere, which protects the Earth from UV radiation[2] . Although the CFC's were deemed safe, this was partly on a local level, on a global level, they had the potential to eradicate the human population if no action was taken and the ozone layer would have disappeared completely. To avoid this, it was decided in 1987 (Montreal protocol [3]) to curb the use of CFC with the goal to stop using all CFC's within 26 years (Last legal production of CFC in Article 5 countries where in 2003[3]). As alternative to the CFC's the refrigerant industry developed the HCFC, which had 10 times less ozone depleting effect compared to the CFC's, these where accepted as an intermediate refrigerant until a better solution was found. The HCFC will be fully phased out by 2040 in Article 5 countries. Since followed the developments of the hydrofluorocarbons - HFC's which have no ozone depleting effect. This was great news for the ozone layer and in recent years there has been some restoring of the ozone layer in the stratosphere [4].

Table 1: Article 5 country phase-out schedule for HCFC production and consumption [3]

Schedule	Year
Baseline	Average of 2009 and 2010
Freeze	2013
90% (reduction of 10%)	2015
65% (reduction of 35%)	2020
32.5% (reduction of 67.5%)	2025
Annual average of 2.5%	2030 to 2040
0% (reduction of 100%)	2040

The HFC's unfortunately raise another potential issue as they have a significant high global warming potential. With increasing temperatures on earth, due to the excessive usage of fossil fuels over the last 100 years it seems not logical to apply such harmful refrigerants. With increased water level and more severe weather phenomena's, there are potentially many deaths in the future related to global warming. This is especially the case if the human population does not manage to keep the goals from the Paris agreement of "keeping global average temperature to well below 2 °C above pre-industrial levels and pursuing efforts to limit the temperature increase to 1.5 °C" [5]. The Paris agreement have been ratified by 185 of the 197 participating countries. It has been followed up by the Kigali amendment [6] in 2016, declaring that all high GWP refrigerants will be phased out by 2047 globally, this will avoid 0.4˚C global warming. The lessons learned is that if it was only the refrigeration industry polluting the world the effect on the global climate would be limited. However, as there are many other sources which effect the global climate, we must be very vigilant regarding the exposure to the global climate as there is only one Planet Earth.

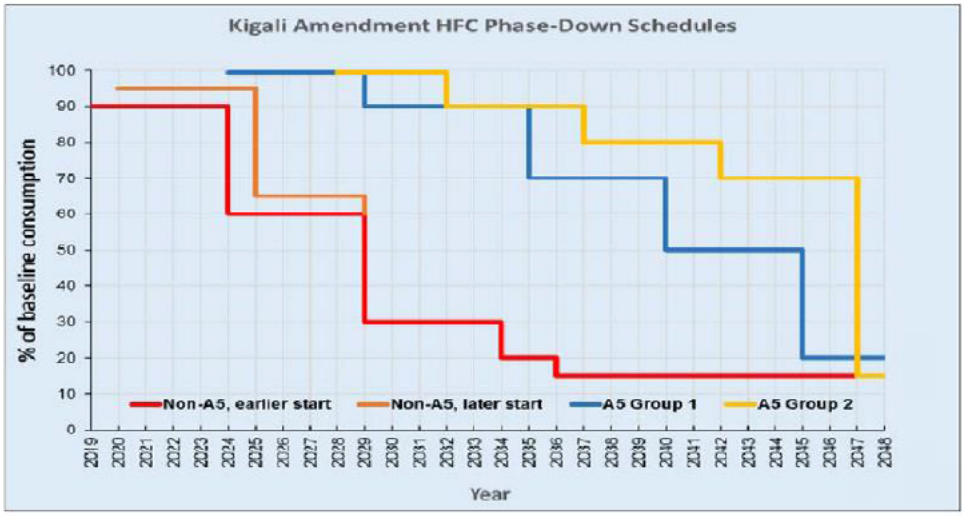


Figure 2: Global phasedown schedule for HFC production and consumption [3].

With growing global demand and sales of refrigerants of more than 15 bn US dollar, the refrigerant manufactures have a huge interest in replacing HFC's and they launched the first alternatives in 2008 [8]. Shortly after, the first articles appeared about the properties of unsaturated HFC's (HFO) refrigerants, which have a very short life in the atmosphere (a few days only). The issue is that HFOs are not safe refrigerant as previous synthetical refrigerants, however, they are flammable and toxic when combusting.

3. How do HFO differ from HFC?

HFC are created of stable molecules bonds, which are difficult to break down. This makes them good refrigerants, but it also gives them high global warming effect, as these stable fluids stay in the atmosphere for a very long time while absorbing radiation. HFO-1234yf is an unstable molecule with a double bond that breaks up quickly in the atmosphere, the degradation produces a 100% molar yield of trifluoroacetic acid (TFA) within days of release. Although TFA is naturally occurring on the oceans there is significant evidence that all TFA found in freshwaters, is human made. R134a does also break down to TFA, but only 20% of the molecules break down to TFA and it's over a much longer period.

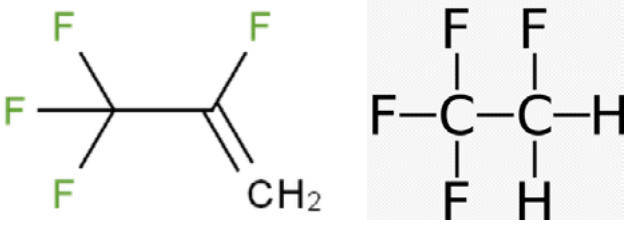


Figure 3: The molecule the left is the unsaturated HFO-1234yf 2,3,3,3-tetrafluoroprop-1-ene, C3H2F4; CF3CF=CH2 with an unstable double bound that breaks down within 10 days[4] in atmosphere. To the right is an HFC-134a 1,1,1,2-Tétrafluoroéthane, $C_2H_2F_4$ molecule, which has a stable structure that stays in the atmosphere for 10 years[4].

Table 2: Table showing the mass amount of TFA created from the refrigerant when decomposed in atmosphere

Molar yields of TFA from degradation of HFO's and HFC's	
HFOs	
R1234ze	<10% (as cited by WMO, 2010)
R1234yf	100% (as cited by WMO, 2010)
HFCs	
R134a	21% (as cited by WMO, 2010)
R227ea	100% (as cited by WMO, 2010)
R245fa	<10% (as cited by WMO, 2010)
R365mfc	<10% (as cited by WMO, 2010)
R236fa	<10% (as cited by WMO, 2010)

4. Toxicity of combustion products from HFO

HFO refrigerants are most commonly categorised as A2L refrigerants as they are so-called mildly flammable. This is a major change from the commonly applied R134a, which is and A1 refrigerant and classified as non-flammable. Although most refrigeration engineers in Europe have been trained since 2007 according to the F-gas regulations a new set of training of the personnel is required to keep themselves and the environment safe when handling HFO refrigerant.

Table 3: Flammability comparison of HFO with other commonly used refrigerants. LFL (lower flammability limit), UFL (upper flammability limit) [8].

Property	R290	R152a	R32	R717	R1234yf
Flame limits (ASTM E681-04) @ 21˚C					
Lower Flammability Level (vol% in air)	2.2	3.9	14.4	15.0	6.2
Upper Flammability Level (vol% in air)	10.0	16.9	29.3	28.0	12.3
Delta UFL – LFL	7.8	13.0	14.9	13.0	5.8
Minimum Ignition energy (mJ)	0.25	0.38	30 – 100	100 – 300	5.000 – 10.000
Burning velocity (cm/s)	46	23	6.7	7.2	1.5

The new refrigerants also require new standard from the equipment suppliers. They need to thoroughly assess the component used to ensure enough effort is made to make the system leak tight. Unfortunately, a lot of global economy is driven by lowest capital cost and not life cycle cost. With most heat pump installation being used where there is a continued heat demand for more than 20 years, there should be a greater focus on durability than only fit for purpose throughout the warranty period. With the heat pump industry mainly using flammable refrigerant it could backfire on the industry not focusing on quality if there is an increase in fatal failures.

Based on test made by Umaa University in 2016 the following findings are reported when investigating the products from combustion of HFO-1234yf "Amongst the detected chemicals with relatively high emission factors, COF_2, HF and CO are of greatest health concern. COF_2 (which is about three times as potent as chemical warfare agent phosgene used in World War I) reacts immediately with water to form HF. This will take place in the airways upon contact with the lung lining fluid; mucus and surfactants. HF is highly toxic and corrosive. HF may induce pulmonary edema upon inhalation and may cause severe burns following skin exposure. It can be adsorbed and penetrate tissues, and by binding to calcium HF may cause hypocalcemia. CO binds to haemoglobin and forms carboxyhaemoglobin which inhibits the transport of oxygen in the body resulting in hypoxia in many tissues of organs." [10]

$$CF_3CFCH_2 + 2.5(O_2 + 3.76N_2) \Rightarrow 2CO_2 + 2HF + COF_2 + 9.4N_2 \qquad (1)$$

Formula 1: This is the chemical process that takes place when combusting HFO-1234yf

Due to the slow burning of HFO-1234yf it is difficult to create conditions where you get 100% combustion of the refrigerants. Most of the by-product are unburned HFO-1234yf (220-480 mg/g), but there is also a significant amount of carbonyl difluoride (170-360 mg/g), carbon dioxide (120-320 mg/g) and hydrogen fluoride (70-240 mg/g) which all can cause a health risk in very small quantities.

Table 4 [11]: There are three categories of Protective Action Criteria (PACs) representing concentrations at or above which the general population may experience health effect based on 60 minute exposure. PAC-1: Mild, transient health effect, PAC-2: Irreversible or other serious health effect that could impair the ability to take protective action, PAC-3: Life-threatening health effects [12].

	PAC-1 (mg/m^3)	PAC-2 (mg/m^3)	PAC-3 (mg/m^3)
HFO-1234yf; 2,3,3,3-Tetrafluoropropene	10,000	11,000	66,000
Carbonyl difluoride (COF_2)	0.069	0.76	2.2
Hydrogen fluoride (HF)	0.82	20	36

In case of a fire in a car with (typically around 700g refrigerant) HFO-1234yf within a tunnel (cross section area 10 x 5 m), there is a potential health risk to anyone within 154 m (based on HF, PAC-2 level).

$$\frac{220\frac{mg}{g}HF\times 700\ g\ of\ R1234yf}{(10\times 5\ m^2)\times 20\frac{mg}{m^3}} = 154\ m \qquad (2)$$

Formula 2: Calculation of the distance the air will contain more than 20 mg/m^3 HF, based on Umaa University's combustion test.

If this is transferred to industrial refrigeration where centrifugal chillers can contain up to 10,000 kg of refrigerant the health risk of the HFO-1234yf becomes very apparent. HFO refrigerants should not be treated as safe refrigerant as they are flammable and the combustion products are highly toxic.

5. Environmental impact of fluorinated gasses

Nordic Council of Ministers [13] highlighted in their report that almost all people have fluorinated substances in their bodies today. It is estimated that this leads to an annual health-related costs to 52 – 84 billion EUR for all EEA countries. Exposure occurs primarily through contamination of drinking water. Most of this pollution is not from refrigerant releases, however, as for the global warming gasses and ozone depletion gasses it is part of the puzzle and we need to take responsibility.

HFO refrigerants breaks down to trifluoroacetic acid (TFA) within days in the atmosphere, which is toxic in larger amount to humans and can affect the reproduction [14]. Although TFA is naturally occurring in the oceans it has only become detectable in fresh water in Europe within the last 10 years.

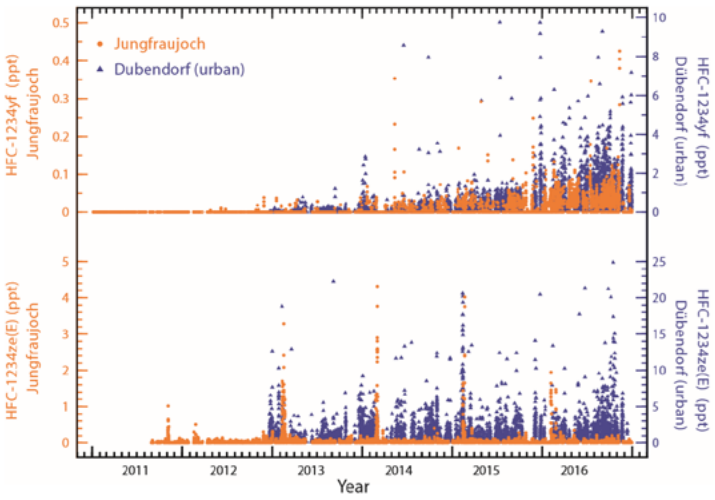


Figure 3: The table shows the increase amount of HFO found in the atmosphere at 2 European sites, The Mountaintop site Jungfraujoch (3,580 meteres above sea level) and urban Dubendorf site. The different colours indicate results from different sites. By mid-2016, 1 – 4 ppt of R1234yf and ~1 ppt of R1234ze(E) were regularly observed at Dubendorf, with pollution events containing up to 20 ppt of R1234ze(E), suggesting that it is more prevalent used in this region.

Several studies of the increased level of TFA in our drinking water due to refrigerant gas releases have shown that at the current amount of release there is very limited concerns. However, with the projected rise in

release over coming years (See figure 1), in 20 years' time when the release to atmosphere is at the same level as at the peak of Ozone depletion substances a review will be needed. This is under the assumption that only refrigeration will add to the TFA pollution, however, we need to realise that many other processes are adding to the fluoride acid pollution and we need to act. The Norwegian Environment Agency recommend in their report from 2017[14] "phasing out HFOs (and consequently TFA), or emission reduction strategies along with best practise measures that help ensure efficient capturing of HFO/TFA during recycling operations"

After 90 years of different type of synthetical refrigerants it is time to realise that there is not such a thing as "safe refrigerant". Some refrigerant poses a local risk if not handled with due care and others pose a global risk. HFO poses both a local and global risk if not handled safely and kept inside the refrigeration system until disposed. All refrigerants should be handled with due care. Refrigerant charge should be minimised in all systems. Systems should be made "leak tight" and everyone handling refrigerants should have proper training. In IEA Annex 54[18] "Heat pump systems with low GWP refrigerants" more investigation has been made into handling refrigerant with due diligence.

6. The economic dilemma

The global market for synthetical refrigerant gasses exceeds $15 bn US dollars per year[7] and it is forecasted to continue to grow in the coming years. Every time a new generation of synthetical refrigerants have entered the marked the specific price per kg have increased. The 4th generation of refrigerant is priced at around £70 per kg which is almost 50 times more than = the most commonly used natural refrigerants.

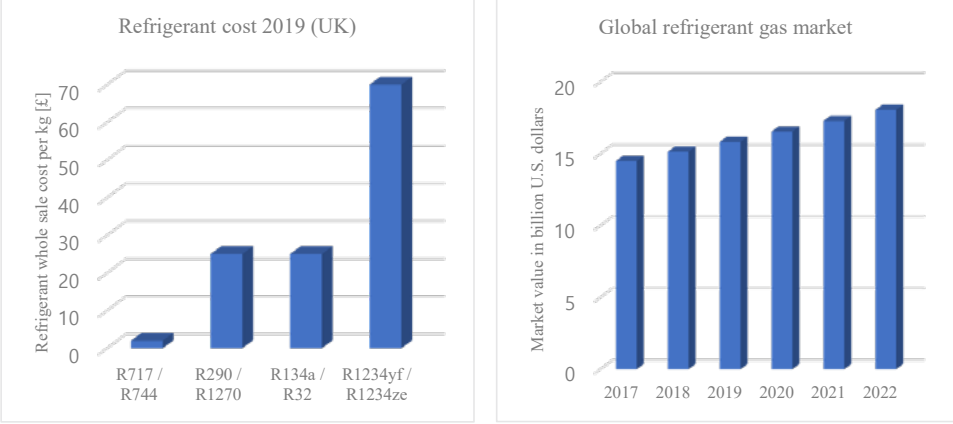


Figure 4: On the graph to the left is the retail cost of refrigerant in the UK 2019 (Source: BOC/Wolseley), to the right is a forecast of the global value of refrigerant sales in billion US dollars [7]

If the refrigeration and heat pump industry hypothetically would stop all production of synthetical refrigerants it would have a huge impact on the turnover for the companies producing and selling refrigerant gasses globally. The main question is whether the global and local consequences of increased releases of HFO are acceptable for the society, since only a few companies are benefitting economically. The next generation will have to tackle the consequences, in the same way as we have had to pay the price for replacing the ozone depletion substances (CFC's) in the first place and global warming fluids (HFC's) lately. Is it worth the risk and is it fair?

Many end-users have been forced to change their refrigeration / heat pump installation before the end of service life due to phase-out of previous generation of synthetical refrigerants. We saw a large replacement of industrial refrigeration system before 2015 in Europe due to the phase-out of HCFC-22. The same is now happening in commercial refrigeration with the phase-out of R404A in 2020 in EU. This will also happen in the rest of the World as they get closer to their deadline for phase out of these refrigerants. This is an added cost to the end-user, which was not communicated at the time of sales. There is no guarantee from the current sales people of refrigerant that this will not happen again in the near future with the HFO's. Does the refrigeration industry need this detour?

7. What are the alternatives?

The fake argument is often used that there is no alternative to HFO and that the alternatives are too costly. But is this true? As HFO are classified as A2L refrigerants they are not "safe" refrigerants so the quality of the components and assembly of heat pumps using HFO should be the same as used for natural refrigerants like CO_2, Ammonia or propane. If HFO heat pumps units are only build as "fit for purpose" throughout the warranty period then there is high risk to the end-user of the system, as small leaks can go undetected for a while until the ignition limit is reached with risk of fire and the toxic by-products from this.

For hydrocarbon refrigerants like R1270, R290 and R600a which all are classed A3 refrigerants, there are additional ATEX requirement to the electrical installation. However, this has been proven by many suppliers to have a very small impact on the cost and is outweighed by the significant lower cost of the refrigerant compared to HFO refrigerants.

For industrial heat pumps where customers do not only evaluate the equipment based on purchase price but also consider the service and operation costs as part of a total life cycle cost analysis, ammonia heat pumps do have significant advantages.

Table 5: Comparison for natural refrigerant (ammonia) industrial heat pump with an industrial heat pump using R1234ze refrigerant. Whereas the ammonia heat pump has a refrigerant charge of 41 kg, there is 140kg of R1234ze refrigerant on the synthetical refrigerant option. This is based on the industry standard for these type of heat pumps. Carrier have informed that they would have 210kg of R1234ze on a 1200 kW heat pump.

Example	RedGenium 1100 heat pump (source: GEA)	HFO Heat pump (Source: Oilon)
Chilled water inlet:	15˚C	15˚C
Chilled water outlet:	10˚C	10˚C
Cooling duty:	557 kW	494 kW
Heating water in:	45˚C	45˚C
Heating water out:	65˚C	65˚C
Heating duty:	716 kW	701 kW
Heating COP:	4.06	3.31
Refrigerant charge	41 kg	140 kg
Capital cost:	£177,000	£120,000
Refrigerant cost:	£80	£10,000
Service cost (20 year):	£125,000	£145,000
Running cost (20 years, £0.1 per kWh, 5000 h per year):	£1,724,137	£2,114,803
Total life cycle cost:	**£2,026,217**	**£2,389,803**

When taking into consideration that for large industrial heat pumps where the refrigerant charge can be up to 10,000 kg, there is also a considered financial risk. In case of a catastrophic failure where the entire charge of the plant is lost the customer would need to spend £700,000 on new refrigerant.

Currently there is a lot of research ongoing in developing high temperature (>100˚C) heat pumps. Where some HFO refrigerant can be used due to their relatively low saturated pressure at high temperature. However similar results can be achieved which R600a and R600, which has been proven by experimental investigations at NTNU / Sintef in Norway[17].
For car AC units many of the manufactures have now introduced alternatives to HFO. Fiat have launched a model with propane and both Daimler and Volkswagen [15] have introduced car models with CO_2 as refrigerant, so there certainly are alternatives to HFO. CO_2 air conditioning and heat pumps have also been proven to be very efficient in electric busses where Valeo[16] has demonstrated that the CO_2 heat pump can add up to 30% extra kilometres in temperatures as low as -20˚C.

For domestic heat pumps many manufacturers also have models with hydrocarbon. For ground source heat pumps there are manufacturer like Heliotherm, and Kensa who has introduced hydrocarbon heat pumps and for airsource heat pumps Nibe and Innotec have introduced a range of airsource heat pumps with hydrocarbons.

For split units air-conditioning and heat pumps there is also many suppliers globally, although some of the main suppliers have been reluctant to include hydrocarbon refrigerant models in their portfolio as they claim

that there is added risk of using these refrigerants. Fact is that there is a larger risk by installing a leaking HFO system than a tight hydrocarbon split unit.

References

[1] Edelmann, Frank T: The life and legacy of Thomas Midgley Jr, Papers and proceedings of the Royal Society of Tasmania, Volume 150(1), 2016
[2] Pienitz, Reinhard and Vincent, Warwick F. : Effect of climate change relative to ozone depletion and UV exposure in subarctic lakes, Nature 404, International journal of science, 2000
[3] UN Environment programme, Ozone Secretariat, Refrigeration, Air Conditioning and Heat Pumps, Technical options Committee, 2018 Assessment Report, 2018
[4] World Meteorological Organisation, Global Ozone Research and Monitoring Project – Report No. 58, Scientific assessment of ozone depletion: 2018, 9.2.2019
[5] Paris Agreement, United Nations, Framework Convention of Climate Change, 26.1.2016
[6] United Nations Kigali Amendment to the Montreal Protocol on substances that deplete the ozone layer 2016
[7] Statistica 2019: https://www.statista.com/statistics/819414/global-market-value-forecast-of-refrigerants/
[8] Minor, Babara and Spatz, Mark: HFO-1234yf Low GWP Refrigerant update, Purdue University, 2008
[9] Pearson, Dr. AB, R1234ze for variable speed centrifugal chillers, The Institute of refrigeration 11.4.2013
[10] Magnusson, Roger, Hagglund, Lars, Gustafsson Aasa, Bergstrom, Ulrika and Lejon, Christian: Identification and brief toxicological assessment of combustion products of refrigerant HFO-1234yf, Umaa University 2016
[11] US Department of Energy, Protective Action criteria https://sp.eota.energy.gov/pac/Search
[12] Alberta Health, Public Health Compliance, January 2017
[13] Nordic ministers council, Cost of Inaction, March 2019
[14] the Norwegian Environment Agency, Study on environmental and health effect of HFO refrigerants
[15] Klima reporter, VW wechselt das Klima, https://www.klimareporter.de/verkehr/vw-wechselt-das-klima
[16] R744.com, Valeo launches CO2 heat pump for buses at Busworld, October 2017
[17] Bamigbetan, O. The development of a hydrocarbon high temperature heat pump for industrial heating applications. https://ntnuopen.ntnu.no/ntnu-xmlui/handle/11250/2584930
[18] https://heatpumpingtechnologies.org/annex54/

13th IEA Heat Pump Conference
April 26-29, 2021 Jeju, Korea

Fundamental Study on a Green Roof Building Air-conditioning System – Experimental Analysis of Summer Mode using a Reduction Model Apparatus

Tzuwei Yeh[a*], Toshio Otaka[b]

[a]Graduate School of Engineering, Kokushikan University, 4-28-1, Setagaya, Setagaya-ku, Tokyo, 154-8515, Japan
[b]School of Science & Engineering, Kokushikan University, 4-28-1, Setagaya, Setagaya-ku, Tokyo, 154-8515, Japan

Abstract

In recent years, urban areas in Japan have been experiencing a phenomenon called the heat island effect, which causes the temperature in cities to increase to a few degrees warmer than the surrounding suburban areas. It has attracted attention as one of many environmental issues. By utilizing the green roof units as thermal storage tanks and combining it into the building air-conditioning system which has an auxiliary heat source apparatus, a new air-conditioning system with low energy consumption can be designed, and there is the possibility that this technology could provide a solution to both the heat island effect and global warming. This paper relates to an experimental apparatus as a reduction model which we produced to evaluate the effectiveness of this compound system. The reduction model apparatus has a heat storage planter, a tank of hot water, artificial solar heat and an air conditioner.

In this paper, we presented operation characteristics of summer mode on this reduction model apparatus, and results show that the green roof building air-conditioning system is one promising candidate as a new building air-conditioning system.

Keywords: Heat pump; Green roof; Heat storage; Artificial sun; Heat recovery

1. Introduction

In recent years, urban areas in Japan have been experiencing a phenomenon called the heat island effect, which causes the temperature in cities to increase to a few degrees warmer than the surrounding suburban areas. It has attracted attention as one of many environmental issues. The heat island effect is a phenomenon in which atmospheric temperature is elevated due to increases in artificial heat releases and artificial land surfaces. In urban areas, the heat release rate is high because of the higher energy consumption rate. Additionally, since the coverage of artificial land surfaces such as roads or concrete buildings is extensive in urban areas, these materials act as a thermal storage medium through energy consumption, causing temperature increases in these areas. Especially in summer time, there is concern about health issues related to heat exhaustion, etc. caused by the temperature rise, and it becomes a serious environmental issue when a vicious spiral occurs due to the temperature rise driving up energy consumption. As a preventive measure, attention is being given to green roof projects that allow for a reduction in asphalt or concrete surface coverage in urban cities and are expected to promote the transpiration effect of plants. Consequently, various types of green roof units have actually been made available for practical use.

In addition to the remedial measure against the heat island effect, green roofs are also expected to provide other positive impacts including prolonging a building's life span and saving energy consumption as a result of reductions in air conditioning usage, since it increases building insulation. One of the global environmental problems of importance is global warming. To suppress global warming requires a decrease in load in the power plants.

* Corresponding author. Tel.: +81-80-7304-2482 ;
E-mail address: s9me005g@kokushikan.ac.jp

Thus, increasing the energy efficiency of electrical equipment is an important policy. Especially, the energy efficiency of air-conditioning systems for buildings should be improved immediately, because they are less efficient than household air conditioners. From these facts, the author and other staff have been conducting fundamental researches by focusing on a combined system of a green roof and air-conditioning for buildings [1]. And the heat transfer characteristic of lightweight soil was clarified [2]. Current building air-conditioning systems are operated under excessive heat loads, and when a green roof unit is used as a thermal storage tank, the excessive heat can be utilized by establishing an energy saving type air-conditioning system which produces efficient energy use. However, a combined system of a green roof and air-conditioning is currently not on the market. By utilizing the green roof units as thermal storage tanks, and combining it into the building air-conditioning system which has an auxiliary heat source apparatus, a new air-conditioning system with low energy consumption can be designed, and there is the possibility that this technology could provide a solution to both the heat island effect and global warming. Furthermore, we developed an experimental apparatus of a reduction model which is designed to evaluate the effectiveness of this compound system [3].

This paper relates to the green roof air-conditioning system under summer times conditions by using collector as a function of a water retention rate by lightweight soil from results of experiments using this reduction model apparatus.

2. Reduction Model Apparatus

2.1. Outline of a system to target

Figure 1 shows expected summer and winter mode of a system with a green roof unit for a building. If a green roof unit is utilized as a thermal storage unit for air conditioning, an air-conditioning system for a building can be made energy efficient. In winter time, excess waste heat is transferred from the interior to a green roof unit in the building, which allows the plants to grow without dying all year. A green roof improves the thermal insulating properties of the building, which increase the energy efficiency of the air conditioning. A green roof can also receive solar energy to heat water. The efficiency of these co-generation systems for buildings is around 0.5 as COP of a trial calculation which was predicted with an assumption.

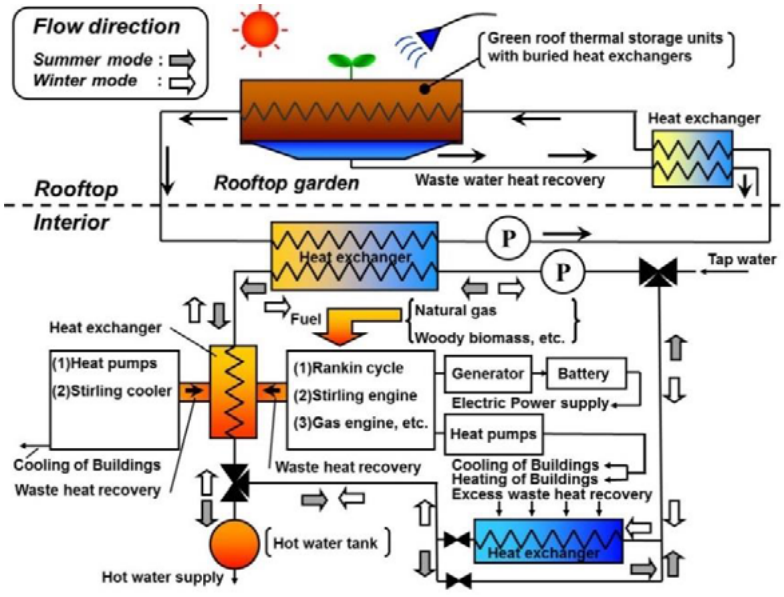


Fig. 1. Structure of a system

2.2. Reduction Model Apparatus

The author has designed an apparatus as a reduction model which we produced to evaluate the effectiveness of this compound system based on basic experimental results. We assumed a building which has 8 rooms of 23 m^2 and total floor area of 200 m^2. The reduction model reduced this to 1/15. Table 1 shows specifications of the reduction model apparatus.

Figure 2 shows the reduction model apparatus. Then also Figure 3 shows a circuit diagram of this model. This apparatus has a heat storage planter, a tank of hot water, and an air conditioner. The heat storage planter is heated by artificial solar heat, and collected heat is done heat storage of by hot water tank. The hot water tank is united with an air-conditioning system through a heat exchanger.

Table 1. Specifications of the reduction model

	A building to assume	A reduction model
Floor area	200 m^2	13.3 m^2
Planter area	3.75 m^2	0.25 m^2
Hot water supply	28 L/min.	1.8 L/min.
Capacity of air conditioner	40 – 46.8 kW (2 HP ×8)	2.5 – 2.8 kW (1 HP)
Waste heat from a building	6.51 kW	0.43 kW
Solar irradiance from an artificial solar		800 W/m^2 (max.)

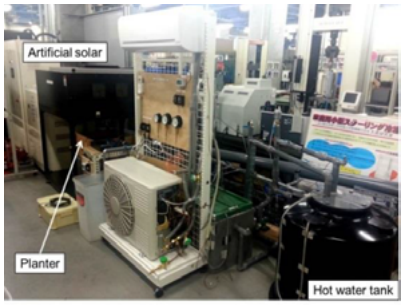


Fig. 2. The reduction model

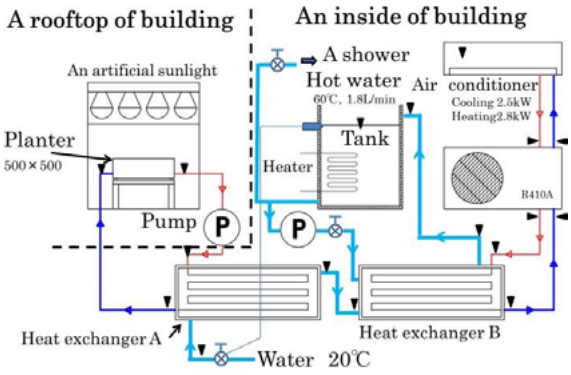


Fig. 3. Circuit diagram of the reduction model

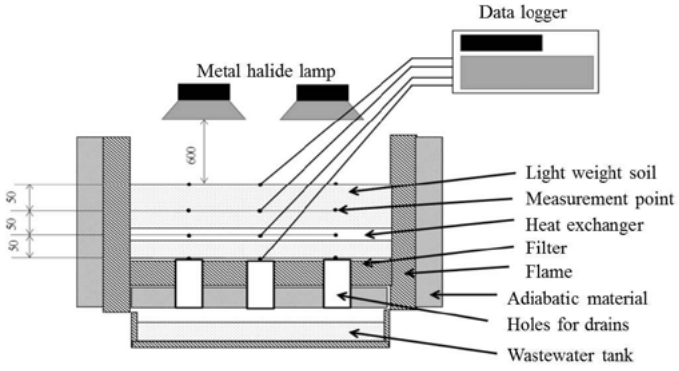


Fig. 4. Schematic view of the planter

A design of the planter used for the reduction model apparatus is shown in Figure 4 for greening units, the bottom part has holes for drains so that the excess water could always be discharged from the unit. Furthermore, on the ground, thermocouples are placed at five places numbered as No.1 to No.5, each place has depths of 0 mm, 50 mm, 100 mm, and 150 mm from the surface. Instead of the sun, we use artificial sunlight to adjust solar irradiance. The adjustment of solar irradiance was set between 700 and 800 W/m^2. The metal halide lamp has a distance of 600 mm from the soil surface. To avoid temperature effects from the outer environment, insulation materials are set at the side and bottom surface of the greening unit. The copper pipes are buried to 100 mm depth as a heat exchanger, and water passes through in it consecutively.

3. Experimental

3.1. Experimental conditions

Table 2 shows the experimental conditions. The selection of water retention rate is on the mass of water to be 0 kg, 3kg, 6kg, 9kg and through Formula (1) to calculate the water retention rate.

Table 2. Experimental conditions

	Conditions
Water retention rate (%)	0%, 33%, 50%, 60%
Solar irradiance (W/m^2)	700~800 (W/m^2)
Temperature of water (˚C)	15(˚C)
Flow rate of water (L/min.)	4.0~4.5 (L/min.)
Time of measurement (hours)	6 (hours)
Mass of dry soil (kg)	6 (kg)

Here, the definition of water retention rate is shown as

$$u = W_w/(W_w + W_s) \times 100\% \quad (1)$$

where
u = Water retention rate (%), W_w = Mass of water (kg), W_s = Mass of dry soil (kg)

3.2. Experimental results

The experimental results are shown in Figure 5 to Figure 7.

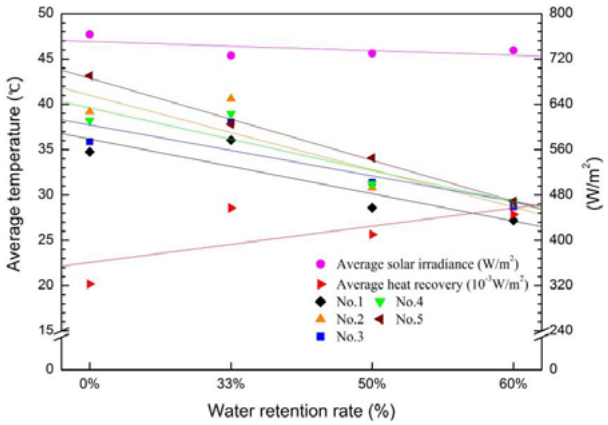


Fig. 5. Water retention rate affects average temperature and average heat recovery

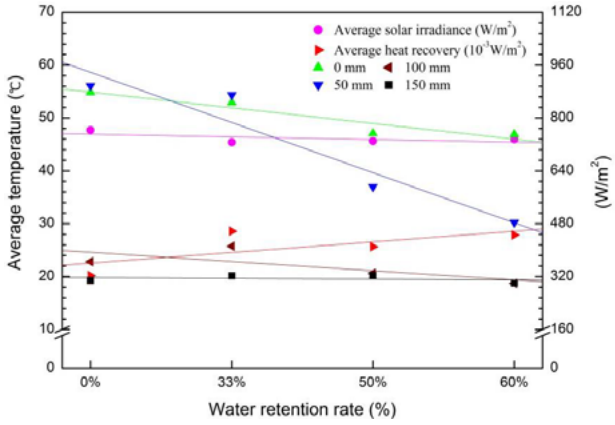


Fig. 6. Water retention rate affects different depth measurement point average temperature and average heat recovery

In Figure 5 to Figure 7, each point represents the average measurements in 6 hours and each linear regression is drawn by its points. The measurement point in average heat recovery represents the copper pipe with tap water which buried in the planet is heat-exchanged with the waste heat generated by the artificial sun.

As shown in Figure 5, a soil average temperature decrease as the water retention rate increase. In contrast, there is an increasing trend for average heat recovery. Also, at a water retention rate of 60%, the average temperature of No.1 to No.5 (about 28.7 ˚C) is more uniform than others.

In Figure 6, 0 mm and 50mm has a relatively large average temperature difference. The copper pipe with tap water is buried in depth 100 mm which has the average heat recovery about 0.45 (W/m^2) at a water retention rate of 60%.

Figure 7 shows the higher a water retention rate, the higher an average heat recovery efficiency tends to be. Finally, the average heat recovery efficiency has about 0.06% at a water retention rate of 60%.

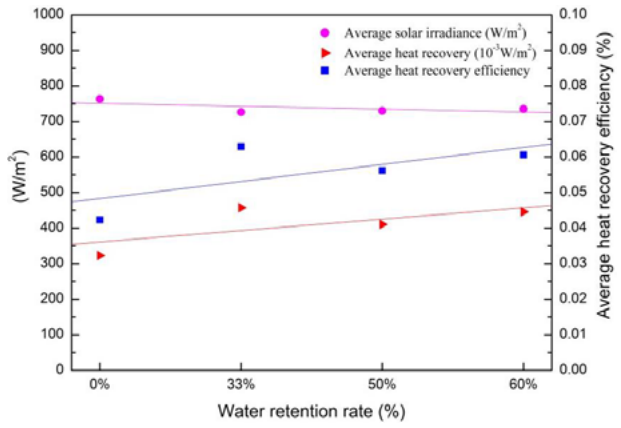


Fig. 7. Average heat recovery and average heat recovery efficiency

4. Conclusion

The thermal energy stored in the planter unit as a function of moisture content was recovered and a basic experiment was conducted to clarify the heat storage characteristics of this model device. In addition, since practicality is confirmed in this system, the function utilization test of this reduction model device is carried out and the result is reported. From this experiment result, it was seen that the heat recovery efficiency increased in proportion to the water retention rate. These results show that the green roof building air conditioning system is one promising candidate as a new building air conditioning system.

5. Acknowledgement

We gratefully acknowledge the work of past member, Taishi Miyahara, and present members, Toshiaki Yanagawa, Taro Horiguchi, Tomoya Watanabe of our laboratory for helpful discussions and comments on the manuscript.

6. Reference

[1] T.Otaka, Study of a Green Roof Building Air-conditioning System with Thermal Energy Storage Unit using Light Weight Soil, Proc. The International Conference on Power Engineering-2009, (2009), pp.299-303

[2] H.Yokobayashi, D.Kim, T.Otaka, Basic Study on a Thermal Design of a Green Roof Planter –Thermal Properties of a Thermal Energy Storage Unit Using Light Weight Soil, Proc. Design Symposium 2012, (2013), pp.203-206

[3] T. Otaka, Study of an Air-conditioning System Combining a Green Roof as Heat Storage Unit - Analysis of Operating Characteristic of a Reduction Model Apparatus, Proc. 12th IEA Heat Pump Conference 2017, (2017)

[4] Taishi Miyahara, Yosuke Ishida, Ryusei Ebine, Toshio Otaka, Heat Storage Characteristics of a Planter Unit for a Green Roof Building Air-conditioning System, Proc. 2019 The International Conference on Engineering and Applied Sciences （ISBN 978-986-5654-07-8)

13th IEA Heat Pump Conference
April 26-29, 2021 Jeju, Korea

Effect of evaporating temperature rising operation for multi-split type air-conditioner on energy conservation and thermal comfort

Hiroshi NAKAYAMA[a*], Yuji NAKA[a], Masaaki MIURA[b], Hideki TANAKA[c]

[a]Chubu Electfric Power co., Inc., 20-1, Kitasekiyama, Midori-ku, Nagoya, Aichi, 459-8522, Japan
[b]Chubu Electfric Power co., Inc., 6-1, Ushijima-cho, Nishi-ku, Nagoya, Aichi, 451-6090, Japan
[c]Nagoya University, Furo-cho, Chikusa-ku, Nagoya, Aichi, 464-0814, Japan

Abstract

In commercial buildings, the energy consumption by air conditioning amounts to 30% -40% of the entire building. Therefore, the energy saving of air-conditioning in those buildings is important to reduce their total energy consumption. In this background, the evaporating temperature rising operation of multi-split type air conditioner during cooling have been applied as one of the energy saving operations.

In general, the increase of the evaporating temperature can improve the efficiency of the air conditioner, and the reduction of the energy consumption can be expected. On the other hand, since the cooling latent heat capacity decreases in this operation, the humidity of the air-conditioned room may increase and the thermal comfort may decrease.

In this study, the energy saving effect and the thermal comfort of evaporating temperature rising operation in the air conditioning system for offices and a store were investigated by simulation. It was found that 7% - 17% cooling energy saving effect can be obtained by the rising the evaporating temperature in consideration of thermal comfort in the room, and larger energy saving effect can be obtained in the building having a high cooling sensible heat ratio.

Keywords: Air conditioner, Evaporating temperature, Energy saving, Thermal Comfort ;

1. Introduction

In order to prevent global warming, it is important to reduce air conditioning energy, which accounts for a large proportion of building energy. In this background, the performance improvement of air conditioners and appropriate air conditioning operation have been conducted. As examples of energy saving operation of multi-split type air conditioner, rising operation of the evaporating temperature during cooling or reducing operation of the condensation temperature during heating have been reported[1][2]. Among them, the rising of the evaporating temperature is attracting operation because a greater effect can be expected.

In general, the evaporating temperature for cooling is controlled to be about 6 °C due to dehumidify indoor air and create a comfortable environment. As shown in Fig.1, by rising the evaporating temperature of the refrigerant, the efficiency of the air conditioner can be improved and the equipment energy consumption can be reduced. On the other hand, since the cooling latent heat capacity is reduced, the humidity of the air conditioned area increases depending on the state of the air conditioning load, and the thermal comfort of the resident is impaired.

Conventionally, commercial multi-air conditioners have been adjusted for capacity by the “refrigerant circulation rate control” method in order to perform individual operation for each indoor unit and to maintain the comfort of each indoor unit. In this method, the refrigerant temperature (evaporating temperature) cannot basically be changed, but it is possible to reduce the equipment energy consumption by forcibly increasing the

* Corresponding author. Tel.: +81-52-621-6101; fax: +81-52-624-9234.
E-mail address: Nakayama.Hiroshi2@chuden.co.jp.

evaporating temperature with a control software. Recently, it has been developed some air conditioning systems that can increase the evaporating temperature when the refrigerant evaporating temperature is controlled by the dedicated controller of the air conditioner manufacturer according to the air conditioning load and it is determined that the air conditioning load becomes low.

This study focuses on the effect of the rising in the evaporating temperature of the commercial air conditioner on the energy saving effect and the thermal comfort of the air-conditioned room. In particular, the energy efficiency and thermal comfort were evaluated for the building type and air conditioner capacity as parameters.

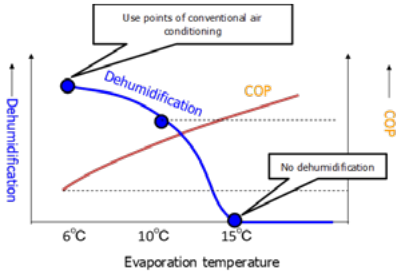


Fig. 1. Relation between evaporating temperature, dehumidification and COP

2. Calculation conditions

2.1. Building conditions

It is considered that the energy saving effect due to the increase in evaporating temperature is greater for buildings with higher sensible heat loads. Therefore, energy simulations are conducted for the office and the business store models which have different cooling sensible ratios (annual cooling sensible heat load/ total cooling load) with total floor area of about 1,000m^2.

Table 1 shows the calculation conditions for these buildings. Two cases for offices are considered. One is Office A which has a conventional specification and the other is Office B which has a nearly ZEB (net Zero Energy Building) specification as next-generation building. Office B not only has better skin performance than Office A, but also has low emissivity (low-e) glass and light shelf near the ceiling (Fig. 2.), which actively uses daylight and has reduced internal air-conditioning load.

These offices are operated to light up from 8:00 to 19:00 except from 12:00 to 13:00, and the occupancy rate and equipment usage rate gradually decrease from 17:00. The specifications of the store model were determined with reference to the previously reported home appliance mass sales store [3]. In this study, we used meteorological data in Nagoya area of Japan. AMeDAS(Automated Meteorological Data Acquisition System) were used for the data [4].

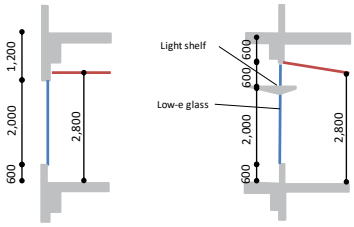


Fig.2 Window shape comparison (Left: Office A, Right: Office B)

Table 1. Model of buildings

		Office A	Office B	Store
Air-conditioning area		1,038m^2	1,038m^2	1,000m^2
Ceiling height		2.8m	2.8m	4m
Outer wall performance	Thickness of insulation	25mm	50mm	-
	Glass	6mm (Single layer)	Low-e (Double layer)	8mm (Single layer)
	Blind	Blind	No Blind	Blind
	Gap wind	0.2number/h	0.1number/h	0.1number/h
	Eaves	No eaves	Eaves	No eaves
Internal heat generation	Lights	14W/m^2	1.6W/m^2	25W/m^2
	Equipment	20W/m^2	10W/m^2	20W/m^2
	Standby power	5W/m^2	2.5W/m^2	-
	Human density	0.1human/m^2	0.1human/m^2	0.1human/m^2
Outside air condition	Amount of outside air	3CMH/m^2	3CMH/m^2	4CMH/m^2
	Outside air cut	Summer 1h Winter 2h	Summer 1h Winter 2h	Summer 1h Winter 2h
Air-conditioning condition	Period	Cooling May~Octobar Heating November~April	Cooling May~Octobar Heating November~April	Cooling April~November Heating December~March
	Operation time	Cooling 8~19 Heating 7~19	Cooling 8~19 Heating 7~19	Cooling 9~21 Heating 9~21
	Inside air condition (Tem./Relative Humidity)	Summer 26°C/50% Winter 22°C/40% Mid-season 24°C/45%	Summer 26°C/50% Winter 22°C/40% Mid-season 24°C/45%	Summer 26°C/60% Winter 20°C/40% Mid-season 24°C/60%

2.2 Air conditioning load

At first, the air-conditioning loads for each hour were calculated using the BEST (Building Energy Simulation Tool) program for the conditions of Table1[5]. The BEST program was developed in Japan as a simulation tool for building air conditioning load and annual energy consumption. The program has the same accuracy in terms of room temperature and air conditioning load of the building as the simulation tools (BLAST, DOE2, ESP, SERIRES, etc.) which commonly used in Europe and the United States [6],[7].

Figure 3 shows the calculation results of the annual air conditioning load in each case. Generally, latent heat is affected by amount of outside air and human density, and sensible heat is affected by internal heat generation and the insulation performance of buildings. Since the store has a longer operating time and larger internal heat generation than the offices, the air-conditioning load and cooling sensible heat have the largest among them. In Office B oriented to nearly ZEB, the internal heat generation is smaller than that of Office A, so that the cooling sensible heat load is small and the heating sensible heat load is large. As a result, the sensible heat ratio during the cooling period (= cooling sensible heat load/cooling total load) tends to be Store> Office A> Office B.

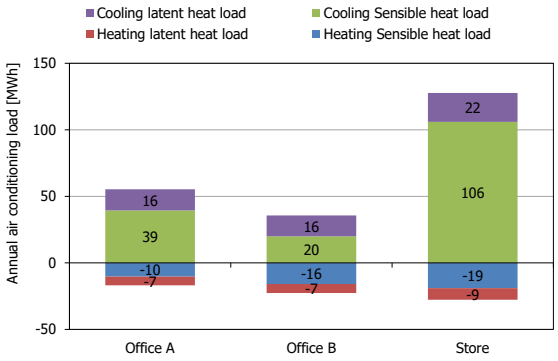


Fig.3. Comparison of annual air-conditioning load

2.3 Air conditioner assumption

In general, the capacity of air conditioners is set with a margin for the maximum air conditioning load. In this calculation, the capacities of 100%, 120%, 140%, and 160% were set for the maximum air conditioning load calculated in each case in order to confirm the effect of the installed capacity.

Figure 4 shows the relationship between the evaporating temperature and the cooling capacity normalized by the total cooling capacity at 6 °C. This relationship between the cooling capacity of the air conditioner and the evaporating temperature of refrigeration which published by the manufacturer were used [8]. As the evaporating temperature rises, the total cooling capacity gradually decreases, reaching a capacity of about 60% at an evaporating temperature of about 15 °C. Although the sensible heat capacity does not change much, latent heat capacity decreases as the amount of dehumidification decreases, and the latent heat capacity becomes 0 at 15 °C.

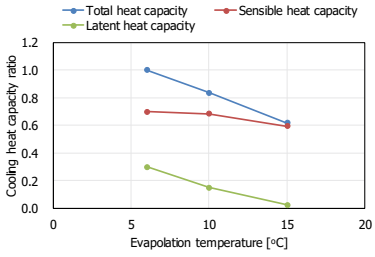


Fig.4. Relationship between the evaporating temperature and the cooling capacity

2.4 Energy consumption / comfort calculation method

Figure 5 shows the calculation procedure. At first, we determined the air-conditioner rated capacity based on the air-conditioning maximum (peak) load calculated by the BEST program. And then, the capacity was corrected by the evaporating temperature and the outside air temperature at each time, and the sensible heat capacity/latent heat capacity and power consumption of the equipment were calculated. Here, when the sensible heat/latent heat capacity is insufficient with respect to the air-conditioning load, the indoor temperature and humidity air-conditioning are changed. When the air conditioning load cannot be processed at the calculation time, the unprocessed load was added to the next time. PMV (Predicted Mean Vote) which considered to be most recognized in thermal comfort standard was used as the thermal comfort index in the air-conditioned room [9]. PMV was calculated with indoor temperature, humidity, radiation temperature, wind velocity and so on, and the values based on experimental results in Table 2 were used for this calculation.

We calculated four conditions for the evaporating temperature. Three of these conditions fixed the evaporating temperature at 6 °C, 9 °C, and 12 °C, and one of them changed the evaporating temperature. That is, the evaporating temperature was changed within ± 0.5 which is the comfortable range of PMV. In this paper, this condition is called “PMV control”.

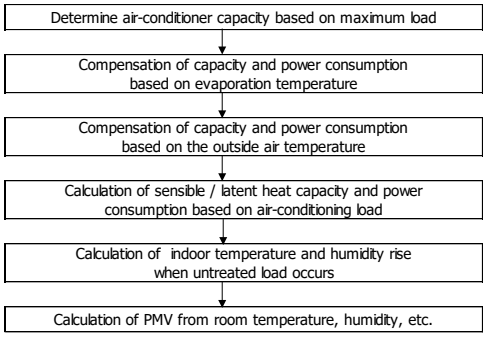


Fig.5. Calculation procedure

Table.2. Calculation condition of PMV

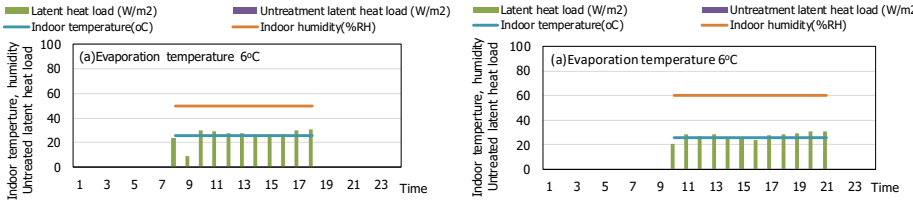
	Indoor temperature and humidity	Radiation temperature (°C)	Wind Velocity (m/s)	clo	Mets
Office	Calculated value	Indoor temperature+0.5	0.05	0.43	1.1
Store	Calculated value	Indoor temperature	0.05	0.3	1.4

3. Calculation results

3.1 Calculation results for Office A

Figures 6(a) to (d) show temporal changes of latent-heat load, untreated latent heat load, indoor temperature, and indoor humidity on the summer representative day (August 1) when the evaporating temperature is fixed at 6 °C (standard), 9 °C, and 12 °C and PMV controlled. Figure 7 shows temporal changes of PMV in each case. In all cases, the capacity of the air conditioner is 120%, which is close to the actual condition. As shown in Fig. 6(a), at the standard evaporating temperature of 6 °C, all the sensible heat and latent heat load can be processed, so the temperature and humidity do not change during the day. When the evaporating temperature is set as high as 9 °C and 12 °C, though the sensible heat load is processed, the untreated latent heat load increases with time, and the indoor humidity and PMV shift to the warmer side. In particular, when the evaporating temperature is fixed at 12 °C, the untreated load increases, and the indoor humidity becomes extremely high at 10:00 (Fig.6(c)).

Actually, humidity is not expected to rise to nearly 100% due to mixing of outside air and room air due to ventilation not considered in this calculation, but it is expected that the environment will become extremely uncomfortable. On the other hand, in the case of PMV control as shown in Fig. 5(d) and Fig.6, the PMV is maintained within 0.5, and although untreated load occurs, thermal comfort is maintained. It is noted that similar treads were seen in Office B.



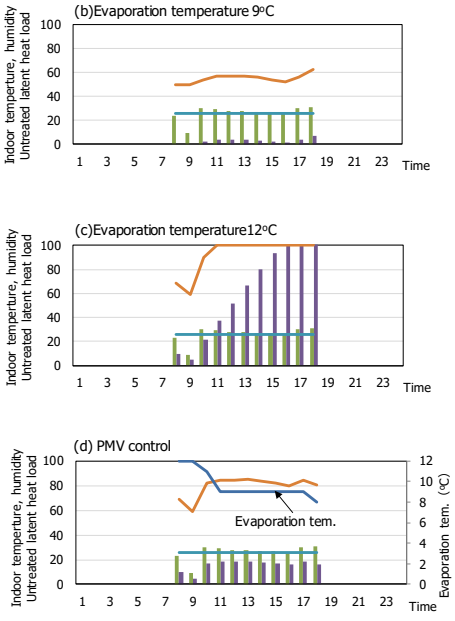


Fig.6. Temporal change of temperature/humidity and latent heat load (Office A)

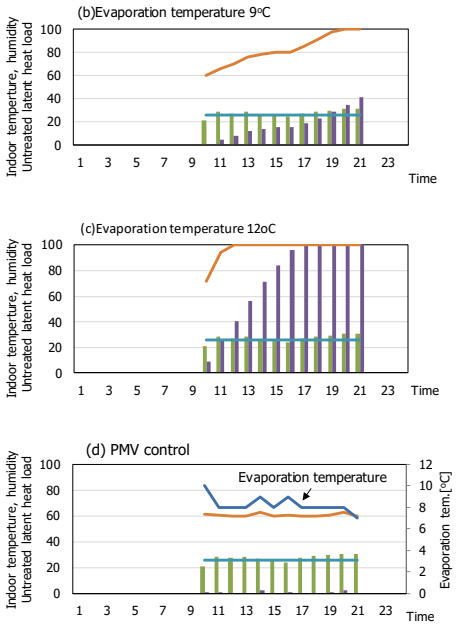


Fig.8. Temporal change of temperature/humidity and latent heat load (Store)

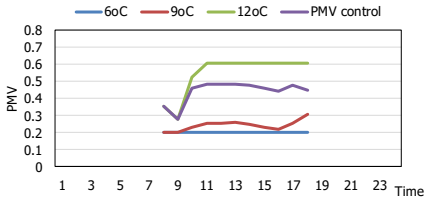


Fig.7. Temporal change of PMV (Office A)

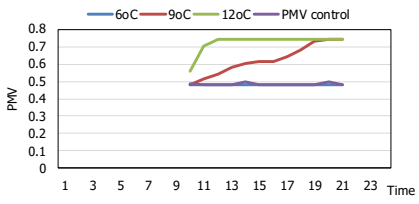


Fig.9. Temporal change of PMV (Store)

3.2 Calculation results for Store

Figures 8(a) to (d) show temporal changes of latent-heat load, untreated latent heat load, indoor temperature, and indoor humidity on the summer representative day (August 1) when the evaporating temperature is fixed at 6 °C (standard), 9 °C, and 12 °C and PMV controlled, and Figure 9 shows temporal changes of PMV. Similar to Office A, in the case of the evaporating temperature 6 °C, the sensible heat and latent heat load can be processed, so both the temperature and humidity are stable. However, when the evaporating temperature is set to 9 °C and 12 °C, the untreated latent heat load increases with time, the indoor humidity and PMV shift to the warmer side, and PMV finally becomes about 0.75 as shown in Fig.9. On the other hand, in the case of PMV control, since PMV is high at the time of air conditioning start-up, the air conditioner quickly decreases the evaporating temperature and almost no untreated load occurs.

3.3 Influence on power consumption and thermal comfort (Office A)

Figure 10 shows a comparison of the cooling power consumptions in Office A. In these case, cooling period is from May to October. Comparison parameters are evaporating temperature and air-conditioner capacity.

When the evaporating temperature is increased from 6 °C to 9 °C and 12 °C, the power consumption during cooling decreases. For example, in the case of 100% for air-conditioner capacity, cooling power consumption is reduced by 26% at evaporating temperature of 12 °C compared to evaporating temperature of 6 °C. In the

case of PMV control, a reduction effect of 17% can be obtained.

Figure 11 and Fig.12 show time that PMV exceeds 0.5 (uncomfortable time) and cooling COP, respectively. In the case of evaporating temperature 12 ° C, the time that PMV exceeds 0.5 increases in the midsummer season, and the uncomfortable time increases significantly. Basically, the air-conditioner load which can be processed increases as the installed air-conditioner capacity increases. Therefore, as shown in Fig. 10 and Fig.11, an increase in the air-conditioner capacity leads to a decrease uncomfortable time and an increase in the cooling power consumption.

When the evaporating temperature is fixed, the COP is almost the same regardless of the capacity of the air conditioner. This is because air-conditioning capacity is small relative to the air-conditioning load, and high-load operation continues. On the other hand, in the case of PMV control, as the air conditioner capacity increases, the cooling power consumption decreases and COP increases as shown in Fig.10 and Fig.12. This is because the air conditioner is operated at an efficient medium load.

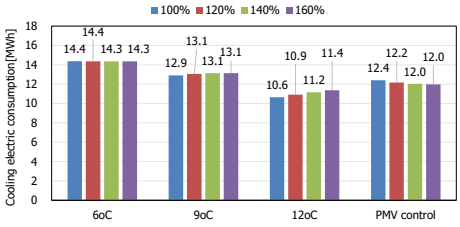


Fig.10. Cooling power consumption

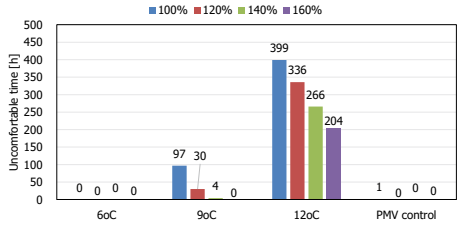


Fig.11. Uncomfortable time

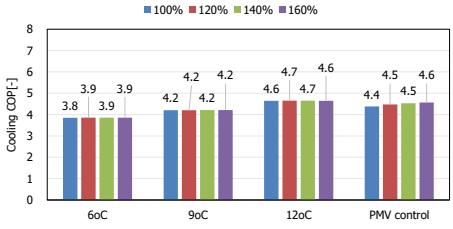


Fig.12. Cooling COP

3.4 Considerations for further energy saving

In order to investigate further energy saving effect by PIV control, the cases where PMV is allowed to 0.6(slightly uncomfortable region) were calculated. Table 3 shows comparison of the power consumption reduction rates at Office A, Office B, and Stores in the case of PMV<0.5 and PMV<0.6. These power consumptions at each case were normalized by that of the evaporating temperature 6 °C. Compared to the standard evaporating temperature of 6 °C, the power consumption can be reduced by 7-17% in the case of PMV<0.5 considering energy saving and thermal comfort. In either case, even if PMV<0.6 is allowed, the energy saving effects only increase by 1 to 4 points compared to those in the case of PMV<0.5.

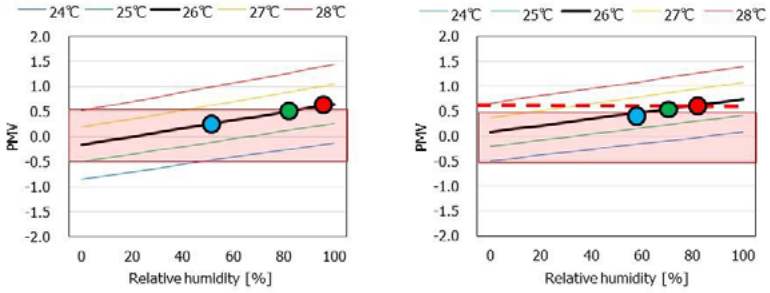
Figure 13(a) and (b) show the relationship among indoor temperature, relative humidity, and PMV in the Office and Store, respectively. In this calculation, the sensible heat load could be processed in all cases, so the room temperature did not change from 26 °C and only the relative humidity increased. In addition, even if PMV=0.5 (green circle in the figure) or PMV=0.6 (red circle in the figure) is allowed for the standard temperature and humidity conditions (blue circle in the figure) in this calculation, there is no significant difference. Therefore, it seems that the increase in energy saving effect has become small. However, if the temperature/humidity setting is set to a low value, the temperature/humidity control range is increased, and it is considered that a large energy saving effect can be obtained by introducing PMV control.

Figure 14 shows the relationship between the cooling sensible heat ratio and the cooling power consumption reduction rate in the PMV control. Although there is a difference in the power consumption reduction rate due to the difference in temperature and humidity settings between the office and the store, the higher the sensible heat ratio in summer, the higher the energy saving effect. Therefore, a large power consumption reduction effect can be expected in commercial buildings such as warehouses and data centers with large sensible heat ratio.

Table.3. Power consumption reduction rate (Cooling season)

	Office A		Office B		Store	
Air-conditioning	PMV<0.5	PMV<0.6	PMV<0.5	PMV<0.6	PMV<0.5	PMV<0.6

Capacity						
100%	-14%	-15%	-7%	-10%	-11%	-13%
120%	-15%	-16%	-8%	-10%	-14%	-15%
140%	-16%	-17%	-9%	-12%	-15%	-16%
160%	-17%	-17%	-9%	-13%	-16%	-17%



(a) Office (b) Store

Fig.13. Relationship among temperature, relative humidity, and PMV

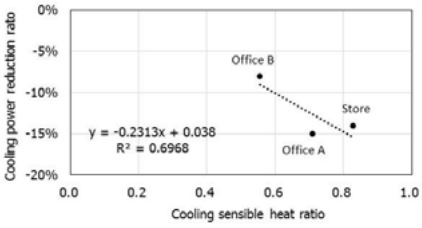


Fig.14. Relationship between cooling sensible heat ratio and cooling power reduction ratio

4. Summary

In this study, we calculated on the effect of the rising in the evaporating temperature of the multi-type air conditioner on the energy saving effect and the thermal comfort of the air-conditioned room. The main results are as follows,

Compared to the standard evaporating temperature of 6 °C, the power consumption can be reduced by about 21-26% in the case of the evaporating temperature 12 °C, and 7-17% in the case of PMV control considering energy saving and thermal comfort. When the evaporating temperature is fixed at 12°C, a large energy saving effect is obtained, but the thermal comfort is significantly deteriorated.

When the evaporating temperature is fixed, the COP is almost the same regardless of the capacity of the air conditioner. An increase in the air-conditioner capacity leads to a decrease uncomfortable time and an increase in the cooling power consumption.

When PMV control is used, a large energy consumption reduction effect can be expected in commercial buildings with a large cooling sensible heat ratio.

References

[1] Zhang, G., Xiao, H., Zhang, P.,Wang, B, Li, X.,Shi, W., and Cao, Y., 2019. “Review on recent development of variable refrigerant flow systems since 2015”, Energy and Buildings, 198, p.444-466.

[2] Zhao, D., Zhang X., Zhong M., 2015. “Variable evaporating temperature control strategy for VRV system under part load conditions in cooling mode”, Energy and Buildings, 91, p.180-186.

[3] Nakayama, H., Miyaoka, Y., Hirota, M.,Onishi, M., 2015. “A Study on the Effect of LED Lamps on Air-Conditioning Load in Business Related Building”, Proceedings of the International Commision on Illumination 2015 (CIE2015), Manchester, UK, paper no.OP64.

[4] Akasaka, H. 2005, “Expanded AMeDAS weather data 1981-2000”, Architectral Institute of Japan.

[5] The BEST Program, Institute for Building and Energy Conservation, http://www.ibec.or.jp/best/english/index.html

[6] Hirabayashi, K.,Murakami, S., Ishino, H., Kohri, K., Utsumi, Y., Nimiya, H., "Development of an Integrated Energy Simulation Tool for Buildings and MEP Systems, the BEST Validation by BESTEST and the Case Study", Proceedings of The Society of Heating, Air-Conditioning and Sanitary Engineers of Japan, OS-14, 2008 (in Japanese)
[7] Judkoff, R.; Neymark, J., "International Energy Agency building energy simulation test (BESTEST) and diagnostic method", United States: N. p., 1995. Web. doi:10.2172/90674.
[8] Technical manual of multi split type air conditioner, Mitsubishi Electric., 2018 (in Japanese)
[9] Fanger PO., 1970. "Thermal comfort", Danish Technical Press, Copenhgen.

13th IEA Heat Pump Conference
April 26-29, 2021 Jeju, Korea

Study on Short Circuit of Airflow in Outdoor Unit of Air Conditioner

Hiroyuki Miyazaki[a*], Tsubasa Ito[b], Hiroshi Nakayama[a], Masafumi Hirota[b]

[a]Chubu Electric Power Co.,Inc., 20-1, Kitasekiyama, Midori-ku, Nagoya city, Aichi, 459-8522, Japan
[b]Mie University, 1577, Kurimamachiya-cho, Tsu-city, Mie, 514-0102, Japan

Abstract

In air conditioners installed in commercial buildings, their efficiencies are often deteriorated by short circuits of airflows in which hotter (cooling operation) or cooler (heating operation) air blown out from the outdoor units is sucked again in the outdoor units. From viewpoints of energy savings of air conditioners, it is necessary to understand the influence of short circuits of airflows on operations of air conditioners quantitatively and to take measures against them. The purpose of this study is to make clear the influence of installation conditions of the outdoor unit of an air conditioner on the short circuit of airflow issued from it.

We made laboratory measurements and field measurements of airflow temperatures around the outdoor unit of a packaged air conditioner. The short circuit of the airflow from the front face to the side face of the outdoor unit was enhanced when there was a wall near the side face. In such cases, linear relationships were found between suction air temperatures of the outdoor unit and outdoor air temperatures.

Keywords: Air conditioner, Outdoor unit, Airflow, Short circuit, Suction air temperature ;

1. Introduction

Individual distributed air conditioner may cause a short circuit of air flow in which high-temperature air blown from its outdoor unit (cooling operation) is directly sucked by its suction face, depending on the outdoor unit installation situation (close to walls, under the roof, concentrated equipment installation, etc.). It is known that the performance of the air conditioner is deteriorated by this short circuit. In addition, there are cases in which the air conditioner shuts down due to capacity control when the impact of the short circuit becomes large. In order to save energy and keep proper operation, it is required to quantitatively understand the influences of short circuits and take measures against them.

Several papers on short circuits have been reported so far [1][2], but there are few reports on the influences of outdoor unit installation conditions, changes in outdoor air temperature and load factors on short circuits and capacity degradation of an air conditioner.

The purpose of this study is to quantitatively understand the influences of short circuits of air flow in the outdoor unit on the performance of air conditioners, taking the outdoor unit installation conditions, outdoor air temperature and load factor as parameters.

In the first half of this paper, we show the results obtained in the environmental test laboratory in which influences of a building wall or an obstacle on the performance of a packaged air conditioner were examined to clarify the relationship between the outdoor unit's suction temperature and the outdoor air temperature. In the second half, we will clarify the effect of short circuits when two or more air conditioners installed in an actual building are operated with walls around the outdoor unit.

* Corresponding author. Tel.: +81-52-621-6101; fax: +81-52-624-9234.
E-mail address: Miyazaki.Hiroyuki2@chuden.co.jp.

2. Laboratory Test

2.1. Test Method

This test was conducted in the environmental test laboratory of the Chubu Electric Power Co., Inc. by installing one side blown 5-horsepower packaged air conditioner with a specification shown in Table 1. Figure 1 shows the outdoor unit installation conditions. Pattern 1 is a standard installation in which there are no obstacles around the suction face (back and side faces) and the blowing face (front face) of the outdoor unit.

On the other hand, since many outdoor units are often installed near the building walls, a test was performed on Pattern 2 in which walls simulating building walls were installed near the back and side faces (suction faces) of the outdoor unit. Here, the distances between the wall and those faces were set to effective spaces of 0.3 m as described in the manufacturer's installation manual. In addition, a test was also conducted on Pattern 3 that simulated an installation in a small space with walls near the back, side (suction) and the front (blowing) faces of the outdoor unit. The distance between the front face of the outdoor unit and the wall was set at 1.0 m as described in the manufacturer's installation manual.

Figure 2 shows the positions of thermo-sensors set on the suction and the blowing faces with the wall setting situation of Pattern 2 in the environmental test laboratory.

Table 1. Specifications of test air conditioner

5 HP packaged air conditioner (manufactured in 2017)		
	Cooling operation	Heating operation
Rated capacity	12.5 kW	14.0 kW
Rated power consumption	3.31 kW	3.30 kW
APF*(2015)	6.3	

*APF: Annual Performance Factor

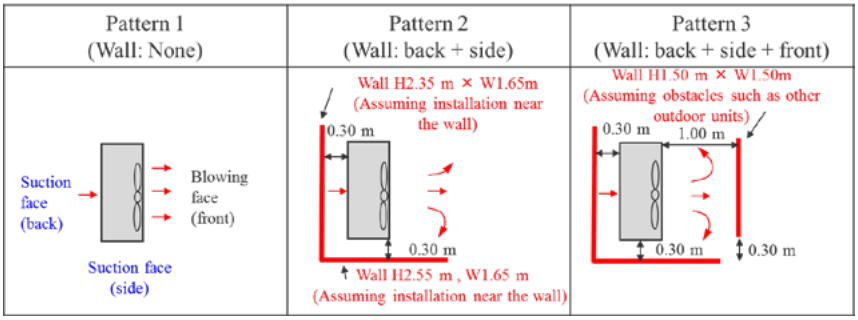


Fig. 1. Wall installation patterns around the outdoor unit of the air conditioner

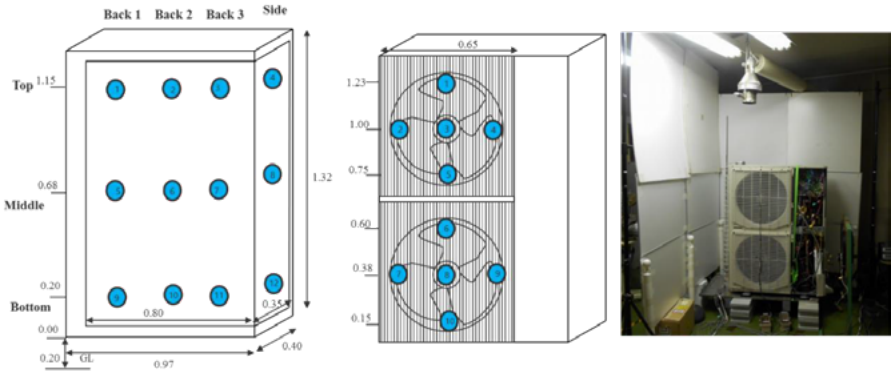


Fig. 2. Positions of sensors on the outdoor unit and wall installation condition of Pattern 2

2.2. Test Conditions

The air conditioning capacity was measured by the indoor enthalpy method. Test conditions are shown in Table 2, the air dry bulb temperature in the outdoor test room was set at 35 ºC, 30 ºC or 25 ºC in the cooling performance test, and at 12 ºC, 7 ºC or 2 ºC in the heating performance test.

A part of tests was conducted considering the situation that the air conditioning load is large and the air conditioner is always operating at full power (100%). In these tests, the indoor test room was controlled at 27 ºC and the remote control temperature was set to 18 ºC in the cooling operation, and the indoor test room was controlled at 20 ºC and the remote control temperature was set to 30 ºC in the heating operation.

Tests were also conducted assuming the situation that the air conditioning load is reduced in the intermediate period. In the case of cooling, the air conditioning load was set at 25% and 50% of the actual rated cooling capacity of the tested air conditioner, and the air temperature of the indoor test room was controlled at 27 ºC by the air conditioner itself. In the heating performance test, the indoor air temperature was controlled at 20 ºC with the heating load corresponding to 25% and 50% of the actual rated heating capacity.

Measurement data were sampled at 10-second intervals, and they were averaged in 60 minutes for the steady operation and in one cycle for the intermittent (on-off) operation.

Table 2. Test conditions (dry bulb temperature / wet bulb temperature)

Operations	Outdoor temperature conditions	Indoor temperature conditions	Load factor
Cooling	35 ºC / -	27 ºC /19 ºC	100%
Cooling	30 ºC / -	27 ºC /19 ºC	50%
Cooling	25 ºC / -	27 ºC / 19 ºC	25%
Heating	12 ºC / 11 ºC	20 ºC / -	25%
Heating	7 ºC / 6 ºC	20 ºC / -	50%
Heating	2 ºC /1 ºC	20 ºC / -	100%

2.3. Results

2.3.1. Influence of Wall Installation

Table 3 shows the results of average suction air temperatures (back, side, and overall average) and Table 4 shows the average blowing air temperature in each pattern in the cooling performance test at the outdoor air temperature of 35 ºC with full power operation.

In Pattern 1, the suction air temperatures on the back and side faces are about 37 ºC, and the difference from the outdoor air temperature is not so large. It should be noted that the temperature sensor position for setting the test room was different from the positions of the thermo-sensors on the suction face, so there was a difference between the test room setting temperature and the suction air temperature in Pattern 1.

In Pattern 2 in which the walls are installed on the back and side of the outdoor unit, the suction temperature is about 2 ºC higher than Pattern 1 on average. In particular, the suction air temperature is as high as 41.2 ºC on the side face, and it can be seen that the influence of the short circuit is greatly reflected on the side of the outdoor unit. Pattern 3 shows a similar trend to Pattern2.

Regardless of the change in the suction air temperature, the blowing air temperature is almost constant at about 48 ºC in all patterns as shown in Table 4.

Table 3. Average of suction air temperature during cooling operation at the outdoor air temperature of 35 ºC with 100% operation

Suction air temperature	Pattern 1	Pattern 2	Pattern 3
Back	37.0ºC	38.6ºC	39.1ºC
Side	37.6ºC	41.2ºC	42.3ºC
Overall	37.1ºC	39.2ºC	39.9ºC

Table 4. Average of blowing air temperature during cooling operation at the outdoor air temperature of 35 ºC with 100% operation

	Pattern 1	Pattern 2	Pattern 3
Blowing air temperature	48.1ºC	47.9ºC	48.6ºC

For more detailed changes in the air temperature on the suction face, Table 5 shows differences between suction air temperatures in Pattern 2 and Pattern 1, and Table 6 shows a comparison with Pattern 3. Here, the positions described in these tables correspond to the sensor positions shown in Figure 2. As can be seen from Table 5, the place where the temperature change is particularly large is from the center to the bottom of the back and side faces of the outdoor unit, rising by 6-7 ºC. Table 6 of Pattern 3 shows a similar tendency. It is thought that hot air blown from the front face of the outdoor unit stayed around the bottom of the side face where there was little air flow.

In addition, from the overall average temperature change in Table 5 and Table 6, it rises to 2.1 ºC by wall setting on the back and side, whereas it rises to 2.8 ºC by wall setting on the back, side and front. It can be seen that the influence of the back and side walls on the short circuit is greater than that of the front wall.

Table 5. Difference of suction temperatures of pattern 2 from pattern 1 at the outdoor air temperature of 35 ºC with 100% operation

	Back 1	Back 2	Back 3	Side
Top	-0.1ºC	-0.3ºC	-0.6ºC	-0.5ºC
Middle	-0.9ºC	0.8ºC	3.6ºC	5.1ºC
Bottom	1.3ºC	3.5ºC	7.2ºC	6.2ºC
Average of Back		1.6ºC		-
Average of Side		-		3.6ºC
Average of Overall		2.1ºC		

Table 6 Difference of suction temperatures of pattern 3 from pattern 1 at the outdoor air temperature of 35 ºC with 100% operation

	Back 1	Back 2	Back 3	Side
Top	0.2ºC	0.5ºC	0.7ºC	0.7ºC
Middle	-0.8ºC	1.7ºC	5.2ºC	6.3ºC
Bottom	1.5ºC	3.5ºC	6.4ºC	7.2ºC
Average of Back		2.1ºC		-
Average of Side		-		4.7ºC
Average of Overall		2.8ºC		

Table 7 shows the power consumption, cooling capacity and COP of the air conditioner during 100% cooling operation at the outdoor air temperature of 35 ºC for each pattern. From these results, the power consumption increased by 2-4%, the cooling capacity decreased by 1-3% and consequently COP decreased by 3-6% in Patterns 2 and 3 compared to Pattern 1, due to the short circuit.

Table 7 Power consumption, Cooling capacity and COP at the outdoor air temperature of 35 ºC with 100% operation

	Pattern 1	Pattern 2	Pattern 3
Power consumption	4.43kW	4.54kW	4.62kW
(Rate of change)	(Basis)	(+2.36%)	(+4.12%)
Cooling capacity	14.19	14.04	13.81
(Rate of change)	(Basis)	(-1.06%)	(-2.68%)
COP	3.20	3.09	2.99
(Rate of change)	(Basis)	(-3.34%)	(-6.53%)

2.3.2. Influence of Partial Load Operation

In actual use an air conditioner is often operated under a partial load. Therefore, we conducted partial load performance tests. In order to understand the influence of the short circuit under partial load, the setting of outdoor temperature and lord factor of the environmental test laboratory was changed, and the relationship between the suction average temperature, the outdoor air temperature and load factor was investigated. As mentioned in Section 2.3.1, there was a difference between the test room setting temperature and the suction air temperature in Pattern 1, in which the influence of the short circuit was negligibly small. Hence, in order to clarify the difference between Patterns 2 and Pattern 3 that have a strong influence of short circuit, the suction air temperature of Pattern 1 was used as the outdoor air temperature.

2.3.2.1 Cooling Operation

Figure 3 shows the relationship between the outdoor air temperature and the mean suction air temperature at each load factor close to actual operations measured under the test conditions shown in Table 2.

In Pattern 2, it can be seen that the lower the outdoor air temperature and the load factor, the smaller the difference from Pattern 1 and the smaller the influence of the short circuit. As for Pattern 3, only the result of one high outdoor air temperature is shown, and the difference from Pattern 2 is negligibly small. This suggests that the wall installed in the side of the outdoor unit is more dominant in the occurrence of the short circuit than that installed in the front. From this result, it should be noted that the short circuit of airflow may occur even if the outdoor unit is installed at a distance from the building wall recommended by the manufacturer. It is recommended that the distance between the suction face of the outdoor unit and the building wall be set larger than the manufacturer's recommendation value.

Table 8 shows the difference between the blowing air temperature and the suction air temperature. Compare to low outdoor air temperature and the load factor, the difference is large at high outdoor air temperature and the load factor.

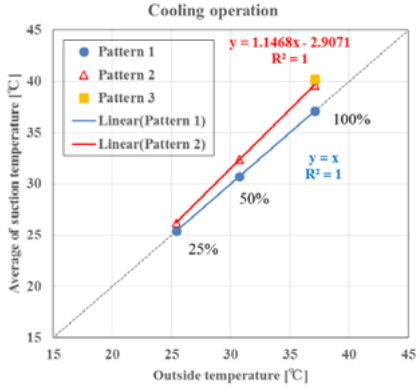


Fig. 3. The relationships between outdoor air temperature and suction air temperature in cooling operation

Table 8. Blowing air temperature during cooling operation

Outdoor temperature conditions	Pattern 1	Pattern 2	Pattern 3
25ºC	28.6ºC (+3.1)	29.0ºC (+2.8)	-
30ºC	36.1ºC (+5.3)	37.3ºC (+4.9)	-
35ºC	48.1ºC (+11.0)	47.9ºC (+8.3)	48.6ºC (+8.4)

( ) Indicates the difference between the blowing air temperature and the suction air temperature

In order to quantitatively express the influence of the short circuit, the short circuit ratio (SCR) [3] shown in Equation (1) was calculated.

$$SCR[\%] = \frac{Suction\ air\ temperature - Outdoor\ air\ temperature}{Blowig\ air\ temperature - Outdoor\ air\ temperature} * 100 \quad (1)$$

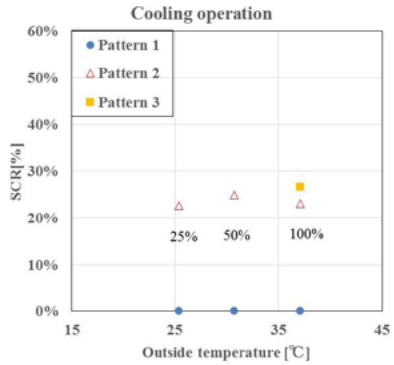


Fig. 4. SCR during cooling operation

Figure 4 shows the results of SCR under the low load conditions in each pattern. It can be seen that the SCR is about 20-25% in Patterns 2 and 3.

2.3.2.2 Heating Operation

Next, the influence of the short circuit during heating operation is examined. Figure 5 shows the suction air temperature during heating operations at 100% load at 2 ºC and partial loads shown in Table 2. It can be seen that there is no significant difference among the results for three patterns. The reason why the influence of the short circuit (decrease in the suction air temperature) was small in comparison with the cooling operation may be that the difference between the suction air temperature and the blowing air temperature was small in the heating operation. In 100% cooling operation, the difference between the blowing air temperature and the suction air temperature was as large as 8 ºC to 11 ºC (Table 8). On the other hand, the difference in the heating operation was smaller than 3 ºC (Table 9).

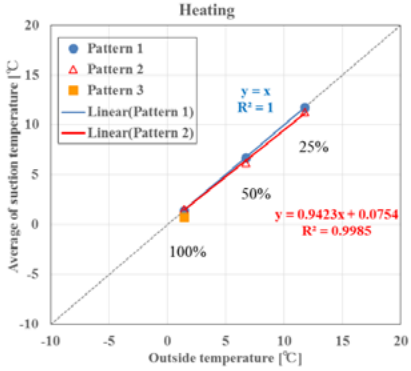


Fig. 5. The relationships between outdoor air temperature and suction air temperature in heating operation

Table 9 Blowing air temperature during heating operation

Outdoor temperature conditions	Pattern 1	Pattern 2	Pattern 3
2ºC	-1.7ºC (▲3.1)	-1.3ºC (▲2.8)	-2.2ºC (▲2.9)
7ºC	4.4ºC (▲2.3)	4.1ºC (▲2.1)	-
12ºC	10.4ºC (▲1.4)	10.2ºC (▲1.0)	-

( ) Indicates the difference between the blowing air temperature and the suction air temperature

3. Field Test

3.1. Test Method

In this test, we used two packaged air conditioners installed in a building of Mie University. By measuring the blowing air temperature, suction air temperature, outdoor air temperature, etc. of the outdoor unit, the occurrence of the short circuit was examined. We also examined the installation conditions of outdoor units where short circuits are likely to occur. The measurements were conducted mainly in September and October to avoid the cooling capacity shortage in midsummer that might be caused by the short circuit.

The air conditioner used for the measurement was a packaged air conditioner with a rated cooling capacity of 8 kW (manufactured in 2009). As shown in Figure 6, the left side (air conditioner No.1) of two adjacent outdoor units was the main measurement target. As for the air conditioner on the right side (air conditioner No.2), we measured only power consumption in order to understand its operating state.

As can be seen from this figure, there were building walls on the back side of these outdoor units, but there were no walls on the side and front. Therefore, as shown in Figure 7, a partition wall (height 2.0 m, width 1.0 m) simulating the building wall was put on the side and/or front of the outdoor unit of air conditioner 1 to generate the short circuit artificially. An experiment was conducted based on the air conditioner installation manual, and the distance between the outdoor unit and the partition wall was set at 0.15 m when the wall was installed on the side of the outdoor unit and 1.0 m when it was installed on the front.

Figure 8 shows the positions of the thermos-sensors installed in the outdoor unit of air conditioner 1. The temperatures of the blowing and suction air were measured at 1 minute intervals. In addition, the outdoor air temperature was measured at a position away from the outdoor unit, and the power consumptions of both air conditioners were also measured.

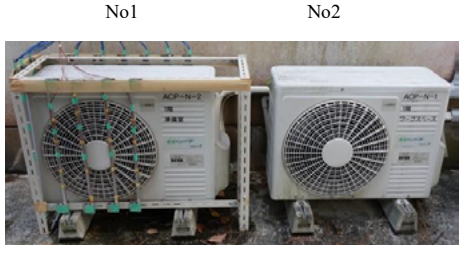


Fig. 6 Air conditioner installation condition (the air conditioner 1 to be measured is on the left)



Fig. 7 Wall installation conditions (left: Side, right: Side + Front)

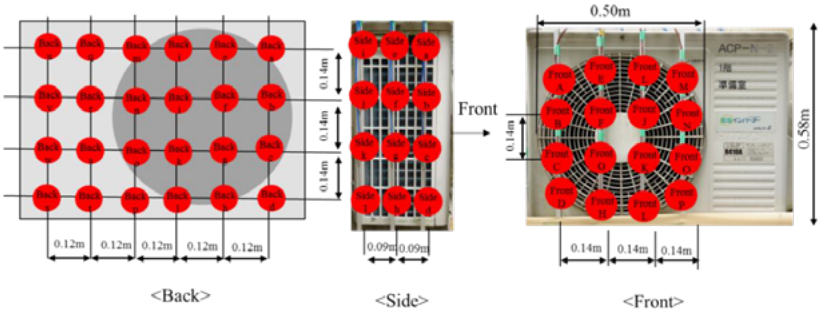


Fig. 8 Measurement position of suction (Back and Side) and blowing (Front) air temperature

3.2. Results

3.2.1. Influence of Wall

Table 10 shows the results of temperature measurements. When the adjacent air conditioner 2 was not operating and the wall was installed on the side, the suction air temperature on the side face increased by 4.6 ºC. On the other hand, the temperature rise on the back face was not so much. The same tendency is observed when the wall was installed in the front. These results are very similar to those of the laboratory tests.

When the air conditioner 2 was operating, the temperature rise in the side and back faces is remarkable. The situation when the air conditioner 2 was operating is described in detail in the next chapter.

Table 10 Rise of average suction air temperature under each condition

Wall	Air-conditioner 2	Side suction temperature – Outdoor air temperature	Back suction temperature – Outdoor air temperature
None	OFF	-0.2ºC	-1.1℃
	ON	0.7 ºC	0.8℃
Side	OFF	4.6 ºC	1.0 ºC
	ON	6.1 ºC	3.2 ºC
Side + Front	OFF	5.0 ºC	1.4 ºC
	ON	4.3 ºC	2.4 ºC

3.2.2. Influence of Adjacent Air-Conditioner

Figure 9 shows the temporal change of the suction air temperature at the representative point "Back 1" on the back of the air conditioner 1 when the air conditioner 2 was operated without any walls. Here Δt on the ordinate denotes the difference between the suction air temperature and the outdoor air temperature. For comparison, the suction air temperature of “Back 1” when the air conditioner 2 was stopped is also shown. The suction air temperature at “Back l” with the operation of air conditioner 2 is 2 ºC higher than that without the operation of air conditioner 2. From this result, it is presumed that when the adjacent air conditioner 2 is in operation, the air blown from the air conditioner 1 wraps around the back of the outdoor unit due to the influence of air blown from air conditioner 2.

Next, let us describe the case where the wall was installed on the side of the outdoor unit. Figure 10 shows the blowing air temperature and the suction air temperature on the back face ("Back a" to "Back d") when the air conditioner 2 was operating. Figure 11 shows changes in the power consumption of the air conditioner 2 and the suction air temperature at the back of the air conditioner 1. The rise of the suction air temperature at the back of the outdoor unit increases compared to the results without the wall (Figure 9). In addition, the influence of air conditioner 2 is more noticeable.

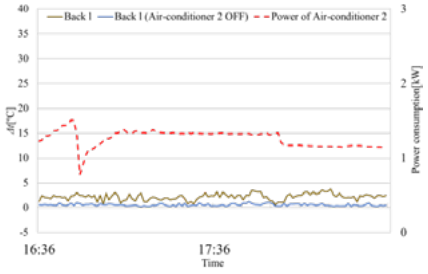


Fig. 9 Comparison of suction air temperature on the back-face and power consumption of air conditioner 2 (No walls)

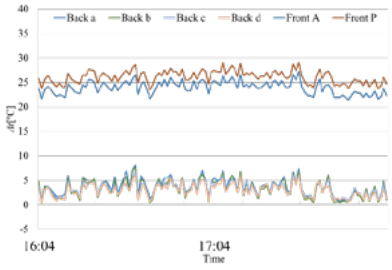


Fig. 10 Comparison of blowing air temperature and back-face suction air temperature (Wall: side installation)

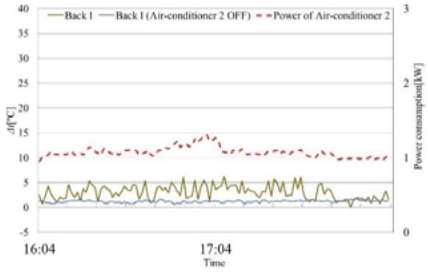


Fig. 11 Comparison of suction air temperature on the back-face and power consumption of conditioner 2 (Wall: side installation)

Table 11 Example of correlation coefficients between blowing air temperature and suction air temperature

Wall	Blowing position	Suction position	Correlation coefficient (Air-conditioner 2 OFF)	Correlation coefficient (Air-conditioner 2 ON)
None	Front D	Side a	0.147	0.258
		Side b	0.128	0.464
		Side c	0.509	0.437
		Side d	-0.008	0.760
Side	Front D	Side a	0.239	0.896
		Side b	0.454	0.832
		Side c	0.020	0.746
		Side d	0.091	0.780
Side + Front	Front D	Side a	0.540	0.775
		Side b	0.535	0.718
		Side c	0.413	0.523
		Side d	0.272	0.715

3.2.3. Correlation Coefficient between Blowing Air Temperature and Suction Air Temperature

In this study, we obtained the correlation coefficient of the time-series changes of the blowing air temperature and the suction air temperature. Based on this correlation coefficient, we can estimate the position at which the air blown from the front of the outdoor unit was easily sucked.

As an example of the correlation coefficient calculation results, Table 11 shows the correlation coefficient calculated between "Front D" (blowing air) on the front face of the outdoor unit and "Side a" to "Side d" (suction air) on the side face. The correlation coefficient between the blowing position "Front D" and the suction position "Side a" is expressed as follows.

$$\text{Correlation coefficient} = \frac{\overline{t_D' \cdot t_a'}}{\sqrt{\overline{t_D'^2}} \cdot \sqrt{\overline{t_a'^2}}} \quad , \quad t_D' = t_D - \overline{t_D} \quad \text{and} \; t_a' = t_a - \overline{t_a}$$

Here t_D and t_a are instantaneous air temperatures at "Front D" and "Side a" measured at every one minute, and overbar means time-averaged values. Therefore, t_D' and t_a' designate the temperature fluctuations of blowing and suction air with time. The value of the correlation coefficient was calculated based on air temperatures measured in two hours.

The correlation coefficient with the wall installation is generally higher than that without the wall. In addition, when the air conditioner 2 was in operation, the correlation coefficient further increases. This suggests that a short circuit tends to be strengthened due to the synergistic effect of the wall and air blown from air conditioner 2. When there were no walls, the correlation coefficient tends to be higher on the lower side face, whereas when the wall was installed, the correlation coefficient on the upper region of the side face tends to be higher. It is thought that the air tends to go to the upper side by the influence of the wall.

4. Conclusions

In this report, in the environmental test laboratory and in an actual building, a wall simulating a building wall or an obstacle was installed near the outdoor unit of the air conditioner, and the relationship between the outdoor air temperature, load factor and the performance degradation were investigated. Due to the influence of the wall installation, SCR and power consumption increased, and COP decreased. The main results are shown below.

1. In the cooling operation, when there are walls near the back and side faces of the outdoor unit, the suction air temperature becomes higher than the case of no wall installation. The increase in the suction air temperature is particularly remarkable on the side face of the outdoor unit.
2. Short circuit is more likely to occur when the wall is installed on the side than when the wall is installed on the front of the outdoor unit.
3. COP decreased by 6.5% in the case of patern3, high outdoor air temperature and the load factor in cooling operation.
4. In the cooling operation, a short circuit may occur in 100% load operation even at low outdoor air temperatures, but the influence of the short circuit is reduced under lower load operation.
5. Under the partial load operation, the influence of the short circuit is large in the cooling operation, whereas the influence of the short circuit is small in the heating operation.
6. In the cooling operation, the suction air temperature also increases on the back face of the outdoor unit, and the temperature rise becomes more remarkable when the adjacent air conditioner is operating.

References

[1] Yumoto,Y., Ichikawa,T., Nobe,T., Kametani,S., Study on Performance Evaluation of a Split Air Conditioning System Under the Actual Conditions, International Refrigeration and Air Conditioning Conference 2006,R067.

[2] Narumi,D.,Tanaka,K.,Shimoda,Y.,Mizuno,M., Improvement of the Thermal Environment around the Air-cooled Outdoor Units of Air Conditioning System. Transactions of the Japan Society of Refrigerating and Air Conditioning Engineers, 2011,Volume 26, Issue 1, pp. 81-92.

[3] Kotani,H.,Yamanaka,Y.,Momoi,Y.,Sagara,K., Study on Short-Circuit Phenomenon around Outdoor Air-Conditioning Units Part 3 Short-Circut Ratio using Inlet Air Temperature by Wind Tunnel Test. The Society of Heating, Air-Conditioning and Sanitary Engineers of Japan 2012, I-64, in Japanese.

13th IEA Heat Pump Conference
April 26-29, 2021 Jeju, Korea

Study on Short Circuit of Airflow in Outdoor Unit of Air Conditioner

Hiroyuki Miyazaki[a*], Tsubasa Ito[b], Hiroshi Nakayama[a], Masafumi Hirota[b]

[a]Chubu Electric Power Co.,Inc., 20-1, Kitasekiyama, Midori-ku, Nagoya city, Aichi, 459-8522, Japan
[b]Mie University, 1577, Kurimamachiya-cho, Tsu-city, Mie, 514-0102, Japan

Abstract

In air conditioners installed in commercial buildings, their efficiencies are often deteriorated by short circuits of airflows in which hotter (cooling operation) or cooler (heating operation) air blown out from the outdoor units is sucked again in the outdoor units. From viewpoints of energy savings of air conditioners, it is necessary to understand the influence of short circuits of airflows on operations of air conditioners quantitatively and to take measures against them. The purpose of this study is to make clear the influence of installation conditions of the outdoor unit of an air conditioner on the short circuit of airflow issued from it.

We made laboratory measurements and field measurements of airflow temperatures around the outdoor unit of a packaged air conditioner. The short circuit of the airflow from the front face to the side face of the outdoor unit was enhanced when there was a wall near the side face. In such cases, linear relationships were found between suction air temperatures of the outdoor unit and outdoor air temperatures.

Keywords: Air conditioner, Outdoor unit, Airflow, Short circuit, Suction air temperature ;

1. Introduction

Individual distributed air conditioner may cause a short circuit of air flow in which high-temperature air blown from its outdoor unit (cooling operation) is directly sucked by its suction face, depending on the outdoor unit installation situation (close to walls, under the roof, concentrated equipment installation, etc.). It is known that the performance of the air conditioner is deteriorated by this short circuit. In addition, there are cases in which the air conditioner shuts down due to capacity control when the impact of the short circuit becomes large. In order to save energy and keep proper operation, it is required to quantitatively understand the influences of short circuits and take measures against them.

Several papers on short circuits have been reported so far [1][2], but there are few reports on the influences of outdoor unit installation conditions, changes in outdoor air temperature and load factors on short circuits and capacity degradation of an air conditioner.

The purpose of this study is to quantitatively understand the influences of short circuits of air flow in the outdoor unit on the performance of air conditioners, taking the outdoor unit installation conditions, outdoor air temperature and load factor as parameters.

In the first half of this paper, we show the results obtained in the environmental test laboratory in which influences of a building wall or an obstacle on the performance of a packaged air conditioner were examined to clarify the relationship between the outdoor unit's suction temperature and the outdoor air temperature. In the second half, we will clarify the effect of short circuits when two or more air conditioners installed in an actual building are operated with walls around the outdoor unit.

* Corresponding author. Tel.: +81-52-621-6101; fax: +81-52-624-9234.
E-mail address: Miyazaki.Hiroyuki2@chuden.co.jp.

2. Laboratory Test

2.1. Test Method

This test was conducted in the environmental test laboratory of the Chubu Electric Power Co., Inc. by installing one side blown 5-horsepower packaged air conditioner with a specification shown in Table 1. Figure 1 shows the outdoor unit installation conditions. Pattern 1 is a standard installation in which there are no obstacles around the suction face (back and side faces) and the blowing face (front face) of the outdoor unit.

On the other hand, since many outdoor units are often installed near the building walls, a test was performed on Pattern 2 in which walls simulating building walls were installed near the back and side faces (suction faces) of the outdoor unit. Here, the distances between the wall and those faces were set to effective spaces of 0.3 m as described in the manufacturer's installation manual. In addition, a test was also conducted on Pattern 3 that simulated an installation in a small space with walls near the back, side (suction) and the front (blowing) faces of the outdoor unit. The distance between the front face of the outdoor unit and the wall was set at 1.0 m as described in the manufacturer's installation manual.

Figure 2 shows the positions of thermo-sensors set on the suction and the blowing faces with the wall setting situation of Pattern 2 in the environmental test laboratory.

Table 1. Specifications of test air conditioner

5 HP packaged air conditioner (manufactured in 2017)		
	Cooling operation	Heating operation
Rated capacity	12.5 kW	14.0 kW
Rated power consumption	3.31 kW	3.30 kW
APF*(2015)	6.3	

*APF: Annual Performance Factor

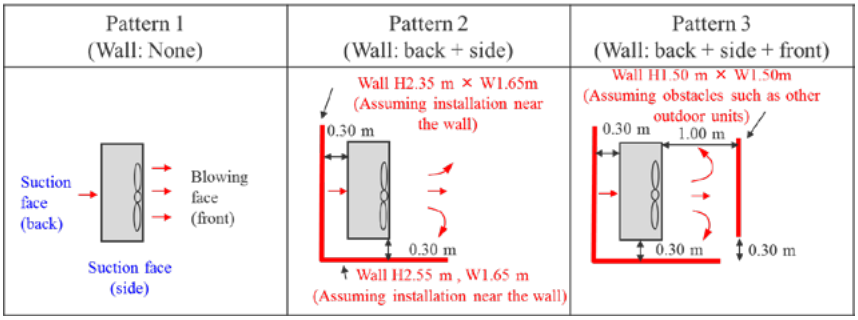


Fig. 1. Wall installation patterns around the outdoor unit of the air conditioner

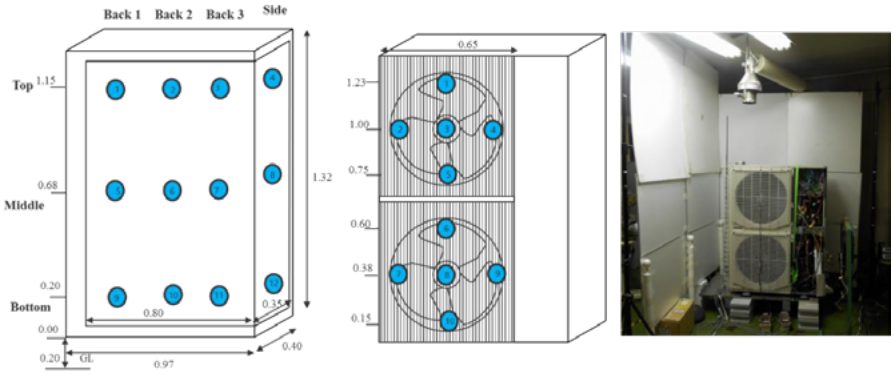


Fig. 2. Positions of sensors on the outdoor unit and wall installation condition of Pattern 2

2.2. Test Conditions

The air conditioning capacity was measured by the indoor enthalpy method. Test conditions are shown in Table 2, the air dry bulb temperature in the outdoor test room was set at 35 ºC, 30 ºC or 25 ºC in the cooling performance test, and at 12 ºC, 7 ºC or 2 ºC in the heating performance test.

A part of tests was conducted considering the situation that the air conditioning load is large and the air conditioner is always operating at full power (100%). In these tests, the indoor test room was controlled at 27 ºC and the remote control temperature was set to 18 ºC in the cooling operation, and the indoor test room was controlled at 20 ºC and the remote control temperature was set to 30 ºC in the heating operation.

Tests were also conducted assuming the situation that the air conditioning load is reduced in the intermediate period. In the case of cooling, the air conditioning load was set at 25% and 50% of the actual rated cooling capacity of the tested air conditioner, and the air temperature of the indoor test room was controlled at 27 ºC by the air conditioner itself. In the heating performance test, the indoor air temperature was controlled at 20 ºC with the heating load corresponding to 25% and 50% of the actual rated heating capacity.

Measurement data were sampled at 10-second intervals, and they were averaged in 60 minutes for the steady operation and in one cycle for the intermittent (on-off) operation.

Table 2. Test conditions (dry bulb temperature / wet bulb temperature)

Operations	Outdoor temperature conditions	Indoor temperature conditions	Load factor
Cooling	35 ºC / -	27 ºC /19 ºC	100%
Cooling	30 ºC / -	27 ºC /19 ºC	50%
Cooling	25 ºC / -	27 ºC / 19 ºC	25%
Heating	12 ºC / 11 ºC	20 ºC / -	25%
Heating	7 ºC / 6 ºC	20 ºC / -	50%
Heating	2 ºC /1 ºC	20 ºC / -	100%

2.3. Results

2.3.1. Influence of Wall Installation

Table 3 shows the results of average suction air temperatures (back, side, and overall average) and Table 4 shows the average blowing air temperature in each pattern in the cooling performance test at the outdoor air temperature of 35 ºC with full power operation.

In Pattern 1, the suction air temperatures on the back and side faces are about 37 ºC, and the difference from the outdoor air temperature is not so large. It should be noted that the temperature sensor position for setting the test room was different from the positions of the thermo-sensors on the suction face, so there was a difference between the test room setting temperature and the suction air temperature in Pattern 1.

In Pattern 2 in which the walls are installed on the back and side of the outdoor unit, the suction temperature is about 2 ºC higher than Pattern 1 on average. In particular, the suction air temperature is as high as 41.2 ºC on the side face, and it can be seen that the influence of the short circuit is greatly reflected on the side of the outdoor unit. Pattern 3 shows a similar trend to Pattern2.

Regardless of the change in the suction air temperature, the blowing air temperature is almost constant at about 48 ºC in all patterns as shown in Table 4.

Table 3. Average of suction air temperature during cooling operation at the outdoor air temperature of 35 ºC with 100% operation

Suction air temperature	Pattern 1	Pattern 2	Pattern 3
Back	37.0ºC	38.6ºC	39.1ºC
Side	37.6ºC	41.2ºC	42.3ºC
Overall	37.1ºC	39.2ºC	39.9ºC

Table 4. Average of blowing air temperature during cooling operation at the outdoor air temperature of 35 ºC with 100% operation

	Pattern 1	Pattern 2	Pattern 3
Blowing air temperature	48.1ºC	47.9ºC	48.6ºC

For more detailed changes in the air temperature on the suction face, Table 5 shows differences between suction air temperatures in Pattern 2 and Pattern 1, and Table 6 shows a comparison with Pattern 3. Here, the positions described in these tables correspond to the sensor positions shown in Figure 2. As can be seen from Table 5, the place where the temperature change is particularly large is from the center to the bottom of the back and side faces of the outdoor unit, rising by 6-7 ºC. Table 6 of Pattern 3 shows a similar tendency. It is thought that hot air blown from the front face of the outdoor unit stayed around the bottom of the side face where there was little air flow.

In addition, from the overall average temperature change in Table 5 and Table 6, it rises to 2.1 ºC by wall setting on the back and side, whereas it rises to 2.8 ºC by wall setting on the back, side and front. It can be seen that the influence of the back and side walls on the short circuit is greater than that of the front wall.

Table 5. Difference of suction temperatures of pattern 2 from pattern 1 at the outdoor air temperature of 35 ºC with 100% operation

	Back 1	Back 2	Back 3	Side
Top	-0.1ºC	-0.3ºC	-0.6ºC	-0.5ºC
Middle	-0.9ºC	0.8ºC	3.6ºC	5.1ºC
Bottom	1.3ºC	3.5ºC	7.2ºC	6.2ºC
Average of Back		1.6ºC		-
Average of Side		-		3.6ºC
Average of Overall		2.1ºC		

Table 6 Difference of suction temperatures of pattern 3 from pattern 1 at the outdoor air temperature of 35 ºC with 100% operation

	Back 1	Back 2	Back 3	Side
Top	0.2ºC	0.5ºC	0.7ºC	0.7ºC
Middle	-0.8ºC	1.7ºC	5.2ºC	6.3ºC
Bottom	1.5ºC	3.5ºC	6.4ºC	7.2ºC
Average of Back		2.1ºC		-
Average of Side		-		4.7ºC
Average of Overall		2.8ºC		

Table 7 shows the power consumption, cooling capacity and COP of the air conditioner during 100% cooling operation at the outdoor air temperature of 35 ºC for each pattern. From these results, the power consumption increased by 2-4%, the cooling capacity decreased by 1-3% and consequently COP decreased by 3-6% in Patterns 2 and 3 compared to Pattern 1, due to the short circuit.

Table 7 Power consumption, Cooling capacity and COP at the outdoor air temperature of 35 ºC with 100% operation

	Pattern 1	Pattern 2	Pattern 3
Power consumption	4.43kW	4.54kW	4.62kW
(Rate of change)	(Basis)	(+2.36%)	(+4.12%)
Cooling capacity	14.19	14.04	13.81
(Rate of change)	(Basis)	(-1.06%)	(-2.68%)
COP	3.20	3.09	2.99
(Rate of change)	(Basis)	(-3.34%)	(-6.53%)

2.3.2. Influence of Partial Load Operation

In actual use an air conditioner is often operated under a partial load. Therefore, we conducted partial load performance tests. In order to understand the influence of the short circuit under partial load, the setting of outdoor temperature and lord factor of the environmental test laboratory was changed, and the relationship between the suction average temperature, the outdoor air temperature and load factor was investigated. As mentioned in Section 2.3.1, there was a difference between the test room setting temperature and the suction air temperature in Pattern 1, in which the influence of the short circuit was negligibly small. Hence, in order to clarify the difference between Patterns 2 and Pattern 3 that have a strong influence of short circuit, the suction air temperature of Pattern 1 was used as the outdoor air temperature.

2.3.2.1 Cooling Operation

Figure 3 shows the relationship between the outdoor air temperature and the mean suction air temperature at each load factor close to actual operations measured under the test conditions shown in Table 2.

In Pattern 2, it can be seen that the lower the outdoor air temperature and the load factor, the smaller the difference from Pattern 1 and the smaller the influence of the short circuit. As for Pattern 3, only the result of one high outdoor air temperature is shown, and the difference from Pattern 2 is negligibly small. This suggests that the wall installed in the side of the outdoor unit is more dominant in the occurrence of the short circuit than that installed in the front. From this result, it should be noted that the short circuit of airflow may occur even if the outdoor unit is installed at a distance from the building wall recommended by the manufacturer. It is recommended that the distance between the suction face of the outdoor unit and the building wall be set larger than the manufacturer's recommendation value.

Table 8 shows the difference between the blowing air temperature and the suction air temperature. Compare to low outdoor air temperature and the load factor, the difference is large at high outdoor air temperature and the load factor.

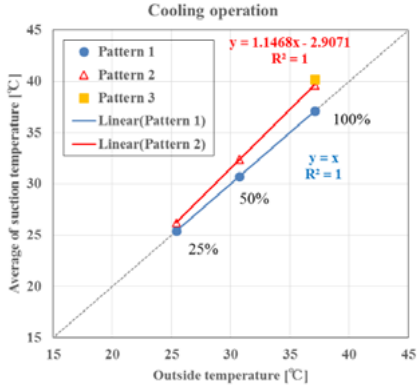


Fig. 3. The relationships between outdoor air temperature and suction air temperature in cooling operation

Table 8. Blowing air temperature during cooling operation

Outdoor temperature conditions	Pattern 1	Pattern 2	Pattern 3
25ºC	28.6ºC (+3.1)	29.0ºC (+2.8)	-
30ºC	36.1ºC (+5.3)	37.3ºC (+4.9)	-
35ºC	48.1ºC (+11.0)	47.9ºC (+8.3)	48.6ºC (+8.4)

( ) Indicates the difference between the blowing air temperature and the suction air temperature

In order to quantitatively express the influence of the short circuit, the short circuit ratio (SCR) [3] shown in Equation (1) was calculated.

$$SCR[\%] = \frac{Suction\ air\ temperature - Outdoor\ air\ temperature}{Blowig\ air\ temperature - Outdoor\ air\ temperature} * 100 \quad (1)$$

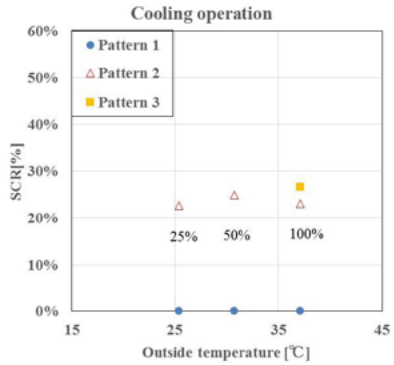


Fig. 4. SCR during cooling operation

Figure 4 shows the results of SCR under the low load conditions in each pattern. It can be seen that the SCR is about 20-25% in Patterns 2 and 3.

2.3.2.2 Heating Operation

Next, the influence of the short circuit during heating operation is examined. Figure 5 shows the suction air temperature during heating operations at 100% load at 2 ºC and partial loads shown in Table 2. It can be seen that there is no significant difference among the results for three patterns. The reason why the influence of the short circuit (decrease in the suction air temperature) was small in comparison with the cooling operation may be that the difference between the suction air temperature and the blowing air temperature was small in the heating operation. In 100% cooling operation, the difference between the blowing air temperature and the suction air temperature was as large as 8 ºC to 11 ºC (Table 8). On the other hand, the difference in the heating operation was smaller than 3 ºC (Table 9).

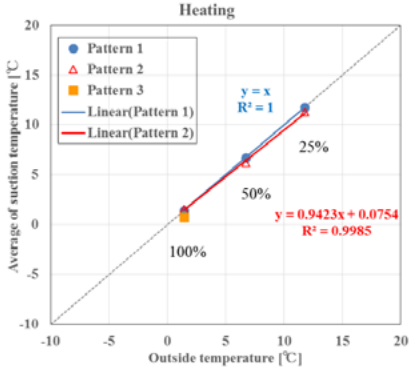


Fig. 5. The relationships between outdoor air temperature and suction air temperature in heating operation

Table 9 Blowing air temperature during heating operation

Outdoor temperature conditions	Pattern 1	Pattern 2	Pattern 3
2ºC	-1.7ºC (▲3.1)	-1.3ºC (▲2.8)	-2.2ºC (▲2.9)
7ºC	4.4ºC (▲2.3)	4.1ºC (▲2.1)	-
12ºC	10.4ºC (▲1.4)	10.2ºC (▲1.0)	-

( ) Indicates the difference between the blowing air temperature and the suction air temperature

3. Field Test

3.1. Test Method

In this test, we used two packaged air conditioners installed in a building of Mie University. By measuring the blowing air temperature, suction air temperature, outdoor air temperature, etc. of the outdoor unit, the occurrence of the short circuit was examined. We also examined the installation conditions of outdoor units where short circuits are likely to occur. The measurements were conducted mainly in September and October to avoid the cooling capacity shortage in midsummer that might be caused by the short circuit.

The air conditioner used for the measurement was a packaged air conditioner with a rated cooling capacity of 8 kW (manufactured in 2009). As shown in Figure 6, the left side (air conditioner No.1) of two adjacent outdoor units was the main measurement target. As for the air conditioner on the right side (air conditioner No.2), we measured only power consumption in order to understand its operating state.

As can be seen from this figure, there were building walls on the back side of these outdoor units, but there were no walls on the side and front. Therefore, as shown in Figure 7, a partition wall (height 2.0 m, width 1.0 m) simulating the building wall was put on the side and/or front of the outdoor unit of air conditioner 1 to generate the short circuit artificially. An experiment was conducted based on the air conditioner installation manual, and the distance between the outdoor unit and the partition wall was set at 0.15 m when the wall was installed on the side of the outdoor unit and 1.0 m when it was installed on the front.

Figure 8 shows the positions of the thermos-sensors installed in the outdoor unit of air conditioner 1. The temperatures of the blowing and suction air were measured at 1 minute intervals. In addition, the outdoor air temperature was measured at a position away from the outdoor unit, and the power consumptions of both air conditioners were also measured.

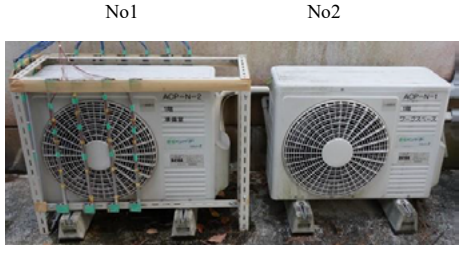


Fig. 6 Air conditioner installation condition (the air conditioner 1 to be measured is on the left)



Fig. 7 Wall installation conditions (left: Side, right: Side + Front)

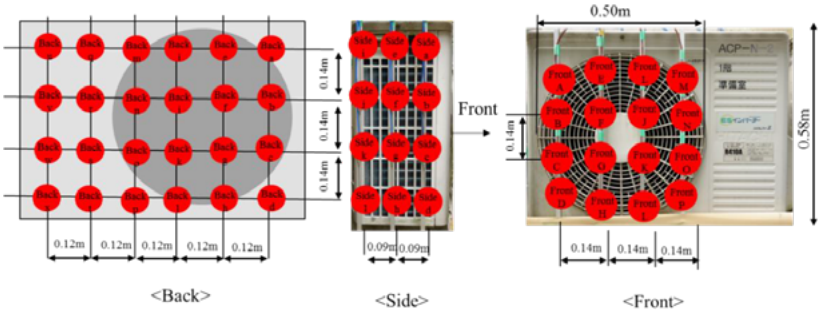


Fig. 8 Measurement position of suction (Back and Side) and blowing (Front) air temperature

3.2. Results

3.2.1. Influence of Wall

Table 10 shows the results of temperature measurements. When the adjacent air conditioner 2 was not operating and the wall was installed on the side, the suction air temperature on the side face increased by 4.6 ºC. On the other hand, the temperature rise on the back face was not so much. The same tendency is observed when the wall was installed in the front. These results are very similar to those of the laboratory tests.

When the air conditioner 2 was operating, the temperature rise in the side and back faces is remarkable. The situation when the air conditioner 2 was operating is described in detail in the next chapter.

Table 10 Rise of average suction air temperature under each condition

Wall	Air-conditioner 2	Side suction temperature – Outdoor air temperature	Back suction temperature – Outdoor air temperature
None	OFF	-0.2ºC	-1.1℃
	ON	0.7 ºC	0.8℃
Side	OFF	4.6 ºC	1.0 ºC
	ON	6.1 ºC	3.2 ºC
Side + Front	OFF	5.0 ºC	1.4 ºC
	ON	4.3 ºC	2.4 ºC

3.2.2. Influence of Adjacent Air-Conditioner

Figure 9 shows the temporal change of the suction air temperature at the representative point "Back 1" on the back of the air conditioner 1 when the air conditioner 2 was operated without any walls. Here Δt on the ordinate denotes the difference between the suction air temperature and the outdoor air temperature. For comparison, the suction air temperature of “Back 1” when the air conditioner 2 was stopped is also shown. The suction air temperature at “Back l” with the operation of air conditioner 2 is 2 ºC higher than that without the operation of air conditioner 2. From this result, it is presumed that when the adjacent air conditioner 2 is in operation, the air blown from the air conditioner 1 wraps around the back of the outdoor unit due to the influence of air blown from air conditioner 2.

Next, let us describe the case where the wall was installed on the side of the outdoor unit. Figure 10 shows the blowing air temperature and the suction air temperature on the back face ("Back a" to "Back d") when the air conditioner 2 was operating. Figure 11 shows changes in the power consumption of the air conditioner 2 and the suction air temperature at the back of the air conditioner 1. The rise of the suction air temperature at the back of the outdoor unit increases compared to the results without the wall (Figure 9). In addition, the influence of air conditioner 2 is more noticeable.

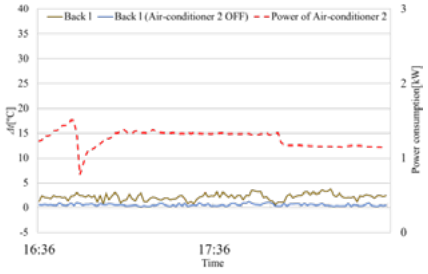


Fig. 9 Comparison of suction air temperature on the back-face and power consumption of air conditioner 2 (No walls)

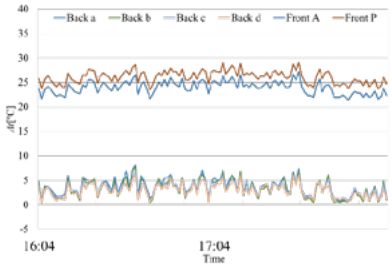


Fig. 10 Comparison of blowing air temperature and back-face suction air temperature (Wall: side installation)

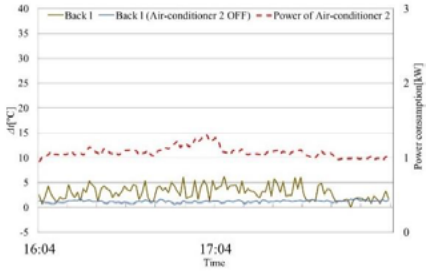


Fig. 11 Comparison of suction air temperature on the back-face and power consumption of conditioner 2 (Wall: side installation)

Table 11 Example of correlation coefficients between blowing air temperature and suction air temperature

Wall	Blowing position	Suction position	Correlation coefficient (Air-conditioner 2 OFF)	Correlation coefficient (Air-conditioner 2 ON)
None	Front D	Side a	0.147	0.258
		Side b	0.128	0.464
		Side c	0.509	0.437
		Side d	-0.008	0.760
Side	Front D	Side a	0.239	0.896
		Side b	0.454	0.832
		Side c	0.020	0.746
		Side d	0.091	0.780
Side + Front	Front D	Side a	0.540	0.775
		Side b	0.535	0.718
		Side c	0.413	0.523
		Side d	0.272	0.715

3.2.3. Correlation Coefficient between Blowing Air Temperature and Suction Air Temperature

In this study, we obtained the correlation coefficient of the time-series changes of the blowing air temperature and the suction air temperature. Based on this correlation coefficient, we can estimate the position at which the air blown from the front of the outdoor unit was easily sucked.

As an example of the correlation coefficient calculation results, Table 11 shows the correlation coefficient calculated between "Front D" (blowing air) on the front face of the outdoor unit and "Side a" to "Side d" (suction air) on the side face. The correlation coefficient between the blowing position "Front D" and the suction position "Side a" is expressed as follows.

$$\text{Correlation coefficient} = \frac{\overline{t_D' \cdot t_a'}}{\sqrt{\overline{t_D'^2}} \cdot \sqrt{\overline{t_a'^2}}} \quad , \quad t_D' = t_D - \overline{t_D} \quad \text{and} \; t_a' = t_a - \overline{t_a}$$

Here t_D and t_a are instantaneous air temperatures at "Front D" and "Side a" measured at every one minute, and overbar means time-averaged values. Therefore, t_D' and t_a' designate the temperature fluctuations of blowing and suction air with time. The value of the correlation coefficient was calculated based on air temperatures measured in two hours.

The correlation coefficient with the wall installation is generally higher than that without the wall. In addition, when the air conditioner 2 was in operation, the correlation coefficient further increases. This suggests that a short circuit tends to be strengthened due to the synergistic effect of the wall and air blown from air conditioner 2. When there were no walls, the correlation coefficient tends to be higher on the lower side face, whereas when the wall was installed, the correlation coefficient on the upper region of the side face tends to be higher. It is thought that the air tends to go to the upper side by the influence of the wall.

4. Conclusions

In this report, in the environmental test laboratory and in an actual building, a wall simulating a building wall or an obstacle was installed near the outdoor unit of the air conditioner, and the relationship between the outdoor air temperature, load factor and the performance degradation were investigated. Due to the influence of the wall installation, SCR and power consumption increased, and COP decreased. The main results are shown below.

1. In the cooling operation, when there are walls near the back and side faces of the outdoor unit, the suction air temperature becomes higher than the case of no wall installation. The increase in the suction air temperature is particularly remarkable on the side face of the outdoor unit.
2. Short circuit is more likely to occur when the wall is installed on the side than when the wall is installed on the front of the outdoor unit.
3. COP decreased by 6.5% in the case of patern3, high outdoor air temperature and the load factor in cooling operation.
4. In the cooling operation, a short circuit may occur in 100% load operation even at low outdoor air temperatures, but the influence of the short circuit is reduced under lower load operation.
5. Under the partial load operation, the influence of the short circuit is large in the cooling operation, whereas the influence of the short circuit is small in the heating operation.
6. In the cooling operation, the suction air temperature also increases on the back face of the outdoor unit, and the temperature rise becomes more remarkable when the adjacent air conditioner is operating.

References

[1] Yumoto,Y., Ichikawa,T., Nobe,T., Kametani,S., Study on Performance Evaluation of a Split Air Conditioning System Under the Actual Conditions, International Refrigeration and Air Conditioning Conference 2006,R067.

[2] Narumi,D.,Tanaka,K.,Shimoda,Y.,Mizuno,M., Improvement of the Thermal Environment around the Air-cooled Outdoor Units of Air Conditioning System. Transactions of the Japan Society of Refrigerating and Air Conditioning Engineers, 2011,Volume 26, Issue 1, pp. 81-92.

[3] Kotani,H.,Yamanaka,Y.,Momoi,Y.,Sagara,K., Study on Short-Circuit Phenomenon around Outdoor Air-Conditioning Units Part 3 Short-Circut Ratio using Inlet Air Temperature by Wind Tunnel Test. The Society of Heating, Air-Conditioning and Sanitary Engineers of Japan 2012, I-64, in Japanese.

13th IEA Heat Pump Conference
April 26-29, 2021 Jeju, Korea

Disruption to heat business models: from shifting boxes to selling comfort

Cate Lyon [a*], Lindsay Sugden [b], Roxanne Pieterse [c]

[a]Delta-EE Ltd, Argyle House, 3 Lady Lawson Street, Edinburgh, EH3 9DR, UK
[b]Delta-EE Ltd, 8000 Aarhus C, Denmark
[c]Delta-EE Ltd, Future Business Centre, King's Hedges Road, Cambridge, CB4 2HY, UK

Abstract

While heat pumps are gaining ground in the new build market in Europe, the replacement market remains challenging. Emerging alternative business models - like 'Heat as a Service' – tackle key consumer barriers and promise to open up new market opportunities in retrofit for technologies like heat pumps. The authors assess how alternative propositions are gaining traction in Europe, assess customer response to such models based on our own primary research, and discuss what this trend means for the heat pump industry.

Keywords: heat pump; Europe; business model; alternative propositions; heat as a service; asset leasing; services; consumers; overcoming barriers; market opportunities; replacment market; retrofit.

1. Introduction

The heat pump market in Europe has shown >10% growth per year for the past 4 years [1] but it is far from reaching its potential. There are ~12 million heat pumps installed in Europe [1], a number dwarfed by the more than 100 million fossil fuel boilers installed [2]. This is primarily because of limited success in the retrofit (existing buildings) market, where heat pumps continue to struggle to gain traction against "traditional" heating systems (primarily fossil fuel boilers). Alternative, service-based customer propositions for heat are emerging, in particular Heat as a Service, which promise to overcome some of the retrofit challenges, and could enable heat pumps to capture a greater share of the existing buildings market.

Such propositions typically involve a residential building occupier signing up to a contract for heating provision and/or heating equipment (plus related services and maintenance) for a fixed (or variable) monthly fee, rather than purchasing their heating appliance outright. Similar heat contracting business models based on ongoing rather than upfront fees are already common in the commercial and industrial sectors, where heating and hot water demand is relatively more predictable than in the domestic sector, reducing the risk to the provider.

1.1 Heat pumps are established in new build – but existing buildings remain the biggest challenge

Heat pumps are already the heating system of choice for housing developers in many markets – in markets such as France and Germany, heat pumps account for 40-50% of heating systems in new single family homes (and in Sweden this is >90%) [2]. Tightening building regulations, and political goals to phase out the use of fossil fuels in new homes promise a bright future for heat pumps in new build, even in gas-dominated markets such as the Netherlands and UK [3]. But the majority of heating systems are installed in existing buildings, and it is here that heat pumps need to gain traction. In some of Europe's biggest heating markets (UK, Netherlands, Germany) heat pumps capture just a 1 - 5% share of the retrofit single family home market – which should be the initial target for heat pumps. This is compared to a >90% share for fossil boilers. A combination of low end-user awareness of heat pumps, lack of end-user trust in heat pumps and entrenched

* Corresponding author. Tel.: +44-131-625-3338 (direct), +44-131-625-1011 (main switchboard).
E-mail address: cate.lyon@delta-ee.com.

preference for 'like-for-like' replacement, and economic concerns, make gaining traction in retrofit very challenging.

1.2 What are the challenges to the growth of heat pumps in existing buildings, and how can 'Heat as a Service' help to overcome these?

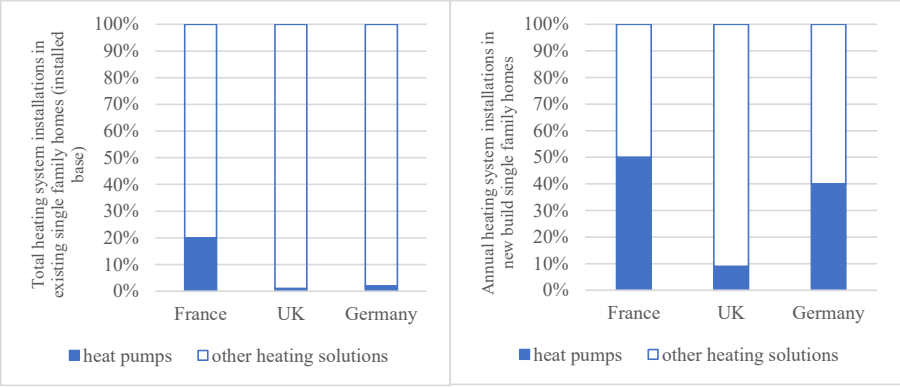


Figure 1: Share of heat pumps in existing (left) and new (right) single family homes

Source: [2], [1]

There are many barriers for heat pumps in displacing traditional heating systems (usually fossil boilers) in existing homes, in particular:

- Upfront cost of heat pump to end-user (can be 2-4 x the upfront cost of a new boiler, and more if heat distribution systems need to be replaced)
- Running costs compared to a boiler (varies by market, but high electricity prices versus gas & oil is a critical issue in many markets, and uncertainty about future energy prices make the idea of switching fuel risky for the end-user)
- End-user confidence/trust in heat pumps' ability to perform (though there are exceptions in markets such as Sweden and Switzerland, end-users are still cautious about switching from a familiar heating system like a boiler, to an 'unknown' system like a heat pump – despite the fact the technology is well-established)

'Heat as a Service' type models, by reducing the amount of risk taken on by the end-user, can potentially help to overcome some of the retrofit barriers:

- Upfront cost of heat pump to end-user: 'Heat as a Service' removes – or reduces - the upfront cost barrier, as the cost is borne by the service provider rather than the end-user. The service provider can get better economies of scale, and potentially get volume discounts for purchase of many heat pumps at once.

- Running costs compared to a boiler: 'Heat as a Service' usually gives a fixed rate heat cost to the end-user, meaning there is less uncertainty about running costs. There are also various ways the service provider might reduce heat pump running costs – through for example including microgeneration for self-consumption such as PV, and through optimisation of the heat pump running times to run when electricity is cheaper.
- End-user confidence/trust in heat pumps' ability to perform: 'Heat as a Service' removes the risk of poor heat pump performance and break-downs from the end-user, by providing maintenance, remote monitoring, and guaranteeing the heat outcome

'Heat as a Service': A definition

'Heat as a Service' usually means either/both of the following:

- *Paying an ongoing monthly fee rather than a one-off upfront fee* (the monthly fee usually includes payment for the heating system, the heat delivered, and the ongoing servicing)
- *Paying for outcomes rather than inputs* (paying for heat or comfort delivered rather than fuel input)

Delta-EE defines 'Heat as a Service' as a service where the provider takes on the following 'risks' usually borne by the end-user:

- *financial risk* – The service provider takes on credit risk by providing a heating appliance for a monthly fee and little or no upfront payment.
- *technical risk* – The monthly fee charged by the service provider includes: routine maintenance, repairs, and appliance replacement if necessary within the contract period.
- *performance risk* – The service provider charges per unit of output (heat) or for the outcome (warmth) provided by the heating appliance (or guarantees savings on heating costs).
- *energy price risk* – The service provider offers a fixed price per unit of heat or warmth generated for a period of time, typically a year.
- *behaviour risk* – the service provider charges for the outcome (warmth) provided, thereby taking on the risk that customers use heating inefficiently by, for example, opening windows.

Sub categories of 'Heat as a Service' exist, where the provide takes on only some (but not all) of the above risks. These include:

- Asset leasing
- Efficient asset leasing
- Energy payment plan
- Warmth payment plan

There are also further developments possible, beyond 'Heat as a Service', including:

- Comfort as a Service: where the outcome is a level of year-round thermal comfort in a home, including providing cooling in summer, when needed
- Energy as a Service: where the offer to the customer includes energy use for other appliances (e.g. including other electricity needs).

2. The 'Heat as a Service' landscape in Europe – who is doing what?

Over the past 3-5 years, an increasing number of new 'Heat as a Service' type offerings have emerged in the domestic sector, being offered from providers including energy suppliers, heating manufacturers and specialist start ups. The majority of these are still pre-commercial and at trial stage, but several have been commercialised successfully, and we estimate that the number of customers currently using a Heat as a Service type model is in the low 1,000s across Europe [4]. Figure 2 highlights some of the main activity in Heat as a Service offerings in the domestic sector. Heating systems employed in these offerings include heat pumps, hybrids (heat pump & boiler), and traditional heating systems, sometimes packaged together with building fabric renovation, PV and other technologies. It should be noted that heat contracting business models, based on ongoing rather than upfront fees, are already common in the commercial and industrial sectors (where heating and hot water demand is relatively more predictable than in the domestic sector, reducing the risk to the provider).

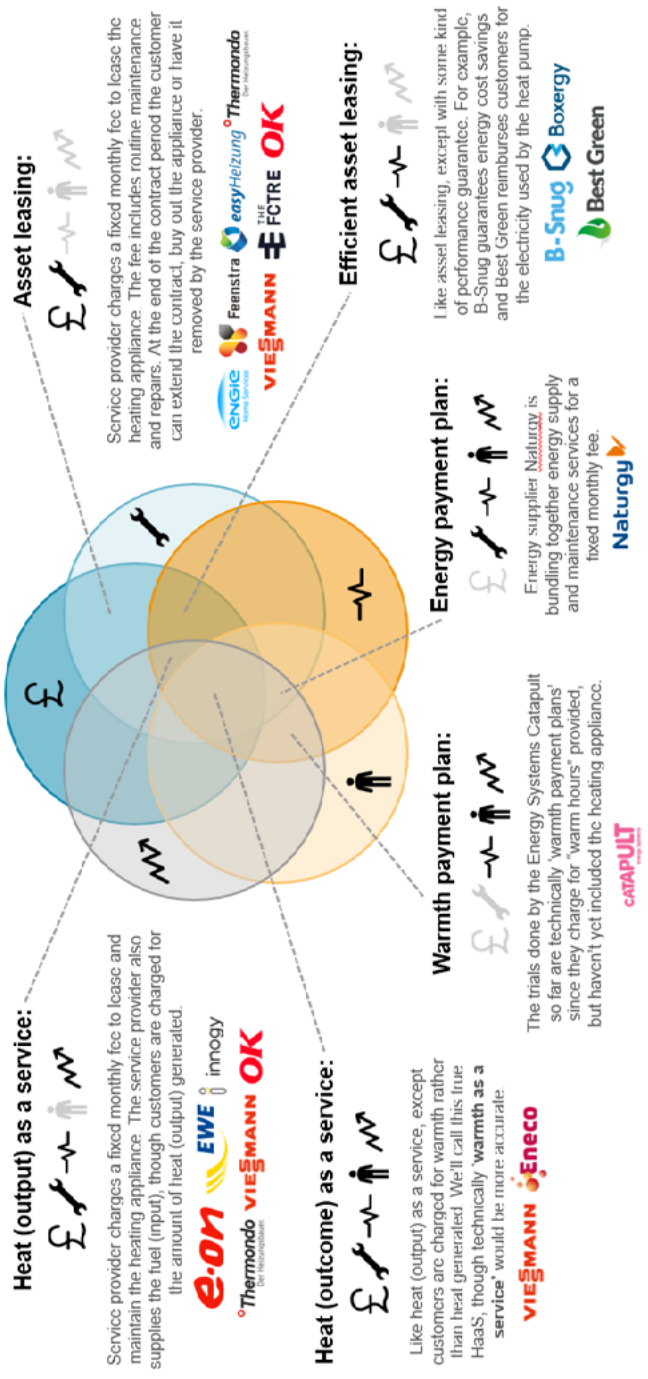


Figure 2: The 'Heat as a Service' landscape. Source: [4].

We highlight examples of three of these models in the case studies below – from specialist service provider The FCTR E in the Netherlands, oil supplier OK in Denmark, and heating manufacturer Viessmann in Germany. (Please note that the use of these examples does not represent an advertisement for any of the companies mentioned, or show any form of endorsement).

CASE STUDY: The FCTR E "e-home" package – Efficient Asset Leasing, moving towards Energy as a Service
Type of provider: Independent service provider
Stage of development: Commercial
Location: Netherlands
Heating appliance: Air-to-water heat pump with water tank and solar PV
Initial target customers: Larger, privately-owned homes (typically 150m^2 or above)
Number of installations: Aiming for 1,000 in 2019

The FCTR E is a Dutch company established in 2016. It replaces gas heating with a package of electric technologies for a fixed monthly fee, at no upfront cost.

The FCTR E could ultimately offer relatively low-risk 'Energy as a Service'. With its customers needing little to no residual electricity* from the grid (as the solar PV is sized to match the heat pump's expected needs), the FCTR E has limited electricity price risks, so user behaviour risks are less of a concern. If it can include electricity supply at a fixed fee as planned, it will be an example of true Energy as a Service.

Key details:

FCTR E e-home package	
Price:	Fixed monthly fee, typically ~€250, properly dependent. No upfront cost.
Contract:	1 year, automatically renewed unless cancelled more than 3 months before contract ends. On cancellation, customers can: ▪ Pay the residual value to purchase the equipment; ▪ Pay for the equipment to be removed; ▪ Transfer the contract free of charge.
Includes:	1) Design and installation of "e-home" system, including a NIBE heat pump, water tank, solar PV (optional) and smart controls. 2) Routine maintenance and repairs.
Savings:	Total cost ~25% less than current energy bill (not guaranteed).

The average system equipment costs ~€35k. This is financed by banks and the company founders.

Contracts are calculated based on a 15 year equipment lifespan, but are **effectively indefinite.**

EV charging and battery storage options are also available.

Residual electricity supply is not currently included, but the FCTR E is planning to white label electricity supply in 2019/20 to meet customer demand. **

The FCTR E is looking into **additional services** it can provide, such as home energy management and grid services.

* Residual electricity means the additional electricity required from the grid, on top of that produced by onsite PV.
** White labelling is where the service supplier has an agreement with another company e.g. the electricity supplier, to sell electricity on its behalf. In this case, the service supplier (The FCTR E) would buy electricity from the electricity supplier and sell it on to the end-user – so the end-user relationship remains with the service supplier.

CASE STUDY: OK – Leasing and Heat (output) as a Service
Type of provider: Oil supplier
Stage of development: Commercial
Location: Denmark
Heating appliance: Air-to-water heat pump
Initial target customers: Privately-owned homes; often those currently using oil for heating
Number of installations: 500/year for leasing model (launched in 2012), 200/year for Heat as a Service model (launched in 2017).

OK offers heat pump leasing and subscription packages, including energy supply for a fixed monthly fee (revised annually based on heat use) and a complete end-to-end service for heat pumps including the design, planning and installation of heat pumps. Customers are offered the options to:

- Buy the heat pump upfront, for a cost of around 100k-120k DKK;
- Lease the heat pump from OK
- Get the heat pump on a subscription service that includes energy supply.

Key details:

	Heat pump leasing	Heat pump subscription
Price:	▪ Upfront fee of DKK 25,000 or DKK 50,000 for installation. ▪ Monthly rental fee from DKK 995, depending on contract length and heat pump capacity.	▪ Upfront fee of DKK 20,000 for installation. ▪ Fixed monthly usage fee for kWh heat consumed, around 2,000 DKK.
Contract:	Flexible contract period, up to 10 years.	15 years. Contract can be transferred to a new owner if moving house, or customers can buy themselves out by paying the residual value of the heat pump.
Includes:	1) Installation of a heat pump. 2) Routine maintenance and repairs.	1) Installation of a Vølund or Vaillant air source heat pump. 2) Routine maintenance and repairs. 3) Energy supply for the heat pump.
Savings:	Can be calculated.	Can be calculated.

The leasing model has been popular, particularly for distress purchases.

The monthly usage fee is **revised annually** based on actual heat use.

OK has a Heat Pump Calculator that shows customers the cost to buy and operate a heat pump, and the energy cost savings over 15 and 20 years (including a 30% discount on electricity prices that customers can apply for).

CASE STUDY: Viessmann –Heat (output) as a Service
Type of provider: Heating manufacturer
Stage of development: Commercial
Location: Germany
Heating appliance: Gas boiler
Initial target customers: Privately owned homes, and private landlords
Number of installations: Offer launched in late 2019; trial of 200 homes already completed.

Viessmann's Heat Fix package is the first commercial offering taking on all five 'risks' by offering a fixed price for energy, albeit with gas boilers rather than low carbon alternatives. As part of Viessmann's aim to realign itself as an "integrated solutions provider for the entire living space", the company has launched three new heat packages in Germany:

- Heat Basic: gas boiler and maintenance for a fixed monthly price (asset leasing);
- Heat Flex: Heat Basic + gas supply with variable billing;
- Heat Fix: Heat Basic + gas supply for a fixed monthly price (Heat (output) as a Service).

Key details:

Viessmann Heat Fix	
Price:	No upfront cost; fixed monthly base price for appliance and maintenance; fixed monthly price for gas consumption.
Contract:	10 years, automatically extended for a further 5 years unless customer gives notice. If notice is given, the customer can: ▪ Pay the residual value to buy the appliance; ▪ Have it removed; or ▪ The contract can be transferred to a new property owner/tenant
Includes:	1) Installation of new gas boiler. 2) Routine maintenance and repairs, including chimney sweep costs, and replacement if necessary 3) Gas supply.
Savings:	Example shows lifetime cost savings of 30%.

The fixed monthly price is calculated on a **case-by-case basis** by the installer at the start of the contract. Changes in consumption are likely accounted for in annual price adjustments.

Installation services are delivered through Viessmann's strong network of **independent installers**, who also handle the subsequent maintenance work. This way installers earn the same for installation and maintenance as they would normally.

Installers find they can also achieve higher conversion rates by offering the heat packages as financing options.

Viessmann sources gas from both local and national energy suppliers, enabling it to get the **best gas prices**.

3. Will 'Heat as a Service' offerings engage end-users and fulfil their potential in driving the growth of low carbon heating such as heat pumps?

Experience from the market and feedback from customer research indicates a strong potential role for 'Heat as a Service' in driving decarbonisation in existing buildings – though there are barriers to implementation to overcome, and considerations to be made regarding how to manage the risk(s) borne by the provider.

Offerings currently being trialled and commercialised show generally positive responses from participants (with no known cases where a customer has asked to end the contract early). But the numbers of customers currently using Heat as a Service-type offerings across Europe is in the low 1,000s, compared with the tens of millions of customers across Europe who have bought heating systems upfront.

Delta-EE has carried out primary customer research across ~800 end-users in the UK, France, Germany, Italy and the Netherlands [5], who currently do not have such a service, assessing their attitudes to different heat propositions (Figure 3). This research shows that, while the majority still prefer the traditional payment upfront option, around 30% of all participants stated that they would be likely to take up a 'Heat as a Service' proposition if available, and this proportion increases with younger participants (to closer to 50%). This is a positive indication of the potential attractiveness of such models – and their growth potential.

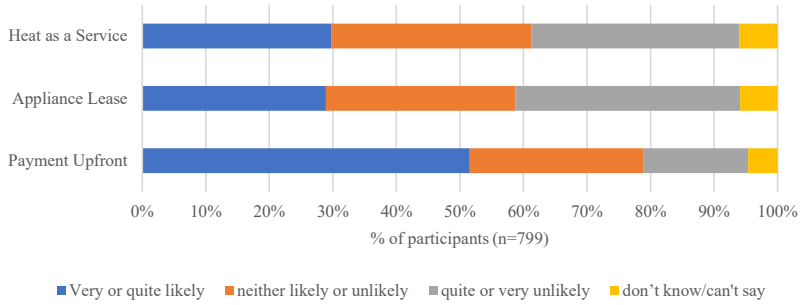


Figure 3: How likely would you be to take up one of the following propositions if it was available to you?

Source: [5]. Based on a sample of 799 domestic customers in the UK, France, Germany, Italy and the Netherlands. (Survey restricted to those who own their home outright or with a mortgage, and make decisions jointly or solely about the heating system in the household).

To develop a more detailed view of the optimal proposition designs, Delta-EE carried out Focus Groups with participants in the UK, the results of which are highlighted in Table 1 below. Ultimately, a flexible approach to proposition design is necessary, to meet the widest range of customer needs and expectations. But the research indicates that key pillars of the proposition should - ideally – be:

- a heat contract length of under 5 years
- offer bundled with maintenance and repairs plus an energy supply contract
- and guaranteed running cost savings, or lowest tariff guarantee.

Table 1. High level results from Delta-EE Focus Groups exploring proposition design

What participants liked in a proposition	What participants did not like in a proposition
• Having maintenance and insurance included in the monthly fees	• Long contract periods – over 5 years is not appealing to many customers
• Bundling in other services/solutions like solar panels or insulation	• Being tied into an energy supply contract so it could be difficult to switch energy supplier
• Paying a fixed monthly fee for energy/heat	• Paying extra to use heating outside of pre-set hours

Source: [6]. Based on focus groups with 38 domestic customers in the UK (all home-owners).

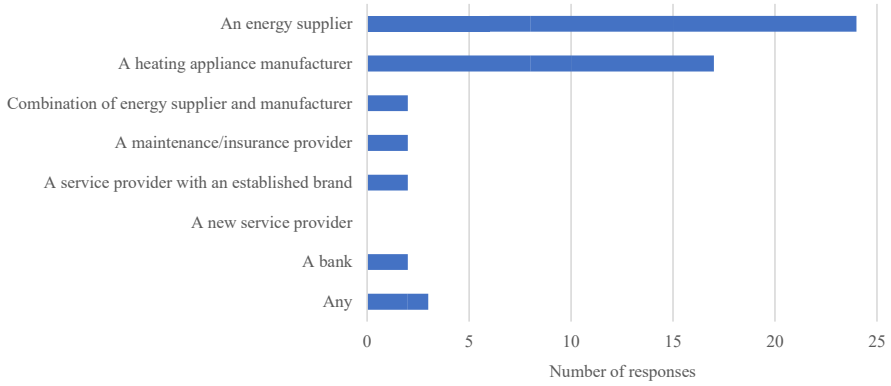
4. What does Heat as a Service mean for the heat pump industry?

'Heat as a Service' shows promise as an enabler of growth for low carbon technologies like heat pumps in the existing building market, for the following reasons:

- The concept is already well-proven: many have been commercialised for a number of years, and trials are yielding further insights into the ideal proposition designs.
- Such service models can overcome some key end-user barriers to uptake of new technologies, such as the relatively high upfront cost compared to the typical heating appliance, and concerns over performance or running cost.
- The concept is appealing to a significant share of end-users, according to our customer research. Awareness of these concepts is currently low (due to the limited number of commercial offerings available today in each country), so familiarity is also low. It is conceivable that as familiarity with these offerings rises, the appeal could also grow.

'Heat as a Service' offers a new opportunity for manufacturers, either as equipment suppliers to a service provider, or as a service provider themselves. While the majority of offerings on the market today are from energy suppliers (and specialist start ups), Delta-EE's focus groups research indicate that a heating manufacturer could be an appealing provider, along with energy suppliers (Figure 4).

Figure 4: Who would you choose to purchase a 'Heat as a Service' type package from?



Source: [6]. Based on focus groups with 38 domestic customers in the UK (all home-owners).

5. Recommendations & Conclusions

There is a huge opportunity for innovative 'Heat as a Service' models to enable real growth in the heat pump market – particularly in retrofit, where heat pumps generally still struggle to compete. To capture this opportunity, the heat pump industry can prepare by, for example:

- Identifying a 'Heat as a Service' provider to supply – potentially taking part in trials. This would provide manufacturers with additional equipment sales, and could potentially offer additional opportunities to installation & maintenance partners.
- Considering the product functionalities which will best meet the service providers needs - e.g. connectivity, interoperability of the heat pump and other appliances/controls in the home, minimising maintenance requirements and costs, and providing remote diagnostics. Focussing on these aspects could provide heat pump manufacturers & suppliers with a competitive edge over rivals, in securing equipment supply contracts with service providers.
- Making a strategic decision to become the organisation offering Heat as a Service-type offerings - providing a service to end-users, rather than shifting boxes. This will likely require action on some or all of: identifying partners; strengthening installation and maintenance networks and supply chains; arranging necessary financing and developing customer-facing

tools like billing and support. While this option requires the most effort (and involves the most risk) it also has the potential to bring the highest rewards (through providing the most opportunities for revenue generation, and strengthened brand positioning).

The implementation of 'Heat as a Service' models could be a critical step in unlocking parts of the extensive European domestic retrofit heat pump market to heat pumps, because it would overcome some of the biggest end-user barriers for heat pumps – high upfront cost, risk of high running costs, and lack of trust in the technology. The concept is well-proven, and is gaining ground in the domestic heat pump market, with several large players engaging. We expect this type of model to become much more widespread in the future heating market – and heat pumps can be one of the key beneficiaries.

References

[1] EHPA, European Heat Pump Market and Statistics Report, EHPA 2019
[2] Delta-EE, European Heating Market Database 2019
[3] Delta-EE, Viewpoint: The end of the road for fossil fuel boilers in new build? Delta-EE Heat Services, November 2019
[4] Delta-EE, Heat as a Service report, Delta-EE Heating Business Service, August 2019
[5] Delta-EE, European Customer Research Report, Delta-EE Electrification of Heat Service, September 2019
[6] Delta-EE, Heat as a Service Focus Groups Report, Delta-EE Heating Business Service, August 2019

13th IEA Heat Pump Conference
April 26-29, 2021 Jeju, Korea

Electrification of heat and decarbonisation of the electricity system: Sector coupling is creating opportunities for heat pumps

Cate Lyon [a*], Lindsay Sugden [a]

[a]Delta-EE Ltd, Argyle House, 3 Lady Lawson Street, Edinburgh, EH3 9DR, UK

Abstract

As the electricity sector decarbonises, the need for energy system flexibility is rising – and electric heating and cooling have a role to play in providing this flexibility. The flexible operation of residential electric heating and cooling products – including heat pumps – is beginning to move from trial stage to commercial reality in some European markets, potentially creating value for customers, networks and energy suppliers. Where are the opportunities today, how will these change in the future, and how can the heat pump industry be part of a future world of flexible energy? The authors present their latest research into the emerging opportunities and business models for heat pumps arising from 'sector coupling', home energy management, and demand-side response.

Keywords: heat pump; Europe; sector coupling; decarbonisation; flexibility; home energy management; demand-side response; business models; opportunities; customers; networks; energy suppliers; aggregators.

1. Introduction

As the electricity sector in Europe decarbonises, the need for energy system flexibility is rising, due to the greater share of electricity coming from intermittent renewable sources such as solar PV or wind generation (versus traditional, dispatchable fossil-fuel based generation). Smarter control of the level and timing of demand-side electrical loads (so-called demand-side response) can provide an important source of this flexibility, and one which can also generate value for a number of players in the energy system.

At the same time, the penetration of electrically-driven heating and cooling in homes and businesses in Europe is also increasing, driven by: a desire for forms of heating that are more efficient and lower carbon than traditional forms using fossil fuels; rising average summer temperatures; and increasing consumer expectations on year-round thermal comfort in buildings.

This convergence of the heating and electricity sectors in Europe (so-called 'sector coupling') – and the growing need for energy system flexibility – therefore presents an opportunity for heat pumps in Europe to become a more attractive technology to end-users, energy suppliers, aggregators, network operators, governments and other players, through their role in providing demand-side response. The flexible operation of residential electric heating and cooling products – including heat pumps – is beginning to move from trial stage to commercial reality in some European markets today.

However, as this is a space which is still in development, there are challenges associated with understanding the exact nature and timing of the opportunity, and the associated developments needed to realise it. It is therefore pertinent for those involved in the design, development, manufacture and sale of heat pumps (and related components & services) to understand where these opportunities are today in Europe, how they might change in the future, and what role heat pumps can play in a future world of flexible energy, in order to make the right strategic decisions for their businesses.

Delta-EE here presents its latest research into the emerging opportunities and business models for heat pumps arising from 'sector coupling', home energy management, and demand-side response in Europe.

2. Heat pumps and other HVAC loads represent an important potential source of flexibility

2.1 There is a growing need for energy system flexibility in Europe, leading to greater consideration of the potential for demand-side response

As the electricity sector in Europe decarbonises, the need for energy system flexibility is rising, due to the greater share of electricity coming from intermittent renewable sources such as solar PV or wind generation (versus traditional, dispatchable fossil-fuel based generation). This flexibility could be provided by various means, including additional dispatchable generation or electricity storage solutions.

Smarter control of the level and timing of demand-side electrical loads (so-called demand-side response) can also provide an important source of this flexibility, and one which can generate value for several different players in the energy system – plus end-users.

2.2 Heat pumps and other electric HVAC loads could provide many GWs of energy system flexibility – if appropriately connected

Delta-EE estimates that within Europe in 2019, the installed base of electrical heating, cooling and hot water appliances within residential properties represents over 220GW of installed capacity (table 1). We also estimate that the expected replacement of older electric HVAC appliances – or installation of new appliances – within Europe will likely represent 10's of GWs of 'new' capacity in the next five years, in the markets studied [1].

Table 1. Electrical heating, cooling and hot water loads in Europe in residential properties in 2019. An estimate of installed capacity, % of installed based with connectivity enabled, and potential for flexibility of timing of use. (Markets considered: UK, Germany, France, Italy, Norway, Sweden, Denmark and Finland).

	Space Heating	Hot Water
Capacity of installed base (GW)	110	110
% of installed base with connectivity enabled	<1%	<1%
Potential for flexibility of timing of electricity demand (qualitative)	Low to medium	Medium to high

Space heating loads – including heat pumps – offer low to medium potential to be flexible with regards to the timing of electricity demand. This can be increased by the provision of additional thermal storage, and/or smarter control regimes.

In order to be used to provide demand-side response to the wider energy system, it is necessary for an electricity-using appliance (such as a heat pump) to have the ability to receive signals from an external source which can influence the operation of the appliance (e.g. turn off, turn on, modulate power usage up or down). Delta-EE estimates that today, a very low percentage of the installed base of heat pumps in Europe (<1%) has the necessary connectivity installed - and enabled - in order to allow them to be used for demand-side response. However as new appliances are installed and sold, we expect that this percentage will rise, as it is easier for new appliances to be sold with the necessary equipment and control protocols already installed (preventing the need for costly retrofitting). We also expect to see a growing number of commercial offerings to residential customers emerging in the coming years, which will increase the user awareness and acceptance of such models.

3. How this flexibility can create value for energy system players, and end-users

3.1 There are several potential sources of value from sector coupling

Transmission system operators (TSOs), distribution system operators (DSOs) and electricity suppliers all benefit from having flexibility in the energy system. The value to these players of demand-side flexibility (demand-side response) includes the opportunity to avoid costs, or to generate revenue (figure 1).

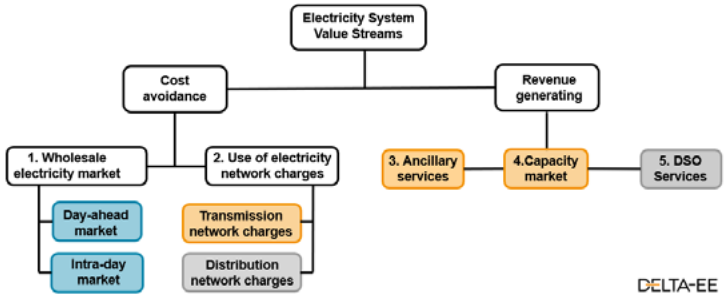


Fig. 1. Value streams typically available in European countries from demand-side response [2].

Demand-side flexibility can help market players to avoid costs by improving their trading in the wholesale electricity market, and/or avoiding charges arising from the use of the electricity networks.

- **Wholesale electricity market:** the majority of electricity on the wholesale market is traded by generators, suppliers and traders, on the day-ahead and intra-day markets. In the day-ahead market, trading takes place one day ahead of when the electricity will be delivered. The intra-day market is used by market members to fine-tune their market positions and account for any unforeseen circumstances which occurred once the day-ahead market has closed. Energy market players can choose to use demand-side flexibility to reduce the costs associated with this trading, by – for example – shifting the time of electricity use by their customers into a time period when it is cheaper for them to generate or purchase that electricity.
- **Electricity network charges**: are fees charged to network users (e.g. end customers) to recover costs associated with building, operating and maintaining the electricity transmission and distribution systems. The fees are related to the volume of electricity consumed, the connection capacity, or the timing of the electricity consumption (with higher charges often associated with periods of peak demand on the networks). Energy market players can use demand-side flexibility to reduce these charges – especially where the flexibility can be used to shift consumption into times of lower demand on the networks.

Alternatively, demand-side flexibility can be used to generate revenue from ancillary services payments, capacity market payments, or providing services to distribution system operators (DSOs).

- **Ancillary services payments:** are payments made by the Transmission System Operator to energy market players on the agreement the player provides services which maintain the proper function of the electricity system, by helping to maintain grid frequency, or enable the efficient handling of imbalances or congestion. Traditionally, these payments have been awarded to energy market players who can turn on or turn up electricity generation assets in order to provide the necessary services. However, in an increasing number of markets in Europe, these payments can now be awarded to players who can provide the necessary services via demand-side flexibility.
- **Capacity market payments**: are market subsidies paid to owners of electricity generation assets to ensure they can provide electricity generation to meet peak demands. As with ancillary services payments, an increasing number of European markets are allowing energy market players to use demand-side flexibility to bid to provide this service.
- **DSO services**: some distribution system operators (DSOs) are beginning to pay energy market players for demand-side flexibility, where this can help the DSO to avoid costs such as reinforcing their network or paying for constraint management.

Heat pumps can – in theory – be used to access all these value streams. In reality, the opportunity to access them is dependent on several factors in each European market, including:

- Minimum load size needed to access each stream (residential heat pumps will normally need to be aggregated into a larger portfolio of assets than individual appliances)
- Whether regulations permit the value stream to be accessed by residential loads in that country

- The penetration of smart meters, which are often a key enabler of residential demand-side response offerings.

In addition to the above value streams, heat pumps can also be used to provide value to end-users by optimizing heat pump operation within the building itself - e.g. by improving the self-consumption of electricity and/or integrating with other loads within a building. This can be done either using intelligence within the heat pump itself, intelligence off-site (within a cloud computing service) or intelligence within a home energy management unit – or a combination of several of these.

We have illustrated these potential uses for heat pumps (and other electrical heating and cooling loads) within a residential property in figure 2.

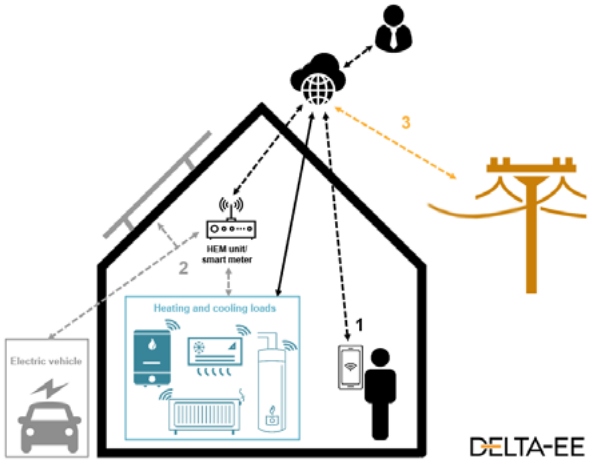


Fig. 2. Illustration of different uses for connected heat pumps (and other electrically-driven heating and cooling loads). 1: connected individual appliance providing greater control & visibility to end-user. 2: integration with other loads, at building level, for optimizing self-generated electricity. 3: providing services to the wider energy system (demand-side response).

3.2 Over time, more value streams are expected to become accessible, in more European markets

Delta-EE has surveyed a number of major European energy markets, using a mixture of desk-based research, and conversations with relevant industry experts and players. Delta-EE has found that today in Europe, the number of demand-side response value streams which are open to residential loads – including heat pumps – varies by country (table 2).

Based on our observations, and conversations with industry experts, Delta-EE expects that in the coming years, more markets within Europe will open an increasing number of value streams to residential loads, driven by increasingly favourable policy and improving regulation. This will open up a growing commercial opportunity for players in the energy market to use aggregated fleets of residential heat pumps for demand response.

Table 2. Number of demand-side response value streams which can be accessed by residential loads in selected European markets in 2019. (Excludes improved self-consumption within one residential property). [1].

	#
Finland	3 or more
France	3 or more
United Kingdom	3 or more
Germany	2
Denmark	2
Sweden	2
Norway	2
Netherlands	2
Switzerland	1

3.3 End-users can gain value from sector coupling in a number of ways

In-home optimization of the heat pump operation can bring value to the end-user (as above) via improving self-consumption of electricity, and/or integrating with other building loads. In addition to this, the end-user of a heat pump (or other HVAC appliance) can also benefit from the appliance being used for demand-side response.

Depending on the value stream(s) being accessed and the business model used, companies wishing to influence heat pump operation in order to provide demand-side response may choose to offer one or several of the following financial benefits to the heat pump end-user:

- Access to a lower-cost electricity tariff
- Access to a time-of-use electricity tariff, where the cost of electricity (price per kWh) varies by time. These can be fixed time periods within each 24yr period (static time-of-use tariff) or variable (dynamic time-of-use tariff). Time of use tariffs allow the heat pump end-user the opportunity to change their times of electricity consumption, in order to lower their electricity bills.
- Some companies offer an additional service whereby they will provide an optimization service to the end-user, automatically shifting the heat pump operating times into periods of lower cost electricity (where possible without affecting user comfort).
- A small number of companies will reward end-users with a financial payment for allowing their heat pump to be used for demand response, either in the form of a direct payment, or a discount on their energy bill.

As well as financial rewards, companies can also choose to reward the end-user of the heat pump through offering non-financial rewards, such as:

- Improved controls, such as via a smartphone app
- Improved visibility of energy usage (energy insights provision) via a smartphone app, or website
- Optimising the heat pump to run at the times of lowest electricity carbon dioxide intensity, thereby helping to reduce the end-user's 'carbon footprint'
- The positive emotional benefit from explaining that their heating appliance is helping to decarbonize Europe's electricity supply, by helping to accommodate more renewable sources of electricity.

4. Commercial examples and learnings from using heat pumps in Europe to provide demand-side response

4.1 Commercial examples already exist in Europe, and more are likely to emerge in the coming years

Our review of the European market has revealed several commercial offerings in Europe which use residential heat pumps to provide demand-side response, generating value for the company providing the offering, and also financial and/or non-financial rewards to the end-user. The key metrics are provided in table 3, and the following sections give three commercial examples available in Europe today. (Please note that the

use of these examples does not represent an advertisement for any of the companies mentioned, or show any form of endorsement).

Table 3. A summary of commercial offerings using residential heat pumps for demand response in Europe in 2019. There are numerous further projects which are in pre-commercial or trial stage; information for these is not presented here. [3].

Metric:	
Number of fully commercial offerings with heat pumps as the main asset:	7 offerings
Number of countries:	5 countries
Number of assets being steered for demand-side response (majority of which are heat pumps):	>20,000 assets
MWs of capacity provided by these assets:	>160MW

4.2 Commercial examples 1 & 2: Time of use tariff optimization in Sweden & Austria

In 2017, the Swedish government passed a law requiring energy suppliers to offer half-hourly electricity tariffs (with prices tied to market spot prices). A similar law has now been passed in Denmark. This has given rise to heat pump manufacturers such as NIBE and IVT (Bosch) introducing a service whereby the heat pump can automatically respond to price signals and generate heat to store when it is cheapest to do so. Customer savings are in the range of 5-10% on the variable part of their electricity bill. While this may have minimal impact in the Nordic countries, where wholesale prices are relatively stable, in countries such as Germany and the UK, where wholesale prices are more variable, the saving could be much greater. A dynamic time of use tariff for residential customers was recently launched in the UK, from supplier Octopus Energy.

In Austria, an energy supplier called aWATTar offers hourly time-of-use electricity tariffs to residential end-users. The company also offers end-users an additional hardware and software package which can automatically shift their heat pump operating hours into lower-priced hours, where this is possible without reducing their comfort. End-users pay a fee of around €149 for this additional package, and the company claims it will reduce the end-user's yearly energy bills by around 10%, through this load-shifting

4.3 Commercial example 3: heat pumps for ancillary services in Switzerland.

In Switzerland, company TIKO gains revenue from the ancillary services market. It controls the operation of a fleet of residential heat pumps throughout the country to provide grid balancing services to the Swiss electricity network. The offer to the end-user is reduced-price access to a smart phone app, which allows them to remotely adjust their preferred heating times, view their heat pump's energy consumption and performance, and alert them to possible faults.

5. Further development of several enabling factors would help the heat pump industry fully realise the opportunity across Europe provided by sector coupling

Our research has shown that only a small share of today's installed base of heat pumps in Europe is being used for demand-side response. There remains an - as yet - largely untapped potential for residential heat pumps to be used for sector coupling, allowing such appliances to be fully part of a future world of flexible, low carbon energy.

The further development of a number of enabling factors would help to increase the number of commercial offerings available, including (but not limited to):

- Greater wholesale & retail energy price variation
- Increased value from electricity system revenue streams, in order to mitigate the associated costs of aggregating and managing the assets
- Regulatory frameworks allowing residential assets to be (more easily and more commonly) used to provide demand-side response
- Reduced cost of associated hardware (including cost of retrofitting, where applied to an existing installed heat pump)
- Greater standardization of communications protocols among devices
- More use of real load profiles by energy suppliers to settle residential customer electricity bills

- More wide-spread use of home energy management systems, to control and optimize electricity loads within residential buildings

Creating a compelling proposition for the end-user was voted as being the most important area for development, in a poll of energy & heating industry professionals conducted by Delta-EE (figure 3).

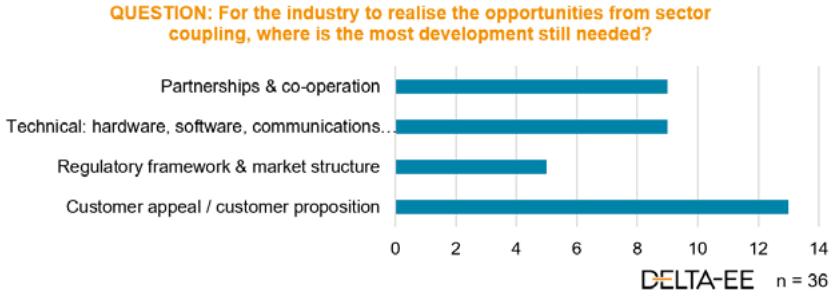


Fig. 3. Results of a poll among energy & heating industry experts by Delta-EE in September 2019. Respondents could select one of the four possible options shown.

Acknowledgements

With thanks to our colleagues in the Delta-EE Flexibility Research Service, the participants in our Delta-EE Heat Summit 2019 who took part in our poll, and the industry contacts we contacted for our research into this topic.

References

[1] Delta-EE. Residential DR market status. Delta-EE, Flexibility Research Service. 2019.
[2] Delta-EE. Value streams for flexibility – a non-expert's guide. Delta-EE, Flexibility Research Service. 2019.
[3] Delta-EE. Residential DR infobase. Delta-EE, Flexibility Research Service. 2019.

13th IEA Heat Pump Conference
April 26-29, 2021 Jeju, Korea

Design and Experimental Results of a Two-Stage Steam Producing Industrial Heat Pump

Marina, A.[a,*], Smeding, S.F.[a], Wemmers, A.K.[a], Spoelstra, S.[a], Kremers, P.[b]

[a]TNO, Westerduinweg 3, 1755 LE, Petten, The Netherlands
[b]IBK B.V., Duwboot 19, 3991 CD, Houten, The Netherlands

Abstract

This paper describes the design and experimental analysis of a steam producing industrial heat pump system. The heat pump is a two-stage flooded system with a thermal capacity of 150 kW_{out}, capable of producing medium pressure steam (4.8 bar_{abs}, 150°C) with up to 90°C temperature lifts. The heat pump takes up heat at two distinct temperature levels and in this way can take advantage of temperature glides, typical of waste heat streams in industrial processes. It has been tested with a single working fluid, namely the hydrocarbon Pentane. The heat pump is tested using a specially designed test rig, capable of simulating conditions typical of numerous industrial processes. Experimental results are presented for various operational conditions (temperatures, powers) using both the single-stage and dual-stage cycle. The heat pump is shown to be capable of producing steam temperatures at the design point of 150°C. The results demonstrate that steam producing heat pumps are a feasible technology option for industrial applications. There are however steps needed for mass uptake, especially related to upscaling powers to the 1-5 MW range.

Keywords: Industry; High temperature heat pump; Waste heat; Pentane; Pilot scale system;

Nomenclature

Symbols		out	Stream flow out of system
β	Heat source ratio (-)	sink	Thermal sink
η	Efficiency (-)	source	Thermal source
$\dot{Q}$	Heat transfer rate (W)	steam	Steam production
T	Temperature (K)	th	Thermal
$\dot{W}$	Rate of work, power (W)		
		Abbreviations	
Subscripts		COP	Coefficient of performance
abs	absolute	GHG	Greenhouse gas
Carnot	Carnot cycle, theoretical maximum	GWP	Global warming potential
elec	Electrical	HP	High pressure
in	Stream flow into system	LP	Low pressure
LT	Low temperature	MP	Middle pressure
MT	Middle temperature	ODP	Ozone depletion potential

1. Introduction

The European Union and its 28 member states (EU28) have set the ambitious target of reducing greenhouse gas (GHG) emissions by 80-95% relative to 1990 levels by 2050. In order to achieve this, there is the requirement to transform the current energy system, primarily by switching to renewable energy sources and implementing energy efficiency measures. This will be particularly relevant for the industrial sector in the coming years, which at present (2018) is responsible for 11,590 PJ or 25% of final energy consumption in EU28 [1].

* Corresponding author. Tel.: +31 (0) 6 5000 9632.
E-mail address: andrew.marina@tno.nl.

Industrial energy usage in EU28 is dominated by the demand for thermal energy, which is estimated to be responsible for 73% of total consumption (2012) [2]. The heating demand is at present covered almost entirely by fossil sources, namely natural gas, oil and coal. The remaining energy demand, covered by electricity, is mostly required for mechanical work, for example to drive fans, compressors, pumps and other machinery. Based on this, it can be determined that large reductions in GHG emissions from industry will only be achievable through radical changes in the supply and use of heat, implying the need for significant changes to existing processes. The challenge for industry to transform their heat supply is made greater by the requirement for heat use at different temperature levels, from below 100°C, to well above 1000°C, depending on the given process or sector.

The use of heat pump technology in an industrial setting is an option which has the potential to cover a large share of the low temperature (<200°C) heat supply, estimated to be 45% of total industrial heat demand (incl. space heating) [3]. Heat pumps are a technology which take waste heat, typically discarded to ambient due to the low temperature level, and upgrade this to temperatures required by the process. This is done with the input of electricity. When renewable electricity is used as an input source, the GHG emissions from the process can be reduced to zero. In any case, the electricity input required is less than the original energy input (gas, oil, etc.) to the process, meaning that implementing heat pumps will necessarily lead to reductions in the final energy consumption.

One of the main drivers currently prohibiting heat pumps in industry, is the fact that the majority of commercially available heat pumps are currently limited to supplying process heat up to temperatures of approximately 90°C. There is currently a limited demand for heat in industry up to this temperature level. Increasing the maximum heat supply temperature of heat pumps above 100°C such that they have the capability to produce steam will increase the market potential of the technology significantly. Further increases in the maximum temperature towards 200°C will lead to further application potential, making the technology appropriate for numerous processes particularly in the chemical, paper and food sectors.

Whilst there has recently been increased focus in industrial heat pump technology in both academia and the refrigeration and heat pump sectors, the developing nature of the market ensures that further demonstration of the technology is needed. In the Dutch nationally funded project 'Sustainable sTEam Production for induStry' (STEPS), a pilot scale, steam producing industrial heat pump was designed, constructed and tested. The goals of this development project were as follows:

- To demonstrate that an industrial heat pump, producing steam at temperatures up to 150°C (4.8 bar_{abs}), can be manufactured from components which are currently available in the market
- To identify if there are necessary developments needed from component and equipment manufacturers as well as system suppliers
- To accelerate acceptance and uptake from industrial end-users of heat pump technology

The project was carried out with a consortium of partners consisting of a research institute, equipment manufacturers and system suppliers, as well as industrial end-users of the technology from multiple industrial sub-sectors (paper, chemical, refinery, food and beverage). Of this consortium, the design and construction of the heat pump was realized by refrigeration and heat pump system supplier IBK, whilst testing and subsequent analysis of results was conducted at the industrial heat pump test centre at TNO. This remainder of this paper provides details relating to the design of the heat pump system (section 2) as well as results from testing under representative industrial conditions (section 3).

2. Heat Pump Design

Details relating to the design and technical characteristics of the heat pump are given in this section. Firstly, a description is given on how design conditions for the heat pump were determined and the effect this has on the system requirements. Following this, information is provided on the physical system itself, including the process scheme and component information. Finally, details are provided on the specially designed test rig, which was connected to the heat pump to simulate the conditions that would be imposed on the heat pump by an industrial process.

2.1. Design Conditions

Full scale industrial heat pump systems will be characterised by large thermal powers, typically in the range of 1-5 MW_{out}. With the intention in the project to develop a pilot scale heat pump system, a nominal thermal power of 150 kW_{out} was targeted.

Design conditions for the constructed industrial heat pump were selected based on input received from the multiple industrial end-users involved in the project. The end-users were requested to provide data relating to typical conditions (process and waste heat quantities as well as temperature levels) whereby a heat pump could be applied within their process. On the basis of the information received, the design conditions and requirements of the heat pump were determined.

It was determined that to satisfy the requirements of the multiple end-users, the heat pump should be designed to function with three operational concepts:

1. Single evaporator, single compressor
   The evaporator temperature varies between 52°C and 97°C, whilst the target steam temperature varies between 120°C and 150°C. The use of a single compressor ensures this operation mode is most suitable for low to moderate temperature lifts.
2. Single evaporator, two compressors
   The evaporator temperature varies between 52°C and 97°C, whilst the target steam temperature varies between 120°C and 150°C. The use of two compressors in series ensures this operation mode is most suitable for moderate to high temperature lifts. Furthermore, this cycle implementation provides efficiency (coefficient of performance - COP) enhancement when compared with the single compressor cycle.
3. Two evaporators, two compressors
   The single system operates with two evaporators which have two distinct pressure (temperature) levels. The low temperature evaporator varies between 52°C and 97°C, whilst the high temperature evaporator varies between 97°C and 111°C. The target steam temperature in this case is also in the range of 120°C to 150°C.

Whilst conventional heat pump cycles consist of a single source and sink, the requirements of the end-users have necessitated a multi-temperature heat pump whereby waste heat can be input at two locations. There are two main scenarios whereby a multi-temperature (source) heat pump is advantageous for use in a process:

1. Where multiple waste heat sources are available at differing temperature levels.
2. Where the waste heat source has relatively low energy content, leading to a large temperature glide on the waste heat stream in order to produce the required thermal power on the sink side of the heat pump.

The efficiency of a heat pump cycle, also known as the COP relates the heat output in the condenser to the electrical work input. The theoretical maximum COP that can be achieved is determined by the temperature of the heat sink as well as the temperature lift required to be achieved by the heat pump (see section 2.4). Increasing the temperature lift has a detrimental impact on the maximum achievable COP. By implementing a multi-stage (single evaporator, two compressors) or multi-temperature (two evaporators, two compressors) cycle, the COP is enhanced as the entirety of working fluid in the heat pump cycle does not need to be compressed from lowest temperature (pressure) level to highest temperature (pressure) level, therefore limiting the temperature lift for part of the system. This leads to a lower electrical energy input for a given process heat output.

Whilst multi-temperature heat pumps impose additional complexity on the system design and associated control system for operation, their use is not uncommon. There are numerous cycles which can be used to implement multi-temperature heat pump cycles. A comprehensive review of the various multi-temperature heat pump cycles is given by Arpagaus [4].

2.2. High Level Design

The heat pump construction was based on a previously designed, constructed and tested system, an overview of which can be given in the works of Wemmers et al. [5]. The original heat pump design was based on a single stage system (single evaporator and compressor) and used Butane as the working fluid. To fulfil the requirements of the end-users, a number of modifications had to be made to the unit, namely to convert it to a multi-stage and temperature unit, as well as adapt the system to operate with a new working fluid. The new working fluid was needed as the critical temperature of Butane is 152°C, making it unsuitable to operate at the desired sink temperatures of 150°C in a sub-critical cycle.

Pentane was chosen as the new working fluid in the system for the following reasons:

- It is a natural working medium which has zero ODP and low GWP (~4), adding to the sustainable credibility of the technology
- It has a high critical temperature (197°C) and low boiling point (36°C) relative to the range of design and operation conditions (52°C – 150°C) to be tested
- It has good thermal stability, up to the temperatures of interest

As was the case with the heat pump described in [5], the modified unit was constructed inside a container, which allows it to be easily transported and placed at various industrial sites as needed. Rather than test the heat pump directly at an industrial site, the heat pump was tested on a specifically constructed heat pump test rig, also placed within a container unit. There are a number of benefits to this approach, the most important being:

- Issues and delays associated with start-up and commissioning can be resolved without affecting or interfering with the production process
- The heat pump in the first instance is decoupled from the process, making it much simpler to troubleshoot performance or reliability issues
- The performance of the heat pump can be characterised in a controlled environment for numerous operational conditions

An image of the containers housing the heat pump, as well as the test infrastructure can be seen in Figure 1 which follows. These are provided to give the reader an indication of the physical sizing of the systems.



Fig. 1. Containers which house the heat pump (white container) and test infrastructure (blue container) and associated connections

2.3. Process Flow Diagram

A process flow diagram of the heat pump system is seen in Figure 2. As indicated previously, the heat pump is a two-stage system, which allows heat input at two locations. The heat pump is characterised by the two piston compressors as well as the two separator vessels which feed liquid refrigerant to the evaporators in a thermosiphon type arrangement. Additional notable characteristics of the system are described as follows.

Suction Gas Superheaters

A notable characteristic of the working fluid Pentane is that isentropic compression from a (near) saturated vapor will result in the compressed fluid entering the two phase region. Liquid droplets in the compressor can have a large impact on the longevity of the system and may even lead to complete failure. Two suction gas superheater heat exchangers make use of the high temperature liquid from the condenser and middle pressure (MP) separator vessel, transferring heat to the gas in the compressor suction lines. These heat exchangers move the compressor suction gas sufficiently away from the two-phase region, therefore ensuring a limited amount of superheat in the discharge gas for both compressors.

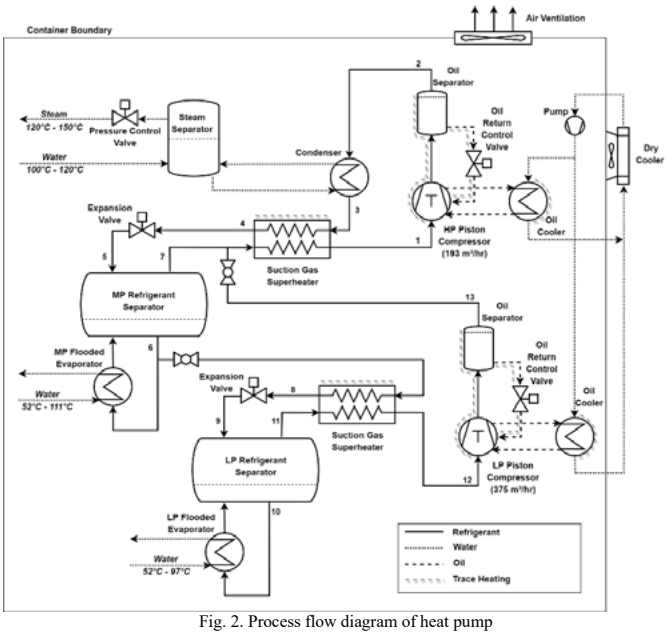


Fig. 2. Process flow diagram of heat pump

Condenser and Steam System

The heat pump utilises a split condenser system (only a single condenser pictured), located parallel to one another. On the water side of the system, the condensers are fed by a steam separator vessel in a thermosiphon type arrangement, with a two phase mixture returned to the vessel from the heat exchanger. The steam separator vessel is fed by the test rig to maintain a fixed liquid level, whilst pressure (and therefore temperature) is controlled by actuating a control valve on the steam return line to the test rig.

Oil Management

Oil discharge from the compressor is separated from the compressor discharge gas in oil separator units. The oil is returned to the compressor through a control valve, which is actuated to limit the return flow rate. Additional oil which manages to pass through the oil separators will make its way to the pentane separators whereby it will accumulate without proper management. Therefore a small amount liquid from the refrigerant separators is entrained intermittently into the suction gas lines, prior to the suction gas superheaters such that it can be evaporated and any residual oil returned to the compressors (feature not pictured in process flow diagram).

In addition to managing the return of oil to the compressors, the high temperatures which characterise this system necessitate external cooling of the oil. This is conducted through two heat exchangers coupled to an external cooling circuit which discards the heat to ambient through use of a dry cooler. The oil is circulated using a pump which is internally located within the compressor housing.

Trace Heating

Trace heating is employed at numerous locations throughout the heat pump, utilised when the heat pump is not in operation. The majority of trace heating in the system is located in the vicinity of the compressor oil system. Trace heating is located on the oil separator and the compressor housing, as well as the lines (both oil and refrigerant) between these components. In addition, trace heating is placed on the oil coolers. The purpose of this trace heating is to prevent refrigerant condensing and mixing with the oil during shut down periods. This can lead to oil foaming on start-up, limiting the oil pressure in the compressor. Trace heating was also placed on both suction gas superheaters to prevent liquid condensing in the suction line when the system is not in operation. Without this trace heating, it is probable that significant amounts of liquid refrigerant would be entrained into the compressor on start-up.

2.4. Theoretical Performance

As indicated in section 2.1, the COP of a heat pump relates the heat output in the condenser to the electrical work input as seen in equation 1. This is valid for both single evaporator and multi-evaporator cycles, in the latter case, the electrical energy from both compressors must be summed.

$$COP = \frac{\dot{Q}_{th-out}}{\dot{W}_{elec-in}} \tag{1}$$

The theoretical maximum COP that can be achieved by a heat pump cycle containing only internally reversible processes is known as the COP_{Carnot} and is defined by the second law of thermodynamics. For a heat pump with a single heat source, the COP_{Carnot} can be simply expressed as a function of the source and sink temperatures, as given in equation 2.

$$COP_{Carnot} = \frac{T_{sink}}{T_{sink} - T_{source}} \tag{2}$$

For a multi-temperature heat pump system, calculation of the COP_{Carnot} becomes non-trivial. The value is dependant not only on temperatures, but also on the fraction of heat input from each evaporator in the system. The equations which define the second law efficiency (COP_{Carnot}) for a multi-temperature heat pump have been defined by Arpagaus [4] and are reproduced in equations 3 to 7 below.

$$COP_{Carnot(LT)} = \frac{T_{sink}}{T_{sink} - T_{source(LT)}} \quad , \quad COP_{Carnot(MT)} = \frac{T_{sink}}{T_{sink} - T_{source(MT)}} \tag{3), (4}$$

$$\beta = \frac{\dot{Q}_{th-in(MT)}}{\dot{Q}_{th-in(MT)} + \dot{Q}_{th-in(LT)}} \quad , \quad \alpha = \frac{\beta}{1-\beta}\frac{COP_{Carnot(LT)} - 1}{COP_{Carnot(MT)} - 1} \tag{5), (6}$$

$$COP_{Carnot(multi-temp)} = \frac{1}{1+\alpha}COP_{Carnot(LT)} + \frac{\alpha}{1+\alpha}COP_{Carnot(MT)} \tag{7}$$

To determine the true efficiency of a heat pump, the COP achieved is related to the thermodynamic maximum through equation 8. For the current project, a η_{Carnot} of 50% was targeted for both single stage and dual stage cycles, which should be feasible for a well designed heat pump system.

$$\eta_{Carnot} = \frac{COP}{COP_{Carnot}} \tag{8}$$

2.5. Component Selection

The system utilises industrial open type piston compressors manufactured by Mayekawa (HP compressor pictured Figure 3). The specifications of these compressors are given in Table 1. Piston compressors were chosen as they match well with the system size requirements (150 kW) and can easily adjust to the differing pressure ratios required for testing. These compressors were able to operate between 900 RPM and 1600 RPM and were lubricated by a polyalkylene glycol (PAG) lubricant with an ISO viscosity grade of 100.

Table 1: Compressor specifications

Component	Type	Swept Volume (cm^3)	Displacement (m^3/hr @ 1450 RPM)
LP Compressor	Mayekawa F8WA	4310	375
HP Compressor	Mayekawa B6HK	2218	193

The heat pump is equipped with numerous sensors to measure physical quantities which combined give the performance of the cycle. The data from the unit is collected at an interval of 1 second using a Siemens SCADA system. There are pressure and temperature sensors at numerous locations, both of which are generally located in each vessel as well as between the major components. Mass (or volume) flows are not measured within the heat pump itself, rather they are calculated from data gathered from the connected test rig (see section 2.7).

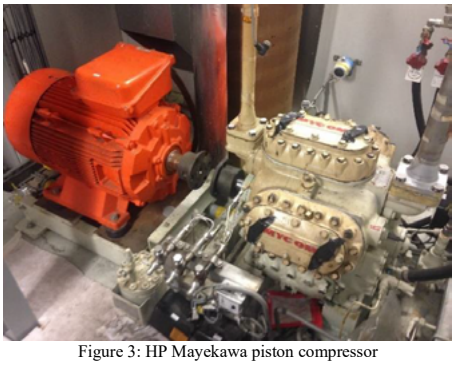


Figure 3: HP Mayekawa piston compressor

2.6. Safety Systems and Measures

The heat pump system inside the container conforms with relevant ATEX requirements. The container is placed in the open air, with the internals ventilated with approximately 2000 m³/hr of fresh air. Pentane detectors in the ventilation ducts will detect leaks at 1400 PPM, roughly 10% of the lower explosive limit.

2.7. Test Rig

A process flow diagram of the test rig used to simulate the industrial process can be seen in Figure 4. The buffer vessel is the central component, with all flows originating from this location. The buffer vessel contains a water steam mixture which is heated in the range of 100°C – 120°C (1 bar_{abs} – 2 bar_{abs}) using an electrical heating element prior start-up. Liquid from this vessel is fed to the steam separator (which subsequently feeds the condenser) as well as the two evaporators. The flow rate for all three circuits are set by a speed controlled pump, whilst the temperatures of the flows to the evaporators can be controlled by recirculating the cooled flows from the exit of the evaporator back to the inlet. The return flows from both the evaporators (liquid) as well as the steam separator (vapor) are returned to the buffer vessel. The heat added to the vessel from the flow from the condenser is greater than that removed from the evaporators, in theory, by the power of the compressors. Therefore, to maintain the temperature of the buffer vessel at a fixed level, it is necessary to remove heat, which is done by condensing steam at the top of the vessel using a simple U tubed heat exchanger. A water glycol mixture is circulated through the heat exchanger with the heat discharged to ambient using a dry cooler. The test rig is equipped with numerous instrumentation (pressure, temperature, flow) to determine the thermal power from the heat pump and fully characterise the process.

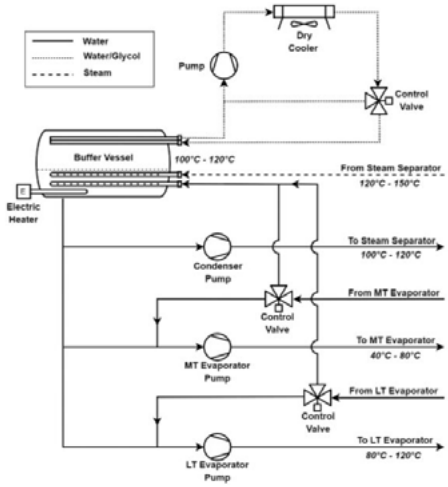


Fig. 4. Process flow diagram of test rig which simulates the industrial process on the heat pump

Figure 5 shows an image of the internals of the test rig system. The buffer vessel is clearly distinguishable in the foreground on the right side of the figure. The connections for the U-tube heat exchanger are located at the top of the vessel, whilst the return lines for the condenser and evaporators are located below. In the background on the left side of the figure, the pumps as well as general flow apparatus (valves, flow meters) are present. After this figure was taken, and prior to testing, the buffer vessel, piping and components were thermally insulated.



Fig. 5. Internals of test rig showing the buffer vessel and ancillary components

3. Experimental Results

This section outlines experimental results obtained from the unit. Firstly, two measurement results (one single stage, one dual stage) are analysed. Following this, a full list of results from the experiments is presented.

3.1. Analysis of Single Stage Results

Single stage results are presented for the heat pump producing steam at 130.6°C from a source heat temperature of 84.9°C cooled to 79.7°C. The measured cycle state points are presented on TS and PH diagrams in Figure 6 and 7 respectively. The numbered points on the diagram make reference to the location in the cycle as seen in Figure 2. Overlaid on the TS diagram is the temperature of the external source and sink to give an indication of the ΔT in the evaporator and condenser heat exchangers. It is noted that the specific entropy information is not relevant to this data.

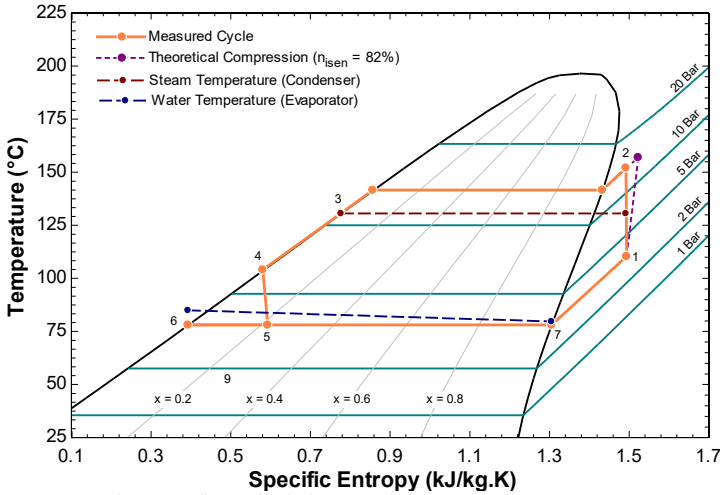


Fig. 6: TS diagram for single stage cycle (T_{steam} = 131°C, T_{source} = 85°C)

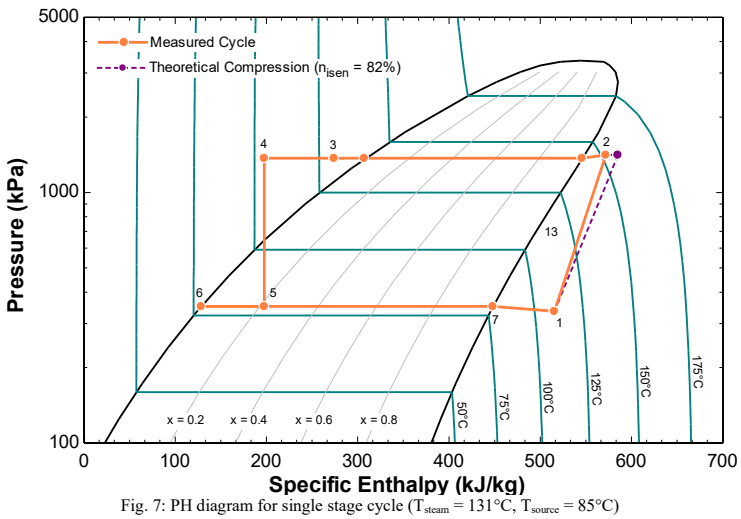


Fig. 7: PH diagram for single stage cycle (T_{steam} = 131°C, T_{source} = 85°C)

The heat pump produced 97.5 kW of heat (steam) with an electrical energy input of 36.3 kW, leading to a COP of 2.69. Based on the maximum/minimum external temperatures of 130.6°C and 79.7°C respectively, the COP_{Carnot} for these conditions is 7.92, leading to a value of η_{Carnot} of 34%. The low efficiency of the system is attributed to three (3) reasons described below with the assistance of the TS and PH diagrams, as well as Figure 8, which presents an energy balance for the cycle.

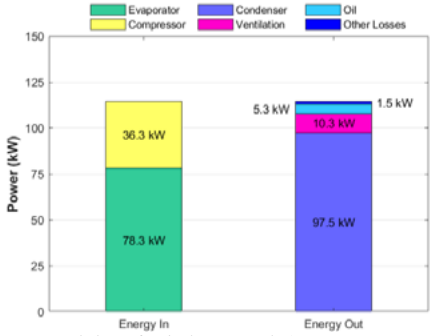


Fig. 8: Energy balance for single stage cycle (T_{steam} = 131°C, T_{source} = 85°C)

1. *Compressor and Electric Motor*

As stated, the measured electrical power to the compressor was 36.3 kW. At the given conditions the compressors should be expected to operate with an isentropic efficiency of 82%. Based on the calculated mass flow for the cycle, the power input is expected to be in the range of 22.2 kW, which obviously varies greatly (10.1 kW) from the measured value. The reason for the large electrical power input is difficult to determine due to the limited sensors which may give a conclusive answer. Likely it is a combination of a lower than expected isentropic efficiency of the compressor, combined with a low electrical motor efficiency, estimated to be in the range of 60%.

2. *Large Temperature Difference in Condenser*

For this experimental condition, the measured condenser temperature was 141.6°C (13.7 bar) whilst the measured evaporator temperature was 78.1°C (3.5 bar). Whilst a small ΔT was measured throughout the evaporator (1.6°C-6.8°C), this was not the case in the condenser (~11°C). The large temperature differences act to increase the work required by the compressor, therefore reducing the total efficiency of the machine.
The large mean temperature difference which acts to reduce the efficiency of the heat pump, has been attributed to air ingress occurring whilst the system is shut down and below atmospheric pressure. This air trapped in the condenser section could not be easily purged.

Thermal Losses

A large amount of heat produced in the system was lost to oil cooling (5.3 kW) as well as the ventilation air (10.3 kW). These thermal losses are visible through inspection of the theoretical compression process overlaid on the measured cycles in Figure 6 and 7. Whilst it would be expected that the theoretical process brings the compressor discharge state closer to the two-phase region than the measured cycle, this is not the case due to the thermal losses which are present. This result emphasizes the case for proper thermal insulation of the heat pump unit and correct selection of the oil temperature when operating at high temperatures. It is noted that a small portion (1.5 kW, 1.3%) of the total heat input could not be accounted for in the energy balance.

3.2. Analysis of Dual Stage Results

The results of the dual stage cycle implementation are presented for the heat pump producing steam at 150.4°C from two heat sources; one cooled from 105.1°C to 102.0°C, and the other from 64.9° to 60.1°C. Once more, the measured cycle state points are presented on TS (source and sink temperatures overlaid) and PH diagrams, seen in Figure 9 and 10 respectively.

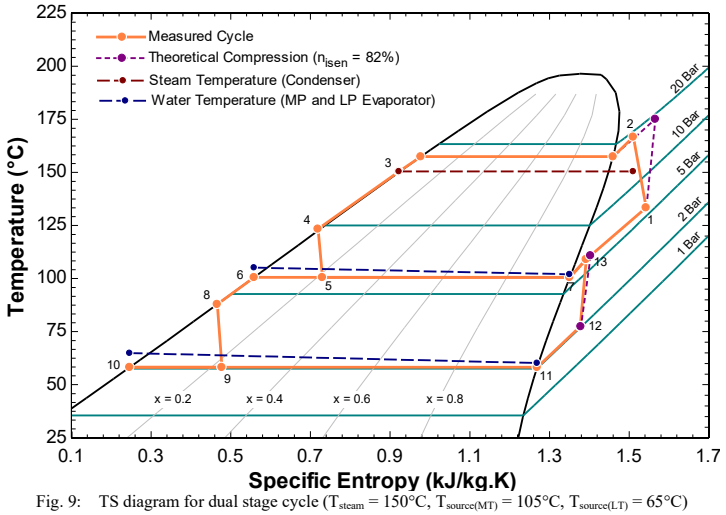


Fig. 9: TS diagram for dual stage cycle (T_{steam} = 150°C, $T_{source(MT)}$ = 105°C, $T_{source(LT)}$ = 65°C)

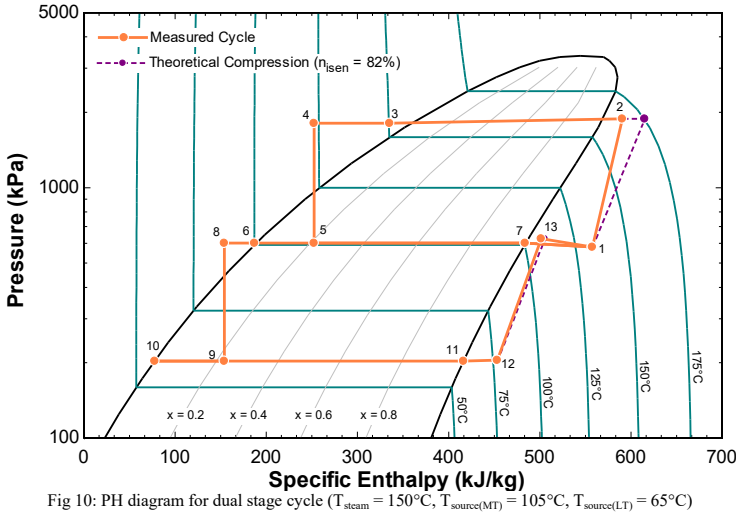


Fig 10: PH diagram for dual stage cycle (T_{steam} = 150°C, $T_{source(MT)}$ = 105°C, $T_{source(LT)}$ = 65°C)

The heat pump produced 144 kW of heat (steam) with an electrical energy input of 63 kW, leading to a COP of 2.06. Utilizing equation (3) through (7), the COP_{Carnot} was calculated to be 5.63 for the dual stage cycle, leading to a η_{Carnot} of 36.5%. Whilst still relatively low, the dual stage cycle performs relatively better than the single stage cycle.

Insights can be gained into the performance of the cycle from the supplied TS and PH diagrams (Figure 9 and 10) as well as the energy balance for the system provided in Figure 11. The theoretical compressor work required for this cycle was 31.2 kW (59% of measured) and 14.3 kW (83% of measured) for the HP and LP compressors respectively. This gives evidence to suggest that the combination of compressor and electrical motor performs better in terms of isentropic and electrical efficiency in the low stage compared to the high stage. Further to this, from the TS and PH diagrams, when viewing the theoretical compression process, it can be seen that for the low stage that the theoretical and actual lines are almost overlapping. This is not the case for the high stage. This indicates that the thermal losses on the low stage are significantly lower than that of the high stage. This could be expected on the basis that the low stage operates at much lower temperature levels than the high stage. These factors, particularly the higher electrical efficiency of the motor, are likely the reason for the slightly higher η_{Carnot} when compared to the single stage cycle. Like the single stage cycle though, thermal losses from the system are still significant, with 12.1 kW lost to the ventilation, 14.0 kW lost to the oil system, and 18 kW being unaccounted for. Similarly, large temperature differences were seen over the condenser, which also increases the internal temperature lift of the heat pump and acts to reduce the COP of the system.

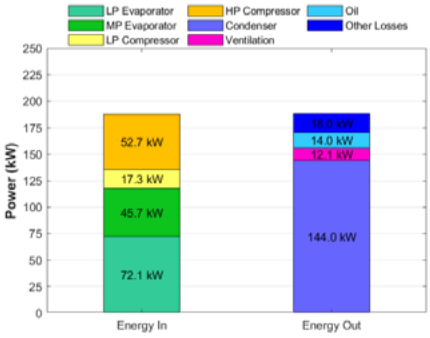


Fig 11: Energy balance for dual stage cycle (T_{steam} = 150°C, $T_{source(MT)}$ = 105°C, $T_{source(LT)}$ = 65°C)

3.3. Summary of Additional Results

A summary of the measurement results from the pilot scale heat pump unit is given in table 2. As was the case with the reference measurements, the system was characterised by low values of η_{Carnot}. Once more, in general, two-stage cycles performed better relative to the single stage cycle.

Table 2: Summary of additional measurement results from the heat pump

LT Evaporator		LP Compressor	MT Evaporator		HP Compressor	Steam Production		Heat Losses		COP	η_{Carnot}
T (°C)	Q̇ (kW)	Ẇ (kW)	T (°C)	Q̇ (kW)	Ẇ (kW)	T (°C)	Q̇ (kW)	Oil (kW)	Air (kW)	(-)	%
60.0	95.8	21.5	100.0	35.0	46.8	133.6	166	13.8	11.3	2.4	38
64.9	72.1	17.3	105.0	45.7	52.7	150.4	144	14.0	12.1	2.1	37
-		-	94.3	91.5	41.6	140.9	110	8.9	13.0	2.6	33
-	-	-	105.0	109.0	49.0	150.5	132	11.2	12.1	2.7	32
-	-	-	85.0	78.3	36.3	130.6	98	5.3	10.3	2.7	34

4. Conclusions and Future Works

This paper gave an overview of the design and experimental analysis of a pilot scale industrial heat pump, designed with a thermal capacity of 150 kW_{out}, able to produce medium pressure steam of 150°C (4.8 bar_{abs}). The heat pump was able to take up heat at two distinct temperature levels through the use of separate flooded evaporators. Pentane was used as a working fluid, allowing the range of evaporating and condensing

temperatures (52°C – 150°C) required by end-users involved the project to be covered with a single working fluid.

To perform an experimental analysis of the heat pump, it was connected to a specially designed test rig, which contained the necessary instrumentation to determine thermal powers and characterise the process. Results were presented for the heat pump operating with both a single heat input as well as a dual heat input at two distinct temperature levels.

The heat pump was in general characterised by low values of η_{Carnot}, in the range of 32-38%. The low efficiencies were attributed to three factors: combined low electrical efficiency of the electrical motor and isentropic efficiency of the compressor; large temperature differences between fluid streams in the condenser and higher than expected thermal losses. In general, the two-stage cycle showed higher values of η_{Carnot} than the single stage cycle, which was demonstrated to be a result of the lower thermal losses in the low (temperature) stage, combined with a compressor and electrical motor performance which better matched to theoretical values. With the absence of the large temperature differences in the condenser, and use of electrical motors with efficiencies in the range of 90%, it is feasible that values of η_{Carnot} exceeding 50% would be feasible.

Despite the lower than expected efficiencies, the results of the experimental analysis demonstrate that it is indeed possible to build an industrial steam producing heat pump utilising equipment currently available in the market. Using this standard equipment, the heat pump demonstrated a maximum steam temperature of 150°C, corresponding to a saturation pressure of 4.8 $bar_{(abs)}$. The condensing temperature in this case exceeded 157°C suggesting higher steam temperatures should be feasible with a better functioning condenser. Another notable result was a maximum external temperature lift of 90°C, achieved using the dual stage cycle with heat input at an intermediate temperature level.

Further work on this topic will involve attempting to gain clarity on the lower than expected performance of the system, particularly determining the exact reason for the higher than expected electrical energy input for the high pressure compressor. Additionally, the unit will be tested with a synthetic working medium, namely, the non-flammable synthetic R1336mzz(Z). The experiments conducted will focus on other process conditions relevant for end-users not yet tested, as well as characterising the heat pump using a single evaporator combined with two-stage compression. Follow-up projects on compression heat pumps will focus on upscaling the technology to full-scale sizes (1-5 MW) relevant for industrial end-users. The focus will be on achieving heat pump units with low specific investment costs (€200/kW_{th}), giving a higher likelihood of mass uptake in the market.

5. Acknowledgements

The project is partially funded by subsidies of the Topsector Energy from the Ministry of Economic Affairs (EZ) – project number TEEI115010.

6. References

[1] Eurostat. Energy Balances 2018. 2019. https://ec.europa.eu/eurostat/web/energy/data/energy-balances (accessed November 11, 2019).
[2] European Commission. Communication from the Commission to the European Parliament, the Council, the European Economic and Social Committee and the Committee of the Regions on an EU Strategy on Heating and Cooling. 2016.
[3] Heat Roadmap Europe. Heating and Cooling: facts and figures 2017.
[4] Arpagaus C, Bless F, Schiffmann J, Bertsch SS. Multi-temperature heat pumps: A literature review. International Journal of Refrigeration 2016;69:437–65. doi:10.1016/j.ijrefrig.2016.05.014.
[5] Wemmers AK, van Haasteren, A.W.M.B., Kremers P, van der Kamp J. Test Results R600 Pilot Heat Pump. 12th IEA Heat Pump Conference, Rotterdam: 2017.

13th IEA Heat Pump Conference
April 26-29, 2021 Jeju, Korea

Acoustic Characterisation of an Air-To-Water Heat Pump for Different Operating Conditions: Inter-laboratory Results

François Bessac [a*], Roberto Fumagalli [b], Henrik Hellgren [c], Thore Oltersdorf [d], Svend Pedersen [e], Thomas Fleckl [f], Christoph Reichl [f]

[a] CETIAT, 25 avenue des Arts, 69100 Villeurbanne, France
[b] Politechnico di Milano, Piazza Leonardo da Vinci, 32, 20133 Milano MI, Italy
[c] RISE Research Institutes of Sweden, Brinellgatan 4, 504 62 Borås, Sweden
[d] Fraunhofer - Institut für Solare Energiesysteme ISE, Heidenhofstraße 2, 79110 Freiburg im Breisgau, Germany
[e] DTI Danish Technological Institute, Gregersensvej 8, 2630 Taastrup, Denmark
[f] AIT Austrian Institute of Technology GmbH, Giefinggasse 4, 1210 Wien, Austria

Abstract

Since the last 5 years the European heat pump market is showing an accelerated growth of outdoor air source heat pumps. The noise emitted by heat pumps is recognised as a drawback of the technology, especially during non-steady state operation of the heat pump.
Within Annex 51 "Acoustic Signatures of Heat Pumps" of the IEA HPT TCP, a dedicated task is the experimental investigations on acoustic performance of air-to-water heat pumps. The measurements of several laboratories on a unit, according to several operating conditions, on standard conditions (EN 14511), part-load conditions (EN 14825) and ERP (EN 12102-1) are compared. Under some conditions, some frost/defrost cycles occur, and a focus is set on the spectrum and sound level changes that can be observed between these cycles. The paper also presents some data about the acoustic directivity of the unit.

Keywords: acoustic emission; inter-laboratory test; heat pump; acoustic test;

1. Introduction

The primary aim with Annex 51 "Acoustic Signatures of Heat Pumps" of the IEA HPT TCP is to further increase the acceptance of heat pumps for comfort purpose with respect to the noise and vibration emissions.

The overall objective of this collaborative work is to gather the knowledge and expertise of the participants in order to forward this knowledge with dedicated recommendations for low-noise heat pumps to different target groups such as manufacturers, acoustic consultants, installers, standardization bodies and policy makers.

To reach this goal, different reasons to reduce sound emissions depending on countries (regulation), locations and applications have to be gathered and understood. The main influencing factors to the acoustic signature of these units will be identified. Collecting and combining research results in these fields on the different implementation levels (component, unit and application level) will finally lead to directions for improved components, units and control strategies including guidelines, as well as training and inputs to future standards.

The work of Annex 51 is divided into six tasks, from standard and legislation aspects to acoustic behavior of individual heat-pump sources (components) and noise synthesis, noise emission for neighborhood, psychoacoustics, etc. One of these tasks is dedicated to the measurement of the heat-pumps noise levels: water heater, air-to-air and air-to-water heat-pumps.

This paper focuses on the acoustic measurement of a split air-to-water unit circulating in six European laboratories, and running on several operating conditions, leading to different sound power levels which are analyzed and compared. In addition, the unit polar directivity is also measured and the effects on the noise between the defrosting phases and the consequences of frosting on the sound level is addressed.

* François Bessac. Tel.: +33 (0)4 72 44 49 00 *E-mail address:* francois.bessac@cetiat.fr

Regarding the expertise in terms of testing of heat pumps, as Annex 51 gathers experts from the major testing laboratories as well as the convenor of the European standardization committee on acoustics for HP (CEN/TC 113 WG9) and considering the new standard EN 12102-1 which is applied in this project, no specific bibliography was conducted for that task.

It has to be noted that many round robin tests are regularly performed within laboratories for ISO 17025 accreditation but without any public data. The European project ECOTEST, aiming at assessing the reproducibility of the standards used for Ecodesign regulations by means of round-robin tests on different types of heat pumps was conducted exactly at the same time than the Annex 51 task. The results of ECOTEST on the acoustic tests will be considered once publically available, if any relevance for this Annex.

2. Sound power levels of heat-pumps in steady-state conditions

2.1. Program

The EN 12102-1 standard specifies the main rules for implementing an acoustic measurement, especially on the installation aspects of the unit, whatever the operating conditions. A measurement program (cf. Table 1) has been defined for the unit, and each laboratory carried out all or part of this program, with thermodynamic measurements in parallel to the acoustic measurement.

The EN 12102-1 Annex A.4 gives the conditions to determine the sound power level of variable speed units for compliance with Ecodesign and Energy labelling regulations (cf. configuration #5 of Table 1).

Table 1. program of tests with the thermodynamic settings and specific settings for the selected air-to-water heat pump

Nr.	Standard	Condition	Air dry bulb (wet bulb) temperatures (°C)	Water inlet/outlet temperatures (°C)	Setting from manufacturer table	Set temperature	Fan	Mode	Liquid circulator setting
1	EN 14511	standard rating	7(6)	30/35	1	30	Auto	Heat (Sun)	max.
2	EN14511	standard rating	7(6)	30/35	1	30	Auto	Heat (Sun)	2
3	EN 14511	standard rating at max frequency	7(6)	30/35	10	21	Auto	Heat (Sun)	max.
4	EN 14825	C	7(6)	*/27	12	29	Medium (3 bars)	Heat (Sun)	max.
5	EN12102-1 A.4	reaching the same capacity as test C	7(6)	30/35				Heat (Sun)	max.
6	EN 14825	D	12(11)	*/24	11	30	Medium (3 bars)	Heat (Sun)	max.
7	EN 14825	B	2(1)	*/30	13	28	Medium (3 bars)	Heat (Sun)	max.
8	EN 14825	A/F (Tbiv)	-7(-8)	*/34	14	27	Medium (3 bars)	Heat (Sun)	max.
9	EN 14825	A/F (Tbiv) and maximum frequency	-7(-8)	*/34				Heat (Sun)	max.
10	EN 14825	E (TOL)	-10(-11)	*/35	15	25	Medium (3 bars)	Heat (Sun)	max.

2.2. Heat-pump under test

A split air-to-water heat-pump was selected as it is representative of a large share of the European market. The unit under test was provided by an European manufacturer: this inverter unit using R410A has a rated heating output of 8 kW according to its label. The outdoor unit size is approx. 800 x 600 x 300 mm.

2.3. Laboratories

This unit circulated in 6 European laboratories, carrying out acoustic and thermodynamic measurements:

- AIT (Wien, Austria),
- CETIAT (Lyon, France),
- DTI (Aarhus, Denmark),
- Fraunhofer ISE (Freiburg im Breisgau, Germany),
- Politechnico Milano (Milan, Italy),
- RISE (Borås, Sweden).

These laboratories implemented the heat pump in different measuring environments, some in a reverberant room, some others in a climatic chamber used as a hard wall room or as a free field room. The measurement

techniques are various, from ISO 3741 in reverberant room and ISO 3743-1 or ISO 3747 (with engineering grade) in hard-wall room (usually a climatic chamber), and ISO 3744 for other environments. They all fulfilled the EN 12102-1 “class A” measurement requirement, which implies ambient conditions to be controlled, and the use of an acoustic standard with at least engineering grade.

One of the laboratories uses a mesh of 55 microphones around and above the unit, allowing directivity measurement.

Several laboratories investigated short time steps acoustic measurements (with less than the 30 seconds average used for standard measurement) to observe the noise variation when frosting and defrosting cycles occur.



Fig. 1. Examples of the heat-pump installation in a test room
(left: reverberant room, right: climatic chamber)

2.4. Inter-comparison results and analysis

Even though the tests results for all the conditions listed in Table 1 can not be presented, it can be said that in most of the cases, the laboratories found similar results. The differences that can occur are acceptable, given the variety of test environment and acoustic test methods. When some larger difference appeared, it was often due to a difficulty of adjusting operating condition rather than an acoustical measurement problem.

The first condition to be tested by 6 laboratories is the standard rating condition, as given in EN 14511 condition (configuration #1) which results are presented in Fig. 2

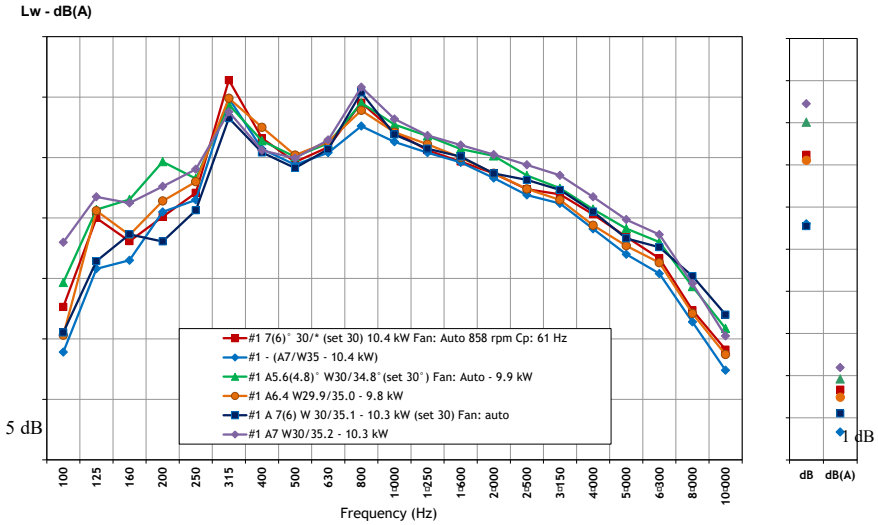


Fig. 2. Spectrum of A-weighted sound power levels for Standard rating conditions EN 14511 (#1) from 6 laboratories

For this operating condition, the spectra are close in the middle range of the spectrum, and the peaks at 315

and 800 Hz are well observed by all laboratories (their origin has not been studied, not being part of this work). As usual, larger differences appear at low frequencies, due to modal behavior of the rooms. The overall dB(A) value remains in a range of 1.4 dB(A). The thermodynamic results are also in a narrow range, from 9.8 to 10.4 kW.

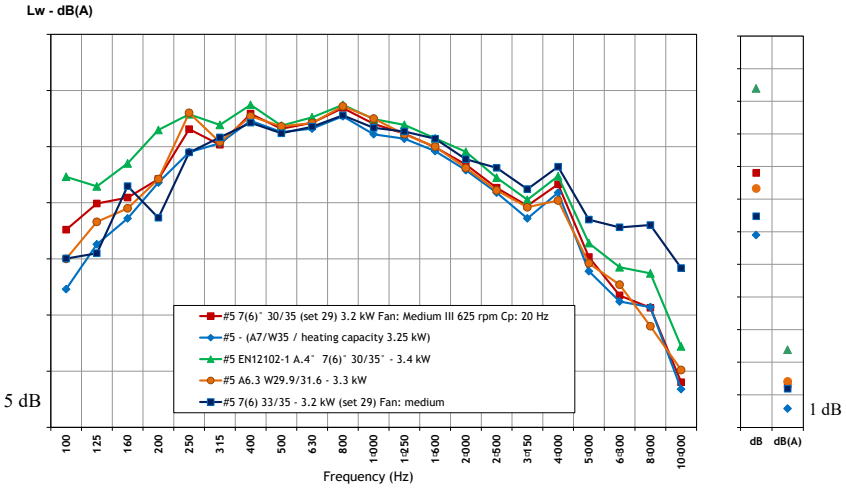


Fig. 3. Spectrum of A-weighted sound power levels for EN 12102-1 7(6)° 30/35° same capacity as for the previous EN 14825 (C) from 5 laboratories

The EN 12102-1 condition requires to set the unit to the same heating capacity as observed for the C point of EN 14825, by reducing the compressor frequency and/or the water temperature difference ΔT if necessary. This procedure is sometimes difficult to achieve as the setting parameters are not reachable, or even though, the requested capacity can not be achieved.

The Fig. 3 shows results from 5 laboratories, leading to convergent results, for the middle range of the spectrum. The low and high frequency ranges exhibit some discrepancies for some laboratories (not investigated in the scope of this study), but the overall dB(A) value remains in a 1.5 dB(A) range. The measured capacity remains in a 0.2 kW range, from 3.2 to 3.4 kW.

2.5. Operating conditions vs sound power levels

The results of one laboratory which measured the rotation speed of compressor and fan are used to show the differences in sound power levels according to the operating conditions.

Different operating conditions lead obviously to variable sound power level and different spectrum shapes. In the present case, the standard rating condition (configuration #1) has a peak at 315 Hz band which disappears for the same condition but with the max frequency setting of compressor and fan. In spite of an average difference of 1.5 to 2.5 dB over the spectrum, the overall value only differs by 0.8 dB(A).

The noise levels for the configuration #6 and configuration #5 are significantly lower, respectively -13 and -10 dB(A) compared to the standard rating conditions (#1).

The noise is more linked to the rotation speeds of the compressor and the fan, than to the heating capacity of the unit, for which no linear relationship can be found for all the laboratories. Fig. 4 shows that configuration #5 is louder by 2.8 dB(A) than #6, due to the higher fan rotation speed (625 vs 558 rpm), despite a lower capacity. Although the two configurations have the same fan rotation speed, configuration #3 is louder by 1 dB(A) than #7, because compressor rotation frequency is 81 Hz instead of 34 Hz.

For all laboratories, configuration #3 (EN 14551 at maximum frequency) gives the highest observed sound power level from all configurations. The negative outdoor air temperature conditions lead to a sound level very close value to the value obtained with configuration #3. For the sake of simplicity, and to avoid acoustic measurement at negative temperatures, this easy-to-implement condition could be considered if the highest sound level would have to be declared. It has to be noted that this value would only be representative of a short period of the heat pump operation.

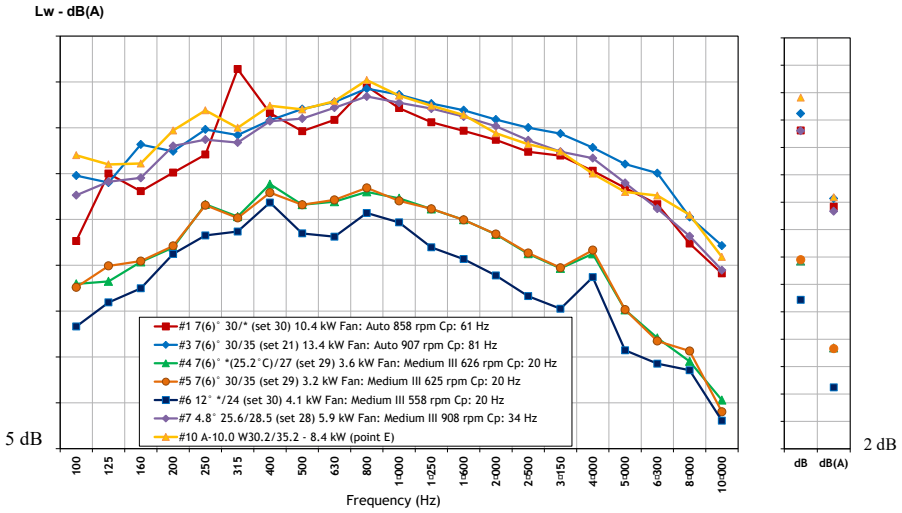


Fig. 4: Spectrum of A-weighted sound power levels for different operating conditions of the heat pump

For the acoustic value measured according to EN 12102-1 Annex A.4 (configuration #5), laboratories found out the procedure difficult to understand and not easily implemented for setting the unit (the heating capacity has to be same than for C point, the compressor frequency being the main parameter to adjust, then the outlet water temperature if necessary). The sound power level obtained is very close to the one obtained for EN 14825 point C (configuration #4). For the 5 laboratories that perform both tests, the overall difference is between 0 and -0.3 dB(A) only. A proposal could be to replace configuration #5 by the configuration #4 for achieving better reproducibility among laboratories.

3. Directivity

One laboratory implemented measurements with a dodecagonal polar frame (approx. diameter 2 m) around the outdoor unit, with 55 microphones. The data from 12 microphones, height 75 cm (third row from the floor, see the yellow arrows for 2 microphones on Fig. 5), allows the plot of the relative directivity diagram, presented in A-weighted overall level on Fig. 6 (an offset was applied to the acoustic data to show directivity values centered on zero).

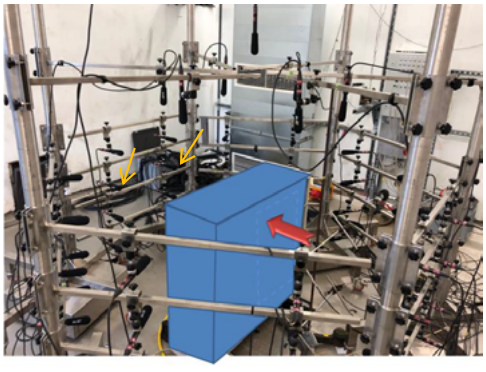


Fig. 5.Dodecagonal frames around the units with microphones

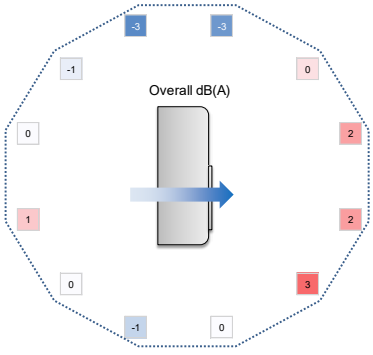


Fig. 6. Directivity for the overall A-weighted sound pressure level at 75 cm height

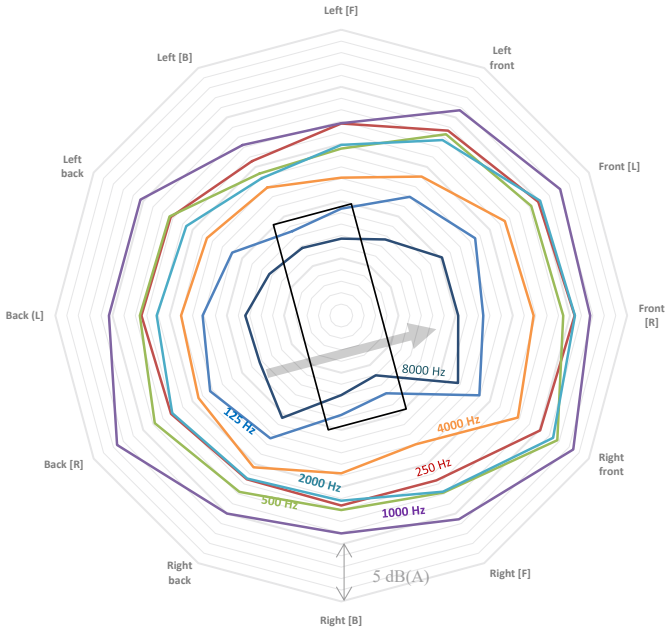


Fig. 7. Directivity for each A-weighted octave band

The directivity diagram in Fig. 7 shows the acoustic radiation directivity of the unit for each A-weighted octave band. Due to the fan located on the right of the casing, the maximum sound level is emitted in this direction ("right front"), and a little bit less on the rear side. The minima can be found on right and left sides, where there are only blind faces. For each octave band, Table 2 gives the amplitude of variation, and the position of the loudest and the quietest microphone.

Table 2. Amplitude of variation of sound pressure level around the unit

Freq.	**125 Hz**	**250 Hz**	**500 Hz**	**1000 Hz**	**2000 Hz**	**4000 Hz**	**8000 Hz**	**Overall**
Max – Min (dB)	6.1	4.8	7.5	6.6	7.5	5.8	5.7	6.2
Max position *	Right front	Front [R]	Right front	Right front	Right front	Right front	Right front	Right front
Min position *	Right [F]	Left [B]	Left [B]	Left [F]	Left [B]	Left [F]	Right [F]	Left [B]

** according to Fig. 7*

As expected the radiation is not omnidirectional, but the directivity amplitude is not huge, with a maximum range of 7.5 dB, meaning a ± 3.75 dB(A) around the mean arithmetical value. The octave bands for which the directivity is the most important are also those which contribute the most to the overall level. Overall range (including the full band) is ± 3.1 dB(A) around the mean arithmetical value.

In the case of an outdoor unit installation close to a neighborhood, this directivity should be considered in order to orientate the quietest side in front of the neighbor. Nevertheless, the effect of this directivity tends to reduce at longer distance.

4. Transient effects (spectral, sound power level)

The experiments also focused on the variation of sound power level when the heat pump operates with frost/defrost cycles. The sound level is rarely measured during this phase as it is generally out of the scope of standardised condition required for national legislations or certifications. In this condition, it is then continuously measured with a short time step (around 1 s) over a series of frost/defrost cycles. According to the temperature conditions, these cycles may have different duration, from 75 minutes to 120 minutes. The variation of acoustic emissions during these phases seems to be repeatable in shape as shown in Fig. 8.

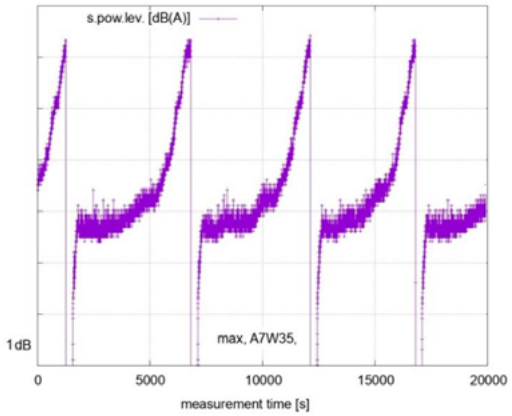


Fig. 8. Time dependent A-weighted sound power levels over 5h30 – configuration #3: EN 14511 freq. max

The simplest analysis for this unit shows that its sound power level measured (averaged over a few seconds) is always lower than the one measured during frosting (almost-steady state operation), without consideration of annoyance which would be studied using a psychoacoustic approach. That is why the acoustic behaviour during the defrosting phase is not investigated in the present paper.

Fig. 9 shows the variation of A-weighted sound power level according to time in seconds, for each octave band and for the overall levels during the frost and the defrost cycle. It can be seen that the overall value slightly increases with the frosting, for almost all frequency bands, except 4000 and 8000 Hz. The most contributing bands to the overall A-weighted value are 1000, 500 and 2000 Hz.

The frosting of the unit leads to an increase up to 3.5 dB(A), before the unit switches to the defrosting cycle. The spectrum at the end of frosting (arrow D) can be compared to the "dry" heat exchanger configuration (arrow H) on Fig. 10. The spectra of Fig. 10 correspond to the arrows time positions on Fig. 9.

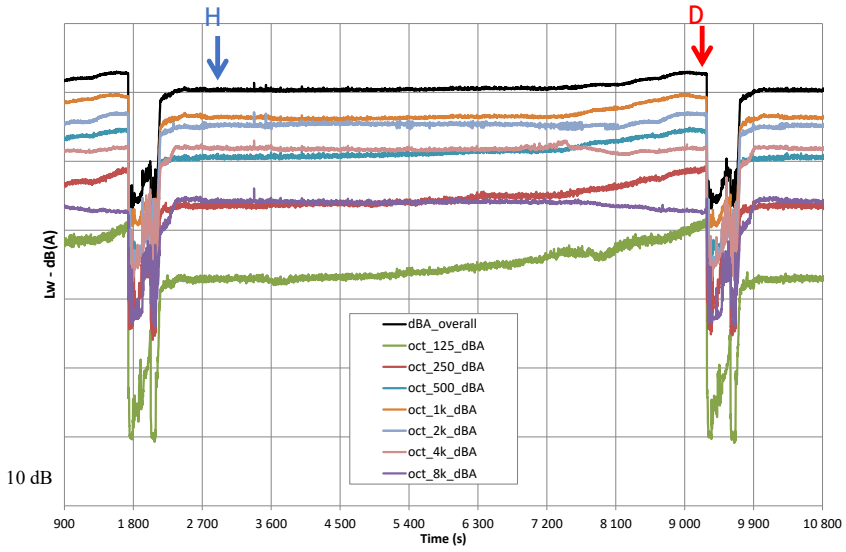


Fig. 9. Time dependent A-weighted sound power levels (in octave bands) between two defrosting phases configuration #3: EN 14511 frequency max

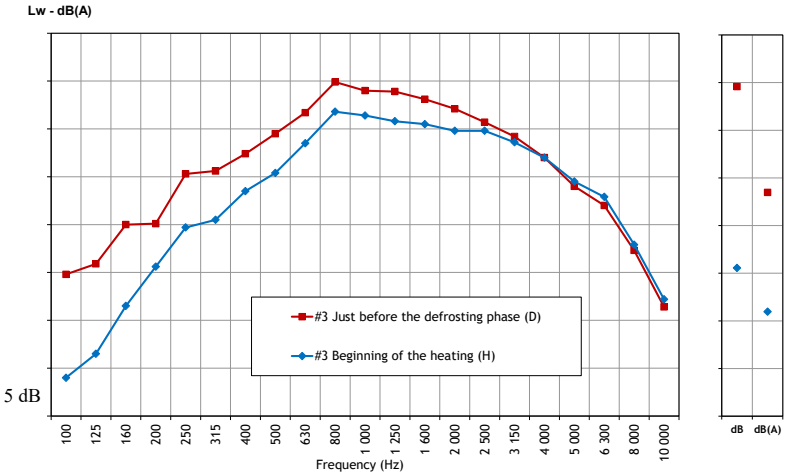


Fig. 10. Comparison of sound spectra before and after defrosting phase (cf. arrows on Fig. 9)

A similar increase of sound power level was observed for the configuration #7 (EN 14825 point B) condition, with a smaller effect on the overall increase, which is around 2 dB(A).

Fig. 11 shows the same quantities as Fig. 9, for negative outdoor air temperatures, leading to different behaviors of the sound power level. These levels are steadier, without noticeable increase before the defrosting starts, even though some accidents on frequency band may occur, but without larger influence on the overall level (see changes at 1800 s). However, this overall level quickly reaches the same magnitude than the one observed at the end of heating of Fig. 9 - arrow "D").

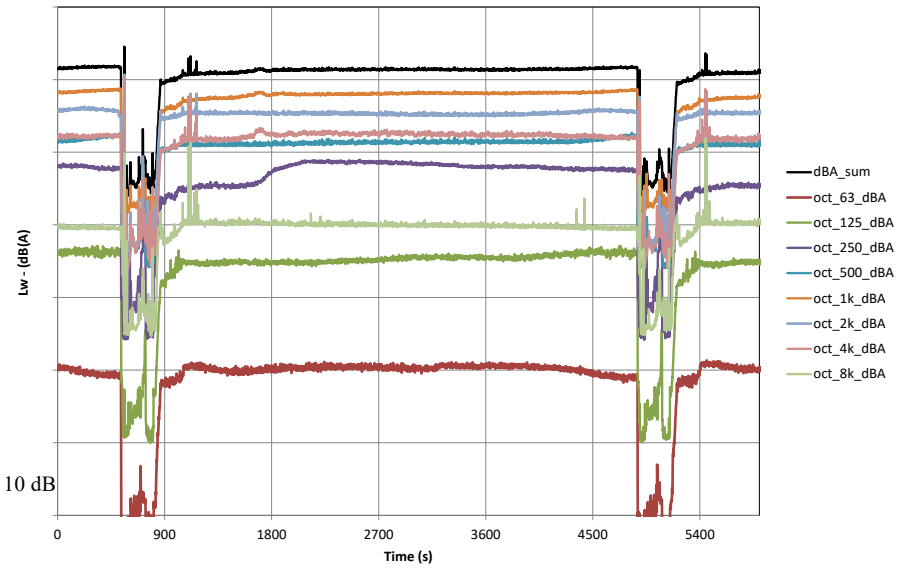


Fig. 11. Time dependent A-weighted sound power levels (in octave bands) between two defrosting phases configuration #8: EN 14825 -7(-8) */34

Conclusions

Acoustic tests have been performed on a split air-to-water heat pump, circulating through six European laboratories, for several operating conditions. The comparison of sound measurements shows a good agreement between results for standard operating conditions (EN 14511 and EN 12102-1). The EN 12102-1 Annex 4 used for Ecodesign compliance requires a unit setting not easy to understand and a clarification from the European Commission could be helpful.

The polar directivity appears to exist with a moderate amplitude (6.2 dB(A) for the overall A-weighted value, and 7.5 dB(A) for middle frequency octave bands), which can be used for an optimized orientation of the outdoor unit in order to limit the noise for the neighborhood. Additional measurements done on the non-steady period between the defrosting phases show that the frosting may increase the sound power level by 3.5 dB(A) for positive outdoor temperatures.

As part of the Annex 51, the results from these round robin tests will be of much help for:

- achieving a better understanding by the manufacturers of the acoustic behaviour of heat pumps in relation with climate conditions
- providing input for the revision of acoustic product standards such as EN 12102-1
- preparing recommendations for installers, namely on the sound directivity
- a better understanding by the policy makers of the complexity to tackle sound power level as it is often a compromise with energy efficiency of the heat pumps.

The results will provide input in order to select the most relevant operating point of the heat pumps and to define corresponding sound power level requirements in ErP regulations.

Acknowledgements

This publication has been developed in the framework of IEA HPT TCP Annex 51 “Acoustic Signatures of Heat Pumps”. We thank the IEA for continuously supporting this topic.

The Austrian Research Promotion Agency (FFG) and the Austrian Climate and Energy Fund (KLIEN) is gratefully acknowledged for funding this work under Grant No. 848891 (program line *'Energieforschung emission 1st call*', project '*SilentAirHP*'). We also want to thank the Federal Ministry of the Republic of Austria for Transport, Innovation and Technology for supporting IEA HPT Annex 51 in Austria in the framework of the IEA Research Cooperation.

CETIAT acknowledges its industrial members as well as Cetim, EDF and GRDF, for co-funding this work.

References

[1] EN 12102-1 (2017) - Air conditioners, liquid chilling packages, heat pumps and dehumidifiers with electrically driven compressors for space heating and cooling – Measurement of airborne noise – Determination of the sound power level

[2] EN 14511-2 (2018) - Air conditioners, liquid chilling packages and heat pumps with electrically driven compressors for space heating and cooling – Part 2: Test conditions

[3] EN 14825 (2018) - Air conditioners, liquid chilling packages and heat pumps, with electrically driven compressors, for space heating and cooling. Testing and rating at part load conditions and calculation of seasonal performance

13th IEA Heat Pump Conference
April 26-29, 2021 Jeju, Korea

Heat pump integration for nZEB–results of IEA HPT Annex 49

Carsten Wemhoener[a*], Fabian Ochs[b], Christina Betzold[c], Arno Dentel[c]

[a]IET Institute of Energy Technology, HSR University of Applied Sciences Rapperswil, Oberseestrasse10, 8640 Rapperswil, Switzerland
[b]Unit for Energy Efficient Building, UIBK, University of Innsbruck, Technikerstrasse 13, 6020 Innsbruck, Austria
[c]TH Nürnberg Georg Simon Ohm, ECN Building Energy efficient system, Fürtherstrasse 250, 90429 Nuremberg, Germany

Abstract

Heat pumps are a promising building technology, especially in nearly Zero Energy Buildings (nZEB), which is believed to be the future building standard in many countries. In IEA HPT Annex 49, participants of nine countries are investigating design and integration options for heat pump application in nZEB. In Task 1, current implementations of nZEB are analysed and a methodology to compare ambition levels in the countries is developed. In Task 2, improvements of the heat pump performance by system integration are investigated by simulations, which are also coupled to the evaluation of real world performance of monitored heat pumps in nZEB in Task 3. In Task 4, the design and control is investigated, which also covers control for demand response. Besides single buildings, also clusters of buildings are included.
Results indicate that heat pumps reach a high performance in nZEB, which is necessary to reach ambitious nZE targets in particular in larger buildings. Furthermore, by simulation and monitoring, further optimization potentials of the heat pump operation have been identified. It is also confirmed that adapted controls can improve self-consumption and grid interaction of on-site electricity generation.

Keywords: Integrated heat pumps; nZEB, system design; energy flexibility; field monitoring

1. Background of nZEB

The recast of the Energy Performance of Buildings Directive [1] in Europe sets the objective that all new public buildings shall be built as nearly Zero Energy Buildings (nZEB) from 2019 on and all new buildings from 2021 on. Also in the USA and Canada Net Zero Energy Buildings (NZEB) are in the focus of the political strategy for high performance buildings, in order to be widely introduced between 2020 and 2030 and in Japan, NZEB are planned to be the standard building by 2030.

Even though political strategies strongly refer to the nearly or Net Zero Energy objectives, there is limited available knowledge and experiences about standardised cost- and performance optimized building technologies to reach nearly or Net Zero Energy consumption. While low- and ultra-low energy houses, e. g. according to the passive house standard, already show considerable market penetration and growth in several European countries and worldwide, nZEB are rather in the pilot and demonstration phase in order to prove a nearly zero, net zero or even plus energy balance. In plus energy buildings a surplus of produced energy compared to the consumed energy is achieved by installed renewables on-site on an annual basis. Especially in the non-residential sector, the nZEB balance can be challenging. Residential buildings have rather moderate energy loads and consumptions, and in particular for single family buildings, there is enough space in the building envelope to reach the balance by on-site renewable production.

In larger buildings, though, both loads may be higher and building envelope may be limited regarding the on-site renewable production, challenging the achievement of the balance and emphasizing the application of high performance components and operation.

Due to the common understanding, an NZEB is a grid-connected building with highly reduced energy needs where the weighted consumed energy can be produced by weighted renewable production on-site on an annual basis. However, this definition is incomplete, e.g. regarding the system boundary (what does on-site mean,

* Corresponding author. Tel.: +41 55 222 43 25
E-mail address: carsten.wemhoener@hsr.ch.

since the EPBD also considers nearby energies), the energies taken into account (including plug loads or just building technology, including mobility, life-cycle consideration) and the weighting system. Moreover, with a broad introduction of the concept as intended in the political objectives, aspects like load match between locally produced and consumed energy as well as interaction with energy grids, in particular the electricity grid should also be considered and buildings should be designed to work in line with the needs of the connected energy grids. Last but not least, the definition of the nZE building has an impact on design and the system configuration.

2. Project outline IEA HPT Annex 49

IEA HPT Annex 49 entitled "Design and integration of heat pumps for nZEB" is carried out in the Heat Pumping Technologies (HPT) Technology Collaboration Programme (TCP) of the International Energy Agency. It deals with integration options and design/control of heat pump application in nZEB, which is investigated both by simulation and monitoring of realized nZEB. Moreover, prototype developments of new integrated heat pumps are included in the Annex 49.

The IEA HPT Annex 49 started in October 2016. The nine countries Austria, Belgium, Estonia, Germany, Norway, Sweden, Switzerland, UK and the USA have joined the Annex 49. The Annex 49 is dealing with a more in-depth evaluation of integration options as well as the design and control of components. Moreover, the building technology may get new tasks, e.g. the provision of flexibility to the connected energy grids, in particular the electricity grid. This may have an impact on future system design and on storage integration. But not only a short-term flexibility, but also the seasonal mismatch has to be taken into account for a holistic assessment of the system solutions.

Furthermore, also the economic boundary conditions are rapidly changing. For instance, PV prices and subsidy schemes are changing, which affects the design and layout of systems and reduction of feed-in tariffs lead to a higher importance of the self-consumption to guarantee an economic operation of the PV system. Decreasing prices of electrical batteries due to e-mobility may additionally have an impact on self-consumption and demand response.

As a further aspect, the investigations in Annex 49 extend the system boundary to clusters of buildings or neighbourhoods. For instance, collective systems connected by micro-grids and load balancing between buildings are implemented.

The work in Annex 49 has been structured into the following tasks:

- Task 1 deals with the state-of-the-art of heat pump application in nZEB in the participating countries. Thereby, the impact of the national definitions on the ambition level in the countries is a topic. Furthermore, implications of the definitions on heat pump use shall be characterized by comparing system solutions and characterizing favourable system layouts and configurations.
- Task 2 is dedicated to an in-depth analysis of integration options of heat pumps in nZEB both on the source side like the ground and active components in the building envelope as well as thermal and electric storage. Moreover, also the integration and coupling to electric and thermal grids shall be considered in terms of load management and grid supportive operation. Thereby, also clusters of buildings and neighbourhoods are evaluated regarding their integration potential for load shift between buildings.
- Task 3 is dedicated to the development of prototype systems and the monitoring of heat pump operation and performance in nZEB, which also includes larger buildings like multi-family houses and non-residential buildings like office buildings, a school and a kindergarten, a hotel and a supermarket in Germany and Norway.
- Task 4 is dedicated to the design and control of heat pumps in nZEB and is closely linked to the system integration in Task 2. Both the on-site control as well as design implications for higher self-consumption of solar energy produced on-site and demand response for grid-supportive operation are aspects of the control. Thereby, potentials of model predictive control are partly assessed, as well.

An overview of the different participating institutions in the countries and the national project contributions is given in Table 1.

Table 1. Overview of contributions of the participating countries to Annex 49

Country/Institution	Contribution to IEA HPT Annex 49
Austria Unit EE building Univ. of Innsbruck, IWT TU Graz, AIT	• Monitoring and simulation of two nZEB buildings for performance optimization • Development of a prototype of a façade integrated heat pump • Evaluation of larger nZEB buildings and districts
Belgium Free Univ. Brussels	• Evaluation of heat pump in office nZEB with sewer heat recovery heat source
Estonia Tallinn Technical Univ.	• Modelling and simulation of ground-coupled heat pumps (energy piles, horizontal collectors) • Design of heat pumps and heat emission systems for the nZEB application
Germany TH Nürnberg, IGS of Univ. of Braunschweig, TEB GmbH	• System integration, design and field monitoring of different nZEB building types • Development of control strategies for smart grid integration
Norway SINTEF, NTNU, Cowi AS	• Developments of heat pumps with natural refrigerants • Investigation/monitoring of nZE demonstration buildings and neighbourhoods in Norway
Sweden RISE	• Monitoring and comparison of heat pump systems in two equal test houses
Switzerland IET HSR	• Integration and design options of solar and heat pump systems • Field monitoring of nZEB with façade integrated PV
UK Glen Dimplex	• Evaluation of design and control of nZEB model houses
USA ORNL, NIST, CEEE Uni Maryland	• Field monitoring of integrated heat pump variants (IHP) • Technology testing and comfort evaluation in NZEB test facility (NZERTF) • Evaluation of a prototype of a personal cooling device to reduce loads in NZEB

In the following, specific results of the single Tasks and national contribution are given as overview of the outcomes of the IEA HPT Annex 49.

3. Results of the different Annex 49 Tasks

3.1. Task 1 on the state-of-the-art of nZEB

In Task 1 the state-of-the-art of nZEB in the different participating countries of the Annex 49 is analyzed. nZEB definition in Europe is elaborated by the EU-member states (MS) and current definitions in the EU-MS vary both in system boundaries, metrics, limits and rating systems as outlined in [2], [3] for different states of implementation. Thus, in the first step, there will not be a common definition of nZEB, even though the EU institutions REHVA and CEN have prepared different documents to support a harmonized definition and implementation of nZEB in the EU. In the USA, a similar system boundary as of the REHVA definition has been proposed by US-DOE [4].

However, current implementations of nZEB may still updated before requirement for all new buildings are enacted on January 1, 2021, even though the deadline for the requirements for all new public buildings is already passed and thereby, definitions are in application.

The different definitions of nZEB are also related to national rating procedures, which use national calculation methods in order to approve compliance with the nZEB requirement according to the national implementation. As consequence, even with a common definition, the implementation in the single countries would vary due to different national boundary conditions, national climate data and calculation methods. Thus, it is hard to compare the ambition level of the different countries to achieve high building performance values in the new sector, which would be a useful information for policy makers to set high ambition levels in the new built sector.

Therefore, in the Task 1 of Annex 49, a methodology to compare the ambition levels of different nZEB definitions is worked out. The term ambition level refers to the ambition of the nZEB rating to reach very high energy performance of the building. For instance in Denmark, there is an ambitious requirement to reach a building envelope in the range of passive house level for the nZEB implementation, thus for the building envelope, Denmark has a high ambition level. The development of the methodology is still in progress, thus in the following, the current state is shortly summarized, details on the state of the methodology can be found in [6]. The methodology is based on a single family building as outline in [5] with some modification in order to turn the building into an nZEB. Since a heat pump is applied as heat generator for space heating and DHW operation, the building corresponds to an all-electric building. As next step, based on the common design, boundary conditions and site of the reference building, the building is transferred to the local conditions.

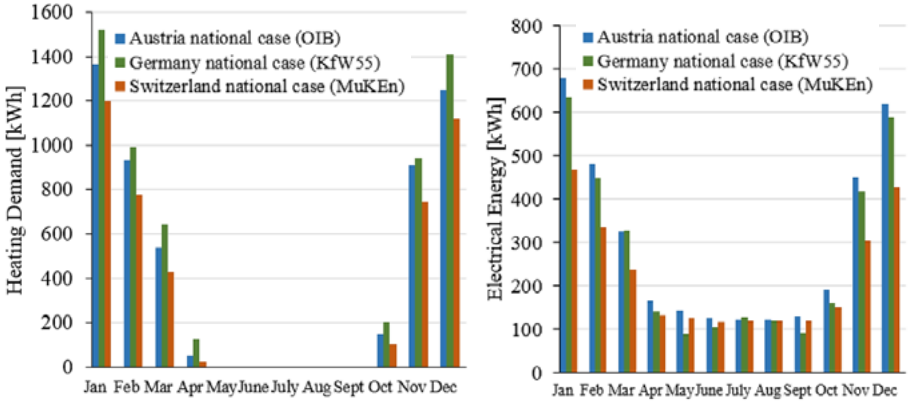


Fig. 1. Comparison of the space heating demand (left) and the electrical energy (right) for the nZEB requirements in the D-A-CH countries Germany, Austria and Switzerland

Thereby, the national nZEB layout related to the national boundary conditions by the rating procedure in the different countries can be evaluated. Afterwards, the building parameters are transferred to a simulation model of the buildings, and boundary conditions and climate data are changed back to the common ones.

This enables the comparison of the national buildings for common boundary conditions regarding internal loads, climate and DHW tapping profiles. Finally, the space heating demand and the delivered energy can be compared in order to get a ranking of the ambition level in different countries. Fig. 1 shows a comparison for the D-A-CH countries Germany (D), Austria (A) and Switzerland (CH), which are in the same climate zone, for the space heating demand on the left and the delivered electrical energy on the right according to the national definitions. It can be seen, that requirements for the nZEB rating in Switzerland results both in a lower space heating demand and in a lower electricity consumption than in the two other countries. Thus, a relative order of ambition levels among the three countries can be evaluated. However, present limitations of the methodology are that only countries in the same climate zone have been compared and the method focuses on the building envelope, while for the nZEB concept, also the on-site renewable production shall be included for the ranking. Thus, the methodology shall be further developed and extended to other examples.

3.2. Task 2 on heat pump integration for nZEB

Task 2 is dedicated to the integration options of heat pumps for nZEB application. The work in Task 2 is carried out by simulation, but is also linked to monitoring projects carried out in Task 3. An example for this link of the implementation of optimization potentials derived by simulations in monitored buildings is a project contribution of the Unit for Energy Efficient Building of the University of Innsbruck

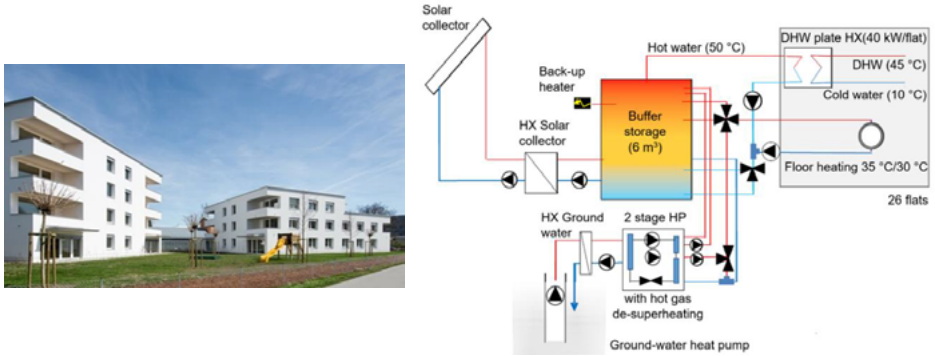


Fig. 2. Two multi-family houses in passive house standard of the project Innsbruck Vögelebichl (left, photo: "NHT Tirol") and principle sketch of the installed system technology (right)

An example for this link of the implementation of optimization potentials derived by simulations in monitored buildings is a project contribution of the Unit for Energy Efficient Building of the University of Innsbruck.

The case study deals with two multi-storey multi-family buildings in passive house standard of the social housing company NHT in Tyrol, Austria (see also [8] for more details). In the following, the main facts are summarized. Fig. 2 left shows a photo of the two buildings in Innsbruck Vögelebichl and Fig. 2 right depicts a principle sketch of the building system technology.

The buildings consist of 10 or 16 flats, respectively, with a total treated area of 2149 m^2 and are designed for a Net Zero Energy balance in terms of space heating, domestic hot water (DHW) production and auxiliary energies for the building technology (i.e. without taking into account appliances and plug loads). The design heat load for both buildings is 24 kW (according to the Passive House Planning Package – PHPP) and additional 12 kW for DHW. The buildings are equipped with 73.6 m^2 solar thermal collectors and a solar PV installation, which covers the entire roof of the one building with an area of 99.8 m^2 and a part of the other roof with 52.5 m^2 besides the solar thermal installation. The system consists of a ground-water source two compressor heat pump of a nominal heating capacity of 58 (52) kW at W10/W35 (W55) and respective COP values of 6 (3.7). The heat pump and the solar thermal system supply heat to a central 6 m^3 thermal buffer storage. The storage is charged at the top in DHW mode and at a relative height of 67% in space heating mode. The combined return flow enters the storage at a relative height of 33% or at the bottom depending on the temperature level. The installed direct electrical back-up heater is currently not in use. The storage delivers the heat to a floor heating system in the flats and the decentralized fresh water systems with plate heat exchangers for the DHW supply at use temperatures of 45 °C, using a primary inlet temperature of 50 °C from the storage.

Additionally, the heat pump is equipped with a de-superheater for simultaneous heating and DHW preparation. The de-superheater is located between the compressor outlet and the condenser inlet and uses the higher temperature of the refrigerant discharge gas for a DHW production at lower condenser pressure level in simultaneous space heating operation (e.g. for a floor heating with typical design temperature of 35 °C/30 °C) instead of the higher pressure level of the DHW-only mode. Thereby, the higher DHW temperature can be produced at high efficiency and no interruption of the space heating operation is necessary. However, the heat extraction is limited to the de-superheating fraction before the condensation begins, see also Fig. 4 below. Furthermore, the actual hydraulic integration is not optimal, see [8] for more details.

The investigations by simulation comprises different aspects of the system as operation modes of the two-compressor heat pump including the evaluation of the performance map, which is not available for all operation modes by the manufacturer. Furthermore, the de-superheater operation, the monitoring system, the nZEB balance including the auxiliaries, the storage stratification and the control of the building technology are investigated. For a detailed analysis, a system model has been set-up, which consists of a simplified refrigerant cycle model of the two-compressor heat pump. Using the model, the performance maps of the missing operation modes have been identified with the monitoring data. Moreover, a model of the central storage has been set-up and compared to monitoring data. There are some deviations, but for the use of investigating the configuration, design and control of the system, the model is applicable. Using the developed system models, the integration of the system functions and the respective control can be simulated and optimized. Selected results are presented in the following, more details are found in [7, 8].



Fig. 3. Monitored heat balance (left) and electrical energy (right) of the three year measurement period of the multi-family buildings Vögelebichl Innsbruck

Results of the monitoring a three-year period are shown in Fig. 3. Operation of the buildings started in winter 2015. The demand for space heating of the buildings was 20.5 kWh/(m²yr) in 2017 and 18.5 kWh/(m²yr) in 2018 and thereby slightly higher than the planned 15 kWh/(m²yr) according to the passive house standard.

The DHW demand was 25 kWh/(m²yr) and thereby in the expected range. Both the space heating demand and the electricity consumption could be successively decreased from year to year.

However, the thermal losses slightly increased in absolute numbers leading to an increased relative contribution of 14%, which is one of the major reasons, why the NZE balance related to the balance boundary of the building technology and the onsite PV production could not be fulfilled, yet. In 2018, for instance, the electricity consumption of the HP was 21 MWh and auxiliary energies were responsible for 14 MWh. The PV field produced in average around 27 MWh, as shown in Fig. 3 right of the electric energy balance for the years 2016 to 2018.

Despite the reduced total energy demand in 2018 (mainly because of the decreased heating demand), the NZE balance was not achieved. Thereby, the PV production was 24.5 MWh in 2018 due to a technical failure of the inverter of the PV field of the north building. A yield between 26.6 MWh and 27.2 MWh can be predicted based on data of 2016 and 2017 for the case without the failure.

Fig. 4, left hand side, shows a more detailed theoretical estimation of the system operation by de-superheating. Potentials for electricity savings are dependent on the ratio of DHW heat demand and space heating demand, which depends on the building standard. While in low energy houses (LEH) the space heating demand is still dominating, the fraction can increase to 50% of the total heat demand in single family passive houses (PH SFH) and even reach a ratio of about two in multi-family passive buildings (PH MFB). The given curves are parametrized by the DHW share produced by de-superheating, which might range from 7.5% to 15%. With increasing DHW fraction, the potential electricity saving decrease from 8% in the best case to about 1% to 2%, since with dominating DHW demand, the simultaneous operation with space heating decreases and thereby also the potential for combined heat production for both building services. In this configuration, the de-superheater could always supply the heat to the buffer storage in the top zone.

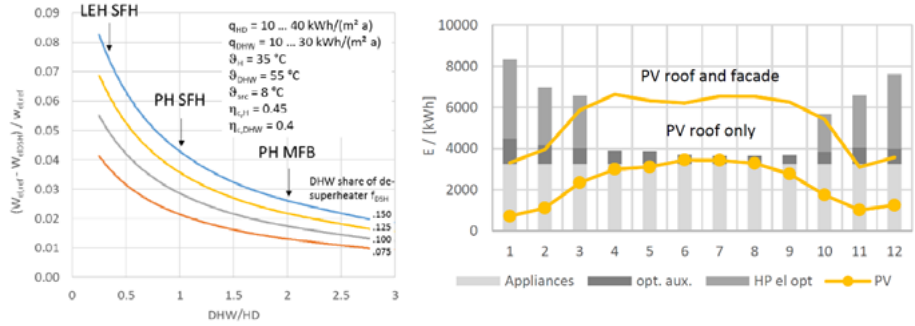


Fig. 4. Theoretical potential of the DHW electrical energy saving by desuperheating for different building types and DHW shares (left) and simulated annual energy balance with improved control and reduced auxiliary losses (right)

Fig. 4, right hand side, depicts a prediction of the monthly energy balance with reduced auxiliary energy consumption for the building equipment (e.g. pumps, fans etc.) and optimized control strategy. A multi-dimensional performance map was developed in Matlab/Simulink environment and is integrated in a system model that allows to simulate different heat pump operation strategies with and without de-superheating, single and double-stage operation as well as optimized hydraulic integration. In this optimal case, the nZE balance for heating, DHW and auxiliary energy for the building equipment can be met with the yield of the PV on the roof. However, it is noteworthy that PV in the façade is required, if also household appliances and plug loads are considered, too, as shown in Fig. 4 right. It is obvious, that the contribution to the winter load is not significant if the annual energy balance is met. A monthly net balance could only be achieved by integration of (very cost intensive) long term energy storage. This demonstrates the importance of reducing the winter load.

3.3. Task 3 on heat pump prototyping and monitoring of heat pumps in nZEB

Task 3 is dedicated to the development of prototype technologies and monitoring of nZEB with heat pumps. Different participating countries in the Annex 49 perform field monitoring projects in order to evaluate the real performance of heat pumps in nZEB.



Fig. 5: Building Black & White with roof and façade integrated PV system in the city centre of Pfäffikon SZ (left) and building use (right, orange – commercial use, green – office use, blue – residential use) (source: AWIAG)

In the following results of a monitoring project in Switzerland are given, which refers to a 5-storey building with mixed commercial (basement, 615 m^2), office (1st and 2nd floor, 615 m^2) and residential use (3rd and 4th floor and attic, 1520 m^2) energy reference areas in the city centre of Pfäffikon (SZ), that has been monitored for one year. The building and the uses are depicted in Fig. 5.

Fig. 6 shows a sketch of the building technology system. As counterpart to the efficient building envelope on passive house level also an efficient building technology was planned and an active solar electricity production was designed to high yields of a net zero energy balance. Therefore, a major part of the building outer surface is used for the solar PV-production. In order to meet a nZE balance, the roof comprises 26 kW$_p$ of monocrystalline PV modules. In the south, east and west direction, thin-film PV modules of a total installed capacity of 48 kW$_p$ are integrated in the façades. The efficiency of the roof modules is with 21% notably higher than the thin film CIS-module in the façade with an efficiency of 11%. Moreover, the building is integrated in the city centre, so that the facades are temporarily shaded by surrounding buildings.

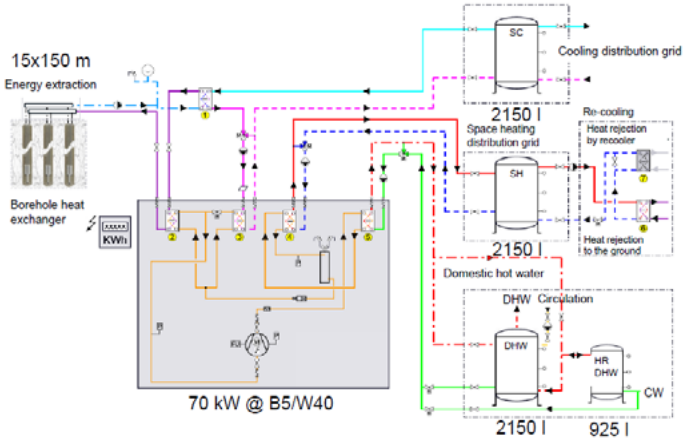


Fig. 6: Building technology concept of the Black & White with ground-coupled heat pump and waste heat recovery in space cooling operation (source: Andy Wickart Haustechnik AG)

As innovative building technology concept, the core component of a 70 kW (B5/W40) ground coupled heat pump has been planned, so that the building corresponds to an „All-electric building“. The heat source is a borehole heat exchanger field of 15 Duplex-ground probes of 40 mm diameter and a depth of 150 m each, which guarantees an efficient space heating and DHW operation, but is also integrated in the cooling concept. For the space cooling operation, a 5-phase-concept is considered: The system is planned in that way, that both the ground and a heat recovery for the DHW and space heating operation cover the re-cooling of the heat pump in cooling operation, i.e. also for the active cooling operation, no re-cooler to the outside air is required.

However, the focus of the cooling concept is a high degree of coverage in ground-coupled free-cooling (phase 1), and only at higher cooling loads, the active cooling with reverse operation of the heat pump is used. The maximum cooling capacity in active cooling mode is 53 kW. Thereby, the re-cooling heat is transferred primarily into the DHW preheating storage (phase 2). At simultaneous space heating and cooling demand, the recooling heat is transferred into the heating buffer storage (phase 3), and only in case of a surplus heat, which cannot be used in the heating buffer or DHW storage, the ground is regenerated (phase 4). If the ground cannot absorb the surplus heat anymore, a re-cooler to the outside air has to be operated (phase 5). For balancing the load and production a heating and cooling buffer storage of each 2,150 l are installed. Additionally, two DHW storages are installed, a preheating storage of 925 l for the use of re-cooling heat and a DHW storage of 2,150 l.

Moreover, for the different uses, ventilation systems with heat recovery are installed, which supply the building with an overall volume flow rate of 8,450 m^3/h. The commercial areas are cooled by cooling ceilings, which enhances the free-cooling use due to the higher possible temperature levels, and henceforth the reverse operation of the heat pump for space cooling can be limited to peak loads in summer. Additionally, the ground probes are used to preheat the ventilation air in wintertime in order to avoid ice formation on the heat recovery heat exchangers.

The year-round monitoring was evaluated from Oct. 2016 – Sept. 2017 and the balance is depicted for the single energy uses in Table 2. The measured energy consumption mainly corresponds to the calculated design values of the building. The space cooling demand is yet a bit lower, since one of the server rooms has not been operated as planned.

The projected production did not reach 20 $kWh/(m^2yr)$ energy reference area (ERA), which would have balanced the energy consumption of the building technology. Reasons are the different type of modules, so the façade could deliver more energy with higher efficiency of the modules. The system performance factors reaches high values of 4.97 in space heating operation and 3.1 in DHW operation at 60 °C charging temperature of the storage. The space cooling operation reaches a seasonal performance of 5.9, whereby the re-cooling heat is entirely used in the space heating and DHW storage or for the regeneration of the ground, so no re-cooler to the ambient air is installed. The PV yield of the façade-integrated modules, though, has not reached the projected values, since different modules than considered in the planning have been used in the real building.

Table 2. Yearly balance of the Black & White building with mixed use in urban environment

Balanced energy	Calculation/Design value	Monitoring value
Space heating and DHW	11.4 $kWh_{el}/(m^2yr)$	9.9 $kWh_{el}/(m^2yr)$
Ventilation	3.2 $kWh_{el}/(m^2yr)$	5 $kWh_{el}/(m^2yr)$
Space cooling	5.2 $kWh_{el}/(m^2yr)$	2 $kWh_{el}/(m^2yr)$
Total electricity building technology	19.8 $kWh_{el}/(m^2yr)$	16.9 $kWh_{el}/(m^2yr)$
Total electricity consumption	49.1 $kWh_{el}/(m^2yr)$	44.4 $kWh_{el}/(m^2yr)$
Electricity yield solar PV	20 $kWh_{el}/(m^2yr)$	13.4 $kWh_{el}/(m^2yr)$
nZEB balance (weighted with 2)	-0.4 $kWh_{el}/(m^2yr)$	7.0 $kWh_{el}/(m^2yr)$

Thus, despite a building envelope on ultra-low energy house level and a good system performance with an overall seasonal performance factor of 5.2 including free-cooling, the net balance based on the system boundary building technology (excluding plug loads) is not entirely reached. Nevertheless, 95% of the energy for the building system is produced on-site on an annual basis including the ground source. The reasons for not reaching the nZE balance is the PV yield of the façade modules, which is below the design values. With an increased efficiency of the façade modules, though, the nZE balance for the boundary of the building technology could be reached, while it would be hard to reach the nZE balance including plug load, which would require a total on-site production of 44.4 $kWh/(m^2yr)$. Since already a large fraction of the façade and roof is covered with PV and the system performance is already high, it would be hard to reach the balance including plug loads for this type of building, since the building envelope is limited and PV yields are also affected by the urban environment due to temporary shading by surrounding buildings.

3.4. Task 4 on Design and control of heat pumps in nZEB

Task 2 on the integration of nZEB building technology and Task 4 on the design and control of heat pumps for the application in nZEB are interlinked. If integrated systems are considered, also the design and control is an important feature to achieve the maximum performance.

The integration also includes the integration of nZEB into connected energy grids in terms of thermal grids or the electrical grid. As example of grid integrated nZEB, a project contribution of Germany is presented which consists of a new built neighbourhood.

At the energy campus of the TH Nürnberg, Germany, the electric and thermal integration is considered for the example of eight single family terraced houses of each 150 m^2 energy reference area, which is called "Herzo Base". The system concept contains two modulating central ground-coupled heat pumps, which are equipped with inverter control and are distributing the space heating energy by a low temperature grid on the level of the supply temperatures for the space heating operation, which is thereby centrally supplied. In contrast, the domestic hot water (DHW) is produced in decentralised 200 liters DHW storages in each house, which are supplied each by decentral 2 kW booster heat pumps, that use the low-temperature grid as heat source.

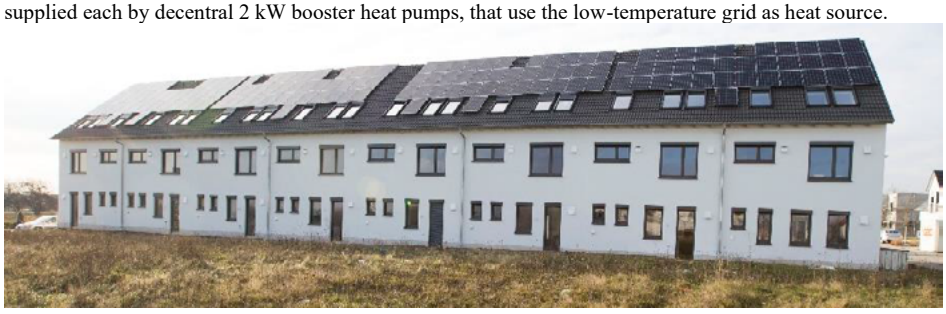


Fig. 7. Terraced houses of the project "Herzo Base" in Germany

In summertime, the ground source is used for free-cooling. The system is also equipped with an electrical battery storage that is installed centrally at the two modulating ground-source heat pumps. Fig. 7 shows a picture of the eight terraced houses.

At daytime, the PV mainly covers the household appliances and plug loads. In case of PV surplus, the battery is charged to mainly cover the illumination of the buildings and electric consumers in the evening.

Additionally, also central thermal buffer storages are installed. Besides a monitoring of the system, it is also investigated by simulations. One task of the simulation study is to evaluate control concepts, how the different storage options and heat pump modulation enhances self-consumption of the on-site generated PV electricity, since thermal storage and electric storage can be combined to increase on-site PV use and diminish grid interaction and grid import as well as to reduce peak loads. Details on control strategies are found in [9].

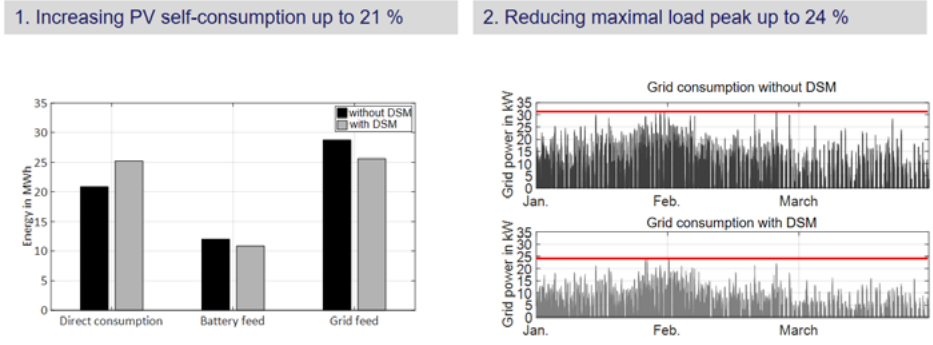


Fig. 8. Simulation results of Demand Side Management (DSM) to increase self-consumption and decreased load peaks and grid import

In Fig. 8, simulation results for the increase of self-consumption are depicted. The direct consumption could be notably increased by 21% due to the control optimisation. Thereby, also the battery feed-in could be decreased by 10%, while grid import is reduced by 11%. Moreover, the impact of the DSM on the grid also led to a reduction of the load peaks in the grid, which were reduced by 24% in the three winter months January to March.

Monitoring results of the system for the year-round monitoring period of April to March confirm the plus energy design of the building. The measured energy for space heating is with 33.2 kWh/(m²yr) slightly higher than the design value of 23.4 kWh/(m²yr) and also the measured DHW energy of 21.8 kWh/(m²yr) surpasses the design value of 18.5 kWh/(m²yr).

The space cooling, though, is with measured 7.3 kWh/(m²yr) a bit lower than the calculated 8.6 kWh/(m²yr). The overall balance in terms of delivered energy, primary energy and CO_2-emissions is given in Fig. 9. In the annual balance a surplus of the delivered energy by the PV production of 26.6 kWh/(m²yr) is achieved, and weighted values of primary energy and CO_2-emissions lead to 47.9 kWh/(m²yr) and 14.0 kg/(m²yr), respectively. This surplus can also be explained by the good performance values of the installed heat pumps, which is depicted in Fig. 10 for different system boundaries.

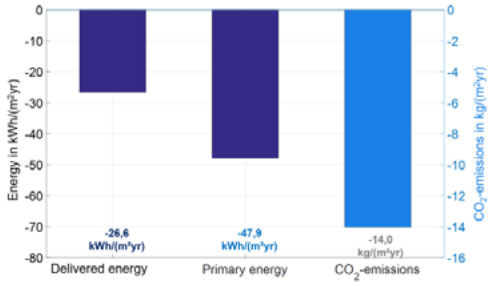


Fig. 9. Annual monitoring results for the Herzo Base system in terms of delivered energy, primary energy and CO_2-emissions

Even higher values than in the simulation have been measured. The two central heat pumps reach values of 5.4 and 6.0 in the boundary of the COP, and including the source system a value of 5.6. The source system by itself reaches a measured performance of an ETA of 175, where ETA refers to the electro-thermal amplification by extracted heat related to pumping energy. The booster heat pumps for the DHW operation reach performance values around 4.

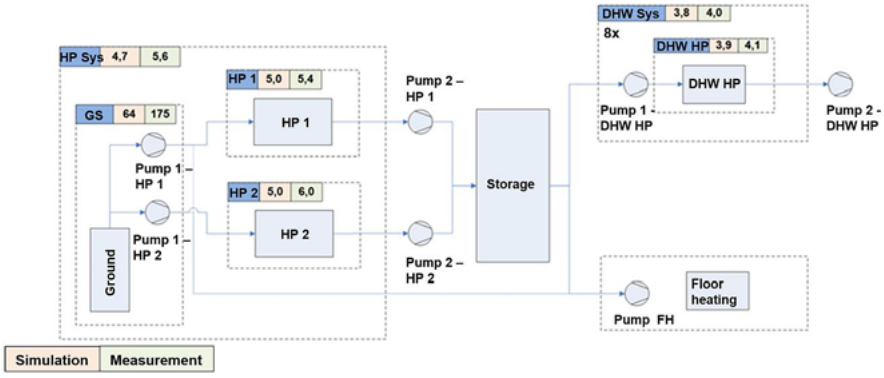


Fig. 10. Seasonal performance factors based on produced energy of the heat pumps

4. Conclusions

IEA HPT Annex 49 has the objective to perform investigations and analysis of the integration options and adapted design and control of heat pumps for the application in nearly Zero Energy Buildings, which are considered as future building standard in many countries around the world. nZEB requirements have already been introduced in the EU member states by Jan 1, 2019 for all new public buildings, which will be extended to all new buildings by the beginning of 2021. Nevertheless, despite different attempts for a harmonisation among countries, the implementations presently differ in metrics, limits and rating procedures, which impede a comparison of ambition levels and the development of standardised system solutions.

Moreover, in this step, not all countries require the nZE balance, but some countries only set requirements on the building envelope or primary energy consumption or have separate requirement for on-site renewable production without explicitly requiring a balance between energy consumption and on-site production.

IEA HPT Annex 49 has set a scope on integration options of the heat pump for nZEB. Regarding the monitoring, integration option yield positive results regarding the energy performance. The monitored integrated heat pumps reach high seasonal performance factors in the range of 5-6, which is also due to internal waste heat recovery by combining different building service in simultaneous operation of the heat pump as well as the integration of sources for free-cooling and regeneration. However, despite a high system performance and a high-performance building envelope, reaching an annual nZE balance may still be challenging in larger buildings, where the building surface area is limited for the renewable production on-site. Thus, a high system performance and an optimised system operation is a prerequisite for approaching the nZE balance in these buildings.

Regarding the design and control, besides the conventional aspects of performance and cost, additional aspects may affect the design of the building technology in nZEB, namely the energy flexibility, which becomes more important in nZEB for two reasons. On the one hand, the economy of on-site PV systems, which are often installed in nZEB to achieve the nearly zero energy balance, is positively affected by a higher degree of on-site consumption of the produced electricity in times of decreasing feed-in tariffs.

On the other hand, with increasing renewable energy in the electricity grids, buildings may also play a role to provide energy flexibility to the grid by reduced or increased consumption according to the grid needs. In this context also the control strategies are an important feature, since future buildings should contribute to a reduction of grid interaction and reduce the stress put on the grid by the increased renewable energy production. Thus, buildings are already seen today as one player for a future smart grid and the nZEB concept of on-site renewable production to balance the building's energy demand can be considered as turning point for buildings from a passive to an active component in the energy system. Design and control of the building technology should thus take into account demand response capabilities. An increase of electrical storage side by side with thermal storage installations raise the question of improved system and building integration of heat sources, generators, storages and sinks, on the single building level as well as on the neighbourhood and district level, where buildings with different use profiles and needs can be integrated by thermal and electrical grids. Presented results of a load shift and peak load reduction, which can be achieved by electric and thermal storage integration are positive from the energy perspective, but it has still to be proven, if this is also economically feasible for the building owners, since currently in most cases the building owner is not refunded for providing energy flexibility. Exception may be found in particular tariff structures, where e.g. a benefit for peak load reduction is granted. However, especially in smaller buildings like single family houses, designing the building technology to larger demand response capabilities, e.g. by larger storage design may not pay off with current electricity tariffs.

Summarising, nZEB are a next step to high performance buildings including renewable energy production, but reaching the balance can still be a challenge in larger building. The high-performance values reached with heat pump integration options and optimised design and control help to achieve ambitious targets of nZEB, and also enhance energy flexibility, which has been proven by the different simulation and field monitoring results of IEA HPT Annex 49.

Acknowledgements

IEA HPT Annex 49 is a collaborative research project and gratitude is expressed for the contributions of all participating countries as well as for the good collaboration within the IEA HPT Annex 49.

The support and funding of the IEA HPT Annex 49 by the Swiss Federal Office of Energy SFOE is highly acknowledged.

References

[1] European Parliament. Directive 2010/31/EU of the European Parliament and Council of May 19, 2010 on the energy performance of buildings (recast), Journal of the European Union, p. L 153/13, 18. 6. 2010, Brussels

[2] BPIE. Nearly Zero Energy Buildings definitions Across Europe - Factsheet. BPIE, Brussels (2015)

[3] IPEEC Building Energy Efficiency Taskgroup. Zero Energy Building Definitions and Policy Activity – An Intenational Review (2018)

[4] Peterson, K., Torcellini, P., Grant, R. A Common Definition for Zero Energy Buildings. Washington DC,

U.S. Department of Energy (US-DOE), (2015)

[5] Dott, R. Haller, M. Y., Ruschenburg, J., Ochs, F., Bony, J. The Reference Framework for System Simulations of the IEA SHC Task 44 / HPP Annex 38 – Part B: Buildings and Space Heat Load. Institut Energie am Bau FHNW, Muttenz (2013)

[6] Wemhoener, C., Rominger, L., Buesser, S., Magni, M., Ochs, F., Betzold, C., Dippel, Th. Simulation-based methodology for comparison of nZEB requirements in different countries including results of model calibration tests, Proceedings Building simulation 2019, IBPSA, 2.-4. Sept., Rome

[7] Ochs, F., Dementzis, G., Monteleone, W. Simulation-assisted Optimization of the HVAC system of NZE Multi-family Buildings, Proceedings Building simulation 2019, IBPSA, 2.-4. Sept., Rome

[8] Ochs F., Monteleone W., Franzoi N., Dermentzis G., Control optimization of a double stage heat pump with desuperheater in multi-family NZEBs, 13th IEA HPC 2020, Korea.

[9] Dentel, A. and Betzold, C. Control Strategies for Geothermal Heat Pump Systems in Combination with Thermal and Electrical Storage Units. Building Simulation 2017.

13th IEA Heat Pump Conference
April 26-29, 2021 Jeju, Korea

Research and development for 200°C compressed water heat pump using exhaust heat with low GWP refrigerant for industrial use

Ryosuke Suemitsu[a*], Masanobu Sakai[a], Yoshie Togano[a], Naoki Kobayashi[b], Hiroyuki Yuki[a], Yasushi Hasegawa[a], Kazuki Wajima[a], Kenji Ueda[c]

[a]Mitsubushi Heavy Industries Thermal Systems, Ltd., 1-1-1 Wadasaki-cho, Hyogo-ku, Kobe, Hyogo 652-8585, Jpana
[b] Mitsubishi Heavy Industries, Ltd., 1, Aza Takamichi, Iwatsuka-cho, Nakamura-ku, Nagoya, Aichi, 453-8515, Japan
[c] MHI Bingshan Refrigeration (Dalian) Co., Ltd., No.106 East Liao He Road, Dalian Technological Development Zone, China

Abstract

According to the Paris Agreement (COP21), the increase in global average temperature should be less than 1.5°C. The industry demands to decrease CO_2 emissions; however, the demand for heat at high temperature "more than 100°C" is mostly met by fossil fuels. Therefore, we have studied the process of introducing heat pumps with heating water to 160°C or higher by utilizing exhaust heat. We filtered industrial processes that are highly effective for installing heat pumps and calculated the effect. The installation of heat pumps was confirmed to reduce the primary energy consumption by approximately 14% and running costs 32% compared with using only fossil fuels. Thus, we have been developing 160°C- and 200°C-type centrifugal heat pumps using a low GWP refrigerant and exhaust heat. By 2023, the performance is going to achieve more than a COP 3.5 by heating high temperature pressurized water to 200°C and using heat source water at 95°C with a heating capacity of 600kW. Furthermore, we have selected a refrigerant suitable for high temperature, and the refrigerant candidates have GWPs of 20 or less and stability.

Keywords: Low GWP refrigerant, Heat pump, Industrial use, High temperature, COP ;

1. Introduction

In December 2015, the 21st Session of the Conference of the Parties to the United Nations Framework Convention on Climate Change (COP21) adopted the Paris Agreement, requiring each country to update and submit its own CO_2 reduction goal every five years. For refrigeration and air conditioning equipment, fluorinated greenhouse gases (F-gases) regulations in Europe, and the Act for Rationalized Use and Proper Management of CFCs and HFCs in Japan were designed to reduce the environmental impacts of these gases.

HFC refrigerants that have a high global warming potential (GWP), such as R134a, have been replaced by new types of low GWP refrigerants. Several aspects of these low GWP refrigerants must be verified, including their physical properties, stability, toxicity and flammability. The choice of refrigerant depends on the capacity, compressor type, operating temperature, and conditions of the heat pump; thus, it is necessary to consider the following items when selecting alternative refrigerants [1].

- Environmental factors: GWP ≤ 100, not an Ozone Depleting Substance
- Low toxicity and non- or mild flammability
- Physical properties: Cycle efficiency equivalent to that of existing refrigerants. Design pressure not to be excessively high.

Several double bond olefin refrigerants are candidates. Table 1 shows a comparison of R-134a and olefin refrigerants. The GWPs of the olefin refrigerants are very low, and their cycle efficiencies are equivalent to that of existing refrigerants.

Heat pumps are increasingly being used for supplying of hot water and heating in the household sector,

* Corresponding author. Tel.: +81-50-3727-7536; fax: +81-78-652-0048.
E-mail address: ryosuke_suemitsu@mth.mhi.co.jp

but their application in the industrial sector has been slower [6]. The adoption of exhaust heat recovery heat pumps offers great potential for improved energy efficiency and a reduction in CO_2 emission in the mechanical and chemical industries. So, investigation of in the mechanical and chemical industries in which high-temperature heat demand and unused exhaust heat exist, and high temperature heat pump systems capable of heating pressurized hot water to 160°C and 200°C with COPs of 3.5 or more, are part of the research and development program of the New Energy and Industrial Technology Development Organization (NEDO).

Table 1. Comparison of R-134a and olefin refrigerants

Refrigerant	HFC	Olefins				
	R-134a	R-1234yf	R-1234ze(E)	R-1234ze(Z)	R-1233zd(E)	R-1336mzz(Z)
Global Warming Potential (GWP)*1	1300	<1	<1	<1	1	2
Ozone-Depleting Substances*2	non	non	non	(non)*4	non	non
Flammability*3	non	mildly	mildly	(mildly)*4	non	non
Toxicity*3	low	low	low	low*5	low	low
Atmospheric lifetime*1	13.8 years	10.5 days	16.4 days	10.0 days	26.0 days	22.0 days
Allowable concentration [ppm] *3	1000	500	1000	-	800	500
Safety class*3	A1	A2L	A2L	(A2L)*4	A1	A1
Standard boiling point [°C] *6	−26.1	−29.5	−19.0	9.7	18.3	33.5
Critical point [°C] *6	101.1	94.7	109.4	150.1	166.5	171.4
Critical pressure [MPa (abs)] *6	4.06	3.38	3.63	3.53	3.62	2.90
Saturated pressure @ 91°C [MPa (abs)] *6	3.31	3.14	2.53	1.11	0.85	0.57
Saturated vapor specific volume @ 25°C [m^3/kg] *6	0.0309	0.0264	0.0380	0.1136	0.1388	0.1968
Theoretical heating COP *6 *7	1.55	1.31	1.56	1.90	1.91	1.77

*1: IPCC Fifth Assessment Report [2], *2: Montreal Protocol, *3: Refrigerant Safety Classification Standard ASHRAE 34 [3],
*4: Expected, *5: YUJICHEM MSDS [4], *6: Refprop Ver10.0 refrigerant thermal property database [5],
*7: Refrigeration cycle efficiency for a single stage cycle, evaporation temperature 25°C, condensation temperature 91°C, super heat 21°C, adiabatic efficiency 90%

2. Investigation and selection of the process of introducing heat pumps

The actual conditions of the heat process are not clear for the machinery and chemical industries, such as the existence of heat demand and exhaust heat, the balance between heat and energy, operating hours, and operating methods to introduce heat pumps. First, as shown in Fig. 1, we evaluated the effect of installing a heat pump from simple information, such as the process temperature, heat demand, and existence of exhaust heat. As shown in Table 2, the drying process and the chemical process were indicated to be particularly effective. As a result of the hearing investigation, it was clarified that the data on the heat demand is organized in detail, but only the supply temperature of the heating source is organized, and there is almost no data on the exhaust heat source. Therefore, we measured the actual conditions of the drying process [Company L] and the chemical process [Company B], which are highly effective when install, and we clarified the heat balance with respect to the measured temperature, flow rate, state, operating time, etc. in the system.

In addition, we examined an exhaust heat recovery system and pressurized water supply system, etc. for the existing facilities and studied the economic effect of installing a heat pump. As shown in Fig. 2, we found that the primary energy consumption and running costs could be reduced.

- Paint drying process [Company L]: As shown in Fig. 3, it is possible to reduce primary energy consumption by 14% and running costs by 32% by installing 160°C heat pump with a COP of 4 to a portion of existing burners into the current air circulation heating process, compared with only using burners.
- Chemical process [Company B]: As shown in Fig. 4, it is possible to reduce the primary energy consumption by 7% and the running costs by 23% by installing 200°C heat pump with a COP of 3 to a portion of the existing boilers heating process of the reactor, compared with only using boilers.

Therefore, we have been developing a 160°C heat pump and process system of air drying and thermostatic chamber and a 200°C heat pump for steam generation and chemical processes, by taking the two steps.

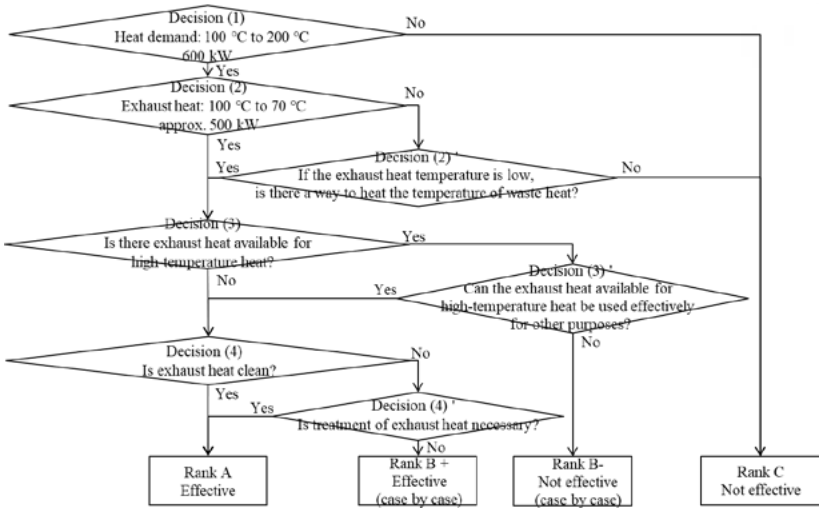


Fig. 1. Flow of assessment of introduction effect

Table 2. Survey results of the process introducing heat pumps

Business Type	Company	Process	Stability of temperature conditions/load		Rank	Remarks
			High temperature heat	Exhaust heat		
Ironmaking	A	Cleaning	200°C	200°C or higher	B -	Suitable heat demand, but too high temperature exhaust heat
Chemistry	B	Heating	135 ~ 190°C	100°C	A	Suitable heat demand and exhaust heat
Refuse incineration	C	Incineration	200°C	200°C or higher	B -	Suitable heat demand, but too high temperature exhaust heat
Sludge incineration	D	Incineration	200°C	200°C or higher	B -	Suitable heat demand, but too high temperature exhaust heat
Chemistry	E	Drying	120°C	35°C	C	Suitable heat demand, but too high temperature exhaust heat
Glass, earth and stone products	F	Drying	100°C or lower	-	C	Too low temperature heat demand
Rubber products	G	Mixing	100°C	40°C	C	Too low temperature heat demand
Chemistry	I	Distillation column	200°C	100°C	A	Suitable heat demand and exhaust heat
Chemistry	J	Rectification [distillation]	100~200°C	100°C	A	Suitable heat demand and exhaust heat
Chemistry	K	Sterilization, drying, distillation	100°C	40°C	C	Too low temperature heat demand
Machinery	L	Paint drying	120°C	100°C	A	Suitable heat demand and exhaust heat

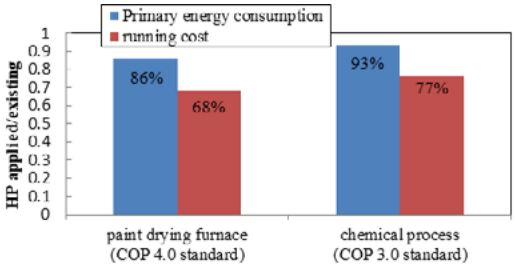


Fig. 2. Primary energy consumption and running costs compared with existing facilities

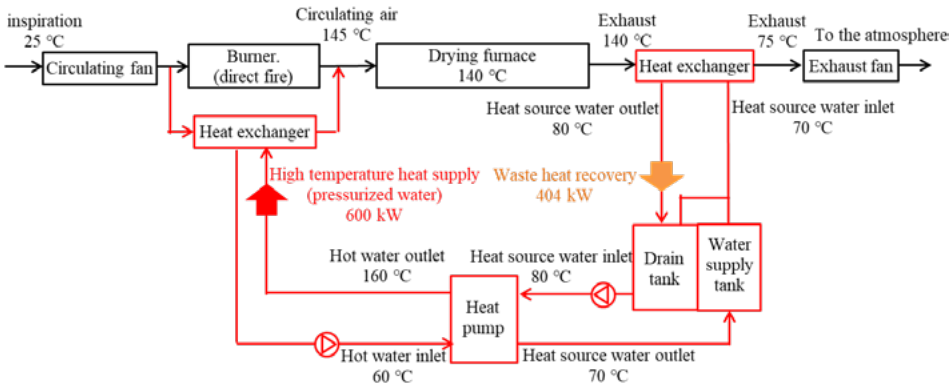


Fig. 3. Proposal for installation into the paint drying process

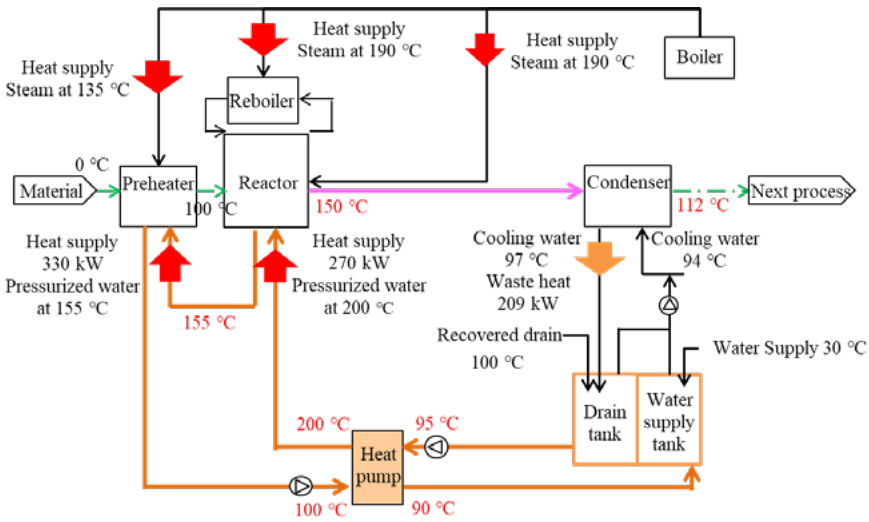


Fig. 4. Proposal for installation into the chemical process

3. Development of centrifugal heat pump heating pressurized water to 160°C

3.1. Selection of refrigerant

For the selection of a refrigerant, the operational temperature range of the heat pump must be considered, and physical properties suitable for the temperature range are required. This requires the following physical properties:

- Stability at high temperature: To prevent of isomerism and decomposition at the operating temperature of the heat pump.
- Standard boiling point: At the operating temperature, it is necessary that the design pressure of the equipment is not significantly high, and the compressor size is not too small to prevent a reduction in the adiabatic efficiency. Therefore, in high temperature, it is better to use a refrigerant which has a high standard boiling point.

R-134a is often used in existing centrifugal heat pumps, and Table 3 shows a comparison between R-134a and olefin refrigerants. If the olefin refrigerants is used for the 160°C heat pump, the refrigerant side pressure of the pressurized water in the heat exchanger can be reduced to approximately 3MPa(abs). It was confirmed that the thermal stability of R-1233zd(E) is poor at 175°C and 200°C. In addition, the internal pressure of the machine using R-1233zd(E) could be below atmospheric pressure when the heat pump is stopped; thus, the incoming air needs to be considered. However, as shown in Table 4, decomposition proceeds in a short period when air is added even at 150°C. Therefore, it is necessary to select R-1234ze(Z) or R-1336mzz(Z) to ensure the stability of the heat pump in the operating temperature range. The pressure on the refrigerant side of the high-pressure water heat exchanger of R-1336mzz(Z) is lower 37% (2.42MPa(abs)), the saturated vapor specific volume at 68°C is 54% higher, and the theoretical heating COP is 3.7% higher (3.61) than that of R-1234ze(Z). Therefore, the design pressure of the equipment is not too high, the compressor size is not too small, and the heat pump performance is expected to be improved. Thus, R-1336mzz(Z) is selected for the 160°C heat pump from the viewpoints of the thermal stability, design pressure, vapor specific volume, and theoretical heating COP.

Moreover, R-1336mzz(Z) is reported to have good stability up to 250°C and suitable for the 200°C heat pump [7].

Table 3. Comparison of R-134a and olefin refrigerants

Refrigerant	HFC	Olefins		
	R-134a	R-1234ze(Z)	R-1233zd(E)	R-1336mzz(Z)
Standard boiling point [°C] *1	-26.1	9.7	18.3	33.5
Critical point [°C] *1	101.1	150.1	166.5	171.4
Critical pressure [MPa (abs)] *1	4.06	3.53	3.62	2.90
Pressure of refrigerant side of pressurized water in heat exchanger [MPa (abs)] *1	10.87*2	3.87*2	3.30*3	2.42*3
Saturated vapor specific volume @ 68°C [m^3/kg] *1	0.0092	0.0323	0.0390	0.0496
Theoretical heating COP *1	3.18*4	3.48*4	3.39*5	3.61*5

*1: Refprop Ver 10.0 refractory thermal property database
*2: Superheated vapor pressure at 161°C and saturated gas entropy @ 68 °C, *3: Saturated pressure @ 161°C
*4: Refrigeration cycle efficiency for a single stage cycle, evaporation temperature 68°C, refrigerant temperature: inlet/outlet 161/71°C of pressurized water heat exchanger, adiabatic efficiency 90%
*5: Refrigeration cycle efficiency for a single stage cycle, evaporation temperature 68°C, condensation temperature 161°C, adiabatic efficiency 90%

Table 4. Thermal stability testing of R-1233zd(E)

Test condition*1		Result		
Air [ppm]	Moisture [ppm]	R-1233zd(E)[wt%]	F^- [ppm]	Cl^- [ppm]
<10	<10	0.0	0.6	0.5
<10	100	0.7	17.5	0.5
100	<10	0.4	0.3	0.4
100	100	0.4	14.3	3.4

*1: Temperature: 150°C, Duration: 168 h

3.2. Selection of lubricant oil and elastomer materials

As with the refrigerant, the lubricant oil must be stable in the high temperature range, and the solubility and viscosity of the lubricant oil with the refrigerant also need to been evaluated.

As a first step, we investigated lubricant oil for the 160°C heat pump using R-1336mzz(Z). The synthetic oil is commonly used with non-chlorine refrigerants, such as HFCs. The polyol ester (POE) oil was therefore selected because of the stability for R-1336mzz(Z). Therefore, as shown in Table 5, we carried out the accelerated thermal stability testing at 220°C and 200°C in consideration of a 200°C heat pump also, and the stability at 220°C was confirmed. Moreover, kinematic viscosity is 175%, compared with the requirements for the bearings of the 160°C heat pump. Thus, we selected the lubricant oil with sufficient high-temperature stability, lifetime, and lubricating performance for the 160°C heat pump.

The POE oil has a kinematic viscosity of 101%, compared with the requirements for the bearings of the 200°C heat pump.

Table 5. Thermal stability testing of POE oil

Test condition*1		Result
Temperature [°C]	Duration [h]	Acid Value [mg kOH/g]
200	168	0.01
220	168	0.01
220	336	0.23
220	672	0.45
250	168	2.25

*1: R-1336mzz(Z)/oil: 50/50, air/moisture [ppm]: 100/1000

We carried out autoclave testing for suitability of the elastomer material and R-1336mzz(Z)/POE oil. Table 6 shows the change in weight, volume, hardness, and refrigerant hue for the test specimens. Those (PTFE, PEEK, EPDM, FKM, FFKM, etc.) were compatible with the R-1336mzz(Z)/POE oil. Thus, we selected the suitable elastomer materials for the 160°C heat pump.

Table 6. Compatibility testing of elastomer material with R-1336mzz(Z)/POE oil

Test condition*1		Results			
Material	Temperature [°C]	Weight [%]	Volume [%]	Hardness [%]	Refrigerant hue
PTFE	175	+3	+4	-13	Transparent
	200	+3	+4	-14	Muddy
PEEK	200	+1	+1	+0	Transparent
POM	175	+0	+3	-6	Muddy
PPS	175	+0	+0	+1	Muddy
EPDM	200	+22	+21	-36	Transparent
NBR	175	+13	+10	-3	Muddy
HNBR	175	+18	+16	-8	Muddy
FKM	200	+17	+23	-20	Transparent
FFKM	200	+15	+24	-13	Transparent

*1: duration：336h

3.3. Drop-in verification test

To verify the component validity for the 160°C heat pump, we modified the verification machine with R-1336mzz(Z) from 90°C hot water heat pump with R-134a. In addition, we designed and manufactured the verification test equipment, so that it could operate with pressurized water up to 200°C, and we conducted a drop-in verification test. Table 7 shows the specifications of the verification machine, Fig. 5 shows the heat pump cycle, and Figs. 6 and 7 show the external appearance.

The evaluation items were as follows.

- Verification test equipment: The test equipment could be operated stably even at 160°C for a pressurized outlet water.
- Aerodynamic performance of the centrifugal compressor: The performance was equivalent to the estimated performance evaluated for the 90°C heat pump using R-134a, even if the refrigerant was replaced from R-134a to R-1336mzz(Z) and the centrifugal compressor was designed for high temperature.
- Heat exchanger performance: The performance was found to be equivalent to the estimated value, even if the refrigerant was replaced from R-134a to R-1336mzz(Z).
- Mechanical loss: The loss of bearings, motors, etc., was the estimated value.

Table 7. Specifications of the element verification test

Refrigerant [filling quantity]	R-1336mzz(Z) [106 kg]
Lubricating oils [filling quantity]	POE oil [20 L]
Heat pump cycle	Economizer cycle
Compressor	Centrifugal two-stage compressor
Evaporator/condenser/intermediate cooler/intercooler	Brazing plate heat exchanger
Size L × W × H	3.5 × 2.0 × 2.7 m
Power supply voltage	400 V
Starting method	Inverter

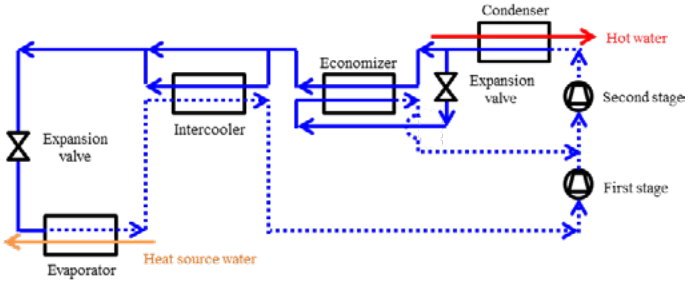


Fig. 5. Heat pump cycle of the verification machine

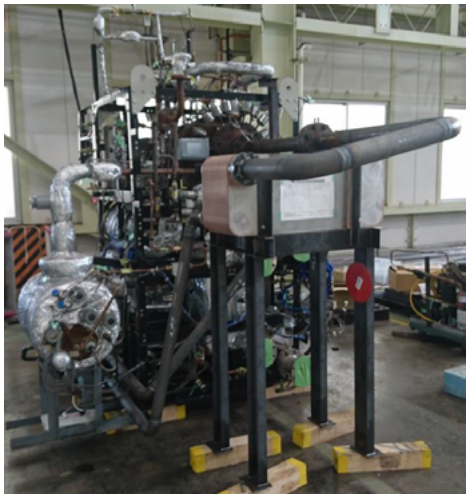


Fig. 6. External view of the verification machine

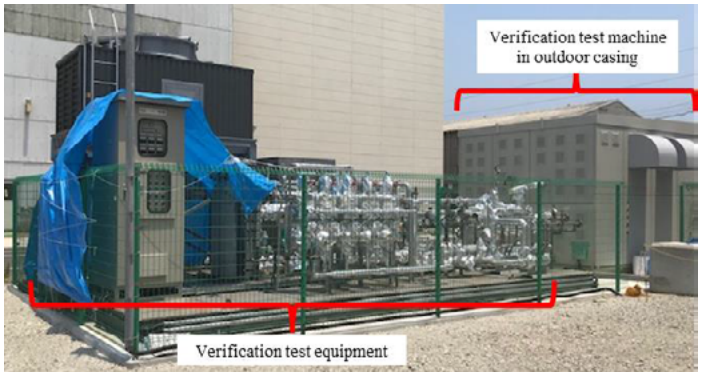


Fig. 7. External view of the verification test machine and equipment

Table 8 shows the result of the drop-in verification test. We confirmed that the verification equipment can be operated stably up to 160°C for pressurized water output, and that the performance of the heat exchanger is equivalent to the estimated value. However, there were discrepancies with regard to the estimated values for the compressor flow performance and the loss of motor. Therefore, after investigating the cause of the discrepancies, we has modified the verification machine as follows, and executed an additional drop-in verification test.

- Centrifugal compressor: To modify the shape, material and assembling method, in order to ensure a flow rate equivalent to the estimated value
- Motor: To modify the cooling system to control the motor temperature properly and the motor with high heat resistance to evaluate the characteristics of the deviation

Table 8. Results of element verification test

Items	Actual measurement value	Estimated value
Heating capacity	267.1 kW	
Hot pressurized water temperature	145.7 °C → 160.1 °C	
Hot pressurized water flow rate	16.9 m^3/h	
Heat source temperature	92.1 °C → 87.9 °C	92.5 °C → 87.9 °C
Heat source flow rate	34.1 m^3/h	
Centrifugal compressor: First stage flow rate ratio*1	0.94	1
Centrifugal compressor: Second stage flow rate ratio*1	0.89	1
Motor windage ratio*1	3.06	1
Motor efficiency ratio*1	0.97	1
Power consumption	117.0 kW	102.5 kW
Heating COP	2.28	2.61 (+ 14.5%)

*1: actual/estimated

3.4. Design of centrifugal heat pump

Heat pumps heating water to 90°C are applied for moderate high temperature, for example, for cleaning and food processes. However, there are thermal demands from 160°C to 200°C in industrial applications, for example, for chemical reactor and drying processes, etc.

160°C heat pumps need drain water as exhaust heat and we estimates exhaust heat (heat source water) temperature is less than 100°C. Therefore, two-stage compressors are planned to be arranged in series, so that one heat pump unit can operate even at the high differential pressure between the condenser and the evaporator.

The 90°C heat pump is adopted a two-stage compression economizer cycle. However, to obtain a higher COP, the two-stage compression bleeding cycle shown in Figs. 8 and 9 is adopted for a high temperature

heat pump [8]. In the case of a process in which the inlet temperature of the hot water can be lowered to the temperature of the heat source water (For example, it is used to raise the temperature of a medium from ambient temperature to high temperature.), the bleeding cycle is highly efficient because it uses some of the refrigerant gas discharged from the low stage compressor for intermediate heating.

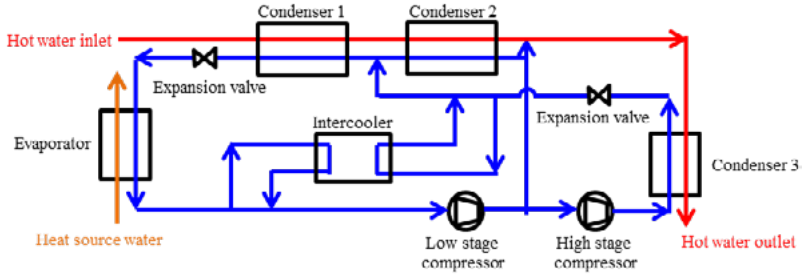


Fig. 8. Two-stage compression bleeding cycle

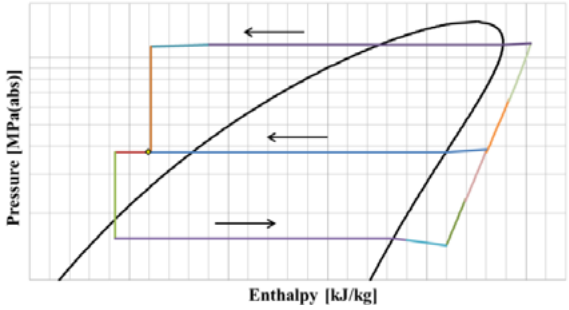


Fig. 9. P-h diagram of two-stage compression bleeding cycle

Table 9 shows the specifications of the 160°C heat pump. Under the conditions of a heating capacity of 600 kW, a hot water inlet/outlet temperature is 70°C/160°C, a heat source water inlet/outlet temperature is 80°C/70°C, and its COP is estimated to be 4.0.

Based on the results of the drop-in verification test, we are going to improve the accuracy of the estimated performance and expand the operational temperature range.

Table 9. Specifications for 160°C heat pump

Rated heating capacity	600 kW
Refrigerant,	R-1336mzz(Z)
Hot pressurized water temperature	70°C to 160°C
Hot pressurized water flow rate	6.0 m^3/h
Heat source water temperature	80°C to 70°C
Heat source water flow rate	40.5 m^3/h
Power consumption	146.7 kW
COP	4.0
Heat pump cycle	Two-stage compression bleeding cycle
Low and high stage compressors	Centrifugal two-stage compressor
Evaporator/condenser 1,2,3/intercooler	Brazing plate heat exchanger
Size L × W × H	3.6 × 2.0 × 2.5 m
Starting method	Inverter

4. Development of elements for centrifugal heat pump heating pressurized water to 200°C

We have been developing step by step 160°C and 200°C heat pumps with low GWP refrigerants. We will try to launch 200°C heat pump with pressurized hot water for practical applications by 2023.

As shown in Chapter 3, R-1336mzz(Z) may be a refrigerant candidate for 200°C heat pumps. A comparison of R-134a and R-1336mzz(Z) is shown in Table 10. The vapor specific volume @ 88°C of R-1336mzz(Z) is smaller at 94% than that of R-134a @25 °C. Under the condition of 200°C pressurized water and heat source water inlet/outlet temperature of 95/90°C, this may lead to be smaller compressor size and reduce in an adiabatic efficiency. Therefore, to prevent a reduction in an adiabatic efficiency, new refrigerant candidates that have a high standard boiling point and proper vapor specific volume for a 200°C heat pump must be selected. The candidates have GWPs of 20 or less and are stable at high temperature. We continue to examine toxicity, cycle characteristics, etc., and will evaluate whether or not to apply to a 200°C heat pump.

For the heat pump cycle of 200°C pressurized high-temperature water, we are going to adopt a two-stage compression bleeding cycle capable of achieving a COP of 3.5 or more, as with the 160°C heat pump.

Table 10. Comparison of R-134a and R-1336mzz(Z)

Refrigerant	Existing		New	
	R-134a	R-1336mzz(Z)	Candidate A	Candidate B
Standard boiling point [°C] *1	−26.1	33.5	During evaluation	
Saturated vapor specific volume @ 25 °C [m^3/kg] *1	0.0309	-		
Saturated vapor specific volume @ 68 °C [m^3/kg] *1	-	0.0496		
Saturated vapor specific volume @ 88 °C [m^3/kg] *1	-	0.0291		

*1: Refprop Ver10.0 refrigerant thermal property database,

5. Conclusion

In response to the industry demands to decrease CO_2 emissions, we are developing 160°C and 200°C heat pumps with pressurized water at 100°C or higher and low GWP refrigerants.

As a result of investigation of the effective process to install the 160°C or 200°C heat pumps, we estimated that primary energy consumption could be reduced by 14%, running costs by 32% for painting drying process, and primary energy consumption by 7%, running costs by 23% for chemical process.

The 160°C heat pump with a heating capacity of 600kW is being developed with an existing refrigerant R-1336mzz(Z), which has a GWP of 2. R-1336mzz(Z) has low GWP, non- flammability and low toxicity, making it a suitable refrigerant for industrial heat pumps. In addition, under the conditions of hot water inlet/outlet temperature of 70°C/160°C and heat source water inlet/outlet temperature of 80°C/70°C, a two-stage compression bleeding cycle in which COP is improved was adopted, it is estimated to achieve COP is 4.0. Furthermore, a drop-in verification test has been started, and the additional drop-in verification test will be executed after modification of the verification machine, and we are going to improve the accuracy of the estimated heat pump performance and expand the operational temperature range.

We are also considering the use of a new refrigerant with a high standard boiling point for the heat pump heating pressurized high-temperature water to 200°C. The refrigerant candidates have GWPs of 20 or less and are stable at high temperature. We are going to continue to examine the toxicity, cycle characteristics, etc. of the refrigerant candidates for the 200°C heat pump. In the future, we will select a suitable refrigerant for the 200°C heat pump. A two-stage compression bleeding cycle has been adopted with the target of COP 3.5 and over, and we will carry out the element design and drop-in test, and proceed with the development of the high temperature heat pump.

Acknowledgements

This work was supported the project of research and development of innovative practical use technologies for unutilized thermal energy by New Energy and Industrial Technology Development Organization.

References

[1] Suemitsu R et al. Development of centrifugal chiller and heat pump using low GWP refrigerant, 12th IEA Heat Pump Conference, 2017.

[2] Intergovernmental Panel on Climate Change (IPCC), Working Group I Contribution To The Ipcc Fifth Assessment Report Climate Change 2013, 2015.

[3] ASHRAE, 2015 Addenda Supplement to ANSI/ASHRAE Standard 34-2013, Designation and Safety Classification of Refrigerants, 2015.

[4] YUJICHEM MSDS, Beijing Yuji Science & Technology Co., Ltd., 2017. http://www.beijingyuji.com/english/product/fluorine/Working-Fluid/HFO-1234ze-Z.html.

[5] Lemmon E.W et al. Reference Fluid Thermodynamic and Transport Properties Database - REFPROP Ver. 10.0, National Institute of Standards and Technology, Boulder, CO, USA, 2018.

[6] Arpagaus C et al. High temperature heat pumps: Market overview, state of the art, research status, refrigerants, and application potentials, Energy 152 (2018) 985-1010, 2018.

[7] Kontomaris K. HFO-1336mzz-Z: High Temperature Chemical Stability and Use as A Working Fluid in Organic Rankine Cycles, 2014 Purdue Conferences, 2014.

[8] Kondou C, Koyama S. Thermodynamic assessment of high-temperature heat pumps using Low-GWP HFO refrigerants for heat recovery, Int J Refrig 2015;53:126–141.

13th IEA Heat Pump Conference
April 26-29, 2021 Jeju, Korea

Today's one million heat pumps are already in essential role in smart energy transition towards carbon neutral Finland

Jussi Hirvonen*

*Finnish Heat Pump Association SULPU ry, Laivurinkatu 13 as 3, 06100 Porvoo, Finland

Abstract

Finland reached one million heat pump installations in year 2019. Heat pump sales and stock in relation to population of 5.5 million is one of the biggest in the world. Heat pumps produce as much as 15% (>10TWh/a) of Finnish heating. Investments in heat pumps now amount to EUR 6 billion. The decarbonisation impact of heat pumps already over 2 million tons CO2 eq. Reasons behind this success story may be useful to understand. Good circumstances such as cold climate, moderate electricity prices, lack of gas network and good drilling conditions help create a very successful heat pump market without subsidies. But very active lobbying and market creating activities by the national heat pump association cannot be overemphasised, along with taking care of sufficient and appropriate information flow to all parties. The quality issues of products and installation have also been all the time under a critical eye. Finnish success story continues. According to recent studies, in 2030 heat pumps will produce 22 TWh/a with those 2 million heat pumps. The Finnish government has decided recently that Finland will be carbon neutral in 2035. In a large Finnish Smart Energy Transition research project a very challenging 35 TWh/a target has been set for heat pumps in 2040.

Keywords: Heat pump market;Finland;lobbying;Heat pump association;market drivers;Smart Energy Transition

1. Introduction

The significance of heat pumps has grown in Finland in the heating of single-family houses, multi-storey buildings as well as large service-facility buildings such as shopping centres and logistics centres. Also, the use of heat pumps is continuously increasing in heat-recovery and process solutions as well as in the production of district heating and cooling. The role of heat pumps as a producer of Finnish renewable energy is much greater than that of, e.g., solar and wind energy.

This article describes the size, development and structure of the Finnish heat pump market as well as its special characteristics. This market has also been adjusted in line with the heat-pump market in other European countries.

The Finnish heat pump market has increased a thousand-fold over the past couple of decades. Annual heat pump purchases made by individual people, worth EUR 600 million in 2019, form the biggest Finnish investment in renewable energy.

This article looks also at the drivers that have had, and still have, an impact on the success of the heat pump sector, and it considers whether those drivers can be influenced. The experiences of the rapid market development in Finland and an analysis of the market drivers, as well as the possibilities to influence those market drivers, may provide a basis for the development of the heat pump market in countries where the significance of heat pumps is not yet this great.

In 2035 Finland should be carbon neutral. For this purpose a study has been published which estimates that heat production by heat pumps should be increased to 38 TWh/a by 2040. In the Finnish heating system district heating plays a very big role, about 50% of the Finnish heating market. Decarbonisation of the heat market by

* Jussi Hirvonen. Tel.: +358 50 500 2751.
E-mail address: jussi.hirvonen@sulpu.fi.

heat pumps means a lot of heat pumps in the production of district heating but also saving district heating and other heat production by enormous amounts of heat pumps installed locally in individual houses.

2. The Heat Pump Market in Finland

2.1 Special Characteristics of the Finnish Heat Pump Market

On a European scale, the Finnish heat pump market is big and quite unique. When looking at the number of heat pumps per type, the heat pump market is dominated by air-source heat pumps, whereas ground-source heat pumps lead the market when looking at the figures in Euros. 75% of single-family house builders choose a heat pump. In over 50% case the choice is Ground Source Heat Pump. Heat is already being extracted from 150 000 geothermal wells, the combined depth of which totals half of the earth's circumference, i.e., 20,000km.

300,000 owners of houses where heating is based on oil and hydronic electricity have not yet replaced their heating with a heat pump even though the return on capital invested is, almost always without exception, 10%/a. More than half a million people who use electric heating are wondering whether the affordable electricity price of 12 cents per kWh will increase.

Efforts have been made to start saving energy also in district heating that has been produced with combined power and heat production (CPH) or other means. This happens more and more often with exhaust-air heat pumps that have been installed in apartment houses and office buildings. Big buildings are also increasingly replacing district heating entirely with ground-source heat pumps. New, large shopping and logistics centres increasingly use large geothermal fields for cooling and heating instead of district heating. The largest geothermal site in Finland, a logistics centre, has 316 geothermal wells, each 300 metres deep, totalling 100km of drill holes.

The role of cooling in the Finnish climate is not great. However, the demand for it in housing, too, has increased due to living-comfort reasons as well as nearly zero-energy buildings. This is beginning to have an impact on the profitability of investments, since heating and cooling is provided through the same investment.

The most important reason behind the success is clear, yet this reason is also distinctive on a European scale. Heat pump systems are a very profitable investment. The return on capital invested is often 10-15%/a. The Finnish government does not offer so far any subsidy to heat pumps apart from the household tax deduction that can be claimed for the installation work of a heat pump.

Heat pumps are easy to use, they are carefree, they require little space and they have a cooling feature. These are arguments that also speak in favour of choosing a heat pump. Affordable electricity, the lack of a gas network, the high consumption of heating energy that is caused by the Nordic conditions, a suitable bedrock for drilling, the customer-friendly heat pump system supply all create favourable preconditions for profitable investments.

2.2. The Finnish Heat Pump Market Is Big, Even on a European Scale

2.2.1 Over 10 TWh per year production with 1,000,000 Heat Pumps

At the end of 2019, the cumulative sales of heat pumps heat reached the limit of one million pumps. We must remember that Finland is a country with a population of only 5.5 million people. A heat pump is by far the most popular form of heating in new single-family houses, and heat pumps are rapidly replacing oil and electric heating as well as district heating in old buildings.

At the end of 2019, as many as 1,000,000 heat pumps have already been sold in Finland. Their total annual output is more than 10 TWh which corresponds to over 15% of the heating of Finland's residential and service building stock. About 7 TWh of renewable energy and waste heat is recovered annually and used in heat pumps [1]. It is noteworthy that this huge investment in the environment and in fighting against climate change has been made mainly by house owners using their own money. The excellent profitability of heat pumps has made consumers' decision-making easier. People have also started to understand the significant role of heat pumps in heat decarbonisation and demand response.

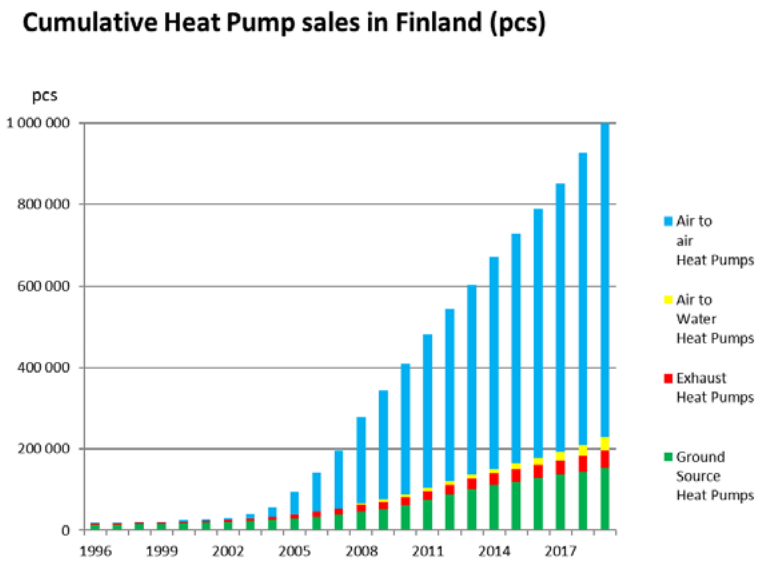


Fig. 1 Number of Heat Pumps Installed in Finland, Cumulative 1996-2019 [1]

75% of single-family house builders choose a heat pump as their main heating system. 53% choose a ground-source heat pump, which apparently is a world record of its own in new construction. Just over 15% of builders choose an exhaust-air heat pump, and approximately 5% choose an air-to-water heat pump. Furthermore, electrically heated houses are most often being fitted with air-source heat pumps as an electricity-saving and cooling fixture.

The greatest potential for heat pumps, however, lies in the already-existing houses. 200,000 oil boilers, more than 100,000 hydronic electric heating users, and 500,000 direct electric heating users most often pay double or triple the price for their heating energy as compared to heat pump heating. With the current interest rates, not making the decision to invest in a heat pump shows only ignorance.

The value of about 100 000 annual heat pump system deliveries is EUR 550 million. When the megawatt-size heat pump systems for district heating/cooling production, industry, shopping centres, and other service buildings as well as other ancillary operations such as planning, delivery supervision, maintenance, and other services (not yet included in the SULPU statistics) are added, the heat pump sector reached annual investment levels exceeding half a billion in 2019. This meant approximately one extra TWh per year to CO2-free heat production. It should be noted that most of this investment consisted of investments made by individual consumers using their own money, as it was a good investment for them.

The heating business concerning residential and service buildings amounts to between 70 and 80 TWh per year. Of this already 15%, over 10 TWh per year, is clean, individual heating generated by heat pumps. This has been achieved through Finland's close to one million heat pumps, in which consumers have invested EUR 6 billion. Heat pump investments in the production end of district heating and cooling as well as in industrial waste heat recovery are also growing.

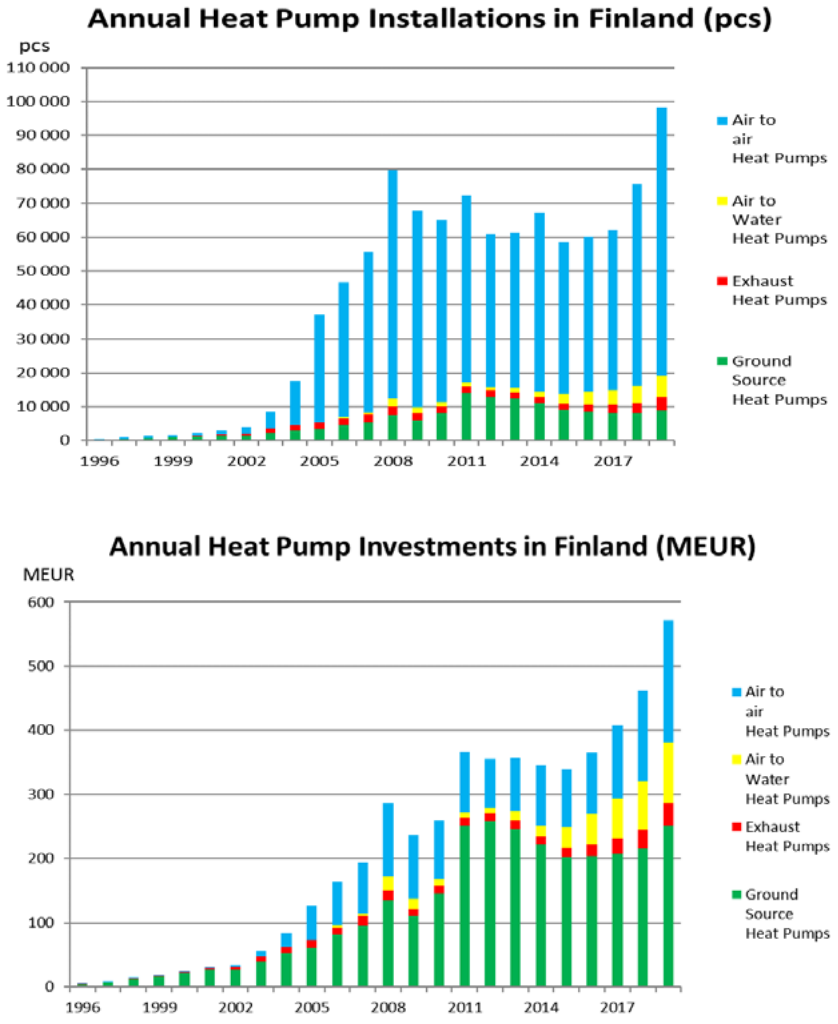


Fig. 2 Heat Pumps Installed in Finland per Type of Heat Pump; Quantities and in Euros, 2005-2019 [1]

2.2.3 On a European Scale, the Heat Pump Market Is Big

When comparing the success of the heat pump market in European countries, the market must considered in proportion to the population or to the number of houses. In the EHPA, the European Heat Pump Association, statistics of 2018, Table. 1, the sales volumes have been presented in proportion to the number of households.

When looking at Fig. 3, two main observations can be made. Firstly, there are roughly three groups of countries. The first group comprises Northern European countries: Norway, Estonia, Finland, Sweden, and Denmark. All of these countries boast sales of more than 20 units per 1,000 households. After these countries, there is rather a large gap. The second group is led by France with sales of 9.5 heat pumps per 1,000 households, followed by Switzerland (9.3), Lithuania (9.0) and Italy (7.8). The last group, mainly Central European countries, is characterised by very low heat-pump market shares, or in other words, very high potential. [2]

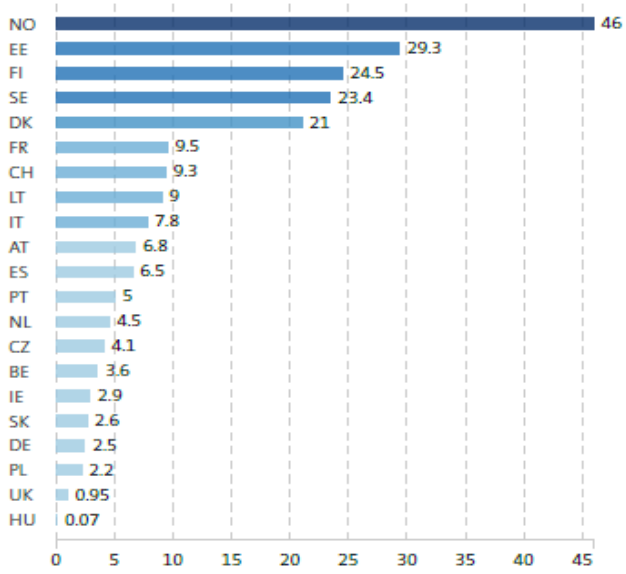


Fig. 3 Heat Pump Sales in Europe per 1000 Households, 2018 [2]

2. Market Drivers and How to Have an Impact on Them

The prerequisites for heat pumps in Finland are excellent. In a cold climate, a lot of energy is needed. In a typical single-family house, the usual annual consumption for heating and domestic hot water is 15,000-25,000 kWh of electricity or 2,000-3,000 litres of oil. Since Finland is a big country with a small population of 5.5 million, having e.g. a comprehensive gas network is unprofitable. The lack of this competitor favours heat pumps.

When considering the recent general developments in the construction business, the heat pump business has clearly strengthened its position in the heating and cooling of houses. However, it is only in the early stages of its success. The direction of the heat pump market development is clear, but the right type of advocacy, lobbying, will have an enormous impact on the degree of this development. The real market drivers have to be identified the means as well with which to influence them. The areas of this lobbying are multifaceted and, therefore, here are a few examples of current, genuine sectors in which lobbying is conducted in practice.

The heat pump market has increased a thousand-fold in Finland for 20 years. It is necessary to investigate the true market drivers and to consider whether they can be influenced and how.

3.1 Profitability

The most important of them is certainly profitability. The investor is a consumer, the user of energy, a house owner, most often a private individual. They must, at least, get the feeling that they are getting a sufficient return on their investment.

This they very often get in Finland. Fig. 3 shows the investments and the savings in both energy as well as in Euros for different types of heat pumps, indicating the price levels of 2019, in single-family houses as compared to electricity and oil heating. Approximately the same investment and savings ratios are reached with larger facilities where the comparison is usually with district heating.

Table. 1 Savings and Investments of Various Heat Pump Types in Single Family Houses [1]

Heat-pump type	Savings per year, kWh	Savings per year, €	Investment, €
Ground-source heat pump	14 000…17 000	1 800…2 200	14 000…20 000
Air-to-water heat pump	8 000…13 000	1 000...1 700	8 000…12 000
Exhaust-air heat pump	3 000…7 000	400…800	6 000…10.000
Air-source heat pump	2 000…7 000	250…800	1 500…2 500

Is it possible to have an impact on profitability? Yes, it is, at least on a long-term basis. As the market grows, market mechanisms bring system investments to the right level. Various subsidies are, in practice, always temporary and may boost the market for a short while but should not be allowed to disturb market-based development in the long run.

The profitability of heat pumps is very dependent on the price of fuels, electricity and district heating. In any case, they include a lot of taxes. Having an impact on these taxation structures is possible in the long run. Indeed, this is one of the foremost objectives of lobbying for the Finnish heat pump industry. For instance, by taking away the tax subsidy for fuel oil and by putting it in the same tax class as diesel transport fuel, heat pumps would receive a 20-30% leap in profitability. This is, after all, what our neighbour Sweden already did in the 1990s. The flourishing of the heat pump business that this, in part, created is something that we as a neighbouring country have been left to envy for a couple of decades now already.

Furthermore, the increase of electricity-price taxation would suit the heat pump business, since the competitiveness of heat pumps would improve in 700,000 electrically heated houses and almost 500,000 holiday homes.

3.2 Information, Communication and Visibility

Consumers, decision-makers and politicians must all have the most accurate information as possible and as much of it as possible. If they do not know that the profitability of heat pumps is excellent, business will not flourish, nor will heat pumps feature in discussion agendas, nor will they be acknowledged in regulations, law, rules or instructions.

Here, if anywhere, is the place for advocacy, for lobbying. The Finnish heat pump interest organisation, the Finnish Heat Pump Association SULPU, has extensively focused on providing this information, both qualitatively as well as quantitatively, in various media, such as the press, TV, radio, social media, with presentations, panel discussions, statements, and expressions of opinion. Regarding the development of the heat pump market, it is also very important to participate in the preparatory work of regulations, laws and instructions in ministries.

The principal messages when relaying this information must be carefully chosen and repeated systematically in the media, regardless of the channel of communication. A heat pump is profitable, the return on capital invested is excellent, it improves Finland's current external balance, it offers employment, and is a major and profitable environmental act. These arguments must be expressed repeatedly in all communication.

There is never enough of this type of lobbying, influencing. Nevertheless, it has been rewarding in Finland and can be seen in the development of the heat pump market.

3.3 Surveys Are the Best Fuel for Lobbying, Increasing Information, and for Quality

The heat pump business has carried out and participated in surveys that shed light on the possibilities of heat pumps and prospects. Here are three survey examples in which the heat pump industry has been involved and has used in its lobbying.

According to a survey conducted by the independent consultants Gaia Ltd, a total of EUR 12 billion will be invested in heat pumps by 2030, creating approximately 3,000 new jobs in the field. By then, heat pumps will be producing 22 TWh/a, 15 TWh of which is renewable energy that is extracted from around the building. These investments will also have a billion-class effect on Finland's current external balance and the value of

its building stock. [3] The breath-taking result of this survey has brought heat pumps a lot of credibility and weight now when, e.g., the Finnish Climate and Energy Strategy is being prepared.

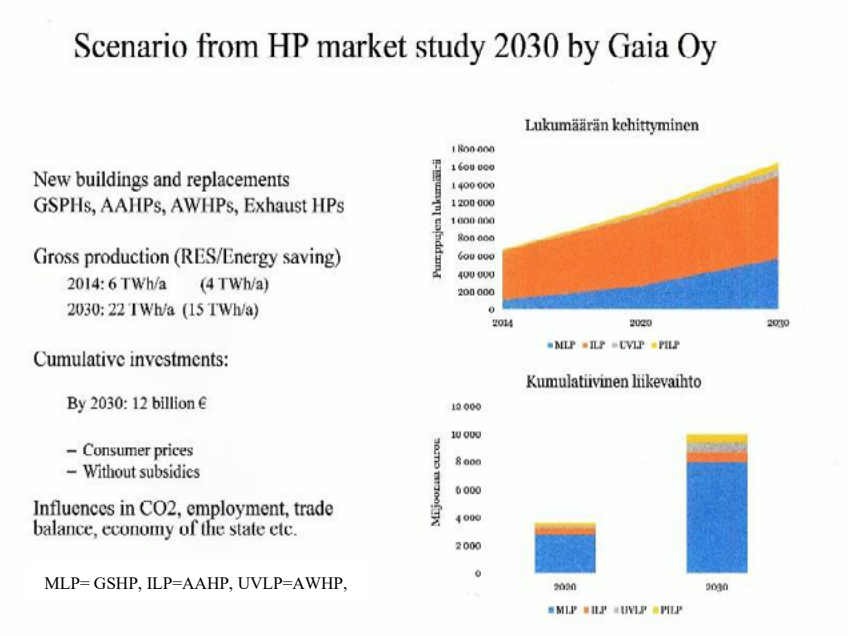


Fig. 4 The Role of Heat Pumps in 2030 [3]

Also, a study of how much exhaust air heat pumps can save of district heating in an apartment building. More than 30,000 apartment buildings release exhaust air that is warmer than 20 degrees Celsius. The entire air volume of the building is changed once every two hours, and that air vanishes up into thin air. Therefore, exhaust-air heat pumps have gradually become more common also in apartment buildings. About 2,000 apartment buildings have already been fitted with a heat pump that retains the heat of the exhaust air. This reduces even as much as 50% of the district-heating or other energy consumption of the building. After the fitting of this heat pump, it is also often decided that the remaining energy need will be covered with a ground-source heat pump, and district heating becomes redundant. Finnish Energy Industry, with the support of the heat-pump industry, commissioned VTT Technical Research Centre of Finland Ltd to study the effects of exhaust-air heat pumps on the district-heating network as well their market potential (3-5 TWh /a) [4].

There are 600,000 air-source heat pumps in Finland, and approximately 50,000 more are installed every year. It is common knowledge that in a Finnish house they save money, they cool the building, they work, and people buy them. There was no reliable information available as to how much energy they extract from around a building. That's why a study on the Energy Saving Potential of Exhaust Air Heat Pumps in Single Family Houses was performed a couple of years ago. Commissioned by the Ministry of the Environment and the heat-pump industry, VTT Technical Research Centre of Finland Ltd modelled an air-source heat pump for the heating system of a few houses and studied their energy-consumption effects in old, new and in the upcoming nearly zero-energy single-family houses. For the first time now, it has been possible to reliably define, in figures, the energy-saving potential of an air-source heat pump in Finnish conditions. The study took into consideration, in detail, the characteristics of the heat pumps and the buildings [5]. The result of this complicated and challenging modelling was that air-source heat pumps can provide 40-60% of the heating of a single-family house. The authorities, constructors and single-family house inhabitants will benefit from these results. These results have been used, e.g., in the nearly zero-energy buildings (NZEB) regulations that will be finalised shortly. Naturally, these results have been used to acquire lots of positive visibility in the Finnish media.

4. Summary

The heat-pump industry has become a significant renewable-energy business in Finland. 1,000,000 heat pumps produce over 10 TWh/a of energy, over 7 TWh of which is energy that is extracted from around the building. This already represents as much as 15% of the heating energy of all Finnish buildings. The prospects for heat pumps are good. The market will certainly develop in the future. The heat pump business can be described as an integrator that operates amidst and between renewable energy, electricity, and heating and cooling production. Heat pump technology and its applications can also be seen as an interface to a carbon-free age.

This paper looked at the Finnish heat pump market, at market drivers and whether they can be influenced. The heat pump industry market drivers must, indeed, be identified in order to be able to influence them. Finnish heat pump industry market drivers include profitability, the quality and quantity of information and communication, visibility, study results, and the quality of operations. It is certain that the significance of the heat pump industry will become greater. However, the degree of that significance can be influenced by influencing these drivers.

Profitability is affected by not only investments but also by the price of energy. The state taxes both fuels as well as electricity heavily. The structure and the scale of taxation are not, however, carved in stone. Taxing of CO2 releases must be accelerated.

The quality and quantity of information and communication as well as visibility have an immediate impact on the market. Increasing these is challenging in terms of resources, know-how and shaping the media environment. It has, however, proved to be possible and rewarding. Research that supports the development of the heat pump industry, research that is preferably conducted close to the market interface, plays a significant role in the management of this information. Developing quality and training schemes alongside the development of the heat pump market is important, and it is also a means for lobbying.

All too often, the importance of lobbying is forgotten, even though it is a very essential aspect in creating the preconditions for a new industry. The material required for lobbying, and the vision and goal for the heat pump industry, can be acquired from, e.g., surveys that are conducted by independent consultants. But also, close co-operation and communication on an international (IEA HPT TCP) and European scale (EHPA) and, of course, at a wider national level provide the basis for lobbying.

According to one of those above-mentioned independent surveys in 2030, there will be 2 million heat pumps in Finland producing 15 TWh worth of renewable energy. By then, a total of EUR 12 billion will have been invested in heat pumps, and 3,000 new jobs will have been generated. The savings that will have been made will by then be in the region of one billion euros per year.

More pressure or possibilities for heat pumps have been created by the political promise to make Finland carbon neutral by 2035. For this purpose, the Smart Energy Transition consortium has published a study estimating that heat production by heat pumps should be increased to 38 TWh/a by 2040 [6]. In the Finnish heating system district heating plays a very big role, about 50% of the heating market. Decarbonisation of the heat market by heat pumps means a lot of heat pumps in the production of district heating but also saving district heating by heat pumps installed locally in individual houses.

After fulfilling one million heat pump vision in 2020, the next target of two million heat pumps can be set for 2030.

References

[1] The Finnish Heat Pump Association SULPU ry, Statistics 2019.
[2] EHPA, European Heat Pump Market and Statistics Report 2018.
[3] Pesola, A.,Karttunen, V., Vanhanen, J.,2015, Lämpöpumppuinvestointien alueellinen ja kansataloudellinen tarkastelu, Gaia Group report,.
[4] Rämä, M.,Niemi, R.,Similä, L., 2015. Poistoilmalämpöpumput kaukolämpöjärjestelmässä, VTT, asikasraportti p.4.
[5] Laitinen,A., 2016, Energy Saving Potential of Air-to-air Heat Pumps in Detached Houses in Nordic Climate, CLIMA 2016-proceedings of the 12th REHVA Wolrd Congress
[6] Rinne, S., Freda, A., Auvinen, K., Ruggiero, S., Temmes, A.,2018, Discussion paper: Clean district heating – how can it work? (pdf). Publication of the Smart Energy Transition project funded by the Academy of Finland's Strategic Research Council.

13th IEA Heat Pump Conference
April 26-29, 2021 Jeju, Korea

Energy flexibility of capacity-controlled air-source heat pumps using rule-based control in residential nZEB

Lukas Rominger[a], John Clauß[b,c], Carsten Wemhoener[a*], Laurent Georges[c]

[a]IET Institute of Energy Technology, HSR University of Applied Sciences Rapperswil, Oberseestrasse10, 8640 Rapperswil, Switzerland
[b]SINTEF Community, Høgskoleringen 7B, 7034 Trondheim, Norway
[c]Norwegian University of Science and Technology, Kolbjørn Hejes vei 1a, 7034 Trondheim, Norway

Abstract

The reduction of operational heating costs by deploying the building flexibility is investigated using a predictive rule-based control and building simulations. This paper focuses on the applicability of a proposed price-based control strategy in different buildings and climate zones where also electricity spot prices differ. More specifically, the operational costs of a heat pump system in a Norwegian and Swiss residential single-family house are compared. The aim of the price-based control is to shift the operation of an air-to-water heat pump to times when electricity spot prices are low. The results show, that the success of the control strategy with regard to operational cost savings is highly dependent on the hourly fluctuations of the electricity spot price. Furthermore, it is shown that also the design of the heating system as well as the chosen temperature set-points of the control influence the outcome substantially. Results show, that a 5% cost reduction can be achieved even though the electricity use increases.

Keywords: heat pump system; price-based control; capacity-controlled heat pump

1. Introduction

With the growing share of renewable energies in the electricity mix, demand side flexibility gets more important to enable the full potential of the renewables [1][2]. Heat pumps are more often applied to heat buildings and their share among other building heating systems is growing, especially in highly energy-efficient buildings [3]. The application of capacity-controlled heat pumps has become more common during the last decade as the increased efficiency during part-load operation leads to distinct benefits compared to on-off heat pumps. Detailed studies on heat pump systems are usually performed for one specific country, whereas there is a lack of studies that evaluate similar control approaches for heat pump systems for different countries.

Clauß et al. [4] tested different price-based control strategies for heating a residential building located in Norway. In their study, they evaluated price-based heating control strategies for different building insulation levels. The implemented price-based control aims at reducing operational costs by deploying the energy flexibility potential of the building. To evaluate how the heating strategies proposed by Clauß et al. work for the Swiss climate and Swiss national boundary conditions, the control strategies are applied to a Swiss building. The Swiss building is described in detailed in Rominger et al. [5], where different building insulation levels and thermal masses have been applied to the Swiss building.

2. Methodology

Two different residential buildings have been simulated. In a previous study, Clauß et al [4] studied a Norwegian residential single-family house using the dynamic building performance simulation tool IDA ICE

* Corresponding author. Tel.: +41 55 222 43 25
E-mail address: carsten.wemhoener@hsr.ch

Version 4.8 The Swiss residential building is simulated using Matlab Simulink and the CARNOT-toolbox [6]. A brief comparison of both buildings in presented in Table 1.

It is mentioned here that there are distinct differences for the building and heating, ventilation and air-conditioning (HVAC) system models for the original Norwegian study and the study performed in this paper. The main differences are the building location, the building size and thus the load profiles and the layout of the HVAC system. The original work of Clauß et al. [4] considers a water tank for space heating (SH). In this study, the heat pump is in many cases connected directly to the floor heating (FH) system.

However, the same heat pump, HOVAL Belaria SRM 4, is chosen for both studies. To be able to provide a meaningful comparison of the results from this work and the previous work by Clauß et al. [4], the U-values of the building envelopes are aligned, as also shown in Table 2. The same price-based control strategies are implemented in both studies to research the effect of the spot price signals on the operational costs. Furthermore, the temperature set-points (TSP) for SH and domestic hot water (DHW) heating are varied (1) within the same range (+10 K; -5 K for DHW) to compare both case studies and (2) within a lower range (+3 K; -3 K for DHW) to also show the influence of TSP choices on the energy system performance and operational costs. The TSP for SH depends on the fact whether a SH storage tank is used or not.

Table 1. Comparison of the case study buildings.

Parameter	Unit	Norwegian (Clauß et al. [4])	Swiss
Area	m²	105	200
Floors	-	1	2
Basement	-	No	Yes
Window fraction	%	10	29
Number of persons	-	4	4
Location	-	Trondheim, Norway	Zurich, Switzerland



Figure 1 Pictures of Norwegian building (left) and the drawing of the Swiss building (right)

2.1. Building envelope

The characteristics of the building envelope are according to the Norwegian passive house (PH) standard for residential buildings, NS 3700 [7]. This building standard also requires a balanced mechanical ventilation with a heat recovery effectiveness of the air handling unit of 85% at nominal conditions. The constant air volume ventilation has a nominal air flow rate of 120 m^3/h and a supply temperature set-point of 19 °C. The Norwegian PH building is a wooden lightweight building. For the Swiss PH, the same building structures are used as for the Norwegian PH, but the geometry of the building remains the same. However, the basement of the Swiss PH is a concreate construction. The Swiss heavyweight construction (HC) building is designed to meet the new building requirements of Switzerland MuKEn 2014 [8]. Except for the roof, everything is in heavyweight construction. Table 2 summarizes the building envelope and HVAC characteristics.

Table 2. Insulation level and HVAC characteristic

Component	Parameter	Unit	Building insulation type		
			Norwegian	Swiss	
			PH	PH	HC
Building envelope	$U_{exterior\ Wall}$	W/(m²K)	0.10	0.10	0.16
	$U_{inner\ Wall}$	W/(m²K)	0.34	0.34	0.70
	$U_{Basement\ Wall}$	W/(m²K)	-	0.17	0.17
	U_{Roof}	W/(m²K)	0.09	0.09	0.15
	U_{Floor}	W/(m²K)	0.09	0.09	0.71
	$U_{Floor\ Basement}$	W/(m²K)	-	0.17	0.17
Infiltration	$V_{dot,i}$	ACH	0.6	0	0
Air exchange	V_{dot}	m³/h	120	96	96
Thermal bridges	ψ	W/(m²K)	0.03	0.02	0.02
Windows	U_{Total}	W/(m²K)	0.8	0.8	1.0
AHU	η_{HR}	%	85	80	80
Water tank	DHW	l	215	500	500
	SH	l	243	243	243
	$Q_{dot,Aux,DHW}$	kW	3	0	0
	$Q_{dot,Aux,SH}$	kW	9	0	0
SH needs	Q_{SH}	kWh/(m²yr)	34	19	27

2.2. HVAC system

The HVAC systems of the previous work by Clauß et al. [4] and this case study are slightly different. The main difference is the use of a SH tank. In this case study, two system layouts have been considered: (1) the heat pump is directly connected to the heat distribution system and (2) the heat pump is connected to a SH tank, like in the Norwegian study.

The HVAC system simulated in this study consists of an air-source heat pump that is connected to a DHW storage tank, while the heat pump is directly connected to a FH system to provide SH. The heat pump runs at full load in DHW mode, whereas it modulates between 30 % and 100 % of the nominal compressor capacity in SH mode. Regarding DHW mode for the Norwegian case study, at the beginning of a heat pump cycle the heat pump is operated at full load and the mass flow through the circulation pump is adjusted by a P-controller to meet the temperature set-point at the condenser outlet. As soon as the mass flow is at its maximum, the speed of the heat pump compressor is adjusted to stay close to the required DHW temperature set-point. In the Swiss building the DHW storage is charged by step-charging with a constant mass flow. For the SH, the mass flow is kept constant for both building cases while the heat pump modulates to achieve the required floor heating supply temperature. For the Swiss case study, the FH supply temperature is kept constant throughout the whole year and is not dependent on the outdoor air temperature. A simplified sketch of the heating system configuration is presented in Figure 2.

For the case where a SH tank is used, the volume of the SH storage tank is aligned to the volume of the previous Norwegian case study, being 243 liters (l). However, the DHW storage tank of the Swiss buildings has a chosen capacity of 500 l, compared to 215 l for the Norwegian case study. To ensure a minimal tapping temperature of 45 °C, the heat pump switches on as soon as the temperature at a relative tank height of 0.8 drops below 50 °C. The heat pump is switched off again as soon as the temperature of 50 °C is reached at a relative tank height of 0.4. For the Swiss building, the internal heat exchanger is placed at the bottom of the DHW storage tank. The same strategy as for the DHW storage tank is used for the SH storage tank with a temperature set-point of 30 °C and relative heights of 0.8 and 0.2. For the cases without a SH storage, the heat

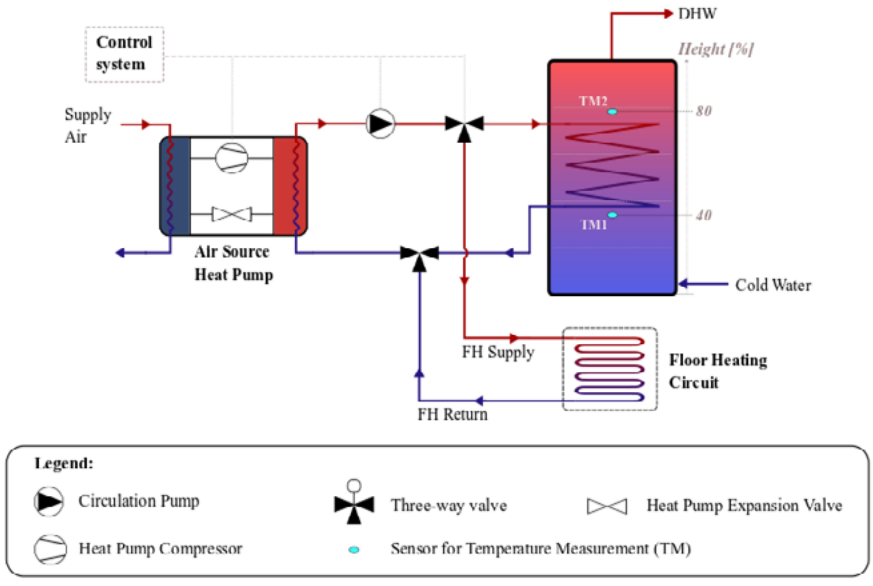


Figure 2. Configuration of the heating system

pump is switched on based on the room temperature. The temperature set-point (TSP) of the room is 21 °C with a hysteresis of 2 K.

2.3. Power sizing

The performance map of the selected air-source heat pump HOVAL Belaria SRM 4 is shown in Figure 3.

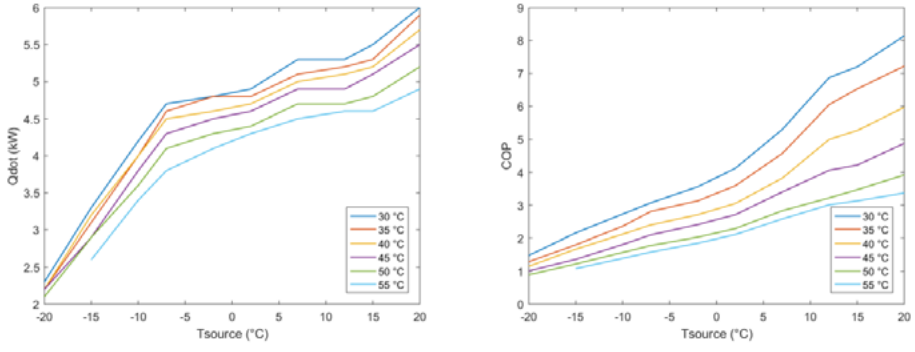


Figure 3. Performance map of HOVAL Belaria SRM 4 at 100 % compressor speed

The heat pump is designed for a monovalent operation, but it can be used as a bivalent/mono-energetic system where an auxiliary heater would cover peak loads. In Switzerland, a heat pump is designed for monovalent operation according to the building regulation, which does not allow bivalent heat pump systems with a direct electric heater. In Norway, a heat pump system can also be sized as a bivalent system. This difference will be important when comparing the price-based controls of both studies in Section 5.

For all cases, the same heat pump is used, although the heat pump is generally oversized for the PH cases. However, since there are no heat pumps on the market, which are significantly smaller than the chosen one, it seems to be a realistic assumption that this heat pump can also be applied to PH cases.

To simulate the inverter-controlled behavior, the heating capacity of the heat pump can be controlled from 30 % to 100 % of its maximal capacity, while the mass flow of the floor heating circuit is kept constant. The detailed control strategies are described by Clauß et al. [4] and Rominger et al. [5]. For the sake of simplicity, the COP increase during part-load operation is not modeled. The COP is held constant over the whole part-load range.

2.4. Boundary conditions

Weather data as well as electricity spot prices were taken for one year. In the previous study by Clauß et al. [4], simulations were performed for the year 2015, whereas this Swiss case considers the data for 2018. By using spot prices and weather data from the same year, it can be ensured that possible weather dependencies of the electricity price are taken into account.

For the Swiss cases the internal user profiles for occupancy and electric appliances (including lighting) are taken from the Reference Framework for System Simulations [9]. However, these profiles are scaled according to the pre standard SIA 2024 [10] for single-family houses.

Based on Fanger`s Predicted Mean Vote (PMV) / Predicted Percentage Dissatisfied (PPD) method, it is assumed that indoor operative temperatures can be varied between 20 °C and 24 °C while still keeping a similar comfort level. According to EN15251:2007 [11], this temperature range corresponds to $-0.5 < PMV < 0.5$ and a $PPD < 10\%$ for a clothing level of 1.0 and an activity level of 1.2 MET.

3. Simulation scenarios

3.1. Reference strategy

In the reference case, called business as usual (BAU), temperature set-points for DHW heating and SH are kept constant at all time at 50 °C and 21 °C, respectively. Constant temperature set-points are chosen for the reference scenario, because heating systems in residential buildings are usually controlled in this way.

3.2. Control Strategy Price, CSP

This work investigates demand response scenarios, where the DHW and SH set-points are modulated depending on the hourly spot price. Electricity spot prices vary throughout the day, which means that operational costs could be reduced, if a heating system is operated during low-price periods and/or if the operation during high-price periods is avoided. The TSPs for SH are either increased by 3 K or decreased by 1 K depending on the current spot price and the spot price trend for the next 24 hours. In the case without a SH storage, the switch-off hysteresis is decreased by 1 K during high-price periods. Therefore, the heat pump switches off earlier. On the contrary, the temperature set-point is increased by 1 K during low-price periods. Two temperature ranges for TSP variation are investigated for DHW: (1) the TSPs for DHW heating are increased by 10 K or decreased by 5 K, or (2) the TSPs are increased or decreased by 3 K respectively. The capacity control of the heat pump is not affected by the price signal.

To generate the price-based control signal, two principles are applied and compared, control strategy price principle (a), CSP-a and principle (b), CSP-b. Both principles are illustrated in Figure 4 [4]. The spot price of the prospective 24 hours can be divided into three price segments (i.e. low, medium and high price segments) using two price thresholds. The heating set-points can then be adjusted based on the spot price of the current hour relative to the price segment. A 24 hours sliding horizon is considered to determine a low-price threshold (LPT) and a high-price threshold (HPT). The determination of the thresholds follows the approach presented in [4]: describing the maximum and minimum spot prices for the next 24 hours as SP_{max} and SP_{min}, the HPT can be determined by $SP_{min} + 0.75\ (SP_{max} - SP_{min})$ and the LPT by $SP_{min} + 0.30\ (SP_{max} - SP_{min})$. The choice of thresholds is important for the operation of the heating system, as different thresholds will lead to a different number of hours per price segment and thus the respective heating set-points.

CSP-a aims at charging the thermal storage during periods with the lowest prices and simply increases TSPs when the current price is below the LPT and decreases TSPs as soon as the current spot price is above the HPT.

CSP-b aims at charging the thermal storages just before high-price periods. For this case, the control signal is also based on the three price segments and additionally considers whether the spot price will be increasing or decreasing in the next two hours. The TSPs are increased, if the current spot price is between the two thresholds and if the spot price is increasing the next two hours. On the contrary, the temperature set-points

are decreased, if the current spot price is between the HPT and LPT and is decreasing the next two hours. The TSPs remain at the reference set-point if the current spot price is below the LPT.

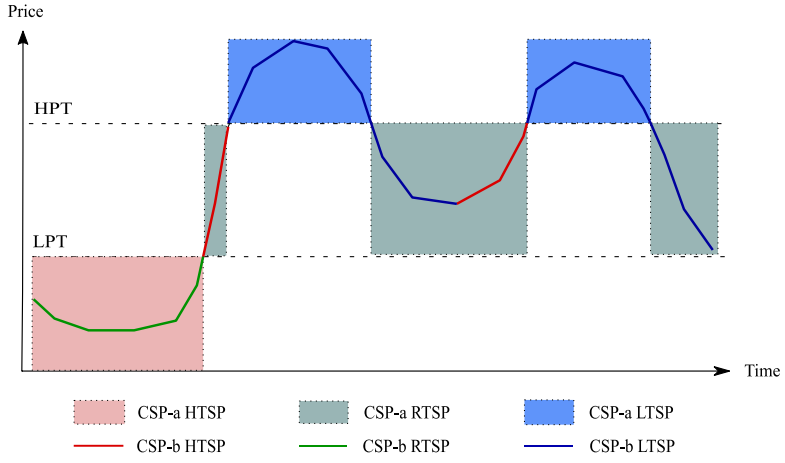


Figure 4. Determination of price-based control signals for control strategies CSP-a and CSP-b (HTSP – High temperature set-point, RTSP – Reference temperature set-point, LTSP – Low temperature set-point) [4]

4. Key performance indicators

The results are evaluated with the help of the following key performance indicators (KPI):

- Annual energy use for heating in kWh, consisting of the delivered electricity ($El_{del,i}$) to the heat pump compressor
- Annual heating costs for the operation of the heat pump system, calculated by

$$E_{Costs}\left[\frac{€}{year}\right] = \sum_{i=1}^{n} El_{del,i}[kW] \cdot 1h \cdot Spot\ Price_{el,i}\left[\frac{€}{kWh}\right] \quad (1)$$

Other performance indicators such as primary energy or CO_2-emissions are not considered in this study.

5. Results

It is shown in Table 3 that CSP-a performs better than CSP-b for the Swiss case study, whereas in Norway CSP-b shows a better performance than CSP-a. For all cases, the used electrical energy increases with the CSP compare to the BAU. That is obvious, since TSP are increased to charge the thermal storages when electricity prices are low. Higher storage temperatures also lead to higher storage losses and lower COP for the heat pump (as a result of higher temperature lift).

It is possible to reduce the energy costs with CSP-a using the Swiss spot prices. Applying the Norwegian electricity spot prices to the Swiss building and energy system, the annual operational costs increase. It can therefore be concluded that CSP-a works well, if the spot price varies strongly enough. The Swiss spot price in 2018 has a difference from the average to the 0.75 quantile and the 0.25 quantile of 10.8 €/MWh respectively 11.0 €/MWh. Whereas the Norwegian spot price only varies 5.9 €/MWh respectively 6.0 €/MWh from the average spot price to the 0.75 quantile and the 0.25 quantile. However, also with the Swiss electricity prices, the measure of increase and decrease of the TSP is decisive for a decrease of the costs.

With the comparison between the Swiss PH with and without a SH storage it can be determined that the cost reduction is bigger without a SH storage tank. This is due to the fact that the thermal heat storage capacity to which the heat pump is connected to, is bigger for the building thermal mass compared to the SH storage tank, although the building thermal mass is also for the case with the SH storage tank indirectly connected to the heat pump. The higher thermal mass of the Swiss HC compare to the Swiss PH does not lead to an increase in cost savings. Furthermore, the Swiss electricity spot prices in combination with CSP-b do not cause cost savings.

In the Norwegian case study by Clauß et al [4], a bivalent heat pump system was used. They found that the

electric auxiliary heater operated more often, if price-based control strategies were applied for both, SH and DHW heating, which was due to the fact, that the heat pump prioritized DHW heating over SH. If there was a demand for DHW and SH at the same time, the heat pump was heating DHW and the electric auxiliary heater provided SH.

Table 3. General Results (PH – Passive house, BAU – Business as usual, CSP – Control strategy price, SH – space heating, SPF – Seasonal performance factor, NSP – Norwegian spot price, SSP – Swiss spot price, Swiss HC – Swiss solid construction)

Set points	Building	Spot price	Control strategy	Electrical energy		Cost	
				kWh	%	NOK*/€	%
Variant 1	Norwegian PH	NSP	BAU	2199	-	484*	-
(TSPs for DHW +10 K or –5 K)			CSP-a	3057	+39	605*	+25
			CSP-b	2657	+21	585*	+21
	Swiss PH with SH Storage	SSP	BAU	1741	-	93	-
			CSP-a	2050	+18	97	+4
			CSP-b	2006	+15	107	+15
	Swiss PH without SH storage	SSP	BAU	1760	-	95	-
			CSP-a	2063	+17	94	-1
			CSP-b	1992	+13	107	+13
	Swiss PH without SH storage	NSP	BAU	1760	-	744*	-
			CSP-a	2084	+18	816*	+10
			CSP-b	1974	+12	829*	+11
	Swiss HC without SH storage	SSP	BAU	2109	-	115	-
			CSP-a	2428	+15	116	+1
			CSP-b	2345	+11	127	+11
Variant 2	Swiss PH	SSP	BAU	1741	-	93	-
(TSPs for DHW +3 K or –3 K)			CSP-a	1850	+6	90	-3
			CSP-b	1822	+5	95	+2
	Swiss PH without SH storage	SSP	BAU	1760	-	95	-
			CSP-a	1871	+6	88	**-7**
			CSP-b	1805	+3	95	+0
	Swiss PH without SH storage	NSP	BAU	1760	0	744*	-
			CSP-a	1897	+8	756*	+2
			CSP-b	1803	+2	747*	+0
	Swiss HC without SH storage	SSP	BAU	2109	0	115	-
			CSP-a	2226	+6	109	**-5**
			CSP-b	2162	+2	116	+1

6. Conclusions

The results of this paper show that a sufficient hourly fluctuation of the spot prices is necessary to achieve cost savings for the proposed demand response strategies. The additional energy use due to charging the thermal energy storages are only outweighed, if the difference in the electricity spot prices are sufficient. However, a stable electricity price indicates, that there is no incentive for a price-based control.

Since the total electrical power of all the electrical heat pumps in Switzerland is about 1.5 GW [12] and the maximal electricity power of the hydro storage power plants are 11 GW [12] it is hard to say how much the spot price would be influenced, if all heat pumps would use the CSP-a controller. In addition, the Swiss electrical grid is well connected with its neighbours, which makes it even more difficult to predict the influence of the CSP-a control on the spot price.

This study confirms the conclusions found by Fischer et. al. [13]. The success of a demand response strategy is highly dependent on the sensor position and the control strategy to run the heat pump. In the Norwegian

case, with the lower sensor being positioned relatively high in the SH storage, the potential of shifting the load is limited. However, for the Swiss building and HVAC layout, the best results were achieved for a system without a SH storage tank. Due to the fact that the thermal mass of the building is bigger than the thermal mass of the water storage tank and the building thermal mass is directly accessible, more energy can be shifted for the case without a SH storage tank. For the Swiss PH with its lightweight structure there is no need of a SH storage tank regarding the run time of a capacity-controlled heat pump. Therefore, in this case an HVAC system layout without a SH storage tank is preferable.

Furthermore, the procedure/regulations for sizing a heat pump are an important factor that influences the success of a control strategy. For the Norwegian case study by Clauß et al. [4], the system was designed as a bivalent system with a direct electric heater as an auxiliary heater. On the contrary, building regulations in Switzerland do not allow bivalent sizing of the heat pump with a direct electric heater. Therefore, the efficiency loss due to higher TSPs is smaller in Switzerland than in Norway, where it is possible to run the heat pump and the direct electric heater at the same time to provide DHW heating and SH. Thus, for a bivalent heat pump system, the price-based control strategy should be improved to prevent the electric heater from switching on too frequently. Regarding the choice of the TSPs and their influence on the operational costs, it can be concluded that a too large TSP variation lowers the efficiency too much so that it impairs the operational cost savings. This also shows that the potential cost savings with a sensible heat storage is limited, due to the efficiency decrease with temperature increase. Therefore, a latent heat storage might be suitable to increase the flexibility and the operational cost savings, if the charging and discharging power of it is sufficient.

Acknowledgements

The authors would like to acknowledge the international research collaboration "IEA HPT Annex 49 - Design and Integration of Heat Pumps for nZEB" which provided the framework for this work. The support and funding of the IEA HPT Annex 49 by the Swiss Federal Office of energy SFOE is highly acknowledged.

References

[1] S. Ø. Jensen et al., “IEA EBC Annex 67 Energy Flexible Buildings,” Energy Build., 2017.
[2] K. O. Aduda, T. Labeodan, W. Zeiler, G. Boxem, and Y. Zhao, “Demand side flexibility: Potentials and building performance implications,” Sustain. Cities Soc., 2016.
[3] B. für E. BFE, “Schweizerische Elektrizitätsstatistik 2018,” 2019.
[4] J. Clauß, S. Stinner, I. Sartori, and L. Georges, “Predictive rule-based control to activate the energy flexibility of Norwegian residential buildings: Case of an air-source heat pump and direct electric heating,” Appl. Energy, vol. 237, pp. 500–518, Mar. 2019.
[5] L. Rominger, C. Wemhoener, and S. Buesser, “Investigations of speed controlled heat pumps for NZEB in IEA HPT Annex 49,” in Journal of Physics: Conference Series 1343 012078, 2019.
[6] S. I. Juelich, “CARNOT-Toolbox,” 2018.
[7] Standard Norge, NS 3700:2013 Criteria for passive houses and low energy buildings - Residential buildings. 2013.
[8] K. K. Energiedirektoren, “Mustervorschriften der Kantone im Energiebereich,” Bern, 2018.
[9] R. Dott, M. Y. Haller, J. Ruschenburg, F. Ochs, and J. Bony, “The Reference Framework for System Simulations of the IEA SHC Task 44 / HPP Annex 38,” 2013.
[10] Schweizerische Ingenieur und Architektenverein, Raumnutzungsdaten für die Energie- und Gebäudetechnik. 2015.
[11] European Committee for Standardization, Indoor environmental input parameters for design and assessment of energy performance of buildings addressing indoor air quality, thermal environment, lighting and acoustics. 2007.
[12] B. für E. BFE, “Schweizerische Gesamtenergiestatistik 2018,” Bern, 2019.
[13] D. Fischer, J. Bernhardt, H. Madani, and C. Wittwer, “Comparison of control approaches for variable speed air source heat pumps considering time variable electricity prices and PV,” Appl. Energy, 2017.

13th IEA Heat Pump Conference
April 26-29, 2021 Jeju, Korea

Cost optimized design of ground probe fields with solar regeneration

Simon Buesser[a], Carsten Wemhoener[a*], Lukas Rominger[a]

[a]IET Institute of Energy Technology, HSR University of Applied Sciences Rapperswil, Oberseestrasse10, 8640 Rapperswil, Switzerland

Abstract

Solar regeneration is often used to raise the temperature of the ground above the natural level in order to enable a more efficient operation of heat pumps. The aim of this simulation study was to find the most cost-effective configuration of ground probes in combination with solar regeneration. The results show that with the help of regeneration not only the costs, but also the efficiency of the heat supply can be improved in comparison to the case without regeneration. Besides that, good conditions are achieved for freecooling with the ground probes despite the regeneration, as well.

Keywords: Ground source heat pump, regeneration, ground probe field design, cost-optimal design

1. Introduction

Heat pump systems enable low-carbon heating of buildings. The ground is often used as a heat source. The advantage of ground-source heat pump systems compared to air-to-water systems, which are also widely used, is the low noise emission, even in large systems, and the lower electrical power requirement in colder weather conditions. However, higher initial investment cost is required for ground-coupled systems. Another problem can occur with large construction projects or refurbishments. For space reasons, the probes may have to be arranged in compact fields, which can lead to a strong temperature decrease in the ground.

One way to prevent this problem is to regenerate the ground using a second heat source. This can limit the long-term temperature degradation during the use of the ground probes over several decades. In addition, the lowering of temperatures during a single winter can be reduced. Furthermore, it was also assumed that the use of solar collectors would result in cost advantages. On the one hand, since the number of probes could be reduced, on the other hand since a part of the domestic hot water can be heated directly and thus less electrical energy and less source energy is needed for the operation of the heat pump.

In practice, the aim of a solar regeneration is usually to raise the temperature of the ground above the natural level in order to enable a more efficient operation of the heat pump. This requires a heat input to the ground that exceeds the heat extraction in the annual balance. The focus thereby is on energy efficiency rather than on cost efficiency.

To determine the potential of a strictly cost-optimized design, a simulation study has been carried out. A residential complex consisting of six buildings with a totally heated area of 16,800 m^2 is used as a case study. Active cooling operation with the heat pump used as chiller was not analyzed for this application, as active space cooling is not common in residential buildings in Switzerland, yet. However, the free cooling potential by the ground are addressed based on the evaluated ground temperatures. Nevertheless, the system configuration has also cooling potential and indeed, in the luxury residential segment also active cooling is more often asked on the market. Thus, further investigations shall also include the space cooling operation as further operation mode of the system.

* Corresponding author. Tel.: +41 55 222 43 25
E-mail address: carsten.wemhoener@hsr.ch.

2. Method

The aim of the simulation study was to determine the minimum number of probes required as a function of the collector area. In addition, the power consumption of the heat pumps and the pumps for the source circuit were determined. In this way, the level of investment and operating costs as well as the consumption of electrical energy could be determined. The same model has been used for all simulation variants.

The only parameters varied were the number of probes, the distance between the individual probes and the area of the collectors.

The simulation model was created with Matlab/Simlink and the Carnot Toolbox [1]. The model contains very well insulated buildings. The heat demand for DHW (19.8 kWh/(m^2yr)) is slightly lower than the heat demand for space heating (21.2 kWh/(m^2yr)), but in the same range. The location of the buildings is Zurich. The heating period lasts from the beginning of October to the middle of May. Each building has two storage tanks for the hot water system and collectors on the roof. The collectors are oriented to the south with an inclination of 30°. One storage tank serves to preheat the water through the collectors, the second tank is supplied by the heat pump. In order to shorten the calculation time, the buildings were not modelled in detail. Instead, load profiles created in advance were used. In this profiles, space cooling is not taken into account.

An unglazed, selective collector was used. In the first priority, the collectors preheat the domestic hot water, in the second priority they deliver heat to the ground probes. The collectors were distributed evenly on the roofs of the six buildings.

The heat source is a central ground probe field with a bidirectional low-temperature network with a cold and a warm distribution pipe to which all heat pumps and collectors are connected. Each building has its own heat pump. The temperature difference between the warm and cold conductor is 5 K.

A self-developed model is used for the ground probes, which is based on the EWS model developed by Huber [2] for the probe tube and the close range (3 m around the ground probe). For the boundary conditions, the method for the analytical calculation of the g-functions according to Lamarche and Beauchamp [3] was used. In addition, the probe loads are superposed for half a year at an interval of seven days. The probes are installed to 200 m depth, the mean ground surface temperature is 9 °C and the geothermal gradient is 0.03 K/m. Further parameters of backfill and ground are listed in Table 1. The probes are always arranged in squares.

Table 1. Material properties of the backfill and the ground

Component	Backfill	Ground
Thermal conductivity (W/m/K)	0.81	2.4
Specific heat capacity (J/kg/K)	3040	1000
Density (kg/m^3)	1180	2600

The collector area required for differently sized ground probe fields was determined so that the ground does not cool down too much. The design criterion was that the temperature of the cold distribution pipe must not fall below -3 °C during the first 50 years of operation, according to the Swiss standard SIA 384/6:2010 [4].

In order to evaluate the configurations from an energetic point of view, the electrical consumption of the heat pumps and the pumps in the source circuit is evaluated. The characteristic diagram of a commercially available speed-controlled heat pump was used. When calculating the electrical consumption of the frequency controlled circulating pumps, only the pressure drop by the ground probes was taken into account according to the pressure drop calculation tool of Huber et al. [5]. The pressure loss of the horizontal connecting pipes was neglected. The pipes of the ground probes have a diameter of 32 mm. The efficiency of the circulating pumps is 0.5.

Configurations of the following combinations of ground probe fields and probe distances were investigated:

- ground probe fields: 3×3 / 4×4 / 5×5 / 6×6 / 7×7 / 8×8
- ground probe distances: 6 m / 8 m / 10 m / 20 m

An attempt was made in each case to select the collector area in such a way that the minimum temperature in the cold distribution pipe is as close as possible to -3 °C. The exact values for the collector area, the power consumption, the system efficiency and the regeneration share were finally interpolated. The following definitions were used:

- Power consumption: Average electricity consumption of heat pumps and source pumps over 50 years
- System efficiency: Quotient of heat demand for space heating and domestic hot water and power consumption

- Regeneration share: Total collector yield divided by the total source heat demand for space heating and domestic hot water. The source heat demand includes the heat that was directly used for preheating the domestic hot water and heat for the heat pump extracted of the ground probes.

As a comparison, the number of probes necessary to achieve the design criterion without regeneration was also determined for the various probe distances. The results were also interpolated. For this reason, a number of probes can result for the required probes that cannot be arranged in a square.
The system costs are calculated from the interpolated values for the collector surfaces and the number of probes. The following values which are common in Switzerland, were assumed:

- Electricity: 0.15 €/kWh
- Investment costs ground probes: 80 €/m
- Investment costs for collectors: 400 €/m² (includes planning, mounting system, piping and installation work)

3. Results

Fig. 1 shows the values for the minimum temperature of the cold distribution pipe in the first 50 years of operation of all simulation variants. The range of the marked square on the left is enlarged in the right figure.

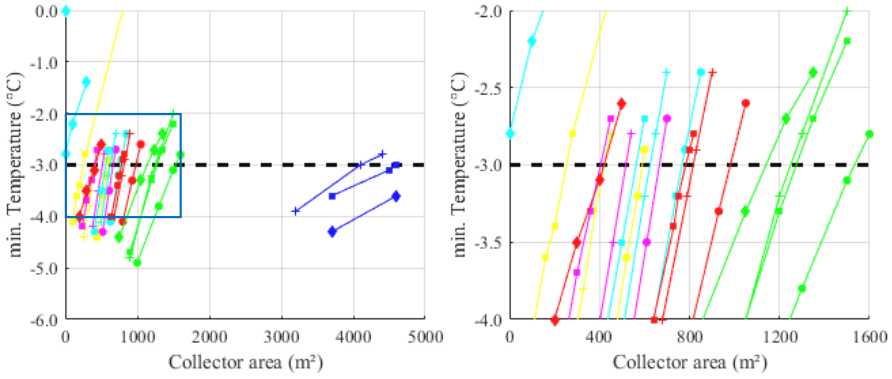


Fig. 1. Minimum temperature of the cold conductor in the first 50 years of operation. (Fields: blue: 3×3, green: 4×4, red: 5×5, cyan: 6×6, violet: 7×7, yellow: 8×8 / Distances between ground probes: dots: 6 m, crosses: 8 m, squares: 10 m, diamonds: 20 m)

Fig. 2 shows the temperature curves of the cold and the warm distribution pipe of a case with and without regeneration as a comparison. It can be seen, that by the reduction of the ground probe length, the system reaches negative temperatures already after a few years of operation, but the temperatures remains more or less constant from then on. The non-regenerated system does not come close to a stationary state even after 50 years. The difference between the maximal and minimal temperature is significantly higher in the regenerated case, because of the smaller usable heat capacity of the ground compared to the larger, non-regenerated field.

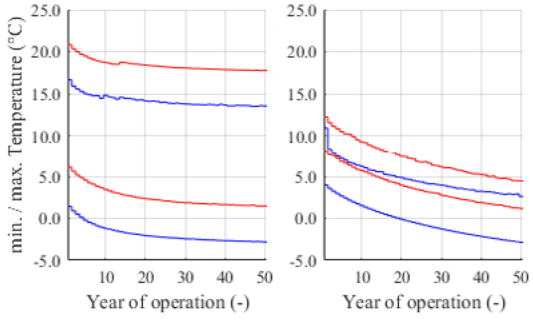


Fig. 2. Plot of the maximum and minimum temperature of the cold (blue) and the warm (red) conductor per year.(left: 5×5 ground probes in a distance of 10 m with 820 m² collector area, right: 10×10 ground probes in a distance of 10 m without regeneration)

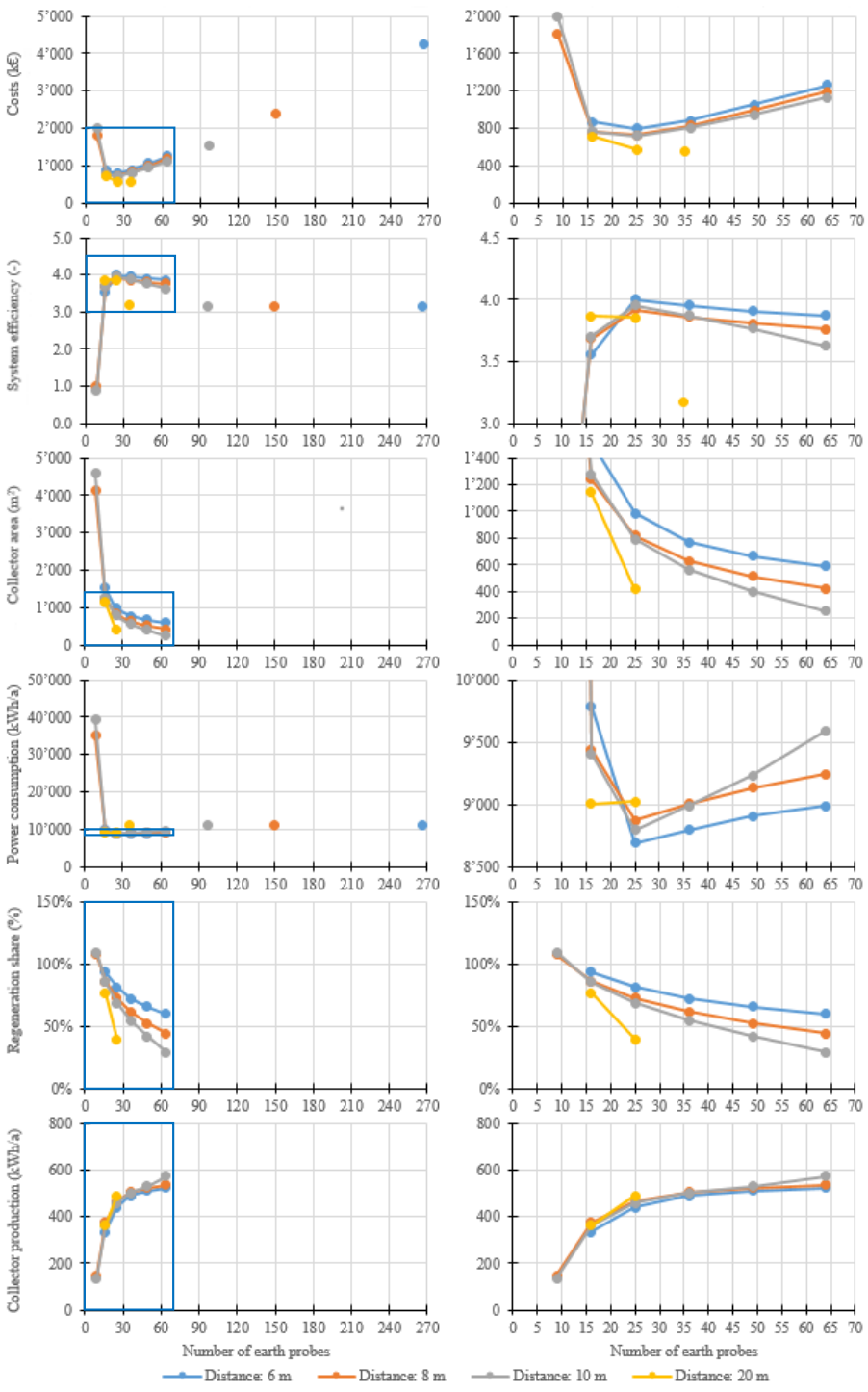


Fig. 3. Costs, System efficiency, collector area, power consumption and regeneration share as a function of the ground probe field

Fig. 3 shows the interpolated values for the required calculated costs, the system efficiency, the collector area, the power consumption and the regeneration share for the various system configurations. The single points represent the cases without regeneration. The marked area in the left figure is depicted enlarged in the right figure.

The results demonstrate that by means of regeneration not only the total cost can be reduced, but also the efficiency of the heat supply can be improved. Besides that, there are still good conditions for free cooling with the ground probes, since the regenerated field is operated colder than with higher shares of regeneration.

The distance between the probes has a large influence on the reduction potential of the cost. The smaller the distance between the probes, the higher the saving potential, which can be evaluated by a comparison of the cost curve with regeneration and the single points without regeneration. In the case with a distance of 10 m, the cost optimum is achieved with approximately 16-25 probes. Compared to the case without regeneration with 97 probes, this is a 74-84% reduction in probe length and about 42% in costs. This can be advantageous for refurbishments when space is limited. But, it can also be beneficial for new buildings. By reducing the need for ground probes with the help of regeneration, the distance between the ground probes can possibly be increased. That could allow a further reduction of the number of ground probes. The lowest overall cost is reached, however, for the largest distance of 20 m.

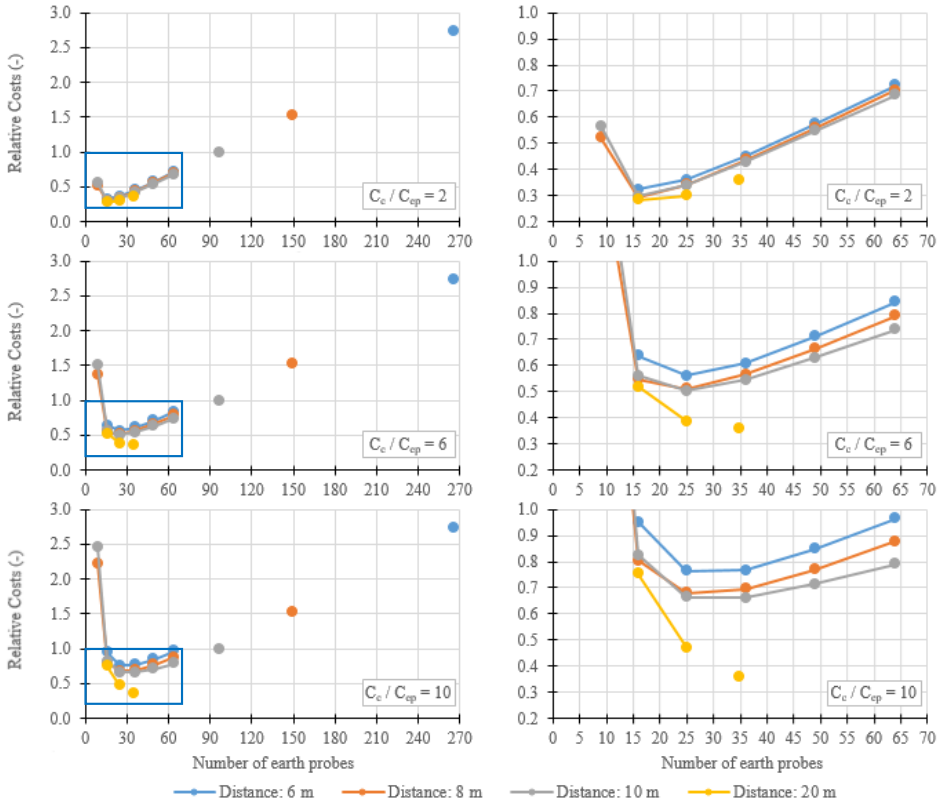


Fig. 4. Relative costs for different ratios of the cost per square meter of collector area (C_c) to the cost per meter of ground probe with the cost of a 5×5 field with a 10 m borehole distance as a basis.

The system efficiency is increased, although the temperatures in the cold distribution pipe in winter already reach negative values after a few years. One reason for this is the partly direct supply of hot water by the collectors, the other reason is the temporarily high source temperatures for the heat pumps. Fig. 2 on the left shows the case with the ground probe field 5×5 and a ground probe distance of 10 m and a collector surface of 820 m^2, which is close to the cost optimum. Fig. 2 right shows the case without regeneration with 100 probes arranged in a square of 10 m distance, corresponding to the minimum number of probes without regeneration.

Due to the lower number of probes the temperatures are lower only during the heating period. During the other seasons, the domestic hot water can be produced very efficiently at higher source temperatures. In the described case, the DHW share produced by the collectors is 49%. Thus, a performance increase can be expected in particular in larger new buildings, where the DHW share reaches the same energy amount or is even higher than the space heating needs.

The energy consumption of the pumps has a significant influence on the total power consumption only for small fields. With the 3×3 fields it can reach up to 80%. With the 4×4 fields it is 6-25% and with the 5×5 fields it is reduced to less than 5%. The higher power consumption with the small fields is due to the higher pipe resistance, since the mass flow is kept the same as in larger fields. Additionally, due to the larger collector area, a higher collector yield has to be transferred to the ground. This is also the reason, why for the small fields the system performance is notably reduced, since the fraction of auxiliary energy expenditure for the pumping of the fluid rapidly increase up to low overall system performance. Due to the large regeneration shares, also the system cost increases disproportionally. These system designs are thus not reasonable neither from the energy performance nor from the cost viewpoint and are henceforth not considered for the evaluation of the results.

The cost of ground probes and collectors can vary significantly depending on the region and system size. Therefore, in Figure 4 the relative costs were calculated as a function of the ratio of the price per square meter of collector area (C_c) to the price per meter of ground probe (C_{ep}). The electricity price was set to 0.00 €/kWh in all cases. The influence of the electricity price in the range of 0.00 €/kWh - 0.20 €/kWh on the total costs is in all cases less than 0.5% and is therefore negligible. The costs for the case with a 5×5 probe array with 10 m probe spacing were taken as a basis. In graph 3 the ratio is $C_c / C_{ep} = 5$.

It can be seen that the results do not fundamentally change even for large and small ratios C_c/C_{ep}. But, the cheaper the geothermal probes are, the less advantageous is a substitution by collectors.

4. Conclusion and Perspective

Results of the investigations show that a design of the ground source to shorter length by regeneration can yield cost and performance increase, which is also due to a direct production of used energy by the regeneration system, in this case the direct solar DHW operation of the collectors. Since for this investigation, selectively coating unglazed solar collectors have been considered, DHW use temperatures can be reached by the collector in summer operation. However, current investigations only reflect one particular weather data set, load situation and system configuration. Therefore, further investigations are necessary, also e.g. regarding longer cold periods. Due to the smaller number of ground probes compared to a conventional configuration without regeneration, the system is more vulnerable to cold periods. During cold periods lasting several days, the area around the probes can cool down considerably. Due to the lower number of probes, the available heat around the probes is smaller, which leads to a stronger cooling.

For the considered buildings the system performance is increasing with the regeneration, in particular in case of limited space for the ground probes. However, for the considered case, the annual DHW demand is in the same range as the energy demand for space heating, and thus the summer operation is more pronounced. Therefore, for different buildings loads, the effect on the system performance should also be considered. Since the minimal temperature level in winter is lower for the considered regenerated cases than in the reference case without regeneration, see comparison in Fig. 2, the system efficiency could decrease for certain times compared to the reference case.

Moreover, for the regeneration with unglazed solar collectors, a large collector area is needed. The influence of alternative heat sources for regeneration, such as outside air, waste water or free cooling of the connected buildings should also be examined in more detail.

In this context also the low system performance in case of only a few ground probes is to be analyzed in more detail, which, however, is according to the present evaluation not cost-effective due to a very large regeneration need.

Acknowledgements

The research project is financially supported by the Swiss Innovation Agency Innosuisse and is part of the Swiss Competence Center for Energy Research SCCER EIP.

References

[1] CARNOT-Toolbox 6.1 for the use with Matlab-Simulink. 2018. Solar Institute Juelich, FH Aachen
[2] Huber A, Schuler O. Berechnungsmodul für Erdwärmesonden. Forschungsprogramm Umgebungs- und Abwärme, Wärmekraftkopplung, Bundesamt für Energie Bern. 1997.
[3] Lamarche L, Beauchamp B. A new contribution to the finite line-source model for geothermal boreholes. Ecole de Technologie Supérieure. 2006.
[4] SIA 384/6:2010 Erdwärmesonden. Schweizerischer Ingenieur- und Architektenverein Zürich. 2010
[5] Huber A, Ochs M. Hydraulische Auslegung von Erdwärmesondenkreisläufen mit der Software„EWSDruck“ vers. 2.0. Bundesamt für Energie Bern. 2007.

13th IEA Heat Pump Conference
April 26-29, 2021 Jeju, Korea

Evaluation of solar heat source and sink in multi-functional heat pump operation

Carsten Wemhoener[a*], Simon Buesser[a], Roman Schwarz[ab], Lukas Rominger[a]

[a]HSR University of Applied Sciences Rapperswil, Oberseestrasse 10, CH-8640 Rapperswil, Switzerland
[b]Basler und Hofmann AG, Forchstrasse 395, CH-8032 Zürich

Abstract

With increasing heat pump use, heat sources gain importance. For high performance, the heat source should deliver high temperature levels. Compared to outdoor air solar installations like unglazed collector or photovoltaic/thermal installations can extract energy from the ambient air, but also yield higher temperatures at solar irradiation.
To overcome cost barriers compared to cheaper outside air heat pumps, a multi-functional operation for direct solar space heating/domestic hot water (DHW) generation at high solar irradiation has advantages. During nighttime, also space cooling by heat rejection to the colder ambient temperatures/night sky can be provided which increases performance of the overall system by multi-functional integration.
Test rig measurement of solar components as heat sink are evaluated and seasonal performance calculations are performed by simulation. Results indicate that in particular in buildings with higher space cooling and DHW shares, solar components can yield higher overall seasonal performance factors than outdoor-air heat pumps. Night cooling capacities can be enhanced by an evaporation on the collector, which also enables to vary surface properties to adapt to DHW production during daytime and space cooling during nighttime.

Keywords: Solar heat source, evaporative cooling, nZEB, multifunctional heat pump design

1. Introduction

Currently, residential buildings are seldom cooled actively in central European countries like Switzerland, while in office buildings, there is already a cooling demand due to higher internal gains. However, recent studies indicate, that due to increasing outdoor air temperatures, rising number of electric devices and higher comfort requirements, also residential cooling demands will increase notably until the mid of the 21st century.

In [1] an increase of the cooling demand in residential buildings in Switzerland of 300% to 700% for the reference year of 2060 has been evaluated by simulations, see Fig. 1. Since buildings have a long life cycle, it is thus important to consider changing boundary conditions already in the planning phase. In addition to purely passive measures regarding the design of the building envelope, efficient cooling processes must also be developed in order to maintain comfort conditions, but limit the electrical expenditure for the cooling function.

Free cooling methods have already been introduced, but mainly in non-residential buildings. In residential buildings free cooling methods are often limited to nighttime ventilation or ground-coupled free cooling when a ground-coupled heat pump is used as heat generator. A possibility of free cooling in residential buildings, which is not much applied so far, is the heat dissipation by activated outer surfaces of the building envelope, e.g. those installed with solar thermal components. These components, which are designed to generate heat, can also reject heat to the ambiance during nighttime operation, under the condition that there is a good thermal connection to the ambiance.

* Corresponding author. Tel.: +41 55 222 43 25
E-mail address: carsten.wemhoener@hsr.ch

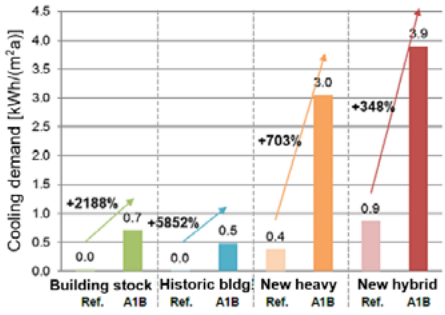


Fig. 1. Longterm development of residential cooling demands in Switzerland to the reference year 2060 [1]

In addition to pure heat dissipation to the outside air by convection, heat dissipation by infrared radiosity to the ambiance and particularly to the sky is used, since a cloudless night sky has a significant lower equivalent sky temperature that is up to 20 K colder than the outdoor air temperature.

Fig. 2 shows the cooling mechanisms that can be used for nighttime cooling on the outer surfaces of buildings. The heat emission is especially favourable for uncovered solar components, which are in direct contact to the ambiance. An increase in the cooling capacity of these components can be achieved by an additional evaporative cooling, if the surface of the components is wetted with water. In order to have a sustainable water source, reuse of decentralized treated grey- and wastewater is investigated as water for wetting the absorber.

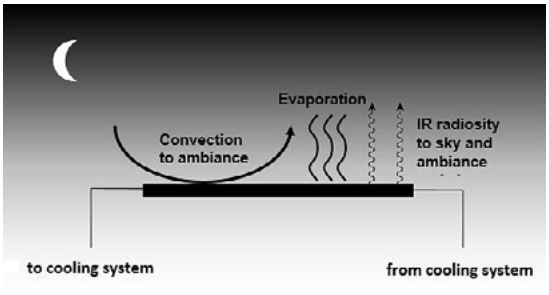


Fig. 2. Different cooling mechanisms on building outer surfaces

2. Simulation case study

In order to evaluate the feasibility of free cooling by the outer building surfaces, simulation studies were carried out for residential and office buildings. The simulations for residential buildings were carried out for a single- and multi-family house. For both types of buildings, energy-efficient new buildings have been considered that meet the requirements of the Swiss building directive MuKEn 2014 [5]. Summarizing, the following building cases were considered in the simulation study:

- Single family building as low energy (according to Swiss label MINERGIE) and passive house level (according to the Swiss label MINERGIE-P)
- Multi family building as low energy (according to Swiss label MINERGIE) and passive house level (according to the Swiss label MINERGIE-P)
- Office building according to the future Swiss building directive MuKEn 2014

The varied building parameters are given in chap. 2.1. In this publication, the investigations of the residential buildings, in particular in single-family buildings, are presented. Results for the office buildings examined show that high free cooling fractions of 80% to almost 100% can be achieved for Zurich Meteoschweiz weather station according to the Swiss guideline SIA 2028 [2] and boundary conditions of use according to SIA 2024 [3], depending on comfort requirements and properties of the outer building surface. This means, that active cooling by a chiller can be significantly reduced to back-up operation for the cases of adverse weather conditions with high nighttime temperatures.

Since typical nighttime air temperatures in Zurich Meteoschweiz weather are in the range of 15 °C, there is a good potential for cooling by outer surfaces, and the mentioned high fractions of 80 – 100% can be reached.

2.1 Building parameters

The single-family house has an energy reference area of 200 m^2. The U-value of the outer walls with U_{AW} of 0.17 W/(m^2K) corresponds to the requirements of the Swiss building directive MuKEn 2014. The window fraction of 40% is evenly distributed across all façade orientations. The windows are triple glazed with an U_w-value of 1.0 W/(m^2K) and a low fraction of the frame of only 10%. The g-value of 0.5 is in the typical range for triple glazing. For shading, variants are calculated that reflect the user behavior.

With optimal shading, from 200 W/m^2 irradiance and a room temperature of 23.5 °C, the total energy transmission is reduced to a g-value of 0.1. Irradiance of 400 W/m^2 and 600 W/m^2 are considered as variants for non-optimal shading and 1000 W/m^2 as unshaded case. For the hot water consumption, 150 l or 37.5 l/person with a used temperature of 55 °C were kept constantly throughout the year, which corresponds to an energy consumption of 2900 kWh or 14.5 kWh/(m^2yr) used energy for the hot water demand.

The multi-family building has five stories with a total of 10 flats. The total energy reference area is 1500 m^2. The U-value of the outer walls is with a U-value of 0.185 W/(m^2K) just above the limit value according to MuKEn 2014 and the U-value of the triple-glazed window with a frame proportion of 10% with U_w of 1.2 W/(m^2K) is also slightly higher than the requirement for single building components. The g-value is 0.5, which is reduced to 0.14 when shading is activated. Shading is controlled dependent on the façade orientation. The activation of the shading of 200/400/600 W/m^2 irradiance on the façade is also varied in order to model different user behavior. The occupancy of the flats with 5 persons or one person area of 30 m^2/person is higher than in a single-family house with a person specific area of 50 m^2/person. Hot water consumption is assumed to be a slightly lower consumption of 30 l/person inline with the standards for multi-family buildings at a hot water temperature of 55 °C.

The residential buildings are equipped with mechanical ventilation and heat recovery, which has a thermal efficiency of 80%. In summer mode, heat recovery is reduced to 10% for modelling a summer bypass. The residential buildings are also both equipped with floor heating, which corresponds with 0.1 m pipe spacing to a rather large dimensioned floor heating, which enables low flow temperatures and thus creates favourable conditions for renewable energy use. The floor heating serves as emission system for both heating and free cooling operation.

2.2 System configuration

The building technology consists of a solar absorber, which is connected to a water-glycol source storage tank and serves as the only heat source for the heat pump. The heat pump operates in both heating and hot water mode. If the temperature level of the solar absorber is high enough, the hot water generation can also be switched-over to the absorber and be carried out directly with the solar absorber. In this study a selective absorber is considered, which can reach the hot water temperatures in summer operation due to the reduced radiative losses at higher temperatures. Furthermore, both a buffer tank for heating operation and the hot water tank are integrated. In cooling mode, the source storage is used as a cold storage. Then the absorber circuit is operated during the night for heat losses to the ambiance in order to cool down the storage tank. When charging the storage tank with the heat extracted from the building by the floor heating, the comfort limit of a floor surface temperature of at least 19 °C must be considered. Table 1 summarizes the parameters of the single-family and multi-family house.

Table 1. Building and system parameters for the single-and multi-family building

Building and system parameters	Single-family house	Multi-family house
Residents/People	4	50
Window fraction	40%	40%
Energy reference area (ERA) [m^2]	200	1500
Annual heating demand [kWh/(m^2_{ERA}yr)]	25	15
Annual hot water demand [kWh/(m^2_{ERA}yr)]	14.5	19.5
Annual cooling demand [kWh/(m^2_{ERA}yr)]	4-6	4-6
Absorber area [m^2_{ABS}]	11-18	71-178

The hot water demand of the multi-family building exceeds the heating energy demand due to a low space heating demand of 15 kWh/(m²yr) on average among the flat, ranging from 9.3 kWh/(m²yr) of a flat on the third floor in south orientation to 27.4 kWh/(m²yr) of a flat in north orientation on the top floor. The low space heating demand is due to the lower area-to-volume ratio of the multi-family house.

In addition, the multi-family house has a higher occupancy with 30 m²/person, which increases the hot water requirements and also lowers the space heating needs due to about two-thirds higher internal gains compared to the single-family house. However, the loads for equipment and lighting remain the same. The cooling requirement is with an average of 4 kWh/(m²yr) still moderate and ranges from 2.6 to 4.8 kWh/(m²yr) among the flats. It is slightly lower than for a single-family house, partly for similar reasons as for heating, e.g. due to the smaller outer surface area compared to the energy reference area and also due to slightly lower window area per energy reference area. In Switzerland, the energy reference area comprises all treated areas for heating or cooling of the building storeys as gross area, i.e. including the insulation layer thickness.

3. Results of the feasibility study

In the following results for the single family house are presented in more detail. Results on the multi-family house are discussed in more detail in [7] and are shortly summarised in chapter 3.3.

3.1 Energies and seasonal performance factors single-family house

For the single family house, the following variants are considered:

- Variation of collector area 10.7 m² (6 absorbers) and 17.8 m² (10 absorbers)
- Variation of activation of the shading of 200/400/600 W/m². Moreover, an unshaded case (activation at 1000 W/m²) is considered.
- Variation building envelope according to the Swiss low energy and ultra-low energy house labels MINERGIE®- and MINERGIE-P® [4]
- Variation of weather boundary conditions Zurich Meteoschweiz normal and warm data set

The MINERGIE®-single family house has shading of 200 W/m² and an effective space heating demand including the ventilation heat recovery of 26.1 kWh/(m²yr). The DHW demand is 14.6 kWh/(m²yr) and the space cooling demand is by the good shading moderate with a 4 kWh/(m²yr). With a MINERGIE-P®-building envelope the space heating demand decreases to 17.1 kWh/(m²yr) and the space cooling demand increases to 4.8 kWh/(m²yr). Thereby, the space heating demand approaches the DHW demand. Despite the moderate space cooling demands at optimal shading the cooling demand surpasses on single days the DHW demand in the summer months of June - August, where peaks in the cooling demand are observed.

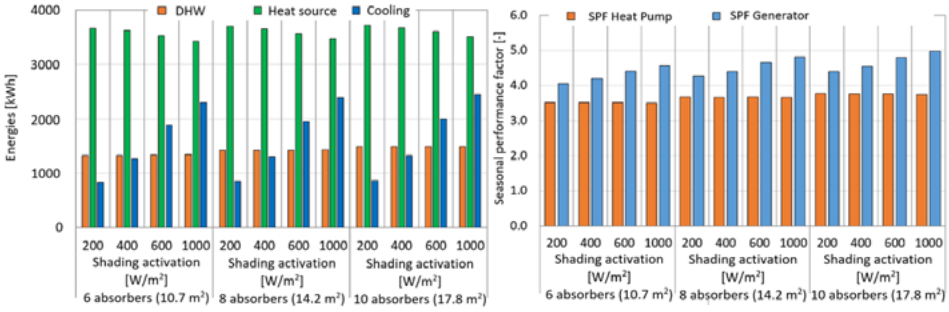


Fig. 3. Collector yield of different operation modes (left) and seasonal performance factor of the heat pump and overall (right)

Even without solar thermal DHW production, which reduces the heat pump operation in summer time, to cover the cooling demand only in simultaneous operation with the heat pump in DHW operation would be difficult. Fig. 3 left shows the collector yield for the different collector areas at variation of the shading activation of 200 W/m² to 1000 W/m² (unshaded). The space heating operation is not affected by the higher solar gains in the case of lower shading. The DHW yield is only dependent on the absorber area, and is independent of the shading. At lower absorber area the solar DHW fraction is about ca. 40%, at higher absorber areas it increases to ca. 46%. In the summer months, it is about 75-90%.

The yield of the absorber in the space cooling operation, though, is directly correlated to the shading of the building, since the space cooling loads increase with reduced shading of the building. In the unshaded case, the absorber yield in cooling is about 3 times of the space cooling energy with optimal shading. In Fig. 3 right, the performance factors of the heat pump and the overall performance factor of all generators is contrasted. As expected the shading affects the performance factors of the heat pump only slightly. The performance factor in space heating operation is almost 4, in DHW operation almost 3, which corresponds to an overall performance of 3.5-3.8.

At higher absorber area, the performance factor increases due to higher source temperatures in space heating and DHW operation by about 0.1-0.2, leading to an overall performance of 3.8.

For the ultra low energy building (MINERGIE-P building), which is not depicted, the required yield in space heating is reduced by 25%. The solar fraction corresponds to the low energy single family house (MINERGIE building). The absorber yield in cooling operation corresponds at optimal shading to the low energy house, in the unshaded case, it increases by 15%.

With smaller absorber areas and lower outside temperature with little solar irradiation, problems with the lower operation limit of the heat pump may occur, which may require an emergency heating or a second heat source, which, however, has not been modelled. At larger absorber areas, the source temperature level in the source storage increases, and thereby also the performance factor of the heat pump, which mitigates problems with the lower temperature limit of the heat pump.

For the consideration of the overall seasonal performance factor of the heat pump and the direct solar and free cooling operation, the seasonal performance of the generator (SPF_{gen}), which is depicted in Fig. 3 right. The SPF_{gen} describes the overall efficiency with the application of multiple generators and relates the thermal energy to the electricity input. In this case the condenser heat and the direct solar thermal yield of the collector is related to the electricity for the heat pump and the collector pump. Pumping energy for the source energy of the heat pump, the DHW production and free cooling is taken into account. For all operation modes, values up to around 5 can be optained for the SPF_{gen}, which is by 0.6-0.8 higher than the SPF_{HP}, as shown in Fig. 3 left.

3.2 Thermal comfort single family house

The comfort evaluation is depicted uniformly for an absorber area of 17.8 m^2. The comfort is evaluated by the operative temperature according to the requirement of the SIA 180 [6] for air-conditioned buildings, even though the building is not actively conditioned, but just free cooling is applied. The impact of the humidity is not evaluated, since with free cooling operation, the relative humidity cannot be affected. As the winter room temperatures are well in the comfort range of SIA 180 (temperature band 20.5 °C to 24.5 °C), the summer comfort only is depicted in the following. Here, the operation of the shading as well as the free cooling operation is decisive.

Fig. 4 shows the room temperatures in the summer season of mid of April until the end of September without (Fig. 4 left) and with optimal shading (Fig.4 right), with and without free cooling operation in both figures. Without shading, a maximum temperature in the range of 33 °C is reached. By a free cooling operation without shading, the temperature can be limited to a maximum of 28 °C. However, thereby, single comfort violation also occur with free cooling, as the comfort limit is set to 26.5 °C in the standard SIA 180., see also Fig. 5. By an optimal shading without free cooling, maximum temperatures are limited to 29 °C.

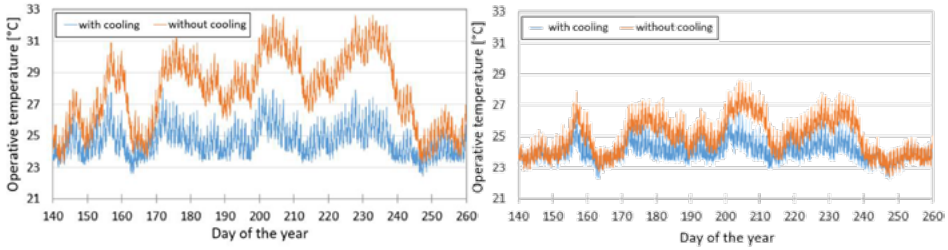


Fig. 4. Room temperatures in the summer without shading (left) and with optimal shading (right) with and without free cooling

With optimal shading starting with irradiation values of 200 W/m^2 and free cooling operation the temperatures stay in the comfort range. In Fig. 5 the hourly averaged room temperatures are depicted in the comfort range of SIA 180 for the annual period based on the moving average of the last 48 h of the ambient temperature.

In winter operation the temperature are well in the comfort range with temperatures of 22-23 °C, which are often measured in monitoring projects.

In Fig. 5 left the room temperatures with optimal shading and no free cooling operation are depicted. The 340 overheating hours outside the comfort range mainly occur in summer operation. In Fig. 5 middle the room temperatures without shading, but with free cooling are depicted. The overheating hours are reduced to 260 with about 150 hours occurring in the mid-season and about 110 hours in the summer. The overheating hours in the mid-season indicate optimisation potentials in the control, as the capacity of the collector at colder outdoor condition should be sufficient. Free cooling allows to reduce significantly the number of overheating hours that occur during summer time. Fig. 5 right shows the comfort range at optimal shading and free cooling operation.

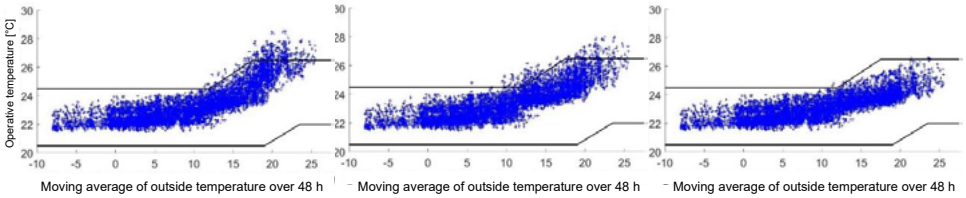


Fig. 5. Room temperature with shading and without free cooling (left) and without shading but with free cooling (middle) as well as with optimal shading and free cooling (right)

No overheating occurs anymore and there is even a reserve until the comfort boundary is reached. Thus, the free cooling operation can compensate a non-optimal shading within limits. But a shading cannot be entirely replace with the considered design of the free cooling system, in particular at high outdoor temperatures.

3.3 Summary of results of the multi-family house

For the multi-family building similar indicators are evaluated as for the single family building. The main results are summarised below. However, the energy demands and system efficiencies are affected by the specific building parameters and load. For instance, the multi-family building has a more compact building envelope with a lower surface-to-volume ratio paired with a higher occupancy of 30 m^2/person and thereby higher internal gains. This lowers the space heating demand to an average of 15 kWh/(m^2yr). Nevertheless, depending on the location in north or south orientation, the space heating demand varies among the flats. But, due to the higher occupancy, the specific DHW demand increases to 19.7 kWh/(m^2yr) and has a higher impact on the overall performance. Cooling demand is thereby considered the same as in the single family house. The same variations as for the single family house are considered.

The seasonal performance factor of the heat pump in the multi-family house is in the range of 4.5–4.9 depending on the collector area. For larger collector area the source temperature for the space heating operation increases. In the DHW operation the average SPF is 2.8, with a moderate increase of 0.1 with larger collector areas, as due to the direct solar fraction, the heat pump is producing the water at higher temperature levels. Meanwhile, the higher impact of the DHW operation the performance factor increases by 0.2-0.3 with larger collector area leading to performance factor of the heat pump SPF_{HP} in the range of 3.5–3.8.

The solar fraction increases with doubled collector area only moderately from 33% to 40%. The moderate increase is due to the limited DHW storage volume. With an extension of the storage size, the solar fraction could be increased up to 50%. The overall performance factor including heat pump, direct solar fraction and the free cooling operation SPF_{gen} yields higher performance values in the range of 4.5–5.0. Thereby, also the shading has an impact, since with reduced shading the cooling demand and the free cooling fraction increases.

Also the thermal comfort shows the same tendencies as in the single family building, but the difference between shading-only and free cooling operation becomes more distinct. The thermal comfort in winter can be maintained quite well. For a collector area of 107 m^2, optimal shading and no free cooling, about 1000 overheating hours are observed, so shading-only is not sufficient. With free cooling operation overheating hours can be limited to 100, and violations of the comfort range are mainly in the mid-season and may be further reduced with optimised control. With a combination of optimal shading and free cooling operation the comfort range can be maintained the whole summer with temperatures up to 26 °C, and still holding a little reserve regarding the comfort limit. For warmer boundary conditions of a warm summer some overheating hours result even with optimised shading and free cooling. An additional active cooling by the heat pump would have to be applied to entirely stay in the comfort range.

4. Test rig results for the space cooling operation

In order to further characterise the space cooling operation with test rig results, measurement have been performed on a selectively coated unglazed solar collector on the accredited test rig of the HSR Institute SPF, which is the national test centre of Switzerland for solar thermal collector. Fig. 6 left shows the unglazed solar collector on the test rig and Fig. 6 right depicts a sketch of the measurement system including a legend of the measurement points. In order to determine the capacity of the absorber in free cooling mode, the inlet and outlet temperatures of the absorber fluid are measured. With the measured volume flow the enthalpy change on the fluid side and thereby the cooling capacity can be evaluated. The fluid is a water-glycol mixture.

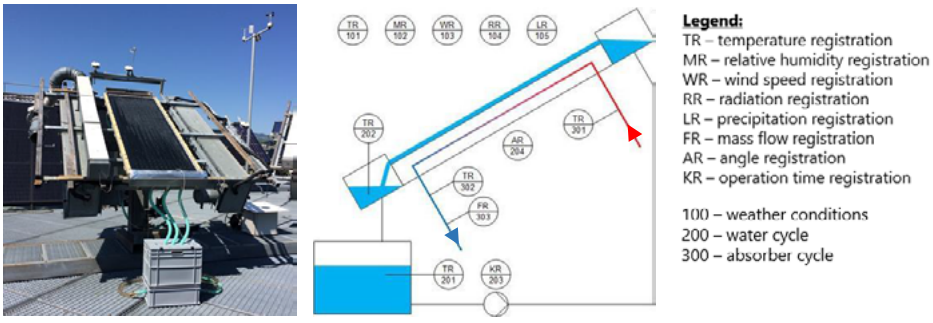


Fig. 6. Unglazed solar collector on the test rig (left) and sketch of the test rig with measurement points including the legend of the measurement points (right)

Additionally, the weather boundary conditions of the short wave solar irradiation, the downward long wave radiation, the ambient temperature and relative humidity as well as the wind speed and precipitation are measured in order to characterize the impact on the cooling capacity. As expenditure for the free cooling operations the electricity input to the pump is measured. For the operation of the system, continuous and cyclic operation can be run. During continuous operation, the absorber surface is continuously wetted by a water film running down on the absorber surface. In cyclic operation, the film is only continued for 10 seconds every 2 minutes, which saves pump electricity.

In the following figures, the cooling capacity for different weather boundary conditions is depicted. Fig. 7 left shows the temperatures linked to the nighttime absorber operation in cooling mode. The inlet and outlet temperature are decisive for the evaluation of the cooling capacity. The inlet temperature is kept constant at about 20 °C. By the high volume flow rate of 200 l/h, the temperature difference between inlet and outlet is limited to 2 K. With a lower mass flow rate, the temperature difference can be increased, but the capacity is reduced, since the average temperature difference to the ambient is decreased. Thus, as in space heating, a lower mass flow decreases the outlet temperature, but also the cooling capacity. The temperature of the tank characterizes the temperature of the water film on the absorber. In this case, a night with a moderate ambient temperature and a clear sky is depicted. This can be seen at the temperature difference to the (fictive) sky temperature that characterizes the long wave radiation exchange between the absorber and the sky.

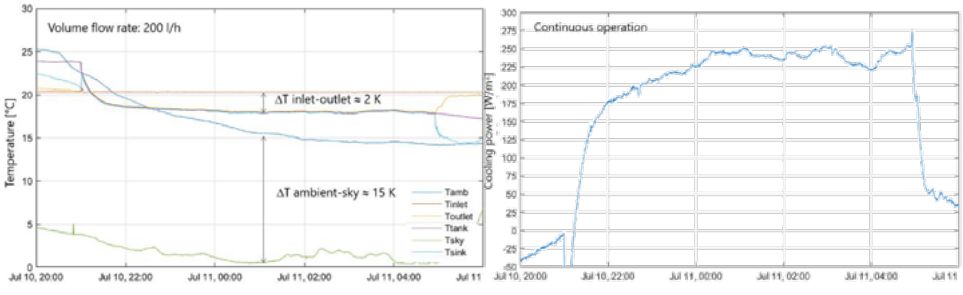


Fig. 7. Temperatures (left) and cooling capacity (right) of the unglazed solar collector on the test rig at favourable nighttime ambient conditions with clear sky and moderate ambient temperature

Since the water vapour in the atmosphere absorbs long wave radiation and reemits it as long wave downward radiation, a clear sky is a more favourable weather condition than a cloudy sky and the sky temperature reaches values up to 20 K lower than the ambient air temperature.

Fig. 7 right depicts the cooling capacity of the absorber. At favourable conditions a cooling capacity in the range of 250 W/m^2 is reached. Until about 10 p.m., the ambient temperature is still higher than the average absorber temperature, which limits the cooling capacity. Nevertheless, even at warmer ambient temperatures, a cooling capacity by radiation and evaporation surpasses the convective gains by the ambient temperature. During the night, the cooling capacity is increased with the decrease of the ambient temperature, which is in line with the decrease of temperatures from the building as well as the inlet temperature to the collector in real operation.

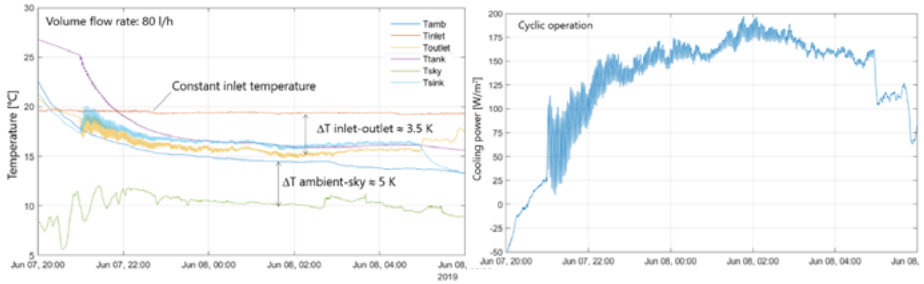


Fig. 8. Temperatures (left) and cooling capacity (right) of the unglazed solar collector on the test rig at moderate nighttime ambient conditions with cloudy sky and moderate ambient temperature

Fig. 8 depicts a cyclic operation with cloudy sky conditions and a lower mass flow rate of 80 l/h, which is the nominal mass flow of the collector at heating conditions. In this case, the temperature difference between the ambient and the sky temperature decreases to only 5 K, which is due to a higher long wave downward radiation from the sky. Despite the lower cooling capacity, which is depicted in Fig. 8 right, a temperature difference for 3.5 K over the absorber is reached due to the lower mass flow rate.

The cooling capacity is not constant due to the cyclic operation. The water on the collector surface is partly evaporating, which has also influence on the radiation properties, since the collector has a selective coating. If water is on the collector, the long-wave emissivity in the infrared spectrum ε_{IR} is defined by the water to values around ε_{IR}=0.95. However, if the water is evaporated, the emissivity changes to the one of the selective coating, which has an emissivity around ε_{IR}=0.15. Thus, the evaporative and radiative cooling capacity is reduce at dry parts of the collector surface, which leads to a decrease of the cooling capacity in cyclic operation. In the beginning of the night, the water for the wetting of the absorber is still warm, which leads to the higher swing in the temperatures. The swing is successively reduced down to differences of about 20 W/m^2. This effect of the selective coating is depicted in Fig. 9. In this case, the inlet temperature to the collector is adapted to the ambient temperature. Until about 1:30 am the collector is wetted. Then, the water film is stopped for two hours until 3:30 am, and the collector is drying completely. In the drying process cooling capacity successively decreases, and for the dry collector, the cooling capacity is strongly decreased from initially 125 W/m^2 before the drying process down to values around 10 W/m^2 after complete drying of the collector surface.

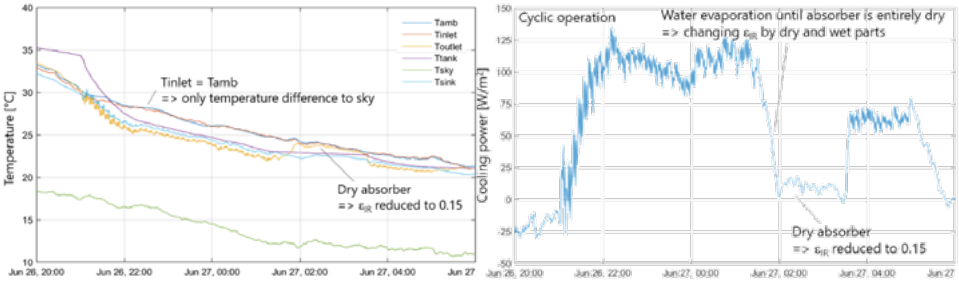


Fig. 9. Temperature difference for wet and dry absorber (left) and respective cooling capacity (right)

At the test rig, there is also the option to switch-on artificial wind in the range of wind speed of 1-3 m/s. The ventilator is located directly along the long side or the absorber and shown as a white box in Fig. 6. As the wind changes both the convective and evaporation heat transfer coefficients, a significant increase of the cooling capacity is measured with artificial wind. Fig. 10 left depicts the temperatures and Fig. 10 right the cooling capacity at clear sky conditions and artificial wind of 3 m/s. A cooling capacity up to 450 W/m^2 is measured at ambient temperature of 13 °C and a temperature difference to the sky of 15 K.

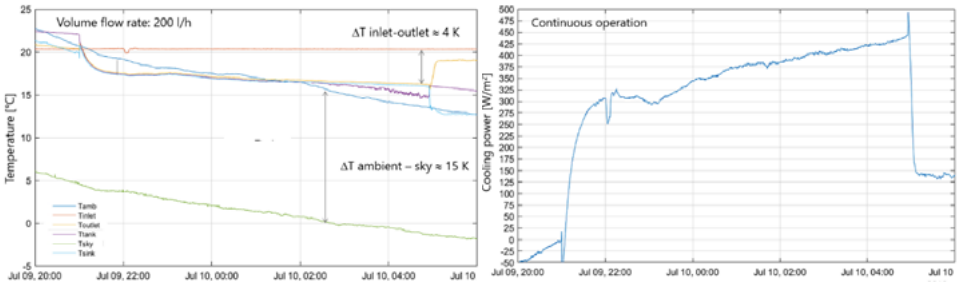


Fig. 10. Temperatures (left) and cooling capacity (right) with 3 m/s artificial wind on the absorber surface at clear sky conditions

5. Conclusion and Outlook

Result of a feasibility study for different building types and heat pump systems with solar heat source confirm a good performance of the heat pump in space heating and DHW operation with an overall SPF in the range of 3.5 – 3.8. By direct solar operation in DHW mode during the summer with higher solar irradiation values, the DHW performance can be increased above the pure heat pump operation to values above 4. Moreover, the unglazed solar collector can also be used for the integration of the free cooling operation during nighttime, where the collector rejects heat by convection, radiation and evaporation, if the collector surface is wetted. Besides the evaporative cooling effect by wetting the collector surface, also radiative properties can be changed in case of a selective coating of the collector. Thereby, a selective coating helps to reach higher temperature in the DHW operation during daytime due to a reduction of the radiative losses, while it enhances radiation losses due to the high emissivity of water up to 95% in nighttime of the free cooling operation. The overall performance including the free cooling operation can reach overall SPF values above 5 in low energy buildings depending on the space cooling and DHW loads.

For the feasibility study, however, only limited test data including the evaporative cooling were available. Therefore, test rig measurements have been carried out at the accredited test rig of the national Swiss solar test center for solar thermal systems at the HSR Rapperswil, which confirm good specific cooling capacities in the range of 100 – 300 W/m^2 depending on the ambient conditions, which are even higher than the values used in the feasibility study. Wind on the collector surface enhances the convective and evaporative heat transfer to the ambiance and values up to 450 W/m^2 have been measured at a wind speed of 3 m/s at the collector surface. However, in summer, low wind speeds at night are predominant, thus the potential for higher cooling capacities by wind is limited.

In the frame of the project, also the application of treated greywater as water source for the space cooling operation is investigated in collaboration with the Institute of Ecopreneurship of the University of Applied Sciences Northwestern Switzerland FHNW in the frame of the Swiss Competence Centre for Energy Research, Efficiency of Industrial Processes (SCCER-EIP). First results indicate that fouling and scaling on the collector surface can be effectively avoided by the water treatment in a decentral membrane bioreactor (MBR) water treatment process, and cooling capacities are not affected. Also, bacteria growth meets the requirements for evaporative cooling, so treated wastewater can be a sustainable water source for the evaporative free cooling. Experiments and respective simulation studies will be carried on in order to further characterize the process and free cooling potentials.

Acknowledgements

The research project is financially supported by the Swiss Innovation Agency Innosuisse and is part of the Swiss Competence Center for Energy Research SCCER EIP.

References

[1] Settembrini et al. 2017. ClimaBau – Planen angesichts des Klimawandels, Schlussbericht BFE Forschungsprogramm Gebäude und Städte, Hochschule Luzern Technik und Architektur, Horw
[2] SIA 2028. 2010. Klimadaten für Bauphysik, Energie- und Gebäudetechnik, Schweizerischer Ingenieur- und Architektenverband, Zürich
[3] SIA 2024. 2015. Raumnutzungsdaten für die Energie- und Gebäudetechnik, Schweizerischer Ingenieur- und Architektenverband, Zürich
[4] Verein MINERGIE. 2018. Produktreglement zur Nutzung der Marke MINERGIE, Bern
[5] MuKEn 2014. 2018. Musterverordnung der Kantone im Energiebereich, Version 2014, Konferenz der kantonalen Energiedirektoren EnDK, Bern
[6] SIA 180. 2014. Wärmeschutz, Feuchteschutz und Raumklima in Gebäuden, Schweizerischer Ingenieur- und Architektenverband, Zürich
[7] Wemhoener, C., Schwarz, R. Space cooling application with unglazed solar absorber, Proceedings Eurosun 2018, 13. – 16. Sept. 2018, Rapperswil

13th IEA Heat Pump Conference
April 26-29, 2021 Jeju, Korea

Medium capacity low charge ammonia chiller and heat pump.

Valentin Salgado Fuentes[a*], Wiebke Brix Markussen [a], Erasmus Damgaard Rothuizen[a], Jóhannes Kristófersson[b], Claus Madsen[b], Brian Elmegaard[a].

[a]Department of Mechanical Engineering, Technical University of Denmark, Nils Koppels Allé Building 403, Kgs. Lyngby, DK-2800, Denmark.
[b]Danish Technological Institute, Gregersensvej, DK-2630 Taastrup, Denmark.

Abstract

Large-scale ammonia refrigeration and heating systems have been widely used in industry due to their high efficiency, broad temperature ranges of operation and innocuous environmental effects. However, implementation of this technology in small to medium systems has not yet been very successful. Factors like the toxicity of the refrigerant and prices of ammonia equipment are some of the obstacles that this technology must overcome before being able to enter a market dominated by systems running on HFC refrigerants. This paper presents a concise review of the research and development of ammonia systems designed to supply small to medium capacity applications. Based on this review, a low charge ammonia chiller and heat pump unit intended to supply both needs providing 180 kW of cooling and 200 kW of heating was proposed. A market overview was performed to find the available equipment that can guarantee proper operation with the lowest possible refrigerant charge. Furthermore, a numerical study of three concepts for this system was performed to study the performance, as well as refrigerant charge estimation and distribution within the equipment. The analysis laid the foundation to propose a suitable configuration to embrace the intended market segment not only considering the high coefficient of performance but also specific refrigerant charge.

Keywords: Low charge, Ammonia, Chiller, Heat Pump;

1. Introduction

The latest regulations promoting the phase-out of HFC refrigerants e.g. The Kigali Amendment [1], are forcing the refrigeration and heating industry to develop new systems that make use of refrigerants with low or preferably zero GWP. Thus, systems with natural refrigerants like ammonia are a suitable option to keep supplying cooling and heating demands. Ammonia has proven to be an efficient and environmentally harmless refrigerant. That is why industrial-sized refrigeration systems have used ammonia since the beginning of the refrigeration industry. Besides, district energy applications have increased the use of ammonia systems in the last decades. Thus, in large-scale systems, shifting from HFC towards ammonia can prove to be a viable solution for manufacturers and industrial consumers. However, toxicity is an issue that has excluded this refrigerant from smaller scale refrigeration and heating applications for many years. Consequently, the re-introduction of small (≈10 kW) to medium-sized (≈200 kW) ammonia systems as a replacement for HFC systems, would require the development of new methods to prevent hazards from leakages. Hence, as presented by Ciconkov [2], researchers and companies have recognised that one main improvement to keep embracing the use of ammonia systems is the reduction of refrigerant charge.

Regardless of the system's application, most of the studies and developments to minimize charge or improve performance and security during operation are for large ammonia systems and, to a low extent, studies for small-scale ammonia systems. However, the optimization of medium capacity ammonia systems has not received much attention. Moreover, there are few reference cases about the construction or performance of this kind of equipment on the market. The present paper will present a concise review of the current research to minimize charge in ammonia systems. This acquired knowledge allows the introduction of a medium-capacity chiller-heat pump unit concept. A numerical model of the system will show not only the performance but also the specific charge of the system when using the equipment available in the market.

1.1. Review of Ammonia Chiller and Heat Pump Research

The application of ammonia cooling and heat pump systems has been a topic of interest in the last decades. Stoecker [3] introduced expanded applications for ammonia within the refrigeration industry. The author presented water chiller and ice thermal storage applications that, at the time, were considered as prototypes of what is now recognised as conventional systems. Furthermore, the effects of ammonia leakages from the systems was also a topic of concern in the study. Thus, the author presented methods and numerical models to analyse the consequences of releasing ammonia into the atmosphere. Similarly, Korfitsen [4] showed the suitability of applying ammonia heat pumps in several food refrigeration applications. Not only they presented case studies to assess the advantages of ammonia over other refrigerant systems but also, they are the ones who introduced the high-pressure/temperature (40 bar) ammonia heat pump concept, which nowadays is a standard operation mode in high-temperature heat pump applications. The market and technology development have increased the acceptance of large scale ammonia systems in the last decades, as a matter of fact, Skačanová et al. [5] showed that by 2017, more than 90% of the large refrigeration installations in Europe use ammonia as working fluid. Besides, Skačanová et al. discussed the substantial increment of low charge ammonia systems in industrial applications and regions. Low charge systems have also received attention from researchers mainly related to industrial applications. Chapp [6] and Poggi [7] describe the possibilities of charge reduction with emphasis on industrial refrigeration systems and the effect of charge minimization in each component. Likewise, Pearson [8] explained the advantages and disadvantages of charge reduction in industrial ammonia systems. These three studies [6]–[8] concluded that industrial systems tend to accumulate substantial amounts of refrigerant within the liquid lines. Furthermore, inappropriate charge reduction could have a counterproductive effect on the operation and performance of the system. From a component-oriented perspective, Hrnjak [9] demonstrated that ammonia has the best potential for being used in low charge systems if a rational approach to minimize charge within the components is applied. Similarly, Ayub [10] showed the reduction of charge and price of an industrial heat pump through optimizing the selection of the evaporator.

On the other hand, low charge small ammonia systems have also received attention from researchers. Palm [11] proposed a 9 kW ammonia heat pump with a specific charge of 11 g/kW. The author also performed a market analysis to spot different components that can be embedded in this kind of systems concluding that there is a lack of proper components for small ammonia systems. Similarly, Hrnjak [12] proposed an air to water ammonia chiller concept with a 13 kW capacity and specific charge of 18 g/kW. Hrnjak also compared the specific refrigerant charge of the prototype with different chillers available in the market to show how commercial systems are still not optimized in terms of refrigerant charge. These works have proven that there is plenty of opportunities to reduce refrigerant charge in ammonia systems, thus improving the competitiveness of this refrigerant in the market. Nevertheless, approximately a decade has passed since these last two studies were published and it is still not possible to embrace small ammonia systems and their entrance in the market. For instance, Zajacs [13] introduced a small-scale ammonia heat pump concept for space and water heating. They also recognized that the lack of components for small-scale ammonia systems still is a drawback on introducing them to the market. In the same way, Wu [14] presented a study of the progress in the development of ground source heat pumps with natural refrigerants. In this comprehensive survey, Wu showed that large-scale systems are still embracing the market. However, they were not able to recognise further improvements in small ammonia systems. Among the literature related to medium capacity ammonia chillers or heat pumps, Nielsen [15] modelled the performance of a 150 kW heat pump with different refrigerants. Aside from proving that the heat pump performance is higher when using ammonia as a refrigerant, the author also performed a charge estimation concluding that the ammonia system with a specific charge of 23 g/kW was the one with the lowest refrigerant charge needed to operate. Furthermore, Nelson [16] examined the long-term suitability of medium-sized ammonia chillers. Using a 280 kW unit as a case study, Nelson showed the economic benefits of replacing HFC units with ammonia ones. The two afore-mentioned papers are recent and do not refer to prior studies of suitability or optimization of systems working with these capacities.

Few companies produce medium-capacity ammonia systems. Most of these companies do not have a complete description of the operating conditions or sizes. On top of that, few companies can provide systems with the so-called "very low" refrigerant charge, ranging 100 g/kW to 200 g/kW. However, the approach used to assure low charge seems to be the same, a compact designed system with plate heat exchangers as evaporator and condenser. Moreover, manufacturers agree that the proper implementation of the receiver helps to minimize the amount of ammonia within the system. Based on the performed review related to ammonia chiller and heat pumps, the current work presents a concept that could be a suitable option to supply medium-capacity cooling and heating applications. The inspiration for the current concept comes from a real case study in which there is a need to provide cooling for different industrial processes of a mineral wool manufacturer plant. On

the other hand, the heat pump mode will serve a district heating network of a municipality located in the vicinities of the plant. The concept proposes a combined ammonia chiller and heat pump with a nominal cooling capacity of 180 kW and a heating capacity of 200 kW.

2. Methods

2.1. Medium Capacity chiller-heat pump concept

The rating test conditions for process chillers of the European standard EN 14511:2018 [17] was used as an inspiration to define the operating conditions of the evaporator and condenser when the system is working in chiller mode. However, the current standards developed for heat pumps are focused on space heating applications, which are not the same as district heating applications. Thus, the specifications of heat pumps available in the market that have been used in district heating applications were used as an inspiration to define the operating conditions of the condenser when the system is working in heat pump mode. Moreover, in the design of the evaporator, the temperature difference is maintained in both chiller and heat pump modes. Thus, when the system is working in heat pump mode, the temperature difference in the evaporator is maintained as the one from the chiller mode operation. Finally, the chosen evaporator and condensation temperatures entail the same design pressure ratio in both chiller and heat pump mode. Table 1 compiles the design operating conditions of the proposed concept.

Table 1. Operating conditions of the Chiller-heat pump concept

	Chiller		Heat Pump	
Data	Value	Units	Value	Units
Capacity	180	kW	200	kW
Evaporation Temperature	0	°C	30	°C
Temperature of inlet/outlet water in evaporator	12/7	°C	42/37	°C
Condensing Temperature	40	°C	80	°C
Temperature of inlet/outlet water in condenser	30/35	°C	65/75	°C

With the operating conditions defined, the three configurations presented in figure 1 were analysed to quantify the difference in performance and refrigerant charge. First, a direct expansion (DX) configuration (figure 1a) was studied to define the minimum charge needed by the system to operate. However, there will be a difference in the amount of refrigerant needed by the cooling and heating modes. Consequently, a receiver is required to store the excess refrigerant [18]. That is why the second configuration analysed was the DX system with the addition of a high-pressure receiver (figure 1b). Finally, Pearson [8] proposed a suitable configuration to minimize refrigerant charge in industrial ammonia systems. Thus, using this concept as inspiration, a flooded evaporation system with a low-pressure receiver was analysed (figure 1c). The analysis of these three systems required additional operating conditions to be defined. For the DX systems, superheating of 10K at the outlet of the evaporator was assumed to guarantee stable operation whereas, subcooling is not considered.

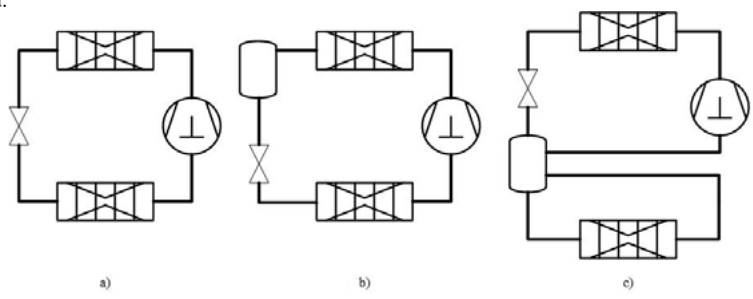


Fig. 1. Proposed configurations to study charge distribution. a) Direct Expansion, b) Direct expansion with high-pressure receiver, c) Flooded evaporator with low-pressure receiver.

The main components in the system were selected based on the market availability of equipment for ammonia systems. In the case of the compressor, it is necessary to find a compressor that fulfils the operating conditions of both chiller and heat pump modes. The considered reciprocating compressors available in the market and developed for ammonia chiller applications were not able to operate with the current cooling capacity proposed for the system. Thus, an open screw compressor seemed to be the only option for the current application. However, according to the manufacturers, these compressors can only operate under the chiller operating conditions, not the heat pump conditions.

On the other hand, suppliers of ammonia heat pump compressors also offer open screw compressors that can be used in the current heat pump application. Nevertheless, they do not assure that the compressors could operate within the chiller mode operating conditions. In the current concept, the pressure ratio of both chiller and heat pump operation modes are similar. Thus, it is assumed that if a screw compressor can operate in chiller mode, it would also be possible for it to operate in heat pump mode. Finally, at the current condensation temperatures, the discharge temperature is high. Consequently, manufacturers restrict the discharge temperatures to a lower value with the addition of oil cooling systems to the compressor. In this case, the suggested temperatures by the manufacturers of the compressors were used as a reference. The important dimensioning specifications of the compressor are summarized in Table 3.

Table 2. Compressor specifications

Type	Displacement [m^3/h]	RPM	Isentropic Efficiency	Discharge Temperature Chiller mode [°C]	Discharge Temperature Heat pump mode [°C]
Screw Compressor	250	2900 (50Hz)	0.6	80	110

Regarding the evaporator and condenser, plate heat exchangers were analysed. The supplier used as a reference for the plate heat exchangers was SWEP, which recommends the use of stainless steel plate heat exchanger for the proposed application. The specifications of the chosen heat exchangers are summarized in Table 2. In the case of the evaporator, the same heat exchanger was used in all the configurations, with the difference that the pressure drop will be lower for the flooded evaporator with low-pressure receiver configuration. Moreover, for the flooded evaporator, SWEP also stated that the circulation number for the brazed plate heat exchanger should be around 1.1 (outlet quality of 0.9) which is the value used for the current concept. The condenser is smaller in dimensions when compared with the evaporator. Since ammonia has a high heat transfer coefficient during condensation, the condenser needs smaller heat transfer areas than the evaporator.

Table 3. Plate heat exchangers specifications

Heat Exchanger	Heat Load [kW]	Heat Transfer Area [m^2]	# Plates	# Channels	Volume [dm^3]
Evaporator	180	11.9	94	93	7.9
Condenser	200	3.9	100	99	4

2.2. Numerical Model

The analysis was based on a numerical model of the chiller-heat pump unit to study the thermodynamic cycle for the operating conditions presented in Table 1. This calculation yielded an estimation of the expected coefficient of performance for both chiller and heat pump modes. The model was implemented in Matlab R2018b making use of ammonia properties from REFPROP 10. The compressor used in this concept is a generic proposal based on different specifications from manufacturers. That is why it was not possible to obtain performance curves given as polynomials. A simple model was used for the compressor in which the assumed isentropic efficiency is used to estimate the difference between an ideal compression and a real compression process. Moreover, the heat loss from the compressor was also calculated based on the assumed discharge temperatures and the theoretical discharge temperature. Finally, the amount of refrigerant in the compressor was calculated based on the method proposed by Poggi [7] making use of the volumetric displacement.

For the evaporator and condenser, detailed models were implemented for analysing component performance and refrigerant inventory. The detailed models accounted for the specifications provided by the manufacturers of each component. The models utilized a 1D-discretization approach with a Newton-Raphson solver in which the heat exchanger was divided into 100 control volumes of equidistant enthalpy steps during the phase change of ammonia through the plate heat exchangers. Mass and energy balances as well as heat transfer equations were formulated for each control volume. Calculation of the heat transfer coefficient for two-phase flow was based on the correlations from Amalfi [19] for the evaporator and Yan [20] for the condenser. In case of single phase heat transfer coefficient, the correlation of Longo [21] was used for ammonia and Kim [22] for water. The models also computed the pressure drop along the plates based on the correlations for the fanning friction factor of Amalfi [19] in case of the evaporator and Arman [23] for the condenser. For the single phase friction factor, Martin [24] was used for ammonia and Kim [22] for the water. The calculation of refrigerant mass inside the evaporator and condenser needs the implementation of a void fraction model. However, there is no model developed for ammonia within plate heat exchangers. In this case, aside from the homogeneous model, the void fraction models of Zivi, Smith, Rouhani-Axelsson, Premoli, Hughmark, Yashar and Boher, presented by Godbole [25] and Poggi [7], were selected as suitable models for the current application. The component models for compressor, condenser and evaporator were coupled to simulate the operating conditions of the units when working in the chiller and heat pump mode as well as to simulate the dependency of the refrigerant charge between these components.

The dimensioning of the receiver is based on its capacity to store the excess of refrigerant during a change of operation mode. However, in the current study, we were mainly interested in the amount of refrigerant needed to act as a seal between the incoming and outgoing refrigerant streams at design conditions. Following a conservative approach, Rajapaksha [18] recommends that the amount of refrigerant in the receiver has to be one-sixth of the charge needed by the system in design conditions. Finally, the piping between the different components was also considered as part of the charge estimation. In this case, a fixed pipe length of 1 m was assumed for suction and discharge pipes of the compressor and 0.5 m for the liquid lines. However, the pipes that connect the low-pressure receiver with the flooded evaporator were dimensioned to have a suitable driving force to run the evaporator with thermosiphon effect. Moreover, standard pipe diameters for ammonia systems were used considering that the flow velocities of the refrigerant would not exceed the values recommended for ammonia systems by Granryd [26].

3. Results

The coefficient of performance (COP) of the vapour compression cycle with ideal compression for chiller mode using the temperatures specified in table 1 is 5.6 and likewise 5.6 for the heat pump mode using the temperatures specified for the heat pump mode. However, the use of real components specifications and the different configurations will affect this ideal COP. For instance, as can be seen in figure 2, the operating cycle for the DX systems (dashed red line) for both chiller and heat pump, varies considerably from the ideal compression cycle (blue line).

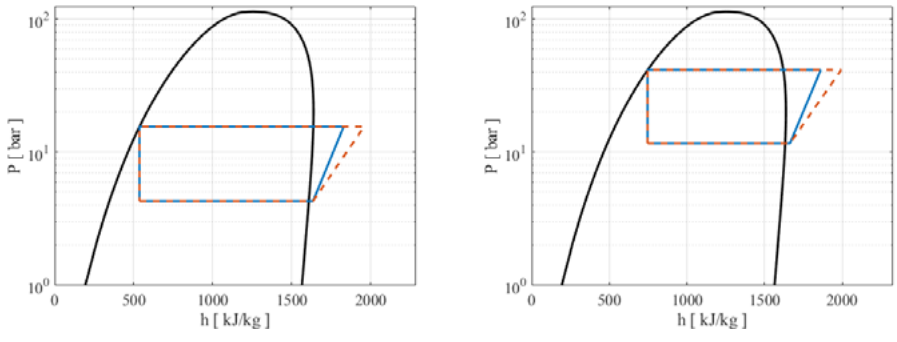


Fig. 2. Log-ph diagram of the Ideal compression cycle and the DX cycle configuration for: a) Chiller operating mode, b) Heat pump operating mode.

For each system configuration presented in figure 1, the mass calculation with the eight void fraction models was applied. Table 4 shows the COP and the average total charge for chiller and heat pump modes and, for the different configurations.

Table 4: COP and refrigerant charge of the systems

	Chiller			Heat Pump		
	DX	DX-HPR	Flooded-LPR	DX	DX-HPR	Flooded-LPR
COP	3.4	3.4	3.5	3.0	3.0	3.2
Average Total Charge [kg]	1.0	1.2	2.2	1.2	1.5	2.7

A quantitative comparison of refrigerant charge presented in Figure 3 for the chiller and Figure 4 for the heat pump, shows the estimation in each component as well as the total refrigerant charge for the three proposed configurations. As can be seen, the refrigerant charge in the compressor is negligible when compared to the total charge of the systems. On the other hand, there is a significant amount of refrigerant that the system accumulates inside the pipes that connect the condenser, expansion valve and evaporator, where the refrigerant is mainly in the liquid phase. Thus, the distance, as well as diameters of these pipes, should be optimized to accumulate the least possible amount of liquid. In the case of evaporator and condenser, the mass distribution shows that most of the refrigerant charge is located inside the evaporator. On the contrary, the charge inside the condenser remains steady despite the type of system. The results for the DX system with high-pressure receiver showed that the addition of the receiver imposes and increment of refrigerant charge due to the liquid level needed at the bottom of it. Besides, more pipe is needed to connect the receiver with the condenser and evaporator. Hence, the share of liquid refrigerant accumulated inside the pipes increases. The flooded configuration presents a different tendency in the charge distribution compared with the previous configurations. In this case, the largest share of refrigerant is still inside the evaporator. However, the share of the pipes slightly increased mainly due to the addition of more pipe circuits to connect the low-pressure receiver.

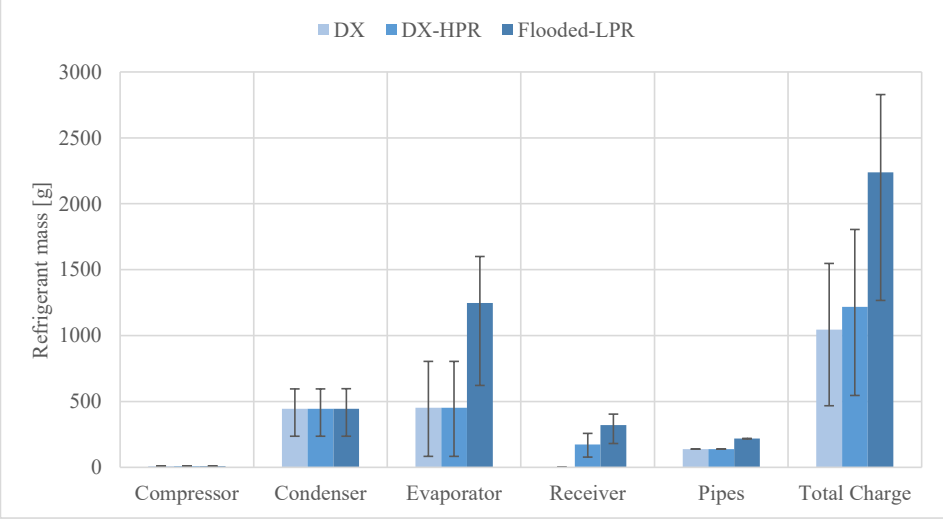


Fig. 3. Refrigerant inventory of the proposed configurations working as a Chiller

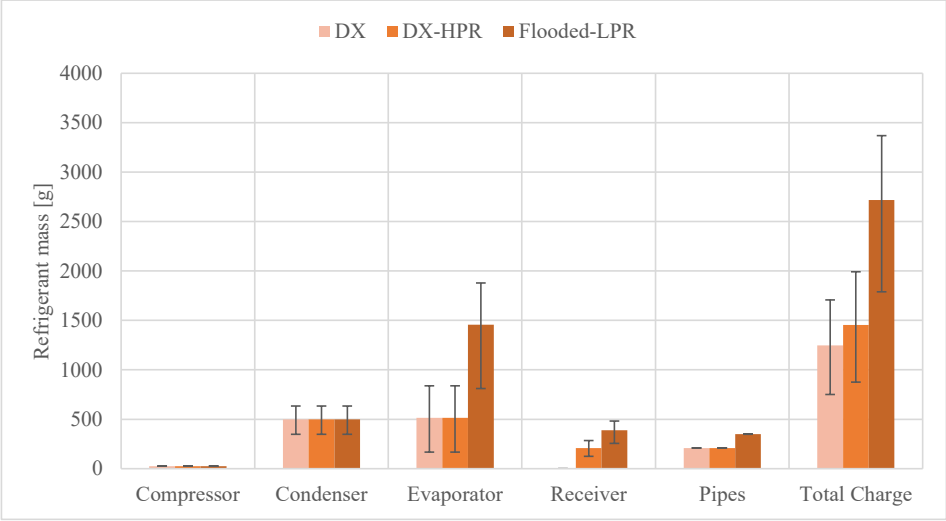


Fig. 4. Refrigerant inventory of the proposed configurations working as a Heat Pump

The error bars shown in Figure 3 and Figure 4, represent the variation that can be expected in the refrigerant charge estimation based on the different void fraction models. To properly depict this dependency on the calculations, Figure 5 shows the eight void fraction models used for a saturation temperature of 0 °C and a saturation temperature of 80 °C. When increasing operating saturation temperature of ammonia, the void fraction models tend to estimate a lower fraction of the heat exchanger being occupied by the vapour phase. Thus, a higher share of the liquid phase is present inside the heat exchangers. Even though between the saturation temperature of 0 °C and saturation temperature of 80 °C, there is a reduction of 20% in liquid density, there is more than 800% increment in vapour density. Therefore, a larger refrigerant charge estimation would be obtained when the concept is operating as a heat pump.

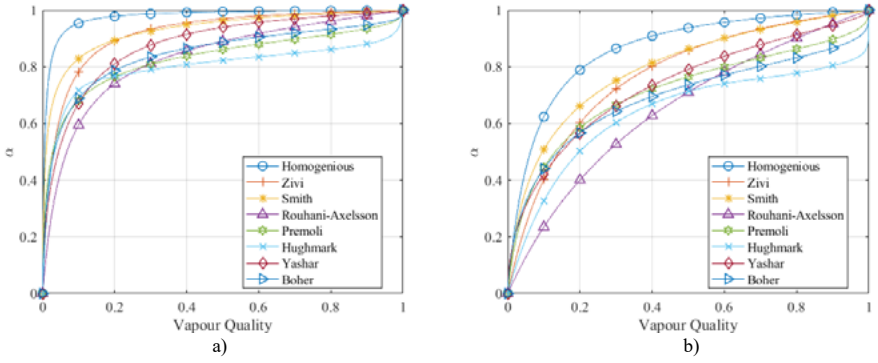


Fig. 5. Void fraction models for Ammonia at: a) Evaporation temperature of 0 °C, b) Condensation temperature of 80 °C.

For each system configuration presented in figure 1, the minimum, average and maximum specific refrigerant charge is presented in table 5. Moreover, the table shows the values of specific charge presented in the introduction to verify the current results.

Table 5: Specific refrigerant charge comparison

	Chiller			Heat Pump			Literature			
	DX	DX-HPR	Flooded-LPR	DX	DX-HPR	Flooded-LPR	Palm [11]	Hrnjak [12]	Nielsen [15]	Industry
Minimum Specific Charge [g/kW]	2.6	3.0	7.0	4.2	5.0	10.0				
Average Specific Charge [g/kW]	5.8	6.8	12.4	7.0	8.0	15.0	11.0	18.0	23.0	100-200
Maximum Specific Charge [g/kW]	8.6	10.0	15.7	9.5	11.0	19.0				

4. Discussion

The COP of the three systems is considerably lower when compared with the Carnot COP. The explanation for this is because of the current selection of equipment for the three configurations. The isentropic efficiency of the compressor plays an important role for the performance of the system. Regarding the calculated refrigerant charge of the three configurations, the average values of specific charge presented in Table 5 are remarkably low when compared with the refrigerant charge of the systems designed by Palm [11], Hrnjak [12], Nielsen [15] or the available systems in the market. The amount of refrigerant charge calculated in this study has a direct dependency on the void fraction model used to estimate the refrigerant charge inside the plate heat exchangers. The results of the simulations showed that the homogeneous model yields the lower estimation for both evaporator and condenser in either chiller or heat pump mode. The higher estimation for evaporator and condenser of the DX systems, in either chiller or heat pump mode, was obtained with the Hughmark model. However, for the flooded evaporator, the highest charge estimation was obtained with Rouhani-Axelsson. Moreover, among the three proposed configurations, the major variation in the refrigerant charge estimation is on the evaporator. Nonetheless, if the values of maximum specific charge are considered as valid, the specific charge will be within the same range as the results presented by Palm [11] or Hrnjak [12].

The selection of larger evaporator and condensers will substantially increase the charge accumulated inside of them. Besides, the pressure drop through these components will decrease and the COP of the system will increase. Hence, a further study to analyse the trade off between the increment in COP and the increment in refrigerant mass will define the optimum size of the system. The amount of refrigerant accumulated in the receiver is also an assumption that affects the charge estimation of the proposed systems. If a higher value for the excess refrigerant in the receiver was assumed, a higher refrigerant inventory would have been estimated. However, the receiver needs further analysis to account for its influence on the performance of the system. In a more detailed study, simulations of the system at different operating conditions are essential to estimate the difference in refrigerant mass needed for the components. Thus, a more accurate value of refrigerant mass within the receiver can be determined. Finally, the consideration of more components that are normally part of these type of systems like liquid or oil separators will improve the estimation of the refrigerant charge. Furthermore, the analysis of more configurations would help to improve the knowledge of the charge distribution of medium capacity ammonia chiller and heat pumps.

5. Conclusion

Medium capacity ammonia systems still need to be developed and optimized to keep improving components as well as the portfolio of ammonia systems within the market. Furthermore, it will facilitate the inclusion and development of small ammonia systems. Three concepts of a medium-capacity low charge ammonia chiller and heat pump able to provide 180 kW of cooling capacity and 200 kW of heating capacity were analysed. The calculation showed that the average amount of refrigerant needed for the system to operate either in cooling or heating mode is 1.2 kg for a DX system, 1.5 kg for a DX with a high-pressure receiver and 2.7 kg for a flooded system with a low-pressure receiver. Even though the flooded system will tend to accumulate a higher amount of liquid refrigerant than the DX system, it is still possible to conceive a flooded system with a low refrigerant charge. The main conclusion from the refrigerant inventory calculation is that industrial or commercial ammonia systems can still be optimized to reduce the amount of refrigerant. Nonetheless, the study of more complex configurations will extend the knowledge and development of low charge ammonia systems.

Acknowledgements

This paper presents part of the work developed for the CLAUS project (64018-0100) partially funded by the EUDP Energy development and demonstration program of the Danish Energy Agency.

References

[1] Nations Industrial Development Organization, "Kigali Amendement," Vienna, 2017.
[2] R. Ciconkov and Z. H. Ayub, "New technologies in ammonia refrigerating and air-conditioning systems," Heat Transf. Eng., vol. 30, no. 4, pp. 324–329, 2009.
[3] W. F. Stoecker, "Expanded applications for ammonia - coping with releases to atmosphere," Int. J. Refrig., vol. 13, no. 2, pp. 86–94, 1990.
[4] E. Korfitsen and A. P. R. Kristensen, "Ammonia high pressure heat pumps in food refrigeration applications," Int. J. Refrig., vol. 21, no. 3, pp. 212–218, 1998.
[5] A. G. Klára Skačanová, Alvaro de Oña, "Global market and policy trends for CO2 and ammonia in refrigeration.," in 13th IIR Gustav Lorentzen Conference on Natural Refrigerants, 2018.
[6] T. L. Chapp, Low Ammonia Charge Refrigeration Systems for Cold Storage. 2014.
[7] F. Poggi, H. Macchi-Tejeda, D. Leducq, and A. Bontemps, "Refrigerant charge in refrigerating systems and strategies of charge reduction," Int. J. Refrig., vol. 31, no. 3, pp. 353–370, 2008.
[8] A. Pearson, "The Advantages and Disadvantages of Charge Reduction in Industrial Systems," in 11th IIR Gustav Lorentzen Conference on Natural Refrigerants, GL 2014, 2014.
[9] P. Hrnjak, "Rational approach to refrigerant charge reduction," in 25th International Congress of Refrigeration, 2019.
[10] Z. Ayub and A. Ayub, "Low Charge Evaporators for Industrial Heat Pumps," Heat Pump Technologies Magazine, vol. 37, no. 1, pp. 27–30, 2019.
[11] B. Palm, "Ammonia in low capacity refrigeration and heat pump systems," Int. J. Refrig., vol. 31, no. 4, pp. 709–715, 2008.
[12] P. Hrnjak and A. D. Litch, "Microchannel heat exchangers for charge minimization in air-cooled ammonia condensers and chillers," Int. J. Refrig., vol. 31, no. 4, pp. 658–668, Jun. 2008.
[13] A. Zajacs, A. Lalovs, A. Borodinecs, and R. Bogdanovics, "Small ammonia heat pumps for space and hot tap water heating," Energy Procedia, vol. 122, pp. 74–79, 2017.
[14] W. Wu and H. M. Skye, "Progress in ground-source heat pumps using natural refrigerants," Int. J. Refrig., vol. 92, pp. 70–85, 2018.
[15] S. Nielsen, S. W. Christensen, R. S. Thorsen, and B. Elmegaard, "Comparison of Heat Pump Design and Performance for Modern Refrigerants," in Proceedings of 13th IIR Gustav Lorentzen Conference on Natural Refrigerants, 2018.
[16] C. Nelson, S. W. Higgins, and A. Ste, "Analysis of the Long-Term Suitability of Ammonia Chillers," in Proceedings of 13th IIR Gustav Lorentzen Conference on Natural Refrigerants, 2018.
[17] European Committee for Standardization, "EN 14511 - Air conditioners , liquid chilling packages and heat pumps for space heating and cooling and process chillers, with electrically driven compressors," 2018.
[18] L. Rajapaksha and K. O. Suen, "Influence of liquid receiver on the performance of reversible heat pumps using refrigerant mixtures," Int. J. Refrig., vol. 27, pp. 53–62, 2004.
[19] R. L. Amalfi, F. Vakili-Farahani, and J. R. Thome, "Flow boiling and frictional pressure gradients in plate heat exchangers. Part 2: Comparison of literature methods to database and new prediction methods," Int. J. Refrig., vol. 61, pp. 185–203, 2016.
[20] Y. Y. Yan, H. C. Lio, and T. F. Lin, "Condensation heat transfer and pressure drop of refrigerant R-134a in a plate heat exchanger," Int. J. Heat Mass Transf., vol. 42, no. 6, pp. 993–1006, 1999.
[21] G. A. Longo, "Refrigerant R134a condensation heat transfer and pressure drop inside a small brazed plate heat exchanger," Int. J. Refrig., vol. 31, no. 5, pp. 780–789, 2008.
[22] M. B. Kim and C. Y. Park, "An experimental study on single phase convection heat transfer and pressure drop in two brazed plate heat exchangers with different chevron shapes and hydraulic diameters," J. Mech. Sci. Technol., vol. 31, no. 5, pp. 2559–2571, 2017.
[23] B. Arman and T. Rabas, "Condensation Analysis for Plate-Frame Heat Exchangers," Argonne, 1995.
[24] H. Martin, "A theoretical approach to predict the performance of chevron-type plate heat exchangers," Chem. Eng. Process. Process Intensif., vol. 35, no. 4, pp. 301–310, 1996.
[25] P. V Godbole, C. C. Tang, A. J. Ghajar, P. V Godbole, C. C. Tang, and A. J. Ghajar, "Comparison of Void Fraction Correlations for Different Flow Patterns in Upward Vertical Two- Phase Flow," Heat Transf. Eng., vol. 7632, no. May, pp. 843–860, 2011.

[26] E. Granryd, Refrigerating Engineering. Stockholm: Royal Institute of Technology, KTH, Department of Energy Technology, Division of Applied Thermodynamics and Refrigeration, 2005.

13th IEA Heat Pump Conference
April 26-29, 2021 Jeju, Korea

High-temperature vapor compression heat pump using butane (R600) – development of a prototype and first measurements

Manuel Verdnik[a,*], René Rieberer[a]

[a]Graz University of Technology, Institute of Thermal Engineering, Inffeldgasse 25B, 8010 Graz, Austria

Abstract

The application of industrial heat pumps for waste heat recovery can reduce the usage of fossil fuels and increase the energy efficiency of industrial processes. Utilizing a trans-critical vapor compression cycle extends the operating range of refrigerants beyond their critical temperature, enabling high heat sink temperatures with natural refrigerants, which are characterized by zero ozone depletion potential and a negligible global warming potential.
To prove the concept of a trans-critical vapor compression cycle using butane as refrigerant, a prototype to achieve a nominal heating capacity of 30 kW at heat sink outlet temperatures of up to 160 °C for utilizing waste heat (at 60 °C) was developed. The one-stage cycle with a suction gas cooled reciprocating compressor is equipped with a low-pressure accumulator and an internal heat exchanger (IHX) for suction gas superheating. First measurements of sub-critical and trans-critical operation show remarkable coefficients of performance (COPs) and confirm that optimum high-side pressures yielding the maximum COP exist. In trans-critical operation the optimum pressure can be shifted towards lower pressures by increasing the suction gas superheat in the IHX.

Keywords: industrial heat pump; high-temperature application; hydrocarbons; optimum high-side pressure; trans-critical cycle;

Nomenclature

1…9	state point	p_{hp}	high-side pressure (bar)
accu	low-pressure accumulator	$\pi = p_{ref,1}/p_{ref,2}$	pressure ratio of the compressor (-)
COP	Coefficient of Performance	$\dot{Q}_{SI}$	heating capacity on water side (kW)
$\eta_{is,ov}$	overall isentropic efficiency (-)	ref	refrigerant
$\eta_{is,i}$	internal isentropic efficiency (-)	ρ	density (kg·m³)
η_{FI}	frequency inverter efficiency (-)	s	isentropic change of state
EXV	electric expansion valve	sat	saturated state
h	specific enthalpy (kJ/kg)	SI	heat sink
IHX	internal heat exchanger	sim	simulated
in	inlet	SO	heat source
λ_{vol}	volumetric efficiency	ΔT_{sup}	suction gas superheat (K)
meas	measured	t	temperature (°C)
$\dot{m}_{ref}$	refrigerant mass flow (kg/h)	t_{cond}	condensation temperature (°C)
out	outlet	$\dot{V}$	volume flow
p	absolute pressure (bar)	VIHX	3-way-valve internal heat exchanger
P_{el}	electric power of compressor and inverter (kW)	$\dot{V}_{swept}$	compressor swept volume flow (m³/h)

* Corresponding author. Tel.:+43 316 873-7304; fax: +43 316 873-7305.
E-mail address: manuel.verdnik@tugraz.at.

1. Introduction

Improving the efficiency of energy systems is a key to decrease energy consumption. Implementing all available energy efficiency measures between now and 2040 would allow to double the global gross domestic product by 2040 while limiting the increase in primary energy demand to levels only slightly higher than those today [1]. Through the application of high-temperature heat pumps, the utilization of waste heat to cover industrial process heat demands can be accomplished. A trans-critical vapor compression cycle as proposed by Lorentzen [2] offers the possibility to extend the operating range of refrigerants beyond their critical temperature. While this process is state-of-the art for CO_2, the application of other refrigerants is very limited. Besbes et al. [3] developed a high temperature trans-critical heat pump utilizing R32, capable of producing hot air at 120 °C. Abi Chahla et al. [4] extended the supply temperature to 150 °C by using the HFO 1234ze(E). Regarding natural refrigerants Kimura et al. [5] developed a test apparatus of a trans-critical cycle for R600 using oil-free turbocompressors enabling heat supply temperatures of 180 °C according to simulations.

This work is based on the development of a prototype of a vapor compression heat pump utilizing a natural refrigerant in a trans-critical cycle enabling heat supply temperatures higher than 150 °C. In a trans-critical cycle, the refrigerant is compressed to a supercritical state and the heat rejection occurs at high-side pressure levels exceeding the critical pressure of the refrigerant at gliding temperature. Considering the available components with respect to the necessary pressure, R600 was chosen as refrigerant. The influence of the operating parameters on the efficiency of the prototype were investigated by means of simulation. Measurement data of the prototype is compared to results from the simulation model. The prototype, simulation model and results from experiment and simulation as presented by Verdnik et al. [6] are analyzed in more detail and used to derive an improved simulation model.

2. Prototype of the trans-critical vapor compression heat pump

The development of the prototype was based on a study by Verdnik et al. [7] on the application of R600 in a trans-critical vapor compression cycle. The application specific challenges such as the required suction gas superheat due to the overhanging two phase region of the refrigerant and safety measures due to the flammability of the refrigerant were addressed during the design of the prototype.

2.1. Hydraulic layout

Fig. 1. shows the realized hydraulic layout and a picture of the prototype.

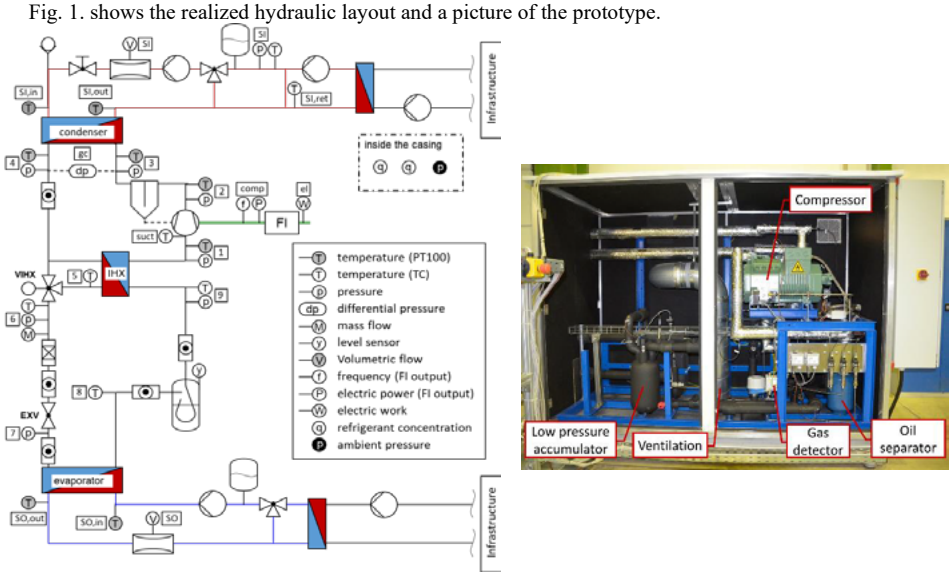


Fig. 1. Hydraulic layout including sensor positions of the high-temperature heat pump (left) and the prototype with opened casing (right)

The single stage cycle utilizes an inverter driven suction gas cooled reciprocating compressor. In order to maximize the evaporation temperature and to accomplish the necessary suction gas superheating in the internal heat exchanger (IHX) saturated refrigerant at the evaporator outlet is targeted. This is accomplished by using a low-pressure accumulator (accu) and the corresponding refrigerant charge to allow for a liquid level in the accumulator.

Experimental data from the prototype is shown in t/h-diagrams with operating points in sub-critical (Fig. 2 left) and trans-critical operation Fig. 2 (right). The state points are corresponding to Fig. 1.

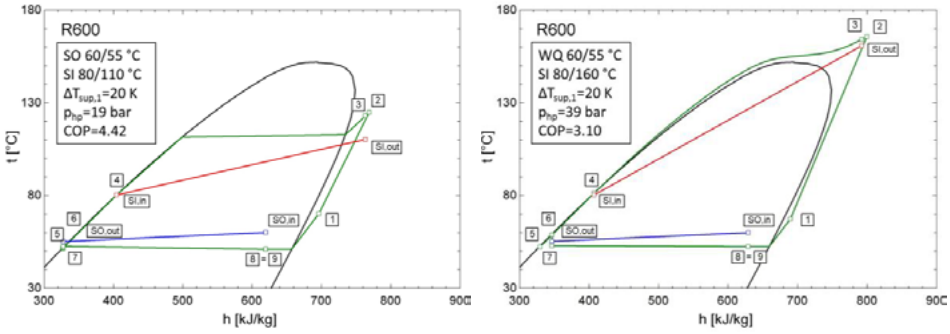


Fig. 2. t/h-diagrams of a measured sub-critical operating point (left) and trans-critical cycle operating point (right)

Refrigerants with an “overhanging” two phase region require a certain degree of suction gas superheat in order to avoid a compression into the two-phase region. According to Moisi and Rieberer [8], the required suction gas superheat for R600 is 18 K assuming a positive evaporation temperature and isentropic compression. At the prototype, the suction gas superheat is evaluated at the compressor suction port as well as before the refrigerant flows into the cylinder after cooling the electric motor according to equation (1) and (2), respectively. While the superheat before the cylinder acts as a threshold for the minimum superheat, the value at the control inlet is used as the control variable for the VIHX.

$$\Delta T_{sup,1} = t_{ref,1} - t_{sat}(p_{ref,1}) \tag{1}$$

$$\Delta T_{sup,suct} = t_{ref,suct} - t_{sat}(p_{ref,1}) \tag{2}$$

The three-way-valve (VIHX) controls the degree of suction gas superheat at state point 1. The electronic expansion valve (EXV) is used to control the high-side pressure. Assuring saturated vapor at the outlet of the evaporator and inlet of the IHX by using an accumulator also decouples the control loops for high-side pressure and suction gas superheat. In order to keep the pressure throughout the condenser above the set pressure and to dampen pressure oscillations from the compressor the condenser outlet pressure is used as the control variable for the high-side pressure control loop.

The auxiliary hydraulic cycles representing the heat source and heat sink use pressurized water at 10 bars which is corresponding to a boiling point of 180 °C. A hydraulic separator with a bypass pump is used in the sink cycle to avoid high return temperatures ($t_{SI,ret}$) at the heat exchanger connecting the test rig with the infrastructure.

Due to the flammability of the refrigerant, two gas detectors are installed in the machine casing. If the concentration of R600 reaches 20% of the lower flame level, an explosion proof ventilation system is activated and the power supply to the rest of the prototype is cut.

With exemption of the prototype compressor, off-the-shelf parts as listed in Table 1 are used in the trans-critical heat pump.

Table 1. Main components used in the refrigerant cycle

Component	Manufacturer	Specifications
Compressor	Bitzer	$\dot{V}_{swept}$ @50Hz 34.7 m³/h
Oil separator	ESK Schultze	V=7.5 l
VIHX	Siemens	p_{max}=43 bar
EXV	Carel	t_{max}=70 °C
Accumulator	Frigomec	V=7.8 l
Heat exchangers	Alfa Laval	Brazed plate with asymmetric channels
		Brazed plate
		Brazed plate

2.2. Measurement equipment and evaluation

The used measurement equipment is listed in Table 2 including the expected uncertainties of reading at the measured operating points of the prototype. The accuracy of the temperature sensors was determined through calibration. For the other measured quantities manufacturers' specifications regarding the accuracy of the sensor as well as the acquisition system were taken into consideration. The uncertainty of measurement of evaluated quantities have been estimated using the Gaussian Error Propagation implemented in the Engineering Equation Solver (EES) [9]. Properties of R600 and water are evaluated with EES.

Table 2. Measurement equipment used for evaluating the capacities and evaporation temperature

Measured quantity	Location	Sensor	Uncertainty of reading
Temperature	SI,in; SI,out	Pt100	± 0.1 K
Volumetric flow rate	SI	Electromagnetic flow meter	± 0.0015 l/s
Electric power consumption	el	Wattmeter	± 1% of reading
Pressure	4	Strain-Gauge	± 0.25 bar
Pressure	7	Strain-Gauge	± 0.09 bar

The systems COP is evaluated according to equation (3) by averaging 10 minute long measurements of steady operating points at a measurement interval of 1 second.

$$COP = \frac{\dot{Q}_{SI}}{P_{el}} = \frac{\dot{V}_{SI,in} \cdot \rho_{SI,in} \cdot (h_{SI,out} - h_{SI,in})}{P_{el}} \quad (3)$$

The power consumption of the heat pump is measured at the terminal of the frequency inverter with a wattmeter.

2.3. Experimental investigation of optimum high side pressure

In order to determine the influence of the high-side pressure on the COP the high-side pressure was varied while the heat sink and source temperatures, the suction gas superheat and the compressor speed were set constant. It was found that an optimum value for the high-side pressure exists. Fig. 3 shows t/h-diagrams of measured sub-critical operating points at a pressure lower than the optimum pressure, close to the optimum pressure and at a too high pressure from left to right. During sub-critical operation the location of the pinch point in the condenser is determined by the sink temperature levels and the condensing temperature. Through controlling the high-side pressure, the EXV determines the condensation temperature. At too low high-side pressures, as shown in Fig. 3 (left), the pinch point occurs at the refrigerants dew line, i.e. within the condenser. This limits the heat transfer leading to an increased refrigerant temperature at the condenser exit (state point 4) which reduces the heating capacity. Increasing the high-side pressure increases the compressor outlet temperature to the cost of increased compression work. Too high pressure levels as seen in Fig. 3 (right) decrease the COP since the pinch point at the condenser outlet limits the heat transfer and the increase in

heating capacity is outmatched by the increase in compression work. In between these two cases an optimum high-side pressure, as depicted in Fig. 3 (middle), yielding the maximum COP can be found.

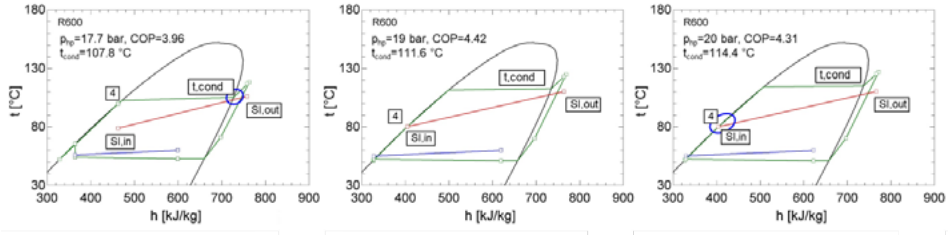


Fig. 3. t/h-diagrams of measured sub-critical operating points at different high-side pressures at source inlet/outlet temperatures of 60/55 °C, sink inlet/outlet temperatures of 80/110 °C and a suction gas superheat of $\Delta T_{sup,1}$=20 K

Similar observations can be made during trans-critical operation. At a constant compressor inlet state, the compressor outlet temperature and subsequently the condenser inlet temperature (state point 3) depend on the high-side pressure. The location of the pinch point in the condenser depends on the condenser inlet state, thus the heat transfer in the condenser is affected by the high-side pressure.

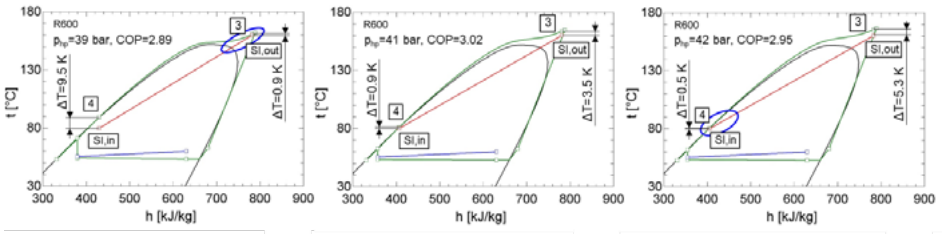


Fig. 4. t/h-diagrams of measured trans-critical operating points at different high-side pressures at source inlet/outlet temperatures of 60/55 °C, sink inlet/outlet temperature of 80/160 °C and a suction gas superheat of $\Delta T_{sup,1}$=10 K

The second operating parameter studied experimentally is the suction gas superheat. Fig. 5 shows the dependency of the COP on the high-side pressure for 10 K, 15 K and 20 K of suction gas superheat at the compressor inlet.

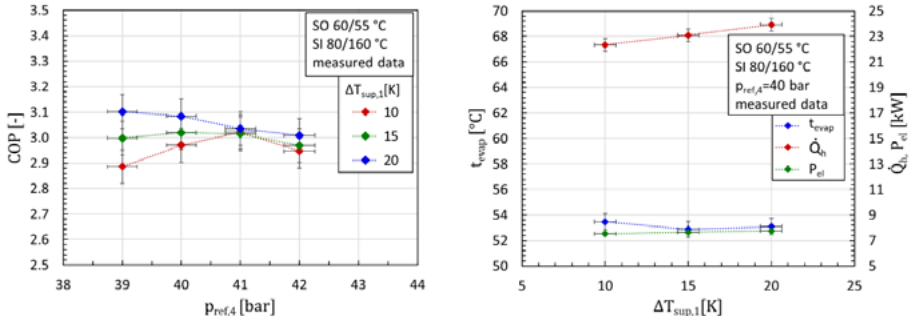


Fig. 5. Measured COP at source inlet/outlet temperatures 60/55 °C and sink inlet/outlet temperatures 80/160 °C for different values of suction gas superheat (left) and the influence of the superheat on evaporation temperature and capacities (right)

It can be seen that by increasing the suction gas superheat in the IHX the levels for optimum high-side pressure can be shifted to lower values while an increase of the COP is possible, which is in agreement with

the simulation study conducted by Verdnik et al [7]. This is possible because the increase in suction gas superheat established in the IHX does not lead to a drop in the evaporating temperature as can be seen in Fig. 5 (right). The increased condenser inlet temperature lead to an increase in the heating capacity which is larger than the increase in compressor power, which subsequently leads to the observed increase in the COP.

3. Simulation model

The TIL Suite package [10] was used to develop a simulation model of the trans-critical heat pump. This Dymola library contains models for components and media properties in the object-based Modelica language, Predefined models of the package have been modified or extended with user specific geometries or correlations for heat transfer and pressure drop.

3.1. Compressor model

The compressor is modeled using the overall isentropic efficiency, inner isentropic efficiency and volumetric efficiency according to equation (4), (5) and (6) respectively. The efficiencies are based on data extracted from the manufacturers' software [11]. As first experiments showed a stronger decline in the volumetric efficiency, the slope of the gained approximation was increased by 30 %. In order to calculate the power consumption at the terminal of the frequency inverter, an inverter efficiency of 95% is assumed according to equation (7), yet all simulations and measurements in this work have been conducted at an inverter frequency of 50 Hz.

$$\eta_{is,ov} = \frac{\dot{m}_{ref} \cdot (h_{ref,2s} - h_{ref,1})}{P_{comp}} = 0.684 - 0.002 \cdot \pi - 0.0004 \cdot \pi^2 \quad (4)$$

$$\eta_{is,i} = \frac{h_{ref,2s} - h_{ref,1}}{h_{ref,2} - h_{ref,1}} = 0.76 - 0.002 \cdot \pi - 0.0004 \cdot \pi^2 \quad (5)$$

$$\lambda_{vol} = \frac{\dot{m}_{ref}}{\rho_{ref,1} \cdot \dot{V}_{swept}} = 1.04 - 0.05 \cdot (1 + 30\%) \cdot \pi = 1.04 - 0.065 \cdot \pi \quad (6)$$

$$P_{el} = \frac{P_{comp}}{\eta_{FI}} = \frac{P_{comp}}{0.95} \quad (7)$$

3.2. Modelling of the heat exchangers

The TIL-Suite includes models for plate heat exchangers based on a finite volume approach. For the IHX and evaporator these models were used with a discretization of 10 cells. The model for the condenser was adopted to account for the asymmetric channel widths of the refrigerant and the water side and a discretization of 80 cells was used. A sinusoidal chevron pattern with an inclination angle of 60° was assumed for all heat exchangers. Table 3 shows the used geometry for the heat exchanger models as well as the correlations for the heat transfer coefficients (HTC) and pressure drops (Δp).

Table 3. Correlations used in the heat exchanger models

		Condenser		Evaporator	IHX		
		Refrigerant	Water				
Refrigerant	HTC	Forooghi and Hooman [12]		Longo [13]	Refrigerant	HTC	Forooghi and Hooman [12]
	Δp	Martin [14]		Longo [15]	high-pressure side	Δp	Martin [14]
Water	HTC	Martin [14]		Martin [14]	Refrigerant	HTC	Longo [13]
	Δp	Martin [14]		Martin [14]	low-pressure side	Δp	Martin [14]

3.3. Simulation study on variation of the operating parameters

The influence of suction gas superheat, heat source temperature level and heat sink inlet and outlet temperatures on the COP have been studied over a range of high-side pressures.

An increase of the suction gas superheat lowers the optimum high-side pressure and increases the COP as can be seen in Fig. 6. Since the heat sink inlet/outlet temperatures of 80/160 °C, as depicted in Fig. 6 (left), can be reached with pressures slightly above the critical pressure (37.96 bar), this effect can be seen clearer at sink inlet/outlet temperatures of 80/170 °C, as depicted in Fig. 6 (right).

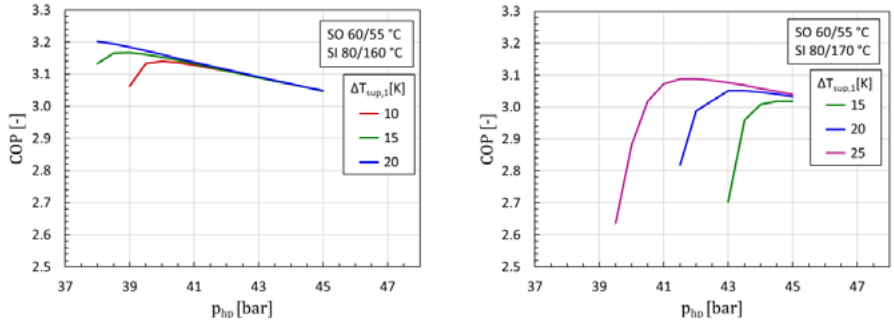


Fig. 6. Simulated COP for different high-side pressures at varying suction gas superheat for source inlet/outlet temperatures 60/55 °C, sink inlet/outlet temperatures 80/160 °C (left) and heat sink inlet/outlet temperatures 80/170 °C (right)

A variation of the sink inlet temperature, as depicted in Fig. 7 (left), shows that an increase of the sink inlet temperature leads to a decrease of the COP, but the value of the optimum high-side pressure is not influenced. Varying the sink outlet temperature, as illustrated in Fig. 7 (right), shows that higher high-side pressures are necessary to achieve higher sink outlet temperatures, which leads to a decrease of the maximum COP. By comparing the two graphs it can be seen, that the system COP is more sensitive in a change of sink inlet temperature than sink outlet temperature.

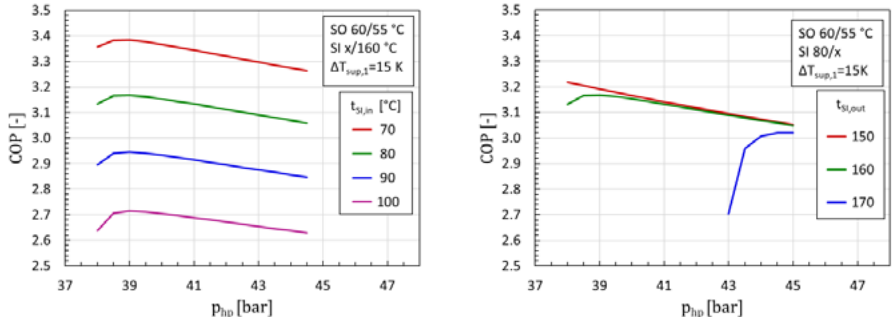


Fig. 7. Simulated COP for different high-side pressures at varying suction gas superheat for varying sink inlet temperature (left) and varying sink outlet temperature (right)

The last operating parameter to investigate is the heat source temperature. Fig. 8 shows a variation of the heat source temperature with a constant difference between inlet and outlet temperature of 5 K. As can be seen in Fig. 8 (left), an increase of the heat source temperature leads to an increase of the COP because of the reduced pressure ratio the compressor has to overcome. The level of the optimum high-side pressure is slightly shifted towards higher pressures but is very close to the minimum pressure needed to reach the set heat sink outlet temperature. As the heat source temperature determines the evaporation temperature, an increase of the heat source temperature leads to a strong increase in compressor power and heating capacity, as can be seen in Fig. 8 (right.)

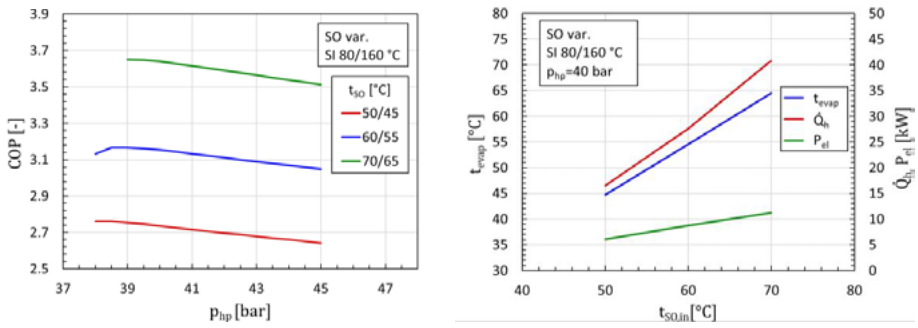


Fig. 8. COP for different high-side pressures at varying suction gas superheat at varying source temperatures (left) and the influence of the source temperature on evaporation temperature and capacities (right)

4. Simulation vs. measured data

Fig. 9 compares the results of the simulation model with the experimental data gathered with the prototype for the same operating point and different values of suction gas superheat. The simulation reflects the characteristic relation of the COP on the high-side pressure, although the value of the optimum high-side pressure is not exactly reproduced.

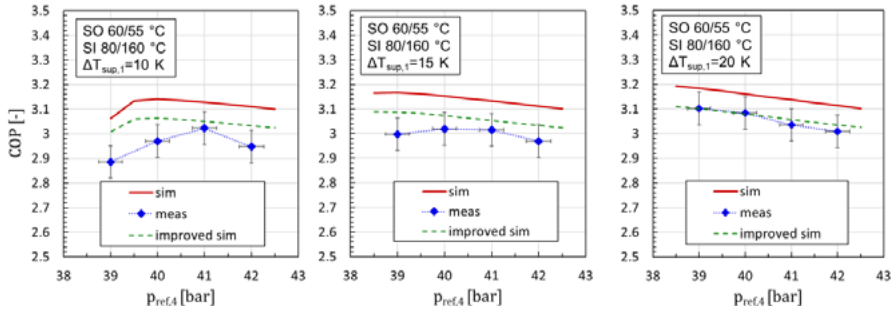


Fig. 9. Measured and simulated COP for heat source inlet/outlet temperatures 60/55 °C, heat sink inlet/outlet temperatures 80/160 °C and suction gas superheat of $\Delta T_{sup,1}$=10 K (left), 15 K (middle) and 20 K (right)

A direct comparison of the simulated and measured values for the COP, the heating capacity and the electric power consumption in Fig. 10 shows a deviation between simulation and experiment of +7%, +20% and +15% respectively which is caused by a slight overestimation of the evaporation temperature and compressor volumetric efficiency in the simulation. As first steps to improve the simulation model, the vapor quality at the accumulator outlet, the compressors volumetric efficiency, the pressure drop and assumptions regarding the plate pattern geometry in the evaporator were investigated. In the improved simulation model, the vapor quality at the outlet of the low-pressure accumulator was modelled with values less than unity depending on the filling level instead of the ideal behavior of saturated vapor. In the evaporator, momentum, manifold and port, and gravity pressure drop according to Longo et al. [13] were considered on the refrigerant side. The assumption regarding corrugation angle and pitch were altered to 10° and 10 times the corrugation height, respectively. The compressors volumetric efficiency was modelled with equation (8).

$$\lambda_{vol} = 0.945 - 0.056 \cdot \pi \tag{8}$$

The results of the improved simulation model yield a deviation to experimental data of less than 5% in COP, less than 7% for the heating capacity and less than 5% for the electric power consumption as can be seen in Fig. 10.

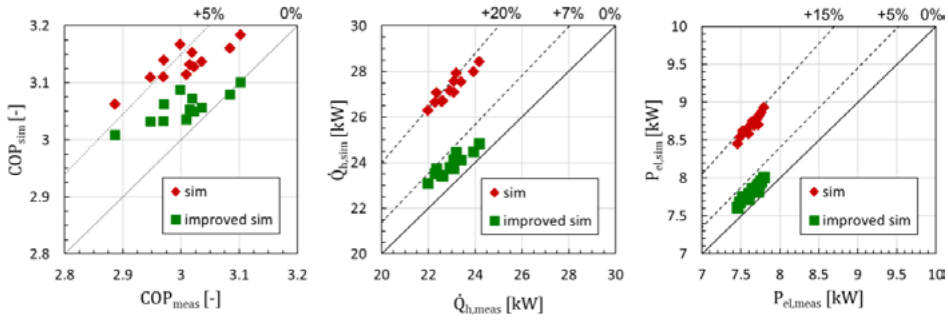


Fig. 10. Comparison of simulated and measured COP (left) heating capacity (middle) and electric power consumption (right)

5. Conclusions and Outlook

A prototype of a high-temperature vapor compression heat pump utilizing R600 in a one-stage cycle using a reciprocating compressor, low-pressure accumulator and IHX for suction gas superheating has been developed. First measurements prove the concept of using R600 in a trans-critical cycle. Tests conducted at heat source inlet/outlet temperatures of 60/55 °C showed a COP of 4.42 for heat sink inlet/outlet temperatures of 80/110 °C in sub-critical operation. Increasing the high-side pressure to values exceeding the critical pressure of the refrigerant enabled heat sink inlet/outlet temperatures of 80/160 °C, yielding a COP of up to 3.10 depending on the suction gas superheat and high-side pressure. Energy balances over the IHX showed that the refrigerant vapor quality at the outlet of the low-pressure accumulator is in the range of 0.9 depending on the operating point, which reduces the possible suction gas superheating in the IHX.

The originally introduced simulation model reproduced the system COP with a deviation of less than 7%, while the heating capacity and electric power consumption were overestimated by 20% and 15%, respectively. After further considerations regarding refrigerant vapor quality at the accumulator outlet, volumetric efficiency of the compressor and evaporator geometry and pressure drop, the deviation was reduced to less than 5%, 7% and 5% in COP, heating capacity and electric power consumption, respectively.

The next steps will be to conduct further measurements to evaluate the compressor and system efficiency as well as more detailed investigations regarding the refrigerant charge and pressure drop in the condenser. The simulation model will be refined and validated using experimental data. The operational envelope in terms of heat source temperatures, suction gas superheat and inverter frequency will be experimentally determined with respect to the compressor power and sufficient cooling of the electric motor. These insights should serve to develop a control strategy for the optimal high-side pressure and suction gas superheat depending on the operating conditions of the high-temperature heat pump.

Acknowledgements

This work has been conducted in the course of the cooperative project “TransCrit” (FFG No.: 865083) under the cooperation of Graz University of Technology and Frigopol Kälteanlagen GmbH. The project is funded by the Austrian Climate and Energy Fund and carried out within the Austrian Energy Research Program 2017.

References

[1] International Energy Agency. Energy Efficiency 2019. https://webstore.iea.org/market-report-series-energy-efficiency-2019 (4.11.2019).
[2] Lorentzen, G., 1990. Trans-critical vapour compression cycle device. Patent WO/07683.
[3] Besbes, K., Youghaib, A., De Carlan, F., Peureux, J.-L., 2015. A R-32 transcritical heat pump for high temperature industrial applications. 24th IIR Congress of Refrigeration, Yokohama, Japan, paper id: 599.
[4] Abi Chahla, G.; Beucher, Y., Zoughaib, A., De Carlan, F., Pierucci, J., 2019. Transcritical industrial heat pump using HFO’s for up to 150 °C hot air supply. 25th IIR Congress of Refrigeration, Montreal, Canada,

paper id: 1184.
[5] Kimura, T,, Fuchikami, H., Nishida, K., Kudo, M., Machida, A., Saito, K., Ohta, Y., Katsuta, M., 2018. Development of a high temperature heat pump using reusable heat as the heat source. JRAIA International Symposium 2018, Kobe, Japan.
[6] Verdnik, M., Rieberer, R., & Baumhakel, A. (2020). Entwicklung einer transkritischen R600-Hochtemperaturwärmepumpe. 45th Annual Meeting of the Deutscher Kaelte und Klimatechnischer Verein 2019: Deutsche Kaelte-und Klimatagung 2019 Ulm, Germany, pp. 1325-1334
[7] Verdnik, M., Rieberer, R., Moisi, H., 2019. Trans-critical vapor compression cycle using butane (R600) as refrigerant for industrial waste heat recovery. 25th IIR Congress of Refrigeration, Montréal, Canada, paper id: 1186.
[8] Moisi, H., Rieberer, R., 2017. Refrigerant Selection and Cycle Development for a High Temperature Vapor Compression Heat Pump. 12th IEA Heat Pump Conference 2017, Rotterdam, Netherlands, paper id: O.3.4.3.
[9] EES, 2019. Engineering Equation Solver v. 10.644, F-Chart Software, Madison, Wisconsin.
[10] TLK-Thermo, 2018. TIL Suite v.3.8.0, TLK-Thermo GmbH, Braunschweig, Germany
[11] Bitzer, 2018. Bitzer Software v. 6.9.2074, BITZER Kühlmaschinenbau GmbH, Sindelfingen, Germany.
[12] Forooghi, P., Hooman, K., 2014. Experimental analysis of heat transfer of supercritical fluids in plate heat exchangers. International Journal of Heat and Mass Transfer 74, p. 448-459
[13] Longo, G. A., Mancin, S., Righetti, G., Zilio, C., 2015. A new model for refrigerant boiling inside Brazed Plate Heat Exchangers (BPHEs). International Journal of Heat and Mass Transfer 91, p. 144–149.
[14] Martin, H., 2013. Druckverlust und Wärmeübergang in Plattenwärmeübertragern. Verein Deutscher Ingenieure, VDI-Wärmeatlas, Springer Vieweg, Berlin, p. 1687-1693
[15] Longo, G. A., 2012. Hydrocarbon Refrigerant Vaporization Inside a Brazed Plate Heat Exchanger. Journal of Heat Transfer (134).

13th IEA Heat Pump Conference
April 26-29, 2021 Jeju, Korea

Analysis of the impact of different HVAC configurations andcontrol strategies on primary energy and cost savings for an office building

Mara Magni[a], Fabian Ochs[a]

[a]University of Innsbruck, Technikerstraße 13, Innsbruck 6020, Austria

Abstract

In order to mitigate climate change, sustainable and responsible use of resources is required. In the present study, different technologies applicable for the renovation of an office building are evaluated considering, both economic feasibility and environmental impact for the climates of Rome Stuttgart and Stockholm. Decentralized heating and cooling systems represented by different types of heat pumps (i.e. air-to-air On/Off and modulating) are considered in combination with photovoltaic panels (PV), battery and efficient lighting (LED) in order to investigate the achievable energy savings and the additional cost. The environmental impact is evaluated in terms of electricity and total primary energy (PE) savings calculated with constant and monthly conversion factors representing different scenarios with different share of renewables in the electricity mix.
It was observed that the energy savings calculation method influences the ranking of renovation packages. High-energy savings with low additional cost are achievable with HP in combination or not with LED and PV, in Stockholm and Stuttgart, and with LED and PV in combination with electric heating in Rome. Battery brings additional energy savings with high additional cost.

© HPC2020.
Selection and/or peer-review under responsibility of the organizers of the 13th IEA Heat Pump Conference 2020.

Keywords: Cost optimality; Energy simulations; Office building renovation; HVAC;

1. Introduction

In spite of higher efficiency, the energy consumption of buildings has increased over the past decades and the European Union has set restrictive targets. To reach these goals, buildings have to be transformed from energy consumer to energy provider. In non-residential buildings, the available façade area for the installation of a renewables based system is limited and an optimization of the building system is required in order to reduce the primary energy demand.

The recast of the Energy Performance of Buildings Directive [1] states that member state (MS) must ensure that minimum energy performance requirements for buildings are set “with a view to achieve cost-optimal levels” in terms of global cost and primary energy need. The cost-optimal level must be calculated in accordance with a comparative methodology.

In the literature, some studies dealing with both economic feasibility and environmental impact for office buildings are present but they do not consider different scenarios for the evaluation of the influence of the electricity mix. Pikas E. et al. [2] is focused on the building envelope considering different fenestration design solutions. Gustafsson M. et al. [3] investigated energy renovation packages involving centralized heating and cooling system, windows, envelope insulation and solar photovoltaics (PV), for European office buildings. Sanja Stevanović presented a cost optimality study [4] for an office building located in Serbia where the cooling demands is predominant.

* Corresponding author. Tel.: +43-512-507-63619
E-mail address: Mara.Magni@uibk.ac.at

Ochs F, et al. [5] introduces a PE evaluation method considering different future development of the load (i.e. building stock) and electricity mix (share of REs) with seasonal variations. This works highlight the need of an appropriate evaluation method for comparing and ranking different passive and active technologies on micro- and macro- economic scale. Different EU MS adopts different national conversion factors for PE/CO_2, which are subject to change [5]. Seasonal variations are not considered at all, although the share of renewables within the period of consideration (e.g. 20 years) should be included [5].

In this work different HVAC retrofit solutions (i.e. HP, PV, Batteries, LED etc..) are compared against a reference case involving an electric heating system with an On/Off split unit for cooling and fluorescent lamps combining both economic and environmental analysis. A sensitivity analysis is carried out in order to evaluate the influence of input parameter (i.e. interest rate, investment cost and electricity price) on the results of the economic analysis. The environmental analysis is performed using different share of renewables in the electricity mix showing the impact of the development of increasingly share of RE on the ranking of the different retrofit solutions.

2. Method

2.1. Building model and boundary conditions

The reference building is chosen in order to be representative of a typical European office cell located in middle floor of a high-rise building [6]. Three different European climates are considered in this study: Rome (Mediterranean), Stuttgart (cold moderate) and Stockholm (cold climate). Fig. 1 shows the considered office cell, which has a heated area of 27 m^2 and a volume of 81 m^3. All the surfaces are considered adiabatic, except for the façade oriented toward South (with window-to-wall ratio of 60%) where ambient boundary conditions are applied. Shading from adjacent obstacles is not considered, whereas an external movable shading, able to block 70% of the incoming radiation, is activated when direct solar radiation impinging the south façade is higher than 120 W/m^2.

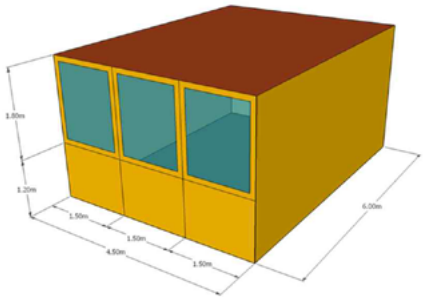


Fig. 1. View of the reference office zone [6]

Table 1 shows the yearly average ambient temperature ($T_{amb,av}$), yearly global irradiation over a horizontal surface ($I_{g,h}$) and yearly irradiation over a south oriented vertical surface (I_{south}) for each climate.

The thermal transmittance of the façade elements ($U_{ext,wall}$) and the characteristics of the windows such as the thermal transmittance (U_{win}), the solar heat gain coefficient (g-value) and the solar transmittance (τ_{sol}) depend on the three climates, as shown in Table 1. The internal walls are typical plasterboard walls, the exterior wall is a three layer structure with different insulation thicknesses depending on the climate.

User behavior (e.g. occupancy, appliances and lighting) is taken into account by means of hourly profiles, different for week and weekend days [7]. A contemporaneity index of 0.8 is used for occupancy and appliances. Three persons are present during the working time and a sensible and latent heat of 70 W/person and 0.08 kg/h/person are considered. The internal gain due to appliances is assumed to be 7 W/m^2 and the electric gain due to lighting is 10.9 W/m^2. The lighting schedule follows occupied hours and is defined considering a non-daylight responsive system

The natural infiltration rate is assumed to be constant and equal to 0.15 1/h. A fresh air supply of 40 m^3/h/person is covered by a mechanical ventilation system with heat recovery (70% sensible efficiency), which is active only during the working time (i.e. from Monday to Friday from 8:00 am until 08:00 pm).

Table 1. Main properties of the south oriented façade and climates [6]

	$T_{amb,av}$ [°C]	$I_{g,h}$ [kWh/m^2]	I_{south} [kWh/m^2]	$U_{ext,wall}$ [W/m^{2}K]	U_{win} [W/m^{2}K]	g-value [-]	τ_{sol} [-]
Rome	15.8	1632	1253	0.80	1.26	0.33	0.462
Stuttgart	9.9	1101	889	0.40	1.35	0.59	0.426
Stockholm	7.8	952	884	0.20	0.90	0.63	0.260

An anti-freezing resistance is heating up the ambient air when the external temperature falls below 0°C while a bypass of the heat recovery is activated when the temperature of the zone is higher than 23 °C and the ambient temperature is lower than the indoor temperature. The set point temperature for the indoor convective temperature during the wintertime and summertime are 21°C and 25°C. A detailed description of the boundary conditions is reported in D'Antoni, et al. [6]. The building model is developed in Matlab/Simulink and it has been validated against other dynamic simulation tools [8].

2.2. Renovation packages

The renovation packages discussed in this paper include the combination of different heating, cooling and lighting technologies optionally combined with PV and battery without modifying to the envelope. In addition, the effect of different control strategies is considered.

Table 2 reports all the technologies involved in this study highlighting in bold the reference system used for the comparison (i.e. electric heating and On/Off HP for cooling with a standby consumption running for the entire year, fluorescent lighting and the reference control system for the ventilation and free-cooling described in section 2.1). The electric heating system can be retrofitted with either a simple On/Off or improved modulating HP that might cover also the cooling load.

In the reference case the free cooling can be activated only during the working time therefore savings in terms of cooling demand can be achieved when the free cooling is activated every time the internal and external conditions makes it effective.

Switching off completely the cooling system during the winter season, enable savings by reducing the standby consumption. Switching off the heating and cooling systems during non-occupied periods (night set-back) might enable further savings. Moreover, using modern LED instead of fluorescent lamps can approximately halve the electricity consumption for lighting purpose.

Table 2. Characterization of the investigated renovation components

	Options	Description
Heating	**Direct electric**	Electric resistance, efficiency equal to 1.
	On/Off (Split type) HP	See Fig. 2. Two different On/Off HP sizes are considered.
	Modulating (Split type) HP	See Fig. 2.
Cooling	**On/Off** (Split type) Air-Con.	See Fig. 2. Two different On/Off HP sizes are considered.
	Modulating (Split type) Air-Con.	See Fig. 2.
PV	Mono-crystalline silicon	PV installed in the available wall area (5.4 m^2) in the south façade with an efficiency of 17.7% and a peak power of 877 Wp.
Battery	Ideal battery	Efficiency of 90% (4kWh capacity).
Control	HP and mechanical ventilation	**On/Off HP** and PI for the modulating HP, for the mechanical ventilation see the building description.
	Free cooling 7/7	Free cooling can be activated every time the internal and external conditions makes it effective.
	Improved standby consumption	Standby consumption of 10W accounted only during the working season of the considered technology (instead of the whole year).
	Night set back	The heating and cooling systems are switched off during non-occupied periods and restarted 4h before the working time.
Lighting	**Fluorescent**	10.9 W/m^2 (500 lux on the working desk, 8 luminaire).
	LED	5.45 W/m^2 (500 lux on the working desk, 8 luminaire).

As specified in Table 2, two On/Off HP with different sizes and one modulating HP are considered in this work. The main characteristics (i.e. COP, EER, heating and cooling power and air volume flows) are reported in Table 3 and the maps of performances in Fig. 2.

Table 3. Main characteristics of the modulating and On/Off heat pumps. The heating power and COP are specified for the external air temperature of 15°C and internal of 22°C while the cooling power and EER are specified for the external air temperature of 35°C and internal of 27°C. For the modulating HP the performances are specified for the maximum f_{max} and minimum f_{min} frequency.

	Internal air volume flow [m³/h]	External air volume flow [m³/h]	Heating power (15°C/22°C) [W]	Cooling power (35°C/27°C) [W]	COP (15°C/22°C) [-]	EER (35°C/27°C) [-]
Modulating HP	648	1872	f_{max}: 4006 f_{min}: 1006	f_{max}: 2510 f_{min}: 1248	f_{max}: 5.44 f_{min}: 5.86	f_{max}: 5.29 f_{min}: 5.05
On/Off HP low power	187	1872	523	1250	4.12	4.28
On/Off HP high power	648	1872	3923	2510	5.38	5.29

Fig. 2 shows the performances of the modulating, On/Off low (lp) and high (hp) power heat pumps in cooling and heating operation used in the simulations. The COP of the On/Off HP (Fig. 2.2b) considers a degradation of the performance due to deicing when the ambient temperature is between 7°C and 2°C. The modulating HP is modelled with a separated deicing model therefore the COP reported in Fig. 2.1b does not consider the losses due to deicing operation.

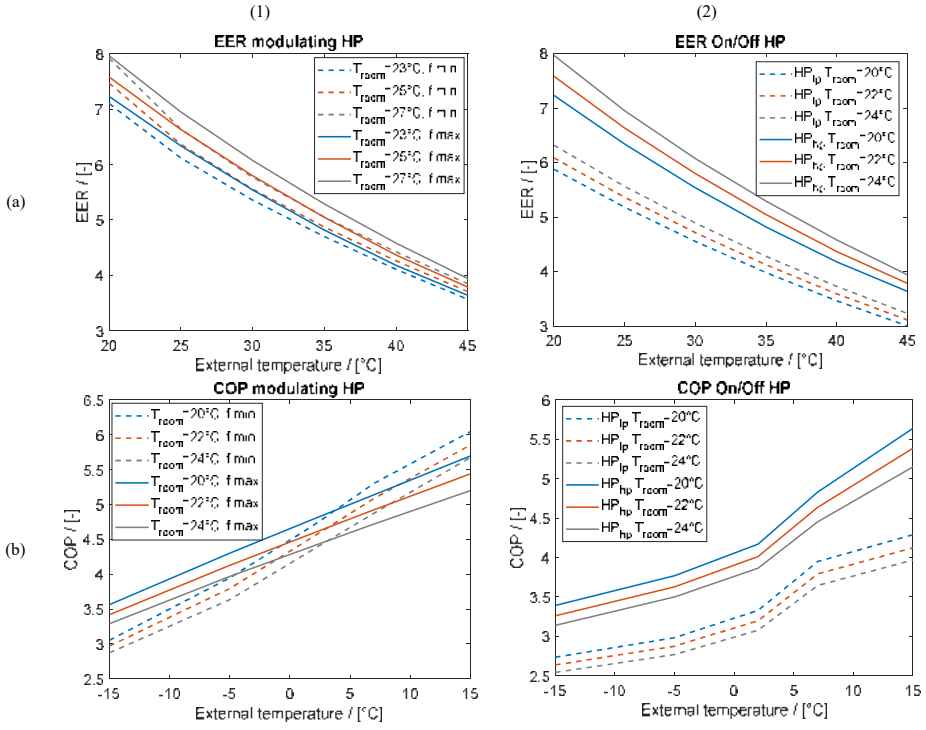


Fig. 2. Maps of performances of the modulating (1) and low power (lp) and high power (hp) On/Off (2) heat pump in cooling (a) and heating (b) mode

The schemes of the control system used for the On/Off and modulating HP are reported respectively in Fig. 3a and Fig. 3b. The On/Off HP is controlled with an hysteresis (±0.5 K) having as input the temperature difference between the heating set point and the air temperature ($T_{set,H}$-T_{air}) during the heating mode and the temperature difference between the air temperature and the cooling set point (T_{air} -$T_{set,C}$) during the cooling mode. The Look-up-Tables (LuT) deliver as output the COP/EER, the absorbed electric power (P_{el}) and the delivered thermal power ($\dot{Q}_{th}$). The transfer function (TF) with a time constant of 130 s is necessary to slow down the

system response and makes the heat pump behaviour more realistic. The LuT have as input the control signal, the air temperature (T_{air}) and the ambient temperature (T_{amb}).
The modulating HP is controlled with a proportional integral (PI) control having as input $T_{set,H}$-T_{air} during the heating mode and T_{air}-$T_{set,C}$ during the cooling mode. The equation (1) shows the PI control rule where the proportional parameter K_p is equal to 1 and the integral time constant T_n is equal to 418.7 s.

$$f(t) = K_p \cdot \left(err\ (t) + \frac{1}{T_n} \cdot \int err\ (t)\, dt \right) \quad (1)$$

The control system of the modulating HP includes also a minimum run (t_{ON}) and off (t_{OFF}) time and the deicing ($dt\ r_{deic}$). The deicing cycle, which last 600 s, starts only when the time counter reaches the defined waiting time that is a function of the ambient temperature (i.e. 11460 s for an ambient temperature of -7°C and 2406 s for an ambient temperature of 5°C). During the deicing cycle, the HP absorbs electric energy without delivering any thermal energy to the room. When the HP is switched on and is not performing the deicing cycle, it is forced to remain in operation with a frequency between the minimum and the maximum until the minimum run time counter reaches the threshold of 300 s. In the same way, when the HP is switched off, it is forced to remain in this status until when the minimum off time counter reaches the threshold of 600 s.

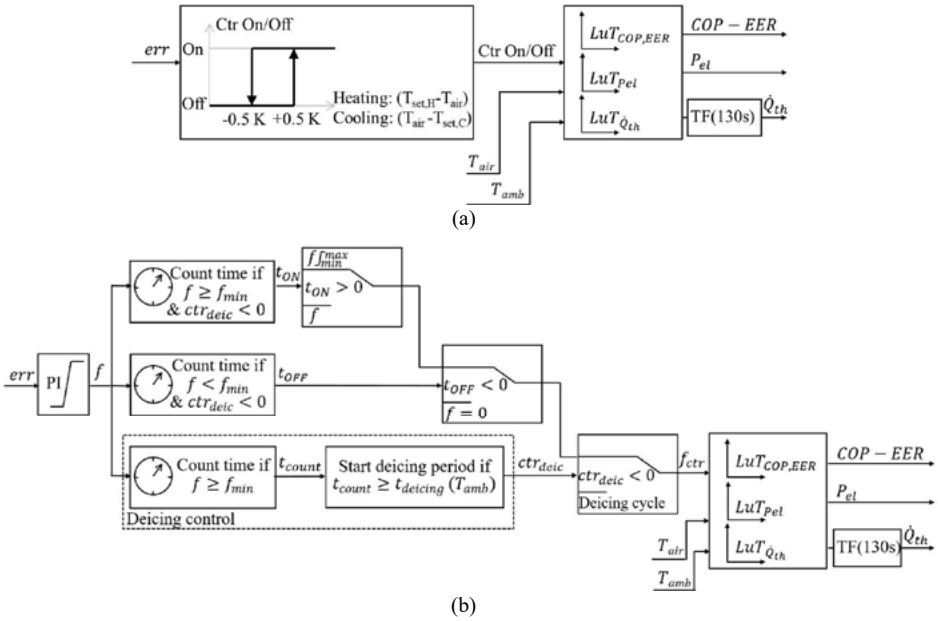


Fig. 3. Control of (a) On/Off and (b) modulating HP

The PV model from the Matlab/Simulink CARNOT library [9] is based on equation (2) and (3).

$$\text{Power}_{PV} = \left((25 - T_{\text{m odule}}) \cdot \Delta W_{p,T} + 1 \right) \cdot W_p \cdot f_{gen} \cdot \frac{Q_{solar}}{1000} \quad (2)$$

$$T_{\text{m odule}} = \frac{Q_{solar}}{1000\ \left(\frac{w}{m^2}\right)} \cdot 40 + T_{\text{am b}}\ [°C] \quad (3)$$

Where:

- $\Delta W_{p,T} = 0.00375$ is the temperature coefficient [1/K];
- $W_p = 877\ W$ is the peak power [W];
- $f_{gen} = 1 - 0.03$ is the efficiency of the PV considering losses in diodes, power mismatch and dirt;
- Q_{solar} is the solar irradiation impinging the PV panel corrected with the Incidence Angle Modifier (IAM).

The model of the inverter is provided by the CARNOT library [9]. It considers a standby consumption of 1 W and the efficiency is a function of the output power (i.e. when the output power is between 300 W and 3600 W the efficiency is above 0.95).

2.3. Economic analysis

The economic analysis adopted in this work is based on the Equivalent Annual Cost (EAC), considering investment and running costs over a reference lifetime (N). EAC is the annual cost of owning, operating, and maintaining an asset over its entire life, it allows comparing the cost-effectiveness of various assets that have unequal lifespans. Equation (4) shows the calculation of the EAC:

$$\mathrm{EAC} = \frac{\mathrm{C} \cdot \mathrm{r}}{1-(1+\mathrm{r})^{-\mathrm{N}}} \tag{4}$$

Where r is the real interest rate (3%). The total annual cost is calculated, for electrically driven systems, as:

$$Total\ \ annual\ \ cost\ \ = EAC + MC + FE \cdot el_{price} \tag{5}$$

Where MC is the yearly maintenance cost, FE is the final electric energy and el_{price} is the electricity price that is assumed to be 0.2 €/kWh. An escalation rate of the energy price of 2% is considered. A sensitivity analysis is carried out varying the interest rate, the investment cost and the electricity price in order to assess the sensitivity of the economic results to the input data. The annual interest rate is varied ±1% point from the default value (3%), the electricity price and the investment costs are varied ±20%. In Table 4 the investment, installation, maintenance costs, the technical lifetime and the resulting EAC for each technology are reported. The data for HP and PV are all taken from [3] except the investment cost of PV which is taken from [10] where mono-crystalline silicon PV are considered.

The reference technology for the cooling is the On/Off low power HP therefore when the modulating HP or the On/Off high power HP are considered, as a cooling technology, only the additional costs are accounted for (ΔEAC=143.5€).

The data for battery and LED are assumed considering the current price of different sellers. The battery are usually guaranteed for 10 years while LED for 50000 hours that correspond to a lifetime of 15 years.

The PV self-consumption contributes to the reduction of the electricity demand of the building system. When the battery is considered, the PV surplus energy is stored and later used by the building, otherwise the benefit of selling the surplus to the main grid is disregarded.

Table 4. Investment costs, installation costs, maintenance costs and EAC of the studied renovation measures

Renovation measure	Investment costs [€]	Installation costs [€]	Maintenance costs [€/y]	Technical lifetime [y]	EAC [€]
On/Off HP low power	500 [3]	100 [3]	16 [3]	12 [3]	76.3
On/Off HP high power	1400 [3]	290 [3]	50 [3]	12 [3]	219.8
Modulating HP	1400 [3]	290 [3]	50 [3]	12 [3]	219.8
PV (877 Wp)	2322 [10]	380 [3]	34.2 [3]	20 [3]	215.8
Battery (4.8 kWh) with Inverter	4000	1400	0	10	663.1
LED light (8 luminaire)	640	300	0	15	78.7

2.4. Environmental analysis

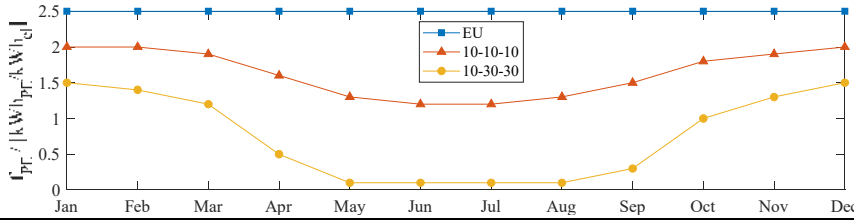
In this case study all the analyzed solutions are using electricity as input, therefore they can be compared considering the savings in terms of electricity demand. In order to compare the savings in terms of primary energy there is the need to define the proper conversion factors.

The increasing share of renewables in the electricity mix affects the definition of the PE/CO_2 conversion factors especially because the energy production from renewables is not constant during the year but rather has a seasonal trend. Significantly increased share of RE electricity can be expected in the near future in particular in summer, while in winter only a moderate increase is likely, unless there is a significant further extension of wind power or seasonal storage capacities are strongly build up [5].

For this reasons, different scenarios for the PE conversion factor are taken into account.

Fig. 4 shows the monthly PE conversion factors considering a constant coefficient defined in [11], a simplified

scenario with an energy mix of 10% hydro, 10% wind and 10% PV and an energy mix of 10% hydro, 30% wind and 30% PV. The difference between the EU conversion factor and the 10-10-10 or 10-30-30 scenarios is higher during the summer than during winter. This means that using the EU conversion factor the same value is given to savings obtained in summer and winter while using the monthly conversion factors (i.e. 10-10-10 and 10-30-30) less importance is given to the energy savings occurring in summer.



	Jan	Feb	Mar	Apr	May	Jun	Jul	Aug	Sep	Oct	Nov	Dec
EU	2.5	2.5	2.5	2.5	2.5	2.5	2.5	2.5	2.5	2.5	2.5	2.5
10-10-10	2	2	1.9	1.6	1.3	1.2	1.2	1.3	1.5	1.8	1.9	2
10-30-30	1.5	1.4	1.2	0.5	0.1	0.1	0.1	0.1	0.3	1	1.3	1.5

Fig. 4. Monthly total PE conversion factor defined according to (EU) European definition, (10-10-10) scenario where a share of 10 % hydro, 10 % wind, 10 % PV and 70 % fossil is considered in the electricity mix, and (10-30-30) scenario where a share of 10 % hydro, 30 % wind, 30 % PV and 30 % fossil is considered in the electricity mix *[5]*

3. Results

3.1. Reference case and PV yield

The reference case is composed of a direct electric heating system and an On/Off HP_{lp} without PV. Fig. 5a shows, for each climate, the monthly electricity demand per square meter of floor area (27 m^2) for each component of the balance (i.e. heating, cooling, appliances, lighting, anti-freezing resistance of the heat exchanger and fans of the mechanical ventilation). The PV production in each climate is reported by the straight blue line. The cross (EU conversion factor), triangle (10-10-10 scenario) and square (10-30-30 scenario) markers refer to the right vertical axes reporting the primary energy consumption. As highlighted in section 2.4, increasing the renewables share in the grid leads to a reduction of the primary energy demand especially during the summer time.

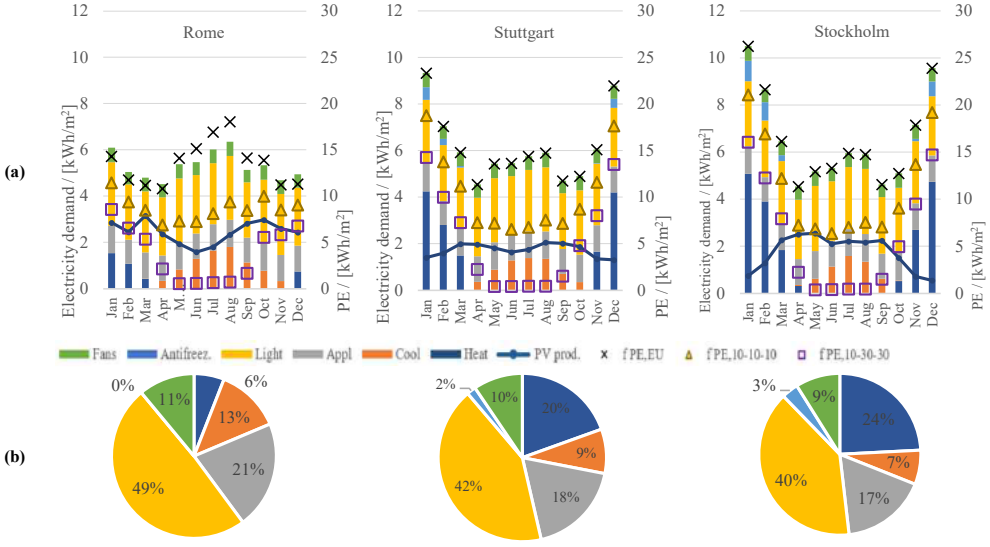


Fig. 5. Results for the reference case (direct electric heating and split HP) for the climates of Rome, Stuttgart and Stockholm. (a) Electricity demand for each end use and PV production; (b) share of electricity required by each end use.

Fig. 5b shows the share of electricity required by each end use, highlighting that the lighting is prevailing in each climate.

Table 5 reports the annual electricity consumption required by each end use and PV production for the climates of Rome, Stuttgart and Stockholm. The total electricity consumption of the reference case is 64 kWh/(m^2y) in Rome, 74 kWh/(m^2y) in Stuttgart, and 79 kWh/(m^2y) in Stockholm. The PV total production would cover the 46%, 28% and 26% of the total consumption in Rome Stuttgart and Stockholm respectively. From this analysis is already clear that the installation of PV in the façade (BIPV) in this case study would bring important energy savings.

Table 5. Annual electricity consumption required by each end use and PV production.

	Heating	Cooling	Appliances	Lighting [kWh/(m^2y)]	Antifreez.	Fans	PV
Rome	4	8	14	31	0	7	29
Stuttgart	14	6	14	31	1	7	21
Stockholm	19	5	14	31	3	7	21

3.2. Pareto solutions

The results of the dynamic simulations investigating different HVAC and lighting solutions (see section 2.2) are compared to the base case considering the additional capitalized cost and energy savings. The latter are expressed in terms of electric energy (E_{EL}) and of total PE calculated with the constant conversion factor (PE_{EU}), with the 10-10-10 scenario ($PE_{10\text{-}10\text{-}10}$) and with the 10-30-30 scenario ($PE_{10\text{-}30\text{-}30}$).

Fig. 6 shows the energy savings in terms of (A) E_{EL}, (B) PE_{EU}, (C) $PE_{10\text{-}10\text{-}10}$ and (D) $PE_{10\text{-}30\text{-}30}$ versus the additional total annual cost (see Equation (5)) of each technology for the climate of Stockholm. Fig. 7 shows the energy savings in terms of (E, F) E_{EL} and (G, H) $PE_{10\text{-}30\text{-}30}$ versus the additional cost for the climate of Rome and Stuttgart, respectively. In both Fig. 6 and Fig. 7, the square markers represent the results of the different technologies together with the PV panels, while the asterisk markers represent the solutions including battery and PV. The error bars shows the results of the economic sensitivity analysis, indicating the impact on the additional total annual cost by varying the investment cost, energy price and interest rate. The investment cost has the highest impact on the economic evaluation.

In this specific case, the analysis of the results does not change considering the PE_{EU} or E_{EL} since all the compared solutions are using electricity as energy source (see Fig. 6 A and B).

The two objects of this optimization are the minimization of the cost and the maximization of the energy savings under the constraint of maintaining thermal comfort. In such a case, typically a feasible solution that minimizes all objective functions simultaneously does not exist. The optimal cases lay on the Pareto front composed by solutions that cannot be improved in any of the objectives without degrading the second object. In Fig. 6 and Fig. 7, the Pareto front, for the set of solutions considered in this work, is highlighted with a light green underlay. The red underlay highlights solutions that are not optimal since enable lower savings and same cost of at least one solution of the Pareto front. The differences in terms of energy savings between the On/Off low or high power and modulating HP are not significant in all the considered climates but the modulating HP and high power On/Off HP are more expansive than the On/Off low power HP.

The night set back slightly reduces the heating demand, therefore it has a small effect in Stockholm and Stuttgart but no effect in Rome where the heating demand is almost zero.

Switching off the air conditioner, when not in operation, i.e. the during the winter season for the case when the electric heating is active), reduces the standby consumption and comes without any additional costs.

The free-cooling active seven days per week on the one hand reduces the cooling demand while on the other hand increases the energy consumption of the fans, increasing also the overall energy consumption. When the $PE_{10\text{-}30\text{-}30}$ instead of E_{EL} is considered, the results of the cases with free cooling (see violet and dark green markers) are overlapped to the respective cases without free cooling (see yellow and light blue markers).

Since in the reference case almost half of the electricity demand is required for lighting, changing the illumination system from fluorescent to LED has a great benefit at low cost. In fact, the solution with electric heating, HP and LED (see light gray circle marker) is close to the Pareto front in all the climates for both E_{EL} and PE savings plots. The same technology with PV (square light gray marker) is close to the Pareto front only for Rome. Since here, the heating demand is almost zero, the HP technology appears between the cost optimal solutions only when it is combined with PV and LED or PV, LED and battery. The reversible On/Off HP (for heating and cooling) either combined or not with LED, is always between the best solutions for the climate of Stockholm and Stuttgart. When the renovation package involving electric heating, On/Off cooling HP and

LED (see light gray circle marker) is compared with On/Off HP H/C (see yellow circle marker), in Stuttgart and Stockholm, it is noteworthy that the scenario for evaluation of the energy savings (i.e. E_{EL} or $PE_{10\text{-}30\text{-}30}$) might change the ranking of the solutions. In Fig. 6.A and Fig. 7.F, it can be seen that the renovation package with electric heating, On/Off cooling HP and LED (light gray marker) gives the same or even more E_{EL} savings than the On/Off HP H/C, but the situation is reversed when the savings are evaluated in terms of $PE_{10\text{-}30\text{-}30}$ (see Fig. 6.D and Fig. 7.H). The monthly conversion factors of the 10-30-30 scenario are almost zero during summer therefore the savings during the wintertime have higher impact on the calculated yearly energy savings. When the PV is considered together with the HP and LED with or without battery (see square and asterisk light blue markers) these solutions are cost optimal in all the climates.

The Pareto front highlights a set of cost optimal solutions from which one renovation package has to be selected based on economic restrictions and other parameters (e.g. thermal and visual comfort, quickness of the retrofitting, personal preferences, etc.). But there are some clear and remarkable trends that can be noted: in Stockholm and Stuttgart the solution with reversible On/Off HP_{lp} H/C + LED have the same cost but guarantee higher energy savings with respect to other solutions such as reversible On/Off HP_{lp} H/C and El. Heating + On/Off HP_{lp} + LED. Adding PV increases the energy savings but also the cost therefore the selection of this solution depend on the economic restriction. Adding battery only slightly increases the energy savings while the cost substantially increases. In Rome El. Heating + On/Off HP_{lp} + LED with or without PV allows to keep the additional cost near to zero enabling high-energy savings.

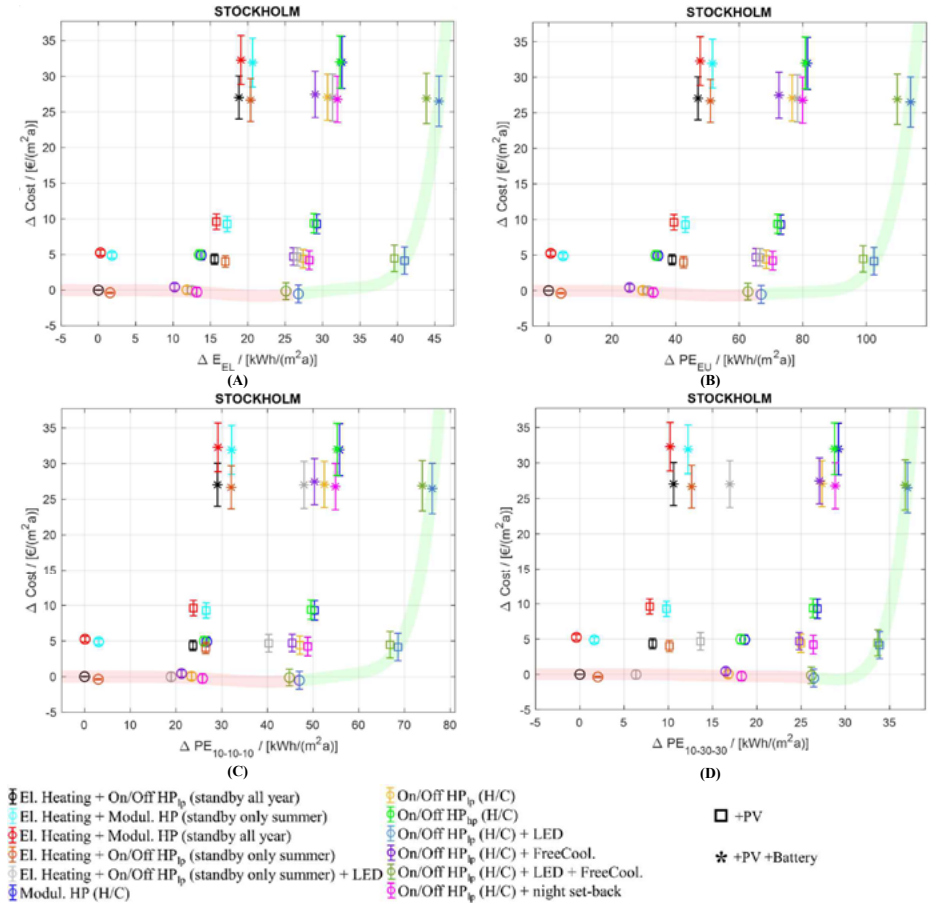


Fig. 6. Savings in terms of (A) Electric energy, (B) Primary energy according to EU conversion factor, (C) Primary energy according to 10-10-10 scenario conversion factors,(D) Primary energy according to 10-30-30 scenario conversion factors vs additional cost of the analysed technologies for the climate of Stockholm

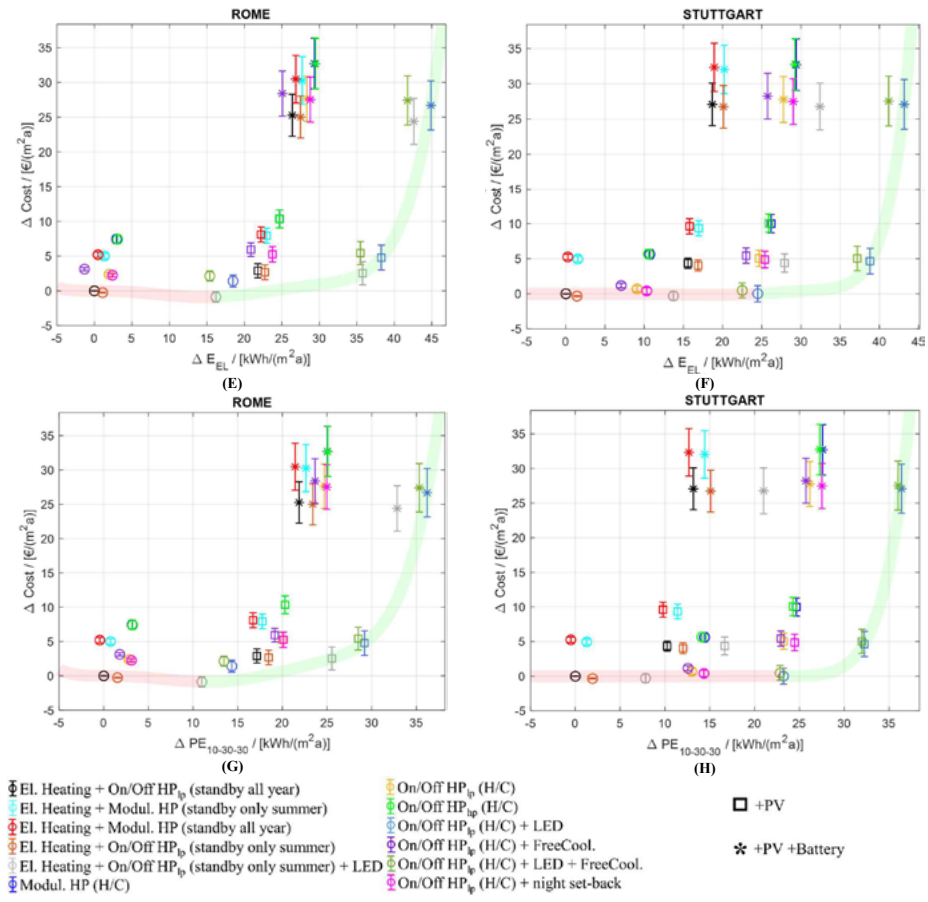


Fig. 7. Savings in terms of (E,F) Electric energy and (G,H) Primary energy according to 10-30-30 scenario conversion factors vs additional cost of the analysed technologies for the climate of Rome and Stuttgart respectively.

Table 6 shows the yearly heating and cooling demands and electricity consumptions for Rome, Stuttgart and Stockholm. Using the HP instead of the electric heating saves around 15% in terms of electricity demand in Stuttgart and Stockholm. The heating demand slightly increases and the cooling demand substantially decreases together with the electricity demand when LED technology is considered. Adding the free cooling to the On/Off HP (H/C) case, reduces the cooling demand while slightly increases the total electricity consumption, this effect is caused by the increased electricity demand of the fans. The night set-back, compared to the case with On/Off HP (H/C), slightly reduces the electricity demand only in Stuttgart and Stockholm.

Table 6. Annual heating, cooling demand and electricity consumption for the climates of Rome, Stuttgart and Stockholm.

	Heating demand [kWh$_{th}$/(m^{2}a)]			Cooling demand [kWh$_{th}$/(m^{2}a)]			Total Electricity demand [kWh$_{el}$/(m^{2}a)]		
	Rome	Stuttg.	Stock.	Rome	Stuttg.	Stock.	Rome	Stuttg.	Stock.
El. Heating+On/Off HP (standby all year)	2.7	13.1	17.2	32.7	26.0	24.5	63.8	73.8	79.0
Modul. HP (H/C)	3.1	13.5	17.6	33.4	26.7	25.0	60.8	63.1	65.2
On/Off HP$_{lp}$ (H/C)	2.7	13.1	17.2	32.7	26.0	24.5	61.8	64.7	67.1
On/Off HP$_{hp}$ (H/C)	2.8	13.1	17.2	32.9	26.2	24.7	60.7	43.3	65.4
On/Off HP$_{lp}$ (H/C) + LED	4.7	17.5	22.8	24.6	19.7	18.7	45.3	49.3	52.2
On/Off HP$_{lp}$ (H/C) + FreeCool	2.8	13.1	17.3	24.9	17.0	14.3	65.1	66.8	68.8
On/Off HP$_{lp}$ (H/C) + LED + FreeCool	4.7	17.5	22.9	17.8	12.0	9.8	48.4	51.3	53.9
On/Off HP$_{lp}$ (H/C) + night set-back	2.2	10.2	14.0	31.3	24.2	23.0	61.4	63.5	65.8

4. Conclusions

Different technologies applicable for the decentral renovation of a typical office building (cell) are evaluated considering, both economic feasibility and environmental impact for the climates of Rome, Stuttgart and Stockholm by means of dynamic building and HVAC simulations. The cost analysis is based on the equivalent annual cost (EAC) and a sensitivity analysis is performed in order to assess the influence of the used inputs on the results. The environmental impact is evaluated in terms of electricity demand and total primary energy (PE) savings calculated with a constant and monthly conversion factors representing different scenarios with different share of renewables in the electricity mix (i.e. 10-10-10: 10 % hydro, 10 % wind, 10 % PV and 70 % fossil and 10-30-30: 10 % hydro, 30 % wind,30 % PV and 30 % fossil). In this specific case study, since all the analyzed technologies require electricity as input, the same conclusion can be derived using the energy savings expressed in terms of electricity or total PE calculated with a constant conversion factor while the results might change if monthly conversion factors for different renewables scenarios are used. In fact, the renovation package with electric heating and LED has the same (in Stockholm) or higher (in Stuttgart) electricity savings than the On/Off HP for heating and cooling without LED but the situation is reversed when the savings are evaluated in terms of PE calculated with the conversion factor of the 10-30-30 scenario. The renovation packages allowing high-energy savings with low additional cost are represented, in Stockholm and Stuttgart, by HP in combination or not with LED and PV and in Rome, by LED and PV in combination with electric heating. Battery in combination with PV, HP and LED brings, in all the climates, additional energy savings with high additional cost. Technologies, which will lead to higher savings in winter with lower availability of renewables and generally higher loads, will be more valuable and this can be quantified by the proposed method.

References

[1] EPBD recast, Directive 2010/31/EU of the European Parliament and Council of May 19, 2010 on the energy performance of buildings (recast), *Journal of the European Union*, 153/13., 2010.

[2] E. Pikas, M. Thalfeldt and J. Kurnitski, Cost optimal and nearly zero energy building solutions for office buildings". *Energy and Buildings*, vol. 74, pp. 30-42, 2014.

[3] M. Gustafsson, C. Dipasquale, S. Poppi, A. Bellini, R. Fedrizzi, C. Bales, F. Ochs, M. Sié and S. Holmberg, "Economic and environmental analysis of energy renovation packages for European office buildings". *Energy and Buildings*, vol. 148, pp. 155-165, 2017.

[4] S. Stevanovic, "Parametric study of a cost-optimal, energy efficient office building in Serbia". *Energy*, vol. 117, pp. 492-505, 2016.

[5] F. Ochs and G. Dermentzis, "Evaluation of Efficiency and Renewable Energy Measures Considering the Future Energy Mix". *7th International Building Physics Conference*, Syracuse, NY,USA, 2018.

[6] M. D'Antoni, P. Bonato, D. Geisler-Moroder, R. Loonen and F. Ochs, "IEA SHC T56 - System simulation Models Part C Office Buildings", 2017.

[7] SIA 2024:2015, Raumnutzungsdaten für di Energie- und Gebäudetechnik, Zurich, Switzerland.

[8] M. Magni, F. Ochs, P. Bonato, M. D'Antoni, D. Geisler-Moroder, S. de Vries, R. Loonen, A. Maccarini, A. Afshari and T. Calabrese, "Comparison of Simulation Results for an Office Building Between Different BES Tools – The Challenge of Getting Rid of Modeller Influence and Identifying Reasons for Deviations". *Bilding Simulation Conference*, Rome, 2019.

[9] S.-I. Juelich, "CARNOT Toolbox," [Online]. Available: https://de.mathworks.com/matlabcentral/fileexchange/68890-carnot-toolbox. [Accessed 12 11 2019].

[10] F. Ascione, N. Bianco, G. Maria Mauro and G. Peter Vanoli, "A new comprehensive framework for the multi-objective optimization of building energy design: Harlequin". *Applied Energy*, vol. 241, pp. 331-361, 2019.

[11] Directive 2006/32/EC of the European Parliament and of the Council of 5 April 2006 on energy end-use efficiency and energy services and repealing Council Directive 93/76/EEC.

13th IEA Heat Pump Conference
April 26-29, 2021 Jeju, Korea

Trends and Recent R&D Activities on Fuel Driven Sorption Heat Pumps

Gerrit Füldner [a*], Edo Wiemken[a], Angeles Rivero Pacho [b], Steven Metcalf [b], Kyle Gluesenkamp [c], Zhiyao Yang [c], Andrea Frazzica [d], Marcello Aprile [c], Tommaso Toppi [e], Mario Motta [c], Robert E. Critoph [b], Peter Schossig [a]

[a]*Fraunhofer ISE, Fraunhofer Institute for Solar Energy Systems, Heidenhofstr. 2, 79110 Freiburg, GERMANY*
[b]*University of Warwick, Coventry CV4 7AL, UK*
[c]*Oak Ridge National Laboratory (ORNL),One Bethel Valley Road, Oak Ridge, TN, USA*
[d]*Consiglio Nazionale delle Ricerche (CNR), Istituto di Tecnologie Avanzate per l'Energia "Nicola Giordano" (ITAE), Via S. Lucia sopra Contesse n. 5, 98126 S. Lucia, Messina, ITALY*
[e]*Politecnico di Milano, via Lambruschini 4, 20156 Milano, ITALY*

Abstract

Over the last 4 years, the IEA-HPP Annex 43 has worked on Sorption Gas Heat Pumps (GHP). GHP have been identified as an efficient solution for space heating and sanitary hot water preparation. There was advance on several ongoing developments both for ad- and absorption technology. A water-ammonia absorption GHP based on plate heat exchangers (PHE) is under development and shows promising results both in terms of compactness and efficiency. An absorption GHP for the residential market is being developed. Another participant is working on the development of an adsorption gas heat pump with active carbon and ammonia as working fluid, using a promising new adsorber design. The development of a zeolite-water based GHP is pursued with a consortium of industry and research partners. The open source SorpPropLib materials database allows evaluation of materials for sorption heat pumps in SorpSim or other platforms. A common view on market requirements and potential was found for different markets.

© HPC2020.
Selection and/or peer-review under responsibility of the organizers of the 13th IEA Heat Pump Conference 2020.

Keywords: Gas Heat Pump;Sorption;Fuel Driven Heat Pump

1. Introduction

Over the last 4 years, the IEA-HPP Annex 43 has worked on Sorption Gas Heat Pumps (GHP). GHP have been identified as an efficient solution for space heating and sanitary hot water preparation, mainly in existing buildings. They are a complementary technology to electrical heat pumps with potential to reduce requirements on the electric grid and to balance the energy consumption in the future energy mix. Annex 43 had the aim to support the technology through cooperation between industry and academia. At present, due to a lack of competitive commercially available products, the market share of sorption heat pumps on the total heating market is marginal. However, it is expected that a potential exists to assist the transition from completely fossil fuel based heating technologies towards technologies, including environmental heat sources and thereby decreasing the demand on fossil fuels.

2. Results on Gas Heat Pump R&D

There was advance on several ongoing developments both for ad- and absorption technology. At Polimi (Italy), a water-ammonia absorption GHP based on plate heat exchangers (PHE) is under development and shows promising results both in terms of compactness and efficiency. Also an Italian company is working on an absorption GHP for the residential market. University of Warwick (UK) is working on the development of an adsorption gas heat pump with active carbon and ammonia as working fluid, using a promising new adsorber

design. Fraunhofer ISE (Germany) works on the development of a zeolite-water based GHP with a consortium of industry partners. At ORNL, research is ongoing on a GHP with salts and ammonia as working pairs.

2.1. Water-Ammonia Absorption GHP based on plate heat exchangers

At Politecnico di Milano research is carried out with the objective of developing an air source gas-fired heat pump for space heating and DHW production for domestic applications. To assure a large potential for market penetration, the target of reducing specific costs and size compared to existing products is addressed. As an additional measure to ease the industrialization of the GHP, it has been decided to rely mainly on components derived from large series production, whose manufacturers actively collaborate to the project. In particular, all heat exchangers, except the desorber, are fusion-bonded plate heat exchangers.

The outcome of the development is a 7.5 kW GAHP prototype, whose diaphragm pump and desorber have been designed to reduce the appliance size to the dimensions of a standard domestic condensing boiler. The effectiveness of different configurations of the refrigerant circuit has been investigated, together with the potential benefits of controlling the flow rate of refrigerant and solution. The achieved performances, measured according to the European Standard EN 12309, are in line with the expectation: a sGUE based on the net calorific value ($sGUE_{NCV}$) of 1.5 has been reached for the average climate (design temperature of -10 °C) and for the high temperature application (supply temperature of 55 °C). However, a detailed analysis shows room for improvements on some of the component, which are expected to boost the $sGUE_{NCV}$ up to about 1.6.

2.2. Active Carbon – Ammonia Adsorption GHP

The overall objective of the research at Warwick was to develop a domestic air source gas-fired heat pump to replace standard condensing boilers cost-effectively. The working pair is ammonia (able to evaporate at sub-zero temperatures, as required for an air-source) and active carbon. A succession of sorption generators have been prototyped, culminating in the 'kebab' design in which monolithic carbon is compressed between aluminium fins on a steel tube containing pressurised water that either heats or cools the adsorbent in a two-bed cycle with heat and mass recovery. The ‘kebabs’ are illustrated in Figs. 1 and 2.



Figure 1: ‘Kebab’ schematic

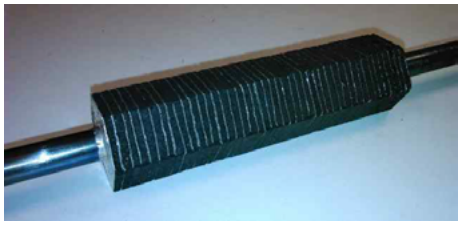


Figure 2: Sample ‘kebab’

A 10 kW system was built and tested. Initial results were poor with Coefficient of Performance (COP) a little above 1. This was due to mass transfer resistance in adsorption being too high, due to an excessive binder fraction. A new formulation has been tested in a single 'kebab' and the results are consistent with an internal COP of 1.40 when delivering 10 kW at 50°C and evaporating at 0°C or 1.34 when delivering 20 kW. Simulation results are given in Fig. 3, illustrating how power may be traded off against efficiency. It is clear that the sensitivity of GUE to power output is significant but there is the prospect of achieving an average GUE of > 1.2 in UK climatic conditions. Whether this is commercially acceptable will depend crucially on the production cost. Previous 4-bed configurations with enhanced internal heat recovery [1] show a GUE of 1.4 to be possible but at the expense of greater complexity and cost. The aim here is to explore simpler, low cost options if at all possible.

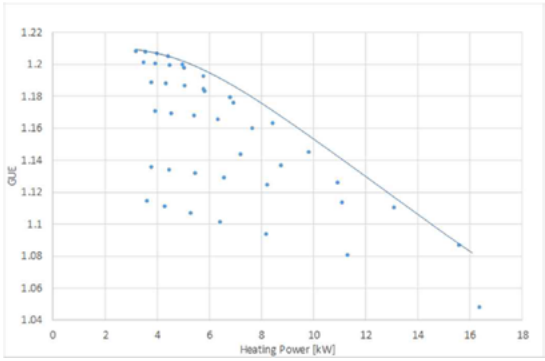


Figure 3: GUE(based on Gross Calorific Value) v. SCP for final design of 208C carbon + organic binder 'kebab'

2.3. Zeolite-water adsorption GHP

Two gas-fired adsorption heat pump products based on the working pair zeolite-water have been on the market by the companies Vaillant and Viessmann. Both are no longer market available, mainly due to high cost and not being able to sufficiently serve the retrofit market with higher needed supply temperatures at reasonable efficiency. Adsorption modules were based on a loose grain configuration and a binder based coating on stainless steel heat exchangers, respectively.

Promising developments with potentially much higher power densities have recently been made at Fraunhofer ISE together with the company Fahrenheit. The combination of an aluminium fibre structure and a direct crystallization coating of a thin zeolite layer on the extremely high surface of such a heat exchanger showed the feasibility of power densities which potentially allow for a wall hung GHP unit [2].

Activities on binder-based coated adsorbers are also being developed by CNR ITAE and University of Messina, mainly focusing on the intensification of heat and mass transfer efficiency with a low-cost and energy intensive manufacturing process [3].

There are yet unresolved issues concerning long-term stability, and proof has to be made that such adsorption modules can be manufactured in a cost-efficient way. One drawback of water as working fluid is the limitation to ambient source temperatures >0°C. A potentially feasible option is the use of exhaust air from a central ventilation unit. Compared to a compression heat pump, a gas heat pump needs only about a third of ambient source power. With a limitation of about 1 kW source power from exhaust air (typical ventilated apartment), a vapour compression heat pump with a COP of 4 could deliver a maximum power of about 1.3 kW, while a gas heat pump with a GUE of 1.3 could deliver about 4 kW.

2.4. Salt-Ammonia GHP

An ammonia-based triple-state sorption heat pump was developed and investigated by ORNL and SaltX to significantly improve the current gas heating efficiency in cold climates. The gas-fired heat pump extracts heat from cold ambient by absorbing ammonia onto salt held in a nano-coated matrix, and it supplies high-temperature heat from heat of adsorption and the heat of ammonia condensation when the salt is heated and desorbs ammonia. A simulation study identified the optimal heat pump sizing as 22-44% of peak heating load for the shortest payback under typical cold climate conditions in the U.S [4,5].

A laboratory prototype with design targets of delivering 54.4°C (130°F) hot water under ambient temperature of -20°C with GUE > 1.0 has been developed a Swedish company and ORNL and evaluated experimentally at ORNL. The prototype has a simple configuration including a salt-containing reactor and a salt-less combined condenser-evaporator. No pump or valves are needed in the fully hermetic ammonia system. The COP and capacity of the prototype progressed with insulation and improved controls in the shakedown tests, and a heating capacity of 4.4 kW at 55°C hot water supply with a cycle GUE of 1.02 was demonstrated in the laboratory with 8°C simulated ambient temperature. A dynamic model using finite-difference method has been developed for the salt-containing reactor and is now being validated with test results.

Another outcome of the Annex is the compilation of vapor pressure properties for sorption working pairs into the open source SorpPropLib materials database developed by ORNL and Purdue University. This allows evaluation of materials for sorption heat pumps in SorpSim or other platforms [6].

3. Performance potential study

A simulation study has been performed to provide performance numbers of gas fired sorption heat pumps in the residential sector in order to assess the impact of such systems with respect to environmental effects, compared to conventional heating systems.

3.1. Scope

A comparative approach is applied in this study: two different fuel driven sorption heat pump technologies based on currently developed technologies are compared with conventional heating technology, representing the exclusive use of a condensing gas boiler (reference system). The phrase ‘current technology’ in this context means one market available technology (ammonia-water absorption technology) as well as present laboratory test status of a water-zeolite adsorption technology. For these technologies, reliable data to execute the comparative calculations are available. Other technologies (e.g. ammonia-active carbon adsorption, ammonia – salt absorption, other ammonia-water absorption cycles) are still under development and may achieve promising performance results in the near future, see sections above.

To assess the potential of the heat pump systems, building loads from typical residential buildings are applied. The loads are generated through building simulation, but on base of well-defined building standards. The applied building models range from non-retrofitted multi-family houses (MFH) to new single family houses (SFH, present building standard). All calculations are executed for meteorological conditions of five European sites.

Economical aspects and life-cycle aspects are not topic of this study. An energetic and economic comparison of absorption and electrically driven compression heat pumps is e.g. shown in [7].

Thus, the performance figures and environmental savings presented in this study reflect the running system operation. The results are presented as annual values of performance (i.e., gas utilization efficiency) and environmental savings in comparison to the reference system (i.e., CO2 and primary energy savings and primary energy ratio).

3.2. Sites and thermal building loads

Climate data of five European sites (London, Potsdam, Paris, Strasbourg, Milano) were applied in the study, to determine the building heat loads. From a meteorological point of view, the sites correspond to the climate classification [8] of Cfb (warm temperate climate, fully humid, warm summer) with the exception of Milano, corresponding to Cfa (warm temperate, fully humid, hot summer) respectively.

Despite of identical or similar climate classification, the site dependent temperature conditions reveal large differences in heating demand for the buildings in the survey. For the calculation of the heat demand, hourly data of ambient temperature and humidity were generated for each site by use of the meteorological engineering software Meteonorm [9].

For four sites, the minimum ambient temperatures are still above -10°C and thus conform with the ‘average climate‘, as classified in the European Standard EN12309, part 7 [9], whereas the Potsdam site normally fits to the ‘cold climate‘ classification. Nevertheless, in the light of the very few hours of falling below -10°C at Potsdam site and for reasons of a better comparison of the results, the heating system temperature curve of the ‘average climate‘ was applied in the calculations to all sites.

The meteorological data set of Strasbourg is additionally used for the performance calculation of a representative European site (EU), applying European conversion numbers for primary energy use and greenhouse gas emission instead of individual national conversion numbers.

In the building sector, multi-family houses (MFH) play an important role in greenhouse gas avoidance strategies, as their share on building stock and on living space area is high. e.g., in Germany, 31% of the living space accounts to small and medium size MFH with 3 to 12 apartments [10]. Another reason for the interest in MFH in the context with this study is that the market available gas fired sorption heat pump from the manufacturer Robur with its capacity of 18 kWth or above yet does not fit to small residential buildings.

For the assessment in this study in the context with a larger gas driven heat pump, an MFH model was applied, which was defined within the activities in the Low-Ex project group [11]. The building model images an MFH with 3 floors and 3 apartments on each floor. The building standard corresponds to the construction period of 1959-1978, as compiled by the Tabula/Episcope Projects (see: http://episcope.eu); the total number of occupants is 13. The building model setup and calculation of thermal loads was performed in the simulation environment of TRNSYS, version 17 [12].

Two versions of the building are applied:

1. MFH as representative for an average German non-retrofitted building (building stock);
2. MFH+ retrofitted in a conventional way according to Tabula/Episcope specifications for Germany, which resemble the requirements of the German EnEV 2014/2016 [13].

The load data are transferred to hourly data of each hour of a representative year of meteorological data for the sites previously specified. Additionally, thermal loads for preparing domestic hot water (DHW) for the buildings are included. The annual share of heat demand for DHW preparation on the total heat demand is shown in Figure 4, revealing the distinctly higher significance of hot water preparation in buildings with higher energy saving standards.

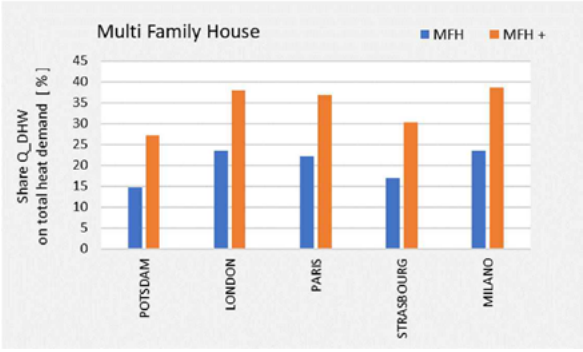


Figure 4: MFH: Share of heat demand for DHW preparation on the total heat demand.

For small capacity gas fired adsorption heat pumps, the market of single family houses (SFH) is of especial interest. Within this comparative study, two single family houses were modelled and heat loads for the sites given in Figure 2.1 have been determined:

1. SFH+ as representative for a retrofitted building with 120 m² living area;
2. SFH_{NEW} as representative of a new building with 150 m² living area.

The load calculations were carried out with a one-node building model according to DIN EN ISO 13790 [14]. The adopted U-values of the key building components are the averages of the published values of the respective countries.

The load data are determined as hourly data of each hour of a representative year of meteorological data for the sites previously specified. An overview on site dependent heating loads is given in Annex A1 of this study. The number of occupants in both buildings is 4; the DHW loads are calculated accordingly on base of the approaches, used for the MFH.

The annual share of heat demand for DHW preparation on the total heat demand is shown in Figure 5. In general, the set value of supply temperature in heating systems is expressed as a function of the ambient temperature. This heating system temperature is essential in the calculations, since the performance of sorption heat pumps as with all heat pumps is very sensitive to the supply temperature level.

In this study, the heating system temperature relations are derived from EN12309, part 7 [9]. The High Temperature curve (max. 55°C) requires moderate effort in exchange of e.g. appropriate radiators and is applied in the calculations of the multifamily buildings (stock and retrofit) in combination with the gas driven ammonia-water heat pump.

The Medium Temperature curve (max. 45°C) requires more ambition in the heating distribution system and is applied in the MFH+ and additionally in the calculations of the single family houses, where adsorption heat pumps are considered.

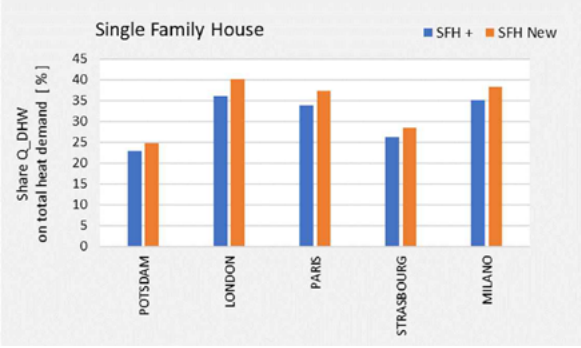


Figure 5: SFH: Share of heat demand for DHW preparation on the total heat demand.

3.3. Thermally driven heat pump models

Ammonia-Water absorption heat pump

The model is based on the gas fired absorption heat pump from Robur, model K18. The machine uses the fluid pair ammonia and water and requires ambient air as low-temperature source. Since the evaporator is integrated into the machine, the heat pump is designed for external installation. The K18 model provides a heating capacity of 18 kWth (some basic data are given in [3.1/1]). Due to the ability to deliver hot water of up to 60°C, DHW can be prepared beside space heating. The simulation model of the Robur K18 heat pump was developed by POLIMI [15] and has been applied in other comparative studies as well, such as [16, 7].

The simulation of the K18 heat pump system reflects a system setup where either the DHW buffer storage is heated or the space heating is served. In the latter case, a backup gas boiler is implemented to cover peak loads on demand. This is especially required in applications with a high exploitation of the heat pump and at colder sites (e.g., Potsdam, Strasbourg).

Water-zeolite adsorption heat pump

The adsorption heat pump model is based on experimental laboratory tests at Fahrenheit GmbH and modelling based on these results by Fraunhofer ISE; the machine is not market available yet. In the experimental setup, the working pair water with the zeo-type material SAPO-34 as adsorbent is applied. The adsorption module consists of two similar heat exchangers, one acting as combined evaporator/condenser (EC) and the other as adsorption heat exchanger (AdHX). The AdHX is coated with SAPO-34 with the partial support transformation technique as by Bauer et al. [17]. The experimental results and the component data were published by Wittstadt et al. [2].

A detailed numerical model of the adsorption module was developed at Fraunhofer ISE and validated with the experimental data. The model allows the variation of geometric key parameters of the components in order to optimize the adsorption module for a given application [18]. The data presented here are obtained with geometrically optimized components for the heating application. One important difference between the experimentally tested module and the optimized module is the size of the EC. The size of the EC was reduced significantly in order to improve the efficiency without worsening the overall dynamics of the module. The model takes into account important loss mechanisms such as condensation of the working fluid on the housing and heat flux from AdHX to EC.

The heat pump for this study is considered to be connected to a ground tube as low temperature source, as low temperatures < 5°C until now cannot efficiently be used with water as working fluid due to freezing in the evaporator.

The following operation boundaries were included in the model:

- Low temperature source temperature: 5°C - 9°C;
- Medium temperature (inlet into AdHP): 25°C – 43°C;
- Desorption temperature (driving heat from gas boiler): 80 °C – 120 °C

The source temperature is determined as a function of the ambient temperature in accordance with VDI 4650, which provides corresponding values for heating operation [19]. The maximum heating capacity of the

AdHP research unit is approx. 7 kWth. However, in the comparative study, the capacity is site dependently adjusted to the building load with the target to maximize the annual overall sGUE (heating and DHW, including gas boiler performance). Thus, the maximum capacity in calculations ranges from 7 to 11 kWth.

To emphasize a special advantage of adsorption modules, the cycling period of the sorption process can be controlled in a variable way. In the model, this period is varied between 75 s (high power output, but moderate to low GUE values) to 500 s, resulting in low power output in part-load situations, but performing at distinctively higher GUE values.

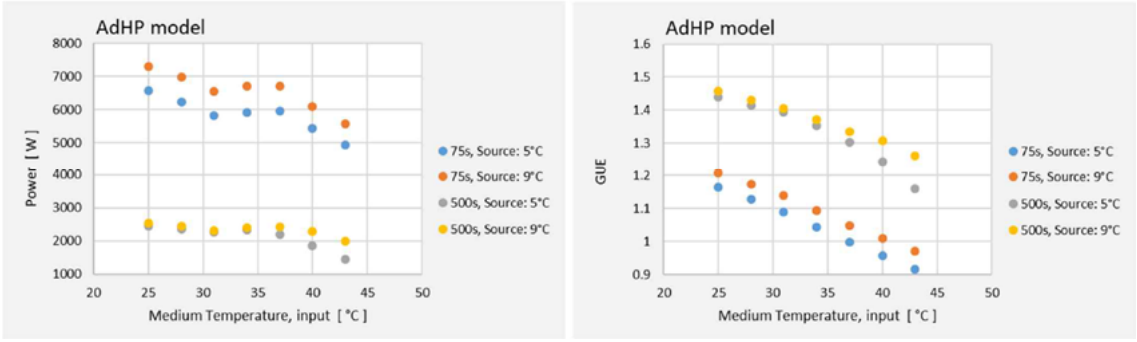


Figure 6: Performance of the AdHP versus the medium temperature input. Displayed for the minimum and maximum cycling period (75s and 500s resp.) and for the low temperature bounderies 5°C and 9°C. The lowest GUE values occur at medium temperatures close the upper limit and at lowest source temperature (5°C) and at short cycling period. In this operation mode, the efficiency is comparative to the gas boiler efficiency.

For the determination of the actual GUE in the simulation, the gas boiler runs in desorption with fixed efficiency of 85%, but additional heat recovery in the flue gas heat exchanger increases the heating capacity and thus the GUE. This is considered through an increase in overall boiler efficiency, using the relation between hot water temperature (Medium temperature) and efficiency as described.

To illustrate the scope of the AdHP performance, Figure 6 shows examples on modelled performance for the minimum and maximum low temperature source and for the minimum cycling period (high capacity) and maximum cycling period (low capacity, high GUE).

In the comparative study, a gas boiler, foreseen to be integrated into the AdHP and actually turning it into a hybrid heat pump being able to run in direct or heat pump mode, serves as high temperature source for desorption. Moreover, the boiler is used as peak-load and backup boiler (e.g., heating to the set point, in case the output temperature of the sorption unit is not matching the set value, given by the heating temperature curve). The boiler additionally covers all of the DHW heat demand, since the inlet temperature range into the heating circuit of the sorption unit is below the temperature levels of the DHW buffer: the lowest temperature level in the DHW buffer in the simulation is 45°C; this corresponds well with field monitoring results, gained in the German 'WP Monitor' project [20].

The system integration, applied in the comparative study for the AdHP development, is shown in figure 7.

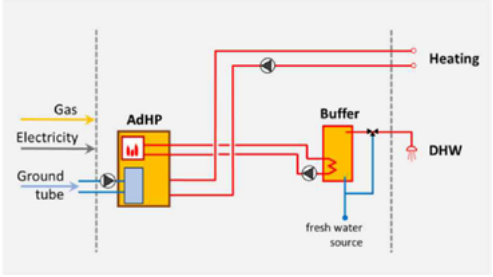


Figure 7: Sketch of the heating system with the Adsorption heat pump (AdHP).

Condensing gas boiler

The GAHP model returns the GUE for each time step; the model is based on test data. Thus, the internal boiler efficiency for heating and DHW preparation with the sorption module is indirectly included. For the external peak load boiler in the GAHP and for the gas boiler in the AdHP system (Figure 7), the efficiency (base: gross calorific value GCV) is simply calculated as function of the hot water input temperature into the boiler. The function is shown in Figure 3.6 and is derived from Haller et al. [21].

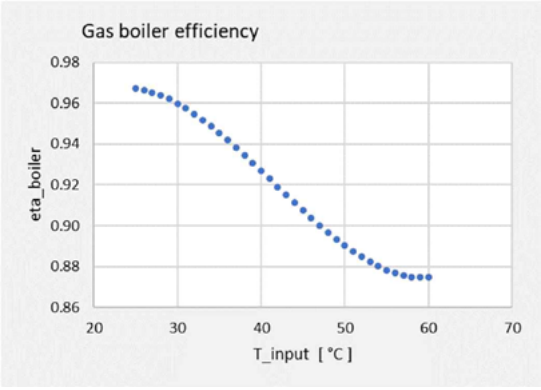


Figure 8: Efficiency model of the gas boiler (peak load use and DHW heating in the AdWP system).

3.4. Results

In the following, annual results from the simulations are depicted for the sites, buildings and heat pump systems as described. For the five sites, national conversion factors for primary energy use and CO_2 emissions were used to determine the environmental performance figures.

For each site and building, a reference calculation is carried out, considering a system without heat pump but with a gas condensing boiler as only heat source for heating and domestic hot water (DHW) preparation. Focus is on the performance (seasonal Gas Utilization Efficiency, sGUE) and on environmental benefits such as CO_2 and primary energy savings (relative to the expenditures in the reference system) and on the primary energy ratio PER. The total annual $sGUE_{total}$ is calculated by including all gas input into the heat pump and peak load boiler for both heating and DHW preparation.

The calculation of environmental benefits includes beside natural gas consumption the electricity consumption in the low temperature sources (fan of air source unit, pump of ground tube circuit respectively) and auxiliary electricity demands, e.g. for the gas boiler fan. Electricity demand for heat distribution in the building is not considered, as no substantial deviations from the reference system for this purpose are expected.

Table 1 summarizes the results by order of the building types. The range of the results expresses site dependent differences.

The results are interpreted in the following way:

Absorption heat pump system (ammonia-water):

- Highest performance is achieved at applications with a high degree of utilization (high workloads), as the heat pump performs more favorable in this operation mode. This is especially the case in the non-retrofitted MFH;
- The performance in combination with MFH+ is comparatively low due to unfavorable part-load operation of the heat pump, since the machine is oversized for this building loads (since the market available Robur 18 kW_{th} is modelled, the capacity is not varied in the simulations). Thus, in an additional calculation two buildings are served by one heat pump in order to achieve more appropriate workloads (case: MFH+, 2 units). This leads to increased performance, comparative to the results obtained in the MFH;
- If in the retrofitted MFH+ the heat distribution systems are additionally replaced by low-temperature distribution systems, allowing the Medium Temperature heating system curve. In this combination,

the highest system performance and environmental benefits are achieved (MFH+, 2 units; Medium heating temperature);
- In the most favorable applications, the sGUE (GCV) exceeds 1.35 and annual CO_2 savings up to 30 % are obtained;
- The high performance in nearly all applications is supported by the ability of the ammonia-water heat pump to cover the DHW demand as well. This is especially important in retrofitted buildings, which show a high share of DHW on the overall heat demand.

Table 1. Summary of the results for the two different heat pump systems, sorted by building types. The range of the results is due to site dependent differences. The most favorable applications are highlighted in blue.
The capacity factor indicates the adjustment of the heat pump capacity, in order to achieve an adequate heat pump operation. The factor is applied to the nominal capacity of the adsorption unit (7 kWth). The absorption heat pump model was not adjusted, as this unit is market available.

	Heating Curve	$sGUE_{total}$	Relative CO2 savings	Relative PE savings	PER / PER_{Ref}	Capacity factor
		-	%	%	%	-
Absorption: Ammonia-Water						
MFH	High	**1.30 – 1.36**	**22.9 – 28.8**	**21.5 – 26.0**	**27.4 – 35.1**	**1**
MFH+	High	1.22 – 1.30	19.2 – 26.3	19.5 – 24.0	21.3 – 31.5	1
MFH+, 2 units	High	1.29 – 1.35	23.0 – 29.2	21.6 – 26.5	27.6 – 36.0	1
MFH+, 2 units	Medium	**1.32 – 1.37**	**24.7 – 30.0**	**23.1 – 27.2**	**30.1 – 37.3**	**1**
Adsorption: Water-Zeolite						
SFH+	High	1.13 – 1.16	16.5 – 18.7	16.4 – 18.0	19.7 – 22.0	1
SFH^{NEW}	High	1.12 – 1.13	15.9 – 17.5	15.7 – 16.7	18.6 – 20.0	1
SFH+	Medium	**1.17 – 1.21**	**18.6 – 21.3**	**18.5 – 20.4**	**22.7 – 25.6**	**1**
SFH^{NEW}	Medium	**1.15 – 1.20**	**17.5 – 20.5**	**17.4 – 19.8**	**21.1 – 24.7**	**1**
MFH	High	1.07 – 1.12	9.8 – 14.6	9.8 – 14.5	10.9 – 16.9	1.5
MFH+	High	1.06 – 1.13	11.0 – 15.8	11.0 – 15.7	12.4 – 18.6	1.5
MFH+	Medium	1.12 – 1.15	14.9 – 17.7	14.9 – 17.1	17.3 – 20.6	1.5

Adsorption heat pump system (water-zeolite):
- The performance is lower than in the ammonia-water systems in some operation modes. However, in part-load operation modes, the adsorption system benefits from the possibility to increase the performance switching to higher cycle periods and thus showing in such operation modes an inverse behaviour than the ammonia-water heat pump. An appropriate layout and control of the adsorption system is therefore essential;
- The performance is affected due to the fact, that DHW demand is not supported by the heat pump, but completely served through the gas boiler. The latter fact is important, since in retrofitted or new buildings the DHW share on the total heat demand increases;
- The heating system temperature curve is more important in the application of this heat pump than in case of the ammonia-water heat pump. Thus, the highest performance is achieved in buildings, allowing the medium heating temperature curve;
- In the most favorable applications, the sGUE is in the range of 1.2 and annual CO_2 savings up to 21% are obtained.
- It needs to be kept in mind that a very simple configuration of an adsorption GHP has been modelled, which does not allow for any kind of heat recovery. Also, the limitations of the zeolite-water working

pair reflect in the fact that the device cannot be run in heat pump mode for LT source temperatures below 0°C due to freezing in the evaporator. Both issues might be overcome by recent technological developments e.g. with Active Carbon – Ammonia as working pair or by making use of an LT heat source >0°C, see above.

Table 2 presents the results by order of the sites. The range thus reflects the influence of building types and applied heating temperature curves.

Table 2. Summary of the results for the two heat pump systems and different buildings and heating system curves, ordered by sites. EU denotes the representative European site, using climate data of Strasbourg and default European conversion factors (primary energy use and CO_2 emissions in electricity consumption).

	Building, Heating Curve	$sGUE_{total}$	Relative CO2 savings	Relative PE savings	PER / PER_{Ref}	Capacity factor
		-	%	%	%	-
Absorption: Ammonia-Water						
Potsdam	all	1.22 – 1.32	19.2 – 24.7	19.5 – 24.9	24.4 – 33.3	1
London	all	1.30 – 1.37	24.3 – 27.6	24.0 – 27.2	31.5 – 37.3	1
Paris	all	1.28 – 1.36	26.3 – 30.0	20.7 – 24.8	26.1 – 33.0	1
Strasbourg	all	1.23 – 1.33	23.4 – 28.1	17.6 – 23.1	21.3 – 30.1	1
Milano	all	1.27 – 1.36	22.4 – 27.1	22.6 – 27.0	29.2 – 37.0	1
EU	all	1.23 – 1.33	20.7 – 25.8	20.4 – 25.6	25.6 – 34.3	1
Adsorption: Water-Zeolite						
Potsdam	all	1.06 – 1.21	9.8 – 20.3	9.8 – 20.4	10.9 – 25.6	1 – 1.5
London	all	1.12 -1.18	14.6 – 18.9	14.5 – 18.8	16.9 – 23.1	1 – 1.5
Paris	all	1.11 -1.18	14.1 – 20.2	12.6 – 18.5	14.4 – 22.7	1 – 1.5
Strasbourg	all	1.07 – 1.20	11.6 – 21.3	10.1 – 19.4	11.2 – 24.1	1 – 1.5
Milano	all	1.08 – 1.17	11.8 – 18.6	11.7 – 18.6	13.3 – 22.8	1 – 1.5
EU	all	1.07 – 1.20	10.9 – 20.4	10.8 – 20.3	12.1 – 25.5	1 – 1.5

Considering the two heat pump systems (absorption and adsorption), a difference occurs at the ‘colder‘ sites Potsdam and Strasbourg: In the ammonia-water heat pump system, the performance at Potsdam and Strasbourg is below the performance at the other sites. This is due to the fact that higher heating supply temperatures in general affect the performance. In principle, this is true as well in the water-zeolite system, but the effect can be superposed by the DHW preparation: due to the high heating loads at these sites, the share of heat demand for DHW is smaller than at other sites. For this reason, the influence of the low-performance DHW preparation done by the gas boiler is smaller as well. Consequently, the overall performance achieves comparatively high values in some applications. In the ammonia-water system this effect is not appearing, since hot water is prepared by the sorption heat pump as well.

4. Summary, Discussion and Future Perspective

The results underline the capability of gas fired heat pumps to distinctly decrease environmental loads in terms of CO_2 emissions and primary energy demand. In currently available applications, savings of 30 % (CO_2)

and an improvement in PER of > 35 % can be obtained. This is a significant increase in efficiency of the overall heat supply in residential buildings.

The highest sGUE value close to 1.4, achieved in the GAHP system at London site in the MFH, corresponds very well to the simulation results of 1.37-1.38, published in the UK summary report on Annex43 [22] for UK houses.

Considering the EU site with default EU conversion factors, highest performance is achieved in the GAHP system, serving two units of the MFH+, and resulting in an annual sGUE of 1.33 and close to 26 % of CO_2 savings (Medium heating temperature).

However, differences between the analyzed technologies, i.e., ammonia-water absorption and water-zeolite adsorption, are obvious. Performance results for the AdHP are throughout below the performances of the GAHP system. The main reason for this difference is the necessity in the AdHP system to use the gas boiler for DHW preparation. This requirement, resulting from present laboratory tests with water-zeolite adsorption technology, lowers the efficiency considerably, as e.g. the share of heat demand for DHW preparation in well retrofitted or new single familiy houses is high. In the mid-term, the focus in the development of adsorption heat pump thus should allow to use the sorption unit for DHW preparation at adequate temperatures as well. It can be seen from the simulations, that the sGUE‘s for space heating only in the AdWP system are very promising and approaching to annual values of 1.4.

Likewise in many heating systems, an appropriate layout of the heating components is essential. As an outcome of this comparative approach, the different part-load behaviour of the heat pump technologies leads to oppositional performances: whereas the GAHP (the market available Robur K18) obviously performs better at high utilization and an oversizing therefore has to be avoided, the AdHP (test bench model) performs much better in part-load situation through the unique possibility of cycle variation in adsorption modules. Thus, undersizing of the AdHP decreases the annual performance.

In general, lower requirements on the heating temperature, e.g., application of the medium heating system temperature curve, improves the performance. This is especially true for the zeolite-water AdHP, which shows advantages in new or retrofitted buildings with fewer requirements on high heating temperatures.

Although the performance figures of the sorption heat pump technologies, analyzed in the context of residential building heating in this study are promising, many steps towards a higher share of market penetration have still to be done. With respect to the adsorption technology, a challenge remains in enabling domestic hot water preparation, i.e., to increase the supply temperature level, and further to allow the use of a more widely available low temperature source, in the best case ambient air or building exhaust air. Identifying proper materials and heat pump design allowing for this, will make the technology complementary to present absorption (i.e., ammonia-water) technologies in the residential sector.

Other obstacles in market penetration are connected with cost, awareness of building planners and building service companies and system integration. These topics are not touched in this study. However, gas fired sorption heat pump systems are still a new technology and demonstrate great potential to decrease the gas consumption considerably on the one hand without stressing the public electricity grids on the other hand. Thus, the technology can assist European and national efforts towards a low-carbon energy supply system transformation.

Gas (natural gas, biogas, hydrogen etc.) heat pumps for domestic use are potentially a huge market if they can become the successor technology to condensing boilers whose worldwide production exceeds 13 million/year. Sorption technology can reduce gas consumption for domestic heating by almost 40% (existing products) and might increase the saving to 60% with corresponding benefits in GHG emissions.

Acknowledgements

The work of Warwick University presented here has been supported by RCUK grant EP/K011847/1, Interdisciplinary Centre for Storage, Transformation and Upgrading of Thermal Energy (i-STUTE) and Department for Business, Energy and Industrial Strategy, BEIS Low Carbon Heating Technology Innovation Fund grant ‘Adsorption gas heat pump’.

The work presented by Fraunhofer ISE and Fahrenheit has been supported by the German federal ministry of Economic affairs and energy (BMWI) under grant number FKZ 03ET1554 and FKZ 03ET1127.

References

[1] Critoph, R. E., Metcalf S., 2011, Development of a Domestic Adsorption Gas-fired Heat Pump, Proc. Inst. R. (2011-12) 1.1 – 1.7.

[2] U. Wittstadt, G. Füldner, E. Laurenz, A. Warlo, A. Große, R. Herrmann, L. Schnabel, and W. Mittelbach, A novel adsorption module with fiber heat exchangers: Performance analysis based on driving temperature differences, Renewable Energy, vol. 110, pp. 154–161, 2017

[3] L. Calabrese, V. Brancato, et al. (2017): Development and characterization of silane-zeolite adsorbent coatings for adsorption heat pump applications. Applied Thermal Engineering 116: 364-371.

[4] Blackman, Corey; Kyle R. Gluesenkamp, Mini Malhotra, Zhiyao Yang (2019). "Study of Optimal Sizing for Residential Sorption Heat Pump System," Applied Thermal Engineering, v. 150, 421-432. (March 2019) https://doi.org/10.1016/j.applthermaleng.2018.12.151

[5] Zhu, Chaoyi; Kyle R. Gluesenkamp, Zhiyao Yang, Corey Blackman (2019). "Unified Thermodynamic Model to Calculate COP of Diverse Sorption Heat Pump Cycles: Adsorption, Absorption, Resorption, and Multistep Crystalline Reactions," International Journal of Refrigeration, v. 99, 382-392.

[6] Yang, Zhiyao, Kyle R. Gluesenkamp, and Andrea Frazzica (2018). "Database of sorption material equilibrium properties," Heat Powered Cycles, Bayreuth Germany, 16-19 September 2018

[7] R. Scoccia et al., Department of Energy, Politecnico di Milano, Italy: Absorption and compression heat pump systems for space heating and DHW in European buildings: Energy, environmental and economic analysis. Journal of Building Engineering 16 (2018) 94-105

[8] M. Kotteck et al.: World Map of Köppen-Geiger Climate Classification updated; 2006. http://koeppen-geiger.vu-wien.ac.at/pdf/Paper_2006.pdf

[9] European Standard EN12309, 2015.
Gas-fired sorption appliances for heating and cooling with a net heat input not exceeding 70 kW – Part 7: Specific provisions for hybrid applications

[10] V.Bürger et al., Klimaneutraler Gebäudebestand 2050 in: Climate Change 06/2016. Published by Umweltbundesamt, Dessau-Roßlau (Germany), 2016.
https://www.umweltbundesamt.de/sites/default/files/medien/378/publikationen/climate_change_06_2016_klimaneutraler_gebaeudebestand_2050.pdf

[11] Ebert, Bernd (2018). Systematische Analyse von Mehrfamilien-Bestandsgebäuden - LowEx-Bestand Analyse Abschlussbericht zu AP 1.1 ; Karlsruhe Institute of Technology, Germany

[12] TRNSYS – transient simulation tool, developed by University of Wisconsin, USA. https://sel.me.wisc.edu/trnsys/ ; Version 17 was used

[13] Energieeinsparverordnung; national framework for requirements on energy saving in residential and non-residential buildings. Regularly updated; requirements not higher than in issue 2016 were applied.
Source: e.g., http://www.enev-online.com/enev_2014_volltext/00_titelseite.htm

[14] DIN EN ISO 13790:2008. Energy performance of buildings - Calculation of energy use for space heating and cooling

[15] Product catalogue of the Robur K18 gas absorption heat pump, providing base data: https://www.robur.com/downloads/2957/499/ROBUR_K18-5-2017_UK_b.pdf

[16] Toppi, M. Aprile, M. Motta, C. Bongs, Seasonal performance calculation and transient simulation of a newly developed 18 kW air-source water-ammonia gas heat pump for residential applications, in: proceedings of the IEA Heat Pump Conference, Montreal, Paper O.3.6.2, 2014

[17] J. Bauer, R. Herrmann, W. Mittelbach, and W. Schwieger, Zeolite/aluminum composite adsorbents for application in adsorption refrigeration, Int. J. Energy Res, vol. 33, no. 13, pp. 1233–1249, 2009

[18] A. Velte, Experimentelle Arbeiten und Entwicklung von numerischen Modellen zur Analyse und Optimierung von erweiterten Adsorptionskreisläufen für die Wärmeversorgung von Gebäuden, PhD Thesis (submitted), Universität Freiburg, 2019

[19] VDI 4650 Blatt 2:2013-01. Simplified method for the calculation of the annual heating energy ratio and the annual gas utilisation efficiency of sorption heat pumps - Gas heat pumps for space heating and domestic hot water

[20] The final report of the WP Monitor project can be found for download at https://wp-monitoring.ise.fraunhofer.de/wp-monitor-plus/german/index/ergebnisse.html; viewed April 2019

[21] Haller, M., J. Paavilainen, et al. (2011): A unified model for the simulation of oil, gas and biomass space heating boilers for energy estimating purposes. Part 11: Parameterization and comparison with measurements. Journal of Building Performance Simulation 4 (1): 19-36

[22] E. Critoph et al., School of Engineering, University of Warwick, UK: UK Summary Report on IEA Heat Pump Annex 43 'Thermally Driven Heat Pumps', August 2018

13th IEA Heat Pump Conference
May 11-14, 2020 Jeju, Korea

Dynamic performance tests of a heat pump cycle integrated latent heat thermal energy storage for optimized DHW generation

Klemens Marx[a,], Johann Emhofer[a], Tilman Barz[a], Johannes Krämer[a], Philipp Mascherbauer[a], Luisa F. Caeza[b], Gabriel Zsembinszki[b], Andreas Strehlow[c], Birgo Nitsch[c], Michael Wiesflecker[d], Raimund Zitzenbacher[d]*

[a]AIT Austrian Institute of Technology, Center for Energy, Giefinggasse 2, 1210 Wien, Austria
[b]GREiA Research Group, INSPIRES Research Centre, Universitat de Lleida, Pere de Cabrera s/n, 25001 Lleida, Spain
[c]AKG Verwaltungsgesellschaft mbH, Am Hohlen Weg 31, 34369 Hofgeismar, Germany
[d]OCHSNER Wärmepumpen GmbH, Krackowizerstraße 4, 4020 Linz, Austria

[*] Corresponding author. Tel.: +43-50550-6033; fax: +43-50550-6679.
E-mail address: klemens.marx@ait.ac.at.



13th IEA Heat Pump Conference
May 11-14, 2020 Jeju, Korea

Abstract

Latent heat thermal energy storage (LHTES) bears the advantage of high energy storage density and balancing demand and supply. A promising application for residential buildings is the use of a compression heat pump (HP) in combination with a LHTES to generate domestic hot water (DHW) with the aid of the hot refrigerant compressor discharge. In this case the LHTES enables load shifting, heat pump operation harmonization and results in energy efficiency improvement. The setup investigated here is built of a compact combination of an air/water compression HP with R32 as refrigerant and a novel 3-media – Refrigerant, Phase Change Material (PCM) and Water – Heat EXchanger (RPW-HEX) which is directly integrated into the HP cycle between compressor and condenser. A key challenge of this combination is the dynamic system operation and control which is experimentally examined in this work. RPW-HEX charging and discharging as well as continuous operation is analyzed based on several weeks of operation. In this work it is proven that the proposed combination is capable to operate stable over a wide operating range and to generate DHW effectively.

© HPC2020.
Selection and/or peer-review under responsibility of the organizers of the 13th IEA Heat Pump Conference 2020.

Keywords: Heat Pump; COP increase; Experimental Analysis; System Performance Tests; Phase Change Material; Domestic Hot Water Generation

1. Introduction

The demand for heating and cooling has seen a tremendous upswing in the past. Solely the cooling demand is reported to have five-folded between 1990 and 2014. For this reason, a great share (approx. 40%) of today's world's final energy consumption is used for heating and cooling applications in buildings as well as industries. In these applications about 65% is attributable to fossil fuels [1,2]. A cut in the fossil fuel consumption and switch to renewable energy sources is inevitable to reach the 20/20/20 target set by the European Union [3,4] and to limit the effects of climate change [5].

The trend towards energy sustainability is a key challenge and at the same time an opportunity for enabling technologies. Among others, the compression heat pump (HP) technology is traded as an enabling technology for a future carbon-emission free world. The technology enables efficient, carbon emission-free heat and cold when embedded into a renewable electricity grid. For this and other reasons the technology has seen a tremendous rise with continuously growing sales - three years in a row double-digit growth rates (2015-2017) have been reported - passing the 1-million-unit sales figure in the EU-21 end 2017 [6].

Compression HPs are particularly interesting in building applications where they serve to deliver cooling in summer, heating in winter and domestic hot water (DHW) all year long. Radiant heating and cooling by means of underfloor heating in office and residential buildings offer superior internal comfort compared to legacy air condition system for heating. The low temperature level for heating can be provided at excellent efficiency by HPs' [7]. On the other hand, DHW must be provided at elevated temperatures to tackle the risk of legionella [8]. These elevated temperatures go hand in hand with lower COPs and therefore with a significant higher electric energy consumption of the HP compared to the operation in heating mode. Hence, concepts, that can lower the electric energy consumption for DHW generation are more than welcome. This transient and high-temperature operation and the resulting inefficiencies for HPs' give rise to novel concepts which include thermal energy storage (TES). By means of load shifting and harmonization of the HP operation they can provide energy savings and result in a cost advantage [9]. TES systems can include sensible energy storage, e.g. water tanks, or latent heat thermal energy storage (LHTES) using phase change material (PCM). LHTES offer high thermal energy storage densities but the selection of the best-suited PCM material is a key issue to take advantage of the technology [10].

A promising application for residential buildings is the use of a compression heat pump (HP) in combination with a LHTES in residential buildings to generate domestic hot water (DHW) with the aid of the hot gas of the refrigerant at compressor discharge. The setup investigated here is built of a compact combination of an air/water compression HP using R32 as the refrigerant and a novel 3-media – Refrigerant, Phase Change Material (PCM) and Water – Heat EXchanger (RPW-HEX) which is directly integrated into the HP cycle after the compressor. High-temperature heat is transferred from the hot compressor discharge gas to the RPW-HEX to charge the PCM during heating or cooling operation. In DHW generation operation, low-temperature heat continues to be delivered from the condenser of the HP and only the remaining energy needed to reach the desired DHW temperature is covered by discharging the PCM inside the RPW-HEX to the water circuit.

The concept was originally presented by Emhofer et al. [11] who proved the considerable annual energy performance advantages compared to legacy systems. More than 120 potential suitable PCM materials for this concept were screened by Zsembinszki et al. [12] and, based on key performance indicators, the most suitable material was selected.

While a detailed techno-economic analysis of the systems is presented at this conference as well [13]. This contribution focuses on the experimental validation of the HP/RPW-HEX system including:

- RPW-HEX charging operation,
- RPW-HEX discharging operation,
- Continuous charging/discharging operation, and
- Continuous charging/discharging operation for DHW generation.

2. Technology

2.1. Heat pump technology

The heat pump is a water/air type heat pump with R32 as the refrigerant and comprises an inside unit, an outside unit, and the RPW-HEX. The schematic process flow diagram of the setup is depicted in Fig. 1.

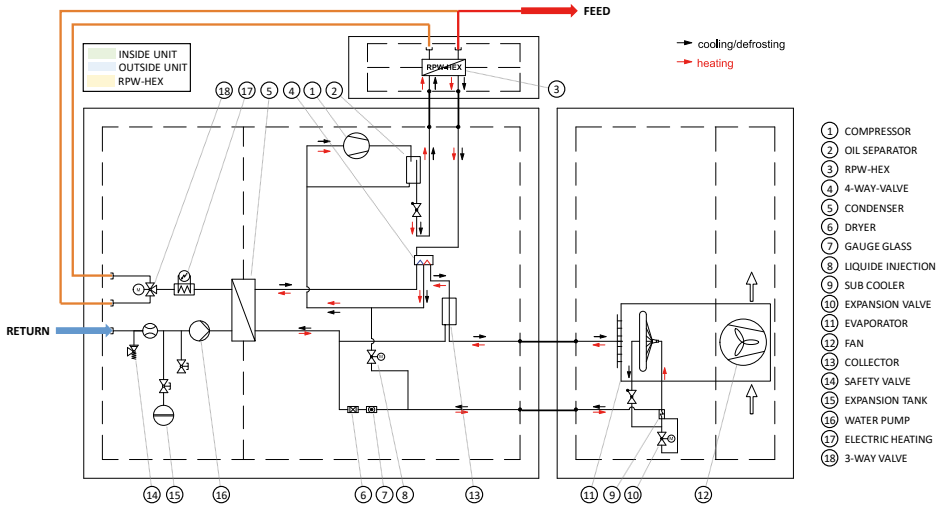


Fig. 1 Process flow diagram of the compression heat pump setup with the inside unit (light green), the outside unit (light blue) and the RPW-HEX (light orange).

In the inside unit, the compressor ① is placed which is driven by a variable speed drive. The frequency converter of the variable speed drive has a DC bus that is routed to the outside and therefore can handle AC and DC-supply as well. This allows for the direct use of DC energy from PV. After passing the oil separator ② the hot compressor exhaust flows to the RPW-HEX ③. Inside the RPW-HEX high-temperature sensible heat is effectively recovered from the refrigerant and stored mainly in the PCM. The 4-way valve ④ allows to reverse the flow of the refrigerant and facilitates either cooling or defrosting operation. In heating mode

operation, the hot refrigerant is directed to the condenser ⑤ to heat the process water flowing to the heat sink. After passing a filter dryer ⑥ and a gauge glass ⑦ the refrigerant is subcooled in the sub-cooler ⑨, expanded in the expansion valve ⑩ before entering the evaporator ⑪. The outside unit is equipped with a variable speed fan ⑫ controlled depending on the operating conditions. A small refrigerant collector ⑬ (pipe in pipe-type) is used to allow operation over a wide operating range while keeping the refrigerant volume low. The 4-way-valve closes the refrigerant cycle and directs the refrigerant to the compressor suction side. To limit the temperature at the compressor exit – a peculiarity of the R32 refrigerant cycle – liquid refrigerant is injected into the compressor suction side using the liquid injection valve ⑧. In cooling or defrosting operation, the 4-way-valve directs the hot refrigerant to the evaporator, where it condenses releasing heat. The cold refrigerant then passes the condenser where it evaporates absorbing low-temperature heat for cooling. In the water circuit a safety valve ⑭ is placed to avoid overpressure in the water circuit of the heat pump. To compensate for the density fluctuation, the expansion tank ⑮ is placed. The water pump ⑯ compensates for the pressure drop of the condenser. After passing the condenser an electric heater ⑰ would allow covering the demand whenever the heat pump delivers insufficient thermal power. However, this additional electric heating was never used in the experiments. To control the feed-water temperature the 3-way valve ⑱ is used allowing to mix the water from the condenser and the RPW-HEX.

2.2. RPW-HEX

The RPW-HEX is a novel 3-passage heat exchanger made of aluminum (110 kg empty mass) and includes a refrigerant passage, a phase change material (PCM) passage and a water passage (a cross-section is illustrated in Fig. 2 right).

The high-temperature heat is extracted from the compressor discharge and, depending on the operating condition, stored inside the PCM and/or transferred to the water directly. To enhance the heat transfer, aluminum fins are placed inside the PCM, the refrigerant passages, and the water passages. The RPW-HEX is filled in total with 40 kg of PCM. The PCM is manufactured by Rubitherm Technologies type RT64HC [14] which melts at 63-65 °C and has a total latent heat storage capacity of about 2.8 kWh. For the experimental evaluation, the RPW-HEX is equipped with in total 14 thin-film PT-100 temperature sensors class A (manufacturer RS-components type 70643577), which are directly applied to the surface of the RPW-HEX. A pressure transmitter is attached to the PCM section to capture the pressure caused by the volume displacement of the melting PCM. A schematic of the RPW-HEX including the position of the temperature sensors is shown in Fig. 2 left.

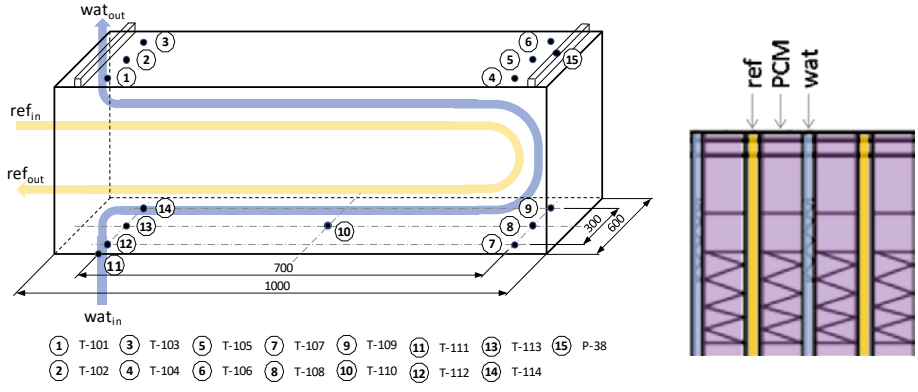


Fig. 2 Left: Schematic of the RPW-HEX showing the refrigerant pass (ref_{in} and ref_{out}) the water pass (wat_{in} and wat_{out}) as well as sensor positions (① to ⑮). Temperature sensors are attached to the surface of the RPW-HEX and include position ① to ⑭. A pressure sensor is attached to the PCM section indicated at position ⑮. Right: Cross-section of the RPW-HEX showing the refrigerant passage (ref), the PCM passage (PCM) and water passage (wat).

2.3. Energy balance calculations

Thermal energies were determined based on temperature, pressure, and flow rate measurements. Measurements were taken in the refrigerant cycle and the water circuit. The following thermal energies were determined:

- E_{Cond}: energy from the condenser either during charging $E_{\text{Cond charge}}$ or discharging $E_{\text{Cond discharge}}$ based on measurements in the water circuit directly at the inlet and outlet of the condenser.
- E_{RPWW}: energy from the RPW-HEX based on measurements in the water circuit directly at the inlet and outlet of the RPW-HEX.
- E_{RPWR}: energy from the RPW-HEX based on measurements in the refrigerant cycle directly at the inlet and outlet of the RPW-HEX.
- E_{RPW}: energy from the RPW-HEX itself (PCM and aluminium) derived from

$$E_{RPW} = E_{RPW_W} - E_{RPW_R} \tag{1}$$

- E_{tot}: energy transferred from the HP/RPW-HEX system to the water circuit based on measurements in the water circuit at the inlet and outlet of the entire system.

3. Experiments

3.1. Experimental setup

To assess the performance of the RPW-HEX integrated in the HP cycle, the system was placed in a controlled laboratory environment at the AIT Austrian Institute of Technology. The laboratory infrastructure allows for high precision control of the temperature and flow rate of water to the system. The outside unit of the heat pump was placed in a climate chamber enabling air temperature and humidity control over a wide range (down to -20 °C). Calibrated water temperature, pressure/pressure drop and flow sensors, air humidity and temperature sensors, as well as electric consumption meters, were used. A mass flow meter (Coriolis type), positioned after the gauge glass ⑦ (see Fig. 1), allows measuring the refrigerant mass flow rate. Note, the refrigerant mass flow rate was not always accessible because of 2-phase flow in the sensor at certain operating conditions. In addition to these sensors, heat pump internal sensors (mainly temperatures, pressures, and flows) were integrated into the laboratory control and data acquisition system via Modbus interface to allow for control and real-time monitoring of the system operation.

For testing, the system was filled with 3.9 kg of R32 and water was used in the hydraulic circuit. The arrangement of the HP and RPW-HEX including hoses and measurements is shown in Fig. 3.

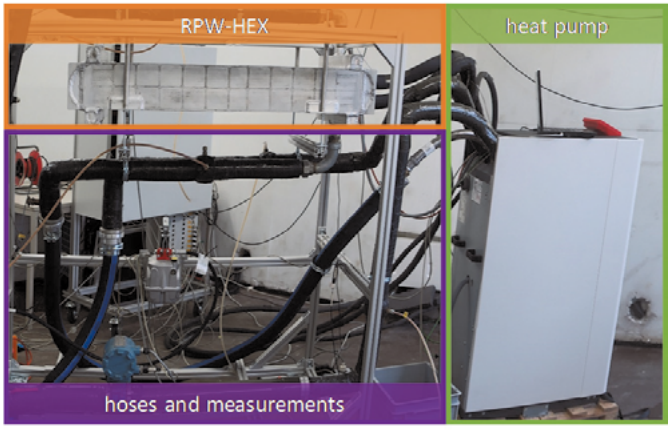


Fig. 3 Experimental setup showing the heat pump inside unit (green), the RPW-HEX (orange) and hoses and sensors for the flow rate measurements (violet).

3.2. Experimental campaign

To gain an understanding of the operation of the HP with an integrated RPW-HEX a series of experiments have been conducted. For these experiments the climate chamber, where the outside unit of the heat pump was located, was operated at -7 °C dry/-8 °C wet bulb temperature, which reflects the requirements prescribed by the EN 14511 for HP testing. The water inlet temperature of the heat pump ("RETURN" in Fig. 1) was held constant to 33 °C while the water mass flow was changed depending on RPW-HEX charging or discharging operation. In the first measurement series solely charging or discharging was investigated, while in the second series the system was operated cyclical (continuous charging/discharging operation). Furthermore, the water mass flow through the RPW-HEX controlled by the three-way valve (⑱ in Fig. 1) was once switched between on/off only (*discharging I* operation) and the other time varied to guarantee a stable outlet temperature to the heat sink (*discharging II* operation). The water flow rates have been selected to meet the requirements in typical operation of such a system. An overview of the experiments is shown in Table 1.

Table 1. Overview of experiments

Series	Description	Compressor speed in %	Water mass flow in kg/s		Flow rate through the RPW-HEX during discharging
			charging	discharging	
1	charging	90	0.245	-	none
1	discharging I	0	-	0.14	constant
1	discharging II	90	-	0.14	constant
2	cyclic operation I	90	0.245	0.14	constant
2	cyclic operation II	90	0.245	0.14	variable

4. Results

4.1. Experiments Series 1

Series 1 focused on the complete charging and discharging behavior of the system considering long term charging and discharging to assess the operating limits of the RPW-HEX.

For the first charging experiment (cf. *charging* in Table 1) the system was operated for more than 20 hours where the measured RPW-HEX temperatures, as well as RPW-HEX refrigerant outlet temperature, is shown in Fig. 4. The RPW-HEX was pre-heated to 33 °C at the beginning with the aid of the external water cycle. The refrigerant inlet temperature to the RPW-HEX was almost constant at approx. 110 °C. After approx. 4, 10.5, and 17 hours of operation, the HP switched to defrosting operation (refrigerant cycle

operated in reverse mode) due to icing of the outside unit. The defrosting operation caused a sharp decrease of RPW-HEX temperatures T-101 to T-103 as well as RPW-HEX refrigerant outlet temperature (T-06) attributable to the drop of compressor outlet temperature in this operating mode. After about 6.5 hours of operation all RPW-HEX temperatures passed the melting temperature of 64 °C of the PCM. The steep increase of T-107 to T-109 (blue lines) as well as T-06 after this event can interpreted as the end of melting of the PCM inside the RPW-HEX.

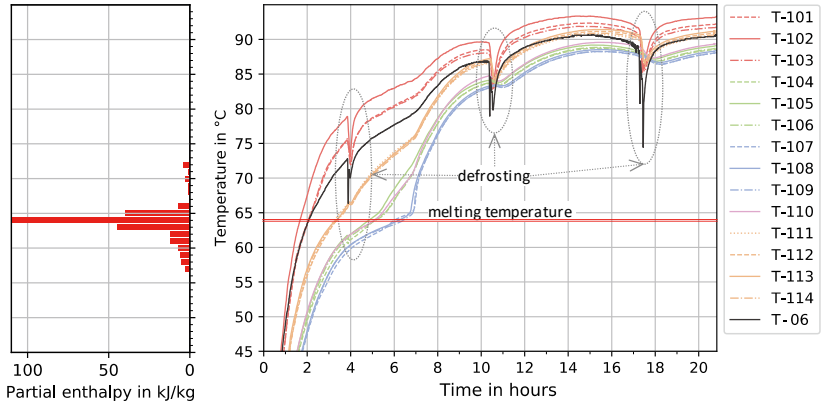


Fig. 4 Experimental results for the *charging* test in Series 1. Left: Partial enthalpy diagram PCM melting [14]. Right: Measured temperature profiles of RPW-HEX surface temperature measurements (T-101 to T-114, cf. Fig. 1) as well as RPW-HEX refrigerant outlet temperature (T-06).

To obtain the thermal energy stored in the RPW-HEX for the first discharging experiment (cf. *discharging I* in Table 1), the heat pump was switched off and the entire water was directed to the RPW-HEX using the 3-way valve (cf. ⑱ in Fig. 1) in the water circuit. Discharging was stopped once the RPW-HEX temperatures reached the level of the water inlet temperature (33 °C) – after about 1 hour. The PCM has two solidification peaks: at 64 °C and 61 °C (cf. Fig. 5 left). The 64 °C solidification peak was very well observed from the RPW-HEX temperature measurements while the second solidification peak at 61 °C appeared later in the experiments at about 57°C (cf. Fig. 5 middle). This may be an indication of delayed solidification which has been observed by others as well [15-17]. The same melting/solidification behaviour was found for a different LHTES application and phenomenological modelling was presented in [18]. However, the experiments revealed that the water temperature at the RPW-HEX outlet can reach up to 85 °C (cf. Fig. 5 right) if the three-way valve is fully open. This must be considered for the implementation in residential buildings where often plastic-compound pipes with a maximum operating temperature of 75 °C are used today. After the 85 °C peak the water reaches a plateau at about 57 °C, which can be attributed to the second solidification peak of the PCM. At the end of the discharging experiment, in total 6.3 kWh thermal energy was extracted from the RPW-HEX if it is cooled from initial approx. 90 °C to 33 °C.

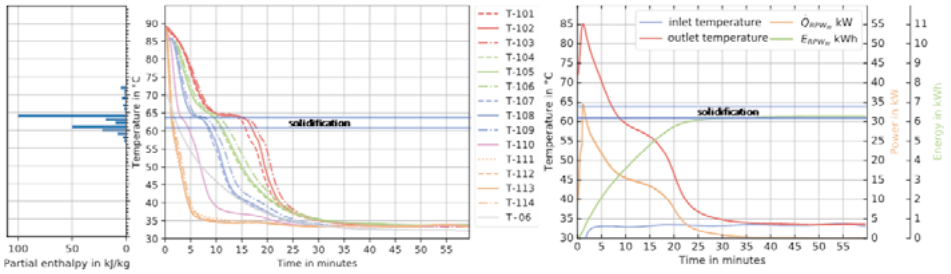


Fig. 5 Experimental results for the *discharging I* test in Series 1. Left: Partial enthalpy diagram PCM melting [14]. Middle: Measured temperature profiles of RPW-HEX surface temperature measurements (T-101 to T-114, cf. Fig. 1) as well as RPW-HEX refrigerant outlet temperature (T-06). Right: Water temperatures at the inlet and outlet of the RPW-HEX as well as thermal power and energy from the RPW-HEX.

The discharging experiment with running compressor (cf. *discharging II* in Table 1) is shown in Fig. 6. Similar solidification plateaus were observed compared to the *discharging I* test. However, for this test the solidification plateau appeared even more pronounced because the water, in this case, was pre-heated by the condenser to about 45 °C and therefore, less energy was drawn from the RPW-HEX compared to *discharging I* at the beginning (cf. orange lines in Fig. 5 and Fig. 6 right). The experiments showed that with running compressor the RPW-HEX is not only discharged but also allows to direct exchange heat between the refrigerant and the water side, transferring approx. 2.5 kW (see $\dot{Q}_{\mathrm{RPW_w}}$ in Fig. 6 right after about 50 minutes).

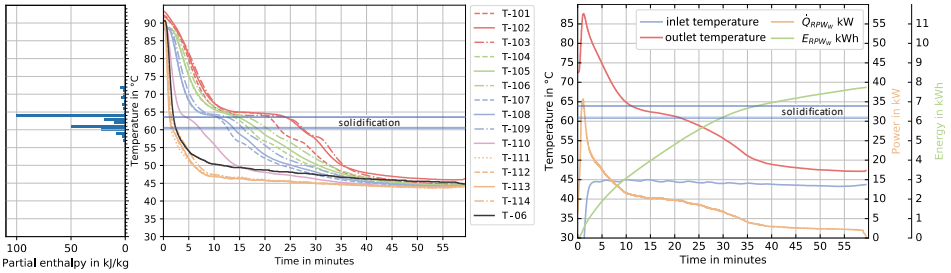


Fig. 6 Experimental results for the *discharging II* test in Series 1. Left: Partial enthalpy diagram PCM melting [14]. Middle: Measured temperature profiles of RPW-HEX surface temperature measurements (T-101 to T-114, cf. Fig. 1) as well as RPW-HEX refrigerant outlet temperature (T-06). Right: Water temperatures at the inlet and outlet of the RPW-HEX as well as thermal power and energy transferred from the RPW-HEX to the water circuit.

4.2. Experiments Series 2

To test the continuous operation of the system, it was operated in subsequent charging/discharging cycles. Based on the results from complete charging/discharging tests both the optimal conditions for switching between both operating modes was identified. Charging of the RPW-HEX should preferably end if all the PCM is molten. As an indicator for this event, the point in time when the average value of T-107, T-108 and T-109 exceeds 70 °C was identified (cf. Fig. 2). Discharging was stopped once the water temperature at the RPW-HEX outlet dropped below 55 °C. This limit was selected since a lower temperature is considered useless for DHW generation and most of the latent energy should already be released from the RPW-HEX at this point (cf. outlet temperature in Fig. 6 right), too.

For the first cyclic operation test run (cf. *cyclic operation I* in Table 1), the 3-way valve (cf. ⑱ in Fig. 1) in the water circuit was not controlled, but rather fully opened or closed. To meet the requirements in a real application, the water flow to the system was reduced for RPW-HEX discharging operation.

For *cyclic operation I* the system was operated for more than 50 hours covering 7 RPW-HEX charging and discharging cycles (see Fig. 7). While the charging cycle took between 6-7 hours, depending on how many defrosting cycles were needed, the discharging cycle always took approx. 30 minutes.

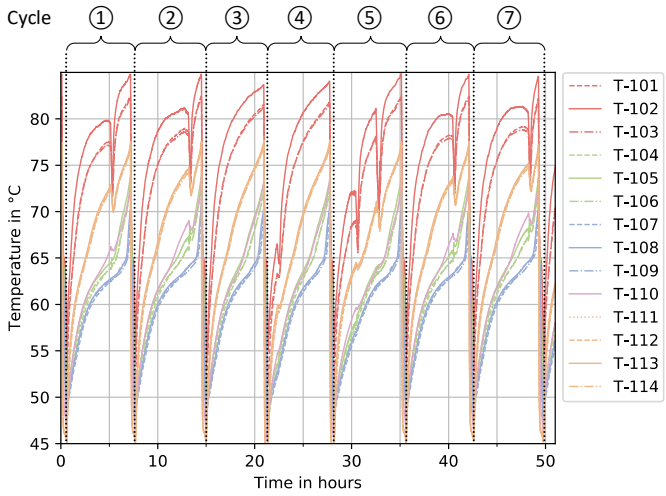


Fig. 7 Experimental results for the cyclic charging I test in Series 2. Shown are the RPW-HEX surface temperatures.

The energy balance for one typical charging/discharging cycle in test run *cyclic operation I* is depicted in Fig. 8 left. While charging the RPW-HEX, about $E_{\text{Cond charge}}$=49.2 kWh is delivered from the condenser, which can be used for heating purposes. During discharging of the RPW-HEX about 60% of the energy is attributable to the RPW-HEX (E_{RPWW}=5.36 kWh). Only about $E_{\text{Cond discharge}}$=3.5 kWh is covered by the condenser which, however, is crucial for efficient DHW generation. During the complete charging/discharging cycle, about E_{tot}=56.7 kWh is delivered to the water circuit, which is 1.37 kWh less than what is recovered from the condenser and the RPW-HEX. This discrepancy is caused by thermal losses in the piping system.

A detailed analysis of the energy balance during discharging is given in Fig. 8 right (shown as stacked plot). Based on the measurements, it is obvious that a share of about 11% is attributable to direct heat transfer from the refrigerant – the hot gas from the compressor – to the water. The analysis also reveals that about 0.86 kWh appears as thermal loss, which is relatively high compared to the total cycle (1.37 kWh). This is because the thermal energy loss is attributable to stagnant water in the piping system to the RPW-HEX, which becomes effective during discharging operation only.

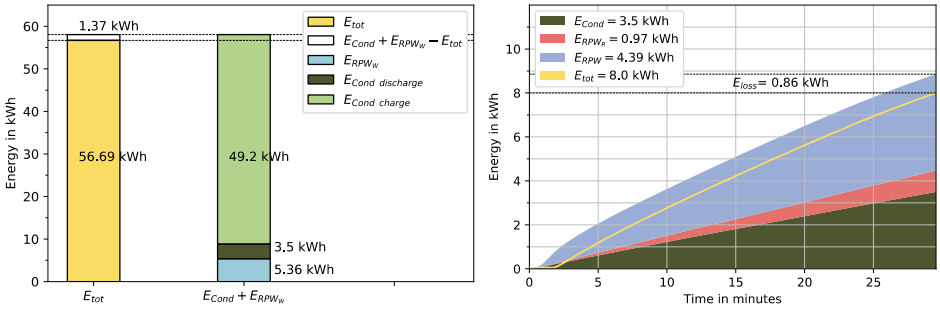


Fig. 8 Energy balance considerations for one typical charging/discharging cycle for test run *cyclic operation I* in Series 2. Left: Energy transferred to the water cycle for one complete charging/discharging cycle. Right: Energy transfer during discharging illustrated as stacked plot.

For the efficient use of the thermal energy stored in the RPW-HEX, the temperature at the outlet of the system must be controlled. This is obtained by controlling the 3-way valve (cf. ⑱ in Fig. 1) and mixing

warm water from the condenser outlet with hot water from the RPW-HEX outlet. Therefore, a control loop was implemented (cf. *cyclic operation II* in Table 1) to reach a target temperature of 55 °C at the system outlet for the use as DHW.

Measured water temperatures for one representative discharging cycle for test run *cyclic operation II* are shown in Fig. 9 left. The discharging time is longer, compared to the test run *cyclic operation I* since only a part of the water passes the RPW-HEX. Due to the reduced water flow for discharging, the condenser outlet temperature immediately increased from 41 °C to 45 °C and then drops to 43 °C later due to increased heat transfer inside the RPW-HEX caused by decreasing PCM temperature during discharging. Similarly, the discharging experiments presented before the RPW-HEX water outlet temperature increases quickly and reaches about 82 °C after about 2 minutes. The water temperature at the system outlet at the beginning decreases quickly reaching a mere at 38 °C due to the stagnant water in the piping system of the RPW-HEX – as mentioned before here as thermal energy loss. However, after about 5 minutes the setpoint (55 °C) at the system outlet is reached and DHW is obtained for about 42 minutes.

The detailed analysis of the energy balance is given in Fig. 9 right. Compared to the test run *cyclic operation I* (cf. Fig. 8 right) the total energy available for DHW increases by 22%, while the contribution from the RPW-HEX (E_{RPW}) is almost equal. This is caused by the increased contribution from the condenser ($E_{Cond\ discharge}$) and the direct heat transfer from the hot gas (E_{RPWR}).

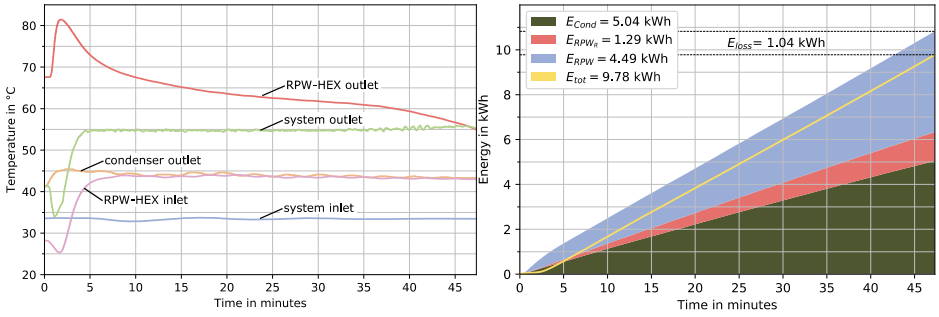


Fig. 9 Left: Temperature profiles in the water circuit for a typical discharging cycle for test run *cyclic operation II* in Series 2. Right: Energy transfer during discharging illustrated as stacked plot.

5. Conclusions and Outlook

In this work, it was experimentally verified that the proposed setup, a LHTES – in the form of an RPW-HEX – integrated in the hot gas section of the refrigerant cycle of a compression HP, allows for effective, parallel generation of heat and DHW for residential buildings at a beneficial *COP*. Startup, normal operation, reverse cycle operation, i.e. outside unit defrosting, shutdown and restart operation were successfully tested without major difficulties. However, it was found that care must be taken to avoid condensation of refrigerant inside the RPW-HEX – a safety measure to avoid refrigerant, and potentially also oil accumulation inside the refrigerant section of the RPW-HEX. This requirement demands adapted startup and operation procedures which shall be implemented on the level of the HP controller.

The RPW-HEX surface temperature measurements turned out to be effective to trigger discharging in an automated system. Certain temperatures can give an idea for the melting and solidification peaks of the PCM inside the RPW-HEX.

The continuous charging/discharging operation of the system revealed that for the selected operating conditions the current design of the RPW-HEX can deliver approx. 8 kWh of DHW per discharging cycle and 3 discharging cycles can be obtained per day. Compared to what is needed according to EN16147 (2017), this is 1.36 times the daily DHW consumption of an average apartment (5.845 kWh) per discharging cycle. Therefore, the RPW-HEX with decentral sensible DHW storages (cf. [11,13]) may serve DHW to in total 4 apartments if a constant return water temperature of 33 °C is assumed. Note, that the return water temperature from the sensible DHW storages in a real-life application strongly affects this temperature value. Switching between heating and DHW generation was smooth and HP operation itself was uninterrupted neither had to be adjusted. This clearly underlines the ability of the system for effectively shifting thermal loads, harmonizing the operation to run the HP at high efficiency although generating high-temperature heat.

Based on the knowledge gained from the experimentation the design of the RPW-HEX, the defrosting operation procedure, and the startup-procedure were adapted. A new optimized design of the RPW-HEX is currently being manufactured to be tested in near future.

Acknowledgements

The authors thank A. Zottl, J. and W. Zach for supporting the experiments. This work was part of a project which has received funding from the European Union's Horizon 2020 research and innovation programme under grant agreement No 768824 (HYBUILD). GREiA is certified agent TECNIO in the category of technology developers from the Government of Catalonia. The authors at the University of Lleida would like to thank the Catalan Government for the quality accreditation given to their research group (2017 SGR 1537). This work is partially supported by ICREA under the ICREA Academia programme.

References

[1] IEA. Energy Technology Perspective 2017. IEA Publications, International Energy Agency; 2017. ISBN: 978-92-64-27597-3
[2] Mengxue, L., Joseph, L. Review on carbon emissions of commercial buildings. Renewable and Sustainable Energy Reviews 119 (2020). DOI: 10.1016/j.rser.2019.109545.
[3] European Council. *2020 climate & energy package*. European Comission.
[4] COP24. *United Nations Framework Convention on Climate Change.* Presented at the 21st Conference of the Parties 2018, Katowice, Poland.
[5] IPCC. Global Warming of 1.5 °C. The Intergovernmental Panel on Climate Change; Special Report; October 2018.
[6] Nowak, T., Westring, P. European Heat Pump Market and Statistics: Report 2018. The European Heat Pump Association AISBL (EHPA); 2018.
[7] Olesen, B. W. Radiant Floor Heating In Theory and Practice. ASHRAE Journal, July 2002.
[8] World Health Organization. *Guidelines for drinking-water quality*. World Health Organization, 2017; 4th edition. ISBN: 978-92-4-154995-0.
[9] Moreno, P., Solé, C., Castell, A., Cabeza, L.F. *The use of phase change materials in domestic heat pump and air-conditioning systems for short term storage: A review.* Renewable and Sustainable Energy Reviews 39 (2014) 1–13. DOI: 10.1016/j.rser.2014.07.062.
[10] Xu, H., Sze, J. Y., Romagnoli, A., Py, X. *Selection of Phase Change Material for Thermal Energy Storage in Solar Air Conditioning Systems*. Energy Procedia 105 (2017) 4281 – 4288. DOI: 10.1016/j.egypro.2017.03.898
[11] Emhofer, J., Barz, T., Marx, K., Hochwallner, F., Cabeza, L. F., Zsembinski, G., Strehlow, A., Nitsch, B., Weiss, M.. *Integration of a compact two fluid PCM heat exchanger into the hot superheated section of an air source heat pump cycle for optimized DHW generation*. 25th IIR International Congress of Refrigeration, Montreal, Canada, August 24−30, 2019. DOI: 10.18462/iir.icr.2019.645.
[12] Zsembinszki, G., Gasia, J., Oró, E., Cabeza, L.F. Phase change material selection for two innovative compact energy storage systems in residential buildings. XI Congreso Nacional y II Internacional de Ingeniería Termodinámica; 2019.
[13] Emhofer, J., Marx, K., Hochwallner, F., Barz, T., Cabeza, L.F., Zsembinszki, G., Strehlowc, A., Nitsch, B., Wiesflecker, M., Pink, W. *Techno-economic analysis of a heat pump cycle including a three-media refrigerant/phase change material/water heat exchanger in the hot superheated section for efficient domestic hot water generation.* 13th International Energy Agency Heat Pump Conference; May 11-14; Korea.
[14] Rubitherm. *Data sheet RT64HC*. Rubitherm Technologies; retrieved on July 22, 2019 from https://www.rubitherm.eu/media/products/datasheets/Techdata_-RT64HC_EN_06082018.PDF
[15] Cabeza, L.F. *Advances in thermal energy storage systems: meth-ods and applications*. Woodhead Publishing, Oxford, 2014
[16] Rathgeber, C., Schmit, H., Miró, L., Cabeza, L. F., Gutiérrez, A., Ushak, S. N., Hiebler, S. *Enthalpy-temperature plots to compare calorimetric measure-ments of phase change materials at different sample scales*. Journal of Energy Storage 15 (2018), p. 32–38. DOI: 10.1016/j.est.2017.11.002.
[17] Mehling, H., Barreneche, C., Solé, A., Cabeza, L. F. *The connection betweenthe heat storage capability of PCM as a material property and their performance in real scale applications*. Journal of Energy Storage 13 (2017), p. 35–39. DOI: 10.1016/j.est.2017.06.007.
[18] Barz, T., Emhofer, J., Marx, K., Zsembinszki, G., Cabeza, L.F. *Phenomenological modelling of phase transitions with hysteresis in solid/liquid PCM.* Journal of Build Performance Simulation. DOI: 10.1080/19401493.2019.1657953.

13th IEA Heat Pump Conference 2020

13th IEA Heat Pump Conference
April 26-29, 2021 Jeju, Korea

Simulation-Based Eco-Economic Assessment Of Heat Pump Systems For Refurbishing All-Electric Non-Residential office building With Complex Energy Demand Structures

Laura Maier*[a], Xuchao Ying[a], Konstantin Finkbeiner[a], Sarah Henn[a], Jan Richarz[a], Markus Nürenberg[a], Tanja Osterhage[a], Dirk Müller[a]

[a] RWTH Aachen University, E.ON Energy Research Center, Institute for Energy Efficient Buildings and Indoor Climate, Mathieustrasse 10, 52074 Aachen

Abstract

Heat pumps (HP) are a key technology to reduce CO_2 emissions in buildings. Yet, profitability of HP-based systems is often poor due to high electricity prices compared to gas prices. Consequently, HP-based systems in new non-residential buildings in Germany only accounted for 17 % in 2018 [1]. However, the German government intends to introduce carbon pricing which could increase HPs´ market penetration.
To evaluate the profitability of all-electric systems in non-residential buildings, the energy system of an old military hospital, which is transformed into a technology and laboratory center called FUBIC, is designed.
We create the building model and analyze the building´s thermal demand using Modelica. Based on this, a HP-based all-electric and a conventional supply scenario are modelled. As KPI, we calculate the annuity and CO_2 emissions in both 2018 and 2030 based on three carbon pricing scenarios.
Results show that, despite its lower emissions, HP-based system´s annuity is lower than that of the conventional scenario regardless of the carbon pricing scenario. The main cost drivers are the demand-related costs which can be decreased by advanced operating strategies.
© HPC2020.
Selection and/or peer-review under responsibility of the organizers of the 13th IEA Heat Pump Conference 2020.

Keywords: Non-residential Buildings; All-electric Heating Systems; Modelica; Building Stock

1. Motivation

Over the last years, the German government introduced measures in order to reduce CO_2 emissions. These measures mainly focus on the electricity sector representing 21 % of the final energy demand in Germany [2]. Here, the share of renewable energies (RE) in total electricity generation reached 37.8 % in 2018, aiming at 80 % by 2050 [3]. In contrast to that, in the heating and cooling sector, which has a share of 50 % of the final energy demand, RE sources only accounted for 14 % in 2018 [2,4]. Obviously, implementing RE sources in the heating sector would contribute strongly to a decrease in total CO_2 emissions in Germany. This is why the German government set the aim for an almost climate-neutral building stock by 2050 [5]. One measure to achieve this is to substitute fossil-based heat generation systems by those utilizing RE sources [5]. In this context, sector coupling plays a key role. By coupling the electricity and the heating sector, the already realized shift towards REs in the electricity sector can be exploited even more. This is why according to [6] and [7], the electrification of the heating sector is crucial for achieving a holistic energy transition and reach the set aims for 2050. In this study, we refer to heating and cooling systems merely utilizing electricity as energy source as all-electric systems.

* Corresponding author. Tel.: +49-241-80-49795; fax: +49-241-80-49769.
E-mail address: laura.maier@eonerc.rwth-aachen.de.

In the context of all-electric systems, heat pumps (HPs) and chillers are key technologies as they can utilize RE sources (electricity supply and ambient energy) and enable sector coupling. However, in non-residential buildings, the primary energy source is gas and HP-based systems only account for 17 % in new buildings, assuming even lower ratios in the building stock [1]. Nevertheless, non-residential buildings´ share in the total energy demand in the building sector was 37 % in 2014 [8]. This trend is also reflected in the poor amount of current research activities on all-electric systems in the non-residential building sector [9].
A major obstacle to the prevalence of all-electric systems is their profitability. Compared to oil or gas prices, electricity is approximately 4 to 5 times more expensive in Germany [10]. However, fuel prices are strongly fluctuating and their development is uncertain. In addition, there have been some recent developments towards pricing of carbon dioxide, which would strongly influence the given comparison.
This paper contributes to the economic profitability of all-electric systems based on HPs by following steps:

- In chapter 2, an overview of typical energy supply systems in non-residential buildings as well as current and future regulatory boundaries are given.
- We present the developed simulation-based approach for economically and ecologically assessing two supply systems in chapter 3. In addition, future scenarios regarding the development of CO_2 factors and CO_2 pricing are discussed.
- In chapter 4, we show that profitability of HP-based all-electric systems strongly depends on regulatory and economic boundary conditions. Despite their potential to reduce CO_2 emissions, all-electric systems are not necessarily profitable regardless of the carbon pricing scenario applied.
- Based on the results, we deduce a break-even point for CO_2 pricing as well as electricity and gas prices and derive measures in order to support the spread of HP-based all-electric systems.

2. State of the art: Energy supply systems and price development

2.1. Energy supply systems in non-residential buildings

In Germany, the majority of energy systems in non-residential buildings is fossil-based [11]. Besides agriculture, gas is the primarily used energy source. District heating is the second leading source whereas electricity has only small shares. Considering the prediction for the shares of energy sources used for space heating given in [12], we detect a decreasing amount of used gas whilst at the same time increasing renewables such as biomass or geothermal energy. According to the forecast, the absolute consumption of electricity used for space heating remains almost constant between 2009 and 2050 indicating that HPs´ share will remain constant as well.

According to the forecasts presented in [12], electricity will not dominate future heating supply. One reason are high electricity prices in comparison to the other energy prices [10]. This results in the decreased integration of HPs despite their higher efficiency in comparison to conventional heat generators. In addition, HPs have higher capital-related cost when compared to conventional boilers even reinforcing this effect. One aspect which might increase the profitability of HP-based energy systems, however, is the development of carbon pricing. Over the last years, different measures to price CO_2 emissions have been introduced which will greatly influence the profitability of energy systems and thus the choice of energy sources. As HPs support the integration of REs, carbon pricing would encourage their implementation.

2.2. Current and future energy and CO_2 prices

When assessing the profitability of energy systems, regulatory and economic boundary conditions strongly influence the results. The following chapter summarizes current and future energy price developments as well as methods of carbon pricing.
A major reason for the prevalence of gas-based heating systems are low gas prices as well as their well-known technology. Over the last 10 years, gas prices even dropped favoring the integration of gas-based energy systems. In 2018, regular customers (20 – 200 GJ/a) paid 6.08 ct/kWh (all taxes included), whereas industrial customers (100 – 1.000 TJ/a) paid 2.65 ct/kWh including consumption taxes (excluding value added tax (VAT)). Since 2009, an average annual gas price decrease of 0.64 % for regular customers and 2.99 % for industrial customers is observed. [7]
In contrast, increasing prices were recorded for electricity. Prices for the German regular customer (2.5 – 5 MWh/a) have risen by an average of 2.77 % per year over the past ten years. In the large customer segment (2

– 20 GWh/a) the increase was slightly lower at 2.19 % per year. In the second half of 2018, German electricity prices amounted to 12.44 ct/kWh for industry (consumption taxes included, VAT excluded), respectively. [7] Obviously, gas prices are 4 to 5 times lower than electricity prices given the current regulatory and boundary conditions. Therefore, HP-based energy systems would have to reach a SCOP of 4 to 5 in order to achieve equal operating costs which is usually not realistic [13].

Nevertheless, the current regulatory and economic boundary conditions are under constant change. A factor which could strongly influence the given conditions is carbon pricing. Over the last years, various forms of carbon pricing have been introduced as a measure to beat climate change in many countries. There are currently two types of CO_2 pricing systems [14]:

- Direct pricing by applying e.g. taxes
- Indirect pricing by introducing certificate trading [15]

In Europe, the latter is realized by the EU Emissions Trading System (ETS). Sectors which are covered by the system are the energy, industrial and EU-aviation sector. Sectors like the traffic, building, small industry, agriculture and waste sector are referred to as Non-ETS sectors. For these, EU member states set the goal for 2030 to reduce emissions by 38 % compared to 2005. In 2018, however, the German government decided to extent the ETS to the heating and traffic sector. They intent to introduce 3 phases in Germany [16]:

1. From 2021 to 2025: CO_2 certificates are sold for fixed prices starting from 10 €/t in 2021 to 35 €/t in 2025.
2. In 2026: A certificate auctioning system is introduced with prices ranging from 35 to 60 €/t combined with a fixed upper limit for overall emissions.
3. From 2027 onwards: Based on the findings of the former phases, the necessity of upper and lower boundary prices is checked and the system will be adapted accordingly.

In contrast to the implemented trading system in Germany, other countries like Switzerland have introduced a direct pricing system realized by a carbon tax. Starting from 2008, the Swiss government has taxed fossil fuels like gas and oil, gradually adapting the price per ton CO_2 depending the overall emission level.
This development will strongly influence the profitability of all-electric systems in comparison to conventional heating systems and might favor the spread of HP-based energy systems.

3. Methodology

In order to economically assess HP-based systems in the non-residential building sectors, a simulation-based approach is adopted to compare two supply scenarios for the refurbishment process of an office and laboratory building called FUBIC. One scenario represents a state-of-the-art set up based on a condensing gas boiler (CGB) whilst the other scenario is a HP-based all-electricity scenario and thus is not common in non-residential buildings.

3.1. Simulation-based assessment of FUBIC

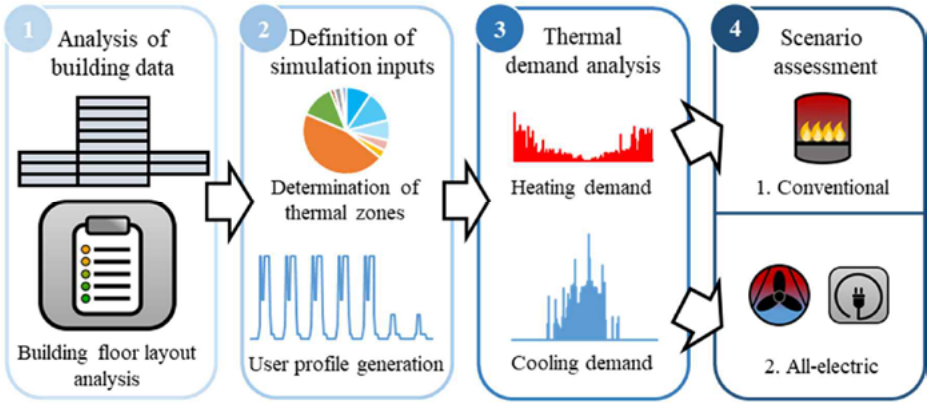


Fig. 1. Simulation-based assessment of a conventional and a HP-based all-electric supply scenario.

The use case is a former military hospital in Berlin, which is transformed into a business, laboratory and innovation center called FUBIC. The center will host start-ups and young companies of the sectors life science, health, communication and IT. FUBIC´s area will be divided into 30 % laboratory spaces, 60 % office spaces and 10 % ancillary areas.

In an early planning phase within the construction process of a building, the operating costs have to be estimated. In practice, this is usually done by applying static calculation methods. However, once the building operation starts, it becomes obvious that a priori estimated energy demand and actual energy consumption often differ greatly [13]. This is especially true for HP-based systems. HPs' efficiency strongly depends on external boundary conditions such as supply and ambient temperatures impeding the prior estimation of energy consumption and thus operating costs.
In this context, dynamic simulations are a promising tool to overcome this obstacle. Dynamic models enable a more realistic assessment of building and energy system performance and behavior. In order to compare the two supply scenarios described before, the two energy systems are implemented in the modelling language Modelica. The used models derive from either the Modelica Standard Library or the AixLib [16]. In this way, we can depict the physically implied dynamics.

In this study, we apply a 4-step approach (s. figure 1). In a first step, we analyze FUBIC´s floor layout deducing zones with similar utilization and boundary conditions (e.g. laboratories, group office, etc.). As a result, we obtain 9 zones which are the basis of the following energetic analysis. For each of these zones, we estimate people presence influencing the use of lights and other electrical devices based on weekly profiles from the Swiss standard SIA 2024 [17]. These boundary conditions serve as inputs for the simulation program and result in both an electrical and a thermal demand in step 3. In the final step, these demands are covered by the supply scenarios. Finally, we can estimate the annuity as well as CO_2 emissions based on the resulting energy demand and maximum thermal loads of the whole system.

3.1.1. Step 1 to 3: FUBIC´s thermal demand
A building model representing the demand side is the first model to be used for the simulation of a building energy system (s. figure 1). It considers various usage purposes of areas inside FUBIC. For modeling such a large multi-zone building, considering various usage purposes of its areas, a reduced order model approach developed by Lauster et al. [17] is applied. The model, which is available in AixLib [16], joins the building physics based on the German Guideline VDI 6007 [18] and the models for internal gains caused by persons, machines and lighting. As described in the guideline, the thermal response of the building can be calculated by using an electric equivalent model with resistances and capacities. In this way, the computation time is reduced considerably resulting from fewer parameters and equations.

For the parametrization of the electric equivalent model, the open-source software tool TEASER [19] is applied. It is used to calculate the resistances and capacities based on information about the geometry and physical properties of the building. Furthermore, TEASER includes a statistical database of representative building setups und thus enables a quick generation of archetype buildings with little input data. The parameters are exported by TEASER in such a structured format that they can be automatically imported into AixLib [16], with which the building model is set up.
The FUBIC building model is extended from an institute building archetype with laboratories. The input data for this archetype is summarized in table 1.

Table 1. Input parameters for simulation tool TEASER for the FUBIC building: Geometry and physical properties.

Number of floors	6 above-ground floors
Net leased area	11,112 m²
Zone layout	Elongated, h = 1 floor
Construction type, year	Heavy, 2018
Ventilation	Mechanical ventilation

With the information extracted from the floor plans, rooms of an equal or similar usage type are classified into one thermal zone, which is assigned with use conditions based on the German standard DIN V 18599 and SIA 2024 [17,20]. The various use conditions determine features like the room set temperatures, air exchange rates, occupancy profiles, internal gains and others. Figure 2 visualizes the resulting zoning of FUBIC

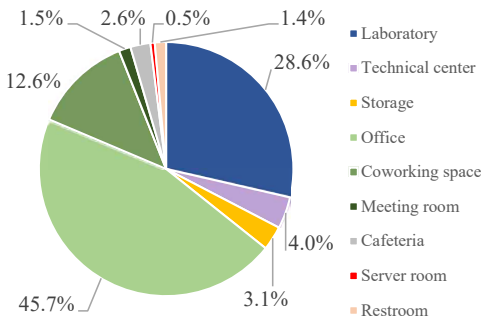


Fig. 2. Classification of FUBIC into thermal zones of equal usage.

The internal gains in the building model include the occupancy of persons, usage of machines and lighting with schedules. The schedules are based on Swiss standard SIA 2024 [17] and are modified for the FUBIC building. For each zone a week profile is defined, considering the difference between weekdays and weekends. The German standard DIN V 18599 [20] also defines the range of indoor comfort temperatures, air exchange rates and conditions of the supply air for each zone. Reference room temperature set points for cooling are given by the German guideline VDI depending on the outdoor temperature to reduce energy demand. [21]
External loads are estimated with weather data given in Test Reference Years (TRY) for Berlin. Germany's National Meteorological Service [22] offers localized weather data of an intermediate TRY as well as special TRYs with a cold winter or a hot summer.
As a simulation result, 4 different thermal demand types are determined in step 3, which are covered by the supply scenarios. The 4 thermal demand types are distinguished as follows:

- Dynamic heating via the ventilation system and static heating via the floor heating system (FHS)
- Dynamic cooling via the ventilation system and additional cooling via recirculation coolers

All in all, 67 % of the heat demand and 22 % of the cooling demand are supplied via the central air handling unit whilst the residual demand is covered by the FHS and the recirculation coolers respectively.

3.1.2. Step 4: Scenario assessment

The main difference between the assessed scenarios is the heat generation system. In the conventional scenario, a CGB is used whilst in the all-electric scenario an air-to-water HP and an electrical backup heater cover FUBIC´s heat demand. The electrical backup heater supports the heat when outdoor temperature drops below a predefined bivalence temperature of -2 °C [23]. Furthermore, the HP is equipped with a modulating compressor (30 to 100 % of design load) as thermal demand is strongly dynamic and thus heat demand can be covered more precisely. In order to guarantee more flexibility, a buffer storage is implemented connecting the HP and the air handling unit (AHU) in parallel. The buffer storage is loaded based on a hysteresis of 5 K while the FHS is controlled by a supply temperature control and a PID controller.
The implemented HP model is taken from the open source library AixLib [16]. It represents a grey box model in which the HP´s COP is based on the Carnot efficiency. The HP´s COP is calculated as follows [16]:

$$COP = \eta_{Carnot} \frac{T_{con}}{(T_{con} - T_{evap})} \quad (1)$$

In equation 1, T_{con} and T_{evap} represent the condenser and evaporator leaving temperatures. The Carnot efficiency η_{Carnot} is assumed to be 50 % and describes the ratio of the HP´s actual COP to the theoretical maximum COP [24]. The implemented model computes transient behaviour using a first order differential relation for the condenser and evaporator water and air volumes. For further information, see documentation of open source model AixLib.Fluid.HeatPumps.Carnot_y [16].

In the given use case, heat has to be supplied at two temperature levels: 50 °C to provide for the AHU´s heat demand and 35 °C for the FHS. These low temperatures support the utilization of HP-based systems, as HP´s COP increases with decreasing supply temperatures (s. equation 1). However, HP´s COP is more significantly influenced by external factors such as the ambient temperature as well as the operating point. In addition, process heating and cooling demand are less flexible demands compared to e.g. space heating. These boundary conditions pose additional requirements for the energy system which is why conventional heat generators are more common in cases like that. Their efficiency does not depend strongly on supply temperatures making prior estimation of energy demands easier. The adopted simulation-based approach, however, enables the detailed analysis of HP´s operation and thus overcomes this obstacle.

3.2. Energy market scenarios

When evaluating the profitability of energy systems, the economic and regulatory boundary conditions strongly influence the outcome. In the following chapter, we analyze important factors that influence the economic assessment of HP-based energy systems focusing on energy prices and CO_2 emissions in Germany.

3.2.1. Development of energy and carbon pricing

Based on the recent development of electricity prices (s. chapter 2.2), a price increase for electricity is assumed for future-related evaluations in this study. Despite the observed decrease in gas prices, the World Energy Outlook New Policies Scenario predicts that gas prices will increase as of 2020 [25]. In the following use case, an increase to 5 ct/kWh for industry (≙ large customers) by 2030 is presumed. Regarding electricity prices, the past trends are extrapolated, resulting in 16 ct/kWh for industrial customers.

Apart from that, carbon prices also influence the economic assessment of energy systems. However, their future development is uncertain as they have just or not yet been introduced in some countries. Nevertheless, they will strongly influence the profitability of energy systems and should thus be included in an economic assessment. In this work, the focus lies on the development in Germany and three scenarios are deduced.
The first scenario reflects an old policies scenario. Here, no carbon pricing is introduced which is referred to as the no costs scenario (NC scenario). In addition, a low costs scenario (LC scenario) is introduced. As the German government discusses the option to introduce a lower boundary of 35 €/t for carbon pricing starting in 2027. In the LC scenario, this is assumed to stay constant until 2030. In contrast to that, a third scenario is evaluated in which the future trend for pricing carbon from 2021 until 2025 is extrapolated resulting in a price of 66 €/t in 2030. We refer to this scenario as high costs scenario (HC scenario).

3.2.2. Future CO_2 factor

When evaluating the costs for carbon, it is necessary to predict the mass of CO_2 emissions caused by the respective energy system. In this context, CO_2 factors play an important role as they allow to estimate the CO_2 emissions per kWh of an energy source.
Since it depends on the chemical properties of an energy source, its CO_2 factor does not underlie time-dependent changes in most cases. This applies, for example, to natural gas (approx. 202 g/kWh) and heating oil (approx. 266 g/kWh).
Due to the Energiewende the composition of the so called electricity-mix in Germany and likewise its CO_2 factor are subject to steady changes. The past development and a prediction of this CO_2 factor is shown in figure 3. As the share of RE in the electricity mix has the highest impact on the CO_2 factor, the prediction is calculated with a linear function of this share. This function is based on past data points of the CO_2 factor and RE share in Germany. The future development of the RE share itself is also a linear function with the goals of the German government being the interpolation points. Obviously, the CO_2 factor will decrease in the next years due to an increasing RE share. Additionally, it is shown that by 2042 the CO_2 factor of electricity will be lower than the factor of gas.

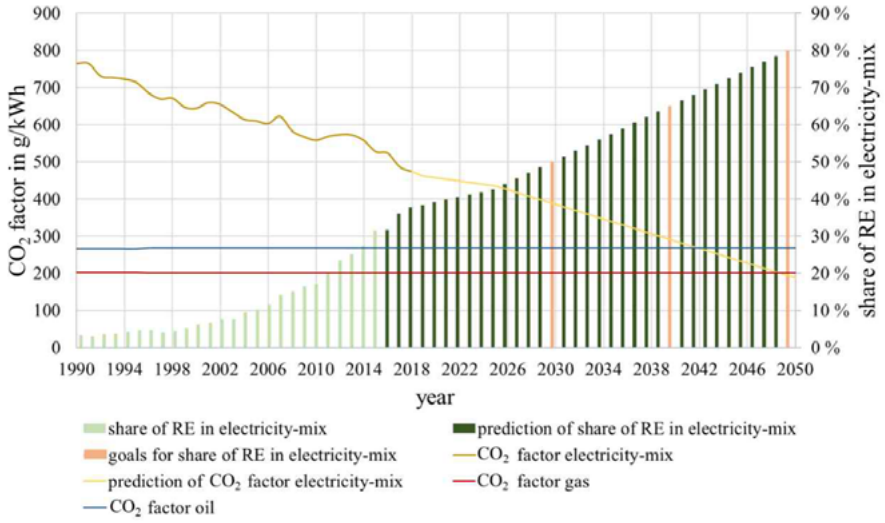


Fig. 3. Development of the CO_2 factor of the average German electricity mix in recent years and in the future. The CO_2 factors of gas and oil are given as benchmarks.

The presented methodology enables the simulation-based assessment of the two developed supply scenarios. As a result, we obtain the operating costs of the system which depend on the energy prices and the CO_2 factor respectively.

3.2.3. Key performance indicators

Based on the deduced energy prices and CO_2 factors the two scenarios are compared. In order to evaluate the systems from an ecological point of view on the one hand, the annual CO_2 emissions caused by the cooling and heating system are calculated. On the other hand, the system´s annuity is used to compare the profitability of the two scenarios. The annuity calculation bases on the German guideline VDI 2067 [26]. According to VDI 2067 the annuity consists of 3 cost types: the capital- (cap), demand- (dem), and operation-related costs (op). The capital-related costs are based on a market analysis on component investment costs. The demand-related costs derive from the simulation results and the electricity, gas as well as carbon prices of the respective year (s. chapter 3.2.1. and 3.2.2.). The operation-related costs are calculated as a fixed percentage of the capital-related costs which depend on the component type [26]. The annuity-based capital-related costs depend on the component service life. The components considered are the HP, the chiller, the CGB and the electrical heater.

Results and discussion

The resulting thermal demands of the FUBIC building are shown in figure 4. The heating power is mostly required in the cold season (September to April). At the start of the simulation, a considerable heat demand is detected as a result of the initialization process but not taken into account for the demand analysis.
Regarding the cooling demand, a base load of around 80 kW covered by the additional cooling can be identified throughout the entire period (additional cooling). This is caused by the cooling demand of the servers. The dynamic cooling demand, however, is primarily required for cooling and dehumidification of the outdoor air in the warm season (May to August).

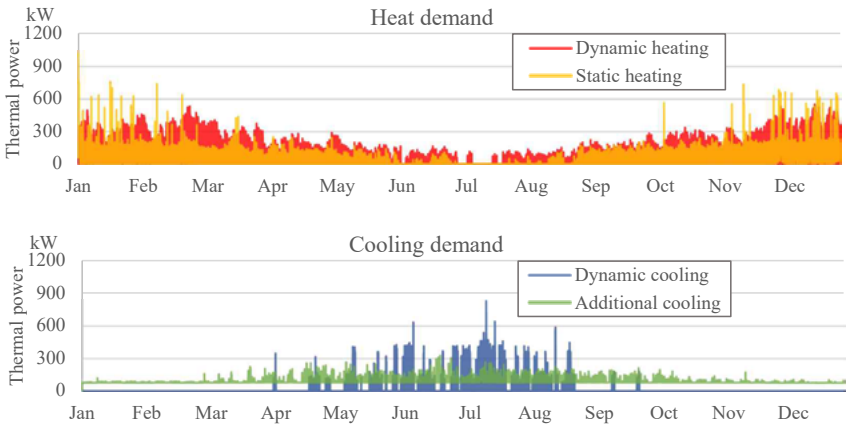


Fig. 4. Simulated heat (above) and cooling (below) demands of the FUBIC building using a TRY with a cold winter.

The presented thermal demands are the basis for the choice of a supply system. The simultaneous occurrence of heating and cooling demand e.g. impedes the use of a reversible HP. This is why a chiller has to be implemented in order to meet the cooling demand throughout the whole year. Nevertheless, a major advantage of HPs over CGBs is that while generating heat at a high temperature level at condenser site they extract heat at evaporator site at a lower temperature level at the same time. Usually, the extracted heat is taken from the ambient air or ground. However, as FUBIC´s heating and cooling demand occur simultaneously, the extracted heat can be used to partially cover the cooling demand. In this use case, the interaction is realized by a hydraulic connection via the ice storage. Here, the HP´s evaporator as well as the chiller´s evaporator are hydraulically connected via the ice storage. Hence, both the HP and the chiller can cover the cooling demand and synergy effects can be realized.

Based on the given energy demand structure, the two presented supply scenarios are assessed. Figure 5 depicts the simulation results. We compare the annual CO_2 emissions as well as the resulting negative annuity of the conventional (C) and the HP-based all-electric scenario (AE) in 2018 and in 2030. The annuity is negative in all scenarios as only costs are considered in this study. The biggest share in total costs are the demand-related costs. They make up 82 to 90 % of the annuity depending on the regarded scenario.
In 2018, the annuity of the conventional scenario is 35 % lower compared to the all-electric scenario. This effect is explained by lower gas prices per kWh in comparison to electricity prices in Germany as well as lower capital-related costs. CBGs´ capital-related costs are 50 % lower than those of HPs.
From an ecological point of view, the conventional scenario leads to an increase in CO_2 emissions of 2 % in 2018. However, this does not have any effect on the operating costs as carbon is not priced yet in Germany. Consequently, given the present boundary conditions, the all-electric system is not more profitable than the conventional scenario. The savings in CO_2 emissions are negligible as the current electricity mix in Germany is still mainly based on conventional energy sources.

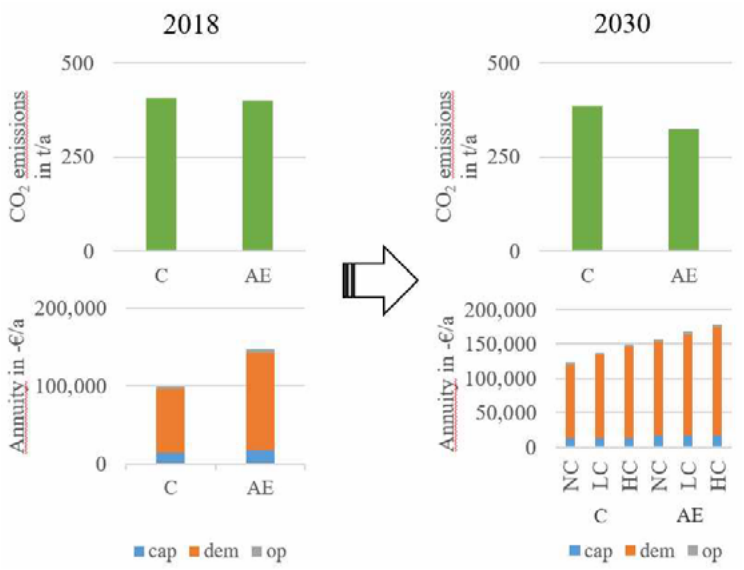


Fig. 5. Comparison of CO_2 emissions and annuity of the conventional and HP-based all-electric scenario for 2018 (left) and 2030 (right). In 2030, two scenarios for future CO_2 pricing are considered (NC = no costs; LC = low costs; HC = high costs). The system annuity is divided into the annual capital- (cap), demand- (dem) and operating-related (op) costs.

In 2030 however, the three introduced carbon pricing scenarios (NC, LC, HC) are taken into consideration which have an effect on the demand-related costs. As the share of REs in the German electricity mix increases, overall CO_2 emissions for both scenarios decrease. So even if the electricity consumption remains the same in 2030, overall emissions will be lower as the CO_2 factor of electricity decreases (s. figure 3). This effect is not applicable for the CO_2 emissions caused by the CGB. As explained in chapter 3.2.2., the CO_2 factor of gas depends on the chemical structure only and thus will remain constant in the future. As a result, the difference in CO_2 emissions in 2030 between the regarded scenarios increases to 18 %. Obviously, all-electric systems lead to higher CO_2 emission savings in the future. The reduction of CO_2 emissions simultaneously leads to decreased operating costs in 2030 due to carbon pricing.

Despite this effect, the system annuity of the conventional system is lower compared to the HP-based all-electric system in all of the regarded carbon pricing scenarios. This can be explained by the low percentage of carbon costs in the total demand-related costs. In the conventional scenario, costs for CO_2 emissions make up 11 and 19 % in the LC and HC scenario respectively. In the HP-based all-electric scenario, however, carbon costs only account for 8 and 14 % (LC and HC scenario respectively). Obviously, even though the carbon costs double in the HC scenario compared to the LC scenario, they do not influence the overall trend significantly.
For the given comparison, we calculate a break-even price for CO_2 of 559 €/t which results in equal annuity in the conventional and the all-electric scenario. Based on the researched forecasts for carbon pricing in 2030, we assume this to be unlikely.

Based on the results, regarding external boundary conditions the development of electricity and gas prices will more importantly influence the profitability of energy systems. In our use case, costs for gas and electricity make up 81 to 92 % of the demand-related costs. Even though the energy price´s influence decreases in the future as CO_2 prices will presumably be introduced, they still account for the biggest percentage in annuity. Nevertheless, in the conventional scenario, the demand-related costs increase by 80 % in the LC and by 99 % in the HC scenario. In the LC (HC) scenario, this increase is caused to an extent of 61 % (66 %) by the introduction of carbon pricing and to 39 % (34 %) by the rising gas prices.
Given the two regarded scenarios, the break-even gas price is 7.2 ct/kWh and the break-even electricity price is 11.1 ct/kWh.
Consequently, the HP-based all-electric scenario can be profitable only considering external boundary conditions in the future if either the gas price increases or the electricity price decreases in the large customer

segment. Another key factor is the system efficiency. HPs´ COP strongly depends on external influences such as the ambient temperature. In our case, a test reference year with a cold winter was chosen which decreases HP´s COP significantly. Advanced energy management systems can increase system efficiency by shifting HP´s operation e.g. to times of higher ambient temperatures. In addition, they enable the efficient coordination of heating rod and HP as we focus on a bivalent system.

4. Conclusions and Outlook

In this study, the assessment of a common conventional CGB-based and a HP-based all-electric energy supply scenario reveals that HP-based energy systems are not necessarily more profitable in the future. It becomes obvious that considering the regarded three cost types, the demand-related costs (CO_2 emissions costs and costs for electricity/gas) make up the highest percentage.
Irrespective of the carbon pricing scenario, the conventional scenario´s annuity is lower despite its higher emissions. The break-even price for CO_2 is 559 €/t which is assumed to be unrealistic. Hence, carbon pricing should be taken into consideration as it influences economic evaluation but it is not the main cost driver. In addition, we calculate the break-even gas price which is 7.2 ct/kWh and the break-even electricity price which is 11.1 ct/kWh for the large customer segment. Obviously, HP-based all-electric supply systems become more profitable once gas prices increase or electricity prices decrease.

Apart from that, we prove that conventional supply systems are not necessarily more suitable for non-residential buildings with complex energy demand structures. In the presented use case, heating and cooling demand occur simultaneously and are highly fluctuating. In this context, a HP-based energy system enables the exploitation of synergy effects between the heating and cooling systems. As HPs supply heat on condenser site while extracting heat on evaporator site, heating and cooling demand can be covered simultaneously. Nonetheless, a chiller and an electrical heater should be integrated to ensure secure energy supply throughout the whole year. This synergy effect cannot be accomplished by a conventional technology such as the CGB and needs an advanced energy management system for efficient operation.

All in all, profitability of HP-based all-electric systems mainly depends on the demand-related costs. Besides from external boundary conditions such as the given prices for electricity and gas, these costs can be decreased by high system efficiency. Intelligent operating strategies and an advanced energy management system support the profitability of HP-based all-electric systems. For the use case presented in this study, the focus should lie on the complex interaction of the heating and cooling system as they are coupled via an ice storage.

Acknowledgements

We gratefully acknowledge the financial support by Federal Ministry for Economic Affairs and Energy (BMWi), promotional reference 03ET1619B.

References

[1] Statistisches Bundesamt (Destatis). Bauen und Wohnen: Baugenehmigungen/Baufertigstellungen von Wohn- und Nichtwohngebäuden (Neubau) nach Art der Beheizung und Art der verwendeten Heizenergie 2018, 2019. Available at: https://www.destatis.de/DE/Themen/Branchen-Unternehmen/Bauen/Publikationen/Downloads-Bautaetigkeit/baugenehmigungen-heizenergie-pdf-5311001.pdf?__blob=publicationFile – [accessed 15.11.2019].
[2] Agentur für Erneuerbare Energien, 2019. Available at: https://unendlich-viel-energie.de/mediathek/grafiken/endenergieverbrauch-2017-nach-strom-waerme-und-verkehr – [accessed 15.11.2019].
[3] V1.5 Energiedaten; Geschäftsstelle der Arbeitsgruppe Erneuerbare Energien-Statistik (AGEE-Stat), Erneuerbare Energien in Zahlen, 2019. Available at: https://www.umweltbundesamt.de/themen/klima-energie/erneuerbare-energien/erneuerbare-energien-in-zahlen#textpart-1 – [accessed 15.11.2019].
[4] Lauf, Dr. T., Memmler, M., Schneider, S., 2019. Emissionsbilanz erneuerbarer Energieträger. Available at: https://www.umweltbundesamt.de/daten/energie/energieverbrauch-nach-energietraegern-sektoren – [accessed 15.11.2019].
[5] Bürger, V., Hesse, Dr. T., Quack, D. , Umweltbundesamt. Klimaneutraler Gebäudebestand 2050, 2016. Available at: https://www.umweltbundesamt.de/sites/default/files/medien/378/publikationen/climate_change_06_2016_klimaneutraler_gebaeudebestand_2050.pdf – [accessed 15.11.2019].

[6] Bundesministerium für Umwelt, Naturschutz, Bau und Reaktorsicherheit, Klimaschutzplan 2050. Klimaschutzpolitische Grundsätze und Ziele der Bundesregierung, 2016. Available at: https://www.bmu.de/fileadmin/Daten_BMU/Download_PDF/Klimaschutz/klimaschutzplan_2050_bf.pdf – [accessed 15.11.2019].
[7] Gerhardt, N., Fraunhofer-Institut für Windenergie und Energiesystemtechnik Geschäftsmodell Energiewende: Eine Antwort auf das "Die-Kosten-der-Energiewende"-Argument, Kassel, 2014.
[8] dena Deutsche Energie-Agentur, Statistiken und Analysen zur Enegieeffizienz im Gebäudebestand. Available at: https://www.dena.de/fileadmin/user_upload/8162_dena-Gebaeudereport.pdf – [accessed 15.11.2019].
[9] Ranft, F., Institut für Technik und Ökologie, Neubau eines energetisch optimierten Bürogebäudes Bob – balanced office building. Endbericht., 2007. Available at: www.enob.info/fileadmin/media/Publikationen/EnBau/Projektberichte/ 19_MonitoringAB_1_p2_BOB_k.pdf. – [accessed 15.11.2019].
[10] BWP-Bundesverband Wärmepumpe e.V., BWP-Branchenstudie 2015: Szenarien und politische Handlungsempfehlungen, 2015. Available at: https://www.waermepumpe.de/fileadmin/userupload/waermepumpe/07_Publikationen/2016-04-08_Branchenprognose_2015_web.pdf. – [accessed 15.11.2019].
[11] Jochum, P., Lempik, J., Böttcher, S., Stelter, D., Krenz, T., Mellwig, P., Pehnt, M., von Oehsen, A., Blömer, S., Hertle, H., Beuth Hochschule für Technik Berlin, ifeu- Institut für Energie- und Umweltforschung Heidelberg GmbH, Ableitung eines Korridors für den Ausbau der erneuerbaren Wärme im Gebäudebereich, 2017.
[12] Nitsch et al., Deutsches Zentrum für Luft- und Raumfahrt (DLR), Institut für Technische Thermodynamik, Fraunhofer Institut für Windenergie und Energiesystemtechnik (IWES), Langfristszenarien und Strategien für den Ausbau der erneuerbaren Energien in Deutschland bei Berücksichtigung der Entwicklung in Europa und global, 2012. Available at: https://www.dlr.de/dlr/Portaldata/1/Resources/bilder/portal/portal_2012_1/leitstudie2011_bf.pdf – [accessed 15.11.2019].
[13] Huchtemann K., Müller D., 2012, Evaluation of a field test with retrofit heat pumps. Building and Environment; p.100–106.
[14] Bundesministeriums für Umwelt, Naturschutz und nukleare Sicherheit, Klimaschutz in Zahlen: CO_2-Bepreisung. Available at: https://www.bmu.de/fileadmin/Daten_BMU/Download_PDF/Klimaschutz/pcd_co2_bepreisung_bf.pdf – [accessed 15.11.2019].
[15] Klimakabinett, Eckpunkte für das Klimaschutzprogramm 2030, 20.09.2018. Available at: https://www.bundesregierung.de/resource/blob/975202/1673502/768b67ba939c098c994b71c0b7d6e636/2018-09-20-klimaschutzprogramm-data.pdf?download=1 – [accessed 15.11.2019].
[16] Müller D., Lauster M., Constantin A., Fuchs M., Remmen P., AIXLIB–An open-source Modelica Library within the IEA-EBC Annex60 framework. In: Grunewald J., Felsmann C., editors. Proceedings of the CESBP Central European Symposium on Building Physics and BauSIM 2016; 2016 Sep 14-16; Dresden, Germany. Fraunhofer IRB Verlag:3-9.
[17] Swiss Society of Engineers and Architects – Raumnutzungsdaten für die Energie- und Gebäudetechnik (SIA 2024), Zürich, Switzerland, 2015.
[18] The Association of German Engineers, Guidline 6007, Part 1: Calculation of transient thermal response of rooms and buildings - Modelling of rooms, Beuth Verlag GmbH, Berlin, Germany, 2012.
[19] Remmen, P., Lauster M., Mans M., Osterhage T., and Müller D. (2016). Citygml import and export for dynamic building performance simulation in modelica. In Proceedings of the 3rd IBPSA-England Conference BSO 2016.
[20] Deutsches Institut für Normung e.V., DIN V 18599 – Energy efficiency of buildings – Calculation of the net, final and primary energy demand for heating, cooling, ventilation, domestic hot water and lighting. Beuth Verlag GmbH, Berlin, Germany, 2018.
[21] Siemens AG, Regeln und Steuern von Lüftungs-/Klimaanlagen, 2018. Availablte at: https://www.downloads.siemens.com/download-center/Download.aspx?pos=download&fct=getasset&id1=A6V10327348 – [accessed 15.11.2019].
[22] Deutscher Wetterdienst DWD, Ortsgenaue Testreferenzjahre von Deutschland für mittlere, extreme und zukünftige Witterungsverhältnisse. Offenbach, 2017.
[23] Deutsches Institut für Normung e.V., DIN 4701-10, Energy efficiency of heating and ventilation systems in buildings – Part 10: Heating, domestic hot water, ventilation, Beuth Verlag GmbH, Berlin, Germany, 2003.
[24] Zottl A., Nordman R., Miara M., Benchmarking method of seasonal performance: D4.4 Benchmarking method of seasonal performance under consideration of boundary conditions. Available at: http://sepemo.ehpa.org/uploads/media/D4_4_reporting_Benchmarking_method_of_seasonal_performance.pdf – [accessed 15.11.2019].
[25] ewi Energy Research & Scenarios gGmbH , Energiemarkt 2030 und 2050 –Der Beitrag von Gas-und Wärmeinfrastruktur zu einer effizienten CO2-Minderung, 2017. Available at: https://www.ewi.research-scenarios.de/cms/wp-content/uploads/2017/11/ewi_ERS_Energiemarkt_2030_2050.pdf – [accessed 15.11.2019].
[26] VDI Verein Deutscher Ingenieure e.V., VDI 2067: Economic efficiency of building installations. Berlin: Beuth Verlag GmbH; 2012.



13th IEA Heat Pump Conference
April 26-29, 2021 Jeju, Korea

Long-term evaluation of an office building with large-scale heat pump and aquifer system in southern Sweden

Tommy Walfridson[a], Martin Larsson[b], Jessica Benson[c], Oskar Räftegård[d], Ola Gustafsson[b], Caroline Haglund Stignor[b], Lovisa Axelsson[c], Pia Tiljander[b]

[a] Energy and Circular economy, RISE Research Institutes of Sweden, Stockholm , Sweden
[b]Energy and Circular economy, RISE Research Institutes of Sweden, Borås, Sweden
[c]Energy and Circular economy, RISE Research Institutes of Sweden, Göteborg, Sweden
[d]Energy and Circular economy, RISE Research Institutes of Sweden, Karlstad, Sweden

Abstract

IEA Annex 52 is the first long-term evaluation of large-scale heat pump systems. The Annex aims to survey and create a library of quality long-term measurements of GSHP system performance for commercial, institutional and multi-family buildings. The IEA Annex 52 also aims to provide a set of benchmarks for comparisons of such GSHP systems around the world.

The GSHP system in this report consists of two serial coupled heat pumps connected to a four-well aquifer and produces both heating and cooling. Total heating capacity is 0.3 MW. Due to a complex system with poor control system the Seasonal Performance Factor, SPF_{H4} is as low as 2.5 for the first year. Several control errors have been identified, including a potential short circuit of the serial DHW heat pump, erroneous operation of it for heating purpose and probable unnecessarily high condensation temperatures of the main heat pump.

The cooling system has high Seasonal Performance Factor, SPF_{C4} is 5.7 the first year. The system mainly uses free cooling, but performance decreases significantly at low load, possibly due to poor pump control. All system boundaries used are the IEA Annex 52 proposal

© HPC2020.
Selection and/or peer-review under responsibility of the organizers of the 13th IEA Heat Pump Conference 2020.

Keywords: System performance; System boundaries; Large-scale heat pump system; Annex 52 long-term evaluation; Performance Factor, Coefficeint of Performance; Office; GSHP; Sweden;

1. Introduction

1.1 Background

Measured long-term performance data for ground source heat pump systems serving commercial, institutional and multi-family buildings are rarely reported in the literature [1].

IEA HPT Annex 52 [2] is focused on long term performance measurement of GSHP systems serving commercial, institutional and multi-family buildings. Performance varies between different plants, and there is a need of more knowledge of the underlying causes. An important part of Annex 52 is to develop a methodology for measurement strategies and common system boundaries for larger heat pump systems. To achieve this 40 GSHP monitoring case are studied, covering a range of applications, located in seven countries.

It is important to make analyses based on a large amount of data and to identify key performance indicators when comparing different heat pumps.

More information with focus on factors that influence the performance is needed, identifying causes of low performance and unnecessary errors that can be avoided in the future. One example that causes low

performance of a GSHP system is for example dimensioning issues and suboptimal control systems. Reasons of low performance needs to become visible, in order to get knowledge and understanding.

The over-all performance of a GSHP system is affected by the performance of the source side ground circuit, as well as the heat pump unit performance and the load side circuit performance, including supplementary heating and cooling. The varying design and complexity of GSHP systems poses challenges in comparable performance factors.

Detailed long-term analyses of large GSHP systems for commercial, institutional and multifamily buildings are rare. This article describes one of the 40 GSHP monitoring case studies and focuses on evaluating an aquifer heat pump system. The system design is described, and Seasonal Performance Factors (SPF) are analyzed from 2 years of measurement data.

1.1.1 System boundaries

The IEA Annex 52 project has identified the need of and proposed system boundaries for large-scale GSHP system [3] based on the 2012 SEPEMO work [4]. The system boundaries are shown in Figure 1 below. The system boundaries used in this report are 0, 1 and 4. System boundary 0 is the aquifer system, including pumps and are discussed in chapter 3.1, system 1 is inside the heat pump cabinet and is estimated in chapter 3.2. The project has good measurements for system boundary 4, this is examined in chapter 3.3

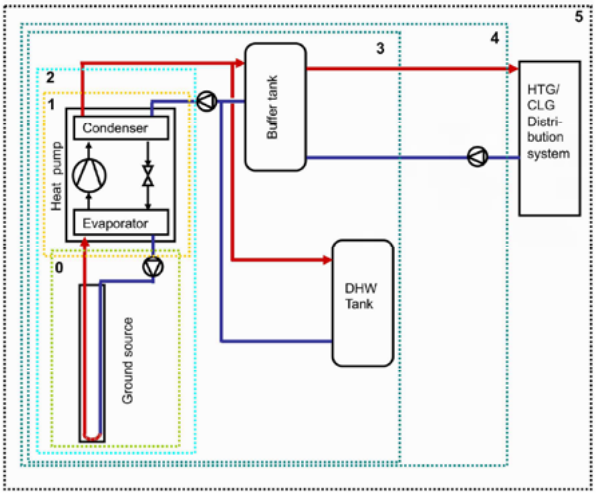


Figure 1 System boundaries according to the IEA Annex 52 project proposal (preliminary)

2 Methodology

One aim of the project is to aid the Annex 52 project in finding relevant system boundaries and test them. Another is to evaluate the performance of the GSHP system and find Performance Factors on the different system boundaries, whenever possible to calculate. This project has historic data from 2012-2014, data that previously was analyzed by RISE in an earlier, different project. No newer measurements have been used, but few changes have been made to the system until today, meaning the data is still valid for the system. The data set consist on electrical energy metering on each heat pump and summed on all circulation pumps and energy metering on aquifer, cooling, heating, subcooler heat and Domestic Hot Water, DHW, all on hourly basis. Temperatures were only measured at the four wells of the aquifer; no additional temperature data is available. Outdoor temperatures were taken from the SMHI [5] weather station at the nearby airport, corrected due to the site's much closer distance to a large lake and the elevation difference (140 m). The temperature was corrected +0,8°C, which was the annual temperature difference between the now closed city weather site and the still operating airport weather site, when comparing historic data. This approach is not perfect, as the variation is great and the temperature difference is slightly higher in the winter, but no better correction was found.

To understand the project a site visit was performed in October 2019.

2.1 Object

The heat pump and aquifer system serving an office building is located in southern Sweden, with undisturbed ground temperature of about 6 °C. One advantage offered by aquifers is the seasonal storage and another that different temperatures effectively could be stored separately, by using cold and warm wells. Essential for good performance is to optimise temperature-levels, for optimal use of the advantageous temperatures of aquifers. The system is described in Figure 2.

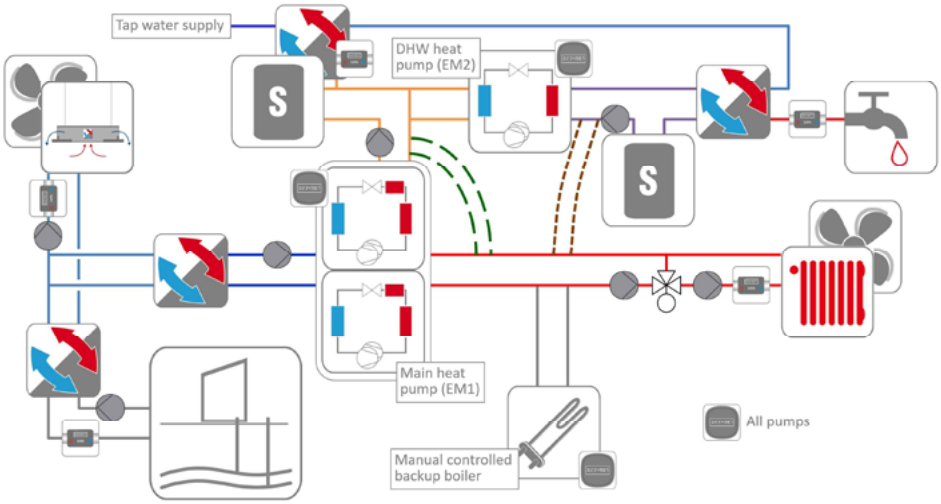


Figure 2 The heat pump and aquifer system. The Main heat pump (EM1) is using the aquifer as its heat source, while the DHW heat pump (EM2) is using the subcooler of the Main heat pump as its heat source. Dashed green and brown lines show possible heat flows, flows that are not intended according to the documentation, but are fully possible. All functionality is not described and especially the dashed lines are symbolically drawn. Pictograms by TU Braunschweig IGS, used with permission within the course of IEA HPT Annex 52

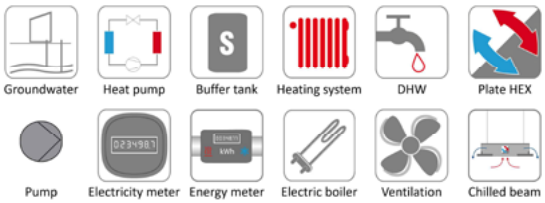


Figure 3 Explanation of pictograms used in Figure 2. Note that the heat pumps used are all dual compressor heat pumps and the main heat pump has subcooler heat exchangers. Pictograms by TU Braunschweig IGS, used with permission within the course of IEA HPT Annex 52

The main heat pump (EM1) has a heating capacity of about 300 kW and has four compressors in two refrigerant circuits, see Figure 2. The main heat pump (EM1) uses the aquifer as the heat source, while the Domestic Hot Water (DHW) heat pump uses the subcooler of the main heat pump as the heat source. The condenser of the main heat pump (EM1) heats the building, but with a change of two valves, the DHW heat pump can also heat the building. At times with to low heating capacity of the subcooler, the condensor has the possibility to heat the DHW as well, see dashed curved lines of Figure 2. The cooling system in the building is, via two heat exchangers, connected to the aquifer and the evaporator of the main heat pump. According to design documentation the main heat pump is used for heating, with temperature aid from the DHW heat pump during winter conditions with need of high heating system temperatures. The subcooler has a setpoint of 20°C, giving the DHW heat pump the possibility of high Coefficient of Performance (COP) when producing DHW.

The setpoints of the heating system is 35°C at an ambient temperature of 0°C and 50°C at dimensioning ambient winter temperature (-18°C), meaning a relatively low temperature system.

The strategy of the control system is to keep the condensing temperature of the Main heat pump (EM1) as low as possible. The main heat pump is used for heating only, the control system can not start it for cooling purpose, regardless of cooling demand. The cooling capacity is regulated by the flow from the aquifer, it has no dependency control wise to the heat pump. There is a need of cooling all year round. The cold wells of the aquifer are used at ambient temperatures above 12 °C, while the warm wells are used below 10 °C. There is no other hysteresis in changing the well of the aquifer, meaning the wells will be changed many days of the year. According to the site visit the wells are now (2019) changed manually instead.

2.2 Method

2.2.1 Calculation method

An estimated Performance Factor for heating on system boundary 1, PF_{H1}, for the main heat pump was calculated using the following formula:

$$PF_{H1} \approx \frac{Q_{Heating\ system} + Q_{Subcooler\ DHW} + Q_{DHW} - P_{EM2}}{P_{EM1}} \quad (1)$$

The only measurement done on the system boundary 1 for the main heat pump (EM1) is its own power consumption, P_{EM1}. The heat from the subcooler to preheat the DHW, $Q_{Subcooler\ DHW}$ and the heat to the heating system, $Q_{Heating\ system}$, are measured on system boundary 4. All energy supplied by the system originates from the main heat pump, the DHW heat pump is only increasing the temperatures. This means that the power consumption of the DHW heat pump, P_{EM2}, should be subtracted from the total heat supplied to calculate the performance factor of the main heat pump (EM1), PF_{H1}. As losses in the system are not stringently taken into account this can only be considered an estimate.

To be able to calculate Performance Factors on system boundary 4 the power consumption of the circulation pumps and the heat pump compressors must be allocated to the heating and the cooling side. This is done based on the heat and cooling produced for each hour of the year, according to the consensus in the Annex 52 project group. Power consumption allocated for cooling is calculated according to:

$$P_{Cooling\ ,allocated} = \left[\frac{Q_{Cooling}}{Q_{Cooling} + Q_{Heating\ system}}\right] \cdot \left(P_{EM1} + P_{pump\ ps}\right) \quad (2)$$

While power consumption allocated for heating is calculated according to:

$$P_{Heating\ ,allocated} = \left[\frac{Q_{Heating\ system}}{Q_{Cooling} + Q_{heating}}\right] \cdot \left(P_{EM1} + P_{pump\ ps}\right) + P_{EM2} \quad (3)$$

All circulation pumps are measured combined with one electrical energy meter; thus, the dedicated cooling or heating system pumps could not be allocated directly to their side of the system. All circulation pump power consumption is thus allocated according to the formulas, as this was the best possible method. The compressor power consumption of the EM2 is only used to produce DHW and does not cool the aquifer, all that power consumption is allocated to the heating side.

The calculation of the Performance Factor for heating on system boundary 4, PF_{H4}, is calculated with the following formula:

$$PF_{H4} = \frac{Q_{Heating\ system} + Q_{Subcooler\ DHW} + Q_{DHW}}{P_{Heating\ ,allocated}} \quad (4)$$

The calculation of the Performance Factor for cooling on system boundary 4, PF_{C4}, is calculated with the following formula:

$$PF_{C4} = \frac{Q_{Cooling}}{P_{Cooling\ ,allocated}} \quad (5)$$

In this paper performance factor SPF and DPF are used, were SPF is calculated over one year and DPF is calculated over 24 hours.

3 Results (Discussion)

The office building has a heating and cooling load according to Figure 4 below, the diagram has 24h average values due to low resolution of energy data.

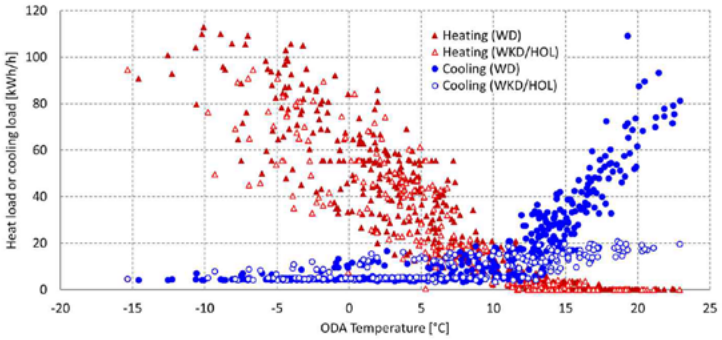


Figure 4 Heat and cooling load as a function of outdoor temperatures, average over 24h

As seen in Figure 4 the cooling load is highly dependent on the activities of the employees, during weekends and holidays the cooling load is a fraction of the workdays. The same is not seen in heating, but the variations at the same outdoor temperatures is very large. This could be due to the weather (sun/cloud) as the building has very few shadowing buildings surrounding it, but no data could verify this.

A thermal balance of the entire system was done, showing good results, see Figure 5. The negative side is sources of heat: The warm well of the aquifer, the compressors of the two heat pumps and the pumps in the system. The positive side is the sink of heat: The cold wells of the aquifer, the heating system and the Domestic Hot Water (DHW)

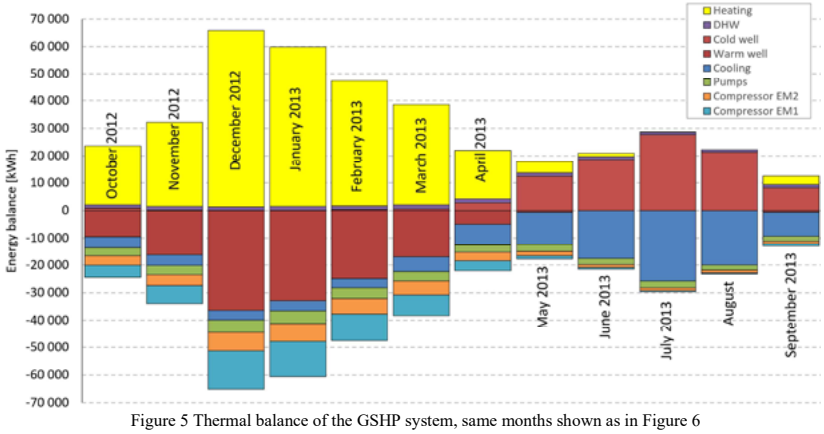


Figure 5 Thermal balance of the GSHP system, same months shown as in Figure 6

Total pump power consumption is high at low load conditions, especially compared to compressor power consumption.

3.1 IEA Annex 52 system boundary 0

The energy extracted and injected into the aquifer was measured, but as seen Figure 6, the resolution is low (100 kWh per pulse). As the pump of the aquifer were not measured separately no Performance Factor could be derived. In order to express the energy in kWh/h a 24-hour average value was calculated.

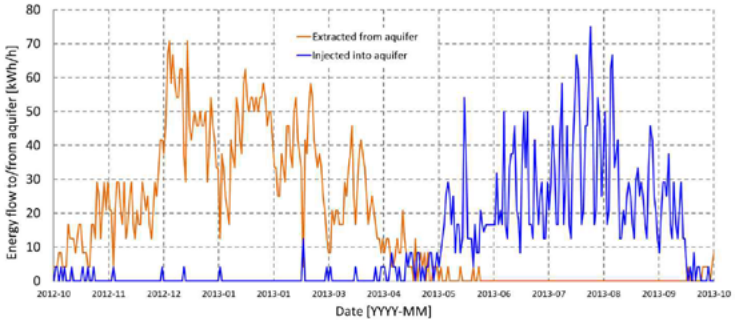


Figure 6 Heat extracted from and injected into the aquifer during one full year, mainly the first year in the time series, 24h average.

As seen in the diagram the pumps are at several occasions reversed, especially in April, May, September and October. The16th of February, a cold day, the pumps reverse, and the cold well was used, clearly seen in Figure 6. The control system didn't handle the aquifer optimal, as mention in chapter 2.1 the flow direction of the aquifer was change just according to ambient temperature, meaning the flow direction changes often in the spring and autumn. According to a site visit (2019) this was now handled manually instead.

3.2 IEA Annex 52 system Boundary 1

3.2.1 Heating

The measured data of the office building is not enough to calculate the performance on individual heat pump level but it could be estimated by subtracting the power consumption of the DHW heat pump (EM2) from the total heat produced, see equation 1 in chapter 2.2.1. The only function of the DHW heat pump is to increase the temperature from the main heat pump (EM1), EM2 has the main heat pump (EM1) as its only heat source, see Figure 2. The heating Seasonal Performance Factor on system boundary 1, SPF_{H1} is estimated to 4.2 the first year and 3.7 the second year, when the DHW heat pump has a better control strategy. See chapter 3.4 for further details and discussion.

3.3 IEA Annex 52 System Boundary 4

On system boundary 4, see to Figure 1 for definition, meaning the entire heat pump installation, excluding the heating, cooling and ventilation system of the building itself, all necessary data has been measured over the period September 2012 to August 2014. The allocation of pump and compressor power consumption is seen in equations 2 and 3, while the Performance Factors are calculated according to equations 4 and 5, all in chapter 2.2.1

3.3.1 Heating

The following diagram over Daily Performance Factor, DPF, see Figure 7, has been developed to fully understand the performance of a heat pump system at a glance. It directly shows that the heat pump system, with four compressors in the main heat pump (EM1) and a total heating capacity of 300 kW, is oversized and only uses one compressor in on/off mode most of the year. The maximum capacity used is 110 kW or 37 % of installed capacity, despite both winters during the period having low temperatures. It also directly shows that the heat pump system has almost the same performance factor regardless of heat output and that it at very low output mainly collapses in performance.

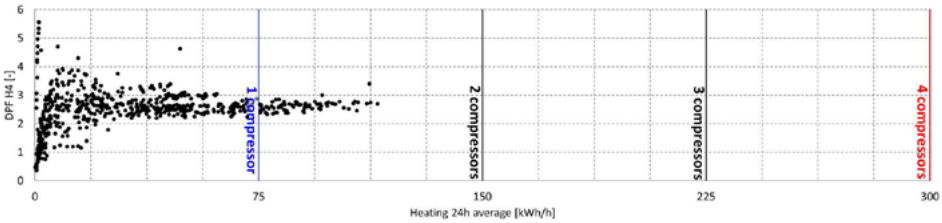


Figure 7 Overview of heat pump system performance factor H4 as a function of heat provided to the office building, blue line shows lowest capacity without ON/OFF operation, red line maximum heating capacity at highest heating system temperatures (winter)

The heat pump system has been compared to a state-of-the-art heat pump system produced by a major Swedish manufacturer in order to show the expected performance for a well-designed system, see Figure 8 below.

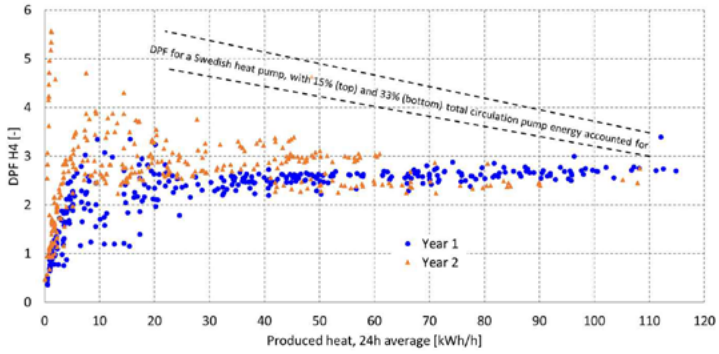


Figure 8 The heat pump system heating Daily Performance Factor, DPF_{H4}, compared a state-of-the-art heat pump system

The second year the control system is changed September 16th, 2013, it is noted as a significant decrease of power consumption of the DHW heat pump (EM2), but exact implication of the change is not known. This clearly increases performance in the medium output region, but the change is reversed between January 15th 2014 and March 4th 2014, giving poor performance in the high output region again. The change is likely done for the system to be able to deliver high enough temperature to the heating system, but that has not been possible to verify, as temperature data is not available.

The heat pump system is within the range of the total pump energy seen in Figure 8 above (dashed lines), 15-33 % of total compressor power consumption, above 40 kWh/h average produced heat. Below 40 kWh/h pump energy increases dramatically and is 90% at lowest heating load. This indicates a systematic error in the control of circulation pumps, which could not be explained by the nature of the aquifer system.

It is difficult to understand that the DPF_{H4} is below one (1) at low capacity, worse than resistive heating, but the control of the aquifer pumps is likely a major cause. The exaggerated pump power then gives very little heat to the brine system, as little is being needed, the losses in the water-cooled pumps basically heats the aquifer instead.

The Seasonal Performance Factor, SPF_{H4}, is calculated to 2.5 for the first year and due to the change in the control system the SPF_{H4} increased to 2.7 the second year. For a well-designed heat pump system, the SPF_{H4} is estimated to be able to reach 4 in the office building, around 50 % higher than the system used.

3.3.2 Cooling

The heat pump system is used to cool the building, it has a fairly constant equipment cooling load of 4-6 kWh/h clearly seen during heating season, but the main cooling load is during the short Swedish summer in June, July and August.

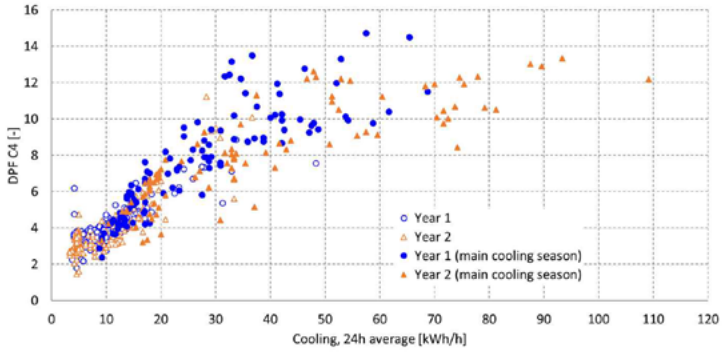


Figure 9 The heat pump system cooling Daily Performance Factor, DPF_{C4}

As seen in Figure 9 the Daily Performance Factor, DPF_{C4}, is high or very high during most of the year, but at low load the performance is in parity with conventional chiller performance. It is clear from the data that the cooling is mainly produced directly from the aquifer, by means of free cooling, else this high performance would be impossible. The low performance at low load is likely due to poor control of the aquifer pumps, note that the performance is low at low load even at the main cooling season, with very low heating demand, see filled markers in Figure 9. The performance is thus not mainly an effect of the method used for allocating the pump electricity. Note that the power consumption of the DHW heat pump (EM2) is not affecting the cooling Performance Factor, it is accounted on the heating side only, see chapter 2.2.1.

A well performing aquifer system, with good pump management at lower load, could perform at the top performance seen in Figure 9 most or all of the cooling season.

The Seasonal Performance Factor, SPF_{C4}, is calculated to 5.7 for the first year and slightly higher 5.8 the second year

3.4 The serial DHW heat pump (EM2)

The DHW heat pump (EM2) has the subcooler of the main heat pump (EM1) as its main heat source, it can not use the aquifer directly as a heat source. The DHW heat pump (EM2) is designed to mainly produce Domestic Hot Water, DHW, but can aid the main heat pump (EM1), only producing heat, to keep high enough temperature in the heating system. This means that the DHW heat pump (EM2), at DHW production, should use significantly less power than the main heat pump (EM1), else the thermal balance is not fulfilled. The reason being the subcooler of the main heat pump produce a fraction of the total condenser heat and varying depending on condensing temperature. The DHW heat pump has temperature wise good possibility to perform well, meaning with low power consumption.

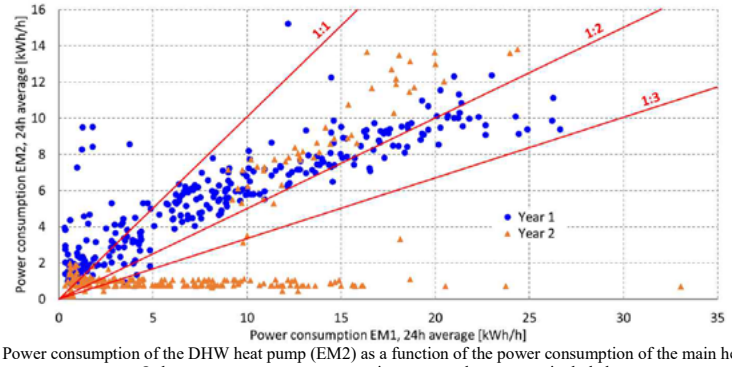


Figure 10 Power consumption of the DHW heat pump (EM2) as a function of the power consumption of the main heat pump (EM1). Only compressor power consumption measured, no pumps included.

Looking at the power consumption of the DHW heat pump (EM2) compared to the power consumption of the main heat pump, see Figure 10, the DHW heat pump (EM2) has too high power consumption. With all heat coming from the subcooler of the main heat pump, in a well-designed system, the ratio would be below 1:3 or at least 1:2 at all time, but mostly significantly lower. This is not the case, the main part of operation is at higher ratios, especially the first year and during the winter the second year. This likely means that the EM2 is heated by the condenser of EM1, causing the lower than necessary Performance Factor seen in Figure 7 and Figure 8. This is possible, circuit and control wise, see green long-dashed lines of Figure 2. Noteworthy is the extreme low ratio in the left side of Figure 10. It is identified that the condenser of the DHW heat pump (EM2) has the possibility, control and circuit wise, to heat its own evaporator, this possible short circuit could be the reason for this extreme operation, see green long-dashed lines in combination with brown dashed lines of Figure 2.

The line of orange rectangles along the x-axis in Figure 10 is likely when the EM2 is focused on producing DHW, meaning the control system is operating correctly. In Figure 11 the DHW production as a function of power consumption of the same heat pump is seen.

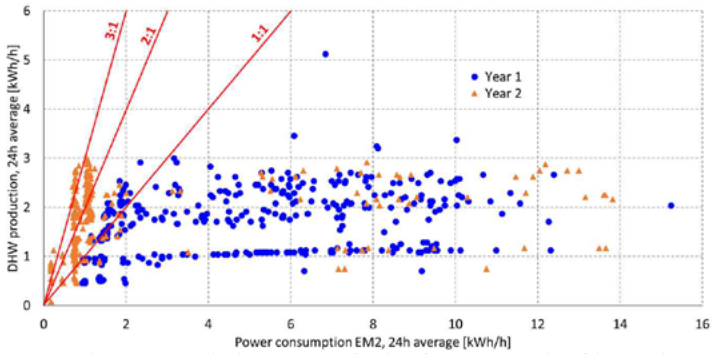


Figure 11 Domestic Hot Water production (DHW) as a function of power consumption of the DHW heat pump (EM2)

It is clear that the DHW heat pump (EM2) is operating in heating mode most of the first year and during the winter of the second year, as the ratio is well below 1:1, meaning extensive unaccounted losses in the DHW system as the only other possible solution. As far from full heating capacity of the main heat pump is not used, see Figure 7, this is not optimal. One possible answer to this poor operation could be found on the nameplate of the main heat pump, it is a chiller with a maximum return temperature of 45°C, meaning the DHW heat pump possibly must aid it at higher heating system temperatures.

According to the nameplate of the DHW heat pump it is also a chiller, not a dedicated heat pump. It has the same maximum return temperature (45°C), meaning about 5-10°C lower than what is necessary to handle legionella temperatures according to Swedish legislation. This means the DHW heat pump continuously is operating outside the envelope stated by the manufacturer, to handle the legionella temperatures, if it does. At the site visit the return DHW circulation temperature was 8°C lower than the legislative requirement, and the cover of the heat pump was removed for simple reset when the machine tripped a high pressure side alarm.

The building used about 15 MWh of DHW per year, including DHW circulation losses, a fraction of the heat supplied (210-290 MWh). The DHW heat pump (EM2) is largely oversized for the purpose, giving it low possibility to handle DHW temperatures accurately.

3.5 The three-port rotary control valve

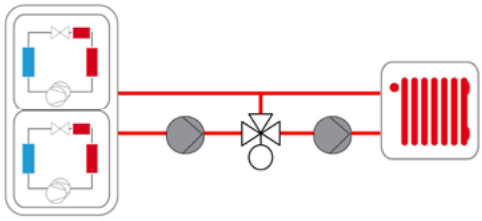


Figure 12 The three-port rotary control valve solution within the heating system, simplification of Figure 2. Pictograms by TU Braunschweig IGS, used with permission within the course of IEA HPT Annex 52

The three-port rotary control valve used between the main heat pump and the heating system, see Figure 12, leads to elevated temperature for the condenser, if not fully open at all time, causing lower Performance Factor, especially at lower load operation, seen in Figure 7 and Figure 8. At the site visit the temperature increased rapidly over the condenser, causing compressor stops after five minutes. Repeated short compressor operating time can cause premature compressor failures and will lead to transient losses [1] that, especially in combination with elevated condenser temperature, will lead to poor performance. The reason for the short compressor operating time is likely that the three-port rotary control valve decreases the working fluid volume for the heat pump to a minimum, by effectively cutting of the heating systems large fluid volume.

This three-port rotary control valve solution is not to be used in a well-designed heat pump system, except for decreasing temperatures to sub heating systems with lower operating temperatures.

3.6 Discussion

The heat pump solution underperforms according to expected performance for a heat pump with an aquifer heat source, heating a state-of-the-art Swedish office building with a low temperature heating system. The unnecessary complexity of the system, with a DHW heat pump in series with the main heat pump and unintuitive circuit layout means it is very difficult to understand when in operation. This was clearly stated by the personnel met at the site visit.

Due to lack of temperature data no relevant uncertainty analysis for the performance factors could be calculated

4 Conclusions

The GSHP solution in this report is complex, with a control system that most likely would need improvements to perform well. The 0.3 MW total heating capacity is almost three-fold the maximum heating demand seen during the two-year measurement period 2012-2014, despite having very cold winter days these years. This means only two of the four compressors in the main heat pump will be used, most of the year there is surplus heating capacity with only one compressor.

The DHW heat pump is seen operating many hours in heating mode, despite its purpose is for DHW. With an unknown change to the control system the second year, made twice, the DHW heat pump heated the heating system significantly less, meaning an overall higher performance factor for the system. Due to system design the DHW heat pump has the ability to heat its own evaporator, it has been identified that it likely does that during the first year. Moreover, the DHW was at times heated by the condenser of the main heat pump, causing lower performance factor, instead of the intention of using the subcooler heat.

A three-port rotary control valve is restricting the flow to the heating system and thus likely elevating the condensing temperatures of the main heat pump. This causes lower performance factors, but also leads to shorter than necessary run time for the compressors, being observed during the site visit. This solution should be avoided in heat pump heating systems. The Seasonal Performance Factor, SPF_{H4} is as low as 2.5 the first year and 2.7 the second year.

The compressors of the heat pump system are not controlled to run actively at cooling operation, the aquifer is then passively supplying the cooling to the building. This means a good potential for high performance factors, but it deteriorated with lower load, suggesting pump management is poor. The pump power

consumption is significantly higher than needed at low cooling demand. The cooling system has regardless high Seasonal Performance Factor, SPF_{C4} was 5.7 the first year and 5.8 the second year.

No temperature data was available; thus no scientifically valid uncertainty analysis was possible to perform. All system boundaries used in the report are the IEA Annex 52 proposal.

Acknowledgements

The support from the Swedish Energy Agency (TERMO research program Grant 45979-1) is gratefully acknowledged. This work is part of the IEA HPT Annex 52, *Long-term performance measurement of GSHP systems serving commercial, institutional and multi-family buildings*.[2].

References

[1] Naicker, S. S. and S. J. Rees.: Performance Analysis of a Large Geothermal Heating and Cooling System. Renewable Energy 122:429–442. https://doi.org/10.1016/j.renene.2018.01.099 (Measurement data available as open access at http://archive.researchdata.leeds.ac.uk/272/). (2018).
[2] IEA HPC.: Annex 52 - Long term performance measurement of GSHP Systems serving commercial, institutional and multi-family buildings . Retrieved Nov. 15, from https://heatpumpingtechnologies.org/annex52/
[3] Gehlin S, Spitler J, 2019, Half-term Results from IEA HPT Annex 52 - Long-term Performance Monitoring of Large GSHP Systems, 13th IEA Heat Pump Conference 2020, Korea
[4] Nordman R, Kleefkens O, Riviere P, Nowak T, Zottl A, Arzano-Daurelle C, Lehmann A, Polyzou O, Karytsas K, Riederer P, Miara M, Lindahl M, Andersson K, Olsson M, 2012, SEasonal PErformance factor and MOnitoring for heat pump systems in the building sector SEPEMO-Build Final report,
[5] Historical temperature data from SMHI. Retrieved Sept. 1, from https://www.smhi.se/data/meteorologi/ladda-ner-meteorologiska-observationer/#param=airtemperatureInstant,stations=all
[6] Spitler, J.D. and S.E.A. Gehlin.: Measured performance of a mixed-use commercial-building ground source heat pump system in Sweden. Energies 2019, 12, 2020; doi:10.3390/en12102020. Open access at: https://www.mdpi.com/1996-1073/12/10/2020 (2019).
[7] Abuasbeh, M., Acuña, J.: ATES System Monitoring Project, First Measurement and Performance Evaluation: case study in Sweden. IGSHPA Research Track 2018, Stockholm, Sweden, September 18th 2018. (2018).

13th IEA Heat Pump Conference 2020



13th IEA Heat Pump Conference
April 26-29, 2021 Jeju, Korea

Design of a gas-driven hybrid adsorption heat pump coupled to geothermal heat exchangers for retrofitting applications

Valeria Palomba[a*], Antonino Bonanno[a], Davide La Rosa[a], Stefan Löwe[b], Ralph Herrmann[b], Andrea Frazzica[a]

[a]Istituto di Tecnologie Avanzate per l'Energia CNR-ITAE, Messina (Italy)
[b]Fahrenheit GmbH, Halle (Germany)

Abstract

The need for retrofitting of residential buildings with energy efficient solutions requires for the development of a wide range of solutions, suitable for different climates and buildings. In the present paper, a concept based on a gas-driven sorption heat pump using geothermal source for evaporation is presented. A dynamic luped-parameter model was implemented in Dymola and used to verify the flexibility of the system in terms of response to variable load and comfort conditions. The outcomes of the activity will be used to propose an improved design of the system.

© HPC2020.
Selection and/or peer-review under responsibility of the organizers of the 13th IEA Heat Pump Conference 2020.

Keywords: sorpion; geothermal; residential.

1. Introduction

The building heating and cooling sector is accounting for a relevant amount of primary energy consumption in Europe. So far, according to EU, less than 20% of heating and cooling is provided by renewable sources. Heat pumps represent an innovative solution to increase the share of renewables at the building scale, thus participating to the decarbonisation of the heating and cooling sector [1]. In order to make them suitable for different climates, keeping high performance in terms of COP/EER also in severe conditions, the exploitation of geothermal energy as ambient heat source/sink is considered of great interest [2]. In particular, advantages of geothermal heat pumps include high efficiencies (COPs of ground source heat pumps are in the range 3–5 while COPs of air source heat pumps are in the range 2.3–3.5) and low operating costs [2]. The application of ground-source heat pumps was investigated and proven in a wide variety of climates, including European Mediterranean and Continental [3,4], Turkey [5], Iran [6] and China [7], as well as in different building typologies, i.e. residential and commercial [4,8]. However, the exploitability of this resource in the built environment, for retrofitting applications, becomes quite challenging due to both, technical and regulatory constraints that limit the drilling procedures for the ground source heat exchangers (GSHEX) installation.

With this mind, the EU funded GEOFIT [9] project aims at the deployment of innovative geothermal heat pump solutions for retrofitting applications. Particularly, an innovative hybrid geothermal heat pump will be developed, tested and installed in two demo sites. Different hybrid geothermal heat pumps have been proposed, such as a solar-geothermal heat pump able to exploit alternatively the heat from vacuum collectors or the ground [10] or a hybrid configuration with the cooling tower and the ground loops connected together [11,12].

Instead, in the present work, the hybrid solution proposed consists of a hybrid gas-driven hybrid adsorption/electric heat pump Indeed, this combination of thermally and electrically driven HP, despite the lower thermal COP compared to an electrical vapour compression chiller, can be efficiently operated with a smaller size GSHEX. This will make the heat pump more suitable for applications with reduced space availability.

In order to assess the feasibility of such a hybrid solution, a detailed dynamic model was developed in Dymola environment. Adsorption heat pump and gas boiler were modelled by means of TIL Media Library, TIL Suite and self-developed components to match the specific characteristics of the hybrid unit developed. Particular focus was put on the control strategy for enhancing the comfort level achievable by the retrofit of existing systems with the hybrid solution proposed. A first prototype will be developed by Fahrenheit GmbH which will be tested at the CNR ITAE lab subsequently.

2. The GEOFIT sorption solution

The core of the hybrid sorption heat pump developed within GEOFIT is a gas-driven sorption heat pump, whose main components are shown in Figure 1. It is based on the two-modules layout from Fahrenheit GmbH commercial system. Each module consists of an adsorber/desorber and an evaporator/condenser. The desorber is connected through the HTF circuit to the gas boiler that allows the regeneration of the sorption material. At the same time, through the vacuum circuit, the refrigerant flows from the desorber to the condenser, that supplies heat at the temperature level requested for space heating. The adsorber is connected in parallel to the condenser through the HTF circuit. The vacuum circuit allows the flow of the refrigerant from the evaporator to the adsorber. The ground heat exchanger allows the use of the soil as heat source for evaporation. The useful effect delivered to the user is represented by the adsorption heat and condensation heat.

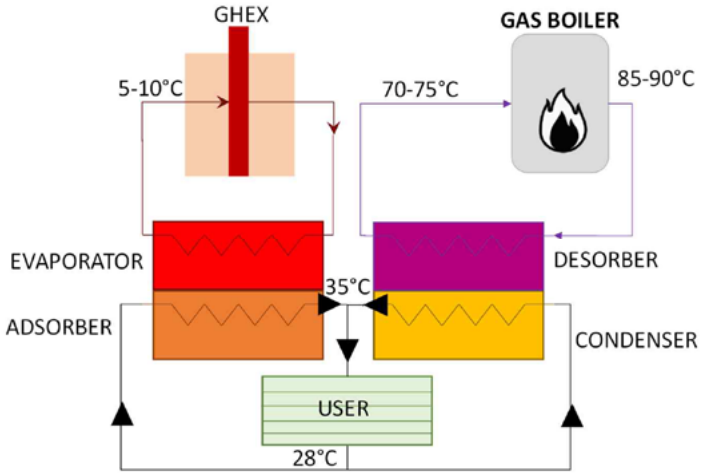


Figure 1: Main layout and thermal levels for GEOFIT hybrid gas-driven heat pump.

The main advantages in the utilization of such thermally-driven heat pumps as retrofitting solutions lies in the possibility of using shallow GSHEXs with a superficial area significantly lower than that needed when the heating system is represented by a vapour compression electrically-driven heat pump.

A schematic of a possible integration of the proposed gas-driven hybrid heat pump is depicted in Figure 2. It is clear that the gas boiler is exploited both to drive the desorption process and to provide domestic hot water (DHW) to the user. The typical distribution system used to increase the heat pump efficiency is a floor heating system, while GHEX is used to provide heat of evaporation in winter and to dump heat of condensation in summer.

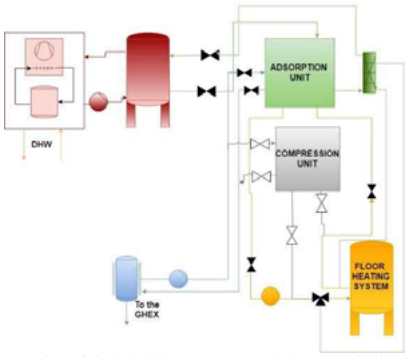


Figure 2: Schematic of the integration of the hybrid heat pump coupled to a gas boiler and the space heating system.

3. The modelling approach

The modelling approach used is schematically shown in Figure 3: Modelica language and Dymola commercial software were chosen as simulation environment. The main reasons for such a choice are the possibility of creating acausal and easily reusable models that, thanks to the FMU functionality of Dymola, can be easily exchanged and integrated in other simulation environments[13,14]. In order to model the refrigerant, the Heat Transfer Fluid (HTF) and the main components of the system, the commercial libraries included in TIL Suite were employed. Correspondently, the same structure as for components already included in the libraries, based on a cell level and a component level was employed also for the self-developed models. In particular, standard models based on liquid cells were employed to model the heat exchanger and heat transfer correlations, whereas self-developed model were used for the sorption equilibrium and the vapour/liquid control volume of the evaporator/condenser. The gas boiler was modelled considering a constant thermal power and an efficiency variable with part load and return temperature. All the components are properly managed thanks to specifically developed controls. The main equations of the model are presented in Table 1, while for a more detailed description of the Dymola model for the sorption unit, the reader is referred to [15].

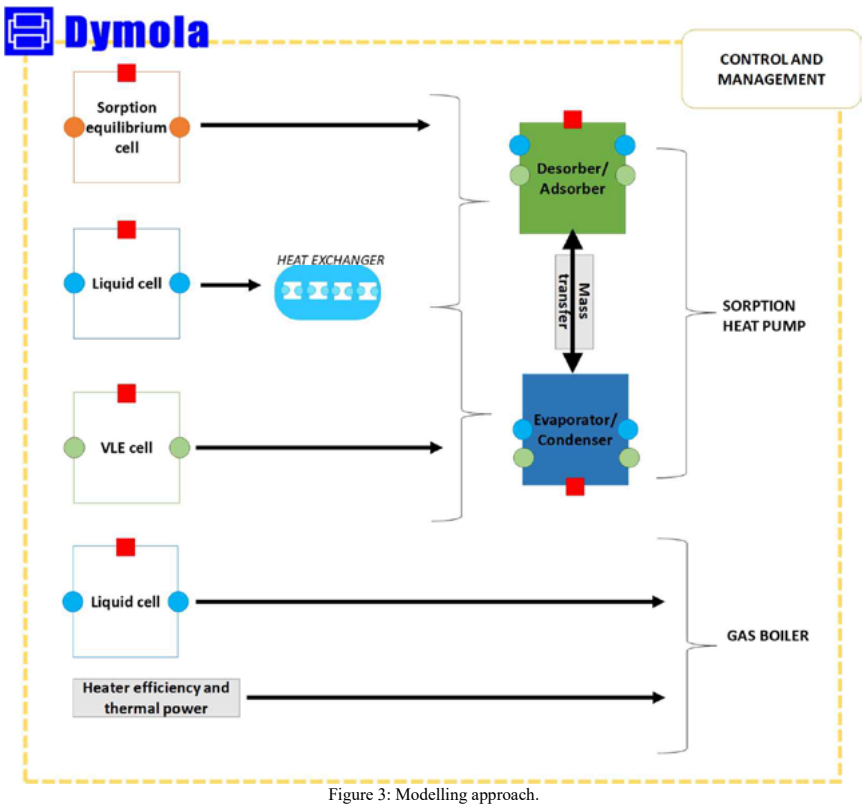


Figure 3: Modelling approach.

4. System control and management

In order to give indications on the best management strategy for the hybrid heat pumps and its integration in retrofitted systems, different controls were implemented and evaluated. In particular, three possible options for controlling the system were considered:

a. Variable flow rate of the pumps according to part load;
b. Step variation of the cycle time of the adsorption unit using the load requested by the user as target variable;
c. Step variation of the cycle time of the adsorption unit using the temperature in the user circuit as target variable.

The models for such components were developed in Dymola using existing components from Modelica Standard Library.

Since the main goal for the system under the GEOFIT activity here presented is the retrofitting of existing heating systems in different climates, two key elements play a particularly significant role:

1. the design of components, that must be as compact as possible;
2. the possibility of ensuring the same level of comfort and a flexible operation, in terms of adaptivity to the load of the building.

The first goal can be achieved thanks to the use of zeolite/water working pair, applying the patented crystallization technique developed by Fahrenheit [16], that has a significant higher power density when compared to standard silica gel/water systems on the market [17].

Instead, the second goal was the focus of the numerical activity here presented. Two key aspects were evaluated: the possibility of delivering a constant temperature to the user under different climatic conditions and the proper management of the sorption unit to be adaptable to user load.

Table 1: List of main equations used for the model implementation.

Component		Equation	
Adsorber	Mass balance sorbent cell	$\dot{m}_{ref} = \dot{m}_{evap} + \dot{m}_{cond}$	(1)
	Energy balance sorbent cell	$\left(m_{sorb}\, c_{p_{sorb}} + w \cdot m_{sorb}\, c_{p_{ref}}\right)\frac{dT_{sorb}}{dt} = \dot{Q}_{fbw} + \dot{m}_{ref}\, h_{ads} - m_{sorb}\, c_{p_{sorb}}\, T_{sorb}\, \frac{dw}{dt}$	(2)
	Mass balance adsorber HEX	$0 = \dot{m}_{in} + \dot{m}_{out}$	(3)
	Energy balance adsorber HEX	$m_{fluid}\, c_{p_{fluid}}\frac{dT_{fluid}}{dt} = \dot{m}_{fluid}\, c_{p_{fluid}}\left(T_{fluid_{in}} - T_{fluid_{out}}\right) + \dot{Q}_{fbw}$	(4)
	Heat transfer sorbent/HEX	$\dot{Q}_{fbw} = (\alpha S)_{ads}\,(T_{sorb} - T_{fluid})$	(5)
	Sorption equilibrium	$w = w_0 \exp(-bA)$	(6)
		$A = -RT_{sorb} \log\frac{p_{ads}}{p_{sat}}$	(7)
Vapor Liquid Equilibrium (VLE) volume evaporator/ condenser	Mass balance	$\frac{dm}{dt} = \dot{m}_v + \dot{m}_l$	(8)
	Energy balance	$\frac{dU}{dt} = \dot{H}_v + \dot{H}_l + Q_{fbw}$	(9)
	Mass balance HEX	$0 = \dot{m}_{in} + \dot{m}_{out}$	(10)
	Energy balance HEX	$m_{fluid}\, c_{p_{fluid}}\frac{dT_{fluid}}{dt} = \dot{m}_{fluid}\, c_{p_{fluid}}\left(T_{fluid_{in}} - T_{fluid_{out}}\right) + \dot{Q}_{fbw}$	(11)
	Heat transfer refrigerant/HEX	$\dot{Q}_{fbw} = (\alpha S)_{evap/cond}\,(T_{VLE} - T_{HEX})$	(12)
	Additional equations	$p_{VLE} = p_{sat}\,(T_{VLE})$	(13)
Mass transfer	Mass balance	$\dot{m}_{ref} = \dot{m}_{in} + \dot{m}_{out}$	(14)
	Linear Driving Force	$\dot{m}_{ref} = m_{sorb}\,\frac{dw}{dt} = m_{sorb}\,\beta(w_{eq} - w)$	(15)
	Mass transfer coefficient	$\beta = \frac{15D}{r_{sorb}^2}$	(16)
Gas boiler	Thermal power output	$\dot{Q}_{fbw} = \dot{Q}_{nominal}\,\eta$	(17)
	Efficiency	$\eta = a * T_{w_{in}} + b * T_{w_{in}}{}^2 + c * T_{w_{in}}{}^3 + d * T_{w_{in}}{}^4 - e * \mathrm{PL} + f * \left(T_{w_{in}} * \mathrm{PL}\right) - g * \left(T_{w_{in}}{}^2 * \mathrm{PL}\right) + h$	(18)

5. Results

To evaluate the adaptability of the heat pump to a variable user load, a signal with changing load (between 4 kW and 8 kW) was used, aiming at simulating a variable user demand. The first approach, based on varying the heat transfer fluid flow rate, resulted not robust enough to let the adsorption machine being properly operated. Accordingly, the control strategy based on the variation of adsorption cycle time as a function of user load was implemented. To this aim, a multi-switch control was used, able to switch between different cycle periods as a function of the expected requested power. Clearly, the higher is the power demand the lower is the cycle time, in order to enhance the average heating capacity provided by the adsorption module, whose behaviour is intrinsically discontinuous due to the physics of the adsorption process[18]. This control is not based on a linear variation of the cycle time, but rather a step variation is investigated. To demonstrate the effect of the variable cycle time on the average power, in Figure 4 the output power provided by the adsorption heat pump is showed. The adsorption/desorption cycle time variation is clearly visible. The average heating power provided increases from about 3 kW at 800 s cycle time up to 5 kW for 200 s cycle time.

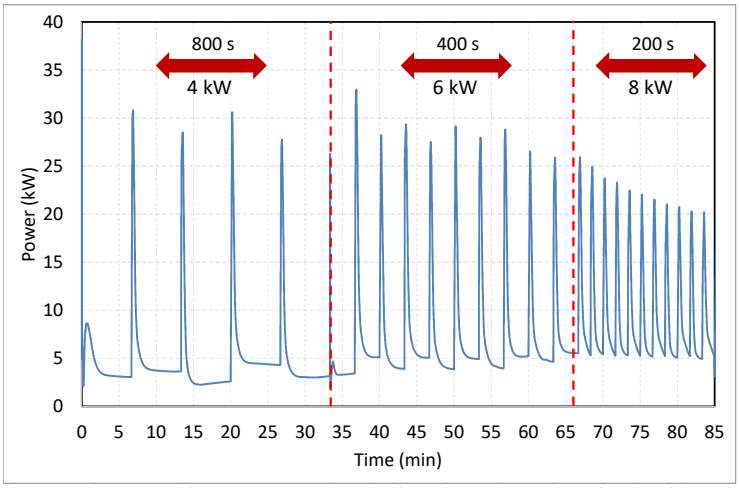


Figure 4: Adsorption machine output power (adsorption/desorption cycle control as a function of the load)

Analysing the temperature of water provided to the user Figure 5) it could be noted that the control works properly when the load is 3 kW and the cycle time is 800 s. Differently, it tends to deviate from the target when the power increases, most probably because the cycle time is reduced too much. This means that, to achieve a proper management, a continuous variation of cycle time according to the measured values of the temperature at each sampling time is needed.

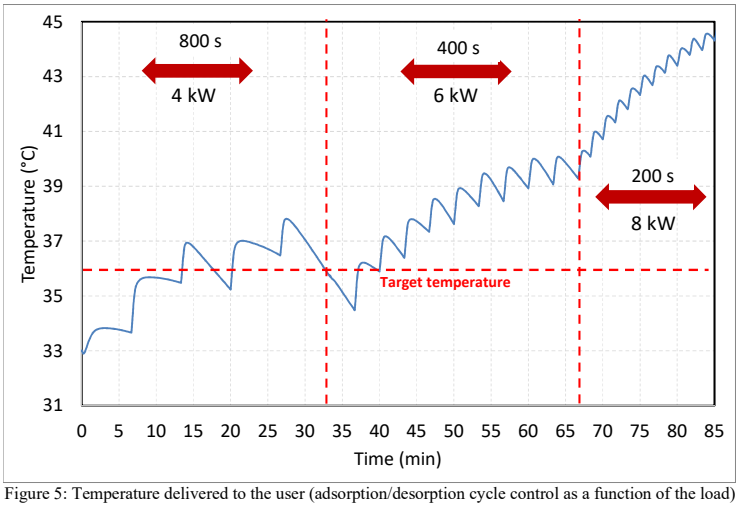


Figure 5: Temperature delivered to the user (adsorption/desorption cycle control as a function of the load)

From such results, it is clear that, to get comfort conditions, it is necessary to use a control that allows a finer tuning in terms of temperatures delivered to the user. Therefore, a second control was developed, that manages in real time the adsorption/desorption cycle time as a function of the temperature delivered to the user. The control compares the signal coming from the T_{user} sensor with the set point (e.g. 35°C); if the measured temperature is lower than the set point, this means that the heating load is higher than the one produced by the adsorption machine, therefore the adsorption/desorption cycle time is reduced. If the measured temperature is higher, than the cycle time is increased, because the requested heating power is decreasing. Compared to the previous case, the cycle time is not imposed a priori, i.e. there is not a predetermined cycle time as a function of the temperature, but rather a user-defined Δt is used for following the user heating demand:

- When the feedback signal $T_{user,measured}$-$T_{user,set}$ is <0, the cycle time is reduced of an amount Δt;

- When the feedback signal $T_{user,measured}$-$T_{user,set}$ is >0, the cycle time is increased of an amount Δt;

Threshold values for minimum and maximum cycle time are imposed as well, to avoid inefficient operation of the unit. Figure 6 reports the power delivered by the adsorption machine for a 30 min operation at variable load with the implemented control. The feedback loop operates changing the cycle time with a Δt of 50 s. The feedback signal is reported in Figure 6 as well. It is possible to notice that the average power output from the sorption heat pump during an overall can be adjusted with this strategy. Furthermore, as confirmed by Figure 7, the proposed approach is able to keep the temperature level delivered to the user close to the target, thus properly operating the adsorption machine. It will be then proposed for the implementation in the prototype to be tested in the lab and then in the demo sites for the GEOFIT project.

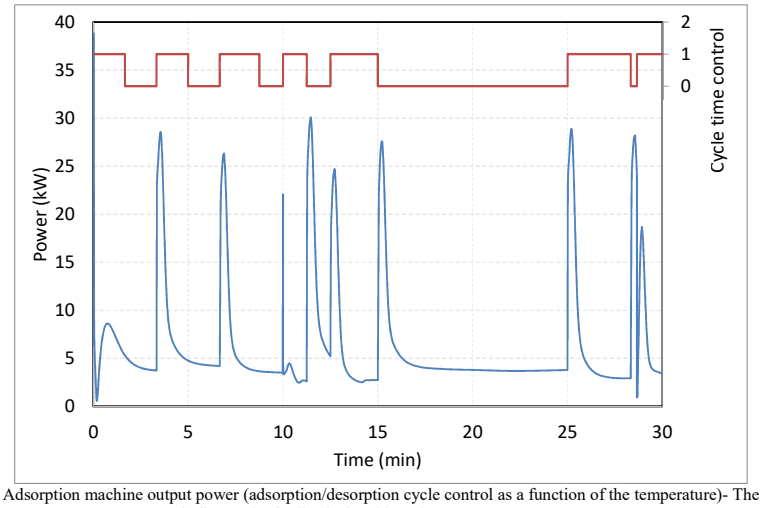


Figure 6: Adsorption machine output power (adsorption/desorption cycle control as a function of the temperature)- The red line indicates the feedback signal based on $T_{user,measured}$-$T_{user,set}$

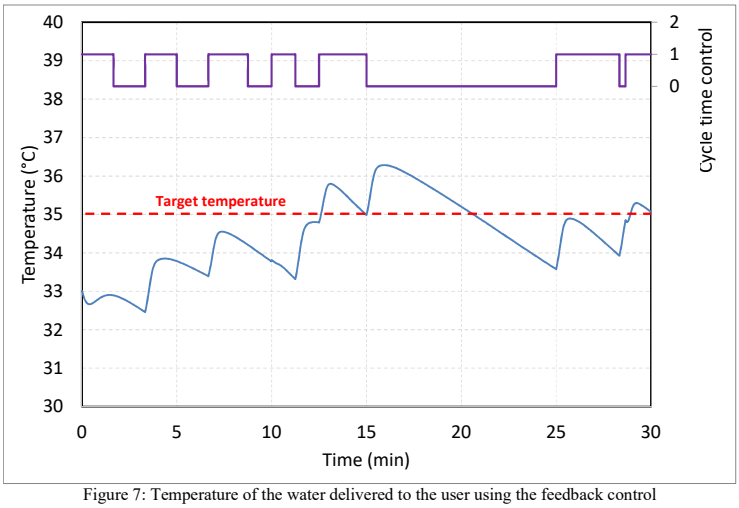


Figure 7: Temperature of the water delivered to the user using the feedback control

6. Conclusions and future activities

The present paper presents the modelling activity of a novel hybrid sorption concept for retrofitting of heating systems in existing buildings, using a gas-driven sorption heat pump and a ground-source HEX as heat

source for evaporation. A dynamic model in Dymola was implemented, including a black-box model of the gas boiler, as well as a detailed adsorption module which comprises heat and mass transfer mode as well as equilibrium data for the given zeolite/water working pair. Particular focus was put on control and management strategies for the system, evaluating the flexibility of the heat pump with variable load and temperature conditions. The best control strategy identified is based on the continuous variation of cycle time according to a feedback control on delivered temperature to the user. As shown in Figure 8, the next steps will include model validation thanks to results from laboratory activity, as well as the definition of an improved design and its adaptation to the pilot sites for the project.

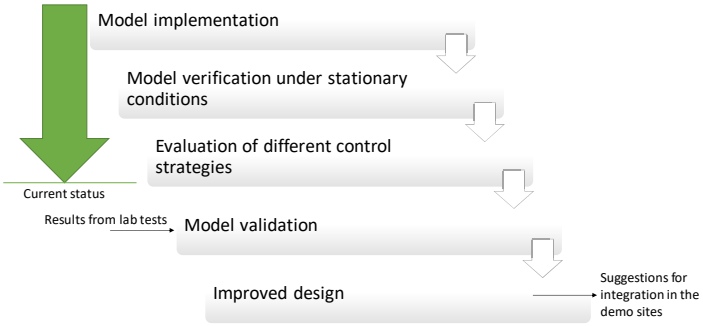


Figure 8: Model development and future steps.

Acknowledgements

This work was funded by the project Geofit: Deployment of novel GEOthermal systems, technologies and tools for energy efficient building retroFITting, which has received funding from the European Commission H2020 Programme under Grant Agreement No. 792210

References

[1] European Commission, COM(2016) 51 final: An EU Strategy on Heating and Cooling | Build Up, (2016). http://www.buildup.eu/en/node/47833 (accessed February 8, 2019).

[2] S.J. Self, B. V. Reddy, M.A. Rosen, Geothermal heat pump systems: Status review and comparison with other heating options, Appl. Energy. 101 (2013) 341–348. doi:10.1016/J.APENERGY.2012.01.048.

[3] D. Antonijevic, M. Komatina, Sustainable sub-geothermal heat pump heating in Serbia, Renew. Sustain. Energy Rev. 15 (2011) 3534–3538. doi:10.1016/J.RSER.2011.05.008.

[4] B. Morrone, G. Coppola, V. Raucci, Energy and economic savings using geothermal heat pumps in different climates, Energy Convers. Manag. 88 (2014) 189–198. doi:10.1016/J.ENCONMAN.2014.08.007.

[5] A. Cetin, Y.K. Kadioglu, H. Paksoy, Underground thermal heat storage and ground source heat pump activities in Turkey, Sol. Energy. (2019). doi:10.1016/J.SOLENER.2018.12.055.

[6] H. Yousefi, H. Ármannsson, S. Roumi, S. Tabasi, H. Mansoori, M. Hosseinzadeh, Feasibility study and economical evaluations of geothermal heat pumps in Iran, Geothermics. 72 (2018) 64–73. doi:10.1016/J.GEOTHERMICS.2017.10.017.

[7] Y. Chang, Y. Gu, L. Zhang, C. Wu, L. Liang, Energy and environmental implications of using geothermal heat pumps in buildings: An example from north China, J. Clean. Prod. 167 (2017) 484–492. doi:10.1016/J.JCLEPRO.2017.08.199.

[8] J. Molavi, J. McDaniel, A Review of the Benefits of Geothermal Heat Pump Systems in Retail Buildings, Procedia Eng. 145 (2016) 1135–1143. doi:10.1016/J.PROENG.2016.04.147.

[9] Geofit project, (n.d.). http://geofit-project.eu/.

[10] J. Choi, B. Kang, H. Cho, Performance comparison between R22 and R744 solar-geothermal hybrid

heat pumps according to heat source conditions, Renew. Energy. 71 (2014) 414–424. doi:10.1016/J.RENENE.2014.05.057.
[11] D.P. Zurmuhl, M.Z. Lukawski, G.A. Aguirre, W.R. Law, G.P. Schnaars, K.F. Beckers, C.L. Anderson, J.W. Tester, Hybrid Geothermal Heat Pumps for Cooling Telecommunications Data Centers, Energy Build. (2019). doi:10.1016/J.ENBUILD.2019.01.042.
[12] L.I. Lubis, M. Kanoglu, I. Dincer, M.A. Rosen, Thermodynamic analysis of a hybrid geothermal heat pump system, Geothermics. 40 (2011) 233–238. doi:10.1016/J.GEOTHERMICS.2011.06.004.
[13] P.A. Fritzson, Introduction to Modeling and Simulation of Technical and Physical Systems with Modelica by Fritzson, Peter A., John Wiley & Sons, Inc, Hoboken, New Jersey, 2011. http://www.amazon.de/Introduction-Simulation-Technical-Sep-30-2011-Paperback/dp/B009KJBU2O/ref=sr_1_1?s=books&ie=UTF8&qid=1376394696&sr=1-1&keywords=fritzson+2011.
[14] Modelica Association, Functional Mock-up Interface, (n.d.). https://fmi-standard.org/ (accessed July 30, 2019).
[15] V. Palomba, E. Varvagiannis, S. Karellas, A. Frazzica, V. Palomba, E. Varvagiannis, S. Karellas, A. Frazzica, Hybrid Adsorption-Compression Systems for Air Conditioning in Efficient Buildings: Design through Validated Dynamic Models, Energies. 12 (2019) 1161. doi:10.3390/en12061161.
[16] Fahrenheit zeolite products, (n.d.). https://fahrenheit.cool/en/zeolite-technology/.
[17] S. Vasta, V. Brancato, D. La Rosa, V. Palomba, G. Restuccia, A. Sapienza, A. Frazzica, S. Vasta, V. Brancato, D. La Rosa, V. Palomba, G. Restuccia, A. Sapienza, A. Frazzica, Adsorption Heat Storage: State-of-the-Art and Future Perspectives, Nanomaterials. 8 (2018) 522. doi:10.3390/nano8070522.
[18] A. Sapienza, V. Palomba, G. Gullì, A. Frazzica, S. Vasta, A new management strategy based on the reallocation of ads-/desorption times: Experimental operation of a full-scale 3 beds adsorption chiller, Appl. Energy. 205 (2017) 1081–1090. doi:10.1016/j.apenergy.2017.08.036.

183

13th IEA Heat Pump Conference
April 26-29, 2021 Jeju, Korea

Heat pump noise – Seasonal averaging and operation dependence

Ola Gustafsson[a], Henrik Hellgren[a], Caroline Haglund Stignor[a]

[a]RISE Research Institutes of Sweden, Box 857, Borås 50115, Sweden

Abstract

This study has developed an improved method for evaluation and new indicators for declaration of noise from heat pumps. The improvements may lead to better informed consumers and an Energy Labeling scheme that better reflect the actual use of the heat pump and thereby deployment of quieter and less disturbing heat pumps. And as a consequence, larger acceptance of this efficient technology.
17 heat pumps of the types; air/water and brine/water were evaluated through field and laboratory measurements to provided information of how the noise from heat pumps varies over time and at different operating conditions.
The results indicate that noise measurements should be performed at the operating conditions representing an outdoor temperature of 2°C according to the European standard EN14825 (alternatively 7°C for air/water heat pumps, but with the capacity of 2°C). The reason is that this operating condition is the one that best coincide with the seasonal averaged noise. In addition, the maximal noise of the heat pump should be measured to show the customer how the noise can vary and to be able to compare the noise from an on/off heat pump and an inverter-controlled heat pump.

© HPC2020.
Selection and/or peer-review under responsibility of the organizers of the 13th IEA Heat Pump Conference 2020.

Keywords: Heat pump; noise; sound power level; seasonal noise; SCOP; evaluation method;

1. Introduction

1.1. Background

Traditionally heat pumps have been controlled with fixed capacity (on/off), but variable capacity heat pumps (inverter) have become more common the latest years. The outcome is that the sound level varies with the change in capacity. Bessac showed that one single operating condition is not enough to evaluate the noise performance of variable capacity heat pump [1]. Gustafsson et al showed that the part load operation of a variable capacity air source heat pump has an important impact on the sound power level [2]. This project previously suggested that it might be necessary to use separate evaluation methods for air/water and brine/water, depending on the noise characteristics experienced in the field [3]. And it is of greatest importance, to identify methods that provide accurate and relevant information to customer and that also pushes the manufacturers to develop products that generates low noise in real operation. However, the aim should be to develop methods that ensure cost effective testing for the manufactures.

For labeling purposes, the sound power level is determined at one operating condition. In the current testing standard EN12102 [4], the heating capacity during the sound test should be within ± 5% according to test point C in EN14825 [5] (method for calculating SCOP). Still the sound power level is determined at a capacity in the lower region of the possible operating range. According to EN14825, test point C corresponds to 35% capacity at 7°C.

In the long-term studies should focus on investigations to identify the correlation of the SCOP and a seasonal noise average. Seasonal averaging of noise is however not that straight forward. It might be difficult to

understand what the average noise level would mean to the consumer, but a way to use it to identify to the best operating condition to perform the standard measurements.

1.2. Scope

The scope of this study was to:

- Define the noise of heat pumps at different state of operation
- Develop and suggest an improved method of evaluation and new indicators for declaration of noise from heat pumps. This would give consumers better guidance and also support the manufacturers in their product development.

1.3. Delimitations

The scope of this study has not been to identify methods that reduces the noise from a heat pump. The focus has instead been on how to develop methods used to measure and evaluate the noise.

2. Methodology

This paper presents results from 17 heat pumps that were investigated in laboratory measurements. The heat pumps included in the study were both on/off- and inverter-controlled heat pumps of type air/water (only monobloc type) and brine/water in heating capacity range up to 18kW. The sound power level was determined at several operating conditions according to standards EN12102, ISO3747 [6] and EN14825. The forward flow temperature was altered and for the heat pump with inverter-controlled compressors the sound power level of different compressor frequency was evaluated, ranging from minimum to maximum frequency. The sound power level depending on heating capacity and part load was compared for both heat pump types, to identify a general noise behavior. From this data a calculation method of seasonal noise averaging was proposed, to identify the most realistic operating condition for standard measurements. The proposed calculation method for seasonal noise average is generally using the same reasoning as the SCOP calculation method defined in EN14825. The noise level is assumed to vary linearly with the heating capacity of the heat pump. The lowest part load assumed to be 30% and the heat pump covers the maximum heating load down to -10°C. A bin-method with bins according to the “average climate” was used to provide a weighting factor for each outdoor condition. Hence, the seasonal noise average, denoted weighted sound power level was defined as the log-based average of the sound power level in each bin multiplied with the corresponding bin hours

The weighted sound power level combined with the linearized sound power level (describing the variation of sound power level depending on the outdoor temperature) gives an indication to what outdoor temperature and its correlated sound power level that best represent seasonal averaged noise. The method is showed graphically in figure 3.

3. Results and discussion

The sound power level for air-source heat pumps is generally higher than for ground source, depending on the fan noise. Hence, the control of the fan is an important factor for the generated noise of an air/water heat pump. For inverter heat pumps the A-weighted sound power level in relation to heating capacity is shown in figure 1, for both air/water and brine/water. The variation in sound power level has a strong connection to the heating capacity. Hence, the sound power level varies more for an inverter heat pump compared to an on/off heat pump. The fan noise of an air/water heat pump adds between 10 to 15 dBA for a corresponding heating capacity.

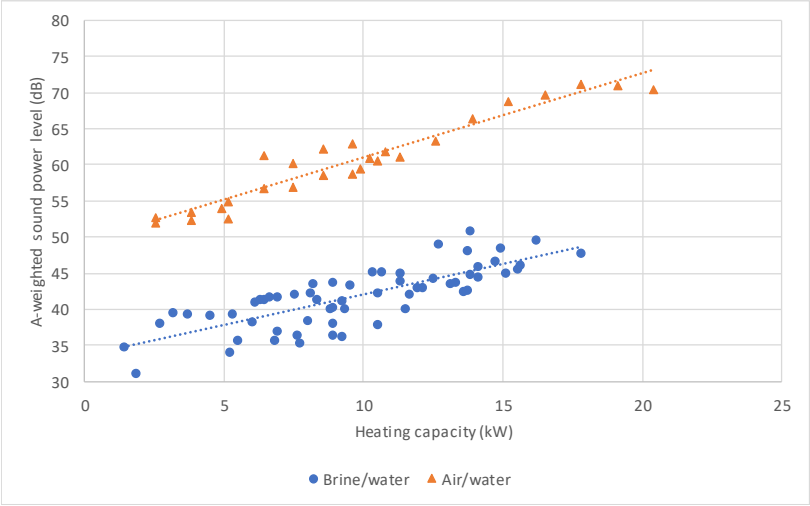


Figure 1. The A-weighted sound power level depending on the heating capacity for both air/water and brine/water. Results from several different heat pumps of each type is shown. The sound power level of air/water heat pumps is up to 15 dBA higher for a corresponding heating capacity of brine/water heat pumps.

The observed variation in sound power level for inverter brine/water heat pumps have both a part load and forward flow temperature effect, shown in figure 2. The part load effect is around 10 dBA between the lowest and highest part load and the flow temperature (condensation temperature) effect around 2 to 3 dBA. The observed increment of the sound power level for an on/off heat pump is around 2 to 3 dBA, when increasing the forward flow temperature from 35 to 55 °C. Hence, the forward flow temperature effect is in the same vicinity for both on/off and inverter heat pumps.

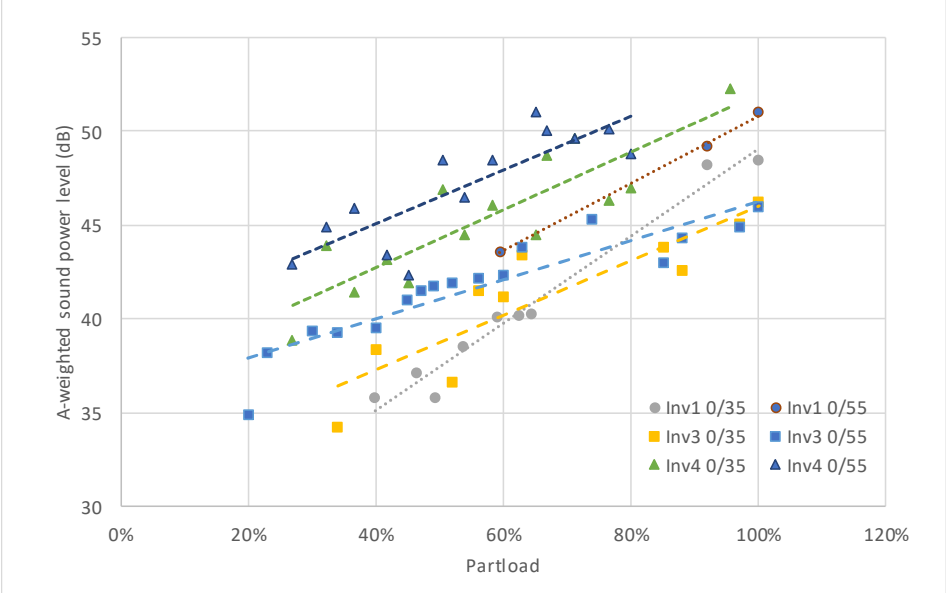


Figure 2. The A-weighted sound power level of inverter 3 brine/water heat pumps depending on part load. There is a part load effect of around 10 dBA and outlet temperature effect of around 2 to 3 dBA.

For labeling purposes, as an alternative to test the sound power level at a multitude of different operation conditions, it would be beneficial to identify a part load condition that correspond to a seasonal noise average. Also, due to the wide range in the observed sound power levels, the maximum sound power level should be stated to inform the consumer about the possible noise variation even though the maximum sound power level might not occur very often depending on the dimensioning of the heat pump. Still, a combination of both seasonal noise average and maximum sound power level would allow for better comparison between different heat pump and especially for differences between inverter and on/off heat pumps.

Based on the assumptions previously described, the lowest part load is set to 30% and given a value of 50 dBA and the maximum heating load at -10 °C is given a value 62 dBA. For the purpose of example is shown in figure 3. The total sound power level range is assumed to be 12 dBA, to account for both the observed part load and outlet temperature effect. To calculate the seasonal noise average, the sound power level is converted to energy levels before multiplying it with the bin hours for average climate according to EN14825. The calculated weighted sound power level (seasonal noise average) in figure 3 takes a value of 53 dBA. The lines of the theoretical and weighted sound power level intersect at a temperature of 2.5°C. Hence, determination of sound power level at test point B 2°C correspond quite well to the seasonal noise average.

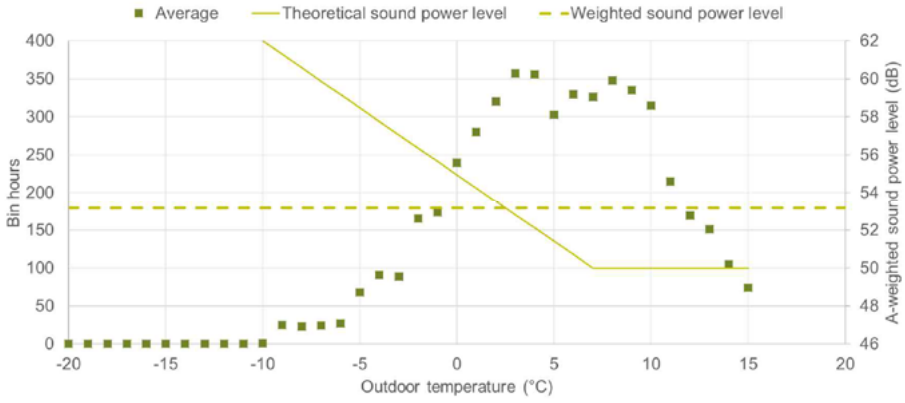


Figure 3. Basis of the calculation method for seasonal noise averaging. The average corresponding the bin hours at each temperature is multiplied with the energy levels of the theoretical sound power level to obtain the weighted sound power level (seasonal noise average). The lines of the weighted sound power level and the theoretical sound power level intersect at 2.5°C.

4. Conclusion

The test condition corresponding best to the calculated seasonal noise average is test point B according to EN14825. To avoid problems with defrosting of air-source heat pumps the determination of sound power level should be performed at 7 °C, but with the capacity of test point B. Determination of maximum sound power level for ground source should be performed at B0/W55 and maximum compressor speed. For air-source heat pumps the determination should be made at test point B and but with maximum compressor speed.

5. Acknowledgements

The study has been funded by the Swedish Energy Agency, through the research programs Effsys Expand and Termo, Bosch Thermoteknik, Danfoss Heat Pumps, NIBE, Enertech and Villaägarnas Riksförbund and they are all kindly acknowledged.

References

[1] Bessac F. How to estimate the sound level of inverter-type air-conditioning units. The 33rd International Congress and Exposotion on Noise Control Engineering. 2004
[2] Gustafsson O. Johansson H. Fahlén P. Axell M. Larsson K. Noise level in relation to energy performance of air-to-air heat pumps. 10th IEA Heat Pump Conference. 2011
[3] Hellgren H. Gustafsson O. Bergman P. Improved measurement method for heat pump noise. 12th IEA Heat Pump Conference. 2017
[4] EN12102-1:2017 Air conditioners, liquid chilling packages, heat pumps, process chillers and dehumidifiers with electrically driven compressors –Determination of sound power level – Part 1: Air conditioners, liquid chilling packages, heat pumps for space heating and cooling, dehumidifiers and process chillers.
[5] EN14825:2016 Air conditioners, liquid chilling packages and heat pumps, with electrically driven compressors, for space heating – Testing and rating at part load conditions and calculation of seasonal performance.
[6] ISO3747:2010 Acoustics – Determination of sound power levels and sound energy levels of noise sources using sound pressure – Engineering/survey methods for use in situ in a reverberant environment.

13th IEA Heat Pump Conference
April 26-29, 2021 Jeju, Korea

CHP-Waste Heat Utilization with Small-scaled Absorption-Resorption Chillers for Supermarket Refrigeration

O Ziegler[a*], U Hesse[a] and C Thomas[a]

[a]Technische Universität Dresden, Bitzer Chair of Refrigeration, Cryogenics and Compressor Technology, 01062, Dresden, Germany

Abstract

The IEA says in its World Energy Outlook 2012, "a key constraint on the deployment of CHP is the difficulty of distributing heat over long distances. Because of this, CHP units must be located close to demand, potentially increasing costs."[1] In the trade and commerce sector, especially the food retailing, it seems to be unfeasible to utilize the entire amount of heat while there is a permanent demand on electric energy provided by a CHP plant. In summer or transitional months there is nearly no demand on heating but the need for air conditioning (A/C) is increasing while the demand for normal refrigeration is almost constant throughout the year. A possible solution to the waste heat problem is the installation of a sorption refrigeration system to compensate the opposite demand for heating and cooling capacity providing both temperature levels of normal cooling and air conditioning. Especially for those applications small-scaled sorption chillers in the range <50 kW are currently not available on the market. In a pilot project a thermally driven refrigeration plant with a cooling capacity of <25 kW using the resorption principle was evolved and installed in a supermarket. Special focus is given to the operating costs, the amortization as well as the CO_2 emissions of the examined system.

© HPC2020.
Selection and/or peer-review under responsibility of the organizers of the 13th IEA Heat Pump Conference 2020.

Keywords: Combined Heat and Power (CHP); Waste Heat Utilization; Resorption Refrigeration; Supermarket; Natural Refrigerants

1. Introduction

"The exergy consumption of the processes necessary for human life thus corresponds to the consumption of primary energy. In order to save primary energy, it is necessary to select exergetically favorable processes, i.e. those with a low exergy demand, and also to try to avoid exergy losses when converting primary energy into the effective energy required." [2]

Supermarkets are structurally complex objects with regard to the supply of effective energy. Electricity and fossil fuels are used to supply the applications for heating, for cooling at different temperature levels, for lighting and for ventilation. The structures of industrial providers of supply technology that have grown over the decades show a highly specialized equipment portfolio. Suppliers can manufacture and install a product specialized on the boundary conditions specified by the customer like ventilation unit, deep freezing- and normal cooling-chillers, gas boiler, etc. The unavoidable problem for the customer is the interface management of these highly specialized systems. If systems, e.g. for room temperature regulation are not coordinated with each other, the resulting losses due to unfavorable controlling are higher than the savings achieved by increasing the efficiency of the single systems.

* Corresponding author. Tel.: +49-351-463-32603; fax: +49-351-463-37247.
E-mail address: oliver.ziegler@tu-dresden.de.

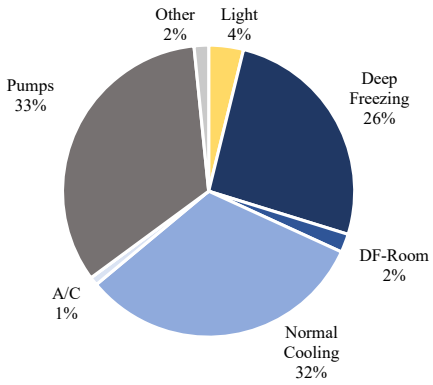


Figure 1: Percentages of electrical energy at the examined supermarket (regarding Table 2)

Table 1: Final and effective energy types in supermarkets

Type of Final Energy	Type of Effective Energy	Specification
Natural gas	Heating heat	Room heating
		DHW
Electricity	Light	Light
	Cooling	Deep freezing
		Normal cooling
		A/C
		Pumps (Brine etc.)
	Others	Ventilation
		Heating

However, since efficiency increases represent one of the implicit actions for global primary energy savings, it is necessary to consider the overall supply system, especially with increasingly complex systems, such as in supermarkets, to control interfaces and to use synergy effects with regard to energy and exergy flows. Looking at a supermarket as an overall system, it is primarily the final energy consumption entering the system that can be identified and can be broken down according to its utilization (see Figure 1 and Table 1).

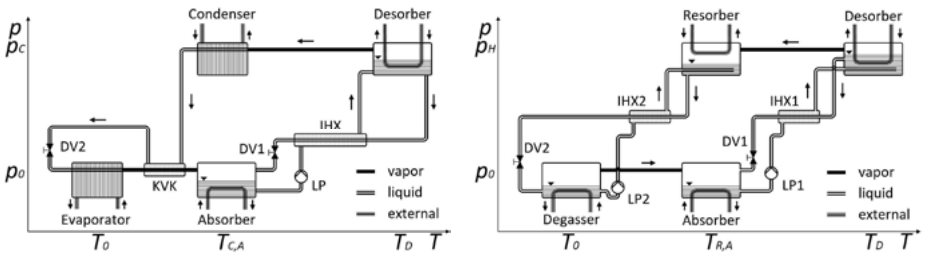
It is obvious that refrigeration and distribution (pumps) account for the major part of the electrical energy consumption (> 90%), which is almost constant throughout the year. Contrary to electrical energy, thermal energy for heating is only required in the colder season, therefore cogeneration plants for supermarkets have not been considered so far. Thermally driven refrigeration systems using the excess heat generated by cogeneration units and providing refrigeration at the normal cooling level could be an acceptable option. As part of a pilot project, such a system was installed in a supermarket in southern Germany and monitored over a period of 1.5 years.

2. Heating and Cooling Technologies for Supermarkets

2.1. Resorption Refrigeration System

Sorption refrigeration systems were developed in the middle of the 19th century with the necessity of industrial cooling. In a much quoted basic work from Altenkirch [3] on continuously operated sorption chillers, the so far very rarely used – and therefore almost unknown – configuration of the *resorption refrigeration system* is presented. Altenkirch describes its essential components and work processes in *p-T*-diagrams (cf. Figure 2). The significant difference in resorption compared to absorption is the second solution cycle with an additional absorber (resorber) instead of a condenser and an additional desorber (degasser) instead of the evaporator. Both absorption and resorption systems are continuously operating systems and are equally suitable for the utilization of waste heat. The decisive factor for the selection is the focus on the respective task to be fulfilled, taking the quality and availability of the driving energy as well as other boundary conditions into account. To select the appropriate system, temperature levels should be considered foremost.

As shown in Figure 2, three temperature levels are required to operate a sorption system – the heating temperature T_D, the recooling temperature $T_{C,A}$ resp. $T_{R,A}$ and the refrigeration temperature T_0. If cooling temperature values above 4 °C are targeted, *Water-LiBr-Absorption* and *Water-Silicagel-Adsorption* systems are available which can achieve higher coefficients of performance (*COP*) than ammonia-water systems. Therefore, they are mainly used for cold water generation in the process industry or for air conditioning, e.g. in office buildings or for server cooling. The use of water as the refrigerant is not suitable for providing a cooling capacity below 0 °C due to its triple point of $T_{TP} = 0.01$ °C, as it would freeze and block the evaporator and eventually also the expansion device in conventional absorption systems. For this case of application, other working fluid pairs are suitable. Usually ammonia-water *absorption refrigeration systems* are used for this purpose. However, due to their high technical and safety requirements, they were almost exclusively implemented for large-scale systems with cooling capacities of $\dot{Q}_0 >> 100$ kW.



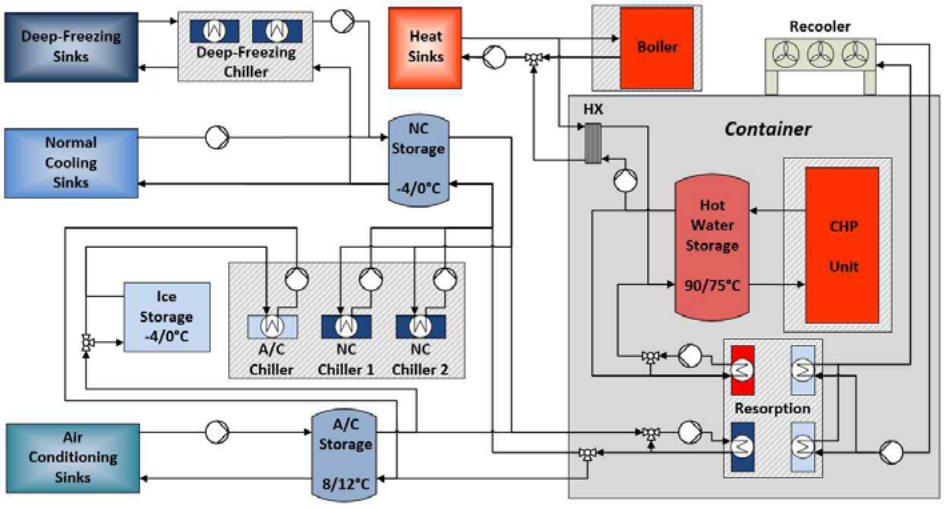
SP…solution pump; TV…throttle valve; IHX…internal heat exchanger; CPC…condensate precooler

Figure 2: Comparison of an absorption refrigeration system without rectification (left) and a resorption refrigeration system (right) according to [3], [4]

The so far almost forgotten technology of the *resorption refrigeration system* (RRS) is the focus of a currently running project. A system for the utilization of waste heat with a small cooling capacity ($\dot{Q}_0$ = 25 kW) and the working fluid pair ammonia-water is investigated. This system has a wide range of operation with regard to part load operation and temperature ranges. The equipment requirements and thus the system costs are significantly reduced. On the one hand, this is due to the fact that rectification and the dephlegmation of the ammonia vapor is no longer necessary. Furthermore, the system pressure is reduced to p_H < 0.6 MPa due to the presence of the ammonia only in aqueous solution. With regard to the thermal boundary conditions, the range of operation is considerably more flexible, even though the temperature of the decoupled cooling capacity is limited to $T_0 \approx$ -10 °C. Current operational experiences also demonstrate that, in particular, operation under short-term varying boundary conditions with regard to temperatures has only minimal effects on the plant performance, which can cause problems with conventional absorption systems. [5]

2.2. Heating and Cooling Network of the examined Supermarket

A supermarket was restructured as a part of a project funded by the German Federal Ministry of Economics and Energy. This includes the installation of a CHP-unit (nominal electrical power of P_{CHP} = 48 kW_{el} and a heating capacity of $\dot{Q}_{CHP}$ = 80 kW_{th}), a brine circuit with connected deep-freezing chillers, propane chillers (3 times $\dot{Q}_{0,PC}$ = 25 kW_{th}) and a resorption refrigeration system ($\dot{Q}_{0,RRS,max}$ = 25 kW_{th}) using waste heat to provide A/C and normal cooling. The network of heating, cooling and electrical energy generators resulting from the retrofitting is illustrated in Figure 3.



NC…normal cooling; A/C…air conditioning; HX…heating heat exchanger; CHP unit…combined heat and power unit

Figure 3: Heating and Cooling Network of the examined supermarket [5]

A special requirement was to assemble the system as a compact unit in the external area of the supermarket. Therefore, the implementation of the CHP unit and the resorption system was realized as a container-solution. In addition, the A/C and NC propane chillers were installed in another nearby container, and the resorption system was coupled into the piping network of these chillers. It can also be seen that a condensing boiler is installed in addition to the CHP unit. This existing unit has been preserved and now serves as failure redundancy for the CHP unit for the heating supply of the supermarket. A special aspect and sub-task of the project was the installation of a latent energy storage tank (ice storage) and the investigation of its influence on the flexibilization of cooling load and cooling generation. Furthermore, various sensitive storage tanks (hot water, A/C and NC) can be seen, which are necessary for the operation of the resorption plant, but also for the temporal decoupling of thermal energy load and generation.

3. Energy cost analysis

3.1. Database

In order to be able to answer the economically interesting question of current energy costs and payback period, it is necessary to have a sufficient database. Comprehensive monitoring of the entire supermarket enables consumption data to be displayed. Figure 4 shows an example of the electrical energy consumption of the supermarket over a period of one month as the sum of the electrical energy generated by the CHP unit and the electrical energy obtained from the grid. In addition, the excess electrical energy generated by the CHP unit and not consumed by the supermarket which is fed into the grid. Especially on Sundays when the market is closed, is shown.

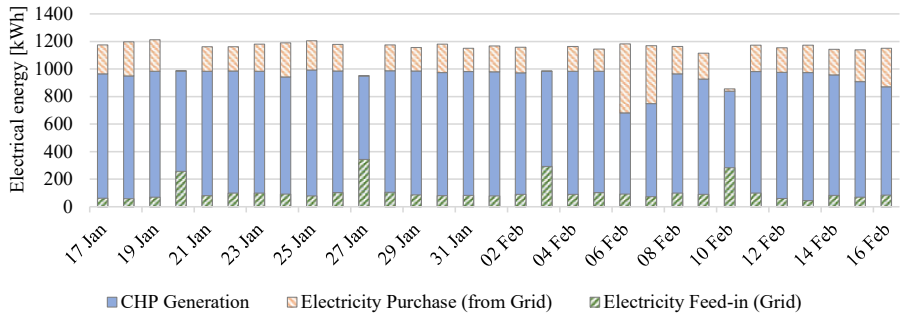


Figure 4: Daily electrical energy generation (CHP unit), purchase and feed-in (grid) for one month (winter period 2019) at the examined supermarket

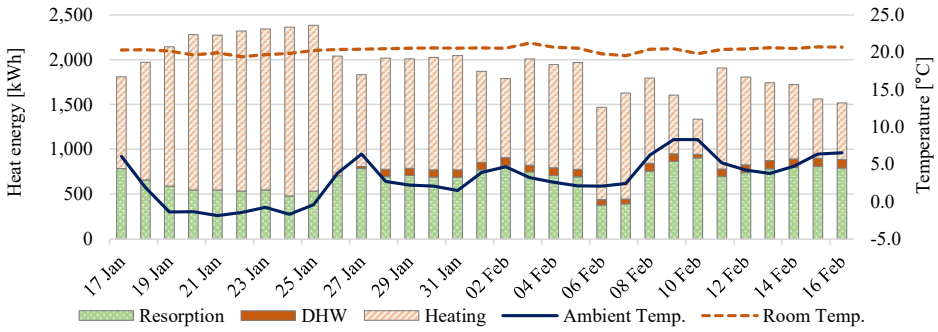


Figure 5: Distribution of heat in the examined supermarket for one month (winter period 2019) at the examined supermarket

The CHP unit is not managed according to electricity consumption, but according to heat consumption. Thus, it is only active if the hot water storage tank to be supplied by it does not exceed a temperature limit. If there is insufficient consumption of thermal energy by the heating system or the resorption system, the

temperature in the storage tank increases and the CHP unit switches off. It is therefore interesting to see how the heat provided by the CHP unit is distributed among the consumers depending on the ambient temperature (cf. Figure 5). It can be clearly seen that with decreasing ambient temperatures the necessary heat demand of the supermarket increases and the available heat for the resorption plant decreases. If the resorption system would consume a continuous heat flow, the hot water storage tank would cool down and the necessary temperature for room heating would no longer be reached. It is therefore necessary to operate the resorption plant at partial load, especially in the winter months, with very low ambient temperatures.

Based on the measurement data, the annual quantities and percentages of the individual electrical energy consumers can be summarized, as shown in Table 2. Particular importance is attached to the distribution of the consumption of electrical energy for the provision of cooling. The reason for this is that the resorption system partially covers the load of normal cooling and air conditioning, whereas the consumption values for lighting, deep-freezing (DF) and others remain constant. Due to the installed brine system, a considerable amount of energy is used to generate pumping power. This proportion can also be reduced by running the resorption system, as the brine pumps of the normal cooling chillers can be operated at partial load during the operation of the resorption system.

Table 2: Annual consumption values in MWh and the distribution in % of electrical energy in the examined supermarket with and without the CHP unit and Resorption system

	Light	*Deep Freezing*	*LT-Storage Room*	*Normal Cooling*	*A/C*	*Resorption*	*Pumps/ Recooler*	*Others*	*Total*
Grid Electricity + Condensing Boiler	14,0 MWh	94,5 MWh	7,5 MWh	117,0 MWh	3,4 MWh	0,0 MWh	122,1 MWh	5,8 MWh	364,3 MWh
	3,8%	25,9%	2,1%	32,1%	0,9%	0,0%	33,5%	1,6%	100,0%
CHP Unit + Resorption Refr. System	14,0 MWh	94,5 MWh	7,5 MWh	58,5 MWh	0,7 MWh	18,6 MWh	108,1 MWh	5,8 MWh	307,6 MWh
	4,6%	30,7%	2,4%	19,0%	0,2%	6,0%	35,1%	1,9%	100,0%

In order to carry out a comparison between the original (condensing boiler and grid electricity) and the new (CHP and resorption system) configuration, the measured values of several representative weeks were extrapolated to the period of one entire year. This was necessary because the CHP plant was not in continuous operation during the entire monitoring period and the originally installed systems thus fulfilled their task not only as additional but also as redundant systems.

3.2. Final energy costs

For an economic analysis it is necessary to know the expenses for the energy consumption of the supermarket. **오류! 참조 원본을 찾을 수 없습니다.** shows the average electricity and natural gas costs per kWh for industrial customers in selected countries of the European Union in the first semester of 2019.

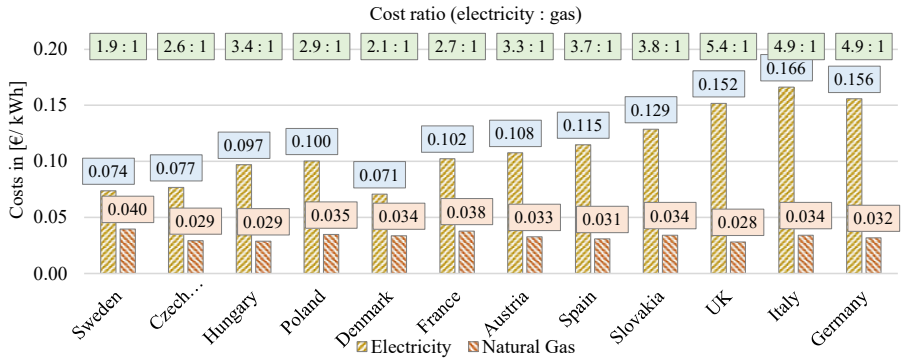


Figure 6: Electricity and natural gas prizes for industrial customers in European countries (excluding VAT and other recoverable taxes and levies), 2019 [6],[7]

It can be seen that the prices for electricity differ strongly, while the price for natural gas is almost constant. It should be noted that the given values exclude VAT and other recoverable taxes and levies, but national additional charges such as the EEG levy (German Renewable Energy Act) are included. This leads to significant price differences between the countries. The decisive factor for the profitability of a CHP unit is the ratio of natural gas price to electricity price, which is highlighted in green in the upper part of **오류! 참조 원본을 찾을 수 없습니다.**. As a result, before calculating the operating costs (chapter 3.3), it becomes clear that the system proposed in this paper is not suitable from an economic point of view in all countries.

3.3. Operating costs

In addition to the energy consumption data shown in Table 2 and the effective energy costs shown in **오류! 참조 원본을 찾을 수 없습니다.**, the efficiencies of the individual systems are also relevant for the calculation of operating costs. The thermal efficiency of the condensing boiler is $\eta_{th,CB} = 0.95$. The electrical efficiency of the CHP is $\eta_{el,CHP} = 0.38$ and the thermal efficiency is only $\eta_{th,CHP} = 0.55$. Nevertheless, the entire thermal energy required by the supermarket for heating and hot water supply is covered by the CHP unit and also provides the input heat for the resorption refrigeration system.

오류! 참조 원본을 찾을 수 없습니다. shows the annual operating costs for electricity and natural gas for the standard system (blue) and the system with CHP + resorption (orange) for the European countries mentioned above. In addition, the green highlighted annual operating cost savings are shown as a percentage. It becomes clear that there is a significant correlation between the price ratio (natural gas to electrical energy) and the annual cost savings. Due to the high effective energy price ratio in countries such as Germany, Italy and the UK almost or even more than half of the annual costs can be saved.

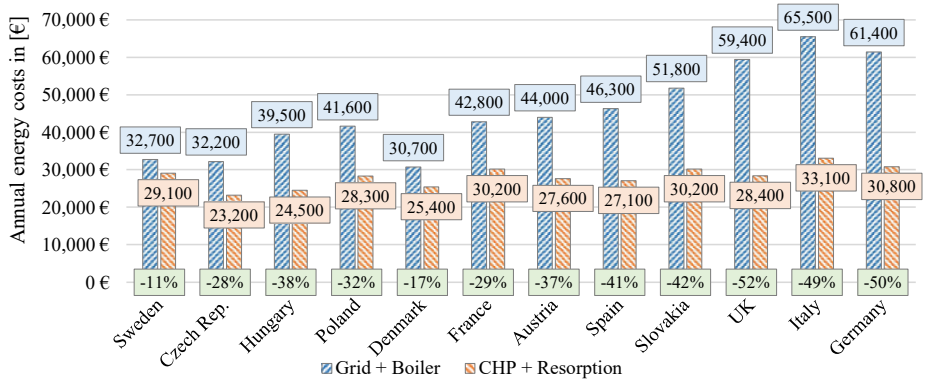


Figure 7: Annual energy costs with and without CHP + Resorption system

4. Amortization

In addition to the consideration of running costs, the necessary investment costs for the installation of such a system are also decisive. Table 3 shows the necessary costs for the various components, based on the investment costs for the pilot project in Germany. In particular, the costs for the resorption system are hypothetical, as there is no supplier for this yet.

Table 3: Investment costs of the CHP + Resorption system

CHP unit	Resorption System	Container, Recooler, Storages, etc.	Other	Engineering	Total
60.000 €	25.000 €	50.000 €	15.000 €	50.000 €	200.000 €

Figure 8 shows the amortization period based on these investment costs. Due to the very low operating cost savings for the operation in Sweden and Denmark, the system will only amortize after more than 25 years, which is not a realistic investment. Considering the previously mentioned countries Germany, Italy and the

UK, the system represents an alternative to existing solutions, as the lifetime of about 10-15 years is longer than the amortization period of the system.

Considering the values in Table 3, it is obvious that the engineering of the plant accounts for 25% of the total investment. Therefore, within the framework of the investigations of the overall system, the idea of a modular design was developed, which should be scalable with regard to electrical energy generation, heating and cooling capacities for each customer. This could significantly reduce engineering costs and shorten amortization periods, thereby opening up new markets.

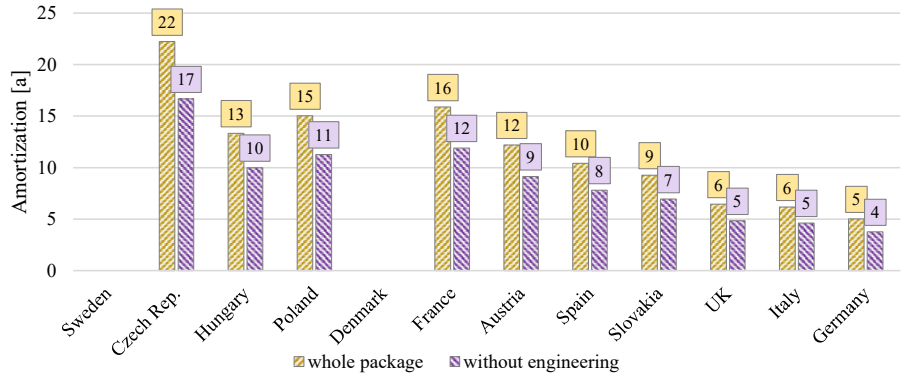


Figure 8: Amortization period of the CHP + Resorption system with and without engineering costs

5. CO_2 emissions

5.1. CO_2 emission factors

In addition to economic considerations, the impact on the environment is also decisive. In this context, the amount of fossil fuels used in the electricity generation chain must be considered first and foremost. As for natural gas and electrical energy prices, also statistics on the CO_2 equivalents of electricity generation can be found as shown in Figure 9. Depending on the main type of generation, the situation in the European countries varies considerably. Countries such as Sweden or France, where electricity is mainly generated from renewable sources or from nuclear power plants, have a significantly lower CO_2 emission factor than countries such as Germany, the Czech Republic or Poland, where a large amount of electricity is generated by fossil-fired steam power plants.

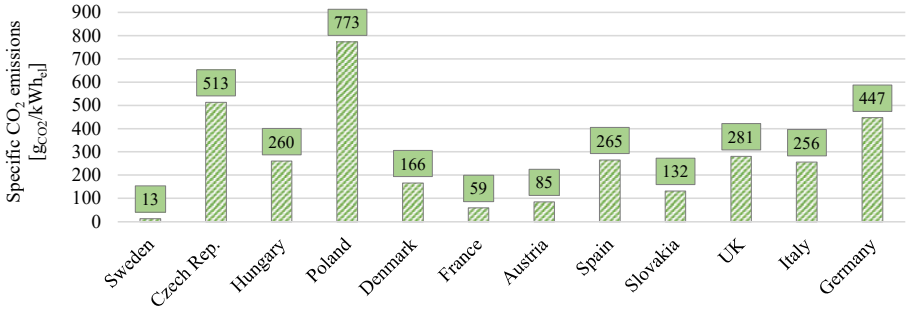


Figure 9: Specific CO_2 emissions for electricity generation in European countries [8]

When generating electrical and thermal energy from a CHP plant natural gas is used. Due to its high specific calorific value at the lowest amount of carbon of all fossil energy sources, natural gas, which consists mainly

of methane (CH_4), has a low emission factor of only ε_{CH4} = 202 g_{CO2}/kWh_{th}, which is however significantly higher than that from regenerative sources such as wind or solar power plants.

5.2. Annual CO_2 emissions

The specific annual emission values of the two system configurations (with and without CHP + resorption) can be calculated using the consumption values from Table 2 and the emission values of the electricity generation shown in Figure 9. Figure 10 shows that in the countries with a threshold value of < 315 g_{CO2}/kWh_{el} the annual emission values with the system solution of CHP + resorption system are above those of the initial configuration. Therefore, they do not represent a sustainable alternative. Key factors to improve the system and to decrease this threshold value are the percentage coverage of the cooling load by the resorption system and the electrical efficiency ratio of the CHP unit.

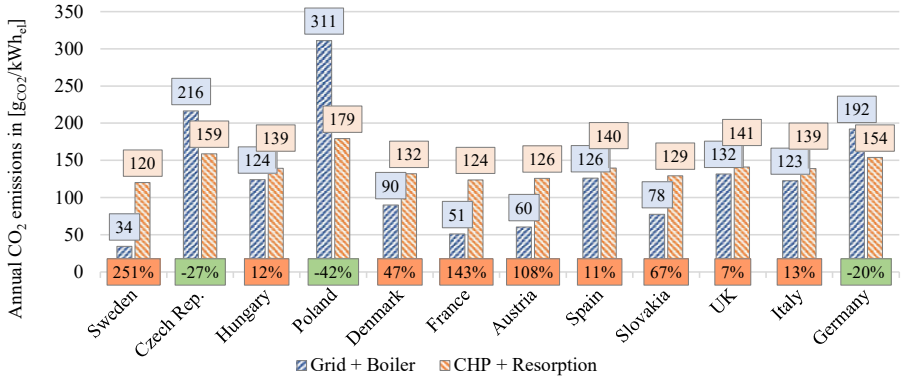


Figure 10: Annual CO_2 emissions with and without CHP + Resorption system

6. Conclusion and Outlook

As part of a pilot project, a supermarket was retrofitted in such a way that a combined heat and power unit (CHP) was installed to supply electricity and heating energy. Especially in the transition and summer months from March to November, only a small amount of thermal energy is needed for heating and domestic hot water supply. In order not to dissipate the co-generated heat to the environment, a thermally driven resorption refrigeration system was additionally installed. This system uses the waste heat from the CHP unit to provide cooling capacity for normal refrigeration and air conditioning of the supermarket, thus reducing the power consumption of the conventional vapor compression refrigeration systems.

The monitoring of the supermarket and the calculations based on it show that a considerable amount of up to 52 % of the annual operating costs could be saved. Based on these values, it was possible to determine an amortization calculation that proves the cost-effectiveness of the technology. In an European comparison, a partly lower economic efficiency can be observed, since the prices for electrical energy differ significantly and thus lead to unfavorable gas/electricity cost ratios, which are reflected in the achievable annual savings.

In addition, the system of a CHP + resorption unit in the supermarket network was investigated with regard to the CO_2 balance. It can be stated that the internationally varying generation strategies for electrical energy have a decisive influence on this. The combined CHP + resorption system emits a lower amount of CO_2 only if the local production of electrical energy has an emission factor of > 315 g_{CO2}/kWh_{el}, which in the future will decrease internationally as production from renewable sources increases.

Finally, it can be said that the use of systems that are individually uneconomical (resorption system) or environmentally harmful with regard to CO_2 emissions (CHP) overcome both disadvantages when they are used in combination. Technologies such as power-to-gas, which convert excess electrical energy, e.g. into synthetically produced methane, will enable the economic and climate-friendly operation of decentralized combustion-based electrical energy generation (e.g. CHP units) using the existing natural gas infrastructure. This shows the advantages of a cross-system approach in the design of energy systems.

Acknowledgements

The presented results were achieved within the scope of the project ResoField supported by the German Federal Ministry for Economic Affairs and Energy (BMWi) (Contract FKZ: 03ET1338A). The authors express their gratitude to the BMWi and the company EDEKA Handelsgesellschaft Südwest mbH for their financial and energetic support.

References

[1] International Energy Agency 2012 World Energy Outlook 2012 (Paris OECD/IEA) pp 351-356
[2] Baehr H D. Thermodynamik. Springer, Berlin usw; 1991, p
[3] Altenkirch E. Absorptionskältemaschinen. VEB Verlag Technik Berlin; 1954, pp 56-73.
[4] Niebergall W. Handbuch der Kältetechnik Band 7 – Sorptionskältemaschinen. Springer Verlag Berlin/Göttingen/New York; 1959, pp 23-71.
[5] Ziegler O, Hesse U, Thomas C. Increased efficiency of combined heat and power plants by utilizing waste heat for resorption chillers and their combination with hydrocarbon chillers. 37th UIT Heat Transfer Conference Padova, 24-26 June 2019
[6] Eurostat. Gas prices for non-household consumers - bi-annual data (from 2007 onwards). https://appsso.eurostat.ec.europa.eu/nui/show.do?dataset=nrg_pc_203&lang=en; 2019
[7] Eurostat. Electricity prices for non-household consumers - bi-annual data (from 2007 onwards). https://appsso.eurostat.ec.europa.eu/nui/show.do?dataset=nrg_pc_205&lang=en; 2019
[8] Koffi B, Cerutti A, Duerr M, Iancu A, Kona A, Janssens-Maenhout G. Covenant of Mayors for Climate and Energy: Default emission factors for local emission inventories– Version 2017, EUR 28718 EN, Publications Office of the European Union, Luxembourg, 2017, ISBN 978-92-79-71479-5, doi:10.2760/290197, JRC107518.

13th IEA Heat Pump Conference
April 26-29, 2021 Jeju, Korea

Augmented reality acoustics of air heat pumps –App development and methods

Gerwin H.S. Drexler-Schmid[a*], Christian H. Kasess[b], Brigitte Blank-Landeshammer[a], Christian Köfinger[a], Johann Emhofer[a], Holger Waubke[b], Christoph Reich

[a]AIT - Austrian Institute of Technoloy GmbH, Center for Energy, Thermal Energy Systems, Giefinggasse 2, 1210 Vienna, Austria
[b]Austrian Academy of Sciences, Acoustics Research Insitute, Wohllebengasse 12-14, 1040 Vienna, Austria

Abstract

To minimize noise immissions in urban areas, methods of sound measurement combined with augmented reality have been developed that enable simple and intuitive access to noise emissions and possibilities to their reduction. These methods allow a virtual representation of a sound emitting device and the resulting sound dispersion in a real environment.
In this work, the methods of sound measurement, to obtain transient directional and frequency-dependent sound emission behavior of a device in addition to the sound power level under different operating conditions, are shown. The focus lies on the development of an application for mobile devices, which visualizes the sound emitting apparatus with direction-dependent sound propagation virtually in a real environment. Using augmented reality this apparatus can be freely positioned and moved to find the acoustically optimal position. The sound pressure level can be determined at any position by the observer. In the future, the technology should facilitate the planning and installation of heating and air conditioning units regarding noise pollution, increase the acceptance of heat pumps and thus lead to a higher proportion of renewable energy.

© HPC2020.
Selection and/or peer-review under responsibility of the organizers of the 13th IEA Heat Pump Conference 2020.

Keywords: augmented reality; acoustics; air heat pumps; sound propagation

1. Introduction

Noise causes stress and thus triggers reactions such as cardiovascular diseases, sleep and concentration disorders and mental illnesses and has an influence on social behavior (aggression) [1]. In urban areas in particular, people are severely affected by noise pollution. In addition to traffic and commercial noise, heating and cooling equipment is particularly important here. Air-conditioning systems, heat pump external units (source) or even noisy control cabinets or fast-charge stations of batteries often lead to conflicts. In addition, noise pollution has increased again in recent years and about 40% of Austrians are affected [2]. In view of the steady expansion of renewable energy sources, the number of air heat pumps in particular will increase strongly in the urban area. Nowadays, sound emissions are usually determined from a single number, the direction- and location-independent sound power level and converted into a location-dependent sound pressure level by simple mathematical methods. This does not take into account the frequency dependence, direction dependency, operating state or the influence of the environment. It is therefore urgently necessary to develop a more intuitive, simpler but at the same time more accurate and more complete approach to the sound issue in order to make cities 100% renewable and at the same time quieter. This approach is based on Augmented Reality (AR) and represents a unique approach to date.

* Corresponding author. Tel.: +43 664 620 78 66; fax: +43 50550-6679.
E-mail address: gerwin.drexler-schmid@ait.ac.at.

The aim of this work is to make sound emissions from noise sources visible and audible in real time before they are installed. This shall be done by means of "Augmented Reality" on site, depending on frequency, direction, operating condition and environment. Noise sources such as recirculating chillers, evaporators, fans, etc. in/around the building as well as noise-insulating measures should be able to be placed virtually before the units are installed on site. Their sound emissions are visualized on the surrounding surfaces in real time and made acoustically perceptible. For the calculations, the automatically detected environment is taken into account in terms of its acoustical properties. With the unique methodology developed, different installation locations, noise reduction measures and facades which are yet to be built can be taken into account, thus virtually optimizing the noise level of the heating and cooling units to be installed in the future, even before the units are ordered.

Several works regarding augmented reality acoustics and acoustic augmented reality have been published so far. However, the approach presented in this work is new to date. Most recently Green and Murphy [3] published a study of an intuitive environmental sound monitoring system that can be used on-site and return meaningful measurements beyond the standard L_{Aeq}. The created iOS-app returns readings indicating the human, natural and mechanical sound content of the local acoustic scene and implements four virtual sound objects which the user can place in the scene to observe their effect on the readings. Other existing concepts in this area of development refer to assigning a sound source to real objects in the environment and making them perceptible with e.g. headphones. The Japanese technology group *NEC*, for example, is pursuing such a concept [4].The system is similarly called "Acoustic augmented reality" and is to be used, for example, for marketing purposes, guidance systems, information for tourists or speaking advertising pillars. The French company *Augmented Acoustics* strives to use the same functional principle for concerts. A similar approach has also been followed at the *Finnish University of Aalto* together with *Nokia* under "acoustic-hear-through" and "microphone-hear-through" approaches [5]. *Microsoft* also follows this approach to help visually impaired people find their way [6]. A different approach is being pursued in the automotive sector. In the future, vehicles will be able to warn drivers of hidden dangers before they are visible [7].

The work presented here includes sound data acquisition, software/hardware selection and app development.

2. Methods

2.1. Experimental setup for acoustic measurements

A large part of the components in the heating & cooling sector, but also switch cabinets, transformers and similar apparatus like charging stations, emit sound waves which are caused by vibrating surfaces or flow effects. Methods are available for the characterization of sound emissions in different depths, e.g. ISO 3741, ISO 3741-1 / ISO 3741-2, ISO 3744, ISO 3745, ISO 3746, ISO 3747. Usually, the sound power level is specified for a sound emitting object, which is determined using an enveloping surface method with standard microphones or intensity probes, using different test environments, e.g. EN 12102-1 for heating and cooling or prNE 12102-2 for heat pumps. In this method, the acoustic information is reduced to a single number - the sound power level. Directional and time-dependent emissions are not taken into account. Tonal components in the signal are only taken into account as a lump sum by the addition of a "penalty surcharge" in some countries [8]. With the help of this sound power level, simple mathematical models can be used to calculate the sound pressure level at observer positions. In Austria, the association *Wärmepumpe Austria* provides a sound propagation calculator for this purpose [9]. In the current variant, a direction factor or the existence of sound insulation measures can also be taken into account. The sound propagation visualization of the *Danish Energy Agency* calculates a sound map based on the sound power level, which is superimposed on Google-Maps [10] (see Figure 1).

In order to characterize the directional dependence of sound propagation and the long-term behavior of components even under different climatic conditions, measurement with a large number of microphones over a large time range is necessary. This can be done with an acoustic dome (Figure 2).

The dome used in this work consists of up to 64 microphones with a 64 channel simultaneous data acquisition system and a sampling rate of up to 192 kHz. This allows measurements for time-dependent sound power determination, but also frequency, location and time-dependent analyses.

For this work an AIT-built heat pump, the SilentAirHP (Figure 3), was put into a climate chamber surrounded by the acoustic dome. The heat pump was measured at several different operating conditions. For the further work a data set was selected, where the evaporator of the heat pump was iced up.



Figure 1: Visualization of the expected sound propagation through the installation of a heat pump on a house wall (stoejberegner.ens.dk) [10]

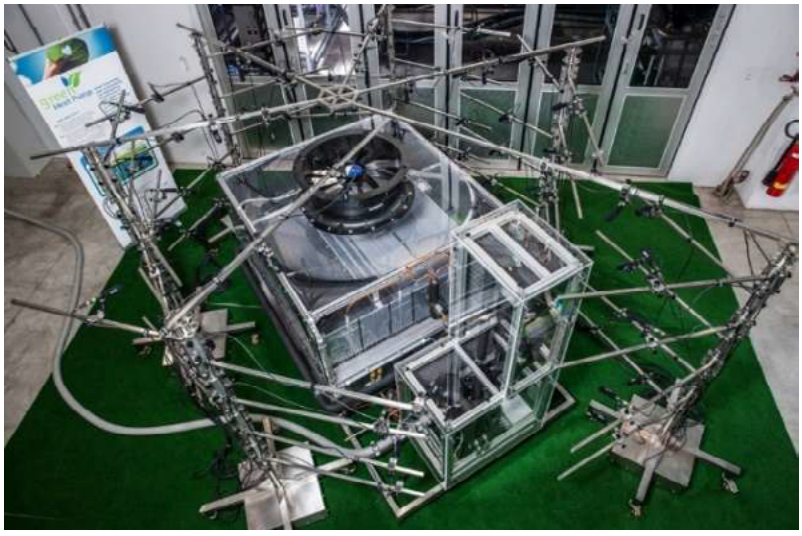


Figure 2: Acoustic dome placed around the *GreenHP [11]* (image by AIT)



Figure 3: SilentAirHP in the AIT climate chambers. The acoustic dome has been setup around the heat pump. In the background the white bags allowing for a very uniform quit inflow air distribution into the climate chamber can be seen.

2.2. Selected hardware and software for augmented reality acoustics

There are a number of SDKs (Software Development Kits) and environments used for the development of augmented reality applications, ranging from vendor-specific solutions only working on their native platforms, like SDKs from BOSE [12] or Apple [13] or Microsoft's MixedRealityToolkit for HoloLense [14], to more general approaches like Vuforia [15], DeepAR [16] or Kudan [17], and from open-source or free projects to commercial offers to new and upcoming solutions still existing as a beta version. They can be further categorized based on their overlaying capability or their tracking, as discussed in [18]. For iOS, Apple's own framework, ARKit, which was released in 2017, is mostly used. Google's Tango was discontinued in 2018 after only three years, shifting the focus to the new project, ARCore [19], for android devices [20] while Facebook's Spark AR public beta was launched in Summer this year [21]. Most SDKs rely on third party 3D engines such as Unity [22], UnrealEngine [23] or SceneKit [24] as development environment [25].

For this project Apples ARKit and Unity were used to create an app running on all devices that support ARKit.

2.3. Methods for sound propagation calculations

There are various methods for calculating sound propagation, which are briefly described in the following.

I) **Ray tracing**: The different methods of ray tracing have proven to be useful for interior problems. The effort is less than with the finite and boundary element method (FEM and BEM, respectively). Therefore, also sound propagation in large spaces with many borders can be calculated [26]. However, the diffraction is

normally not recorded. This is why this method is not suitable for the calculation of the sound propagation in the open air in particular behind sound screens without further corrections.

II) **Methods of noise mapping**: Simplified methods are used for noise mapping which are limited to direct sound and first and second reflections. The direct sound paths (i.e. also deflected by diffraction) are determined according to ÖNORM ISO 9613-2. Diffractions at single or multiple edges are considered only approximately on the basis of experiments and analytical solutions. Due to the relatively simple calculation, these methods can be used on a large scale, whereby the efficiency of the analytical approaches is also limited here [27]. Within the RELSKG program, frequency-dependent correction factors for noise barriers on roads and railways with and without absorbing material have already been determined [28]. However, these values have to be adjusted for the low heights, short distances and shorter lengths, which are usual for the situations considered in this project.

III) **Finite Element Methods**: The calculation of the sound distribution using the FEM [29, 30] is only possible for small rooms, whereas semi-infinite elements or Perfectly Matched Layers (PMLs) also allow the consideration of radiation. This method can therefore only be used to determine correction factors for diffraction behind noise barriers. This is essentially limited to the 2D case.

IV) **Boundary Element Method**: For noise barriers, mainly 2D calculations or 2.5D calculations are performed for the BEM. It is assumed that the geometry is constant in the third dimension, but the source can also be a point source [31]. This method was further developed in terms of efficiency at the Acoustic Research Institute [32]. Nevertheless, the computational effort required for this does not allow an ad-hoc calculation. Thus, this method is also only suitable for the determination of correction factors. 3D-BEM can only be used for small geometries and/or low frequencies due to the much higher effort, and therefore can only be used for special problems in this project.

V) **Further methods**: Beside the mentioned methods there is also the Finite Difference Method, which is unsuitable for external space problems, the Wave Based Method [33], which is also rather used for internal space problems, and transformation methods, which are only used for single bordered areas.

In this work a frequency dependent sound propagation was derived from the measurements. For this purpose, the entire frequency space was divided into third octave bands. For each band, the sound pressure was calculated as a function of the distance.

3. Results & Discussion

3.1. Data processing

For this work the raw data-files of 64 channels were split into ~1.3 seconds wavelets and were further processed using Fast Fourier Transform technique. After applying the A-weighting the data was stored as third octave band transient sets. Integration over the acoustic dome surface per third octave yields the time dependent A-weighted third octave sound power P (see equation 1), where $\overline{p^2}$ is the mean squared sound pressure, ρ the air density, c the sound velocity and dA an area element of the surrounding surface [34].

$$P = \int \frac{\overline{p^2}}{\rho \cdot c} dA \tag{1}$$

The sound power level LwA is calculated with equation 2.

$$LwA = 10 \cdot \log\left(\frac{P}{P_0}\right) \tag{2}$$

Where P_0 is 10^{-12} Watts. The third octave band sound power levels were used for the *SilentAirHP-App*. An additional app, *HVAC Positioner*, was compiled using the sound power level over all frequencies. To calculate the sound power level over all frequencies the third octave sound powers levels are logarithmically summed up.

3.2. App-assembling

3.2.1. SilentAirHP-App

For the *SilentAirHP-App* the resulting sound pressure levels of the different third octave bands were calculated via equation 3, where LpA is the sound pressure level, Q is a geometry factor [35] an r is the distance

from the sound source. The geometry factor Q is 1 for a sound source in mid-air, 2 for a sound source placed on plane surface, 4 near a wall, 8 in a corner. The different geometry factors are shown in Figure 4. For the version of the app at time of writing fixed value of Q was hard coded into the software. This will be changed to allow for user selection or automatic detection. Sound pressure values were assigned to colors for visualization.

$$LpA = LwA - \left|10 \cdot \log\left(\frac{Q}{4\pi \cdot r^2}\right)\right| \quad (3)$$

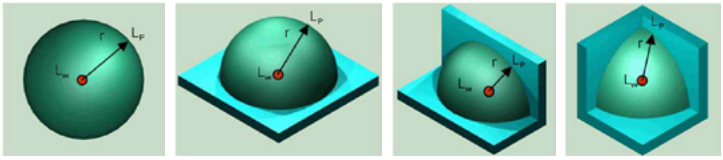


Figure 4: Full sphere $Q = 1$, half sphere $Q = 2$, quarter sphere $Q = 4$, eighth sphere $Q = 8$ (http://www.sengpielaudio.com/calculator-soundpower.htm) [35]

A photorealistic model of the SilentAirHP was created by a third party, i.e. Wunderwerk GmbH. Eventually the app included the following features: i) positioning of the SilentAirHP, ii) switching it on/off, iii) switch to choose either hearing and visualizing all frequencies or a third octave band around a certain frequency, iv) a slider to choose the third octave band frequency, v) a display of the actual dB-value and distance, and vi) audio output. All these features are visible in Figure 5, where the AR-SilentAirHP was positioned in front of a building in Austria. The observer can freely move and change position and has also the possibility to change the position of the heat pump in order to find a more suitable spot with regard to acoustic emissions.



Figure 5: Augmented Reality Acoustics at AIT - current state of development, a laboratory heat pump (SilentAirHP) placed using AR in a real environment with frequency-dependent sound propagation of a point source (without directional characteristic, diffraction or reflection)

3.2.2. HVAC Positioner

The second app that was built includes nearly all heat pumps that can be bought in Austria, but only refers to the overall sound power level for calculating dB(A) values and has no audio output. The data of the heat pumps is stores in an external data base to keep safe storage on the mobile device, requiring an internet connection. This app can be downloaded from the *Apple App Store* and *Google Play Store* [36]. For this app the sound power levels are calculated in real time.

Figure 6 shows a chiller put on the lawn via augmented reality with the corresponding sound power level indicated on the right-hand side of the image. The color code corresponds to guidelines regarding allowed maximal sound power levels for positioning the air heat pump.

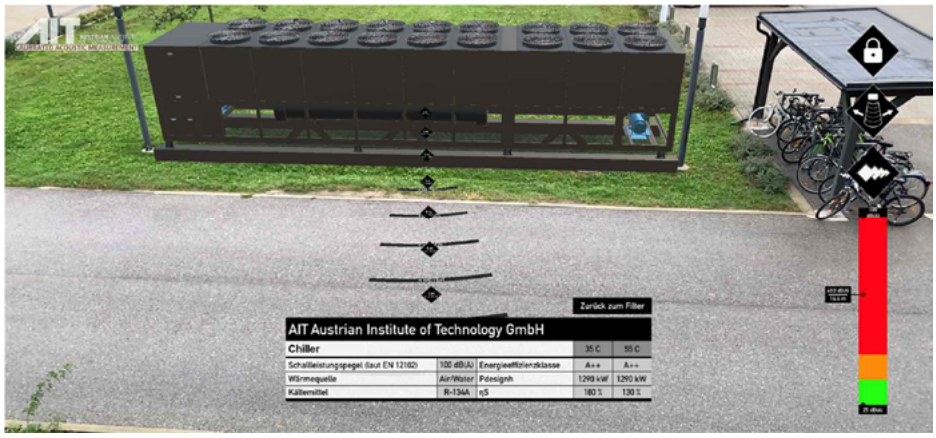


Figure 6: HVAC Positioner

4. Conclusion & Outlook

The base for an intuitive approach to acoustic problems with air heat pumps and chillers was created. This was done by building an app, which made it possible not only to visualize air heat pumps and chillers via augmented reality, but also to make the sound of these machines visible and thus much easier to comprehend. The sound pressure level is calculated from the sound power levels. Guidelines regarding allowed maximal sound pressure levels for positioning the air heat pump are intrinsically included in the via the color code on the right-hand side of the app. A database including nearly all available air heat pumps in Austria was generated and will be extended in the future. Next steps in the projects will be i) a faster raw-data handling algorithm and conversion of noise source measurements into suitable sound profiles, ii) an automatic sound physical detection of the environment (near and far range), iii) calculation of sound propagation based on sound profiles and environmental data, iv) implementation of sound absorption and reflection, and v) an interactive visual and acoustic representation of the calculations using AR, i.e. virtual noise source with virtual sound in real environments.

5. Acknowledgements

The Austrian Research Promotion Agency (FFG) and the Austrian Climate and Energy Fund (KLIEN) is gratefully acknowledged for funding this work under Grant No. 848891 (program line 'Energieforschung e!Mission 1st call', project 'SilentAirHP') and Grant No 873588 (program line 'Stadt der Zukunft 2nd call, project 'RAARA'). We also want to thank the Federal Ministry of the Republic of Austria for Transport, Innovation and Technology for supporting IEA HPT Annex 51 in Austria in the framework of the IEA Research Cooperation.

6. References

[1] T. Münzel *et al.,* "Environmental Noise and the Cardiovascular System," *Journal of the American College of Cardiology*, vol. 71, no. 6, pp. 688–697, http://www.sciencedirect.com/science/article/pii/S0735109717419309, 2018.

[2] A. Aichinger, S. Baud, and E. Milota, "Umweltbedingungen, Umweltverhalten 2015: Ergebnisse des Mikrozensus," 2017.

[3] M. Green and D. Murphy, “Environmental sound monitoring using machine learning on mobile devices,” *Applied Acoustics*, vol. 159, p. 107041, 2020.
[4] M. Kölling and T. Review, *Post aus Japan: AR für die Ohren.* [Online] Available: https://www.heise.de/tr/artikel/Post-aus-Japan-AR-fuer-die-Ohren-3844617.html. Accessed on: Oct. 28 2019.
[5] R. Albrecht, T. Lokki, and L. Savioja, *A Mobile Augmented Reality Audio System with Binaural Microphones: Proceedings of Interacting with Sound Workshop Exploring Context-Aware, Local and Social Audio Applications*. New York, NY: ACM, 2011.
[6] F. Ribeiro, D. Florencio, P. A. Chou, and Z. Zhang, “Auditory augmented reality: Object sonification for the visually impaired,” in *2012 IEEE 14th International Workshop on Multimedia Signal Processing (MMSP)*, Banff, AB, Canada, Sep. 2012 - Sep. 2012, pp. 319–324.
[7] F. Schwarz and W. Fastenmeier, “Augmented reality warnings in vehicles: Effects of modality and specificity on effectiveness,” (eng), *Accident; analysis and prevention*, vol. 101, pp. 55–66, 2017.
[8] C. Reichl *et al., Annex 51 - Acoustic Signatures of Heat Pumps.* [Online] Available: http://heatpumpingtechnologies.org/annex51/.
[9] Verein Wärmepumpe Austria, *Schall-Rechner.* Accessed on: 2020, 7th of Jannuary.
[10] Grontmij A/S, *Styr på støjen – luft/vand varmepumper.* [Online] Available: http://stoejberegner.ens.dk/. Accessed on: 2020, 7th of Jannuary.
[11] Andreas Zottl, *Green Heat Pump.* [Online] Available: www.greenhp.eu. Accessed on: 2020, 7th of Jannuary.
[12] *Bose Developer Portal | Bose AR Beta.* [Online] Available: https://developer.bose.com/bose-ar. Accessed on: Oct. 28 2019.
[13] A. Inc, *ARKit 3 - Augmented Reality - Apple Developer.* [Online] Available: https://developer.apple.com/augmented-reality/arkit/. Accessed on: Oct. 28 2019.
[14] *microsoft/MixedRealityToolkit-Unity.* [Online] Available: https://github.com/Microsoft/MixedRealityToolkit-Unity. Accessed on: Oct. 28 2019.
[15] *Vuforia - Engine.* [Online] Available: https://engine.vuforia.com/engine. Accessed on: Oct. 28 2019.
[16] *SDK | DeepAR.* [Online] Available: https://www.deepar.ai/augmented-reality-sdk. Accessed on: Oct. 28 2019.
[17] *Kudan.* [Online] Available: https://www.kudan.io/. Accessed on: Oct. 28 2019.
[18] D. Amin and S. Govilkar, “Comparative Study of Augmented Reality Sdk's,” *IJCSA*, vol. 5, no. 1, pp. 11–26, 2015.
[19] *ARCore - Google Developers | Google Developers.* [Online] Available: https://developers.google.com/ar/. Accessed on: Oct. 28 2019.
[20] J.-K. Janssen and h. online, *Google ARCore 1.0: Realistische Augmented Reality künftig auf 13 Android-Smartphones.* [Online] Available: https://www.heise.de/newsticker/meldung/Google-ARCore-1-0-Realistische-Augmented-Reality-kuenftig-auf-13-Android-Smartphones-3977662.html. Accessed on: Oct. 28 2019.
[21] *Creativity for all: Facebook’s Spark AR now lets anyone build and share effects on Instagram.* [Online] Available: https://tech.fb.com/creativity-for-all-facebooks-spark-ar-now-lets-anyone-build-and-share-effects-on-instagram/?utm_source=web&utm_medium=spark-ar&utm_campaign=ar-ig-launch&utm_offering=spark-ar&utm_product=spark-ar. Accessed on: Oct. 28 2019.
[22] Unity, *Unity.* [Online] Available: https://unity.com/. Accessed on: Oct. 28 2019.
[23] *Unreal Engine | What is Unreal Engine 4.* [Online] Available: https://www.unrealengine.com/en-US/what-is-unreal-engine-4. Accessed on: Oct. 28 2019.
[24] A. Inc, *SceneKit - Apple Developer.* [Online] Available: https://developer.apple.com/scenekit/. Accessed on: Oct. 28 2019.
[25] M. Romilly, *12 Best Augmented Reality SDKs.* [Online] Available: https://dzone.com/articles/12-best-augmented-reality-sdks. Accessed on: Oct. 28 2019.
[26] Claus Lynge Christensen, *Odeon - Room Acoustics Software.* [Online] Available: www.odeon.dk. Accessed on: 2020, 7th of Jannuary.
[27] W. Wei, T. van Renterghem, and D. Botteldooren, “An-efficient-method-to-calculate-sound-diffraction-over-rigid-obstacles,” https://www.apexacoustics.co.uk/an-efficient-method-to-calculate-sound-diffraction-over-obstacles/, 2015.
[28] C. H. Kasess, W. Kreuzer, and H. Waubke, “Deriving correction functions to model the efficiency of noise barriers with complex shapes using boundary element simulations,” *Applied Acoustics*, vol. 102, pp. 88–99, 2016.
[29] K.-J. Bathe, *Finite element procedures,* 2nd ed. Englewood Cliffs, N.J: Prentice-Hall, 2014.
[30] P. Reiter, R. Wehr, and H. Ziegelwanger, “Simulation and measurement of noise barrier sound-reflection properties,” *Applied Acoustics*, vol. 123, pp. 133–142, 2017.

[31] D. Duhamel, "EFFICIENT CALCULATION OF THE THREE-DIMENSIONAL SOUND PRESSURE FIELD AROUND A NOISE BARRIER," *Journal of Sound and Vibration*, vol. 197, no. 5, pp. 547–571, 1996.
[32] C. H. Kasess, W. Kreuzer, and H. Waubke, "An efficient quadrature for 2.5D boundary element calculations," *Journal of Sound and Vibration*, vol. 382, pp. 213–226, 2016.
[33] E. Deckers *et al.,* "The wave based method: An overview of 15 years of research," *Wave Motion*, vol. 51, no. 4, pp. 550–565, 2014.
[34] J. Emhofer, R. Zitzenbacher, and C. Reichl, "Sound Source Extension Library for Modelica," in *Proceedings of the 12th International Modelica Conference, Prague, Czech Republic, May 15-17, 2017*, 2017, pp. 605–612.
[35] Eberhard Sengpiel, *Compare Sound power, Sound pressure, and Sound intensity in a distance from the sound source.* [Online] Available: http://www.sengpielaudio.com/calculator-soundpower.htm. Accessed on: 2020, 7th of Jannuary.
[36] G. H. S. Drexler-Schmid *et al., HVAC-Positioner: iOS, Android*. https://apps.apple.com/at/app/hvac-positioner/id1462057877, https://play.google.com/store/apps/details?id=at.ac.ait.hvacpositioner&hl=de_AT: AIT - Austrian Institute of Technology, 2019.

13th IEA Heat Pump Conference
April 26-29, 2021 Jeju, Korea

Analysis of a directly gas-fired absorption heat pump with an improved condensing boiler technology

Philipp Wagner[a*], Rene Rieberer[a]

[a]Graz University of Technology, Institute of Thermal Engineering, Inffeldgasse 25/B, 8010 Graz, Austria

Abstract

Residential heating is one of the most important factors for the reduction of fossil energy consumption and CO_2 emissions. A relevant contribution can be expected from directly gas-fired ammonia/water absorption heat pumps (GAHP) when it comes to the replacement of traditional condensing boilers in cold and moderate climatic regions (e.g. Europe). Especially in old buildings, the return flow temperature of the heat distribution system is above the dew point of the flue gas, thus water vapor condensation of the flue gas cannot take place in the flue gas heat exchanger. To ensure water vapor condensation under all operating conditions the flue gas can be cooled by the refrigerant in a refrigerant cooled flue gas heat exchanger, installed between the evaporator and the absorber. A GAHP with a nominal heating capacity of 18 kW was equipped with a water cooled and a novel refrigerant cooled flue gas heat exchanger to experimentally investigate the achievable increase in efficiency by means of the refrigerant cooled flue gas heat exchanger. The GAHP was operated at different heat source temperatures and different cycle configurations.

© HPC2020.
Selection and/or peer-review under responsibility of the organizers of the 13th IEA Heat Pump Conference 2020.

Keywords: Ammonia/Water; Cycle Design; Gas Utilization Efficiency; Flue Gas Heat Exchanger; Space Heating

Nomenclature

Δ	difference	out	outlet
ABS-1, ABS-2	water cooled absorber	*p*	pressure (Pa)
ABS-3	solution cooled absorber	pso	poor solution
CON	condenser	PUMP	solution pump
DEP	dephlegmator	q	vapor quality
EVA	evaporator	*Q*	heat flow rate (W)
FlueHX1	water cooled flue gas heat exchanger	REC	rectification column
FlueHX2	refrigerant cooled flue gas heat exchanger	ref	refrigerant
		rso	rich solution
fuel	fuel (natural gas)	RTH	refrigerant throttle
GAHP	gas-fired absorption heat pump	sink	heat sink (water)
GEN	generator	source	heat source (brine)
GUE	Gas Utilization Efficiency (-)	SRC	source temperature level
H_i	lower calorific value (kJ·m^{-3})	STH	solution throttle
H_s	calorific value (kJ·m^{-3})	*t*	temperature (°C)
in	inlet	*v*	specific volume (m^3·kg^{-1})
λ	combustion-air ratio	*V*	volume flow rate (m^3·s^{-1})
liq	liquid	V_i	needle valve
m	mass flow rate (kg·s^{-1})	vap	vapor
norm	referred to standard conditions	*x*	ammonia mass fraction (kg·kg^{-1})

* Corresponding author. Tel.: +43 316 873 7303; fax: +43 316 873 7305.
E-mail address: philipp.wagner@tugraz.at.

1. Introduction

In order to reach the ambitious targets of the European Unions climate and energy framework the share of renewable energies as well as the energy efficiency of all processes - especially for heating processes - have to be significantly increased. In 2030 the greenhouse gas emissions shall be reduced by at least 40 % below the levels of 1990. Renewables shall be increased by at least 32 % and the energy efficiency shall be increased by at least 32.5 %. [1]

As the energy consumption used for residential heating has a significant share on the total energy consumption - around 26 % of the Europeans total energy consumption [2] - this sector can contribute significantly to reach the climate targets. Especially, the heating demand of buildings has to be reduced and the efficiency of heating technologies has to be increased. Currently the heating demand is mainly covered by condensing gas boilers. E.g. in Germany gas and oil boilers had a market share of 75 % in the year 2017, whereas electrically driven heat pumps only had a market share of 11 % [3].

State-of-the-art condensing boilers provide the heating demand by burning fossil fuels (e.g. gas, oil) and cooling the combustion gas by the return flow of the hydronic heat distribution system. If the return flow temperature is below the dew point of the combustion gas, latent heat can be utilized by water vapor condensation. In this way, with state-of-the-art condensing gas boilers in combination with a low temperature heating system (e.g. floor heating system) an efficiency of up to 109 % (based on the lower calorific value) - which is already the limit - can be achieved [4].

To achieve a 40 % decrease in greenhouse gas emissions a more efficient technology is necessary to replace state-of-the-art condensing boilers. Especially in old buildings it is not realistic to replace all oil and gas fired boilers with electrically driven compression heat pumps due to the high temperature of the hydronic heat distribution system which leads to a low efficiency and a peak demand especially at low ambient temperatures. In this context, it is not meaningful to only use electrically driven heating systems as there is already an existing natural gas network which can be used. According to the current state-of-the-art the storage of natural gas is easier than the storage of electrical energy. It has also taken into account, that in some countries electrical energy is still produced in fossil-fired power stations at low efficiencies.

For old buildings a worthwhile contribution can be expected from directly gas-fired absorption heat pumps (GAHPs). Recently, a lot of research has been carried out in this field to increase the efficiency and/or to reduce the size and/or the complexity and/or the costs [5–9]. A GAHP is driven by a high temperature heat source (combustion of natural gas) and utilizes low temperature heat from the ambient (e.g. air, ground, water) and releases the sum of both heat flows to the hydronic heat distribution system at a medium temperature. Due to the utilization of ambient heat which is “free of charge”, with this promising technology an efficiency of up to 180 % (based on the lower calorific value) is possible [9]. Therefore a reduction of the energy consumption and greenhouse gas emissions of more than 40 % compared to state-of-the-art condensing boilers is possible. To further reduce the environmental impact of GAHPs in the future there are already suggestions to increase the amount of hydrogen in the natural gas network and to supply the natural gas network with renewable gas.

It has to be noted, that such high efficiencies are only possible in combination with a low temperature heating system (e.g. floor heating system) and if the low temperature heat from the ambient is supplied at a rather high level. If the return flow temperature of the hydronic heat distribution system is above the dew point of the flue gas the latent heat of the flue gas cannot be used and dissipates into the environment. This issue can impede the future market penetration of GAHPs as e.g. in Germany around three quarters of the residential buildings were built more than 30 years ago. Under typical operating conditions the return flow temperature is around 55 °C in the heating system of these buildings [10]. With a combustion-air ratio of λ=1.3 the dew point of the flue gas of a natural gas combustion is around 55 °C, which means in most applications the condensing boiler technology cannot be used because water vapor condensation in the combustion gas does not take place.

With a modified cycle GAHPs offer a great possibility to cool the combustion gas with a low temperature fluid to use the condensing boiler technology under all operating conditions. The lowest temperature in a GAHP occurs at the evaporator which results in the possibility of cooling the combustion gas with the refrigerant. As it is not advantageous to (partially) replace the evaporator with a refrigerant cooled flue gas heat exchanger, it makes sense to install it after the evaporator or depending on the cycle design after a refrigerant heat exchanger (internal heat exchanger). Generally, after the evaporator or the refrigerant heat exchanger the temperature is around -15 °C to +20 °C, which is lower and independent from the temperature of the hydronic heat distribution system, which ensures water vapor condensation under all operating conditions. Wagner and Rieberer [5] have shown a simulation study of a GAHP with a conventional water cooled flue gas heat exchanger (cooled by the hydronic heat distribution system) compared to a GAHP with a refrigerant cooled flue gas heat exchanger (cooled by the refrigerant). This study has shown the possibility to

increase the efficiency of a GAHP by up to 12 % depending on the operating conditions and the cycle configuration by installing a refrigerant cooled flue gas heat exchanger.

First measurement results of a GAHP prototype with a novel refrigerant cooled flue gas heat exchanger were recently published by Wagner and Rieberer [6]. An increase in efficiency of around 3 %, which was lower than expected based on the previous work [5], was achieved. Based on this sub-optimal results a first optimization of the integration of the refrigerant cooled flue gas heat exchanger was done.

Currently there are two working pairs used in absorption heat pumps. As heat source temperatures below 0 °C (e.g. air) are usual for heating applications the working pair ammonia/water has been used in the investigated prototype. Ammonia is a natural refrigerant and has the advantage of no ozone depletion potential and no global warming potential. It is classified as hardly inflammable and toxic. Therefore, national standards and regulations have to be observed if ammonia/water absorption heat pumps are operated in residential buildings (e.g. outdoor installation, installation with a ventilated housing, …). The ammonia charge in GAHPs is quite low and mainly dissolved in water, nevertheless it should be kept as low as possible.

Within this work a GAHP prototype with a nominal heating capacity of 18 kW was equipped with a refrigerant cooled flue gas heat exchanger between the evaporator and the absorber. Compared to the previous work by Wagner and Rieberer [6] first results with a modified flue gas flow direction are shown. Different cycle configurations were experimentally investigated and a comparison between a GAHP with a refrigerant cooled flue gas heat exchanger and a GAHP with a water cooled flue gas heat exchanger was performed.

2. System Description

Fig. 1 shows a schematic flow chart of the analyzed GAHP cycle, Fig. 2 shows the laboratory prototype. Rich solution (rso) with a relatively high ammonia mass fraction is brought to the high pressure (condensation pressure p_{CON}) by means of an electrical solution pump (PUMP). The rich solution is used to cool the dephlegmator (DEP) to produce the required reflux for the rectification column (REC) and to achieve a higher ammonia mass fraction in the refrigerant (ref). A bypass (V_{nDEP}) at the dephlegmator gives the opportunity to investigate the influence of the dephlegmator on the ammonia mass fraction and the overall efficiency. Via valve V_{REC}, a part of the rich solution can be fed into the rectification column and be used as an additional reflux. An optimum of the valve settings of V_{REC} and V_{ABS-3} was experimentally determined and kept constant for all investigations. The rich solution that is not fed into the rectification column is preheated in the solution cooled absorber (ABS-3) before it enters the generator (GEN). In the generator the rich solution is partly evaporated by the heat supplied by a natural gas combustion (Q_{GEN}). Ammonia vapor rises upwards in the rectification column, where it is brought into contact with the liquid solution (reflux) flowing downwards.

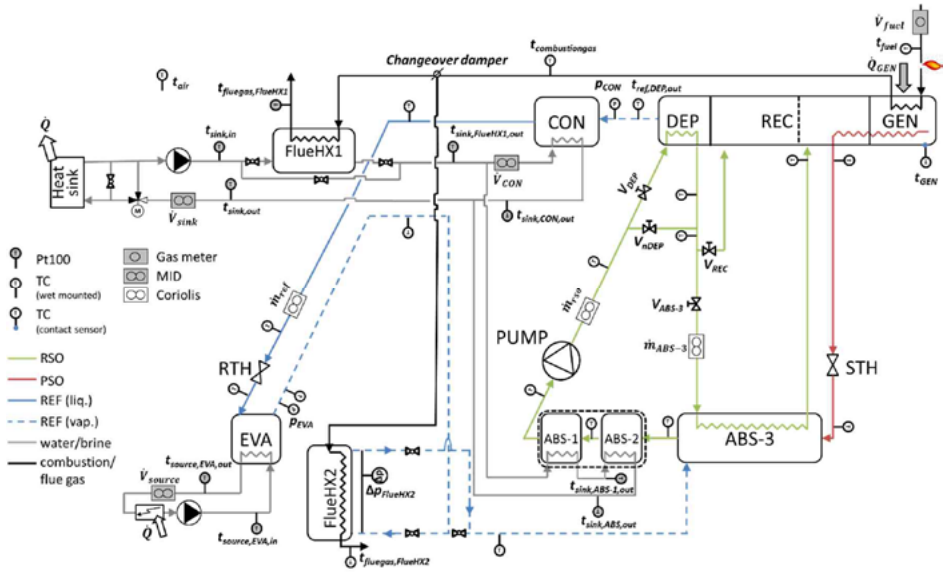


Fig. 1. Schematic flow chart of the analyzed absorption heat pump cycle

The refrigerant vapor leaving the dephlegmator enters the condenser (CON) where it is liquefied by releasing heat to the heat sink. After being expanded in the refrigerant throttle (RTH) to the low pressure (evaporation pressure p_{EVA}), the refrigerant enters the evaporator (EVA) and evaporates by extracting heat from the heat source. If the GAHP cycle is analyzed with a refrigerant cooled flue gas heat exchanger the refrigerant can be further heated by the combustion gas, before it enters the solution cooled absorber.

To further increase the overall efficiency of the GAHP and the transferrable heat in the evaporator a refrigerant heat exchanger can be installed on the warm side between the condenser and the refrigerant throttle and on the cold side between the evaporator and the refrigerant cooled flue gas heat exchanger / solution cooled absorber. Wagner and Rieberer [6] have previously investigated the influence of the refrigerant heat exchanger on the overall efficiency. It was found that the refrigerant heat exchanger had only a minor effect (within the measurement uncertainties) on the overall efficiency of the GAHP and is therefore not investigated within this work.

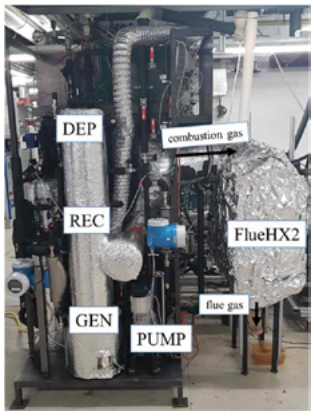


Fig. 2. Laboratory prototype

After partly evaporation of the solution in the generator, the poor solution (pso) with a relatively low ammonia mass fraction (x_{pso}) is taken from the bottom of the generator and cooled by a solution recirculation pipe. After being expanded in the solution throttle (STH), the poor solution enters the solution cooled absorber (ABS-3), where it absorbs the refrigerant. A complete absorption of the refrigerant by the poor solution takes place in the water cooled absorbers (ABS-1 & ABS-2).

The combustion gas which leaves the generator at around 130 °C to 150 °C (depending on the operating condition) can be either cooled by the return flow of the hydronic heat distribution system in a water cooled flue gas heat exchanger (FlueHX1) or by the refrigerant in a refrigerant cooled flue gas heat exchanger (FlueHX2) to reduce the energy losses. By analyzing the GAHP cycle with the water cooled flue gas heat exchanger the return flow of the hydronic heat distribution system is preheated (from $t_{sink,in}$ to $t_{sink,FlueHX1,out}$) before entering the condenser and the water cooled absorbers. If the GAHP cycle is analyzed with a refrigerant cooled flue gas heat exchanger the refrigerant can be further heated by the combustion gas, before it enters the solution cooled absorber.

The refrigerant cooled flue gas heat exchanger prototype is designed like a counterflow fin and tube heat exchanger with a heat transfer area of approx. 16 m² on the flue gas side. The cold refrigerant enters the flue gas heat exchanger at the bottom and the hot combustion gas (leaving the generator) enters at the top. On each level the refrigerant flows through two to three parallel pipes in series before it flows up to the next level. After 24 levels the refrigerant exits the flue gas heat exchanger at the top at a high temperature. The hot combustion gas flows downwards while getting cooled and exits at the bottom of the flue gas heat exchanger as flue gas. Compared to the results shown in Wagner and Rieberer [6] the flow direction of the flue gas and the refrigerant was changed, because it turned out that the condensate which was flowing downwards (against the combustion gas) created an additional layer for the heat transfer and was partially evaporated by the hot combustion gas which entered the refrigerant cooled flue gas heat exchanger at the bottom. Therefore the heat transfer was negatively influenced and reduced by the additional layer and a partial evaporation of the condensate. In addition to these issues, the combustion gas side connection between the generator and the refrigerant cooled flue gas heat exchanger was too long and insufficient insulated which caused non-negligible heat losses. These issues were solved before the experimental investigations with the optimized integration of the refrigerant cooled flue gas heat exchanger were continued.

The standard water cooled flue gas heat exchanger is designed like a finned heat exchanger with a heat transfer area of approx. 0.5 m². The difference in the heat transfer area of the novel refrigerant cooled flue gas heat exchanger is caused by the limited convective heat transfer of superheated refrigerant, which is substantially lower than the one of liquid water.

3. Measurements

Measurements with a GAHP have been conducted. Different cycle configurations with and without the dephlegmator and different flue gas heat exchangers as well as different operating conditions have been investigated. The mass flow rate of the refrigerant (m_{ref}), the rich solution (m_{rso}) and through the solution cooled

absorber (m_{ABS-3}) were measured using Coriolis flow meters. The mass flow rate of the poor solution (m_{pso}) was calculated by applying a mass balance ($m_{ref} + m_{pso} - m_{rso} = 0$) at the solution cooled absorber. The condensation pressure (p_{CON}) was measured at the condenser inlet and the evaporation pressure (p_{EVA}) was measured at the evaporator outlet. The pressure loss of the refrigerant cooled flue gas heat exchanger ($\Delta p_{FlueHX2}$) was determined using a differential pressure transmitter.

The "internal temperatures" (refrigerant & solution, except the temperature at the generator bottom - t_{GEN}) and the combustion gas temperature ($t_{combustiongas}$) were measured by means of wet mounted thermocouples. The temperature at the generator bottom (t_{GEN}) was calculated as an average of the temperatures measured using three contact sensors (thermocouples) mounted at the outer wall where the poor solution enters the solution recirculation pipe. The "external" temperatures, i.e. the heat sink (t_{sink}) and heat source (t_{source}) and the flue gas ($t_{fluegas}$) temperature, were measured using wet mounted Pt100 sensors. The volume flow rates of the heat sink (V_{sink}, V_{CON}) and the heat source (V_{source}) were measured using MID flow meters. The volume flow rate through the water cooled absorbers (V_{ABS}) was calculated by applying a mass balance ($V_{CON} \bullet \rho(t_{sink,FlueHX1,out}) + V_{ABS} \bullet \rho(t_{sink,FlueHX1,out}) - V_{sink} \bullet \rho(t_{sink,out}) = 0$) at the confluence of the condenser and the absorber. The fuels' volume flow rate (V_{fuel}) was measured using a gas meter.

3.1. Methodology

In order to compare the different cycle configurations and flue gas heat exchanger types, measurements were taken at a constant natural gas flow rate. For the experimental investigation different heat source temperatures were combined with a constant heat sink temperature. The ammonia mass fraction of the refrigerant was influenced by the dephlegmator. Investigations were performed with (DEP) and without (nDEP) the dephlegmator. Table 1 shows an overview of the varied parameters during the experimental investigation.

Table 1. Overview of the varied parameters

Parameter	Values
Natural gas flow rate ($V_{fuel,norm}$) in m³/h	0.75
Heat source in/outlet temperature ($t_{source,EVA,in/out}$) in °C	+10/+7, -5/-8
Heat sink in/outlet temperature ($t_{sink,in/out}$) in °C	45/55
Dephlegmator	with (DEP), without (nDEP)
Flue gas heat exchanger	FlueHX1 (water cooled), FlueHX2 (refrigerant cooled)

The evaluation of the measured data was performed with the software Engineering Equation Solver (EES) [11]. The substance data of ammonia/water was taken from the equation of state formulated by Ibrahim and Klein [12], which is implemented in EES as a predefined function. All measurement uncertainties were calculated by means of Gaussion error propagation rule implemented in EES and are indicated by error bars in the figures in chapter 3.2 and chapter 3.3.

The following assumptions were made within the evaluation:

- The ammonia concentration of the refrigerant (x_{ref}) at the dephlegmator outlet was determined by assuming saturated conditions according to Eq. (1).

$$x_{ref} = f(p_{CON}, t_{ref,DEP,out}, q = 1) \quad (1)$$

- The heat flow rates at the condenser and the absorbers were determined using the measured values at the external circuits due to the smaller measurement uncertainty. Eq. (2) shows the calculation of the heat flow rate at the condenser and Eq. (3) and Eq. (4) are showing the calculation of the heat flow rates at the water cooled absorbers.

$$\dot{Q}_{CON} = \dot{V}_{CON} \cdot \rho(t_{sink,FlueHX1,out}) \cdot (h_{sink,CON,out} - h_{sink,FlueHX1,out}) \quad (2)$$

$$\dot{Q}_{ABS-1} = (\dot{V}_{sink} \cdot \rho(t_{sink,out}) - \dot{V}_{CON} \cdot \rho(t_{sink,FlueHX1,out})) \cdot (h_{sink,ABS-1,out} - h_{sink,FlueHX1,out}) \quad (3)$$

$$\dot{Q}_{ABS-2} = (\dot{V}_{sink} \cdot \rho(t_{sink,out}) - \dot{V}_{CON} \cdot \rho(t_{sink,FlueHX1,out})) \cdot (h_{sink,ABS-2,out} - h_{sink,ABS-1,out}) \quad (4)$$

- The mean refrigerant flow velocity at the refrigerant cooled flue gas heat exchanger was estimated according to Eq. (5) as an average of the measured refrigerant side inlet and outlet conditions taking the transferred heat flow rate from the flue gas to the refrigerant into account.

$$w_{ref,mean,sin} = \frac{\dot{m}_{ref}}{A_{pipe}} \cdot \frac{(v_{ref,FlueHX2,in} + v_{ref,FlueHX2,out})}{2} = \frac{\dot{m}_{ref} \cdot 4}{d_{pipe}^2 \pi} \cdot \frac{(v_{ref,FlueHX2,in} + v_{ref,FlueHX2,out})}{2} \quad (5)$$

- Pressure losses were neglected, except the refrigerant side pressure loss in the refrigerant cooled flue gas heat exchanger as well as when determining the theoretically achievable efficiency ($GUE_{FlueHX2,\Delta pFlueHX2\approx0}$, see Fig. 10).
- Heat losses were neglected.

For the assessment of the heat pump process the ratio of the total heating capacity and the fuel input based on the calorific value is relevant according to DIN EN 12309-1 [13]. In this consideration the energy consumption of the solution pump is neglected. Eq. (6) shows the Gas Utilization Efficiency (GUE) according to DIN EN 12309-1 [13], where the calorific value (H_s) is taken as the reference value. Conversely, Eq. (7) shows the calculation of the Gas Utilization Efficiency (GUE) according to DIN EN 12309-4 [14] where the lower calorific value (H_i) is taken as the reference value. Due to the inconsistency in the standard, two ordinates are plotted in the figures that show the efficiency of the GAHP determined with Eq. (6) and Eq. (7). The achievable efficiency $GUE_{FlueHX2,\Delta pFlueHX2\approx0}$ (shown in Fig. 10) was estimated according to the measurements performed and published by Wagner and Rieberer [6]. These results should show the efficiency which could be achieved with an optimized geometry if the refrigerant side pressure loss in the refrigerant cooled flue gas heat exchanger could be omitted.

$$GUE_{Hs} = \frac{\dot{Q}_{sink}}{\dot{Q}_{fuel,norm,H_s}} = \frac{\dot{Q}_{sink}}{\dot{V}_{fuel,norm} \cdot H_{s,norm}} \quad (6)$$

$$GUE_{Hi} = \frac{\dot{Q}_{sink}}{\dot{Q}_{fuel,norm,H_i}} = \frac{\dot{Q}_{sink}}{\dot{V}_{fuel,norm} \cdot H_{i,norm}} \quad (7)$$

3.2. Results

In Fig. 3 - Fig. 8 the measurement results regarding the ammonia mass fraction in the refrigerant (x_{ref}), the refrigerant mass flow rate (m_{ref}), the flue gas temperature at the outlet of the flue gas heat exchanger ($t_{fluegas}$), the Gas Utilization Efficiency (GUE), the heat flow rates in the water cooled absorbers (Q_{ABS-1}, Q_{ABS-2}) and the heat flow rate in the condenser (Q_{CON}) with different cycle configurations (with/without DEP) and different operating conditions (t_{source}) are shown. The heat source in/outlet temperature ($t_{source,in}/t_{source,out}$) is abbreviated with SRC in the following figures (e.g. $t_{source,in}/t_{source,out}$ = +10/+7 °C is abbreviated as SRC 10/7). In Fig. 9 the refrigerant side pressure loss in the refrigerant cooled flue gas heat exchanger and in Fig. 10 the achievable Gas Utilization Efficiency ($GUE_{FlueHX2,\Delta pFlueHX2\approx0}$) if the refrigerant side pressure loss could be omitted are shown.

Fig. 3 shows the ammonia mass fraction in the refrigerant vapor with (DEP) and without (nDEP) the dephlegmator. It can be seen that the ammonia mass fraction is independent of the flue gas heat exchanger type, but dependent on the presence of a dephlegmator. If a dephlegmator is used, the ammonia mass fraction could be increased from 0,964 to 0,994, i.e. by around 3 % (compare “SRC 10/7 DEP” and “SRC 10/7 nDEP” in Fig. 3).

The decrease of the refrigerant mass flow rate shown in Fig. 4 is mainly based on two effects. Firstly, the absorption process is influenced by the superheated ammonia vapor entering the absorber which basically causes an increase of the evaporating pressure due to a worse absorption behavior which has to be considered by the control of the refrigerant and the solution throttle. Secondly, the additional refrigerant side pressure loss had a negative effect on the absorption pressure and therefore on the refrigerant mass flow rate which can be absorbed by the poor solution. The decrease in the refrigerant mass flow rate becomes higher if the refrigerant mass flow rate is higher, which is the case at a higher heat source temperature. These two effects caused a decrease in the refrigerant mass flow rate of up to 11 % (see “SRC 10/7 DEP” in Fig. 4).

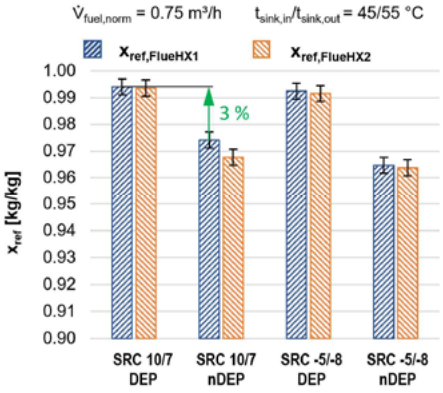


Fig. 3. Ammonia mass fraction depending on the cycle configuration

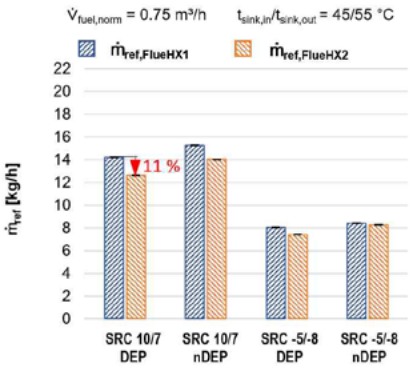


Fig. 4. Refrigerant mass flow rate depending on the cycle configuration

Fig. 5 shows the flue gas temperature at the outlet of the flue gas heat exchanger. The flue gas temperature at the water cooled flue gas heat exchanger ($t_{fluegas,FlueHX1}$) shows only minor changes due to the independence of the flue gas temperature on the cycle configuration and the heat source temperature. The flue gas temperature at the refrigerant cooled flue gas heat exchanger shows a noticeable dependence on the cycle configuration and the heat source temperature. A lower flue gas temperature ($t_{fluegas,FlueHX2}$) could be achieved at a lower ammonia mass fraction in the refrigerant (compare "SRC 10/7 DEP" and "SRC 10/7 nDEP" or "SRC -5/-8 DEP" and "SRC -5/-8 nDEP"). This is caused by a higher temperature glide during the evaporation and therefore a lower vapor quality after the evaporator. Due to a lower ammonia mass fraction a higher heat flow rate can be transferred in the refrigerant cooled flue gas heat exchanger, which – in general – leads to a lower flue gas temperature. I.e., a flue gas temperature of 2 °C instead of 49 °C (see "SRC -5/-8 nDEP" in Fig. 5) could be achieved with the refrigerant cooled flue gas heat exchanger which led to a significant increase in the recovered heat flow rate from the flue gas.

It also turned out that the flue gas temperature for "SRC -5/-8 DEP" ($t_{Fluegas,FlueHX2}$ = 43 °C) is higher than the one at "SRC 10/7 DEP" ($t_{Fluegas,FlueHX2}$ = 11 °C) even though the heat source temperature and therefore the refrigerant inlet temperature of the refrigerant cooled flue gas heat exchanger is lower. This is caused by the high ammonia mass fraction in the refrigerant (see Fig. 3) and the low refrigerant mass flow rate (see Fig. 4) at "SRC -5/-8 DEP".

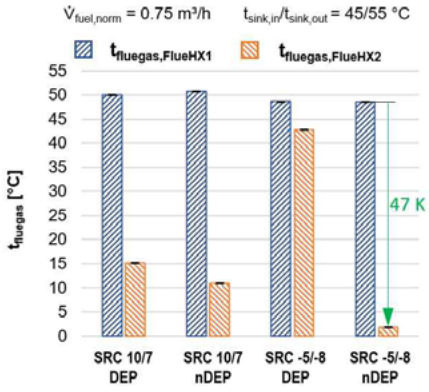


Fig. 5. Flue gas outlet temperatures depending on the cycle configuration

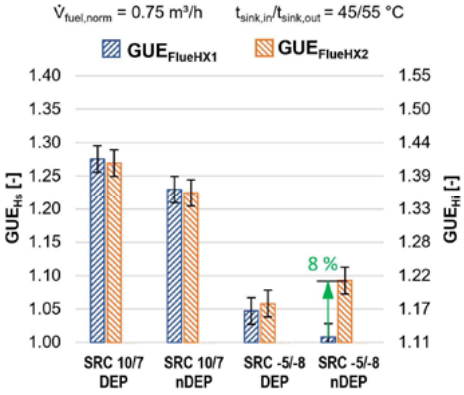


Fig. 6. GUE depending on the cycle configuration

The achieved GUEs at different heat source temperatures and different cycle configurations are shown in Fig. 6. At a heat source temperature of $t_{source,in/out}$ = +10/+7 °C the GAHP with a refrigerant cooled flue gas heat exchanger and the GAHP with the water cooled flue gas heat exchanger are showing nearly the same Gas Utilization Efficiencies. The higher recovered heat flow rate from the flue gas due to the lower flue gas outlet temperature gets compensated by the lower refrigerant mass flow rate and the negative effect of the refrigerant side pressure loss in the refrigerant cooled flue gas heat exchanger. At a heat source temperature of $t_{source,in/out}$ = -5/-8 °C the GAHP with a refrigerant cooled flue gas heat exchanger shows an increase of the GUE with as well as without the dephlegmator. The highest increase of the GUE_{Hs} from 1.01 ($GUE_{FlueHX1}$) to 1.09 ($GUE_{FlueHX2}$), i.e. by around 8 % can be achieved at "SRC -5/-8 nDEP" (see Fig. 6).

In Fig. 7 the heat flow rates at the water cooled absorbers (ABS-1 & ABS-2) are shown. The heat flow at the absorber results from cooling the refrigerant to the saturation state, liquefying the refrigerant, the released heat during the absorption of the refrigerant by the poor solution, and cooling the solution dependent on the heat sink inlet temperature. Fig. 7 should show the change of the heat flow rates in the water cooled absorbers (Q_{ABS-1} & Q_{ABS-2}) if the flue gas is cooled by the refrigerant. The measurements have shown that the temperature of the rich solution at the outlet of the solution cooled absorber does not significantly change if the refrigerant enters the solution cooled absorber at a higher temperature due to the limitation of the heat flow rate (pinch-point) which can be transferred to the rich solution. As the temperature of the rich solution at the water cooled absorber outlet also does not significantly change, the heat flow transferred to the refrigerant in the refrigerant cooled flue gas heat exchanger is rejected to the heat sink in the water cooled absorbers. It can also be seen that the heat flow rate transferred in ABS-1 is much lower compared to the one in ABS-2. The change in the heat flow rate mainly occurred in ABS-2, which means that the heat flow rate supplied in the refrigerant cooled flue gas heat exchanger is mainly rejected in ABS-2. E.g., within the operating condition "SRC -5/-8 nDEP" (see Fig. 7) the total heat transferred to the heat sink in the absorbers increased from 5.3 kW to 6.5 kW, i.e. by around 23 %. Due to the decreased mass flow rate of the refrigerant with the refrigerant cooled flue gas heat exchanger the heat flow rate to liquefy and to absorb the refrigerant is lower compared to the configuration with the water cooled flue gas heat exchanger. Only the capacity to cool the refrigerant from a superheated state to the saturation state increases. Therefore, the increase of the rejected heat flow rate in the absorbers is lower than the recovered heat flow rate in the refrigerant cooled flue gas heat exchanger.

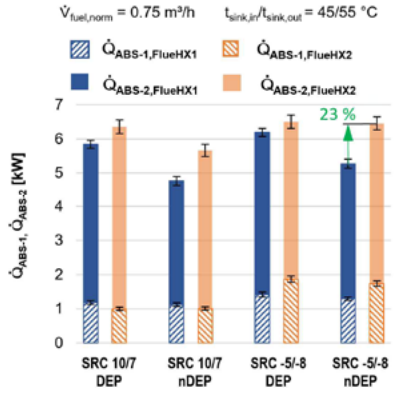


Fig. 7. Comparison of the heat flow rate in the water cooled absorbers

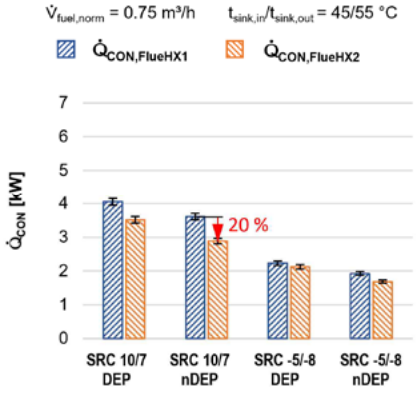


Fig. 8. Comparison of the heat flow rate in the condenser

Fig. 8 shows exemplarily the impact of the reduced refrigerant mass flow rate on the condenser capacity. The impact on the evaporator capacity is similar to the one described at the condenser. In principle the decrease of the condenser capacity is higher if the decrease of the refrigerant mass flow rate is higher, which is the case at a higher heat source temperature (see Fig. 4). For example at the operating condition "SRC 10/7 nDEP" the condenser capacity was reduced from 3.6 kW to 2.9 kW, i.e. by 20 % (see Fig. 8). Basically the reduction of the condenser capacity and the increase of the absorber capacity balance each other at "SRC 10/7" which does not cause an advantage for the refrigerant cooled flue gas heat exchanger in the overall efficiency as explained in context to Fig. 6. At a lower heat source temperature, e.g. "SRC -5/-8 nDEP", the increase of the absorber capacity (from 5.3 kW to 6.5 kW) outperforms the decrease of the condenser capacity (from 1.9 kW to 1.7 kW) which leads to a higher heat flow rate transferred to the heat sink (+1 kW) and therefore to a higher GUE.

3.3. Further optimization potential

As mentioned in chapter 3.2 the refrigerant side pressure loss in the refrigerant cooled flue gas heat exchanger (see Fig. 9) had a negative effect on the GUE. The influence of the pressure loss in the refrigerant cooled flue gas heat exchanger on the GUE was previously experimentally determined by Wagner and Rieberer [6]. In general the pressure loss in the refrigerant cooled flue gas heat exchanger is higher if the ammonia mass flow rate is higher, due to a higher volume flow rate and therefore a higher flow velocity of the refrigerant. In the case of the working pair ammonia/water the ammonia mass fraction has also an influence on the density of the refrigerant and therefore an influence on the volume flow rate and the flow velocity. The mean refrigerant flow velocity in the refrigerant cooled flue gas heat exchanger is shown in Fig. 9 and was calculated according to Eq. (5). Even though the refrigerant mass flow rate at "SRC 10/7 nDEP" is higher than at "SRC 10/7 DEP" (see Fig. 4) the refrigerant velocity is lower at "SRC 10/7 nDEP" due to the higher refrigerant density caused by the lower ammonia mass fraction in the refrigerant (see Fig. 3). Due to the lower refrigerant velocity the pressure loss at "SRC 10/7 nDEP" is slightly lower compared to the pressure loss at "SRC 10/7 DEP". The pressure loss showed a maximum of 0.023 MPa at "SRC 10/7 DEP". At a heat source temperature of "SRC -5/-8" the pressure loss was less than half of the pressure loss at "SRC 10/7" (see Fig. 9), mainly due to the lower refrigerant mass flow rate.

Fig. 10 shows the GUE of the GAHP with the water cooled ($GUE_{FlueHX1}$) and the GUE of the GAHP with the refrigerant cooled flue gas heat exchanger ($GUE_{FlueHX2}$) as shown in Fig. 6. In addition to these values a theoretically determined GUE of the GAHP with the refrigerant cooled flue gas heat exchanger ($GUE_{FlueHX2,\Delta pFlueHX2\approx0}$) is shown if the refrigerant side pressure loss can be omitted. The pressure loss in the refrigerant cooled flue gas heat exchanger caused a decrease of the GUE_{Hs} between 2.5 % ("SRC -5/-8") and 4 % ("SRC 10/7"). Without the pressure loss the highest increase of the GUE_{Hs} from 1.01 ($GUE_{FlueHX1}$) to 1.12 ($GUE_{FlueHX2,\Delta pFlueHX2\approx0}$), i.e. by around 11 % can be achieved at "SRC -5/-8 nDEP" (see Fig. 10).

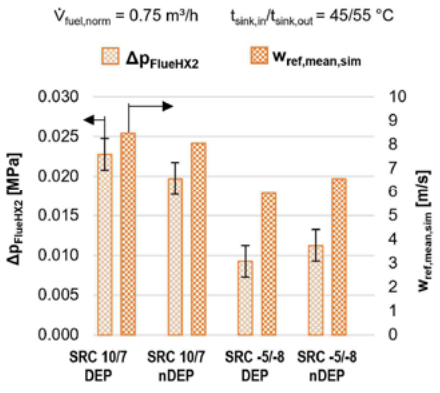


Fig. 9. Refrigerant side pressure loss ($\Delta p_{FlueHX2}$) and mean refrigerant velocity ($w_{ref,mean,sim}$) in FlueHX2

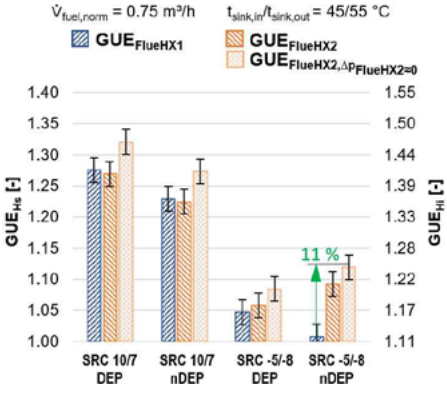


Fig. 10. Effect of the pressure loss in FlueHX2 on the GUE

4. Conclusion

A gas-fired absorption heat pump (GAHP) with a conventional, i.e. water cooled, flue gas heat exchanger was compared to a GAHP with a novel refrigerant cooled flue gas heat exchanger. The influence of the dephlegmator on the ammonia mass fraction in the refrigerant as well as the flue gas exit temperature were analyzed. Furthermore, the Gas Utilization Efficiency (GUE) and the heat flow rates in the condenser and the water cooled absorbers were compared.

The measurements with the refrigerant cooled flue gas heat exchanger have shown that a lower flue gas temperature at the flue gas heat exchanger outlet could be achieved and thus the dissipation of latent heat into the environment was significantly reduced. The highest benefits could be achieved at a lower ammonia mass fraction in the refrigerant, i.e. if no dephlegmator was in use. This means in a GAHP with a refrigerant cooled flue gas heat exchanger components of the desorber, such as the dephlegmator or the rectification column can be smaller or omitted. An increase in efficiency of the GAHP with a refrigerant cooled flue gas heat exchanger

compared to the GAHP with a water cooled flue gas heat exchanger of up to 8 % within the first tests could be achieved. The refrigerant side pressure loss has hindered a higher increase in efficiency. If the pressure loss could be significantly reduced an increase in efficiency of up to 11 % is possible. At an even higher return flow temperature of the hydronic heat distribution system (e.g. 55 °C) the advantage in efficiency can be further increased.

Hence further efforts are required to reduce the size and the refrigerant side pressure loss of the refrigerant cooled flue gas heat exchanger. The know-how gathered from this experimental analysis will be considered in a simulation model of the GAHP. Furthermore, an economical and ecological analysis will be performed to show the advantage of a refrigerant cooled flue gas heat exchanger and to determine the most suitable cycle configuration.

Acknowledgements

This work has been conducted in the course of the cooperative project “FluePump” (FFG-Project No.: 853579). The project is funded by the Austrian Climate and Energy Fund and carried out within the Austrian Energy Research Program 2015. The authors would like to thank the project partner E-Sorp GmbH to make this work possible.

References

[1] European Commission, 2019. 2030 climate & energy framework. European Commission, Brussels. URL: https://ec.europa.eu/clima/policies/strategies/2030_en (2019/10/10).

[2] Fleiter, T., Steinbach, J., Ragwitz, M., Arens, M., Aydemir, A., Elsland, R., Frassine, C., 2016. Mapping and analyses of the current and future (2020 - 2030) heating/cooling fuel deployment (fossil/renewables). Work Package 1: Final Energy Consumption for the Year 2012. European Commission, Brussels.
URL: https://ec.europa.eu/energy/sites/ener/files/documents/Report%20WP1.pdf (2019/08/13).

[3] Umweltbundesamt, 2016. Marktdaten: Bereich Wohnen., Dessau-Roßlau.
URL: https://www.umweltbundesamt.de/daten/private-haushalte-konsum/gruene-produkte-marktzahlen/marktdaten-bereich-wohnen#textpart-1 (2019/10/09).

[4] Wolff, D., Teuber, P., Budde, J., Jagnow, K., 2004. Felduntersuchungen: Betriebsverhalten von Heizungsanlagen mit Gasbrennwertkesseln. Fachhochschule Braunschweig Wolfenbüttel, Wolfenbüttel.

[5] Wagner, P., Rieberer, R., 2017. Untersuchung einer neuartigen Abgaswärmeübertragereinbindung für gasbefeuerte Absorptionswärmepumpen. Proc. Deutsche Kälte-Klima-Tagung 2017, Bremen.

[6] Wagner, P., Rieberer, R., 2019. Experimental analysis of a gas-fired absorption heat pump with a refrigerant cooled flue gas heat exchanger. Proc. 25th IIR International Congress of refrigeration, Montreal.

[7] Glanville, P., Keinath, C., Garrabrant, M., 2017. Development and Evaluation of a Low-Cost Gas Absorption Heat Pump. Proc. ASHRAE Winter Conference, Las Vegas.

[8] Critoph, R. E., Metcalf, S. J., 2019. UK Summary Report on IEA Heat Pump Technology Collaboration Programme (TCP) Annex 43: Thermally Driven Heat Pumps, Warwick.

[9] Wechsler, R., Rieberer, R., Emhofer, J., Zottl, A., Köfinger, C., 2016. Experimentelle Untersuchung einer Gasabsorptionswärmepumpe unter Labor- und Feldtestbedingungen sowie Vergleich mit Simulationsergebnissen. Proc. Deutsche Kälte-Klima-Tagung 2016, Dresden.

[10] Recknagel, H., Sprenger, E., Schramek, R.E. (Eds.), 2008. Taschenbuch für Heizung+Klimatechnik, 73rd edition. Oldenbourg Industrieverlag GmbH, Oldenburg.

[11] EES, 2019. Engineering Equation Solver, V10.644. F-Chart Software, Madison.

[12] Ibrahim, O. M., Klein, S. A., 1993. Thermodynamic Properties of Ammonia-Water Mixtures. ASHRAE Transactions 1993 (99(1)), 1495 - 1502.

[13] DIN EN 12309-1:2015, 2015/03/01. Gas fired sorption appliances for heating and/or cooling with a net heat input not exceeding 70 kW - Part 1: Terms and definitions; German version EN 12309-1:2014. DIN Deutsches Institut für Normung e. V., Berlin.

[14] DIN EN 12309-4:2015, 2015/03/01. Gas-fired sorption appliances for heating and/or cooling with a net heat input not exceeding 70 kW - Part 4: Test methods; German version EN 12309-4:2014. DIN Deutsches Institut für Normung e. V., Berlin.

13th IEA Heat Pump Conference
April 26-29, 2021 Jeju, Korea

Investigation of VRF System under Cooling Mode through Field Testing and Machine Learning-based Modeling

Hanlong WAN[a], Tao CAO[a], Yunho HWANG[a*], Heunghee BAE[b], Saikee OH[b]

[a]4164 Glenn Martin Hall Bldg., Center for Environmental Energy Engineering
Department of Mechanical Engineering, University of Maryland,
College Park, MD., 20742, United States
[b]System Air Conditioning Laboratory, LG Electronics, Seoul, Republic of Korea

Abstract

Variable Refrigerant Flow (VRF) system is widely known for its flexibility and energy efficiency. Nevertheless, most of the research has focused on experiments in laboratory. Limited papers discussed the field test case. To enhance operational efficiency, we investigated details of cooling operational behavior through field testing and developed a machine learning-based model for a better control algorithm. We conducted the test in a university office building. The power consumption under cooling mode was investigated. In addition, a Support Vector Regression algorithm-based model has been built to predict the power consumption of the VRF system. The penalty parameters in the SVR model have been optimized to decrease the generalization error of the model. We found that the compressor frequency and condensing temperature are the two most important parameters for the accurate. The mean relative error of the model was 7% for outdoor unit power consumption when we compared experimental data and modeling results. The modeling results showed that if the compressor frequency, outdoor fan speed, and condensing temperature were the same, the power consumption should be the same.

© HPC2020.
Selection and/or peer-review under responsibility of the organizers of the 13th IEA Heat Pump Conference 2020.

Keywords: support vector regression; variable refrigerant flow system; energy consumption;

1. Introduction

Variable refrigerant flow (VRF) systems have been introduced to the U.S. at around 2002 and are widely used in commercial and office buildings [1]. VRF system is known for its flexibility and energy-efficiency. Some researchers studied the VRF system in the laboratory. For example, Yun et al. [2] conducted a series of experiments in the multi-calorimeter consisting of one outdoor unit chamber and two indoor unit chambers, as part of their work to develop a load responsive control of the evaporating temperature in a VRF system under cooling operations. The results indicate that increasing the evaporating temperature can reduce the energy consumption of the system by up to 35%. However, the system performance in the field test is sometimes different from that in the laboratory due to the following reasons. First, a steady-state condition is hard to achieve in the field test, since the compressor frequency is typically low in this mode, and thus the system is open under cycling. Second, the ambient condition is uncontrolled, which causes the control logic different from that applied in the laboratory. Thus, more study is needed in the field test.

To fill this gap, we conducted field tests of the VRF system under cooling mode (from April to May 2019) in an office building in MD, US, as shown below in Fig. 1. Seven same indoor units were installed in five rooms. The users controlled the indoor units. The system schematic diagram is given in Fig. 2. This figure shows the system operation status when seven indoor units are in cooling mode as an example. We measured

* Corresponding author. Tel.: +1-301-405-5247.
E-mail address: yhwang@umd.edu.

the pressure, temperature, mass flow rate, and power consumption. The sensors' positions are also shown in this figure. We used DAQ system and made the measurement every two seconds. In this research, we mainly measured and compared the outdoor unit power consumption under cooling only mode. To analyze the data under the same ambient and operation conditions, we also set up a machine learning-based data-driven model.

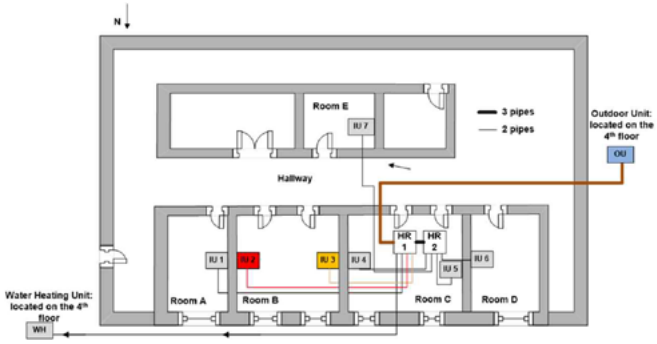


Fig. 1. Room Layout (third floor)

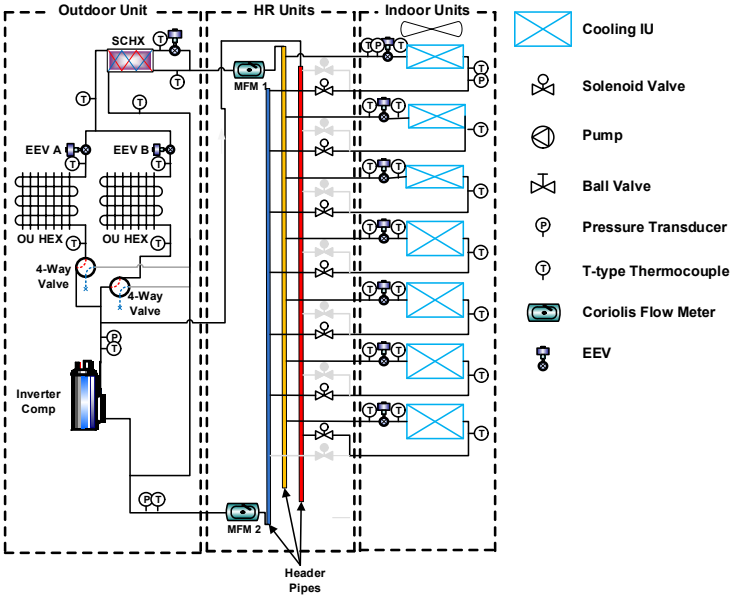


Fig. 2. System Diagram

Recently, the machine learning based model is a hot topic in refrigeration system modeling and fault detection. Kang et al. proposed a Neural Network-based model using weather data including outside temperature, relative humidity, solar radiation, cloudiness, wind speed, and rainfall events as input data to predict the energy consumption [3]. Applying the same algorithm, Chung et al. [4] used ambient temperature, outside humidity, cooling load, saturated temperature, condensate temperature, and condense pressure as input neurons to predict energy consumptions. Shi et al. [5] combined the Bayesian neural network with the ReliefF classifier to detect low refrigerant charge. Yu et al. [6] proposed a VRF charge fault method based on expert modification C5.0 decision tree, and the overall error rate could be decreased by 4%. As a linear regression method, Support Vector Regression (SVR) algorithm is able to build a simple structured model and can be

well explained. According to our literature review survey, Sun et al. [7] proposed a new method based on SVR, which resulted in a decrease in error rate by 2.1%. Li et al. [8] found the various virtual refrigerant charge sensors combined with the SVR could reduce the error rate to 5.5%. Only limited researchers used this algorithm in refrigerant charge fault detection. The SVR algorithm has not been used to predict the system power consumption and COP. In addition, no one discussed the process in penalty parameter optimization of this algorithm in VRF data analysis.

2. Methodology

As mentioned in the introduction part, the first challenge of field test data analysis is searching for semi-steady-state data. A steady-state filter was introduced by some researchers [9]. However, in our field test, this requirement for steady state was so strong that limited data points could be accessed. Thus, we considered the semi-steady state of the data points. The conditions in our study were for the standard deviation of the total mass flow rate to be smaller than 5 g/s in a ten-second time window while the compressor frequency and all the electric expansion valve (EEV) opening degrees kept unchanged. We finally secured 23,323 data points. We defined a two-digit number M. The digit of M means the number of indoor units operating in cooling mode. As an example, “M=3” means that three cooling units operated. Table 1 shows the distribution of the M value of our database. We ignored the group with the count number smaller than 100.

Table 1 Tabulated Data

M Value	Count	Percentage
1	1,167	5.0%
2	6,182	26.5%
3	7,425	31.8%
4	3,191	13.7%
5	371	1.6%

In the field test, the ambient conditions were not controlled. It was challenging to make the system working under the same condition. Thus, modeling work was needed to simulate each working model of the system to compare their performance under the same conditions. In the model, SVR was applied. SVR was a regression algorithm based on a classification algorithm called Support Vector Machine. The objective of support vector machine algorithm is to find a hyperplane in a space that distinctly classifies the data points [10]. For the details of this algorithm, interested readers could read the reference [11]. In a simple two-dimension case, the algorithm was used to solve the following optimization problem:

$$M\dot{n}\left(\frac{1}{2}\|w\|^2 + C\sum_{i=1}^{N}(\xi_i + \xi_i^*)\right) \quad (1)$$

subject to

$$y_i - wx_i - b \le \varepsilon + \xi_i \quad (2)$$

$$wx_i + b - y_i \le \varepsilon + \xi_i^* \quad (3)$$

$$\xi_i, \xi_i^* \ge 0 \quad (4)$$

where symbols, w, and b, are weighting factor and bias, respectively. C and ε are two crucial parameters that would affect the performance of the algorithm. In this study, we conducted a parametric study to optimize the two parameters to build a robust and accurate model. We used Python to conduct this study. Ambient temperature range was from 20 °C to 40 °C.

3. Discussion and results

3.1. Field test

The field test result of the power consumption is shown in Fig. 3. Different rows indicate a different number of cooling units. For example, the first row means that there is only one cooling unit operating. As can be found in Fig. 3, the slope of the data points increases with the number of cooling units. It is because the cooling load is increased with the ambient temperature. In this situation, the system control logic would apply a higher frequency of the compressor. Therefore, the power consumption of the compressor was increased with the

compressor frequency. According to **오류! 참조 원본을 찾을 수 없습니다.**, it is hard to conclude the energy efficiency of different cases. Thus, we conducted a machine learning-based model using the two data sets. The goal was to predict the power consumption under the same ambient and operating conditions.

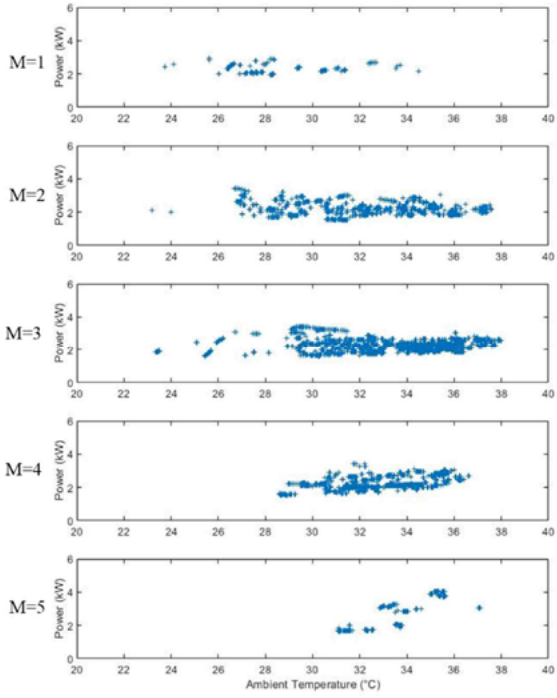


Fig. 3. Power Consumption versus Ambient Temperature

3.2. Modeling results

Typically, the compressor map, which is developed under the steady-state operation at a given ambient condition, is used in VRF system models. However, in the field test, the steady-state point is difficult to find, and the ambient temperature is not controlled so that the compressor map cannot be used. Therefore, we propose the machine learning-based modeling work, which only requires hundreds of field test data points. For this, we conducted data-based modeling work to simulate the power consumption of the system based on the SVR algorithm. This model could be used as a substitution of the compressor map. However, before the modeling work, we need to decide which input parameters should be used. We draw a so-called heatmap to see the effect of seven possible parameters that might affect the outdoor unit power consumption. The parameters selected are outdoor power consumption, compressor frequency, condensing temperature, suction temperature, outdoor fan speed, evaporating temperature, and ambient temperature, respectively. The heatmap shows the covariance between each pair of these parameters. The covariance means the relation between the two parameters. The absolute value of the covariance equals to one means the two parameters are the same, while if the covariance equals to zero, the two parameters had no relationship. In Fig. 4, we used the light color to show a positive relationship, while the dark color to show a negative relationship. We sorted the parameters according to the absolute value of their covariance with the outdoor unit power consumption. The frequency of the compressor was the most significant factor which might affect power consumption. The ambient temperature was nearly not related to outdoor power consumption, at least in certain control logics. It was possible since the significant part of the outdoor unit power consumption is from the compressor. Moreover, the frequency was the essential parameter affecting the compressor power consumption.

The performance of the model was evaluated by Mean Squared Error (MSE), which was defined by the following equation:

$$MSE = \frac{1}{N}\sum_{i=1}^{N}\left(y_{train\ ,i} - y_{pred\ ,i}\right)^2 \quad (5)$$

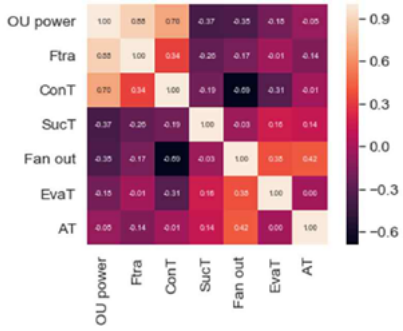


Fig. 4. Covariance Heatmap

It was also known as the loss function in SVR modeling. We built SVR models based on the data sets. All the data were normalized before the modeling. We first used "*C*=1 and *ε*=0.08". The result validation was shown in Fig. 5. The two dash lines in these figures represented "±10%" deviation. The denormalized result is shown in Fig. 5 on the left side. The measured value and the predicted value did not match very well before parameter study. Then we continued to optimize the parameters, C and ε, in the model. We separated the data set into training and testing data set. The training data set has 60% data points, and the testing data set has 40% data points, respectively. The MSE, C, and ε listed here are dimensionless since all the parameters are normalized. From **오류! 참조 원본을 찾을 수 없습니다.**, we could see that for training data set, C should be as large as possible, while for testing data set, the MSE decreased first and then increased as C increased. Thus, C should not be too large. Furthermore, as the right-side figure shows, epsilon should be as small as possible. In this case, *ε* should be small, and C should not be too large. We used "*C*=20 and *ε*=0". The mean relative error, which represented the average percentage error of the prediction, of this case was 7%.

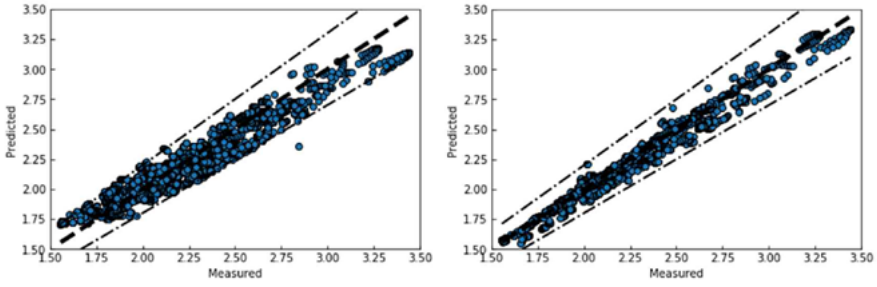


Fig. 5. Model Validation (left: before parametric study; right: after parametric study)

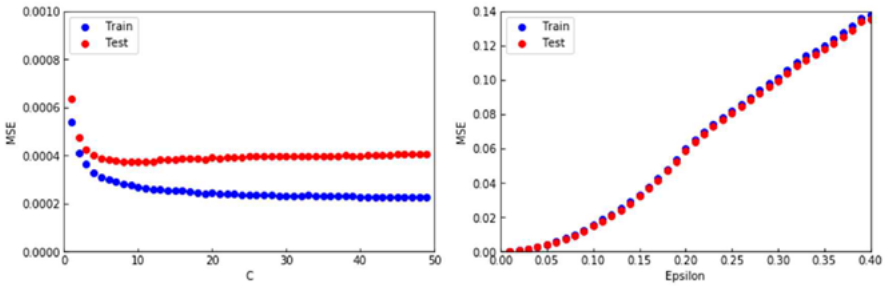


Fig. 6. Parametric study

The final validation result is shown in Fig. 5. As mentioned above, we applied the three operating conditions for the model to predict power consumption. Table 2 shows the modeling results. The columns meant suction temperature, condensing temperature, evaporating temperature, compressor frequency, outdoor fan speed, and outdoor power consumption, respectively. However, the conclusion could not be made without the uncertainty analysis.

Table 2 Modeling results

SucT (°C)	ConT (°C)	EvaT (°C)	Ftra (Hz)	Fan out (RPM)	OU Power (kW)
9.8	45.3	4.5	30	200	2.02
10.2	42.4	6.3	40	200	2.39
12.4	45.4	8.7	50	200	3.18

3.3. Uncertainty analysis and parametric study

We used the method introduced by Lecompte et al. [9] and Koçyigit and Bulgurcu [12] to conduct uncertainty analysis. The uncertainty on the variable y was calculated as a function of uncertainties U_{xi} on each measured variable x_i, as shown in Equation (6).

$$U_y = \sqrt{\sum_i \left(\frac{\partial y}{\partial xi}\right)^2 {U_{xi}}^2} \tag{6}$$

The accuracy of the measurement equipment used was given in Table 3. Since the correlation obtained from the model is complicated, the value of the partial derivative was derived by numerical differentiation. The uncertainty of the modeling power consumption varied when the input values varied. Thus, we only gave the uncertainty of one point, when the suction temperature was 10.2 °C, condensing temperature was 42.4 °C, the compressor frequency was 40 Hz, and the outdoor fan speed was 200 RPM, respectively. We applied a 1% variation to each input parameter, excluding compressor frequency and outdoor fan speed. The condensing temperature and evaporating temperature were calculated by the high pressure and low pressure. Thus, the instrument uncertainty was calculated based on the uncertainty of the pressure sensor.

Table 3 Instrument Uncertainty

Measurement	**Range**	**Uncertainty**
T-type Thermocouples	-200~350 °C	± 0.5 K
Pressure Transducer (High pressure side)	0~6,770 kPa	± 6.34 kPa
Pressure Transducer (Low pressure side)	0~3,339 kPa	± 4.21 kPa
Wattmeter (Outdoor unit)	0~40 kW	± 0.5% FS

Table 4 Uncertainty Analysis

	Instrument uncertainty (℃)	1% Deviation (℃)	OU Power deviation (-)	Uy (-)
SucT	0.5	0.1	0.01%	1.54E-06
ConT	0.1	0.4	0.71%	1.82E-05
EvaT	0.03	0.06	0.06%	6.99E-07
	Uncertainty of the model (B type)			0.5%
	Power meter uncertainty (A type)			0.5%
	Total Uncertainty			0.7%

According to the calculation, the total uncertainty of power consumption should be 0.7%, as shown in **오류! 참조 원본을 찾을 수 없습니다.**. We could further find that the condensing temperature, which also meant the high pressure had the most critical impact on the outdoor power consumption when frequency and outdoor fan speed were fixed. This result was consistent with our result shown in the heatmap.

3.4. Energy efficiency analysis

Fig.7 shows the Coefficient of Performance (COP). Similarly to what we show in Fig.3, the trend of the COP is not apparent when M is small. When M equals 4 or 5, as the ambient temperature increases, the COP of the system decreases. The reason might be that when only 1 or 2 indoor units operated, the cooling load was not high. Thus, the compressor was working under low frequency, which caused the efficiency of the compressor was low. This would make a complicated result for the COP. However, when the compressor frequency was high, the efficiency of the heat exchanger would be a significant factor. When ambient temperature decreased, the heat transfer efficiency of the outdoor unit heat exchanger increased, and the COP of the system should also increase.

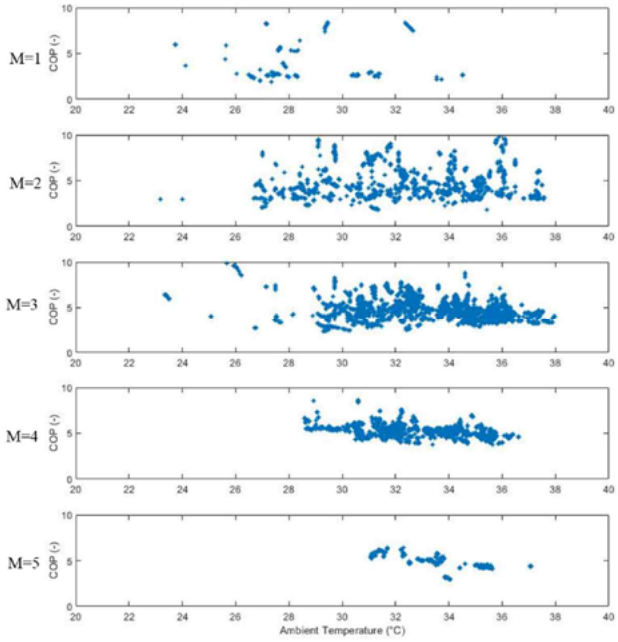


Fig. 7. COP versus Ambient Temperature

4. Conclusions

To enhance the operational efficiency of VRF system, we investigated details of cooling operational behavior through field testing and developed a machine learning-based model for better control logic development. In the test conducted in a university office building, the power consumption under cooling mode was investigated while the number of indoor units operating varied. As the number of indoor units operating increased, the positive linear relationship between power consumption and ambient temperature was increasingly evident for cooling-only mode. Moreover, an SVR algorithm-based model was built to predict the power consumption of the VRF system by five groups of inputs. The penalty parameters in the SVR model were optimized to decrease the generalization error of the model. According to the study, when C is equal to 20, and ε is equal to 0, the model had the best performance. We also found that the compressor frequency and condensing temperature were the two most important parameters for the accurate prediction of outdoor unit power consumption. The mean relative error, which means the average prediction error, of the model was 7% for outdoor unit power consumption when we compared experimental data and modeling results. Based on the field test and modeling work conducted, we found that the power consumptions of cooling only mode were the same if the five groups' inputs were fixed. Future work could be conducted to study heat recovery mode of the VRF system.

Nomenclature

C	penalty parameter
ConT	condensing temperature (°C)
COP	coefficient of performance
EEV	electric expansion valve
EvaT	evaporating temperature (°C)
Ftra	compressor frequency (Hz)
Fan out	outdoor fan speed (RPM)
MSE	mean squared error
OU	outdoor unit
SucT	suction temperature (°C)
SVR	support vector regression
U	uncertainty
VRF	variable refrigerant flow
Greek symbols	
ε	penalty parameter

Acknowledgments

We gratefully acknowledge the support of the Center for Environmental Energy Engineering (CEEE) at the University of Maryland, and System Air Conditioning Laboratory at LG Electronics Inc.

References

[1] L. Kwon, H. Lee, Y. Hwang, R. Radermacher, B. Kim, Experimental investigation of multifunctional VRF system in heating and shoulder seasons, Applied Thermal Engineering. 66 (2014) 355–364. https://doi.org/10.1016/j.applthermaleng.2014.02.032.

[2] G.Y. Yun, J.H. Lee, H.J. Kim, Development and application of the load responsive control of the evaporating temperature in a VRF system for cooling energy savings, Energy and Buildings. 116 (2016) 638–645. https://doi.org/10.1016/j.enbuild.2016.02.012.

[3] I. Kang, K. Lee, J. Lee, J. Moon, Artificial Neural Network–Based Control of a Variable Refrigerant Flow System in the Cooling Season, Energies. 11 (2018) 1643. https://doi.org/10.3390/en11071643.
[4] M.H. Chung, Y.K. Yang, K.H. Lee, J.H. Lee, J.W. Moon, Application of artificial neural networks for determining energy-efficient operating set-points of the VRF cooling system, Building and Environment. 125 (2017) 77–87. https://doi.org/10.1016/j.buildenv.2017.08.044.
[5] S. Shi, G. Li, H. Chen, J. Liu, Y. Hu, L. Xing, W. Hu, Refrigerant charge fault diagnosis in the VRF system using Bayesian artificial neural network combined with ReliefF filter, Applied Thermal Engineering. 112 (2017) 698–706. https://doi.org/10.1016/j.applthermaleng.2016.10.043.
[6] F. Yu, G. Li, H. Chen, Y. Guo, Y. Yuan, B. Coulton, A VRF charge fault diagnosis method based on expert modification C5.0 decision tree, International Journal of Refrigeration. 92 (2018) 106–112. https://doi.org/10.1016/j.ijrefrig.2018.05.034.
[7] K. Sun, G. Li, H. Chen, J. Liu, J. Li, W. Hu, A novel efficient SVM-based fault diagnosis method for multi-split air conditioning system's refrigerant charge fault amount, Applied Thermal Engineering. 108 (2016) 989–998. https://doi.org/10.1016/j.applthermaleng.2016.07.109.
[8] J. Liu, G. Li, H. Chen, J. Wang, Y. Guo, J. Li, A robust online refrigerant charge fault diagnosis strategy for VRF systems based on virtual sensor technique and PCA-EWMA method, Applied Thermal Engineering. 119 (2017) 233–243. https://doi.org/10.1016/j.applthermaleng.2017.03.074.
[9] S. Lecompte, S. Gusev, B. Vanslambrouck, M. De Paepe, Experimental results of a small-scale organic Rankine cycle: Steady state identification and application to off-design model validation, Applied Energy. 226 (2018) 82–106. https://doi.org/10.1016/j.apenergy.2018.05.103.
[10] C. Cortes, V. Vapnik, Support-vector networks, Mach Learn. 20 (1995) 273–297. https://doi.org/10.1007/BF00994018.
[11] G. Li, Y. Hu, H. Chen, H. Li, M. Hu, Y. Guo, S. Shi, W. Hu, A sensor fault detection and diagnosis strategy for screw chiller system using support vector data description-based D-statistic and DV-contribution plots, Energy and Buildings. 133 (2016) 230–245.
[12] N. Kocyigit, Fault and sensor error diagnostic strategies for a vapor compression refrigeration system by using fuzzy inference systems and artificial neural network, International Journal of Refrigeration. 50 (2015) 69–79.

13th IEA Heat Pump Conference
April 26-29, 2021 Jeju, Korea

Low GWP refrigerant for heat pump

Sarah Kim[a,*], Laurent Abbas[b], Leping Zhang[c], Drew Turner[d]

[a]Arkema Inc., 900 First Ave, King of Prussia, PA, 19406, USA
[b]Arkema France, Rue Henri Moissan, Pierre-Benite Cedex, 69493, France
[c]Danfoss China, Gong Ti Bei Lu, Chaoyang District, Beijing 100027, China
[d]Danfoss LLC, 11655 Crossroads Circle, Baltimore, MD 21220, USA

Abstract

Climate change concerns have driven the development of lower Global Warming Potential (GWP) fluorocarbon refrigerants and transition away from incumbent HFC refrigerants is already in progress in multiple applications. In this paper, R-516A, a ternary azeotropic refrigerant with GWP of 131 (AR5) and essentially a near drop-in of R-134a, is evaluated as a refrigerant for air-to-water chiller and heat pump applications. Performance and application map of R-516A are compared to the R-134a baseline as well as other HFO solutions.

© HPC2020.
Selection and/or peer-review under responsibility of the organizers of the 13th IEA Heat Pump Conference 2020.

Keywords: Low GWP refrigerant ; R-516A ; R-134a ; Oil-free compressor ; Low ambient heat pump

1. Introduction

The HVAC&R industry continues to strive to meet stringent energy regulations while transitioning to environmentally friendly refrigerants with lower global warming potential (GWP) in an effort to minimize the carbon footprint. Global regulations such as F-gas Regulation and Kigali Amendment to the Montreal Protocol are also forcing the adoption of refrigerants that lead to lower CO_2 direct emission indicated by the GWP values.

In a typical office building, heating and comfort cooling accounts for approximately 40% of the total energy consumption [1]. Therefore, there is a constant demand in search of more efficient systems. For that reason, there are emerging opportunities for oil-free compressors to be further utilized due to their superior efficiency and lower energy and maintenance cost throughout the life of the compressor. One potential application would be low ambient heat pump systems where typically today, positive displacement compressors are being used with high density refrigerants such as R-410A with relatively high GWP of 1924 (AR5) [2]. In this paper, the potential of using low GWP refrigerant R-516A in low ambient heat pumps will be evaluated.

2. Refrigerant properties

R-516A

R-516A is a mildly flammable (A2L) refrigerant with a low GWP of 131 (AR5) [2]. This fluid and early versions of this fluid (same components of slightly different compositions) have been extensively studied for the possibility of replacing R-134a in medium pressure chillers [3-4]. Results were promising where R-516A was shown to be essentially a drop-in like fluid to R-134a in terms of system design. In this work, we will focus on evaluation of R-516A in low ambient heat pumps as a replacement solution to R-134a.

* Corresponding author. Tel.: +1-610-878-6037 ; fax: +1-610-878-6499 .
E-mail address: sarah.kim@arkema.com .

2.1. Compatibility and stability

R-134a is used with polyol ester (POE) type lubricating oils. The miscibility of R-516A was tested with typical POE lubricants over a wide range of concentrations and temperatures that covers the operating ranges typically encountered in commercial refrigeration and air-conditioning; the operating range of R-516A was found to be comparable to that of R-134a.

The stability of R-516A in the presence of materials that it would likely encounter in practical use was evaluated in sealed tube tests according to the ASHRAE Standard 97-2007. At the evaluated test conditions, R-516A and R-516A/POE blends in the presence of steel, copper, and aluminum showed thermal stability similar to that of R-134a.

2.2. Flammability

R-516A's A2L safety classification indicates that it is a lower toxicity and lower flammability refrigerant. The flammability properties of R-516A are shown in Table 1. The burning velocity was measured using the worst case of formulation for flammability (WCF) as defined by ASHRAE 34.

Table 1. Flammability characteristics of R-516A

Flammability parameters	
LFL (%v/v) @ 23°C	5
UFL (%v/v) @ 23°C	14
Burning velocity (cm/s) @ 23°C	4.8
Heat of combustion (MJ/kg)	11.2

2.3. Thermodynamic properties

The fluid and thermodynamic properties of R-516A are presented in Table 2 and compared to R-134a as well as other lower GWP R-134a replacements. The vapor pressure of R-516A is very close to R-134a for a wide range of temperatures with only minor differences observed at temperatures above 60°C [4].

Table 2. Fluid and thermodynamic properties of R-134a and replacement refrigerants

	R-134a	R-516A	R-513A	R-1234ze(E)
GWP_{100} (AR5) [2]	1300	131	573	<1
Flammability Class	1	2L	1	2L
Bubble point (°C) at 1atm*	-26.3	-29.6	-29.6	-19.0
Dew point (°C) at 1atm*	-26.3	-29.6	-29.5	-19.0
Critical Temperature (°C)*	101.1	96.8	94.9	109.4
Critical Pressure (MPa)*	4.0	3.6	3.6	3.6
Liquid Density at 25°C (kg/m^3)*	1206.7	1069.2	1134.2	1163.1
Vapor Density at 25°C (kg/m^3)*	32.4	34.5	37.6	26.3

*R-134a, R-513A and R-1234ze(E) properties were obtained from REFPROP [5]. R-516A properties were obtained through proprietary measurements and models.

3. Results

In order to be utilized in a low ambient heat pump, the evaporating temperature must be below -25°C, which makes R-516A a suitable refrigerant for this application. R-516A and R-513A were compared to R-134a based on an oil-free R-1234ze(E) optimized compressor model with same electricity power input inside the aero map. This small capacity compressor utilizes a plate heat exchanger economizer.

The performance of the refrigerants were calculated at the following conditions:

Cooling
Evaporation Temperature = 7.2°C
Condensation Temperature = 54.4°C
Temperature approach of economizer = 3K
Evaporator Superheat = 11.1K
Condenser Subcooling = 8.3K

Heating
Evaporation Temperature = -7°C
Condensation Temperature = 50°C
Temperature approach of economizer = 5K
Evaporator Superheat = 5K
Condenser Subcooling = 5K

When the compressor performance of R-516A was compared to that of R-134a and R-513A with same motor design, both capacity and COP for cooling and heating of R-516A and R-513A were found to be slightly lower than R-134a, Figure 1 and 2. R-516A showed very similar performance to R-513A, but with significantly lower GWP. In terms of compressor operation speed, R-516A needs slightly lower speed than R-134a but slightly higher speed than R-513A.

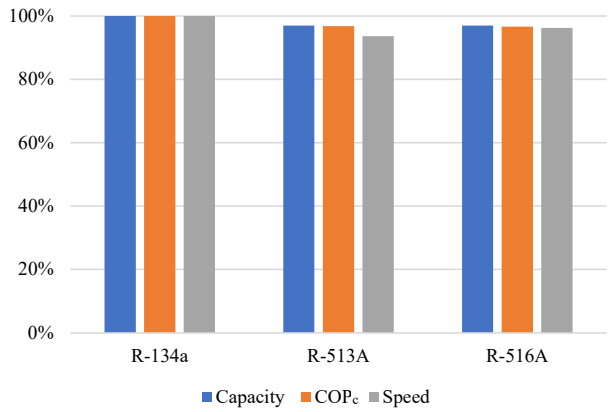


Fig. 1. Cooling mode compressor performance prediction of R-134a, R-513A, and R-516A in a R-1234ze(E) optimized compressor

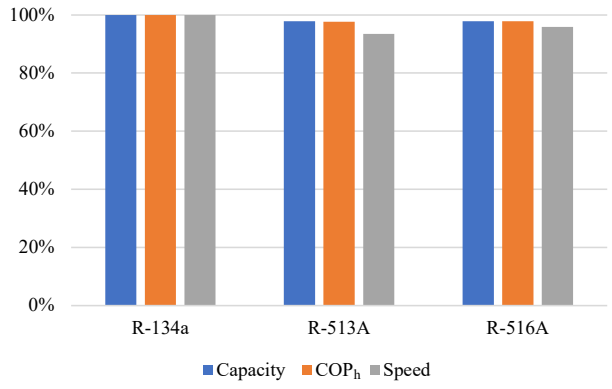


Fig. 2. Heating mode compressor performance prediction of R-134a, R-513A, and R-516A in a R-1234ze(E) optimized compressor

In terms of discharge temperature, both R-513A and R-516A showed similar values that were lower than R-134a by approximately 6K lower at the cooling condition and 8K lower at specific heating condition (Fig. 3).

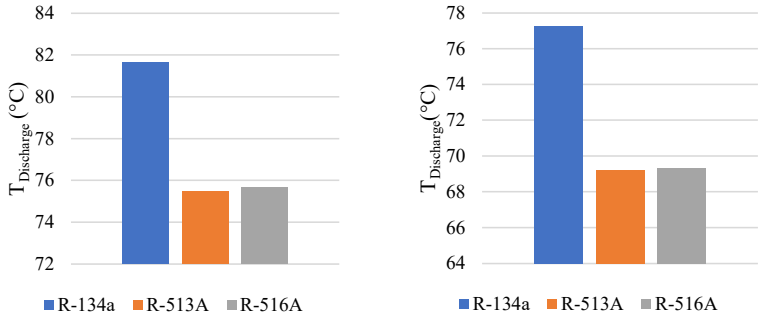


Fig. 3. Cooling (left) and heating (right) mode discharge temperature calculation of R-134a, R-513A, and R-516A in a R-1234ze(E) optimized compressor

The usage of R-516A was also evaluated in a larger capacity oil-free compressor optimized for R-134a and utilizing a flash tank economizer. In general, the trends are similar regardless of whether the compressor was optimized for R-1234ze(E) or R-134a, but the exact values are slightly different.

The capacity/efficiency comparison provides a couple of interesting highlights (Fig. 4 and 5); R-516A is closer to R-134a for heating than cooling with the efficiency within 1% of R-134a in the large capacity compressor. However, cooling with large capacity model was approximately 1.5% lower than with small capacity model, which was optimized for R-1234ze(E).

The closer capacity and efficiency performance of R-516A to R-134a in heating mode becomes critical when optimizing product designs to either cooling or heating, depending on the primary application driver.

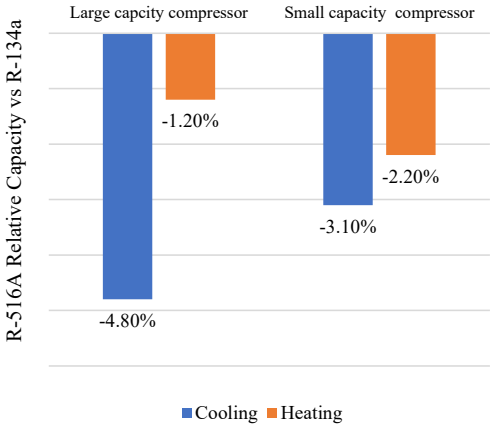


Fig. 4. Relative capacity of R-516A compared to R-134a in a R-134a compressor (left) and R-1234ze(E) compressor (right) in cooling and heating mode

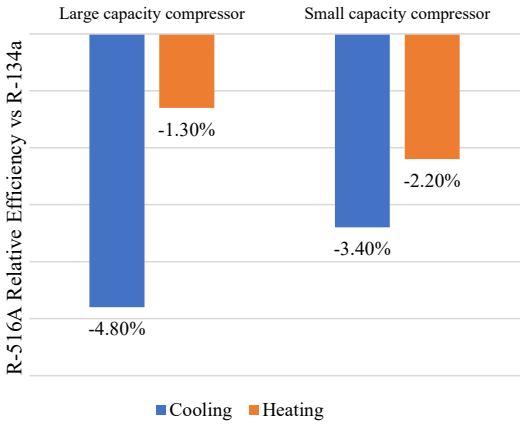


Fig. 5. Relative efficiency of R-516A compared to R-134a in a R-134a compressor (left) and R-1234ze(E) compressor (right) in cooling and heating mode

4. Conclusions

R-516A is a good drop-in alternative directly to R-134a/R-513A compressors with material compatibility qualification and consideration of the mildly flammable nature. R-516A showed matching capacity and efficiency to R-134a both in cooling and heating mode when evaluated in a R-134a optimized oil-free compressor while providing a 90% reduction in CO_2 direct emission. Heating performance of R-516A was closer to R-134a than in cooling mode. Similar stability, compatibility, and oil miscibility of R-516A to R-134a will also allow easy adoption of R-516A as a replacement fluid.

References

[1] Lecamwasam L, Wilson J, Chokolich D. *Guide to Best Practice Maintenance & Operation of HVAC Systems for Energy Efficiency*, Australia: Department of Climate Change and Energy Efficiency; 2012.
[2] Myhre G, Shindell D, Bréon F-M, Collins W, Fuglestvedt J, Huang J, Koch D, Lamarque J-F, Lee D, Mendoza B, Nakajima T, Robock A, Stephens G, Takemura T, Zhang H. *Anthropogenic and Natural Radiative Forcing*. In: Climate Change 2013: The Physical Science Basis. Contribution of Working Group I to the Fifth Assessment Report of the Intergovernmental Panel on Climate Change. Cambridge and New York: Cambridge University Press; 2013.
[3] Schultz, K., Perez-Blanco, M., 2018. "Performance of Low GWP Refrigerant R-516A in an Air-Cooled Chiller", ASHRAE Winter Conference. Chicago, IL, USA.
[4] Abbas, L., Kim, S., Schultz, K., 2016. "Novel Very Low GWP Refrigerant Composition to Replace R-134a in Stationary Air-conditioning and Refrigeration", International Refrigeration and Air Conditioning Conference, Purdue University. West Laffayette, IN, USA, paper #1707.
[5] Lemmon EW, Bell IH, Huber ML, McLinden MO, NIST Standard Reference Database 23: Reference Fluid Thermodynamic and Transport Properties-REFPROP, version 10, National Institute of Standards and Technology, Gaithersburg, MD; 2018.

Disclaimer

The statements, technical information and recommendations contained herein are believed to be accurate as of the date hereof. Since the conditions and methods of use of the information referred to herein are beyond our control, Arkema expressly disclaims any and all liability as to any results obtained or arising from any reliance on such information; NO WARRANTY OF FITNESS FOR ANY PARTICULAR PURPOSE, WARRANTY OF MERCHANTABILITY, OR ANY OTHER WARRANTY, EXPRESS OR IMPLIED, IS MADE CONCERNING THE INFORMATION PROVIDED HEREIN. The user should thoroughly test any application before commercialization. Nothing contained herein constitutes a license to practice under any patent and it should not be construed as an inducement to infringe any patent, and the user is advised to take appropriate steps to be sure that any proposed action will not result in patent infringement.

13th IEA Heat Pump Conference
April 26-29, 2021 Jeju, Korea

Dynamic Modelling and Design Optimization of a Heat-Pipe-Integrated Chemisorption Adsorber

Zhiyao Yang[a], Ming Qu[a], Kyle Gluesenkamp*[b]

[a]Lyle School of Civil Engineering, Purdue University, West Lafayette, IN 47906, USA
[b]Oak Ridge National Laboratory (ORNL), Oak Ridge, TN 37830, USA

Abstract

Thermally driven chemical adsorption (chemisorption) systems have recently seen increased research and development for their potential in novel energy applications such as solar-driven refrigeration and cold-climate heat pumping. The sorbent-containing adsorber is the core of a chemisorption system where the reversible chemical reaction occurs between the sorbent and the refrigerant, generating useful heat and the desired pressure level. Therefore, properly designed adsorbers with enhanced chemical reaction and heat and mass transfer are critical to overcoming the key limitation of chemisorption technology of low power density and energy efficiency.
In this study, a dynamic model using the finite difference method is developed to simulate the heat/mass transfer and chemical reaction in a chemisorption adsorber using stacked heat pipe plates. The model is first used to simulate and analyze the transient desorption and adsorption performance of a baseline design. Then parametric analysis reveals the impact of key design parameters such as the heat pipe spacing and sorbent plate geometry and identifies optimal design for two different expanded graphite composite sorbents.

© HPC2020.
Selection and/or peer-review under responsibility of the organizers of the 13th IEA Heat Pump Conference 2020.

Keywords: chemisorption; adsorption; dynamic simulation; design optimization.

Nomenclature

Ar	Arrhenius term for the chemical reaction [-]	ΔH_{fg}	vaporization enthalpy of ammonia [kJ/kg]
Cp	specific heat [kJ/kg-K]	ΔH_r	reaction enthalpy [kJ/mol]
c.v.	Control volume	ΔS_r	reaction entropy [kJ/mol-K]
COP	Coefficient of performance [-]	P	pressure [kPa]
m	mass [kg]	r	Radius [m]
J	Molar flow [mol/s]	K_T	Thermal conductivity [kW/m-K]
K_D	Permeability [m^2]	V	Volume [m^3]
φ	Porosity [-]	R	gas constant [J/mol -K]
N	number of moles [-]	τ	Time [s]
T	temperature [K]	t	Time [s]
X	Reaction progression [-]	S	Heat source power [kW]
Q	Heat flux [kW]	$S_{v,q}$	Volumetric source power [kW/m^3]
SCP	Specific heating power [kW/kg]	$S_{v,n}$	Volumetric ammonia mole change [mol/m^3]
PD	Power density [kW/m^3]	z	Height [m]

* Corresponding author. Tel.: +1-865-241-2952
E-mail address: gluesenkampk@ornl.gov.

1. Introduction

Thermally driven chemical adsorption (chemisorption) systems have recently seen increased research and development for their unique potential in various novel energy applications, including solar-driven refrigeration [1], high-density thermal energy storage [2], and efficient cold-climate heat pumping [3]. The sorbent-containing adsorber is the most important component in a chemisorption system where the reversible chemical reaction occurs between the sorbent and the refrigerant, generating useful heat and desired pressure level. Therefore, properly designed adsorbers with enhanced chemical reaction and heat and mass transfer are critical to overcoming the key limitation of chemisorption technology of low power density and energy efficiency.

Typical adsorber designs use finned tubes [4] and annular tubes [5-6] to exchange heat between the external heat source and the sorbent. The considerable temperature gradient observed leads to a "reaction front" to propagate across the adsorber during the desorption and adsorption phases and reduce the power density of the system [5]. Heat pipe was applied in several studies in finned tube configurations [4,7] to enhance the heat transfer towards the sorbent without a pump.

An innovative design with an integrated heat pipe was recently proposed for high-performance chemisorption adsorber [8]. The new design uses stacks of heat pipe plates to significantly enhance the heat transfer between the sorbent and the external heat source/sink. On the other hand, there is a trade-off between the heat transfer improvement with larger heat transfer surfaces and energy efficiency loss due to increased thermal mass and reduced sorbent charge. Moreover, the heat and mass transfer in the sorbent is also affected by the height/radius ratio and inner/outer radius ratio of the heat pipe and sorbent assembly. The existing dynamic models of chemisorption adsorbers are dominantly based on annular [5-6] and finned-tube [4] configurations, which have very different heat and mass transfer characteristics compared with the new heat pipe plate design. Therefore, a detailed model for the adsorber is needed to analyze the influence of these design parameters and identify the optimal design for the highest performance.

This study develops such a dynamic model using the finite difference method to simulate the heat/mass transfer and chemical reaction in the heat-pipe-integrated adsorber. The model is first used to simulate and analyze the transient desorption and adsorption performance of a baseline design. Then parametric analysis reveals the impact of key design parameters such as the heat pipe density and sorbent plate geometry using different sorbents and identified the optimal design for the sorbents.

2. Dynamic Model of the Heat-pipe-integrated Adsorber

The adsorber is a cylindrical pressure vessel housing a heat exchanger made up of disc-shaped steel plates engineered in such a way as to allow a heat transfer fluid (steam or pumped water) to flow within the discs. There is a hollow center through all the salt and heat pipe plates from top to bottom, providing extra passage for ammonia vapor to flow in and out of the salt in the center of the plate. The heat exchanger of the adsorber provides thermal energy to or removes thermal energy from a matrix material infused with a salt such as $CaCl_2$ that reversibly adsorbs ammonia vapor. The matrix is hosted in between the heat exchanger discs and in good contact with the heat exchanger surfaces. The adsorber has an opening at the top to allow ammonia vapor to flow to the condenser or back from the evaporator, depending on the operating mode.

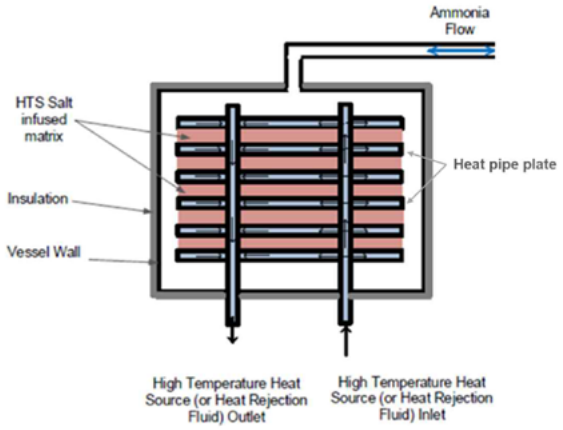


Fig. 1. Schematic of the heat-pipe-integrated adsorber [8]

During operation, the heat pipe discs conduct heat to or from the sorbent plates, leading to the endo- or exothermic chemical reaction between the salt and ammonia vapor to occur. With the proceeding of the reaction, the ammonia molar concentration around the salt grain changes, creating a driving force for the ammonia vapor to diffuse towards the low-concentration region. During desorption, the ammonia vapor accumulated in the interior of the salt plate eventually arrives at the inner or external perimeter of the sorbent plate and gets released into the adsorber chamber. During adsorption, ammonia vapor from the evaporator diffuses into the sorbent plates from the perimeter to get adsorbed by the "dry" salts.

Based on the geometry and operation of the heat-pipe-integrated adsorber, the coupled heat-and-mass transfer and chemical reaction inside the sorbent plates can be described in detail with a system of differential equations. The heat-and-mass transfer differential equations are established on a representative differential control volume (c.v.) as shown in Fig. 2. The salt plate is a typical cylindrical geometry that can be divided into differential "rings." The cross-section of the ring is rectangular, and by using cylindrical coordination $z - r$ the differential c.v. can be described as c.v. P is a representative c.v., with the adjacent c.v. termed east/west/north/south. The distance between the center of adjacent c.v. in the radial direction is defined as dr, and in the vertical direction as dz. The dimensions of the c.v. are determined by the number of c.v., created as well as the absolute radius from the c.v. center to the centerline of the cylinder.

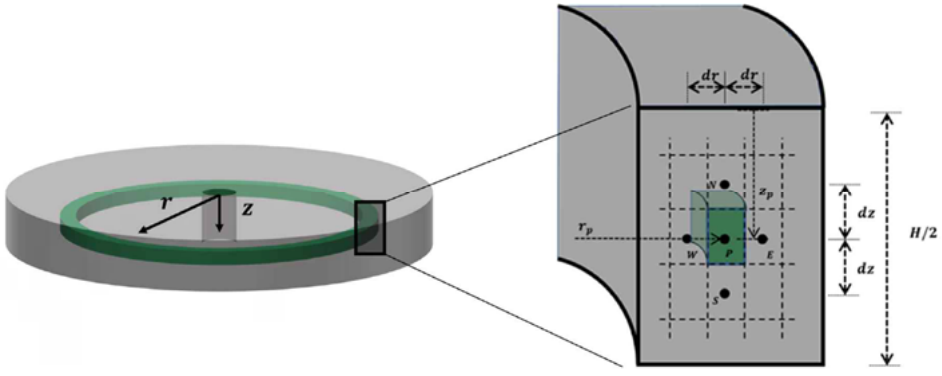


Fig. 2. Schematic of the differential control volume ring

The governing equations to describe the heat and mass transfer process are established based on the following assumptions:

1. The temperature of heat pipe discs is uniform across the entire heat pipe stack;

2. Heat exchanger metal temperature is the same as the steam/water inside;
3. The radiative, convective, and conductive heat transfer between ammonia vapor with the heat exchanger metal and sorbent is neglected;
4. The thermal mass of the adsorber vessel shell is neglected;
5. Uniform pressure around heat pipe/sorbent stack;
6. Ammonia vapor travels inside the sorbent plate only through diffusion;
7. The heating/cooling power through the adsorber heat exchanger during heating-desorption and cooling-adsorption is assumed to be constant, i.e. the temperature difference between the heat transfer medium in the heat exchanger and the adjacent sorbent is constant.

Since the sorbent plates are vertically symmetrical, the model only needs to describe the upper half of the entire plate. The overall energy balance equation for a control volume can be expressed as in equation (1):

$$\Delta Q_{int} = \dot{Q}_z + \dot{Q}_r + \dot{S}_{chem} \tag{1}$$

Where ΔQ_{int} is the change of internal energy, $\dot{Q}_z$ is the net heat inflow in the vertical direction, $\dot{Q}_r$ is the net heat inflow in the radial direction, and $\dot{S}_{chem}$ is the reaction heat. Applying Fourier's law for heat transfer between adjacent c.v., the vertical conduction can be calculated as equation (2):

$$\dot{Q}_z = \dot{Q}_n - \dot{Q}_s = K_T \cdot \frac{\partial^2 T}{\partial z^2} \cdot dr \cdot r \cdot 2\pi \cdot dz \tag{2}$$

Where K_T is the thermal conductivity, and $\dot{Q}_n$ and $\dot{Q}_s$ are heat conduction with the two vertically adjacent c.v. Similarly, for heat conduction in the radial direction can be calculated as in equation (3):

$$\dot{Q}_r = \dot{Q}_e - \dot{Q}_w = K_T \cdot \frac{\partial^2 T}{\partial r^2} \cdot dz \cdot r \cdot 2\pi \cdot dr + K_T \cdot \frac{\partial T}{\partial r} \cdot dz \cdot 2\pi \cdot dr \tag{3}$$

And finally, equation (4) calculates the chemical reaction heat in the c.v., with $N_{NH3,i}$ the ammonia change associated with the reaction, $\Delta H_{r,i}$ the reaction heat, and n_{salt} the volumetric mole density of salt in the c.v.

$$\dot{S}_{chem} = S_{vol} \cdot V = \Sigma \frac{dN_{NH3,i} \cdot \Delta H_{r,i}}{dt} \cdot n_{salt} \cdot dz \cdot dr \cdot r \cdot 2\pi \tag{4}$$

By defining the thermal diffusivity as in equation (5), the energy balance equation (1) can be re-written as equation (6) by inserting equation (1)-(5):

$$\alpha = \frac{K_T}{\rho \cdot Cp} \tag{5}$$

$$\frac{1}{\alpha} \cdot \frac{\partial T}{\partial t} = \frac{\partial^2 T}{\partial z^2} + \frac{\partial^2 T}{\partial r^2} + \frac{1}{r} \cdot \frac{\partial T}{\partial r} + \frac{1}{K} \cdot S_{vol} \tag{6}$$

Similar to heat conduction between adjacent c.v., ammonia vapor in the interconnected pores flows across the boundary of c.v. through diffusion driven by the molar concentration difference. The mass balance can be expressed as in equation (7)

$$\Delta N = J_z + J_r + J_{chem} \tag{7}$$

Where N is the total amount of ammonia vapor in the pores of the c.v., J_z is net mass inflow flux in the vertical direction, J_r for radial direction, and J_{chem} is the ammonia vapor change due to chemical reaction. By assuming Darcy flow, the diffusivity of the sorbent plate can be calculated from its permeability in equation (8):

$$D = -\frac{K_D}{\mu} \cdot P_p \cdot \varphi \tag{8}$$

Applying Fick's first law the diffusion mass flux can be calculated between vertically and horizontally adjacent c.v. as in equation (9) and (10):

$$J_z = J_n - J_s = D \cdot \frac{\partial^2 n}{\partial z^2} \cdot dr \cdot r \cdot 2\pi \cdot dz \tag{9}$$

$$J_r = J_e - J_w = D \cdot (\frac{\partial^2 n}{\partial r^2} \cdot r \cdot 1 \cdot dz + \frac{\partial n}{\partial r} \cdot dz \cdot 2\pi) \cdot dr \tag{10}$$

With the ammonia vapor flux generated from the chemical reaction as in equation (11), the ammonia vapor mass balance equation (7) can be expressed as in equation (12):

$$J_{chem} = S_{v,n} \cdot V = \Sigma \frac{dN_{NH3,i}}{dt} \cdot n_{sat} \cdot dz \cdot dr \cdot r \cdot 2\pi \tag{11}$$

$$\frac{\partial n}{\partial t} = D \cdot \left(\frac{\partial^2 n}{\partial z^2} + \frac{\partial^2 n}{\partial r^2} + \frac{1}{r} \cdot \frac{\partial n}{\partial r}\right) + S_{v,q} \tag{12}$$

The equilibrium of ammonia-based chemisorption reactions can be expressed by the van't Hoff equation as equation (13), and the chemical reaction kinetics can be described by the semi-empirical equation first proposed by Tykodi et al. [9] and used in various chemisorption reaction simulation studies [3-4]:

$$h\left(P_{eq}\right) = -\frac{\Delta H_r}{RT_{sat}} + \frac{\Delta S_r}{R} \tag{13}$$

$$\frac{dX}{dt} = (1 - X)^n \cdot Ar \cdot h\left(\frac{P_{eq}(T_{sat})}{P_{bcal}}\right) \tag{14}$$

For the upper half-plate, the top boundary is the heat pipe heat exchanger, and therefore the boundary condition for the c.v. on the top layer is the heat exchanger temperature. The bottom of the plate is assumed to be isothermal since the plate is symmetrical. These two boundaries are also assumed to allow no ammonia vapor flow. Around the outer perimeter and inner perimeter (around the center vapor channel) of the plate, the sorbent directly contacts with the ammonia vapor in the adsorber chamber. The heat transfer boundary conditions for the c.v. on the perimeter layer is isothermal since the heat transfer between ammonia vapor and solid sorbent is assumed to be negligible. However, the ammonia vapor next to the boundary sorbent is assumed to be at the sorbent temperature and the chamber pressure.

In a typical chemisorption heat pump cycle as in Fig. 3, the adsorber is connected with a condenser to draw and condense the ammonia vapor from the adsorber during the desorption phase, and an evaporator to supply ammonia vapor to the adsorber during the adsorption phase. In the current study, the condenser and evaporator are assumed to provide constant ammonia pressure based on the saturation temperature instantly. The condensing and evaporating heat is calculated directly from the latent heat of ammonia vapor to and from the adsorber.

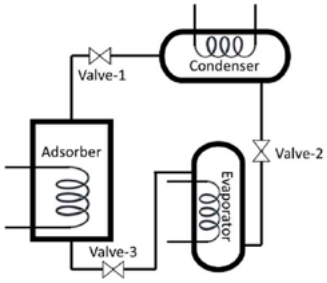


Fig. 3. Schematic of a chemisorption heat pump with one adsorber

A cycle starts with heating and desorbing the sorbent by the high-temperature heat source. At the end of the desorption phase, the heat flux from high-temperature source is stopped and the fluids in the adsorber heat exchanger start to cool the sorbent. Once the condensation is sufficiently reduced, the connection to the

condenser is cut off. The cool and dry salt continuously adsorbs the remainder ammonia vapor in the adsorber chamber until the adsorber chamber pressure reaches the evaporating pressure and the evaporator valve is opened. The operating procedure of a desorption-adsorption cycle of the adsorber is listed in Table 1.

Table 1. operating procedure of desorption-adsorption cycle

Stage	Endpoint	Adsorber heat flow	Valve positions
Desorption	Reached half-cycle time	Heating the sorbent	Valve-1 open, valve-2 and valve -3 closed
Cooldown -1	Condensation stops	Cooling the sorbent	Valve-1 open, valve-2 and valve -3 closed
Cooldown -2	Adsorber chamber reaches evaporating pressure	Cooling the sorbent	Valve-2 open, valve-1 and valve-3 closed
Adsorption	Reached cycle time	Cooling the sorbent	Valve-3 open, valve-2 and valve -1 closed

The performance of the adsorber is evaluated with three parameters: the cooling coefficient of performance (COP), the specific cooling capacity (SCP), and the cooling power density (CPD). The COP is calculated in equation (15) as the ratio of the evaporating heat over the heat transferred from the heat pipe to the sorbent during the desorption phase. The SCP in equation (16) is based on the mass of the sorbent material. The CPD in equation (17) is based on the volume of the heat pipe-sorbent stack enclosure.

$$COP = \frac{Q_{evap}}{Q_{input}} = \frac{\Delta H_{fg} \cdot m_{NH3}}{Q_{input}} \quad (15)$$

$$SCP = \frac{Q_{evap}}{\tau_{cycle}} \cdot \frac{1}{m_{sorbent}} \quad (16)$$

$$CPD = \frac{Q_{evap}}{\tau_{cycle}} \cdot \frac{1}{V_{stack}} \quad (17)$$

3. Modeling Results

In this study, a dynamic model was first developed in MATLAB for a baseline adsorber using the governing equations in the previous section. $CaCl_2$ has been a popular choice in ammonia-based chemisorption systems, and it is selected as the sorbent salt in this study. There are two ammoniate reactions under the assumed refrigeration working condition of evaporating at 0°C and rejecting condensation and adsorption heat at 45°C as listed below. The chemical equilibrium data of $CaCl_2$/ammonia reactions from Neveu et al. [10] and the kinetic coefficients from Wang et al. [11] are listed in Table 2.

$$CaCl_2 \cdot 8NH_3(s) \rightarrow CaCl_2 \cdot 4NH_3(s) + 4NH_3(g)$$

$$CaCl_2 \cdot 4NH_3(s) \rightarrow CaCl_2 \cdot 2NH_3(s) + 2NH_3(g)$$

Table 2. equilibrium and kinetic coefficients for $CaCl_2$ ammoniate reactions

	Parameter	$CaCl_2$-8/4	$CaCl_2$-4/2
Equilibrium	Reaction enthalpy (ΔH_r) [J/mol]	41013	42268
	Reaction entropy (ΔS_r) [J/mol-K]	230.3	229.92
Kinetics	Desorption: Order of reaction (n)	1.005	0.468
	Desorption: Arrhenius term (Ar)	0.0195	0.0045
	Adsorption: Order of reaction (n)	2.104	1.78
	Adsorption: Arrhenius term (Ar)	0.0125	0.0287

To enhance the heat and mass transfer and avoid agglomeration during reactions, the $CaCl_2$ salt is combined with two different porous matrix materials: expanded graphite (EG) and expanded natural graphite treated with sulfuric acid (ENGTSA). Compared with EG, ENGTSA further improves the heat transfer performance at the expense of lower permeability. The physical properties of the composite $CaCl_2$/EG and $CaCl_2$/ENGTSA are

taken from Tian et al. [12] and Jiang et al. [13]. The key parameters of the baseline adsorber and the sorbent materials are listed in Table 3.

Table 3. key parameters of the baseline adsorber and the sorbent materials

Item	Value	Unit
Total height of heat pipe stack	0.6	m
Sorbent plate thickness	0.01	m
Outer diameter of heat pipe and sorbent plates	0.2	m
Inner diameter of heat pipe and sorbent plates	0.01	m
Outer thickness of one heat pipe disc	0.01	m
Density of composite sorbent	450	kg/m3
Porosity of composite sorbent	0.5	-
Salt mass fraction in the composite sorbent	50	%
Thermal conductivity of $CaCl_2$/EG composite	1.	W/m-K
Permeability of $CaCl_2$/EG composite	1×10^{-11}	m^2
Thermal conductivity of $CaCl_2$/ENGTSA composite	40	W/m-K
Permeability of $CaCl_2$/ ENGTSA composite	1×10^{-14}	m^2

The performance of the adsorber is evaluated in one complete desorption-adsorption cycle with a full-cycle time of 40 min, a steam temperature limit of 140°C during desorption, cooling water temperature of 45°C in the adsorber during adsorption. At the start of the desorption phase, all sorbents are at 45°C and $CaCl_2$-$8NH_3$ state. The adsorber contained 40 sorbent plates and 41 heat pipe discs. The sorbent plates consist of 5.63 kg of $CaCl_2$/EG composite, 2.8 kg of which is $CaCl_2$ salt. The desorption lasted the first 1200 seconds of the cycle, followed by 71 seconds of continued condensation in cool down -1 phase, and 200 seconds of standalone cooling down before the final 924 seconds of adsorption. 6989 kJ heat was supplied through the adsorber heat exchanger to the sorbent during the desorption phase to heat the sorbent and support the decomposition of ammoniate salts. During the adsorption phase, 2.1 kg liquid ammonia evaporated, producing 2812.8 kJ cooling. The cooling COP of this baseline setup is 0.402, the SCP is 415.8 W/kg sorbent, and the CPD is 62.2 kW/m^3 based on the heat pipe-sorbent stack volume.

Fig. 4 illustrates the progression of salt state change in the control volume close to the heat pipe through the cycle. Initially, all the salt was in $CaCl_2$-$8NH_3$ state. The salt was heated up to the equilibrium temperature of about 95°C when it started to decompose into $CaCl_2$-$4NH_3$, which later further released ammonia and becomes $CaCl_2$-$2NH_3$ at even higher temperatures. Once the cooling-adsorption starts, the $CaCl_2$-$2NH_3$ compound absorbs ammonia and becomes $CaCl_2$-$4NH_3$ and then $CaCl_2$-$8NH_3$ as the temperature of the salt decreases. The fraction of the $CaCl_2$-$4NH_3$ and $CaCl_2$-$8NH_3$ gradually increases after the desorption-adsorption mode switch in Fig. 4.

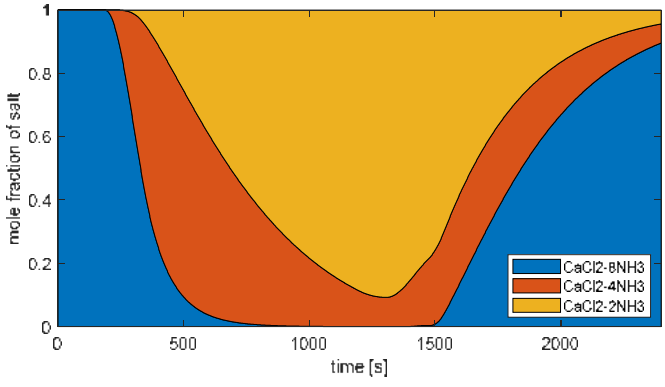


Fig. 4. Different ammoniate salts in control volume at sorbent plate top inner rim

Therefore, the mole fraction of $CaCl_2$-$8NH_3$ in Figure 4 drops quickly after about 300s into initial heating towards the decomposition temperature of the $CaCl_2$-$8NH_3$; then the mole fraction of $CaCl_2$-$4NH_3$ rises due to the 8→4 reaction; its share starts to decline when the 4→2 reaction starts at a higher temperature. The mole fraction of salt in different ammoniate states reverses once the adsorber switched to cool down and adsorption stages.

4. Design optimization

In this section, the performance of adsorbers using different geometries based on the baseline design is evaluated using the dynamic model to identify optimal design for composite sorbents with different heat and mass transfer characteristics and under different cycle times.

Fig. 5. Shows the COP and SCP of adsorbers using the baseline geometry but under cycle time of 20-60 minutes. Generally, the COP increases with cycle time as the reactions have more time to approach completeness, leading to more ammonia evaporation and higher efficiency. On the other hand, the increase of cycle time reduces the averaged cooling power of the EG adsorber as chemical reactions slow down when approaching completeness. In contrast, the SCP of ENGTSA adsorber slightly increases with longer cycle time. It is due to the low reaction completeness constrained by the low permeability of the ENGTSA matrix. Thus, the mass-transfer impeded ENGTSA adsorber requires longer cycle time to reach high reaction completeness under the baseline thin-plate geometry.

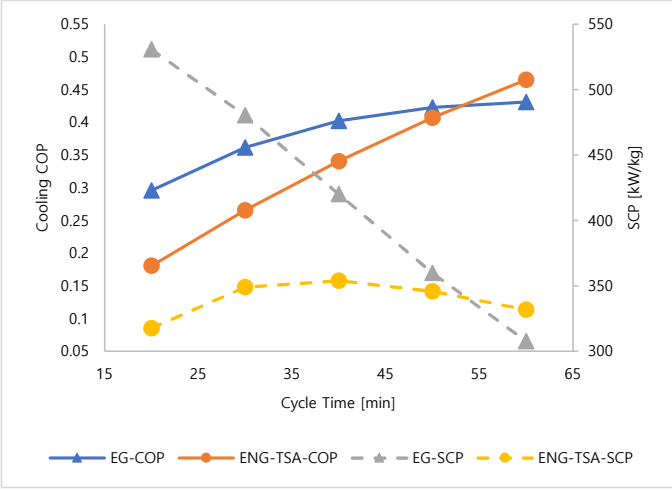


Fig. 5. COP and SCP of the adsorber with baseline geometry under different cycle time

Fig. 6 shows the influence of the sorbent plate thickness on the COP and SCP. Thicker plates contain more adsorbents in the same adsorber, but it also reduces the number of heat pipe discs and thus the heat transfer surface area between the external heat source and the sorbent. Therefore, adsorbers using both types of sorbent demonstrate an optimal sorbent plate thickness about COP and SCP. The performance of the adsorbers with plates thicker than 20mm are limited due to insufficient heat transfer area.

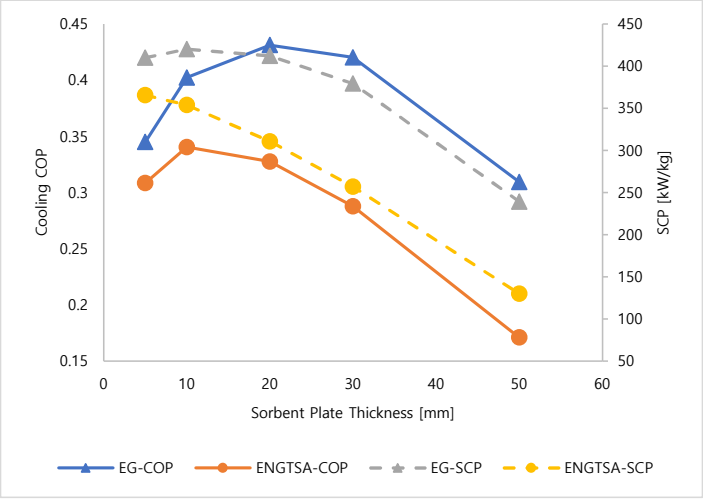


Fig. 6. Different ammoniate salts in control volume at sorbent plate top inner rim

The ENGTSA matrix offers significantly higher thermal conductivity compared with EG at the expense of much lower permeability. Therefore, mass transfer of the ammonia vapor from inside the sorbent to the adsorber chamber could be a limiting factor. Fig. 7 illustrates the influence of the center vent diameter on the adsorber performance. A wider vent leads to more sorbent exposure to the adsorber chamber and therefore better mass transfer. It is manifested by the significant increase of COP for ENGTSA adsorber shown in the left chart in Fig. 7 compared with the flat COP curve of EG. Meanwhile, increasing the vent size reduces the total amount of sorbent in the adsorber, as the outer diameter of the sorbent plate is fixed. Therefore, the power density, as shown in the right chart in Fig. 7 decreases quickly for EG adsorber with little benefit from the improved mass transfer. In contrast, the ENGTSA adsorber sees a peak PD in the trade-off of better mass transfer and less sorbent.

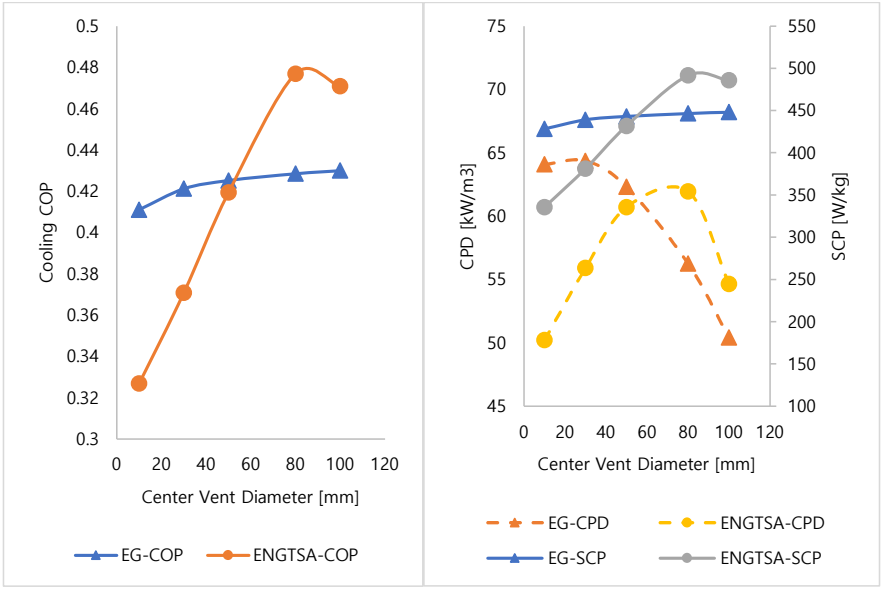


Fig. 7. Different ammoniate salts in control volume at sorbent plate top inner rim

5. Conclusions

This study develops a dynamic model using the finite difference method to simulate the heat/mass transfer and chemical reaction in the heat-pipe-integrated chemisorption adsorber. The model is first used to simulate and analyze the transient desorption and adsorption performance of a baseline design. The dynamic modeling predicts the system performance under different designs, and the effect of each design parameter is examined and the optimal design identified. The sorbent plate thickness affects both the amount of sorbent in the adsorber as well as the available heat transfer surface between the sorbent and the external heat source. Under the overall adsorber geometry constraint, the optimal sorbent plate thickness for EG sorbent is about 20 mm and ENGTSA is about 10 mm. The diameter of the vapor vent at the plate center affects the mass transfer area as well as the amount of sorbent in the adsorber. Since the EG matrix provides sufficient permeability, the widening of the vent doesn't improve the COP noticeably but rather decreases the power density. For ENGTSA with lower permeability, the increase of the mass transfer area by a larger vent significantly improves the COP and the power density of the adsorber, and the optimal vent diameter is found to be 80 mm.

The dynamic model demonstrated its capability of capturing the transient heat mass transfer and chemisorption reaction progression during the adsorber operation for predicting the energy efficiency and power density of the component. The model, once validated with experimental data, can be used for optimizing the design of similar plate-type adsorbers using various sorbent salt and matrix materials of different thermophysical properties.

Acknowledgments

This work was sponsored by the U. S. Department of Energy's Building Technologies (BTO) Office under Contract No. DE-AC05-00OR22725 with UT-Battelle, LLC. The authors would like to acknowledge Mr. Antonio Bouza, Technology Manager for HVAC&R, Water Heating, and Appliance, U.S. Department of Energy BTO.

References

[1] Yu N, Wang R, Wang L. Sorption thermal storage for solar energy. Progress in Energy Combustion Science. 2013;39:489-514.
[2] Yan T, Wang RZ, Li TX, Wang LW, Fred IT. A review of promising candidate reactions for chemical heat storage. Renewable and Sustainable Energy Reviews. 2015;43:13-31
[3] Yang Z, Qu M, Gluesenkamp KR. Model-Based Performance Comparison of Ammonia Chemisorption Heat Pumps for Cold Climate with Different Working Pairs and Cycle Configurations. Oak Ridge National Lab.(ORNL), Oak Ridge, TN (United States); 2018.
[4] Wang LW, Wang RZ, Wu JY, Wang K. Compound adsorbent for adsorption ice maker on fishing boats. International Journal of Refrigeration. 2004;27:401-8.
[5] Lu, H. B., Mazet, N., Coudevylle, O., & Mauran, S. (1997). Comparison of a general model with a simplified approach for the transformation of solid-gas media used in chemical heat transformers. Chemical Engineering Science, 52(2), 311-327.
[6] Lebrun, M., & Spinner, B. (1990). Models of heat and mass transfers in solid—gas reactors used as chemical heat pumps. Chemical engineering science, 45(7), 1743-1753.
[7] Li TX, Wang RZ, Wang LW, Lu ZS, Chen CJ. Performance study of a high efficient multifunction heat pipe type adsorption ice making system with novel mass and heat recovery processes. International Journal of Thermal Sciences. 2007;46:1267-74.
[8] Blackman, C., Gluesenkamp, K. R., Malhotra, M., & Yang, Z. (2019). Study of optimal sizing for residential sorption heat pump system. Applied Thermal Engineering, 150, 421-432.
[9] Tykodi, R. J. (1979). Thermodynamics of Steady States:"Resistance Change" Transitions in Steady-state Systems. Bulletin of the Chemical Society of Japan, 52(2), 564-570.
[10] Neveu P, Castaing J. Solid-gas chemical heat pumps: field of application and performance of the internal heat of reaction recovery process. Heat Recovery Syst CHP. 1993;13:233-51.
[11] Wang, C., P. Zhang, and R.Z. Wang, Investigation of solid–gas reaction heat transformer system with the consideration of multistep reactions. AIChE Journal, 2008. 54(9): p. 2464-2478.
[12] Tian B, Jin ZQ, Wang LW, Wang RZ. Permeability and thermal conductivity of compact chemical and physical adsorbents with expanded natural graphite as host matrix. International Journal of Heat and Mass Transfer. 2012;55:4453-9.
[13] Jiang L, Wang LW, Zhou ZS, Zhu FQ, Wang RZ. Investigation on non-equilibrium performance of composite adsorbent for resorption refrigeration. Energy Conversion and Management. 2016;119:67-74.



13th IEA Heat Pump Conference
April 26-29, 2021 Jeju, Korea

Evaluation of a low charge heat pump circuit using propane

Clemens Dankwerth, Timo Methler, Simon Braungardt, Christian Sonner, Thore Oltersdorf, Marek Miara, Peter Schossig, Lena Schnabel*

Fraunhofer Institute for Solar Energy System - ISE, Department of Heating and Cooling Technologies, Heidenhofstr. 2, 79115 Freiburg, Germany

Abstract

A low refrigerant charge brine-to-water heat pump circuit was evaluated addressing a heating capacity of 5 – 10 kW and using propane as refrigerant. Propane is a natural refrigerant, has a low global warming potential (GWP) of three and attractive thermodynamic properties. No regulations, except for safety, are expected to apply for this refrigerant. Therefore it was chosen as refrigerant for this evaluation, the refrigerant charge of propane was limited to 150g, resulting in 0.45kg of CO_2 equivalent. The reduction of charge was achieved with different design approaches and techniques: The main goal was to minimize the internal volume on the refrigerant side in all components and tubes. The two heat exchangers and the liquid line are the components impacting the charge the most. To reduce the internal volume, different design aspects were taken into account: The condenser and evaporator are designed with an asymmetric plate profile and a long thermal length, the liquid line was designed as short and thin as possible, and the filter dryer in the liquid line was shifted to the suction line. Also, the refrigerant absorption in the oil has a large impact on the refrigerant charge. The majority of the oil is in the compressor sump and the rest in the refrigerant circuit. To reduce the quantity of refrigerant in the oil, the amount of oil was minimized and the arrangement of components in the refrigerant circuit was chosen carefully to prevent oil retention. The charge reduced heat pump circuit was tested with two different inverter-driven compressors (suction gas-cooled scroll compressor and a hot gas-cooled twin rotary compressor) at various points of operation. This paper presents the results of the experimental evaluation and discusses the safety issues and potential for further optimization.

© HPC2020.
Selection and/or peer-review under responsibility of the organizers of the 13th IEA Heat Pump Conference 2020.

Keywords: charge reduction, propane, heat exchanger, heat pump

1. Introduction

The installation and use of heat pumps is increasing worldwide. In parts of Europe, the heat pump has become the dominant heating solution in new buildings. Due to the increasing awareness towards global warming and the need to reduce the use of fossil fuels and environmentally harmful gases, the market share of heat pumps is expected to rise steeply. Heat pumps use electricity for heating purposes with significantly higher efficiency than purely electrical resistance heaters. Combined with electricity from renewable sources, heat pumps can provide building heating without using any fossil fuels. Currently most heat pump systems employ refrigerants with high global warming potential (GWP) refrigerants due to security advantages regarding flammability and toxicity. The global community unanimously banned refrigerants with ODP by the Montreal protocol [13] and is now gradually restricting the maximum GWP for refrigerants. In Europe the F-gas Regulation [9] is implemented to phase out the use of refrigerants with a high GWP. Such regulations encourage and force the shift towards refrigerants with very low GWP, such as natural refrigerants, in a timely

manner. Propane is a well-known refrigerant with excellent thermal dynamic properties and a minimal impact on the environment (GWP =3, ODP =0). Furthermore, no regulations, except for safety, are expected to apply for propane as refrigerant, making it predestined for use in heat pumps. Propane heat pump research and development focuses on developing ***security systems*** [4][5], optimizing ***performance*** [2], reducing ***charge*** [1, 3] and ***comparing*** various ***refrigerants*** i.e. evaluating the different perspectives and making comparisons to other, mainly synthetic, refrigerants [10, 15][12]. This paper will show the first results of a charge-reduced brine-to-water propane heat pump.

2. Baseline for low charge residential heat pump systems

In 2001 and later in 2007, Fernando et al. [7] presented first experimental results of a low-charge propane heat pump. The comprehensive results and findings are part of his PhD thesis [14] on a brine-to-water heat pump with ca. 5 kW heating capacity at -3°C/35°C and a charge of 230g. [6] In 2018, Andersson [1] presented a study on a heat pump capable of 10 kW heating capacity using a refrigerant charge of less than 150g propane (B7/W40) with a non-hermetic compressor. Both studies investigated heat pump concepts, in which unique prototype components as well as an automotive scroll compressor were installed. The employed automotive compressor, however, was neither rated for the use with propane nor was it designed as a hermetic compressor. Another shortcoming was that the source temperature fluctuated strongly because the test environment was too small. The work presented by Andersson provided a baseline for the reduction of charge as well as an identification of the preliminary areas of attention for future research.

There are a few propane-charged systems commercially available, most of which are air-to-water systems for outdoor locations. Outdoor systems are more common due to less security restrictions and concerns. Due to leaking, indoor propane systems could create a hazardous environment. Outdoors any leaked propane would quickly dissipate, thus creating no hazard. Most manufacturers do not employ propane heat pumps for indoor applications due to the high security requirements and the accompanying financial costs. A brief market analysis of available brine-to-water heat pumps from the beginning of 2019 is shown in Figure 1. The black lines show the lines with same charge. The red line marks Fraunhofer ISE's target of a heating capacity between 5 and 10 kW with 150g propane. As seen in the graph, this target results in a specific charge of 15 to 30g/kW, a reduction by a factor of four in comparison to market available heat pumps.

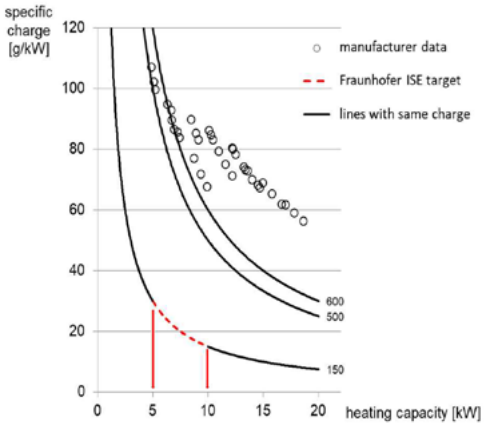


Figure 1: Specific charge over heating capacity of available brine-to-water heat pumps

A more elaborate market study with a wider range of application of air-to-water and brine-to-water heat pumps was done by Palm [11] as part of the LifeFront report [8]. These reports are comparable to the market research done preliminary to this low-charge heat pump development project.

3. Goals and ambitions

The project goal is to create a heat pump using only commercially available components and to achieve 5-10 kW heating capacity with a maximum charge of 150g propane. At the same time, the efficiency of the unit must be maximized for these given boundary conditions. The parameters are marked in red in Figure 1 and give a perspective on the significance of this goal. Additionally the charge-reduced compression cycle shall be analyzed in detail. Specific evaluation criteria for comparison purposes will be defined. The knowledge gained shall be transferred to enable the design of an air-to-water heat pump with similar boundary conditions.

4. Test rig

Main refrigerant circuit

The refrigerant circuit was designed and built as shown in Figure 2. As a side effect of minimizing the pipe length and diameters, the overall dimensions were reduced. With dimensions of 700x500x200mm, the refrigeration circuit is small in comparison to other units with the same capacity. The main components used for the heat pump are shown in

Table 1.

No.	Component
1	Compressor
2	Evaporator: Alfa Laval ACH72- 16AH- F
3	Condenser: Alfa Laval CB65- 16AH- F
4	Filter dryer: ALCO PCN 008925
5	Expansion device: Parker SDR2

Table 1: Main components in the refrigeration circuit.

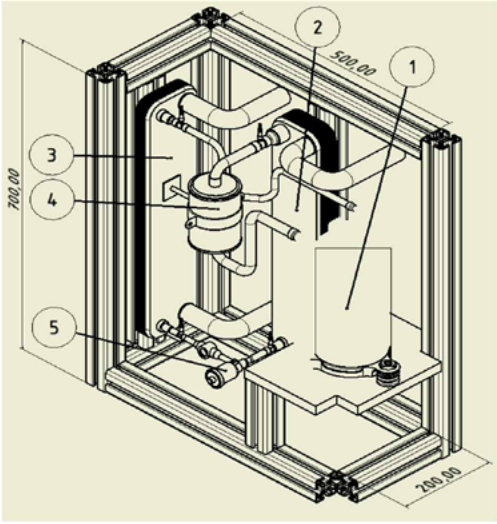


Figure 2: Drawing of the compression cycle

No.	Component
1	Compressor
2	Evaporator: Alfa Laval ACH72- 16AH- F
3	Condenser: Alfa Laval CB65- 16AH- F
4	Filter dryer: ALCO PCN 008925
5	Expansion device: Parker SDR2

During the measurements all changes to the refrigerant circuit have been documented with version numbers. The compressor has been changed during the project duration and from now on will be referred to as system 1 and system 2 respectively. Minor changes result in numbering such as 2.1 ➔ 2.2. This will be clarified if necessary in relevant places.

Measurement procedure

Most measurements were taken in a setup which allowed for variations in charge. First, the initial charge was filled into the heat pump. Operating points were recorded by running the circuit until steady state conditions were reached. Then the measured operation point of the heat pump was run for another 30 minutes in steady state conditions and the mean values during the last few minutes were calculated. The transition to the next operational point was initiated by adding additional 10g of R290 to the system. Once again the system ran until steady state was reached and the described loop was repeated to complete the series of measurements. The temperatures for the secondary circuits were chosen based on typical test parameters in the heat pump sector. For the source temperature -10°C, -7°C, 0°C, 12°C were chosen. These values refer to the inlet temperature. For the sink 35°C, 45°C, 55°C and 65°C were chosen as outlet temperatures of the heat exchanger. For both of the secondary hydraulic circuits, a constant delta T between inlet and outlet of 5K and 3K respectively was maintained as specified in EN14511. Measured data points are designated as "BX/WY" which derives from "brine with temperature X" and "water with temperature Y." The brine always characterizes the source temperature and water the sink temperature.

Test environment

To ensure standardized testing, the conditioning modules, providing the secondary fluids, were used to simulate source and sink and are referred to as secondary modules. These conditioning modules are standardized equipment in the laboratory and have the following adjustable parameters: flow temperature, pressure difference and mass flow. The conditioning module for the sink side is filled with water and the module on the source side with a mixture of ethylene/glycol and water with a freezing temperature of -30°C. Both modules are connected to the building cooling system to ensure operation at all times. All testing was done in a monitored environment with gas detection system and forced ventilation. In case of a propane leakage,

the power supply is switched off and the ventilation enhanced.

5. Results

Simulations

The complete refrigerant circuit was simulated before the physical set up was installed. The simulation software IMST ART was used. Heating capacity simulations are shown in Figure 3. The simulation was done for the operation point B0/W35 with a frequency of 60Hz and 10K superheat. The simulations were based on the available geometric data from the datasheets provided by the manufacturers, excluding compressor volume and oil volume due to stability issues and insufficient available oil data to calculate accurate absorption of the refrigerant in the oil. The simulation predicted the demonstrator would be able to fulfill the goal of a heating capacity of 5-10kW. The output graph of the heating capacity can be seperated in three sections of different operational modes: underfill operation, saturated/flooded operation, overfill operation. Saturated/flooded operation is comonly the operation point for heat pumps and cooling devices. During underfill operation mode, the condenser outflow does not reach a fully liquid state. With increasing charge less vapor is present at the output and a fluid level is established inside the condenser. Therefore, the width of the saturated/flooded area can be extended by the use of a collector or by increasing the inner volume of the condenser. Figure 4 shows the percentage increase in charge for the simulated components, when comparing underfill operation with saturated/flooded operation. The simulations support the assumption of liquid build up inside the condenser.

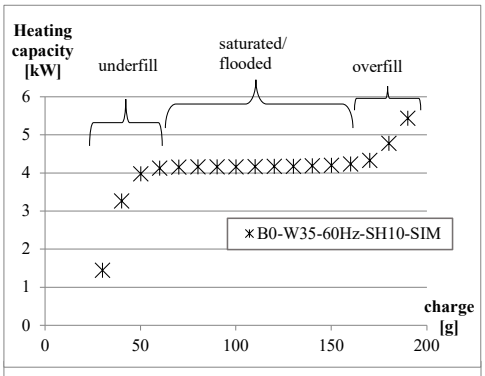


Figure 3: IMST Art results, B0/W35 60Hz SH 10K, system 1

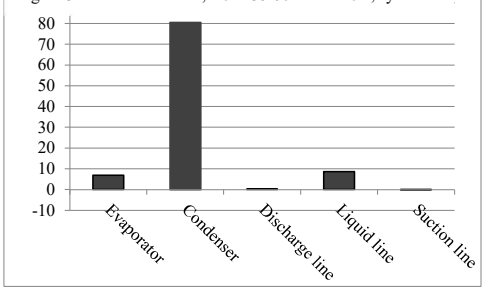


Figure 4: relative percentage charge change for simulated components, comparing underfill operation with saturated/ flooded operation, system 2

Simulation vs. measured values

The results of the simulations and the measurements for the same operation points are compared in Figure 5 and Figure 6. Important to note is the included static 150g charge offset, which was added as a static value to the simulation. Figure 3 and Figure 6 show the same simulation results where the latter includes the static offset, which has a limited number of possible explanations. The following possibilities are considered: inaccurate representation of unused volumes, oil absorption and unknown factors. Nevertheless the liquid accumulation in the condenser mentioned earlier seems to be represented accurately based on the width of saturated/flooded operation. The measurements could not be continued in the over flooded operation state, the refrigerant circuit started to show unstable behavior. The unstable conditions triggered the security shut off of the system. The COP differs significantly as shown in the comparison in Figure 5, however the shape of the curve seems to match roughly. Inefficient behavior, especially of the evaporator, is being considered as the cause for the difference in COP. The prototype is expected to reach the simulated COP values after addressing the known issues like insulation, maldistribution and insufficient EEV. Some of the known issues will be discussed further in the following sections.

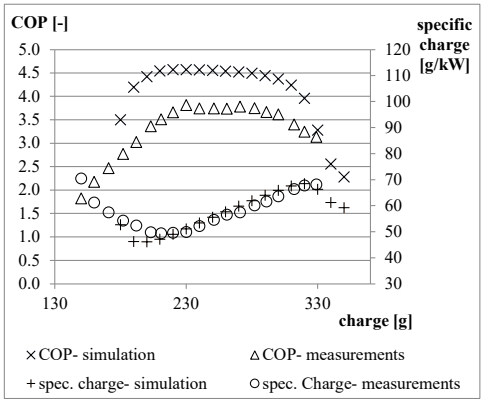


Figure 5: COP and spec. charge, measurement vs. simulation, 150g static offset, in operational point B0/W35 60Hz SH10, system 2

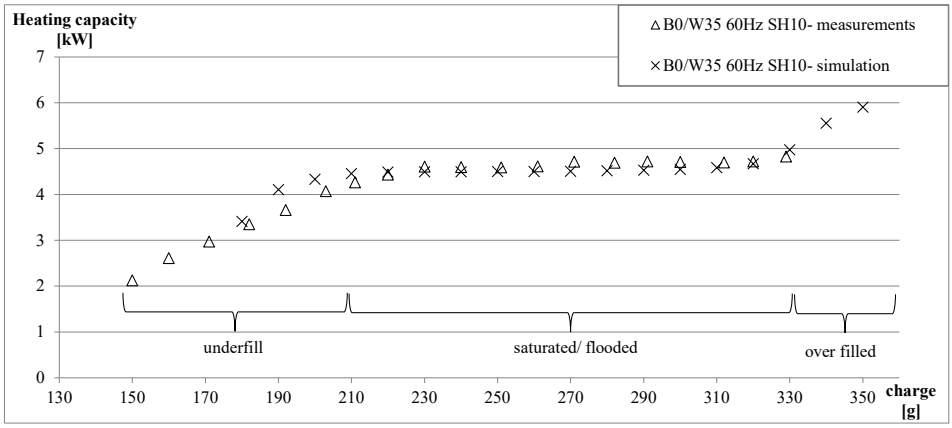


Figure 6: Heating capacity over charge, measurement vs. simulation including a 150g static charge offset, system 2

Measurement results

The simulation showed the three distinct modes of operation. Two of the three distinct modes of operation are also present in the visualization for compressor comparison in Figure 7. The graph also displays the differences between the two systems. For both systems to reach saturated/flooded operation, more charge is needed at operation with lower frequencies. This effect was also present in all measurements. The total range tested was from 30Hz to 120Hz in 10Hz increments. The mass variation measurements shown were not continued with more charge after saturated operation was reached. All measured data points followed the procedure detailed in section Measurement procedure. All measurements shown are done for the temperature pairing of B0/W35. The suction superheat (SSH) has been set to 10K, nevertheless it was not reached for all operation points due to the limited operational window of the EEV. The SSH varied between 5 and 22K. The deviation from 10K is only significant for operation points with the lowest and highest charge. Figure 8 shows the COP values corresponding to the heating capacities of Figure 7. In Figure 7 it can be seen that system 2 reaches a higher heating capacity than system 1 at high frequencies. For lower frequencies the behavior of the two systems is diverse. Until 200g of charge system 1 has a higher heating capacity. Beyond 200g, system 2 has a higher heating capacity. Both systems reach a higher heating capacity with higher charge.

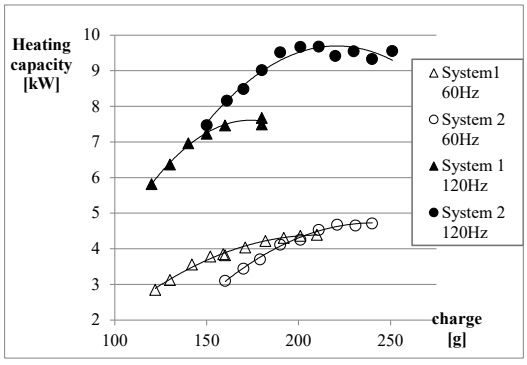


Figure 7: Heating capacity over charge comparing both compressors, all operation points are B0/W35

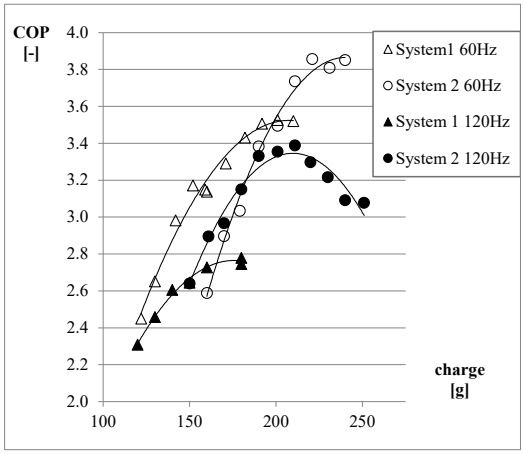


Figure 8: COP over charge graph, comparing both compressors, all operation points are B0/W35

In Figure 8, it can be seen that both systems achieve a higher COP for lower frequencies and both systems achieve their optimal COP in the saturated/flooded operation mode. For lower frequencies, system 1 achieves higher COPs. For higher frequencies it is the other way round.

In order to design an entire heat pump system, stable operation must occur at all possible operating points. Moreover the behavior at all operation points must be well understood in order to give accurate information about performance. For this purpose different parameter variations were measured. In this paper a variation of source temperature and suction superheat will be mentioned.

A reduction of source temperature leads to lower amount of charge necessary to reach saturation/ flooded operation mode. Figure 9 shows the measurement results and the mentioned effect. Possible explanations are different oil absorption and changes in the refrigerant density. The figure also shows the significant impact the source temperature has on the provided heating capacity. Comparing 10°C and -7°C the heating capacity at saturated/flooded operation point drops from 5.9kW to 3.9kW, which corresponds to a difference of 34%. The operation modes underfill and saturated/flooded are once again present in the current visualization.

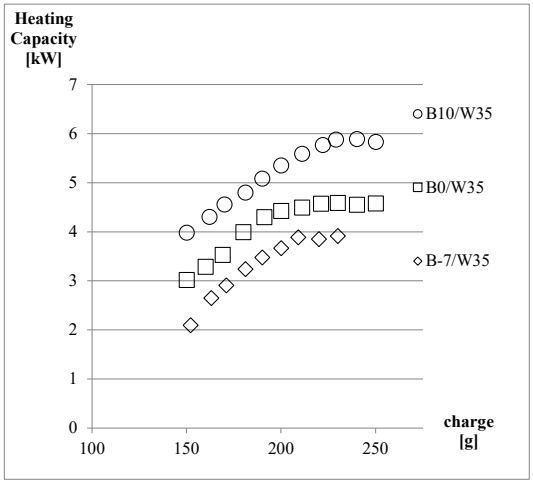


Figure 9: Heating capacity over charge, source temperature variation, system 2, SSH 10K

The second parameter varied is the suction super heat (SSH). Due to the wide range of tested charge, the EEV is not sufficiently sized in either direction to cover all points of operation. Figure 10 shows the operation points in which the EEV was able to perform to the set super heat. Missing points of operation between 140g and 250g did not stick to the set super heat. Figure 10 also illustrates the need for a different means of measuring or indication of performance for EEV's. The superheat does have a significant impact on efficiency. Figure 10 shows the efficiency evolution for the different attempted SSHs. The highest efficiencies around 3.6 were achieved during measurements with an SSH of 10K. Important to note is the different behavior of the COPs during underfill operation. The points for 20K superheat are flat; the points for 10K superheat are steep. Figure 10 illustrates the different operation modes depending on the charge of the system. A possible explanation might be the significantly altered oil sump conditions and therefore different absorption factors. Considering the constant source input temperature and therefore a correlating evaporation temperature, varying superheats have an impact on the suction gas temperature. The varying suction gas temperature has again an impact on the suction gas density and therefore on the mass flow into the compressor. For high superheats the evaporator is used as a gas heater, which lowers the efficiency of the heat exchanger and therefore the entire unit. Any or all of these reasons are possibly part of a high COP optimum at 10K SSH as well as the shifting saturation points. These issues will be addressed in further investigations.

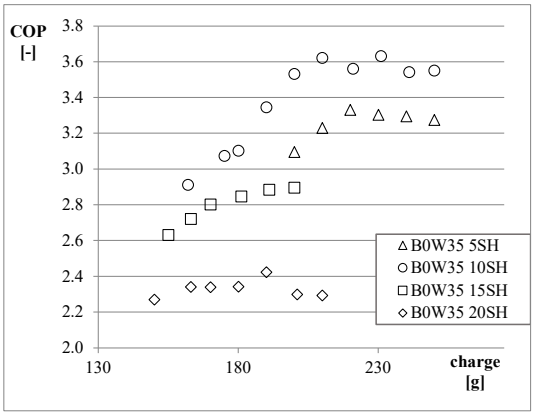


Figure 10: COP over charge, comparing super heat 5K, 10K 15K, 20K, all operation points are B0/W35

Optical analysis

During the measurements, thermography pictures were taken from the condenser as shown in Figure 11 Pictures of the evaporator are shown in
Figure 12. The pictures were taken from a side view onto the heat exchanger plates. Both heat exchangers have 16 plates. The refrigerant flows along the vertical axis of the pictures, running from the inlet to the outlet as marked in Figure 11 and
Figure 12. The thermography pictures were taken with a direct view of the plate heat exchangers with no insulation applied. Therefore the pictures are not taken of a flat surface, thus impairing the resolution and

accuracy of the images. It was attempted to normalize the emissivity, which was set to 1 by applying a thin chalk layer. Based on the relative temperature distribution visible in Figure 11, a maldistribution in the condenser can be assumed. The temperature profile is an u-shaped profile. Perfect distribution would be indicated by a horizontal temperature profile. The evaporator could not be analyzed employing thermography, due to condense water on the surface which washed away the normalizing chalk layer. Due to the low temperatures, ice formed and prevented taking thermography pictures. Therefore, the distribution of the evaporator had to be analyzed by optical information, such as ice formations on its surface. An example of the ice formation is shown in
Figure 12. Only the first few plates show ice formation on the outside of the evaporator. During the testing of the heat pump operation, the last plates seem to be blocked or not charged with any refrigerant which leads to a smaller heat transfer area and a smaller transverse section for the refrigerant to pass through. This results in higher pressure drops and a smaller evaporation temperature to provide the same cooling capacity. Other explanations for the blocked plates could be damaged internal structures. Using water with varying temperatures and surface-mounted temperature sensors, confirmation of no internal damage was obtained.

Due to the maldistribution on both heat exchangers the pressure ratio is higher than necessary. Especially the evaporator showed a very high pressure drop. This results in a higher power consumption of the compressor which again leads to lower COPs of the unit. Both heat exchangers as well as the distribution system of the evaporator will undergo investigation.

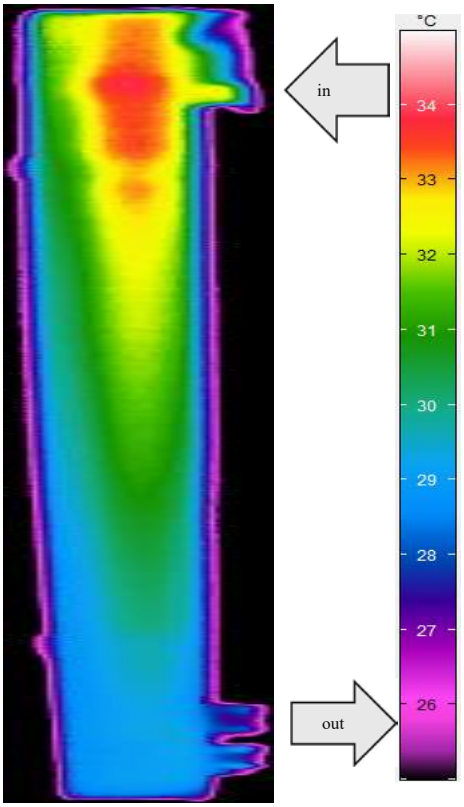


Figure 11: Thermography pictures of the condenser at B0/W35, 60Hz and SH10K, system 1



Figure 12: Ice formation on evaporator at B0/W35, 60Hz and SH10K, system 1

Discussion

The low charge heat pump has successfully shown the potential of charge reduction and the results provide a solid base to accurately define further research areas. Nevertheless a present tradeoff exists between the optimal COP and the optimal specific charge, as shown in Figure 13. The efficiency maximum is located in the low charge regions of saturated/flooded operation whereas the specific charge minimum is located in the slight underfill operation, which is less absolute charge than the COP optimum needs. The main explanation for this is the strong density drop off in the low quality regions compared to the Δh loss. Figure 14 shows a log p – h diagram for a representative optimal compression cycle. The dashed line with connected arrows indicates the expansion after the EEV during underfill operation. The cycle operates non- subcooled before the EEV, which creates the minimum in specific charge, with a trade off in COP.

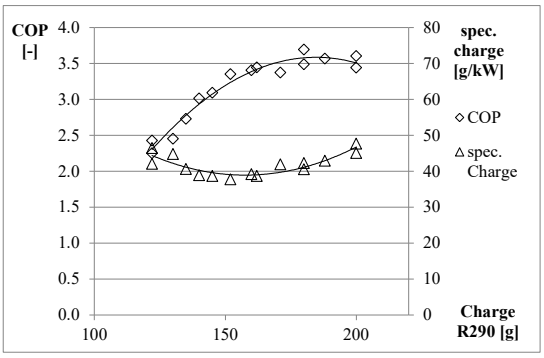


Figure 13: COP and specific charge over total charge, at B0/W35, 60Hz and SSH 10K, system 1

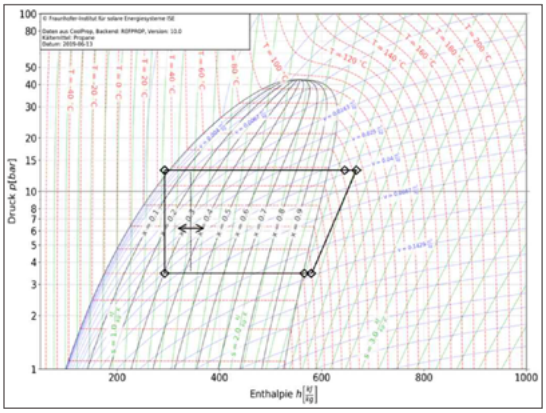


Figure 14 Log p - h diagram, representing the compression cycle

Regarding the charge offset in the simulation results, a few explanations are being considered. The filter dryer material is being tested and evaluated with respect to unknown side effects. Secondly the oil absorption is not yet included in the simulation and this might have a large effect on the offset. Further work will attempt to include the oil absorption in the model to increase the model accuracy.

The work up to this point focused on achieving the targeted heating capacity. The next steps and future focus will be the improvement of COP. The demonstrater is expected to reach competitive COP's within the near future.

Acknowledgment

The authors would like to thank Klas Andersson, Björn Palm and Jose M. Corberan for constructive discussion over the course of the project. Appreciation also belongs to our industry partners for providing the parts for building the demonstrator.

References

[1] ANDERSSON K., GRANRYD E., and PALM B. 2018. *Water to water heat pump minimum charge of propane. DOI*=10.18462/IIR.GL.2018.1264.

[2] Andreas Zottl. *Next Generation heat pump for retrofitting buildings*. *GreenHP Projekt*. AIT Austrian Institute of Technology.

[3] B. Palm, P. Fernando, K. Andersson, P. Lundqvist, O. Samoteeva. DESIGNING A HEAT PUMP FOR MINIMUM CHARGE OF REFRIGERANT.

[4] Colbourne, D. and Suen, K. O. 2014. Characterisation of a leak of flammable refrigerant within equipment enclosures. *11th IIR Gustav Lorentzen Conference on Natural Refrigerants: Natural*

Refrigerants and Environmental Protection, GL 2014, 109–117.

[5] D. Israel Octavio Martínez Galván. 7 de Julio de 2008. *Estudio experimental de las prestaciones de una bomba de calor agua-agua empleando propano como fluido de trabajo*. TESIS DOCTORAL, UNIVERSIDAD POLITÉCNICA DE VALENCIA.

[6] Fernando, P., SAMOTEEVA, O., Palm, B., and Lundqvist, P. 2001. Charge distribution in a 5 kW heat pump using propane as working fluid. *16 Nordiske Kølemøde Og 9*.

[7] Klára Zolcer Skačanová, Anti Gkizelis, Dario Belluomini, Marie Battesti, Thomas Willson. 2018. *IMPACT OF STANDARDS ON HYDROCARBON REFRIGERANTS IN EUROPE. Market research report*.

[8] Official Journal of the European Union. 2014. REGULATION (EU) No 510/2014 OF THE EUROPEAN PARLIAMENT AND OF THE COUNCIL of 16 April 2014 57, L 150.

[9] Omar Abdelaziz, Som Shrestha, Jeffrey Munk, Randall Linkous, William Goetzler, Matthew Guernsey, Theo Kassuga. 2015. *Alternative Refrigerant Evaluation for High-Ambient-Temperature Environments: R-22 and R-410A Alternatives for Mini-Split Air Conditioners*.

[10] Palm, B. 2008. Hydrocarbons as refrigerants in small heat pump and refrigeration systems – A review. *Int. J. Refrig.* 31, 552–563.

[11] Supharuek Konghuayrob, K. K. 2016. Performance Comparison of R32, R410A and R290 Refrigerant in Inverter Heat Pumps Application.

[12] United Nations Foundation. 1987. Montreal Protocol on Substances that Deplete the Ozone Layer.

[13] W. Primal D. Fernando. 2007. *Experimental Investigation of Refrigerant Charge Minimisation of a Small Capacity Heat Pump*. Doctoral Thesis, Royal Institute of Technology, KTH.

[14] Yunho Hwang, Dae-Hyun Jin, Reinhard Radermacher. 2004. COMPARISON OF HYDROCARBON R-290 AND TWO HFC BLENDS R-404A AND R-410A FOR MEDIUM TEMPERATURE REFRIGERATION APPLICATIONS.

13th IEA Heat Pump Conference
April 26-29, 2021 Jeju, Korea

Alternate refrigerants for Heat Pump Water Heater Applications

Kashif Nawaz[a,*], Bo Shen[a], Ahmed Elatar[a], Van Baxter[a], Omar Abdelaziz[a]

[a]Oak Ridge National Laboratory

Abstract

Growing awareness of the potential environmental impacts of conventional refrigerants (CFCs and HFCs) has led to efforts to identify suitable refrigerants for various heat pump applications with minimum environmental impact. This study is focused on the performance evaluation of various hydrocarbon (HC) and hydroflouroolefins (HFO) as drop-in-replacement for R134a for heat pump water heating (HPWH). A component-based model is used to predict the performance. Key performance parameters such as unified energy factor, first hour rating and thermal stratification in the water tank are investigated. Appropriate experiments are conducted to validate the finding from model. Simulation and experimental findings suggest that both alternative refrigerants could provide comparable system performance to that of the baseline system containing R134a. System refrigerant charge and the condenser discharge temperature are established to investigate the potential of hydrocarbon refrigerants to substitute R134a without significant system modifications

Keywords: HFOs, Hydrocarbons, Propane, Hot Water

1. Introduction

Residential and commercial water heating accounts for approximately 10% of all residential and commercial site energy usage in the United States, making it the fourth largest energy end use in homes [1]. On a global scale, in 2015 water heating consumed about 15–20% of residential energy for OEDC and non-OEDC countries as shown in Fig. 1.

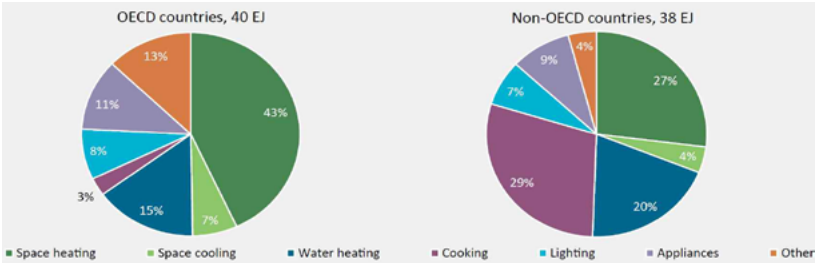


Fig. 1: End uses of residential energy consumed in OECD and non-OECD countries [2]

Despite recent advancements in energy efficiency, most residential water heaters are either conventional natural-gas-fired or electric storage heaters. While such systems are quite simple, they have very low system efficiency. Conversely, under appropriate conditions, electrically driven, vapor compression heat pumps, or

* Corresponding author. Tel.: +1-865-241-0972.
E-mail address: nawazk@ornl.gov

heat pump water heaters (HPWHs), represent a system opportunity with much higher thermal efficiency than conventional electric water heaters, resulting in significant energy savings.

Similar to conventional refrigeration or air-conditioning cycles, HPWHs use a vapor compression refrigeration cycle to transfer heat from a low temperature ambient to a high temperature reservoir, a hot water tank. A key parameter of interest is the working fluid used in the vapor compression cycle. Conventional HPWH systems deployed R-22, which is being phased down due to the high ozone depletion potential (ODP) associated with this fluid. R-134a emerged several years ago as the potential replacement, and most manufacturers have introduced systems with a reasonably higher unified energy factor (UEF) based on this refrigerant. However, concerns about possible global climate change have led to legislative action all around the world to phase down the use of hydrofluorocarbons (HFCs), including R-134a, in a range of heating, ventilation, air conditioning, and refrigeration (HVAC&R) applications, due to their relatively high global warming potential (GWP). Since HPWH systems are essentially heat pumps relying on the vapor compression refrigeration cycle, the technology has been equally affected [3]. Table 1 summarizes some familiar refrigerants with potential impact on the environment.

Table 1: Characteristics and environmental impact of different refrigerants [4]

Refrigerant group	**Refrigerant example**	**ODP**	**GWP_{100}**	**Atmospheric lifetime (years)**	**Flammability**
CFCs	R11, R12, R115	0.6–1	4750–14400	45–1700	Nonflammable
HCFCs	R22, R141b, R124	0.02–0.11	400–1800	1–20	Nonflammable
HFCs	R407C, R32, R134a	0	140–11700	1–300	Nonflammable or mildly flammable
HFOs	R1234yf, R1234ze, R1234yz	0	0–12	-	Mildly flammable
Natural refrigerants	R744, R717, HC (R290, R600, R600a)	< 20	0	Few days	HCs: Highly flammable R717: Flammable R744:Nonflammable

A range of experimental, analytical, and numerical studies have evaluated the performance of HCs for various HVAC&R applications. Broadly, these refrigerant studies used either pure HCs, HC blends, or HC blends mixed with HFCs and hydrofluoroolefins (HFOs). Urchueguia et al. [5] conducted an experimental study of a commercial refrigeration unit using R290 instead of R22. They concluded that the COP increased by 1–3% and the capacity decreased by 13–20% when R290 was used to replace R22. In another similar study. Lee and Su [6] compared the performance of a domestic refrigeration system with R600a to replace R12 and R22. Khalid and Qusay [7] investigated the performance of a residential air-conditioning system under high condensing temperatures using R22, R290, R407C, and R410A. They found that the cooling capacity and the power consumption for R410A were the highest among the four refrigerants and that R290 required less power and refrigerant charge for comparable performance to R22. Song et al. [8] evaluated the performance of an air-conditioning system using R32 and R290 as substitute fluids for R22 and R410A. They found that at the rated conditions, the COP of R32 and R290 was significantly higher than that of R410A and R22. In another similar study, Zhou et al. [9] considered R290 as a potential replacement for R22 in a split air-conditioning unit with different diameters of coiled capillary tubes and various operating conditions. They found that the cooling capacity of the system with R290 was lower than that with R22; however, the energy efficiency ratio was higher.

Multiple studies have focused on using HC mixtures as substitutes for conventional refrigerants. Chao and Teng [10] studied the feasibility of using HC mixtures of R290 and R600a as alternative refrigerants in a small-sized refrigerator originally using R134a. They concluded from a no-load pull-down test that the optimal refrigerant charge for HCs was significantly lower than that for R134a. Rasti et al. [11] used R436A (56% R290 and 44% 600a) as an alternative to R134a in a domestic refrigerator and concluded that the system's on-time ratio was reduced by 13% and that power consumption was reduced by 5.3% as compared to the original system with R134a. Mani and Selladurai [12] conducted an experimental study using R290 and R600a (68% and 32% by mass, respectively) as a drop-in replacement for R12 and R134a and found that the HC mixture had a higher cooling capacity. It is important to note that trans-critical CO_2 HPWH technology also relies on

an environmentally friendly refrigerant, however, issues related to high pressure and variable flow rate pump system along with intermediate heat exchanger makes the technology less feasible compared to HC based HPWH system [13].

2. Analysis strategy

Modelling a HPWH system has been a challenge due to the varying complexities of the subsystems and the integration of the heat pump and water tank. The DOE/ORNL Heat Pump Design Model (HPDM) has been a reliable, public-domain platform for designing, optimizing, and analysing heat pumps of varying complexity for both residential and commercial applications. The platform was used to develop a HPWH system model that included a wrapped tank condenser and accounted for features such as thermal stratification, piston effect, and mixing. The model was calibrated against measured test data and was used to evaluate HPWH performance.

The current study draws upon some component modelling aspects of a previous ORNL HPWH analysis for forced-flow designs [14]. Some of the key HPDM features important to the current study are described here. AHRI 10-coefficient compressor maps have been used to calculate mass flow rate and power consumption as shown by Eqs. (1) and (2), respectively, as functions of evaporation and condensation temperatures [15].

$$\dot{m} = \alpha_1 + \alpha_2 T_{evap} + \alpha_3 T_{cond} + \alpha_4 T_{evap}^2 + \alpha_5 T_{evap} T_{cond} + \alpha_6 T_{cond}^2 + \alpha_7 T_{evap}^3 + \alpha_8 T_{evap}^2 T_{cond} + \alpha_9 T_{cond}^2 T_{evap} + \alpha_{10} T_{cond}^3 \quad (1)$$

$$\dot{W} = \beta_1 + \beta_2 T_{evap} + \beta_3 T_{cond} + \beta_4 T_{evap}^2 + \beta_5 T_{evap} T_{cond} + \beta_6 T_{cond}^2 + \beta_7 T_{evap}^3 + \beta_8 T_{evap}^2 T_{cond} + \beta_9 T_{cond}^2 T_{evap} + \beta_{10} T_{cond}^3 \quad (2)$$

where T_{evap} and T_{cond} are the compressor suction and discharge saturation temperatures, and α and β are the compressor map coefficients for mass flow rate and power respectively. $\alpha_{1,2,...,10}$ and $\beta_{1,2,...,10}$ are the mass flow rate and power coefficients respectively for compressor.

The HPDM uses a segment-to-segment modelling approach, which divides a single tube into numerous mini segments. Each tube segment has individual air-side and refrigerant-side entering states and considers possible phase transition; the ε-NTU approach has been used for heat transfer calculations within each segment. In addition to the functionalities of the segment-to-segment fin-tube condenser model, the evaporator model can simulate the dehumidification process. A wrapped tank condenser model was developed specifically for this investigation, using a segment-to-segment modelling approach. The flow-pattern-dependent heat transfer correlation published by Thome et al. [16] was used to calculate the condenser's two-phase heat transfer coefficient. The tank model includes the thermal conductivity of the thermal paste (used to ensure good contact between the wrapped tank condenser tubes and the tank wall) and the insulation covering the tank. Thus, heat loss from the tank was captured for the full time of the operation. The transient tank model accounts for one-dimensional water temperature stratification due to natural convention. Fig. 2 shows an example case (i.e., mixing caused by advection during water draw) for the CFD model used for the analysis. A residential HPWH was considered as the baseline water-heating unit for performance evaluation and model calibration as shown in Fig 3. The performance of this unit has been evaluated previously at ORNL [17].

3. Results and discussion

The US Department of Energy (DOE) initiated a rulemaking to consider amendments to its old test procedures for covered residential and commercial water heaters, as recommended in the American Energy Manufacturing and Technical Corrections Act. Based on the extensive testing, a new performance evaluation procedure was defined. In the new procedure, the tank water temperature set point is 125°F, and the test conditions for inlet water and ambient air temperature are prescribed as 58°F and 67.5°F (35–45% relative humidity), respectively. Key performance metrics used to evaluate and compare the performance of water heaters (WHs), including HPWHs, are listed below.

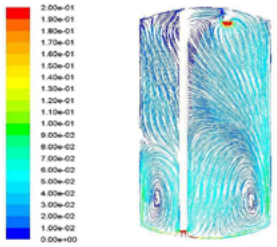


Fig. 2. Streamline for water flow in the tank during draw (m/s).

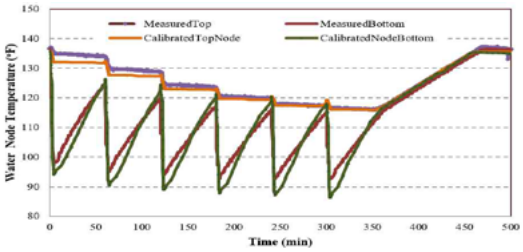


Fig. 3. Temperature stratification variation (measured vs. predicted).

First Hour Rating. FHR is a measure of the available hot water capacity of the WH (in gallons). Per the new DOE test method, hot water (125±15°F) is drawn from the tank as long as the temperature is more than 67±2°F higher than the entering water temperature. Once the temperature drops below the prescribed limit, the supply is stopped until the set point of 125±1.5°F is met again. Following the procedure, the total water drawn from the tank during 1 hour indicates the total capacity of the heat pump and electric resistance heaters.

Unified Energy Factor. UEF is a measure of system efficiency. It is defined as the ratio of the total heat delivered from the system (by heating the water) to the total power required to operate the system. Equation (3) describes the UEF.

$$UEF = \sum_{k=1}^{n} \frac{M_k c_p (T_s - T_i)}{W_i} \quad (3)$$

In Eq. (3) k represents the individual hot water draw, considering that multiple draws are required by the test procedure and that n (total number of draws) can vary according to the method proposed by DOE (small, medium, and large usage pattern), and M is the total mass drawn for each respective draw. T_s, T_i, and W_i represent the supply water temperature, inlet water temperature, and total energy consumed by the unit (power times unit run time), respectively. The previous EF test procedure used a single water draw pattern—six equal water draws of ~10.7 gallons each spaced equally during the first 5 hours of the EF test—and applied it to all WHs (including HPWHs) with a storage tank. In contrast, the new method uses the measured FHR value to define the hot water draw pattern. The FHR analysis concluded that under all parametric conditions, the appropriate draw pattern for the HPWH unit being analysed was for medium usage (FHR varied between 57 and 64 gallons).

4. Parameters for performance evaluation

To optimize system performance, a parametric study was conducted to investigate the impacts of the condenser wrap pattern and the heat loss from the water storage tank. Two representative insulation effectiveness values were considered for the heat loss from the tank, 90% and 95%. The effectiveness is 90% when the tank loses 10% of the energy input to the water. The effectiveness is 95% when half that amount of energy is lost through the tank wall and insulation material to the environment. This essentially accounts for two values for the resistance to heat loss. Similarly, to explore the impact of condenser configuration, two different wrap patterns were considered for analysis as shown in Fig. 4. The counterflow pattern represents the flow of the refrigerant entering from the top section of the tank and moving downwards. In the parallel-counterflow configuration, the refrigerant enters close to the middle of the tank, moves upwards, and then comes back to the middle section to continue downwards (identical to the pattern used by the prototype systems evaluated in the prior experimental study). In both cases, the refrigerant enters the system as superheated vapor, goes through a phase-change process, and exits as a subcooled liquid. Table 2 summarizes the cases considered in current study.

5. Results and discussion

FHR is a direct indication of system capacity. A larger FHR indicates a superior system capacity. It can be observed from Fig. 5 that R290 consistently shows a comparable FHR when compared with baseline R134a values, whereas R600a has an average FHR, close to 57 gallons (lower than R134a). Although the system's design parameters can have some secondary impact, the FHR is a direct indication of the volumetric capacity of the refrigerant. The low value for volumetric capacity for R600a can explain a relatively lower FHR.

Table 2. Simulation cases for parametric analysis

Case number	Wrap pattern	Effectiveness (%)
1	Parallel-counterflow	90
2	Parallel-counterflow	95
3	Counterflow	90
4	Counterflow	95

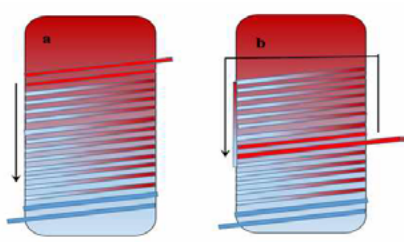


Fig. 4. Condenser wrap configurations: (a) counterflow, (b) parallel-counterflow.

Unified energy factor (UEF) is a direct measure of system efficiency. A larger UEF denotes a better performance. Fig. 6 presents the 24-hour UEF for different refrigerants as the design parameters vary. Heat loss from the tank is seen as a dominant factor, and UEF is higher for the cases with 95% tank insulation effectiveness. On the other hand, the condenser wrap pattern does not have any significant impact, as observed from the values presented in Fig. 6. Among the three refrigerants, R600a has the lowest UEF while for R134a and R290, the values are comparable.

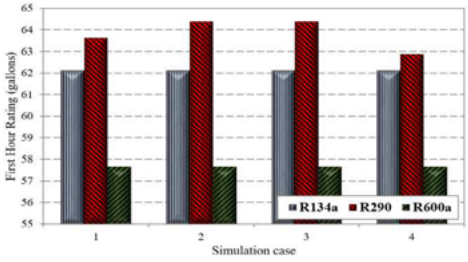


Fig. 5. First hour rating for different refrigerants

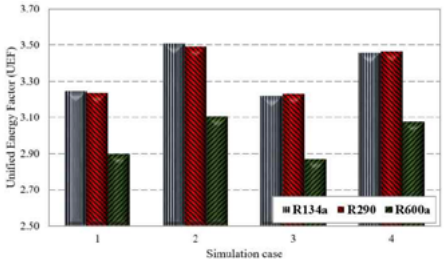


Fig. 6. Unified energy factor for different refrigerants

COP is the typical parameter used to describe the efficiency of a heat pump. It is important to recognize that COP, unlike UEF, represents the efficiency of the heat pump only and cannot be used to indicate the performance of the whole system. However, this is still an important parameter to consider as it shows the stand-alone performance of the heat pump. Fig. 7 presents COP for the different design options. Overall, COP is comparable for all design options, with slightly better performance for parallel-counterflow configuration and 95% tank insulation effectiveness. When the individual performance of different refrigerants is compared for a specific design option, COP is clearly lowest for R600a, as was the case for UEF.

An interesting relationship between insulation effectiveness and supply water temperature is presented in Fig. 8. A higher supply water temperature results in 90% thermal insulation (cases 1 and 3) because of the control mechanism to turn the heat pump on (T = 120°F) and off (T = 125°F), which ultimately lowers the system's UEF. The heat lost with the poorer thermal insulation causes the heat pump's run time to increase, leading to a higher average supply temperature.

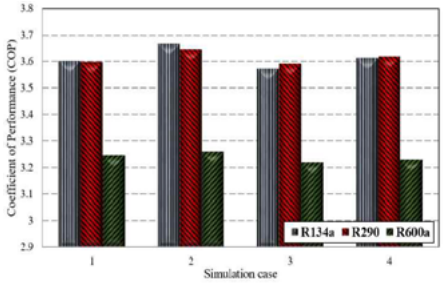


Fig. 7. Coefficient of performance

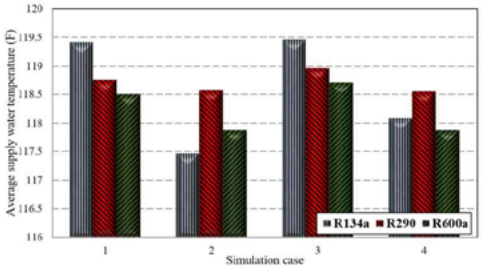


Fig. 8. Average supply water temperature

Total system charge is a critical parameter that has been the focus of continuous effort toward minimization, not only because refrigerants are expensive but also because class A3 refrigerants present serious safety concerns for any HVAC&R application. Fig. 9 compares total system charge in the evaporator and the condenser. Even though there is no significant difference in charge for various design options, it is interesting and encouraging that the charge required for both R290 and R600a is less than half that of the baseline R134a. This can be explained in terms of the lower molecular weights for the R290 and R600a refrigerants which are almost half that for R134a. This shows the potential of HC refrigerants to substitute for R134a and indicates that further development may allow an even smaller charge of flammable refrigerant to be successfully substituted to provide similar performance, thereby reducing safety concerns.

Fig. 10 presents the maximum condenser saturation temperature drop. For better heat transfer performance, a smaller temperature drop, which is directly related to the pressure drop through the condenser, is desired. As shown in Fig. 10, both design options with the parallel-counterflow wrap pattern result in a lower condenser saturation temperature drop, while for the counterflow arrangement, it is higher. The higher condenser temperature drop can be related to the relative amount of condenser containing refrigerant vapor. Since for the counterflow arrangement there is a slower transfer of heat in the top part of the water tank, which contains relatively hot water (due to stratification), a longer heat exchanger length fraction in the vapor (higher pressure drop) region is required. In contrast, for a parallel-counterflow arrangement, vapor refrigerant entering close to the middle of the tank interacts with relatively cold water, ensuring a higher heat transfer rate and shorter vapor region. Analysis of the individual performance of the refrigerants shows that R290 has the lowest values. For counterflow arrangement, both R-134a and R600a show comparable performance; however, for parallel-counterflow configuration, R600a has a higher temperature drop. Since the saturation temperature drop directly depends on the saturation pressure drop, a condenser tube with relatively larger diameter can be helpful; however, this leads to a higher refrigerant charge, which is undesirable for the current application. For a drop-in-replacement study, it is desirable to have a comparable and preferably lower compressor discharge temperature for alternative refrigerants, as this ensures that a similar compressor with existing lubrication can be safely used. The issue is critical due to the flammable nature of refrigerants as well. Fig. 11 compares the compressor discharge temperature for various design options and indicates that maximum compressor discharge temperature is about 10°F lower for R600a and 1–2°F lower for R290 compared to the baseline refrigerant (R134a). This suggests that with respect to oil temperatures for both refrigerants, a safe substitution is possible without significant modification. However, since the volumetric capacity of R600a is lower, a relatively larger compressor is required for comparable performance (i.e., COP and UEF).

Thermal stratification in the storage tank has been studied extensively, and recent findings have shown that higher stratification can lead to improved UEF, a classical feature of CO_2-based HPWHs (Nawaz et al., 2017), since this can provide better heat transfer from the condenser tube to the water. Fig. 12 shows the relative water stratification for different refrigerants and design selections where the difference between the supply water temperature (exiting the water tank) and average tank water temperature is presented. There is no consistent trend when different design selections are compared, though cases 1 and 3 with 90% insulation effectiveness show slightly lower temperature differences. However, the relative water temperature difference is lowest for R600a on average, which is consistent with previous discussion regarding lower UEF and higher heat pump run time for this refrigerant.

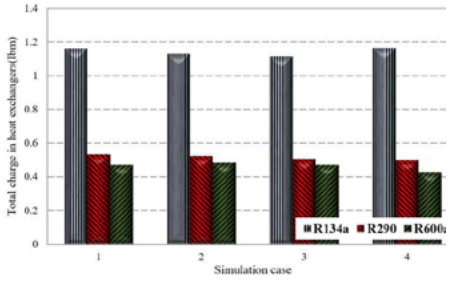


Fig. 9. Total charge in condenser and evaporator

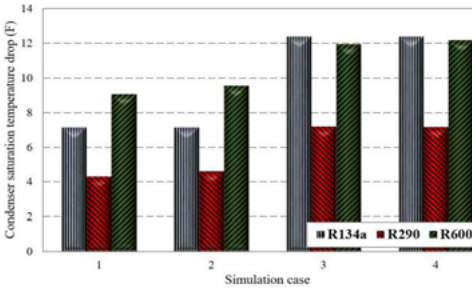


Fig. 10. Maximum condenser saturation temperature drop

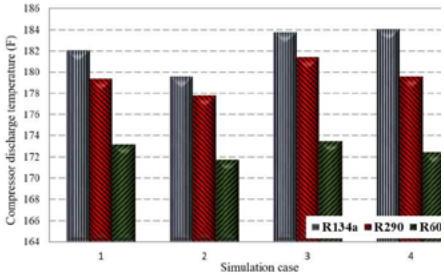


Fig. 11. Maximum compressor discharge temperature

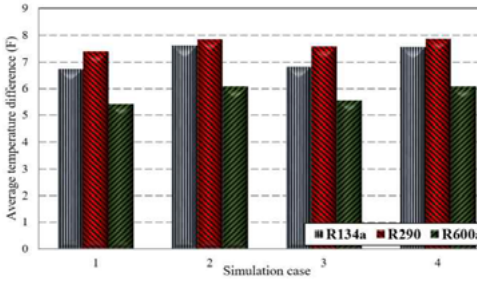


Fig. 12. Average difference between supply and tank bulk temperature

6. Conclusions

A simulation study of a wrapped-tank heat pump water heater has evaluated the feasibility of using R290 (propane) and R600a (isobutane) as natural refrigerants to substitute for R-134a. A model based on the DOE/ORNL Heat Pump Design Model was developed to account for both the heat pump and water tank designs, and it was used to study the impact of various design parameters. It has been found that both R134a and R290 showed comparable FHR and UEF. A relatively lower performance for R600a can be attributed to its relatively lower volumetric capacity, which can be resolved by increasing compressor size. The compressor discharge temperature was lower for R290 and R600a than it was for R134a. This suggests that compressors of similar design can be used with these refrigerants and that existing compressor lubricants are feasible. Total system charge for R290 and R600a was much smaller compared to the baseline system (at least 50% reduction). Considering the potential flammability of replacement refrigerants, which are safety class A3, the substitution of R290 or R600a would reduce safety concerns because a relatively smaller amount would be needed to operate the system. Considering the various performance parameters, R290 showed better prospects as a drop-in replacement for R134a, while R600a required a relatively larger compressor size to meet the baseline performance.

Acknowledgements

This research was supported by the DOE Office of Energy Efficiency and Renewable Energy, Building Technologies Office. The authors thank Mr. Antonio Bouza, program manager for the Building Technologies Office. This manuscript has been authored by UT-Battelle, LLC, under contract DE-AC05-00OR22725 with the US Department of Energy (DOE). The US government retains and the publisher, by accepting the article for publication, acknowledges that the US government retains a nonexclusive, paid-up, irrevocable, worldwide license to publish or reproduce the published form of this manuscript, or allow others to do so, for US government purposes. DOE will provide public access to these results of federally sponsored research in accordance with the DOE Public Access Plan (http://energy.gov/downloads/doe-public-access-plan).

Nomenclature

AHRI	Air-Conditioning, Heating, and Refrigeration Institute		
CFC	chlorofluorocarbon	HC	hydrocarbon
CFD	computational fluid dynamics	HFC	hydrofluorocarbon
COP	coefficient of performance	HFO	hydrofluoroolefin
EF	energy factor	HPDM	Heat Pump Design Model
FHR	first hour rating	HPWH	heat pump water heater
GWP	global warming potential		
HVAC&R	heating, ventilation, air conditioning, and refrigeration		
ODP	ozone depletion potential		
OEDC	Organization for Economic Cooperation and Development		
UEF	unified energy factor		
WH	water heater		

References

[1] Building Technologies Office 2016 Peer Review
[2] International Energy Agency, 2016 (https://www.iea.org/)
[3] McLinden, M. O., Brown, J. S., Brignoli, R., Kazakov, A. F., Domanski, P. A., 2017, Limited Options for Low-Global-Warming-Potential Refrigerants, Nature Communications, 8-14476.
[4] ANSI/ASHRAE STANDARD 34, 2013. Designation and Safety Classification of Refrigerants.
[5] Urchueguıa, J. F., Corberan, J. M., Gonzalvez, J., Dıaz, J. M., 2004. Experimental characterization of a commercial-size scroll and reciprocating compressor working with R22 and propane (R290) as refrigerant. Ecolibrium, 23–5.
[6] Lee, Y. S., Su, C. C., 2002. Experimental studies of isobutane (R600a) as the refrigerant in domestic refrigeration system, Applied Thermal Engineering, 22, 507–19.
[7] Khalid, A. J., Qusay, R. A., 2014. Experimental assessment of residential split type air-conditioning systems using alternative refrigerants to R-22 at high ambient temperatures. Energy Conversion Management, 86:496–506.
[8] Song, C., Shuangfeng, W., Zhongmin, L., 2014, Cycle performance of alternative refrigerants for domestic air-conditioning system based on a small finned tube heat exchanger, Applied Thermal Engineering, 64, 83–92.
[9] Zhou, G., Zhang. Y., Yang, Y., Wang, X., 2010. Numerical model for matching of coiled adiabatic capillary tubes in a split air conditioner using HCFC22 and HC290, Applied Thermal Engineering, 30, 1477–87.
[10] Chao, Y. C., Teng, T. P., 2014. Retrofit assessment of refrigerator using hydrocarbon refrigerants. Applied Thermal Energy, 66, 507–18.
[11] Rasti, M., Hatamipour, M. S., Aghamiri, S. F., Tavakoli, M., 2012. Enhancement of domestic refrigerator's energy efficiency index using a hydrocarbon mixture refrigerant, Measurement, 45,1807–13.
[12] Mani, K., Selladurai, V., 2008. Experimental analysis of a new refrigerant mixture as drop in replacement for CFC12 and HFC134a, International Journal of Thermal Science, 47,1490–5.
[13] Nawaz, K., Shen, B., Elatar, A., Baxter, V. D., Abdelaziz, O., Performance Optimization of CO2 HPWH System, International Journal of Refrigeration, 2017, 85, 213-218.
[14] Baxter, V. D., Murphy, R. W., Rice, C. K., Shen, B., Gao, Z., 2011. Analysis of Highly Efficient Electric Residential Heat Pump Water Heaters for Cold Climates, ORNL/TM-2011/278.
[15] ANSI/AHRI Standard 540-99, 2010, “Positive Displacement Refrigerant Compressors and Compressor Units”, Air Conditioning and Refrigeration Institute, Arlington, VA.
[16] Thome J. R., J. El Hajal and A. Cavallini, 2003, “Condensation in horizontal tubes, part 2: new heat transfer model based on flow regimes”, International Journal of Heat and Mass Transfer, 46(18), Pages 3365-3387.
[17] Murphy, R. W., V. D. Baxter, E. A. Vineyard, and R. L. Linkous, 2011, “Drop-in Evaluation of Refrigerant R1234yf in a Residential Integral Heat Pump Water Heater,” Proceedings of the 10th International Energy Agency Heat Pump Conference.

13th IEA Heat Pump Conference
April 26-29, 2021 Jeju, Korea

Semi-open absorption water heater: experimental results

Kyle R. Gluesenkamp[a]*, Navin Kumar[a], Ahmad Abu-Heiba[a], Viral Patel[a], Zhiyao Yang[a,c], Rohit Bhagwat[b], Sidharth Sanadhya[b], Michael Schmid[b], Richard Rode[b], Basil Anabtawi[b], and Saeed Moghaddam[b]

[a]Oak Ridge National Laboratory, USA
[b]University of Florida, USA
[c]Purdue University, USA

Abstract

Absorption heat pumps are traditionally closed systems, while adsorption dehumidifiers are traditionally open systems. Recently a semi-open heat pump and dehumidifier has been proposed, in which ambient atmospheric humidity is absorbed into a solution, desorbed back to vapor in a desorber, condensed to liquid in a condenser, and released back to the ambient as a liquid. In this work, a semi-open sorption heat pump water heater was evaluated under the standard 24-hour duration test procedure used to evaluate water heaters in the US, the uniform energy factor (UEF) test. The results demonstrated that a cycle COP of 1.22 was achieved at air conditions of 19.7°C (67.5°F) and 50% relative humidity. Over the 24-hour period, the heat pump ran twice, with an average heating capacity of 0.825 kW, and an average cycle heating COP of 1.22. The standard load profile withdrew 209.6 L (55.4 gallons) from a 173.8 L (45.9 gallons) storage tank. The water supplied to the tank was 14.4°C (58°F) and the water withdrawn from the tank was always hotter than 45.3°C (113.5°F).

© HPC2020.
Selection and/or peer-review under responsibility of the organizers of the 13th IEA Heat Pump Conference 2020.

Keywords: semi-open; absorption; ionic liquid; heat pump water heater

1. Introduction

Traditionally, sorption heat pump systems are either: closed (for chilling and heat pumping) or open (for dehumidification). Recent work [1, 2] has explored the possibility of semi-open systems, which utilize ambient humidity as a working fluid of the cycle. This paper presents the performance evaluation of a third generation of semi-open membrane-based sorption heat pump water heater and dehumidifier.

2. Experimental system

2.1. Process and instrumentation diagram

Figure 1 **오류! 참조 원본을 찾을 수 없습니다.** shows a schematic of the experimental heat pump and its coupling to a 46-gallon storage water tank through the water-water heat exchanger. The heat pump has four flow loops: heating oil (state points T1 through T3), solution (state points T5 through T9), process water (state points T10 through T15), and moist air (state points 21 and 22). An additional water loop (state points T16 and T17) exists to isolate the low hydrostatic pressure of the process water loop from the high tap pressure of the

* Corresponding author. Tel.: +1-865-241-2952.
E-mail address: gluesenkampk@ornl.gov

tank. A final water flow path (state points T19 and T20) is the cold tap water source (T19) and hot domestic water supply (T20).

Three fluid loops are present in the absorber: air, process water, and solution. In the absorber, ambient air interfaces with the solution through a membrane that is permeable to water vapor: the solution absorbs water vapor from the air, the temperature of the solution rises, and the solution water content increases. The process water stream flows in the absorber in a counterflow arrangement to the solution, removing heat from the solution. The flow rate of the process water is controlled by adjusting a needle valve downstream of the process water circulation pump. The weak solution leaves the absorber (T7) and is preheated in the SOHX (T8 to T9) before it enters the desorber at T9.

Three fluid loops are present in the desorber-condenser: oil, process water, and solution (condensate may be considered a fourth fluid). In the desorber, the weak solution is heated to desorb some of its water content and increase its concentration. The temperature in the desorber is controlled via the inlet oil temperature (T1) provided by a circulator-heater. Water vapor leaves the solution at high temperature and enters the condenser. The strong solution leaves the desorber at high temperature (T4) and enters the SWHX where it transfers heat to the process water leaving the absorber. The flow rate of the solution is controlled through adjusting the speed of the solution pump. The process water leaves the SWHX (T12) and enters the condenser where it gains heat from the water vapor and condenses it. The process water then leaves the condenser (T13) and enters the water-water heat exchanger (T14) where it heats water that is recirculated from the bottom to the top of the storage tank (T17 to T16). Recirculating from the bottom to the top maintains stratification in the tank to maintain the lowest possible inlet water temperature to the absorber.

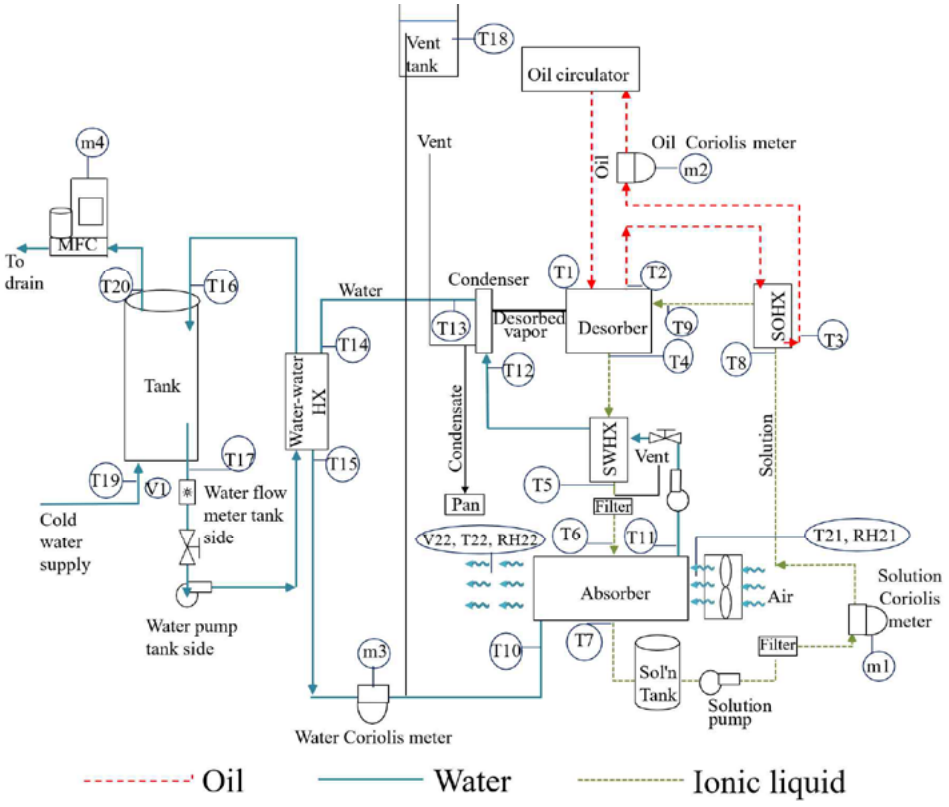


Figure 1: Process and instrumentation diagram of the instrumented experimental test setup.

Cold domestic water flowed to the bottom of the storage tank and hot water was drawn from the top, in a stratified configuration. The inlet temperature of the domestic water was controlled by a water temperature

conditioning unit to within ±0.5°C of the setpoint. The flow rate of the domestic water was controlled through a flow controller with a remotely adjustable setpoint. The water storage tank was outfitted with 16 thermocouples distributed along with the height of the tank. Measurement instruments and sensors and their uncertainties are summarized in Table 1 **오류! 참조 원본을 찾을 수 없습니다.**.

Table 1: Measurements and their systematic uncertainties.

Measured parameter	Instrument/Sensor	Systematic uncertainty
Temperature	T-Type Thermocouple	0.5°C
Relative humidity	Capacitive humidity sensor	1.5%
Airflow rate	Differential pressure	2%
Domestic water flow rate	Mass flow controller	0.224 lpm
Oil flow rate	Coriolis flowmeter	0.5%
Solution flow rate	Coriolis flow meter	0.5%
Process water flow rate	Coriolis flowmeter	0.5%

2.2. Absorber

A schematic and photograph of the absorber are shown in Figure 2. The absorber is of special importance in this system due to its unique design requirements and novel design. The absorber was fabricated with polycarbonate and hydrophobic porous polymeric membranes sheets. Two sheets of polycarbonate with machined channels for water flow were thermally-bonded and chemically treated to make the surface hydrophilic. Following the thermal bonding of internal water channels, the polymeric membrane sheets were thermally-bonded to the fins machined on the reverse side of the polycarbonate sheets. The fins provided structural support to the membranes and assisted in ionic solution flow distribution. The solution and water manifolds were attached to the absorber with adhesive. The air flows across the membranes through a 12mm gap between the membrane panels.

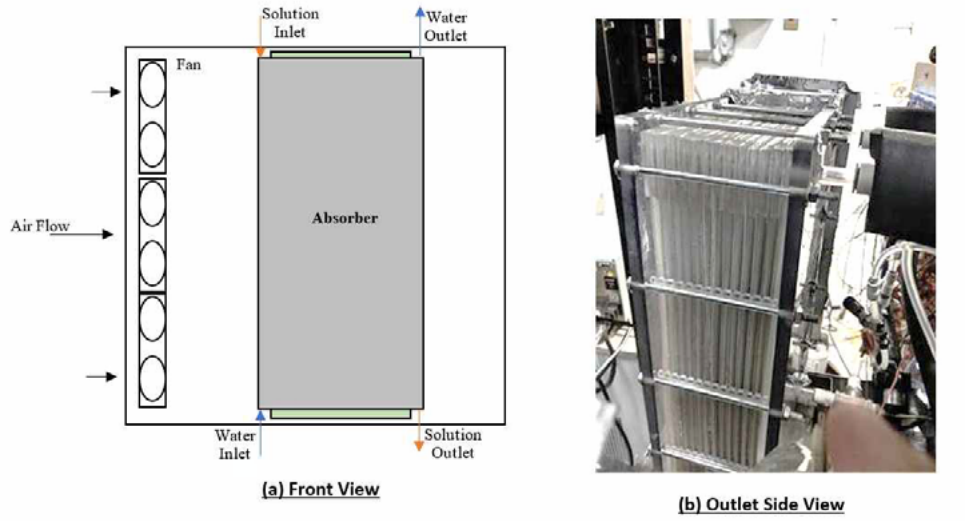


Figure 2: (a) Front view schematic of the absorber. (b) Outlet side view photograph of the absorber.

Table 2 summarizes the difference between the absorbers used in previous experimental studies by Chugh et al. [1], [2]. The table shows that the absorber in this work has approximately double the active absorber mass transfer area, with comparatively less increase in component volume.

Table 2: Comparison of the absorber used in the previous generation and this study.

Absorber	Generation 1 [1]	Generation 2 [2]	This study
Number of panels	4	7	13
Active air surface area [m^2]	0.42	0.92	1.89
Active plate volume [m^3]	0.0084	0.0080	0.0119
Active surface area/volume ratio [m^{-1}]	50	115	159
Material used	Waterside: Metal (Cu/SS frame)	All polymer (polycarbonate)	All polymer (polycarbonate)
	Solution-water interface: stainless steel sheet	Thermal and adhesive bonding, CNC machining	Thermal and adhesive bonding, CNC machining
	Solution-side fins: 1.5 mm tall (additively manufactured polymer)	Solution-side fins: 1 mm tall	Solution-side fins: 0.6 mm
Membrane pore size	1 µm	1 µm	1 µm
	Not bonded on the fins	Thermally bonded on fins	Thermally bonded on fins

2.3. Desorber-Condenser Module

The integrated desorber-condenser module, as shown in Figure 3, used a superhydrophobic membrane to separate the desorber and condenser within one housing. A structure of surface features, similar to what was used in the the absorber, was used to enhance the desorption rate, as reported in previous studies [2], [3]. The desorbing and condensing sides were bolted together with gasket material. The desorber was leak tested with Nitrogen gas up to 5 PSI.

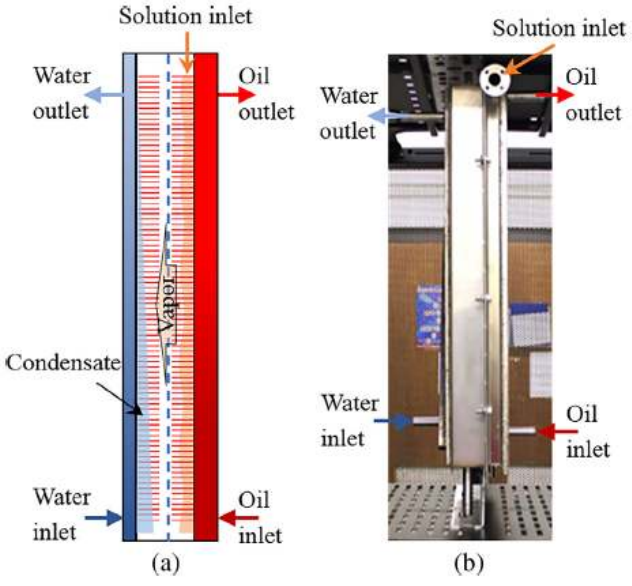


Figure 3: (a) Cross sectional schematic of the desorber-condenser component, with membrane shown as a dotted blue line. (b) Outlet side view photograph of the desorber-condenser. Reprinted with permission from "Experimental evaluation of a semi-open membrane-based absorption heat pump system utilizing ionic liquids," by D.Chugh et al., 2019, Appl. Energy, 239, p.921. *[2].*

2.4. Heat Exchangers

Two counter flow heat exchangers were used in the heat pump section for heating of water and solution. One heat exchanger transfers heat from the solution to water after desorption, and the second one transfers heat from the oil to the solution before desorption. Hot silicone oil was used as the source of energy input. The temperature of the oil was controlled using a temperature-controlled circulating bath.

The heat pump was integrated with a nominal 50-gallon water heater storage tank. The domestic water into the water heater storage tank was conditioned with a laboratory water supply system to deliver water at 58°F ± 2°F (14.4°C ± 1.1°C).

2.5. Data reduction

The COP of the system was calculated using equation (1). The Cp_{oil} was measured using a differential scanning calorimeter (DSC) as 1.8 $kJ^{1}kg^{-1}K^{-1}$ in the relevant temperature range.

$$COP = \frac{Q_{water}}{Q_{oil}} = \frac{\dot{m}_{water} * Cp_{water} * \left(T_{water,cond\ out} - T_{water,abs\ in}\right)}{\dot{m}_{oil} * Cp_{oil} * \left(T_{oil,desorber\ in} - T_{oil,SHX\ out}\right)} \quad (1)$$

3. Test operation

The test procedure for the 24-hour uniform energy factor test is outlined in the Electronic Code of Federal Regulations (e-CFR, [4]). The test procedure outlines all test conditions, sensor requirements and supply/outlet water temperature requirements. When all installation requirements have been met, the first-hour rating test is performed. This was done for the water heater used in the current work and the results showed that a medium usage draw pattern was required. The details of the medium usage draw pattern are given in Table 3.

Table 3: Medium usage draw pattern [4].

Draw No.	Time during test [hh:mm]	Volume [gallons (liters)]	Flow rate [GPM (L/min)]
1	0:00	15.0 (56.8)	1.7 (6.4)
2	0:30	2.0 (7.6)	1 (3.8)
3	1:40	9.0 (34.1)	1.7 (6.4)
4	10:30	9.0 (34.1)	1.7 (6.4)
5	11:30	5.0 (18.9)	1.7 (6.4)
6	12:00	1.0 (3.8)	1 (3.8)
7	12:45	1.0 (3.8)	1 (3.8)
8	12:50	1.0 (3.8)	1 (3.8)
9	16:00	1.0 (3.8)	1 (3.8)
10	16:15	2.0 (7.6)	1 (3.8)
11	16:45	2.0 (7.6)	1.7 (6.4)
12	17:00	7.0 (26.5)	1.7 (6.4)

To initiate the 24-hour simulated-use test, the water in the water heater tank was first conditioned as outlined in the test procedure. The test was initiated by withdrawing the volume of water specified in Table 3 for the first draw. Among other measurements, the average storage tank temperature and ambient temperature were recorded for the entirety of the test. Additional draws were initiated at the required elapsed times as given in Table 3 **오류! 참조 원본을 찾을 수 없습니다.**. The maximum allowable deviation from the specified volume of water removed for any single draw taken at a nominal flow rate of 1 GPM or 1.7 GPM was ±0.1 gallons (±0.4 liters). The mean of the hot water discharge temperature and the cold-water inlet temperature for each draw were recorded, along with the net volume of water removed. The tank, inlet/outlet, and ambient temperatures, water volume withdrawn, and total energy consumption of the heat pump were all used to determine the UEF.

4. Results

4.1. COP and Capacity

The COP of the system during heat pump operation is shown in Figure 4. The heat pump involves coupled heat and mass transfer phenomena in the absorber with three different fluids (air, ionic solution, and water), where the heat pump recovers the latent heat from the humid ambient environment. In this study, the ambient air was conditioned at the UEF test condition requirement of 19.7°C/ 50%RH. The heat pump was operated for a total of 6 hours and 18 minutes during 24 hours of UEF testing. The runtime of the heat pump was divided into two segments with a 6 hour non-operational period between them. The average heating and dehumidification COP during the first four-hour segment of heat pump operation were 1.18 ± 0.04 and 0.36 ± 0.03, respectively. The average and standard deviation in heating COP and dehumidification COP during the second (2 hours and 18 minutes) segment were 1.34 ± 0.14 and 0.45 ± 0.09. These standard deviations represent fluctuations in the value, and is not an instrumentation uncertainty. During the operation of the heat pump, the average water heating thermal power was 853 ± 92 W for the first operation segment and 1002 ± 270 W for the seccond. The increase in COP during the second segment could be attributed to higher solution and water flowrate into the absorber, as summarized in Table 4.

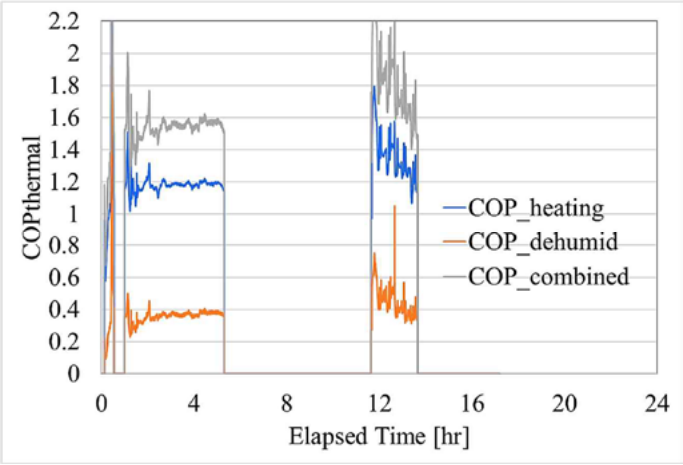


Figure 4: The thermal COP of the system during the operation of the heat-pump.

4.2. Absorber

Table 4 summarizes the absorber performance and its inlet solution and water conditions. The average concentration of the solution at the inlet and outlet of the absorber was around 88% and 84%, respectively. The concentration of the solution was measured with a Milton Roy Benchtop Refractometer at half-hour intervals. During this period, the average condensate rate was 5.66 to 5.76 mL/min. The condition of ambient air during the 24-hour UEF testing is shown in Figure 5. On average, the air absolute humidity dropped through the absorber by 1.36 ± 0.06 to 1.49 ± 0.1 g water vapor per kg dry air, and rose in dry bulb temperature by 2 to 3°C.

Table 4: Average and standard deviation of absorber parameters during operation.

Heat pump on/off	Weak solution concentration [%]	Strong solution concentration [%]	Delta solution concentration [%]	Condensate rate [mL/min]	Solution inlet temperature [°C]	Water inlet temperature [°C]	Solution mass flow rate [g/s]	Water mass flow rate [g/s]
First heat pump segment	83.72 ± 0.4	88.21 ±0.5	4.43	5.66	23.91 ±0.3	17.64 ±0.8	2.32 ± 0.1	5.79 ± 0.3
Second heat pump segment	84.10 ±0.6	88.05 ±0.5	3.95	5.76	24.8 ±0.9	19.69 ±0.9	3.09 ± 0.2	6.79 ± 0.5

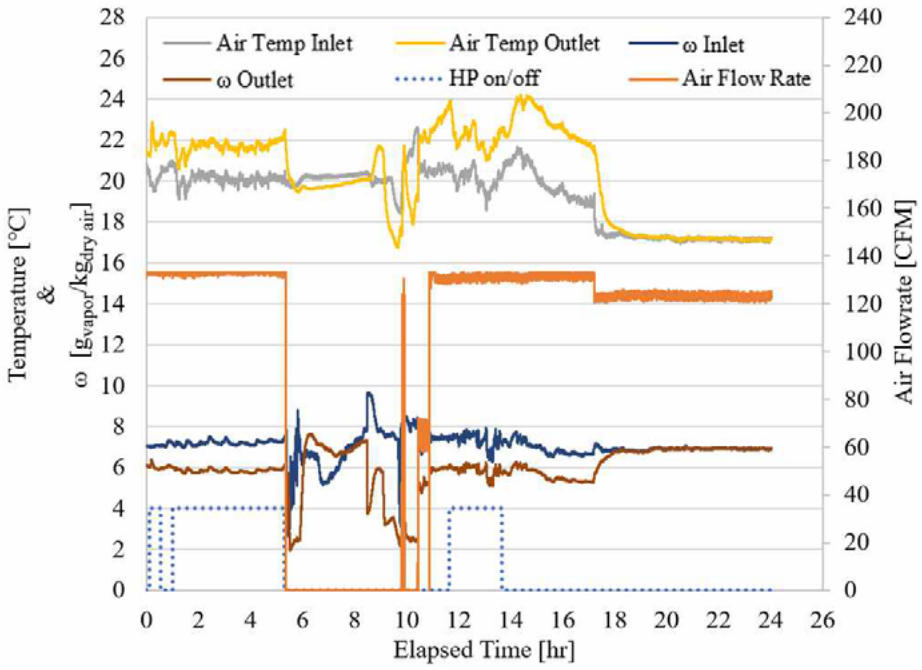


Figure 5: Air conditions during the 24-hour UEF testing. ω is the humidity ratio of the air.

Figure 6 compares the performance of the system evaluated by Chugh et al. [1], [2] and this study. The primary difference between this study and the previous studies by Chugh et al. is the absorber. The difference between the absorbers used in previous studies and this study was previously summarized in Table 2 **오류! 참조 원본을 찾을 수 없습니다.**. Chugh et al. [2] achieved a COP of 1.24 with an inlet water temperature of 18°C and ambient conditions of 21.3°C/60%RH; and a COP of 1.22 with inlet water temperature of 16°C and air conditions of 19.9°C/49%RH. In this study with an improved absorber, we achieved a COP of 1.26 at less favorable airside conditions (19.9°C /49%RH) and less favorable water inlet temperature conditions (18.4°C), and with similar water and solution flowrate. The improvement in the performance of the new absorber is attributed primarily to the increase in the active absorber surface area.

Another point of comparison is that Chugh et al. [2] achieved a COP of 1.22 with inlet water temperature of 16°C and air conditions of 19.9°C/49%RH. The present study achieved a higher COP with much less favorable water inlet conditions (18.4°C).

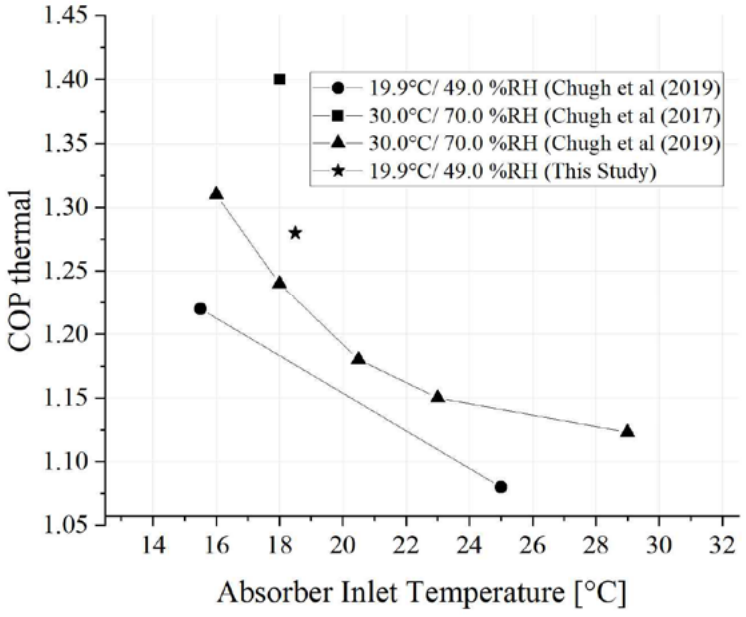


Figure 6: Comparison of the current absorber performance with previous absorber in a similar test set-up. The previous results were from Chugh et al. (2017 [1], Chugh et al. (2019)[2].

4.3. Water Storage Tank

A residential water heater has supply water at 51.7 ± 2.8°C (e-CFR, [4]). Therefore it desirable that the heat pump delivers the requirement temperature lift to the water in the water storage tank during charging and draw. If the heat pump delivers water at any condition below 49°C, the UEF test would be invalidated. The temporal and spatial water temperature distribution is shown in Figure 7. During the UEF test, the tank hot water outlet temperature and top tank temperature was maintained above 48.9°C during draws and charging. This UEF test demonstrates that the heat pump evaluated in this study can deliver water above the current testing standards requirement of 48.9°C at an ambient condition of 19.7 ± 0.6°C and 50 ± 2 %RH.

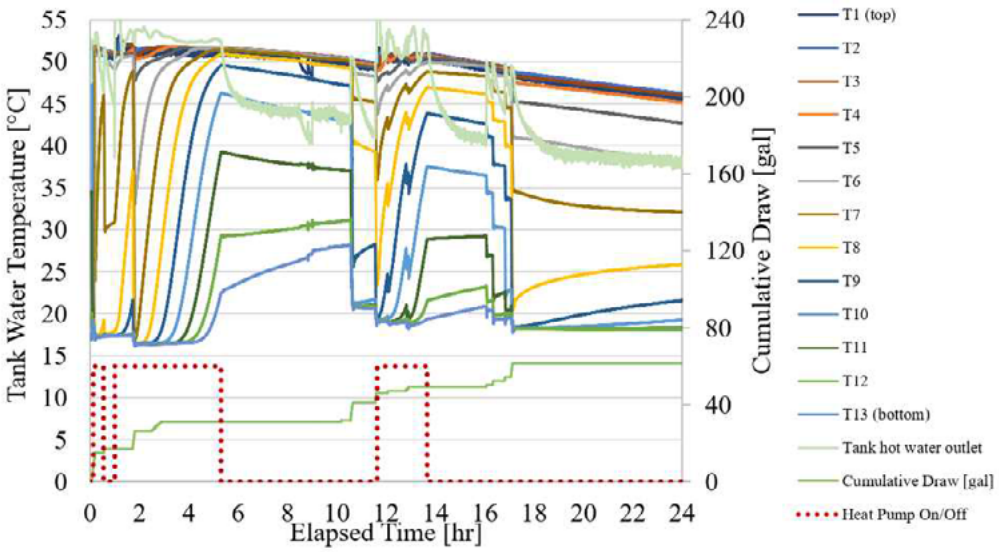


Figure 7: The water temperatures in the 50-gallon water storage tank throughout the 24-hour test.

5. Conclusions

A semi-open, membrane-based heat pump water heater experimentally followed the US standard water heater test method. While directly utilizing water vapor from the surrounding air as a working fluid, the cycle demonstrated an average cycle COP of 1.22 and 825 W water heating capacity, in surroundings of 19.7°C (67.5°F) and 50% relative humidity. The medium use load profile from the US DOE UEF test procedure was met without relying on any other heat source.

NOMENCLATURE

CFM	cubic feet per minute
COP or $COP_{thermal}$	coefficient of performance (useful heat / thermal energy consumed)
$COP_{combined}$	the sum of $COP_{heating}$ and $COP_{dehumidification}$
$COP_{dehumidification}$	useful dehumidifcation capacity / thermal energy consumed
$COP_{heating}$	useful water heating capacity / thermal energy consumed
GPM	gallons per minute
MFC	mass flow controller
$\dot{m}$	mass flow rate [g/sec]
Q	heat flow [kW]
RH	relative humidity [%]
SOHX	solution-oil heat exchanger
SWHX	solution-water heat exchanger
T	temperature [°C]
UEF	uniform energy factor
WWHX	water-water heat exchanger

Subscripts

SHX	solution to oil heat exchanger
cond	condenser
abs	absorber

Symbols

ω humidity ratio [$g_{vapor}/kg_{dry\ air}$]

Acknowledgements

This research was supported by the DOE Office of Energy Efficiency and Renewable Energy, Building Technologies Office (BTO). The authors would like to acknowledge Mr. Antonio Bouza, Technology Manager – HVAC&R, Water Heating, and Appliance, DOE/BTO. This manuscript has been authored by UT-Battelle, LLC under Contract No. DE-AC05-00OR22725 with the U.S. Department of Energy. The United States Government retains and the publisher, by accepting the article for publication, acknowledges that the United States Government retains a non-exclusive, paid-up, irrevocable, world-wide license to publish or reproduce the published form of this manuscript, or allow others to do so, for United States Government purposes. The Department of Energy will provide public access to these results of federally sponsored research in accordance with the DOE Public Access Plan (http://energy.gov/downloads/doe-public-access-plan).

References

[1] D. Chugh, K.R. Gluesenkamp, O. Abdelaziz, and S. Moghaddam, "Ionic liquid-based hybrid absorption cycle for water heating, dehumidification, and cooling," Appl. Energy, vol. 202, pp. 746–754, Sep. 2017.
[2] D. Chugh, K.R. Gluesenkamp, A. Abu-Heiba, M. Alipanah, A. Fazeli, R. Rode, M. Schmid, V.K. Patel, S. Moghaddam. "Experimental evaluation of a semi-open membrane-based absorption heat pump system utilizing ionic liquids," Appl. Energy, vol. 239, pp. 919–927, Apr. 2019.
[3] M. Mortazavi, R. Nasr Isfahani, S. Bigham, and S. Moghaddam, "Absorption characteristics of falling film LiBr (lithium bromide) solution over a finned structure," Energy, vol. 87, pp. 270–278, Jul. 2015.
[4] 10 e-CFR 430, Energy Conservation Program for Consumer Products; Subpart B, Test Procedures; Appendix E, Uniform Test Method for Measuring the Energy Consumption of Water Heaters, US Department of Energy, 2019

13th IEA Heat Pump Conference
April 26-29, 2021 Jeju, Korea

Thermoelectric heat pump performance characterization

Viral K. Patel, Kyle R. Gluesenkamp*, Philip Boudreaux

Oak Ridge National Laboratory, Oak Ridge TN 37831, USA

Abstract

This paper describes the results of an experimental study on the heat transfer characteristics of a commercially available solid-state thermoelectric heat pump device, when applied in an application heating water in minichannels. Each TE device was sandwiched in between two aluminum minichannel heat exchangers, with water flowing through the minichannels in opposite directions. Measurements of the TE substrate temperatures, water temperatures, water flow rates, input voltage and current to the TE were used to determine the heating and cooling capacity and coefficient of performance. The parameters that were varied during the study included the water flow rate, incoming water temperature and current supplied to the TE. These results were compared to manufacturer specifications and theoretical prediction using classical TE equations (based on available TE property data) and showed significant differences. The results are part of a larger study on thermoelectric clothes drying for residential applications.

© HPC2020.
Selection and/or peer-review under responsibility of the organizers of the 13th IEA Heat Pump Conference 2020.

Keywords: Thermoelectric; heat pump

Nomenclature

$\dot{m}_{hw}$	Mass flow rate for hot water, kg/s
$\dot{m}_{cw}$	Mass flow rate for cold water, kg/s
$c_{p,hw}$	Specific heat capacity for hot water, kJ/kg·K
$c_{p,cw}$	Specific heat capacity for cold water, kJ/kg·K
COP_{heat}	Heating coefficient of performance
COP_{cool}	Cooling coefficient of performance
$T_{hs,avg}$	Average hot-side substrate temperature, °C
$T_{cs,avg}$	Average cold-side substrate temperature, °C
$T_{hw,avg}$	Average hot water temperature, °C
$T_{cw,avg}$	Average cold water temperature, °C
ΔT	Temperature difference between average hot- and cold-side substrate temperatures (also DT), K
q_{hw}	Heating capacity, W
q_{cw}	Cooling capacity, W
UA_{hot}	Overall heat transfer coefficient on hot-side, W/K
UA_{cold}	Overall heat transfer coefficient on cold-side, W/K
W_{elec}	Electrical power input to TE, W

* Corresponding author. Tel.: +1-865-241-2952.
E-mail address: gluesenkampk@ornl.gov

1. Introduction

Thermoelectric (TE) modules are ubiquitous devices that rely on the Peltier effect for heat pumping [1]. Although typically less efficient than traditional vapor-compression based heat pumps [2], it is possible to use TE heat pumps for certain applications which take advantage of their modularity and simple design. For example, TEs have been studied in recent years for improving or augmenting existing types of building heating and cooling systems [3-6]. Most recently, Zhao et al studied radiative sky cooling-assisted thermoelectric cooling for building applications [6]. They showed that by integrating TEs with other technologies, the COP could be improved significantly, demonstrating potential large-scale adoption of TE cooling. The use of the integrated TE cooling allowed for better control of the heat transfer fluid temperature (in addition to providing supplemental cooling) and made the performance of radiative sky cooling subsystem less susceptible to changes in ambient conditions. A case study involving a two-story residential building with thermal storage tank, radiative cooling surface and 101 TE modules was able to achieve an annual cooling COP of 1.87. Both daytime and nighttime cooling of the radiative sky cooling subsystem were analyzed.

In addition to building heating and cooling applications, TEs have also been considered for many other types of equipment, including refrigeration [7], personal thermal comfort [8], electronics cooling [9] and appliances such as clothes dryers [10, 11]. For example, Liu et al have conducted a thermodynamic analysis of a transcritical CO_2 refrigeration cycle integrated with thermoelectric subcooler and ejector [7]. They found that a 39% increase in maximum cooling coefficient of performance (COP) was possible by using the thermoelectric subcooler + ejector compared to the baseline cycle. Simultaneously, a lower discharge pressure was achieved. The authors have also conducted past studies on a clothes drying application which utilize TE heat pumps [10, 11]. These studies showed that the energy efficiency of traditional electric clothes dryers (which using heating elements) could be improved by as much as 40% by using a TE heat pump designed in such a way to control temperature lift and achieve optimum TE performance.

Based on current research, it has become increasingly important to properly characterize the performance of TE modules, as this information is valuable to update TE models and predict the overall system performance whenever TEs are used in different applications. Along those lines, the current work describes an experimental effort to measure the heating and cooling performance of a TE module as a function of applied voltage, current and other parameters. The experimental measurements are used to determine heating and cooling COP and overall heat transfer coefficient for a TE module installed in between two minichannels heat exchangers through which water flows. The experimentally measured results are also compared to manufacturer-provided specifications on TE performance.

2. Experimental setup

The experimental setup consisted of a single 40 × 40 mm TE module installed between two flat aluminum minichannel heat exchangers through which water flowed in opposite directions. An aluminum spacer block was used to maintain a small gap in between the hot and cold minichannel heat exchangers, as illustrated in Fig. 1.

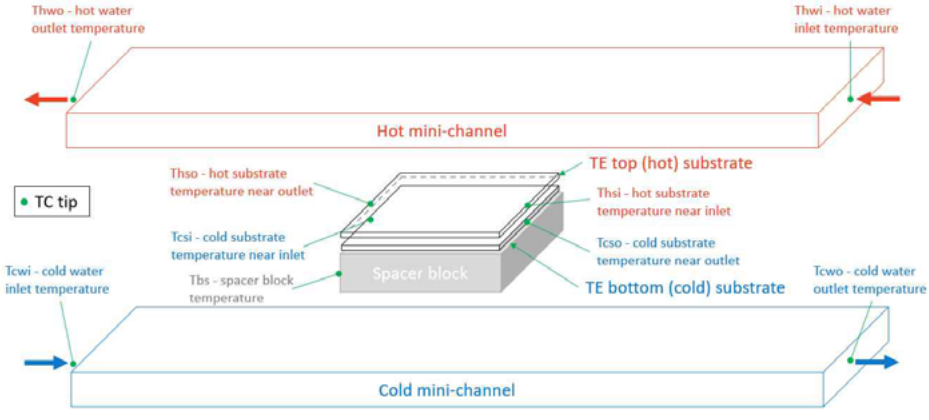


Fig. 1. Schematic showing installation of TE module and thermocouple (TC) locations

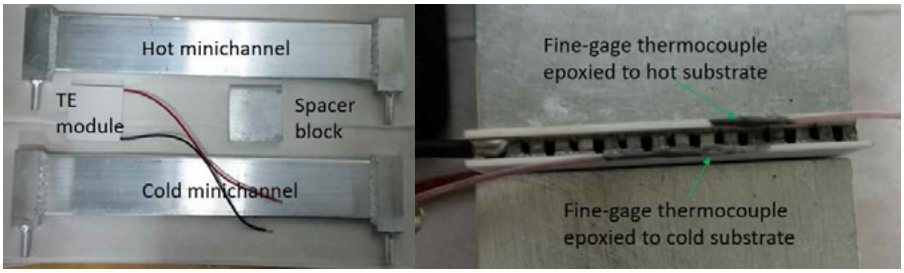
As shown in Fig. 1, various temperature sensors were used in the experimental setup to measure substrate and water temperature. Thermocouple probes were used to measure the water temperatures, while fine-gage thermocouple wires were used to measure surface temperature of the TE substrate and spacer block. Water mass flow rates were measured by using a precision weighing scale and high-accuracy timer to determine that rate at which an empty container was filled. The water temperatures were used with the water mass flow rates to determine the heating and cooling capacity of the TE module. The voltage applied to the TE and current flowing through the TE were used to determine the electrical power consumed. The substrate temperatures were used along with electrical power to determine the overall heat transfer coefficient between the TE and water.

The specifications of the commercially available TE [12] are given below in Table 1. The TE was chosen based on the nominal temperature difference between hot and cold sides, average heating and cooling capacity, operating voltage and current.

Table 1. TE specifications from manufacturer datasheet [12]

Hot substrate temperature, T_h [°C]	27	50
Temperature difference between hot and cold side of the module when cooling capacity is zero at cold side, ΔT_{max} [°C]	74	83
Voltage applied to the module at ΔT_{max}, V_{max} [V]	16.8	18.08
DC current through the modules at ΔT_{max}, I_{max} [A]	8.4	8.4
Cooling capacity at cold side of the module under ΔT = 0 °C, Q_{Cmax} [W]	90.0	98.0
AC resistance [Ω]	1.50	1.66

A photo of the various components in the experimental setup before assembly is shown in Fig. 2a. Figure 2b shows a close-up image of the TE hot and cold substrates and placement of the fine-gage thermocouples.



(a.) (b.)

Fig. 2. (a.) components used in experimental setup before assembly and (b.) close-up photo of thermocouple placement on TE substrate

A single mechanical clamp was used to hold the assembly together, as shown in a photo of the completed experimental setup with insulation (Fig. 3). All mating surfaces were coated with a thermal compound [13] to reduce interfacial thermal resistance.

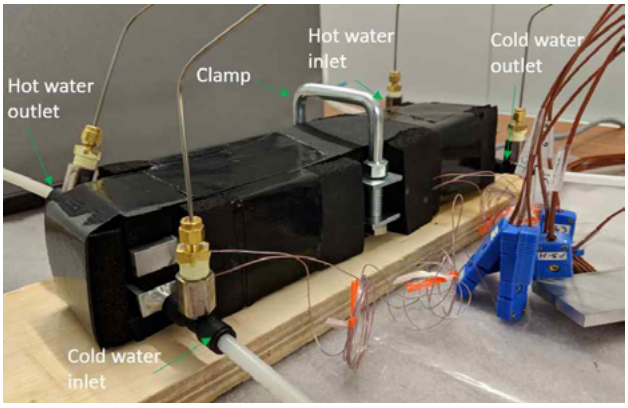


Fig. 3. Completed experimental setup with insulation

A heated recirculating bath was used to maintain a constant inlet temperature on the hot side and tap water was used on the cold side. Needle valves were used on both sides to adjust the water flow rates as needed. An Extech Switching Mode adjustable DC power supply was used to apply a voltage to the TE module. Voltage and current were recorded from the front panel display of the power supply.

3. Experimental method and data reduction

The TE module performance was characterized as a function of the hot-side inlet water temperature and current. The experiment matrix is shown below in Table 2. The quantities for water flow rates and inlet temperatures were based on previous work on thermoelectric clothes drying [11].

Table 2. Experiment matrix for TE module performance characterization

Hot side water mass flow rate [g/s]	Cold-side water mass flow rate [g/s]	Hot-side inlet water temp. [°C]	Cold-side inlet water temp. [°C]	Current [A]
9.66	19.24	40	Tap, ~20	5.00
9.66	19.24	40	Tap, ~20	7.00
9.66	19.24	40	Tap, ~20	8.30
9.66	19.24	55	Tap, ~20	7.00
9.66	19.24	55	Tap, ~20	7.90
9.66	19.20	75	Tap, ~20	7.00
9.66	19.20	75	Tap, ~20	8.30

The experiment was initiated by first measuring the water flow rates on the hot and cold sides and adjusting them to the desired values in Table 2. Next, the setpoint on the heated recirculating bath was adjusted to the desired hot-side inlet water temperature in Table 2. When conditions were steady, the power supply for the TE module was turned on. The power supply functioned in “constant current” mode and current was adjusted to the desired value in Table 2. The steady state voltage and current readings on the power supply front panel were recorded. The changes in substrate and water temperature were recorded continuously at 1 sample/s for a total of 300 s, after which the power supply was turned off for 60 s. This process was repeated three times for each experiment, to ensure that the results were reliable and repeatable.

The overall heat transfer coefficient, UA, between the TE substrates and the water was calculated using Eqs. (1) and (2) for the hot- and cold-sides, respectively (nomenclature for temperatures as defined in Fig. 1):

$$UA_{hot} = \frac{\dot{m}_{hw} c_{p,hw} (T_{hw\,o} - T_{hw\,i})}{(T_{hs,avg} - T_{hw,avg})} = \frac{q_{hw}}{(T_{hs,avg} - T_{hw,avg})} \quad (1)$$

$$UA_{cold} = \frac{\dot{m}_{cw}\, c_{p,cw}\, (T_{cw\,i} - T_{cw\,o})}{(T_{cw,avg} - T_{cs,avg})} = \frac{q_{cw}}{(T_{cw,avg} - T_{cs,avg})} \quad (2)$$

The heating and cooling COPs were calculated using Eqs. (3) and (4), respectively:

$$COP_{heat} = \frac{q_{hw}}{W_{elec}} \quad (3)$$

$$COP_{cool} = \frac{q_{cw}}{W_{elec}} \quad (4)$$

4. Results and discussion

All experiments in Table 2 were completed. Example results of temperatures measured during the first two experiments are shown in Fig. 4 (nomenclature as defined in Fig. 1).

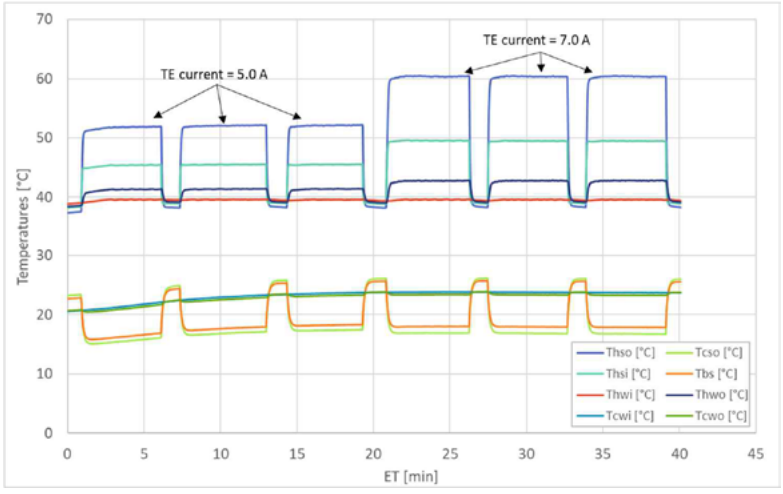


Fig. 4. Results of temperature measurement for experiments for V = 11.2 V, I = 5.0 A and V = 16.1 V, I = 7.0 A (Note: T_{csi} not shown due to erroneous measurements)

As illustrated above, all experiments were performed three times with the exact same conditions to ensure repeatability and reliability of the data. From the measurements in Fig. 4, the highest temperatures occurred on the TE hot substrate; the substrate temperature increased in the direction of the water flow by as much as 11°C (T_{hsi} vs. T_{hso} in Fig. 4). The results also showed that the average temperature of aluminum spacer block was similar to that of the cold side TE substrate. Detailed results of the above experiments are given in Table 3.

Table 3. Detailed results for experimental data shown in Fig. 4

Current [A]	Voltage [V]	Average hot-side substrate temperature [°C]	ΔT [K]	Heating capacity [W]	Cooling capacity [W]	UA_{hot} [W/K]	UA_{cold} [W/K]	Heating COP	Cooling COP
5.0	11.2	48.54	33.00	69.13	31.40	8.48	5.54	1.23	0.56
5.0	11.2	48.78	31.93	71.40	32.38	8.61	5.49	1.28	0.58
5.0	11.2	48.80	31.41	72.30	32.08	8.68	5.33	1.29	0.57
7.0	16.1	54.97	38.08	127.36	34.69	9.23	5.16	1.13	0.31
7.0	16.1	54.93	38.07	128.19	34.33	9.31	5.12	1.14	0.30
7.0	16.1	54.92	38.13	128.82	34.09	9.37	5.09	1.14	0.30

As shown above, the overall heat transfer coefficient on the hot side was greater than on the cold side. The experimental results were found to be consistent from test to test when all conditions were kept the same. To illustrate the comparison between experimentally measured values and manufacturer provided data, an overlay graph was created. Figure 5 shows such an overlay; the manufacturer data [12] shows the cooling capacity of the TE module at a hot-side substrate temperature of T_{hs} = 50°C, as a function of applied voltage, for various temperature differences between the hot and cold TE substrates (DT or ΔT). It is important to note that the manufacturer data are not derived from experimental measurements, but rather from solutions of the classical thermoelectric equations [1] which characterize TE performance as a function of substrate temperatures, TE properties and applied current. The closest experimental results from Table 3 which could be compared to the manufacturer data were for the TE current of 5.0 A (the average hot-side substrate temperature and DT from the three experiments were 48.7°C and 32.1 °C, respectively).

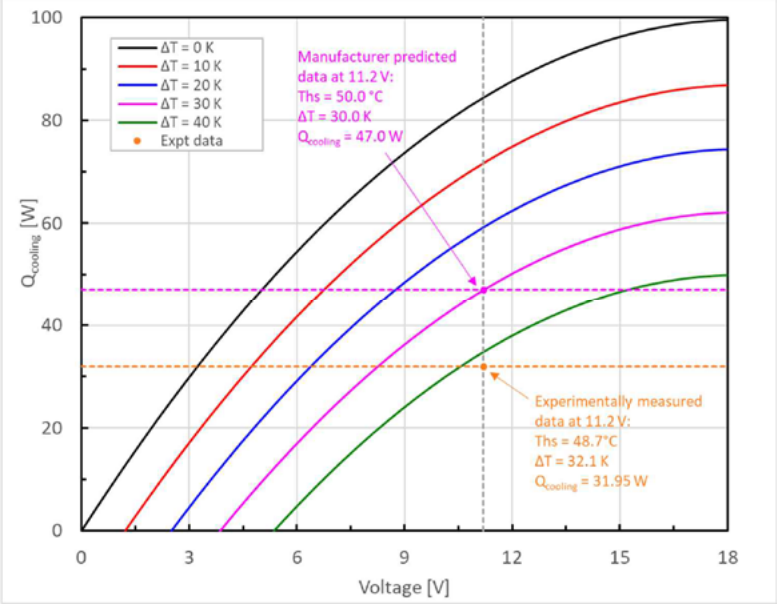


Fig. 5. Experimental data points overlaid on manufacturer data [12] for TE cooling capacity at a hot-side substrate temperature of 50°C as a function of voltage for various DT values (i.e. temperature difference between TE hot and cold substrate)

As shown above, there was a significant difference in the average measured cooling capacity (31.95 W, at a voltage of 11.2 V and DT = 32.1 K) and the cooling capacity expected from manufacturer data (~47.0 W) at the same voltage and DT (magenta line). Furthermore, the average measured cooling COP for this case was 0.57, whereas the manufacturer provided data indicated a cooling COP of 0.86 (51% higher). The results

showed that there was a discrepancy between the experimentally measured values and manufacturer provided data, possibly due to differences in material property values used in the calculations. For the experimental data, heat losses and measurement sensor uncertainty contributed to the overall uncertainty. It should be noted, however, that the above results were for a single operating point averaged over three identical experiments. More experiments will need to be performed with various water flow rates, temperature differences, voltages/currents to obtain an overall performance map. In addition, compensation for any heat losses should be applied in future work to improve the experimental accuracy.

5. Conclusions

The performance characteristics of a single TE module were measured in an experimental setup with water as the heat transfer fluid. The results show that the measured data are consistent and show significant differences compared to manufacturer-provided values for heating capacity, cooling capacity, and COP as a function of input voltage and current. For example, the manufacturer-specified cooling capacity was 51% higher than measured for one operating point. As such, if TE modules are to be used in system models for different applications, care must be taken to accurately characterize their performance for the particular application.

Acknowledgements

This research was supported by the DOE Office of Energy Efficiency and Renewable Energy, Building Technologies Office (BTO). The authors would like to acknowledge Mr. Antonio Bouza, Technology Manager – HVAC&R, Water Heating, and Appliance, DOE/BTO. This manuscript has been authored by UT-Battelle, LLC under Contract No. DE-AC05-00OR22725 with the U.S. Department of Energy. The United States Government retains and the publisher, by accepting the article for publication, acknowledges that the United States Government retains a non-exclusive, paid-up, irrevocable, world-wide license to publish or reproduce the published form of this manuscript, or allow others to do so, for United States Government purposes. The Department of Energy will provide public access to these results of federally sponsored research in accordance with the DOE Public Access Plan (http://energy.gov/downloads/doe-public-access-plan).

References

[1] Rowe, D. M., 2005, Thermoelectrics Handbook: Macro to Nano, CRC press - Taylor & Francis Group, Boca Raton, FL.
[2] Zhao, D., and Tan, G., 2014, "A review of thermoelectric cooling: Materials, modeling and applications," Applied Thermal Engineering, 66(1), pp. 15-24.
[3] He, W., Zhou, J., Chen, C., and Ji, J., 2014, "Experimental study and performance analysis of a thermoelectric cooling and heating system driven by a photovoltaic/thermal system in summer and winter operation modes," Energy Conversion and Management, 84, pp. 41-49.
[4] Ibañez-Puy, M., Bermejo-Busto, J., Martín-Gómez, C., Vidaurre-Arbizu, M., and Sacristán-Fernández, J. A., 2017, "Thermoelectric cooling heating unit performance under real conditions," Applied Energy, 200, pp. 303-314.
[5] Irshad, K., Habib, K., Basrawi, F., and Saha, B. B., 2017, "Study of a thermoelectric air duct system assisted by photovoltaic wall for space cooling in tropical climate," Energy, 119, pp. 504-522.
[6] Zhao, D., Yin, X., Xu, J., Tan, G., and Yang, R., 2019, "Radiative sky cooling-assisted thermoelectric cooling system for building applications," Energy, p. 116322.
[7] Liu, X., Fu, R. S., Wang, Z. Q., Lin, L., Sun, Z. X., and Li, X. L., 2019, "Thermodynamic analysis of transcritical CO2 refrigeration cycle integrated with thermoelectric subcooler and ejector," Energy Conversion and Management, 188, pp. 354-365.
[8] Duan, L., Han, J., Cao, L., and Huo, C., 2017, "Experimental study on heat transfer characteristics of CNTs/Al2O3nanofluids in personal cooling system based on thermoelectric refrigeration," Procedia Engineering, 205, pp. 588-595.
[9] Liang, K., Li, Z., Chen, M., and Jiang, H., 2019, "Comparisons between heat pipe, thermoelectric system, and vapour compression refrigeration system for electronics cooling," Applied Thermal Engineering, 146, pp. 260-267.
[10] Patel, V. K., Gluesenkamp, K. R., Goodman, D., and Gehl, A., 2018, "Experimental evaluation and thermodynamic system modeling of thermoelectric heat pump clothes dryer," Applied Energy, 217, pp. 221-232.
[11] Patel, V., and Gluesenkamp, K. R., 2018, "Thermoelectric Heat Pump Clothes Dryer using Secondary Loop Heat Exchangers: Experimental Evaluation and System Modeling," Proc. 5th International High Performance Buildings Conference at Purdue, West Lafayette, IN.
[12] Thermonamic, 2017, "Specification of Thermoelectric Module - TEHC1-12708," www.thermonamic.com.cn
[13] Arctic Silver Inc., 2019, "Arctic Silver 5 - High-Density Polysynthetic Silver Thermal Compound," http://www.arcticsilver.com/as5.htm

13th IEA Heat Pump Conference
April 26-29, 2021 Jeju, Korea

Impact of Variable Speed Components on the Seasonal Performance of a Residential Air-Source Heat Pump

Fatih Meral[*,a], Oliver Obst[a], Nicholas P. Salts[a], Eckhard A. Groll[a]

[a]Purdue University, School of Mechanical Engineering, Ray W. Herrick Laboratories,
177 S Russell St, West Lafayette, IN 47907, United States

Abstract

Heat pumps utilizing variable-speed compressors and other capacity control techniques offer significant seasonal efficiency improvements over traditional single-speed systems by reducing system cycling losses and corresponding system inefficiencies. However, the majority of residential heat pumps operated in the United States (US) utilize single-speed Permanent Split Capacitor (PSC) compressors and offer few capacity control options. This paper presents testing results of a novel electronic drive that enables the variable-speed control of conventionally single-speed PSC motors in compressors and fans using a low power inverter. The focus of this research is to improve the cooling seasonal performance of a 2-ton (6.7 kW) off-the-shelf residential air-source heat pump by replacing its PSC scroll compressor with a PSC rotary compressor and applying the low power inverter to enable variable speed control of the PSC motors. This paper also presents the impact of a variable speed indoor blower with an electronically commutated motor (ECM) and two variable speed outdoor fans: the first with a variable speed PSC motor enabled by the electronic drive and the second with a conventional variable speed ECM motor. The modified heat pump has been tested in psychrometric chambers for Seasonal Coefficient of Performance (SCOP) / Seasonal Energy Efficiency Rating (SEER). The results show that a SCOP/SEER improvement of nearly 33% is possible using a low power inverter for the PSC compressor combined with variable speed ECM indoor and PSC and ECM outdoor fans. Results also indicate a total SCOP/SEER improvement of 40% is possible by changing from a PSC scroll compressor to a PSC rotary compressor while also utilizing variable speed fans.

Keywords: air-source heat pump, inverter, SEER, Variable Speed Control, PSC

1. Introduction

The increasing demand for energy, which has so far primarily been produced from fossil fuels, represents an enormous burden on the environment and the climate. Fossil fuel power plants generated 82% of the energy worldwide needed in 2018 [1]. CO_2 emissions, amounting to approximately 36 billion metric tons in 2018, must be reduced to a large extent in order to curb global warming [2]. Therefore, the use of fossil fuels must be greatly reduced, but energy costs should not rise to the same extent. This raises the question of ways to save resources. One possibility is to increase the efficiency of existing Heating, Ventilation and Air Conditioning (HVAC) heat pump cycles in order to save energy especially due to the fact that 40% of the total energy consumption in the US is being due to buildings mainly for cooling and heating [2]. The US market for these systems is primarily dominated by fixed-speed single-stage systems with low seasonal energy efficiency ratios (SEER).

* Corresponding author.
E-mail address: fmeral@purdue.edu .

This could be explained in part by the expected useful lifespan of heat pumps, which is estimated between 9 and 15 years, which contributes to the number of single-speed systems due to the fact that systems with variable speed operations have only gained popularity in the last few years. In addition, the SEER requirement for split-system central air conditioners was increased by the department of energy (DOE) to at least 13 for all units which were manufactured after January 1st, 2015 [3]. The SEER requirement is higher in certain areas of the US. Split-system HVAC units typically deliver from 2 tons (6.7 kW) to 5 tons (17 kW) of cooling capacity for US residential installations. A typical residential vapor compression air conditioning and heat pump system contains four primary components. These components are a condenser, evaporator, expansion device, and a compressor and dedicated fans for the heat exchangers both of which are fixed-speed components.

These fixed-speed components have a significant impact on the efficiency which can be achieved by HVAC units. Fixed speed Permanent Split Capacitor (PSC) motors for compressors, outdoor fans and indoor blowers are traditionally used for low SEER systems, whereas high SEER HVAC units have variable speed control of these elements, which is connected to higher manufacturing costs. These high efficiency systems are providing the ability to modulate the system capacity to match the cooling or the heating load depending on the required cooling capacity which avoids cycling losses inherent to fixed-speed systems at part load. The market share of the high efficiency systems is lower than single-stage systems due to the ability of manufacturers to meet the required efficiency regulations through lower cost approaches, such as increasing the heat exchanger surface area [4]. These approaches are limited considering the restricted space of an HVAC system and will become less cost effective for manufacturers due to the increasingly restrictive efficiency regulations instated by the DOE. An alternative method to increase the efficiency of systems, which use fixed-speed PSC components is to use a low power electronic drive that has been designed to enable variable speed operation of conventionally fixed-speed components. The design and operation of such an electronic drive is described in detail by Chretien et al. [5, 6].

This paper focuses on the performance impact of variable speed components by applying the low power electronic inverter drive that is specifically designed to be used as a modification to an existing single-stage heat pump (SSHP). This drive has been connected to a residential off-the-shelf split-system SSHP with a SEER rating of 13. The modified SSHP allows for the control of system capacity via compressor speed, indoor fan speed and outdoor fan speed. The modified system will be referred to as a variable speed heat pump (VSHP) due to the control it provides over component speeds. The SEER has been calculated for the baseline SSHP with a PSC scroll compressor, the baseline SSHP with a PSC rotary compressor and the inverter modified VSHP in order to compare the systems. This comparison is presented, and future work is discussed.

2. Methods

In this work we selected an off-the-shelf SSHP with a PSC scroll compressor and experimentally determined the baseline SEER for evaluating the inverter and its impact on a residential split-system SSHP. Previous research on the topic of the low power inverter have shown that HVAC systems using PSC rotary compressors have a higher SEER than similar systems with PSC scroll compressors when modified with the inverter [7]. Therefore, the PSC scroll compressor has been removed and a PSC rotary compressor was installed. After the baseline SEER for the new compressor is determined, the inverter is installed to enable the variable speed operation for the compressor, indoor fan and outdoor fan. The variable speed SEER was experimentally determined and compared to the fixed-speed SEER of the off-the-shelf system.

2.1 Baseline Heat Pump and Psychrometric Rooms

The air-source heat pump was installed and instrumented in a pair of temperature and humidity-controlled psychrometric chambers for testing both the scroll and rotary compressor. One room of the psychrometric rooms is for simulating indoor conditions and the other for simulating the outdoor conditions. The heat pump was installed and tested according to the AHRI 210/240-2019 [8] standard for the rating of unitary air source heat pump equipment. The SSHP consists of an outdoor and an indoor unit. The outdoor unit contains the compressor, condenser, outdoor fan, and a four-way valve. The indoor unit includes the evaporator, thermostatic expansion valve (TXV), and indoor fan. The baseline system is a 2-ton (6.7 kW) heat pump with a PSC scroll compressor and a SEER rating of 12. The nominal indoor airflow rate is 1360 m^3/h, the nominal compressor speed is 3600 rotations per minute (RPM) and the system is charged with 2.7 kg of R410A to ensure consistent subcooling in the liquid line and therefore an accurate mass flow reading. The compressor is

a fixed speed PSC scroll compressor, the indoor fan is a constant volume flow rate fan using an electronically commutated motor (ECM), and the outdoor fan uses a PSC fixed speed motor, whose speed is 1075 RPM.

2.2 Inverter Mechanism

The inverter allows for variable speed operation of a traditional heat pump, which has fixed-speeds for compressor as well as indoor and outdoor fan. Figure 1 shows the schematic drawing of the inverter and heat pump connection inside the psychrometric chambers. The inverter is installed in series between the power grid and the indoor as well as outdoor unit. The inverter converts the AC voltage from the 230V power supply and a 60 Hz frequency into a DC voltage and allows the voltage and frequency to be changed and therefore allows to change the speed of the individual components. This system allows the independent control of the speeds of the compressor and fans.

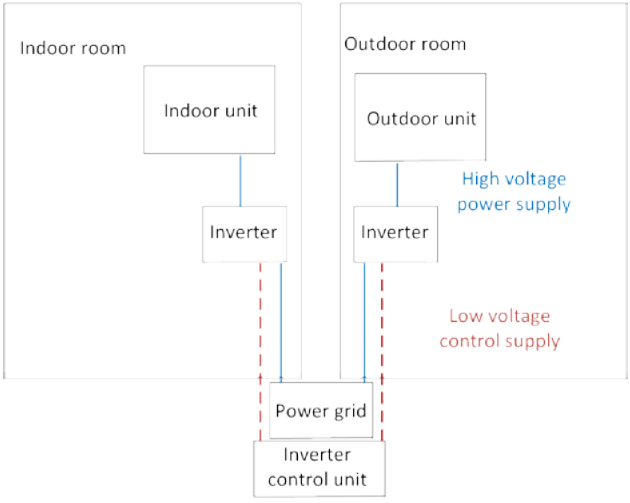


Figure 1. Inverter connection

2.3 Heat Pump modified with an Inverter

The purpose of the modified heat pump with the inverter is to allow the control of the variable speed operation for the compressor, indoor fan, and outdoor fan on existing SSHPs. The main application for such a device is for existing single-speed HVAC systems that are in service, so this experimental characterization captures the actual implementation of this inverter system effectively. The inverter is installed by connecting it in-line between the power source and the components to be controlled, allowing the motor speeds of each component to be adjusted manually and independently of one another during the laboratory experiments. The first modification made to the baseline heat pump was the exchange of the PSC scroll compressor to a PSC rotary compressor, followed by the connection of the inverter to the PSC rotary compressor. The third modification consisted of the connection of the inverter to the PSC outdoor fan, and in the final modification step the PSC outdoor fan was replaced by an ECM outdoor fan. An ECM indoor fan was used during the duration of the laboratory testing. Variable speed operation is inherent to ECM technology and therefore, while the electronic drive was used to control ECM fan speeds, the inverter component, which enables control of PSC motor frequency, was not used in line with the ECM fans.

2.4 Data Collection and Analysis

The data is collected through a National Instruments cRIO-2091 using a visual interface (VI) written in LabVIEW. The power consumption of the indoor fan, the outdoor fan, and the compressor are measured separately with watt transducers. The cooling capacity of the heat pump is determined using the refrigerant and air enthalpy method. A schematic of the refrigerant loop of the heat pump in cooling mode is shown in Figure 2.

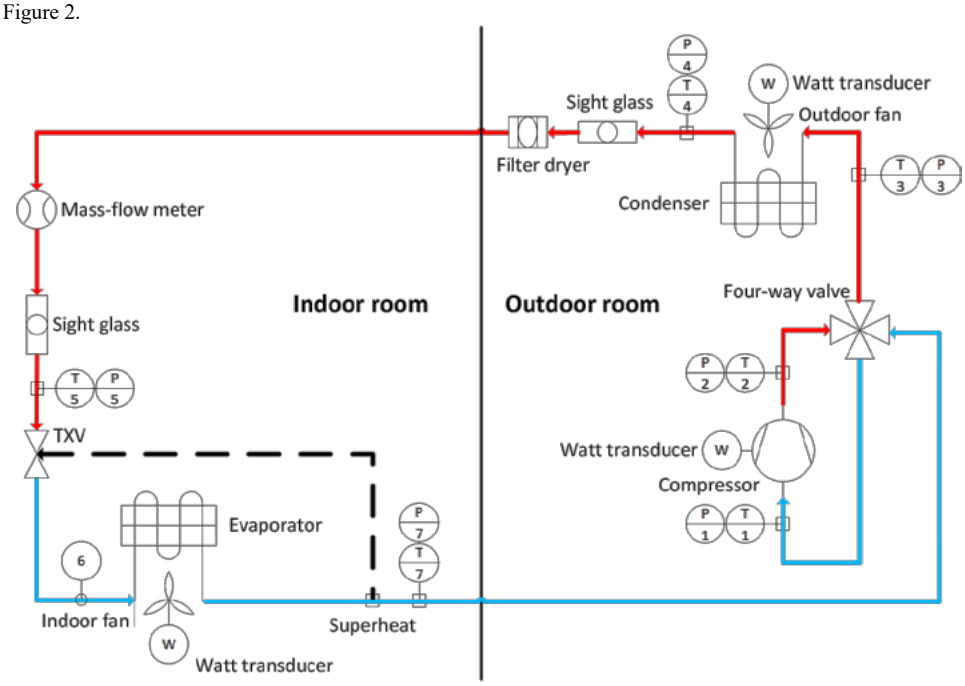


Figure 2. Heat pump schematic

The state points 1 through 5 and 7 in Figure 2 are determined by measuring the pressure and the temperature of the refrigerant. In order to determine the state point 6 between the TXV and the evaporator assumptions of an isenthalpic expansion across the TXV and no pressure drop for the section between the outlet of the TXV and the outlet of the evaporator are made. The mass flow rate of the refrigerant is measured by using a Coriolis-effect mass flow meter oriented for liquid measurement at the outlet of the condenser. All refrigerant and air properties have been determined using the software Engineering Equation Solver (EES) [9].

The cooling capacity of the refrigerant-side of the evaporator can be calculated from an energy balance derived from the first law of thermodynamics and the measured state points along with the listed assumptions resulting in equation 1.

$$\dot{Q}_{\text{evap}} = \dot{m} \cdot \Delta h_{evap} = \dot{m} \cdot (h_7 - h_6) \quad (1)$$

The net capacity is calculated by subtracting the heat added to the air by the indoor fan, which can be assumed to be equal to the power consumption of the indoor unit, from the evaporator capacity shown in equation 2.

$$\dot{Q}_{\text{net}} = \dot{Q}_{evap} - \dot{W}_{indoor} \quad (2)$$

The air-side capacity of the system is calculated from the first-law energy balance across the indoor unit as shown in equation 3. This equation accounts for the change in enthalpy of the air stream and also accounts also for the small amount of water that is condensed out of the air stream.

$$\dot{Q}_{\text{net}} = \dot{m}_{air} \cdot \Delta h_{evap} - \dot{m}_{water} \cdot h_{water} \quad (3)$$

The air volume flow rate is determined using a nozzle box connected to the duct work of the indoor unit and is designed as outlined in ASHRAE Standard 37-2009 [10]. The air volume flow rate is calculated iteratively according to equation 4 using the area of the duct work (A_i). The expansion factor (Y) and the coefficient of discharge (C_i) are also established in ASHRAE Standard 37-2009.

$$\dot{V}_{air} = Y \cdot \sqrt{\frac{2 \cdot \Delta p_{nozzle}}{\rho_{air}}} \sum_{0}^{k} C_i \cdot A_i \quad (4)$$

The mass flow rate of the air is determined by equation 5.

$$\dot{m}_{air} = \dot{V}_{air} \cdot \rho_{air} \quad (5)$$

The dry-bulb temperature of the air is measured with a 3x3 thermocouple grid at the inlet and outlet of the indoor unit. The relative humidity of the inlet air is determined by using a relative humidity sensor. The dew point of the outlet air is determined by sampling the outlet air at a rate of 1 liter/min and passing it through a chilled mirror dew point sensor. The inlet air enthalpy, outlet air enthalpy and outlet water enthalpy are calculated using EES using these measured values. The condensed water mass flow rate is determined as shown in equation 6.

$$\dot{m}_{water} = \dot{m}_{air} \cdot (\omega_2 - \omega_1) \quad (6)$$

The coefficient of performance (COP) is unitless and defined as the ratio of the cooling capacity divided by the total power consumed by the heat pump.

$$\text{COP} = \frac{\dot{Q}_{net}}{\dot{W}_{total}} \quad (7)$$

2.5 Test Matrix

The baseline heat pumps with fixed-speed components as well as the inverter modified heat pumps with variable speed components have been tested according to the guidelines set by AHRI Standard 210/240-2019 [8]. The test matrix shown in Table 1 contains the ratings tests for a SSHP, while Table *2* shows the ratings tests for a VSHP. Temperature values have been co-listed in both English and SI Units because the SEER calculation requires the input of temperatures in °F.

Table 1. ANSI/AHRI test matrix for a heat pump with a single speed compressor and constant volume indoor fan.

Test description	Air entering outdoor unit °F/°C		Air entering outdoor unit °F/°C		Air volume rate
	Dry–bulb	Wet–bulb	Dry–bulb	Wet–bulb	
A (required)	95.0 / 35.0	75.0 / 23.9	80.0 / 26.7	67.0 / 19.4	Full–load
B (required)	82.0 / 27.8	65.0 / 18.3	80.0 / 26.7	67.0 / 19.4	Full–load

Table 2. ANSI/AHRI test matrix for a heat pump with a variable speed compressor and indoor fan.

Test description	Air entering outdoor unit °F/°C		Air entering indoor unit °F/°C		Compressor speed	Air volume rate
	Dry–bulb	Wet–bulb	Dry–bulb	Wet–bulb		
A_2 (required)	95.0 / 35.0	75.0 / 23.9	80.0 / 26.7	67.0 / 19.4	Maximum	Full–load
B_2 (required)	82.0 / 27.8	65.0 / 18.3	80.0 / 26.7	67.0 / 19.4	Maximum	Full–load
E_V (required)	87.0 / 30.6	69.0 / 20.6	80.0 / 26.7	67.0 / 19.4	Intermediate	Intermediate
B_1 (required)	82.0 / 27.8	65.0 / 18.3	80.0 / 26.7	67.0 / 19.4	Minimum	Minimum
F_1 (required)	67.0 / 19.4	53.5 / 11.9	80.0 / 26.7	67.0 / 19.4	Minimum	Minimum

2.6 SEER Analysis

These test matrices are used to determine the SEER for the system. This rating is a standard method used to rate the cooling performance of heat pumps in the US. A seasonal analysis is necessary to characterize the actual benefits of the VSHP, which come in form of the ability to match part load conditions, relative to a SSHP. This research will use the SEER rating to quantify the improvement in performance of the baseline SSHP compared to the inverter modified VSHP.

Each test matrix contains optional tests to determine the coefficient of cyclic degradation (C_D). This factor is used to account for the loss in efficiency of the heat pump during periods of cycling on and off. The standard calls for an assumed value of 0.25 for the coefficient of cyclic degradation if all optional tests are not performed. Due to significant time requirement to carry out the optional tests, a value of 0.25 is assumed in this analysis. This value resulted in the calculated SEER of the baseline SSHP to be equal to the SEER declared by the manufacturer. The same coefficient of cyclic degradation was assumed for the VSHP. The official online calculation tool provided by AHRI was then used to calculate the SEER for the SSHPs and VSHPs. A full description of the SEER calculation can be found in the AHRI Standard 210/240.

3. Results

All heat pumps tests are shown in Table 3. The first test was baseline testing of the off-the-shelf single stage heat pump with the PSC scroll compressor (SSHP1). Next, the PSC scroll compressor was exchanged for a PSC rotary compressor for the second baseline test (SSHP2). Both SSHP1 and SSHP2 tests used a constant volume flow rate setting for the ECM indoor fan. The inverter was then connected to the PSC rotary compressor and the heat pump was tested as a VSHP (VSHP1). After this test, the PSC outdoor fan was connected to the inverter, which enabled the variable speed control for the fan (VSHP2). Finally, the PSC outdoor fan motor was replaced by an ECM motor in order to compare an inverter driven PSC outdoor fan, which is usually installed in SSHPs and a more expensive ECM-powered outdoor fan that enabled the variable speed option without an inverter and is typically installed in VSHPs with a higher SEER rating (VSHP3). All VHSP tests were performed using the ECM indoor fan in variable speed mode. The baseline test results for the SSHP1 are shown in Table 4.

Table 3. Phases of testing the heat pump.

Test	Compressor Type	Outdoor Fan Motor	Variable Speed Components	Fixed Speed Components
SSHP1	Scroll	PSC	None	Compressor Indoor Fan Outdoor Fan 1
SSHP2	Rotary	PSC	None	Compressor Indoor Fan Outdoor Fan 1
VSHP1	Rotary	PSC	Compressor Indoor Fan	Outdoor Fan 1
VSHP2	Rotary	PSC	Compressor Indoor Fan Outdoor Fan 1	None
VSHP3	Rotary	ECM	Compressor Indoor Fan Outdoor Fan 2	None

Table 4. SSHP1 test results.

Test	Indoor Air Flowrate	Static Head	Cooling Capacity	Compressor Speed	Outdoor Fan Speed	Indoor Power	Outdoor Power	Total Power	COP	SCOP
[-]	[m^3/hr]	[Pa]	[kW]	[%]	[%]	[W]	[W]	[W]	[-]	[-]
A	1338.84	142.4	6.7	100	100	206	1755.4	1961.4	3.49	3.88
B	1341.72	143.2	7.3	100	100	213	1509.9	1722.9	4.31	

For the baseline test, the cooling capacity matched the manufacturer value of 2 tons (6.7 kW) with a SCOP rating of 3.88. Overall excellent agreement with rated performance is achieved. The cooling capacity is validated by comparing the refrigerant and air side calculation method. For all tests both calculation methods matched within 7% which indicates accurate cooling capacity readings. Table 5 contains the baseline test results for the SSHP2.

Table 5. SSHP2 test results.

Test	Indoor Air Flowrate	Static Head	Cooling Capacity	Compressor Speed	Outdoor Fan Speed	Indoor Power	Outdoor Power	Total Power	COP	SCOP
[-]	[m^3/hr]	[Pa]	[kW]	[%]	[%]	[W]	[W]	[W]	[-]	[-]
A	1291.68	142.9	7.2	100	100	206.4	1786.4	1992.8	3.6	4.08
B	1323	143.7	7.8	100	100	213.5	1512.3	1725.8	4.54	

By changing the PSC scroll compressor to a PSC rotary compressor the SCOP rating increased by 4.98% to 4.08. The COP for the A-test increased by 3.24% to 3.6 and for the B-Test by 5.34% to 4.54, which indicates a higher cooling capacity for both tests. Table 4 and Table 5 show that the overall SCOP rating of the heat pump with the rotary compressor is higher than the heat pump using the scroll compressor. Typically, a single stage scroll compressor is more efficient than a similarly sized system with a rotary compressor, which is not the case for the tested units. The reason for this is delivered by Figure 3, which indicates that the isentropic efficiency of the rotary compressor is significantly higher than the scroll compressor.

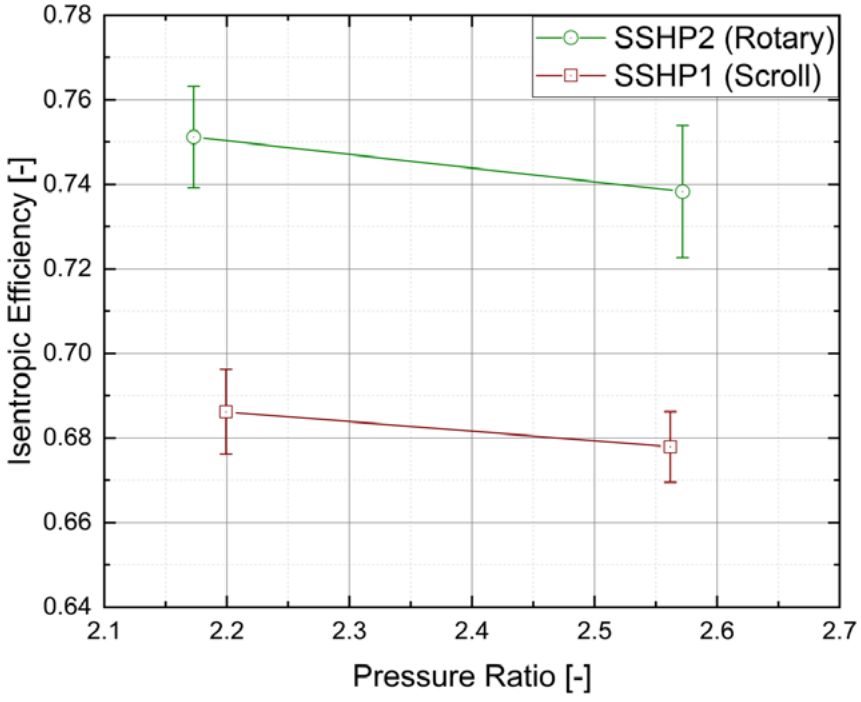


Figure 3. Isentropic Efficiency vs. Pressure Ratio for the A and B test of the AHRI Standard 210/240-2019.

Table 6 shows the results of testing the inverter modified VHSP with only the compressor connected to the inverter, operating in variable speed mode.

Table 6. VSHP1 test results.

Test	Indoor Air Flowrate	Static Head	Cooling Capacity	Compressor Speed	Outdoor Fan Speed	Indoor Power	Outdoor Power	Total Power	COP	SCOP
[-]	[m^3/h]	[Pa]	[kW]	[%]	[%]	[W]	[W]	[W]	[-]	[-]
A_2	1291.68	142.9	7.2	100	100	206.4	1786.4	1992.8	3.6	
B_2	1323	143.7	7.8	100	100	213.5	1512.3	1725.8	4.54	
E_v	1006.92	80.4	4.8	57	100	107.1	921	1028	4.66	4.88
B_1	829.44	59.8	3.4	35	100	75.99	568.9	644.9	5.25	
F_1	828.72	58.4	3.7	35	100	74.98	440.1	515.1	7.12	

The inverter modified heat pump enabled variable speed control over the compressor and the ability to match part load conditions. The SCOP rating of the heat pump was improved by 19.63% to 4.88 by just connecting the compressor to the inverter. An overall SEER improvement of 25.59% was achieved, compared to the SSHP1. Table 7 shows the results of testing the inverter modified VSHP with the compressor and the outdoor fan connected to the inverter and operating in variable speed mode.

Table 7. VSHP2 test results.

Test	Indoor Air Flowrate	Static Head	Cooling Capacity	Compressor Speed	Outdoor Fan Speed	Indoor Power	Outdoor Power	Total Power	COP	SCOP
[-]	[m^3/h]	[Pa]	[kW]	[%]	[%]	[W]	[W]	[W]	[-]	[-]
A_2	1291.68	142.9	7.2	100	100	206.4	1786.4	1992.8	3.61	
B_2	1350	143.7	7.8	100	100	213.5	1512.3	1725.8	4.54	
E_v	1005.84	78.53	4.7	57	79	103.5	892	995.5	4.75	5.18
B_1	854.64	57.35	3.4	35	66	75.09	515.3	590.4	5.83	
F_1	855.36	58.03	3.7	35	66	74.78	372.7	447.51	8.24	

The SCOP rating of the heat pump was improved to 5.18 by adding the variable speed option to the PSC outdoor fan and still providing the same cooling capacity. This SEER improvement is an increase of 27.1% compared to the SSHP2 and 33.43% compared to the SSHP1. The testing results for the inverter modified heat pump with an ECM for the outdoor fan are shown in Table 8.

Table 8. VSHP3 test results.

Test	Indoor Air Flowrate	Static Head	Cooling Capacity	Compressor Speed	Outdoor Fan Speed	Indoor Power	Outdoor Power	Total Power	COP	SCOP
[-]	[m^3/h]	[Pa]	[kW]	[%]	[%]	[W]	[W]	[W]	[-]	[-]
A_2	1324.08	143.1	7.2	100	89	206.4	1786.4	1992.8	3.61	
B_2	1324.44	143.8	7.7	100	89	213.5	1512.3	1725.8	4.54	
E_v	1007.64	79.81	4.8	57	67	103.5	892	995.5	4.75	5.42
B_1	857.88	58.46	3.4	35	53	75.09	515.3	590.4	5.83	
F_1	859.32	60.63	3.4	35	53	74.78	372.7	447.51	8.24	

By using an ECM outdoor fan instead of an inverter modified PSC outdoor fan the SCOP could be improved additionally by 4.52% to 18.48. The seasonal COP (SCOP) and SEER of the different heat pump test cases are shown in Figure 4.

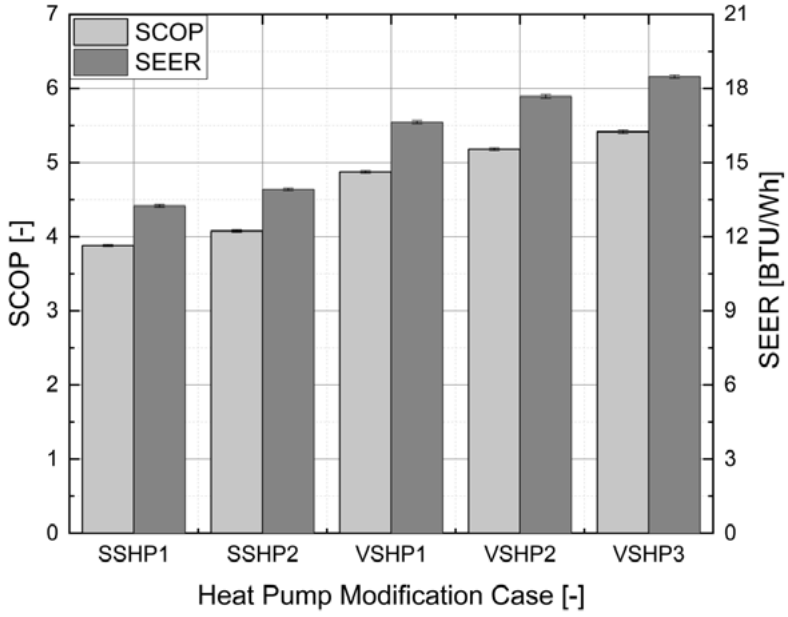


Figure 4. SCOP and SEER of the different heat pump test cases.

Table 9 shows the different heat pump modification cases with the SCOP, the SEER and the improvement in percentage. Table 9 and Figure 4 are indicating that the largest single improvement occurred from SSHP2 to VSHP1 by operating the PSC rotary compressor in variable speed mode along with a variable speed indoor ECM fan. The SEER could be improved by over 19% compared to the same heat pump setup without the electronic drive. Table 9 and Figure 4 also show that operating the PSC outdoor fan in variable speed mode has a significant impact. Operating the PSC outdoor fan in variable speed mode (VSHP2) shows an increase of more than 27.1% compared to SSHP2.

Table 9. Seasonal COP and SEER comparison for all test cases.

Test Case	SCOP	SEER	Improvement compared to SSHP1	Improvement compared to SSHP2
[-]	[-]	[BTU/Wh]	[%]	[%]
SSHP1	3.88 +/- 0.0149	13.25 +/- 0.0508	-	-
SSHP2	4.08 +/- 0.0156	13.91 +/- 0.0533	4.98 +/- 0.96	-
VSHP1	4.88 +/- 0.0187	16.64 +/- 0.0638	25.59 +/- 1.05	19.63 +/- 0.82
VSHP2	5.18 +/- 0.0199	17.68 +/- 0.0678	33.43 +/- 0.97	27.10 +/- 0.73
VSHP3	5.42 +/- 0.0208	18.48 +/- 0.0707	39.47 +/- 1.14	32.85 +/- 0.89

4. Conclusions

The results of this paper indicate that the use of an electronic drive to control the motor speeds of both PSC and ECM components improves the seasonal performance of an existing single-speed heat pump significantly. The highest SEER improvement was achieved by operating the PSC compressor and ECM indoor fan in variable speed mode with the help of the electronic drive. This shows that performance improvements can be made to an HVAC system that uses fixed-speed components by only modifying the power delivery system. In addition, the results clearly show that operating the outdoor fan in variable speed mode has a significant impact

on the SEER rating. Furthermore, operating the PSC outdoor fan using the inverter can be nearly as efficient as a conventional ECM outdoor fan.

Future work on this project is to connect the inverter control unit to the thermostat of a modified variable-speed unit. We would like to provide an automatic control of the inverter by changing the speed of the components depending on the ambient condition without input from the end user. This would be automatically determined by the ambient and user set point temperature with an optimization algorithm. Additional studies should be conducted to investigate the impact of the inverter drive for the heating mode of the heat pump and further the reliability of fixed-speed compressors and outdoor fans being operated in variable speed mode. One way to do this could be done by performing life cycle testing on an inverter modified heat pump with a fixed-speed compressor and outdoor fan paired to an inverter.

Acknowledgements

The authors would like to thank the Center for High Performance Buildings (CHPB) at the Ray W. Herrick Laboratories, Purdue University for the financial support of this study. Riley Barta, Tyler J. Shelly, Cai Rohleder and Dr. Orkan Kurtulus (Herrick Laboratories, Purdue University) provided useful insights on the experiment design and execution. We would also like to extend our deepest gratitude to Frank Lee who was the main technician on this study.

Nomenclature

A	Area	m^3
C	Coefficient of discharge	-
h	Specific enthalpy	$\frac{kJ}{kg}$
$\dot{m}$	Mass flow	$\frac{kg}{s}$
p	Pressure	kPa
$\dot{Q}$	Cooling capacity	W
T	Temperature	K
$\dot{V}$	Volume air flow	$\frac{m^3}{s}$
$\dot{W}$	Power	W
Y	Expansion factor	-

Acronyms

AHRI	Air-Conditioning, Heating, and Refrigeration Institute
COP	Coefficient of Performance
SCOP	Seasonal Coefficient of Performance
DOE	Department of Energy
EES	Engineering Equation Solver
ECM	Electronically Commutated Motor
HVAC	Heating, Ventilation and Air Conditioning
LabVIEW	Laboratory Virtual Instrumentation Engineering Workbench
PSC	Permanent Split Capacitor
RPM	Rotations Per Minute
SEER	Seasonal Energy Efficiency Rating
SSHP	Single Speed Heat Pump
TXV	Thermostatic Expansion Valve
US	United States
VI	Visual Interface
VSHP	Variable Speed Heat Pump

Greek Symbols

ρ	Density	$\frac{kg}{m^3}$
ω	Air Humidity Ratio	–

Subscript

1, 2, 3, …	State Points
air	Air
evap	Evaporator
indoor	Indoor
net	Net capacity
nozzle	Nozzle Box
total	Total
water	Water

References

[1] Cayer, E.; N. u. Nesreddine, H.: Parametric study and optimization of a transcritical power cycle using a low temperature source, *Applied Energy 87* (2010), p. 1349-1357

[2] U.S. Energy Information Administration (EIA): *Annual Energy Outlook* (2019)

[3] Liecau, L.; Chapman, M. G.: Residential Heating and Cooling Systems Initiative Description, *Consortium for Energy Efficiency* (2015)

[4] Goetzler, W.; Sutherland, T.; Reis, C.: Energy Savings Potential and Opportunities for High-Efficiency Electric Motors in Residential and Commercial Equipment, *US Department of Energy, Energy Efficiency & Renewable Energy* (2013)

[5] Chretien, L.; Becerra, R.; Salts, N.; Groll, E. A.: Sesonal Energy Efficiency Rating Improvement of Residential HVAC Systems using a Low Power Inverter with a PSC Compressor, *International Refrigeration and Air Conditioning Conference* (2018), Paper 1896

[6] Chretien, L.; Becerra, R.; Salts, N.; Groll, E. A.: System solution to improve energy efficiency of HVAC systems, *IOP Conference Series: Materials Science and Engineering* (2017), 232 012067

[7] Salts, N. P.; Rohleder, C.; Groll, E. A., Chretien, L., Yang, B.; Becerra, R.: Performance Testing of a Dual Rotary Compressor with Variable Speed PSC Motor, *IOP Conference Series: Materials Science and Engineering* (2019)

[8] AHRI Standard 210/240: Performance Rating of Unitary Air-conditioning & Air-source Heat Pump Equipment, *AHRI Standard* (2017)

[9] Klein, S.: "Engineering Equation Solver", F-Chart Software, v.10.268 (2018)

[10] ASHRAE Standard 37-2009: Methods of Testing for Rating Electrically Driven Unitary Air-Conditioning and Heat Pump Equipment, *ASHRAE Standard* (2009)

13th IEA Heat Pump Conference 2020

13th IEA Heat Pump Conference
April 26-29, 2021 Jeju, Korea

Disproportionation risk study for HFO-1123 compositions as Low-GWP refrigerants

Hidekazu Okamoto*, Tetsuo Otsuka, Hiroki Hayamizu, Tatsuya Ueno

AGC Inc., Marunouchi 1-5-1, Tokyo, 100-8405, Japan

Abstract

In this study, we reported the risk assessment evaluation of the HFO-1123 containing refrigerant mixture that was previously developed as an alternative to HFC-32 and R410A refrigerants. Based on conventional knowledge, the refrigerants containing HFO-1123 might inherent safety risk of an autocatalytic disproportionation reaction. In order to address this issue, we evaluated the probability of air conditioner unit failure by this reaction process using the the risk assessment technique that was previously use for HFC-32. Disproportionation reaction occurs when the refrigerant is exposed to an ignition source under high-temperature and high-pressure conditions similar to the conditions inside the compressor unit. We performed a risk assessment of disproportionation of a HFO-1123/HFC-32 refrigerant mixture (40% /60% by weight). Our study concluded that by adding additional safety measures such as manual recovery unit, the safety risk of HFO-1123/HFC-32 refrigerant mixture at the same level of HFC-32 refrigerant.

Keywords: Refrigerant ; Low-GWP; HFO-1123; Disproportionation; RAC; Risk assessment

1. Introduction

In recent years, HFC-32 has become a popular alternative refrigerant to R410A for residential air conditioners (RACs). According to the ASHRAE classification, R410A is classified as A1 non-flammable substances. HFC-32, however, is classified as A2L mildly flammable substance and therefore must be subjected to flammability risk assessment [1-2]. More recently, hydrofluoro-olefins (HFOs) have accepted as next generation refrigerants with lower global warming potential (GWP) property. And previously we have proposed a refrigerant containing trifluoroethylene (HFO-1123) for residential air conditioning applications. The typical physical properties of HFO-1123 and other refrigerants are shown in Table 1 [3]. HFO-1123 has a boiling point close to that of HFC-32 compared to other HFO refrigerants that have been proposed as an alternative for R410A. It is possible to provide a mixed refrigerant with small temperature glide in a variety of composition range [3]. Figure 1 shows that HFO-1123 can form a mixed refrigerant that has small temperature glide over a wider range than HFO-1234yf and HFO-1234ze(E). Although this excellent property, fluorinated ethylene compounds, such as tetrafluoroethylene (HFO-1114), is known to cause an autolytic disproportionation reaction generating significant heat. There are, in fact, reports on previous explosion accidents at chemical plants [4]. HFO-1123 is also known to und[1]ergo disproportionation in the presence of an ignition source (equation 1) [5]. Therefore the safety issue of HFO-1123 needs to be addressed before introducing them into practical use as adequate refrigerants. To clarify this risk, we evaluated the probability of unit failure by the disproportionation reactions for mixed refrigerants containing HFO-1123, using fault-tree analysis (FTA), a technique used previously in assessing the flammability risk of HFC-32 [2].

$$CHF{=}CF_2 \rightarrow 1.5C\ (amorphous) + 0.5\ CF_4 + HF + 250\ kJ/mol \quad (1)$$

* Hidekazu Okamoto. Tel.: +81-50-9014-1358; fax: +81-45-374-8834.
E-mail address: hidekazu-okamoto@agc.com

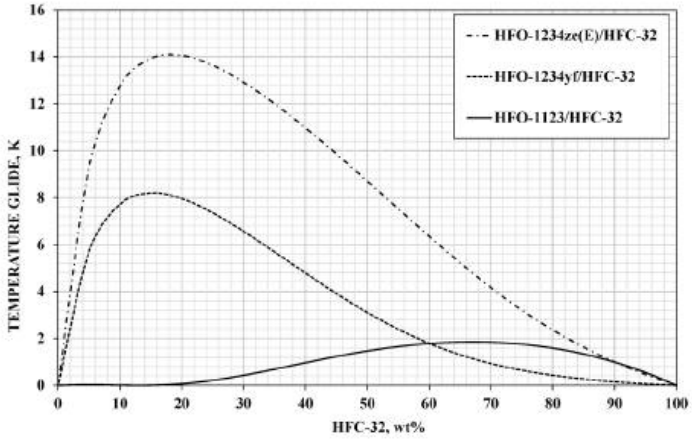


Fig. 1 Temperature glide of HFOs and HFC-32 mixtures

Table 1. Chemical and physical properties of HFOs and HFCs

	HFO-1123	HFO-1234yf	HFC-32	R-410A
Molecular weight, g/mol	82.0	114.0	52.0	72.6
Normal boiling point, K	214.0	243.7	221.5	222.2
Critical temperature, K	331.9	367.9	351.3	344.5
Critical pressure, MPa	4.5	3.38	5.78	4.90
Critical density, kg/m^3	492	476	424	459
Vapour pressure(273K), kPa	1084	316	813	798
Liquid density(273K), kg/m^3	1126	1176	1055	1170
Vapour density(273K), kg/m^3	48.6	17.7	22.1	30.6
Flammable limits (296K, 101.3kPa), vol%	10.4-29.3*/**	6.2-12.3	14.4-29.3	None
LFL, kg/m^3	0.34	0.29	0.31	-
Burning velocity, cm/s	6.6*	1.5	6.7	-
Nominal heat of combustion, MJ/kg	9.9	10.7	10.1	-
Atmospheric lifetime, Year	1.5 Days*	11 Days	4.9	-
GWP(ITH=100), CO_2=1	0.0054*	4	675	2090
Ames test	Negative	Negative	Negative	Negative
LC_{50}, ppm	>200,000	>400,000	>760,000	-
OEL, ppm	750	500	1000	1000
ASHRAE Classification	(A2L) (Expected)	A2L	A2L	A1

* Measured by the National Institute of Advanced Industrial Science and Technology
**35°C, dry air

2. Scope of Risk assessment

2.1. Incident probability allowance

Referning to ISO/IEC Guide 51 of the probability of an incident that is allowed in a risk assessment (“allowance” below), we performed a study using the R-Map methodology proposed by National Institute of Technology and Evaluation (NITE) to estimating incident frequency and to quantifying the frequency of an occurrence. In the case of chemical plants and other large-scale facilities, which are under a variety of regulations, the allowance is set below 10^{-5} events/year. And for household appliances that typically require mimimum maintenance, the allowance is set below 10^{-8} units/year (on a 1-million unit basis) based on the probability of a major incident occurance. In other words, for a product that has 1 million units being distributed per year, there needs to be less than one fatal injury every hundred years. In this study, refering to our previous work on allowances for air conditioners [1-2], we specified a target probability of incidents in use of 10^{-10} units/year or less, because the extent of damage from disproportionation is unclear and we assume the maximum damage under R-Map.

2.2. Possible ignition sources

Disproportionation is known to happen when an ignition source is present under both high temperature and high pressure conditions [6]. Therefore, there is minimum risk of disproportionation when the refrigerant leaks at atmospheric pressure. However the risk is significantly high inside the compressor of air conditioning unit where elevated pressures and temperatures exist. Thus we hypothesized that the ignition sources could be caused by (a) static electricity caused by a refrigerant flow, (b) spark of layer short circuit or lead wire short circuit resulting from melted insulation coating due to either faulty manufacture of the insulation member or abnormally high temperature, and (c) frictional heat by contacting between compressor rotor and casing. The estimated amount of energy of the three respective ignition sources are as follows. In the case of ignition source (a), the possible charge of static electricity in everyday space is up to about 12 kV when the relative humidity is low. When the capacitance is 100 pF, the discharge energy is 7.2 mJ [7]. In safety assessments for flammable gas facilities, the standard for spark energy is that a maximum of 20 mJ (or 40 mJ) is considered good, so we took 40 mJ as the static spark energy. As for (b), we assessed ignition sources comprehensively for this paper using fault-tree analysis (FTA). And lastly, as for (c), since the compressor rotor is metallic and has high thermal conductivity, therefore under normal operations, it has no risk of becoming an ignition source.

3. Results and Discussion

3.1. Risk assessment of disproportionation in constant-speed air conditioners

A mixture of HFO-1123/HFC-32 refrigerants (40% /60% by weight: GWP: 405) was used in our study as the model case of HFO-1123 containing refrigerant system in our risk assessment. For conditions under which an ignition source might appear leading to disproportionation under operating conditions for RACs, we performed a comprehensive analysis by using the FTA methodology [8]. To investigate the cases of abnormal operation, we carried out simulation tests of abnormal operation using actual equipment [8]. As the result, the greatest temperature and pressure rise was observed in the heating operation with either a three-way valve closed or a forgotten opening valve after installation or subsequent regular services (A). Other abnormal operations being considered in our study were the condenser side fan stoppage during operation (B) and contact fusion of compressor relay (C). Figure 2 shows the FTA of possible failure modes that could lead to ignition sources. The failure mode I and the failure mode II show the events that may create ignition sources due to the above abnormal operations, while the failure mode III shows the events that can create ignition sources due to either mechanical failures or the like during normal operation.

In the failure mode I and II, the safety device and controller mounted on the compressor will stop functioning with continuous live current due to intermittent repetition of operation. These will cause the compressor to stall, the motor essentially becoming a low-resistance heater and rapidly heating up with increasing pressure. The compressor's interior would exceed the temperature at which the windings melt, leading to break down of the insulation and current sparking lead to disproportionation.

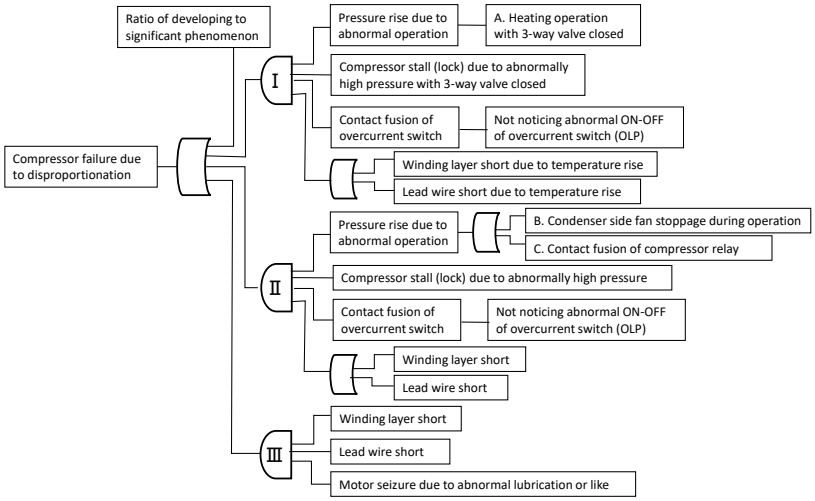


Fig. 2. FTA leading to disproportionation inside residential air conditioners

3.1.1. Risk assessment of disproportionation due to abnormal operation

For values and safety equipment used for our risk assessment, we took the probabilities of functional failure to be at the line between safety-integrity level (SIL) 3 and 4 at safety device that operate high-frequency in Table 2 (10^{-8} times/h). Based on JIS room air conditioner standard (JIS C 9612: 2013), the assessment was held for total yearly running time of a residential air conditioner, we used the 2500 h/year, and based on that get a failure rate for ordinary electrical components of 2.5×10^{-5} ($= 10^{-8} \times 2500$), and we used a human error of 3×10^{-3} [9].

Table 2. Functional safety of electric, electronic, and programmable electronic safety systems under IEC61508 (JIS C0508)

	Safety level	Average probability of functional failure in design per work request
Safety device that operate low-frequency	SIL 4	10^{-5} to less than 10^{-4}
	SIL 3	10^{-4} to less than 10^{-3}
	SIL 2	10^{-3} to less than 10^{-2}
	SIL 1	10^{-2} to less than 10^{-1}
	Safety level	Average frequency of dangerous failure of safety function (times/ h)
Safety device that operate high-frequency	SIL 4	10^{-9} to less than 10^{-8}
	SIL 3	10^{-8} to less than 10^{-7}
	SIL 2	10^{-7} to less than 10^{-6}
	SIL 1	10^{-6} to less than 10^{-5}

Figure 3 shows the flowchart of disproportionation which result from heating operation with the three-way valve closed (abnormal operation mode I). We assessed the probability of an incident resulting from abnormal operations going unnoticed as shown in the Table.3. In this scenario, which assumes the compressor reaching an internal temperature above 250°C, the winding and lead wire have a probability of dielectric breakdown of 1. When using our model refrigerant (HFO-1123/HFC-32:40 wt%/60 wt%), we calculated that disproportionation resulting from a spark ignition source caused by this dielectric breakdown would have a probability of 1 as well. Disproportionation resulting from heating operation with a three-way valve closed has a probability of 9×10^{-9} instances/year.

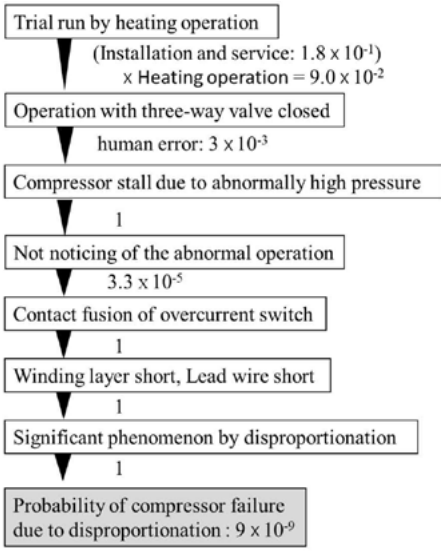


Fig. 3. Flowchart of heating operation with three-way valve closed

Table 3. Probability of anomalous operation going unnoticed

By installers and service personnel			By user		Incidence by mode
Test run	Test run contents	Miss rate	Setting conditions	Miss rate	
done 0.997	Perform until normal operation confirmation (10 min): 0.997	3×10^{-3}	One unit per room 0.9	3×10^{-3}	8.1×10^{-6}
			Several unit per room 0.1	1×10^{-2}	3.0×10^{-6}
	Startup confirmation only (10 sec): 3×10^{-3}	1	One unit per room 0.9	3×10^{-3}	8.1×10^{-6}
			Several unit per room 0.1	1×10^{-2}	8.1×10^{-6}
No test drive was performed 3×10^{-3}		1	One unit per room 0.9	3×10^{-3}	3.0×10^{-6}
			Several unit per room 0.1	1×10^{-2}	3.0×10^{-6}
Total					**3.3×10^{-5}**

Figure 4 shows the flowchart of the probability of disproportionation which result from the fan being stopped on the condenser side during operation (abnormal operation mode II-B). We calculated the probability that abnormal operation would go unnoticed as shown in Table 4.

In this case, in a simulation using only the compressor, the temperature and pressure of refrigerant at the compressor's outlet port would not climb as in the case where the three-way valve is closed; even if there were a short circuit of the winding and lead wire causing a spark ignition source that would not result in disproportionation, and the probability of that happening is calculated as low as 10^{-6} [8]. In addition, the probability of disproportionation resulting from the condenser-side fan being stopped during operations, according to the flowchart, is estimated in the range of 9.3×10^{-14} instances/year.

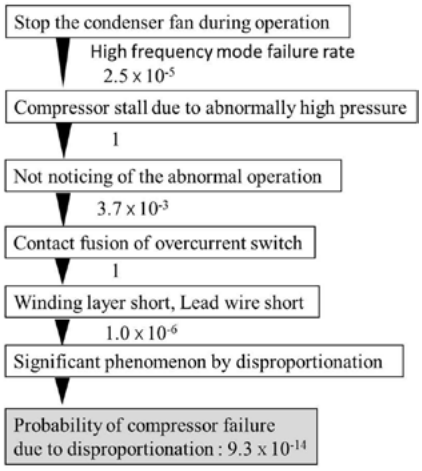


Fig. 4. Flowchart of condenser-side fan stopping during operation

Table 4. Probability of anomalous operation going unnoticed

By user		Incidence by mode
Setting conditions	Miss rate	
One unit per room 0.9	3×10^{-3}	2.7×10^{-3}
Several unit per room 0.1	1×10^{-2}	1×10^{-3}
Total		**3.7×10^{-3}**

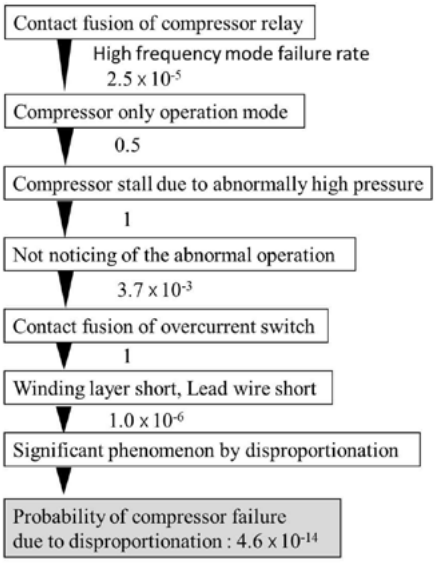


Fig. 5. Flowchart of runaway mode caused by compressor relay spot-welding itself

Figure 5 shows the flowchart of the probability of disproportionation which result from the compressor being in runaway mode due to the compressor relay (an electromagnetic contact device) spot-welding itself (abnormal operation mode II-C). We calculated the probability that abnormal operation would go unnoticed as shown in Table 4. In this case as well, even if there were a dielectric breakdown on the winding and lead wire causing a spark ignition source, the accourance would not result in disproportionation since probability of that happening is as low as 10^{-6}. Following the flowchart, the probability of disproportionation occurring due to its relay spot-welding itself as a result of the compressor being in runaway mode is estimated to be 4.6×10^{-14} instances/year. Combining together the results the above flowcharts, the total probability of an incident during one year that as the probability of a single unit have a disproportionation incident resulting from anomalous operations modes in the classes I, II-B, and II-C is 9×10^{-9} (as shown in Table 5).

Table 5. Probability of disproportionation per unit (total of three anomalous operations modes)

Mode	Probability (instances/year)
I. Cooling operation with three-way valve closed	9×10^{-9}
II-B. Condenser-side fan stopped	9.3×10^{-14}
II-C. Compressor relay spot-fusing	4.6×10^{-14}
Total	9×10^{-9}

3.1.2 Risk assessment of disproportionation due to normal operation

The flowchart in Figure 6 shows mode described in section III of Figure 2, for disproportionation resulting from normal operations. The probability of a lead wire short circuit or a layer short circuit in the windings during operation can be assumed to be 10^{-6}. Conversely, when a short circuit occurs in the temperature and pressure ranges prevailing under normal operations, the likelihood that this would lead to disproportionation is dramatically different due to the ignition energy that would cause spark ignition. We concluded an experiment in order to simulate spark ignition similar to a winding layer short circuit or lead wire short circuit inside a pressure vessel charged with refrigerant, and evaluated for disproportionation in a variety of temperature and pressure ranges [10-11].

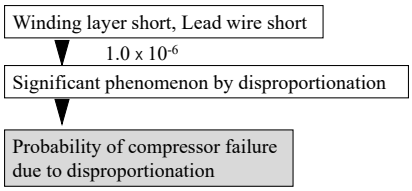


Fig. 6. Flowchart of the disproportionation mode during Nomal operation

Using equipment with ignition electrodes inside a pressure resistant reaction chamber (Figure 7), we confirmed the presence or absence of disproportionation phenomenon by observing temperature and pressure rises after ignition in a chamber with a fixed gap type ignition electrode. With this type of ignition electrodes, the breakdown potential gradient is extremely large in the system where a high-density fluorine-containing refrigerant with large breakdown voltage for use in RACs is present. Thus, it is necessary to apply an extremely high voltage or use a very small inter-electrode distance for generation of sparks. For the purpose of this study, the risk assessment needs to simulate the conditions of home power supply. And it was difficult to employ spark generation by the ignition method specified in the ASTM standard (ASTM E681-94, 1994) [12] because of the problem of easy short-circuiting of electrodes by the soot resulting from the disproportionation reaction (equation 1). Hence, we devised a movable gap type spark ignition system (see an enlarged view in Figure 7) and conducted the evaluation by an ignition method simulating spark phenomena that would occur in the compressor of air conditioners [10]. The spark generation mechanism is described in detail below. When a voltage is applied to one of the copper plates of ignition device, current begins to flow (the insert in Figure 7). A magnetic field is generated in accordance with Ampere's circuital law, and the current flowing due to the generated magnetic field is subjected to outward force of the circuit. By this force, the tungsten screws set on the cupper plate repel each other and separate (the insert in Figure 7). An electrical spark occurs at the moment when they separate. The power source used was an AC power source that is generally used for room air conditioners. In determining the ignition energy, the time change of current and voltage was monitored using an oscilloscope (Tektronix, TDS5054B), and the energy value was calculated using equation (2) by the time integration of current I(t) and voltage V(t) between the point (t_1) where the resistance value rises steeply and the point (t_2) where the resistance value returns back to the original value.

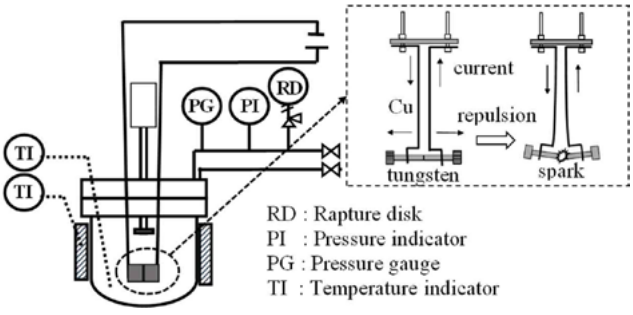


Fig. 7. Explosion apparatus with spark ignition electrode

$$E = \int_{t_1}^{t_2} I(t) \cdot V(t) dt \quad (2)$$

In normal operations, the operating conditions for the mixture refrigerant containing HFO-1123 have a maximum temperature of 130°C and a maximum attainable pressure of 4 MPa, referring to HFC-32's envelope diagram near its boiling point [13]. Based on the calculation using REFPROP [14], temperature of 86°C and pressure of 3.5 MPa, and taking into account a safety margin, we considered that these figures are reasonable.

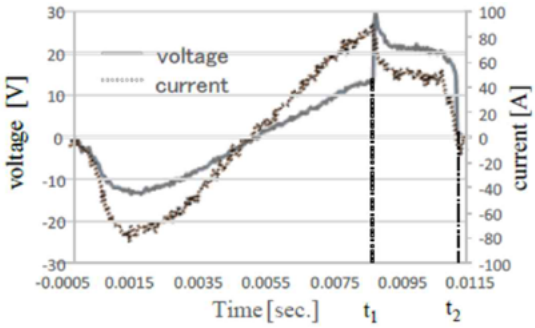


Fig. 8. Voltage and current intensity vs time

Then, we evaluated whether disproportionation occurs in the presence of various kinds of ignition energy at 130°C and 4 MPa. Figure 9 shows the results of 108 spark ignition tests at 130 °C, 4 MPa plotted versus the spark energy of the refrigerant mix with 60% by weight HFO-1123 and 40% by weight HFC-32. Our test was conducted with a composition having a higher amount of HFO- 1123 than the composition that was the subject of this risk assessment (HFO-1123 / HFC-32: 40 wt% / 60 wt%). This is because a very large amount of ignition energy is required to generate disproportionation for that composition. We regard disproportionation as being a phenomenon with the same probability as explosive combustion [4], and calculated a minimum ignition energy (MIE) using statistical analysis. It was difficult to generate consistent spark energy with the spark ignition device used in our experiment, making it difficult to perform the regression analysis used in ordinary statistical analysis. The logistic regresion method has been the major procedure to calculate the ignition probability distribution. But Rudz et al. [15] compared three methods, which are cumulative logistic distribution, cumulative normal distribution, and cumulative lognormal distribution. They concluded that a cumulative lognomal distribution was the most suitable for their experimental results. They reported the ignition probability by a cumulative logistic distribution and a cumulative normal distribution, was not zero when the ignition energy is zero. It was not appropriate to discuss low probability around 10^{-8} for the safety evaluation of this risk assesment. Therefore in our study the lognomal model was used to caluculate the minimum ignition energy distribution of disproportionation. By using the 108 measured values shown in Figure 9, as in the previous report [10], the parameters of equation (3) were determined as follows, and the ignition probability for each energy was calculated. Table 6 shows some ignition probabilities calculated from equation (3) with given ignition energies.

$\mu = 3.863$, $\sigma = 0.233$.

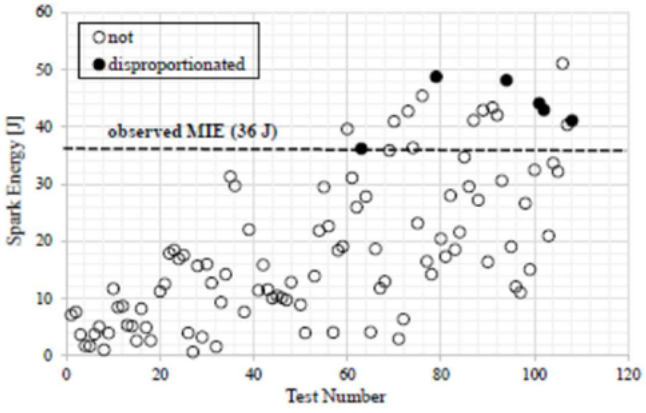


Fig. 9. Plot of 108 tests vs spark energy (HFO-1123/HFC-32:60wt%/40wt%, 130°C, 4MPa)

$$P(x) = \frac{1}{2}\left(1 + erf\left(\frac{ln(x) - \mu}{\sigma\sqrt{2}}\right)\right) \quad (3)$$

Based on these results, we assessed the probability of disproportionation occurring using the flowchart in Figure 6, and determined that the probability of this phenomenon changes depending on the spark ignition energy inside the compressor. Our result suggests that the probability will be even lower than that shown in Table 7 when using the model refrigerant (HFO-1123/HFC-32: 40 wt%/60 wt%) of this risk assessment.

Table 6. Calculated ignition probabilities and given ignition energies at 130°C, 4Mpa (HFO-1123/HFC-32 : 60wt%/40wt%)

130℃, 4Mpa		Spark energy
Observed	Exp.	36 J
Calculated	DEP* 50%	48 J
	DEP* 1%	28 J
	DEP* 0.001%	20 J

* Disproportionation event probability

Table 7. Probability of disproportionation per unit (under normal operations)

Expected spark ignition energy	Probability of winding layer short or lead wire short	Probability of disproportionation from ignition	Probability of disproportionation per unit
48 J	1.0×10^{-6}	0.5	0.5×10^{-6}
28 J		1.0×10^{-2}	1.0×10^{-8}
20 J		1.0×10^{-5}	1.0×10^{-11}

3.2. Summary of risk assessment & safety measures

For residential air conditioner unit, with a mixture refrigerant of HFO-1132/HFC-32, the risk of disproportionation is mainly determined by the spark energy from a winding layer short circuit or lead wire short circuit that might occur in the equipment. There is almost no statistical research into the spark energy from winding layer short circuits in air conditioning equipment, and it can be assumed that this will vary considerably depending on the equipment's design, the usage environment, and etc. For our model case, we assumed a typical compressor used in RACs (constant-speed, 3.48 kW cooling and heating type, single-phase power supply at 50 Hz, using R410A refrigerant) connected to ordinary household lines, in which the compressor rotor is locked and current is flowing causing the windings to heat up, leading in turn to a dielectric breakdown, we measured the spark energy from this. We assessed two kinds of motors, with distributed windings or concentrated windings. Results are shown in Table 8.

Table 8. Evaluation of spark ignition energy occurring within the compressor

	Test conditions		Spark phenomenon result		Conditions on sparking	
	Winding type	Grounded	Spark energy [J]	Number of sparks	Temp. [°C]	Pressure [MPa]
1	Concentrated	Yes	0.01–0.02	Several	233	8.9
2	Concentrated	Yes→No	0.01–0.1	Several	243	9
3	Concentrated	No	0.01	Several	338	9.4
4	Distributed	Yes	0.1–40	7	236	8.7
5	Distributed	No	0.01–20	85	238	9.5
6	Distributed	No	0.01–23	92	245	8.7

Table 8 shows that a concentrated-winding motor produces a maximum spark energy of 100 mJ, while a distributed winding motor can produce up to 40 J. This result shows that the spark energy that can be generated inside the compressor differs greatly depending on the winding system and the compressor design.

To prevent disproportionation in this kind of air conditioner with the refrigerant being studied, it would be necessary for allowance to be quantitively on the order of 10^{-3}, and qualitatively, there would need to be independent protection measures that would allow for one to fail.

Following are possible independent protection measures that would allow for one to fail.

A) A refrigerant mixture that would not disproportionate in the presence of spark energy that would result from normal operations or the worst-case scenario envisioned for abnormal operations (Figure 2, mode I). Specifically, a refrigerant with less HFO-1123 in the refrigerant composition would be one solution, but increasing the ratio of HFC-32 in the refrigerant composition has the disadvantage of increasing the GWP. Instead, another HFO refrigerant (such as HFO-1234yf), which would not increase GWP, should be considered for addition to the refrigerant composition.

B) Refrigerant with restrictions for use

B-1) Require two or more manual-recovery protection devices (detection by pressure, temperature, current, etc.) for at least one instance.

B-2) In addition to an overcurrent switch, require an additional manual-recovery protection device that can directly disconnect the compressor circuit.

Table 9 shows probability of disproportionation when the above measures in place.

Table 9. Revised disproportionation probabilities

Type of problem		Base spec	Remedy		
			1. Auto-recovery safety device	2. Manual-recovery safety device	3. Non-Disproportionating composition
Equipment in cooling operation		9×10^{-2}	9×10-2	9×10^{-2}	9×10^{-2}
Operating with 3-way valve closed		3×10^{-3}	3×10^{-3}	3×10^{-3}	3×10^{-3}
OLP inoperative (short)	trial-run action overlooked	9×10^{-3}	9×10^{-3}	9×10^{-3}	9×10^{-3}
	On/off during operation overlooked (≒ 1 month)	3.7×10^{-3}	3.7×10^{-3}	3.7×10^{-3}	3.7×10^{-3}
2nd protective device inoperative	On/off overlooked (next month)		7×10^{-1}		
	Manual recovery protective device inoperative			3×10^{-4}	
Disproportionation		1	1	1	0.2
Disproportionation leading to serious outcome		1	1	1	1.0×10^{-3}
Probability of disproportionation (incidents per year per unit)		9×10^{-9}	6.3×10^{-9}	2.7×10^{-12}	1.8×10^{-12}

4. Conclusion

This study investigated a risk assessment of a refrigerant consisting of 40 wt% HFO-1123 and 60 wt% HFC-32, which could be adopted as an alternative to R410A with a much lower GWP, as used in RACs. The study calculated the probability of significant incidents resulting from disproportionation while operating the air conditioners. The results show that the probability of a significant incident from foreseeable abnormal operations of the equipment, which have the highest risk mode could not cross the threshold of 10^{-10} units/year. This threshhold is the target of probability for serious incidents being allowed for residential products. In addition, we recommed some kind of additional safety measures, such as the addition of protection measures with manual recovery, which would allow for one to fail, would be necessary to bring the risk below the target threshold.

We conducted a risk assessment of the refrigerant in equipment under normal operations, assessing the energy for a layer short circuit in the windings or a lead wire short circuit, that might occur inside a compressor under normal operations, and the probability of these events. Although the result clearly highlights these important factors and conclusive, because of limited literature on the subject, further assessment of the risk would be necessary.

Acknowledgements

This study was supported by the New Energy and Industrial Technology Development Organization (NEDO).

References

[1] Takaichi K. The safety measures of the mini split air conditioner with A2L refrigerant in JRAIA. *Reito* 2013; **88**: 753-9

[2] Takaichi K. 2012. "Risk Assessment of Mini-Split air-conditioners with A2L Refrigerant in Progress," The International Symposium on New refrigerants and Environmental Technology, Kobe, Japan, p. 90-4

[3] Hashimoto M., Otsuka T., Fukushima M., Okamoto H., Hayamizu H., Ueno K., Akasaka R. Development of new Low-GWP refrigerants-refrigerant mixtures including HFO-1123. *Science and Technology for the Built Environment* 2019; **25**: 776-83

[4] Reza A., Christiansen E. A case study of TFE explosion in PTFE manufacturing facility. *Process Safety Progress* 2007; **26**: 77-82.

[5] Lisochkin Y. A., Poznyak V. I. Evaluation of the explosibility of fluorine-containing monomers and their mixtures according to the minimum ignition pressure for a fixed igniter energy. *Combustion, Explosion, and Shock Waves* 2006; **42**: 140-3

[6] Tanaka T., Okamoto H., Ueno K., Irisawa J., Otsuka T., Nogami T., Dobashi R. 2014. "Development of a New Low-GWP Refrigerant Composed of HFO-1123," Annual meeting of AIChE, Atlanta, USA, paper #256d

[7] Electrostatic Society, *Compact static electricity Handbook*, Tokyo: Ohm; 2006, p. 132

[8] New Energy and Industrial Technology Development Organization. 2016. "Safety assessment of the inherent characteristics of the low-GWP refrigerant," Research report, Japan, Report #20160000000627: p. 50-62

[9] WASH-1400, Reactor Safety Study. *An Assessment of Accident Risks in U.S. Commercial Nuclear Power Plants Rasmussen* 1975

[10] Otsuka T., Ueno K., Okamoto H., Ippommatsu M., Dobashi R. Analysis of disproportionation process of trifluoroethylene using high power spark ignitions over 5J. *J. Loss Prev. Process Ind.* 2018; **51**: 36-41

[11] Okamoto H., Otsuka T., Hayamizu H., Ueno K., Fukushima M., Ippommatsu M. 2018. "Disproportionation risk study for trifluoroethene composition as Low-GWP refrigerants," 1st IIR International Conference on the Application of HFO Refrigerants. Birmingham, UK, paper #1132.

[12] ASTM. E681-94, *American Society for Testing and Materials*, Philadelphia: PA; 1994

[13] Pham H. M., Monnier K. 2016. "Interim and Long-Term Low-GWP Refrigerant Solutions for Air Conditioning," International Refrigeration and Air Conditioning Conferences. Perdue, USA, paper #2402.

[14] Lemmon E. W., Huber M. L., Mclinden M. O. 2013. REFPROP. Version 9.1: NIST Reference Fluid Thermodynamic and Transport Properties

[15] Rudz S., Chetehouna K., Strozzi C., Gillard P. Minimum ignition energy measurements for α-pinene / air mixtures. *Combustion Science and Technology* 2014; **186**: 1597-1605

13th IEA Heat Pump Conference
April 26-29, 2021 Jeju, Korea

Improving Risk Assessment Of Refrigerant Leakage Hazards: Going Beyond Physical Testing

Sangamesh Hosur[a*], Mahmood Tabaddor[b]

[a]UL India Pvt Ltd, Kalyani Platina, Block I, Whitefield, Bengaluru-560066 INDIA
[b]Underwriters Laboratories LLC, 333 Pfingsten Road, Northbrook, Illinois – 60062 USA

Abstract

Simulation based risk assessment of refrigerant leakage hazards calls for accurate prediction of concentrations of the leaked refrigerant gas into an indoor environment. Although computational fluid dynamics (CFD) is seen as a promising tool to model complex dispersion scenarios, it is necessary that it be properly validated against reliable experimental data before the predictions can be used with confidence. In this paper, validation of the model is carried out for some scenarios involving a propane gas leak in to a confined space with various leak flow rate and locations. More importantly, we introduce a new risk metric to measure the probability of fire when there is leakage of a combustible propane gas into a confined space. This risk metric can only be obtained from the rich data generated by CFD modeling. This risk metric tracks the volume of combustible propane gas that lies between the upper and lower flammability limits. The results demonstrate how the risk metric provides a simple of fire risk ranking for different leakage scenarios.

© HPC2020.
Selection and/or peer-review under responsibility of the organizers of the 13th IEA Heat Pump Conference 2020.

Keywords: CFD, Species transport, turbulence, refrigerant leakage, diffusion, fire risk;

1. Introduction

A global effort to reduce the greenhouse warming potential of refrigerants for refrigeration systems has reduced the overall candidate list to refrigerants that exhibit higher flammability than their predecessors. This has required additional investigations to ensure that the potential fire/explosion hazards associated with leakage of a flammable refrigerant are properly addressed and mitigated. The main means to gaining data to support risk assessments has been through physical testing [1].

However, there is a challenge and a limit to using physical testing to methodically understand the potential risks associated with leakage of a combustible refrigerant in confined spaces. One obvious challenge is that physical testing, especially if it could involve fire and explosion, is expensive and time consuming. Yet more importantly, each physical test is only a single data point and so, many tests must be run to cover scenarios of interest, which requires significant funding. Another limitation of physical testing is that it is only possible to capture data at discreet points during the physical test. These discrete points are usually selected to address the specific question the test was designed to answer and so the data collected may not provide sufficient insight into the testing conditions or allow for generalization.

An alternative to physical testing, or rather a complement, is the use of computational modeling tools. These tools have been used sporadically to help understand the risks associated with leakage of combustible refrigerants [2,3]. For modeling, the key challenge is to validate the simulation, that is to demonstrate via experimental evidence that the model predictions are accurate [4,5,6]. In one research report [1], the results of testing and simulation were compared, yet the validation of the simulation was not properly conducted. In other similar research conducted on refrigerant leakage hazard, the published reports [2,3] demonstrated good

* Sangamesh Hosur. Tel.: +91.80.4138.64627; fax: +0-000-000-0000 .
E-mail address: sangamesh.hosur@ul.com

agreement between the model predictions and those from the test, and yet only a single point was selected for this conclusion. This is not enough to establish high confidence validation and could potentially hide flaws in the model that become more prevalent when used for other leakage scenarios.

Also, there is a challenge of using a few discrete points to assess the fire/explosion risk of a combustible refrigerant leakage scenario. When the intent is to determine if ignition of the leaked refrigerant is possible, the exact location of the ignition sources are critical and ignition outcomes could change drastically depending on the location of the ignition source(s) and local gas concentration levels. Also, the risk scenario of an active combustible gas leak is time dependent and therefore, a single fire or no fire outcome from an ignition source activated at an instant of time is not sufficiently informative of the full transient state.

The intent of our research is to demonstrate two things: (1) rigorous validation evidence for a simulation of refrigerant leakage in gaseous form in a confined space. And, (2) a new, simple risk metric for assessing the potential fire/explosion hazards associated with leakage of refrigerant into a confined space. This metric can only be obtained from the rich data provided by such computer-based engineering tools.

2. Physical Test Set-up

The experimental setup that was simulated was carried out at the fire testing facilities at UL [7]. A 3.6 m by 2.4 m by 2.4 m room was constructed within the facility as shown in Figure 1(b). The room was constructed with dimensions in accordance with ISO 9705 [8]. The room contained an obstruction of 1.83 m by 0.91 m by 0.91 m size at the center of the room. The room was equipped with refrigerant sensors at select locations to measure the leaked propane gas concentrations as shown in Figure 1. The location co-ordinates were measured from the experimental set up and transferred on to the computational domain to maintain corresponding sensor locations. The refrigerant was leaked in a gaseous form with controlled mass flow rate. Two locations were selected for leak introduction, one near the top and one near the bottom of the room (red dots shown in Figure 1b). The leak was introduced at one location at a time. Ignition sources were placed at one location in the room where a spark was generated at a specified point in time. Further details about the experiment can be found in the UL test report [7].

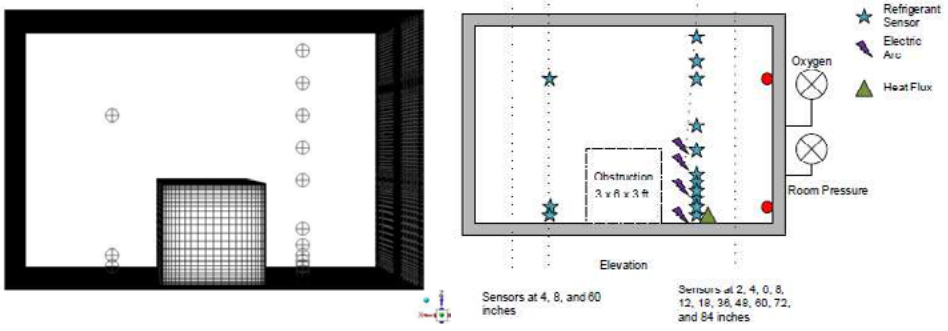


Fig. 1. (a) Sensor locations in computational domain (b) Sensor locations in test ISO room

3. CFD Simulation

The model for refrigerant gas leakage for the physical testing described in previous section was developed using ANSYS Fluent 2019 R2. CFD analysis was carried out to investigate the influence of refrigerant release rate and location on the spatial and temporal refrigerant concentration levels in a test room. The simulation provides predictions of the gas concentrations throughout the room for each scenario. The key challenge is to properly capture the physics of turbulence, diffusion and buoyancy which help determine the concentration gradient within the room. For the purposes of this research, a combustion model was not included as the focus for this simulation is on the gas concentration levels within the room prior to ignition. Though combustion is not modeled, fire risk can be determined by monitoring the gas concentration levels throughout the room over time and by comparing those values to the upper and lower flammability limits for the refrigerant gas.

3.1. CFD Model Description

Refrigerant leakage is modeled in Fluent CFD software which includes the key behaviors such as transient, turbulent species transport, mass diffusion, energy transfer and buoyancy [9]. The concentration of diffused gas is predicted by solving convection-diffusion equation.

$$\frac{\partial(\rho\, Yi)}{\partial t} + \nabla.(\rho\, U\, Yi) = -\nabla.(\boldsymbol{J}) + Ri + Si \quad (1)$$

Where Y_i mass fraction of i^{th} species. R_i is the net rate of production of species by chemical reaction (this is null in this case as no chemical reaction taking place.) and Si is the rate of creation by addition from the dispersed phase plus any user-defined sources. An equation of this form will be solved for $N\text{-}1$ species where N is the total number of fluid phase chemical species present in the system. Since the mass fraction of the species must sum to unity, the N^{th} mass fraction is determined as one minus the sum of the $N\text{-}1$ solved mass fractions.

The mass diffusion due to the mixing action of the chaotic turbulent velocity fluctuations is given as

$$\boldsymbol{J} = -\left(\rho Di,m + \frac{\mu t}{Sct}\right)\nabla.\mathrm{Yi} - Dt,j\frac{\nabla \mathrm{T}}{T} \quad (2)$$

where Sct is the turbulent Schmidt number, μt is the turbulent viscosity and Dt is the turbulent diffusivity. The default Sct 0.7 is used as turbulent diffusion is much higher than the laminar diffusion.

3.2. Geometry and Meshing

The ISO 9705 room was replicated in the computational domain (Figure 2). The room included two inlets which were located at 0.2 m and 1.8 m height from the floor on one wall opposite to a door. Each inlet allowed for controlled leakage of the propane gas. The flow conditions for the experimental project [7] was designed to represent a variable mass release at expected temperature/pressure conditions of a leak point in the subcooled liquid line. The fact that it would release as a gaseous form was confirmed from release temperature and pressure measurements [7]. During each test, only a single inlet was activated. A 3 mm gap between the door and floor was included in the model with the length of the gap being 0.9 m. The obstruction in the middle of the room was also modeled as a no-slip, no-penetration boundary condition of the computational domain.

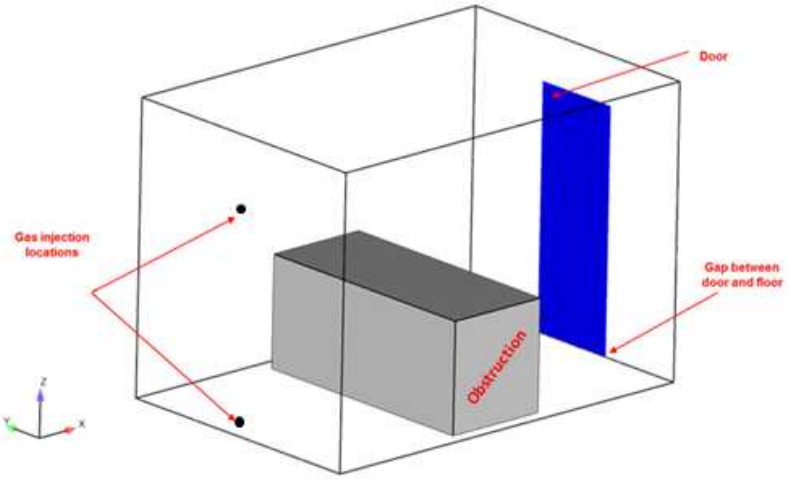


Fig. 2. Geometric model of test room

The entire computational domain was meshed using hex elements employing ANSYS ICEMCFD (Figure 3) [10]. A mesh sensitivity study was carried out with two different mesh sizes. An analysis of the results shows that the difference between the coarser (1.2 million cells) and fine mesh (4.2 million cells) were marginal (Figure 4). The coarser mesh has been applied to all subsequent calculations to reduce computational time.

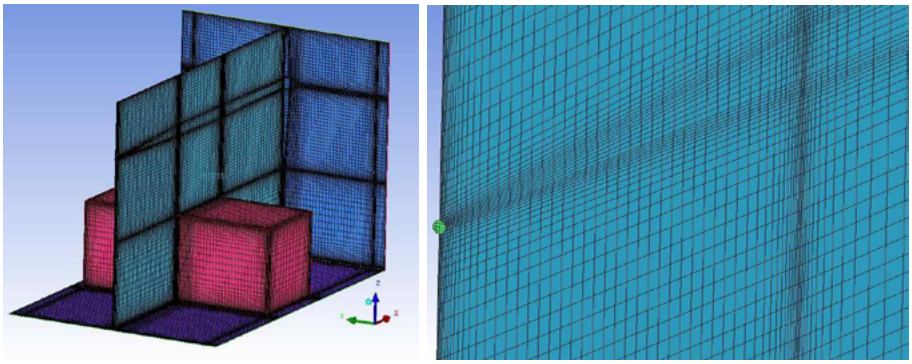


Fig. 3. Mesh of test room with mid plane showing mesh distribution

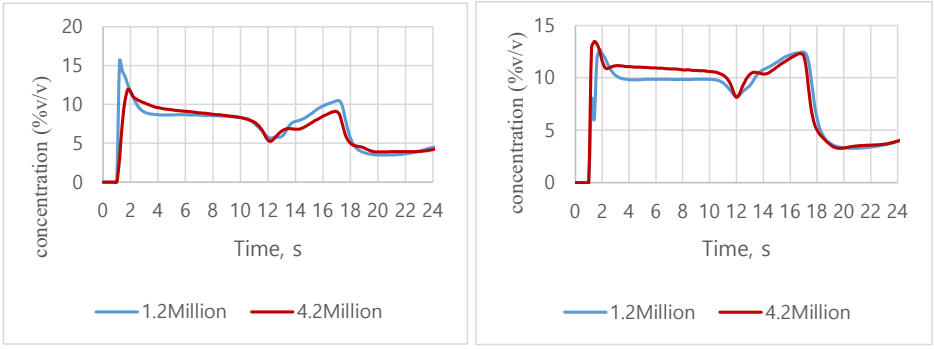


Fig. 4. Mesh sensitivity results for sensor 1 (left) and sensor 2 (right)

3.3. Fluid Properties and Boundary conditions

The fluid properties considered for simulation in accordance with test set up are shown in the Table 1.

Table 1. Thermo-physical Fluid properties

Gas property	Air	Propane
Molecular weight (g/mol)	29	44.1
Density (Kg/m3)	1.225	1.8985
Dynamic Viscosity (N s/m2)	1.789e-05	7.816e-06
Thermal conductivity (W/mK)	0.0242	0.0172
Specific heat Cp (J/K kg)	1006	1646.8
Mass diffusivity (m2/s)	NA	0.1

For this study, four different refrigerant gas leakage scenarios were studied. The factors under consideration were the gas leakage rate, total gas quantity and the location (height) of the leak. The opening size was kept constant at 25 mm diameter. Actual test times varied as the objective of these tests was to introduce varied quantity mass of gas for each scenario (Table 2). As such the test times are variable and were only considered up to the point of ignition in the test in keeping with the physics of the model.

Table 2. Scenarios being modeled

Scenario	Target Mass flow rate (g/s)	Total Mass of gas introduced (g)	Release height (m)	Simulation time (s)	Discharge temperature (°C)
CP06	6.4	97	0.2	15	20.0
CP10	6.7	198	0.2	29	20.5
CP21	6.7	201	1.8	30	18.8
CP26	40	417	1.8	9	15.0

The actual mass flow was obtained from the experimental mass flow meter. A sample variable mass flow plot has been shown in Fig. 5. The variation of mass was observed at fraction of seconds at the beginning and before end of the leaking process. The walls were assigned no slip conditions and adiabatic in nature. The entire room was initialized with air at 1 atm pressure and 25ºC.

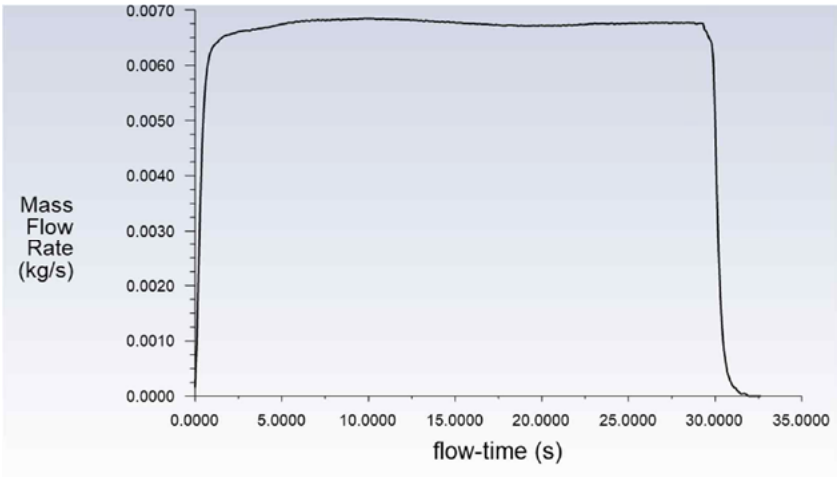


Fig. 5. Variable mass flow for CP21 scenario

4. Model validation

Model validation is essential to check the correctness of solution and its consistent behavior across the different flow conditions [11]. For this project, a rigorous validation was carried out by comparing available experimental concentration values obtained from sensors installed inside the room with simulation concentrations obtained at the same locations over a specified simulation time. Fourteen concentration sensors were located inside the room during physical testing. In this paper, only a single sensor, which was in front of an inlet, will be discussed for each scenario. Yet results hold true for all the other sensors and is not discussed in this report.

The graphs in Figure 6(a, b, c and d) show the variation of propane concentration over time and space. These plots possess a common trend: an initial spike in the concentration values for the simulation as opposed to a gradual increase exhibited by the experimental data. This is due to the fact that when jet of gas hits the sensor points, simulation shows an instantaneous response where as physical test sensors were not local point sensors. Instead, they extracted the gas locally and then transported it to the main sensor that makes the

concentration measurement. To account for this delay, deconvolution of the experimental data was necessary by taking average values of concentrations over certain time period. Nevertheless, some error is expected in the test data, especially when the leak first starts, and unfortunately, test error was not available. Though as time passes, the simulation and experiment values are much closer to each other and follow a similar growth pattern. The important point here is that sometimes modelling is more accurate than the experimental results, or rather, more accurately reflects what is happening within the point of interest.

It is observed in Figure 6(a) that there is an initial rise due to the fact that actual mass flow rate at the inlet was gradually increased to the target value. Whereas, in the other cases, it was almost an impulse input and so the simulation results exhibit a more sudden increase. This is the expected behaviour, though not what is seen in the experimental data. For example, Figure 6(d) shows a very severe and almost impulsive increase in concentration levels in the simulation. This makes sense since it is a very high mass flow rate. The experimental data does not appear to represent what is actually happening inside the room.

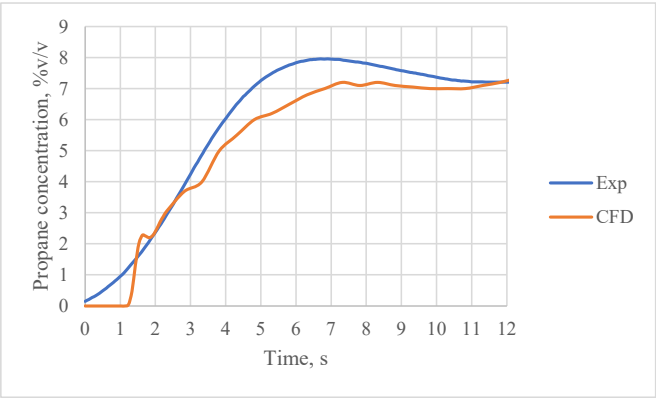


Fig. 6 (a). Comparison of concentration between experiment and CFD at 8 inches height from floor for CP-06 scenario

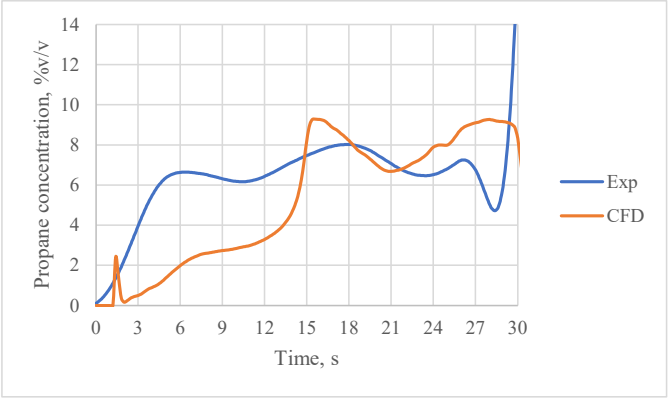


Fig. 6 (b). Comparison of concentration between experiment and CFD at 8 inches height from floor for CP-10 scenario

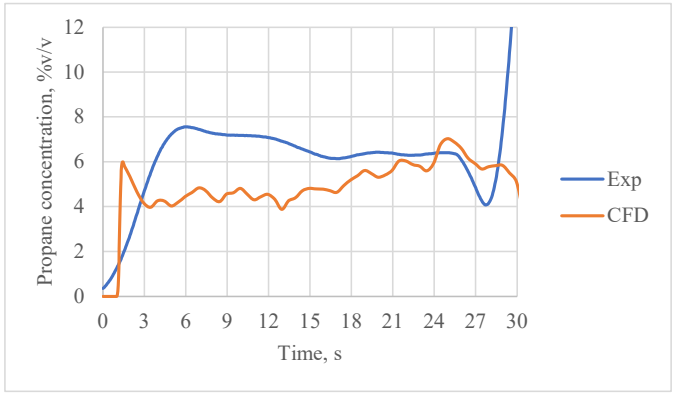


Fig. 6 (c). Comparison of concentration between experiment and CFD at 72 inches height from floor for CP-21 scenario

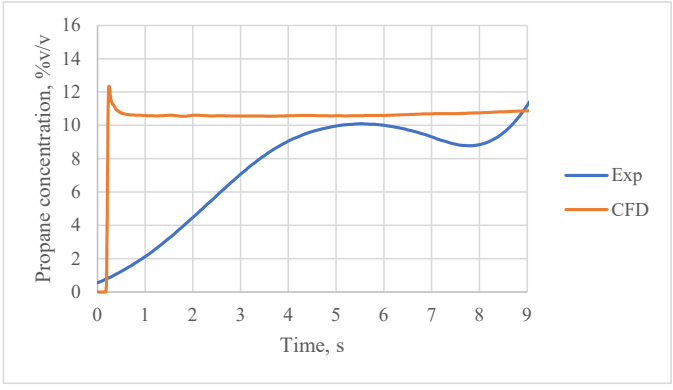


Fig. 6 (d). Comparison of concentration between experiment and CFD at 72 inches height from floor for CP-26 scenario

5. Risk Matrix

When a combustible gas is released into a confined space where an ignition source could be present, there is a possibility of a fire and/or explosion taking place. Part of the risk is determined by the gas concentration levels. For combustion of gases, the concentration level must reside within an interval defined by the lower and upper flammability limits [12]. The upper and lower flammability limits for the refrigerant in this study, propane, are 2.1% and 9.5% by volume, respectively [13]. Concentration volume within these limits is called as Flammable Volume (FV). The power of computer simulation is that it can measure and track the size and location of FV of the leaked gas. This will not only contribute to the probability of a fire, but also to predict the magnitude of an event. By tracking the size and location of the FV and normalizing it by the volume of the room, a new risk measure called Normalized Flammability Volume (NFV) is defined which represents the probability of a fire/explosion occurring assuming the ignition sources are randomly distributed in the domain of interest. In some case, the domain of interest is simply the entire volume of the room.

Though, it is possible that the ignition sources are not distributed throughout the room but within a smaller fraction of the room. In such case, the Flammability Volume is normalized by a portion of the volume of the entire room, called the volume of interest (VOI), where the ignition sources are most likely to reside. The NFV (unitless) values reside between 0 and 1 with a higher value suggestive of a higher probability and risk of fire/explosion. So more generally,

$$NFV = FV\ (in\ VOI)/\ VOI \tag{3}$$

NFV values are calculated by considering full room and bottom half room volumes which are shown in Figure 7(a,b) for three scenarios. It was observed (Figure 7(a)) that CP-26 possessed higher NFV value (full room as VOI) than the other two cases. which was due to the fact that a higher quantity (400 g) of refrigerant was injected. In CP-06 and CP-21, the quantity of injected refrigerant was almost same, yet CP-06 possessed higher NFV (assuming full room as VOI) due to lower injection point in the room and the resulting accumulation of concentration due to the presence of the obstacle. Risk of fire hazard is high in CP-26 compared to CP-06 and CP-21.

But when the VOI was set to the lower half volume of the room, CP-06 possessed higher risk (higher NFV) with null risk for CP-21 and 26. It was observed that, when the refrigerant gas injected from top inlet then the concentration was not built-up at bottom half due to diffusion and turbulent behavior of refrigerant gas flow. But flammable volume was restricted near the inlet zone only.

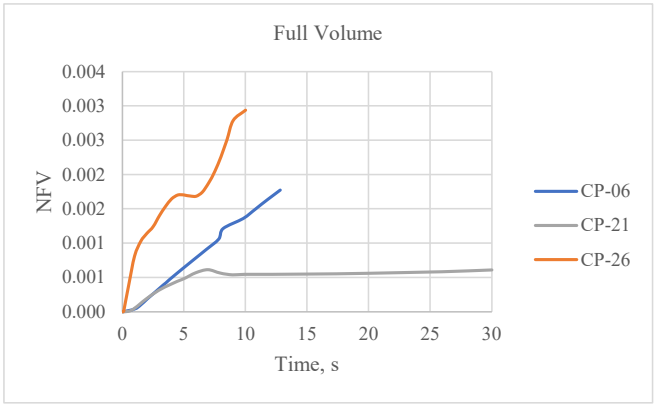


Fig. 7 (a). Comparison of NFV values considering full room between CP-06, 21 and 26 scenarios

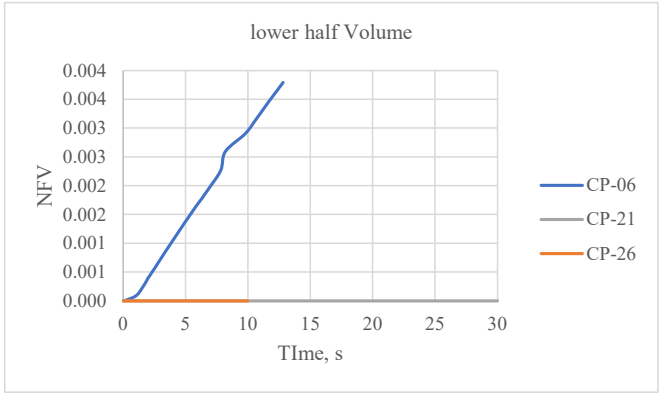
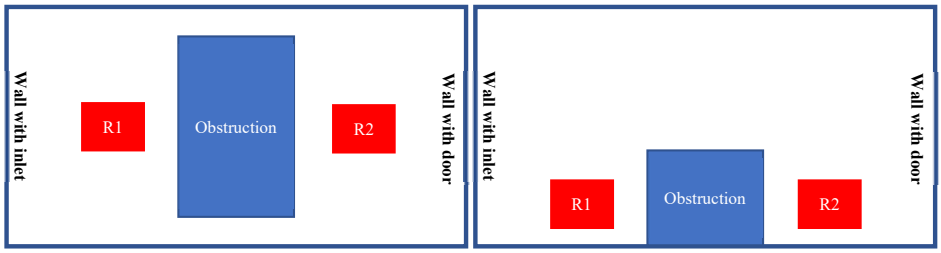


Fig. 7 (b). Comparison of NFV values considering bottom half room between CP-06, 21 and 26 scenarios

To further demonstrate the role of the VOI, two VOIs of dimensions 3 cm by 3 cm by 3 cm were created inside the room. The first region (R1) was placed between wall with inlet and obstruction. The other region (R2) was placed between obstruction and wall with the door as shown in the schematic layout in Figure 8(a and b). These regions are virtual in nature and indicate that the ignition sources exist within them.



(a). Plan view (b). Elevation view

Fig. 8. Schematic layout of room depicting virtual regions

The graphs in Figure 9(a and b) shows some trends for NFV. The scenario, with leakage from the bottom of the room (CP-06), lead to highest values of NFV in R1. In the same scenario, R2 exhibited zero NFV. In other words, R1 has more risk of fire as compared to R2. The scenario with leak from bottom tends to pose high risk of fire in the vicinity of R1 due to the fact the propane gas accumulates around it by obstruction in the form of obstruction. It takes plenty of time for propane gas to recirculate around the obstruction and reach R2. Till then the propane concentration dilutes due to diffusion which results in negligible values of NFV in R2. In other words negligible risk of fire. Among scenarios CP-06 and Cp-26, CP-06 exhibits the highest value of NFV hence high risk of fire, followed by CP-26 with very negligible NFV values. This analysis gives a more refined insight in that if the ignition sources are known to reside in a specific volume then it might be more relevant to reduce the size of the normalization volume as much as possible to get more exact value of NFV.

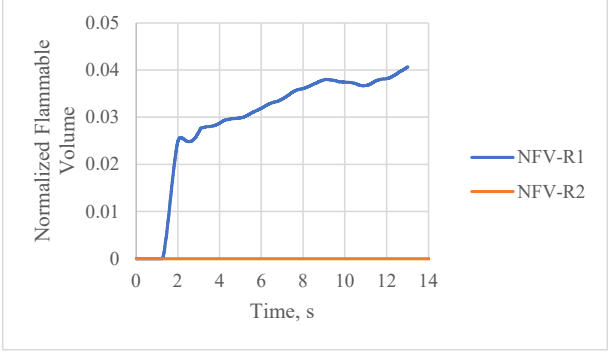


Fig. 9 (a). NFV values over time for CP-06 (Inlet at 0.2m height from floor).

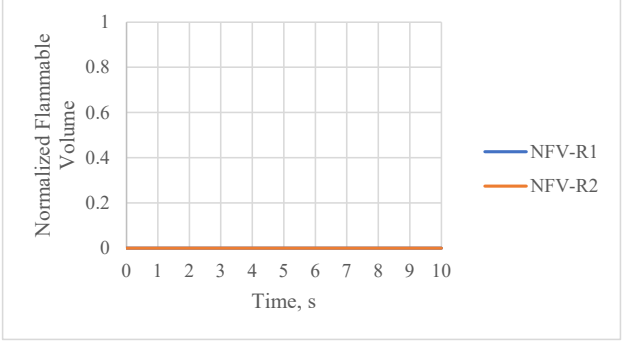


Fig. 9 (b). NFV values over time for CP-26 (Inlet at 1.8m height from floor)

6. Conclusion

In this paper, a new risk metric, normalized flammability volume (NFV), one that represents the probability of fire/explosion during refrigerant gas leakage into a confined space is introduced. The power of this simple, fire risk metric is that it can track the changing nature of the risk (probability of fire) during a leakage event when combustible gas is being introduced into a confined space. The gas concentration levels are determined by the physics of the flow and details of the room. This paper also demonstrated the value in using the risk metric to help rank different scenarios. Of course, if there is knowledge of the locations of potential ignition sources, then the NFV can be finetuned to provide an even more accurate measure. This risk metric is not available from physical testing and can only be obtained from high fidelity and validated CFD models.

Second, though a validation study was carried out to demonstrate the accuracy of the computational model, it turned out that the predictions of the model were more likely to reflect the reality within the leaked compartment versus what was measured in the experimental setup due to challenges of the particular sensor used. So in some cases, computational models can actually be an improvement over data generated by physical tests.

Acknowledgements

The authors would like to acknowledge the technical support by Mohsen Battoie from CADFEM USA. The authors would also like to thank George Hunter and Mark Skierkiewicz from UL LLC.

References

[1] Gradient Corp report 2015, AHRI Project 8009 Final Report : Risk Assessment of Refrigeration Systems Using A2L Flammable Refrigerants.
[2] Navigant corp report 2016, AHRI Project No. 8016: Risk Assessment of Class 2L Refrigerants in Commercial Rooftop Units.
[3] Gradient Corp report 2012, AHRI Project 8004 Final Report Risk Assessment of Residential Heat Pump Systems Using 2L Flammable Refrigerants.
[4] Lizhi Jiaa, Wufeng Jina, and Yan Zhangb, Analysis of Indoor Environment Safety with R32 Leaking From a Running Air Conditioner, 9th International Symposium on Heating, Ventilation and Air Conditioning (ISHVAC) and the 3rd International Conference on Building Energy and Environment (COBEE).
[5] Safety research of A2L/A3 refrigerants and risk assessment in japan by Eiji Hihara https://www.jraia.or.jp/english/side/presentation3.pdf.
[6] https://www.grc.nasa.gov/www/wind/valid/tutorial/valassess.html.
[7] Underwriters Laboratories Research Report, March 2019, AHRTI Report No. 9007-02, Benchmarking Risk by Whole Room Scale Leaks and Ignitions Testing of A3 Refrigerants.
[8] ISO 9705-1: Reaction to fire tests - Room corner test for wall and ceiling lining products - Part 1: Test method for a small room configuration - First Edition.
[9] ANSYS Fluent Theory Guide, Release 18.2, August 2017.
[10] https://www.ansys.com/en-in/services/training-center/platform/introduction-to-ansys-icem-cfd.
[11] Standard for Verification and Validation in Computational Fluid Dynamics and Heat Transfer, V V 20 – 2009, ASME, ISBN: 9780791832097.
[12] Quanyi Liua, Hui Zhanga , Yi Liua , Hong Huanga , Xiaole Zhanga , Zhipeng Lib , Wei Yaoa "Influencing factors of flammable refrigerants leaking in building airconditioning System" The 9th Asia-Oceania Symposium on Fire Science and Technology, Procedia Engineering 62 (2013) 648 – 654.
[13]"Safety data sheet" by National Refrigerants.Inc https://secureservercdn.net/198.71.233.179/m9v.7b6.myftpupload.com/wp-content/uploads/2019/12/SDS-R290-Propane.pdf?time=1580410902
[14] NIST (National Institute of Standards and Testing) https://webbook.nist.gov/chemistry/fluid/

13th IEA Heat Pump Conference
April 26-29, 2021 Jeju, Korea

Experimental comparison of R1224yd(Z) and R1233zd(E) in a high temperature heat pump

Cordin Arpagaus* and Stefan Bertsch

NTB University of Applied Sciences of Technology Buchs, Werdenbergstrasse 4, 9471 Buchs, Switzerland

Abstract

High temperature heat pumps (HTHP) with heat supply temperatures of 100 to 160 °C will increasingly become commercialized in the coming years, especially for drying, sterilization and evaporation processes in the food and chemical industries. There is significant research towards testing new environmental-friendly refrigerants with low GWP for use in HTHPs. Besides natural refrigerants, the synthetic hydrochlorofluoroolefins (HCFO) R1224yd(Z) and R1233zd(E) (GWP < 1) are suitable substitutes for the hydrofluorocarbons (HFC) R245fa and R365mfc (GWP > 800). This paper examines the experimental performance of R1224yd(Z) and R1233zd(E) as a drop-in test in a laboratory HTHP with 5 to 10 kW heating capacity. The developed heat pump is single-stage, operates with a variable speed piston compressor, and contains a continuously adjustable internal heat exchanger (IHX) for superheating control. The performance data were measured at 30, 50, and 70 K temperature lift (40 to 80 °C heat source, 80 to 150 °C heat supply). The integration of the IHX in the heat pump cycle significantly increased the efficiency and the heating capacity over the entire operating map. The experimental results with R1224yd(Z) at W60/W110 indicate a COP of 2.8 (basic cycle) and 3.2 with IHX integration (+14%). The drop-in test showed that the heating capacity of R1224yd(Z) was on average 9% higher than that of R1233zd(E). The measured COP data of R1224yd(Z) were comparable to R1233zd(E) in the whole operating map. The deviations were within the measurement uncertainty of ± 0.2 COP. Moreover, an increase in the temperature glide on the heat sink side from 5 to 25 K further increased the COP by +9%, which is promising in processes with low return temperatures. Overall, the experimental results are promising for use in HTHPs and the developed laboratory HTHP system allows testing alternative HCFO and HFO refrigerants in the future.

© HPC2020.
Selection and/or peer-review under responsibility of the organizers of the 13th IEA Heat Pump Conference 2020.

Keywords: High Temperature Heat Pump; Industrial Heat Pump; Refrigerants; R1224yd(Z); R1233zd(E), HCFO; COP

1. Introduction

The range of electrically driven high-temperature heat pumps (HTHP) for industrial applications has grown steadily in recent years. There are at least 26 industrial HTHP products available on the market that can provide heat at sink temperatures from 90 to 160 °C [1–4]. HTHP technology is expected to play a key role in the decarbonization and electrification of the industrial sector. By switching from fossil fuels to renewable energies and increasing energy and resource efficiency, the CO_2 footprint can be significantly reduced.

The use of industrial HTHP is particularly interesting for heat recovery applications and for various industrial processes such as drying, steam generation, sterilization, paper production or food preparation. From a research perspective, HTHP technology is being further developed and the limits of supply temperatures and performance indicators are being further researched. To further increase system efficiency, multi-temperature heat pump systems are another suitable approach for using several heat sources and heat sinks with different temperature levels [5].

* Corresponding author. Tel.: +41 81 755 34 94
E-mail address: cordin.arpagaus@ntb.ch

Various experimental R&D projects are currently in progress at international level to push HTHP technology from laboratory scale to industry. The main research objectives are: (1) Extending the limits of heat source and sink temperatures to higher levels, (2) improving heat pump efficiency (COP) through advanced multi-stage cycles and oil-free compressors, (3) developing temperature resistant components such as compressors and valves, and (4) developing and testing new environmentally friendly low global warming potential (GWP) synthetic refrigerants.

The partially fluorinated hydrocarbons (HFC) R134a, R245fa and R365mfc have a GWP of 1'300, 858 and 804 [6], and in most industrialized countries are confronted with a "phase-down", i.e. reduction of production and consumption. In Europe, the F-gas regulation [7] prohibits the use and reduces the market availability of greenhouse gases. The goal is to gradually reduce consumption by 79% by 2030. From 2022 on, only refrigerants with a GWP < 150 may be used in new commercial heat pumps. In Switzerland, the permissible use of refrigerants is regulated in the Chemicals Risk Reduction Ordinance (ChemRRV) and industrial heat pumps with a (cooling) capacity of >600 kW are affected by the HFC ban.

Natural refrigerants such as water (R718) [8–10], CO_2 (R744), ammonia (R717), or hydrocarbons like butane (R600) [11–13], propane (R290) or pentane (R601) [14] are promising environmentally friendly substitutes. However, special heat pump cycle designs with multi-stage compression (e.g. vapour compression) or sophisticated safety measures due to flammability (A3) are required, which can increase system costs.

In recent years, the 4th generation of new synthetic refrigerants has been developed consisting of various hydrofluoroolefins (HFO) and hydrochlorofluoroolefins (HCFO), which have very low GWPs, are non-flammable and have great potential for use as refrigerants in HTHP. The thermodynamic properties of these synthetic refrigerants such as R1336mzz(Z), R1233zd(E) and R1224yd(Z) allow heat pump operation at condensation temperatures from 140 to 160 °C [15,16]. Although HCFO refrigerants like R1233zd(E) and R1224yd(Z) contain a chlorine atom in their structure and do not comply with the legal requirements of the Montreal Protocol (Zero Ozone Depletion Potential, ODP), there are national regulations, such as the Swiss ChemRRV, which allow the use of HCFO refrigerants with an OPD <0.0005 (e.g. refrigerant R1233zd(E) or R1224yd(Z)) since 1 June 2019.

At the NTB Buchs, an HTHP on a laboratory scale was developed as part of the SCCER-EIP project [17]. The HTHP has a single-stage design, works with a reciprocating compressor with variable speed and contains a variable internal heat exchanger (IHX) for superheat control. A viscous POE oil (173 mm²/s at 40 °C) was used to achieve sufficient lubrication with the refrigerants at high temperatures. The basic functionality of the HTHP and first experimental results with R1233zd(E), R1224yd(Z) and R1336mzz(Z) have already been presented at several conferences [18–24].

The aim of this study is to experimentally investigate the efficiency of R1224yd(Z) (AMOLEA®1224yd, AGC Chemicals, 99.9% purity, 99.7/0.3 Z/E isomer ratio) and R1233zd(E) (Solstice®zd from Honeywell) in the same HTHP laboratory plant using a drop-in test. Starting from a reference point at W60/W110 (50 K temperature stroke), a parameter study is performed to measure the operating characteristics (i.e. heating capacity and COP) as a function of the temperature lift of the heat pump in the range from 30 to 80 °C heat source and 70 to 150 °C sink temperature. In addition, an overview of the thermophysical, environmental and safety aspects of the refrigerants is given.

2. Refrigerants

Table 1 shows the essential thermodynamic, environmental and safety properties of the tested HFO / HCFO refrigerants R1336mzz(Z), R1233zd(E), R1224yd(Z) in comparison to HFC R245fa.

R1233zd (E) has a critical temperature of 165.6 °C, a critical pressure of 36.2 bar and is available under the brand name Solstice®zd from Honeywell [25] or as Forane®HTS 1233zd from ARKEMA [26]. Although R1233zd(E) contains a chlorine atom that may participate in the catalytic destruction of the ozone layer, the atmospheric lifetime is sufficiently short, i.e. about 14 days [27] or 40.4 days [28], so that the fluid does not reach the stratosphere after leakage and thus does not participate in ozone depletion. Depending on the study, an ODP of 0.00034 [28]or 0.00030 [29] is estimated.

Today R1233zd(E) is mainly used as a blowing agent for duroplastic foams and aerosols. In air conditioning it is used for large chillers with radial compressors [30]. It is recommended for applications in HTHP and Organic Rankine Cycles (ORC). At high operating temperatures, a small portion of R1233zd(E) can isomerize to R1233zd(Z). Wissam et al. [26] confirm the efficacy of a stabilizer with R1233zd(E) over pure unstabilized R1233zd(E) to significantly reduce Z-isomer formation at high temperatures. The stabilized product showed high stability at 180 °C after 14 days aging with metals and oils. At 220°C and 14 days aging, a very low degree of isomerization (< 0.5%) was observed.

So far there are only limited experimental studies on the use of R1233zd(E) in HTHP applications [31]. First results were presented at the DKV Conference 2018 [18], the ICR 2019 [20] and the 2nd HTHP Conference [24] with the laboratory HTHP developed at NTB Buchs. Compared to a simple cycle, the integration of an IHX led to a 15% increase in COP under W60/W110 conditions [20]. The maximum sink temperature tested was 150 °C, whereby a COP of 2.1 was achieved at the operating point W80/W150 (70 K temperature range).

Another HTHP test facility is being developed at the University of Ulster to test R1233zd(E) within the CHESTER project [31,32]. Simulation results from Shah et al. [31] showed up to 8% higher COP than with R245fa. Further investigations are underway to test R1233zd(E) and oil miscibility.

Table 1. Thermophysical, environmental and safety properties of R1224yd(Z), R1233zd(E), R1336mzz(Z) and R245fa suitable for HTHP applications [6,19,36–42,25–29,33–35]

Refrigerant	R1224yd(Z)	R1233zd(E)	R1336mzz(Z)	R245fa
Product (Manufacturer)	AmoleaTM1224yd (AGC Chemicals) [19,42]	Solstice®zd (Honeywell) [25] Forane®HTS 1233zd (ARKEMA) [26]	Opteon™ MZ (Chemours)	Genetron®245fa (Honeywell)
Molecular structure	Z-CF_3-CF=CHCl	E-CF_3-CH=CHCl	Z-CF_3-CH=$CHCF_3$	CHF_2-CH_2-CF_3
Boiling point at 1,013 bar [°C]	14,6	18,0	33,4	14,9
Critical temperature [°C]	155,5	165,6	171,3	154,0
Critical pressure [bar]	33,4	35,7	29,0	36,5
GWP_{100} (CO_2 = 1, 100 years) [-]	0,88 [36]	1 [6], <5 [29]	2 [6]	858 [6]
ODP (CFC-11 = 1)	0,00023 [36]	0,00034 [28]; 0,00030 [29]	0	0
Lifetime in atmosphere (days)	20 [36]	~14 [27]; 26 [6]; 36 [29]; 40,4 [28]	22 [6]	7,7 years [39]
LC_{50} (rat, 4 h) [ppm v/v]	>213'000	120'000	102'900	>203'000
Occupational Exposure Limit (OEL) [ppm v/v]	1'000	800	500	300
Safety group (ASHRAE 34, A1 = non-flammable)	A1	A1	A1	B1
End products from degradation in the atmosphere [41]	$CF_3C(O)OH$, CO_2, HF	CO_2, HF, HCl	CO_2, HF	CO_2, HF
Molar yield of TFA during degradation in the atmosphere	97% [43]	~ 2% [29]	< 20% [40]	< 10% [39]

R1224yd(Z) is another HCFO refrigerant developed for use in centrifugal chillers [19,30,33,35], for power generation in ORC applications [34], and in HTHP for waste heat recovery [33]. AGC Chemicals (Asahi Glass) markets the product as Amolea™1224yd [42], where AMOLEA stands for "AGC Makes Hydrofluoroolefins as Alternatives". R1224yd(Z) differs from R1233zd(E) by a slightly different molecular structure (Table 1). The physical properties are close to R245fa. The equations of state and mass transport data were evaluated by Akasaka et al. [44] and Miyara et al. [45]. The critical temperature is 155.5 °C and the saturation vapour pressure is slightly lower compared to R245fa (about 13% at 120 °C) [46]. With an ODP of almost zero (0.00023 [36]), a GWP of 0.88 and an atmospheric lifetime of 20 days, the environmental impact is estimated to be low [36]. In addition, AMOLEA™1224yd is non-combustible (A1) and toxicity is given with an occupational exposure limit (OEL) of 1'000 ppm [47].

At the ICR 2019 conference Kaida et al. [46] presented first experimental results on R1224yd(Z) in a commercial SGH165 heat pump from KOBELCO (with economiser cycle and internal heat exchanger). "Drop-in" tests at operating point W50/W95 (45 K temperature increase) showed a 3% higher heat capacity and 12 % higher COP compared to R245fa. The performance increase was attributed to a higher refrigerant mass flow, a lower viscosity and a lower required pressure ratio (higher adiabatic compressor efficiency). In addition, R1224yd(Z) is also well compatible with the most common metals, plastics and elastomers [30,34,48] and has good miscibility for various types of oils [46,48,49]. The chemical resistance and compatibility of AMOLEA™1224yd is comparable to that of R245fa. Overall, R1224yd(Z) has been suggested as a suitable R245fa alternative for HTHP.

R1336mmz(Z) has a higher critical temperature of 171.3 °C than R1233zd(E) and R1224yd(Z). This allows condensation at temperatures up to about 160 °C. Chemours has been marketing R1336mzz(Z) since 2018 under the brand Opteon™ MZ for HTHP in process technology and special applications in the high temperature range. The safety class is A1 (non-flammable) and the GWP is 2. The ODP is 0 and the service life in the atmosphere is only 22 days [6]. The refrigerant is thermally stable up to 250 °C and is suitable for ORC and applications for heat recovery and steam generation [50–53]. Laboratory tests have shown that the material compatibility with copper and steel is similar to that of R245fa. Highly viscous polyol ester (POE) is recommended as lubricant as it is completely miscible over wide temperature ranges and compositions [51,53].

Figure 1 shows the vapour pressure curves and the pressure enthalpy and temperature entropy diagrams of the refrigerants. The thermophysical properties were calculated using the Engineering Equation Solver Software (EES) [54] from F-Chart. Figure 1 shows that R1233zd(E) and R1224yd(Z) have a slightly lower vapour pressure than R245fa. Furthermore, the critical pressure of R1224yd(Z) is about 3 bar lower than that of R245fa, while the critical temperatures are almost the same (see also Table 1). In the case of R1233zd(E), the saturated steam pressure is slightly lower than that of R1224yd(Z), while the critical temperature is about 11 K higher. The p-h diagram indicates that R1224yd(Z) has a lower evaporation enthalpy than the other fluids.

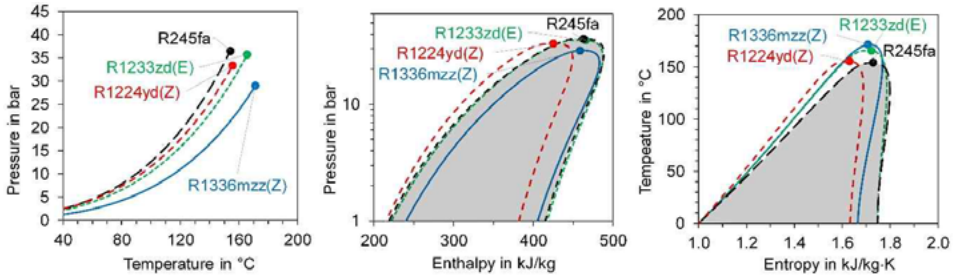


Fig. 1. Vapour pressure curve (p-T diagram), pressure enthalpy (p-h) and temperature entropy (T-s) diagrams of the refrigerants R1336mmz(Z), R1233zd(E) and R1224yd(Z) compared to R245fa (substance data from [54])

Another topic that is repeatedly in the media, apart from GWP and ODP, is the decomposition products of refrigerants in the atmosphere and their effects on human health and the environment [55]. In the EU, this topic has been become public, mainly by the use of HFO R1234yf in car air conditioning systems. The atmospheric degradation of HFC, HCFC and HFO refrigerants is initiated by reaction with OH radicals, resulting in halogenated carbonyl compounds which are further oxidised to hydrofluoric acid (HF), hydrochloric acid (HCl), formic acid (HC(O)OH), or CO_2 and in some cases form trifluoroacetic acid (TFA, $CF_3C(O)OH$) [29,39–41,56].

For comparison, the >C=C< double bond in HFO and HCFO reacts with OH radicals two orders of magnitude faster than HFC R134a [41]. The molar yield of TFA in R134a is about 7 to 21%, while for R245fa it is <10% [39]. Due to the long atmospheric lifetime of 13.4 and 7.7 years [39], the gaseous TFA can spread widely in the atmosphere, descend to earth via rainfall and accumulate in various waters such as rivers, streams, lakes and wetlands, as well as terminal sinks such as salt lakes, playas and oceans [55,56]. HF and HCl neutralize quickly due to the buffer capacity of the surface water [41].

Since HFO and HCFO decompose much faster into their final products, they can occur locally at the point of emission and have direct effects. The molar yields of TFA formation from degradation depends on the refrigerant type [20]. HFO R1234yf leads to a 100% molar yield of TFA. R1233zd(E) decomposes to max. 2% TFA [29], whereas the yield for R1336mzz(Z) (with two CF_3-CH= groups) is likely to be <20% [40]. Since R1224yd (Z) has a similar molecular structure to R1234yf, the molar yield of the degradation to TFA is 97% [43].

The effects of TFA on the environment have been investigated in various studies and found to be negligible, since TFA occurs in large quantities in oceans [41,56]. The oceans already contain more than 200 million tons of TFA from natural sources such as volcanic activity. Henne et al. [40] considered a worst-case scenario for Europe in which all car air-conditioning systems are filled with R1234yf, which has 100% TFA as a decay product, and this is emitted. This would have an impact of 0.04% on the global TFA content in the oceans, which is well below the no-effect level of the most sensitive algae.

Solomon et al. [56] estimated in the worst case of unregulated use of HCFCs, HCFCs and HFOs up to 2050 with an additional amount of maxiaml 15.3 ng TFA per litre of sea water in the oceans compared to the average 200 ng existing at the beginning of the millennium. The risk for aquatic organisms was classified as negligible.

Nevertheless, according to current knowledge, studies on the precise effects of TFA accumulation in freshwater and on land on human health and the environment are still in their early stages.

3. Experimental setup of the HTHP laboratory facility and test procedure

Figure 2 illustrates the setup of the HTHP laboratory plant with the principle diagram. All components used are commercially available without modifications. A semi-hermetic reciprocating compressor (Bitzer, 2DES-3Y New Ecoline) with variable speed drives the HTHP. An external frequency converter (Vacon 100) adjusts the compressor speed within the permissible limits (30 to 60 Hz corresponds to 870 to 1'750 rpm). An integrated temperature sensor prevents the motor windings from overheating. The switch-off temperature is approx. 110 °C. The fan of the compressor was not in operation during the experiments.

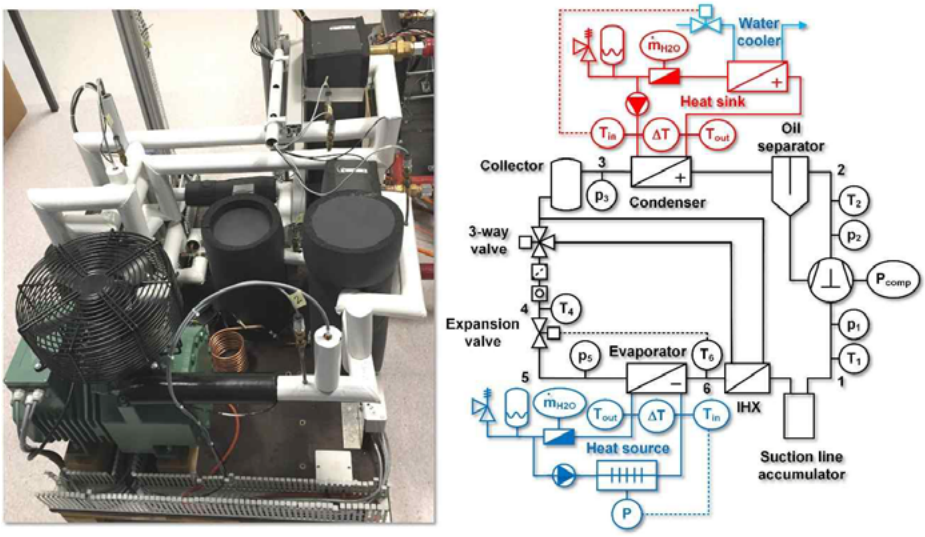


Fig. 2. Experimental setup of the HTHP laboratory facility with principle diagram

The HTHP consists of a simple heat pump cycle with condenser, evaporator and an IHX. The heat exchangers used are compact plate heat exchangers (SWEP) with low pressure drop. The IHX transfers the heat from the hot liquid refrigerant to the suction gas after the condenser outlet, thereby increasing the suction gas temperature (T_1) and ensuring sufficient superheating. The superheat is measured between the evaporator and the IHX (T6) and was set to 5 K for all tests. The superheat was controlled by the expansion valve (Siemens, MVL661.15-0.4) and a PI control in LabVIEW™.

The refrigerant mass flow through the IHX is continuously adjustable from 0 to 100% via a three-way valve (Siemens, M3FK15LX15). A setting of 0% IHX corresponds to the operation of a simple heat pump cycle without IHX, while at 100% the IHX is fully integrated into the cycle. A liquid receiver (Bitzer FS56) serves as a refrigerant collector after condensation and provides liquid refrigerant upstream of the expansion valve. A suction gas accumulator (ESK Schultze, FA-22) prevents the direct penetration of liquid refrigerant into the compressor. The filling quantities of the refrigerants R1233zd(E) and R1224yd(Z) were 4.2 kg and 3.6 kg respectively.

A POE oil (Fuchs, Reniso Triton SE 170) with a viscosity of 173 mm²/s at 40 °C (17.6 mm²/s at 100 °C) was used to achieve sufficient lubrication at the high operating temperatures. An oil separator (Temprite, Coalecent 922M) is installed on the high-pressure side to collect the oil and return it to the compressor via a cooling pipe. As safety measure, a high pressure/low pressure pressostat protects the compressor and all other components. A filter dryer is integrated in the system to absorb residual moisture. The copper pipes and the circuit components are insulated with temperature-resistant Armaflex®HT.

The inlet temperature of the heat source ($T_{source,in}$) can be set between 30 and 80 °C and the outlet temperature of the sink ($T_{sink,out}$) between 70 and 150 °C. The heat source circuit simulates potentially available waste heat from an industrial process and includes a controllable electric heater (Backer ELC, 10 kW), a water pump (Speck Pumpen, HT-AY-2251-PM.0005) with adjustable flow and an expansion vessel with safety valve. The electric heater controls the inlet temperature of the heat source and a control valve (BELIMO, 2-way zone valve with rotary actuator) at the inlet of the water cooler controls the inlet temperature of the heat

sink to the condenser (both by PI controls in LabVIEW™). The heat sink is a potential application (e.g., steam generation or drying process) and includes a water cooler that releases the generated heat to the environment.

The temperatures are measured with thermocouples (type K, class 1) calibrated in a silicone oil bath of 20 to 110 °C with an accuracy of ± 0.1 K. Thermocouples with differential temperature measurement are installed at the inlets and outlets of the heat pump. The water mass flow meter in the heat sink circuit is a calibrated Coriolis sensor (E+H, Promass 300 F) with a measurement error of ± 0.05%. A power sensor (Infratek, ITL101) measures the electrical power consumption of the compressor with an accuracy of ± 3%. A CompactRIO® from National Instruments (cRIO-9022 with 8 card slots) in combination with LabVIEW™2017myRio is used for data acquisition and control of the test setup with a sampling time of one second. Further details on the components and sensors are described in Arpagaus et al. [21,23].

4. Test procedure

After heating up the heat pump system to a desired operating point (heat source and sink temperatures), a temperature spread of 3.0 ± 0.1 K at the heat source and 5.0 ± 0.1 K at the heat sink (based on standard DIN EN 14511 [57]) was manually adjusted by means of the water pumps speed (mass flow) in the two hydraulic circuits. The HTHP was operated for several minutes per operating point in a stationary state and average values of at least five minutes were used for the data analysis.

The COP and the 2nd law efficiency (η_{2nd}) of the HTHP were determined from the measured heating capacity ($\dot{Q}_{sink}$) and the electrical power consumption of the compressor (P_{comp}) according to equations (1) and (2), where $\dot{m}_{H_2O}$ corresponds to the water flow and ΔT_{sink} corresponds to the temperature difference between output and input of the heat sink. The temperature dependence of the specific heat capacity of water $c_{p,H_2O}(T)$ was considered according to [58]. The electrical power consumption of the control system of the heat pump system (approx. 110 W) and the water pumps in the hydraulic circuits (between 0.25 and 1.75 kW) are not taken into account in the COP calculation. According to error propagation, the measurement uncertainty is maximum ± 0.2 COP over the entire measurement campaign.

$$COP = \dot{Q}_{sink} / P_{comp} = \left(\dot{m}_{H_2O} \cdot c_{p,H_2O}(T) \cdot \Delta T_{sink}\right) / P_{comp} \quad (1)$$

$$\eta_{2nd} = COP / COP_{Carnot} \quad \text{with} \quad COP_{Carnot} = T_{sink,out} / \left(T_{sink,out} - T_{source,in}\right) \quad (2)$$

Starting from a reference point (Ref) at W60/W110, a parameter study was carried out to measure the operating characteristics of the heat pump for the two HCFO refrigerants R1224yd(Z) (AMOLEA®1224yd, AGC Chemicals) and R1233zd(E) (Solstice®zd from Honeywell). The influence of the external temperature lift between heat source and heat sink ($\Delta T_{lft} = T_{sink,out} - T_{source,in}$) on the COP and 2nd Law efficiency was investigated. The inlet temperature of the heat source was varied between 30 and 80 °C and the sink temperature between 70 and 150 °C.

The refrigerant change in the HTHP for the drop-in test from R1233zd(E) to R1224yd(Z) was carried out professionally. First, the old refrigerant was extracted with an evacuation station, then an oil change was carried out. The circuit was evacuated overnight to minimize residual moisture in the system. Then the tightness was checked and the system was filled with new refrigerant via the suction line in steps of about 200 g using a scale. In order to determine the optimum filling quantity, the heat pump was put into operation at the reference point W60/W110 during the filling process and the COP was checked as a function of the filling quantity. To accelerate the filling process, the refrigerant gas cylinder was slightly heated from the outside.

5. Experimental test results

Figure 3 (A to F) summarizes the main results of the parameter studies with the refrigerants R1224yd(Z) and R1233zd(E). Figure 3 (A) and (B) show the experimentally measured COP data of the HTHP laboratory plant as a function of the investigated heat sink temperature ($T_{sink,out}$) at different temperature lifts (ΔT_{lft}); in (A) for R1224yd(Z) and in (B) for R1224yd(Z) compared to R1233zd(E) in the IHX cycle. As expected, the COP increases with a smaller temperature lift. At the reference point W60/W110 a COP of 3.2 and 3.0 was reached for R1224yd(Z) and R1233zd(E), respectively.

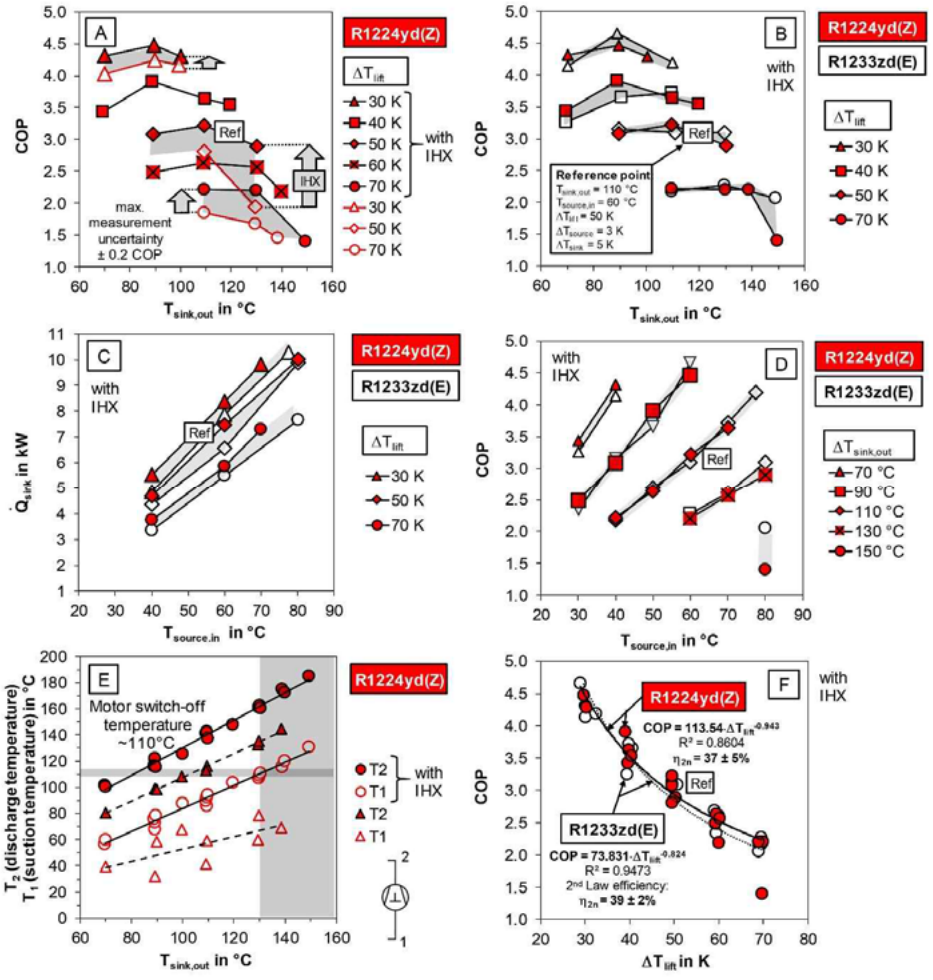


Fig. 3. Experimental test results with R1224yd(Z) and R1233zd(E) in the laboratory HTHP.
(A) Influence of the IHX integration on the COP at different temperature lifts with R1224yd(Z),
(B) Comparison of R1224yd(Z) and R1233zd(E) COPs as a function of heat sink temperature and temperature lift in the IHX HP cycle,
(C) Comparison of R1224yd(Z) and R1233zd(E) heating capacity with IHX cycle at 30, 50 and 70 K temperature lift,
(D) Comparison of R1224yd(Z) and R1233zd(E) COPs as a function of heat source and sink temperature with IHX cycle,
(E) Discharge and hot gas temperature in function of sink temperature with R1224yd(Z),
(F) COP fit curves of the measurement data with 2nd Law efficiency and IHX cycle

The slightly decreasing COP curves at higher sink temperatures are a result of the smaller enthalpy of vaporization for condensation near the critical temperature and the increasing heat loss of the system due to natural convection and radiation. Depending on the temperature, heat losses of about 35 ± 12% are estimated from the energy balance of the heat pump ($\dot{Q}_{bs} \approx \dot{Q}_{source} + P_{com\,p} - \dot{Q}_{sink}$). This means that there is potential for optimisation in insulation (especially at the compressor) and room for efficiency increase.

Overall, the measured COP data of R1224yd(Z) are comparable with R1233zd(E). The deviations lie within the measurement uncertainty of ± 0.2 COP. At operating point W80/W150, near the critical temperature of 155.5 °C of R1224yd(Z), the COP decreased due to the narrowing of the two-phase region (see p-h diagram in Figure 1). The maximum sink temperature tested in this study was 150 °C. R1233zd(E) achieves potentially higher condensation temperatures due to the higher critical temperature of 165.6°C compared to 155.5°C of R1224yd(Z).

Figure 3 (A) with R1224yd(Z) shows that the integration of the IHX into the heat pump circuit leads to a significant increase in COP over the entire operating map. Compared to the basic cycle (0% IHX), the suction gas in the IHX is additionally superheated and the liquid refrigerant is subcooled more strongly. When the IHX is added, both the suction gas (T_1) and hot gas temperatures (T_2) (see Figure 3, E) as well as the heating capacity increase. At the operating point W60/W110, the COP increased by about 15 % (from 2.8 to 3.2) with IHX addition, at W80/W130 even by 48 % (COP from 1.9 to 2.9) compared to the basic cycle. This is in line with earlier work [59] where R1233zd(E) showed an average efficiency increase of 11% and 19% under the same conditions.

Figure 3 (C) compares the heating capacity ($\dot{Q}_{sink}$) of the two HCFO refrigerants in the IHX cycle as a function of the heat source temperature ($T_{source,in}$) at 30, 50 and 70 K temperature lift. The heating capacity increases steadily with higher source temperature according to the Carnot relation. Under (Ref)-conditions the heating capacity with R1224yd(Z) is about 6.6 kW, with R1233zd(E) about 7.5 kW and at operating point W80/W110 about 10 kW. At this point, the HTHP laboratory system reaches its experimental capacity limits. The data show that the heating capacity of R1224yd(Z) is on average 9% higher than that of R1233zd(E). This is consistent with simulation studies [60], where for R1224yd(Z) also about 8% higher VHC values were calculated than for R1233zd(E) at W60/W110. Theoretical results confirm that R1224yd(Z) and R1233zd(E) lead to similar COP as R245fa. The VHCs are 7 to 15% lower than with R245fa. For R1233zd(E) a compressor with a slightly larger displacement volume would be required to achieve similar heating performance as R1224yd(Z). Depending on the refrigerant, a compromise must be found between COP and VHC.

Figure 3 (D) shows the COP data as a function of the heat source and sink temperature. The increase in efficiency at higher source temperatures is obvious. The COP data of R1224yd(Z) are comparable with R1233zd(E). In addition, a greater temperature glide on the heat sink from 5 to 25 K (at W60/W110) has further increased the COP by 9%, which is advantageous for processes with low return temperatures. Heat transfer in the condenser improved with increasing temperature glide.

Figure 3 (E) shows the discharge gas and suction gas temperatures in function of the sink temperature with R1224yd(Z). The measured suction gas temperatures in the basic cycle without IHX were clearly below the motor switch-off temperature of approx. 110 °C (grey line). In the IHX cycle the suction gas temperature exceeded the motor limit temperature at approx. 130 °C and higher. However, short-term tests over several minutes at 150 °C were possible.

Figure 3 (F) shows the determined COP data of the experiments as a function of the respective temperature lift. As expected, the COP values decrease with a higher temperature lift according to the Carnot relationship and follow a fit curve ($COP = A \cdot \Delta T_{lift}^{B}$)) with a 2nd Law efficiency of 39 ± 2% for R1233zd(E) and 37 ± 5% for R1224yd(Z) in the IHX cycle. These values are comparable with results with R1336mzz(Z) (34 ± 3%) in the same HTHP plant [20,24], as well as in another HTHP laboratory setup of Helminger et al. [61] with R1336mzz(Z).

Finally, but still important, the neutralization number of the synthetic POE oils was determined after approx. 100 operating hours in the HTHP after the refrigerant tests by titration according to DIN 51558-1 in mg KOH/g oil. The neutralisation number indicates the content of acid components in the lubricant and is a measure of ageing. Strong acidification of the oil is undesirable. Fresh oil was also measured for comparison. Visual inspections revealed a slightly yellowish discoloration of the oils after operation in the HTHP. The neutralisation number for fresh POE oil was 0.04, for R1233zd(E) 0.06 and for R1224yd(Z) 0.25. This is well below the warning value of 0.5 for HTHP applications assumed by the oil supplier Fuchs. The data shows that the POE-based oil (Reniso Triton SE 170) is suitable for use with HCFO refrigerants. However, long-term tests were not the aim of this study. At best, even more viscous POE oils (SE 220) and the addition of thermal stabilizers would have to be tested. Temperature-resistant compressors and stable lubricating oils are decisive components for the further development and commercialization of HTHP.

6. Conclusions

The two HCFO refrigerants R1224yd(Z) and R1233zd(E) were successfully tested in a single-stage laboratory scale HTHP with basic and IHX cycle. Operation of the HTHP was demonstrated at heat source inlet temperatures of 30 to 80 °C and heat sink outlet temperatures of 70 to 150 °C at 30 to 70 K temperature lift. The temperature levels simulate possible industrial applications of waste heat recovery, steam generation or drying. The laboratory plant was built with standard components.

A COP of 3.2 and 3.1 for R1224yd(Z) and R1233zd(E) was measured at the operating point W60/W110 (50 K temperature lift). Due to the higher critical temperature, R1233zd(E) was more efficient at 150 °C than R1224yd(Z). Otherwise, the differences were within the measurement uncertainty of ± 0.2 COP.

By connecting an IHX to the circuit and thus subcooling the refrigerant more strongly, the COP increased by 15 to 48% with R1224yd(Z) compared to the basic cycle. The IHX additionally superheats the suction gas and subcools the liquid refrigerant more. A further COP increase of around 9% was achieved by a higher temperature glide on the heat sink from 5 K to 25 K, which is advantageous for industrial processes with low return temperatures, such as steam generation or drying processes.

At a heat sink outlet temperature of 130 °C and higher, the motor switch-off temperature of about 110 °C was exceeded. The limit of the compressor's temperature resistance was reached. Short-term tests up to 150 °C were nevertheless possible.

The drop-in test also showed that the heating capacity of R1224yd(Z) was on average 9% higher than that of R1233zd(E), which in practice requires slightly larger compressors to achieve a comparable heating capacity. At operating point W80/W110, a heating capacity of up to 10 kW was achieved. At this point, the HTHP laboratory system reaches its experimental capacity limits.

Overall, the experimental results of the two HCFO refrigerants R1224yd(Z) and R1233zd(E) with the POE oil are promising for use in HTHP. Both refrigerants are characterized by a very low global warming potential, non-flammability (safety group A1), stability with polymers and metals, miscibility with POE oils, negligible decomposition products in the atmosphere, and good thermodynamic efficiency. The refrigerants therefore have a high potential for future use as refrigerants in HTHP applications as drop-in replacement refrigerants for R245fa, which is affected by a phase-down due to the stricter F-gas regulations.

In the future, the HTHP developed will make it possible to test other alternative HFO and HCFO refrigerants with stabilizing additives, HFCs such as R245fa or R365mfc for direct comparison or other oils based on polyol ester or polyalkylene glycol. Further efficiency gains could be achieved by reducing heat losses at high temperatures through better insulation of components and piping.

Acknowledgements

This research project is part of the Swiss Competence Center for Energy Research – Efficiency of Industrial Processes (SCCER EIP) of the Swiss Innovation Agency Innosuisse. The authors also thank Debra Carolina Cortés Gómez from the Institute for Micro- and Nanotechnology at NTB Buchs for measuring the acid numbers of the POE oils. The refrigerant R1224yd(Z) (AMOLEA®1224yd 99.9% purity, 99.7/0.3 Z/E isomer ratio) was kindly donated by AGC Inc.

References

[1] C. Arpagaus, F. Bless, M. Uhlmann, J. Schiffmann, S.S. Bertsch, High temperature heat pumps: Market overview, state of the art, research status, refrigerants, and application potentials, Energy. 152 (2018) 985–1010. doi:10.1016/j.energy.2018.03.166.

[2] C. Arpagaus, F. Bless, J. Schiffmann, S.S. Bertsch, Review on High Temperature Heat Pumps – Market Overview and Research Status, in: Int. Work. High Temp. Heat Pumps, Sept. 9, 2017, Copenhagen, Denmark, 2017: pp. 1–25.

[3] C. Arpagaus, F. Bless, M. Uhlmann, J. Schiffmann, S.S. Bertsch, High temperature heat pumps: Market overview, state of the art, research status, refrigerants, and application potentials, in: 17th Int. Refrig. Air Cond. Conf. Purdue, July 9-12, 2018, 2018: pp. 1–10. doi:10.1016/j.energy.2018.03.166.

[4] C. Arpagaus, Hochtemperatur-Wärmepumpen: Marktübersicht, Stand der Technik und Anwendungspotenziale, 138 Seiten, ISBN 978-3-8007-4550-0 (Print), ISBN 978-3-8007-4551-7 (E-Book), VDE Verlag GmbH, Offenbach, Berlin, 2018.

[5] C. Arpagaus, F. Bless, J. Schiffmann, S.S. Bertsch, Multi-temperature heat pumps: A literature review, Int. J. Refrig. 69 (2016) 437–465. doi:10.1016/j.ijrefrig.2016.05.014.

[6] G. Myhre, D. Shindell, F.-M. Bréon, W. Collins, J. Fuglestvedt, J. Huang, D. Koch, J.-F. Lamarque, D. Lee, B. Mendoza, T. Nakajima, A. Robock, G. Stephens, T. Takemura, H. Zhang, Anthropogenic and natural radiative forcing, in: Clim. Chang. 2013 Phys. Sci. Basis. Contrib. Work. Gr. I to Fifth Assess. Rep. Intergov. Panel Clim. Chang., Cambridge University Press, Cambridge, United Kingdom and New York, NY, USA, 2013: pp. 659–740.

[7] EU, Regulation (EU) No 517/2014 of the European Parliament and of the Council of 16 April 2014 on fluorinated greenhouse gases and repealing Regulation (EC) No 842/2006, (2014) L150/195-230. http://eur-lex.europa.eu/eli/reg/2014/517/oj.

[8] S. Bertsch, C. Arpagaus, F. Bless, A. Weickgenannt, J. Schiffmann, Theoretical Investigation of a High Temperature Heat Pump using a Micro Turbo Compressor and Water as a Refrigerant, Paper ID 201, in: 13th IIR-Gustav Lorentzen Conf. Nat. Refrig. 18-20 June 2018, Valencia, Spain, 2018: pp. 1–9.

[9] M. Chamoun, R. Rulliere, P. Haberschill, J.-L. Peureux, Experimental and numerical investigations of a new high temperature heat pump for industrial heat recovery using water as refrigerant, Int. J. Refrig. 44 (2014) 177–188. doi:10.1016/j.ijrefrig.2014.04.019.

[10] P. De Larminat, D. Arnou, P. La Sausse, F. Clunet, J.-L. Peureux, A high temperature heat pump using water vapor as working fluid, in: 11th IIR Gustav Lorentzen Conf. Nat. Refrig. GL 2014, China, 31 August - 2 Sept. 2014, 2014. doi:10.1046/j.1365-2222.2000.00820.x.

[11] O. Bamigbetan, T.M. Eikevik, P. Nekså, M. Bantle, Development of propane-butane cascade high temperature heat pump: Early test rig results, in: Int. Work. High Temp. Heat Pumps, Sept 9, 2017, Copenhagen, Denmark, 2017: pp. 1–12. http://www.sintef.no/heatup.

[12] H. Moisi, R. Rieberer, Refrigerant Selection and Cycle Development for a High Temperature Vapor Compression Heat Pump, in: 12th IEA Heat Pump Conf. 2017, Rotterdam2, 2017: pp. 1–10.

[13] A.K. Wemmers, A.W.M.B. van Haasteren, P.K.J. van der Kremers, Test results R600 pilot heat pump, in: 12th IEA Heat Pump Conf. Rotterdam, May 14-17, 2017, 2017: pp. 1–9.

[14] T. Yamazaki, Y. Kubo, Development of a High-Temperature Heat Pump, IEA Heat Pump Centre, Newsletter, Vol. 3, No. 4. (1985) 18–21.

[15] F. Helminger, K. Kontomaris, J. Pfaffl, M. Hartl, T. Fleckl, Hochtemperatur-Wärmepumpen-Messergebnisse einer Laboranalage mit HFO-1336MZZ-Z bis 160°C Kondensationstemperatur, in: 14. Symp. Energieinnovation, 10. Bis 12. Febr. 2016, Tech. Univ. Graz, 2016. www.tugraz.at/events/eninnov2016.

[16] T. Fleckl, M. Hartl, F. Helminger, K. Kontomaris, Pfaffl, Performance testing of a lab-scale high temperature heat pump with HFO-1336mzz-Z as the working fluid, in: Eur. Heat Pump Summit 2015, Oct. 20-21, Nuremberg, Ger., 2015: pp. 1–25.

[17] Innosuisse, SCCER Efficiency of Industrial Processes (SCCER EIP), (2019). www.sccer-eip.ch.

[18] C. Arpagaus, M. Prinzing, F. Bless, M. Uhlmann, E. Büchel, S. Frei, R. Kuster, J. Schiffmann, S.S. Bertsch, Hochtemperatur Wärmepumpe mit HFO und HCFO Kältemitteln - Systemdesign, Simulation und erste experimentelle Ergebnisse, in: Dtsch. Kälte- Und Klimatagung 2018 (DKV-Tagung), 21.-23. Nov. 2018, Aachen, 2018.

[19] AGC Inc., New Generation Low GWP Refrigerant AMOLEA 1224yd, in: Chill. Nuremberg, Oct. 16-18, 2018, 2018.

[20] C. Arpagaus, F. Bless, M. Uhlmann, E. Büchel, S. Frei, J. Schiffmann, S.S. Bertsch, High temperature heat pump using HFO and HCFO refrigerants - System design, simulation, and first experimental results, ICR 2019, 25th IIR Int. Congr. Refrig. August 24-30, Montréal, Québec, Canada. (2019) 1–9. doi:10.18462/iir.icr.2019.242.

[21] C. Arpagaus, F. Bless, M. Uhlmann, E. Büchel, S. Frei, J. Schiffmann, S.S. Bertsch, High temperature heat pump using HFO and HCFO refrigerants - System design , simulation, and first experimental results, in: 17th Int. Refrig. Air Cond. Conf. Purdue, July 9-12, 2018, 2018: pp. 1–10.

[22] C. Arpagaus, F. Bless, S.S. Bertsch, J. Schiffmann, Wärmepumpen für die Industrie: Eine aktuelle Übersicht, in: 25. Tagung Des BFE-Forschungsprogramms “Wärmepumpen Und Kälte”, 26. Juni 2019, BFH Burgdorf, Schweiz, 2019: pp. 1–15.

[23] C. Arpagaus, M. Prinzing, F. Bless, M. Uhlmann, E. Büchel, S. Frei, R. Kuster, J. Schiffmann, S.S. Bertsch, Hochtemperatur-Wärmepumpe mit HFO- und HCFO-Kältemitteln, KI Kälte Luft Klimatechnik, 12/2018. (2018) 45–53.

[24] C. Arpagaus, S.S. Bertsch, Experimental results of HFO / HCFO refrigerants in a laboratory scale HTHP with up to 150 °C supply temperature, in: 2nd Conf. High Temp. Heat Pumps, Sept. 9, 2019, Copenhagen, 2019: pp. 1–9.
[25] Honeywell, Solstice 1233zd(E) Technical Information, (2013) 1–8.
[26] W. Rached, S. Kim, L. Abbas, Stable R-1233zd (E) for energy recovery applications, in: 1st IIR Int. Conf. Appl. HFO Refrig. Birmingham, UK, 2-5 Sept. 2018, 2018: pp. 1–7. doi:10.18462/iir.hfo.2018.1137.
[27] L.L. Andersen, F.F. Østerstrøm, M.P. Sulbaek Andersen, O.J. Nielsen, T.J. Wallington, Atmospheric chemistry of cis-CF3CHCHCl (HCFO-1233zd(Z)): Kinetics of the gas-phase reactions with Cl atoms, OH radicals, and O3, Chem. Phys. Lett. 639 (2015) 289–293. doi:10.1016/j.cplett.2015.09.008.
[28] K.O. Patten, D.J. Wuebbles, Atmospheric lifetimes and Ozone Depletion Potentials of trans-1-chloro-3,3,3-trifluoropropylene and trans-1,2-dichloroethylene in a three-dimensional model, Atmos. Chem. Phys. 10 (2010) 10867–10874. doi:10.5194/acp-10-10867-2010.
[29] M.P. Sulbaek Andersen, J.A. Schmidt, A. Volkova, D.J. Wuebbles, A three-dimensional model of the atmospheric chemistry of E and Z-CF3CH=CHCl (HCFO-1233(zd) (E/Z)), Atmos. Environ. 179 (2018) 250–259. doi:10.1016/j.atmosenv.2018.02.018.
[30] S. Kujak, K. Schultz, E. Sorenson, Experiences with next generation low GWP refrigerants in centrifugal chillers, in: 1st IIR Int. Conf. Appl. HFO Refrig. Birmingham, UK 2-5 Sept. 2018, 2018: pp. 1–8. doi:10.18462/iir.hfo.2018.1110.
[31] N.N. Shah, D. Cotter, N.J. Hewitt, Overview on HCFO-R1233ZD(E) use for high temperature heat pump application, in: ICR 2019, 25th IIR Int. Congr. Refrig. August 24-30, Montréal, Québec, Canada, 2019: pp. 1–8. doi:10.18462/iir.icr.2019.
[32] N.J. Hewitt, D. Cotter, M.J. Huang, N. Shah, Industrial Heat Pumps in the UK Current Constraints and Future Possibilities, in: ICR 2019, 25th IIR Int. Congr. Refrig. August 24-30, Montréal, Québec, Canada, 2019: pp. 1–8. doi:10.18462/iir.icr.2019.
[33] M. Fukushima, Next Generation Low- GWP Refrigerants AMOLEA, in: JRAIA Int. Symp. 2018, 2018: pp. 1–5.
[34] S. Eyerer, F. Dawo, J. Kaindl, C. Wieland, H. Spliethoff, Experimental investigation of modern ORC working fluids R1224yd(Z) and R1233zd(E) as replacements for R245fa, Appl. Energy. 240 (2019) 946–963. doi:10.1016/j.apenergy.2019.02.086.
[35] M. Fukushima, H. Hayamizu, M. Hashimoto, Thermodynamic properties of low-GWP refrigerant for Centrifugal Chiller, in: 16th Int. Refrig. Air Cond. Conf. Purdue, July 11-14, 2016, 2016: pp. 1–10. http://docs.lib.purdue.edu/iracc/1631.
[36] K. Tokuhashi, T. Uchimaru, K. Takizawa, S. Kondo, Rate Constants for the Reactions of OH Radical with the (E)/(Z) Isomers of CF3CF=CHCl and CHF2CF=CHCl, J. Phys. Chem. A. 122 (2018) 3120–3127. doi:10.1021/acs.jpca.7b11923.
[37] ARKEMA, FORANE HTS 1233zd - Refrigerants, Excellent Choice for Centrifugal Chillers, Product Datasheet, SDC/08.2017, 2017.
[38] Honeywell, Solstice 1233zd(E) Technical Brochure, 2013.
[39] WMO (World Meteorological Organization), Scietific Assessment of Ozone Depletion 2010, Global Ozone Research and Monitoring Project - Report No. 52, Geneva, Switzerland, 2011.
[40] S. Henne, D.E. Shallcross, S. Reimann, P. Xiao, S. Boulos, A.C. Gerecke, D. Brunner, Environmental impacts of HFO-1234yf and other HFOs, ASHRAE/NIST Refrig. Conf. Mov. Towar. Sustain. (2012) 182–194.
[41] T.J. Wallington, M.P. Sulbaek Andersen, O.J. Nielsen, Atmospheric chemistry of short-chain haloolefins: Photochemical ozone creation potentials (POCPs), global warming potentials (GWPs), and ozone depletion potentials (ODPs), Chemosphere. 129 (2015) 135–141. doi:10.1016/j.chemosphere.2014.06.092.
[42] AGC Chemicals, AMOLEA® 1224yd, Technical Information, ASAHI Glass Co., Ltd., (2017) 1–18.
[43] Q. Guo, L. Chen, J. Mizukado, Atmospheric degradation mechanism of Z/E-CF3CF=CHCl, CF3CF=CCl2, and CF2=CFCl initiated by OH radicals using a smog chamber with long-path FT-IR at 298 K, Atmos. Environ. 218 (2019) 116991. doi:10.1016/j.atmosenv.2019.116991.
[44] R. Akasaka, M. Fukushima, E.W. Lemmon, A Helmholtz Energy Equation of State for Cis-1-chloro-2,3,3,3-tetrafluoropropene (R-1224yd(Z)), in: 21st Eur. Conf. Thermophys. Prop. Graz, Austria, Sept. 3-8, 2017, 2017: pp. 1–26.

[45] A. Miyara, M.J. Alam, K. Kariya, Miyara A, Alam MJ, Kariya K. Measurement of transport properties of low GWP refrigerant HCFO-1224yd(Z) (cis-1-chloro-2,3,3,3-teraflouropropene;, in: 1st IIR Int. Conf. Appl. HFO Refrig. Birmingham, UK 2-5 Sept. 2018, 2018: pp. 1–8. doi:10.18462/iir.hfo.2018.1139.

[46] T. Kaida, M. Fukushima, K. Iizuka, Application of R1224yd(Z) as R245fa alternative for high temperature heat pump, in: ICR 2019, 25th IIR Int. Congr. Refrig. August 24-30, Montréal, Québec, Canada, 2019: pp. 1–8.

[47] OARS (Occupational Alliance for Risk Science), Workplace Environmental Exposure Level of HCFO-1224yd(Z), 2017. https://med.uc.edu/docs/default-source/default-document-library/hcfo-1224yd(z)-weel-document-final-2017.pdf?sfvrsn=0.

[48] T. Soga, H. Hayamizu, M. Fukushima, Compatibility of Low-GWP refrigerant HCFO-1224yd(Z), F312 (in Japanese), in: JSRAE Annu. Conf. (Japan Soc. Refrig. Air Cond. Eng. Tokyo, Sept. 26-29, 2017, 2017: pp. 1–5.

[49] R. Saito, S.G. Sundaresan, Refrigeration oils for low GWP refrigerants in various applications, IOP Conf. Ser. Mater. Sci. Eng. 232 (2017) 012093. doi:10.1088/1757-899X/232/1/012093.

[50] K. Kontomaris, Zero-ODP, Low-GWP, Nonflammable Working Fluids for High Temperature Heat Pumps, in: ASHRAE Annu. Conf. Seattle, Washington, July 1, 2014, 2014: pp. 1–40.

[51] K. Kontomaris, HFO-1336mzz-Z as low GWP working fluid for transcritical rankine power cycles, in: Jraia Int. Symp. 2014, 2014: p. 6. https://www.chemours.com/Refrigerants/en_US/products/Opteon/Stationary_Refrigeration/assets/downloads/201411_ORC-Kobe-paper.pdf.

[52] K. Kontomaris, A non-flammable, zero-ODP, low GWP working fluid for high temperature heat pumps: DR-148, in: 11th IEA Heat Pump Conf. May 12-16, 2014, Montréal Canada, 2014: pp. 1–10.

[53] K. Kontomaris, HFO-1336mzz-Z: High Temperature Chemical Stability and Use as A Working Fluid in Organic Rankine Cycles, Paper 1525, Int. Refrig. Air Cond. Conf. Purdue, July 14-17, 2014. (2014).

[54] S.A. Klein, Engineering Equation Solver (EES), V10.6.43, F-Chart Software, (2019). www.fchartsoftware.com.

[55] M. Garry, HFOs - How much is too much? Cover story, ACCELERATE Magazine, September 2019, (2019) 30–37.

[56] K.R. Solomon, G.J.M. Velders, S.R. Wilson, S. Madronich, J. Longstreth, P.J. Aucamp, J.F. Bornman, Sources, fates, toxicity, and risks of trifluoroacetic acid and its salts: Relevance to substances regulated under the Montreal and Kyoto Protocols, J. Toxicol. Environ. Heal. Part B. 19 (2016) 289–304. doi:10.1080/10937404.2016.1175981.

[57] DIN EN 14511, Luftkonditionierer, Flüssigkeitskühlsätze und Wärmepumpen für die Raumbeheizung und -kühlung und Prozess-Kühler mit elektrisch angetriebenen Verdichtern, 2019.

[58] VDI, VDI-Wärmeatlas, 10. Auflage, Stoffwerte von Wasser, Dba, Springer, Berlin Heidelberg, 2006.

[59] C. Arpagaus, M. Prinzing, F. Bless, M. Uhlmann, E. Büchel, S. Frei, R. Kuster, J. Schiffmann, S.S. Bertsch, Hochtemperatur Wärmepumpe mit HFO und HCFO Kältemitteln – Systemdesign, Simulation und erste experimentelle Ergebnisse, DKV-Tagung 2018, Aachen, 21.-23. Nov. 2018. IV.05 (2018).

[60] C. Arpagaus, M. Prinzing, R. Kuster, F. Bless, M. Uhlmann, J. Schiffmann, S.S. Bertsch, High temperature heat pumps -Theoretical study on low GWP HFO and HCFO refrigerants, in: ICR 2019, 25th IIR Int. Congr. Refrig. August 24-30, Montréal, Québec, Canada, 2019: pp. 1–8. doi:10.18462/iir.icr.2019.259.

[61] F. Helminger, K. Kontomaris, J. Pfaffl, M. Hartl, T. Fleckl, Measured Performance of a High Temperature Heat Pump with HFO-1336mzz-Z as the Working Fluid, in: ASHRAE 2016 Annu. Conf. St. Louis, Missourii, 25-29 June 2016, 2016: pp. 1–8.

13th IEA Heat Pump Conference
April 26-29, 2021 Jeju, Korea

Roadblocks to heat pump use in residential buildings with Model Predictive Control for demand response and ancillary markets and potential solutions

Ramanunni Parakkal Menon[a,*], Frederic Amblard[b,c], Jessen Page[b]

[a]Concordia University, Montreal, Quebec, Canada
[b]HES-SO Valais-Wallis, Sion, Switzerland
[c]EPFL, Lausanne, Switzerland

Abstract

Demand Response and use of residential buildings for peak shaving and load balancing has been proposed as a popular method towards providing security and increasing efficiency for the electrical grids. Use of heat pumps to shift peaks of electricity and thermal demands is one of the possibilities available for this purpose. This is only possible through the use of advanced control algorithms which are capable of interfacing with the thermal and electric devices available at the residences. However, usage of devices like heat pumps for load shifting and/or peak shaving would imply discomfort for the tenants in the residential building. Thus, demand response only becomes an attractive option to the residential user if there are financial incentives available to them. This is only possible in present-day by providing end-users with access to the ancillary markets. The paper studies the implementation of a control framework (using Model Predictive Control and Machine Learning) on a group of buildings with water-water heat pumps. The paper looks at the practical roadblocks that limit the implementation of advanced control algorithms on heat pumps. The paper, then, looks at solutions towards these roadblocks and the hardware and software that is required to ensure successful implementation of demand response for heat pumps. The paper then looks at the data requirements for creating grey-box models of the heat pumps within a Model Predictive Control Framework such that end-users can actively participate in the ancillary market. Finally, the paper discusses possible changes to the ancillary market for better integration of thermal devices for demand response and changes to redress the difficulties in using heat pump use for demand response.

© HPC2020.
Selection and/or peer-review under responsibility of the organizers of the 13th IEA Heat Pump Conference 2020.

Keywords: Demand Response; Heat Pumps; Buildings; Model Predictive Control; End-user; Ancillary markets

1. Introduction

Distributed Energy Resources (DER) like solar panels and wind turbines have forced a re-think on not only the structure of the grid but also the grid code which exists in today's top-down grid architecture. Demand Response (DR) has often been touted as a great solution to many of the problems faced by the electricity grid. Demand Response has been defined by the Department of Energy (DoE) of USA[1] as, "Changes in electric usage by end-use customers from their normal consumption patterns in response to changes in the price of electricity over time, or to incentive payments designed to induce lower electricity use at times of high wholesale market prices or when system reliability is jeopardized". This definition of DR has been taken as the guideline and the motivation for the rest of the paper. End-use customers, at present, do not have an active role in the electric grid. They are treated as consumers, who only consume and do not have much leeway in changing their consumption patterns. They are as a result, not given an active role in the market and pay fixed tariffs to the consumers.

* Corresponding author. Tel.: +1-4383788386.
E-mail address: ramanunni.menon@protonmail.com.

With nearly 45% of the total energy consumption coming from the end-users and buildings, and with 50% of that coming from thermal energy consumption, there is definitely a role that end-users and end-user buildings can play in demand response [2]. Recent papers and concepts like the microgrid [3] and the EnergyHub [4] are concepts that have put forward the idea of the prosumer who not only consumes but also produces and participates in improving the efficiency and efficacy of the grid, by playing an active role in the electricity market. Prosumers are able to produce electricity through Combined Heat and Power (CHP) systems and storage devices like batteries, and are able to consume in a flexible manner through the use of P2H (Power-to-Heat) devices which have controllable consumptions. The heat is stored either in the building mass or in thermal storages used for space heating and Domestic Hot Water (DHW) needs.

1.1. Heat Pumps in Europe

Thermal demand satisfaction is a vital part of energy consumption in buildings in Europe. Heat pumps are one of the technologies, albeit not the predominant one, in use for thermal demand satisfaction in Europe. Most countries use a mix of boilers, electric heating and heat pumps for satisfaction for all their space heating and DHW purposes. European Heat Pump Association (EHPA) estimates that there are over 12 million heat pumps installed across the European countries for heating, accounting for around 12% of the heating market alone [5]. The heat pump installation rates vary between the countries, with countries like France, Italy and Sweden having high penetration, while others like Hungary and Lithuania having extremely low heat pump penetration. EurObserv'er estimates that a total of around 34.4 million heat pumps have been installed in total in Europe for both heating and cooling purposes combined [6].

Heat pumps are being given huge emphasis within DR strategies as they are one of a small number of P2H (Power to Heat) devices able to utilize electrical power and provide thermal power. Thus, they offer a powerful option to shifting and changing a large portion of the energy consumption in buildings, while also making it possible to actively participate in the electricity market.

DR strategies and algorithms developed for thermal systems have typically looked at electric heaters. This is as they are easier to control and model. When algorithms have looked at heat pumps, the typical approach has been to either model them akin to batteries or to use physical models that rarely account for the limitations of controlling the heat pumps remotely and their non-linear behavior.

With this in mind, the aim of this paper is to look at how model predictive control maybe implemented in heat pumps currently existing in the building stock and understand the data requirements, the current roadblocks preventing implementation of DR using heat pumps, and propose solutions towards alleviating these issues. The paper is structured as follows for that purpose: Section 2 details on the implementation of Model Predictive Control (MPC) for heat pumps, through application within a site in Switzerland and the preliminary findings and problems faced when implementing the algorithm on actual buildings. Section 3 identifies the roadblocks that present-day heat pumps create, preventing DR implementation for end-users. Section 4 and 5, identify proposals and potential solutions towards alleviating said roadblocks, followed by a Conclusion and References.

2. Model Predictive Control for heat pumps

Model Predictive Control (MPC) is an often-used optimization method found in recent scientific literature, for forecast and management of building thermal and electric power demand satisfaction. It has also been used for maintaining thermal comfort and minimizing the cost associated with electricity and gas that is spent by the consumer. Some implementations of MPC and the associated theory can be seen in [7], [8], [9], [10].

Model Predictive Control utilizes a Receding Horizon (RH) principle. For the MPC implementation in this paper, we have used a finite time horizon of 24 hours. The optimization utilizes a certain (typically between 15 minutes and one hour) time step depending on the use case. The MPC is used to minimize the energetic costs and discomfort of tenants in these buildings. The objective function is structured such that usage of energy demand is optimized for each of the buildings. More details on the MPC implementation and associated data requirements can be found in the subsequent sections.

2.1. Naters

The block of buildings modelled are based on data collected from a group of 12 buildings of a pilot site in Naters, Switzerland. Each of the buildings at the site are used for either residential or mixed purposes. They were either constructed or renovated between the periods of 1960 and 2015. The buildings have been fitted

with heat pumps and thermal storages of different capacities (as deemed appropriate for building requirements) such that their respective thermal needs can be satisfied. The net capacity of the installed heat pumps come to around 700 kW_{th} peak output when working together in a concerted manner (very rare).

Their electricity and thermal demands vary daily depending on the inter- and intra-seasonal weather fluctuations and user consumptions. The heat pumps are all water-water heat pumps (WWHPs) which utilize a Low-Temperature Heating (LTHN, Anergy) Network as the heat source. The building mass is heated using either radiators and/or through floor heating. The temperatures of the LTH network stay relatively fixed between 9-11°C throughout the year. The water volume within the DHW (Domestic Hot Water) tank is kept constant by refilling from the bottom using clean water at 15°C. When hot DHW is required, the 15°C water is heated up by heat transfer through a plate heat exchanger and fed into the DHW tank. The DHW tank is heated to 60°C once every day to prevent legionella growth and associated health problems. The schematic of the heating systems installed can be seen in Figure 1.

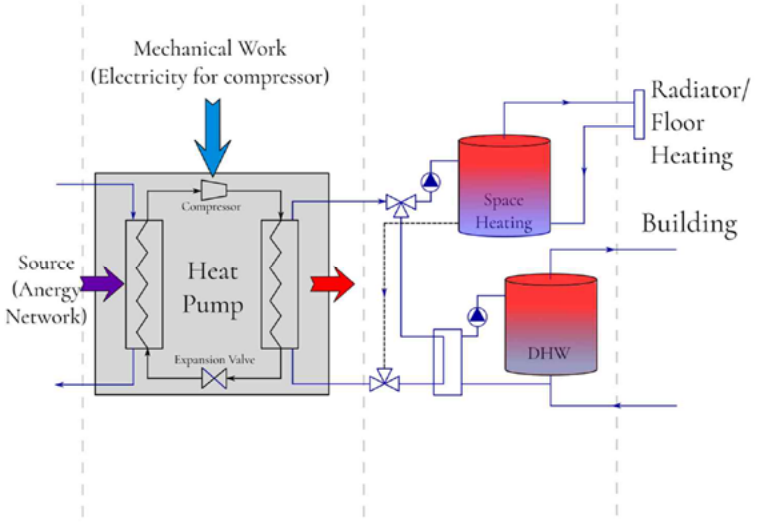


Fig. 1. Conventional Heat Pump set-up in European end-user buildings

2.2. Cluster Manager and Model Predictive Control Implementation

The MPC for the buildings at Naters was implemented in a centralized manner. The MPC is designed to be run by a Cluster Manager (CM). The Cluster Manager is an entity created for the purpose of the EU H2020 (Horizon 2020) research project, Sim4blocks. This entity is charged with the responsibility of monitoring and controlling the heat pumps and other systems within the building stock while, simultaneously, interacting with the aggregators/market. This entity was also created to allow for aggregation of multiple systems to satisfy and/or surmount the high entry barriers to the electricity market. Currently, there are very few end-users who qualify the prerequisites of the existing market. The Cluster Manager agglomerating on behalf of the end-users, is seen as a entity created to surmount these barriers, while also acting as the responsible entity ensuring that the devices are safe from damage due to over-use or being operated under sub-par component conditions. The algorithm was solved such that the end-user buildings can provide ancillary services in the electricity market.

The MPC models are created such that it maximizes the data available from the buildings. As a result, the MPC uses simple two/three node models for the building. The building parameters used are based on the information available from the building construction data and the architectural standards. The models for the storage tanks for space heating and domestic water purposes are single node models. This is a departure from previous work where 3-5 nodes for the storage tanks were chosen, based on the need for stratification or full mixing. This was abandoned as thermal storages in existing buildings only have one sensor (or at best two) measuring the temperature within, making it difficult to create good representations of the stratifications within the tank. Also, single node models are easier to solve.

The equations listed here are mostly generic representations describing an MPC. As can be seen from the equations 1a, 1b, and 1c, the objective function consists of minimization of operating costs and the penalty costs associated with discomfort for the users in the building. The equations 2 represents the forecasted states of the state with reference to the present state and control variables and equation 3 represents the constraints imposed on the systems. The actual models are variations of the equations used in [11] and [12].

$$min \sum_{k=0}^{T} J(x_k, u_k) \tag{1a}$$

$$\sum_{k=0}^{T} J(x_k, u_k) = \sum_{k=0}^{T} l(x_k, u_k) + V(x_T) \tag{1b}$$

$$\sum_{k=0}^{T} J(x_k, u_k) = \sum_{i=0}^{12} \sum_{k=0}^{T} OPC + Penalty \tag{1c}$$

$$x_{k+1} = f_k(x_k, u_k) = Ax_k + Bu_k \tag{2}$$

$$G(x_k, u_k) \leq 0 \tag{3}$$

$$x(0) = x_0, k = 1, 2, 3, \ldots . T - 1 \tag{4}$$

$$u_k \in \{0, 1\} \tag{5}$$

The equations of the state at any starting time is represented as shown in equation 4 and equation 5 highlights that the control variable is a binary variable. Thus, the problem is solved as a Mixed-Integer Linear Programming Problem (MILP).

However, what is different from the conventional heat pump models are the additional constraints that have been imposed on the problem and the post-processing that is required for transforming the MPC results to ensure that the strategy is implemented for each of the buildings.

Conventional heat pump internal logic units use dead-band controls on the temperatures within the storage tanks and the distribution systems to prevent lack of DHW and heat for space heating during winters and use specific programs for heating that change from season to season. These dead-band limits were added to the MPC problem as constraints, as they reflect the actual HP heating ability versus what is theoretically possible. In addition, it is important to know the program that the heat pump is running on (whether it is for both space heating and DHW, or just DHW; whether it is running on a Winter/Summer program etc.) as that will change these dead band values. These factors were also added to the MPC as constraints. In addition, the problem constraints were varied depending on the building end-users' subjective comforts (based on assumptions on internal temperature constraints and historic data observations) and their space heating systems as well.

However, adding these constraints have a direct impact on the tractability, convergence rates and convergence time required for solving the problems. The addition of these constraints was observed to increase the convergence times from a few seconds for each timestep to anything from a few minutes to the maximum allowed 15 minutes to solve (15 mins as the electricity balance markets use 15 minutes as actuation time limit). The 15-minute time limit and the additional constraints make the problem difficult to solve in time, for a site with HPs. As a result, it makes it difficult to be part of the bidding process that is mandatory for participation in the electricity markets.

Other factors and problems associated with such an MPC implementation on HPs is mentioned in detail in the next section.

3. Problems with Heat Pump integration for Demand Response

Heat Pumps have always proven to be difficult devices to use towards DR applications. Heat Pumps are non-linear in behavior and as a result, making linear models which provide time-series of the electric power consumption and thermal power output within time constraints imposed by electricity markets has always been difficult.

This is made, even more difficult by certain practices in the industry, practices seen in installation and the existing internal logic within heat pumps.

These can be broadly divided to five main categories: (1) Installation issues, (2) Monitoring and sensor issues, (3) Standards and communication issues, (4) Feedback of states within installed systems issues and finally, (5) Management system/algorithm design and market issues.

3.1. Installation Issues

For most existing buildings, heat pump installation is performed by certified installers. The existing certification framework is managed by each HP manufacturer (e.g. Each company have a set number of configurations for certain types of buildings and the installer must conform to these configurations). On paper, this seems like a good idea. As building standards change, all that the HP manufacturers need to do is to upgrade the HP installation configurations and train the installers to install accordingly.

However, the reality is that, many a times, the peculiarity of the location of the building, the orientation of the building to the cardinal directions and as a result the sun, and geometrical peculiarities of a building over or underestimates the thermal demands of a building. There are also situations where the blueprint of the thermal installation will still conform to the certified configurations, however, the actual location of the thermal sensor (e.g., for measuring the outdoor temperature or the temperature within the storage tank) will be different from what it says on the schematic owing to space and architectural limitations.

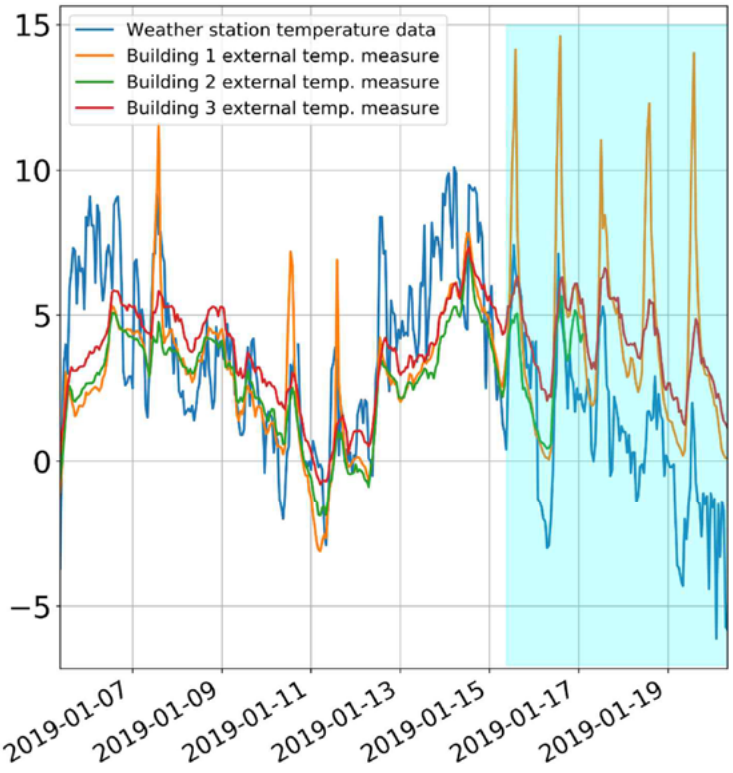


Fig.2. The comparison of the external temperature readings between three buildings at Naters and the weather station data. In the area, highlighted in cyan, one can observe the huge spikes in external temperature reading registered by the heat pumps for one of buildings because of exposure of the external temperature sensor to solar irradiation.

This might seem trivial as a problem, however, during the project, such a faulty installation was seen to measure outdoor temperatures above 20°C during winter days in Naters where the external temperature was measured to be sub-zero. This has drastic effects on the heating done by the heat pumps.

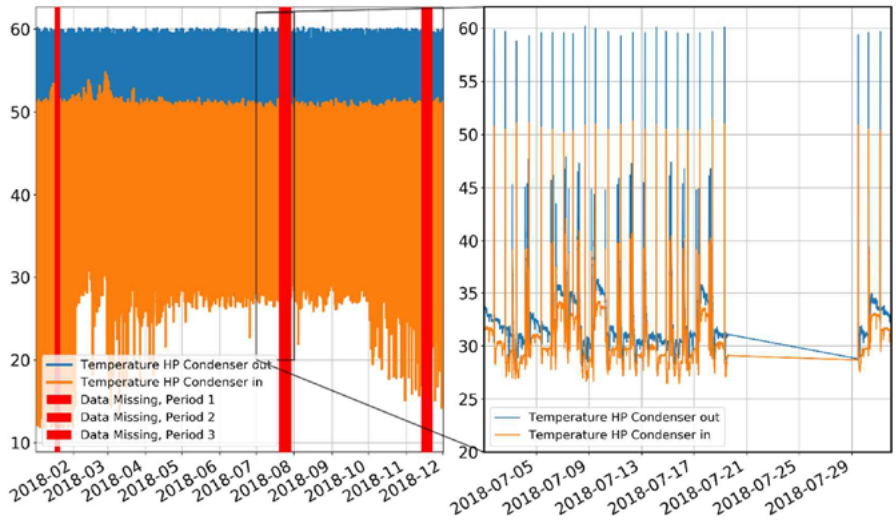


Fig. 3. The temperature of the water that goes into the condenser and comes out of the condenser collected over a year for a building in Naters highlighting the inconsistencies in monitoring

3.2. Monitoring Issues

Monitoring issues are a problem that is only partially attributable to the heat pumps and the manufacturers. However, this is a vital aspect when it comes to functioning alongside the new smart devices and an essential factor that will decide on whether HPs will be able to participate in the electricity market.

Monitoring and monitoring problems are a direct by-product of the participation of devices in the various markets and coming-of-age of the Internet-of-Things (IoT) paradigm. A fundamental marker that signifies the successful participation of any system within the electricity market is the proof of implementation of promised behavior. This is only possible through continuous monitoring.

However, as things stand, heat pumps and many of the thermal and electrical devices that exist in buildings are not prepared for the IoT paradigm and are not fit for continuous monitoring. This maybe owing to implementation of proprietary standards or siloed standards that are industry-standard in certain sectors, but are virtually unknown in IT and other sectors. This issue with monitoring reliability was continuously noticed in the Sim4blocks project, as can be seen in Figure 3, where the temperature of the water going into and coming out of the HP condenser dropped for long periods (49 days in 2018) during a year owing to hardware and software problems of the monitoring framework.

Another factor that plagues the monitoring quality is the calibration of the sensors. This has also been found to be inconsistent and there seems to be a lack of consensus on the general number of sensors that need to be present to get a concrete and consistent quantification of the state of charge in thermal storages and within the building mass. Quite often, due to financial reasons, the bare minimum was installed as standard. In the case of thermal storages, quite often the presence of only a single sensor within the storage tanks and installation errors rendered the monitored data meaningless. The presence of erroneous sensor readings can make certain algorithms ineffective, especially when storages only have one reading per tank (as can be seen in the highlighted blue and red bands in Figure 4).

For MPC implementation, this remains one of the most important issues that needs to be tackled, an MPC is only as good as the model you can make from the data you collect. The more reliable the data is, and the better the frequency of data collected, the better the MPC will perform.

3.3. Standards and communication Issues

The monitoring issues in the previous sub-section is partially owing to the sudden burst of IoT to the fore and the resulting impact of the sudden interconnectivity of systems that were previously not connected. Many standards in different fields were instituted separately in each sector over time. This historical separation has meant that there are still many standards and protocols in use in different sectors that remain industry standards, but, don't translate well in the age of the IoT and for use with DR. Proprietary standards are the biggest obstacle in preventing devices like HPs from being used for DR, followed by lack of conversion interfaces of the proprietary standards to interoperable standards like ModBus. The need for removal of vertical silos of standards to be replaced by OneM2M and ETSI standards for successful participation of devices have been highlighted by [13], [14] and [15].

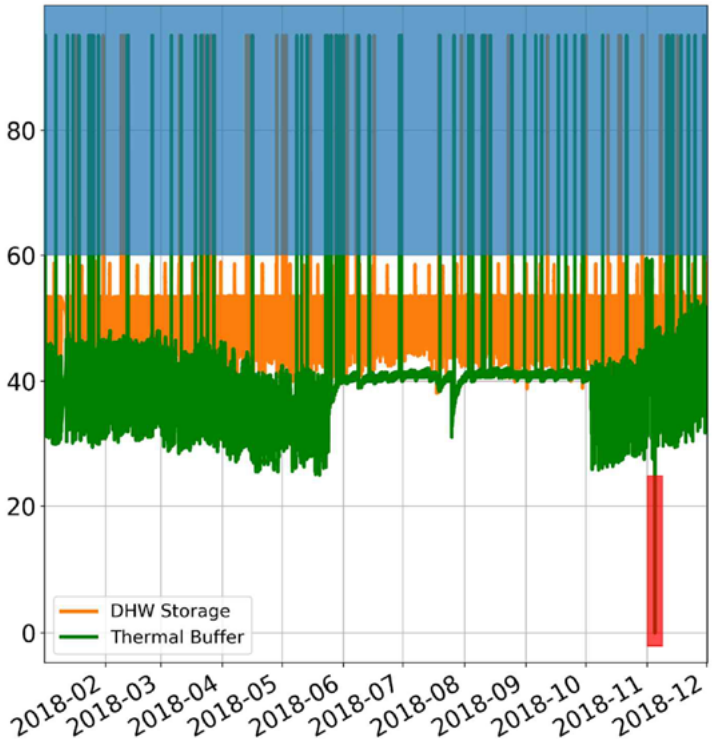


Fig. 4. Faulty water Temperature in the thermal storages (registering 95°C and 0°C, area highlighted in blue and red respectively) in one of the buildings in Naters

Of the existing HP manufacturers, most offer interfaces that can convert the internal logic and standards to ModBus or BACNet signals. This is the first step in the right direction. However, quite a few manufacturers provide this facility solely for monitoring and not towards reading and writing of variables remotely for control purposes. In addition, even number of monitored values available varies from company to company. Of the 12 buildings at Naters, only 8 buildings are equipped with HPs which can be controlled remotely for DR purposes. The other 4 have heat pumps which provide data of very low quality and only for reading purposes.

Presently, most HP manufacturers are more interested in integrating new protocols only for the latest batch of Heat Pumps (HPs). However, this leaves a large swathe of already existing Heat Pumps installed in the existing building stock that are unable to communicate optimally. As many of these devices won't be replaced overnight, it becomes vital to come up with strategies for these heat pumps in addition to the new HPs.

The removal of the standard and communication issues will also have a direct impact on the monitoring issues and thus, the removal of a large obstacle towards participation of HPs in the electricity market for DR and other services.

3.4. Issues concerning feedback over states within installed systems

The class of issues concerning long-term feedback are a result of the previous three issues mentioned working together. However, this is important for estimation of the quality of the heat supply within the buildings by the heat pumps over a year. Quite often, the installed systems behave properly for a certain season/period of time, but perform woefully during other periods of the year. This effect is presented even if the installer adheres to the certified configurations and conforms to the best monitoring standards. This can only be studied and ameliorated through consistent observation over long periods of time.

Currently, this is not performed at all. The only occasions when corrections are made are when the users within the building complain of exorbitant bills or of over/under-heated living spaces.

Conducting long-term monitoring and correction based on data feedback may be too expensive or not possible for manufacturers and/or installers. However, this may be of interest and of value to third-party entities that may also be interested in providing demand response as a service to the end-users.

Providing such services would not only save money spent in maintenance or upgrade in the long-run, but also, provide valuable input on the building's feasibility to participating in DR without losing money in the market by being an active part from the get-go.

3.5. Management system/algorithm design and market issues

All markets currently in existence, have clearly demarcated rules and constraints for participation. However, these rules and constraints were drawn up with the electrical devices in mind. Thermal devices with higher inertia struggle to keep up with the time constraints imposed.

This is often made better through the presence of efficient control and management systems with algorithms that aid further. However, all of the algorithms and control systems that are designed to-date, either follow rules or models (regardless of whether they are white, grey or black). In addition, each algorithm have different data requirements.

These control/management systems are presently unable to provide a solution that fits all buildings and all users. This means, that the best systems need to be equipped to be flexible and adapt to the buildings, the devices and users within. This is only possible through more data, better monitoring, better and more open communication standards. What would also be required is the presence of controllable variables that are readable and writable.

At present, the existing Heat Pumps are woefully under-equipped to handle anything other than scenario-based management systems leaving them either unable to participate in the market or only in a very limited manner.

4. Proposed Solutions for Heat Pump participation for DR and MPC

The following are the proposed solutions to facilitate heat pump participation for DR (in particular for MPC):

- Better standardization across the heat pumps, vis a vis, use of non-proprietary/universal/open-source protocols for communication and control.
- Improvement on variables that can be written by management systems preferably with a range, rather than discrete options.
- Understanding of minimum number of sensors required for reliable data monitoring and algorithm implementation.
- Better standardization on the location of sensor installation and the calibration of sensors, where installed and feedback on the state of the systems and modification of the systems for optimal functioning.
- Third-party certification of the building installation over multiple and sustained periods of time.

With what we have seen from the previous sections, it is fairly obvious that the first thing to address in the heat pumps would be improved access to data within the systems. At the moment, the data access and the use of vertical standards within the devices isolate the heat pumps and the larger thermal distribution system from being accessed and controlled in a reasonable manner. In addition, use of proprietary control and communication protocols leave very little room for the system to be controlled remotely. Use of ETSI, oneM2M and other horizontal layers of standards that aid monitoring and control would greatly aid heat pump participation in markets.

Once, participation is possible, the second aspect that needs to be tackled is the quality of the data that is being collected and the consistency of monitoring of the devices to see whether the installations are performing to the mark that they were built and installed for. There needs to be a framework to study the behavior of the systems over a set period of time and make changes to the system if need be, so that they work as they are listed and not under sub-par conditions.

Finally, there needs to be concerted effort and collaboration between the market monitors, heat pump manufacturers, installers and the designers of the latest machine learning and control algorithms to come up with the software and hardware necessary, which are flexible enough to adapt depending on the needs of the markets and the needs of the users in the buildings. This will also inform the market policy makers as to how relax or tighten the rules to make it easier for HPs to participate.

5. Proposed Changes to ancillary market to aid thermal device participation

The following are the proposed solutions to improve thermal device participation within the ancillary markets:

- Relaxation of certain actuation constraints of devices, while tightening monitoring constraints
- Encouragement of auto-consumption with systems such as solar panels and batteries that are locally available.
- Creation of blocks of periods where thermal devices have priority/advantage (like during night)
- Lowering of base entry size within balance markets and certain ancillary markets
- Continued liberalization of the market to introduce third-party entities that control aggregated end-user buildings

Thermal devices like heat pumps, unlike electrical devices, have high inertia. This is owing to the vast building mass within each building: within the concrete, the air in the buildings and the insulation that reduces loss of heat to the atmosphere. The flow of heat through the distribution system and the dynamics of the thermal transfer from the source to the sink and then to the storage tanks within the buildings and finally to the distribution system and to the buildings themselves take time.

This is very different from the electric systems which have low inertia and consume and/or produce electricity within seconds. This puts thermal devices on the back foot from the outset.

As things stand, the ancillary and balance markets in Switzerland [16], even the slowest market constraints require the systems to have proof of actuation from 30 seconds to within a minute and be satisfying the power promised within 5 minutes. This is an exceedingly difficult proposition for thermal devices and is a high barrier for consistent HP participation in the market.

So, the active role of thermal systems within an electricity market is only possible if there is a rethink on the rules of participation within the market. Another option would be allowing for the thermal devices to be used to offset electrical devices like PV and batteries.

During nights and certain periods of the day, it might also be possible to prioritize use of thermal devices to offset electricity produced elsewhere in the grid such that they heat the storage tanks and the building mass in advance.

Finally, participation of third-party entities who can control many disparate systems, various thermal devices and in a geographically-wide area, while being able to disaggregate their actuation signals successfully would greatly improve the ability of thermal devices to participate in the market. This would require liberalization of the market to allow for such actors such as aggregators and the cluster manager described in the previous sections.

6. Conclusion

This paper hopes to shine some light on how to better utilize heat pumps within end-user buildings, with a priority on the existing building block, rather than the newly constructed buildings. This is of vital importance as the yearly retrofit/upgrade rate of the existing building stock has been found to be less than 2% throughout Europe.

The authors realize that the conclusions and the proposals that have been made are based solely from a small subset of the heat pump installations in the residential and mixed-use building sectors. This may not reflect the rest of the heat pump installations in Europe or the world. However, based on the similarities seen between the different heat pumps and the similar problems faced by the different pilot sites within the

Sim4blocks project and also from conversations with partners and other players in the industry, the authors believe that the suggestions made could be used as a good baseline to improve the participation of thermal devices, especially Heat Pumps in the electricity market, especially for Demand Response.

Further analysis of the ongoing MPC experiments within the Sim4blocks project and the resulting data will only strengthen the observations made here and shed further light on the ability and shortcomings of MPC for DR with HPs. It will also reinforce the need for more sensors, reliable monitoring data and more tests in other real pilot sites located in actual communities situated in various countries.

This paper is a distillation of the lessons learnt on the value of good sensors, the quality, reliability and type of data, the standardization of communication and monitoring protocols which will be required to ensure successful and optimal thermal device participation in electricity markets. It also shows a possible direction to the evolution of the markets and the grid when used with modern algorithms and management systems.

In addition, the authors hope to highlight the great need for concerted effort between engineers, scientists and policy makers across different fields to ensure successful evolution of the present electrical and thermal systems to create more efficient and greener grid, cities and future.

Acknowledgements

This project has received funding from the European Union's Horizon 2020 research innovation program under grant agreement No. 695965. The authors would also like to thank the partners of the Sim4Blocks project for their invaluable support and help without which this paper would not have been possible.

References

[1] DoE, U. S. (2006). Benefits of demand response in electricity markets and recommendations for achieving them. A report to the United States Congress pursuant to section 1252 of the Energy Policy Act of 2005. In *US Washington, DC: Department of Energy.[http://eetd. lbl. gov/ea/EMP/reports/congress-1252d. pdf](26 July 2009)*.

[2] Yang, Liu, Haiyan Yan, and Joseph C. Lam. "Thermal comfort and building energy consumption implications–a review." Applied energy 115 (2014): 164-173.

[3] R. H. Lasseter and P. Paigi, "Microgrid: a conceptual solution," *2004 IEEE 35th Annual Power Electronics Specialists Conference (IEEE Cat. No.04CH37551)*, Aachen, Germany, 2004, pp. 4285-4290

[4] Geidl, M., Koeppel, G., Favre-Perrod, P., Klöckl, B., Andersson, G., & Fröhlich, K. (2007, March). The Energy Hub–A powerful concept for future energy systems. In *Third annual Carnegie mellon conference on the electricity industry* (Vol. 13, p. 14).

[5] EHPA, European Heat Pump Association, http://www.ehpa.org/

[6] Observ, E. R. Heat pumps barometer-EurObserv'ER 2018.

[7] Fernandez-Camacho, E., & Bordons-Alba, C. (1995). *Model predictive control in the process industry*.

[8] P. Stadler, A. Ashouri and F. Maréchal, "Distributed model predictive control of energy systems in microgrids," *2016 Annual IEEE Systems Conference (SysCon)*, Orlando, FL, 2016, pp. 1-6

[9] Halvgaard, R., Poulsen, N. K., Madsen, H., & Jørgensen, J. B. (2012, January). Economic model predictive control for building climate control in a smart grid. In *2012 IEEE PES innovative smart grid technologies (ISGT)* (pp. 1-6).

[10] Bertsekas, Dimitri P., et al. *Dynamic programming and optimal control*. Vol. 1. No. 2. Belmont, MA: Athena scientific, 1995.

[11] Menon, R. P., Amblard, F., & Page, J. (2019, April). Implementation of demand response for a block of buildings for active participation in the electricity market. In *Proceedings of the 10th ACM/IEEE International Conference on Cyber-Physical Systems* (pp. 330-331). ACM.

[12] Energy, S. S. R. T. D3. 1–Optimization strategies for the use case scenarios.

[13] Park, H., Kim, H., Joo, H., & Song, J. (2016). Recent advancements in the Internet-of-Things related standards: A oneM2M perspective. *ICT Express*, *2*(3), 126-129.

[14] E. Kovacs, M. Bauer, J. Kim, J. Yun, F. Le Gall and M. Zhao, "Standards-Based Worldwide Semantic Interoperability for IoT," in *IEEE Communications Magazine*, vol. 54, no. 12, pp. 40-46, December 2016.

[15] Främling, K., Kubler, S., & Buda, A. (2014). Universal messaging standards for the IoT from a lifecycle management perspective. *IEEE Internet of things journal*, *1*(4), 319-327.

[16] Abrell, J. (2016). The Swiss wholesale electricity market. *tech. rep., wiss Competence Center for Energy Research*.

13th IEA Heat Pump Conference
April 26-29, 2021 Jeju, Korea

Single Source "Solar Thermal" Heat Pump for Residential Heat Supply: Performance with an Array of Unglazed PVT Collectors

Christian Schmidt, Arim Schäfer *, Korbinian Kramer

Fraunhofer-Institute for Solar Energy Systems ISE, Freiburg 79110, Germany

Abstract

This work deals with the results of experimental measurements of a novel solar heat pump based heating supply concept for residential heat supply. The constructed load case aims at supplying heat for a single-family house with a moderate heat demand of 45 kWh per m² and year. An system design case was measured comprising an array of rear insulated uncovered photovoltaic thermal (PVT) collectors, a brine/water heat pump with deactivated resistance heaters and extended temperature range on the evaporator side, and a two-zone combi storage. The main innovation is to operate the PVT array as the sole heat source for the heat pump and accordingly with extended collector loop temperatures below the freezing point. Performance analysis was carried out on two characteristic cold winter test days. Measurement results show that the present system configuration is able to cover the heat demand comprising domestic hot water and space heating. Analysis of the cold winter test days reveal that insignificant icing occurred on the surface of the collectors. Temperature comfort levels were reached. Improper system design was detected, discussed and several concrete optimization potential measures were identified.

© HPC2020.
Selection and/or peer-review under responsibility of the organizers of the 13th IEA Heat Pump Conference 2020.

Keywords: solar thermal; heat pump; solar only; single source; photovoltaic thermal collector; PVT

1. Introduction to solar thermal heat pump systems

1.1 System Concepts

In residential heating systems comprising domestic hot water preparation, solar thermal collectors are usually combined with a fossil back up. Replacing the fossil boiler with a heat pump provides the possibility to boost the renewable share of these heating systems. In such a solar and heat pump (SHP) system, solar thermal collectors and the heat pump supply energy for space heating and/or hot water independently of the source(s) of the heat pump. Heating systems with this kind of operation mode were defined as "parallel" within the work of the Task 44/Annex 38 "Solar and Heat Pump" of the Solar Heating and Cooling program of the International Energy Agency (T44A38). In the "serial" configuration the solar thermal collector acts as a source of the heat pump, either exclusively or additionally (Hadorn, 2015). In general, in SHP systems, both, parallel and serial operation modes can be realized within one system (Fig. 1, left). The SHP system investigated in this work is

* Corresponding author. Tel.: +49 761 4588 5623
E-mail address: arim.schaefer@ise.fraunhofer.de.

a combined parallel/serial solar thermal heat pump system (Fig. 1, right) with an array of unglazed PVT collectors.

1.2 Market barriers

The T44A38 market research conducted in 2011/2012 found 135 solar thermal heat pump system configurations offered by different suppliers and manufacturers (Ruschenburg, Herkel et al., 2013). Results of T44A38 have shown that there are promising systems in terms of energy performance in both, serial and parallel (and regenerative) configurations (Hadorn, 2015). For illustration purposes, Fig. 2 shows the operating temperatures of the main components, solar part and heat pump with either air or ground source, of said SHP configurations ("state of the art"). It can be seen that in (regenerative and) serial SHP configurations, controller and system design rule out operation temperatures below zero degrees in the solar loop.

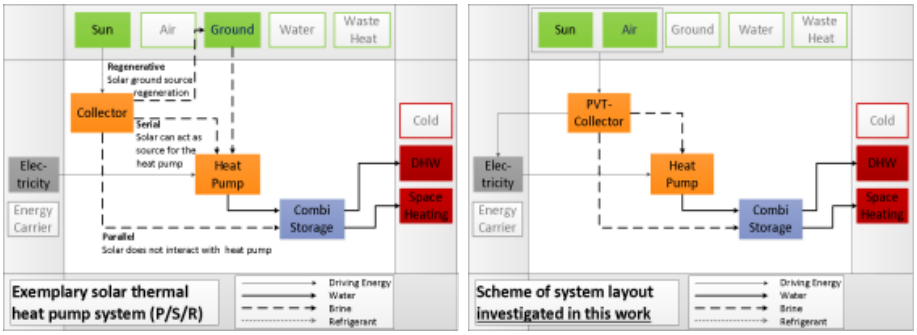


Fig. 1: The left scheme shows an exemplary parallel/serial solar thermal heat pump system according to T44A38 visualization scheme with costly energy sources on the left bar, free energy sources on the top bar, and useful energy sinks on the right bar. The right scheme shows the combined parallel/serial solar thermal heat pump system investigated in this work. Similar to the example on the left, this system has access to two heat sources via the PVT collector array.

Manufacturers may shy away from the risk of formation of ice. On the one hand, the performance of unglazed solar collectors under operating conditions below the frost point was investigated in the past i.e. in (Massmeyer and Posorski, 1982) or more recently in (Bunea, Perers et al., 2015), but studies with operation of entire systems are still rare. Hence, a second heat source is required to cover the remaining (high) heat demand during cold weather periods. A consequence is that the utilization ratio of the solar array is greatly reduced by limiting the operating temperatures of the collector field above the freezing point (i.e. < 2 °C). As a result, the solar fraction of these systems would be in a similarly (low) range as for conventional solar thermal combi systems with fossil back up heater.

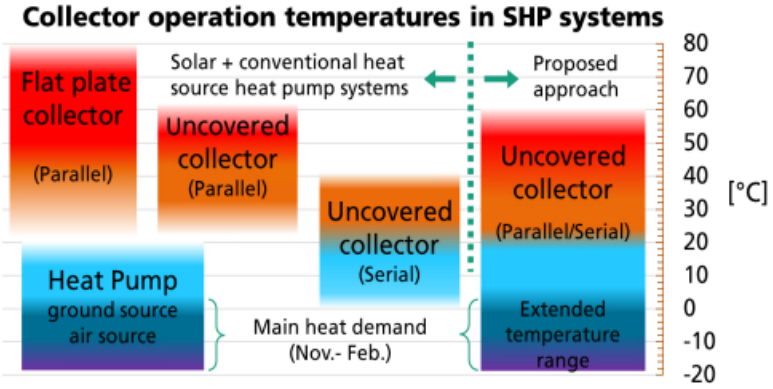


Fig. 2: Most SHP configurations investigated within T44A38 (i.e. market study) do not substitute a conventional heat source. Hence, solar does not cover the main heat load: This design approach limits the solar utilization ratio, thus leading to low fractional energy savings.

Whereas improved system performance can be achieved, the additional investment cost for the solar thermal part (solar collector array, hydraulics and pump group, installation and initial operation, etc.) forms a market barrier: Considering the extra cost of the "optional solar thermal add-on" and its limited saving potential, investors might question its meaningfulness. To date, solar thermal and heat pump systems – if at all – play a niche role in the national heat pump markets. In order to improve the cost efficiency solar thermal heat pump systems, it seems in the nature of the case to substantially increase the utilization ratio of the solar part by extending its temperature operation range below zero degrees Celsius, hence, making the conventional heat pump heat source and cost for its activation obsolete (Fig. 2, "Proposed approach").

2. Single source SHP systems

2.1 Solar thermal and PVT: Previous developments

Only six out of 135 configurations of said T44A38 market study can be called single source SHP systems employing an array of solar collectors as sole source of the heat pump (Table 1). All systems but one use unglazed solar collectors to operate below ambient temperatures. The majority of systems allow for operation below the frost point. All but two systems rely on smaller or larger source side storages, mostly using water as a phase change material, which results in additional cost. None of the systems use PVT collectors. On the one hand, PVT collectors in T44A38 system configurations are only employed as additional low-temperature heat and electricity source for space heating and DHW or to regenerate a heat pump source (ground probe or brine storage). On the other hand, the prospect of a heat pump heating system with a single component PVT collector as heat and electricity generator for the heat pump seems attractive.

Table 1: Overview of collector types, operation temperatures and storage types of all identified single source solar thermal "only" heat pump system configurations of T44A38 market study. Only systems providing space heating and domestic hot water (DHW) are listed. For comparison, the system investigated in this work is shown at the end.

#	Available modes	Collector type	Collector array operated		Storage on heat pump ... side	
			as ambient heat exchanger	below freezing point	source	sink
1	Parallel/ Serial	Flat plate	Presumably not	-	wet sand (large, outdoor)	DHW
2	Serial	Absorber	yes	yes	-	DHW
3	Serial	Absorber	yes	?	ice (large, outdoor)	DHW
4	Serial	Absorber	yes	yes	ice (320 l)	Combi storage
5	Serial	Absorber	yes	yes	-	DHW
6	Serial	Flat plate with integrated fan	yes	yes	ice (320 l)	Combi storage
This work	Parallel/ Serial	PVT	yes	yes	-	Combi storage

While in R&D, the heat supply concept of PVT collectors applied as sole heat source for a heat pump gained increased interest (Zhang, Zhao et al., 2012), especially for DHW applications (Wang, Guo et al., 2017), efficient application in combined space heating and DHW still seems to pose a challenge. To date, the authors are aware of only one single source PVT heat pump system configuration for space heating application which is about to enter the market (Leibfried, 2018).

2.2 Objectives of the study

The objective of this study was therefore to check the principal meaningfulness and furthermore the potential of the single source PVT heat pump as a heat supply concept for residential buildings.

1. Is the array of PVT collectors able to sufficiently supply heat for the heat pump during cold weather periods, including extreme cold and snowfall?
2. To what extent can icing be expected due to the continuous low-temperature operation?

3. Which optimization potential can be derived?
4. How to integrate the electric benefit of PVT into established performance figures?

3. Experimental setup

3.1 Single source PVT heat pump system configuration

A parallel/serial solar thermal heat pump system with an array of PVT collectors, power inverter, combi storage, heat pump, and hydraulics was installed at the system test rig at Fraunhofer ISE in Freiburg, Germany and put into operation in December 2017 (Fig. 3). The main system components are described in further detail in Table 2.



Fig. 3: Investigated single source SHP system with an array of PVT collectors in two rows totaling 20 collectors installed on top of the system test stand at Fraunhofer ISE (left). The photo on the right shows the installed combi storage and the heat pump including a hydraulic unit. The power inverter is installed as well (not shown in the photo).

Table 2: Description of the main components of the measured solar thermal heat pump system.

Component	Subcomponent	Description
Solar PVT array 31,4 m² 5,2 kWp,	Collector type	The array consists of 20 rear-insulated uncovered and therefore infrared and wind-dependent PVT collectors (“2Power HM 1000, 1Power 260 Mono Black”). Rated power is 260Wp (PV), area is 1,57m².
	Electric side	The modules are connected to an SMA inverter, which is connected to the grid. The inverter is powered only by the PV array.
	Thermal side	The array is subdivided into four arrays with five modules each. The hydraulic connectors of the modules are connected according to the Tichelmann system; hence all collectors are flowed through in parallel.
	Control	The parallel mode is set as first priority. Charging is triggered if the temperature of the solar array is above the lower storage tank temperature. Serial mode is triggered by heat pump control settings based on heat demand.
Heat pump P_{rated}: 5,1 kW	Type	Brine-water heat pump with extended temperature operation range on the source side from -20 °C to +30°C.
	Heating rods	Resistance heaters (backup) on source/sink side deactivated during measurements.
	Control	Storage tank temperatures trigger the serial heat pump operation using the solar array. After parallel mode, serial mode is second priority: The heat pump should provide temperatures above 48°C in the DHW section of the combi storage. If this criterion is fulfilled, the space heating section of the combi storage is charged. The required temperature depends on the ambient temperature.
Storage	Type	850 liter combi storage provided with a permeable partition plate to avoid temperature mixing of space heating and domestic hot water zones. Inner outlets in the space heating zone are provided with diffusors (cf. Fig. 4).

3.2 Description of load emulation and measurement equipment

Fig. 4 shows the experimental setup of this work comprising the solar thermal heat pump system (equipment

under test), with its main thermal components and hydraulics as well as the interface to the test rig. In total, almost 60 sensors were installed, of which 41 were calibrated for the characterizing measurements, the remaining form part of the equipment under test. Table 3 and Fig. 4 refer to (and show) selected sensors relevant to this work only: Table 3 shows the applied sensor types and accuracies; Fig. 4 shows the denominations of the sensors used in result diagrams (Fig. 5) in chapter 4.

Table 3: Properties of selected sensors used for the measurements and presented in this work.

Sensor	Manufacturer	Type	Accuracy
Temperature (fluid)	TMH	PT 100	0,1 K
Flow Rate	Krohne/Siemens	magnetic inductive (Optiflux 5000/ Sitrans FM MAG 1100)	0,5 %
Solar radiation	Kipp&Zonen	CMP 11	2 %
Relative humidity	B&B Thermo-Technik GmbH	HA-ANA-10V	2 %
Electricity (summer test day only)	EMU	Allrounder 3/75	1 %

Fig. 4 shows the load side on the right side of the dashed line, comprising a space heating loop (radiator) and domestic hot water loop with a freshwater station (heat exchanger and shower head symbol). In both cases, hot water tapping from the combi storage is realized by directly connected hydraulic loops with eccentric worm pumps. Details of the volume flow control specifications are given in Table 4.

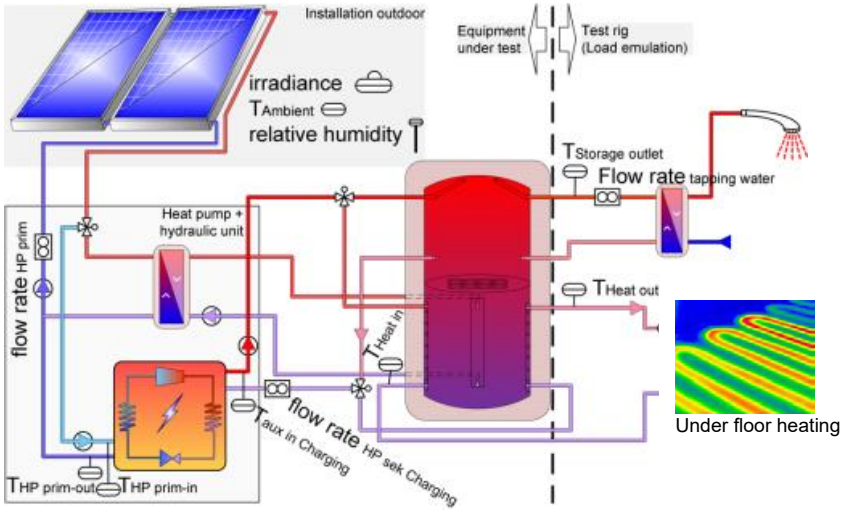


Fig. 4: Experimental setup of this work comprising the solar thermal heat pump system, with its main thermal components and hydraulics, interface to the test rig and sensor positions. The electric side of the solar array is connected to a power inverter (not shown). Sensor denominations given in this illustration are used in Fig. 5 of the next chapter.

Table 4: Set up for the domestic hot water (DHW) and space heating heat loads.

Type	Load description
DHW load:	7,7 kWh at 45 °C carried out in 23 draw offs (shower, small draw offs, dishwashing, bathtub). The load profile is equal for every day and based on the EU tapping cycle "M" with 23 draw-offs, ~5,8kWh (Ecodesign Regulation 814/2013, 2013). The following T44A38 modifications according to (Haller, Dott et al., 2013) were adopted: • Since a daily 3,6 kWh "bathtub" draw off was added to the EU tapping cycle, the energy demand for the other draw-offs was reduced (Total: 7,7kWh instead of 9,4kWh). • Required draw off temperatures were set to 45 °C.

	Deviations from the T44A38: • The bathtub draw-off is every day (not every 7th day) • The dishwasher draw-off is as well at 45 °C (instead of 55 °C) The temperature loss of the freshwater station was assumed 3 K. Hence, the heat pump control was set to provide temperatures of least 48°C in the DHW zone of the combi storage.
Heating load:	65 kWh "Winter peak case" for winter and spring test days based on SFH45 building with underfloor heating (ΔT = 4K) in the climate of Strasbourg. A maximum heating load "winter load case" was defined for all test days except summer. The load is based on T44A38 simulation results for an "SFH 45" building with an underfloor heating in the climate of Strasbourg (45 kWh/m²a) and a heated area of 140m². Based on simulated monthly values given in (Dott, Haller et al., 2013), the mean daily heat demand for the coldest months December and January was obtained (51 kWh/d and 54 kWh/d). Since there are positive (and negative) deviations from these mean values throughout these months, an increased daily space heat load of 65kWh was chosen for said winter load case. The temperature of the space heating zone of the combi storage (hence, indirectly $T_{Heat\ out}$) is controlled dynamically by a heating curve dependent on ambient temperature, as usual in heating systems. The heat load of 65 kWh is achieved as follows: Underfloor heating loops are often operated without night setback because of their inertia; accordingly, the eccentric worm pump operates 24 h with a (constant) volume flow of 10 l/min. Assuming a temperature difference of 4K between $T_{Heat\ out}$ and $T_{Heat\ in}$, ~65kWh is discharged from the combi storage within 24h. $T_{Heat\ in}$ was set dynamically to $T_{Heat\ out}$ - 4 K with a minimum temperature admitted by the thermostat at 20°C.

3.3 Test days

In response to the questions raised in section 2.2 (Objectives of the study), characteristic test days were selected from the measurement period and analyzed accordingly. Refer to the next chapter for test day description and system performance analysis.

4. Results: Performance analysis on test days and optimization potential

4.1 Presentation of measurement results on test days

Result diagram description: Result diagrams of all test days are shown in Fig. 5. The characteristic operating behavior of the system is shown by pairs of diagrams showing the key sensor values of the charging (left) and discharging (right) side of the combi storage. Discharging is carried out via the domestic hot water and/or the space heating loop. Refer to Fig. 4 of the previous chapter for sensor positions. Irradiance and ambient temperature are shown on the left side.

Load side - DHW tapping emulation: 23 draw offs were performed on every test day, with the desired characteristics. Energy quantities as provided by the test rig are presented (Table 5). DHW tapping was carried out as intended: The targeted energy load of 7,7kWh was either met or slightly surpassed presumably due to a temperature level above 48°C in the DHW zone of the combi storage on test days spring and summer.

Load side - space heating load emulation: Due to inappropriate control settings of the thermostat, which in turn lead to temperature differences lower than 4K between $T_{Heat\ out}$ and $T_{Heat\ in}$, the targeted "winter peak case" heat demand of 65 kWh was met only on the second winter test day (03th of March), caused by the control of the test rig. Nevertheless, heat demand is still appropriate: 57.2 kWh is still above the mean heat demand of December (51kWh/d) and January (54kWh/d, cf. Tab 4, "heating load").

Table 5: Measured heat loads for DHW and space heating for given test days. Measurements were carried out in 2018.

Unit [kWh]	1st winter day 28th Feb.	2nd winter day 03th Mar.	Spring day 09th Apr.	Summer day 19th Aug.
DHW: Total	7.6	7.5	8.1	9.1
DHW: Tapping, shower	4.1	4.0	4.6	5.4
DHW: Bathtub	3.6	3.6	3.6	3.7
Space heating: Total	**57.2**	**66.9**	55.7	0.0

General remarks regarding the system behavior – combi storage charge: Charging is carried out either via the heat pump (serial mode) or via the solar plate heat exchanger (parallel mode). In serial mode, the heat pump is

charging the DHW and space heating zone of the combi storage alternately (cf. $T_{aux\text{-}in\ -\ charging}$). Depending on the heat demand, this occurs continuously, as on the 2nd winter test day, or with interruptions when the combi storage is fully charged (cf. spring test day from ca. 07:30). During these periods, it can be seen that the heat pump control "checks" the source temperature level three times per hour, sending a volume flow of about one minute to the source side pump. On the summer test day, the occurrence of the parallel mode can be observed, starting at about 11:30 (cf. flow $rate_{solar\ -\ charging}$, $T_{HP\ prim\text{-}in\ =\ sol\ out}$ $T_{HP\ prim\text{-}out\ =\ sol\ in}$).

General remarks regarding the system behavior – combi storage discharge: Regarding the achieved temperatures of the space heating temperatures, the two winter test days are relevant only (Refer to the following section 4.2). Regarding the achieved DHW temperatures, a general problem can be observed which concerns the heat pump charging behavior: DHW temperature comfort level ($T_{Minimum\ demand}$ = 48°C) is generally met for all draw offs apart from the bathtub where discharge temperatures always drop to about 43 - 44 °C. That this is a storage tank specific issue can be seen on the summer day, where the combi storage is fully charged by the solar array in parallel mode. The heat demand for the entire bathtub is met without any temperature drop. Further malfunctions due to bad control/system layout are discussed in chapter 4.4, Tab 5.

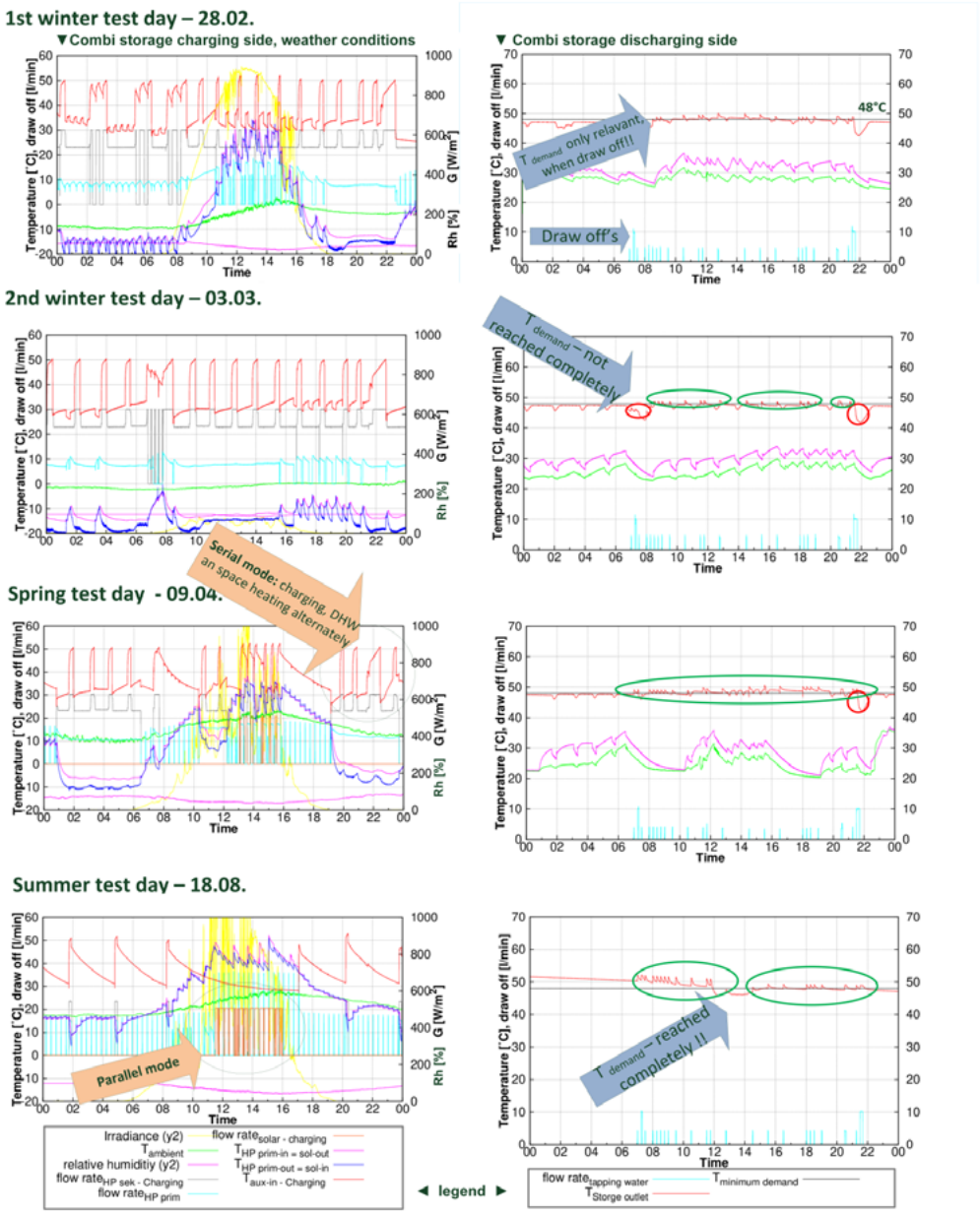


Fig. 5: Diagrams of the following test days: Winter (1st: 28.02.18 and 2nd: 03.03.18), Spring (09.04.18) and Summer (18.08.18). Diagrams on the left show the charging side of the combi storage, diagrams on the right show the discharging side of the combi storage. Legend applies to all diagrams above. Refer to Fig. 4 for positions of the sensors within the system.

4.2 Performance under cold weather conditions

This section deals with the question, whether the array of PVT collectors is able to sufficiently supply heat for the heat pump during cold weather periods, including extreme cold, snowfall, and icing. In response, system performance on two typical winter situations is analyzed.

- 1st winter day (28.02.) Clear sky day/night with ambient temperature ranging from -5 °C to -10 °C. 27th and 28th of February 2018 were the coldest days of the entire winter period 2017/2018 in Freiburg (Fig. 5,6).
- 2nd winter day (03.03.) Cloudy day/night with an ambient temperature between -2°C to 1°C (Fig. 5,7).

Icing: Fig. 6 shows the maximum level of ice formation at 04:53 the early hours of the 1st winter test day. The layer of ice is in places and superficially only (< 1 mm). Similar behavior was observed during measurements of other cold days, as well as in the climate chamber (Schmidt, Schäfer et al., 2018). **"Ice-production" on the module surfaces did not exceed 1cm of thickness (precipitation) on the front side during the entire system measurement phase (Dec. '17 to Aug. '18). No slipping of ice could be detected (tilt angle of 35°).** The comparably low ice formation can be explained due to the low flow of humidity being transported to the surface of the PVT collectors by means of natural convection. In contrast, icing occurs usually in external air units, where humidity is permanently supplied by means of a forced air flow to the compact heat exchanger of the external unit. In consequence, significant amounts of icing on the PVT collector array should only be expected if transport of humidity is assured in large quantities (i.e. precipitation). It could also be observed, that surface ice would melt within a few minutes under direct solar irradiation.



Fig. 6: Maximal observed ice cover on the surface of the solar array in the clear sky night from 27th/28th of February with a thickness approximately below one millimeter (left). On the coldest two days of the winter 2017/2018, the solar array reached operation temperatures above 20 °C from noon to the early afternoon.

The layer of snow on the solar array on the 2nd winter test day (Fig. 7) originates from snowfall on the previous day. It persisted for the entire test day on the solar array due to: low irradiance, the cooled PVT collectors operating as ambient heat exchanger and ambient air temperatures close to the freezing point. As explained below, such a layer of snow still allows for ambient heat exchange with the collector fluid. Measurements on absorbers under comparable conditions (Bunea, Perers et al., 2015) revealed that heat exchange can be increased due to the "naturally" increased collector surface**. The heat pump allows for manual reversing the heat pump cycle to heat the collector with energy by cooling the space heating zone of the combi storage. The mechanism was successfully tested on a layer of snow (+5 cm) on the solar array**: The layer of snow started melting on the side touching the collector array and slipped afterwards to the test rig floor.



Fig. 7: The solar array was covered with a layer of snow with a thickness of ~2 cm on the solar array for the period of 24h of the first winter test day (03.03.). The photos show the first row of the solar array in the morning (07:02) and in the evening (17:41).

System performance on the 1st winter day (cf. Fig. 5): On the second coldest day of the winter period 2017/2018, a space heat demand of 57.2 kWh is covered. Mean temperatures of the space heating loop ($T_{heat\ in}$ + $T_{heat\ out}$)/2 range from 26°C to 33°C. DHW energy demand is met as well; comfort levels are met with exceptions in the morning and in the evening (cf. section 4.2, last paragraph and section 4.5, Table 6, Area "DHW").

Throughout the day, the heat pump is operating most of the time in serial mode (cf. flow $rate_{HP\ Sek\ –\ Charging}$). Due to the cold ambient temperatures, when the evaporator outlet temperature $T_{HP\ prim\text{-}out}$ reaches -20 °C, the heat pump switches to frost protection mode and combi storage charging is interrupted. This occurs frequently from midnight to about 8am in the morning. During this time, it can be seen how space heating loop temperatures decline gradually. Interestingly, during the sunny day, mean evaporator temperatures ($T_{HP\ prim\text{-}in}$ + $T_{HP\ prim\text{-}out}$)/2 increasing along with the sunrise to peak values above 20 °C between 12:00 and 15:00 and decreasing back to low night time values after sunset. Hence, on clear sky days, the single source heat pump can play out its advantage by means of high source temperatures compared to air or ground source heat pumps.

System performance on the 2nd winter day (cf. Fig. 5): On this cloudy winter day, where a layer of snow covers the solar array, a space heat demand of 66.9 kWh is covered. Mean temperatures of the space heating loop ($T_{heat\ in}$ + $T_{heat\ out}$)/2 range from ca. 26°C to 30°C. DHW energy demand is met as well; comfort levels are met with exceptions due to an unknown charging interruption of the heat pump between ca. 7:45 to 8:45 (see also section 4.2, last paragraph and section 4.5, Table 6, Area "DHW").

Likewise, to the first winter day, the heat pump is operating most of the time in serial mode (cf. flow $rate_{HP\ Sek\ –\ Charging}$), charging DHW and space heating zone alternately (cf. $T_{aux\text{-}in\ –\ charging}$). Mean evaporator temperatures ($T_{HP\ prim\text{-}in}$ + $T_{HP\ prim\text{-}out}$)/2 are below -10°C during the whole day reaching minimum values at night time between -15° and -18°C. Apart from two frost protection cycles (at about 01:15 and 03:15), the solar array provides low-temperature energy to the heat pump at all times.

Assessment of system performance under cold weather conditions: Heat demand was met completely. The heat was delivered at the required temperature levels for space heating and with few limitations for domestic hot water.

4.3 Performance indicators used in the project (SPF or AZ)

Measurements in summer, autumn and winter where continued. The test days where repetitive days like mentioned before. The heating demand was adapted to the demand developed in IEA TASK44A38 (Summer: no heating; spring/autumn: 35 kWh/d; winter: 55 kWh/d). The daily DHW draw offs where
8 kWh/d split in the 23 taps based on Erp.

Representative test days where used to determine (daily) performance indicators.

Fig. 8 is based on IEA TASK44A38. The boundaries for the different AZ-values are shown.

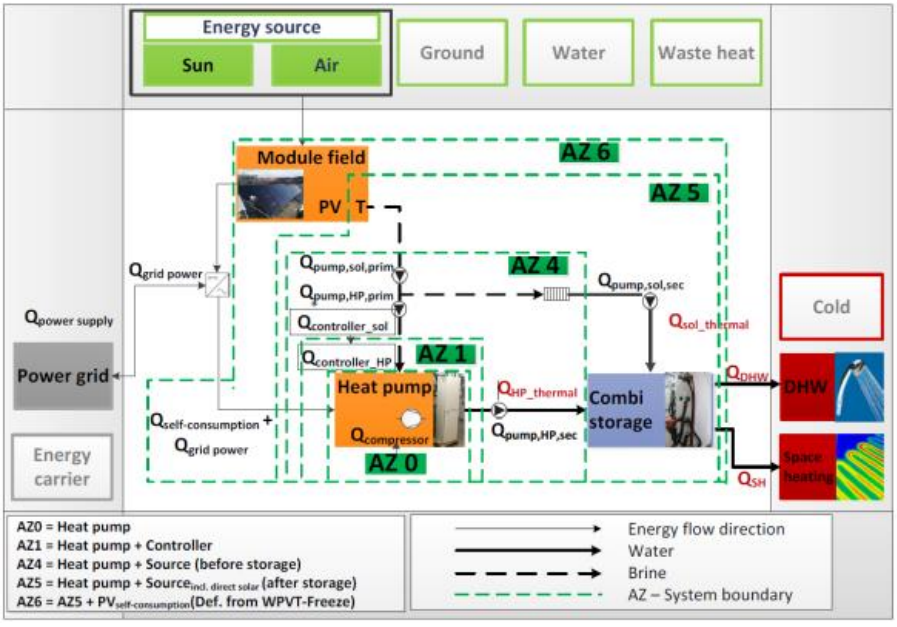


Fig. 8: Boundaries for the performance indicators based on T44A38.

AZ0 – AZ5 are known performance indicators. AZ6 is introduced to show the performance indicator by considering the PV- self consumption.

	Date:	18.08.2018	24.08.2018	27.10.2018	06.11.2018	03.11.2018	24.01.2019	29.01.2019	
Day type	Characteristics of the day	Summer-sunny	Summer-cloudy	Autumn-Rain	Autumn-cloudy	Autumn-sunny	Winter-cold	Winter - sunny	Seasonal Performance Factor
Load	Domestic hot water [kwh]	9.1	9.1	8.3	8.0	8.4	8.5	8.5	(ISE-internal Extrapolation - Weighting of reference/test days)
	Target value (23 Tapping cycles, ErP)	8	8	8	8	8	8	8	
	Heating load [kwh]	-	-	34.8	33.9	34.2	53.8	51.6	
	Target value (acc. to TASK44)	-	-	35	35	35	54	54	
Seasonal Performance Factor	AZ 0	4.0	3.9	3.5	3.5	3.7	2.9	3.2	3.6
	AZ 1	2.6	2.7	3.3	3.3	3.5	2.8	3.1	3.1
	AZ 4	1.7	2.4	2.7	2.6	2.9	2.3	2.5	2.5
	AZ 5	2.9	2.4	2.4	2.6	2.2	2.0	2.2	2.4
	AZ 6 incl. PV self-consumption	5.3	3.4	2.5	2.8	2.6	2.1	2.5	3.2
PV	PV - Daily yield [kwh]	19.7	7.9	2.1	1.7	8.6	0.6	6.4	
	PV - Self-consumption [kwh]	1.4	1.1	1.1	1.1	2.8	0.5	3.3	
	PV - Share of self-consumption from daily yield	7%	14%	54%	66%	32%	95%	52%	
	PV - Share (self-consumption) of electricity demand	45%	29%	6%	7%	15%	2%	12%	rough first estimation
Meteo	Irradiation - Daily total [MJ/m²]	18.0	6.7	1.8	0.4	12.5	1.1	9.7	
	T_amb min [°C]	16.7	14.3	5.0	4.8	6.5	-2.8	0.0	
	T_amb max [°C]	28.5	24.2	10.2	13.1	12.5	-1.3	6.0	
	Rain - Daily total [mm]	0	0	14	0	0	0	0	

Fig. 9: Performance indicators, with boundary conditions (daily and a yearly, projected based).

Fig. 9 shows the daily performance indicators with it's boundary conditions. Theses values are based on real

measurements. The last column shows the seasonal performance indictors. The base for this are the test days shown in the table, extrapolated to reach a rough first estimation.

4.4 Optimization potential

The realized system has optimization potential. The main points are the following:

- Storage tank design not satisfying. The ErP "bathtub" tapping could also be reached completely by a better use of the buffer volume (readiness volume) for the DHW.
- A controller concept with focus on higher amount of PV self consumption could increase the seasonal performance factors
- PVT modules without back insulation for higher use of latent heat and thermal convection could increase the energy coming from the PVT source

4.5 Key performance indicators according IEA TASK60

Within the IEA TASK60 (PVT systems) Subtask D, key performance indicators are under development. The report of this Subtask D was supposed to be published in January 2020. All formulas with description will be content of this report. A presentation of the Subtask D leader Daniel Zehnhäuser showed a list of KPI's, which are wished "at least". The following chapters show the application of these KPI's, based the measurements on the PVT-heat pump system of project WPVT-Freeze.

4.5.1 Area-specific thermal yield

(listed in the presentation; but no defined calculation method in the Subtask D report)

$$Area\ specific\ yield = \frac{Q\ thermal\ taken\ from\ PVT - field}{Areagross\ (31{,}4\ m^2)} = 312\ \frac{kWh}{m^2 a}$$

Aspects of the PVT-module-field:

- System controlling was not optimized on using solar
- Thermal absorber is glued on the back side of the PV
  -> solar is absorbed by PV and heat conduction to absorber could be optimized
- Back side insulation of the module causes less use of environmental energy
  -> later PVT prototype in the project is without back side insulation

4.5.2 Thermal utilization ratios

$$\omega_{PVT,\,th}^{gross} = \frac{Q_{PVT}}{\int G_{col}\,dt \cdot A_{PVT}^{gross}}$$ Equation 3 (Report – Subtask D)

$$Thermal\ utilisation\ ratio = \frac{Q\ thermal\ taken\ from\ PVT - field}{Qsolar\ *\ area\ gross\ (31{,}4\ m^2)} = 0{,}28$$

Aspect:

- $Q_{thermal}$ contains heat taken from sun and environment

4.5.3 Average of the collector mean fluid temperature

$$\overline{\vartheta_m} = \frac{\int_{\substack{collector\ field \\ in\ operation}} dt\ \vartheta_m}{\int_{\substack{collector\ field \\ in\ operation}} dt} = 0.4\ °C\ \ (mean\ value\ /year)$$ **Equation 11** (Report – Subtask D)

Aspects:

- Main service time of heat pump during space heating season
- Main heat source of this PVT-application is using environmental energy
  -> low surrounding temperatures during winter

4.5.4 **Solar thermal fraction**

$$f_{sol,th}^{total} = \frac{Q_{PVT,*}}{Q_{*,primary}+Q_{PVT,secondary}} = 1 \quad (has\ to\ be\ 1)$$ **Equation 18** (Report – Subtask D)

Expl.: Thermal energy PVT / (Energy delivered to heat pump + Energy delivered directly to the storage)

$$f_{sol,th}^{secondary} = \frac{Q_{PVT,secondary}}{Q_{H\,P,*}+Q_{PVT,secondary}} = 0.1$$ **Equation 19** (Report – Subtask D)

Expl.: Thermal energy PVT (direct charge of storage tank) /
(Heat pump energy delivered to storage tank+ Thermal energy PVT, direct charge of storage tank)

Aspects:

- The calculation according to TASK60 seems to focus on multi source systems (see Eq. 18)
- Main heat source of this PVT-application is using environmental energy -> low surrounding temperatures during winter (low value of 0,1 considers only solar)

4.5.5 Performance Factor – heat pump system

$$SPF_{SHP+}^{(total)} = \left[\frac{Q_{HS}}{E_{*,HS}}\right]_{SHP+} = \frac{used\ heat}{electricity\ for\ heat\ pump} = 2.4$$ Equation 28 (Report – Subtask D)

Remark: See also chapter 4.3 (it corresponds to AZ5=2.4)

4.5.6 Performance Factor – heat pump system incl. grid

$$SPF_{SHP+}^{(Grid)} = \left[\frac{Q_{HS}}{E_{Grid,HS}}\right]_{SHP+} = \frac{used\ heat}{electricity\ for\ heat\ pump - PV\ self\ consumption} = 3.2$$

Equation 28 (Report – Subtask D)

Remark: See also chapter 4.3 (it corresponds to AZ6 = 3.2)

4.5.1 Investment cost per square meter

$$i_0^{PVT} = \frac{[I_0]_{PVT}}{A_{gross}^{PVT}} = 378\ €/m^2$$ Equation 48 (Report – Subtask D)

The following costs are considered:

(PVT-modules, inverter, controller, piping and mounting equipment, solar fluid)

4.5.2 Levelized Cost of Heat

$$LCoH = \frac{\left[\sum_{t=1}^{T=25}(I_t+OM_t-RV_t)\cdot(1+r)^{-t}\right]_{HS}}{\sum_{t=1}^{T=25}Q_{HS,t}\cdot(1+r)^{-t}}$$ Equation 44 (Report – Subtask D)

	PVT incl. PV self-consumption **incl. PV costs**	Thermal system (PV-system deducted)
I_0 = Investment costs	31 985 €	21 985 €
C_t= O&M costs	320 €	220 €

T = Service years	25	25
E_t = DHW and heating energy [kwh/a]	8483	8483
AZ6 (SPF) (3.2) or AZ5 (SPF)(2.4)	3.2	2.4
LCoH	28 ct/kWh	25 ct/kWh

Remark: System is not yet optimized, not energetically and not yet on use of PV self-consumption.

Example values for other technologies (based on internet research – whole system costs):

Heat pump deep bore	31 ct / kWh
Heat pump - air heat	24 ct / kWh
Heat pump - surface collector	23 ct / kWh
Oil central heating - calorific value	26 ct / kWh
Oil central heating calorific value	25 ct / kwh
Gas central heating calorific value	18 ct / kWh
Gas central heating calorific value	17 ct / kWh
Firewood central heating	15 ct / kWh
District heating wholesale customer tariff	17 ct / kWh
Central pellet heating	23 ct / kWh
Direct electrical heating	22 ct / kWh

4.5.3 Saved fuel and grid electricity cost

(according to chapter 2.5 of report – Subtask D)

Costs based on calculation, if the whole energy demand would have to be supplied by oil.

Saved **fuel** costs = **9.00 €/a m²** module area
= **282.65 €/a** system

Calculation basis:

saved energy/avoided primary energy	4 948.5	kWh/a	system
	157.6	kWh/a m²	module area
heating oil - calorific value	11.8	kWh/l	
saved fuel	419.4	l/ a	system
	13.4	l/m² a	module area
price for heating oil	67.40	€ /100l	

Saved cost for **electricity** = **47.28 €/a m²** module area
= **1 484.55 €/a** system

(whole energy demand supplied by electricity – 0.30 €/ kwh)

4.5.4 Avoided primary energy depletion

(according to chapter 2.3.5 of report – Subtask D)

Avoided primary energy (based on oil) = **157.6 kwh/a m²** module area
= **4 948.5 kwh/a** system

4.5.5 Avoided global warming impact

(according to chapter 2.4.2 of report – Subtask D)

Avoided primary energy depletion = **44.1 kg CO_2/a m²** module area
= **1 385.6 kg CO_2/a** system

Calculation basis:

saved energy/avoided primary energy	4 948.5 kWh/a system
	157.6 kWh/a m² module area
Example values:	1 litre heating oil ≙ 3.17 kg CO_2
	or 1 kwh ≙ 0.28 kg CO_2

5. Conclusion

Up to date, combined solar thermal heat pump (SHP) systems form a niche in the heat pump markets. The hypothesis is raised that an ineffective integration of the solar collector array forms a market barrier due to increased cost but little-added value, because solar thermal collectors are inactive during the cold periods of a year when heat demand is large. While such inactivity is inevitable in a conventional solar thermal system with a fossil backup heater, the solar array of a SHP system should be active, operating as heat exchanger to ambient during low irradiation conditions and night time. Hence, in order to exploit the full saving potential in SHP systems, it is suggested to substitute other conventional heat pump sources entirely by the solar thermal array. To date, such single source SHP systems typically rely on solar absorbers. The objective of this work was to check the principal meaningfulness and potential of an array of photovoltaic thermal (PVT) collectors in a single source SHP system configuration with a residential heat demand: On the one hand, a PVT collector can provide electricity for the heat pump. On the other hand, the thermal performance is lower compared to a solar thermal absorber.

Results suggest that the single source SHP with PVT collector array is a promising heat supply concept for residential buildings. An extreme case with an array of rear-insulated PVT collectors was investigated. A brine/water heat pump with extended temperature range on the evaporator side and deactivated resistance heaters as well as two-zone combi storage form the other components of the SHP system configuration. The analysis of cold winter test days reveals that insignificant icing occurred on the surface of the collectors and heat demand was met completely. Temperature comfort levels were also met for space heating and with few limitations for domestic hot water delivery. Improper system design was detected and discussed and concrete optimization potential measures identified. The most obvious measure is to replace the solar array with rear non-insulated PVT collectors. A significant temperature increase of source temperatures can be expected. The main aspects are:

- Wider source temperature range down to – 20°C incl. condensation and ice has a big potential
- **PVT Single Source Heat Pump concepts can work!**
- New system concept was designed by project partner PA-ID
- Position of backup heater on the demand side of the fresh water station is recommended
- 2-3 mm max. ice thickness on the front of the PVT-modules during test period
- Key performance indicators for the system where calculated according IEA TASK60 formulas

Acknowledgements

This work was supported by the Federal Ministry for Economic Affairs and Energy (0325854A). Support is gratefully acknowledged.

References

Bunea, M., Perers, B., Eicher, S., Hildbrand, C., Bony, J., Citherlet, S., 2015. Mathematical modelling of unglazed solar collectors under extreme operating conditions. Sol Energy 118, 547–561. DOI: 10.1016/j.solener.2015.06.012

Dott, R., Haller, M., Ruschenberg, J., 2013. The Reference Framework for System Simulations of the IEA SHC Task 44 / HPP Annex 38 Part B: Buildings and Space Heat Load A technical report of subtask C - Report C1 Part B. URL: http://www.taskx.iea-shc.org/data/sites/1/publications/T44A38_Rep_C1_B_ReferenceBuildingDescription_Final_Revised_ 130906.pdf.

Ecodesign Regulation 814/2013, 2013. Commission regulation (EU) No 814/2013 of 2 August 2013 implementing Directive 2009/125/EC of the European Parliament and of the Council with regard to ecodesign requirements for water heaters and hot water storage tanks. Official Journal of the European Union. URL: https://eur-lex.europa.eu/LexUriServ/LexUr iServ.do?uri=OJ:L:2013:239:0162:0183:EN:PDF.

Hadorn, J.-C. (Ed.), 2015. Solar and Heat Pump Systems for Residential Buildings, 1st ed. Ernst, Wilhelm & Sohn, Berlin, Online-Ressource. ISBN: 978-3-433-03040-0.

Haller, M., Dott, R., Ruschenberg, J., Ochs, F., Bony, J., 2013. The Reference Framework for System Simulations of the IEA SHC Task 44 / HPP Annex 38 Part A: General Simulation Boundary Conditions. A technical report of subtask C Report C1 Part A. URL: http://www.taskx.iea-shc.org/data/sites/1/publications/T44A38_Rep_C1_B_ReferenceBuildingDescription_Final_ Revised_130906.pdf.

Haller, M.Y., Haberl, R., Carbonell, D., Philippen, D., Frank, E., 2014. SOL-HEAP Solar and Heat Pump Combisystems. URL: https://www.researchgate.net/publication/272093420_SOL-HEAP_Solar_and_Heat_Pump_ Combisystems

Leibfried, U., 2018. Energieschub für Wärmepumpen. Innovatives PVT-Energieversorgungssystem für Heizungstechnik in Verbindung mit Sole-Wasser-Wärmepumpen. Sonnenenergie: Offizielles Fachorgan der Deutschen Gesellschaft für Sonnenenergie e.V. (02/2018), 54–55. URL: http://www.sonnenenergie. de/sonnenenergie-redaktion/SE-2018-02/Layout-fertig/PDF/Einzelartikel/SE-2018-02-s054-Innovationen-Energies chub_fuer_Waermepumpen.pdf.

Massmeyer, K., Posorski, R., 1982. Wärmeübergänge am Energieabsorber und deren Abhängigkeit von meteorologischen Parametern. Zentralbibliothek d. Kernforschungsanlage, Jülich, II, 155 S. ISSN 0343-7639. URL: https://www.researchgate.net/profile/Klaus_Massmeyer/publication/318901737_Warmeubergange_am_Energieabsorber_und_deren_Abhangigkeit_von_meteorologischen_Parametern/links/59a9714d458515d09ccfed2d/Waermeuebergaenge-am-Energieabsorber-und-deren-Abhaengigkeit-von-meteorologischen-Parametern.pdf

Ruschenburg, J., Herkel, S., Henning, H.-M., 2013. A statistical analysis on market-available solar thermal heat pump systems. Sol Energy 95, 79–89. DOI: 10.1016/j.solener.2013.06.005.

Schmidt, C., Schäfer, A., Thoma, C., Rajkiran Jayachandran, E., Lämmle, M., Geimer, K., Kramer, K., 2018. Quellenseitig in Wärmepumpen-Heizsystem integrierte PVT Kollektoren – Experimentelle Messungen am Einzelmodul und am Gesamtsystem., Thermische Solarenergie, 10. bis 12. Juni 2018, Kloster Banz, Bad Staffelstein.

Wang, Z., Guo, P., Zhang, H., Yang, W., Mei, S., 2017. Comprehensive review on the development of SAHP for domestic hot water. Renewable and Sustainable Energy Reviews 72, 871–881. DOI: https://doi.org/10.1016/j.rser. 2017.01.127.

Zhang, X., Zhao, X., Smith, S., Xu, J., Yu, X., 2012. Review of R&D progress and practical application of the solar photovoltaic/thermal (PV/T) technologies. Renewable and Sustainable Energy Reviews 16 (1), 599–617. DOI: https://doi.org/10.1016/j.rser.2011.08.026.

13th IEA Heat Pump Conference
April 26-29, 2021 Jeju, Korea

A study on the heat pump system for removing white plume of cooling tower and recovering water vapor

Chulwoo Roh*, Gilbong Lee, Beomjoon Lee, Eun Seok Wang, Young-Jin Baik, Hyung-ki Shin, Jongjae Cho, Junhyun Cho, Bongsu Choi

Korea Institute of Energy Research, Yusung-gu Gajengro 152, Daejeon, South Korea

Abstract

A study on the system applying a heat pump technology to remove the white plume from a cooling tower and recover the water vapor is carried out. The proposed system firstly cools the discharged humid air stream (38 ℃, RH 95%) from a cooling tower by using a cool outside air and secondly cools the humid air stream by the evaporator of the heat pump system to recover water vapor. The recovered water is re-supplied to the cooling tower's water basin. The thermal energy absorbed in the evaporator is released to the condenser of the heat pump system. The condenser is located at the final stage of the cooling tower to heat the air stream discharging into the atmosphere. The final discharging air stream is cooled by the cold outside air as soon as it is released, but the probability of white plume generation is significantly low, owing to the thermal buffer which is provided by the condenser of the heat pump.

© HPC2020.
Selection and/or peer-review under responsibility of the organizers of the 13th IEA Heat Pump Conference 2020.

Keywords: Cooling tower; White plume; Abatement; Heat pump; COP

1. Introduction

A Cooling tower is an important facility in various industrial fields such as power generation and air conditioning that can supply a heat sink at 28~32 ℃ by using the latent heat of water evaporation [1]. The cooling tower discharges heat energy into the atmosphere by evaporating the fresh water under forced direct-contacted convection. The humid air which is discharged from the upper part of the cooling tower in fall or winter generates the form of cloud, usually called white plume. The white plume from a cooling tower can pose several issues. It may affect visibility and safety as well as public perception [2]. Even though the cooling tower plume is made up of water vapor, a community may perceive it as unwanted or smoke-related. This may affect the use of nearby land or decrease property values.

Another issue about recent cooling tower technology is related to the huge consumption of fresh water for cooling. The water consumption in cooling towers may lead to lower efficiency of facilities and a decrease in industrial production in certain seasons especially when drought occurs. Large inland power plants with cooling towers generating electricity by using water supplies in large quantities should pay high attention to water saving in drought season.

Water conservation is highly related to energy conservation. It takes a considerable quantity of water to generate electricity [3]. Likewise, it takes a considerable amount of energy to produce fresh water and to treat wastewater. This article discusses a water-saving modification using a heat pump in the upper part of the cooling tower. The heat pump condenses the water vapor discharged from the cooling tower for the recovery of fresh water and heats the final discharging flow to reduce white plume.

* Corresponding author. Tel.: +82-42-860-3379; Fax.: +82-42-367-5067
E-mail address: chulwoo.roh@kier.re.kr.

2. System schematic and experimental results

2.1. System schematics

Fig. 1 shows a schematic diagram of the heat pump dehumidification system for a cooling tower. The humid air flow at DB (dry-bulb) 36 °C – RH (relative humidity) 95% is generated in a duct system by using a thermo-hygrostat and additional humidifiers. The air flow rate was 1000 CMH. The heat pump system makes hot and cold water circulating for heat exchangers. In order to simplify the system configuration and to consider the actual installation conditions of the cooling tower, the cold and hot water stream are separately circulated. For better performance, it is necessary to adopt a method of direct heat exchange of the refrigerant with the humid air, so further studies are currently underway. The temperatures of the cold water and hot water were 24 °C and 61 °C, respectively.

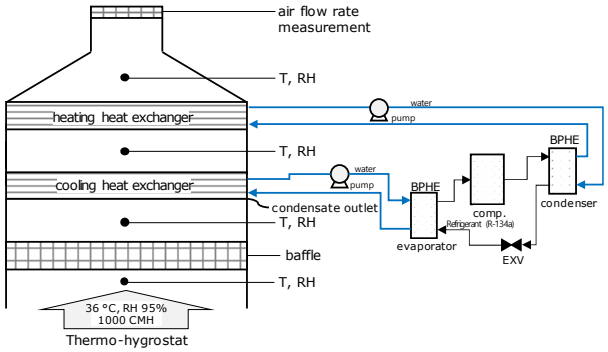


Fig. 1. Schematic of the cooling tower test system with a heat pump dehumidifier

2.2. Experimental Results

Table 1 presents the experimental results of the targeted system. Approximately 18% of water vapor was recovered by the heat pump system from the humid air flow. The final air flow was heated by the heat pump condenser to DB 52 °C and RH 34%. This final state of the air flow does not cause white plume even under the conditions of the outside DB 0 °C and RH 95%.

Table 1. Performance results of the heat pump system for a cooling tower discharging flow

Evaporator inlet	Evaporator outlet	Water recovery	Condenser outlet	Heat pump capacity	Power consumption of heat pump
DB 36 °C RH 98%	DB 33 °C RH 95%	30 g·kg$_{DA}^{-1}$ (-18.1%)	DB 52 °C RH 34%	Evaporator: 3.2kW Condenser: 4.5kW	1.46kW

Energy is required to condense the water vapor in the air. The energy recovered by the heat pump as water vapor condenses into the water can be used to abate the white plume as in this study, or it can be used for the purpose of supplying hot water for district heating. In order to apply the recovered heat from the water vapor for the district heating system, it is necessary to consider the cost-effectiveness of the electric power consumption of the heat pump system versus the fuel cost to operate a separate peak boiler in a conventional district heating system.

It is difficult to secure economical effectiveness in recovering the water vapor by the heat pump system to simply reduce the water usage cost. The presented approach should be recognized as a disaster response technology that can cope with serious water depletion, desertification or frequent occurrence of drought. In terms of socioeconomic costs of whit plume problem in cooling towers, the presented technology must ensure compatibility in the operation of public infrastructure.

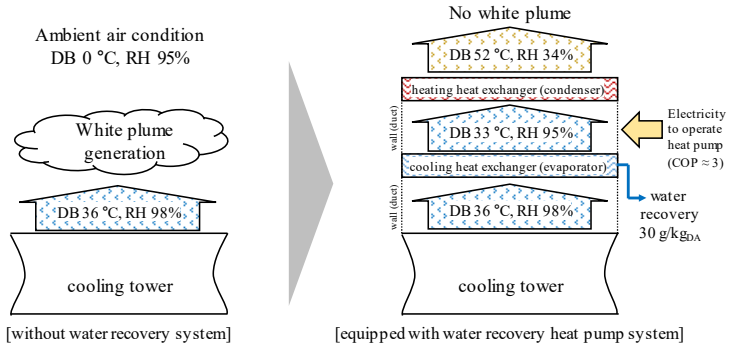


Fig. 2. Schematic of the heat pump system to remove white plume from cooling tower outlet

2.3. Economic Analysis

The power plant that produced 100MW of electricity with 40% efficiency generates 150MW of heat. Assuming a capacity factor of 80% and the plant is cooled by evaporating 15 °C of water, the annual cooling water requirement is estimated at 1.44 million tons. South Korea's industrial water cost is approximately $0.34 per ton. Assuming the additional flow rate for the drain of the cooling tower is 80% of the absolute coolant requirement, the annual cooling water cost is expected to be $927,280. There is sewage fee for drainage of the cooling tower, which is $0.487 per ton of water. Sewage rate of cooling tower is estimated by $563,000 annually. Therefore, annual cooling water usage costs are estimated to be $149 million, taking into account sewage rates. However, this figure is an absolute small cost of $0.002, calculated as the cost of cooling tower in power generation costs per kWh.

From an operator's point of view, unless there is an absolute shortage of water, there seems to be a lack of factors to try to reduce the use of cooling tower with additional investment. It may be better to have an infrastructure with high externalities that can draw water to prepare for an emergency case. This aspect suggests that various technical options should be considered from a policy perspective.

3. Conclusions

In this study, we propose a dehumidification system using a heat pump to recover water by condensing from the humid air discharged from a cooling tower. The experimental results are as follow.

1. As the heat pump system operates in the condition of COP 3 for the cooling tower exhaust air flow (DB 36 °C, RH 95%), 28.5% of water was condensed and recovered from the incoming air-water mass flux.
2. The latent heat which is absorbed from the heat pump's evaporator was utilized for producing hot water by the heat pump, so the final exhaust humid air flow can be in a state of DB 51 °C and RH 31%.
3. The proposed approach can effectively recover water by condensation and prevent a white plume in cold air conditions, but consumes energy required for driving the heat pump. A follow-up study will be conducted to ensure optimum performance of the heat pump in response to various cooling tower exhaust flow and ambient conditions.

Acknowledgements

This work was supported by the National Research Council of Science & Technology (NST) grant by the Korea government (MSIT) (No. CRC-15-07-KIER)

References

[1] Chu, K. D., Yoon, J. I., Kim, J. D., & Lee, C. J., 1999. An Experimental Characteristics of Thermal Performance of Cross Flow Type Cooling Tower. Proceedings of SAREK, pp. 271-276.
[2] Jung, J., Jung, J., & Choi, Y. K., 2014. Program development for the prediction of cooling tower performance. Korean Journal of Air-Conditioning and Refrigeration Engineering, 26(3), pp. 130-136.
[3] Macknick, J., Newmark, R., Heath, G., & Hallett, K. C., 2011. Review of Operational Water Consumption and Withdrawal Factors for Electricity Generating Technologies (No. NREL/TP-6A20-50900). National Renewable Energy Lab. (NREL), Golden, CO (United States).

13th IEA Heat Pump Conference
April 26-29, 2021 Jeju, Korea

Experimental investigation of a rolling piston compressor operated with a hydrocarbon refrigerant mixture

Melanie Cop[a]*, Ramona Nosbers[a], Christiane Thomas[a], Ullrich Hesse[a]*

[a] Technische Universität Dresden, Bitzer Chair of Refrigeration, Cryogenics and Compressor Technology, 01062 Dresden, Germany

Abstract

Theoretical considerations indicate enhanced system performance of household appliances when using zeotropic mixtures compared to R134a. This paper describes the experimental investigation of the performance behavior of a rolling piston compressor used in a heat pump tumble dryer and operated with a zeotropic zeotropic blend.

The experimental investigations demonstrate the change in operation conditions and compressor performance of the substitute refrigerant in comparison with the hydrofluorocarbon R134a. The compressor is tested on a compressor test rig according to DIN EN 13771-1 to measure and determine power consumption, cooling resp. condensing capacity, pressure ratio and cycle temperatures. The measured data of the reference setup with R134a and the substitute setup with a hydrocarbon refrigerant mixture will be compared with each other for a better understanding of their influences under different operation conditions.

Keywords: Rolling Piston Compressor; Compressor Performance;Liquid Slugging; Zeotropic Refrigerant Blend; Drop-in Refrigerant

1. Introduction

The Kigali Amendment to the Montreal Protocol [1] entering into force on January 1, 2019 regulates the global phase down of hydrofluorocarbons (HFC) with a high global warming potential. It confirms the European F-Gas Regulation from 2015 that already controls the phase down of fluorinated substances, e.g. refrigerants, based on their global warming potential (GWP). Consequently, hydrofluorocarbons (HFCs), for instance R134a, are limited in their availability and alternative solutions need to be investigated. Such solutions can include the development of new refrigeration systems designed to the specifics of the chosen low GWP refrigerant or retrofitting an existing system to said low GWP refrigerant. The latter is widely favored in terms of investment cost. The difficulty in retrofitting is to match the thermo-physical properties of one refrigerant with an entirely different substance not compromising the efficiency.

Having identified a refrigerant matching the boundary conditions, refrigeration cycle calculations follow to assess the system performance. However, the effects and consequences of a refrigerant change have to be tested in real systems. The influences of geometry or the compatibility with the lubricant and the behavior in the existing components are parameters difficult to appraise analytically. Therefore, an experimental investigation is necessary to achieve a deeper understanding e.g. of the effects on the compressor performance of an alternative solution.

A series of measurements on a test rig according to the DIN EN 13771-1 was carried out using a commercial rolling piston compressor designed for household heat pump applications. This paper presents the results of the performance measurements of the reference set-up with R134a and the substitute refrigerant blend of RE170 and R290. Three test conditions were examined corresponding to the operating range of the compressor.

* Corresponding author.
E-mail address: melanie.cop@tu-dresden.de.

2. Experimental Method

2.1. Experimental Setup

The present test rig setup is designed for performance tests of small capacity refrigerant-compressors in accordance with the ASHRAE standard 23.1 [2], resp. DIN EN 13771-1 [3]. Based on a standard vapor compression cycle the test bench includes a calorimeter evaporator and a flow meter to determine the refrigerant mass flow rate. Besides the main components like the compressor, the condenser, and an electronic expansion device, the cycle is additionally equipped with an oil separator, a filter dryer, sight glasses, and an accumulator (see Fig. 1). The compressor and the condenser are each integrated in the circuit with a detachable screw connection ensuring the adaption of the test bench to varying compressor capacities. Additionally, a small 12 V-fan installed next to the compressor may optionally cool it with ambient air to prevent too high discharge temperatures.

There are five measuring points for temperature and pressure, one of them monitoring the state of the secondary fluid in the calorimeter. The numbering of the locations refers to the designated point of state of the refrigerant in the cycle. All temperature sensors are PT100 resistance thermometers with class A accuracy [4]. The pressure transducers have a measurement inaccuracy of ±0.1 %FS. Table 1 lists the measuring range of the installed pressure sensors, which is necessary to calculate the absolute value of the uncertainty. A power meter separately plots the electrical input power of the compressor and the resistance heating element of the calorimeter. Finally, the mass flow rate and the ambient temperature complete the set of measured data.

In this specific study, the compressor mounted onto the test bench is a rolling piston compressor with the following characteristics:

- displacement of 7.8 cm³/rev,
- 2 pole induction motor, grid frequency of 50 Hz,
- voltage range of 187 to 264 V.

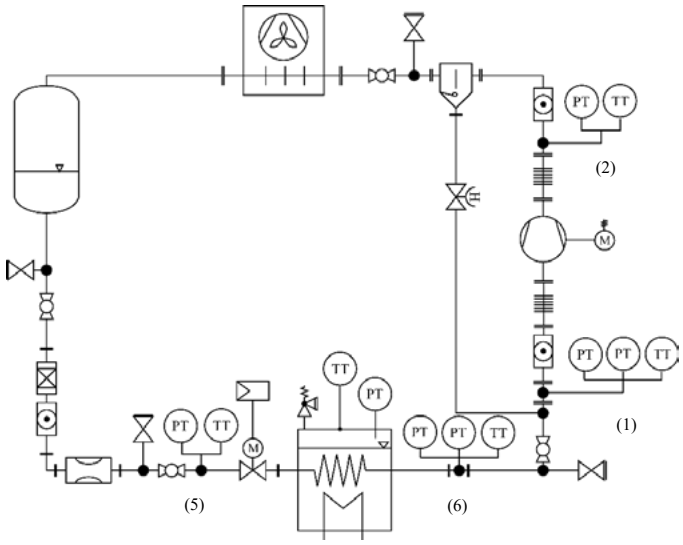


Fig. 1. Process and instrumentation chart of the test bench

Table 1. Installed Pressure Transducers

Measuring point	Range	Output
discharge line (2), inlet of the expansion device (5)	0 … 25 bar	4 … 20 mA
outlet of the evaporator (6), inlet of the compressor (1)	0 … 16 bar and 0 … 3 bar	4 … 20 mA
inner volume of calorimeter	0 … 25 bar	4 … 20 mA

Besides the pressure range of the sensors, the design of the evaporator calorimeter limits the operation range of the test bench. The maximum heat input capacity is 2 kW that is equivalent to the maximum cooling capacity. Secondly, the opening pressure of the safety relief valve is 20 bar, which leads to a maximum calorimeter temperature of 67.48 °C with liquid R134a as a secondary fluid.

2.2. Test Conditions

This paper investigates a rolling piston compressor used in a heat pump tumble dryer application. The objective is to compare the nowadays-used R134a with the substitute refrigerant blend RE170/ R290 at certain operating conditions. Besides the performance data supplied by the manufacturer, American and European standard rating conditions were considered to identify consistent parameters for the tests. The American AHRI standard 540, table 1, [4, p. 5] defines rating conditions for positive displacement refrigerant compressors. Next, the DIN EN 12900, table 5, [5, p. 10] states rating conditions of performance data as well but differing from the AHRI conditions. However, both standards distinguish three refrigeration appliances:

- "H" – high evaporation temperature,
- "M" – medium evaporation temperature,
- "L" – low evaporation temperature.

Figure 2 shows the manufacturer's data on the compressor operating pressure range with R134a. Considering those limits, the number of possible rating conditions decreases eminently leaving four rating conditions.

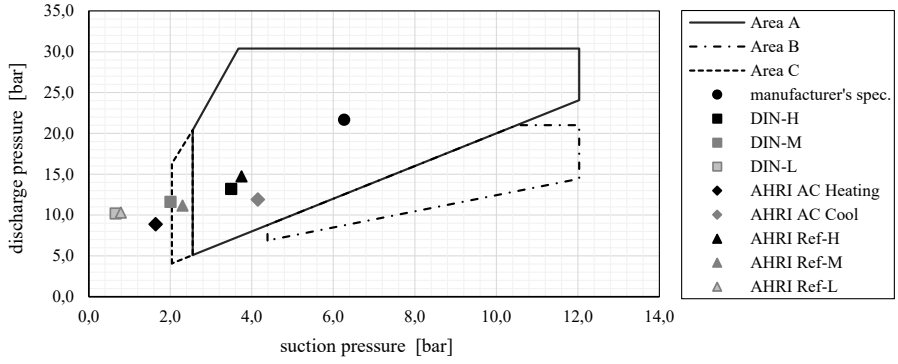


Fig. 2. Compressor operating range for R134a (Area A: normal operating zone; Area B: High density flow zone - running time less than 3 minutes; Area C: Low pressure zone - running time less than 3 minutes) with possible rating conditions

Out of the four points within area A, the "AHRI AC Cool" condition is neglected in the tests because it refers to an air-conditioning application not corresponding to the compressor's appliance. Since an adjustment of the refrigerant subcooling temperature and the ambient temperature is not possible with the described set-up of the test bench, those parameters are not specified in the rating conditions. Instead of the "AHRI Ref-H" point, the manufacturer defines a condition called "ASHRAE" condition. This state has similar temperature levels but different superheating which is included in the experimental investigation. Each test condition has a distinctive feature giving it merit for testing. The manufacturer specification refers to a heat pump application. The "DIN-H"-condition derives from a refrigeration appliance and the "ASHRAE"-condition adds a large superheating to similar refrigeration characteristics. The test conditions retained for the comparison of the two refrigerants are given in Table 2.

Table 2. Performance rating conditions for the rolling piston compressor in accordance with the manufacturer's data

	Suction dew point T_0 [°C]	Discharge dew point T_C [°C]	Suction gas T_1 [°C]
manufacturer's specification	23	71	35
ASHRAE	7.2	54.5	35
DIN-H	5	50	20

2.3. Experimental proceeding

The preparation for the test consists of evacuating the circuit and charging the cycle with refrigerant and the compatible oil (Table 3). The charged mass is measured indirectly by weighing the refrigerant bottle. Uncertainties result from the non- measurable liquid level of the receiver (see Table 3).

Table 3. Tested refrigerants, their charged amounts and the corresponding compressor oil

Refrigerant	Composition [%w]	refrigerant charge	Oil charge
R134a	100	434.8±20 g	prefilled, POE VG65
RE170/R290	69.86/30.14	383.8±20 g	200 ml of POE VG 100

The DIN test procedure [3] stipulates the recording of the measured data once the cycle reaches steady state. Therefore, the expansion device and the calorimeter heat input are adjusted according to the set temperature and the pressure at the suction side of the compressor. The condenser fan speed, respectively the swept air-volume flow, is the regulating variable for the compressor discharge pressure. When using a flow meter to determine the mass flow rate one must ensure that the minimum subcooling of the refrigerant is $\Delta T_{C,sc} = 3\,K$. Increasing or decreasing tendencies larger than 50% of the allowed deviation of the test parameter, as listed in Table 4, indicate that no steady state has been reached. The minimum duration of data recording is 15 minutes and at least one set of measurements per minute is required. Having established steady state conditions, several consecutive measurements of 15 minutes each are recorded. The same test is repeated in another session.

Table 4. Permitted deviation of measured values for the duration of a test series

Measured parameter	allowed deviation
pressure (absolute)	±1%
temperature	±3.0 K
calorimeter heat input	±1% of cooling capacity

2.4. Evaluation of the Data

The general processing of the acquired data for this experimental investigation follows the European standard on compressor rating [3]. If the measurement meets the criteria of the steady state, the mean values of the logged parameters are the basis for the calculation. Due to the diversion between the experimental data and the ideal rating condition, the consideration of corrective factors is vital for an objective comparison of the rated compressor performance. In addition to the COP, the isentropic efficiency is also determined using this test procedure.

The described data evaluation applies on the average values of a 15-minute-measurement. The first step is to determine the refrigerant mass flow rate. Therefore, the present test rig is equipped with the evaporator calorimeter (method A) and a refrigerant flow meter (method E), thus representing two standard methods [3] indicated in Fig. 3.

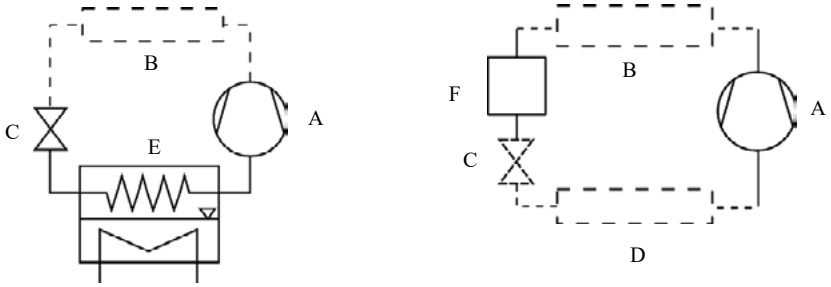


Fig. 3. Schematic of DIN 13771-1 test methods A (left) and E (right): A – compressor; B – condenser; C – expansion device; D – evaporator; E – evaporator calorimeter with heat source; F – mass flow meter

According to method A, the mass flow rate $\dot{m}_A$ is calculated using a calorimeter energy balance (1) considering the calorimeter heat loss F, the electrical input power of the heater $\dot{Q}_n$, the saturation temperature

of the secondary fluid t_s'' and the enthalpy difference of the inlet (h_6) and outlet (h_5) state. The measured refrigerant mass flow $\dot{m}_E$ is assumed to be oil-free due to the installed oil separator (2). Subsequently, the average of those two values is referred to as the actual mass flow rate $\dot{m}_a$ (3). The multiplication with a corrective factor regarding the ratio of the actual density at the compressor inlet $v_{1,a}$ and the ideal density v_1 leads to the refrigerant mass flow at the specified rating conditions (4).

$$\dot{m}_A = \frac{\dot{Q}_n + F*(t_{amb} - t''_s)}{h_6 - h_5} \quad (1)$$

$$\dot{m}_E = \dot{m}_{flow\ meter} \quad (2)$$

$$\dot{m}_a = \frac{1}{2}(\dot{m}_A + \dot{m}_E) \quad (3)$$

$$\dot{m} = \dot{m}_a * \frac{v_{1a}}{v_1} \quad (4)$$

The compressor's cooling capacity $\dot{Q}$ is obtained by multiplying the mass flow with the enthalpy difference between the ideal state at the compressor inlet h_1 and the boiling point enthalpy h_{f2} at the ideal compressor discharge pressure.

$$\dot{Q} = \dot{m} * (h_1 - h_{f2}) \quad (5)$$

The calculation of the power consumption at the ideal rating condition regards the ratio of the isentropic compressor power P_i at the specified rating conditions (6) and the isentropic power at the measured conditions P_{ia} (7). This ratio multiplied with the measured compressor power consumption P_a equals the input power at the specified rating conditions P.

$$P_i = \dot{m} * (h_{i1-2} - h_1) \quad (2)$$

$$P_{ia} = \dot{m}_a * (h_{i1-2a} - h_{1a}) \quad (7)$$

$$P = \frac{P_i}{P_{ia}} * P_a \quad (8)$$

Finally, the characteristic values are determined putting the previously calculated figures into relation.

$$COP_R = \frac{\dot{Q}}{P} \quad (9)$$

$$\eta_i = \frac{P_{ia}}{P_a} \quad (10)$$

The evaluation of a 15-minute-measurement solely gives a momentary impression. The average of the consecutive measurements and the results of the repetition experiment performed on another day as well as the corresponding standard deviation of each parameter represent the performance characteristics categorised by the refrigerant and the test condition.

3. Results and Discussion

The investigation of the compressor performance consists of three aspects. First, the difference between the two refrigerants at the theoretical nominal rating condition is examined, second the values calculated from the measured data are investigated and finally the compressor performance with regard to the refrigerant substitution is discussed.

3.1. Nominal Conditions

The experimental investigation comprises three operating points defined by the suction pressure dew point temperature, the discharge pressure dew point temperature, and the actual suction gas temperature as described above. Applying two refrigerants calls for a closer examination of the fluids properties regarding the specific refrigeration capacity, the specific volume of the compressor inlet state, and the pressure ratio assuming an ideal refrigeration cycle.

Fig. 3 (left) illustrates the specific refrigeration capacity of both refrigerants at the three operating points. Generally, the refrigerant mixture of RE170 and R290 possesses a distinctively larger specific refrigeration capacity than R134a. It indicates that less refrigerant mass flow is required to obtain the same cooling capacity. The large superheat of the "ASHRAE"-condition leads to a slight increase of capacity while the high dew point temperatures of the manufacturer's condition significantly decreases the specific refrigeration capacity. The latter observation is rather unsurprising as the latent heat decreases with rising temperature, respectively pressure.

As a rule, the volumetric refrigeration capacity (see Fig. 4, right) is an indicator for the compressor size. The mixture of RE170 and R290 exhibits a slightly larger volumetric capacity, indicating that an adjustment of the compressor size is necessary for future endeavours. Overall, the prospective reduction of the refrigerant mass flow due to the increased specific refrigeration capacity in combination with comparable volumetric refrigeration capacity leads to the conclusion that using the zeotropic blend reduces the refrigerant charge maintaining the compressor size or rather the compressor model. This observation corresponds to the actual refrigerant charge of the test bench in Table 3 and further supports the substitution of R134a.

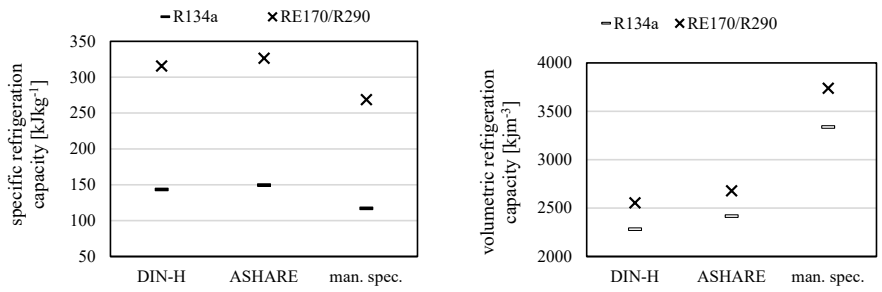


Fig. 4. Specific refrigeration capacity (left) and volumetric refrigeration capacity (right) of R134 and RE170/ R290 at the specified rating conditions

The last nominal parameter to discuss in terms of compressor performance is the pressure ratio depicted in Fig. 5. This value mainly influences the required compression work and gives an idea of the discharge temperature too. Ideally calculated according to the specified rating conditions, the pressure ratios of the two refrigerants are in a similar range supporting a substitution. Yet, it even suggests a slightly lower work input in the case of the zeotropic blend. Still, there are more influencing factors to the power consumption like the mass flow rate, the pressure ratio, and internal friction that should be analysed.

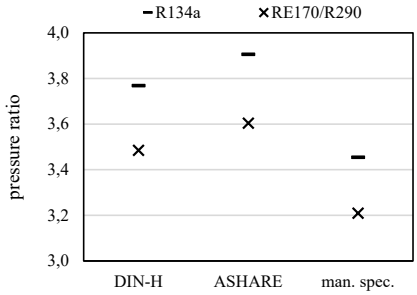


Fig. 5. Ideal pressure ratio of R134 and the mixture RE170/R290 at the specified rating conditions

3.2. Experimental Data

The evaluation of the experimental raw data follows the calculation described in section 2.4. All discussion points of the experimental results refer to the average value over the number of consecutive measurements at the same nominal conditions performed on one day and their repetition on another day. The standard mean error is shown to depict the deviation within the measured or calculated figure.

In general, the rating consists of the refrigerating capacity, the power input and the refrigerant mass flow rate. However, this paper refrains from discussing the refrigeration capacity, as it is the product of the ideal refrigeration capacity and the determined refrigerant mass flow rate. Boundary conditions not specified upfront or different from the standard condition must be stated as well (see Table 5).

The boundary conditions such as the ambient and the subcooled refrigerant temperature affect the compressor performance comparability but cannot be influenced at the present state of the test bench. The experiments were performed during the summertime causing fluctuating and, in some cases, elevated ambient temperatures. As it solely matters in terms of the compressor-shell cooling and the condenser fan speed, the latter being of low importance to the compressor performance, the relatively small divergence is negligible. The subcooled temperature of the refrigerant-mixture tends to be around 2 K cooler than the baseline refrigerant tracing back to the temperature glide of the refrigerant blend. As stated before, the subcooled state is a boundary condition that influences the calculation of the mass flow rate (1). There is no direct link to the rating of the compressor power due to the mentioned corrective factors.

Table 5. Boundary conditions for the performed compressor test

Test condition		DIN-H		ASHRAE		manufacturer's specification	
Refrigerant		R134a	RE170/R290	R134a	RE170/R290	R134a	RE170/R290
ambient temperature T_{amb}	[°C]	26.04±0.34	24.84±0.36	27.19±1.45	25.0±0.31	28.77±0.99	25.11±0.09
subcooled refrigerant T_5	[°C]	45.41±0.29	43.90±0.33	50.03±0.07	48.22±0.33	66.50±0.13	64.94±0.06

The discussion of the experimental data regards the determined mass flow rate as depicted in Fig. 5 (left diagram) and the standard mean error shown in Table 6. It supports the suggestion of a reduced mass flow of the alternative refrigerant. Given the fact that the compressor runs at a constant speed thus having a constant suction volume flow, the mass flow determined from the measured data according to equations (1) to (4) of the zeotropic mixture is on average 47 % lower than the one of R134a. In terms of the comparability of this value with other testing facilities, one must bear in mind that the mass flow rate is highly dependent on the expansion device and its inlet state. The measured mass flow rate of the test bench is the result of the valve lift and the expansion device's inlet state resp. the subcooled temperature, the priority of the valve lift being the setting of the suction pressure. Consequently, the measured flow rate might differ for other test benches for other subcooled temperatures. The examination of the product of the mass flow rate and the previously compared specific refrigeration capacity of both refrigerants combined lead to an on average 17.7 % higher refrigeration capacity with the zeotropic blend.

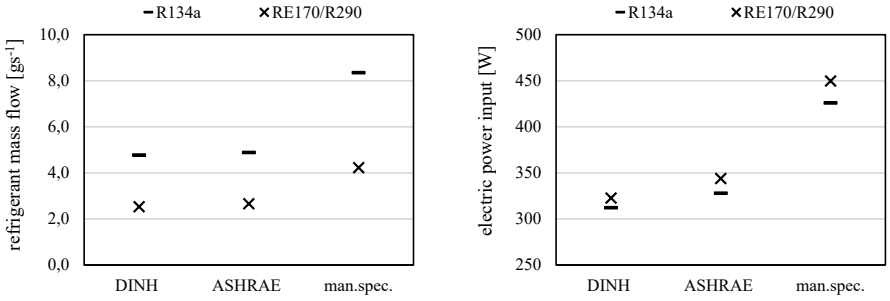


Fig. 6. Calculated refrigerant mass flow rate and electric power input at the specified rating conditions

Table 6. Relative standard mean error of averaged results in percentage [%]

Test condition	DIN-H		ASHRAE		manufacturer's specification	
Refrigerant	R134a	RE170/R290	R134a	RE170/R290	R134a	RE170/R290
power consumption	0.80	1.00	1.17	0.55	0.26	0.38
mass flow rate	1.42	0.46	0.98	0.09	1.24	0.59

In spite of the favorable pressure ratio and mass flow rate as stated before, the power consumption of the compressor (see Fig. 6, right diagram) in the case of the zeotropic mixture is on average elevated by 4.6 %. However, the trend for both refrigerants at the specified test conditions is the same. The refrigeration conditions "DIN-H" and "ASHRAE" have comparable pressure levels while the suction gas temperature is considerably higher for the latter condition. As a result, the power consumption increases while the mass flow rate remains rather constant. This observation testifies that a large superheating of the refrigerant is not beneficial to the compressor power consumption. The analysis of some compressor characteristics such as the discharge temperature, the oil sump temperature, and the isentropic efficiency in Fig. 7 helps to understand the mechanism behind this difference in the compressor input power for both refrigerants. The actual compressor input power is subject to thermal and mechanical losses. While thermal losses of the refrigerant gas affect the isentropic efficiency, friction causes the compressor material temperature to be elevated thus decreasing the heat loss of the compressed gas to the compressor shell. This chain of cause and effect helps to understand the observations made in Fig. 7. The left diagram reveals a higher isentropic efficiency at all operating conditions using RE170/ R290 compared to R134a. Meanwhile, the oil sump temperature of R134a is considerably below the one occurring during the tests with the refrigerant blend as the discharge temperature ranges among the same high values. The rather large thermal gradient over the shell of the compressor respectively the oil sump and the compressed gas supports the low isentropic efficiency. In return, the oil sump temperature of the tests with RE170/ R290 is close to the measured discharge temperature resulting in small to no thermal losses of the compressed gas. However, the elevated oil sump temperature indicates friction of the mechanical parts. Given the fact that the described behavior can be observed throughout all operating conditions it is the evidence that the lubricant is not favorable for the compressor although it was selected for the refrigerant blend due to the higher solubility.

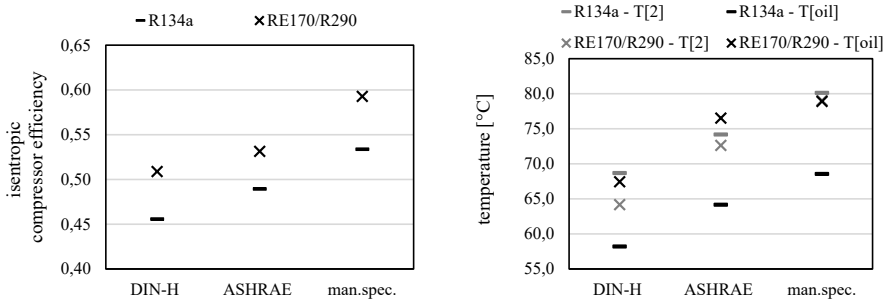


Fig. 7. Compressor characteristics – calculated isentropic efficiency based on measured values (left), refrigerant discharge temperature and oil sump temperature (right)

Finally, all evaluated data at the reference rating conditions come together when discussing the rated coefficient of performance COP_R depicted in Fig. 8. Despite the elevated power consumption of the compressor with the refrigerant blend, its coefficient of performance is greater than of the base line refrigerant at the three tested rating conditions. On the other hand, the results of the R134a tests reveal an upward trend throughout the rating conditions. Given the fact that the compressor is designed for the heat pump application, the observation of the highest COP using R134a-at the manufacturer's condition is not surprising. However, the COP of the substitute refrigerant is on average 12.6 % higher than the baseline.

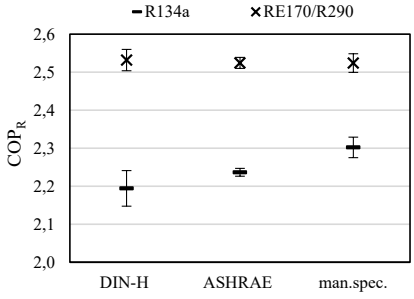


Fig. 8. Rated coefficient of performance at the specified rating conditions

4. Conclusion

In comparison to the high GWP refrigerant R134a, the tested natural refrigerant blend of RE170 and R290 shows favorable results e.g. the COP is significantly higher and the volumetric cooling capacity is in the same level of magnitude. Under this precondition, the experimental outcome supports the substitute refrigerant blend. The reduction of the charge and the increased performance at three different rating conditions are the core findings. The standard mean deviation proves the repeatability of the tests with respect to the stated boundary conditions like the ambient temperature. However, the increase of input power testing the alternative refrigerant raises interest for further optimization of the lubrication.

To conclude, the performed compressor tests reveal the potential of the natural refrigerant blend RE170/ R290 directly substituting R134a. It has merit to regard it for future cycle designs because the adaption of the compressor size, the heat exchangers or, the expansion device might affect the cycle efficiency positively. Further, the general acceptance of the natural yet flammable refrigerants must grow respecting the appropriate security measures since these refrigerants are inevitable for sustainable solutions.

Nomenclature

symbols		*Unit*	**subscripts**	
COP_R	rated coefficient of performance (cooling)		0	evaporation
F	thermal loss coefficient of calorimeter	$W\ K^{-1}$	1	compressor inlet
h	specific enthalpy	$kJ\ kg^{-1}$	2	compressor outlet
h_{i1-2}	specific enthalpy of the refrigerant gas at the compressor discharge port assuming an isentropic compression (specified rating conditions)	$kJ\ kg^{-1}$	f2	discharge bubble point of specified rating conditions
$\dot{m}$	mass flow rate	$kg\ s^{-1}$	5	inlet expansion device
P	power	W	6	outlet evaporator
p	pressure (absolute)	bar	a	actual, measured
Q	cooling capacity at rating conditions	W	amb	ambient
Q_n	electrical power input of the heater (calorimeter)	W	i	ideal isentropic
T	temperature	$°C\ or\ K$	s	secondary fluid
V_{SW}	theoretical swept volume flow of the compressor	m^3s^{-1}	v	volumetric
v_1	specific volume	m^3kg^{-1}		
η	efficiency			

Acknowledgements

The presented results were achieved within the scope of the project REFMIX supported by the German Federal Ministry for Education and Research (BMBF) and the German Aerospace Centre (DLR) (Contract FKZ: 01DL17003A). The authors express their gratitude to the DLR and BMBF for the financial support. The authors would like to thank the anonymous reviewers for their valuable comments and suggestions to improve the quality of the paper.

References

[1] UNEP, "Amendment to the Montreal Protocol on substances that deplete the ozone layer," 15 October 2016. [Online]. Available: https://treaties.un.org/doc/Publication/CN/2016/CN.872.2016-Eng.pdf.

[2] ASHRAE, *ASHRAE Standard 23.1-2010: Methods of Testing for Rating the Performance of Positive Displacement Refrigerant Compressors and Condensing Units that Operate at Subcritical Temperatures of the Refrigerant,* 2010.

[3] DIN - Deutsches Institut für Normung e.V., *DIN EN 13771-1: Compressors and condensing units for refrigeration - Performance testing and test methods – Part 1: Refrigerant compressors,* 2017.

[4] AHRI - Air-Conditioning, Heating and Refrigeration Institute, *Performance Rating of Positive Displacement Refrigerant compressors and Compressor Units,* 2015.

[5] DIN - Deutsches Institut für Normung e.V. , *DIN EN 12900 - Rating Conditions, tolerances and presentation of manufacturer's performance data,* 2013.

13th IEA Heat Pump Conference
April 26-29, 2021 Jeju, Korea

Residential Split Heat Pump Using Low GWP Refrigerants

Bo Shen*, Moonis Ally

Building Equipment Research Group, Building Technologies Research and Integration Center, Oak Ridge National Lab, TN, USA

Abstract

Conventional refrigerants, e.g. R-410A have high global warming potentials (GWP) > 1800. They are being phased out to protect the environment. The candidates to replace R-410A include R-32, R-452B, R-454B and R-466A for heat pump applications. These candidates are intended for drop-in replacement, i.e. having minimum modifications on existing systems. The paper investigates the low GWP refrigerants drop-in application via system simulations using a well-regarded, hardware-based heat pump model. A baseline heat pump having all fin-and-tube heat exchangers and a two-speed compressor was used. Cross-comparisons were made under rated conditions of ambient temperatures, compressor speeds, indoor air flow rates, respectively for cooling and heating operations. The seasonal performance indices, i.e. SEER and HSPF are presented.

© HPC2020.
Selection and/or peer-review under responsibility of the organizers of the 13th IEA Heat Pump Conference 2020.

Keywords: Heat Pump, Low GWP Refrigerant, System Simulation.

1. Introduction

The earth continues to see a record increase in temperatures and extreme weather conditions that is largely driven by anthropogenic emissions of warming gases such as carbon dioxide and other more potent greenhouse gases such as refrigerants. The cooperation of 188 countries in the 21st Conference of the Parties in Paris 2015 (COP21) resulted in an agreement aimed to achieve universal agreement on climate, with the aim of keeping global warming below 2°C by the end of the century. A global phasedown of hydrofluorocarbons (HFCs) can prevent 0.5°C of warming by 2100.

To replace HCFC and HFC refrigerants in existing air conditioner/heat pump equipment, selections of alternative lower GWP refrigerants are subject to a few key factors. The candidates are expected to have similar volumetric capacity, so that available compressors would provide similar cooling capacity, and equal or higher energy efficiency. In addition, a selected refrigerant should accommodate the same or wider working envelope, i.e. an adequately high refrigerant critical temperature for high ambient operation. Similar or moderately higher compressor discharge temperature levels are also important, to prevent the need to change compressor lubricant and maintain good reliability.

Potential low GWP refrigerants for R-410A used in the study are introduced in Tables 1. The R-410A replacements are mostly blends containing R-32 and an HFO (Hydrofluoroolefins) of R-1234yf, as well as a pure refrigerant of R-32. They have approximately 70% lower GWPs than R-410A. On the other hand, the compositions of R-32 and R-1234yf cause minor flammability and are classified as A2L. It should be noted that R-466A is an A1 refrigerant, i.e. non-flammable. These refrigerant blends have negligible temperature glides. All the alternatives have higher critical temperatures than R-410A, making them more suitable for high condensing temperature operation.

* Corresponding author. Tel.: +1-865-574-5745.
E-mail address: shenb@ornl.gov.

Table 1. Alternative Low GWP Replacements for R-410A

Refrigerant	GWP AR4[a]	GWP AR5[b]	Safety Class	Temperature glide [K]	Critical T [C]
R-410A[c]	2088	1924	A1	0.1	71.34
R-32	675	677	A2L	0.0	78.12
R-452B[d]	698	676	A2L	1.3	79.68
R-454B[e]	466	467	A2L	1.5	77.0
R-466A[f]	733	733	A1	1.5	83.8

a. IPCC 2007.
b. IPCC 2013.
c. R-410A has mass-based compositions of R-32 (0.5)/R-125 (0.5).
d. R-452B has mass-based compositions of R-32 (0.67)/R-125 (0.07)/R-1234yf (0.26).
e. R-454B has mass-based compositions of R-32 (0.689)/R-1234yf (0.311).
f. R-466A has mass-based compositions of R-32 (0.49) / R-125 (0.115) / R-13I (0.395).

2. Refrigerant Properties

The temperature-enthalpy diagram of a refrigerant illustrates two critical properties: the span between the saturated liquid line and saturated vapor line (i.e. latent heat of vaporization per unit mass of refrigerant) and the critical temperature (working range). Volumetric vaporization heat, i.e. latent heat × vapor density at an average saturation temperature of dew point and bubble point, indicates the evaporating capacity per unit volumetric flow rate. Refrigerants with smaller volumetric vaporization heat have reduced cooling capacities at a fixed compressor displacement volume.

Figure 1 illustrates the temperature-enthalpy diagram of R-410A and its alternative refrigerants. All the R-410A alternatives (except R-466A) have wider domes and higher critical temperatures, indicating that they are better refrigerants for high ambient operations. Figure 2 shows the volumetric vaporization heat versus the average saturation temperature. R-32 has noticeably larger vaporization heat than R-410A, and R-466A is slightly larger. R-452B and R-454B have similar vaporization heat, which are slightly lower than R-410A. When approaching to the critical temperature, all the refrigerants' vaporization heat drops.

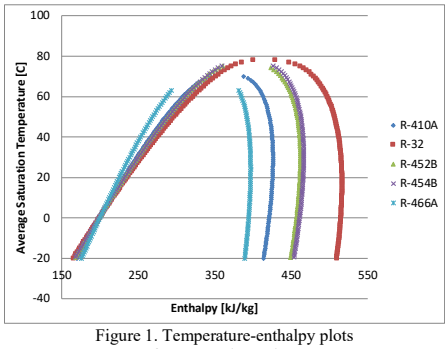


Figure 1. Temperature-enthalpy plots of R-410A alternatives.

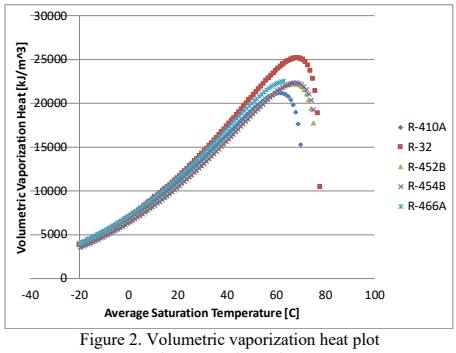


Figure 2. Volumetric vaporization heat plot of R-410A alternatives.

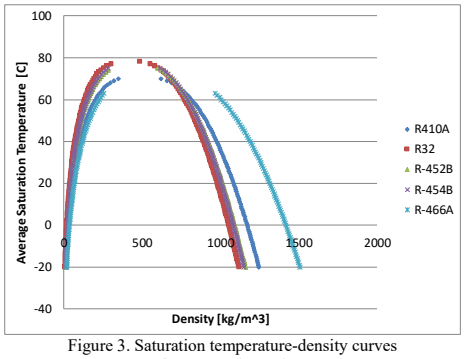


Figure 3. Saturation temperature-density curves of R-410A alternatives.

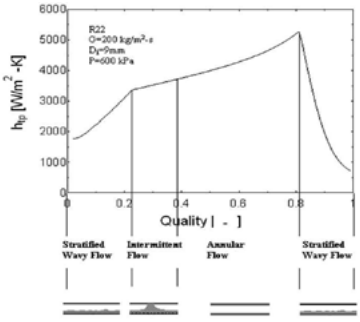


Figure 4: Local flow boiling coefficient predicted with the Thome (2002) [1] flow-pattern-dependent evaporation model.

Figure 3 shows curves of saturation temperature versus density of the R-410A alternatives. Most of the R-410A alternatives, except R-466A, have lower suction vapor density and lesser refrigerant mass flow rate if using a fixed compressor displacement volume.

At an average saturation temperature, a refrigerant with a lower volumetric vaporization heat results in smaller cooling capacity during a drop-in replacement. The saturation temperature is also impacted by the heat transfer performance and refrigerant pressure drop of the refrigerant. Lower saturation temperature leads to smaller cooling capacity if using the same compressor. And thus, whether an alternative low GWP refrigerant leads to higher or lower capacity depends on the trade-off between its volumetric vaporization heat and the resultant suction saturation temperature impacted by its heat transfer characteristics.

3. Model Description

A public-domain HVAC equipment modeling and design tool (HPDM, Shen 2016 [2]) was used to model a baseline heat pump. Some features of the HPDM, related to this study, are introduced below:

Compressor model:

AHRI 10-coefficient compressor maps (ANSI/AHRI 540-99, 2010 [3]) are used to calculate mass flow rate and power consumption, and enable calculation of the refrigerant-side vs. air-side energy balance from inlet to outlet by inputting a compressor shell loss ratio relative to the power input. It also considers the actual suction state to correct the map mass flow prediction.

We obtained the original compressor maps, developed for R-410A. For modeling the alternative refrigerants, it is assumed that the compressor would maintain the same volumetric and isentropic efficiencies at the same suction and discharge pressures. Thus, the efficiencies were reduced from the original R-410A map as a function of the suction and discharge pressures. The volumetric efficiency is defined in Equation 1, and isentropic efficiency is shown in Equation 2.

$$m_r = Volume_{displacement} \times Speed_{rotation} \times Density_{suction} \times \eta_{vol} \quad (1)$$

$$Power = m_r \times (H_{discharge,s} - H_{suction}) / \eta_{isentropic} \quad (2)$$

Where $\boldsymbol{m_r}$ is compressor mass flow rate; $\boldsymbol{Power}$ is compressor power; $\boldsymbol{\eta_{vol}}$ is compressor volumetric efficiency; $\boldsymbol{\eta_{isentropic}}$ is compressor isentropic efficiency; $\boldsymbol{H_{suction}}$ is compressor suction enthalpy; $\boldsymbol{H_{discharge,s}}$ is the enthalpy obtained at the compressor discharge pressure and suction entropy. The approach converting the compressor map of a baseline refrigerant to be used by its drop-in replacements has been extensively validated in Shen et al. (2018) [4].

Heat Exchanger Models:

Segment-to-segment fin-&-tube condenser: It uses a segment-to-segment modelling approach, which divides a single tube to numerous mini segments; each tube segment has individual air side and refrigerant side entering states and considers possible phase transition. An ε-NTU approach is used for heat transfer calculations within each segment. Air-side fin is simplified as an equivalent annular fin. Both refrigerant and air-side heat transfer and pressure drop are considered. The coil model can simulate arbitrary tube and fin geometries and circuitries, any refrigerant side entering and exit states, maldistribution, and accept two-dimensional air side temperature, humidity and velocity local inputs; the tube circuitry and 2-D boundary conditions are provided by an input file.

Segment-to-segment fin-&-tube evaporator: In addition to the functionalities of the segment-to-segment fin-tube condenser, the evaporator model is capable of simulating the dehumidification process. The method of Braun et al. (1989) [5] is used to simulate cases of water condensing on an evaporating coil, where the

driving potential for heat and mass transfer is the difference between enthalpies of the inlet air and saturated air at the refrigerant temperature. As noted, the segment-to-segment modelling approach can reveal the glide of a zeotropic refrigerant, since the temperature increment is accounted by each individual segment along the refrigerant flow path.

Through an extensive literature survey, we identified heat transfer and pressure drop correlations suitable for modeling and optimizing air conditioners and heat pumps, to assess various low GWP refrigerants. The correlations are listed in Table 2.

Table 2. Selected correlations for two-phase heat transfer and pressure drop

Application	Correlation
Fin-&-tube heat exchanger (FTC) -Evaporation heat transfer	Thome (2002) [1]
FTC-Condensation heat transfer	Cavallini et al. (2006) [6]
FTC-Evaporation pressure drop	Kedzierski and Choi (1999) [7]
FTC-Condensation pressure drop	Kedzierski and Choi (1999) [7]

The two-phase heat transfer correlations developed by Thome (2002) [1] and Cavallini (2006) [6] account for local flow patterns, considering refrigerant properties. The idea of the flow-pattern dependent evaporation model is to first estimate the wetted surface inside a horizontal smooth tube using a flow map prediction. The model covers stratified flow, stratified-wavy, annular-wavy, intermittent, annular flow, annular flow with partial dryout, and mist flow in evaporation. The general expression for local evaporating heat transfer coefficient is of the form,

$$h_{tp} = \frac{\theta_{dry} h_v + (2\pi - \theta_{dry}) h_{wet}}{2\pi} \tag{3}$$

$$h_{wet} = (h_{nb}^3 + h_{cb}^3)^{1/3} \tag{4}$$

In Equation 3, θ_{dry} is the dry angle corresponding to the dry circumference of the tube, which is determined from the flow pattern and void fraction. The void fraction model for this correlation is Rouhani (1970). h_{wet} is the heat transfer coefficient at the wet circumference of the tube, which is composed of a nucleate boiling term h_{nb} and a convective boiling term h_{cb}. h_v is the heat transfer coefficient at the dry circumference of the tube.

The local evaporation heat transfer coefficient calculated with the Thome (2002) [1] correlation is shown in Figure 4. The Thome (2002) correlation reasonably predicts degradation of heat transfer coefficient at high quality due to dry out of the liquid film, while most of the other correlations are not able to do this. This model can also reveal the effect of heat flux.

The condensation correlation of Cavallini (2006) [6] is given in Equation 5,

$$h_{tp} = \frac{\theta_{film} h_f + (2\pi - \theta_{film}) h_c}{2\pi} \tag{5}$$

θ_{film} is the falling film angle around the perimeter of the tube, which is dependent on the local flow pattern and void fraction. h_f is the Nusselt film condensing coefficient, and h_c is the convective condensation heat transfer coefficient. The Cavallini (2006) [6] condensation model also starts with the flow pattern prediction.

It is reported that azeotropic refrigerant mixtures have the same heat transfer performance as pure refrigerants. Thus, pure refrigerant correlations are able to work for an azeotropic refrigerant mixture such as R-410A. However, zeotropic refrigerant mixtures with large temperature glides, have different behaviors.

Heat transfer correlations developed for pure refrigerants must be corrected if they are to be used for zeotropic refrigerants. Stephan et al. (1992) proposed a correction method for condensation as well as evaporation. In this method, the mixture heat transfer coefficient h_m is defined as,

$$h_m = [1/h_f + (\delta Q_{SV} / \delta Q_T)/h_g]^{-1} \tag{6}$$

where h_f is the heat transfer coefficient computed from a pure refrigerant heat transfer model and h_g is the heat transfer coefficient of the vapor phase, which can be calculated with the Dittus-Boelter equation. $\delta Q_{SV} / \delta Q_T$ is the ratio between the sensible heat transfer and the total heat transfer. Bell and Ghaly (1973)

suggested that if the total isobaric temperature glide is around 7-8 °C, then the ratio could be approximated as,

$$(\delta Q_{SV} / \delta Q_T) \approx x Cp_g (\Delta T / \Delta h_m) \quad (7)$$

Where ΔT is the temperature glide, Δh_m is the enthalpy of latent heat of the mixture, x is the quality, and Cp_g is the vapor specific heat.

We adopted air side heat transfer correlations specific to individual fin types, respectively for dry and wet surface. Dittus-Boelter correlations was adopted to modelled single-phase refrigerant tube side heat transfer.

Expansion Devices:

The compressor suction superheat degree and condenser subcooling degree or system charge are explicitly specified. As such, the expansion device is not solved here – a simple assumption of constant enthalpy process is assumed.

Fans and Blowers:

The air flow rate and power consumption were direct inputs from the laboratory measurements for the model calibrations.

Refrigerant Lines:

Temperature changes and pressure drops of suction, discharge and liquid lines were specified using the measured data from the experiments.

Refrigerant Properties:

We programmed interface functions to call REFPROP 10.0 (Lemmon, 2018) [7] directly; our models accept all the refrigerant types in the REFPROP 10.0 database, and also we can simulate a new refrigerant by making the refrigerant definition file according to the REFPROP 10.0 format, or look-up tables.

4. Baseline Heat Pump and Rating Conditions

The DOE/ORNL heat pump design model (HPDM) was used for analytical evaluations for a baseline heat pump having a two-speed compressor. The two-state heat pump has the total cooling capacity of 5-ton/17.6 kW at 35°C ambient temperature/26.7°C indoor dry bulb temperature (DB) and 19.4°C indoor wet bulb temperature (WB). The high and low speeds of the scroll compressor provide 100%/67% capacity. The indoor and outdoor heat exchangers are described in Table 3. For the system modeling, the condenser exit subcooling degree was set at 10 R (5.6 K) for cooling mode and 20 R (11.2 K) for heating mode; the evaporator exit was assumed to have a constant superheat degree of 10 R (5.6 K).

Table 3: Parameters of Indoor and Outdoor Units

Parameters (heating mode)	Indoor Fin-&-Tube Coil	Outdoor Fin-&-Tube Coil
Face area, ft2 (m2)	3.30 (0.307)	22.3 (2.07)
Total Tube Number	84	64
Number of rows	3 (cross counter-flow)	2 (cross counter-flow)
Number of parallel circuits	9	6
Fin density, fins/ft (fins/m)	168 (551)	264 (866)
	Indoor Blower (High/Low[1])	Outdoor Fan
Flow Rate, cfm (m3/s)	1670/1380 (0.790/0.653)	3500 (1.652)
Power [W]	322/203	300

1. The indoor blower has two speed levels, corresponding to the compressor low/high speeds respectively.

Following the AHRI 210/240 standard [9] to rate a two-speed heat pump. In cooling mode, the heat pump should provide performance indices at 35°C, 27.8°C ambient temperature and indoor condition of 26.7°C DB/19.4°C WB. In heating mode, the heat pump should be rated at the indoor dry bulb temperature of 21.1°C. At the low speed, the ambient temperature should vary at 16.7°C DB/13.6°C WB, 8.3°C DB/ 6.1°C WB, 1.7°C DB / 0.6°C WB and -8.3°C DB / -9.4°C WB. The high speed should be rated at 8.3°C DB/ 6.1°C WB, 1.7°C DB / 0.6°C WB and -8.3°C DB / -9.4°C WB.

Since HPDM is a steady-state system model, it doesn't predict cyclic performance and frost/defrost penalty. We adopted a typical degradation coefficient of 0.1 for the high speed, and 0.15 for the low speed. AHRI 210/240 quantifies frosting/defrost loss at the outdoor condition of 1.7°C DB / 0.6°C WB. If no frost effect is

correlated by an analytical model, the standard recommends a 98% factor to scale the power consumption and a 91% factor to scale the heating capacity. AHRI 210/240 assumes no frost formation at the ambient temperature above 8.3°C DB/ 6.1°C WB and below -8.3°C DB / -9.4°C WB. At other ambient conditions, the performances are interpolated between 8.3°C DB/ 6.1°C WB, 1.7°C DB / 0.6°C WB; and interpolated between 1.7°C DB / 0.6°C WB and -8.3°C DB / -9.4°C WB. For the ambient conditions below -8.3°C DB / -9.4°C WB, the results are extrapolated based on the predicted results at 8.3°C DB/ 6.1°C WB and -8.3°C DB / -9.4°C WB.

5. Cooling Performance

Table 4 below presents predicted cooling performances of the heat pump using R-410A at the low (_L) and high speed (_H) levels, including cooling capacities [kW], cooling COPs [W/W], compressor discharge temperature [F] and compressor isentropic efficiency reduced from the compressor map in the form of Equation 2. The two-speed scroll compressor uses the full displacement volume at 100% capacity. At 67% capacity, only part of the scroll is utilized, which causes more loss factors. As a result, the compressor efficiency of the low speed is roughly 7% lower than the high speed.

Table 4: Predicted Cooling Performance Indices Using R-410A

Outdoor Condition	Capacity [kW]	COP [W/W]	Compressor Disc T [F]	Isentropic efficiency
35C_H	17.6	3.7	164.1	74%
27.7C_H	18.7	4.5	147.4	73%
35C_L	13.0	3.9	158.7	67%
27.7C_L	13.9	4.8	140.5	67%

Figure 5 show cooling capacity increments of the alterative refrigerant in comparison to R-410A, dropping into the same equipment. Corresponding to the vaporization plots in Figure 2, R-32 and R-466A result in 4% to 6% higher cooling capacities at all the conditions. On the other hand, R-452B and R-454B lead to approximately 2% smaller capacities. Figure 6 show increments in cooling COPs. With the same heat exchangers, larger capacity tends to cause higher condensing temperature and lower evaporating temperature, degrading the efficiency. Consequently, R-32 and R-466A have large capacities at the expense of reduced COPs. R-452B and R-454B result in higher COPs. Figure 7 presents compressor discharge temperatures. R-32 have significantly higher discharge temperatures, up to 30R. The other alternative refrigerants lead to minorly high temperatures, up to10R. At the low speed, the discharge temperatures are lower than those at the high speed, because the condensing temperature is reduced at the part-load operation. Figure 8 compares the seasonal cooling COPs, calculated from AHRI 210/240. They differ minorly, ranging from 4.45 to 4.58. R-454B results in the highest COP and R-466A results in the lowest COP.

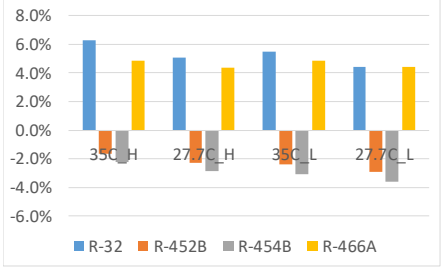


Figure 5. Capacity increments in cooling mode

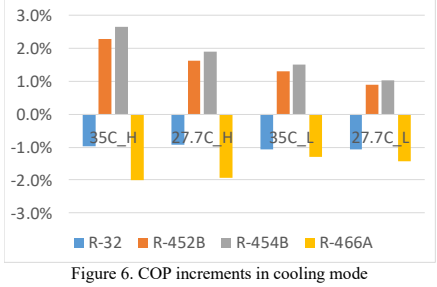


Figure 6. COP increments in cooling mode

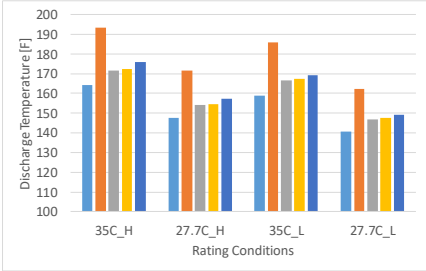


Figure 7. Compressor discharge temperatures in cooling mode

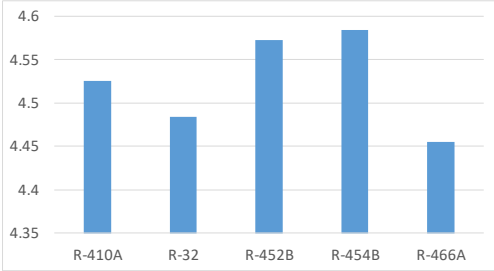


Figure 8. Seasonal cooling COPs

6. Heating Performance

Table 5: Predicted Heating Performance Using R-410A

Outdoor Condition	Capacity [kW]	COP [W/W]	Compressor Disc T [F]	Isentropic efficiency
8.3C_H	17.6	3.9	167.1	72%
1.7C_H	15.0	3.6	166.7	70%
"-8.3C"_H	11.4	3.0	172.8	64%
16.7C_L	15.8	4.5	165.7	66%
8.3C_L	12.8	3.9	165.7	63%
1.7C_L	10.8	3.4	170.1	59%
"-8.3C"_L	7.9	2.6	190.8	50%

Table 5 predicts heating performances using R-410A at the low (_L) and high speed (_H), including heating capacities [kW], heat pump heating COPs [W/W], compressor discharge temperatures [F] and the compressor isentropic efficiencies. Comparing the high speed with the low speed at low ambient temperatures, the efficiency degradation is more pronounced because the loss factors ascend with the compressor pressure ratio. At -8.3°C, the isentropic efficiency decreases from 64% to 50% when the pressure ratio increases from 3.4 to 4.2.

A typical heat pump sized to meet the building cooling load can't satisfy heating load at low ambient temperatures. Figure 9 compares the heat pump capacities as a function of the ambient temperature, versus the building load line of DHR_{min} defined in AHRI 210/240 in the ASHRAE climate zone IV. DHR_{min} indicates a well-insulated building. Even in the adequately insulated home, the heat pump total capacity still can't provide enough heating capacity. The high speed will be called at the ambient temperature below 25°F. Below 15°F, the high-speed operation can't meet the building heating load, and then, supplemental resistance heat will be used.

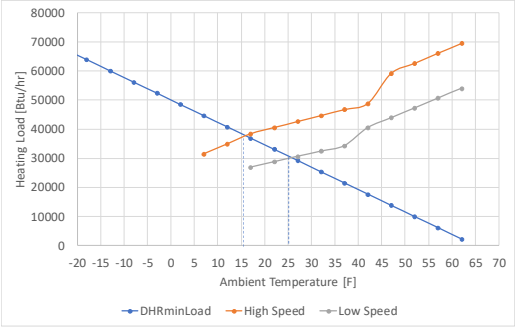


Figure 9: Heat Pump Capacities versus building load line

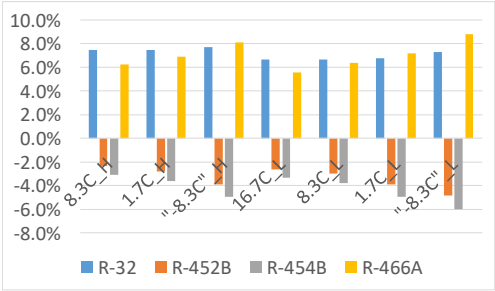


Figure 10. Capacity increments in heating mode

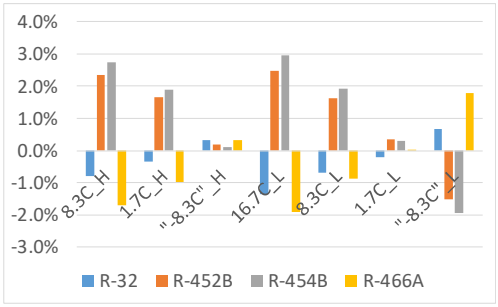


Figure 11. COP increments in heating mode

Figure 10 shows capacity increments of the alterative refrigerants versus R-410A in heating mode. R-32 and R-466A result in 6% to 8% higher heating capacities, which increase with decreasing the ambient temperature. On the other hand, R-452B and R-454B lead to approximately 2% to 6% smaller capacities, which decrease with the ambient temperature. Figure 11 shows increments in the heat pump heating COPs. R-32 and R-466A lead to 2% lower COPs due to the increased heating capacities. R-452B and R-454B lead to 2% higher COPs. Figure 12 presents compressor discharge temperatures. Because of the noticeably lower isentropic efficiency of the low speed at low ambient temperatures, more compressor power is converted to heat the refrigerant vapor than providing more useful pressure energy. Thus, the compressor discharge temperatures at low speed are higher than those at high speed. This is opposite to the trend, shown in Figure 7 regarding the cooling mode.

The discharge temperature increases with the pressure ratio, which tends to be higher in heating mode. Limit of discharge temperature is the major reason preventing heat pump operating below a certain ambient temperature. The higher discharge temperatures of the R-410A replacements would narrow the working envelope. The significantly higher discharge temperatures of R-32 (>210°F at -8.3°C) would require compressor lubricant change for the heat pump application. Figure 13 compares the seasonal heating COP, i.e. HSPF calculated by AHRI 210/240. Larger heating capacity causes degradation in heat pump COP, however, it decreases the supplemental resistance heat use at low ambient temperatures. As a result, the seasonal heating COPs are almost identical, regardless of the variations in heating capacity.

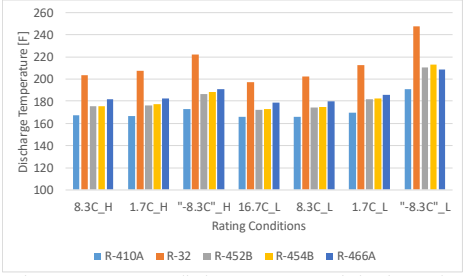


Figure 12. Compressor discharge temperatures in heating mode

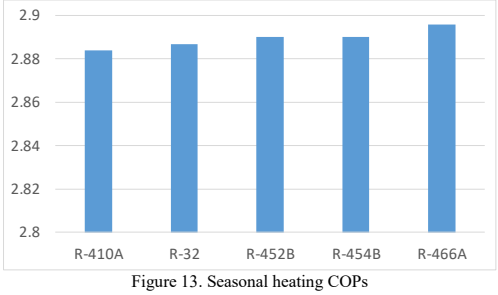


Figure 13. Seasonal heating COPs

7. Summary

This study starts with a hardware-based heat pump system simulation and design model, which adopted fundamental flow-pattern-dependent heat transfer correlations to represent variations in refrigerant properties. A method, to convert a baseline refrigerant compressor map used by alternative refrigerants in the similar pressure range, was developed and validated. Using the advanced analytical tool, we assessed lower GWP refrigerants to replace R-410A, in a drop-in application with respect to a two-speed heat pump. The alternatives include R-32, R-452B, R-454B and R-466A. The performance indices were predicted at the rating conditions of the AHRI 210/240 standard. Additionally, the seasonal cooling efficiency (SEER) and heating efficiency (HSPF) were compared.

In summary,

1) In cooling mode, R-32 and R-466A led to higher capacities, but slightly lower COPs than R-410A. R-452B and R-454B had very similar performance, having slightly lower capacities but higher COPs. R-454B resulted in the highest seasonal COP, and R-466A resulted in the lowest seasonal COP. In general, they differ minorly, ranging from 4.45 to 4.58.
2) In heating mode, R-32 and R-466A led to higher capacities, which degraded the heat pump heating COPs. R-452B and R-454B had slightly lower capacities but higher COPs. Larger heating capacity causes degradation in heat pump COP, but reducing the supplemental resistance heat use at low ambient temperatures. As a result, the seasonal heating COPs are almost identical among these refrigerants.
3) R-32 causes significantly higher discharge temperatures; R-466A, R-452B and R-454B results in moderately higher discharge temperatures. The higher discharge temperatures may narrow the operation envelope, particularly in heating mode. It is necessary to change the compressor lubricant for R-32, to tolerate the high discharge temperature during heating mode or cooling mode at elevated ambient temperature.

Acknowledgements

This research was supported by the DOE Office of Energy Efficiency and Renewable Energy, Building Technologies Office (BTO). The authors would like to acknowledge Mr. Antonio Bouza, Technology Manager – HVAC&R, Water Heating, and Appliance, DOE/BTO. This manuscript has been authored by UT-Battelle, LLC under Contract No. DE-AC05-00OR22725 with the U.S. Department of Energy. The United States Government retains and the publisher, by accepting the article for publication, acknowledges that the United States Government retains a non-exclusive, paid-up, irrevocable, world-wide license to publish or reproduce the published form of this manuscript, or allow others to do so, for United States Government purposes. The Department of Energy will provide public access to these results of federally sponsored research in accordance with the DOE Public Access Plan (http://energy.gov/downloads/doe-public-access-plan).

References

[1] Thome J.R. and Jean Ei Hajal, "Two-phase flow pattern map for evaporation in horizontal tubes: lastest version", 1st International Conference on Heat Transfer, Fluid mechanics, and Thermodynamics, 8-10 April 2002, Kruger Park, south Africa TJ2
[2] Shen, B. and Rice, K., 2016, DOE/ORNL Heat Pump Design Model, Web link: http://hpdmflex.ornl.gov/
[3] ANSI/AHRI Standard 540-99, 2010, “Positive Displacement Refrigerant Compressors and Compressor Units”, Air Conditioning and Refrigeration Institute, Arlington, VA.
[4] Bo Shen, Omar Abdelaziz, Som Shrestha, Ahmed Elatar, Model-based optimizations of packaged rooftop air conditioners using low global warming potential refrigerants, International Journal of Refrigeration, Volume 87, 2018, Pages 106-117, ISSN 0140-7007
[5] Braun. J.E., Klein. S.A, and Mitchell, J.W., 1989, “Effectiveness models for cooling towers and cooling coils”, ASHRAE Transactions, Vol. 95, Pt. 2, pp. 164-174.
[6] Cavallini, A, D.D. Col, L. Doretti, et al., Condensation in horizontal smooth tubes: a new heat transfer model for heat exchanger design, Heat Transfer Eng. 27 (8) (2006) 1–38.
[7] Lemmon E. W., Huber M. L., 2018 “NIST Reference Fluid Thermodynamic and Transport Properties Database (REFPROP): Version 10.0”, http://www.nist.gov/srd/upload/REFPROP10.pdf
[8] Kedzierski, M. A. and Choi J. Y., 1999, “A generalized pressure drop correlation for evaporation and condensation of alternative refrigerants in smooth and micro-fin tubes”, NISTIR 6333.
[9] AHRI 2008. ANSI/AHRI Standard 210/240-2008, “Performance Rating of Unitary Air-Conditioning and Air Source Heat Pump Equipment,” Air-Conditioning, Heating, and Refrigeration Institute, Arlington, VA, USA.

13th IEA Heat Pump Conference
April 26-29, 2021 Jeju, Korea

Experimental Setup and Test of a Desalination System Using a Heat Pump

Soo-Kwang Yang[a], Hae-Eun Song[b], Young-Chull Ahn[c*]

[a]Pusan national University, 2, Busandaehak-ro 63beon-gil, Geumjeong-gu, Busan, Republic of Korea
[b]Pusan national University, 2, Busandaehak-ro 63beon-gil, Geumjeong-gu, Busan, Republic of Korea
[c]Pusan national University, 2, Busandaehak-ro 63beon-gil, Geumjeong-gu, Busan, Republic of Korea

Abstract

This study aimed to analyze the mechanism and the basic performances of a heat pump desalination system. As a kind of evaporation method, a heat pump system using cascade cycles of R410A and R134a generates 80℃ of heat to the heat pump condenser and transfers it the plate type heat exchanger. Heat generated by the heat pump is transferred through the plate type heat exchanger and the fin tube type exchanger. Through the 3-way valve installed in the seawater supply system to reduce the heating time, water below set temperature 60℃ is recycled and water above the set temperature is discharged to the storage tank. The hot water discharged into the storage tank is evaporated and passed through the cyclone and the bag filter to the fin tube type heat exchanger by using the vacuum pump, which condenses into fresh water by heat exchange with the low temperature air of the heat pump evaporator. The amount of hot water that can be produced is about 20ℓ/min and the power consumption used for the entire system is estimated to be 9.3 kWh/㎥.

© HPC2020.
Selection and/or peer-review under responsibility of the organizers of the 13th IEA Heat Pump Conference 2020.

Keywords: Desalination; Heat Pump; Evaporation; 3-Way Valve

1. Introduction

Currently, more than 40% of the world's population suffers from water shortages. In addition, due to global warming and deepening climate change, uncertainties in water resource use and management are increasing. Korea, which is relatively rich in water resources, is also concerned about the lack of water in mountainous and coastal areas due to climate change [1]. Along with these problems, various measurements are needed for the independence of the building facilities in the island area. While the development of alternative water resources is needed, seawater desalination technology is receiving the most attention, and the reverse osmosis method, which consumes less energy than the conventional evaporation method, is increasing. According to Kim et al. [2], the reverse osmosis system occupies about 90% in the overseas seawater desalination plant market, and 87.5% of seawater desalination facilities in Korea use reverse osmosis. Kesieme at al. analyzed desalination technologies in the context of carbon pricing and found that the cost of desalination schemes increased by introduction of a price for carbon, but RO still remain the lowest cost [3]. However, reverse osmosis also has a limitation in that a pretreatment facility is essential, energy recovery cannot be more than 50%, and maintenance costs are high due to membrane replacement [4]. In addition to maintenance costs and energy aspects, existing seawater desalination systems are difficult to apply to island areas due to their large size. This study aimed to analyze the mechanism for the optimal design of seawater desalination system using heat pump that is a compact facility and can be applied as an independent water supply system for island buildings.

* Corresponding author. Tel.: +82-51-510-2492 ;
E-mail address: ycahn@pusan.ac.kr.

2. Experiment apparatus and method

To study the performance of heat pump desalination system, the experimental apparatus is setup, which consists of a heat pump system, cyclone, bag filter and seawater supply system. The heat pump system is a commercial product of LG Electronics and refrigerant cycle uses R410a and R134a cascade cycles. The seawater supply system consists of a seawater tank, a circulation pump, 3-way valve and check valve, as shown in Fig.1. Heat generated by the heat pump is transferred through the plate type heat exchanger and the fin tube type exchanger. A vacuum pump was installed to adjust the evaporation pressure, and a demister was installed to capture the uncondensed vapors being discharged through the vacuum pump. The blowout air temperature of the heat pump evaporator and the water temperature in seawater tank were measured using a thermocouple wire (T type). The inlet and outlet water temperatures between the heat pump condenser and the plate type heat exchanger and water temperature at 3-way valve were measured by automatic temperature sensor.

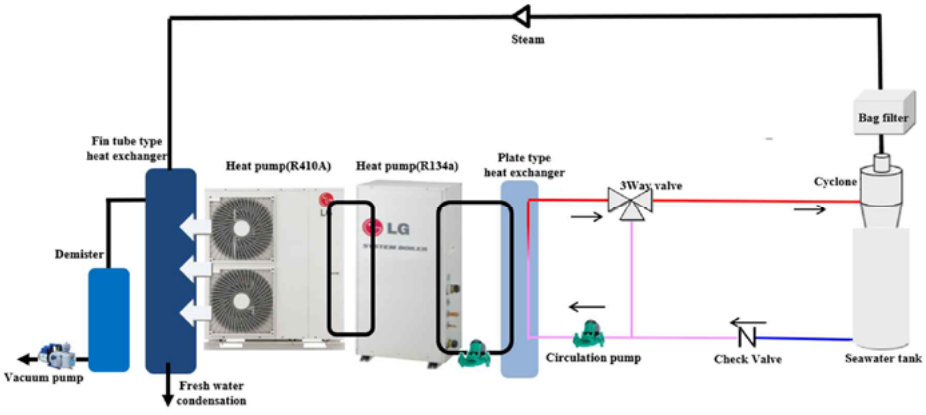


Fig. 1. Schematic diagram of heat pump desalination system



Fig. 2. Photo of the experimental apparatus

3. Results

3.1. Experiment apparatus analysis

Schematic diagram of the heat pump desalination system is shown in Fig.1. A heat pump system using cascade cycles of R410A and R134a generates 80℃ of heat to the heat pump condenser and transfers it the plate type heat exchanger. The seawater circulated in the seawater supply system receives heat from the plate type heat exchanger and is heated to the storage tank. Through the 3-way valve installed in the seawater supply system to reduce the heating time, water below set temperature 60℃ is recycled and water above the set temperature is discharged to the storage tank. The hot water discharged into the storage tank is evaporated and passed through the cyclone and the bag filter to the fin tube type heat exchanger by using the vacuum pump, which condenses into fresh water by heat exchange with the low temperature air of the heat pump evaporator.

3.2. Fluid state inside system

The inlet and outlet water temperature variations between the heat pump condenser and the plate type heat exchanger and water temperature variations at 3-way valve are shown in Fig.2. After the heat pump starts up, the temperature is continuously increased, and 70℃ hot water is passed through the 3-way valve to produce a storage tank.

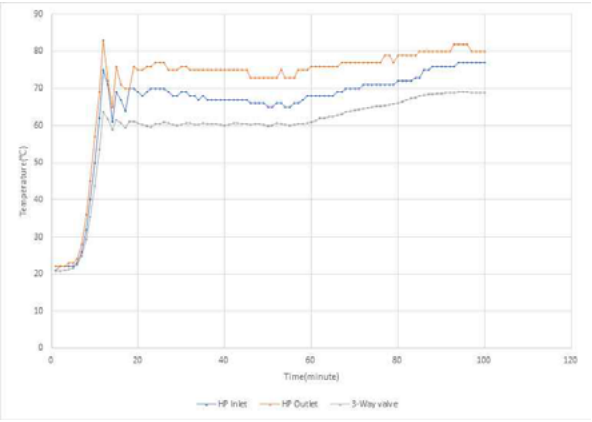


Fig. 2. Temperature variations in each point

3.3. Productivity and Energy consumption

After 90 minutes of a heat pump operation, the amount of hot water produced is about 20ℓ/min and the power consumption used for the entire system is estimated to be 9.3 kWh/㎥. The conditions of the produced hot water are shown in Table 1.

Table 1. Condition of produced hot water

Temperature	Water flow rate	vacuum pressure	Energy consumption
70℃	20ℓ/min(1.2 ㎥/h)	0.3077 atm	9.3 kWh/㎥

.

4. Conclusions

This study aimed to develop a high-efficiency seawater desalination system using heat pump. The heat pump condenser heats seawater and generated steam condenses through heat exchange with the heat pump evaperator. Heat pump cycles were constructed using refrigerants R410A and R134a. The vapor is condensed by removing impurities as it passes through the cyclone and bag filter. The mechanism analysis results are as follows.

1. A heat pump system using cascade cycles of R410A and R134a generates 80℃ of heat to the heat pump condenser and transfers it the plate type heat exchanger. The hot water discharged into the storage tank is evaporated and passed through the cyclone and the bag filter to the fin tube type heat exchanger by using the vacuum pump, which condenses into fresh water by heat exchange with the low temperature air of the heat pump evaporator.
2. By installing 3-way valve, hot water can be produced quickly and it can produce hot water of 70 ℃ continuously.
3. After 90 minutes of a heat pump operation, the amount of hot water produced is about 20ℓ/min and the power consumption used for the entire system is estimated to be 9.3 kWh/㎥.

Experimental results show that energy consumtion of heat pump desalination system for fresh water production is 9.3kW/㎥, which requires more energy than reverse osmosis and large-scale evaporaton plants. But it will increase the efficiency by expanding the scale of heat exchanger and heat storage tank. The price of production water during the short term is expected to be least considering the construction cost, pertreatment cost and facility maintenance cost.

Funding

This research was supported by the National Research Foundation of Korea(NRF) grant funded by the Korea government(MSIT)(No.2018R1A2B6004137)

References

[1] Water Information Portal.Trends and Implications of Global Seawater Desalination.2016.
[2] In-Soo Kim, Moon-Hyun Hwang, Chang-Gyu Choi, Sung-Jo Kim, Seung-Ho Kook, Do-Sun Han, Jin-Woo Lee. A Study on the Development of High-efficiency Low-Energy Seawater Desalination Plant Technology using Renewable Energy. Gwangju Institute of Science and Technology. 2016.
[3] Kesieme U.K, Milne N, Aral H, Cheng C.Y, Duke M. Economic analysis of desalination technologies in the context of carbon pricing and opportunities for membrane distillation. Desalination, vol.323, pp66-74. 2013.
[4] Seung-gwan Hong , Sang-ho Lee, Joon-ha Kim, Jung-hoon Kim,Young-gil Ju. Evolution of Reverse Osmosis Process for Green Future. Industrial Chemistry Prospect. 2011,Vol. 14, No. 6.
[5] Young-Hwang Hwang, Young-In Kim, Moon-Hee Jang. Optimization of SMART Desalination Plant. Korea Atomic Energy Research Institute. Technical Report. 2002.
[6] Chi-Sung Song. Energy Consumption of Evaporative Desalination Plant. Korean Society of Marine Engineers. 2014. Vol.38 (9).
[7] Jurn Hur, Suk-Jong Lee, Jae-Yong Sung, Myeong-Ho Lee, Jai-Dong Yoon. Performance Test of Pressure and Flow Rate in a Hot Water Heating System with 3 Way Valves for Flow Bypass. Korea Journal of Air-Conditioning and Refrigeration Engineering. 2007. Vol.19, pp269-274.
[8] Moon-Hyun Hwang, In S Kim. Comparative Analtsis of Seawater Desalination Technology in Korea and Overseas. Korean Soc Environ Eng. 2016. Vol.38, pp255-268.

13th IEA Heat Pump Conference
April 26-29, 2021 Jeju, Korea

Application of a deep reinforcement learning algorithm in household inverter air-conditioner temperature control

Myung Sup YOON[a,*], Won Sik YOON[a], Jong-Seok LEE[b]

[a]Energy Technology Center, Korea Testing Laboratory, 87 Digital-ro 26-gil, Guro-gu, Seoul, 08389, Republic of Korea
[b]School of Integrated Technology, Yonsei Unviersity, 85 Songdogwahak-ro, Yeonsu-gu, Incheon, 21983, Republic of Korea

Abstract

A deep reinforcement machine learning algorithm was applied to household inverter air-conditioner precision temperature control. Generally, air-conditioner temperature control aspects rely on the specific technology of the product, cooling room area size, outdoor temperature variation, and indoor building load variation when the set temperature is fixed. In this study, we fixed the test product and room size, and used the given variations of outdoor temperature and indoor building load over the course of one day. Even though the test product showed satisfactory performance at the remote controller set temperature of 26°C without a machine learning algorithm, we experimented with deep reinforcement learning performances to check whether the test product could follow general product performances or surpass the product ability in the precision temperature control by applying only high and low set temperatures alternatively. Training started with no disturbances of constant building cooling load and outdoor temperature. It resulted in reasonably accurate temperature control with the real training environments of Korean and Middle Eastern climates.

Keywords: Air-conditioner; Smart home; Deep reinforcement learning; Machine learning; Temperature control; AI

1. Introduction

Smart home appliances are a rapidly expanding industry. Korea is one of the leading countries in the smart home market, especially in the home appliance division. Premium air-conditioner and refrigerator products in Korea are now expected to embed smart-phone applications that can monitor energy consumption and be controlled from outside the house. However, there is further scope to improve them by adopting AI technology. Korean manufactured high-quality air-conditioners currently make it possible to perform target cooling by learning the occupant's positioning area and operating commands from the occupant's voice. But until now, these products seem to only borrow existing AI technology of vision and voice recognition from other fields.

Many HVAC (Heating, Ventilation, and Air-Conditioning) studies predict building cooling loads using a time series method and neural networks [1–4], fuzzy logic [5–7], and applying machine learning techniques in central air- conditioning systems [8–13]. However, it is not easy to find machine learning research in the field of household air-conditioners. For the energy usage comparison between inverter and constant speed air-conditioner technology, Yoon et al. [14,15] tested an air-conditioner under the actually varying temperature condition in an accurately controlled test chamber over a prolonged period. Referring to international standards such as ISO or EN, they suggested a one-point environmental test energy efficiency ratio (EER) or a more complicated multi-point interpolated energy efficiency ratio (seasonal EER) for the test of air-conditioner energy performance. These methodologies, however, cannot capture the dynamically improved performances of an AI driven air-conditioner because test chamber environments are statically fixed at each test point. Therefore, Yoon et al. [14,15] suggested a more realistic experiment. They simulated varying outdoor

* Corresponding author.
E-mail address: msyun95@ktl.re.kr

temperature and indoor building load conditions over the course of a day. This approach was analogous with a realistic car fuel economy test under real road load circumstances rather than a fixed high-speed condition.

In our study, a deep reinforcement learning algorithm was applied to a household inverter air-conditioner under an experimentally simulated varying environment (outdoor temperature, indoor building load). The purpose of this study was to check whether the machine learning algorithm could be applied to the household inverter air-conditioner temperature control and surpass the normal usage of the product.

2. Related work and background

Reinforcement learning (RL) is one of the most exciting and also one of the oldest areas of the machine learning discipline [16]. The problem of reinforcement learning is expressed in the Markov decision process (MDP), which is popular in the theory of dynamic programming [17]. Dynamic programming using value iteration or policy iteration evolved into the SARSA (State, Action, Reward, State, Action) on-policy problem, and later, the Q-learning (SARSA off-policy) [18].

A deep neural network (DNN) is an artificial neural network (ANN) consisting of several hidden layers between the input and output layers. One ANN study goes back to the Fukushima's convolution neural network (CNN) paper [19], and DNN is now used in various fields related to vision recognition [20,21]. In addition, language recognition studies use the modified DNN methods, which are RNN (Recursive Neural Network) or LSTM (Long Short-Term Memory) in machine learning [22–24].

In this study, we used the well-known DQN (Deep Q-learning Network) method that uses DNN for the Q-learning [18,25,26].

$$Q(S_t, A_t) \leftarrow Q(S_t, A_t) + \alpha[R_t + \gamma \cdot max_{a'} Q(S_{t+1}, a') - Q(S_t, A_t)] \quad (1)$$

where, (S_t, A_t) is the current state and action, (S_{t+1}, a') is the next state and action, $Q(S_t, A_t)$ is the quality of the agent in (S_t, A_t), R_t is the reward obtained by taking an action A_t from state S_t, and α and γ are the learning rate and the discount factor, respectively. In the iteration i, Q-learning updates by the following loss function

$$L_i(\theta_i) = \left(R_t + \gamma \cdot max_{a'} Q(S_{t+1}, a', \theta_{i-1}) - Q(S_t, A_t, \theta_i)\right)^2 \quad (2)$$

where, θ_i is the parameter of the Q-network at iteration i and θ_{i-1} is the network parameter from the previous iteration.

3. Methodology

3.1. Artificial neural network model

In this study, we used one input layer of 3 nodes, two hidden layers of 24 nodes each, and one output layer of 2 nodes. The input layer consists of three elements of state [$(T_{in}(t) - 26)$, dT_{in}/dt, $T_{dis}(t)$]. Each element represents indoor temperature (T_{in}), indoor temperature derivative (dT_{in}/dt), and air-conditioner discharge temperature ($T_{dis}(t)$) according to ISO 5151 [27] and ASHRAE 116 [28].

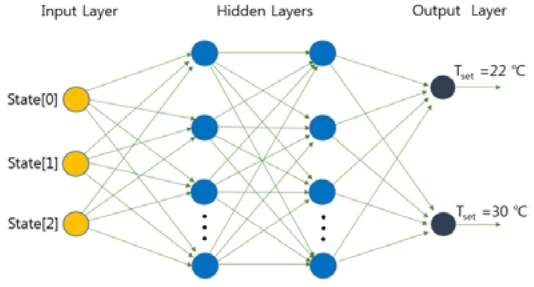


Fig. 1. DNN model for the inverter air-conditioner temperature control

The output layer gives action outputs to the remote controlled air-conditioner with the selected set temperature of each low and high product temperature [22, 30] °C. Even though the real test product has a wider controllable temperature range (16–31°C), we define action states here as two cases of set temperature to simplify the problem definition and reduce the calculation time when the target temperature is 26°C. These input, hidden, and output layers' artificial neural networks are generated by TensorFlow [29].

3.2. Simulation of the test chamber environment

Air-conditioner power consumption depends on indoor-side and outdoor-side environment conditions simultaneously. An indoor unit has an evaporator heat exchanger, and an outdoor unit usually has a condenser heat exchanger and a compressor component. If the outdoor-side temperature rises and the indoor cooling load is high, then the air-conditioner instantaneous power input usually increases. Therefore, international test standards such as ASHRAE and ISO request the exact fixing of the indoor and outdoor environment (temperature or humidity) for the rating test [28,29]. For example, the standard test condition (T1) of summer periods is (DBT/WBT) = 35°C/24°C and 27°C/19°C at each outdoor- and indoor-side chamber, respectively.

For the AI training of the product, we need time-varying real environment conditions rather than fixed-temperature conditions. Here, we assumed a summer situation of a typical region in Korea and the Middle East for the TRNSYS simulation [14,15]. The TRNSYS simulation program was used to obtain indoor building load $q_{build}(t)$ and outdoor temperature variation $T_{out}(t)$. The average temperature and building load variations during a summer's day can be obtained using TRNSYS climate data and analysis. The TRNSYS simulation condition is shown in Table 1.

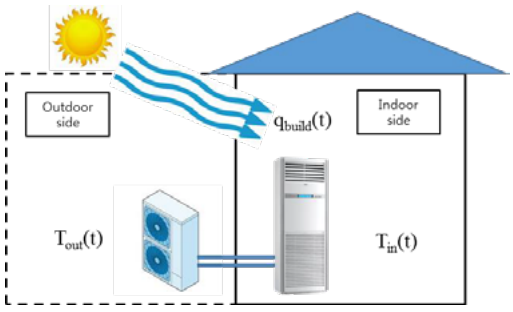


Fig. 2. Environment simulation concept (reproduced from Yoon et al. [14,15])

Table 1. TRNSYS simulation condition in Seoul & Middle East

Input variable	Simulation condition in Seoul	Simulation condition in M.E.
Space (single zone)	10m × 8m × 2.5m	10m × 8m × 2.5m
Window	60% of the southern wall area (15 m^2)	30% of the southern wall area (7.5 m^2)
Floor of space	Located between floors – up and down insulations	Located between floors – up and down insulations
Glass insulation	1.20 W/m^2K	1.720 W/m^2K
Wall insulation	0.21 W/m^2K	0.345 W/m^2K
Room temp. & humidity	26°C & 60%R.H.	26°C & 60%R.H.
Heating & light element	25 W/m^2	25 W/m^2
Persons	4 persons	4 persons
Infiltration	0.4 (1/h)	0.4 (1/h)
Ventilation	0.6 (1/h)	0.6 (1/h)

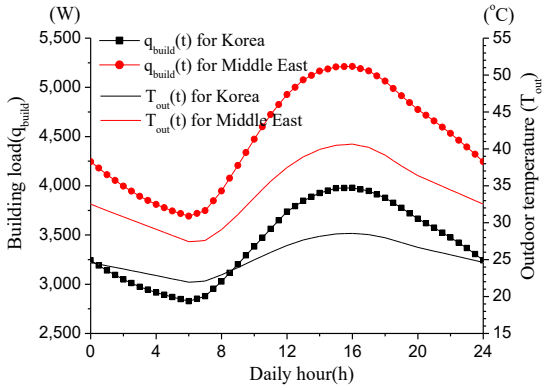


Fig. 3. Environment simulation result

3.3. Air-conditioner selection

A household room air-conditioner is categorized largely by constant speed compressor type and inverter compressor type. This study prepared an inverter compressor split wall mount air-conditioner. A constant speed air-conditioner's compressor turns off and on according to whether the room environment temperature satisfies the remote controller set temperature or not. In contrast, an inverter air-conditioner can control compressor speed to adjust the needed cooling capacity, which varies over time [14,15]. In this study, we simply control the set temperature by using an IR remote controller because each component's control method or signals (e.g., compressor speed, fan speed, expansion valve openness) are usually hidden by the manufacturer.

Even though the thermostat switching method of an inverter air-conditioner differs depending on the technology of each manufacturer, a dead band thermostat is usually used. This means that an air-conditioner starts to change the operation state when a certain activation range of temperature difference is satisfied between the measured room temperature and the product set temperature.

Table 2. Specifications of test air-conditioner

Contents	Name plate values
Air-conditioner type	Split wall mount
Compressor type	Inverter type
Electricity	Single phase, 220 V, 60 Hz
Rated cooling capacity	6 500 W
Rated power input	1 750 W
Max. power input	2 900 W
Min. power input	500 W
Refrigerant	R410a, 2kg

3.4. Deep reinforcement learning algorithm coding

The problem definition is:

- State : $[(T_{in}-26), dT_{in}/dt, T_{dis}]$
- Action : [22°C, 30°C]
- Reward : +1 pt, when T_{in} in the range of (26 ± 0.5)°C
- Penalty : –100 pts, when T_{in} out of (26 ± 0.5)°C

- Each episode ending : when penalty
- Environments during simulation time:
  - Day 1 : constant T_{out} = 28°C, q_{build} = 3,000 W
  - Day 2 : constant T_{out} = 28°C, q_{build} = 3,000 W (repeat one more day)
  - Day 3 : Korean summer climate, as Fig. 3
  - Day 4 : Middle Eastern summer climate, as Fig. 3
- Reset : T_{set} is reset within (26 ± 0.2)°C when each episode ends.

The coding flow is shown in Fig. 4. The basic algorithm is the same as established deep Q-learning, with experience replay [25], but differs by the addition of the training condition, T_{in} = (26 ± 0.5)°C, and reset condition T_{in} = (26 ± 0.2)°C.

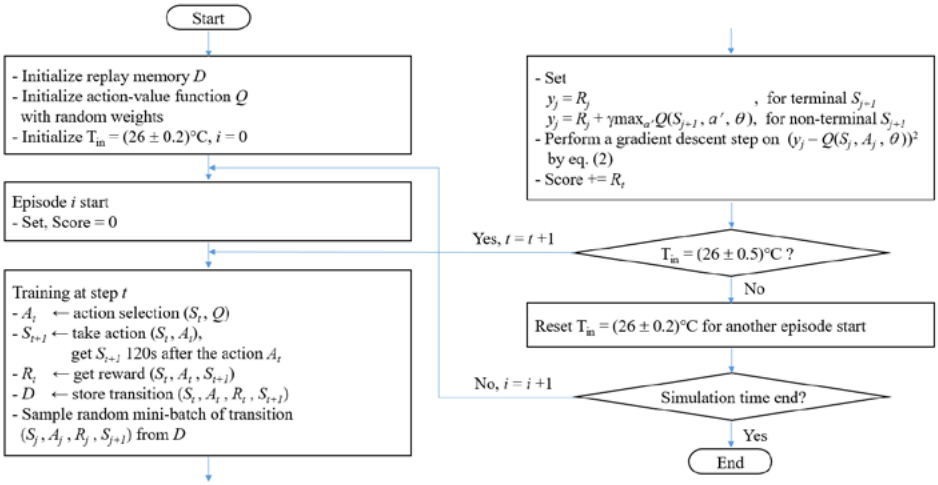


Fig. 4. Deep reinforcement learning coding flow

3.5. Air-conditioner remote control

Our deep reinforcement learning algorithm generates two cases of agent action, which are the remote controller setting temperatures of up and down. One of these action signals is transferred to the Arduino-based IR signal emitter. The IR signal changes the setting temperature of the air-conditioner. Before undertaking the IR operations, we need to record the infrared signals for each setting temperature of the remote controller. These Arduino IR signal-receiving and emission codes are well established in the Arduino-IRremote github library (https://github.com/z3t0/Arduino-IRremote). Figure 5 presents circuit diagrams of the IR signal receiver and emitter.

The block diagram for the experiment set-up is shown in Fig. 6. The test facility has one computer system for the facility environment simulation and data acquisition. The necessary data for the machine learning state inputs are transferred to a second PC. The second PC conducts a machine learning calculation and sends action output to the Arduino IR signal emitter.

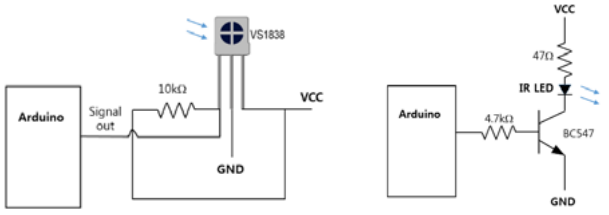


Fig. 5. IR signal receiver (left) and emitter (right) circuit

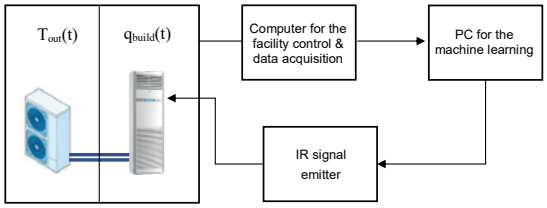


Fig. 6. Block diagram for the experiment set-up

4. Experiments and results

Even without AI, today's commercially available inverter air-conditioner technology is well established and can adjust building cooling demand to the desired room temperature. It offers satisfactory performance for the customer. However, this study aims to show that combining an inverter air-conditioner with RL machine learning can demonstrate better performance, especially in temperature precision control. First, normal usage of an air-conditioner with the fixed set temperature case, T_{set}=26°C, was experimented. Second, a simple thermostat algorithm was applied using computer control. Third, DQN RL training was started with a reward at T_{in}=(26±0.5)°C. Fourth, the same environment as the third case was maintained to check training reliability. Fifth, Korean summer climate environment variation was applied as a disturbance. Sixth, a Middle Eastern climate environment was applied as a harsh condition.

4.1. Without machine learning (normal usage of the product)

The recommended temperature setting for air-conditioners varies from country to country. In Korea, 26°C indoor room temperature is recommended. In order to compare the effect of RL machine learning, here we set the remote controller to 26°C without a machine learning algorithm and checked the indoor room temperature ($T_{in}(t)$) variation pattern under the Korean climate environment of outdoor temperature ($T_{out}(t)$) and building load ($q_{build}(t)$) change over the course of a day.

We introduced an inverter compressor-type air-conditioner to fine tune the indoor temperature, but the results in Fig. 7 are not very precisely controlled. Searching for other papers' results of different household inverter air-conditioner models does not change this fact [14,15]. The reason for this temperature control pattern is that ordinary HVAC products perform dead band control in order to reduce the switching frequency and increase the operating efficiency of the product [30]. During one day (24 h), as shown in Fig. 7, the maximum of T_{in} was 27.46 and the minimum was 25.00°C. Although the remote controller set temperature was fixed at 26°C, room temperature T_{in} oscillates with a deviation of approximately ±1°C.

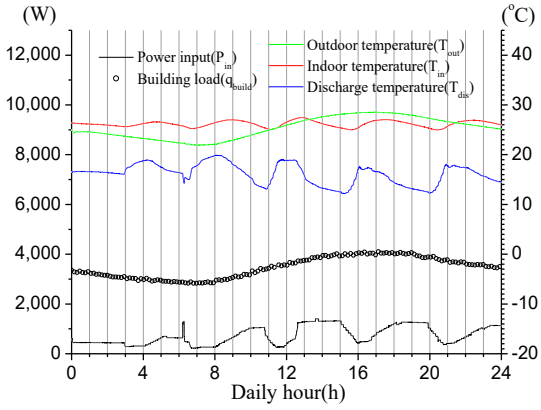


Fig. 7. Normal operation of the air-conditioner with T_{set} = 26°C

4.2. Simple computer thermostat algorithm control

In this case, the behavior of the product was identified by applying a simple thermostat algorithm rather than allowing the product to operate on its own. In Fig. 8(a), if the indoor temperature (T_{in}) was below 26°C, the product was remote controlled by an Arduino LED emitter at the value of 27°C. When T_{in} was over 26°C, the remote control value was set as 26°C. That is, a simple thermostat operation was implemented by computer algorithm. As another case of simple computer thermostat control, in Fig. 8(b), if T_{in} was below 26ºC, the product was remote controlled at the value of 30°C. When T_{in} was over 26°C, the remote control value was set as 22°C immediately.

Compared with Fig. 7, showing the normal operation under the T_{set} = 26°C, Fig. 8(a) of the simple thermostat algorithm shows similar graph patterns with some more fluctuations in indoor temperature (T_{in}), power input (P_{in}), and product discharge temperature (T_{dis}). Peaks in discharge temperature (T_{dis}) near 2, 6, and 10 hours were caused by the abrupt decrease of P_{in}. This abrupt change of P_{in} was due to the T_{set} signal of 27°C. To speculate on the control behavior of the product, we analyzed the point where the 26°C gray baseline meets T_{in}. At the 1.5 hour position, the room temperature (T_{in}) meets the downward 26°C line, and the automatic program changes the T_{set} set point to 27°C, but only slightly reduces power. In practice, the point at which power is drastically reduced is around 1.7 hours where the room temperature is at the local minimum. At 12 and 16 hours, T_{in} declines and meets the 26°C line. But, P_{in} does not decrease abruptly. For this reason, even though we cannot know the exact control design information of the original product, we can infer that the product uses dead band thermostat control.

Figure 8(b) shows the result when we use T_{set} of 22 and 30°C, instead of 26 and 27°C for the simple thermostat control. Because 22 and 30°C of T_{set} are far from our target of 26°C, immediate control is possible regardless of the dead band control of the product. The on and off graph line of the power input (P_{in}) and oscillating indoor temperature (T_{in}) are typical control aspects of a constant speed (or fixed speed) compressor air-conditioner. It is similar with the constant speed air-conditioner result (Fig. 3) of Yoon et al. [14].

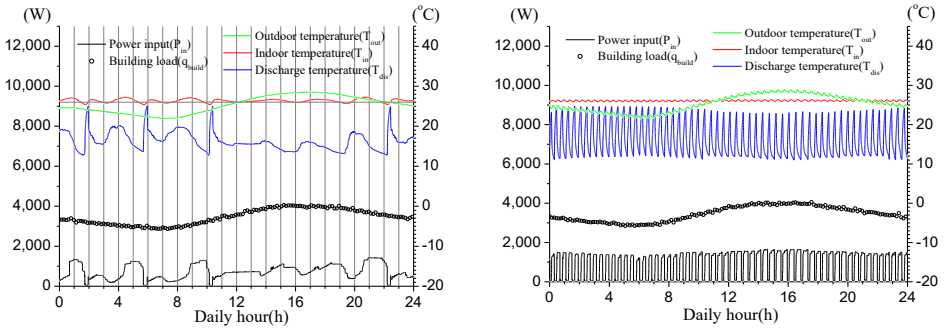


Fig. 8. Simple computer thermostat algorithm of (a) T_{set} = 26°C & 27°C (b) T_{set} = 22°C & 30°C

4.3. With machine learning algorithm (day 1 of RL)

On day 1 of reinforcement learning (RL), the test chamber environment was maintained at a constant outdoor temperature (T_{out}) of 28°C and a building load (q_{build}) of 3 000 W to reduce disturbances, as shown in Fig. 9. Even though the tested air-conditioner is an inverter type, which has typically small adjustment characteristics of power input (fine saw-tooth shape increase or decrease), such as in Figs. 7 and 8(a), in this case, Fig. 9 shows on and off switching characteristics as the indoor temperature was only controlled by the action of T_{set} high (30°C) and low (22°C).

Usually, pure computer RL machine learning such as in Atari games [25,26] takes less than a few hours. But real-world machine learning can take much longer, especially in the thermo-fluid system, which has a slow response time. Fortunately, this real-world air-conditioner RL study "only" took 16 hours to solve the problem. T_{in} in Fig. 9 is stabilized after 16 hours. The graph patterns of air-conditioner discharge temperature (T_{dis}) and power input (P_{in}) are irregular prior to 16 hours, so that sometimes the large time span of power-on duration can be seen (e.g., 9~10 h, 13 h). After 16 hours, P_{in} and T_{dis} show regular graph patterns.

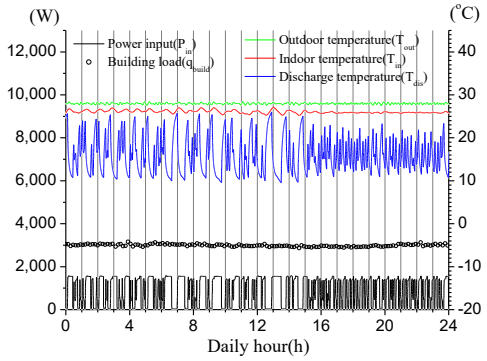


Fig. 9. Day 1 of RL result under the constant environment

An enlarged picture of the indoor temperature (T_{in}) is shown in Fig. 10. The red portions of the graph reflect the region where the reward +1 pt is taken. If T_{in} escapes the (26±0.5)°C range, each episode of training ends. For the restart of the training, the program algorithm forces the temperature down or up to reset T_{in} within (26±0.2)°C. The obtained scores at each episode are shown in Fig. 11. In this study, approximately one episode matches one hour before problem stabilization (16 h). It shows fluctuation from 2 to 25 scores. Even though Fig. 11 has no score information after 17 hours, episode 18 recorded 1,518 pts at the moment near the start time of day 4 (Fig. 15) when the environment changes abruptly to a harsh Middle Eastern climate condition.

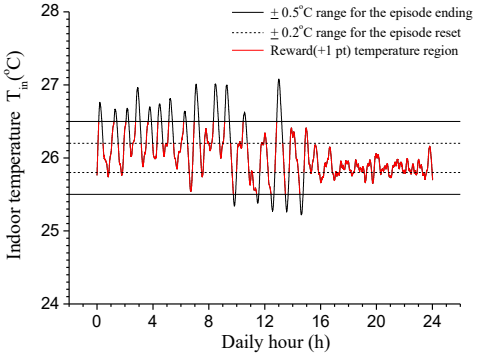


Fig. 10. Enlargement of the indoor temperature (T_{in}) graph during day 1

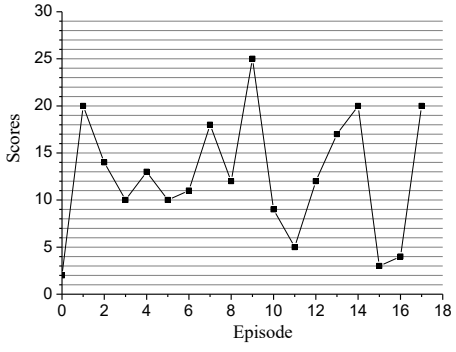


Fig. 11. Scores at each episodes during day 1

4.4. With machine learning algorithm (day 2 of RL)

On day 2 of RL, we repeated the same environment of constant T_{out} (28°C) and q_{build} (3 000 W) as day 1 of RL. Figure 12 shows a very well-trained and stabilized situation, and episode 18 continued during day 2 of RL. One thing to mention here is that throughout this work, there is a slight micro-vibration of the outdoor temperature (T_{out}) as a whole. This phenomenon is caused by the vibration of the condenser heat from the outdoor unit as the air-conditioner is turned on and off. Therefore, the fluctuation time matches between T_{out} and P_{in}. Normally, there are no such temperature interferences because air-conditioners are operated in a steady state on mode when products are tested according to ISO standard.

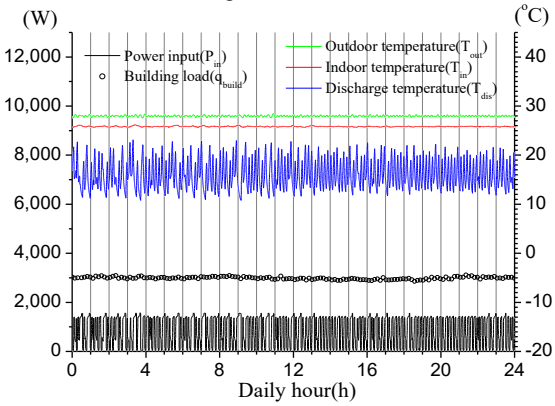


Fig. 12. 2nd day of RL result under the constant environment

4.5. With machine learning algorithm (day 3 of RL)

On day 3 of RL, a Korean summer climate (Fig. 3) was applied to the outdoor temperature ($T_{out}(t)$) and building cooling load ($q_{build}(t)$) as disturbance variations. Some other papers [2–4] have used these kinds of thermal variation as LSTM periodic state inputs, but in this study we did not use them as state inputs. Therefore, $T_{out}(t)$ and $q_{build}(t)$ variables act as unknown disturbances. From Fig. 13, $T_{out}(t)$ and $q_{build}(t)$ have minimum values near 6–7 a.m. and maximum values near 3–4 p.m. Indoor temperature (T_{in}) seems to converge well without change. However, the discharge temperature (T_{dis}) and power input (P_{in}) exhibit some different aspects with the constant environment case of Fig. 12. P_{in} near the maximum variation (3–4 p.m.) shows more on mode time span rather than minimum variation interval (6–7 a.m.). Also by the same reason, T_{dis} records a lower discharge temperature near 3–4 p.m. than 6–7 a.m. This means RL machine learning DNNs are adapted to the environment.

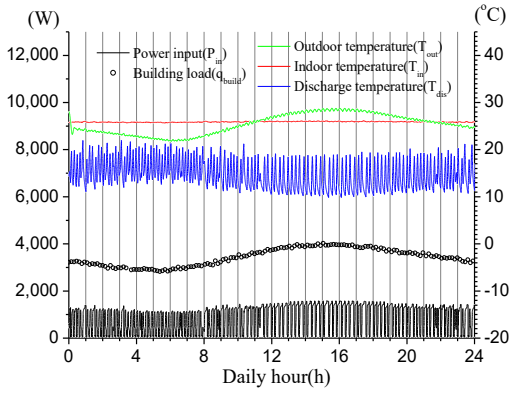


Fig. 13. Day 3 of RL result under Korean summer climate

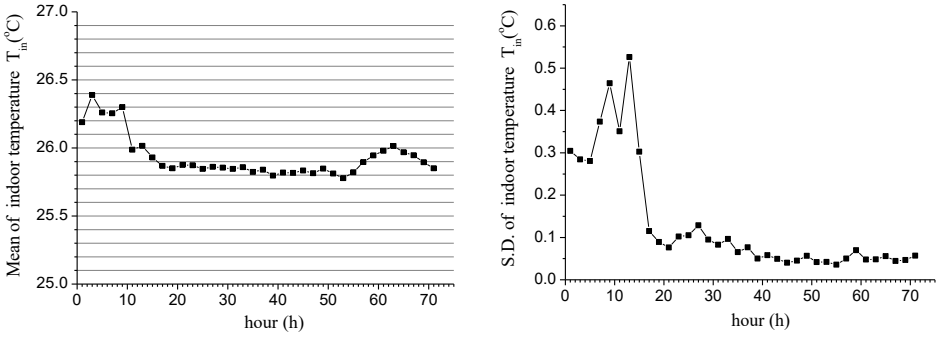


Fig. 14. Mean (left) and S.D. (right) of indoor temperature (T_{in}) during total three days at every 2 hour

The quality of T_{in} data during over the three days of RL was compared in Fig. 14. Because the training was stabilized after 16 hours of day 1, the mean value and standard deviation of T_{in} also show stabilization after 16 hours. However, the mean value shows one high peak at 64 hours (= 2 days and 16 h). This peak is due to environmental variations (T_{out} and q_{build}) during day 3 of RL. In any event, T_{in} exhibits a high accuracy when comparing the RL case of Figs. 12 and 13 with the normal usage (T_{set} = 26°C) case of Fig. 7.

4.6. With machine learning algorithm (day 4 of RL)

In this section, the environmental conditions of the Middle East were applied successively after the Korean environment, since summer temperatures in the Middle East are the harshest on the planet, which can act as big environmental disturbances in this study. In Fig. 15, because the start value of $q_{build}(t)$ abruptly changed from the Korean climate ending $q_{build}(t)$ value 3 250 W to the Middle East start value of 4 250 W, it shows disturbed T_{in} temperature near the start time. Therefore, we obtained a renewal of episode number by 19 at this moment. Episode 18 ended with the score of 1,518 pts at this position.

During the day time, there is a time interval in which power input (P_{in}) shows only an on mode without off mode. This means that the tested air-conditioner cooling capacity is insufficient to cover the building load (q_{build}). Notably from 13.5 hours to 19.8 hours, the indoor temperature (T_{in}) is over 26.5°C, even with the full operation of the product. Because the specification of the tested product (Table 2) is for moderate temperature condition (ISO T1 condition), the high temperature condition (ISO T3 condition) of the Middle East cannot be applied to this product. Nevertheless, this study conducted tests in the Middle East temperature condition to identify the limitations of RL machine learning due to harsh environmental conditions. Results show that even though the product capacity is insufficient, the trained deep neural network (DNN) continues to send 22°C of signal to cool the room.

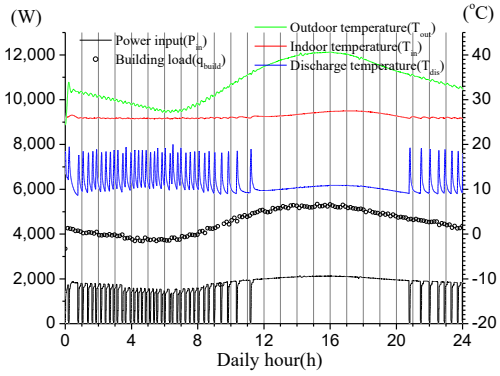


Fig. 15. Day 4 of RL results under the Middle Eastern summer climate

Table 3. Temperature mean, S.D., minimum, maximum values and power consumptions

Case	Mean of T_{in}	S.D. of T_{in}	Min. of T_{in}	Max. of T_{in}	P_{24h} (kWh)
Normal usage of T_{set} =26ºC (Fig. 7)	26.19	0.600	25.00	27.46	17.63
Simple thermostat of T_{set} =26ºC, 27ºC (Fig. 8(a))	26.39	0.431	25.34	27.29	17.52
Simple thermostat of T_{set} =22ºC, 30ºC (Fig. 8(b))	26.09	0.163	25.78	26.37	21.74
Day 1 of RL (Fig. 9), no climate disturbance	26.07	0.362	25.22	27.08	20.39
Day 2 of RL (Fig. 12), no climate disturbance	25.83	0.081	25.65	26.18	19.33
Day 3 of RL, Korean climate (Fig. 13)	25.90	0.088	25.66	26.12	20.23
Day 4 of RL, Middle Eastern climate (Fig. 15)	26.29	0.551	25.69	27.51	38.99

Finally, the temperature control qualities and power consumptions for each day are summarized in Table 3. The mean value and standard deviation of the T_{in} temperature show good results on day 2 and day 3 of RL. Similarly, the minimum and maximum deviations from the target temperature (26°C) also show minimum errors on day 2 and day 3 of RL. It shows that the application of DQN reinforcement learning in this study can surpass the temperature control ability of the product in normal usage or simple thermostat control cases. In terms of power consumption during one day (P_{24h}), this RL study case (about 20 kWh) is not energy efficient than normal usage case (17.63 kWh). This is because the product was machine-learned only using two action control temperatures of 22 and 30°C to avoid the dead band control zone inherent in the original air-conditioner product and to simplify the RL problem.

5. Conclusion

Reinforcement learning (RL) using a DQN (Deep Q-learning Network) method was applied to household inverter air-conditioner temperature precision control. Three state variables of $[(T_{in}(t) -26), dT_{in}/dt, T_{dis}(t)]$ and two actions of 22, 30°C remote control are used in the DQN model. The practical application of DQN RL to home appliances is seldom found in papers. In this study, after 16 hours of training, we obtained a stabilized indoor temperature close to 26°C. Environmental disturbances were applied during the training using Korean and Middle Eastern summer climates. The Korean climate conditions, which can be covered by product capabilities, showed a more stable and accurate temperature control pattern. Comparing with the normal usage result of T_{set}=26°C (T_{mean}=26.19°C, S.D.=0.600°C, T_{min}=25.00°C, T_{max}=27.46°C) or computer simple thermostat control of T_{set}=22 and 30°C (T_{mean}=26.09°C, S.D.=0.163°C, T_{min}=25.78°C, T_{max}=26.37°C), this study's DQN reinforcement learning recorded more accurate temperature control results (T_{mean}=25.90°C, S.D.= 0.088°C, T_{min}=25.66°C, T_{max}=26.12°C).

Acknowledgement

The authors highly appreciate the financial support from Korea Testing Laboratory (Project No. CBS1826).

References

[1] D. L. Marino, K. Amarasinghe, and M. Manic, "Building energy load forecasting using deep neural networks," in Proceedings of the IEEE Industrial Electronics Society (IECON), 2016, pp. 7046–7051.

[2] A. Rahman, V. Srikumar, and A. D. Smith, "Predicting electricity consumption for commercial and residential buildings using deep recurrent neural networks," vol. 212, Applied Energy, 2018, pp. 372–385.

[3] A. S. Ahmad, M. Y. Hassan, M. P. Abdullah, H. A. Rahman, F. Hussin, H. Abdullah, and R. Saidur, "A review on applications of ANN and SVM for building electrical energy consumption forecasting," vol 33, Renewable and Sustainable Energy Reviews, 2014, pp. 102–109.

[4] M. Manivannan, B. Najafi, and F. Rinaldi, "Machine learning-based short-term prediction of air-conditioning load through smart meter analytics," vol. 10, Energies, 2017, pp. 1905.

[5] S. K. Jeong, C. H. Han, L. Hua, and W. K. Wibowo, "Systematic design of membership functions for fuzzy logic control of variable speed refrigeration system," vol. 142, Applied Thermal Engineering, 2018, pp. 303–310.

[6] H. Yan, Y. Xia, X. Xu, and S. Deng, "Inherent operational characteristics aided fuzzy logic controller for a variable speed direct expansion air conditioning system for simultaneous indoor air temperature and humidity control," vol. 158, Energy and Buildings, 2018, pp. 558–568.

[7] Z. Li, X. Xu, S. Deng, and D. Pan, "A novel neural network aided fuzzy logic controller for a variable speed (VS) direct expansion (DX) air conditioning (A/C) system," vol. 78, Applied Thermal Engineering, 2015, pp. 9–23.

[8] X. Xu, Z. Zhong, S. Deng, and X. Zhang, "A review on temperature and humidity control methods focusing on air-conditioning equipment and control algorithms applied in small-to-medium-sized buildings," vol. 162, Energy and Buildings, 2018, pp. 163–176.

[9] A. Kusiak, and G. Xu, "Modeling and optimization of HVAC systems using a dynamic neural network," vol. 42, Energy, 2012, pp. 241–250.

[10] P. V. Fazenda, K. Veeramachaneni, P. Lima, and U-M. O'Reilly, "Using reinforcement learning to optimize occupant comfort and energy usage in HVAC systems," vol. 6, J. of Ambient Intelligence and Smart Environments, 2014, pp. 675–690.

[11] K. Yan, C. Zhong, Z. Ji, and J. Huang, "Semi-supervised learning for early detection and diagnosis of various air handling unit faults," vol. 181, Energy and Buildings, 2018, pp. 75–83.

[12] W. Vallandares, M. Galindo, J. Gutierrez, W. C. Wu, K. K. Liao, J. C. Liao, K. C. Lu, and C. C. Wang, "Energy optimization associated with thermal comfort and indoor air control via a deep reinforcement learning algorithm," vol. 155, Building and Environment, 2019, pp. 105–117.

[13] C. C. Cheng, and D. Lee, "Artificial intelligence-assisted heating ventilation and air conditioning control and the unmet demand for sensors: Part 1. Problem formulation and the hypothesis," vol. 19, Sensors, 2019, pp. 1131.

[14] M. S. Yoon, J. Lim, T. S. Qahtani, and Y. Nam, "Experimental study on comparison of energy consumption between constant and variable speed air-conditioners in two different climates," in Proceedings of the Asian Conference on Refrigeration and Air-conditioning (ACRA), 2018, E342.

[15] J. Lim, M. S. Yoon, T. S. Qahtani, and Y. Nam, "Feasibility study on variable-speed air conditioner under hot climate based on real-scale experiment and energy simulation," vol. 12, Energies, 2019, pp. 1489.

[16] R. S. Sutton, and A. G. Barto, Reinforcement learning: An introduction (2nd edition). MIT Press, Cambridge, MA, 2018.

[17] R. Bellman, Dynamic programming. Princeton University Press, 1957.

[18] C. J. Watkins, Learning from delayed rewards, PhD thesis, King's College, Cambridge, England, 1989.

[19] K. Fukushima, "Neocognitron: A self-organizing neural network model for a mechanism of pattern recognition unaffected by shift in position," vol. 36, Biol. Cybernetics, 1980, pp. 193–202.

[20] O. Russakovsky, J. Deng, H. Su, J. Krause, S. Satheesh, S. Ma, Z. Huang, A. Karpathy, A. Khosla, M. Bernstein, A. C. Berg, and L. Fei-Fei, "ImageNet large scale visual recognition challenge," vol. 115, Int. J. of Computer Vision, 2015, pp. 211–252.

[21] I. J. Goodfellow, J. Pouget-Abadie, M. Mirza, B. Xu, D. Warde-Farley, S. Ozair, A. Courville, and Y. Bengio, "Generative Adversarial Nets," vol. 27, Advances in NIPS, 2014, pp. 2672–2680.

[22] D. E. Rumelhart, G. E. Hinton, and R. J. Williams, "Learning representations by back propagating errors," vol. 323, Nature, 1986, pp. 533–536.

[23] H. Sak, A. W. Senior, and F. Beaufays, "Long short-term memory recurrent neural network architectures for large scale acoustic modeling," in Proceedings of Interspeech, 2014, pp. 338-342.

[24] H. Sak, A. W. Senior, K. Rao, and F. Beaufays, "Fast and accurate recurrent neural network acoustic models for speech recognition," in Proceedings of Interspeech, 2015, pp. 1468-1472.

[25] V. Mnih, K. Kavukcuoglu, D. Silver, A. Graves, I. Antonoglou, D. Wierstra, and M. Riedmiller, "Playing atari with deep reinforcement learning," arXiv preprint arXiv:1312.5602, 2013.

[26] I. A. Hosu, and T. Rebedea, "Playing atari games with deep reinforcement learning and human checkpoint replay," arXiv preprint arXiv:1607.05077, 2016.

[27] ISO 5151, "Non-ducted air conditioners and heat pumps–Testing and rating for performance," International Organization for Standardization, Geneva, Switzerland, 2017.

[28] ASHRAE 116, "Methods of testing for rating seasonal efficiency of unitary air-conditioners and heat pumps," American Society of Heating, Refrigerating and Air-conditioning Engineers, Atlanta, GA, USA, 2010.

[29] M. Abadi, et. al, "TensorFlow: Large-scale machine learning on heterogeneous systems," 2015, https://www.tensorflow.org

[30] A. Afram, and F. J. Sharifi, "Effects of dead-band and set-point settings of on/off controllers on the energy consumption and equipment switching frequency of a residential HVAC system," vol. 47, J. of Process Control, 2016, pp. 161–174.

13th IEA Heat Pump Conference
April 26-29, 2021 Jeju, Korea

The role of electric heat pumps in the decarbonisation of the heating sector in Europe

Martin Forsén, Laure Meljac

NIBE Energy Systems, Post box 14, SE-28521 Markaryd, Sweden

Abstract

Mitigation of greenhouse gases, dependency of fossil fuel and security of energy supply are on top of the agenda in all energy discussions. This sets the focus on energy efficiency and the use of renewable energy in all sectors. The European Union has set ambitious targets to improve energy efficiency, increase the use of renewable energy and reduce greenhouse gas emissions by 2030. Up until recent years most of the focus has been on the electricity and transport sector. The building sector has largely been overlooked. However as approximately 40% of the total energy use in Europe is related to buildings, this sector has one of the largest potential for reducing greenhouse gas emissions. The objective of this paper is to present a general methodology on how to determine greenhouse gas emissions related to different sources of heating and to what extent a wide introduction of electric heat pumps will contribute to a decarbonisation of the heating sector. The methodology is additionally used to calculate primary energy savings as well as to give an indication of potential operating cost savings by use of available statistics for different energy sources. The results show that electric heat pumps has a significant potential to improve energy efficiency (53 – 81%) and reduce greenhouse gas emissions (57 – 99%) while replacing old inefficient boilers in Europe.

© HPC2020.
Selection and/or peer-review under responsibility of the organizers of the 13th IEA Heat Pump Conference 2020.

Keywords: heat pump; decarbonise; greenhouse gas emissions; primary energy; final energy; primary energy factor;

1. Introduction

This paper explains the development of a methodology to estimate the potential for a reduction of green housegas (GHG) emissions when heat pumps are replacing conventional heating systems. The main objective of this paper is to make an assessment on GHG-emission reduction and primary energy savings that may be accomplished while replacing old fossil boilers by electric heat pumps. Other types of heat pumps such as thermally driven and fuel engine driven heat pumps are commercially available but not included in the study that serves as a basis for this paper. At local and regional level emission reduction of particles, SOx and NOx may be just as important drivers to phase out the use of old boilers. The model used for all calculations allow for the use of different assumptions of efficiency at appliance level as well as the generation of electricity on national level. The GHG-emission savings are calculated and expressed in terms of carbon dioxide equivalents (kg CO_2eq). The calculations are performed by use of emission factors (ef_{xx} [kg CO_2eq/kWh]) for different energy carriers and national emission factors for the generation of electricity. The example calculations of primary energy savings are, where existing, based on official primary energy factors for different energy carriers.

2. On how to compare energy efficiency of different heating systems

When we are to compare the energy efficiency of heating systems, we need to realise that the result will depend on the boundaries for the system in view. Different stake holders would set the boundaries from different perspectives. The end user of a heating system would naturally define the efficiency as the useful heat in

relation to the amount of energy that needs to be purchased. This is however not sufficient when energy systems are studied from a broader perspective, as energy losses and emissions from different types of heating systems appear at different stages in the energy chain. An electric boiler might seem very efficient from the perspective of the end consumer, but if we take into account for distribution losses and losses at point of electricity generation and even further up the energy chain, it is evident that electric heating is not as efficient as the customer might perceive. In order to obtain an impartial comparison of the energy efficiency and total emissions for different types of systems, it is essential to extend the system boundary beyond the external wall of the heated building.

If we start with the actual energy needed to heat a building and add all the losses in the heating appliance, distribution and if applicable power generation as well as energy use for extraction, refinement and transportation of fuels we end up at a final value that gives a better representation of the energy needed to supply one unit of heating. The total amount of energy including the energy content of the energy carrier itself and all the energy required for extraction, refinement, transformation and distribution is often referred to as primary energy. An assessment of primary energy use is often required in order to enable a fair comparison of different heating systems using different energy carriers. In order to simplify a primary energy assessment, it is common to use a set of precalculated primary energy factors (PEF) for different energy carriers. The primary energy use is given by the purchased energy multiplied by the PEF for the energy carrier in use. The European standard EN 15603 defines a methodology, including a few alternatives, on how to calculate PEF.

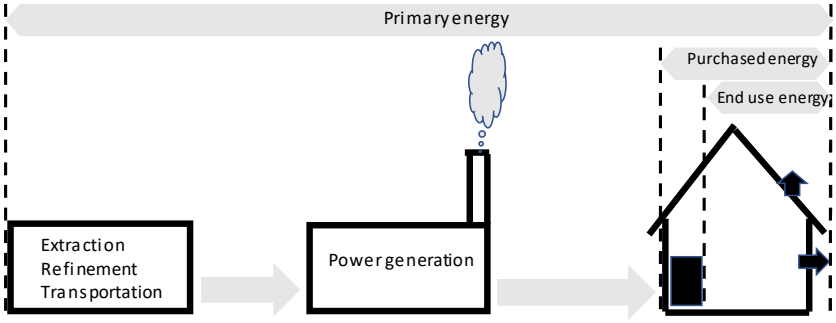


Figure 1 System boundaries for primary energy definition

2.1 The use of primary energy factors, PEF

Within the European Union there are several policy instruments e.g. the Energy Efficiency Directive and the Energy Performance of Buildings Directive [1, 2] that requires the use of PEF for different energy carriers. The default value for the primary energy factor for electricity for all Member States has recently been reviewed and changed from 2,5 to 2,1. The revision was based on a study initiated by the European Commission and finalised 2016 [3]. The study presents 4 principal methods that may be used to calculate the PEF and elaborate pros and cons for each method. It is evident that the applicable system boundaries and time frames chosen for the calculation of the PEF will vary from country to country and thus result in different values. It is however vital that the calculations of the PEFs are made in a transparent manner avoiding arbitrary assumptions chosen to fit a predefined purpose. As this study is focusing on the transformation of the heating in buildings, we have chosen to use the PEFs that have been established for use in the building codes in different countries.

3. Calculation of primary energy savings

While assessing the potential primary energy savings that can be achieved by replacing conventional boilers with electric heat pumps we need to take into account for the efficiency of the appliances we are addressing as well as the primary energy factors for electricity and the energy carrier of the system we are considering to

replace. Even though the model we are describing in this paper is generic and may be used for any type of heating system, the derivation is given for the example of replacement of an existing gas boiler.

The primary energy use of a gas boiler may be expressed as follows;

$$E_{Prim\ Gas} = \frac{Q_H \times PEF_{gas}}{\eta_{gas}} \quad (1)$$

Where;

$E_{Prim\ Gas} = Primary\ \ energy\ \ use\ \ of\ \ a\ gas\ boiler$

$Q_H = Annual\ \ heating\ \ demand$

$PEF_{gas} = Primary\ \ energy\ \ factor\ \ for\ \ gas$

$\eta_{gas} = Annual\ \ efficiency\ \ \ \ of\ \ the\ gas\ boiler$

The primary energy use of an electric heat pump may be expressed as follows;

$$E_{Prim\ HP} = \frac{Q_H \times PEF_{el}}{SPF} \quad (2)$$

Where;

$E_{Prim\ HP} = Primary\ \ energy\ \ use\ \ of\ \ the\ heat\ \ pump$

$Q_H = Annual\ \ heating\ \ \ demand$

$PEF_{el} = Primary\ \ energy\ \ factor\ \ for\ \ electricity$

$SPF = Seasonal\ \ performance\ \ factor\ \ of\ \ the\ heat\ \ pump$

By use of equation 1 and 2 we may now deduce the relative primary energy savings.

$$\frac{\frac{Q_H \times PEF_{gas}}{\eta_{gas}} - \frac{Q_H \times PEF_{el}}{SPF}}{\frac{Q_H \times PEF_{gas}}{\eta_{gas}}} = \frac{\frac{PEF_{gas}}{\eta_{gas}}\left(1 - \frac{PEF_{el}\ \eta_{gas}}{PEF_{gas}\ SPF}\right)}{\frac{PEF_{gas}}{\eta_{gas}}} \quad (3)$$

Thus, the relative primary energy savings are given by the relation between the primary energy factors and the relation between the annual efficiencies of the appliances.

$$Relative\ \ \ primary\ \ energy\ \ savings = \left(1 - \frac{PEF_{el}}{PEF_{gas}}\frac{\eta_{gas}}{SPF}\right) \quad (4)$$

Equation (4) is in its form general and may be used to calculate the relative primary energy savings that may be achieved while replacing any type of heating system with a heat pump. In order to make the calculation for replacement of oil or solid coal the primary energy factor for gas (PEF_{gas}) and the annual boiler efficiency (η_{gas}) shall be replaced by the respective constant for the relevant system.

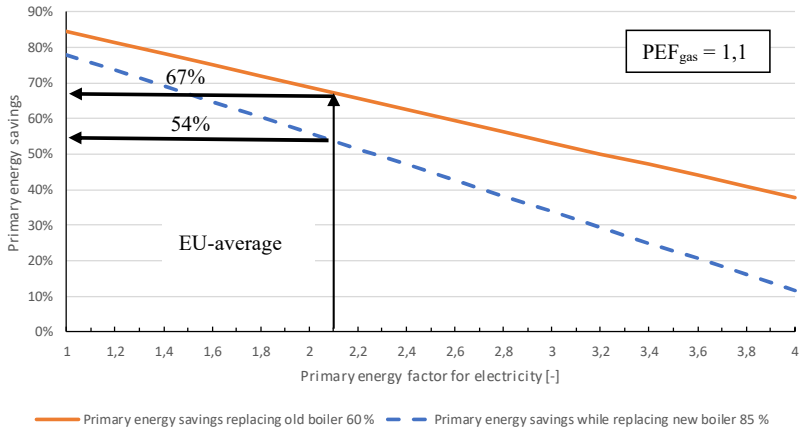


Figure 2 Primary energy savings - heat pump replacing boiler

Figure 2 illustrates the primary energy savings that will be achieved by replacing boilers with an electric heat pump operating at an annual SPF of 3,5. The European Union has established that the average of European electricity generation corresponds to a primary energy factor of 2,1. This value may be used by the Member States to assess national improvements of energy efficiency. However, Member States are free to establish their own primary energy factor based on the national mix of the generation of electricity. The ongoing transition of the electricity sector characterised by an increasing share of renewables is improving the efficiency over time and thus leading to a lower primary energy factor. These improvements enhance the primary energy savings further.

Table 1 below depicts the calculated primary energy savings that will be achieved for 9 different Member States. The calculations are based on the primary energy factors for electricity that has been established in each country to be used in the building codes.

*Table 1 Primary energy savings; old boiler (60%), new boiler (85%), * PEF for Sweden = 1,85 is to be confirmed during 2020*

Country	PEF$_{elec}$	Primary energy savings, old boiler	Primary energy savings, new boiler
France	2,58	60%	43%
Germany	1,8	72%	60%
The Netherlands	2,56	60%	43%
The United Kingdom	1,5	77%	67%
EU-average	2,1	67%	54%
Czech	3,0	53%	34%
Slovakia	2,2	66%	51%
Poland	3,0	53%	34%
Finland	1,2	81%	74%
Sweden*	1,85	71%	59%

The results reveal that significant energy savings may be achieved by replacement of old inefficient boilers (53 – 81%). Furthermore, it can be seen that a replacement of more efficient boilers contributes to an improvement in the heating sector (34 – 74%).

4. Calculation of reduction of greenhouse gas (GHG) emissions

While addressing the greenhouse gas emissions, expressed in the form of CO_2-eqvivalents, we may in an analogous manner derive a general equation as depicted below.

The GHG-emissions generated by a gas boiler may be expressed as follows;

$$GHG_{gas} = \frac{Q_H \times e_{gas}}{\eta_{gas}} \tag{5}$$

Where;

$GHG_{gas} = green\ \ house\ \ gas\ \ emissions\ \ \ \ generated\ \ \ \ by\ a\ gas\ \ boiler$

$Q_H = Annual\ \ heating\ \ \ \ demand$

$e_{gas} = Emission\ \ \ \ factor\ \ \ \ for\ \ gas$

$\eta_{gas} = Annual\ \ efficiency\ \ \ \ \ \ of\ \ the\ gas\ \ boiler$

The GHG-emissions generated by a heat pump may be expressed as follows;

$$GHG_{HP} = \frac{Q_H \times e_{elec}}{SPF} \tag{6}$$

Where;

$GHG_{HP} = green\ \ house\ \ gas\ \ emissio\ \ ns\ \ generated\ \ \ \ by\ a\ heat\ \ pump$

$Q_H = Annual\ \ heating\ \ \ \ demand$

$e_{elec} = Emission\ \ \ \ factor\ \ \ \ for\ \ electricity$

$SPF = Seasonal\ \ \ \ performance\ \ \ \ factor\ \ \ \ of\ \ the\ heat\ \ pump$

By use of equation 5 and 6 we may deduce the relative reduction of greenhouse gases that may be achieved while replacing a gas boiler with a heat pump.

$$\frac{GHG_{gas} - GHG_{HP}}{GHG_{gas}} = \frac{\frac{\cancel{Q_H} \times e_{gas}}{\eta_{gas}} - \frac{\cancel{Q_H} \times e_{elec}}{SPF}}{\frac{\cancel{Q_H} \times e_{gas}}{\eta_{gas}}} = \frac{\frac{\cancel{e_{gas}}}{\cancel{\eta_{gas}}}\left(1 - \frac{e_{elec}}{e_{gas}}\frac{\eta_{gas}}{SPF}\right)}{\frac{\cancel{e_{gas}}}{\cancel{\eta_{gas}}}} \tag{7}$$

Thus, the relative reduction of greenhouse gases is given by the relation between the primary energy factors and the relation between the annual efficiencies of the appliances.

$$Relative\ \ \ \ GHG\ emission\ \ \ \ savings\ \ \ = \left(1 - \frac{e_{elec}}{e_{gas}}\frac{\eta_{gas}}{SPF}\right) \tag{8}$$

Figure 3 below illustrates the reduction of greenhouse gas emissions that will be achieved by a replacement of gas boilers with electric heat pumps (SPF = 3,5) as a function of the emission factor for the generation of electricity. Results show that an electric heat pump that replace a gas boiler will contribute to a reduction of GHG-emission by the order of 65 – 75% if we base the calculation on the European average emission factor for generation of electricity (295,8 gCO_{2eq}/kWh_{elec}) [4].

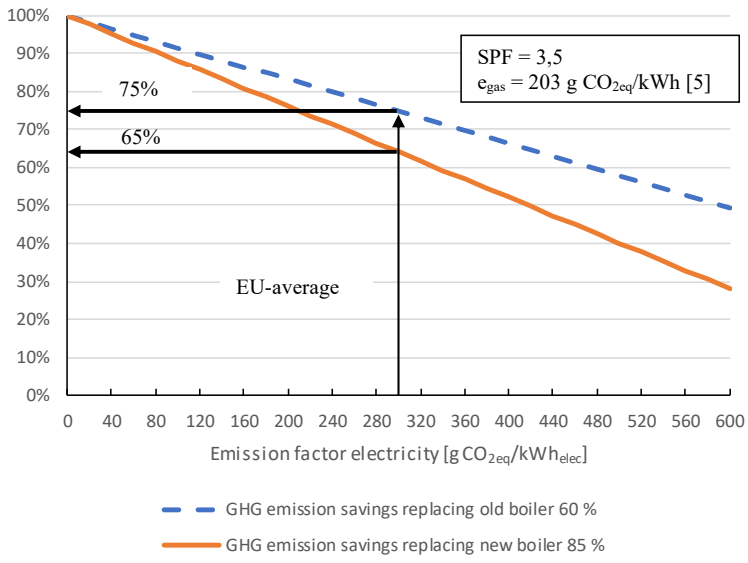


Figure 3 Reduction of greenhouse gases

Figure 3 visualise the impact of the carbon intensity of the electric grid. The reduction of greenhouse gas emissions by retrofitting old boilers with electric heat pumps are significant in all European countries, but varies a great extent depending on the carbon content of electricity. Poland is one of the countries that has one of the highest emission factors for electricity in Europe (773,3 gCO_2/kWh_{elec}) [4] show the lowest potential, but in this case it might be relevant to perform the assessment based on the assumption that the heat pump replace an old coal-fired boiler which is still used to a large extent. In this case a heat pump retrofit will decrease the greenhouse gas emissions by the magnitude of 60% and the benefits will increase over time as the greening of the grid will come into effect. Table 2 below show the potential of reduction of GHG-emissions in 9 European countries, based on the latest available data of the carbon intensity in the national grid. The calculations are based on replacements of gas boilers in the gas dominated countries (France, Germany, The Netherlands, The United Kingdom and EU-average) and a replacement of coal boilers in Czech, Slovakia and Poland. As none of these systems are common in Finland nor Sweden the calculations are based on oil boilers in this case.

Table 2 Reduction of greenhouse gases; old boiler (60%), new boiler (85%), (e_{elec}= emission factor for electricity 2016 [4], e_{gas}= 203 g CO_{2eq}/kWh, e_{gcoal}= 334 g CO_{2eq}/kWh, e_{oil}= 267 g CO_{2eq}/kWh [5])

Country	Energy source being replaced	e_{elec} [g CO_{2eq} /kWh_{elec}]*	GHG-emission reduction, old boiler	GHG-emission reduction, new boil
France	Gas	58,5	95%	93%
Germany	Gas	440,8	63%	47%
The Netherlands	Gas	505,2	57%	40%
The United Kingdom	Gas	281,1	76%	66%
EU-average	Gas	295,8	75%	65%
Czech	Coal	512,7	74%	63%
Slovakia	Coal	132,3	93%	90%
Poland	Coal	773,3	60%	44%
Finland	Oil	112,8	93%	90%
Sweden	Oil	13,3	99%	99%

Table 2 reveal the significant emission reduction that may be achieved by a replacement of boilers with electric heat pumps. Improvements in heat pump technology and the phase out of carbon intensive electricity generation will increase the benefits even further with time. The current trend in the electricity sector is positive and is expected to continue at an even higher pace in several countries. Figure 3 depicts the evolvement of the

national emission factor for the generation of electricity [4]. In 2016 the share of renewable electricity reached 29 % in Europe. The share of renewable electricity is by now higher than coal and lignite. The transition from fossil fuels to renewable electricity in conjunction with increased efficiency has led to a decrease of the emission factor of 43 % between 1990 and 2016.

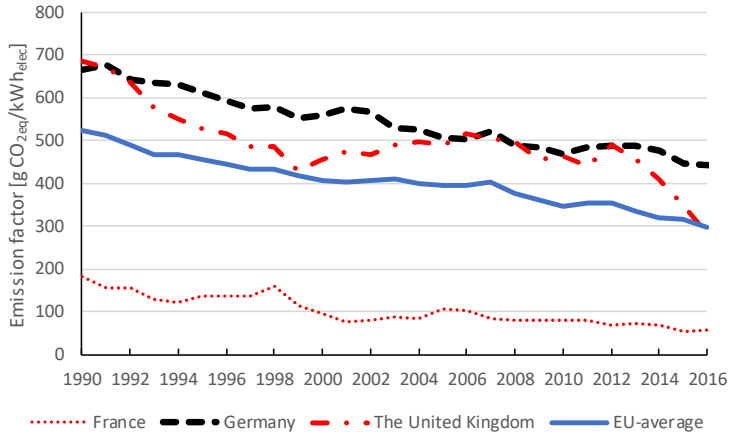


Figure 4 Development of the emission factor for electricity generation 1990 – 2016 [4]

5. Economical aspects

In view of the Paris agreement and binding European targets it is evident that there is an urgent need to transform the heating sector. Up until recently there has been a strong focus on how to decarbonise electricity and transport. The heating and cooling sector has so far not attracted the attention it deserves and requires, but changes are on their way. The European Directive on energy performance of buildings (EPBD) sets a requirement that all new buildings within the European Union need to meet a "nearly zero energy building" definition by 1 January 2021. The member states of the European Union are presently at the point of re-defining their building codes to meet this requirement. The EPBD is expected to serve sufficiently for new construction but as this will only address a minor fraction of the energy use of the whole building stock it is essential to implement comprehensive renovation programs. The European Commission published a "green deal" communication in December 2019 [6] which states that the European Union and its Member States should engage in a "renovation wave". The European Union will enforce the legislation related to the energy performance of buildings that will start with an assessment of the national long-term renovation strategies in 2020. The annual renovation rate of the building stock varies in between the Member States from 0,4 – 1,2 %. This rate will need to at least double in order to reach the energy efficiency and climate targets [6]. Several Member States are aware of the significant benefits that are offered by heat pumps but the economical incentives for end consumers to make a shift differ greatly between the Member States.

The relative savings of the operational costs that may be achieved by a replacement of an existing boiler with an electric heat pump is largely determined by the energy price ratio between electricity and the energy carrier to be replaced. In analogy with the expressions for primary energy savings and reduction of greenhouse gases the potential annual savings of the operational costs may be expressed as;

$$Relative\ \ savings\ \ of\ annual\ \ operation\ \ costs\ \ = \left(1 - \frac{Price_{elec}}{Price_{gas}} \frac{\eta_{gas}}{SPF}\right) \tag{9}$$

Where;

$$Price_{elec} = Price\ of\ electricity \quad \left[\frac{euro}{kWh}\right]$$

$$Price_{elec} = Price\ of\ gas \left[\frac{euro}{kWh}\right]$$

The quota between the energy prices for electricity and the relevant energy carrier we are comparing with constitute the previously mentioned energy price ratio. By use of equation (9) we may draw a chart of the potential savings of the annual operational costs as a function of the energy price ratio.

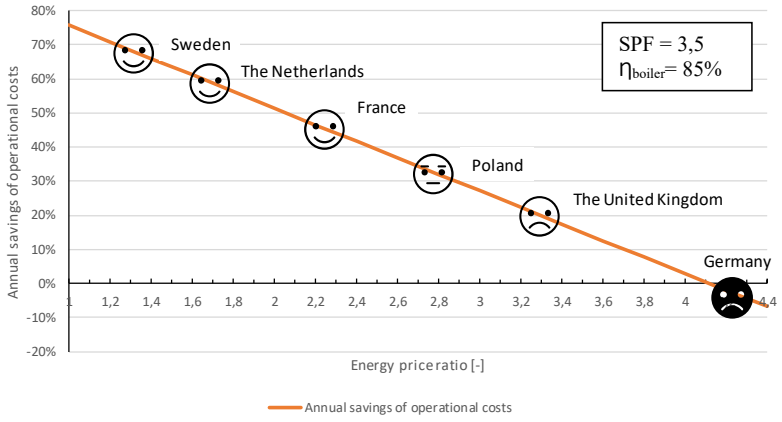


Figure 5 Annual savings of operational costs

Figure 5 depicts the potential annual operational cost savings that may be achieved by a heat pump compared to a modern boiler while taking into account for relevant energy price ratios 2018 [7] on a few selected markets. As these calculations are based on average energy prices and rough estimations on annual efficiencies the results may only be seen as an indication of the level the economic attractiveness of heat pumps. In reality substantial differences may prevail both in terms of energy prices and efficiencies. It is however evident that the low energy price ratio for Sweden has served as the single most important economic driver for the development of the Swedish heat pump market. As of today, heat pumps are used in more 50% of the single-family houses and the use of heating oil that for decades was the dominant source of heating is almost entirely abandoned. The low energy price ratio in Sweden is to a large extent the result of the introduction of a carbon tax 1991. On the other side of the scale the German heat pump market is suffering from high energy price ratios partly because of the energy price policy induced the “energy turnaround” (energiewende) that introduced additional taxes on electricity in order to finance the development of renewable electricity. Given the good example of Sweden it is evident that some sort of progressive energy price policy may play a very important role in order to stimulate the transformation of the heating sector. The energy price policy may as in Sweden be in the form of a carbon tax or as mentioned in EU Green Deal Communication [6] an inclusion of the heating sector into the emission trading system.

References

[1] Energy Efficiency Directive, European Directive (EU) 2018/2002 of the European Parliament and of the Council of 11 December 2018.
[2] Energy Performance of Buildings Directive, DIRECTIVE (EU) 2018/844 of the European Parliament and of the Council of 30 May 2018.
[3] Final report - Evaluation of primary energy factor calculation options for electricity, A. Esser, F. Sensfuss, 2016.
[4] Overview of electricity production and use in Europe, Indicator Assessment, European Environmental Agency, 2019.
[5] 2019 Government Greenhouse Gas Conversion Factors For Company Reporting, Methodology Paper for Emission Factors Final Report, Department for Business, Energy & Industrial Strategy, United Kingdom.
[6] European Commission, Communication on The European Green Deal, 2019,
[7] European Heat Pump Market and Statistics report 2019, T. Nowak, P. Westring, EHPA 2019.

13th IEA Heat Pump Conference
April 26-29, 2021 Jeju, Korea

Lubrication management of a reversible compressor-expander-unit in a combined HP-ORC-plant

Daniel Steger[a*], Markus Zwiefler[a], Eberhard Schlücker[a]

[a]Institute of Process Machinery and Systems Engineering,
Friedrich-Alexander-Universität Erlangen-Nürnberg (FAU),
Cauerstraße 4, 91058 Erlangen, Germany

Abstract

Combining a heat pump cycle with an Organic Rankine cycle and adding a thermal storage enables an innovative and reversible energy storage concept. As both processes use similar components, it is conceivable to combine these in one single cycle with two operation modes.
Within an ongoing research project at University Erlangen-Nuremberg, a combined HP-ORC pilot plant is designed and constructed. One focus in the research is the combination of the compressor of the heat pump and the expander of the ORC in one single machine (e.g. screw-type). Besides the pressure ratios and temperature levels, the lubrication is an interesting challenge, as it differs in quantity and function.
Several innovative designs of the lubrication system are conceivable. The oil separator is an essential component of the lubrication circuit. With methods of CFD-simulation, a close look at the separation in both operation modes (HP and ORC) is possible. This paper describes preliminary considerations, shows design methods and identifies solutions for the lubrication management of a reversible compressor-expander unit.

© HPC2020.
Selection and/or peer-review under responsibility of the organizers of the 13th IEA Heat Pump Conference 2020.

Keywords: Combined HP-ORC; Carnot-Battery; Lubrication; Combined compressor-expander; CFD; Simulation

Nomenclature

HP	Heat Pump
ORC	Organic Rankine Cycle
CFD	Computational Fluid Dynamics
E	Energy
PV	Photovoltaics
Π	pressure ratio
p	pressure
θ	volume ratio
κ	isentropic exponent
C	compressor
E	expander
S	separator
VOF	Volume of Fluid
DPM	Discrete Phase Model
η	efficiency
n	number

* Corresponding author. Tel.: +49 9131 8529440; fax: +49 9131 8529449.
E-mail address: Daniel.Steger@ipat.fau.de

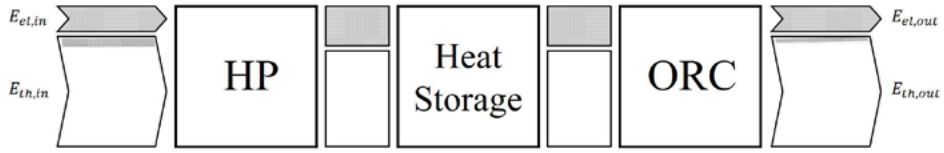


Fig. 1. Diagram of energy flows for the HP-ORC-concept (el.: electric, th.: thermal)

1. The combined HP-ORC-concept

1.1. Fluctuating renewable energies and the need for energy storages

Reaching the goals of the *Paris Agreement*, a significant increase in the electrical power production coming from renewable energy sources takes place. Due to the fluctuating character of renewables (especially PV, wind) improvements of energy distribution and storage are strongly required [1]. Several storage concepts are known, which differ greatly in storage capacity, efficiency and lifecycle-costs, so that there is a different area of application for each. *Pumped Thermal Energy Storage* is a big scale medium-term concept group that includes the *Carnot Battery,* a combination of heat pump and Organic Rankine Cycle.

1.2. The HP-ORC-concept (Carnot Battery)

The heat pump cycle (HP) is a well-known method to lift a medium's temperature by using electrical energy in a very efficient way. The Organic Rankine cycle (ORC) is a system that converts heat or thermal energy to mechanical energy and (via a generator) electrical energy. Using both concepts together and adding a thermal energy storage leads to the combined HP-ORC-concept (see figure 1). The concept also known as *Carnot Battery* can act as medium-term electrical energy storage. Electrical energy to be stored runs a heat pump cycle using waste heat energy to increase the temperature level of a thermal storage medium. In case of need, an Organic Rankine cycle converts the thermal energy of the storage medium (lowering the temperature level again) back into electrical energy. The achievable power-to-power efficiency and storage capacity strongly depends on the temperature levels of the application [2]. As both processes consist of similar components, it is possible to combine the cycles using the components reversibly and save investment costs.

2. Reversible use of a compressor and expander

The combination of a heat pump cycle and an Organic Rankine cycle requires some further considerations. The heat exchangers, being the most expensive parts of the cycles, can already reduce the investment costs significantly when used reversibly [3]. A diverse task is the combination of the compressor (HP) and the expander (ORC) in one single machine. The combination is conceivable for any type of volumetric machine [4]; in the current case, a screw type is investigated. Comparing the two operation modes of the concept, the outstanding differences are the temperature and pressure levels of condensing and evaporating and thus the inlet and outlet conditions of the machines. While the temperature variations are manageable, the different pressure levels are a relevant factor for process design. One fundamental number of the compression or expansion step is the pressure ratio Π, which is defined as the ratio of the higher pressure to the lower pressure:

$$\Pi_{com\ pression} = \frac{p_{out}}{p_{in}} \quad (1)$$

$$\Pi_{expansion} = \frac{p_{in}}{p_{out}} \quad (2)$$

During the heat pump mode, the working fluid's temperature rises from the temperature level of the waste heat (where the evaporation takes place) to the upper storage temperature (where the condensation takes place). Applying the ORC, the working fluid reduces its temperature from the upper storage level (evaporation) nearly

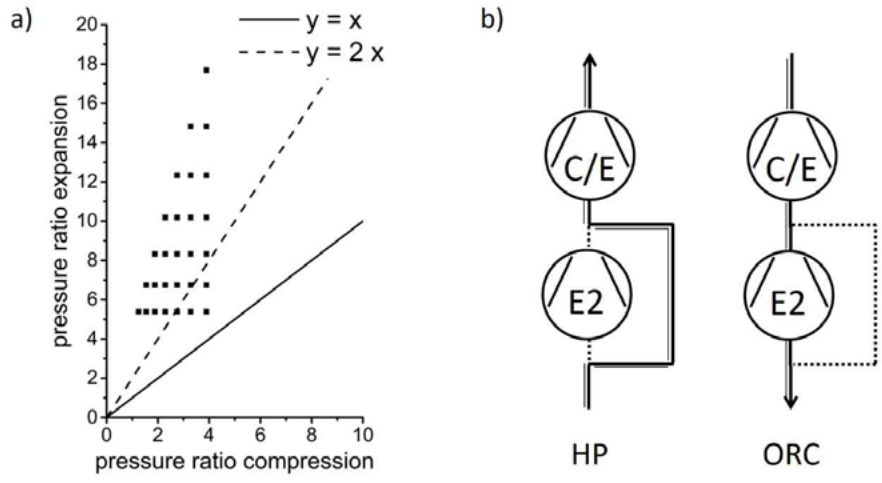


Fig. 2. Comparison of pressure ratio for compression and expansion (a) and concept of combined machine layout (b)

down to ambient temperature (condensation). Since the temperature levels of the phase changes differ in the two modes, the pressure ratios at the machines differ significantly, being much higher in the ORC-case. Figure 2a) shows these numbers for different temperature scenarios (dots) of the storage concept. The full line in the figure indicates the symmetrical case, when the pressure ratio at expansion equals the pressure ratio at compression. Regarding the location of the typical operation scenarios of a combined HP-ORC-application, apparently this case does not occur. The location of the operation field is much more in the range of

$$\Pi_{expansion} = n \cdot \Pi_{compression} \quad ; with\ n = 2;3 \tag{3}$$

Particularly for volumetric machines (e.g. screw compressor, screw expander), there is a fluid sensible relation between the built-in volume ratio θ and the pressure ratio, with κ being the isentropic exponent [5]:

$$\Pi = \theta^{\kappa} \tag{4}$$

Equation (4) shows the challenge to select a single machine, which meets the requirements of both compression and expansion having different pressure ratios. A solution to this is a serial approach as seen in figure 2b). Adding an extra expansion unit (E2) to the reversible machine (C/E) in expansion case (ORC) and bypassing it in compression case (HP) enables two different pressure ratios. These can be adjusted to the main operating point by the selection of proper machinery.

3. Lubrication of a combined machine

The lubrication of screw machines brings several advantages (no need of gears, better sealing, temperature regulation) thus an oil-injected compressor or expander is frequently used. Still the lubrication comes with some challenges especially for a reversible use. It differs for compressors and expanders due to the reversion of the thermodynamic process. In the compressor, the main function of the lubricant is the heat transport: the cooling of the compressed gas is necessary to increase the efficiency and lower the thermal load on the component parts. In contrast, there is no cooling necessary for the expander case, because expansion of the gas already lowers its temperature. That leads to a difference in the mass flow of the lubricant, being smaller in the expander-case.

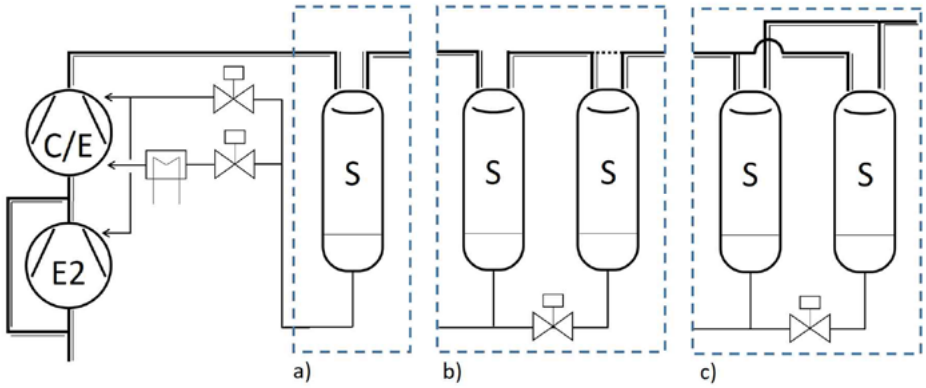


Fig. 3. Lubrication chart of combined compression-expansion-machine with: a) single separator, b) two serial separators, c) two parallel separators

One main part of the lubrication circuit is the oil separator, which divides the refrigerant vapour from the oil. Here again, two different approaches have to be compared: While in the HP-case, it is straightforward to locate the separator downstream of the compressor, cool the separated lubricant and re-inject it at the low-pressure side, the separation process for an expander is often quite different. Locating the separator downstream as well would lead to a huge apparatus because of the bigger volume flows at low pressure. To avoid this, it can be placed upstream. That leads to the fact, that the lubricant follows the refrigerant's way all through the ORC and is separated just before the expander, to be injected into the proper places. Due of the relatively low mass flow, the lubricant does not affect the refrigerant circuit too much. Furthermore, this setup enables the combination of the lubrication for a combined compressor-expander-unit very well (see figure 3a)).

Nevertheless, the different mass flows of lubricant and different volume flows of refrigerant influence the design of the separator particularly. Several layouts are conceivable: to adapt the performance to each case it might be necessary to add a second separator. It can be placed as a serial (figure 3b)) or parallel setup (figure 3c) improving the separation efficiency or halving the volume flow respectively. For further investigations of the fluid dynamics in a vapor-liquid-separator, numerical analysis was carried out.

4. Fluid dynamics in oil separators

4.1. CFD model

The main function of this setup is to enable vapor-liquid separation for the HP-mode and ORC-mode. Therefore, it is necessary to use a symmetrical separator design. In general, the vertical vapor-liquid separator consists of four sections [6]: the inlet diverter, the gravity settling section, the liquid collection section and the mist extractor. In this study, both the vapor-liquid inlet (diameter 0.03 m) and the vapor outlet (diameter 0.03 m) are placed on top of the vessel (diameter 0.12 m, height 0.4 m), which are separated by a divider to prevent short cut flow. Droplets of liquid settle in the liquid collection section, where an outlet for the liquid is placed at the bottom of the vessel.

To predict the fluid flow behavior inside the separator and to calculate the separation efficiency, Computational Fluid Dynamics (CFD) is used. There are two approaches for multiphase flow modeling: Euler-Euler and Euler-Lagrange. For the Euler-Euler method, continuous-continuous phase interactions form a discrete interphase between them. They are immiscible with each other and it focuses on the fluids motion in a specific location. With the Euler-Lagrange method, the fluid is considered as continuous phase, while the disperse phase can be solid particles liquid droplet or gaseous bubbles. Each particle is tracked separately and the motion can be predicted.

Studies of vertical gas-liquid separators [7,8] have shown a combination of the volume of fluid (VOF) model, as a simplified version of the full Eulerian model, with the discrete phase model (DPM) is suitable for simulation of multiphase separation processes. Hereby oil-droplets as a dispersed phase are solved under a

Lagrangian frame until it reaches the final destination where boundary conditions apply and the vapor as continuous phase is solved using an Eulerian frame of reference.

4.2. Boundary conditions

In this study, a steady vapor-liquid simulation is implemented in ANSYS FLUENT 19.1. With the criteria of quality and skewness of the mesh, a computational mesh-grid-independent solution was performed. Prism layers were set at the wall and tetrahedral elements placed inside the separator. To save computational time, a symmetric boundary condition was placed. The Reynold Stress Model (RSM) calculates turbulence. The inlet mass flow was defined accordingly to table 1 for the liquid and vapor phase for the following simulated cases. As it typically appears for the storage concept, the mass flow in the ORC-case is slightly smaller than in the HP-case. The droplet size of the oil in the vapor stream follows a particle size distribution. As there is no physical data for the specific case available, the mean droplet size is assumed to be 250 microns. This will be valuated experimentally in a pilot plant set up. For the serial HP-mode, just the second apparatus was simulated, as the first one is identical to the single HP-mode. The inlet conditions at the second separator are equal to the outlet conditions of the first; the droplet size is reduced to 150 microns, assuming the smaller particles to be less separated in stage one. In the parallel HP-mode, vapor and oil mass flow is halved. Static pressure was set at the outlets as for the bottom outlet hydrostatic pressure was set. Furthermore, phase interaction, Ishii Zuber drag forces and virtual mass are included. The surrounding fluid flow remains unaffected by the droplet motion. Physical transport processes, which take place at the phase boundary surface (warm and cold transport), are not considered in this work.

Table 1: Fluid properties for HP- and ORC-modes

	HP- mode, single	ORC-mode, single	HP- mode, serial (2)	HP- mode, parallel (1/2)
Gas flow rate	0.3 kg s^{-1}	0.2 kg s^{-1}	0.3 kg s^{-1}	0.15 kg s^{-1}
Liquid flow rate	0.04 kg s^{-1}	0.02 kg s^{-1}	0.004 kg s^{-1}	0.02 kg s^{-1}
Operating pressure	163800 Pa	91300 Pa	163800 Pa	163800 Pa
Operating temperature	411 K	368 K	411 K	411 K
Gas density	83.61 kg m^{-3}	48.78 kg m^{-3}	83.61 kg m^{-3}	83.61 kg m^{-3}
Liquid density	1048.48 kg m^{-3}	1048.48 kg m^{-3}	1048.48 kg m^{-3}	1048.48 kg m^{-3}
Droplet size	250 µm	250 µm	150 µm	250 µm

4.3. Simulation results and discussion

Stochastic model of turbulent dispersion is included in the particle trajectory calculations. 10500 particles were injected at the inlet. Through the DPM, escape zones and trapped areas were assigned to count the particles, which reached the liquid collection section. Equation 5 provides the predicted separation efficiency with the number of oil droplets at inlet and outlet:

$$\eta = \left(\frac{n_{oil,in} - n_{oil,out}}{n_{oil,in}}\right) \cdot 100\ \% \tag{5}$$

Table 2 shows the calculated separation efficiencies for the considered cases.

Table 2: Separation efficiency

Case	HP-mode, single	ORC-mode, single	HP-mode, serial (2)	HP-mode, parallel (1,2)
Separation Efficiency	89.4 %	98.6 %	86.9 %	84.3 %

Figure 4 shows the particle velocity magnitude for the four different cases. The inlet is on the left for HP and on the right for ORC. According to the simulation results, separation in HP-case could reach an efficiency of about 89 %. An improvement because of parallel use of two similar separators cannot be seen, even though the volume flow halves (84 %). Conversely, a second serial apparatus can increase the separation efficiency furthermore (89 % at first stage, 86 % at second stage) reaching in total a number of 98.6 %. Having a symmetrical geometry, the reversible use of the separator in the ORC-case is not an issue per se. Yet the inlet conditions change (lower pressure and therefor lower density), resulting in different flow conditions. Here a separation efficiency of about 98 % results. Further simulation results show a strong dependence of the particle size.

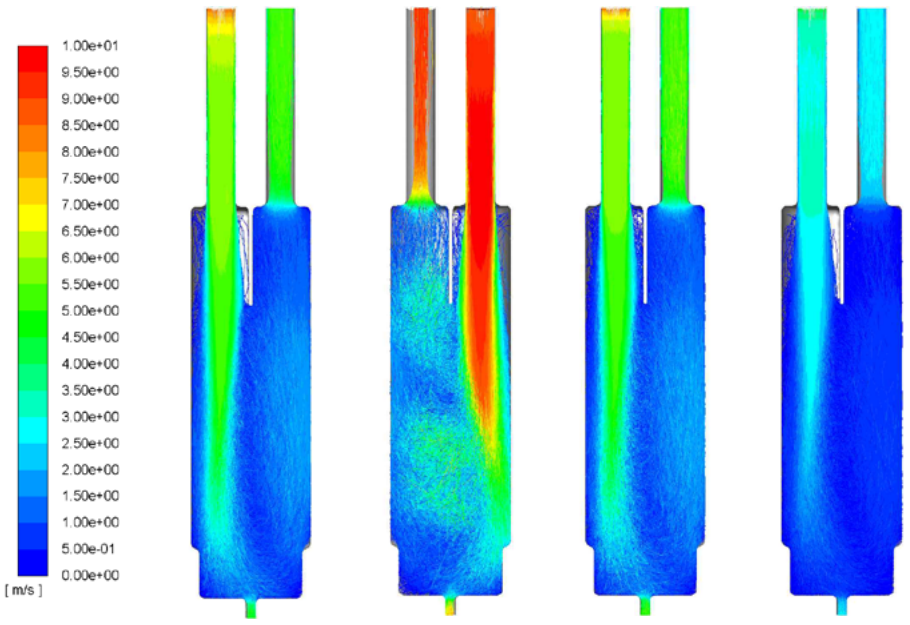


Fig. 4. Particle velocity magnitude of oil droplets in different separation setups

To sum up, the separation efficiency is mainly a function of particle size, volume flow and lubricant mass flow. Combining a heat pump compressor and an Organic Rankine cycle expander two different lubrication situations meet. Of course, it is feasible to find an optimal separator for each task, but combining the function in just one separator comes with smaller declines. The study shows that separation in ORC-mode is slightly more efficient; hence, the separation apparatus should be bigger in HP-mode. This challenge can be resolved by adding a second apparatus. Here the study shows an advantage of the serial setup compared to the parallel one. Even though the results are valid in general, the droplet size assumption has to be confirmed experimentally and updated to the simulation. Therefore, a pilot plant setup of the combined HP-ORC concept will be launched in 2020.

Acknowledgements

The authors would like to offer their special thanks to BITZER SE, SWEP International AB and Honeywell International Inc. for the support with products and to the Bayerische Staatsregierung for financing the project within the *Energie Campus Nürnberg*.

References

[1] Cebulla, F., Haas, J., Eichman, J., Nowak, W., & Mancarella, P. (2018). How much electrical energy storage do we need? A synthesis for the U.S., Europe, and Germany. Journal of Cleaner Production, 181, 449–459. http://doi.org/10.1016/j.jclepro.2018.01.144

[2] Staub, S., Bazan, P., Braimakis, K., Müller, D., Regensburger, C., Scharrer, D., … Karl, J. (2018). Reversible Heat Pump–Organic Rankine Cycle Systems for the Storage of Renewable Electricity. Energies, 11(6), 1352. http://doi.org/10.3390/en11061352

[3] Steger, D., Regensburger, C., Eppinger, B., Will, S., Karl, J., Schlücker, E. (2019). Combining an Organic Rankine Cycle and a Heat Pump Cycle in a Test Plant for Reversible Storage of Energy. 5TH International Seminar on ORC Power Systems, September 9-11, 2019, Athens, Greece
[4] Dumont, O. (2017). Investigation of a heat pump reversible into an organic Rankine cycle and its application in the building sector, (September). http://doi.org/10.13140/RG.2.2.19499.13604
[5] Rinder, L. (1979). Schraubenverdichter / Laurenz Rinder. Wien, New York: Springer
[6] M. Stewart and K. Arnold, Chapter 3: Two-Phase Gas–Liquid Separators, in Gas-Liquid and Liquid-Liquid Separators, 2008, pp. 65–130.
[7] A. Pourahmadi Laleh, W. Y. Svrcek, and W. D. Monnery, Computational Fluid Dynamics Simulation of Pilot-Plant-Scale Two-Phase Separators, Chem. Eng. Technol., vol. 34, no. 2, pp. 296–306, 2011.
[8] J. C. Mendez, A. E. Efendioglu, and J. L. Guevara, Numerical investigation of vertical gas–liquid separators using computational fluid dynamics and statistical techniques, WIT Trans. Eng. Sci., vol. 120, no. December, pp. 103–114, 2018.

13th IEA Heat Pump Conference
April 26-29, 2021 Jeju, Korea

Development and Implementation of Industrial High Temperature Heat Pumps for Waste Scrubbing Process

Gilbong Lee*, Beomjoon Lee, Junhyun Cho, Ho-Sang Ra, Young-Jin Baik, Eun Seok Wang, Hyung-Ki Shin, Young-Soo Lee, Chulwoo Roh

Thermal Energy Systems Laboratory, Korea Institute of Energy Research, 152, Gajeon-ro, Yuseong-gu, Daejeon, 34129, Korea

Abstract

In this study, industrial heat pump which can generate low pressure steam was developed. The heat pump uses process waste heat of 50-60℃ to generate 120℃, 2kgf/cm2 steam. By implementing this, the overall thermal energy efficiency of a factory can increase. In case of R134a, the discharge temperature and pressure of compressor was expected to be in supercritical state around 200℃/10 MPa. To locate operation points in lower temperature and pressure zone, R245fa was selected as a working fluid. Cycle and system design was performed based on R245fa properties. With the experiment results of small-scale, reciprocating-compressor system, large scale system design of screw-compressor was carried out. Since this system was to be applied to actual operation, control logic with high reliability was also developed. After in-lab tests, the heat pump was installed to supply steam for waste scrubbing process in a chemical factory.

© HPC2020.
Selection and/or peer-review under responsibility of the organizers of the 13th IEA Heat Pump Conference 2020.

Keywords: Low Pressure Steam; High Temperature Heat Pump; R-245fa

1. Introduction

Emission of greenhouse gases is largely related to energy consumption and energy efficiency is expected to play as an important role as renewable energy to deal with global warming issues.[1] Among residential, commercial, industrial and transport sectors, the industrial sector generally contributes the largest portion in energy consumption. For South Korea industrial sector consumed about 61.7% of final energy in 2012.[2] Energy consumption by functions in manufacturing showed that feedstock accounted for the largest portion of 57.2% followed by heat energy of 29.1%.[3] (Table 1) Therefore it is an important research target to find methods of reducing heat energy in industrial sector. Conventional heating methods like combustion and electric heating is considered to reach limit in efficiency. Alternative heating methods are being sought to improve thermal efficiency. Among them heat pump is considered as one of the most prominent candidates. Heat pump system satisfies heat demand by transferring energy from low temperature source to high temperature sink. Energy is used in changing pressure and temperature of working fluid – refrigerant in heat pump. The total transferred heat is sum of energy input and extracted energy from low temperature source. Therefore heat pump can deliver more heat than input energy.
Heat pump can be applied to use low temperature heat source to generate hot temperature energy such as space heating and hot water. As a low temperature heat source, heat pumps can use air, river, lake/sea water or even ground (underground) energies.[4] This versatility of energy source has made heat pump to be considered as a renewable energy system. In EU, heat pump satisfying minimum SPF (Seasonal Performance Factor) is regarded as renewable energy system.[5] Some countries have implemented subsidy programs to expand installation of heat pump since it can emit less greenhouse gases than conventional boilers using fossil fuels.

* Corresponding author. Tel.: +82-42-860-3293; fax: +82-42-367-5067
E-mail address: giblee@kier.re.kr.

Table 1. Energy consumption in manufacturing industry by functions in 2010, South Korea

Function	PJ (10^{15} J)	Portion (%)
Heat	1,312	29.1
Power	398	8.8
Feedstock	2,574	57.2
Miscellaneous	216	4.8
Total	4,501	100

Currently main market of heat pump is residential, commercial and district heating/cooling market. The penetration status of heat pump in the industrial sector is very low. In one milk powder factory in Denmark, a compression/absorption heat pump was installed to preheat process air up to 80ºC by extracting heat from coolant of 40ºC.[6] In England one chocolate factor installed heat pump system to simultaneously heat the process water and cool glycol mixture.[7] Most of heat pump application in industrial sector are in production of hot water for processes. For a higher temperature application, Andrea et al. proposed the application of absorption heat pump type 2 to reduce middle pressure steam in pulp factory and showed high potential in energy saving.[8]

Table 2 is the temperature distribution of heat demand in German in C. Lauterbach's report.[9] According to the report, heat demand of 100ºC or less occupies 9% and that of 100-200ºC was 8% of similar contribution. Temperature distribution of heat demand however showed different pattern among industrial sectors. For example, paper and rubber product sector need almost twice amount of heat in 100-200ºC as that in below 100ºC zone. Fig. 1 is thermal energy demand distribution in French industry by D. Bobelin et al.[10] The analysis focused on heat demand below 140ºC. The heat demand below 100ºC was reported to be small compared to heat demand of above temperature.

Table 2 Breakdown of the industrial heat demand with detailed temperature distribution between 100 and 500ºC[9]

Industrial sector	Hot water	Space heating	Process heat [TWh]					sum
			<100℃	<200℃	<300℃	<500℃	>500℃	
Chemicals and chemical products	0.2	6.7	13.5	9.5	5.9	5.5	55.7	96.9
Food products and beverages	0.3	8.3	11.8	13.7	0.9	0	0	35
Motor vehicles and trailers	1	7.3	2.7	1.1	0	0.8	3.7	16.8
Paper and paper products	0.1	2.4	2.7	5.6	0.2	4.1	0	15.1
Fabricated metal products	0.9	6.3	2.3	1	0	0.8	3.4	14.8
Machinery and equipment	0.6	4.5	1.6	0.7	0	0.5	2.3	10.3
Basic metals	0.2	4.4	0.9	1.5	0.1	1.1	154.9	163.1
Non-metallic mineral products	0.1	3.5	1.2	1	0	0.7	82.7	89.3
Rubber and plastic products	0.1	1.6	0.9	2	0.1	1.4	0	6.1
Electrical equipment	0.3	2.4	0.9	0.6	0	0.5	1.1	5.8
Textiles	0.1	1.2	2	0	0	0	0	3.3
Printing and recorded media	0	0.4	0.2	1.5	0.1	1.1	0	3.3
Wood and wood products	0	0.3	1.5	0.2	0	0.2	0	2.1
Furniture and other goods	0	0.7	0.4	0.6	0	0.4	0.2	2.4
Computer, electronic, optical products	0.1	0.9	0.3	0.1	0	0.1	0.4	2
Other transport equipment	0.1	0.9	0.3	0.1	0	0.1	0.4	2
Leather and related products	0	0.1	0.2	0	0	0	0	0.3
Wearing apparel	0	0.1	0.2	0	0	0	0	0.3
Tobacco products	0	0	0	0	0	0	0	0.1
Sum	**4.2**	**52**	**43.6**	**39.3**	**7.5**	**17.4**	**304.9**	**468.9**
Share	1%	11%	9%	8%	2%	4%	65%	100%

Most of the thermal energy in industrial processes is supplied in the form of steam in order to maintain a stable temperature. Typically, steam below 140ºC is termed as low pressure steam. Since there is high demand of heat above hot water temperature, many researches have been conducted to increase the temperature of heat pump cycle. In this paper, high temperature heat pump cycle to generate low pressure steam was developed. The design temperature of heat sources are 60-70ºC waste heat and the product target was120ºC low pressure steam. In addition to basic cycle design, application of internal heat exchanger was considered. Test rig of 40 kW scale steam heat pump was constructed and performance evaluations were conducted.

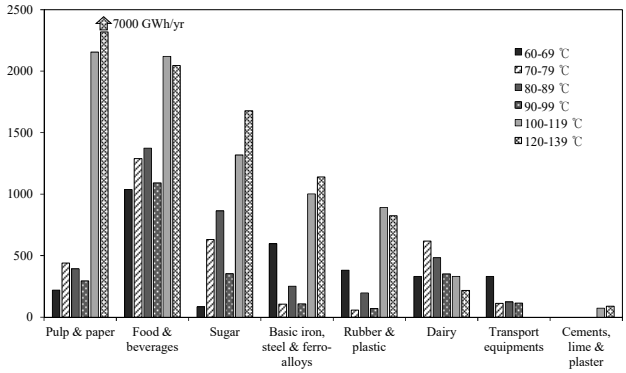


Figure 1 Distribution of the heat demand per industrial branch[10]

2. Design of high temperature heat pump cycle for steam generation

2.1. Basic Cycle Design

As a base cycle for high temperature heat pump, vapor-compression cycle was applied. In this cycle, compressor increases the pressure and temperature of refrigerant by transforming mechanical energy. The discharged refrigerant releases heat energy to high temperature heat sink in condenser. The temperature difference between heat sink and refrigerant in condenser is generally in order of 10ºC. The lower the temperature difference is, the lower the input energy compressor requires. This eventually increases the efficiency of system. The optimization of heat pump system is directed to the minimization of temperature difference in condenser.
Fig. 2 is heat and mass transfer diagram of steam generation heat pump cycle. In closed loop, the generated steam will be circulated to boiler again, while in open loop additional water should be supplied as the steam is exhausted to low temperature process or in the air. Fig. 2 is open loop configuration. Steam can be produced by either direct heating or by pressure reduction in circulating water (flashing method). Since the density difference between saturated liquid and saturated vapor of water is so large, the condenser of heat pump may become too bulky under direct heating method. Therefore in this study, pressure reduction method was used for steam production. In this method, only small portion of circulating water is transformed to low pressure saturated vapor. (less than 10%) Large amount of saturated liquid is recirculated to condenser and make-up water is mixed along the circulation. After circulation pump the pressure of process water is increased. Since the portion of saturated liquid is very high, the circulating water undergoes single phase heat transfer in condenser.

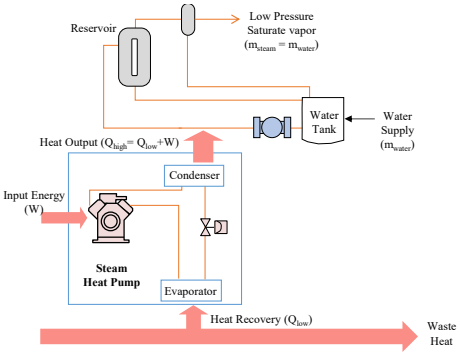


Figure 2 Cycle diagram of steam generation heat pump

To produce low pressure steam with heat pump, the condensation temperature should rise up to 130ºC. Table 3 gives characteristics of refrigerant candidates for high temperature application.[11] R134a is one of the most commonly used refrigerant in current market. It has critical temperature around 100ºC. This means that heat pump cycle of R134a would undergo supercritical process to generate steam. If refrigerants have critical temperature above 130ºC, they would have advantage in efficiency. R1234ze(Z), R245fa and R365mc satisfy

this requirement for critical temperature. Among them R245fa was chosen since it has no flammability and is easily purchased.

Table 3 Basic characteristics of refrigerants for high temperature heat pump applications

Refrigerant	GWP	Flammability	T_c [℃]	P_c [MPa]
R134a	1430	-	101.1	4.06
R755	1	-	31.0	7.38
R1234yf	4	Low	94.7	3.38
R1234ze(E)	6	Low	109.4	3.64
R1234z3(Z)	<10	Low	153.7	3.97
R245fa	1030	-	154.0	3.65
R365mfc	794	Low	186.9	3.27

Heat pump system of R134a makes hot water with low temperature heat source (such as geothermal energy, sea water, ambient air). The target heat pump of R245fa makes low pressure steam with waste heat source of 60-70ºC. Considering the difference in the operation temperature range R245fa and R134a have similar operation pressure. Thermo-physical properties related to heat transfer are listed in Table 4 with different saturation pressures. Chen suggested boiling heat transfer as combination of convective heat transfer and nucleate heat transfer.[12] Column 10 and 11 of table 4 are the relative convective heat transfer coefficient when values of R134a are assumed as 1. The velocity was assumed to be the same. Dittus-Boelter correlation was used to calculate heat transfer coefficient. From the relative values, R245fa may show similar heat transfer performance in vapor phase but have poor performance in liquid phase. This is because R245fa has disadvantage in thermal conductivity and viscosity in liquid phase. For the enhancement factor of convection heat transfer many researchers suggested Martinelli parameter as key parameter.[12] Since R245fa has higher density in saturated vapor phase than R134a, enhancement factor of R245fa will decreases in evaporation heat transfer compared to R134a. In condensation, R245fa may show similar heat transfer performance as R134a.
Although the final product of steam heat pump cycle is vapor, the heat transfer in condenser is single phase if pressure reduction method is applied. Considering the working temperature difference, the condensation heat transfer will not change much compared to R134a. All of these will imply that conventional cycle design approach of R134a could be applied to the design of R245fa based heat pump design with only minor modification. Therefore refrigerant change approach from R134a to R245fa was applied in the construction of test apparatus for the preliminary research.

Table 4 Properties of R134a and R245fa at saturation conditions

P (MPa)	R134a				R245fa						
	T (K)	ρ_{liq} (kg/m^3)	ρ_{vap} (kg/m^3)	h_{gf} (kJ/kg)	T (K)	ρ_{liq} (kg/m^3)	ρ_{vap} (kg/m^3)	h_{gf} (kJ/kg)	$\alpha_{liq,relative}$	$\alpha_{vap,relative}$	$X_{tt,relative}$
0.3	274	1293	15	198	319	1281	17	178	0.87	1.05	1.09
0.5	289	1241	24	186	336	1228	28	166	0.88	1.05	1.09
0.7	300	1200	34	176	348	1187	39	156	0.88	1.05	1.09
0.9	309	1165	44	168	358	1151	50	148	0.88	1.05	1.09
1.1	316	1134	54	160	367	1118	62	140	0.89	1.05	1.09
1.3	323	1105	65	152	374	1088	75	133	0.89	1.06	1.09
1.5	328	1077	77	145	381	1059	88	126	0.90	1.06	1.09
1.7	334	1051	88	139	387	1031	102	119	0.90	1.07	1.09
1.9	338	1024	101	132	392	1003	117	113	0.91	1.08	1.09
2.1	343	998	114	125	397	975	134	106	0.92	1.09	1.09
2.3	347	972	129	118	402	947	151	99	0.92	1.11	1.10

ρ: density, h: enthalpy, liq: liquid, vap: vapor, gf: fluid to gas
"relative" means values of R245fa compared to R134a under same pressure

Dittus-Boelter correlation: $\alpha_{liq} = 0.023\,\mathrm{Re}_{liq}^{0.8}\,\mathrm{Pr}_{liq}^{0.4}\left(\frac{k_{liq}}{d_i}\right)$

Martinelli parameter: $X_{tt} = \left(\frac{1-x}{x}\right)^{0.9}\left(\frac{\rho_{vap}}{\rho_{liq}}\right)^{0.5}\left(\frac{\mu_{liq}}{\mu_{vap}}\right)^{0.1}$

2.2. System Reliability and Efficiency

The most common causes of compressor failure are refrigerant flood back, flooded starts, liquid slugging, overheating, lack of lubrication, etc.[13] Refrigerant flood back occurs when refrigerant is not heated up to superheated phase in the evaporator. This is caused by low evaporation load or failure of evaporator. Under compression with refrigerant flood back, foaming phenomenon in lubricant of compressor is generally occurred. Flooded start is when compressor starts its initial operation with a large amount of liquid refrigerant within the compressor shell. This happens when the system is over-charged with refrigerant or the system is stayed for a long period. Under flooded start, massive and instant exit of lubricant occurs. This causes temporal lack of lubrication of compressor. Overheating operation is caused by high compression ratio, low suction pressure, high superheat, etc. High compressor temperature causes negative effect to lubrication.
Adequate superheat is needed for the protection of refrigerant flood back. It is also important to secure lubrication performance in compressor. Compressor lubricant performs roles such as sealing, anti-friction, cooling, etc. Under normal operation lubricant mixes with refrigerant in compressor. Daniel chart shows trends of lubricant/refrigerant mixture with isobaric curves.[14] It shows refrigerant concentration, viscosity with different temperature and pressure of lubricant and Fig. 3 is an example for R32.[15] Since the pressure of lubricant is same as that of refrigerant the difference between lubricant temperature and refrigerant saturation temperature can be used as the index of reliability. This definition is similar to the definition of superheat. In practical application, superheat would be used as an alternative index to lubricant superheat. Under constant pressure, concentration ratio of refrigerant stiffly increases as temperature approaches saturation temperature of refrigerant. Since the viscosity of HFC refrigerants is much lower than pure lubricant, lubrication performance was impaired as superheat becomes small.[16] Whether using suction superheat or discharge superheat as the criteria of reliability depends on the position of oil reservoir in compressor. In low pressure shell, oil reservoir is placed in suction part. Low suction superheat may tremendously increase the concentration of refrigerant damaging the lubrication performance. However in high pressure shell compressor, the oil reservoir is placed in discharge part. Therefore the negative effect of low suction superheat can be compensated in high pressure shell type compressor.[17] In summary, adequate superheat where the oil reservoir is placed should be maintained to secure lubrication performance.

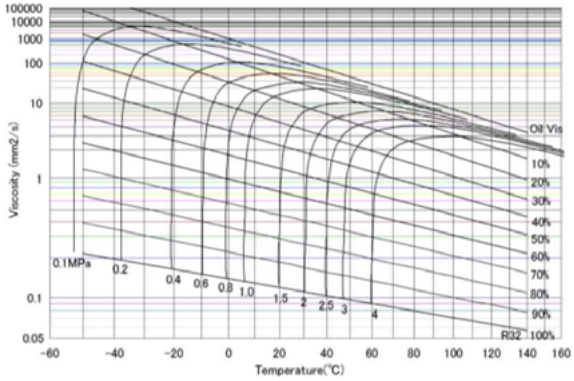


Figure 3 Daniel chart of New-PVE68 with R32 [15]

For commonly used R134a the isentropic line moves away from saturated vapor line (bubble line) as the pressure increases. However R245fa shows different trend, moving toward the bubble line (Fig. 4) Discharge superheat affects lubrication of high pressure part in compressor. Therefore certain amount of discharge superheat should be maintained for reliability.
Fig. 5 shows discharge superheat trends with different suction superheat and operation pressures. The suction pressure was fixed as 400 kPa and the isentropic efficiency of compressor was assumed as 0.8. If compressor has to have adequate superheat for the entire operation range, more suction superheating is required for R245fa. This means that the design point of suction superheat of R24fa should be higher than R134a. High suction superheat requires large temperature difference between refrigerant and secondary fluid in evaporator. This causes low evaporation pressure and low efficiency.

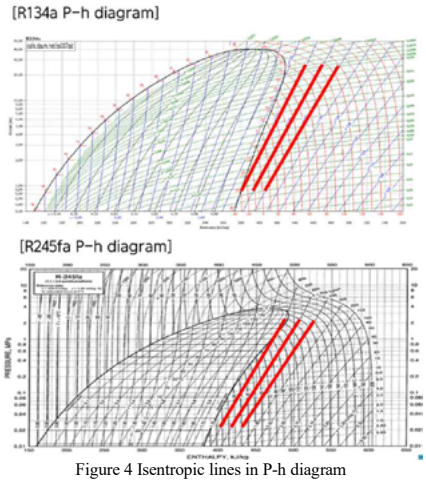


Figure 4 Isentropic lines in P-h diagram

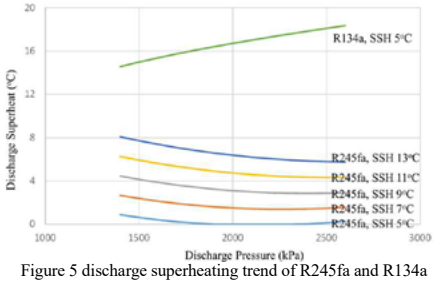


Figure 5 discharge superheating trend of R245fa and R134a

2.3. Application of Internal Heat Exchanger

In the previous chapter it was shown that the requirement of superheat of R245fa may cause performance decrease in heat pump cycle. With evaporator only, the temperature gradient of refrigerant will increase to meet the requirement. The temperature difference between heat source and evaporator will also increase. To meet this, evaporation pressure of heat pump system will drop resulting in high compression work and low capacity. High temperature heat pump system of 40 kW for steam generation was designed to examine this trend. Fig. 7 shows system performance changes under different suction superheat. If the minimum value of discharge superheat is set as 10ºC, about 7% of COP was decreased due to high suction superheat.
Internal heat exchanger (IHEX) transfers heat between condenser outlet fluid and evaporator outlet fluid. With this, system has additional suction superheat and heating capacity. As IHEX provides superheat for compressor, unnecessarily low pressure in evaporator can be eliminated. The cycle diagram of IHEX integrated heat pump is fig. 8. Table 5 shows performance comparisons with and without IHEX. IHEX increased evaporation pressure by 0.4 bar.



Figure 6 Experimental apparatus of steam generation heat pump development (40kW scale)

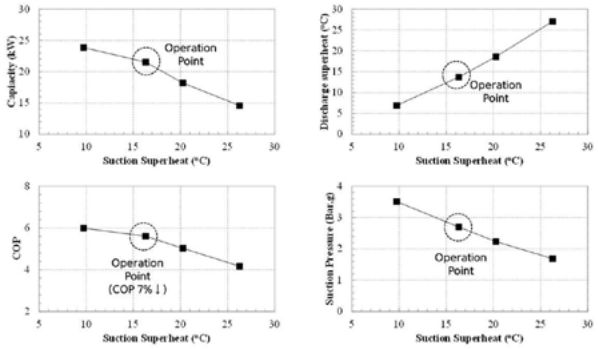


Figure 7 Performance characteristics of R245fa heat pump cycle with various suction superheat

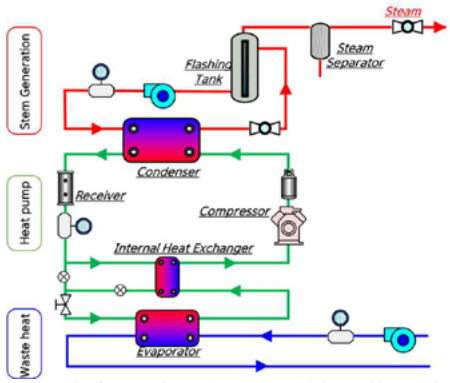


Figure 8 Cycle diagram of steam heat pump with internal heat exchanger

To further analyze the effect of IHEX simple parametric analysis was performed for R134a and R245fa to see effect of suction superheat. Condensation pressure and evaporation pressure were set as 2200 kPa and 400 kPa. Isentropic compression, constant volumetric efficiency, and no subcooling were assumed. Under these conditions, performance with 5ºC suction superheat was selected as reference point. The relative performances with different suction superheat were listed in Table 6. According to the table, increasing superheating also increase the compression work. However it also increase the heating capacity of the system. Therefore the heating COP is to have a tendency to increase as well. More improvement is seen in R245fa cases. This is due to higher specific heat at vapor phase and relatively low latent heat. R245fa has lower sensitivity in discharge superheat and higher sensitivity in efficiency than R134a. Therefore R245fa has more advantage in applying IHEX than R134a.

Table 5. Performance comparisons between with and without internal heat exchange

Parameters		W/O IHEX	W IHEX	Difference
Evaporation Pressure	bar, g	2.88	3.64	0.76
Condensation Pressure	bar, g	11.09	11.50	0.41
Subcooling	℃	2.06	13.67	11.61
Discharge Superheat	℃	15.21	25.82	10.51
Evaporator Superheat	℃	17.29	11.82	-5.47
Suction Superheat	℃	16.21	30.21	14.00
Heating Capacity	kW	21.52	24.55	3.03
Heating COP	-	5.60	6.22	0.61

Table 6. Effects of suction superheat on discharge superheat and COP

Suction superheat (K)	R134a		R245fa	
	Discharge superheat(K)	Relative COP	Discharge superheat(K)	Relative COP
11	15.63	1.013	0.02	1.037
13	17.36	1.018	1.42	1.050
15	19.10	1.022	2.85	1.062
17	20.86	1.027	4.33	1.074
19	22.64	1.031	5.83	1.086
21	24.42	1.036	7.37	1.097
23	26.22	1.040	8.93	1.109
25	28.03	1.045	10.52	1.120

3. Field Test and Evaluation of High Temperature Heat Pumps for Waste Scrubbing Process

In the industry field, steam is widely used in the processes such as refining, extraction, and food processing. Many researchers have been working on developing energy saving method of steam generation using low temperature waste heat. High temperature heat pump which can generate low pressure steam is one of the technical candidates for this. In this study, a heat pump system that produces steam of over 100ºC with capacity of 0.5 ton/h was developed based on cycle design methods in chapter 2. The steam heat pump utilizes waste heat of 50-70ºC, producing 110-120°C steam using a flash tank. Then, the developed steam heat pump system was tested at a Chemical Polycarbonate (PC) production line in Yeosu Industrial Complex.

Fig. 9 shows a conceptual diagram of the steam heat pump apparatus, which receives heat from the heat source water on the left side and produces steam through a flash tank on the right side. The evaporator superheat of the heat pump unit was controlled by the EKC315 superheat controller. The target value was 5°C based and the measuring point was the evaporator outlet. An ICM valve was used as an expansion valve to since the outlet temperature of condenser is normally about 100ºC. The control of the flash tank is the most important factor for the stable operation of the steam heat pump. The main factors of flash tank control are the pressure of the steam generated and the flash tank level. The pressure of the flash tank determines the temperature of the steam generated.

The manufactured steam heat pump system is shown in Fig. 10. Performance improvement and stability evaluation were conducted in the laboratory prior to the installation in the demonstration site. To maintain the stability of the system, control of flash tank pressure and liquid level in the tank are important. The level control of the flash tank is conducted with the differential pressure gauge, the pressure reducing valve, the two-way valve and the GH1000 controller. Stable make-up water supply is required to reduce the pressure fluctuations of the generated steam. To do this, it is necessary to properly set the pressure reducing valve, select the suitable inner diameter of the two-way valve, and set the PID gain of the GH1000 controller. In the performance improvement process, the several modifications were conducted such as refrigerant amount optimization, unit insulation, EKC operation optimization, steam pressure optimization and flashing pressure reducing valve optimization operation. The final performance in the laboratory was Steam 118.3ºC, capacity 362.6 kW, and COP 3.73.

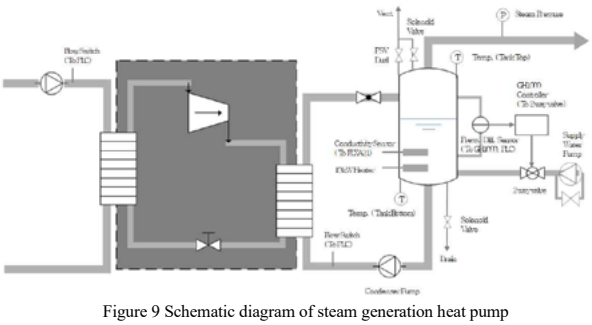


Figure 9 Schematic diagram of steam generation heat pump



Figure 10 Steam generation heat pump unit

The pressure of the steam line of the target process was about 0.16 MPa, which corresponds to steam temperature of 115ºC. The pressure control of the steam outlet of the flash tank became unnecessary because the main steam supply line maintained stable pressure. Fig. 11 shows the high temperature heat pump package installed in the demonstration site of a chemical factory. It consists of a heat pump unit and a flash tank unit. The installation in the chemical plant took about two months, and the operation of the steam pump system started in February 2018. The performance of the steam heat pump during the test run period is as follows; Steam output: approx. 0.53 ton/h, steam heat pump performance: calorie 348 kW, COP 3.03. Fig. 12 shows steam production and heat source water temperature during the period.



Figure 11 Field test and evaluation of steam heat pump at LG Chem.

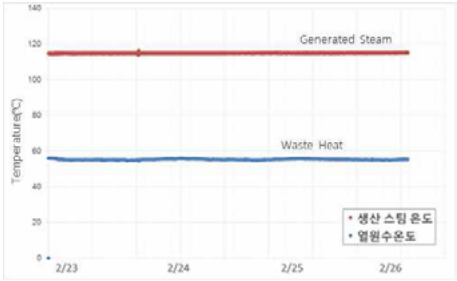


Figure 12 Generated steam temperature and heat source temperature of heat pump during field test

4. Conclusions

In this study cycle characteristics of high temperature heat pump cycle were analyzed. As the demand for energy saving has increased in the industrial sector, interest for heat pump which recycles waste heat to produce low pressure steam has increased. R245fa was considered as suitable refrigerant of heat pump cycle for steam generation condition since the critical temperature of R245fa is above the operation temperature of steam

generation condition. Similar design concepts of R134a hot water heat pump could be applied to design steam heat pump cycle when steam is produced through flashing process.
Superheat is an important index for reliability and efficiency. In compressor, lubricant mixes with refrigerant. Small temperature difference to saturation temperature implies stiff concentration increase of refrigerant - high solubility of refrigerant to lubricant. Therefore certain amount of superheat should be maintained in oil reservoir part of compressor. R245fa tends to decrease superheat under compression process which is contrary to R134a. In designing R245fa cycle, design point of suction superheat must be higher because of this characteristic.
With internal heat exchanger, discharge superheat can be secured without increasing temperature difference in the evaporator. Simple parametric analysis was performed for R134a and R245fa to see effect of suction superheat. The results showed that R245fa has more favorable thermo-physical characteristics in applying internal heat exchanger compared to R134a. Therefore internal heat exchanger can be suggested as an essential component in R245fa heat pump cycle. The steam heat pump manufactured through this study was installed at a chemical plant and verified the performance. The heating capacity of the system was 350 kW and COP was 3.03 from the operation in the demonstration site.

ACKNOWLEDGMENT

This work was jointly supported by the National Research Council of Science & Technology (NST) grant by the Korea government (MSIP) (No. CRC-15-07-KIER) and the Energy Efficiency & Resources Core Technology Program of the Korea Institute of Energy Technology Evaluation and Planning (KETEP), granted financial resource from the Ministry of Trade, Industry & Energy, Republic of Korea (No. 2017010000850).

REFERENCES

[1] Energy Technology Perspectives 2012 – Pathways to a Clean Energy System. IEA. France
[2] Energy Info. Korea. Korea Energy Economics Institute; December 2013.
[3] Annual Report 2011. Korea Energy Management Corporation
[4] Park JT, Jang GC. An investigation on quantity of unused energy using temperature difference energy as heat source and its availability. *Energy Eng. J*. 2002; 11:106-113.
[5] IEA-ETSAP and IRENA© Technology Brief E12. Heat Pumps – Technology Brief;January 2013.
[6] Annual Report 2012. Danish Technological Institute
[7] Application of Industrial Heat Pumps, Task 4: Case Studies, IEA Industrial Energy-related Systems and Technologies Annex13/ IEA Heat Pump Programme Annex 35. Final Report;2014.
[8] Costa A, Bakhtiari B, Schuster S, Paris J. Integration of absorption heat pumps in a Kraft pulp process for enhanced energy efficiency. *Energy* 2009; 34:254-260.
[9] Lauterbach C. Potential, system analysis and preliminary design of low-temperature solar process heat systems. Kassel university press GmbH. Kassel; 2014
[10] Bobelin D, Bourig A, Peureux J. Experimental results of a newly developed very high temperature industrial heat pump (140°C) equipped with scroll compressors and working with a new blend refrigerant. *Proceedings of International Refrigeration and Air Conditioning Conference at Purdue* July 2012.
[11] Application of Industrial Heat Pumps, Task 3: R&D Projects, IEA Industrial Energy-related Systems and Technologies Annex13/ IEA Heat Pump Programme Annex 35, Final Report; 2014.
[12] Thome JR. Engineering Data Book III. Wolverine Tube. Inc.
[13] Why compressors fail part 1-7. Danfoss: http://danfoss.com.
[14] Henderson DR. Solubility, viscosity and density of refrigerant/lubricant mixtures – Final technical report. Spauschus Associates, Inc.;1994: DOE/CE/23810-34.
[15] Matsumoto T, Kaneko M, Kawaguchi Y. Development of PVE Refrigeration Lubricants for R32. *Proceedings of International Refrigeration and Air Conditioning Conference at Purdue* July 2014.
[16] Dossat R. Principles of Refrigeration. fifth edition. Prentice Hall. Columbus, Ohio.
[17] Tanawittayakorn W, Phrajunpanich P, Siwapornphaisarn S. Heat Pump Efficiency Improvement by Discharge Superheated Control. *Proceedings of International Refrigeration and Air Conditioning Conference at Purdue* July 2012.

13th IEA Heat Pump Conference
April 26-29, 2021 Jeju, Korea

Method for a quick economic assessment of vapor compression heat pumps

Dominik Seliger[a,*], Daniel Lange[a], Veronika Wilk[b], Jürgen Fluch[c], Karl Ponweiser[a]

[a]TU Wien, Institute for Energy Systems and Thermodynamics (IET), Getreidemarkt 9/302, 1060 Wien, Austria
[b]AIT Austrian Institute of Technology GmbH, Sustainable Thermal Energy Systems, Giefinggasse 2, 1210 Wien, Austria
[c]AEE – Institue for Sustainable Technologies, Feldgasse 19, 8200 Gleisdorf, Austria

Abstract

Renewable energy systems play a major role in the reduction of CO_2 emissions in industrial processes. However, selecting a suitable renewable energy system is difficult since the development of standardized concepts for assessing the ecological and techno-economic performance of such a system is lagging behind the advances made in the technologies themselves.
This article introduces a diagram-based approach for the quick evaluation and comparison of energy systems by using the vapor compression heat pump cycle as an example. On the basis of known technical key parameters of the heat pump cycle, transparent and highly flexible performance indicators are deduced like the relative energy cost and CO_2 savings during heating operation. The proposed evaluation concept demonstrates efficient practical use for economic and ecological technology comparison in several example scenarios. A parameter study shows the influence of key parameters in the heat pump cycle with regards to the system savings.

© HPC2020.
Selection and/or peer-review under responsibility of the organizers of the 13th IEA Heat Pump Conference 2020.

Keywords: heat pump, techno-economic analysis, cost savings, ecological assessment, graphical assessment;

1. Introduction

The consumer driven demand for sustainable products is steadily increasing, forcing companies to overthink their ecological impact. Therefore, companies are faced with the task to develop business models with sustainable replacements for technologies that are affecting the environment [1-2]. However, there are currently no standardized tools to give comprehensive and reliable statements about the impact of switching between technologies. This slows down the implementation process and market penetration of renewable energy systems. Comprehensible performance indicators are needed to develop a common understanding of the economic potential of switches between technologies. Furthermore, time and money constraints rarely justify in-depth system studies like a pinch analysis during pre-projects and business case development. Industrial stakeholders and consultants therefore need easily accessible tools for the quick assessment of the economic and ecological potential of new technologies for their evaluation and decision making process.

This article formulates an effective approach to compare different heating technologies. The premise is to give a clear indication for the more beneficial system by calculating its potential relative savings. The proposed method expands on considerations made by Lange [3]. It is based on observations for energy technologies in general and is then refined for vapor compression heat pump systems. Key parameters are used to customize the method for heat pump cycles and a comprehensive graph is presented that further emphasizes the practicability of the approach. The approach can be used for either economic or ecological purposes by using suitable specific costs in the calculation which is demonstrated with several example scenarios. These scenarios

* Corresponding author. Tel.: +43-1-58801-302316; fax: +43-1-58801-302399.
E-mail address: dominik.seliger@tuwien.ac.at.

are examples for the effectiveness and comprehensibility of the relative savings as a key figure as well as the approach itself. Furthermore certain parameters are discussed to understand how these should be adapted to have positive impact on the overall relative savings.

2. Derivation of economic performance indicators

In order to evaluate and compare two different technologies the same framework must be applied: Every considered technology has the function to fulfill a certain heat demand, Q_D, in a certain time period Δt. During the defined time period Δt all considered technologies are working in a steady state, meaning that every process variable is assumed to be constant.

2.1. Comparison of two energy technologies

Any technology for heat supply causes costs mainly due to the consumption of other energy sources, Q_i. Each of these energy sources has a specific cost c_i. Therefore, the operating costs C to provide a certain heat demand Q_D are:

$$C(Q_D) = \sum_i Q_i(Q_D)\, c_i \tag{1}$$

However, most technologies only consume one type of energy to meet a certain heat demand. These technologies shall be named direct conversion technologies from this point onward. Operating costs as defined in equation 1 can be expressed for these direct conversion technologies as follows:

$$C = Q\, c \tag{2}$$

Equation 2 is also valid for technologies which use only one energy source with significant specific costs, making the costs for other energy sources negligible. Furthermore, for direct conversion technologies the efficiency η is defined as:

$$\eta = \frac{Q_D}{Q} \qquad \text{or} \qquad Q = \frac{Q_D}{\eta} \tag{3}$$

One indicator for a beneficial technology are lower operating costs in comparison to reference technologies. An easy criterion, that identifies technology A as superior to B is:

$$\frac{C^A(Q_D)}{C^B(Q_D)} < 1 \tag{4}$$

If this criterion is used to compare two direct conversion technologies, equation 2 and 3 can be used to transform equation 4 to a cost-efficiency-ratio:

$$\frac{\eta^B\, c^A}{\eta^A\, c^B} < 1 \tag{5}$$

Finally, the relative savings $\hat{S}$ by using technology A instead of B can be calculated as:

$$\hat{S} = \frac{C^B - C^A}{C^B} = 1 - \frac{C^A}{C^B} \tag{6}$$

If only direct conversion technologies are considered, equation 6 can be modified by using the cost-efficiency-ratio:

$$\hat{S} = 1 - \frac{\eta^B\, c^A}{\eta^A\, c^B} \tag{7}$$

Equation 7 shows that the relative savings for switching between any two given technologies may be calculated using only the specific costs for input energies and efficiencies, regardless of the heat demand Q_D.

2.2. Relative savings with a vapor compression heat pump system

One of the main technical parameters for a vapor compression heat pump system is the coefficient of performance, COP. In a steady state the supplied heat, Q_D, and the required work, W^{HP}, are proportional to their process variables, $\dot{Q}_D$ and $\dot{W}^{HP}$. Therefore the COP can be calculated as follows:

$$COP = \frac{Q_D}{W^{HP}} \tag{8}$$

For every vapor compression heat pump system exists an ideal reverse Carnot cycle for comparison [4] The ideal cycle is based upon isentropic changes of state in the compressor and throttle as well as upon isotherm changes of state in the condenser and evaporator. For this ideal system the coefficient of performance reaches its maximum, COP_{max}. Due to the first and second law of thermodynamics, COP_{max} can be calculated by using only the temperatures in the evaporator, T_{eva}, and the condenser, T_{con}:

$$COP_{max} = \frac{T_{con}}{T_{con} - T_{eva}} \tag{9}$$

Like most other efficiencies, the COP relates benefit to cost. However, typical values for the COP are above 1 and the range varies due to the temperature levels of the system, making a direct comparison difficult. As a universal performance indicator the second law efficiency η^{HP} is introduced. This factor compares the ideal performance, COP_{max}, to the actual performance of a heat pump system, COP:

$$\eta^{HP} = \frac{COP}{COP_{max}} \tag{10}$$

If equations 8 and 10 are combined, W^{HP} is calculated as follows:

$$W^{HP} = \frac{Q_D}{\eta^{HP}\, COP_{max}} \tag{11}$$

The relative savings $\hat{S}$ can be derivated by combining considerations analogue to chapter 2.1 with the established technical parameters of a heat pump system and. The operating costs for a heat pump system are:

$$C^{HP} = W^{HP}\, c_W^{HP} + Q^{HP}\, c_Q^{HP} \tag{12}$$

Additionally to electrical work W^{HP}, each heat pump system is supplied with a low grade heat Q^{HP} that is either waste heat or taken from the environment. Therefore Q^{HP} causes no costs in most cases, reducing the specific costs c_Q^{HP} to 0. Equation 12 is then reduced to:

$$C^{HP} = W^{HP}\, c_W^{HP} \tag{13}$$

Inserting equation 11 into 13 leads to the operating costs for heat pumps with regards to heat demand Q_D:

$$C^{HP} = \frac{Q_D}{\eta^{HP}\, COP_{max}}\; c_W^{HP} \tag{14}$$

Equation 14 calculates the operating costs based upon general key technical parameters of a heat pump system. These costs may also be compared to other systems using equations 4 and 6. For a reference system based on a direct conversion technology, equation 4 yields:

$$\frac{1}{COP_{max}} \frac{\eta^{ref}\, c_W^{HP}}{\eta^{HP}\, c^{ref}} < 1 \qquad \text{or} \qquad \frac{\eta^{ref}\, c_W^{HP}}{\eta^{HP}\, c^{ref}} < COP_{max} \tag{15}$$

Finally, the relative savings $\hat{S}$ for operating a heat pump system instead of a reference system are:

$$\hat{S} = 1 - \frac{1}{COP_{max}} \frac{\eta^{ref}\, c_W^{HP}}{\eta^{HP}\, c^{ref}} \tag{16}$$

Which can also be transformed to:

$$\hat{S} = 1 - \frac{1}{COP} \frac{\eta^{\mathrm{ref}} c_W^{\mathrm{HP}}}{c^{\mathrm{ref}}} \tag{17}$$

Figure 1 shows a graph illustrating $\hat{S}$ for higher practicability. The graph is based on the two main components of equation 16 and 17 which are a coefficient of performance, either COP or $COP_{\max}$, as well as the according cost-efficiency-ratio. Note that the term for the cost-efficiency-ratio changes with the according coefficient of performance. Therefore the use of Figure 1 is more flexible depending on which technical key parameters for the heat pump system are known.

The linear nature of equations 16 and 17 makes Figure 1 easily to use. Straight lines for a constant COP or $COP_{\max}$ can be added at will due to the following rules:

- $\hat{S} = 1$: Relative savings of 100% are only possible if the relative cost savings are 0 regardless of the coefficient of performance. Therefore any straight line has to cross the y-axis exactly at 1.0.
- $\hat{S} = 0$: For relative savings of exactly 0%, the cost-efficiency-ratio is equivalent to the coefficient of performance. Consequently, a line for a constant value of COP or $COP_{\max}$ crosses the x-axis at that value.

These characteristics strongly increase the overall applicability of the diagram since it is also possible to make rough sketches and estimations on the go. Furthermore, several approaches to use the equations 16 and 17 or Figure 1 exist, depending on the required result. Aside from calculating relative savings it is possible to show necessary technological or economic thresholds to guarantee an economic benefit.

2.3. Ecological assessments and inclusion of a pollutant tax

The operational ecological costs of technologies are mainly represented by their production rate of environmental pollutants such as CO_2. For an ecological assessment the equation system above may be used by simply inserting the specific production rate p of a pollutant instead of the specific economic costs c of an energy source Q in equation 2. This amount for the ecological costs C_{ecol}

$$C_{\mathrm{ecol}} = Q\, p \tag{18}$$

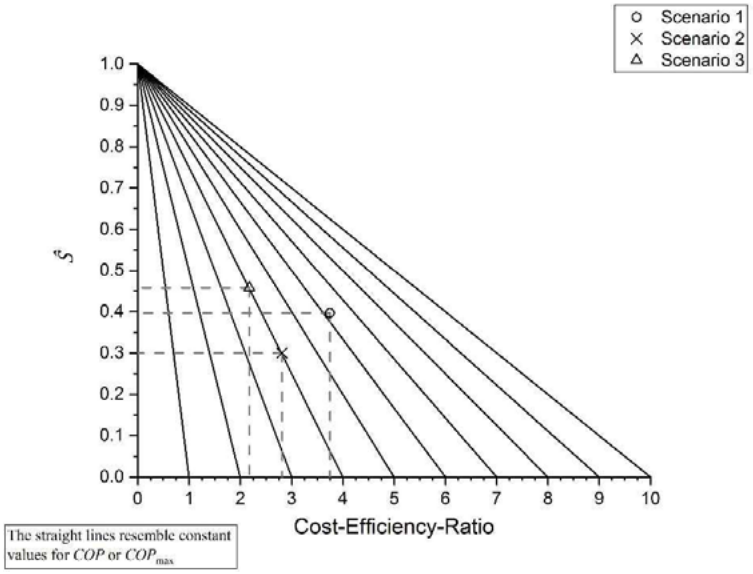


Fig. 1: The relative cost savings as a function the cost-efficiency-ratio for an array of constant $COP_{\max}$ or COP values as calculated with equation 16 or 17 respectively. The marked points show results for example scenarios given in section 3. By using the corresponding cost-efficiency-ratio, Figure 1 can be applied for equation 20 and 23 as well.

This allows the use of the same approach as shown in chapter 2.1 and 2.2 for the calculation of the relative savings in pollutant production, $\hat{S}_{\mathrm{ecol}}$, resulting from a technology switch:

$$\hat{S}_{\mathrm{ecol}} = 1 - \frac{\eta^{\mathrm{B}}\, p^{\mathrm{A}}}{\eta^{\mathrm{A}}\, p^{\mathrm{B}}} \tag{19}$$

$$\hat{S}_{\mathrm{ecol}} = 1 - \frac{1}{COP}\,\frac{\eta^{\mathrm{ref}}\, p_W^{\mathrm{HP}}}{p^{\mathrm{ref}}} \tag{20}$$

For future considerations the inclusion of a pollutant tax t might also be of relevance. By using the pollutant production rate p and the specific costs c of the energy source Q, the overall economic costs result in:

$$C_{\mathrm{econ}} = Q\,(c + p\,t) \tag{21}$$

By using equation 21 instead of equation 2, the relative economic costs savings change to:

$$\hat{S}_{\mathrm{econ}} = 1 - \frac{\eta^{\mathrm{B}}\,(c^{\mathrm{A}} + p^{\mathrm{A}}\,t)}{\eta^{\mathrm{A}}\,(c^{\mathrm{B}} + p^{\mathrm{B}}\,t)} \tag{22}$$

$$\hat{S}_{\mathrm{econ}} = 1 - \frac{1}{COP}\,\frac{\eta^{\mathrm{ref}}\,(c_W^{\mathrm{HP}} + p_W^{\mathrm{HP}}\,t)}{(c^{\mathrm{ref}} + p^{\mathrm{ref}}\,t)} \tag{23}$$

Equation 20 and 23 are of similar structure as equation 17 and therefore Figure 1 may also be used if the correct cost-efficiency-ratio is applied. However, note that equations 20 and 23 can be only applied if the used waste heat source for the heat pump, Q^{HP}, does not result in additional pollutant production.

To use this method it is necessary to know the specific production or emission rate of the considered pollutant for the used energy sources. Energy suppliers usually reference their used energy mix but not necessarily their specific impact on environmental resources. Aside from rough key figures about certain energy types it is possible to perform a system analysis for further information. Nevertheless, one of the more efficient approaches is to use tools like GEMIS. GEMIS is an open source database plus an analysis model to determine energy and resource flows. It considers the life-cycle for processes and scenarios and therefore includes secondary contributions like raw material and transportation. However, for quick calculations the GEMIS database delivers key figures for the main energy sources as well [5].

3. Evaluation of example scenarios

The set of equations derived in chapter 2 as well as Figure 1 can be used to examine possible applications for heat pumps. Depending on the requirements they may be used either to calculate the relative cost savings coinciding with a technology switch, or to determine the necessary technical boundaries for predefined minimum savings. Several predefined scenarios are analyzed in the following section to demonstrate the approach for practical applications.

3.1. Scenario 1 – comparison of a heat pump system and purchased saturated steam

The first scenario considers an industrial process that is currently supplied with saturated steam at $100\ °C$. The steam, which is bought from an external supplier at $10\ \mathrm{cent/kWh}$, provides thermal energy for an industrial dryer at constant temperature. An unused waste heat source allows a theoretical evaporator temperature of $40\ °C$ and enables the implementation of a heat pump system. The company pays $15\ \mathrm{cent/kWh}$ for electrical energy including secondary costs. Experimental data shows second law efficiencies for high temperature heat pumps between 0.40 and 0.60 [6], therefore it is safe to assume a minimum second law efficiency of 0.40. The relative cost savings are required to justify a technology switch.

To use Figure 1, the cost-efficiency-ratio and the according COP_{max} have to be calculated. Due to the fact that steam is bought and used directly for heating the dryer at a constant temperature, the corresponding efficiency is 1.

$$\frac{\eta^{\text{steam}}\, c_W^{\text{HP}}}{\eta^{\text{HP}}\, c^{\text{steam}}} = \frac{1.00 \cdot 15\ \text{cent/kWh}}{0.40 \cdot 10\ \text{cent/kWh}} = 3.75$$

$$COP_{\max} = \frac{T_{\text{con}}}{T_{\text{con}} - T_{\text{eva}}} = \frac{(100 + 273)\ \text{K}}{(100 - 40)\ \text{K}} = 6.22$$

To evaluate the relative economic cost savings, either equation 16 or the graph for $\hat{S}$ can be used. Inserting the calculated $COP_{\max}$ and cost-efficiency-ratio in Figure 1 shows that the implementation of a heat pump system instead of purchasing steam leads to relative cost savings of about 40% for the given boundaries. As shown in equation 15 the economic threshold for the implementation of a heat pump system is the equilibrium of $COP_{\max}$ and the cost-efficiency-ratio. In this particular case the specific costs for the electrical energy have to increase by approximately 66 % in order to reach this equilibrium. Furthermore, Figure 1 allows to identify the required cost-efficiency-ratio in order to meet a given relative economic saving. This procedure is shown in scenario 2.

3.2. Scenario 2 – comparison of a heat pump system and a natural gas heater

This scenario examines a heat pump system that may be used as an alternative to a natural gas heating system for a household. The gas furnace uses condensing technology and has an average fuel utilization efficiency of 0.90 [7] at a cost of $8\ \text{cent/kWh}$. Electrical power is supplied at a cost of $25\ \text{cent/kWh}$. The heat pump system must lead to relative cost savings of at least 30% to ensure a reasonable return of investment. Point of investigation is the COP.

Again the cost-efficiency-ratio is calculated first, but in regards to COP, not $COP_{\max}$:

$$\frac{\eta^{\text{gas}}\, c_W^{\text{HP}}}{c^{\text{gas}}} = \frac{0.90 \cdot 25\ \text{cent/kWh}}{8\ \text{cent/kWh}} = 2.81$$

Using the graph for $\hat{S}$, and a calculated cost-efficiency-ratio of 2.81 leads to a minimum of 4.0 as COP for any profitable heat pump system as shown in Figure 1. At this point the versatility of the diagram based approach can be demonstrated. Assuming that the heat pumps available on the market only reach a COP of 3, the relative cost savings decrease to approximately 5%, making their implementation less feasible.

3.3. Scenario 3 –ecological evaluation of scenario 2

Aside from the relative energy cost savings it is also possible to evaluate the ecological impact of a technology switch as defined in scenario 2 by using the specific CO_2 production of the energy sources. Key figures taken from the GEMIS-database show that burning natural gas emits about $250\ \text{g}_{\text{CO2}}/\text{kWh}$ whereas using electric power produces $605\ \text{g}_{\text{CO2}}/\text{kWh}$ [8].

This can be translated into a cost-efficiency-ratio as well:

$$\frac{\eta^{\text{gas}}\, p_W^{\text{HP}}}{p^{\text{gas}}} = \frac{0.90 \cdot 605\ \text{g}_{\text{CO2}}/\text{kWh}}{250\ \text{g}_{\text{CO2}}/\text{kWh}} = 2.18$$

Using the minimum COP of 4.0 as estimated in scenario 2 and the new cost-efficiency-ratio of 2.18 leads to minimum CO_2 savings of about 45% during operation as seen in Figure 1. Due to the fact that the idea to give emissions a certain economic value is gaining popularity, it is important to make these upcoming changes quantifiable. Scenario 4 demonstrates the economic impact of a tax on emissions for a change of technology.

3.4. Scenario 4 –considering a pollutant tax for scenario 2 and 3

A CO_2 emission tax of $0.01\ \text{cent/g}_{\text{CO2}}$ is introduced to study the impacts of a pollutant tax on the future profitability of the technology switch as demonstrated in scenario 2.

Considering equation 23, the cost efficiency ratio including a pollutant tax is as follows:

$$\frac{\eta^{\text{ref}}\,(c_W^{\text{HP}} + p_W^{\text{HP}}\, t)}{(c^{\text{ref}} + p^{\text{ref}}\, t)} = \frac{0.90 \cdot (25\ \text{cent/kWh} + 605\ \text{g}_{\text{CO2}}/\text{kWh} \cdot 0.01\ \text{cent/g}_{\text{CO2}})}{8\ \text{cent/kWh} + 250\ \text{g}_{\text{CO2}}/\text{kWh} \cdot 0.01\ \text{cent/g}_{\text{CO2}}} = 2.66$$

The new cost-efficiency-ratio is lower than without a CO_2 tax when compared with scenario 2. This leads to several main conclusion:

- Using the same COP as calculated in scenario 2, 4.0, leads to relative cost savings of about 33%, which is higher than without a CO_2 tax.
- With minimum savings of 30%, as suggested in scenario 2, and the new cost-efficiency-ratio, the new minimum COP is 3.8. A pollutant tax would therefore lower the technical requirements for the heat pump system.

These considerations clearly indicate, that the heat pump system is economically better when a CO_2 tax is introduced. However, this relates mainly to the higher CO_2 savings calculated in scenario 3. If the CO2 tax would be raised indefinitely, the threshold for the relative cost savings would be the same as the relative CO_2 savings.

4. Parameter study

The presented example scenarios highlight the ease of the approach. However, the key parameters are further examined to develop an understanding how the system would behave if certain inputs are changed. These considerations can also be facilitated when analyzing potentials or optimizing systems in general.

4.1. Influence of condenser and evaporator temperature on relative cost savings

In regard to vapor compression heat pumps the main technical parameters are the temperatures in the condenser and evaporator, T_{con} and T_{eva}. These temperatures determine the ideal Carnot process that is used for comparison and therefore determine the $COP_{\max}$ as seen with equation 9. To understand the influence of the temperatures, equation 9 is combined with equation 16:

$$\hat{S} = 1 - \frac{T_{\mathrm{con}} - T_{\mathrm{eva}}}{T_{\mathrm{con}}} \frac{\eta^{\mathrm{ref}}\, c_W^{\mathrm{HP}}}{\eta^{\mathrm{HP}}\, c^{\mathrm{ref}}} = 1 - \left(1 - \frac{T_{\mathrm{eva}}}{T_{\mathrm{con}}}\right) \frac{\eta^{\mathrm{ref}}\, c_W^{\mathrm{HP}}}{\eta^{\mathrm{HP}}\, c^{\mathrm{ref}}} \tag{24}$$

Equation 24 shows a linear dependence between the temperature ratio $T_{\mathrm{eva}}/T_{\mathrm{con}}$ and the relative cost savings $\hat{S}$. This is also presented with various cost-efficiency-ratios in Figure 2. Several statements can be made by analyzing equation 24 and Figure 2:

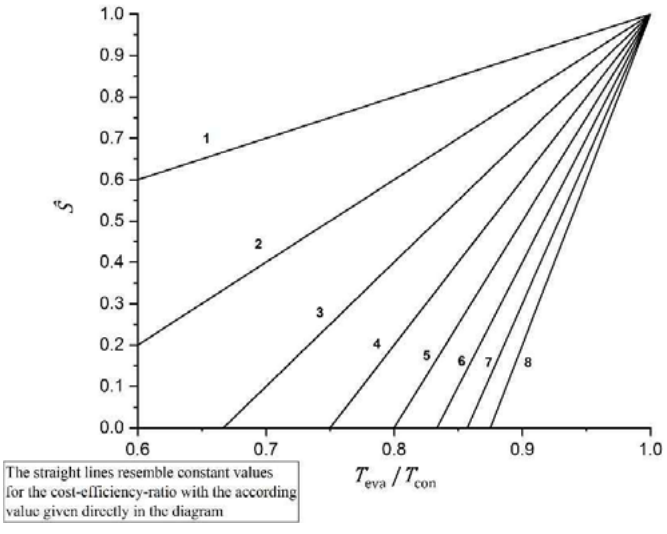


Fig. 2: Relative cost savings as a function of the temperature ratio of the vapor compression heat pump cycle for an array of constant cost-efficiency-ratios. $T_{\mathrm{eva}}/T_{\mathrm{con}} \leq 0.6$ is equivalent to $COP_{\max} \leq 2.5$ which is currently outside of feasible heat pump applications.

Several statements can be made by analyzing equation 24 and Figure 2:

- Increasing T_{eva} or decreasing T_{con} improves the relative cost savings whereas decreasing T_{eva} or increasing T_{con} reduces the relative cost savings. More specifically, smaller differences between T_{eva} and T_{con} lead to higher cost savings.
- For $T_{eva} = T_{con}$ the relative cost savings are always 100% because the utilized waste heat can theoretically be used directly and without a heat pump.
- Each cost-efficiency-ratio has temperature combinations that allow positive relative cost savings. However, the maximum profitable temperature difference between T_{con} and T_{eva} may be very small, depending on the temperature level. More specifically, higher cost-efficiency-ratios reduce the economically beneficial temperature difference.
- The same temperature difference at higher temperature increases the temperature ratio and therefore results in better relative savings as long as the cost-efficiency-ratio remains constant.
- The theoretically lowest temperature ratio is 0 which coincides with a COP_{max} of 1. A COP_{max} below 1 is therefore impossible.

4.2. Considerations about the cost-efficiency-ratio

The cost-efficiency-ratio has a significant influence on relative savings aside from the temperatures of the heat pump cycle. Any change in the specific costs or technology efficiencies leads to a change in the overall ratio. Statements about changes in the cost-efficiency-ratio can therefore be translated to each of its parameters if their position in the numerator or denominator is considered.

Relevant for considerations about the cost-efficiency-ratio are equations 15 and 16. Moreover, equation 16 can be developed into a graph aside from Figure 1 as shown in Figure 3. This allows the following statements:

- Relative savings are guaranteed when equation 16 is used and the cost-efficiency-ratio is below 1 due to COP_{max} always being greater or equal to 1. However, the regular COP theoretically may still be below 1.
- In order to have positive relative cost savings, the coefficient of performance has to be higher than the respective cost-efficiency-ratio.
- Both, an increase of the coefficient of performance or a decrease of the cost-efficiency-ratio, lead to improved relative savings. However, it is more beneficial to lower the cost-efficiency-ratio by a certain percentage, e.g. 5%, than to improve the respective coefficient of performance by the same percentage.

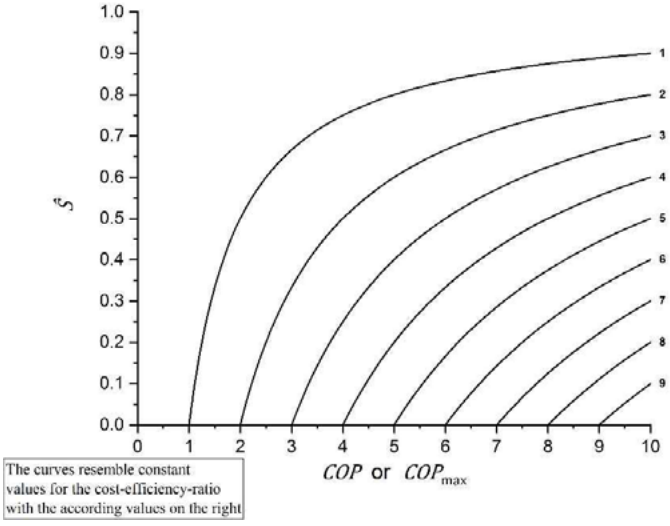


Fig. 3: Relative cost savings as a function of the COP or COP_{max} with an array of curves for constant cost-efficiency-ratios.

5. Conclusion

The derived equations are an accessible and fast tool for assessing and comparing vapor compression heat pump systems with other heating technologies. Based on general known key parameters the relative savings are a clear indicator for the more viable system. Companies may use either the established equation system itself or the graph shown in Figure 1 for estimations about economic potential and therefore for their decision making.

Aside from economic use, the here shown system may also be used for an ecological comparison. The structure of the cost-efficiency-ratio allows the comparison of any number of aspects, as long as the specific costs are of the same type. Comprehensive and reliable statements about ecological effects may be given in combination with databases like GEMIS. If taxes for CO_2-production are introduced in the future, the shown method for a fast economic and ecological evaluation will become even more useful.

Future research in the course of the project CORES (COmbind Renewable Energy Systems) will link the heat pump with other renewable energy technologies like solar thermal energy, photovoltaics and thermal energy storages for optimization in industrial applications. For further improvements the approach may be extended to include a comprehensible assessment about investment costs and amortization periods.

Acknowledgements

The present article was developed as part of the research project “CORES”. This project is funded by the Austrian Climate and Energy Fund and is carried out as part of the Energy Research Programme 2018.

References

[1] GlobeNewswire. CGS Survey Reveals Sustainability Is Driving Demand and Customer Loyalty, 2019. https://www.globenewswire.com/news-release/2019/01/10/1686144/0/en/CGS-Survey-Reveals-Sustainability-Is-Driving-Demand-and-Customer-Loyalty.html. Accessed October 28, 2019

[2] Kiron D, Kruschwitz N, Reeves M, Goh E. The Benefits of Sustainability-Driven Innovation. *MIT Sloan Management Review.* 2013; **54**:69-73.

[3] Lange D., Ponweiser K. *Bewertung der Leistungsfähigkeit von Wärmepumpen im Heiz- und Kühlbetrieb*. Düsseldorf, VDI-Verlag, 2020, p 50-63, ISBN 978-3-18-316319-9

[4] Eder W, Moser F. *Die Wärmepumpe in der Verfahrenstechnik.* Vienna, Springer, 1979, p. 5-7. ISBN 978-3-7091-2252-5

[5] IINAS. About GEMIS. http://iinas.org/about-gemis.html. Accessed October 28, 2019

[6] Arpagaus C, Bless F, Uhlmann M, Schiffmann J, Bertsch SS. High temperature heat pumps: Market overview, state of the art, research status, refrigerants and application potentials. Energy 2018; **152**:985-1010

[7] Lekov AB, Franco VH, Wong-Parodi G, McMahon JE, Chan P. Economics of residential gas frunaces and water heaters in US new construction market. *Energy Efficiency* 2010; **3**:203-222

[8] IINAS. Introduction to selected results from GEMIS Version 4.95. 2017 iinas.org/tl_files/iinas/downloads/GEMIS/2017_GEMIS-results.xlsx. Accessed October 28, 2019

13th IEA Heat Pump Conference
April 26-29, 2021 Jeju, Korea

It works - long-term performance measurement of ground source heat pump systems

Franziska Bockelmann*[a], Christian Kley[b]

[a]Steinbeis-Innovationszentrum (SIZ) energie+, Mühlenpfordtstraße 23, 38106 Braunschweig, Germany
[b]TU Braunschweig, Institut für Gebäude- und Solartechnik, Mühlenpfordtstraße 23, 38106 Braunschweig, Germany

Abstract

Long-term studies of GSHP heating and cooling systems for six different buildings (commercial, institutional and multi-family buildings) have been conducted in Germany by SIZ energy+. Three of them are equipped with borehole heat exchangers and the others use energy piles as a heat exchanger. The paper deals with a demonstration of the investigated buildings, the measured values and performance and the obtained results that include important findings and experiences, problems encountered and possible preventive measures to avoid mistakes.
After ten years of operation it can be stated that the systems work and achieve their planned efficiency but require constant control and regulation to avoid faulty operation. An analysis of the implemented control strategies shows that, for all these heating and cooling systems, holistically coordinated control strategies that are verified during commissioning are required.

© HPC2020.
Selection and/or peer-review under responsibility of the organizers of the 13th IEA Heat Pump Conference 2020.

Keywords: GSHP systems; long-term performance measurement; efficiency

1. Introduction

The integration of heat pumps in the energy supply of buildings is an increasingly applied technology for heating but also for cooling applications. As the number of available and installed heat pump systems increases, the number of possible usable low-temperature heat sources is also increasing.

In practice, heat pumps still often function unsatisfactorily or at least sub-optimally today. The reasons for this are often insufficient connection to the low-temperature heat source and/or incorrect dimensioning of the corresponding heat exchanger. In some cases, heat pumps are not operated in accordance with the design conditions, which is often due to overoptimistic assumptions during planning, but also partly to user-dependent operating errors. In many cases, the primary energy, ecological and economic potential of a heat pump system is greater than achieved in practice. [1-3]

In Germany, the geothermal systems for heating and cooling of office and non-residential buildings have been implemented since 1990. While the first buildings were still pilot projects, most of the systems used nowadays are state-of-the-art. When the monitoring started in 2004 [1-3], there were no examinations or comparative studies from real operation dealing with the functionality and efficiency of the installed heat pumps and their system components. The advantages of a monitoring during operation have been recognized over time in practice, so that nowadays a pronounced increase in knowledge can be stated.

Within the framework of the IEA HPT Annex 52, the Steinbeis-Innovationszentrum (SIZ) energie+ is investigating the interaction between heat pumps and geothermal borehole heat exchangers as well as energy piles using six different buildings (commercial, institutional and multi-family buildings) in a long-term monitoring period of up to > 10 years. The aim is to obtain and document reliable knowledge about the actual

*Franziska Bockelmann. Tel.: +49-531-3913557; fax: +49-531-3918125.
E-mail address: franziska.bockelmann@stw.de.

performance of the buildings with regard to energy consumption, user comfort and operation. Such measurements can also be used to gain insight in how the various system components and control strategies affect overall performance, to identify best practices, design and installation issues that lead to poor performance and to give guidance on how unanticipated consequences of the design can be partially or totally avoided.

For the majority of the examined systems, errors have been analyzed and rectified so that operation-as-planned could be implemented. Subsequently, optimization measures were carried out with regard to a more efficient operation of the geothermal heat storage system in heating and cooling mode, where it was feasible.

2. Monitoring buildings and systems

Within the framework of a "low-level monitoring", four office buildings as well as a school and a multi-family house are measured and analyzed more precisely (Table 1). The six buildings are newly constructed buildings in different locations in Germany. Three building are equipped with borehole heat exchanger and the other three with energy piles, which serve as heat sources for the heat pump system.

The year of construction and commissioning of the buildings took place in the years 2002 to 2016. However, most of the measurement data is not available from the beginning of the building's use. The buildings will be evaluated in the period from 2006 to 2018. For some buildings, however, the data is only available since 2011 or 2017 (commissioning of the building or data transmission). The geothermal systems are integrated in the buildings for heating via a heat pump and for cooling in free cooling mode and via a reversible heat pump [1,3].

The energy concepts for all buildings contain the combination of floor heating or another low-temperature system to heat the building with a heat pump. In the building, heat and cold are distributed resp. transferred via concrete core activation and ventilation systems. In some buildings, high-temperature distribution systems with convectors or radiators are implemented to cover the peak loads of the heating. These building are either connected to the district heating network or use a gas condensing boiler [1,3].

Concerning the school, it is necessary to add, that in addition to the energy piles, a so-called "Agrothermiefield" was installed beneath the sports field. Agrothermie is basically an area collector, that is installed in a new and innovative process using a special plowing technology. The pipe system is plowed with a newly developed sword plow up to 2 m depth under the sports field of the school.

As part of the monitoring of the six buildings, all relevant data will be collected in order to be able to describe the buildings and their plant technology with sufficient accuracy. The measurement concept provides the recording of all essential heat flows and electricity consumption, so that a balanced assessment including the individual producers and consumers is possible.

For older or already commissioned buildings, additional measuring equipment had to be installed. For the other buildings, the monitoring and measuring concept was already defined during the construction phase so that the data can be obtained directly from the system control. For reasons of cost and time, the additional equipment was installed on top of the existing system technology in such a way that data access was given without intervening the building services or structural changes. Depending on the requirements, this could be achieved through the use of mobile digital measurement technology (additional heat meters with temperature and volume flow sensor at relevant points). The measured datasets mainly were recorded on-site either by a computer or by the building management system. Via remote access, the recorded data could be retrieved.

The measured values are recorded every 15 minutes so that parameters of the system components can also be mapped. The measurements and analysis include among other things operating modes, control strategies, the ground source heat extraction and injection, fluid temperatures as well as seasonal performance factors.

Depending on the building, the monitoring extends over two to more than 10 years, so that at least two heating and/or cooling periods are available for evaluating the performance of individual system components and for determining characteristic values.

Table 1. Buildings, heat exchanger systems and supplied systems of the buildings investigated in the monitoring

	Building (anonymized building code)			Ground heat exchanger		Heat supply system
Borehole heat exchanger	AOV Office building	Year: Net floor area: Heating load: Cooling load: Add. heat source:	2010 6750 m² 262 MWh per year 62 MWh per year Gas boiler	Quantity: Length of borehole: Overall length: Extraction / Injection:	25 100 m 2500 m 174 / 206 MWh per year	radiator concrete core activation ventilation
	GEW Office building	Year: Net floor area: Heating load: Cooling load:	2004 6200 m² 554 MWh per year 166 MWh per year	Quantity: Length of borehole: Overall length: Extraction / Injection:	36 150 m 5400 m 155 / 110 MWh per year	heating/cooling ceiling ventilation floor heating
	KON multi-family house	Year: Net floor area: Heating load: Cooling load:	2016 1100 m² 66 MWh per year -	Quantity: Length of borehole: Overall length: Extraction / Injection:	9 100 m 900 m 60 / - MWh per year	floor heating domestic hot water
Energy piles	EFB Office building	Year: Net floor area: Heating load: Cooling load: Add. heat source:	2003 20700 m² 828 MWh per year 62 MWh per year District heating	Quantity: Length of pile: Overall length: Extraction / Injection:	196 8,50 m 1666 m 85 / 85 MWh per year	concrete core activation
	VGH Office building	Year: Net floor area: Heating load: Cooling load: Add. heat source:	2002 4000 m² 350 MWh per year 24 MWh per year District heating	Quantity: Length of pile: Overall length: Extraction / Injection:	101 17,50 – 21,50 m 1926 m N/A	concrete core activation ventilation
	WGG school	Year: Net floor area: Heating load: Cooling load: Add. heat source:	2015 11500 m² 340 MWh per year 100 MWh per year Gas boiler	Quantity: Length of pile: Overall length: Extraction / Injection:	4400 m² Agroth. / 96 energy piles 8 – 12 m 1004 m Agroth. 61,5 / 70,7 MWh per year energy piles 101,7 / 102,3 MWh per year	concrete core activation ventilation floor heating

3. Monitoring

In addition to technical practicability, energy as well as ecological and economic aspects play a central role in the decision for or against a particular heating or cooling system. When comparing geothermal systems with

conventional systems, the question arises as to whether they can guarantee a similarly high level of thermal comfort in buildings and what usable advantages they offer with regard to the above-mentioned aspects.

In the following sections, the monitoring results of the six buildings and systems are used to discuss energy yields and system efficiency as well as system performance.

Some of the systems had already been in operation for several years before they were analyzed in more detail as part of this project. Therefore, in some of the buildings and plants faults were hidden for a long time and were only discovered during monitoring and corrected as far as possible. The measurement results reflect the fault detection and correction as well as the subsequent operational optimization and therefor vary considerably from year to year in some cases.

The results documented in the following are therefore not target or guideline values for other projects, but rather are intended to show optimization successes and potentials as well as possibilities and limits of the geothermal systems.

3.1. Seasonal performance factor

In order to ensure a uniform basis in the evaluation of the heat pump performance, the boundaries for the calculation of the Seasonal Performance Factor (SPF) are set in advance in according to the boundaries defined by SEPEMO [4]. The boundaries can be found in Figure 1.

In the evaluation and comparison of the monitored plants, only SPF2 is described more detailed in this paper. In addition, depending on the available measurement data, the heating and cooling cases are considered separately, so that a seasonal performance factor is determined for both heating and cooling cases.

$$SPF\,2 = \frac{\text{thermal energy of heat or cold supply of the heat pump and free cooling}}{\text{electrical energy of the compressor of the heat pump and circulating pump on earth side}} \quad (1)$$

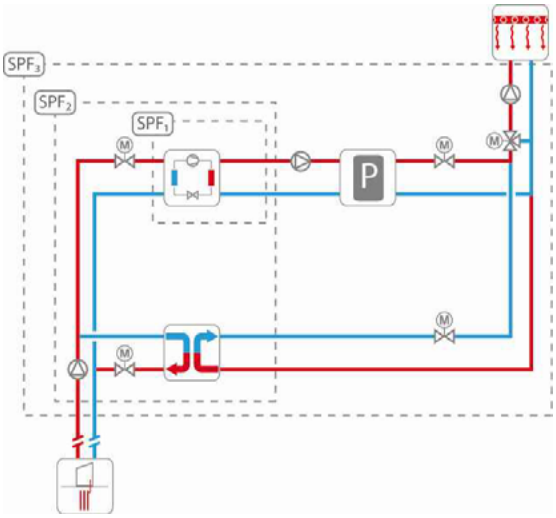


Fig. 1. Boundaries for the calculation of the seasonal performance factor

The seasonal performance factor of heat pumps, free cooling and cooling machines vary widely in their magnitude. From a primary-energy perspective, heat pump operation with a SPF greater than 3 is considered efficient. In active cooling mode, the SPF should reach a value greater than 2.5. Free cooling operation is particularly efficient. Here, electrical energy consumption on the generator side is only required for driving the circulating pumps of the geothermal system. With correct dimensioning and mode of operation, SPFs of 20 to 50 – or higher - can be achieved [1].

With seasonal performance factors of less than 3, the operation of some of the monitored plants was not as efficient as planned when the monitoring started. Within the scope of the monitoring, the systems and the operation could be optimized to such an extent that all plants achieve seasonal performance factors between 3

and 6 (Figure 2 and 3). Larger leaps in the seasonal performance factor, e.g. in the energy pile system of the VGH or the GEW system, are usually due to system optimizations or hydraulic changes. Causes for slight fluctuations, such as in the energy pile system of the EFB building, are, for example, due to varying requirements depending on the weather as well as varying underground temperatures. A decisive influence on the seasonal performance factor of the cooling system is the proportion of the very efficient free cooling operation in relation to the active cooling mode.

The comparatively low seasonal performance factors of the borehole heat exchanger system of the GEW building with almost optimized operation are related to the deviating objective. The building is heated and mainly cooled by the geothermal system. Only the supply air is cooled to room temperature in summer by an independent system. In order to cover the cooling loads from the building even on extreme summer days, the heat pump is reversible and can therefore also provide active cooling during the summer. Since the GEW borehole heat exchanger system, unlike the other systems, is not designed primarily for basic but also for peak load coverage, the reversible heat pump run a large part of the operating time in less efficient partial load operation. Furthermore, this heat pump is not a standard product and was individually designed at the time. According to the age and the construction method, seasonal performance factors > 3 are not to be expected.

The results of the EFB, AOV, KON and WGG buildings show that targeted quality assurance and operational monitoring pay off right from operational start-up. Up to now, seasonal performance factors of up to 5 have been achieved here. (Figure 2 and Figure 3) It should also be noted that operational monitoring is also helpful after a calibration phase. Thus, it can be stated that after the end of the actual research project and the optimization phase (2010/2011), the seasonal performance factor at the VGH fell below 3.0 again. The faults here relate to the plant technology.

On the basis of the evaluations of the buildings and heat pump systems, it can be summarized that (Figure 2 to 5)

- the majority of the buildings meet the consumption calculated in the planning and there are no major user-dependent changes,
- the heat pump systems are generally reliable and efficient,
- for the heating mode, seasonal performance factors larger than 3 are achieved for most systems. SPF over 5.0 were determined for two systems. For one building, the seasonal performance factor is below 3.0 according to the measured data, which is due to the design and the plant itself.
- for cooling operation, seasonal performance factors of around 4 can be achieved for most systems if there is a priority active cooling process (reversible heat pump). The free cooling operation of the EFB system alone leads to seasonal performance factors of around 40 in cooling mode.

The reasons for the low seasonal performance factors include, among others

- the continuous operation of the system (running times),
- non-coordinated operating strategies as well as heating and cooling curves between the operating states of heating, active cooling and free cooling, and
- changed setpoints, e.g. outdoor air temperature as the starting value of the cooling mode, were not reset to standard mode after changes in the settings due to defective equipment, and
- faulty measurement.

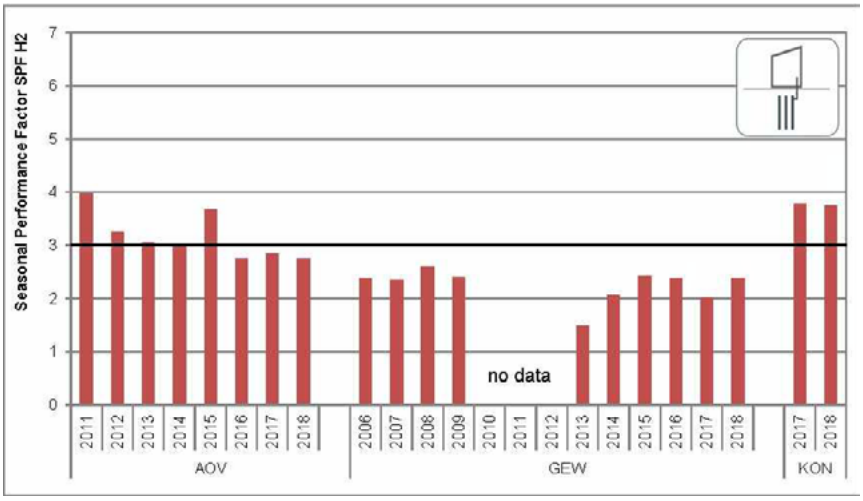


Fig. 2. Seasonal performance factors heating for the monitored buildings with borehole heat exchangers

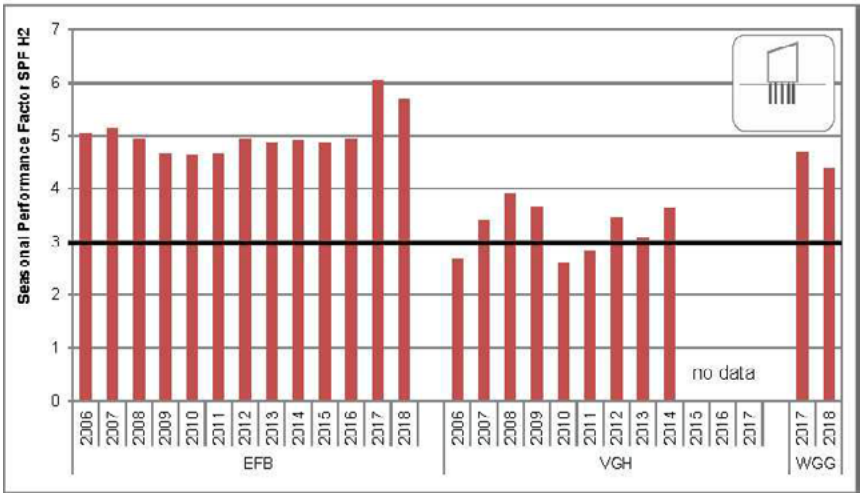


Fig. 3. Seasonal performance factors heating for the monitored buildings with energy piles

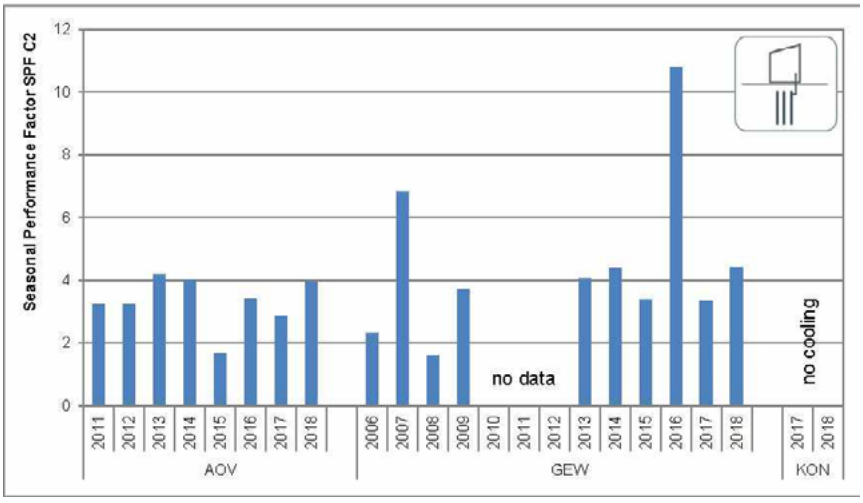


Fig. 4. Seasonal performance factors cooling for the monitored buildings with borehole heat exchangers

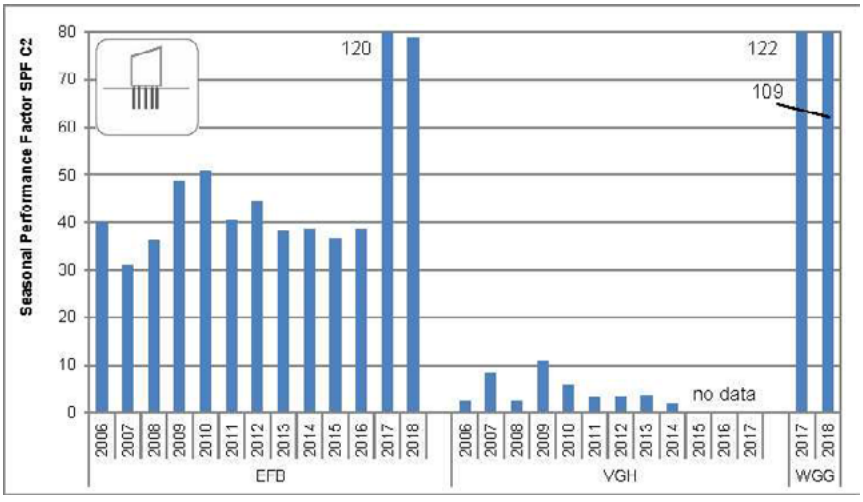


Fig. 5. Seasonal performance factors cooling for the monitored buildings with energy piles

3.2. Heat extraction and injection

The specific annual energy yields for the various heat sources and heat exchanger systems are shown in Figure 6 per meter of borehole heat exchanger or energy pile.

The largest specific energy extraction occurs in the KON and WGG. In one year up to 170 kWh/(m a) and 107 kWh/(m a) are extracted from the ground. The AOV and GEW have the highest specific heat injection. A maximum of 120 kWh/(m a) and 96 kWh/(m a) are injected into the ground. The average specific heat extraction for borehole heat exchangers is 80 kWh/(m a) and for energy pile systems 50 kWh/(m a). The values for heat injection are 75 kWh/(m a) for the borehole heat exchangers and around 34 kWh/(m a) for the energy piles.

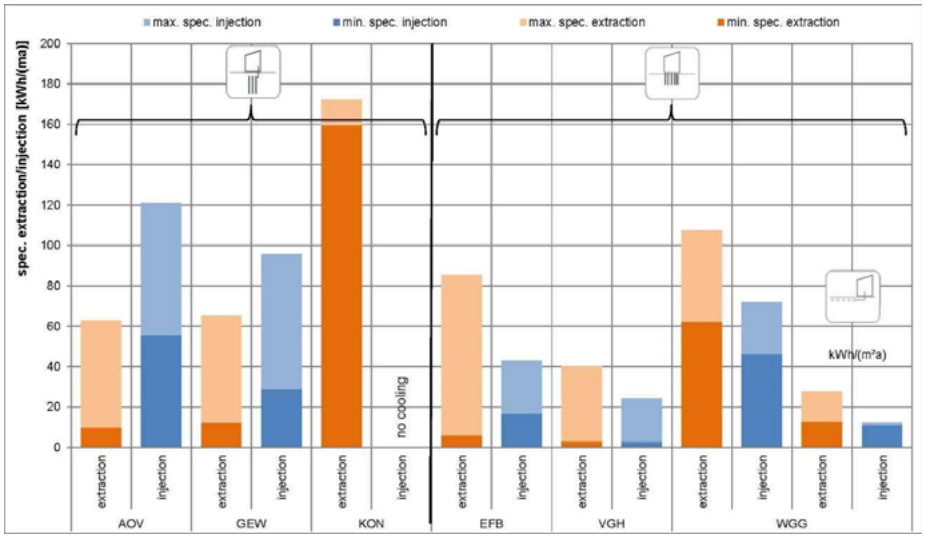


Fig. 6. Specific heat extraction and injection of the monitored heat exchangers

Ground storage systems are planned with the aim of achieving a constant temperature level in the ground over the years and a permanently stable operation for approximately equal yields of heat extraction and injection. The energy yields recorded as part of the monitoring vary from year to year, mainly because of the system optimizations, but also as a result of the influence of the weather and the resulting varying consumption. Overall, the extracted heat corresponds approximately to the planned values. The heat injection, on the other hand, deviates considerably from the planned values for some plants. The reasons for this are faults in current operation or an excessively high temperature level in the ground for free cooling operation as a result of operating faults immediately after start-up. In order to achieve a constant temperature level over the years, some systems require a higher heat extraction than heat injection due to higher than expected temperatures of the underground.

For inner-city areas, monitoring has shown that less deep systems, such as energy piles, which are used as seasonal storage systems, usually require a higher heat extraction rate than the heat injection. Due to the high density of buildings and the high degree of surface sealing, the near-surface layers in inner-city areas are relatively warm. With a well-adjusted balance between heat extraction and heat injection, the temperature level of the heat sink is usually too high for free cooling operation in summer.

For the AOV, it can be noted that the heat injection is noticeably higher than the heat extraction (in 2015: 3.5 times). A well-adjusted heat balance is therefore not available, despite an almost 100% heat supply via the heat pumps. It is therefore essential to ensure that more heat is extracted from the ground or that significantly less heat is injected into the ground due to server cooling. On the basis of the total energy quantities, it can be seen from the annual balance sheets that since 2011 significantly less heat has been extracted than assumed in the planning / design. It can also be seen, however, that the optimizations and modifications to the heat pump have increased heat pump operation and have thus also enabled significantly more heat to be extracted from the ground since 2013. The heat injection could be significantly reduced by outsourcing the servers and the associated server cooling (2017). In 2018, a good balance between heat injection and heat extraction can now be established. (Figure 7)

In the case of the GEW building, heat extraction was significantly increased from 2009 onwards. For the years 2009 to 2018, heat extraction is between 230 and 330 MWh/a. During the years 2011 to 2017, reduced active cooling mode and an increased proportion of free cooling will lead to a reduction in heat injection into the ground. During this period, the heat injections were between 220 and 270 MWh/a. In 2018, 405 MWh/a were injected into the ground as a result of the further increase in cooling machine operation. (Figure 7)

For the EFB, it can be noted that around two times more heat is being extracted from the ground than being injected during the summer. The aim is to cool down the underground and enable a higher proportion of free cooling in summer. In 2009, the heat extraction of 142 MWh/a was almost three times higher than the heat injection which was 53 MWh/a. Both heat extraction and heat injection were significantly reduced in the years

2013 to 2018 due to errors in the heat pump and control problems and amount to 10 MWh/a to 33 MWh/a for extraction and 28 MWh/a to 55 MWh/a for injection. (Figure 8)

At VGH, the planned heating and cooling operation was implemented during the monitoring process until 2009. From 2014, heat extraction from the ground was reduced to between 5 MWh/a and 43 MWh/a due to a new control system and new software for the heat pump. No scheduled operation has been restored since the software changeover. (Figure 8)

The alternating heating and cooling operation of the WGG requires a coordination between the Agrothermie and energy piles. For the years 2017 and 2018 the energy piles have a heat extraction of 63 MWh/a and 107 MWh/a as well as a heat injection of 46 MWh/a and 72 MWh/a. The extraction and injection values of the Agrothermie in the same period are 56 MWh/a and 121 MWh/a for the extraction and 48 MWh/a and 53 MWh/a for the injection. Since beginning of the building's use, adjustments have been made to the control strategies of the two sources on the basis of the brine entry and exit temperatures of the geothermal low-temperature heat sources and their heat exchangers. The inefficient year-round continuous operation of both sources (parallel operation), which was implemented at the beginning, was replaced by a prioritization (addition / removal of one source). To increase the efficiency, the two sources have been controlled separately in the winter months since the changeover. The changeover is based on the higher brine outlet temperatures per source system. During the heating period, the heat pumps primarily use the energy piles (higher brine temperature level). To ensure that the piles are kept frost-free, they are only operated up to a brine entry temperature of > 3 °C. Afterwards the heat is removed from the Agrothermie. A reverse priority is planned for the cooling period. The Agrothermie will act as a priority and then the bored piles will be controlled to ensure, among other things, regeneration of the energy piles.

For an assessment of the efficiency of the Agrothermie, the energy piles were deactivated during the heating period 2018/2019. The control adaptation serves to determine the heat injection and extraction in a heat pump system with the sole heat source of an Agrothermie. It has been shown that the field can serve as the sole source for the heat pumps up to and including December (and beyond). For the future operation of both heat sources, however, it must be ensured that there is a balance in both sources and that the soil is overcooled neither in the Agrothermie nor in the energy piles. Regeneration is necessary in both cases. (Figure 8)

The KON system is running according to plan and without any incidents. The heat extraction amounts to about 150 MWh/a in the years 2017 and 2018. (Figure 7)

The success of the optimization measures and error corrections carried out can be clearly seen in the buildings. Nevertheless, a well-adjusted balance was not fully achieved.

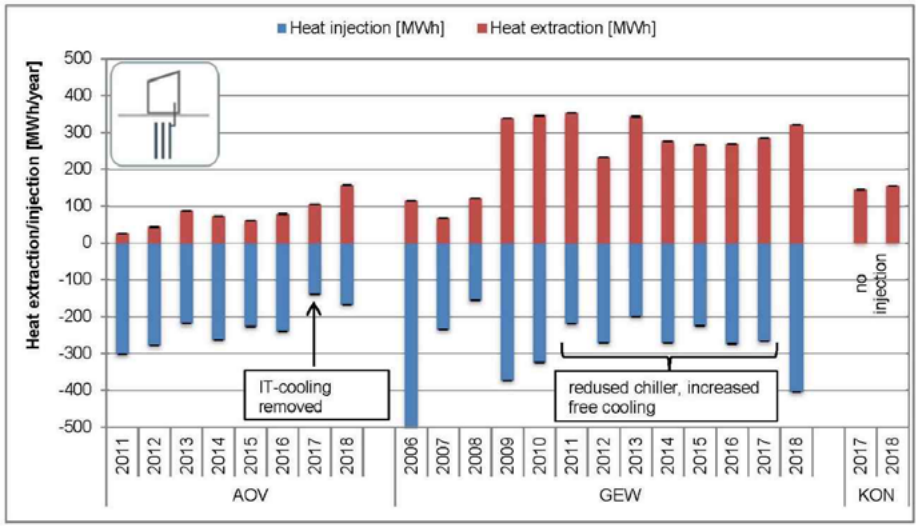


Fig. 7. Annual heat injection and extraction of the borehole heat exchangers systems

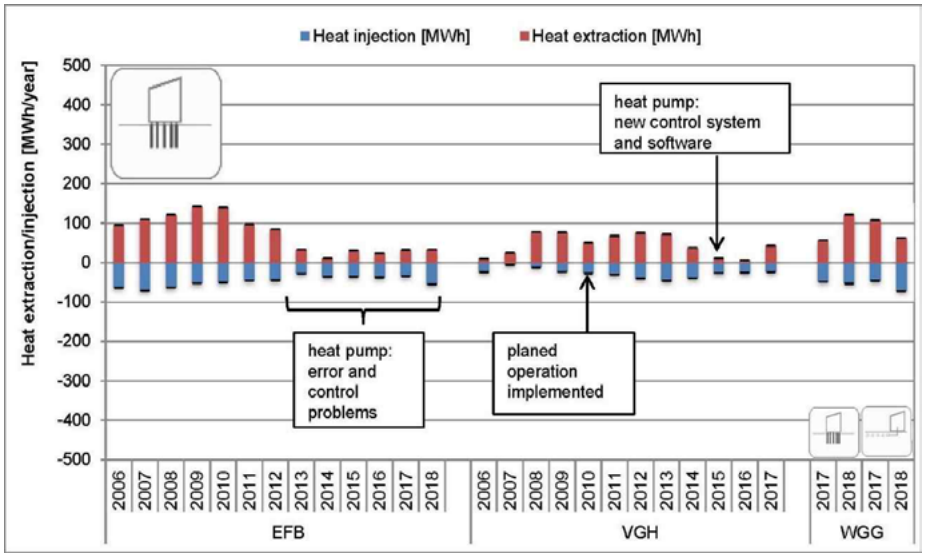


Fig. 8. Annual heat injection and extraction of the energy pile systems

4. Operating experiences

The experience gained from the project monitoring shows that it is possible and sensible to integrate geothermal systems into innovative energy concepts for office buildings as well as schools and multi-family houses. However, a regulation phase is required during which the direct interaction between the geothermal system, the building, other thermal conditioning systems and not least the users is optimized. A lack of experience of contractors and plant operators often significantly prolongs this regulation phase. Compared to conventional heating and cooling systems, geothermal low-temperature sources are subject to a special feature with regard to the detection of system and operating faults due to their inertia and the interaction of base and peak load components. Without targeted operational monitoring, errors due to system inertia remain unnoticed until defined operating parameters can no longer be achieved. As this usually only happens after years, the ground is -in the worst case- already significantly undercooled or overheated. Once the fault has been rectified, the ground may no longer be usable for the intended operating mode - heating or cooling - for a longer period of time. The ground must first be thermally regenerated.

Many of the results presented in this paper have been generalized, as they have not only been found in individual buildings. In one building, the points listed may have been more serious/amplified than in another. We would like to consider the following statements generally valid, although they should also be checked/monitored for all buildings in the future.

Essential points of the performed defect and error removal at the buildings and plants examined by measuring technology and the resulting problems were among others:

- Hydraulic investigation: like incorrect installation of valves and check valves or opening valves without heating or cooling medium.
- Defects in dimensioning and design: system components dimensioned / designed too small, e.g. plate heat exchanger, circulating pumps.
- Control of the geothermal system: poorly coordinated control strategies or circulation pumps running 24/7.
- Coordination of the individual exchange systems and components.
- Faulty operation is usually not due to the geothermal system, but to the technical and operational integration of the single system modules in the complex overall system.
- Errors in design and implementation but particularly faults in control and operation.

Important findings and experience:

- Heat is drawn from other sources instead of using the ground (district heating, internal loads, etc.). In some buildings, an unequal energy balance in the ground was recorded. In addition, other installations did not function reliably, so that no continuous and controlled heat extraction and injection into the ground could be recorded. This led to overheating or cooling of the ground. The supply of district heating or similar must be limited exclusively to covering peak loads.
- Faulty operation: under- or overheated soil, free cooling not possible and temperature level between heat sink and building often not tuned. Adaptation of heating and cooling curves as well as control and release limits of heat pumps, rev. heat pump and free cooling during operation is mandatory.
- Adaptation of room set points and general set points to the actual boundary conditions.
- Control and recording of the function of a building combined with installation of geothermal system is important, it is not a system that works for itself.
- Constant control required: Changes in the operation modes will be forgotten to reset.
- Slow system →late fault detection, long-term consequences.

Fault prevention:

- "Keep it as simple as possible" – simple energy concepts with simple systems and modules are needed.
- Quality assurance during the construction phase as well as comprehensive final inspection and commissioning after completion.
- Improved and early integration of geothermal systems into building concept and control strategies.
- We have to talk! Consultation between architect, building services planner and geothermal planning.
- Monitoring:
  By monitoring the operating condition of most buildings, it is possible to prove that they are not in accordance with the design. For this reason, error analyses and error corrections are necessary at the beginning of monitoring in order to transfer the buildings to regular operation. Only then can the operating data be used for the objective of the project and the actual measurements and evaluation can begin.
  - Minimum measurement equipment for monitoring of operation.
  - Monitoring of operation to detect and eliminate performance faults >> adjust operation to real boundary conditions.
  - Monitoring of annual energy amount (heat injection and extraction) as well as brine temperatures.

5. Conclusion

In addition to reducing the energy requirements of buildings, the sustainable (e.g. CO_2-neutral) coverage of energy requirements is a focus of research and development. From the perspective of the use of regenerative energies and energy-efficient construction, in recent years, the ground has increasingly been integrated into energy concepts as a supplier of heat and cooling in conjunction with a heat pump for the heating and cooling of modern office and administration buildings as well as multi-family houses. Heat pump technology will therefore continue to play an important role in the future supply of heat and cooling. In order to exploit the potential of this energy supply variant as efficiently as possible, the choice of a low-temperature heat source and the most suitable heat exchanger for the respective application is of decisive importance.

The results from the research work and the scientific monitoring of the projects, as well as their implementation in practice—presented in the paper—show that it is generally possible and sensible to integrate ground-coupled heat pumps into innovative energy concepts. By monitoring six buildings and their geothermal systems for more than 10 years, it has been shown that, for a successful and permanent operation of energy pile and borehole heat exchanger systems, a high-quality standard has to be maintained during planning, implementation and operation.

It also becomes clear that it is not only a harmonious energy concept and innovative plant technology that lead to an energy-efficient building. Even with detailed, careful planning, malfunctions often occur during operation, which can cause rising energy consumption or cause discomfort. For this reason, quality assurance (operational analysis and optimization) is of crucial importance for ground-coupled supply concepts, especially in the first years of operation and beyond the project phases. This is the only way to ensure that buildings and systems achieve their planning objectives and long-term functionality, as well as progress in system energy efficiency and user comfort. For all heating and cooling systems in this study, it was found that holistically coordinated control strategies are required, and these must be double-checked and monitored during operation

until regular operation is achieved. In cooperation with the building management, possible errors and optimization potentials could be identified step by step, the operation of the systems optimized and the balancing phase shortened. Most of the considered buildings and their ground-coupled heat pumps could be brought into operation as planned and now operate efficiently with an SPF H2 between 2.5 and 6 and in cooling mode between 4 and greater than 100 (depending on the proportion of free and active cooling). The results also show that there is generally no significant difference in operation and performance between a borehole heat exchanger and an energy pile.

In general, it should be stated for all buildings that a balancing phase and continuous monitoring of the injection and extraction quantities should not be neglected. As found in earlier monitoring projects and also in the buildings currently under investigation, it is only possible to detect errors and inconsistencies which have a decisive influence on the operation of the plant through long-term monitoring. Continuous monitoring, adjustment and maintenance is therefore necessary to ensure the intended operation of the plant.

Acknowledgements

The research projects (032736A, O3ET1024A and 03ET1605) were funded by the German Federal Ministry for Economic Affairs and Energy. We would like to thank all building owner and operator for their help and support as well as providing measurement data and information about the monitored buildings.

References

[1] Bockelmann, F., Kipry, H., Fisch, M. N.: WKSP – Wärme- und Kältespeicherung im Gründungsbereich energieeffizienter Bürogebäude, final report: BMWi Fkz 032736A, TU Braunschweig Institut für Gebäude- und Solartechnik, November 2010, Braunschweig, Germany

[2] Bockelmann, F., Kipry, H., Fisch, M. N.: Erdwärme für Bürogebäude nutzen, BINE-Fachbuch, Fraunhofer IRB Verlag, Stuttgart, Germany, ISBN 978-3-8167-8325-1, 2010

[3] Bockelmann, F., Fisch, M. N., et al: geo:build - Systemoptimierung erdgekoppelter Wärme - und Kälteversorgung von Bürogebäuden - reversible Wärmepumpen und freie Kühlung, final report: BMWi Fkz O3ET1024A, TU Braunschweig Institut für Gebäude- und Solartechnik, Dezember 2015, Braunschweig, Germany

[4] Zottl, A., Nordman, R., Miara, M., Huber, H.: System boundaries for SPF calculation, 10th IEA Heat Pump Conference, Tokyo, Japan, 16 - 19 May 2011.

13th IEA Heat Pump Conference
April 26-29, 2021 Jeju, Korea

Study on the frosting phenomena between concavity and convexity plate under forced convection - The prediction of frost layer growth using the observation from the frost and defrost multi-cycle experiment-

Masafumi Katsuta[a],Shota Ikutaya[b], Yuki Terakado[b], Junya Yamagishi[b], Rio Asakawa[b] , Sangchul Bae[a]

[a]*Department of Modern Mechanical Engineering, Waseda University, Shinjuku-ku, Tokyo, 169-8555, Japan*
[b]*Graduate School of Environment and Energy Engineering, Waseda University, Shinjuku-ku, Tokyo, 169-8555, Japan*

Abstract

Recently, the development of hybrid and electric vehicles has been promoted. Along with this, since the impact reduction for cruising distance and the securing of the heat source are problems, changes are also required for the air conditioner. Therefore, high efficiency of the air conditioning system by improving efficiency of the heat exchanger has become more necessary. However, due to frost formation of the outside heat exchanger in a cold climate region, increase of pressure drop and decrease of heat transfer rate are supposed to be an application difficulty of HP systems.

The objective of this study is to analyze the mechanism of frosting phenomenon in a fin-less heat exchanger. This is intended to clarify the advantage in terms of frost strength and defrosting performance of a fin-less heat exchanger.

In this research, the frost and defrost multi cycle experiment are established and the qualitative characteristics are investigated. Through observation of frost layer growth in the continuous experiment, ice column growth such as initial ice column diameter and ice column distance is grasped and influence of wettability on ice column growth is also confirmed.

© HPC 2020.
Selection and/or peer-review under responsibility of the organizers of the 13th IEA Heat Pump Conference 2020.

Keywords : Frosting and Defrost Phenomena under Convection, The effect of Wettability Frost Layer Growth, Finless Heat Exchanger;

1. Introduction

Currently, as a power train alternative to gasoline and diesel vehicles in the automotive industry, the development of hybrid and electric vehicles has been promoted. Along with this, since the impact reduction for cruising distance and the securing of the heat source are problems, changes are also required for the air conditioner. Therefore, high efficiency of the air conditioning system by improving efficiency of the heat exchanger and changing to hat pump system has become more and more necessary. However, due to frost formation of the outside heat exchanger by using in the cold climate region, increase of pressure drop and decrease of heat transfer rate are expected to be a problem on HP systems.

Multi-flow type heat exchanger having a corrugated-louvered fin is the mainstream of the heat exchanger for a vehicle, and the fin and tube miniaturization is progressing in order to improve the performance. Thereby, since the retention amount of the condensed water or melting water between the fins increases, frost strength and defrosting performance is feared to be reduced. As improved method for these problems, fin-less type heat exchanger has been proposed to prevent the retention of condensate. This study is to analyse the mechanism of frosting phenomenon in fin-less heat exchanger, it is intended to clarify the advantage in terms of frost strength and defrosting performance fin-less heat exchanger for the current heat exchanger.[1)-3)]

2, Methodology

2.1. Experimental Apparatus

Fig.1 is a schematic diagram of experimental apparatus. Experimental apparatus is composed of constant temperature and humidity air chamber, blower, orifice flow meter, test section and the duct. The air controlled by temperature and humidity from the chamber, is flowing into the test section by the blower and then returned to the chamber. Air temperature and humidity before and after the test section is measured by the temperature and humidity sensors. In addition to the area of frost layer, diameter and interval distance of crystal columns were measured by using an image processing. Experimental system is almost same as previous paper.(paper number) To establish the defrosting condition, the hot water heating is adopted and its system is shown in Fig.2.

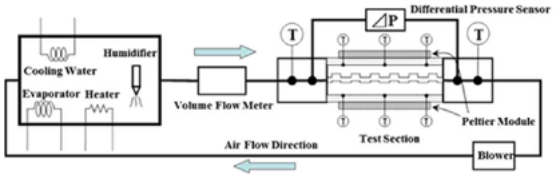


Fig. 1. Schematic of Experimental Apparatus

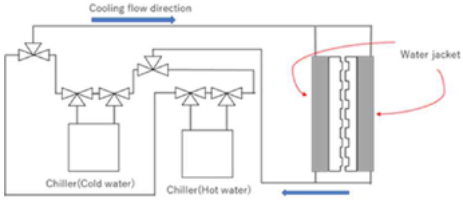


Fig. 2. Circuit diagram including Water Jacket (Defrost)

2.2. Test Section

Fin-less heat exchanger has a shape like Fig.3. In this study, we focus on the air side passage, and a test section focusing on only one flow path is prepared as shown in Fig.4. Test section has a periodic convex-concave shape as shown in Fig.5, and the size of each part is defined as shown in Fig.6.

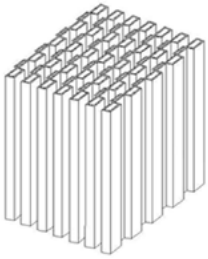


Fig.3. General View of Heat Exchanger

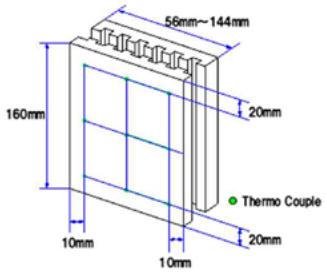


Fig.4. Test Section Plate

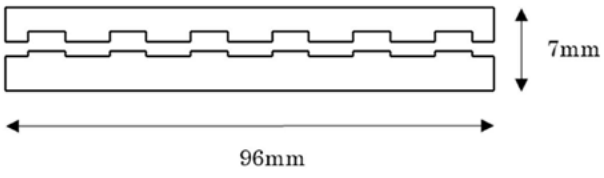


Fig.5. Flow Channel of Test Section

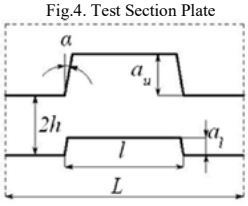


Fig.6. Detail of Flow Channel

2.3 Experimental methodology and condition

First, air conditions in the air chamber are adjusted to the experimental aimed value as shown in table 1. Turn off the blower after confirmation of the steady state, and the test section was cooled down to a set temperature. The experiment started after reaching the set temperature, and to measure the temperature, humidity and pressure drop across the test section until channel blockage, and the state of frost growth was taken by camera. Then, the test section was removed, and frost weight was measured. Air flow rate decreases in accordance with frost growth, however the blower output was fixed. Design parameters of test section are shown in Table 2.

After the end of each experiment, the height of the frost layer was taken by camera from the top of test section, and the height of the frost layer was measured. The captured image can be incorporated into image processing and analysis software, and then the height of frost layer is measured.

Table 1. Experimental Conditions

Temperature	℃	7.0
Temperature of Cooling Surface	℃	−10.0
Relative Humidity	%	86.0
Initial Air Flow Rate	m^3/h	5.0

Table 2. Design Parameters of Test Section

			No.1	No.2	No.3	Hydrophilic	Hydrophobic
Height of Convexity Portion	a_l	mm	2.0	1.2	2 .8	2.0	2.0
Depth of Concavity Portion	a_u	mm				2.8	
Length of convex-concave portion	l	mm				8.0	
Pitch of convex-concave	L	mm				16.0	
Taper Angle of Unevenness	α	deg				10	
Number of convex-concave	N	—				6	
Contact Angle (Wettability)	-	deg		60~90		~10	150~

3. Result and Discussion

3.1. The heat transfer rate and pressure drop

The channel blockage time is the time until the air flow rate becomes zero or the increase rate of the approximate curve of the air flow rate becomes zero.

The purpose of the experiment was to clarify the effects of the height of the convex part and the surface treatment, focusing on the pressure loss and the amount of heat absorption, in the air flowing through the test section simulating a row of concave and convex plate. Obtained experimental result is substituted for the following equation and the heat transfer rate is calculated.

$$\dot{Q} = \dot{Q}_s + \dot{Q}_l = \dot{m}_a C_p \Delta T + \dot{m}_a \Delta W (\hbar_{fg} + \hbar_{fg}') \quad (1)$$

h_{fg}: Latent heat of condensation h_{fg}': Latent heat of solidification

However, since the amount of water whose state changed from water to ice is unknown from the experimental results, Equation (1) is calculated on the assumption that all the water amounts obtained from the absolute humidity difference are frozen instantly.

3.2. The heat transfer rate of each flat plate

This experiment consists of 2 cycle frost and defrost experiment. The result of the convex-concave flat plate with different heights and the wettability is shown from Fig.7. to Fig.11. Fig.12. and Fig.13. show total heat flow rate.

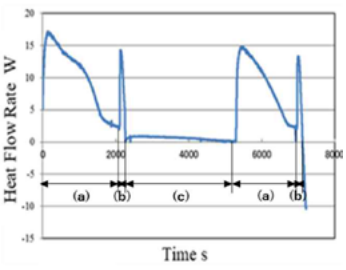


Fig. 7 Heat Flow Rate of No.1 Plate

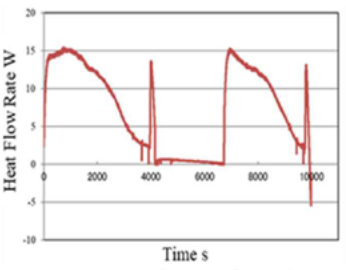


Fig. 8 Heat Flow Rate of No.2 Plate

(a)Frosting Period
(b)Defrosting Period
(c)Preparing Period

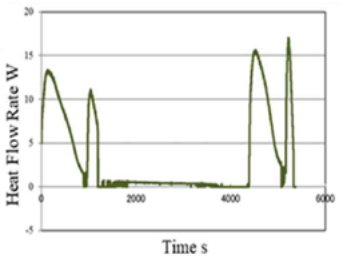


Fig. 9 Heat Flow Rate of No.3 Plate

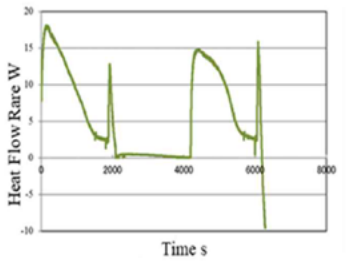


Fig. 10 Heat Flow Rate of Hydrophilic Surface

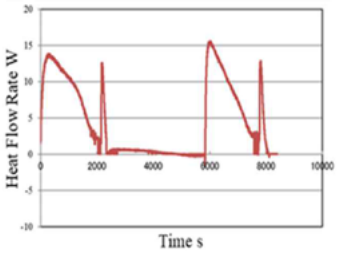


Fig. 11 Heat Flow Rate of Hydrophobic Surface

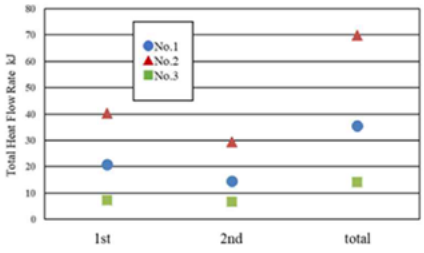


Fig. 12 Total Heat Flow Rate (Comparison with Convex Height)

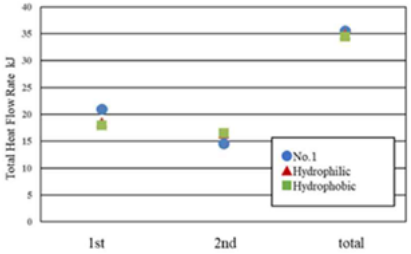


Fig. 13 Total Heat Flow Rate (Comparison with Surface Condition)

From Fig. 12, No.2 experimental convex-concave plate having the lowest height achieves the highest heat flow rate. Also, from Fig.13, the surface treatment (difference wettability) does not have the clear effect on heat flow rate.

3.3. Blockage arise time of each experimental convex-concave plate

The channel blockage time is the time until the air flow rate becomes zero or the increase rate of the approximate curve of the air flow rate becomes zero. Fig.14. to Fig.22. show that the pressure drop of second cycle compared with height and wettability as the parameter.

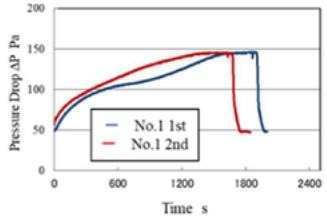


Fig. 14 Pressure Drop of No.1 Plate

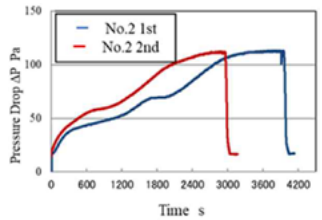


Fig. 15 Pressure Drop of No.2 Plate

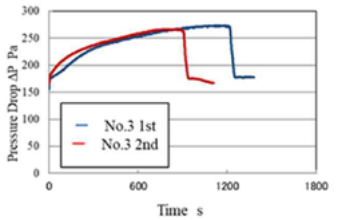


Fig. 16 Pressure Drop of No.3 Plate

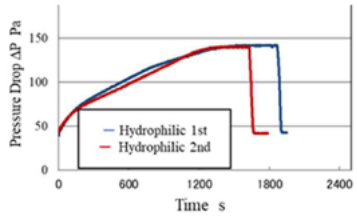


Fig. 17 Pressure Drop of Hydrophilic Surface

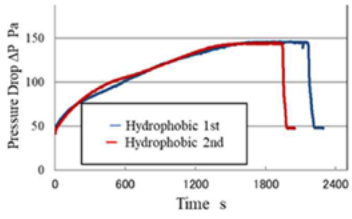


Fig. 18 Pressure Drop of Hydrophobic Surface

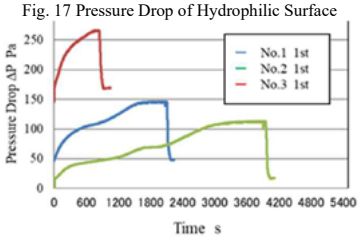


Fig. 19 Pressure Drop of 1st Cycle

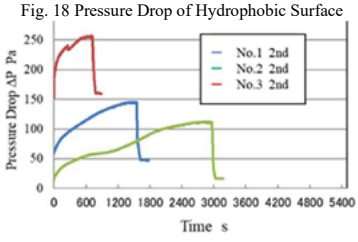


Fig. 20 Pressure Drop of 2nd Cycle

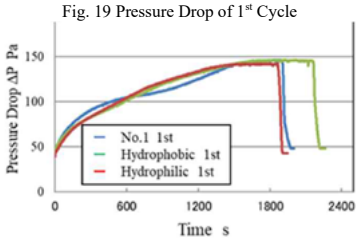


Fig. 21 Pressure Drop of 1st Cycle

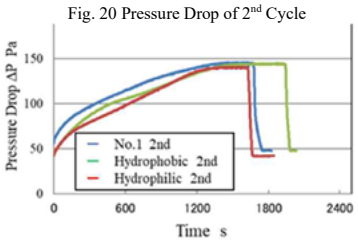


Fig. 22 Pressure Drop of 2nd Cycle

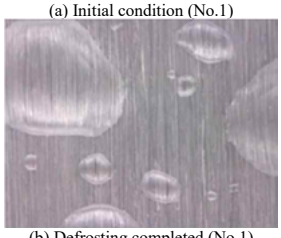
Each test piece plates, second cycle experiment is earlier to close as shown from Fig.14. to Fig.20. Comparison is made by wettability; the hydrophilic plate is earlier to close than other test pieces (Fig.21 and Fig.22).

3.4. Observation of Frost Crystals Growth

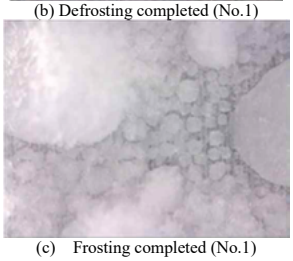
By changing the one side of the aluminium plate to acrylic plate, the test section was visualized. After frost crystals appear, the interval distance and diameter distance were measured. Fig.23. is shown No.1 plate, Fig.24. is shown hydrophobic plate and Fig, 25. is shown hydrophilic plate.



(a) Initial condition (No.1)



(b) Defrosting completed (No.1)

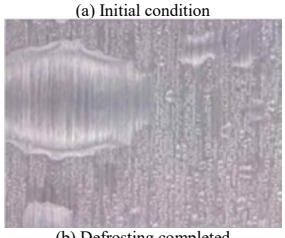


(c) Frosting completed (No.1)

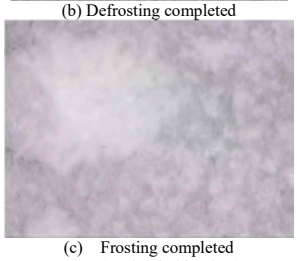
Fig. 23. Observation of Frost Crystals Growth (No.1)



(a) Initial condition



(b) Defrosting completed

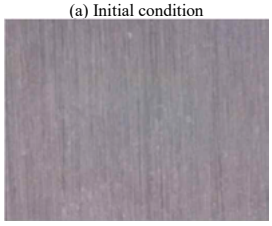


(c) Frosting completed (Hydrophobic Plate)

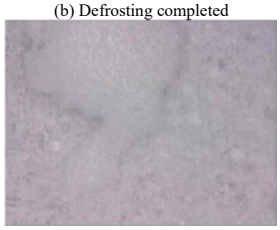
Fig.24. Observation of Frost Crystals Growth (Hydrophobic)



(a) Initial condition



(b) Defrosting completed



(c) Frosting completed (Hydrophilic plate)

Fig.25 Observation of Frost Crystals Growth (Hydrophilic)

The air flows from right to left on test piece. The hydrophilic test section has different trend to compare with other test pieces. In the first cycle, it is confirmed that droplets are generated like the other test pieces and ice crystals grow from there. However, in the second cycle, it is confirmed that the frost crystals are growing as they were without small droplets coalescence each other. Moreover, after the defrosting is completed, the generation of droplets is observed in other test pieces, but this hydrophilic test piece is not so clear as compared with the other test pieces. Much more in detailed observation movies will present in conference.

Next, the initial crystal column diameter and ice column interval are measured using image processing in the same manner as the frost layer area measurement for the frost column in each channel taken by frost layer growth observation. The initial crystal column diameter is measured when the formation of frost columns is confirmed growing with ice droplets as the nucleus. The number of ice droplets is counted for the crystal interval, and the interval is defined as the distance between crystals assuming that it is uniformly distributed in an image area. However, since it is difficult to count the number of ice droplets in the second cycle of hydrophilic test piece, the distance between the ice drops that could be confirmed is taken as the ice column interval. The future task is to improve the accuracy of the measurement method of ice column diameter and ice column interval. The measured ice column diameter and ice column interval are summarized in Table 3.

Table 3. Various amounts of initial frost crystals forming

	1st Initial crystal column diameter (mm)	1st Crystal column interval (mm)	2nd Initial crystal column diameter (mm)	2nd Crystal column interval (mm)
No.1	0.015	0.051	0.022	0.063
Hydrophobic	0.025	0.065	0.021	0.060
Hydrophilic	0.013	0.054	0.007	0.036

3.5 Analysis of frost layer growth

The growth process of the frost layer is classified into “Crystal growth stage”, “Frost layer growth period”, and “Frost layer full growth stage”. Crystal growth stage: Needle-like crystals are generated with ice droplets as nuclei, forming crystals, forming a frost layer with a large porosity and rough surface. Frost layer growth stage: Side branches occur on the side of the frost column, filling the voids, forming a frost layer with a small surface roughness and a flat surface The calculation is based on Yamashita's model[7], which is obtained by multiplying a constant to Tao et al [6]. Water vapor transport through the frost layer considered to be a porous layer and is divided into a frost layer density increasing component and a frost layer height increasing component that diffuse inside the frost layer according to the concentration gradient. As mentioned, using analysis method is almost same as previous paper[4]. Here important key equations[5)-8)] are summarized as below .

$$(\delta L_f/\delta t) = C_2 \times (h_D / \rho_I) \times (X_a - X_{fs}) \quad (2)$$

$$(\delta d/\delta t) = C_3 \times 2 \times (h_D / \rho_I) \times (X_{\ddot{y}} - X_I) \quad (3)$$

$$T_Y = k_\alpha \times T_\alpha + (1 - k_\alpha) \times T_w \quad (4)$$

$$\rho_f = \frac{\int_0^{Lf} [\frac{\pi}{4} d^2 \rho_I + (l^2 - \frac{\pi}{4} d^2) \times \rho_a] \times dz}{l^2 \times Lf} \quad (5)$$

h_D = Mass transfer coefficient [kg / m^{2}sΔX] , X_{fs} = Absolute humidity of Frost Layer Surface [kg / kg´] X_f = Absolute humidity of frost layer [kg / kg´], k_a ・ C_2 ・ C_3: Constant , X_a = Absolute humidity of air [kg /kg´] d = Crystal column [m] , X_l = Absolute humidity crystal column [kg / kg´]

$$\dot{m} = \dot{m}_d + \dot{m}_h = h_D \times (X_a - X_{fs}) \quad (6)$$

$$\varepsilon = \frac{\rho_i - \rho_f}{\rho_i - \rho_a} \quad (7)$$

$$\dot{m}_d = D_{eff} \times \frac{d\rho_v}{dz} = D_{eff} \times \frac{M_v}{RT_f} \times \frac{dP_v}{dz} \quad (8)$$

$$D_{eff} = \mu \times D_v = \frac{\varepsilon}{\tau} \times D_v \quad (9)$$

$$\partial \rho_f / \partial t \times (t_f \times A_w) = \dot{m}_d \times A_w \quad (10)$$

Table 4. The Suggested Formulas of Tortuosity

Year	Name	Tortuosity
1969	Brian et al	$\tau=1.1$
1986	Auracheret al	$\tau=1-0.58\times(1-\varepsilon)$
1993	Taoet al	$\tau=1/1.1$
1997	Le Gall et al [9)]	$\tau = \frac{\varepsilon}{\frac{\varepsilon}{1-0.58\times(1-\varepsilon)} + F\times 10\times(1-\varepsilon)\times\varepsilon^{10}}$
2002	Mezedure et al	$\tau = \frac{\varepsilon}{1-(1-\varepsilon)^{0.5}}$

$\dot{m}$: Mss flux kg/m^{2}s $\dot{m}_d$:Mass flux by using density increment kg/m^{2}s $\dot{m}_h$:Mass flux by using increment of the frost height kg/m^{2}s D_{eff}: Effective diffusion coefficient m^2/s Aw : Cooling surface area m^2 μ: Diffusion resistance coefficient ε: Porosity Dv: Diffusion coefficient m^2/s τ:Trtuosity

3.5 Results of analysis

Ice column interval and initial ice column diameter is set as initial value referred to experimental result in Table 3. Table 5 shows the value used in calculation, Fig.26 and Fig. 27 shows the calculation results of the frost density, and Fig. 28 and Fig. 29 show the calculation results of the frost height, respectively.

Table 5. Calculation Parameter

	Transition Region		Crystal Growth Stage				Frost Layer Growth Period
	Starting Time	Closing Time	1st Initial ice column diameter mm	1st Ice column interval mm	2nd Initial ice column diameter mm	2nd Ice column interval mm	Tortuosity
No.1	60s	1170s	0.015	0.051	0.022	0.063	Le Gall et al eq.(F=1)
Hydrophobic			0.025	0.065	0.021	0.060	Le Gall et al eq.(F=1)
Hydrophilic			0.013	0.054	0.007	0.036	Le Gall et al eq.(F=1)

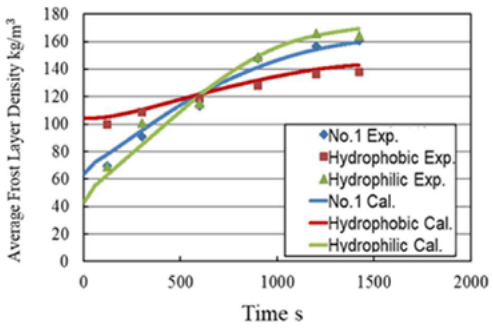


Fig.26. Average Frost Layer Density as Function of Time (1st)

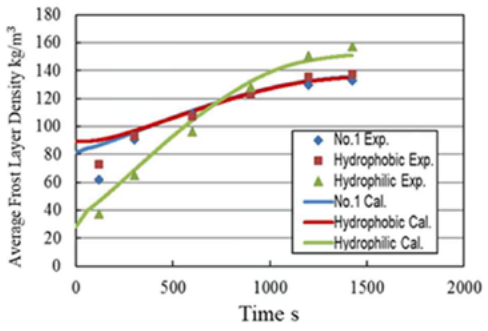


Fig.27. Average Frost Layer Density as Function of Time (2st)

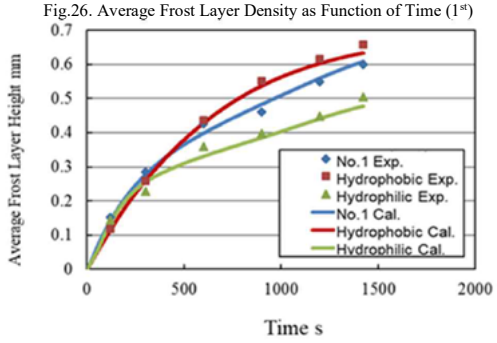


Fig.28. Average Frost Layer Height as Function of Time (1st)

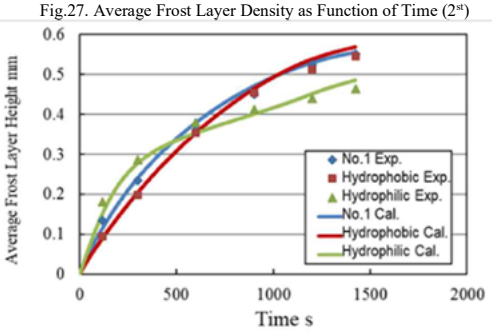


Fig.29. Average Frost Layer Height as Function of Time (2nd)

From Fig. 26. to Fig. 29, it is confirmed the difference between experimental value and calculated value in crystal growth stage are large. Therefore, it is necessary to improve accuracy of the analysis model of this stage.

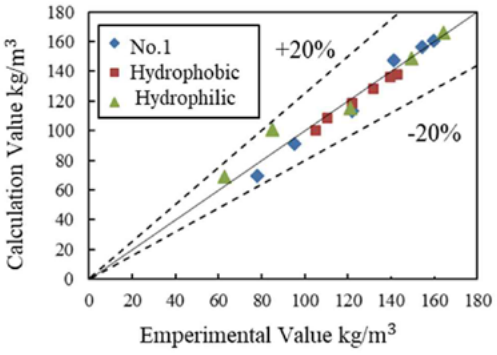


Fig. 30. Error Band of Frost Layer Density (1st)

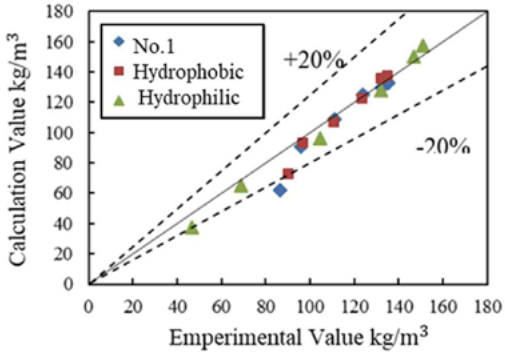


Fig. 31. Error Band of Frost Layer Density (2nd)

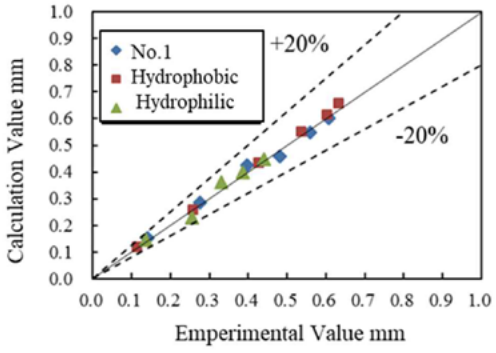


Fig.32. Error Band of Frost Layer Height (1st)

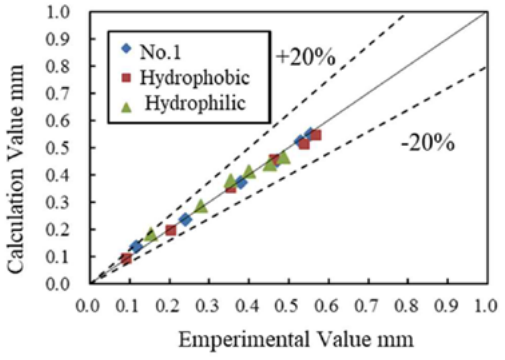


Fig. 33. Error Band of Frost Layer Height (2nd)

From Fig. 30. to Fig.33. show the error band of frost layer density and frost layer height, respectively. Table 6 shows the average error rate.

Table 6 Average Error Band

	No.1		Hydrophobic		Hydrophilic	
	1st	2nd	1st	2nd	1st	2nd
Ave. Frost Density	5.91%	8.79%	3.15%	2.23%	7.48%	5.92%
Ave. Frost Height	4.27%	4.04%	6.09%	3.01%	10.1%	5.95%

From Fig. 30. to Fig. 33., the error band of calculated value is about 10%. Particularly, the average error band is about 2% in No.1.

4. Conclusion

(1) A multi-cycle frost and defrost experiment using a water-cooled jacket is established, and the qualitative frost and defrost characteristics are grasped.
(2) By frost layer growth observation in multi-cycle experiments, the growth of crystal such as initial crystal diameter and spacing is determined, and the effects of convex height and wettability on crystal growth are confirmed.
(3) The calculation results of the analytical model of the frost layer growth on the convex-concave plate are summarized with an error of less than 10% on average, using experimental values as the setting values in the calculation.

(4) Within the scope of this study, the combination of No. 1 plate and the hydrophobic surface treatment had the most frost resistance.

5. Reference

[1] Adachi T, Mizushima J. 1998, The transfer to the stability and the turbulent flow of a flow in rectangular tube. *RIMS Kokyuroku published*. 1051: p. 202-214.

[2] Adachi T, Uehara H. 2000, Pressure Drop and Heat Transfer Characteristics of Flow in Channels with Periodically Grooved Parts, *Transactions of the JSME*. B67(657).

[3] Yang D. 2006, Frost formation on a cold surface under turbulent flow, *International Journal of Refrigeration*. 29(2): p. 164-169.

[4] Yasui K., Katsuta M., Doshida H. and Miyashita R., Study on the Frosting Phenomena between Concavity and Convexity Plate under Forced Convection-Detailed Observation and Analysis of Frost Layer Grouth-,*12th IEA Heat Pump Conference*, Rotterdam Netherland, (2017.5.15).

[5] Tao Y, Besant R, Mao Y. 1993, Characteristics of frost growth on a flat plate during the early growth period. *ASHRAE Transactions*. 99: p. 746-753.

[6] Tao Y, Besant R, Mao Y. 1994, Frost growth characteristics on heat exchanger surface: measurement and simulation. *HTD*, 286: p. 29-38.

[7] Yamashita K. 2009, Frosting phenomenon in low temperature environments. *Doctor's degree of Tamagawa University*.

[8] Fukusako S, Inaba H. 1996, *Heat transfer phenomenon under the cool temperature environment and applicability*. Yokendo, Tokyo, 14 p.

[9] Le Gall, J.M. Grillot and C. Jallut, "Modelling of Frost Growth and Densification", I*nt. J. of Heat Mass Transfer.* 28, (7) (1997),3177-3187.

13th IEA Heat Pump Conference
April 26-29, 2021 Jeju, Korea

The study of secondary loop system with efficient and flammable refrigerants in MAC

Inguk Hwang, Haejun Lee, Gumbae Choi, Jaeyeon Kim, Manju Oh*

Hanonsystems, 95, Sinilseo-ro, Daedeok-gu, Daejeon, 34325, Korea
Hyundai Motor Group, 150, Hyundaiyeonguso-ro, Namyang-eup, Hwaseong-si, Gyeonggi-do, 18280, Korea

Abstract

In EV market, two key factors are driving range and cost. The conventional heat pump system can extend driving range in cold season, but it has lots of components and has complicated structures. The cost of heat pump is also more expensive than normal air-condition system with air PTC heater.
To solve these challenges, secondary loop system has been considered for EV thermal management system based on coolant system. However, it has weak point in regard to fast cool down, warm up and maximum performance due to heat loss. To solve those problems, some refrigerant is in study, and we did drop in test with efficient & flammable refrigerants (R1234yf, R152a, R290). Test result shows the possibility of secondary loop system & challenges.

Keywords: Secondary loop; Heat Pump; Flammble refrigerant; R152a; R290

1. Introduction

In the EV market, which is growing in size over time, EVs are valued as mileage and price. Among them, many electric vehicles use heat pump system to increase the mileage, but the heat pump system has a large number of parts and a complicated system configuration, which makes it less competitive in terms of price. On the other hand, electric heaters are often used in general A / C systems to solve electric car cooling / heating at low prices. In winter, the use of electric heaters is the biggest factor in reducing the mileage of electric cars.

After all, in order to increase the competitiveness of electric vehicles, a simple configuration and a low-cost heat pump system are required. As a solution, a secondary loop heat pump system is attracting attention these days. However, the secondary loop heat pump system has a heat transfer process of refrigerant-cooling water-air, and in this process, heat exchange efficiency is reduced, and performance is lower than that of a direct system for refrigerant-air heat exchange.

In this study, the refrigerant was studied as a method to improve the performance of the secondary loop heat pump system. Drop-in evaluation was performed on three refrigerants R1234yf, R152a, and R290 with different characteristics, and the cooling / heating performance of each refrigerant was compared.

* Corresponding author. Tel.: +82-42-930-5947; fax: +82-42-930-6992.
E-mail address: ihwang@hanonsystems.com.

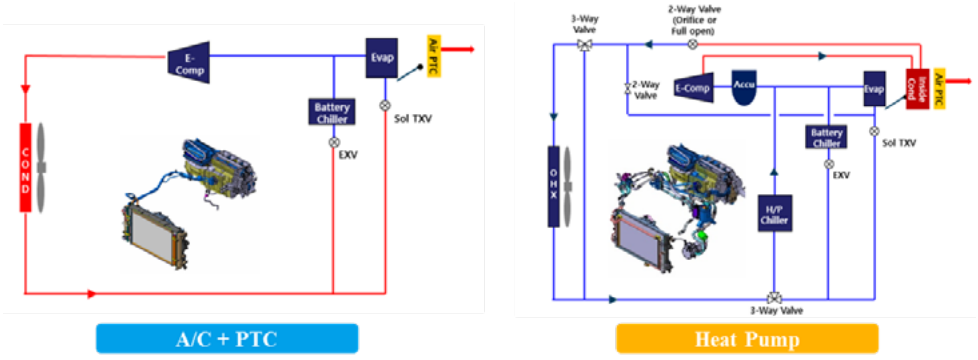


Fig. 1. A/C+PTC System / Heat Pump System

2. Body

2.1. *Secondary Loop System Definition*

Comparing current direct heat pump systems with secondary loop systems shows a number of differences in component count and pipe connections. The current heat pump system has a large number of heat exchangers for cooling and heating, and includes a plurality of refrigerant valves for changing the direction of the refrigerant, and the increase in the number of components increases the price of the heat pump system. Secondary loop systems can reduce the number of components because there is no need to switch the refrigerant direction, which leads to a lower price.

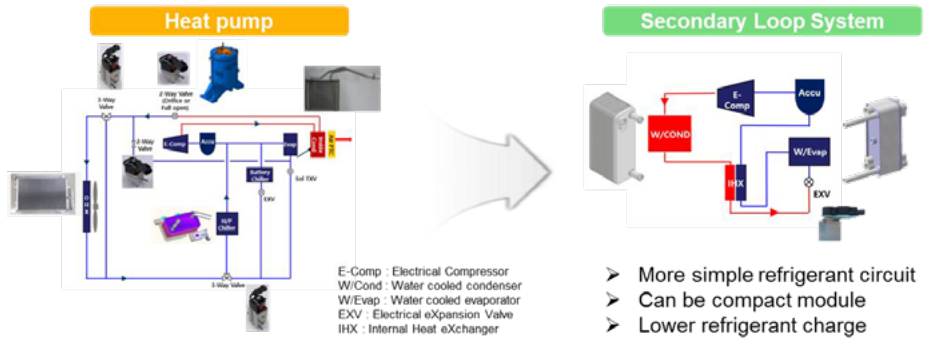


Fig. 2. Direct heat pump system / Secondary loop system

In a secondary loop system, cooling and heating are operated by circulation of the coolant. When cooling, the coolant heat exchanged from the evaporator is drawn to the heat exchanger in the HVAC, and when heating, the coolant heat exchanged from the condenser is drawn. Figure 3 shows the coolant circuit at A/C mode and H/P mode.

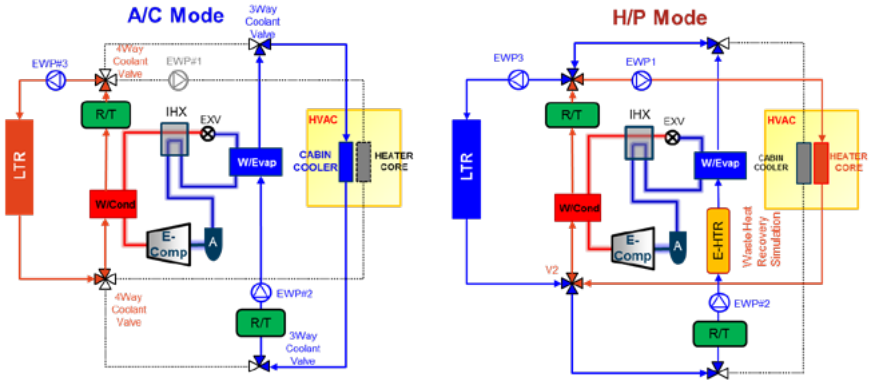


Fig. 3. Cooling mode and heating mode in secondary loop system

The advantage of the secondary loop is that the system is simpler in construction, and the disadvantage of the secondary loop is that the performance is degraded due to the heat exchange process. In fact, when R1234yf refrigerant used in the current heat pump is used in the secondary loop, cooling performance is reduced by about 22% and heating performance is reduced by about 15%.

2.2. Refrigerant Characteristics Comparison

With R1234yf refrigerant, it is difficult to satisfy the performance in the secondary loop system. There are limitations in refrigerant characteristics. In this study, we applied the refrigerant of R152a and R290 to check whether the performance can be satisfied in the secondary loop. R152 and R290 are low-GWP eco-friendly refrigerants and low cost. In addition, the heat of vaporization is large relatively, which can lead to higher performance.

Table 1 Refrigerant characteristic comparison

	Market Application	Environmental Regulation (GWP)	Safety Regulation	Estimated Cost ($/kg)	Heat of vaporization (kJ/kg) at 0°C	Heat of vaporization (kJ/kg) at 60°C	System Matching
R134a	Current (will Phase down)	1430	A1	3.4	198.6	139.1	Direct
R1234yf	Launched (Global)	3	A2L	66.8	163.3	110.4	Direct
R152a	TBD	124	A2	-	307.1	229.3	Indirect
R290	TBD	3	A3	3.1	374.9	259.2	Indirect

The p-h diagram (Fig. 4) shows that the heat of vaporization of these two refrigerants is large, and in particular, R290 has a relatively lower saturation temperature at the same pressure, which improves the cooling performance and heating performance.

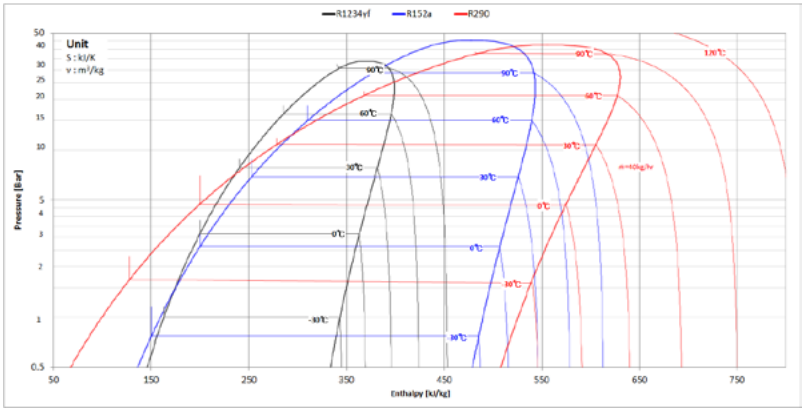


Fig. 4. p-h Diagram of Refrigerants

2.3. Bench Rig Test Result

Figure 5 shows the results of the refrigerant charge amount determination test. The test was on A/C high load condition, 35°C ambient temperature and 50% relative humidity. The refrigerant charge amount is reduced by 45% in the secondary loop system compared to the direct heat pump system. Where R152a and R290 are further reduced by 27% and 58%, respectively. If 1000g of refrigerant is charged in the R1234yf direct heat pump system, the refrigerant charge amount of the R290 secondary loop system is about 230g. This is half of the IEC standard 500g (self-contained).

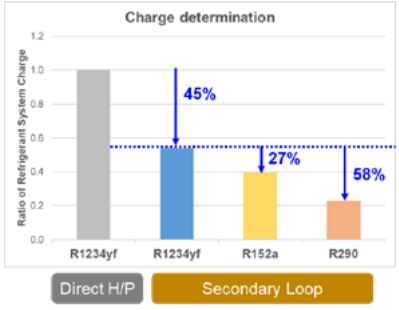


Fig. 5. Results of refrigerant charge determination test

Cooling performance test was performed under an ambient temperature of 35°C, humidity 40% RH conditions. The air flow rate on the HVAC side was 450cmh, and the air flow rate on the air cooled condenser and radiator side was 2.5 m/s. The compressor is a 33cc electric scroll type compressor and was operating 7000rpm.

Figure 6 and 7 show the results of the A/C test. The secondary loop system based on the R1234yf reduces 22% performance over the direct system. The air discharge temperature at the evaporator shows that the direct system is 8.5°C, while the secondary loop system is 11.8°C, because coolant is in between the refrigerant and the air. In more detail, the refrigerant temperature of the evaporator under the above conditions is about 5°C, and in heat exchanger refrigerant cools the air to 8.5°C. On the other hand, in the second loop, when the refrigerant temperature of the evaporator reaches 5°C, and it makes the coolant temperature about 8.5°C, and the 8.5°C coolant makes the air 11.8°C.

In this case, when R152a refrigerant is used, the heat of vaporization is large, and a cycle is formed at a lower pressure and a temperature in the evaporator, thereby improving cooling performance by about 4%. At

the same pressure, the saturation temperature is slightly higher than R1234yf, but the heat of vaporization is relatively large, so performance can be secured at a small flow rate.

When using R290 refrigerant, the effect of the refrigerant characteristics is very huge. Cooling performance is improved by 30%, which is equivalent to a direct system using R1234yf. R290 has a high heat of vaporization and a low saturation temperature at the same pressure. So it is possible to make refrigerant at lower temperature, coolant at lower temperature, and discharge air at lower temperature. However, Pd is formed relatively high, so the compressor power is consumed more, and the COP is lowered, but this COP is similar to the secondary loop system of the R1234yf, which is not a disadvantage of the R290.

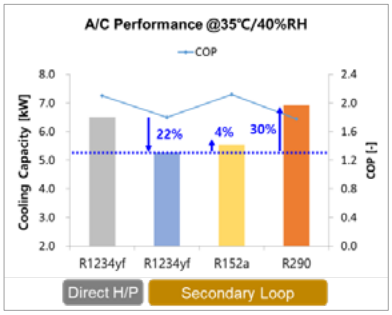


Fig. 6. Results of A/C performance test

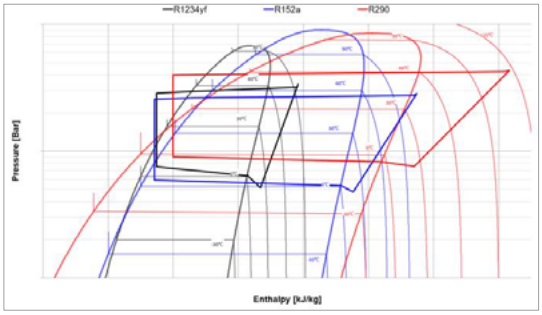


Fig. 7. p-h diagram comparison in A/C mode

Figure 8 and 9 show the results of the H/P test. Heating performance test was performed under an ambient temperature of -20°C. The air flow rate on the HVAC side was 300cmh, and the compressor was operating 5000rpm. The waste heat of the electrical equipment was simulated, and 2 kW of energy was supplied to the evaporator. Since the same heat absorption amount of waste heat was applied, the performance difference was not large. However, the low pressure side refrigerant state at this time can confirm the performance impact of the refrigerant characteristics. R1234yf and R152a have a refrigerant temperature of -20°C or -19°C based on compressor suction side, whereas R290 has refrigerant temperature of -30°C.

What the refrigerant temperature is lower than outside air means that additional heat absorption from outside air is possible. Because the refrigerant temperature on low pressure side of R1234yf and R152a is similar to outside air, heat absorption from outside air is not possible, it makes limited heating performance. However, R290 is lower than outside air by 10°C, so additional heat absorption from outside air is possible, which can improve heating performance.

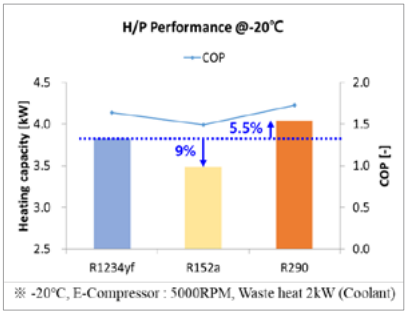


Fig. 8. Results of H/P performance test



Fig. 9. p-h diagram comparison in H/P mode

Figure 10 shows the comparison of heating performance with only outside air heat absorption of R1234yf direct system and R290 secondary loop system. In -20°C condition, the air flow rate on the HVAC side was 300cmh, and the air flow rate on the air cooled condenser and radiator was 2.5m/s. The compressor was operating 5000rpm. Even though R290 is a secondary loop system, the heating performance is about 17%

higher than the R1234yf of the direct system. Because of the temperature and pressure characteristics of R290 described above, it is possible to absorb more outside heat sources than when operating a heat pump with R1234yf.

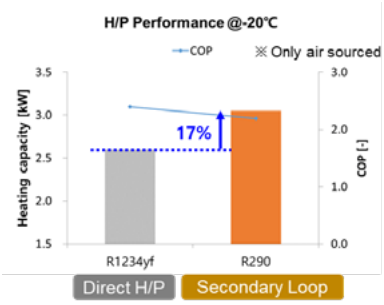


Fig. 10. Results of H/P performance test with only outside heat source

3. Summary/Conclusions

In order to improve the performance of the secondary loop heat pump system, the study was done about the refrigerants. Drop-in test was performed on three refrigerants R1234yf, R152a, and R290 with different characteristics, and the cooling / heating performance for each refrigerant was compared. Changing from direct heat pump system to secondary loop heat pump system based on R1234yf reduces cooling performance by about 22% and heating performance by about 15%. However, using R290 refrigerant improves cooling performance by 30%, equivalent to the direct system of R1234yf. The heating performance is above the direct system of R1234yf due to the increase of outside air heat absorption. The R290 refrigerant can overcome the performance shortcomings of the secondary loop system, which can help reduce the cost of electric vehicles through the application of the secondary loop system.

References

[1] Kemp, J.D.; Egan, C.J., Hindered rotation of the methyl groups in propane. The heat capacity, vapor pressure, heats of fusion and vaporization of propane. Entropy and density of the gas, J. Am. Chem. Soc., 1938, 60, 1521-1525.
[2] Johnson, E, “Global warming from HFC”, Environ. Impact assessment. Rev, 18, 485-492. 1998
[3] B.O. Boloji, Experimental study of R152a and R32 to replace R134a in a domestic refrigerator, Energy, vol. 35, Iss. 9, pp. 3793-3798, Sept 2010.
[4] Huber, M. L. and McLinden, M. O., "Thermodynamic Properties of R134a (1,1,1,2-tetrafluoroethane)" (1992). International Refrigeration and Air Conditioning Conference. Paper 184.
[5] Col DD, Torresin D, Cavallini A, Heat transfer and pressure drop during condensation of the low GWP refrigerant R1234yf. Int. J. Refrigeration 2010; 33:1307-18.

13th IEA Heat Pump Conference
April 26-29, 2021 Jeju, Korea

Increasing flammable refrigerant charge size without compromising safety

Laure Meljac[1,*], Martin Forsen[1], Daniel Colbourne[2]

[1]NIBE, Hannabadswägen 5, Markaryd 285 21, Sweden
[2] c/o HEAT GmbH, Seilerbahnweg 14, 61462 Königstein, Germany

Abstract

Propane, namely R290, is a perfect candidate to replace hydrofluorocarbon that can help the European Union reaching the 2050 target in terms of CO_2 emissions. However, wide introduction of R290 in products are effectively hindered by international safety standards that limit the allowable charge size of flammable refrigerants.
LIFE, the European Union financing instrument for the environment and climate action is financing a project aiming at establishing technical evidence demonstrating that safety is not compromised while increasing the refrigerant charge size of R290 in heat pumps provided that adapted mitigation measures are in place.
Within the LIFE FRONT project, a test procedure aiming at assessing the risk that may be induced by a heat pump using R290 in case a leak is occurring has been defined. Two water based heat pump prototypes designed to operate with R290 were then tested according to the defined procedure. The tests demonstrate that an appropriate design can ensure a safe operation of a heat pump while increasing the refrigerant charge size well above the 150g limit recommended in the safety standard.

Keywords: LIFE FRONT; heat pump; R290; standards; safety

1. LIFE FRONT project

1.1. LIFE programme

"The LIFE programme is the EU's funding instrument for the environment and climate action created in 1992. The current funding period 2014-2020 has a budget of €3.4 billion.

The LIFE programme is divided in two sub-programmes, one for environment (representing 75% of the overall financial envelope) and one for climate change (representing 25% of the envelope).

The climate action sub-programme supports projects in the areas of renewable energies, energy efficiency, farming, land use, and peatland management.

It provides action grants for best practice, pilot and demonstration projects that contribute to the reduction of greenhouse gas emissions, the implementation and development of European Union (EU) policy and law, best practices and solutions. The European Commission is particularly looking for technologies and solutions that are ready to be implemented in close-to-market conditions, at industrial or commercial scale, during the project duration."[1]

1.2. EU legislative framework

In the context of the world fight against climate change the EU ratified the Kigali agreement and committed to take appropriate measures to reduce the CO2 emissions gradually until achieving net zero emission by 2050.

Actual targets in terms of CO2 emissions are set for 2030 and are associated with several overarching pieces of legislation such as the Energy Efficiency Directive, Renewable Energy Directive and the Energy Performance of Buildings Directive…. Among the pieces of legislation published by EU, the commission regulation 517/2014 (F-GAS regulation) regulating the use of hydrofluorocarbon (HFC) fluids has a major

* Corresponding author. Tel.: +33 6 07 98 45 28

impact on the refrigeration, air conditioning and heat pump industry. Indeed, the F-GAS regulation sets the plan for the usage limitation and phase out of the HFCs having a high global warming potential.

The refrigerants commonly used in refrigeration, air conditioning and heat pump applications are HFCs having a high warming power impact (>2000 kgCO2equivalent). Thus, while restricting the use of HFC, the EU works at ensuring that technical options will be available on due time. These options should replace HFC by low global warming potential (GWP) refrigerants providing high energy efficiency and a high level of safety.

1.3. LIFE FRONT project

LIFE FRONT project constitutes one of the EU initiative to facilitate the switch to low GWP refrigerant in refrigeration, air conditioning and heat pump. Indeed, most of the suitable refrigerants for replacing the commonly used HFC are flammable. However, the EU and international standards, which main concern is safety, set strong restrictions on the use of flammable refrigerants, making it very difficult to introduce appliances using flammable refrigerants on the EU market.

"The LIFE FRONT project aims to remove "barriers posed by standards" for flammable refrigerants in refrigeration, air conditioning and heat pump applications. It strives to improve system design to address flammability risk and encourage thereby wider uptake of climate-friendly alternatives to fluorinated gases."[2]

The LIFE FRONT project gathers several partners: Shecco, HEAT, ECOS, AHT, AIT-Deutschland and NIBE.

AHT, AIT and NIBE are industrial companies, manufacturing RACHP appliances, some of which has been using R290 for years. These companies have a long experience in using R290 and will to share their experience to help overcome the existing limitation for flammable refrigerant usage.

AHT mainly produces commercial refrigerating cabinets. AIT and NIBE are manufacturers of water based heat pumps: air to water, ground source heat pump and exhaust air heat pumps.

1.4. Project objectives

The LIFE FRONT work programme is divided in several steps including;

- Review of existing flammable refrigerant standards and literature review on refrigeration, air conditioning and heat pump safety in relation with flammable refrigerant
- Field survey addressing type and cause of refrigerant leakages including leak hole size and leak flowrate
- Equipment design with improved safety

The outcomes from these steps will serve as a basis for drafting proposed requirements for the standards on flammable refrigerants (such as IEC 60335-2-40:2018). The standard and literature review reports are publicly available on the LIFE FRONT project website http://lifefront.eu.

This paper is more focusing on the third step of the project consisting in building and testing prototypes of heat pumps, specifically designed to operate with R290.

2. Barriers to usage of flammable refrigerants

Barriers to the usage of flammable refrigerants are present in standards and sometimes in national regulation within the EU. Barriers coming from standards can be easily identified whereas it is difficult to get a clear picture of the barriers posed by national regulation. This work only focusses on standard barriers.

Refrigeration, air conditioning and heat pump equipment are covered by safety standards of two kinds: product standards and group standards. The product standards are specific for a type of product whereas group standards cover a broad spectrum of systems and equipment in a generic manner.

Compliancy to safety standards does not necessarily constitute a legal requirement, however, compliancy to product or group safety standards often ensure conformity to the applicable EU legislation and CE marking in particular. Thus, in practice, requirements of safety standards are strictly followed by the industry and shape the products being placed in the EU market.

The existing safety standards related to refrigeration, air conditioning and heat pump equipment are listed in the table below:

Table 1. refrigeration, air conditioning and heat pump safety standards

Standard type	Group		Product		
Standard	ISO 5149	EN 378	EN/IEC 60335-2-24	EN/IEC 60335-2-40	EN/IEC 60335-2-89
Domestic refrigeration			x		
Commercial refrigeration	x	x			x
Industrial systems	x	x			
Transport refrigeration	x	x			
Heat pumps, air conditioners and chillers	x	x		x	

IEC 60335-2-89 has recently been revised and maximum A3 flammable refrigerant charge increased from 150g to approximatively 500g of R290 (13xLFL, Lower Flammability Limit) without adding specific requirements on the product design. As a result the practical cooling capacity of refrigerating circuit using A3 flammable refrigerant has been increased significantly.

In IEC 60335-2-40, the maximum A3 flammable refrigerant charge size depends on the location of the equipment. Maximum refrigerant charge for equipment located outdoors (approximatively 5kg of A3 flammable refrigerant) is enough to provide heating capacity suitable for the EU heating demand in single household dwellings. Maximum refrigerant charge size for refrigeration circuits located in an occupied space indoor depends on the surface area of the room where the equipment is installed and the height at which the part of the equipment containing the refrigerant circuit is positioned.

For heat pumps, in particular ground source and air to water heat pumps, having floor installation, the charge size cannot exceed 150g of R290 unless the room size exceed 35m². As a consequence, ground source or air to water heat pumps designed to be installed indoor cannot use a flammable refrigerant as the provided heating capacity will not fit the usual heat demand of a single dwelling apartment or house in the EU. There is an option defined in the standard to use a so-called “ventilated enclosure” where the charge limit is about 5 kg of A3 refrigerant (irrespective of floor area) but this option is not applicable to air to water or ground source heat pumps.

The requirement on the room size set in the safety standard has been theoretically established to prevent an explosive atmosphere under the assumption of a leak flowrate corresponding to the complete refrigerant charge being released in 4 minutes.

This assumption does not leave any scope for innovation nor option for protective measures that could effectively prevent formation of a flammable mixture using other means and thus ensure that the equipment can operate without compromising safety.

3. Experimental work

3.1. General approach

As of today, according to EN/IEC 60335-2-40, whatever is the heat pump design, with the exception of ventilated enclosure, the maximum charge size of flammable refrigerant cannot exceed 150g if the room where the product is installed does not exceed the minimum floor area. Thus, the safety standard is widely considered a barrier to innovation as it does not allow the manufacturer to develop systems using flammable refrigerant. Similarly, it is not possible to implement appropriate design or mitigation measures that can ensure that flammable atmosphere can be avoided irrespective of the refrigerant charge size.

Within the LIFE FRONT project it is intended to develop a robust test methodology that permits to evaluate whether a product using flammable refrigerant can operate without compromising safety whatever the charge size and the room surface area.

It is the intention to demonstrate that an obligation of providing evidence that a refrigerant leakage under a certain flowrate will not increase the concentration of flammable substances above a certain level could well replace the charge limits.

One part of the LIFE FRONT project work is based on experiments simulating R290 leakages occurring from indoor heat pumps whereby measuring R290 concentrations at the product surrounding. Before performing such tests, two questions demand an answer: what is a valuable criteria while assessing that an equipment does not compromise safety in regards to refrigerant charge size and which leak flowrates can be representative of leakages occurring in refrigeration, air conditioning and heat pump systems?

3.2. Definition of a "tolerable risk level"

Within the LIFE FRONT project, it was needed to define a "tolerable risk level" that needs to be achieved by a heat pump in regards to the use of flammable refrigerant. It was decided that a heat pump reaches this "tolerable risk level" if, in the event of a complete loss of the refrigerant charge, the R290 concentration surrounding the heat pump does not exceed 50% of the lower flammability limit (LFL). In addition, would one or several heat pump parts contain a potential ignition source, and if the components are under Ex-type standards, R290 concentration in the concerned areas shall not exceed 50% of LFL.

Note that, these criteria permit to assess whether a product reaches a "tolerable risk level" at its design phase. The assessment of the heat pump risk level presented in this report does not encompass a risk analysis of the heat pump that covers its complete life cycle including manufacturing, installation, maintenance and dismantling.

Note that the risk associated with the heat pump should be considered in light of the background fire risk arising with electric heat pumps, irrespective of the refrigerants used. Whilst such data is not readily available, that for other refrigerating systems (such as domestic refrigerators and air conditioners) is public. This data infers the additional risk from flammable refrigerant should be less than 1 per 100,000 units per year [4].

3.3. Leak cause analysis and associated leak flowrate

Before starting the experimental test, it was needed to assess what could be a reasonable basic assumption for the refrigerant leak flowrate.

To answer that question, a thorough analysis of the leak causes has been performed. The analysis is based on decades of experience of the project partners in manufacturing heat pumps and are based on the feedback and records from the field and after sales and quality departments. As industrial project partners manufacture hermetically sealed equipment that do not need any refrigerant piping work at installation, the leak causes that may affect the piping work done on site are not shown in table 2.

In parallel of the leak causes analysis, hundreds of leaking parts coming from refrigeration, air conditioning and heat pump equipment installed in the field were collected and analyzed by the project partner HEAT. The data has been stored in a database (http://lifefront.eu/databases). For each leak, the leak cause, leak hole size and leak flowrate are detailed so that it is possible:

- To highlight what is the typical leak flowrate occurring in the field
- To correlate leak flowrate and leak cause

The inputs that came out from both the analysis and the data collection are depicted in the table below. Every leak hole and leak flowrate shown in the table come from field measurements; some of them come from the LIFE FRONT project database and some other from the industrial partners own data bank.

Table 2. leak causes and associated leak flowrate

Component	**Cause of leakage**	**Leak features**		**Associated risk**	**Existing mitigation measures in IEC 60335-2-89 and IEC 60335-2-40 Note that the latest version of the IEC standards have not yet be approved by the EU**
		Hole size	**Flowrate**		
Fins and tubs heat exchanger	Any type of corrosion: galvanic, microbiological…	Small hole: 1 to 100 µm	Small : 1-2 g/day	None	No need for mitigation measures
Air to water heat exchanger (plate, co-axial…)	Crack du to frost of the heat exchanger	Large: more than 1mm²	Catastrophic: 88g/min	Refrigerant is flowing on the hydraulic system and can be ignited when hydraulic system will be vented	Disconnexion of hydraulic system from refrigerant circuit or refrigerant vented outside in case the leak occur: IEC/EN 60335-2-40/A1 section GG.6

	Electrical short circuit with copper pipes	Large: more than 1mm²	Catastrophic: 88g/min	Hole is created on the pipe and refrigerant is ignited by the electrical arc: Fire or explosion	No electrical cable shall be installed close to a refrigerant pipes. For cables installed on site, cable passway shall be clearly marked. Revision IEC 60335-2-40:20xx (not published yet)
Brazing and pipes located in the heat pump enclosure	Defective bending	0,17mm²	22g/min	Risk of fire in case of ignition source	•
	Fatigue rupture due to vibration	0,17mm²	22g/min	Risk of fire in case of ignition source	Mitigation measures given in IEC60335-2-89: 2019: vibration test, section 22.108
	Defective brazing	0,7mm²	Catastrophic 65g/min	Risk of fire in case of ignition source	•
	Fritting, repetitive rubbing of surface	<0,1mm²	<3g/min	Risk of fire in case of accumulation and ignition source	•
	Icing of pipes	0,17mm²	22g/min	Risk of fire in case of ignition source	•
Other components	Schrader valve; expansion valve, 4 way valves, pressure sensor….	Small hole	Low flowrate <3g/year	None	•

One can observe that some of the causes for leakages may be eliminated already at design phase by appropriate mitigation measures, already defined in the existing or upcoming standards. However, adapted design requirements cannot prevent any leak from occurring as equipment material can be altered over time in an unpredictable manner.

Based on these analysis, two heat pump prototypes were tested: one packaged air to water heat pump and one ground source heat pump, both heat pump prototypes designed to be installed indoor. The above table highlights that 88g/min is the maximum flowrate that has been identified. However, this leak flowrate has only been observed in the case of a hole created by an electric short circuit. Considering that this leak cause can be avoided by design, the first test done was based on the maximum flowrate of 65g/min which corresponds to a defective bending. For the second test, it was decided to assess the efficiency of the proposed testing method with a flowrate equal to the maximum: 88g/min (rounded to 100g/min for the sake of simplification).

The objectives of the tests are:

- to define a proper test protocol that is appropriate to evaluate whether an equipment design permits a usage of a flammable refrigerant at a tolerable risk.
- to demonstrate that adapted mitigation measures can be implemented to prevent the refrigerant concentration surrounding the heat pump from exceeding 50% of the LFL in case a leak is occurring.

It is essential to adopt a reasonable leak hole size and associated flowrate. If a too small hole is used then it is likely that the implemented protective measures will be insufficient to mitigate the hazard arising from all leaks. If a too large hole is used then the protective measures would be unnecessarily over-designed.

3.4. Test method

3.4.1. General features

The test method described in this section has been finalised after the tests were performed as experience was gained throughout the tests. Thus, the tests performed over the LIFE FRONT project do not strictly follow the described test method.

3.4.1.1. Test space and arrangement

The appliance to be tested shall be positioned within a test room. The room height shall be no less than 2.2m. The room shall be “tight”. The appliance shall be installed at a height and location as prescribed by the instructions manual, selected to yield the least favourable result.

3.4.1.2. Gas sensors number and positioning

Sampling points to measure gas concentration shall be positioned around the heat pump, no more than 30mm above floor level. There shall be one sampling point at a distance of no more than 0.5m from each exposed side of the heat pump. **오류! 참조 원본을 찾을 수 없습니다.** 1 shows a possible arrangement of the sampling points. The gas sensors shall be suitable for the gas to be detected and under calibration control.

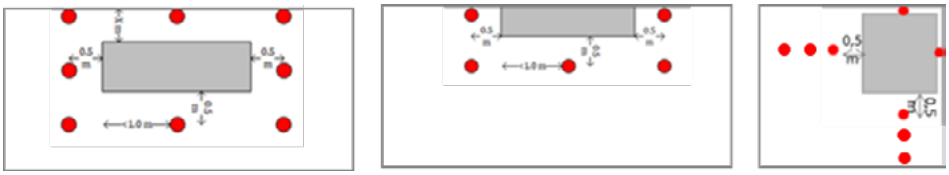


Fig 1. Possible test room set up and positioning of the sampling points; plan view showing the RACHP equipment (grey block) and floor level sensors (red dots)

Note that the gas sensor positioning is only valid where refrigerant density is higher than air density.

3.4.1.3. Leak generation and location

A simulated leak shall be made at the most unfavourable positions on refrigerant containing parts. Several locations might be chosen to be representative or to determine the least favourable one. The jet direction which leads to the highest concentration shall be chosen.

The refrigerant is released through an orifice in vapour phase at a pressure of at least 2bar (gauge), or whatever is necessary for choked flow.

3.4.1.4. Leak flowrates and released mass

Two mass flowrates shall be used: 10g/min and 100g/min. It might be interesting to test an additional intermediate flowrate, 45g/min, to get the concentration developing trend around the product.

The mass released is the refrigerant charge.

3.4.1.5. Test procedure

The tightness of the test room shall be assessed prior any test on the heat pump is performed. Sufficient tightness is demonstrated by a mass of refrigerant equating to about 50% of LFL being released into the room and mixed using a circulating fan. The average concentration at six sampling points throughout the room shall be within ±5% of the arithmetic mean and the mean value shall not decline by more than 5% within a five-minute duration.

For each flowrate and leak location, the refrigerant charge shall be released. The test shall be repeated no fewer than three times at each flowrate and leak location. The heat pump shall be switched off during the test, only the devices that are in operation at all time (fan….) might be operating

3.4.1.6. Recorded data

Measurements of gas concentration shall be recorded at time increments of no more than 5 seconds apart from the time at which the release begins and until the concentration at all sampling points declines for at least three minutes.

3.4.1.7. Criteria

None of the refrigerant concentration detected by the gas sensors surrounding heat pump shall be greater than 50% of LFL. In case gas sensors are installed within the heat pump enclosure, none of them shall detect a gas concentration higher than 50% of LFL.

3.4.1.8. Specific arrangements used for the LIFE FRONT tests

For the tests performed over the project, an enclosure of a size, 3m x 2m x 2.5m height, intended to mimic a typical utility room is built and serves as test room.

R290 is supplied to the leak positions from a cylinder fed into the enclosure via refrigerant hoses **오류! 참조 원본을 찾을 수 없습니다.**. The hose terminates with a 1mm (0.8mm2) diameter orifice fitting in order to ensure choked flow. The mass flowrate and total released mass is modulated with a mass flow controller, calibrated for R290.

To assess the tightness of the enclosure mimicking the utility room, 400g of R290 were released in the enclosure. The air in the enclosure was mixed using a circulating fan. The R290 concentration was then recorded during 30 minutes. Over these 30 minutes, the R290 concentration remained stable, it was concluded that the enclosure that sufficiently tight for the purpose of the tests to be performed.

R290 sensors are used to measure R290 concentration. Some of them are aspired sensors and others are positioned on a gas stand and are diffusion operated.

While tests are on-going it may happen that R290 concentration gets so high that the R290 sensors get saturated; in that event, the gas sensors are disconnected to avoid poisoning them. This is the reason why in the charts shown in the following clauses some curves are interrupted. In order to highlight the impact of the specific heat pump design on the tolerable risk level, the first test was performed on a heat pump designed to operate with a non-flammable refrigerant such as R410A or R407C.

Each performed test starts with a clean room: no R290 neither in the mock utility room nor in the heat pump enclosure. R290 is then released and the test stops after the defined R290 mass has been released. After each test, the R290 is evacuated from the testing enclosure and from the heat pump. The following test starts when the R290 sensors do not detect any R290.

3.4.2. Ground source heat pump prototype

A ground source to water heat pump prototype has been specifically designed to be used with R290. Ground source heat pumps are generally designed to be installed indoor, in a garage or a utility room. The prototype has been tested at NIBE AB facilities at Markaryd, Sweden with the support of HEAT. During the tests, the heat pump has not been in operation.

3.4.2.1. Installation

Three zones, represented on figure 2, are defined as:

- zone A: upper part of the heat pump contains the hydronic components, immersion heater, power supply and all electrical components,
- zone B contains the refrigerating circuit,
- zone C represents the heat pump surrounding. Zone A and zone C represent the zones were R290 concentration shall not exceed 50% of LFL (components in zone A do not comply with ATEX legislation). The red dots represent the gas sensors.

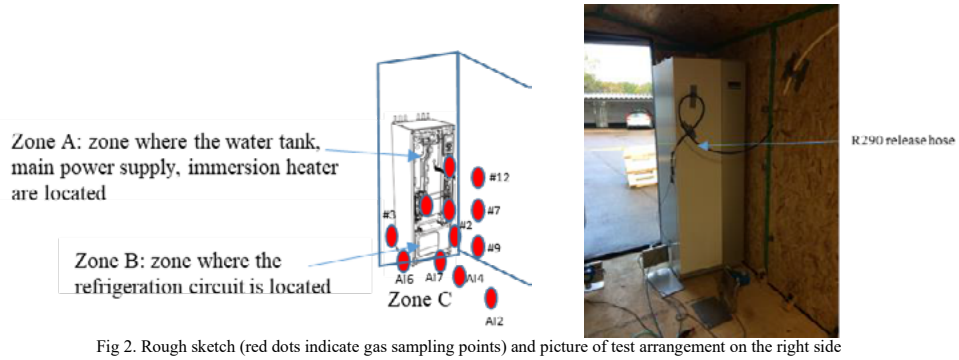


Fig 2. Rough sketch (red dots indicate gas sampling points) and picture of test arrangement on the right side

3.4.2.2. Selection of release locations

The refrigerant is contained in zone B. The leak hose is placed at the centre of zone B. For assessing whether R290 could get into zone A, the leak orifice was oriented first toward the top of zone B. Then, the leak orifice was oriented towards the side panel of zone B against the wall of the room.

3.4.2.3. Selection of flowrates and mass of R290 to be released

Two mass flowrates were selected. The two mass flow considered are: 20g/min and 100g/min. 88g/min is the highest leak flowrate observed according leak the cause analysis, for this test, it was decided to evaluate what will happen in case this catastrophic leak occur (88g/min was rounded to 100g/min).
800g of R290 was released at each test. After the 800g were released, the R290 concentration continued logging for several more minutes.

3.4.2.4. Test conditions

Table 3. test condition for ground source heat pump

Test no.	Release mass flow rate [g/min]	Release location	Orifice height [m]	Released quantity [g]
Tests performed on a ground source heat pump designed for R407C				
1	100	Oriented towards zone A	0.3	400
Tests performed on a ground source heat pump designed for R290				
2	100	Oriented towards zone A	0.3	800
3	100	Centre	0.3	800
4	20	Centre	0.3	800

3.4.2.5. Test results

In the following charts, the doted blue line represents 50% of LFL.

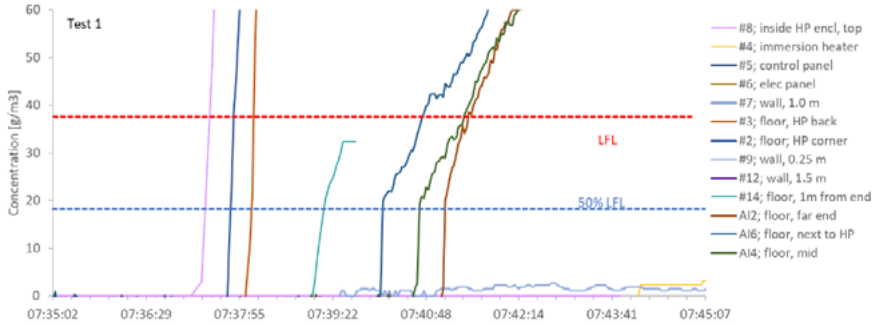


Fig 3. results of test 1 performed on ground source heat pump designed for R407C - 100g/min

For this first test, one sensor was positioned within part B, in the refrigeration enclosure. R290 release starts at 7:36 and ends at 7:40. Only 400g were released. 50% of the LFL is reached everywhere in the room at floor level. One can notice that as there is no ventilation in the room, R290 stagnates at floor level and the concentration remains lower than 50% of LFL at 0.25m height whereas no R290 is detected by the sensors positioned at 1m and 1.5m.

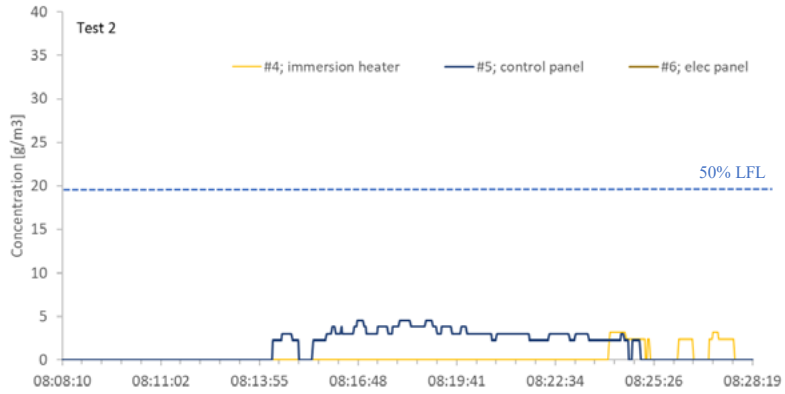


Fig 4. results of test 2 performed on the ground source heat pump prototype designed for R290 – 100g/min

R290 release starts at 8:10 and stops at 8:18. R290 concentration remains far below 50% LFL on zone A. No R290 is detected in the electrical panel where the relays are located.

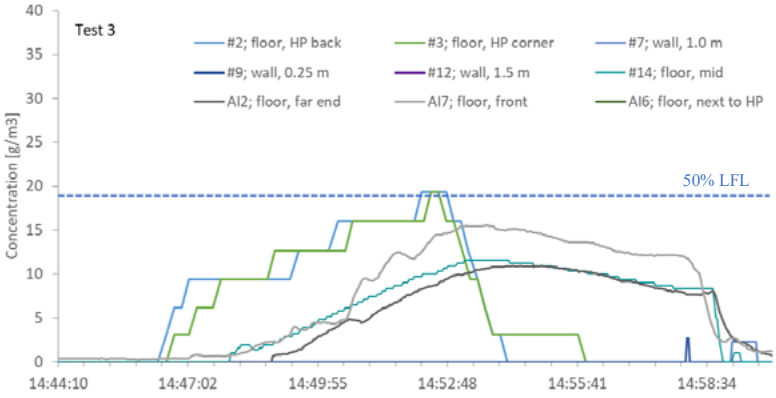


Fig 5. results of test 2 performed on the ground source heat pump prototype designed for R290 – 100g/min

R290 is released at 14:44. The 800g are released after 8 minutes. R290 concentration increases first at the side of the heat pump which is by the wall as well as at the back. Then, the R290 is propagating into the room.

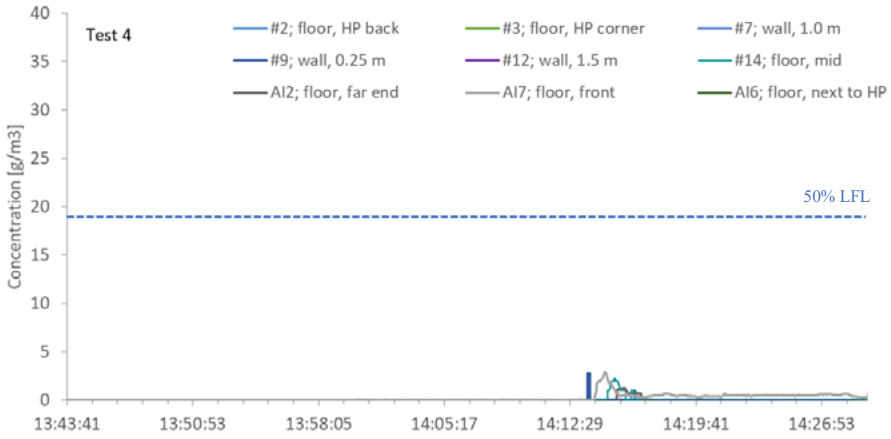


Fig 6. Results of test 3 performed on the ground source heat pump prototype designed for R290 – 20g/min

R290 release starts at 13:43 and ends at 14:23. R290 concentration remains far below 50% of LFL.

From the three tests performed, one can conclude that R290 is not penetrating zone A, where potential ignition sources could be found. The tests also demonstrate that in case there is no air movement in the room, R290 stagnate at floor level. Finally, the test demonstrates that the ground source heat pump design is efficient in preventing the creation of an explosive atmosphere around the heat pump either in the event of a catastrophic leak is occurring in the refrigerating circuit or in the event of a small leak is occurring.

3.4.6. Indoor packaged air to water heat pump prototype

An indoor packaged air to water heat pump prototype has been specifically designed for operating with R290. This prototype has been tested at the AIT technology centre in Kasendorf, Germany with the support of HEAT.

During all tests, the heat pump is not in operation, the compressor and the fan are always off. Generally the heat from the compressor will create convection currents which helps to disperse any releases, the test conditions are thus conservative.

3.4.6.1. Installation

The heat pump consists of three zones: the hydronic unit, which contains the hydraulic and electrical components, the condensing enclosure that contains the refrigerating circuit except evaporator, and the evaporating enclosure that contains the evaporator, the fan and the ducts. Heat pump surrounding, namely zone C, represents the zone where the R290 concentration shall not exceed 50% of the LFL. The red dots on **오류! 참조 원본을 찾을 수 없습니다.**7 represent the R290 sensors, the orange arrows represent the location where R290 is released.

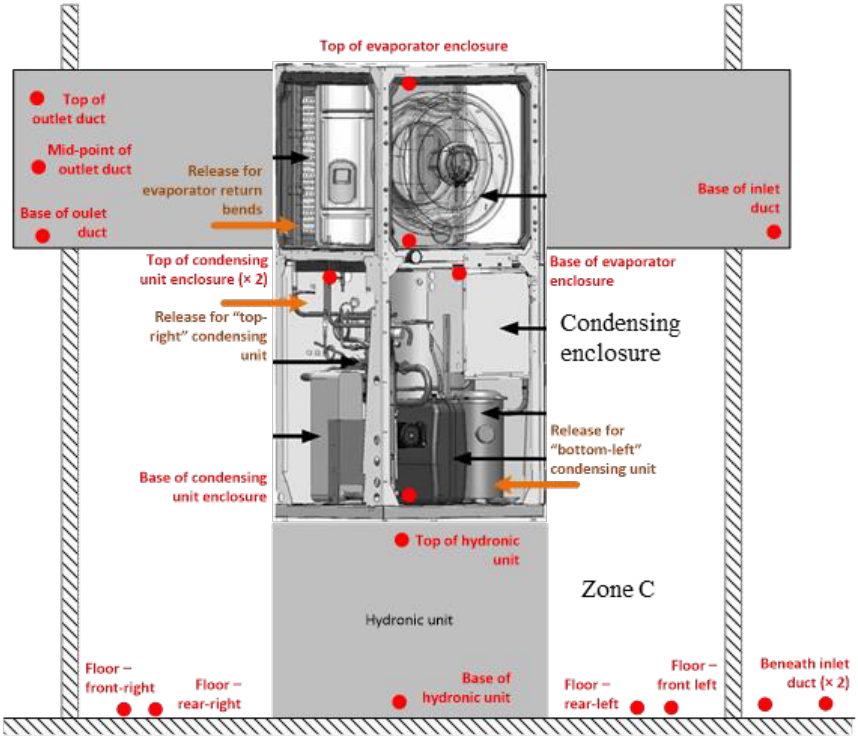


Fig 7. Rough sketch of test arrangement: red dots indicate sampling points and orange arrows are release positions

3.4.6.2. Selection of release locations

Three R290 release locations were defined as being the most unfavourable locations for a leak to occur: one in the evaporator enclosure and two in the condensing enclosure: one on top and one at the bottom.

All releases involved a jet at choked flow conditions, directed horizontally, to impinge against a nearby surface in order to remove momentum from the jet and thus to minimise mixing.

3.4.6.3. Selection of flowrates and mass of R290 to be released

The three mass flowrates considered were: 20g/min, 45g/min and 65g/min. 20g/min corresponds to the leak flowrate that might be obtained in case of defective bending, fatigue rupture or pipe icing, 45 g/min corresponds to the assumed low-side R290 leak rate within the draft amendment 61D/421/CD to IEC 60335-2-40 for enhanced tightness systems and 65g/min correspond to the highest leak flowrate, considering that electrical arc can be avoided by construction.

500g of R290 was released at each test. After the 500g were released, the R290 concentration records last for another couple of minutes.

3.4.6.4. Test conditions and test results

Table 4. test conditions and results obtained for indoor packaged air to water heat pump

Test no.	Release mass flow rate [g/min]	Release location	Orifice height [m]	R290 concentration reached during the test surrounding the product – zone C
1	40	Evaporating enclosure	1.5	Lower than 50% of LFL
2	20	Condensing enclosure: bottom	0.8	Higher than LFL
3	40	Evaporating enclosure	1.5	Lower than 50% of LFL
4	65	Evaporating enclosure	1.5	52% of LFL was reached
5	20	Evaporating enclosure	1.5	Lower than 50% of LFL
6	20	Condensing enclosure: bottom	0.8	Lower than 50% of LFL
7	45	Condensing enclosure: bottom	0.8	Lower than 50% of LFL
8	65	Condensing enclosure: bottom	0.8	Lower than 50% of LFL
9	20	Condensing enclosure: top	0.95	Lower than 50% of LFL
10	65	Condensing enclosure: top	0.95	Lower than 50% of LFL

Test 1 and 2 were performed on a heat pump designed for R410A. When released in the evaporating enclosure, the concentration of R290 in zone C remains lower than 50% of LFL. However, when released in the condensing enclosure, R290 concentration get higher than LFL in zone C.

Starting from test 3, all tests were performed on a heat pump specifically designed for R290.

During test 3, 4 and 5; R290 was released in the evaporating enclosure. When released at 65g/min, the concentration of R290 reaches 52% of the LFL in zone C. The 50% LFL criteria is not strictly met; however, at this phase of the project it was decided to go on with the test. When released in the evaporating enclosure, R290 concentration remains lower than 52% of LFL surrounding the product, however, it has been observed that the higher is the flowrate, the higher the R290 concentration gets surrounding the heat pump.

From test 6 to test 8, R290 was released at the bottom of the condensing enclosure. Whatever is the released mass flowrate, 20g/min, 45g/min or 65g/min, the concentration of R290 in zone C remained below 50% of LFL.

Results obtained when R290 was released at the top of the condensing enclosure, test 9 and 10, gave very similar results as to the ones obtained over tests 6, 7 and 8.

From the eight tests performed on the heat pump specifically designed for R290, one can conclude that the indoor packaged air to water design is sufficient to avoid creating an explosive atmosphere around the product. However, some adjustments would be needed as a little more than 50% LFL is reached where R290 is released in the evaporating enclosure.

4. Conclusion

The LIFE FRONT project aims to remove barriers posed by standards for flammable refrigerants in refrigeration, air conditioning and heat pump applications. It strives to improve system design to address flammability risk and thereby encourage wider uptake of climate-friendly alternatives to fluorinated gases.

In the scope of the LIFE FRONT project, two heat pump prototypes designed to operate with R290 were built and tested. The objective of the tests was to evaluate the efficiency of the prototype design in limiting R290 concentration at 50% of LFL surrounding the heat pump and in parts of the heat pump where an ignition source can be present, in the event of a leak is occurring within the refrigerating circuit. Note that during the tests, the compressor was off, thus, the impact the air temperature within the refrigeration enclosure may have on the R290 flow was not evaluated.

The two major outcomes of the tests performed are the following:

- Mitigation measures can be implemented that permits the use of R290 in larger quantities than those imposed by the safety standards without compromising safety. The tests demonstrate that it was possible to limit the concentration surrounding the product and in heat pump parts containing potential ignition sources below 50% of the LFL.
- A suitable test method, described in section 3.4.1, has been developed and evaluated that permits the evaluation of the efficiency of the mitigation measures. The test method assesses whether the heat pump can generate an uncontrolled explosive atmosphere surrounding the heat pump in the event of a refrigerant leak.

According to the current safety standards, residential indoor packaged air to water heat pumps and ground source heat pumps containing more than 150g of flammable refrigerant cannot without difficulty be placed on the European market. However, the tests performed within the LIFE FRONT project on a residential indoor packaged air to water heat pump and on a ground source heat pump show that appropriate mitigation measures can guarantee that the flammable refrigerant concentration surrounding the heat pump and in any part of the heat pump that may contain potential ignition source remains lower than 50% of the LFL. The tests demonstrate that substantially more than 150g of flammable refrigerant can be used in indoor heat pumps without compromising safety.

As an outcome of the work done, we would like to suggest that the safety standards, EN378 and EN/IEC 60335-2-40, are revised in a way that offers several possible approaches, at least a “simple” approach, based on existing requirement: 150g as a maximum charge size, and an “advanced” approach that would imply that the manufacturer performs the test as described in the above section.

References

[1] https://ec.europa.eu/easme/en/life
[2] http://lifefront.eu/
[3] Klára Zolcer Skačanová, Anti Gkizelis, Dario Belluomini, Marie Battesti, Shecco Impact of Standards on Hydrocarbon Refrigerants in Europe – Market research report
[4] Comparative risk assessment of hydrocarbon refrigerant in a refrigerator and split air conditioner; Daniel Colbourne

13th IEA Heat Pump Conference
April 26-29, 2021 Jeju, Korea

Analysis of the mixture refrigerant R600/R245fa using in high temperature heat pump

Xiaohui Yu*, Chang Xu

School of Energy and Environment Engineering, Hebei University of Technology, Tianjin 300401, PR China

Abstract

High temperature heat pump (HTHP) is an effective equipment to recovery industrial waste heat and it has a wide application potential. The choice of refrigerant has important influence on the efficiency of HTHP. In this paper, the performance parameters of the mixture refrigerant R600/R245fa using in HTHP were tested. Compared with the R245fa, the mixture refrigerant R600/R245fa has higher heating capacity and lower COP. But the COP of the HTHP system also can maintain above 3.0 when the temperature of condenser outlet water is at 100 ℃ and 35 ℃ temperature lift. Analysis shows that R600/R245fa is suitable for HTHPs with higher condenser outlet water temperature and heating capacity demand. And its low GWP also has good environmental benefits.

Keywords: mixture refrigerant; High temperature heat pump; cycle performance

Nomenclature		**Greek symbols**	
COP	coefficient of performance	η	efficiency (%)
C_p	specific heat capacity (kJ/(kg.K))	Subscripts	
HTHP	high temperature heat pump	1,2,3,...,6	state point
GWP	global warming potential	a	available
ODP	ozone depletion potential	b	boil
h	enthalpy (kJ/kg)	con	condenser
m	mass flow rate (kg/s)	h	high temperature
T	temperature (°C)	i	inlet
s	entropy (kJ/(mol.K))	l	low temperature
P	power (kW)	o	outlet
Q	heating (kW)	r	refrigerant

1. Introduction

The problem of energy and environment has become a serious problem facing all countries in the world. The environmental pollution caused by energy consumption has become an important obstacle to global

* Corresponding author. Tel: +86 15102282362
E-mail address: 2018133@ hebut.edu.cn

economic growth and social progress. Industrial energy consumption accounts for nearly half of the world's total energy consumption [1]. Many industrial processes produce a large amount of waste heat and directly discharge to the environment, resulting in energy waste and environmental pollution. Therefore, waste heat utilization is an effective way to energy saving. On the one hand, the utilization of waste heat can reduce the thermal pollution. On the other hand, it can reduce the consumption of high-grade energy and achieve multiple purposes. HTHP is one of the reliable waste heat recovery devices. It can improve the quality of low-grade heat energy to higher quality by producing high temperature water or steam. Metallurgy, chemical industry, food, paper and other industries have a large demand for 100-130℃ hot water [2]. Therefore, HTHP has a good application prospect and has some new researches in recent years.

The research on refrigerant selection was also widely carried out, which lays a solid foundation for the selection of HTHP working medium. Guido et al. [3] conducted extensive screening on the working medium of steam compression high temperature heat pump, there were 27 kinds of preliminary selection under the environmental protection requirements and technical restrictions. Bobelin et al. [4] verified that a new mixed refrigerant ECO3 and it could effectively raise the outlet water temperature of HTHP to 125 ℃ . Chamoun et al. [5] designed and tested a new type of heat pump which raised the outlet water temperature to 130~140 ℃ when using R718 as refrigerant. Bamigbetan et al. [6] proposed that pasteurization process, drying, distillation and so on all need the working temperature of 100-125 ℃. After screening, R600 and R1233zd(E) have better performance and basically suitable for the mainstream compressor. In addition to the pure substance, the research of mixed refrigerant has gradually become another direction. Yu et al. [7] conducted a binary near-azeotropic mixture named BY- 4. The COP was 2.8-3.6 when the temperature of outlet water was 90-110 ℃ and 40 ℃ temperature rose. Guo et al. [8] analyzed a series zoetropic mixture, proposed that N-hexane/propene and R4310mee/R32 are superior alternative to CO2 heat pump.

R245fa has been theoretically calculated or experimentally verified in some literatures to show that it is a kind of HTHP refrigerant with good performance, safety and stability [9],[10]. R245fa is widely used because of its high COP, low compressor discharge temperature and discharge pressure. The obvious disadvantage of R245fa is that its volumetric heating capacity is lower compared with the conventional heat pump refrigerant [11]. R600 is a recognized refrigerant which is suitable for HTHP, but its application is greatly restricted due to its inflammable and explosive characteristics [12]. R1234ze(Z) and R1233zd(E) are considered as potential substitutes for R245fa in some studies from the perspective of pure refrigerant [13]. In this paper, from the perspective of mixture refrigerant, a binary mixture substance R600/R245fa is proposed to provide more refrigerant choices for users of HTHPs. Most studies on the refrigerants of HTHP adopt the method of theoretical calculation, while in this study, the mixture refrigerant R600/R245 is tested on the experimental platform. For comparison, pure refrigerant R245fa with the same injection mass is also tested at the corresponding working conditions. According to the research of Zhou et al. [14], the theoretical cycle calculation results show that the mixture refrigerant prepared on R245fa has a higher COP when the mass ratio of R245fa is 0.5-0.7. Therefore, the ratio of R600/R245fa is defines as 0.3/0.7 in this experiment. The experimental results show that the two refrigerants R600 and R245fa can complement each other. After the two constitute a mixture refrigerant, the COP of the HTHP system decreases and the heating capacity increases. Compared with pure refrigerant R245fa, the compressor discharge temperature and discharge pressure of mixture refrigerant increases, the compression ratio decreases obviously. The GWP of the mixture refrigerant decreases compared with the pure refrigerant R245fa due to the low GWP of R600. The inflammable and explosive properties of R600 are also weakened because of its low proportion in the composition. The experiment setup are presented in Section 2. The thermodynamic analysis methods are described in Section 3. The results and discussions are arranged for Section 4. Conclusions are summarized in the last section.

2. Experiment setup

A HTHP system was designed and built for testing the performance of the proposed mixture refrigerant R245fa/R600. The schematic diagram of the HTHP system is shown in Fig. 1. The main equipment of the system is evaporator, condenser, electronic expansion valve and scroll compressor. A vapor-liquid separator is installed between the evaporator and the compressor to prevent the refrigerant liquid from entering the compressor and causing liquid hammer. The electronic expansion valve and the condenser are equipped with dry filter and liquid storage tank. Some other accessories together with the main equipment constitute the whole HTHP system. The heat source of the system is an adjustable electric heating tank. The temperature in the heating water tank can be maintained constant through the control cabinet to satisfy the requirements of

the evaporator's stable inlet temperature. The heat sink side of the system uses the fan-coil unit to discharge heat to outdoor air and maintain the heat balance of the system.

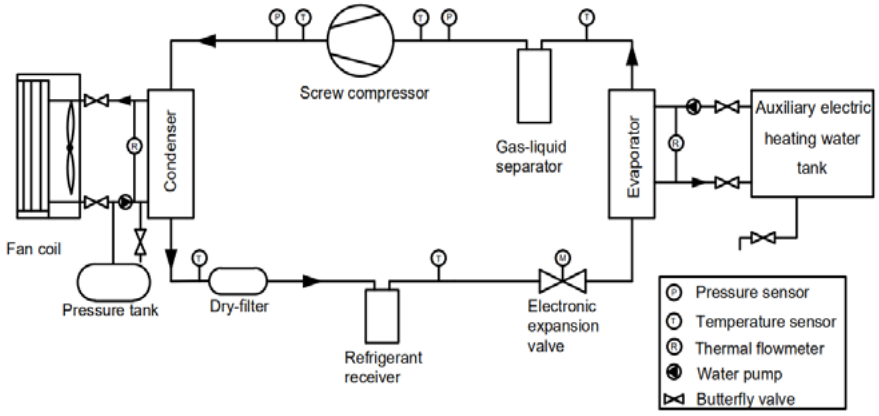


Fig. 1. Schematic diagram of the HTHP system

The detailed parameters of main equipment of HTHP are listed in Table 1. And the information of measuring instruments are listed in Table 2. Some parameters of the refrigerants are listed in Table 3.

Table 1. The main equipment parameters of the HTHP

Equipment	Type	Specification
Evaporator	EB12P3823	Heat transfer rate: 13.3 kW
Condenser	CB12P3823	Heat transfer rate: 14.7 kW
Electronic expansion valve	DPF(Q01)2.4	Diameter: 2.4 mm
Screw compressor	HRH049U4LP6	Rated power: 4.04 kW Nominal refrigeration capacity: 12110 W
Water pump	PUM200	Rated flow: 2.5 m^3/s; Pump head: 12 m; Power: 0.25 kW.
Fan coil	KFR-35GW/MHAB1	Specification: 1280×195×295 mm
Auxiliary electric heating water tank	SX-1000	Volume: 1 m^3

Table 2. The information of measuring instruments

Name	Type	Accuracy grade

Pressure transmitter	MIK- P50- 2 (low- pressure side) MIK- P100- 8 (high- pressure side)	± 0.5% FS included nonlinearity hysteresis and temperature drift
Digital power meter	RK9900N	± 0.5% FS
Turbine flow meter	LWY-25	± 1.0L
Pressure gauge	YTZ-150	± 1.5% FS
Temperature sensor	PT1000	A

Table 3. Some parameters of the refrigerants

Substance	Molar mass (g/mol)	Tb (℃)	Tc (℃)	Pc (MPa)	ODP	GWP (100yr)
R600	58.12	- 0.49	151.98	3.796	0	4
R245fa	134.05	15.14	154.01	3.651	0	858
R600/R245fa (3:7)	96.31	/	132.74	3.557	0	/

3. Analysis method

The circulating principle of high temperature heat pump is reverse Carnot cycle, as shown in Fig. 2. The blue and red lines represent the temperature changes of the circulating water in the evaporator and the condenser respectively. The whole refrigerant cycle includes four thermodynamic processes: endothermic process (5-1) , compression process (1-2) , condensation process (2-4) , throttling process (4-5) . In order to simplify the calculation, the following assumptions are made as follows.

(1) All components of the system are operated under steady- states and steady- flow conditions.

(2) The changes in kinetic energy and potential energy of the refrigerant are ignored.

(3) The temperature loss and pressure loss of the refrigerant during pipeline circulation are ignored.

(4) The evaporation and condensation processes are isobaric.

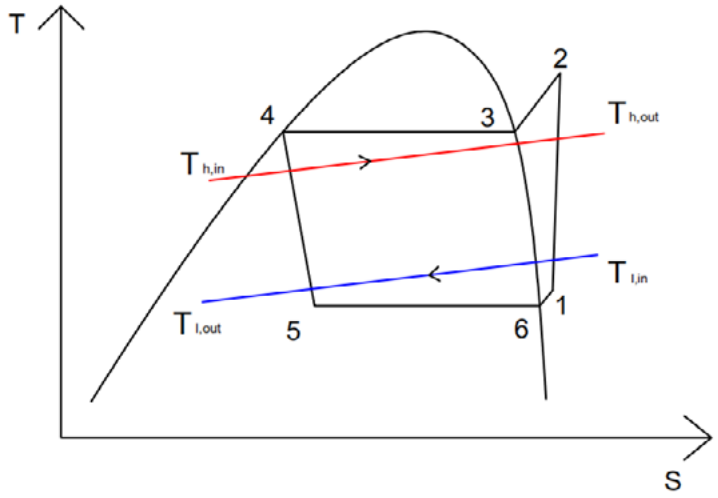


Fig. 2. T-s diagram of the HTHP

The energy equation of some components of the system, based on the first law of thermodynamics, can be calculated as follows.

(1) Condenser

The heating release of the refrigerant in the condenser can be calculated as follows：

$$Q_{con} = m_r(h_2 - h_4) = m_{hw}C_{p,hw}(T_{h,in} - T_{h,out}) \quad (1)$$

Where h2 is the enthalpy of the refrigerant at the condenser inlet, h4 is the enthalpy of the refrigerant at the condenser outlet, mr is the mass flow rate of the refrigerant, mhw is the mass flow rate of the high temperature water passing through the condenser, Th,in is the temperature of high temperature water at the condenser inlet, Th,out is the temperature of high temperature water at the condenser outlet, Cp,hw is the constant pressure specific heat capacity of the high temperature water.

(2) Scroll compressor

Scroll compressor is suitable for small units because of its high efficiency and strong stability. The efficiency of compressor can be calculated as follows:

$$\eta = \frac{P_a}{P_{in}} \quad (2)$$

Where η is the compression efficiency, Pin is the input power of the compressor which can be measured directly, Pa is the available power which can be expressed as:

$$P_a = m_r(h_2 - h_1) \quad (3)$$

Where h1 is the enthalpy of refrigerant at the evaporator outlet.

In conclusion, the COP of the system can be calculated as follows:

$$COP = \frac{Q_{con}}{P_{in}} \tag{4}$$

4. Results and discussions

The evaporator inlet water temperature of the experiment ranged from 45 ℃ to 65 ℃ and the temperature interval is 5 ℃ . The temperature lift between evaporator inlet water and condenser outlet water remains constant at 35 ℃ . When the operating condition is stable, the HTHP performance is tested and investigated under different operating conditions. For the convenience of the following description, R600/R245fa is denoted by R1 and R245fa is denoted by R2.

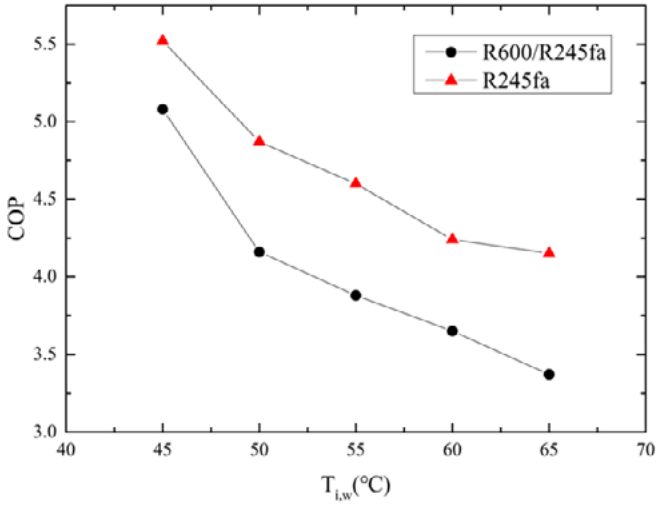
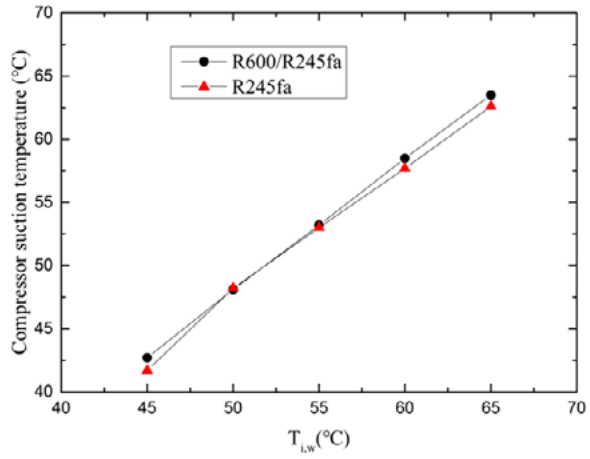
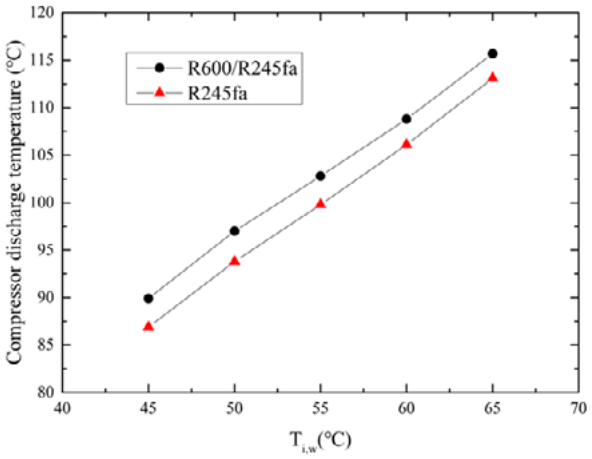


Fig. 3. The COP of HTHP varied with different inlet water temperature of the evaporator

As shown in Fig. 3, the COP of R1 and R2 decreases gradually with the increase of evaporator inlet water temperature. When the inlet water temperature increased from 45 ℃ to 65 ℃ , the COP of HTHP using R1 and R2 decreases by 1.71, 1.37 respectively. It means that the COP of the HTHP system decreases by 1.68 % and 1.24% on average with the evaporator inlet water temperature increased by 1 ℃ . Among them, the COP decreases faster in the temperature interval 45-50 ℃ , and the other temperature intervals decrease evenly. The average COP of using R1 decreases about 13.9% compared with R2. Considering the experimental error, the R1 also can maintain the average COP not less than 3.0 when the water temperature lift is 35 ℃ and the outlet water temperature at 100 ℃.



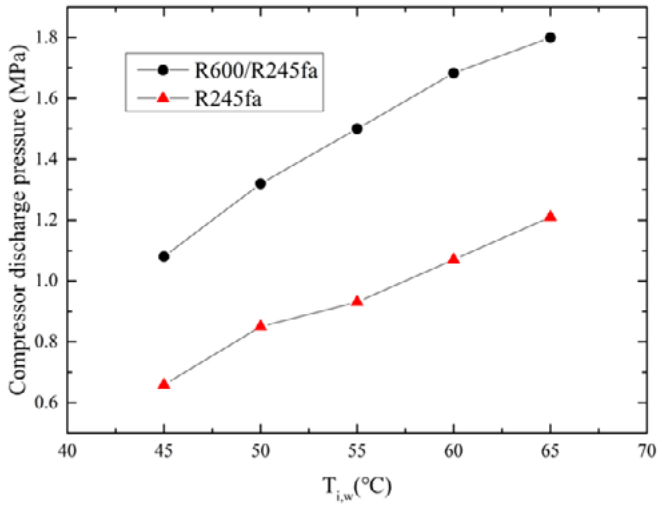
(a) The compressor suction temperature changed with different inlet water temperature of the evaporator



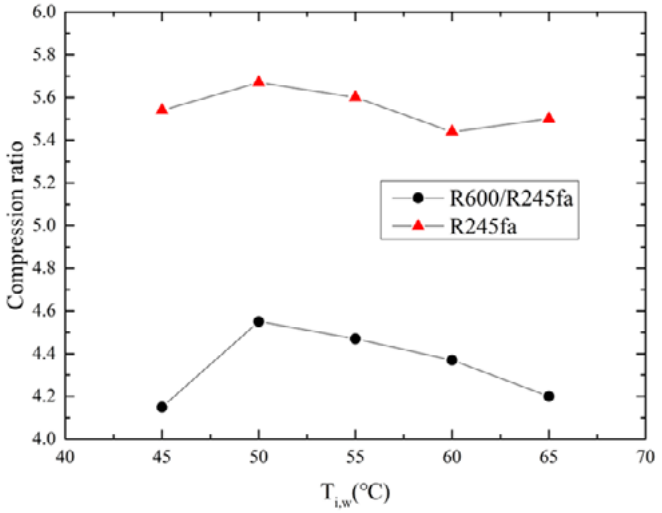
(b) The compressor discharge temperature changed with different inlet water temperature of the evaporator

Fig. 4. The compressor suction temperature and discharge temperature changed with different working conditions

As shown in Fig. 4 (a), the compressor suction temperature varies with different inlet water temperature of the evaporator. R1 has a slightly higher compressor suction temperature than R2 in this experiment. The compressor suction temperature is lower than the evaporator inlet water temperature, which may be due to a little amount of liquid refrigerant evaporates and absorbs heating at the inlet of the compressor. The Fig. 4 (b) shows the change of compressor discharge temperature under different evaporator inlet water temperatures. The compressor discharge temperature corresponding to R1 is significantly higher than that to R2, and the average temperature overshoot is 2.9 ℃. The difference between the compressor suction temperature and the discharge temperature will rise with the increase of the evaporator inlet water temperature in this experiment.



(a)



(b)

Fig. 5. The variation of the discharge pressure of the compressor (a) and compression ratio (b) changed with different inlet water temperature of the evaporator

Fig. 5 shows the variation of the compressor discharge pressure and compression ratio under different working conditions. As shown in Fig. 5(a) , the compressor discharge pressure of R1 is 0.533MPa higher than R2 on average. The maximum of the difference between the two pressures occurs when Ti,w is 60 ℃ and the value is 0.613 MPa. Despite the higher compressor discharge pressure of the R1, it can been seen from Fig. 8

5(b) that the compression ratio is lower. The average compression ratio of R1 is 4.35 and the average compression ratio of R2 is 5.55. The different of the mean value is 1.2. It seems that R1 may be suitable for higher heating temperatures form the trend. In general, R1 is superior to R2 in term of compression ratio.

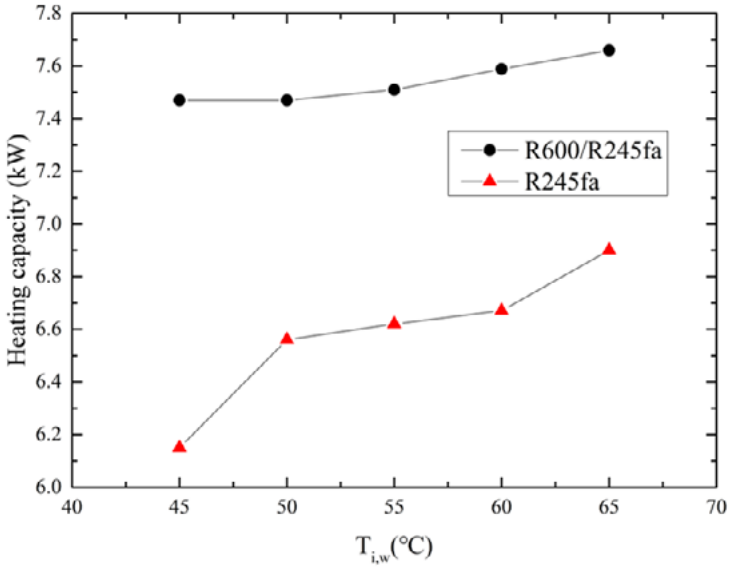


Fig. 6. The heating capacity of HTHP varied with different inlet water temperature of the evaporator

As shown in Fig. 6, the heating capacity of the HTHP using R1 as refrigerant is significantly higher than that of R2. The value of using R1 is on average 14.7% higher than that of R2. This suggests that R1 is better suited to higher heating capacity requirements of HTHPs than R2. The heating capacity of the HTHP is negatively correlated with the compression ratio. In this experiment, with the increase of the evaporator inlet water temperature, the compression ratio of the two refrigerant decreases gradually. It makes the compressor volume efficiency lift, resulting in the increase of the actual compressor gas transmitting volume. Meanwhile the volumetric heating capacity decreases with the rise of condensation temperature, but the product of volumetric heating capacity and refrigerant steam volume at the outlet of the compressor will still increase, that is, the heating capacity of the HTHP will continue to increase.

5. Conclusion

The operating performance of the HTHP system using R600/R245fa and R245fa as refrigerant are obtained by experimental test under different running conditions. We analyzed these data and reach the following conclusions:

1. From the point of the COP, the mixture refrigerant R600/R245fa is less than R245fa and the COP dropped by an average of 13.9%. But the mixed refrigerant R600/R245fa can keep the COP at least 3.0 when the temperature lift is 35 ℃ and outlet water temperature at 100 ℃. Therefore, this kind mixture refrigerant can be accepted for HTHPs.

2. The compressor discharge temperature and compressor discharge pressure of HTHP using R600/R245fa will be higher than that of R245fa. However, R600/R245fa has advantages in terms of compression ratio and heating capacity, in which the compression ratio decreases 1.2 on average and the heating capacity increases 14.7% on average.

3. Compared with the R245fa, the mixture refrigerant R600/R245fa is more suitable for HTHPs with higher heating capacity demand and higher temperature working conditions.

4. The mixture refrigerant R600/R245fa has lower GWP than the R245fa, which has certain advantages in environmental protection.

Reference:

[1] Cordin Arpagaus, Frederic Blessa, Michael Uhlmann, J ü rg Schiffmann, Stefan S. Bertsch. High temperature heat pumps: Market overview, state of the art, research status, refrigerants, and application potentials. Energy 2018; 152: 985-1010.

[2] Carlos Mateu-Royo, Adrián Mota-Babiloni, Joaquín Navarro-Esbrí, et al. Multi- objective optimization of a novel reversible High-Temperature Heat Pump- Organic Rankine Cycle (HTHP - ORC) for industrial low-grade waste heat recovery. Energy Conversion and Management 2019; 197: 111908.

[3] Guido Francesco Frate, Lorenzo Ferrari, Umberto Desideri . Analysis of suitability ranges of high temperature heat pump working fluids. Applied Thermal Engineering 2019; 150: 628-640.

[4] D. Bobelin, A. Bourig. 2004. Experimental results of a newly developed very high temperature industrial heat pump (140°C) equipped with scroll compressors and working with a new blend refrigerant. International Refrigeration and Air Conditioning Conference, Paper #1299.

[5] M. Chamoun, R. Rulliere, P. Haberschill, et al. Experimental and numerical investigations of a new high temperature heat pump for industrial heat recovery using water as refrigerant.International Journal of Refrigeration 2014; 44: 177-188.

[6] Opeyemi Bamigbetan, Trygve M. Eikevika, Petter Nekså,et al.Theoretical analysis of suitable fluids for high temperature heat pumps up to 125 °C heat delivery.International Journal of Refrigeration 2018; 92: 185-195.

[7] Yu Xiaohui, Zhang Yufeng, Deng Na, et al. Experimental performance of high temperature heat pump with near-azeotropic refrigerant mixture. Energy and Buildings 2014; 78: 43-49.

[8] Hao Guo, Maoqiong Gong, Xiaoyu Qin. Performance analysis of a modified subcritical zeotropic mixture recuperative high-temperature heat pump. Applied Energy 2019; 237: 338-352.

[9] Opeyemi Bamigbetan, Trygve M. Eikevik, Petter Nekså, Michael Bantle, Christian Schlemminger. Theoretical analysis of suitable fluids for high temperature heat pumps up to 125 °C heat delivery. International Journal of Refrigeration 2018; 92: 185-195.

[10] Xuelian Ma, Yufeng Zhang, Lei Fang, Xiaohui Yu, Xiaoqiong Li, Ying Sheng, et. al. Performance analysis of a cascade high temperature heat pump using R245fa and BY-3 as working fluid. Applied Thermal Engineering 2018; 140: 466-475.

[11] Fukuan Tian. Experimental investigation on mixed refrigerants for moderately high temperature heat pump. Thesis for the Master Degree. China: School of energy power and mechanical engineering; 2018.

[12] Baojun Luo, Peng Zou. Performance analysis of different single stage advanced vapor compression cycles and refrigerants for high temperature heat pumps. International Journal of Refrigeration 2019; 104: 246-258.

[13] Giovanni A. Longo, Simone Mancin, Giulia Righetti, Claudio Zilio, J. Steven Brown.Assessment of the low-GWP refrigerants R600a, R1234ze(Z) and R1233zd(E) for heat pump and organic Rankine cycle applications. Applied Thermal Engineering 2020; 167: 114804.

[14] Fu Zhou, Weiwei Yang, Xingqi Cao, Yaling He. Theoretical study of three zeotropic mixtures for high temperature heat pump. Journal of engineering thermophysics 2015; 36: 703-708.

13th IEA Heat Pump Conference
April 26-29, 2021 Jeju, Korea

Performance evaluation by simulation of refrigerated display cabinets using HFO refrigerant

Yoichi Miyaoka[a,*], Takaoki Suzuki[b], Kosuke Bizen[b], Koichi Kitamura[b]
Seiichi Yamaguchi[a], Kiyoshi Saito[a]
Tadao Watanabe[c], Takahiro Iwasaki[c], Koji Takiguchi[c]

[a]Interdisciplinary institute for thermal energy conversion engineering and mathematics, Waseda University, Shinjuku-ku, Tokyo, 169-8555, Japan
[b]Dept. of Applied Mechanics, Waseda University, Shinjuku-ku, Tokyo, 169-8555, Japan
[c]Mie Factory, Food & Beverage Distribution Business Group, Fuji Electric Co., Ltd., Yokkaichi, Mie, 510-8631, Japan

Abstract

For protecting the global environment, low GWP refrigerants are to be incorporated in air conditioning systems and refrigerating devices, such as refrigerated display cabinets (RDCs) commonly used in convenience stores and supermarkets. R290 (propane), as a natural refrigerant, has been receiving attention as a potential working fluid alternative but poses safety issues due to its flammable characteristic. As the demand for safe refrigeration systems with easy maintenance is increasing, this study evaluated the utilization of HFO-1234yf for RDCs, and its performance was compared to R290 and other commonly used refrigerants. Simulations were conducted based on actual ambient temperature data from a convenience store. Results showed that the COP of HFO-1234yf was slightly lower than those of R290 and R134a, but higher than those of R410A, R32, and R744. The annual power consumption and the annual performance factor of HFO-1234yf were very similar to those of R290. Hence, it is expected that RDCs using HFO-1234yf will perform as efficiently as those using R290.

Keywords: Showcase; Performance Evaluation; Refrigerants; HFO-1234yf; Simulation

1. Introduction

Recent trends in global warming prevention have been revised by the Kigali Amendment in the Montreal Protocol [1], and an obligation was established to reduce HFCs by 85% by 2036. Therefore, to achieve the reduction obligation by 2029, before the amount of HFCs becomes severe in Japan, refrigeration equipment using low GWP refrigerant and reduction of refrigerant leakage is to be developed. However, if a low GWP refrigerant is used without preliminary evaluation of the equipment performance, then it can result in (1) inefficient operation, and (2) increased energy required for manufacturing.

Apart from the proper selection of the working fluid focused on natural refrigerants to lessen direct CO2 emissions, systems that utilize these refrigerants must work efficiently to avoid over power consumption that results in indirect CO2 emissions. As of March 2019, 58,000 convenience stores operate in Japan, with annual sales exceeding 10 trillion yen [2]. Most of the energy consumption at convenience stores is due to lighting, air conditioning, and refrigeration equipment [3]. There is a high demand for refrigerated display cabinets (RDCs) as one of the commonly used refrigeration equipment to hold and preserve perishable goods while offering ease of accessibility to the customers. There are two types of RDCs: “built-in type” and “separate type.” In the former, a condensing unit, with mechanical parts such as a compressor and a condenser, is integrated with a device for displaying and cooling the product, while the latter features the separation of the evaporating and condensing units at the indoor and outdoor, respectively. Convenience stores often use built-in RDCs because they can easily accommodate changes in store layout and restrictions on the location of condensing units. Convenience store owners are also keen on the operational safety of the refrigerated display cabinets.

In this study, a simulator was built and used to evaluate alternative working fluids that can conform to the environmental standards, operational safety, and system efficiency, particularly for built-in type RDCs. The results can be used for benchmarking and preliminary assessment of the performance before manufacturing and utilization of the systems. In particular, this study evaluated the potentiality of HFO-1234yf refrigerant as a low GWP refrigerant to replace commonly used high GWP refrigerants, such as R134a, R410A, and R32. Furthermore, the performance of HFO-1234yf was compared to that of R290, as the latter has received attention for possible usage despite its high flammability that poses safety issues.

2. Methods

The annual energy performance of RDCs using various refrigerants was evaluated. Here, an annual performance evaluation simulator for RDCs was constructed based on the annual interior conditions at a store in Japan. Furthermore, the simulator evaluated the annual performance by changing the refrigerant. This feature makes it easy to assess the performance of a variety of refrigerants without incorporating them in actual equipment.

2.1. Simulator Overview

The annual performance simulator was input with specifications and conditions of the RDCs, and the store interior temperature conditions (in case of the built-in type) and the outdoor temperature conditions (in case of the separate type). The simulator provided the annual performance as output. For analyzing the applicability of low GWP refrigerants to RDCs, the annual performance of showcases was evaluated. Therefore, the annual power consumption of the RDCs, the annual average COP, and the time-series data of the operating state such as compressor discharge temperature, were obtained as output. Fig. 1 shows the input/output relationship of the annual performance simulator. The annual performance was calculated by the simulator that used the thermodynamic cycle analysis. This simulator applied pinch temperature analysis as its calculation principle [4]. For subcritical cycle refrigerants, the pinch temperature was applied at the condenser refrigerant outlet. The subcooled condition was determined by the temperature difference between the condensation temperature and ambient temperature, and the pinch temperature. In the case of R744 (CO_2), the pinch temperature was used at the gas cooler refrigerant outlet.

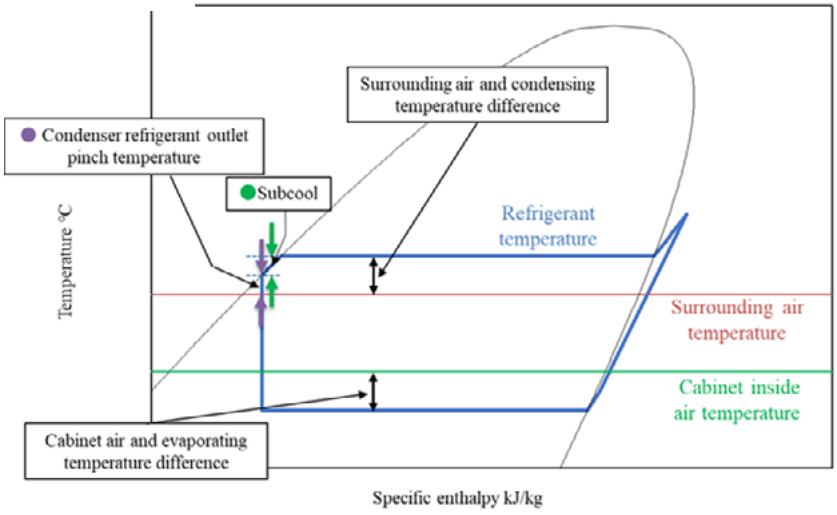


Fig. 1. Temperature-enthalpy diagram

2.2. Calculation prerequisites

The performance of RDC systems using various refrigerants can be compared in the thermodynamic cycle. Table 1 shows the computational elements used for the performance calculation.

Table 1 Computational elements

Computational elements
Difference between the evaporating temperature and the surrounding air temperature
Evaporator outlet superheat
Difference between the condensing temperature and the surrounding air temperature
Compressor adiabatic efficiency
Isenthalpic process at the expansion valve

The procedure to determine the cycle is as follows:

1. Determine the evaporation temperature from the cabinet air temperature.
2. Determine the condenser temperature from the surrounding air temperature and the refrigerant outlet pinch temperature.
3. Determine the refrigerant properties of the compressor suction considering the evaporator superheat.
4. Determine the refrigerant properties at the compressor outlet considering compressor adiabatic efficiency.

A fixed temperature difference between the heat exchanger and the ambient temperature was employed, where the difference in heat transfer performance and pressure loss due to the physical properties of the refrigerant was not considered. This is because the thermal resistance on the air side is dominant and there is no significant difference in the temperature difference between refrigerants.

3. Results and Discussion

3.1. Annual exterior and interior temperatures at an actual store

Various measurement data obtained at an actual convenience store were examined to conduct the simulation under conditions that represent those in an actual store. Fig. 2 shows the exterior and interior store temperatures measured for one year in an actual store. This data was measured at one-hour intervals between June 1, 2017, and May 31, 2018. However, there are some missing data.

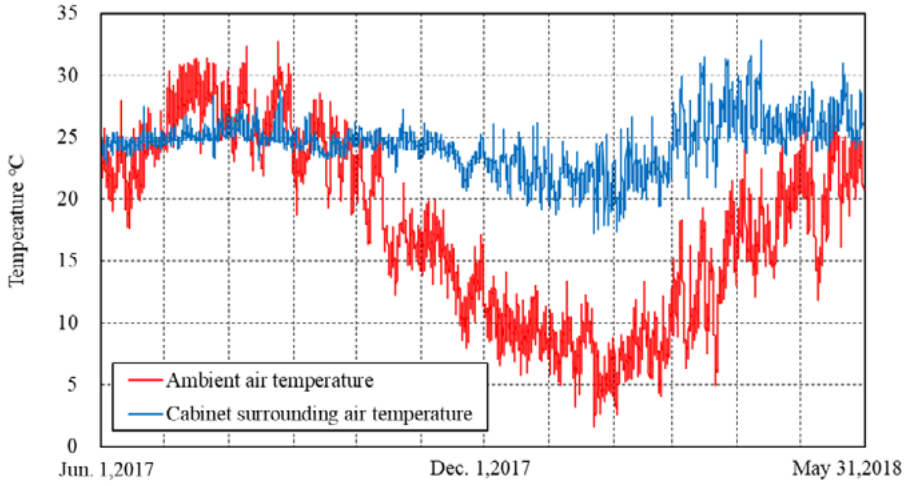


Fig. 2. Indoor and outdoor air temperature of an actual store

The simulator used the physical properties of the refrigerants based on the data from the NIST REFPROP [5]. Tables 2 and 3 list the physical properties, GWP, and the safety classifications of the refrigerants considered in the study.

Table 2 Physical properties, GWP, and safety class of various refrigerants (1/2)

Refrigerant	GWP [6]	Critical temperature °C	Critical pressure MPa	Safety class
R134a	1430	101.06	4.059	A1
R1234yf	< 1	94.70	3.382	A2L
R290	3.3	96.74	4.251	A3
R410A	2088	71.34	4.901	A1
R32	675	78.11	5.783	A2L
R744	1	30.98	7.377	A1

Table 3 Physical properties of various refrigerants (2/2)

Refrigerant	Condensing pressure MPa	Evaporating pressure MPa	COP	Volume capacity kJ/m^3	Suction density kg/m^3	Capacity kJ/kg Refrigerant
R134a	0.887	0.243	4.01	1865	11.780	158.30
R1234yf	0.895	0.266	3.89	1806	14.556	124.05
R290	1.218	0.406	3.96	2597	8.686	298.99
R410A	2.144	0.678	3.78	4440	25.111	176.80
R32	2.190	0.691	3.84	4815	18.176	264.93
R744	8.019	3.046	2.66	12446	79.064	157.42

Table 4 lists the preconditions of the RDC set for the calculation. These input conditions do not necessarily reflect actual machine data, but by maintaining these uniform conditions, a calculation can be performed to an approximate refrigeration system in accordance with the physical properties of various refrigerants. As the condensation temperature of R744 cannot be defined under the calculation conditions shown in Table 4, the pinch temperature of the gas cooler outlet temperature sets the pressure at which the COP is maximum as the high operating pressure [7].

Fig. 3 shows COP calculation results of various refrigerants. In terms of the COP, the results confirm that R1234yf is slightly inferior to R134a and R290, equivalent to R32, and superior to R410A and R744.

Table 4 Specifications of the calculation

Condition	Value
Difference between condensing temperature and the surrounding air temperature °C	10
Cabinet temperature °C	25
Surrounding air temperature °C	5
Difference between evaporating temperature and the surrounding air temperature °C	10
Evaporating temperature °C	-5
Evaporator outlet superheat °C	5
Compressor adiabatic efficiency	0.7

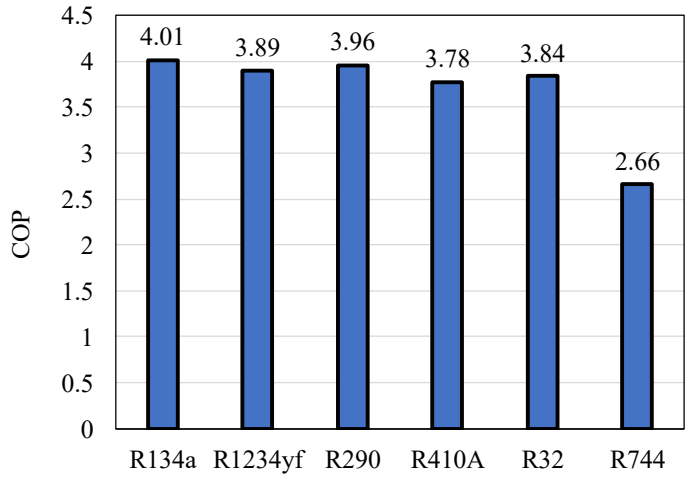


Fig. 3. COP calculation results of various refrigerants

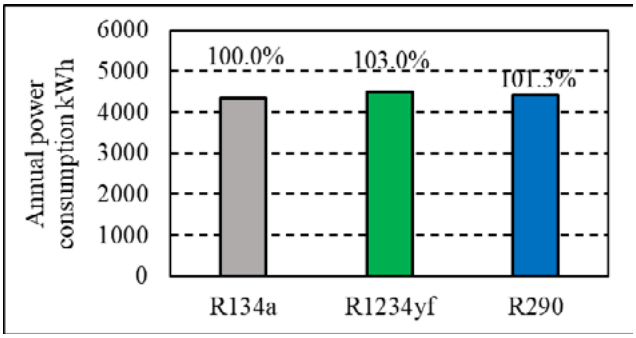
3.2. Annual performance evaluation with fixed heat load

The performance of RDC systems were evaluated from two sets of simulations: with fixed heat load and with heat load variation when the type of refrigerant was changed based on the indoor temperature and the inside of cabinet temperature data measured at an actual store. The result for one year was calculated at hourly intervals. For the cabinet temperature of the refrigerated showcase, the actual average value of one-minute interval data per day for each season was considered, because there were no hourly data throughout the year.

At first, we simulated the performance of RDC systems with fixed heat load. The heat load was fixed at 2 kW. Linear interpolation was applied to account for some missing time-series data. The comparisons were focused mainly on R1234yf and R290 with R134a as the baseline, as these refrigerants have shown better COP values compared to the other working fluids presented in the previous section. Additionally, these three refrigerants exhibit similar critical temperatures and properties. Fig. 4 shows the ratio of the annual power consumption of R1234yf and R290 with respect to R134a, and Fig. 5 shows the annual average COP obtained by dividing the annual total refrigeration load by the power consumption. Table 5 shows the assumed specifications of the RDC set.

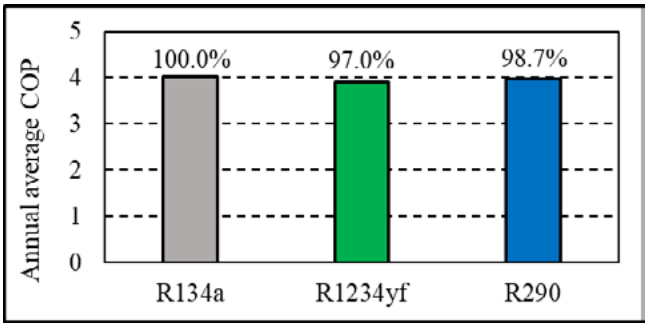
Table 5. Specifications of the RDC set

Specifications	
Rated refrigeration load	2 kW
Type	Built-in type
Physical size	Standard size (specific size is not considered)



Refrigerant	Annual power consumption (kWh)
R134a	4343
R1234yf	4475
R290	4400

Fig. 4. Annual power consumption calculation results for three refrigerants at 2kW heat load



Refrigerant	Annual average COP
R134a	4.03
R1234yf	3.92
R290	3.98

Fig. 5. Annual average COP calculation results for three refrigerants at 2kW heat load

Fig. 6 shows the results of calculating the hourly change in the COP of three refrigerants for one year. From Fig. 4–6, it is evident that the performance of R1234yf is similar to that of R290.

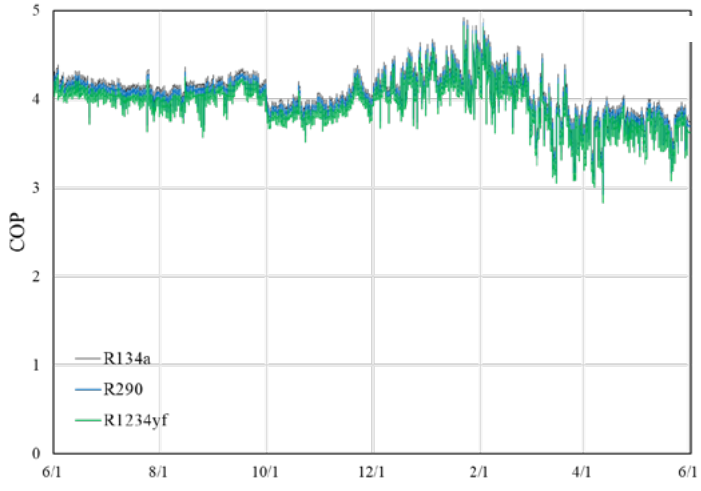


Fig. 6. Hourly COP for one year for three refrigerants at 2kW heat load

3.3. Annual performance evaluation with varying heat load

Next, we simulated the performance of RDC systems with varying heat load. This is because the surrounding air temperature at RDC changes in the case of an open refrigerated display cabinet. The heat load is assumed to change due to cold air leaks from the RDC while an outside air infiltrates [8]. Varying the heat load was obtained from the correlation between the difference of the inside and surrounding air temperature of RDC, and the heat load calculated from the experimental values. The experimental measurements were taken using the actual machine during three periods with varying temperatures at the surrounding environment of the RDC: summer, mid-term, and winter, and the heat load was calculated from the evaporator inlet/outlet temperature and airflow rate.

Table 6 shows the results of the heat load during the three periods. The calculated heat load from the experimental values was linearly approximated.

Fig.7 presents the results of the correlation for the difference between the surrounding air and inside temperature of the RDC, against the heat load.

As observed from Fig. 7, the heat load of the target RDCs was less than 1kW.

Table 6. Calculated heat load during the three periods

	Summer	Mid-term	Winter
RDC surrounding air temperature ℃	27	25	19.3
RDC inside temperature ℃	5	4.6	4.6
Heat Load kW	0.953	0.831	0.464

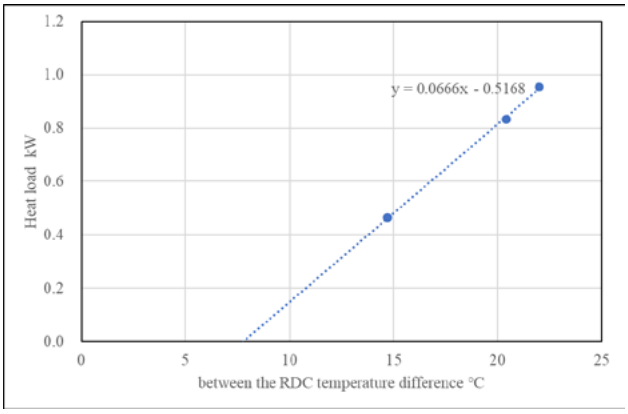
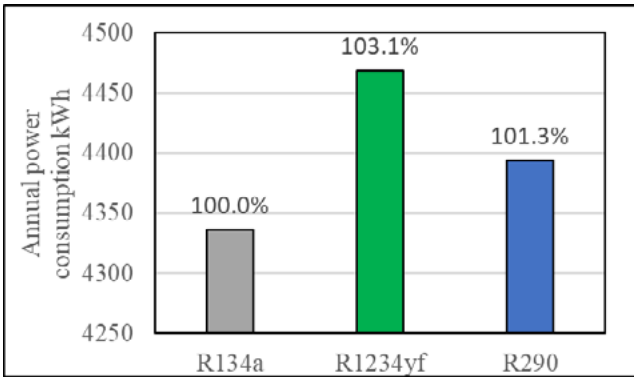


Fig. 7. Correlation between the RDC temperature difference and heat load

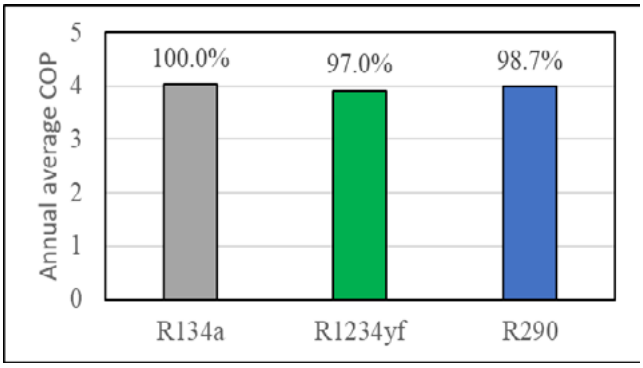
To compare the annual power consumption and annual average COP for fixed and variable loads, the correlation equation shown in Fig. 7 was scaled up so that the average heat load conforms to 2 kW. The results are shown in Fig. 8 and Fig. 9. Furthermore, the correlation equation between the heat load and heat exchange temperature difference does not apply because it varies with the geometry of each equipment and refrigerant, hence the set of preconditions of the RDC from Table 4 was used for the calculation.

Fig. 8 shows the ratio of the annual power consumption of R1234yf and R290 with respect to R134a, while Fig. 9 shows the annual average COP.



Refrigerant	Annual power consumption (kWh)
R134a	4336
R1234yf	4468
R290	4394

Fig. 8. Annual power consumption calculation results for three refrigerants with varying heat load



Refrigerant	Annual average COP
R134a	4.04
R1234yf	3.92
R290	3.98

Fig. 9. Annual average COP calculation results for three refrigerants with varying heat load

Table 7 shows the calculated values for the annual power consumption and the average annual COP for fixed and variable heat load. The results show that the error in the average annual power consumption figure is about 0.15%, and the average annual COP changed insignificantly.

Table 7 Comparison of annual energy consumption and annual average COP at fixed and variable heat loads

Refrigerant	Heat load fixed		Heat Load Variation	
	Annual energy consumption	Annual average COP	Annual energy consumption	Annual average COP
R134a	4343	4.03	4336	4.04
R1234yf	4475	3.92	4468	3.92
R290	4400	3.98	4394	3.98

Fig. 10 shows the results of calculating the hourly change in the COP of three refrigerants for one year. As in the case of fixed heat load, the performance of R1234yf is similar to that of R290.

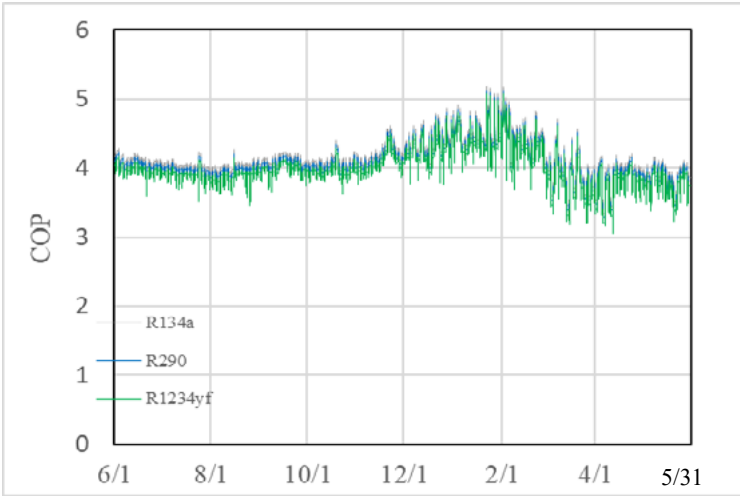


Fig. 10. Hourly COP for one year for three refrigerants with varying heat load

These results show that the annual power consumption and the average annual COP for fixed and variable heat loads are almost the same. One of the reasons for this is that the surrounding air temperature at RDC does not change much because the target is built-in RDCs, and the heat load does not consequently change much throughout the year.

3.4. Parameter study

A simulation calculation was performed to examine the effect of varying the cabinet temperature of the RDC on the annual power consumption and annual average COP. This simulation was performed with a fixed heat load of 2kW. Table 7 and Table 8 list the calculation results of annual power consumption and annual average COP, respectively.

Table 7 Annual power consumption (kwh)

Refrigerant	Cabinet temperature		
	4 ℃	5 ℃	6 ℃
R134a	4388	4271	4151
R1234yf	4522	4398	4271
R290	4445	4328	4207

Table 8. Annual average COP

Refrigerant	Cabinet temperature		
	4 ℃	5 ℃	6 ℃
R134a	3.99	4.10	4.22
R1234yf	3.87	3.98	4.10
R290	3.94	4.05	4.16

It is evident from Table 7 that when the cabinet temperature is lowered by 1 °C, the annual power consumption increases, and annual average COP decreases by approximately 3%. Table 7 and Table 8 indicate that the power consumption of R1234yf increases by approximately 1–2% compared to that of R290, and annual average COP decreases by 1–2%. Thus, it can be concluded that the performance of R1234yf is closely equivalent to that of

R290.

4. Conclusion

Simulations were performed to compare the performance of HFO-1234yf refrigerant to those of various refrigerants when used for refrigerated display cabinets. The COP of HFO-1234yf refrigerant was slightly lower than R134a and R290, but higher than conventionally used high GWP refrigerants such as R410A, and even R32. HFO-1234yf also outperformed R744 (CO_2). Based on the annual power consumption and annual average COP results, and it was confirmed that HFO-1234yf performed as efficiently as R290. Therefore, RDCs using HFO-1234yf are expected to exhibit a system performance that is as efficient as those using R290. Owing to the safety desired from integrated RDCs installed in stores and supermarkets, the low GWP refrigerant, R1234yf, is considered to be more suitable than R290.

In the future, as the built-in type refrigerated display cabinet was considered in this study, the separated type will be considered. Furthermore, to verify the accuracy of the simulation results, we plan to conduct more experiments to evaluate the performance with actual machines.

References

[1] https://www.unenvironment.org/news-and-stories/press-release/montreal-protocol-celebrates-another-milestone-agreement-reduce [Accessed on Oct. 8, 2019]

[2] https://www.jfa-fc.or.jp/particle/320.html (Japan Franchise Association (in Japanese)) [Accessed on Oct. 8, 2019]

[3] https://www.tokyo-co2down.jp/cmsup/pdf/conveni201303.pdf (Power saving guide for convenience store managers, Tokyo Environment Bureau (in Japanese) [Accessed on Oct. 8, 2019]

[4] Suzuki T, Miyaoka Y, Yamaguchi S, Saito K, 2020. “Annual Performance Assessment of Heat Pump Water Heater Technology based on Thermodynamic Properties of Various Refrigerants,” 13th IEA Heat Pump Conference. Jeju, Korea 2020

[5] https://www.nist.gov/srd/refprop [Accessed on Sep. 27, 2019]

[6] IPCC Fifth Assessment Report: Climate Change 2013（AR5）

[7] “Guide for Subcritical and Transcritical CO_2 Applications,” Emerson Climate Technologies, Inc.2016

[8] Redo M.A., Ohno K., Giannetti N., Yamaguchi S., Saito K., 2019. “Seasonal Performance Evaluation of CO_2 Open Refrigerated Display Cabinets,” Applied Thermal Engineering Vol. 163, 114354.

13th IEA Heat Pump Conference
April 26-29, 2021 Jeju, Korea

A Techno-Economic Assessment of Air-Source Heat Pumping Technologies in the Canadian Residential Sector

Justin Tamasauskas[a,*], Stéphanie Breton[a], Martin Kegel[a]

[a]CanmetENERGY in Varennes, Natural Resources Canada, 1615 Lionel Boulet Blvd, Varennes, Quebec, Canada, J3X 1P7

Abstract

While heat pump systems have strong potential to reduce energy use in the Canadian residential sector, the optimal system type and configuration can vary greatly depending on local climate and economic conditions. This paper applies techno-economic analysis to compare three market available air-to-air heat pumps (single stage, conventional variable capacity, and cold climate variable capacity) and examine their relative potential under different climate and utility rate structures. Using an improved, data-driven heat pump model, the economic and energy performance of each system is assessed for new construction housing in three Canadian regions. Results demonstrate the energy savings benefit of cold climate heat pumps in harsher winter climates, and the challenging economic context faced by heat pumps under current low natural gas rates in some Canadian regions. Key design concepts, including the sensitivity of the results to changes in estimated operating COP, and the strong link between peak loads and the combined control of the heat pump and auxiliary systems, are also discussed in order to promote an improved integration of heat pumps in Canada.

Keywords: Variable capacity heat pumps; Cold climate heat pumps; Techno-economic analysis; Canadian residential sector

1. Introduction

As the world transitions towards a decarbonized economy and infrastructure, efficient renewable energy technologies are of great importance. In recognition of this context, the Government of Canada has developed a Market Transformation Roadmap [1], which presents a framework for an increased adoption of the high efficiency mechanical systems needed to drive decarbonisation of the built environment. Heat pumps play an important role within the Roadmap, responding to key aspirational goals regarding future high efficiency space heating systems (Target energy performance[1] >100%) and the integration of renewable energy. However, to fully capitalize on this strong potential, appropriate heat pump system selection is of critical importance.

The Canadian context represents a particularly challenging set of circumstances for heat pump integration. Significant variations in both climate (mild maritime to extreme cold) and utility rate structures (vast differences in natural gas vs. electricity rates) often mean that the optimal system choice is highly dependent on local climate and economic conditions. Selection can be further complicated when considering the peak load impacts of heat pumps, an aspect of growing importance given the increasing electrification of building systems and more widespread heat pump adoption.

The current Canadian residential heat pump market is dominated by air-source (air-to-air) heat pumps, driven by their lower costs and relative ease of installation [2]. However, traditional single stage systems suffer significant performance degradations at colder temperatures while cycling frequently at milder conditions, making it difficult to meet comfort needs in Canadian climates. The last decade has seen important technological advances in the market, including the increased availability of inverter-driven variable speed compressors, and the introduction of cold climate air-source heat pumps, which combine variable capacity

* Corresponding author. Tel.: +1-450-652-4822; fax: +1-450-652-5177.
E-mail address: Justin.Tamasauskas@Canada.ca.

[1] Energy performance here refers to how efficiently a selected technology delivers space heating, quantified using the COP and Heating Season Performance Factor (HSPF) (heat pumps) or annual fuel utilization efficiency (AFUE) (gas and oil-fired equipment) [1]. These targets provide important motivation for increased heat pump adoption in Canada.

technology with larger outdoor coils and other cycle improvements such as vapour injection [3,4]. These advancements allow the heat pump to provide increased heating capacities at lower ambient temperatures, while still efficiently modulating at milder conditions. While previous studies have examined the energy performance of these systems and their economics in isolation [5,6], there is little information available regarding when the added investment for cold climate and variable capacity technologies is most appropriate, or how the economics of different air-source heat pump technologies compare across Canada.

This paper presents a simulation-based approach, driven by extensive testing and measured data, to assess the relative benefits of three types of market available air-source heat pumps: conventional single speed systems, conventional variable capacity units, and cold climate (variable capacity) heat pumps. A new data-driven heat pump model, capable of appropriately capturing the unique performance characteristics of variable capacity heat pumps, is used as a base for system assessment. Each heat pump integration is examined for newly constructed housing in three Canadian regions (Montreal, Edmonton, and Vancouver) to identify the potential for energy and lifecycle cost savings. A grid interaction analysis is also performed to more fully understand the implications of a given system selection.

2. Development of Base Case Housing Models

Climate, utility rate structure, and the type of heat pump integration (ducted or ductless) can vary greatly across Canada. In order to highlight these effects, three Canadian regions were selected, each representing a unique set of boundary conditions. Key climate parameters for each region are provided in Table 1 [7].

Table 1 Summary of climate characteristics

Characteristic	Montreal	Edmonton	Vancouver
Heating Design Temperature (°C)	-23	-30	-7
Heating Degree Days Below 18°C	4,200	5,120	2,825
Climate Type	Cold & Humid	Cold & Dry	Cool & Humid

Housing models used in the analysis were selected to be representative of typical single family housing, with building geometry based on the Canadian Centre for Housing Technology (CCHT) test homes located in Ottawa, Canada [8]. The modelled home included two above ground floors and a finished basement, with a total heated floor area of 284 m^2. The building envelope was modified to represent new construction housing in each region using National Building Code of Canada (NBC) minimum requirements for the appropriate climate zone [7]. Building mechanical systems were based on typical configurations in each region, and included both centrally ducted systems (Edmonton, Vancouver) and non-ducted configurations (Montreal). It is important to note that Montreal does include small flexible ducting to distribute a low volume (65 CFM) of ventilation air from the HRV, with a small electric duct heater used to ensure a suitable ventilation supply air temperature. A summary of key housing characteristics for each base case is provided in Table 2, with further details available in Kegel *et al.* [9].

Table 2 Key housing characteristics for base case models

Characteristic	Montreal	Edmonton	Vancouver
Central Air Distribution	No	Yes	Yes
Primary Heat Fuel & System	Electric Baseboard Heaters	Natural Gas Forced Air Furnace	Natural Gas Forced Air Furnace
Heating Efficiency	100%	92%	92%
Space Cooling System	Split AC Unit COP = 3.3*	Central AC COP = 3.5*	Central AC COP = 3.5*
DHW Fuel	Electric	Natural Gas	Natural Gas
Heat Recovery Ventilator (HRV)	Yes	Yes	Yes

*At AHRI rating conditions

3. Heat Pump System Integrations

Each base case model serves as a platform to assess three different heat pump technologies:

I. Conventional Single Stage Air-Source Heat Pump (**SSHP**)
II. Conventional Variable Capacity Air-Source Heat Pump (**VCHP**)
III. Cold Climate (Variable Capacity) Air-Source Heat Pump (**CCHP**)

It is important to note that the method of heat distribution within the home can vary depending on whether central ducting is available. As such, for each system type listed above (SSHP, VCHP, CCHP), both ducted and non-ducted configurations were examined. For locations with existing central ducting (Edmonton, Vancouver), a ducted heat pump configuration is proposed, with the indoor coil of the heat pump integrated into a central air handling unit. For homes without central ducting (Montreal), a ductless configuration is proposed, with a wall mounted indoor unit located in the stairwell connecting the first and second floors of the home. In this configuration, the basement is heated only using electric baseboards, as per the base case.

For all heat pump cases, system sizing was chosen to match the capacity used in the CCHP analysis. This decision was made to provide a common base of comparison for all systems, and to avoid cross-effects from different sizing methodologies. System sizing for the CCHP case was based on the heat pump acting as the primary source of heating for the building, supplemented by limited auxiliary heating operations if needed.

System sizing in Montreal is limited to 1.5 tons, the largest market available system size for the ductless CCHP *used in the simulations*. As outlined later in this paper, the simulation model for this heat pump was based on extensive test data, with the tested model not available in sizes > 1.5 tons. This limitation is better understood by noting the type of ductless system used: A single-split (one indoor unit, one outdoor unit) ductless configuration. Although a multi-split unit (multiple indoor units, one outdoor unit) is a more likely choice given the size of the home in this study, the single-split unit is modelled due to the availability of extensive performance data derived from detailed testing at the CanmetENERGY facility. Given that similar data was not available for multi-split systems, the single-split was used instead to avoid employing additional modelling assumptions, while more closely representing as-installed performance.

Single Stage Air-Source Heat Pump

The single stage heat pump represents the most basic system available in the current market, and is included in the analysis to provide a point of reference for the other technologies.

Single stage heat pumps encounter two significant challenges when operating in many Canadian climates:

I. Heating capacity drops drastically at colder ambient temperatures, increasing auxiliary energy use
II. Available capacity at milder conditions is often far greater than the building heating load, leading to frequent and inefficient on/off cycling.

Given the reduced heating performance at colder ambient temperatures, fully sized auxiliary systems (sized to meet the peak heating loads) are required. For ductless configurations, auxiliary heating is achieved using electric baseboards located in each thermal zone, while for centrally ducted configurations, an electric duct heater is used to supplement heat pump operations as required. Key SSHP parameters are provided in Table 3.

Table 3 Performance characteristics for single stage heat pump

	Montreal	**Edmonton**	**Vancouver**
HP Size	1.5 Ton	3 Ton	2 Ton
HP Configuration	Ductless	Ducted	Ducted
Heating COP*	3.2	3.7	3.7
Cooling COP*	3.5	3.4	3.4
Min. Outdoor Operating Temperature, Heating Mode (°C)	-8	-20	-20
% of Rated Capacity @ Cut-Off	62%	27%	27%

*At AHRI Rating Conditions

Conventional Variable Capacity Air-Source Heat Pump

Variable capacity units account for a growing share of the Canadian market, driven by increased energy savings resulting from the ability to efficiently modulate the capacity of the unit to match heating or cooling demand. However, variable capacity technology alone does not necessarily constitute a cold climate heat pump: Many market available units provide less than 50% of rated capacity at outdoor air temperatures of -20°C or -25°C. This integration examines these more conventional variable capacity systems in each region.

Variable capacity heat pumps are defined both by their full capacity at maximum speed, and their ability to modulate to meet reduced loads. Fig. 1 presents the heating capacity and COP as a function of outdoor air temperature for a representative ducted variable capacity heat pump [10]. Capacity curves are normalized based on AHRI rating conditions (i.e. capacity at 47°F (8.3°C)). It is important to note the increase in COP at lower compressor speeds, which allows this type of heat pump to operate at improved efficiencies during times of lower heating demand while also limiting on/off cycling.

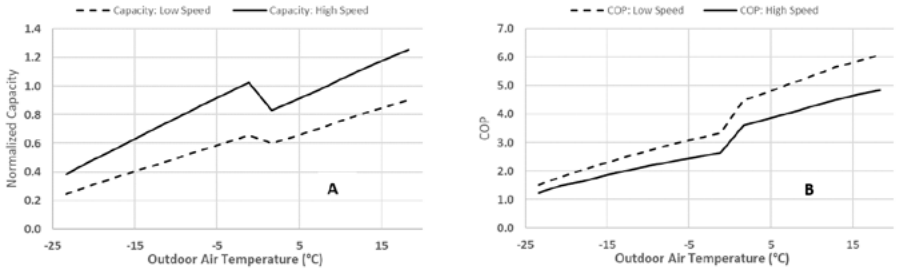


Fig. 1. Variation of (A) heating capacity and (B) COP at minimum and maximum capacity for a typical VCHP [10]

A summary of key variable speed heat pump parameters for each region is provided in Table 4.

Table 4 Key performance characteristics for variable capacity (non-cold climate) heat pumps

	Montreal	**Edmonton**	**Vancouver**
HP Size	1.5 Ton	3 Ton	2.5 Ton
HP Configuration	Ductless	Ducted	Ducted
Heating COP*	3.3	4.1	3.7
Cooling COP*	4.1	4.1	3.9
Min. Outdoor Operating Temperature, Heating Mode (°C)	-17	-23	-23
% Capacity at Cut-Off Temperature (Max Speed)	51%	38%	38%
Average Min: Max Capacity Ratio	0.32	0.30	0.30

*At AHRI Rating Conditions

Cold Climate Variable Capacity Air-Source Heat Pump

Cold climate heat pumps combine variable capacity technologies with other cycle improvements (e.g., larger outdoor coils, vapour injection cycles) to maintain a larger portion of heating capacity at low outdoor air temperatures. While several definitions for cold climate heat pumps are available in the literature [11,12], in this study they have been classified based on an ability to operate to a minimum outdoor air temperature of -25°C, while still maintaining over 65% of their rated capacity. These performance characteristics make cold climate units well suited to space heating in many Canadian regions, albeit at added initial investment.

Fig. 2 (A) shows a representative normalized heating curve for a ducted cold climate heat pump at minimum and maximum speed [13]. A representative curve for a non-cold climate variable capacity unit at maximum speed is also presented. It is clear that the cold climate unit is able to maintain a far greater percentage of its heating capacity, reducing the amount of auxiliary energy input required. Fig. 2(B) shows the COP of the same representative cold climate unit over its range of operating conditions.

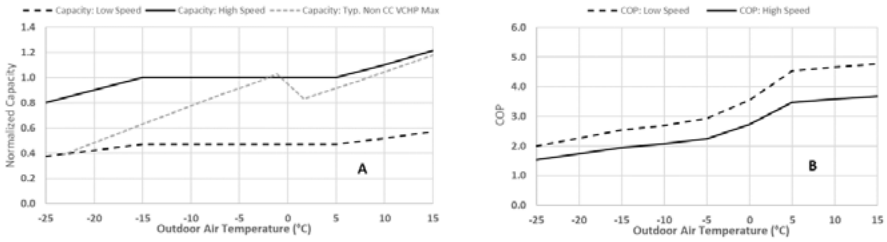


Fig. 2. Summary of (A) heating capacity and (B) COP for cold climate variable capacity heat pump [13]

A summary of key cold climate heat pump characteristics is provided below in Table 5.

Table 5 Key performance characteristics for cold climate variable capacity heat pumps

	Montreal	**Edmonton**	**Vancouver**
HP Size	1.5 Ton	3 Ton	2.5 Ton
HP Configuration	Ductless	Ducted	Ducted
Heating COP*	4.1	3.7	3.6
Cooling COP*	4.2	3.7	3.7
Min. Operating Temperature, Heating Mode (°C)	-25	-25	-25
% Capacity at Cut-Off Temperature (Max Speed)	66%	80%	80%
Average Min: Max Capacity Ratio	0.33	0.47	0.56

*At AHRI Rating Conditions

4. Heat Pump System Energy Models

Accurately modelling each heat pump system is critical in order to properly estimate the energy and economic benefits of each integration. In this study, all systems were modelled with TRNSYS v.17 using the appropriate Canadian Weather for Energy Calculations (CWEC) weather file. Each simulation was run with a time step of 2.5 minutes to better simulate the control logic of the heat pump and auxiliary systems.

Heat Pump Performance Modelling

One of the main strengths of TRNSYS is its ability to support the development and integration of custom components models for different HVAC equipment. This capability was leveraged to develop a new variable capacity heat pump model, Type 3255 [6], which was designed to more closely represent variable capacity performance in system level simulations. The component model is based on extensive experience with a heat pump test bench at the CanmetENERGY facility in Varennes, and integrates a number of new capabilities including performance variation with compressor speed, and short term characteristics such as defrost and compressor behaviour during start up. Further details regarding model development and capabilities can be found in Breton *et al.* [6].

Type 3255 uses a data driven approach to heat pump simulation, requiring the user to provide a detailed map of how capacity and power consumption vary with compressor speed. Wherever possible, systems simulated in this paper use experimental data to inform heat pump simulations. However, given the variety of systems examined in this study, certain models have been developed using manufacturer data at rated conditions, with performance at lower compressor speeds estimated using typical curves relating heat pump power to the ratio of delivered and rated heating capacities [14, 15]. A summary of the data sources used for each heat pump integration is summarized in Table 6.

Table 6 Summary of data sources for heat pump modelling

	Ductless Systems		Ducted Systems	
Heat Pump System	**Rated Performance**	**Part Load Performance**	**Rated Performance**	**Part Load Performance**
SSHP	Manufacturer [16]	Literature [15]	Manufacturer [17]	Literature [15]
VCHP	Manufacturer [18]	Literature [14]	Test [3]	Test [3]
CCHP	Test [19]	Test [19]	Manufacturer [13]	Literature [14]

Representing Heat Pump Control

Heat pump control was simulated using a PID controller, which estimated the required compressor frequency (or heat pump capacity, for SSHP) to maintain the desired temperature setpoint of 21°C in heating, or 23°C in cooling. Additional controls ensure that the heat pump only operates within its intended range of outdoor temperatures. Compressor frequency spikes to maximum during start up after a defrost or shutdown event when in heating mode, based on observations noted during testing at the CanmetENERGY facility.

Auxiliary heating elements (electric baseboards for ductless cases, electric duct heater for central systems) are a key component of each heat pump integration, and play an important role in defining the peak loads of the system. Auxiliary systems have three operating modes, depending on heat pump operations:

I. Heat pump is defrosting: For central systems, the auxiliary duct heater turns on at a constant, fixed, limited capacity to minimize occupant discomfort during defrost. No special control is used for the ductless system, as the system modelled is not equipped with internal heating elements. Defrost length is fixed at 5 minutes in the current model (future work will add varying defrost lengths).
II. Heat pump is operating: Auxiliary heaters operate with a slightly lower setpoint (20°C vs. 21°C for the heat pump) to ensure space temperatures are maintained within an acceptable range while still prioritizing heat pump operations. The heat pump and auxiliary system may operate in parallel.
III. Heat pump is unable to operate: When ambient temperatures are too cold for the heat pump to operate, auxiliary heating maintains the desired setpoint of 21°C.

5. Lifecycle Cost Analysis

In addition to examining energy performance, it is also important to understand the economics of each system to fully assess their potential in the Canadian market. With this in mind, each system integration has been assessed over a 20 year lifespan, with a focus on the associated capital, maintenance, and operational costs. No replacement costs are included. All lifecycle calculations were performed using an inflation rate of 1.8% and a discount rate of 3.3%, based on current Canadian financial markets.

System capital costs were estimated at the component level, and included all required equipment, controls, and ducting. A listing of all equipment included in the cost analysis is provided in Table 7.

Table 7 Summary of components included in capital cost calculations

Category	**Components**
Equipment	Heat Pump (Both Indoor & Outdoor Sections)
	Auxiliary Electric Baseboards (Ductless Cases)
	Auxiliary Electric Duct Heaters (Ducted Cases)
Controls	Thermostat
Distribution	Ductwork (Ducted Cases)

Component costs were derived from available suppliers [20-22], and RS Means [23], and included both material and labor. Wherever possible, prices were compared from the same source for all three system integrations to ensure that relative pricing between each remained consistent. Equipment and labour costs were adjusted for each region using factors presented in RS Means [23]. Capital costs for each integration and region are presented in Table 8, with values in Canadian Dollars. Annual maintenance includes typical tasks (inspection, coil & filter cleaning), but not replacement of major components (e.g. refrigerants or compressors).

Table 8 Summary of capital and maintenance costs for each system integration by region

System	Cost	Montreal	Edmonton	Vancouver
Base Case	System	$8,400	$12,300	$11,600
	Annual Maintenance	$114	$237	$225
SSHP	System	$8,500	$12,400	$10,900
	Annual Maintenance	$114	$123	$117
VCHP	System	$9,200	$17,200	$14,200
	Annual Maintenance	$114	$123	$117
CCHP	System	$10,100	$19,800	$16,000
	Annual Maintenance	$114	$123	$117

Utility rates used in the study were based on current rates and structures for each selected region [24-28]. This included all daily/monthly fixed charges, tiered rate structures, and appropriate rate riders. Energy escalation rates were estimated using information from the National Energy Board of Canada [29]. A summary of utility rates used in the analysis are provided in Table 9. Natural gas rates are not presented for Montreal, as this source of energy is not used in the base case or any heat pump integration.

Table 9 Summary of utility rate structures in each selected region [24-29]

Utility	Charge	Montreal	Edmonton	Vancouver
Electricity	Daily Charge	$0.4064/day	$0.8283/day	$0.205/day
	Energy Charge	$0.0591/kWh (First 36 kWh/day) $0.0912/kWh (> 36 kWh/day)	$0.1132/kWh	$0.0928/kWh (First 1,350 kWh/2 Month) $0.1392 (> 1,350 kWh/2 Month)
	Escalation Rate	0.1%	2.8%	0.3%
Nat. Gas	Daily Charge	--	$0.965/day	$0.409/day
	Energy Charge	--	$4.23/GJ ($0.015/kWh$_{Eq}$)	$7.36/GJ ($0.026/kWh$_{Eq}$)
	Escalation Rate	--	1.0%	0.2%

6. Results and Discussion

The developed models provide an important base to assess the energy and economic performance of each system, and to study the peak load implications of the three selected technologies.

Energy Performance

Table 10 summarizes the annual energy performance of each ductless heat pump integration in Montreal. Integrating a heat pump system results in a notable reduction in the energy used for heating and cooling, with savings ranging from 19% to 31%. While these savings represent an important reduction in energy use, the total energy required for heating still remains quite high in all cases. This can be attributed to the fact that, in the ductless system configuration, the heat pump only serves the first and second floors of the home, with the basement still heated using electric baseboards (Elec. BB). Comparing the energy used to heat the two above ground floors, each heat pump system is able to demonstrate heating energy use reductions of greater than 32%. The CCHP unit in particular demonstrates strong performance, reducing heating energy use for the first and second floors by nearly 50% while almost completely eliminating operations of the electric baseboards. Energy use reductions are more limited for the SSHP and VCHP cases, primarily due to reduced heating capacities and inefficient cycling of the SSHP at milder ambient conditions.

Readers may note the significant decrease in cooling energy use for the CCHP and VCHP cases, which can be attributed to the higher sensible heat factor (SHF) and the improved operating COPs of these two units in cooling. Given that cooling control in the model is based on the dry bulb space temperature, a system with a higher SHF is able to more rapidly reach the setpoint temperature, reducing system operations and energy use.

Table 10 Summary of annual energy performance for each ductless heat pump system in Montreal

End Use	Base Case	SSHP	VCHP	CCHP
Total Heating (kWh)	16,090	12,910	11,850	11,200
Heat Pump	--	2,500	3,960	4,790
Aux: Elec BB (1st, 2nd)	10,000	4,300	1,690	220
Other: Elec. BB Basement + HRV Elec. Duct Heater	6,090	6,110	6,200	6,190
Cooling (kWh)	1,050	1,030	630	600
Fans (kWh)	490	690	700	670
DHW (kWh)	4,270	4,270	4,270	4,270
Lighting/Equip. (kWh)	9,520	9,520	9,520	9,520
Total Energy Use (kWh)	31,420	28,420	26,970	26,260
Total Savings (kWh)	--	3,000	4,450	5,160
% Savings for Htg&Clg	--	19%	27%	31%
Seasonal Heating COP*	1.0	1.25	1.35	1.44

*Seasonal Heating COP for whole home. Seasonal COP higher when considering only zones served by HP

Table 11 summarizes the energy performance of the ducted heat pump systems in Edmonton and Vancouver. Energy savings are noticeably larger than in Montreal, given that each heat pump is now integrated into a ducting network serving all three levels of the home and sized to meet a larger portion of the heating load. In both cities, the CCHP offers the strongest energy savings, driven by greater available heating capacity at colder outdoor temperatures, and improved operating efficiencies over the most common winter temperatures (-10°C to +5°C). Cooling energy use is higher in all heat pump cases, as the selected heat pumps are able to provide cooling over a larger operating window (down to ambient temperatures of 18°C vs. 24°C for the base cases), a capability which is used primarily during the shoulder seasons.

Table 11 Annual energy performance for each ducted heat pump system in Edmonton and Vancouver

	Edmonton				Vancouver			
End Use	Base Case	SSHP	VCHP	CCHP	Base Case	SSHP	VCHP	CCHP
Total Heating (kWh)	19,310	10,600	10,340	8,590	12,690	4,500	4,740	3,830
Heat Pump	--	6,190	8,060	7,220	--	4,330	4,570	3,680
Aux: Elec. Duct Heater	--	4,410	2,280	1,370	--	170	170	140
Cooling (kWh)	280	370	320	320	260	350	320	340
Fans (kWh)	3,970	4,180	3,000	3,500	3,640	2,770	2,090	2,140
DHW (kWh)	7,490	7,490	7,490	7,490	5,870	5,870	5,870	5,870
Lighting/Equip. (kWh)	9,520	9,520	9,520	9,520	9,520	9,520	9,520	9,520
Total Energy Use (kWh)	40,570	32,160	30,670	29,420	31,980	23,010	22,540	21,700
Total Savings (kWh)	--	8,420	9,900	11,150	--	8,970	9,440	10,280
% Savings for Htg&Clg	--	44%	46%	55%	--	63%	61%	68%
Seasonal Heating COP	0.9	1.7	1.8	2.1	0.9	2.7	2.5	3.1

It is interesting to note that VCHP and SSHP performance is similar in both regions, with the VCHP actually consuming more energy for heating in Vancouver. This result is not related to the impact of variable capacity technology, but instead to the operating COP of the VCHP used in this analysis over the most common winter temperatures. To illustrate this point, Table 12 summarizes the operating COP of each heat pump integration by ambient temperature in Vancouver. Even when including cycling losses, the SSHP offers improved COPs for outdoor air temperatures from -10°C to +5°C in comparison to the VCHP. This result highlights the importance of examining not only the rated COP of the unit, but, wherever possible, the estimated operating COP at various points along the heating load line. Further details regarding the impact of these performance curves and operating COPs is presented later in this section.

Table 12: Operating COP of heat pump systems by temperature in Vancouver

Temperature Range	SSHP COP	VCHP COP	CCHP COP
-10°C to -5°C	2.8	2.0	2.6
-5°C to 0°C	2.9	2.3	2.9
0°C to 5°C	3.0	2.8	3.5
5°C to 10°C	3.0	3.5	4.6
10°C+	2.6	4.0	4.9

Techno-Economic Performance

Table 13 summarizes the economic performance of each system in Montreal. All three heat pump systems offer lifecycle utility and total cost reductions, with total lifecycle cost savings ranging from 8% for the SSHP to 11% for the CCHP unit. Results in Montreal are aided by (1) the fact that heat pumps are replacing a less efficient base case system using the same energy source, and (2) the relatively small incremental cost between ductless split system air-conditioners and heat pumps of the same capacity. Relatively low electricity costs and higher capital costs mean that the added energy savings provided by the CCHP yield marginal total cost savings vs. the VCHP, although both systems offer strong lifecycle cost reductions vs. the base and SSHP cases.

Table 13 Summary of lifecycle economic performance in Montreal

	Base	SSHP	VCHP	CCHP
Capital Cost	$8,350	$8,490	$9,240	$10,090
Lifecycle Utility Cost	$38,150	$34,120	$32,170	$31,220
Lifecycle Maintenance Cost	$1,670	$1,670	$1,670	$1,670
Total Lifecycle Cost	$48,170	$44,270	$43,080	$42,980

Table 14 summarizes the economic performance of each system in Edmonton and Vancouver. Results for these two regions are significantly different than those presented for Montreal, primarily because heat pumps are now replacing less expensive natural gas-based heating. Despite the much higher efficiency of the heat pumps in comparison to the furnaces used in the base cases, all heat pump cases still result in increases in total lifecycle utility costs. In Edmonton, for example, the ratio of electricity to natural gas rates (per unit of energy) is so high (> 7:1) that a seasonal COP of more than 7 is needed just to achieve *any* utility cost savings.

When comparing only the heat pump systems, it is evident that VCHP and CCHP systems are challenged by their higher capital costs. Although energy savings can significantly reduce annual electricity costs vs. the SSHP case (e.g., *annual* savings of over $300 CAD for the CCHP in Edmonton), this is not enough to outweigh the large increase in capital costs for these systems. Despite these currently challenging conditions, it is likely that increased market adoption of higher efficiency systems will gradually reduce initial costs and make these system integrations more financially viable in the coming years. The implementation of carbon pricing may also increase fuel-based utility costs, and further improve the economics of heat pumps systems.

Table 14 Summary of lifecycle economic performance in Edmonton and Vancouver

	Edmonton				Vancouver			
	Base	SSHP	VCHP	CCHP	Base	SSHP	VCHP	CCHP
Capital Cost	$12,290	$12,410	$17,220	$19,810	$11,630	$10,870	$14,170	$16,030
Lifecycle Utility Cost (incl. N.G & elec.)	$44,710	$63,520	$60,310	$57,610	$33,010	$35,750	$34,800	$33,040
Lifecycle Maintenance Cost	$3,450	$1,800	$1,800	$1,800	$3,280	$1,710	$1,710	$1,710
Total Lifecycle Cost	$60,450	$77,730	$79,330	$79,220	$47,920	$48,330	$50,680	$50,780

Grid Interaction

With increased adoption of onsite renewable energy generation and electrification of building systems, it is becoming important to assess not only energy and economic performance, but also the impact that each system integration can have on the local electricity grid. This is particularly important in many areas of Canada, where displacing current fossil fuel furnace systems with heat pumps can have significant peak demand implications.

In order to illustrate this aspect of system performance, the electrical load of the HVAC system (heat pump, auxiliary heaters, and fans) is examined for the first 60 days of the year (starting Jan. 1), representing the coldest winter conditions. Results are provided as a box plot in Fig. 3. The edges of each box denote the 25th and 75th percentiles, providing an idea of the variation in loading. The line across each box shows the median value. Whiskers in each plot show the maximum and minimum HVAC electrical load.

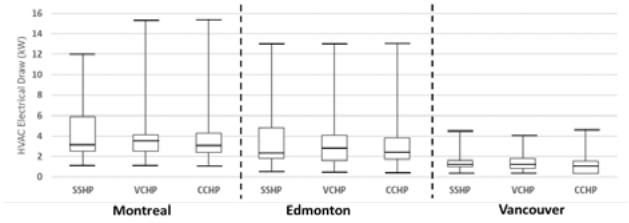


Fig. 3. Box plot of HVAC system power for each heat pump integration and region

An initial examination of the results shows median loads tend to be similar across all system types for a given region, which can be expected given the similar system sizing and operating efficiencies used in the study. However, a closer examination of the results by region reveals some key details regarding the impact of each heat pump configuration on the electricity grid. In Edmonton, the SSHP case shows a larger spread of data between the median and 75th percentile, meaning that this system spends a greater portion of time at a higher electrical draw in comparison to the other two heat pump systems. This increased draw is related to the reduced heating capacity of the SSHP at lower ambient temperatures in comparison to the CCHP, and the higher minimum operating temperature in comparison with the VCHP case (-20°C vs. -23°C). Maximum loads are identical for all three heat pumps, as these peak demands occur during the coldest winter days when outdoor air temperatures are below the minimum operating temperature of each heat pump.

Milder winter conditions in Vancouver present differing performance trends vs. the Edmonton case. These milder conditions result in similar HVAC electrical demands for all three heat pump systems, as the extra capacity and extended operating range of the CCHP and VCHP systems are not required. Peak loads in Vancouver are driven by the defrost process, when the auxiliary duct heaters (all sized identically) turn on to limit temperature drops in the conditioned space. Loading is reduced for the SSHP and VCHP cases due to their lower estimated heat pump power draws during this defrost process.

Results for Montreal underline important considerations regarding the control of the heat pump and auxiliary units. Similar to Edmonton, the SSHP shows greater variation between the median and 75th percentile, due to its reduced heating capacity and operating range. However, the VCHP and CCHP units actually have higher peak loads, due to the combined control of the heat pump and electric auxiliary.

The higher peaks for the VCHP and CCHP systems are best explained with the aid of Fig. 4, which shows several key performance criteria for the CCHP case over a four hour window starting at 3:00 AM Jan. 26th (day of maximum loading). Although the heat pump operates continuously until 5:20AM, its reduced capacity during this cold day means that it is unable to meet the setpoint temperature of 21°C. While auxiliary heating is still available during this portion of heat pump operations, the auxiliary system operates with a setpoint of 20°C to prioritize use of the heat pump. However, when outdoor air temperatures fall below the minimum cut-off for the heat pump (at 5:20 AM), the auxiliary then becomes the sole source of heating. Now operating with a new setpoint of 21°C, the auxiliary system attempts to rapidly raise the indoor temperature, causing the peak loads seen for the CCHP and VCHP cases. This behavior is not seen for the SSHP case due to its higher cut-off (i.e., minimum operating) temperature.

In addition to this peak loading, it is also interesting to note the potential issues caused by parallel heat pump/auxiliary operations. Just past 4:00 AM, the heat pump goes into defrost, cooling the space down to around 19.5°C. This translates into a strong increase in baseboard power demand, which, when combined with the heat pump operating at maximum frequency after the defrost event, also causes an unintendedly high peak power draw. In regions where the heat pump always operates above its minimum cut-off temperature, this behavior could become a major driver of peak electrical loading for the system, especially if backup baseboard temperatures setpoints are close to the temperature setpoint of the heat pump.

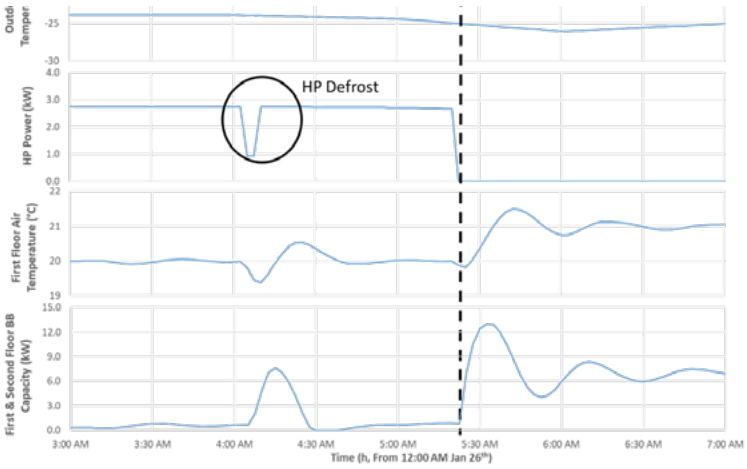


Fig. 4. Summary of key performance indicators for CCHP case in Montreal during peak load event

The importance of considering the interaction of the heat pump and auxiliary systems is clearly evident from the analysis. As demonstrated above, unforeseen operation of these two sub-systems can cause a significant increase in the peak electrical demand, and pose potential issues for the electrical grid in regions with more widespread heat pump adoption. Several simple workarounds can help facilitate a smoother interaction between these two system components, including limiting available auxiliary capacity to a reasonable amount when the heat pump is in operation (e.g., the difference between heat pump capacity and building load at the heat pump cut-off temperature), and using a ramped setpoint change when the system transitions from parallel heat pump/auxiliary operations to solely using auxiliary heating. In any case, more sophisticated controls should be carefully considered to optimize heat pump interaction with the grid. The integration of thermal storage could also afford an increased degree of flexibility by decoupling thermal supply and demand, allowing for peak shifting and demand reduction capabilities.

Sensitivity Analysis

While the above results show the potential of heat pump systems, it is clear that the conclusions are highly dependent on the performance data and control strategies used in the analysis. An appropriate selection of the heat pump is vital in order to maximize the energy savings potential of the system. In order to better illustrate this point, two additional cases were run in Edmonton:

(1) VCHP from Literature: A VCHP (with very similar SEER and HSPF ratings to the previously presented VCHP case) modelled using performance curves developed from manufacturer data [9]
(2) VCHP from SSHP: A variable capacity unit, with maximum performance derived from the ducted SSHP [17], and power consumption at lower compressor speeds estimated with typical part load equations for VCHPs [14]. Capacity modulation ratios were based on the original VCHP case.

Simulation results for each case, along with the original SSHP and VCHP simulations, are compared in Table 15. By replacing the original VCHP performance curves (while keeping all other simulation settings the same), annual heating energy use was reduced by between 6% and 12%, primarily driven by higher COPs between outdoor air temperatures from -10°C to +5°C. The *VCHP From SSHP* case is particularly interesting, as it demonstrates the isolated impact of adding variable capacity technology to a single stage heat pump (a reduction in heating energy use of 9%). Given the significant development work in the field of variable speed drives and heat pump technologies, it is likely that the performance benefits of variable capacity units will continue to grow in the coming years, and may even be underestimated in the current analysis.

Table 15 Sensitivity analysis for VCHP systems in Edmonton

End Use	SSHP	VCHP	VCHP Lit.	VCHP From SSHP
Total Heating (kWh)	10,600	10,340	9,110	9,680
Heat Pump	6,190	8,060	6,780	5,390
Aux: Duct Heater	4,410	2,280	2,330	4,290

7. Conclusions

This study has examined the techno-economic potential of three market available heat pump technologies in new construction Canadian housing. Using an improved, data-driven component model, single stage, variable capacity, and cold climate variable capacity systems were simulated over a full year in the Canadian cities of Montreal, Edmonton, and Vancouver. Cold climate heat pumps offered the strongest energy savings in all three regions, with heating/cooling energy use reductions ranging from 31% in Montreal to 68% in Vancouver. Despite these energy savings, higher capital costs and low natural gas rates made it difficult to achieve lifecycle cost savings for heat pumps in all regions except Montreal. An assessment of the distribution of HVAC electrical demand showed the potential of cold climate systems to reduce electrical loads by mitigating auxiliary energy use, but also highlighted the critical importance of appropriately considering the interaction between the heat pump and any auxiliary heating systems, and the value of more sophisticated controls. While the information presented in this study offers insight into the Canadian market, it is important to be aware of the sensitivity of the results to the economic parameters and performance characteristics used. Future work will explore the economics and grid impacts of these systems in other Canadian regions and housing vintages, and obtain additional test data to more accurately represent the heat pump technologies presented in this study.

References

[1] Natural Resources Canada. Paving the Road to 2030 and Beyond: Market transformation road map for energy efficient equipment in the building sector. Ottawa, CA: Govt. of Canada; 2017.
[2] Canada Energy Regulator, 2019. Market Snapshot: Steady growth for heat pump technology. Ottawa, CA: Govt. of Canada. Available at: https://www.cer-rec.gc.ca/nrg/ntgrtd/mrkt/snpsht/2018/02-03htpmps-eng.html [Accessed Oct. 2019]
[3] Sager, J., Mackintosh, T., St-Onge, G., McDonald, E. and Kegel, M., 2018. “Detailed performance assessment of variable capacity inverter-driven cold climate air source heat pumps,” 9th International Cold Climate Conference. Kiruna, Sweden.
[4] Bertsch, S., Groll, E., 2006. Air Source Heat Pump for Northern Climates Part I: Simulation of Different Heat Pump Cycles. International Refrigeration and Air Conditioning Conference. West Lafayette, IN, USA, paper #783.
[5] Kegel, M., Sunye, R., Tamasauskas, J., 2012. Life Cycle Cost Comparison and Optimisation of Different Heat Pump Systems in the Canadian Climate. eSim 2012: 7th Conference of IBPSA-Canada. Halifax, Canada, paper # 1110.
[6] Breton, S., Tamasauskas, J., Kegel, M., 2019. An Evaluation of Cold Climate Variable Capacity Air-Source Heat Pumps in Canadian Residential Buildings Using an Enhanced Component Model. Building Simulation 2019. Rome, IT, paper #211116.
[7] National Research Council of Canada. National Building Code of Canada. 13th ed. Ottawa: NRC; 2010.
[8] Swinton, M.C., Entchev, E., Szadkowski, F., Marchand, R. Benchmarking twin houses and assessment of the energy performance of two gas combo heating systems. Ottawa, CA: Canadian Centre for Housing Technology.
[9] Kegel, M., Tamasauskas, J., Sunyé, R., Giguère, D, 2017. Heat Pump Water Heaters in the Canadian Residential Market. IEA Heat Pump Conference 2017. Rotterdam, NE, paper #329.
[10] Daikin Manufacturing Company. DZ20VC Specification Sheet. Houston, USA: Daikin Manufacturing Company; 2019. Available at: https://daikincomfort.com/products/heating-cooling/whole-house/heat-pumps/dz20vc [Accessed Oct. 2019]
[11] Northeast Energy Efficiency Partnerships (NEEP). CCASHP Specification and Product List. Lexington, MA, USA: NEEP; 2019. Available at: https://neep.org/ASHP-Specification [Accessed November 2019]
[12] Northwest Energy Efficiency Alliance (NEEA). Cold Climate DHP Specification and Recommendations. Portland, OR, USA: NEEA;2019. https://neea.org/our-work/cold-climate-dhp-specification [Accessed Jan. 2020]
[13] Mitsubishi Electric. PUZ-HA Series Engineering Manual. Atlanta, GA, USA: Mitsubishi Electric Trane HVAC; 2019. Available at: http://mylinkdrive.com/ [Accessed Jan. 2019].

[14] Filliard, B., Guiavarch, A. and Peuportier, B., 2009. Performance Evaluation of an Air-to-Air Heat Pump Coupled with Temperate Air Sources Integrated Into a Dwelling. Building Simulation 2009. Glasgow, UK.
[15] U.S Department of Energy. DOE-2 Engineers Manual. Berkeley, California, USA: Lawrence Berkeley Laboratory; 1982.
[16] Carrier. Carrier 40QNQ/38QRF Product Data. Indianapolis, IN, USA: Carrier Corporation; 2008.
[17] Daikin Manufacturing Company. DZ14SN Specification Sheet. Houston, USA: Daikin Manufacturing Company; 2019. Available at: https://daikincomfort.com/products/heating-cooling/whole-house/heat-pumps/dz14sn [Accessed Oct. 2019]
[18] Carrier. Carrier 38 MHRB Product Data. Indianapolis, IN, USA: Carrier Corporation; 2018. Available at: https://www.carrier.com/residential/en/ca/products/ductless-systems/38mhrbq/ [Accessed Oct. 2019]
[19] Kegel, M., Sager, J., Thomas, R., Giguère, D., Sunyé, R., 2017. Performance Testing of Cold Climate Air Source Heat Pumps. IEA Heat Pump Conference 2017. Rotterdam, NE, paper #340.
[20] Ductless.ca. Mitsubishi M Series. Toronto, CA: Ductless.ca; 2019. Available at: https://ductless.ca/products [Accessed Apr. 2019]
[21] AC Direct. AC/Heat Pump and Ductless Single Zone Systems. Winter Park FL,USA: ACDirect.com; 2019. Available at: https://www.acdirect.com/ [Accessed Oct. 2019]
[22] Pick HVAC. Heating & Cooling Guide: Carrier, Lennox & Bryant Heat Pumps. Pick HVAC; 2019. Available at: https://www.pickhvac.com/heat-pump/ [Accessed Oct. 2019]
[23] RS Means. RS Means Mechanical Cost Data 2017. Norwell, USA: Reed Construction Data; 2017.
[24] Hydro Quebec. Domestic Rates. Montreal, QC: Hydro Quebec; 2019. Available at: http://www.hydroquebec.com/residential/customer-space/rates/ [Accessed Apr. 2019]
[25] EPCOR. Regulated Residential Rates & Fees. EPCOR; 2019. Available at: https://www.epcor.com/products-services/power/rates-tariffs-fees/Pages/regulated-residential-power-rates.aspx [Accessed Apr. 2019]
[26] AltaGas Utilities. Rates & Rate Riders: Small General Service. Calgary, AB, CA: Alta Gas; 2019. https://www.altagasutilities.com/rates-and-rate-riders [Accessed Apr. 2019]
[27] BC Hydro. Residential Conservation Rate. Vancouver, BC, CA: BC Hydro; 2019. https://app.bchydro.com/accounts-billing/rates-energy-use/electricity-rates/residential-rates.html [Accessed Apr. 2019]
[28] FortisBC. Residential Natural Gas Rates. Vancouver, BC, CA: FortisBC; 2019. www.fortisbc.com/accounts-billing/billing-rates/natural-gas-rates/residential-rates [Accessed Apr. 2019]
[29] National Energy Board of Canada. Energy Markets. Ottawa, CA: National Energy Board of Canada; 2016. Available at: https://www.neb-one.gc.ca/index-eng.html [Accessed Nov. 2016]

13th IEA Heat Pump Conference
April 26-29, 2021 Jeju, Korea

Replicable Water Source Heat pumps for A Zero Carbon Future

Nicky Jason Cowan[a*]

[a]Star Renewable Energy, Thornliebank, G46 8JW, Scotland

Abstract

The United Kingdom (UK) is beginning to invest heavily in the construction of district heating networks as it recognises their potential for decarbonisation. Unfortunately, the vast majority of these are designed around burning fuel in one form or another, but with the undeniable effects of climate change being constantly reported and the surge in public awareness, alternative technologies are being sought after, primarily, heat pumps.

Although there is huge success in European countries regarding heat pump projects, the UK is still hesitant in deploying the technology even though the majority of large towns and cities are built on the backs of rivers.

By analysing the key sections required to deliver a successful water source heat pump (WSHP) for large urban district heating networks, a simplified methodology for repeating similar projects has been developed. Based on the learnings gathered from designing Scotland's largest, hottest WHSP being installed in Clydebank, utilising the river Clyde as a source, real examples of design and technology will be detailed.

Keywords: Water source heat pump, Design, District Heating

1. Introduction

Time is running out for every country to fulfill the agreements and pledges signed on 22nd April 2016: The Paris Agreement [1]. Some countries have went further declaring climate emergences [2], however little to no real progress has been made. With so many technologies confusing the pathway to decarbonising the UK it is not surprising that most towns and cities end up either doing nothing or "quick wins" which see a small impact made on the overall challenge. It is time to start taking large chucks out of our carbon footprint and this paper will describe how, by utilising a natural resource that almost every town and city has, we can achieve this.

2. Heat Pump Sections

An unavoidable fact about water source heat pump (WSHP) projects is that every location is different therefore we must look to simplify, where possible, the methodology to approaching each project and equipment selections. A WSHP heat pump project can be split into its basic constituent sections that can be further refined.

Table 1.

Section 1	Section 2	Section 3	Section 4
Water Source	Heat Pump	Heat Network	Secondary Network

* Corresponding author. Tel.: +44 141 3028143
E-mail address: ncowan@neatpumps.com.

2.1. Section 1: The Water Source

Every river that flows through a town or city is unique but there are some basic questions that help begin selections:

1. Is the river fresh water or salt water?
   This determines pipework and heat exchanger materials and selections on the source water side.
2. Is the river tidal or controlled through weirs?
   Determines filtration equipment location and pipe routes, helps determine abstraction pump style.
3. River depth at abstraction location?
   Determines abstraction location and pump style.
4. Is there information relating to the flora and fauna of the water abstraction area?
   This has knock on effects to the filtration requirements. Eels and Mussels can impact on pre filtration quite significantly and so can migrating Salmon if this happens to be at the same time you intend to disrupt the water course.
5. Yearly water temperature profile?
   Allows more accurate heat pump performance data to be calculated.
6. Annual river flowrate profile?
   Determines the amount of available water for abstraction.

Engagement with the environmental agency is crucial at as early a stage as possible for any project as they will have their own requirements to follow such as; Allowable water volume than can be abstracted (based on Q95 or Q50 value etc.), temperature change allowed on the water, velocity at discharge location.

A decision will have to made about the handling of the source water side. There are different techniques being put forward for this such as:

1. Glycol pipework loop in the river.
2. A hydraulic break loop: River water is abstracted and fed to a heat exchanger where it transfers its heat to a glycol loop. The glycol loop is then sent to the heat pump evaporator.
3. Open loop: The river water is sent directly to the heat pump evaporator.

As the focus is on multi MW district heating, the glycol loop can be discarded as the size and amount of pipework would not be viable. A hydraulic break loop is considered to be a sound option however the inclusion of one has multiple negative effects such as extra installation costs, additional running cost (glycol pump circuit) and a negative effect on the heat pumps performance (heat transfer required across the break loop heat exchanger which results in a lower evaporating temperature at the heat pump). Pumping river water direct into the evaporator is viewed as risky but with the right technology installed this risk can be contained.

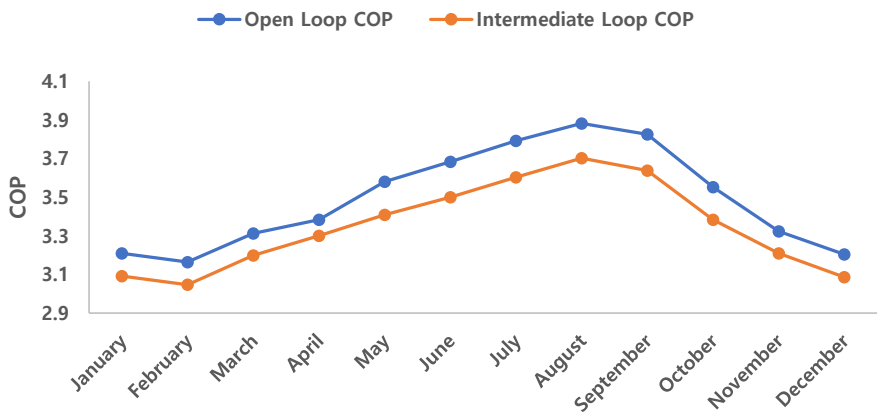


Fig. 1. COP performance graph of open loop style abstraction Vs including a hydraulic break loop

When looking at an open loop style system, there are multiple methodologies for achieving water abstraction:

1. Cutting away a section of the riverbank and inserting an abstraction chamber.
2. Floating a pipe out with concrete sections and sinking it to a desired depth.
3. Laying a pipe along the bottom and upturning the end.
4. Design a building to sit on a pontoon or floating barge where the abstraction pumps sit directly above the water. If made big enough you could house the entire abstraction system inside.

For the Clydebank heat pump project, the abstraction chamber will sit at the edge of the basin where pipework will vertically enter the water. The following basic layout describes the source side of the heat pump system

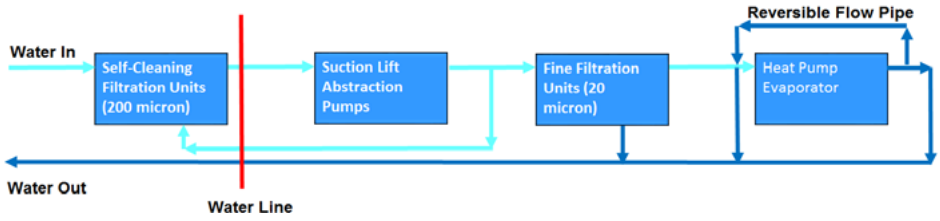


Fig. 2. Abstraction Layout

Due to the location of the project three major challenges had to be overcome: Salt water, extreme tidal fluctuations and mussels being present.

Challenge 1 – Salt Water:
The heat pump is an open loop style, so the river water from the Clyde enters directly into the heat pump evaporator. To overcome the issues of salinity in the heat exchanger a Spray Chiller Evaporator style was selected with Titanium tubes, titanium coated tube plates and super duplex end boxes. The evaporator itself is self-cleaning as explained in challenge 3.

Challenge 2 – High Tidal Fluctuations:
At the abstraction location the river can vary in height from over 4m to under 1m during the course of the tides. To ensure abstraction can continue the filters are placed under the minimum height expected from the lowest tide. A second problem was foreseen due to the abstraction point being in a manmade basin where silt could build up if the filters were placed on the river bed. To avoid this the filters are held 300mm off the river bed.

Challenge 3 – Silt and Mussels:
The river Clyde has mussels which means there are mussel seeds. These seeds are around 20 microns in size so very fine filtration is required. There are three types of filtration on the source water side to help combat this. First there are self-cleaning backwash style filters in the river. These are made self-cleaning as a small portion of the water being delivered to the heat pump, is sent back to the filters where a rotating bar with nozzles ejects the water back through the mesh. The second piece of filtration is a bank of spinning disk style units which are sized to stop the mussel seeds from progressing in the system.

The final piece of filtration is on the spray chiller evaporators. Each evaporator contains 770 tubes which are externally and internally enhanced as per figure 3. Each tube is fitted with a brush (figure 4) and a cage on both sides to catch the brush as it travels through the tube (figure 5).

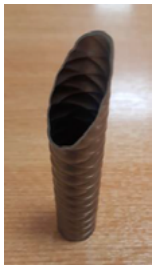


Fig. 3. Spray Chiller Enhanced Tube



Fig. 4. Spray Chiller Brushes [3]



Fig. 5. Spray Chiller Cages

As water flows through each tube, the brushes settle at one side of the evaporator. Silt and other fouling can accumulate in the tubes, leading to a negative effect on heat transfer. To use the brushes a series of valves and pipework reverse the flow allowing the brushes to be pushed to the other end of the evaporator, dislodging any fouling that has accumulate. The water is then discharged back to the river.

.



Fig. 6. Flow Reversal Pipework On the Side of the Spray Chiller Evaporator

2.2. Section 2: The Heat Pump

The heat pump while complicated in its own right, is by far the simplest piece of equipment to put together in this type of project. Its working conditions are preset on one side by nature and the other by desiring a calculated outcome.

To narrow in on a design, there are always three initial questions for the selection of any water source heat pump:

1. Source water: flow and return temperature (°C)?
2. Heating network: flow and return temperature (°C)?
3. Capacity required (MW)?

Advanced selection criteria that can influence the design of the heat pump are:

4. Refrigerant Type?
5. Electric Voltage?
6. Variable Speed Required?
7. Source Water and style of abstraction?
8. Source Side and Hot Side fluids?
9. Does COP meet project requirements?

Using Clydebank as an example

1. Source water: Varies from 4°C in winter to 18°C in Summer. Based around conversations with SEPA we are allowed a 3K ΔT.
2. Heating network: 80°C/60°C then dropping to 75°C to 45°C
3. Capacity required: 5.2MW
4. R717 as refrigerant (GWP<1, ODP 0)
5. 690V electric motor
6. Salt water, open loop abstraction and treated water for the district heating loop.
7. Average COP of >3



Fig. 7. 2-off 2.6MW Water Source Heat Pumps for Clydebank

Each heat pump at Clydebank consists of a positive displacement, oil injection, twin screw compressor with the rotation provide from an air cooled electric motor. Once the ammonia is compressed, the oil and ammonia mix is sent to an oil separator where the ammonia carried on to a desuperheater, condenser, subcooler, expansion valve and evaporator before being drawn back into the compressor. The oil is sent from the oil separator to an oil cooler, filters, oil pump and finally re-injected back into the compressor.

The district heating water is fed into the heat pump where it is split so that some water goes to the oil cooler and the rest passes through the subcooler, condenser and the desuperheater. The water from the oil cooler and desuperheater are then joined back together and returns to the district heating network.

The source water is as per fig. 2.

Currently the United Kingdom (UK) offers the Renewable Heat Incentive (RHI) to compliant heat pump systems. This is a tariff paid over 20 years for every kWh of heat generated renewably and the heat pump must conform to certain requirements such as an average COP of 2.5. This has been put in place to not only help stimulate the marked but offset against the cost of cheap gas and expensive electricity (known in the UK as the spark gap). The cut off point for projects is that they must be installed and commissioned by March 2021.

2.3. Section 3: The District Heating Network

District heating networks come in all different shapes, sizes and most importantly for the heat pump, temperature ranges. The temperature ranges are often referred to as Generations [4], with the flow temperature of the 3rd generation being (<100°C) and 4th (≤70°C). There are other styles being examined such as ambient loops however as detailed in section 2.4. this does not provide the least intrusive method for the consumer in a retrofit procedure.

Project networks can be devised into several categories:

1. Existing networks: These are already in place, delivering heat to existing building stock where the heat is generated, typically, by the burning of fossil fuel. This a very challenging case for heat pumps to fit into due to the networks predominantly being on a high flow and return temperature, typically with a poor ΔT. The high temperature is normally a function of reducing end consumer impact (changing building internals)
2. New networks for existing buildings. This is the most challenging case to make heat pumps fit in as typically in the UK, each building has its own gas boiler connected to the gas network. Finding ways to encourage people to move away from cheap gas to what is seen as a new methodology for delivering heat (district heating) can be very complicated.
3. New network for new buildings: Network temperature is designed specifically for the heat pump from the beginning and so are the consumers building internals (radiators, heat interface units etc).
4. New network serving new builds and existing stock: The heat pump will be deployed to serve existing building stock while new builds come online. Existing buildings will transition to a lower network temperature and wider ΔT. Careful consideration needs to be given to heat pump heat exchanger design as flowrates can half so extra passes may have to be designed in.

The Clydebank project falls under point 4. Currently existing stock to be included in the district heating project is the West College Scotland Clydebank campus and the Clydebank leisure center (The pink section of Figure 2. The red section is for all the new builds: 1063 dwellings, 80 bed care home, NHS medical center, a hotel, food store and various other retail and commercial facilities.



Fig. 8. Clydebank Project Sections.

Due to the Clydebank project looking to secure RHI, the heat pumps are going to be installed before the majority of the site has been completed which leads to some complications.

5. Stage one of the project is to send heat to the college and leisure center while waiting for the new development to bring buildings online. The college and leisure center will be retrofitted to work on the lower district heating network temperature however the heat pumps will begin operating on 80°C flow and 60°C return before this work is carried out.
6. When the network comes online the college and leisure center will be retrofitted and the whole system will operate on 75°C flow and 45°C return. This has two positive impacts on the heat pump as the output temperature has been lowered and the ΔT has been increased, allowing for more subcooling on the units. See section 3 for more details.

In reality if water source heat pumps are going to tackle dense urban city centers then projects fall under point 1 or 2. If we look at point 2 and take Glasgow city center as an example, how can you roll out district heating when each building is currently served off the gas grid, operates individually and has no incentive to switch. The main schools of thought are around providing concession areas for district heating companies and setting air quality limits (which are within Scotland's devolved powers).

2.4. Section 4: The Secondary Network (The Consumer)

There are several examples of what to expect when faced with a consumers internal building network

1. Currently existing with no plans to retrofit.
2. Currently existing with plans to retrofit.
3. New build where a desired temperature can be installed form the start.

Ultimately, the temperature required on the consumer's network is what sets the district heating network flow and return temperature and to decarbonise a city center, the major challenge will be changing customers with the mindset of point 1 to point 2 especially if the intent is to run the network from heat pumps.

Customers who fall under point 1 have the biggest detrimental effect to the heat pumps performance. They will typically be served by a gas boiler and have an internal network of 82°C flow and 71°C return. Most buildings do not even achieve this ΔT and it can be as little as 1 or 2K.

A key starting point to minimise disruption would be to survey the buildings internals and calculate if the equipment installed can operate on lower temperatures (was it over sized when it was installed?).

If the network serves multiple different consumers and for example one of them is an industrial heat consumer and requires very high temperature heat., instead of designing the network based on that one consumer's requirements, design for the majority at a lower temperature and look at installing a booster heat pump at the client's location to deliver site specific requirements. This could allow the industrial consumer heat up to 150°C if required.

Ambient loop networks are being discussed as a solution instead of district heating. Similar in concept to a district heating network except the water sent to each building is around 15°C, this water is then used as the source to an individual heat pump placed in each building. Each building takes a bit of heat out of the loop and the loop is cooled. A large heat pump would be required to balance out the ambient loop. Ideally buildings would equally be heating and cooling to self-balance the loop, however in Winter there is little cooling demand. A drawback for this style of system in a city center is where you want to minimise end consumer building internal changes as everything is a function of cost. The individual heat pumps placed at each building will be small capacity and so limited in outlet temperature (around 65°C) so a full retrofit will probably be required and unlikely given the scale of existing building stock.

3. Heat Pump Performance

Although heat pumps can achieve reliably 85°C/90°C for district heating, they generate the best performance at lower temperatures on the hot side and higher temperatures on the cold side. In this instance the cold side is the river and although this is variable throughout the year, it is a fixed point that cannot be altered. This leaves manipulating the hot side where possible to increase performance. There are two areas to strive for improvement:

1. Reduction of the network temperature
2. Increasing the network ΔT

Figure 9 below shows a yearly trend for COP based on a typical river profile for 3 different heating scenarios.

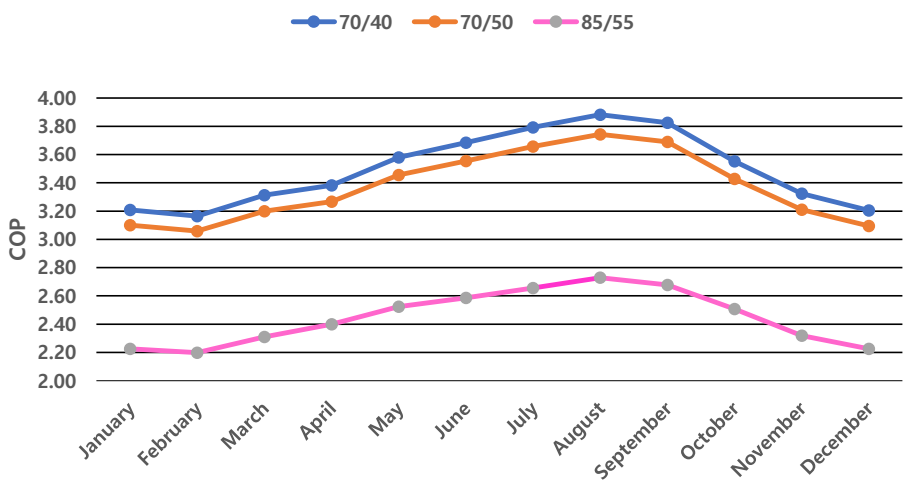


Fig. 9. COP variations for changing Network temperature and the network ΔT

4. Advanced Thinking

Like many types of projects there are ways to further optimise a system. With a heat pump led district heating network the following areas can greatly enhance the viability and efficiency of a system:

1. Thermal storage.
2. Flexible electricity tariff (half hourly).
3. Off-peak/ surplus electricity consumption.
4. Incorporate the cooling generated by the heat pump.
5. Lower the network temperature.
6. Reduce network heat losses.

Points 1, 2 and 3 work together as heat consumption from a district heating network is not constant. Low periods of heat consumption generally coincide with lower electricity prices, so if you are on a flexible tariff, instead of operating the heat pumps at 50%, run them at 100% (achieving the best COP), consuming the cheap electricity to fill a thermal store. You have then developed a buffer that if sized correctly could allow the heat pumps to be switched off at peak network consumption, avoiding expensive electricity charges. The same point applies to the electricity grid if it is being supplied with more electricity than it requires. Heat pumps could be switched on to fill thermal stores, avoiding the constraint payments wind farms are paid to switch off during over production.

Point 4 highlights the fact that to generate heating on one side of the heat pump you have created a cold source that can either be returned to the river or sent to a process that requires cooling. If the heat pumps are strategically placed this cooling can be sent to a data center or a hospital for example, offsetting their own electrical consumption and increasing the heat pumps overall COP. This can form another revenue stream for the district energy company making project more viable.

5. Environmental

The pathway to decarbonising the UK, can at best be described as complex. With so many technologies on the market providing quick wins in reducing carbon (but not fully decarbonising) or providing the illusion of decarbonising while having a negative impact as the grid decarbonises (Gas CHP) it has never been more confusing to pick a solution that is right. Mix in the vested interests from major oil and gas companies that would push the introduction of hydrogen into the gas grid or a full relaying of the pipework to have 100% hydrogen sent to homes it is not surprising that very few projects begin.

Heat pumps operate by consuming electricity so their carbon footprint is inherently tied to that of the electricity grid feeding them. If a heat pump has a COP of 3 then you take the electrical grids carbon content per kWh and divide by 3 to obtain each unit of heats carbon footprint. If your grid is 0gCO_2/kWh, then so is your heat. This make heat pumps one of the only scalable zero carbon methods for generating heat.

Even though the UK has made great strides to decarbonise its electrical grid, unfortunately documentation in the building sector is lacking in supporting the deployment of heat pumps. New projects have to use documentation published in 2012 which states the electrical grid has a footprint 519gCO_2/kWh [5] even though planned updates in 2016 (showed grid at 398gCO_2/kWh) [6], 2018 (Showed grid at 233gCO_2/kWh) [7] and now 2019 (Shows grid at 136gCO_2/kWh) [8]; all of which, have yet to be implemented.

6. Conclusion

With cities such as Glasgow and Edinburgh setting a target of net zero carbon by 2030 [9],[10], Scotland by 2045 and the rest of the UK by 2050 drastic changes have to be taken now if there is any hope at succeeding.

The main barriers that often block project conception range from a lack of understanding though to the complexity of aligning all the appropriate project partners. There any many companies that can assist local authorities in how to get projects moving and can even take on the whole project scope leaving the local authority in charge on the network at the end.

Although challenging, water source heat pumps provide a real way to decarbonise a cities carbon footprint now and every day that projects like these are delayed in conception, another day is lost in preventing further climate change.

References

[1] https://unfccc.int/process-and-meetings/the-paris-agreement/what-is-the-paris-agreement
[2] https://www.thenational.scot/news/17603494.read-nicola-sturgeons-full-speech-from-the-snp-spring-conference/
[3] http://www.kalvo.de/en/brushes.html
[4] Henrik Lund , Sven Werner, Robin Wiltshire, Svend Svendsen, Jan Eric Thorsen, Frede Hvelplund, Brian Vad Mathiesen 4th Generation District Heating (4GDH) Integrating smart thermal grids into future sustainable energy systems
[5] SAP 2012, The Governments Standard Assessment Procedure for Energy Rating of Dwellings.
[6] SAP 2016, The Governments Standard Assessment Procedure for Energy Rating of Dwellings.
[7] SAP 10, The Governments Standard Assessment Procedure for Energy Rating of Dwellings.
[8] SAP 10.1, The Governments Standard Assessment Procedure for Energy Rating of Dwellings.
[9] https://www.glasgow.gov.uk/article/25066/Council-Sets-Target-Of-Carbon-Neutral-Glasgow-by-2030
[10] https://www.edinburgh.gov.uk/news/article/12648/capital-sets-ambitious-neutral-carbon-target-of-2030

13th IEA Heat Pump Conference
April 26-29, 2021 Jeju, Korea

In-situ analysis of a centralized wastewater heat pump for a complex of high energy standard buildings

Simon Callegari*, Fleury de Oliveira, Pierre Hollmuller, Carolina Fraga

Energy Systems Group, University of Geneva, 66 Bd Carl Vogt, 1211 Genève, Switzerland

Abstract

While heat pump systems combined with district heating could reduce the CO_2 emissions of Geneva's heating sector, it is crucial to know and control their performance in real condition of use. This paper concerns detailed monitoring (hourly data, entire year) of a new low energy multifamily buildings complex, with centralized heat pump on wastewater (200 kW) and complementary gas boiler (600 kW). Heat production is covered at 45% by the heat pump (SPF: 3.03), with 55% complement by the gas boiler (85% efficiency). At the level of the buildings, domestic hot water supply (39.5 kWh/m^2) accounts for 59% of the demand, against 41% for space heating (27.3 kWh/m^2). For space heating, the gap between measured and climate corrected design values can be explained by operation conditions which differ from the norm (indoor temperatures, window openings), but remains quite lower than benchmark values on the recent building stock. Domestic hot water supply is also above the normed value, but coherent with a benchmark on other buildings. Finally, we highlight some issues and recommendations for optimized system integration and control concerning this type of innovative solution.

Keywords: wastewater heat recovery ; district heating ; multi-family buildings ; in-situ monitoring ; performance gap

1. Introduction

Nomenclature

DH	district heating
DH1	district heating network with the 4 studied buildings
DH2	district heating network with the last 3 buildings under construction
DHW	domestic hot water
HEX	substation heat exchanger
HP	heat pump
MFB	multifamily building
SH	space heating
SPF	seasonal performance factor (annual or seasonal value)
VHR	ventilation heat recovery by dual flow
WW	wastewater
WW-HX	wastewater heat exchanger

* Corresponding author. Tel.: +41 22 379 0646.
E-mail address: simon.callegari@unige.ch.

1.1. Context and issues

In Geneva, the heat demand is mainly covered by fossil fuels, with individual gas or heating oil boilers. One of the most realistic and expected option for renewable heat integration in this dense urban area is the development of district heating (DH), along with integration of centralized or individual heat pumps (HP) [1].

The potential and performance of HP systems is however linked to the temperature range of available heat sources such as ground, ground water, lake water or air, and its adequacy to the related heat demand in terms of quantity and temperature level [2]. A further key point for HP integration in heating systems is its eventual combination with other resources, typically fossil boilers, which requires carful system design planning and regulation [3].

Moreover, on the heat demand side, actual values of energy demand usually turn out to be higher than project values, as well for retrofit of old buildings [4], as for new buildings with high energy standards [5]. Concerning new buildings, the heat demand for domestic hot water (DHW) production represents a growing share compared to the space heating (SH), and becomes a key point for HP integration, as it requires relatively high temperatures levels.

In this context, in particular in the case of innovative systems, it is important to understand real conditions of use and operating constraints through system monitoring, which is also an opportunity to highlight optimization issues and possibilities.

1.2. Objectives

This paper concerns a new low energy MFB complex located in Geneva, whose heat is produced by a centralized 200 kW_{th} HP on wastewater (WW) with a complementary 600 kW_{th} gas boiler, and distributed via a local DH network.

Based on detailed hourly monitoring over an entire year of operation, we derive the annual energy balance of the entire system and analyze the annual daily dynamic of heat production and demand. We then display daily heat production temperatures, and highlight their impact on operating constraints, especially for the HP. Finally, we focus on the performance gap of SH and DHW supply, as compared to project values.

2. Case study

2.1. Buildings and system layout

Situated in Geneva, the case study concerns the first 4 buildings of a complex of 7 new MFB, built according to the *Minergie* low energy demand standard. The studied buildings have a total heated area of 17'400 m^2, of which 16'150 m^2 for housing and the rest for extracurricular activities for school kids. Note that the 4 buildings have an identical heated surface area (4'350 m^2), structure and form (9 storeys), as well as thermal envelope.

The simplified schematic of the heat production and distribution system is depicted in Figure 1. Base load production is supplied by way of a 200 kW_{th} wastewater HP, which is connected to a centralized wastewater tank with immerged heat exchanger system (WW-HX) [6]. On condenser side, the HP delivers its heat to a 20m^3 buffer. Complementary peak load is supplied by a 600 kW_{th} gas boiler.

Heat distribution to the buildings is provided by way of 2 local DH networks, one for the 4 buildings of the case study (DH1), the second for the 3 buildings still under construction (DH2). At the level of each building, supply is delivered by way of a heat exchanger (HEX) on a secondary circuit, which supplies a DHW storage tank (in priority) and the SH floor heating circuit (connected to the outlet of the DHW supply).

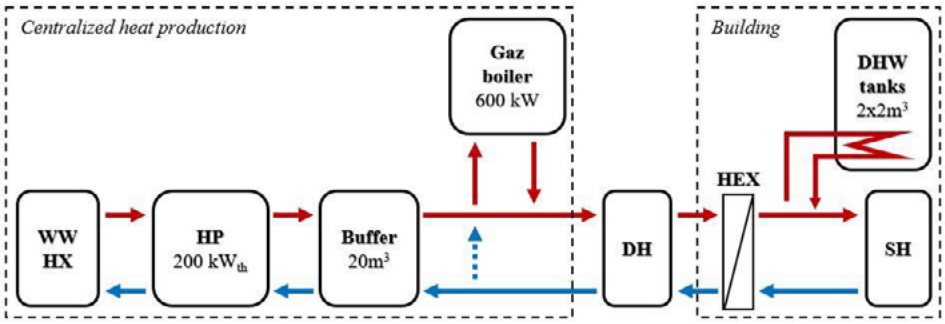


Fig. 1. Simplified schematic of heat production and distribution

2.2. Monitoring

The main data in 20 min time step is collected from the centralized control system, and aggregated in hourly and daily values. In terms of energy flows, it concerns: i) electricity for the HP and related circulation pumps; ii) heat production of HP and gas boiler; iii) in each building, heat supply for DHW (at storage inlet) and for SH. The associated temperatures, as well as the wastewater temperatures (tank inlet and outlet, evaporator in and outlet) are also collected.

As a complement: i) spot monitoring of the mechanical ventilation system (temperatures and air flows) allows to characterize the corresponding heat recovery and loss; ii) weekly reading of the gas consumption is used to determine the boiler efficiency.

3. Results

The results presented in this paper concern the first year of operation (2018) with complete hourly data on centralized heat production and heat demand of the 4 buildings under consideration (DH1).

3.1. Annual heat production and demand

The annual heat production and demand flows are depicted in following Sankey diagram (Figure 2).

The HP production (613 MWh) accounts for 45% of the total production, with a seasonal performance factor (SPF) of 3.03, including ancillary electricity of circulation pumps on evaporator and condenser side. This SPF can be related to an annual energy weighted average temperature of 56°C (at condenser outlet) and 7°C (at evaporator inlet), corresponding to 45% of the Carnot performance factor. The 55% complement by the gas boiler (761 MWh) is produced with an 85% efficiency (on higher heat value).

The produced heat is mainly distributed to the 4 buildings under consideration (DH1), while the remaining part goes for the last 3 buildings, which were already partially heated while under construction (DH2), and for storage and distribution losses.

At the level of the 4 buildings, DHW supply (687 MWh) accounts for 59% of the total, against 41% for SH (474 MWh). As a complement to direct SH, ventilation heat recovery by dual flow (VHR) with a measured 80% efficiency, contributes with 420 MWh to compensation of heat losses through the building envelope.

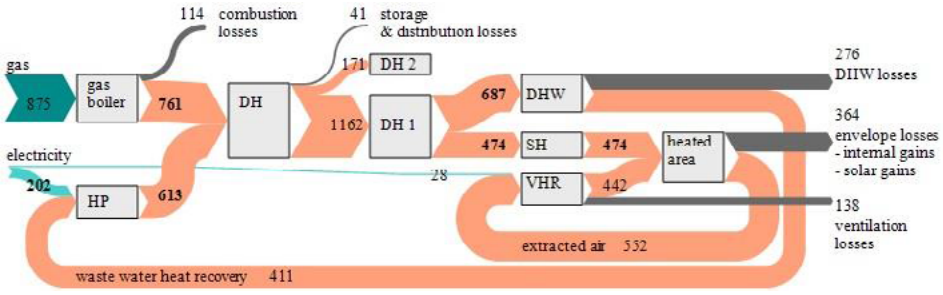


Fig. 2. Sankey diagram, 2018 (unit: MWh; bold font: completely monitored values; normal font: derived values and/or spot monitoring)

3.2. Seasonal dynamic

The seasonal dynamic of heat production and demand is presented in Figure 3. In summer the HP is able to fully furnish the DHW supply, except for a weekly temperature rise of 1 h, for legionella prevention, done by the gas boiler. The HP production slightly drops during winter, and is complemented by a high heat fraction from the gas boiler. Unlike what could be understood at first sight, winter HP production actually doesn't cover the DHW supply, but rather part of the SH supply at lower temperatures, as clarified below.

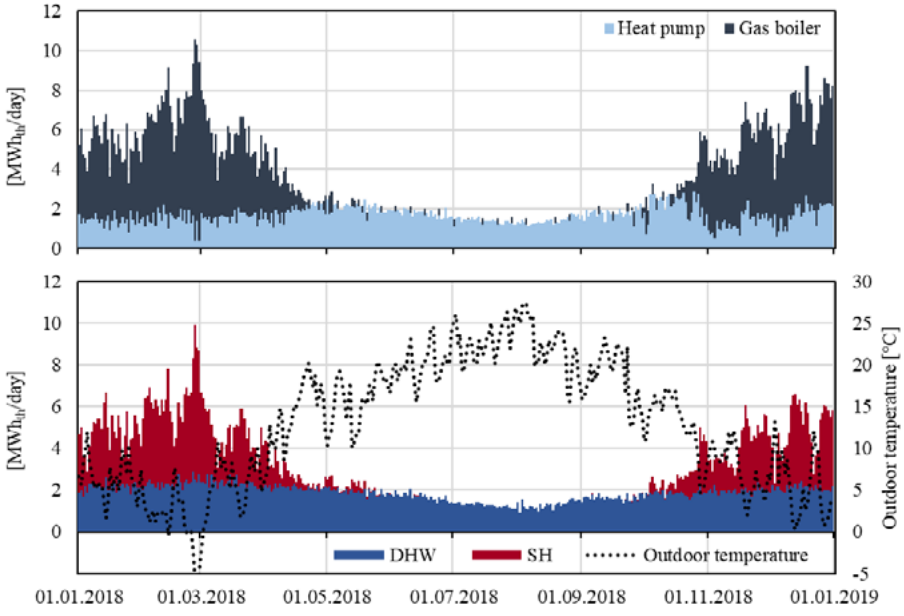


Fig. 3. Heat production (top) and demand (bottom), Jan – Dec 2018 (daily values)

The related dynamic of the daily average heat production temperatures is presented in Figure 4, which highlights differentiated operation modes and set points between summer and winter. During the summer, the HP production is set to its maximum at 63°C, which is sufficient for DHW supply (except during the above-mentioned anti-legionella treatment at 75°C by the gas boiler). During winter, the HP production temperature varies between 45 and 55°C, according to the upper and lower buffer set points, while the gas boiler produces at an average of 65°C (including the 1h anti-legionella treatment).

On the cold source side, we notice a relatively stable temperature at wastewater tank inlet (in the range of 20-25°C), while the evaporator inlet as well as tank outlet are quite lower (5-10°C). This surprising drop is

possibly linked with recurrent fouling of the wastewater heat recovery system, an issue which is still under investigation.

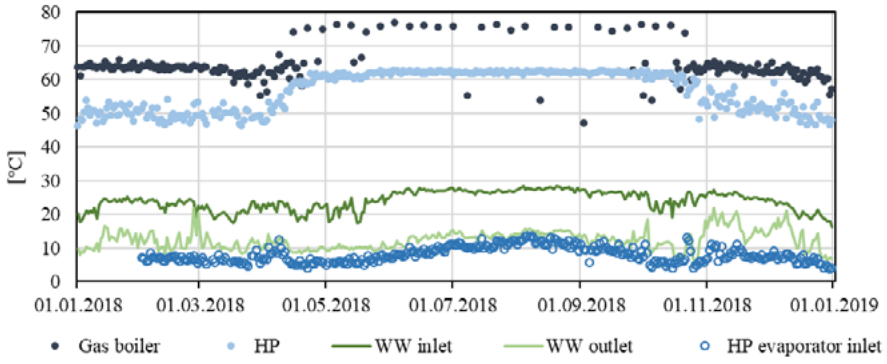


Fig. 4. Heat production temperatures, Jan – Dec 2018 (daily values)

3.3. Heat production issues

The above described differentiated summer/winter operation mode induces a distinct use of the HP and gas boiler, as explained (but not depicted) hereafter. In winter, due to the lower HP production set point, it can no longer cover the DHW supply. Latter is hence produced by the gas boiler, which induces return temperatures higher than those of the HP buffer. As a consequence, to avoid heating of the HP buffer with the gas boiler, the HP and its buffer are isolated from the DH distribution. Once the DHW storage tanks of all the buildings are fully charged, the DH drops to a SH supply temperature of around 35°C, which is again compatible with the HP and buffer temperatures.

Note that the differentiated winter operation mode was planned for SPF optimization reasons, with the objective to take advantage of the lower SH temperatures. However, it does in fact limit the operation duration of the HP to short periods, between DHW supply cycles. As a result, the HP share is lower than expected. In this regard, it could be worth using the same set points and operation mode as in summer, which would probably induce a higher share of HP production. Despite a possible drop in SPF, latter could actually lead to a better system performance in terms of CO_2 emissions, when takin into account the related reduction in gas consumption. This issue is currently being tackled by way of numerical simulation.

3.4. Heat demand issues

Figure 5 shows the disaggregated SH and DHW supply by building. We observe a strong variability, despite identical heated surface areas and thermal envelopes (note: as a unique difference, the ground floor of building no 3 has apartments instead of extracurricular activities). This variability, as well as the discrepancy with the projected and available benchmark values, will be discussed here after.

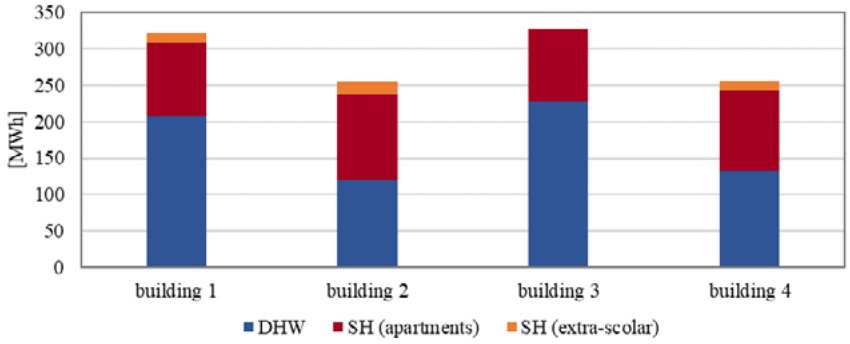


Fig. 5. Disaggregated heat demand by building, 2018

SH supply and performance gap are analyzed by way of a sensitivity analysis carried out with the Lesosai thermal balance calculation tool [7], with following scenarios (Table 1):

1. *Project*, simulated with the project design values, taking into account standard weather data, as well as normed indoor temperature and ventilation rates (without heat recovery).
2. *Real weather*, simulated with the actual weather data of 2018.
3. *Real weather & indoor temperature*, simulated with actual weather data of 2018, as well as actual indoor temperatures (as measured on the exhaust air of the ventilation system of each building).
4. *Measured*, simulated with actual weather and indoor temperatures, as well as adjusted ventilation rates, so as to reproduce the actual monitored SH of 2018.

Note that for the sake of simplicity and coherence, this analysis only concerns SH related to apartments (and not the one for extracurricular activities).

Table 1 Main input parameters for SH performance gap analysis

Scenario	Meteorological year	Indoor temperature [°C]	Air flow [m³/h/m²]
Project	Standard	20.0	0.7
Real weather	2018	20.0	0.7
Real weather & indoor temperature	2018	[22.3 - 22.7][1]	0.7
Measured	2018	[22.3 - 22.7][1]	[0.9 - 1.3][2]

[1] Based on extracted air temperature measurements [per building]
[2] Adjusted air flow to reach the measured heat demand [per building]

The results are depicted in Figure 6 and yield following comments. As 2018 was warmer than the standard weather (2'347 instead of 2'894 heating degree days), the SH demand for the *Real weather* scenario turns out around 20% lower than for *Project*. The demand however rises when taking into account the actual indoor temperature. Finally, reproduction of the actual monitored SH implies to adjust the ventilation rate to 0.9 - 1.3 $m^3/h.m^2$ (instead of the normed value of 0.7 $m^3/h.m^2$, without heat recovery). Latter adjustment could be related to window openings. In this regard, of the average adjusted value of 1.1 $m^3/h.m^2$, 0.2 $m^3/h.m^2$ actually correspond to mechanical ventilation (i.e. 1.0 $m^3/h.m^2$ subject to 80% heat recovery efficiency). The remaining 0.9 $m^3/h.m^2$ is equivalent to 9 constantly open windows of 1x1m per building (as given by a standardized airflow chart). So as to corroborate the plausibility of such window openings, we conducted an infrared photography campaign of the total 768 windows, at a rate of 289 pictures per day over a typical winter week. As a result, we observed an average per building of 3.5 open windows, 8.4 partially open windows and 5.9 open windows behind shutters (i.e. an order of magnitude which could explain the gap between *Measured* and *Real weather & indoor temperature* scenarios).

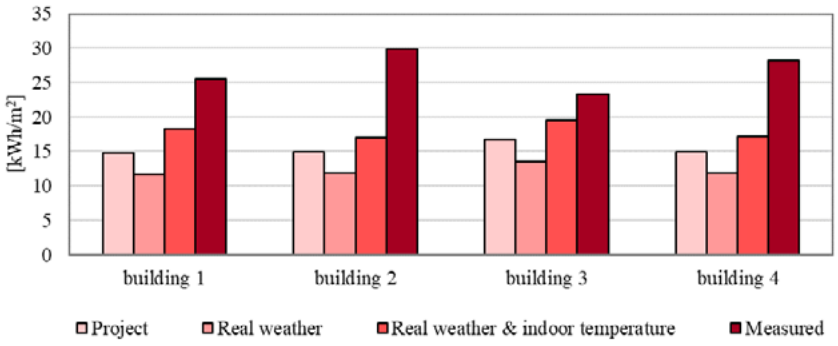


Fig. 6. SH demand, calculated and monitored values

Preceding results lead to following remarks:

- The ratio between *Measured* and *Real weather* (1.7 - 2.5, depending on the building) can in principle be explained by: i) higher indoor temperatures than the ones given by the norm; ii) window openings which over-compensate heat recovery by the mechanical ventilation.
- While this performance gap may seem relatively important, it is in the order of magnitude of other monitored buildings [5]. Furthermore, despite this gap, the actual SH demand (27.3 kWh/m^2) is quite lower than the 68 kWh/m^2 average value of Geneva's MFB stock constructed between 2001 and 2010 [4].

Finally (Figure 7), the measured DHW supply is compared to normed values concerning as well supply to the storage [8], as end use at taps [9]. The measured average (39.5 kWh/m^2) is above the normed supply value (32 kWh/m^2), but in between the median and 3rd quartile of a benchmark on 61 sub-station of Geneva's main DH network [10]. Also note that the important discrepancy between the 4 buildings, which cannot be explained by distinct number of inhabitants, still is in the dispersion range of latter benchmark.

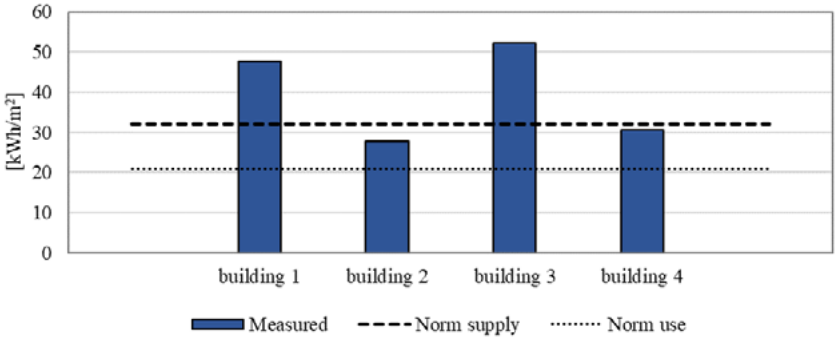


Fig. 7. DHW supply: measured and normed values

4. Conclusions

This paper concerns a new low energy MFB complex in Geneva, whose heat is produced by a centralized HP on wastewater with a complementary gas boiler, and distributed via a local DH network. Detailed hourly monitoring over an entire year of operation yields following main results.

At production level:

- The HP production accounts for 45% of the total production, with a seasonal performance factor of 3.03, including ancillary electricity of circulation pumps on evaporator and condenser side.
- The dynamic and annual energy balance of the system show a lower HP production than expected, especially during winter. This is due to operational constraints linked to distinct temperatures set points between summer and winter, as well as to high return temperature from the gas boiler. Note that this issue is currently being tackled by way of numerical simulation.
- While the wastewater resource temperature is relatively high all year round (20-25°C), the evaporator inlet temperatures is quite lower (5-10°C). Such is possibly linked to recurrent fouling of the wastewater heat recovery system, an issue which is still under investigation.

At demand level:

- At the level of the buildings, DHW supply (39.5 kWh/m^2) accounts for 59% of the total, against 41% for SH (27.3 kWh/m^2).
- As a complement to direct SH, ventilation heat recovery by dual flow, with a measured 80% efficiency, contributes by 24.1 kWh/m^2 to compensation of heat losses through the building envelope.
- The ratio between measured and climate corrected design values (1.7 - 2.5) can in principle be explained by: i) higher indoor temperatures than the ones given by the norm; ii) window openings which over-compensate heat recovery by the mechanical ventilation. While this performance gap may seem relatively important, it is in the order of magnitude of other monitored buildings, and the actual SH demand is quite lower than the average for Geneva's multifamily buildings constructed between 2001 and 2010.
- Finally, the measured DHW supply is above the normed supply value, but in between the median and 3rd quartile of a benchmark on 61 sub-station of Geneva's main DH network.

As a conclusion of this case-study, centralized HP systems on wastewater can play a substantial role for the combined SH and DHW heat production of low-energy multifamily buildings. Implementation and operation however need adequate system integration, control and commissioning.

Acknowledgements

The authors are thankful to following entities, who are funding this evaluation: Services Industriels de Genève (SIG), Office cantonal de l'énergie de Genève (OCEN), Fondation Emma Kammacher (FEK), as well as the diverse stakeholders (engineers, technicians, HP and WW-HX manufacturer) for participating in the follow-up group as part of this case-study.

References

[1] QUIQUEREZ, Loic (2017). Décarboner le système énergétique à l'aide des réseaux de chaleur: état des lieux et scénarios prospectifs pour le canton de Genève. Université de Genève – Thèse. https://archive-ouverte.unige.ch/unige:93380

[2] DE SOUSA FRAGA, Carolina (2017). Heat pump systems for multifamily buildings: which resource for what demand? Université de Genève – Thèse. https://archive-ouverte.unige.ch/unige:94939

[3] ROGNON, Fabrice, YUSHCHENKO, Alisa and RUETSCHI, Matthias (2017). Retrofitting fossil-based heating systems with air to water heat pumps in multifamily houses. 12th IEA Heat Pump Conference, Rotterdam, the Netherlands. http://hpc2017.org/wp-content/uploads/2017/05/P.1.5.4-Retrofitting-fossil-based-heating-systems-with-air-to-water-heat-pumps-in-multifamily-houses.pdf

[4] KHOURY, Jad (2014). Rénovation énergétique des bâtiments résidentiels collectifs: état des lieux, retours d'expérience et potentiels du parc genevois. Université de Genève – Thèse. https://archive-ouverte.unige.ch/unige:48085

[5] ZGRAGGEN, Jean-Marc (2010). Bâtiments résidentiels locatifs à haute performance énergétique : objectifs et réalités. Université de Genève – Thèse. https://archive-ouverte.unige.ch/unige:13093

[6] FEKA (2019). Energie aus Abwasser. http://feka.ch/

[7] Lesosai (2019). Lesosai: certification and thermal balance calculation for buildings. http://www.lesosai.com/fr/01_spec.html

[8] OCEN (2012). Directive relative au calcul de l'indice de dépense chaleur. Office cantonal de l'énergie, Genève. https://www.ge.ch/document/directive-relative-au-calcul-indice-depense-chaleur/telecharger

[9] SIA (2009). Norme SIA 380/1: 2009, L'énergie dans le bâtiment.

[10] QUIQUEREZ, Loic (2017). Analyse comparative des consommations de chaleur pour la production d'eau chaude sanitaire estimées à partir de relevés mensuels: Etude sur un échantillon de bâtiments résidentiels collectifs alimentés par un réseau de chaleur à Genève. https://archive-ouverte.unige.ch/unige:91218

13th IEA Heat Pump Conference
April 26-29, 2020 Jeju, Korea

Air-to-water heat pumps as a substitution of oil-boiler in a non-retrofitted multi-family building of the 70's. In-situ monitoring, actual energy balance and performance.

Omar Montero D., Carolina Fraga, Simon Callegari*, Pierre Hollmuller

Energy Systems Group, University of Geneva, 66 Bd Carl Vogt, 1211 Genève, Switzerland

Abstract

In Geneva, CO_2 emissions are mainly related to the heat supply in the residential sector, in particular in multifamily buildings (MFB). In this context, air-source heat pumps (HP) could help to reduce emissions and replace fossil-based heating systems, especially in dense existing urban areas where air is the only available renewable energy source. This study concerns the analysis of an existing non-retrofitted MF building of 1972 (4´047 m^2 heated area), whose original fossil heat supply was recently replaced by two industrial air-to-water HPs (2 x 140 = 280 kW). Based on a detailed monitoring campaign covering 15 months of operation, the main findings show that the HP system was able to cover the entire heat demand, except for a short breakdown. Thanks to optimizations in the system regulation and the choice to use only one HP in summer, the COP_{sys} increased from 1.3 in the early stage, up to 3.4 during the last summer. Based on the latter performances, we estimated that the SPF could reach an annual value of 2.3 (instead of the measured value of 1.9).

Keywords: air-to-water heat pump, multi-family building, retrofit, in-situ monitoring, energy balance, performance gap.

1. Introduction

Nomenclature

COP_{HP}	coefficient of performance of the heat pump
COP_{sys}	coefficient of performance of system, including related auxiliary electricity
DHW	domestic hot water
E_{HP}	electricity consumption of heat pump
E_{sys}	electricity consumption of heat pump and auxiliary electricity
HP	heat pump
MFB	multifamily building
Q_{HP}	heat production of heat pump
SH	space heating
SPF	seasonal performance factor (annual or seasonal value)
ΔT_{HP}	Differential temperature between HP heat source and sink temperatures

1.1. Context and issues

In Geneva, the CO_2 emissions related to the energy sector represent 4.2 ton of emitted CO_2 per capita, of which 2.2 emitted by the heating sector, 1.1 by the transport sector (not including the airport) and 0.8 by the electricity sector [1]. Consequently, the main CO_2 emissions reduction potential lies in the heating sector, which represents about half of the final energy consumption in Geneva.

* Corresponding author. Tel.: +41 22 379 0646.
E-mail address: simon.callegari@unige.ch.

Even though multifamily buildings (MFB) only constitute 27% of the Geneva building stock, they represent almost half of the heated floor area of the canton, namely 19.3 out of 40.9 million m^2 [2]. About half of these MFB, which were built between 1946 and 1980, are nowadays in need of retrofit and possess a strong energy saving potential. In parallel to reducing of the heat demand of the building stock, in particular by way of retrofit, reducing of the CO_2 emissions can also be achieved by replacing fossil fuels by renewable energies, in particular via heat pump (HP) systems.

However, although the market share of HPs in the Swiss residential sector grew from nearly zero in the 1990s to about 50% today, only 10% corresponds to MFB [3]. This can be explained by the fact that the implementation of HP systems in MFB is more complex than in single family buildings [4], especially because of: i) multiple households, with diluted decision power and related problems of governance; ii) buildings often located in highly dense urban areas, with limited access to renewable heat sources other than air; iii) if not threated carefully, noise emissions can easily become a barrier; iv) higher shares of domestic hot water (DHW) in overall heat demand and related high temperature, which can affect the HP performance.

1.2. éco21- HP program for multifamily buildings

Within this context, the local public utility Services Industriels de Genève (SIG) is developing a series of pilot projects concerning the replacement of fossil-based heating systems by air to water HP in MFB. These projects, which are developed under SIG's portfolio éco21, are implemented in the form of energy contracting [4].

Feasibility studies revealed the difficulties of the task: solar is not technically possible (due to complicated old roof, building being under historical heritage protection, no place available for water storage), geothermal energy and often wood and biomass are not authorized by law (due to water and air protection regulations). Air to water HPs are therefore the only solution for integrating renewable energy supply into the buildings. The challenge is important: buildings are old, there is little space, the heat distribution systems within the buildings are old, and investment costs are high [4]. Due to the age of the buildings and the restrictions to insulate the buildings envelope, the distribution temperatures are not always compatible with the ones needed for the high efficiency of the air to water HPs.

One of the major technical challenges is related to unavailability of air to water HPs specially designed for MFB. Most of the residential HPs currently have a capacity below 30 kW and are suited for single-family houses, while industrial HPs with higher capacities are not specifically designed for integration in residential buildings, specifically on noise aspects.

1.3. Objective

This paper aims to analyze one of the pilot projects of the éco21 program, in actual conditions of use. After description of the considered case study, we analyze the results of a detailed monitoring campaign covering 15 months of operation (July 2018 – Sep 2019). A particular focus is set on the diverse optimizations which had to be done so as to reach an acceptable system performance. Basing on the results obtained by way of this optimization process, we finally estimate an optimized SPF over an entire year of operation.

2. Case study

Located in Geneva and built in 1972, the MFB under consideration has a total heated surface of 4´047 m^2 (114 residents). While its envelope has not undergone any retrofit, the existing oil boiler (319 kW) was replaced by two industrial air-source heat pumps (312 kW). Each one has a heating capacity of 156 kW and COP of 3.42 (7°C evaporator and 45/40°C condenser side) as well as four scroll compressors offering four capacity stages in response to the load or source temperature [5]. Before system replacement, the climate corrected oil consumption (final energy) for production of space heating (SH) and domestic hot water (DHW) was 158 kWh/m^2 per year.



Fig. 1. Studied collective multifamily building (left) and industrial air-source heat pumps (right)

The oil boiler was kept as backup for the first years of operation but will eventually be dismantled. The distribution includes two storage tanks in parallel for DHW (500 L each) and one for SH tank (1000 L).

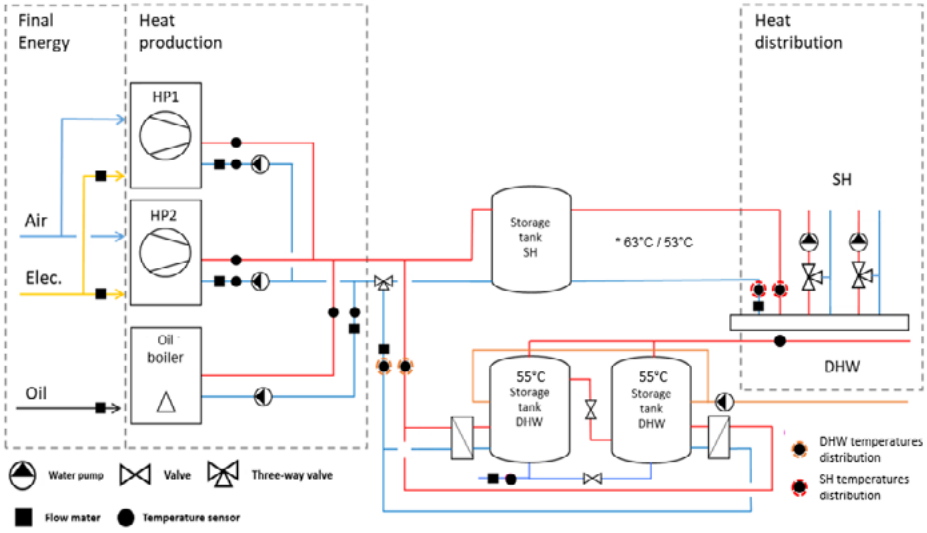


Fig. 2. Heating system (simplified diagram). * Defined at an outdoor temperature of -7°C

3. Monitoring

Instrumentation of the system is depicted in Figure 2. The monitored data are: i) electricity of each HP, including auxiliary electricity of the circulation pump on condenser side; ii) heat production of each HP; iii) heat distribution for SH (before the three-way mixing valve) and for DHW (at storage inlet); iv) DHW consumption (storage outlet).

The monitoring campaigned started in July 2018 for a period of 15 months (until December 2019). Data is acquired in 5 min time step, and aggregated in hourly and daily values.

4. Results and discussion

4.1. Building demand

The annual demand is 125 kWh/m^2 (Sep 2018 – Aug 2019), of which 47% for DHW (58 kWh/m^2) and 53% for SH (67 kWh/m^2). Latter DHW demand corresponds to the highest benchmarked values on Geneva's MFB stock [6]. On the other hand, despite the envelope not having been retrofitted, SH is well below Geneva's average for buildings from the 70's (101 kWh/m^2) and rather matches the average of the decade of 2000s [7].

The energy signature of the entire bundling shows a non-heating temperature of 17°C and SH rises to 20 W/m^2 at an outdoor temperature of 0°C (Figure 3).

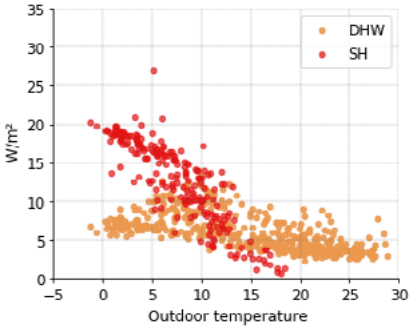


Fig. 3. Daily heat demand vs the outdoor temperature

The peak daily demand is around 25 W/m^2 (Figure 4). In daily average, DHW varies between 3 and 12 W/m^2 (summer vs winter), with an unexplained increase from February 2019 onwards.

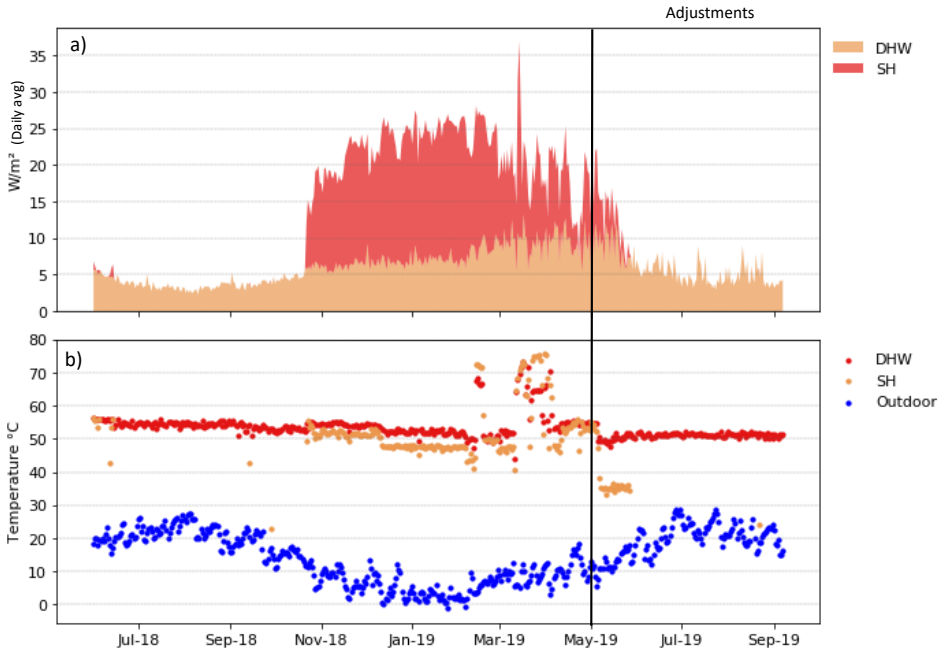


Fig. 4. Daily heat demand (a) and daily distribution temperatures (b)

Daily distribution temperatures are also depicted in Figure 4. The DHW temperature (at storage inlet) has a constant value of 50 – 55°C (except during HP breakdown in Feb and Mar 2019, see further down). Up to May 2019, the SH temperature (before the mixing valve) was relatively constant and similar to DHW. This was due to internal HP setpoints not taking into account the heating curve defined at the level of the centralized automation. This problem could finally be identified and resolved at the end of the heating season (May 2019), with a SH temperature dropping to 35°C (for an outdoor temperature above 10°C).

4.2. Heat production

The daily heat production is depicted in Figure 5. The heat production was entirely covered by both HPs, except during the HP breakdown (Feb and March 2019) when the oil boiler had to be turned on. During the first summer (up to Sep 2018), both HPs were run in parallel. From there on, priority was given to HP2 (master), with HP1 turned on for loads above approximately 15 W/m^2. During the adjustments of May 2019, priority was given to HP1, and HP2 was completely switched off for the summer period (for electricity savings on unnecessary standby mode).

Note that the HP breakdown could have been handled faster if the local technicians were used to/trained for this type of heating systems and had available spare changes, which underlines the importance of professional training.

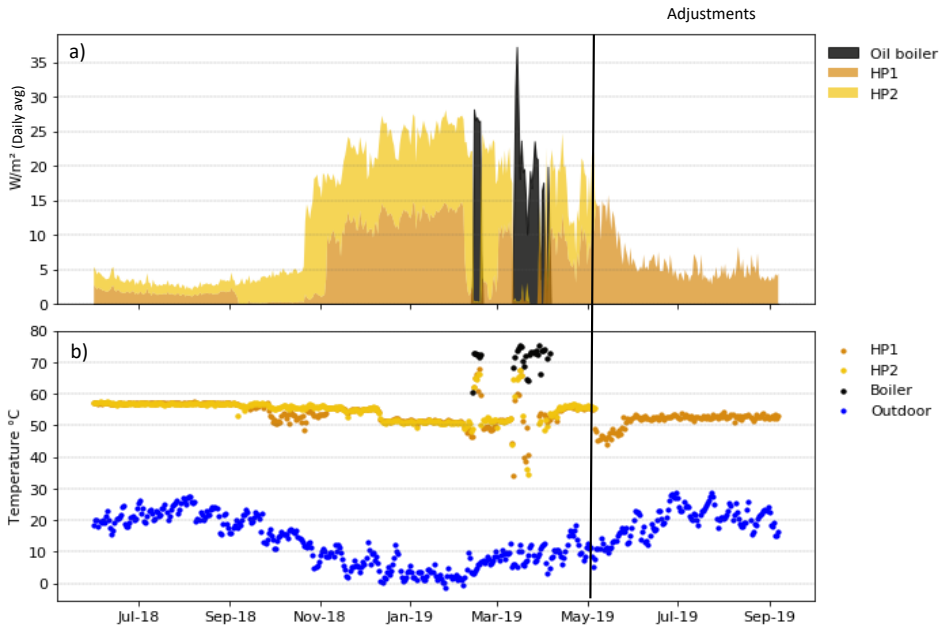


Fig. 5. Daily heat production (a) and production temperatures (b)

As pointed out before, the HP production temperature is relatively constant until the adjustments in May 2019 (Figure 5). Afterwards a short drop is observed due to the adjustments SH heating curve, followed by the DHW production during summer. During the HP breakdown, the oil boiler production temperature raised to 70°C, which is standard for this type of technology.

4.3. HP performance

For the purpose of this section, the HP performance indicators are based on the HP heat production and electricity use, and they are defined as follows:

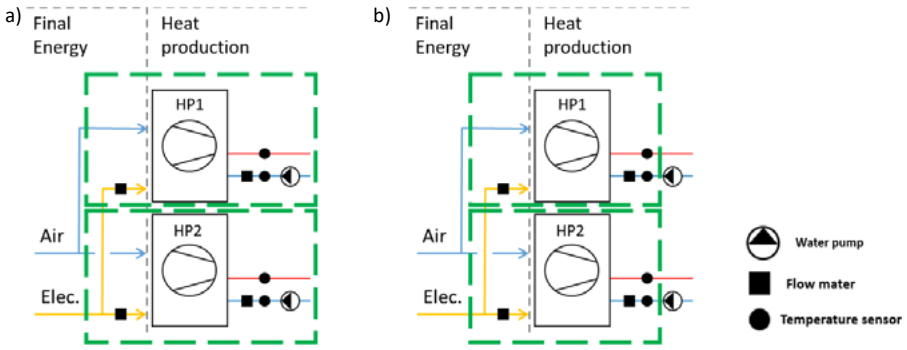


Fig. 6. Boundaries of the system performance (a) and heat pump performance (without water pump) (b)

- HP performance (Figure 6 - b) : Ratio between heat production and electric consumption of the heat pump, without auxiliary electricity consumptions, for short time periods (hourly or daily):

$$COP_{HP} = \frac{Q_{HP}}{E_{HP}} \quad (1)$$

- HP system performance (Figure 6-a) : Ratio between heat production and electric consumption of the heat pump and its circulation pump on condenser side, for short time periods (hourly or daily):

$$COP_{sys} = \frac{Q_{HP}}{E_{sys}} \quad (2)$$

- Ratio between heat production and electricity consumption of the heat pump and the circulation pump for a given period (annual or seasonal):

$$SPF = \frac{\sum Q_{HP}}{\sum E_{sys}} \quad (3)$$

Note: As temperature sensors used to calculate Q_{HP} are close to the HP, distribution losses are included in the heat production.

4.4. System performance

The evolution of the HP system performance during the monitored period is depicted in Figure 7, along with different adjustments. Summer 2018 has the lowest COP_{sys}, below 1.5, despite high air temperatures. This is due to a constant activation of the HP1 circulation pump (condenser side), even when the HP was off. An increase in performance is observed from Oct 2018 onwards when the constant flowrate is adjusted to follow the heat production, but COP_{sys} remains mostly below 2, due to constant SH temperature distribution and HP standby mode. After May 2019, the COP_{sys} increased significantly (2.4 - 3.4) due to the adjustment of the SH production temperature, the variable flowrate, high summer outdoor temperatures, as well as the choice to switch off the second HP during the summer period.

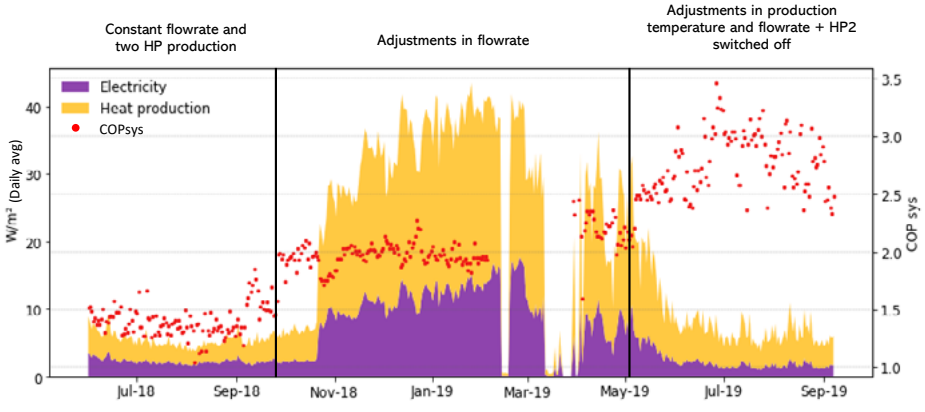


Fig. 7. Daily heat production and electricity consumption of the two HP as well as COP system performance (note: performance during the breakdown period is not considered).

The daily COP_{sys} decreases with the increase of the ΔT_{HP} as show in Figure 8. For the winter 2018-2019 and summer 2019, the COP_{sys} ranges between 3.7 to 1.8 for a ΔT_{HP} of 20 and 50 K, respectively. Note the lower performance during summer 2018 is due to the high electricity consumption induced by the constant flowrates, unrelated to temperature levels.

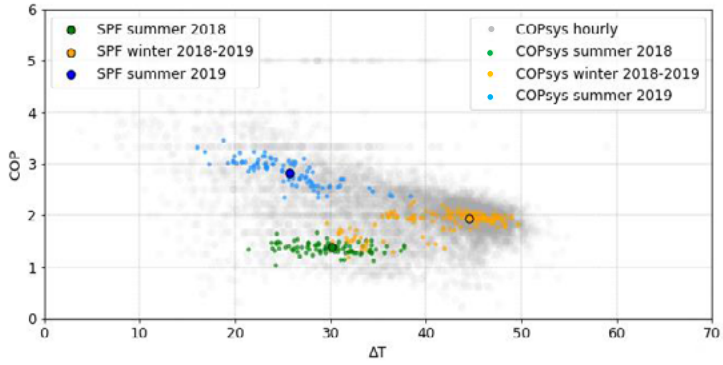


Fig. 8. COPsys and SPF as a function of ΔT_{HP}, for each season (Summer: 1st June - 31st Aug; Winter: 1st Sep - 31st Jan).

4.5. Heat pump performance

In this section, the monitored performance is compared to the one announced by the manufacturer, which is done at HP level. In the case of the manufacturer values, the COP_{HP} is given for continuous HP operation, at full power capacity (four compressors) and without auxiliary electricity consumptions. In order to approach these conditions, the hourly monitored data was filtered to identify the hours when the HP worked at least 30 minutes (note: in the case of summer 2018, the filter was reduced to 18 min, due to the higher power capacity of the two HP set-up which induced shorter durations of heat production). Furthermore, the electricity consumption of the circulation pumps (estimated to approx. 3 kW each) was deducted from the monitored electricity consumption, according to the type of flow rate of each period (constant / variable).

As a result, COP_{HP} (Figure 9) has higher values than COP_{sys} (Figure 8). In addition, the values of summer 2018 are now aligned with the ones of following periods, which highlights the fact that the poor COP_{sys} of that period was due to constant operation of the circulation pumps. Finally, a monitored COP_{HP} has the same trend as the one by the manufacture, with slightly lower values as is frequently observed difference between in situ

monitored versus lab measured values [8, 9, and 10]. In conclusion, the low COP_{sys} observed was not due to a deficiency in the HP machine but to a non-optimal system operation.

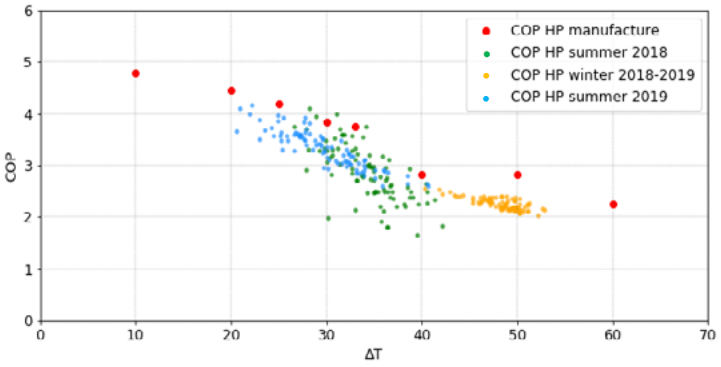


Fig. 9. Daily COP_{HP} filtered for each season and COP manufacture as a function of the ΔT_{HP}.

This analysis further suggests that HP systems should have a dedicated electrical energy meter for the HP (without auxiliary electricity), in order to verify the proper performance according to the manufacture values and help identify auxiliary electricity issues.

4.6. Optimized system performance

As observed above, the system optimizations in May 2019 lead to a clear increase of the COP_{sys} (Figure 7). Given this increase, we finally estimate an optimized SPF over an entire year of operation (Sep 2018 – Aug 2019), based on daily values, with the following hypotheses:

- The heat production is supplied by the HPs year-round (no HP breakdown).
- The daily COP_{sys} is estimated by way of the quadratic regression in Figure 10, on the optimized period, which allows to calculate the related daily electricity consumption.
- Throughout the year, as the ΔT varies between 20 and 55 K, the regression is only applied to this range. The temperature difference outside of this range are not considered.

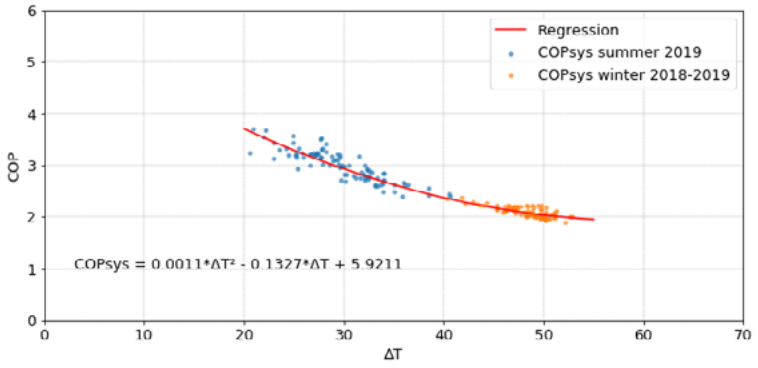


Fig. 10. Quadratic regression of the COP_{sys} as a function of the ΔT_{HP} on the optimized period (Nov 2018 - Aug 2019).

As a result, Figure 11 shows a slightly decrease of the electricity consumption (54.7 to 54.3 kWh/m^2). Note that latter still is a conservative value, because it does not include the adjustment of the SH production temperature. The total heat production increases to replace the breakdown period (HPs production year-round). It shows that a SPF of 2.3 could potentially be achieved (instead of a measured value of 1.9).

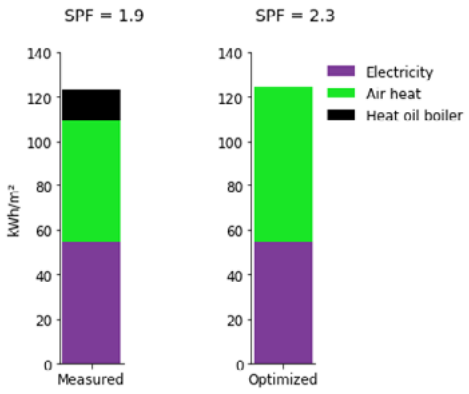


Fig. 11. Measured and optimized HP system electricity and absorbed heat (Sep 2018 – Aug 2019)

5. Conclusions

This paper focuses one a pilot project of the local public utility, concerning the replacement of fossil-based heating systems by air to water heat pumps in multifamily buildings. In the building under consideration (4´047 m^2), heat production by way of a centralized oil boiler was replaced by two industrial air-source heat pumps (2 x 156 kW = 312 kW).

A detailed monitoring campaign covering 15 months of operation (July 2018 – Sep 2019) shows that even in an existing and non-retrofitted building, a fossil boiler can be replaced by an industrial air-source HP system, without decrease of the thermal comfort for the tenants. However, based on the monitored data, improvements in the control system were implemented to improve the overall performance of the system, including:

i) Avoid constantly running of HP circulation pump in absence of production as they have a significant power consumption.
ii) Guarantee that HP set points take into account the heating curve defined at the level of the centralized automation.
iii) Turning off the second heat pump if a single HP is able to cover the entire demand, in order to improve the remaining HP's load factor.

As far as electrical consumption and related SPF is concerned, implementation of such systems however still needs adequate professional training, as well as careful commissioning. Future work will focus on exploring possible optimizations in the hydraulic and control system using numerical simulations.

Acknowledgements

The authors would like to thank SIG for financing of this study and handing over of the main monitoring data, as well as the diverse stakeholders (building owner, engineers, technicians, HP manufacturer) for participating in the follow-up group in turn of this case-study.

References

[1] QUIQUEREZ, Loic et al. The role of district heating in achieving sustainable cities: comparative analysis of different heat scenarios for Geneva. In: The 15th International Symposium on District Heating and Cooling. Seoul (South Korea). [s.l.] : [s.n.], 2016. https://archive-ouverte.unige.ch/unige:88423

[2] KHOURY, Jad. Assessment of Geneva multi-family building stock: main characteristics and regression models for energy reference area determination, 2016. https://archive-ouverte.unige.ch/unige:88423

[3] CSD (2017), IEA Annex 50, Task 1: Market overview - country report for Switzerland.

[4] ROGNON et al. Retrofitting fossil-based heating systems with air to water heat pumps in multifamily houses, 12th IEA Heat Pump Conference, 2017.

[5] AERMEC, Reversible heat pumps high efficency - Technical manual NRK 0200-0700, 2016, https://aeroventic.com/heat-pumps-anl-aermec

[6] QUIQUEREZ, Loic. Décarboner le système énergétique à l'aide des réseaux de chaleur: état des lieux et scénarios prospectifs pour le canton de Genève. Université de Genève. Thèse, 2017. https://archive-ouverte.unige.ch/unige:933

[7] KHOURY, Jad. Rénovation énergétique des bâtiments résidentiels collectifs: état des lieux, retours d'expérience et potentiels du parc genevois. Université de Genève. Thèse, 2014. https://archive-ouverte.unige.ch/unige:4808

[8] DE SOUSA FRAGA, Carolina et al. Large solar driven heat pump system for a multifamily building: Long term in-situ monitoring. In: Solar Energy, 2015, vol. 114, p. 427-439. https://archive-ouverte.unige.ch/unige:48138

[9] MERMOUD, Floriane et al. Suivi énergétique du bâtiment tertiaire Polimmo, 5 route des Jeunes à Genève, rénové MINERGIE® et équipé de pompes à chaleur couplées à des sondes géothermiques - Aspects techniques et économiques, 2014. https://archive-ouverte.unige.ch/unige:41178

[10] TORNARE, Guy et al. Rapport technique et de communication du projet d'assainissement Minergie-P des immeubles « La Cigale » (GE) – Chauffage par pompes à chaleur solaires couplées à des stocks à changement de phase, 2017. https://archive-ouverte.unige.ch/unige:92770

13th IEA Heat Pump Conference
April 26-29, 2021 Jeju, Korea

Performance Characteristics of Cascade Multi-Functional Heat Pump in Cooling-Hot Water Mode With Variation in Secondary Fluid Temperature Conditions

Selorm Kwaku Anka[a], Samuel Boahen[b], Kwesi Mensah[a], Won Hee Kang[c], Min Kyeong Park[c], Kwang Ho Lee[d], and Jong Min Choi[e*]

[a]Graduate School of Mechanical Engineering, Hanbat National University, Daejeon 34158, Korea
[b]Department of Mechanical Engineering, Cape Coast Technical University, P.O. Box DL 50, Cape Coast, Ghana
[c]Graduate School of Department of Architecture, Korea University, Seoul 02841, Korea
[d]Department of Architecture, Korea University, Seoul 02841, Korea
[e]Department of Mechanical Engineering, Hanbat National University, Daejeon 34158, Korea

Abstract

Cascade multi-functional heat pumps have gained much attention in recent times due to their ability to simultaneously meet the cooling, heating and hot water demands of residential buildings. However, the effect of heat source and sink temperature on the performance of cascade multi-functional heat pumps is lacking in open literature. This study experimentally analyzed the performance characteristics of a water-to-water cascade multi-functional heat pump operating in cooling-hot water mode according to variation of indoor heat exchanger entering water temperature (ID EWT), outdoor heat exchanger entering water temperature (OD EWT) and hot water heat exchanger entering water temperature (HW EWT). Capacity of the cooling cycle was affected by variation in ID EWT and OD EWT while capacity of the hot water cycle was affected significantly by variation in OD EWT and HW EWT. Furthermore, system COP decreased with increase in HW EWT and OD EWT, and increased with increase in ID EWT.

Keywords: Cascade multi-functional heat pump, Cooling-hot water mode, Entering water temperature, Capacity, COP

1. Introduction

Heat pumps have been identified as energy efficient systems for space cooling, space heating and hot water generation [1]. While space cooling and heating are needed during summer and winter seasons respectively, hot water is needed all year round. A single heat pump that can simultaneously provide cooling/heating and hot water is of great importance in the aspect of cost, energy savings and efficient space utilization especially in apartment and high rising residential buildings. Multi-functional heat pumps have therefore been developed over the years for this purpose [2, 3]. However, most of the studies done on multi-functional heat pumps have focused on single stage heat pumps with few works on cascade multi-functional heat pumps. Performance characteristics of cascade multi-functional heat pumps is therefore lacking in open literature. This study analyzes the performance characteristics of water-to-water cascade multi-functional heat pump according to variation in secondary fluid temperature. This will provide pathway for the design and control of energy efficient cascade multi-functional heat pumps.

2. Experimental condition and test procedure

The study was done to analyze the performance characteristics of cascade multi-functional heat pump with variation in entering water temperature (EWT) in cooling-hot water mode. The experimental setup used in the study is a multi-functional water-to-water cascade heat pump consisting of a single stage cycle connected in

*Corresponding author. Tel.: +82-42-821-1731 ; fax : +82-42-821-1462
E-mail address: jmchoi@hanbat.ac.kr.

parallel with the low stage (LS) side of a cascade heat pump cycle as shown in Fig. 1. The single stage cycle was used for cooling, and generally consisted of the outdoor heat exchanger (OD HX), compressor, indoor heat exchanger (ID HX) and expansion device. The cascade cycle consisted of low stage (LS) side and high stage (HS) side interconnected by cascade heat exchanger, which acted as condenser to the LS side and evaporator to the HS side. Brine with ethylene glycol of 40% concentration was used as secondary fluid, with constant temperature water bath and magnetic pump used to simulate the secondary fluid flow loop.

When in operation, refrigerant from LS compressor divides into two and go through the cascade HX and the OD HX. The divided refrigerant combine, after expansion, and go through the ID HX for cooling. Also, HS refrigerant gains heat from LS refrigerant in the cascade HX, gets compressed and goes into HW HX for hot water generation. Refrigerant from HW HX is then expanded into the cascade HX for the cycle to continue. Different refrigerants were used in the LS and HS cycles due to their different critical pressure and temperature properties.

Test was conducted by varying the outdoor heat exchanger entering water temperature (OD EWT), indoor heat exchanger entering water temperature (ID EWT) and hot water heat exchanger entering water temperature at reference secondary fluid flow rates as shown in Table 1. Sensors were installed in the test rig to measure the performance parameters of the cascade multi-functional heat pump. Capacity of the cooling cycle (Q_C) and capacity of the hot water cycle (Q_{HW}) were calculated using mass flow rate of secondary fluid ($\dot{m}$), leaving water temperature (LWT) and EWT across the ID HX and HW HX respectively as shown in Eq. (1), while COP of the cascade multi-functional heat pump was calculated using Q_C, Q_{HW} and power consumption of LS (W_{LS}) and HS (W_{HS}) as shown in Eq. 2.

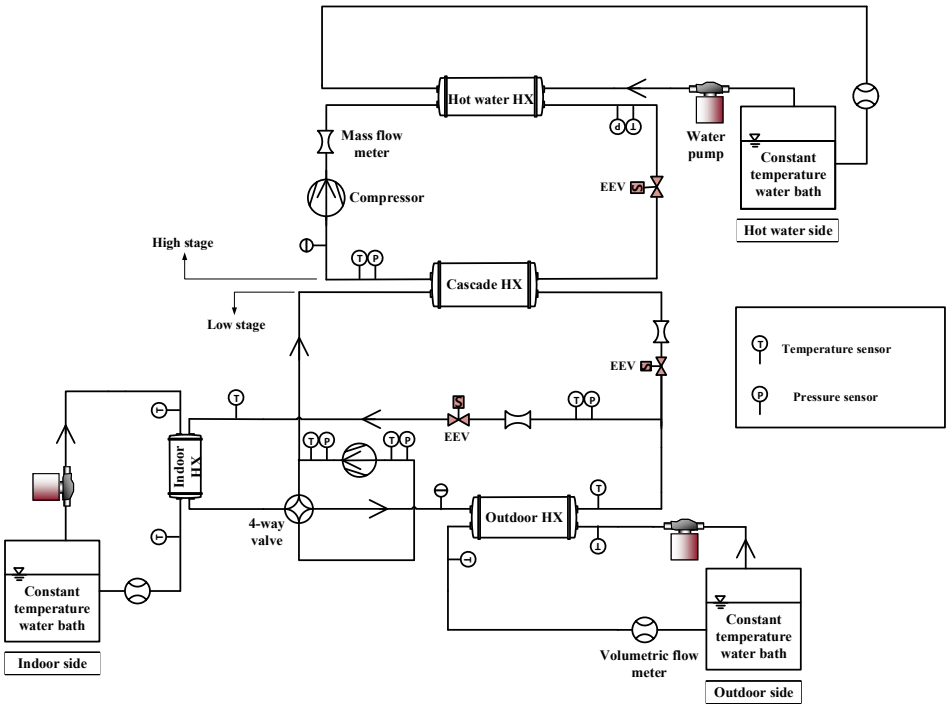


Fig. 1. Schematic diagram of experimental setup

$$Q_C/Q_{HW} = \dot{m} \cdot |LWT - EWT| \quad (1)$$

$$COP = \frac{Q_C + Q_{HW}}{W_{LS} + W_{HS}} \quad (2)$$

Table 1 Test conditions for cooling-hot water mode

Parameter	Unit	Low stage	High stage
Refrigerant	**	R410A	R134a
Optimum charge amount	g	4700	2300
OD EWT	℃	20, 25, 30, 35	-
ID EWT	℃	2, 7, 12, 17	-
HW EWT	℃	-	40, 50, 55, 60, 65
ODHX flow rate	LPM	10	-
IDHX flow rate	LPM	8	-
HWHX flow rate	LPM	-	6
EEV opening	%	Adjusted	Adjusted

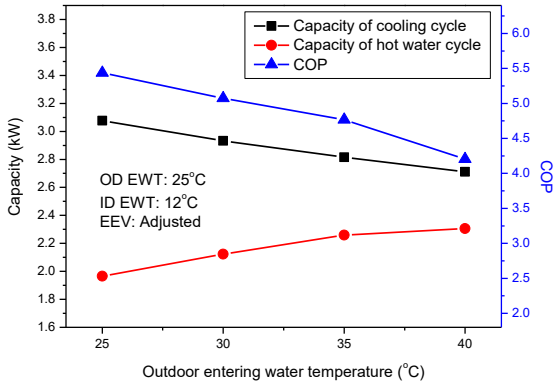


Fig. 2. Capacity and COP variation according to OD EWT

3. Results and discussion

3.1. Performance characteristics according to OD EWT variation

Figure 2 shows capacity and COP variation of the cascade multi-functional heat pump according to OD EWT. Capacity of the cooling cycle decreased with increase in OD EWT due to decrease in heat transfer rate in the evaporator. Capacity of the hot water cycle increased as OD EWT increased due to increase in LS condensing temperature and heat transfer from the LS to the HS while COP of the cascade multi-functional heat pump decreased with increase in OD EWT due to great increase in LS power consumption. Cooling capacity and COP decreased by 13.5% and 29.3% respectively, while capacity of the hot water cycle increased by 14.8% as OD EWT increased from 25℃ to 40℃.

3.2. Performance characteristics according to ID EWT variation

Figure 3 shows variation of capacity and COP according to ID EWT. Capacity of the cooling cycle increased with increase in ID EWT due to increase in refrigerant mass flow rate in the ID HX while COP of the cascade multi-functional heat pump increased with increase in ID EWT due mainly to increase in capacity of the cooling cycle and slight decrease in power consumption of the HS cycle. Furthermore, capacity of the heating cycle was slightly affected by variation in ID EWT. Capacity of the cooling cycle and COP increased up to 27.9% and 26% respectively as ID EWT increased from 2℃ to 17℃.

3.3. Performance characteristics according to HW EWT variation

Capacity and COP variation of the cascade multi-functional heat pump according to HW EWT is shown in Fig 4. Capacity of the cooling cycle was not affected by HW EWT variation. However, capacity of the hot water cycle decreased with increase in HW EWT due to decrease in heat transfer to secondary fluid in the HW HX. Furthermore, COP of the system decreased due to decrease in capacity of the hot water cycle and increase in HS power consumption. Capacity of the hot water cycle and COP decreased up to 15.9% and 28.4% respectively, as HW EWT increased from 40℃ to 65℃.

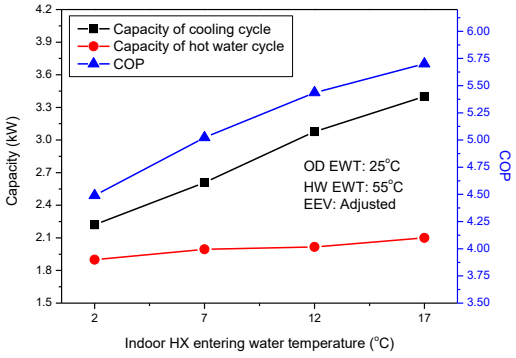


Fig. 3. Capacity and COP variation according to ID EWT

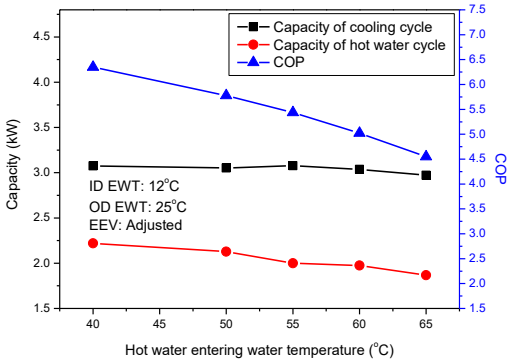


Fig. 4. Capacity and COP variation according to HW EWT

4. Conclusion

This study analyzed the performance characteristics of cascade multi-functional heat pump according to variation of OD EWT, ID EWT and HW EWT in cooling-hot water mode. Heating capacity of hot water cycle increased by 14.8% while cooling capacity and system COP decreased by 13.5% and 29.3% respectively, as OD EWT increased by 15℃ of the standard value. Furthermore, cooling capacity decreased by 27.9% while system COP increased by 27% as ID EWT decreased by 10℃ of the standard value. Capacity of the hot water cycle and system COP decreased by 15.9% and 28.4% respectively as HW EWT increased from 40℃ to 65℃. However, variation of ID EWT and HW EWT had insignificant effect on capacity of the hot water cycle and performance of the cooling cycle respectively.

Acknowledgement

This work was supported by the National Research Foundation of Korea(NRF) grant funded by the Korea government (MSIT) (No. 2019R1A2C2087157).

References

[1] Kim DH, Kim MS. The effect of water temperature lift on the performance of cascade heat pump system. *Applied Therm. Eng* 2014;**64**:273-282.
[2] Liu X, Lau SK, Li H. Optimization and analysis of a multi-functional heat pump system with air source and gray water source in heating mode. *Energ Buildings* 2014;**69**:1–13.
[3] Jung HW, Kang H, Yoon WJ, Kim Y. Performance comparison between a single-stage and a cascade multi-functional heat pump for both air heating and hot water supply. *Int J Refrig* 2013;**36**:1431 – 1441.

13th IEA Heat Pump Conference
April 26-29, 2021 Jeju, Korea

Development of a dynamic model of a heat pump system and fault detection

Yechan Yun[a], Dongwon Han[b], Young Soo Chang[c,*]

[a] Graduate School of Mechanical Engineering, Kookmin University, 77 Jeongneung-Ro, Seongbuk-Gu, Seoul, 02707, Korea
[b] Graduate School of Mechanical Engineering, Korea University, 145 Anam-ro Seongbuk-Gu, Seoul, 02841, Korea
[c] School of of Mechanical Engineering, Kookmin University, 77 Jeongneung-Ro, Seongbuk-Gu, Seoul, 02707, Korea

Abstract

Progressive fault such as refrigerant leakage in a heat pump system is difficult to diagnose at an early stage. If the faulty system is operated for a long time, it may lead to serious fault such as compressor break down as well as performance deterioration. If the dynamic characteristics of the system caused by refrigerant leakage can be predicted, it is possible to prevent the progress of faults and to reduce maintenance cost by early fault detection. This study presents a dynamic model to analyze the dynamic characteristics of the heat pump system. Experiments were conducted by varying the operating conditions such as indoor and outdoor air temperatures, cooling load, and refrigerant charge amount. The developed model can predict the temperature variations of the condenser and evaporator and the dynamic characteristics of the system due to load change under normal or faulty operating conditions. It is expected that the control performance of the system can be enhanced, and refrigerant leakage can be quantitatively diagnosed by predicting the dynamic characteristics using developed model in this study.

Keywords: Heat Pump, Refrigerant charge amount, Dynamic characteristics, Dynamic model, Fault detection;

1. Introduction

Recent advances in variable-speed compressor opened new possibilities in improving system performance and energy efficiency. The compressor speed can be continuously changed to meet the target capacity, and the expansion valve opening is adjusted to maintain the optimized system efficiency. [1]

Various researches for capacity and optimum control of a heat pump system have been carried out. Shah et al. [2] developed a novel controller based on system identification in which a simulation model for a practical air-handling system was developed. He et al. [3] reported on the use of MIMO control of a vapor compression cycle that had multiple actuators and sensors for regulating multiple outputs. They used a low-order dynamic model of the vapor compression cycle that produced a physical meaning to model order reduction.

Faults of heat pump system can be divided into two categories; hard failures and soft failures.[4] Hard failures occur abruptly and cause the system to stop functioning such as compressor and electrical faults. These kinds of faults can be easily detected and diagnosed by electrical on/off relay and alarm signals. However, soft failure such as improper refrigerant charge is more difficult to detect and diagnose. Even though soft faults do not stop a system from working, they lead to decrease in energy efficiency and finally, a fatal failure of the system.[5]

It is required to adopt control methods considering dynamic characteristics of the system models for overall operating region. And, it is needed to develop new control algorithm, which can discriminate dynamic characteristics of heat pump system and indoor load and fault detection. In this study dynamic characteristics of heat pump system and fault detection study were carried out and performed sensitivity analysis of fault detection for improper refrigerant charge of heat pump system.

* Corresponding author. Tel.: +82-2-910-5731; fax: +82-2-910-4839.
E-mail address: yschang@kookmin.ac.kr.

2. Test apparatus and conditions

Figure 1 shows the inverter type heat pump system. Rated cooling and heating capacity of the heat pump system is 3.5 kW and 4.0 kW, respectively. The heat pump system has an outdoor unit and an indoor unit with fin-tube type heat exchangers and variable speed rotary type compressor using R410A refrigerant. Fin-tube type heat exchanger of the outdoor unit consists of wavy fin and smooth tube. Fin-tube type heat exchanger of an indoor unit is consisted of strip fin and smooth tube. Figure 2 shows schematic diagram of test equipment for the heat pump system. Heat pump system was installed in 3RT capacity of environmental chambers. 16 temperatures, 3 pressures, relative humidity and refrigerant flow rate were measured.

Table 1 shows test conditions for obtaining dynamic characteristics of the heat pump system using central composite design method. 25 test conditions were selected by varying outdoor and indoor air temperature, compressor speed and indoor fan speed.

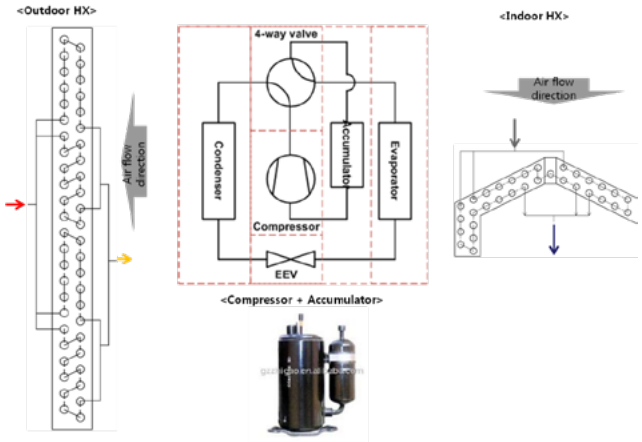


Fig. 1. Inverter type heat pump system.

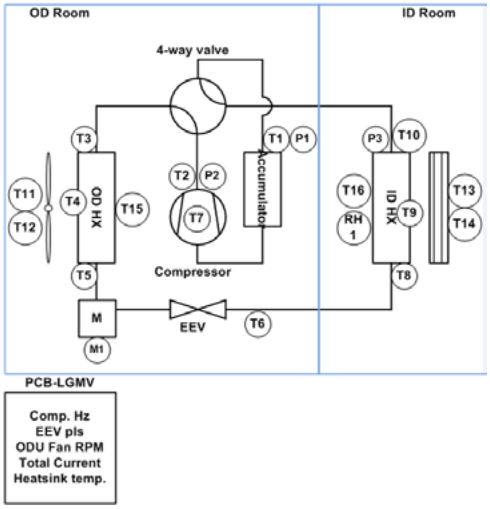


Fig. 2. Schematic diagram of the operation characteristics test equipment for the heat pump system

Table 1 Operation characteristics test condition using central composite design method

Parameter	+α	+1	0	-1	- α
OD temp. (DB/WB, ℃)	48/29	41/50%RH	35/24	28/50%RH	21/15
(ODU Fan speed (RPM))	(810)	(760)	(710)	(660)	(610)
ID temp. (DB/WB, ℃)	32/23	30/40%RH	27/19	24/40%RH	21/15
IDU Fan speed (mode)	Fast	Fast	Middle	Slow	Slow
Comp. Speed (Hz)			25 ~ 100		

Table 2 shows experimental condition for a development of fault-free reference model and for simulated fault mode of improper refrigerant charge. The rated refrigerant charge is 1000g, and the refrigerant charge is varied from 600g to 1100g at intervals of 100g and the experiment was conducted under various operation conditions.

Table 2 Experimental condition for a development of fault-free reference model

Parameter	Experimental condition
Outdoor air temperature (DB/WB)	21/15, 35/24, 48/29
Indoor air temperature (DB/WB)	21/15, 27/19, 32/23
Compressor Hz	Min~Max (5point)
Refrigerant charge	600, 700, 800, 900, 1100g

3. Development of the dynamic model of the system

In this study, the independent variable of the dynamic characteristic model is compressor speed and condensing and evaporating temperatures are considered as input variables that represent external influences on the system according to operating condition. The control variables include compressor discharge temperature, evaporating temperature, condensing temperature, and total current of heat pump system that show the effect of the system by the input variables.

Dynamic model that approximates dynamic characteristics of the system with compressor speed variation was developed using MATLAB. Figure 4 shows system response of four control variables such as compressor discharge temperature, condensing temperature, evaporating temperature and total current by compressor speed change. The dynamic characteristic of control variables was modelled and model outputs for four control variables are compared to actual responses in Fig. 4

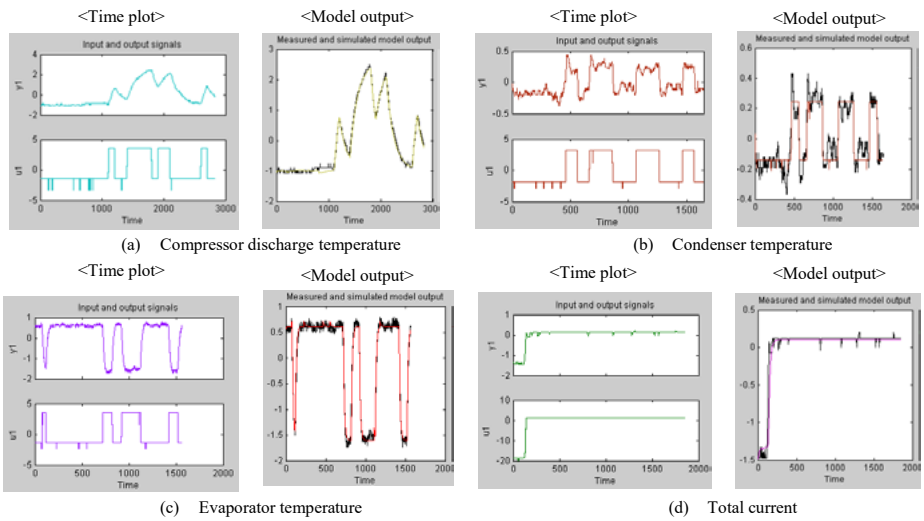


Fig. 3. Development of the dynamic characteristics model

4. Sensitivity analysis according to refrigerant charge

In this study, sensitivity analysis of fault detection was carried out with respect of fault progress. Figure 4 shows the variation of normalized distance according to refrigerant inventory of heat pump system. When refrigerant charge amount is normal, normalized distance is below 6. When fault progress increasingly, normalized distance is over 6 and built up. Fault detection using normalized distance method [6] proposed in this study predicts accurately failure mode for improper refrigerant charge.

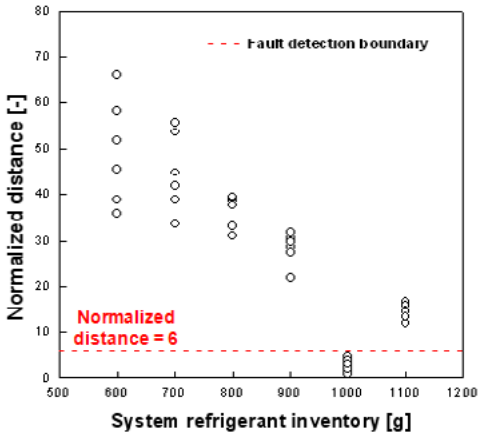


Fig. 4. Fault detection for a fault mode of refrigerant charge

5. Conclusion

In this study, a dynamic model was developed to analyze the dynamic characteristics of the heat pump system. The developed model can predict the temperature variations of the condenser and evaporator and the dynamic characteristics of the system due to load change under normal or faulty operating conditions. It is expected that the control performance of the system can be enhanced, and refrigerant leakage can be quantitatively diagnosed by predicting the dynamic characteristics using developed model.

Acknowledgements

This work was supported by the National Research Foundation of Korea (NRF) grant funded by the Korea government (MSIT) (No. 2019R1F1A1062125).

References

[1] J.W. Choi, G. Lee, and M.S. Kim, 2011, Capacity control of a heat pump system applying a fuzzy control method, Applied Thermal Engeering 31: 2332-2339.
[2] R. Shah, B.P. Rasmussen, A.G. Alleyne, 2004, Application of a multivariable adaptive control strategy to automotive air conditioning systems. International Journal of Adaptive Control and Signal Processing 18: 199-221.
[3] X. He, S. Liu, H.H. Asada, H. Itoh, 1998, Multivariable control of vapour compression system, HVAC&R Research 4: 205-240.
[4] Matthew, C. C., Braun, J. E. and Groll, E. A., 2002, A survey of common faults for chillers, ASHRAE Transaction, pp. 819-825.
[5] Katipamula, S. and Brambley, M. R., 2005, Methods for fault detection, diagnostics and prognostics for building system-a review, Part I, *HVAC&R Research*, Vol. 11, No. 1, pp. 3-25.
[6] D.W. Han, Y.S. Chang, and Y.C. Kim, 2015, Fault Symptom Analysis and Diagnosis for a Single-Effect Absorption Chiller, Korean Journal of Air-Conditioning and Refrigeration Engineering, Vol. 27, No. 11, pp. 587-595.

13th IEA Heat Pump Conference
April 26-29, 2021 Jeju, Korea

Development of AHP, the Integrated Climate System Module for EV

Dae Bok Keon[a] , Jae Chun Ryu[a], Ki Young Shin[b], Sung Je Lee[a]

, Dong Woo Hwang[a*]

[a]Hanon Systems, 95 Shinilseo-ro, Daedeok-gu, Daejeon 34325, Korea
[b]Hyundai Motor Group, 150 Hyundaiyeonguso-ro, Namyang-eup, Hwaseong-si, Gyeonggi-do 18280, Korea

Abstract

This paper presents the results of AHP (Air-controlled Heat Pump), a new concept of climate system for electric vehicle developed in order to overcome the disadvantages of conventional heat pump system to be applied to an electric vehicle for better efficiency. Unlike conventional heat pump system gets cooling and heating by change the refrigerant flow, AHP changes only the air flow path by door control to get cooling and heating functionality. The cooling performance of AHP at 45°C ambient temperature was a little better at high speed driving mode and much better at idle condition than current EV heat pump systems in spite of less power consumption. Also, heating performance at -20°C ambient was satisfied with reduction of power consumption which can achieve 15~27% EV driving range extension compared to electric heater system.

Keywords: Air-controlled Heat Pump System; Air Cooled Condenser; Water Cooled Condenser; Electric Vehicle;

1. Introduction

In recent years, market trends in automotive industry are changing to eco-friendly vehicles due to the lack of fossil fuel energy and global warming issues. The eco-friendly vehicles (Hybrid Vehicle, Plug-In-Hybrid and Battery Electric Vehicle) are being actively developed and rapidly spread out. Despite those wide spread trends, the EV(Electric Vehicle) has still remained technical issues - driving range, high cost and electric charging infra issues.[1] Among these issues, the driving range decrease caused by operating cooling and heating system in the EV cabin is the most pessimistic point to invigorate market.

The EV does not have a heating heat source from engine, unlike conventional internal combustion engine vehicles. It is common to solve the problem using a high voltage PTC electric heater. In this way, while minimizing changes in the existing air conditioning system, due to low efficiency, it has a big problem of reducing the driving range up to 50% in cold weather.[2]

Many vehicle makers and researchers on various types of heat pump system applied in a direction that compensates this non-efficiency with concept of heat recovery from ambient air or using vapor injection compression.[3-4] While the heat pump system is currently applied in vehicle products, the performance is significantly reduced in very cold (-10℃ or less) ambient conditions due to the characteristics of the R134a/R1234yf refrigerant, so it is common to correspond to the heating load with an additional high voltage PTC electric heater. Also heat pump system has frosting problem that happens in heating mode occurring system performance and driving distance decreases due to block of exterior heat exchanger. Some experimental study was conducted to solve the outside condenser frosting problem with various heat exchanger design.[5]

Another case of the heat pump system applied to vehicle products is as following; it is possible to operate the heat pump cycle at -20°C by applying a technology of utilizing the waste heat from vehicle power devices such as driving motors, inverters and so on. This technology can achieve a power reduction of

* Corresponding author. Tel.: +82-42-930-6641 ; fax: +82-42-930-6992 .
E-mail address: DHWANG@hanonsystems.com

battery more than 20% to 25% compared to the high voltage PTC heater only system. Despite the good efficiency of this heat recovery concept, system layout have to have a complex configuration of valves and piping to control the refrigerant path including additional high voltage electric heater and still have the problems caused by outside heat exchanger frosting.

In this study, we proposed an air-controlled heat pump system (AHP) concept to solve the complexity of conventional heat pump systems and improve heating performance with the feasible performance evaluation including vehicle test.

2. AHP System overview

2.1. Basic concept of AHP

There are various types of air conditioning systems for currently EV application which are shown in Fig.1. The first one, applying a high voltage PTC heater only system, has a simple configuration similar to the existing internal combustion engine vehicles. The general heat pump system, the second one, and heat recovery system from vehicle power system consist of a complex piping and a number of refrigerant path switching valves for getting advantages of heating power saving with the heat recovery from ambient air and sometimes waste heat from electric driving power system such as driving motor(s), inverter, etc.

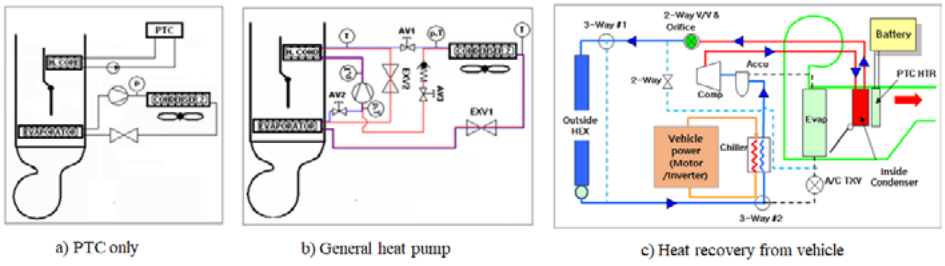


Fig. 1. Various type of electric vehicle air conditioning system

For more efficient and popular market trend, new concept of air conditioning systems for electric vehicles that can achieve weight savings by reducing the number of parts through simplifying the system configuration is required. The basic concept of the integrated air conditioning system "AHP (Air controlled Heat Pump)" developed for EV is the same as the concept of the air conditioning system since it uses hot air through the condenser as a heating heat source. Unlike the existing heat pump system changes the refrigerant flow path to implement the cooling and heating function, the refrigerant flow of AHP is always the same, while keeping the air flow into the cabin room according to the passenger's needs to implement the comfort of the cabin inside.

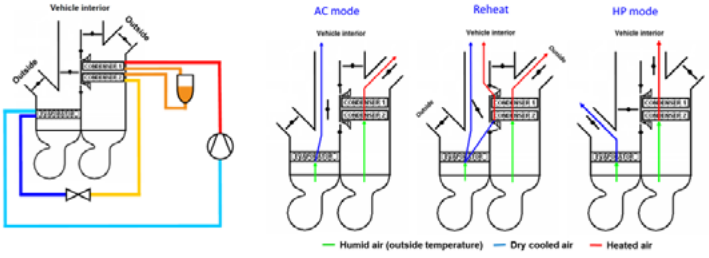


Fig. 2. Schematics and airflow path of AHP system

Fig.2 shows a schematics of AHP system and how it works. Unlike the conventional Heat Pump system as mentioned before, the refrigerant flow path is always in the same direction in cooling or heating mode. Only the airflow is changed depending on which mode user chooses. In A/C mode, cold air through evaporator goes in to the cabin room by control of door opening/closing and the warm air through the condenser is exhausted out to ambient. Vice versa in heating mode of cabin. Every valve is controlled in a HVAC system. For other mode as like dehumidifying function, it can be realized with another reheat door system.

The other word, AHP is an integrated air conditioning system by placing the condenser in one HVAC and make every function in cabin air conditioning with 1-directional and simple refrigerant system; So it can be called the integrated climate system module and is also referred to as the "Air controlled Heat Pump, AHP".

2.2. AHP system construction

For final target of this study, vehicle level performance and driving range extension evaluating, we try to apply the basic concepts of AHP system to electric vehicle. With this goal, the vehicle package and component capacity evaluating study with various type was done.

For better condensing performance and COP in A/C mode, the compact AHP model has a water-cooled condenser, while the air-cooled condenser is installed in HVAC for heating function for cabin. Fig.3 is a comparison of the AHP system in vehicle layout, and it shows the configuration of the actual system application. Depending on the location, the compressor may vary, but the overall refrigerant piping length is shorter and simpler configuration is possible.

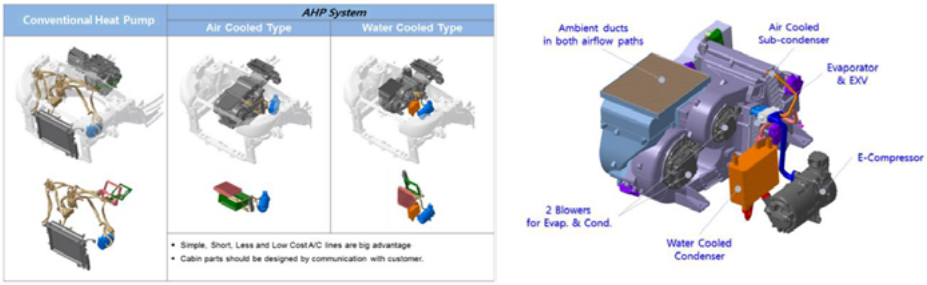


Fig. 3. AHP system construction and vehicle layout

3. Performance evaluation

3.1. Bench rig test

We did bench rig test with previously mentioned water-cooled type AHP prototype sample and evaluated it with conventional heat pump system's performance. The performance-related goals of this research were aimed at the same level of A/C performance and compressor power consumption compared to the conventional EV. The heating performance reached the same as conventional type (Cabin room average temperature 20 °C after 20minutes driving @ ambient -20°C) but the power consumption reduced as details shown in Table 1.

Table 1 Performance target of bench rig test

		Target (@-20°C Ambient)	Conventional system		AHP system
			PTC only	Heat Pump	
Average cabin room temp. (°C)		20	26.2	23.1	**Over 20**
Power consumption (kWh)	PTC heater	-	3.93	1.99	**Improve 20%**
	e-Compressor	-	0	1.07	
	Total	-	3.93	3.06	

Fig.4. shows the comparison of the test results from the bench performance evaluation at ambient temperature 45°C conditions in the cooling mode of the AHP and conventional heat pump systems. The initial

two simulated driving conditions, 50KPH and 100KPH vehicle speed, are judged to have similar cooling performance and COP. The third case, idle simulated conditions, relatively shows 15% higher cooling capacity and 30% better COP.

These evaluating results are the advantages of the system having a dual condensing, secondary air-cooled condenser of the water-cooled condenser with better sub-cool region due to characteristic configuration of AHP. In the other words, the AHP system configuration can have the advantage of being able to introduce the external air directly into the condenser not affecting heat pick-up in vehicle in-front located condenser.

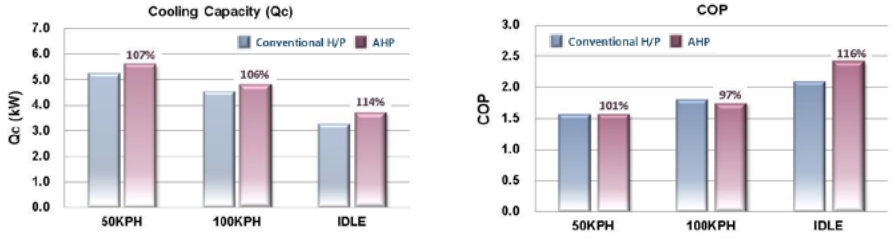


Fig. 4. Comparison of bench rig performance test

With regards to special design and construction of AHP system, this system can have the other advantage of a chance to get more heat recovery from cabin room exhausted waste heat. As is in conventional vehicle air conditioning system, there is some waste heat by extracting air process which can be recovered by recirculation to evaporator inside HVAC in heat pump mode as shown in Fig.7. The case a) conventional system already has partial recirculation logic for better heating performance, such as a certain portion of the air is recirculated to heater (or inside condenser) with fresh air from cabin outside and the remaining is extracted out to ambient. While in case of b) AHP system, some portion of extract air induced to evaporator located in HVAC and makes it possible to recover the waste heat so that refrigerant cycle works in low ambient temperature.

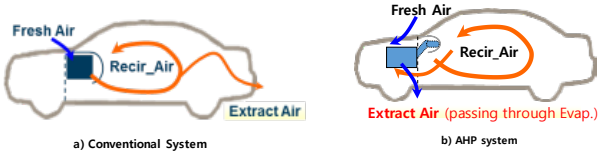


Fig. 5. Outdoor discharge air waste heat recovery in heating mode

Fig.6. shows the bench performance evaluation results of EHR (Exhaust air Heat Recovery) effect on AHP system compared to conventional heat pump system. Although conventional system has heat recovery from electric driving power system, EHR concept has better performance up to 32% and same level of COP. This effect would be more increased in low ambient temperature condition with increasing refrigerant flowrate in system.

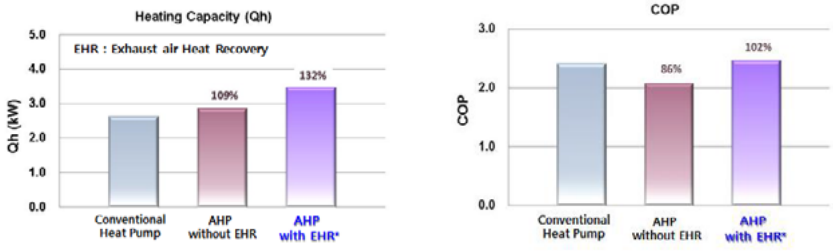


Fig. 6. Effect of EHR in bench rig heating performance test

3.2. Vehicle performance test in climate chamber

In previous section, we got the results of better performance level of AHP system in bench rig test to evaluate the effect of power consumption in real vehicle application. AHP concept sample was equipped to EV product and tested in climate chamber. Table 2. shows detailed test condition of cabin heating and cooling including performance target.

Table 2. Test condition and performance target of vehicle chamber test

	Test condition	Driving mode / Check time	Target performance ; (Cabin interior temperature)
Max cool-down	Ambient temperature : 45℃	50 KPH / 5 min.	Under 38 ℃
	Relative humidity : 40%	50 KPH / 30 min	25 ℃
	Sun load : 1,000 W/m^2	100 KPH / 60 min	22 ℃
	Vehicle full soaking	IDLE / 90min	29 ℃
Max heat-up	Ambient temperature : -20℃	50 KPH / 20 min.	Over 20 ℃
	No sun load	IDLE / 25 min	-
	Vehicle full soaking	100 KPH / 40 min	29 ℃

Fig.7. shows the results of the actual vehicle max cool-down test evaluation. In the case of AHP each temperature is satisfied with the target performance in the entire driving mode, 0.3℃ ~ 0.7℃ difference compared to the conventional system, and especially in the IDLE mode it has a dominant performance of more than 4℃. This can be seen as the advantages of the dual condensing system with water-cooled and auxiliary air-cooled condenser. Also we can consider IDLE performance is much better with less heat pick-up effect which is AHP system characteristics of no front-end located condenser. Despite this better A/C performance, its power consumption was confirmed to be 97% compared to conventional system.

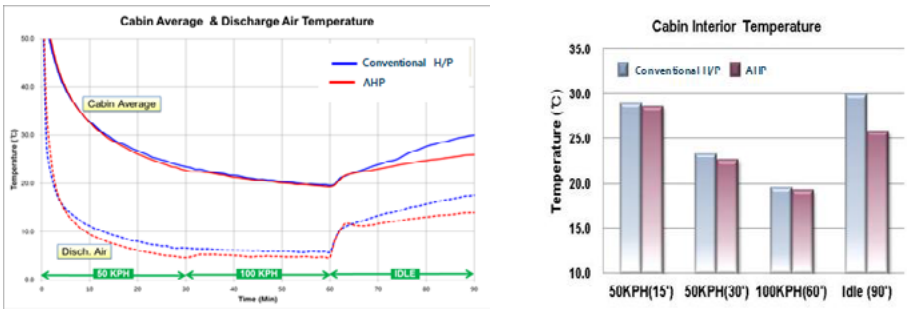


Fig. 7. Comparison of climate chamber vehicle cool-down test

As discussed, it is very serious issue that EV cabin heating requirement makes driving range decreased. For this reason, AHP system development is focused on heat pump efficiency and how to control the electric heater in initial driving mode. With EHR concept and optimized control logic of electric PTC heater operation, AHP system can get more efficiency with same cabin heating performance as shown in Fig. 8. The heating performance of AHP system meets target of average cabin temperature in driving modes and shows somewhat better discharge temperature compared to conventional H/P. In addition, the total power consumption of AHP is 2.39kWh for all the vehicle test modes which is 15% reduction from conventional H/P system power consumption of 2.8kWh. Those results can be achieved with EHR system's characteristic concept for more heat recovery that cause more refrigerant flow in low ambient temperature condition. And another contributor can be electric heater operation control that optimized usage portion in initial mode right-after vehicle start with soaking status. Fig 9. shows power consumption of e-compressor and electric heater (high voltage PTC heater) of different operation logics with regards to test time flow and driving modes.

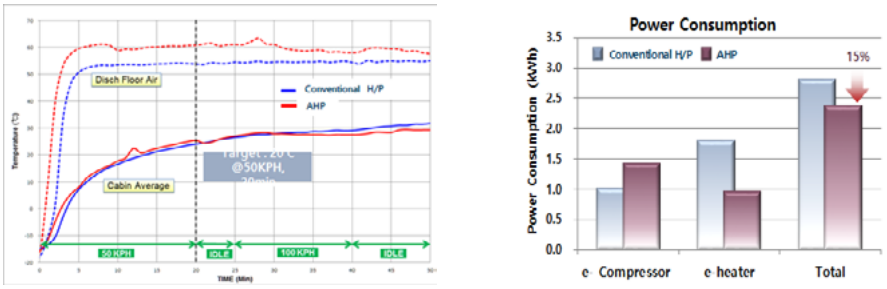


Fig. 8. Comparison of climate chamber vehicle heat-up test

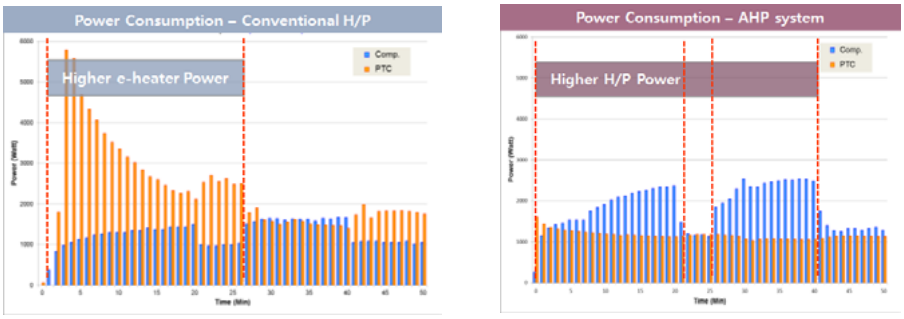


Fig. 9. Comparison of power consumption in vehicle heat-up test

3.3. Vehicle fleet test for driving range evaluation

The main target of this study is EV driving range extension effect with more efficient air conditioning system. With this purpose, we did vehicle fleet test with 3 type of air conditioning system; PTC heater only system, conventional heat pump system and AHP system. The fleet test was conducted at the same time with auto temperature setting for 3 different vehicles with each air condition system and driving range was evaluated with vehicle battery SOC measurement and power consumption calculation. Fig. 10 shows the fleet test course, ambient condition of early winter season and test vehicle status.

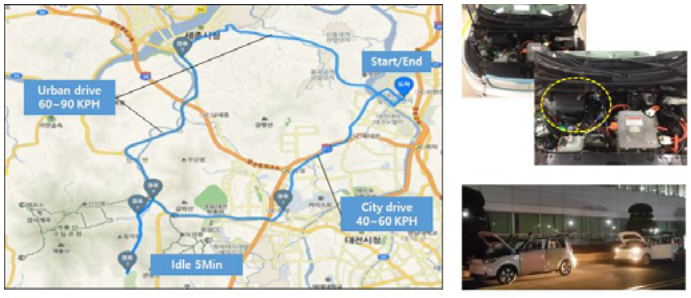
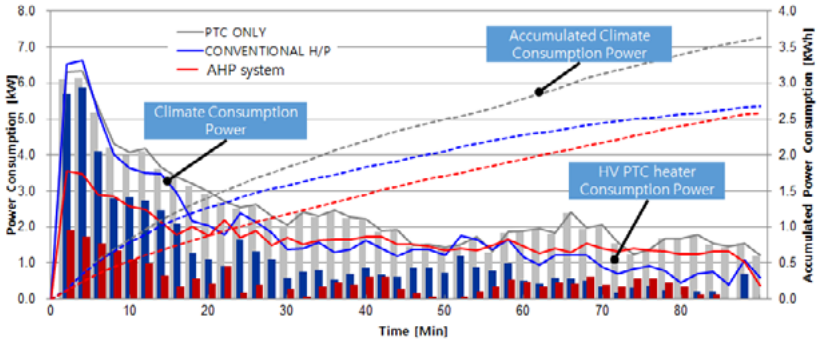


Fig. 10. Vehicle fleet test course and condition

We conducted vehicle power consumption and driving range calculation with real time battery SOC and air conditioning power measurement as shown in Fig. 11. The AHP system has 30.5% less power consumption and 27% driving range extension compared to PTC heater only system. When compared to conventional heat pump system, driving range extension effect is not much higher but this effect may become better in lower ambient condition test. Of course, cabin heating performance is at the same level in all type of vehicles but AHP system shows best performance.



Model	Accumulated Power Consumption			
	Comp.(kWh)	PTC (kWh)	Blower(kWh)	Total (kWh)
PTC ONLY	-	3.65	0.07	3.72
Conventional H/P	0.96	1.68	0.07	2.71 (-27.2%)
AHP system	1.67	0.75	0.17	2.59 (-30.5%)

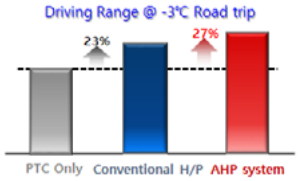


Fig. 11. Power consumption and driving range extension in vehicle fleet test

We may get more improvement in driving range extension after engine room thermal insulation, optimizing cabin room temperature control logic and fast-activated refrigerant cycle through EXV control improvement.

4. Conclusion

A new concept air conditioning system for electric vehicles is evaluated with air controlled heat pump system. In the bench rig, climate chamber vehicle and real road vehicle performance test, AHP system has better efficiency in cool-down and heat-up performance which can be a positive effect on driving range extension. Followings are the detailed conclusions.

- Through the bench rig and vehicle climate chamber test, AHP system cooling performance is better than the current heat pump system, particularly in idle performance.
- The heating performance in bench rig and vehicle test are almost same and efficiency is 3~15% higher, especially in lower ambient temperature condition. This higher efficiency of AHP system affect positively on driving range with the extension of 15~27% compared to electric heater only system.
- The improvement with more efficient component control logic and vehicle package study will be followed for future application in electric vehicle industry.

Acknowledgements

This study supported and funded from Hyundai motor company as co-development project.

References

[1] Hertzke, P., Müller, N., Schaufuss, P., Schenk, S. and Wu, T., *Expanding electricvehicle adoption despite early growing pains*, McKinsey Center for Future Mobility, Aug. 2019
[2] Christof Böttcher and Martin Konz, *The influence of heating and ACsystems on the range of battery electric vehicles*, Forschungsvereinigung Automobiltechnik, June 2011
[3] Asakura, *The RAV 4 EV and its adaptability to the Real Market*, Proc.of EVS-13, 1996
[4] Higuchi, Y., Kobayashi, H., Shan, Z., Kuwahara, M. et al., *Efficient Heat Pump System for PHEV/BEV*, SAE Technical Paper 2017-01-0188, 2017, doi:10.4271/2017-01-0188.
[5] Song, J. Y., Lim, H. Y., Shin, S.H. et al., *Study on the frost phenomenon of the exterior heat exchanger for the vehicle heat pump system in accordance with louvered fin,* Proceedings of the 3rd International Conference of Saving Energy in Refrigeration and Air-Conditioning, ICSERA2013, Oct. 2013

13th IEA Heat Pump Conference
April 26-29, 2021 Jeju, Korea

Next stop: the mass market! Heat pumps on the verge of large-scale deployment in Europe

Thomas Nowak[a]

[a]Secretary General, European Heat Pump Association AISBL, Rue d'Arlon 63-67, 1040 Brussels, Belgium

Abstract

Heat pump sales have been growing since 2013, and the last four years even showed double-digit growth. By the end of 2018, 11.8 million heat pumps were operating in Europe. Jointly they used 128 TWh of renewable energy to provide heating and reduced final energy demand by 164 TWh. Heating related CO_2 emissions declined by 33 Mt/year. The technology is now everywhere – from whitegoods via industrial processes to residential and commercial heating and cooling systems as well as in district energy systems. In applications with an energy label, heat pump-based systems score highest on energy efficiency. In some implementations, like dryers and heating, the top category can only be achieved with heat pump-based systems. Heat pumps have achieved prominent recognition not only in policy but also with scientists and researchers, many of them pointing at the importance of this technology for a decarbonised heating and cooling sector. Heat pumps are covered in the renewables, energy efficiency and building efficiency legislation. Their contribution will become even more visible, once the different planning and reporting mechanisms put in place. But is this enough? Europe has between 115 and 120 million buildings in different categories. With heating heat pumps operating in approx. 5% of the building stock, fossil fuels still provide the majority of heat. To change this, the status quo needs to be reversed – instead of 75% of gas and oil using devices, we should see the deployment of 75% of heat pumps. That means between 86 and 90 million heat pumps, none of which has yet been installed. Consequently, the current annual sales of slightly above 1 million heating heat pumps must triple, ideally overnight. The paper will explore the underlying logic, look at the market developments over the last 10 years and present policy instruments that could help to make the much-needed growth a reality
.

Keywords: heat pump;, market development; sustainable energy system; decarbonisation; Europe; Green Deal; statistics; policy

1. Status quo

The need to address climate change in a meaningful way is picking up speed. While the United Nations Climate Change Conference meets for the 25th time [1], local, national and international legislators declare "climate emergencies" [2] and the general population, led by iconic figures like Greta Thunberg ask for science based action[3], the single measure indicating in increase in global mean temperature seems unaffected.

Global primary energy demand has increased by 2,9% in 2018 and CO_2 emissions have increased by 2 %, the fastest increase since 2010 and 2007 respectively.[4] It is safe to say: "we are not on track".

2. Legislation for decarbonisation: Clean energy for all Europeans

From a European perspective, tackling climate change means decarbonising heating and cooling. This sector is responsible for approx. 50% of final energy demand and 27% of CO_2 emissions. The sector cannot be handled as lightly as it has been handled, if Europe is to become the first decarbonised continent, as recently re-iterated by the new president of the European Commission, Ursula von der Leyen at the COP25 conference.[5]

Corresponding author: Thomas Nowak. Tel.: +49 17663201140 ; fax: +32 24001018.

A first climate and energy package rolled out between 2007 and 2014 consisting of legislations and directives on

- renewable energy,
- energy efficiency,
- energy performance of buildings,
- minimum performance standards of buildings and related labelling,
- re-design of the electricity grid,
- emissions trading and the related scheme.

In addition, heat pump technologies are subject to product-based energy efficiency and labelling directives, the regulation on fluorinated gases and a number of legal provisions on the national level including those defining the requirements for support schemes and subsidies as well as those on vocational training, skills and university level education.

The European Parliament and the Council have recently passed the "Clean energy for all Europeans"-package in order to update and shape Europe's energy and climate policy until 2030 and to deliver the EU's obligations under the Paris agreement.[6]

This package acknowledges the importance of involving the individual citizen in the endeavour to make Europe carbon neutral. Thus several articles inside the eight legislative acts address the participation of this stakeholder group. The Member States now have up to two years to implement the directives into national law. The package also contributes towards the proposed Long Term Strategy (LTS) which covers the necessary measures until 2050.[7]

The clean energy package is a mix of revised and new legislation:

1. The recast renewable energy directive [8]
2. The amended energy efficiency directive [9]
3. The amended energy performance of buildings directive [10]
4. A directive and a regulation on the design of the electricity market [11]
5. A newly introduced regulation on the governance of the energy union and climate action [12]
6. A regulation on risk preparedness in the electricity sector [13]
7. A regulation establishing a European Union agency for the cooperation of energy regulators (ACER) [14]

The first four pieces of legislation listed here will directly affect the decarbonisation of heating and cooling in general, as well as the building sector [15]. Consequently, a high ambition in these areas will affect the market development of heat pumping technologies, as they are not only mentioned as technologies to use renewable energy but do contribute to energy demand reduction and are listed as one of the "high efficiency alternatives" to be considered in new construction and renovation of the building stock.[16]

The existing pieces of legislation affect the development of heat pump demand on different levels of the energy system in parallel and are expected to mutually reinforce each other (see figure 1).

1. **System level**: the focus on **energy efficiency** and the promotion of the use of **renewable energy sources** will result in a parallel reduction of energy demand and an increase in the share of renewable energy to cover it. Both directives apply to all sectors: electricity, transport and heating/cooling.
   The directives set **new targets** for the reduction of final energy demand (against a forecast value) of 32,5% and a share of 32% of renewable energy to cover that said total final energy demand. Both are to be achieved by 2030. For the first time, the renewable heating directive is giving 'cooling' more prominent recognition, allowing also renewable cooling to be counted in the renewable energy statistics. However a definition is yet to be found.

   Impact: As heat pumping technologies are contributing to the renewables and energy efficiency targets, they can expect to receive increasing political recognition and support. The importance of energy efficiency including in cooling will give additional attention to heat pumps offering a heat-recovery / cooling-recovery function to the market.
2. **Sector level:** The **energy efficiency** directive (EED) sets energy saving obligations (art. 7). Under this requirement, measures to reduce the energy demand of existing buildings can be counted (Annex V).

Impact: As the technology development has made heat pumps much more suitable to be deployed in the building stock and as their installation exceeds the status quo of building renovation, resulting savings can be counted. This fact should increase the technologies recognition as a tool to achieve the energy efficiency target of 2030.

3. **Sector level:** The **renewable energy** directive [17] sets forth a specific growth trajectory in art. 23 for the use of renewable energy in heating and cooling. Member States are encouraged to take measures to increase this share by 1,3 percentage points per year. Article 24 obliges Member States to ensure also an increased share of renewable energy in district heating and cooling grids.

   Impact: Comparing the target to the growth of renewable energy over the past 10 years shows that this sector target will have a tremendous impact if executed on the Member State level. The current growth rate needs to be nearly tripled on an annual basis which requires a broader effort in the national implementation. As the potential of heat pumps is currently underused, support and incentives for this technology will help policy makers to achieve even more ambitious targets. Large industrial heat pumps, as a relatively new segment are now manufactured in capacities of up to 35MW being able to provide temperature levels up to 160°C. Both – smaller residential and larger industrial heat pumps can be expected to move to the centre of attention as a key solution to quickly integrate significant amounts of renewable energy to the system.

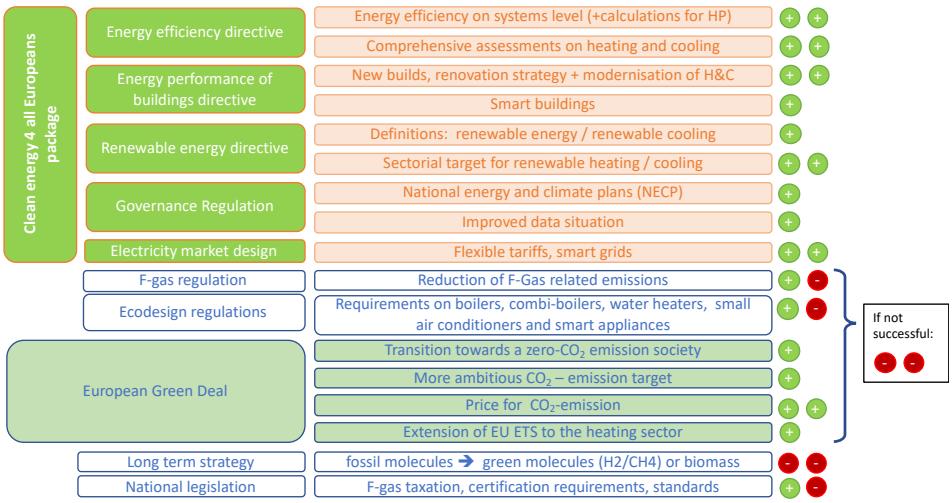


Fig. 1. Qualitative assessment of the impact of European energy and climate-based legislation on heat pump technology.

4. **Sub-system level**: the **energy performance of buildings** directive (EPBD) focussed first on new buildings. The introduced minimum efficiency targets for this building category were making near-zero energy buildings (NZEB) the standard for private (2021) and public (2019) buildings. With the introduction of the first directive in 2010 the requirement to reduce the energy demand of a building and to consider highly efficient heating and cooling solutions was established. In 2018, the amendment to the directive obliges Member States in art. 2a. to develop long-term renovation strategies that move the whole building stock – residential and non-residential, independent of ownership – to nearly zero-energy buildings.[18] These strategies were previously mentioned in art. 4 of EED and have now been moved to the EPBD to ensure a more coherent legislation.[19] Further reference is made to the provision of advisory tools (art. 20), financing solutions (art. 2a (3)), in particular for low income households and the recognition of indoor air quality, fire safety and possible impact from seismic activity.
   It is surprising, that no reference is made to adapt buildings to the possible impacts from climate change, namely the need for cooling, resistance against storms or heavy rainfall / floods.

With reference to buildings becoming active nodes in an increasingly smart electric grid (see the electricity market design directive), EPBD also requires the European Commission to develop a smart readiness indicator (art. 8 (10) and Annex I A) that should rate the ability of the building to adapt to the grid while fulfilling the needs of the occupant. This can be seen as a bridge to the electricity market design directive.

Impact: The lower the energy demand for a building the easier it is to deploy heat pumping technologies. In areas where at least some cooling demand exists, the dual functionality to provide heating and cooling makes the installation of a single heat pump also a cost-efficient solution. Where heat demand is moving towards passive house levels, a combination system to provide ventilation, heating/hot water and cooling can efficiently be provided. A concept that is found already in the market and is meant to be optimised by the joint IEA HPT/ECES annex 55/34 (also part of mission innovation #7).[20]

5. **Consumer level:** The consumer is addressed in many areas. The electricity market design directive [11] aims at ensuring affordable and transparent energy prices as well as supply security. It also defines an active consumer as a generator of energy in the market (chapter 3). Among the rights defined for the consumer is the "entitlement to a dynamic electricity price contract" (art. 11) and the right to purchase and sell electricity services independent of their supply contract (art. 13), enabling them to become active customers in the market (art. 15). The precautions taken in these articles will give a value to demand side flexibility and will enable users that can provide such services to benefit economically. In case of heat pumps and storage systems, the heating and electricity sectors will be connected (sector integration) giving the heating sector a European dimension, as it will be able to contribute to grid stability and contribute from this service in a way that helps reduce operating cost for the end user and system cost for society.

   Impact: It is expected, that this new consumer-centric market design will lead to the creation of new business models helpful to overcome the investment burden of heat pumps vs. incumbent fossil technologies and the technical uncertainty of end users, as most likely such models will be offered by service companies and or aggregators.

6. **System level**: The **governance regulation [12]** defines the cooperation between the European Union and the Member States. As Member States are free to decide on their energy policy but have to apply the related regulations and implement the different directives the governance regulation connects the European energy and climate targets to action 'on the ground'. The different planning tools in connection with monitoring and reporting allow for a better management of the energy transition and a timely evaluation of the status of the Member States and the Union in achieving the 2030 targets. The regulation introduces national energy and climate plans (NECP) to govern the 10-year planning cycle. They integrate previously separate reporting obligations on a) renewable energy, b) energy efficiency, and c) greenhouse gas emission reductions. Based on a common template, Member States of delivered draft versions of their plans covering the period from 2021 to 2030. The European Commission has reviewed these draft versions and has sent improvement suggestions which have to be implemented in the final version [21]. Similarly, the community of non-governmental organisations active in Brussels supported the assessment. Much higher ambition seems to be possible.[22]
   Member states must include their long-term renovation strategies into the NECPs and set indicative milestones and estimates on the amount of energy saved and the share of own building stock renovated (within the 3% renovation obligation).
   Beyond the buildings sector, Member States are obliged to establish Long Term Strategies (LTR, art. 15) to plan and execute necessary action to make national societies carbon neutral. The governance documents reference multiple times to the need for a multi-level dialogue between different stakeholders in order to activate civil society and achieve public acceptance. The deadlines for these plans are overlapping and should be aligned in the future.

   Impact: The NECPs and the Long-Term Renovation Strategy will improve knowledge about the energy demand in buildings and will help and encourage Member States to focus more on the need to address the decarbonisation of their societies in general making use in particular of the opportunities in the building stock. The required "evidence-based" estimates will make an improved

data basis for the building sector essential. As this is lacking today, an estimate of the impact of technology deployment is often difficult to achieve or not coherent. Thus, better building and technology statistics will make market assessments and forecast easier, an improvement that should be beneficial to all renewable heating technologies, including heat pumps.
The Long-Term Strategies create the bridge to connect Member State ambition with the Long-Term Strategy of the European Union, which aims at creating a decarbonised continent by mid-century.

In summary, the clean energy for all Europeans package establishes a multi-level framework to decarbonise society in general and the building sector in particular. Heat pump technologies will benefit, as they contribute to the renewable energy, energy efficiency and CO_2 emission reduction targets as well as providing flexibility to the grid, thus supporting its stability. The technology is readily available in volume and recent developments in research and innovation have opened industrial applications and the build environment for its deployment. From a societal perspective, most of the value chain is still local providing employment and paying taxes. Thus the technology can expect further positive recognition in the upcoming industrialisation strategy which should improve demand from end-users. What is the status of development and what needs to be done to accelerate?

3. The need for a fast acceleration of heat pump deployment

The European Heat Pump Market has grown continuously since 2012. By the end of 2018, a total of 11.8 million heat pump units have been installed in the 21 countries covered by the EHPA statistics [26]. This is a plus of 12% or 1.26 million units over 2017.

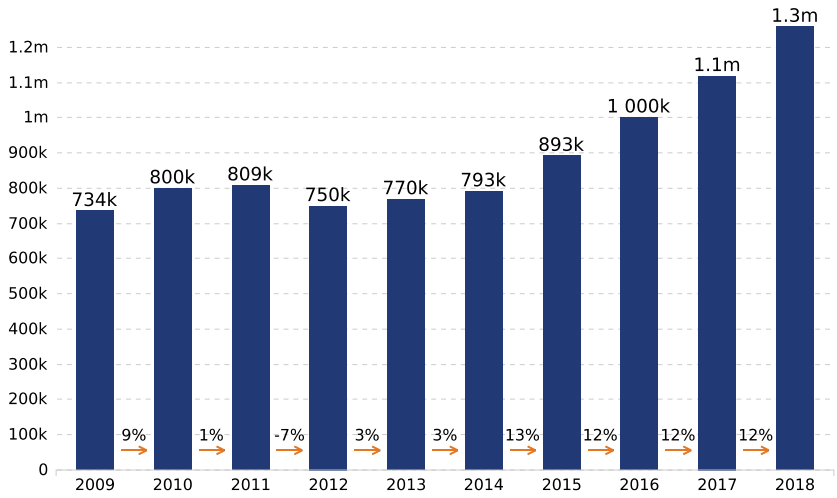


Fig. 2. Sales development of heat pumps in Europe Source: EHPA [26]

The leading markets continue to be France, Italy and Spain. Together they are responsible for more than half of the annual heat pump sales in Europe. Most remarkable – France is now close to completing an uninterrupted 10 year growth path and continues to be the engine for further growth. A recent assessment by AFPAC (Association Française pour la Pompe à Chaleur) has revealed a bullish outlook of +30% in a market that has been growing very strong in the past. Other countries are about to follow. The Netherlands has declared its aim to become "gas free" in residential heating, the UK has announced a ban of oil and gas boilers in new buildings, Ireland has put heat pumps at the centre of its efforts in decarbonizing the building stock. Even those countries that have no specific policy in place see a positive market development.

In 2018, heat pumps with a thermal capacity of 10.6 GW were installed producing approx. 20.7 TWh of useful energy and integrating 12.9 TWh of renewables in heating and cooling while avoiding 3.3 Mt of CO_2-equivalent emissions.

In order to produce the 2018 sales volume and to maintain the installed stock, a total of 68 277 man-years of employment were necessary. Obviously real employment related to the heat pump market is larger, as not all employees work full-time on heat pumps only.

In aggregated terms, the 11.80 million heat pump units sold since 1996 have an installed thermal capacity of 102.2 GW. The stock of heat pumps produces 201.5 TWh of useful energy, 128.5 TWh of which being renewable. Their use saved 164.1 TWh of final and 75.7 TWh of primary energy.

While heat pumps by now are the #1 heating technology in the new build segment of many national markets, they are also making an inroad into the renovation sector. Improved technologies and new business models help their deployment and prepare the technology for continues growth. This will be further fuelled by the implementation of the "Clean energy for all Europeans"-package as described in chapter 2 of this paper.

4. Position of heat pumps in the European heating and cooling market

In principle, heat pump technology can be used in most buildings and in many industrial processes. Precise data on these sectors is however difficult to find.

In 2019 Europe had 223 million dwellings [23]. No official figure exists on the number of buildings, but it can be estimated at around 115 and 120 million units based on the following assumptions:

1. On January 1st 2019 Europe had 513 million inhabitants [24]. With an average household size of 2,3 people, Europeans inhabit 223 million dwellings.
2. The number of single-family buildings is determined at approx. 90 million units, consequently, 207 million inhabitants live in single-family buildings.
3. The remaining 306 million inhabitants require 133 million dwellings.
4. If the typical multi-family building consists of 8 dwellings, 133 million dwellings are distributed across 16 million multi-family buildings
5. A separate statistic states that there are 10 million commercial buildings in Europe.

Europe's building stock would thus consist of 90 million single family buildings, 16 million multifamily buildings and 10 million non-residential buildings – in total approx.116 million units.

The majority of these buildings is today still being heated by fossil sources (see figure 3). A meaningful decarbonisation will require

a) the replacement of the fossil technologies with renewable heating and cooling technologies, and/or
b) the change of energy carrier from fossil to renewable sources, which may include green gases and hydrogen.

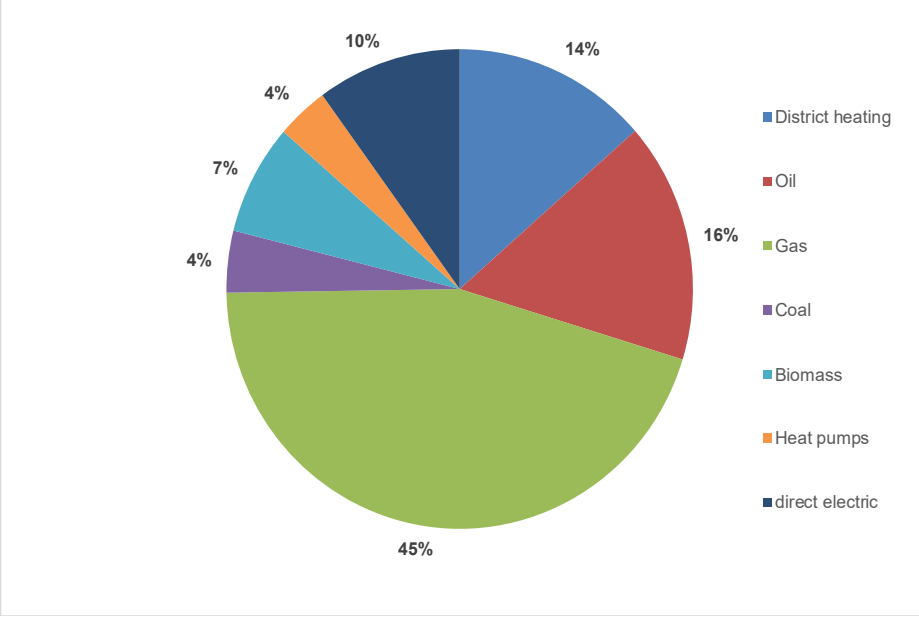


Fig. 3. Decomposition of European building stock by energy source used. Sources: Odysssee [25] and EHPA [26]

In order to evaluate the challenge a quick look the European heater market is essential. Combining data by BRG Ltd (UK) and EHPA results in an estimated market size for heaters of around 7 million units [BRG + EHPA]. This figure can be further dissected into the share of heaters installed in new build and in renovation projects as well as the number of units simply replacing existing heaters.

While this split is not part of available data, it can be deducted from a number of individual pieces of information.

- EUROCONSTRUCT estimates a rate of new construction of around 1,5% per year [29] [30]
- The renovation rate is generally reported as being too low without consistent data being available per member state. A typical figure found in the discussion is a rate around 1% [27] [28, p. 4]
  ➔ based on 116 million buildings, approx. 1,16 million buildings are renovated per year

Thus the 2018 heater market of 7,16 million units can be split into 661 400 heat pump units in new builds, and 478 600 units in renovation project and 1 743 500 other heaters being installed in new and renovation projects. The remaining 4 270 000 units are replacements of existing heaters without significant renovation of the building.

Already today, all new buildings are fit for heat pump deployment (with a very few exemptions) and this will even be truer after 2020, when all new buildings have to comply with near zero energy performance standards. Consequently, a technical market potential of around 1,8 million units in new construction can be estimated. The same argument can be made for renovation projects: All buildings undergoing moderate to deep renovation are fit for heat pump deployment (while there is no definition for deep renovation, see [32, p. 36] for a typology).

No good data exist on heat pump opportunity in the case of like-for-like boiler replacement. It is not known, in how many existing boilers could be replaced with a heat pump (which would be considered a “minor renovation”), but anecdotal evidence shows that this is also successfully happening in many projects in Europe. An “installer rule of thumb” states that a building can be efficiently be heated with a heat pump, if on some of the coldest days in the year, the user is comfortable while the radiators can be touched by hand without burning the skin. In technical terms this means a feed-in temperature to the system of around 55°C.

Assuming around half of the direct heater replacements to be possibly executed with heat pumps results in an additional potential of 2,1 million units. Figure 4 gives an overview of the last 5 years of sales development and an outlook until 2021.

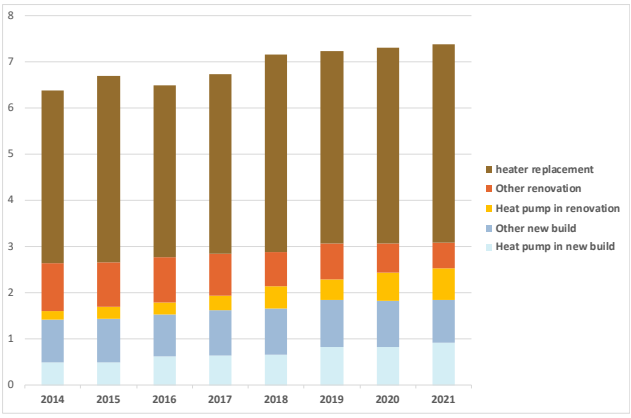


Fig. 4. The split of heat pumps in the European Heater Market (in million units).

However, these numbers are expected to increase as a result of the proposed legislation, as

- more renovated buildings create possibilities for heat pumps and
- technology development makes more heat pumps capable of efficiently providing also temperatures above 65°C.

5. Potential of heat pumps in a decarbonised European heating and cooling market

The impact assessment to the Energy performance of buildings directive estimates a necessary multiplication of today's renovation rate to min. 3% in order to significantly decarbonise the building stock. The in-depth analysis of the data on which the European Commission's long-term strategy is based expects a reduction of buildings energy demand of 48% by 2030 compared to 2015 and based on current policies. The assessment further expects a share of electrical appliances (mainly heat pumps) of 28%. [31, p. 94]

The two scenarios compatible with a 1,5°C mean temperature increase target foresee high shares of electrification in both residential and non-residential buildings. Translating the electrification share into heat pumps would result in an increase of the currently installed heat pump stock by a factor of 5 for residential buildings and about 4 – 4,5 for non-residential buildings. Based on a useful life of 20 – 25 years, all heat pumps expected to be installed in 2050 still have to be build and consequently the necessary production numbers are somewhere between 50 – 60 million units, to be manufactured and installed in the next 30 years. As production would not only have to cover new installations, but also the replacement of older units, it would require an average annual production of more than 2 million units. Compared to today's sales numbers the market would at least have to double, to fulfil this expectation.

Scientific studies looking at feasible pathways to fully decarbonize Europe's energy system similarly conclude that a high share of efficiently electrified heating and cooling is necessary. A technology specific assessment by Lappeenranta university and the energy watch group estimates the share of heat pumps in providing heat to be 44% of final energy demand. Applying this figure to today's building stock would result in 51 million units, very close to the in-depth assessment of the European Union.

Thus, the key question is: **How can the European Union and its Member States support a faster deployment?**

Over the past 10 years, the European Heat Pump market grew by 6,4% per year on average with the last four years seeing a growth of 12%. At the end of 2019, a total installed base for all heat pumps of 13 million will be reached, 12,4 million of which are expected to be heating units, the rest are hot water heat pumps. In the current very positive market environment experts expect growth to continue for the next 5 – 10 years and growth rates around 10% seem entirely feasible. This maybe pessimistic, considering that all measures of the

Clean energy for all Europeans are only currently translated into national law, thus their impact can only be expected to unleash starting in 2021.

However even if only the long-term average growth rate could be maintained, the annual heating heat pump market would arrive at approx. 2 million units around 2030, thus being able to deliver the estimated 50 – 60 million units by 2050.

An even faster growth could be achieved if not only the legal framework would be shaped more heat pump friendly, but if also the fundamental economics would be addressed and changed. The market growth over the previous years was achieved in many Member States of the European Union without significant subsidies and against an often-difficult economic framework. In particular the comparison of the cost of one unit of heat generated from fossil energy with one unit of heat provided by a heat pump shows that reveals an advantage of fossil-based heating. This disadvantage limits further heat pump deployment, as it adds an operations cost disadvantage to the still higher investment cost of heat pump technology.

The price ratio is directly affected by the taxation of the different energy carriers and thus the result of government action. The fact that in absolute terms electricity is taxed (much) higher than gas creates a disadvantage for (efficient) electric heating in the marketplace.

Against the backdrop of the need to reduce CO_2-emissions also from heating a economic disadvantage for heat pumps results from the fact that the negative environmental impacts of using fossil energy for heating are not internalised and thus are not reflected in the price of the energy carrier. Thus, heat pumps, whose main energy source is subject to the precautions of the European emission trading scheme (EU ETS), operate based on internal effects of their environmental impact, while fossil fuel boilers as the main competing technology are not subject to the same conditions. Instead, fossil heating is perceived as cheap while at the same time environmental pollution and health cost are born by society.

The heat pump industry is requesting a correction of both a) relative energy prices and b) cost of CO_2-emissions in order to be able to compete also economically with fossil heaters. It is expected that the European Green Deal, which is shortly to be presented by the European Commission, will address the need for an internalisation of external effects. Prices, taxation and subsidies must reflect the environmental impact of the respective energy carrier and in order to send the right behavioural signal to the end-user.

6. Conclusion

The outlook for heat pumps is positive for three reasons: a strong market foundation, a first legislative acceleration and an expected legislative booster.

1. The continued growth of heat pump technologies over the past decade has led to the technology representing nearly 10% Europe's heating equipment stock. This share was mainly achieved without (sometimes even despite of) government intervention. If the current growth only continued on a business as usual trajectory, heat pumps would be used in more than 1/3 of Europe's buildings by mid-century.

Fortunately, the currently implemented and the proposed legislative framework is recognizing heat pumping technologies more broadly across all sectors and functions and will thus have a re-enforcing effect on market growth, making heat pumps the dominant heating and cooling technology:

2. The clean energy for all package sets the right legislative framework for more energy efficiency and the deployment of renewable energy, leading to overall CO_2 emissions within the timeframe from 2020 to 2030. The unified reporting obligations will provide more detailed data enabling better modelling and more precise governance. The packages transposition to national law should **accelerate the development** of national heat pump markets by 2022, building on an already robust current growth path.
3. The long-term strategy has presented scenarios that make a decarbonised society by 2050 not only possible but also affordable. Its recognition of heat pumps as a robust contribution to a sustainable society will serve as a **booster to market development.** The upcoming European Green Deal is expected to also develop the necessary climate law. It is expected to include a re-assessment of the CO_2-emission reduction target, a discussion on how to apply a price on CO_2-emissions as well as additional legislation to increase ambition level in light of visible climate change.

Without doubt, the transition towards a decarbonised society is possible. In such a future, the typical answer to "what technology heats/cools your building?" or "which technology is used to run an industrial process or a district energy system" is answered simply by "a heat pump"!

References

[1] https://unfccc.int/cop25
[2] European Parliament (2019): The European Parliament declares climate emergency. Press release from 29.11.2019. Download https://www.europarl.europa.eu/news/en/press-room/20191121IPR67110/the-european-parliament-declares-climate-emergency; The climate mobilization (2019): Climate emergency campaign. Download: https://www.theclimatemobilization.org/climate-emergency-campaign.; BBC (2019): UK Parliament declares climate change emergency. Download: https://www.bbc.com/news/uk-politics-48126677
[3] Bloomberg (2019): Teen activist Greta Thunberg to World leaders: 'How Dare You!'.Download: https://www.bloomberg.com/news/articles/2019-09-23/teen-activist-greta-thunberg-to-world-leaders-how-dare-you.
[4] BP (2019): BP statistical review of world energy 2019, 68. Edition. Download: https://www.bp.com/content/dam/bp/business-sites/en/global/corporate/pdfs/energy-economics/statistical-review/bp-stats-review-2019-full-report.pdf
[5] European Commission (2019): UN Climate Conference in Madrid: President von der Leyen presents climate ambitions to world leaders. Press release 2.12.2019. Download: https://ec.europa.eu/clima/news/un-climate-conference-madrid-president-von-der-leyen-presents-climate-ambitions-world-leaders_en
[6] European Commission (2019): Clean energy for all Europeans package. 20.11.2019. Download: https://ec.europa.eu/energy/en/topics/energy-strategy-and-energy-union/clean-energy-all-europeans
[7] European Commission (2018) 2050 long term strategy. https://ec.europa.eu/clima/policies/strategies/2050_en
[8] European Commission (2018): Directive 2018/2001 on the promotion of the use of energy from renewable energy sources. OJ L 328, p82 - 209
[9] European Commission (2012): Directive 2012/27/EU on energy efficiency. OJ L 315, p. 1-56 of 14.11.2012 amended by Directive 2018/2002, OJ L328, p.210 – 230.
[10] European Commission (2010): Directive 2010/31/EU on the energy performance of buildings. OJ L 153, p. 13-35 of 18.6.2010 amended by Directive 2018/844. OJ L 156, p. 75 - 91.
[11] A directive and a regulation on the design of the electricity market
[12] European Commission (2018): Regulation on the governance of the energy union and climate action. 2018/1999. OJ L 328 p. 1 - 77. Download: https://eur-lex.europa.eu/legal-content/EN/TXT/PDF/?uri=CELEX:32018R1999&from=EN
[13] A regulation on risk preparedness in the electricity sector
[14] A regulation establishing a European Union agency for the cooperation of energy regulators (ACER)
[15] Buildings performance institute Europe (2019): Building renovation in the clean energy package: implications at the local, national and EU levels. http://bpie.eu/wp-content/uploads/2019/11/Build-Upon2_Clean-Energy-Package-National-Renovation-Strategies_Nov2019-3.pdf
[16] Article 6 of Directive 2010/31/EU on the energy performance of buildings lists "high efficiency alternative systems" such as decentral renewable energy systems, cogeneration, district heating based on renewable energy sources and heat pumps.
[17] Cf. Article 23 of Directive 2018/2001. OJ L 328, p. 123f. which mandates an increase in the share of renewable heating and cooling, as well, art. 24 of the same Directive that mandates an increase of renewable energy in district heating, most likely with a positive effect on the development of large heat pumps.
[18] Article 2a of Directive 2018/844
[19] European Commission (2012): Directive 2012/27/EU on energy efficiency. OJ L 315, p. 1-56 of 14.11.2012
[20] IEA (2019): Annex 55: Comfort and Climate box – speeding up market development for integrating heat pumps and storage packages. https://heatpumpingtechnologies.org/annex55/
[21] European Commission (2019): National energy and climate plans: draft plans, reocmmendations, assessment reports and factsheets. Download: https://ec.europa.eu/energy/en/topics/energy-strategy-and-eenergy-union/governance-energy-union/national-energy-climate-plans#content-heading-1
[22] Climate action network Europe (2019): National energy and climate plans. Download: http://www.caneurope.org/national-energy-and-climate-plans-necps
[23] Eurostat on dwellings
[24] Eurostat (2019): Population. Table demo_pjan. https://ec.europa.eu/eurostat/web/population-demography-migration-projections/data/database
[25] Odyssee database. https://www.indicators.odyssee-mure.eu/energy-efficiency-database.html
[26] EHPA (2019): European Heat Pump market and statistics report 2019. Brussels. https://www.ehpa.org/market-data/
[27] European Parliament (2016) : Boosting building renovation: what potential and value for Europe. Studie for the ITRE committee. https://www.europarl.europa.eu/RegData/etudes/STUD/2016/587326/IPOL_STU(2016)587326_EN.pdf
[28] BPIE (2017): Building renovation passports. http://bpie.eu/wp-content/uploads/2017/01/Building-Passport-Report_2nd-edition.pdf
[29] Dorffmeister, L; Kocijan, M. (Wohnungsbauaktivitäten in Europea: Neubau legt 2016 kräftig zu. https://www.ifo.de/DocDL/sd-2016-14-dorffmeister-kocijan-europaeischer-wohnungsbau-2016-07-28.pdf
[30] Dorffmeister, L. (2019): Europäische Bauwirtschaft bleibt bis 2021 auf Expansionskurs. https://www.ifo.de/DocDL/sd-2019-02-dorffmeister-bauwirtschaft-2019-01-24.pdf
[31] European Commission (2018): In-depth analysis in support of the commission communication com (2018) 773. P 115
[32] Grasset, H. ; Scoditti, E. (2019) : D4.1 EE renovation market mechanisms, trands and barriers. Report for the stunning project. Download: https://www.stunning-project.eu/fileadmin/user_upload/data_repository/WP4/D4.1_FINAL.pdf
[33] Ram M., Bogdanov D., Aghahosseini A. et al. (2019): Global Energy System based on 100% Renewable Energy – Power, Heat, Transport and Desalination Sectors. Study by Lappeenranta University of Technology and Energy Watch Group, Lappeenranta, Berlin.

13th IEA Heat Pump Conference
April 26-29, 2021 Jeju, Korea

From smarties, ice-cream and flowers

Thomas Nowak[a], Eirini Litina[b]

[a] Secretary General, European Heat Pump Association AISBL, Rue d'Arlon 63-67, 1040 Brussels, Belgium
[b] Communication manager, European Heat Pump Association AISBL, Rue d'Arlon 63-67, 1040 Brussels, Belgium

Abstract

For the longest time, heat pump technology has been presented based on its technical merits. Good for the environment (renewable heat), energy efficient, low CO2 emissions and sometimes even cost savings. But are these really the keywords that have triggered a change in opinion? The presentation will explain a different approach as charted and deployed by the European Heat Pump Association. Aiming at a positive emotional perception of the technology while trying to achieve a high level of recognition, the association has shaped a communications campaign that re-coded the benefits of heat pump technology in colours: green for renewable energy, orange for energy efficiency, blue for GHG emission reduction, red for security of supply, yellow for smart grids and purple for employment. These were then produced as chocolate candies (m&m) and packed together with a mug that said "I love HP". The backside of the mug listed the term "heat pump" in the 24 official languages of the EU plus Japanese, Mandarin and Russian. A pack of candies and a mug were sent to each member of the relevant committees in the European Parliament and to the European Commission. The paper will explain the underlying reasoning and execution of this communication campaign over the last four years and aims at encouraging new approaches of heat pump lobbying.
.
Keywords: Public affairs; communication; emotional approach; heat pumps; energy transition

1. From facts to fiction: a new narrative for heat pump related communication

Over the past 20 years, heat pump technology has arrived in the marketplace in Europe. Positioning was not equally successful in the different member states. Obstacles that had to be overcome ranged and range from general understanding, terminology, connectivity of information to the knowledge level of the target groups to doubts and outrights rejection of technical details.

Corresponding author: Thomas Nowak. Tel.: +49 17663201140 ; fax: +32 24001018.

Table 1 Heat pump-myth levels to be overcome by communication

General	Conceptual	Technical
What is a heat pump?	Heat pumps are not using renewable energy. They are just an energy efficiency technology.	Which temperature levels can a heat pump provide?
How does a heat pump work?	Heat pumps are not increasing energy efficiency. Certainly not on a primary energy basis!	Can heat pumps efficiently be employed in the build environment?
Why is it called heat pump if it can also cool?	Heat pumps are only a marketing tool to push for higher electricity sales!	Can heat pumps provide the high temperature levels needed in industrial applications?
How can a heat pump work at temperatures below 0°C?	Heat pumps compete with district heating!	Heat pumps cannot provide the high temperatures and capacities needed in district heating.
Electricity is too valuable to be used for heating!	Can a heat pump really provide heating and cooling? Why is it called a heat pump then?	
Will large heat pump deployment not lead to black outs?		
Heat pumps are too expensive. They are not affordable, in particular for low-income households.		

Around the year 2000, heat pumps were a niche technology in the European heating market hardly recognized by policy makers. Even though a 1997 white paper by the European Commission [1] considers contributions from biomass, hydro power, wind energy, solar thermal, photovoltaics, passive solar and geothermal and geothermal heat pumps to be relevant, the authors expected a number of 180 000 units to be installed in the EU-15 countries by 2010. Using energy from ambient air and water resources was not considered renewable. The reality surpassed the study with 800 000 heat pump units installed in 2010, 116 000 of which using geothermal energy.[2]

In this first phase of communication the main focus was on

a. explaining the working principle of the technology
b. application examples – which were mainly showcasing the use of heat pumps in new buildings
c. highlighting the fact that heat pumps could also use air, water and (later) waste-water.
d. Highlighting that heat pumps provide heating and cooling at the same time.

The main target group where the European Commission, members of the European Parliament and representatives of the Council. Convincing them was not easy, as scepticism against the technology was widespread, often based on national perceptions and the respective political orientation. Members of the Green party, particularly those from Germany, rejected heat pumps as a tool to increase electrification of heat and thus to facilitate new nuclear power generation facilities.

A second line of argument was focussing on the difference between primary and final energy. While the energy efficiency and energy services directive [3] suggested a conversion factor of 2,5 (an average efficiency of thermal powerplants of 40%), this value was often questioned as being too low. In combination with the doubt of the true efficiency of heat pumps the technology was deemed less efficient than the direct combustion of fossil energy. Rejection of heat pump technology was based on the argument, that the technology would have to be added to the existing load of the grid and would thus result in switching additional generation capacity, usually dirty, hard and brown coal (pollution from marginal emissions).

A third argument applied on the technical feasibility of heat pumps in providing heat and hot water to the build environment. It was argued, that the supply temperatures of heat pumps were not sufficient to heat buildings efficiently and thus a heat pump was just a direct electric heater in disguise. This argument was originally applied to all heat pumps. Later it was modified by accepting geothermal heat pumps in new buildings and it took until 2009 for policy makers to agree to and decide that all heat pumps are in principle

feasible to heat buildings. Even today, after more than 10 years of fast track technology development and despite many successful examples it is still questioned whether heat pump technology can be deployed in the existing building stock or in industrial processes.

As a latest area of scepticism, it is now argued, that the electric grid is not fit to accommodate a much larger share of heat pumps and their deployment will endanger black-outs.

From 2007 to 2009 communication efforts were entirely based on facts focusing on a change of perspective with regards to these arguments. It was continuously argued that the heat pump technology worked, often using the example of developed markets like Sweden, Norway and Switzerland and in which not only air was successfully used as energy source, but also these markets had a significant share of heat pump deployment in renovation and in multi-family buildings.

Eventually the so-called Renewables Directive [4] acknowledged aerothermal, hydrothermal and geothermal energy in its definitions (article 2), to be used by heat pump technology. Besides officially stating that heat pump technology uses renewable energy sources, it also set down the need for educated installers and prescribed a calculation method for renewable energy generation by heat pumps. The Directive was a huge leap forward, as it established a legal basis and a reference point for policy makers and administrators.

In the following years, communication efforts focussed on the technical details of

- The energy performance of buildings [5],
- Improving energy efficiency of the whole energy system [6]
- Implementing measures of the Ecodesign Directive [7] and the energy label [8] for boilers
- The regulation on the use of fluorinated gases. [9]

The underlying discussions where mainly led by experts and where often backed by scientific justification of the different claims and by studies elaborating on the impact of each measure on the market. From an industry perspective a typical communication would start by highlighting the benefit of the technology towards the aims followed by the different pieces of legislation and the targets put forward.

EHPA established such fact-based communication by connecting claims to its statistics and enhancing sales numbers by calculating the renewables contribution of all heat pumps, the energy savings of their deployment and the related CO_2-reduction.

After the implementation of the Ecodesign requirements on boilers and the energy label the association realised that the communication needed to change – in order to achieve a more widespread impact, decision makers would need to consider heat pump technology as a solution that they needed to recognize in order to shape a favourable legislative framework.

2. A stakeholders heart is through its stomach

While the early years of heat pump related communication focused on the technical facts stressing its contribution potential towards Europe's climate and energy targets, they were not able to overcome a "feeling based" and sometimes deep-rooted scepticism against the technology. Stating the obvious seemed never to be good enough.

Thus, inside the association, new communications approaches were deemed necessary to create a fundamentally positive perception of the technology even with hesitating stakeholders. Likewise, it was clear that a shift was needed from fact based to more emotional communication. As the association did not want to risk its reputation as a reliable source of information, all considerations circled around "saying the same, just different" [9].

A multi-annual campaign was crafted based on this new approach. It used an emotional approach wrapping the factual benefits of heat pump technologies into a layer of emotion and executing this approach from different angles, using the effects of repetition and recognition to create anchor points for positive acknowledgement.

As the campaign consisted of different phases, a cut-off would have been possible between the different phases in case of failure.

Table 2 Facts presented and emotional layer used to change the perception of heat pump technology

Campaign phase	Fact layer	Emotional layer	Main target group
Chocolate and coffee	Renewables Energy efficiency CO_2 emission reduction	Tastiness of chocolate and coffee	Members of the European Parliament and the Commission active in the field of energy / heating.
It's cool to like heat pumps	Supply security Smart grids	Tastiness and comfort of ice-cream	Larger group of stakeholders in the energy transition
Plan(t) for the future	Local employment	Planning for a nice, flowery garden	Cities mayors and energy consultants

The different campaign phases addressed a range of stakeholders starting with members of the European Parliament (MEPs), continuing via a wider audience interested in EU sustainable energy issues (Sustainable Energy Week), concluding with a focus on EU mayors. Representatives of the EU Commission and the Council were also targeted in the action. Our goal was to make heat pumps appealing on the emotional level, to make them easy to like, and their advantages to be remembered.

This approach was executed via

- chocolate and coffee,
- ice cream, and
- flowers.

The main contribution of heat pumps to the EU climate and energy targets were colour coded and repeated in all campaign phases.

These six advantages of heat pump technologies were highlighted and promoted:

- GHG emission reduction (blue as in "blue skies")
- Renewable Energy (green)
- Energy Efficiency (orange)
- Energy Security (red)
- Creation of local jobs (purple)
- Smart grids (yellow)

Starting in 2014 every year a different communication angle was chosen. The message was transported via chocolate candies presented together with the "I love HP"-coffee mug (2014), via ice cream flavours (2015, 2017 and 2018) eventually via tulip bulbs (2017).

2.1. Chocolate candies and "I love HP"-mug

In 2014 we created the basic concept of the campaign and its first phase. The decision on the initial colour coding of heat pump technology benefits was taken. They were applied in white type to chocolate lentils (similar to the well-known M&M brand (Mars Inc)) and packed into a transparent box.



Fig. 1. Benefits of heat pumps presented via chocolate candies

How often have you asked people to discuss something "over a coffee/tea"? Connecting heat pump benefits to the prevailing habit of having a hot drink and some sweets resulted in the creation of a mug that stated "I love HP*" similar to the "I love NY" meme, adding an asterisk (*) explaining that "HP stands for heat pump". On the back of that mug we printed the word heat pump in several European languages to enable an easy recognition for members of the target group from different language background.



Fig. 2. "I love HP"-mug

As support and explanation, we asked our designers to design a postcard that pictured the six candy colours in a very reduced visual design explained each benefit in a few words. The motto of the postcard was "It's easy to like heat pumps". But the postcard not only explained the technologies, but also

a) asked recipients for testimonials on their own experience with heat pumps,
b) offered recipients to request more information,
c) invited them to contact us by email, to follow us on twitter or to participate in our annual Forum

Finally, we packaged 1) a box of candies, 2) the postcard and 3) the mug and sent it to all members of the ITRE and ENVI Committees of the European Parliament. In order to avoid any conflict of interest, the recipients were informed about the value of the package (less than 10 €).[10]

In a second communication round, we sent the postcard as PDF by mail to all MEPs and informed them, that those that would return the mail, would receive a mug and a box of candies in the mail as well.

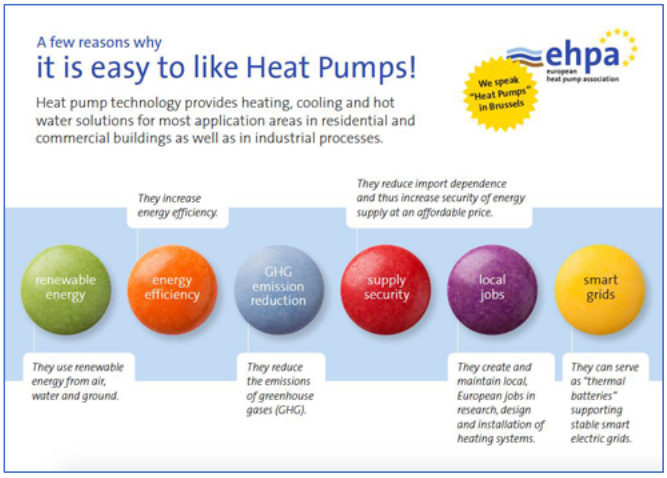


Fig. 3. “It’s easy to like heat pumps”-postcard

Evaluation:

This first campaign phase proved very successful. On the one hand we received very positive feedback in writing, on the other hand MEPs that we visited and talked to throughout the year remembered the mug and the chocolate. Many of them had the mug still on the tables in their offices. Even today can we point to this activity and people recognize us as “the heat pump guys that sent the nice mug and the smarties”.

2.2. Adding cooling: from energy stakeholders to EU policy makers at EUSEW

Based on the successful first phase, it was decided not only to continue to phase II, but also to change the target group. Looking for a different angle, we decided to stress the dual provision of heating and cooling via a heat pump and as it was summer and one of our events took place during the European Sustainable Energy Week (EUSEW) [11], **ice cream** was chosen as the transport medium of the message.

Looking at the first phase of the campaign, we decided to stick with the explanatory format and asked our designers to design a postcard that would picture six ice cream scoops in different colours, again showing each benefit in different colours.

We searched for and found an ice cream company that not only agreed to manufacture the ice cream for us, but also to come with a typical sales booth and to hand out the ice cream. Due to production limitations, we had to adjust the selected colours slightly:

- Vanilla = smart grids
- Pistachio = renewable energy
- Chocolate = GHG emissions
- Red fruit sorbet = energy security
- Lemon sorbet = energy efficiency
- Blueberry = local jobs



Fig. 4. Explanatory postcard: "It's tasty to like heat pumps"

Participants were then invited to use these titles when ordering an ice cream. This created a lot of laughter, when ie. the Director of the General Directorate for energy (DG ENER ordered) "one scoop of renewables and one scoop of smart grid".



Fig. 5. The ice cream booth at EUSEW 2017

In the second and third year, we slightly modified the text on the postcard. Cooling had entered the political agenda and we thought it to be a smart idea to enhance the focus of the campaign from "heating" to "cooling", continuously highlighting the fact that heat pumps provide heating and cooling at the same time.

Evaluation

This idea is still remembered in Brussels lobby circles. The impact was of such a nature, that the organizers of EUSEW asked us to repeat the activity in the years 2017, 2018 and 2019 as it was reported to them as a great success by participants and session organizers. From 2017 onwards, the booth was set up prominently in the lunch area of the Residence Palace (one of the two central event locations of EUSEW) and we handed out more than 600 scoops of ice-cream in each year, with even more people recognizing the activity.

2.3. Flower Campaign: Plan(t) now for the future!" – targeting EU Mayors

At the end of 2015 we started the preparation for the 3rd phase of the campaign. As we had identified cities as important actors of the energy transition, we did some brainstorming on what measure would resonate with city majors. We agreed, that a main characteristic of a city government is long term perspective, in particular for spatial planning and that this resonated well with planting. But how could we connect this idea to our colour scheme? We considered different plants and vegetables but either the execution was too complicated, too costly or the plant would not be available in the colours that we wanted. In fact, this proofed to be the most stringent restriction. And then we turned to tulips and came up with the idea to package 6 tulip bulbs in a nicely designed box and to send them to Mayors of EU capital cities as well as cities that have been using green solutions in transport, energy, etc.

While preparing the third phase of the campaign took longer than expected, we received very positive feedback for the ice cream idea and were invited back to the Sustainable Energy Week to offer the ice cream both to a wider audience in a more prominent location.



Fig. 6. The box with 6 tulip bulbs

In order to finalise the visuals, we asked our graphic designers to illustrate and to explain the campaign with a postcard using the headline "Plan(t) now for the future!". On the backside of the postcard we invited mayors to contact us if they required more information on what heat pumps could contribute to sustainable cities and to send us pictures of the tulips as soon as they bloomed.

Evaluation

In fall 2017, we sent batch of 50 boxes of tulips to the majors of the capitals of Europe and some additional cities that we had been pointed to as particularly active and ambitious in the attempt to green their cities. Not only did we receive 4 invitations to have meetings with the energy departments (London, Madrid, Riga, Budapest), but after 6 months we also received photos of blooming tulips. One package was given to Park Won Soon, Mayor of Seoul and then also president of ICLEI, who later sent his appreciation to the idea by mail.

The idea of the campaign was multiplied by some of our national heat pump associations who translated the postcard and sent the tulips to cities in their own country.

3. Impact of the campaign on the association and its lobbying strategy

The European Heat Pump Association considers the campaign a full success. It increased the recognition of heat pump technology and of the association with the designated stakeholders. It was perceived as innovative and fun, opening a communication channel to also talk about the details of technology.

While each phase could have stood by itself, the connection via the colour coding and their slight modification each year have resulted in very positive recognition and continuity reducing the effort needed to execute.

From a cost perspective, the investment in the campaign was comparatively small, costing less than 10 000 € over the first four years but the material is still used at various occasions helping us to illustrate the benefits of heat pumps in a creative and colourful way in the ongoing discussions with different stakeholders.

The overall result is even better than expected:

- Several Members of the European Parliament (MEPs) confirmed that they have been using the "I Love Heat Pump" mugs and we receive this feedback even today, after 5 years. Just recently, a member of the Commission stated, that the Mug had been "stolen" from him and he would appreciate a new one.
- The idea of the mug is so well received, that now a Chinese, German, Finnish and Slovak versions exist; done by the national heat pump associations respectively. For the next version on the EU level, we will add the term heat pump also in Kyrilic as well as Chinese and Japanese Kangxi. The ice cream campaign at EUSEW is now a classic and participants enjoy ice cream while getting to know the benefits of heat pumps, also understanding that heat pumps provide heating and cooling. For the next edition, an extension to two days is planned.
- The flower campaign has been picked up by 3 National Heat Pump Associations (Austrian, Finnish and Slovak) which approached their target groups with the same concept and motto. In addition, we managed to book 4 meetings with 4 mayors and their energy experts who wanted to discuss further about heat pump applications in cities.
- EHPA is recognized as an association that does not only do lobbying but does it with a fresh approach. This has resonated very well with existing members but has also attracted new members.
- The campaigns have helped the secretariat of the association to establish itself as a creative, forward thinking group of people using innovative yet very cost-efficient approaches to promote the interest of its members.

In 2019 the association was awarded the European associations award in gold in the category "Best associations communications campaign". [12]

The campaign has added a new dimension to heat pump lobbying. Using an emotion-based communication approach it combines technical advantages of the technology with human attributes creating a positive technology perception on a personal level. Attributes like "tasty" and "cozy" (see chocolate, coffee, flowers) were connected to heat pump technology making it easier to remember its benefits (see our selected motto in the postcard "it's easy to like heat pumps"). The importance of planning for the future in the context of creating a decarbonized society was stressed via the flower campaign.

The campaign proved that emotional-based communication does not contradict fact-based communication. Instead it strengthens the argument by using a human dimension to transmit complicated facts.

As a result, the association uses the new approach to deliver its messages to its target groups. We have moved to employing more advanced techniques to raise further awareness of the technology and it's multiple benefits.

Most recently we have deployed the "party heat pump", a device making the cooling and heating dimension of carnot-cycle technology directly tangible. Using the cold part to cool drinks and the hot part to heat sausages (vegetarian and meat based) allowed the discussion on the functioning principle in a comfortable and relaxed atmosphere.

Acknowledgements

The five years of work on this campaign were a real team effort. We would like to express many thanks to Pieter-Jan Cluyse, who helped to bring the original idea to life in a conference room in Stockholm, our design agency Ebmeyer and Ebmeyer from Munich (http://www.2-se.de), who brought our ideas to life and delivered

clear and direct communication tools, the team at EHPA under guidance of Eirini Litina who executed the campaigns with a meticulous eye for detail as well as the rest of the EHPA team and the different communications interns that helped us spread the word. Last, we would like to thank the board of the association for giving us the freedom to experiment with new formats and develop ideas like the ones presented here.

References

[1] European Commission (1997): Communication from the Commission Energy for the future: Renewable sources of energy (COM(97)599 final (26/11/1997). Download at: https://europa.eu/documents/comm/white_papers/pdf/com97_599_en.pdf
[2] European Heat Pump Association (2019):
[3] European Commisison (2006): Directive 2006/32/EC on energy end-use efficiency and energy services and repealing Council Direcitve 93/76/EEC. OJ L 114 p. 64-85 of 27.4.2006. Download at: https://eur-lex.europa.eu/legal-content/EN/TXT/PDF/?uri=CELEX:32006L0032&from=EN
[4] European Commission (2009): Directive 2009/28/EC on the promotion of the use of energy from renewable sources. OJ L 140, p. 16-62 of 5.6.2009
[5] European Commission (2010): Directive 2010/31/EU on the energy performance of buildings. OJ L 153, p. 13-35 of 18.6.2010.
[6] European Commission (2012): Directive 2012/27/EU on energy efficiency. OJ L 315, p. 1-56 of 14.11.2012.
[7] European Commission (2009): Directive 2009/125/EC establishing a framework for the setting of ecodesign requirements for energy-related products (recast). OJ L 285, p. 10-35 of 31.10.2009.
[8] European Commission (2010): Directive 2010/30/EU on the indication by labelling and standard product information of the consumption of energy and other resources by energy-related products OJ L153, p. 1-21 of 18.6.2010.
[9] European Commission (2014): Regulation 517/2014 on fluorinated greenhouse gases and repealing Regulation (EC) No 842/2006F-gas. OJ L 150, p 195 – 230 of 20.5.2014.
[10] This idea was inspired by the campaign “the power of words” by UK based agency purplefeather ltd. https://youtu.be/Hzgzim5m7oU. Downloaded 20.11.2019.
[11] The “code of conduct for Members of the European Parliament with respect to financial interests and conflicts of interest” finds a gift value of less than 150€ to be not compromising the independence of a Member of the Parliament: https://www.europarl.europa.eu/pdf/meps/201305_Code_of_conduct_EN.pdf. The same limit is set by the European Commission in article 6 (4) of the commission decision of 31.1.2018 on a Code of conduct for the members of the European Commission (2018/C 65/06). Download at https://ec.europa.eu/info/about-european-commission/service-standards-and-principles/ethics-and-good-administration/commissioners-and-ethics/code-conduct-members-european-commission_en on 20.11.2019.
[12] https://eusew.eu/
[13] https://europeanassociationawards.com/winners/

13th IEA Heat Pump Conference
April 26-29, 2021 Jeju, Korea

Research on Energy Saving Calculation Combining Load of Air Conditioner and Load of Refrigerated Display Case in a Grocery store

Miwako FUJITA[a,b*], Daisuke NARUMI[a]

[a]Graduate School of Environment and Information Sciences, Yokohama National University,
79-7 Tokiwadai, Hodogaya-ku, Yokohama, 240-8501, Japan
[b]Chubu Electric Power Co.,Inc., 20-1, Kitasekiyama, Midori-ku, Nagoya, Aichi, 459-8522, Japan

Abstract

In this study, the relationship between the enthalpy characteristics and the refrigeration characteristics of five typical refrigerated display cases in a grocery store were clarified by experiments. Based on the results, we devised a method to calculate the energy saving amount considering the interaction between the load of space conditioning and the load of refrigerated display case. Lower the store temperature by space-conditioning has the effect of reducing the total power consumption of refrigeration and space-conditioning, but it has been found that the store temperature needs to be lowered to 22 ℃ or below. Under the same store temperature and humidity conditions, the energy saving effect is greater at a low outside air temperature than at a high outside air temperature. It is important to control the space conditioning and shift the load of display cases to the load of space conditioning in early summer and early autumn.

Keywords: Grocery store, Space conditioning, Refrigerated display case, Energy saving

1. Introduction

From changes in Japan's final energy consumption, the overall increase rate from 1973 to 2013 was 1.2 times, but the increase in business divisions wahot.4 times, so that energy saving is required [1]. Manufacturers are actively developing energy-saving equipment for space-conditioning and lighting, which are typical energy-consuming equipment for business use. On the other hand, refrigeration equipment with a high energy consumption density is exposed to cost competition in the food store industry, so that energy-saving equipment is slow to spread. Therefore, it is important to save energy by devising operation and design.

From the advantage of easy to get products, many open display cases are installed in food stores. The open display case maintains the internal temperature with the air curtain, but from a part of the air curtain cold air in the refrigerator leaks from the display case and the surrounding air enters the display case. Leaked cold air stays in the lower part of the store, affects the air enthalpy in the store and worsens comfort. At the same time, air enthalpy entering display case affects the display case refrigeration load. For these reasons, the load of the open type display case interacts with the space conditioning load, making it difficult to consider energy saving.

There have been many reports on energy conservation in food stores [2]. Narumi created a prediction formula from the store's actual measurement data and calculated the energy saving effect when the display case type was changed or when the store's environmental temperature was changed [3]. Nakayama has reported the energy-saving effect of stores when the operation of space conditioning with high COP is increased by measuring food stores [4]. CFD analysis is effective to examine the effects of space conditioning and ventilation on store energy savings in detail [5], on the other hand the CFD analysis's cost is high, it is also important to develop the method that can be easily calculated.

In this report, the relationship between enthalpy characteristics and refrigeration characteristics of five typical refrigerated display cases in a grocery store was clarified through experiments. Based on the results, an

*Corresponding author. Tel.: +81-52-621-6101; fax: +81-52-624-9234.
E-mail address: Fujita.Miwako@chuden.co.jp.

energy saving calculation method was devised that takes into account the interaction between the space conditioning load and the refrigeration load. Using the devised method, the summer energy calculation was performed on a store model with a total floor of 2127m^2.

2. Outline of space conditioning and refrigeration energy calculation

Since display case power consumption is greatly affected by environmental enthalpy, it is important to adjust the enthalpy in the store by space conditioning and ventilation. Combining with space-conditioning load calculation and display case load calculation (refrigeration load regression formula), we calculated annual space-conditioning and display case power consumption at food stores. Figure 1 shows the calculation flow.

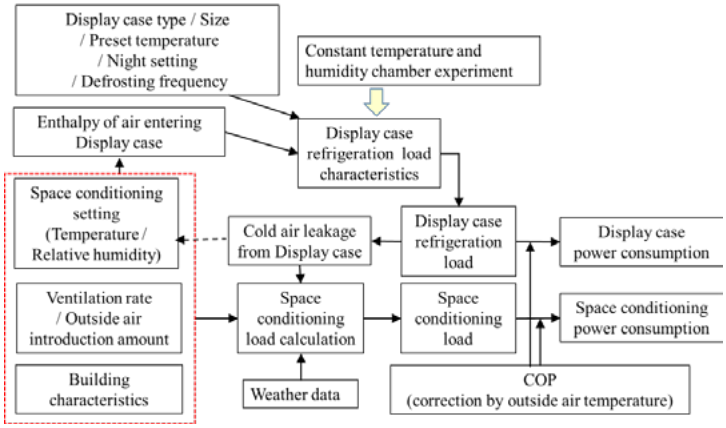


Fig.1. Calculation method of power consumption required for space conditioning and refrigeration

3. Energy consumption calculation for refrigeration

3.1. Energy consumption calculation for refrigeration

The display case refrigeration load characteristics were measured at constant temperature and humidity in the laboratory. There are two types of refrigerated temperature zones (multi-deck (MD (RE)) and semi-multi-deck (SMD (RE))) and three types of freezing temperature zones (multi-deck (MD (FR)) and flat tub (TUB (FR)) and glass door attachment (RI (FR))). Table 1 shows the outline of display case specifications, and Table 2 shows the specifications of refrigeration machines.

Table 1 Specification of the display cases refrigeration systems

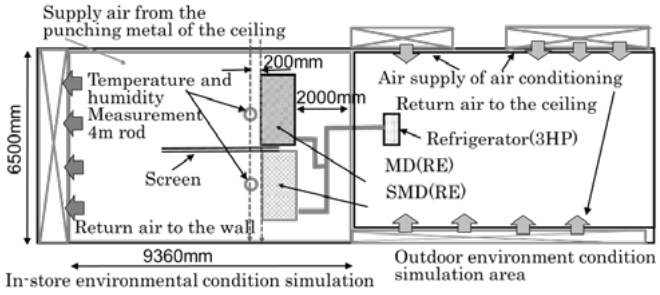
TYPE※1	MD(RE)	SMD(RE)	MD(FR)	TUB(FR)	RI(FR)
Operating Temperature (℃)	-2～2	-2～2	-20～-18	-20～-18	-20～-18
Effective Unobstructed Capacity(L)	1940	1477	1507	1180	1077
Outside Dimension(mm)	W 2440 H 1890 D1100	W 2440 H 1700 D1100	W 2440 H 1880 D1100	W2440 H810 D1810	W1430 H1905 D760
Required Refrigerating Capacity(kW)	2.22	3.04	3.75	1.84/1.47	0.6/0.5
Evaporating Temperature (℃)	-10	-10	-40	-40	-40
Defrosting Method	Off cycle	Off cycle	Heater	Heater	Heater

※1 MD(RE): an open refrigerated multi-deck display case SMD(RE): an open refrigerated semi multi-deck display case
MD(FR): a frozen multi-deck display case TUB(FR): a frozen tub display case
RI(FR): a frozen glass door reach-in display case

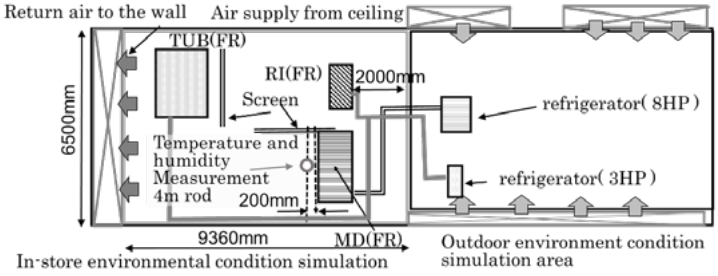
Table 2 Specification of refrigerator (Outdoor Environment: Temperature: 32 ºC Relative Humidity: 40%)

Items	refrigeration machine (3 HP)	efrigeration machine (8 HP
Working refrigerant	R410a	R410a
Evaporating Temperature (ºC)	-10	-40
Freezing capacity (kW)	7.77	6.70
Power consumption (kW)	3.5	6.5

MD (RE) and SMD (RE) were combined with a refrigeration machine (3HP), MD (FR) was combined with a refrigeration machine (8HP), and TUB (FR) and RI (FR) were combined with a refrigeration machine (3HP). The experimental equipment layout is shown in Figure 2, and the measurement items are shown in Table 3. For display case in the refrigerated temperature zone, the refrigeration load (total heat) was obtained from the sensible heat of the circulating air and the amount of drain discharged. For the freezing temperature zone display case, the refrigeration load was determined from the refrigerant enthalpy difference before and after the evaporator and the refrigerant flow rate.



(a) Experimental apparatus for refrigerated display case



(b) Experimental apparatus for frozen display case

MD(RE): an open refrigerated multi-deck display case
SMD(RE): an open refrigerated semi multi-deck display case MD(FR): a frozen multi-deck display case
TUB(FR): a frozen tub display case RI(FR): a frozen glass door reach-in display case

Fig.2 Layout of experimental equipment

Table 3 Measurement item and implementation method

Items	Measuring Location and method
Power consumption	Each device (refrigerator, case blower fan, Case lighting, heater)
Environmental measurement	Measurement 4m rod (8 points in temperature + 6 points in temperature and humidity)
Temperature and humidity Wind speed	Air curtain air supply and inlet (2 to 4 points for each display case air supply and inlet)
Refrigerant flow rate	Refrigerant piping for each display case
Weight of drain water	Continuous measurement of drain water of each display case

The experimental photograph of the multi-deck type is shown in Figure 3. Figure 4 shows the relationship between the display case refrigeration load at the time of stability and the enthalpy of the air entering the display case, obtained from experiments. If the enthalpy that enters the display case calculated from the enthalpy of the store air is input to these relational expressions, the refrigeration load of the display case can be calculated.

In order to correspond to the calculation for 24 hours, in addition to the steady load characteristics, the defrost time changed by the in-store air enthalpy, the load characteristics after defrost, and the load characteristics when installing the night cover in display case were also obtained from the experiment.

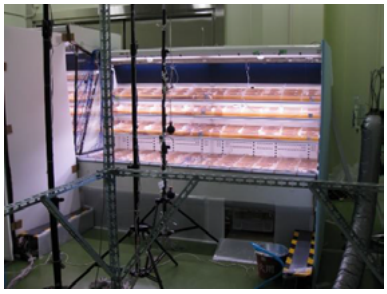
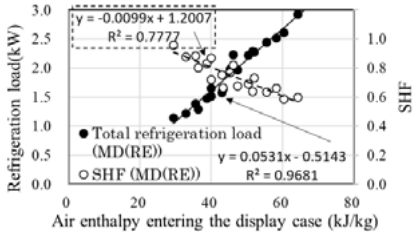
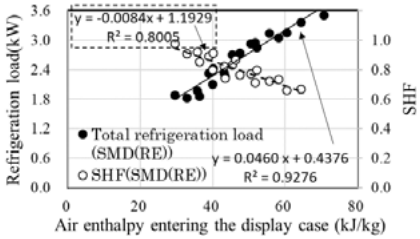


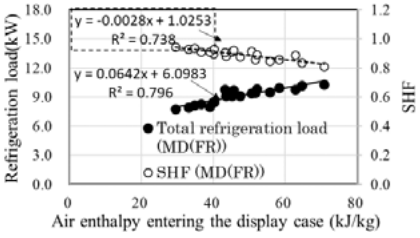
Fig.3 Experimental photo of the multi-deck display case



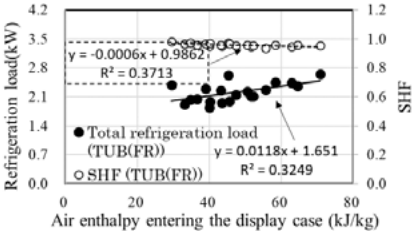
(a) MD(RE)



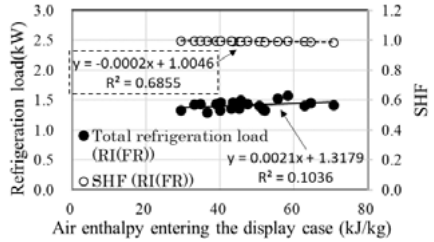
(b) SMD(RE)



(c) MD(FR)



(d) TUB(FR)



(e) RI(FR)

Fig.4 Relationship between refrigeration load, sensible heat factor and laboratory enthalpy

3.2. Calculation of power consumption for display case (refrigerator)

Various parameters are required to calculate the power consumption from the refrigeration load. In this study, (1) COP change due to evaporation temperature determined from display case preset temperature, (2) COP outside air temperature correction, and (3) refrigeration capacity decrease correction due to pipe length were formulated from manufacturer catalog values. In addition, a correction was made to increase the evaporation temperature when the display case load is small.

In order to confirm the validity of the calculation, the calculated value of the refrigerator power consumption was compared with the actual measurement value using the refrigeration load calculation and the refrigerator power consumption calculation method described above. The enthalpy of the store air which is used for the calculation, are the measured values on August 10, 2017. Table 4 shows the calculation conditions, and Figure 5 shows the calculation results. It was almost reproduced the load drop and the power consumption at night due to defrost.

Table 4 Display case load calculation conditions

Items	Calculation conditions
MDC(RE)	7℃ setting:18m / 0℃ setting:7.2m / -1℃ setting:9.6m
SMD(RE)	0℃ setting:9.6m / -1℃ setting:2.4m / -2℃ setting:9.6m / -2℃ setting:2.4m
Night setting	Setting to cover at night / Increase set temperature by 4 ° C
Defrosting times	4 times / day

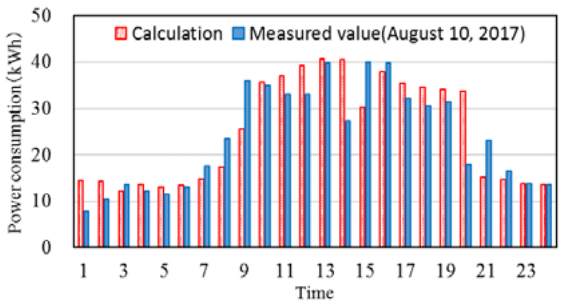


Fig. 5. Comparison of calculated and measured values for refrigerated power consumption

4. Energy consumption calculation for space conditioning

4.1. Outline of space conditioning load calculation

The space conditioning load is calculated by the building structure, ventilation, internal heat generation, indoor air temperature and humidity in the building as same. However, the space-conditioning of grocery stores is affected by the cold air leaking from the display case, so that the store temperature is not uniform. Although the horizontal temperature distribution does not become uniform depending on the arrangement of display case and the position of the entrance, we devised a calculation method that gives only the upper and lower temperature distribution with the horizontal temperature distribution being uniform.

First, the temperature and humidity near the ceiling were given, and the vertical temperature distribution was calculated. The building space conditioning load is calculated using the calculated vertical temperature distribution. Next, the intrusion enthalpy into the display case is calculated, and the refrigeration load is calculated using the enthalpy. The load obtained by subtracting the display case internal load (lighting and fan) from the refrigeration load becomes leakage cold, which reduces the building space conditioning load. The amount of heat obtained by subtracting the display case leakage cold air from the building space conditioning load is the net space conditioning load. A schematic diagram of the relationship between the vertical temperature distribution and the thermal load is shown in Figure 6. When the net space-conditioning load is negative, the temperature and humidity near the ceiling given first are lowered so that the net space-

conditioning load becomes zero. In this report, the food retail store shown in Table 5 was used as a model, and the load was calculated using a general-purpose load calculation program (BEST).

Table 5 Prerequisites for calculating space conditioning load

Items	Prerequisites	
Software	BEST program (Thermal load calculation function)	
Weather data	Extended AMEDAS (2010 edition) standard year Nagoya	
Sales floor area	2172m^2	
Floor height	5.6m（Ceiling height 4.0m）	
coefficient of overall heat transmission	Outer wall	1.26W/m^2・K
	Inner wall glass	4.27 W/m^2・K
	Inner wall	3.31 W/m^2・K
	Ceiling	0.73 W/m^2・K
Ventilation	Ventilation frequency 1 time / hour Gap Wind 0.1 times / hour	

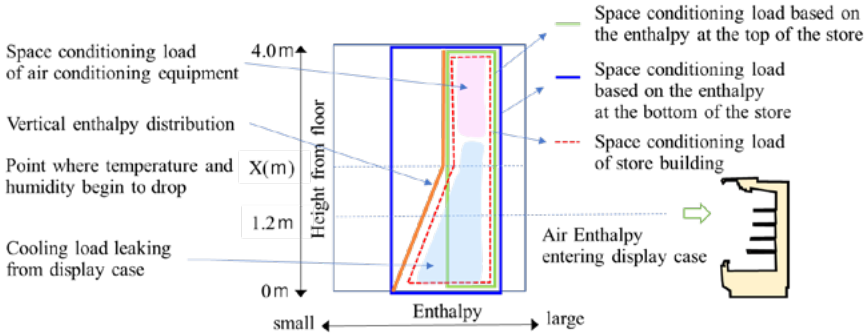


Fig. 6. Relationship between vertical temperature and humidity distribution, leakage heat from display case and space conditioning load

4.2. Determination method of vertical temperature and humidity distribution

The vertical temperature and humidity distribution were measured at the 24 points of the store in the November, where there was no space conditioning load. It is a grocery store with a sales floor area of 2172m^2 and a ceiling height of 4.0m. A floor plan view of the sore is shown in Figure 7. MD (RE) is installed on the wall of the store, and TUB (FR) and RI (FR) are installed. The average value of the measurement results is shown in Figure 8. Using the measurement results, it was assumed that the temperature and humidity would drop from FL + 2.0 m with a ceiling height of 4.0 m, and the space conditioning load calculation described above was performed. The building space conditioning load was 79 kW, and the cooling heat from display case was 70 kW, confirming that the two values were roughly balanced. In the subsequent calculations, it was assumed that temperature and humidity gradients occurred from FL + 2.0 m regardless of the season. The temperature / humidity gradient was calculated from the relationship between FL + 3.9m and FL + 1.2m obtained from annual measurement data.

4.3. Calculation method of space-conditioning power consumption

The calculation of power consumption required for space-conditioning was performed using a space-conditioning COP (outside air temperature correction only), assuming that no unprocessed load was generated and that all space-conditioning loads were processed by the space conditioner. It does not take into account the partial load characteristics resulting from the decrease in space conditioning load factor or the margin for space conditioning equipment. The rated COP is assumed to be 3.5 for cooling and 4.0 for heating.

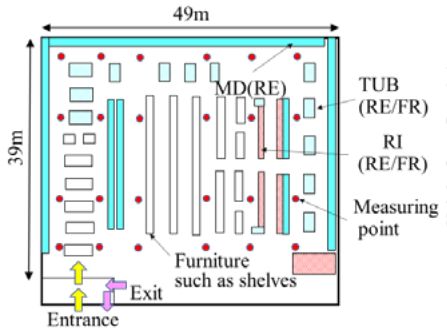


Fig. 7. Store floor plan and measurement points

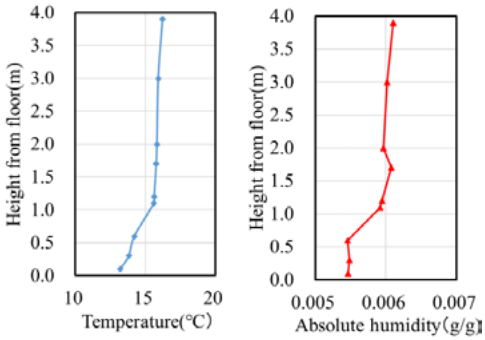


Fig. 8. Vertical distribution of average temperature and average absolute humidity

5. Calculation of power consumption for air conditioning and refrigeration energy

5.1. The validity evaluation of the calculation

The validity of the proposed energy calculation method was evaluated. For space conditioning and refrigeration energy, the results calculated using the standard weather data model (August 4) were compared with the measured data (August 10, 2017). As shown in Figures 9 and 10, the values and changes of space conditioning and refrigeration power consumption are well reproduced. Using this method, the energy saving effect by changing the space conditioning operation in summer was calculated.

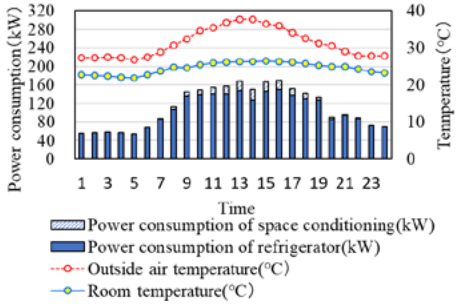


Fig. 9. Actual measurement (August 10, 2017)

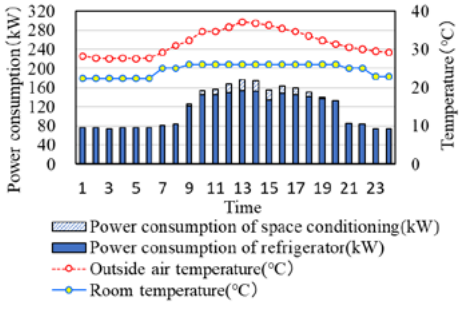


Fig. 10. Calculation (meteorological data August 4 Nagoya, Japan)

5.2. Calculation model and calculation cases

The space conditioning load calculation conditions are shown in Table 5 described above. Table 6 shows the display case conditions in the store. As shown in Table 7, there were 8 types of calculation cases. The weather model was a hot summer day (hot day: August 4) and a slightly cool day (cool day: September 25) in Nagoya, Japan. The space condition near each ceiling was set to 26 °C 60% to 20 °C 60%.

Table 6 Store display case conditions

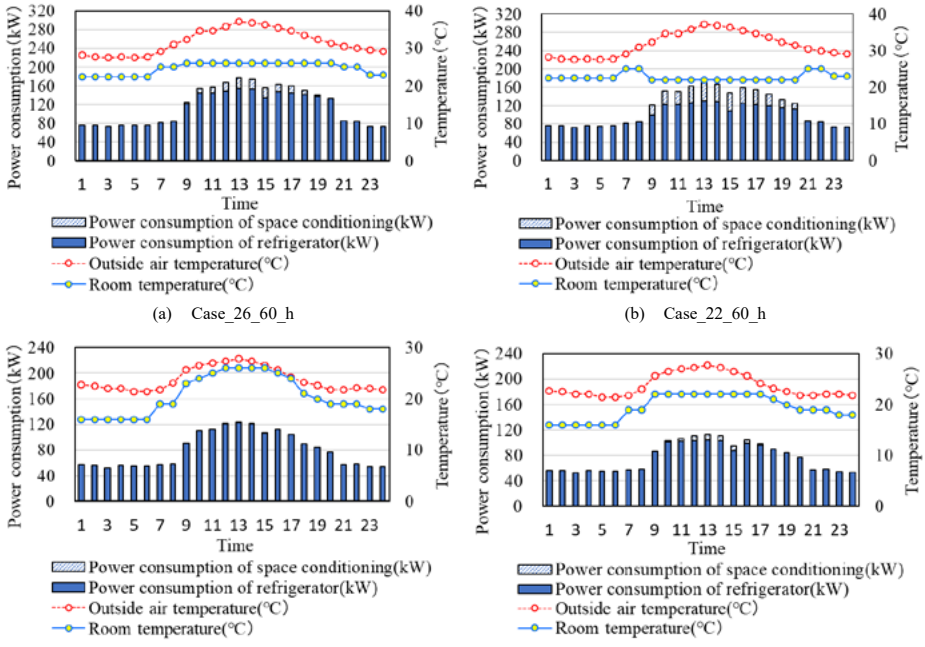
Items	Conditions
MD(RE)	3～9℃ setting:108m / -3～0℃ setting:50m
TUB(FR)	-3～0℃ setting:11m / -20℃ setting:14m
TUB(RE)	7℃ setting:43m
RI(FR)	-20℃ setting:33m
Night setting	Setting to cover at night / Increase set temperature by 4 ° C
Defrosting times	Refrigerated display case: 4 times / day Freezing zone display case: 2 times / day

5.3. Calculation results

Figure 11 shows the time changes for case_26_60 and case_22_60. Even on a hot day in summer, at 26 ° C near the ceiling, the display case leakage cold and the building space conditioning load balance, and there is almost no true space conditioning load. Under any conditions, increasing the space conditioning load decreases the total power consumption of refrigeration and space conditioning. The shape of the energy consumption curve, which is the sum of refrigeration and space conditioning, shows almost no change in any condition, indicating that the display case load has moved to the space conditioning. Japan's electricity charges are greatly affected by the annual peak power. For this reason, it is important to shift the display case load to the space conditioning load to suppress the peak of power consumption. Moreover, if the load shared by space conditioning increases, operation control for peak suppression can be performed by space conditioning instead of display case. This increases the ease of control.

Table 7 Calculation case

Case name	Temperature and humidity near the ceiling	Weather conditions (Extended AMEDAS)
Case_26_60_h	26℃ 60%	(2010 edition) standard year Nagoya August 4, 2006 Lowest Temperature : 27.6℃ Highest temperature : 37.2℃
Case_24_60_ h	24℃ 60%	
Case_22_60_h	22℃ 60%	
Case_20_60_h	20℃ 60%	
Case_26_60_c	26℃ 60%	(2010 edition) standard year Nagoya September 25, 2006 Lowest Temperature : 21.4℃ Highest temperature : 27.8℃
Case_24_60_c	24℃ 60%	
Case_22_60_c	22℃ 60%	
Case_20_60_c	20℃ 60%	



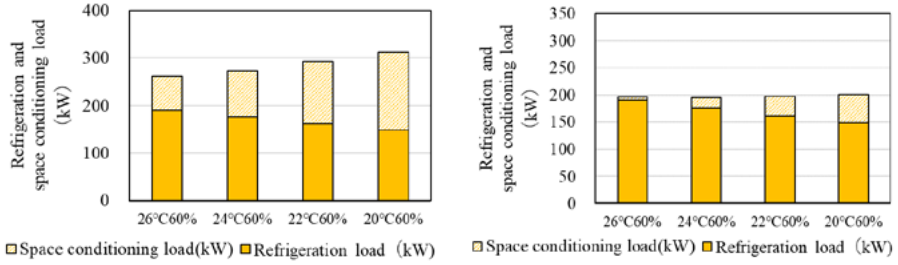
(a) Case_26_60_h (b) Case_22_60_h

(c) Case_26_60_c (d) Case_22_60_c

Fig. 11. 24-hour transition of power consumption for space conditioning and refrigeration

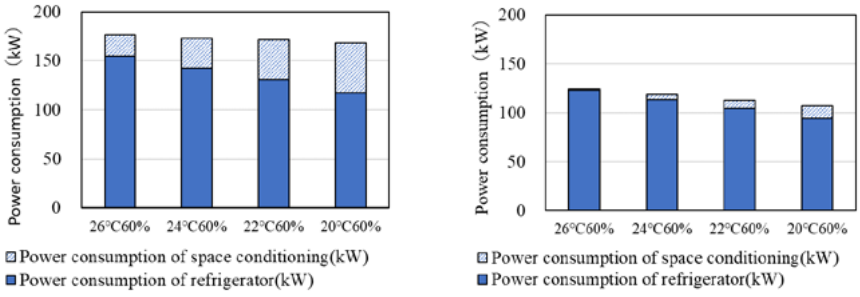
Take the time of 13:00 in each calculation case and compare in detail (Figures 12 and 13). As the temperature near the ceiling decreases, the rate at which the display case load shifts to the space conditioning load increases, and the energy consumption is suppressed by the difference between the display case and the

COP of the space conditioning. Energy savings due to the shift to display case load space conditioning are smaller in hot day where the temperature is high than in cool day where the temperature is low. The reason is that the COP of the space conditioner is more susceptible to the outside air temperature than the COP of the refrigerator, and the space conditioning load for controlling the store temperature and humidity is increased. Compare the amount of power saved each day in each case based on case_26_60 (Figure 14). Compared to hot day, the total power consumption of space conditioning and refrigeration in cool day decreases as the outside air temperature decreases, but the amount of energy saving increases compared to hot day. In grocery stores, the thermal environment has deteriorated due to cold air leakage from display case, so it is difficult to reduce significantly the space conditioning temperature in the store when the outside air temperature is high. However, if the outside air temperature decreases, the amount of clothes increases, so it is easier to reduce the store temperature than in midsummer. In order to save energy in the summer, it is important to control the space conditioning and shift the display case load to the space conditioning load in early summer and early autumn.



(a) Hot day (b) Cool day

Fig.12 Relationship between temperature and humidity near the ceiling, refrigeration load and space conditioning load



(c) Hot day (d) Cool day

Fig. 13. Relationship between temperature and humidity near the ceiling, refrigerated power consumption and space conditioning power consumption

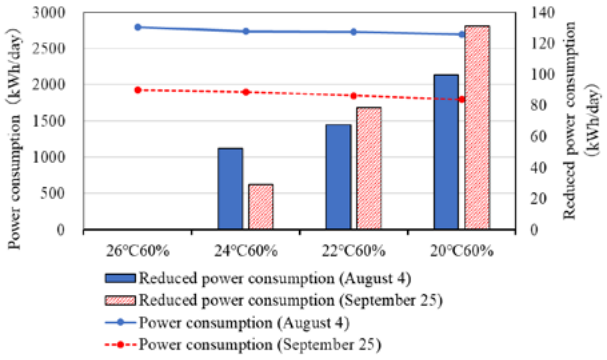


Fig. 14. Comparison of power saving of daily power consumption of refrigeration and space conditioning for each temperature and humidity near the ceiling

6. Conclusions

In this report, we proposed a method to give ingress air enthalpy to display case considering the vertical temperature and humidity distribution in the store. We changed the temperature and humidity in the store, and calculated the energy consumption in summer using a real store as a model. We investigated how changes in store temperature and humidity affect the relationship between space conditioning and display case load, and obtained the following knowledge. In the future, we proceed with consideration for the heating conditions.

1) If the temperature and humidity in the store are lowered by space conditioning, the total power consumption of refrigeration and space conditioning will be reduced.
2) It was found that the temperature inside the store decreased due to the cold leaked from the display case, and the space conditioner hardly operated under the condition of 26 °C near the ceiling. In order to save energy by operating space conditioning, it is necessary to greatly reduce the temperature to 22 °C or 20 °C.
3) Under the same store temperature and humidity conditions, the energy saving effect is greater at a low outside air temperature than at a high outside air temperature. Further, when the outside air temperature is low, it is easy to set the store temperature low, and energy saving can be expected. For this reason, it is important to use space conditioning well during the intermediate period such as early summer and early autumn.

Acknowledgements

For the research, we received a great deal of cooperation from the supermarket headquarters / stores and many other related parties. I would like to express my deep appreciation here.

References

[1] Agency for Natural Resources and Energy “Annual Report on Energy in FY2015” (Energy White Paper 2016) in Japanese.
[2] Varela.D.A, Redo.M.A,Giannetti.N,Ohno.k,Yamaguchi.S and Saito.K:Annual Performance Evaluation of CO_2 Refrigerated Display Cabinets Relative to Geographical Location. Proceedings on the Japan Society of Refrigerating and Air conditioning Engineers Annual Conference 2017, C214
[3] Narumi Daisuke: Impact of energy conservation measures of refrigerated fixtures on energy consumption at Grocery stores. The Society of Heating, Air-Conditioning and Sanitary Engineers of Japan 2015, pp29-32, in Japanese.
[4] Nakayama Taku: A report on demonstration experiment of the Air-Conditioning control methpd in consideration of influnce of refrigerated display cases in the store for Demand Response, Technical Committee on Production Equipment Management (The Institute of Electrical Engineers of Japan), January 2014,PFC-14-002 in Japanese.
[5] WEI Chenghao : Study on Energy Consumption of the Food Retail Store, Part12 Evaluation of

Interaction between Cold Air from Showcase and Heating using CFD. The Society of Heating, Air-Conditioning and Sanitary Engineers of Japan 2019, A-11, in Japanese.

13th IEA Heat Pump Conference
April 26-29, 2021 Jeju, Korea

Which performance indicators should we provide to policy makers to switch from gas boilers to air to water heat pumps?

Carolina Fraga[a,b], Alisa Freyre[a], Pierre Hollmuller[b], Rodrigo de Pablo[a], Matthias Rüetschi[a]

[a] Services Industriels de Genève, Chemin du Château-Bloch 2 – 1219 Le Lignon, Switzerland
b University of Geneva, Boulevard Carl-Vogt 66 – 1205 Genève, Switzerland

Abstract

The most commonly used performance indicator (PI) of heat pump (HP) systems is the COP. But is it a good PI? If so, does it have a minimum threshold? This article covers the potentials and constraints of different PIs for HP systems implemented in non-renovated residential buildings from an environmental, economic and social acceptability point of view, based on real case studies situated in Geneva, Switzerland. After describing the Geneva context and listing the most common PIs, we first compare a traditional gas boiler to an air to water HP system for space heating and domestic hot water of single-family building (SFB). We then follow by a similar comparison for multifamily buildings (MFB). For this particular building demand, a hybrid system is also analyzed (HP combined with gas for the peak loads) and specific PIs are included. Finally, the most pertinent PIs for air to water HP systems are identified and the minimum COP value of 2.5 is recommended to insure the reliability of the system in the 3 mentioned fields in the swiss context.

Keywords: COP; Air to water heat pump; performance indicators; residential buildings; hybrid systems.

1. Introduction

Renewable energy development is one of the main energy policy priorities nowadays. In the past, main efforts were put into renewable electricity, but the adoption of carbon emissions reduction targets as shifted the focus into renewable heat. In Switzerland, carbon emissions originate mainly from transport (32% of overall emissions), buildings (26%) and industry (22%). The country adopted the target of 20% carbon emissions reduction by 2020 compared to 1990 (40% in buildings, 15% in industry, 10% in transport,10% in other sectors) and it has currently announced a new ambitious climate policy target: 50% reduction of carbon emissions in 2030 compared to 1990 [1].

At a federal level, a variety of policy instruments (carbon tax and subsidy) were implemented to achieve carbon emissions reduction and promote renewable heat solutions. Nevertheless, they are now officially recognized as not sufficient to achieve the desired goals. Note that Switzerland's share of renewables in heat supply is about 16% (including 11% of wood-based systems, 5% of other renewables). Most of the heat (75%) is supplied by imported fossil fuels (40% heating oil, 33% natural gas, 2% coal). At the canton level, some actions were put into place. For example, in Geneva canton, the local public utility *Services Industriels de Genève (SIG)* has an energy efficiency program portfolio – *éco21* – that supports renewable heat uptake by final consumers from both single family and multifamily housing sectors [2].

The distinction between these two sectors (single-family buildings – SFB – and multifamily buildings – MFB) is important because in Switzerland, 55% of the existing building stock is composed of MFB, against 45% for SFB [3]. While MFB have the largest potential of CO_2 emissions reduction, SFB are easiest to tackle. For SFB, Geneva canton and *éco21* offer subsidies that cover about 20% of initial investment costs (including equipment and installation services). For MFB, this type of support is not suitable due to the peculiarities of Swiss housing legislation. Contrary to SFB, the majority of inhabitants of MFB are tenants. Tenants are responsible for payment of the energy bills, while it is the responsibility of the owners to invest in heating system. Investment costs cannot be transmitted to tenants via heating bills. Currently for existing buildings the

investment costs of the renewable heat systems such as heat pumps are from three to five times higher compared to the conventional solutions (fossil fuel-based). The owners therefore have no incentive to opt for renewables. [1].

Technically, the replacement of fossil heat by a renewable heat solution – more precisely a HP system – is also harder to tackle in MFB than in SFB. This is reflected in the market share of HPs in the residential sector that grew from nearly zero in the 1990s to about 50% today, but only 10% corresponds to MFB (CSD, 2017). For SFB, the HP market is mature, standard hydraulic schemes guaranteeing a good system performance are used, the whole process can be handled by one professional service. For MFB this process is more complex [1,4]:

- multiple households, with diluted decision power and related problems of governance;
- buildings often located in highly dense urban areas, with limited access to renewable heat sources other than air;
- if not threated carefully, noise emissions can easily become a barrier;
- higher shares of DHW in overall heat demand and related high temperature, which can affect the HP performance;
- absence of standard hydraulic schemes and system regulation guaranteeing a good system performance;
- multiple professional services (energy concept development; noise, static and building physics assessment; planning and implementation of heating, electricity and sanitary works; administrative procedures).

The aim of this work is to study performance indicators and their importance in the transition from fossil heat to renewable heat, more precisely Gas to HP heat. In order to do so, economic, environmental and social indicators are defined. Their values are then presented for different heat solutions (a gas boiler, HP system and HP+Gas system) and for both SFB and MFB. The indicators importance is discussed, solutions to improve economic, environmental and social barriers are presented. The positive and/or negative impact of these solutions on the remaining fields is also discussed. Finally minimum system performance value for the Swiss context is proposed, for both SFB and MFB.

Nomenclature

CHF	Swiss francs (0.91 €; 1.01 US$)
COP	Coefficient of performance
DHW	Domestic hot water
HP	Heat-pump
MFB	Multi-family building
PI	Performance indicator
SFB	Single family building
SIG	Industrial Services of Geneva

2. Methodology

We perform the analysis for three types of buildings: single-family, average and large multifamily. The reasoning for the respective distinction is based on two major motives:

- Contrary to the case of SFB, integration of HP heating systems in MFB is currently still more complicated than in SFB;
- The average-size MFBs do not have access to liberalized electricity market and therefore face relatively high electricity tariffs nowadays, compared to large MFBs.

2.1. Economic PI

To evaluate the performance of various heating solutions from economic perspective, we studied the available estimates of initial investment, operation and maintenance costs per unit of installed thermal capacity (CHF/kW, Fig. 1) [1]. These estimates are based on data from heating supply contracting projects provided by

Swiss ESCOs (24 air-to-water heat pumps), combined with heating modeling tools developed by Services Industriels de Genève (SIG).[1] We adjusted the available estimates, based on the available field data.

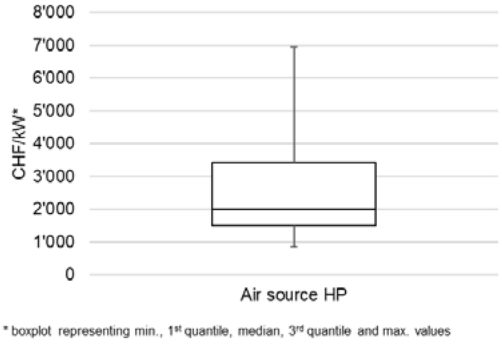


Fig. 1. Initial investment costs of heap pumps per unit of installed thermal capacity.

We calculate the levelized heating costs for an assumed lifetime of 20 years, based on the current average natural gas and electricity tariffs; and the average values of current initial investment costs, as well as average maintenance costs (Table 1). We performed the calculations with the carbon tax rate of 96 CHF/ tCO_2, and the current subsidy level of 70 and 28 CHF/tCO_2 for SFB and MFB respectively. We assumed a natural gas boiler efficiency of 85%. An annual air to water HP system performance (here on called COP) of 2.5, 3 and 3.5 for SFB [5], 2, 2.5 and 3 for MFB (for sensitivity analysis purposes).

For the HP + Gas system, we assumed the HP system would cover 80% of the heat demand and Gas the remaining 20%.

Table 1 Assumptions used in calculations of levelized heating costs of natural gas and heat-pump solutions

Item	Single-family building		Average multifamily building		Large multifamily building	
	Natural gas	Air-Water HP	Natural gas	Air-Water HP	Natural gas	Air-Water HP
Heat demand [kWh/year]	26’400		226’667		500’000	
Heated surface [m^2]	198		1700		3750	
Initial investment [CHF/kW]	600	2200	600	2200	600	2200
Maintenance [CHF/kW/year]	55	25	27	27	28	28
Energy tariff incl. carbon tax [CHF/kWh]	0.090	0.212	0.080	0.205	0.075	0.160

2.2. Social PI

In Switzerland (62%), even more so in Geneva (84%), most inhabitants of residentials buildings are not owners but tenants [6]. These buildings are heated by a centralized heating system that then distributes both SH and DHW to the apartments. The owner is obliged to provide a functioning heating system, and the tenants pay charges that cover the costs of energy consumption, maintenance and CO_2 tax.

In this context: i) owners have no financial benefit when investing in a renewable solution (higher investment costs and no benefits from the reduction of energy consumption); ii) tenants have no interest in investing in a property that they don’t own, even though they could eventually benefit from a reduction of energy consumption and CO_2 tax.

[1] Swiss ESCO datasets and SIG modelling tools are not publicly available.

Given this paradigm, the solution studied in this work is to define the tenant charges as being equivalent to the fossil system's, with a maximum increase of 10% if the fossil system is replaced by a HP solution. This way, the tenant has at maximum a rise of 10% of its charges while the owner can pay back his investments.

2.3. Environmental PI

In the case of HP systems, induced CO_2 emissions are calculated on the basis of a recent study concerning the carbon content of the Swiss electricity consumption mix [7], which uses hourly available data concerning the production of the various European countries, per type of production, as well as hourly data on imports/exports between the countries.

In a follow-up paper, the same authors analyze the induced CO_2 emissions of HP systems, for covering the heat demand of a sample of 6 different multifamily buildings [8]. Therefore, the authors combine the hourly dynamic of: i) the electricity used by the HPs; ii) the CO_2 content of the Swiss electricity mix. As a result, they derive the hourly CO_2 content of the electricity used by HP systems. For air-source HPs, the annual average of this mix finally amounts to 150 g CO/kWh_{el} (lower CO_2 mix), or 303 g CO_2/kWh_{el} (upper CO_2 mix).

The discrepancy between latter 2 values arises from a specific controversy concerning the carbon content of electricity generation from blast furnace gas units in Germany, which represent only a small share of the generation capacity of the total market, but play an important role in compensating for capacity shortages at the European level in the winter period.

In the case of gas boilers, emissions are related to natural gas consumption, by way of a constant emission factor of 228 g CO_2/kWh_{th} given by the Swiss Coordination Conference of Building Services [9].

3. Results and Discussion

3.1. Economic

The costs of heating supply for the SFB are presented in Fig. 2. These values result from the hypothesis described in section 2.1 and are shown for the 2 studied technological solutions and 3 different system performances.

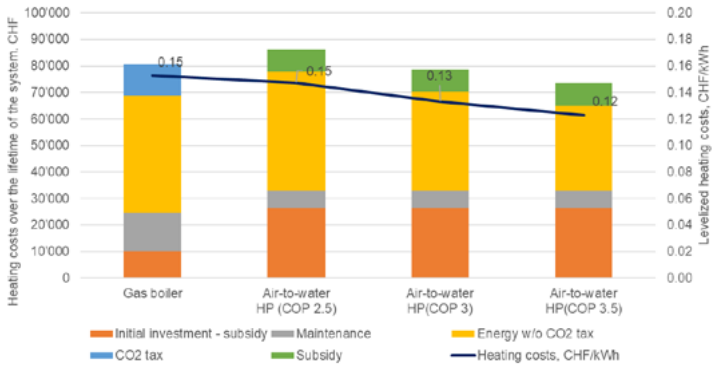


Fig. 2. Heating costs by technological solution and system performance for a single-family house (heat demand 25 MWh/year, 200 m^2 of heated surface), with CO_2 tax rate 96 CHF/t CO_2, w/o a subsidy; the assumed tariffs are 0.09 CHF/kWh for natural gas, 0.2118 CHF/kWh for electricity used for heat pumps.

The results are very positive for the air-to-water HP compared to gas boiler in the SFH. Of all solutions, Gas is the more expensive over the lifetime. It is probably explained by the well-known technology and standardized air-to-water HP systems available in the market for heating powers under 30 kW. There is no need for further engineering costs and material adaptation when installing these HP solutions.

We can consider that the subsidy granted in Geneva covers the risks of a hypothetical gap performance, which is not ideal if we aim for better performances.

From an economic point of view, this subsidy (about 20% of the initial investment) is no longer useful to cover the lifetime costs but still essential to reduce the initial investment.

The costs of heating supply for both average and large MFB are presented in Fig. 3 and Fig. 4 respectively. These values result from the hypothesis described in section 2.1 and are shown for the 3 studied technological solutions and 3 different system performances.

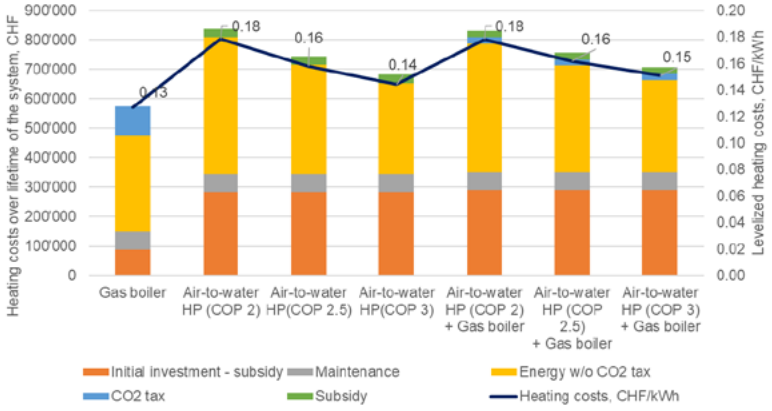


Fig. 3. Heating costs by technological solution and system performance for an average multifamily building (heat demand 225 MWh/year, 1700 m² of heated surface), with CO_2 tax rate 96 CHF/t CO_2, w/o a subsidy; the assumed tariffs are 0.08 CHF/kWh for natural gas, 0.205 CHF/kWh for electricity used for heat pumps.

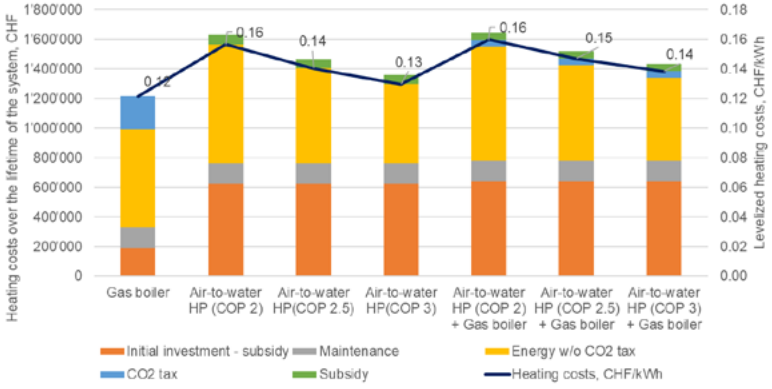


Fig. 4. Heating costs by technological solution and system performance for a large multifamily building (heat demand 500 MWh/year, 3750 m² of heated surface), with CO_2 tax rate 96 CHF/t CO_2, w/o a subsidy; the assumed tariffs are 0.075 CHF/kWh for natural gas, 0.16 CHF/kWh for electricity used for heat pumps.

For an average building, the heating costs over the lifetime of the gas system are 575 kCHF, of the HP system it's between 655 and 810 kCHF and of the HP+Gas system between 685 and 810 kCHF, depending on system performance. For a large MFB these values are: Gas 1'215; HP between 1'300 and 1'565; HP+Gas between 1'385 and 1'595 kCHF.

As seen by the figures, the big discrepancy between the Gas boiler and HP systems is mainly due to the current level of initial investment: HP heating solutions have a 3 times higher initial investment costs than the gas boiler solution. The gap between these solutions is shortened by the CO_2 tax, subsidy and increase of system performance: for example, in the average MFB, a HP system with a COP of 3 is only 80 kCH more expensive than a gas boiler solution, whereas a COP of 2 system would be 230 kCHF.

From all heating solutions, the gas boiler is the cheapest, both in terms of initial investment as well as levelized costs. This is true for both building sizes and despite of the system performance and CO_2 tax. With

this discrepancy, current CO_2 tax and subsidies are not enough to make HP heating solutions economically attractive.

When comparing both figures, large MFB have lower levelized costs than average MFB. This is explained by a liberalized market price to electricity consumers above 100 MWh/yr in Switzerland (0.16 CHF/kWh instead of 0.21 CHF/kWh). This electricity tariff for bigger consumers leads to a HP solution that is more attractive for large MFB than average MFB.

3.2. Social

The costs of heating supply for SFB are presented in Figure 5, including the tenants charge and owner investments. These values result from the hypothesis described in sections 2.1 and 2.2.

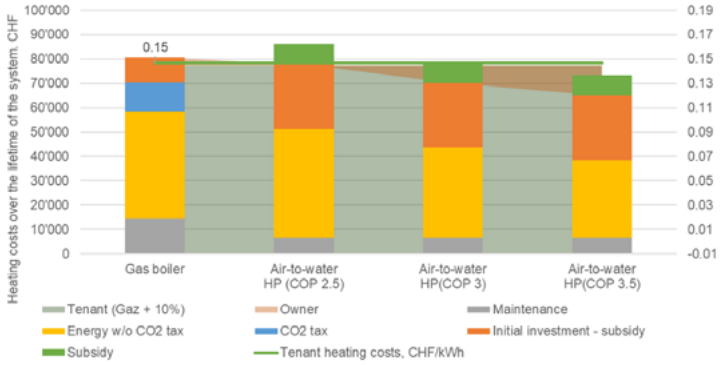


Fig. 5. Heating costs by technological solution and system performance for a single-family house (heat demand 25 MWh/year, 200 m^2 of heated surface), with CO_2 tax rate 96 CHF/t CO_2, w/o a subsidy; the assumed tenant charges are the equivalent to the gas boiler system (energy consumption, maintenance and CO_2 tax), with a maximum increase of 10%.

With the replacement of a gas system by a HP system, and tenant charges equal to the Gas solution +10%, the owner can, in all performances, pay back his investment and the HP system performance becomes crucial to the owner: the better the performance, the more he will be able to benefit from his initial investment.

One could argue that, with current subsidy and a CO_2 tax payed by the tenant, the 10% increase in tenant charges is not needed because the owner can still payback his investment with an average system performance.

Note that, in SFB if the tenant is planning to live in the same house in the very long term, he may assume some (or all) of the investment for a HP system. This unusual situation may occur when there is a good relationship between the owner and the tenant in place, for example when the house is owned by a family member.

The costs of heating supply for both an average and large multifamily building are presented in Fig. 6 and Fig. 7 respectively, including the tenants charge and owner investments. These values result from the hypothesis described in sections 2.1 and 2.2.

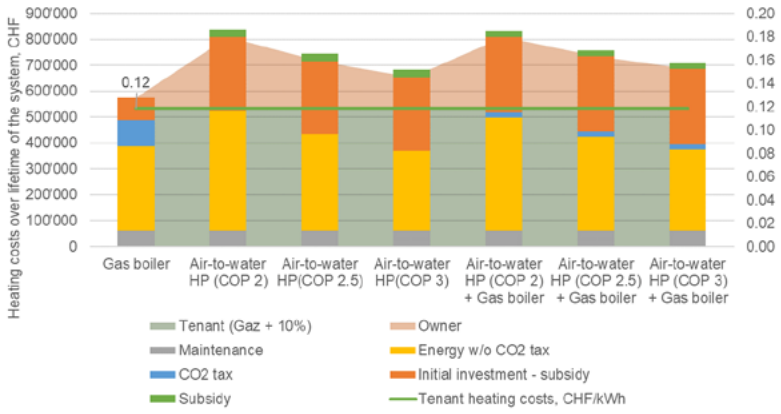


Fig. 6. Heating costs by technological solution and system performance for an average multifamily building (heat demand 225 MWh/year, 1700 m² of heated surface), with CO_2 tax rate 96 CHF/t CO_2, w/o a subsidy; the assumed tenant charges are the equivalent to the gas boiler system (energy consumption, maintenance and CO_2 tax), with a maximum increase of 10%.

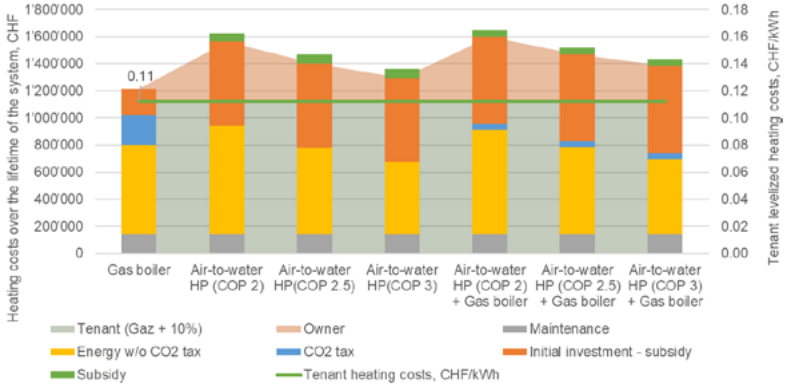


Fig. 7. Heating costs by technological solution and system performance for a large multifamily building (heat demand 500 MWh/year, 3750 m2 of heated surface), with CO2 tax rate 96 CHF/t CO2, w/o a subsidy; the assumed tenant charges are the equivalent to the gas boiler system (energy consumption, maintenance and CO_2 tax), with a maximum increase of 10%.

As seen in the figures, the tenant charges remain acceptable – 0.12 CHF/kWh for average and 0.11 CHF/kWh for large MFB. The 10% increase leading to a small increase of 0.01 CHF/kWh in the levelized costs of the Gas system.

With the replacement of a gas system by a HP system, and tenant charges equal to the Gas solution +10%, the owner can pay back part but not all of his initial investment. In this case, the HP system performance becomes crucial to the owner: the better the performance, the more he will be able to payback his initial investment.

All in all, to promote the replacement of a gas system by a HP system, the best system performance should be achieved and one or more of the following policy instruments could be used:

- increase in the CO2 tax, to increase the levelized heating costs of natural gas solution. In this case, it is important that the carbon tax is paid by the owner, and not the tenants who pay energy bills and have no voice in the choice of the heating systems. In addition, in the context of uncertain future energy prices, it is questionable whether building owners make their choice of a heating systems based on levelized costs only. In fact, operational costs including the carbon tax are paid on an annual basis. Investment costs are paid upfront from own savings or a loan and are recovered during

the years of heating system operation. Alternatively, a contracting mechanism should be introduced to resolve landlord-tenant dilemma and mitigate potential negative effects of long payback time on owner decisions.

- an increase of subsidies, to reduce the levelized costs of heat pump solutions. However, it is important to consider increased public expenditure or potential distributional effects related to increased financing of the energy programs, as well as the risks of increased investment costs due to induced market distortions.
- legal obligations put on building owners with regard to the maximum level of emissions or energy consumption (e.g., max. tCO2/m2/year, max. kWh/m2/year). This policy measure can put a significant burden on building owners, and should be carefully thought to avoid unnecessary market distortions. Namely, it is important not to subscribe a concrete technology into the legal obligations, to incentivize innovation and market competition on different levels (e.g., between technological solutions, contractors).

In practice, a combination of different policy instruments, constantly adapting according to the market developments, may be more efficient. The proposed policy measures require adjustments in current legislation.

3.3. Environmental

The CO_2 emissions of the studied solutions, for a SFB, are presented in Fig. 8. Note that this figure displays the upper CO_2 mix of 300g/kWh$_{el}$ described in section 2.3 - the least favorable scenario for HP systems. The CO_2 emissions for both upper and lower CO_2 mixes are shown in Table 2.

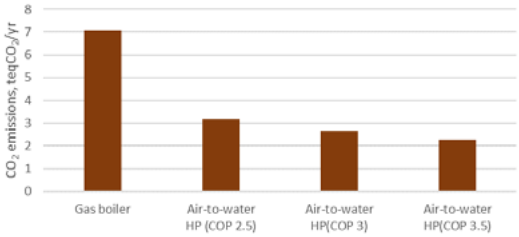


Fig. 8. CO_2 emissions (300 g CO_2/kWhel; 228 g CO_2/kWh$_{th}$) by technological solution and system performance for a single-family building.

Table 2 SFB CO2 emissions of all studied solutions for both upper (300g/kWhel) and lower (150g/kWhel) CO2 mixes in teqCO2/yr.

	upper CO_2 mix (300g/kWh$_{el}$)	**lower CO_2 mix (150g/kWh$_{el}$)**
	SFB, teqCO_2/yr	**SFB, teqCO_2/yr**
Gas boiler	7.1	7.1
Air-to-water HP (COP 2.5)	3.2	1.6
Air-to-water HP (COP 3)	2.6	1.3
Air-to-water HP (COP 3.5)	2.3	1.1

As seen by the figure, a HP system reduces CO_2 emissions by a factor of 3 in SFH, by a factor of 5 if we consider the lower CO_2 mix of 150g/kWh$_{el}$. In addition, more and more individual houses combine heat pumps with photovoltaic solar panels, which tends to lower CO2 emissions due to the grid electricity consumption.

The improvement in HP system performances can lead up to 30% savings. Note that, since the CO_2 emissions of these systems are already quite low, these savings are also low in absolute values (from 0.9 to 0.2 teqCO_2/yr.).

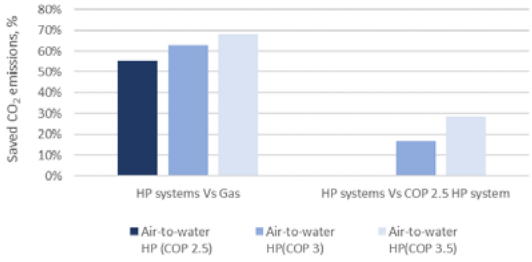


Fig. 9. Saved CO_2 emissions (300 g CO_2/kWh$_{el}$; 228 g CO_2/kWh$_{th}$) for a single-family building when comparing: i) HP solution to Gas solution; ii) HP system performance to lowest COP of 2.5.

The CO_2 emissions of the studied solutions, for both an average and large MFB, are presented in Fig. 10. Note that this figure displays the upper CO_2 mix of 300g/kWh$_{el}$ described in section 2.3 - the least favorable scenario for HP system. The CO_2 emissions for both upper and lower CO_2 mixes are shown in Table 3.

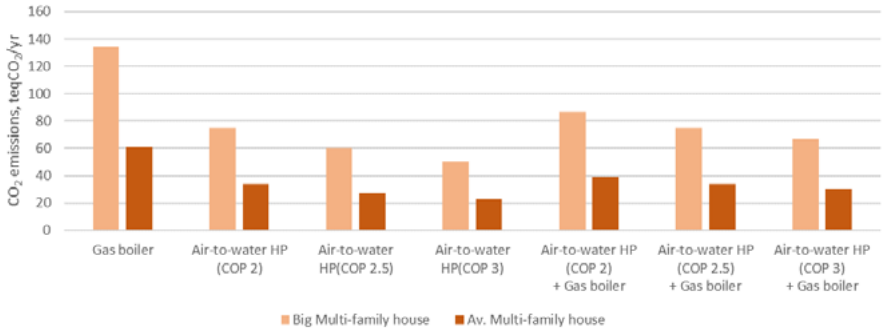


Fig. 10. CO_2 emissions (300 g CO_2/kWhel; 228 g CO_2/kWh$_{th}$) by technological solution and system performance for both average and large multifamily building.

Table 3 CO_2 emissions of both MFBs and all studied solutions, for both upper (300g/kWh$_{el}$) and lower (150g/kWh$_{el}$) CO_2 mixes.

	Upper CO_2 mix (300g/kWh$_{el}$)		**Lower CO_2 mix (150g/kWh$_{el}$)**	
	Large MFB [teqCO_2/yr.]	**Average MFB [teqCO_2/yr.]**	**Large MFB [teqCO_2/yr.]**	**Average MFB [teqCO_2/yr.]**
Gas boiler	134	61	134	61
Air-to-water HP (COP 2)	75	34	38	17
Air-to-water HP (COP 2.5)	60	27	30	14
Air-to-water HP (COP 3)	50	23	25	11
Air-to-water HP (COP 2) + Gas boiler	87	39	57	26
Air-to-water HP (COP 2.5) + Gas boiler	75	34	51	23
Air-to-water HP (COP 3) + Gas boiler	67	30	47	21

The solution with highest CO_2 emissions is the Gas system, followed by the HP + Gas system and lastly the HP system. The HP systems (both HP and HP+Gas) have around half of the CO_2 emissions of the gas system, around a quarter if we consider the lower CO_2 mix.

The CO_2 emissions of the HP+Gas system with COP of 3 are approximately the same as the HP system with a COP of 2.

Fig. 11 shows, in percentage and for the upper CO_2 mix of 300g/kWh_{el}, the saved CO_2 emissions when comparing: i) HP and HP+Gas solutions to Gas solution; ii) HP and HP+Gas performances to the lowest performance (COP of 2); iii) HP solution to HP+Gas solution. These values are valid for both average and large MFB.

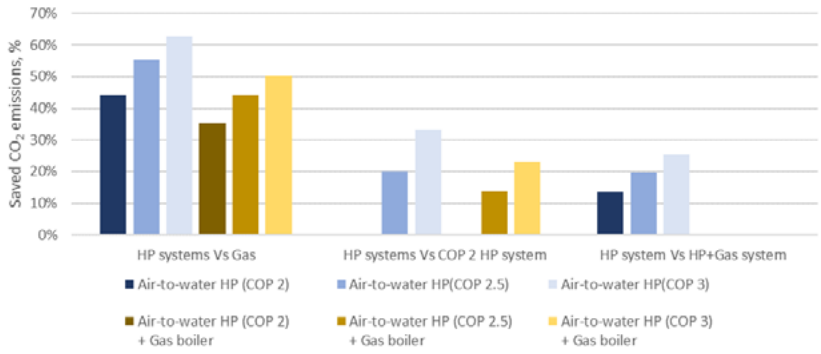


Fig. 11. Saved CO_2 emissions (300 g CO_2/kWhel; 228 g CO_2/kWh_{th}) for both average and large multifamily building when comparing: i) HP and HP+Gas solutions to Gas solution; ii) HP system performance to lowest COP of 2; iii) HP solution to HP+Gas solution.

As seen in the figure, when a Gas system is replaced by a HP+gas system around 45% of CO_2 emissions are saved, and if replaced by a HP system, the savings are around 55% (depending on the system performance). For the lower CO_2 mix, these values would be around 60% and 75 % respectively.

Within systems with HPs, the improvement in system performance can lead up to 33% savings in HP systems and up to 23% in HP+Gas systems. Note that, since the CO_2 emissions of these systems are already quite low, these savings are also low in absolute values (for a large MFB, 25 teqCO_2/yr. for a HP system, 20 teqCO_2/yr. for a HP+Gas system).

When comparing HP+Gas system to HP systems, the latter saves 14 to 25% of CO2 emissions (12 to 17 teqCO_2/yr. for a large MFB).

3.4. Overall

According to previous results, in SFB in Switzerland the replacement of gas boilers by HP systems is both environmentally, economically and socially reliable for the lowest studied system performance of 2.5. Economically, the subsidy (which helps with the high initial investment) and the absence of CO_2 tax helps the owner payback is investment in the lifetime of the equipment; the better the performance of the system, the more he will be able to save in energy costs. Environmentally, the replacement of gas by HP is positive but the increase from a COP of 2.5 to 3.5 is less impactful. Nevertheless, the benefits from better performances in peak electricity consumption should not be forgotten. Socially, with current subsidy and a CO_2 tax payed by the tenant, the 10% increase in tenant charges is not needed. Lastly, the aim of having better system performances and less CO_2 emissions is pursued, not for environmental or social reasons but because it is economically beneficial.

Regarding MFB in Switzerland, the replacement of gas boilers by HP systems is only economically and socially reliable for system performances above 2.5, particularly for average MFB. Economically, in order to payback the investment, the highest performance should be achieved and other tools should be applied (increase in subsidy and/or increase of CO_2 tax and/or obligation to have a share of renewable heat/limited CO_2 emissions). Socially, an increase of the CO_2 tax should be avoided because it would mean higher tenant charges (unless the CO_2 tax would be partially or entirely payed by the building owner), increase of subsidy and/or obligation to have a share of renewable heat and/or contracting solution could be implemented. Environmentally, similar to SFH, the replacement of gas by HP is positive but the increase from a COP of 2 to 3 is less impactful. Nevertheless, the benefits from better performances in peak electricity consumption should not be forgotten.

In other words, in MFB, system performance is critical for Social and Economic reliability but not for Environmental.

The difference between SFB and MFB results could be explained by the fact that available air-to-water HP on the market are optimized in terms of regulation for SFB. Due to lack of high-power HPs in the market, scaling up small HPs for MFB implies a more complex regulation to control all the low power HPs which in turn increases the risks of system underperformance. Standardized hydraulic schemes guaranteeing the HP system performance do not exist yet for MFB. Optimal regulation is not yet defined (production during day time – higher air temperatures – would lead to better performances and avoid running the system at nighttime when noise levels are limited).

Lastly, if policy measures are implemented (CO2 tax, subsidies, renewable heat share/limited CO2 emissions obligation), feedback mechanisms about those policies should be implemented in order to guarantee that those measures are achieving their goal.

4. Conclusion

This article covers a comparative analysis of the potentials and constraints of different performance indicators for HP systems implemented in non-renovated residential buildings from an environmental, economic and social acceptability point of view, for both single-family and multifamily buildings in, Switzerland.

In SFB, the replacement of gas boilers by HP systems is both environmentally, economically and socially reliable for the lowest studied system performance of 2.5.

Regarding MFB in Switzerland, the replacement of gas boilers by HP systems is only economically and socially reliable for system performances above 2.5, especially for average MFB. Economically, in order to payback the investment, the highest performance should be achieved and other tools should be applied (increase in subsidy and/or increase of CO_2 tax and/or obligation to have a share of renewable heat/limited CO_2 emissions). Socially, an increase of the CO_2 tax should be avoided because it would mean higher tenant charges (unless the CO_2 tax would be partially or entirely payed by the building owner), increase of subsidy and/or obligation to have a share of renewable heat and/or contracting solution could be implemented. Environmentally, similar to SFH, the replacement of gas by HP is positive but the increase from a COP of 2 to 3 is less impactful. Nevertheless, the benefits from better performances in peak electricity consumption should not be forgotten.

In conclusion, system performance is critical for Social and Economic reliability but not for Environmental and, for Switzerland, a system performance above 2.5 is highly recommended.

Acknowledgements

The authors would like to thank SIG program éco21 for financing this study and providing the data used in this study.

References

[1] Freyre, A. Energy programs for buildings: analysis in the context of the Swiss energy transition. Université de Genève, PhD Thesis ; 2019.
[2] Rognon F, Yushchenko A, Rüetschi M. Retrofitting fossil-based heating systems with air to water heat pumps in multifamily houses, 12th Heat Pumping conference; 2017.
[3] Schneider, S., Khoury, J., Lachal, B., Hollmuller, P. Geo-dependent heat demand model of the swiss building stock, Sustainable Built Environment (SBE) regional conference, Zurich; 2016
[4] Fraga, C, Hollmuller, P, Schneider, S, Lachal, B. Heat pump systems for multifamily buildings: Potential and constraints of several heat sources for diverse building demands., Applied Energy, vol. 225, p. 1033-1053, 2018.
[5] Miara, M, Günther, D, Langner, R, Helmling, S, Wapler, J. 10 years of heat pumps monitoring in Germany. Outcomes of several monitoring campaigns. From low-energy houses to unretrofitted single-family dwellings, 12th Heat Pumping conference; 2017
[6] Taux de logements occupés par leur propriétaire, 01.11.2019, https://www.bfs.admin.ch/bfs/fr/home/statistiques/construction-logement/logements/conditions-habitation.assetdetail.7346293.html
[7] Romano E., Hollmuller P., Patel M. (submitted 2019). Hourly carbon emission due to electricity consumption – an incremental approach for an open economy. The case of Switzerland.
[8] Romano E., Fraga C., Hollmuller P. CO2 emission savings from heat-pumps in the residential sector. Case study for multifamily buildings in Geneva. In: 13th IEA Heat Pump Conference, May 2020, Jeju, Korea.
[9] KBOB. Empfehlung Ökobilanzdaten im Baubereich 2009-1-2016 (1). Koordinationskonferenz der Bau- und Liegenschaftsorgane der öf- fentlichen Bauherren c/o BBL Bundesamt für Bauten und Logistik.

13th IEA Heat Pump Conference
April 26-29, 2021 Jeju, Korea

Heat pump and thermal energy storage integration in non-continuous processes – an application to the food industry

Edward J. Lucas[a], Jan A. Stampfli[a], Lorenz P. Rast[a], Raphael Agner[a], Beat Wellig[a*]

[a]Lucerne University of Applied Sciences and Arts, Technikumstrasse 21, 6004 Luzern, Switzerland

Abstract

Industrial sectors routinely represent a considerable share of a countries total energy demand. An increasing emphasis is on heat recovery across the sector and reducing greenhouse gases (GHG). Heat pump (HP) integration offers the potential to realize energy efficiency and GHG reduction, but is often challenging as a significant portion of energy demand is allocated to non-continuous processes. Consequently, heat recovery measures involving thermal energy storage integration are frequently the only option to recover heat indirectly. Additionally, careful consideration of available condensation and evaporation duties using the grand composite curve, and HP operational parameters such as evaporation and condensation temperatures, are required to perform HP integration within the system. A practical procedure for combined heat pump and thermal energy storage (HPTES) integration into non-continuous processes is presented. HPTES parameter selection is addressed using a graphical approach based on pinch analysis. The approach is demonstrated through application to a candy production plant, which produces in three daily shifts of similar duration and procedure. Up to 74.1% utility reduction can be achieved through HPTES integration, with internal rate of return of 11%.

Keywords: pinch analysis; heat pump; thermal energy storage; integration; COP curves; non-continuous processes

1. Introduction

Industrial sectors across the globe consume a considerable share of total energy demand (EU avg. 24.6%, 2017) [1], and represent a substantial share of total greenhouse gas (GHG) emissions. A large portion of this demand is in the form of thermal energy. Increasingly in industry, emphasis is placed on reducing total energy consumption in order to realize energy and cost savings, and on the consequential reduction of GHGs in accordance with stringent climate-change targets.

Process integration is an established method of accomplishing energy optimization, whereby pinch analysis (PA) is used to determine cost-optimal energy targets for process heat recovery and process hot and cold utility demands [2]. This systematic analysis differentiates processes into two thermodynamically separate sub-systems, separated in temperature by a pinch point. Typically, only heating is required above the pinch point and cooling below, allowing a direct calculation of the maximum potential for increasing process energy efficiency.

After exploiting the potential for energy efficiency through direct heat exchange, further savings may be available via indirect heat recovery using thermal energy storage (TES), and heat pump (HP) integration [3]. The latter requires processes still contain considerable amounts of low-grade excess heat and heating demands at suitable temperature levels. Appropriate methods are needed to assess whether HP integration in industrial processes is thermodynamically and economically feasible. Methodologies based on PA have been developed for HP integration using composite curves (CCs) [4], and later grand composite curves (GCCs) [5], which display the deficit heat above the pinch and heat surplus below the pinch [6][7]. While these methodologies were originally constrained to the analysis of continuous process only, later developments of the time slice model (TSM) [8] allowed non-continuous processes to be included in the analysis. Recently, approaches based

* Corresponding author. Tel.: +41 41 349 37 44
E-mail address: edward.lucas@hslu.ch.

on the TSM for complete heat pump and thermal energy storage (HPTES) integration using graphical techniques and mathematical programming have been developed [9].

Multiple challenges face HP integration in industry which has prevented widespread adoption of the technology however [10]. Non-continuous processes present particular difficulties when selecting a heat pump with appropriate operational characteristics such as evaporation and condensation temperatures, as well as evaporator and condenser duties for optimal placement across the pinch point [11]. Furthermore, limited expertise and experience represent barriers to entry for the technology and directly affect adoption of the HP technology in industry because of the uncertainty and subsequent financial risks. This is despite such systems being shown to be economically viable, e.g. waste heat recovery from batch reactor systems [12], and a small but growing number of non-continuous process HP integration case studies [13]. Consequently, HP integration has often been relegated to the integration of continuous processes only, restricting the possible contributions of heat pump technology to the reduction in energy consumption across the industrial sector.

This paper aims to reduce these barriers to entry by providing experience and expertise in the form of a case study, helping to support the application of heat pump technology in industry. A procedure based on an optimization approach [9] has been employed to integrate a heat pump into a non-continuous process in the Swiss food and beverage industry.

2. Heat pump integration procedure

An overview of the procedure and a concise description is presented here. For brevity, only the most pertinent parts of the procedure are explained to allow readers to understand how the case study data are treated and the results are produced. Only the graphical method of the full hybrid approach has been used here for heat pump integration. A detailed description of the complete hybrid approach including mathematical optimization can be found in Stampfli et al. [9].

2.1. Overview of procedure and initial steps

The procedure for integrating a heat pump thermal energy storage (HPTES) system proceeds in 6 steps (Fig. 1). The first step considers the extraction of process data using process control systems, process schematics, and direct measurements where necessary, in order to characterize the process requirements (Step 1). Process scheduling, heating and cooling demands and the economic framework are all required. These

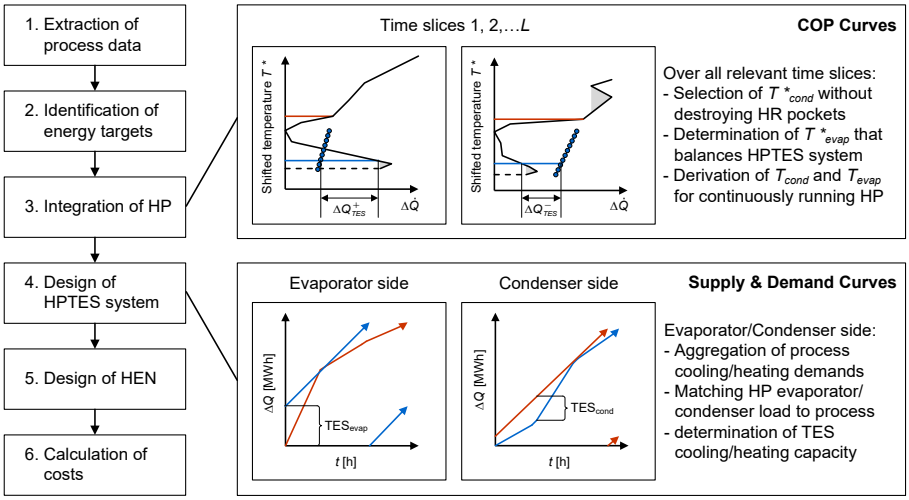


Fig. 1. Procedure for HPTES integration into non-continuous processes

factors form the basis for determination of the energy and cost targets for the process (Step 2) using pinch analysis. Process scheduling directly informs the identification of energy targets through use of the TSM [8].

The process is split into a series of time slices (TSs), according to where the process can be taken as continuous, i.e. periods of time where no streams are beginning or ending in operation, and the available process streams are continuous for the duration of the TS. A change in process heating or cooling requirements dictates the end of the current TS and the beginning of the next. A heat cascade is then calculated for each TS, allowing determination of TS energy targets as well as a pinch temperature during the pinch analysis. When an overall ΔT_{min} is selected, a GCC for each TS is produced. The GCC shows the amount of surplus heat below the pinch [6][7], and can be used for HP integration (Step 3). The required condenser and evaporator temperature and maximum duties for each TS are calculated using the GCC and COP curves, as well as the amount of thermal energy that must be covered by the storage system to complete the energy balance across all TSs. This information is used to size the smaller condenser and evaporator duties of the continuously running heat pump that will be integrated using supply and demand curves (Step 4). These curves also allow the calculation of the required storage capacities. Once sizing is completed, a heat exchanger network (HEN) for the system that functions across all TSs can be designed (Step 5). As a final step (Step 6), the costs of the HPTES system are estimated. This includes investment and yearly operational costs, and an estimation of the yearly energy and cost savings.

2.2. Heat pump integration using COP curves

The GCCs are used to identify feasible and constant HP evaporation and condensation temperatures despite the varying operational demands of the process. Heat recovery loops (HRLs) incorporating thermal energy storage (TES) are used to cover these variations in the process heating and cooling demands. The storages are often, but not limited to, stratified tanks containing two layers of thermal storage media at near-constant temperature. As the HRL contain HEXs themselves, heat pump evaporation or condenser temperature is shifted from the process stream temperature by several instances of ΔT_{min} (Eq. 1).

$$\Delta T = \underbrace{\frac{1}{2}\Delta T_{min} + \frac{1}{2}\Delta T_{min}}_{\text{process stream} \leftrightarrow \text{HRL}} + \underbrace{\frac{1}{2}\Delta T_{min} + \frac{1}{4}\Delta T_{min}}_{\text{HRL} \leftrightarrow \text{HP}} = \frac{7}{4}\Delta T_{min} \tag{1}$$

Between the process streams and the HRL normal heat transfer coefficients are assumed, and therefore two standard temperature contributions of 1/2 ΔT_{min} are applied [6][7]. For feasible heat transfer between the HRL and the HP, given the high film heat transfer coefficients that occur during phase change of the refrigerant, the temperature contributions are reduced to 1/2 ΔT_{min} and 1/4 ΔT_{min}. The resulting temperature differences between process streams and HP is thus a total of 7/4 ΔT_{min}.

Evaporation and condensation temperatures T^*_{evap} and T^*_{cond} determined from the GCC are already shifted with respect to the process streams by 1/2 ΔT_{min}. The shift from these temperatures to the real temperatures of the evaporator T_{evap} and condenser T_{cond} are thus 5/4 ΔT_{min}:

$$T_{evap} = T^*_{evap} - \frac{5}{4}\Delta T_{min} \tag{2}$$

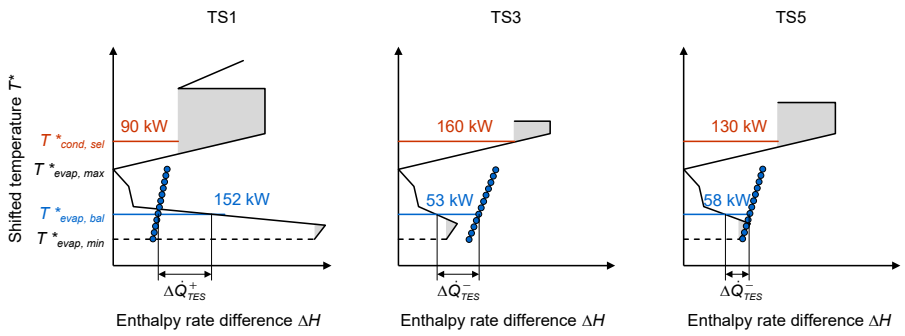


Fig. 2. GCCs of time slices (ΔT_{min} = 5 K) showing COP curves, taken from case study (transitional period)

$$T_{cond} = T^*_{cond} + \frac{5}{4}\Delta T_{min} \tag{3}$$

The heat pump operating evaporation temperature is found graphically using the COP curves (Fig. 2, blue dots). These curves describe the absorbed heat flow of the HP as a function of the evaporation temperatures and chosen condensation temperature. A condensation temperature $T^*_{cond,sel}$ is first selected that ensures the heat flow emitted by the HP is maximized (in order to maximize heat recovery) without destroying self-sufficient pockets, and that is as close to the pinch temperature as possible to reduce the temperature lift of the HP and maintain efficiency. An evaporation temperature is then searched between the bounds of $T^*_{evap,\max}$ and $T^*_{evap,min}$. An estimation of the amount of heat absorbed is made for each evaporation temperature and plotted on the GCC (blue dots), creating the COP curves. The calculation assumes the HP operates in a reduced-efficiency Carnot cycle with a second-law efficiency of 0.5 (Eq. 4). Usual values for second-law efficiency are around 0.55 [15]. Absorbed heat (evaporation duty) is calculated from the COP_{HP} (Eq. 5).

$$\mathrm{COP_{HP}} = \eta_{2nd\ law,HP}\,\mathrm{COP_{Carnot}}\ ;\quad \mathrm{COP_{Carnot}} = \frac{T_{cond}}{T_{cond} - T_{evap}} \tag{4}$$

$$\dot{Q}_{evap} = \dot{Q}_{cond}\,\frac{\mathrm{COP_{HP}} - 1}{\mathrm{COP_{HP}}} \tag{5}$$

Provided the COP curve and GCC intersect, the process cooling demand is exactly equal to the absorbed heat flow by the evaporator. For evaporation temperatures where the absorbed heat is less than the TS cooling demand at this temperature (Fig. 2, TS1), surplus from the process $\Delta\dot{Q}^{+}_{TES}$ must be stored in TES. For evaporation temperatures where absorbed heat exceeds the TS cooling demand at this temperature (Fig. 2, TS3&5), heat deficit $\Delta\dot{Q}^{-}_{TES}$ has to be provided by storage. The evaporation temperature which satisfies the energy balance of the storage across all time slices $T^*_{evap,bal}$ is located where the sum of all heat surpluses and deficits across all TSs ($l = 1 \ldots L$) is equal to zero, given by:

$$\sum_{l=1}^{L} \Delta Q^{+}_{TES,l}\left(T^*_{evap,bal}\right)\cdot\Delta t_l + \sum_{l=1}^{L} \Delta Q^{-}_{TES,l}\left(T^*_{evap,bal}\right)\cdot\Delta t_l = 0 \tag{6}$$

Where Δt_l represents the TS duration. Once these discontinuous heat flows to and from the TES are known, the TES and HP can be sized using supply & demand curves.

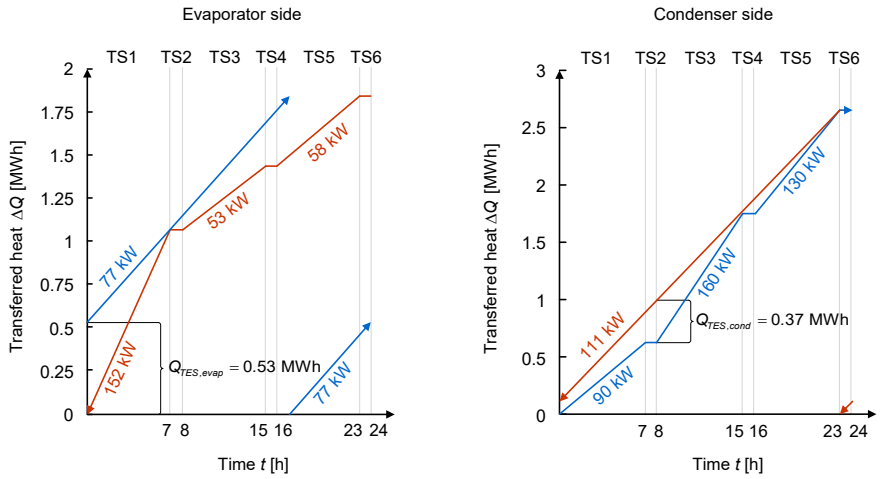


Fig. 3. Supply & demand curves for sizing of HPTES system; values taken from case study

2.3. HPTES sizing using supply & demand curves

Supply & demand curves [14] were developed for the sizing of utility systems of non-continuous processes and are used to size the heat pump for continuous operation, as well as size the necessary capacities of the TESs. For the HRL, two such plots exist, one for the evaporator (Fig. 3, left) and one for the condenser (Fig.3, right). Values are taken directly from the case study data. The diagrams plot the relative flows of heat provided by the HP and demanded by the process across all time slices, which allows calculation of the heat load supplied to or demanded from the TES in order to energetically balance the system.

For the cold HPTES evaporator side, the process TS cooling demands (152 kW, 53 kW, 58 kW) are drawn in red and the HP cooling supply (77 kW) in blue. The maximum discrepancy between the demanded cooling load and the supplied cooling load equals the required TES cooling capacity (0.53 MWh). For the hot HPTES condenser side, process TS heating demands (90 kW, 160 kW, 130 kW) are drawn in blue and the HP heating supply (111 kW) in red. Here, the maximum discrepancy corresponds to the required TES heating capacity (0.37 MWh). It should be noted that during time slices 2, 4, and 6, while no heating or cooling demands are made by the process of the HPTES system, the HP is still in operation. This causes an increase in the heating capacity (hot side) and cooling capacity (cold side) available after these time slices, and hence an increase to the overall required storage capacities on either side of the system.

Without storage, the HP would have to be capable of meeting the process demands directly and would have to be sized according to the maximum demands from the process (evaporator side, 152 kW, condenser side, 160 kW). With TES, the heat pump can run continuously and hence provide the required heat load over a longer duration, reducing the required heat load of the HP.

2.4. Heat pump and storage calculations

Storage volume is calculated from the required mass inventories, which are found using the capacities given by the supply & demand curves (0.53 MWh, 0.36 MWh) and the specific heat capacity of the storage media. The inventories must meet the amount of mass needing be transferred during each TS to cover the heating and cooling demand of the streams. A brief summary of pertinent equations is given for the case of the cold HRL i.e. heat transfer to the storage from the hot process streams. For the hot HRL and condenser equations, see [9]. The required mass of storage media in the HRL to cover the heat transfer demands is given by:

$$m_{C,HRL} = \frac{Q_{TES,evap}}{c_{p,HRL}\left(T_{C,h} - T_{C,c}\right)} \tag{7}$$

Where, $c_{p,HRL}$ is the specific heat capacity of the media, $Q_{TES,evap}$ the required cooling capacity, and $T_{C,h}$ and $T_{C,c}$ the hot and cold temperature levels of the cold storage.

HP electrical power P_{el} can then be calculated by completing the energy balance between the emitted heat of the condenser $\dot{Q}_{cond}$, the absorbed heat of the evaporator $\dot{Q}_{evap}$, and the input power P_i, assuming a drive efficiency η_{drive} (Eq. 8). An assumption is made that when considering heat pumps of significant size, open type compressors are often used. For open type compressors, where frictional losses to heat are lost to the environment, drive efficiency is assumed to be around 0.9. For closed type compressors, assuming almost all electrical power going into the system is transferred to the refrigerant, this value can be taken as approximately unity ($\eta_{drive} \approx 1$).

$$\dot{Q}_{cond} = \dot{Q}_{evap} + P_i \approx \dot{Q}_{evap} + P_{el}\eta_{drive} \tag{8}$$

3. Case Study

3.1. Introduction

The case study chosen for analysis is based on a site that manufactures confectionary for the Swiss and European food and beverage markets. To demonstrate more clearly the procedure, the case study data have been simplified, focusing primarily on the parts of the production processes that have substantial heating and cooling demands. The seasonal dependency of certain process streams has been retained, splitting the analysis into three operating cases: Summer (S), Transition Period (TP), and Winter (W). Additionally, the scheduling of the daily production shifts has been modified. The main areas of consideration are:

- Bonbon (BB) Candy Production
- Soft Fruit Candy (SFC) Production
- Hard Fruit Candy (HFC) Production
- Utility Systems

The site produces three types of candy daily, in three consecutive shifts. Although the exact process requirements of each candy variety vary, their manufacture involves the common stages of syrup preparation, mixing, and boiling, as well as casting, drying, and final treatment of the candies. The heating and cooling requirements of these stages are provided for by the on-site utility systems, which consist of hot, warm and cool water circuits. The hot water circuit is heated using stream purchased from off-site, and provides heating to the candy production, the warm water circuit, as well as the domestic hot water and building air handling.

3.2. Process description and requirements

In order to proceed with the pinch analysis, the process requirements must be extracted. While the stream data have been adapted for this paper, they originate from stream measurements conducted directly on-site. Process diagrams, monitoring systems and online measurements were consulted to characterize the thermal energy demands of the process. The adapted process requirements are found in Table 1. Where stream identifiers (IDs) have been duplicated between streams, this reflects a sharing of the process equipment between seasons or shifts.

Table 1 Process requirements (AY All Year, S Summer, TP Transition Period, W Winter)

Process Stream	**Stream ID**	**Process period**	**Inlet T. (°C)**	**Outlet T. (°C)**	**CP (kW/K)**	**$\dot{Q}$ (kW)**	**α (W/m^{2}K)**
Exhaust Air	H2	AY	55	25	2.43	73	100
Drying Air	C3	S	20	64	2.27	100	50
	C3	TP	12	41	1.92	56	50
	C3	W	5	64	1.27	75	50
BB Vapor 1 bar(a)	H1	AY	99.7	99.6	1200	120	5000
BB Hot Water	C1	AY	95	110	6.0	90	1000
BB Warm Water	C2	S	50	70	20.0	400	1000
	C2	TP	50	70	10.5	210	1000
	C2	W	50	70	13.0	260	1000
BB Cooling Water	H4	S	35	25	28.0	280	1000
	H4	TP	35	25	8.0	80	1000
	H4	W	35	25	6.5	65	1000
BB Cooling	H3	AY	35	25	18.0	180	1000
SFC Vapor 0.5 bar(a)	H1	AY	81.4	81.3	500	50	5000
SFC Warm Water	C2	S	50	70	20.0	400	1000
	C2	TP	50	70	10.5	210	1000
	C2	W	50	70	13.0	260	1000
SFC Cooling Water	H4	S	35	25	17.5	175	1000
	H4	TP	35	25	5.0	50	1000
	H4	W	35	25	3.0	30	1000
HFC Vapor 0.75 bar(a)	H1	AY	91.8	91.7	800	80	5000
HFC Warm Water	C2	S	50	70	20.0	400	1000
	C2	TP	50	70	10.5	210	1000
	C2	W	50	70	13.0	260	1000
HFC Cooling Water	H4	S	35	25	21.0	210	1000
	H4	TP	35	25	6.0	60	1000
	H4	W	35	25	3.5	35	1000

During candy production of any variety, vapor is produced during the boiling and cooking of the gelatin mixtures and according to the temperatures of the cook, the produced vapors vary in pressure (0.5, 0.75, and 1.0 bar absolute). BB production demands the hottest boiling temperatures, and therefore produces the highest vapor pressures. During modelling, all vapor streams are handled as simplified phase changes, having a small temperature difference and a large heat capacity flowrate (CP). After cooking, the candies are formed using cornstarch casts. Before casting can commence the casts must be air-dried, which produces a stream of humid air (Table 1, "Exhaust air"). This humid air is cooled in order to dehumidify it. During dehumidification partial condensation occurs and causes the stream coefficient of heat transfer to increase, as reflected in the table (100 W/m^2K).

Drying air is also required for candy drying, which takes place immediately after casting. The candies are moved to a drying room where a mixture of fresh air and re-circulated room air is cooled and dehumidified via an adsorption process to maintain the room at a specific temperature and humidity. The fresh air used in this drying process must itself first be cooled and dehumidified, before being sent to the drying room. The candies are left in this room for up to 72 hours at a time, meaning this room is in use throughout the day. Dehumidification processes for building air handling also operate, however only during the summer period.
In the final hour of each shift, after the cooking and processing equipment are no longer required, CIP water is used to clean and purge the entire system before the next shift. This cleaning produces wastewater, which is currently used for regenerative heating of the CIP water in a newly constructed heat recovery system. Therefore, the CIP and wastewater were not considered during the integration analysis.

Throughout candy production, warm water and cooling water are both used to provide general heating and cooling, and their requirements vary between seasonal periods. In summer, the dehumidification process for building air is active, and significantly increases both heating and cooling demands compared to winter and the transitional period. In addition to this, warm water demands are higher in winter than the transitional period as a result of lower ambient temperatures. Depending on the variety of candy produced, the cooling water requirements also differ due to differences in the production methods. For BB production an additional hot water stream is used during an intensive cooking phase not required during SFC and HFC production.

3.3. Process scheduling

Process scheduling is displayed as a Gantt chart (Fig. 4), which shows the daily production shifts of the plant. Candy production takes place in three shifts, each approximately eight hours in length. This includes an hour for cleaning after production equipment is out of use. The streams associated with heating and cooling during production are assumed continuous over the shift duration, although this is a simplification. Many batches of candies are produced within their 8-hour shift. According to the TSM, the process is divided into six identified Time Slices (TS), although only time slices 1, 3 and 5 are used as the basis for the HP integration. Time slices 2, 4, and 6 were omitted during HP integration as once the wastewater streams were discounted, the exhaust air and drying air streams did not provide enough remaining heat integration for inclusion in the HPTES system according to the pinch analysis.

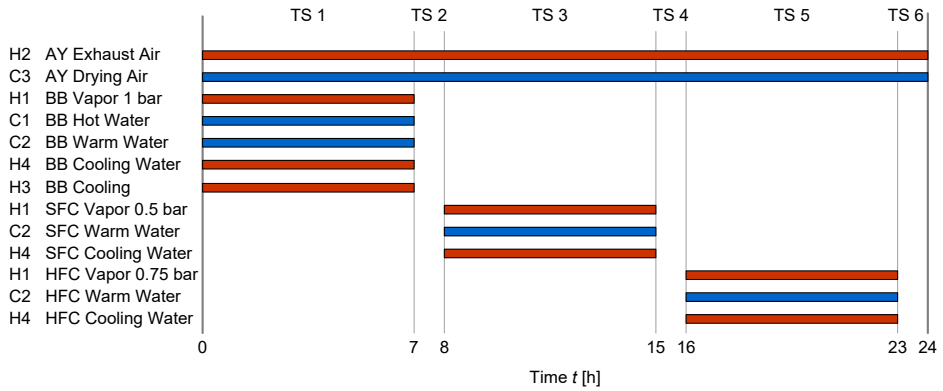


Fig. 4. Gantt-Chart of the daily operating schedule for all seasonal periods

The site is assumed to be in continuous operation 6,000 hours annually. This excludes process downtime such as weekends, in order to simplify the energy targeting analysis [16]. The process hours per individual variety of candy are 438 hours of production and 62 hours of cleaning during summer and winter. During the transitional period, these increase to 875 hours of production and 125 hours of cleaning per candy variety.

3.4. Results

Heat pump and storage sizing

The heat pump was initially sized using generated time slice GCCs of TS1, TS3, and TS5, displayed in section 2 (Fig. 2). A ΔT_{min} of 5 K was selected for all TSs, to avoid the possibility of causing untenably impractical design solutions which require extensive control systems in order to operate successfully. The shown GCCs correspond to the surplus and deficit heat available during the transitional period, which was chosen as a basis for sizing as it is the longest period of seasonal operation. A condensation temperature was selected ($T^*_{cond,sel}$ = 67.75°C, $T_{cond,sel}$ = 74.0°C) that allowed the majority of the required heating demands of all TSs (90 kW, 160 kW, 130 kW) to be satisfied, while remaining as close as possible to the pinch temperature (52.5°C). The COP curves for these time slices were then constructed to locate the initial evaporation temperature. For TS1 there is a relatively large amount of available heat below the pinch point (Fig. 2, TS1), as compared to the later time slices. The heating demands of the process increase from 90 kW in TS1 to 130 kW TS5, peaking at 160 kW during TS3 (Fig. 2, TS3&5). An evaporation temperature was searched (T^*_{evap} = 27.6°C, T_{evap} = 21.35°C) which satisfied the energy balance, resulting in needing TES cooling capacity to cover the cooling demand (152 kW) during TS1, and TES heating capacity to cover the demand for the later time slices (53 kW, 58 kW). These values were then used to construct the supply and demand curves, enabling final sizing of the heat pump condenser (Fig. 3, right, 110 kW) evaporator (Fig. 3, left, 77 kW) as well as the required capacities of the cold and hot side thermal storages (Fig.3, 0.53 MWh, 0.36 MWh). Expressed in cubic meters of water storage, the required storages are 91.3 m^3 (hot side) and 60.0 m^3 (cold side).

The same approach is used to size the storages and the heat pump for winter and summer operation. However the resulting storage capacities were found to be impractically large requiring in excess of 200 m^3 of storage, as high energy demands of summer dehumidification processes come online. This amount of storage is only required during summer, and would remain unused during the other seasonal periods which require significantly less energy due to the absence of taxing dehumidification processes. Therefore, it was decided that in order for the system to remain practically viable, the system was sized according to the period of longest duration (transitional period). This still allows significant savings to be realized during summer and winter although does not completely exploit the savings potential inherent therein. Sizing according to the transitional period only provides some additional economic benefit, as storage and heat pump investment costs are relatively reduced and as the system is designed around one continuous operational point, system complexity and control issues are minimized. As a consequence, the full capacity of the storage is in constant use which helps to reduce thermocline degradation.

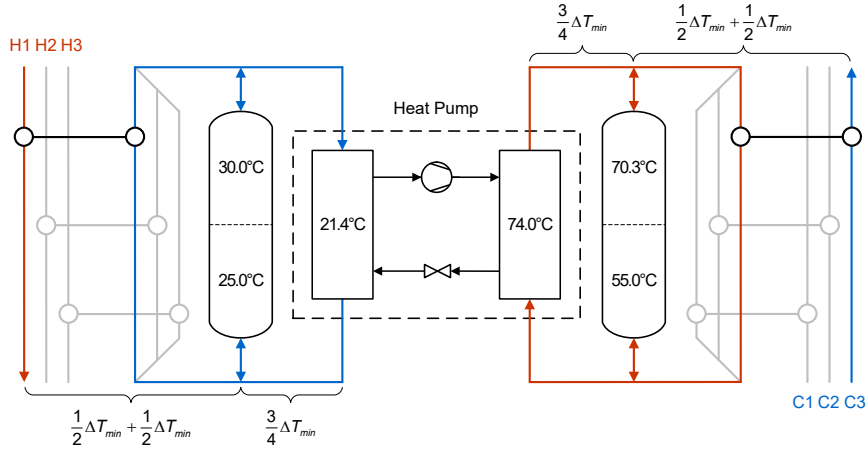


Fig. 5. Conceptual design of the HPTES superstructure

Design of HPTES system

The conceptual design of the HPTES system is given (Fig. 5) showing the heat pump evaporation and condenser temperatures and the temperatures of the storage layers. A summary of the HPTES specifications appear in Table 3.

Table 3 Heat pump and TES specifications

Pinch T. (°C)	Evaporation /Condenser temperature (°C)	Heat pump COP (-)	Condenser load (kW)	TES Hot storage layer temperatures (°C)	TES Cold storage layer temperatures (°C)	TES Hot storage Volume (m^3)	TES Cold storage Volume (m^3)
52.5	21.4/74.0	3.3	111	55.0/70.3	25.0/30.0	60.0	91.3

Design of HEN

The HEN design for the integration of the heat pump and TES system into the process is given (Fig. 6). Integrated streams appear on the right side of the diagram, including the streams HPTES Hot and Cold which represent the intermediate loops of the HPTES system. The design shows the overall HEN with maximum HEX areas, rather than any TS specific HEN where utilized HEX areas may be less than the maximum. HEX areas are displayed beneath their icons. The temperature ranges of the streams are displayed as target and supply temperatures, which begin and end at the pinch (T_p = 52.5°C). The drying air (C3) temperatures are given for each seasonal period (W/TP/S). Utility HEXs have been demarked using arrowed HEXs. The cold utility HEXs have been greyed out, as these are pre-existing heat exchangers which are not considered in the cost calculations. The exhaust air (H2) is a so-called "soft" stream which can provide heating during TSs where this heat can be utilized. If not, the heat is expelled directly to the environment (dotted grey cooler). When calculating energy and cost savings, the cold utility use of this stream is ignored.

Energy savings of the HPTES integration

The hot and cold utility savings after HPTES integration are tabulated (Table. 6). The utility demands of the process per seasonal period have been summed and are presented alongside the required electrical input to the HP. After HPTES integration, there is a large HU (65.3%) and CU (74.1%) utility reduction, equaling an overall utility reduction of 68.8%. This includes the savings from direct heat recovery measures.

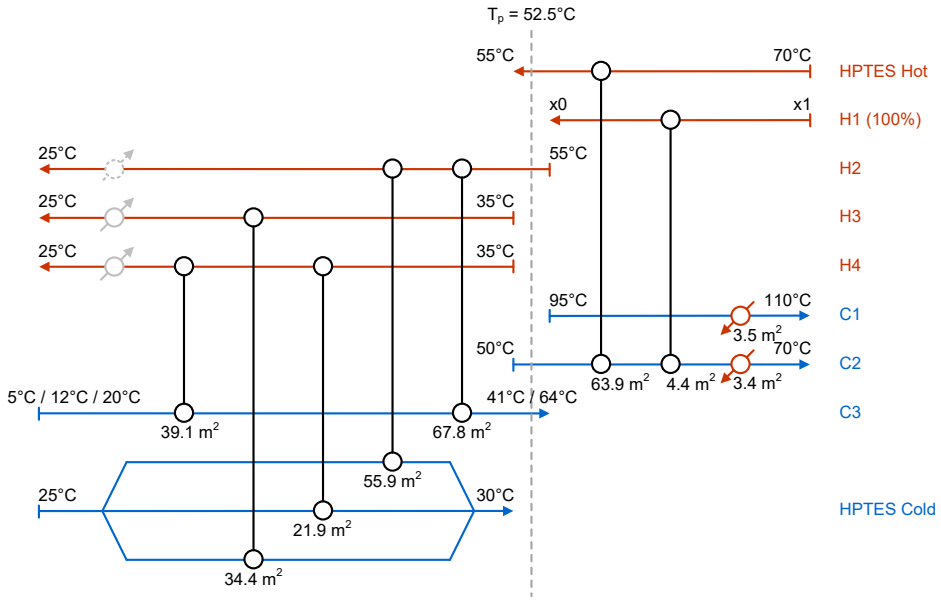


Fig. 6. Conceptual HEN design for candy production (maximum HEX areas)

Table 6 Seasonal energy savings

	Current state		**With HR and HPTES**		
Seasonal Period	Hot Utility (MWh)	Cold Utility (MWh)	Electrical input (MWh)	HU savings (MWh)	CU savings (MWh)
Summer	651.4	429.1	51.2	283.1	177.9
Transitional Period	651.0	494.5	102.4	568.8	486.2
Winter	436.3	205.1	51.2	284.3	171.9
Total	1,738.7	1,128.7	204.8	1,136.2	836.0

Financial analysis

The economics of the HPTES system have been analyzed using prices of hot utility (80 CHF/MWh), cold utility (25 CHF/MWh) and electricity (100 CHF/MWh) provided by the industrial partner. A detailing of the finances are found in Table 7. The system requires an investment of CHF 564,000 (including transport, installation, and VAT) which can be paid back within 6.2 years with annual savings of CHF 91,000. The electricity costs of the installation are CHF 21,000. The calculated return on investment for the HPTES and heat recovery system is approximately 11%.

Table 7 Payback and return on investment calculation of heat recovery measures and heat pump integration. Prices include VAT (8%).

Equipment		**Investment cost**
HEXs of heat recovery measures (incl. HRL)	CHF	202,000
Heat pump	CHF	147,000
TES	CHF	215,000
Total investment	**CHF**	**564,000**
Life time		15 years
Interest rate		3%
Annuity	**CHF**	**47,000**
Total savings of heat recovery measures per year	CHF/y	47,000
Total savings of HPTES system per year	CHF/y	44,000
Total savings	**CHF/y**	**91,000**
Operational costs of HPTES system per year	CHF/y	21,000
Total operational costs	CHF/y	**21,000**
Payback		6.2 years
Net income during payback period	CHF/y	23,000
Net income after payback period	CHF/y	70,000
Return on investment		11%

4. Conclusions

A practical procedure for heat pump integration into a non-continuous candy manufacturing process in Switzerland has been presented. The work allows for integration of a continuously running heat pump and thermal energy storage system that can meet daily variations in process demands. The combined heat pump (condenser 111 kW, evaporator 77 kW) and thermal energy storage system achieves an average utility reduction of 68.8% (65.3% cold utility, 74.1% hot utility) and can be paid back within a reasonable economic time frame of 6.2 years., with an internal rate of return of 11% per year. Whilst not a strictly optimal integration, the procedure has provided a practical, workable, and profitable solution for the case study, that is readily understood by the intended end users in industry. As future work it is recommended to apply a complete thermo-economic optimization, using the extended hybrid method which includes mathematical optimization of the HPTES parameters, in order to locate any potential designs which could further increase energy and cost savings without compromising practicability and controllability.

Acknowledgements

This research project is financially supported by the Swiss Federal Office of Energy SFOE (contract no. SI/501822-01). It is part of the accompanying research in the Swiss Competence Center for Energy Research SCCER EIP.

References

[1] EU ODP, 2017. European Union Open Data Portal. [online] available from <https://bit.ly/2NzqQPA> [Accessed 12 Nov. 2019]
[2] Linnhoff B., 1993. Pinch Analysis – A state-of-the-art overview. *Trans IChemE* 71, 503–22
[3] Townsend D.W., Linnhoff B., 1983. Heat and power networks in process design. Heat and power networks in process design. Part I: Criteria for placement of heat engines and heat pumps in process networks, *AIChE J.* 29, 742-748.

[4] Wallin E., Franck P.Á., Berntsson T., 1990. Heat Pumps in Industrial Processes – an Optimization Methodology, *Heat Recovery Systems & CHP* 10, 437-446
[5] Wallin E., Berntsson T., 1994. Integration of Heat Pumps in Industrial Processes, *Heat Recovery Systems & CHP* 14, 287-296
[6] Kemp I.C., 2007. *Pinch analysis and process integration - a user guide on process integration for the efficient use of energy*. 2nd Edition, Oxford, UK, Elsevier Ltd, 25–27
[7] Smith R., 2016. *Chemical Process Design and Integration*, 2nd Edition, Chichester, UK, John Wiley & Sons, 475-477
[8] Linnhoff B., Ashton G.J., Obeng E.D.A., 1988. Process integration of batch processes. *IChemE symposium series*, 109, 221-237.
[9] Stampfli J.A., Atkins M.J., Olsen D.G., Walmsley M.R.W., Wellig B., 2019. Practical heat pump and storage integration into non-continuous processes: A hybrid approach utilizing insight based and nonlinear programming techniques. *Energy*, 182, 236–253
[10] Lambauer J., Fahl U., Ohl M., Blesl M., 2008. Large scale industrial heat pump – market analysis, potentials, barriers and best - practice examples, 9th IEA Heat Pump Conference. Zürich, CH
[11] Olsen D., Abdelouadoud Y., Liem P., Hoffmann S., Wellig B., 2017. Integration of Heat Pumps in Industrial Processes with Pinch Analysis, 12th IEA Heat Pump Conference. Rotterdam, NL
[12] de Boer R., Smeding S., Biesheuvel K., 2017. Waste heat recovery in industrial batch processes: analysis of combined heat storage and heat pump application, 12th IEA Heat Pump Conference. Rotterdam, NL
[13] Schlosser F., Arpagaus C., Walmsley TG. 2019. Heat Pump Integration by Pinch Analysis for Industrial Applications: A Review. *Chem. Eng. Trans* 76, 7-12
[14] Wang YP., Smith R. 1995. Time pinch analysis. *Chem Eng Res Des* 73, 905–914.
[15] Becker HC. 2012. *Methodology and thermo-economic optimization for integration of industrial heat pumps*, PhD Thesis, École Polytechnique Féderale de Lausanne. Lausanne, CH
[16] Brunner F., Krummenacher P. 2015. *Einführung in die Prozessintegration mit der Pinch-Methode– Handbuch für die Analyse von kontinuierlichen Prozessen und Batch-Prozessen*, Bundesamt für Energie, CH

Nomenclature

$c_{p,HRL}$	Heat capacity of storage media [kJ/kgK]	T^*_{evap}	Evaporation temperature (shifted) [K]
l	Time slices ($l \in \{1..., L\}$	$T^*_{evap,min}$	Minimum evaporation temperature (shifted) [K]
$m_{C,HRL}$	Cold storage media mass [kg]	$T^*_{evap,max}$	Maximum evaporation temperature (shifted) [K]
$\dot{Q}$	Heat flow [kW]	$T^*_{evap,bal}$	Evaporation temperature for energy balance(shifted) [K]
$\dot{Q}_{cond}$	Condenser heat flow [kW]	T_p	Pinch temperature [K]
$\dot{Q}_{evap}$	Evaporator heat flow [kW]	α	Heat transfer coefficient [W/m²K]
$\dot{Q}_{C,HRL}$	Cold storage cooling load [kW]	$\Delta\dot{Q}^-_{TES}$	Heat flow to thermal storage [kW]
P_{el}	Heat pump electrical power [kW]	$\Delta\dot{Q}^+_{TES}$	Heat flow from thermal storage [kW]
Pi	Heat pump input power [kW]	Δt_l	Time slice duration [s]
$T_{C,h}$	Cold storage hot temperature [K]	ΔT_{min}	Pinch temperature difference [K]
$T_{C,c}$	Cold storage cold temperature [K]	$\eta_{2nd\ law,\ HP}$	Second-law efficiency [-]
T_{cond}	Condenser temperature [K]	η_{drive}	Drive efficiency [-]
T^*_{cond}	Condenser temperature (shifted) [K]		
$T^*_{cond,sel}$	Selected condensation temperature (shifted) [K]		
T_{evap}	Evaporation temperature [K]		

Abbreviations

AY	All year	GCC	Grand composite curve
BB	Bonbons	GHG	Greenhouse gas
CC	Composite curve	Hx	Hot stream x
CIP	Clean in place	HEN	Heat exchanger network
COP	Coefficient of performance	HEX	Heat exchanger
CP	Heat capacity flowrate	HFC	Hard fruit candy
Cx	Cold stream x	HP	Heat pump
CU	Cold utility		

HPTES	Heat pump thermal energy storage system
HRL	Heat recovery loop
HU	Hot utility
ID	Identifier
IRR	Internal rate of return
PA	Pinch analysis
S	Summer
SFC	Soft fruit candy
TES	Thermal energy storage
TP	Transition period
TS	Time slice
TSM	Time slice model
W	Winter

13th IEA Heat Pump Conference
April 26-29, 2021 Jeju, Korea

High-efficiency low temperature lift heat pump with novel oil-free, gas-bearing turbo compressor

Dominic Zajonc[a], Stefan Flück[a], Edward J. Lucas [a], Andreas Lehr[b], Beat Wellig[a,*]

[a]Lucerne University of Applied Sciences and Arts, Horw 6048, Switzerland
[b]Teqtoniq GmbH, Horw 6048, Switzerland

Abstract

The Coefficient of Performance (COP) of a heat pump and the Energy Efficiency Ratio (EER) of a chiller are strongly dependent on the internal temperature lift, which corresponds to the difference between the condensation and evaporation temperatures. In modern and efficient building heating and cooling systems, low temperature lifts can be achieved. Turbo compressors have high efficiencies at low pressure ratios during full and part-load operation, thus suiting low temperature lift building heating/cooling applications well. This paper presents the results of experimental investigations on a prototype low temperature lift heat pump/chiller with a heating capacity of 500 kW. The heat pump/chiller is equipped with four novel oil-free turbo compressors built with patented, self-acting gas bearings. High efficiency values during full and part-load operation were measured. Second-law efficiencies for building heating applications of up to 62% were determined. Further increases in efficiency during part-load operation are possible by implementing inlet guide vanes or by shifting the design point of the compressor to lower capacities.

Keywords: turbo compressor; oil-free; low temperature lift; water/water heat pump

1. Introduction

1.1. Background

The development of highly efficient processes and products to significantly reduce CO2 emissions and reach stringent climate targets is one of the biggest challenges of this century. The heating and cooling of buildings requires large amounts of energy, reaching up to 73% of regional energy demands [1]. Experts agree that there is still substantial potential to increase the efficiency of heat pump and chiller systems. The efficiency of heat pumps or chillers is specified by the Coefficient of Performance (COP) or the Energy Efficiency Ratio (EER) and is strongly dependent on the internal temperature lift, which corresponds to the difference between the condensation and evaporation temperatures. The required internal temperature lift depends on the heat source and sink of the system. For modern and efficient building heating systems low temperature lifts between 15 K and 30 K are often sufficient: For efficient building cooling systems even lower temperature lifts between 10 K and 20 K are possible. However, heat pumps and chillers only achieve high second-law efficiencies at low temperature lifts if they are specially designed for the corresponding operating conditions. With the development of low temperature lift heat pumps and chillers, the potential of low temperature lift applications can be exploited.

Moreover, moderate to poor part-load efficiencies often diminish the annual efficiency of building heating and cooling systems, which is a frequent issue as maximum capacity is required only rarely during the year. Turbo compressors have high efficiencies at low pressure ratios during both full and part-load operation, thus suiting low temperature lift building heating and cooling applications well. Resultantly, annual efficiencies of heat pumps and chillers that employ turbo compressors can be significantly higher as compared to systems that employ other compressor types.

1.2. Temperature lifts of building heating and cooling

A short summary of temperature lifts in building heating and cooling applications is presented below. For further details, a comprehensive overview can be found in Gasser et al. [2].

Heating applications

The internal temperature lift of a heat pump used for building heating depends substantially on the heat source and the heat delivery system. In most applications, the temperature lift is typically around 15 K to 75 K (Fig. 1, left). For an efficiently heated low-energy building, desirable temperature lifts range from 15 K to 30 K. This would entail, for example, geothermal heat probes or ground water as the heat source and a modern low-temperature heat distribution and delivery system such as an underfloor heating system. The COP_{ideal} of an ideal heat pump (i.e. Carnot heat pump between the evaporation and condensation temperatures) as a function of the temperature lift for a constant evaporation temperature of 10°C is shown (Fig. 1, right). For a temperature lift of 20 K, a COP_{ideal} of 15.2 is possible. If a system with a second-law efficiency of 60% were implemented, a COP of 9.1 would result.

Cooling applications

The temperature lift of a chiller used for building cooling depends substantially on the space cooling and re-cooling system. In most applications, the temperature lift is typically around 10 K to 55 K (Fig. 2, left). For an efficiently cooled low-energy building located in central Europe, desirable temperature lifts range from 10 K to 30 K. This would entail, for example, space cooling using chilled ceilings, concrete core activation or highly efficient fan coil units and an efficient hybrid/adiabatic re-cooling system. The EER_{ideal} of an ideal chiller (i.e. Carnot chiller between the evaporation and condensation temperatures) as a function of the temperature lift for a constant evaporation temperature of 14°C is shown (Fig. 2, right). For a temperature lift of 12 K, an EER_{ideal} of 24 is possible. If a system with a second-law efficiency of 60% were implemented, an EER of 14.4 would result.

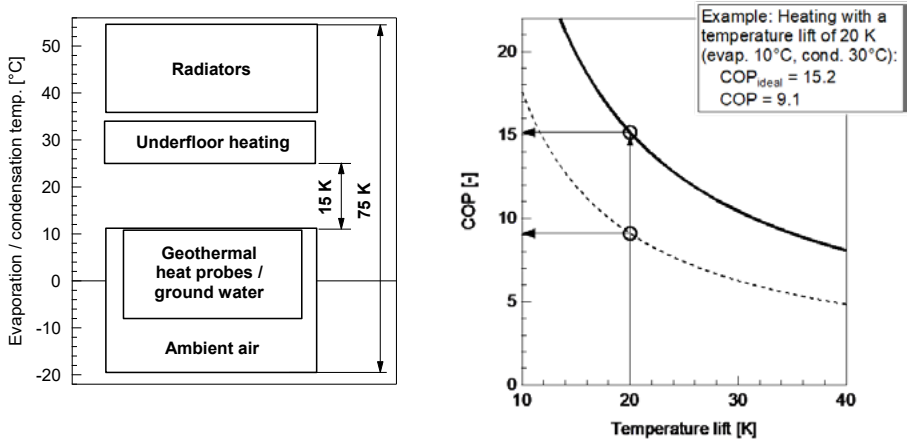


Fig. 1. Left: Typical evaporation and condensation temperatures and temperature lifts of different heat pump systems
Right: COP of an ideal heat pump and a real heat pump with a second-law efficiency of 60% as a function of the temperature lift for a constant evaporation temperature of 10°C [2]

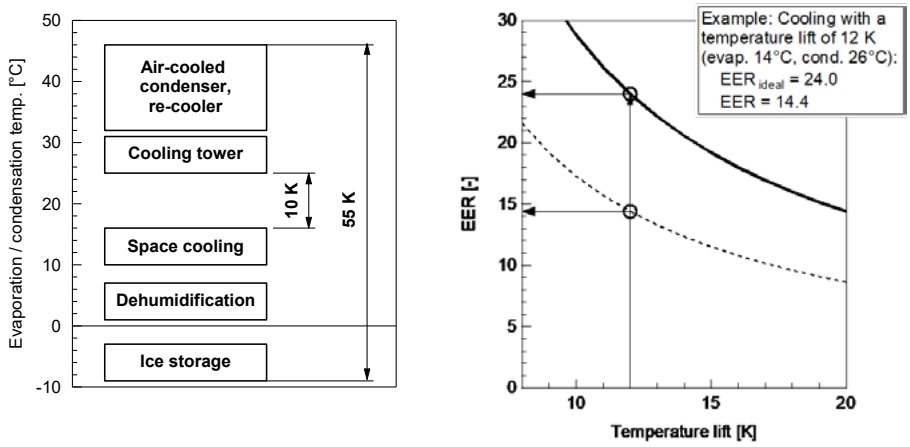


Fig. 2. Left: Typical evaporation and condensation temperatures and temperature lifts of different chiller systems
Right: EER of an ideal chiller and a real chiller with a second-law efficiency of 60% as a function of the temperature lift for a constant evaporation temperature of 14°C [2]

1.3. State-of-the-Art and recent research

The use of turbo compressors in compression heat pumps and chillers originates in 1922 when the first centrifugal refrigeration compressor was presented [3]. Today, turbo compressors are mainly widespread in larger heat pumps and chillers with up to several megawatts of heating/cooling capacity. Prestigious manufacturers include Carrier, Danfoss Turbocor, Friotherm and Mitsubishi Heavy Industries.

The smallest available compressors from these manufacturers are about 200 kW nominal cooling capacity. Most compressors above 200 kW nominal cooling capacity were found not to utilize gas bearings, requiring oil lubrication. As an exception, Danfoss Turbocor uses magnetic bearings and is thus the only manufacturer providing oil-free compressors within this capacity range. For heat pumps/chillers with lower capacities, the use of turbo compressors is rather rare. The manufacturers Celeroton and Fischer offer oil-free refrigerant turbo compressors in the range of 20 kW nominal cooling/heating capacity and utilize gas bearings. Accordingly, there is a market gap in capacity of available turbo compressors.

In recent years, various turbo compressors for heat pump and chiller systems have been introduced across several IEA Heat Pump Conferences. Generally, the presented turbo compressors can be split amongst two groups, those with nominal heating capacities in the range of 20 kW, and those with nominal heating capacities greater than 500 kW, with exception to that presented by Kim et al. (ca. 130 kW heating capacity) [4].

For nominal heating capacities in the range of 20 kW, it is noticeable that the rotational speeds are relatively high with 160-280 krpm [2], [5], [6]. For this application and these rotational speeds, Arpagaus et al. already presented self-acting gas bearings which remove the need for oil lubrication [6]. At heating capacities above 130 kW the rotational speeds are often significantly lower with 11-24 krpm [4], [7]. Accordingly, ball and rolling bearings [4], [8], and seldomly, magnetic bearings [9], are used.

Only Gasser et al. indicates the resulting second-law efficiency (determined with the operating condensation and evaporation temperatures) when operating the turbo compressor in a heat pump, which was found to be at maximum 64% [2].

The presented turbo compressors for small heating capacities are intended for use in heat pumps for building heating [2], [6]. For higher heating capacities, the turbo compressors are often used to generate hot water in the range of 75-95°C [9], [10], [11].

From a research perspective, much of the work conducted regarding turbo compressors follows the same trends as the market, tending not to focus on the 20 to 200 kW capacity range.

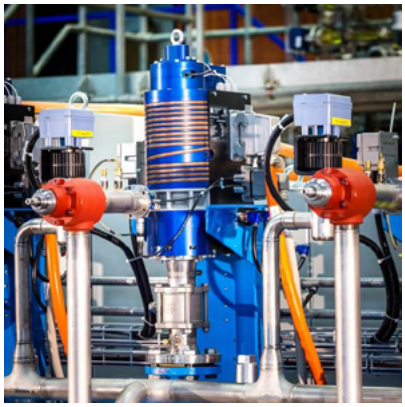


Fig. 3. Novel oil-free, gas-bearing turbo compressor by Teqtoniq GmbH installed in a heat pump/chiller

1.4. Objectives

The goal of this paper is to demonstrate the efficiency of a heat pump/chiller equipped with a novel oil-free, gas-bearing centrifugal turbo compressor. The overall project aim is the development of a marketable and highly efficient centrifugal turbo compressor for heat pumps and chillers with a cooling capacity of 20-100 kW per compressor.

2. Novel oil-free, gas-bearing turbo compressor

The novel, oil-free and gas-bearing centrifugal turbo compressor presented is a development of the Swiss company Teqtoniq GmbH in collaboration with the Lucerne University of Applied Sciences and Arts. The compressor has been developed for use in heat pump and chiller systems with temperature lifts up to 40 K. The cooling capacity of a single compressor can be increased from about 20 kW to 100 kW. Patented self-acting gas bearings are used to support the shaft and impellers at rotational speeds of up to 60 krpm. The gas bearings eliminate the need for oil lubrication, allowing the compressor to operate completely oil-free. Due to the similar gas properties, the compressor can be used with the refrigerants R1234ze, R513a and R134a. In this paper, only the refrigerant R1234ze is considered. The technical data of the compressor are summarized in Table 1.

Table 1 Technical Data of the novel oil-free, gas-bearing turbo compressor by Teqtoniq GmbH

Type	**centrifugal, two-stage**
Electrical power	max. 28 kW
Rotational speed	variable, max. 60 krpm
Refrigerant	R1234ze
Nominal cooling capacity	100 kW
Pressure ratio	max. 4.0
Mass flow rate	max. 0.8 kg/s

3. Experimental setup

3.1. Test rig

The test rig located at the Lucerne University of Applied Sciences and Arts allows the experimental investigation of various thermal systems. Such systems include chillers and heat pumps (up to a cooling capacity of 600 kW) as well as heat exchangers or thermal energy storages.

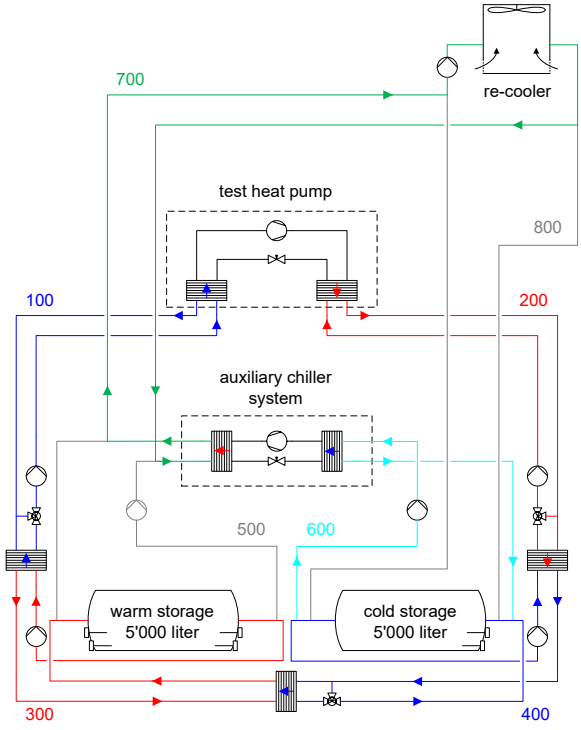


Fig. 4. Simplified schematic view of the test rig at the Lucerne University of Applied Sciences and Arts; application “testing a water/water heat pump/chiller”; cooling of the infrastructure via auxiliary chiller system

With this infrastructure, it is possible to provide heating and cooling within a temperature range of -20°C to +80°C. The core are two separate warm and cold storage tanks, each with capacities of 5,000 litres and filled with an aqueous glycol mixture. Depending on the application, the storage tanks can be conditioned using an auxiliary chiller system, a re-cooler, or electric heating rods. The heat is distributed in various circuits, which are equipped with variable-speed pumps and flowmeters for flow control. The temperatures of some individual circuits are controlled via 3-way mixing valves. With this test rig it is possible to experimentally investigate heat pumps and chillers according to the test standard EN14511. The requirements for control and measurement accuracy can be easily met. Fig. 4 shows a simplified schematic view of the test rig for the application "testing a water/water heat pump/chiller".

When testing a water/water chiller, in circuit 100 the water temperature and mass flow into the evaporator of the test heat pump are adjusted to the specified nominal values. This allows the simulation of a real heat source. In circuit 200, the water temperature and mass flow into the condenser of the test heat pump are adjusted, thereby simulating the heat sink. The two circuits 100 and 200 are connected with the two “inner” circuits 300 and 400 via three heat exchangers. This allows the heat generated at the condenser of the test heat pump to be partially fed to the evaporator of the test heat pump, resulting in maximum heat recovery. The excess heat generated by the larger condenser heat flow in the test heat pump is stored in the cold storage tank, which heats up as a result. When a maximum target temperature is reached, the cold storage tank is cooled to a minimum target temperature via circuit 600 with the auxiliary chiller system. The condenser waste heat from the auxiliary chiller system is released to the ambient air via circuit 700 with the aid of a re-cooler. The task of the warm storage tank is to compensate for temperature fluctuations that occur in circuits 200 and 400. This ensures a constant temperature at the inlet to the heat exchanger, which separates circuits 100 and 300.

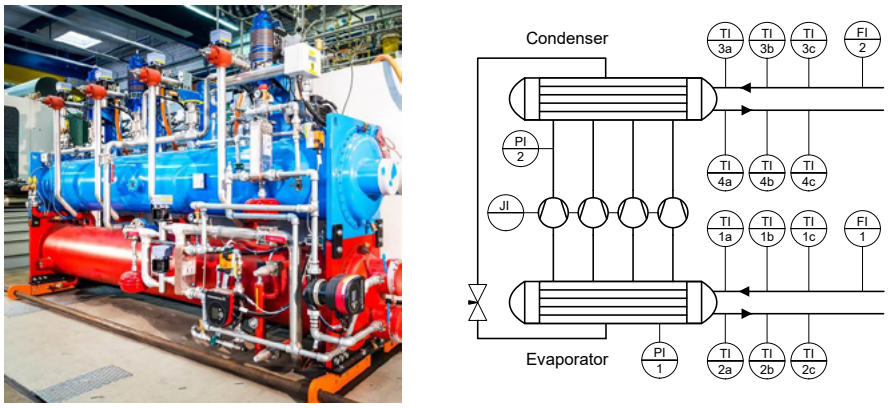


Fig. 5. Left: Water/Water heat pump/chiller with four novel oil-free, gas-bearing turbo compressors by Teqtoniq GmbH
Right: Measurement scheme for the heat pump/chiller; PI: pressure indicator, TI: temperature indicator, FI: mass flow rate indicator, JI: electrical power indicator

3.2. Heat pump/chiller prototype

The tested heat pump/chiller prototype (Fig. 5, left) is equipped with four novel oil-free turbo compressors with self-acting gas bearings. Each turbo compressor has a nominal cooling capacity of approximately 100 kW, resulting in an overall nominal cooling capacity of 400 kW or 500 kW heating capacity, respectively. The capacity of the heat pump can be regulated by the rotational speed of the turbo compressors and by switching compressors on and off. The measurement scheme for the heat pump is also given (Fig. 5, right).

3.3. Test conditions

Heat pump application

The seasonal performance of a heat pump for building heating is determined in compliance with the EN14825 standard [12]. Depending on the heat source and sink, the standard specifies operating points with different part-load ratios for the heat pump. The experimentally determined COP values at the respective operating points can then be used to calculate the expected seasonal performance factor associated with climatic conditions of a location. This paper presents a water/water heat pump designed for low temperature lifts. Hence, only low-lift operating conditions of the EN14825 standard are tested. The operating conditions for a heat pump that works with a heat source such as ground water (10°C) and provides heating water with low temperatures (max 35°C) for an efficient new building therefore apply (Table 2). The water flow rates of heat source and sink in evaporator and condenser are determined by adjusting them such that the water inlet and outlet temperatures match the specified temperatures (10/7°C, 30/35°C) for full load operation (see Table 2). For every other operating point, the determined flow rates are kept constant, resulting in a decreasing temperature differential between inlet and outlet as part-load is reduced.

Chiller application

The seasonal performance of a chiller for building cooling is stated frequently using an index called the European Seasonal Energy Efficiency Ratio (ESEER), which is based on the EN14511 standard. This index represents an average annual efficiency of chillers for building cooling purposes in Europe. To achieve this, EER values at full load and in different part-load operating points are combined using different weighting coefficients. The operating points differ depending on the heat source and heat sink used. The water flow rates of heat source and sink in evaporator and condenser are determined as before (see Table 3). For every other operating point, the determined flow rates are kept constant.

Table 2 Test conditions for the test heat pump in heating applications in compliance with the EN14825 [12] standard

Part-load	Water temperatures evaporator in/out [°C]	Water temperatures condenser in/out [°C]
100%	10 / 7	30 / 35
88%	10 / -	- / 34
54%	10 / -	- / 30
35%	10 / -	- / 27
15%	10 / -	- / 24

Table 3 Test conditions for the test chiller in cooling application in compliance with EN14511 [13] and Eurovent [14] standards

Part-load	Water temperatures evaporator in/out [°C]	Water temperatures condenser in/out [°C]
100%	12 / 7	30 / 35
75%	- / 7	26 / -
50%	- / 7	22 / -
25%	- / 7	18 / -

4. Results and discussion

Heat pump application

For heat pump application measurements, the heat pump presented in Section 3.2 was operated with only three turbo compressors. This is because one turbo compressor was demounted for inspection at the time of the measurements. The nominal heat output at 100% load ratio is accordingly related to three turbo compressors and corresponds to approximately 370 kW heat output. The operating points listed in Table 2 are measured based on the EN14511 standard. The results are shown in Fig. 6. The characteristic values COP and second-law efficiency are determined according the following equations:

$$\mathrm{COP_{HP}} = \frac{\dot{Q}_{cond}}{P_{el}} \; ; \; \mathrm{COP_{Carnot}} = \frac{T_{cond}}{T_{cond} - T_{evap}} \tag{1}$$

$$\eta_{2nd\ law,HP} = \frac{\mathrm{COP_{HP}}}{\mathrm{COP_{Carnot}}} \tag{2}$$

It can be seen that the COP increases from 6.12 to 8.48 by lowering the internal temperature lift from 31 K to 16 K (Fig. 6). The second-law efficiency (related to the evaporation and condensation temperature, i.e. internal behavior of the heat pump) decreases from 0.62 to 0.46. This behavior can be attributed to the design point of the turbo compressor, which lies at higher refrigerant volume flows and pressure ratios. This effect is further intensified by the inlet guide vanes, which are not in operation with the current prototype.

The efficiency of a turbo compressor at lower volume flows than at the design point can be increased by the correct use of inlet guide vanes. It can be seen in the right-hand plot of Fig. 6 that the second-law efficiency is the lowest at the operating point with the lowest heating output, by a considerable margin. This behavior can be explained again with reference to the design point of the turbo compressor. The required heating capacity is too small for the turbo compressor at the given temperature lift, resulting in a lower efficiency. If the nominal heat output of the heat pump had been determined with four compressors, the required heat output for one compressor in this operating point at 15% part-load ratio would have been significantly higher, and the resultant second-law efficiency would have been similarly elevated.

In summary, given a second-law efficiency within the range of 46-62% the heat pump with three novel turbo compressors shows remarkable efficiency values despite its prototype status. With optimization measures such as the tuned operation of the already installed inlet guide vanes, the efficiency of the system could be further improved. Additional increases in efficiency are possible by shifting the design point of the turbo compressor to smaller refrigerant volume flows and temperature lifts. Especially in view of the fact that the part-load operating points have a higher share of operation during the year, therefore having a larger impact on the annual efficiency.

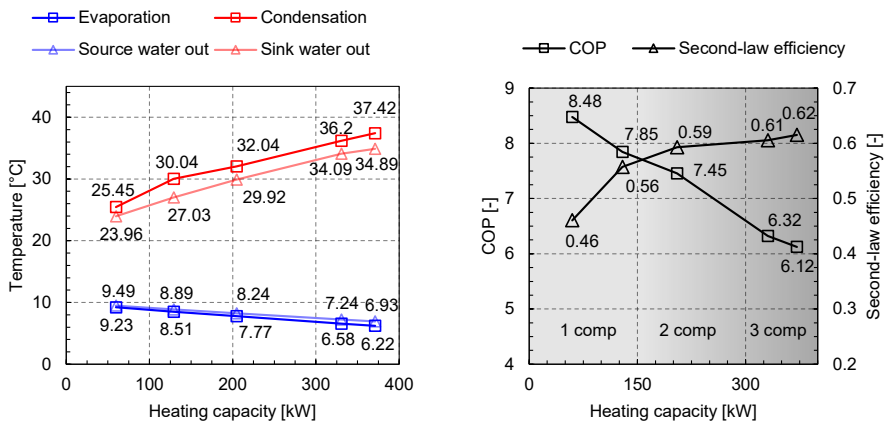


Fig. 6. Left: Water outlet temperatures of evaporator and condenser and corresponding evaporation and condensation temperature depending on the heating capacity at the operating conditions mentioned in Table 2
Right: Corresponding COP and second-law efficiency

Chiller application

The chiller presented in Section 3.2 was operated using all four turbo compressors for the chiller application measurements. The nominal cooling capacity of the system corresponds to approximately 400 kW. The chiller operating points listed in Table 3 are measured based on the EN14511 standard. The measurement scheme of the test heat pump stays the same and can be seen in Fig. 5. The results are shown in Fig. 7. The characteristic values EER and second-law efficiency are determined according to equations (3) and (4):

$$\mathrm{EER_{Ch}} = \frac{\dot{Q}_{evap}}{P_{el}} \; ; \; \mathrm{EER_{Carnot}} = \frac{T_{evap}}{T_{cond} - T_{evap}} \tag{3}$$

$$\eta_{2nd\ law,Ch} = \frac{\mathrm{EER_{Ch}}}{\mathrm{EER_{Carnot}}} \tag{4}$$

In general, similar behavior in the performance of the turbo compressor between the two applications was observed. Noticeably, the second-law efficiency has significantly increased constancy across all operating points. Here, too, the chiller with four novel turbo compressors shows remarkable efficiency values despite its prototype status. Similarly, achieving heightened efficiencies for chiller applications can be accomplished by adjusting the design point of the turbo compressor.

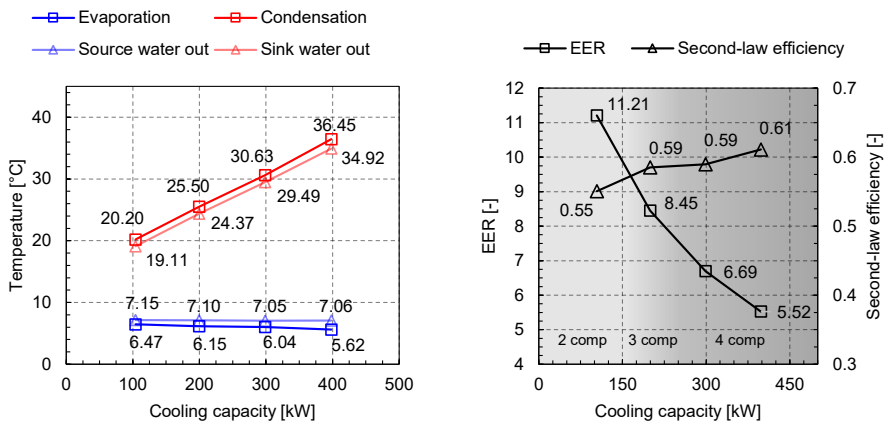


Fig. 7. Left: Water outlet temperatures of evaporator and condenser and corresponding evaporation and condensation temperature depending on the heating capacity at the operating conditions mentioned in Table 3
Right: Corresponding EER and second-law efficiency

5. Conclusions

The consistent use of available low temperature lifts in building heating and cooling can save considerable amounts of electricity. A prerequisite is that the implemented heat pump or chiller be specifically designed for these operating conditions, thus enabling high second-law efficiencies.

The heat pump prototype with four novel, oil-free and gas bearing turbo compressors shows efficiency values which are in the top range for comparable products on the market. For typical temperature lifts encountered in modern building heating and cooling systems, second-law efficiencies around 60% can be achieved for both heating and cooling applications. Overall, the prototype performs better for building cooling purposes than building heating, although is generally well suited to both. Results also indicate potential to increase the efficiency further, by ensuring that compressor part-load performance is optimized for the operating conditions most frequently encountered throughout the year. Increases in efficiency values of several percentage points would be expected, and further work is already being conducted in this area.

Finally, in order to achieve highly efficient building heating and cooling, not only must the heat pump or chiller be efficient, the entire system has to be designed to function efficiently. A non-exhaustive list of design concerns includes the hydraulic circuits, the heat exchange on the source and sink side, building dynamics, and controls systems. Considered implementation of all these measures together with efficient low-lift heat pumps and chillers will lead to a significant reduction in both exergy consumption and on-going operating costs for the heating and cooling of buildings.

Acknowledgements

We thank CTI (Commission for Technology and Innovation, Switzerland) for co-funding the project and Teqtoniq GmbH for the partnership.

References

[1] D. Ürge-Vorsatz, L. F. Cabeza, S. Serrano and C. Barreneche, “ Heating and cooling energy trends and drivers in buildings,” in Renewable and Sustainable Energy Reviews 41, 2015.
[2] L. Gasser, S. Flück, M. Kleingries, C. Meier, M. Bätschmann, and B. Wellig, “High efficiency heat pumps for low temperature lift applications,” in *12th IEA Heat Pump Conference*, 2017.

[3] National Museum of American History, “Carrier Centrifugal Refrigeration Compressor.” [Online]. Available: http://americanhistory.si.edu/collections/search/object/nmah_846092. [Accessed: 23-Aug-2018].
[4] J. Kim, Y. You, H. Jang, U. Seo and T. Kom, “Variable Speed Centrifugal Compressor,” in *7th IEA Heat Pump Conference*, 2002.
[5] J. Schiffmann, J.B. Carré, C. Arpagaus and S. Bertsch, “Turbocompressors for Domestic Heat Pumps – A Critical Review,” in *12th IEA Heat Pump Conference*, 2017.
[6] C. Arpagaus, F. Bless, S. Bertsch, A. Javed, J. Schiffmann, “Heat Pump driven by a Small-Scale Oil-Free Turbocompressor – System Design and Simulation,” in *12th IEA Heat Pump Conference*, 2017.
[7] H. Liu, B. Hu, R.Z. Wang, Z. Zhiping, L. Hongbo, W. Sheng, “Permanent-magnetic Synchronous Frequency-convertible Centrifugal Compressor and Heat Pump System,” in *12th IEA Heat Pump Conference*, 2017.
[8] W. Seki, K. Ueda, Y. Shirakata, K.Nishii and Y, Hasegawa, “Development of a High-Performance Turbo Chiller,” in *8th IEA Heat Pump Conference*, 2005
[9] P. Larminat and D. Arnou, “High Temperature Magnetic Bearing Centrifugal Heat Pump,” *in 11th IEA Heat Pump Conference*, 2014.
[10] S. Umezawa T. Nakayama and Y. Ebinuma, “Field Test of Newly Developed Turbo Heat Pump For Hot Water,” in *10th IEA Heat Pump Conference*, 2011.
[11] K. Wajima, K. Ueda, S. Okuda, N. Matsukura and J. Miyamoto, “Development of Heat Recovery Centrifugal Heat Pump for Industrial-Use,” in *11th IEA Heat Pump Conference*, 2014.
[12] SNV Schweizerische Normen-Vereinigung, “SN EN14825 Luftkonditionierer, Flüssigkeitskühlsätze und Wärmepumpen mit elektrisch angetriebenen Verdichtern zur Raumbeheizung und –kühlung – Prüfung und Leistungsbemessung unter Teillastbedingungen und Berechnung der saisonalen Arbeitszahl,“ 2016.
[13] SNV Schweizerische Normen-Vereinigung, “SN EN14511 Luftkonditionierer, Flüssigkeitskühlsätze und Wärmepumpen mit elektrisch angetriebenen Verdichtern für die Raumbeheizung und –kühlung,“ 2013.
[14] Eurovent, “Eurovent Certification Programme, Liquid Chilling Packages for Air Conditioning.” [Online]. Available: www.eurovent-certification.com/de/Programme/Merkmale.php?lg=de&rub=03&srub=01&select_prog=LCP-HP. [Accessed: 23-Aug-2017].

13th IEA Heat Pump Conference
April 26-29, 2021 Jeju, Korea

CO_2 emission savings of heat-pumps in the residential sector. Case study for multifamily buildings in Geneva

Elliot Romano*, Carolina Fraga, Pierre Hollmuller

University of Geneva, 66 Bd Carl Vogt, 1211 Genève, Switzerland

Abstract

The present paper assesses the CO_2 emissions of air-source and groundwater-source HP systems, with and without complementary PV, for a sample of multifamily buildings (new, retrofitted and non-retrofitted) located in Geneva. HP performance is evaluated by way of numerical simulation in hourly time step, and is cross-cut with the hourly grid CO_2 content of the Swiss electricity mix (taking into account both domestic generation and imports from the neighbor countries). Given the seasonal trend of both the building heat demand and the grid CO_2 content, latter turns out to strongly underestimate the CO_2 content of the HP system electricity. Nonetheless, when compared with a gas boiler, both HP systems induce important annual CO_2 savings (air: 61 - 81% depending on the accounting method; groundwater: 75% - 87%). Finally, while PV can substantially contribute to the summer HP demand, the related annual CO_2 savings remain relatively marginal, also due to seasonality of the grid CO_2 content.

Keywords: heat pump (HP); photovoltaic (PV), multifamily building; CO_2 emissions

1. Introduction

Acronyms

DHW	domestic hot water
HP	heat pump
MFB	multifamily building
PV	photovoltaic
SH	space heating

Symbols

COP	coefficient of performance (kWh_{th}/kWh_{el})
Cbld	CO_2 content of building heat demand, area related (kg/m^2)
Cel	CO_2 content of HP system electricity (kg/kWh_{el})
Cgrid	CO_2 content of electrical grid (kg/kWh_{el})
Cth	CO_2 content of building heat demand (kg/kWh_{th})
Esys	system electricity (kWh_{el}/m^2)
Qdem	building heat demand (kWh_{th}/m^2)
Qdhw	DHW demand (kWh_{th}/m^2)
Qsh	SH demand (kWh_{th}/m^2)
SPF	seasonal performance factor (kWh_{th}/kWh_{el})

* Corresponding author. Tel.: +41 22 379 0657; Email: elliot.romano@unige.ch.

1.1. General issue

An increasing number of authors are evaluating the environmental impact of massive heat-pump (HP) introduction, but only few consider the temporal dynamic of the carbon content of electricity-generation. As a notable exception, [1] shows that introducing direct heat pump heating along with combined cycle gas plants could generate significant reductions of greenhouse gas emissions, when compared with classic fossil-fuel heating and electric resistance heating. Similarly, [2] analyze the temporal load curves of heat pump water heaters and air-source heat pumps in the context of temporal grid-level emissions data. However, while the previous two studies do consider the carbon content of electricity at hourly scale, latter is based on the production accounting principle, which doesn't take into account the impact of electricity imports and exports on the carbon content of the electricity mix. In a country like Switzerland, which relies on a high share of electricity exchanges with the neighboring countries, such an approach is not satisfactory.

1.2. Local context

While the space-heating (SH) and domestic hot water (DHW) production for the building sector of the Canton of Geneva rely at 93% on fossil sources, the energy policy objective is to reduce this share to 66% by 2035. Given important low temperature resources, in particular in terms of surface and subsurface water, one of the major foreseen contributions for this change consists in massive introduction of centralized HPs, at building level as well as integrated in district heating networks [3].

Even though multifamily buildings (MFB) only constitute 27% of the Geneva building stock, they represent almost half of the heated floor area of the canton, namely 19.3 out of 40.9 million m2 [4]. About half of these MFB, which were built between 1946 and 1980, are nowadays in need of retrofit and possess a strong energy saving potential. In parallel to reducing of the heat demand of the building stock, in particular by way of retrofit, reducing of the CO_2 emissions can also be achieved by replacing fossil fuels by renewable energies, in particular via heat pump (HP) systems. However, in addition to HP performance issues, the CO_2 content of the electricity needed to run such HP systems, as well as the complementarity with local PV production remain a fundamental issue.

1.3. Objective

In this context, [5] performed a numerical simulation study which compares the potentials and constraints of different heat sources exploited by HP systems, with and without complementary PV, implemented in various types of multifamily buildings located in Geneva. As a complement, a recent study evaluates the hourly CO_2 content of the Swiss electricity consumption mix [6], taking into account both domestic production and imports to Switzerland from the neighbor countries.

Objective of the present paper is to cross-cut these 2 studies, for assessing the CO_2 emissions of air-source and groundwater-source HP systems, with and without complementary PV, for a sample of multifamily buildings (new, retrofitted and non-retrofitted), located in Geneva.

1.4. Method and results

The methodological part of the paper is organized as follows: i) Presentation of the building sample and related heat load profiles, which are rescaled to 2017, the reference meteorological year for which hourly CO_2 content of electricity is available; ii) Characterization of the considered heat sources (air and groundwater), HP system layout and simulation algorithm, as well as complementary PV system; iii) Characterization of the hourly CO_2 content of the Swiss electricity consumption mix, which is given for two distinct accounting approaches (lower and upper grid CO_2 content).

The results are discussed as follows: i) HP performance, in terms of daily *COP* and annual *SPF*, for the distinct heat demands; ii) CO_2 emissions of the stand-alone HP systems (without PV) and comparison with the CO_2 emissions of a gas boiler; iii) effect of PV production on the daily and annual consumption/production of electricity, as well as related CO_2 savings.

2. Building sample and heat load

2.1. Building sample

The present study is based on the same multi-family building (MF) sample which was used in [5]: i) 2 new buildings with identical low SH demand, but differentiated DHW demand; ii) 3 retrofitted buildings, of which one with low SH and the other ones with intermediate SH demand but differentiated SH distribution temperature; iii) 1 non retrofitted building. The main characteristics of the building sample (with SH demand corresponding to standard weather data) are summarized in Table 1. Note that 4 of the buildings correspond to real case studies situated in Geneva (*New, RetBest, RetRef, NoRet*), while the 2 other are combinations thereof, in terms of DHW demand (*NewLow*) or of SH distribution temperature (*RetAvg*).

Table 1 Building sample.

Building	Qsh kWh/m²	Qdhw kWh/m²	Qdem kWh/m²	Tsh.0 °C
New	20.8	47.7	68.5	30
New Low	20.8	28.3	49.1	30
Ret Best	37.8	34.6	72.4	40
Ret Avg	69.3	28.3	97.6	40
Ret Ref	69.3	28.3	97.6	50
No Ret	110.0	28.3	138.3	50

Qdhw, Qsh, Qdem: DHW, SH and total annual heat demand (with climatic correction to standard weather).
Tsh.0: SH distribution temperature, at 0° outdoor temperature.

Comparison with a benchmark on the SH demand of the MF building stock of Geneva [4] shows that, except for *NoRet*, all our buildings are in the 1st decile, meaning that they are representative of the best cases in their respective construction periods. *NoRet* is in the 3rd quartile, close to the 4th quartile, meaning that it is representative of a lower than average building envelope.

Similarly, comparison with a benchmark on the DHW demand of the MFB stock of Geneva [7] yields following results: *New* is in the 4th quartile, amongst the highest values; *RetBest* is slightly above the median; all other cases (which by definition have the same DHW demand) are in the 2nd quartile, closer to the 1st quartile than to the median.

2.2. Heat load profiles

For the sake of the present study, the above building demands are rescaled to 2017, the reference meteorological year for which hourly CO_2 content of electricity is available (see further down). To do so we consider that: i) DHW demand is independent of the meteorological year and is therefore the same as for standard weather data; ii) SH demand is multiplied by 1.03, the ratio between 2017 and standard weather degree days.

In agreement with [5], the hourly demand profile is then defined as follows: i) For DHW, the hourly profile is given by the monitored data of a typical multifamily building [8]. It is adjusted by a multiplication factor, so that the integral of the load corresponds to the annual DHW demand of the building under consideration; ii) For SH, the hourly load is given by a linear function of the outdoor temperature, defined by a set point above which SH is off and a nominal heat load at 0°C outdoor temperature (which is adjusted so that the integral of the load corresponds to the annual SH demand of the building under consideration); iii) For SH distribution temperature, it is given by a linear function of the outdoor temperature. The DHW distribution temperature is considered constant, at 55°C. The limits of this methodology, in particular in terms of load curve, was discussed in details in [9]. For the particular case of a HP system on a low-energy building, it was shown that simulation results with the modelled heat demand are very similar to simulation results with the monitored heat demand, at least at aggregated system level.

The resulting heat load profiles of the building sample are presented in Figure 1, in daily values. We observe the relatively constant DHW demand at outdoor temperatures above 18°C, below which the distinct SH demands of the building sample are visible (with linear patterns corresponding to the above construction).

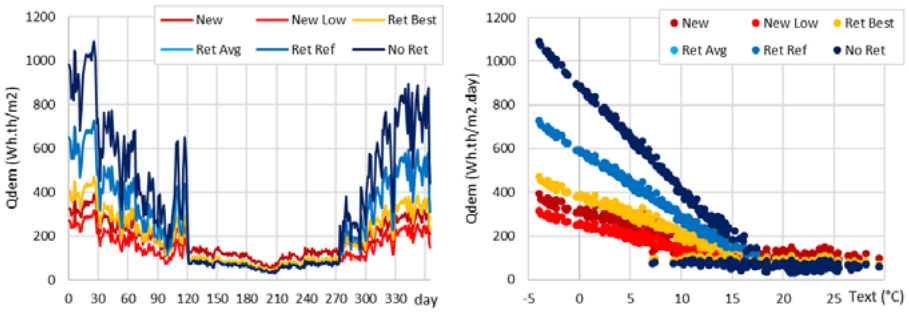


Fig. 1. Heat load of the building sample, profile and relation to outdoor temperature (2017, daily values).

3. HP systems and electrical load

3.1. Heat sources

The above described building sample was previously used for assessing of HP performance for a variety of heat sources [5]: i) ambient air; ii) geothermal boreholes; iii) water from lake of Geneva, pumped from a depth of 35 m; iv) Rhône river, corresponding to the top layer of the lake; v) shallow groundwater; vi) unglazed solar thermal collectors, used as HP heat absorbers in case of insufficient solar irradiation for direct solar production.

As expected, the simulated HP seasonal performance factors (*SPF*) turned out to be strongly related with the heat source temperature: groundwater yielded the highest *SPF* values (4.3 - 4.8, depending on the building heat demand) followed by river (3.9 - 4.5) and lake (3.8 - 4.3). The geothermal borehole performed slightly lower (3.6 - 4.0), while solar and air were at the bottom, with very similar values (solar: 2.9 - 3.5; air: 3.0 - 3.4).

In the present study, we will focus on the two extreme cases: i) air, which is characterized by a strong seasonal and daily variability (hourly values ranging from -5°C to 34°C); ii) groundwater, with a constant temperature of 13°C.

3.2. HP system

The considered system layout (Fig. 2) is similar for the air source HP and the groundwater source HP. Sizing of the components (HP, storage) depends on the maximal hourly heat load of the building under consideration.

Operation of the system obeys following scheme of priorities: i) maintaining the DHW tank above 50°C; ii) covering of the SH demand by way of: a) storage discharge; b) activation of the HP, with surplus production used to charge the heat storage; c) direct electric heating, which is activated only in case of simultaneous SH and DHW without possible storage discharge.

The components are modelled according to energy balance equations, which are integrated in the TRNSYS. simulation software package, taking into account the above defined priority rules [9]. The HP is modelled by an input/output table based on the working temperatures (evaporator input, condenser output), as given by manufacturer data (which, for the air-source HP, includes electricity for de-icing). Each of the storage tanks is modelled by way of a one-node model (disregarding stratification effects, which should be negligible, given the relatively small heat storage capacities), taking into account heat losses to the technical room. Direct electric heating covers the instantaneous difference between demand and production. Auxiliary electricity for circulation pumps is not taken into account. Simulation results were previously validated with monitored values of a solar heat pump system, at component and system level [9]. So as to properly take into account the dynamic of the HP-system, simulation is performed in 6 min time step, with output values stored in hourly time step.

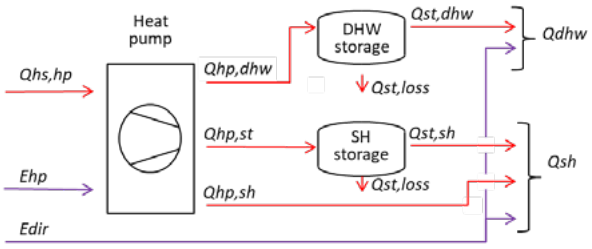


Fig. 2. HP system layout and associated energy flows.

3.3. Reference scenario with gas boiler

As a "business as usual" alternative to the above described HP systems, and for the sake of comparison in terms of CO_2 emission savings, we also consider heat production by way of a centralized gas boiler. In this case the heat production (including storage loses) is considered to match the hourly output of the groundwater HP (plus occasional direct electric heating).

4. PV production

As a complement to the HP system, we study the benefits of adding photovoltaic panels on the available building roof area. In order to do so, we consider following two cases [5]: i) an available roof area of 0.2 m^2 per m^2 heated floor area, corresponding to a "low-rise" multifamily building in Geneva (4 floors, under hypothesis of an 80% ratio between the available roof area, in m^2, and the floor specific heated area, in m^2 per floor); ii) an available roof area of 0.1 m^2 per m^2 heated floor area, which corresponds to a "high-rise" building in Geneva (8 floors).

PV production is based on a 12 % efficiency applied directly to the hourly global horizontal solar irradiation, corresponding to an annual electricity production of 162 kWh per m^2 of PV (2017).

5. CO_2 emissions

5.1. HP systems

In the case of HP systems, induced emissions are calculated on an hourly basis, by way of the 2017 hourly grid CO_2 content of the Swiss electricity consumption mix evaluated by [6]. Latter study takes into account both domestic production and inflows to Switzerland from each of the neighbor countries. To do so, it uses hourly available data concerning the production mix of the various European countries, per type of production, as well as hourly cross-border flows between them. Based on merit-order considerations, it takes into account the impact on the incremental generation mix due to import/export with the neighbor countries.

Finally, the CO_2 content of the resulting electricity mix is calculated by way of the carbon intensity of each production type, as given by the ecoinvent life cycle inventory database [10]. While this method is relatively straightforward for most of the production types (renewables, nuclear, fossils), a specific issue concerns electricity generation from blast furnace gas units in Germany. While latter represent only a small share of the generation capacity of the total market, it plays an important role in compensating for capacity shortages at the European level in the winter period and hence significantly contributes to Swiss imports. In this regard, it should be noted that the CO_2 content of electricity from German blast furnaces is controversial, leading to two distinct accounting approaches: i) on the one hand, such gases can be considered as "waste" from the iron and steel industry, in which case the related CO_2 content is attributed to latter sector and not to electricity generation; ii) on the other hand, in respect to specific economic considerations regarding the decision to flare the gases or to produce electricity, it can also be argued that the corresponding emissions should be attributed to the electricity sector [6].

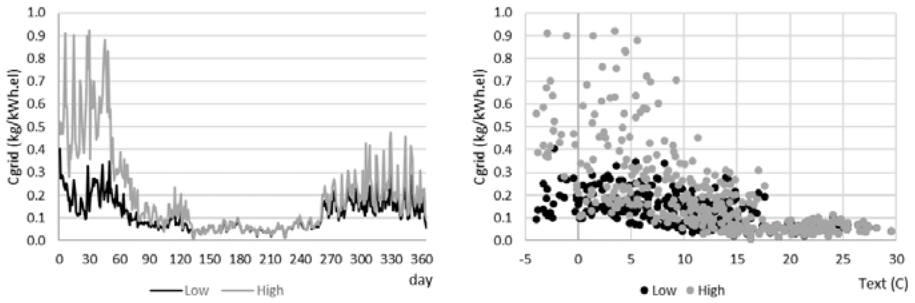


Fig. 3. Grid CO_2 content of the Swiss electricity mix, profile and relation to outdoor temperature (2017, daily values).

Finally, for both of these approaches, the dynamic of the grid CO_2 content (year 2017) is depicted in Figure 3, in daily values. Both approaches reveal a strong seasonal pattern, which results from the seasonality of electricity production and demand in Switzerland and its neighboring countries and the related imports and exports. We further note the fundamental issue of the accounting method for blast furnace gases, with an approximative factor 2 between the resulting annual average (lower grid CO_2: 108 g/kWh$_{el}$, upper grid CO_2: 196 g/kWh$_{el}$).

5.2. PV production and gas boiler

As for the HP systems, avoided emissions related to PV production are calculated on an hourly basis, by way of the above hourly grid CO_2 content. In the case of gas boilers, emissions are directly related to the produced heat, by way of a constant emission factor of 249 g/kWh$_{th}$ given by the Swiss Coordination Conference of Building Services [11].

6. Results and discussion

6.1. Performance and emission indicators

The results will be discussed on the basis of aggregated values of the hourly building heat demand *Qdem* (kWh$_{th}$/m^2), the HP system electricity demand *Esys* (kWh$_{el}$/m^2) and the CO_2 content of grid *Cgrid* (kg/kWh$_{el}$).

Performance of the HP system will be discussed in terms of daily *COP* (kWh$_{th}$/kWh$_{el}$) and annual *SPF*. (kWh$_{th}$/kWh$_{el}$), defined accordingly to their respective daily or annual aggregation level:

$$COP = \frac{\sum Qdem}{\sum Esys} \quad (1)$$

$$SPF = \frac{\sum Qdem}{\sum Esys} \quad (2)$$

Emissions will be discussed in terms of the area related CO_2 content of the heat demand *Cbld* (kg/m^2), the thermal CO_2 content of the heat demand *Cth* (kg/kWh$_{th}$) and the electrical CO_2 content of the HP system electricity *Cel* (kg/kWh$_{el}$). Latter are defined as follows (with daily or annual aggregation level):

$$Cbld = \sum Esys \cdot Cgrid \quad (3)$$

$$Cth = \frac{\sum Esys \cdot Cgrid}{\sum Qdem} \quad (4)$$

$$Cel = \frac{\sum Esys \cdot Cgrid}{\sum Esys} \quad (5)$$

6.2. HP performance

Figure 4 depicts the daily *COP* values of both HP systems. In the case of the air-source HP, when the air temperature is above 10°C the *COP* is mainly in the range of 3 - 4, while it drops for lower temperatures (due to lower resource temperature, as well as related de-icing). In the case of the groundwater-source HP, the *COP* is mainly in the range of 3.5 - 5.5, and is not so sensible to the outdoor temperature.

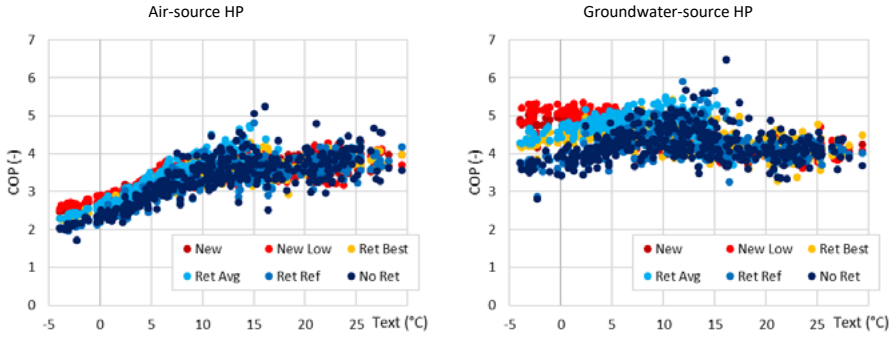


Fig. 4. COP of air and groundwater HP systems (daily values).

The corresponding annual *SPF* values are given in Table 2, with an average of 3.06 for the air-source HP and 4.42 for the groundwater-source HP (not including ancillary electricity for circulation pumps).

Table 2 Annual heat demand and SPF (2017).

Heat demand and SPF		New	New Low	Ret Best	Ret Avg	Ret Ref	No Ret	Average
Qdem	kWh.th/m2	67.12	47.72	69.51	92.23	92.23	129.82	
SPF air	kWh.th/kWh.el	3.24	3.26	3.10	3.11	2.83	2.80	3.06
SPF gw	kWh.th/kWh.el	4.51	4.68	4.46	4.65	4.10	4.12	4.42

air: air-source HP; gw: groundwater-source HP

6.3. CO_2 emissions, without PV

Figure 5 shows the daily values of the system electricity consumption (top) and the area related heat CO_2 content for the lower grid CO_2 content (bottom). While there is a strong correlation between electricity consumption and outdoor temperature, similar to the heat demand (Fig. 1), a much larger dispersion appears for the area related CO_2 content, as induced by the dispersion of the grid CO_2 content (Fig. 3).

The corresponding annual CO_2 emissions are summarized in Table 3, both for the lower and upper grid CO_2 content, as well as for the alternative gas boiler.

While the area related CO_2 content (*Cbld*) obviously depends on the building under consideration, the heat related CO_2 content (*Cth*) turns out relatively constant. In the case of the gas boiler it amounts to 256 g/kWh$_{th}$ (i.e. 3% more than the content of the heat at boiler outlet, see section 5.2, due to storage losses). In comparison, and when considering the lower grid CO_2 mix of electricity, it amounts to an average of 49 g/kWh$_{th}$ for the air-source HP (81% savings as compared to the gas boiler), respectively 33 g/kWh$_{th}$ for the groundwater-source HP (87% savings). When considering the upper grid CO_2 content, it amounts to twice higher values (air: 100 g/kWh$_{th}$ – 61% savings; groundwater: 64 g/kWh$_{th}$ – 75% savings).

Finally, given the seasonal trend of both the heat demand (Fig. 1) and the CO_2 content of the grid (Fig. 3), latter turns out to strongly underestimate the CO_2 content of the HP system electricity (*Cel*). Such is the case both for the lower grid content (grid: 108 g/kWh$_{el}$; air-source HP: 150 g/kWh$_{el}$; groundwater-source HP: 144 g/kWh$_{el}$), as for the upper grid content (grid: 196 g/kWh$_{el}$; air-source HP: 303 g/kWh$_{el}$; groundwater-source HP: 282 g/kWh$_{el}$). While these results confirm the necessity to assess HP emissions by way of hourly values of the grid CO_2 content, the annual derived CO_2 content of the HP system electricity could in principle be used for other annual *SPF* values than the ones considered in this study.

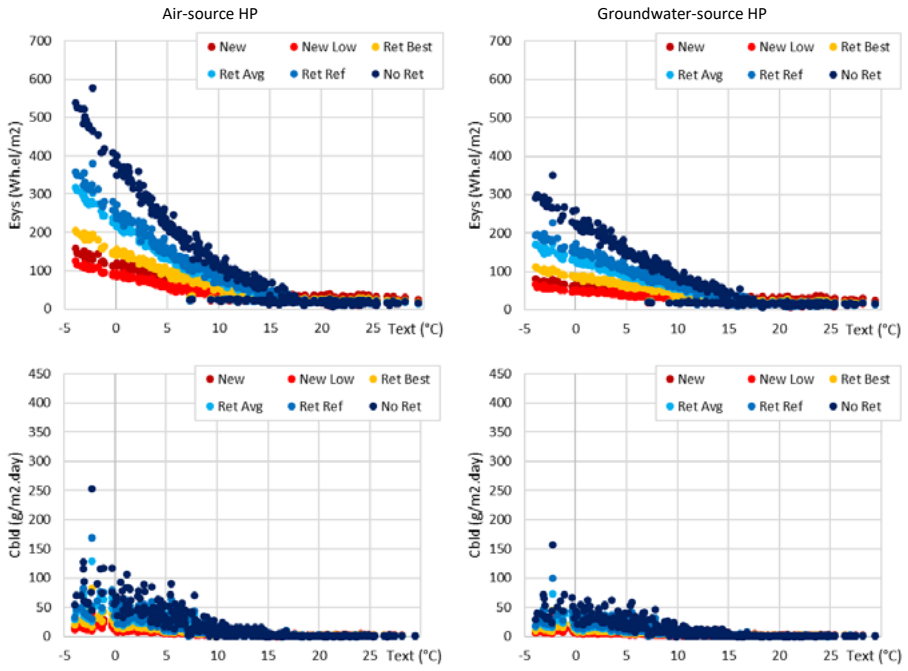


Fig. 5. HP without PV: electricity consumption (top) and area related CO_2 content of the heat demand, for the lower grid CO_2 content (bottom), as a function of outdoor temperature (daily values).

Table 3 Gas boiler and HP (without PV): annual CO2 emissions, for lower and upper grid CO2 content.

Gas boiler			**New**	**New Low**	**Ret Best**	**Ret Avg**	**Ret Ref**	**No Ret**	**Average**
Cbld		kg/m2	17.17	12.25	17.83	23.61	23.72	33.34	
Cth		kg/kWh.th	0.256	0.257	0.256	0.256	0.257	0.257	0.256
HP – lower grid CO_2			New	New Low	Ret Best	Ret Avg	Ret Ref	No Ret	Average
Cbld	air	kg/m2	2.79	2.03	3.28	4.63	5.19	7.54	
	gw	kg/m2	1.90	1.36	2.19	2.98	3.47	5.00	
Cth	air	kg/kWh.th	0.042	0.043	0.047	0.050	0.056	0.058	0.049
	gw	kg/kWh.th	0.028	0.028	0.031	0.032	0.038	0.039	0.033
Cel	air	kg/kWh.el	0.135	0.139	0.146	0.156	0.159	0.163	0.150
	gw	kg/kWh.el	0.128	0.133	0.140	0.150	0.154	0.159	0.144
HP – upper grid CO_2			New	New Low	Ret Best	Ret Avg	Ret Ref	No Ret	Average
Cbld	air	kg/m2	5.42	4.09	6.55	9.54	10.58	15.62	
	gw	kg/m2	3.55	2.58	4.26	5.98	6.89	10.07	
Cth	air	kg/kWh.th	0.081	0.086	0.094	0.103	0.115	0.120	0.100
	gw	kg/kWh.th	0.053	0.054	0.061	0.065	0.075	0.078	0.064
Cel	air	kg/kWh.el	0.262	0.280	0.292	0.321	0.325	0.337	0.303
	gw	kg/kWh.el	0.239	0.253	0.273	0.302	0.307	0.319	0.282

air: air-source HP; gw: groundwater-source HP

6.4. Complementary PV

In this section we analyze the performance of combined HP and PV systems. For a PV system of 0.2 m^2 per m^2 heated area (low-rise building, see section 4), Figure 6 depicts the HP-PV system electricity balance (top) and the area related CO_2 emissions of the heat demand, calculated with the lower grid CO_2 content (bottom).

When considering the HP-PV electricity balance (HP consumption – PV production), and when comparing to the case without PV (Fig. 5), we observe the seasonal mismatch between both technologies: for temperatures below 5°C, consumption is very similar to the case without PV; for temperatures above 10°C, PV production reaches much more important values than HP consumption, resulting in PV injection to the grid.

When considering the area related CO_2 emissions, the situation is quite different. As a matter of fact, while PV injection to the grid results in negative CO_2 emissions (savings), the related values remain relatively small, since such happens when the grid CO_2 content is already low (Fig. 3).

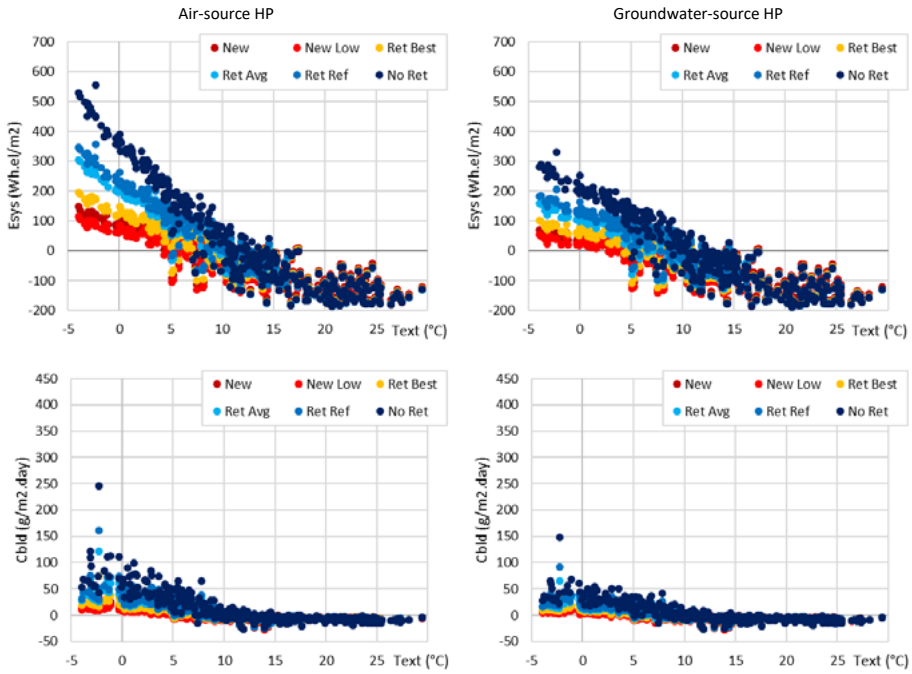


Fig. 6. HP with PV (0.2 m^2 per m^2 heated area): HP-PV electricity balance (top) and area related CO_2 content of the heat demand, for the lower grid CO_2 content (bottom), as a function of outdoor temperature (daily values).

Finally, figure 7 summarizes the annual area related CO_2 content of the 3 production systems (gas boiler, air-source HP, groundwater-source HP) in conjunction or not with PV (0.1 and 0.2 m^2 per m^2 heated area), both for the lower and upper grid CO_2 content of the Swiss electricity consumption mix.

In all cases, the area related CO_2 content is strongly corelated to the building heat demand, with a linear relation between the two. As already pointed out, the CO_2 content of the HP system in all cases smaller than the one of the gas boiler. Finally, while PV can contribute substantially to the summer HP demand, the related annual CO_2 savings remain relatively marginal. Only in the case of buildings with a low heat demand (< 90 kWh/m^2), and in particular for low-rise buildings (0.2 m^2 PV per m^2 heated area), does the annual CO_2 content of the combined HP-PV system lead to CO_2-positive buildings (however not taking into account electricity other than for the HP).

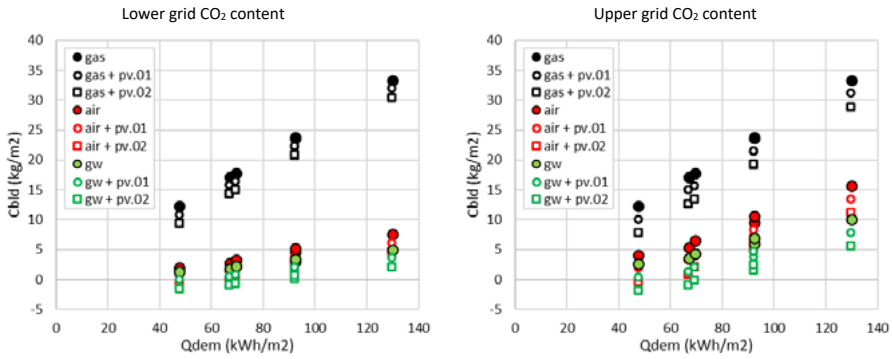


Fig. 7. Gas boiler and HP (with and without PV): Annual area related CO_2 emissions as a function of the building heat demand (for lower and upper grid CO_2 content).

7. Conclusions

The present paper assesses the CO_2 emissions of air-source and groundwater-source HP systems, with and without complementary PV, for a sample of multifamily buildings (new, retrofitted and non-retrofitted) located in Geneva. HP performance is evaluated by way of numerical simulation in hourly time step, and is cross-cut with the hourly CO_2 content of the Swiss electricity mix (taking into account both domestic generation and imports from the neighbor countries).

Latter assessment is done by way of two distinct accounting approaches: i) lower grid CO_2 content, which considers electricity from German blast furnaces CO_2 free (the related CO_2 content being attributed to the iron and steel industry); ii) upper grid CO_2 content, for which the corresponding emissions are attributed to the electricity sector.

The main results are as follows:

- The annual SPF has an average of 3.06 for the air-source HP and 4.42 for the groundwater-source HP (not including ancillary electricity for circulation pumps).
- In both cases, the daily electricity consumption bears a strong relation to the outdoor temperature, with patterns depending on the annual heat demand. A much larger dispersion appears in the case of the CO_2 content of the produced heat, as induced by the dispersion of the grid CO_2 content.
- When comparing with the emissions of a gas boiler, the considered HP systems induce very important annual CO_2 savings, at least for the lower grid CO_2 content of electricity (air-source HP: 81% savings; groundwater-source HP: 87% savings). These savings are somewhat reduced when considering the upper grid CO_2 content of electricity (air: 61%; groundwater: 75%).
- Given the seasonal trend of both the heat demand and the CO_2 content of the grid, latter turns out to strongly underestimate the CO_2 content of the HP system electricity. Such is the case both for lower grid content (grid: 108 g/kWh$_{el}$; air-source HP: 150 g/kWh$_{el}$; groundwater-source HP: 144 g/kWh$_{el}$), as for the upper grid content (grid: 196 g/kWh$_{el}$; air-source HP: 303 g/kWh$_{el}$; groundwater-source HP: 282 g/kWh$_{el}$).
- While PV can substantially contribute to the summer HP demand, the related annual CO_2 savings remain relatively marginal. As a matter of fact, for temperatures below 5°C consumption is very similar to the one without PV; for temperatures above 10°C PV production reaches much more important values than HP consumption, resulting in PV injection to the grid, but related CO_2 savings remain relatively small since such happens when the grid CO_2 content is already low.

Finally, it should be stressed that preceding results are based on numerical simulation, which assumes optimized conditions of HP integration and control, and disregards ancillary electricity of the circulation pumps.

Acknowledgements

This research was co-funded by CTI within the SCCER FEEB&D and SCCER CREST projects.

References

[1] Luickx P.J. et al. (2008). Influence of massive heat-pump introduction on the electricity-generation mix and the GHG effect: Comparison between Belgium, France, Germany and The Netherlands. Renewable and Sustainable Energy Reviews 12, 2140-2158.

[2] Brockway A.M. et al. (2018). Emissions reduction potential from electric heat pumps in California homes. The Electricity Journal 31, 44-53.

[3] Quiquerez L. et al. (2017). The role of district heating in achieving sustainable cities: comparative analysis of different heat scenarios for Geneva. 116, 78-90.

[4] Khoury J. (2014). Rénovation énergétique des bâtiments résidentiels collectifs: état des lieux, retours d'expérience et potentiels du parc genevois. PhD thesis, University of Geneva.

[5] Fraga C. et al. (2018). Heat pump systems for multifamily buildings: Potential and constraints of several heat sources for diverse building demands. Applied Energy 225, 1033-1053.

[6] Romano E. et al. (2019). Real-time carbon emission due to electricity consumption - a marginal approach for an open economy. The case of Switzerland. Université de Genève, Switzerland, submitted paper.

[7] Quiquerez L. (2017). Analyse comparative des consommations de chaleur pour la production d'eau chaude sanitaire estimées à partir de relevés mensuels: Etude sur un échantillon de bâtiments résidentiels collectifs alimentés par un réseau de chaleur à Genève. Université de Genève.

[8] Zgraggen J.-M. (2010). Bâtiments résidentiels locatifs à haute performance énergétique: objectifs et réalités. PhD thesis, University of Geneva.

[9] Fraga C. et al. (2017). Solar assisted heat pump system for multifamily buildings: Towards a seasonal performance factor of 5? Numerical sensitivity analysis based on a monitored case study. Solar Energy 146, 543-564.

[10] Frischknecht R. et al. (2005). The ecoinvent database system: a comprehensive web-based LCA database. Journal of Cleaner Production. 2005;13:1337-43.

[11] KBOB (2016). Empfehlung Ökobilanzdaten im Baubereich 2009-1-2016. Koordinationskonferenz der Bau- und Liegenschaftsorgane der öffentlichen Bauherren. Bundesamt für Bauten und Logistik, Schweiz.

13th IEA Heat Pump Conference
April 26-29, 2021 Jeju, Korea

Heat pumps in existing residential buildings

Marek Miara[a], Danny Günther[a], Robert Langner[a]

[a]Fraunhofer ISE, Heidenhofstrasse 2, 79110 Freiburg, Germany

Abstract

Several reasons speak for using of heat pumps in residential buildings. They can provide heating, domestic hot water und cooling in an ecologically friendly and, in the majority of countries, an economical way. Particularly straightforward is the implementation in new residential buildings, typically equipped with a low temperature underfloor heating system. In a number of European countries heat pumps are the predominant heating technology in the new residential buildings.

However, the real challenge, as regards reaching the goals related to climate changes and higher energy efficiency, is to secure heating in existing residential buildings. Despite several technological solutions allowing for implementation of heat pumps in existing buildings, the number of end consumers choosing heat pumps when replacing an old heating system is still very low.

What is the minimal energetic standard of a building suitable for a heat pump? Are heat pumps able to deliver required temperature and expected thermal comfort? What is the efficiency achieved under real operation conditions? When are heat pumps better than fossil systems from energetical, ecological and economical point of view? Is technological development of heat pumps in recent years recognizable in the real field operation?

The author will attempt to answer these questions on the basis of the evaluation of the latest field monitoring program encompassing more than 60 single-family existing residential buildings in Germany.

Keywords: residential building; retrofitting; field efficiency; monitoring;heating systrem supply temperatures, CO_2 evaluation

1. Introduction

Heat pumps will play the major role providing the heat for space heating and domestic hot water in the residential sector of the future CO_2 reduced energy system. A wide range of studies [1-3] consider heat pumps as a crucial technology on the way to energy system transition and targeted CO_2 neutrality.

In a number of European countries, heat pumps are already now the dominating heating technology in new residential buildings. The real challenge for reaching the goals related to climate changes and higher energy efficiency, is to provide for heating in existing residential buildings. Despite several technological solutions allowing for implementation of heat pumps in existing buildings, the number of end consumers choosing heat pumps when replacing an old heating system is still very low.

In the discussion about the applicability of heat pumps in existing buildings, the main argument against this solution is the assumed high heating supply temperature, leading to poor performance of heat pumps and consequently to exclusion criteria. To verify this assumption, in the newest field test the Fraunhofer ISE examined sixty air-to-water and ground source heat pumps under real operation conditions in existing buildings. Extensive measurement setting and high frequency data acquisition system allowed for detailed analyses of the efficiency of the systems, including the temperatures of the heating system.

2. Heat pumps field tests

Since 2006, the Fraunhofer ISE from Freiburg, Germany has been investigating electric heat pumps in single-family dwellings. Nearly 250 air-to-water and brine-to-water heat pump systems have been investigated under real operating conditions in houses with various energetic standards (from low-energy to un-retrofitted stock buildings with high energy demand).

The characteristic of the projects including the characteristic of the investigated buildings, measurement technology, main results and particular aspects, have already been presented during the 11th and 12th Heat pump Conference [4, 5].

The newest program "Smart Heat Pumps in Existing Buildings" includes heat pumps in older, usually un-retrofitted buildings. The measurement period was closed in June 2019. All investigated heat pumps units cover the heating demand, as well as the domestic hot water demand. In the majority of cases it concerns a mono-energetic systems - the heat pump is supported in emergency cases by a direct electrical back-up heater and is the only heat supplier in the building. One of the goals of the project was the investigation of hybrid heat pumps units; however the results of this investigation will not be consideration of the paper.

The heat pumps examined within the frame of the project "Smart HP in Existing Buildings", were installed in single-family houses built between 1850 and 2005. The range of their retrofitting covers from not retrofitted to retrofitted to the energy high efficient standard. This setting was necessary to investigate heat pumps in different operating conditions, including heating system supply temperature.

3. Overview of the efficiency results

3.1. System boundaries

Figure 1 shows the scheme of a typical heat pump installation and illustrates the system boundaries. There are various possibilities to calculate the efficiency of a heat pump system. The outcomes of efficiency calculations presented in sections 3.2 were based on the boundary SPF 2. The same calculation boundary was suggested as a main boundary for presenting the efficiency outcomes of heat pump systems in the European project SEPEMO-BUILD [6].

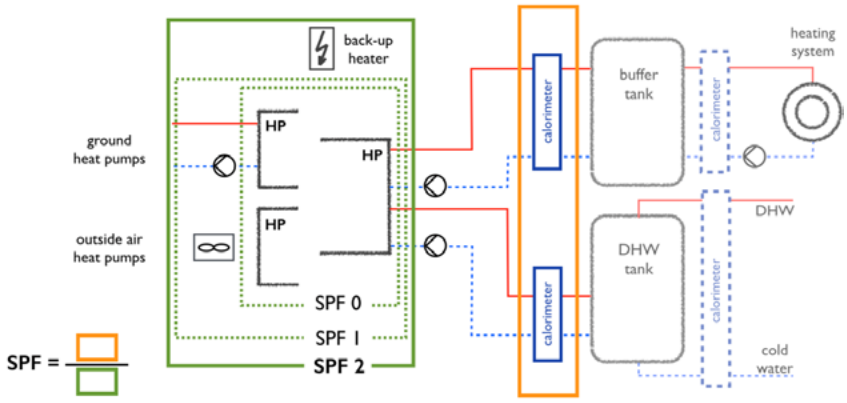


Fig. 1. Heat pump installation and the system boundaries for calculation of SPF values

The SPF is the ratio of the heat energy produced by the heat pump (not including the losses of the heat distribution system and the buffer tanks) and the back-up heater and the corresponding electric need of the heat pump, back-up heater and source fans in case of the A/W heat pump, brine pump in case of the B/W heat pump and well pump in case of W/W heat pump.

3.2. SPF values

Figure 2 shows average values of SPF values among individual projects, as well as the ranges of individual results for all heat pumps units grouped for different heat sources and projects. The comparison takes into

account outside-air heat pumps and ground-source heat pumps. Ground-water heat pumps were omitted due to a neglectable number of the examined installations. Calculation periods differ and are indicated for each project.

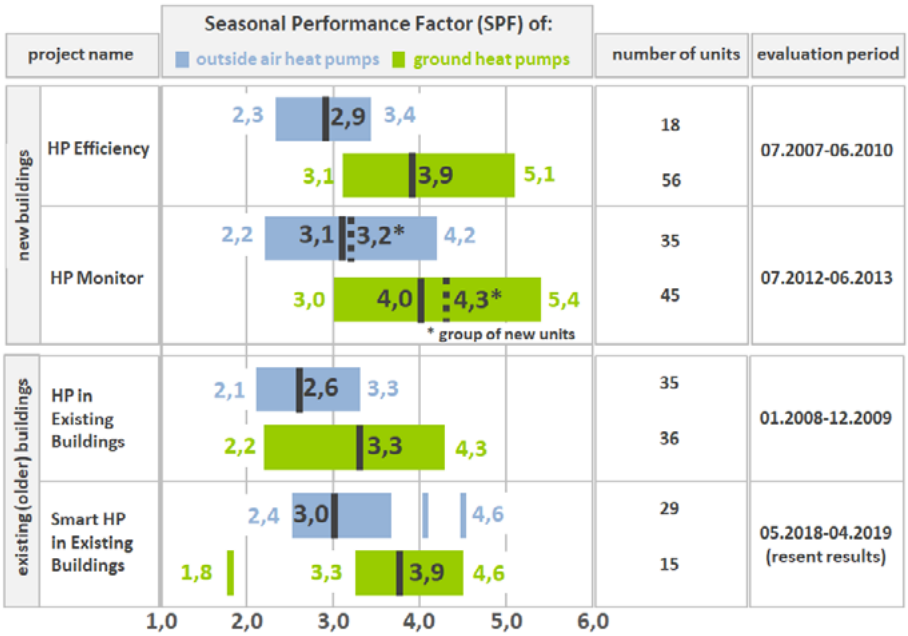


Fig. 2. Averages values and ranges of the SPF in existing residential houses in Germany

The differences in the average SPF values depend on a type of a heat source, type of a building and the period of installation (indicating improvement of technology). The difference between outside air heat pumps and ground heat pumps is evident to the benefit of ground source heat pumps. The ground as a heat source is more beneficial from the point of view of its temperature in the coldest periods with the most demand for heating.

Another important difference was noted between older and newer buildings. It results mainly from a type of the used heat distribution system. Underfloor systems, mostly used in newer buildings, enable lower supply temperatures compared to systems based on radiators in older buildings. Lower supply temperatures contribute significantly to higher efficiency of heat pumps.

In the framework of the "HP Monitor" project, a group of newly installed units (as opposite to the units transferred from the older project "HP Efficiency") was investigated separately (on the graph shown with the symbol *). The outcomes from this group indicate the improvement in the heat pump efficiency resulting from technology development in the recent years.

The results of all projects indicate smaller range of outcomes for individual systems with air-water heat pumps, compared with ground heat pumps. The wide range of SPF achieved by ground heat pumps (at least 2.0 points) indicates a high potential of efficient functioning of ground heat pumps. On the other hand, it shows that the choice of a heat source would not automatically guarantee a high efficiency. Errors in designing, installation and/or running process, result in a decrease of potential efficiency and diminish economical and ecological benefits of theoretically more efficient, but at the same time more expensive, heat source.

The newest results originate from the project "Smart HP in Existing Buildings". One year of evaluation shows following results:

- air-to-water heat pumps achieved the average SPF value of 3.0 with the range between 2.4 and 3.7. Two units with highest results reached the values of 4.1 and 4.6 and have not been reflected in the average value calculation.
- ground source heat pumps achieved average SPF value of 3.9 with the range between 3.3 and 4.6. The unit with the smallest value of 1.8 has not been reflected in the average value calculation.

Compering the results from the latest project with the older project “HP in Existing Buildings”, which has been performed 10 years ago also in existing buildings, the average efficiency increase is significant.

With all restrictions of the direct comparison of various projects (different houses, diverse average heating systems temperatures, unique weather condition for the year of evaluation), it may still be concluded that the efficiency of heat pumps increased in the recent years. Coincidently, the average efficiency results from the latest project with older existing buildings mirrored the results from the project in newly build residential houses conducted 10 years before.

4. Heating systems supply temperatures

The previous section discussed average data from all investigated heat pumps. The focus of this section will be analysis of a group of air-to-water heat pumps. The data are based on a one-year measurement period. The selection criteria for this group was the average heating system temperature. Only units with the temperature 36 °C [97 °F] and above were chosen for the evaluation, in total 16 units.

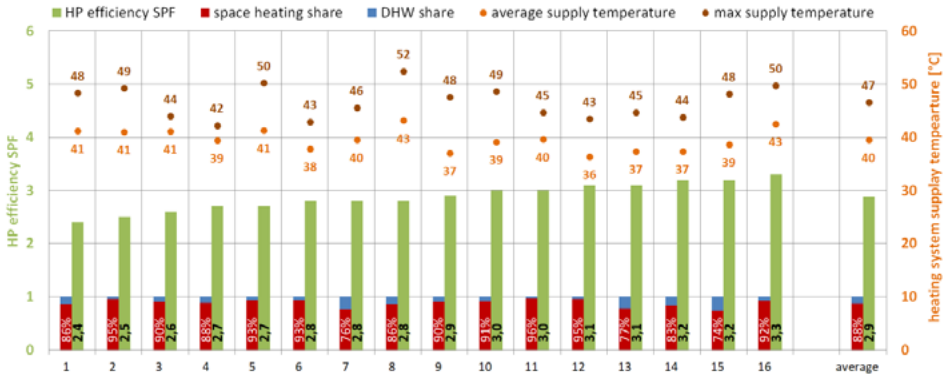


Fig. 3. Heat sink characteristic of 16 air-to-water heat pumps operating in existing residential houses in Germany evaluated over a one-year period

Fig. 3 shows the sink side (heat distribution side) characteristic of the 16 air-to-water heat pumps including their efficiency (green columns). The average SPF value for the whole group of installations amounts to 2.9 with the range from 2.4 to 3.3. The percentage share of the delivered heat in space heating mode (in red) and DHW (domestic hot water) mode (in blue) have been shown on the left side of each efficiency column. The extreme right columns symbolize the average values of all systems. In average, the share of the heat delivered for the space heating equals 88% and the share of DHW heat equals 12%.

Above the columns, two types of the heating system supply temperatures have been shown. The lower one (in orange) indicates the average heating system temperature (supply minus return temperature) over the whole period of evaluation. The higher values (in brown) indicate the maximal daily heating system supply temperatures (only in space heating mode) measured during the heating season.

For the further considerations, it is important to differentiate between three types of heating system temperatures. First one, and usually the highest one, the *design temperature*, is determined by the planning of the heating system and planned for the normative regional lowest outside air temperature. The second one, the lowest, is the *average temperature calculated (or measured) for the whole heating season*. This temperature, indicated on the fig. 3, is significant for the average efficiency of the heat pump and consequently for the ecological and economical results of the system. The third one is the *highest (daily) measured temperature*. This temperature indicates the best the real weather condition, respectively the real lowest outside temperatures.

The investigated group of heat pumps shows considerable low average heating system temperatures, in particular in the light of the fact that the heat distribution in rooms is based on radiators in the majority of the systems. The average value of all units equals to 40 °C (104 °F). The highest average temperature, in the units numbered 8 and 16 equals to 43 °C (109 °F).

The highest maximal daily temperatures are in average 7 K higher. The highest maximal temperature is observed in the unit 8 and equals to 53° C (127 °F). The highest delta between average and maximal temperature is observed in unit 9 and equals to 11 K. In general, the maximum temperatures measured during the heating season are lower than the design temperatures of the systems. The one reason for this situation is

the lower real outside temperature than the normative one used during the planning. The second reason is link to the features of radiators in older buildings. Very often their size is over dimensioned and the actual temperatures required to deliver the necessary amount of heat to the rooms, can be lower than those designed.

Detail analysis of the heating system temperature for exceptional heat pump system is conducted in the next section.

5. Maximal heating supply temperatures

In the discussion about the applicability of heat pumps in existing buildings, the main argument against this solution is the assumed high heating supply temperature, leading to poor performance of heat pumps and consequently to exclusion criteria.

The previous section presented and discussed the average and the maximal heating supply temperatures for a group of heat pumps installations. Bellow, one exemplary installation will be analyzed. It concerns the air-to-water variable speed heat pump installed in a partly retrofitted building. The space heat distribution system bases on radiators (water based system). The investigated time period is the heating season 2018/19.

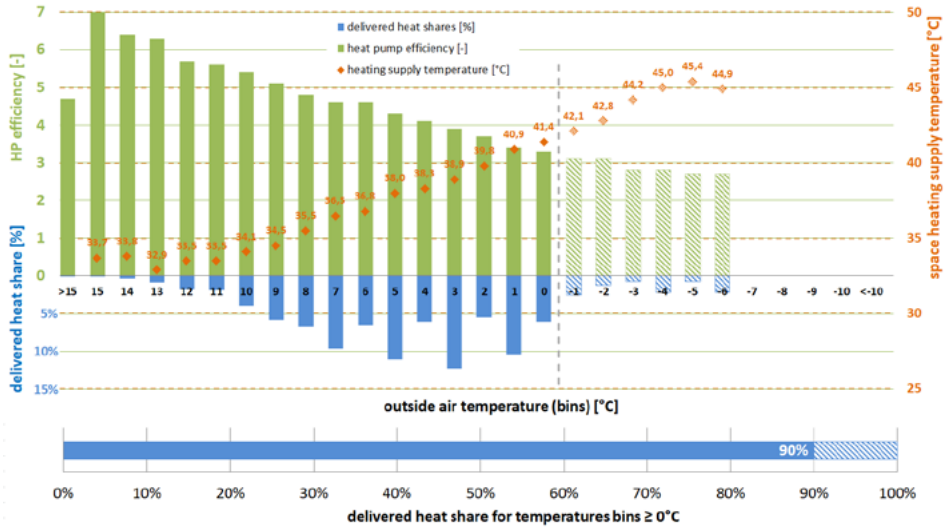


Fig. 4. Delivered heat share for temperature bins in dependency of the efficiency of the heat pump and space heating supply temperature (heating season 2018/2019 in Germany)

Fig. 4 shows the share of delivered heat (blue bars), for space heating, for each temperature bin. The distribution shows a typical bell-shape with the largest share of heating energy delivered by the outside air temperature of 3 °C (37 °F). The shares for the temperature bins below 0 °C and higher than 9 °C, are in the range of 1% to 4% of the total delivered heat and thereby play only a secondary role. The heating energy delivered for the outside air temperatures below 0 °C (32 °F) amounts only to 10% of the total delivered heating energy, which is shown in the lower part of the graph.

Fig. 4 shows additionally the heating system supply temperature (in orange) for each temperature bin and corresponding heat pump efficiency (in green). The supply temperature is clearly depending on the outside temperature and rises from approximately 33 °C (91 °F) to 45 °C (113 °F), which means a temperature rise of 12 K. Obviously, the highest supply temperatures of more than 42 °C (108 °F) are needed for the lowest outside air temperatures (below 0 °C). Also the efficiency of the heat pump clearly depends on the outside air temperature and, consequently, on the supply temperature (delta between evaporating and condensing is getting higher). The overall average efficiency of the heat pump equals to 4.2. The efficiency calculated for the temperature bins 0 °C and higher (without the coldest outside temperatures and highest heating system supply temperatures) equals to 4,0.

As expected, the highest supply temperatures of the heating system meet the lowest outside temperatures, causing the lowest efficiency of the heat pump. However the amount of delivered heat under these conditions

(in the presented example 10%) is rather small and affects the total efficiency of the heat pump only in a minor way.

It has to be noticed, that similar behavior has been noted in several further examples, even if the absolute values of the supply temperature differed.

6. Ecological assessment of the heat pumps efficiency results

The comparison of various heating technologies may be performed by using several indicators. The three most used ones are: economy, ecology and primary energy. The results of such comparison are strongly linked with the local situation and vary considerably from country to country and sometimes from region to region. To illustrate how differently the some technology may be evaluated, following section will show the CO_2 emissions saving potential of heat pumps when compared to a natural gas boiler, in different geographical boundaries.

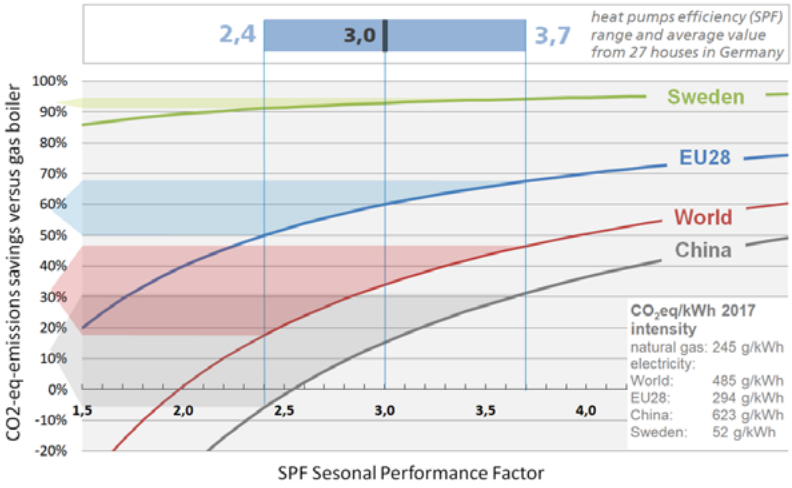


Fig. 5. CO2 emissions saving with heat pumps in dependency of CO2 electricity production intensity

Fig. 5 shows the dependency between the efficiency of a heat pump (impressed in SPF – Seasonal Performance Factor) and CO_2 emissions savings versus natural gas boiler. Crucial for that comparison is the CO_2 intensity of the electricity production in a particular region. The source for the values used for the calculation is the "IEA CO_2 emissions from fuel combustion statistics 2019" and the aggregated data from www.ElectricityMap.org, who track real-time carbon-intensity.

Following geographical regions have been taken in to account: global (the world), 28 European Union countries (EU28), China and Sweden. The CO_2 electricity intensity values are indicated on the lower right corner of the graph. The CO_2 values for the heat generation with natural gas have been taken equal for all regions. To simplify the calculation, the efficiency of the gas boiler has been assumed as 100%. Each colored line on the graph indicates one region (from the top: green – Sweden, blue – EU28, red – the world and grey – China).

The crossing point between virtual vertical line symbolizing the efficiency of the heat pump and the "region" line indicates the CO_2 savings. For example the efficiency of 3.0 means for the EU28 boundary CO_2 savings of 60% compared to natural gas boiler. Second example – the efficiency of 2.0 means for "the world" an even situation (no savings).

The efficiency results from the field measurement of air-to-water heat pumps systems in existing buildings (described in detail in the previous sections), have been indicated in the upper part of the graph.

It is clearly visible, that the same efficiency value leads to varied CO_2 comparison findings. Considering the average efficiency value of 3,0; the saving in China equals to 15%, in "the world" to 34%, in the EU28 – 60% and in Sweden, with the cleanest electricity production, even to 93%.

Also consideration of the efficiency range from 2,4 to 3,7 leads to fully different savings ranges. The largest range from -6% to 31% can be noted in China. The next one – 18% to 47% globally, 50% to 68% in the EU28 and finally 91% to 95% in Sweden.

Concluding, heat pumps or their efficiency may be judged in a diverse way depending on the CO_2 electricity intensity in a particular country or region. The same rule equally applies to the economical evaluation.

Second conclusion is that the "greener" the electricity, the lesser impact has the heat pump efficiency on the CO_2 savings. The countries or regions with less clean electricity have much larger potential for a considerable increase of the savings through increasing the heat pumps efficiency, even if in absolute terms it would be on a lower level (i.e. the increase of CO_2 savings in Sweden may be achieved solely in single percentage, reaching already more than 90%),

7. Case studies

On the website of the project "Smart Heat Pumps in Existing Buildings" in the section "Live Data" (https://wp-monitoring.ise.fraunhofer.de/wp-smart-im-bestand/german/index/live_visu.html) a number of heat pump installations has been visualized. The "live" data are updated daily. The user of the website has the possibility to read description of the house and the heat pump and analyze the hydraulic schema of the installation (including measured values from the sensors). It is also possible to see the efficiency results for different periods of evaluation, and "play" (changing the calculation boundary, for example with or without domestic hot water or back-up heater) with the efficiency results diagram. In addition, the real costs, as well as the ecological and energetical comparison with other heating technologies are shown.

8. Conclusions

Heat pumps are able to provide the required heat for space heating and domestic hot water not only in new but also in partly-retrofitted or even not-retrofitted residential buildings. It has been proven in the field test with sixty heat pump systems in existing buildings in Germany, which investigated both ground source and air-to-water heat pumps.

As evidenced by the field test, the average efficiency for the air-to-water heat pumps amounts to 3.0 with the range from 2.4 to 3.7. Ground source heat pumps reach the average efficiency of 3.9 with the range from 3.3 to 4.6. The efficiency results are very close to the results reached in previous field test project performed six years earlier in new buildings. This indicates the positive development of the technology and of the installations processes. Due to the variety of investigated units and of other influencing aspects, it is not possible to accurately quantify the mentioned developments.

Both measured average heating system temperatures and maximal supply temperatures for space heating in investigated houses are lower than generally expected in existing (oft not-retrofitted houses). The majority of heat for space heating is delivered not in the days with the lowest outside air temperatures. This explains the relatively low average heating systems temperatures. The delta between the real maximal temperature and the design heating system temperature may be explained by milder than assumed weather during the year of investigation, general oversizing of the radiators in older buildings and lower energy demand through renovation measures applied to the house envelope.

Heat pumps or their efficiency may be judged in various ways depending on the CO_2 electricity intensity in a particular country or region. The same rule equally applies to the economical evaluation. Taking as a basis for the evaluation the efficiency reached during the field test performed by the Fraunhofer ISE in the last 15 years in Germany, heat pumps perform well under real operation conditions ensuring in most cases significant CO_2 savings compared to natural gas boilers. It applies to the vast majority of the countries and world´s regions.

Acknowledgements

The implementation of a monitoring project is a challenging and complex task. The execution of the projects and the evaluation of the test results required participation of more than a hundred persons assisting for several years. Thus, special thanks are directed to all employees and former employees who assisted in this task, as well as to all industrial and institutional partners who made the whole implementation possible. This work was supported by the German Ministry of Economics and Technology (BMWi), under the Grant 03ET1272A upon decision of the German Bundestag and supervised by the Project Manager Jülich (PTJ).

References

[1] Buck, M.; Graf, A.; Graichen, P., Agora Energiewende (2019): European Energy Transition 2030: The Big Picture. Ten Priorities for the next European Commission to meet the EU's 2030 targets and accelerate towards 2050."; March 2019
[2] Ausfelder et al. (Hrsg.): Sektorkopplung - Untersuchungen und Überlegungen zur Entwicklung eines integrierten Energiesystems (Schriftenreihe Energiesysteme der Zukunft), München 2017. ISBN: 978-3-9817048-9-1.
[3] IRENA (2018), Global Energy Transformation: A roadmap to 2050, International Renewable Energy Agency, Abu Dhabi.
[4] M. Miara, D. Günther, R. Langner, S. Helmling, " The outcomes and lessons learned from the wide-scale monitoring campaign of heat pumps in family dwellings in Germany" in 11th IEA heat pump conference, Montreal 2014.
[5] M. Miara, D. Günther, R. Langner, S. Helmling, J.Wapler, "10 years of heat pumps monitoring in Germany. Outcomes of several monitoring campaigns. From low-energy houses to un-retrofitted single-family dwellings." in 12th IEA heat pump conference, Rotterdam 2017.
[6] Zottl, Andreas, and R. Nordman. 2012. "Project SEPEMO, D4.2./D2.4. Concept for Evaluation of SPF." www.sepemo.eu.

13th IEA Heat Pump Conference
April 26-29, 2021 Jeju, Korea

Effects of tube shape on boiling heat transfer of low-pressure refrigerantR1233zd(E) outside horizontal tubes

Sho Fukuda[a,*], Yuki Shimizu[b], Noya Miyoshi[b], Yasushi Hasegawa[b]

[a]Kyushu Sangyo University, 3-1 Matsukadai 2-chome, Higashi-ku, Fukuoka 813-8503, Japan
[b]Mitsubishi Heavy Industries Thermal Systems, Ltd., Hyogo-ku, Kobe-shi, Hyogo 652-8585, Japan

Abstract

Hydro-fluoro-olefins and hydro-chloro-fluoro-olefins, such as R1234ze(E), R1234ze(Z), and R1233zd(E), are anticipated to become low global warming potential refrigerants to replace R134a and R245fa for industrial heat pump systems. Experimental data on the heat transfer coefficient of saturated pool boiling of R1233zd(E) on a horizontal fin tube were obtained in this study. The test tube was 19.05 mm in diameter and 400 mm in heat transfer length. The heat transfer coefficients in the two kinds of fin tube were compared. The heat transfer characteristics differed according to the slit on cover of tunnel structure.

Keywords: evaporation, heat transfer coefficient, pool boiling, expansion ;

1. Introduction

Hydro-fluoro-olefins (HFOs) and hydro-chloro-fluoro-olefins (HCFOs), such as R1234ze(E), R1234ze(Z), and R1233zd(E), are expected to become low global warming potential (GWP) refrigerants, which will replace R134a and R245fa for industrial heat pump systems. The normal boiling points of most alternative refrigerant candidate in HFOs and HCFOs are higher than those of hydrofluorocarbons (HFCs). Therefore, suitable tube shape for HFOs and HCFOs is different from that for HFCs. However, the heat transfer characteristics of HFOs and HCFOs have not been investigated.

In this study, experimental data on the heat transfer coefficient (HTC) of saturated pool boiling of R1233zd(E) on a horizontal fin tube are presented.

2. Experiment

2.1. Experimental Apparatus

Fig. 1 shows an experimental apparatus to measure the condensation and pool boiling HTC on a horizontal smooth tube. This is a natural circulation system, in which the liquid refrigerant condensed on a test tube (4) and subcondensers (6) flows down to a boiling chamber, while the vapor evaporated on the test tube and electric heaters (8) returns to a condensation chamber. The flow rate of the condensate flowing down a drain pan (5) is measured by a Coriolis mass flow meter (7). The heat transfer on the test tube is obtained from the temperature change measured in the mixing chambers and the flow rate of the water flows in the test tubes. To determine the refrigerant saturation temperature, the pressure is measured very close to the test tube. The saturation temperature is checked with the temperature measured by K-type thermocouples installed in those chambers. An electric current of 40 A is conducted to the test tube, so that the mean wall temperature is calculated as a function of the electric resistance measured by a voltage meter. The wall temperature is calibrated in the preliminary test; meanwhile, the heat loss from the chambers to ambient air is also measured. The heat flux on the tube wall is defined as follows:

* Corresponding author. Tel.: +81-92-673-5626 ; fax: +81-92-673-5090 .
E-mail address: s.fukuda@ip.kyusan-u.ac.jp

$$q_{\text{wall}} = \frac{V_{\text{H}_2\text{O}}\rho_{\text{H}_2\text{O}}\left(h_{\text{H}_2\text{O,o}} - h_{\text{H}_2\text{O,i}}\right) - Q_{\text{loss}}}{\pi D_{\text{o}} L} \tag{1}$$

where V_{H2O}, ρ_{H2O}, and h_{H2O} are the volumetric flow rate, density, and specific enthalpy of water, respectively, evaluated at the arithmetic mean of $T_{\text{H2O,i}}$ and $T_{\text{H2O,o}}$. Q_{loss} is the heat loss correlated to the temperature difference between water and ambient air. D_{o} and L are the outer diameter and effective heat transfer length of the test tube. Therefore, the HTC is expressed as follows:

$$\alpha = \frac{q_{\text{wall}}}{T_{\text{sat}} - T_{\text{wall}}} \tag{2}$$

where T_{sat} is the saturation temperature evaluated at the measured pressure. T_{wall} is the tube wall temperature correlated to the electric resistance. The thermodynamic and transport properties of R1233zd(E) are calculated by REFPROP Ver. 10 [1] with the incorporated coefficients optimized by Akasaka et al. [2].

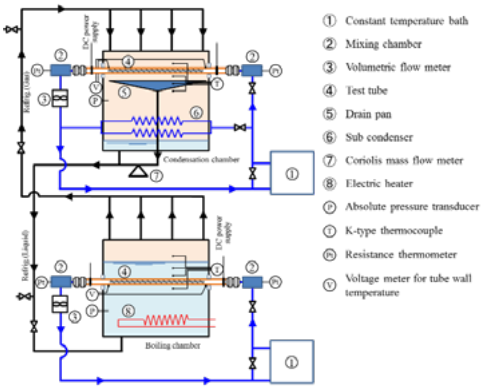


Fig. 1. Schematic diagram of experimental apparatus

2.2. Experimental condition and method

The test refrigerant was R1233zd(E). The HTC was quantified at a saturation temperature of 10°C. The measurement range of heat flux was from 3 to 20 kW·m^{-2} for pool boiling.

2.3. Test tubes

The three kinds of test tubes, which were made of copper, had 19.12-mm outer diameter and 400-mm heat transfer length (tubes A, B, and C), and they were set in a perfectly horizontal configuration. As an example, Fig. 2 shows the external appearance of tube B. The three enhanced tubes had different fin geometries, including the tunnel structure. The difference of the tubes was the size of slit on cover of tunnel structure, as shown Fig. 3. In the order of tubes A, B, and C, the slit on the cover became smaller. For all tubes, the tunnel structure sizes were approximately the same.



Fig. 2. External appearance of tube B

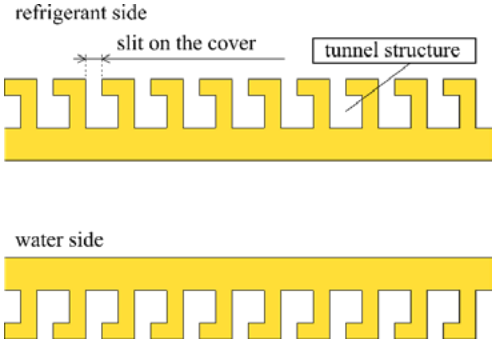


Fig. 3. Schematic diagram of test tubes

3. Results and discussion

Fig. 4 shows the variation in boiling HTC with heat flux in test tubes A, B, and C. The circle, triangle, and square represent tube A, tube B, and tube C, respectively. The symbols are the experimental values of HTC, with the vertical bars indicating the measurement uncertainty of HTC. In general, boiling HTC increases with increase in heat flux.

Boiling HTC of tube B was considerably higher than that of tube A. This was caused by the promotion of the nucleate boiling and the boiling by a thin liquid film. In tube B, when the refrigerant boiled, local pressure became higher by the cover of the tunnel structure. However, in tube A, local pressure did not increase, because the slit on the cover was wide. Then, the nuclear boiling in tube B was promoted. Furthermore, the heat transfer in tube B was promoted by the thin liquid film. In tube B, most of the generated bubbles were exhausted from the upper part of the tube through the tunnel structure, because the slit on the cover was small (a small number of generated bubbles were exhausted by the slit on the cover). A thin liquid film was formed by surface tension as bubbles moved along the tunnel structure. However, in tube A, the generated bubbles were exhausted from the slit on the cover. Then, the heat transfer in tube A was not promoted.

Boiling HTC of tube B was considerably higher than that of tube C. The slit on the cover of tube C was smaller than that of tube B. Then, nuclear boiling in tube C was promoted, as with tube B. However, the HTC of tube C decreased because of a dry patch. In tube C, dryout occurred on part of the heat transfer surface because the slit on the cover was too small, making it difficult for the bubbles to be exhausted.

Therefore, boiling HTC of tube B was considerably higher than those of tubes A and B, because there was an appropriate size in the slit on the cover.

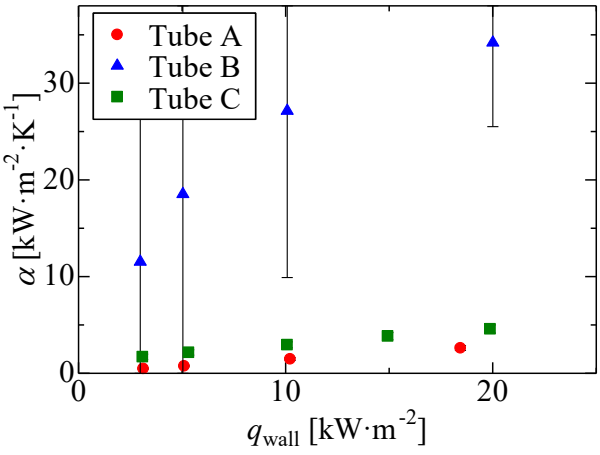


Fig. 4. Variation in boiling HTC with heat flux

4. Conclusion

The experimentally determined HTCs of low-GWP refrigerants of R1233zd(E) on three horizontally installed enhanced tubes were presented. The main conclusions are as follows:

- The HTC was improved by nuclear boiling as well as boiling by the thin liquid film promoted by the tunnel structure and slit on the cover of tunnel structure.
- The slit of the cover of tunnel structure had an appropriate size.

References

[1] Lemmon, E. W., Huber, M. L., and McLinden, M. O., 2018, Reference Fluid Thermodynamic and Transport Properties - REFPROP Ver. 10, National Institute of Standards and Technology, Boulder, CO, USA.
[2] Akasaka, R., and Lemmon, E. W., 2018, Helmholtz equation of state for R-1233zd(E), Refprop Ver. 10.

13th IEA Heat Pump Conference 2020

13th IEA Heat Pump Conference
April 26-29, 2021 Jeju, Korea

Investigation of model predictive control for fifth generation district heating and cooling (5GDHC) substations

Simone Buffa[a,*], Anton Soppelsa[a], Mauro Pipiciello[a], Gregor P. Henze[b,c], Roberto Fedrizzi[a]

[a] Eurac Research, Institute for Renewable Energy, Viale Druso 1, 39100 Bolzano, Italy
[b] University of Colorado Boulder, Department of Civil, Environmental and Architectural Engineering, Boulder, Colorado 80309 USA
[c] National Renewable Energy Laboratory, Golden, Colorado 80401 USA

Abstract

This work investigates the performance of a model predictive controller for customer-sited energy transfer substations, installed in fifth generation district heating and cooling networks (5GDHC) that include electrically driven heat pumps and thermal energy storage systems. Using heat pumps effectively couples the thermal and electrical distribution networks at the individual building level, which opens the door to new scenarios in terms of smart management of urban energy systems. The model predictive controller (MPC) implemented includes two key elements based on artificial intelligence: a composite model of the 5GDHC substation based on several artificial neural networks (ANN) and a constrained optimization solver based on particle swarm optimization (PSO). This study focuses on the analysis performed to test the predictive controller and to understand how it affects the substation energy performance and the building owner's energy bill under different boundary conditions. Moreover, the capacity of the MPC in providing demand flexibility to the power grid has been evaluated through a load shifting strategy obtained by exploiting the capacity of the substation's thermal energy storage.

Keywords: Smart energy systems; Artificial neural networks; Receding horizon control.

1. Introduction

District heating and cooling is acknowledged as a sustainable solution to meet heating and cooling demands in high-density urban areas. This technology has evolved in the last decades towards low distribution temperature in the network and decentralized active plants and substations. These developments enhance the inclusion of renewable heat sources, a reduction of heat losses with the consequence of a more complicated energy system. Fifth-generation district heating and cooling (5GDHC) systems operate at a temperature range between 0÷30°C that is not suitable for direct heating purposes even with low-temperature heat emission systems like floor heating or ceiling panels. Because of the neutral temperature of the network with respect to the ground, heat losses are minimized, and all available urban low-temperature excess heat can be recovered and reused according to circular economy principles. These pros are paid for with the fact that water-source heat pumps, usually electrically driven, are needed in the customer-sited energy transfer stations to boost the temperature of the supplied heat to satisfy the user comfort as shown in Fig. 1. 5GDHC substations can be hydraulically complicated compared to traditional district heating (DH) user substation and in general, are operated to supply space heating (SH) and domestic hot water (DHW) or active/passive space cooling (SC). Consequently, a reversible 5GDHC substation can be considered a "prosumer" that can extract heat from the thermal network in heating mode as a common end-user, or that can supply heat to the network in cooling mode as a producer.

The interest in 5GDHC systems is growing in Europe with an installation rate of three systems per year on average in the last decade [1]. Existing 5GDHC networks will be expanded and new ones will be built in the

* Corresponding author. Tel.: +39-0471-055636; fax: +39 0471 055 699
E-mail address: simone.buffa@eurac.edu

framework of the Interreg project D2grid [2] and H2020 REWARDHeat [3], both launched in 2019. Several utility companies have started exploiting the advantages of supplying simultaneously heating and cooling by means of a single network, extending the operation of the DHC system and their economic revenues all year round.

This study focuses on the development of an advanced decentralized controller for 5GDHC substations with a focus on the optimization of DHW production. The method adopted for the controller implementation is presented in Section 2 whereas the results of preliminary tests are discussed in Section 3.

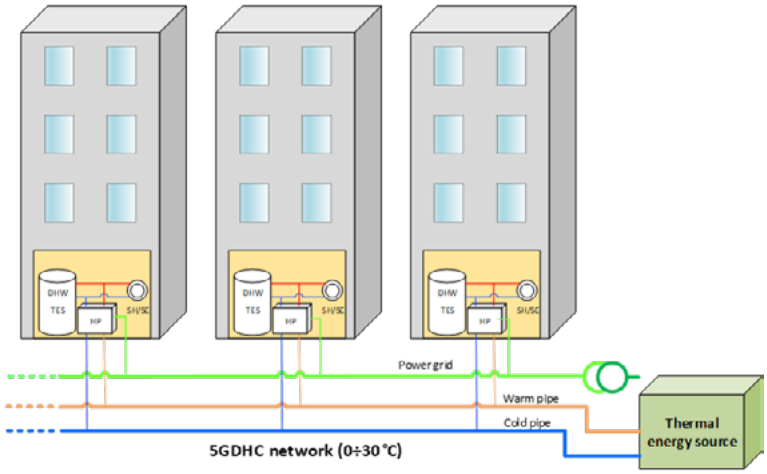


Fig. 1. Layout of a 5GDHC system.

2. Methodology

The advanced controller for 5GDHC substations has been implemented in the form of artificial neural network-based model predictive control (ANN-MPC). A literature review about the MPC application for HVAC systems can be found in Afram and Janabi-Sharifi (2014) [4].

In general, MPC employs an explicit model of the system whose identification phase is usually demanding in terms of development time and effort. At each control timestep, the state of this model is updated from measurements, and the model is used to make several predictions of the future behaviour of the system according to a sequence of the control inputs $\bar{u}(t)$ that are applied. MPC is a form of optimal control since it involves an optimization algorithm that solves in real-time a constrained optimization problem providing the sequence of the control variables that minimises (or maximises) a given objective function over a time window, satisfying the problem constraints. At the current time-step t, only the first value of the optimal trajectory identified by the MPC is applied to the system. At the next control timestep $t+1$, the procedure is repeated with a prediction horizon window shifted by one control timestep. This methodology is known as receding horizon model predictive control approach. To limit the computational effort of the controller, it is a common practice to apply a move blocking strategy so that the length M of the control input vector $\bar{u}(t)$ is shorter than the prediction horizon length N and the last element of control input vector $\bar{u}(t)$ is kept constant for the remaining timestep of the prediction horizon.

MPC can be applied in general in the form of a multi-input multi-output (MIMO) system that aims at minimising an objective function that includes a tracking error with respect to a reference value and the control effort over the prediction horizon. Conversely, as in this study, MPC can be also employed as a supervisory controller developed in the form of an economic MPC since the objective function to be minimised includes system economics. A black-box model of the considered system has been developed in the form of artificial neural networks (ANNs). This reduced-order model (ROM), presented in the next section, has been used as a surrogate model of the real system to perform at each control timestep t a prediction of its performance over the prediction horizon.

2.1. Reduced order model (ROM) of the 5GDHC substation

Reduced order models (ROMs) is the term used for simplified models of complex systems that can capture the system performance maintaining adequate accuracy. The growing application of machine learning algorithms in building energy systems allow the development of ROMs that in general exhibit the following advantages (+) and disadvantages (-) with respect to fully defined physics-based building energy models:

(+) the building and the energy system feature do not need to be fully defined;
(+) simplified models can be aggregated to build complex models with a bottom-up approach;
(+) they have a short simulation runtime that is important especially in real-time systems;
(+) a predefined model architecture can be employed in different case studies;
(-) to create the model a diverse training dataset is needed so that the model can experience different possible conditions;
(-) the model outputs depend on the temporal resolution of the training dataset;
(-) the model outputs cannot be explained by physical laws and must be interpreted.

There are several ways to build data-driven ROMs of HVAC systems. In particular, in Afram and Janabi-Sharifi (2015) [5] artificial neural networks (ANNs) outperform different black-box models as well as grey-box models of the same HVAC components installed in a single-family house. Moreover, in Esen and Inalli (2010) [6], [7] and in Li et al. (2011) [8] it was shown that adaptive network-based fuzzy inference system (ANFIS) models overperform ANN models for a ground-source heat pump (GSHP) system and for the prediction of the building electricity, hot and cold water loads, respectively. Nevertheless, ANFIS models require more complicated architectures as well as more complicated training algorithms. For this reason, the present study focuses on the development of ROMs based on ANNs that can be used in a real-time control system for a 5GDHC substation.

ANN-based MPC consists of the application where a single ANN model or a group of interconnected ANN models are used as a surrogate model of the system in an MPC controller [9]. Afram et al. (2017) [10] performed an extensive review of the application of ANN-MPC for the optimization of HVAC systems operation. The authors highlighted that this approach has been applied especially in commercial, public and office buildings in the last years because the HVAC systems of such large buildings are usually equipped with a building energy management system that can handle the outputs of an MPC controller. This is not the case for residential buildings that represent the largest share of the building stock. Nevertheless, residential buildings can harness several economic and environmental advantages through the exploitation of MPC technology and can provide flexibility to both electrical and thermal grids. Since 5GDHC systems pave the way for decentralised sector coupling exploiting customer-sited energy transfer substations, the ANN-MPC technology has been developed to operate a substation of this kind supplying a small multifamily house.

2.2. Optimization algorithm

As is described in Afram et al. (2017) [10], different nonlinear optimization methods have been used in the field of ANN-MPC like genetic algorithms (GA), Newton-Raphson, branch and bound, etc. Nevertheless, among the metaheuristic methods, GA is the most widely used in ANN-MPC studies. It is able to solve both constrained and unconstrained problems and to deal with integer values. These pros are paid for with slow convergence for complex problems so that it can be not suitable for real-time implementation. Particle swarm optimization (PSO) algorithm is considered a well-balanced method to solve both single and multi-objective optimization problems with low computational time [10]. For this reason, this optimization algorithm has been chosen in this study for the implementation of a real-time MPC controller.

PSO is a biologically inspired meta-heuristic methodology. This population-based algorithm is useful in solving optimization problems where the analytical expression of the gradient of the cost function is not available or difficult to assess. It consists of a population of interacting agents that directly search for the minimum of the cost function in a multi-dimensional domain with no information about the gradient (unknown environment). It is inspired by the collective behaviour of species like birds (flocking) and fishes (shoaling and schooling). This concept is part of the artificial intelligence discipline under the name of “swarm intelligence”. The LabVIEW code used in this work was derived from the “perturbed Particle Swarm Optimization” (pPSO) algorithm that is part of the Advanced Metaheuristics Algorithms library implemented by Derouiche M. L. (2015) [11] on the basis of the work of Xinchao Z. (2010) [12], and available at [13].

The algorithm implemented by Derouiche M. L. (2015) has been designed to have as output a real number. Nevertheless, since the HP of the 5GDHC substation operates in ON-OFF mode the algorithm has been modified to handle a binary output. This has been done according to the proposal of Kennedy and Eberhart (1997) [14] where the velocities of the particles are treated as "probabilities of change" and their position results in a 0 or 1 state.

2.3. Physical model of a 5GDHC substation

In order to build the reduced order model (ROM) of the 5GDHC substation, a physical model in TRNSYS [15] has been set up in order to create a dataset used for training the data-driven model based on artificial neural networks (ANNs). The physical model of the 5GDHC substation has been built using Type 927 of the TESS library to model the water-source heat pump (WSHP) system and Type 534 of the TESS library to model the DHW TES and the SH/SC buffer tanks. The 5GDHC network is not modelled and it is considered an ideal thermal energy source that supplies the substation at a constant temperature of 15°C. The 5GDHC substation has been sized to meet the space heating (SH) and domestic hot water (DHW) demands of a small multi-family house located in Rome and has a thermal capacity of about 23 kWth. The residential building has a total of 10 apartments divided into 5 floors. Every single apartment has a floor area of 50 m2 and an energy net demand level of about 45 kWh/m2 per year for space heating (SH) according to the study performed in Fedrizzi et al. (2015) [16]. Accordingly, the specific DHW load results in 24 kWh/m2 per year and it has been obtained by generating the DHW draw profile by means of the tool DHWcalc V.2.02b [17] considering an occupancy level of 2 people/apartment and specific hot water demand of 40 l/(person day). The building heat emission system consists of ceiling radiant panels that are supplied by the 5GDHC substation. The SH demand profile has been obtained from a separate dynamic numerical simulation of the building using Type 56 and used as a boundary condition for the substation.

The performance map of the water source heat pump (WSHP) has been calibrated and validated by means of dedicated tests at the Energy Exchange Laboratory of EURAC Research in Bolzano-Bozen (Italy) [18]. The tests have been performed by first fixing a constant inlet temperature at the evaporator and varying the inlet temperature at the condenser, thereafter fixing a constant inlet temperature at the condenser and varying the inlet temperature at the evaporator. The results of the calibrated HP model concerning the thermal power measured at the evaporator and condenser as well as the electricity consumption fall within the measurement uncertainty band under almost all operating conditions.

2.4. Reduced order model (ROM) of a 5GDHC substation

The reduced order model (ROM) of the 5GDHC substation has been built by adopting a modular approach and using one ANN to model each single component. The composite model of the 5GDHC substation is obtained by connecting, in a proper way the input-output of an ANN model of the DHW TES system and an ANN model of the HP. To achieve this goal, the two ANN models have been trained separately using a dataset of 20 days obtained from the TRNSYS simulation of the validated 5GDHC substation model. The time resolution adopted to model the system is 10 minutes, short enough to capture the system dynamics and allowing the possibility of taking into account a "cost" for the change of state (ON-OFF) of the HP. This timestep is also large enough to keep the computational effort acceptable. The same control timestep of 10 minutes has been adopted for the optimization problem of the MPC. It is important that the ANN models are developed with the same timestep of the optimization problem so that during the MPC real-time simulation the variables exchanged, that are in this case thermal energy, are the results of the integration of thermal power profiles over the same control timestep. The ANN structure adopted in this study for the two models is the same: nonlinear autoregressive network with exogenous inputs (NARX). This kind of ANN differs from the standard multilayer perceptron (MLP) because includes feedback from the outputs.

The variables considered in the development of a 5GDHC substation ANN model are listed in Table 1. The thermal energy delivered by the HP to the DHW TES ($E_{th,HP,DHW}$) in one control timestep (4 kWhth) represents the control variable and its trajectory is provided according to the binary output of the MPC. During the MPC simulation, the trajectories of $E_{th,HP,DHW}$ are provided to the ANN model to perform an on-line simulation. This variable is provided to both the TES and HP models, simultaneously. The DHW TES system ANN model inputs are the thermal energy supplied to the DHW TES by the HP ($E_{th,HP,DHW}$) and the DHW load covered by the DHW TES ($E_{th,load}$). The two outputs are the temperature at the top (T_{top}) and at the bottom (T_{bot}), respectively. The ANN has 15 neurons in the hidden layer where the tangent-sigmoid activation function has been used, whereas for the output layer the linear activation function has been adopted.

The ANN model of the HP has 15 neurons in the hidden layer. The tangent-sigmoid and the linear activation functions have been adopted in the hidden and output layer, respectively. The model inputs are three: the thermal energy provided by the HP to the DHW TES ($E_{th,HP,DHW}$), the inlet temperature of the HP at the condenser ($T_{in,load}$) and the inlet temperature of the HP at the evaporator ($T_{in,source}$). The model provides as outputs the electricity consumption of the substation ($E_{el,SUB}$) and the thermal energy extracted by the HP from the DHC network ($E_{th,SUB}$).

Table 1 Inputs and outputs description of the implemented ANN models.

		ANN Model of the TES		**ANN Model of the HP**	
		Input variables	Output variables	Input variables	Output variables
Input at	$t = t_k$	1- $E_{th,HP,DHW}$ $[kWh]$ 2- $E_{th,load}$ $[kWh]$	1- T_{top} $[°C]$ 2- T_{bot} $[°C]$	1- $E_{th,HP,DHW}$ $[kWh]$ 2- $T_{in,load}$ $[°C]$ 3- $T_{in,source}$ $[°C]$	1- $E_{el,SUB}$ $[kWh]$ 2- $E_{th,SUB}$ $[kWh]$
Input TDL at	$t = t_{k-1}$	3- $E_{th,HP,DHW}$ $[kWh]$ 4- $E_{th,load}$ $[kWh]$		4- $E_{th,HP,DHW}$ $[kWh]$ 5- $T_{in,load}$ $[°C]$ 6- $T_{in,source}$ $[°C]$	
Output TDL at	$t = t_{k-1}$	5- T_{top} $[°C]$ 6- T_{bot} $[°C]$		7- $E_{el,SUB}$ $[kWh]$ 8- $E_{th,SUB}$ $[kWh]$	

The validation of the ANN models has been performed comparing the outputs with a dataset from a physical model simulation of 24 hours (144 timesteps of 10 minutes) not used for the ANN training. The performance metrics assessed for this purpose over the entire simulation are the normalised mean bias error and the coefficient of variation of the root mean square error for the variable ζ_j presented in Equations 1 and 2, where m_i the measured value and s_i is the simulated one of the variable ζ_j.

$$NMBE_{\zeta_j} = \frac{1}{\bar{m}_j} \frac{\sum_{i=1}^{n}(m_{j,i} - s_{j,i})}{n} \cdot 100(\%) \quad (1)$$

$$CVRMSE_{\zeta_j} = \frac{1}{\bar{m}_j} \sqrt{\frac{\sum_{i=1}^{n}(m_{j,i} - s_{j,i})^2}{n-1}} \cdot 100(\%) \quad (2)$$

For the ANN model of the DHW TES a CVRMSE of 2.1% has been obtained for the temperature at the top (T_{top}) and a CVRMSE of 4.9% for the temperature at the bottom (T_{bot}). For the ANN model of the HP a CVRMSE of 1.3% has been achieved for the electricity consumption ($E_{el,SUB}$) and a CVRMSE of 0.8% has been achieved for the thermal energy extracted by the HP from the source ($E_{th,SUB}$). The NMBE for all the variables resulted in less than 1%.

2.5. Cost function

The MPC controller has been implemented as an economic MPC task since the objective function to minimise is the operating costs of the 5GDHC substation over the prediction horizon with N timesteps $[t_0, \dots, t_k, \dots, t_{k+N-1}]$. As shown by Equation 3 the operating cost calculation considers at each timestep t_j, $E_{el,SUB}(t_j)$: the electricity consumption of the substation and its auxiliaries, $c_{el}(t_j)$: the specific cost of electricity, $E_{th,SUB}(t_j)$: the thermal energy supplied by the 5GDHC network to the substation and $c_{th,dhc}(t_j)$: its specific cost.

$$J(t_j) = \sum_{j=k}^{k+N-1} c_{el}(t_j) E_{el,SUB}(t_j) + \sum_{j=k}^{k+N-1} c_{th,dhc}(t_j)\, E_{th,SUB}(t_j) \quad (3)$$

Moreover, in order to minimise the number of ON-OFF switching events of the HP that are cause of inefficiencies and stress for both electrical and mechanical components as shown by Curtis and Pine (2012) [19], a "state change cost" $K(t_j)$ has been added in the cost function and implemented according to Equation 4: the state variations of the HP over the prediction horizon N are counted and weighted by a factor β that has been set equal to 1 in this study.

$$K(t_j) = \beta \sum_{j=k}^{k+N-1} \left| s(t_j) - s(t_{j-1}) \right| \quad (4)$$

The PSO algorithm used here has been conceived to solve unconstrained problems. To handle the MPC problem, the constraints have been included in the cost function in the form of soft constraints as suggested by Derouiche et al. (2016) [11]. The method applied here is the external static penalty technique so that the value of the objective function increases proportionally to the degree of constraint infeasibility. The constrains must be verified over the control horizon and are implemented as follows:

- the temperature at the top of the DHW TES must be higher than 45°C to satisfy the comfort needs as described by Equation 5:

$$\min_{t_j \geq 0} T_{top,DHW}(t_j) > T_{top,DHW,min} = 45°C \quad (5)$$

- the temperature at the top of the DHW TES must be lower than 55°C to satisfy the operating limits of high temperature and high pressure of the refrigerant at the HP condenser that has been verified through dedicated tests at the Energy Exchange Laboratory:

$$\max_{t_j \geq 0} T_{top,DHW}(t_j) < T_{top,DHW,max} = 55°C \quad (6)$$

The overall cost function is implemented so that at each control timestep it is called by the optimization algorithm and it is assessed considering the different trajectories of the ANN model outputs and of the boundary conditions over the prediction horizon N. To increase the robustness of the controller, the MPC outputs are filtered through a back-up rule-based controller (RBC) so that the DHW TES is charged if the temperature at the top accidentally drops below 45°C or it is no longer charged if the temperature at the top could reach a value higher than 55°C.

In the next section, the results of two separated tests are presented with a perfect prediction of the DHW load. In both cases, a prediction horizon of three hours $(N = 18)$ and a control horizon of one hour $(M = 6)$ have been selected. Test 1 deals with the assessment of the behaviour of the MPC controller both with and without model mismatch between the model used in the MPC and the one used to simulate the controlled system. In Test 2 the results of different scenarios over a simulation of one month (January 2017) are presented. The boundary conditions include a time-of-use (TOU) electricity price variation as a form of demand response (DR) strategy based on the Italian tariff D1 taken as a reference. According to this, the peak period is defined as the time between 8:00 and 19:00 on work days. The aim is to compare the results of a standard rule-based control (RBC) strategy versus MPC only to cover the DHW load through the assessment of the following KPIs:

- $T_{top,max}$ and $T_{top,min}$ are the maximum and minimum temperature value at the top of the DHW TES (controlled variable) over the simulation period;
- T_{ave} is the volume average temperature the DHW TES over the simulation period;
- $E_{el,sub}$ and $E_{th,sub}$ are the electricity and thermal energy consumptions of the substation coming from the electrical and thermal grids during the DHW operation mode;
- E_{load} is the DHW load covered by the substation;
- COP_{sub} is the coefficient of performance of the substation including the HP and auxiliaries in DHW operation mode calculated as the ratio between E_{load} and $E_{el,sub}$;
- N_{on} is the total number of the HP start-ups in DHW operation mode;
- $E_{el,sub,off\text{-}peak}$ and $E_{el,sub,peak}$ are the electricity use of the substation during the off-peak and peak hours;
- t_{disc} is the percentage of time with respect to the entire simulation period where the DHW is available for the user at a temperature lower than 44°C. This limit has been fixed as a threshold to assess a form of discomfort for the final user.

The simulations of Test 2 are performed in TRNSYS and have a time step of one minute that allows observing with enough resolution the interaction between the HP and the DHW TES that influence the TES stratification process. The controller that includes the MPC and the backup controller is implemented in LabVIEW. The MPC optimization problem is solved with a control timestep of 10 minutes. To exchange information between TRNSYS and LabVIEW in real-time a dynamic link library (DLL) connection has been developed.

3. Results and discussion

3.1. Test 1: No model mismatch vs. model mismatch

The first test involving the MPC controller aims at comparing its operation through the two platforms developed for the debugging phase: the first one realised completely in LabVIEW and the second one includes a co-simulation between TRNSYS and LabVIEW. A model to emulate the real system is needed in the debugging phase to test the ANN-MPC. In both cases, the emulator is updated at each control timestep by receiving the first input u* of the optimal trajectory resulting from the MPC calculations and returns back state information about the "virtual system" to update the state of the MPC model before the optimization process starts again. In the first platform, the same ANN model of the MPC controller is used as an emulator of the 5GDHC substation (no model mismatch) whereas in the TRNSYS platform a physical model of the substation is used for the same purpose with the introduction of a mismatch between the MPC model and the system emulator.

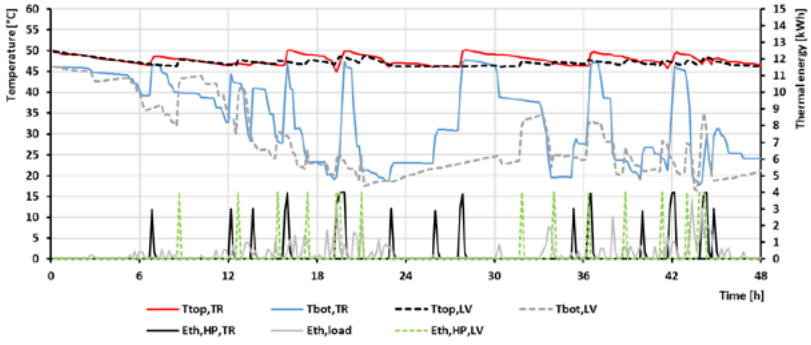


Fig. 2. Simulation results of the "no model mismatch" case VS the target values.

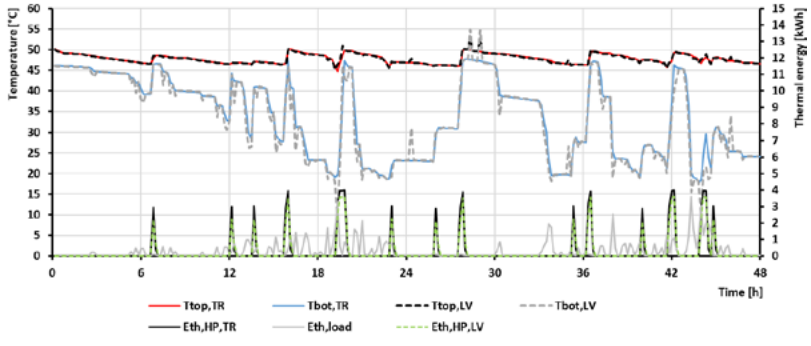


Fig. 3. Simulation results of the "model mismatch" case VS the target values.

In Fig. 2 the simulation results of the two cases with model mismatch (TRNSYS platform) and without model mismatch (LabVIEW platform) are compared under the same boundary conditions for testing the MPC during a simulation duration of 48 hours: the DHW TES model starts with the same state-of-charge in the two

simulations and the identical DHW load is applied. On the primary axis, there are shown the temperature profiles at the top and at the bottom of the DHW TES. The solid lines Ttop,TR, Tbot,TR represent the target temperature profiles that are the result of the physical model of the substation developed in TRNSYS. The dashed lines Ttop,LV, Tbot,LV represent the temperature profiles of the ANN model of the substation developed in LabVIEW. On the secondary axis, there are shown the thermal energies supplied by the HP to the DHW TES in the two cases (Eth,HP,TR, Eth,HP,LV) and the DHW load considered (Eth,load) with a timestep of 10 minutes. It can be noticed that after a few hours of simulation the temperature profiles of the ANN model in LabVIEW (no model mismatch case) diverge from the true profiles that one obtains from the TRNSYS model (model mismatch case). A normalised error for the temperature at the top ($CVRMSE_{Ttop,LV}$) of 3% and for the bottom one ($CVRMSE_{Tbot,LV}$) of 28% for the entire simulation is observed. These results are a consequence of the use of NARX ANNs models that propagate the errors for the output variables at the current timestep to the model inputs at the next timestep.

In Fig. 3 the same profiles of the previous case are shown, but the comparison is made between the outputs of the TRNSYS model and the real-time outputs of the surrogate ANN model of the MPC (model mismatch case). It can be noticed that since at each control timestep the ANN model state is initialised from the true measurements of the system (output of the TRNSYS model) the error that it provides to the outputs is very small and is not propagated along the simulation. This small error is also due to the delay of one simulation timestep (1 minute) that occurs during the exchange of information between the TRNSYS-LabVIEW co-simulation process. The errors of the temperature profiles are reduced to a value of 0.7% for $CVRMSE_{Ttop,LV}$ and a value of 6.3% for $CVRMSE_{Tbot,LV}$. Beyond this comparison, it can be observed that the MPC satisfies the constraints of the top temperature of the TES described by Equation 5.

3.2. Test 2: rule-based control vs. model predictive control

The test of the MPC controlled described in this study aims at comparing its performance with respect to a baseline that represents a simulation with the same boundary conditions where the 5GDHC substation is operated by a rule-based control strategy. Three scenarios have been developed to test the MPC operation and to perform an energetic and economic performance assessment of the 5GDHC substation for supplying the DHW load. The difference between the three MPC scenarios is the profile of the electricity price. It is flat and equal to 0.15 [EUR/kWh] for the scenario 1, whereas it is 0.15 [EUR/kWh] during the off-peak hours and equal to 0.30 [EUR/kWh] and 0.60 [EUR/kWh] during the peak-hours for the TOU scenario 2 and 3, respectively. The price of the thermal energy extracted from the 5GDHC grid has been considered constant and equal to 0.05 [EUR/kWh]. Thus, a TOU-based demand response is implemented only in scenarios 2 and 3 since in scenario 1 the electricity price is constant and the MPC operates to minimise the energy consumptions and state change of the substation.

The results listed in Table 2 show that in scenarios 1, 2 and 3 the MPC operates by charging the DHW TES more frequently with respect to the baseline scenario. In fact, the number of start-up signal (Non) of the HP in DHW mode increases by about 70.3%, 57.4%, and 67.3%, respectively. Thus, on average it results that less thermal energy is provided by the HP to the DHW TES during a single charge with respect to a standard charging process that occurs in the baseline scenario. The same occurs for the average electricity extracted by the HP from the power grid in a single charging process. The MPC always operates to further increase the temperature of the TES when a peak in the load is predicted. This occurs also in scenario 1 where the electricity price is flat. Nevertheless, the temperature at the top of the TES never reaches the upper bound of 55°C. The extra-charging process of the MPC has an impact on the average temperature of the TES over the simulation period that increases between 1.4% and 1.9% for the different scenarios with respect to the baseline with resultant higher thermal losses of the TES but achieving a reduction of the discomfort period (tdisc) for the occupant. Since the temperature at the evaporator is maintained constant, a higher temperature at the condenser has a negative impact on the COPsub that drops by about 3÷3.7% in the different scenarios with respect to the baseline. Lower COPsub and higher thermal energy losses have a direct impact on the energy consumed to run the 5GDHC substation. In fact, there is an increase of the consumptions of electricity and thermal energy from the 5GDHC grid between 3.2÷4.2%.

It is also important to highlight how the MPC operation contributes to the electricity peak-load shaving by comparing the electricity consumption of the substation for the different scenarios during the off-peak and peak hours defined according to the TOU demand response strategy. It can be noticed that, in scenario 1 where a TOU price variation is not implemented, the effect of the MPC is to reduce the electricity consumption during the peak hours by 2.1% and to increase the one during the off-peak hours by 7.7%. Because a peak DHW load occurs in the morning between 7:00 and 9:00, the prediction of the MPC leads to the production of DHW

before the peak load occurs. When the TOU price variation is implemented in scenarios 2 and 3, this shift is further boosted. The higher the price variation, the higher is the amount of electricity consumption that is shifted to off-peak hours.

The economic performance of the different scenarios is summarised in Table 3. For the different cases, the total costs of the electrical (CEel,tot) and thermal energy (CEth,tot) consumption over the simulated period are calculated for the baseline scenario with the corresponding energy tariffs. For scenario 1 with a flat electricity price, the extra-charging processes with a peak temperature above 50°C due to the MPC outputs lead to higher electrical and thermal energy consumption with a total utility energy bill (UEBtot) that is higher than the baseline one by 3.7%. With the introduction of a TOU electricity tariff in scenario 2, the 5GDHC substation operation due to the MPC implicates a shift in the costs with a small reduction of the electricity bill and an increment of 3.2% of the thermal energy bill. Nevertheless, the relative difference in UEBtot is less than 1%. This means that a TOU energy tariff of that kind is still not effective for a final user that would like to install a predictive controller as already presented in a previous study [20]. This because the saving obtained by the limited price variation between off-peak and peak hours that occurs only two times a day during working days, does not compensate for the additional energy consumptions due to the drop in the 5GDHC substation performance and additional thermal losses of the TES. Finally, in scenario 2 it can be noticed that the situation is changed. The peak hours electricity tariff is four times that of off-peak hours. Here, the electricity bill savings achieved is about 6% whereas the thermal energy bill increases by 4.1% with respect to the baseline. The UEBtot has a reduction of 3.5% with respect to the baseline that makes the MPC system attractive with respect to a standard RBC system.

Table 2 Energy assessment of the parametric simulations.

Scenario	$c_{el,off\text{-}peak}$ [EUR/kWh]	$c_{el,peak}$ [EUR/kWh]	$T_{top,max}$ [°C]	$T_{top,min}$ [°C]	T_{ave} [°C]	$E_{el,sub}$ [kWh]	$E_{th,sub}$ [kWh]	$E_{th,load}$ [kWh]	COP_{sub} [-]	N_{on} [-]	$E_{el,sub,off\text{-}peak}$ [kWh]	$E_{el,sub,peak}$ [kWh]	t_{disc} [%]
Baseline			50.4	41.7	40.7	439.6	993.1	1224.0	2.78	101	258	182	2.1%
1	0.15	0.15	54.1	43.7	41.2	455.8	1029.1	1226.1	2.69	172	278	178	1.6%
			7.5%	*4.7%*	*1.4%*	*3.7%*	*3.6%*	*0.2%*	*-3.4%*	*70.3%*	*7.7%*	*-2.1%*	*-24.7%*
2	0.15	0.3	54.3	42.0	41.3	454.3	1025.2	1227.0	2.70	159	290	165	1.6%
			7.7%	*0.6%*	*1.5%*	*3.3%*	*3.2%*	*0.2%*	*-3.0%*	*57.4%*	*12.4%*	*-9.5%*	*-26.9%*
3	0.15	0.6	54.3	43.5	41.4	458.2	1033.6	1228.3	2.68	169	302	156	1.5%
			7.8%	*4.3%*	*1.9%*	*4.2%*	*4.1%*	*0.3%*	*-3.7%*	*67.3%*	*17.3%*	*-14.2%*	*-32.2%*

Table 3 Economic assessment of the parametric simulations.

	$c_{El,off\text{-}peak}$ [EUR/kWh]	$c_{El,peak}$ [EUR/kWh]	$c_{Eth,dhc}$ [EUR/kWh]	$C_{El,tot}$ [EUR]	$C_{Eth,tot}$ [EUR]	UEB_{tot} [EUR]
Baseline	0.15	0.15	0.05	65.9	49.7	115.6
Scenario 1	0.15	0.15	0.05	68.4	51.5	119.8
Rel. var.				*3.7%*	*3.6%*	*3.7%*
Baseline	0.15	0.3	0.05	93.2	49.7	142.9
Scenario 2	0.15	0.3	0.05	92.8	51.3	144.1
Rel. var.				*-0.4%*	*3.2%*	*0.8%*
Baseline	0.15	0.6	0.05	147.9	49.7	197.5
Scenario 3	0.15	0.6	0.05	139.0	51.7	190.7
Rel. var.				*-6.0%*	*4.1%*	*-3.5%*

4. Conclusions

This work presents the implementation of an MPC controller that has been developed to optimise the operation of a 5GDHC substation to cover the DHW load by exploiting the thermal capacity of the DHW thermal

energy storage system. The controller structure is based on artificial neural networks (ANN) that have been used in a modular approach to create a surrogate model of the 5GDHC substation and the binary particle swarm optimization (BPSO) algorithm has been used in the optimizer to find the best trajectory over the prediction horizon according to the boundary conditions. The investigation reported in this study deals with two preliminary tests of the MPC controller. The results of test 1 highlight that using the same ANN model of the system as an emulator of the system can be useful in the debugging phase of the controller. Nevertheless, the results of the simulation are not representative for an accurate assessment of the system performance since the use of NARX ANN models involves the propagation of the errors of the outputs onto the input at each simulation timestep. To overcome these drawbacks, a platform that includes a co-simulation TRNSYS-LabVIEW has been developed. It includes a physical model of the system as an emulator and allows a reliable and accurate assessment of the MPC operation and system performance under close-to-reality boundary conditions.

The results of the second test presented in this study deal with the energetic and economic performance assessment of the 5GDHC substation comparing the system operation under a model predictive control (MPC) strategy compared to a standard rule based controller. Different scenarios have been analysed considering different electricity prices. In particular, a comparison between a flat electricity tariff with respect to time-of-use tariff is performed considering two different peak prices. The results show that the extra-charging process of the TES leads to a drop in system performance due to lower COP and higher thermal energy losses. This results in additional energy consumption of electricity and thermal energy that are not always compensated economically by the savings achieved by charging in a smart way the TES during the off-peak hours. In the best scenario, total bill savings of 3.5% have been achieved thanks to the MPC controller. Nevertheless, it is important to highlight how the MPC operation contributes to shaving the electricity peak-load providing flexibility to the power grid. For the two TOU scenarios, part of the electricity consumption is shifted to the off-peak period achieving a reduction of 9.5% and 14.2% in the peak-hours period with respect to the baseline. Further research is needed to extend the analysis to annual simulations and considering the MPC operation under real-time pricing (RTP) programs.

Acknowledgements

This work is part of the research activities of the project REWARDHeat funded by the European Union's Horizon 2020 research and innovation programme under grant agreement No 857811.

References

[1] S. Buffa, M. Cozzini, M. D'Antoni, M. Baratieri, and R. Fedrizzi, "5th generation district heating and cooling systems: A review of existing cases in Europe," *Renew. Sustain. Energy Rev.*, vol. 104, pp. 504–522, 2019.
[2] "Interreg project D2Grids." [Online]. Available: http://www.nweurope.eu/projects/project-search/d2grids-increasing-the-share-of-renewable-energy-by-accelerating-the-roll-out-of-demand-driven-smart-grids-delivering-low-temperature-heating-and-cooling-to-nwe-cities/.
[3] "REWARDHeat H2020 project." [Online]. Available: https://cordis.europa.eu/project/rcn/224317/fact-sheet/en. [Accessed: 13-Nov-2019].
[4] A. Afram and F. Janabi-Sharifi, "Theory and applications of HVAC control systems – A review of model predictive control (MPC)," *Build. Environ.*, vol. 72, pp. 343–355, Feb. 2014.
[5] A. Afram and F. Janabi-Sharifi, "Black-box modeling of residential HVAC system and comparison of gray-box and black-box modeling methods," *Energy Build.*, vol. 94, pp. 121–149, 2015.
[6] H. Esen, M. Inalli, A. Sengur, and M. Esen, "Predicting performance of a ground-source heat pump system using fuzzy weighted pre-processing-based ANFIS," *Build. Environ.*, vol. 43, no. 12, pp. 2178–2187, Dec. 2008.
[7] H. Esen and M. Inalli, "ANN and ANFIS models for performance evaluation of a vertical ground source heat pump system," *Expert Syst. Appl.*, vol. 37, no. 12, pp. 8134–8147, 2010.
[8] K. Li, H. Su, and J. Chu, "Forecasting building energy consumption using neural networks and hybrid neuro-fuzzy system: A comparative study," *Energy Build.*, vol. 43, no. 10, pp. 2893–2899, 2011.
[9] M. Lawrynczuk, *Computationally efficient model predictive control algorithms: a neural network approach*. New York: Springer, 2013.
[10] A. Afram, F. Janabi-Sharifi, A. S. Fung, and K. Raahemifar, "Artificial neural network (ANN) based model predictive control (MPC) and optimization of HVAC systems: A state of the art review and case study of a residential HVAC system," *Energy Build.*, vol. 141, pp. 96–113, Apr. 2017.

[11] M. L. Derouiche, S. Bouallègue, J. Haggège, and G. Sandou, "LabVIEW Perturbed Particle Swarm Optimization Based Approach for Model Predictive Control Tuning," *IFAC-Pap.*, vol. 49, no. 5, pp. 353–358, 2016.
[12] X. Zhao, "A perturbed particle swarm algorithm for numerical optimization," *Appl. Soft Comput. Elsevier*, vol. 10, pp. 119–124, 2010.
[13] "Advanced Metaheuristics Algorithms by ENIT." [Online]. Available: http://sine.ni.com/nips/cds/view/p/lang/it/nid/216789. [Accessed: 25-Oct-2018].
[14] Kennedy J. and Eberhart R.C., "A discrete binary version of the particle swarm algorithm," presented at the IEEE International Conference on Systems, Man, and Cybernetics. Computational Cybernetics and Simulation, Orlando, FL, USA, 1997.
[15] University of Wisconsin--Madison. Solar Energy Laboratory, *TRNSYS, a Transient Simulation Program.* Madison, Wis. :The Laboratory, 1975.
[16] R. Fedrizzi *et al.*, "FP7 INSPIRE project D6.3c: Performance of the Studied Systemic Renovation Packages – Multifamily Houses." 2015.
[17] U. Jordan and K. Vajen, "DHWcalc: Program to generate domestic hot water profiles with statistical means for user defined conditions," in *ISES Solar World Congress*, 2005, pp. 1–6.
[18] Eurac Research, "Energy Exchange Lab." [Online]. Available: http://www.eurac.edu/en/research/technologies/renewableenergy/Infrastructure/Pages/Energy-Exchange-Lab.aspx. [Accessed: 15-Dec-2017].
[19] R. Curtis and T. Pine, "Effects of cycling on domestic GSHPs. Supporting analysis to EA Technology Simulation / Modelling.," Mimer Geoenergy, Cornwall, 2012.
[20] Buffa S., Cozzini M., Henze G.P., Dipasquale C., Baratieri M., and Fedrizzi R., "Potential study on demand side management in district heating and cooling networks with decentralised heat pumps," presented at the International Sustainable Energy Conference - ISEC 2018, Graz, Austria.

13th IEA Heat Pump Conference
April 26-29, 2021 Jeju, Korea

Performance analysis of ground source heat pump system with vertical borehole heat exchangers affected by rapid groundwater flow

Hobyung Chae[a,*], Katsunori Nagano[a], Yoshitaka Sakata[a],

Takao Katsura[a], Takeshi Kondo[b]

[a]Graduate School of Engineering, Hokkaido University, N13-W8, Kita Ku, Sapporo 060-8628, Japan
[b]NIKKEN SEKKEI Research Institute, 3-737, Kanda Ogawamachi, Chiyoda-ku, Tokyo 101-0052, Japan

Abstract

The objective of this study is to estimate a cooling and heating performance of the ground source heat pump system with the borehole heat exchangers affected by rapid groundwater flow. The performance prediction is especially performed according to the required length of the borehole heat exchangers. For the evaluation of the performance, the measured data are analyzed in a three-floor building installed on the ground source heat pump system with four borehole heat exchangers (BHE s) in Kazuno City, Japan where the area has the groundwater flow actively. Based on the thermal properties of the soil and the groundwater velocity analyzed by the thermal response test, the measured circulating fluid temperature corresponding with the building load is compared with the calculated circulating fluid. The calculated fluid temperature was in agreement with the measurement data when an effective thermal conductivity of soil and a groundwater velocity were 4.7 W/(m K) and 120 m/y. An average coefficient of performance in a cooling/heating period was 4.5 and 7.8 respectively.

Keywords: Performance analysis, ground source heat pump system, groundwater, borehole heat exchanger;

1. Introduction

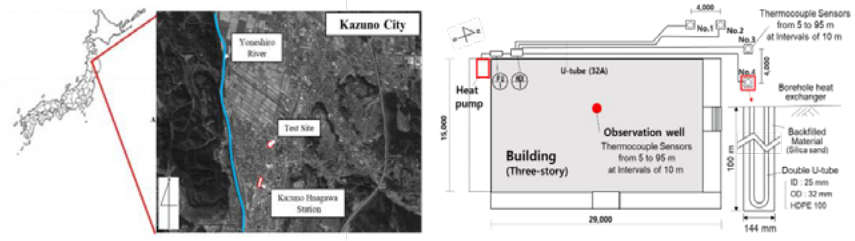
Ground source heat pump system (GSHPs) has been used to supply heating and cooling to buildings, using the ground as a heat source or a heat sink. The GSHPs installed in some areas with groundwater flow can achieve high performance. Some areas in Japan have an active groundwater flow owing to a steep slope of the mountains and the coefficient of permeability of the soil. Since the effect of the groundwater flow makes the ground temperature constant, the length of the ground heat exchanger (GHE) and initial cost can decrease. Ingersoll et al. [1] mentioned that the 286 m/y of the groundwater velocity results in the heat exchange rate (HER) to increase by 19 %.

A lot of research has been analyzed a coefficient of performance (COP) of the GSHP system to deliberate the optimal design of the GSHP system under widely divergent conditions. However, there is little research reflecting the effect of the groundwater velocity estimated from the thermal response test to consider the COP of the GSHP system. This study is carried out the calculation of the circulating fluid temperature at inlet and outlet pipes, based on the building load and the soil properties from the TRT results reflecting the effect of the groundwater flow. As a result of the previous study [2], the groundwater velocity and effective thermal conductivity were estimated at 120 m/y and 4.7 W/(m･K)), respectively. The calculated fluid temperatures are compared with the measurement data. The performance prediction is especially performed according to the required length of the borehole heat exchangers.

* Corresponding author. Tel.: +82-011-706-6288 ; fax: +82-011-706-6288 .
E-mail address: hobyung@eis.hokudai.ac.jp .

2. Site description

The test site was located in Kazuno city (40°19'N and 140°78'E), Akita Prefecture where the groundwater flow was expected to move actively by surrounding mountains and Yoneshiro River in Figure 1 (a). Figure 1 (b) shows the ground plan of the target building. The target building was a three-floor building, and the floor area was 435 m^2. The four GSHPs were installed for cooling and heating at intervals of 4 m. The diameter and length of the borehole were 144 mm and 100 m. A double U-tube was inserted in the borehole. The U-tube was high-density polyethylene, and an outer and an inner diameter of the U-tube was 32 and 25 mm respectively. A grout material was filled from a ground surface toward a bottom side of the borehole. The soils of the test site were mainly composed of gravel, gravelly sand and sandy gravel, and the effective thermal conductivity of the soil calculated by the thickness-weighted average of the soils was 2.4 W/(m·K). The experiment data was measured from 1st to 14th January 2018 in the heating period and from 1st to 14th July 2018 in the cooling period. Table 1 shows the description of the building in test site.



(a) Location of test site (b) Ground plana of target building

Fig. 1. Location of test site and Ground plana of target building

Table 1. Description of the building in test site

Category	Description
Total floor area	435 m^2 (Three floor building)
Total length of BHEs	400 m (Four BHEs)
Borehole diameter/U-tube size	144 mm / Double U-tube (outer:32 mm, inner:25 mm)
Measurement period	Heating (January 1 - 14th, 2018) / Cooling (July 1 - 14th, 2018)

3. Method

3.1 Analysis method of the measurement data

In the heating period, the heating load of the building is the sum of the HER and the power consumption of the heat pump in Eq (1). on the other hand, in the cooling period, the sum of the HER equals the sum of the cooling load of the building and the power consumption of the heat pump in Eq (2). The HER is calculated in Eq (3) or (4).

$$Q_c \approx Q_{inj} - W_{hp} \quad (1)$$

$$Q_h \approx Q_{ext} + W_{hp} \quad (2)$$

$$Q_{\mathrm{inj}} = \dot{m}_{\mathrm{f}} c_{\mathrm{f}} (LWT - EWT) \quad (3)$$

$$Q_{\mathrm{ext}} = \dot{m}_{\mathrm{f}} c_{\mathrm{f}} (LWT - EWT) \quad (4)$$

Here, Q_{c} and Q_{h} are the cooling/heating load of the building. Q_{inj} and Q_{ext} are the heat injection/extraction rate from/to the ground. W_{hp} is the power consumption of the heat pump. LWT and EWT are the leaving water temperature from the heat pump and the entering water temperature to the heat pump respectively. $\dot{m}_{\mathrm{f}}$ is the flow rate of the circulating fluid and c_{f} is the specific thermal capacity of the circulating fluid.

The coefficient of performance (COP) of the GSHP in the cooling period and the heating period is calculated as follows;

$$COP_c = \frac{Q_c}{W_{hp}} \approx \frac{Q_{inj} - W_{hp}}{W_{hp}} \quad (5)$$

$$COP_{\mathrm{h}} = \frac{Q_{\mathrm{c}}}{W_{\mathrm{hp}}} \approx \frac{Q_{\mathrm{ext}} + W_{\mathrm{hp}}}{W_{\mathrm{hp}}} \quad (6)$$

Here, W_{cp} is the power consumption of the circulating pump.

3.2 Calculation of the fluid temperature with the groundwater flow

The moving line source theory is applied for calculation of the fluid temperature, considering the groundwater flow. The soil in this method is treated as homogeneous medium which do not change physical properties with the temperature in Eq (7) [3,4].

$$\theta(r, \varphi, \tau) = \frac{q}{4\pi\lambda_{\mathrm{S}}} \exp\left(\frac{Ur}{4\alpha_{\mathrm{s}}} cos\varphi\right) \int_0^{\frac{r^2}{4\alpha_S \tau}} \frac{1}{\beta} \exp\left(-\frac{1}{\beta} - \frac{U^2 r^2 \beta}{16\alpha_{\mathrm{S}}^2}\right) d\beta \quad (7)$$

Here, θ is the temperature rise in medium, $\theta = T - T_0$, T_0 is an initial temperature of the soil, $\boldsymbol{r}$ is radius coordinate, φ is a polar angle, q is a heat flux per meter, λ_{S} is an effective thermal conductivity of the soil and α_{s} is a thermal diffusivity, U is a Darcy velocity, β is an integration parameter.

The previous study of the authors [2] analyzed the thermal response test data in the same field and estimated the groundwater velocity and the effective thermal conductivity of the soil. The fluid temperature was calculated by applying superposition of the thermal response with hourly heat extraction and heat injection and the estimated groundwater velocity and the effective thermal conductivity. The calculated results were compared with measured data. The estimated groundwater velocity and the effective thermal conductivity were 120 m/y and 4.7 W/(m K)

4. Results and discussion

4.1 Measurement data of the units

Figure 2 shows the outdoor temperature, the mean ground temperature in the observation wall and the heating/cooling load. During the measurement period, the minimum and maximum temperatures of the outside were -4.5 and 33.9 ℃. On the other hand, the average soil temperatures in the observations well, which is 15 m away from the BHEs, were constant to be 11.2 ℃. The results indicate that the outdoor temperature and the BHEs injecting/extracting the heat to/from the ground do not affect the temperature of the observation wells due to the effect of the groundwater flow. During the heating period, the GSHPs was operated continuously, and the average heating load was 9.8 kW. On the other hand, in the cooling period, the GSHPs was operated intermittently, and the average cooling load was 2.5 kW.

Figure 3 illustrates the power consumption of the heat pump and the circulating pump and the flow rate. The power consumption of the heat pump of the heating period was higher than that of the cooling period because of the relative high-temperature difference between the outdoor temperature and the indoor temperature. The mean power consumption of the heat pump in the heating period and the cooling period was 3.1 and 0.6 kW respectively. The power consumption of the circulating pump was constant to be 0.2 kW regardless of the period. The mean flow rate in the heating period and cooling period was 48.5 and 40.7 L/min respectively.

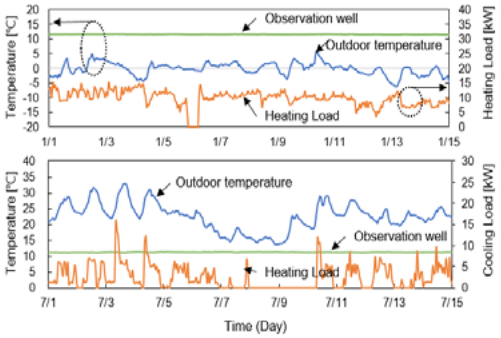


Fig. 2 Outdoor temperature, the mean ground temperature in the observation wall and the heating/cooling load.

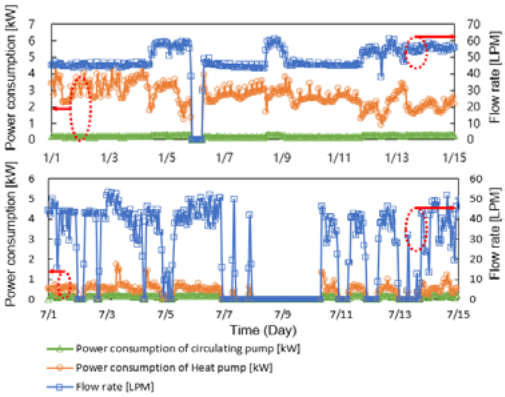


Fig. 3. Power consumption of the heat pump and circulating pump and the flow rate.

4.2 Temperature variation of the circulating fluid

Figure 4 indicates the temperature variation of the LWT and the EWT in the heating/cooling period. The LWT showed large fluctuations due to the ununiform power consumption of the heat pump whereas the fluctuation of the EWT was relatively constant. Especially, the results were regarded that the effect of the groundwater flow makes the EWT constant despite the continuous operating for the heating in the heating period.

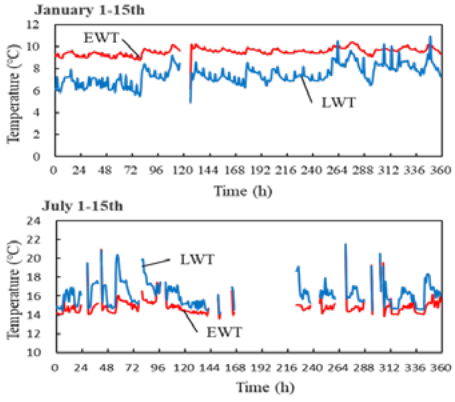


Fig. 4. Temperature variation of the LWT and the EWT

4.3 Performance analysis of ground source heat pump system

Figure 5 shows the variation of the heat exchange rate, the COP. Each result was calculated in Eq (4), (5), (6) and (7). The mean COP during the heating/cooling period was calculated to be 8.4 and 4.0 respectively. The heating load was bigger than the cooling load over 3.9 times, and the heat exchange rate of the heating period was also bigger that of the cooling period over 2 times. On the other hand, the average COP of the heating/cooling period was 3.6 and 6.2 because the power consumption of the heat pump of the heating period was lower than that of the cooling period over 5 times.

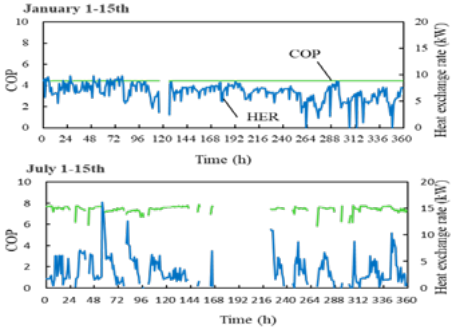


Fig. 5. Variation of the heat exchange rate, the COP

Table 2. The results of COP, Heat exchanger, EWT and LWT

Period	COP	Heat exchange rate [kW]	EWT [℃]	LWT [℃]
Heating period	4.5	6.7	9.5	7.5
Cooling period	7.8	3.3	15.0	16.2

4.4 Variation of EWT and LWT each case

Figure 6 shows the variation of EWT and LWT each case. The Cases were classified by the analysis method of the TRT, and the results of estimated parameter each case show in Table 3. As results, the calculated temperature results of the case 1 reflecting the groundwater velocity were similar to that of the measurement data. The temperature error between the case 1 and measurement data was under 6 % and 1 % during the heating period and cooling period, respectively.

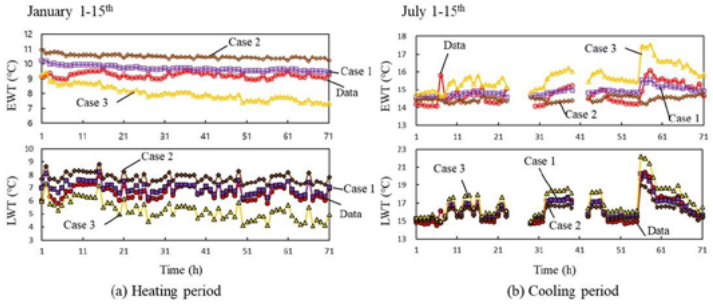


Fig. 6. Variation of EWT and LWT each case.

Table 3. Cases classified by the analysis method of the TRT

Case	λ_{eff} $(W/(m \cdot K))$	v (m/y)
Case 1 (Results calculated by MLS theory)	4.7	120
Case 2 (Results calculated by ILS theory)	8.9	0
Case 3 (Results from the column section)	2.4	0

4.5 Variation of EWT and COP according to total borehole length

Figure 7 shows the variation of EWT and COP according to the required total length of the borehole heat exchanger. Based on the parameters of the case 1, the EWT and COP were calculated according to the total borehole length. The shorter total borehole length resulted in the more significant fluctuation of EWT. In the analysis of the COP according to the total borehole length during the short-term period, the variation of COP during the heating period was insignificant, but the variation of COP during the cooling period was significant. Each COP according to the total borehole length was summarized in Table 4.

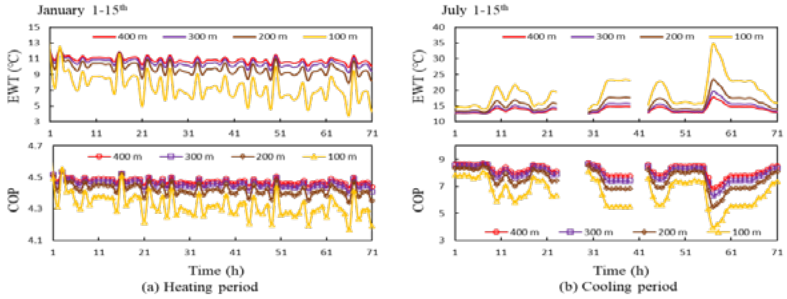


Fig. 7. Variation of EWT and COP according to total borehole length

Table 2. Variation of EWT and COP according to the required total length of the borehole heat exchanger.

Period	COP	Heat exchange rate [kW]	EWT [℃]	LWT [℃]
Heating period	4.5	4.5	4.4	4.3
Cooling period	7.8	7.7	7.5	6.6

5. Conclusion

The main objective of the present study is to investigate the cooling and heating performance of the ground source heat pump system with the borehole heat exchangers affected by groundwater flow. The EWT and LWT calculated by the MLS model based on the thermal properties of the ground (groundwater velocity= 120 m/y, effective thermal conductivity=4.7 W/(m･K)) [2] according to the building loads were compared with that of measurement data. The following is a summary of this study.

1) The performance analysis of the GSHP system was conducted by using the field data which is measured in the three-floor building located in Kazuno City.
2) The COP in measured heating and cooling period was 4.5 and 7.8.
3) The variation of EWT and LWT calculated by the MLS theory with the estimated parameters in the previous study was similar to that of measurement data.
4) In the analysis of the COP according to the total borehole length during the short-term period, the variation of COP during the heating period was insignificant, but the variation of COP during the cooling period was significant.

The decrease in the total length of the BHEs during the short-term period did not affect the COP of the GSHP system significantly when groundwater flows. therefore, the initial cost can be saved by decreasing the total length of the BHEs.

Acknowledgement

Tohoku Electric Power Co., Inc. gave us a generous support to demonstrate the experiment.

References

[1] L.R.Ingersoll, F.T.Adler, Madison Wis, H.J.Plass : Theory of Earth Heat Exchangers for the Heat Pump, Heating, Piping and Air Conditioning, pp.113-122, 1950
[2] H. Chae, K Nagano, Y Sakata, T Katsura, M Nakamura, T Kondo : Simultaneous evaluation of effective thermal conductivity and groundwater velocity from thermal response test data, 2019 conference of SHASEJ
[3] H.S. Carslaw, J.C. Jeager : Conduction of Heat in solids, Oxford University Press, Oxford, 1959.
[4] N. Diao, Q. Li, Z. Fang : Heat transfer in ground heat exchangers with groundwater advection, International Journal of Thermal Sciences 43, pp. 1203–1211, 2004

13th IEA Heat Pump Conference
April 26-29, 2021 Jeju, Korea

Next-Generation Residential Space Conditioning System in the United States

Ammi Amarnath[a,*], Sara Beaini[a], Aaron Tam[a], Jerine Ahmed[b]

[a] Electric Power Research Institute, 3420 Hillview Avenue, Palo Alto, CA, 94304, USA
[b] Southern California Edison, 1515 Walnut Grove Ave., Rosemead, CA, 91770, USA

Abstract

This paper reports on ongoing work integrating a variable-capacity heat pump with additional heating and cooling technologies to provide efficiency and other benefits for residential customers. The Next-Generation Residential Space Conditioning System (Next-Gen RSCS) was tested in three leading U.S. laboratories as well as field evaluated at three homes in California. The Next-Gen RSCS integrates advanced HVAC technologies, including a variable-capacity compressor and variable-speed indoor blower, auto demand response, fault detection and diagnostics, intelligent dual-fuel heating, integrated heat recovery ventilation, and zonal control. An alternative refrigerant, R-32, was evaluated in laboratory testing as a possible future enhancement. An assessment was also performed on duct losses for single- versus multi-zone duct configurations with variable-capacity equipment. The field evaluation saw positive customer feedback, with users appreciating how quiet the units were, how quickly they cooled or heated the space, and their ability to control the temperature in individual spaces. The paper also begins a discussion to extrapolate project results beyond California climates, conditions, and demographics.

Keywords: Variable-capacity heat pump; alternative refrigerant; auto demand response; zonal control; field demonstration; energy savings; non-energy savings

1. Introduction

Cooling and heating of buildings to achieve comfortable temperature and humidity levels accounts for a large portion of the residential energy use in the United States (48%) and California (31%). Improving cooling and heating system efficiency are clear targets for improving residential energy use. Many emerging space conditioning technologies offer improvements in efficiency, but they were not integrated into a single heating, ventilation, and air-conditioning (HVAC) system, nor were they optimized for local climates. This project evaluated individual heat pump technology improvements and integrated them into a variable-capacity heat pump system that could provide higher efficiency space conditioning for California climate zones.

Results of early project work were presented at the American Council for an Energy-Efficient Economy (ACEEE) Summer Study in 2018 [1] followed by a presentation of updated project results at the American Society for Heating Refrigeration and Air Conditioning Engineers (ASHRAE) Winter Meeting in January 2019 [2]. Both papers and presentations focused on laboratory results for the Next-Gen RSCS obtained at three leading U.S. laboratories (Electric Power Research Institute in Knoxville, TN, Pacific Gas & Electric Applied Technology Services in San Ramon, CA, and Western Cooling Energy Center in Davis, CA). A final report, issued in April 2019 [3], documented project findings and included early field test results obtained at three residential sites in California. This IEA paper uses information presented in the final report and additional field test data obtained since April 2019 to provide a discussion of heating and cooling field test results. Also

* Corresponding author. Tel.: +1-650-855-1007.
E-mail address: aamarnath@epri.com.

included in this paper is a discussion of Next-Gen RSCS advantages: how they can satisfy customer needs and provide utility benefits and how they might be extrapolated beyond California applications.

2. Next-Gen RSCS System Features

The portfolio of advanced features incorporated into the Next-Gen RSCS (See Figure 1) included a variable-capacity compressor and variable-speed fan using state-of-the-art inverter technology; integrated heat recovery ventilation to exchange heat between the incoming air and the exhaust air to and from the conditioned space; intelligent dual-fuel technology to select the most economical means of heating to decrease energy cost and empower consumers to choose between electricity and natural gas; zonal control using mechanical dampers controlled by thermostat setpoints to avoid conditioning unoccupied rooms; demand-response strategies that take advantage of variable capacity to save energy; advanced fault detection and diagnostics to facilitate proper installation, operation, and maintenance; and alternative refrigerants for improved efficiency and reductions in global warming. Figure 2 summarizes which features were evaluated in the laboratory (Phase 1 and Phase 2) and field evaluation (Phase 3) portions for the study.

Fig 1. Next-Generation Residential Space Conditioning Enhancing Features

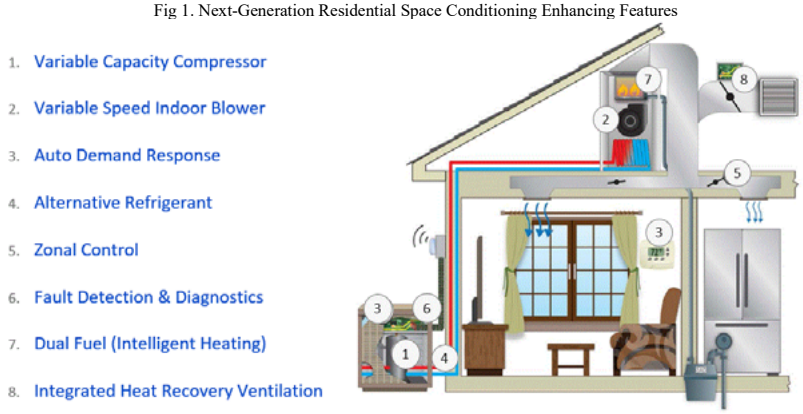


Fig 2. Technology Features Evaluated in Lab (Phase 1 and 2) and Field (Phase 3)

Technology	Phase 1	Phase 2	Phase 3
Variable-Capacity Compressor	✓		✓
Variable-Speed Blower	✓		✓
Integrated Ventilation	✓		
Demand Response	✓		✓
Dual Fuel (intelligent heating)	✓		✓
Duct-loss assessment for single-zone	✓		✓
Alternative Refrigerants		✓	
Fault Detection & Diagnostics		✓	
Zonal Control		✓	✓
Duct-loss assessment for multi-zone		✓	✓

2.1 Benefits and Potential Barriers

An assessment of the benefits and potential barriers of the Next-Gen RSCS features was performed as part of the technology transfer planning effort and is summarized in Table 1.

Table 1 Benefits and Potential Barriers of Next-Gen RSCS Features

Feature	Benefits	Potential Barriers
Variable Capacity	Greater comfort, lower energy costs, improved noise, smoother operation, possible reliability improvements	Higher equipment cost and complexity, harmonics
Alternative Refrigerants	Lower Global Warming Potential (GWP), performance improvement, and lower energy cost	Requires regulatory approval
Dual Fuel	Lowest possible heating costs based on fuel selection	Higher equipment costs
Fault Detection and Diagnostics	Improved maintenance and reliability, lower energy costs	Higher cost of control systems
Integrated Ventilation/Heat Recovery Control	Lower energy costs	Higher equipment costs
Zonal Control	Lower energy costs, better controllability, greater comfort	Higher equipment costs require additional user training
Auto Demand Response	Lower demand charges, greater comfort	Higher equipment costs

2.2 Energy Cost Savings

The testing and analysis in this project and the literature review provided information on the potential operating savings resulting from deployment of the Next-Gen RSCS. In summary, the energy savings for each feature determined by this project, and in a cursory review of the literature review, are provided in the following paragraphs. (More details are provided in Section 6.3 of the Final Report [3] regarding the work reported in the literature on each system feature.)

- Variable capacity[1] – Current study - 22% to 32% energy savings; 35% [4] and 36% [5] energy savings in other studies.
- Alternative refrigerant – Current study - R-32 shows 1.2% to 3.0% improvement in cooling efficiency and improvement in heating capacity by 5% at 25°F and by 10% at 62°F; 1% [6] to 9% [7] energy savings in other studies.
- Dual fuel – Current study - for average electric and gas prices, the highest energy cost savings were 22% for California climate zone 3 (Oakland); no quantitative results were found in the recent literature.
- Fault detection & diagnostics – Current study - Inform maintenance alerts to avoid inefficient operation (no quantitative results obtained): High energy reductions were found to be possible in the literature depending on the nature and severity of the faults detected and resolved [8].
- Integrated heat recovery ventilation control – Current study - 1.3% to 3.8% energy savings in this study; 30% or more energy efficiency improvement in other studies [11, 12].[2]
- Zonal control – Current study - up to 50% savings at 40% capacity; 10% load reduction would result in 12.8% power reduction; 16% to 25% [13, 14] in other studies.
- Auto demand response – Current study - 50% power reduction resulted in only a 38.2% capacity reduction, and a 70% power reduction resulted in only a 61.8% capacity reduction; savings depend on specific utility and customer conditions.

[1] The efficiency savings obtained with variable speed are due to reduced temperature differences in the system at part-load conditions as the compressor speed is reduced as well as reduction/elimination of start and stop transients as the load is followed compared to on-off modulation with a single-speed system.

[2] Energy savings were greatest when the climate was extreme (very hot or very cold) and the residence was tight and well insulated.

Examining and accumulating the savings achieved by each feature indicates that energy savings of approximately 50% are achievable by integrating all the features studied.

2.3 Non-Energy Cost Savings

The technologies deployed in the Next-Gen RSCS will generally have higher first costs than the technologies they are replacing, but these costs will be offset by lower energy costs and lower maintenance costs as well as other benefits discussed below, including improved reliability and greater comfort.

2.4 Reliability

The use of fault detection and diagnostics (FDD) will increase reliability of the units by anticipating failures and alerting the occupant and contractor to permit timely maintenance and repair to reduce system downtime. Variable capacity should provide smoother operation, reducing equipment stops and starts, thus reducing stress on components, resulting in increased equipment life.

2.5 Safety

The anticipated higher reliability of the Next-Gen RSCS should provide greater occupant safety when comfort is a safety issue (as in extreme climate situations). Since R-32 is classified as A2L refrigerant (lower flammability and lower toxicity), regulation will need to provide the appropriate usage guidelines to address flammability issues in the equipment design, placement, and operation to ensure that safety is equivalent to or better than the equipment that it is replacing.

2.6 Consumer Appeal

In addition to the reduced operating cost, improved reliability, and safety issues aforementioned, the following Next-Gen RSCS advantages should appeal to consumers:

- The Next-Gen RSCS will provide greater comfort during normal operation due to use of variable capacity to permit load following, closer temperature control, and less on-off cycling.
- The timely use of FDD will increase reliability of the units, reducing downtime, repair bills, and intermittency of space-conditioning.
- The use of a furnace and a heat pump as heating options affords the user with the opportunity to take advantage of the lowest price source of heating. This should appeal to cost-conscious consumers.

2.7 Demand Benefits

According to California's Energy Efficiency Strategic Plan [15], HVAC is the single largest contributor to peak power demand in the state, comprising up to 30% of total demand in the hot summer months. The auto demand response and variable-capacity features of the Next-Gen RSCS can significantly reduce HVAC system peak demand.

Intelligent, variable-capacity space-conditioning equipment has been demonstrated to reduce power by 60% during peak events, while continuing to provide cooling to the conditioned space [16]. Variable-capacity systems have the unique attribute of going to a state of higher operating efficiency when the compressor speed is reduced. This Next-Gen RSCS project confirmed that power reductions would exceed capacity reductions when operating the unit below maximum speed. This provides demand savings and increased cooling capacity compared to equivalent single-speed units. According to the Strategic Plan, the California Energy Commission estimates that a peak demand reduction of 1,096 MW in the residential and small commercial sectors could be achieved through high-quality HVAC installations by 2020. (Next-Gen RSCS installations would certainly qualify as high-quality installations.) Assuming market penetration of 20% and the ability of the system to reduce peak demand by 60%, the cumulative peak demand reduction for California would be approximately 1.5 GW. Thus a 1–1.5 GW in demand reduction due to deployment of units similar to the Next-Gen RSCS appears to be an aggressive but potentially achievable goal. These savings, if achieved, will enable electric utilities to avoid building new power plants and consequently avoid adding substantial capital costs to their systems. Customers will benefit accordingly as reduced utility system costs should result in lower rates than would otherwise be mandated.

2.8 Energy and Environmental Benefits

As indicated in Section 2.2, energy cost savings of 50% appear to be technologically achievable when deploying the Next-Gen RSCS compared to commonly used residential HVAC systems. This could result in savings of 475 GWh/yr or $83 million annually in California, assuming market penetration of 20%, 4750 GWh/yr for single-family HVAC energy use in California in 2014 [17], and an average residential electric rate of $0.176/kWh. Assuming an equipment life of 15 years, the Next-Gen RSCS could save California ratepayers over $1 billion over the lifetime of the equipment. Based on the standard emission factor (0.331 kg/kWh saved) and energy savings of 475 GWh/yr or 475 million kWh/yr, the Next-Gen RSCS could provide a reduction of 157 million kg of CO_2 emission per year in California.

In addition to these CO_2 emissions savings, use of a refrigerant such as R-32 could also contribute to a reduction in global warming. Assuming typical leakage rates, an R-32 system (GWP of 675) will emit only 33% as much CO_2-equivalent direct emissions as the equivalent R-410A (GWP of about 2100) system over its lifetime. This value may be even lower in reality because systems using R-32 will have a lower refrigerant charge than R-410A systems. These global warming savings, while substantially less than the equivalent CO_2 emissions savings due to lower energy use, are still significant.

The environmental benefits achieved by deploying the Next-Gen RSCS compared to commonly used residential HVAC systems could be a major step in helping utilities achieve their environment mandates.

3. Field Evaluation

A field evaluation of the Next-Gen RSCS was performed in three occupied residential households, one in each of the California investor-owned utilities (IOU) service territories (Pacific Gas & Electric [PG&E], Southern California Edison [SCE], and San Diego Gas & Electric [SDG&E]). The field study included retrofitting each home with a new ducted split variable-capacity heat pump unit (VCHP) with refrigerant R-410A, provided by Daikin/Goodman. Table 2 lists the specifications of the three homes that participated in the field evaluation.

Table 2 Field Testing Host Sites Specifications

Host Site	**West Sacramento**	**Chino Hills**	**San Diego**
Utility	PG&E	SCE	SDG&E
CA Climate Zone	12	10	7
Area (ft^2)	2507	1850	1906
Home Vintage	2008	1993	1980
Existing Ducting, Heating System (pre-install)	Ducted AC with Gas Furnace	Ducted AC with Gas Furnace	Ducted AC with Gas Furnace
Location of Ducts	Attic	Attic	Attic
AC Size (tons) (pre-install)	3-ton Condenser 4-ton AHU	4	4
Floors	2	2	1
Number of Residents	4 + 1 pet	4 + 1 pet	1 + 3 pets

The objective of the field evaluation was to assess the functionality of the Next-Gen RSCS features in residential homes and evaluate the performance with respect to the customer experience. For the field evaluation, each home—depending on its configuration and climate—evaluated a subset of the key features discussed next. After installing the Next-Gen RSCS with new ducting insulation, each home was instrumented with power meters for the indoor and outdoor units, temperature and relative humidity sensors in each zone, and pressure differential sensors across each zone damper in the attic ducting. Data collection spanned over one year to capture both the heating and cooling season. Data analysis included comparing variable-capacity heat pump performance to a single-speed Seasonal Energy Efficiency Ratio (SEER) 14 HVAC unit, as well as comparing the field-testing data with the lab-testing data.

3.1. Variable-Capacity Compressor and Blower Field Performance

The cooling and heating seasonal analysis of the field data for the Next-Gen RSCS both show energy consumption within 20% of the lab data model, which was developed with steady-state testing. A 2-ton model

of the system was tested in laboratories at outdoor temperatures at 10˚F increments from 65˚F to 105˚F for cooling, and at 62˚F, 47˚F, 35˚F, 25˚F, and 15˚F for heating. The indoor condition was kept constant at 75˚F dry bulb and 63˚F wet bulb for cooling and 70˚F and 57˚F, respectively, for heating, and each condition was tested at high (100%), intermediate (50%), and low (30%) compressor speed. While the lab- and field-tested systems are of different rated capacities and different setpoints may have been used, the efficiency of the system should be comparable. The cooling performance of the units shows a range of Energy Efficiency Ratio (EER) between 10 and 25, which agrees with the range of EER found in the laboratory testing performed earlier in the study. Figures 4, 5, and 6 show the West Sacramento site field data compared to the laboratory testing results as well as a SEER 14 baseline system. The results clearly illustrate the benefits of a variable-capacity system, with much higher efficiency as the system reduces its compressor speed to intermediate and low stage.

Fig 4. West Sacramento Site High-Stage Field Data

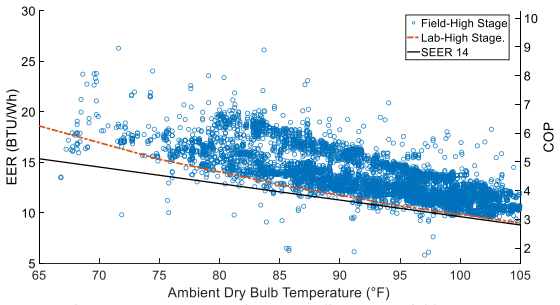


Fig 5. West Sacramento Site Intermediate-Stage Field Data

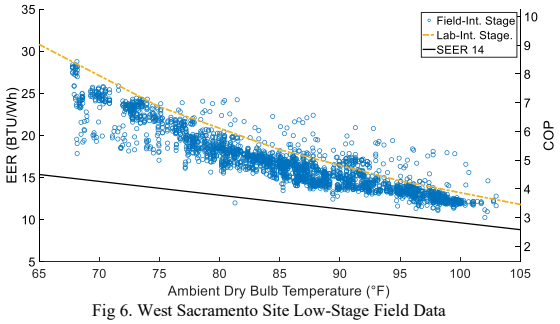
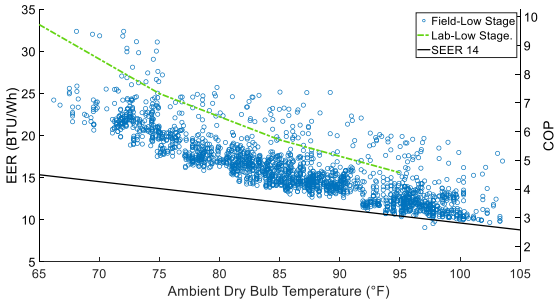


Fig 6. West Sacramento Site Low-Stage Field Data



3.2. Dual-Fuel (Intelligent Heating) Field Performance and Operation

Once the breakeven temperature[3] was set for each of the three host sites, the Next-Gen RSCS performed as expected in the heat pump mode and gas furnace mode throughout the duration of the heating season. The Next-Gen RSCS dual-fuel capability provides an important choice for the residential customer to adjust the unit settings based on economic factors (utility rates), efficiency factors (heat pump vs. gas furnace), or environmental factors (reduction of carbon footprint).

Having a controller that automatically receives pricing information and sets the breakeven temperature accordingly would minimize the need for customer interaction (unless they chose to do so.) Future work is needed to develop a versatile/intelligent heating controller that can receive a signal based on utility prices and customer choice/preference (price, efficiency, fuel mix distribution), which would optimize the Next-Gen RSCS's performance in the heating mode.

3.3. Auto Demand Response (ADR) Field Performance

The unit capacity reduction is less than the unit power reduction when operating below maximum speed and capacity; therefore, customer comfort is not as compromised while energy and demand savings can be realized during a utility-led demand response event.

Field ADR testing was conducted in both the heating and cooling mode. Heating mode demand response of 30% or 50% demand reduction both resulted in 4.9% variation between power and capacity change (the power reduction was 4.9% more than capacity reduction). During the cooling mode test, a 50% demand reduction resulted in 8.4% variation between power and capacity change.

3.4. Zonal Control Field Performance

The three host sites for the field evaluations were set up with variable-speed heat pumps and new insulated ducting that was zoned into either two, three, or four zones depending on the housing configuration and square footage. An important observation learned from the field evaluation is the significance of setting up the zoning controls through the zone weightings to minimize the possibility of overflow in small zones.

When installing variable-capacity equipment with ductwork located in unconditioned space, zoning controls provide added system efficiency where the system would operate in part-load capacity when not all the zones are called on for conditioning.

3.5. Customer Feedback Regarding Field Test Units

The following summarizes the homeowners' feedback on their experience with the Next-Gen RSCS:

- They appreciate how much quieter the Next-Gen RSCS operates compared to their previous single-speed AC unit.
- They like how quickly it cools or heats the space.[4]
- They like having an app-based controller for the thermostats to turn on and set the temperature of individual zones.
- They like the ability to control temperatures in individual spaces (that is, an advantage and nice attribute of zonal control is to control zones independently).
- While zonal control is a convenient feature for the occupants, it added complexity to the VCHP system when there were more than two zones. Airflow was too forceful in certain zones, making it noisy in some rooms. Once the weighting of the zones was adjusted, this mitigated the effect of the airflow imbalance.

The laboratory and field evaluation of the Next-Gen RSCS features in residential homes resulted in recommendations to extend the benefits of the Next-Gen RSCS concept, which are summarized in Section 4.

4. Configuring the Next-Gen RSCS into Different Models

Two of the recommendations made in the study final report [3] are worth exploring in this forum and in terms of extending the scope of the project beyond California. The first is to examine the suitability of each

[3] The *breakeven temperature* is defined as the temperature at which the cost of heating using the gas furnace and the electric heat pump is equal. Above the breakeven temperature, it is more economical to run the heat pump; below the breakeven temperature, it is more economical to run the furnace.

[4] This is in comparison to the older, poorly operating system that was replaced.

feature of the Next-Gen RSCS for the conditions being considered: climate, customer demographics,[5] electricity rates, configuration, and delivery system. The second is to integrate the most desirable features into a model of the Next-Gen RSCS most suitable for those conditions.

The premise of both recommendations is that each feature will differ in value depending on customer demographics, utility rates, and climate. What features are most likely to be of value, and what are the variables affecting this value? The reported study focused on forced air delivery systems for single-family residential systems in California climates.[6] How would the features perform if incorporated into other delivery systems and in other climates?

Variable-capacity inverter-driven technology is the key to many of the system advantages. Being able to vary the compressor and fan speed to follow the load provides smooth, efficient, unobtrusive operation. It is also the key to efficient **demand response**, providing more efficient operation while also reducing demand. Capacity modulation is also the key to efficient zonal control. Variable capacity is the cornerstone of the Next-Gen RSCS and is likely to be incorporated into all models of future units.

Variable capacity can be, and is, used with other delivery systems, including systems using refrigerant piping for distribution as well as hydronic systems. As such, it should be applicable to a wide range of HVAC configurations in the United States and abroad.

The advantages of variable capacity are most apparent at off-design conditions and may not be useful when many hours occur at high-temperature conditions. Nonetheless there should be sufficient hours in "shoulder" periods and the need for zoning and demand response to make this feature valuable.

Fault detection and diagnostics are a robust technology that, with proper sensors and controls, should be viable across the entire range of customer demographics, climates, and delivery systems. Early detection of inefficient operation and impending failures is needed for all HVAC systems. Potential savings are likely to be highest when the need for heating and cooling are highest, but FDD systems should be generally applicable across the United States and abroad.

Zonal control can be managed effectively with a variable-capacity system that can respond to changes in occupancy. Matching the Next-Gen RSCS to operate with a variety of delivery systems should make it applicable across the United States and abroad. Climate and demographic differences should not hamper its operation.

Integrated heat recovery ventilation preheats or precools the air entering the conditioned space, providing fresh air ventilation efficiently by exchanging heat between a fresh air and exhaust air stream. This system requires a heat exchanger and flow path that can be independent or integrated with the HVAC system and thus can be effectively added to any delivery system that requires a forced ventilation system. Energy savings should be highest at extreme temperatures (high outdoor temperatures for cooling and low outdoor temperature for heating), but the savings are modest compared to the savings achievable by other features.

R-32 as an **alternative refrigerant** to R-410A appears to have cooling mode performance advantages over R-410A that are highest at high outdoor temperature and thus would be most advantageous as a replacement in hotter climates. This could apply to other climates in the United States and abroad but not typically in heavily populated areas of Europe. R-32 has already been approved and has seen wide adoption in Japan and is seeing more penetration in China and European countries. The environmental advantages of R-32 compared to R-410A are clear, and performance appears comparable for milder cooling and heating conditions.

Dual fuel is the feature that is most sensitive to electricity and gas rates and climate. Dual fuel using a gas furnace or other gas heating device and an electric heat pump works best economically when there are many heating hours at moderately cold temperatures where the both the furnace and the heat pump can each operate for enough hours to offset their capital cost. If most of the heating is at low temperature and gas prices are economical, it would likely pay to just have a furnace for heating. Where most of the heating is at mild temperatures and the electricity prices are economical, just a heat pump with or without electric resistance backup might be most economical for heating.

Economical operation of the dual-fuel option depends on both the gas and electric rates and the climate. Since heat pump efficiency degrades as the outdoor temperature is reduced and gas furnace efficiency is relatively constant with outdoor temperature, there is a temperature at which the heat pump and furnace operating costs are the same—the breakeven temperature. If gas prices are very low or electric prices are very high, the breakeven temperature will be high and the furnace will carry the crux of the heating load. The

[5] Pertinent customer demographics include number, mobility, and age of occupants and how it affects factors such as occupancy and the usefulness of zoning and sensitivity to temperature settings.

[6] For the most part, the results in the study were obtained for relatively dry climates. For hot, humid climates, coils will need to be designed for greater latent load removal, and thus, likely need to be deeper. The RSCS's integration of the multiple features studied should remain applicable to such climates.

opposite is true when electric prices are low and gas prices are high. Gas and electric prices vary dramatically globally as does local climate, so the operation of the dual-fuel heat pump needs to be evaluated on a case-by-case basis with regard to these variables.

In configuring the Next-Gen RSCS for a particular customer segment or climate, the features discussed above should be considered and built upon to develop a model best suited for the demographics, configuration, and climate of interest.

A premium model might include all energy efficiency features of the Next-Gen RSCS. The base model could be a variable-capacity heat pump with demand response, fault detection and diagnostics, and zonal control—all of which are crucial features to benefit from the efficient operation of variable-capacity heat pump. The intermediate model could include intelligent heating as an additional feature to the base model.

5. Concluding Remarks

While the current project conducted the testing and evaluation of each of the features to quantify the potential for energy savings and performance benefits, a future project would be needed to develop a model that evaluates the cost effectiveness of each feature. The model would need to evaluate energy and demand cost savings for each feature for different climate zones for representative housing, demographics, and occupancy situations.

Acknowledgments

The authors would like to acknowledge the California Energy Commission for its support and funding of this project under award number CEC EPC-14-021. Also, they would like to acknowledge Daikin/Goodman who supplied the variable-capacity heat pump units and provided research guidance.

References

[1] Beaini S, Amarnath, A, Hunt W, Domitrovic R, Krishnamoorthy S, Harrington C, Modera M, Davis R, Hinokuma R, "Evaluation of the Next Generation Residential Space Conditioning System for California," 2018 ACEEE Summer Study on Energy Efficiency in Buildings.

[2] Beaini S, Amarnath A, Hunt W, Domitrovic R, Krishnamoorthy S, Harrington C, Modera M, Davis R, Hinokuma R, Blatt M, "Next Generation Residential Space Conditioning System for California," (AT-2019-C035). ASHRAE 2019 Winter Conference Proceedings, January 14, 2019.

[3] Amarnath A , Beaini S , Hunt W, Domitrovic R, Tam A, Vaddiraj A, Davis RA, D'Albora MD, Modera M, Harrington C, Krishnamoorthy S, Blatt M, Development and Testing of the Next Generation Residential Space Conditioning System for California. Final Project Report, CEC-EPC-14-021, April 2019.

[4] Yunhua L, "Variable Frequency Drive Applications in HVAC Applications", in New Applications of Electric Drives, book edited by Miroslav Chomat, ISBN 978-953-51-2233-3, December 9, 2015.

[5] Lawrence R, Blatt M, Adjustable Speed Drives in Residential Appliances, White Paper, EPRI for CEC/PIER 500-10-022, March 14, 2014.

[6] Li H, and By B, Soft-optimized System Test of Refrigerant R-32 in 3-ton Split System Heat Pump, Goodman Manufacturing for AHRI Low-GWP AREP, December 19, 2012.

[7] Xu X, Hwang Y, Rademacher R , Performance Measurement of R32 in Vapor Injection Heat Pump System, University of Maryland, International Refrigeration and Air Conditioning Conference at Purdue, July 16-19, 2012.

[8] Mowris R, Eshom R, Jones E, "Laboratory Measurements of Residential HVAC Installation and Maintenance Faults", Fault Detection Diagnosis and Repair of Residential HVAC Systems, September 10, 2013 – Davis, CA.

[9] Francisco PW, "Measuring residential duct efficiency with the short-term co-heat test methodology", University of Illinois, Energy and Buildings 38 (2006) 1076–1083.

[10] Modera, MP, Remote Duct Sealing in Residential and Commercial Buildings: "Saving Money, Saving Energy and Improving Performance, Lawrence Berkeley National Laboratory, April 21, 2006.

[11] Hekmat D, Feustel HE, Modera MP, "Ventilation Strategies and their Impacts on the Energy Consumption and Indoor Air Quality in Single-Family Residences", Energy and Buildings, Vol. 9, p. 239-251, 1986.

[12] Jokisalo J, Kurnitska J, Torkki A, "Performance of balanced ventilation with heat recovery in residential buildings in cold climate", International Journal of Ventilation, Vol. 2. 2003.

[13] Oppenheim, P., Energy Implications of Blower Overrun Strategies for a Zoned Residential Forced-Air System, University of Florida, ASHRAE Transactions, Vol. 97, Part 2, 1991.

[14] Electric Resistance Heating, DOE http://energy.gov/energysaver/electric-resistance-heating Accessed July 6, 2016.

[15] California's Long Term Energy Efficiency Strategic Plan – September 2008 - http://www.cpuc.ca.gov/WorkArea/DownloadAsset.aspx?id=5305 California Public Utilities Commission.

[16] Variable-Speed Heat Pumps for Energy Efficiency and Demand Response: Field Testing High-Efficiency Systems in a Simulated-Occupancy Home in Knoxville, Tennessee. EPRI, Palo Alto, CA 3002003925, 2014.

[17] Advancing Water and Energy Efficient Strategies and Technologies in California, Attachment 12, Energy Efficiency Data, GFO-15-317, November 2015.

13th IEA Heat Pump Conference
April 26-29, 2021 Jeju, Korea

Research and analysis on influence factors of accuracy of geotechnical thermal response test

Yang Lingyan[a,*], Li Jintang[a], Fu Yijun[a], Ma Ning[b], Wei Wei[b], Bian Mengmeng[a]

[a]China Academy of Building Research, Beisanhuandonglu 30, Beijing 100013, China
[b]Shandong Yimeike Energy Conservation Service Co.,Ltd., No.1577, Longao North Road, Jinan City, Shandong 250001, China

Abstract

In this paper, simulation model of thermophysical properties test have been established and the accuracy of which have been verified by actual test data. Using linear heat source model to process simulation data for the analysis of different factors influences on simulation results. It shows that when using linear heat source model as the regression model for rock-soil thermophysical properties, in order to improve the thermophysical property accuracy identification, test duration should be 72 hours with elimination of the first 12 hours data and ensure a strong turbulent state for the flow velocity in pipes.

Keywords: Borehole heat exchanger；thermophysical properties test；linear heat source model

1. Background

Technology of thermophysical properties of rock-soil test is the premise and foundation of the highly efficient and energy-saving operation of the ground source heat pump (GSHP) system. By simulating the heat transfer characteristics of the borehole heat exchanger under the actual working conditions and with the help of theoretical analysis model or professional simulation software, an effective bridge is built between obtaining thermophysical properties of rock-soil and guiding the design of the actual GSHP system which effectively promote the scientific nature and rationality of GSHP system design.

The common test methods of under-ground rock-soil thermophysical properties include geotechnical types identification method, steady-state plate test, probe test and thermal response test, etc. [1,2], among which the most widely used type is the thermal response test. And currently, the most commonly used ones are the constant heat flow method and constant temperature method. The constant heat flow method was first proposed by C.eklof in 1996 [3-6], which has been recommended by the IGSHPA and ASHRAE standards as the international practice. This method only test the exothermic condition which uses the electric heater to provide stable heating quantity, records the water temperature at the inlet and outlet of the buried tube at each time, and uses the mathematical model to obtain the thermophysical properties of the rock and rock-soil, that is easy to operate and widely used and is also applied by the national standard of GB50366 *Technical code for ground source heat pump system* for thermophysical properties measurement of soil and rock [7].

The main calculation method of rock-soil thermophysical property test is to deduce the thermophysical parameters by inverse algorithm which requires input of the test results in the computer and compare them with the simulation results. By repeatedly adjusting the thermophysical parameters of the rock-soil in the heat transfer model until the variance of the average temperature value and the minimum value are obtained, it is considered that the thermophysical parameters in the heat transfer model are exactly those of the rock and soil in the location.

* Corresponding author. Tel.: +86-10-84275107 ; fax: +86-10-84283555.
E-mail address: yly8111@163.com

2. Model establishment and verification

In this paper, simulation model of the soil and rock thermophysical properties test has been established through TRNSYS as is shown in Fig.1. Duct Ground Heat Storage Model (DST) has been applied for borehole heat exchanger which is a typical mixed solution of both analytical and numerical methods. Verified by the actual test results, reliability of the model has been confirmed, and input conditions are changed to obtain the operation results under different boundary conditions. Taking simulation results as the true value, influence of different test factors on the accuracy of identification results is analyzed by using linear heat source model to process the data.

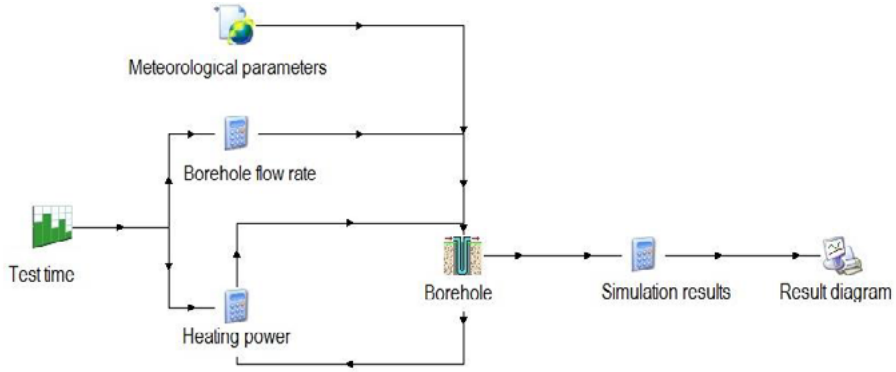


Fig. 1. TRNSYS Simulation model

In order to verify the simulation model of rock-soil thermophysical test, simulation study on an actual GSHP test was conducted for comparison between simulation and test results. In the thermal response test, the constant heating power is 5.938kw, the fluid carrying capacity is 0.854m3/h, and the structural parameters of DN32 single U-type borehole heat exchanger are shown in Table 1. In order to measure the temperature of rock-soil, 10 temperature sensors are arranged along the depth, with an interval of 10 meters between each two temperature sensors. After 48 hours, the values of the 10 temperature sensors are added and averaged. The initial temperature of rock-soil is 20.05℃, and its physical parameters are shown in Table 2.

Table 1 Structural parameters of buried tube heat exchanger

Drilling depth/m	Hole radius/mm	Tube internal diameter/mm	Tube wall thinkness/mm	Center distance/mm
100	65	26	3	64

Table 2 Physical parameters of borehole heat exchanger

Substance	Density/kg/m^3	Specific heat capacity /J/(kg·K)	Thermal conductivity /W/(m·K)
Soil and rock	1600.0	1645	2.71
Backfill	1860.0	840	2.00
Buried tube	950.0	2300	0.44
Fluid carrying	998.2	4182	0.60

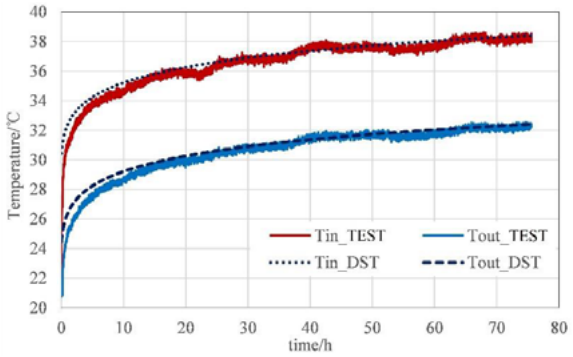


Fig. 2. Comparison between simulation and test values of inlet and outlet temperature

Fig.2 shows that during the 75 hours of simulation calculation, Simulation values of the model (based on DST) have a good agreement with the heat response test data which verifies the accuracy of simulation model.

3. Influence factors of thermophysical properties identification

Using the simulation model to calculate thermophysical properties of the borehole heat exchanger, simulation results are taken as the true values. Comprehensive thermal conductivity of rock-soil based on the simulation results is obtained by using the linear heat source theory to process the data for the analysis of the pattern of various influence factors on thermal response test results.

According to the characteristics of large length to diameter ratio of borehole heat exchanger, the model assumes that heat transfer process is between an underground linear source and the surrounding semi-infinite rock and soil. Therefore, the linear heat source model not only ignores the vertical heat transfer, but also omits the heat capacity inside the hole, namely, the linear heat source model cannot reflect the transient heat transfer process inside the hole, so that when data processing is carried out for the thermophysical property test of rock and soil, linear heat source model fails to process the data before a to-be-steady state inside the hole. In this paper, factors such as test duration, abandoning the early data period, heating power, flow velocity of the fluid inside the tubes are have been respectively analyzed, and the influence of these factors on thermophysical parameters identification of rock-soil are studied.

According to the linear source model, after taking the natural logarithm of the test duration (T), the average temperature T of the carrying fluid corresponding to each time point has a linear relationship with the logarithm value ln (T) of time.

Linear heat source model formula is shown as follows：

$$T = k \cdot \ln(t) + b \tag{1}$$

$$k = \frac{Q}{4\pi\lambda H} \tag{2}$$

$$b = \frac{Q}{4\pi\lambda H}\left[\ln\left(\frac{4\alpha}{r_b^2}\right) - \gamma\right] - \frac{Q}{H} \cdot R_b + T_0 \tag{3}$$

Where T is the average value of the temperature at the inlet and outlet of the fluid in the ground heat exchanger, ℃；

Q is the total heating power under the test condition, W;

H is the buried pipe depth, m;

λ is the thermal conductivity of soil and rock, w / (m.k);

α is the thermal diffusivity of soil and rock and, m^2/s;

t is the test duration, s;

r_b is the drilling radius, m;

R_b is the thermal conductivity, (m.K)/W;

T_0 is the incipient soil and rock temperature, ℃;

γ is the Euler constant, （γ=0.5572）。

The T-ln (T) curve of the average water temperature at the inlet and outlet of the buried pipe and the test time can be obtained according to the simulation data of the thermophysical properties test of the rock-soil. Least square method is used to estimate the parameters of the simulation data, which minimized the variance between the average temperature and the simulation value of the regression model of the carrier fluid to obtain the slope of the T-ln (T) curve, and thus, acquiring the K value in the formula. Finally, the K value can be calculated. Finally, comprehensive thermal conductivity of rock-soil is obtained. For the convenience of data analysis, the relative error of comprehensive thermal conductivity of rock-soil is defined as follow:

$$EER = \frac{\lambda - \lambda_0}{\lambda_0} \times 100\% \tag{4}$$

Where λ represents the comprehensive thermal conductivity obtained through simulation calculation of linear heat source model; λ_0 represents thermal conductivity of rock and soil set in simulation model W/(m-K).

3.1. Test duration influence

The stable value of comprehensive thermal conductivity of rock-soil needs certain calculation time interval, and the guarantee of such calculation time interval needs a certain test duration first which is related to the test conditions of specific project. In this paper, based on the simulation model, the linear heat source model is used for data regression, and the curve of comprehensive thermal conductivity of rock-soil with the test duration is shown in Fig.3.

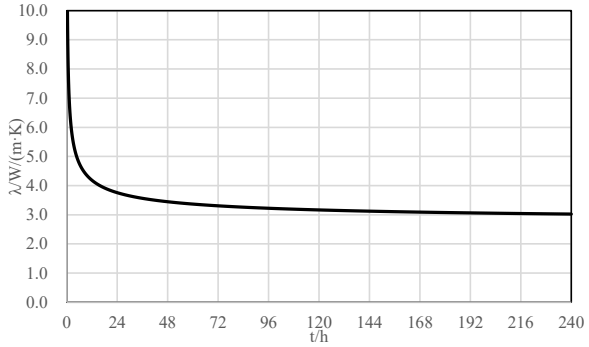


Fig. 3. Curve of comprehensive thermal conductivity of rock and soil with test duration

Fig.3 shows that with the extension of test duration, comprehensive thermal conductivity of rock-soil became closer to the true value. The relative error in early stage of the test decreases rapidly with the increase of time (the early time slope is larger) which indicates that in order to ensure the accuracy of the test results, it is necessary to extend the test duration as much as possible. When test duration is longer than 48h, the comprehensive thermal conductivity of rock-soil has become stable, and the error is within the acceptable range of the project. If the duration is 72h, the error will be further reduced. According to the regression calculation results and the relevant research results at home and abroad, it can be seen that 48h is the necessary test duration, and the optimal one is 72h [8,9].

3.2. Elimination length of transient data influence

From the above calculation, it can be seen that the linear heat source model cannot reflect the transient heat transfer process inside the hole, and the comprehensive heat transfer coefficient obtained from the data regression in this stage changes dramatically which has great deviation from the true value. If part of the transient heat transfer process data is removed, and data under steady state heat transfer process is used for regression simulation, the obtained thermophysical parameters will be more reliable. In this paper, influence of different elimination length of transient data on thermophysical parameters of soil is analyzed as is shown in Figure 4, the comprehensive thermal conductivity curve of rock-soil varies with the length of elimination time, and the accuracy is positively related with this elimination length.

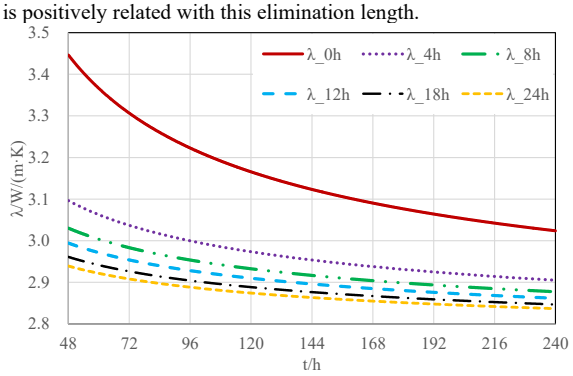


Fig. 4. Curve of rock-soil thermal conductivity under different elimination length of transient data

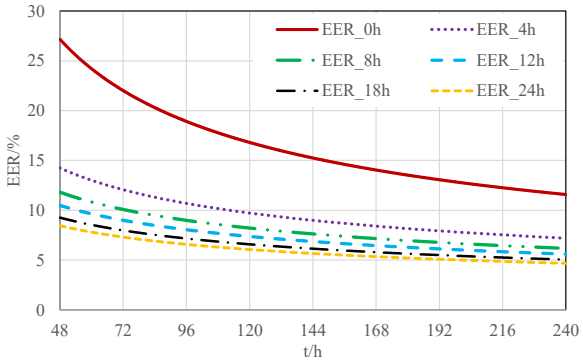


Fig. 5. Curve of rock-soil thermal conductivity relative error under different elimination length of transient data

Error change between rock-soil comprehensive thermal conductivity and the true value caused by the elimination length of transient time is shown in Figure 5. It can be seen for that when eliminating length is 12h, error rate is within 10%, and then with the increase of eliminating time, the error rate is significantly reduced. When the rock-soil comprehensive thermal conductivity is obtained by the inverse calculation of linear heat source model with the elimination of the first 12 hours of unsteady test data, more scientific and reasonable

results can be obtained.

3.3. Influence of different heating power

Influence of different heating power on the identification results of rock-soil thermophysical properties test are analyzed. Under the same flow rate, heating power difference is realized through different inlet and outlet temperature ΔT, as shown in Figure 6, the following conditions are set as: 2 ℃, 4 ℃, 6 ℃, 8 ℃, 10 ℃. When different heating power is used, comprehensive thermal conductivity of rock-soil changes as shown in Figure 7.

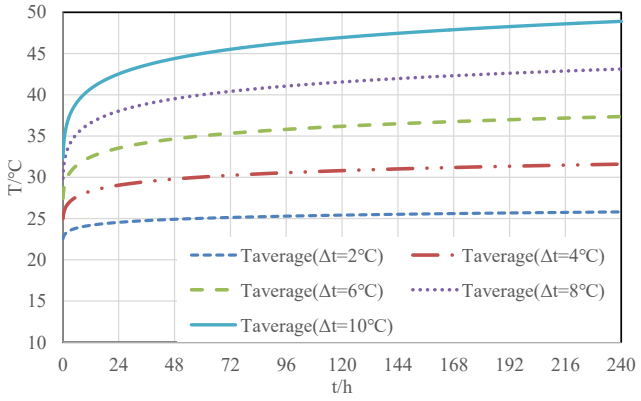


Fig. 6. Curve of average temperature under different heating power by different inlet and outlet temperature ΔT

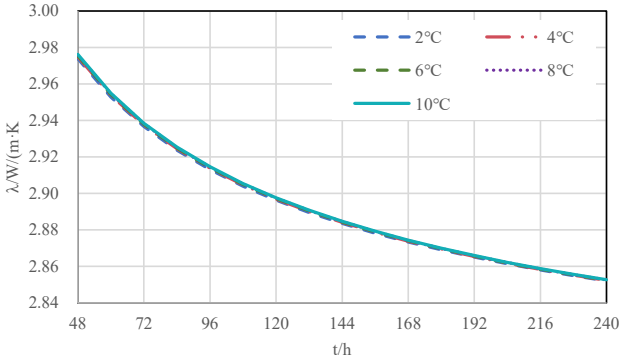


Fig. 7. Curve of rock-soil comprehensive thermal conductivity under different heating power by different inlet and outlet temperature ΔT

It can be seen from Figure 7 that under different heating power conditions, linear heat source model is used to regress the thermophysical parameters of rock-soil, and the results obtained by analyzing and comparing the comprehensive thermal conductivity are basically the same which indicates that the identification results of soil and rock thermophysical properties are not affected by heating power.

However, in the actual thermal response test, with the increase of the power of the heater, the thermal conductivity of the rock and soil tend to increase, which is caused by the leakage of groundwater. Because the buried depth of the underground tube is generally 50-200m where groundwater exists, heat transfer process inside and outside the hole will both be affected, thus the test results of rock-soil thermophysical properties are influenced. When using linear heat source regression calculation, the influence of groundwater is not considered, so the calculation results are not significantly different because of heating power. Therefore, the influence of groundwater leakage must be considered in the thermal response test. When there is no or little ground water leakage, the influence of the power of the heater can be ignored.

3.4. Flow velocity influence

Under the same condition of temperature difference between the inlet and outlet of the buried tube heat exchanger, influence of different velocity in the tube on the back calculation results of the thermophysical properties test is analyzed. The flow velocity in the pipe is set as follows: 0.1m/s, 0.15m/s, 0.2m/s, 0.3m/s, 0.4m/s, 0.6m/s, and the corresponding Reynolds number is shown in Table 3. Obtained comprehensive thermal conductivity curve of rock and soil is shown in Figure 8.

Table 3 Working condition group of simulation

No.	Velocity m/s	Flow rate kg/h	Re
1	0.1	190.79	3238.1
2	0.15	286.19	4857.1
3	0.2	381.58	6476.2
4	0.3	572.37	9714.2
5	0.4	763.16	12952.3
6	0.6	1144.74	19428.5

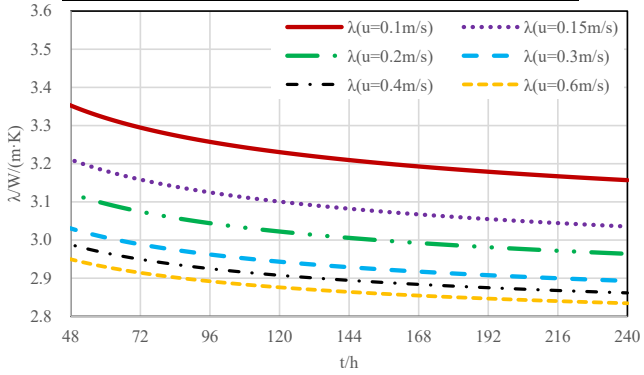


Fig. 8. Variation of rock-soil comprehensive thermal conductivity with test duration under different velocity

It can be seen from the above figure that when the velocity in the tube is in the laminar flow and transition area, error between the simulation and testing value of rock-soil comprehensive thermal conductivity is large with slow change. After turning into turbulence area, the deviation from the true value is rapidly reduced. Therefore, in order to get the most accurate parameters of thermal properties of rock-soil in limited testing duration, it is necessary to increase the flow velocity in the buried tube to maintain a strong turbulent flow.

4. Conclusions

In this paper, the simulation model of rock-soil thermophysical properties has been established, the linear heat source model is used to process the data. Influence of four factors on the accuracy of the identification results of thermophysical properties of rock-soil is analyzed including test duration, eliminating length of transient data, heating power and flow velocity. Results show that test duration is positively related to the accuracy of identification results of soil and rock thermophysical parameters. In order to ensure the accuracy of identification of these parameters, it is necessary to ensure a no-less-than 48hours test duration. Eliminating length of transient data is also positively related to the accuracy of identification results of soil thermophysical parameters, but considering the operability and accuracy of the test, the transient data in the first 12 hours is eliminated which can effectively improve the accuracy of parameter identification and have better operability. Under the linear heat source model with no or little groundwater leakage, heating power has no effect on the

identification results of rock-soil thermophysical properties. By increasing flow velocity in the tubes and maintaining a strong turbulent flow state, the accuracy of identification results can be effectively improved and with less test duration.

Through the analysis of the four factors above, it can be seen that in order to achieve the accurate identification of rock-soil thermophysical parameters, it is necessary to emphasize the setting of several key influencing factors in the test link, and provide more scientific and reasonable basic data of thermophysical parameters for the design of ground source heat pump.

Acknowledgements

The authors acknowledge the support from the Science and Technology Program of Ministry of housing and urban-rural development of China: Research on Key Technologies of multi-energy complementary of renewable energy application in large public buildings (2019-K-036).

References

[1] Liang Shen. Comparison And Analysis Of Test Technology Of Thermal Response Of Soil [J]. Heating and Cooling，2015，(7)：60-63 (in Chinese).

[2] Jintang Li. Parameter Analysis of Thermal Response Test and Research of Heat Transfer for Ground Source Heat Exchanger [D]. Master's thesis.Chongqing University. 2014(in Chinese).

[3]Mogensen P. Fluid to Duct Wall Heat Transfer in Duct System Heat Storages. Proc. Int. Conf. On Subsurface Heat Storage in Theory and Practice. Stockholm, Sweden, June 6-8, 1983, p. 652~657.

[4] Austin III, W A, C Yavuzturk, J D Spitler. Development of an in-situ system for measuring ground thermal properties [J]. ASHRAE Transactions. 2000, 106(1): 365~379.

[5] Gehlin S. and B. Nordell. (1998). Thermal Response Tests of Boreholes – Results from In-Situ Measurements. Proc. Second International Stockton Geothermal Conference. 15-16 March 1998. Richard Stockton College of New Jersey, Pomona, USA.

[6] Kavanaugh S P. Field Tests for Ground Thermal Properties Methods and Impact on Ground-Source Heat Pumps [J]. ASHRAE Trans, 1998, 104(2):347~355.

[7] Qingyu Zhu.Interpretation of Some Points in the Revised Technical Code For Ground Source Heat Pump System [J]. Heating Ventilating & Air Conditioning,2010,40:40~43(in Chinese).

[8] Hu Pingfang, Sun Qiming, Lei Fei, et. Al. Discussion on Some Problems of Rock-Soil Thermal Properties Test[J].Referigeration and Air-conditioning.2012，12(4)：109-111(in Chinese).

[9] Sarah Sigorelli, Simone Bassetti. Numerical Evaluation of Thermal Response Tests [J]. Geothermics 36(2007):141-166.

13th IEA Heat Pump Conference
April 26-29, 2021 Jeju, Korea

Evaluation of Interaction Between Load of Refrigerated Display Cases and Air Conditioners in a Grocery Store Using CFD

Chenghao WEI[a,*], Miwako FUJITA[a,b], Daisuke NARUMI[a]

[a]Graduate School of Environment and Information Sciences, Yokohama National University, 79-7 Tokiwadai, Hodogaya-ku, Yokohama, 240-8501, JAPAN
[b]Chubu Electric Power Company, Nagoya, Aichi, 461-8680, JAPAN

Abstract

In this paper, the cooling load of refrigerated display cases and the load of air conditioners in a grocery store were simulated by using computational fluid dynamics (CFD) models to understand the relationship between the loads of refrigerated display cases and air conditioners in summer and winter. In the summer, the results show that a higher preset temperature of the air conditioner led to an increase in the cooling load of the display cases and a decrease in the cooling load of the air conditioners. For this reason, the total electricity consumption was minimized when the preset temperature was set to 25℃, and the temperature was neither the highest nor the lowest explored. In the winter, the total electricity consumption of both display cases and air conditioners increased with increasing preset temperature. Furthermore, by replacing the frozen multi-deck display cases with frozen reach-in cases in the summer, the electricity consumption of the display cases decreased to half, while that of the air conditioners somewhat increased; in the winter, the electricity of the display cases and air conditioners both decreased.

Keywords: Grocery store; Air conditioner; Refrigerated display case; Energy consumption; CFD

1. Introduction

Supermarkets and grocery stores play an important and energy-intensive role in the commercial sector. The average electrical energy intensity of these stores varies from 1500 kWh/m^2 to 850 kWh/m^2 per year as the sales area increases from 280 m^2 to 1400 m^2 [1]. In Japan, grocery stores occupy 8% of the energy consumption in the commercial sector [2].

Refrigerated and frozen display cases (DCs) are widely used in grocery stores. According to the research data presented by Narumi, 84% of the energy consumption of grocery stores was related to chillers [3], while another study in the UK reported that the power consumption ratio of refrigeration and HVAC (heating, ventilation, and air conditioning) equipment was 60% and 26%, respectively [4].

In addition, HVAC equipment and refrigerators can influence each other in energy consumption, but most studies investigate air conditioners and DCs separately rather than regarding them as a combined working system. Hence, it is essential to explore the interaction between the load of refrigerators and air conditioners in grocery stores. To achieve this goal, the energy consumption of stores should be measured. However, the energy consumption measurement in stores is not easily performed because of the high costs and difficulties in controlling conditions.

CFD models can simulate the leakage of DCs and airflow of air conditioners; thus, the abovementioned obstacle can be overcome. Based on a series of experimental results, we built models of DCs in this study that can imitate their load and low-temperature air leakage under different temperatures or humidity environments.

* Corresponding author. Tel.: +81-080-9522-0437 .
E-mail address: wei-chenghao-wd@ynu.jp.

Nomenclature

$Q_{MD\text{-}R}$	Cooling load of an open refrigerated multi-deck display case [kW]
$Q_{SMD\text{-}R}$	Cooling load of an open refrigerated semi-multi-deck display case [kW]
$Q_{MD\text{-}F}$	Cooling load of a frozen multi-deck display case [kW]
$Q_{RI\text{-}F}$	Cooling load of a frozen glass door reach-in display case [kW]
$Q_{TUB\text{-}F}$	Cooling load of a frozen tub display case [kW]
H_{in}	Influx absolute humidity of a measurement point in front of a display case [kg/kg]
T_{in}	Influx temperature of a measurement point in front of a display case [°C]

Abbreviations

DC	Display case
HVAC	Heating, ventilation, and air conditioning
A&C	Air conditioner
MD-R	Open refrigerated multi-deck display case
SMD-R	Open refrigerated semi-multi-deck display case
MD-F	Frozen multi-deck display case
RI-F	Frozen glass door reach-in display case
TUB-F	Frozen tub display case
DAG	Discharge air grille of a display case
RAG	Return air grille of a display case

A small grocery store situated in Kobe, Japan, was chosen to be simulated to evaluate the interaction between the load of the DCs and air conditioners in the store. The DC CFD models were arranged in the CFD model of the store.

2. Methodology

The main contents of this study can be divided into three parts: (1) setting up an experiment to measure the performance of 5 kinds of DCs at different temperatures and humidities, (2) building the CFD models of the DCs from the data obtained in experiments, and (3) evaluating the interaction between the load of the DCs and that of the air conditioners in a grocery store at different air conditioner preset temperatures and applying energy-saving strategies. These details are provided in the following sections.

2.1. Performance of Display Case Measurements

The experiment measuring the performance of DCs in a laboratory with constant temperature and humidity was divided into 2 types: refrigerated and frozen experiments. The refrigerated DCs measured in the experiment consisted of one open refrigerated multi-deck DC (MD-R) and one open refrigerated semi-multi-deck DC (SMD-R); the frozen DCs consisted of a frozen multi-deck DC (MD-F), a frozen glass door reach-in DC (RI-F) and a frozen tub DC (TUB-F). Table 1 lists specifications of the 5 kinds of DCs. The 2 experimental plans are separately shown in Fig. 1(a) and Fig. 1(b). Plastic cardboard of approximately 1.7 m in height were fixed at the air exhaust to simulate a real store environment. A series of experiments were conducted to evaluate the effect of indoor air temperature and relative humidity on the cooling load of the 5 kinds of DCs, and the environment of the outdoor chamber remained at steady-state conditions (32°C and 40% relative humidity). The experimental conditions are summarized in Table 2. To build CFD models and to check the reliability, temperature and humidity and flow rate of the inlet and outlet vents of the DCs, the room temperature distribution and the cooling load of the DCs were measured.

Table 1 Specifications of the display cases

Display case	MD-R	SMD-R	MD-F	RI-F	TUB-F
Effective unobstructed capacity (L)	1940	1477	1507	1077	900
Outside dimension (mm)	Length 2440, Width 1100 Height 1890	Length 2440, Width 1100 Height 1700	Length 2440, Width 1100 Height 1880	Length 1430, Width 760 Height 1905	Length 1810, Width 1520 Height 810
Required refrigerating capacity (kW)	2.22	3.04	3.75	0.6/0.5	1.20/1.51
Evaporating temperature (℃)	-10	-10	-40	-40	-40

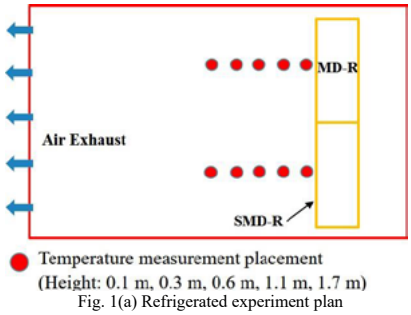


Fig. 1(a) Refrigerated experiment plan

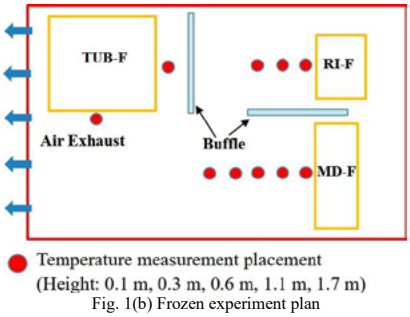


Fig. 1(b) Frozen experiment plan

Table 2 Experimental conditions

Item	Conditions
Outdoor environment	Temperature: 32℃ Relative humidity: 40%
Temperature	DC preset temperature: MD-R, SMD-R: 1℃; MD-F, RI-F: -28℃; TUB-F: -25℃ Indoor: 19℃, 22℃, 25℃, and 28℃
Indoor humidity	30%, 40%, 60%, and 70%
Cases	16 cases
Measurements	(1) Temperature, flow velocity and humidity of DCs RAG and DAG (2) Indoor temperature distribution (Measuring placements and heights are shown in Fig. 1 (a), (b)) (3) Cooling load of DCs

Table 3 Conditions of the CFD analysis of DCs

Items	Conditions
Employed code	STREAM Ver.14 (Software Cradle Co., Ltd)
Dimension	9.36 m (X)*6.5 m (Y)*4.0 m (Z)
Object	Air (Incompressible)
Analysis method	Steady-state analysis (Interval: 0.1 s)
Turbulent model	RANS (high-Reynolds)
Vapor	Diffusivity: 0.0000256 m2/s, Power law: 0.67
Number of mesh	From 2.1 to 6.6 million (Depending on DCs)
Boundary surface	No-slip surface
Boundary heat transfer	Thermo insulation
Air influx of the air conditioner	Speed: 0.065 m/s Turbulent: k=0.0001 m^2/s^3, ε=0.0001 m^2/s^3 Temperature: 19℃, 22℃, 25℃, and 28℃ Humidity: 30%, 40%, 60%, and 70%
Air exhaust	Natural outflow and inflow with aperture ratio while under 1.7 m (5% for refrigerated DCs and 10% for frozen DCs)
Radiation	View factor radiative heat transfer

2.2. Display case CFD Model

2.2.1. Detailed CFD Model

The laboratory model is shown in Fig. 2, which was built on the basis of the real laboratory. Detailed DC models, using the MD-R as an example shown in Fig. 3, were built based on the data obtained from the experiments. The commercial code STREAM Ver. 14 (November 2018. Software Cradle Co., Ltd. Oosaka, Japan) was employed for calculations in this study, and a high-Reynolds number-type κ-ε turbulence model was used to solve a steady-state simulation because the inaccurate imitation of viscous sublayers close to solid walls can be ignored in this study. A termination criterion of 10^{-4} is used for all variants in this study. The view factor method was used to calculate radiation. Additional details of the conditions are summarized in Table 3.

As the boundary conditions, the heat was insulated at all boundaries between the defined and undefined areas. The speed of flow from the air conditioner outlet surfaces was maintained at a constant speed. The air

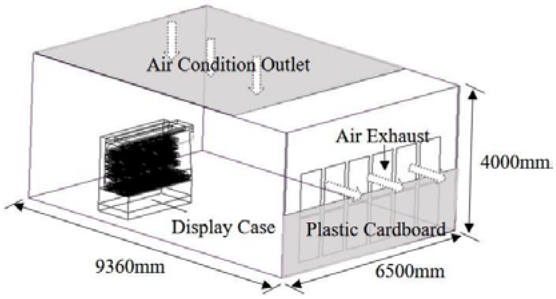


Fig. 2. Laboratory CFD model

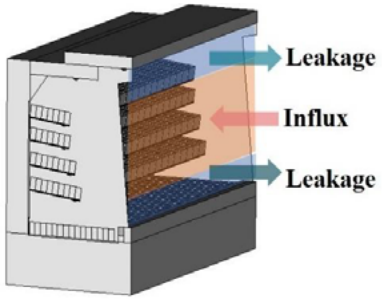


Fig. 3. Detailed model of MD-R

conditioner outlet temperature and relative humidity conditions were in accordance with the experiment (Table 3). The air conditioner exhaust surface was fixed as natural air outflowing and inflowing (the aperture ratio was fixed while under 1.7 m to simulate the plastic cardboard). Because plastic cardboard is not spliced tightly, the aperture may not remain constant through experiments. The aperture ratio values of the refrigerated and frozen experiments are discussed separately and determined as shown in Table 3. The DAG and RAG settings are shown in Fig. 4, using the MD-R as an example. The flow rate, temperature, and humidity of RAG and DAG were based on data measured from the experiment.

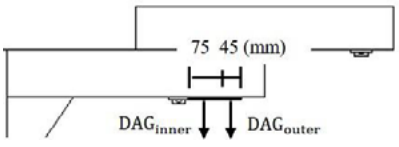
It was found that the air in front of a DC model was always divided into two air leakage parts and an influx part, as shown in Fig. 3.

The cooling load, which was calculated from enthalpy differences between the DAG and RAG of a DC, and vertical temperature distribution in front of the DC were used to inspect the reliability of the detailed DC CFD model. The MD-R is taken as an example, whose results are presented in Figs. 5 and 7. The positive reliability of the detailed DC CFD models was confirmed.

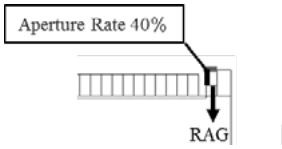
2.2.2. Simplified CFD Model

If the scale of a domain expands, the computational load increases when simulating the energy consumption of the store by using CFD with detailed DC models. Hence, a simplified DC CFD model was used to decrease the computational load.

Without building models in detail, such as shelves and goods, only leakage and influx surfaces are set, as shown in Fig. 6. The airflow volume, temperature, humidity of leakage and influx surface were fixed from the association between them and the average temperature of the influx surface. The relations were obtained from the results of the detailed models. Fig. 8 displays the volume of influx surfaces as an example. Formula (1)-Formula (5) show the relationships between the cooling load of the DCs and the average temperature and humidity of the influx surface, which can be used to obtain the energy consumption of the stores.



(a) Discharge air grille (DAG)



(b) Return air grille (RAG)

Fig. 4. DAG & RAG settings of the MD-R model

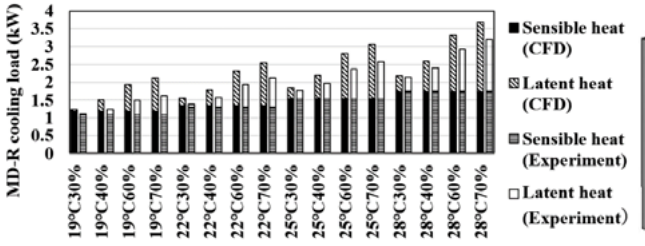


Fig. 5. MD-R cooling load reliability

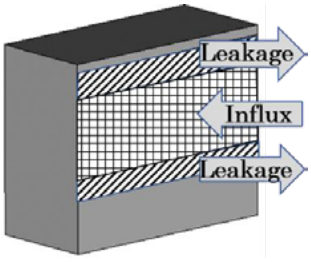


Fig. 6. Simplified model of the MD-R

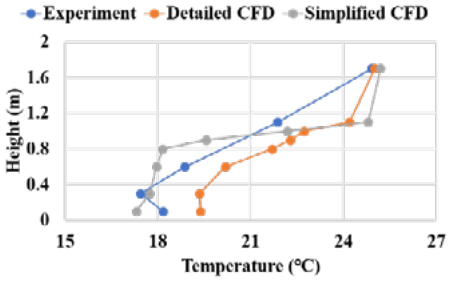


Fig. 7. Vertical temperature distribution (2 m away from the MD-R)

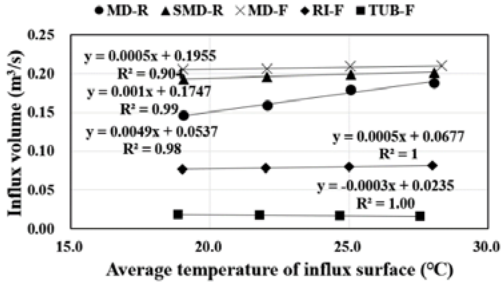


Fig. 8. Relationship between the influx volume and a measurement point temperature

The vertical temperature distribution in front of the DC were used to inspect the reliability of the simplified DC CFD model. The MD-R is taken as an example, whose results are presented in Figs. 7. The positive reliability of the simplified DC CFD models was confirmed.

$$Q_{MD-R} = 143.75 \times H_{in} + 0.083 \times T_{in} - 1.02 \quad (1)$$

$$Q_{SMD-R} = 182.17 \times H_{in} + 0.070 \times T_{in} - 0.67 \quad (2)$$

$$Q_{MD-F} = 124.62 \times H_{in} + 0.099 \times T_{in} + 7.43 \quad (3)$$

$$Q_{RI-F} = 0.070 \times H_{in} + 0.00215 \times T_{in} + 2.5 \quad (4)$$

$$Q_{TUB-F} = 4.286 \times H_{in} + 0.0022 \times T_{in} + 2.54 \quad (5)$$

2.3. Evaluation of the Energy Consumption of a Grocery Store

2.3.1. Description of the Grocery Store

The grocery store simulated in this study is a typical small grocery store that is approximately 261 m^2 in size and is located in Kobe. The plan of the store is provided in Fig. 9. There are 9 open refrigerated multi-deck DCs (MD-R), an open refrigerated semi multi-deck DC (SMD-R), 2 frozen multi-deck DCs (MD-F) and 2 hybrid-type frozen DCs, which were regarded as 2 frozen tub DCs (TUB-F) in this study. For the HVAC equipment, there are 4 four-way cassette indoor air conditioner units, 3 ducted exhaust ventilation fans used in the summer and a ducted in-line ventilation fan with four vents used in the winter.

2.3.2. Grocery Store CFD Model

Fig. 10 displays an exploded view of the CFD store model. The model consisted of refrigerated and frozen DCs, unrefrigerated DCs, HVAC equipment, architecture components, and people. The architecture components were external walls, an internal wall, the ceiling, the roof, the floor and windows, whose detailed settings are provided in Table 4.

A high-Reynolds number-type κ-ε turbulence model was used because the inaccurate imitation of viscous sublayers close to solid walls can be ignored in the store. Additional details of the basic conditions are summarized in Table 5. Radiation analysis was omitted due to the limitations of the CFD analysis code employed in this analysis, where radiation analysis and solar radiation cannot be activated simultaneously. Both surfaces of the DCs and HVAC devices were fixed as boundary conditions; therefore, only the walls and floors were influenced by radiation. Therefore, the error induced by neglecting radiation slightly influenced the airflow and temperature distribution results in this study.

The simulation time was set to Aug. 8th and Dec. 21st, whose solar radiation data were input from a database called METPV-11 [5]. In this paper, we only simulated starting at 12:00 by transient analysis whose interval time was 0.1 s per calculation cycle. The number of guests generating heat from bodies and leading to influx

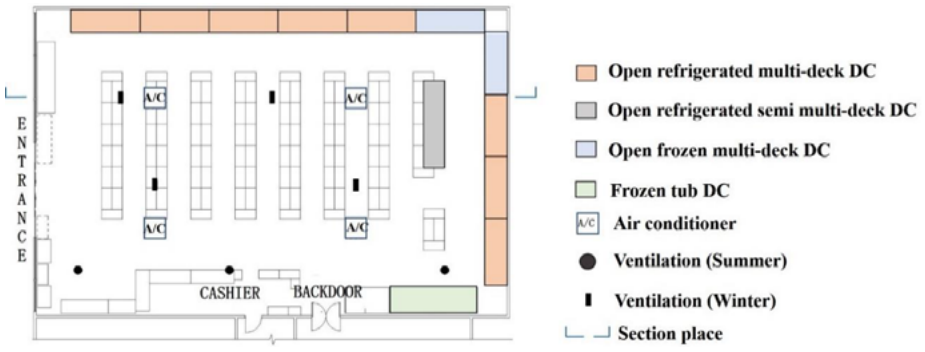
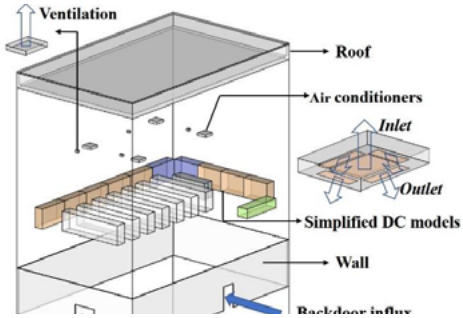


Fig. 9. Plan of the grocery store

Table 4 Architecture components conditions

Component	Material	Thickness (mm)	Thermal conductivity (W/(m K))
External wall	Tile	10	1.3
	Glass wool	100	0.034
	Gypsum	10	0.14
Internal wall	Tile	10	1.3
	Air layer	30	Temperature-dependent
	Gypsum	10	0.14



Ceiling and roof	Stainless	5	16
	Air layer	975	Temperature-dependent
	Glass wool	10	0.034
	Gypsum	20	0.14
Floor	Tile	20	1.3
	Concrete	200	1.2
	Glass wool	100	0.034
Window	Glass	50	0.75

Fig. 10. Exploded view of the CFD store model

Table 5. Conditions of the CFD analysis of the store

Items	**Conditions**
Employed commercial code	STREAM Ver.14 (Software Cradle Co. Ltd)
Dimension of domain	19.82 m (X)*13.14 m (Y)*4.15 m (Z)
Object	Air (Incompressible)
Analysis Method	Transient Analysis (Interval: 0.1 s)
Turbulent model	RANS (high-Reynolds), k= 0.0001 m^2/s^3, ε=0.0001 m^2/s^3
Boundary surface velocity	No-slip surface
Boundary heat transfer	Thermo insulation
Inflow boundary	(1) Outlet surfaces of air conditioners (2) Leakage surfaces of simplified DC models (3) Outside influx surfaces of entrance and backdoor
Outflow boundary	(1) inlet surfaces of air conditioners (2) air exhausted surfaces of ventilation fans
Vapor	Diffusivity: 0.0000256 m^2/s Power law: 0.67
Meshes	1,699,629 meshes
Human	Body temperature: 36.5°C Number: Change by the hour and 63 people in total in the case of 12 o'clock
Solar radiation	City: Kobe Time: 12:00, Aug. 8^{th} and Dec. 21^{st} Database: METPV-11

from outside was determined to be 631 people per day based on the *Annual Statistical Report on Supermarkets* [6]. The total amount was distributed per hour according to the guest distribution of the store, which was obtained from Google Maps data [7]. The average time of stay of each guest was fixed as 10 minutes, which matched the size of the store. In addition, a staffer was set in the model. As a result, there were 63 people in total being set in the store model at the start of simulation at 12:00. The surface temperature of the guests and the staff was maintained constant at 36.5°C (Table 5).

As the boundary conditions, the heat was insulated in all boundaries between the defined and undefined areas. Inflow and outflow boundaries are shown in Fig. 10. Additional details of the boundary conditions are summarized in Table 5. The inflow boundaries consisted of the outlet surfaces of the air conditioners, the leakage surfaces of the abovementioned simplified DC models, and the outside influx surfaces of the entrance and backdoor. The outflow boundaries consisted of the inlet surfaces of the air conditioners and air exhaust surfaces of the ventilation fans. Additional details are supplied in the following sections.

Simplified refrigerated and frozen DC CFD models were arranged in accordance with the real store Although there is a range of set temperatures in the real store, the set refrigeration temperature was unified at 1°C, and the freezer temperature was at -28°C in the simulation because an accurate reproduction is not the purpose of this study. Unrefrigerated cases were placed in the center of the store. Moreover, to simulate the gap between goods placed in unrefrigerated cases, the refrigerated cases were built by surfaces with an opening ratio of 60%.

For air conditioner models, the outlet temperature and humidity were calculated from those of the inlet flow, which can be determined in a solver during the simulation. The power of the air conditioners set up in the store model was controlled by the inlet temperature. The power changed linearly over a range of ± 0.5°C around the set temperature from 0 kW to the maximum temperature and remained at constant values outside the temperature range. For example, when the preset temperature was 25°C in the summer, the power remained at 0 kW before 24.5°C, then the power increased as the temperature rose and was maintained at a maximum after 25.5°C. For the purpose of making the computations easy to converge, the power control function was set in a simplified way despite being different from the real function. Other detailed settings of the HVAC system, such as the ventilatory volume, are shown in Table 6.

Table 6 HVAC system and influx conditions

Item	Season	Conditions
Air conditioner	Summer	Mode: Cooling Volume: 0.0875*4=0.35 m^3/s, Maximum power: 14 kW
	Winter	Mode: Heating Volume: 0.15*4=0.6 m^3/s, Maximum power: 15 kW
Ventilation fan	Summer	The number of vents: 3 Total volume: 2115 m^3/h
	Winter	The number of vents: 4 Total volume: 610 m^3/h

Regarding the outside influx volume from the entrance or backdoor, 3 assumptions were considered in this study: (1) the automatic door at the entrance keeps opening for a duration of 10 s once someone passes, (2) the influx only originates from the entrance when the door keeps opening; in the other situation, the influx originates from the backdoor where the temperature remains at 22℃ in the winter and 25℃ in the summer, (3) without simulating the door opening and closing, the influx originates from both the backdoor and the entrance all the time in the CFD model to make the computation converge easily. Hence, the influx volume compensating for the outflow ventilation volume was separated from the backdoor and the entrance by the ratio of the time of the door opening and not opening.

The calculations were conducted for six cases each season, as summarized in Table 7. They were divided into two types: various preset temperature experiments and energy-saving strategies experiments. CASE3 was the standard of these cases. Four preset temperature experiments (from CASE1 to CASE4) were adopted to evaluate the effectiveness of the air conditioner temperature changes in the energy consumption of the store. One energy-saving strategy was halving the ventilation volume in the summer and tripling it in the winter (CASE3-V), and the other strategy was replacing the frozen multi-deck DCs with frozen glass door reach-in DCs (CASE3-R). In each case, an initial temperature indoor was set to be the preset temperature of air conditioners to make the computations faster to converge.

Table 7. Cases list

Experiment type	Case name	Display cases	Ventilation Volume(m^3/h)	Preset temperature
Temperature experiment	CASE1	MD-R, SMD-R, MD-F, TUB-F	Summer: 2115, Winter: 610	19℃
	CASE2	MD-R, SMD-R, MD-F, TUB-F	Summer: 2115, Winter: 610	22℃
	CASE3	MD-R, SMD-R, MD-F, TUB-F	Summer: 2115, Winter: 610	25℃
	CASE4	MD-R, SMD-R, MD-F, TUB-F	Summer: 2115, Winter: 610	28℃
Energy-saving strategies	CASE3-V	MD-R, SMD-R, MD-F, TUB-F	Summer: 1058, Winter: 1830	25℃
	CASE3-R	MD-R, SMD-R, RI-F, TUB-F	Summer: 2115, Winter: 610	25℃

2.3.3. Energy and Electricity Calculation Method

The energy (load) consumption calculation was divided into 2 parts: DC and air conditioner. The formulas summarized above were used to calculate the cooling load of the DCs. For air conditioners, the cooling load or the heating load was calculated from enthalpy differences between the outlet air and inlet air.

The electricity can be calculated from the load by using the coefficient of performance (COP). In the summer, the COP of the air conditioners was 3.59, the refrigerated DC COP was 1.90, and the frozen DC COP was 0.75. In the winter, the COP of air conditioners was 4.06, the refrigerated DC COP was 1.86, and the frozen DC COP was 0.79.

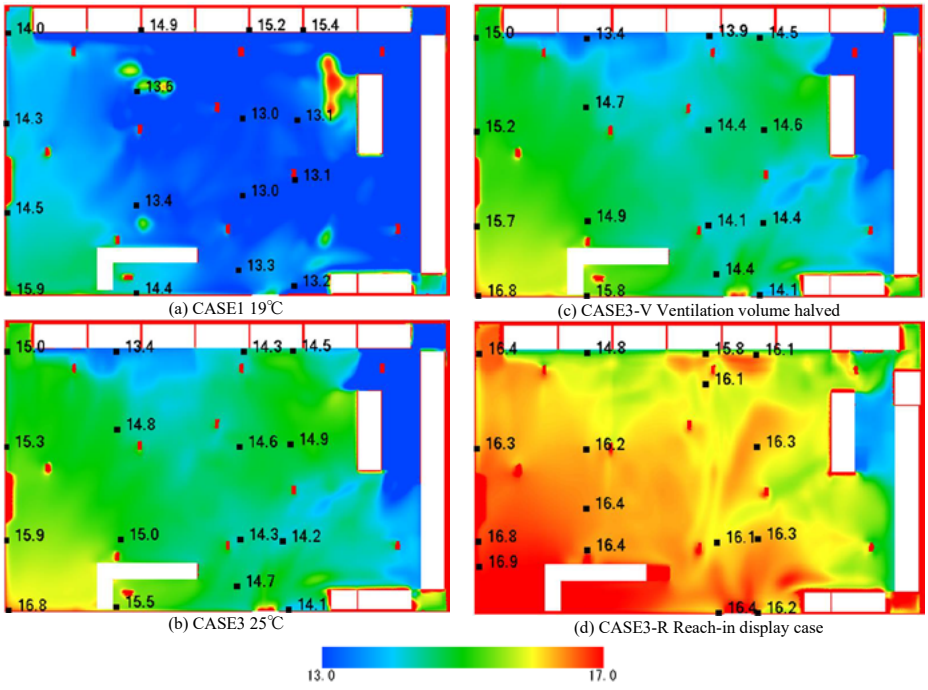


Fig. 11. Temperature plan distribution at the height of 0.7 m

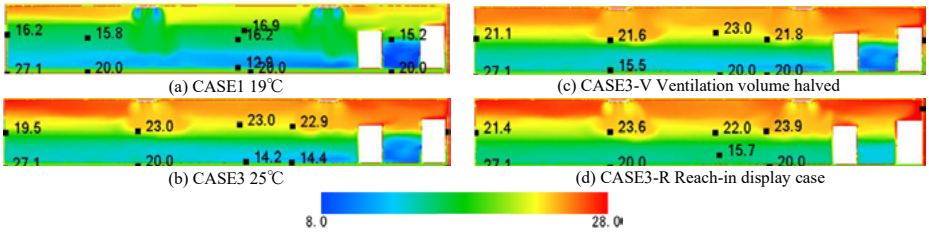


Fig. 12. Section plan temperature distribution

3. Results

3.1. Summer

3.1.1. Stability

The transient temperatures of the air conditioner outlet air and an indoor measurement point at a height of 1.6 m were used to check the stability of the simulations. The outlet air temperatures remained stable after 1000 cycles, while the indoor air temperatures remained stable after 6000 cycles. Therefore, the results of 10000 cycles were stable enough to be adopted.

3.1.2. Temperature

Fig. 11 compares the temperature plan distribution at a height of 0.7 m for different cases, and the temperature distribution of the section plan shown in Fig. 9 is provided in Fig. 12.

As a result, the higher the preset temperature was, the higher the temperature was in the upper part of the store, where high-temperature air accumulated. On the other hand, low-temperature air accumulated in the lower part of the store and hardly changed as the preset temperature increased. Therefore, the vertical temperature distribution was obviously separated into a low-temperature part and a high-temperature part. The

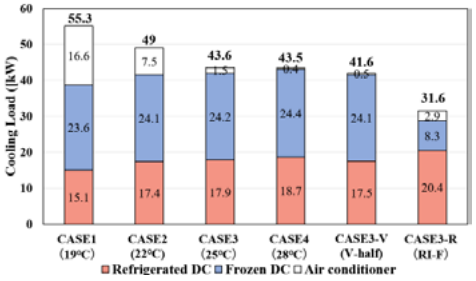


Fig. 13. Cooling load of the air conditioner & the DCs in the summer

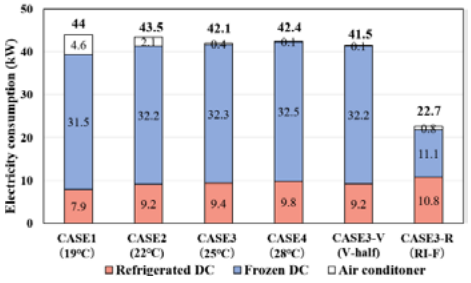


Fig. 14. Electricity consumption in the summer

maximum difference can reach 10℃. For the temperature plan distribution, the temperature decreased from the entrance to the innermost part of the store in every case. The average temperature of the 0.7 m plan was 13.6℃ when the preset temperature was 19℃, and it increased to 15.2℃ as the preset temperature increased to 28℃, which illustrates that the average plan temperature increased as the preset temperature increased.

When the ventilation volume was halved, the high-temperature part of the store became cooler because of the lower high-temperature influx air from outside; in contrast, the low-temperature part of the store hardly changed. The low-temperature part of the store became warmer when the frozen multi-deck DCs were replaced with frozen reach-in DCs.

3.1.3. Load and Electricity Consumption

The energy and electricity consumption in the summer are shown in Fig. 13 and Fig. 14, respectively. The result shows that with an increase in the preset temperature, the cooling load of the DCs increased while the space cooling load of the air conditioner decreased. The total cooling load of the DCs and the air conditioner increased with the increasing preset temperature of the air conditioners. Although the highest preset temperature of air conditioners and the highest total cooling load of DCs and the air conditioner were in the 28°C case, the total electricity consumption was minimized when the preset temperature was set to 25°C. Furthermore, the frozen multi-deck DCs strongly affected the total energy consumption of the store. By replacing the frozen multi-deck DCs with frozen reach-in DCs, the indoor air temperature increased. Therefore, the electricity consumption of DCs was halved, while that of air conditioners somewhat increased. In the aggregate, the total electricity consumption of the DCs and air conditioners obviously decreased while replacing the frozen multi-deck DCs with frozen reach-in DCs.

3.2. Winter

3.2.1. Stability

In the winter, the outlet air temperature remained stable after approximately 1000 cycles. Therefore, the results of 3000 cycles can be adopted.

3.2.2. Temperature

Fig. 15 compares the temperature plan distribution at a height of 0.7 m for different cases, and the temperature distribution of the section plan is provided in Fig. 16.

The results were similar to those for summer; the higher the preset temperature was, the higher the temperature was in the upper part of the store, where high-temperature air was accumulated. Simultaneously, low-temperature air accumulated in the lower part of the store and increased as the preset temperature increased, which is different from the summer. Also, with winter having a general opposite temperature compared to the summer temperature, the temperature increased from the entrance to the innermost part of the store. The indoor temperature decreased slightly when the ventilation volume was tripled. The low-temperature part of the store became warmer when the frozen multi-deck DCs were replaced with frozen reach-in DCs.

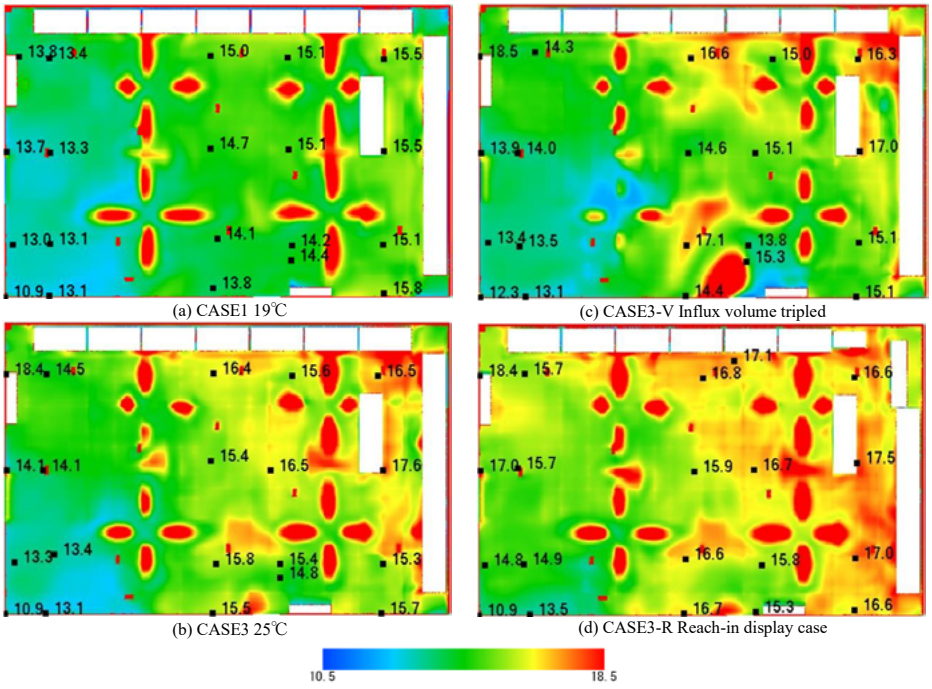


Fig. 15 Temperature plan distribution at the height of 1.4 m

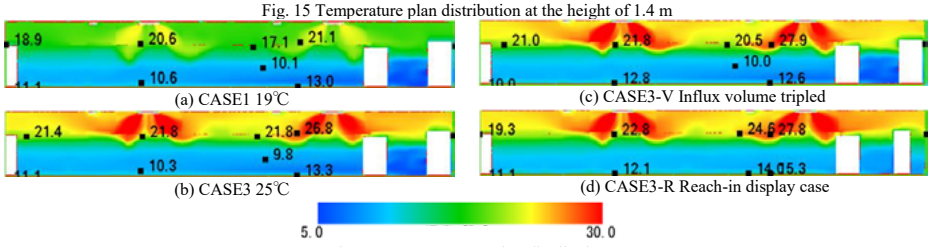


Fig. 16 Temperature section distribution

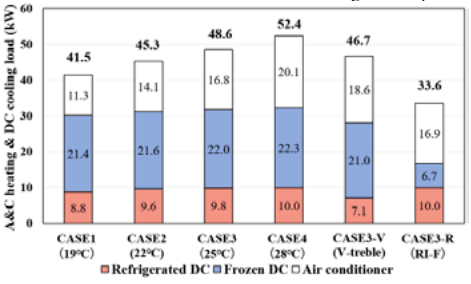


Fig. 17. Air conditioner heating & DC cooling load in the winter

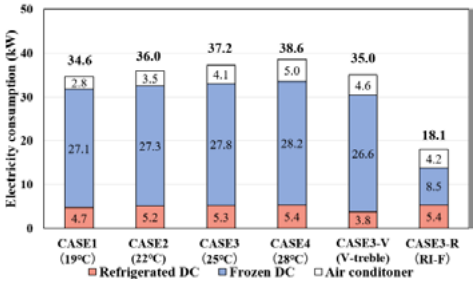


Fig. 18. Electricity consumption in the winter

3.2.3. Energy and electricity consumption

The energy and electricity consumption in the winter are shown in Fig. 17 and Fig. 18. The cooling load of the DCs and the heating load of the air conditioner both increased with increasing preset temperature. Additionally, the total electricity consumption of the DCs and air conditioners increased. Similar to summer, frozen multi-deck DCs also strongly affected the total energy consumption of the store in the winter. The total electricity consumption of the DCs and air conditioners decreased to half by replacing frozen multi-deck DCs with frozen reach-in DCs. In addition, the total load and electricity consumption both decreased when the

ventilation was tripled.

4. Discussion

We have shown that the CFD method can assist in simulating the energy consumption of DCs and air conditioners in a store and evaluating the interaction between them without assuming that the temperature is uniform anywhere indoors. By applying simplified DC CFD models, which can be adopted to calculate the cooling load of DCs in different conditions, to study changes in the energy consumption of a grocery store under different conditions, we found that the total energy consumption of the store changed when changing the preset temperature of air conditioners or adopting other energy-saving strategies. In the summer, the result shows that a higher preset temperature of the air conditioner leads to increases in the cooling load of the display cases and a decrease in air conditioners cooling load. In the winter, both the total electricity consumption and the total load increased with increases in the preset temperature. Furthermore, by replacing the frozen multi-deck DCs with frozen reach-in DCs in the summer, the electricity consumption of DCs decreased to half, while that of air conditioners somewhat increased; in the winter, the electricity and the load of the DCs and air conditioners both decreased.

The main cause of the load interaction between the DCs and air conditioners may be explained by the fact that the indoor temperature distribution changed under various conditions. It is surprising that the total electricity consumption in the summer was minimized when the preset temperature was set to 25°C, and the temperature was neither the highest nor the lowest explored. In contrast, the total cooling load of air conditioners and DCs became largest when air conditioners were set to 28°C. This is because the COP of air conditioners is larger than that of the DCs. Tripling the ventilation in the winter, which can lead to a more low-temperature air influx from outside, reduces the energy consumption of the store. An explanation is that the influx air restrained the cooling load of the DCs and comparatively induced a slight increase in the heating load of air conditioners because of the delamination of air. We believe that there might be an appropriate ventilation volume that can lead to the lowest energy consumption of the store, which is worth investigating in the future.

The method we adopted to build the DC CFD models was partly successful because it was able to simulate the cooling load under different temperatures and humidity environments. However, the limitation of the models we built is that they can only be applied under a particular condition, where the preset refrigerant evaporation temperature is -10°C and -40°C for refrigerated DCs and frozen DCs, respectively.

We also found that a vertical air temperature distribution was obviously separated into a low-temperature part and a high-temperature part. Research by Endo et al. shows a similar result [8]. A possible explanation for this is that the density of high-temperature air is lower than that of low-temperature air, which makes the lower air easily accumulate in the upper part of a room. In addition, to make the store model easy to converge computationally, we ignored the air mixing caused by guests moving or doors opening and closing, which might be able to strengthen the delamination in this study. The influence of air mixing should be evaluated in the future.

5. Conclusion

This study set out to develop a CFD store model to imitate the cooling load of DCs and air conditioners in a store and to evaluate the interaction between them. We changed the preset temperature of air conditioners and applied some energy-saving strategies to understand the interaction between the load of air conditioners.

The findings clearly indicated that changing the air conditioner preset temperature or altering the equipment arrangement in stores is in favor of reducing the energy consumption of stores.

- The DC CFD models in this study can be used to calculate the cooling load of DCs under different conditions and to imitate the transient energy consumption of grocery stores.
- If the temperature was increased by the air conditioners, both the load of the DCs and air conditioners increased in the winter; however, in the summer, the load of the DCs increased, while that of air conditioners decreased. The lowest electricity consumption occurred when the preset temperature was 25°C in the summer. An appropriate temperature should be set to save energy rather than being set as high as possible in the summer.
- Replacing open DCs by reach-in door DCs can obviously reduce the load of the store. Reducing the ventilation volume in the summer or increasing it in the winter can also help save energy in the store.

- In the future, factors such as people moving and doors opening should be considered to improve the precision of store CFD models.

References

[1] Tassou, S.A., Ge, Y., Hadawey, A., Marriott, D., 2011. Energy consumption and conservation in food retailing. Applied Thermal Engineering 31, p.147–156.

[2] Agency for Natural Resources and Energy, Japan. Energy White Paper. 2014.in Japanese.

[3] Narumi, D., 2015. Examination of Characteristics of Energy Consumption in Retail Stores with Refrigeration Facilities and its Modeling. Summaries of technical papers of Annual Meeting, Architectural Institute of Japan (Kanto), p1075-1076. in Japanese.

[4] Mylona, Z., Kolokotroni, M., Tassou, S.A., 2017. Frozen food detail: Measuring and modelling energy use and space environment systems in an operational supermarket. Energy and Buildings 144, p.129-143.

[5] NEDO. METPV-11. https://www.nedo.go.jp/ library/nissharyou.html

[6] Japan Supermarket Association. Annual Statistical Report on Supermarkets. 2017. in Japanese

[7] https://www.google.co.jp/maps

[8] Endo, M., Nagano, S., Suzuki, H., 2006. Improvement of indoor temperature distribution of food store by use of KHP, Part2 Measurement results in winter and evaluation by CFD to the effect of air circulator. Summaries of technical papers of Annual Meeting, Architectural Institute of Japan (Hiriku), p.249-252. in Japanese.

13th IEA Heat Pump Conference
April 26-29, 2021 Jeju, Korea

Analytical study on performance of R134a, R404A, and R744 refrigeration truck system

Yunchan Shin[a], Yeonghun Kim[a], Minjun Kim[b], Honghyun Cho[b,*]

[a]Graduate school of Chosun University, Gwangju, 501-759, Korea.
[b,*]Department of Mechanical Engineering, Chosun University, Gwangju, 501-759, Korea.

Abstract

An automotive air-conditioning system and refrigeration truck is normally used refrigeration R134a and R404A. The natural refrigerant R744 is one of alternative refrigerant for refrigeration truck. In this study, the theoretical study on the performance comparison between R744, R134a, and R404A for the refrigeration truck. The cooling capacity, compressor work, and COP of R744 refrigeration system were analyzed according to outdoor air temperature and compressor rotating speed. Also, those are compared with those of R404A and R134a system. As a result, the performance of all systems with the outdoor temperature was rapidly decreased. The performance decrement of R404A is relatively higher than that of other system. In the change of RPM, the increasing rate of cooling capacity and compressor work of the R404A, R134a, and R744 system reached the highest at 1500 RPM. The data of this study is to provide the basic performance data of refrigeration system of refrigeration truck.

Keywords: Compressor work; COP; R134a; R404A; R744; Refrigeration capapcity

1. Introduction

As parcels and distribution supply recently increased, energy consumption for the storage and transport of parcels is increasing. In particular, the energy consumption for delivery has increased even more as the demand for delivery has increased compared to the storage of items. In addition, as the delivery of products requiring freshness from among the delivered products increases, the demand for a refrigeration truck using a refrigeration system is increasing to keep the temperature of the product storage room constant at all times.

Refrigeration trucks consume more energy than general trucks by using a refrigeration unit to maintain a constant temperature in the product storeroom. Therefore, research on improving the performance of refrigeration truck is essential for energy saving. The Ozone Depletion Potential (ODP) of R404A and R134a refrigerants, which are widely used in the refrigeration industry, is currently 0, but the Global Warming Potential (GWP) is very high at 4,700 and 1300, respectively. Regarding refrigerants used in automotive air conditioning systems, the European Commission has decided to regulate the use of refrigerants more than GWP of 150 for new vehicles since 2022. R744 refrigeration system can miniaturize because R744 refrigerant has a smaller specific volume than R404A and R134a. In addition, it can be used even at low temperatures since the boiling point is low. Table 1 showed the properties of refrigerant used in this study.

In this study, R404A, R134a and R744 refrigerants were applied to the refrigeration system of refrigeration trucks, and the performance of refrigeration truck refrigeration system was compared under various operating conditions. The results of this study may provide basic data on the performance of refrigeration truck refrigeration system with alternative refrigerants.

* Corresponding author. Tel.: 82-62-230-7050; fax: 82-62-230-7055.
E-mail address: hhcho@chosun.ac.kr.

Table 1 Refrigerant properties

Refrigerant	R134a	R404A	R744
Molecular weight [kg/kmol]	102.03	97.6	44.01
Boiling point [K]	247.08	319.15	194.65
Critical temperature [K]	374.2	345.1	304.25
Critical pressure [MPa]	4.06	3.73	7.38
Latent heat of vaporization at 25℃ [kJ/kg]	177.8	140.3	119.9
Flammability	Inflammable	Inflammable	Inflammable
Ozone depletion potential	0	0	0
Global warming potential	1300	4700	1

2. Simulation modeling and analysis

The refrigeration truck refrigeration system used in this study was developed by selecting the refrigeration truck currently operating on the road as the main analysis model. And the developed system shown in Fig. 1 is consist of compressor, condenser, expansion valve and evaporator. This simulation is conducted using the EES program and the flow of performance analysis was carried out as shown in Fig. 2.

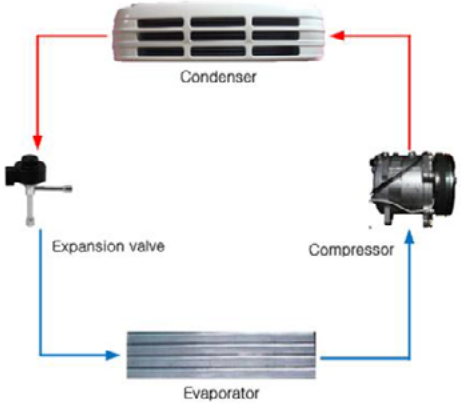


Fig. 1. Refrigeration cycle of refrigeration truck

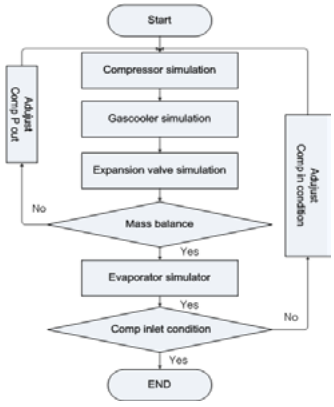


Fig. 1 Flow chart for the refrigerator cycle

2.1. Compressor modeling

The compressor of R404A, R134a and R744 used in the analysis of this study was selected due to its durability and widely used as swash plate compressor of automobile air conditioning systems. In the case of R744, as the rate of heat capacity is bigger than R404A and R134a, the stroke volume of the compressor is controlled to obtain the same refrigeration capacity from the system. The equation (1) was used to calculate the mass flow rate of R404A, R134a and R744. The volumetric and isentropic efficiency of R404A, R134a, and R744 in this study was used based on the experiment of previous study [1-3]. The volumetric and isentropic efficiency of the refrigeration system for R404A were used the equation (2) and (3) [1], respectively. In case of the refrigeration system with R134a, It was calculated by the equation (4) and (5) [2]. The volumetric and compression efficiency of refrigeration system for R744 was calculated by the equation (6) and (7) [3].

$$M_r = n\frac{\pi}{4}d_c^2 S_p N\frac{\eta_v}{v_s} \tag{1}$$

$$\eta_{v,R404A} = 0.3596 + 1.1072 \times S_p - 0.08132 \times \varepsilon + 0.0001175 \times N - 0.4025 \times S_p^2 - 2.449 \times 10^{-8} N^2 \tag{2}$$

$$\eta_{i,R404A} = 0.2402 + 1.4187 \times S_p - 0.09698 \times \varepsilon + 0.000123 \times N - 0.5852 \times S_p - 2.457 \times 10^{-8} N^2 \quad (3)$$

$$\eta_{v,R134a} = 0.8263 \left[1 - 0.09604 \left(\varepsilon^{\frac{1}{\gamma}}\right) - 1\right] \quad (4)$$

$$\eta_{i,R134a} = 0.9343 - 0.04478 \times \varepsilon \quad (5)$$

$$\eta_{v,R744} = 1.149768 + 0.001025 \times P_{c,in} - 0.003592 \times P_{c,in} - 13.660815 \times V_s + 0.000059 \times N \quad (6)$$

$$\eta_{c,R744} = 0.781749 - 0.000956 \times P_{c,out} - 0.003812 \times SH_{c,s} - 0.003565 \times T_{c,s} + 0.000033 \times N \quad (7)$$

2.2. Heat exchanger modeling

The condenser consists of four rows and is divided into two tubes. And the evaporator is divided into six tubes and consists of eight rows each. Detailed specifications of the heat exchanger are shown in Table 2. In this study, the heat transfer and pressure drop correlation of single-phase and two-phase used for modeling of R404A, R134a and R744 system is shown Table 3. In addition, the heat transfer coefficient and pressure drop for the analysis of air side used the correlation of the Wang [14].

Table 2 Specification of heat exchanger

Specification	Condenser	Evaporator
Fin interval [mm]	2.1	4.56
Fin height [mm]	25.78	22.64
Fin width [mm]	24.83	26.13
Tube diameter [mm]	9.5	9.5
Tube thickness [mm]	0.5	0.5
Total size [mm]	760.2(L)×283.5(H)×99.3(W)	864.6(L)×135.8(H)×209(W)

Table 3 Heat transfer coefficient and pressure drop of R404A, R134a, R744 for heat exchanger modeling

	R404A		R134a		R744	
	Single- phase	Two- phase	Single-phase	Two-phase	Gascooler	Evaporator
Heat transfer coefficient	Wang[4]	Traviss[6]	Dittus and Boelter[8]	Gungor and Winterton[10]	Gnielinsk [11]	Yoon et al [13]
Pressure drop	Blasius[5]	Fridel[7]	Fanning and Pierre[9]	Fanning and Pierre[9]	Churchill [12]	Yoon et al[13]

2.3. The expansion device modeling

The expansion device used in the R404A, R134a, and R744 system used the electron expansion valve. The electron expansion valve is comprised of the orifice, needle and the drive stepping motor. The orifice diameter used to the modeling of R404A and R744 system was 1.6 mm. It used the equation of the Hwang and Kim [15]. The orifice diameter of the R134a system was 1.4 mm and it used the equation of the Chung et al [16].

2.4. The frost analysis

The frost growth in the evaporator has an bad effect on the system efficiency due to the decrease of heat transfer area in the heat exchanger. The thermal resistance and heat transfer coefficient of the frost layer was applied to the heat exchanger analysis of the R404A, R134a and R744. Thermal conductivity and density of the frost layer was calculated according to the equation proposed by Lee at al. [17] and those are calculated by the equations (8) and (9).

$$k_f = k_{ice} \times 0.26259 (Re_d)^{0.49406} (Fo)^{0.18733} (w_a)^{-0.25087} (T_a^*)^{-7.20328} (T_c^*)^{5.5004} \quad (8)$$

$$\rho_f = \rho_{ice} \times 0.00008 (Re_d)^{0.44785} (Fo)^{0.21083} (w_a)^{-0.53939} (T_a^*)^{23.90830} (T_c^*)^{5.69576} \quad (9)$$

3. Results and discussion

In this study, the performance characteristics of the system were investigated the performance for refrigeration cycle of the designed refrigeration truck refrigeration system using R134A, R404A, and R744 refrigerant. Fig. 3 showed the variation of COP, compressor work, and cooling capacity according to the change of outdoor air temperature. As the outdoor air temperature increased from 25℃ to 35℃, the compressor work of R404A, R134a, and R744 system increased by 19.1%, 13.1%, and 16.8%, respectively and the refrigeration capacity ratio decreased by 43.1%, 9.0%, and 41.5%, respectively.

Fig. 4 showed the variation of COP, compressor work, and cooling capacity according to the change of compressor rotating speed. As the compressor rotating speed increased from 1000 rpm to 3000 rpm, the ratio of compressor work and of refrigeration capacity rapidly increased at the system of R404A, R134a, and R744. Accordingly, the ratio of COP decreased because compressor work more increased than refrigeration capacity. The COP ratio of R404A and R744 system showed maximum value at the compressor rotating speed of 1500 rpm.

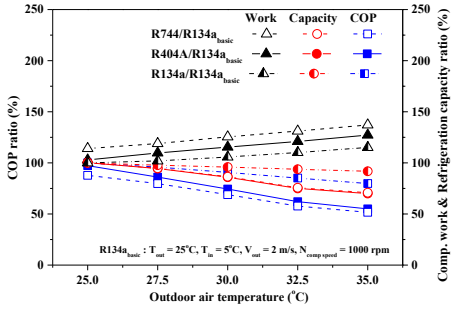


Fig. 3. Variations of compressor work, capacity, COP with outdoor air temperature

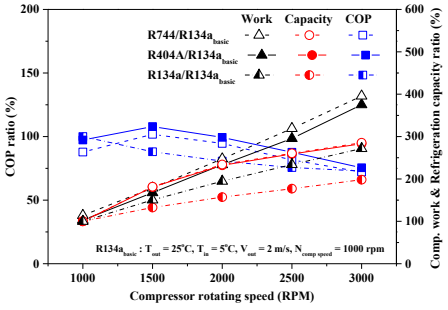


Fig. 4. Variations of compressor work, capacity, COP with compressor rotating speed

4. Conclusions

In this study, R404A, R134a and R744 refrigerants were applied to the refrigeration system of refrigeration trucks, and the performance of refrigeration truck refrigeration system was compared under various operating conditions. An automotive air-conditioning system and refrigeration truck is normally used refrigeration R134a and R404A. The natural refrigerant R744 is one of alternative refrigerant for refrigeration truck. In this study, the theoretical study on the performance comparison between R744, R134a, and R404A for the refrigeration truck. The cooling capacity, compressor work, and COP of R744 refrigeration system were analyzed according to outdoor air temperature and compressor rotating speed. Also, those are compared with those of R404A and R134a system. As a result, the performance of all systems with the outdoor temperature was rapidly decreased. The performance decrement of R404A is relatively higher than that of other system. In the change of RPM, the increasing rate of cooling capacity and compressor work of the R404A, R134a, R744 system reached the highest at 1500 RPM. The data of this study is to provide the basic performance data of refrigeration system of refrigeration truck.

Acknowledgements

This work was supported by “Human Resources Program in Energy Technology” of the Korea Institute of Energy Technology Evaluation and Planning (KETEP), granted financial resource from the Ministry of Trade, Industry & Energy, Republic of Korea (No. 20194030202410).

References

[1] Changqing, T., Yunfei, L., Xianting, Li., 2006. “A mathematical model of variable displacement swash plate compressor for automotive air conditioning system,” International Journal of Refriger

ation, Vol. 29, p. 270-280.
[2] Brown, J Steven., Yana-Motta, Samuel F., Domanski, Piotr A., 2002. "Comparative analysis of a n automotive air conditioning system operating with CO_2 and R134a," International of Refrigerat ion Vol. 25, Issue 1, p. 19-32.
[3] Sanchez, D., Torrella, E., Cabello, R., Liopis, R., 2010. "Influence of the Superheat Associated t o a Semihermetic Compressor of a Transcritical CO_2 Refrigeration Plant," Applied Thermal Engi neering, Vol. 30, Issue 4, p. 302-309.
[4] Wang C, C., 2001. "A Comparative Study of Compact Enhanced Fin-and-Tube Heat Exchangers," Heat and Mass Transfer, Vol. 44, p. 3565-3573.
[5] Blasius, H, Z., 1913. "Das Ahnlichkeitsgesetz bei Reibungsvorgangen in Flussigkeiten," Forschg. Arb. Ing. Wes., No.131, Berlin.
[6] Traviss D, P., Rohsenow W, M., Baron A, B., 1972. "Force convection condensation inside tube : a heat transfer equation for condenser design," ASHRAE Transactions, Vol. 79, p. 157-165.
[7] Friedel, L., 1979. "Improved friction pressure drop correlation for horizontal and vertical two-ph ase pipe flow," European two-phase flow group meeting, p. E2.
[8] Dittus F, W., Boelter L, M, K., 1930. "Heat Transfer in Automobile Radiators of the Tubular T ype," Publications in Engineering, University of California, Berkeley, Vol. 2, p. 443.
[9] Pierre, B., 1964, "Flow resistance with boiling refrigerants - part1," ASHRAE Journal, p. 58-65.
[10] Gungor, K, E., Winterton R, H, S., 1986. "A general correlation for boiling in tubes and annul i," International Journal of Heat Transfer, Vol. 19 p. 351-358.
[11] Gnielinski, V., 1976. "New Equation for Heat and Mass Transfer in Turbulent Pipe and Channel Flow," Int. J. Chemical Engineering, Vol. 16, p. 359-368.
[12] Churchill, S., 1997. "Friction Factor Equation Spans all Fluid Flow Regimes," Journal of Chemi cal Engineering, Vol. 7, Issue 24, p. 91-92.
[13] Yoon, S, H., Cho, E, S., Kim, M, S., 2004. "Characteristics of Evaporative Heat Transfer and P ressure Drop of Carbon Dioxide and Correlation Development Near the Critical Point," Proceedi ngs of the SAREK, Vol. 16, No. 6, p. 530-534.
[14] Wang C, C., Chi K, Y., Chang C, J., 2000. "Heat transfer and friction characteristics of plain fi n-and-tube heat exchanger, part II: Correlation," Vol. 43, p. 2693-2700.
[15] Hwang, Y, W., Kim, O, J., 2007. "Experimental Study on the CO_2 Flow through Electronic Exp ansion Valves," SAREK, p. 1237-1241.
[16] Choi, J, M., Chung, J, T., Kim, Y, C., 2004. "A generalized correlation for two-phase flow of a lternative refrigerants through short tube orifices," International Journal of Refrigeration, Vol. 27, p. 393-400.
[17] Lee, K, S., Kim, J, S., Yang, D, K., 2008. "Dimensionless correlations of frost properties on a cold cylinder surface," International Journal of Heat and Mass Transfer, Vol. 51, p. 3946-3952.

13th IEA Heat Pump Conference
April 26-29, 2021 Jeju, Korea

Energy Efficiency Research of an Air-source Heat Pump for Floor Heating System in Winter Test

Chenxi Ni[a,*], Haihong Huang[a,*], Lei Yang[b], Tiejun Wang[b]

[a]School of Mechanical Engineering, Hefei University of Technology, No. 193 Tunxi Road, Baohe District, Hefei, 230009, P. R. China
[b]School of Automobile and Transportation Engineering, Hefei University of Technology, No. 193 Tunxi Road, Baohe District, Hefei, 230009, P. R. China

Abstract

An air-source heat pump for floor heating system was developed and tested which produced hot water for heating the floor of residential buildings by heat pump cycle. The field test of the air-source heat pump for the floor heating system has been conducted in winter for 93 days. During the test, the compression ratio (π) was controlled stable based on the exergy performance analysis. The theoretical η_x of the system decreases with the increase of the compression ratio (π). The values of π were maintained as small as possible from 2 to 6 approximately in the ideal control method in the winter test. Based on the control strategy, the system was proved to be robust. The energy efficiency ratio (EER) ranged from 2.32 to 4.71 while the heat capacity ranged from 3.8 to 10 kW. Especially, the performances of the system in the warmest and coldest days were compared. The results indicate good environmental adaptability of the heat pump system.

Keywords: heat pump; floor heating system; field test

1. Introduction

Building energy consumption has become an important aspect that cannot be ignored. Some studies have shown that energy consumption can be saved by 20% to 30% via optimizing system operation and efficient energy management without changing the building structure and internal equipment [1]. Heating ventilation and air conditioning (HVAC) system is the main energy consumption system in residential buildings, which generally accounts for 30%~50% of the total energy consumption [2]. At present, heat pumps are widely used for domestic hot water (DHW) preparation and space heating (SH), which can offer the possibility to substitute conventional heating systems (direct electric, oil boiler, gas boiler, etc.) and reduce the primary energy consumption [3]. Especially, air-source heat pumps (ASHP) are widely used in residential heating and cooling systems due to the low installation costs and high efficiency [4]. In this paper, an air-source heat pump system used for floor heating was proposed and tested. The operation performance was evaluated.

2. System description

A schematic diagram of the proposed air-source heat pump system is shown in Fig. 1. The system consists of an inverter compressor, an electronic expansion valve, a fin-tube heat exchanger in the airside, and a plate heat exchanger in the waterside. When the heating model is operated, hot water is produced through the plate heat exchanger by the heat pump cycle.

The adaptive defrosting strategy is applied in the system for improving the adaptation to environmental variations [5]. The whole defrosting process is conducted in time and barely does not affect the indoor temperature. The operation test was conducted and the main working conditions are shown in Table.1.

* Chenxi Ni. Tel.: +8617730224199
*E-mail address:*1025079429@qq.com.
* Haihong Huang. Tel.: +8613955138301.
E-mail address: allenhuanghaihong@163.com.

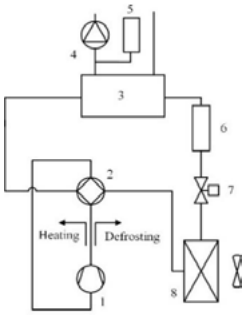


Fig. 1. The air-source heat pump for floor heating system (1.Compressor 2. Four-way reversing valve 3. Plate heat exchanger 4. Circulating water pump 5. Expansion tank 6. Reservoir 7. Expansion valve 8. Fin-tube heat exchanger)

Table 1 Test condition of the air-source heat pump for floor heating system

Nominal Condition	Outdoor dry/wet bulb temperature (T_{od}/T_{ow}:)	Water flow rate(Q)	Outlet water temperature (T_o)	Refrigerating/ Heating capacity(C_R/C_H)	Inlet power(P_{in})	EER
Refrigerating	35/- ºC	1.2 m^3/h	7 ºC	2 kW	2.77 kW	3.08
Heating	7/6 ºC	1.2 m^3/h	45 ºC	9.02 kW	2.87 kW	3.14
			35 ºC	9.56 kW	2.38 kW	4.02

3. Application test in winter

The air-source heat pump system is used on the third floor of a 6-storey unit building in Chuzhou, Anhui Province, China，in which the building area is about 120 m^2. The whole heating load in the winter season is calculated to 2.19KW. In Fig. 2, residential structure and geothermal hot water circuit design can be seen that four separated hot water circuits are respectively installed in the master bedroom A, second bedroom B, master bedroom C and study room D. Besides, the temperatures of the water inlet and outlet were tested outside to control the condensing temperature for the stable air temperature in the room, and the evaporating temperature varied with ambient temperature by the fin-tube evaporator in Fig. 2.

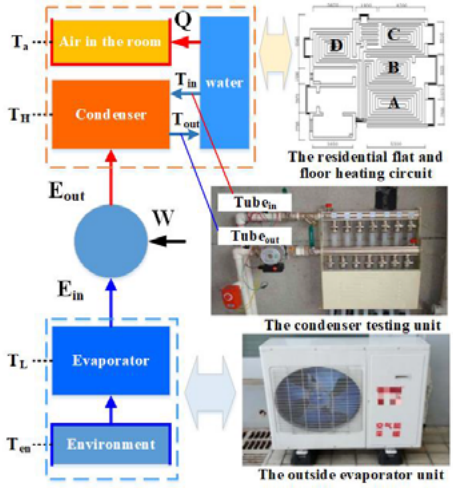


Fig. 2. The diagrammatic sketch of the principle of the air-source heat pump for floor heating system

The Energy efficiency ratio (*EER*) of the heat pump unit is the long-established evaluation parameter that is the ratio of heating energy and energy consumption of the system. Energy consumption (W) is the inlet

electric energy, and heating energy (Q) is the energy from the environment (E_{in}) plus electric energy (W) shown in Fig. 2. W is measured by the power meter every one minute.

3.1. Exergy efficiency

For the vapor compression system, the external power is supplied by the compressor for the major components: evaporator, condenser, and expansion valve. Heat transfer between the chiller and the environment shown as Qcond in Fig. 3 takes place at a finite temperature difference, which is a major source of energy losses for the cycle. Irreversibility causes system performance to degrade. The irreversibility in the cycle is supposed to be evaluated considering individual thermodynamic processes that composed the cycle. To show the individual process energy balances, exergy calculations provide increased and deeper insight into the process for improvements. Exergy analysis of the heat pump system for heating floor is performed by analyzing the components of the system separately. Identifying the main sites of exergy destruction shows the direction for potential improvements. The goal of exergy analysis for the system is to find the minimum power required for a certain desired result. The expressions for the exergy efficiency and exergy loss for the individual processes that make up the cycle as well as the energy efficiency ratio (EER) and second law efficiency for the entire cycle are analyzed.

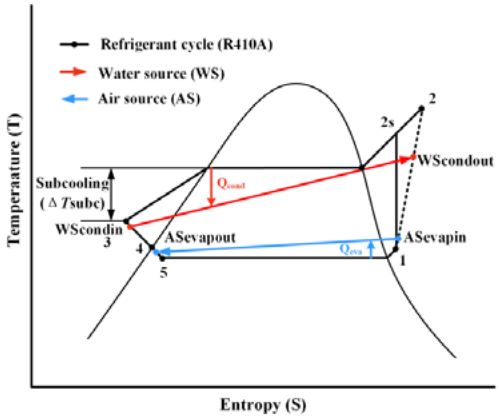


Fig. 3. T–s diagram of the refrigerant cycle and heat sources (water and air sources).

T–S diagram of the system is shown in Fig. 2. In the diagram, process 1-2s is isentropic compression in the compressor. The real compression process is the state 1-2. The other states viz. 2-3, 3-5, and 5-1 show condensation, throttling in the expansion valve, and evaporation in the evaporator respectively. The special lines in red and blue of the refrigerant (R410A) states in Fig. 2 indicate the heat exchange processes of air source and water source.

The mathematical formulation for exergy analysis in different components can be arranged in the following way:

Specific exergy in any state is:

$$\psi = (h - h_d) - T_d(s - s_d) \tag{1}$$

where h is the specific enthalpy, s is the specific entropy, and T_d, h_d and s_d are the temperature, the enthalpy, and the entropy at the dead state.

For evaporator, the heat addition in the evaporator is:

$$Q_{evap} = \dot{m}(h_1 - h_5) \tag{2}$$

The exergy destruction of the evaporator is:

$$I_{evap} = \dot{m}(\psi_5 - \psi_1) + Q(1 - \frac{T_d}{T_{ev}}) \\ = \dot{m}(h_5 - h_1) - T(s_5 - s_1) + Q(1 - \frac{T_d}{T_{ev}}) \quad (3)$$

For the compressor, the compressor work is:

$$W_{com} = \dot{m}(h_2 - h_1) \quad (4)$$

For non-isentropic compression, the electrical power is:

$$W_{el} = \frac{W_{com}}{\eta_{mech}\eta_{el}} \quad (5)$$

where the mechanical efficiency (η_{mech}) and the electrical efficiency (η_{el}) of the motor are 90% respectively.

The exergy efficiency (η_x) is:

$$\eta_x = \frac{\psi_1 - \psi_5}{W_{el}} \quad (6)$$

The energy efficiency ratio (*EER*) is:

$$EER = \frac{h_1 - h_5}{W_{el}} \quad (7)$$

To improve the *EER* of the heat pump, the refrigerant cycle should be controlled for enlarging (h_1-h_4) based on equation (7) and reducing (h_2-h_1) based on equations (4) and (5). It could be concluded that h_1 is positively correlated with *EER*. Based on equations (1), (5), and (6), the η_x could be improved by controlled for the proper h_5 which is mainly controlled by point 3 in the cycle under varied ambient conditions. To improve the *EER* of the heat pump, the refrigerant cycle should be controlled for enlarging (h_1-h_4) based on equation (7) and reducing (h_2-h_1) based on equations (4) and (5). It could be concluded that h_1 is positively correlated with *EER*. Based on equations (1), (5), and (6), the η_x could be improved by controlled for the proper h_5 which is mainly controlled by point 3 in the cycle under varied ambient conditions. In conclusion, points 1 and 3 should be controlled for closing the states of inlet air (point ASevapin in Fig. 3) and inlet water (point Wcond in Fig. 3) to decline the temperature difference between the heat sinks and the heat sources. Based on the researches for the best performance according to the energy and exergy efficiency of the system, exergy efficiency can be improved by controlling sub-cooling temperature to 5 °C. It can be done for reducing the pressure rises in the compressor and hence reduce the irreversibility in the compressor because it is found that most of the irreversibility occurs in the compressor parts. The temperature difference of the evaporating and condensing temperature should be reduced because exergy loss increases as the temperature of the evaporator decrease. For a fixed indoor temperature heated by the condenser, the condensing temperature varies with the inlet water source temperature. The components that contribute most to the heat pump exergy efficiency improvement with the sub-cooling state are the expansion valve and the condenser. To decline irreversibility which can lead to the reducing exergy destruction ratio (*EDR*) and the increasing exergy efficiency of the heat pump system, the sub-cooling temperature should be maintained close to 5 °C, also the compression ratio (π) is kept stable. The inlet water temperature for the test in winter varied from 2 to 12 °C, and the inlet air temperature varied from -10 to 12 °C. Therefore, π of the compressor unit should be maintained from 2 to 6 and the actual π in the practical test is controlled from the range of 2.67 to 5.73 by the expansion valve and the variable frequency compressor in the test.

3.2. Operation test

The approach of the air-source heat pump for the floor heating system has been implemented in TRNSYS software for accurately modeling the dynamic simulation of the system. The simulating data for 93 days in winter were performed in Fig. 5 (a) to verify the theory of the ideal control method. The field test of the air-

source heat pump for the floor heating system has been conducted comparing with the simulating data in winter for the 93 days. Based on the fixed compression ratio (π) controlled by the system, the tested heating capacity (*HC*(Test)) and energy efficiency ratio (*EER*(Test)) of the heat pump system, which nearly are the same as those of simulation (*HC*(Sim) and *EER*(Sim) in Fig. 5 (a)), showed opposite variation trends. The tested heating capacity of the system ranged from 3.8 kW to 10 kW, while *EER* ranged from 2.32 to 4.71. It means that the required heating capacity varied with the change of environmental temperature, and the relatively stable temperature field can be obtained due to the fixed π during the heating period.

As shown in Fig. 5 (b), the average measured temperatures at different height of 0.1m, 1m, 1.5m, and 2m were 20.5ºC, 19.5ºC, 19ºC, and 18.4ºC in the heating periods, during which the outdoor temperatures were ranging from -10ºC to 14ºC with the average temperature of 3.7ºC. Therefore, people could feel comfortable owing to the relatively stable temperature field in the house.

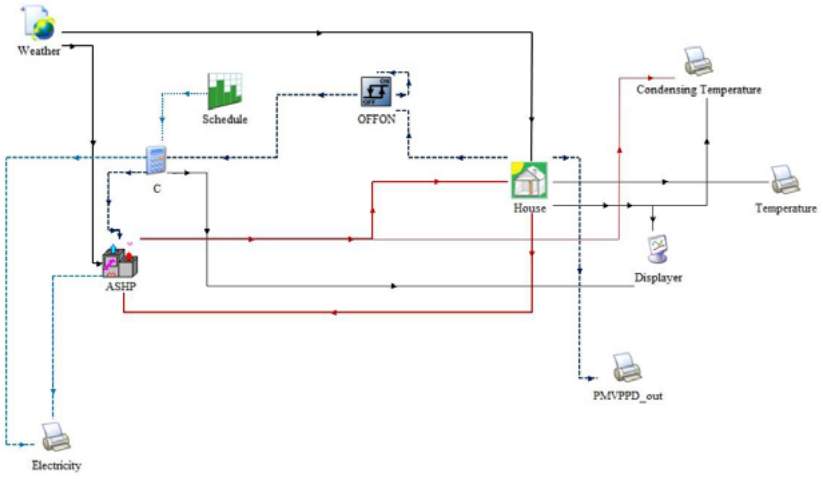
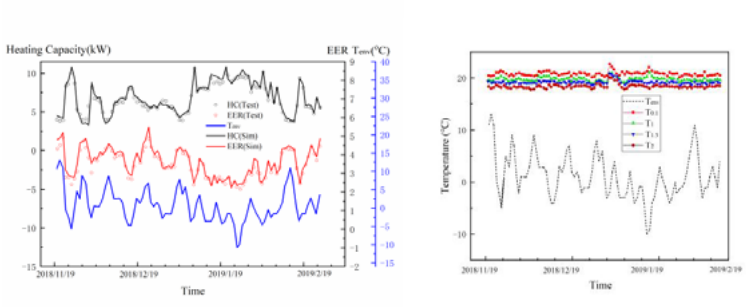


Fig. 4. The diagrammatic sketch of air source heat pump for floor heating system in TRNSYS software



(a) (b)

Fig. 5. The performance of the air-source heat pump in winter (a. Tested temperatures b. EER and *Q* in winter)

The operation performances of the heat pump system in the coldest and warmest days were listed in Table.2 based on the tested data. The results show that: 1) In the whole period, there was a great difference between the outdoor temperatures on the coldest and warmest days. The indoor temperature keeps relatively stable at about 19 ºC which indicates good environmental adaptability of the heat pump system. 2) The heating capacity and *EER* on the coldest day are relatively stable, while the fluctuation is relatively larger on the warmest day. The average *EER* in the warmest day is much higher than that of the coldest day by 159%. 3) The difference between suction pressure and exhaust pressure in the coldest day and the warmest day is small and within a reasonable range based on the required stable indoor temperature.

Table 2 The operation data of the heating system on the typical days during the heating period

Typical weather day	Environmental temperature(T_{env})	Heating capacity(Q_h)	EER	Suction/Exhaust pressure(P_s/P_e)	Condensing/Evaporating temperature(T_c/T_e)
The coldest day(2019/1/23)	-4.3~-10.0ºC	8.6~9.61 kW	2.01~2.54	0.44/2.52MPa	48.3/-16.3 ºC
The hottest day(2018/11/21)	8~16 ºC	2.1~6.03 kW	3.62~5.33	0.79/2.11 MPa	37.9/-0.3 ºC

4. Conclusion

The air-source heat pump system for floor heating was presented. Based on the theoretical analysis of the exergy efficiency (η_{ex}), the related simulation and operation tests were conducted and its performance was analyzed. Some conclusions are shown as follows.

(1) The theoretical η_x of the system decreases with the increase of the compression ratio (π). According to the actual demand, the sub-cooling temperature should be maintained close to 5 ºC, also the compression ratio (π) should be kept stable theoretically. The values of π were maintained as small as possible from 2 to 6 approximately in the ideal control method in the winter test.

(2) The average measured temperatures in different heights show a relatively stable and uniform indoor temperature field during the heating period in the winter test. Under the different outdoor temperatures, the heating capacity of the presented heat pump varied from 3.8 to 10 kW with the *EER* changed from 2.32 to 4.71. The required heating capacities in the coldest and warmest days can be both satisfied owing to the controlled compression ratio (π), which shows the good environmental adaptability of the system.

(3) The actual *EER* is not only correlated with η_{ex} but also the coefficient of performance and rate of the heating of evaporator, condenser, and water source. There is a clear positive correlation among them, and thus η_{ex} could be the only objective function theoretically. The real gap between *EER* and η_{ex} is the ignored error in measurement and the product of the coefficient of performance and rate of the heating source which could be researched further.

Acknowledgments

The work of this paper is financially supported by China YangziGroup Chuzhou Yangzi Air Conditioner Co., LTD and Independent Innovation Specialized Fund Project of Anhui Province (2012XKJH0003).

References

[1] Guan X, Xu Z, Jia Q. Energy-efficient buildings facilitated by micro grid. *IEEE Transactions on Smart Grid*, 2010; **1(3)**: 243-252.
[2] Pérez-Lombard L, Ortiz J, Pout C. A review on buildings energy consumption information. *Energy and Buildings*, 2008; **40(3)**: 394-398.
[3] Chua K J, Chou S K, Yang W M. Advances in heat pump systems: a review. *Appl Energy* 2010; **87**: 3611–3624.
[4] Heo J, Jeong M W, Baek C, Kim Y. Comparison of the heating performance of air-source heat pumps using various types of refrigerant injection. *Int J Refrig*. 2011; **34**: 444–453.
[5] Ni C , Wang T , Jiang B , et al. Experimental investigation of the Time-Temperature difference (t-dT) defrosting control method in frost-free household refrigerators. *Science and Technology for the Built Environment*, **2019(6)**:1-16.

13th IEA Heat Pump Conference
April 26-29, 2021 Jeju, Korea

High-resolution surface plasmon resonance imaging of an evaporating droplet on the surface

Chan Ho Jeong[a], Hyung Joo Lee[a], and Seong Hyuk Lee[a,*]

[a]School of Mechanical Engineering, Chung-Ang University, 221 Heukduk-dong, Dongjak-gu, Seoul 156756, South Korea

Abstract

The present study aims to investigate the characteristics of evaporating thin film (ETF) in the interfacial region during evaporation. High-resolution imaging technology was used for visualization of a sessile droplet based on the surface plasmon resonance phenomena. In particular, the influence of surface wettability on the depinning behavior and the evaporation flux near the edge of a sessile droplet was examined. To resolve the singularity problem occurring at the edge of a droplet, the current study suggests a single-valued boundary limit which can be imposed at the edge, based on the experimental data. From the result, it is found that the estimated ETF distribution shows a similar order of magnitude to the profiles predicted by the Maxwell equation. There is also little influence of droplet volume on the ETF thickness and width, indicating that interfacial phenomena in the contact line region are affected mainly by wettability, not by droplet volume.

Keywords: Evaporating thin film (ETF); Surface plasmon resonance (SPR) imaging; depinning behavior;contact line region

1. Introduction

Droplet evaporation is regarded as one of commonly occurring processes in the surrounding nature and an important physical phenomenon that controls heat and mass transfer through a phase change. It can also be applied to various industrial fields such as spray cooling, direct injection engines, and heat exchangers [1]. As a matter of fact, a lot of studies have reported the dynamic behavior of droplet evaporation, related to heat transfer enhancement [2]. Using the theoretical equation based on Fick's law, the infinite flux was shown at the edge of a droplet showing singularity [3]. This singularity wouldn't be real because finite but maximum evaporation takes place in the contact line region. Cachile et al. [4] obtained the local flux distribution explicitly for the droplet with very high wettability, and Hu and Larson [3] estimated the local evaporation flux which rapidly increased at the edge of the droplet. Xie at al. [5] tried to resolve this singularity by using the molecular dynamics simulations on hydrophilic and hydrophobic surfaces, and they showed there is finite evaporation flux in the contact line. Physically, the contact line region has three regions such as adsorbed film, evaporating thin film (ETF), and bulk meniscus regions [6]. The ETF represents a liquid thin film evaporating between adsorbed film and bulk meniscus. Due to the sub-micron scale, it is very difficult to directly visualize the ETF region. Instead, most of the studies on the ETF have been carried out by theoretical and numerical manners [7].

Hence, the near-field visualization methods should be adopted for showing the ETF and examining its characteristics. As one of earlier efforts, we used the confocal microscopy for visualization of the ETF [8], successively showing micro-scale thin film emanating from the bulk droplet. The present study used the surface plasmon resonance (SPR) imaging to capture the sub-micron scale ETF because this method is capable of being of very high vertical resolution with a few tens nanometer. Indeed, we have successfully visualized the sub-micron frost layer between the frozen droplets and conducted quantitative measure of frozen layer thickness by using the surface plasmon resonance imaging microscope (SPRIM) [9]. Based on the previous study, the present study aims to visualize the ETF region of the sessile droplet on the surface and to estimate

* Corresponding author. Tel.: +82 2 820 5254; fax: +82 2 820 5254
E-mail address: shlee89@cau.ac.kr

the thin film thickness by using the SPR imaging. In particular, we suggested the new evaporation flux model with the measured length of the ETF region by estimating a finite boundary limit. In the following sections, the present study describes the details of experiments and the theoretical modeling, and also presents the experimental results. In the end, the results are summarized in the conclusion.

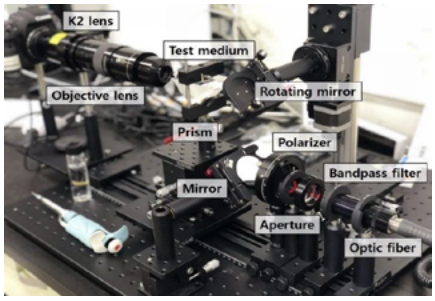


Fig. 1. Experimental setup (SPRI system).

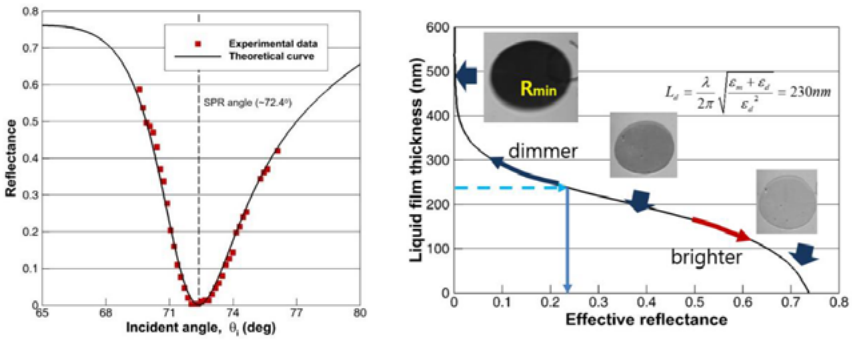


Fig. 2. a) reflectance variation with incident angle, b) liquid film thickness with respect to effective reflectance.

2. Experiment and modeling

To determine the flux profile along the liquid-vapor interface of the sessile droplet, most of the previous works have adopted the diffusion-limited model, assuming that the transfer rate depends on the diffusion of saturated vapor during evaporation [10]. Moreover, the evaporation flux along the liquid-vapor interface of the droplet is eventually determined by the overall shape of droplet [11]. So, we used the analogy between vapor concentration and electrostatic distribution, the evaporation flux can be expressed by [12]. We can estimate the evaporation flux along the interface by

$$J(r) = \frac{D(1-RH)c_{sat}}{R_i}\left[\frac{1}{2}\sin\theta + \sqrt{2}(\cosh\alpha + \cos\theta)^{3/2} \times \int_0^\infty \frac{\cosh\theta\tau}{\cosh\pi\tau}\tanh[(\pi-\theta)\tau]P_{-1/2+i\tau}(\cosh\alpha)\tau\, d\tau\right] \quad (1)$$

where J is evaporation flux, D is diffusivity of 26.1 mm^2/s [13], c_{sat} is saturated vapor concentration of 2.32 $\times$ 10^{-8} g/mm^3 [3], RH is relative humidity, R_i is droplet contact diameter, r is the radial position, θ is contact angle of the sessile droplet, and P is the representation of Legendre function.

As shown in Fig. 1, the present study uses the surface plasmon resonance imaging (SPRi) system because this method has very high vertical resolution, making it possible to visualize the evaporating thin films in the contact line region. The long-distance K2 lens with 9.6× magnification was attached to CMOS camera (CANON, EOS 7D), with a pixel resolution of 680 nm. The CMOS camera captured the single-wavelength light reflected from the prism at one frame per second. The right-angle prism consists of BK7 glass (Edmund Optics), and its corresponding refractive index is 1.516 (at λ = 632 nm). The coverslip with a 50 nm gold thin layer (Platypus Tech., Au.0500.CSS) on the 2.5 nm titanium adhesion layer was attached to the prism by using an index

matching liquid (Norland, IML150) with the same refractive index of the BK7 glass. The light irradiated from the halogen lamp (Dolan-Jenner) is converted into a single wavelength light beam through a bandpass filter (632 ± 5 nm, Edmund Optics). A collimation lens array is installed to convert the diverging light beam into a parallel light beam.

As shown in Fig. 2(a), the measure reflectance shows very good agreement with the theoretical solutions from Maxwell equation and thin film optics theory. The surface plasmon is representing the energy carrier being charged, and the evanescent wave propagates along the interface between two dissimilar layers. For water phase, the incident angle of 72.4 degree is called SPR angle at which the minimum reflectance occurs, indicating that mostly absorbed energy is converted into evanescent waves. At this condition, SPRi system enables to capture the images with different contrast levels between zero and 256 based on 8 bits. Figure 2(b) shows the change of liquid film thickness estimated theoretically with the reflectance. This figure indicates that the liquid film thickness can be directly matched with the corresponding reflectance. It means once the reflectance is measured, the liquid film thickness can be estimated through the relationship shown in Fig. 2(b). As the captured image gets dimmer, the liquid film gets thicker, vice versa. Interestingly, we can get 500 nm thickness with very high vertical resolution, being of approximately 1.8 nm based on our facility. We used Kretschmann's configuration for SPR imaging with the white light illuminated from an LED light source which was passed through the optic arrays. A single wavelength light (632 ± 5 nm) and p-polarized ray was used for visualization. The ray is guided onto the prism by using the rotatable mirror with a specific incident angle (72.4°). The gold coated thin film is attached to the prism.

Once the liquid film thickness is measured with SPRi system, the evaporation flux at the droplet edge can be modeled as illustrated in Fig. 3. Geometrically, the inflection point on the droplet interface can be estimated by using the measured film thickness. Hence, we finally determine the width of evaporating thin film as shown in Fig. 3. Here, we suggest a new parameter called the averaged evaporation flux (AEF), as shown in Eq. (2). Using this equation, we can get the averaged value over the contact line region by mass conservation, showing the finite (not infinite value) evaporation flux limit can be obtained.

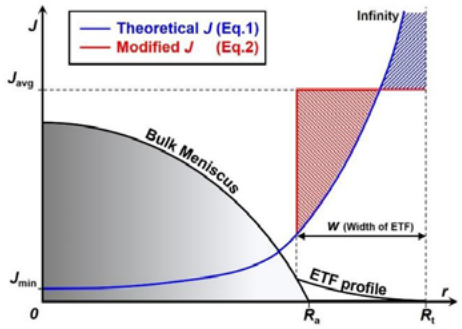


Fig. 3. Concept of the averaged evaporation flux modelling based on the measured width.

$$J_{avg} = \left(\int_{R_t - w}^{R_t} J \, dr \right) / w \tag{2}$$

where R_t is total contact radius of droplet considering ETF region, and R_a is apparent contact radius of spherical cap, w means the width of ETF, and J_{avg} denotes the AEF in the ETF which is treated as the boundary limit mathematically. For closing this equation, it is necessary to get the experimental measures of width and thickness of ETF. Those measures were obtained by the SPRIM system used in the present study.

3. Results and discussion

Figure 4 shows the measured ETF profiles. The measurements were made five times for getting the averaged values with relative errors. A convex shape was observed consistently at different droplet volumes. Indeed, the shape of ETF has been explained by the force balance along the triple lines according to Young-Laplace model and kinetic theory. As shown in Fig. 4, we can see that a slight change in liquid film thickness is observed, indicating that the shape of ETF does not change with time by interacting with the bulk droplet region.

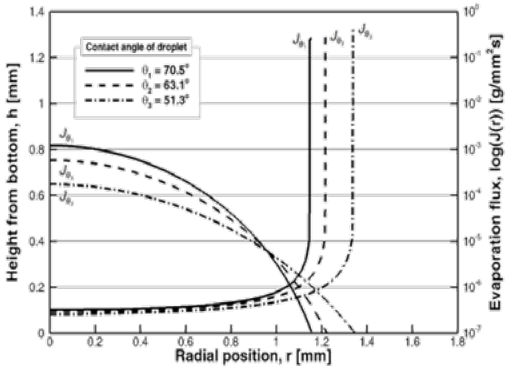
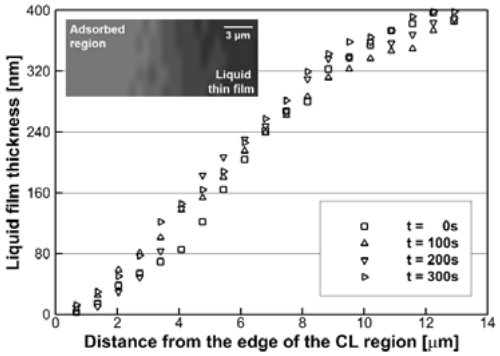


Fig. 4. The measured liquid film thickness with respect to time.

Based on this result, we can estimate the averaged evaporation flux as shown in Fig. 5. For validation, the evaporation flux at the apex of droplet showed being of the same value compared with the data from Hu and Larson [3]. The maximum evaporation flux was estimated to be 0.2547 g/mm^2·s, 0.2486 g/mm^2·s, and 0.2486 g/mm^2·s for the droplet volume of 2 μl, 4 μl, and 6 μl, respectively. It shows that the averaged evaporation flux predicted in the ETF becomes getting higher for smaller drops. That is, the smaller the droplet volume, the greater the absolute amount of evaporation flux in the ETF region. It means the portion of evaporation flux in the ETF region cannot be ignored for smaller droplet.

Fig. 5. Real-scale droplet meniscus and scaled evaporation flux considering ETF region with respect to drop volume at the initial stage.



4. Conclusions

This study reported that there exists the evaporating thin film clearly in the contact line region by the SPR imaging method. We also suggested the new approach to estimate the averaged evaporation flux. The following conclusions were drawn.

1) We observed the existence of an ETF and measured its profile in the contact line region. It indicates that the current SPR system can successfully measure the submicron liquid film thickness.
2) The present study investigated the effect of droplet volume on the ETF profile, but it was negligible. Although the droplet volume increased, the profile of ETF remains consistent shape in the contact line region because it was affected by the interfacial forces with the bulk region. Also, we estimated the averaged evaporation flux in the contact line by using the measured data. It could be used to overcome the singularity problem of the diffusion-limited model. It was shown that the contribution of ETF to evaporation was dominant as the droplet volume decreased. It is also noted that the smaller droplet was

significantly affected by the ETF which cause the higher mass transfer.

Acknowledgements

This work was supported by a National Research Foundation of Korea (NRF) grant funded by the Korea government (MSIT) (No. 2017R1A2B2006943). Also, this research was partially supported by the development of human resources for design specialists in applications of functional materials (Brain Korea (BK) 21).

References

[1] D. Mampallil and H. B. Eral, A review on suppression and utilization of the coffee-ring effect, Advances in Colloid and Interface Science, 252 (2018) 38-54.
[2] R. D. Deegan, O. Bakajin, T. F. Dupont, G. Huber, S. R. Nagel, and T. A. Witten, Contact line deposits in an evaporating drop, Physical Review E, 62 (2000) 756-65.
[3] H. Hu and R. G. Larson, Evaporation of a sessile droplet on a substrate, Journal of Physical Chemistry B, 106 (6) (2002) 1334-1344.
[4] M. Cachile, O. Benichou, C. Poulard, and A. M. Cazabat, Evaporating droplets, Langmuir, 18 (2002) 8070-8078.
[5] C. Xie, G. Liu, and M. Wang, Evaporation flux distribution of drops on a hydrophilic or hydrophobic flat surface by molecular simulations, Langmuir, 32 (2016) 8255-8264.
[6] V. P. Carey, Liquid Vapor Phase Change Phenomena. Taylor & Francis, (2007).
[7] M. Potash Jr and P. Wayner Jr, Evaporation from a two-dimensional extended meniscus, International Journal of Heat and Mass Transfer, 15 (10) (1972) 1851-1863.
[8] D. H. Shin, J. S. Allen, C. K. Choi, and S. H. Lee, Visualization of an evaporating thin layer during the evaporation of a nanofluid droplet, Langmuir, 31 (4) (2015) 1237-1241.
[9] C. H. Jeong, D. H. Shin, V. Konduru, J. S. Allen, C. K. Choi, and S. H. Lee, Quantitative measurements of nanoscale thin frost layers using surface plasmon resonance imaging, International Journal of Heat and Mass Transfer, 124 (2018) 83-89.
[10] Y. O. Popov, Evaporative deposition patterns: spatial dimensions of the deposit, Physical Review E, 71 (2005) 036313.
[11] J. M. Stauber, S.K. Wilson, and B.R. Duffy, Evaporation of droplets on strongly hydrophobic substrates, Langmuir, 31 (2015) 3653-3660.
[12] N. N. Lebedev, Special functions and their application, Prentice-Hall: Englewood Cliffs, New Jersey, 1965.
[13] R. C. Weast and M. J. Astle, CRC handbook of Chemistry and Physics, 62nd ed.; CRC Press: Boca Raton, FL, 1981-1982.

13th IEA Heat Pump Conference
April 26-29, 2021 Jeju, Korea

Annual performance assessment of heat pump water heaters applying various refrigerants

Takaoki Suzuki[a], Zheng Ge[a], Muhamad Yulianto[b] Yoichi Miyaoka[c], Seiichi Yamaguchi[c], Kiyoshi Saito[c,*]

[a]Dept. of Applied Mechanics, Waseda University, Shinjuku-ku, Tokyo, 169-8555, Japan
[b]Waseda Research Institute for Science and Engineering, Waseda University, Shinjuku-ku, Tokyo, 169-8555, Japan
[c]Interdisciplinary institute for thermal energy conversion engineering and mathematics, Waseda University, Shinjuku-ku, Tokyo, 169-8555, Japan

Abstract

In order to help prevent global warming, greenhouse gas emissions must be reduced. Equivalent CO_2 emissions can be reduced by using heat pump water heaters instead of conventional gas boilers or electric-resistance water heaters. We focused on the differences in annual performance of heat pump water heaters using different refrigerants, including those that contained CO_2 and R32. When assessing different refrigerants, the effect of different climates in relation to the specific application area was taken into consideration. To this end, water supply and ambient temperatures were varied according to the particular climatic conditions to calculate annual performance. As a result, the effect of different refrigerants and climates on the annual performance of heat pump water heaters was revealed.

Keywords: Annual performance; Climate; Thermodynamic property; Refrigerants; Simulation;

Nomenclature

COP_h	Coefficient of Performance (heating)
c_p	Isobaric mass heat capacity kJ/kgK
E	Power consumption kWh
G	Mass flow rate kg/s
h	Specific enthalpy kJ/kg
K	Constant
P	Pressure MPa
$\dot{Q}$	Heating capacity kW
Q	Amount of heat transferred to water kWh
s	Specific entropy kJ/kgK
T	Temperature ° C
$\dot{W}$	Power input kW
ΔT	Temperature difference ° C
η	Efficiency

Subscripts

ad	Adiabatic
amb	Ambient
annual	Annual
ave	Average
con	Condenser
comp	Compressor
eva	Evaporator
i	i th hourly data in time series
pinch	Pinch
R	Refrigerant
series	time series
SH	Super heat
vap	Saturated vapor
W	Water
winlet	Water inlet

1

* Corresponding author. Tel.: +81-3-5286-3259; fax: +81-3-5286-3259.
E-mail address: saito@waseda.jp

1. Introduction

To build a sustainable society and address recent environmental problems such as increasing energy demand and global warming, it is necessary to save energy. Widely applied heat pump technologies, which include highly energy-saving refrigeration, air-conditioning, and heating technologies, can contribute to energy conservation in society and alleviate environmental problems. The vapor compression heat pumps occupy an important position in energy conservation due to their energy saving performance and high versatility.

However, many refrigerants used in vapor compression heat pumps have adverse effects on the environment. In order to protect the environment, international efforts are being made to switch from conventional refrigerants with high environmental impact to refrigerants with low global warming potential (GWP). Various types of low GWP refrigerants, including mixed refrigerants, have been proposed with varying thermodynamic properties, transport properties, and environmental performance. However, the performance of a heat pump system optimized for newly developed refrigerants has not been clearly understood; thus, it is necessary to select a suitable refrigerant and to evaluate and compare the performance of each new refrigerant.

To evaluate and compare the performance of different heat pump systems, systems designed for different types of refrigerants must be considered. However, the typical drop-in test that is currently performed on new refrigerants is not sufficient to clarify the performance of the system. During drop-in tests, it is common that component specifications like dimensions of heat exchangers are not suitable for the target refrigerants. To deal with this problem, a heat pump performance simulation model, where the heat transfer performance of heat exchanger is considered by relying on the pinch temperature approach, is developed.

This study aims to establish a simulation-based performance evaluation method for vapor compression heat pumps. This method evaluates the energy consumption of heat pumps and compares their performance in various operating conditions and regions. The proposed evaluation method is developed with the aim of easily selecting suitable refrigerants and establishing system configuration guidelines.

2. Research target

This report covers heat pump water heaters using various refrigerants. A simulator was developed to evaluate the annual performance of heat pump water heaters. This simulator was built to compare the performance of different refrigerants, even when there was no actual machine designed for new refrigerants.

2.1. Heat pump water heaters

Compared to conventional electric-and gas water heaters, heat pump water heaters can release several times more heat than the input energy. An example of a widely used residential heat pump water heaters in Japan is the EcoCute. The EcoCute uses a supercritical CO_2cycle, enabling a highly efficient hot water supply under specific operating conditions. The CO_2 refrigerant has the advantages of a low GWP and high safety. However, there are disadvantages such as special measures being required for the refrigerant circuit due to high operating pressure and decreasing performance under conditions of higher inlet water temperature.

The performance of a heat pump varies in relation to the climatic conditions such as the ambient air temperature and the inlet water temperature. Accordingly, the beneficial effect of implementing a heat pump water heater can be expected to vary depending on the region. In addition, as suggested by the example of the EcoCute, the most suitable refrigerant for residential heat pump water heaters may vary depending on the region and application. Therefore, it is critical to assess the performance of residential heat pump water heaters using low GWP refrigerants in different climatic regions.

2.2. Low GWP refrigerants

In order to mitigate global warming, the production and use of refrigerants with high GWPs are limited, and the use of low GWP refrigerants is promoted. Currently, hydrofluorocarbons (HFCs) are popular refrigerants; however, they often have a high GWP. Various alternative refrigerants have been proposed to satisfy conflicting requirements, and evaluated for different application cases by simulations and experiments. [1] [2] [3]

However, the heat pump system tested with an alternative refrigerant was designed for operating with the existing refrigerant. Therefore, when a new refrigerant is proposed, the system is not operated in a state that is suitable for the specific refrigerant. Namely, performance assessments performed when other refrigerants are applied to a system designed for a different working fluid are not providing sufficient information for guiding the choice on which new refrigerant to use.

3. Method

The performance of the heat pump water heater was evaluated for various refrigerants. Hot water supply demand and climate vary depending on the region and season. To evaluate the energy saving and environmental performance of heat pump water heaters, it was necessary to evaluate the performance throughout the year.

Therefore, an annual performance simulator for heat pump water heaters was constructed, which used the annual climatic conditions and hot water demand in each region as input data. Then, the annual performance could be calculated by simply specifying the refrigerant. This feature made it easy to evaluate a variety of new refrigerants that did not have actual equipment and could serve as guidelines for refrigerant selection.

3.1. Simulator overview

In the annual performance simulator, the specifications of the water heater, the climatic conditions, the demand for hot water supply, etc. are provides as the input and the annual operating state fluctuations and the annual performance are the output. Heat pump water heaters are expected to operate throughout the year. Thus, in order to judge the applicability of low GWP refrigerants to water heaters, it is important to evaluate the performance of water heaters throughout the year. Therefore, the annual power consumption of the water heater and the annual average COP, along with the time series data of the operating state, such as compressor discharge temperature, are given as the output. Fig. 1 shows the input/output relationship of the annual performance simulator. The subscript i is used to represent certain hourly data in the time series. The annual performance simulator includes a simulator that analyzes the thermodynamic cycle.

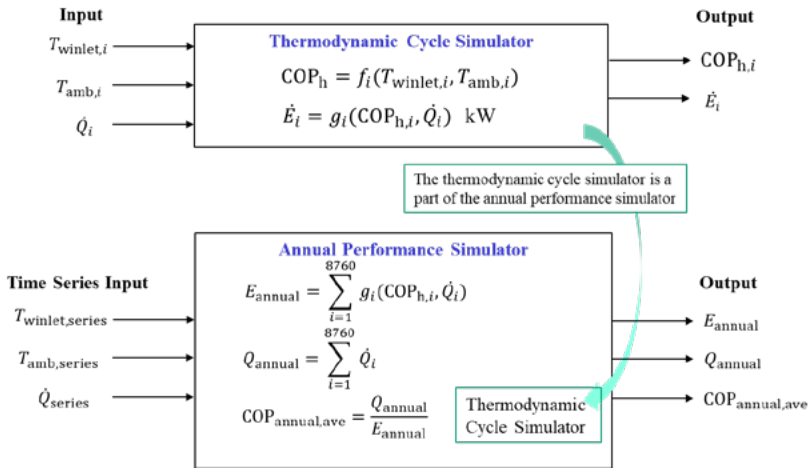


Fig. 1. Annual performance simulator overview

3.2. Thermodynamic Cycle Simulator

In order to design heat pump equipment suitable for the region and application, it is necessary to compare candidate refrigerants and select an appropriate refrigerant. To evaluate the annual performance in each region when a new refrigerant is applied to the heat pump water heater, commonly, a considerable amount of time is spent setting the design parameters for various new refrigerants and performing simulations and experiments.

Therefore, in this report, a mathematical model that emphasizes the calculation speed and ease of setting the design parameters of the equipment was developed for thermodynamic cycle analysis and incorporated into the annual performance simulator. This section describes this mathematical model.

Fig. 2 shows the flow diagram of the heat pump water heater and the corresponding Ph diagram of the heat pump cycle. The numbering of each point indicated by the arrows in Fig. 2 is used throughout this paper.

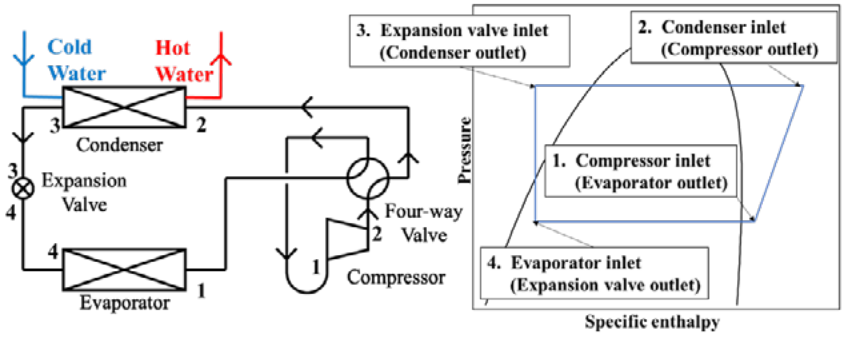


Fig. 2. Heat pump cycle flow diagram and Ph diagram

The heating coefficient of performance (COP) of the heat pump cycle is defined by the following formula.

$$\mathbf{COP_h} = \frac{\dot{\boldsymbol{Q}}_{\mathbf{con}}}{\dot{\boldsymbol{W}}_{\mathbf{comp}}} \tag{1}$$

To clarify the mass and energy balance of each component of a heat pump, the balance equations for each component are described below. The mass balance equation and energy balance equation in the compressor are

$$G_{\mathrm{R1}} = G_{\mathrm{R2}} \tag{2}$$

$$\dot{\boldsymbol{W}}_{\mathbf{comp}} = \boldsymbol{G}_{\mathbf{R2}}\boldsymbol{h}_{\mathbf{R2}} - \boldsymbol{G}_{\mathbf{R1}}\boldsymbol{h}_{\mathbf{R1}} \tag{3}$$

The compressor suction temperature and compressor suction enthalpy are given by

$$\boldsymbol{T}_{\mathbf{R1}} = \boldsymbol{T}_{\mathbf{Rvap,eva}} + \boldsymbol{\Delta T}_{\mathbf{SH}} \tag{4}$$

$$\boldsymbol{h}_{\mathbf{R1}} = \boldsymbol{h}_{\mathbf{R1}}(\boldsymbol{T}_{\mathbf{R1}}, \boldsymbol{P}_{\mathbf{eva}}) \tag{5}$$

For zeotropic refrigerants, $T_{\mathrm{Rvap,eva}}$ is given by the evaporator dew point. The compressor adiabatic efficiency is

$$\boldsymbol{\eta}_{\mathbf{comp}} = \frac{\boldsymbol{h}_{\mathbf{R1}} - \boldsymbol{h}_{\mathbf{R2,ad}}}{\boldsymbol{h}_{\mathbf{R1}} - \boldsymbol{h}_{\mathbf{R2}}} \tag{6}$$

Using equation (6), the compressor discharge enthalpy can be calculated by

$$h_{\mathrm{R2}} = h_{\mathrm{R1}} + \frac{h_{\mathrm{R2,ad}} - h_{\mathrm{R1}}}{\eta_{\mathrm{comp}}} \tag{7}$$

η_{comp} is a constant and is given to the simulator as an input. The value of η_{comp} is assumed from typical value of actual compressor adiabatic efficiency. Here, in order to calculate $h_{\mathrm{R2,ad}}$ by the equation of state, the compressor discharge entropy of the reversible process is used.

$$\boldsymbol{s}_{\mathbf{R2,ad}} = \boldsymbol{s}_{\mathbf{R1}} \tag{8}$$

$$\boldsymbol{h}_{\mathbf{R2,ad}} = \boldsymbol{h}_{\mathbf{R2,ad}}(\boldsymbol{P}_{\mathbf{con}}, \boldsymbol{s}_{\mathbf{R2,ad}}) \tag{9}$$

The same formula is used for the condenser in the subcritical cycle and the gas cooler in the transcritical cycle. As heat pump water heaters are the target of this study, a mathematical model of a counter-flow heat exchanger is constructed. The mass balance and energy balance equations of the refrigerant in the condenser

(or, gas cooler) are

$$\boldsymbol{G_{R2} = G_{R3}} \tag{10}$$

$$\boldsymbol{\dot{Q}_{con} = G_{R2}h_{R2} - G_{R3}h_{R3}} \tag{11}$$

For the water,

$$\boldsymbol{G_{W2} = G_{W3}} \tag{12}$$

$$\boldsymbol{\dot{Q}_{con} = G_{W2}c_{pW}T_{W2} - G_{W3}c_{pW}T_{W3}} \tag{13}$$

The condenser (or, gas cooler) refrigerant outlet temperature is

$$\boldsymbol{T_{R3} = T_{W3} + \Delta T_3} \tag{14}$$

The mass balance and energy balance equations for the expansion valve are as follows.

$$\boldsymbol{G_{R3} = G_{R4}} \tag{15}$$

$$\boldsymbol{G_{R3}h_{R3} = G_{R4}h_{R4}} \tag{16}$$

The mass balance and energy balance equations in the evaporator are

$$\boldsymbol{G_{R4} = G_{R1}} \tag{17}$$

$$\boldsymbol{\dot{Q}_{eva} = G_{R1}h_{R1} - G_{R4}h_{R4}} \tag{18}$$

The refrigerant dew point temperature in the evaporator is

$$\boldsymbol{T_{Rvap,eva} = T_{amb} - \Delta T_{eva}} \tag{19}$$

ΔT_{eva} is given to the simulator as a positive constant. This is used to calculate the compressor suction temperature in equation (4). The refrigerant evaporation pressure is calculated from the equation of state as follows.

$$\boldsymbol{P_{eva} = P_{eva}(T_{Rvap,eva})} \tag{20}$$

We focus on the pinch temperature in the condenser in order to build a model that determines the state of the refrigerant in the condenser from the temperature conditions of the hot water inlet and outlet. There is at least one pinch temperature in the condenser, usually two. It is impossible from the viewpoint of heat transfer to have a pinch temperature below 0 ° C. Therefore, a constraint condition that takes a positive finite value as the pinch temperature is set. K_1 and K_2 are positive constants. The inequality constraints on the condenser refrigerant outlet pinch temperature ΔT_3 and the condenser internal pinch temperature $\Delta T_{\mathrm{con,pinch}}$ (see Fig. 3) are represented by

$$\Delta T_3 \geq K_1 \tag{21}$$

$$\boldsymbol{\Delta T_{con,pinch} \geq K_2} \tag{22}$$

Here, $\Delta T_{\mathrm{con,pinch}}$ is the pinch temperature in the condenser that can exist other than ΔT_3, and is defined as follows using the temperatures $T_{\mathrm{R,con}}$ and $T_{\mathrm{W,con}}$ of the refrigerant and hot water, respectively, that exchange heat with each other. [4]

$$\boldsymbol{\Delta T_{con,pinch} = T_{R,con,pinch} - T_{W,con,pinch}} \tag{23}$$

The simulator input values of K_1, K_2 and ΔT_{eva} are assumed from typical value of domestic heat pump hot water heaters. The heat exchange and pinch temperature in the condenser will be explained using Fig. 3 with

the heat exchange on the horizontal axis and the temperature on the vertical axis.

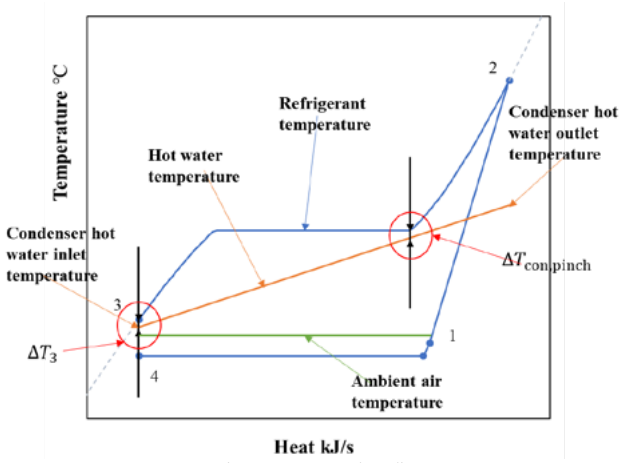


Fig. 3. Temperature heat diagram

From the mathematical model of the condenser model described above, the absolute value of exchanged heat of both fluids in the condenser is equal. Therefore, the horizontal width of the thermal composite line of water and the thermal composite line of refrigerant are equal, and the start and end points are at the same position on the horizontal axis. As the flow rates of both fluids are directly related to the heat capacity, the curves (including straight lines) representing the heat exchange process of both fluids can be scaled with respect to the horizontal axis, depending on the mass flow rate of each fluid. The relationship between heat exchange and temperature is expressed in Fig. 3.

$$\boldsymbol{T_{\mathrm{R,con,pinch}} = T_{\mathrm{R,con,pinch}}\left(P_{\mathrm{con,pinch}}, h_{\mathrm{con,pinch}}\right)} \tag{24}$$

$$\boldsymbol{T_{\mathrm{W,con}} = \frac{T_{\mathrm{W2}} - T_{\mathrm{W3}}}{G_{\mathrm{W2}} h_{\mathrm{W2}} - G_{\mathrm{W3}} h_{\mathrm{W3}}} \left(G_{\mathrm{W}} h_{\mathrm{W}} - G_{\mathrm{R}} h_{\mathrm{R}}\right) + T_{\mathrm{W3}}} \tag{25}$$

Under these conditions, the COP maximization problem, with the condenser pressure as the optimization parameter, is solved. A cycle is constructed using the solution of this maximization problem as the condenser pressure P_{con}.

4. Discussion

4.1. Fundamental characteristics of heat pump water heater

Several refrigerants are evaluated using the thermodynamic simulator in order to clarify similar and significantly different characteristics. As R410A refrigerant, which is currently widely used in heat pumps, has a high GWP of 1924, alternative low GWP refrigerants have been proposed. R32 and R446A are compared as substitute refrigerants for R410A. In addition, R134a and propane are also included in the comparison to understand the characteristics that differ significantly depending on the refrigerant.

Japan's average climatic conditions are adopted as reference conditions, and the COP, compressor discharge temperature, and refrigerant mass flow of each refrigerant compared. The standard conditions are an inlet water temperature of 16.5 ° C, outlet water temperature of 65 ° C, and an ambient air temperature of 16 °C. Fig. 4 shows the results of the comparison.

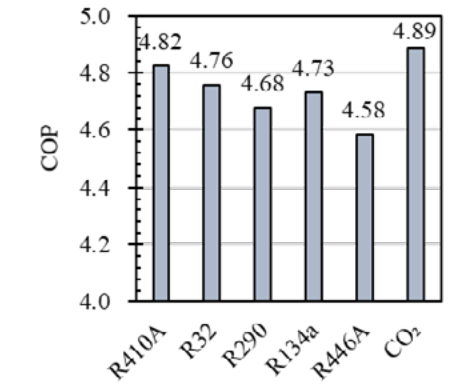
The refrigerant with the highest COP (4.89) is CO_2, and the refrigerant with the lowest COP (4.58) is R446A. CO_2 refrigerant is a transcritical cycle under these operating conditions. R410A has the highest COP of the subcritical cycle refrigerants. The compressor discharge temperature is the highest for R32, at 113.2 °C. R290 is the refrigerant with the lowest discharge temperature of 82.6 °C. R134a also has a low temperature of 83.7 °C. The mass flow rate of R134a is the largest, but R410A and CO_2 feature similar values. Conversely, R290 has the smallest mass flow rate, and the value of R32 is close to it.

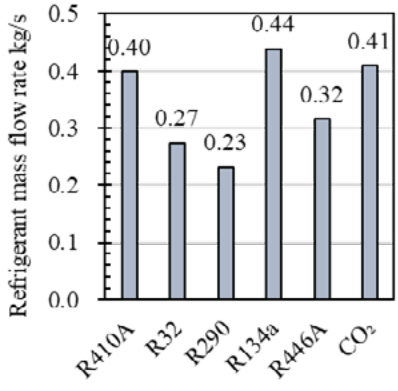
A parameter study is conducted for COP, compressor discharge temperature, and refrigerant flow temperature. Fig. 5 shows the results for the feed water temperature, Fig. 6 shows the results for the condenser outlet water temperature, and Fig. 7 shows the results for the ambient air temperature.

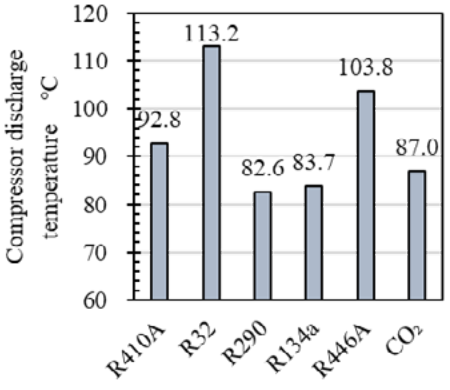
First, we focus on COP. With one exception, all refrigerants show similar trends for water supply, hot water, and ambient air temperature. Generally, the COP decreases with respect to the feed water temperature and condenser outlet water temperature and rises with respect to the ambient air temperature. In the region where the feed water temperature is low, the COP of the CO_2 refrigerant is higher than that of other refrigerants. However, when the feed water temperature exceeds 20 °C, the COP of other refrigerants may increase. The COP of the CO_2 refrigerant is the lowest at around 30 °C.

Next, we focus on the compressor discharge temperature. Although the discharge temperature values differ between refrigerants, there is no significant difference in the tendency for parameter changes except for CO_2. The compressor discharge temperature with CO_2 refrigerant rises more than other refrigerants when the feed water temperature is high and the ambient air temperature is low.

Finally, the refrigerant mass flow rate is described. Here, the CO_2 refrigerant also shows a different tendency. Compared with other refrigerants, the increase in mass flow rate is remarkable when the feed water temperature and the ambient air temperature become high.







Calculation condition (Standard condition, defined in text)	
Ambient air temperature	16 °C
Water inlet temperature	16.5 °C
Water outlet temperature	65 °C
ΔT_3	3°C
$\Delta T_{con,pinch}$	3°C

Fig. 4. Refrigerant comparison under standard conditions

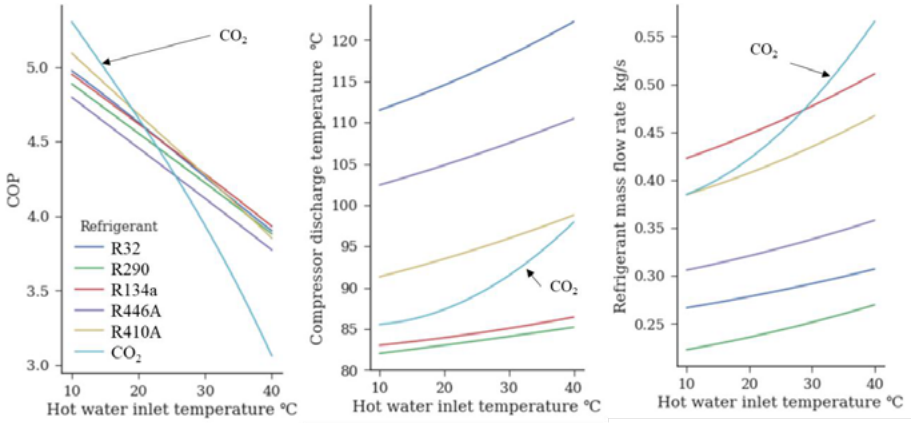


Fig. 5. Parametric study on influence of hot water inlet temperature on COP, Compressor discharge temperature, and Refrigerant mass flow rate

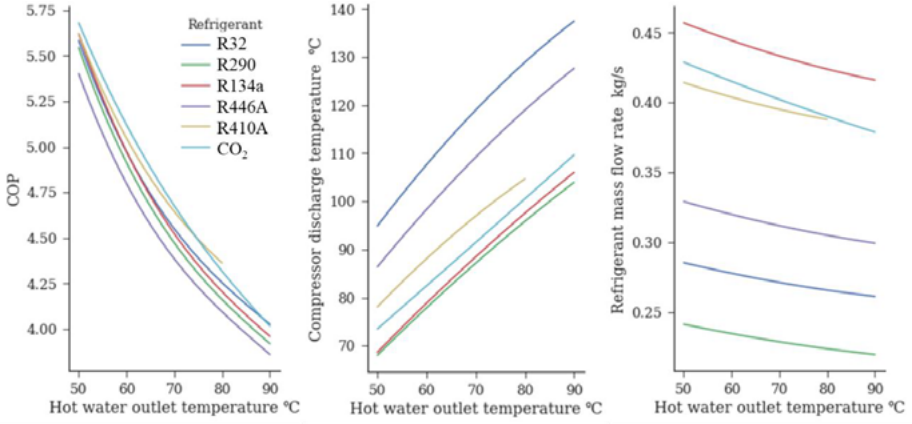


Fig. 6. Parametric study on influence of hot water outlet temperature on COP, Compressor discharge temperature, and Refrigerant mass flow rate

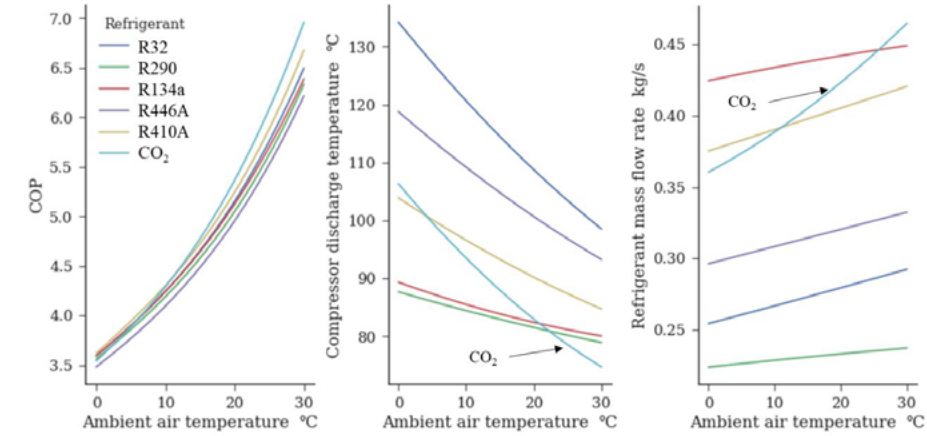


Fig. 7. Parametric study on influence of ambient air temperature on COP, Compressor discharge temperature, and Refrigerant mass flow rate

4.2. Annual performance evaluation

A simulation is conducted to investigate the effect of differences in area, climate, and refrigerant on the annual performance of heat pump water heaters. The condenser hot water outlet temperature is fixed at 65 ° C, and the ambient air temperature, water inlet temperature, and hot water demand were input in time series. In this report, the supply water temperature is given by a direct relation to the ambient temperature, and the same daily pattern is used for the hot water demand in each region. The hot water demand pattern is based on table B.6 of JIS C9220:2011 Annex B. [5]

The target refrigerants are CO_2 and R32, which have been used as refrigerants for domestic hot water heaters in Japan. Sapporo, Tokyo, and Naha are selected as three representative cities for Japan's high, middle, and low latitudes. These three cities are indicated in Fig. 8. The climatic data on the ambient air temperature are from 2018 [6]. Fig. 9 shows the ambient temperature fluctuations in these three cities. For ease of understanding, the trend of annual fluctuation in Fig. 9 uses monthly averaged data, while input data to the simulator refer to the hourly data.

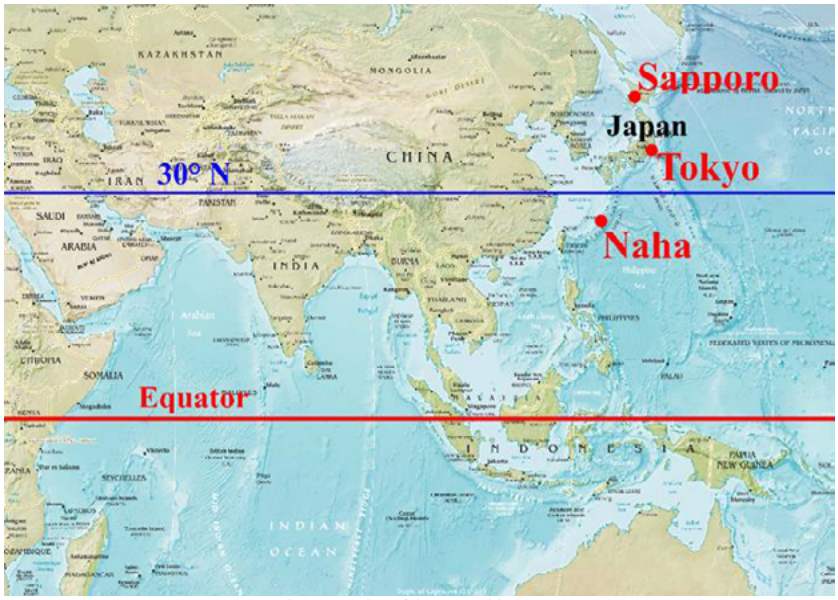


Fig. 8. Location of the target cities **[7]**

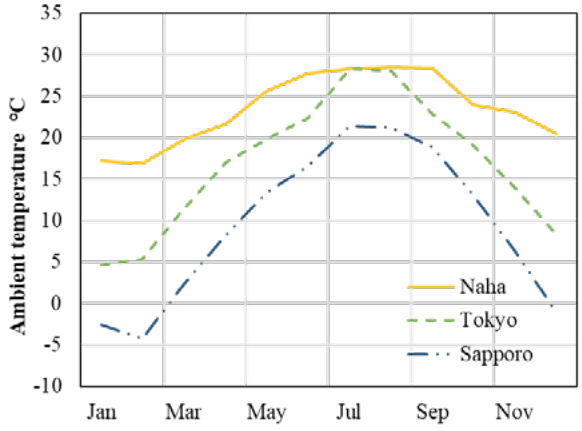


Fig. 9. Annual ambient temperature at Sapporo, Tokyo, and Naha

Fig. 10 shows the evaluation results of the annual power consumption and annual average COP of the water heater. Generally, the annual power consumption decreases and the annual average COP tends to increase as the latitude of the region decreases. When the CO_2 refrigerant is used as a reference, the annual power consumption of the R32 refrigerant increased by a maximum of 2.53%, and annual average COP decreased by 2.46%. Focusing on the regional characteristics, the annual power consumption in Sapporo was approximately twice that of Naha. This is not only because of the lower heat load due to the higher ambient temperature of Naha, but also because the COP is higher here than in Sapporo almost throughout a year, as described later.

Fig. 11 shows the annual COP change. The graph on the left is for the CO_2 refrigerant, and the right is for the R32 refrigerant. For all refrigerants, it is demonstrated that the COP is higher in summer than in winter. Naha has shown that it can operate at a high COP throughout the year and there is almost no COP difference between the two refrigerants.

To compare the trend of the COP variation for each refrigerant in detail, Fig. 12 shows the COP fluctuation for the first week of 2018 and Fig. 13 shows that of the first week of the second half of same year. Thus, the difference in COP trend for each refrigerant is not significant. According to Fig. 7, regarding the ambient air temperature, the performance difference is considered to increase in the hot season and regions. However, as shown in Fig. 5, CO_2 has a significantly larger COP drop than other refrigerants with respect to the water inlet temperature. Accordingly, the COP of CO_2 refrigerant is slightly higher in any of these three regions during winter, however, the COP of R32 refrigerant come to almost same at Tokyo and Naha in summer, as shown in Fig. 12 and Fig. 13. Therefore, it can be considered that the COP is reversed with other refrigerants in hot seasons and regions.

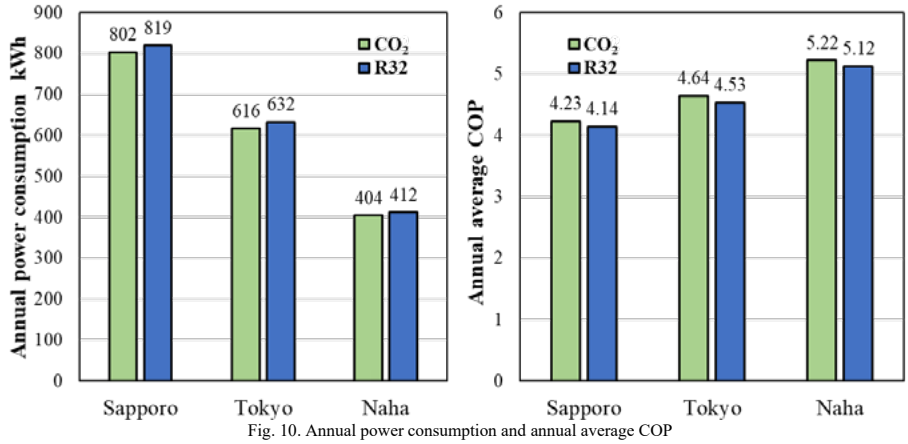


Fig. 10. Annual power consumption and annual average COP

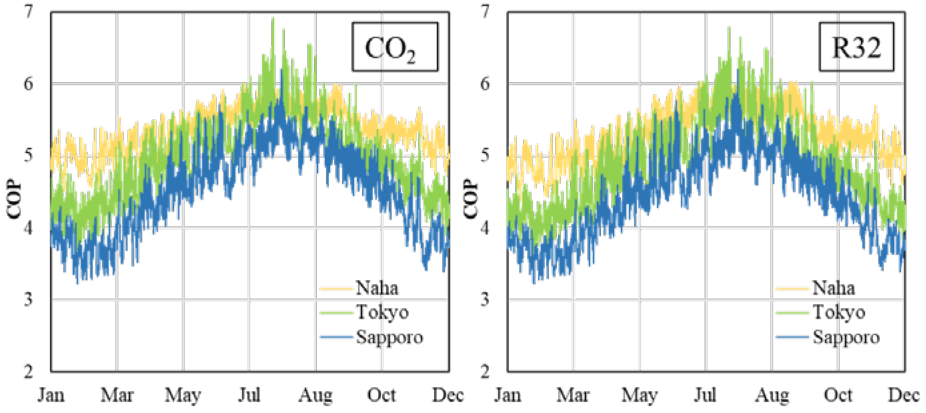


Fig. 11. Annual COP fluctuation (Left: CO_2, Right: R32)

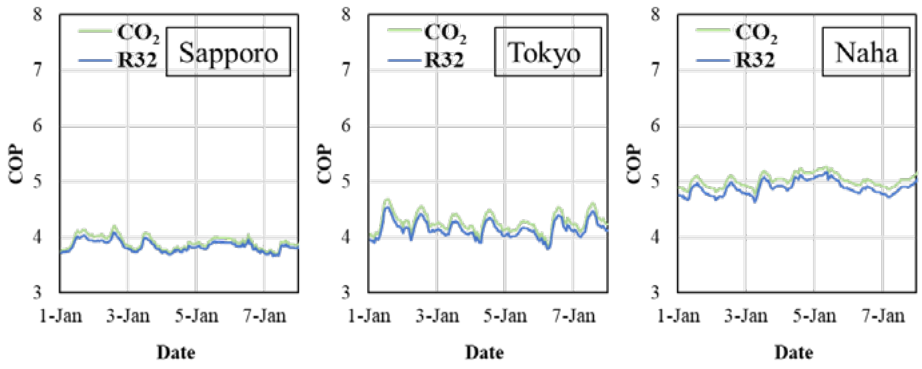


Fig. 12. Weekly COP fluctuation (Winter, Comparison by refrigerant)

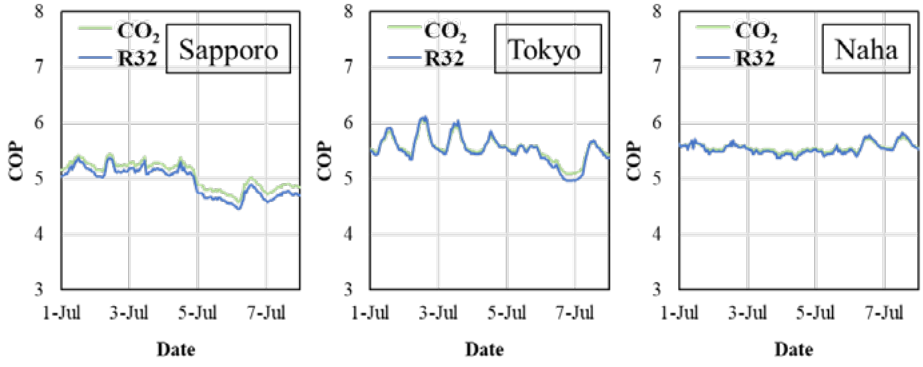


Fig. 13 Weekly COP fluctuation (Summer, Comparison by refrigerant)

5. Outlook for the future

Currently, in practice, a domestic heat pump water heater requires a water tank for the following two reasons. First of all, water usage during a shower is around 10 L/min for 10 to 20 minutes. Thus, the power output required in order to provide instant heating for a shower is about 10 to 20 kW. The higher the power output is, the more expensive the price of a heat pump is. As a result, it is impractical to use high output power heat pumps for domestic water heating. Secondly, due to the daily fluctuations of the electricity pricing in Japan, using electricity at night is cheaper and in order to lower the cost, heat pump systems are designed to operate and store hot water during that period.

This report focuses on the heat pump cycle itself rather than the water tank. However, using a water tank can result in the temperature of water supplied to condenser or gas cooler to be higher than that of the tap water. This is believed to have some influence to the system's performance. Other than that, the time of operation should also be carefully considered since factors like ambient air temperature, water supply temperature and heat loss can be different between day and night, and, thus, affect the system's efficiency. Therefore, in the future, we would like to build a model that considers the hot water storage tank and perform more accurate and versatile annual performance evaluation based on this model.

6. Conclusion

An annual performance simulator was constructed to compare the performance of various refrigerants

and heat pump water heaters in different regions. The actual climate data of different Japanese cities were inputted into the simulator to compare the heater performance in different regions and with different refrigerants.

As a result, it was confirmed that the water heater performance was higher in lower latitude areas. In addition, it was suggested that the lower the latitude, the smaller the fluctuation of the driving condition, and the more stable the operation. The comparison of R32 and CO_2 suggests that the performance of the CO_2 refrigerant is higher in all regions of Japan. However, the results of the basic performance analysis suggest that the performance can be reversed in warmer areas, and in applications where the water supply temperature is high.

Acknowledgements

This study was supported by The Kansai Electric Power Co., Inc., The Federation of Electric Power Companies of Japan, and Heat Pump & Thermal Storage Technology Center of Japan. The authors would like to express their gratitude here.

References

[1] K. Nawaz, B. Shen, A. Elatar, V. Baxter and O. Abdelaziz, "R1234yf and R1234ze(E) as low-GWP refrigerants for residential heat pump water heaters," *International Journal of Refrigeration,* vol. 82, pp. 348-365, 2017.

[2] Z. Li, L. Kun and J. Hanying, "Experimental study of R1234yf as drop-in replacement for R134a in an oil-free refrigeration system," *Applied Thermal Engineering,* vol. 153, pp. 646-654, 2019.

[3] C. Bai, Z. Han, H. Wei, X. Ju, X. Meng and Q. Fu, "Simulation study on performance of a dual-source hybrid heat pump unit," *Energy and Built Environment,* vol. 1, pp. 1-10, 2020.

[4] M. Saikawa, "Development of CO2 Refrigerant Residential Heat Pump Water Heater," Kyushu University, 2017.

[5] Japanese Industrial Standards Committee, *Japanese Industrial Standards JIS C 9220:2011.*

[6] Japan Meteorological Agency, "Past weather data [Translated from Japanese.]," [Online]. Available: https://www.data.jma.go.jp/gmd/risk/obsdl/index.php. [Accessed 1 2019].

[7] Central Intelligence Agency, "The World Factbook," 24 10 2019. [Online]. Available: https://www.cia.gov/library/publications/the-world-factbook/docs/refmaps.html. [Accessed 28 10 2019].

[8] The Japan Refrigeration and Air Conditioning Industry Association, *JRA 4050:2007R.*

[9] H. Tatsumi and K. Matsuda, Pinch Technology [Translated from Japanese.], 2002.

13th IEA Heat Pump Conference
April 26-29, 2021 Jeju, Korea

Control strategy assessment of a small GSHP sourced DH system with end user DHW booster heat pumps

Wim Boydens[a], Sigrid Feyaerts[b], Annelies Vandermeulen[b,c,d] , Lieve Helsen[b,d]

[a]boydens engineering, Kooidam 6, 8200 Bruges, Belgium
[b]KU Leuven, Celestijnenlaan 300, 3001 Leuven, Belgium
[c]VITO, Boeretang 200, 2400 Mol, Belgium
[d]EnergyVille, Thor Park 8320, 3600 Genk, Belgium

Abstract

A small thermal grid for historic Almshouses 'the Schipjes' in Bruges was designed in 2016 and is nearing the final phase of construction while partly in operation. The houses' building envelopes were retrofitted with respect to the monumental character to decrease the heating demand and the required temperature levels.
The houses are connected to a low temperature thermal grid supplied by a hybrid of a ground source heat pump (GSHP), solar thermal panels (ST) and a condensing gas boiler (not installed after predesign simulation).
Domestic hot water (DHW) at higher temperature in the individual houses is provided by booster HP's, while room heating (RH) is provided by floor heating and radiators.

A limitation of thermal power creates a challenge to verify which rule based control (RBC) operates optimal for this case.

The study simulates the project using Modelica. RBC variations are simulated in which temperature levels in the system, anticipation, building integrated or central vessel storage are implemented. For each variation the resulting comfort, the share of renewable energy supply (RES) and the electrical energy use (COP) are quantified. Conclusions are a.o. that building integrated storage is needed for the load management, as well as a heating curve for the further increase of the RES system performance. The individual variations lead to a decrease of discomfort by 17%, an increase of RES by 7.4% and a decrease of electrical energy use of 25% on an annual basis.

Keywords: simulated control impact assessment, thermal grid, ground source HP, fossil free system approach, residential retrofit

1. Introduction

This paper describes a study that optimizes the operation of a residential renovation project that combines a thermal micro grid, a centralized ground source heat pump, centralized thermal solar collectors and booster heat pumps in each of the houses for domestic hot water. The concept decisions, design and sizing phases were supported by dynamic system simulations, aiming at a balanced performance increase by system approach and building retrofit. The overall aim was to realize a future oriented integrated solution towards zero fossil fuel concepts in historical city centres, which could have a large replication factor throughout Europe and beyond. The project is partly in operation, and the handover is approaching, so this study aims to define the Rule-based Control (RBC) to be programmed in order to provide thermal comfort with minimal environmental impact of the system.

2. Context

The Almshouses ‘the Schipjes’ is a social housing neighbourhood in Bruges, Belgium (Fig 1). It was built in the beginning of the 20th century (1907, arch René Cauwe). Today it is the property of Mintus, the social welfare organization of the city of Bruges, and houses 12 small households. In 1999 a limited retrofit was realized, providing a thin insulation layer in the roof, renewing the electrical installation and installing an

individual gas fired stove (with an efficiency of less than 80%) in each house, with integrated heat exchanger to distribute heat to radiators in the kitchen, bedroom and bathroom. The domestic hot water (DHW) was delivered by a direct electrical boiler. The Schipjes has been classified as heritage in 2009, Bruges is a Unesco acknowledged historical city.

Due to non-compliance with contemporary comfort expectations a deeper renovation was planned, thereby thoroughly upgrading the energetic and ecologic aspects of the houses. The research project, funded by VLAIO (Flemish Agency for Innovation and Entrepreneurship) started in 2014, by a consortium of two universities, three companies and two social organisations (Fig 2). Several configurations of thermal supply of the thermal grid and retrofit options for the houses themselves were investigated and compared. After an experience-based long list approach, four system configurations were shortlisted and simulated, and after adding investment and operational cost evaluation the results have been leading to the finally chosen concept (Aertgeerts, Boydens & Helsen, 2016). In the study phase only 11 houses were connected to the thermal grid, during execution one house was added leading to a total of 12.



Fig. 1. Almshouses the Schipjes, birdsview



Fig. 2. Almshouses the Schipjes, the consortium partners of the renovation guidance project on site

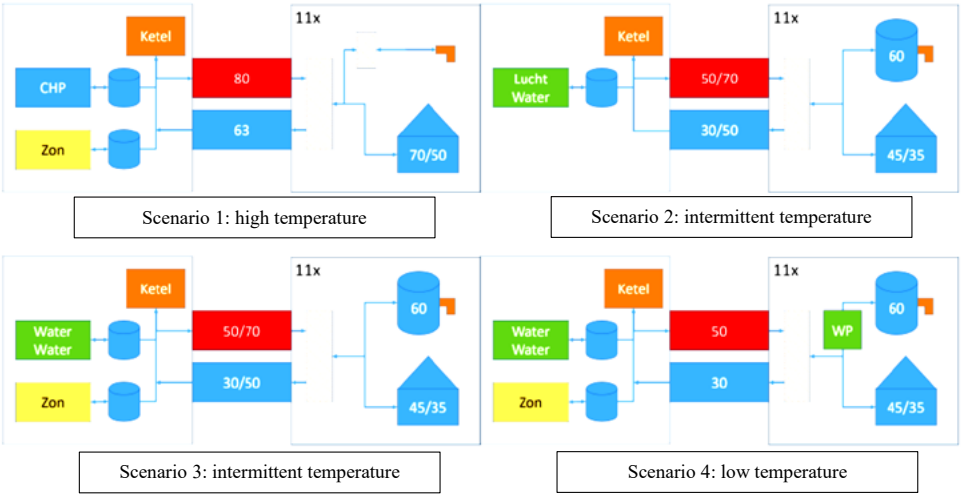


Fig. 3. Schematics of the four shortlisted system configurations

The four scenarios as illustrated in Figure 3 were selected in order:

- to assess the impact of efficiency gains and losses, among them: thermal grid operating temperatures, affecting (1) associated heat losses to the ground, (2) injection potential of the solar thermal system, (3) the COP of the heat pump;
- to compare different heat supply technologies in different configurations and operating modes with regard to their system efficiency (cogeneration (CHP), gas fired condensing boiler (GCB), air to water heat pump (AWHP), ground source heat pump (GSHP), solar thermal (ST), water to water booster heat pump (BHP)).

The gas fired CHP scenario 1 was used as a reference case, since this configuration was considered and observed the most feasible in the market for small scale collective system solutions in Belgium, around 2010-2014, by boydens engineering. Main disadvantages are the dependency on fossil fuels and the local air pollution in the city centre, as well as the maintenance cost and high system temperatures.

Scenario 2 aimed at lowering the investment cost, share of fossil fuels and system temperatures by using the AWHP as dominant supply, and applying intermittent higher system temperatures (if needed through support of a condensing gas boiler) for DHW demand, storing higher temperatures in individual storage tanks in these periods.

Scenario 3 applies the same intermittency, but using the GSHP as main thermal supply. The ST was added to temper ground source depletion, and prevent gas boiler operation for DHW in sunny periods.

Scenario 4 is implementing the same centralized supply as scenario 3 but focusses on a permanent low temperature in the thermal grid of maximum 50°C. The DHW is boosted to the required 60°C in the individual storage tanks, with decentralized BHP's in the houses.

Scenario 4 was chosen as final concept, since multiple criteria, i.e. share of renewables, solar heat supply, total primary energy demand reduction and fossil fuel reduction reached optimal levels in the system simulations, performed by The Thermal Systems Simulation research group of KU Leuven (A. Aertgeers, L. Helsen). These simulations also showed the condensing gas boiler was superfluous in this case (fig 4).

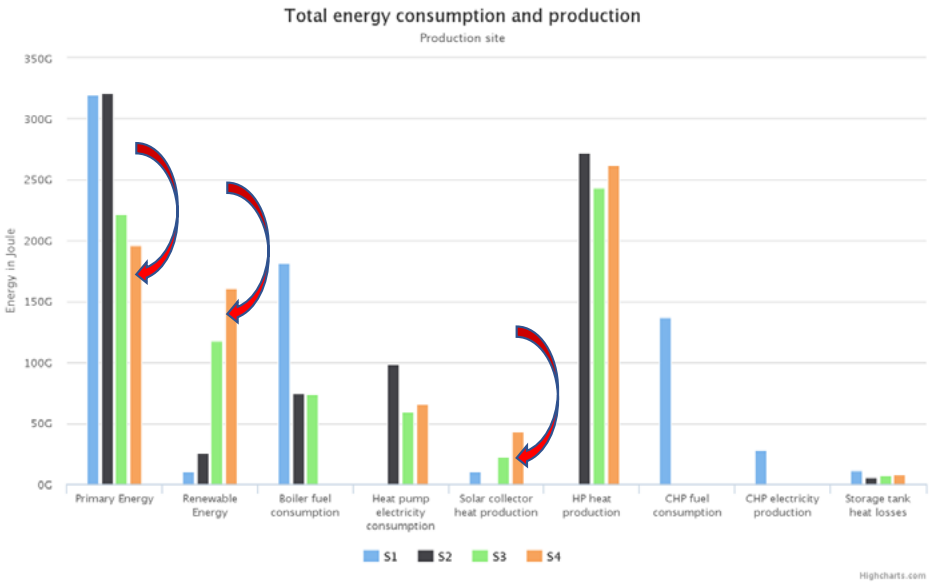


Fig. 4. Results of the first predesign simulation based comparisons, leading to the preferred scenario 4

The renovation started in 2016 and will be finalized in spring 2020. It was realized in phases, and 8 houses are already in operation since September 2019. Illustrations below show: the site plan with the thermal grid and the position of the 8 boreholes, double U, each 125 m deep (Figure 5), the supply cabin in the garden that houses the heat pump, storage tanks and pumps (Figure 6) and the booster heat pump with DHW storage mounted in the individual houses (Figure 7).

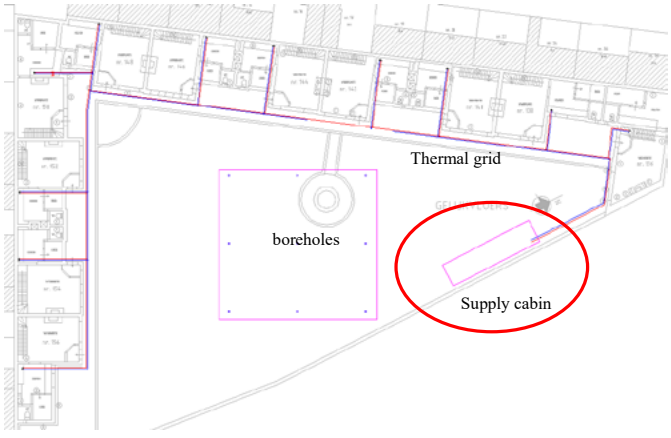


Fig. 5. The site plan with the thermal grid, and the position of the 8 boreholes, double U, each 125 m deep



Fig. 6. The supply cabin in the garden that houses the ground source heat pump, storage tanks and pumps



Fig. 7. The booster heat pump with DHW storage mounted in the individual houses

The design being consolidated and under construction, a performant RBC programming of the system is targeted and therefore this simulation based study was performed.

Furthermore, adding one house to the system in the course of the project, without changing the system sizing, raised the question whether thermal comfort would be endangered, and whether the condensing boiler would be needed anyhow. Or, in case, if a smartly implemented RBC could avoid this move back to fossil technologies.

This synthesizes the main research question: What is the impact of the control on the operation and the sizing of a heat pump based thermal grid, or alternatively stated, can we correct a given undersizing by a smarter control in a real environment?

3. Methodology

The houses and the supply, distribution and emission systems were dynamically modelled and simulated in more detail than in the predesign stage. The RBC as foreseen from designers experience was implemented in the model and the resulting thermal comfort was evaluated, together with other performance indicators, such as: share of renewable energy sources (RES) and primary energy use.

All simulations have been performed in the Modelica simulation environment using Dymola, and component models from the Modelica libraries IDEAS, Buildings and IBPSA. The explicit Euler solver was used instead of the DASSL solver (however a comparison was made in one case). For more detailed information we refer to the master thesis of Sigrid Feyaerts [1].

The hydraulic scheme of the thermal system is shown in fig 8.

Analysis of the results according to the engineered design (reference case) led to expected shortcomings, and to the creation of alternative controls. These alternative control strategies were implemented in the model and the results were compared to the reference design case.

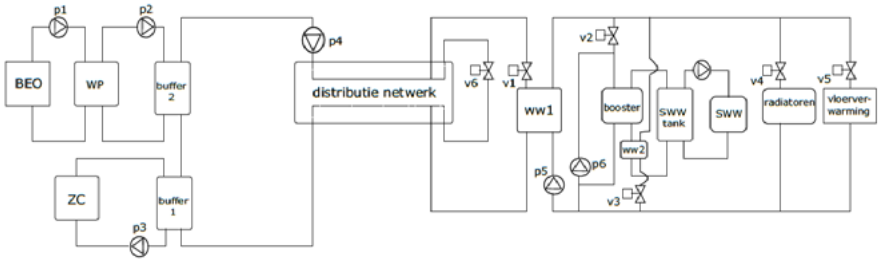


Fig. 8. Hydraulic scheme of the thermal grid, supply systems on the left side, situation in one of the twelve individual houses on the right side. BEO refers to the ground source, WP to the heat pump, ZC to the solar thermal collector, distributie netwerk to the thermal grid, ww to a heat exchanger, SWW to domestic hot water and vloerverwarming to Floor heating

The main assumptions and simplifications in the simulation model are (1) single zone modelling of the houses, (2) fixed ground source temperature of 7°C, with a COP of 3.67 (for the real installed unit) when supplying 50°C at the condenser side, (3) DHW user behaviour according to the StROBe stochastic approach [2] (however the monitored DHW use showed lower loads than the StROBe approach), (4) no internal heat gains taken into account, (5) TMY Uccle (BE) as weather data, as well as a comparison with monitored data (KU Leuven, 2017).

The reference RBC can be summarized as an on/off control of the heat pump activated by the HP buffer temperature (on if lower than 50°C-3°C for 3 min and demand in one of the houses, off if 50°C + 5°C is reached in the buffer for 5 min). ST injects if a 3°C surplus towards the solar buffer tank is noticed for 2 min, off if the ST temperature becomes lower than the buffer temperature). The secondary side of the heat exchanger of the house uses a heating curve for the radiators/floor heating (40°C, -10°C / 20°C, 20°C). Hysteresis is applied for the DHW booster HP (60/45°C) and thermostatic valves are used on the radiators.

The RBC performance for multiple scenarios (using different control strategies) is assessed using the following criteria:

1. Thermal discomfort: Kelvin-hours with temperatures below the setpoint (defined by the StROBe model).
2. Share of RES (renewable energy sources in supply):
   (solar energy supplied by ST + ground source extracted heat) / the total heat supplied
3. Total electricity demand for heating: electricity use for the GSHP and the booster HP's

4. Results and discussion

4.1 Reference RBC

Figure 9 shows how the heat supply and demand are distributed over the system components for the reference RBC. Important to stress are: (1) the centrally supplied heat to the grid (Enet) on a yearly basis , (2) the electricity supplied to the heat pumps (EhpEl, EboosEl), and (3) the dissipated heat loss in the grid (Edis). For this reference case the yearly electricity use by the heat pumps (geothermal and booster) is 154.2 GJ.

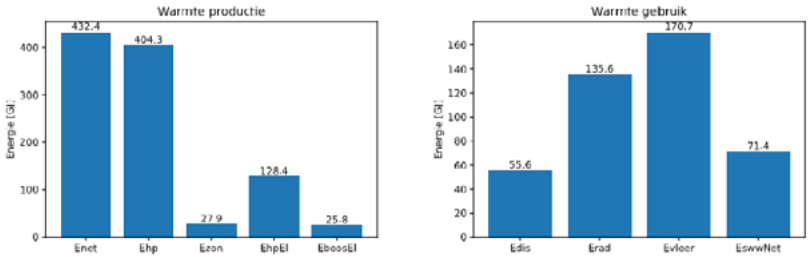


Fig. 9. Heat supply and emission per system element for the reference case

Figure 10 (left) presents the energy sources used for heat generation and (right) the distribution over the different users (grid losses, radiators, floor heating and DHW). The reference RBC results in a RES share of 66.3%, distributed as 60.2% GSHP (Egrond) and 6.1% ST (Ezon).

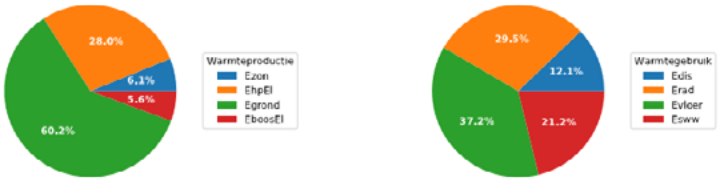


Fig 10: Heat supply and emission share for the reference case

The aggregated thermal discomfort for all houses is 17084 Kh for the full year. This result is not as such directly interpretable. However, according to ISO7730 class A buildings allow maximum 100 Kh/a outside the +/- 1°C bound thereby guaranteeing the PPD is limited to 5% [3]. Therefore, to give insight in the discomfort level, the number of Kelvin-hours that the indoor temperature set point – 1°C is not achieved is assessed, hereby not considering the first two start up hours in the morning, resulting in an average of 83 Kh/a for an individual house. Better understanding of this occurring discomfort is achieved by zooming in on a cold period in January (see Figure 11).

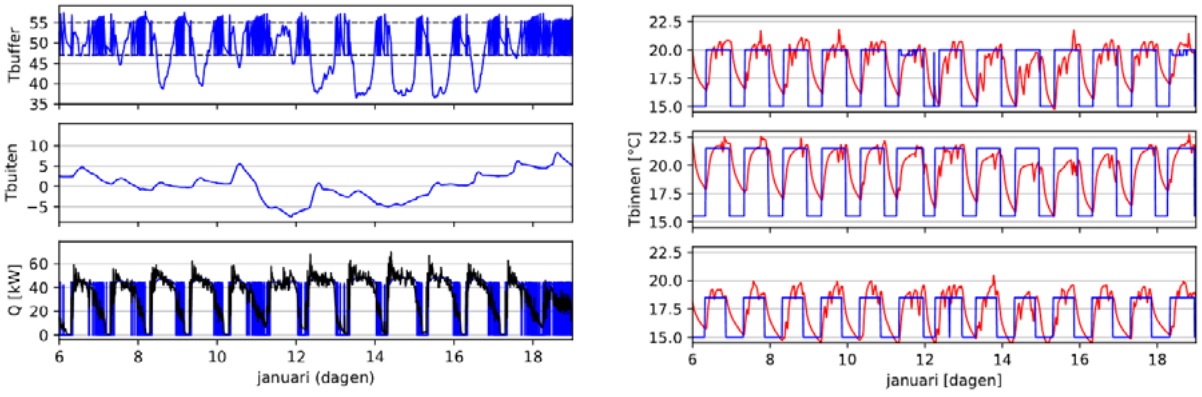


Fig. 11. Total heat (left, demand in black, supply in blue) and comfort (right, for different set points) profiles in a cold winter period for the reference RBC case

It is very clear that the night setback of the RH (room heating) creates a demand profile that varies between the peak demand (around 60 kW) and no demand over 24 hours. As the demand for DHW is prioritized in the reference RBC, and at these times the supply to the radiators and floor heating is temporarily shut off, this can affect severely the discomfort for the room heating in the morning, since the reheating of the local DHW storage takes 62 min on average. Therefore an adapted strategy for DHW reheating is an obvious goal in the advanced RBC. It is clear that simply following the peak demand would require additional thermal supply, and stepping back to adding the condensing gas boiler the most evident measure.

4.2 Alternative RBC - Adapted DHW reheating strategies:

Several variations for the DHW reheat rules have been investigated:

1. More frequent and time limited reheating of the DHW tanks can be achieved by adapting the reheat set point to 50°C instead of 45°C. Of course a higher average DHW temperature during reheat will decrease the booster HP COP. The reheating time is observed to decrease to 43 min on average. However no significant improvement is observed in the aggregated thermal discomfort.
2. Preheating DHW during night time to a higher temperature was also implemented, using a set point of 70°C. The overlap of RH and DHW demand in morning hours was as such reduced, resulting in a decrease of thermal discomfort by 10%. A decrease of the average COP of the booster HP's from 3.8 in the reference case towards 3.4 was noticed, as well as a small decrease of RES share from 66.3% to 65.9%.
3. A strategy with simultaneous RH by the radiators (only FH is off) during DHW reheating results in a lower discomfort (-17%). Especially during the day the combination of the stored heat in the FH, shut off (of FH) during DHW demand, and the available power of the radiators succeeds in maintaining indoor thermal comfort (Fig 12). In the morning hours the night setback control prevents this action.

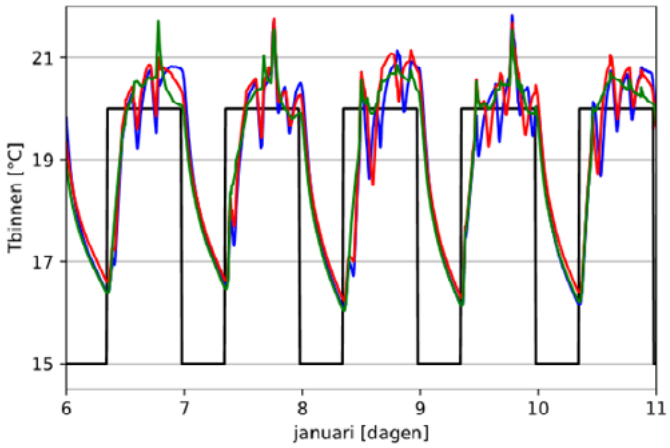


Fig. 12. Effect on indoor temperature by keeping the radiators (green line), or the floor heating (red line) activated during DHW demand (booster HP in operation), the reference RBC result is the blue profile

4.3 Alternative RBC - Anticipation:

Anticipation in cold periods of the year, where logically the limited thermal power results in more frequent discomfort hours, is a next approach. Based on the research of Basciotti and Schmidt [4] some variations have been set up. Anticipating the start-up and peaks in the morning by thermal storage in the central storage tanks at higher temperatures did not give any relevant results, due to the limited storage potential. Night storage in the houses, however, by reducing the night setback for floor heating proved to be far more effective. It decreases the required supply capacity and improves thermal comfort, with an extra electricity supply of only 1.2%. The RES share remains 66% and the total heat demand of the grid rises by only 0.3%. The higher demands during the night are largely compensated by the decrease of start-up energy use (see Figure 13), as

studied by Frederiksen and Werner [5], even in this case where the insulation level of the historic houses is rather limited.

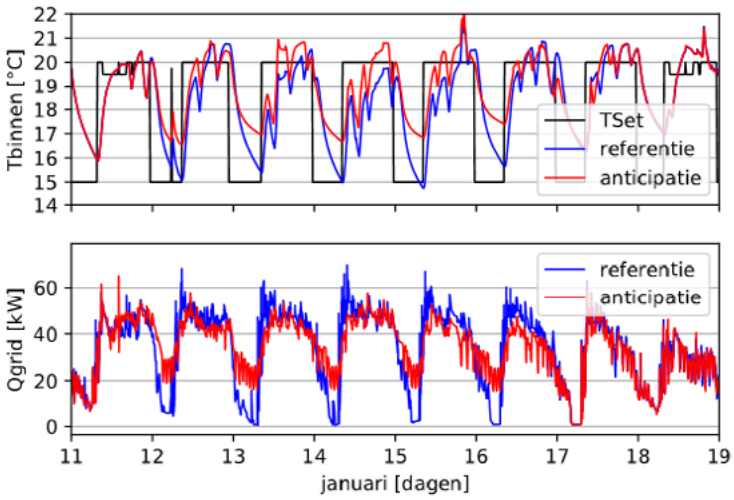


Fig. 13. The effect of reduced night setback on achieved indoor temperatures and supply peaks during cold periods

4.4. Alternative RBC - Adapted heating curves:

As a final exercise the effects of adapted heating curves are studied. Previous research of Ommen et al. [6] already resulted in optimization of supply temperatures in thermal grids with central HP supply and decentralized booster HP's. Inspired by those results, the grid is controlled by two different heating curves, selected as: (1) 50°C, -10°C / 25°C, 20°C and (2) 50°C, -10°C / 30°C, 15°C. The first led to inlet temperatures at the booster HP, which are not within the boundary constraints of the manufacturer. Both heating curves lead to a higher amount of injected solar energy and a higher COP of the GSHP. The total electricity supply decreases by 25%. The (dis)comfort however is not affected.

4.5. Summary: overview of variations investigated

An overview of the results of the described individual variations to the reference RBC is shown in Table 1. Results for the reference case applied to the measured climate data (Leuven, 2017), have been added as well. In the thermal discomfort column the improvements can be seen for the individual variations, and one should keep in mind the considerations put forward in the beginning of this section, prior to Fig 11.

Table 1 Overview of results of implemented variations to the reference RBC

RBC variation	RES share (%)	Thermal discomfort (Kh)	COP-HP	COP-booster HP	Thermal grid heat demand (GJ/a)
Reference	66.3	17.1 k	3.13	3.78	432.4
Preheating DHW	65.9	15.4 k	3.13	3.44	433.9
Simultaneous RH	66.6	14.1 k	3.14	3.78	433.8
Continuous FH	66.0	16.1 k	3.11	3.78	433.7
Heating curve (2)	73.7	16.9 k	4.37	3.54	414.3
Weather data 2017	66.4	11.9 k	3.09	3.78	360.9

5. Conclusion

The research case investigated handles individual variations in the RBC approach for the hybrid heat supply and emission systems in Almshouses 'the Schipjes' in Bruges, a practical case that is nearing completion. As the given installed power is limited and challenged towards the extension of the connected houses during construction the possible improvements by variations in the reference rule based control design were studied. Individual changes have shown that reasonable impact on the expected discomfort is possible, without decreasing, in some cases even increasing other performance criteria such as the share of RES and COP of the global system. Thus the degree of impact of the control on the required size of the supply systems, taking into account storage and dynamic effects, has been clarified for this specific case. This study moreover shows that a fully RES-based thermal network is feasible, even in historic city centres, provided that also the electricity used is based on RES technologies. Given the large amount of historic centres in Europe and beyond, the replication factor of this concept can be substantial.

Future work will consist in evaluating combined variations that improve the targeted criteria. The combination of continuous FH, adapted heating curve and simultaneous RH with radiators seems to be the best case to evaluate.

Acknowledgements

The authors acknowledge the Flemish Agency for Innovation and Entrepreneurship (VLAIO) for funding the research work within the living lab 'De Schipjes' (grant number 140125). Also Mintus is acknowledged for their front-running investments and project coordination.

References

[1] Sigrid Feyaerts, Impact van de regeling op de performantie van een klein thermisch net voor godshuizen, De Schipjes, te Brugge, Master Thesis, KU Leuven, 2019..
[2] Ruben Baetens, On externalities of heat pump-based low-energy dwellings at the low-voltage distribution grid, PhD Thesis, KU Leuven Belgium, 2015.
[3] ISO7730
[4] D. Basciotti and R.-R. Schmidt, "Peak reduction in district heating networks: a comparison study and practical considerations," in The 14th International Symposium on District Heating and Cooling, (Stockholm, Sweden), September 2014.
[5] S. Frederiksen and S. Werner, District heating and cooling. Lund: Studentlitteratur, 2014
[6] T. Ommen, J. E. Thorsen, W. B. Markussen, and B. Elmegaard, "Performance of ultra low temperature district heating systems with utility plant and booster heat pumps," Energy, vol. 137, pp. 544–555, 2017.

13th IEA Heat Pump Conference
April 26-29, 2021 Jeju, Korea

Heat pump assisted drying of flower bulbs

Sjors Wagenaar[ab], Carlos Infante Ferreira[a*]

[a]Delft University of Technology, Department Process & Energy, Leeghwaterstraat 39, 2628 CB Delft, The Netherlands
[b]Wagenaar Koeltechniek, Zaadmarkt 17, 1681 PD Zwaagdijk-Oost, The Netherlands

Abstract

Within the agriculture sector, drying of food and flowering products is a required production step. Most companies use hot air dryers where the heat is obtained by combustion of natural gas. This paper proposes a heat pump assisted drying system as an alternative. Flower bulb carrying boxes containing just harvested products have been approximated as packed beds filled with spherical products. A heat pump is proposed which includes a cross flow heat exchanger and allows for recirculation of the drying air while maintaining its operating temperature and humidity at optimal conditions to guarantee the required drying rate while preventing damage of the product. Simulink is used to optimize the operating conditions of the system guaranteeing both the product quality and a low energy consumption. The heat pump has been sized to dry 10 flower bulb carrying boxes of about 800 kg each in 24 hours. The performance of the heat pump (170 kWh/day renewable electricity) is compared to the performance of conventional fossil fuel based drying systems (350 kWh/day fossil fuel). Understanding heat and mass transfer mechanisms during drying allows optimization of the heat pump design.

Keywords: heat pump, drying of horticulture products, moisture removal, experimental drying rates;

1. Introduction

1.1. Energy needs in field horticulture

Drying is an energy intensive process. It accounts for 10 to 20% of the total consumption of energy by industry in most developed countries [7]. Drying of agricultural products is commonly accomplished using hot air convective drying, where air is preheated by a gas burner or indirectly by a gas boiler. The Paris agreement from 2015 imposes the banning of fossil fuels as heat sources for drying processes. Heat pumps are currently the most appropriate technique to replace gas boilers. Heat pumps can both be used for heating and dehumidification purposes making its users less dependent on weather conditions, lowering the energy consumption and guaranteeing a constant high product quality. When renewable electricity is used to drive the heat pumps, its operation is fully independent of fossil fuels.

The agricultural sector can be divided in field horticulture (production and processing of food and flowers), greenhouse horticulture, animal farms, wood processing and fishing. These sectors, in the Netherlands, consume 140 PJ of primary energy corresponding to CO_2 emissions of 7.3 Mton. The strategy of the Dutch government [4] to fulfill to the Paris agreement by 2030 imposes a CO_2 emission reduction of 40% for the agricultural sector. According to Wildschut [18] the field production and processing of flowers and flower bulbs is responsible for about 5 PJ of primary energy. It is also expected that this sub-sector contributes to the CO_2 emission reduction with 40% . The sector has signed an agreement with the government that by 2023 16% of the energy use will come from renewable sources [18]. Implementation of heat pumps for drying needs in the sector making use of renewable energy will give significant contributions to these goals.

Nomenclature

* Corresponding author. Tel.: ++31-15-278-4894.
E-mail address: c.a.infanteferreira@tudelft.nl.

Roman characters			*Greek characters*		
A	Area	-	α	Heat transfer coeff.	$W/m^{-2}K^{-1}$
a_w	Water activity	-	Δh_{fg}	Evaporation heat	$kJkg^{-1}$
COP	Coefficient of performance	-	ε	Void fraction	-
c_p	Specific heat	$kJkg^{-1}K^{-1}$	ε_{CFHE}	Effectiveness CFHE	-
D	Diffusivity	m^2s^{-1}	λ	Thermal conductivity	$Wm^{-1}K^{-1}$
d_{bulb}	Bulb diameter	m	μ	Viscosity	Pa s
G	Mass flux	$kgs^{-1}m^{-2}$	ρ	Density	kgm^{-3}
k	Mass transfer coefficient	ms^{-1}	ω	Humidity ratio	$kg_{H2O}kg_a^{-1}$
L	Length	m			
$\dot{m}$	Mass flow	kgs^{-1}	*Subscripts*		
M	Molecular weight	$kgkmol^{-1}$	a	(Dry) air	
Nu	Nusselt number	-	c	Cross flow	
NTU	Number of transfer units	-	char	Characteristic	
p	Pressure	kPa	eq	Equilibrium	
Pr	Prandtl number	-	evap	Evaporation	
R	Universal gas constant	$kJkmol^{-1}K^{-1}$	G	Humid air side	
Re	Reynolds number	-	in	Inlet	
Sc	Schmidt number	-	int	Interface	
$SMER$	Spec. moisture extraction	$kgkWh^{-1}$	L	Liquid	
T	Temperature	K or °C	out	Outlet	
t	Time	s	sat	Saturated	
u	Velocity	ms^{-1}	v	Water vapor	
x	Moisture content bulb	$kg_{H2O}kg_{bulb}^{-1}$	w	Wetted effective	

1.2. Flower bulb processing

This study focus on flower bulbs. Flower bulbs generate heat by metabolism, absorb water and attract diseases when wet. After harvesting the flower bulbs need to be quickly dried to prevent that germs and fungi develop. Flower bulbs need to be conserved at specific temperature, water content and water activity. The water activity, a_w, gives the ratio between partial and saturated water vapor pressure at the surface of a product and is influenced by the temperature and humidity of the surrounding air. Also the concentration of CO_2 and ethylene around the flower bulbs need to be controlled to prevent health issues and contamination with external viruses. According to Wildschut et al. [19], a small amount of ventilation is, however, sufficient to prevent harmful concentrations. According to Rockland & Beuchat [14] a high water activity supports the growth of microorganisms, germination of spores and participation in several types of chemical reactions. Bacteria usually require at least a water activity of 0.91 and fungi of 0.60. So a flower bulb drying system should bring and maintain the water activity close to values just below 0.60. Every 1% of prevented product loss due to better conditioning of the drying and storage conditions results in savings of about € 16500. per year for the average farmer.

The transportation and storage of flower bulbs is usually realized in large cubic boxes of 0.8 to 1.2 m^3. These can be easily transported using forklift trucks. These boxes have a perforated bottom through which drying air can be circulated. Fig. 1 illustrates how the drying air flow from a central air treatment system can be distributed to a large number of these cubic boxes.

At the end boxes the forklift openings are blocked with foam creating a pressure rise which forces the air through the flower bulbs in the boxes. The return air is discarded or dehydrated and heated before being recirculated. The air temperature is maintained in the range 20 to 25 °C, depending on the cultivar. The average drying time of one batch is 24 to 36 hours and the amount of water that needs to be removed is around 50 kg per box [5].

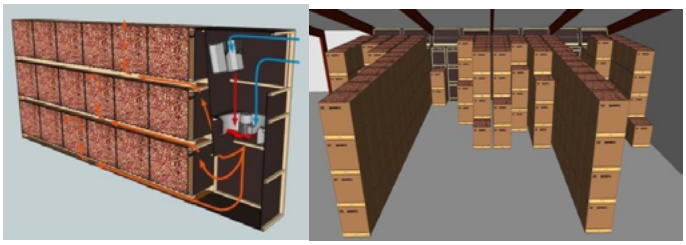


Fig. 1. Drying distribution arrangement for multiple flower bulb boxes.

1.3. Modeling of drying processes of agricultural products

Tzempelikos et al. [15] and Agrawal and Methekar [1] modeled the heat and mass transfer processes during drying of quince slices and pumpkin, respectively. Alnaimat et al. [2] and Li et al. [8] studied the heat and mass transfer processes in a structured packed bed column to determine temperature and humidity of air as it rises in countercurrent flow to cooled water. Minea [11] has reviewed the advances in heat pump drying technologies and its modeling approaches. Although these studies concern different drying processes, they have been used as the basis for the development of the flower bulb drying model introduced in this paper.

2. Drying of flower bulbs

The drying process starts by conditioning the air that is circulated along the bulbs to the required conditions (20 to 25 ºC; low humidity < 5 g/kg_{dry_air}). If possible heat recovery should be used. Then heat is transferred from the drying air to the surface of the bulbs while at the same time water evaporates from the surface of the bulb into the drying air flow. In this evaporation process surface water, or bounded water inside the product which has diffused into the surface, is removed from the bulb surface into the drying air flow. The resulting colder, humid air flows back into the conditioning system and is brought back to feed conditions. Mujumbar [12] distinguishes two drying rate regimes. In the begin of the process unbounded water is evaporated from the surface at a constant rate. When bounded water from the core of the bulb starts to be removed, at a critical moisture content of the bulb, the drying rate starts to decrease. This rate will then generally linearly decrease with the moisture content of the bulb until equilibrium is attained and the drying process stops.

2.1. Flower bulb properties

Bulbs are structured in multiple layers and have a strong solid surface which protects them against damage and diseases. Their structure is similar to the structure of onions and garlic which have been more frequently investigated. The effective moisture diffusivity of the flower bulbs, D, expressed in m^2/s has been assumed to be identical to the moisture diffusivity in onions as reported by Mujumbar [12] and is given in eq. 1 where the moisture content per kg bulb, x, is expressed in kg_{H2O}/kg_{bulb} and T, is the bulb temperature, in K.

$$D = \frac{1}{1+x} \cdot 1.45E-08 \cdot e^{\left[-\frac{70.2}{8314}\left(\frac{1}{T}-\frac{1}{333.15}\right)\right]} \quad (1)$$

Density, specific heat and thermal conductivity of onions reported by van Hiele et al. [16] have been assumed to apply for flower bulbs. Moisture content dependent values have been adopted from Kalbasi [6]. Its values are given in Table 1.

Table 1. Density, ρ, specific heat, c_p and thermal conductivity, λ of flower bulbs. x in kg_{H2O}/kg_{bulb} and T in K.

Properties of flower bulbs based on properties onions	$\rho_{product}$ (kgm^{-3})	$c_{p_product}$ ($kJkg^{-1}K^{-1}$)	$\lambda_{product}$ ($Wm^{-1}K^{-1}$)	ρ_{bulk} (kgm^{-3})	c_{p_bulk} ($kJkg^{-1}K^{-1}$)	λ_{bulk} ($Wm^{-1}K^{-1}$)
Van Hiele et al. [16]	882	3.77	0.48	575	3.77	0.35
Kalbasi [6]		1.84+2.34*x	0.445+0.309*x-0.005*T			

In this study the water activity is obtained making use of the Chung-Pfost equation with the coefficients proposed for garlic bulbs by Madamba et al. [9]. The water activity is obtained using eq. 2 in which T is expressed in ºC.

$$a_w = e^{\left[-\frac{203.4}{T+76.5}\cdot e^{(-0.072\cdot x)}\right]} \tag{2}$$

The equilibrium moisture content of the bulbs can be related to the water activity. The Guggenheim-Anderson-de Boer equation predicts this relation over a wide range of water activity. For onions, Mujumbar [12] proposed eq. 3 with the parameters given in Table 2.

$$x_{eq} = \frac{b_0 \cdot b_1 \cdot b_2 \cdot a_w}{(1-b_1 \cdot a_w)\cdot(1-b_1 \cdot a_w + b_1 \cdot b_2 \cdot a_w)} \tag{3}$$

Table 2. Parameters proposed by Mujumbar [12] for the equilibrium moisture of onions in the Guggenheim-Anderson-de Boer equation. R in kJkmol^{-1}K^{-1} and T in K.

b_0	b_1	b_2	$b_{10}*10^5$	b_{11}	b_{20}	b_{21}
20.2	$b_{10}\cdot e^{\frac{b_{11}}{RT}}$	$b_{20}\cdot e^{\frac{b_{21}}{RT}}$	2.3	32.5	5.79	6.43

2.2. Modeling of drying process

The model has been developed for a single flower bulb carrying box. Fig. 2 illustrates how the box with coordinates x, y and z has been considered. The properties of flower bulbs and air flow are only changing in z-direction so that a control volume considers the whole x-y cross section of the box. The model is transient considering an one-dimensional step Δz in space and a time step Δt. The flow passage area of the box is constant along the height of the box and results in $z/\Delta z$ control volumes. Each control volume contains a volume fraction of flower bulbs, liquid and air. Multiplying each volume fraction with the corresponding material density results in the total mass in the control volume.

Fick's law allows for the determination of the mass transfer over the height of each control volume. This rate of mass transfer can be converted into the rate of humidity ratio change per control volume [17] as given in eq. 4.

$$\frac{d\omega}{dz} = \frac{k_G A_w}{G_a}\cdot\frac{M_v}{R}\left[\frac{p_v^{sat}(T_{\text{int}})}{T_{\text{int}}} - \frac{\omega}{0.622+\omega}\cdot\frac{p}{T_G}\right] \tag{4}$$

In this equation M_v is the molecular weight of the water vapor, R the universal gas constant, T_G (K) the air temperature, T_{int} (K) is the interface temperature (the flower bulb surface temperature), k_G (m/s) is the mass transfer coefficient, A_w (m^2/m^3) is the wetted effective surface area per unit volume. G_a is the mass flux of air through the cross flow area of the box, A_c, and p is the total system pressure.

The change in air temperature is obtained from the energy balance [17] and is given in eq. 5.

$$\frac{dT_a}{dz} = \frac{\frac{d\dot{m}_v}{dz}\cdot\Delta h_{fg} - \alpha\cdot(T_G - T_L)\cdot A_w\cdot A_c - \frac{d\dot{m}_v}{dz}\cdot(2501.1+1.8135\cdot T_{a_in})}{\dot{m}_a\cdot c_{p_a} + 1.8135\cdot\dot{m}_v + 1.8135\cdot\frac{d\dot{m}_v}{dz}} \tag{5}$$

where

$$\frac{d\dot{m}_v}{dz} = \frac{d\omega}{dz}\cdot\dot{m}_a \tag{6}$$

and T_L is the flower bulb surface temperature. The heat transfer coefficient between flower bulb surface and air, α, has been obtained from the correlation proposed in Mills [10] for spherical shaped packed beds.

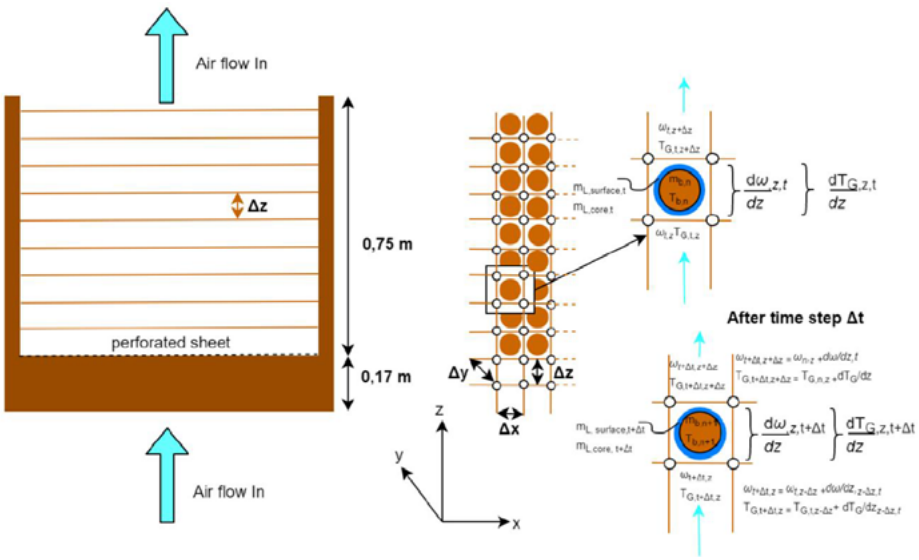


Fig. 2. Discretization of the flower bulb box considering it as a packed bed of flower bulbs.

$$\alpha = \frac{\lambda_a}{L_{char}} \cdot Nu = \frac{\lambda_a}{L_{char}} \cdot (0.5 \cdot \mathrm{Re}^{0.5} + 0.2 \cdot \mathrm{Re}^{0.67}) \cdot \mathrm{Pr}_a^{0.33} \tag{7}$$

With the characteristic length L_{char} obtained from eq. 8.

$$L_{char} = d_{bulb} \cdot \frac{\varepsilon}{1-\varepsilon} \tag{8}$$

With ε the void fraction of the packed flower bulb bed which was initially assumed to be 0.26 [3]. The Reynolds of the flow is calculated using eq. 9:

$$\mathrm{Re} = \frac{G_a \cdot L_{char}}{\mu_a} \tag{9}$$

The mass transfer coefficient is obtained making use of the Chilton-Colburn analogy.

$$k_G = \frac{\alpha}{\rho_a \cdot c_{p_a}} \cdot \left(\frac{\mathrm{Pr}}{Sc}\right)^{0.67} \tag{10}$$

The wetted effective surface area per unit volume is obtained considering that the flower bulbs are spheres and taking the void fraction into account.

$$A_w = \frac{6}{d_{bulb}} \cdot (1-\varepsilon) \tag{11}$$

The pressure drop through the packed flower bulb bed has been predicted making use of the Ergun equation for packed beds, as proposed by Mills [10].

$$\frac{dp}{dz} = \frac{150 \cdot \mu_a \cdot u_{char}}{L_{char}^2} + \frac{1.75 \cdot \rho_a \cdot u_{char}^2}{L_{char}} \tag{12}$$

With the characteristic velocity obtained from eq. 13.

$$u_{char} = \frac{G_a}{\rho_a \cdot \varepsilon} \tag{13}$$

During the second drying regime mainly internal diffusion dominates the process. To take this into account the volume of the flower bulb has been discretized into several nodes between which diffusion is calculated. Details of the approach have been reported in Wagenaar [17].

3. Experimental data

During the summer of 2018 experimental data of the drying period have been collected at two different companies: Niels Kreuk BV and Gebr. Boon Hem BV. Data have been collected of temperature, relative humidity, total mass and pressure drop for batches of flower bulb boxes. Here only the data obtained at Niels Kreuk BV is discussed.

A schematic of the drying chamber and drying arrangement is shown in Fig. 3. This company makes use of a heat pump to dry its flower bulbs. In this arrangement dry air enters the flower bulb boxes from the top and the humid air leaves at the bottom. The air is then dried and heated by a heat pump. The figure shows the position of the boxes which have been measured.

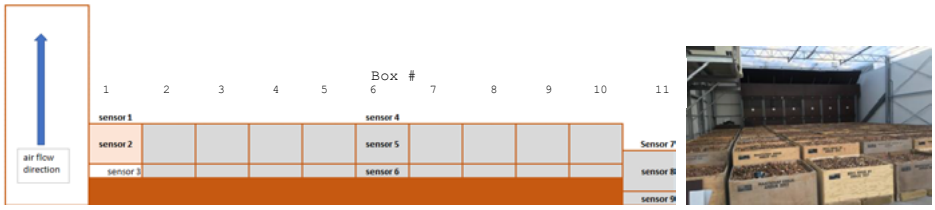


Fig. 3. Schematic of the heat pump based drying chamber of Niels Kreuk BV.

Table 3 shows the mass reduction of the different flower bulb boxes after 15 h and after 62 h of operation. The initial mass is the mass of the boxes just arriving from the field and before starting the drying operation.

Table 3. Mass reduction during the drying period of flower bulb boxes at Niels Kreuk BV. Data collected in July 2018.

	Initial mass [kg]	Mass after 15 h [kg]	Reduction [kg]	Reduction [%]	Mass after 62 h [kg]	Reduction [kg]	Total Reduction [%]	Total mass removed [kg]
Box 1	830	804	26	3.1	794	10	4.3	36
Box 6	790	772	18	2.3	762	10	3.5	28
Box 11	816	799	17	2.1	788	11	3.4	28

The table makes clear that the amount of moisture (and probably remaining soil) in each box is different so that in average the drying percentage is 4.1% but that the contents of some boxes dry 3.4% while of others dry up to 4.3%. The temperature and relative humidity have been measured by installing Lascar EL-USB-2 temperature and humidity data loggers in the different boxes. The temperature is measured with an accuracy of ± 0.5 K and the relative humidity with an accuracy of ± 2%. Fig. 3 shows that for some boxes the temperature and humidity change of the air flow as it passes the boxes have been measured. Fig. 4 illustrates how temperature and humidity change with time at inlet, halfway and at outlet of box 11. The air volume flow rate has been measured making use of an anemometer from Testo-air and mounting a plate with anemometer size perforations above the boxes. The measuring probe of Testo-air 435 has an accuracy of ± 0.1 m/s. The air volume flow through the boxes varies linearly with the position with the largest flow through box 1 (1600 m^3/h) and the lowest through box 11 (1200 m^3/h).

Fig. 4 makes clear that the control of the air inlet temperature and humidity was not able to maintain the air inlet conditions during the experimental period. In the first hour of operation, the air leaving the first half of the box was already saturated with water so that the relative humidity halfway the box is already identical to the relative humidity at the outlet of the box. It is only after about 20 minutes that the orange line starts decreasing. During some periods it is clear that the air inlet and outlet humidity did not change indicating that there was no humidity removal during these periods.

The pressure drop across the flower bulb box was 220 Pa for a volume flow rate of 1417 m^3/h and, respectively, 180 Pa and 100 Pa for volume flow rates of 1259 m^3/h and 917 m^3/h. These data have been used to calibrate the value of the void fraction. This was done by adjusting the value of the void fraction in eq. 13 until the result of eq. 12 corresponded with the experimental data. A value of 0.196 was derived for the void fraction which is slightly lower than the value proposed by Conway & Sloan [3] which was 0.26. A void fraction of 0.196 has been further used in the model.

The experimental wetted effective surface area per unit volume taking the eventual dirt in the void between the flower bulbs into account has also been derived from the experimental data. Since the rate of mass transfer is constant during the first hour of operation, A_w can be derived from eq. 4 when it is assumed that the bulb surface is at wet bulb conditions. From the experimental data, a value of 0.198 is calculated for A_w. This corresponds to assuming an average flower bulb diameter of 4.1 cm in eq. 11, what is quite reasonable.

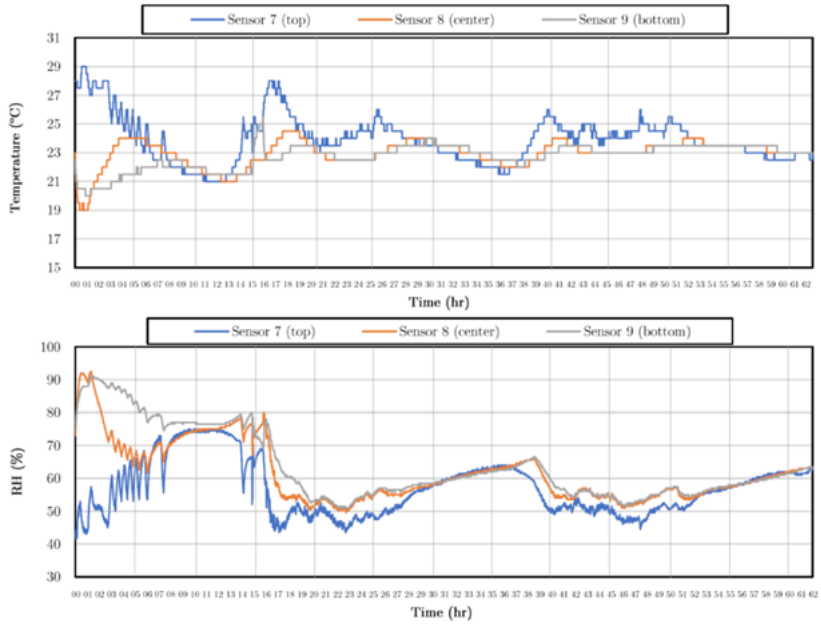


Fig. 4. Temperature (top) and relative humidity (bottom) of the air flow through the flower bulb box 11. Blue is inlet, orange halfway and grey is outlet. The time scale goes from 0 (start time) to 63 h (end of drying process).

4. Model validation

In Fig. 5 (left) the prediction of the model (light blue line) for the air outlet temperature is compared to the experimental outlet temperature (green line). The experimental inlet temperature (red line) is used as input for the model. The agreement is quite good. In Fig. 5 (right) the prediction of the model (light blue line) for the absolute humidity of the air at the outlet is compared to the experimental outlet absolute humidity (green line). The experimental inlet absolute humidity (red line) is used as input for the model. In the center the comparison of the relative humidity. The agreement is quite good.

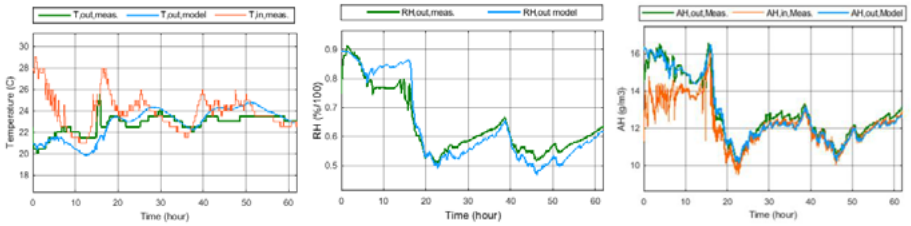


Fig. 5. Temperature (left) and absolute humidity (right) of the air flow through the flower bulb box 11. Red is inlet (experimental and also used as model input), light blue the outlet condition predicted by the model and green is experimental outlet. The time scale goes from 0 (start time) to 60 h (drying period).

Fig. 6 compares the progress of the drying process with the experimental data. The orange line gives the experimental data, the blue line gives the model prediction taking the flower bulb discretization into account and the purple line gives the model prediction based on the absolute humidity change and the air volume flow rate.

Using the flower bulb discretization to take the internal diffusion into account clearly improves the accuracy of the prediction. The model has been validated making use of the root mean square error method. Details of the validation have been reported by Wagenaar [17].

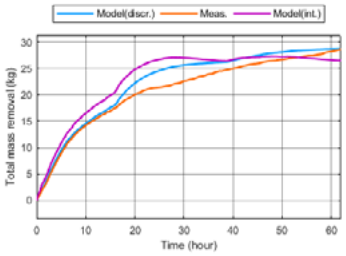


Fig. 6. Mass removed from box 11 as a function of time. The orange line shows the experimental data while the other two lines give the model prediction calculated in two different ways.

5. Heat pump dryer design

The flower bulb heat pump dryer proposed in this study is a typical vapor compression cycle assisted with a cross flow heat exchanger (CFHE). Its schematic and operating conditions are illustrated in Fig. 7. The system has been designed to remove the surface water of 10 flower bulb boxes in 8 h. Depending on the return temperature and humidity of the air after removing moisture from the boxes (state 1 in Fig. 7) the required evaporator capacity will vary from 40 to 60 kW. The heat pump should be able to remove 30 kg/h of water.

The heat pump has been modelled using simplified models for each component. Propane (R290) has been selected as the working fluid as it, as a natural refrigerant, has low environmental impact. A pressure ratio dependent isentropic efficiency has been adopted for the compressor, leading to efficiencies in the range 0.70 to 0.72 for the studied conditions. The evaporator and condenser dimensions and capacities have first been determined using the NTU-method. UA values of 3.55 and 3.20 kW/K have been obtained respectively for the evaporator and for the condenser. The heat exchanger effectiveness has then been used to predict the evaporating and condensing temperatures for different operating conditions, assuming these processes have infinite heat capacity. This is illustrated for the evaporator in eq. 14.

$$T_{evap} = \frac{T_{a_out} - T_{a_in} \cdot e^{-NTU}}{1 - e^{-NTU}} \tag{14}$$

The CFHE has also been modelled using the NTU-method as proposed by Ogulata & Doba [13] and its effectiveness is given in eq. 15.

$$\varepsilon_{CFHE} = 1 - 0.447 \cdot NTU^{-0.4} \tag{15}$$

The output temperature is then obtained from eq. 16 in which the indexes refer to states in Fig. 7.

$$T_2 = T_1 - 0.8 \cdot \varepsilon_{CFHE} \cdot (T_1 - T_3) \tag{16}$$

The 0.8 correction factor has been proposed by the CFHE manufacturer to take into account the condensation that takes place as the air passes the cold surface.

The heat pump dryer model has been implemented in Simulink. The schematic of the model is given in Fig. 8 and illustrates the links between the different components and the air flow conditions.

6. Heat pump dryer performance prediction

To prevent the air temperature to attain values above 35 ºC, what may damage the flower bulbs, the heat pump dryer is modelled with a constant air volume flow of 10000 m^3/h (1000 m^3/h per flower bulb box). Assuming that the air leaving the flower bulb boxes is almost saturated (95% relative humidity), the corresponding temperature and enthalpy at the evaporator outlet can be obtained. Then the required cooling

capacity can be determined and with it the required mass flow of refrigerant. The rotational speed of the compressor can then be adjusted to deliver the required cooling capacity.

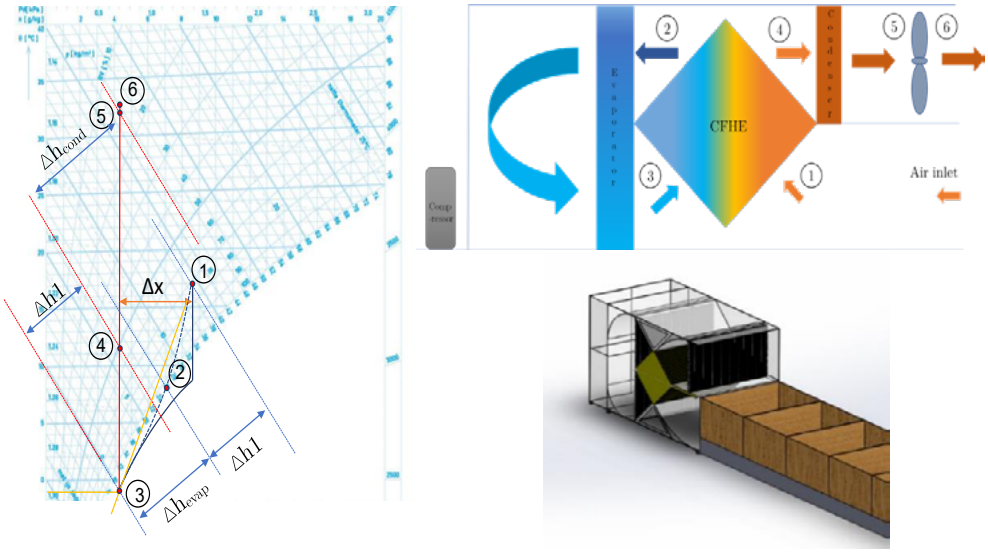


Fig. 7. The drying process in a Mollier diagram and schematic of the heat pump dryer. Between states 2 and 3 the air flow passes the evaporator of the heat pump and between 4 and 5 passes its condenser. State 1 is the return condition after removing moisture from the product. State 6 is the air condition as it enters the flower bulb boxes.

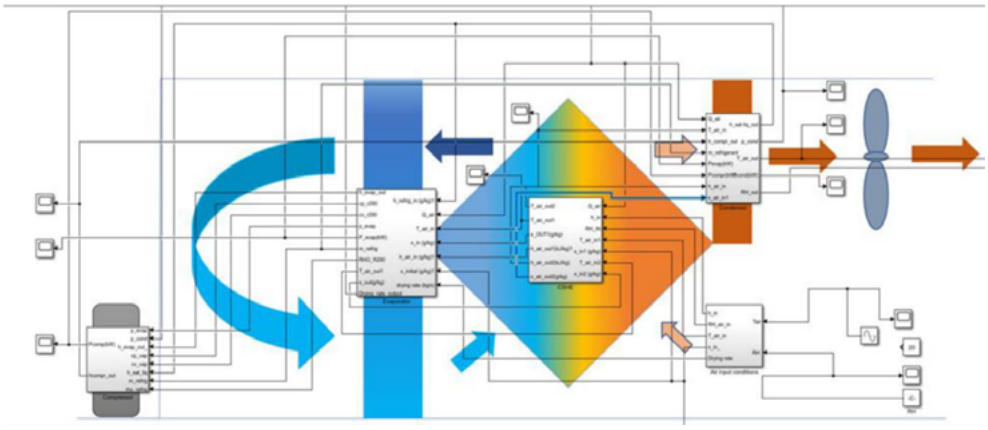


Fig. 8. Simulink model of the heat pump dryer showing the interaction between the different components of the system.

Fig. 9 shows, in the center, the predicted temperatures in the different positions of the heat pump system (the states are indicated in Fig. 7). The left hand side gives the temperature and relative humidity at the inlet and outlet of the heat pump dryer. The conditions of the air stream leaving the flower bulb carrying box (Fig. 5) are used as input for the heat pump dryer model. In the final stages of drying the humidity ratio remains practically unchanged between in- and outlet. Air enters at high temperature and low relative humidity and leaves at lower temperature and higher relative humidity. The right hand side of Fig. 9 gives the condensation and evaporation temperatures of the heat pump as predicted by the model. The evaporating temperature never goes below 0 ºC so that frost formation and associated problems are prevented. The condensation temperature reaches up to 40 ºC, a temperature about 7 K higher than the air outlet temperature and 15 K higher than the

air inlet temperature. The condensation temperature could be lowered by implementing a larger / external condenser to remove excess heat and with it the COP of the system would be improved.

The heat loads of the different components as predicted by the model and the corresponding coefficient of performance (*COP*) are given in Fig. 10 with left the heat loads, in the center the *COP* and the specific moisture extraction rate (*SMER*) expressed in kg/kWh and right the required mass flow of refrigerant. The refrigerant mass flow variation with time indicates that the compressor needs to operate between full-load and about 60% part-load. A range with very acceptable part-load performance.

Typical drying walls just increase the moisture removal capacity by preheating the drying air making use of hot water heat exchangers. The temperature of the drying air is conventionally increased with 4 K as the air passes these heat exchangers. Taking a boiler efficiency of 90% into account, heating 10000 m^3/h air requires a fuel heating power of 14.6 kW. This corresponds to a fossil fuel based energy consumption of 352 kWh per day. The left end side of Fig. 10 shows that during the first 24 hours the compressor of the heat pump (light blue line) consumes approximately 170 kWh renewable electricity. This is an energy consumption reduction of 57%. A CO_2 emission reduction will only be attained if the compressor is driven by renewable electricity. With an average energy conversion efficiency of 0.42 in the Dutch fossil fuel driven power stations, using electricity generated by these power stations will result in approximately the same CO_2 emissions.

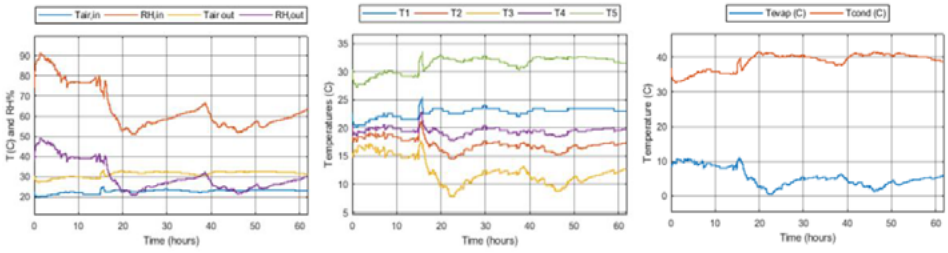


Fig. 9. Simulation results of heat pump performance. Left the air temperature and relative humidity at inlet and outlet of the heat pump dryer. In the center the air temperature changes along the different components (see Fig. 7 for positions). Right the condensation and evaporation temperatures of the heat pump.

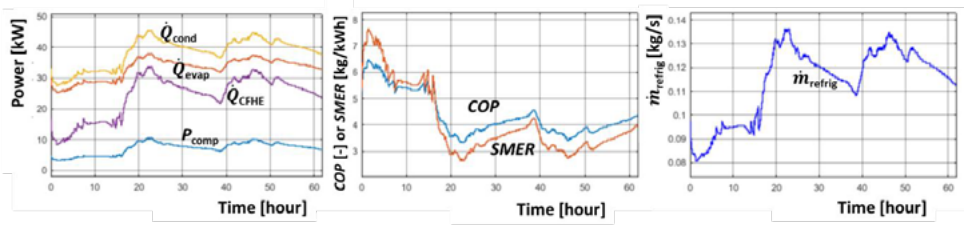


Fig. 10. Simulation results of heat pump performance. Left the heat exchanged in the different components. In the center the *COP* and *SMER* of the system. Right the required mass flow of refrigerant as a function of time.

7. Conclusions

In this study a Simulink model has been developed for the drying process of flower bulbs which includes a vapor compression heat pump assisted with a cross flow heat exchanger for heat recovery. The model results have been validated making use of experimental data collected at a flower bulb company. The main conclusions of this study are as follows:

- The drying process of the flower bulbs distinguishes two regimes: first the unbounded water is evaporated from the surface of the bulbs at a constant rate after which the water from the core of the bulbs starts to be removed and the moisture removal rate linearly decreases until an equilibrium is attained.
- Approaching the flower bulb boxes as packed beds of spherical shaped bulbs with void fraction of 19.6% and average diameter of 4.1 cm gives results comparable to the experimental values for what concerns the drying rate.

- To prevent too high temperatures of the air entering the flow bulb boxes, compressor speed control is required. The expected load conditions are in the range 60 to 100%.
- In the first 15 hours of operation the *COP* of the heat pump reaches values in the range of 6. However, improvement of the design of the condenser and evaporator is possible since, in the present design, the temperature driving forces across these heat exchangers are quite large.
- During the first 15 hours of operation the heat pump removes around 25 kg of moisture per flower bulb box. This is around 3% of the total weight per box.
- During the first 15 hours of operation the heat pump extracts 6 kg of moisture per kWh of energy consumed.
- While a conventional fossil fuel driven drying system consumes 350 kWh per day, the proposed heat pump dryer consumes 170 kWh renewable electricity per day.
- Implementation of heat pumps for drying purposes in the agriculture sector results in energy savings combined with improved product quality while burning of fossil fuels is prevented.

Acknowledgements

The authors would like to thank Niels Kreuk BV and Gebr. Boon Hem BV for facilitating the experimental work and Wagenaar Koeltechniek for delivering the data-collecting equipment.

References

[1] Agrawal SG, Methekar RN, 2017. Mathematical model for heat and mass transfer during convective drying of pumpkin. Food and Bioproducts Processing **101**: 68-73.
[2] Alnaimat F, Klausner JF, Mei R, 2011. Transient analysis of direct contact evaporation and condensation within packed beds. International Journal of Heat and Mass Transfer **54-15-16**: 3381-3393.
[3] Conway JH, Sloane NJA, 1999. Sphere packings, lattices and groups. 3rd Edition. Springer-Verlag New York.
[4] ECN & CBS, 2017. *Nationale energieverkenning*. ECN-O-14-036; The Netherlands.
[5] Hand R, Ernens B, 2014. Voorstudie: duurzaam drogen van bloembollen middels een droogsysteem met zuigende ventilatoren en actieve ontvochtiging. Report 13985.
[6] Kalbasi M, 2003. Heat and moisture transfer model for onion drying. Drying Technology **21-8**: 1575-1584.
[7] Kemp IC, 2014. Fundamentals of energy analysis of dryers. *Modern Drying Technology* **4-4**:1–45.
[8] Li Y, Klausner J, Mei R, Knight J, 2006. Direct contact condensation in packed beds. International Journal of Heat and Mass Transfer **49-25-26**: 4751-4761.
[9] Madamba PS, Driscoll RH, Buckle KA, 2007. Predicting the sorption behaviour of garlic slices. Drying Technology **12-3**: 669-683.
[10] Mills AF, 1999. Basic heat & mass transfer. 2nd Edition. Prentice Hall, New Jersey.
[11] Minea V, 2016. Advances in heat pump-assisted drying technology. CRC Press, New York.
[12] Mujumbar, AS, 2014. Handbook of industrial drying. 4th Edition. CRC Press, New York.
[13] Ogulata RT, Doba F, 1998. Experiments and entropy generation minimization analysis of a cross-flow heat exchanger. International Journal of Heat and Mass Transfer **41-2**: 373-381.
[14] Rockland LB, Beuchat LR, 1987. Water activity: theory and applications to food. 2nd Edition. Marcel Dekker, New York.
[15] Tzempelikos DA, Mitrakos D, Vouros AP, Bardakas AV, Filios AE, Margaris DP, 2015. Numerical modeling of heat and mass transfer during convective drying of cylindrical quince slices. Journal of Food Engineering **156**: 10-21.
[16] van Hiele T, Koster GJ, van Male J, Nunes EL, 1986. Handboek voor de koudetechniek. Uitgeverij P.C. Noordervliet BV, Zeist. The Netherlands.
[17] Wagenaar S, 2019. Feasibility study of a heat pump assisted flower bulb drying system. MSc thesis in Mechanical Engineering. Delft University of Technology.
[18] Wildschut J, 2018. Energiemonitor van de Nederlandse Bloembollensector 2016. Bleiswijk: Wageningen University & Research, BU Glastuinbouw - Bloembollen. 38 p. (Report Wageningen Plant Research; no. WPR-816).
[19] Wildschut J., Dijkema M, van der Lans A, 2013. Ventilatie, Ademhaling en CO_2-schadedrempels. Praktijkonderzoek Plant & Omgeving B.V. Report PPO nr. 32 36156400.

13th IEA Heat Pump Conference
April 26-29, 2021 Jeju, Korea

Heating system based on heat recovery from sewage

Maneesh Avadhani[a], Roland van Rooyen[b], Carlos Infante Ferreira[a*]

[a]Delft University of Technology, Department of Process & Energy, Leeghwaterstraat 39, 2628 CB Delft, The Netherlands
[b]City of Rotterdam, Postbus 6575, 3002 AN Rotterdam, The Netherlands

Abstract

Buildings consume 40% of the total global energy and contribute to over 30% of all CO_2 emissions. Space heating forms a significant part of energy consumption in buildings. A possible solution is to recover waste heat from sewage and to upgrade its exergy using a heat pump. Polymers reduce cost and energy required for manufacturing the heat exchangers. The impact of sewage flow and temperature, heat exchanger dimensions and thermal enhancement of polymers on heat recovery is studied using a Matlab model. The model integrates a sewage heat exchanger with a heat pump and optimizes heat recovery from sewage. A heat pump is used to obtain hot water at 55°C for space heating. Heat recovered from sewage and overall COP are quantified. In case of HPDE with graphite filler, increase in filler content from 0% to 30% increases thermal conductivity from 0.46 to 1.89 $Wm^{-1}K^{-1}$ increasing the heat recovery with 34%. The heat transfer coefficient becomes twice as large when polymer with no filler is enhanced with 30% filler content. Large heat exchange area and variability of sewage level limit the recovered heat.

Keywords: enhanced polymer; sewage heat recovery; heat pump; building heating.

1. Introduction

Buildings consume about 40 % of the total global energy and contribute to over 30 % of all CO_2 emissions [17]. Space heating and cooling and domestic hot water supply form the largest part of the energy consumed in residential buildings [2]. Use of fossil fuels to cope with heating and air-conditioning demands of buildings leads to a series of critical problems such as pollution, climate change and energy shortage [9]. Next to this, the Dutch government has set goals to phase out the use of natural gas and wants to be free from natural gas in 2050. The city of Rotterdam has set a sub target for 2030: 49% CO_2 reduction. Thus, it is vital to develop sustainable technology that can assist in reducing this energy consumption.

A possible route to reduce the energy consumption from buildings is to recover heat from sewage (waste) water. Water that has been affected in quality due to anthropogenic influence is called waste water. According to Hepbasli et al. [5] more than 15% of the thermal energy supplied to buildings is lost through the sewer system. Waste water can be used as a heat source for heat pumps to fulfill the heating and cooling requirements of buildings. These streams are suitable heat sources because, as reported by Frijns et al. [3], in the Netherlands, these flows reach to 1928 Mm^3 per year so that by cooling the flow with 5 K 40.4 PJ heat can be extracted from the flow. Additionally its temperature is higher than ambient in the winter and lower in the summer and daily temperature changes are small.

Currently, mainly in Europe, about 500 Waste Water Source Heat Pumps (WWSHP) are estimated to be in operation with thermal rating in the range of 10 - 20,000 kW. Installation of WWSHP systems can be either in the sewer system or after the waste water treatment plant (WWTP).

Nomenclature

Roman symbols	*Greek symbols*		
		req	Required

* Corresponding author. Tel.: ++31-152-784-894.
E-mail address: c.a.infanteferreira@tudelft.nl .

A	Area	m^2	α	Heat transfer coef.	$Wm^{-2}K^{-1}$	s	Tube surface
c_p	Specific heat	$kJkg^{-1}K^{-1}$	Δ	Difference		sub	Submerged
d	Diameter	m	λ	Thermal conductivity	$Wm^{-1}K^{-1}$	sw	Secondary water
l	Length	m	μ	Dynamic viscosity	Pa s	t	Tube
$LMTD$	Log. Mean ΔT	K	ρ	Density	kgm^{-3}	tot	Total
$\dot{m}$	Mass flow rate	Kgs^{-1}				ww	Waste water
N	Number	-	*Subscripts*				
P	Perimeter	m	act	Actual	*Abbreviations*		
Q	Energy	kWh	c	Cross sectional	HDPE	High density polyethylene	
$\dot{Q}$	Heat flow	kW	ch	Sewage channel	LDPE	Low density polyethylene	
r	Radius	m	comp	Compressor	MEG	Mono-ethylene glycol	
T	Temperature	°C or K	cond	Condenser	PC	Polycarbonate	
U	Overall heat transfer coef.	$Wm^{-2}K^{-1}$	elec	Electrical	PPS	Polyphenylene sulphide	
v	Velocity	ms^{-1}	hyd	Hydraulic	PS	Polystyrene	
W	Work	kJ	in	Inlet	WWHEX	Waste water heat exchanger	
$\dot{W}$	Power	kW	o	Outer diameter	WWSHP	Waste water source heat pump	
YTS	Yield strength	MPa	out	Outlet	WWTP	Waste water treatment plant	

Although recovering heat after WWTP would eliminate the risk of bio-film growth in the heat exchanger, the maximal temperature of waste water is usually at the initial stages of the sewer system. Moreover, heat recovery location in the sewer is closer to the consumers than waste water treatment plants [16].

A WWSHP consists of three components (i) Waste Water Heat Exchanger - Heat is recovered from waste water (ii) Heat pump - The heat recovered is upgraded to be used in the heating system of buildings (iii) Distribution system of heating and cooling in buildings.

Waste water can lead to the fouling of the waste water heat exchanger. Fouling occurs when fluid degrades near heat transfer surface or solids deposit on surface. Sometimes, microorganisms create bio-film matrices on heat exchange surface which will also result in reduced heat transfer performance of the heat exchanger [2]. Liu et al. [9] have reported that the convective heat transfer and fouling resistances on the sewage side of the waste water heat exchanger accounted for 80% of the total thermal resistance of their system.

In this paper, sustainable and economic system design is considered to recover waste heat from sewage for heating / cooling of buildings to reduce their carbon footprint. The ”Doelen” case in Rotterdam is considered to illustrate the benefits of heat recovery in terms of renewable energy, economics and sustainability of installing such systems in sewers. The Doelen is a concert venue and convention center in Rotterdam, Netherlands. The heat recovered from sewage will contribute to the heating requirements of ’Doelen’. Furthermore, polymer sewage heat exchangers are considered for heat recovery due to their advantages such as low cost, lesser weight, lower fouling and higher corrosion resistance. It is estimated that the energy required to produce a unit mass of polymers is two times lower than of common metals, which makes polymer heat exchangers environmentally friendly [1].

The objective of this study is to develop technology that provides a strong basis for scaling up sewage waste heat recovery systems for large urban areas. The scope includes designing, modeling and validation of the most suitable polymer heat exchangers for heat recovery from sewage systems.

2. State-of-the-art

2.1. Sewage heat recovery potential

About 70% of the total drinking water produced in the Netherlands is used for domestic purposes [6, 15] and contributes most to the temperature of the sewage flow. Roest et al. [12] report that drinking water enter the sewage at around 27 ºC and the water from bathing and showers at 38 to 40 ºC. Tap water and water from the dish washer and washing machine enter the sewage at approximately 40 ºC. According to Hofman et al. [6] these flows correspond to 40 % of the total energy losses from modern Dutch dwellings. The temperature of the effluent leaving the WWTP was found to be roughly 15 ºC. Cooling the total effluent flow (1928 Mm^3/year, [3]) with 5 K ΔT from 15 ºC to 10 ºC delivers 40.4 PJ low temperature energy available as heat source for heat pumps. With a COP of 4 these heat pumps could deliver 53.9 PJ of heat at 55 ºC at national level and 1.6 PJ for a town with 500,000 inhabitants. This is sufficient to cover 12% of the heating requirements of the built environment (448 PJ in 2015).

2.2. Possible sewage heat recovery locations

Heat recovery from sewage can be done in three locations of the sewage network [2]. Heat can be recovered at the source of sewage (buildings), or in the sewage line or after the treatment of sewage.

Waste water temperature affects the water treatment process. Nitrification, one of the steps of water treatment, is a temperature dependent process. Growth of nitrifying bacteria is impeded at lower waste water temperatures [16].

Looking at the pros and cons of each location, recovering heat from the sewage network is more advantageous since waste water flow is higher and continuous in comparison to the decentralized domestic sewage system. The problem with recovering heat after treatment is that the WWTPs are located far away from residential buildings, implying additional investment on pipelines and insulation.

2.3. Waste Water Heat Exchangers

Liu et al. [9] report the COP of a WWSHP system designed for the (partial) heating supply of a residential building with 10,000 occupants in Dalian, China. The system can be used for heating and cooling. Heat recovery is of the indirect type so that the waste water exchanges heat with a secondary flow in a heat exchanger, after which it is sent back to the municipal sewage pipeline. This system uses a shell and tube heat exchanger.

Spriet and Hendrick [14] developed a simulation to evaluate the potential of heat recovery from waste water. The model has been validated using experimental data of an installation located in Myrtes (Brussels), Belgium. The sewage heat exchanger is installed in the sewer while the heat pump is placed in a machine room. The recovered heat is used for heating of a conditioned space. The waste water heat exchanger is of the multi-row tube type. HDPE tubes are connected in series in multiple tube rows. A solution of glycol in water (MEG 33 %) is used as the heat transfer medium inside the tubes to recover heat from waste water.

Among the two WWSHP systems described, the first one used a metallic shell and tube heat exchanger for heat recovery from waste water. The use of shell and tube was only possible because the sewage was cleaned off of the fouling elements using complex anti-clogging equipment. The anti-clogging system requires regular maintenance and adds to the overall cost of the system. Thus, considering the overall system complexity, space requirements and the cost of metallic heat exchangers, the system used in Myrtes was selected for further investigation in this study. Experimental data and simulation results of the Myrtes site can then be used for validation purposes.

2.4. Polymer materials

Different polymers have been compared based on the values of three of the most important features : thermal conductivity, λ, yield strength (YTS) and cost of raw materials. The four polymers with the highest thermal conductivity are listed in Table 1. PS is included because it is commonly used in heat exchangers.

The fillers used in polymer composites are particles, fibers, flakes and laminas. Chen et al. [1] provide a list of some composites with their matrix material, filler material, filler volume and the resulting thermal conductivity values. For instance, the thermal conductivity of PS (0.14 $Wm^{-1}K^{-1}$) rises to 0.25 $Wm^{-1}K^{-1}$ when 10 % graphite is added as filler to the material and to 0.90 $Wm^{-1}K^{-1}$ when 30% graphite is added.

Table 1. Commonly used polymers with highest thermal conductivity. Please consult the list of abbreviations in the nomenclature for the polymer specifications. The thermal conductivity of copper, a frequently used material in heat exchangers, is 401 $Wm^{-1}K^{-1}$ and copper costs around 5.54 €/kg.

Polymer	λ_t [$Wm^{-1}K^{-1}$]	YTS [MPa]	Cost [€kg^{-1}]
HDPE	0.46	25.9	0.54
LDPE	0.30	10.8	0.57
PPS	0.30	68.9	1.10
PC	0.20	62.0	1.10
PS	0.14	43.9	0.90

The advantage of having high YTS is that the thickness required to withstand pressure can be lower. Low thickness leads to higher *U*-values. When compared to metals, the benefit of low cost of polymers far outweighs that of high thermal conductivity of metals. Among the remaining options, HDPE shows the highest λ value and a relatively high YTS. For this reason, HDPE has been selected for application in the sewage heat exchanger.

3. System model

3.1. Local characteristics of sewage network

The model concerns a specific sewage channel in the center of Rotterdam. The data required for modeling of the sewage heat recovery system such as sewage channel dimensions, sewage temperature and sewage flow has been provided by the Municipality of Rotterdam.

The dimensions of the sewage channel considered for the installation of waste water heat exchanger are as shown in Fig. 1. The sewage channel is located in the center of Rotterdam near the 'Doelen'. The sewage channel is approximately oval shaped with the flow passage area spanning 1.5 m in width and 1.44 m in height.

Number of tubes of heat exchanger actually submerged in sewage flow, hydraulic diameter of the channel, flow cross-sectional area and sewage flow velocity are all dependent on the sewage level. These parameters are dynamically evaluated for each sewage level. The angle between the horizontal and l_2 is 30°. When the sewage level is higher than l_4, the flow area is divided into a trapezium with sides l_1; l_2; l_5; l_3 and a rectangle with area l_5 x l_6. In that case, the length of the sides l_6=l_7 is calculated as the difference in sewage level and l_4. For sewage level lower than l_4, the flow area is just a trapezium and length of sides l_6=l_7 is 0. From a measurement in 2018, the highest sewage level that can be attained is 0.5 m. Thus, the maximum possible value for l_4 + l_6 is 0.5 m. Dimensions of the sewage channel calculated for the sewage level of 0.5 m are provided in Table 2.

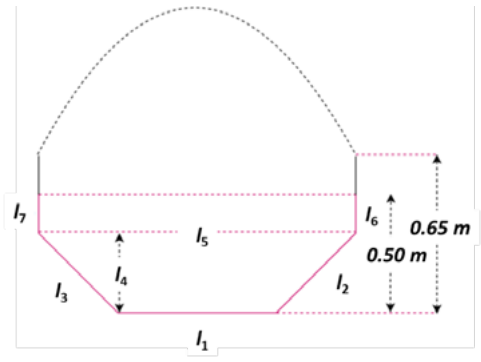


Fig. 1. Schematic of the cross section of the sewage channel.

Table 2. Dimensions of the sewage channel for a sewage level of 0.5 m.

l_1 [m]	l_2 [m]	l_3 [m]	l_4 [m]	l_5 [m]	l_6 [m]	l_7 [m]	$P_{tot,ch}$ [m]	P_{ch} [m]	$d_{hyd,ch}$ [m]	$r_{hyd,ch}$ [m]	$A_{c,ch}$ [m^2]
0.50	0.58	0.58	0.29	1.50	0.21	0.21	3.58	2.08	0.68	0.17	0.61

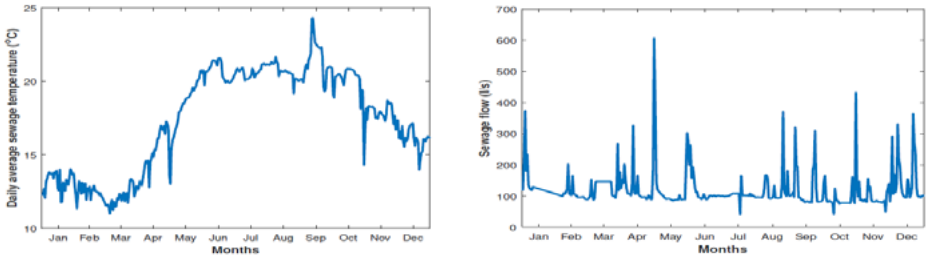


Fig. 2. Daily averaged temperature (left) and volumetric flow rate (right) of the sewage flow in 2018.

Sewage temperature values were available in intervals of 5 minutes for each day of the year 2018. Since the daily variation of sewage temperature was not significant, daily average was calculated for each day of the year and was considered to be the sewage temperature for that day. Variation of daily average sewage temperatures throughout the year is plotted in Fig. 2 (left). Sewage temperature was found to vary between a maximum of 24.3 ºC to a minimum of 11 ºC. It can be seen that sewage temperatures are higher in the summer (June, July and August) and lower in the winter.

The volume flow rate is given in Fig. 2 (right) and, in 2018, varied between a maximum of 606.8 l/s to a minimum of 41.5 l/s. Sewage flow velocity and level were calculated based on flow data and channel dimensions. From the known data that the highest sewage level in 2018 was 0.5 m, sewage levels for all other flow rates were interpolated linearly with sewage flow. The sewage level variation is plotted in Fig. 3 (left). Velocity of sewage flow was estimated from sewage flow rate, sewage level and the corresponding channel dimensions. Flow area is dependent on the sewage level and sewage level is dependent on flow. Fig. 3 (right) shows the variation of sewage velocity along the year. It can be observed that on the day of the highest sewage level, flow velocity is the lowest. Sewage velocity varied between a minimum of 1 m/s to a maximum of 2.17 m/s. The corresponding Reynolds number varied between 15000 and 76000, indicating turbulent flow.

The mass flow rate of sewage can be obtained from its velocity using eq. (1).

$$\dot{m}_{ww} = \rho_{ww} \cdot A_{c,ch} \cdot v_{ww} \tag{1}$$

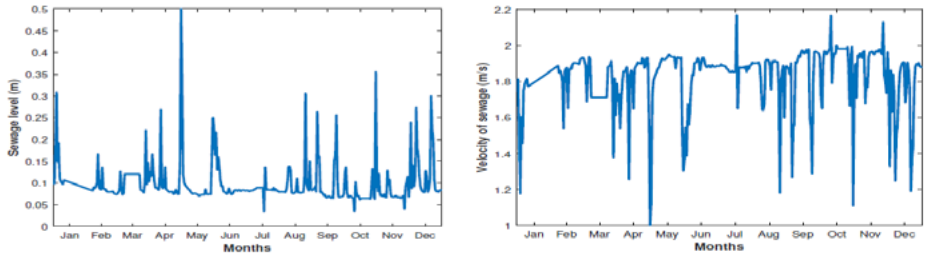


Fig. 3. Daily averaged sewage level (left) and velocity (right) of the sewage flow in 2018.

3.2. Waste water source heat pump (WWSHP) system

The waste water source heat pump systems considered in this work are schematically illustrated in Fig. 4. In the winter, heat is recovered from the sewage and in the summer rejected to the sewage. For this reason a reversible heat pump is used. Polymer waste water heat exchangers (WWHEX) are used to transfer heat with the sewage. Four heat exchangers are installed in parallel inside the sewage channel as illustrated in Fig.4.

Secondary water (a solution of glycol in water) is used as an intermediate fluid between the heat pump and the WWHEXs.

During the winter secondary water transfers the heat recovered from the sewage to the refrigerant in the evaporator of the heat pump. In the evaporator, the hot secondary water is cooled to a temperature 2 K higher than the evaporation temperature. The heat required by 'Doelen' is supplied by the condenser of the heat pump. The condensation temperature is set at 55 °C. The water used for heating in the 'Doelen' is heated from 25 °C to about 53 °C in the condenser and then supplied to the heating network of the 'Doelen'. In the summer, the heat pump is operated in reverse. Chilled water from the cooling network of 'Doelen' is cooled from 14 °C to 10 °C in the evaporator of the heat pump which operates at 8 °C. The condensation temperature of the heat pump is varied such that the secondary water inlet temperature to the waste water heat exchanger is higher than the sewage temperature.

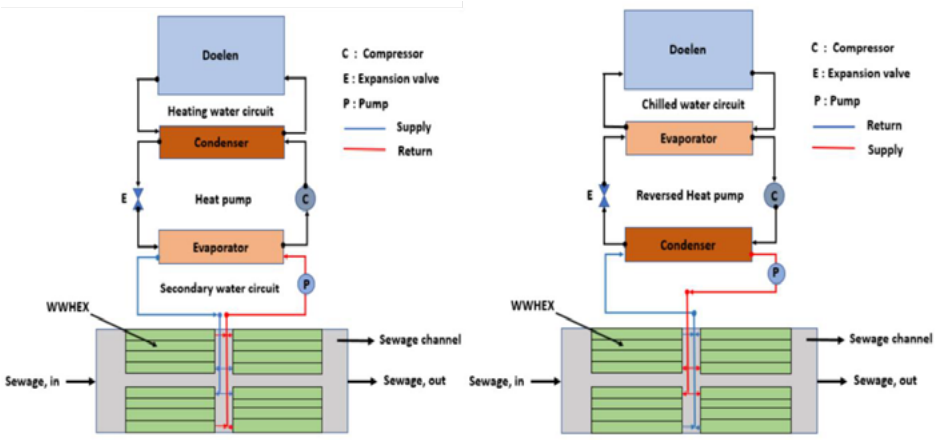


Fig. 4. WWSHP system as connected during the winter season (left) and summer season (right).

Winter and summer situations are simulated separately due to the differences in operation. For each combination of tube length and diameter of the waste water heat exchanger, the winter model is simulated on a daily basis for nine months of winter. In the heat recovery system, the sewage and heat pump condensation temperature are the only known values while all other temperatures are unknown. Based on the sewage temperature, the secondary water outlet temperature ($T_{sw,out}$) is set. The secondary water inlet temperature ($T_{sw,in}$) is varied from 0 °C to a temperature 2 K lower than $T_{sw,out}$. The evaporation temperature of the heat pump is set 2 K lower than $T_{sw,in}$. For each of the 9 months, a primary inner loop was run for the number of days of that month while a secondary inner loop ran over all combinations of temperatures until the increase in *COP* of the system was less than 5% (convergence criterion). Once the combination of temperatures with the optimized *COP* is found, the secondary inner loop is terminated and the calculations for the next day start. After the winter model has been simulated for 9 months, the total heat recovered, heat supplied, required pump and compressor power and seasonal *COP* are calculated. After that, the same calculations were repeated for the next combination of tube dimensions. At the end, all the seasonal performance parameters are compared to find the most optimal heat exchanger tube dimensions.

The same set of optimized tube dimensions are used for the summer model since the waste water heat exchanger installation is the same in the summer. In the summer, the secondary water rejects heat to the sewage, thus its temperature is set higher than the sewage temperature. The increase in secondary water temperature ($T_{sw,in} + \Delta T$) at the inlet of waste water heat exchanger over $T_{ww,in}$ is varied from 10 K to 50 K to study the effect on system performance. Thus, the summer model was simulated for different secondary water inlet ($T_{sw,in}$) temperatures. For each $T_{sw,in}+ \Delta T$, a primary inner loop iterated over the summer months. A secondary inner loop iterated over all the days of the summer where the condensation temperature was set to be equal to $T_{sw,in}$ + 2 K and the secondary water outlet temperature ($T_{sw,out}$) is set 2 K higher than the daily average sewage temperature. Similar to the winter model, all the seasonal values of the system performance indicators are calculated to find the most optimum value for $T_{sw,in}$.

3.3. Waste water heat exchanger

The WWHEX has sewage on the hot side and secondary water on the cold side in the winter and vice-versa in the summer. Multi-row polymer tube heat exchanger is selected as the WWHEX type. The polymer tubes are arranged in series. To reduce the pressure drop, the total secondary water flow required is distributed among 4 parallel heat exchangers which have tubes arranged in series. All the tube rows are installed against the surface of the sewage channel, so that the sewage flows directly over the polymer tubes. From initial analysis, it was concluded that, due to low thermal conductivity of the polymer tubes, a large number of tubes is required. For this reason the tubes are closely packed. Fig. 5 illustrates the cross sectional view of an indicative tube arrangement to assist the understanding of modeling of the heat exchanger. All the dimensions in the diagram are in mm. Fig. 5 indicates the tube arrangement for a sewage level of 0.5 m and depicts two heat exchangers placed symmetrically. In each heat exchanger, the tubes are connected in series. One heat exchanger is on the RHS and another on the LHS. A small separation between the two can be seen on the bottom side. Two more heat exchangers are placed along the channel adjacent to these two heat exchangers. A common header was used to carry the total secondary water flow, which was split into the 4 heat exchangers.

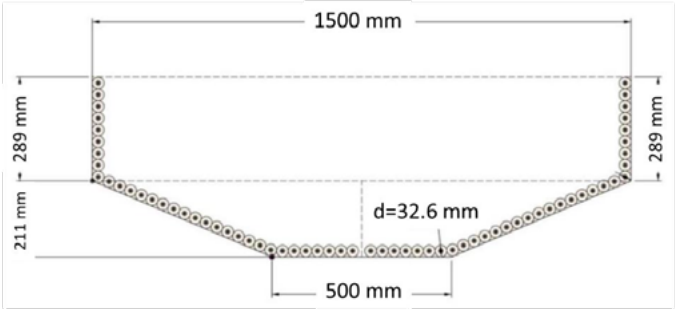


Fig. 5. Cross section of the sewage channel showing the arrangement of the polymer tubes along the surface of the channel. Fig. 3 shows that the liquid level is generally lower so that preferably only the trapezium part of the channel should be covered with tubes.

3.4. Design duty for WWHEX

The WWHEX has been designed to exchange (recover/reject) 180 kW from the sewage. It should recover 180 kW during the day with the lowest temperature in the winter and to reject 180 kW to the sewage during the hottest day in the summer. The months of September to May are the months requiring heating (winter). The rest of the months, June to August are the months requiring cooling (summer). The required heat duty of the waste water heat exchanger was considered to scale linearly with the ambient temperature. Thus, 180 kW should be recovered from sewage during the day with the lowest outside temperature while no heat should be recovered ($\dot{Q}_{ww} = 0$ kW) when the ambient temperature is above 20 ºC in the winter. In the summer, 180 kW should be rejected to the sewage on the hottest day and cooling is not required on those days when ambient temperature is lower than 20 ºC. Heat recovered from the sewage was considered to be equal to the capacity of the evaporator in the winter and the heat rejected to sewage to be equal to condenser capacity in the summer. Fig. 6 (left) depicts the variation of ambient temperature in 2018 and the required heat exchange with sewage in the winter and Fig. 6 (right) indicates the heat to be rejected to the sewage in the summer. A horizontal line marking 20 ºC is shown in both plots. It can be seen that in the winter when the ambient temperature crosses the 20 ºC line, the heat duty goes to zero and in the summer, the heat duty goes to zero when the ambient temperature is below the 20 ºC.

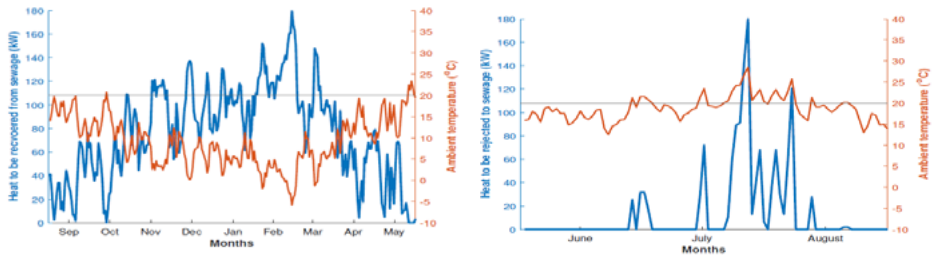


Fig. 6. Heat to be extracted from the sewage in the winter season (left) and rejected to the sewage in the summer season (right).

Due to the large sewage flow, reduction in sewage temperature was negligible after heat extraction. Thus, the physical properties of sewage at inlet and outlet of waste water heat exchangers were considered to be the same. Due to the fact that exact data indicating the quantitative and qualitative analysis of the sediments in the sewage of Rotterdam was not available, properties of water were considered for sewage water calculations. Measurements by the Municipality indicated that the sediments were low in the sewage channel considered. Properties of water have been evaluated as a function of the sewage temperature.

Flow of sewage in the sewage channel was approximated to flow through tubes. Hydraulic diameter of the channel based on the sewage level was considered to be the diameter of the channel for Nusselt number calculation. Thus, the convective heat transfer coefficient on the sewage side (α_{ww}) was calculated based on sewage flow velocity (v_{ww}) and hydraulic diameter of the channel ($d_{hyd,ch}$). Properties of sewage such as λ_{ww}, μ_{ww}, ρ_{ww} and $c_{p,ww}$ required for the calculation of (α_{ww}) were calculated at the sewage temperature.

The secondary fluid was a mixture of water and mono-ethylene glycol with a concentration leading to a freezing point of -20 ºC. The properties of this mixture have been obtained from Melinder [10]. The mass flow of secondary water has been obtained with eq. (2) where the heat duty is obtained from Fig. 6 and ΔT_{sw} is the temperature change of the secondary water as it passes the heat exchanger.

$$\dot{m}_{sw} = \frac{\dot{Q}_{ww}}{c_{p,sw} \cdot \Delta T_{sw}} \tag{2}$$

The velocity of the secondary water through the heat exchanger tubes follows from the cross section of the flow, the density and the number of heat exchangers in parallel (4). The convective heat transfer coefficient on the secondary water side α_{sw} was calculated using the same correlations as for the sewage side [11]. A fouling resistance of 0.00067 m^2KW^{-1} [9] has been assumed on the sewage side and of 0.0002 m^2KW^{-1} [13] on the secondary water side. These extra resistances have been included in the calculation of the overall heat transfer coefficient based on the external area of the tubes, U_o.

Based on the value of U_o, LMTD and the heat duty per heat exchanger, the external surface area of the tubes ($A_{tot,t}$) required per heat exchanger was obtained from eq (3).

$$A_{tot,t} = \frac{\dot{Q}_{ww,req,1}}{U_o \cdot LMTD} \tag{3}$$

This allowed for the calculation of the required number of tubes. The number of tubes must be even to ensure that the return line can be connected from the same side as that of the supply line. The number of tubes required per heat exchanger was compared with the total number of tubes that were submerged in sewage at any given time ($N_{t,sub}$) to see if it was feasible. $N_{t,sub}$ depends on sewage level with corresponding wetted perimeter, tube diameter and tube pitch. The actual heat recovered from the sewage per heat exchanger is then obtained from eq. (4).

$$\dot{Q}_{ww,act,1} = U_o \cdot \frac{N_{t,sub}}{2} \cdot A_{s,t} \cdot LMTD \tag{4}$$

With $A_{s,t}$ the surface area of a single tube. The pressure drop on the secondary flow side was obtained from the number of tubes and connecting elbows, length of the tubes, connecting header and mass flow through the

heat exchanger. This pressure drop allowed for calculation of the power consumption of the pump. For the heating period, the instantaneous COP was then obtained from eq. (5).

$$COP = \frac{\dot{Q}_{cond}}{\dot{W}_{sw,pump} + \dot{W}_{comp}} \quad (5)$$

The working fluid of the heat pump was propane (R290). In the winter season the condensation temperature of the cycle was maintained at 55 ºC. The temperature of the refrigerant at the outlet of the compressor was then around 64 ºC. In the condenser, the refrigerant was cooled from 64 ºC to a sub-cooled temperature of 30 ºC. Water from the 'Doelen' heating system was heated from 25 ºC to 53 ºC with a pinch of 5 K in the condenser. The secondary water temperature $T_{sw,in}$ at the outlet of the evaporator was the limiting factor for the evaporation temperature. The evaporation temperature of the heat pump was set 2 K lower than $T_{sw,in}$ to prevent temperature cross-over. $\dot{Q}_{cond}$ and $\dot{W}_{comp}$ were obtained from the heat pump model making use of Refprop [8] for the propane properties.

4. Model results

4.1. Validation

The data reported by Spriet and Hendrick [14] collected in Myrtes has been used for validation purposes. This test plant makes use of 30 HPDE tubes of 6 m long with internal diameter of 32 mm and a wall thickness of 2.13 mm. The recovered heat is upgraded making use of a R410A heat pump. During the experiments, the sewage flow varied between 5 and 60 m^3/h and its temperature from 6 to 18 ºC. The secondary water (MEG) was pumped over 230 m. Table 3 compares the reported experimental data with the results of the model proposed in this work.

Table 3. Comparison of the experimental data of the Myrtes plant and the proposed model.

Parameter	Myrtes plant data	Present model
Heat recovered from sewage [kW]	2.5 – 5.5	1.2 – 5.5
Heat delivered by heat pump [kW]	3.2 – 7.0	2.7 – 7.4
COP	3.7 – 5.0	3.9

In general the model predicts reasonably well the peak values recovered and delivered by the system. The lower values of the recovered heat and delivered heat are lower in the present model. The reason for this deviation is that the sewage design of Rotterdam was assumed to apply for Myrtes since its real geometry was not reported by the Spriet and Hendrick [14].

4.2. Tube dimensions of waste water heat exchanger

The winter model was run for 6 combinations of tube lengths and diameters. Standard HDPE tube lengths of 12 m and 30 m and tube inner diameters of 17 mm, 29 mm and 58 mm were selected for these simulations. The lowest COP value was observed for the combination of l_t = 30 m and $d_{i,t}$ = 17 mm while the highest COP was observed for $d_{i,t}$ = 58 mm options. Smaller tube diameters resulted in more heat recovery due to higher secondary water velocity (hence higher U_o). The highest amount of heat recovered from the sewage was for l_t = 30 m and $d_{i,t}$ = 17 mm. The lowest amount of heat recovered was for the l_t = 12 m and $d_{i,t}$ = 58 mm combination. Table 4 provides the seasonal values of COP, heat recovered from sewage, total electrical energy required to run the pump and the compressor along with a cost comparison. The cost column includes the cost of the waste water heat exchanger and the cost of electricity. The cost of heat exchanger is based on the weight of material used in the heat exchanger and the specific price of the material. It is assumed equal to three times the material cost. The cost of electricity was considered to be 50.7 €/MWh [4]. The system performance was quantified as the amount of heat delivered to 'Doelen', Q_{cond}, per unit cost (kWh/€).

Table 4. Optimization of tube dimensions for the waste water heat exchanger.

Dimensions		Q_{cond}	Q_{ww}	W_{elec}	N_t	Cost [€]			kWh/€	*COP*
l_t [m]	$d_{i,t}$ [mm]	[MWh]	[MWh]	[MWh]		WWHEX	W_{elec}	Total		
	17	236	181	66	200	396	3346	3742	63	3.6
12	29	131	103	30	128	415	1521	1936	**68**	**4.5**
	58	43	34	9	64	403	456	859	50	4.6
	17	535	405	331	200	989	16782	17771	30	1.6
30	29	486	374	126	128	1037	6388	7425	**65**	**3.9**
	58	188	148	41	64	1007	2079	3085	61	4.6

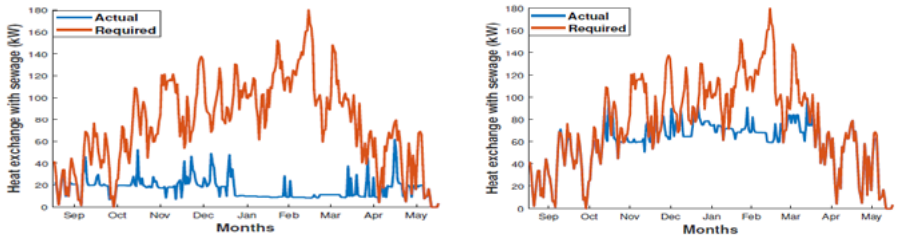


Fig. 7. Difference between the required (red) and recovered (blue) heat from the sewage for the 29 mm tube. Left for tubes of 12 m; right for tubes with 30 m.

The best two options were $d_{i,t}$ = 29 mm, l_t = 12 m and $d_{i,t}$ = 29 mm, l_t = 30 m. The 12 m option delivered 68 kWh/€, while the 30 m option delivered 65 kWh/€ which is only 4.6% lower. Thus, to make a choice between l_t = 12 m and l_t = 30 m, a comparison between the actual heat recovered and the required heat exchange with the sewage was compared as shown in Fig. 7. The heat recovered in the case of l_t = 12 m option was much lower than what was necessary (Fig. 7 left), while it was much better in the case of l_t = 30 m (Fig. 7 right). Thus, making use of just one heat exchanger with l_t = 12 m was not sufficient to recover the required amount of heat. Thus, l_t = 30 m and $d_{i,t}$ = 29 mm were chosen as the optimized tube dimensions.

Based on the time dependent sewage temperature values, secondary water inlet and outlet temperatures were determined. Based on secondary water inlet (to waste water heat exchanger) temperature, the heat pump evaporation temperature was determined (2 K lower). Condensation and evaporation temperature of the heat pump, sewage inlet and outlet temperatures and secondary water temperatures for the winter season are plotted in Fig. 8 left. The optimum COP of the system was obtained when the temperature of the secondary water increased by 10 K. Fig. 8 right shows how the COP of the system changes during the heating season.

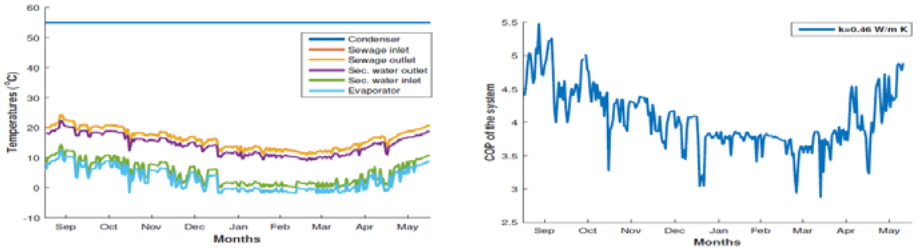


Fig. 8. Change of the operating temperatures during the heating season (left). Notice that in and outlet of sewage are the same. Right: the change of system COP during the heating season.

4.3. Effect of using enhanced polymers

Table 5 shows a comparison of WWSHP system performance in the winter and summer. Increase in thermal conductivity of the polymer tubes from 0.46 to 1.89 $Wm^{-1}K^{-1}$ enhances heat recovery in the winter much more

than in the summer. The electrical energy consumption was higher in the winter due to longer period of operation (9 months) and more heat recovery. Seasonal COP value of summer was higher than winter for both the cases (of thermal conductivity). The increased U_o in both the cases was almost two times the initial value.

Table 5. Optimization of tube dimensions for the waste water heat exchanger.

Season	λ_t	U_o	Q_{cond}	Q_{evap}	W_{elec}	Cost [€]			kWh/€	COP
	[$Wm^{-1}K^{-1}$]	[$Wm^{-2}K^{-1}$]	[MWh]	[MWh]	[MWh]	WWHEX	W_{elec}	Total		
Heating	0.46	149	486	374	126	1037	6388	7425	65.5	3.9
Cooling		143	26	23	3		152	1189	19.3	7.3
Heating	1.89	296	650	495	211		10698	11735	55.4	3.1
Cooling		290	30	27	4		203	1240	21.8	6.9

5. Conclusions

The feasibility of using locally the sewage network to deliver heat to buildings in the center of Rotterdam has been investigated. Polymer heat exchangers to be submerged along the sides and bottom of the sewage channel have been proposed in combination with a heat pump delivering heat at 55 °C. The following has been concluded:

- Using HDPE tubes 8.1 MWh/m_{sewage} heat at 55 °C can be delivered yearly. The system yearly averaged COP is then 3.9. To deliver 1 PJ of heat 34.3 km of sewage need to be equipped with such heat exchangers.
- Using thermally enhanced HDPE tubes 10.8 MWh/m_{sewage} heat at 55 °C can be delivered yearly. The system yearly averaged COP is then 3.1. To deliver 1 PJ of heat 25.7 km of sewage need to be equipped with such heat exchangers.
- The heat exchangers can be designed to deliver local heating requirements during the whole heating season.

Acknowledgements

The authors would like to thank the Municipality of Rotterdam for providing the relevant sewage data.

References

[1] Chen X, Su Y, Reay D, Riffat S. Recent research developments in polymer heat exchangers - A review. Renewable and Sustainable Energy Reviews; 2016; **60**:1367–1386.
[2] Culha O, Gunerhan H, Biyik E, Ekren O, Hepbasli A. Heat exchanger applications in waste water source heat pumps for buildings: A key review. Energy and Buildings; 2015; **104**: 215–232.
[3] Frijns J, Hofman J, Nederlof M. The potential of (waste)water as energy carrier. Energy Conversion and Management; 2013; **65**:357–363.
[4] Greunsven J, Derks M. Tennet - Annual Market Update. page 3, 2018.
[5] Hepbasli A, Biyik E, Ekren O, Gunerhan H, Araz, M. A key review of waste water source heat pump (WWSHP) systems. Energy Conversion and Management; 2014; **88**:700–722.
[6] Hofman J, Hofman-Caris R, Nederlof M, Frijns nJ, van Loosdrecht M. Water and energy as inseparable twins for sustainable solutions. Water science and technology; 2011; **63**:88–92.
[7] Hussain ARJ, Alahyari AA, Eastman SA, Thibaud-Erkey C, Johnston S, Sobkowicz MJ. Review of polymers for heat exchanger applications: Factors concerning thermal conductivity. Applied Thermal Engineering; 2017; **113**:1118–1127.
[8] Lemmon, E. W., Huber, M. L. and McLinden, M. O. NIST Standard Reference Database 23: Reference Fluid Thermodynamic and Transport Properties-REFPROP, Version 9.1, National Institute of Standards and Technology, Standard Reference Data Program, Gaithersburg. 2013.
[9] Liu Z, Ma L, Zhang J. Application of a heat pump system using untreated urban sewage as a heat source. Applied Thermal Engineering; 2013; **62**:747–757.
[10]Melinder A. Properties of secondary working fluids for indirect systems. International Institute of Refrigeration, 2010.
[11]Mills AF. Basic heat and mass transfer. Prentice Hall, New Jersey, 1999, p. 269-280.

[12]Roest K, Hofman J, van Loosdrecht M. De Nederlandse watercyclus kan energie opleveren. H_2O; 2010: **47**(25/26):47–51.
[13]Sinnott RK, Towler G. Chemical Engineering Design. Elsevier. Butterworth-Heinemann, 5th edition, 2009. Chapter 12 – Heat transfer equipment, p. 815-978.
[14]Spriet J, Hendrick P. Waste water as a heat source for individual residence heating: A technoeconomic feasibility study in the Brussels capital region. Journal of Sustainable Development of Energy, Water and Environment Systems; 2017; **5**:289–308.
[15]van der Hoek JP, de Fooij H, Struker A. Wastewater as a resource: Strategies to recover resources from Amsterdam's waste water. Resources, Conservation and Recycling; 2016; **113**:53–64.
[16]Wanner O, Panagiotidis V, Clavadetscher P, Siegrist H. Effect of heat recovery from raw waste water on nitrification and nitrogen removal in activated sludge plants. Water Research; 2005; **39**(19):4725–4734.
[17]Yang L, Yan H, Lam JC. Thermal comfort and building energy consumption implications - A review. Applied Energy; 2014; **115**:164–173.

13th IEA Heat Pump Conference
April 26-29, 2021 Jeju, Korea

Seasonal thermal energy storage for large scale district heating

Just Remmelts[a], Sander Tensen[b], Carlos Infante Ferreira[a*]

[a]Delft University of Technology, Department Process & Energy, Leeghwaterstraat 39, 2628 CB Delft, The Netherlands
[b]Eneco Industrial & Heat, Postbus 19020, Rotterdam, The Netherlands

Abstract

Seasonal thermal energy storage (STES) systems in combination with heat pumps can significantly reduce the impact of peak loads in large scale district heating systems and allow for the application of renewable heat sources in these networks. This paper investigates technologies with the highest potential for implementation in large scale district heating networks and identifies high temperature aquifer thermal energy storage (HT-ATES) as the most suitable technology. The HT-ATES has been applied at the primary side of the network (90 to 110 ºC) and at the secondary side (72 to 92 ºC). Suitable locations for the STES have then been identified. A control volume approach is used in Matlab to predict heat transfer and pressure drop in the HT-ATES wells considering porosity, permeability, grain size and geometry of the aquifer. The temperature distribution and extraction temperature are predicted as function of time. The yearly heating demand of a network has been used in combination with different operating modes to identify the required size of the HT-ATES. The simulations indicate that it will take 5 years to reach steady temperature supply.

Keywords: heat pump; high temperature aquifer energy storage; district heating.

1. Introduction

In the Netherlands, the built environment creates about 20% of the entire national energy demand. The heat consumption of the sector amounted 574 PJ in 2015 [12] and the majority of this heat is produced by gas-fired boilers. The national and international climate agreements together with policies concerning gas production in Groningen (the Netherlands) require substantial changes in the thermal energy supply of the built environment. A significant increase of the use of district heating networks (DHN) is one of the measures proposed to move away from gas-fired heating systems. Several studies predict that by 2050 a large share of the heating supply in the built environment will make use of DHNs. Hoogervorst [8] predicts a share of 57%, Roelofsen et al. [15] of 27% and Wielders et al. [27] of 61%.

Currently, most of the heat delivered by DHNs does not originate from renewable sources. Although DHNs are suitable to transport renewable energy, the thermal energy is currently mostly produced by fossil-fueled plants such as combined heat and power plants (CHP) and backup boilers (BUB). According to Schoots et al. [18], 75% of the thermal energy supplied by large scale DHNs in the Netherlands is based on fossil fuels. Renewable heat production units, such as solar heat, industrial waste and geothermal energy plants, need to be added to the thermal energy supply. The increasing variety of heat production units causes a decrease in flexibility of the heat supply. Waste heat from industrial processes does not fluctuate over the seasons but is determined by industrial activity. Solar thermal energy and energy from geothermal plants are determined by the amount of sun hours and limitation in pumping rates. For all heat sources, long operating times have a strong impact on the levelized cost of energy (LCOE). LCOE quantifies the cost of unit energy produced including the investment and operational costs of the system.

Nomenclature

Roman symbols					
	V	Volume	m^3	hot	Hot well

* Corresponding author. Tel.: ++31-152-784-894.
E-mail address: c.a.infanteferreira@tudelft.nl .

A	Area	m^2	z	Coordinate	m	in	At inlet
c_p	Specific heat	$kJkg^{-1}K^{-1}$	*Greek symbols*			out	At outlet
E	Thermal energy/year	$kJyear^{-1}$				r	At radius r
			Δ	Difference	-		
h	Heat transfer coeff.	$kWm^{-2}K^{-1}$	η	Efficiency	-	sto	Storage
m	Mass	kg	ρ	Density	kgm^{-3}	th	Thermal
Q	Heat	kJ	*Subscripts*			tot	Total
$\dot{Q}$	Heat flow	kW				w	Water
r	Radial coordinate	m	aq	Aquifer		well	Well
T	Temperature	°C or K	ave	Average		z	At position z
t	Time	s	cold	Cold well			

Seasonal thermal energy storage systems (STES) are able to store surplus heat. In winter, when the demand is higher than the supply, STES can function as an extra heat source. STES allows DHNs to operate in a sustainable and efficient way. In order to balance the heat demand and renewable heat supply at all times, thermal energy storage systems in DHNs seem inevitable. Fig. 1 shows the heat demand of the DHN of Utrecht in 2017 and 2018. The blue area shows the effect of STES on the required thermal energy production. In the summer the heat supply can be increased and the surplus heat (above the thermal energy demand curve) is stored.

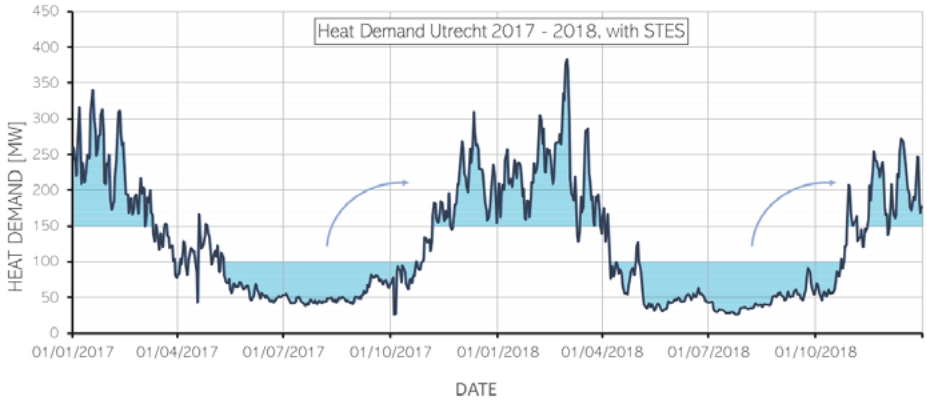


Fig. 1. Daily heat demand of the DHN of Utrecht in 2017 and 2018. The blue filled areas indicate the effect of STES on the installed capacity. In summer the heat production is increased so that the surplus can be stored to be used during winter as an extra heat source.

The transformation of a large scale mainly fossil-fueled DHN into a mainly renewable heat based system will generally reduce the flexibility of the DHN. Optimally sized STES can balance demand and supply of heat and to a certain extent provide flexibility to the DHN. The renewable heat sources can then always operate at optimal conditions while the surplus heat can be stored for later use.

The supply temperatures of most of the existing DHNs in the Netherlands is between 70 and 90 °C [27]. Low temperature DHNs, with supply temperatures <70 °C, perform thermally better since heat losses are lower [2]. While more heat sources become available when the DHN makes use of low temperatures, in the current built environment infrastructure high temperature DHNs can have a better economic performance. The existing infrastructure has been designed to deliver heat at high temperature and does not require end-user investments. Also, the high temperature DHN requires smaller distribution pipes leading to lower costs [26]. This study focuses on large scale (>2,000 consumers) high temperature supply (>70 °C) DHNs similar to the DHN of Utrecht.

The DHN of Utrecht is the third largest in the Netherlands [8]. It supplies thermal energy to more than 40,000 users. Presently the network is entirely supplied by fossil-fueled heat sources and needs to transition to renewable energy sources in the coming years. Internal scenarios from the owner, Eneco, indicate that seasonal storage is required from an economic perspective. The district heating network of Utrecht can be divided into two networks: the transport network and the distribution network. The transport network carries hot water generated at the heat source to the heat transfer station (HTS). The heat source and the HTS both have heat exchangers to transfer the heat from and towards the transport network. At the HTS the hot supply water transfers thermal energy to the distribution network. The colder water leaving the HTS is sent back to the heat source to be reheated. The supply temperature of the water is determined by the maximum thermal energy demand of the day [6]. This ensures a constant daily supply with an average lower supply temperature. As the heat demand is higher in the winter than in the summer, the temperature of the water in the transport network is higher in the winter to provide enough thermal energy. The DHN always needs to deliver safe and sufficient heat to the end-users. Safe means that the water temperature should always be high enough to prevent legionella to develop. These two characteristics determine the supply temperature of the DHN. The daily set-point is determined by a dedicated prediction software [5]. The BUBs can supply extra heat to the distribution network if the power from the source is insufficient. In the HTS the heat is transferred to the distribution network making use of heat exchangers. The distribution network's supply temperature is determined by the ambient temperature. The hot water exchanges heat at the end-user before it returns to the HTS. Fig. 2 shows left the relation between the delivered thermal power and the supply temperature in the transport network and right the relation between environmental temperature and supply temperature of the distribution network. The major heat sources are located in the transport network and consist of two CHP plants of 180 MW each and a BUB of 105 MW. Additionally a few BUBs are installed in the distribution network with capacities in the range 58 to 90 MW. Goal is to substitute these fossil-fuel driven heat sources by renewable heat sources. In the first phase mainly bio heat and green gas combustion systems will be implemented. In the second phase renewable heat sources without combustion will be implemented.

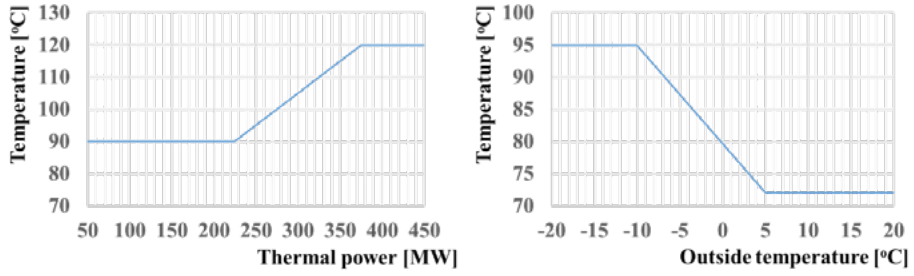


Fig. 2. Temperature levels of the supply water in the network: left in the transport network as a function of thermal power requirement and right in the distribution network as a function of the environmental temperature.

The International Energy Agency (IEA) gives an overview of previous high temperature storage systems [16]. Existing high temperature storage systems connected to district heating are predominantly located in the north of Europe. Wolfgramm [28] reports that in Neubrandenburg (Germany) a geothermal installation has been converted to a 4 MW high temperature aquifer thermal energy storage (HT-ATES) system. In the winter the system supplies heat to a low temperature district heating network. In the district heating of Braedstrup (Denmark) several pit thermal energy storage (PTES) and tank thermal energy storage (TTES) have been successfully implemented [20-21]. Several caverns are under construction to store 120 MW of hot water of the DH of Helsinki [23]. The Drake Landing project (Canada) provides almost the entire heat demand of a district by combining solar thermal heat with thermal storage [19]. The European project HeatStore plans to demonstrate underground thermal energy storage in five different countries [10].

The objective of this paper is to investigate the technical feasibility of the implementation of a seasonal heat storage system in an existing large scale DHN. The approach followed is schematically illustrated in Fig. 3. First the most suitable technology is identified, then suitable geographical locations are determined. A model for an HT-ATES system combined with a heat pump to load and unload the storage is developed in Matlab. The performance of the storage system in combination with the load profile of the DHN of Utrecht is then predicted and analysed.

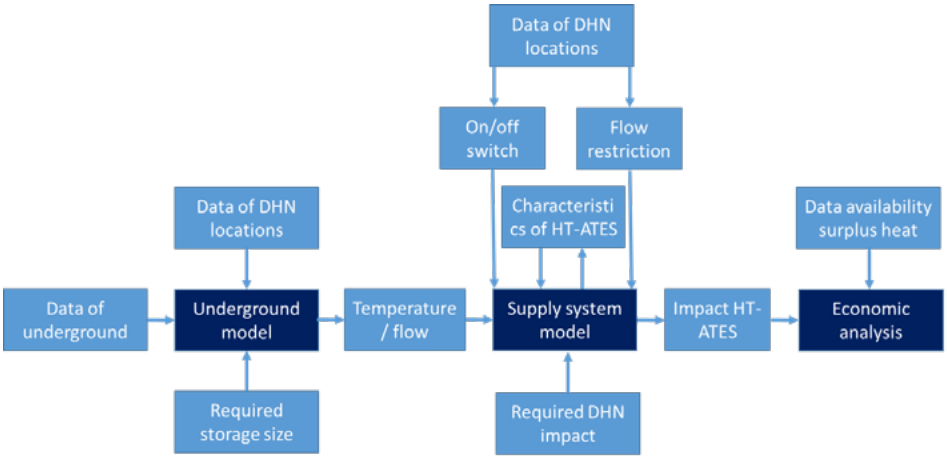


Fig. 3. Schematic of the approach used. A model was first developed for an HT-ATES taking the underground data for the different possible locations and the required storage size into account. This model allows for the prediction of inlet or outlet well temperatures and flow as a function of time. Then a supply system model including a heat exchanger and a heat pump was developed which is coupled to the HT-ATES model and allows for the prediction of the storage conditions as a function of time. Finally these results were used to estimate the economic performance of the storage facility.

2. Seasonal thermal energy storage (STES) systems

Three different groups of storage can be adopted for thermal energy storage (TES): sensible heat storage, latent heat storage and thermochemical heat storage. Fig. 4 (left) illustrates the three groups with corresponding storage capacities and temperature range [17].

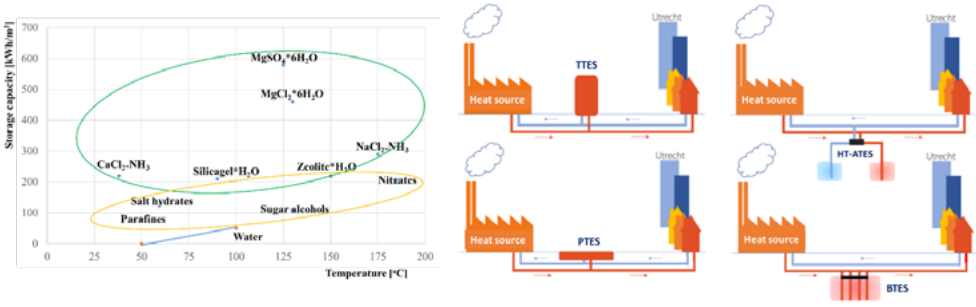


Fig. 4. Left the three groups of TES with sensible heat in blue, latent heat in yellow and thermochemical in green showing that latent heat storage can be twice compacter and thermochemical heat storage up to 7 times compacter. Right the four promising STES systems for district heating integration.

Sensible heat storage is the simplest to apply. The stored amount of energy is obtained with eq. (1).

$$Q = m \cdot c_p \cdot \Delta T \tag{1}$$

Where m is the mass of storage medium (frequently water), c_p its specific heat and ΔT the temperature difference between initial and final temperature of the storage medium. The most frequently used methods of storage of sensible heat are illustrated in Fig. 4 (right): tank thermal energy storage (TTES), pit thermal energy storage (PTES), high temperature aquifer thermal energy storage (HT-ATES) and borehole thermal energy storage (BTES). The optimal STES system stores heat at low cost and high efficiency and can be implemented in dense urban areas without too many constraints.

The bigger the storage volume, the smaller the relative area through which heat losses can take place. Increasing the size generally increases the construction costs. Especially for TTES and PTES the costs increase significantly. The increasing costs for HT-ATES are however smaller as the subsurface itself functions as the insulating material. Fig. 5 shows that the costs reduce with increasing storage volume [11].

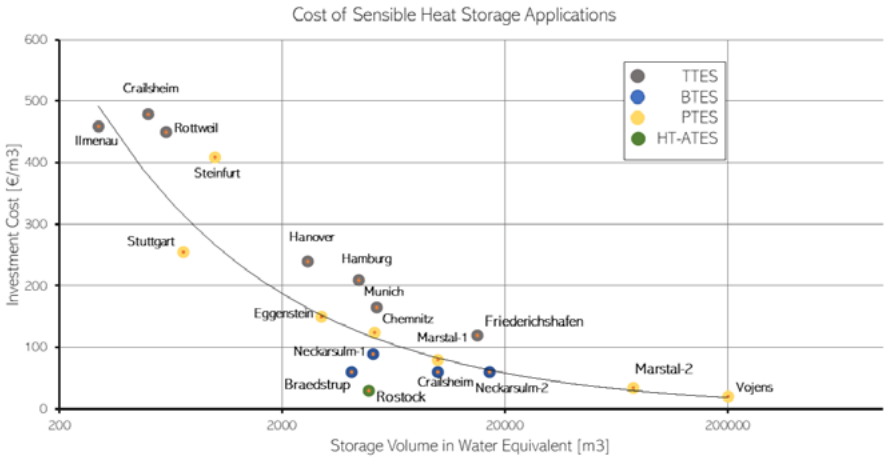


Fig. 5. Relation between specific investment costs and volume of TES based on existing plants in Denmark and Germany [11].

The largest TES, the PTES of Vojens, has a volume of 200,000 m^3 and supplies heat to 2,000 consumers [24]. According to the Danish Energy Agency [3] the costs of this plant are 113 €/GJ. The larger the STES systems, the more economic attractive the systems become. According to de Wit-Blok [7] TTES is expected to have the highest large scale investment costs (139 €/GJ) while HT-ATES is expected to have the lowest costs (14 €/GJ).

Latent heat storage uses the phase change energy of a material to store heat. The melting enthalpy is significantly larger than the sensible change of enthalpy so that the same amount of energy can be stored in a much smaller volume, see Fig. 4 (left). Additional advantage is that the phase change takes place at almost isothermal conditions which depend on the material and can be selected in the temperature range of the DHN (50 ºC to 150 ºC). The most important drawback of latent heat storage is its costs which are currently significantly higher than for sensible heat storage. According to the IEA [9] the costs are 2,778 €/GJ and need to reduce significantly before latent heat storage becomes competitive. A reduction of at least 50% is required for applications in DHNs [22].

Thermochemical energy storage uses chemical energy preserved in the bonds of molecules to store heat [13]. The energy added to the system is used to dissociate a material into other components [1]. Thermochemical storage systems have very high energy densities, see Fig. 4 (left), and are optimal for dense urban areas. Yu et al. [29] claim that storage volumes can be up to 30 times smaller than for sensible heat storage systems and the IEA [9] claims that theoretically storage efficiencies of 100% can be attained. The challenges of applying this storage system for large DHNs are the low technical readiness level and the system costs. The lowest reported potential cost is 2,222 €/GJ [9]. Remmelts [14] has compared the largest PTES storage in Vojens (200,000 m^3) assuming a storage efficiency of 60% for the sensible PTES and a storage efficiency of 100% for the thermochemical storage. The storage costs for Vojens are 113 €/GJ while the costs for the thermochemical storage are 2,222 €/GJ or 1,111 €/GJ, assuming a 50% cost reduction. As the cost of heat increases, a storage technique with a higher storage efficiency (thermochemical) will have a faster increasing economic potential. However, assuming a relatively high cost of heat (the current consumer market price of 24 €/GJ), the total yearly costs of the thermochemical storage are still 2.3 and 1.4 times higher than for the PTES.

From the previous discussion it becomes clear that presently sensible heat storage seems to be the most competitive STES and, taking into account the required size of the DHN storage, the HT-ATES solution seems the most appropriate. It occupies the least surface area of all the sensible heat storage solutions. Presently, in

the Netherlands, subsurface regulations only allow pilot high temperature storage projects and allowance for commercial projects is being investigated.

The HT-ATES can be installed in the transport network (centralized) or at several locations of the distribution network. This is illustrated in Fig. 6. The largest difference between the two locations is that the centralized location affects all distribution networks while the decentralized affects only the respective distribution network. The centralized location requires higher supply temperatures then the decentralized locations.

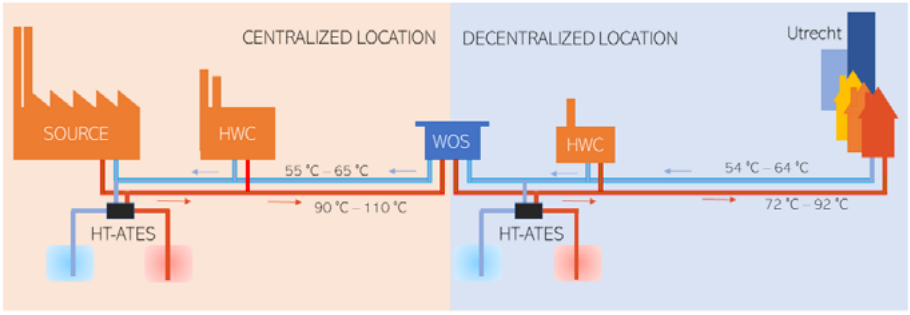


Fig. 6. Possible locations for the HT-ATES STES. At the surface, heat pumps bring the guarantee that heat can be delivered to the network (discharging phase) or to the heat storage (charging phase).

ATES system should not interfere with drinking water or other protected sub-ground areas so that those areas are excluded as possible HT-ATES locations. To prevent conflicts with protected areas the usable aquifers are more than 150 m below the surface. Below 500 m under the surface the mining law applies and the installation costs of the wells increase so that the usable aquifers must be above this level. HT-ATES systems consist of at least three layers: two confining impermeable layers and a permeable aquifer. The confining layers function as an insulator for the stored heat. The heat is stored in the aquifer layer which consist of water and sand. In the subsurface of Utrecht the impermeable and aquifer layers are stacked alternatively.

Remmelts [14] has identified suitable underground layers. These aquifers have suitable permeabilities in the range 5 m/day and 20 m/day [4]. The ground water flow is 3.5 m/year so that it will hardly affect the heat recovery of the storage.

3. Modelling of STES system

3.1. Underground thermal performance model

The thermal performance of an aquifer can be evaluated by determining its thermal recovery efficiency. This efficiency gives the ratio of extracted and injected thermal energy, see eq. (2). The non-recovered heat is the heat loss of the aquifer. This heat loss results in a higher efficiency for the next cycle.

$$\eta_{th} = \frac{T_{out,ave} \cdot V_{out}}{T_{in,ave} \cdot V_{in}} \tag{2}$$

Where T_{ave} is the average temperature during the charging or discharging period. The thermal recovery depends on the heat transport phenomena in the aquifer and impermeable layers (aquitards). Fig. 7 (left) illustrates the forms of heat transfer that have been taken into account.

The right hand side of Fig. 7 shows how the energy conservation equations have been locally used to determine the temperature. Further details of the underground model can be found in Remmelts [14]. Fig. 8 illustrates the results obtained with the underground model.

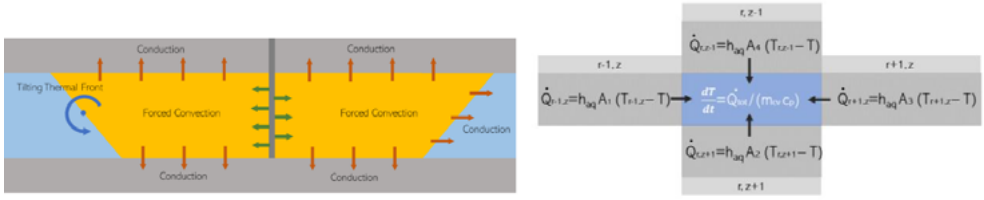


Fig. 7. Heat transfer phenomena considered in the modelling of the aquifer: convection, conduction and tilting of the thermal front. The vertical line indicates the position of the well while the yellow area represents the hot water stored in the aquifer. Right the control volume approach to determine the local temperatures in the aquifer.

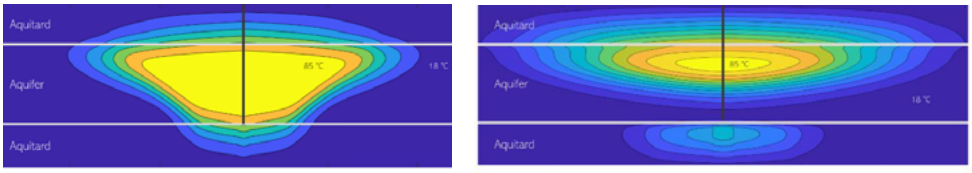


Fig. 8. Typical temperature profiles predicted by the underground model. Left at the end of the injection stage (charging) and right at the end of the extraction stage (discharging). An aquitard is an impermeable layer.

3.2. HT-ATES size

The heat available for storage originates from heat that otherwise would be wasted and from heat produced by increasing the base load of the heat sources of the DHN during the summer. Goal is to size the HT-ATES to deliver 400,000 GJ/year. The HT-ATES should be able to deliver heat for a period of 120 days with a maximum power output of 50 MW and an average of 38 MW. It is expected that there will be approximately 185 days charging time, 30 days buffer time, 120 days extraction time and again 30 days buffer time, depending on the thermal energy demand. The desired size of the HT-ATES is given by eq. (3).

$$V_{sto} = \frac{E}{\rho_w \cdot c_p \cdot (T_{well,hot} - T_{well,cold})} \approx \frac{400{,}000{,}000{,}000}{983 \cdot 4.185 \cdot (73 - 18)} = 1{,}767{,}862 m^3 \quad (3)$$

The hot well is charged with water at 85 °C but its temperature drops to 55 °C during the discharging period. The HT-ATES has been designed with a storage volume of 1,300,000 m^3 since the compressor of the heat pump delivers part of the required heating capacity. The volume extracted from the hot well should be equal to the injected volume. Otherwise the recovery efficiency for the next cycle will be lower. Also the discharging must be limited to a maximum of 180 days so that there is enough time left to recharge the HT-ATES.

The maximum allowable flow velocity in an aquifer so that the well filter does not get blocked determines its total capacity [25]. This implies that several wells are required for the required size of the storage.

3.3. Connection to DHN

The water from the HT-ATES system cannot be directly used in the DHN. It has a different chemistry than the DHN water and it must be pumped back into the same ground layer. In order to transfer the heat from the HT-ATES to the DHN a heat exchanger and a heat pump are used. Due to the large temperature difference between cold and hot wells, a heat exchanger is not sufficient. To return the flow at the desired temperature a heat pump must be used. For each doublet (pair of cold and hot wells) a pump is required to overcome the pressure difference between both wells. Fig. 9 illustrates the system connections for a decentralized supply system.

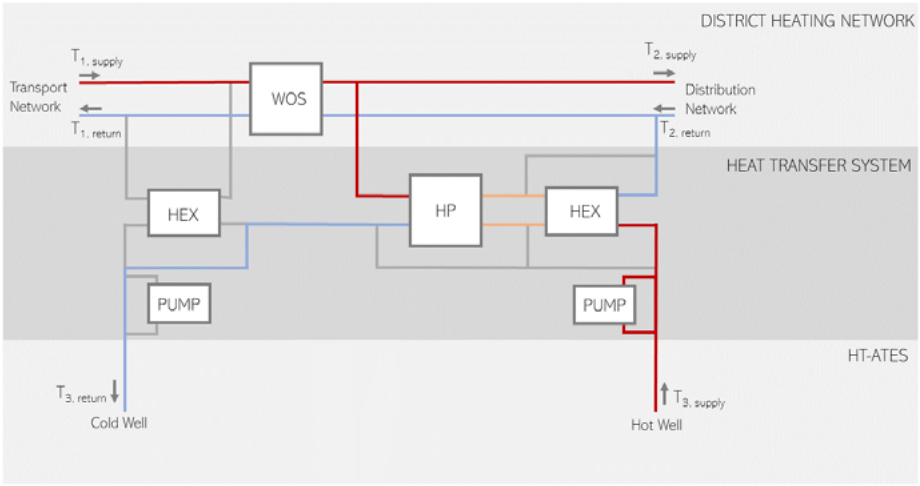


Fig. 9. Schematic of decentralized heat transfer system. The HT-ATES is operating in the beginning of the winter so that both heat exchanger (HEX) and heat pump (HP) are in operation. In red the hot water streams, in blue the cold water streams and in grey the inactive lines.

The electrical power consumed by the well pump is obtained from the extraction volume flow rate and the total pressure difference that the pump has to overcome. This pressure drop consists of the pressure drop in HEX and HP, the pressure drop between the doublet, the pressure drop in the vertical wells and the pressure drop in the transportation lines. A pump efficiency of 74% and an electric efficiency of the electric motor drive of 88% are further assumed. For the heat exchangers, the minimum temperature difference between the hot inlet and the outlet is assumed to be 5 K. If the temperature of the extracted flow becomes too low for the heat exchanger, the flow is guided through a by-pass directly to the heat pump.

Butane (R600) has been selected as the working fluid of the heat pump. An isentropic efficiency of 70% has been assumed for the compressor of the heat pump. The heat rejection from the heat pump takes place in three steps: de-superheating, condensation and sub-cooling. The condensation takes place at a 3 K higher temperature than the supply temperature to the DHN. Also at the sub-cooling side, the condenser outlet temperature is 3 K higher than the water returning from the DHN. Table 1 gives the design conditions of the heat pump and its corresponding COP.

Table 1. Design operating temperatures of heat exchanger and heat pump.

	$T_{source,out}$ [°C]	$T_{source,in}$ [°C]	$T_{sink,in}$ [°C]	$T_{sink,out}$ [°C]	$T_{condensation}$ [°C]	$T_{evaporation}$ [°C]	*COP*
Decentralized	18	60	60	76	75	15	3.99
Centralized	18	60	62	105	98	15	3.27

3.4. Heat load in DHN

The daily thermal energy demand data of the DHN and the corresponding supply and return temperatures have been linked to the thermal model of HT-ATES side of the system. The switching point for the discharging of the HT-ATES follows from the required thermal energy of the DHN. The ATES model predicts the time dependent extraction temperature. As discussed in section 1, the supply temperature of the DHN follows from its operating conditions so that the temperature delivered by the heat pump is also time dependent. The injection temperature into the cold well is fixed at 18 °C so that the evaporating temperature of the heat pump is also fixed. The extraction temperature and the temperature of the return flow from the DHN determine if the bypass of the heat exchanger is activated.

4. Results

4.1. Performance of ATES

The properties of aquifers at different locations in the area covered by the DHN of Utrecht have been used to determine the corresponding recovery efficiency. Charging and discharging cycles as discussed in section 3.2 have been applied for a total of 15 cycles for each of the possible locations. The most promise ATES in a decentralized network area had a recovery efficiency of 80% at the end of the 15th cycle and in the centralized area of 77%.

During the first years of operation the aquifers have a lower recovery efficiency because the soil needs to heat up. Fig. 10 shows the temperature of the water injected into the hot well / extracted from the hot well as a function of time for a period of 15 years. The extracted temperature at the end of the discharging period increases every year. The constant parts of the temperature line correspond to the injection period at constant temperature (85 ºC).

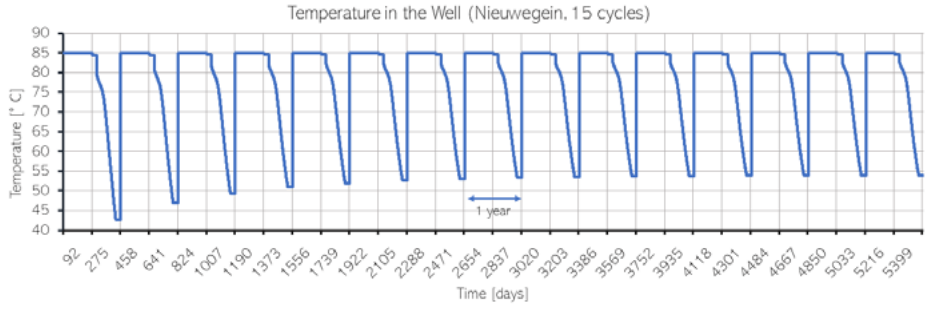


Fig. 10. Change of the extraction temperature from the HT-ATES during a period of 15 years.

4.2. Performance of STES in combination with the DHN

The locations with best performing aquifers have been tested to determine its potential for three different operating strategies:

- "Peak shaving" where the peak thermal energy demand during the winter is supplied from the HT-ATES;
- "Winter base load" where a constant base load is delivered by the HT-ATES during the winter season;
- "Total winter coverage" where the entire winter thermal energy demand is supplied by the HT-ATES.

Fig. 11 (top) shows the results of the three operating strategies for a decentralized district of the DHN with local thermal energy demand that is close to the size of the HT-ATES (1,300,000 m^3 storage). It is clear that the "total winter coverage" can nicely fit the demand of this district. Part of the storage capacity would remain unused if the "peak shaving" and "winter base load" strategies would be applied. Fig. 11 (bottom) shows that for the transport network side (centralized) of the DHN the "total winter coverage" strategy would lead to a very short operating period. Both the "peak shaving" and "winter base load" strategies could be applied at central level. However the "peak shaving" option leads to very high mass flow fluctuations in both HT-ATES and DHN sides. Such operation may lead to problems in the wells and should be prevented. For this reason the "winter base load" strategy would be the preferred one for the centralized storage. In both applications, at the end of the discharging period, the mass flow from the HT-ATES increases to provide the desired thermal power as the temperature of the extracted water decreases.

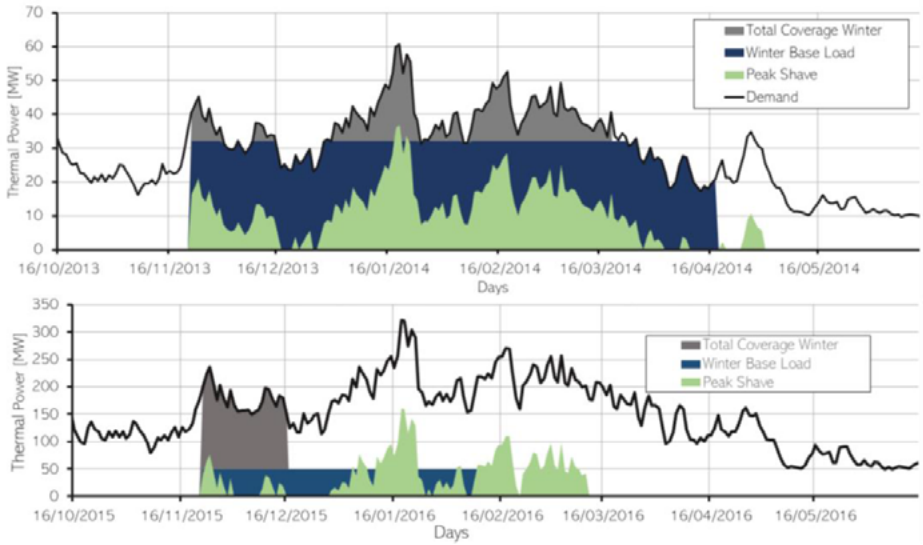


Fig. 11. Supplied thermal energy during the winter of 2015-2016 making use of an HT-ATES with 1,300,000 m^3 storage volume making use of different strategies: "peak shaving" (green), "winter base load" (blue) and "total winter coverage" (grey). Top: decentral location; Bottom: central location.

Fig. 12 shows the contribution of the heat exchanger (blue) and of the heat pump (green) during the discharging period of the winter of 2013 – 2014. Left the results for the decentral application and right for the central application. Due to the higher temperature required at the transport side, the contribution of the heat exchanger is smaller for the centralized solution. The heat exchanger can only deliver a small share of the total delivered heat. Without a heat pump the system would not be feasible.

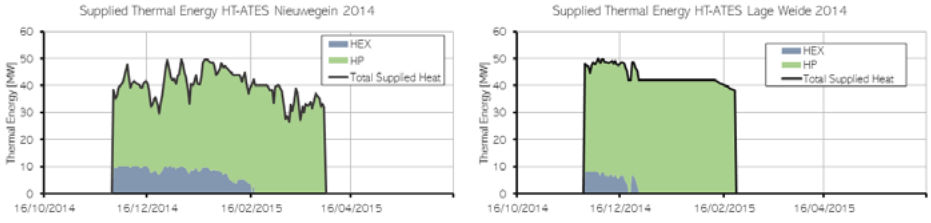


Fig. 12. Contribution of heat pump and heat exchanger to the total supplied heat to the DHN. Left: decentral location; Right: central location.

5. Conclusions

This study confirms that it is technically feasible to implement a seasonal thermal energy storage system in an existing large scale district heating network. Both application at the transport side (centralized) and distribution side (decentralized) result in solutions with comparable advantages for the whole DHN.

- The storage volume of the HT-ATES should be selected taking the local energy demand and the availability of surplus heat into account.
- The maximum thermal power should be selected in agreement with the storage volume available.
- The heat pump plays a major role in the feasibility of the concept. Just using a heat exchanger would significantly limit the energy that can be recovered from the storage.

Acknowledgements

The authors would like to thank ENECO for providing relevant data of the considered DHN.

References

[1] Abedin AH, Rosen MA. A critical review of thermochemical energy storage systems. The Open Renewable Energy Journal. 4: 42–46, 2011.
[2] Corel A, Roos J, Kleiwegt E. 2017. Wegwijs in warmte*: Kansen en risico's voor woningcorporaties bij aansluiten op een warmtenet*. Platform31, Infinitus Energy Solutions & Rebel Groep. 2017.
[3] Danish Energy Agency. Technology data for energy storage. 2018.
[4] de Boer S, Kleinlugtenbelt R. Position paper hoge temperatuur opslag. Walenberg & van Os Communicatie. IF Technology. 2013.
[5] de Keijzer PC. Warmteboek. Warmte- en koudesystemen bij Eneco. Eneco. 2018.
[6] de Vries AJ. Implementation and optimisation of thermal storage in existing, large-scale district heating networks. MSc thesis. Delft University of Technology. Process & Energy. 2018.
[7] de Wit-Blok M. (2017). Duurzame warmte 'de meerwaarde van (hogetemperatuur) warmteopslag voor warmtenetten'. VV+.
[8] Hoogervorst N. *Toekomstbeeld klimaatneutrale warmtenetten in Nederland*. Uitgeverij PBL, Report 1926. Den Haag. 80 p. 2017.
[9] IEA. Energy technology system analysis programme IEA-ETSAP. 2013.
[10] Juhl A, Vangkilde-Pedersen T, Nielsen JE, Sørensen PA, Egermann P, Rey C, Maragna C. HEATSTORE Underground thermal energy storage (UTES)–state-of-the-art, example cases and lessons learned. 2019.
[11] Mangold D, Deschaintre L. Seasonal thermal energy storage- Report on state of the art and necessary further R+D. p.1–48, Solar Heating & Cooling Programme. 2015.
[12] Menkveld M, Matton R, Segers R, Vroom S, Kremer AM. *Monitoring warmte 2015*. Report ECN-E-17-018, ECN & CBS. 2017.
[13] Prieto C, Cooper P, Fernández AI, Cabeza LF. Review of technology: Thermo chemical energy storage for concentrated solar power plants. Renewable and Sustainable Energy Reviews, 60:909–929, 2016.
[14] Remmelts JJR. Seasonal thermal energy storage in large scale district heating networks. MSc thesis. Delft University of Technology. Process & Energy. 2019.
[15] Roelofsen O, de Pee A, Speelman E.. *Versnellen van energietransitie: kostbaar of kansrijk?* McKinsey & Company. 2016.
[16] Sanner B, Knoblich K. 1998. New IEA-activity ECES Annex 12 – High temperature underground thermal energy storage. Journal of Underground Thermal Storage and Utilization, 1. 1998.
[17] Sarbu I, Sebarchievici C. A comprehensive review of thermal energy storage. Sustainability (Switzerland), 10(1), 2018.
[18] Schoots K, Hekkenberg M, Hammingh P. 2017. *Nationale energieverkenning*. ECN-O-17-018; ECN & PBL, The Netherlands.
[19] Sibbitt B, Mcclenahan D, Djebbar R, Paget K. Groundbreaking Solar: Drake Landing Solar Community, ASHRAE - High Performing Buildings, Summer 2015, 36-46.
[20] Sørensen A, Schmidt T. Design and construction of large scale heat storages for district heating in Denmark. 14th International Conference on Energy Storage. 25-28 April 2018, Adana, Turkey. 2018a.
[21] Sørensen A, Schmidt T. Monitoring results from large scale heat storages for district heating in Denmark. 14th International Conference on Energy Storage. 25-28 April 2018, Adana, Turkey. 2018b.
[22] Thomson A, Claudio G. The technical and economic feasibility of utilising phase change materials for thermal storage in district heating networks. Energy Procedia, 159:442–447, 2019.
[23] Uitto J. Helen world's best city energy. 2019.
[24] Ulbjerg F. Heat storage pit. 2015.
[25] van de Weerdhof B. Meervoudige ontwerp- en effectenstudie van koude- warmteopslagsystemen in de binnenstad van Den Haag. MSc thesis. Delft University of Technology. Faculteit Civiele Techniek en Geowetenschappen. Afdeling Watermanagement. 2005.
[26] Verhaegh N. *Slim van het gas af met lage temperatuur warmte in de bestaande bouw*. DNV-GL. 2018.
[27] Wielders L, Schepers B, Schuurbiers M. *Gastransitie en warmtenetten*. Report 16.3J04.45. CE Delft. 2016.
[28] Wolfgramm M. Aquifer thermal energy storage in Neubrandenburg. 2015.
[29] Yu N, Wang RZ, Wang LW. Sorption thermal storage for solar energy. Progress in Energy and Combustion Science. 39, Pages 489-514. 2013.

13th IEA Heat Pump Conference
April 26-29, 2021 Jeju, Korea

Low temperature district heating based on low temperature geothermal heat (30 ºC)

Sebastiaan Knepper[a], Ivo Pothof[a,c], Laure Itard[b], Carlos Infante Ferreira[a*]

[a]Delft University of Technology, Department Process & Energy, Leeghwaterstraat 39, 2628 CB Delft, The Netherlands
[b]Delft University of Technology, Faculty of Architecture and the Built Environment, Julianalaan 134, 2628 BL Delft, The Netherlands
[c]Deltares, Hydrodynamics for Industry and Infrastructure, Boussinesqweg 1, 2629 HV Delft, The Netherlands

Abstract

A comparative study for a representative case district in the Netherlands with around 2500 dwellings has been executed with the purpose of identifying the best solution for a Low Temperature District Heating (LTDH) with Low Temperature Geothermal Heat (LTGH) as the main heat source. The district is presently connected to the Dutch gas network. Its heat demand and building typologies are used as departing points. The comparison is based on 3 key performances indicators (KPI's): CO_2 emissions, levelized costs of energy (LCOE) and peak electricity use. The following LTDH designs have been considered: Central heat pump and collective peak supply at 70 ºC / 50 ºC; Central heat pump and decentral peak supply at 70 ºC / 50 ºC; Decentralized heat pumps using 30 ºC supply temperature. Individual air source heat pumps for space heating and electric boilers for domestic hot water purposes are taken as reference. The LTDH concept with decentralized heat pumps saves 19.5 %, 16.8 % and 36 % on the CO_2 emission, LCOE, and electricity use in peak load hours compared to the reference concept.

Keywords: heat pump; low temperature district heating;low temperature geothermal heat source;

1. Introduction

In 2015, 34% of the total energy use in the Netherlands originated from the built environment. 70% of the energy use in this sector was for heating dwellings, cooking food and the preparation of hot water, while the remaining was for electricity use [15]. With the current climate developments, earthquakes as a result of natural gas extraction in the northern parts of the Netherlands and a transition in public thinking towards making the world more sustainable, an investigation of alternative ways of supplying heat to Dutch dwellings has become increasingly relevant.

According to Kremer et al. [15], in 2015, 78% of the total heating requirement originated from natural gas combustion. In Dutch households, 219 PJ of natural gas was used for heating homes, 60 PJ was used for domestic hot water supply, and 6 PJ for cooking. The Dutch government aims to disconnect Dutch houses from the existing gas distribution network by 2050, and wants to stop natural gas extraction in Groningen by 2022. New solutions are required on short term to deliver the heating requirements. District heating systems, together with heat pumps, are the most commonly suggested solution for replacing the natural gas distribution network in the densely populated urban areas of the Netherlands. Low Temperature District Heating (LTDH) is one of the proposed solutions which is claimed to have high efficiency and to be easy to connect to sustainable heating sources [18].

Nomenclature

Roman characters *Subscripts*

* Corresponding author. Tel.: ++31-152-784-894.
E-mail address: c.a.infanteferreira@tudelft.nl .

A	Area	m^2	ATES	Aquifer thermal storage
COP	Coefficient of performance	-	C	Cold source
c_p	Specific heat	$kJkg^{-1}K^{-1}$	Carnot	2nd law of thermodynamics
F	Fuel costs	€	demand	Demand side
I	Investment costs	€	elec	Electrical
M	Maintenance costs	€	H	Hot sink
$\dot{m}$	Mass flow rate	kgs^{-1}	HP	Heat pump
n	Number of years	-	injection	Injection well
Q	Energy	kWh	loss	Related to heat losses
$\dot{Q}$	Power	kW	LTDH	Low temperature DH
r	Interest rate	-	LTGH	Low temperature GH
T	Temperature	ºC	peak	Peak load conditions
U	Overall heat transfer coefficient	$kWm^{-2}K^{-1}$	recovery	Recovery of ATES
$\dot{W}$	Shaft power	kW	return	Return line
Greek character			supply	Supply line
η	Efficiency	-	well	Production well

Several researchers have investigated the feasibility of the implementation of LTDH in the Netherlands [25, 30, 31]. The results seem promising but the proposed solutions are not capable of delivering the peak duty during cold periods. European studies [18, 21, 23] have however concluded that LTDH would provide a sustainable way of supplying heat to dwellings. Most houses in the Netherlands are equipped with radiators designed for high temperature heat delivery which limit the use of low temperature heating systems. According to Østergaard [20], in Denmark, such radiators are oversized and can still be used in LTDH. This, however, still needs to be confirmed to apply for the Dutch situation.

This study investigates how a low temperature (30 ºC) geothermal source (originating from aquifers in the drilling range between 500 to 1250 m below ground level) can best be used for heating purposes in urban areas by considering a specific area in the Netherlands. The use of such geothermal heat sources for heating of greenhouses has recently been reported by Schepers et al. [25].

Geothermal installations consist of two wells, a production well and an injection well. Hot water is extracted from an aquifer at elevated temperature by the production well. The hot water is pumped from the production well to a heat exchanger (HEX), which may be part of a heat pump, at surface level. The HEX, eventually after temperature upgrading by a heat pump, transfers the heat to a secondary water network. The cooled production water is pumped back into the aquifer via the injection well. The amount of heat, which is extracted by the installation, depends on the mass flow of the ground water and the temperature difference across the HEX. The temperature of the water extracted depends on the depth of the aquifer. Water with a higher temperature is extracted at deeper reservoirs [2]. The mass flow through the HEX is determined by the pump in the production well. An important part of the geothermal installation are the filters in the geothermal reservoirs. The filters remove solids out of the water in order to protect the heat exchanger and the wells of the geothermal plant. The well pump must run between a minimal flow and maximum flow. If the flow rate is too low, the reservoir becomes clogged. If the flow rate is too high, the filter installation will be damaged [13]. The heat production from geothermal sources is therefore poorly adjustable and cannot be adjusted to large fluctuations of the heat demand. For this reason, geothermal systems cover generally a base load and the peak demands need to be supplied by other sources [10].

District heating systems (DHS) are networks which collect heat from producers and provide heat for the collective heating demand of buildings and industry. DHS can be divided in High Temperature (HT), with supply temperature > 70 , Medium Temperature (MT, [45 - 70 ºC]) and Low Temperature (LT), with supply temperature below 45 ºC, networks [17, 21].

A distinction is made between space heating demand and domestic hot water heating (DHW) demand. Heat gains and losses inside a building depend on transmission, ventilation & infiltration, internal gains and solar gains [29]. DHW is needed for the bathroom and for cooking purposes. The sum of these two demands for the whole neighborhood is the heat demand of the district.

Lundström & Wallin [19] have shown that the peak heat demand of a district is mainly caused by the space heat demand in the winter, provided that a boiler is used for DHW storage and peak shaving. In the summer,

the peak heat demand is caused by the DHW use. In 2016, the Biesdonk district of Breda (the Netherlands), with 1650 homes, consumed 14813 MWh for heating purposes and 3451 MWh for DHW [31]. When designing a DHS making use of data for a single dwelling, the heat demand of the DHS can be estimated by multiplying these data with the number of dwellings in a district making use of the corresponding simultaneity factor. The heat demand determines the type and size of the pipes [19]. Because LTDH use low supply temperature, the temperature difference between the supply and return pipe is small. To supply the same amount of heat through an LTDH instead of a HTDH, the diameters should be larger. If the peak heat requirement is supplied through the pipe network, the diameters of the pipes need to take the peak load conditions into account. If only the basis heating demand goes through the pipe network and the peak heat demand is produced near the dwellings, the diameters of the pipes can become smaller [19]. Another limitation is the supply of DHW. In the Netherlands DHW should be delivered at least at 60 °C, otherwise legionella can possibly develop in the water. For LTDH this is difficult to realize, so a need for post-heating is required. Post-heating can be done with a Booster Heat Pump (BHP) or an electric heating element. If the DHS water enters the house with 60 °C or higher, only a heat exchanger (HEX) is needed.

The heating needs differ on daily base and on seasonal base. Peak demands occur in the morning and evening on a daily base. Residents wake up in the morning and prepare to start their day. During the day, fewer people are present in a neighborhood, resulting in a lower heat demand. Most of the residents come back to their homes in the evening increasing the heat use. On a daily base, the peaks depend mainly on when the residents are at home. Occupancy level of people can be estimated using Ahmed et al. [3]. Seasonal peaks are different. These are based on the weather. In the winter, when the temperature is lower, heat demand is higher than in the summer.

According to Rezaie & Rosen [22], an DHS can be divided into three subsystems: heat production, heat transportation and heat consumption. The heating system for a neighborhood can be done collectively or decentralized [22]. The difference is the location of the heat source. In a collective heating system, the heat is produced far from the location of the end-users and it produces heat for the whole district and distributes the heat via a large distribution network. A decentral heating system produces heat close to the end-user and has a smaller or no distribution network. The same applies for storage methods. Collective storage is located far from the end-user and decentral storage is located close to the end-user. Collective storage depends on the seasonal heat demand and decentral storage depends on hourly demand [4]. In general, it can be said that decentral heating systems become more relevant for low density neighborhoods and collective heating is relevant for high density neighborhoods.

According to Alva et al. [4] and Lund et al. [18], the aquifer thermal energy storage (ATES) and hot water tank storage are currently the most suitable storage methods for an LTDH, because these systems have low installation costs and are more frequently applied than other technologies. ATES is a technology which is used for seasonal storage. Heat is extracted from the ATES during the winter and heat is injected during the summer. ATES works as follows. An ATES consists of two wells (a doublet) or multiple doublets. Groundwater from the cold well is injected at increased temperature in the warm well, when there is an excess heat production from the LTGH. In winter, when the warm well is charged, heat from the warm well is transferred to the grid and cooled groundwater is injected in the cold well. The recovery efficiency of an ATES is defined as the amount of injected thermal energy that is recovered after the injected volume has been extracted [5]. The recovery efficiency increases when the storage temperatures of the DHS decrease. The heat loss that occurs is due to displacement by groundwater flow and by dispersion and conduction.

To investigate which LTDH design can supply the peak demand most efficiently and sustainably, the following KPIs have been considered.

- CO_2 emission: the CO_2 emission of the system should be as low as possible.
- Levelized cost of energy (LCOE): the costs of produced kWh of heat should be as low as possible.
- Electricity use: Electricity use should be as low as possible to prevent overloading of the electricity net.
- Availability: the supply (including stored heat) should always meet the demand.

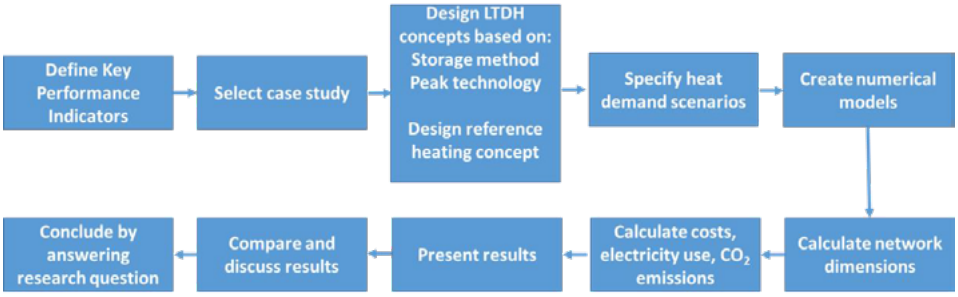


Fig. 1. Methodology used in the present study.

As illustrated in Fig. 1, this study starts with the definition of the key performance indicators (KPI) used for the evaluation of the different LTDH systems, the definition of the types of housing in the urban area considered and the quantification of the related heating requirements in these buildings. The alternative network designs considered for the LTDH network are created. The typology of the considered district allows for the determination of the required distribution line lengths and sizes. Numerical models are introduced to quantify the yearly energy requirements of the different options. Finally, the predicted electricity use, costs and CO_2 emission of the different network designs are compared to identify the most suitable solution.

2. Case study and LTDH designs

2.1. District heating location and heating requirement

Biesdonk, a district of Breda dating from the 1970's, has been selected for the present case study. In 2015, Biesdonk had 4995 residents and 2230 dwellings. The heat demands of 650 terraced houses and 1000 apartments are known. The terraced houses are low-rise buildings. Other buildings, such as shopping centers, schools, and churches are also present in the area. Heat demands for those buildings are not known and are outside the scope of this study. A map of Biesdonk and its heating demand are presented in Fig. 2. In the figure the space heating is given by the blue line and the water heating consumption by the red line.

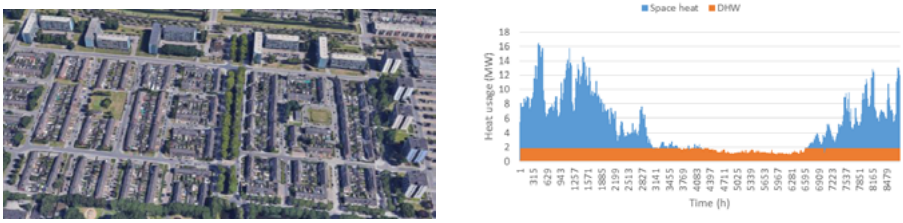


Fig. 2. District Biesdonk in Breda selected for implementation of the LTDH designs (left) and heating requirement for 650 terraced houses and 1000 apartments in 2016 (right).

2.2. Network designs

The LTGH source considered in this study is located in an aquifer 750 m below surface level and delivers 150 m^3/h (41.7 kg/s) in the heating season and 90 m^3/h in the summer of ground water with a constant temperature of 30 °C. This flow can be directly delivered to the district network making use of a heat exchanger at the well head or can be directly upgraded with a heat pump at the well head and delivered to the network at higher temperature.

Since the flow delivered by the LTGH source is continuous throughout the year, a heat storage facility is required which could be an aquifer closer to the surface maintained at the temperature level of the distribution system. This aquifer serves then the whole district and can cover the season peak needs. Alternatively, a hot water tank can be used on a decentral level to cover the daily peak heating needs. Additionally, the network

requires an auxiliary boiler to cover peak loads which cannot be covered by the storage facilities. This boiler can be installed at collective level or decentral at user level.

The return temperature for the designs which use central heat pumps is 32 ºC. Existing radiators can create a return temperature of 30 ºC, but the return water will be increased by 2 ºC due to losses in the supply set at home level [20]. If the ATES provides cold water to the return pipes, the temperature will increase as well. The return temperature for the designs without central heat pumps is 18 ºC. This can be achieved by the decentral heat pumps [30].

Table 1 gives an overview of the considered network designs.

Table 1. Evaluated designs of the network with individual air source heat pumps as alternative to the network (design 6).

Design	LTDH supply temperature	Collective storage	Decentral storage	Collective peak	Decentral Peak	DHW heating
1 – HT boiler	70 ºC	ATES	none	boiler	None	HEX
2 – HT elect.	70 ºC	ATES	water tank	none	electrical	HEX
3 – MT boiler	50 ºC	ATES	none	boiler	None	booster HP
4 – MT elec.	50 ºC	ATES	water tank	none	electrical	booster HP
5 – LT HP	30 ºC	ATES	none	none	HP	HP
6 – air HP	none	none	none	none	HP	HP

Fig. 3 gives a schematic representation of design 1 which consists of a central heat pump that upgrades the heat from the geothermal source to 70 ºC, an aquifer that collects the excess heat available from the network to deliver it when needed, a (biomass) boiler to cover the collective peak requirement and a HEX to deliver the individual DHW needs.

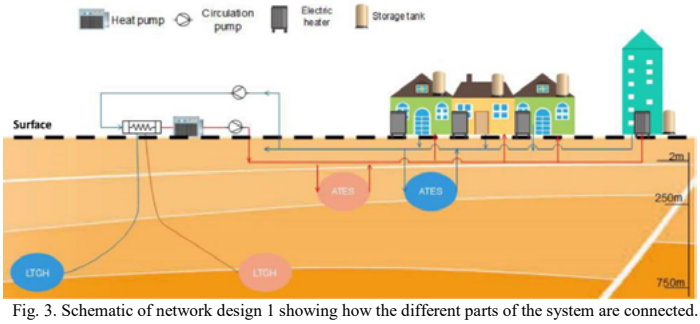


Fig. 3. Schematic of network design 1 showing how the different parts of the system are connected.

Fig. 4 is a simplified flow diagram of the network illustrating the log-mean temperature differences (LMTD) during heat exchange in the different parts of the system.

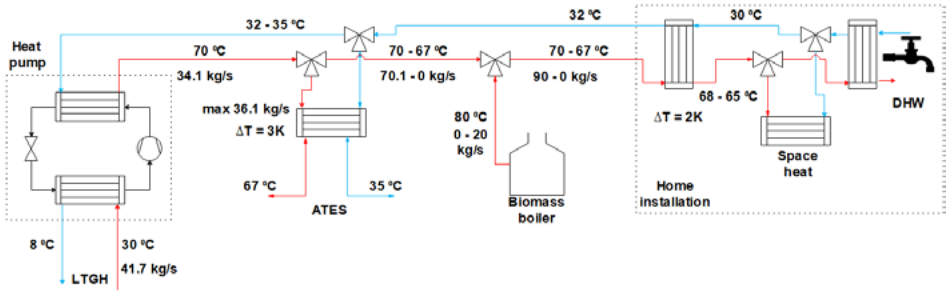


Fig. 4. Flow diagram of network design 1 showing flows and corresponding temperature levels. The supply line is given in red while the return line is printed in blue. The mass flow to / from the aquifer is limited to 130 m^3/h [9, 27].

3. Matching energy demands to energy availability

3.1. Network sizing

The heat supplied by the LTGH source can be obtained with eq. (1) where the temperature of the production well is constant at 30 °C and the injection temperature depends on the network design. The volume flow of the geothermal well is 150 m³/h (41.7 kg/s) in the heating season and 90 m³/h (25 kg/s) in the summer period.

$$\dot{Q}_{LTGH} = \dot{m}_{LTGH} \cdot c_{p_LTGH} \cdot (T_{well} - T_{injection}) \quad (1)$$

When a heat pump is used, the heat supplied to the network is enlarged as given in eq. (2) with *COP* the performance of the heat pump.

$$\dot{Q}_{LTDH_HP} = \frac{COP \cdot \dot{Q}_{LTGH}}{COP - 1} \quad (2)$$

The mass flow through the LTDH follows then from eq. (3).

$$\dot{m}_{LTDH} = \frac{\dot{Q}_{LTDH_HP}}{c_{p_LTDH} \cdot (T_{supply} - T_{return})} \quad (3)$$

The type of network material and size is determined by the heating demand per pipe line. First a network is created. The approach is based on Frederiksen & Werner [12]. The LTGH is located in the center of the district, since in this way the distances between the heat supply plant and each substation are as short as possible and therefore heat losses are smallest. For the district Biesdonk, the LTGH can be located in a small park. The network is divided into 4 sectors; A in north-west (with 360 apartments and 150 terraced houses), B in north-east (with 240 apartments and 200 terraced houses), C in south-west (with 300 terraced houses), and D in south-east (with 320 apartments and 100 terraced houses). According to Verhaegh [31], in 2016 sector A had a heating requirement of 5355 MWh, B of 6358 MWh, C of 3293 MWh and D of 4200 MWh. Pipes leaving the LTGH station are large and decrease step by step to small pipes as the network approaches the individual users. The heat transported through the pipes depends on the number of homes in a street. The heat demand is calculated for the worst case scenario. If the flow velocity exceeds 3 m/s or the pressure drop exceeds 400 Pa/m diameter adjustments need to be done. The Wanda software of Deltares [8] is then used to develop the physical infrastructure for the heat distribution network including pipe diameters and circulating pump selection. Fig. 5 illustrates the approach.

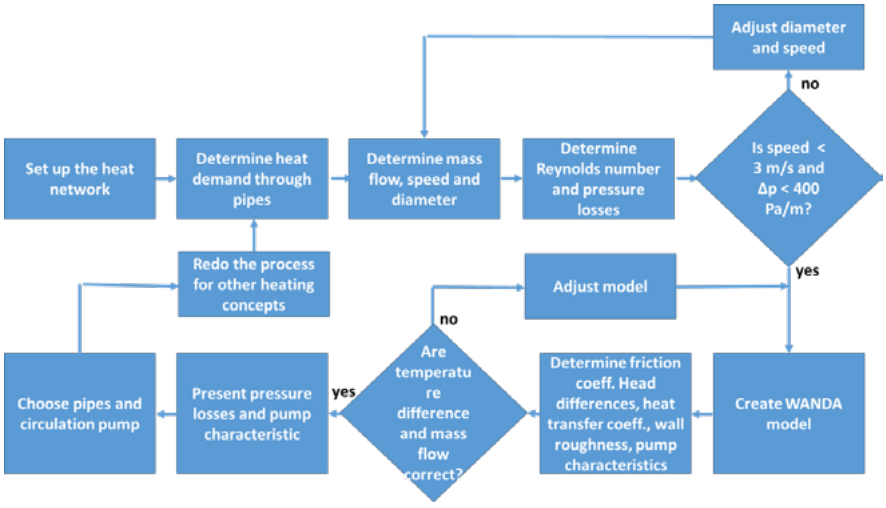


Fig. 5. Flow chart of the network sizing making use of the software Wanda of Deltares (2019).

3.2. Energy balance

Since the LTGH source delivers a fixed amount of energy, a yearly energy balance is obtained by varying the number of users connected to the network and so changing $\dot{Q}_{demand}$ in eq. (4).

$$\dot{Q}_{demand} + \dot{Q}_{loss} = \dot{Q}_{LTGH} + \dot{Q}_{peak_supply} \tag{4}$$

where the losses result from losses in the aquifers, in the network pipe lines and in the heat exchangers. The heat losses from the aquifer have been considered by assuming storage temperature dependent recovery efficiencies as proposed by de Wit-Blok [7]. The ATES at HT (67 ºC, designs 1-2) is assumed to have a heat recovery of 65%, at MT (47 ºC, design 3-4) of 75% and at LT (27 ºC, design 5) of 85%. The pipe lines losses have been adapted from Thermaflex [28], a company specialized in the manufacturing of insulated tubes for LTDH networks. The losses depend mainly on tube size and temperature level of the network and vary from a factor larger than 3 for 70 ºC in comparison to 30 ºC for the smaller inner diameters (14.4 mm) to a factor 2 for the larger tubes (138 mm). The losses from heat exchangers are generally small and have been determined by estimating its *UA* values from external surface to environment and the temperature difference to the environment. The heat exchangers are assumed to be insulated so that the *U* value is around 1.5 $Wm^{-2}K^{-1}$ and its surface is around 12 m^2. Fig. 6 in combination with eq. (5) illustrates how the capacity of the ATES storage has been determined.

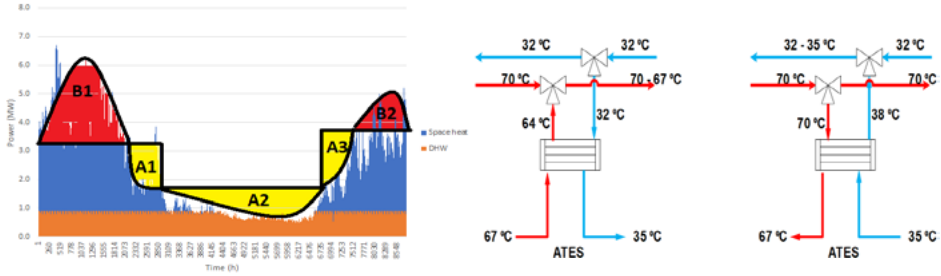


Fig. 6. Peak shaving with ATES. The extra heat delivered by the well given in yellow can be stored to be used to cover the peak loads marked in red (left). Temperatures differences in heat exchanger during discharging and charging of the ATES (right).

$$Q_{ATES} = \frac{(B_1 + B_2)}{\eta_{recovery}} = (A_1 + A_2 + A_3) \tag{5}$$

The sizing of the ATES is based on Drijver et al. [9] and Sommer [27]. The ATES is installed at 250 m depth and the maximum mass flow rate is 130 m^3/h, consistent with the geo-hydrological conditions in the Netherlands. The supplied power is calculated with eq. (6).

$$\dot{Q}_{ATES} = \dot{m}_{ATES} \cdot c_{p_{ATES}} \cdot (T_{ATES_supply} - T_{ATES_return}) \tag{6}$$

The COP of the collective heat pumps is obtained from eq. (7) with T_H the thermodynamic average temperature at the DH side and T_C the thermodynamic average temperature at the geothermal well side. The second law efficiency, η_{Carnot}, has been taken as 0.30, in agreement with de Vrieze [6]. The COP of the collective heat pumps (designs 1-4) is then 3.2 for the 70 ºC network and 3.9 for the 50 ºC network. The decentralized water-water heat pumps (network design 5) will have COPs of 4.2 and 3.6 respectively for space heating and DHW purposes.

$$COP = \eta_{Carnot} \cdot \frac{T_H}{T_H - T_C} \tag{7}$$

In network design 6, air to water heat pumps are used to deliver the heating requirement. These heat pumps extract heat from the environmental air and convert it into useful heat for a water circulation circuit. The *COP* therefore depends on the outside temperature. Table 2 presents experimental *COP* values of air – to – water heat pumps at different outside temperatures. The temperature at the inlet of the radiators is 55 ºC. At ambient temperatures below 5 ºC, frost develops on the surface of the evaporator which reduces the performance of the heat pump. The frost layer reduces the rate of heat transfer in the evaporator because it acts as a thermal insulation. Furthermore, the frost layer blocks part of the air flow passage through the evaporator which causes

a further reduction of the performance. To prevent this phenomenon, an electrical resistance is installed in the heat pump which is activated when the ambient temperature is lower than 5 ºC. The power consumed by the resistance causes a decrease of about 10% in the COP [26].

Table 2. *COP* of an air-water heat pump delivering heat at 55 ºC, adapted from Ertesvåg [11].

Ambient temperature [ºC]	-9	-7	-5	-3	-1	1	3	5	7	9	11	13
COP_{HP}	1.9	2.1	2.2	2.4	2.5	2.6	2.7	2.8	3.2	3.3	3.5	3.8

If the network has a supply temperature below 60 ºC, a booster heat pump (BHP) is required to prepare the DHW. According to Kleefkens et al. [14], when the supply temperature to the BHP is 45 ºC, the COP is 4.2. The required electricity is calculated with eq. (8), where $\dot{Q}_{HP}$ is the power delivered by the heat pump.

$$\dot{W}_{elec} = \frac{\dot{Q}_{HP}}{COP_{HP}} \tag{8}$$

The CO_2 emission considered in this study is only caused by the use of electricity and biomass. Regular geothermal sources produce extra CO_2, because natural gas is released. However, the considered LTGH source is drilled only at 750 m depth and in aquifers where no natural gas is available [25]. The emission factor of electricity and biomass in the Netherlands are currently 0.649 kg/kWh and 0.093 kg/kWh [24].

The price of electricity has been taken as 0.18 €/kWh and of biomass fuel as 0.04 €/kWh [1].

3.3. Levelized cost of energy (LCOE)

The *LCOE* calculates the costs per amount of energy delivered over a certain time. This is summarized in eq. (9).

$$LCOE = \frac{\sum_{t=0}^{t=n} \frac{I_t + M_t + F_t}{(1+r)^t}}{\sum_{t=0}^{t=n} \frac{Q_t}{(1+r)^t}} \tag{9}$$

Where *LCOE* is expressed in €/kWh, the delivered energy (Q) is the heat delivered to the users of the LTDH network. The life time (n) is the number of years the systems runs (here assumed to be 30 years). The years are expressed in (t) and run from year 0 to year 30. The interest rate (r) is assumed to be 6%, because a transformation in energy supply is a risk-full project [16]. The investment costs (I), maintenance costs (M), and fuel costs (F) are the total costs in a certain year. The costs in year 0 are the investment costs (CAPEX). During all the other years the costs consist of operational and maintenance costs (OPEX).

4. Results and discussion

4.1. Amount of auxiliary heat required

The values of all relevant variables have been calculated on an hourly basis for the whole year. As an example of the results, the difference between the power delivered by the LTGH in the two coldest weeks of the year and required by the users of the network is shown in Fig. 7 (a) for network design 1 (70 ºC). The figure makes clear that in these two weeks most of the time the power delivered by the geothermal source is not sufficient to cover the heating requirement. Some of this extra power can be delivered from the ATES as shown in Fig. 7 (b). The remaining power needs to be delivered by the auxiliary boiler. This contribution is shown in Fig. 7 (c).

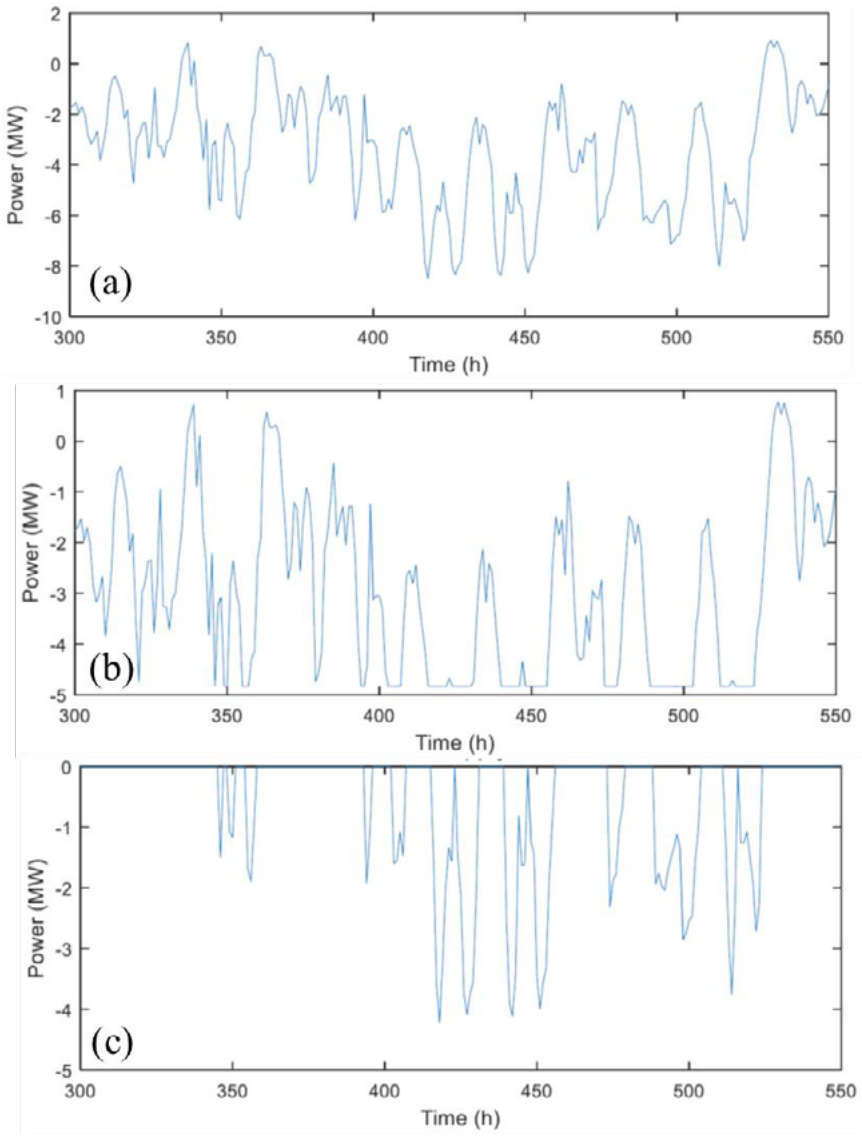


Fig. 7. Difference between available LTGH power and required thermal power by the network users during the two coldest weeks (a) for network design 1 (70 ºC). Power delivered by the ATES in these two weeks (b) and power provided by the auxiliary boiler to compensate for the shortage of power (c).

In a similar way the amount of power delivered by the auxiliary boiler has been determined for the whole year and for the different network designs.

4.2. Impact of temperature level of the network

Operating the network at a lower temperature imposes the use of larger flows and so larger tube sizes and pumps. Table 3 illustrates the impact of network design (and so its temperature level) on flows, pressure drop and tube sizes.

Table 3. Impact of network design in relevant parameters of the network. The details of the designs are listed in Table 1.

	Design 1	Design 2	Design 3	Design 4	Design 5
Flow rate [m³/h]	6 x 55.0	6 x 30.7	6 x 108.5	6 x 56.0	6 x 110.4
Largest internal tube size [mm]	102	90	138	102	138
Pressure drop [bar]	5.4	4.8	6.5	5.7	7.0
Yearly heat losses network [MWh]	3741	3346	2724	2637	1682
Peak power of LTDH [MW]	13.47	10.25	13.47	8.76	10.21

4.3. Results for KPIs

Table 4 shows the values obtained for the KPIs defined in section 1 applied for the different designs. In bold the best performing designs.

Table 4. KPIs for the different network designs. The details of the designs are listed in Table 1.

	Design 1	Design 2	Design 3	Design 4	Design 5	Design 6
CO_2 emission in 30 years [ton CO_2]	52.5	52.2	48.5	48.8	**31.8**	39.5
LCOE [€/kWh]	0.198	0.186	0.222	0.201	**0.168***	0.202*
Yearly electricity in peak [MWh]	**509**	613	528	785	527	823
Yearly heat peak source [MWh]	233	**29**	741	392		
Yearly operation peak source [h]	135	**18**	259	151		

*This assumes that the heat pump [€ 2500. (design 5) and € 7800. (design 6)] is invested twice (once in the 15 years).

Fig. 8 summarizes the performance of the different designs in comparison with the use of individual air-water heat pumps per user (design 6). The figure only considers the most relevant KPIs: CO_2 emissions and *LCOE*.

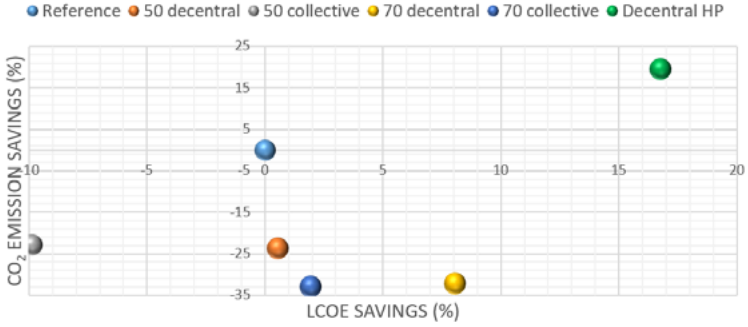


Fig. 8. Visualization of the performance of the different network designs in comparison to design 6 (no network). See Table 1 for network design details. Design 1 is indicated as 70 collective, 2 as 70 decentral, 3 as 50 collective, 4 as 50 decentral and 5 as decentral HP.

Fig. 8 shows that only design 5 (network at 30 ºC) performs better on both CO_2 emissions (19.5% less emissions then reference design) and *LCOE* (16.8% lower *LCOE* then reference design). Design 2 also leads to a significant but lower *LCOE* reduction (7.9%) but at the same time leads to a significant increase of the CO_2 emissions: +32.5%.

5. Conclusions

The supply temperature of the LTGH source has an influence on the *COP* of the heat pumps. Since the heat pumps of the LTGH use most of the total electricity, the electricity use depends a lot on the supply temperature of the LTGH source. This can be seen in the *LCOE* and CO_2 emissions as well. If the supply temperature of the LTGH source can be increased, the heat pumps require less electricity what reduces the CO_2 emission and costs for the complete system.

The best way to meet the heat demand in existing Dutch dwellings, with LTDH and an LTGH as main source is an LTGH with decentral heat pump for every single home. This LTDH concept saves 19.5 %, 16.8 %,

and 36.0 % on the CO_2 emission, *LCOE*, and electricity use in peak load hours compared to an all-electric scenario.

Acknowledgements

The authors would like to thank Mr. M. de Vrieze of Visser & Smit Hanab for his support and advise.

References

[1] ACM. (2018). Warmtetarieven. Retrieved 15 December 2018, from https://www.acm.nl/nl/warmtetarieven
[2] Agemar, T, Weber J, Schulz R. (2014). Deep Geothermal Energy Production in Germany. Energies, **7**, 4397-4416.
[3] Ahmed K, Akhondzada A, Kurnitski J, Olesen B. (2017). Occupancy schedules for energy simulation in new prEN16798-1 and ISO/FDIS 17772-1 standards. Sustainable Cities and Society, **35**, 134–144.
[4] Alva G, Lin Y, Fang G. (2018). An overview of thermal energy storage systems. Energy, **144**, 341–378.
[5] Bloemendal M, Hartog N. (2018). Analysis of the impact of storage conditions on the thermal recovery efficiency of low-temperature ATES systems. Geothermics, **71**, 306–319.
[6] de Vrieze M. (2018). Personal communication on September 30, 2018 at Visser & Smit Hanab. Papendrecht.
[7] de Wit-Blok M. (2017). Duurzame warmte 'de meerwaarde van (hogetemperatuur) warmteopslag voor warmtenetten'. VV+.
[8] Deltares (2019). Wanda, advanced water hammer software, designed for engineers by engineers. Deltares, Delft.
[9] Drijver B, van Aarssen M, Zwart BD. (2012). High-temperature aquifer thermal energy storage (HT-ATES): sustainable and multi-usable. In Conference proceedings Innostock (Vol. 2012).
[10] Erlingsson T, Jóhannesson T, Olafsson E, Axelsson G. (2010). Geothermal district heating system in XianYang, Shaanxi, China. In Proceedings World Geothermal Congress (pp. 25–29).
[11] Ertesvåg IS. (2011). Uncertainties in heat-pump coefficient of performance (COP) and exergy efficiency based on standardized testing. Energy & Buildings, 43, 1937–1946.
[12] Frederiksen S, Werner S. (2013). District Heating and Cooling. Studentlitteratur AB. Sweden.
[13] Hirschberg S, Wiemer S. (2015). Energy from the earth deep geothermal as a resource. Report TA-SWISS 62/2015, Hochschulverlag AG an der ETH Zürich.
[14] Kleefkens O, van Berkel J, Geelen C, Bos M. (2017). Booster heat pump, development of test procedure and calculation methodology in order to estimate the energy performance in various domestic applications. In Proceedings of the 12th IEA Heat Pump Conference, Rotterdam, The Netherlands.
[15] Kremer AM, Menkveld M, Matton R, Segers R, Vroom J. (2017). Monitoring warmte 2015. ECN & CBS. Report ECN-E--17-018, 66 pages.
[16] Kumar R. (2015). Valuation. Academic Press.
[17] Lauenburg P. (2016). Temperature optimization in district heating systems. Advanced district heating and cooling (DHC) systems. Elsevier Ltd.
[18] Lund H, Werner S, Wiltshire R, Svendsen S, Thorsen JE, Hvelplund F, Mathiesen BV. (2014). 4th Generation district heating (4GDH). Integrating smart thermal grids into future sustainable energy systems. Energy, **68**, 1–11.
[19] Lundström L, Wallin F. (2016). Heat demand profiles of energy conservation measures in buildings and their impact on a district heating system. Applied Energy, **161**, 290–299.
[20] Østergaard, D. S. (2018). Heating of existing buildings by low-temperature district heating. PhD thesis DTU. DTU Civil Engineering Report 396.
[21] Østergaard D, Svendsen S. (2017). Space heating with ultra-low-temperature district heating - A case study of four single-family houses from the 1980s. Energy Procedia, **116**, 226–235.
[22] Rezaie B, Rosen MA. (2012). District heating and cooling: Review of technology and potential enhancements. Applied Energy, **93**, 2–10.
[23] Sayegh MA, Danielewicz J, Nannou T, Miniewicz M, Jadwiszczak P, Piekarska K, Jouhara H. (2017). Trends of European research and development in district heating technologies. Renewable and Sustainable Energy Reviews, **68**, 1183–1192.
[24] Schepers B, Scholten T. (2016). Ketenemissies warmtelevering. Report 16.3H06.06. CE Delft.
[25] Schepers B, Scholten T, Willemsen G, Koenders M, de Zwart B. (2019). Beyond gas. Report 19.3K61.096. CE Delft. In cooperation with IF Technology.
[26] Schmidt EØ, Kristensen MS. (2014). Optimisation of defrost strategy for an air-to-water heat pump. Dynamic modelling and experimental study of frost formation on cross-flow heat exchanger surface. MSc Thesis Aalborg University. Department of Energy Technology.
[27] Sommer W. (2014). Modelling and monitoring of aquifer thermal energy storage. WUR.
[28] Thermaflex. (2017). Technical data sheet Flexalen ® 600, 1–2.
[29] van Bueren E, van Bohemen H, Itard L, Visscher H. (2012). Sustainable urban environments: An ecosystem approach. Dordrecht: Springer.

[30]van Vliet E, de Keijzer J, Slingerland E, van Tilburg J, Hofsteenge W, Haaksma V. (2016). Collectieve warmte naar lage temperatuur. Ecofys & Greenvis. TKI project number UENNL16481. Utrecht.
[31]Verhaegh N. (2018). Slim van het gas af met lage temperatuur warmte in de bestaande bouw. DNV-GL.

13th IEA Heat Pump Conference
April 26-29, 2021 Jeju, Korea

Performance analysis of a vapor-extraction heat-pump system for district heating/cooling applications

Malick Kane[a*], Aziz Mbaye[b]

[a]Laboratory for Thermal Energy (LTE), University of Applied Sciences and Arts of Western Switzerland Boulevard de Pérolles 80, CH-1700, (Fribourg) Switzerland
[b]He-Tech Suisse, Route du Jura 37B – CP 304, CH-1701, (Fribourg) Switzerland,

Abstract

This paper describes a new concept of a high temperature (HT)/low-temperature (LT) network integration by using an advanced heat pump technology able to integrate and manage various renewable and residual energy sources with different temperature levels. It is based on a vapor extraction (VE) compression cycle, which integrates two well-known cycles: a vapor compression heat pump cycle and an organic Rankine cycle (ORC). To perform a comparison with existing heat pumps, an energy/exergy analysis has been carried out by using R134a as a working fluid. Thus, for a given extraction ratio of 25%, results show that an increased heating/cooling capacity of about 30% and a high exergy efficiency of 59.7% can be achieved, compared to the 55.5% obtained for conventional compression heat pumps. A global coefficient of performance (COP) between 2.5 and 3.5 (corresponding to a vapor extraction ratio between 10% and 30%) is also obtained and compared to the 1.3-1.7 values given in the literature for existing thermally driven heat pumps (e.g. absorption heat pumps or double orc-orc heat-pump cycles) working with high temperature levels of hot sources.

Keywords: **:** *District Heating/cooling Network;, Heat pumps; Organic Rankine Cycle; Vapor compression Cycle; Thermally driven heat pump cycle; Vapor extraction compression heat pump*

1. Introduction

Heating and cooling represent around 40-50% of the total end-use energy consumption in Switzerland [1]. In their vast majorities, useful heating and hot water preparation demand in Buildings are supplied by using fossil-fuel centralized energy conversion systems like boiler or combined heat and power units (CHP) driven district heating (DH) networks [2]. These existing types of networks operate in general with relatively low thermal efficiencies related to high operating temperature levels (e.g. around 80-200°C). As an alternative or complement to pollutant control technologies to mitigate the emissions of fossil-fuel-based district heating networks, consumers, public interest groups and some local and state governments advocates a shift away from polluting energy systems to low-grade district heating/cooling systems using residual and/or renewable sources like geothermal, solar thermal, heat-pumps or waste heat [3-5].

* Corresponding author. Tel.: +41 (0)26 429 68 42.
E-mail address: malick.kane@hefr.ch.

Depending on the type of sources, such low-grade district heating/cooling networks operate at temperature levels between 10 and 35°C and use generally decentralized heat pump (HP) units to raise the temperature in buildings for heating and domestic hot water production [6-7]. These advanced networks have the advantage of being able to serve both for heating (up to 35°C in winter) and cooling (15°C in summer) if their temperature levels could be alternately adapted between seasons [9]. However, the time dependence of temperature levels of these renewable energy sources and the increasing numbers of small installations providing both heating or cooling to connected buildings will considerably affect the temperature levels of the network and therefore influence both the performance of thermal networks and decentralized heat pumps units. The high differential temperature between the DH network and the supply temperature level for heating and hot water process in the building corresponds to an important consumption of electricity in the decentralized HP units. The control of these temperature levels can be easily done in the networks by using existing HT district heating networks. Such integration of HT/LT networks can be realized by using an intermediate station unit (or Cluster). The Cluster station system could be represented by a simple heat exchanger to separate HT and LT circuits or an energy conversion system based organic Rankine cycle (ORC) cogeneration units or thermally driven heat pump (THP) cycles [10]. Figure 1 shows an application of thermally driven heat pump cycles using a HT network system (temperature between 80-280°C) to supply heat to a low-grade district heating/cooling network (20-35°C). The cold source of the THP could be renewable like solar thermal or geothermal or residual heat. A new concept of THP system able to integrate HT/LT networks with better efficiency (or COP-coefficient of performance) and can be operated with hot sources at relatively low temperature levels (even below 50°C) is the object of this paper (Figure 3).

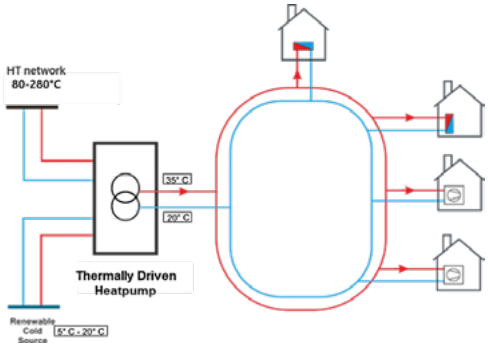


Fig. 1. An Integrated DH network application with thermally driven heat pumps

2. Existing thermally driven heat pump systems

Existing THP technologies such as absorption heat-pumps (single-effect and double-effect) [11,12], ORC driven heat pumps (ORC-ORC) [13] and ejector refrigeration technologies [14] operate in general with high temperature level are in general limited in term of capacity of heating and cooling, and efficiency (coefficient of performance). Figure 2 shows the coefficient of performance (COP) of a broad range of thermally driven heat pumps operating together in the range of hot sources with high temperature levels (between 95 and 275°C) which are more difficult to achieve using residual or renewable energy sources.

A global coefficient of performance between 1.3 and 1.7 have been demontrated for some existing commercial or experimental prototype units working with hot sources at relatively high temperature levels. We can indeed mention a) the gas fired absorption chiller units, commercialized by the company ROBUR S.A and operating at 150°C on the generator with a COP of 1.7 [15] and b) the various solar thermal prototype units based ORC driven heat pumps, demonstrated by several authors. So based on experimental studies on the ORC driven heat pumps, Prigmore and Baraber [16] showed that a COP of 1.5 can be reached with a hot source temperature of 95°C. Strong [17] worked on an ORC driven heat pump that can operates at, with a relatively high temperature level (277°C) with a COP of 1.43. He demonstrated a COP of 1.17 at 229°C. Another experimental study carried out by Biancardi et al. [18] specified a COP of 1.6 for a generator operating at 145°C. Wang et al. [13] have tested an ORC driven machine that produce a COP of 1.5 for a high temperature of 190°C.

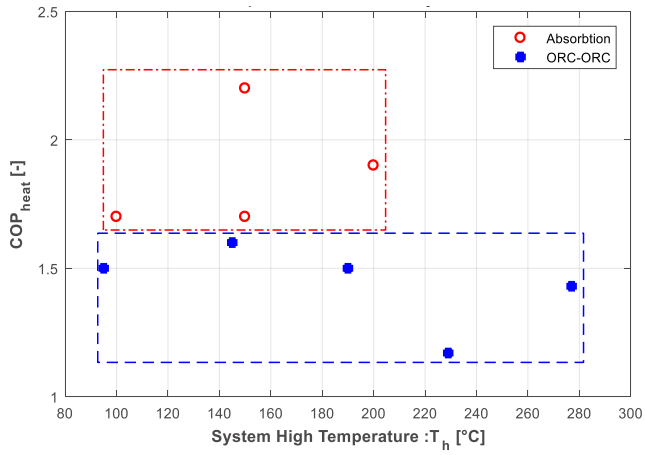


Fig. 2. Coefficient of performance of some existing and theoretical THP based absorption and orc-orc systems given in the literature

Besides those experimental investigations, some other theroretical studies have been performed mainly for absorption cycles. Grossmann [19] studied the performances of both single-effect and double-effect absorption machines for heating applications. His results showed that the single-effect absorption heat pump operating at a temperature level of 100°C can achieve a COP of 1.7 while the double-effect machine delivers a COP of 2.2 at 150°C. Critoph [20] investigated theoretically a forced convection adsorption cycle, which produced a COP of 1.9 at 200°C.

In addition to their low efficiencies and capacity for heating and cooling, such thermally driven heat pumps are limited in term of power density because of the size and the increasing number of components used in the cycle. The new ORC-ORC solution of thermally driven heat-pumps using high speed centrifugal compressor directly coupled with a radial turbine [21] are promising but needs important further developments to demonstrated efficiency, reliability and the ability to work with low temperature heat sources. Theoretical and experimental investigations have been done recently for space heating and hot water preparation in small residential building by using a gas fired boiler. A coefficient of performance of 1.3 has been demonstrated for a differential temperature of 20°C between the evaporator and the condenser and with supercritical thermodynamic cycle using R134a as a working fluid [22].

As the cost-competitiveness of existing thermally driven heat pumps is not yet feasible for applications of low temperature hot sources (below 50°C) because of the costs, efficiency and size of the units, renewable applications will shift towards increasing numbers of vapor compression heat pump technologies mainly adapted for low temperature heating and cooling [6–7]. The solution described in this paper is an original concept of "hybrid drive heat pump systems", developed by the company He-Tech. The hybrid heat pump uses both a primary heat and electricity to run a vapor compression cycle with intermediate pressure extraction for both providing heat from the condenser and recovering heat from the generator. It is based on two well-known cycles: a vapor compression heat pump cycle and an organic Rankine cycle. The system offers more flexibility to integrate and manage different renewable and residual energy sources (such as solar thermal, biomass, geothermal and waste heat) and ability to work with low-temperature heat sources (even below 50°C). One object of this present paper is to evaluate the performances (capacity for heating and cooling, coefficient of performance and exergy efficiency) of such a vapor extraction compression cycle concept and compare results to those of existing heat pump cycles.

3. Vapor-extraction heat pump cycle technology

The proposed new solution of heating/cooling is based on an innovative concept of hybrid drive heat pump technology based on a vapor compression cycle with partial flow extraction (VE heat pump cycle) that would enable to provide cost effective heating. Moreover, the system can provide significant environmental benefits by using renewable energy sources (e.g. solar thermal, geothermal and or biomass) and energy benefits by allowing the valorization of low-temperature residual heat from buildings. It is based on two well-known

thermodynamic cycles: The Organic Rankine Cycle (ORC) and the vapor compression cycle. It is able to perform energy tri-generation, which means, depending on the application, it can provide heat, cold and/or electricity. A flowsheet diagram showing the main refrigerant circuit of the proposed system is given in Figure 3.

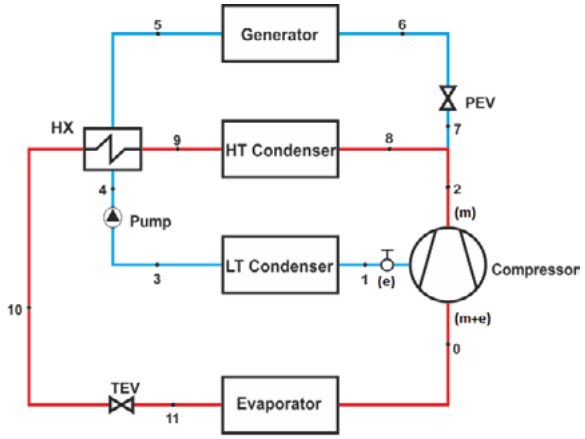


Fig. 3. Flowsheet diagram showing the main refrigerant circuit of a VE heat pump cycle

The new working fluid like R1234yf can be a good solution for such a type of advanced heat pumps. However, for the basis of this comparison with existing vapor compression heat pumps, the refrigerant R134a is considered as a working fluid for calculations. Figure 4 shows the T-s diagram of the VE heat pump cycle.

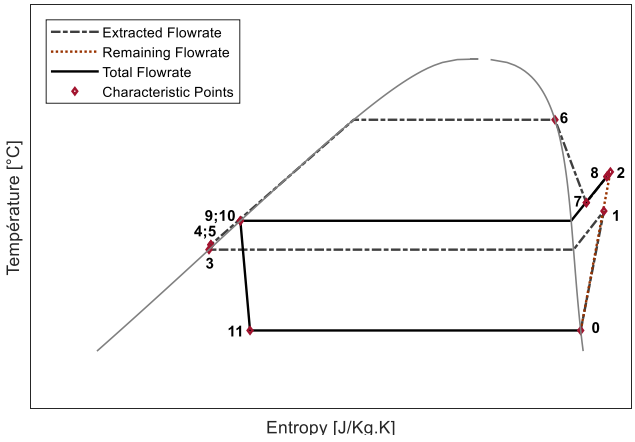


Fig. 4. T-s diagram of a VE heat pump cycle

A portion of the compressed vapor (e) is extracted from the compressor at an intermediate pressure level (fig. 3). After condensation (in the LT condenser), the liquid is pumped to feed the generator via an internal heat exchanger (HX) which acts as a preheater. The fluid vapor produced within the generator is expanded through a pressure expansion valve (PEV) controlling the outlet pressure. After mixing with the high-pressure vapor coming from the compressor (m), cooling and condensation within a heat exchanger (HT condenser), the total liquid (m+e) is cooled into the internal HX, which acts as a subcooler and then expanded through an expansion valve (TEV) into the evaporator. In order to minimize the electricity consumption, the high-pressure expansion valve (PEV) could be replaced by an expander operating at higher temperature levels compared to the PEV and able to generate a part of electricity needed for the heat pump.

To point out the contribution of the heat recovered at the generator in the overall amount of heat produced by the VE heat pump we defined a parameter named extraction ratio (ER) which represents the extracted flowrate (ė) over the compressor inlet flowrate ($\dot{m} + \dot{e}$). For a standard heat pump system, the ER is equal to zero.

$$ER\ [\%] = \frac{\dot{e}}{\dot{m} + \dot{e}} \tag{1}$$

4. Performance analysis and results

As mentioned above, a low-grad district heating (DH) network application is considered where the centralized VE heat pump is used to supply the required heat and to control the temperature of the network. Thermodynamic calculations have been made to compare the system with existing heat pumps (vapor compression standard heat pump and thermally driven heat pumps) used for the same application.

4.1. Model of the vapor extraction heat pump cycle

A simplified R134a thermodynamic model have been considered for the VE-HP. To establish such model, we made the following assumptions:

- The heat exchangers operate at the saturation level (e.g. without superheating on the evaporator and no subcooling on the LT condenser) and the system is considered in steady state;
- The expansion process through the valves TEV and PEV is considered isenthalpic;
- A global isentropic efficiency of 70% is assumed for both the pump and the compressor;
- The motor efficiency and the mechanical efficiency the pump and the compressor stages are set to 1;
- The pressure losses as well as the heat losses are ignored

The models of the VE-HP are then obtained by performing energy and mass balances on each component (Eq. 2 - 5):

$$\dot{Q}_{gen} = \dot{m} \cdot (h_{gen,out} - h_{gen,in}) \tag{2}$$

$$\dot{Q}_{evap} = (\dot{m} + \dot{e}) \cdot (h_{evap,out} - h_{evap,in}) \tag{3}$$

$$\dot{Q}_{LT_cond} = \dot{m} \cdot (h_{LT_cond,in} - h_{LT_cond,out}) \tag{4}$$

$$\dot{Q}_{HT_cond} = (\dot{m} + \dot{e}) \cdot (h_{HT_cond,in} - h_{HT_cond,out}) \tag{5}$$

where $\dot{m}$ is the mass flowrate through the generator; $h_{gen,out}$, $h_{gen,in}$, $h_{evap,out}$, $h_{evap,in}$, $h_{LT_cond,out}$, $h_{LT_cond,in}$, $h_{HT_cond,out}$ and $h_{HT_cond,in}$and h_5 are respectively the refrigerant enthalpy at the outlet and the inlet of the generator, evaporator, low temperature condenser and high temperature condenser and $\dot{e}$ is the extracted flowrate. The extracted flowrate is calculated by using the extraction ratio ER:

$$\dot{e} = \dot{m} \cdot \frac{1 - ER}{ER} \tag{6}$$

To determine the compressor total electric power, we take account of the work delivered to the fluid by the two compression stages:

$$\dot{E}_K = \dot{m} \cdot (h_{K,out,ext} - h_{K,in}) + \dot{e} \cdot (h_{K,out} - h_{K,in}) \tag{7}$$

where $h_{K,in}$, $h_{K,out,ext}$, $h_{K,out}$ are the refrigerant enthalpy at respectively the compressor inlet, extraction outlet and second stage outlet.

In the same way, the power of the pump is calculated by Eq (8):

$$\dot{E}_p = \dot{m} \cdot (h_{p,out} - h_{p,in}) \quad (8)$$

where $h_{p,out}$ and $h_{p,in}$ are the enthalpy at the pump discharge and succion.

In order to assess the contribution of the heat recovered at the generator, two definitions of coefficient of performance (COP) are considered:

- the net electric coefficient of performance (COP_{el}) given by the ratio between the output of condensers and the total electric power consumed by the system (compressor and pump)
- the hybrid (or global) coefficient of performance (COP_{gl}) taking into account both the electric power consumption and the recovered heat rate at the generator

$$COP_{el} = \frac{\dot{Q}_{LT_cond} + \dot{Q}_{HT_cond}}{\dot{E}_k + \dot{E}_p} \quad (9)$$

$$COP_{gl} = \frac{\dot{Q}_{LT_cond} + \dot{Q}_{HT_cond}}{\dot{E}_k + \dot{E}_p + \dot{Q}_{gen}} \quad (10)$$

For the classical heat pump, since the extraction ratio is zero the COP_{el} and the COP_{gl} are the same. In order to be able to compare the two technologies (standard vapor compression cycle and hybrid vapor compression cycle) with the same criterion, an exergy efficiency was defined as in equation 11. $\dot{e}_{LT_cond}$, $\dot{e}_{HT_cond}$, $\dot{e}_k$, $\dot{e}_p$, $\dot{e}_{gen}$ are respectively the heating exergy provided by the LT condenser and the HT condense, the compressor exergy consumption, the pump exergy consumption and the exergy received at the generator; T_{LT_cond}, T_{HT_cond}, T_{gen}, T_o are respectively the temperature of the LT condenser, the temperature of the HT condenser, the temperature of the hot source at the generator and the outside ambient temperature.

$$\eta_{ex} = \frac{\dot{e}_{LT_cond} + \dot{e}_{HT_cond}}{\dot{e}_k + \dot{e}_p + \dot{e}_{gen}} \quad (11)$$

$$\eta_{ex} = \frac{\dot{Q}_{LT_{cond}} \cdot \left(1 - \frac{T_o}{T_{LT_{cond}}}\right) + \dot{Q}_{HT_{cond}} \cdot \left(1 - \frac{T_o}{T_{HT_{cond}}}\right)}{\dot{E}_k + \dot{E}_p + \dot{Q}_{gen} \cdot \left(1 - \frac{T_o}{T_{gen}}\right)} \quad (12)$$

The set of equations is implemented and solved with Matlab®. At each point of the cycle, the refrigerant properties are evaluated using the thermodynamic state equations.

4.2. Performance simulation

A case study of a DH network operating at a temperature level of 35°C and with a heating nominal demand of 100% is considered for the simulation.

Table 1. An example of a table

	Pressure [bar]	Temperature [°C]
Evaporator	3.74	7
LT-condenser	8.87	38
HT-condenser	11.6	48
Generator	26.3	77

The generator of the VE heat pump is connected to the hot source with a maximum temperature of 80°C and which can come from process waste heat, solar thermal, or biomass. The VE heat pump uses the

atmosphere or a geothermal cold source for which the temperature is supposed to be constant at 10°C. Table 1 shows pressure and temperature levels of evaporation and condensation of the working fluid (R134a). The same thermodynamic cycle is used to evaluate the performance of the standard vapor compression heat pump cycle by setting the extraction ratio at 0%.

4.3. Capacity and efficiency of the VE heat pump

Figure 5 shows the variations of the VE heat pump coefficient of performance (blue curves) and exergy efficiency (red curve) in function of the extraction ratio. A net exergy efficiency of about 63% (e.g. 50% extraction ratio) can be achieved for this application. The minimum value of 55.5% corresponding to a zero extraction ratio represents the exergy efficiency of a standard vapor compression heat pump.

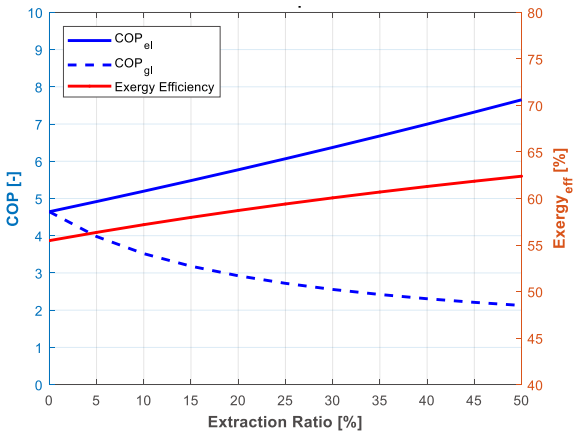


Fig. 5. Coefficient of performances and exergy efficiency of the VE heat pump cycle for various extraction ratio

Note that the global coefficient of performance decrease at high extraction ratio can be explained by the primary heat consumption, which is then too high at the generator of the cycle. As shown in figure 5 the net electric coefficient of performance increase also with the vapor extraction ratio. It can be pointed out that the compressor is used at very partial flow (operation between the LT and HT condensing pressures), requiring then less electric power consumption for the same demand or corresponding to an important gain of heating/cooling capacity when compared to the standard vapor compression cycle with same electricity consumption. Figure 6 represents the variation of heat supply vs electricity consumption with the two configurations. Results show that an increased heating/cooling capacity of about 30% is achieved for a given extraction ratio of 25% (which corresponds also to an exergy efficiency of 59.7% according to the figure 5).

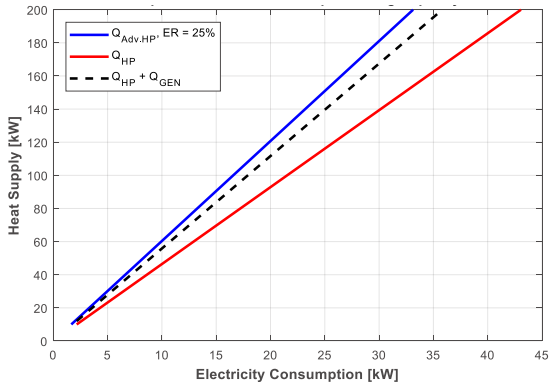


Fig. 6. Heating capacity of the VE heat pump cycle for an extraction ratio of 25% and the standard vapor compression cycle

Other sources of improvements that can influence the capacity of the VE heat pump are related to the internal heat exchanger (HX). The additional subcooling increases the evaporator cooling capacity by reducing the evaporator inlet enthalpy of the fluid. The additional condenser mass flow (**e+e**, for both the LT and HT condenser) increases also considerably the heating capacity of the installation. These added capacities are achieved with less electrical power consumption in the compressor because the amount of vapor extracted (**e**) is compressed only from the suction pressure to the intermediate pressure. Due to this increase in capacity, it could be required to specify a smaller compressor (low displacement) for a given heating and/or cooling demand. For a given extraction ratio of 25%, an increased capacity of 30% is achieved compared to a conventional vapor compression heat pump.

Fluctuations of both the amount of heat recovered at the generator, the hot source temperature and/or outside ambient temperature can be coped with the adaptation of the extraction mass flow rates of the HP working fluid. This flexibility of operation whoud allow to better integrated various sources of renewable energy such as solar thermal application.

4.4. Comparison with commons thermally driven heat pumps

A good way to analyze the performances of such technology is to compare them with those of other tri-therm machines that could be potentially used in this particular application. Figure 7 shows the coefficient of performance of the VE heat pump in function of the temperature levels at the generator compared to existing thermally driven heat pumps.

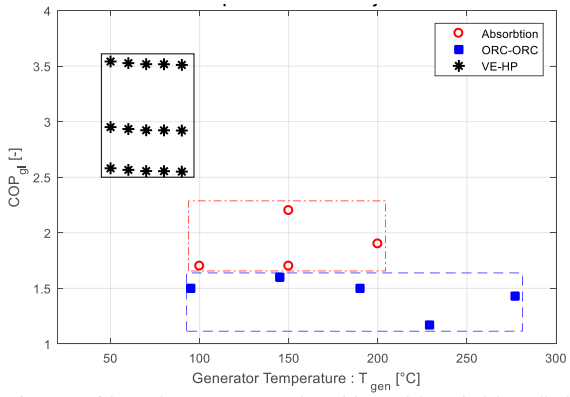


Fig. 7. Coefficient of performance of the VE-heat pump compared to exisitng and theoretical thermally driven heat pumps based absorption and orc-orc systems given in the litterature

Efficiency with vapor extraction heat pump is always higher than conventional thermally driven heat pumps (like absorption heat pump and orc-orc heat pump) when providing the same capacity for heating and cooling. Because, only the small portion (**e**) of refrigerant, extracted from the compressor (less than 30% of the main flow rate) is used to feed the generator, requiring then less heat consumption compared to other systems. A global coefficient of performance (COP) between 2.5 and 3.5 (corresponding to a vapor extraction ratio between 10 and 30%) is obtained and compared to the 1.3-1.7 of existing thermally driven heat pumps working with high temperature levels.

The results show that there is no advantage to work at relatively high temperature levels on the generator of the cycle. Such a situation corresponds in fact to a high difference of temperature between the HT condensing temperature and the generator evaporation temperature reducing then the global coeffient of performance because of losses on the pressure expansion valve (PEV). A high difference of temperature corresponds also to a high difference of pressure on the pump that is accompanied by a significant consumption of the electric power. This makes the cycles work at higher temperature on the generator, which is then detrimental for the coefficient of performance.

5. Conclusions

A new concept of hybrid drive heat pump technology based on a vapor compression heat pump cycle with partial flow extraction has been proposed and applied to control the temperature level of a low-grade district heating/cooling network **(**VE heat pump cycle**)**. The system offers more flexibility to integrate and manage different renewable and residual energy sources (such as solar thermal, biomass, geothermal and waste heat) and ability to work with low-temperature heat sources (even below 50°C). For the comparison with standard vapor compression heat pump the refrigerant R134a have been considered and a simplified thermodynamic model was performed to simulate and evaluate the performances (capacity for heating and cooling, coefficient of performance and exergy efficiency) of such a vapor extraction compression cycle concept and compare results to those of existing heat pump cycles. Results show that an increased heating/cooling capacity of about 30% and a high exergy efficiency of 59.7% (instead of 55.5%) can be achieved for a given extraction ratio of 25%, compared to the 55.5% obtained for conventional compression heat pumps. A global coefficient of performance between 2.5 and 3.5 (corresponding to a vapor extraction ratio between 10 and 30%) is also obtained and compared to the 1.3-1.7 given values in the literature for existing thermally driven heat pumps (e.g. single or double effect absorption heat pumps or double orc-orc heat-pump cycles). Future work could be devoted to experimental investigations on the VE heat pump and a comparative thermo-economical study with other solutions available for district heating/cooling application.

Acknowledgements

The authors gratefully acknowledge the support of InnoSuisse [Grant number 33741.1 INNO-EE].

References

[1] Kirchner A., Kemmler A. Hofer P. Keller M. Jakob M. Catenazzi G.**:** Analyse des schweizerischen Energieverbrauchs 2000-2009 nach Verwendungszwecken. Swiss Federal Office of Energy, (2010).
[2] Rezaie B., Rosen MA.**:** District heating and cooling: review of technology and potential enhancements. Applied Energy, 93 : 2-10, (2012).
[3] Ostergaard PA., Lund H.**:** A renewable energy system in Frederikshavn using low-temperature geothermal energy for district heating. Applied Energy, 88: 479-87, (2011).
[4] Hallera M-Y., Bertramb E., Dottc R., Afjeic T., Ochsd F., Hadorn J-C.: Review of component models for the simulation of combined solar and heat pump heating systems. SHC, Energy Procedia 30 (2012) 611 – 622
[5] Noussan M., Jarre M., Degiorgis L., Poggio A.: Data Analysis of the Energy Performance of Large Scale Solar Collectors for District Heating. Energy Procedia, Volume 134, October 2017, Pages 61-68
[6] Molyneaux A., Leyland G., Favrat D.**:** Environomic multi-objective optimization of a district heating network considering centralized and decentralized heat pumps. Energy, 35(2): 751-758, (2010).
[7] Østergaard P-A and Andersen A-N.: Booster heat pumps and central heat pumps in district heating. Applied Energy 184 (2016) 1374–1388
[8] Henchoz S., Chatelan P., Marechal F., Favrat D.**:** Key energy and technological aspects of three innovative concepts of district energy networks, Energy, 117 (2016) 465-477, (2016).
[9] Kane M., Grosjean S., Kaempf J.: Energy integration and performance evaluation of a new concept of advanced solar district heating/cooling networks for energy supply in buildings. 5th International Solar District Heating/Cooling (SDH) conferences, April 2018 (Graz, Austria)
[10] Lake, Andrew & Rezaie, Behanz & Beyerlein, Steven: "Review of district heating and cooling systems for a sustainable future," Renewable and Sustainable Energy Reviews, Elsevier, vol. 67(C), pages 417-425 (2017).
[11] Wang R.Z. and Oliveira R.G.**:** Absorption refrigeration-An efficient way to make good use of waste heat and solar energy. Progress in Energy and Combustion Science, 32(4): 424-458, (2006).
[12] Schossig P.**:** Thermally driven heat pumps (Foreword). IEA Heat Pump Center Newsletter, 29(1): 18-22, (2011).
[13] Wang H., Perterson R., Harada K., Miller E., Ingram-Goble R., Fisher L., Yih J., and War C.**:** Performance of a combined organic Rankine Cycle and vapor compression cycle for heat activated cooling. Energy, 36(1): 447-458, (2011).
[14] Abdulateef J.M., Sopian K., Alghoul M. A. and Suaiman**:** Review on solar-driver ejector refrigeration technologies. Renewable and Sustainable Energy Reviews, 13(6-7): 1338-1349, (2009).
[15] ROBUR SA, Association Swiss Gas Industry [On ligne]. - 2018. - http://www.gaz-naturel.ch/.

[16] Prigmore D., Barber R.: Cooling with the sun's heat: Design considerations and test data for a Rankine Cycle prototype. Solar Energy.
[17] Strong D.T.G.: Ph.D. Thesis, University of Oxford, 1980.
[18]0Biancardi F.R., Sitler J.W., Melikian G. : Development and test of solar Rankine cycle heating and cooling systems. International Journal of Refrigeration.
[19] Grossmann G.: Solar powered systems for cooling, dehumidication and air-conditioning. Solar Energy.
[20] Critoph R.E.: Forced convection adsorption cycle with packed bed heat regeneration. International Journal of Refrigeration.
[21] Demierre J.: Theoretical and Experimental Study of a Thermally Driver Heat Pump Based on a Double Organic Rankine Cycle. PhD. Thesis No. 5201, Suisse Federal Institute of Technology, EPFL-Lausanne, Switzerland, (2012).
[22] Morvaj B., Evins R., Carmeliet J.: Optimizing urban energy systems: Simultaneous system sizing, operation and district heating network layout. Energy 116 (2016) 619e636

13th IEA Heat Pump Conference
April 26-29, 2021 Jeju, Korea

Evaluation of a Hybrid AC/DC Powered Residential Split-System Heat Pump Performance using a DC Nanogrid

Jonathan Ore[a,*], Fatih Meral[a], Oliver Obst[a], Orkan Kurtulus[a], Eckhard A. Groll[a]

[a]Purdue University, Ray W. Herrick Laboratories 177 S. Russell St., West Lafayette 47907, USA

Abstract

Many benefits have been observed from the employment of Direct Current (DC) distribution schemes over those of traditional Alternating Current (AC) within building architectures, ranging from enhanced system efficiency, increased reliability, reduced points of failure, and more convenient integration with renewable energy generation systems. The objective of this research is to demonstrate the emulation of a DC Nanogrid system supporting the largest categorical energy consumer in the residential building-space: the HVAC system. Through the avoidance of unnecessary energy losses due to power conversion, a DC-driven heat pump affords a significant opportunity for energy savings and overall improved efficiency. This paper presents the results from laboratory testing a hybrid AC/DC powered air-source heat pump fashioned to operate separately on either an AC or DC electrical supply. The corresponding residential DC Nanogrid system is simulated with a psychrometric chamber integrating a variable voltage DC power supply. Initial psychrometric testing of both AC and DC configurations are presented, along with corresponding thermal and electrical performance analysis. Future work will consider individual characterization of the heat pump components under DC supply, comparison of line losses between AC and DC load conditions, and additional environmental heating and cooling test cases.

Keywords: DC Power; Direct Current; Nanogrid; Heat Pump

1. Introduction

Within the U.S., the advent of ever-increasing energy demands has resulted in escalating strain on the power grid, often pressuring it to the limits of its capabilities. Modern technological innovations have fostered a greater dependency on the grid, coupling it with nearly every aspect of contemporary society. Unfortunately, the grid has not experienced a parallel rate of growth alongside technology, with some estimates reporting in the range of trillions of dollars necessary for repairs and upgrades to return to a nominal performance level. During the previous decade, the American Society of Civil Engineers scored the U.S. energy system with a grade of a "D+" for overall reliability, describing outdated distribution systems, limited system capacity, and undesirable environmental side-effects as the leading factors in their evaluation [1]. Further challenging these conditions is the increasing dependency on internet technology and cellular networks, resulting in a proportional rise in vulnerability of the electrical grid. A recent Wall Street Journal article concludes that a failure of just nine substations (via targeted attack, electrical failure, etc.) could result in a significant destabilization of the entire electrical grid [2].

These concerns have stimulated investigations into other potential solutions, including the feasibility of individual micro and nanogrids existing in both residential and commercial spaces. These grids, while still connected to the outside "main" electrical grid, possess the ability to operate autonomously and mitigate loads in an islanding-mode without relying on the external grid. Such capabilities are highly beneficial in the face of emergencies or other failures, but also offer advantages in energy costs through the employment of renewable energy sources (e.g. wind, solar, geothermal, etc.). The electrical infrastructure afforded by a micro/nanogrid is typically that of Direct Current (DC), as opposed to the traditional infrastructure of Alternating Current (AC)

* Corresponding author. Tel.: +1-765-494-2132.
E-mail address: jore@purdue.edu.

currently in place. Unfortunately, nearly all appliances and devices, particularly in a residential setting, require DC power at terminal endpoints; as a result, the AC power being supplied to them must first be converted to DC, resulting in a loss of energy. This problem is further exacerbated when renewable energy is integrated, which naturally generates DC power. To provide compatibility with the existing infrastructure, energy generated from renewable resources must first undergo a conversion from DC to AC, resulting in energy loss, and then experience a second conversion from AC back to DC at the point of use, resulting in additional energy loss. Such penalties are primary drivers for interest in a DC-based micro/nanogrid solution, with some modeling estimations revealing a potential conversion loss reduction of up to 30% in a commercial building with an integrated battery [3].

The residential setting in this paper serves as the foundation for a novel type of nanogrid, which seeks to achieve a complete home conversion from AC to DC power. Nanogrid terminology is employed to differentiate the intra-building scope of the design, as opposed to a microgrid which often encapsulates multiple buildings and distributed energy generation sites and storage. The dwelling under scrutiny is a two-story 1920's era home entitled "The DC House", housing three graduate students and located in West Lafayette, IN. The DC House is situated on a 595 m^2 lot with a detached garage, and contains 208 m^2 of floor space. As part of the conversion process from AC to DC, a DC infrastructure will be designed and installed, and supplied by renewable energy sources using solar panels on the roof of the house. Modeling and simulation are planned to verify and validate the hardware solution, as has been performed in similar setups [4].

With the house serving as a "living lab", baseline AC energy consumption among the residents was evaluated for an entire year. Analysis of data collected during 2018 revealed the heat pump system to be the largest categorical energy consumer of all appliances present.

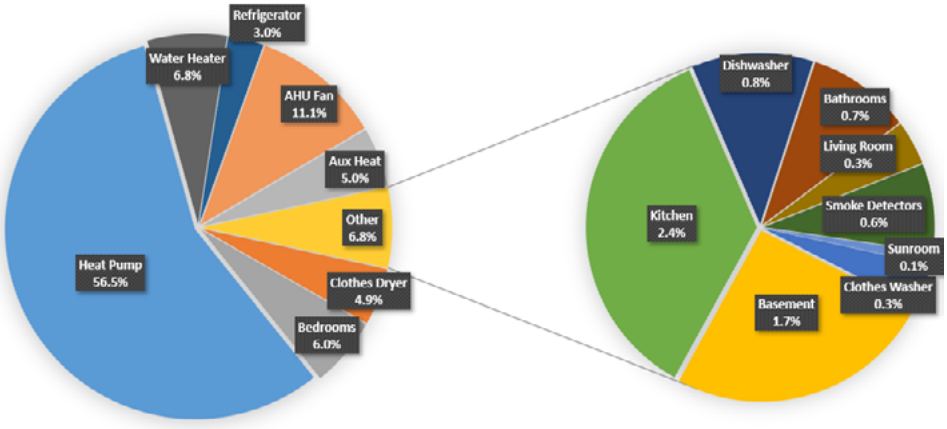


Fig. 1. DC House Categorical Comparison of Appliance Energy Consumption in 2018

A survey performed by the IEA confirms the findings in Fig. 1, estimating that space heating and air conditioning represent up to 49% of average U.S. household energy consumption [5]. As a result, electrical retrofitting of the heat pump from an AC to DC configuration affords a significant opportunity for energy savings and an increase in efficiency.

In this paper, the DC Nanogrid is simulated through the use of a variable-voltage 15 kW DC power supply. The environmental conditions inside and outside the DC House are emulated using two adjacent psychrometric chambers, capable of replicating conditions between -20 °C (-4 °F) and 55 °C (130 °F), and 15% to 100% humidity. AC and DC electrical configurations using a retrofitted hybrid heat pump are tested under a variety of cooling conditions, and compared with thermal and electrical performance metrics. Further testing conditions and topics of investigations are then considered for future study.

2. Specifications and Methods

To provide a basis for comparison across the various electrical configurations, an off-the-shelf variable speed heat pump with scroll compressor was selected and retrofitted to accept both AC and DC electrical

supply inputs. Using conventional residential AC power, the modified unit operates on a nominal split-phase 240 VAC input. Under the DC configuration, the modified unit operates on nominal bi-polar 350 VDC input, with undervoltage and overvoltage limits at 250 VDC and 400 VDC, respectively. The internal thermal configuration in the modified unit remained unchanged in order to ensure commonality. The results within this paper evaluate thermal and electrical performance with both AC and DC power conditions using the retrofitted AC/DC hybrid unit. Future investigation will then consider this data against an unmodified unit installed at the DC House operating on standard 240 VAC.

2.1. Electrical Configuration and Conversion Losses

A specific advantage of the DC-based electrical configuration arises from the difference in current consumption of the heat pump. The maximum power of the heat pump is rated at 6.96 kW, which can be used to determine the maximum current load under a 120 VAC split-phase configuration.

$$P_{AC} = I_{AC} \cdot \Delta V_{AC} \quad (1)$$

Under this relationship, the maximum current is found to be approximately 29 A. If the voltage is then increased to 350 VDC for the DC connection, the maximum current is proportionally decreased to 20 A instead. Eq. 1 can be rewritten to describe the loss of power with respect to the line resistance, as is shown in Eq. 2.

$$P_{Loss} = I^2 \cdot R \quad (2)$$

From this relationship, it is clear that the loss of power associated with resistance in the system is reduced in proportion to the squared inverse of current. As a result, halving the current requirement for a component could potentially reduce its electrical line transmission power losses by a factor of one-fourth. In the specific case of the heat pump under study in this paper, the decrease in current requirements from 29 A to 20 A affords a theoretical maximum reduction in line power loss of up to 52%, assuming equivalent resistances.

Although the line power consumption represents only a small portion of the energy consumed by the heat pump system, the savings become more significant over larger distances and across numerous appliances. These losses also reduce result in a voltage drop between supply and appliance, potentially reducing performance and introducing system instability. Additional current requirements also impose an increase in the wire gauge, resulting in higher costs and even further possible line losses. These factors will be closely analyzed in future studies to numerically quantify differences between AC and DC configurations, and their corresponding transmission losses under a variety of line lengths.

In a traditional electrical design, input three-phase AC voltage is passed through a bridge rectifier, converting it to a usable DC voltage as shown in Fig. 2.

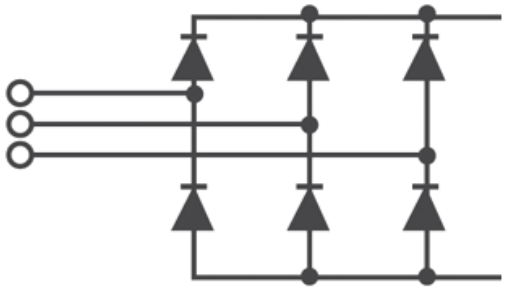


Fig. 2. Standard Three-Phase Bridge Rectifier Circuit

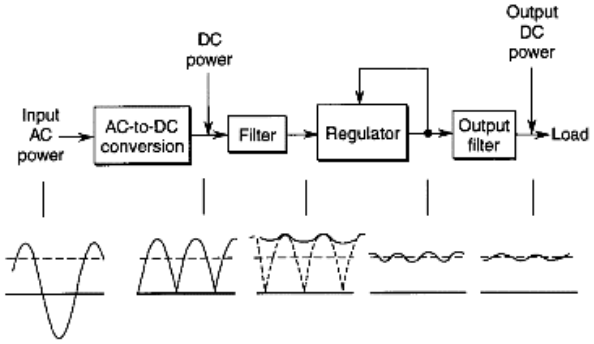


Fig. 3. Complete Power Conversion Process from AC to DC [6]

The entire conversion process can be summarized using the flow diagram in Fig. 3, with the corresponding electrical waveform shown immediately underneath. The rectification stage in Fig. 2 is represented in Fig. 3 by the "AC-to-DC conversion" block. As Fig. 3 illustrates, this first stage of rectification results in the largest source of energy lost. Through the ratcheting-effect of the diodes in the rectifier, the negative phase of the AC waveform is removed in the first step towards the DC conversion. The collective result of each stage in Fig. 3 can yield a net loss of 10% to 15% or more in energy efficiency.

The internal control mechanisms of the modified heat pump have been designed to accept both conventional AC voltage and DC input. The hybrid nature of the modified heat pump is made feasible in part by the capability of the bridge rectifier in Fig. 2 to allow DC voltage to pass through without significant impedance. In the case of a pure DC voltage, which is constant without any sinusoidal component, the diodes have no impact on the path of current outside of a small voltage drop, and therefore do not inhibit the processing of the DC input. The remaining conversion stages (filter, regulator, etc.) also have no significant impact on an input DC voltage, and thus the final output DC power shown in Fig. 3 is still achieved.

2.2. Hybrid Heat Pump Setup and Specifications

Initial experimental data for the hybrid heat pump was collected using a 230 VAC connection available within the psychrometric chambers. Within the U.S., 220 VAC to 240 VAC are generally understood as synonymous, and thus the DC House and psychrometric laboratory setting can be considered electrically equivalent for future studies. The hybrid heat pump under study is a 14.07 kW (4 ton) air-source split-system design, accepting either 240 VAC or 350 VDC as inputs. Indoor and outdoor components of the heat pump were installed separately in individual psychrometric chambers to properly emulate realistic environmental conditions at the DC House. The outdoor unit contains a compressor, condenser, outdoor fan, and a four-way valve, while the indoor unit includes the evaporator, thermostatic expansion valve (TXV), and indoor fan. The heat pump unit contains a scroll compressor, and a manufacturer Seasonal Energy Efficiency Ratio (SEER) value of 18. The nominal indoor airflow rate is 2379 m^3/h, and the hybrid system is charged with 6.1 kg of R410A. The heat pump system is composed of a variable speed compressor, an indoor fan with variable volume flow rate, and an outdoor fan with a variable speed motor. The specifications are summarized in Table 1.

Table 1. Hybrid Heat Pump Configuration Summary

Available electrical configurations	Cooling capacity	SEER rating	Refrigerant	Testing environment
240 VAC / 350 VDC	14.07 kW (4 ton)	18	R410A	Psychrometric Chambers

2.3. Equipment Setup and Data Collection

Laboratory data from the hybrid heat pump was collected using a National Instruments cRIO-2091 data acquisition system (DAQ) with a LabVIEW based visual interface for inspection and logging. Watt transducers were individually installed to monitor the AC power consumption of the indoor unit fan, and the outdoor unit fan and compressor. When employing the DC power configuration, cumulative system power was monitored

using the 15 kW MagnaPower variable-voltage DC power supply. DC power was distributed to the indoor unit using 20 m of 10 AWG wire, and to the outdoor unit using 10 m of 6 AWG wire.

Thermal data collected was evaluated using both air and refrigerant enthalpy methods to determine the cooling capacity. A schematic summarizing the psychrometric chamber layout and refrigeration loop configuration is provided in Fig. 4, with the state point descriptions given in Table 2.

Table 2. Hybrid Heat Pump State Point Definitions

State Point	Description
1	Compressor Inlet
2	Compressor Outlet
3	Condenser Inlet
4	Condenser Outlet
5	EXV Inlet
6	EXV Outlet
7	Evaporator Inlet
8	Evaporator Outlet

Thermophysical properties from the psychrometric test setup were determined through the use of the Engineering Equation Solver (EES) software [7]. In addition, state points 1 through 5 and 7 in Fig. 4 could be calculated from the measured pressure and temperature values of the refrigerant. State point 6 between TXV and the evaporator was obtained assuming both an isenthalpic expansion across the TXV device and negligible pressure drop at the outlet of the TXV and evaporator. The refrigerant mass flow was determined using a Coriolis mass flow meter configured for liquid phase between state points 4 and 5.

Cooling capacity of the hybrid heat pump could be calculated through two separate means, and then compared to determine the accuracy of the system measurements. Using a First Law energy balance and the given assumptions at each state point, the evaporator cooling capacity can be computed from Eq. 3.

$$\dot{Q}_{evap} = \dot{m}\Delta h_{evap} = \dot{m}(h_7 - h_6) \tag{3}$$

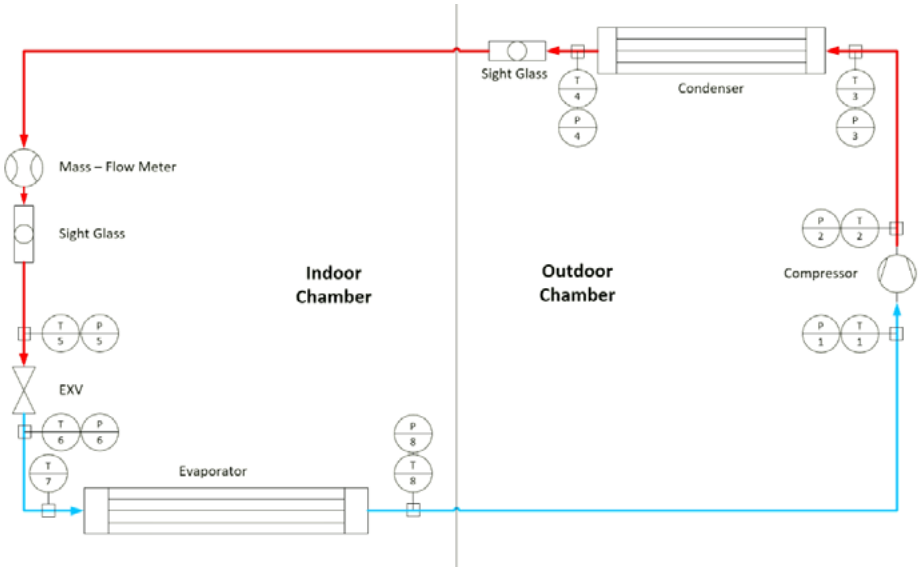


Fig. 4. Hybrid Heat Pump Cooling Configuration Schematic – Psychrometric Chamber Setup

The net capacity is then calculated by taking the difference between the cooling capacity of the evaporator from Eq. 3, and the additional heat added to the system from the indoor fan. The amount of heat was assumed approximately equivalent to the overall power consumption of the indoor unit, resulting in the relationship given by Eq. 4.

$$\dot{Q}_{delivered} = \dot{Q}_{evap} - \dot{W}_{indoor} \tag{4}$$

Alternatively, the hybrid heat pump cooling capacity could also be determined using an air-side approach. In this evaluation, the overall air-side capacity can be calculated again by considering a First Law energy balance applied to the indoor unit. Within this energy balance, the difference in enthalpy of the air flow is accounted for, along with the phase change of water condensed within the unit, yielding Eq. 5.

$$\dot{Q}_{delivered} = \dot{m}_{air}\Delta h_{evap} - \dot{m}_{water}h_{water} \tag{5}$$

In order to evaluate Eq. 5, calculation of the mass of air flow is needed. This can be determined by analyzing the volume flow rate of the nozzle box in line with the indoor unit's duct work of the indoor unit, which is designed in compliance with ASHRAE Standard 37-2009 [8]. The volumetric flow rate is calculated iteratively using Eq. 6.

$$\dot{V}_{air} = Y\sqrt{\frac{2\Delta p_{nozzle}}{\rho_{air}}}\sum_{0}^{k} C_i A_i \tag{6}$$

The expansion factor (Y) and coefficient of discharge (C_i) in Eq. 4 are defined in ASHRAE Standard 37-2009, and the area of the duct work (A_i) was specified during system installation [8]. With the volumetric flow rate obtained, the air flow mass can be solved by multiplying by the air density, and illustrated in Eq. 7.

$$\dot{m}_{air} = \dot{V}_{air}\rho_{air} \tag{7}$$

In addition to the mass of the air flow, the mass of the condensed water flow is also needed to evaluate Eq. 5. EES is used to calculate the inlet air enthalpy, outlet water enthalpy, and outlet air enthalpy, provided the necessary inputs are given. This includes the air dry-bulb temperature, which is measured with a 3x3 thermocouple grid situated between the inlet and outlet of the indoor unit, the relative humidity of inlet air using a relative humidity sensor, and the dew point of the outlet air. The dew point is determined through a periodic sampling of the air at the rate of 1 L/min, which is then processed through a chilled mirror dew point sensor. The relationship between these values calculated in EES is detailed in Eq. 8.

$$\dot{m}_{water} = \dot{m}_{air}(\omega_2 - \omega_1) \tag{8}$$

Finally, the heat pump coefficient of performance (COP) can be tabulated by dividing the system cooling capacity by its power consumption, as defined in Eq. 9.

$$\mathrm{COP} = \frac{\dot{Q}_{delivered}}{\dot{W}_{total}} \tag{9}$$

2.4. Testing Methodology

The hybrid heat pump with variable-speed components was tested in accordance with the guidelines set by AHRI. To establish common baseline testing conditions for both the AC and DC electrical configurations, psychrometric indoor and outdoor room conditions were specified from test conditions A, B, C, D, and E from Table 8 of the AHRI Standard 210/240 [9]. The compressor was operated near full speed during each test, but not explicitly controlled under either AC or DC configuration.

The test conditions performed are collected into a matrix shown in Table 3, with temperature values provided in both English and SI Units because SEER calculations require the input of temperatures in °F. Each test case was performed under both the 230 VAC and 350 DC configuration under steady state conditions, and monitored for thermal and electrical characteristics every few seconds. This data was subsequently post-processed using the EES software at the conclusion of the testing.

Table 3. Hybrid Heat Pump Psychrometric-Based Test Matrix

Test Case	Cycle Configuration	Indoor Temperature [°F/°C]	Indoor Relative Humidity [%]	Outdoor Temperature [°F/°C]	Indoor Relative Humidity [%]
1	Cooling	80/26.7	51.10	95/35	39.60
2	Cooling	80/26.7	51.10	82/27.8	39.90
3	Cooling	80/26.7	51.10	87/30.6	40.20
4	Cooling	80/26.7	51.10	82/27.8	39.90
5	Cooling	80/26.7	51.10	67/19.4	40.30

2.5. COP and EER Analysis

The test matrix described in Table *3*. Hybrid Heat Pump Psychrometric-Based Test MatrixTable 3 is also leveraged to evaluate the COP and the Energy Efficiency Ratio (EER) ratings for the hybrid heat pump system. These ratings, along with the SEER calculation, are standard methods used to rate the heating and cooling performance of U.S. heat pumps. A seasonal analysis is necessary to characterize the benefits of a variable speed system, which come in form of the ability to match part-load conditions. The COP and EER ratings are used in this study to quantify the thermal performance of each test case under the AC and DC configurations of the hybrid heat pump.

3. Results

The results of the hybrid heat pump testing under the AC and DC electrical configurations of the test matrix in Table 3 are detailed in Table 4 and Table 5.

Table 4. Hybrid Heat Pump 230 VAC Test Results

Test Case	Electrical Configuration [VAC]	Cooling Capacity [kW]	Indoor Power [kW]	Outdoor Power [kW]	Total Power [kW]	COP [-]	EER [-]
1-AC	230	12.8	0.4478	3.6204	4.0682	3.15	10.8
2-AC	230	14	0.4515	3.1088	3.5603	3.93	13.4
3-AC	230	13.6	0.3357	3.2627	3.5984	3.78	12.9
4-AC	230	14.1	0.3238	3.0835	3.4073	4.14	14.1
5-AC	230	15.4	0.3568	2.5475	2.9043	5.30	18.1

Table 5. Hybrid Heat Pump 350 VDC Test Results

Test Case	Electrical Configuration [VDC]	Cooling Capacity [kW]	Total Power [kW]	COP [-]	EER [-]
1-DC	350	13.3	3.9050	3.38	11.3
2-DC	350	14.1	3.3260	4.24	14.1
3-DC	350	13.9	3.4557	4.02	13.9
4-DC	350	14.3	3.2429	4.41	14.3
5-DC	350	15.8	2.8138	5.62	15.8

The cooling capacity, COP, and EER measured in each of the test cases was acquired using the refrigerant method calculation. Although these capacities were similar in magnitude between AC and DC configurations, the thermal state points of the refrigeration cycle maintained some significant differences, especially at the compressor suction temperature. To consider these more closely, the thermal characteristics of the first test case under both the AC and DC configurations are presented in Table 6.

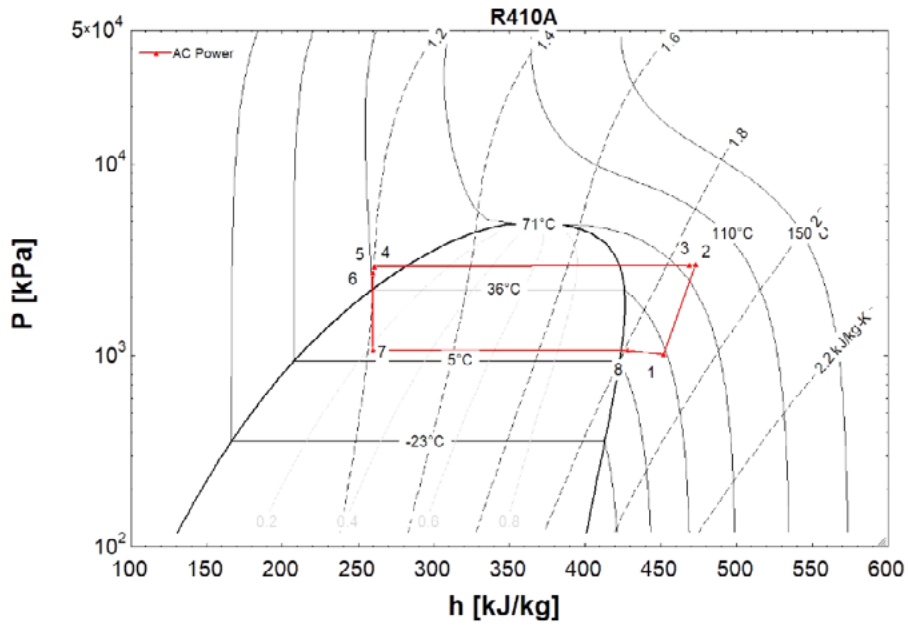


Table 6. Hybrid Heat Pump Test Case 1 Thermal Characteristics

Test Case	Electrical Configuration [-]	Indoor Air Flow [m^3/s]	Compressor Suction Superheat [C]	Compressor Suction Temperature [C]	Compressor Suction Pressure [kPa]	Compressor Discharge Temperature [C]	Compressor Discharge Pressure [kPa]
1-AC	230 VAC	0.6269	24.6	33.9	1016	81.2	3003
1-DC	350 VDC	0.6892	6.1	15.0	997.6	81.6	3002

As Table 6 reveals, the DC configuration maintained a higher indoor air flow rate under steady state conditions and a significantly lower compressor suction temperature. The state points for the AC and DC configurations under test case 1 are further illustrated in the P-h diagram shown in Fig. 5 and Fig. 6.

Since the compressor speed was controlled automatically by the heat pump, this may have resulted in the differences observed. In addition, the drive operation under DC conditions could not be readily evaluated against those under the AC configuration without supplemental manufacturer data. As a result, these factors demonstrated a need for further instrumentation and analysis to determine the source of the differences. Additional DC-watt transducers are planned for installation on the indoor and outdoor unit for increased fidelity of the power consumption, as well as coordination with service data to extract the compressor speeds in post-processing.

Fig. 5. P-h Diagram for the AC Configuration Running Test Case 1

3.1. DC Measurement Uncertainty Analysis

The DC power supply served as both the representative DC Nanogrid supply for the hybrid heat pump, and the monitoring device to capture the heat pump total power consumption. As a result of the significant dependence on this unit, uncertainty of the supply and monitoring capabilities is considered. From the supply side, the manufacturer specifications indicate an output load regulation of ±0.01% of full-scale voltage under a voltage control mode. In addition, an input line regulation of ±0.004% of full-scale voltage is maintained under the same voltage control. Load regulation in this case refers to the capacity of the power supply to maintain a specified output voltage while the load is varying, and line regulation describes the ability of the power supply to maintain the same specified output voltage while the input supply power to the power supply is varying. Collectively, these represent a combined uncertainty of ±0.011%. This is calculated using a

quadratic sum, which describes the uncertainty in measurements x, …, y, which are used to compute an uncertain output, δf. This is given below in Eq. 10.

$$\delta f = \sqrt{(\delta x)^2 + \cdots + (\delta z)^2} \tag{10}$$

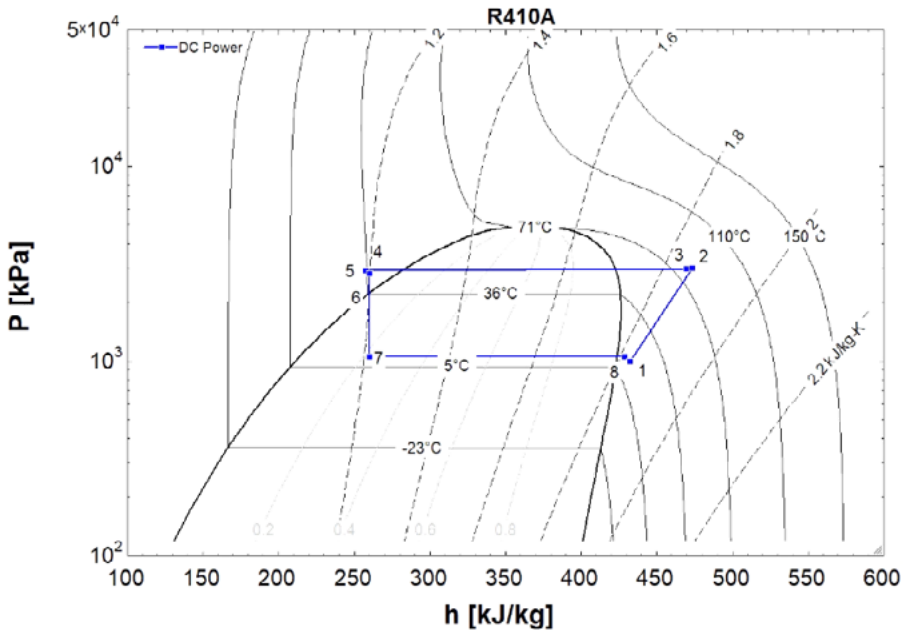


Fig. 6. P-h Diagram for the DC Configuration Running Test Case 1

Defining the full-scale voltage of the power supply to be 500 VDC, the output supply to the heat pump is calculated with an uncertainty of 0.054 VDC. These results are summarized in **오류! 책갈피가 자신을 참조하고 있습니다.**, where $\Delta V_{Controlled}$ represents the 350 VDC measured operating condition.

Table 7. DC Power Supply Output Uncertainty

Uncertainty Condition	Uncertainty [%]	Voltage Error [VDC]
Line Regulation	0.01	$V_{controlled} \pm 0.05$
Load Regulation	0.004	$V_{controlled} \pm 0.02$
Output Supply	0.011	$V_{controlled} \pm 0.054$

Using the power supply to monitor the heat pump power consumption, the measurement accuracy must then be considered. The manufacturer specifies a voltage readback uncertainty of ±0.2% of full-scale voltage, and a current readback uncertainty of ±0.02% of full-scale current. Defining the full-scale current of the power supply to be 30 A, the cumulative power measurement uncertainty reading can be tabulated as shown in Table 8. Since the power is calculated by the multiplication of the DC voltage and current, the resulting uncertainty is defined as the quadratic sum multiplied by the power measurement.

Table 8. DC Power Supply Measurement Uncertainty

Uncertainty Condition	Uncertainty [%]	Error
Voltage Reading	0.02	$V_{measured} \pm 0.1$ [V]
Current Reading	0.02	$I_{measured} \pm 0.006$ [A]
Power Measurement	0.011	$P_{measured} \pm 0.100$ [W]

4. Conclusions and Future Studies

This research presented the psychrometric evaluation of a retrofitted hybrid heat pump unit under a variety of environmental conditions using both AC and DC electrical configurations. The intent of this research is to demonstrate the feasibility of DC retrofits of devices traditionally configured for AC inputs, and to analyze improvements in performance and energy efficiency through the avoidance of AC and DC conversions. The DC power was supplied using a variable voltage power supply, which was implemented to represent a DC Nanogrid operating in a residential setting. The unit functioned successfully using a 350 VDC input, and was able to perform under each of the five test conditions described in Table 3. Based on the thermal and electrical measurements obtained, a need for additional instrumentation and further testing was identified. DC-based watt transducers are planned for installation on the indoor and outdoor units to provide insight into their representative energy consumption. This data coupled with supporting manufacturer measurements will be used to both verify the results obtained within this paper and analyze the difference in behavior between the AC and DC modes of operation. These results, along with additional test conditions and repeated trials, will be provided in a follow-on paper.

Beyond the laboratory setting, additional studies will analyze the hybrid heat pump results described here against an unmodified heat pump unit installed in the DC House using load-based testing methodology. These subsequent investigations will assist in confirming the hybrid heat pump AC and DC data obtained in this paper, and further support the potential energy improvement opportunities under DC operation. In addition, coordinated testing between the hybrid heat pump and unmodified heat pump is planned in order to establish a proportional relationship between testing results. Under this methodology, ambient temperature and humidity from the residential testing environment will be relayed in real-time to the test setup in the psychrometric chambers, allowing it to be recreated and applied to the heat pump under scrutiny there. These test results will be described in a future paper.

Nomenclature

Variable	Description	Units
A	Area	m^3
C	Coefficient of discharge	-
h	Specific enthalpy	kJ/kg
$\dot{m}$	Mass flow	kg/s
p	Pressure	kPa
$\dot{Q}$	Cooling capacity	W
T	Temperature	K
$\dot{V}$	Volume air flow	m^3/s
$\dot{W}$	Power	W
Y	Expansion factor	-

Greek Symbol	Description	Units
ρ	Area	m^3
ω	Coefficient of discharge	-
δ	Uncertainty	-

Acronyms

AC	Alternating Current
AHRI	Air-Conditioning, Heating, and Refrigeration Institute
COP	Coefficient of Performance
DAQ	Data Acquisition System
DC	Direct Current
EER	Energy Efficiency Ratio
EES	Engineering Equation Solver
EXV	Electronic Expansion Valve
HVAC	Heating, Ventilation and Air Conditioning
LabVIEW	Laboratory Virtual Instrumentation Engineering Workbench
RPM	Rotations Per Minute
SEER	Seasonal Energy Efficiency Rating
US	United States
VAC	Voltage AC
VDC	Voltage DC

Subscripts

1, 2, 3, …	State Points
air	Air
controlled	Controlled Quantity
delivered	Net capacity
evap	Evaporator
indoor	Indoor
measured	Measured Quantity
nozzle	Nozzle Box
total	Total
water	Water

Acknowledgements

The authors would like to thank the Center for High Performance Buildings (CHPB) at the Ray W. Herrick Laboratories, Purdue University for the financial support of this study. In addition, the authors express their sincere gratitude to Parveen Dhillon and Rob Hughes for their excellent assistance in testing and troubleshooting equipment.

References

[1] Lacey S. 2013. America Gets a D in Energy Infrastructure, *Greentech Media*.
[2] Tweed K. 2014. Attack on Nine Substations Could Take Down U.S. Grid, *IEEE Spectrum*.
[3] Hofer J, Svetozarevic B, Schlueter A. 2017. Hybrid AC/DC building microgrid for solar PV and battery storage integration, *IEEE Second International Conference on DC Microgrids*. 2:188-191
[4] Jie LR, Naayagi RT. 2019. Nanogrid for Energy Aware Buildings. *IEEE PES GTD Grand International Conference and Exposition Asia.* 92-96.
[5] Baxter V, Sikes K, Domitrovic R., Amrane K. 2014. IEA HPP Annex 42: Heat Pumps in Smart Grids. Task 1: Market Overview. ORNL/TM-2014/73.
[6] Fowler K. 2000. Power Supply Design and Distribution. *IEEE Instrumentation and Measurement.* 3(4):42-46.
[7] Klein S. 2018. "Engineering Equation Solver", F-Chart Software, v.10.268.
[8] ASHRAE Standard 37. 2009. Methods of Testing for Rating Electrically Driven Unitary Air-Conditioning and Heat Pump Equipment, *ASHRAE Standard*.
[9] AHRI Standard 210/240. 2017. Performance Rating of Unitary Air-conditioning & Air-source Heat Pump Equipment, *AHRI Standard*.

13th IEA Heat Pump Conference
April 26-29, 2021 Jeju, Korea

Lubricant-impregnated surfaces (LIS) incorporated with the oil supply system for enhanced durability and condensation heat transfer performance

Donghyun Seo, Jaehwan Shim, Choongyeop Lee and Youngsuk Nam*

Department of Mechanical Engineering, Kyung Hee University, Yongin 446-701, Korea

Abstract

Recently, lubricant-impregnated surfaces (LIS) has been introduced as a promising advanced condenser surface due to easy shedding of droplets and rapid clearing of nucleation sites induced by the infused lubricant layer. However, such surfaces have faced the critical limitation on the durability that the oil layer impregnated within surface structures can be depleted during condensation. Here we suggest a LIS condenser integrated with an oil supply system (LIS_O) which can achieve remarkable improvement in the durability and the condensation heat transfer coefficient. The stationary brush, which physically contacts onto the rotational tube condenser, is used to replenish the lost oil onto the LIS surface. The oil in the brush hairs are spontaneously and quickly recharged from the oil reservoir using the principle of the capillary rise effect. Using a controlled environmental chamber, the improved durability and condensation heat transfer of LIS_O are quantitatively compared to the conventional LIS surface. We experimentally demonstrate 86–232% and 26–61% higher condensation heat transfer coefficients compared to the untreated bare and the hydrophobic surfaces, respectively.

Keywords: Condensers; Condensation heat transfer; Lubricant-impregnated surfaces; Oil supply system; Lubricant oil depletion

1. Introduction

The improvement in heat transfer performance of condensers can provide significant energy and cost savings to various energy applications. Recently, lubricant-impregnated surfaces (LIS) have attracted much attention due to very high droplet mobility on LIS resulting from the extremely small contact angle hysteresis (< 5°)[1-3]. A suitable lubricant oil infused into hydrophobic micro/nanostructures offers a smooth and water-repellent interface, facilitating droplet shedding along with rapid reactivation of nucleation sites. Thanks to these advantages, LIS was reported to improve the condensation heat flux by ~400% and ~30% over the conventional filmwise and dropwise condensation, respectively[4-9].

However, there have been concerns about the depletion of the infused lubricant, which is closely linked to the durability of the surface. For example, a shear stress caused by the liquid flow can eliminate the infused oil layer from the surface[10]. Also, due to the difference in the interfacial tensions between the lubricant oil and condensate, a thin oil layer wraps over the condensed droplet, while the oil ridge forms around the droplet. This geometric configuration contributes to the concomitant oil loss when droplets were removed from the surface[4,8]. Nevertheless, few studies have focused on such oil depletion problem during condensation.

In this study, we propose an active oil supply system for tubular LIS condensers, which enable us to achieve remarkable improvement in both the surface durability and the condensation heat transfer coefficient. Our approach, which is schematically shown in Figures 1a and 1b, combine three schemes: the rotational motion

* Corresponding author. Tel.: +82-31-201-3652.
E-mail address: ysnam1@khu.ac.kr.

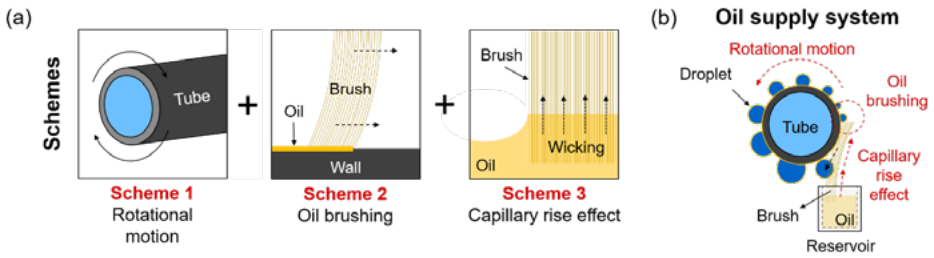


Fig. 1 (a) Concept of the oil supply system. (b) The principle of operation of an oil supply system.

of a tube (Scheme 1), oil brushing (Scheme 2) and oil refilling within brush by capillary rise (Scheme 3). The physical contact between the rotational tube wall and the soft brush hairs ensures lost oil on the condenser to be reliably replenished, while the oil within the brush hairs are spontaneously refilled from the oil reservoir by the capillary rise effect. Note that, in addition to the oil replenishment, LIS_O (LIS incorporated with the oil supply system) can impart additional benefit to heat transfer performance by facilitating the droplet removal via brush sweeping (Fig. 1c). These two characteristics can provide the significant improvement in both the LIS durability and the condensation heat transfer over the conventional LIS.

To evaluate the effectiveness of the proposed schemes, we study the longevity of LIS_O under various condensation rate conditions. Then, a long-term condensation performance of LIS_O: the sliding droplet size and condensation heat transfer coefficient is presented along with those on other control surfaces with different wettabilities, including LIS, hydrophobic surface (HPo) and superhydrophobic surface (SHPo). Unlike other control surfaces, a long-term, stable dropwise condensation mode on LIS_O is maintained up to 48 h without any sign of deterioration.

Then, the improved heat transfer performance on LIS_O over other surfaces is explained based on additional droplet sweeping by brushing. Finally, using a well-controlled environmental chamber, we demonstrate that LIS_O provides the highest condensation heat transfer coefficient (> 72 $kW/m^2 \cdot K$) at a wide range of supersaturation levels, achieving up to 61% heat transfer enhancement over hydrophobic surfaces.

2. Experimental setup and sample fabrication

All condensation experiments are conducted under well-controlled environmental conditions, shown in Figure 2. Non-condensable gases, which significantly deteriorate the condensation heat transfer process by acting as a diffusion barrier for water vapor at the droplet interface, are carefully controlled by using a vacuum pump. A stainless steel frame of this chamber is wrapped by resistive silicone rubber heater lines and then is insulated. A KF flanged bellow connected to an angle valve is integrated on the top of the chamber for a vacuum pump (BT-35A oil rotary vacuum pump, BESTECH). A liquid nitrogen cold trap is connected between the bellow line and the vacuum pump to block the inflow of moisture to the vacuum pump. A pressure gauge (275 Convectron Pirani Vacuum Gauge, MKS) is used to monitor vacuum pressure in the chamber.

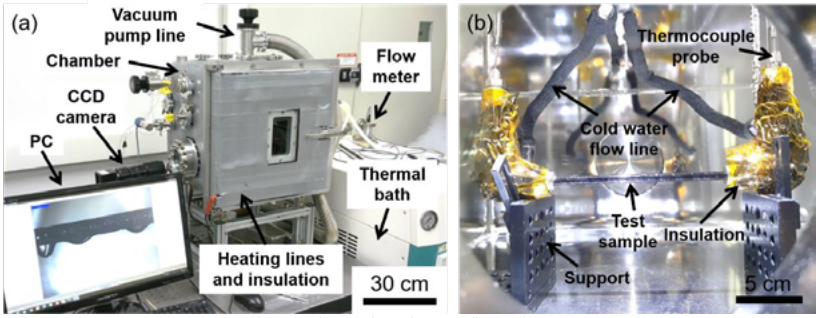


Fig. 2. (a, b) Condensation experimental setup.

Cooling water from a thermal bath (maximum flow rate of 40 L/min, maximum pump pressure of 3.3 bar, cooling capacity of 0.9 kW at 0 °C and temperature accuracy of ± 0.1 °C at 15 °C, Lab Companion, Korea) is circulated along two insulated water flow lines which are fed into the chamber. A flow meter (FLEX-HD1K, Honsberg Instruments, Germany) is integrated to monitor the flow rate.

Degassed water vapor is introduced into the chamber from a stainless steel water reservoir. This reservoir is wrapped by a bend heater and its temperature was controlled by a heater controller. Two needle valves are connected to two stainless steel tubes incorporated with a cover of the reservoir. The first tube is used to fill DI water into the reservoir. This tube line connects the bottom of the reservoir to the ambient. The second tube is used to supply degassed water vapor into the chamber. This tube line connects the top of the reservoir to the inside of the chamber, and it is wrapped by a heating tape.

Tube inlet and outlet temperatures are measured by two thermocouple probes. A saturation vapor temperature in the chamber is measured by a thermocouple probe wrapped with a wet bulb wick. All the thermocouples are calibrated before the experiment. The temperatures and the pressure information are monitored by using DAQ system. Condensation behavior is recorded by a CCD camera.

We use commercially available copper tubes (99.9% purity) with outer diameter, d_o = 6 mm, inner diameter d_i = 4 mm and length L = 125 mm. During all chemical fabrication, the tubes are capped by nipples to prevent any functionalization of their inside. Once capped, the samples are cleaned in an ultrasonic bath with acetone and ethanol for 5 min, respectively and rinsed with de-ionized (DI) water at room temperature. Then the tubes are dipped into a 2.0 M hydrochloric acid solution for 10 min to eliminate any native oxide layers on the surface. Once complete, the tubes are thoroughly rinsed with DI water and then are dried with clean N_2 gas. The CuO nanostructures are fabricated by immersing the cleaned tube inside a hot alkaline solution of ~95 °C composed of $NaClO_2$, NaOH, $Na_3PO_4 \cdot 12H_2O$, and DI water (3.75:5:10:100 wt.%) for 15 min. Sharp and knife-like CuO oxide structures fabricated by this method have height h of 1.0 ± 0.30 μm, pitch p of 300 ± 17 nm, solid fraction ϕ of ~0.023 and roughness factor r of ~10.2. After the oxidation process, the CuO nanostructured tubes are thoroughly rinsed with ethanol and DI water and are dried with clean nitrogen gas.

To render the surface hydrophobic, the samples are coated with self-assembled monolayers (SAMs). The substrates are treated by oxygen plasma to create hydroxyl group on the surfaces, and then they are dipped into a 1.0 wt.% hexane solution of HTMS (1H,1H,2H,2H-Perfluorodecyltrimethoxysilane, Sigma-Aldrich) for 2 h at room temperature. After the SAMs coating processes, the samples are strictly rinsed with ethanol and DI water and then sonicated in hexane for 5 min to remove excess polymerized monolayers on the surfaces. As the conventional LIS, the functionalized nanostructures are fully impregnated with the fluorinated oil of Krytox 1506 (oil-vapor interfacial energy γ_{ov} for Krytox 1506 is ~17 mJ/m^2 at 20 °C). SEM (scanning electron microscope) images of the fabricated CuO nanostructures can be found in the Supplementary Note 6. We chose the Krytox 1506 as the lubricant oil for LIS since it has a very small vapor pressure $P_{v,Krytox}$ of < 10^{-12} mmHg, which allows us to test LIS in our vacuum-based condensation chamber where P_{vacuum} is lowered down to < 0.5 Pa. In addition, Krytox satisfies the essential thermodynamic requirements for forming a stable and water-repellent lubricant interface on the nanostructured surface.

The smooth hydrophilic (Bare) tube for the filmwise condensation is achieved by the oxygen plasma treatment of the cleaned tube for 10 min. The smooth hydrophobic (HPo) tube for the dropwise condensation is obtained by depositing the SAMs on the plasma-cleaned Bare tube.

Advancing θ_a, static θ_s and receding contact angles θ_r for the tested surfaces are follow. Bare: θ_a < 10°, θ_s < 10°, and θ_r = 0°. HPo: θ_a = 123.2 ± 2.7°, θ_s = 111.2 ± 0.8°, and θ_r = 90.7 ± 2.7°. SHPo: θ_a = 168.2 ± 2.9°, θ_s = 167.0 ± 2.1°, and θ_r = 165.9 ± 2.1°. LIS: θ_a = 111.9 ± 1.7°, θ_s = 110.0 ± 1.3°, and θ_r = 108.2 ± 1.4°.

3. Results and discussion

3.1. Durability

We evaluate whether the oil replenishment can help sustain dropwise condensation mode on LIS_O without the oil depletion issue. To quantify the durability of LIS_O, the dropwise condensation behavior on LIS_O is compared with other dropwise condensing surfaces including HPo, SHPo and LIS. Figure 3a compares condensation images of HPo, SHPo, LIS and LIS_O over time at a high supersaturation level of S = ~1.5. All surfaces initially show dropwise condensation; however, HPo, SHPo and LIS undergo the gradual change in condensation mode from dropwise to filmwise condensation due to coating degradation (HPo), flooding (SHPo) or oil depletion (LIS), respectively. The ultra-thin hydrophobic coating layer cannot sustain long-term

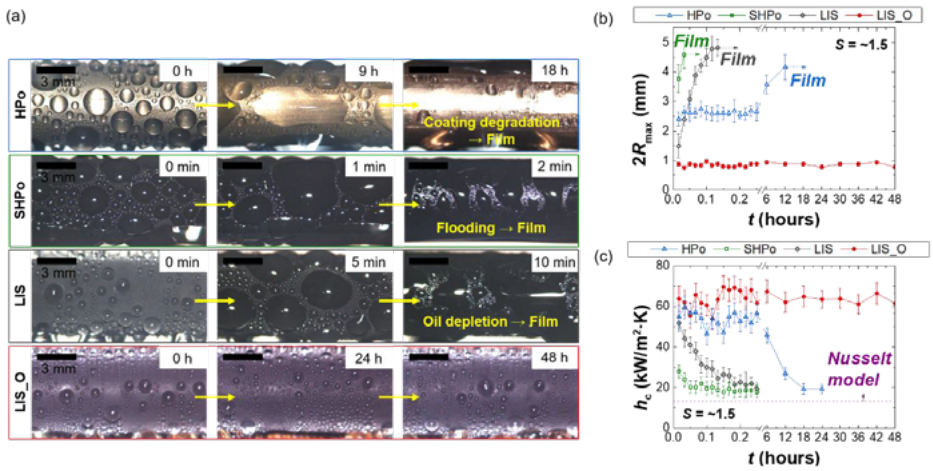


Fig. 3. Oil replenishment effect of LIS_O. (a) Condensation images of hydrophobic (HPo), superhydrophobic (SHPo), LIS and LIS_O over time. (b, c) Changes in $2R_{max}$ and the condensation heat transfer coefficient h_c at S of ~1.5 over time.

dropwise condensation at high supersaturation levels, as shearing by droplet movement and water penetration near the contact line gradually degrade the coating quality[11,12]. The presence of nanostructures on SHPo accelerates the transition into the filmwise condensation since the random nucleation within the nanostructures leads to irreversible surface flooding at a relatively high supersaturation level[11,13]. LIS also suffers flooding after underlying nanostructures are exposed after the complete oil depletion. Stable and long-term dropwise condensation is only observed on LIS_O. LIS_O maintains stable dropwise condensation up to 48 hours without any indication of surface degradation. The high durability of LIS_O can be quantitatively verified by measuring the temporal changes in the maximum hanging droplet size $2R_{max}$ and the condensation heat transfer coefficient h_c over time at S = ~1.5, as shown in Figures 3b and 3c. $2R_{max}$ for HPo, SHPo and LIS markedly increases and finally reaches the maximum value before the transition into the water film. During this transition process, h_c for the surfaces also quickly decreases and approaches to Nusselt model for filmwise condensation. Meanwhile, LIS_O displays nearly invariant $2R_{max}$ and h_c due to the successful oil replenishment by the oil supply system.

The oil replenishment effect is maintained as long as the oil remains in the reservoir, which means that the amount of oil in the reservoir determines the lifetime for LIS_O. We predict the minimum amount of oil required for sustaining LIS_O by measuring the amount of lost oil on LIS. Figure 4 displays the duration time t of LIS as function of the condensation heat flux q_c". In this figure, the symbols denote the experimental data and the solid line indicates the best fit to the experimental data with the correlation of $\log_{10}(t) \propto -\log_{10}(q_c")$. This correlation shows that t is inversely proportional with q_c"; the lifetime for LIS is shortened as the condensation rate increases. Based on t at the different q_c", we deduce the depletion rate of the oil volume such as $v_o = V_o / t$, where V_o is the volume of the impregnated oil. The V_o is given by $V_o = A_{O.D.}\delta_o$, where $A_{O.D.}$ is the tube outer surface area and δ_o is the thickness of oil covering the surface. δ_o is measured by the difference in the mass of the tube before and after oil impregnation (δ_o is ~1.3 μm in this study). This calculation predicts

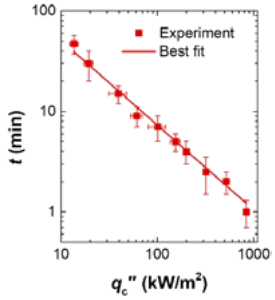


Fig. 4. The durability is evaluated as t as a function of q_c".

that under the present test tube dimension, the amount of the oil loss at q_c" of 839 kW/m^2 is about ~9.9 × 10^{-12} m^3/s, which translates to ~0.58 kg per a year (density ρ_{Krytox} for Krytox is ~1.86 × 10^3 kg/m^3). If condensers are operating in a lower q_c" (= 39 kW/m^2) in the presence of NCGs, LIS_O could work for a year just with < 0.05 kg.

3.2. Heat transfer performance

The heat transfer performance is directly evaluated by measuring condensation heat transfer coefficient h_c at various condensation conditions. Note that the precise measurement of the condensation heat transfer is possible only when NCGs are sufficiently removed from the environment, i.e. P_{vacuum} < 1 Pa. In this pure vapor environment, high q_c" more than 320 kW/m^2 can be obtained, but the heat transfer coefficient of LIS at such a high q_c" cannot be reliably measured because of too fast oil depletion. Therefore, the heat transfer of LIS_O is only compared with Bare, HPo and SHPo. Figure 5a displays representative condensation images of the tested surfaces at S = ~1.5. Figure 5b shows h_c as a function of S. Here, the symbols represent the experimentally measured data and the lines denote the prediction values estimated from the heat transfer model. The heat transfer data shows that LIS_O has the highest heat transfer coefficient at a wide range of supersaturation levels, e.g., h_c for LIS_O is 86–346% and 26–61% higher than HPi and HPo at the tested supersaturation ranges (1.1 < S < 1.6), respectively. Even though SHPo displays the highest h_c at S = ~1.1 by the coalescence-induced droplet jumping, h_c dramatically decreases below the value for LIS_O as a higher S due to the surface flooding limit. As such, LIS_O shows 75–153% higher h_c than the flooded SHPo at 1.1 < S < 1.6.

To understand the heat transfer results, we investigate the heat transfer model that incorporates the thermal resistance model for droplet growth, the emergent droplet wetting morphology, and droplet distribution theory. We obtain the prediction line for LIS_O in good agreement with the experimental data by using experimentally determined the droplet removal diameter $2\hat{R}$ of ~0.9 mm and contact angles. The nucleation density n for LIS_O is determined on the basis of the best fit between the analytical model and the experimental data. The predicted n for LIS_O is achieved by assuming $n_{LIS_O} = 3 \times n_{HPo}$, which means that the stable lubricant interface and the droplet sweeping effect by physical contact of the brush provide ~3 times higher nucleation density on LIS_O compared to HPo. h_c for HPi and flooded SHPo follows the Nusselt model due to the water film formation during condensation. This filmwise condensation provides much smaller h_c compared to dropwise condensation due to the water film acting as the dominant conduction resistance. The higher h_c for LIS_O than that for HPo is attributed to the smaller $2\hat{R}$ and the higher n resulting from the enhanced surface sweeping effect (note that $2\hat{R}$ for HPo is ~2.7mm). The smaller $2\hat{R}$ and higher n result in a higher distribution of smaller droplets, which helps reduce the overall conduction resistance on the surface and promote droplet growth, both of which lead to the increase in heat transfer rate.

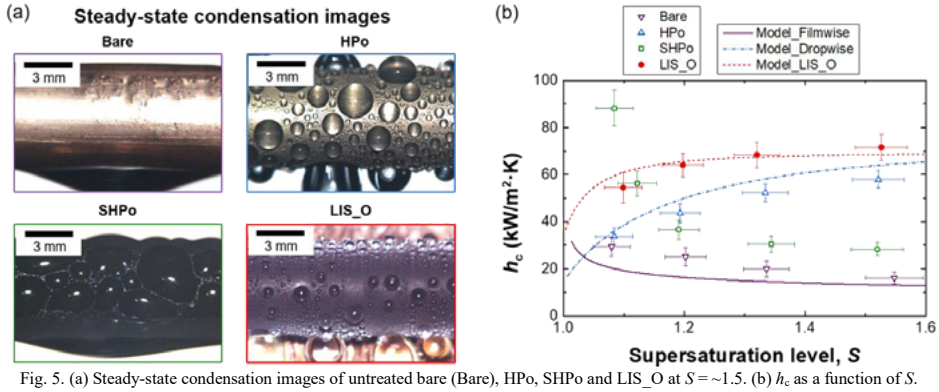


Fig. 5. (a) Steady-state condensation images of untreated bare (Bare), HPo, SHPo and LIS_O at S = ~1.5. (b) h_c as a function of S.

4. Conclusion

In summary, we demonstrated that LIS_O can achieve the remarkable improvement in the durability of LIS by reliably replenishing the depleted oil during condensation, while providing additional benefit to the

condensation heat transfer coefficient by brush sweeping. The traditional LIS suffered the unavoidable oil depletion limit during condensation, while undergoing the rapid degradation in the condensation heat transfer performance. Even typical dropwise condensing surfaces such as HPo and SHPo have showed critical limitations in sustaining long-term high heat transfer performance at high supersaturation levels due to the coating degradation and surface flooding. LIS_O overcomes this critical limit by incorporating the active oil brushing system, which can provide highly durable, superior heat transfer performance at a wide range of supersaturation levels. We believe that LIS_O can be a promising candidate for advanced condenser surfaces of various applications operating at a wide range of supersaturation levels, such as air conditioning, water collection, desalination, distillation towers, heat pipes, and power generation. In addition, we expect that the proposed oil brushing concept can contribute a wide variety of other applications utilizing LIS, such as anti-fouling, anti-corrosion, anti-freezing and self-cleaning, as providing the long-term durable lubricant interface.

Acknowledgements

This work was supported by Basic Science Research Program (2017R1A2B4008028, 2019R1A2C2004607) through the National Research Foundation of Korea (NRF) funded by the Ministry of Science.

References

[1] Wong, T. S., Kang, S. H., Tang, S. K., Smythe, E. J., Hatton, B. D., Grinthal, A., Aizenberg, J., 2011. Bioinspired self-repairing slippery surfaces with pressure-stable omniphobicity. *Nature*, *477*(7365), 443.
[2] Quéré, D., 2005. Non-sticking drops. *Reports on Progress in Physics*, *68*(11), 2495.
[3] Lafuma, A., Quéré, D., 2011. Slippery pre-suffused surfaces. *EPL (Europhysics Letters)*, *96*(5), 56001.
[4] Anand, S., Paxson, A. T., Dhiman, R., Smith, J. D., Varanasi, K. K., 2012. Enhanced condensation on lubricant-impregnated nanotextured surfaces. *ACS nano*, *6*(11), 10122-10129.
[5] Smith, J. D., Dhiman, R., Anand, S., Reza-Garduno, E., Cohen, R. E., McKinley, G. H., Varanasi, K. K., 2013. Droplet mobility on lubricant-impregnated surfaces. *Soft Matter*, *9*(6), 1772-1780.
[6] Xiao, R., Miljkovic, N., Enright, R., Wang, E. N., 2013. Immersion condensation on oil-infused heterogeneous surfaces for enhanced heat transfer. *Scientific reports*, *3*, 1988.
[7] Seo, D., Lee, J., Lee, C., Nam, Y., 2016. The effects of surface wettability on the fog and dew moisture harvesting performance on tubular surfaces. *Scientific reports*, *6*, 24276.
[8] Preston, D. J., Lu, Z., Song, Y., Zhao, Y., Wilke, K. L., Antao, D. S., Louis, M., Wang, E. N., 2018. Heat transfer enhancement during water and hydrocarbon condensation on lubricant infused surfaces. *Scientific reports*, *8*(1), 540.
[9] Seo, D., Oh, S., Moon, B., Kim, H., Kim, J., Lee, C., Nam, Y., 2019. Influence of lubricant-mediated droplet coalescence on frosting delay on lubricant impregnated surfaces. *International Journal of Heat and Mass Transfer*, *128*, 217-228.
[10] Wexler, J. S., Jacobi, I., Stone, H. A., 2015. Shear-driven failure of liquid-infused surfaces. *Physical review letters*, *114*(16), 168301.
[11] Shim, J., Seo, D., Oh, S., Lee, J., Nam, Y., 2018. Condensation Heat-Transfer Performance of Thrmally Stable Superhydrophobic Cerium-Oxide Surfaces. *ACS Applied Materials & Interfaces*, *10(37)*, 31765-31776.
[12] Seo, D., Shim, J., Moon, B., Lee, K., Lee, J., Lee, C., Nam, Y., 2019. Passive Anti-flooding Superhydrophobic Surfaces. *ACS Applied Materials & Interfaces*, *doi:10.1021/acsami.9b17943*.
[13] Seo, D., Oh, S., Shin, S., Nam, Y., 2017. Dynamic heat transfer analysis of condensed droplets growing and coalescing on water repellent surfaces. *International Journal of Heat and Mass Transfer*, *114*, 934-943.

13th IEA Heat Pump Conference
April 26-29, 2021 Jeju, Korea

Refrigerant circuitry optimization of an outdoor unit heat exchanger based on partial load operating conditions

Shehryar Ishaque[a], Man-Hoe Kim[b]

[a,b]School of Mechanical Engineering & IEDT, Kyungpook National University, Daegu, 41566, South Korea

Abstract

Finned tube heat exchangers have been widely used as a condenser and an evaporator in a residential air conditioning and heat pump system. These heat exchangers are mostly designed based on peak load operating points. Heat pump systems operate considerably for a longer period of time at partial load operating conditions rather than peak load design point. This study investigated refrigerant circuitry optimization based on rated and partial load operating conditions. The achieved optimal refrigerant circuitry for each operating condition is different from the other due to different outdoor conditions. The results revealed that significant performance improvement of 4.70% and 2.40% have been achieved in average heat exchanger capacity using optimized refrigerant circuitry based on the highest weighted partial load operating condition rather than peak load design point in cooling and heating modes respectively.

Keywords: Finned tube heat exchanger; refrigerant circuitry; optimization; partial load; operating condition

1. Introduction

The International Energy Agency (2013) has stated that air conditioning (AC) and heat pump systems account for almost 700 million metric tons of CO_2 equivalent direct (7%–19%) and indirect emissions (74%) per year, which is responsible for global warming and ozone depletion. This percentage is expected to increase drastically in the next half-century as the demand for AC and heat pump systems around the globe is increasing day by day due to the rapid rise in temperature and humidity [1]. Direct emissions can be reduced by introducing low GWP refrigerants, whereas, indirect emissions can be controlled using more efficient heat pump systems [2].

One of the main components of a residential air conditioning (AC) and heat pump system are the finned tube heat exchangers that are used as a condenser or evaporator. Thermo-hydraulic performance of these heat exchangers is influenced by several geometric parameters including tube length, tube diameter, number of tube rows, tube pitch, fin pitch, and fin configuration. One of the important design parameter is the sequence in which the tubes are connected in order to exchange heat efficiently with the air [3]. There are n! possible connections for n number of tubes and is, therefore, not possible to evaluate each design manually. Hence, more sophisticated optimization techniques are required to numerically investigate the optimized refrigerant circuitry. One such method is using a genetic algorithm (GA) that has been employed in Intelligent System for Heat Exchanger Design (ISHED) [4], which produces an optimal refrigerant circuitry for evaporators and condensers based on the applied operating conditions. This tool is commercially available in a simulation package EVAP-COND [5] developed by NIST 2003. It has the capability to cope with different parameters and the non-uniform airflow distribution which results in significant heat exchanger performance improvement [6]. Furthermore, optimal refrigerant circuitry also reduces the size, cost and amount of refrigerant [7-8]. Liu et al also reported an optimization technique to improve heat transfer capacity with minimized cost [9]. Peng et al applied particle swarm algorithm technique on multi-stream plate-fin heat exchangers to investigate the effect of non-uniform inlet flow distribution along with pass arrangement [10].

Most of the heat exchangers up to the date had been designed based on peak load operating conditions that occur for about 1%-2.5% of the year. Such heat exchangers performs well under rated load condition but are generally oversized and ineffective in conditions other than peak load [11]. Therefore, the focus has been shifted on maximizing part-load efficiencies of the heat exchangers which required peak load operating point

* Corresponding author: Man-Hoe Kim. Tel.: +82-53-950-5576; fax: +82-53-950-6550.

alongside the load profile [12]. Outdoor unit heat exchangers are exposed to environmental conditions that keep changing throughout the year. A refrigerant circuitry is sensitive to non-uniform airflow distribution along with other geometric and operating conditions. In many cases, the heat exchanger optimization process focuses on identifying refrigerant circuitry that provides the maximum heat transfer rate for given environmental constraints [13,14]. Thus, optimized refrigerant circuitry based on one set of technical and operating conditions may not perform well in other conditions. Therefore, the current study emphasizes developing an optimized refrigerant circuitry based on partial load operating conditions with the highest weighting factor that leads to significant heat exchanger seasonal performance improvement.

2. Physical description

Finned tube heat exchangers have been used as an outdoor unit with refrigerant R410A as a working fluid, inside the tubes circulating throughout the closed cycle. It consists of three depth rows with 30 tubes in each row. Louver wide fins have been used in the current study. Figure 1 is a basic model showing refrigerant flow path, with red circles indicating the inlets and blue circles indicating the outlets. The lower graph of air flow velocity distribution serve as an input to the EVAP_COND [5] in order to solve heat exchanger along with other geometric details i.e. tube length, tube diameter, fin pitch, etc. as given in Table 1.

Table 1. Geometric details of outdoor unit heat exchanger

Items	Outdoor unit
No. of tube rows	3
No. of tubes per row	30
Tube length	1720 mm
Tube inner diameter	6.3 mm
Tube outer diameter	7 mm
Fin pitch	1.7 mm
Fin thickness	0.092 mm
Fin type	Φ7 Louver(Wide)
Airflow	Non-uniform

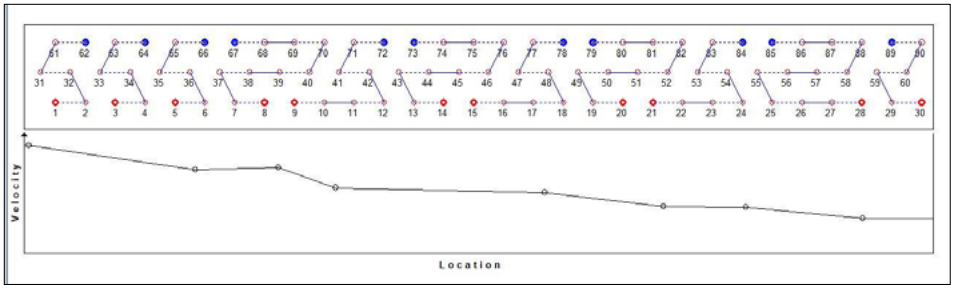


Fig. 1. Refrigerant path of outdoor unit heat exchanger used as a basic model

3. Operating conditions

Outdoor unit of a heat pump systems are exposed to environmental conditions and non-uniformly distributed air flows interact with the tubes. The magnitude and distribution of the flow velocity varies for each seasonal outdoor condition [15]. Heat pump and air conditioning systems operate in different outdoor seasonal conditions throughout the year. The actual weighting factor of the partial load operating condition is difficult to determine as it depends on the application and environment conditions of the AC and heat pump system. Alternatively, few standards are used nowadays, for better determination of the reflecting time of each load condition. One such method adopted in the current study is to utilize the weighting factors of the European standard EN14825 to calculate the average heat exchanger performance as given in Eqs. (1) and (2) for cooling and heating standards.

$$SEER = 0.03A + 0.33B + 0.41C + 0.23D \quad (1)$$

$$SCOP = 0.03A + 0.24B + 0.23C + 0.5D \quad (2)$$

where A, B, C, and D represent EER under 100%, 75%, 50%, and 25% load conditions for cooling mode and 100%, 84%, 51%, and 33% load conditions for heating mode respectively. Detailed partial load operating conditions in cooling and heating modes are summarized in Table 2 and Table 3.

Table 2. Partial load operating conditions in a cooling mode

S No	Part load ratio	Dry bulb Temperature (°C)	Wet bulb Temperature (°C)	Weighting coefficients	Airflow rate (m^3/min)	Average airflow velocity (m/s)	Refrigerant mass flow rate (kg/h)
Case 1	100	35	30	3%	182	3.18	430
Case 2	75	30	26	33%	135	2.36	323
Case 3	50	25	22	41%	112	1.96	209
Case 4	25	20	18	23%	65	1.14	112

Table 3. Partial load operating conditions in a heating mode

S No	Part load ratio	Dry bulb Temperature (°C)	Wet bulb Temperature (°C)	Weighting coefficients	Airflow rate (m^3/min)	Average airflow velocity (m/s)	Refrigerant mass flow rate (kg/h)
Case 1	100	-7	-8	3%	149	2.61	176
Case 2	84	2	1	24%	135	2.36	159
Case 3	51	7	6	23%	86	1.50	95
Case 4	33	12	11	50%	65	1.14	65

4. Numerical methodology

The current study has been carried out using commercially available software EVAP-COND version 4. This program uses the tube by tube method, where outlets from the first tube are considered as inputs to the second tube, and the outlets of the second tube are considered as an inlet to the third one and so on. Parametric tube details; inlet conditions, properties, and mass flow rates for air and refrigerant are known parameters and provide input for the first tube. Airside heat transfer rate can be expressed as Eq. (3)

$$Q_a = \dot{m}_a C_{p_a} \left(DBT - T_{ri}\right)\left(1 - \exp\left(-\frac{U_{an} A_i}{\dot{m}_a C_{p_a}}\right)\right) \quad (3)$$

where $\dot{m}_a$ is the air mass flow rate, C_{p_a} is the specific heat capacity of air-side, DBT is the air dry-bulb temperature, T_{ri} is the refrigerant inlet temperature, where U_{an} is the overall heat transfer coefficient, A_i is the surface area exposed to air. Based on heat transfer, outlet parameters are evaluated, with subsequent pressure drop calculations across each circuit.

Refrigerant side heat transfer and pressure drop correlations are based on flow quality i.e. annular flow ($0< x \leq 0.8$), dispersed flow ($0.8< x \leq 1$) or superheated flow ($x>1$). Overall heat transfer coefficient can be calculated using Eq. (4).

$$1/U_{an} = R_t = R_i + R_t + R_o + R_f = \sum R \quad (4)$$

where U_{an} is the overall heat transfer coefficient, R_t is the total thermal resistance, R_i is the inside tube resistance, R_t is the tube thermal contact resistance, R_o is the outside tube resistance and R_f is the fin to tube contact resistance. These variables are defined as follows,

$$R_i = \frac{A_i}{A_{i_ht} h_{an}}, R_t = \frac{A_i t}{A_{pm} k_t}, R_o = \frac{A_i}{A_{o_ht} h_{co}}, R_f = \frac{1}{h_t (1 - \frac{A_{fs}}{A_i})(1 - \phi)}$$

where A_{fs} is fin surface area, A_{i_ht} is tube inside surface area, A_{pm} is mean surface area, A_{o_ht} is tube outside surface area, t is tube thickness, k_t is tube thermal conductivity, h_{an} is inside tube heat transfer coefficient, h_{co} is air side heat transfer coefficient, ϕ is the fin efficiency. Two phase heat transfer coefficient can be found using Gungor Winterton [16] correlation as given by Eq. (5).

$$h_{an} = Eh_l + Sh_{pool}, \tag{5}$$

where E is the enhancement factor, h_l is the liquid heat transfer coefficient, S is the suppression factor, and h_{pool} is pool boiling heat transfer coefficient. Similarly air side heat transfer coefficient for louvered fins can be calculated using Eq. 6.

$$h_{co} = \frac{jGC_{pa}}{\Pr^{\frac{2}{3}}}, \tag{6}$$

Where j-factor for louvered fins can be found using J. Dong [17] air-side heat transfer coefficient correlation. G is refrigerant mass flux, Pr is the Prandtl number and C_{pa} is the specific heat capacity of air-side. Finned tube heat exchangers have several numbers of refrigerant circuits, with different lengths. Hence each circuit will have different refrigerant mass flowing through it. Fraction of refrigerant through each circuit can be expressed as Eq. (7)

$$F_i = \frac{m_i}{m_{tot}} = \frac{1}{\sum_{j=first}^{last} \left(R_i / R_j \right)^{0.571}}, \tag{7}$$

where $R_i = \Delta P_i / \Delta G_i^{1.75}$ is the total refrigerant flowing through the i-th circuit, $R_j = \Delta P_j / \Delta G_j^{1.75}$ is the total flow resistance for all branches splitting from that point. The first iteration loop estimates R_i. Resistance in each tube is assumed to be the same regardless of flow quality. Therefore, initial Ri depends on the number of refrigerant circuits and their paths. Subsequent iterations update R_i and F_i values. Iteration continues until the pressure drop across each circuit becomes uniform.

5. Results and discussion

ISHED is an optimization tool that provides optimized refrigerant path with maximum heat exchanger capacity as an objective function. Figure 2(a) shows optimized designs for different outdoor cooling conditions according to the European standard EN14825. Each optimized design differs from the other based on non-uniform airflow velocity distribution, outdoor air temperature, and refrigerant mass flow rate. In each case, different flow velocity profile interacts with the tubes which leads to different optimized design. Figure 2(b) shows a significant increase of 4.64%, 6.97%, 4.42%, and 10.36% in heat exchanger capacity for optimized designs as compared to the basic model under cooling conditions A, B, C, and D respectively.

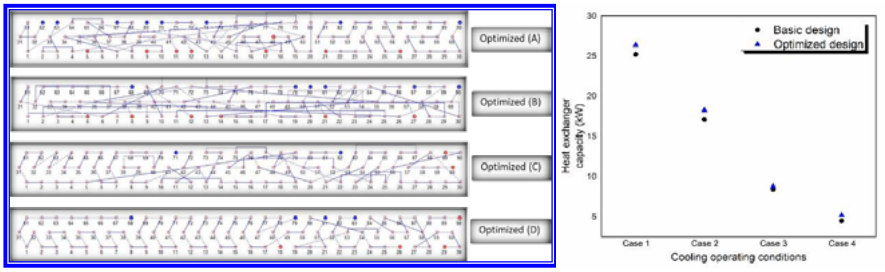


Fig. 2. Cooling mode (a) Optimized refrigerant paths, (b) Heat exchanger capacities for each optimized design

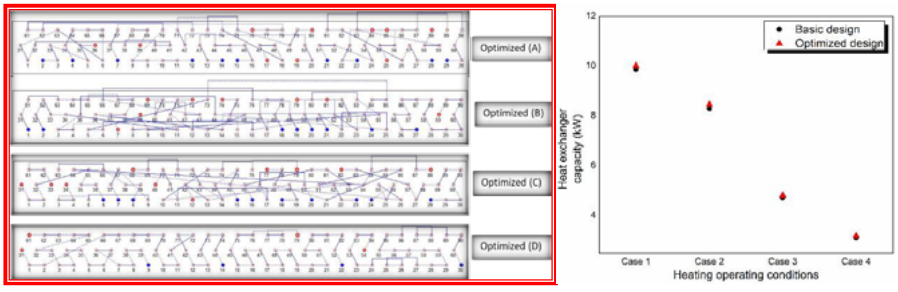


Fig. 3. Heating mode (a) Optimized refrigerant paths, (b) Heat exchanger capacities for each optimized design

Figure 3(a) shows optimized designs for different heating conditions according to the European standard EN14825. The optimized designs differ from the cooling mode as the outdoor operating conditions are changed. Figure 3(b) shows a significant increase of 1.52%, 2.05%, 2.96%, and 2.25% in heat exchanger capacity for optimized designs as compared to the basic model under heating conditions A, B, C, and D respectively.

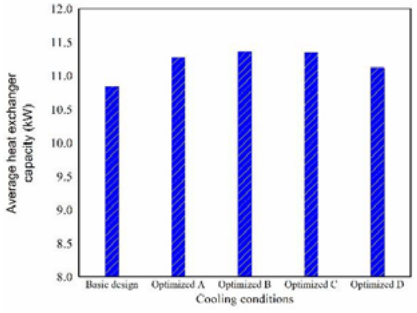


Fig. 4. Average heat exchanger capacities for each optimized design in cooling mode

Heat exchangers worked under different load conditions and are usually designed based on rated load conditions that worked for about 1%-2.5% of the time. In order to choose an optimal refrigerant path, the best approach is to determine an optimized refrigerant circuitry that worked well under all conditions. One similar approach is used here by finding the optimal refrigerant paths for all partial load operating conditions. Once all optimized paths have been achieved, the same paths are used for each condition and the average cooling capacities based on their weighting factors are calculated. Although it is difficult to accurately reflect the operating time under each load condition as it varies with respect to the application and environmental conditions. Alternatively, European standard EN14825 has been utilized to emphasize on the importance of refrigerant circuit optimization based on the most weighted load factor.

In the current study, the same outdoor unit has been optimized for all operating conditions and based on their weighting factor the average heat exchanger capacities have been calculated using Eq. (1). Figure 4 reveals that refrigerant circuitry optimized for the partial load operating condition with the highest weighting factor can significantly increase up to 4.70% in the average heat exchanger cooling capacity. Heat exchanger

capacities based on weighted load factor does not increase linearly with optimized designs. A maximum heat exchanger capacity has been found for using optimized design B in all conditions. Similarly, optimized design C is also better than optimized design A and D because the performance under part-load conditions of B and C were more highly weighted than the others. Therefore, it is recommended to use an optimized refrigerant circuitry based on the highest weighting factor throughout the year instead of the peak load.

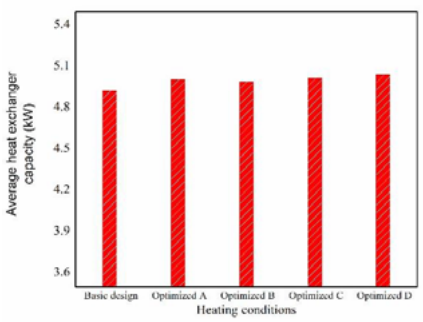


Fig. 5. Average heat exchanger capacities for each optimized design in heating mode

Similarly, Fig. 5 shows the average heat exchanger capacities using optimized designs A, B, C, and D. Each optimized design is tested for all four partial load operating heating conditions and the average heat exchanger capacity in each case has been calculated using the weighting factors of Eq. (2). The results reveal that the average heat exchanger capacity based on an optimized design for the highest weighted factor can improve heat transfer performance up to 2.4%. Sometimes the optimized design based on rated load condition shows more improvement but that is not realistic as the same design performs poorly in other more weighted partial load conditions.

6. Conclusion

The current study has been carried out to determine an optimized refrigerant path of an outdoor unit heat exchanger under rated as well as partial load operating conditions. One basic outdoor unit heat exchanger model has been selected with non-uniform airflow distribution. Heat exchanger capacity has been determined using a commercially available software EVAP-COND. The built-in refrigerant circuitry optimization tool ISHED was utilized to find the optimal refrigerant paths for all partial load operating conditions. Each partial load operating condition is applied to the obtained optimized designs. Average heat exchanger capacities have been calculated using weighting factors of the European standard EN14825. The findings of the present study have been listed below.

- A significant increase of 4.64%, 6.97%, 4.42%, and 10.36% in heat exchanger capacity have been achieved for optimized designs as compared to the basic model under cooling conditions A, B, C, and D respectively.
- A significant increase of 1.52%, 2.05%, 2.96%, and 2.25% in heat exchanger capacity have been achieved for optimized designs as compared to the basic model under heating conditions A, B, C, and D respectively.
- A maximum percentage increase of 4.70% has been achieved in average heat exchanger capacity using optimized refrigerant circuitry based on the highest weighted factor among the partial cooling loads.
- A maximum percentage increase of 2.40% has been achieved in average heat exchanger capacity using optimized refrigerant circuitry based on the highest weighted factor among the partial heating loads.

The current study is limited to the optimization of refrigerant circuitry using ISHED that optimized the refrigerant path for a single condition at a time. Further studies will extend the matrix by optimizing different geometric parameters based on the partial load operating conditions rather than a single peak load. Designing heat exchangers based on rated as well as partial load conditions can reduce huge energy consumption. A similar idea can also be extended to other types of heat exchangers used in industrial applications.

References

[1] G. Blanco, R. Gerlagh and S. Suh (eds). Drivers, Trends and Mitigation. In: Climate Change. 2014;351–412.
[2] B. Metz, O.R. Davidson, P.R. Bosch, R. Dave LAM (eds). Climate Change. Mitigation. 2007.
[3] P. A. Domanski, D. Yashar, 2007. Optimization of finned-tube condensers using an intelligent system. International Journal of Refrigeration 30, p.482-488.
[4] P. A. Domanski, D. Yashar, M. Kim, 2005. Performance of a finned-tube evaporator optimized for different refrigerants and its effect on system efficiency. International Journal of Refrigeration 28, p.820-827.
[5] P.A. Domanski, D.A. Yashar, EVAP-COND Version 3-Simulation Models for Finned Tube Heat Exchangers with Circuitry Optimization, National Institute of Standards and Technology, Gaithersburg, MD, 2010. http://www.nist.gov/el/building_environment/evapcond_software.cfm.
[6] D.A. Yashar, S. Lee, P.A. Domanski, 2015. Rooftop air-conditioning unit performance improvement using refrigerant circuitry optimization. Applied Thermal Engineering 83, p.81-87.
[7] Z. Wu, G. Ding, K. Wang, M. Fukaya, 2008. A general steady state mathematical model for fin-and-tube heat exchanger based on graph theory. International Journal of Thermal sceince 47, p.985-997.
[8] Z. Wu, G. Ding, K. Wang, M. Fukaya, 2008. Knowledge-based evolution method for optimizing refrigerant circuitry of fin-and-tube heat exchangers. HVAC&R Research. 14, p. 435-451.
[9] J. Liu, W.J. Wei, G.L. Ding, C.L. Zhang, M. Fukaya, K.J. Wang, T. Inagaki, 2004. A general steady state mathematical model for fin-and-tube heat exchanger based on graph theory. International Journal of Refrigeration 27, p. 965-973.
[10] X. Peng, Z. Liu, C. Qiu, J. Tan. 2016. Effect of inlet flow maldistribution on the passage arrangement design of multi-stream plate fin heat exchanger. Applied Thermal Engineering 103, p.67–76.
[11] Whole Building Design Guide. High-Performance HVAC. http://www.wbdg.org/resources/hvac.php (accessed June 9, 2010).
[12] United States Department of Energy Office of Energy Efficiency and Renewable Energy. How to Buy an Energy-Efficient Commercial Boiler.
http://www1.eere.energy.gov/femp/technologies/eep_boilers.html (accessed June 11, 2010).
[13] P. A. Domanski, D Yashar, K. A. Kaufman, R. S. Michalski, 2004. An optimized design of finned-tube evaporators using the learnable evolution model. Ventilating, Air-Conditioning and Refrigerating Research 10, p. 201–211.
[14] M.-H. Kim, S.Y. Lee, S.S. Mehendale, R.L. Webb, 2003. Microchannel Heat Exchanger Design for Evaporator and Condenser Applications. Advances in Heat Transfer 37, p. 297-429.
[15] F.A. Tereda , N. Srihari , B. Sunden, S. K. Das, 2007. Experimental Investigation on Port-to-Channel Flow Maldistribution in Plate Heat Exchangers. Heat Transfer Engineering 28, p.435-443.
[16] K.E. Gungor and R.H.S. Winterton, 1985. A general correlation for flow boiling in tubes and annuli. International Journal of Heat and Mass Transfer 29, p.351-358.
[17] J. Dong, J. Chen, Z. Chen, W. Zhang, Y. Zhou, 2007. Heat transfer and pressure drop correlations for the multi-louvered fin compact heat exchangers. Energy Conversion and Management 48, p.1506-1515.



13th IEA Heat Pump Conference
April 26-29, 2021 Jeju, Korea

Status on the Electric-thermal Energy Storage Technology and Application of a Supercritical Carbon Dioxide Power Cycle

Junhyun Cho[a], Chulwoo Roh[a], Hyungki Shin[a], Gilbong Lee[a], Bongsu Choi[a], Jongjae Cho[a], Beomjoon Lee[a], Ho-Sang Ra[a], Young-Jin Baik[a,*]

[a]Thermal Energy Systems Laboratory, Korea Institute of Energy Research, Daejeon 34129, South Korea

Abstract

A large-scale energy storage system becomes more essential as a proportion of the renewables increases in the future electricity supply mix. Intermittent electricity supply characteristics by renewables causes instability of a grid, therefore electricity time shift technologies are needed. Batteries are representative electricity energy storage system, however, it is hard to expand for large-scale system, because of high cost, short discharge duration characteristics. The electric-thermal energy storage technology, recently called as a Carnot Battery, has been focused as a solution for the large-scale grid level energy storage applications, because it uses conventional robust heat engine technologies suitable for large-scale system. It is composed of electricity-to-heat, heat storage and heat-to-electricity system. In case of heat-to-electricity, a supercritical carbon dioxide power cycle (sCO2) is attractive option because of its potentials of wide operation range, dry-cooling, high efficiency and small foot print. Korea Institute of Energy Research (KIER) has been developed a sCO2 power cycle test loop with the turbomachinery. In this paper, concept of the electric-thermal energy storage and the technical development highlights of the sCO2 power cycle in KIER are presented.

Keywords: Carnot Battery, Electric-Thermal Energy Storage, ESS, Supercritical Carbon Dioxide Power Cycle

1. Introduction

The interest in renewable energy sources (RES) such as solar and wind has been growing due to its climate change mitigation and economic benefits. Based on REN21's 2018 report, RES accounted for approximately 18.2% of global energy consumption and the ratio have been rising gradually. In addition, in 2017, South Korea's Ministry of Trade, Industry and Energy announced the "Renewable Energy 3020" implementation plan which aims to increase a share of renewable energy from 7% to 20% of the total energy mix by 2030. Therefore, Korea will need additional 63.8 GW capacity of renewable power sources which is similar to present Korea power plant capacity (~100 GW) in 2030.

Energy storage systems (ESS) are essential because of the intermittent power generation features of renewable generation sources that can generate electricity only when the sun is there and when it is windy. The battery-based small-capacity energy storage system is applied to the small-scale new renewable power generation source, and serves as voltage correction and frequency adjustment. However, if large-scale renewable of GW class are introduced in the future, a commercially appropriate large-capacity energy storage system is required. Obviously, this will be limited by existing high-cost battery-based storage devices.

Therefore, in order to continuously use these large-capacity renewable energy sources with reliability and stability of the electric grid, low-cost, long-term energy storage devices are required. In this way, it is necessary to develop a large-capacity energy storage device that can make a time-shift of intermittent power generation at the grid level to enable renewables as a base power source uses.

* Corresponding author. Tel.: +82-42-860-3226; fax: +82-42-367-5067.
E-mail address: twinjin@kier.re.kr.

Electrochemical energy storage technologies such as a battery, a super-capacitor and a flow battery have characteristics of high efficiency, high energy density, no geographic limitation and relatively simple configuration. However, the system capacity is several kW-MW, the capacity is limited to cope with the grid and the discharge time is under several hours so that it is limited to use for a long-term storage purpose. Therefore, these are suitable for voltage correction/frequency adjustment with short discharge time. The efficiency is high, but the cost corresponding to LCOE (Levelized Cost of Electricity) is about 10 times of the pumped storage hydropower (PSH) [1].

Recently, a Carnot Battery concept is proposed for a large-capacity energy storage system. The Carnot cycle is a reversible heat engine thermodynamic cycle, the Carnot Battery uses thermodynamic cycles for the purpose of electricity storage. To use a power cycle when the ESS system generates electricity, the electricity has to be stored as a thermal type which is enough to drive a turbine. Therefore, an electric heater or a heat pump have to be used to convert the electricity to the heat. The heat pump is well known thermodynamic system for efficient heat conversion. The electric heater is simple and cheap conventional technology.

Currently, 70% of the electricity used in Korea is obtained by the steam turbine power generation cycle method that generates electricity by using steam from coal and nuclear fuel to drive turbines, and 22% is gas turbine power generation cycle is used in which the turbine is driven by high temperature air obtained from the heat of combustion of natural gas [2]. In other words, 92% of electricity is obtained through thermal-power conversion heat engine technology: power cycle, which is suitable for a large capacity plant of hundreds of MW.

In this point of view, energy storage systems that can cope with future GW-class distributed power supply systems should use technically and commercially proven power cycle technology, and have a minimum unit of several MW to several hundred MW system. Therefore, when the surplus electricity generated from the renewable is stored in the form of a large amount of thermal energy in the conditions that can generate electricity by driving a turbine, which means the Carnot Battery, it is possible to implement an energy storage system capable of low-cost/long-term power generation.

It is early stage of research, so in this paper as an introductive purpose, the concept of the Carnot Battery, technical issues and its status of global research trends are described. There are several configuration of the Carnot Battery corresponding to the heat storage temperatures, various types of heat pumps and power cycles can be used. A supercritical carbon dioxide power cycle (sCO2) which is recently studied for a promising power cycle, is attractive option for the Carnot Battery due to its high efficiency, small footprints, fast response, dry cooling and wide heat source temperature range. A turbine, a compressor, a heat exchanger and thermodynamic devices for the supercritical carbon dioxide could be also used for the supercritical carbon dioxide heat pump for the Carnot Battery. Korea Institute of Energy Research (KIER) have developed core technologies of the sCO2 from 2013. And KIER try to apply sCO2 to the Carnot Battery. Brief research history and accomplishments of sCO2 in KIER are described.

2. Carnot Battery

The Carnot Battery as shown in Fig. 1 is composed of three parts: electricity-to-heat, heat storage and heat-to-electricity sub-systems. The methods of heat-to-power are (1) electric heater and (2) heat pump technology. The electric heater is a relatively simple method of converting electricity into heat to drive a heat engine. In this case, efficiency of the conventional resistive electric heater is 95-98%, then, the thermodynamic charge-discharge round-trip efficiency (RTE) is dominantly affected by efficiency of the heat-to-electricity unit which is a power cycle. In case of power cycle, ideal thermodynamic efficiency is expressed as a Carnot efficiency according to the heat source and sink temperature, in this case, the storage temperature. If a practical maximum efficiency of the power cycle is near 70% of the Carnot efficiency as temperature, at least 800℃ heat storage is required to actually implement a 50% of RTE system. The heat engine that can be used above 800℃ is a combined gas turbine power cycle. When the electric heater is used as the charging technology for simple configuration, a layout in which ultra-high heat storage and gas turbine power cycle can be used.

On the other hand, if power cycle (discharge) using a high temperature heat storage and convert to a low temperature storage, then a low temperature heat can be pumped back to a high temperature heat by using a heat pump (charging), as shown in Fig. 1. Assuming an ideal reversible process without loss (Carnot cycle), a closed charging-discharging cycle without energy loss can be configured, so called as a Carnot Battery. However, due to the presence of irreversible losses (heat losses, mechanical losses, etc.) in the actual energy utilization process, the actual round-trip efficiency of the charging and discharging process decreases.

When the layout using a heat pump is actually implemented, proper high and low temperature storage configuration is an important technical issue because trade-off of heat pump performance expressed by a

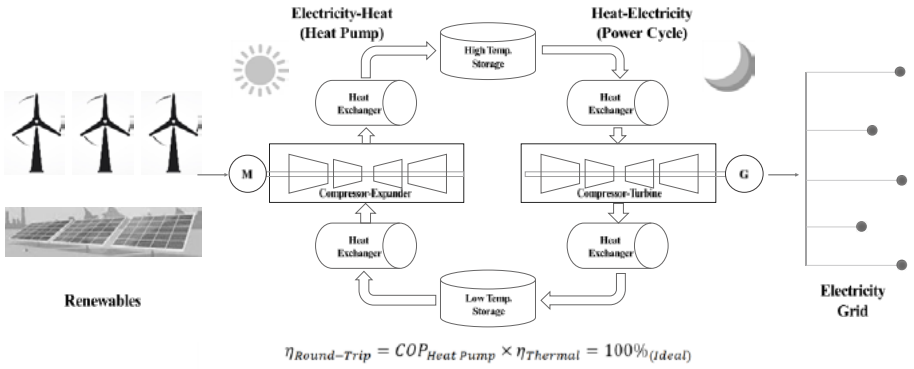


Fig. 1. Concept of the Electric-thermal energy storage system [3]

coefficient of performance (COP) and power cycle efficiency occurs. For example, if the high temperature heat storage temperature is increased to increase the efficiency of the power cycle unit, the COP of the heat pump will be reduced. This layout can be configured using by conventional steam power generation system of turbine inlet temperature 500-600℃, but there is a new technical issue of the development of ultra-high temperature heat pump. The current maximum production temperature of conventional heat pump is about 180℃ based on compressor discharge temperature by using a refrigerant.

Heat storage medium is also a technical issue. In case of high temperature heat storage, it is important to select a heat storage material according to the heat storage temperature. In case of molten salt, which is currently being used in Concentrating Solar Power (CSP) application, the operating temperature is about 280-550℃. Therefore, the molten salt is used in combination of a steam power cycle using the sensible heat of molten salt. Sand or rock may be used to store the high temperature of 800℃ or higher, which has the advantage of being inexpensive but has a disadvantage of poor heat exchange performance. In addition, the power cycle (discharge) system, the heat pump (charging) system, the low temperature heat storage material, the heat exchanger types are changed according to the temperature of the low temperature storage device, and thus, various system layouts can be configured according to the configuration and operating conditions of the entire cycle. [3]

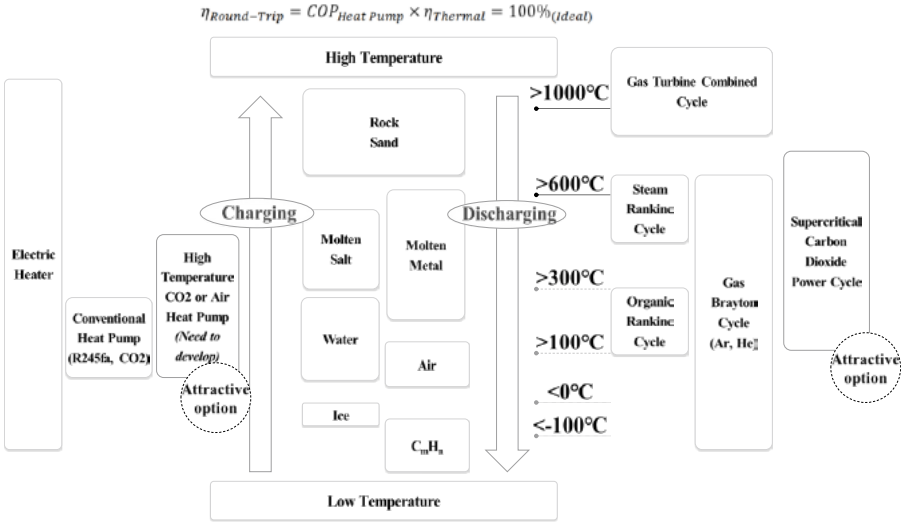


Fig. 2. Technical candidates for an electric-thermal energy storage system according to temperature [3]

Figure 2 shows technical candidates for the Carnot Battery system according to temperature. In case of thermal storage medium, a molten metal such as Tin, Sodium can be used for relatively wide operation range of the power cycle. Water is the attractive thermal storage medium due to its advantages of low cost, stability,

reliability and safety for relatively low temperature range for high temperature storage. In that case, an organic Rankine cycle (ORC) and a supercritical carbon dioxide power cycle (sCO2) can be used. Although efficiency of the power cycle is low due to low heat source temperature, the COP of the heat pump is high, therefore, RTE can be achieved by using a conventional heat pump devices.

Gas Brayton cycle using an Ar or Ne or He is possible power cycle which can make wide temperature differences between hot side and cold side of heat storage. In particular, this layout can utilizing cryogenic heat sink, so temperature difference between high and low temperature of the power cycle could be increased which means it can get a better power cycle efficiency.

Recently, a supercritical carbon dioxide power cycle has been focused on a promising power cycle technology due to its advantage of high efficiency, reduced size, small foot-print, fast response, low cost, dry-cooling, and wide operation range suitable to various heat sources. In addition, core components of the sCO2 power cycle such as a turbine, a compressor, a heat exchanger, a valve, a pipe and so on could be applied in the high temperature supercritical carbon dioxide heat pump. Therefore, a sCO2 heat pump-sCO2 power cycle Carnot Battery layout is possible.

An important consideration in this Carnot Battery concept is the cost issue. It is important to evaluate the leveled cost of storage (LCOS) value considering the costs of charging and discharging stages as well as heat storage. Economic Carnot Battery will survive in the future large-scale capacity ESS market because it will utilize surplus or cheap electricity in the off-peak time and then generate electricity in the peak time. Therefore, LCOS of Carnot Battery is a key factor for electricity time shift in the electricity grid. Since this value is determined by the hot/cold operating temperature of the cycle, the cycle working fluid, the heat storage system and the cycle layout, the optimal cycle design to minimize the LCOS value is a major technical issue. [3]

3. Research Trends

The Carnot Battery which utilize the heat pump and the heat engine for large-capacity ESS have been studied recently, and now preliminary feasibility studies were started by governments and global power system companies.

In terms of the heat pump, a supercritical or transcritical carbon dioxide heat pumps were considered by GE and ABB.

GE investigated a hybrid type of Carnot Battery using the electric heater and the supercritical carbon dioxide heat pump cycle as a part of power-to-heat unit as shown in Fig.3. Since this configuration utilize the conventional steam power cycle in the heat-to-power part that turbine inlet temperature of near 500℃, the

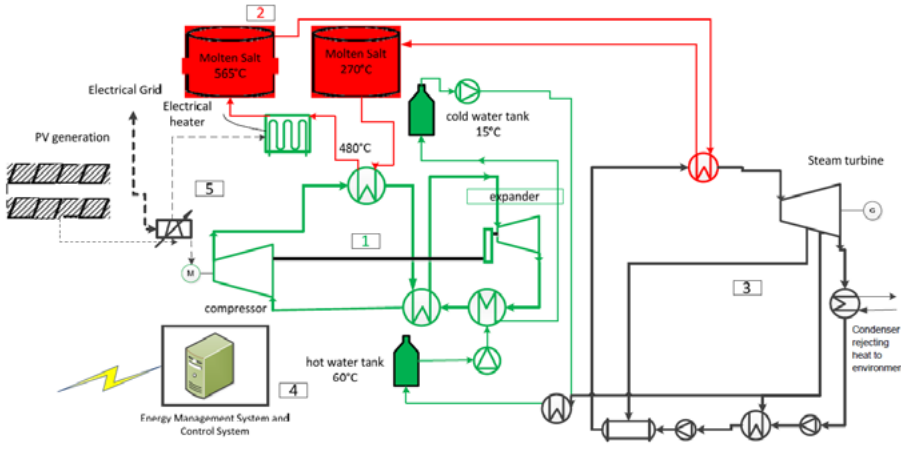


Fig. 3. GE's Carnot Battery concept using a supercritical carbon dioxide heat pump [4]

molten salt is used as a high temperature heat storage like CSP application. The molten salt storage uses

sensible heat transfer between about 250-550°C, a supercritical carbon dioxide heat pump in attractive because heat exchange profile is well matched with a sensible heat application. Also, natural refrigerants have to be used in such high temperature application of the heat pump. However, there is no high temperature supercritical carbon dioxide heat pump in these days yet, so GE suggest additional electric heater for power-to-heat purpose reducing development risk of a high temperature of supercritical carbon dioxide heat pump. [4]

ABB investigated the carbon dioxide heat pump in the Carnot Battery, however, a Transcritical carbon dioxide heat pump and a Transcritical carbon dioxide power cycle are configured as shown in Fig.4. Since, about 120°C temperature of carbon dioxide heat pump is conventional technology, all commercially available thermodynamic systems are easily configured in this Carnot Battery concept. A -2°C ice storage is used for low temperature storage. The RTE of commercial scale this Carnot Battery is evaluated up to 65% from their calculation, however, a carbon dioxide expander, a compressor and a turbine have to be developed sophisticatedly for commercialization. [5]

Recently, preliminary pilot plant scale Carnot Battery system have being constructed in Germany by Siemens. A rock is used as a high temperature heat storage, an electric heater is used for power-to-heat unit and a conventional steam power cycle is used for heat-to-power. It has lower RTE because it uses an electric heater than a heat pump, however, it is very cheap and simple so that LCOS is favourable.

US DOE have started feasibility concept studies for various Carnot Battery system layouts. NREL is investigating an electric heater – sand – gas turbine combined cycle, Brayton Energy is investigating a molten salt-gas Brayton cycle concept and Echogen is investigating concept using a supercritical carbon dioxide power cycle. [6]

DLR in Germany, has started a project for the Carnot Battery technology focusing on the power plant retrofit. Since, a coal-fired or a nuclear power plant have a steam power block so the Carnot Battery configuration would be easily constructed by substituting a boiler or a nuclear steam generator to a heat pump or an electric heater. [7]

A project called Malta, which is being promoted as a future technology by Google (Google Project X), is a Laughlin-Brayton Carnot Battery that stores electricity in the form of thermal energy in molten salt and discharges it into the power generation cycle. The company is developing the Brayton cycle and has designed the turbomachinery required for the system. [8]

4. Supercritical Carbon Dioxide Power Cycle (sCO2) in KIER

In these Carnot Battery concepts, a supercritical carbon dioxide power cycle (sCO2) is an attractive option for both medium-high and low temperature of hot storage source. In addition, small foot print of the sCO2 system due to high pressure operating condition makes Carnot Battery to be compact and modular design. Dry-cooling is also important advantage of the sCO2 because lots of PV complex would be constructed inland area.

Korea Institute of Energy Research (KIER) has developed a fundamental sCO2 test loop from 2013, now, KIER is operating a kWe-class and a tens of kWe-class sCO2 experimental test loops and is commissioning the final hundreds of kWe-class test loop. In this paper, brief descriptions of our test loops are presented.

(1) kWe-class, 500°C turbine inlet temperature (TIT), Transcritical test loop, Radial turbo-generator
(2) tens of kWe-class, 200°C turbine inlet temperature, Transcritical test loop, Axial turbo-generator
(3) hundreds of kWe-class, 500°C turbine inlet temperature, Dual Brayton test loop, 2 Axial turbo-generators, Centrifugal compressor

Figure 5 and 6 show a kWe-class for 500°C TIT(turbine inlet temperature) radial turbo-generator, a tens of kWe-class for 200°C TIT axial turbo-generator its test loops with operational results respectively.

Both test loops were developed as a transcritical cycle by using a liquid carbon dioxide pump for focusing on the developing a turbo-generator driven by a supercritical carbon dioxide, investigating cycle characteristics and developing operation and control strategy of sCO2 cycle.

In case of small kWe-class turbo-generator, a radial type of turbine was designed with a 10% of partial admission nozzle to reduce rotational speed of the rotor. Designed rotational speed was a 120,000 RPM. An angular contact ball bearing lubricated by oil mist was installed to support both radial and thrust force of the rotor due to high operating condition of the sCO2 turbomachinery. Designed capacity of the turbine was a 4.5 kW without mechanical loss.

The main components of the test loop are two pumps, a turbo-generator, two immersion type of electric heaters, a printed circuit heat exchanger (PCHE), a recuperator, a settling chamber, a chiller, and pressure vessels. The two pumps pressurized liquid CO2 into supercritical state. The supercritical CO2 flows through

the recuperator and is heated by the residual heat of turbine outlet flow. In the two electric heater, CO2 is more heated until the turbine inlet condition is reached and then, its flow characteristic becomes uniform at the settling chamber. Next, the heated sCO2 drives the turbo-generator by the expansion work and the generated power is measured with a power meter. In the turbine outlet, because the supercritical CO2 still has a large amount of energy, it is cooled down at the recuperator. In the cooler PCHE, it is cooled to make a pump inlet condition which is equal to the minimum temperature of the cycle. A separator is used to divide two phase CO2 into liquid and gas because pump can pressurize the liquid CO2 only. A reservoir and an inventory are used to control the filling amount of CO2 in the test loop.

In 2017, power generating operation was successful, a 287 We of electricity was obtained at TIT of 401℃. There were rotordynamics issues induced by high axial force at high temperature and high rotating speed condition. After modification, a 30 minutes of continuous power generating results were obtained over 300℃ of TIT condition.

Through this very small sCO2 test loop, basic characteristics of closed sCO2 cycle were investigated. In particular operation strategy of sCO2 cycle was developed including inventory control to fine proper mass flow rate of working fluid. [9]

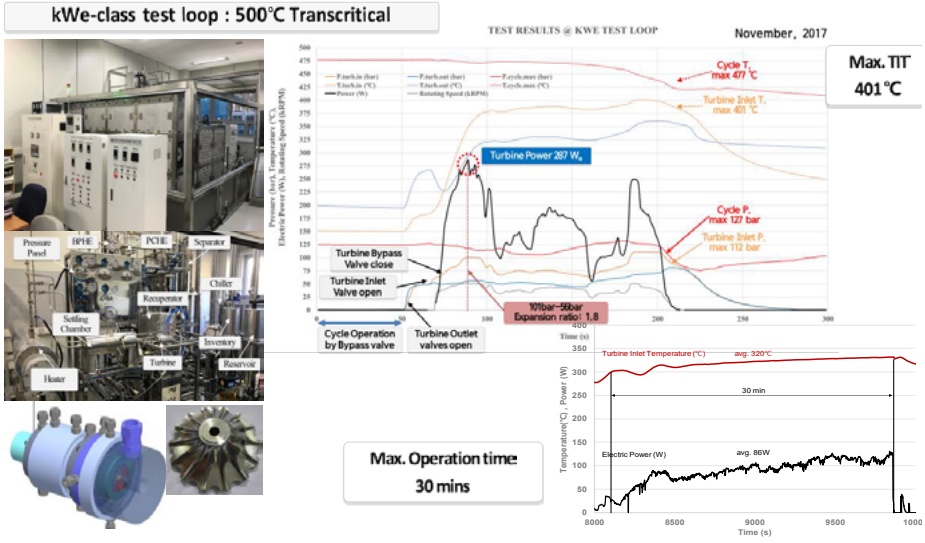


Fig. 5. 500℃ kWe-class radial turbo-generator and Transcritical test loop with operation results

Figure 6 shows a tens of kWe-class for 200℃ TIT axial turbo-generator and its test loop. The axial turbo-generator was actually designed for 392℃ TIT condition for KIER's final target test loop. Before constructing whole test loop, the low temperature turbine was firstly fabricated and was tested under off-design condition by using existing test facilities. In this approach, in order to overcome reported failure problems of the radial-type turbine induced by high rotational speed and axial force, an axial-type impulse turbine and partial admission nozzle was designed and manufactured to reduce the rotational speed by up to 45,000 RPM, as well as the axial force. Thereafter, the turbine wheel part was separated by carbon ring-type mechanical seals to use the commercial oil-lubricated tilting-pad bearings. As these bearings place a limitation on the rotational speed, it was important to reduce the shaft rotational speed. The rotor mean diameter was 73 mm and the blade height was 8.36 mm. A 60 kWe permanent magnet (PM) generator type was also designed. Using an axial-type turbine with a mechanical seal similar to the dry-gas-seal and oil-lubricated bearings, the design is meaningful as it can be applied to further MW-scale turbo-generator designs.

In order to develop a step-by-step, systematic technology, a transcritical cycle was constructed at the turbine inlet at 200°C in one step, and the turbine was operated to obtain data under relatively stable temperature conditions through power production operation. The maximum temperature was 200°C as the first step target, which is a relatively mild condition for the piping, valves, and pressure vessels of the system. Liquid CO2 at 20°C, 57 bar, and 1.566 kg/s was pressurized into a supercritical state at 135 bar using a plunger-type reciprocating liquid CO2 pump (Catpumps, USA) with an inverter-controlled electric motor in order to

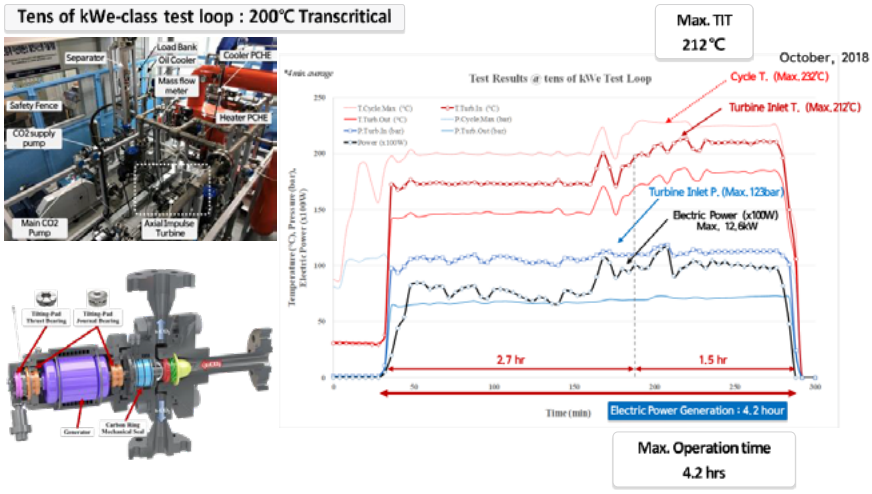


Fig. 6. 200℃ tens of kWe-class axial turbo-generator and Transcritical test loop with operation results

test the various flow conditions. An LNG-fired thermal oil boiler heated the CO2 to 200°C through a printed circuit heat exchanger (PCHE), and after driving the turbine the CO2 was cooled through the PCHE.

In order to use a technically stable oil-lubricated bearing, a mechanical seal was installed in the turbo-generator, which inevitably leads to turbine leakage flow. In the current turbo-generator design, a 2 to 3% leakage flow was estimated; therefore, the leakage management system was constructed to re-inject CO2 into the system. An oil separator, cooler, and buffer tank were constructed for cooling the hot leakage flow and removing incoming bearing oil. A three-stage reciprocating oil-free-type CO2 compressor was constructed for pressurizing up to 80 bar in order to recharge the atmospheric leakage flow into the main loop. The leakage flow amount was measured with a Coriolis mass flow meter.

In 2018, a 4.2 hours continuous electricity generating operation was successful under TIT of 212°C. A robust turbo-generator design, a leakage make-up system and operation strategy leads success of safe operation. [9]

In 2019, a 500°C hundreds of kWe-class two axial turbo-generator and Brayton test loop was commissioning. In this test loop, 650°C, 1.75 MWth burner was developed for heat source and a shell-and-finned-tube type heat exchanger was also fabricated for heating a 135 bar of supercritical carbon dioxide. In addition, for Brayton cycle, a centrifugal supercritical carbon dioxide compressor was developed and fabricated. A compressor was driven by high-speed motor connected with a coupling. A design rotating speed of the compressor was 70,000 RPM. In this compressor, in order to reduce leakage flow, a dry gas seal (DGS) was fabricated in the rotor. In addition, in order to supply dried carbon dioxide into seal face, an additional DGS supply control system consists of a booster, a heater and so on was developed.

Two axial turbo-generator for 500°C and 392°C of TIT were developed for this test loop. As described above, the second low temperature turbo-generator for 392°C already fabricated and tested in the previous tens of kWe-class transcritical test loop. In this final test loop, new 500°C of TIT axial turbo-generator was developed which is composed of an oil-lubricated tilting pad journal and thrust bearing that operates at 70,000 RPM. In this turbo-generator, a balancing piston which is driven 6 bar of compressed air was fabricated to reduce axial force on the rotor. By controlling a pressure of supply air, semi-active axial force balancing is possible.

Two PCHEs were fabricated for recuperators and one PCHE was fabricated for a cooler. Since there are leakages from two turbo-generator and one compressor, one leakage recompressing system was developed in the loop, and a 600 L of inventory tank was fabricated for supplying carbon dioxide corresponding to leakage. All piping were constructed as ASME standard. All test loop was assembled. Now commissioning progress is conducted. After investigating these core components of supercritical carbon dioxide power cycle, a part of preliminary Carnot Battery system would be constructed and tested in the future.

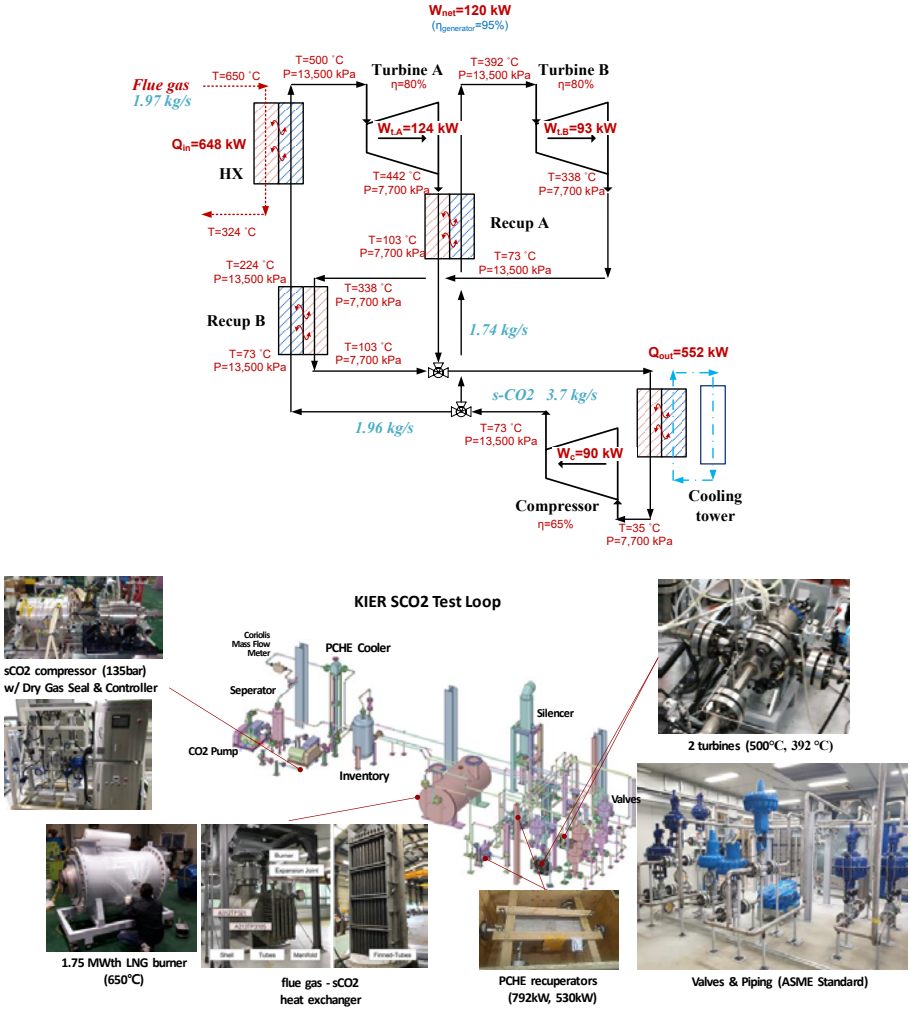


Fig.7. 500℃ hundreds of kWe-class two axial turbo-generator and Brayton test loop

5. Summary and Future Works

There are several layout options for the Carnot battery as a hot storage temperature. A conventional gas turbine combined cycle and a conventional steam turbine cycle can be utilized. In addition, a supercritical carbon dioxide power cycle is an attractive option in the Carnot battery concept due to its advantages. KIER has been developed sCO2 power cycle technology for future power generation system. Various capacities of sCO2 turbomachinery and test loops have been developed and operated as shown in this paper.

Therefore, KIER is now considering sCO2-Carnot Battery concept utilizing our sCO2 technology. Further studies on cycle layouts, economics and development of a small-scale test loop of the Carnot battery would be done as a next step.

Acknowledgements

This work was conducted under the framework of Research and Development Program of the Korea Institute of Energy Research (KIER) (C0-2410, C0-2450) and National Research Council of Science & Technology (NST-CPS-19-07).

References

[1] IEA, Technology Roadmap, Energy storage (2014).
[2] Ministry of Trade, Industry and Energy in Korea, 8th Basic Plan for Electricity Supply and Demand (2017).
[3] Cho J, Shin H, Cho J, Choi B, Roh C, Lee B, Lee G, Ra H-S and Baik Y-J. Electric-thermal Energy Storage for Large-scale Renewables and a Supercritical Carbon Dioxide Power Cycle, SolarPACES 2019, Daegu, Korea.
[4] Aga V, Conte E, Carroni R, Burcker B and Ramond M. Supercritical CO2-Based Heat Pump Cycle for Electrical Energy Storage for Utility Scale Dispatchable Renewable Energy Power Plants, 5th International Symposium - Supercritical CO2 Power Cycles, March 28-31, 2016, San Antonio, Texas.
[5] Mercangoz M, Hemrle J, Kaufmann L, Z'Graggen A and Ohler C. Electrothermal energy storage with transcritical CO2 cycles, Energy 2012;**45**:407-15.
[6] US DOE, ARPA-E, DE-FOA-0001906, CFDA Number 81.135 (2018).
[7] Geyer M. DLR, Webinar on Carnot Batteries
[8] https://x.company/projects/malta/
[9] Cho J, Shin H, Cho J, Choi B, Roh C, Lee B, Lee G, Ra H-S and Baik Y-J. Development and power generating operation of the supercritical carbon dioxide power cycle experimental test loop in KIER, 3rd European supercritical CO2 Conference, September 19-20, 2019, Paris, France

13th IEA Heat Pump Conference
April 26-29, 2021 Jeju, Korea

Condensation heat transfer and pressure drop characteristics of R-513A as an alternative refrigerant of R-134a

Andreas Karageorgis[a], George Hinopoulos[a], Man-Hoe Kim[b*]

[a] Halcor-Copper Tube Division, ElvalHalcor Company, 32011 Oinofyta –Viotia, Greece
[b]School of Mechanical Engineering & IEDT, Kyungpook National University, Daegu, 41566, South Korea

Abstract

Two phase condensation heat transfer and pressured drop characteristics of R-513A in a 9.52 mm O.D. horizontal microfin copper tube are investigated experimentally. Test facility has a straight test section with a length of 2.0 m and is cooled by cold water circulated in a surrounding annular space. The water-side annular space heat transfer coefficients are measured using the Wilson plot method. Average heat transfer coefficients and pressure drop data are reported at the condensation temperature of 35°C in range of 100-440 kg/m^{2}s mass flux. The test data of R-513A are compared with those of R-134a, R-1234yf and R-1234ze(E).

Keywords: Microfin tube; low-GWP refrigerants; condensation heat transfer; R-513A; R-1234yf; R-1234ze(E)

1. Introduction

In recent years, the use of energy systems including refrigeration and air conditioning systems is gradually increasing due to the advancement of technology and improvement of living standards, and energy supply and demand and environmental problems are emerging as important issues. Among the energy systems, the environmental impact of the refrigeration and air conditioning systems is the global warming effect that occurs in generating the working fluids of the system and power required for the system operation. The global warming is highly affected by air-conditioning, refrigeration and heat pump systems which account 700 million metric tons of CO_2 equivalent direct (7%–19%) and indirect emissions (74%) per year [1]. Therefore, it is very important to increase the energy efficiency of the system, and use eco-friendly alternative refrigerants such as carbon dioxide and HFO refrigerants with a small global warming potential [2-3]. Heat exchangers in air conditioning and heat pump applications play an important role on system efficiency and physical size. Finned round tube or flat tube heat exchangers are widely used for the evaporators and condensers in residential air-conditioning and heat pump systems. To investigate the overall performance of the finned tube heat exchangers, tube-side heat transfer and pressure drop characteristics as well as air-side performance should be investigated simultaneously. Several investigators [4–10] conducted investigations on two phase thermal and hydraulic performance in smooth and enhanced tubes. Kim and Shin [5, 6] investigated experimentally evaporation and condensation heat transfer characteristics using R-22 and R-410A in 9.52mm OD smooth and microfin tubes. They found that average evaporation and condensation heat transfer coefficients of R-410A for microfin tubes were 1.86-3.27 and 1.7-3.19 larger than those of smooth tubes, respectively. And they also reported that the evaporating heat transfer coefficients for R-410A were 97–129% of R-22 when compared to R-22 at the same test conditions. Due to the EU Regulation No 517/2014, the refrigerant R-134a is already banned in mobile air-conditioning and household refrigerator-freezer systems and will be also prohibited for commercial refrigerator-freezers from 2022 [7]. Hence studies to find low-GWP alternative refrigerants for R-134a have attracted to prevent negative effects on climate change by many researchers. Table 1 and Fig. 1 show general properties and vapor pressures of R-134acompared to alternative refrigerantsR-1234yf, R-1234ze(E), and R-513A. GWP values of R-1234yf and R-1234ze(E) are significantly lower than R-134a. However, R-1234yf and R-1234ze(E) are mildly flammable and classified as A2L. R-1234ze(E) has a lower saturation pressure than R-134a (75% of R-134a at a saturation temperature of 35°C), so it the design of the system requires to be modified and the pressure drop is relatively

* Corresponding author: Man-Hoe Kim. Tel.: +82-53-950-5576; fax: +82-53-950-6550.

Table 1. General properties of R-134a alternative refrigerants

	R-134a	R-513A	R-1234yf	R-1234ze(E)
Chemical Formula	CF3CH2F	R-1234yf/134a (56/44 wt %)	CH2CFCF3	C3H2F4
Molar mass [g/mol]	102	108	114	114
ODP	0	0	0	0
GWP	1430	573	4	6
Flammability	A1	A1	A2L	A2L
NBP[oC]	-26	-29	-29	-19
Tc [oC]	101	96.5	94.7	109.4
Pc [kPa]	4059	3648	3381	3632
qv* [kJ/m3]	7293	7373	6891	5608

* Volumetric capacity calculated at the condensing temperature of 35°C

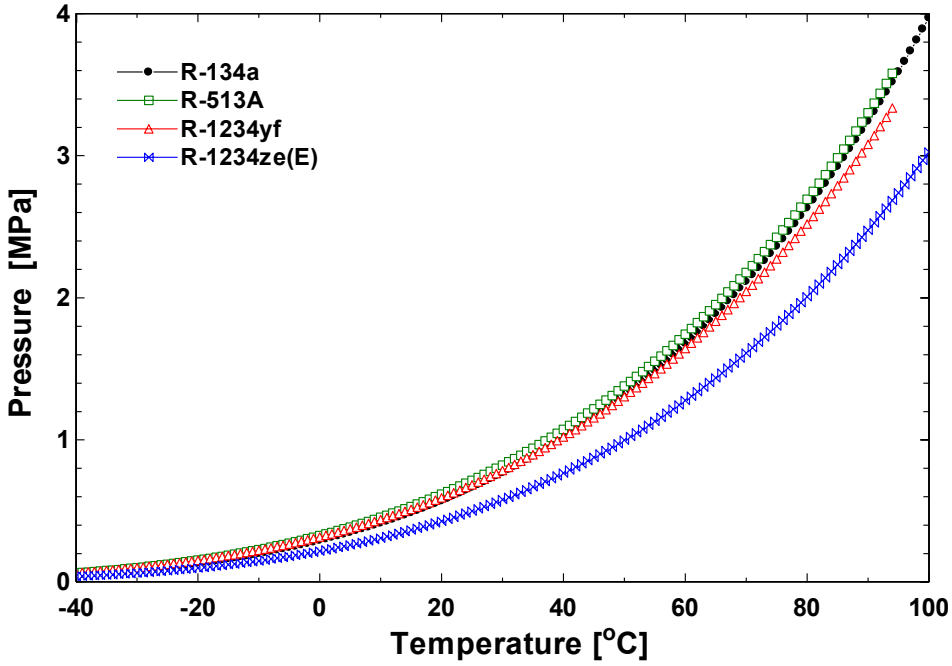


Fig. 1. Saturation vapor pressures for R-134a alternative refrigerants

high. R-513A refrigerant is an azeotropic mixture with a mass ratio of R-1234yf and R-134a of 56 to 44, and its GWP value is slightly higher at 573, but it is not flammable and has an advantage that is very similar to R-134a in thermodynamic properties. Yang et al. [8] and Diani et al. [9] conducted experimental studies on condensation heat transfer of R-1234yf and R-1234ze refrigerants in small diameter microfin tubes, respectively. Diani et al. [10] investigated condensation heat transfer of R-513A at the saturation temperatures of 30 and 40 °C in the range of 100-1000 kg/m^{2}s mass fluxes inside 3.5 mm ID smooth and microfin tubes.

In this study, condensation heat transfer and pressure drop characteristics in a 9.52 mm OD microfin tube are experimentally performed for R-513A, R-1234yf, R-1234ze(E), and R-134a at a condensation temperature of 35°C in the range of 100-440 kg/m^{2}s mass fluxes. The correlation equation of the heat transfer coefficient for the annular space of the test section is obtained using the Wilson plot, and the condensation test results of the refrigerant R-513A are compared with those of R-134a, R-1234yf and R-1234ze(E).

2. Experiments

2.1 Experimental facility

A schematic diagram of the experimental facility is shown in Fig. 1. The facility consists of one refrigerant loop and two water loops. The refrigerant loop is designed to measure the mean heat transfer coefficient of refrigerant condensing inside a micro fin tube. It is mainly composed of a gear pump, a pre-heater, a test section, a heat exchanger and a receiver tank. Refrigerant in liquid state is pumped from the bottom of the receiver tank to the preheater where it is heated up until it reaches a state of superheated vapour. With the preheater, it is possible to control the refrigerant superheat when it enters the test section. The refrigerant enters the test section in superheated vapor state and leaves in subcooled liquid. The test section with a length of 2m as shown in Fig. 2 consists of a simple tube-in-tube counter flow heat exchanger. The refrigerant inside the inner tube condensates and the water that flows in the annular duct between the two tubes is heated. Chiller 1 (6) is designed to control the conditions of the water entering the test section. After the test section, the refrigerant enters the plate heat exchanger as a subcooled liquid. The role of the plate heat exchanger is to control the system pressure. Chiller 2 (7) controls water temperature and flow rate at the inlet of the plate heat exchanger.

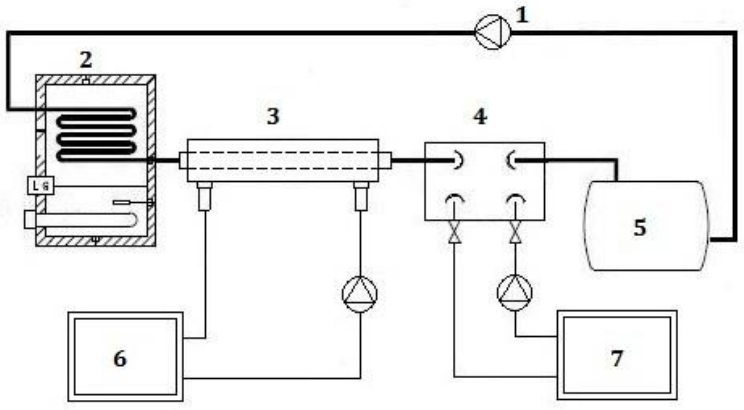


Fig. 2. Schematic diagram of experimental facility (1. Refrigeration pump, 2. Preheater, 3. Test section, 4. Plate heat exchanger, 5. Receiver tank, 6. Chiller1, 7. Chiller2

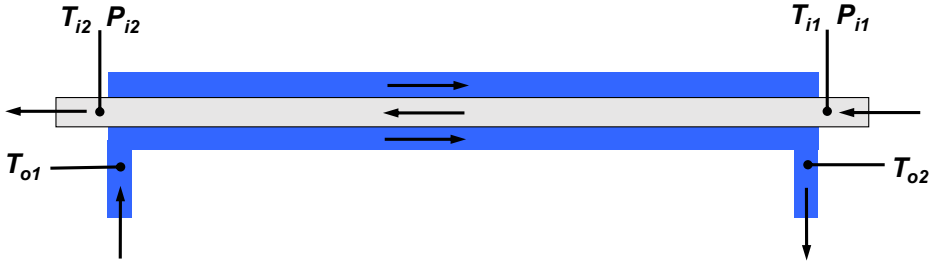


Fig. 3. Schematics of test section

The refrigerant pump (1) is a positive displacement gear pump with the maximum flow of 100 kg/h liquid refrigerant. Special attention is given to the refrigerant inlet pressure and temperature conditions to ensure that the refrigerant's pressure is higher than its vapor pressure at any point in the pump and avoid any bubble

formation within the pump. For that reason, the refrigerant's pressure and temperature is measured at the suction line to ensure that the refrigerant remain in liquid state. The pre-heater (2) is an insulated tank that contains a coil of the main loop refrigerant on the top, electrical resistances on the bottom and a low-pressure fluid; its role is to heat up the liquid refrigerant to a superheated vapor state. The electrical resistor heaters heat the low-pressure refrigerant which evaporates on the bottom of the tank. Then, low-pressure refrigerant vapor condensates on the surface of the main refrigerant loop coil on the top of the tank. The test section (3) can be described as a simple tube in a tube heat exchanger. It consists of an inner grooved tube mounted inside an outer shell tube, so that the refrigerant flows counter-current through the inner tube, with the cooling water around it. Refrigerant condensates in the test section under fully controlled conditions. The pressure and temperature are measured at the inlet and outlet of the test section. Both inlet and outlet state of the refrigerant are single phase, thus the inlet-outlet specific enthalpies can be determined using thermodynamic data. The condensation heat capacity is calculated as the product of the mass flow and the differential enthalpy. The plate heat exchanger (4) role is to control the refrigerants pressure; this is accomplished by heating or cooling the refrigerant loop with water as a secondary mean. The heating or cooling rates at the plate heat exchanger are small in order to accomplish a high precision pressure regulation. The water flow rate and temperature are controlled. The receiver tank (5) contains refrigerant in both liquid and vapor state at the bottom and top respectively. The refrigerant outlet is located on the bottom of the receiver tank so that only liquid refrigerant is pumped.

2.2 Experimental methods and conditions

The test conditions are described in Table 2. The condensation experiments are conducted at the saturation temperature of 35 °C for the mass flux of 100-440 kg/m^{2}s with R-134a, R-513A, R-1234yf and R-1234ze(E). The inlet superheat and outlet subcooling of condenser are 5 and 2 °C, respectively. The refrigerant flow is regulated by controlling the input power of the variable speed magnetic gear pump. The test conditions and data to be collected were monitored throughout the test, and data sets were recorded and averaged over 10 min after test conditions reached steady state. Before the condensation experiment, a series of water-to-water experiments are first performed to find the correlation of the heat transfer coefficient of the annular space. Water to water test data are collected with increasing the water flow rate of the annular space from 200 to 800 kg/h in increments of 100 kg/h. The tested microfin tube has 60 fins with fin height of 0.25 mm, an apex angle of 60°, and bottom wall thickness of 0.35mm.

Table 2. Test conditions

Refrigerants	R-134a, R-513A, R-1234yf, R-1234ze(E)
Condensing temp. [°C]	35
Mass flux [kg/m^{2}s]	100-440
Degree of superheat/subcooling [°C]	5/2

2.3 Data reduction

Condensation heat transfer coefficients can be calculated using the following equations

$$\frac{1}{U_o A_o} = \frac{1}{h_i A_i} + R_w + \frac{1}{h_o A_o} \quad (1)$$

Where U_oA_o is the overall heat transfer coefficient. R_w is the thermal conduct resistance of the tube wall and it can be neglected because the tube material is copper and the thickness of the tube wall is very thin.

$$Q = U_o A_o \, LMTD \quad (2)$$

Where Q is the heat transfer rate of the test section and the arithmetic mean of tube- (Q_i) and annular-side (Q_o) heat transfer rates that obtained from the following equations

$$Q = \frac{Q_i + Q_o}{2} \quad (3)$$

$$Q_i = m_i c_p \, (T_{i1} - T_{i2}) \quad (4)$$

$$Q_o = m_o c_p \, (T_{o2} - T_{o1}) \quad (5)$$

And the *LMTD* is the log mean temperature difference which is defined as

$$LMTD = \frac{(T_{i2} - T_{o1}) - (T_{i1} - T_{o2})}{\ln\left[\frac{(T_{i2} - T_{o1})}{(T_{i1} - T_{o2})}\right]} \quad (6)$$

If the heat resistance ($1/h_oA_o$) of the annular space is known from Eq. (1), the heat transfer coefficient (h_i) in the tube can be obtained from the heat resistance ($1/h_iA_i$) in the tube. Refrigerant properties were calculated using NIST REFPROP [11].

3. Results and discussion

Figs. 4 and 5 show the Wilson plot and the correlation equation for obtaining the heat transfer coefficient of the annular space with variation of water flow rate of 200-800 kg/h, respectively. As shown in Fig. 4, the total thermal resistance value ($1/U_oA_o$) of the test section is well expressed as a function of the tube-side thermal resistance ($1/h_iA_i$). The total thermal resistance value decreases with the increase of the flow rate of the annular space at the same flow rate in the tube-side, because the heat transfer coefficient of the annular flow path increases with the increase of the flow rate. The refrigerant-side heat transfer coefficients are calculated from Eq. (1) using correlation of $1/h_oA_o$ from Fig. 5.

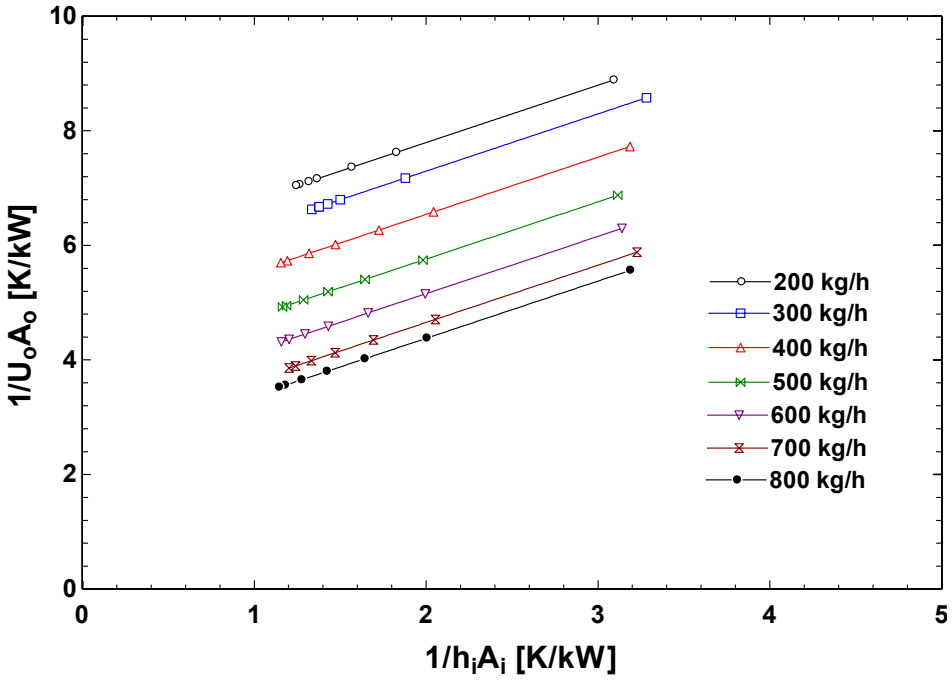


Fig. 4. Wilson plot with variation of annular-side mass flow rate

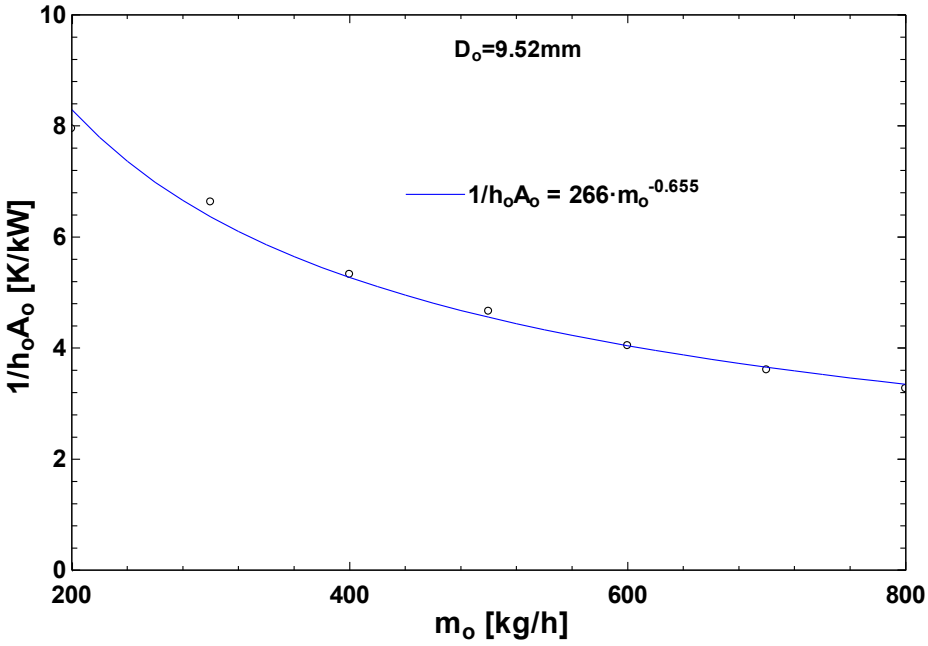


Fig. 5. Heat transfer coefficient for annular side as function of water mass flow rate

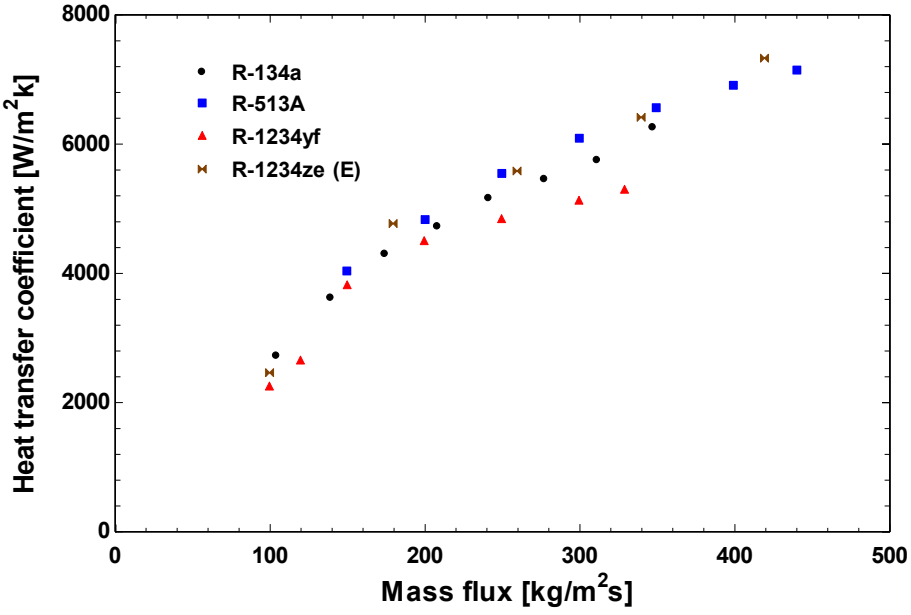


Fig. 6. Heat transfer coefficient for refrigerant side with variation of refrigerant's mass flux

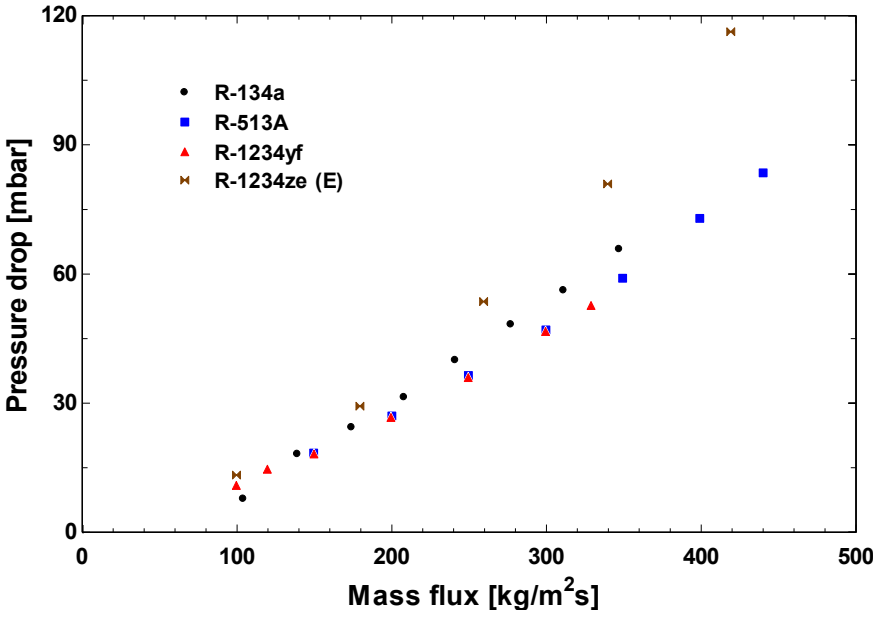


Fig. 7. Pressure drops with variation of refrigerant mass flux

Table 3 Thermodynamic and transport properties of R-134a alternative refrigerants [11]

Properties [Units]	Refrigerants			
	R-134a	R-513A	R-1234yf	R-1234ze(E)
Saturation temperature [°C]	35	35	35	35
Saturation pressure [kPa]	887	941	895	667
Latent heat [kJ/kg]	168	147	137	159
Liquid viscosity [μPa-s]	172	147	135	168
Vapor viscosity [μPa-s]	12.1	12.0	12.0	12.8
Liquid thermal conductivity [mW/m-K]	76.9	66.3	60.5	70.9
Vapor thermal conductivity [mW/m-K]	14.9	15.1	14.9	14.5
Liquid density [kg/m^3]	1167	1095	1054	1129
Vapor density [kg/m^3]	43.4	50.2	50.3	35.3
Liquid specific heat [J/kg-K]	1471	1464	1443	1422
Vapor specific heat [J/kg-K]	1103	1131	1124	1023
Liquid Prandtl number [-]	3.29	3.23	3.23	3.37
Vapor Prandtl number [-]	0.90	0.90	0.90	0.91
Surface tension [mN/m]	6.74	5.47	4.97	7.56
Reduced pressure [-]	0.18	0.26	0.26	0.18

Figs. 6 and 7 present average heat transfer coefficients and pressure drops at the condensing temperature of 35°C in ranging of 100-440 kg/m^{2}s mass flux, respectively. The heat transfer coefficients of the test refrigerants including R-513A increase with the refrigerant mass flux as expected, and all four refrigerants have similar heat transfer coefficient values at low mass flux. However as the mass flux increases, the heat transfer coefficient of R-513A has a similar value to that of R-1234ze(E), while it is about 10% higher than that of R-134a. The heat transfer coefficient of R-1234yf represents the lowest value among the test refrigerants, and the difference in heat transfer coefficient with other refrigerants becomes larger as mass flux increases. Table 3 presents the major thermodynamic and transport properties of R-134a alternative refrigerants. These properties are attributed to the higher R-513A and R-1234ze(E) heat transfer coefficients and lower R-1234yf heat transfer coefficient compared to R-134a [12,13]. The pressure drops for all test refrigerants are increased with mass flux as expected as shown in Fig. 7. The pressure drops of R-513A and R-1234yf are smaller than that of R-134a when the mass fluxes are larger than 150 kg/m^{2}s, while the pressure drops of R-1234ze(E) are

relatively higher than that of R-134a. This is partly due to the higher vapor viscosity of R-1234ze(E) compared to R-134a as shown in Table 3.

4. Conclusion

The present study has been conducted to investigate two-phase condensation heat transfer and pressure drop characteristics in a horizontal 9.52 mm OD microfin tube with refrigerant R-513A. The experimental results are compared with those of R-134a, R-1234yf and R-1234ze. The findings of the present study have been listed below.

- The average condensation heat transfer coefficients of R-513A and R-1234ze (E) are similar to that of R-134a in the lower range of tested mass fluxes (100-150 kg/m^{2}s). As mass flux increases, the heat transfer coefficients of R-513A and R-1234ze (E) become higher than that of R-134a.
- The average condensation heat transfer coefficients of R-1234yf is lower than that of R-134a for the full range of tested mass fluxes.
- The pressure drop of R-513A is similar to R-1234yf and lower compared to that of R-134a
- R-1234ze(E) pressure drops are higher compared to that of R-134a.

References

[1] G. Blanco, R. Gerlagh and S. Suh (eds), 2014. Drivers, Trends and Mitigation. In Climate Change 2014, Cambridge University Press, Cambridge, United Kingdom and New York, NY, USA. p. 351–412.
[2] M.-H. Kim, J. Pettersen, and C.W. Bullard, 2004. Fundamental Process and System Design Issues in CO_2 Vapor Compression Systems. Progress in Energy and Combustion Science, 30, p. 119-174.
[3] M.-H. Kim, S.Y. Lee, S.S. Mehendale, R.L. Webb, 2003. Microchannel Heat Exchanger Design for Evaporator and Condenser Applications. Advances in Heat Transfer 37, p. 297-429.
[4] L. Lin, M. Kedzierski, 2019. Review of low-GWP refrigerant pool boiling heat transfer on enhanced surfaces. Int. J. Heat Mass Tran.131, p. 1279-1303.
[5] M.-H. Kim and J.S. Shin, 2005. Evaporating heat transfer of R22 and R410A in horizontal smooth and microfin tubes. Int. J. of Refrig, 28, p. 940-948.
[6] M.-H. Kim and J.S. Shin, 2005. Condensation heat transfer of R22 and R410A in horizontal smooth and microfin tubes. Int. J. of Refrig, 28, p. 949-957.
[7] A. Mota-Babiloni, P. Makhnatch, R. Khodabandeh, J. Navarro-Esbrí, 2017. Experimental assessment of R134a and its lower GWP alternative R513A. Int. J. Refrig, 74, p. 682-688.
[8] C.-Y.Yang, H. Nalbandian, 2018. Condensation heat transfer and pressure drop of refrigerants HFO-1234yf and HFC-134a in small circular tube. Int. J. Heat Mass Tran. 127, p. 218-227.
[9] A. Diani, M. Campanale, L. Rossetto, 2018. Experimental study on heat transfer condensation of R1234ze(E) and R134a inside a 4.0 mm OD microfin tube. Int. J. Heat Mass Tran. 126, p. 1316–1325.
[10] A. Diani, P. Brunello, L. Rossetto, 2020. R513A condensation heat transfer inside tubes: Microfin tube vs. smooth tube. Int. J. Heat Mass Tran. 152, p. 119472.
[11] E. Lemmon, M. McLinden, M. Huber, 2018. NIST Reference Fluid Thermodynamic and Transport Properties Database: REFPROP Version 10, NIST Standard Reference Database 23.
[12] C.-C. Wang, 2013. An overview for the heat transfer performance of HFO-1234yf. Renewable and Sustainable Energy Reviews. 19, p. 444-453.
[13] A. Karageorgis, G. Hinopoulos, M.-H. Kim, 2021. A comparative study on condensation heat transfer and pressure drop characteristics of R134a and alternative refrigerants in a horizontal microfin tube – technical note. Fluids, under review.

13th IEA Heat Pump Conference
April 26-29, 2021 Jeju, Korea

An Experimental Study on Thermal Comfort Improvement For Residential Air Conditioner Applying a Wind-free Technology

Youngju Joo[a], Jun Hwang[a*], Hyeongjoon Seo[a], Byongguk Lim[a]

[a]Samsung Electronics, Suwon-si, Gyeonggi-do, 16677, Republic of Korea

Abstract

This paper focused on the indoor thermal comfort improvement by the wind-free air conditioner. Evaluate the indoor thermal comfort and air quality to meet the growing demands of the occupants, a hybrid flow path was applied to the air conditioner. There are various parameters which are influenced thermal comfort, Especially, Air flow is the most essential parameter to achieve comfort condition. This study presents the thermal comfort improvement for wall mount type, floor-standing type and ceiling type air-conditioner, respectively. When the occupant zone reached to comfort condition, the air flow can be changed to the wind-free mode, it can be reduced cold draft and energy consumption. The air flow visualization and temperature distribution was measured compare general cooling mode with wind-free mode.

Keywords: Wind-free; Thermal comfort; Air-conditioer;

1. Introduction

With improved living standards and the increase in the desire and importance for comfortable indoor environment, the penetration rate of residential air conditioners in South Korea is increasing every year. According to the survey report on home appliance penetration rates published by the Korea Power Exchange, the penetration rate of residential air conditioners increased from 2% in 1985 to 61% in 2011 and to 75% in 2015[1]. The cause of this increase is the increase in the various desires of consumers for indoor thermal comfort. While air conditioners were recognized as summer products for reducing the indoor air temperature in the past, the development of air conditioners is being expanded from temperature-oriented air conditioning to comprehensive comfort air conditioning by reinforcing various additional functions, such as heating, dehumidification, and air cleaning.

Indoor thermal comfort not only improves personal satisfaction but also has the economic effect of increased productivity. Dorgan[2] estimated that the annual profit resulted from the productivity improvement and medical cost savings caused by indoor air quality improvement is $62.7 billion, and Fisk[3] reported that the economic effect of the reduction in diseases and the increase in work efficiency caused by the improvement of indoor environment amounts to $40.0 - $200 billion. It can be said that indoor thermal comfort is a basic and essential condition in modern society.

1.1 Principles of wind-free air conditioners

Indoor thermal comfort can be secured by controlling the four elements of air conditioning, i.e. the indoor temperature, humidity, airflow, and cleanliness. Among them, the airflow acts as a positive element by rapidly forming a comfort condition in the space during the initial operation. The airflow, however, has double-sidedness because it acts as a negative element that induces cold draft after the formation of the comfort condition. [4][5]

To maintain continuously comfortable environment for indoor occupants without the discomfort caused by the airflow, wind-free air conditioners were developed using the hybrid flow path.

* Corresponding author. Tel.: +82-31-8062-2500; fax: +82-31-8062-2500.
E-mail address: neojun.hwang@samsung.com

For the wind-free air conditioners, the hybrid flow path is constructed so that the indoor temperature can be rapidly reduced with the opening of wind doors during the initial operation and the internal flow path can be changed with the closing of the wind doors when the wind-free mode is selected after a comfort condition is reached in the residential space. The airflow is uniformly discharged at low speed through micro-holes to maintain the comfort of the residential space without the feeling of airflow.

In this study, the cases of residential and system air conditioners with the hybrid flow path for wind-free cooling and the effect of wind-free cooling on the improvement of indoor thermal comfort were analyzed.

2. Theories on Indoor Thermal Comfort and Their Application

2.1 PMV and PPD

To quantify human thermal sensation, Fanger (1970) presented the predicted mean vote (PMV) by combining the results of the experiment performed with 1,300 participants and the heat balance equation for the human body.

PMV is determined by six elements, including four environmental elements (room air temperature, mean radiation temperature, relative humidity, and air velocity), metabolism, and thermal resistance of clothing. It can be expressed as a function of the human body thermal load (L) calculated with the body surface temperature and sweat evaporation rate that provides neutral thermal sensation in the metabolism (M) as shown in equation (1).

$$\mathrm{PMV} = 0.303\exp(-0.036\mathrm{M}) + 0.028 \tag{1}$$

The PMV value was set based on the seven-point thermal sensation scale of ASHRAE. The predicted percentage of dissatisfied (PPD) represents the expected percentage of people who are not satisfied with the given environment. There is a correlation between PMV and PPD as shown in equation (2). The given environment is evaluated as "comfortable" if PMV is within ±0.5 and PPD is less than 10%.[6]

$$\mathrm{PPD} = 100 - 95\exp[-(0.03353PMV^4 + 0.2179PMV^2)] \tag{2}$$

2.2 Application of PMV and PPD

For the calculation of PMV and PPD, equations (1) and (2) were automatically calculated by programming. The input parameters required for the calculation are shown in Table 1.

Table 1. Input parameters of PMV-PPD Program

Input Parameter	Unit
Metabolism (M)	met=W/m^2
External work (W)	W/m^2
Thermal resistance of clothing (I_{clo})	clo=m^2°C/W
Room air temperature (Ta)	°C
Mean radiation temperature (Tr)	°C
Air velocity (Va)	m/s
Relative humidity (Rh)	%

The environmental elements, i.e. the room air temperature, mean radiation temperature, air velocity, and relative humidity, were automatically obtained using sensors, and the elements related to the human body that could not be measured were treated as constants as shown in Table 2.

Table 2. Constants of PMV-PPD Program

Parameter	constant
Metabolism	1.2met = 69.84 W/m^2 (Office, Home)
External work	0W/m^2 (for everyday activities)
Thermal resistance of clothing	0.5 clo = 0.078m^2°C/W(Summer)

3. Experimental Setup and Method

3.1 Experimental setup

Experiments were performed in a residential environment laboratory that simulated the actual environment. The residential environment laboratory consisted of an outdoor environment chamber for simulating various outdoor environments and a model house.

The model house simulated the living room and main room of an apartment. Fig. 1 shows the schematic diagram of the model house. Thermocouples were installed in three dimensions to measure the temperatures inside the model house, and indoor thermal environment elements were measured using relative humidity sensors, radiation thermometers, and wind speed measuring instruments.

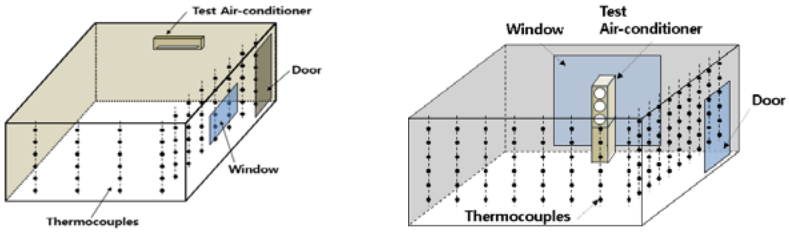


Fig. 1. Schematic diagram of model house

3.2 Experimental method

Table 3 shows the experimental test conditions in model house. The initial outdoor load conditions were a dry-bulb temperature of 35℃ and a wet-bulb temperature of 24℃ (relative humidity 39%). Tests were conducted after both the model house and the outdoor environment chamber were stabilized. The air conditioners were operated after the windows and doors had been closed to minimize the entry and exit of heat, and the indoor temperature, relative humidity, mean radiation temperature, and air velocity were measured every 20 seconds. To analyze the effect of the hybrid flow path on indoor thermal comfort, the cooling set temperature was fixed at 24℃ and the air conditioners were operated while the air volume setting was varied. In the case of residential and system air conditioners, they adopt inverters and maintain a constant indoor temperature by varying the cooling capacity through the control of the revolutions of the compressor when the indoor temperature reaches the set temperature. When the indoor temperature was stabilized at 24℃, the indoor temperature distribution, air velocity, and thermal comfort for each air volume setting were compared.

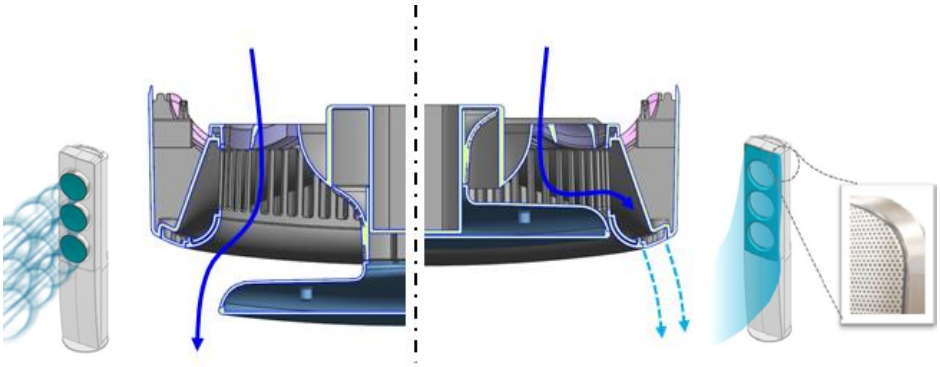
Table 3. Experiment test conditions

Parameter	Value
Initial Dry bulb temperature	35
Initial wet bulb temperature	24

Set temperature of air-conditioner 24

4. Experiment Results and Discussion

4.1 Stand-type wind-free air conditioner



(a) Cooling mode (b) Wind-Free mode

Fig. 2. Schematic of hybrid flow path

For residential air conditioners, the airflow is essential for creating comfortable conditions through the suction of hot and humid air indoors and air conditioning. Most indoor occupants, however, have the perception that direct exposure to the cold airflow from an air conditioner is harmful to their health.

Considering this double-sidedness of the airflow, the hybrid flow path was applied to stand-type air conditioners, which dominate the domestic market, to rapidly reduce the indoor temperature with powerful cooling during the initial operation and to generate comfortable environment without the feeling of airflow after the set temperature is reached.

When the hybrid flow path is applied, powerful and fast airflow is discharged from the front with wind doors opened for rapid cooling during the initial operation as shown in Fig. 2(a). When the wind-free mode is selected after the residential space reached a comfort condition, the internal flow path is changed as the wind doors are closed as shown in Fig. 2(b). In this case, the airflow is uniformly discharged at low speed through the 135,000 micro-holes in the front panel.

4.1.1 Indoor temperature and air velocity

To analyze the indoor thermal comfort of a stand-type residential air conditioner in an indoor residential space (the indoor activity range of occupants: less than 1.8m height from the floor, more than 0.3m distance from the external wall, and within 1 m from the air conditioner) [7], the air velocity and indoor temperature distributions at the cooling and wind-free modes are shown in Figs. 3 and 4, respectively.

When the air velocities at 1.5 m from the air conditioner were compared, the air velocity exceeded 0.5 m/s at all points even at the low airflow mode, resulting in non-uniform indoor temperatures. ASHRAE defines the air velocity of 0.15 m/s or less in a residential space as still air [8].

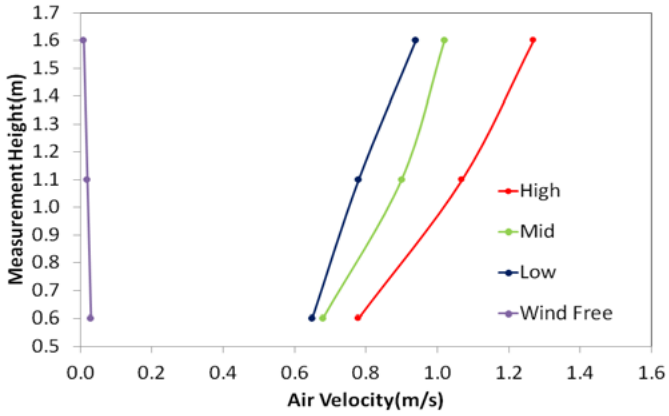
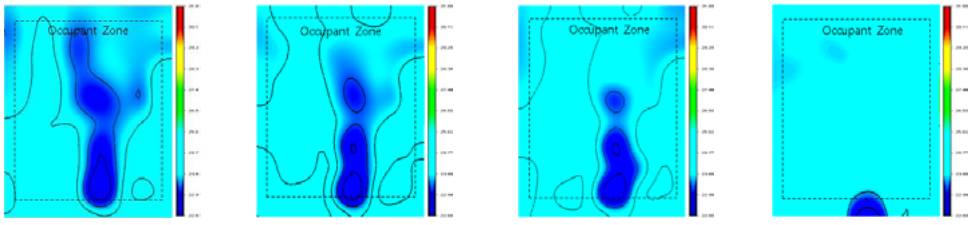


Fig. 3. Air flow velocity distribution of cooling mode and Wind-Free mode



(a) High Airflow mode (b) Mid Airflow mode (c) Low Airflow mode (d) Wind-Free mode

Fig. 4. Temperature distribution of cooling mode and Wind-Free mode

At the wind-free mode, the air velocity was 0.15 m/s or less, and thus the airflow could not be felt. As the indoor temperature was maintained while the air velocity in the residential space was 0.15 m/s or less, a uniform indoor temperature distribution was formed as shown in Fig. 4(d).

4.1.2 PMV and PPD

To compare the indoor thermal comfort of the cooling mode with that of the wind-free mode, PMV and PPD were shown in Figs. 5 and 6, respectively. In the case of the cooling mode, as the air volume setting decreased while the indoor temperature was maintained at 24℃, the air velocity decreased and the PMV and PPD values slightly increased to thermal neutrality. Even at the low airflow mode, however, it is expected that at least 30% of the occupants exposed to the discharged airflow will experience discomfort caused by the cold.

At the wind-free mode, the air velocity was 0.15 m/s or less and the influence of the airflow was minimized. As PMV approached zero, thermal neutrality was closer, and PPD was also in the comfort zone of10 or less. Uniform thermal comfort was secured in the residential space because the air velocity was no more than 0.15 m/s and the indoor temperature was uniformly maintained as shown in Fig. 4(d).

4.2 Wall-mounted wind-free air conditioner

As wind-free air conditioning is also required in personal spaces, such as bedrooms and studies, the hybrid flow path was applied to wall-mounted residential air conditioners. When the hybrid flow path is applied, the wind doors are opened and rapid cooling is performed with powerful and fast airflow as shown in Fig. 7, and

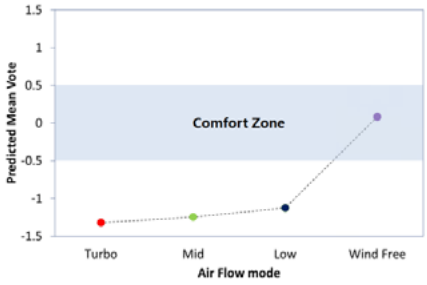


Fig. 5. Comparison of the PMV at cooling mode and Wind-Free mode

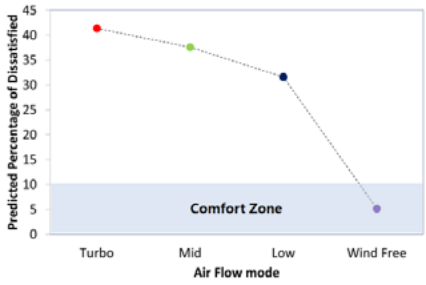
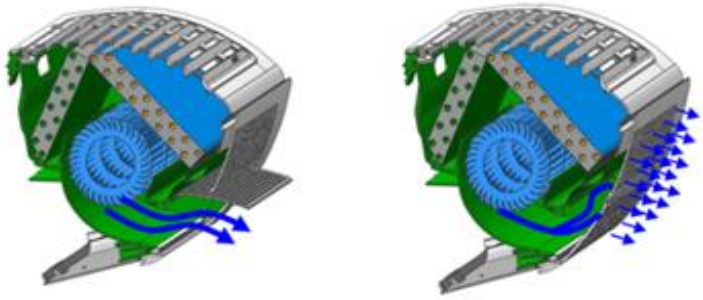


Fig. 6. Comparison of the PPD at cooling mode and Wind-Free mode

the internal flow path is changed as the wind doors are closed when comfortable cooling is required after the set temperature is reached. The residential space can remain comfortable without wind as the airflow is uniformly discharged at low speed through the micro-holes in the front panel.

To analyze the indoor thermal comfort of a wall-mounted wind-free air conditioner, it was installed in the residential environment laboratory, and the indoor temperature and air velocity were analyzed in the same manner as the stand-type wind-free air conditioner.



(a) cooling mode (b) Wind-Free mode

Fig. 7. Schematic of hybrid flow path

4.2.1 Indoor temperature and air velocity

To analyze the indoor thermal comfort of the wall-mounted air conditioner in an indoor residential space (the indoor activity range of occupants: less than 1.8m height from the floor, more than 0.3m distance from the external wall, and within 1 m from the air conditioner) [7], the air velocity and indoor temperature distributions at the cooling and wind-free modes are shown in Figs. 8 and 9, respectively.

When the air velocities at 1.5 m from the air conditioner were compared, the air velocity exceeded 1.0 m/s at the cooling modes, including the high, mid, and low airflow modes, thereby causing non-uniform indoor temperatures (Fig. 9(a), (b), (c)).

At the wind-free mode, the air velocity was 0.15 m/s or less and thus the airflow could not be felt. As the indoor temperature was maintained while the air velocity in the residential space was 0.15 m/s or less, a uniform indoor temperature distribution was formed as shown in Fig. 9(d).

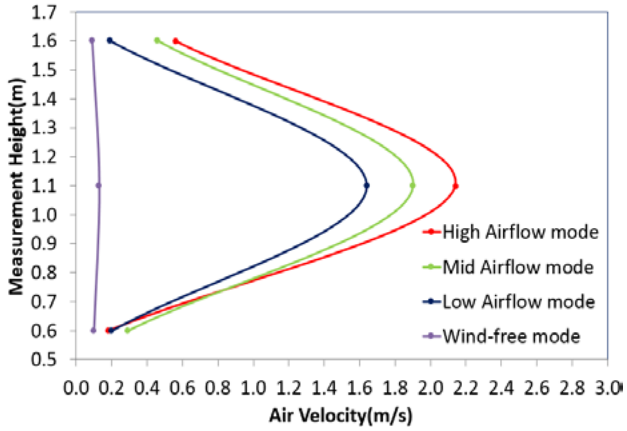
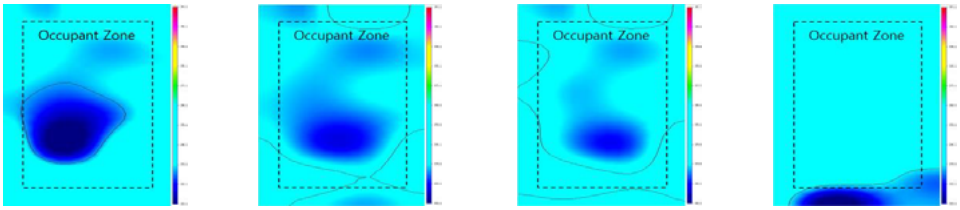


Fig. 8. Air flow velocity distribution of cooling mode and Wind-Free mode



(a) High Airflow mode (b) Mid Airflow mode (c) Low Airflow mode (d) Wind-Free mode

Fig. 9. Temperature distribution of cooling mode and Wind-Free mode

4.2.2 PMV and PPD

To compare the indoor thermal comfort of the cooling mode with that of the wind-free mode, PMV and PPD were shown in Figs. 10 and 11, respectively. In the case of the cooling mode, as the air volume setting decreased while the indoor temperature was maintained at 24℃, the air velocity decreased and the PMV and PPD values were slightly improved to thermal neutrality. Even at the low airflow mode, however, it is expected that at least 20% of the occupants will experience discomfort caused by the cold.

At the wind-free mode, the air velocity was 0.15 m/s or less and the effect of the airflow was minimized. As PMV approached zero, thermal neutrality was closer, and PPD was in the comfort zone of 10 or less. Uniform thermal comfort was secured in the residential space because the air velocity was no more than 0.15 m/s and the indoor temperature was uniformly maintained as shown in Fig. 9(d).

4.3 Ceiling-type 1-way cassette wind-free air conditioner

To expand the wind-free function from residential air conditioners to system air conditioners, the hybrid flow path was applied to 1-way cassette air conditioners, which are mostly built-in products, as shown in Fig. 12.

In the case of 1-way cassette air conditioners, the airflow arrival distance is important for uniform and fast cooling due to their installation characteristics. The conventional 1-way cassette air conditioners exhibited an approximately 40% flow loss due to the airflow resistance caused by blades when remote-distance airflow was implemented. In the case of the wind-free 1-way cassette air conditioners with the hybrid flow path, however, the air volume loss could be reduced to approximately 20% by raising the flow path by 10° compared to the

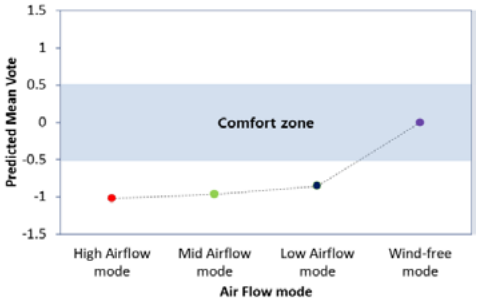


Fig. 10. Comparison of the PMV in the cooling mode and wind-free mode

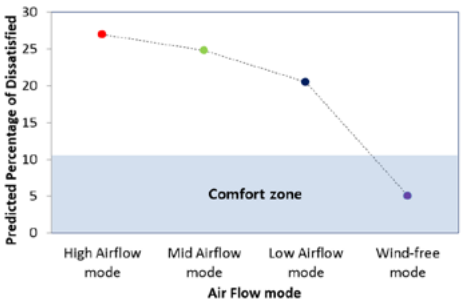
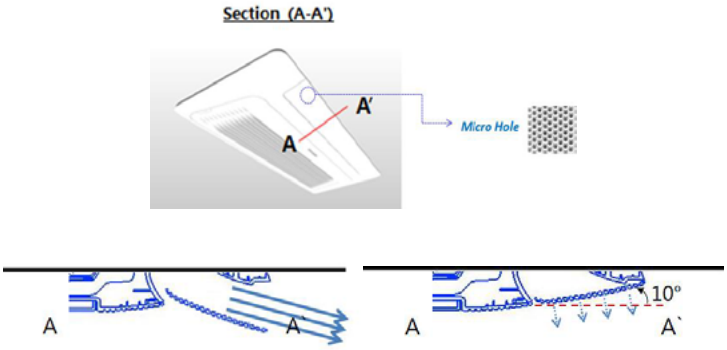


Fig. 11. Comparison of the PPD in the cooling mode and wind-free mode

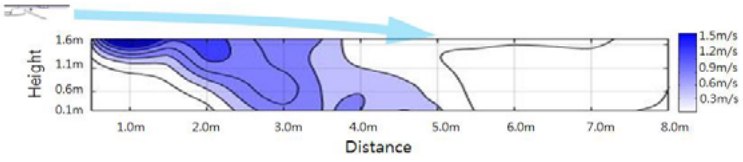
conventional flow paths. Moreover, while the geometry of the internal flow path of the conventional 1-way cassette air conditioners was almost perpendicular to the ceiling surface, that of the wind-free 1-way air conditioners was inclined according to the angle of the discharged airflow.

As a result, the remote-distance airflow of the wind-free 1-way cassette air conditioners with the hybrid flow path increased by approximately 60% compared to that of the conventional 1-way cassette air conditioners as shown in Fig. 13(b).

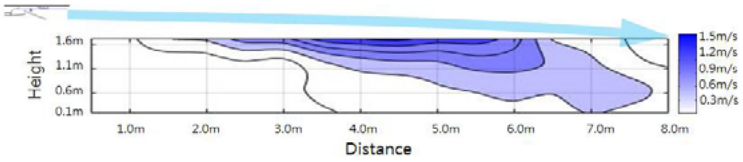


(a) Long air flow mode (b) Wind-Free air flow mode

Fig. 12. Schematic of hybrid flow path



(a) Conventional 1-way CST



(b) Wind-Free 1-way CST

Fig. 13. Air flow velocity distribution

4.3.1 Indoor temperature and air velocity distribution

To compare the thermal comfort according to the airflow when a comfort condition is formed after reaching the set temperature, the air velocity and temperature distributions under the cooling mode of a conventional 1-way cassette air conditioner and the wind-free mode of a wind-free 1-way cassette air conditioner were shown in Figs 14 and 15, respectively.

When the air velocities at 1.5 m from the air conditioner were compared, the air velocity of the conventional 1-way cassette air conditioner exceeded 0.7 m/s as shown in Fig. 13, and non-uniform indoor temperatures were maintained because the temperatures at the points through which the air flew were low as shown in Fig. 14(a). On the other hand, the air velocity of the wind-free 1-way cassette air conditioner at the wind-free mode was 0.15 m/s or less as shown in Fig. 14, and a uniform temperature distribution was maintained in the residential space as shown in Fig. 15(b).

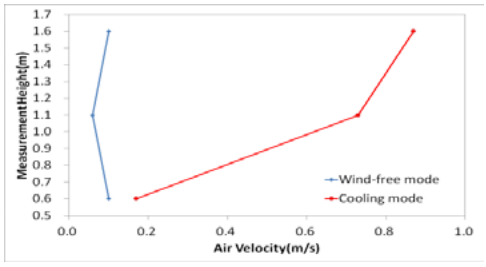
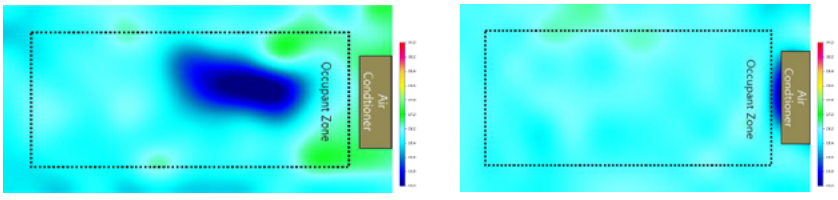


Fig. 14. Air flow velocity distribution of cooling mode and Wind-Free mode



(a) Cooling mode (b) Wind-Free mode

Fig. 15. Temperature distribution of cooling mode and Wind-Free mode

4.3.2 PMV and PPD

To compare the indoor thermal comfort of the cooling mode with that of the wind-free mode, PMV and PPD were shown in Figs. 16 and 17, respectively. In the case of the conventional 1-way cassette air conditioner, the indoor temperature was not uniform and PMV was approximately -1.49 due to the discharged airflow. Therefore, discomfort caused by the cold is predicted and it is expected that approximately 50% of the

occupants will experience discomfort when PMV is converted to PPD. In the case of the wind-free 1-way cassette air conditioner at the wind-free mode, on the other hand, the air velocity was 0.15 m/s or less in the residential space and a uniform indoor temperature distribution was formed. Therefore, it is expected that the occupants will be comfortable regardless of their positions.

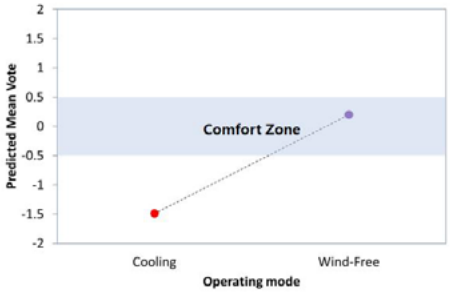


Fig. 16. Comparison of the PMV in the cooling mode and Wind-Free mode

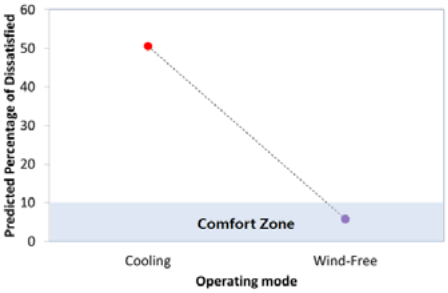


Fig. 17. Comparison of the PPD in the cooling mode and Wind-Free mode

5. Conclusion

In this study, the thermal comfort of the wind-free air conditioners that applied the hybrid flow path to residential and system air conditioners was analyzed to implement powerful cooling during the initial operation and comfortable environment without discomfort caused by the cold airflow from the air conditioner after reaching the set temperature. To this end, experiments were performed in the residential environment laboratory that simulated the actual environment, and the results of the air velocity, indoor temperature distribution, predicted mean vote (PMV), and predicted percentage of dissatisfied (PPD) at the conventional cooling mode and the wind-free mode were compared.

In the case of the stand-type wind-free air conditioner, the indoor temperature distribution was not uniform due to the discharged airflow faster than 0.5 m/s at the cooling mode when the indoor temperature was maintained at 24°C, and it is expected that at least 30% of the occupants will experience discomfort caused by the cold. At the wind-free mode, the air velocity in the residential space was no more than 0.15 m/s and a uniform indoor temperature distribution was confirmed.

In the case of the wall-mounted wind-free air conditioner, an experiment was performed under the same conditions as those of the stand-type wind-free air conditioner. At the cooling mode, the indoor temperature distribution was not uniform due to the discharged airflow of 1.0 m/s or faster, and it is expected that at least 20% of the occupants will experience discomfort caused by the cold. At the wind-free mode, the air velocity in the residential space was 0.15 m/s or less and a uniform indoor temperature distribution was confirmed.

To expand the wind-free function to system air conditioners, the hybrid flow path was applied to 1-way cassette air conditioners, which dominate the built-in market. As a result, the airflow arrival distance increased by approximately 60% compared to the conventional 1-way cassette air conditioners, making it possible to rapidly and uniformly cool a large space during the initial operation.

Under the condition of maintaining the same indoor temperature when a comfort condition is formed after reaching the set temperature, the air velocity of the conventional 1-way cassette air conditioner exceeded 0.7 m/s, resulting in non-uniform indoor temperatures. In addition, it is expected that approximately 50% of the occupants will experience discomfort due to the discharged airflow. In the case of the wind-free 1-way cassette air conditioner, still air (with an air velocity of 0.15 m/s or less) defined by ASHRAE was formed in the residential space at the wind-free mode, confirming that a uniform indoor temperature distribution was maintained.

When the hybrid flow path is applied to residential and system air conditioners and wind-free cooling is performed, it is expected that occupants can secure uniform thermal comfort in their residential spaces because discomfort and non-uniform indoor temperatures caused by the discharged airflow are removed.

References

[1] Korea power exchange, 2013, Electricity market trends and analysis 2013 annual report.
[2] C.B Dorgan, C.E. Dorgan, M.S. Kanared and A.J. William, 1998, health and productivity benefits of improved indoor air quality, ASHRAE Transactions Atlanta 104
[3] W.J. FISK, 2002. How IEQ affects health productivity, ASHRAE Journal 44(5)
[4] Kang, Ki-Nam, Song, Doo-Sam, 2013, A study on the effects of the characteristics of fluctuation in air current on the comfort sensibility of human, Architectural Institute of Korea Spring Annual conference 2013
[5] Hyung Chul Kim, 2001, A Study on variable airflow selection in air conditioned space, SAREK Winter Annual conference 2001
[6] ASHRAE, 1993, ASHRAE Handbook-1993 Fundamentals
[7] ASHRAE Standard 55-2013
[8] Edward Arens, Stephen Turner, Hui Zhang, ASHRAE Journal May 2009, Moving Air For Comfort

13th IEA Heat Pump Conference
April 26-29, 2021 Jeju, Korea

Categorization of industrial heat pump for integrated simulation technology

Akihiro ICHIKAWA[a,*] , Jongsoo JEONG[b] ,Yoichi MIYAOKA[b], Seiichi YAMAGUCHI[b] and Kiyoshi SAITO[b]

a Dept. of Applied Mechanics, Waseda University, Shinjuku-ku, Tokyo, 169-8555, Japan
b Interdisciplinary institute for thermal energy conversion engineering and mathematics, Waseda University, Shinjuku-ku, Tokyo, 169-8555, Japan

Abstract

Recently, the demand for high-temperature heat in the industrial field has increased. Hence, improvement in conversion efficiency to generate thermal power is strongly required for surplus steam heat that is of significant value along with a process with low heat generation efficiency in factories. Given the aforementioned problems, a significant energy saving effect for the complete process is expected by introducing a heat pump to the thermal process. However, it is extremely difficult to experimentally examine the energy saving of the system due to cost and installation space. The final goal of the study is to construct integrated analysis technologies that can realize optimization of the system including the design and control system from the selection of various refrigerants and cycles via simulations. The study compared and examined introduction model cases applied to high temperature heat pump and confirmed that the annual simulation results were reasonable when compared to measured values.

Keywords: Waste heat recovery, Industrial heat pump, integrated simulation, Annual performance evaluation;

1. Introduction

With the development of heat pump technology, there is an increasing interest the introduction of heat pump technology to save energy in the industrial field. However, the existing factory is large in scale and includes a complicated configuration with many devices. Thus, it is necessary to quantitatively clarify several parameters including the type of heat pump and temperature zone that are required for a factory. Therefore, it is difficult to evaluate the effect of experimental heat pump introduction. Hence, the introduction method of heat pump and evaluation method of introduction effect are not established to date.

Therefore, in the study, we propose a heat pump introduction method and evaluation of the introduction effect in the industrial field via simulations. First, it is necessary to model a large and complex factory to realize this type of a simulation. Additionally, annual performance evaluation is performed when conducting simulations in countries with four seasons, such as Japan, and hence a significant amount of calculation is expected from the simulation period and size of the factory. In the analysis logic in the simulation, it is necessary to increase calculation speed while maintaining calculation accuracy. Furthermore, it is necessary for the built simulator to entail ease of use for the user to operate and output energy saving and economic efficiency prior to and after the introduction of the heat pump.

Given the aforementioned factors, the purpose of the study is to construct a general-purpose evaluation tool on the effects of introducing industrial heat pumps. The study focuses on the construction of basic system configuration patterns and construction of general-purpose analysis logic for the model.

* Corresponding author. Tel.: +81-3-5286-3259; fax: +81-3-5286-3259.
E-mail address: amnos-9am19az8@akane.waseda.jp

2. Method

2.1. Simulation overview

Fig. 1 shows the overall algorithm to evaluate the effects of introducing a heat pump. In the simulation in the study, the method to evaluate the effect of introducing heat pump is determined via dividing it into three main processes.

First, the target systems are classified by basic patterns. It is difficult to perform calculations with a model that divides element devices such as boilers and heat pumps into smaller elements, such as valves, heat exchangers, and compressors, because of the large scale of the target system. (In this paper, combustion-type heating devices including burners are collectively referred to as “boilers”) Additionally, accuracy can be obtained to analyze long-term performance such as annual performance although it is not practical due to the significant calculation time involved. Therefore, although the details are subsequently described, we aim to increase the calculation time by classifying the basic pattern proposed in the study with the boiler and heat pump as an element. Second, the target system is constructed by combining the classified patterns, and input variables are set for each pattern. Here, in order to correspond to the patterns classified in the previous stage, it is necessary to select variables that can be calculated even if the model of each pattern is divided. Finally, the heat pump introduction effect is calculated from the model of the target system and the input variables. Thus, even if the target is divided and modeled, it is still necessary to construct a method that decreases the calculation time by assuming annual performance calculations. Based on the aforementioned flow, it is possible to verify the effect of introducing the heat pump to the target system. The system before and after the introduction is compared, the performance parameters are graphed and displayed, and the user evaluates the introduction effect. Additionally, we construct a simulator that can be handled easily by any user and experts on heat pumps as a whole to save energy in the entire industrial field.

The following sections describe each process.

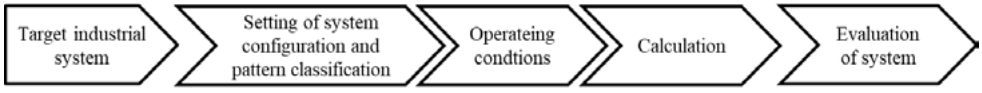


Fig. 1. Overall logic in the study

2.2. Pattern classification

In order to organize a complicated system configuration, a basic pattern is constructed based on various systems in which heat pumps are already introduced. In the study, we propose a patterning method based on four indicators (i.e., device, heating method, introduction use) via surveys of heat pump products developed for existing industries, literature surveys, and interviews with experts.

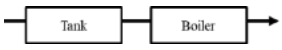
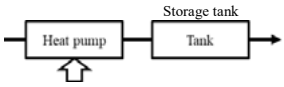
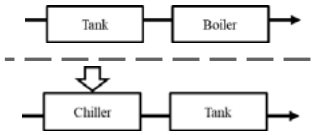
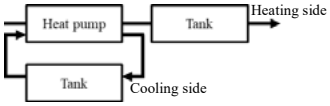
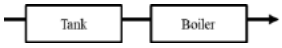
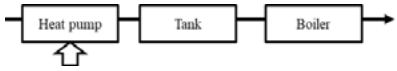
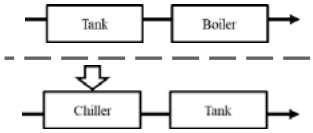
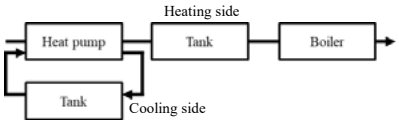
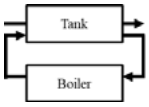
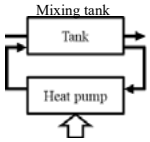
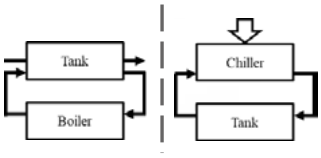
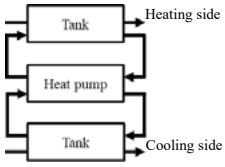
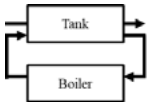
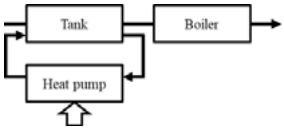
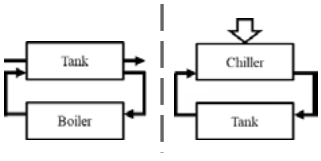
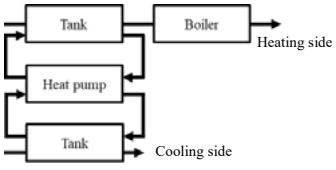
First, in order to compare the use of a conventional boiler with a heat pump, the former “device” is set to “boiler” and the latter is set to the “heat pump”. We then consider an eco-cute system that supplies hot water as a system that includes a heat pump. Household water heaters are popular although large-scale industrial eco-cutes were developed to generate hot water instead of boilers. This corresponds to an introduction example targeted in the study. In this type of a water heater, there is a difference in the heating method between storing hot water in the tank and temporarily supplying hot water. Therefore, the former “heating method” is set to “circulation” and the latter is set to “non-circulation”. Furthermore, the CO2 hot air generation heat pump was developed as an industrial heat pump that generates hot air without burning fuel like a boiler. The product makes it is possible to generate hot air at a higher temperature that consumes less fuel than before by replacing the boiler with a heat pump or heating the hot air preheated with a heat pump with a conventional heater. Therefore, the former “introduction use” is set as “replacement” and the latter is set as “preheating”. Finally, heat pumps that can realize applications including cold / hot water generation, hot water supply, and hot water tank heating with a single unit were developed using waste heat recovery technology. The heat pump can simultaneously extract cold and warm heat from the high temperature side and low temperature side such as recovering the heat released to the atmosphere during cooling operation by a conventional air conditioning system and using it as a heat source for hot water supply. Therefore, the “cold heat utilization” is set as “cold heat generation” and otherwise “hot heat generation” is set.

In the present study, a total of 16 patterns are proposed by combining the aforementioned "used equipment" (boiler, heat pump), "heating method" (circulation, non-circulation), "introduction use" (preheating, replacement), and "cool use" (cold heat generation, heat generation). However, if it corresponds to “cold heat

generation" and the device used is a boiler, then it is assumed that a refrigerator is present at the same time. The outline of the 16 patterns is listed in Table 1.

The user inputs the target system configuration via a combination of the 16 basic patterns. Similarly, it is possible to perform a comparison with the case where the heat pump is introduced by using the basic pattern and to clarify various effects of introduction.

Table 1. Basic pattern of system configuration

Type No.	Conventional type	Heat pump type
Type1 ・Non-circulation ・Replacement ・Hot heat generation		
Type2 ・Non-circulation ・Replacement ・Cold/Hot heat generation		
Type3 ・Non-circulation ・Preheating ・Hot heat generation		
Type4 ・Non-circulation ・Preheating ・Cold/Hot heat generation		
Type5 ・Circulation ・Replacement ・Hot heat generation		
Type6 ・Circulation ・Replacement ・Cold/Hot heat generation		
Type7 ・Circulation ・Preheating ・Hot heat generation		
Type8 ・Circulation ・Preheating ・Cold/Hot heat generation		

In these patterns figure, a white arrow indicates a heat source input. Each tank functions either as a storage tank or as a mixing tank, which is indicated in Table 1. If there is no tank, apply the pipe model to the tank. In all patterns proposed in this study, heating source is basically needed for heating process in the system, and cooling heat source is adjusted to get hot water or air as much as possible considering the heat balance between high and low temperature heat sources.

2.3. Simulation input and calculation

After classifying the target system configuration into patterns, input variables for boiler and heat pump elements in each basic pattern are set. Input and output variables for each element are shown in Tables 2 and 3, and the expressions used are shown below. Given that each pattern consists of a boiler, heat pump, and tank, models were created for the same. Various methods are available for mathematical model creation. In the study, in order to evaluate the annual performance, a model based on the pinch temperature was established in the heat transfer part of the heat pump to ensure sufficient validity while focusing on the calculation speed. As an example, the heat pump calculates variables including the heating capacity, COP, and primary energy consumption from the input variables listed in Table 3. In order to quantitatively evaluate the introduction effect under the same temperature and flow conditions in the heat pump type as compared with the boiler type, the simulator in the study mainly calculates the primary energy consumption as the output of each pattern.

Table 2. Input and output variables (Boiler)

Input			Output		
Variable	Code	Unit	Variable	Code	Unit
Boiler efficiency	η_{Boiler}	%	Heating capacity	Q	kW
Rated heating capacity	Q_{rated}	kW	Primary energy consumption	W_{prim}	kW
Inlet temperature	T_{in}	℃	Load factor	η_{load}	%
Outlet temperature	T_{out}	℃			
Mass flow	G	kg/s			

$$Q = G c_p (T_{out} - T_{in}) \tag{1}$$

$$W_{prim} = \frac{Q}{\eta_{boiler}} \times 100 \tag{2}$$

$$\eta_{road} = \frac{Q}{Q_{rated}} \tag{3}$$

Table 3. Input and output variables (Heat pump)

Input			Output		
Variable	Code	Unit	Variable	Code	Unit
Rated heating capacity	Q_{rated}	kW	COP	COP	
Inlet temperature at condenser	$T_{con,in}$	℃	Heating capacity	Q	kW
Outlet temperature at condenser	$T_{con,out}$	℃	Load factor	η_{load}	%
Mass flow	G	kg/s	Energy consumption	W	kW
Source temperature	T_{source}	℃	Primary energy consumption	W_{prim}	kW
Refrigerant	-	-			
Isentropic efficiency	η_{ad}	%			
Pinch point temperature at condenser	ΔT_{con}	℃			
Pinch point temperature at evaporator	ΔT_{eva}	℃			
Primary conversion efficiency	η_{prim}	%			

$$COP = \frac{h_{con,in} - h_{con,out}}{h_{con,out} - h_{eva,in}} \quad (4)$$

$$Q = Gc_p(T_{con,out} - T_{con,in}) \quad (5)$$

$$W = \frac{Q}{COP} \quad (6)$$

$$W_{prim} = \frac{W}{\eta_{prim}} \times 100 \quad (7)$$

2.4. Simulation output

By passing the system configuration and input variables with the aforementioned patterns to the analysis algorithm, simulation results including the total primary energy consumption and reduction rate of the entire system are output from each basic pattern of the input system. From the results output from the simulator, the effect varies based on how the heat pump is introduced into the target system, it is possible to evaluate and examine the overall system configuration that can achieve the maximum effect after the introduction of the heat pump. Additionally, it is possible to compare systems that already include heat pumps installed and changing the type, cycle configuration, and refrigerant used. For annual performance evaluation, there is a method to evaluate from the performance of each season, a method to evaluate from the performance of the representative day set every month, and a method to evaluate 365 days every minute or every hour. Thus, it is necessary to output data that can correspond to the output desired by the user and evaluation method. The simulator constructed in the study outputs time-series calculation results for each variable of the input system.

2.5. Verification

A prototype was specifically constructed for the simulator that enables evaluating the effects of introducing the industrial heat pump proposed above. Using the simulator, the measurement data of a factory where an industrial heat pump is already introduced was input to the simulator, and the analysis logic and calculation accuracy were verified. Figure 2 shows the flow chart of the target factory. In the factory, hot air from a gas burner is mainly used in the product drying process although a heat pump is used as part of the heating. Therefore, the classification described in 2.2 corresponds to Type4. Given that the measured values corresponding to the input items set in 2.3 are 1-minute intervals, the power consumption of the heat pump at 1-minute intervals is calculated for each representative day of 12 months. Furthermore, given that the measured value of power consumption corresponds to the total every 30 min, the calculated value was converted to an average every 30 minutes for comparison purposes. The results and measured values are compared to verify the accuracy of the simulator constructed in the study. The annual performance by the representative day of each month was calculated, and the representative day was set on the third Wednesday, which is used as the average value of each month. Additionally, we analyze the case of assuming a system configuration in which heating by a heat pump in the target factory is performed by a boiler. Based on the results, we evaluate the extent to which the primary energy consumption as a heat pump introduction effect can be annually reduced from the use of conventional boilers.

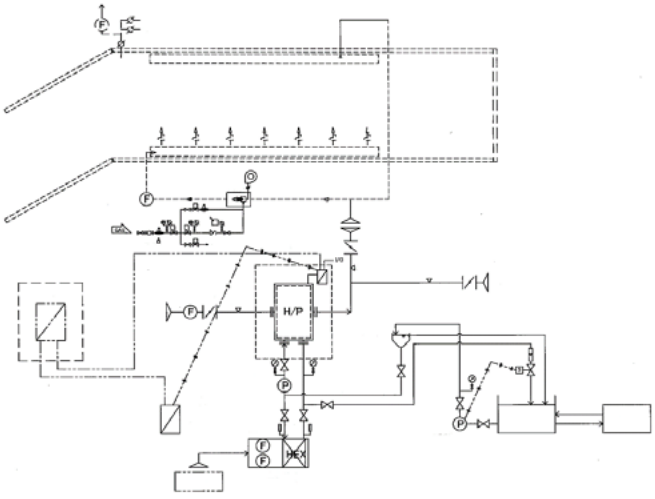


Fig. 2. Flow of the target factory

3. Simulation results and discussion

With respect to the power consumption of the heat pump, Fig. 3 shows the simulation results and measured values of daily transition for each representative day of the month and the total relative error of the day. Based on the results, in the analysis logic constructed in the study, the total annual power consumption multiplied by the number of factory operating days in each month corresponds to 5.47 GWh for the simulation result, 5.76 GWh for the measured value, and the relative error corresponds to 5.19%. With respect to Fig. 3, the power consumption on the representative day of each month is calculated lager than measured value except for March although the analytical values and the measured values exhibit similar fluctuation trends. Most of the time when the heat pump is operating in a stable manner, it exhibits an error of approximately 5%. Therefore, the analysis logic and calculation model of the simulator constructed the time exhibit sufficient calculation accuracy in practice. The reason why the calculated value exceeds the measured value is that the pinch temperature in the heat exchanger was set as constant to match the capability under the rated operating conditions defined by JIS. The COP is calculated as low, and thus it is necessary to set the pinch temperature as the performance of the heat exchanger smaller than the value determined in the rated operating conditions and set it based on the conditions of every minute. Hence, more accurate calculation results can be obtained via correcting the fluctuation of the heat exchanger pinch temperature under actual operating conditions. Henceforth, in order to achieve the specifically, we plan to set the pinch temperature input and investigate and correct the calculation logic.

Additionally, Fig. 4 shows a comparison of changes in the primary energy consumption before and after the introduction of the heat pump in June, when the relative error was the smallest, as the output of the simulator. Fig. 5 shows a comparison of annual primary energy consumption before and after the introduction of the heat pump.

As shown in Fig. 4, the primary energy consumption decreases by 35% per year with an error of 5.19% per year by introducing the heat pump to the target factory. In the simulation, a heat pump with a single-stage vapor compression cycle was modeled. However, in order to quantitatively evaluate the effects of introducing the heat pump in a wider range, it is necessary to model other models in the same manner as the proposed method.

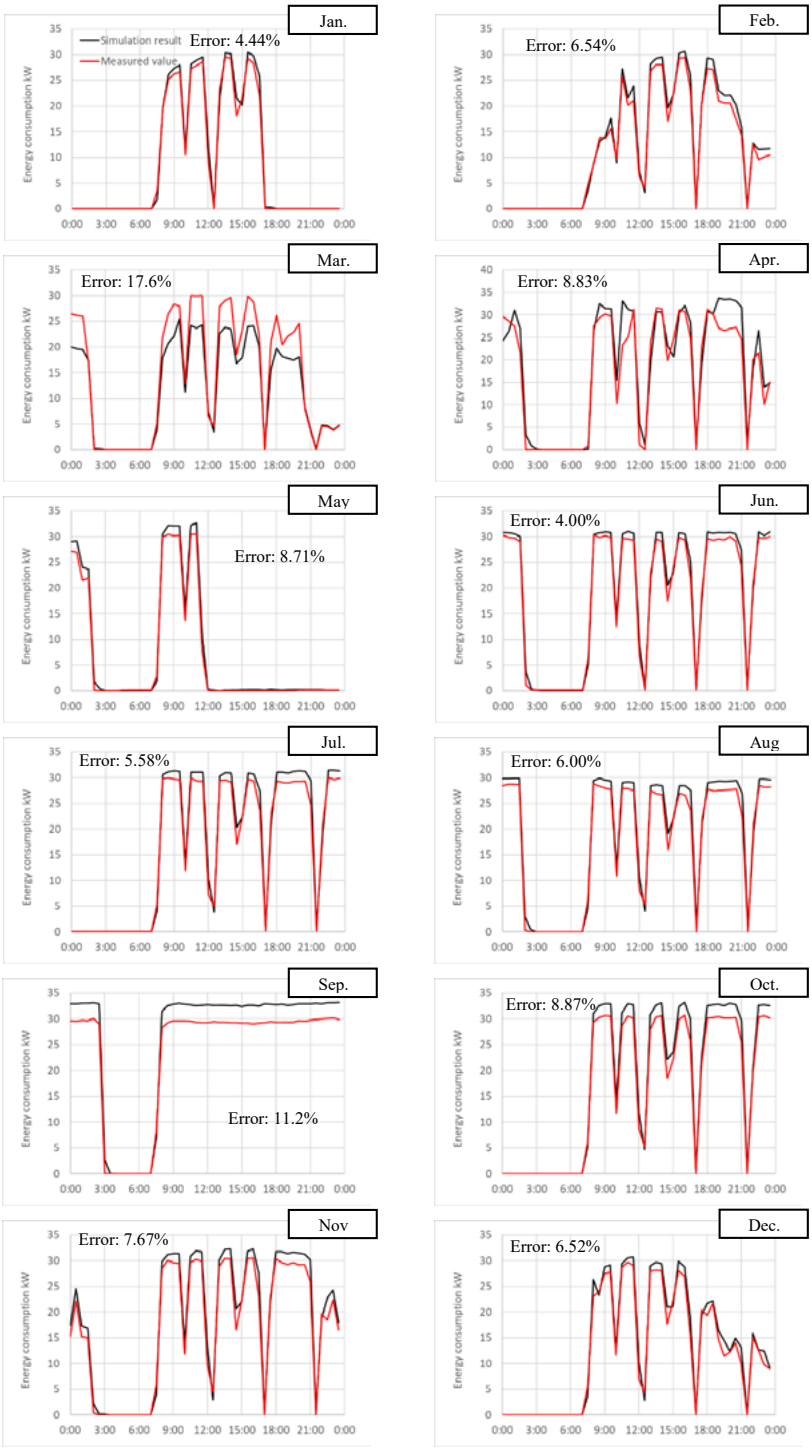


Fig. 3. Annual energy consumption fluctuation

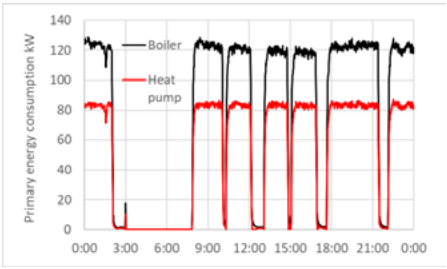


Fig. 4. Primary energy consumption fluctuation (June)

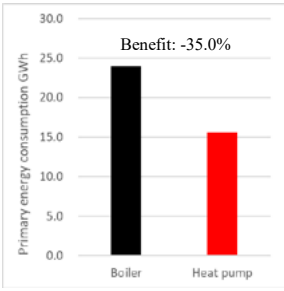


Fig. 5. Annual effect of introducing heat pump

4. Conclusions

In the study, we proposed 16 basic patterns that can categorize heat utilization systems including almost all boilers and heat pumps. Additionally, by incorporating the basic pattern model into the analysis logic, various system simulations are possible. Therefore, it was possible to quantitatively compare the primary energy consumption between a conventional system and new heat pump introduction system. In the study, we created an example that served as the basis for a simulator that incorporated the basic patterns and the built model and verified the accuracy by comparing the actual measurement data and simulation results at a factory where an industrial heat pump was already installed. Thus, the results that the annual power consumption (which is the output of the simulator) can be calculated with a relative error of 5.19% when compared to the actual measurement. Under the accuracy, the results indicated that the primary energy consumption decreased by 35% per year when compared to the case where the target factory was operated with a boiler under similar operating conditions. Henceforth, in order to further improve the accuracy of simulation calculations, we plan to develop and extend the model and specifically develop a simulator.

Acknowledgements

The study was the result of commissioned work by the New Energy and Industrial Technology Development Organization (NEDO). Additionally, when verifying the accuracy of the simulation, we received significant cooperation from Minami Denki Seisakusho Co., Ltd., Shikoku Electric Power Co., Ltd., and Shikoku Research Institute, Inc. for installation of measurement equipment and provision of various measurement data. The authors express their sincere appreciation to the aforementioned institutions.

Nomenclature

c_p	specific heat at constant pressure, kJ·kg^{-1}·K^{-1}
G	mass flow, kg·s^{-1}
h	specific enthalpy, kJ·kg^{-1}
Q	cooling capacity, kW
W	energy consumption, kW
T	Celsius temperature, ℃
η	efficiency, %

Subscript

In	inlet
Out	outlet
source	heat source

Air	air flow
Con	condenser, condensation
Eva	evaporator, evaporation
prim	primary
rated	rated
load	load

References

[1] Energy White Paper 2018, available from < https://www.enecho.meti.go.jp/about/whitepaper/2018pdf/>, (accessed on Oct. 29, 2018).
[2] ELECTRO-HEAT 2010 No.171, available from JAPAN ELECTRO-HEAT CENTER <http://www.jeh-center.org/eh_171.html＞

13th IEA Heat Pump Conference
May 11-14, 2020 Jeju, Korea

Development of LNG Vaporization Systems Applying Hybrid Ground Source Heat Pumps Combined Ground Heat Exchangers with Air-water Heat Exchangers

Takao Katsura[a*], Yutaka Shoji[a], Hitoshi Akai [a,b], Katsunori Nagano[a], Jun Shishido[c], Mitsuhiro Ishikawa[d], Yuichi Yashima[e], Koji Tanifuji[f]

[a] Hokkaido Univerisity, Kita13-Nishi 8, Kita-ku, Sapporo, 060-8628, Japan
[b] Fukushima Univerisity, Kanayagawa1, Fukushima, 960-1296, Japan
[c] Tohoku Electric Power Co., Inc., 1-7-1 Honcho, Aoba-ku, Sendai, 980-8550, Japan
[d] Hokkaido Electric power Co., Inc., Odori-Higashi 1, Chuo-ku, Sapporo 060-8677, Japan
[e] NIPPON GAS DEVELOPMENT CO., LTD, 4-2-1 Kyutaromachi, Chuo-ku, Osaka 541-0056, Japan
[f] ZENERAL HEATPUMP INDUSTRY CO., LTD., 121 Mishinden Odaka-cho, Midori-ku, Nagoya, 459-8001, Japan

Abstract

In order to reduce the gas consumption in LNG satellite stations, the authors have developed LNG vaporization systems applying hybrid ground source heat pumps (HGSHPs) combined ground heat exchangers (GHEXs) with air-water heat exchangers (AWHEXs). The heat pumps can vaporize the LNG with high efficiency because it is possible to vaporize the LNG by using the low-temperature hot water of around 25ºC. The ground source heat pumps (GSHPs) can supply the hot water stably even in the winter season due to no need of defrosting operation. In addition, the HGSHP system with AWHEXs can prevent the decrease of ground temperature due to the excess heat extraction. The authors constructed the field experimental apparatus and carried out the vaporization experiment with a HGSHP. The results indicated that it is possible to vaporize the liquid Nitrogen (Instead of LNG) by using hot water with the temperature of 25ºC and the low-temperature hot water supply with GSHP yields the reduction of energy consumption.

Keywords: Hybrid ground source heat pump; LNG vaporization; Ground heat exchanger; Air-water heat exchanger; Field experiment

1. Introduction

Recently, the number of facilities applying LNG satellite station is increasing in the case where the facilities has high gas demand such as factories. In some LNG satellite stations, it is necessary to burn the vaporized natural gas in order to supply the natural gas stably. In this case, 3~5% of the vaporized natural gas is used for burning, therefore, it is required to reduce the gas consumption for energy saving.

It is possible to reduce the energy consumption by applying the heat pump system because the natural gas can be vaporized by using the hot water with lower temperature compared to the usual hot water with the temperature of 60ºC. Especially, installation of GSHP systems is effective because of no need of the de-frosting operation. However, if the GSHP systems are applied for LNG vaporization, in which the heating demand is generated through the year, there may be a long-term decrease of ground temperature due to the excess heat extraction.

Therefore, the HGSHP system with AWHEXs is applied to prevent the decrease of ground temperature. Although the solar collectors that can absorb the solar heat are also used in the hybrid GSHP system [1], [2], the efficiency of the solar system drops during cloudy and rainy days. In addition, the solar heat cannot be collected during the night. In comparison, the AWHEXs can extract the heat from air even in the condition of

* Corresponding author. Tel.: +81-11-706-6284 ; fax: +81-11-706-6284.
E-mail address: katsura@eng.hokudai.ac.jp

cloudy or rainy weather if the air temperature is higher than the temperature of heat carrier fluid. It can recover the ground temperature by injecting heat regardless of the weather condition. In addition, the efficiency of heatpump can be improved compared to the conventional GSHP system if the hybrid GSHP provides heating in summer season. The authors constructed the field experimental apparatus of gas vaporization system with HGSHP and the experimental proof of gas vaporization with HGSHP was carried out. In addition, the energy saving effect of HGSHP was evaluated by using the result of experiment.

2. Outlines and advantage of system

Figure 1 shows a concept diagram of LNG vaporization system applying HGSHP. The system consists of heat pump units, GHEXs, AWHEXs, and LNG vaporization heat exchangers. Depending on the outside air temperature conditions, it is possible to select only the GHEXs or a combination of GHEXs and AWHEXs as the heat source. Then, the heat pump units supply hot water to the LNG vaporization heat exchangers and the LNG is vaporized. Here, the LNG vaporization heat exchangers are designed so that the hot water does not freeze even in the case where the hot water with lower temperature is supplied.

The following advantages of LNG vaporization system applying HGSHP are mentioned;

A. It is possible to obtain the heating output to stably vaporize the LNG.

B. There is no decrease of heating output and heating COP occurred by the de-frosting operation.

C. In summer season, the outside air with high temperature can be utilized as the heat source. In addition, the ground temperature surrounding GHEX can be recovered by injecting the surplus heat to the ground.

D. The hot water with temperature of 25ºC can be supplied from heat pump units because the LNG is vaporized with the hot water. Therefore, the energy efficiency and energy saving effect are larger than those in the common heating in which the hot water with temperature of 35~45ºC is supplied.

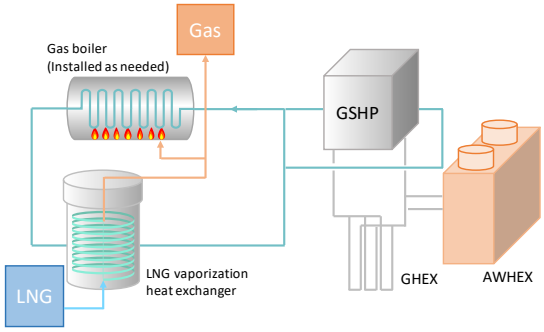


Fig.1 Concept of LNG vaporization system with hybrid GSHP system

3. Field experiment of gas vaporization system with HGSHP

3.1 Outlines of field experimental apparatus

The experimental apparatus of gas vaporization system with HGSHP shown in Figure 2 was constructed in the field of Hokkaido University in Sapporo city. The apparatus is a cut-down version of actual LNG vaporization system. In the experiment, the liquid nitrogen was used instead of LNG. Table 1 indicates the specification of heat pump unit (HP in Figure 2). The heat pump unit has two inverter compressors. The heat pump unit was connected to the two GHEXs with length of 100 m in the primary side and the vaporization heat exchanger in the secondary side, respectively. In addition, the AWHEX was connected between the heat pump unit and GHEXs. Therefore, it is possible to switch only the GHEXs or a combination of GHEXs and an AWHEX as the heat source. Table 2 indicates measurement points in the field experiment. The inlet and outlet temperatures and the flow rates in the primary side and the secondary side of heat pump unit were measured. By using the measured values of temperatures and flow rates, the heating output and the heat extraction rate were calculated. Additionally, the mass flow rate of vaporized nitrogen gas and the temperatures

before and after vaporization were measured, so that the consistency between the heating output from heat pump unit and the amount of heat used for vaporization could be confirmed. The heat pump COP and system COP were also evaluated by measuring the electric powers of a heat pump unit, circulation pumps, and a fan of AWHEXs.

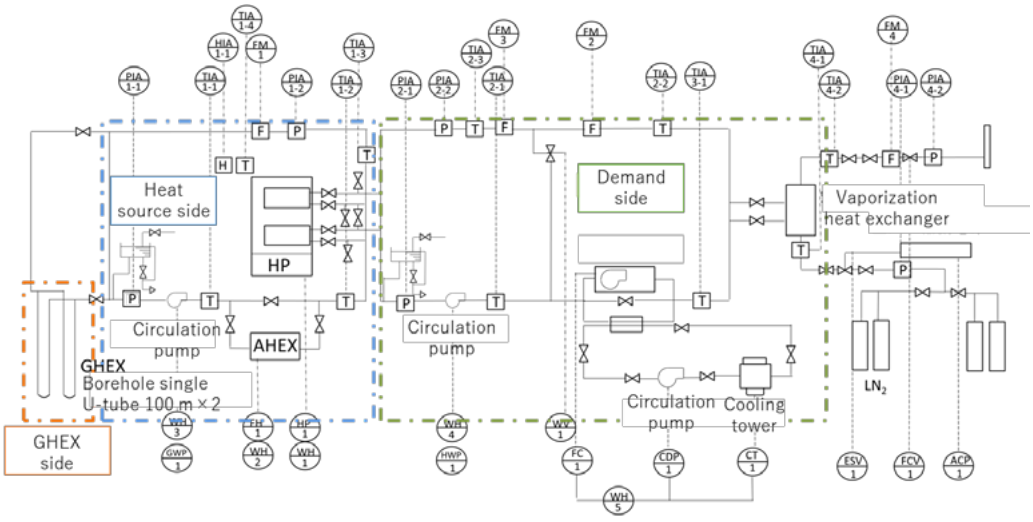


Figure 2 Diagram of field experimental apparatus

Table 1 Specification of heat pump unit

Heat exchanger	Plate heat exchanger
Flow rate	21 L/min
Rated heating output	13.6 kW
Rated electric power	4.2 kW

Table 2 Measurement items

Equipment (Number)	Measuring items	Unit
Pt-100 sensor TIA1-1	Outlet temperature of GHEXs	°C
Pt-100 sensor TIA1-2	Inlet temperature of HP in the primary side	°C
Pt-100 sensor TIA1-3	Inlet temperature of GHEXs	°C
Pt-100 sensorTIA1-4	Outlet temperature of HP in the primary side Ambient temperature	°C
Pt-100 sensor TIA2-1	Outlet temperature of HP in the secondary side	°C
Pt-100 sensorTIA2-2	Outlet temperature of vaporization heat exchanger or fan-coil unit	°C
Pt-100 sensor TIA2-3	Inlet temperature of HP in the secondary side	°C
Pt-100 sensor TIA4-1	Liquid nitrogen temperature	°C
Pt-100 sensor TIA4-2	Nitrogen gas temperature	°C
Flow meter FM-1	Flow rate in the primary side of HP	L/min
Flow meter FM-3	Flor rate in the secondary side of HP	L/min
Flow meter FM-4	Flow rate of nitrogen gas	Nm^3/h
Power meter WH-1	Electric energy of HP	kWh
Power meter WH-2	Electric energy of fan of AWHEX and circulation pump	kWh

3.2 Conditions of field experiment

Table 3 indicates conditions of field experiment. The experiments V1-1~V1-5 were carried out in winter season and only the GHEXs were used as heat source. The supply temperature of hot water and the mass flow rate of nitrogen gas were changed. The experiments V2-1~V2-3 were carried out in summer season and a combination of GHEXs and an AWHEX were used as heat source. The mass flow rate of nitrogen gas was changed.

Table 3 Conditions of field experiment

Test number	Test period	Heat source	Hot water temperature [°C]	Nitrogen flow rate [Nm³/h] (Load ratio)
V1-1	19/1/23 10.30-11.00	Ground	45	90 (100%)
V1-2	19/1/23 11.37-12.07		35	90 (100%)
V1-3	19/1/23 14.00-14.30		25	90 (100%)
V1-4	19/1/23 14.30-14.50			68(75%)
V1-5	19/1/23 15.06-15.36			45(50%)
V2-1	18/8/8 11:20~12:00	Ground +Air	25	90 (100%)
V2-2	18/8/8 12:00~13:00			45(50%)
V2-3	18/8/8 13:00~14:00			30(33%)

3.3 Results and discussions

Figure 3 shows the inlet and outlet temperatures (TIA2-1, TIA2-3) and the flow rates (FM-3) in the secondary side of heat pump unit in the experiments V1-3~V1-5. The variations of nitrogen gas temperature (TIA4-2) and mass flow rate of nitrogen gas (FM-4) are also drawn in Figure 3. The mass flow rate was close to the set value and the gas temperature changed from 10°C to 20°C. The liquid nitrogen temperature was about -170°C, therefore, it was confirmed that the liquid nitrogen was vaporized. Next, the outside air temperature (TIA1-4), the inlet and outlet temperatures (TIA1-2, TIA1-3), and the flow rates (FM-1) in the primary side of heat pump unit in the experiments V1-3~V1-5 were demonstrated in Figure 4. Although the inlet temperature in the primary side decreased, the temperature was higher than the outside air temperature. In addition, Figure 5 indicates the heating output, the heat extraction rate, and the electric power of system (Heat pump unit + Circulation pump in the primary side) in the experiments V1-3~V1-5. In the experiment V1-3, the heating output was approximately 12 kW and the electric power of system was approximately 2.2 kW, respectively. The system COP, which is the ratio of heating output to electric power of system, was approximately 5.5. This result indicated that the high value of system COP was obtained by supplying the hot water with temperature of 25°C even in the winter season.

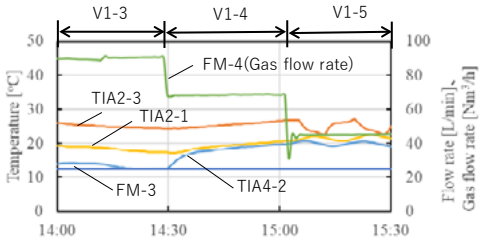


Figure 3 Variation of temperature and flow rate in the secondary side

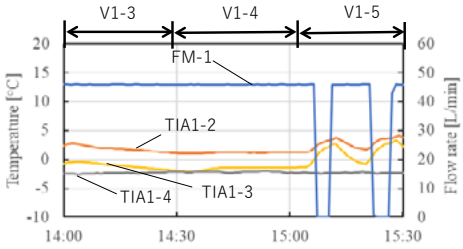


Figure 4 Variation of temperature and flow rate in the primary side

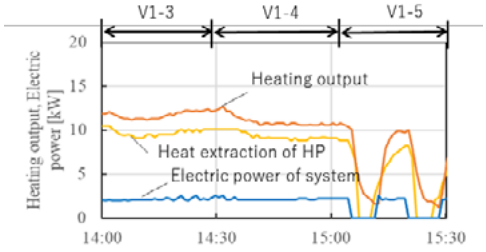


Figure 5 Variation of heating output, heat extraction and electric power

Figure 6 shows the inlet and outlet temperatures (TIA2-1, TIA2-3) and the flow rates (FM-3) in the secondary side of heat pump unit in the experiments V2-1~V2-3. The variations of nitrogen gas temperature (TIA4-2) and mass flow rate of nitrogen gas (FM-4) are also drawn in Figure 6. The mass flow rate was almost kept at the set value and the gas temperature varied from 10ºC to 25ºC. Therefore, the liquid nitrogen was stably vaporized as well as the experiments V1-3~V1-5. The outside air temperature (TIA1-4), the inlet and outlet temperatures (TIA1-2, TIA1-3), and the flow rates (FM-1) in the primary side of heat pump unit in the experiments V2-1~V2-3 were demonstrated in Figure 7. The inlet temperature was approximately 20ºC higher than the temperature in the experiments V1-3~V1-5. This was due to the heat extraction from the AWHEX. In addition, Figure 8 indicates the heating output and the electric power of system (Heat pump unit + Circulation pump in the primary side + Fan of AWHEX) in the experiments V2-1~V2-3. Although the heating output was not constant, the average heating output in the experiment V2-1 was almost as much as the heating output in the experiment V1-3. Figure 9 shows the heat extraction rates of heat pump unit, GHEXs, and AWHEX. The heat extraction rate of AWHEX were much higher than the heat extraction rate of heat pump unit. This result indicated that the surplus heat from AWHEX was injected to the ground via the GHEXs.

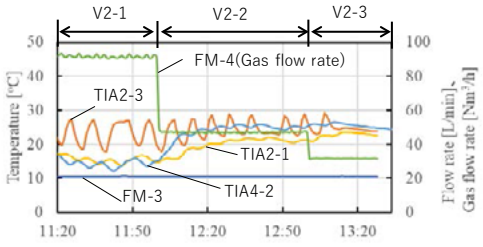


Figure 6 Variation of temperature and flow rate in the secondary side

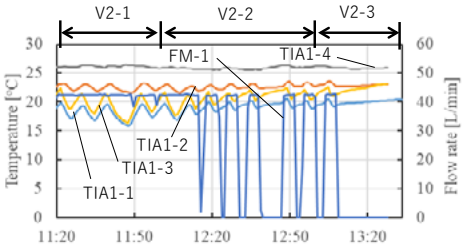


Figure 7 Variation of temperature and flow rate in the primary side

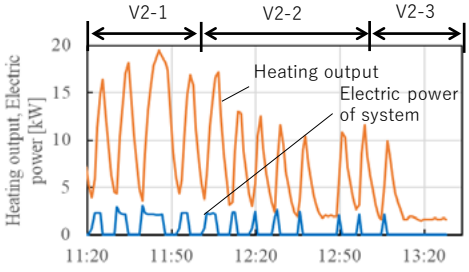


Figure 8 Variation of heating output, and electric power

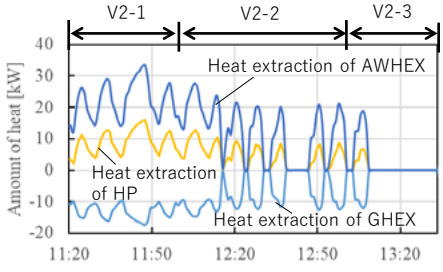


Figure 9 Variation of heat extraction

Table 4 summarizes the heating output from heat pump unit, the heating output for vaporization, the electric power of system, and the system COP(SCOP). The heating output from heat pump unit and the heating output for vaporization were almost equality. Therefore, the heating output from heat pump was used for vaporization. When the SCOPs in the experiments V1-1~V1-3 were compared, the SCOP in V1-3 (Hot water temperature: Approx. 25ºC) was approximately 1.3 times of the SCOP in V1-2 (Hot water temperature: Approx. 35ºC) and approximately 1.7 times of the SCOP in V1-1 (Hot water temperature: Approx. 45ºC). From this result, the improvement of SCOP by supplying the hot water with lower temperature was confirmed. In addition, the SCOPs in the experiments V2-1~V2-3, in which the AWHEX was used in summer season, were more than 10. Basis on these results, the primary energy consumptions in V1-3 and V2-1 were calculated and were compared to the conventional gas boiler system (Boiler efficiency: 0.85). If the primary energy consumption per the electric energy was set as 9.76 MJ/kWh [3], the energy saving effects were approximately 57% in V1-3 and approximately 76% in V2-1, respectively.

Table 4 Summary of field experiment

Test number	Heating output from GSHP [kW]	Heating output for vaporization [kW]	System electric power [kW]	SCOP
V1-1	13.3	13.6	4.2	3.2
V1-2	12.6	13.1	2.9	4.3
V1-3	11.9	12.6	2.2	5.4
V1-4	11.0	10.0	2.4	4.6
V1-5	5.5	6.5	1.1	5.0
V2-1	11.4	12.4	1.1	10.8
V2-2	6.7	6.2	0.5	13.4
V2-3	3.0	3.5	0.2	15.0

4. Summary

1) The outlines and advantages of LNG vaporization system with HGSHP were explained.

2) By using the field experimental apparatus of vaporization system with HGSHP, the authors tested the vaporization of nitrogen liquid instead of LNG. As the result, it was possible to stably vaporize the liquid nitrogen by supplying the hot water with temperature of 25°C. In addition, when the hot water temperature was kept at around 25°C, the SCOP of HGSHP system was 5.4 in the winter season. This SCOP was approximately 1.7 times of the SCOP in the case where the hot water temperature was around 45°C.

3) The SCOPs in the experiments V2-1~V2-3, in which the AWHEX was used in summer season, were more than 10.

4) Basis on the field test result, the primary energy consumptions were calculated and were compared to the conventional gas boiler system. When the hot water temperature was around 25°C, the energy saving effects were approximately 57% in winter season (Only GHEX was used) and approximately 76% in summer season (Combination of GHEX and AWHEX was used), respectively.

References

[1] Farzin M. Rad, Alan S Fung, Wey H. Leong: Feasibility of combined solar thermal and ground source heat pump systems in cold climate, Canada. Energy and Buildings, Volume 61, 2013, pp. 224-232
[2] Aleksandar Georgiev, Rumen Popov, Emil Toshkov: Investigation of a hybrid system with ground source heat pump and solar collectors: Charging of thermal storages and space heating, Renewable Energy, 2018,
[3] List of coefficients in global warming measure report system http://www8.kankyo.metro.tokyo.jp/ondanka/report/pdf/keisuuitiran.pdf, 2019-3

13th IEA Heat Pump Conference
April 26-29, 2021 Jeju, Korea

Feasibility of using ground source heat pumps in heating and cooling of residential buildings

Seama Koohi-Fayegh*
OntarioTech University, 2000 Simcoe St. N, Oshawa, ON L1G 0C5 Canada

Abstract

In many building types, heating and cooling demands are often unbalanced and using a single ground source heat pump (GSHP) to meet both heating and cooling demands introduces various options to designers in sizing the ground heat exchangers coupled to the heat pumps. Due such unbalanced heating and cooling demands, use of ground source heat pumps may not be feasible, or not financially feasible if coupled with a supplementary system. In this study, the impact of heating and cooling demands typical of a residential building on the feasibility of use of ground source heat pumps is studied. A typical residential building block in Ontario, Canada is modeled in eQuest 3.65. Simulation results of the models for space heating and cooling demand are used in RETScreen to arrive at a combination of technologies that may be able to provide heating and cooling to the buildings. Comparison of the approximate cost estimations for the various design options show the importance of employing customized coupling strategies in order to take maximum advantage of ground source heat pump systems and promoting their financial feasibility.

Keywords: Ground-source heat pumps; Heating and cooling; Balanced; residential; eQuest; RETScreen;

1. Introduction

As governments place more stringent requirements on energy performance of buildings and provide financial incentives for construction of sustainable buildings, use of more efficient heating and cooling energy systems in building designs is becoming more popular compared to a decade ago. For example, City of Toronto has mandated employment of renewable energy technologies in city properties [1]. Ground source heat pumps (GSHPs) seem to be suitable options to promote sustainable building designs and their financial and technical feasibility is assessed with varying levels of detail in several studies [2][3][4]. For example, in order for their use to be financially feasible over the system life cycle, the variation in heating and cooling load of the building need to be reviewed. Accurate estimation of building energy performance is possible with computer programs that are able to perform hourly building energy simulations, such as eQuest 3.65 and Hourly Analysis Program (HAP) [4]. eQuest 3.65 is a computer program based on a solver engine developed for the US Department of Energy and performs hourly building energy simulations [5]. While it has been used in a number of scholarly articles to show building energy performance and/or to calculate building heating and cooling loads [3,6-7], it has not been used in combination with other software to show financial feasibility of GSHPs. RETScreen [8] provides a tool to perform technical and financial feasibility analyses of various energy system types and has been used in several scholarly studies [4,9-12]. This software is used for many feasibility analyses in early stages of the design when various heating and cooling options are explored. Another software used for analysis of the systems when system details are available is TRNSYS; however, this software is often used by scholars aiming to evaluate existing designs or systems [3]. Except a few studies on economic analysis of GSHPs [13], their financial feasibility has not been widely studied and not compared for various design options as the current study has.

In the preliminary stage of building design, i.e., design development stage, a preliminary feasibility assessment is sometimes performed to estimate the financial feasibility of use of geothermal heat pumps. The

* Corresponding author. Tel.: +1-905-721-8668x5518
E-mail address: seama.koohi@ontariotechu.ca.

1

outcome of this feasibility study is important since it would consequently impact the decision whether to select geothermal heat pumps as the optimum candidate for a given building type or not. The objective of the current article is to show how sensitive such preliminary analysis outcome is to the selection of parameters such as building loads, design strategy studied for a given building load, and system component costs. Some details are intentionally not included in the study to ensure that the conclusions are based on what is indeed the limited inputs in the ground source heat pump feasibility analyses. If geothermal heat pumps are shown to be financially feasible, further detailed analysis needs to be performed. However, in some cases, the preliminary feasibility analysis may not show satisfactory financial feasibility for incorrect reasons. It may be concluded that some parameters need to be the subject of more focus to ensure the preliminary feasibility analysis shows results that are accurate enough. In this study, the impact of heating and cooling demands typical of a residential building in Ontario, Canada, selected design strategy, and system component costs on the financial feasibility of use of ground source heat pumps is studied.

2. Method

The method used in this study consists of two parts: estimation of heating and cooling energy requirements and feasibility of providing such energy, fully or partially, through ground-source heat pump(s).

2.1.Building energy consumption

In this section, information regarding the characteristics of typical newly-built residential buildings in Ontario, Canada, such as floor area and HVAC systems used are included. In addition, the general method used in estimating the heating and cooling energy consumptions of the building block is provided.

The information used in the models includes the total residential building area (total and square footage), building envelope characteristics, building use characteristics and number of residential units. A summary is provided in Table 1. Note that while much detail is included in the model to generate hourly heating and cooling demands of the building, only main ones are included in this section. Further details on the building are deemed unnecessary for the purpose of discussions in this article and the level of accuracy aimed.

Table 1: Building general characteristics

Building Specification	Value
Site location	Toronto, Ontario[1]
Total building area	3135 m^2
Building footprint	784 m^2
Percentage of building residential area	90%
Number of houses	32
Floor height	3.0 m

[1] weather file for Toronto in 2016 is used in the eQuest model.

Using the information in Table 1, the heating and cooling demands of the building block is calculated in eQuest 3.65. The eQuest model inputs are categorized in three section and are selected from building standards currently used in Ontario, Canada (see Table 2). They are building envelope characteristics, internal gains, outdoor air requirements and air distribution systems.

Table 2: Building envelope and use characteristics

Building characteristic	
Weather file	Toronto, Ontario
Envelope	NECB[1] 2015 standards
Internal gains	NECB 2015 standards
Window-to-wall ratio	20%

[1] National Energy Code of Canada [14]

2.2.Heating and cooling provision using ground source heat pumps

Once the space heating and cooling loads are estimated for the building block, the model is further developed in RETScreen to include the heating and cooling systems. A base case and four cases with various ground source heat pump strategies are investigated (see Table 3). Note that the information listed in the table are based on RETScreen database that is supported by available heat pump models. However, performance details of such heat pumps are not included in the analysis as in [15][16]. For example, an average COP for heating is used for calculation of the electricity requirements of the heat pump in the heating mode and seasonal load variations and their impacts on the performance of the heat pump is not accounted for. As a result, much of the details of a heat pump system such as refrigerant type and compressor type are not included in the current article. Such technical detail on various heat pump models can be found on the heat pump manufacturer websites such as the one used in the current article [17], but is not included in preliminary feasibility models. It is only after a feasibility analysis shows positive results of feasibility of use of ground source heat pumps that inclusion of details of heat pump performance are included in the model. The systems used as the base case, are heating and cooling systems typical of those used in conventional townhomes built in Canada. The strategies are selected based on individualized versus centralized systems. Individual systems refer to heating and cooling systems that that are installed in each townhome and only meet the needs of that individual townhome. Central systems refer to one system for heating and/or cooling all townhomes. The strategies are also based on how heating and cooling energy demand is covered. In many locations such as in Toronto, Ontario, annual heating and cooling demands of residential buildings cannot be covered using a single ground source heat pump with heating and cooling capacities equal to the demand. In such cases, GSHP systems can either be sized for cooling demand or the heating demand. In Toronto, Ontario, residential buildings have larger heating demands than cooling ones. However, when using a heat pump to provide heating and cooling to the building, the amount of heat that is exchanged with the ground is larger during cooling than during heating. This is due to the fact that the energy that is transferred to the ground via a heat pump in the cooling season includes the compressor energy as well as the energy extracted from the space which increases the energy transfer to the ground. Similarly, the energy that is delivered to the space in the heating season includes the compressor energy as well which reduces the amount of energy needed from the ground. In order to keep the heat exchange between the building and the ground balanced, two strategies arise in sizing the GSHP: sizing for heating demand and for cooling demand. When the systems are sized for cooling demand, theoretically all the heat removed from the space is transferred to the ground and only some of that is used to meet the heating demand in the heating season while the rest is rejected to the outside air when not needed. This is to avoid temperature rise in the ground as the cycle repeats seasonally. In this case, the energy transferred to the ground in the cooling season is first calculated as

$$Q_{g,inj} = Q_{sp,c} + \frac{Q_{spc,c}}{COP_C} \quad (1)$$

where $Q_{g,inj}$, $Q_{sp,c}$, and COP_C are heat to be transferred to the ground (heat injection), space cooling needs, and coefficient of performance of the heat pump in cooling mode, respectively.

In this case, the heat available for heating is more than needed in the space and is calculated as:

$$Q_{g,ext} = Q_{g,inj}\left(\frac{COP_H}{COP_H - 1}\right) \quad (2)$$

where $Q_{g,ext}$ and COP_H are heat to be extracted from the ground and coefficient of performance of the heat pump in heating mode, respectively.

Table 3: Building envelope and use characteristics

		Heating system	Cooling system	Peak cooling system
Case 0		Furnace	AC [3]	
Base system	Ind.[1]	80% efficiency	COP 3	
Energy source		Gas	Electricity	
Case 1		GSHP [4]	GSHP	
	Ind.	COP_H 3.2	COP_C 4.5	
Energy source		Electricity	Electricity	
Case 2		GSHP	GSHP	AC

3

	Ind.	COP_H 3.2	COP_C 4.5	COP 3
Energy source		Electricity	Electricity	Electricity
Case 3		GSHP	GSHP	
	Cen.[2]	COP_H 3.2	COP_C 4.5	
Energy source		Electricity	Electricity	
Case 4		GSHP	GSHP	AC
	Cen.	COP_H 3.2	COP_C 4.5	COP 3
Energy source		Electricity	Electricity	Electricity

[1] Ind. Individual system for each dwelling

[2] Cen. Central system for all dwellings

[3] AC Vapor compression air conditioner

[4] GSHP Ground source heat pump

The additional heat that need to be rejected to the outside air is calculated as

$$Q_{additional\ heating} = Q_{g,ext} - Q_{spc,h} \tag{3}$$

where $Q_{spc,h}$ is the space heating need.

Alternatively, when the systems are sized for heating demand, only part of the heat removed from the space in the cooling season is transferred to the ground via a GSHP. The amount of heat corresponds to the heating energy demand during the heating season. The rest of the space heat in the cooling season could be removed via a vapor compression air conditioning unit. In this case, the energy transferred from the ground in the heating season is first calculated as

$$Q_{g,ext} = Q_{sp,h} + \frac{Q_{spc,h}}{COP_H} \tag{4}$$

In this case, the heat allowed to be rejected to the ground, in order to maintain balanced ground temperature over one heating and cooling cycle, ($Q_{\mathrm{spc,c,al}}$) is less than space cooling demand as and is calculated as:

$$Q_{spc,c,al} = Q_{g,ext}\left(\frac{COP_C}{COP_C + 1}\right) \tag{5}$$

where $\mathrm{COP_C}$ is the coefficient of performance of the heat pump in cooling mode. The additional heat that needs to be provided via a cooling system other than the ground source heat pump (e.g., and air conditional unit) is calculated as

$$Q_{cooling\ deficit} = Q_{spc,c} - Q_{spc,c,al} \tag{6}$$

Note in Table 3 that the values used for efficiency of systems, are those typically found in many manufactured systems available in Canada. In addition, it must be noted that that the use of seasonal COPs in the current feasibility analysis is only acceptable for analysis done in design development stage where no detailed design information is available. Once detailed designs are available, a more thorough analysis must be performed to validate the COPs used for the ground source heat pump that vary based on ground temperature variation as heat is stored and collected from the ground.

In cases 2-4, a ground heat exchanger component is modeled in RETScreen which uses the heating and cooling demand calculated in the previous section and approximates the size of heat exchangers needed to exchange the required heat with the ground. Such analysis could become very complex and required use of specialized numerical methods and tools to estimate the size of the heat exchanger. Such accurate analysis is often encouraged for detailed design of ground source heat pump systems, but is often not used for preliminary feasibility analyses preceding the design stage. For this reason, the simplified method used to approximately estimate the heat exchanger length in RETScreen is considered satisfactory for this study. In the current study, boreholes, i.e., vertical ground heat exchangers (shown in Figure 1), are used in the model due to their small land area requirements compared to horizontal ground heat exchangers. While horizontal heat exchangers offer better financial benefits, their use in buildings with small outdoor land area (e.g., backyard) may not be technically feasible. Ground properties for clay rich soil are used in the model as they are closest to the type

of soil observed in north Toronto area when reviewing cross-section of geological conditions in Toronto [21]. The soil properties used in the model are listed in Table 5. Assumptions made in the heat exchanger model as well as estimated calculated length for the boreholes are included in Table 6.

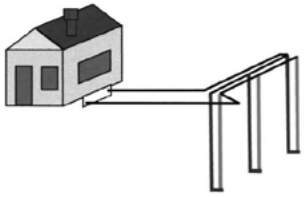


Figure 1: Schematic of vertical ground heat exchangers [22]

2.3.Other system assumptions

The pumping head is calculated based on the length of the boreholes and 15 m of head is added to the pumping head to account for the pressure losses in piping. The mean ground temperature is assumed to vary from 7.5°C by an altitude of 21.4°C on the ground surface with variations decreasing to zero at depths more than 15 m. The temperature of the water flowing into the heat pump is assumed as 0°C and 25°C for heating and cooling modes, respectively. The variation in the ground temperature as heat is injected and extracted from the ground is not accounted for in RETScreen. Such detailed analysis would not be performed at the early stages of design and is therefore neglected in the current study.

2.4.System cost estimation

Once technical specifications regarding the heating and cooling systems are included, capital and operating costs are included in the RETScreen model to analyse the impact of various system selection strategies on financial feasibility of the systems. A summary of the cost information used to compare the various selection strategies is provided in Table 4.

Table 4: Capital and operating costs used in the model [8, 18-20]

Item	Cost
Electricity	$0.13 /kWh
Natural gas	$0.30 /m^3
Fuel cost escalation rate	4.5%
Natural gas furnace	$88 /kW Heating
Heat pump	$350 /kW heating[1]
Vapor compression air conditioner	$350 /kW cooling[1]
Ground heat exchanger loop - pipe	$4 /m
Ground heat exchanger loop – drilling and grouting	$21 /m
Ground heat exchanger pump	$800/kW
Townhouse unit sub-meter	$400 /house
Central heating/cooling plant (sub-meter and piping)	$6000
Operation and maintenance cost	$2-3/ m^2 [2]
Inflation rate	2%
Discount rate	3.5%
Debt ratio	30%
Debt interest rate	3%
Debt term	20 years

[1] 10% reduction in capital costs are assumed for central systems

[2] space unit area

In the next section, a summary of preliminary findings of the RETScreen model (e.g., as system size information) are provided.

3. Results and Discussions

The method described in the previous section is used for a base case and four cases with various ground source heat pump design strategies to compare their financial performance.

Table 5: Thermal properties of soil

Characteristic	Value	
Conductivity	1.3	W/m°C
Diffusivity	6.45 x 10^{-7}	m^2/s
Density	2100	kg/m^3
Heat capacity	0.96	kJ/kg°C

Table 6 Ground heat exchanger characteristics

Characteristic	Value
Borehole diameter	150 mm
Borehole total length	920-1420 m[1]
Borehole distance	12 m

[1] Estimated in RETScreen

Conventional furnace heating and compression cooling were assumed as a baseline for the townhouses. As shown in Table 3, the baseline energy systems use natural gas and electricity to operate.

Simulation results of heating and cooling loads in eQuest are shown in Figure 2. As expected in Ontario, Canada, the heating and cooling maximum space demand for the building in the occurs in months of January and July and are approximately 73 kW and 77 kW, respectively. This is typical of residential systems in Ontario, Canada, weather where the cooling loads are larger than the heating loads. Such effect is often magnified in other building use types such as office buildings where there is much internal heat gains to be removed by the cooling systems.

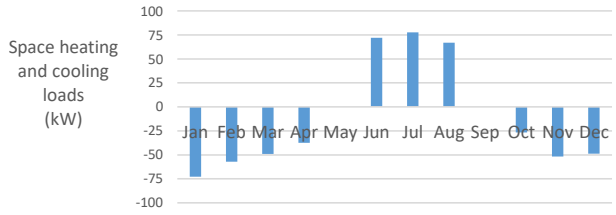


Figure 2: Simulation results of heating and cooling loads for the residential building block

As explained in the previous section, in order to keep the heat exchange between the building and the ground balanced, either the heat pump needs to be sized for cooling and be oversized for heating, or the system must be sized for heating and a supplementary air conditioning unit be used for cooling. In this study, both options are investigated since the first has reduced the capital and operating costs due toavoidance of a secondary cooling system in addition to the ground source heat pump, but has larger ground heat exchangers which generally contribute to about 80% of capital costs. The latter case, i.e., sizing for heating and using a supplementary cooling system, results in a smaller size ground heat pump, and therefore, fewer boreholes that would need to be installed for the smaller heat pump. The distribution of cooling design capacities are shown in Figure 3 for Cases 1 and 2, respectively. It is seen that compared to sizing the GSHP for cooling (Figure 3a), when the system is sized for heating, only a portion of cooling demand can be met by the GSHP and an additional cooling system, in this case a vapor compression air conditioner, is needed to cover the remaining cooling demand (Figure 3b). If heating and cooling loads were each 10% lower and higher than the case modeled in the current study, respectively, the size of the supplementary cooling system would become more pronounced. It is shown in Figure 3c that the additional 3% cooling demand covered by a supplementary

system in Figure 3b would increase to 23% in such case. This would affect the cost and financial feasibility of the hybrid system design where the cooling loads are met by GSHP and a supplementary cooling system.

It should be noted that the distribution of cooling loads for the 10% lower and higher heating and cooling demands would resemble that of Figure 3a for Case a where GSHP is sized for cooling demand. Such case, however, would result in a much more oversized system for heating.

Figure 4 shows the amount of heat available in the ground to meet the building heating needs. The additional heat available must be removed from the ground to ensure balanced ground temperatures over the annual operation of GSHPs. In cases where there is no use for this additional heat, it can be transferred to the outside air. Comparing Case 1 and Case 2 with cooling distributions in Figs. 4a and 4b shows how a perfect balance of heat exchange with the ground may never be achieved when using a GSHP. As expected, Figure 3c and the 10% cases in Figure 4 show that the larger the imbalance between space heating and cooling demands, the larger the supplementary system capacity is when sizing the GSHP for heating, or the larger the amount of heat that needs to be removed from the ground when it is not needed when sizing the GSHP for cooling.

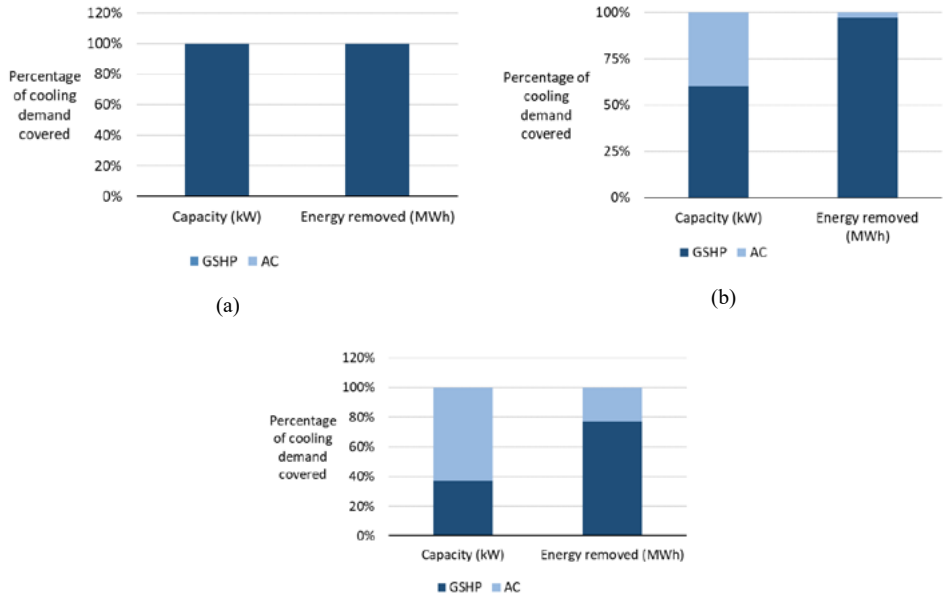


Figure 3: Distribution of cooling design capacities for (a) Case 1, GSHP sized based on cooling demand, (b) Case 2, GSHP sized based on heating demand, (c) Case 2, Case 2 for 10% more cooling demand and 10% less heating demand.

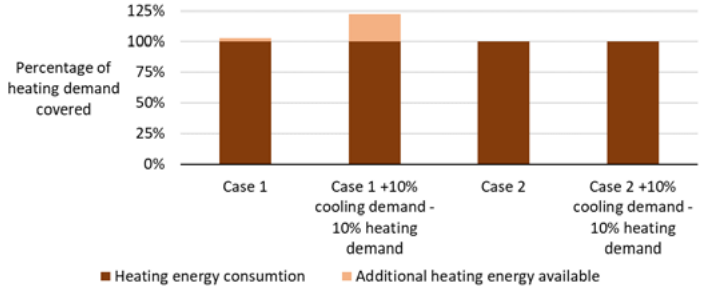


Figure 4: Distribution of heating energy available from the GSHP in four cases

To understand how these various design options contribute to the cost of the system and to its financial feasibility, Figure 5 shows the cumulative cash flow diagram for Case 1, when GSHP is used for heating and cooling with no supplementary cooling system. It is shown that the payback period for this case is about 7 years which could lead to the conclusion that the GSHP alone with no supplementary cooling system and oversized for heating would be profitable. Similar analysis on Cases 2-4 were made and the results for estimated payback periods are shown in Figure 6. It is seen in Figure 6 that although sizing for cooling demand and use of a supplementary cooling system (Case 2) is expected to result in lower capital costs due to smaller ground heat exchangers (estimated 18% lower size of the ground heat exchangers), it would still result in higher costs for the case in the current study. This is due to the higher costs associated with maintenance of air conditioners compared to GSHPs as well as the larger capital costs associated with two cooling systems as opposed to one GSHP (Case 1).

To examine how such conclusions would vary if a central system was used for Cases 1-2, Cases 3-4 were analyzed which included 10% reduced capital costs for the GSHP and supplementary systems. Such assumption was made due to lower design oversizing factors needed for systems serving more than one residential units. However, the costs of metering each residential unit within the block were estimated to be higher than that of individual systems. This led to the overall capital cost of the central systems for Cases 3 and 4 to be larger than their individual system equivalents (Cases 1 and 2, respectively), as seen in Figure 6. Lower metering costs and a larger block size may contribute to their improved financial performance. Such detailed focus is part of ongoing research and is outside of the scope of the current analysis. Another parameter that could greatly impact the comparisons made between the various cases is the coefficient of performance (COP) of the GSHP in heating and cooling modes and that of the supplementary cooling system. In the current study standard values were selected (see Table 4), but it is suggested that the results of the current study be used in cases with comparable heat pump and air conditioner COPs.

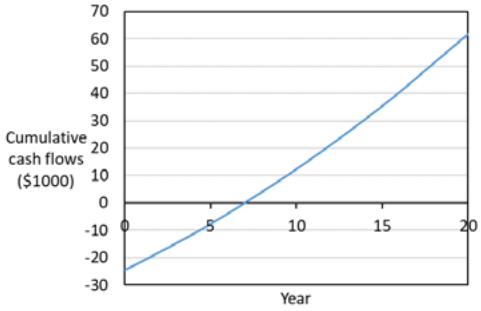


Figure 5: Cumulative cash flow for Case 1, GSHP used for heating and cooling with no supplementary cooling system

Lastly, the four cases described in Table 3 were compared against four cases with an increased unbalance between heating and cooling demands, i.e., 10% lower heating demand and 10% higher cooling demand compared to the demands simulated in eQuest 3.65 in the current study. It was found that although more unbalanced demands may result in more unbalances in system design and heating and cooling system sizing (see Figure 3c and Figure 4), their impact on system financial performance and payback period would remain relatively the same. More unbalanced systems with larger cooling demands and smaller heating demands may results in slightly lower payback periods for Cases 1 and 3 where the amount of heating demand directly affects the cooling via the GSHP and the ground heat exchanger. A lower heating demand, in the case of sizing the GSHP on heating demands, will result in lower amount of heat transferred to the ground in the cooling season. As a result, the GSHP and the ground heat exchanger sizes are reduced compared to the case of the current study. The cooling load would have to be covered using a larger supplementary system, but the decrease in capital costs due to smaller GSHP and smaller ground heat exchanger sizes would dominate the impacts and would result in slightly lower payback periods. However, the variation in payback periods observed in this case is considered negligible (less than 5%) and it is concluded that the results of Figure 6 could represent such unbalanced cases as well. From a more general perspective, this could refer the importance of coupling loads of various building types in order to maximize financial advantage of using ground source heat pump systems.

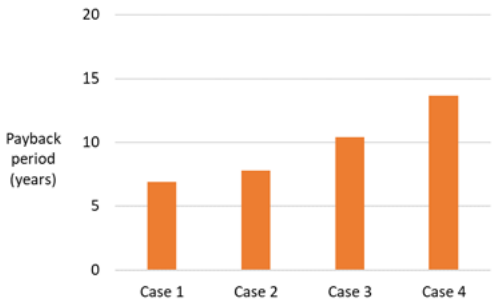


Figure 6: Payback periods estimated for various GSHP cases (refer to Table 3 for details of each design case)

For example, central geothermal heat pumps designed for a number of buildings of more than one type with various load profile characteristics could result in an overall heating and cooling load whose distribution is closer to one corresponding to an optimum geothermal heat pump design. Such optimum load profile could avoid use of supplementary cooling devices or oversized geothermal heat pumps which negatively impact financial feasibility of geothermal heat pump use.

4. Sensitivity Analysis

Here, the calculated payback period for the four cases (shown in Figure 6) are analyzed using a sensitivity analysis to verify the impact of a number of system cost components on the overall feasibility of using geothermal heat pumps for heating and cooling residential building use in the current study.

In the current analysis, it is assumed that heat pumps and chillers will have the same cost and that the additional cost of a geothermal heat pump systems is related to the ground heat exchanger costs. However, in some countries, higher costs are involved with heat pumps. In order to examine how the variation in cost affects the results of the analysis, a sensitivity analysis is performed to examine the variation in results of Figure 6 when the cost of heat pumps are 20% higher than the cost of chillers. It is found that a 20% increase in the cost of the heat pump compared to a chiller results in approximately 9-17% increase in the payback period, i.e., 8-15 years. The effect of variations in cost of geothermal heat pump compared to the cost of a vapor compression air conditioner is considered relatively small on the overall outcome of the feasibility analysis. With more advances in heat pump technologies and their increased use, it is estimated that the payback period would not exceed their current-day values and that geothermal heat pumps will become more favorable in the future.

In addition to varying the cost related to the heat pumps and chillers, the cost of electricity and gasoline is also expected to greatly impact the results of the analysis. Since Ontario has one of the higher electricity rates in Canada, a sensitivity analysis is performed by decreasing the cost of electricity up to 20%. It is seen that, compared to the capital costs associated with the geothermal heat pump and the air conditioner, the cost of electricity has a much higher impact (approximately 40-60% increase) on the payback period in the current case calculated for use of geothermal heat pump and consequently on the decision whether to use geothermal heat pumps or not. This is due to the fact that the large capital costs of geothermal systems are often compared to the annual operating costs of the base system, in this case the furnace and the vapor compression air conditioner that operates using electricity. A lower electricity price would result in a longer payback periods making geothermal heat pumps less favorable and in some cases financially infeasible (Case 4 in the current study). Similarly, it is expected that higher costs of gas in regions where gas heating is typical will result in lower payback periods for use of geothermal heat pumps (approximately 15-45% decrease for 20% increase in gas price in the current case). This is result is important as the cost of electricity and gas in various regions around the world vary and could make the feasibility of use of geothermal heat pumps for residential heating and cooling vary greatly in addition to the design strategy discussed earlier in this section.

The largest component contributing to the cost of geothermal heat pump systems is the cost of grouting and filling for installation of ground heat exchangers. A sensitivity analysis is performed to estimate the impact of 20% reduction in costs of filling and grouting on the financial feasibility of the system. It is seen that up to 17% reduction in payback period for Case 1, i.e., less than 6 years payback period, is resulted for the building under study.

5. Conclusions

A preliminary feasibility assessment is performed to estimate the importance of parameters used in such analysis on the financial feasibility of use of geothermal heat pumps. Such feasibility study is often performed at the early stages of design and its outcome would consequently impact the decision whether to select geothermal heat pumps as the optimum design for a given building type or not. The impact of parameters such as building loads, design strategy studied for a given building load, and system component costs on the outcome of such feasibility analysis is examined in the current study. Financial feasibility of geothermal heat pumps is decided using payback periods calculated when using geothermal heat pumps as opposed to a typical heating and cooling system used in Ontario, Canada, over the life of the system. It is concluded that some parameters such as the price of gasoline and electricity over the life cycle of the technology need to be the subject of more focus to ensure the preliminary feasibility analysis shows results that are accurate enough. Knowledge of such information could guide designers, developers, and energy modelers in equipment recommendation, infrastructure and operational requirements, constraints, estimated costs and off-site opportunities. They are listed as follows:

5.1.Building loads

A few GSHP design strategies are examined in the current study. They are mainly sizing the GSHP and its coupling ground heat exchanger

- solely based on building heating demands, or
- based on building cooling demands while including in the design a peaking cooling system to be used with the GSHP.

Based on industry standard design assumptions and cost estimates for the capital and operating costs of the systems in Ontario, Canada, it is found in this study that using ground source heat pump systems for residential building blocks in Ontario, Canada, are feasible with a payback period of about 7 to 14 years. It is concluded that the range of payback periods varies depending on the specific heating and cooling demand characteristics of the building. In a broader perspective, this emphasizes the importance of employing smart building coupling strategies in order to maximize financial advantage of using ground source heat pump systems. Strategies could consist of designing geothermal heat pumps to serve buildings of more than one type with various load profiles in order to avoid use of supplementary cooling devices or oversized geothermal heat pumps which negatively impact financial feasibility of geothermal heat pump use.

5.2.Design strategies

Comparison of various GSHP design options in the current study shows that the range of payback periods varies significantly depending on the strategies that are employed in designing GSHPs to meet building heating and/or cooling demands. This emphasizes the importance of employing various design strategies in order to maximize financial advantage of using ground source heat pump systems.

5.3.Component costs

A sensitivity analysis of operating costs and capital costs show that cost of fuel used for heating and cooling in the base case (i.e., electricity and gas in the current case) may have the largest impact on financial feasibility of using geothermal heat pumps. Other costs such as cost of geothermal heat pump or cost of grouting and filling of the ground heat exchanger, while still impactful, may have lower impact on the outcome of the feasibility analysis performed at this level.

References

[1] Renewable energy policy for city facilities - City of Toronto (2014) https://www.toronto.ca/wp-content/uploads/2017/11/9056-Renewable-Energy-Policy-For-City-Facilities-September-2014.pdf, Accessed on 25 November 2019.

[2] Roy D., Chakraborty T., Basu D., Bhattacharjee B., 2020. Feasibility and performance of ground source heat pump systems for commercial applications in tropical and subtropical climates. Renewable Energy 152, 467-483.

[3] Liu Z., Xu W., Zhai X., Qian C., Chen Z., 2017. Feasibility and performance study of the hybrid ground-source heat pump system for one office building in Chinese heating dominated areas, Renewable Energy 101, 1131-1140.
[4] Yousefi H., Ármannsson H., Roumi S., Tabasi S., Mansoori H., Hosseinzadeh M., 2018. Feasibility study and economical evaluations of geothermal heat pumps in Iran, Geothermics 72, 64-73.
[5] eQuest, the quick energy simulation tool. http://www.doe2.com/equest/ Accessed on 25 January 2020.
[6] Wang, S., Liu X., Gates S., 2015. An introduction of new features for conventional and hybrid GSHP simulations in eQUEST 3.7, *Energy and Buildings 105*, 368-376.
[7] Bellos, E., Tzivanidis C., Kouvari A., Antonopoulos K.A. Comparison of Heating and Cooling Loads of a Typical Building with TRNSYS and eQUEST. In: Grammelis P. (eds) Energy, Transportation and Global Warming. Green Energy and Technology. Springer: 2016.
[8] RETScreen Software Online User Manual (2019) Natural Resources Canada, http://publications.gc.ca/collections/Collection/M39-118-2005E.pdf, Accessed on 25 November 2019.
[9] Moya, D., 2018. Technical, financial, economic and environmental pre-feasibility study of geothermal power plants by RETScreen – Ecuador's case study, *Renewable & sustainable energy reviews 92*, 628-637.
[10] Pan, Y., 2017. Feasibility analysis on distributed energy system of Chongming County based on RETScreen software, *Energy (Oxford) 130*, 298-306.
[11] Aristizábal Cardona, A.J., Páez Chica C.A., Ospina Barragán D.H. Integrated Photovoltaic System Sizing and Economic Evaluation Using RETScreen™ for a Building of 40 Apartments. In: Building-Integrated Photovoltaic Systems (BIPVS). Springer: 2018.
[12] Aleksandar I.J., Nevenka N., Nataša Lj L., 2019. Feasibility of closed loop ground source heat pump for residential heating and cooling applications in Serbia. *Thermal Science* 00, 279-279.
[13] Lu Q., Narsilio G.A., Aditya G.R., Johnston I.W., 2017. Economic analysis of vertical ground source heat pump systems in Melbourne, *Energy 125*, 107-117.
[14] National Energy Code of Canada (NECB) (2015) National Research Council Canada, https://www.nrc-cnrc.gc.ca/eng/publications/codes_centre/2015_national_energy_code_buildings.html, Accessed on 15 January 2019
[15] Unal F., Temir G., Koten H., 2018. Energy, exergy and exergoeconomic analysis of solar-assisted vertical ground source heat pump system for heating season. Journal of Mechancial Science and Technology 32, 3929-3942.
[16] Ally M.R., Munk J.D., Baxter V.D., Gehl A.C., 2012. Exergy analysis and operational efficiency of a horizontal ground-source heat pump system operated in a low-energy test house under simulated occupancy conditions. *International Journal of Referigeration* 35, 1092-1103.
[17] ClimateMaster. https://www.climatemaster.com/news/building-and-living-green/2018-07-11-ground-source-heat-pump-systems-by-climatemaster. Accessted on 25 January 2020.
[18] Enbridge, https://www.enbridgegas.com/Understanding-gas-rates, Accessed on 25 November 2019.
[19] Toronto Hydro, https://www.torontohydro.com/sites/electricsystem/residential/rates/Pages/resirates.aspx, Accessed on 25 November 2019.
[20] Enbridge, https://www.enbridgegas.com/Understanding-gas-rates, Accessed on 25 November 2019.
[21] Ontario Geological Survey, http://www.geologyontario.mndm.gov.on.ca/index.html, Accessed on 25 November 2019.
[22] Florides, G., Kalogirou S., 2007. Ground heat exchangers—A review of systems, models and applications. *Renewable energy 32(15)*, 2461-2478

13th IEA Heat Pump Conference
April 26-29, 2021 Jeju, Korea

Large Heat Pumps for Decarbonized District Heating

Torben Funder-Kristensen[a1], Drew Turner[b], Leping Zhang[c]

[a] Ph.D. Head of Public and Industry Affairs , Danfoss, Nordborgvej 81, 6430 Nordborg, Denmark
[b]M.Sc. lobal Marketing Manager, Danfoss, Crossroads Cicle 11665, 21220 Baltimore, USA
[c]M.Sc.System Architect, Danfoss, Gong Ti Bei Lu Pacific Centre Place 2A, 100027 Beijing, China

Abstract

Large scale heat pumps constitute one of the most important technologies to pursue a future decarbonized heating supply. In this paper a quantitative overview is given for the EU based on Heat Roadmap Europe (HRE4) also referred in the IEA report Annex 47. Based on this future heating challenge it is important that the suppliers and technology developers of the large scale heat pumps take up the challenge and replies to the opportunities and challenges to obtain the best scenarios. The conditions for district heating grids and heat sources for addressing the appropriate heat pump technologies are described. Applications using low GWP refrigerants like CO2, Ammonia and HFO are compared. The paper also considers the opportunities for addressing decentralized heating providers like supermarkets and chillers traditionally intended for cooling only.

Keywords: Large Heatpump; Oil Free systems; Low noise level; Efficiency

1. Introduction

The EU energy targets for 2030 and the long term 2050 decarbonization aspirations call for the most efficient and innovative cross sectorial solutions. Some countries are already moving beyond previous targets e.g. Denmark has now a domestic target of 70% emission reduction by 2030 and more countries will likely follow with strengthened targets to decrease emissions. Heating of buildings is the largest energy consumer and CO2 emission source focus is on planning for a resilient and efficient system which can provide affordable heat for all. To minimize investments the energy demand must be reduced by energy efficiency measures on buildings and performance optimization of technical building systems – the second factor is to establish efficient heating supply system and to make it decarbonized, with focus on renewable electricity The nature of renewable primary energy supply will force the demand and supply sector to become much more integrated and this will ultimately call for new applications and technologies like demand side flexibility and thermal or electrical energy storage. In the Heat Roadmap Europe (HRE) studies [1],[2] it has been shown that increasing the district heating to cover 50% of the total heat demand together with a 40 GW heat pump capacity in average can address up to 15 % of total heat demand. In periods with a surplus of renewable electricity heat pumps are supposed to supply most heat and utilize thermal storage. The large-scale heat pumps are estimated to produce 520 TWh/year with a coefficient of performance (COP) of 3, see figure 1 and 3. Such an increase enables a much larger utilization of alternative sources of heat like ground source thermal heat and waste heat from data centers and at the same time can utilize of renewable intermittent electricity.

[1] Torben Funder-Kristensen. Tel.: +45 74 88 41 27
E-mail address: tfk@danfoss.com.

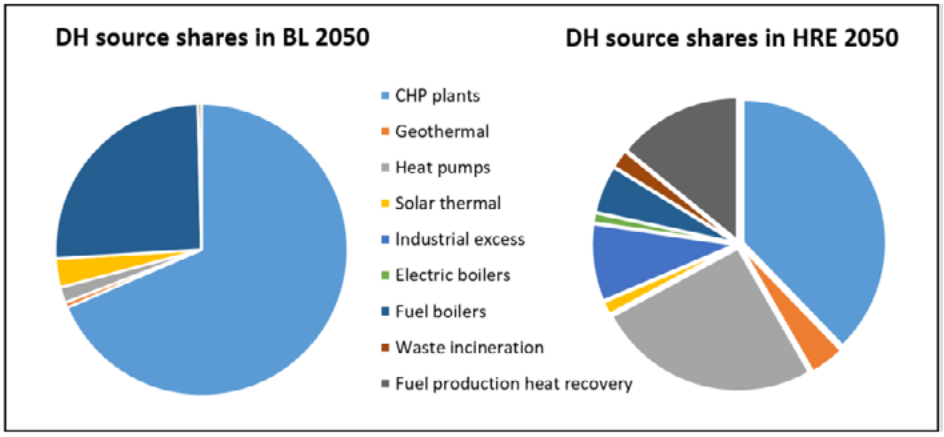


Fig. 1. 2050 DH source share. HRE is the decarbonised scenario [1], likely to increase the HP share with new emission targets

While realized COP in *cooling systems* is important though not a primary business factor (due to existing business models) – it becomes obvious that in heating the 'realized COP' of the heat pumps is a primary business factor for DH operators. The realized COP depends on some basic factors like *temperature lift* and also the *technology* behind the Heat Pump systems. Reported COP values for large heat pumps can be seen in figure 4 [1]. It is obvious that the realized COP values depend on the temperature lift.

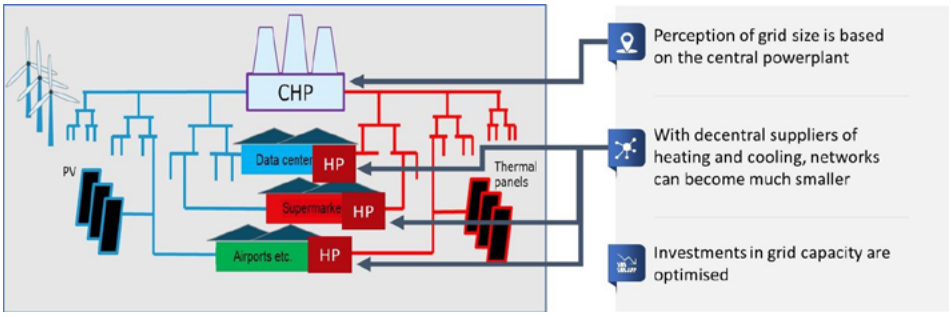


Fig. 2. Decentral large heat pumps can source energy from various utilities. Advantages are listed on the right part of figure

2. Temperature lift

The temperature lift is the difference of the temperature of the heat source inlet and the temperature supplied to the DH system (outlet). DH grids have developed through more than 130 years and can be divided into 4 generations. For simplicity, systems are called by generation names like 3G or 4G. The main parameter characterizing the G-level of the system is the flow line temperature. 3G systems have a flow temperature below 100°C while new 4G systems will go as low as 40°C [4]. The overall system efficiency increases with the lowering of temperature and the opportunities for adding decentral heat sources like heat pumps - or waste heat from supermarkets - can be applied. The first parameter determining how low the flow temp can go is the size of the heating surfaces in buildings. Large surfaces e.g. using floor heating can utilize 40°C water while old radiators in poorly insulated buildings will demand 80°C – at least in cold periods.

Low temp heating is still a rare case for the majority of the building stock in the EU but is expected to grow as renovation of the old building stock takes place. For new city areas low temperature DH is an obvious choice. Specific high temperature needs will then be handled by dedicated heat pumps.

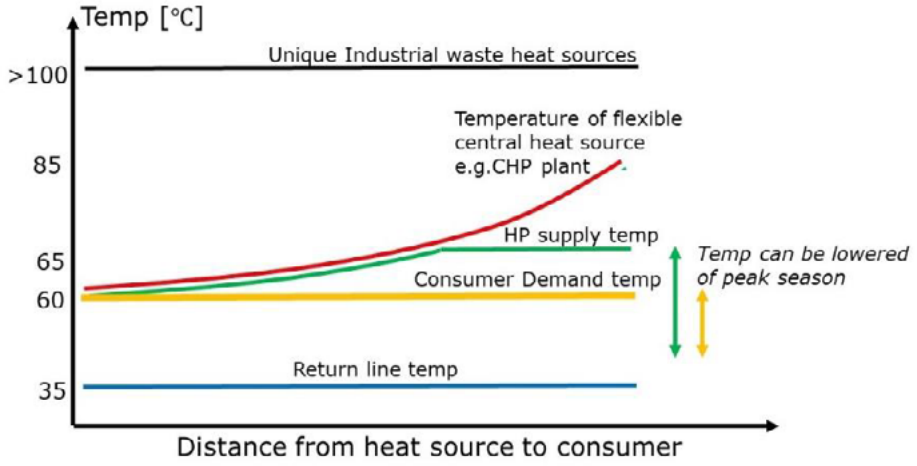


Fig. 3. DH flow line temp compared to demand needs

Another parameter determining the DH flow temperature is the architecture of the DH system layout i.e. pipe diameter, distance between heat supply sources and the density of end consumers. Seasonal variations in heat demand will set the constraints for the flow line temperatures – but the trend is to lower temperatures even during winter. Good practice is to lower the temperature until the most demanding heat consumer will call. Then specific action can be taken towards raising the performance of that specific consumer like better insulation etc. Each City has special opportunities for unique large heat sources i.e. CHP plants, industrial plants, data centers, sea water etc. This will of course reflect the outline of the DH system and likely the flow temperature as some heat sources may have higher temperatures than others. Figure 3 shows a qualitative connection between flow and return line temperatures dependent on distance from heat source and also the heat source type (unique centralized or decentralized heat pumps).

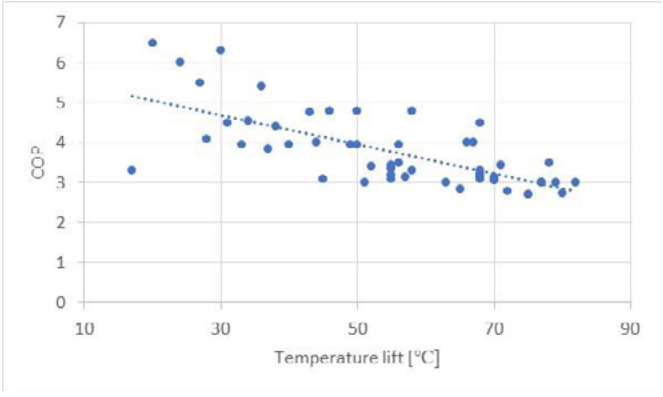


Fig. 4. HP COP versus temperature lift; data from [1]

The flow line temperature is not necessarily reflecting the demand from end consumers but may often be based on the grid piping constraints or specific heat sources. A lower temperature – ensuring sufficient capacity throughout the grid - can be obtained by having multiple and decentralized distributed energy sources like heat pumps. Smaller heat pumps can boost 4G flow temperatures for apartments or multi apartments buildings or

large heat pumps can supply heat to the grid via ground source. Also, the tertiary sector as supermarkets have shown to be able to deliver extra heat to the DH. This issue has already shown to be an important factor to discuss when planning the introduction of heat pumps to the district heating grid and the learning is that the necessary temperature lift may often be smaller than the official flow temperature. This is an important parameter to consider when discussing heat pump heat delivery.

System type	Tws [°C]	TDH°C	WW-HP COP	System/Refrigerant
1	26/19 19/12 12/5	55-65 45-55 35-45	4,7	Centr. Oil free 1234ze(E)
1	26/19 19/12 12/5	55-65 45-55 35-45	4,0	Screw/NH_3
2	26/19 19/12 12/5	35/65	3,9	Recip/CO_2
3	*26;19*	55-65 45-55 35-45	*5.4*	Centr. Oil free 1234ze(E)
3	*15;8*	55-65 45-55 35-45	*3,9*	Centr. Oil free 1234ze(E)
4	26/19	35/65	4.6	Recip/CO_2
4	*15;8*	*35/65*	*3,5*	Recip/CO_2

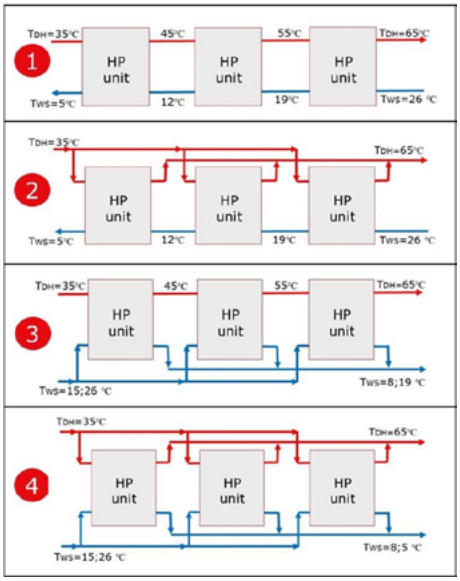


Fig. 5. System type versus refrigerant comparison

3. Technology behind the low GWP heat pump systems

Heat pumps larger than 1 MW are often based on well-known ammonia technology and described in various papers. Also, CO_2 heat pumps can be a good source for high temperature DH but is rarely seen yet. The HFO refrigerant; R1234ze(E), has been introduced to the market during the last years and has a very good HP performance due to its high critical point (165°C). Furthermore, it can be utilized for centrifugal compressors due to its high molecular weight. Assuming a temperature lift of 30-50 °C normally two-three stages of compression are suitable; however, CO2 can due to its transcritical properties, utilize counterflow heat exchanger technology and be effective also for one stage compression. A survey [1] shows COP values from 149 large HP installed in the EU with capacities ranging up to 230 MW and average capacities >10 MW. Looking at figure 6, even with a clear trend line, a high deviation variance of reported COP is evident and can be explained by numerous factors dependent on system architecture, On/off duty cycle or VSD, level of maintenance, etc. As a rule of thumb, the higher the capacity of the system the higher the efficiency due to higher level of complexity and optimization procedures. It should be noticed that potential future rollout of large ground source heat pumps would have capacity limits around 5-10 MW and call for more modular system designs.

4. System comparison

The oil free Air Conditioning chillers using centrifugal compressors have a superior energy efficiency, small size and low noise levels due to high compressor RPM and contact free operation. Even though oil free systems have not yet been used for large scale heat pumps they are notoriously interesting due to high efficiency and the low noise levels which make them suitable to be placed in dense populated areas. To evaluate the efficiency compared to other low GWP refrigerants we did some basic simulations comparing, CO_2 reciprocating

technology and NH_3 screw compressor technology, with the state of art oil free systems for heat pumps around 2 MW capacity. Increased efficiency can likely be obtained in the future due to the ongoing research on utilizing tailor made low GWP refrigerant blends suitable for counterflow heat exchangers [5].
All systems use economizer. The CO_2 and NH_3 system are more complex due to oil management. CO_2 systems evaluated do not use ejectors nor parallel compression. The results in figure 5 show system COP values ranging from 3.5-5.4 depending on the water supply temperatures of 15 °C (high temp level ground source) and 26 °C (Data Center source). The oil free system shows significant good results and the complexity is low which makes it suitable for large scale system production.

5. Conclusion

The energy outlooks for Europe calls for an ambitious increase and investment in district heating networks. District heating will facilitate large scale heat pumps necessary to adopt to the increasing amount of renewable electricity.

The temperature demands of the District Heating grid have continuously decreased during history and it is anticipated that future DH grids will go as low 40°C allowing for decentral heat suppliers like super markets.

Heat pumps can effectively be introduced on a mass scale as decentral zero carbon heat suppliers.

The simplicity of systems and the noise levels and refrigerant safety are qualifying factors to establish MW sized pumps within the cities.

Efficiency of the heat pumps are the business parameter to deliver affordable heat. Efficient, safe and low noise heat pumps can be ensured with oil free heat pump systems.

6. References

[1] Andrei David et al; Heat Roadmap Europe: Large-Scale Electric Heat Pumps in District Heating Systems; Energies 2017, 10, 578; www.mdpi.com/journal/energies
[2] Connolly, D. et al; Heat Roadmap Europe: First Pre-Study for EU27; Aalborg University: Aalborg, Denmark, 2012. 7.
[3] Connolly, D. et al; Heat Roadmap Europe: Second Pre-Study; Aalborg University: Aalborg, Denmark, 2013.
[4] Lund, H. et. al. (2014) 4th Generation District Heating (4GDH). Integrating Smart Thermal Grids into Future Sustainable Energy Systems. Energy 68(2014) 1-11.
[5] Zühlsdorf B., et al, Heat pump working fluid selection—economic and thermodynamic comparison of criteria and boundary conditions, International Journal of Refrigeration 98 (2019) 500–513.

13th IEA Heat Pump Conference
April 26-29, 2021 Jeju, Korea

Study on Aging of Heat Pump based on Long-term Assessment

Nobuhiro TAKAHASHI[a,c,*], Masashi MOMOTA[a], Masahiko KUMAGAI[c],

Tadahiko IBAMOTO[a], Takashi INOUE[b]

[a]Tokyo Denki University, 5, SenjuAsahiCho Adachi-ku, Tokyo 120-8551, Japan
[b]Tokyo University Of Science, 2641 Yamazaki, Noda, Chiba 278-0022, Japan
[c]JAPAN FACILITY SOLUTIONS,Inc, 6-4, Osaki 1-Chome, Shinagawa-ku, Tokyo 141-0032, Japan

Abstract

In this study, we focused on the aging degradation of heat pumps and developed an efficiency evaluation method. From the analysis result of the COP fluctuation factor by the typical CR, it was confirmed that the partial load and the cooling water temperature affected the fluctuation of COP. We developed a method to create a multiple regression equation using these variables as explanatory variables, and analyzed 72 centrifugal refrigerators. As a result, we confirmed the possibility of the efficiency evaluation with this method. Also, it was found that more than 5,000 hours of operation data was necessary to ensure the accuracy of the correction method using the multiple regression equation. In addition, our analysis showed that little aging was observed in CRs under proper maintenance.

Keywords: Long-term Assessment; centrifugal refrigerators; COP;

1. Introduction

1.1. Background of the study

The efficiency of heat pumps for air-conditioning applications, which occupies a large proportion of energy consumption in buildings, should be maintained properly. Therefore, regular inspection and proper maintenance are needed to maintain their initial efficiency. The aging of common equipment is generally represented by a schematic diagram shown in Figure 1. This figure is well known in many fields, however actual investigation on heat pumps are very few. Because, evaluating the changes of actual operation efficiency is not easy. In actual operation, every parameters such as cooling water temperature or partial load change from moment to moment. Complicating things further, seasonal changes also affects to efficiency. According to this background, the evaluation method of heat pumps for stakeholders are demanded.

1.2. Outline of the study

Evaluating efficiency change is worthful for compressing the maintaining cost which to the life cycle management. Considering this issue, the efficiency evaluation method for heat pumps is developed in this study. In particular, focusing correcting the coefficient of performance (COP) of heat pumps against the efficiency fluctuation during operation, long term assessment by maintenance was examined.

* Corresponding author. Tel.: +81-363-712-555; fax: +81-363-712-561.
E-mail address: n.takahashi@j-facility.com.

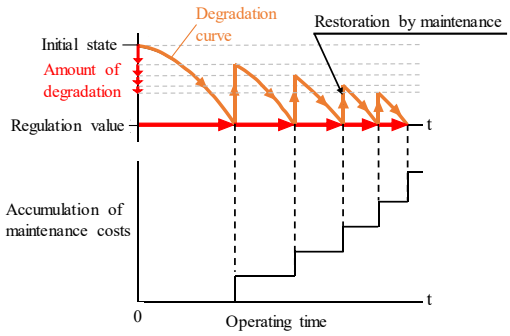


Fig. 1. Schematic diagram of maintenance and costs of recovery from deterioration

1.3. Property of analyzed centrifugal refrigerators

The data of actual operation result used in this study was provided by an energy service company (ESCO) that collaborated in this study and was collected from 73 centrifugal refrigerators (CRs) installed at 30 locations as an ESCO service utilizing thermal energy storage systems. The data was stored on a building automation and control system (BACS) every hour from April 2000 to March 2019. Figures 2 - 5 show outline of the CRs. Many of them have been in operation for more than 10 years. The ESCO includes a maintenance contract for most CRs with the CRs' manufacturers to ensure a supply of chilled water to the users, and it performs satisfactory manufacturer-recommended maintenance at recommended intervals. Since the data contained a large amount of data that was unnecessary for the COP assessment, we had to select the appropriate data before starting the analysis. Table 1 shows the requirement of COP analysis. For this study, not only calculating COP but also functional analysis was main issue, this requirement includes such as the cooling water temperature. In practice, most CRs met this requirement and as a result 72 of CR data was remained.

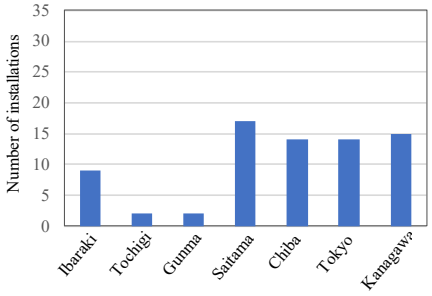


Fig. 2. Number of units installed by prefecture

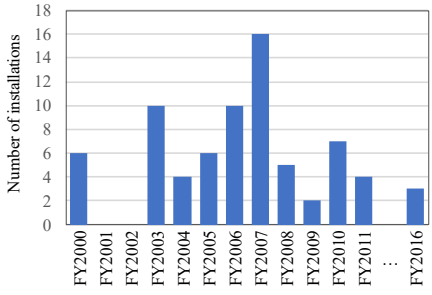


Fig. 3. Number of units installed by year from April

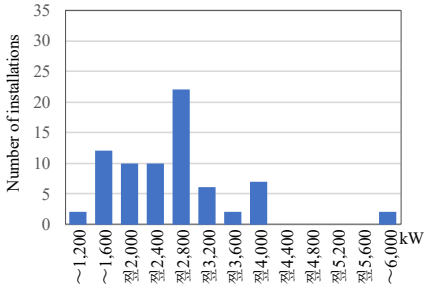


Fig. 4. Number of units installed by capacity (kW)

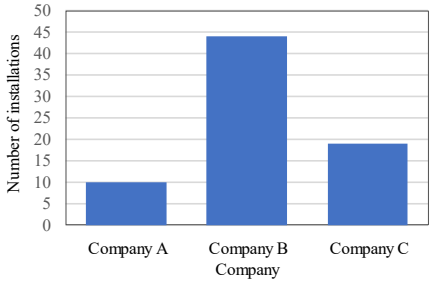


Fig. 5. Number of units installed by supply company

Table 1. Requirement of COP analysis on BACS data

Measurement item
Chilled water inlet and outlet temperature
Chilled water flow
Cooling water inlet and outlet temperature
Power consumption
Heat production
* Hourly data stored in the BACS

2. Analysis on COP fluctuation and factors

2.1. Confirmation of the operation trend

Before the development of the correction of COP, the operation result of all the CRs was analyzed to confirm the trend. Figure 6 shows the operation result of NO.19-01 as a typical example. This CR which installed in FY2006, capacity of 2,700kW, had a decade operation data. This time series COP fluctuation plots are distinguished into colour which indicates the cooling water temperature. Focusing on these colors, it was confirmed that COP fluctuation has a strong relationship along to fluctuation of the cooling water inlet temperature (here in after, "cooling water temperature") which depending on a change of season, same as a theoretical behavior. On the other side, COP was enhanced at the point of 3,000 hour after the operation started. Through the other detailed analysis, it was confirmed that this behavior was caused by the set point change of the chilled water outlet temperature. Considering above, the correlation of the COP with factors which selected in Table 1 was investigated.

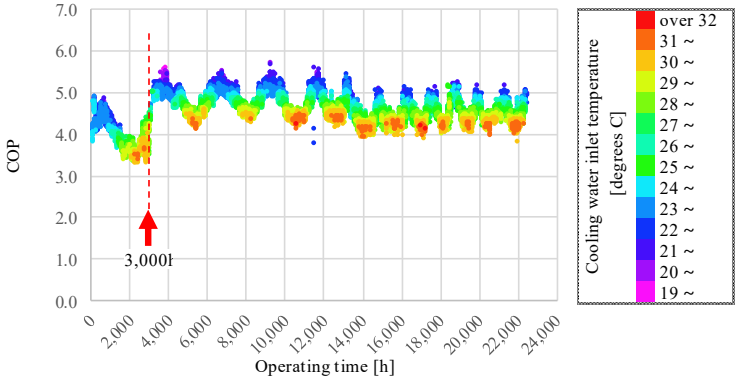


Fig. 6. Operation result of NO.19-01 as a typical example.

Figures 7 - 11 show the correlation of the COP of the CR NO.19-01 over the measurement period for each parameter. The partial load in Figure 8 indicates the ratio of the actual generated heat to the rated capacity of the CR. As shown in Figures 7 - 11, a strong correlation was confirmed between the COP and the partial load as well as the cooling water temperature. On the other side, considering the thermal energy storage system, it is able to be thought that the chilled water temperature is stable in operation except the set point change. Therefore, as the first step of this study, factors which are the partial load and the cooling water temperature were picked up for the correction of COP fluctuation.

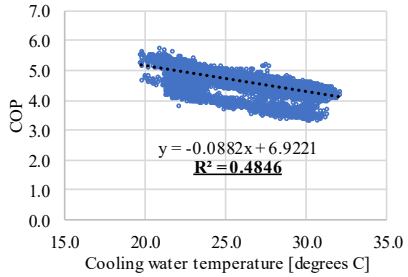


Fig. 7. Correlation between cooling water temperature and COP

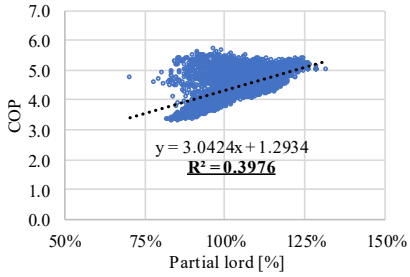


Fig. 8. Correlation between partial lord and COP

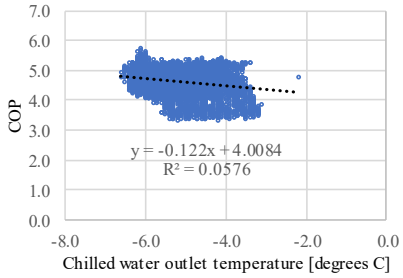


Fig. 9. Correlation between chilled water outlet temperature and COP

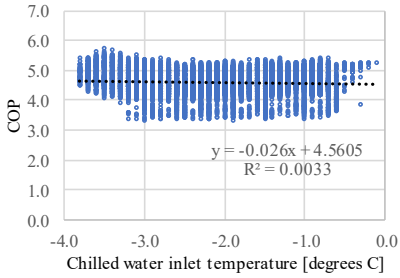


Fig. 10. Correlation between chilled water inlet temperature and COP

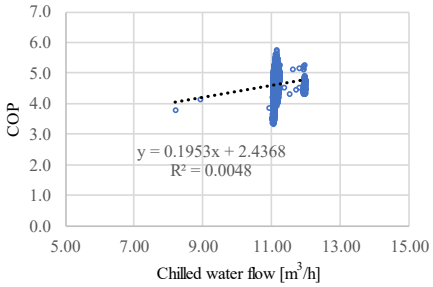


Fig. 11. Correlation between chilled water flow and COP

3. Correction of the COP

3.1. Method of correcting the COP

Table 2 shows the procedure of COP correction. Conception of this method is based on the performance curve generated from an actual operation data. Basically, utilizing the generated curve, the cancellation against fluctuation of factors is realized by correcting the COP of a certain operation state to the data of the reference state. Concrete process utilizing a multiple regression equation is following.

First, to derive a multiple regression equation, a regression analysis of the data for the baseline period is conducted using the partial load and the cooling water temperature as explanatory variables.

The COP obtained by substituting the partial load and the cooling water temperature into the multiple regression equation is defined as the "COP on the performance curve". At this step, we defined the baseline period as three years from the initial fiscal year. If the fluctuation on the cooling water temperature during the

three years is fine degree, another three years with a larger degree of fluctuation were selected to improve the accuracy of the multiple regression equation.

The variability ratio of COP is the value obtained by dividing the actual COP by the COP on the performance curve and subtracting 1 from the resultant value. The multiple regression equation produced in previous step is summarized in the form of equation (1). The coefficients for each variable differ for each CRs. Table 3 shows the coefficients for typical CR.

Figure 12 shows a comparison between the performance curve obtained by the multiple regression equation and the actual operation COP. A few outliers are seen at lower cooling water temperatures, but they are generally similar.

Table 2. COP correction procedure

Step	Contents (Implementation / calculation)
Step.1	Create a correlation diagram between partial lord and COP for each cooling water temperature in the base year
Step.2	Create a multiple regression equation with the partial lord and cooling water temperature as explanatory variables
Step.3	Calculate the COP at each time by substituting the actual cooling water temperature and partial lord every 100 hours into the multiple regression equation * The COP calculated here is defined as COP on the performance curve.
Step.4	The actual COP divided by COP on the performance curve and subtracted 1 is the variability ratio of COP

$$f(x,y) = (C_{11}x^3 + C_{12}x^2 + C_{13}x + C_{14})y^3 + (C_{21}x^3 + C_{22}x^2 + C_{23}x + C_{24})y^2 + (C_{31}x^3 + C_{32}x^2 + C_{33}x + C_{34})y + (C_{41}x^3 + C_{42}x^2 + C_{43}x + C_{44}) \quad (1)$$

$f(x,y)$: COP on the performance curve
x : Cooling water temperature [degrees C]
C_{nm}: Constants
y : Partial lord [%]

Table 3. Coefficient list of typical CR

		m			
		C_{n1}	C_{n2}	C_{n3}	C_{n4}
n	C_{1m}	-8.69283E-02	6.88748E+00	-1.80476E+02	1.56145E+03
	C_{2m}	1.99511E-01	-1.58588E+01	4.17038E+02	-3.62289E+03
	C_{3m}	-1.15261E-01	9.19175E+00	-2.42631E+02	2.12142E+03
	C_{4m}	1.89280E-04	-1.50236E-02	3.92556E-01	-3.36224E+00

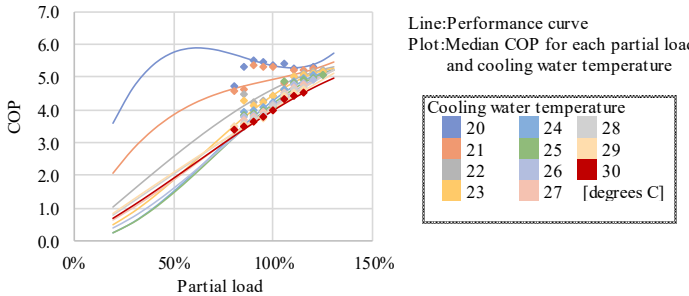


Fig. 12. Comparison of performance curve and actual operation COP

Figure 13 shows the variability ratio of COP for the typical CR (No.19-01). The fluctuation of efficiency concerned with the cooling water temperature and the partial lord was suppressed, effectiveness of this correcting method is confirmed.

On the other side, the variability ratio of COP became a positive value after 6,000 hours. From the point of view of theory, as shown in Figure 13 positive value is not suitable. However, this trend might be caused by the set point change of the chilled water outlet temperature. Also, this trend is able to guess from the correlation of Figure 9. Considering the ordinary circumstances, the chilled water outlet temperature should be involved into the factor of a multiple regression equation. However, all of CRs which picked up in this study are connected to thermal energy storage system, is able to maintain the temperature in stable state, the exclusion effect of the chilled water outlet temperature was estimated not strong issue to evaluate the overview of the trend. Therefore, here in after, two factors which are the cooling water temperature and the partial load were adopted for the correction considering as a first step of this study.

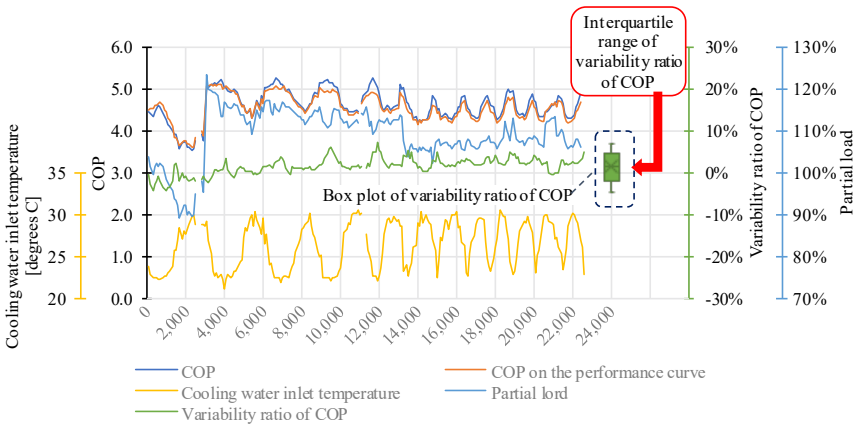


Fig. 13. No.19-01 Changes in variability ratio of COP and COP, etc.

3.2. Correction results of all the COP

Before the evaluation for all the variability ratio of COP, for each CR, it was calculated the interquartile range (the height of the boxplot) of the variability ratio of COP as shown in Figure 13 in previous. This is for the confirmation of the factors that cause a significant fluctuation on the variability ratio of COP.

Figure 14 shows the correlation between the operating (cumulative) time of each CR and the interquartile range of the variability ratio of COP. As shown in the figure, the interquartile range converges after 5,000 hours of the operating time. In other words, a minimum operating time should be decided to maintain the accuracy of the multiple regression equation. Therefore, from point of view of this, these 4 of CRs which are less than 5,000 hours were excluded from the next evaluation.

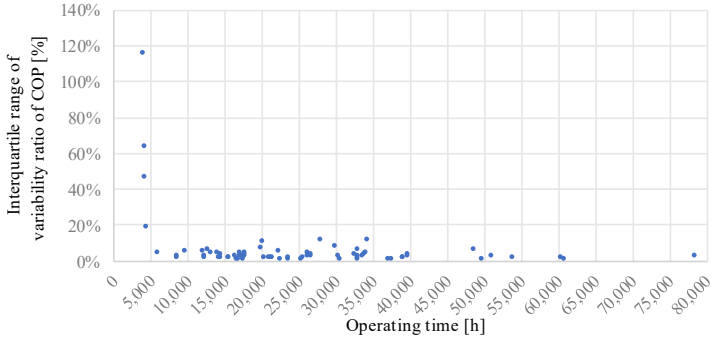


Fig. 14. Correlation diagram of Interquartile range of variability ratio of COP and operation time

Figure 15 shows the variability ratio of COP which averaged in 100 hours for 68 CRs in total, excluding the four CRs mentioned above. Since grasping the overview of the trend was difficult from this figure, statistical processed result was shown in Figure 16. This is boxplot for each 1,000 hours average. Concretely, the evaluation on the variability ratio of COP was performed in the interquartile range to quantitatively determine whether the correction was effective. The range was within roughly ± 5%, indicating that the fluctuation due to the partial load and the cooling water temperature has suppressed by the correction.

Figure 17 shows a comparison between the interquartile range of change in the actual COP for each CR (Red plot) and that of the variability ratio of COP (Blue bar chart). Except for three CRs, the interquartile range is smaller for the variability ratio of COP, it was confirmed that correction method to be effective to almost CRs.

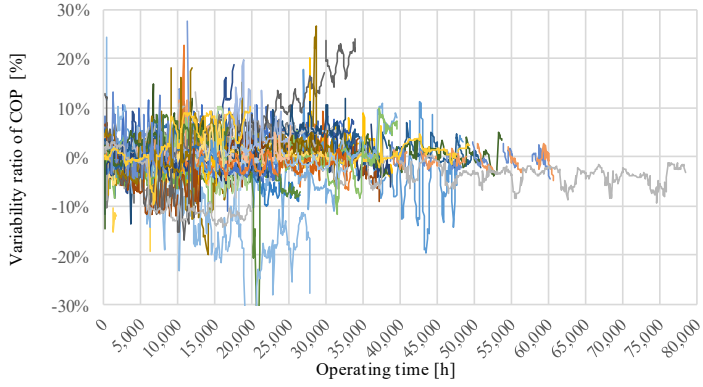


Fig. 15. Trend of variability ratio of COP of 68 units every 100 hours

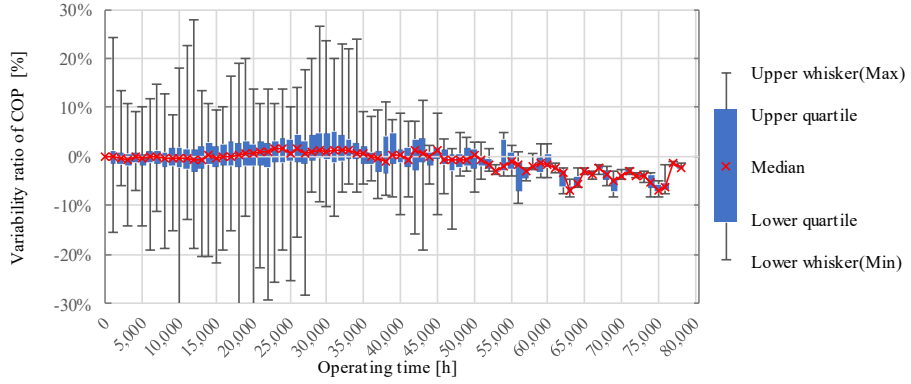


Fig. 16. Box plot for each 1,000 hours

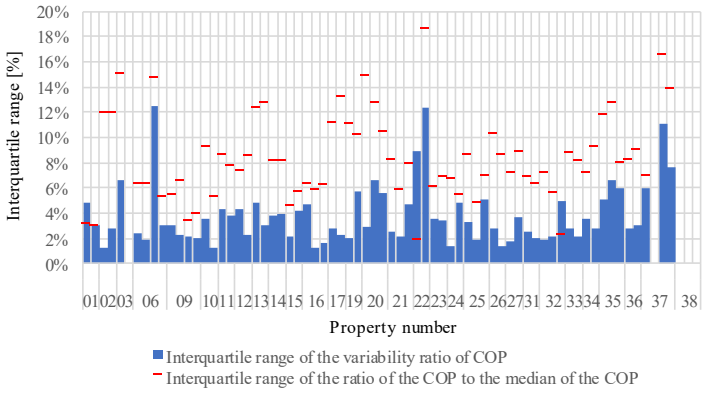


Fig. 17. Interquartile range of the ratio of the COP to the median of the COP and the interquartile range of the variability ratio of COP

4. Conclusions

Focusing on the aging of heat pumps, the efficiency evaluation method is developed in this study. In particular, the correcting COP method against the efficiency fluctuation during operation, long term (longest is 10 years) assessment for centrifugal refrigerators was examined. As a result, following was shown.

- Possibility was confirmed to correct the COP to evaluate the variability COP utilizing developed method which with a multiple regression equation.
- The partial load and the cooling water temperature was explicable factors for the correcting. On the other side, considering other type of refrigerator or HVAC system, it was estimated that the chilled water temperature is one of the effective factor.
- Only in the scope of this study, but more than 5000 hours of operation data is required to ensure the accuracy of the multiple regression equation for the correction method. In addition, from our analysis, almost no aging was observed on CRs under the proper maintenance.

References

[1] Akira Tkakusagi Study on maintenance cost for restoring physical degradation of air−conditioning system. j.Archit. Plann. Environ.Eng.,AIJ, No.459,27-36,May,1994(Japanese paper)

13th IEA Heat Pump Conference
April 26-29, 2021 Jeju, Korea

Proof-of-Concept Testing of Adhesive Joints for HVAC&R Applications

Haotian Liu[a*], Patrick J. Geoghegan[b], Justin A.Weibel[a], Davide Ziviani[a], Eckhard A. Groll[a]

[a]Purdue University, 610 Purdue Mall, West Lafayette, IN 47907, USA
[b]Oak Ridge National Laboratory, 1 Bethel Valley Rd, Oak Ridge, TN 37890, USA

Abstract

The formation of joints is a critical process in HVAC&R component manufacturing and system assembly. Brazed joints are the most commonly used, but there are several alternative methods including mechanical compression, press, and push joints. Adhesive joints have not been widely explored or evaluated for use in HAVC&R systems. In this study, a review of different joint types reveals that adhesive bonding is a promising joining method due to potential benefits in energy use, cost savings, and leakage reduction. In order to demonstrate an application procedure and explore the feasibility of adhesive joints, two proof-of-concept tests were performed. First, tube-to-tube joints were installed in a heat pump dryer system to confirm that adhesive can hold the system pressure without affecting performance. Second, adhesively bonded U-bend joint samples were tested using a shaker table following an ISO standard and benchmarked against brazed joint samples. There was no failure or wear observed for the adhesive or brazed joints. These proof-of-concept tests indicate that there is potential for use of adhesive joints to replace brazed joints in HVAC&R applications, which merits further investigation.

Keywords: ; HVAC&R system, Joints; Adhesive joints; Heat pump dryer; Vibration test

1. Introduction

In heating, ventilation, air conditioning, and refrigeration (HVAC&R) systems, joints are commonly used to connect the refrigerant lines to other system components (such as compressors, condensers, evaporators, and filter dryers) and in the assembly of components such as tube-and-fin heat exchangers. The joints are critical to avoiding system leakage throughout the lifetime of operation. Refrigerant leakage is a direct greenhouse gas emission, but also results in additional indirect emissions by reducing the system energy efficiency and equipment lifetime. Leaks most typically occur at the locations of joints and connections in the system, and are usually caused by fatigue failures associated with temperature cycling, pressure cycling, vibration, or mechanical wear. According to a recent EPA report [1], HVAC&R equipment across many different application categories are facing leakage issues. Several of the common HVAC&R equipment categories shown in Table 1 have leakage rates of 10% per year or more due to faults in joining techniques, system design, and operations/ maintenance practices. Supermarket refrigeration systems can have up to 25% leakage per year due to the nature of field installing long line sets.

In order to address these issues, one of the critical tasks is to investigate, evaluate, and explore both existing and new joining technologies to reduce the leakage of refrigerant from HVAC&R equipment. Currently, brazed joints are the most commonly used, but there are several alternative methods including compression joints, press joints, push joints, and adhesive joints. Among these alternatives, adhesive joints have not been widely explored for use in HAVC&R systems and there has been a lack of evaluation and testing. This paper first reviews and compares different joint types and then reports two proof-of-concept tests performed using adhesive joints.

* Corresponding author. Tel.: +1-765-409-7529; fax: N/A.
E-mail address: liu1460@purdue.edu.

Table 1. Estimated annual HFC leakage rates for common HVAC&R categories, according to the EPA [1].

Equipment Category	Estimated Annual HFC Leakage Rates (%)
Supermarkets and Other Retail	1-25
Mobile Air Conditioners	2-18
Cold Storage	15
Residential Unitary AC	12
Industrial Process Refrigerant	4-12
Centrifugal Chillers	2-11
Commercial Unitary AC	8-9
Packaged Terminal AC / Heat Pump	4
Refrigerated Appliances	< 1

2. Overview of Joining Technologies

A typical HVAC&R system consists of various individual components connected by tubes and joints to form a closed-loop piping system for cycling of the refrigerant. The components usually include compressors, heat exchangers, valves, and additional accessories such as filters, pumps, and sight glasses. In addition to the connections between these components, there are subassemblies consisting of numerous parts that must be joined together. For example, tube-and-fin heat exchangers are manufactured by joining individual tubes and metal sheets together with U-shape bends. In the majority of HVAC&R systems, copper tube-to-tube joints make up most of the connections. The review below focuses on joining technologies for copper, if not otherwise specified.

At each location where two components meet, joining technologies need to provide a mechanically adequate bond between the surfaces without any damage to the original part. These joints must meet structural requirements for load-bearing (if required) and to withstand the operating pressure of the system, allowing refrigerant to flow through unobstructed. Strong and reliable joints provide stable, efficient, and leak-free system operation; failures in joining cause refrigerant leakage having negative consequences including safety concerns, wasted energy due to system efficiency reductions, and pollution to the environment.

2.1. Brazed joints

Brazing is the most common joining technology in the HVAC&R industry. It is a well-established commercial process capable of producing strong joints between most metallic and ceramic materials, which has led to its widespread adoption in industry. Brazing can be performed both manually as well as in automated production processes. As defined by the American Welding Society [2], the term brazing encompasses a group of joining processes that bond materials by heating to a brazing temperature in the presence a filler metal having a melting point above 450 °C (840 °F); the brazing temperature does not cause melting of the base materials. The brazing filler metal becomes molten and is distributed by capillary action within the tight clearance between the two surfaces that are being joined. The assembly is then cooled, and the molten filler solidifies. The filler metal anchors the surfaces together owing to metallurgical reactions that lead to atomic bonding. For most tube-to-tube joints, a separate coupling tube, having a slightly larger diameter than the tube end being joined, is placed so that both tube ends have an overlapping area with the coupling where the bond is established. Alternatively, the two components can be connected directly without an overlapping coupling to form a butt joint.-Strong, uniform, leak-proof joints can be made rapidly and inexpensively with brazing, especially for joints that are inaccessible or for parts and components that may not be joined using other methods.

2.2. Mechanical joints

Mechanical joints can be categorized into several different types including compression joints, press-connect joints, and push-connect joints [3]. Mechanical joints are an alternative for brazed joints when using an open flame is either not desired or impractical. All mechanical joint types form a seal using mechanical

pressure to physically close the leakage path. Mechanical joints are commercially available from several manufacturers.

Compression joints are usually composed of an outer compression nut and an inner compression ring or ferrule made of brass or copper. Ferrules most commonly have a shape of a ring with beveled edges. The longest sloping face of the ferrule usually faces the opposite direction of the nut. In the joining process, the nut is tightened and the ferrule is compressed between the nut and the tube. The ferrule will seal the gap between the tube and nut, producing a tight joint by clamping the end of the ferrule around the tube [3].

Press-connect joints rely on the excellent malleability of copper, forming a seal using a special gasket, usually of an O-ring shape, for joining. Using approved special pressing tools and jaws, the copper fittings are flattened into thin sheet on the tube that are being joined to form a leak-proof connection. [3].

A push-connect joint is another available type of mechanical joint that does not require heating or specialized tools, and can be made by hand. These joints are similar in principle to press-connect joints. On the inner diameter of the fitting, an integral elastomeric gasket or seal and stainless-steel gripping ring help to produce a leak-free joint. Once pushed on, the gripping ring and the gasket together provide a seal on the outer diameter of the insertion tube; the use of the gripping ring avoids the need for a pressing tool as in the press-connect joint.

2.3. Adhesive joints

Adhesive joining processes use an adhesive substance that holds materials together by surface attachment [4]. It is a widely used industrial joining method that has been adopted and proven reliable in several industry sectors, such as in automotive and electronics. While there are many types of adhesives, the ones used for structural bonding are typically cured in order to have adequate strength to transfer the loads through the joints. One-part adhesives need to be heated up before application and two-part adhesives need to be evenly mixed. Based on the application and assembly process requirements, there is freedom to design and develop adhesives with different characteristics such as the curing temperature/time, assembly time, or drying temperature/time.

A review of the scientific literature and survey of available products in the market reveals that adhesive joining (tube-to-tube or otherwise) is not a mature technology for application in HVAC&R systems. There is a lack of research and little information on product development and qualification standards specific to this industry. Most of the existing products focus on quick repair, instead of initial manufacture. Based on our product research, the few examples of adhesives used for HVAC&R joint repairs are two-part epoxies requiring heat curing. Epoxies are widely used as high-performance structural adhesives because of their ability to cure without producing volatile byproducts, high resistance to chemicals, and low shrinkage during curing [5,6]. When employed, the epoxy resin is mixed with hardener at a certain mass ratio to form a homogeneous mixture, which must be applied to a prepared/cleaned surface within a working time before it cures. The strength of the adhesive joint largely depends on the design of the joints, thickness of the adhesive, bonding area, and surface modifications the bonding area.

2.4. Summary comparison of different joint types

A qualitative comparison of brazed, compression, press-connect, push-connect, and adhesive joints are summarized in Table 2. In comparison with the other joining technologies, adhesive joints provide some unique features that are key to overcoming challenges facing the HVAC&R industry. Compared to brazed joints, using adhesive joints can potentially reduce the manufacturing energy and cost, and also avoids the risk of galvanic corrosion between dissimilar metals [7]. In addition, unlike the mechanical joints that are only available for very specialized geometries, the process of using an adhesive material to join between any surfaces is similar in nature to the use of a brazing material. This offers the potential to form adhesive joints in mass production with a similar assembly line as brazing. Being aware that the primary disadvantage of adhesive joints is the lack of established procedures for application and assembly, as well as their unknown reliability, this study aims to demonstrate a joining procedure to explore the feasibility of adhesive joints. A complete joining procedure is developed including surface preparation, adhesive preparation, adhesive application, and curing. Proof-of-concept tests are performed using adhesive joints in a heat pump dryer system and by placing joints on a vibration shaker.

Table 2. Summarized comparison among different types of joints considered for use in HVAC&R systems

Joint type	Various geometry	No open flame	Permeant fittings	No clamping tools	No extra components	Joining of dissimilar metals	Long-term reliability
Brazed	✓	×	✓	✓	✓	×	✓
Compression	×	✓	×	×	×	✓	×
Press-connect	×	✓	✓	✓	×	✓	✓
Push-connect	×	✓	×	✓	×	✓	×
Adhesive	✓	✓	✓	✓	✓	✓	?

3. Heat Pump Dryer System Demonstration

A proof-of-concept test is performed to demonstrate the use of adhesive joints in an HVAC&R system under normal working conditions. In addition to evaluating any potential effects on the system performance, the tests may expose any unexpected issues in the assembly process. The proof-of-concept test uses an adhesive to form tube-to-tube joints in a commercial heat pump dryer test stand, simulating an installation or repair in the field.

3.1. Experimental system

A heat pump system taken from a commercial clothes dryer is selected as the test system. The system components are summarized in Table 3. Fig.1 shows an image of the test stand alongside a schematic diagram of the flow loop with the primary components labelled. The system is a vapour compression cycle: the refrigerant vapour comes out of compressor and is condensed to liquid against ambient air through the subcooler and condenser. A separate fan is used to provide the airflow for the subcooler and to cool down the compressor. The liquid out of the condenser expands through a capillary tube and evaporates in the evaporator which then goes back to the compressor and closes the cycle. There is a blower that provides airflow for both the condenser and evaporator through the same air duct.

Table 3. Component specifications and materials in the heat pump dryer system

Component	Description
Compressor	HIGHLY (Shanghai Hitachi) BSD122DN-H3BDA
Condenser	Tube-and-fin type (Material: Aluminum)
Subcooler	Tube-and-fin type (Material: Aluminum)
Capillary Tube	Material: Copper
Evaporator	Tube-and-fin type (Material: Aluminum)
Filter Dryer	Material: Copper
Tubing	1/4-inch for discharge and 3/8-inch for suction (Material: Copper)

The commercial system introduces various factors that may influence the adhesive joint performance. The system has a relatively high pressure of up to 15 bar at 55 °C with R134a as the refrigerant. The tubing is exposed to sudden pressure changes and random vibrations when the compressor and blower are running. It is an oil-lubricated system with oil passing through the tubing along with the refrigerant. There is tension and torque on the joints caused by thermal expansion and contraction as the system heats and cools as it is cycled on and off. All of these factors simultaneously act on the adhesive joints in a manner that is hard to simulate through standardized testing.

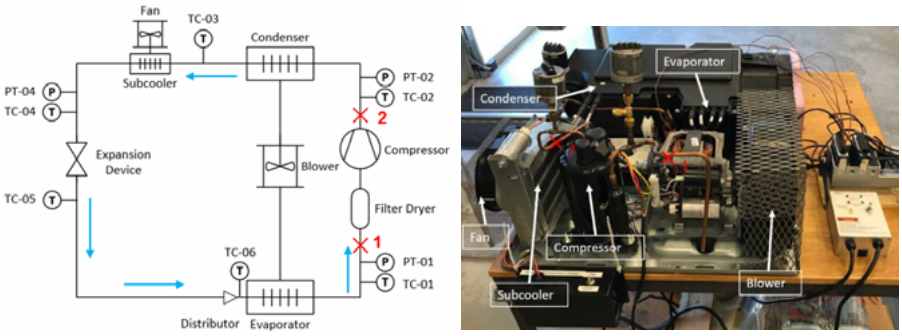


Fig. 1. Schematic drawing (left) and photograph (right) of the custom-instrumented heat pump dryer test stand with the locations of the pressure transducers (P) and thermocouple measurements (T) indicated. The adhesive joints are placed at the locations labelled "1" and "2".

The system was also selected due to its simplicity in system control. The system consists of a single speed compressor, blower and fan with a capillary tube. There is no active control, and hence, the system operating conditions are only determined by the refrigerant charge amount and environmental temperature. Within a lab-testing environment, the temperature stays relatively constant. The operating conditions can thereby be used as an indicator for the system refrigerant charge amount.

The system is custom-instrumented with sensors to monitor the operating conditions. Three pressure transducers and five thermocouples are installed to measure the pressure at several selected locations and the temperatures at the inlet/outlet of each component, as labelled in Fig.1. The pressure transducers measure from 0 – 500 psig with an accuracy of ± 0.65 psig. The thermocouples are copper-constantan (T) type with ± 1 ℃ uncertainty. Two different locations are selected for insertion of the adhesive joint based on the operating conditions of the system, as marked by red crosses in Fig. 1. Location "1" is at the compressor outlet where there is the highest temperature and pressure in the system; location "2" is at the compressor inlet, with the lowest temperature and pressure. At each location, the original tubing is cut with a chip-free tube cutter in the middle, leaving two open ends. A copper coupling is used to form a new tube-to-tube connection using the adhesive, as will be described in the subsequent section.

3.2. Adhesive joining procedure

A structural adhesive two-part epoxy was used as the bonding material for the application process. As suggested by the manufacturer, a manual applicator with a static mixing nozzle were used to evenly mix and apply the adhesive to the surface.

The outer tube surfaces were prepared by a traditional method of acetone cleaning, followed by sanding, and lastly a second acetone cleaning. The coupling is only acetone-cleaned because the inner surface of the small-diameter tube is inaccessible for sanding. Note that the coupling is a standard size for brazing purposes and is not specifically designed for adhesive joining. The gap size between the tube outer diameter and coupling inner diameter at both locations is measured to be 0.85 mm; this is within the recommended working range for the adhesive, which will guarantee a strong adhesive bond. Fig. 2 shows the location "1" tube cut, with the two open ends aligned after preparing the bonding surface; the coupling is shown slid onto the left-side tube end. The difference in color of the copper tube near the coupling indicates that the surface preparation removed the oxide layer and other contaminants. Before applying the adhesive, the two tube ends are aligned coaxially and pressed against each other to decrease the possibility of adhesive leaking into the inner surface of the copper tubing. The adhesive is circumferentially applied on the cleaned tube area to cover a region the same length as the coupling. The coupling is slowly slid along the tube until the cut is at the center of the coupling. It is ensured that the adhesive fills the gap between the tube and the coupling, with no visible openings; the assembled joint is shown in Fig. 2. Because the tube is in a horizontal orientation, the adhesive accumulates at the bottom of the tube due to the effect of gravity. The adhesive is left to cure at room temperature for 24 hours. After curing, an aluminum safety shield is placed around the joints in case of a catastrophic failure. The other adhesive joint in location "2" is manufactured following the same procedure.

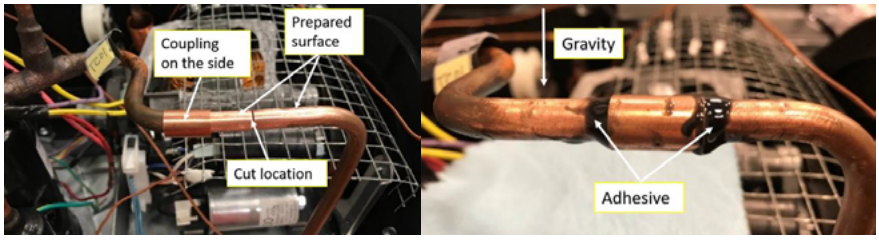


Fig. 2 Photographs of the cut location "1" for the tube-to-tube joint after preparing bonding surface (left) and within the coupling in place over the cut after application of the adhesive (right).

3.3. Testing procedure

Before cutting the tubes, a baseline test was performed to measure the system operating conditions. The system was charged with 428 g of refrigerant R134a, which is recommended by the manufacturer. All of the system components (e.g. the compressor, fan, and blower) were run at a fixed speed that was maintained constant for the duration of the test until steady-state operating conditions were achieved.

After recording the standard operating condition benchmark, the tubes were cut and re-assembled with adhesive joints as described in the previous section. Before recharging the system with refrigerant, a leakage check was performed by charging the lines with high-pressure nitrogen and pulling a vacuum on the system. The system high-side operating pressure is approximately 960 kPa and it was charged with nitrogen to 1900 kPa. After 72 hours, the pressure dropped by ~1% to 1880 kPa and then held steady. When a vacuum was pulled on the system, no pressure increase was observed after 6 hours. These tests confirm that the system was leak-free after the initial adhesive joining and ready for testing.

The system was charged with the same amount of refrigerant as during the baseline testing. After charging, a long-term test plan was followed for the adhesive joints: the system was run for several hours every one or two weeks, similar to the anticipated operation of the device, with the pressure and temperature recorded after reaching a steady operating point. The procedure evaluates whether the prototype adhesive joints can hold the pressure over a long time while being subjected to normal running cycles. The system pressures and temperatures are compared with baseline results, which would differ if there was a significant loss of charge.

3.4. Results and discussion

The operating conditions for the baseline and the case with adhesive joints case are compared in Fig. 3. The baseline condition is defined as the standard operating condition, achieved by the initial charge without any modification with adhesive joints. Several assumptions were made to calculate all state points where there is not a direct measurement, namely: no pressure drop in the condenser, constant enthalpy across the expansion devices, and two-phase operation the condenser and evaporator. Due to the long tubing and distributor before evaporator, there is an additional pressure drop between the capillary tube (point 5) and evaporator (point 6). This was treated as a second expansion device to accurately capture the pressure and temperature at the evaporator inlet.

The data presented in Fig 3. indicates that there is a consistent operation before and after installation of the adhesive joints. In both cases, between state points 5 and 6, there is additional pressure drop with the according temperature decrease. Also, note that the there is pressure drop across the evaporator, which explains the temperature decrease from state point 6 to 1. A small variation in the pressure and temperature, comparing the baseline and adhesive data, are attributed to slightly different charge amounts due to the refrigerant scale uncertainty and difference in the room temperature (21.9 ℃ for the baseline versus 22.4 ℃ in the adhesive case).

In order to further evaluate the feasibility of this concept, the system was operated periodically over the next 6 months per the testing procedure described in the previous section. The corresponding temperature-entropy (T-s) and pressure-enthalpy (P-h) diagrams are shown in Fig. 4, with the adhesive test operating points overlaid on a plot of the baseline condition. As shown in Fig. 4, the system performed consistently with each subsequent test after sealing the joints with adhesive. The consistent pressure level and system performance indicates that there was no leakage over the testing period and that the adhesive joints operate successfully under the temperature changes and vibrations associated with operation of the system using refrigerant R134a. Despite the limitations of testing only two adhesive joints over a moderate temperature/pressure range for a

period shorter than the typical lifetime, as a proof-of-concept test, this suggests that adhesives may be feasible and practical to replace brazed joints in HVAC&R systems. Further testing is recommended to evaluate the performance of adhesive joints in HVAC&R systems to the point of failure or leakage.

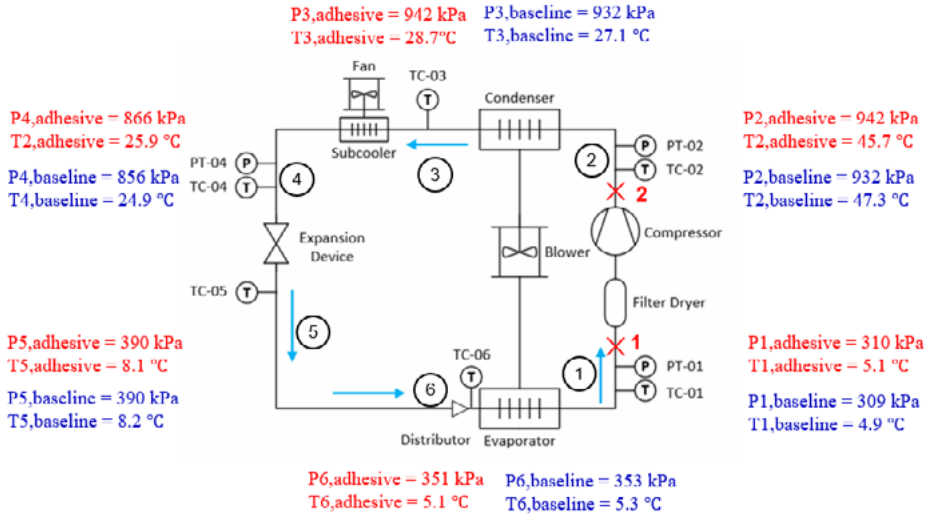


Fig. 3 Schematic diagram of the heat pump system showing the pressure and temperature values measured or calculated at each state point. The baseline data are shown in blue and the data for the tests with the adhesive joints are shown in red.

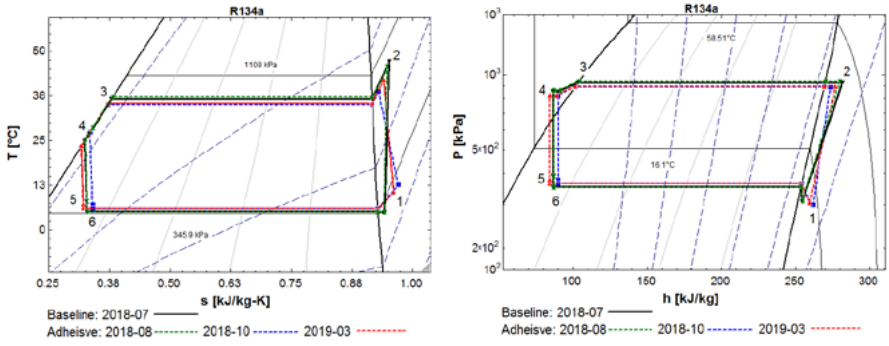


Fig. 4 T-s (left) and P-h (right) diagrams of heat pump system operation conditions at the baseline condition and for three selected tests over a 6-month period after installing the adhesive joints.

4. Vibration Testing

Failure in HVAC&R joints caused by vibration is one of the major concerns. Although the heat pump dryer testing showed that the joints can function in a real operating system under vibrations from the compressor and cooling loop flow, an accelerated test involving more intense and controlled vibrations is performed to evaluate whether a leakage may occur. Vibration testing is performed following the ISO standard 14903 [6], with the test parameters as given in Table 4. The vibration displacement and number of excitations are specified based on the tube size and require precise control.

Table 4 Vibration test parameters from ISO standard 14903 used to evaluate the survivability of the adhesive joints.

Pipe Diameter (mm)	Length (mm)	Displacement (mm)	Frequency (Hz)	Number of excitations
< 10	200	0.30	≤ 200	2 000 000
≥ 10 and < 20		0.25		
≥ 20 and < 30		0.20		
≥ 30 and ≤ 50		0.15		

4.1. Experimental setup

The separate vibration test is performed using a shaker test stand. The test system produces controlled vibrations to evaluate the reliability of components used in various applications.

Due to the large number of U-joints that are present in tube-and-fin heat exchangers, this joint geometry is selected for vibration testing. For this geometry, a U-bend tube is joined at both ends to straight tubes, as shown in Fig. 5. These two tube-to-tube joints are formed by flaring the straight tube for insertion of the U-bend with adhesive, rather than using a coupling. The outer tube diameters are 9.525 mm (3/8 inch) and the straight tube lengths are 152.4 mm (6 inches). A custom adhesive formulation from an industry collaborator (with characteristics similar to the previous one) is used for the joining process, which was performed by the industry partner. Two different sets of U-joints were tested: one set of 8 samples with adhesive joints and another set of 8 samples having brazed joints. Two types of joints are tested simultaneously for comparison.

The vibration exciter generates the vibrations of a specified frequency and displacement to drive the base plate. It is important to firmly clamp the U-joints to the base plate for both safety and accuracy of the testing. For this purpose, aluminum fixtures are custom-designed and fabricated to clamp the extended straight tubes while leaving the U-joints to hang freely at the end, similar to their configuration in tube-and-fin heat exchangers. The 3D drawings of the fixtures are shown in Fig 6. The bottom plate of the fixture is affixed to the shaker base plate using bolted connections through two large clearance holes. The bottom and top fixture plates are attached using bolted connections; eight bolts pass through clearance holes in the top plate and thread into the bottom plate. At the interfacing surfaces between these two plates, there are 16 half cylinder cavities designed to clamp the extended tubes of the samples. Black rubber sheets taped on the extended tubes between the plates and samples provide cushioning and fix the samples in place. The diameter of the cavity is sized to be slightly smaller than the outer tube diameter plus the thickness of the rubber sheet, such that the copper tubes are pushed firmly into place with compression of the black rubber sheets. Fig 5 shows a photograph of the two sets of U-joints with fixtures installed on the shaker test stand.

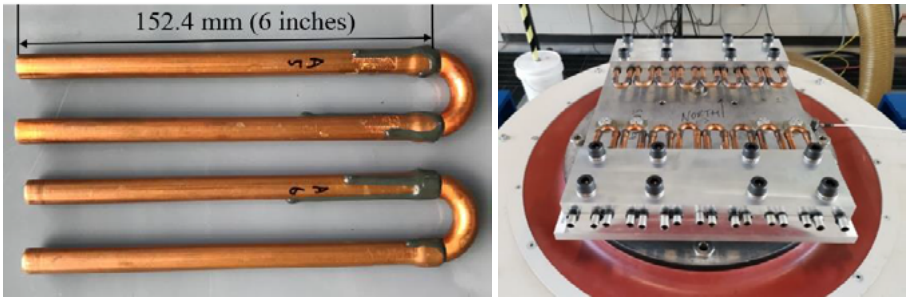


Fig. 5 Photographs of the U-shape joints with adhesive (left) and the fixtures containing a set of 8 samples each installed on the vibration shaker test stand.

4.2. Testing procedure

Following Table 4, the fixtured joints are subjected to vibrations with 0.3 mm displacement at a frequency of 125 Hz. The total number of the excitations is 2,000,000. The displacement and frequency of the test section are monitored and measured throughout the test. The joints are not pressurized with any fluid during the vibration testing in case of failure.

Before and after the vibration testing, the U-joint samples are each visually inspected and checked for leakage. Before vibration testing, fittings are soldered to the open end of the extended tubes to allow charge the samples with high-pressure nitrogen. During the soldering process, the U-joints were cooled using wet cloths to keep the temperature near room temperature. The samples with fittings are charged to 1700 kPa (approximately 250 psi) and immersed in water to observe if there are any air bubbles. The fittings are unsoldered and removed before placing the sample into the fixtures. The same process is repeated after the vibration testing.

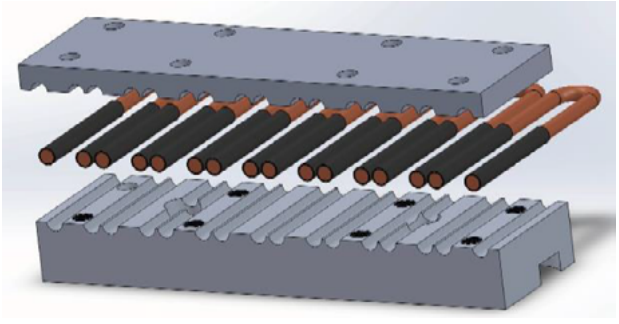


Fig. 6 3D Drawing of the fixture assembly with U-shaped joints wrapped with black rubber sheet.

4.3. Results and discussion

Before vibration testing, there were no cracks or imperfections in the adhesive or brazed joints, and all the samples were leak-free. The in-situ test stand measurements confirmed that the samples were subjected to 0.3 mm displacement vibrations at 125 Hz; the acceleration for the shaker was 21.2 g. The test stand ran continuously for 4.5 hours, which resulted in a total of 2,025,000 excitations. After testing, the rubber sheets used for fixing the samples into place were worn as expected, but the copper surface and the joints appeared the same as before testing for both brazed joints and adhesive joints as shown in Fig. 7. All the samples were confirmed to be leak free after testing. The results demonstrate that the adhesive joints are able to survive these extreme vibration conditions just as the brazed joints without any failures.



Fig. 7 Photographs of the U-shape joints after the vibration test for adhesive joints(left) and vibration joints compared with brazed joints (right).

5. Conclusions

Adhesive joints have the potential to replace brazed joints and improve system efficiencies in the HVAC&R industry. Compared to existing brazed and mechanical joints, the use of adhesives offers lowers cost, increase the ease of manufacturing without an open flame, and provides the flexibility to be applied to various materials and geometries. To demonstrate the application procedure and explore the feasibility of an adhesive joint, two separate proof-of-concept tests were performed using a heat pump dryer system and a vibration shaker test stand. An adhesive joining procedure is presented including surface preparation, adhesive preparation, adhesive application, and curing. For the heat pump dryer system, tube-to-tube adhesive joints were installed

at the inlet and outlet of the compressor. The system was first pressurized to check for initial leaks and then charged with refrigerant for performance testing over a 6-month period. Results showed that the adhesive joints hold the refrigerant pressure without leaks and the system performs consistently before and after the installation of adhesive joints. For the vibration testing, copper U-bend samples were joined to straight tubes using either an adhesive or with a standard brazing method as a benchmark. These joints were fixed on an industrial shaker table and tested following an ISO standard for joints with 0.3 mm displacement at 125 Hz for 2,025,000 vibrations. The joints were leak checked before and after the vibration testing and no failures were observed for the adhesive or brazed joints. These proof-of-concept tests indicate that there is potential for use of adhesive joints to replace brazed joints in HVAC&R applications, which warrants further investigation.

Acknowledgements

This research was supported by the DOE Office of Energy Efficiency and Renewable Energy, Building Technologies Office (BTO) through the Buildings Energy Efficiency Frontiers & Innovation Technologies (BENEFIT) program. The authors would like to thank Antonio Bouza (DOE BTO HVAC, Water Heating, and Appliances Technology Manager) for his support and Prof. Jeff Rhoads and Allison Range for their assistance in performing the vibration testing. This manuscript was coauthored by UT-Battelle, LLC staff under Contract No. DE-AC05-00OR22725 with the U.S. Department of Energy. The United States Government retains and the publisher, by accepting the article for publication, acknowledges that the United States Government retains a non-exclusive, paid-up, irrevocable, world-wide license to publish or reproduce the published form of this manuscript, or allow others to do so, for United States Government purposes. The Department of Energy will provide public access to these results of federally sponsored research in accordance with the DOE Public Access Plan (http://energy.gov/downloads/doe-public-access-plan).

References

[1] EPA. Inventory of U.S. greenhouse gas emissions and sinks: 1990-2013. U.S. Environmental Protection Agency. EPA 430-R-15-004. 2015, April 15.
[2] AWS Committee on Definitions. Standard welding terms and definitions, including terms for adhesive bonding, brazing, soldering, and thermal spraying, AWS, Miami, American Welding Society; 2001, p. 5.
[3] Copper Development Association Inc., Copper Tube Handbook 2019, CDA Publication A4015-14-19; 2019, McLean, VA.
[4] ASTM D 907. Standard definitions of terms relating to adhesives. American society for testing and materials; 2015, Conshohocken, PA.
[5] R.C.L. Tai, Z. Szklarskasmialowska, 1993. Effect of fillers on the degradation of automotive epoxy adhesives in aqueous solutions: Part I absorption of water by different fillers-incorporated automotive epoxy adhesives. Journal of Materials Science, 1993, vol. 28, p. 6199-6204.
[6] International Organization for Standardization ISO 14903: 2017, Refrigerating systems and heat pumps - Qualification of tightness of components and joints; 2017, Geneva, Switzerland.
[7] W. Goetzler, M. Guernsey, J. Yound, Research & Development Opportunities for Joining Technologies in HVAC&R. Navigant Consulting, Inc. 2015, Burlington, MA.

13th IEA Heat Pump Conference
April 26-29, 2021 Jeju, Korea

Experimental investigation of condenser with small diameter copper tube in air source heat pump water heater

Tiantian Wang[a], Zhanpeng Liu[a], Naiping Gao[a,*], Tingwei Fan[b], Hengyi Zhao[c], Yifeng Gao[c]

[a]School of Mechanical Engineering, Tongji University, Shanghai, 201804, China
[b]Gomon New Energy Ltd. of Jiangsu Province, Taizhou, 214500, China
[c]International Copper Association, Shanghai Representative Office, Shanghai, 200020, China

Abstract

In this paper, a series of experimental tests on system coefficient of performance (COP) of air source heat pump water heater (ASHPWH) working with R22 were carried out. ASHPWH equipped the condenser which was wrapped around copper tubes with different inner diameters of 4.5 and 6.4mm and variable types of smooth tube and internal threaded tube. Besides, the economic cost of aforementioned systems were compared and analyzed. The results show that the system performance of ASHPWH with small diameter copper tubes of 4.5mm is improved compared with the large diameter copper tube of 6.4mm, meanwhile the total costs are greatly reduced. Given that the inner diameter is constant, the internal threaded tube has a significant improvement in system COP compared with the smooth tube. Moreover, COP of ASHPWH with internal threaded tubes whose inner diameter is 4.5mm can reach 4.17, therefore the small diameter copper tube has a good application prospect in ASHPWH.

Keywords: heat pump water heater; coefficient of performance (COP); condenser; small diameter copper tubes.

1. Introduction

With the rapid rise of Chinese economy and advancement of urbanization, the "energy bottleneck" problem is becoming increasingly serious. The energy cost of Chinese construction operation was 864 Mtce (million tons of standard coal equivalent) in 2015 excluding biomass energy [1], accounting for about 20% of the total energy consumption in China. As for urban dwelling, the urban residential energy consumption was 192 Mtce in 2015 excluding northern heating, and the energy consumption of domestic hot water was equal to 27 Mtce, accounting for about 14% of total residential energy consumption.

The concentrated supply of urban residential hot water in China mainly depends on electricity, fuel (coal, oil, gas) and solar energy. With increasing awareness of energy saving and emission reduction, the advantages of heat pump water heater, including air source [2-4], ground source [5-6] and solar source [7-8], are significantly obvious in medium-sized centralized hot water supply and small domestic hot water supply. ASHPWH is one of the most widely used style in the market due to its energy-savings, environmental friendliness, flexibility and convenience over the recent decades.

In general, the analysis of the dynamic system characteristics under different working conditions of ASHPWH can be carried out by means of modelling and experiments. Ibrahim et al. [9] proposed a dynamic simulation model to predict the performance of an ASHPWH. The developed model was utilized to assess its performance from the perspective of energy savings and greenhouse gas emissions. Peng et al. [10] developed an ASHPWH model to work under wide operating conditions using different expansion devices, such as electronic expansion valve (EEV), capillary tube and short tube orifice, it was found that the EEV throttling system performed best. Zhang et al. [11] investigated the system performance of an ASHPWH via calculating

* Corresponding author. Tel.: +86-021-65983867, +86 13817847420.
E-mail address: gaonaiping@tongji.edu.cn.

and testing, it pointed out that the refrigerant filling quantity played an important role in heat pump system running.

Some investigations were conducted to compare the different types of refrigerant used in the air source heat pump (ASHP) system. Wang et al. [12] presented a novel frost-free ASHP system working with R134a and R407C as an R22 alternative, the results showed that R134a was more promised alternative than R407C to R22 for the novel ASHP system. Li et al. [13-14] compared the effects of R22, R134a and R744 on the solar-air hybrid heat source heat pump water heater, it was found that the COP of R744 was highest within the ambient temperature of 5~13°C while the COP of R134a was best when the ambient temperature was higher than 13°C.

Moreover, the condenser characteristics were also paid special attention. Yang et al. [15] analyzed the flow condensation heat transfer and pressure drops of R1234yf and R134a in a small circular tube. The results showed that both pressure drop and condensation heat transfer performance depended on the fluid properties, flow conditions and flow patterns. Yan et al. [16] investigated the characteristics of condensation heat transfer and pressure drop of R134a flowing in a horizontal small circular pipe with an inside diameter of 2.0mm, it was found that the condensation heat transfer coefficient of small pipe was about 10% higher than that of large pipe with the inside diameter of 8.0mm. Son et al. [17] experimentally studied the condensation heat transfer of R22, R134a and R410a flowing in the horizontal copper tube of 1.77, 3.36 and 5.35mm inner diameter, respectively. In case of two-phase flow, the condensation heat transfer coefficient for R22, R134a and R410a increased with increasing mass flux and decreasing tube diameter.

The literatures listed above mainly attached importance to the system COP related with expansion devices, refrigerant and its filling quantity. And special attention was paid to the condenser characteristics. But the effects of structural parameters of copper tubes in the condenser on system COP have rarely been investigated. Accordingly, the purpose of this study is to carry out new experimental research on copper tube with different inner diameters, lengths and types used in the condenser of ASHPWH. The effects of aforementioned parameters on system COP are analyzed and these parameters are optimized in order to improve the COP of system. Meanwhile the economic analyses between copper tubes and aluminum microchannel are also taken into consideration.

2. Experimental apparatus and procedures

2.1. ASHPWH experimental system description

The experimental apparatus established in the present study is schematically shown in Fig.1. And the theoretical *P-h* diagram is depicted in Fig.2. The picture of experimental bench is illustrated in Fig.3. The ASHPWH consists of three main loops: the air loop, the refrigerant R22 loop and the water loop. More special attention are paid to the refrigerant R22 circle. As can be shown in Fig.2, its basic components include compressor, condenser, expansion valve and evaporator. The superheated refrigerant vapor is produced in the evaporator, then it flows into the compressor and turns into high temperature and pressure refrigerant vapor via the isentropic compression process 1-2. Next it is sent to the condenser to release heat to the water tank and itself is cooled down to the liquid state, thereby the domestic water at a certain temperature can be obtained through the isobaric cooling process 2-3. Subsequently the liquid refrigerant turns into a gas-liquid mixed state after passing through the expansion valve and then it flows into the evaporator. The refrigerant absorbs heat from the outside air through the isobaric evaporation process 4-1, and enters the compressor again to start a new cycle.

The thermodynamics of ASHPWH can be calculated according to Fig.2. In the actual operation process, the electric energy consumed by the compressor can be expressed by the following equation (1).

$$W = \frac{m_f(h_2 - h_1)}{\eta_o} \tag{1}$$

And the mass flow rate of refrigerant R22 can be calculated according to equation (2).

$$m_f = \frac{NV_{cp}\rho_1\eta_v}{60} \tag{2}$$

Then the released heat from the refrigerant R22 to water in the condenser can be calculated according to equation (3). Equally, this part of heat is absorbed by the water in the condenser.

$$Q_c = m_f(h_2 - h_3) = \frac{\rho_w V_w C_p (T_{out} - T_{in})}{t} \quad (3)$$

Meanwhile the absorbed heat from the ambient air is defined as the equation (4).

$$Q_e = m_f(h_1 - h_4) \quad (4)$$

Finally the system COP can be expressed as the following equation (5).

$$COP = \frac{Q_c}{w} \quad (5)$$

In the above equation (1) ~ (5), m_f represents the mass flow rate of refrigerant R22. The values of rotating speed N, displacement volume rate V_{cp} and volumetric efficiency η_v are 2880rpm, 17cm^3/rev and 91%. h_1, h_2, h_3 and h_4 stand for the enthalpy of point 1, point 2, point 3 and point 4 in Fig.2 respectively. η_o represents the overall efficiency of compressor and the value of it is 0.7 [18] in this study. ρ_w stands for the average density of domestic hot water in the heating process. V_w represents the volume of domestic hot water. C_p represents the average specific heat capacity of water. T_{in} and T_{out} mean the initial temperature and final temperature of water during the heating process. t represents the time of heating process. It is worth mentioning that the enthalpy of refrigerant R22 can be obtained according to the measured temperature and pressure in the corresponding position.

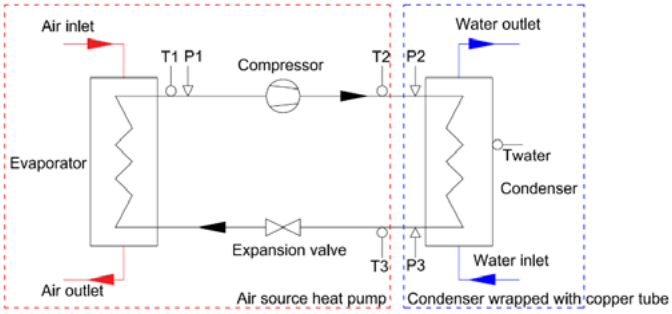


Fig. 1. Schematic diagram of the experimental system.

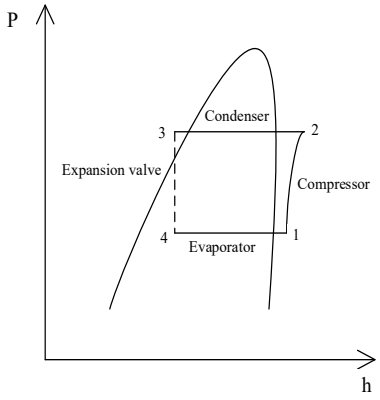


Fig. 2. Theoretical *P-h* diagram of ASHPWH.

2.2. Testing procedure and measuring sensors

The main goal of these experiments is to investigate the effects of different structural parameters of copper tubes on COP of ASHPWH. In this process, 200L water is heated from 15°C to 55°C, and the electric energy consumed by the compressor can be obtained due to the detected voltage and current. Besides, the heat exchange capacity in the condenser can be calculated according to Equation (3). Therefore the system COP can be obtained based on Equation (5). Meanwhile the economic analysis is also taken into consideration for practical application. In this study, the experimental tests are carried out via combining the water tank wrapped around copper tubes in different cases with the host of ASHP system. It should be noted that the dry bulb temperature and the wet bulb temperature of the ambient environment are 20°C and 15°C respectively. The performance parameters of the host are listed in Table 1.

Fig.4 (a) and (b) depict the geometrical and physical diagram of the water tank wrapped around copper tubes respectively. Table 2 illustrates five variable winding schemes of copper tubes outside the water tank in experimental tests. According to Table 2, group A and B study the effects of variable diameters and lengths of copper tubes on system performance. Group B and C pay special attention to copper tube arrangements. Group C and D investigate the effects of length of copper tube and refrigerant charge. Moreover, group D and E compare the effects of type of copper tube on system performance.



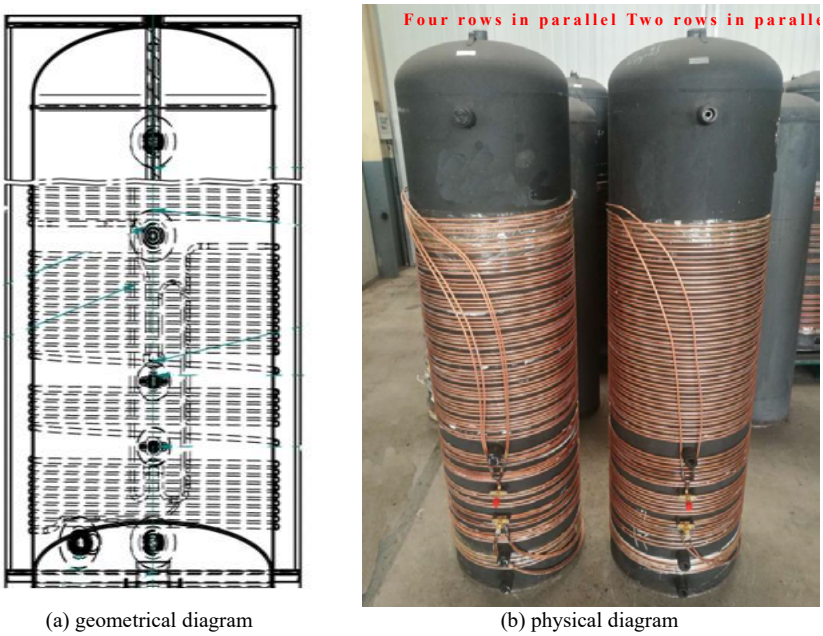
Fig. 3. Picture of the ASHPWH experimental bench.

Table 1. Performance parameters of host of ASHP system

Parameters	Value
Type	KF35E
Rated heating capacity (kW)	3.5
Domestic hot water output (L/h)	80
Rated input power/current (kW/A)	0.83/4.0
Maximum input power/current (kW/A)	1.3/6.0
Refrigerant/rated charge volume (-/g)	R22/1050
Maximum allowable pressure on high/low pressure side (MPa)	3.0
Allowable working overpressure on exhaust side (MPa)	3.0
Allowable working overpressure on suction side (MPa)	0.7

Table 2. Five winding schemes of copper tubes outside the water tank

Group	Inner diameter (mm)	Type	Length (m)	Arrangement	Refrigerant charge (g)
A	6.4	Smooth tube	60	Two rows in parallel	1050
B	4.5	Smooth tube	80	Two rows in parallel	1050
C	4.5	Smooth tube	80	Four rows in parallel	1050
D	4.5	Smooth tube	100	Four rows in parallel	1130
E	4.5	Internal threaded tube	100	Four rows in parallel	1130



(a) geometrical diagram (b) physical diagram

Fig. 4. Picture of water tank wrapped around copper tubes.

As can be seen in Fig.1, the experimental bench equips 4 thermocouples (T1-T3 and Twater), 3 pressure sensors (P1-P3). They are used to analyze the system characteristics under variable conditions. The specific information about these measuring sensors, such as the instrument type, measuring range and accuracy are given in Table 3.

Table 3. Major measuring sensors used in the experimental system

Parameter	Instrument type	Measuring range	Accuracy
P	diffused silicon pressure sensor	0-2MPa	±0.2% of MV
T	K-type thermocouple	0-1000°C	±1.5°C

3. Results and discussion

3.1. System performance of ASHPWH

The performances of five winding schemes of copper tubes outside the water tank are experimentally investigated using the host of ASHP system. The results of these tests are shown in Table 4. It is found that the COP of group A is 3.95 and it is higher than that of group B (3.66) and group C (3.82). Given that the refrigerant charge and the copper tube type are fixed in these three groups, the heat exchange area of group A is larger than group B and C because of the variable diameters and lengths of copper tube. Besides, comparing

group B and C, the arrangement of copper tubes can also affect the system performance. Obviously the arrangement of four rows in parallel runs better than that of two rows in parallel under the same condition. It can be clearly seen in Table 4 that the values of power consumed by compressor of group B and C are 0.83kW and 0.84kW respectively, which are nearly the same. However, the heating capacity of group C is 3.21kW and it is obviously higher than that of group B (3.04kW). Meanwhile the heating time of group C is a little shorter compared with group B. Furthermore, the type of copper tube is also a significant factor affecting system performance. It can be easily found that the internal threaded tube in group E can make the COP of ASHPWH increase by 5% compared with smooth tube in group E considering other things being equal. This is because the internal threaded tube increases the heat exchange area while also enhancing the heat transfer effect on the refrigerant side, thus increasing the heat transfer coefficient of the refrigerant side. Therefore the heating time required for group E is greatly shortened to 9310s compared with 10160s in group D when heating the same volume of water.

Table 4. Experimental results of five variable winding schemes of copper tube

Group	Volume of water tank (L)	Heating time (s)	Heating capacity (kW)	Power consumption (kW)	COP
A	200	9640	3.47	0.88	3.95
B	200	11000	3.04	0.83	3.66
C	200	10420	3.21	0.84	3.82
D	200	10160	3.29	0.83	3.96
E	200	9310	3.59	0.86	4.17

Further to say, the variation of supercooling degree of refrigerant at the outlet of condenser is also taken into consideration. The variation ranges of five different cases are shown in Fig.5. Moreover, special attention is paid to the flow resistance of refrigerant in the copper tubes. The flow resistance of these five groups are depicted in Fig.6. What worth mentioning is that flow resistance in this paper represents the temperature difference corresponding to inlet and outlet pressure of condenser.

As can be seen from Fig.5, the supercooling degree of refrigerant in group A, B, C and D is basically between 5~10°C while the supercooling degree in group E is much higher. It means that the internal threaded tube makes heat transfer coefficient of refrigerant higher compared with the smooth tube, the heat exchange is so sufficient that energy efficiency of ASHPWH is greatly improved.

As shown in Fig.6, flow resistances of group B and E are larger than 3°C. It indicates that longer length, arrangement of two rows in parallel and internal threaded tube have adverse effects on flow characteristics in the copper tubes. Honestly speaking, although the COP of group E is highest, more attention should be paid to reduce the flow resistance in the future study in order to have a better system performance.

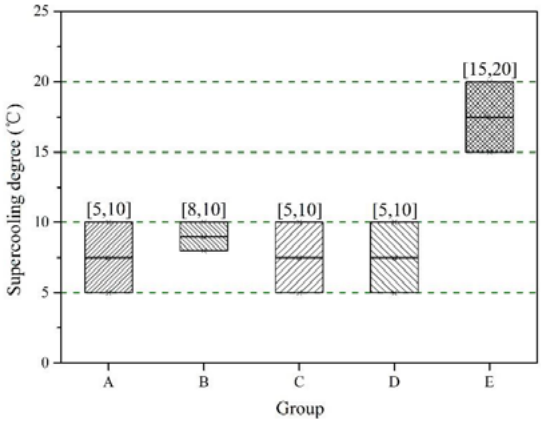


Fig. 5. Variation ranges of supercooling degree of five different groups.

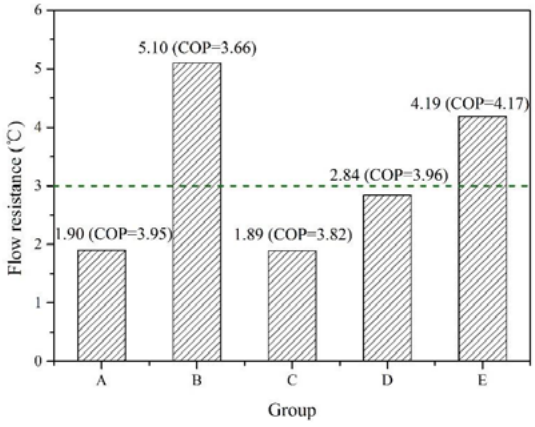


Fig. 6. Flow resistance of these five different groups.

3.2. Economic analysis of tubes

Generally speaking, the total costs of copper tubes consist of material cost and processing cost. And material cost takes a large proportion of total costs, while processing cost only accounts for 10%-20% of material cost. According to the survey, the material cost of copper is ¥45,000 per ton. The processing cost of smooth copper tube is ¥4,500 per ton, and that of internal thread copper tube is ¥6,500 per ton. The total costs of group A, D and E are listed in Table 5. Meanwhile the total cost of aluminum microchannel (group F) is also considered and compared with that of copper tubes.

As for the smooth copper tubes (group A and D), it indicates that copper tubes with smaller diameter can make ASHPWH run better while reducing the total costs. Besides, it is obvious that the total costs of internal threaded copper tubes with the inner diameter of 4.5mm in group E reduce by 17% compared to the smooth copper tubes with 6.4mm in group A. Meanwhile the COP of system increases by 5%. The main reason is that the internal thread copper tubes with smaller diameter can increase the heat exchange area while enhancing the convective heat transfer on the refrigerant side, thereby improving the system energy efficiency. However, what worth mentioning is that the smaller the diameter, the thinner the wall. Considering that the refrigerant pressure is relatively high within high temperature range, if the tube wall is too thin, it is easy to make the D-type copper tube change into O-type, thus reducing the heat exchange area. With regard to the water tank using aluminum microchannel, it is well-known that the unit cost of aluminum is lower than that of copper, but the processing cost of the former is too high. The values of COP in group D and F are 3.96 and 3.95 respectively, the total costs of smooth copper tubes with smaller diameter of 4.5mm reduce by 29% compared to that of aluminum microchannel. Moreover, the internal threaded copper tubes in group E can both increase the system COP and reduce the total costs. In summary, the copper tubes with smaller diameter are relatively more cost-effective, and can also improve the system COP. Thus it has a good application prospect in the area of ASHPWH in the future.

Table 5. Economic analysis of tubes in variable groups

Group	Type	Inner diameter (mm)	Weight per unit length (kg/m)	Length (m)	Total weight (kg)	Total costs (¥)	COP
A	Smooth copper tube	6.4	0.0537	60	3.22	159	3.95
D	Smooth copper tube	4.5	0.0317	100	3.17	157	3.96
E	Internal threaded copper tube	4.5	0.0256	100	2.56	132	4.17
F	Aluminum microchannel	--	--	--	--	220	3.95

4. Conclusions

In this study, the system performance of ASHPWH with variable water tanks using five winding schemes of copper tubes are experimentally investigated. Besides, special attention has been paid to the economic analysis of tubes utilized outside the water tank. The effects of inner diameter and type of copper tubes on system COP have been studied. Moreover, the total costs of copper tubes and aluminum microchannel have been analyzed. The following conclusions can be drawn:

1. As for the smooth copper tubes with different inner diameters (6.4 and 4.5mm), the smaller diameter copper tubes dominate in terms of system performance and economic cost of ASHPWH. Besides, the arrangement of four rows in parallel runs better than that of two rows in parallel considering all other things being equal.
2. With regard to the internal threaded tubes and smooth tubes with same inner diameter, the former can increase the heat exchange area while enhancing the heat transfer effect on the refrigerant side. Therefore the highest COP of ASHPWH can reach 4.17 using the internal threaded copper tubes with the inner diameter of 4.5mm. However, the internal threaded tubes have an adverse effect on system operation, meanwhile the flow resistance increases accordingly.
3. Small diameter copper tube outweighs aluminum microchannel in terms of economic cost of ASHPWH. The total costs of smooth copper tubes with inner diameter of 4.5mm reduce by 29% compared to aluminum microchannel when the system COP of these two cases are almost the same.

Nomenclature

C_p	average specific heat capacity (kJ/(kg·K))	*Subscripts*	
h	specific enthalpy (kJ/kg)	1-4	state point
m	mass flow rate (kg/s)	c	condenser
N	rotating speed (rpm)	cp	compressor
Q	heat transfer amount (kW)	e	evaporator
t	time (s)	f	working fluid
T	temperature (°C)	in	initial
V	volume (L)	o	overall
W	power (kW)	out	final
Greek symbols		out	v
ρ	density (kg/m^3)	w	water
η	efficiency		

References

[1] China annual development research report of building energy conservation in 2017. Beijing: China building industry press. 2017, p. 1-28.
[2] Wang ZH, Wang FH, Wang XK, Ma ZJ, Wu XZ, Song MJ. Dynamic character investigation and optimization of a novel air-source heat pump system. *Appl Therm Eng* 2017;**111**: 122-33.
[3] Guo JJ, Wu JY, Wang RZ, Li S. Experimental research and operation optimization of an air-source heat pump water heater. *Appl Energy* 2011;**88**:4128-38.
[4] Fardoun F, Ibrahim O, Zoughaib A. Quasi-steady state modeling of an air source heat pump water heater. *Energy Procedia* 2011;**6**:325-30.
[5] Esen H, Esne M, Ozsolak O. Modelling and experimental performance analysis of solar-assisted ground source heat pump system. *J Exp Theor Artif In* 2015;**29**:1-17.
[6] Zhai XQ, Cheng XW, Wang RZ. Heating and cooling performance of a minitype ground source heat pump system. *Appl Therm Eng* 2017;**111**:1366-70.
[7] Kong XQ, Zhang D, Yang QM. Thermal performance analysis of a direct-expansion solar-assisted heat pump water heater. *Energy* 2011;**36**:6830-38.
[8] Moreno-Rodriguez A, Gonzalez-Gil A, Izquierdo M, Garcia-Hernando N. Theoretical model and experimental validation of a direct-expansion solar assisted heat pump for demestic hot water applications. *Energy*. 2012;**45**:704-15.
[9] Ibrahim O, Fardoun F, Younes R, Louahlia-Gualous H. Air source heat pump water heater: Dynamic modeling, optimal energy management and mini-tubes condensers. *Energy* 2014;**64**:1102-16.

[10] Peng JW, Li H, Zhang CL. Performance comparison of air-source heat pump water heater with different expansion devices. *Appl Therm Eng* 2016;**99**:1190-200.
[11] Zhang J, Wang RZ, Wu JY. System optimization and experimental research on air source heat pump water heater. *Appl Therm Eng* 2007;**27**:1029-35.
[12] Wang Z, Wang FH, Ma ZJ, Song MJ. Numerical study on the operating performances of a novel frost-free air-source heat pump unit using three different types of refrigerant. *Appl Therm Eng* 2017;**112**:248-58.
[13] Li SS, Li SH, Zhang XS. Simulation research of a hybrid heat source heat pump using R134a, R744 instead of R22 for domestic water heating in residential buildings. *Energ Buildings* 2015;**91**:57-64.
[14] Li SS, Li SH, Zhang XS. Comparison analysis of different refrigerants in solar-air hybrid heat source heat pump water heater. *Int J Refrig* 2015;**57**:138-46.
[15] Yang CY, Nalbandian H. Condensation heat transfer and pressure drop of refrigerants HFO-1234yf and HFC-134a in small circular tube. *Int J Heat Mass Tran* 2018;**127**:218-27.
[16] Yan YL, Lin TF. Condensation heat transfer and pressure drop of refrigerant R134a in a small pipe. *Int J Heat Mass Tran* 1999;**42**:697-708.
[17] Son CH, Lee HS. Condensation heat transfer characteristics of R-22, R-134a and R-410A in small diameter tubes. *Heat Mass Transfer* 2009;**45**:1153-66.
[18] Li YW, Wang RZ, Wu JY, Xu YX. Experimental performance analysis on a direct expansion solar-assisted heat pump water heater. *Appl Therm Eng* 2007;**27**:2858-68.

Responses to Reviewers' Comments

Dear Editor and Reviewers,

We quite appreciate the comments concerning our manuscript entitled "Experimental investigation of condenser with small diameter copper tube in air source heat pump water heater". Those comments are all valuable and very helpful for revising and improving our paper, as well as the important guiding significance to our researches. We have studied comments carefully and have made correction which we hope meet with approval. Revised portion are marked in red in the paper. The main corrections in the paper and the responses to the reviewer's comments are written in blue as following:

Reviewer #1

1. The description of symbols should add their units.

Discussion: Thanks very much for reviewer's careful suggestion. The "Nomenclature" section has been supplemented in order to describe the symbols in details and marked in red in the manuscript.

2. From the introduction, I can not understand the need of your research. The knowledge gap should be properly issued.

Discussion: Thanks for reviewer's valuable advice. The purpose of this study is to investigate the effects of structure parameters of copper tubes in the condenser on the COP of system throught experiments, which has rarely been studied before. Besides, it can provide the guidance for copper tubes applied in the area of ASHPWH. According to the reviewer's suggestion, we have supplemented the "Introduction" section and the modified texts are marked in red in the manuscript.

3. The overall efficiency of compressor η, how did you calculate it?

Discussion: Thanks for reviewer's question. According to some published literatures[1-3], the recommended range of overall efficicncy of compressor η_o is 0.7~0.75. In our experimental bench, the power consumed by the compressor can be detected directly by the dynamometer, the enthalpy of working fluid R22 at the inlet and outlet of compressor can be determined by the measured pressures and temperatures in the corresponding position. And the mass flow rate of working fluid can be calculated according to the following equation.

$$m_f = \frac{NV_{cp}\rho_1\eta_v}{60}$$

The value of rotating speed N, displacement volume rate V_{cp} and volumetric efficiency η_v are 2880rpm, 17cm^3/rev and 91%. The density of R22 at the inlet of compressor ρ_1 can be obtained through Refprop 9.0 according to T_1 and P_1. Then the average overall efficiency of compressor in our experiments can be calculated accroding to equation (1) in the manuscript and the value of it in this study is 0.7, which is within the recommended range.

According to the reviewer's question, we have modified the section 2.1 and made explanations in the manuscript.

[1] Li YW, Wang RZ, Wu JY, Xu YX. Experimental performance analysis and optimization of a direct expansion solar-assisted heat pump water heater. *Energy* 2007;**32**:1361-74.

[2] Li YW, Wang RZ, Wu JY, Xu YX. Experimental performance analysis on a direct expansion solar-assisted heat pump water heater. *Appl Therm Eng* 2007;**27**:2858-68.

[3] Moreno-Rodríguez A, González-Gil A, Izquierdo M, Garcia-Hernando N. Theoretical model and experimental validation of a direct-expansion solar assisted heat pump for domestic hot water applications. *Energy* 2012;**45**:704-15.

4. There are still some English grammar mistakes in your paper. Maybe a native speaker is needed.
Discussion: Thanks a lot for reviewer's suggestion. We have examined the grammar in details and modified the full paper carefully. There are some minor modifications but they are **not** marked specifically in the manuscript.

5. Some quantitative analysis data should be given in the text of results section, especially when comparing performance.
Discussion: Thanks very much for reviewer's valuable suggestion. We have modified section 3.1 and 3.2 in the manuscript accordingly and the modified texts are marked in red.

Reviewer #2
This paper presented experimental tests on system coefficient of performance (COP) of air source heat pump water heater (ASHPWH) working with R22 in new experimental research of copper tube with different inner diameters, lengths and types used in the condenser. The author clearly shows the experimental apparatus, procedures, system performance and economic analysis. The paper is well-organized and the quality of English is satisfactory. The paper can be accepted.
Discussion: We appreciate for the reviewers' warm work earnestly.

We tried our best to improve the manuscript and made some changes in the manuscript. We appreciate for Editors/Reviewers' warm work earnestly, and hope that the correction will meet with approval.
Once again, thank you very much for your comments and suggestions!
Naiping Gao

13th IEA Heat Pump Conference
April 26-29, 2021 Jeju, Korea

Investigation on system performance of air source heat pump water heater with phase change material

Zhanpeng Liu[a], Tiantian Wang[a], Naiping Gao[a,*], Hengyi Zhao[b], Yifeng Gao[b]

[a]School of Mechanical Engineering, Tongji University, Shanghai, 201804, China
[b]International Copper Association, Shanghai Representative Office, Shanghai, 200020, China

Abstract

In this paper, a series of experimental tests on air source heat pump water heater (ASHPWH) using a novel heat battery module with phase change material (PCM) were carried out. The melting temperature of PCM is 58°C. Meanwhile special attention has been paid to the optimization of heat transfer in heat battery module by means of computational fluid dynamics (CFD). The results indicate that the instant coefficient of performance (ICOP) of ASHP is up to 3.82 but the operation of ASHP is unstable and in poor condition with a 1.3 mm caliber electronic expansion valve. The latest experiment shows that using 1.5 mm caliber electronic expansion valve can not only make ASHP run more smoothly but also increase ICOP to 4.08. During the discharge process of heat battery module, 106.5L domestic water can be heated from 15°C to 40°C. The CFD simulation testifies copper fins applied in heat battery module can greatly enhanced the heat transfer coefficient compared with aluminum fins.

Keywords: Heat pump water heater; phase change material; CFD; system performance

1. Introduction

With the rapid development of the economy to stimulate people's demands for high-quality life, water heaters have become an indispensable device in today's homes. Because of its characteristics of energy saving, high efficiency and comfort, ASHPWH has gradually been favored by domestic and foreign markets. China's ASHP industry has developed rapidly since the beginning of the 21st century. In the latest decade, China has become the world's second largest ASHP producer next to Japan. According to the statistical data in 2015, ASHPWH share in China is only 3%, but with the promulgation of relevant energy conservation policies and the improvement of consumers' environmental awareness, ASHPWH has unparalleled application prospect.

Some researches on ASHPWH have been conducted for several decades. For example, the host of ASHPWH needs frequent start and stop, which not only causes a large amount of energy waste but also greatly affects the life of the heat pump system, which will limit the further development of ASHPWH. However, PCM has the advantages of large latent heat and suitable phase transition temperature, which can replace the bulky water tank and further enrich the application scenario [1] of ASHPWH. Moreover, ASHPWH with PCM can make rational use of electric power cost between on-peak and off-peak, saving the cost of electricity and balancing the grid load.

Moreover, PCM has problems such as low thermal conductivity and unstable heat storage performance [2]. Therefore, strengthening the heat transfer of PCM in the endothermic and exothermic process has become a research focus of PCM. At present, the research on the application of highly conductive nanomaterials [3] coupled with PCM to improve the thermal conductivity of PCM has made significant progress. Motahar et al. [4] experimentally studied the thermal conductivity and viscosity of n-octadecane/TiO_2 nanoparticles [5-6] and found that the thermal conductivity is non-monotonic in both solid and liquid phases. In the solid phase, when the mass fraction of nanoparticles is 3%, the thermal conductivity increases the most. In the liquid phase, when

* Corresponding author. Tel.: +86-021-65983867, +86 13817847420.
E-mail address: gaonaiping@tongji.edu.cn.

the mass fraction of nanoparticles is 4%, the thermal conductivity increases the most. In addition, the maximum average thermal conductivity of the two stages was enhanced by about 5%.

The use of microencapsulated of phase change material (MPCM) [7-8] can be effective in reducing the reactivity of PCM with the external environment, increasing the heat transfer area and the heat transfer rate, which makes MPCM has great application potential in the fields of heat storage, temperature control and heat protection. Luo et al. [9] first applied the miniemulsion polymerization method to the synthesis of nanocapsule phase change materials, and prepared nanocapsules with paraffin as the core material, styrene and methyl methacrylate copolymer as the shell material [10-11]. The obtained nanocapsules have a complete core-shell structure and a particle size of less than 100 nm. Park et al. [12] also synthesized stable spherical nanocapsules with paraffin as core and polystyrene as shell by miniemulsion polymerization. The DSC freeze-thaw cycle shows that it has good thermal stability and exothermic properties, and the latent heat of phase change can reach up to 145 J/g.

When there is an electric current passing through the loop composed of different conductors, the endothermic and exothermic phenomena will appear respectively at the joints of different conductors with the direction of the current. Accordingly, Selvam et al. [13] used the Peltier effect [14] to enhance the heat transfer of PCM. Experiment has shown that the cold junction temperature of a PCM Peltier cooler under pulse operation is significantly reduced from -14.5°C to -17.5°C compared to a Peltier cooler without PCM under pulsed operation. It is also found that, there is no significant reduction in COP of the Peltier cooler under pulse operation with PCM as compared to pulse operation without PCM.

Therefore, the purpose of this study is to explore the feasibility and stability of the combination of ASHPWH and PCM by means of thermodynamic performance analysis. Based on the preliminary experimental work and the test data of the prototype, system performance of ASHPWH is analyzed. Moreover, the heat transfer optimization of heat battery module has been conducted via CFD simulation, the comparison between copper tubes and aluminum tubes is illustrated in this paper.

2. Experimental setup

2.1. ASHPWH with PCM experimental system description

The schematic diagram of present experimental setup is shown in Fig. 1. Its basic components include compressor, heat battery module, expansion valve and evaporator. In order to enhance the heat transfer process in battery module, CFD simulation is applied to optimize the structure of heat battery compared with traditional ASHPWH, the main difference is that the condenser is replaced by a heat battery module. Due to the confidentiality agreement with a partner company, the details of heat battery module are not available in this paper. As can be shown in Fig. 2, the superheated refrigerant vapor, which is produced in the evaporator, flows into the compressor and turns into high temperature and pressure refrigerant vapor via the isentropic compression process 1-2. Then the refrigerant undergoes an isobaric cooling process 2-3 to transfer heat to PCM in the heat battery module. The supercooled refrigerant flowing out from the heat battery is throttled by the expansion valve and turns into a gas-liquid mixed state. The refrigerant then re-enters a new cycle through isobaric evaporation process 4-1 in the evaporator. During the valley electric charge time, ASHPWH starts to work and provide heat. Most of the heat released by the refrigerant is stored in PCM in the form of latent heat. When the hot water is needed, the cold water flows into the heat battery module that absorbs a large amount of heat and becomes hot water that can be used immediately. The time of hot water demand is mostly in peak time period, because of the difference of electric price between the peak and the valley, it can reduce electricity costs.

The thermodynamic performance of ASHPWH with PCM can be calculated according to Fig.2. First of all, the mass flow in ASHP can be calculated through the volume flow of the compressor multiplied by the refrigerant density at compressor inlet. The specific calculation equation is as follows:

$$\dot{m} = \dot{V}_s \cdot \rho \tag{1}$$

In the actual compression process, the electric energy used to compress the refrigerant vapor can be calculated by the following equation (2).

$$W = \frac{\dot{m}(h_2 - h_1)}{\eta_o} \tag{2}$$

Then the released heat from the refrigerant R22 to PCM in the heat battery can be calculated by using the following equation (3).

$$Q_b = \dot{m}(h_2 - h_3) \tag{3}$$

The instant coefficient of performance (ICOP) of ASHP, which is defined as the ratio of heat release of refrigerant in heat battery to power consumption of compressor, can be calculated as follows:

$$ICOP = \frac{Q_b}{W} \tag{4}$$

In the above equation (1) ~ (4), $\dot{m}$ represents the mass flow rate of refrigerant R22. ρ and $\dot{V}_s$ stand for the density and volume flow of refrigerant individually. h_1, h_2, h_3 and h_4 stand for the enthalpy of point 1, point 2, point 3 and point 4 in Fig. 2 respectively. η_0 represents the overall efficiency of compressor. It is worth mentioning that the enthalpy and condensation temperature of refrigerant R22 can be obtained according to the measured temperature and pressure in the corresponding position.

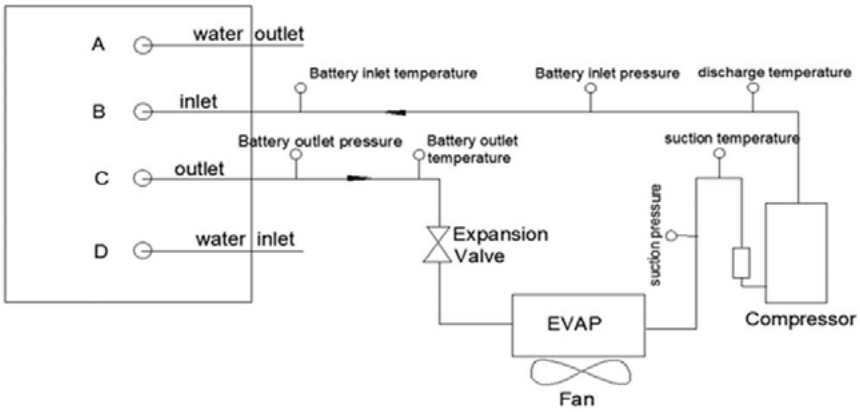


Fig. 1. Schematic representation of experimental setup

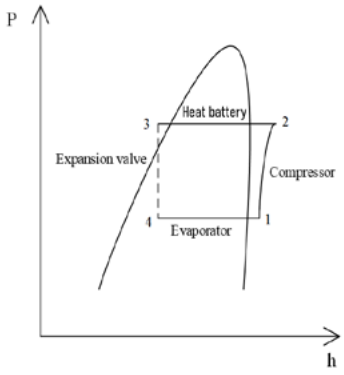


Fig. 2. Theoretical P-h diagram of ASHPWH with PCM

2.2. Testing procedure and measuring sensors

The main goal of these experiments is to test the stability and feasibility of ASHPWH using PCM. During the charge process, the refrigerant R22 releases the heat to the heat battery module whose initial temperature is about 20°C to a fully charged state. It can be measured that the dry bulb temperature and the wet bulb temperature of the ambient environment are 21°C and 19.5°C respectively. During the discharge process, 15°C cold water flows into the heat battery, and the obtained high-temperature hot water is mixed with 15°C cold water at the exit to obtain domestic hot water with 40°C. When the outlet temperature of water has reached 40°C without mixing with cold water, it is considered that the heat battery module is in a completely discharged state. The heat exchange capacity in the heat battery module can be calculated according to Equation (3), and the electric energy consumed by the compressor can be obtained due to the detected voltage and current. Accordingly, the system ICOP can be acquired by using Equation (4).

The performance parameters of the host are listed in Table 1. The experimental bench is shown in Fig. 3. It should be noted that the heat battery module is the most important part of the ASHPWH with PCM and the biggest difference from the traditional ASHPWH.

Table 1. Performance parameters of host of ASHP system

Parameters	Value
Rated heating capacity (kW)	3.2
Rated input power/current (kW/A)	0.88/4.2
Maximum input power/current (kW/A)	1.4/6.5
Refrigerant	R22
Rated charge volume (g)	1700
Caliber of electronic expansion valve (mm)	1.3/1.5



Fig. 3. Picture of the ASHPWH with PCM experimental bench.

As can be seen in Fig. 1, the experimental bench equips 4 thermocouples (suction temperature, discharge temperature, battery inlet temperature, battery outlet temperature), 3 pressure sensors (suction pressure, battery inlet pressure, battery outlet pressure). These sensors are used to measure the instantaneous change in refrigerant and to analyze the thermodynamic properties of the system. The specific information about these measuring sensors, such as the instrument type, measuring range and accuracy are given in Table 2.

Table 2. Major measuring sensors used in the experimental system

Parameter	Instrument type	Measuring range	Accuracy
P	diffused silicon pressure sensor	0-2MPa	±0.2% of MV
T	K-type thermocouple	0-1000°C	±1.5°C

3. Results and discussion

3.1. Experimental optimization

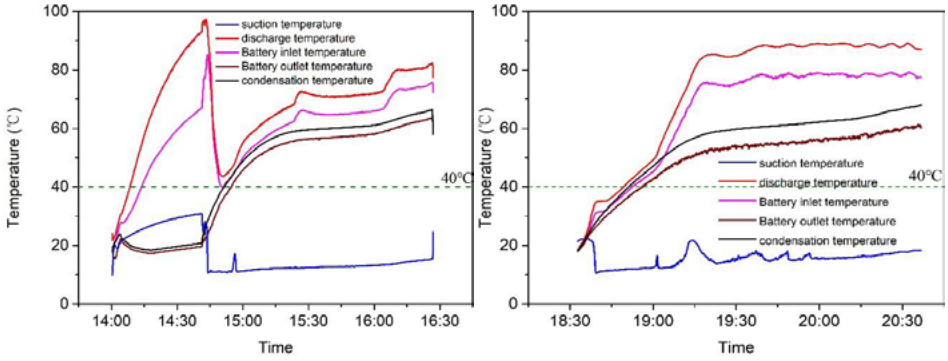
In the experimental investigation, the effect of two different calibers of expansion value on system performance has been studied, as shown in Table 3. The main performance parameters of the two experiments are shown in Table 4. The system thermodynamic performance of these two experiments are illustrated in Fig. 4 and Fig. 5. Due to the property of PCM, the temperature will not change when it is in a phase change state. Therefore, when the temperature of the refrigerant is constant, the PCM is approximately considered to be in a molten state. According to Fig. 4(a), in the first 45 minutes, the mass flow rate of the refrigerant is small and unstable, resulting in a sharp rise in discharge temperature and battery inlet temperature. When the PCM melts, the temperature and enthalpy of the heat battery inlet are 65°C and 423.3 kJ/kg respectively, and the enthalpy of heat battery outlet is 273.15 kJ/kg. The mass flow rate of refrigerant is calculated as 26 g/s, so the heat exchange capacity in the heat battery is 3.89 kW. The ICOP of the first experiment can reach 3.82. After the previous electronic expansion valve with a caliber of 1.3mm is replaced by that with a caliber of 1.5mm, the second experiment shows that using the electronic expansion valve with a caliber of 1.5mm can not only make ASHP run more smoothly but also substantially increase discharge temperature and battery inlet temperature. It can be calculated that the ICOP of the system is improved by 6.8% to reach 4.08. During the exothermic process of heat battery module, PCM heats 106.5 L water from 15°C to 40°C. It can be concluded that ASHPWH with PCM is feasible.

Table 3. Main parameters of the ASHP after the expansion valve is replaced

Case	Host	Refrigerant	Rated charge volume (g)	Caliber of expansion valve (mm)
1	Haipu (1p)	R22	1700	1.3
2	Haipu (1p)	R22	1700	1.5

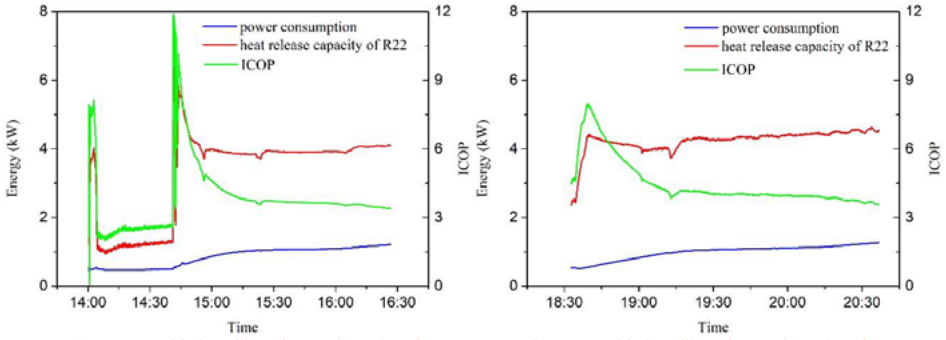
Table 4. Main performance parameters of the two experiments

Parameters	Case 1	Case 2
Discharge temperature (°C)	71	88
Battery inlet temperature (°C)	65	78
Battery inlet enthalpy (kJ/kg)	423.3	437.8
Battery inlet enthalpy (kJ/kg)	273.5	270.8
Mass flow rate (g/s)	26	25.8
Heat release capacity of R22 (kW)	3.89	4.34
ICOP	3.82	4.08
Hot water supply (L)	100	106.5



(a) system with the caliber of expansion valve of 1.3 mm (b) system with the caliber of expansion valve of 1.5 mm

Fig. 4. System temperature variation with different expansion valves



(a) system with the caliber of expansion valve of 1.3 mm (b) system with the caliber of expansion valve of 1.5 mm

Fig. 5. System performance variation with different expansion valves

3.2. Numerical simulation optimization

At present, one of the main problems of heat battery module is poor heat transfer effect, so enhancing the heat transfer between the PCM and refrigerant/water is the major optimization object. The structure of heat battery module used in this experiment is a fin-and-tube heat exchanger, in which the material of the fin is aluminum, and the material of the heat exchange tube is copper. Aluminum has a relatively good thermal conductivity with an acceptable price. It is one of the most commonly used materials for fin materials. However, when it is connected with a copper tube in heat exchangers, the contact thermal resistance between the two is not conducive to the heat exchange between the PCM and refrigerant/water. Therefore, the simulation analysis of the effect of using copper fins instead of aluminum fins on heat transfer in a heat exchange unit was carried out. The two center sections, as shown in Fig. 6, are selected for observation.

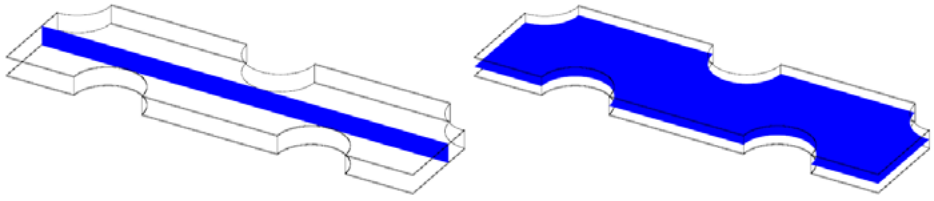


Fig. 6. Two center sections for observation

In the process of simulating the endothermic melting of PCM, in order to simplify the model, the boundary condition on the refrigerant side is set to a constant temperature of 346K, and the initial temperature of the phase change material is 293 K. The CFD simulation results are shown in Fig. 7 and Fig. 8.

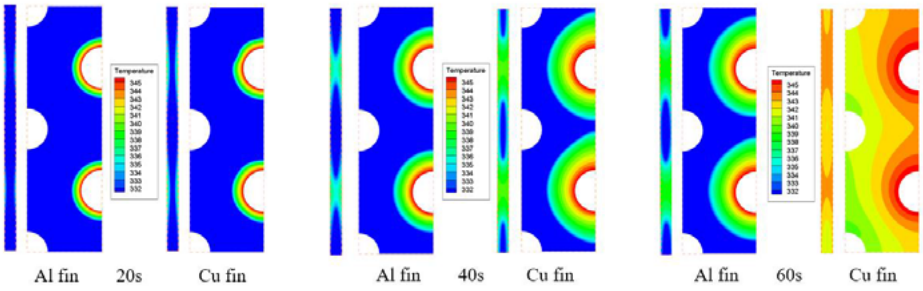


Fig. 7. Temperature distribution of two kinds of fins at different times

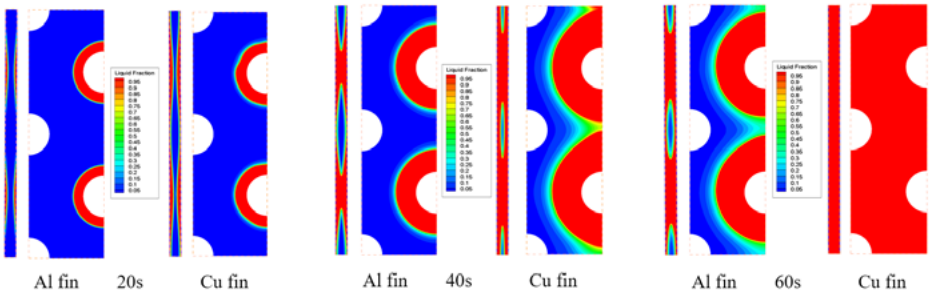


Fig. 8. Liquid fraction distribution of two kinds of fins at different times

It can be seen that the heating rate of PCM increases significantly when using copper fins in the heat battery module. When the heating time reaches 60 s, PCM in heat battery with copper fins almost turned into a liquid state, while a considerable part of PCM of that with aluminum fins was still in solid state. On the one hand, the copper fin can be completely welded together with the copper tube to effectively avoid the adverse effect of contact thermal resistance in heat transfer process; on the other hand, the thermal conductivity of copper is much higher than that of aluminum. Therefore, the use of copper fins can further reduce the thermal resistance of heat transfer and enhance the heat transfer coefficient between the fins and PCM. However, the price of copper is higher than that of aluminum. It is conceivable to replace some of the fins with copper fins to reduce the cost burden.

4. Conclusions

In this paper, a series of experimental tests on a novel heat battery module with PCM applied to ASHPWH were carried out. Based on the preliminary experimental work and the test data of the prototype, the integrated system performance is analyzed. In order to enhance the heat transfer process in battery module, CFD simulation is applied to optimize the structure of heat battery. The following conclusions can be drawn:

1. From the theoretical analysis and experimental results, in the first experiment, the ICOP of ASHP is up to 3.82 but the operation of ASHP is unstable and in poor condition. After the previous electronic expansion valve with a caliber of 1.3 mm is replaced by that with a caliber of 1.5 mm, the latest experiment shows that using 1.5 mm caliber electronic expansion valve can not only make ASHP run more smoothly but also increase ICOP by 6.8% to 4.08. It indicates that ASHPWH with PCM system has a good application prospect and is feasible for practical application in production activities.
2. Copper fins can effectively avoid the adverse effect of contact thermal resistance and greatly enhance the heat transfer coefficient between PCM and refrigerant/water according to the CFD simulation. Considering that copper is more expensive than aluminum, it is conceivable to replace some of the fins with copper fins to balance the cost burden and heat transfer efficiency of heat battery module.

References

[1] Gholipour B. The promise of phase-change materials. *Science* 2019;**366(6462)**: 186-187.
[2] Kim HG, Kim YS, Kwac LK, Shin HJ, Lee SO, Lee US et al. Latent Heat Storage and Thermal Efficacy of Carboxymethyl Cellulose Carbon Foams Containing Ag, Al, Carbon Nanotubes, and Graphene in a Phase Change Material. *Nanomaterials* 2019;**9(2)**:158.
[3] Seulgi Y, Su GJ, Okyoung C, Sumin K. Bio-based PCM/carbon nanomaterials composites with enhanced thermal conductivity.*Sol Energ Mat Sol C* 2014;**120**:549-554.
[4] Manar AJ, Syeda HT, Shohel M, Animesh D. Nano-PCM filled energy storage system for solar-thermal applications.*Renew Energ* 2018;**126**:137-155.
[5] Zhu HT, Han DX, Meng ZG, Wu DX, Zhang CY. Preparation and thermal conductivity of CuO nanofluid via a wet chemical method. *Nanoscale Res Lett* 2011;**6(1)**:181.
[6] Barahoei M, Hezave ZA, Sabbaghi S, Ayatollahi S. Copper oxide nano-fluid stabilized by ionic liquid for enhancing thermal conductivity of reservoir formation: Applicable for thermal Enhanced Oil Recovery processes. *Chem Ind Chem Eng Q* 2016;**22**:211-225.
[7] Li XG, Sun LY,Sui H, He L,Yuan W, Han ZW. A Novel Polymeric Adsorbent Embedded with Phase Change Materials (PCMs) Microcapsules: Synthesis and Application. *Nanomaterials* 2019,**9(5)**:736.
[8] Liu WY, Li FZ, Liu WH. Numerical Analysis on Thermal Function of Clothing with PCM Microcapsules.*Transactions of Nanjing University of Aeronautics and Astronautics* 2019;**36(02)**:320-329.
[9] Luo YW, Zhou XD. *Polymer Science,Part A:Polymer Chemistry* 2004;**42(9)**: 2145–2154.
[10] Jessica GP, Mònica M, Luisa FC. Types,methods,techniques,and applications for microencapsulated phase change materials (MPCM):A review. *Renew Sust Energ Rev* 2016;**53**:1059-1075.
[11] Octavian P, Lucian FT, Mugur B. Numerical model for solidification and melting of PCM encapsulated in spherical shells. *Energy Procedia* 2017;**112**:336-343.
[12] Park SJ, Kim KS, Hong SK.*Polymer–Korea* 2005;**29 (1)**: 8–13.
[13] Selvam C, Manikandan S, Kaushik SC, Lamba R, Harish S. Transient performance of a Peltier super cooler under varied electric pulse conditions with phase change material. *Energ Convers Manage* 2019;**198**.
[14] Jin WL, Liu LY, Yang T, Shen HG, Zhu J, Xu W et. al. Exploring Peltier effect in organic thermoelectric films. *Nat commun* 2018;**9(1)**:3586.

Responses to Reviewers' Comments

Dear Editor and Reviewers,

We quite appreciate the comments concerning our manuscript entitled "Investigation on system performance of air source heat pump water heater with phase change material". Those comments are all valuable and very helpful for revising and improving our paper, as well as the important guiding significance to our researches. We have studied comments carefully and have made correction which we hope meet with approval. Revised portion are marked in red in the paper. The main corrections in the paper and the responses to the reviewer's comments are written in blue as following:

Reviewer #1

This paper made experimental tests on air source heat pump water heater (ASHPWH) using a novel heat battery module with phase change material (PCM), and CFD simulation testifies copper fins applied in heat battery module. It is a good topic to explore the feasibility and stability of the combination of ASHPWH and PCM. The content of the paper is well-organized and the quality of the English is satisfactory. The author clearly explains the experimental setup, analysis of experimental and simulation results. Acceptance of this paper after minor revision is reasonable.

1) Would you please add some detailed description of the specifications of heat battery module with PCM used in the paper?

Discussion: Thanks very much for reviewer's suggestion. We deeply agree with the reviewer. However, the detailed information of heat battery module with PCM is inconvenient to provide in the paper due to the confidentiality agreeement with a partner company. Accordingly we have made the explanation in section 2.1.

Reviewer #2

1) In Table 1 and 3, Has caliber of electronic expansion valve unit? It's better to supply it.

Discussion: Thanks very much for reviewer's careful suggestion. The unit of caliber of electronic expansion is **mm**. According to the reviewer's advice, we have supplemented the unit of caliber of electronic valve in Table 1 and 3. Moreover, the corresponding text has also been modified and marked in red.

We tried our best to improve the manuscript and made some changes in the manuscript. We appreciate for Editors/Reviewers' warm work earnestly, and hope that the correction will meet with approval.

Once again, thank you very much for your comments and suggestions!

Naiping Gao

13th IEA Heat Pump Conference
April 26-29, 2021 Jeju, Korea

Experimental investigation of heat transfer coefficient of R1234yf during condensation inside multiport mini-channel tube

Quang Vu Pham[a], Jong-Taek Oh[b*]

[a] Faculty of Energy Technology, Electric Power University, 235 Hoang Quoc Viet, Hanoi 10000, Vietnam
[b] Dept. of Refrigeration and Air-conditioning Engineering, Chonnam National University, Yeosu 59626, South Korea.

Abstract

R1234yf is an Hydrofluro-Olefins (HFO) that is used as a good candidate for replacing R134a in automotive air conditioning, and it has a low global warming potential of 4 and zero ozone depletion potential (ODP). R1234yf has cooling performance that is 5 % less than R134A but is significantly better for the environment. This research report measured and analyzed the heat transfer performances of R1234yf in the condensation process inside two different multiport mini-channel tubes. Experimental data was obtained for mass fluxes from (50 to 500) kg/m2s, and heat fluxes from (3 to 12) kW/m2 at a fixed saturation temperature of 48 °C. The flow distribution of the R1234yf effect on the heat transfer coefficient was analyzed. Finally, a new heat transfer coefficient correlation was developed from the experimental data.

Keywords: R1234yf, heat transfer coefficient, condensation, multiport tube.

1. Main text

The R-1234yf refrigerant is a low global warming potential of 4 and zero ODP; it has physical properties similar to R-134A and also has the potential as a retrofit refrigerant in existing HFC-134a systems. R-1234yf is classified as slightly flammable., so it is carefully to ensure safety during operation and maintenance of the system included that. R-1234yf has a cooling performance 5% less than R-134A, but significantly better for the environment.

Many available experimental studies compare the heat transfer performance between R134a and R1234yf. Yang and Nalbandian [1] measured the condensation heat transfer and pressure drop of R1234yf and R134a in a 4 mm inner diameter (ID) circular tube. They found that for high vapor qualities, the heat transfer coefficients of R134a are higher than those of R1234yf, but for low vapor qualities, almost the same. Moreover, the authors concluded that the effect of two-phase flow patterns shows strongly on the condensation heat transfer coefficient. [2]'s experimental study on the condensation of R1234yf inside 0.96 mm circular tube compared it with that of R134a at the same test conditions. They found that R134a showed higher performance than R1234yf by about (15–30) % of heat transfer coefficients, and (10–12) % of adiabatic two-phase pressure drop. The experimental data were compared with the correlation of Cavallini et al.[3] . Wang et al. [4] also measured the condensation heat transfer coefficient of R1234yf inside a 4 mm ID tube, compared it with that of R134a and R32, and concluded that strong effects of the mass flux and vapor quality on the heat transfer coefficient are observed in the shear force dominated flow regimes. Also, due to the differences in density ratio, viscosity ratio, and thermal conductivity, the heat transfer coefficients of R1234yf are lower than those of R134a. Illán-Gómez et al. [5] investigated the condensation heat transfer coefficient and pressure drop inside a multiport tube with R1234yf and R134a with large ranges of mass flux and saturation temperature. They

* Corresponding author. Tel.: +82-61-659-7273; fax: +82-61-659-7270.
E-mail address: ohjt@chonnam.ac.kr

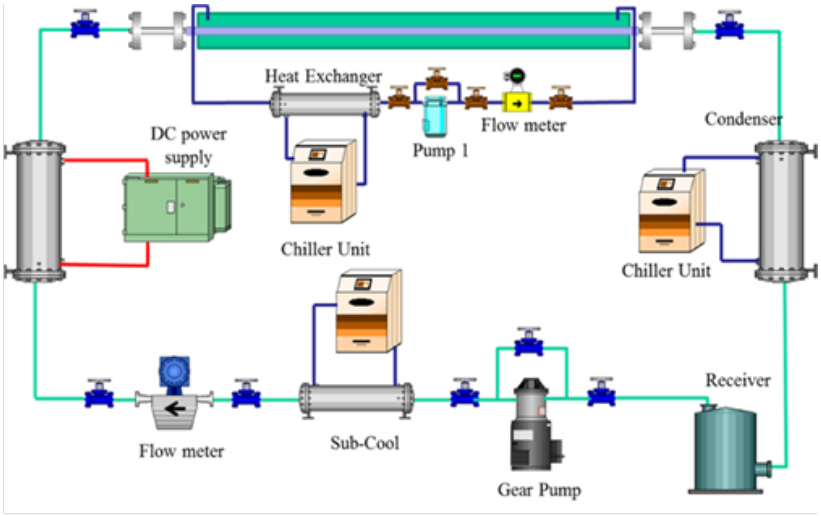


Figure 1 Schematic of the experimental apparatus

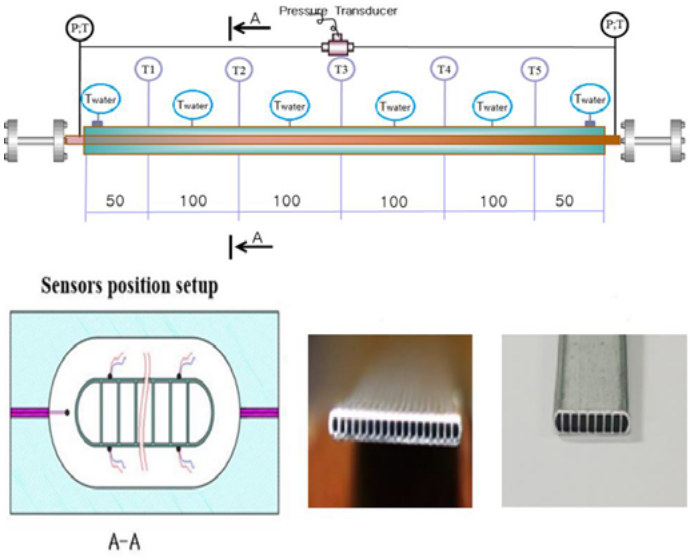


Figure 2 Detail of the test sections setup

compared the experimental data with some heat transfer coefficient and pressure drop models available in the literature, which showed good agreement. Based on the model proposed by Koyama et al. [6], a readjusted model for the heat transfer coefficient has been proposed to improve the agreement with the original model.

Much of the previous research has been conducted and models developed for limited refrigerants and test tubes, while there is a lack of research in the literature that pays attention to the R1234yf inside the multiport minichanel tube. In this study, the condensation heat transfer coefficients of R1234yf inside two types of multiport minichannel tubes of (0.83 and 0.97) mm of hydraulic diameter are investigated experimentally. The effect of mass flux, heat flux, vapor quality, and the geometry of the test section are analyzed, and compared with some existing models.

Table 1 Specification dimensions of the multiport mini-channel tubes

Parameters	PFC	FME
Number of channels	18	8
Width of channel (mm)	0.58	0.69
Height of channel (mm)	1.3	1.42
Hydraulic diameter (mm)	0.846	0.969
Internal cross- sectional area (mm^2)	28.105	19.46
Wetted perimeter surface (mm)	64.52	36.12

2. Experimental apparatus and data reduction

Figure 1 shows the experimental apparatus, which consists of a refrigerant loop, cooling water loop, and water–glycol loop. The experimental apparatus was designed to measure the heat transfer coefficient and pressure drop during the condensation process of refrigerant inside the test section tubes. The refrigerant loop is composed of four major sections: the sub-cooled, the pre-heater, the test section, and the post-condensers. The sub-cooled includes a sub-cooler, a refrigerant gear pump, and a Coriolis-type mass flow meter. The sub-cooler is a tube-in-tube heat exchanger with refrigerant flow inside of the tube and a cooling water loop; the refrigerant is cooled by a water–glycol loop to achieve a subcooled state. The subcooled temperature of refrigerants is controlled by setting the temperatures of constant temperature baths connected to the sub-cooler. The refrigerant is circulated in the refrigerant loop by a magnetic micro gear pump. A Coriolis-type mass flow meter for a maximum mass flow rate of 80 kg/h is installed to measure the mass flow rate of refrigerant. The mass flow rate of refrigerant is independently controlled by adjusting the rotation speed of the drive for the gear pump. The aims of the sub-cooled part provided for the subcooled state refrigerant and required mass flow rate. The pre-heater is used for the multiport tubes test, which is 4 m long, and of 1/4" outer diameter (OD) stainless steel tube. It is connected with a DC power supply for a maximum capacity of 1,500 W. The refrigerant vapor quality in the test section is determined by the heat applied in the pre-heater, which can be controlled by adjusting the voltage and current in the DC power supply unit.

Figure 2 details the test section setup and test section tubes. The test sections are the tube-in-tube heat exchanger in which the refrigerant vapor condenses inside the inner test tubes, while cooling water flows in the annulus. Two types of aluminum multiports were used to have 8 and 16 rectangular channels in hydraulic diameters of (0.969 and 0.846) mm, respectively. The effective lengths of the test section are 200 mm with mass fluxes of (50, 100, and 200) kg/m^2s; and 500 mm with mass fluxes of (300 and 500) kg/m^2s. The local heat transfer coefficients are calculated from the measurements of average heat flux on the test section and the local tube wall temperatures. Twenty T-type thermocouples were equispaced at fixed 5 points along the test sections length, on both the top and bottom sides, to measure the outside tube wall temperature.

Four high-accuracy resistance temperature detectors were attached at the inlet and outlet of refrigerant side and cooling waterside in the test section. The energy balance in the test section is verified by initial testing with the liquid water–water in the test section; the heat balance between the outside fluid and inside fluid was always less than ±3 %. Table 1 shows the dimensions of the two types of aluminum multiport tube.

The vapor quality at the inlet of the test section was defined from the voltage and current of the DC power supply unit in the preheater, which can be determined as follows:

$$x_{inlet} = \frac{1}{h_{fg}}\left[\frac{Q_{pre-heater}}{m_{ref}} - C_p\left(T_{sat} - T_{p,inlet}\right)\right] \quad (1)$$

where, Q_{pre} is the heating power applied in the pre-heater by the DC power supply. The saturation temperature T_{sat} was computed from the measured saturation pressure at the inlet of the test section. The average heat flux in the test section was determined as:

$$q = \frac{m_{water} c_{p,water} \Delta T_{water}}{A_{external}} \tag{2}$$

where, m_{water} is the cooling water mass flow rate, T_{water} is the temperature difference between the inlet and outlet of the cooling water side, and $A_{external}$ is the external surface area of the test section tube. The cooling water mass flow rate in all cases is fixed at 1 kg/min to maintain the water flow distribution on the annulus side. Two test section lengths were used with different mass flux conditions to control the vapor quality difference in the test section at approximately (0.011–0.16). Therefore, it can be assumed that the variation in vapor quality on the test section is linear over the length of the test section. The following equation calculates the vapor quality in the test section:

$$x = x_{inlet} - \frac{m_{water} c_{p,water} \Delta T_{water}}{2 m_{ref} h_{fg}} \tag{3}$$

The Fourier steady-state one-dimensional heat conduction calculated the inner wall temperatures of the tube through the tube wall:

$$T_{w,i} = T_{w,o} + \frac{q\delta}{k_{aluminum}} \tag{4}$$

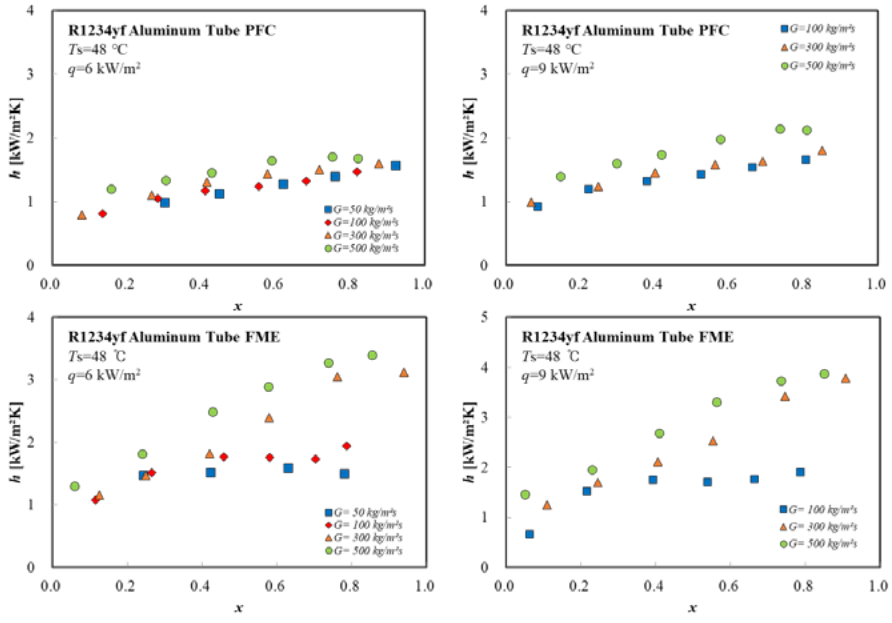


Figure 3 Effect of mass flux on the heat transfer coefficient

where, k is the thermal conductivity of the aluminum. Through all the data reduction processing, the different temperature between inside and outside wall tubes was less than 0.025 K.

The average condensation heat transfer coefficient is obtained as:

$$h = \frac{A_{\text{external}}}{A_{\text{internal}}} \frac{q}{\left(T_{sat} - T_{w,i}\right)} \tag{5}$$

3. Result and discussion

Condensation heat transfer of R1234yf inside the aluminum multiport tubes is carried out at fixed 48 °C, mass flux ranging (50 to 500) kg/m^{2}s, and heat flux ranging (3 to 12) kW/m^2. The vapor quality at the inlet of the test section varied from (0.9 to 0.1), and approximately (0.011–0.16) vapor quality change in the test section, depending on the mass flux and heat flux conditions. The relations of vapor quality, mass flux, and heat flux with the condensation heat transfer coefficient of refrigerant were discussed.

Figure 3 shows the heat transfer coefficient influence of mass flux with both test tubes. The increase of vapor quality and mass flux leads to the rise of the condensation heat transfer coefficient, because of the forced convection mechanism. The effect of vapor quality on the condensation heat transfer coefficient can be explained by flow models. The flow models proposed by Coleman and Garimella [7] show bubbly flow and plug flow in the case of low vapor quality, and annular flow for high vapor quality. Liquid film during condensation is thick in the bubbly and plug flow, and thin in the annular flow. In addition, the effect of liquid film thermal resistance predominates in the condensation heat transfer coefficient, where the heat transfer coefficient increases as the thickness of the liquid film decreases. This effect is more evident in high mass flux and high vapor quality, but weaker in low mass flux and vapor quality.

At low mass fluxes, the results showed that the data of (50, 100, and 150) kg/m^{2}s mass fluxes almost overlap with those figures of (3–12) kW/m^2 of heat flux. Jige et al. [8], Matkovic et al. [9], and Del Col et al. [10] reported that the heat transfer coefficients of (100 and 200) kg/m^{2}s mass velocity were almost similar, which may be explained by the decrease in the shear stress at a certain point and increase at the interface, so that the effect of surface tension in the rectangular channels dominates. The explanation is similar to the theoretical analysis reported by Bortolin et al. [11]. Kim & Shin [12] considered the condensation heat transfer of R134a inside mini channel tubes, and concluded that the low mass flux regime had a weak effect on the heat transfer coefficient. However, at high mass fluxes, the surface tension does not dominate, because the vapor shear stress is much stronger.

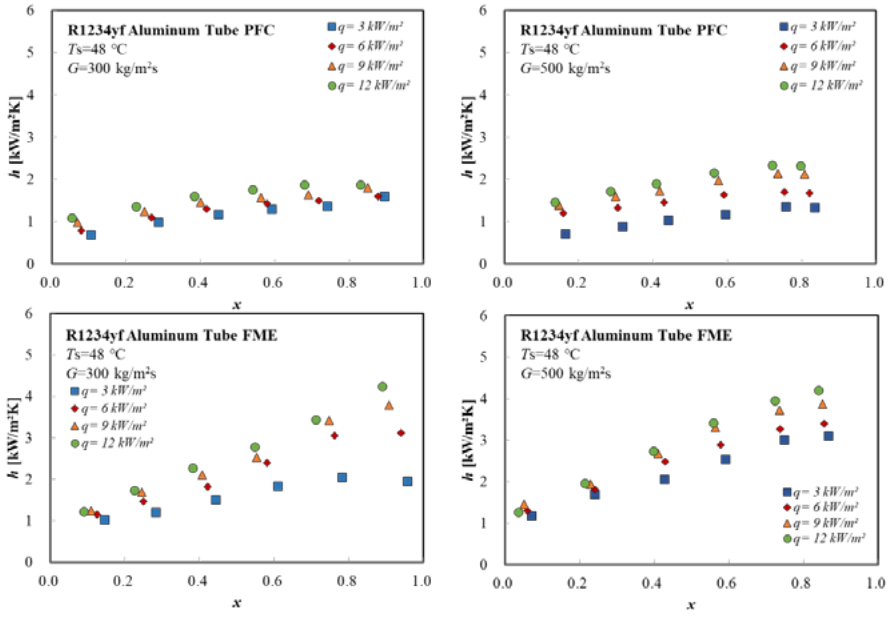


Figure 4 Effect of heat flux on the heat transfer coefficient

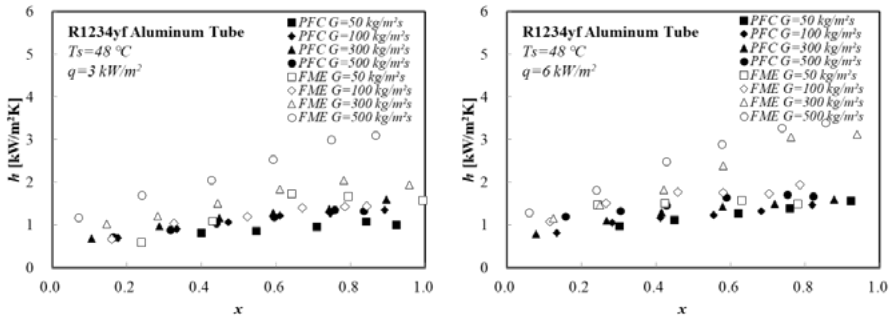


Figure 5 Comparison of the heat transfer coefficient between two types of multiport tubes

Figure 4 shows the effects of heat flux on the measured condensation heat transfer coefficient. The results show that the condensation heat transfer coefficients increase with increasing heat flux. In the present experimental study, the average heat flux approximated uniform heat flux on the test section length, due to keeping 1 kg/min past the cooling water mass flow rate for all test cases. Zhang et al. [13], Sakamatapan et al. [14], and Yan and Lin [15] also reported similar behavior of the heat flux effect. They concluded that the main reasons are the interface temperature between the liquid film and vapor core, and even the effects of the change of momentum of the liquid and vapor phases on the change of heat flux.

Figure 5 compares the condensation heat transfer coefficients of the two types of multiport tube. These show that the heat transfer coefficients of FME are higher than those of PFC at similar test conditions. For conventional round tubes, the heat transfer coefficient increases with decrease of hydraulic diameter of the tubes, but many researchers, such as Pham et al. [16], Kaew-On et al. [17], and Nema et al. [18], suggest that the heat transfer behavior inside multiport rectangular channel tubes is quite different. In the present study, the experimental data show that the heat transfer coefficient is not an observed effect of the hydraulic diameter. However, the widths and aspect ratio of each rectangular channel influence the heat transfer coefficients. Table 1 shows the details of the tube dimension. The condensation heat transfer coefficients of refrigerant inside a rectangular tube are dependent on the surface tension and the shear stress interface of vapor and liquid phases. The condensed liquid film at the top and bottom of the channel is thinner as the width of the rectangular channel increases. These results show that due to surface tension, the condensed liquid drainage to the edges generated a thin liquid film.

4. Conclusions

The condensation heat transfer coefficients of R1234yf inside two types of multiport minichannel tubes were investigated experimentally over a large range of test conditions. The installation and data reduction were described and defined; the results were analyzed and discussed. The condensation heat transfer coefficient increases with increasing vapor quality, mass flux, and heat flux. The effects of cross-section geometry on the condensation heat transfer characteristic are dependent on the surface tension and vapor shear stress.

References

[1] C. Y. Yang and H. Nalbandian, “Condensation heat transfer and pressure drop of refrigerants HFO-1234yf and HFC-134a in small circular tube,” *Int. J. Heat Mass Transf.*, vol. 127, pp. 218–227, 2018.

[2] A. Cavallini, D. Del Col, and L. Rossetto, “Heat transfer and pressure drop of natural refrigerants in minichannels (low charge equipment),” *Int. J. Refrig.*, vol. 36, pp. 287–300, 2013.

[3] A. Cavallini, S. Bortolin, D. Del Col, and L. Rossetto, “Condensation and Vaporization of Halogenated Refrigerants Inside a Circular Minichannel,” 2008.

[4] L. Wang, C. Dang, and E. Hihara, “Experimental study on condensation heat transfer and pressure drop of low GWP refrigerant HFO1234yf in a horizontal tube,” *Int. J. Refrig.*, vol. 35, no. 5, pp. 1418–1429, 2012.

[5] F. Illán-Gómez, A. López-Belchí, J. R. García-Cascales, and F. Vera-García, "Experimental two-phase heat transfer coefficient and frictional pressure drop inside mini-channels during condensation with R1234yf and R134a," *Int. J. Refrig.*, vol. 51, pp. 12–23, 2015.
[6] S. Koyama, K. Kuwahara, K. Nakashita, and K. Yamamoto, "An experimental study on condensation of refrigerant R134a in multi-port extruded tube," *Int. J. Refrig.*, vol. 26, no. 4, pp. 425–432, 2003.
[7] J. W. Coleman and S. Garimella, "Two-phase flow regimes in round, square and rectangular tubes during condensation of refrigerant R 134a," *Int. J. Refrig.*, vol. 26, no. 1, pp. 117–128, 2003.
[8] D. Jige, N. Inoue, and S. Koyama, "Condensation of refrigerants in a multiport tube with rectangular minichannels," *Int. J. Refrig.*, vol. 67, pp. 202–213, Jul. 2016.
[9] M. Matkovic, A. Cavallini, D. Del Col, and L. Rossetto, "Experimental study on condensation heat transfer inside a single circular minichannel," *Int. J. Heat Mass Transf.*, vol. 52, no. 9–10, pp. 2311–2323, 2009.
[10] D. Del Col *et al.*, "Effect of inclination during condensation inside a square cross section minichannel," *Int. J. Heat Mass Transf.*, vol. 78, pp. 760–777, 2014.
[11] S. Bortolin, E. Da Riva, and D. Del Col, "Condensation in a Square Minichannel: Application of the VOF Method," *Heat Transf. Eng.*, vol. 35, no. February 2015, pp. 193–203, 2014.
[12] M. H. Kim and J. S. Shin, "Condensation heat transfer of R22 and R410A in horizontal smooth and microfin tubes," *Int. J. Refrig.*, vol. 28, no. 6, pp. 949–957, Sep. 2005.
[13] H. Y. Zhang, J. M. Li, N. Liu, and B. X. Wang, "Experimental investigation of condensation heat transfer and pressure drop of R22, R410A and R407C in mini-tubes," *Int. J. Heat Mass Transf.*, vol. 55, no. 13–14, pp. 3522–3532, 2012.
[14] K. Sakamatapan, J. Kaew-On, A. S. Dalkilic, O. Mahian, and S. Wongwises, "Condensation heat transfer characteristics of R-134a flowing inside the multiport minichannels," *Int. J. Heat Mass Transf.*, vol. 64, pp. 976–985, 2013.
[15] Y. Y. Yan and T. F. Lin, "Condensation heat transfer and pressure drop of refrigerant R-134a in a small pipe," *Int. J. Heat Mass Transf.*, vol. 42, no. 4, pp. 697–708, 1999.
[16] Q. V. Pham, K.-I. K.-I. Choi, J.-T. J.-T. Oh, and H. Cho, "An Experimental Investigation of Condensation Heat Transfer Coefficients and Pressure Drops of Refrigerants Inside Multiport Mini-channel Tubes," *Int. J. Air-Conditioning Refrig.*, vol. 25, no. 02, p. 1750013, Mar. 2017.
[17] J. Kaew-On, K. Sakamatapan, and S. Wongwises, "Flow boiling heat transfer of R134a in the multiport minichannel heat exchangers," *Exp. Therm. Fluid Sci.*, vol. 35, no. 2, pp. 364–374, 2011.
[18] G. Nema, S. Garimella, and B. M. Fronk, "Flow regime transitions during condensation in microchannels," *Int. J. Refrig.*, vol. 40, pp. 227–240, 2014.

13th IEA Heat Pump Conference
April 26-29, 2021 Jeju, Korea

Energy saving pre-cooling pattern search of an inverter air conditioner using a deep reinforcement learning algorithm

Myung Sup YOON[a,*], Won Sik YOON[a]

[a]Energy Technology Center, Korea Testing Laboratory, 87 Digital-ro 26-gil, Guro-gu, Seoul, 08389, Republic of Korea

Abstract

In this study, we experiment with the energy saving pre-cooling operation of an inverter air conditioner using a deep reinforcement learning algorithm under a fixed going out time duration. An air conditioner with a rated cooling capacity of 6500 W is used. An indoor building load of 4500 W sensible heat and an outdoor temperature of 35°C are continuously applied throughout the study. During the going out time, three remote control temperature options (21, 26, 31°C) are given for simplicity, and a remote controlling pattern (set temperature sequences) that minimizes power consumption upon arrival home while satisfying the arrival target temperature condition is searched using deep reinforcement learning. For a given going out time duration, the power consumptions of the temperature operation pattern found by the computer deep reinforcement learning algorithm and a human are compared. Although the artificial intelligence searches for the power consumption operation pattern over a long period (7 ~ 9 days), depending on the learning environment, it identifies a more accurate and more energy saving and an unexpected operation pattern than by human analysis.

Keywords: Air conditioner; Deep reinforcement learning; Pre-cooling; AI; Energy saving; Smart HVAC; Set temperature sequences

1. Introduction

Due to the development of artificial intelligence (AI) technology, many of us will soon live in more comfortable and energy efficient smart homes, with pre-cooling/pre-heating before returning home that incorporates data from smart vehicles. With the development of high efficiency inverter air conditioners at part-load condition, more energy can be saved by operating an air conditioner gradually before arrival than to operate an air conditioner suddenly on arrival if certain conditions are met [1]. Studies on building energy prediction, management, and heating, ventilation, and air conditioning (HVAC) system control using deep learning technology have been actively conducted [2–20]. However, research that applies deep learning technology to household air conditioners is scarce. Some AI platform companies such as Google Nest and global electronics companies are developing deep learning technology for household air conditioning, but they tend not to publicly release their research findings. Precision temperature control for an air conditioner and optimal operation point search of air conditioner components for maximum energy efficiency (EER) using a deep reinforcement learning algorithm have been conducted in previous research [21–22]. However, there is no air conditioner deep learning research for energy saving pre-cooling operation during the time at which all household occupants are away from home.

Figure 1 shows a conceptual diagram of a comfortable and energy saving HVAC pre-cooling or pre-heating system in conjunction with location information of occupants. The arrival time varies depending on the means of transportation and traffic conditions of the day. Pre-cooling or pre-heating should also vary according to the arrival time of family members, outdoor atmospheric conditions, and the internal building loads of the day. If

* Corresponding author.
E-mail address: msyun95@ktl.re.kr

sufficient data exist for these variables, or a well-defined environment exists, it seems that optimal operation is possible using a deep learning algorithm.

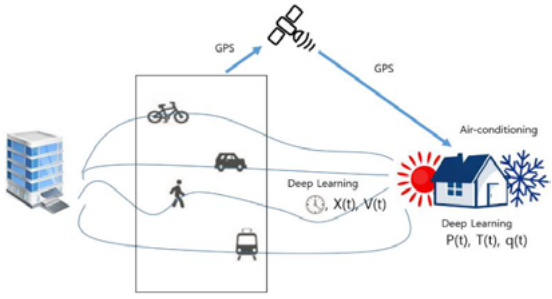


Fig. 1. Concept of pre-cooling or pre-heating using deep learning

2. Experimental Approach

2.1. Problem setup

In this study, in order to minimize the AI learning time, a deep reinforcement learning algorithm is applied under certain assumptions in a well-defined test chamber environment [23–24]. First, cases where the fixed going out time is 2.5 and 3.5 hours are calculated. Second, the building load (q_{build}) during non-occupancy is assumed to be constant at 4500 W of constant sensible heat, and the outdoor side temperature is assumed to be constant at 35°C. Third, it is assumed that there is no latent heat consideration. Fourth, in order to minimize learning obstacles in the dead band zone, which is a feature of the product control, only three signals of set temperature (21, 26, 31°C) are considered. Fifth, the initial temperature (T_0) of the indoor room temperature (T_{in}) in most of the learning episodes is near 26°C. Sixth, temperature variations are considered only when a single agent (actor) exists as one resident (Fig. 2(a)). Seventh, linear distance movement is assumed in all episodes during learning (Fig. 2(b)).

Figure 2(a) shows the temperature change of a room (dashed lines) over the going out time duration ($t_2 - t_1$). Three set temperatures (T_{set}) of the remote controller (21, 26, 31°C) can be given in various sequences over the going out duration at about every 2 minutes. If T_{set} is fixed as 26°C throughout the problem, then the indoor room temperature will ideally be horizontal. To simplify the problem, two cases of the going out time duration (2.5 h and 3.5 h) are scrutinized. Figure 2(b) shows the remaining distance to the destination over time. Linear approximation for the simplicity of the problem is assumed regardless of the various paths according to the traffic and traffic conditions (Fig. 1). A non-linear remaining distance (Ls(t)) pattern also can be considered if there is time-dependent GPS information of multiple agents (family members). Here, only linear profiles are assumed, and $t_{arrival(1)}$ corresponds to 2.5 h and $t_{arrival(2)}$ to 3.5 h, respectively.

The purpose of this study is to find T_{set} sequences over the going out time duration to minimize energy consumption (kWh) using a deep reinforcement algorithm. Of course, T_{in} should be in the target temperature (24 ~ 28°C) on the arrival time (t_2), regardless of the temperature variations during the going out time.

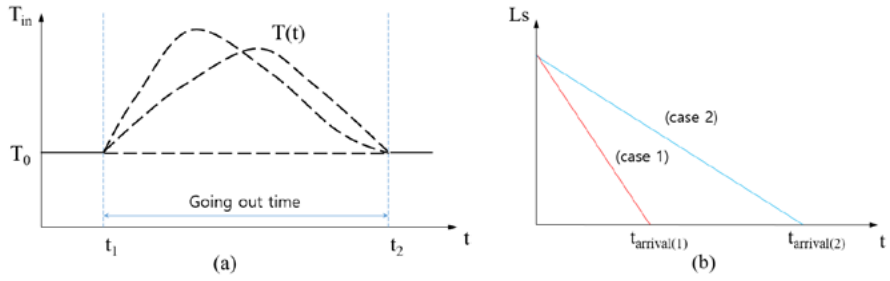


Fig. 2. Variations of (a) indoor temperature (T_{in}) and (b) remaining distance (Ls)

2.2. Air conditioner selection

Air conditioners differ in precision control from model to model and from brand to brand [1]. Minimized dead band zone and precision controlled products are good for reinforcement learning (RL), but unfortunately, the latest models are locked from obtaining IR signals for controlling remote signals using Arduino [21]. Therefore, the old inverter products of Fig. 3 and Table 1 are used throughout this study.

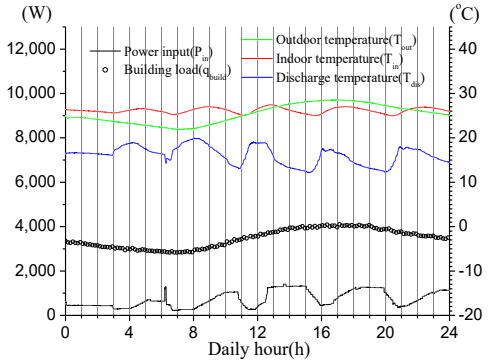


Fig. 3. Operating characteristics of the air conditioner under test (reproduced from Yoon et al. [1, 21])

Table 1. Specifications of test air-conditioner (reproduced from Yoon et al. [21])

Contents	Name plate values
Air-conditioner type	Split wall mount
Compressor type	Inverter type
Electricity	Single phase, 220 V, 60 Hz
Rated cooling capacity	6500 W
Rated power input	1750 W
Max. power input	2900 W
Min. power input	500 W
Refrigerant	R410a, 2 kg

3. Methodology

3.1. Artificial neural network (ANN) model

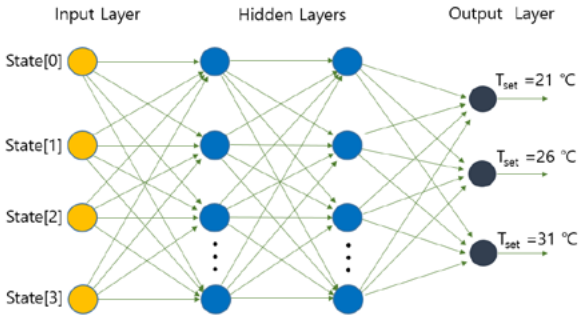


Fig. 4. ANN model for the inverter air conditioner pre-cooling

For the deep reinforcement learning (RL) algorithm, we use one input layer of four nodes, two hidden layers of 24 nodes each, and one output layer of three nodes. The input layer consists of four elements of state [(T_{in}(t) –26), dT_{in}/dt, Pws(t), t]. Each element represents indoor temperature (T_{in}), indoor temperature derivative (dT_{in}/dt), and cumulative power consumption (Pws(t)) at time t, and time t. Here, Pws is same as the Pwh divided by 3600 seconds (Pws = Pwh / 3600). If the movement change due to traffic is non-linear, the above state variable t can be changed into the distance state variable of Ls(t), or it can be replaced with x(t) and y(t), that is, GPS coordination information.

3.2. Reward strategy

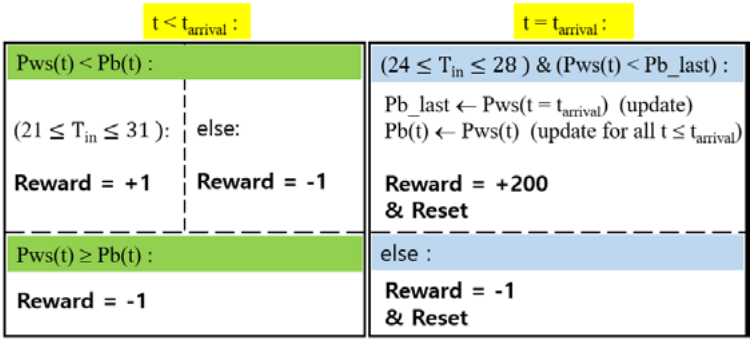


Fig. 5. Regions for the rewards

Figure 5 shows the reward strategy for this problem set-up. Pws(t) is the cumulative power consumption [Ws] measured at each time step, Pb(t) is the cumulative power consumption as a baseline at time t, and Pb_last is the baseline cumulative power consumption at the last time step. If the indoor room temperature (T_{in}) satisfies the target temperature (24–28°C) at the arrival and the Pb($t_{arrival}$) records the minimum power consumption, then a big reward (+200) is given and Pb(t) and Pb_last are updated as new data in this episode, that is, baseline information is updated as the minimum power consumption case. In the first episode (episode = 0), Pb_last starts with 1.e+25, and Pb(t) starts with null values. Before arrival ($t<t_{arrival}$), the target temperature is looser as (21–31°C) under the Pws(t) < Pb(t) condition at each time step, and reward is 1 if satisfied. The reward +1 region induces an air conditioner operation pattern that consumes less power than the previous episode in each time step and consequently induces the reduced cumulative power consumption at the last time of arrival. In other regions, except for the reward +200 and +1 regions, –1 reward is given. Every time, steps have real time progresses according to the linear movement of Fig. 2(b).

3.3. Deep reinforcement learning algorithm coding

The problem definition is:

- State: [(T_{in}–26), dT_{in}/dt, Pws(t), t]
- Action: [21°C, 26°C, 31°C]
- Reward: +200 pt, when T_{in} in the range of (26 ± 2.0)°C and Pws is reduced than ever existing minimum power consumption value (Pb_last) at the arrival time
- Reward: +1 pt, when T_{in} in the range of (26 ± 5.0)°C and Pws(t) is reduced than Pb(t)
- Penalty: –1 pt, in other regions except positive reward regions
- Each episode ending and reset: when t = $t_{arrival}$

The coding flow is shown in Fig. 6. The basic algorithm is the same as established deep Q-learning, with experience replay [25], but it differs by the addition of the reward and reset condition according to Figs. 5 and 6. In Fig. 6, time progresses as real time (t = t + dt) until t = $t_{arrival}$. The initializing condition of T_{in} = (26 ± 0.05)°C is specially applied only to Section 4.4 to compare with the Section 4.3 case of non-exact temperature initializing (fixed time initializing case). The simulation time end is judged by human sense when it seems impossible to achieve more energy saving even with enough repetitive episode training.

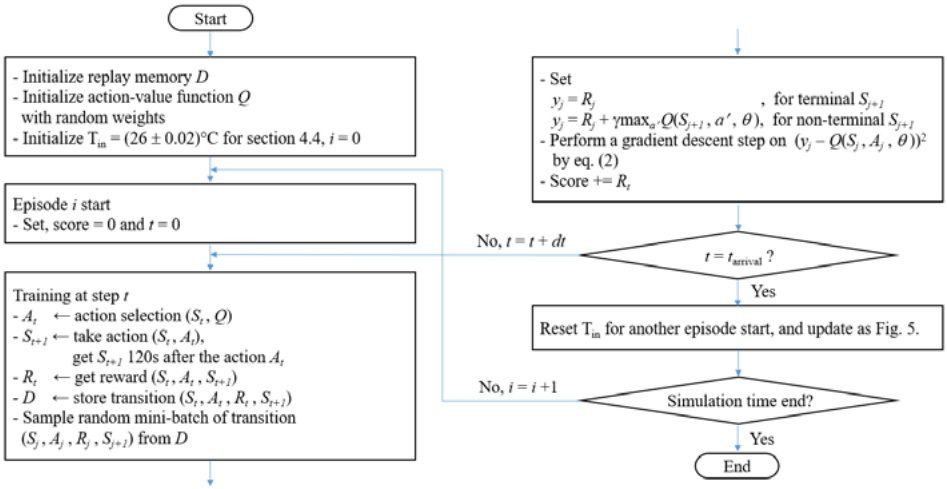


Fig. 6. Deep reinforcement learning coding flow

4. Experiments and results

4.1. Without machine learning (human operation)

Before operation using RL, the amount of minimum power consumption is checked during 2.5 hours and 3.5 hours of going out time by a human. Half an hour is initialized to a set temperature of 26°C before going out at 2.5 hours. Each case of Figs. 7(a), (b), and (c) shows a slightly different T_{in} initializing graph even though the T_{set} temperatures are the same at 26°C. This is generally due to the rough control behavior of air conditioning products, including dead band control. Table 2 summarizes the manual control method. In Fig. 7(b), in order to bring the temperature at t = 3.0 to the target temperature of exactly 28°C, the target range is (24–28°C), T_{set} = 31°C is extended to t = 1.83 h as opposed to 1.33 h in the case of Fig. 7(a). As a result, in Fig. 7(b), the power consumption is reduced to Pwh = 2930 Wh rather than Pwh = 3441 Wh in Fig. 7(a). In Fig. 7(c), instead of lowering the temperature by T_{set} = 26, it is lowered to T_{set} = 21°C. But there is no difference in how the product actually cools due to the (T_{set} –T_{in}) difference detection control.

Figure 8 shows the manual control pattern when the going out time is 3.5 hours. An hour is initialized to a set temperature of 26°C before going out. In Fig. 8(c), T_{set} = 26°C is continuously maintained and changes to 31°C at t = 4.1 h, so that the temperature is near T_{in} = 28°C at the arrival point. Figure 8(c) shows a relatively large electric consumption of 4761 Wh due to poor air conditioner operation.

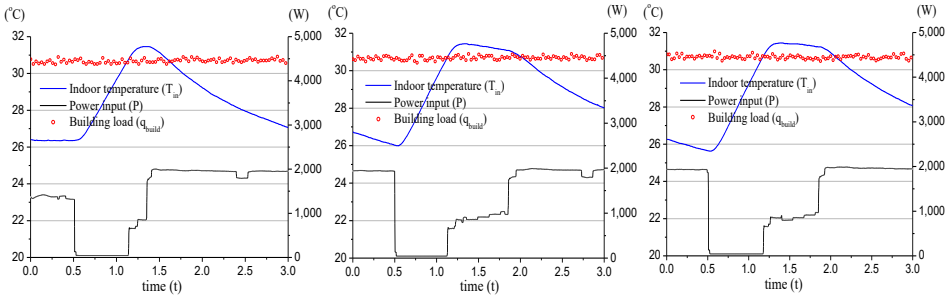


Fig. 7. Human operation during 2.5 h (power accumulation starting at t = 0.5 h): (a) Pwh = 3441, (b) Pwh = 2930, (c) Pwh = 2951

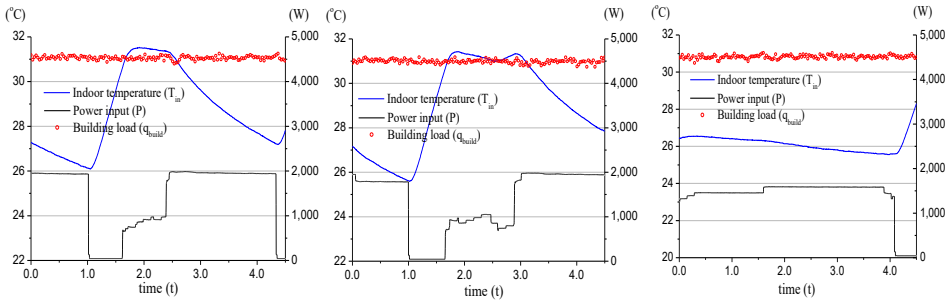


Fig. 8. Human operation during 3.5 h (power accumulation starting at t = 1.0 h): (a) Pwh = 4520, (b) Pwh = 4318, (c) Pwh = 4761

Table 2. Human operation case results

Going out time	Operation case	Operation method	Pwh during going out
2.5 h (Fig. 7)	Fig. 7(a)	26°C(t=0), 31°C(t=0.5h), 26°C(t=1.33h)	3441 Wh
	Fig. 7(b)	26°C(t=0), 31°C(t=0.5h), 26°C(t=1.83h)	2930 Wh
	Fig. 7(c)	26°C(t=0), 31°C(t=0.5h), 21°C(t=1.83h)	2951 Wh
3.5 h (Fig. 8)	Fig. 8(a)	26°C(t=0), 31°C(t=1.0h), 26°C(t=2.5h) , 31°C(t=4.3h)	4520 Wh
	Fig. 8(b)	26°C(t=0), 31°C(t=1.0h), 26°C(t=3.0h)	4318 Wh (4437 Wh)
	Fig. 8(c)	26°C(t=0), 31°C(t=4.1h)	4761 Wh

In the case of Fig. 8(b), due to the manual operation error of the initial temperature adjustment, the initial temperature at the beginning of the power measurement (t =1.0) starts at 25.6°C, which is advantageous for calculating the accumulated power consumption. The time of 430 seconds, which is 26.0°C after t = 1.0, is compensated for the power consumption under the part-load operation assumption (see the power consumption around t = 2.0 in Fig. 8(b)) of 1 kW (430 × 1000 / 3600 = 119 Wh). The 4437 (= 4318 + 119) Wh in the parentheses is a reasonably minimally compensated value for the human operation error.

4.2. Deep reinforcement learning (2.5 hours going out)

The air conditioner operation of 2.5 hours' going out time is solved by RL. It is operated throughout 7.5 days of 59 episodes (Figs. 9 and 10). When we see the entire results graphs (Fig. 9) of 7.5 days, it is difficult to see what the meaningful results are. Therefore, the scores and the cumulative power consumption at each episode are taken by a quick glance from Fig. 10. The red dots in Fig. 10 refer to the results where the episode acquired a +200 reward at the arrival time. The red dots of power consumption decrease until episode 42 and no more episode cases, which gains a +200 reward, appear until the last episode (episode 59).

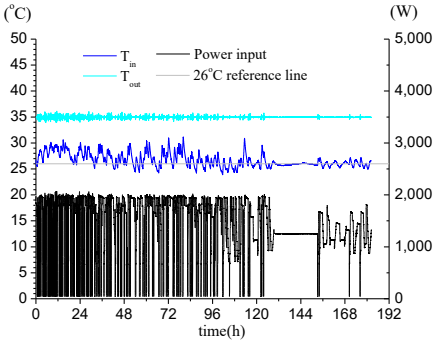


Fig. 9. Total of 7.5 days' deep reinforcement learning for the 2.5 h going out problem

Among the red dot episodes, a representative of three episodes cases (episodes 6, 34, 42) are carefully analyzed (Fig. 11). Commonly, an episode is forcibly stabilized by the 26°C remote control setting during the initial 0.5 hours. However, in the case of Fig. 11(a), the initial value of 26°C is not stably reflected because 0.5 hours are insufficient to stabilize in some cases. In Fig. 12(a), the action outputs for the 21, 26, and 31°C settings are even. In the case of episode 34 (Fig. 12(b)), however, most of the action output maintains the set temperature of 21°C or 26°C, with the exception of the 31°C action output at the 51st time step. In episode 42 (Fig. 12(c)), only the remote control signal of 26°C is continuously maintained. This means that it is more effective to keep the air conditioner at the same initial temperature for a relatively short going out time, which is 2.5 hours in this case. When we compare the human operation case of Table 2, episode 42 of deep reinforcement learning finds smaller power consumption (Pwh = 2766 Wh) than the human (Pwh = 2930 Wh). A human is prone to missing the idea of maintaining the same temperature, but AI finds the answer exactly.

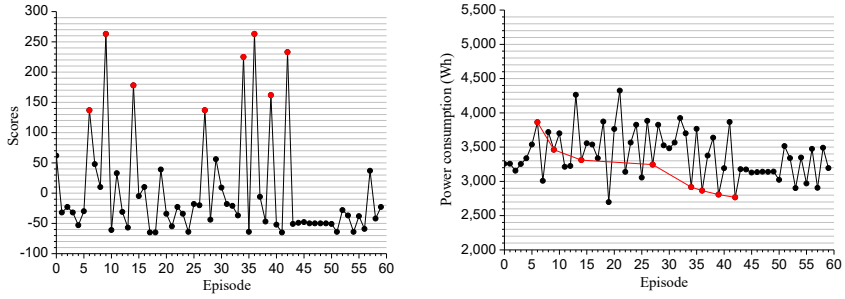


Fig. 10. Variations of (a) scores and (b) power consumption at each episode for the 2.5 h going out problem

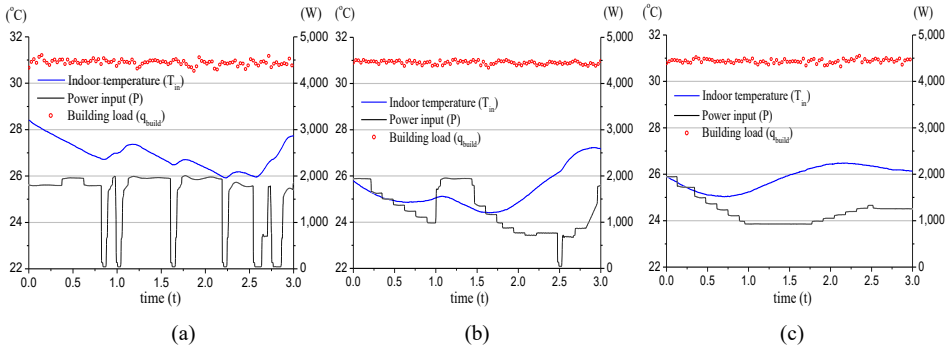


Fig. 11. The RL operation during 2.5 h (power accumulation starting at t = 0.5 h): (a) episode 6, (b) episode 34, (c) episode 42

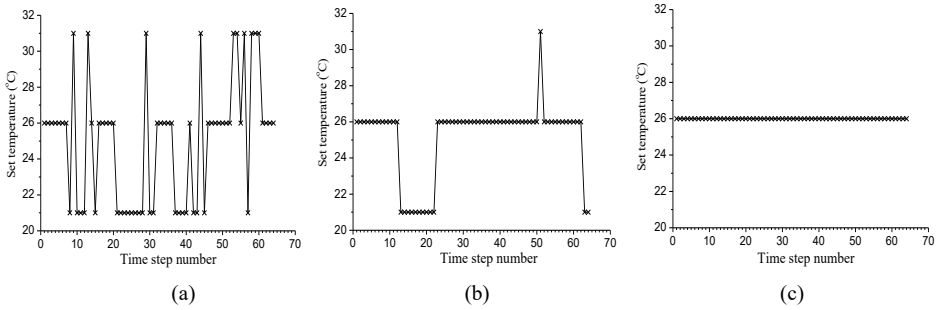


Fig. 12. Set temperature sequences for: (a) episode 6, (b) episode 34, (c) episode 42

4.3. Deep reinforcement learning (3.5 hours going out)

The air conditioner operation of 3.5 hours' going out time is solved by RL. It is operated throughout nine days of 47 episodes (average 0.19 days per one episode, that is, one hour initializing and 3.5 hours training). Because the going out time is longer than the 2.5 hours' going out case, it takes more training time (nine days) than Section 4.2 described (7.5 days of 59 episodes, average 0.127 day per one episode, that is, 30 minutes' initializing and 2.5 hours' training).

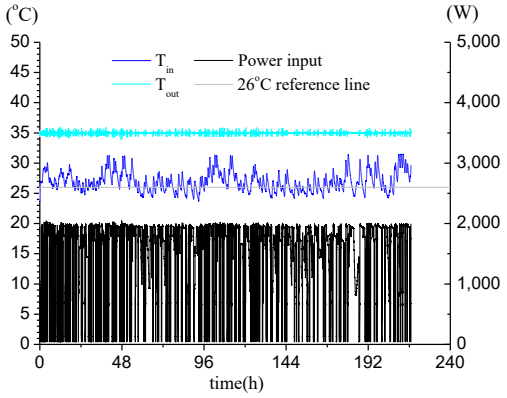


Fig. 13. Total of nine days' deep reinforcement learning for the 3.5 h going out problem

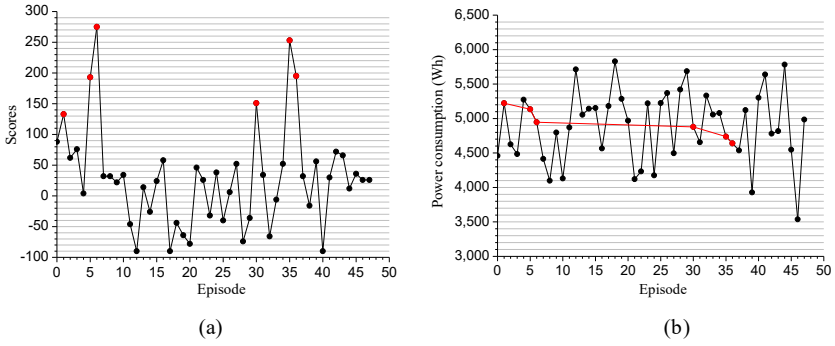


Fig. 14. Variations of (a) scores and (b) power consumption at each episode for the 3.5 h going out problem

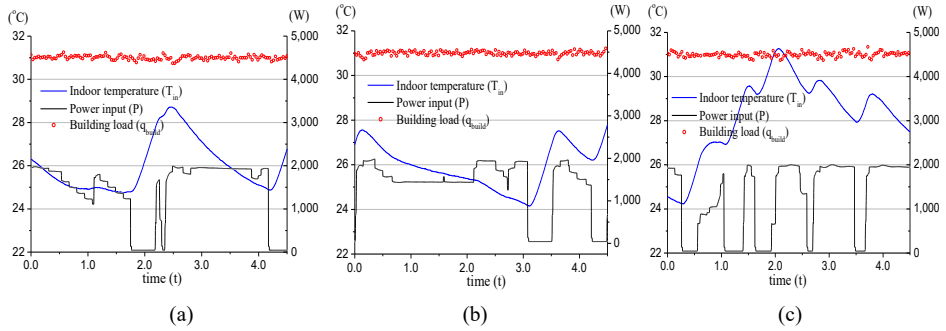


Fig. 15. The RL operation during 3.5 h (power accumulation starting at t = 1.0 h): (a) episode 35, (b) episode 36, (c) episode 42

The RL finds red dots, which satisfies minimized power consumption and in the range of target temperature on the arrival, at episodes 1, 5, 6, 30, 35, and 36 until episode 47. Figures 15 and 16 show the power consumption and remote control signal analysis at episodes 35 and 36 of the energy saving red spot and at episode 42, where there is no energy saving effect. Episodes 35, 36, and 42 record the power consumption of 4739, 4639, and 4780 Wh, respectively. Compared with the results of human analysis in Fig. 8 and Table 2, the cases of human operation (4437 or 4520 Wh) save more energy than the result of RL (4639 Wh). Considering the time it took (9 days), the RL results look comparatively poor.

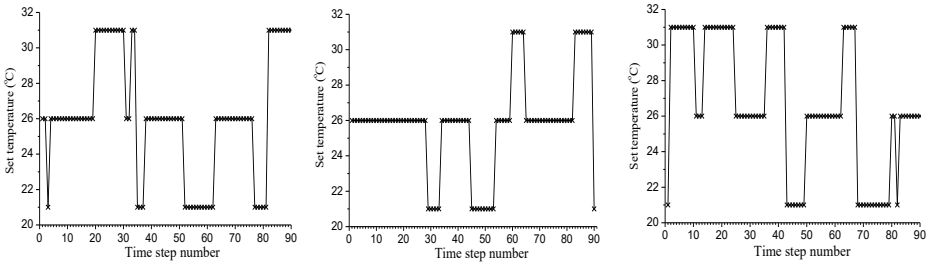


Fig. 16. Set temperature sequences for: (a) episode 6, (b) episode 34, (c) episode 42 (no red dot position of Fig. 14)

4.4. Deep reinforcement learning (3.5 hours going out) with accurate initial condition (T_0 =26 ℃)

The former RL work of Section 4.3 (3.5 hours going out) does not fare well compared with the RL case of Section 4.2 when the going out time is 2.5 hours. The reason for the difference can be guessed by comparing Figs. 11 and 15. In Fig. 11, as the episode progresses, it converges to the 26°C remote control setting value at the arrival time, and in the next episode the learning starts stably at the initial temperature around 26°C. However, in Figs. 15(b) and (c), learning starts slightly away from the initial value of 26°C. The importance of a consistent initial value for RL is well known in the grid world problem or in Atari games [25–26].

With this in mind, 3.5 hours' going out problem is re-solved by modifying the program to start the RL in each episode when the indoor room temperature (T_{in}) is within (26 ± 0.05)°C. If the initial value is under 26°C, then the 31°C remote signal is sent. In the opposite case, a 21°C remote signal is transmitted before starting each episode of learning. The RL is operated fully throughout seven days of 39 episodes, as in Fig. 17.

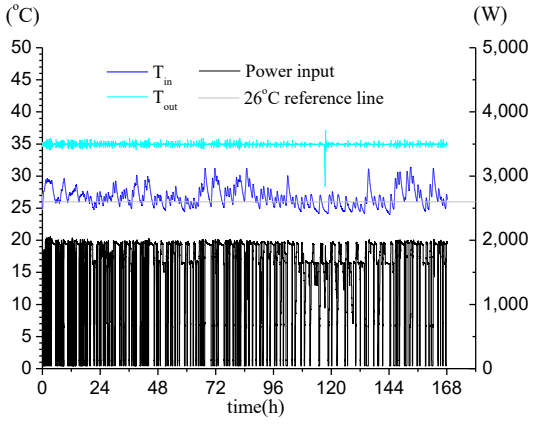


Fig. 17. Total of seven days' deep reinforcement learning for the 3.5 h going out problem

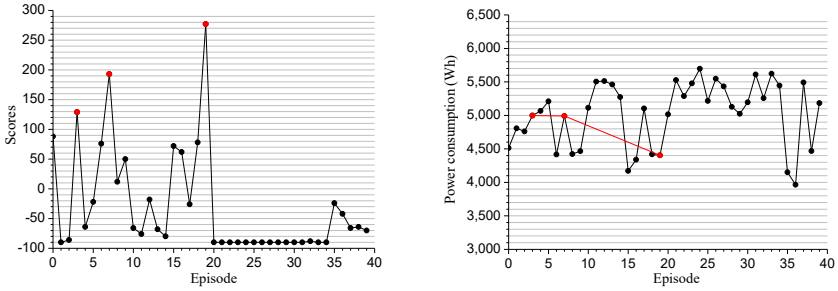


Fig. 18. Variations of (a) scores and (b) power consumption at each episode for the 3.5 h going out problem with accurate initial condition of T_{in} = 26°C

Although learning is performed for seven days, the meaningful RL practically ends within 3.6 days of 19 episodes, as in Fig. 18. At episodes 3, 7, and 19, a reward of +200 (Fig. 5) is recorded, and the power consumption is 4998, 4991, and 4405 Wh, respectively. When compared with the former case of Fig. 14, Fig. 18 converges fast (episode 19) and finds less power consumption (4405 Wh) than the Fig. 14 case (episode 36, 4639 Wh). In Fig. 18(a), it is not easy to get even a smaller reward of +1 (Fig. 5) after episode 19, since the results of episode 19 seem to be optimal.

Compared with the manual result of 4437 Wh in Table 2 and Fig. 8(b), the RL result of 4405 Wh in episode 19 saves more energy. What is more noticeable is that unlike the common sense used in the air conditioner operation method in the operation case of Fig. 8(b) in Table 2 (minimize operation of the air conditioner when going out and then drive again before arrival), RL finds an energy saving method that cannot be found by a human (Fig. 19(c)). Conversely, by comparing the results of Fig. 19(c) and Fig. 8(b), the strategy of RL is analyzed from a human point of view. In Fig. 8(b), after the room temperature reaches 31°C or higher at t = 1.7 h, the air conditioner runs with a part-load of 1 kW to satisfy the 31°C set temperature. After t = 3.0 h, in order to satisfy the final target temperature 28°C (the target range is 24–28°C), the temperature starts to drop by full-load operation. On the other hand, in Fig. 19(c), since the temperature must drop after reaching 31°C anyway in some moment, the temperature drops immediately without delay at the point of 31°C. In addition, energy saving is achieved by aiming for the effect of turning off the air conditioner in (1.8 ~ 2.0) hours and (3.25 ~ 3.5) hours.

In summary, this kind of RL approach is surely useful to find an energy saving operation method when we run an air conditioner. However, we also need more studies about when such an algorithm should be stopped, because in this problem there is no determined answer like the grid world problem or the precision temperature control problem. The grid world problem [26] has a clear goal of reaching the target position, and the air conditioner precision temperature control problem [21] also has an obvious target range of temperature. However, this study has no deterministic minimum energy consumption value. If we have found an energy saving operation method such as in this study, we need to think carefully about how to verify that this minimum solution is a real optimum.

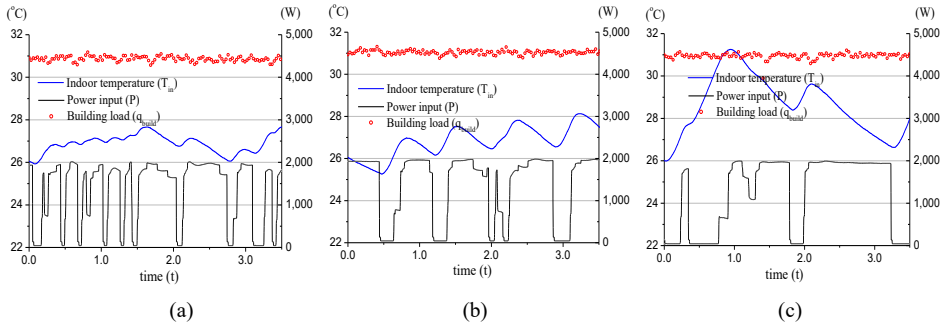


Fig. 19. The RL operation during 3.5 h (power accumulation starting at t = 0 h): (a) episode 3, (b) episode 7, (c) episode 19

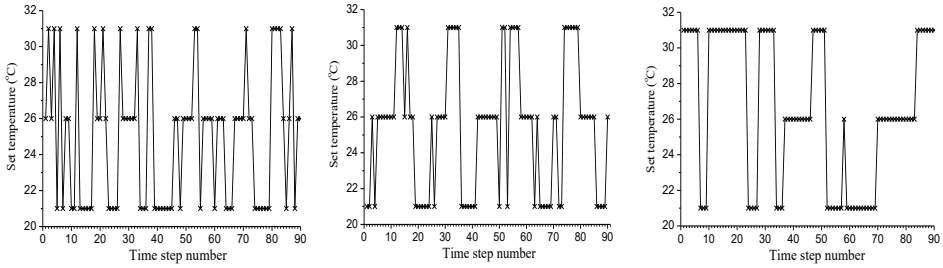


Fig. 20. Set temperature sequences for: (a) episode 3, (b) episode 7, (c) episode 19

5. Conclusion

Reinforcement learning (RL) using a DQN (Deep Q-learning Network) method is applied to a household inverter air conditioner energy saving operation pattern search while occupants are out. Four state variables of [(T_{in}(t) −26), dT_{in}/dt, Pws(t), t] and three actions of 21, 26, 31°C remote control are used in the DQN model. To simplify the problem, some assumptions are made. The indoor building load (q_{build}) and outdoor temperature (T_{out}) are set to be constant at 4500 W and 35°C. Then, assuming that the moving path of the mover (person going out) is linear, only the going out time ($t_{arrival}$) is involved in the problem. For the two going out times of 2.5 and 3.5 hours, the case of manual operation by a human and the case of artificial intelligence operation using RL are compared. The objective of this problem setup is to find remote controller signal sequences during the going out time that save electricity and satisfy the target temperature (24 ~ 28°C) on arrival. In applying RL, it is important to maintain a fixed initial room temperature (T_0 = 26° C) at each episode for fast and stabilized RL results. For the 3.5 hours' going out time problem, two cases of initial condition treatments are given: i) fixed stabilization time as one hour regardless of the start temperature, and ii) accurate initial temperature condition. The latter identifies the energy saving pattern twice as fast as the former, and the result is also better (less energy consumption).

Compared to manual operation based on human judgement, RL finds an exact method that is easy for humans to miss. When the going out time is 2.5 hours, RL derives continuous operation of the air conditioner by fixing the remote controller temperature as 26°C. And when going out time is 3.5 hours, RL shows an operation strategy that induces longer periods of off-mode or part-load mode. In the future, this work can be expanded by merging non-linear movement information with multi-agents and more realistic environmental conditions.

Acknowledgement

This work was supported by the Ministry of Trade, Industry and Energy (MOTIE) and Korea Institute for Advancement of Technology (KIAT) (P0014268, Smart HVAC demonstration support).

References

[1] M. S. Yoon, and W. S. Yoon, "Study on the smart operation approach of an air conditioner when occupants go out," in Proceedings of the 13th IEA Heat Pump Conference (HPC 2020), 2021.

[2] J. V. Canteli, S. Ulyanin, J. Kämpf, and Z. Nagy, "Fusing TensorFlow with building energy simulation for intelligent energy management in smart cities," vol. 45, Sustainable Cities and Society, 2019, pp. 243–257.

[3] K. Grolinger, A. L'Heureux, M. Capretz, and L. Seewald, "Energy forecasting for event venues: Big data and prediction accuracy," vol. 112, Energy and Buildings, 2016, pp. 222–233.

[4] Z. Zhang, A. Chong, Y. Pan, C. Zhang, S. Lu, and K. P. Lam, "A deep reinforcement learning approach to using whole building energy model for HVAC optimal control," in Proceedings of the ASHRAE and IBPSA-USA SimBuild Building Performance Modeling Conference, 2018.

[5] L. Yu, W. Xie, D. Xie, Y. Zou, D. Zhang, Z. Sun. L. Zhang, Y. Zhang, and T. Jiang, "Deep Reinforcement learning for smart home energy management," vol. 7, IEEE IoT Journal, 2020, pp. 2571–2762.

[6] T. Liu, C. Xu, Y. Guo, and H. Chen, "A novel deep reinforcement learning based methodology for short-term HVAC system energy consumption prediction," vol. 107, Int. J. Refrigeration, 2019, pp. 39–51.

[7] D. L. Marino, K. Amarasinghe, and M. Manic, "Building energy load forecasting using deep neural networks," in Proceedings of the IEEE Industrial Electronics Society (IECON), 2016, pp. 7046–7051.

[8] A. Rahman, V. Srikumar, and A. D. Smith, "Predicting electricity consumption for commercial and residential buildings using deep recurrent neural networks," vol. 212, Applied Energy, 2018, pp. 372–385.

[9] A. S. Ahmad, M. Y. Hassan, M. P. Abdullah, H. A. Rahman, F. Hussin, H. Abdullah, and R. Saidur, "A review on applications of ANN and SVM for building electrical energy consumption forecasting," vol 33, Renewable and Sustainable Energy Reviews, 2014, pp. 102–109.

[10] M. Manivannan, B. Najafi, and F. Rinaldi, "Machine learning-based short-term prediction of air-conditioning load through smart meter analytics," vol. 10, Energies, 2017, pp. 1905.

[11] S. K. Jeong, C. H. Han, L. Hua, and W. K. Wibowo, "Systematic design of membership functions for fuzzy logic control of variable speed refrigeration system," vol. 142, Applied Thermal Engineering, 2018, pp. 303–310.

[12] H. Yan, Y. Xia, X. Xu, and S. Deng, "Inherent operational characteristics aided fuzzy logic controller for a variable speed direct expansion air conditioning system for simultaneous indoor air temperature and humidity control," vol. 158, Energy and Buildings, 2018, pp. 558–568.

[13] Z. Li, X. Xu, S. Deng, and D. Pan, "A novel neural network aided fuzzy logic controller for a variable speed (VS) direct expansion (DX) air conditioning (A/C) system," vol. 78, Applied Thermal Engineering, 2015, pp. 9–23.

[14] X. Xu, Z. Zhong, S. Deng, and X. Zhang, "A review on temperature and humidity control methods focusing on air-conditioning equipment and control algorithms applied in small-to-medium-sized buildings," vol. 162, Energy and Buildings, 2018, pp. 163–176.

[15] A. Kusiak, and G. Xu, "Modeling and optimization of HVAC systems using a dynamic neural network," vol. 42, Energy, 2012, pp. 241–250.

[16] P. V. Fazenda, K. Veeramachaneni, P. Lima, and U-M. O'Reilly, "Using reinforcement learning to optimize occupant comfort and energy usage in HVAC systems," vol. 6, J. of Ambient Intelligence and Smart Environments, 2014, pp. 675–690.

[17] K. Yan, C. Zhong, Z. Ji, and J. Huang, "Semi-supervised learning for early detection and diagnosis of various air handling unit faults," vol. 181, Energy and Buildings, 2018, pp. 75–83.

[18] W. Vallandares, M. Galindo, J. Gutierrez, W. C. Wu, K. K. Liao, J. C. Liao, K. C. Lu, and C. C. Wang, "Energy optimization associated with thermal comfort and indoor air control via a deep reinforcement learning algorithm," vol. 155, Building and Environment, 2019, pp. 105–117.

[19] C. C. Cheng, and D. Lee, "Artificial intelligence-assisted heating ventilation and air conditioning control and the unmet demand for sensors: Part 1. Problem formulation and the hypothesis," vol. 19, Sensors, 2019, pp. 1131.

[20] S. J. Cox, D. Kim, H. Cho, and P. Mago, "Real time optimal control of district cooling system with thermal energy storage using neural networks," vol. 238, Applied Energy, 2019, pp. 466–480.

[21] M. S. Yoon, W. S. Yoon, and J. S. Lee, "Application of a deep reinforcement learning algorithm in household inverter air-conditioner temperature control," in Proceedings of the 13th IEA Heat Pump Conference (HPC 2020), 2021.

[22] M. S. Yoon, W. S. Yoon, M. K. Seo, S. Y. Ryu, and J. S. Lee, "Air conditioner component optimum opeartion point search through a deep reinforcement learning algorithm," in Proceedings of the 20th International Conference on Control, Automation and Systems (ICCAS 2020), 2020.

[23] M. S. Yoon, J. Lim, T. S. Qahtani, and Y. Nam, "Experimental study on comparison of energy consumption between constant and variable speed air-conditioners in two different climates," in Proceedings of the Asian Conference on Refrigeration and Air-conditioning (ACRA), 2018, E342.

[24] J. Lim, M. S. Yoon, T. S. Qahtani, and Y. Nam, "Feasibility study on variable-speed air conditioner under hot climate based on real-scale experiment and energy simulation," vol. 12, Energies, 2019, pp. 1489.

[25] V. Mnih, K. Kavukcuoglu, D. Silver, A. Graves, I. Antonoglou, D. Wierstra, and M. Riedmiller, "Playing atari with deep reinforcement learning," arXiv preprint arXiv:1312.5602, 2013.

[26] R. S. Sutton, and A. G. Barto, Reinforcement learning: An introduction (2nd edition). MIT Press, Cambridge, MA, 2018.

13th IEA Heat Pump Conference
April 26-29, 2021 Jeju, Korea

Part Load Capability of a High Temperature Heat Pump with Reversed Brayton Cycle

Johannes Oehler[a1], Jens Gollasch[a], A. Phong Tran[a], Eberhard Nicke[a]

[a] Institute of Low-Carbon Industrial Processes, German Aerospace Center, 03044 Cottbus, Germany

Abstract

This paper studies the part load behavior and capability of a high temperature heat pump that operates with the Brayton cycle. A novel concept of a high temperature heat pump which is currently under construction in Cottbus (Germany) is presented. It goes far beyond temperature levels of current high temperature heat pumps and will provide process heat at above 250 °C. The heat pump uses a closed Brayton cycle driven by axial turbomachinery and provides up to 200 kW of thermal energy. The thermal output can be adjusted by variation of compressor shaft speed, use of internal recuperation and additionally by variation of the fluid inventory. The latter allows operation of our prototype within a broad part load range down to 25 % of the nominal power at nearly constant efficiencies and output temperatures. Brayton cycle heat pumps can be adapted to a wide range of industrial processes and enable highly efficient thermal energy storage systems to balance grid fluctuations.

Keywords: high temperature heat pump; reverse Brayton cycle; fluid inventory control; process heat; electrification

1. Introduction

Industrial processes account for about 25 % of the primary energy used and 20 % of greenhouse gas emissions in the EU-28 countries. Two thirds of this energy are used to meet the process heat demand [1]. Together with space heating in domestic and industrial applications heating and cooling account for 51 % of the final energy consumption in Europe [2]. Current technology relies mainly on fossil fuels such as coal, natural gas and petroleum products [3]. In order to transition to a climate-neutral economy by 2050 which is the declared goal of the European Union [4] all these heat requirements must be met by net zero carbon technologies within 30 years. Heat pumps have been identified as a key technology towards this goal [5].

When using electricity from conventional fossil sources, power to heat technologies are only interesting if either highly efficient or in applications where combustion and emissions are undesired. Otherwise, the losses and the complexity of two conversions from fuel to electricity to heat can hardly be justified. Therefore, conventional heat pumps for low temperature applications such as domestic warm water and space heating are the only field where heat pumps find widespread use as of now [6].

Heat pumps are an important component in energy storage concepts and a possible power-on-demand tool in a more flexible energy system [5, 7, 8]. Efficient part load operation increases the grid balancing capability of heat pumps and is also a selling point for heat pumps in industrial processes where they compete with boilers. Variation of the working pressure is a common tool for changing the power level of a thermodynamic cycle process without having to adapt the geometry [9, 10]. In this paper, the part load capability of a closed loop Brayton cycle heat pump using fluid inventory control is analyzed.

Table 1 shows different technologies to electrify process heat demand. They all rely on renewable electricity which must be generated emission-free in order to reach a climate-neutral economy.

[1] Corresponding author. Tel.: +49 30 67055 8155; *E-mail address:* johannes.oehler@dlr.de

Nomenclature

Abbreviations

DLR	German Aerospace Center
FI	Fluid inventory
FIC	Fluid inventory control
GTlab	Gas Turbine Laboratory
HT	High temperature
HTHE	High temperature heat exchanger
HTHP	High temperature heat pump
LT	Low temperature
LTHE	Low temperature heat exchanger
NTU	Number of transfer units
PTC	Performance Test Code
SSC	Shaft speed control

Variables

a	Fraction of Reynolds independent losses [-]
A	Flow area [m²]
c	Flow velocity [m/s]
COP	Coefficient of performance [-]
M_{Fluid}	Fluid mass [kg]
$\dot{m}$	Mass flow [kg/s]
n	Reynolds dependency of losses [-]
P_C	Compressor power [W]
P_T	Turbine power [W]
p	Total pressure [Pa]
$\dot{Q}$	Heat flow [W]
q_c	Specific heat absorbed at heat source [J/kg]
q_h	Specific heat provided at heat sink [J/kg]
Re	Reynolds number [-]
T_0	Heat source temperature [K]
T_1	Compressor inlet temperature [K]
T_2	Compressor outlet temperature [K]
T_3	Turbine inlet temperature [K]
T_4	Turbine outlet temperature [K]
w	Specific work [J/kg]
V	Volume [m³]
Δp	Pressure drop [Pa]
ζ	Loss coefficient [-]
η	Efficiency [-]
η_{th}	Thermal efficiency [-]
κ	Isentropic exponent [-]
ρ	Density [kg/m³]

Using resistance heating one unit of electrical power is converted to the same amount of thermal energy. When burning substitute natural gas (SNG) or green hydrogen, conversion losses cannot be avoided [11]. Less than one kWh of process heat is generated per kWh of renewable electricity used. With heat pump technology, it is possible to convert one unit of renewable electricity into several units of usable thermal energy. In order to decarbonize process heat demand efficiently, heat requirements at low temperature levels should be met with emission-free technologies first. Process heat at high temperature levels needs a larger investment of renewable electricity per energy unit of heat which can be seen from the low conversion ratio in high temperature applications (see Table 1). Rehfeldt et al. [3] show that a relevant portion of process heat is required at temperature levels from 100 °C to 500 °C.

Heat pumps for sink temperatures of up to 160 °C are already available on the market [6]. The feasibility of heat pumps with sink temperatures as high as 280 °C [12] and 465 °C [7] has been proven utilizing currently available compressor technology. Zühlsdorf et al. [12] suggest a reverse Brayton or Rankine cycle for heat-pumps with very high sink temperatures (> 250 °C) and suggest that coefficients of performance (COP) of nearly two are possible. The German Aerospace Center's (DLR) Institute of Low-Carbon Industrial Processes is currently constructing prototype heat pumps with sink temperatures above 250 °C researching both Rankine and Brayton cycle technology. This paper focuses on the reverse Brayton cycle.

Table 1: Overview of power to heat technologies for process heat demand

Technology	Temperature level	Conversion ratio from net electrical power (COP for heat pumps)	Heating demand for industrial processes in Europe [3]**
Green hydrogen	only material limit	70% [11]	3726 PJ (> 500 °C)
Green gas (SNG)	only material limit	55% [11]	
Resistance heating	At least 850 °C [13]	<100 %	
Ultra-high temperature heat pump	250-500 °C	130-200 %* [7] [12]	2542 PJ (100 – 500 °C)
High temperature heat pump	100-160 °C	200-500 %* [6]	
Conventional heat pump	20-100 °C	300-600%* [6]	821 PJ (<100°C)

* Conversion ratio strongly depends on heat source temperature

** numbers for EU-28 plus Norway, Switzerland and Iceland in 2012, heat demand for space heating not included

2. Thermodynamics of high temperature heat pumps

The reversed Brayton and Rankine cycles are the thermodynamic models of the most commonly used closed cycle compression heat pumps. The Rankine process is preferred in refrigeration and heat pump processes in

the temperature range from -40 °C to 160 °C [6, 14]. It makes use of the phase transition of its working fluid (refrigerant) but is for this reason limited by the physical properties of the refrigerant. The Brayton-process has no phase transition and no temperature limit if air or noble gas is used as a working fluid.

2.1. Brayton process

The Brayton process models a gas turbine process. Operating it reversely (counterclockwise) turns it into a heat pump [14]. Isentropic compression ($T_1 \rightarrow T_2$) happens at a higher temperature level than isentropic expansion ($T_3 \rightarrow T_4$). Sensible heat q_h is provided during an isobaric state change between temperatures T_2 and T_3. The cycle absorbs sensible heat q_c from the environment in an isobaric state change from T_4 to T_1. T_1 is therefore limited to the temperature of the heat source T_0.

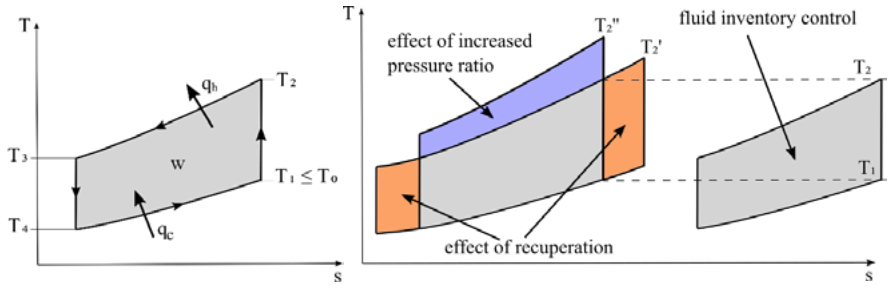


Figure 1: Temperature-entropy diagram of the Brayton cycle (left) and effect through variation of pressure ratio, recuperation or fluid inventory control adapted from [9, 14] (right)

The power turnover of a Brayton cycle can be changed in two ways. By changing the similarity parameters of the cycle and thereby the specific work w or by varying the amount of working fluid exercising the thermodynamic process. Changing the pressure ratio or introducing recuperation affects the temperature levels and the area inside the loop process which represents the specific work w (see Figure 1). With means of fluid inventory control, the process can be shifted sideward in the T-s diagram. When shifted to the right to lower pressure isobars the specific work and temperatures remain constant but the amount of working fluid is reduced. The total power as product of specific work and mass flow is also decreased. Fluid inventory control therefore enables part load operation at constant process temperatures.

2.2. Coefficient of performance

The coefficient of performance (COP) of heat pumps is defined as the ratio between heat delivered from the cycle to the heat sink q_h and work consumed in the thermodynamic cycle process w. The COP is the inverse of the thermal efficiency η_{th} of the equivalent thermal engine [14].

$$COP = \frac{q_h}{w} = \frac{1}{\eta_{th}} \tag{1}$$

For the ideal Brayton cycle with constant isentropic exponent κ the specific work w can be expressed as the difference between heat provided q_h and heat absorbed q_c and $\mathrm{COP_{Brayton}}$ is a sole function of the compressor inlet temperature T_1 and the compressor outlet temperature T_2 [14].

$$COP_{Brayton} = \frac{q_h}{w} = \frac{q_h}{q_h - q_c} = \frac{T_2}{T_2 - T_1} \tag{2}$$

High values of T_1 increase $\mathrm{COP_{Brayton}}$, but T_1 is limited to the temperature T_0 of the available heat source which can be ambient temperature or an exhaust air stream. It is visible from Eq. (2) that the COP

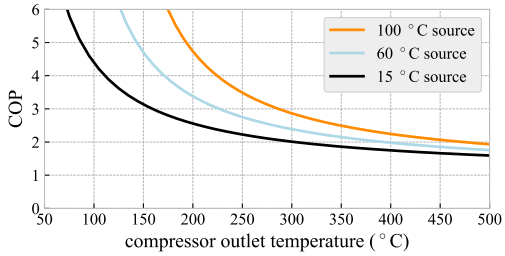


Figure 2: Brayton-cycle COP for high compressor outlet temperatures T_2

decreases with a rising heat sink temperature level and approaches the value of direct electrical heating $COP_{deh} = 1$ for very high T_2.

Figure 2 shows the COP levels of an ideal Brayton cycle heat pump as a function of T_2 for different heat source temperatures $T_0 = T_1$. It shows clearly that the use of exhaust streams is an important aspect when increasing the energy efficiency of industrial processes. The trend of low COP for high sink temperatures also holds for Carnot or Rankine cycle heat pumps [6] and explains why high temperature heat pumps tend to have a lower COP than heat pumps for domestic purpose and low temperatures (see Figure 2 and Table 1).

3. Technical specifications of the DLR-CoBra prototype

With the construction of the prototype 'CoBra' (**Co**ttbus **Bra**yton-cycle heat pump) the German Aerospace Center (DLR) aims at researching the key parameters of a high temperature heat pump with air as working fluid. The high temperature heat pump is designed to provide up to 200 kW of useful heat at temperature levels above 250 °C [15]. Figure 3 shows a model of the heat pump with its most important components. The heat pump has a conditioning unit to control the amount of working fluid in the system consisting of a buffer storage and vacuum pump. Dry air will be used for safety reasons in the research environment. It is non-toxic and has zero global warming potential unlike other common refrigerants [6]. The air in the heat pump must be dried in order to prevent condensation and icing of the turbine at low temperatures.

3.1. Working principle

The compressor increases the pressure and temperature of the working fluid which is the equivalent to state change 1 → 2 of the reverse Brayton cycle (see Figure 1). The high temperature heat exchanger (HTHE) transfers heat to the secondary process which is simulating the industrial process that requires heat. In the turbine, the working fluid is expanded 3 → 4 and power is recovered. The low temperature heat exchanger (LTHE) simulates the heat source which can be ambient air or an exhaust gas stream at higher temperatures. The inlet temperature of the cooling cycle is set to T_0=15 °C for all simulations. The low temperature secondary cycle can also be used for refrigeration at temperatures below 0 °C. The recuperator increases temperature lift at the cost of increased power consumption as shown in Figure 1. It allows to research different operation modes and temperature levels of the heat pump.

Red lines indicate high pressure, blue lines indicate low pressure. Both are fully independent of the ambient air pressure. By filling more working fluid from the buffer storage into the primary circuit the overall pressure level, mass flow and power can be increased. This technique is called fluid inventory control and can be used in closed cycle Brayton engines without combustion [9]. The air buffer also accounts for leakages of the working fluid in the turbomachines and ensures a constant pressure level for repeatable operating conditions.

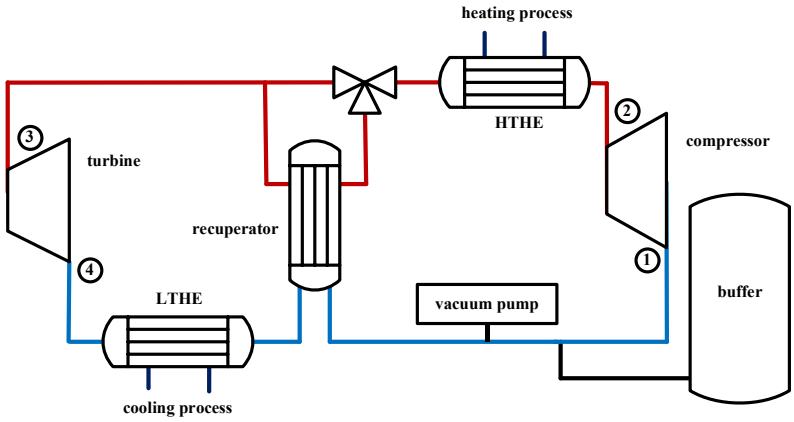


Figure 3: Simplified piping and instrumentation diagram of the Brayton cycle heat pump of the DLR Institute of Low-Carbon Industrial Processes in Cottbus (Germany)

3.2. Part load strategy

In order to meet a reduced heat demand below nominal load, the heat pump can adjust the thermal output with two different control strategies:

- Shaft speed control (SSC)
- Fluid inventory control (FIC)

Reducing the compressor shaft speed yields lower pressure and temperature ratios, lower mass flow and reduces the heat delivery of the heat pump. The compressor outlet temperature T_2 is reduced (see Figure 1). Using fluid inventory control the temperature levels of the thermodynamic process can be kept constant at different load levels. Pradeep Kumar et al. [9] have shown for a closed Brayton cycle gas turbine that fluid inventory control as a part load strategy allows much higher efficiencies than changing temperature levels or bypassing parts of the gas stream.

4. Methodology

In order to simulate the part load performance of the heat pump, a thermodynamic performance model of the system has been developed. The performance model accounts for the effects that occur during part load operation of a closed-cycle heat pump system. The following subsections outline the methods used for the analysis.

Simulations were mainly carried out on a system level. Detailed component simulations are not required to assess the system behavior and were left out of the present work. As the development of the heat pump and simulation tools progresses, higher-fidelity methods will be developed for more in-depth analyses.

4.1. Heat pump cycle simulation

The steady-state heat pump model on which the present analyses are based was created using the DLR in-house performance code GTlab-Performance developed by Becker et at. [16]. In the 0D thermodynamic cycle simulation, the main components of the heat pump are represented as modules, which in turn model the changes of thermodynamic state in the working medium.

For off-design calculations, a performance map of the compressor particularly developed for the CoBra prototype heat pump was used. The map is the result of detailed 3D CFD simulations of the flow in the compressor stages, which used the exact geometry of the blades. The turbine performance map was generated by scaling an existing turbine map of a gas turbine to match the turbine performance of the CoBra prototype based on 3D CFD simulation data computed with the preliminary turbine geometry.

In order to estimate the transferred heat of the shell-and-tube heat exchangers, an approach based on the Number of Transfer Units (NTU) method has been implemented using correlations from VDI Heat Atlas [17].

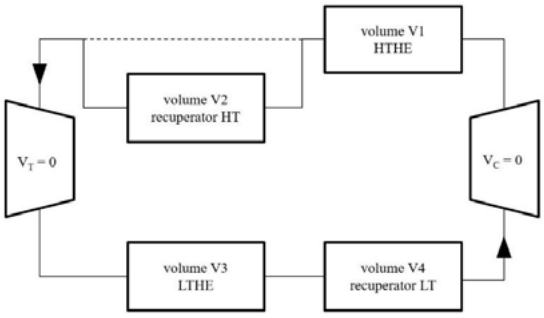


Figure 4: Heat pump component volumes for calculation of pressure levels

The heat transfer is calculated from the two inlet flows and the heat exchanger geometry and accounts for variations in similarity parameters such as Nusselt and Reynolds number. The thermodynamic cycle simulation is coupled with the heat transfer simulation in order to model the system behavior under different operating conditions.

4.2. Pressure level estimation depending on fluid inventory

A simplified heat pump model is used to calculate fluid mass on the high and low pressure side of the heat pump under stationary operating conditions. The volumes are mainly determined by the geometry of the heat exchangers and piping. The pipe volume is lumped to the heat exchangers. According to this, four volumes represent the heat pump components as shown in Figure 4. Due to their small size turbomachine volumes are neglected. Fluid mass is calculated using the semi-ideal gas model of GTlab-Performance, which provides values for density at the inlet and outlet stations of these volumes.

$$M_{Fluid} = \sum_{i=1}^{n=4} V_i \, \bar{\rho}_i \tag{3}$$

M_{Fluid} is approximated with the approach shown in Eq. (3) by using the arithmetic mean value of densities $\bar{\rho}_i$ for each volume V_i. This method is coupled with the GTlab-Performance solver by an iterative correction of lower pressure level for a user-defined fluid inventory. At nominal load the total pressure at compressor inlet is set to the design value of $p_{1,nominal} = 101325\ Pa$.
Part load operating conditions lead to a variation of compressor inlet flow conditions. Reducing compressor shaft speed shifts the operating point to lower pressure ratios, which in most cases induces rising lower pressure levels in hermetic systems. For system level simulations of Brayton cycle heat pumps, it can be important to consider this effect to correctly predict power input and operating limits.

4.3. Pressure drop approximation at partial load

In addition to the isentropic efficiency of turbomachines, pressure drop is a significant factor for the overall heat pump performance. In Brayton cycle heat pumps, the energy recovery of the turbine strongly depends on the pressure losses in the system. This effect is taken into consideration by a pressure loss coefficient ζ_i for each component:

$$\Delta p_i = \zeta_i \frac{\rho_i}{2} c_i^2 \tag{4}$$

Pressure drop is mainly driven by friction losses in heat exchangers, valves and piping. As the heat pump is still under development, not all component geometries and no experimental data are available. Therefore, a simplified approach is used to approximate part load pressure drop in this work. A reference pressure drop for the high and low pressure side of the heat pump is calculated for design operating conditions based on data from the component manufacturers. Pressure drop coefficient ζ is considered to be constant because relevant Reynolds numbers are sufficiently high in all operating conditions (see Moody chart e.g. [17]).

$$\frac{\zeta}{2\,A^2} = \Delta p_{ref}\,\frac{\rho_{ref}}{\dot{m}_{ref}^2} = const. = C_\zeta \tag{5}$$

Off-design pressure drop is estimated by deriving the part load value from the reference state depending on actual mass flow and fluid density. This approach allows a calculation with the parameter set of the GTlab-Performance model:

$$\Delta p = C_\zeta\,\frac{\dot{m}^2}{\rho} = \Delta p_{ref}\,\frac{\dot{m}^2}{\dot{m}_{ref}^2}\,\frac{\rho_{ref}}{\rho} \tag{6}$$

According to the method introduced, pressure losses are approximated for each stationary operating point. On the high pressure side the resulting pressure drop is applied upstream of the turbine inlet and on low pressure side upstream of compressor inlet.

4.4. Reynolds number effect on efficiency of turbomachinery

In compressor and turbine maps, the effect of Reynolds number on the performance of turbomachinery is usually neglected. However, the increased kinematic viscosity at low Reynolds numbers results in additional losses or lower efficiencies. Multiple efficiency scaling correlations have been proposed to account for the Reynolds number effect. The general form of the efficiency correction follows [18]:

$$\frac{1-\eta}{1-\eta_{ref}} = a + (1-a)\left(\frac{Re}{Re_{ref}}\right)^n \tag{7}$$

In Eq. (7), the coefficient a denotes the fraction of the losses that are independent of the Reynolds number. The exponent n is a measure for the Reynolds number dependence of the losses. The effect of Reynolds number on turbomachine efficiency is shown in Figure 5 for three commonly used correlations taken from Wiesner [18] .

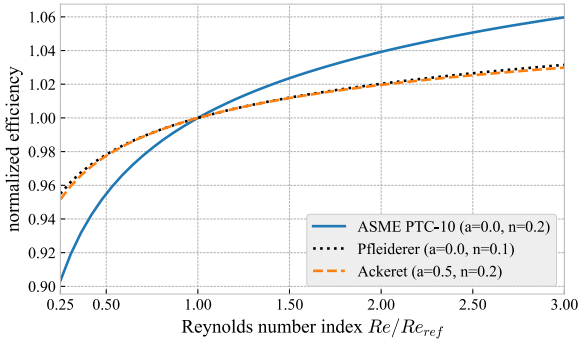


Figure 5: Effect of Reynolds number on turbomachine efficiency based on selected correlations [18]

The ASME Performance Test Code 10 [19] provides Reynolds number correction correlations for axial and centrifugal compressors. Axial compressor efficiencies are assumed to scale only with the Reynolds number ratio, resulting in values of $a = 0$ and $n = 0.2$. Since experimental data of the turbomachines were not available at the time of this study, the coefficients proposed in ASME PTC-10 were applied for the present analyses.

5. Results and discussion

To investigate the part-load capability of closed-cycle high temperature heat pumps two strategies are evaluated (see section 3.2):

- Shaft speed control (SSC): Operating areas of HTHP for non-recuperated and recuperated cycle
- Fluid inventory control (FIC): Comparison with SSC for a scenario with constant temperature requirement and load reduction by 75%

5.1. Operating limits of Brayton cycle heat pumps controlled by shaft speed

The permissible operating range of the CoBra prototype heat pump is bounded by several operating limits:

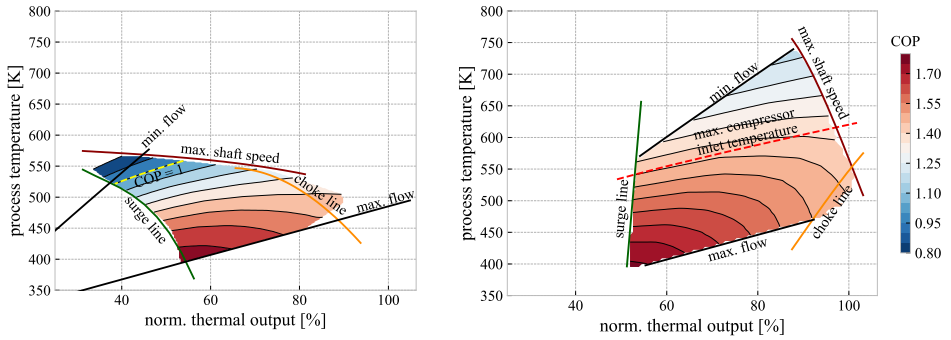
- Compressor surge: The surge line marks the operating limit beyond which no stable flow can be sustained in the compressor due to flow separation at the blades. A certain safety margin must be kept during operation.
- Maximum shaft speed: The absolute shaft speed is typically limited by the mechanical strength of the rotor blades.
- Secondary mass flow: The secondary mass flow rate at the heat exchanger's secondary side is bounded by the minimum and maximum delivery rate of the fan.
- Maximum compressor inlet temperature: Due to the used instrumentation, the compressor inlet temperature must not exceed a maximum value.
- Compressor choke: At high corrected mass flow rates, the flow reaches sonic velocities, preventing further increase of mass flow rate.

Using the methods presented in section 4, the operating envelopes have been calculated for the CoBra prototype heat pump in non-recuperated and recuperated operating mode. The results are shown in Figure 6 (a) and (b), respectively.

The COP used for the following analysis is defined in Eq. (8) and computed with consideration of pressure drop and component efficiencies as described in section 4:

$$COP = \frac{\dot{Q}_{HTHE}}{P_C - P_T} \tag{8}$$

A comparison of the operating modes shows that the recuperated cycle allows for operation at higher process temperatures and thermal output. In accordance with the assessments in section 2.2, both envelopes show a decrease of COP when higher temperatures are demanded. It should be noted that the non-recuperated cycle shows an operating area where the COP drops below 1: At these operating points, the turbine outlet temperature exceeds the temperature of the heat source level $T_0 = 15\,°C$. Therefore, heat is rejected at both heat exchangers and the system is not working as a heat pump. When comparing the operating envelopes, the recuperated cycle shows higher COPs at the same delivered heat flows and temperatures.



(a) Non-recuperated (b) Recuperated

Figure 6: Operating envelopes with COP

Figure 7 illustrates the heat pump's permissible operating range with the current instrumentation for a given fluid inventory in a single diagram. The achievable temperatures are currently limited by the instrumentation at the compressor inlet. Higher delivery temperatures may be achieved by modifying the installed sensors. It is noticeable that the delivered heat flow cannot be reduced below a minimum value by shaft speed control.

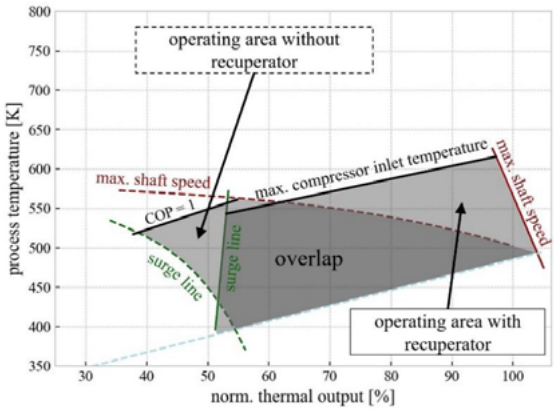


Figure 7: Comparison of operating areas depending on process architecture

Consequently, if a process requires a wider operating range, additional control options are necessary. This is shown in the following section, where the limitations of the recuperated process with fixed amount of working fluid are compared to a system with fluid inventory control.

5.2. Fluid inventory control

As discussed in section 5.1 load reduction of shaft-speed-controlled high temperature heat pumps is limited e.g. due to instability of the compressor. Fluid inventory control has the potential to significantly expand the operating range with little variation in engine efficiency (see section 3.2).

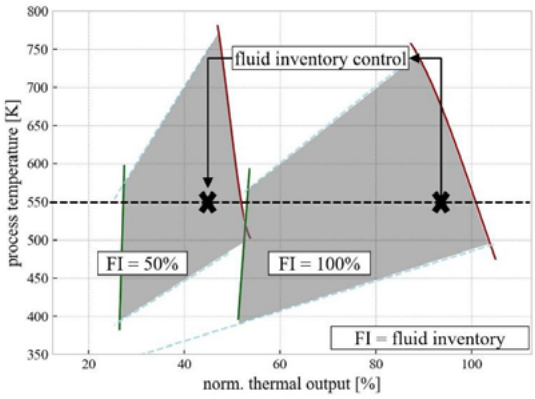
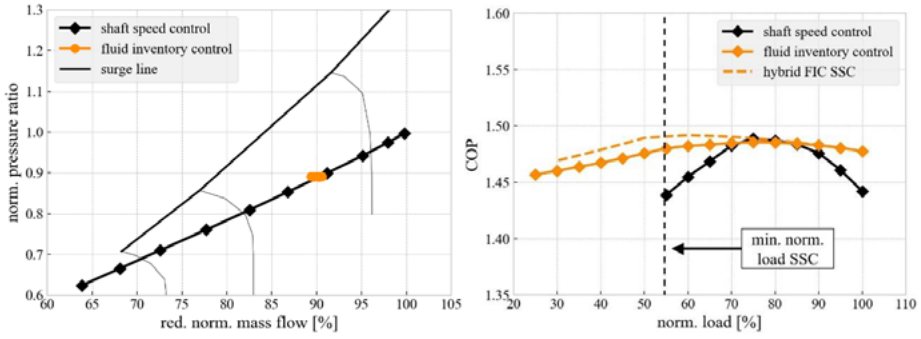


Figure 8: Effect of fluid inventory variation on operating limits of recuperated cycle

Figure 8 shows the effect of a variable fluid inventory on the operating envelope of a HTHP. Altering fluid mass shifts the resulting operating area to corresponding power outputs. When reducing the fluid inventory from a reference state to 50% as shown in the example, the thermal output scales almost linearly with the fluid mass while the temperature range remains almost identical.
For the investigations presented in this paper, a required process temperature of 550 K is assumed. The thermal output range extends from the nominal load to a reduction of 75%. However, the recuperated process architecture only allows a reduction to approx. 55% of nominal load via control of compressor rotational speed.



(a) Compressor map (b) COP

Figure 9: Fluid inventory control vs. shaft speed control for load reduction

If the process requires greater flexibility, the fluid inventory must be adjusted accordingly. This is demonstrated in this figure by shifting an operating point through FIC to low thermal output, which could not be reached by reduction of shaft speed.

Figure 9 demonstrates the advantages of part load operation with fluid inventory control. Figure 9 (a) shows a section of the compressor map. The black working line connects the operating points in the case where part load operation is controlled by varying the compressor rotational speed. For each operating point, the required process temperature is set to 550 K. The inlet temperature of the secondary side of both heat exchangers (HTHE and LTHE, see Figure 3) is 15 °C. The amount of working fluid is optimized for best COP in this range.

When thermal output is controlled by adjusting the fluid inventory, the operating conditions in the turbomachines remain almost identical for the requested performance range. The resulting operating point has been determined by optimization of COP near nominal load conditions and is highlighted in orange in Figure 9 (a).

Figure 9 (b) compares the COP for the entire operating range of shaft speed control and FIC. It becomes clear, that an adjustment of fluid inventory is not only able to extend the operating range but also leads to only minor deviation of heat pump performance even for very low thermal output. The decreasing COP is mainly evoked by Reynolds corrections (see section 4.4) which lead to lower efficiencies of the turbomachines for low-power operating conditions. This trend coincides well with the results by Pradeep Kumar et al. [9], who investigated fluid inventory control for closed cycle gas turbines. There is also some optimization potential by introducing a hybrid method where fluid inventory is controlled as well as compressor shaft speed. This is shown by the dotted orange line. Therefore, fluid inventory control should be considered to increase flexibility of future high temperature heat pumps and extend the scope of their potential applications.

6. Conclusion and outlook

High temperature heat pumps can cover a wide range of industrial process heat requirements. They highlight a very efficient decarbonization strategy for process heat temperatures up to at least 500 °C. Closed cycle Brayton heat pumps capable of thermal output regulation by fluid inventory control provide high flexibility while operating with almost constant efficiency. It is shown that heat pumps are limited to a certain operating range depending on the available methods to control part load operation. Maximum output is mainly determined by thermal and mechanical load capacity of the components.

Two strategies for load reduction have been investigated in the scope of this work. If the heat pump is solely controlled by variation of shaft speed, the permissible minimum load is limited e.g. by compressor stability. The overall operating range for non-recuperated and recuperated process architecture is demonstrated by the introduction of HTHP envelopes. For the CoBra prototype heat pump the recuperator invokes higher output temperatures and better COP.

In order to demonstrate the field of application for fluid inventory control, a scenario with constant output temperature and a load reduction down to 25% has been investigated. The simulation results indicate that fluid inventory control incurs only minor reduction of heat pump performance over the entire operating range. On the other hand, the shaft speed controlled heat pump with fixed amount of working fluid can only operate down to 55% load with varying operating conditions and efficiency.

Fluid inventory control is a promising method to control thermal output of highly flexible future heat pumps. It offers an effective mechanism to react to heat demand changes and address grid fluctuations. Its effect on the transient stability of the compressor will be researched during the operation of the CoBra. In order to investigate fluid inventory control in more detail, studies based on this work with a higher-fidelity model base and experimental examinations are planned.

Acknowledgements

The authors thank Enrico Jende, Leander Schleuss, Panagiotis Stathopoulos and all members of the department of high temperature heat pumps for their support.

References

[1] R. de Boer, A. Marina, B. Zühlsdorf, C. Arpagaus, M. Bantle, V. Wilk, B. Elmegaard, J. Corberán and J. Benson, "Industrial Heat Pump Whitepaper," SINTEF, 2020.

[2] Fraunhofer Institute for Systems and Innovation Research, Fraunhofer Institute for Solar Energy Systems, "Mapping and analyses of the current and future (2020-2030) heating/cooling fuel deployment (fossil/renewables)," report prepared for the European Commission, 2016.

[3] M. Rehfeldt, T. Fleiter and F. Toro, "A bottom-up estimation of the heating and cooling demand in European industry," *Energy Efficiency,* pp. 11:1057-1082, 2018.

[4] European Union, "Long-term low greenhouse gas emission development strategy of the EU and its Member States," 06 03 2020. [Online]. Available: https://unfccc.int/documents/210328.

[5] Prognos, Öko-Institut, Wuppertal-Institut, "Towards a Climate-Neutral Germany," Executive Summary conducted for Agora Energiewende, Agora Verkehrswende and Stiftung Klimaneutralität, [Full study in German language only], 2020.

[6] C. Arpagaus, F. Bless, M. Uhlmann and J. Schiffmann, "High temperature heat pumps: Market overview, state of the art, research status, refrigerants, and application potentials," *Energy,* pp. 985-1010, June 2018.

[7] V. Aga, E. Conte, R. Carroni, B. Burcker and M. Ramond, "Supercritical CO2-Based Heat Pump Cycle for Electrical Energy Storage for Utility Scale Dispatchable Renewable Energy Power Plants," in *5th Int. Supercrit. CO2 Power Cycles Symp*, San Antonio Texas, 2016.

[8] R. B. Laughlin, "Pumped thermal grid storage with heat exchange," *Journal of Renewable and Sustainable Energy,* 02 August 2017.

[9] K. Pradeep Kumar, A. Tourlidakis and P. Pilidis, "Performance review: PBMR closed cycle gas turbine power plant," International Atomic Energy Agency, Vienna (Austria), 2001.

[10] E. Agelidou, M. Henke, T. Monz and M. Aigner, "Numerical Investigation of an Inverted Brayton Cycle Micro Gas Turbine based on Experimental Data," in *Proceedings of ASME Turbo Expo 2018 - Turbomachinery Technical Conference and Exposition*, Oslo, Norway, 2018.

[11] M. Götz, J. Lefebvre, F. Mörs, A. McDaniel Koch, F. Graf, S. Bajohr, R. Reimert and T. Kolb, "Renewable Power-to-Gas: A technological and economic review," *Renewable Energy,* pp. 1371-1390, 2016.

[12] B. Zühlsdorf, F. Bühler, B. M. and B. Elmegaard, "Analysis of technologies and potentials for heat pump-based preocess heat supply above 150 °C," *Energy Conversion and Management: X,* 2019.

[13] BASF, "BASF Carbon Management," 07 2020. [Online]. Available: https://www.basf.com/global/en/who-we-are/sustainability/we-produce-safely-and-efficiently/energy-and-climate-protection/carbon-management.html. [Accessed 12 11 2020].

[14] B. Weigand, J. Köhler and J. von Wolfersdorf, Thermodynamik kompakt, Heidelberg Dordrecht London New York: Springer, 2010.

[15] L. Schleuss, T. Lorenz, D. Wenzke, C. Hensel, S. Panagiotis, E. Nicke and U. Riedel, "Decarbonisation of industrial processes - New DLR institute in Cottbus and Zittau," in *4th International Conferene on Energy Supply and Energy Efficiency*, Baku (Azerbaijan), 2020.

[16] R.-G. Becker, F. Wolters, M. Nauroz and T. Otten, "Development of a Gas Turbine Performance Code

and Its Application to Preliminary Engine Design," *DLRK,* 27-29 09 2011.

[17] VDI e. V., VDI Heat Atlas, Berlin: Springer, 2010.

[18] F. Wiesner, "A New Appraisal of Reynolds Number Effects on Centrifugal Compressor Performance," *Journal of Engineering for Power,* pp. 384-392, 07 1979.

[19] The American Society of Mechanical Engineers, Performance Test Code on Compressors and Exhausters (ASME PTC-10), New York: ASME, 1997.

13th IEA Heat Pump Conference
April 26-29, 2021 Jeju, Korea

Dynamic simulations of an absorption refrigeration system for automobile application

Hai Trieu Phan[a,*], Mathilde Wirtz[a], Julien Hergott[b] and François Boudehenn[a]

[a]Univ. Grenoble Alpes, CEA, LITEN, DTBH, 38000 Grenoble, France
[b]Faurecia Clean Mobility, R&D Center, 25550 Bavans, France

Abstract

This study was aimed at evaluating the technological feasibility of an absorption refrigeration system using heat from the exhaust gases to cover the needs of air conditioning in automobiles. In the first step, architecture of a single-stage ammonia-water absorption cycle was designed for a case study with a standard 2.0L gasoline turbo-engine vehicle. Then, a new dynamic model of the absorption cycle was built based on the TIL Modelica library to simulate the transient behaviour of the cycle during start/stop and change in driving regime. The simulation results show two major limitations of the absorption refrigeration: insufficient cold production for low wheel power (urban cycle); and slow start up compared to a conventional compression system. The dynamic of the absorption cycle is slow enough to make the engine speed fluctuations (including the stop & start function) imperceptible by the users. Analysis of the ammonia mass flow rate in the system exhibits that the inertia of the absorption cycle mainly depends on high-pressure components such as generator and condenser. This study provides some insight to optimize the performance and the dynamic of the absorption refrigeration system for automobile application.

Keywords: absorption refrigeration; dynamic simulation; heat recovery

1. Introduction

Today, compression refrigeration system (CRS) is the most used refrigeration system in automobiles, requiring approximately 8% to 12% of the engine rated power for air-conditioning. As a result, the average fuel oil consumption increases approximately 16% to 20% when driving automobile with air-conditioning in operation [1]. As automobiles have 35% to 40% thermal efficiency rate, the remaining primary energy is consumed for cooling liquid/lubricant, and in exhaust gases [2]. Nowadays, studies focus on the improvement of thermal efficiency by achieving a better fuel consumption. While utilization of the heat dissipated in exhaust gases for turbo charging and cabin heating has been browsed, more and more studies [3 – 4] focus on air-conditioning by waste heat refrigeration system (WHRS). However, WHRS is a crucial topic still not at a maturity state, because of specific technical requirements. WHRS should be compact and light to fit the narrow space of automobiles. They need to be cooled by air directly and must operate whenever the vehicle runs, under any road/driving conditions. Furthermore, the working fluids should be low toxic, low flammable, able to work under the operating pressure and provide good heat and mass transfers [3]. Ammonia-water absorption refrigeration system (ARS) is a promising solution, with the ammonia filling all the working fluids constraints.

Horuz [5] experimentally proved the possibility of using absorption refrigeration system (ARS), feed by the waste heat in exhaust gases from a 6L diesel vehicle. The prototype is a 10kW commercial single-stage NH3-H2O system. The author shows ARS can replace both the internal combustion (IC) system and the compressor of the CRS. Kaewpradub & al. [6] investigate a single-stage LiBr-H2O absorption refrigeration system. Experiments are led at different engine speeds, expansion valve openings, condenser-outlet temperatures and solution flow rates. The coefficient of performance (COP = Cold produced power/Sum of thermal and electricity input powers) and cooling load increase with the engine speed, and the drop of condenser outlet temperature. The cooling load and COP reach maximal values of 700W and 0.28 respectively, at 1400 rpm and 25°C at condenser outlet. When the solution mass flow rate increases, the cooling load capacity increases

* Corresponding author. Tel.: +33 4 79 79 23 72; fax: +33 4 38 78 53 96.
E-mail address: haitrieu.phan@cea.fr.

too, but the COP drops. Koehler & al. [7] developed a detailed model and designed a breadboard prototype of a single-stage NH3-H2O absorption system for truck refrigeration. The heat is provided from the exhaust-gases, at a temperature of around 460°C and a mass flow rate of 360 kg/h. The evaporation temperature varies between -20°C and 0°C, while ambient temperature is from 20°C to 30°C. The prototype COP is from 0.23 to 0.30 with a cooling capacity of 6-10kW.

Charate & al. [4] provide a literature review on air-conditioning in a car, using absorption refrigeration supplied by exhaust heat. Chandrakar & al. [8] designed a NH3-H2O absorption refrigeration system for a 4-cylinder car. Evaporator can produce 2.6 kW of cold, from 4.5 kW of heat; with a COP of 0.57. Rixon & al. [9] designed and built a NH3-H2O absorption refrigeration system from pieces recovery. COP reaches 0.14, with exhaust gases temperature between 100°C and 180°C. Vicatos & al. [10] conducted a theoretical analysis, and developed a unit tested in a laboratory and on road. COP reaches only 0.09. Talom & Beyene [11] led an experimental study on a 10.6 kW absorption chiller, modified to be supplied by a 2.8L V6 IC engine. Results show the concept feasibility and the increase of the system performances.

Most of the authors [5, 4; 8-10] highlight that the use of exhaust gases for air-conditioning allow to reduce IC, fuel consumption, noise and atmospheric pollution, while maintaining efficiency of the engine. However, in most of the studies, the COP is low, about 0.1 to 0.3, which means that further researches for cycle improvement are necessary. According to [5], some points need to be strengthened: pressure variations, and fluctuations of cooling capacity regarding the vehicle speed. An important issue, underlined by [5, 7, 8], is when the vehicle is parked or move slowly: ARS is not sufficient, an alternative solution or a complementary heater is needed. In [7], the authors insist that this system is promising for long distance driving, but is not robust when exhaust gases are low. In [4; 8-10], the authors show that NH3/H2O is the best working fluid couple compromise, being environment friendly and efficient enough.

Xu & al. [3] propose an interesting alternative solution for stationary problem: a novel absorption–compression hybrid refrigeration cycle (ACHRC) driven by gases and power from vehicle engines. R124–DMAC mixture is used as a working fluid. The ARS is powered by exhaust gases; and the CRS, driven by power, runs only if ARS cannot supply enough cooling capacity. For ambient and evaporator temperatures of 35°C and 3°C respectively, the maximum air-conditioning power is 30 kW, while rated generator load in the ARS is 58.68 kW. When the waste heat load recovered by the generator reaches its rated value, air-conditioning is fully supplied by ARS and the maximum integration COP is 0.5. Otherwise, CRS operates to cover the lack of cooling capacity and the COP is reduced. Ambient temperature greatly affects the operating characteristic of the ACHRC: when it rises, the maximum value of the integration COP reduces significantly.

The previous studies focus on the feasibility of ARS process for automobile applications. This process has been proved efficient for monotonic driving at a cruise speed, but an important lock remains to be lifted: the good operation of the ARS during stationary immobile period, start/stop and fluctuations of the vehicle speed. Most of the studies about ARS system for automobile do not consider the dynamic performance of the chiller, which is yet significant for the whole system performances. Indeed, stabilization is deeply affected by transient processes [14]. Even though they are not focus on automobile applications, some studies about dynamic modelling of absorption chiller have been led so far.

Kim and Park [12] and Cai & al. [13] presented dynamic simulations of single-effect NH3-H2O absorption refrigeration system. The numerical model of [12] was applied to a 10.5 kW commercial chiller, to observe the behaviour of several parameters during start-up operation, and find the best conditions for the shortest time constant, with optimal cooling production. A low mass of solution in a large generator volume, combined with a stepwise turn-up/turn-down flue of gas flow rate seems to be the ideal solution for start-up operation. In [13], the authors studied the dynamical response to a pressure step change, and showed that mass flow and heat rates as well as COP oscillated during approximately two loops circulation times before reaching a steady state. Wang & al. [14] analysed the performances of a dynamic model of a single-effect H2O-LiBr absorption chiller, under different parameters. The time required to reach steady-state increases when generator inlet temperature widely change, when cooling water inlet temperature rises, and when evaporator inlet temperature drops. Viswanathan & al. [15] developed a model able to simulate the transient behaviour of an absorption chiller, exploring the entire start-up and shutdown processes for step change of several parameters. Flow rates, pressures and concentrations were stable after 3 minutes. Evaporator and condenser took longer times to reach steady state conditions.

As a continuous of the literature studies, this work aims at bringing further investigation to evaluate the performance of an absorption refrigeration in automobile. A new dynamic model of an absorption cycle feed by exhaust gases was developed to simulate the transient behaviour of the cycle during start/stop and change in driving regime. The simulation results gave the dynamic profiles of hydrodynamic and thermal parameters in different component as well as the system characteristic times. Analysis of the refrigerant mass flow enabled us to identify the key processes and components affecting the dynamic of absorption refrigeration system. Based on this, some ideas are suggested in order to improve the system performance and inertia.

2. Case study and architecture

The present study focuses on evaluating the feasibility in term of the dynamic performance of an absorption refrigeration in order to respond to a given cold request. The other constraints related to the integration of the machine into the vehicle such as vibration, acceleration, deceleration, geometrical layout, weight, fluid charge, etc. are not considered. The case study is a standard 2.0 L gasoline turbo-engine vehicle, which requires a maximum cold production of 5 kW at 5°C of air temperature in the passenger compartment. The driving cycle presented in Fig. 1 corresponds to FTP-75 cycle [16], which has been used for emission certification and fuel consumption testing of light duty vehicles in the United States. This cycle is interesting for this study because of level of acceleration and number of start/stop phase. The first step of thermal system design suited for transient heat sources is to select the power design point, which is important to size all the components, especially heat exchangers. To support design point selection, we have developed a methodology based on analysis of exhaust energy distribution on the cycle. Main output of this methodology are the time fraction, exhaust energy fraction, and average values of parameters such as exhaust temperature and mass flow, on given exhaust power range, as shown in Table 1. It is observed that the available power of the exhaust gases strongly depends on the exhaust-gas flow rate, which depends directly on the engine power. During 62% of time, the vehicle stops or runs at low speed (Point 0 and Point 1), giving low exhaust-gas power.

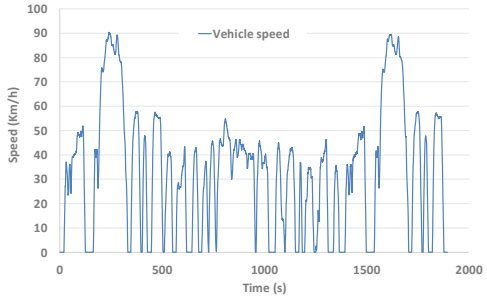


Fig. 1. Typical profile of the vehicle speed

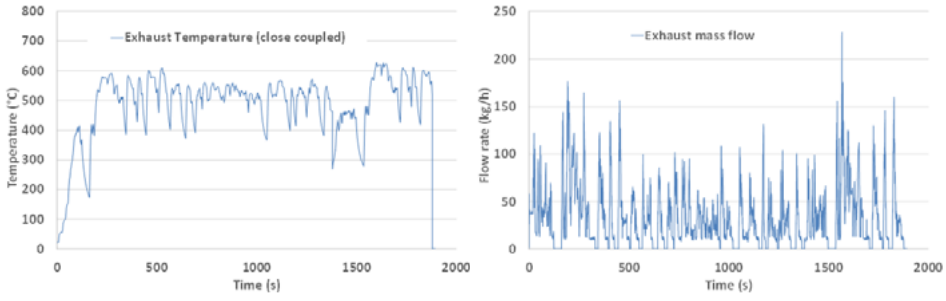


Fig. 2. Evolution of the temperature and flow rate of the exhaust gases

Table 1. Time fractions and average parameters of different range of exhaust power. T_{air} is the ambient temperature.

Point	Range of Available Exhaust Power with T_{air} = 20 °C [kW]	Time fraction	Exhaust Energy Fraction	Average of Vehicle speed [km/h]	Average of Exhaust mass flow [kg/h]	Average of Exhaust Temperature [°C]	Average of Available Exhaust Power with T_{air} = 20 °C [kW]
0	= 0	17,41%	0,00%	0,0	0,0	385,4	0,0
1	]0-5]	44,49%	21,24%	32,9	19,1	468,9	2,4
2	]5-10]	23,19%	32,73%	46,4	44,3	534,3	7,1
3	]10-15]	8,17%	19,87%	48,4	73,6	551,1	12,2
4	]15-20]	4,09%	13,96%	56,0	100,2	564,0	17,1
5	]20-25]	2,10%	9,21%	60,6	128,0	567,2	22,0
6	]25-30]	0,49%	2,65%	56,5	156,7	566,6	27,0
7	]30-35]	0,04%	0,24%	50,6	202,1	526,6	32,2
8	]35-40]	0,02%	0,11%	50,0	224,8	525,8	35,8

Fig. 3 shows the architecture of the absorption refrigeration of this study. It contains a generator, directly heated by the exhaust gases; an absorber, a rectifier and a condenser, which evacuate heat to the ambiance; an evaporator directly produces cold air; a solution heat exchanger (also called economiser); two expansions valve (one for the refrigerant and one for the weak solution) and a solution pump. The system also includes several tanks: T2 and T3 for liquid-vapour separation, T1 for solution storage and T4 for refrigerant storage. Using a standard air heat exchanger with a difference temperature between the air and the fluid of around 10K. The production of cold air at 5°C requires a negative evaporation temperature of the refrigerant. That is the reason why we investigated the absorption refrigeration using the couple NH_3/H_2O as working fluids.

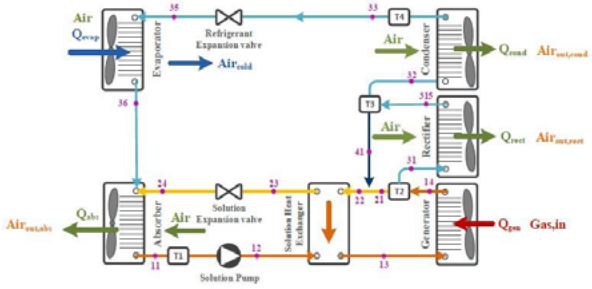


Fig. 3. Schematic view of the architecture of the absorption-refrigeration system

3. Dynamic model

A dynamic model of the above architecture was developed based on Modelica language using the commercial TIL library of TLK-Thermo GmbH, which contains a number of pre-set components and fluid property (based on REFPROP). The component diagram of this model is shown in Fig. 4.

We considered the following hypothesis in different components:

- Heat exchangers:
  - ✓ Air heat exchangers (generator, absorber, rectifier, condenser and evaporator) are fin-and-tube type with tube wall in stainless steel and fins in aluminium;
  - ✓ Liquid-liquid heat exchanger (economiser) is plate type with wall in stainless steel;
  - ✓ The heat exchange coefficients in the exchangers are imposed. On the gas side, the heat exchange coefficient is in the order of magnitude of 100 W/m²/ K on design point. On the liquid side, the heat exchange coefficient is in the order of magnitude of 1000 W/m² K. On the two-phase side, the heat exchange coefficient is in the range of 2000-4000 W/m²/ K;
  - ✓ The geometries of the heat exchangers were previously determined by static calculations to target heat exchanger efficiencies around 0.85 at Point 2 (see Table 1);
  - ✓ The pressure drops are not calculated;
- Expansion valves: a linear relationship between the pressure drop and the mass flow rate is used: $\dot{m} = open \times \Delta P$, *open* is the effective valve opening;

- Tanks: only tanks T2 and T3 where there are separation of liquid and vapour phases are simulated. An artificial pump is used to impose a stable liquid level in tank T3 as observed experimentally with the absorption-chiller prototypes in our laboratory. In reality, the liquid in tank T3 returns to the poor solution due to gravity;
- Air flow: the inlet temperature of air is fixed at 30°C. The air-flow rates were previously determined by static calculations to target a variation in temperature of about 15°C from inlet to outlet for absorber, condenser and rectifier;
- Regulation parameters: pump flow rate and expansion-valve openings;
- Initial conditions: the initial conditions of dynamic simulations are set as below:
  - ✓ Pressures : 10 bar (based on experimental data);
  - ✓ Wall temperatures : 30 °C (equal to the ambient temperature);
  - ✓ NH_3 mass fractions in different components given by static simulations.

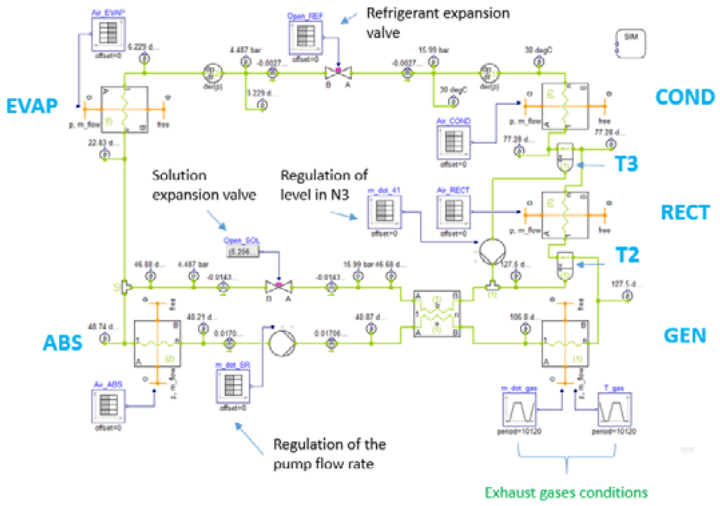


Fig. 4. Component diagram of the dynamic model of the absorption-refrigeration system

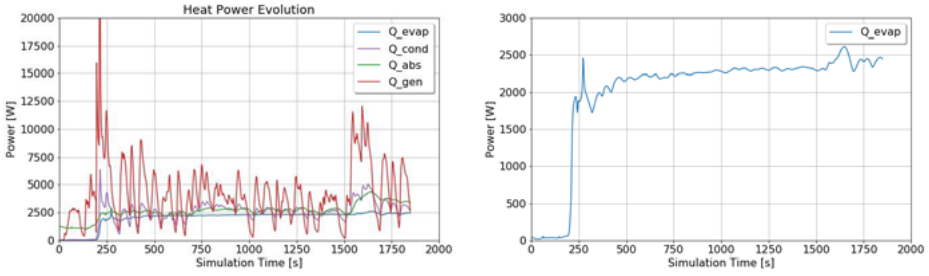
4. Simulation results

4.1. Constant pump flow rate and valve openings

For this case, we set the pump flow rate to the average value given by static simulations (45 kg/h) and fixed the valve openings to obtain the target difference of the pressures in the system. We performed simulations with the exhaust inputs as shown in Fig. 2 and obtained the evolutions of the power in different components: evaporator, condenser, absorber and generator. As shown in Fig. 5, the power at the generator fluctuates significantly due to fluctuations in the exhaust conditions. Since the condenser and the generator are connected at the same pressure level (high pressure), they show similar dynamic behaviour. At the low-pressure side, the absorber and the evaporator show smoother curves. After 250 s (~ 4 minutes), we observe a sudden increase of the cold power to 80% of the stabilized value, mainly due to the highly increase of the generator power. The cold production is maintained even when the vehicle stops. The system dynamic is slow enough to make imperceptible by the customer the fluctuations in engine speed/load. The stabilized cold power is around 2.3 kW, significantly lower than the maximum power required of 5 kW.

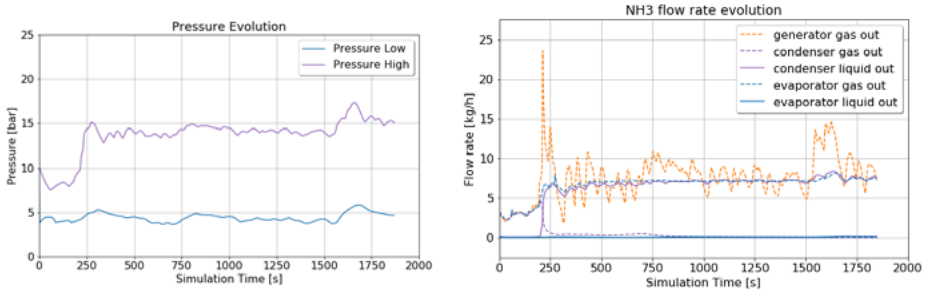
For a better understanding of the main factors affecting the system dynamic, we analyse the evolution of the pressure and the ammonia flow rates in different components. As shown in Fig. 6a and Fig. 6b, there is high peak of ammonia-vapour production at the generator outlet between 200s and 250s, leading to a sudden increase of the high pressure. At 250s, the high pressure approaches 15 bar, generating condensation inside the condenser. Then, the liquid flow rate remains stable at the condenser outlet due to hydrodynamic constraint.

The rest of the produced ammonia liquid is accumulated in the condenser (see Fig. 6c). In reality, this amount of ammonia liquid is stored in tank N4 (see Fig. 3) to do not degrade the condenser performance. Passing through the expansion valve, the ammonia liquid enters the evaporator at nearly saturated condition and therefore it is rapidly evaporates. That is the reason why only a small amount of ammonia-liquid presents in the evaporator.

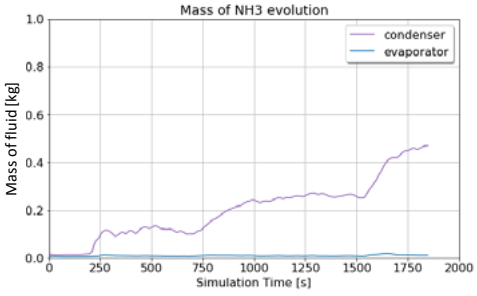


a) b)

Fig. 5. Evolutions of power: a) Q_evap at evaporator, Q_cond at condenser, Q_abs at absorber and Q_gen at generator; b) a zoom on power at evaporator



a) b)



c)

Fig. 6. Evolution of a) pressures; b) ammonia flow rates and c) ammonia mass in the heat exchangers

The above analysis shows that the absorption refrigeration dynamic strongly depends on hydrodynamic in the system. Different from a mechanical-compression machine, during the starting phase, the pressure in an absorption chiller increases by ammonia-vapour production from the generator. The starting time corresponds to the time required for the high pressure to reach the saturation value so that condensation occurs in the condenser. Once ammonia liquid is generated, cold power can be rapidly produced since the ammonia liquid enters the evaporator at nearly saturated condition.

4.2. Regulated pump flow rate and valve openings

To investigate the impact of the regulation parameters, we perform simulations with the following conditions for pump flow rate and valve openings:

- The pump flow rate is regulated to maintain a constant temperature of the weak solution at the generator outlet with the following laws (as illustrated in Fig. 7):
  - Start (t < 250 s) : $\dot{m}_{pump} = \dot{m}_{pump,\,mean} = 45\ kg/h$
  - After start (t ≥ 250 s) :
    - ✓ $\dot{m}_{pump} = \frac{\dot{m}_{pump,mean}}{\dot{m}_{gas,mean}} \dot{m}_{gas} = 1.4 \times \dot{m}_{gas}$ if $\dot{m}_{gas} > \frac{\dot{m}_{gas,mean}}{2} = 16.2\ kg/h$
    - ✓ $\dot{m}_{pump} = \frac{\dot{m}_{pump,mean}}{2} = 22.5\ kg/h$ if $\dot{m}_{gas} \leq \frac{\dot{m}_{gas,mean}}{2}$
- The valve openings are regulated to maintain a constant difference between high and low pressures :
  - Refrigerant valve : $Open_{ref} = k1 \times \dot{m}_{pump,\,mean}$ with $k1 = 160 \times 10^{-9}$ [1/Pa]
  - Solution valve : $Open_{sol} = k2 \times Open_{ref}$ with $k2 = 5.26$

Fig. 8 shows comparison of cold production with constant and variable pump flow rates. After the start-up, the cold production reacts rapidly with the change in pump flow rate. Because the regulation of the valves is fast enough (~ 1s) to adjust the pressure levels in the system so that condensation and evaporation of the refrigerant occur continuously. At high exhaust gas power, an increase in the pump flow rate will lead to an increase in the refrigerant flow rate and thus improve the cold production. For future works, better regulation laws can be developed to optimize the machine performance.

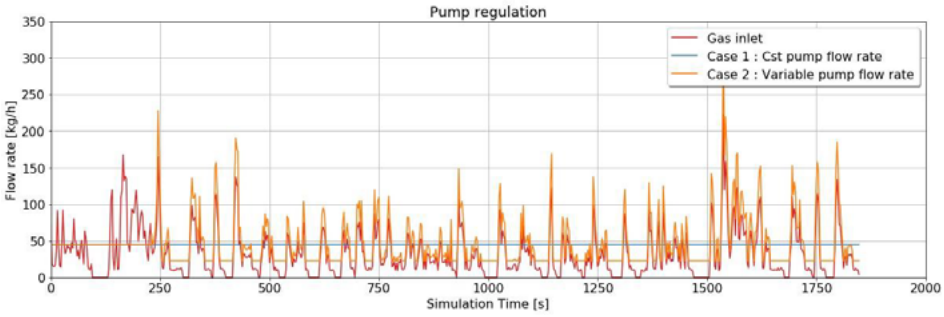


Fig. 7. Pump regulation with case 1: constant flow rate and case 2: variable flow rate

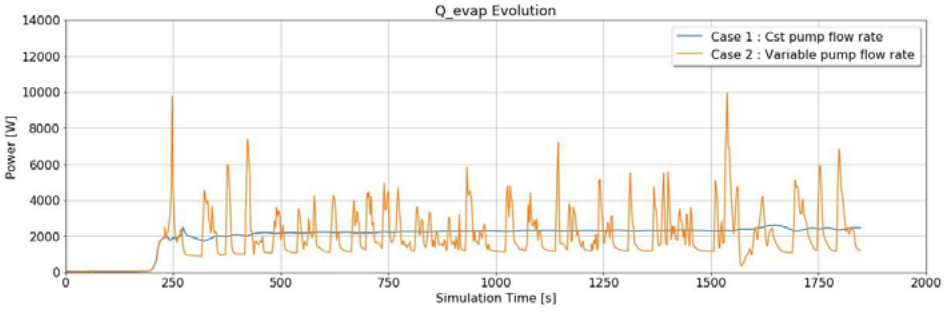


Fig. 8. Cold power productions with constant and variable pump flow rates

5. Conclusions

This study investigates the dynamic performance of an absorption refrigeration heated by exhaust gases. The case study is a standard 2.0L gasoline turbo-engine vehicle running on FTP-75 driving cycle. In agreement

with the literature, dynamic simulations confirm insufficient cold production when the vehicle runs at low engine power (low speed and/or low torque). Another technological limitation is the high inertia of the system that causes long start-up time, around 4 minutes in the present case study. The key factor affecting the absorption refrigeration dynamic is the high-pressure level, which mainly depends on the vapour generation at the generator. For the system to start, the high pressure should reach the necessary value allowing condensation in the condenser. Boosting the generator power (for example by adding complementary heat) for fast vapour production could be a solution to reduce the start-up time. After the start-up, the cold production reacts rapidly with the regulations of pump flow rate and valve openings. Smart regulation law could be a solution to improve the machine performance.

Acknowledgements

The French Alternative Energies and Atomic Energy Commission (CEA) and FAURECIA Clean Mobility for their supports to this work.

References

[1] Fang, GY, Li, H, Automotive air conditioning technology. *China Machine Press*: Beijing, 2002

[2] Horuz, I, Vapor absorption refrigeration in road transport vehicles. *Journal of Energy Engineering* 1999;**125**:48-58.

[3] Xu, S, Li, J, Liu, F. An investigation on the absorption–compression hybrid refrigeration cycle driven by gases and power from vehicle engines. *International journal of energy research,* 2012

[4] Charate, T, Awate, N, Padir, S, Dubey, D, Kadam A. A review of Absorption refrigeration in vehicles using waste exhaust heat. International *Journal of scientific & engineering research*, volume 8, March 2017

[5] Horuz, I. An Alternative Road Transport Refrigeration. *Journal of engineering and environmental science* 1998

[6] Kaewpradub, S, Sanguanduean, P, Katesuwan, W, Chimres, N, Punyasukhananda, P, Asirvatham, LG, Mahian, O, Dalkilic, AS, Wongwises, S. Absorption refrigeration system using engine exhaust gas as an energy source. *Case studies in thermal engineering*, 2018;**12**:797-804

[7] Koehler, J, Tegethoff, WJ, Westphalen, D, Sonnekalb, M. Absorption refrigeration system for mobile applications utilizing exhaust gases. *Heat and Mass Transfer,* 1997;**32**:333–340.

[8] Chandrakar, D, Saikhedkar, NK. Design of ammonia water vapor absorption air conditioning system for a car by waste heat recovery from engine exhaust gas – *Advance physics letter*, volume 3, 2016, ISSN:2349-1108

[9] Rixon, KL, Sanoj, T, Mathew, C, Thomas, T. Air cooling inside vehicles using vapor absorption refrigeration system. *International journal of engineering research & technology*, volume 4, 2015. ISSN:2278-0181

[10] Vicatos, G, Gryzagoridis, J, Wang, S. A car air-conditioning system based on an absorption refrigeration cycle using energy from exhaust gas of an internal combustion engine. *Journal of energy in southern Africa* 19, 2008

[11] Talom, H, Beyene, A. Heat recovery from automotive engine. *Applied thermal engineering* 2009;**29**:439-444

[12] Kim, B, Park, J. Dynamic simulation of a single-effect ammonia-water absorption chiller. *International journal of refrigeration*, 2007;**30**:535-545

[13] Cai, W, Sen, M, Paolucci, S. Dynamic simulation of an ammonia-water absorption refrigeration system. *Industrial & engineering chemistry research*, 2012;**51**:2070-2076

[14] Wang, J, Shang, S, Li, X, Wang, B, Wu, W, Shi, W. Dynamic performance analysis for an absorption chiller under different working conditions. *Applied sciences*, 2017;**7**:797

[15] Viswanathan, V, Rattner, A, Determan, M, Garimella, S. Dynamic model for small-capacity ammonia-water absorption chiller. *International refrigeration and air conditioning conference*, 2012

[16] DieselNet, Emission Test Cycles, FTP-75, https://www.dieselnet.com/standards/cycles/ftp75.php

13th IEA Heat Pump Conference
April 26-29, 2021 Jeju, Korea

Experimental Investigation of Parameters Affecting Drying Time and Power Consumption of a Heat Pump Tumble Dryer

Mehdi Rasti[a], Ji Hwan Jeong[a,*]

[a]School of Mechanical Engineering, Pusan National University, Geumjeong-Gu, Busan 46241, South Korea

Abstract

A heat pump clothes dryer comprises of two closed loops, namely, the heat pump cycle and the air cycle. Clothes dryers are among the most energy-intensive home appliance. This study experimentally investigated how the textile type, textile size, textile weight, fan speed, and compressor frequency influence the drying time and power consumption. A heat pump tumble dryer with a 9 kg rated capacity was selected for experimental investigations. The following values were selected for experiments: textile weight: 3, 6, 9 kg; textile type: sheet, pillowcase, towel; fan speed: 2850, 3150, 3450 rpm; and compressor frequency; 27, 35, 40 Hz. Results showed that the drying time and power consumption were increased by increasing the textile weight and the textile size. The drying time of 9 kg sheets was 42.2% and 22.5% higher than that of pillowcases and towels, respectively. Moreover, the drying time was decreased by increasing the fan speed and compressor frequency.

Keywords: Heat pump clothes dryer; drying time; experimental study; textile weight; textile size.

1. Introduction

Clothes dryers can be categorized as open-loop such as vented dryers or closed-loop such as heat pump dryers and condenser dryers depending on exhausting drum outlet air outdoors. Condenser clothes dryers and vented clothes dryers use an electric heater to heat up the air entering the drum while heat pump clothes dryers use condenser heat rejection to heat up the air. Shrinkage of clothes as a result of high air temperature and high energy consumption are disadvantages of clothes dryers that use an electric heater. Because energy consumption of heat pump clothes dryers is almost half of conventional dryers, their market share has grown rapidly [1]. It should be noted that drying time of heat pump clothes dryers is longer than conventional clothes dryers because of lower drying air temperature [2].

In 2019, the worldwide sale market of clothes dryers was $7.3 billion and it is expected to reach $10.8 billion by 2023 [3]. In 2015, the Energy Information Administration reported that total electricity consumption of clothes dryers were 57.4 billion kWh [4]. The number of clothes dryers in Northern Europe and North America is increasing because of small space requirement and dry clothes regardless of weather conditions [5]. It is expected to reach number of clothes dryers to 105.8 million by 2025 in the US [6]. Since the energy consumption of clothes dryers is considerable, energy efficiency enhancement of clothes dryers is crucial. Stawreberg and Nilsson [7] established a mathematical model for energy efficiency enhancement of drying small loads. Their results showed that by reducing the heat supply and the airflow rate, it is possible to improve the clothes dryer's specific moisture extraction rate by 6% when drying small loads. Braun et al. [8] experimentally compared performance of a heat pump tumble dryer with conventional electric dryers. They reported that energy consumption of a heat pump tumble dryer was 40% and 14% lower that an electric clothes dryer and a conventional electric dryer using heat recovery heat exchangers, respectively. Bengtsson et al. [9] reported that by increasing the cylinder volume of compressor by 50%, drying time of heat pump clothes dryer decreased by 14% without increasing in energy consumption. Erdem [10] developed a model to investigate effects of evaporator geometry on the energy consumption and drying time of heat pump clothes dryers. Their

* Corresponding author. Tel.: +82-051-510-3050; fax: +82-051-512-5236.
E-mail address: jihwan@pusan.ac.kr.

simulation results showed that energy consumption reduced by 12% and 8% by increasing number of evaporator rows and columns from 2 to 4, respectively. Moreover, energy consumption increased by 18% and 21% by increasing tube outer diameter from 6 to 10 mm and increasing the longitudinal tube pitch from 10 to 30 mm, respectively.

The purpose of this study was to investigate the effect of a wide range of textile type, textile weight, fan speed, and compressor frequency on the drying time and power consumption of heat pump tumble dryers.

2. Experimental study

A heat pump tumble dryer with 9 kg rated capacity was selected for experimental investigations. The heat pump tumble dryer was equipped with twenty-three thermocouples with the uncertainty of ±0.3 °C, and three "SHT85 model" relative humidity and temperature sensors with the uncertainties of ±1.5 %RH and ±0.1 °C. The schematic of heat pump tumble dryer is shown in Fig. 1.

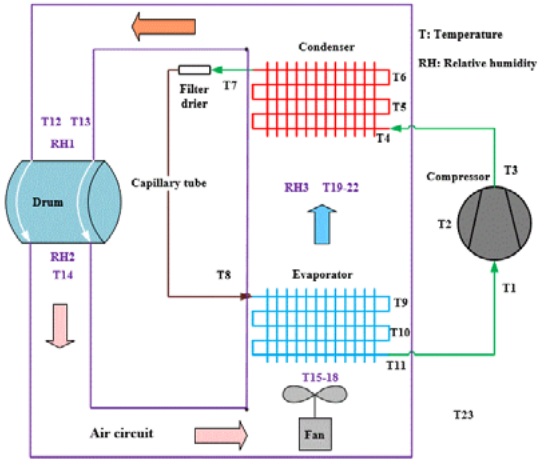


Fig. 1. Schematic of equipped heat pump tumble dryer

All experiments were conducted at the ambient temperature of 23±2 °C. According to IEC 60456 [11], the bone dry method was used for the conditioning of textiles to define the nominal mass of textiles at the start of experiments. The conditioned weight of textiles was defined as:

$$m_{cond,t} = m_{bd,t} \times F_{bd} \tag{1}$$

where $m_{cond,t}$ is the conditioned weight of textiles, $m_{bd,t}$ is the bone dry weight of textiles and the bone dry factor F_{bd} is bone dry factor which experimentally was found equal to 1.072. The difference between $m_{cond,t}$ and $m_{bd,t}$ is equal to the amount of moisture absorbed by textiles from surrounding for more than 15 hours at the ambient temperature of 20±2 °C and relative humidity of 65±5 %. All experiments started at the initial moisture content (IMC) of 60%. The initial moisture content "IMC" can be calculated as below:

$$IMC = \frac{m_{add,w}}{m_{cond,t}} \times 100\% \tag{2}$$

where $m_{add,w}$ is the weight of water added to the conditioned textile. In the present study, the effect of textile weight (3, 6, 9 kg), textile type (sheet, pillowcase, towel), fan speed (2850, 3150, 3450 rpm), and compressor frequency (27, 35, 43 Hz) on the drying time were experimentally investigated. To examine the effect of textile size on the drying time, three cotton base textiles were selected according to IEC 61121 [12]. Specifications of sheets, pillowcases, and towels are given in Table 1.

Table 1. Specifications of textiles used in the experiments.

Parameter		Unit	Sheets	Pillowcases	Towels
Length		mm	2400±150	800±50	1000±50
Width		mm	1600±40	800±20	500±30
Area		m^2	3.84±0.342	0.64±0.057	0.5±0.056
Weight per piece		g	725±15	240±5	110±3
Mass per unit area		g/m^2	185 ± 10	185 ± 10	220 ± 10
Substrate		---	Long staple pure cotton	Long staple pure cotton	Long staple pure cotton
Yarn		---	Ring spun	Ring spun	Ring spun
Weave			Plain weave linen 1/1	Plain weave linen 1/1	Huckaback
Water uptake in		%	138 ± 10	138 ± 10	250 ± 15
Yarn twist	Warp	T/m	600 ± 20	600 ± 20	610 ± 20
	Weft		500 ± 15	500 ± 15	490 ± 15
Yarn Count	Warp	tex	33 ± 1	33 ± 1	36 ± 1
	Weft		33 ± 1	33 ± 1	97 ± 1
Pick count	Warp	pick/cm	24 ± 1	24 ± 1	20 ± 1
	Weft		24 ± 1	24 ± 1	12 ± 1

A list of experiments is shown in Table 2. It should be noted that the heat pump tumble dryer was comprised of a fan-drum motor for rotating both the laundry drum and drying air fan. The drum rotation speed was 49.12 RPM when the fan rotational speed was 2850 RPM and it was 54.29 RPM for the fan rotational speed of 3150 and 3450 RPM.

Table 2. List of experiments used for the development of correlation.

Case	Conditioned weight of textile (kg)	Textile type	Fan speed (rpm)	Compressor frequency (Hz)
1	3	towel	3150	35
2	6	towel	3150	35
3	9	towel	3150	35
4	3	pillowcase	3150	35
5	6	pillowcase	3150	35
6	9	pillowcase	3150	35
7	3	sheet	3150	35
8	6	sheet	3150	35
9	9	sheet	3150	35
10	3	1 sheet/ 4 pillowcases/ 12 towels	3150	35
11	6	2 sheets/ 8 pillowcases / 24 towels	3150	35
12	9	3 sheets/ 12 pillowcases / 36 towels	3150	35
13	9	4 sheets/ 14 pillowcases / 26 towels	2850	27
14	9	4 sheets/ 14 pillowcases / 26 towels	3150	27
15	9	4 sheets/ 14 pillowcases / 26 towels	3450	27
16	9	4 sheets/ 14 pillowcases / 26 towels	2850	35
17	9	4 sheets/ 14 pillowcases / 26 towels	3150	35
18	9	4 sheets/ 14 pillowcases / 26 towels	3450	35
19	9	4 sheets/ 14 pillowcases / 26 towels	2850	43
20	9	4 sheets/ 14 pillowcases / 26 towels	3150	43
21	9	4 sheets/ 14 pillowcases / 26 towels	3450	43

3. Results and discussion

Drying time and total power consumption for cases 1 to 12 are presented in Figs. 2 and 3, respectively. It should be noted that the fan speed and compressor frequency were the same for cases 1 to 12 while the textile weight and textile composition were different. Results showed that the drying time and power consumption increased by increasing the weight of textiles. The shortest and longest drying time was related to towels and sheets because of the smallest size and largest size, respectively. Due to rolled up or rolled inside another, thus trapping moisture, the drying time of sheets was significantly more than towels and pillowcases. In other words, the stagnant core of sheets in the drum was bigger than pillowcases and towels. Therefore, the molecular diffusion which is slower than convection diffusion in the sheets was dominant. Results showed that the drying time of 3, 6, and 9 kg sheets was 7.2%, 28.4%, and 52.3% higher than that of a mix of textiles, respectively. Moreover, the total power consumption of 3, 6, and 9 kg sheets was 11.2%, 34.2%, and 56% higher than the total power consumption of a mix of textiles, respectively.

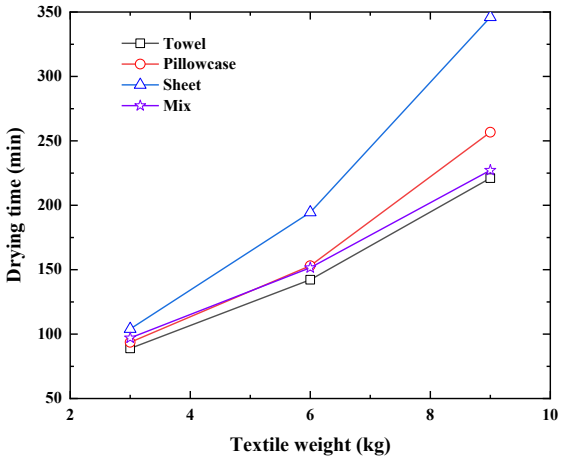


Fig. 2. Effect of textile weight and textile composition on the drying time

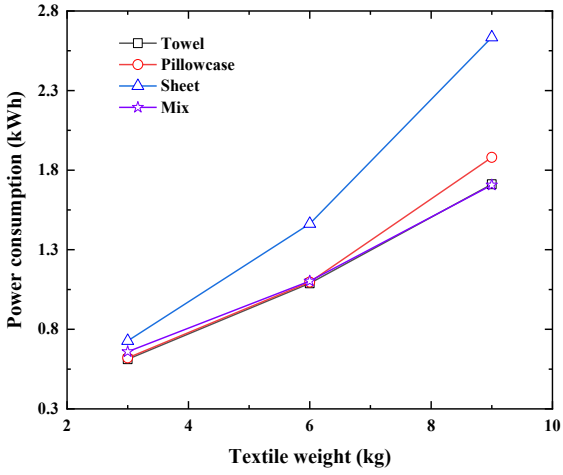


Fig. 3. Effect of textile weight and textile composition on total power consumption

Figs. 4 and 5 present the drying time and total power consumption for cases 13 to 21, respectively. The textile composition for 9 kg textile was selected according to the IEC 61121. The fan speed was changed from 2850 to 3450 rpm and the compressor frequency was changed from 27 to 43 Hz. Results showed that with increasing the compressor frequency from 27 to 43 Hz, the power consumption increased and the drying time decreased because of increasing the air temperature at the inlet of the drum. As shown in Fig. 4, the drying time decreased with increasing the airflow rate because of increasing the moisture evaporation rate in the drum. Manufacturers of clothes dryers are seeking to reduce the power consumption and the drying time. The results showed that although energy consumption decreased with decreasing the compressor frequency, the drying time increased. The power consumption was maximum while the heat pump dryer was working with the highest compressor frequency (43 Hz) and lowest fan speed (2850 rpm). Also, the power consumption was minimum while it was working with the lowest compressor frequency (27 Hz) and the highest fan speed (3450 rpm).

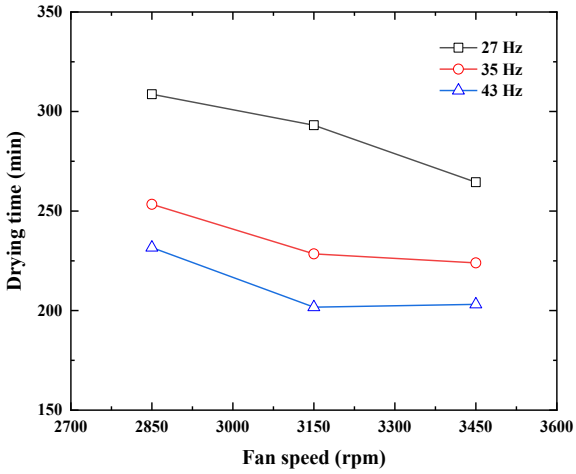


Fig. 4. Effect of fan speed and compressor frequency on drying time

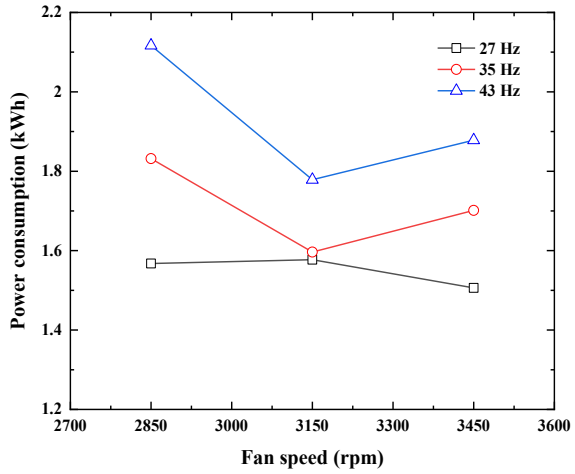


Fig. 5. Effect of fan speed and compressor frequency on total power consumption

The Energy Efficiency Index (EEI) was selected to determine the optimum condition and it was calculated according to the EU 392/2012 standard [13]. The energy efficiency of household tumble dryers is rated in terms of a set of energy labels from *A*+++ to *D*, *A*+++ being the most energy efficient, and *D* the least efficient as shown in Table 3.

Table 3. Energy efficiency classes.

Energy Efficiency Class (EEC)	Energy Efficiency Index (EEI)
A+++ (most efficient)	EEI < 24
A++	24 ≤ EEI < 32
A+	32 ≤ EEI < 42
A	42 ≤ EEI < 65
B	65 ≤ EEI < 76
C	76 ≤ EEI < 85
D (least efficient)	85 ≤ EEI

The EEI and EEC for 9 kg textiles are presented in Table 4. Results showed that case 15 (mix of textiles, fan speed: 3450 rpm, compressor frequency: 27 Hz) was the most energy efficient and case 9 (sheets, fan speed: 3150 rpm, compressor frequency: 35 Hz) was the least efficient. Moreover, the EEC was A+++ and A++ for all experiments while the heat pump dryer was working with the compressor frequency of 27 Hz and 43 Hz, respectively.

Table 4. Energy Efficiency Index of exeriments with 9 kg textile.

Case	weight of textile (kg)	Textile type	Fan speed (rpm)	Compressor frequency (Hz)	EEI	EEC
3	9	towel	3150	35	23.9	A+++
6	9	pillowcase	3150	35	26.3	A++
9	9	sheet	3150	35	35.9	A+
12	9	3 sheets/ 12 pillowcases / 36 towels	3150	35	23.5	A+++
13	9	4 sheets/ 14 pillowcases / 26 towels	2850	27	22.6	A+++
14	9	4 sheets/ 14 pillowcases / 26 towels	3150	27	22.7	A+++
15	9	4 sheets/ 14 pillowcases / 26 towels	3450	27	21.7	A+++
16	9	4 sheets/ 14 pillowcases / 26 towels	2850	35	26.4	A++
17	9	4 sheets/ 14 pillowcases / 26 towels	3150	35	23	A+++
18	9	4 sheets/ 14 pillowcases / 26 towels	3450	35	24.5	A++
19	9	4 sheets/ 14 pillowcases / 26 towels	2850	43	30.4	A++
20	9	4 sheets/ 14 pillowcases / 26 towels	3150	43	25.6	A++
21	9	4 sheets/ 14 pillowcases / 26 towels	3450	43	27	A++

4. Conclusion

This study presented effects of textile type (sheet, pillowcase, towel), conditioned weight of textiles (3, 6, 9 kg), fan speed (2850, 3150, 3450 rpm), and compressor frequency (27, 35, 43 Hz) on the drying time and power consumption of a heat pump tumble dryer. Twenty-one experiments were conducted on a heat pump tumble dryer with a 9 kg rated capacity. All experiments were conducted at the ambient temperature of 23±2 °C and initial moisture content of 60%. The results showed that the drying time and the power consumption increased by increasing the weight of textiles and the size of textiles. The drying time and power consumption of 9 kg sheets were 52.3% and 56% higher than that of a mix of textiles, respectively. Moreover, the drying time decreased and the power consumption increased by increasing the compressor frequency. The results showed that the lowest EEI was belonged to drying 9 kg of a mix of textiles while the heat pump dryer was working with the lowest compressor frequency (27 Hz) and highest fan speed (3450 RPM).

References

[1] Ng, AB, Deng, S., 2008. A new termination control method for a clothes drying process in a clothes dryer. Applied Energy 85, p. 818-829.
[2] Gatarić, P, Širok, B, Hočevar, M, Novak, L., 2019. Modeling of heat pump tumble dryer energy consumption and drying time. Drying Technology 37, p. 1396-1404.
[3] https://wwwprnewswirecom/news-releases/electric-dryers-market-set-to-reach-10-8-billion-by-2023---insights-by-type-of-dryer-type-of-vent-distribution-channel-end-user-and-geography-301005177html.
[4] U.S. Energy Information Administration: *2015 Residential Energy Consumption Survey*; 2015.
[5] Ahn, SP, Kim, SH, Park, YG, Ha, MY., 2019. Experimental study on drying time and energy consumption of a vented dryer. Journal of Mechanical Science and Technology 33, p. 2471-2480.
[6] TeGrotenhuis, W, Butterfield, A, Caldwell, D, Crook, A, Winkelman, A., 2017. Modeling and design of a high efficiency hybrid heat pump clothes dryer. Applied Thermal Engineering 124, p. 170-177.
[7] Stawreberg, L., Nilsson, L., 2013. Potential energy savings made by using a specific control strategy when tumble drying small loads. Applied energy 102, p. 484-491.
[8] Braun, J.E., Bansal, P.K., Groll, E.A., 2002. Energy efficiency analysis of air cycle heat pump dryers. International Journal of refrigeration 25(7), p. 954-965.
[9] Bengtsson, P., Berghel, J., Renström, R., 2014. Performance study of a closed-type heat pump tumble dryer using a simulation model and an experimental set-up. Drying Technology 32(8), p. 891-901.
[10] Erdem, S., 2015. The effects of fin-and-tube evaporator geometry on heat pump performance under dehumidifying conditions. International Journal of Refrigeration 57, p. 35-45.
[11] IEC60456. *Clothes washing machines for household use–Methods for measuring the performance*; 2010.
[12] IEC61121. *Tumble dryers for household use–methods for measuring the performance*; 2013.
[13] EU 392/2012, 2012. Energy labelling of household tumble driers. Official Journal of the European Union 55, p. 1-26.

13th IEA Heat Pump Conference
April 26-29, 2021 Jeju, Korea

Thermodynamic analysis of refrigerant selection for high temperature heat pump cycles

Takenobu Kaida[a,*]

[a] Central Research Institute of Electric Power Industry (CRIEPI), Yokosuka 240-0196, Japan

Abstract

Industrial heat pump is recognized as one of decarbonization technologies in industry by a couple of its high efficiency and electrification with low carbon electricity. For expanding applications of heat pumps into various industrial heating processes, it is necessary to increase the supply temperature of heat pumps. Recently, some new refrigerants have been developed, which allows to increase the choice of refrigerants expected to be applied to higher temperature heat pumps. The purpose of this study is to illustrate working domain maps which can determine the promising refrigerant and the upper limit of heat pumping temperature lift for each supply temperature. First, with thermodynamic analysis for simple heat pump cycle, refrigerant selection in the wide range of the heat pump supply temperature from 60°C to 200° C is analyzed comprehensively for 17 pure refrigerants currently available on the market. Then, the effect of a high efficiency improvement by two-stage cycle with economizer are examined on the refrigerant selection.

Keywords: Industrial heat pump ; High temperature heat pump ; Refrigerant selection ; Low GWP ; Thermodynamic analysis

1. Introduction

Industrial heat pump is recognized as one of decarbonization technologies in industry by a couple of its high efficiency and electrification with low carbon electricity. Figure 1 shows the distribution of heat demand by temperature in the Japanese industrial sector [1]. The high temperature heat demand above 200°C is limited to energy-intensive industries such as steal, metals, cement and petrochemicals, and most of the heat is used as combustion by burner. On the other hand, below 200°C, various industries exist, having various types of heat demands such as drying, washing, sterilization, distillation and concentration. Another feature is that it is used mainly as a form of steam. This heat demand area below 200°C accounts for 28% of the total industrial heat demand and is expected to be applied to heat pumps.

For expanding the heat pump application range, it is necessary to prepare heat pumps with various supply temperatures up to 200°C for use in various heating processes. In general, heat pump performance largely depends on the refrigerant selection, and thus it is desirable to select the appropriate refrigerant. Recently, some new refrigerants have been developed for corresponding to lowering the global warming potential (GWP), which allows to increase the choice of refrigerants expected to be applied to higher temperature heat pumps.

The purpose of this study is to provide working domain maps which can determine the promising refrigerant and the upper limit of heat pumping temperature lift for each supply temperature. Brunin et al. investigate the working domain of many refrigerants in the heat pump supply temperature range up to 200°C [2]. However, majority of the investigated refrigerants are banned today (CFCs, HCFCs) and will be restricted in near future use (HFCs). Ommen et al. investigate the working domains focusing on 4 natural refrigerants (R290, R600a, R744 and R717) [3]. They consider not only technical and thermodynamic constraints but also economic constraints, however the investigated heat pump supply temperature is limited up to 120°C.

* Corresponding author.
E-mail address: kaida@criepi.denken.or.jp.

In this study, for 17 pure refrigerants currently available on the market including newly developed HFOs and HCFOs, refrigerant selection in the wide range of the heat pump supply temperature from 60°C to 200°C is analyzed comprehensively with thermodynamic analysis for simple heat pump cycle. In addition, the effect of a high efficiency improvement by two-stage cycle with economizer are examined on the refrigerant selection.

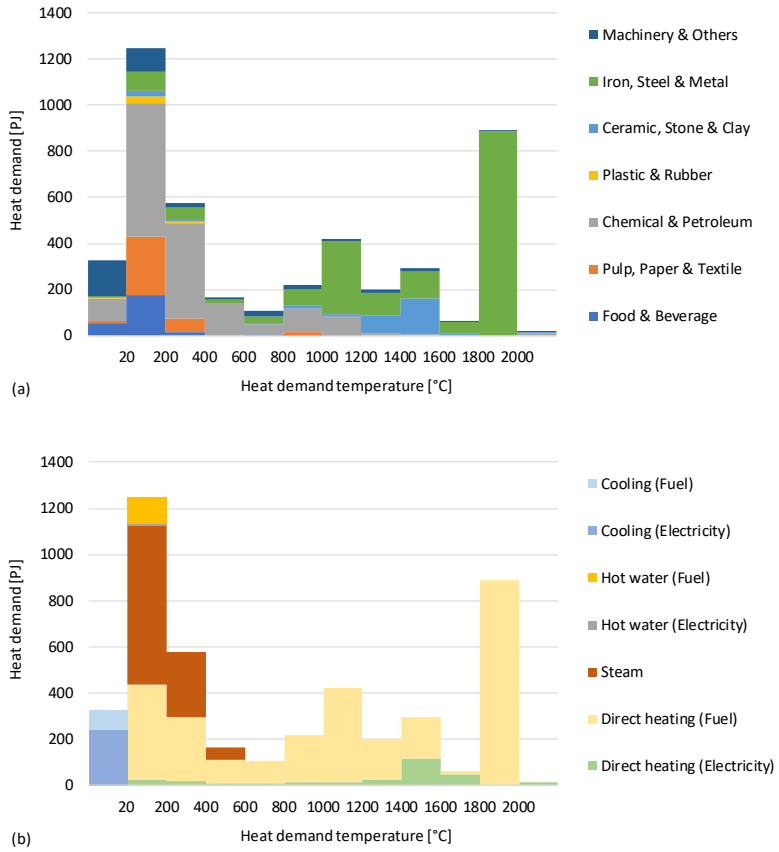


Fig. 1. Heat demand in the Japanese industry (a) by industry and (b) by heat use form

2. Refrigerants for high temperature heat pumps

Table 1 shows the basic properties of 17 refrigerants investigated in this study. Although 3 HFCs (R32, R134a and R245fa) have relatively high GWPs and will be restricted in near future use, they are included in this study for comparison. Other 14 refrigerants have very low GWPs. Among them, 2 HCFOs (R1224yd(Z) and R1233zd(E)), 1 HFO (R1336mzz(Z)) and 2 natural refrigerants (R718 and R744) are classified as A1 in ASHRAE Standard 34 safety group classification, which indicates low-toxicity and non-flammability. The ozone depletion potentials (ODPs) of the HCFOs are not zero but recognized negligible small. Thus, they are not listed as ozone depleting substances (ODSs) in the Montreal Protocol. 3 HFOs (R1234yf, R1234ze(E) and R1234ze(Z) are classified as A2L of low-toxicity and mild-flammability. 5 HCs (R290, R600, R600a, R601 and R601a) are classified as A3 of low-toxicity and high-flammability. R717 is classified as B2L of high-toxicity and mild-flammability.

Table 1. Basic properties of 17 pure refrigerants

Type	Refrigerant	Chemical formula	Molar mass [g/mol]	ODP	GWP	Safety	Critical temperature [°C]	Critical pressure [MPa]
HFC	R32	CH_2F_2	52.0	0	677	A2L	78.1	5.78
	R134a	$C_2H_2F_2$	102.0	0	1300	A1	101.1	4.06
	R245fa	$C_3H_3F_5$	134.0	0	858	B1	153.9	3.65
HCFO	R1224yd(Z)	C_3HF_4Cl	148.5	0.00023	~1	A1	155.5	3.34
	R1233zd(E)	$C_3H_2F_3Cl$	130.5	0.00025	~1	A1	166.5	3.62
HFO	R1234yf	$C_3H_2F_4$	114.0	0	~1	A2L	94.7	3.38
	R1234ze(E)	$C_3H_2F_4$	114.0	0	~1	A2L	109.4	3.63
	R1234ze(Z)	$C_3H_2F_4$	114.0	0	~1	A2L	150.1	3.53
	R1336mzz(Z)	$C_4H_2F_6$	164.1	0	~2	A1	171.4	2.90
Natural	R290	C_3H_8	44.1	0	3	A3	96.7	4.25
(HC)	R600	C_4H_{10}	58.1	0	3	A3	152.0	3.80
	R600a	C_4H_{10}	58.1	0	3	A3	134.7	3.63
	R601	C_5H_{12}	72.1	0	4	A3	196.6	3.37
	R601a	C_5H_{12}	72.1	0	4	A3	187.2	3.38
Natural	R717	NH_3	17.0	0	0	B2L	132.4	11.4
(Others)	R718	H_2O	18.0	0	0	A1	373.9	22.1
	R744	CO_2	44.0	0	1	A1	31.0	7.38

Figure 2 shows the relation between the molar mass and the critical temperature for these refrigerants. Focusing on HCs, it can be seen that the critical temperature becomes higher as the molar mass becomes larger. However, some refrigerants have the same molar mass but the different critical temperatures, which is because of the isomers. The same tendency applies to HFCs, HCFOs and HFOs, however the molar mass is larger than that of HC when viewed at the same critical temperature. Therefore, because of its large molar mass and complicated molecular structure, the development possibility of new refrigerants for high temperature heat pumps is relatively high. On the other hand, it can be seen that R717, R718 and R744 show peculiar characteristics.

The relatively large molar mass is a characteristic of the refrigerant for high temperature heat pump. This characteristic affects the shape of saturated vapor curve. It is known that the slope of the saturated vapor curve on *T-s* diagram becomes positive from negative when the value of specific heat becomes relatively large. Morrison investigates the shape of saturation curves [4]. From general thermodynamic relation, the slope of the saturation curve on *T-s* diagram can be written as follows:

$$\left.\frac{dT}{ds}\right|_{sat} = \left[\frac{c_v}{T} + \left(\frac{\partial p}{\partial T}\right)_v \left.\frac{dv}{dT}\right|_{sat}\right]^{-1} \tag{1}$$

Here the value of c_v/T is always positive and the value of $(\partial p/\partial T)_v$ is generally positive. The value of $dv/dT|_{sat}$ is generally positive for liquid and negative for vapor. Therefore, the slope of the liquid saturation curve is generally positive, but the slope of the vapor saturation curve can be positive or negative mainly depending of the value of c_v. When the molar mass becomes relatively large and the specific heat c_v becomes relatively large, the slope of saturated vapor curve changes from negative to positive.

As an example, Figure 3 shows the comparison of the saturated curves of R134a and R1336mzz(Z) on *T-s* diagram. It can be seen that the slope of the saturated vapor curve of R134a (molar mass: 102.0 g/mol) is negative, but the slope of R1336mzz(Z) (molar mass: 164.1 g/mol) is positive. Therefore, when using R134a, there is no concern that liquid compression will occur even if the compressor suction superheating is zero, but when using R1336mzz(Z), liquid compression will occur unless the sufficient superheating is secured. Hence, it is necessary to secure the suction superheating when using some refrigerants for high temperature heat pumps, for example, by installing an internal heat exchanger.

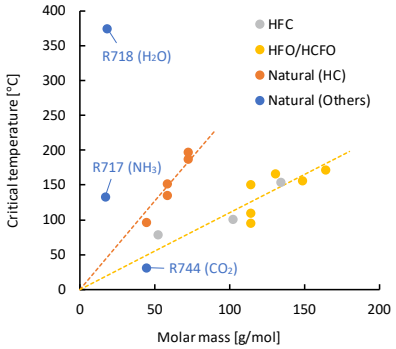


Figure 2. Relation between molar mass and critical temperature

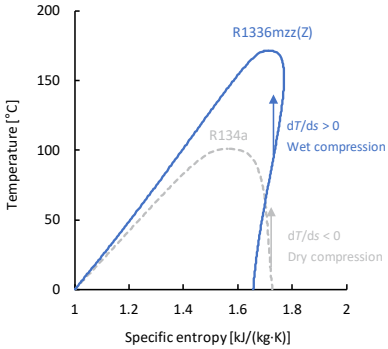


Figure 3. Slope of saturated vapor curve

3. Analysis for simple heat pump cycle

This study analyzes subcritical heat pump cycles using pure refrigerants, assuming that the temperature glides on both of heat source and heat sink are relatively small. Therefore, among the refrigerants shown in Table 1, 16 refrigerants were targeted, excluding R744, which has a lower critical temperature than 60°C.

3.1. Method

Figure 4 and Table 2 show the schematic diagram and calculation condition of the heat pump cycle, respectively. The temperature lift (ΔT_{lift}) is defined by the difference between the heat sink outlet temperature (T_{h2}, heat supply temperature) and the heat source inlet temperature (T_{c1}). The temperature glides on both of heat source (ΔT_{c}) and heat sink (ΔT_{h}) are fixed at 5 K. The pinch temperature differences on both of evaporator ($\Delta T_{\mathrm{pinch,evp}}$) and condenser ($\Delta T_{\mathrm{pinch,cnd}}$) are fixed at 2 K. Strictly speaking, the pinch point of the condenser occurs somewhere in the condenser, but in order to simplify the calculation, it is defined by the difference between the condensation temperature (T_{cnd}) and the heat sink outlet temperature (ΔT_{h2}). The evaporator superheating ($\Delta T_{\mathrm{sh,evp}}$) and the condenser subcooling (ΔT_{sc}) are fixed at 5 K. As mentioned above, depending on the type of refrigerant, the discharge superheating may be smaller than the suction superheating. Thus, the smaller superheating of them (ΔT_{sh}, minimum superheating) is fixed at 5 K. When the discharge superheating is smaller, the insufficient superheat amount covered with an internal heat exchanger. Compressor isentropic efficiency (η_{cmp}) generally depends on the pressure ratio of discharge pressure to suction pressure, but it is set to a constant value of 0.8 in this calculation. The thermophysical properties of each refrigerant are calculated using REFPROP Ver. 10.0 by NIST [5].

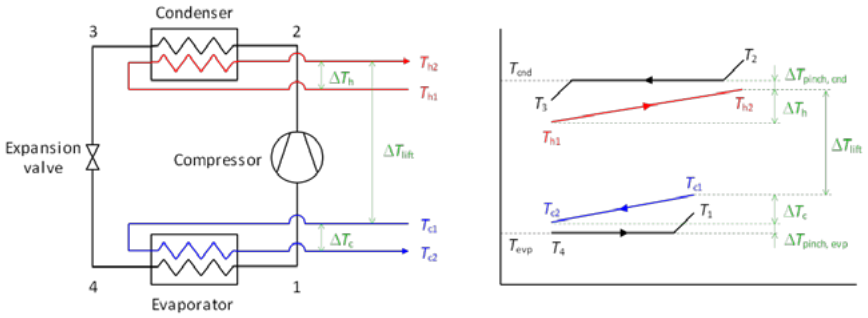


Figure 4. Schematic diagram of simple heat pump cycle and temperature profile

Table 2. Definition of temperature differences and calculation condition

Symbol	Value	Unit	Definition
ΔT_{lift}	Variable	K	$= T_{\mathrm{h2}} - T_{\mathrm{c1}}$
ΔT_{c}	5	K	$= T_{\mathrm{c1}} - T_{\mathrm{c2}}$
ΔT_{h}	5	K	$= T_{\mathrm{h2}} - T_{\mathrm{h1}}$
$\Delta T_{\mathrm{pinch,evp}}$	2	K	$= T_{\mathrm{c2}} - T_{\mathrm{evp}}$
$\Delta T_{\mathrm{pinch,cnd}}$	2	K	$= T_{\mathrm{cnd}} - T_{\mathrm{h2}}$
$\Delta T_{\mathrm{sh,evp}}$	5	K	$= T_{1} - T_{\mathrm{evp}}$
ΔT_{sc}	5	K	$= T_{\mathrm{cnd}} - T_{3}$
ΔT_{sh}	5	K	$= \min\{T_{1} - T_{\mathrm{evp}}, T_{2} - T_{\mathrm{cnd}}\}$
η_{cmp}	0.8	-	$= (h_{2,\mathrm{is}} - h_{1}) / (h_{2} - h_{1})$

When selecting a refrigerant, it is necessary to take into consideration all of the following 5 items:

- Thermodynamic performance
- Safety
- Stability
- Economy
- Environmental friendliness

In this study, first, thermodynamic constraints are set from the viewpoint of energy and economic performances. Specifically, the constraints are placed on the coefficient of performance (COP) and the volumetric heating capacity (VHC). Assuming the current condition of industrial heat pump installation in Japan, the lower limits of COP and VHC are roughly set to 4 and 2 MJ/m^2, respectively. Next, it is conceivable to set a restriction on the discharge temperature from the viewpoints of thermal and chemical stabilities of refrigerant and lubricant and viscosity of lubricant, however in this study the restriction is not set because the limitation is not clear at this moment. For example, the upper limit temperature could be increased by newly development of addition agent. Then, considering the safety and environmental friendliness of refrigerant, this analysis divided into the following 3 cases; (1) the case of selecting from low GWP and A1 refrigerants, (2) the case of selecting from low GWP and A1 or A2 refrigerants, and (3) the case of selecting from natural refrigerants.

3.2. Results

As an example of the calculation result, Figure 5 shows the working domain in the case of R245fa. The maximum heat pump supply temperature is determined only by the critical temperature because there is no restriction set on the discharge temperature. This heat pump can operate competitively in the range of the temperature lift of about 50 K or less due to the constraint of COP of 4 or more. Then, it can be seen that there is a region where the VHC is less than 2 MJ/m^2, even when the COP is 4 or more.

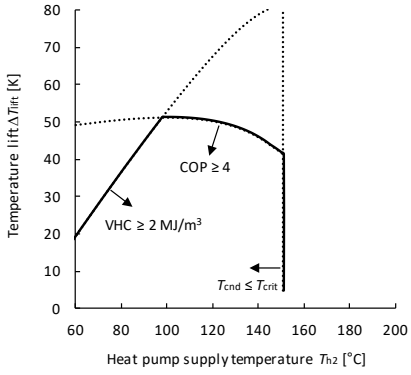


Figure 5. Constraints and working domain of simple heat pump cycle with R245fa

Figure 6 shows the working domains of each refrigerant. The left figure (a) illustrates HFC, HCFO and HFO refrigerants, and the right figure (b) illustrates natural refrigerants. It can be seen that the upper sides of the working domains of R1234yf and R1234ze(E) are close to R32 and R134a, respectively, and the right ends can be expanded. R1234ze(Z) and R1224yd(Z) have similar working domain to R245fa. R1233zd(E) and R1336mzz(Z) have the working domains on relatively higher temperature side.

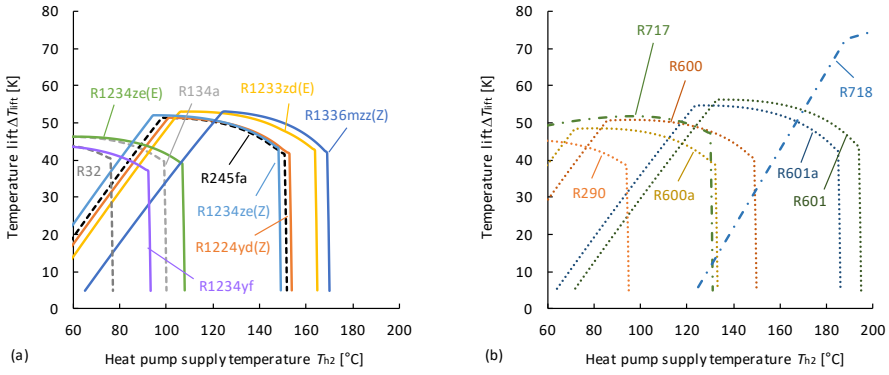


Figure 6. Working domains of simple heat pump cycles with 16 pure refrigerants

Figure 7 shows the composite diagrams so that the working domain is maximized when selecting refrigerants from each case of HFCs, HCFOs or HFOs, and natural refrigerants. It can be seen that the development of the new refrigerants (HCFOs and HFOs) has expanded the working domain and made it possible to construct competitive heat pumps under the conditions where the heat pump supply temperature is higher than before. On the other hand, natural refrigerant has the wide working domain. This indicates high temperature heat pumps can be constructed in a wide temperature range using only natural refrigerant in terms of thermodynamic performance.

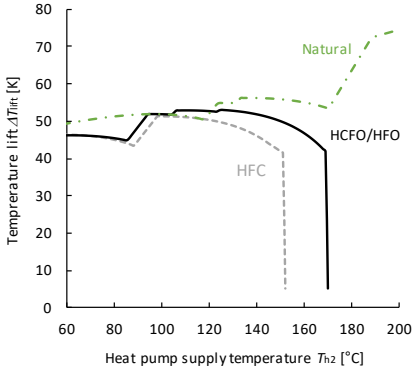


Figure 7. Maximum working domain of simple heat pump cycle

Next considers the safety and environmental friendliness of refrigerant. Figure 8 shows the maximum working domain in the following 3 cases; (1) the case of selecting from low GWP and A1 refrigerants, (2) the case of selecting from low GWP and A1 or A2L refrigerants, and (3) the case of selecting from natural refrigerants.

When selecting from low GWP and A1 refrigerants shown in the figure (a), R1224yd(Z) is promising in the heat pump supply temperature range below 105°C, R1233zd(E) from 105°C to 125°C, R1336mzz(Z) from 125°C to 165°C, and R718 over 165°C.

Then, when approving A2L refrigerants shown in the figure (b), R1234ze(E) becomes a candidate in the heat pump supply temperature range below 85°C, R1234ze(Z) from 85°C to 105°C, and then the working domain of R1224yd(Z) disappears.

On the other hand, when selecting from natural refrigerants shown in figure (c), R717 is promising below 120°C, R601a from 120°C to 130°C, R601 from 130°C to 170°C, and R718 over 170°C. However, it should be noted that the discharge temperature of R717 becomes relatively high. For example, the discharge temperature is 182°C when the heat pump supply temperature is 100°C. In the practical use, it would be necessary to cool the discharge vapor in some way.

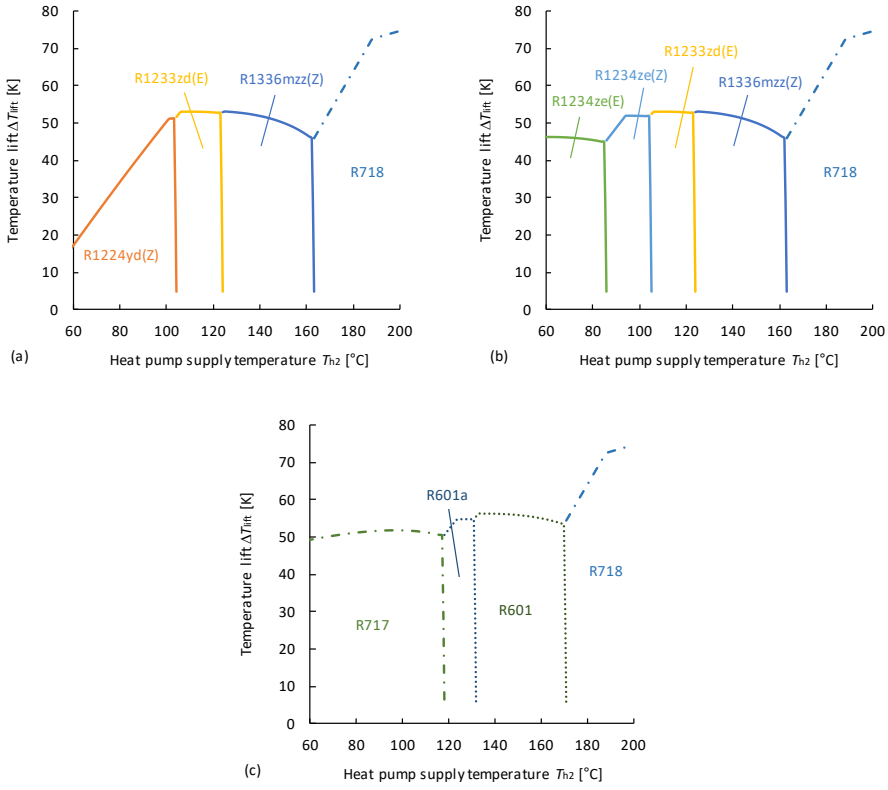


Figure 8. Maximum working domain of simple heat pump cycle (a) selecting from low GWP and A1 refrigerants (b) selecting from low GWP and A1 or A2L refrigerants (c) selecting from natural refrigerants

4. Analysis for two-stage heat pump cycle with economizer

Next, the effect of a high efficiency improvement by two-stage cycle with economizer are examined on the refrigerant selection.

4.1. Method

Each of the minimum superheating of the high-stage compressor and the low-stage compressor is fixed at 5 K. An internal heat exchanger is installed when the discharge superheating is smaller than the suction superheating. The compressor isentropic efficiency of each stage is set to a constant value of 0.8. The

intermediate pressure is defined by the square root of the product of the discharge pressure and the suction pressure. The ratio of refrigerant mass flow rate in the high-stage and low-stage is fixed at 1.5.

4.2. Results

Figure 9 shows the maximum working domain in the following 3 case; (1) the case of selecting from low GWP and A1 refrigerants, (2) the case of selecting from low GWP and A1 or A2L refrigerants, and (3) the case of selecting from natural refrigerants.

When selecting from low GWP and A1 refrigerants shown in the figure (a), R1224yd(Z), R1233zd(E), R1336mzz(Z) and R718 are promising in ascending order of heat pump supply temperature like the case of simple heat pump cycle.

On the other hand, when approving A2L refrigerants shown in the figure (b), R1234yf in the heat pump supply temperature range below 70°C and R1224yd(Z) in a narrow range around 120°C become candidates unlike the case of simple heat pump cycle. This would be because R1234yf has a larger effect of improving COP by the two-stage compression with economizer than R1234ze(E) and R1224yd(Z) has the larger effect than R1234ze(Z).

When selecting from natural refrigerants shown in figure (c), the working domain of R717, which has a relatively small performance effect by the two-stage compression with economizer, becomes narrowed, and R600 becomes a candidate.

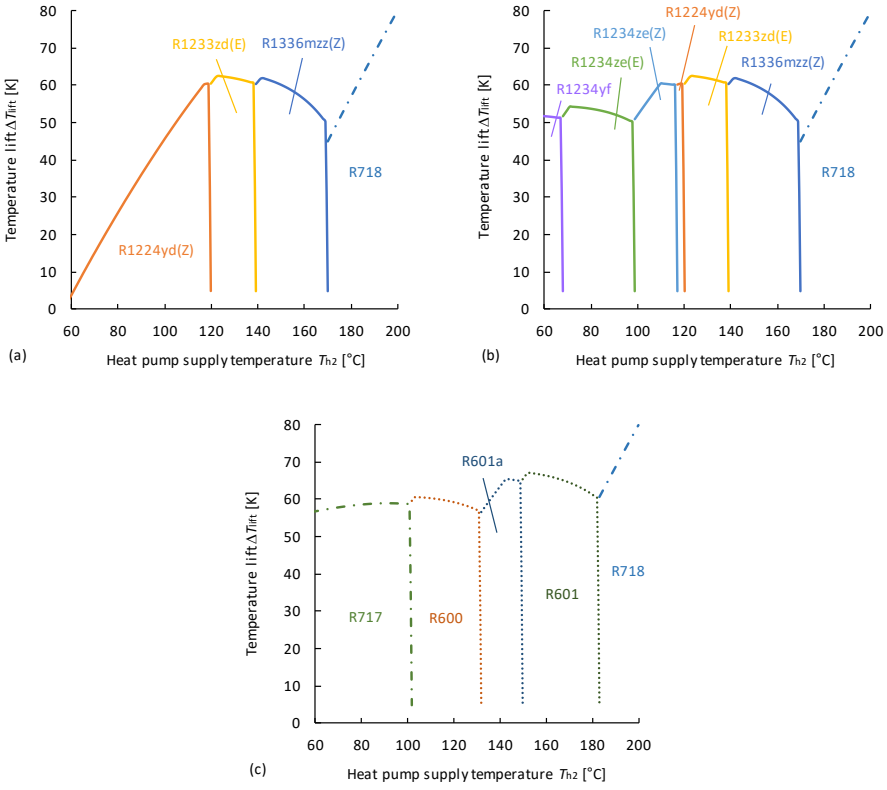


Figure 9. Maximum working domain of two-stage heat pump cycle with economizer (a) selecting from low GWP and A1 refrigerants (b) selecting from low GWP and A1 or A2L refrigerants (c) selecting from natural refrigerants

Figure 10 shows the comparison in maximum working domain between simple heat pump cycle and two-stage heat pump cycle with economizer. In any of the 3 cases, it can be seen that the temperature lifts expand by about 10 K thanks to the higher efficiency, although the improved ranges are limited; the range from 110°C to 160°C when selecting from low GWP and A1 refrigerants, the ranges below 85°C and from 110°C to 160°C when selecting from low GWP and A1 or A2L refrigerants, and the ranges below 115°C and from 140°C to 170°C when selecting from natural refrigerants. In other words, it means that the thermodynamic performance can be kept even when the heat source temperature become about 10 K lower than in the case of the simple heat pump cycle.

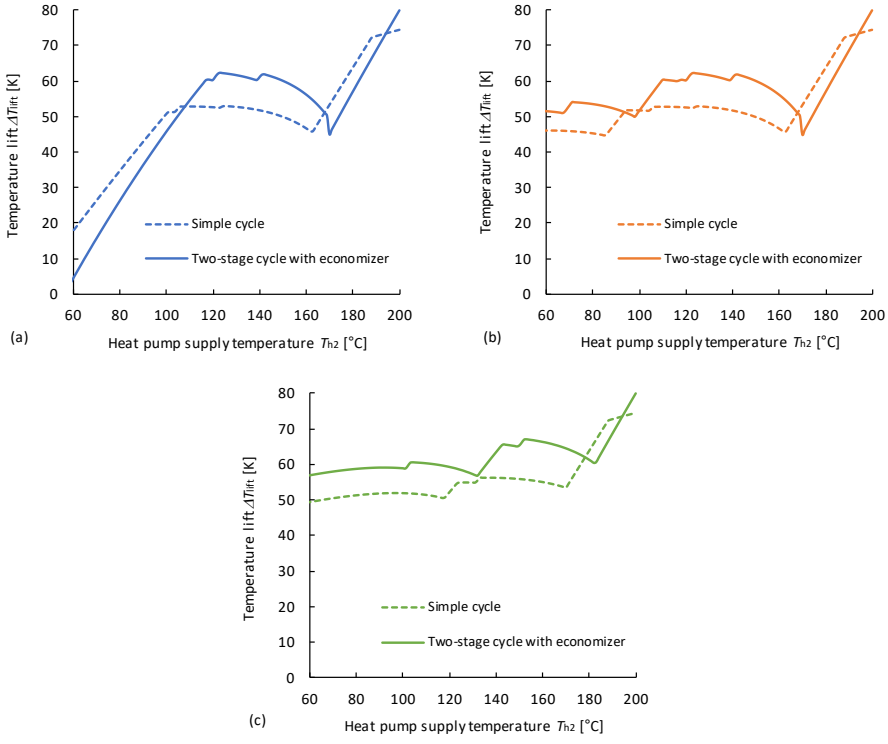


Figure 10. Comparison in maximum working domain between simple heat pump cycle and two-stage heat pump cycle with economizer (a) selecting from low GWP and A1 refrigerants (b) selecting from low GWP and A1 or A2L refrigerants (c) selecting from natural refrigerants

5. Conclusion

In this study, refrigerant selection for high temperature heat pump cycles is analyzed thermodynamically for the purpose of providing working domain maps which can determine the promising refrigerant and the upper limit of heat pumping temperature lift for each supply temperature. The following results are obtained:

- In terms of thermodynamic performance, high temperature heat pumps can be constructed in a wide temperature range from 60°C to 200°C using only natural refrigerant. R717, R601a, R601 and R718 are promising in ascending order of heat pump supply temperature. By improving the heat pump cycle with two-stage compression with economizer, R600 becomes a candidate and the working domain of R717 becomes narrowed.
- Considering the safety of the refrigerant, when selecting from low GWP and A1 refrigerants, R1224yd(Z), R1233zd(E), R1336mzz(Z) and R718 are promising. When approving A2L refrigerants, R1234ze(E) and R1234ze(Z) become candidates and the working domain of R1224yd(Z) disappears.

- By improving the heat pump cycle with two-stage compression with economizer, R600, R1234yf and R1224yd(Z), which have relatively larger effects, become candidates. And the temperature lift expands by about 10 K by the higher efficiency.

However, this study did not set the restriction on the discharge temperature. And this study focuses on the case where the temperature glides on both of heat source and heat sink are relatively small. Therefore, the following items are listed as the future issues:

- To set the restriction on the discharge temperature by considering the limitation of refrigerant stability and lubricant viscosity
- To analyze cases where the temperature glides on heat source and heat sink are relatively large by including transcritical heat pump cycle and other cycles with zeotropic mixed refrigerants

References

[1] Mitsubishi Research Institute (MRI), Survey report on heat demand and heat supply equipment, commissioned by Agency for Natural Resources and Energy, February, 2018. [in Japanese]
[2] Brunin, O., Freidt, M., Hivet, B., Comprison of the working domains of some compression heat pumps and a compression-absorption heat pump, International Journal of Refrigeration, Vol. 20, No. 5, 308–318, 1997.
[3] Ommen, T., Jensen, J. K., Markussen, W. B., Reinholdt, L., Elmegaard, B., Technical and economic working domains of industrial heat pumps: Part 1 – Single stage vapour compression heat pumps, International Journal of Refrigeration, Vol. 55, 168–182, 2015.
[4] Morrison, G., The shape of the temperature-entropy saturation boundary, International Journal of Refrigeration, Vol. 17, No. 7, 494–504, 1994.
[5] Lemmon, E., Bell, I., Huber, M., McLinden, M., National Institute of Standards and Technology (NIST) Reference Fluid Thermodynamic and Transport Properties Database (REFPROP), Ver. 10.0, 2018.

13th IEA Heat Pump Conference
April 26-29, 2021 Jeju, Korea

Effect of shape change in the flow dirction of mini-channel on the flow patterns

Haruki Mitarai[a], Tetsuya Kobayashi[a], Koji Enoki[a], Kosaku Nishida[b] and Ikuro Akada[b*]

[a]The University of Electro-Communications 1-5-1, Chofugaoka, Chohu-shi, Tokyo 182-8585, Japan
[b]MAYEKAWA MFG. CO. LTD 2000, Tetsuzawa, Moriya-shi Ibaraki 302-0118, Japan

Abstract

As a method of improving the heat transfer of vapor-liquid two-phase flow in a mini-channel, there is the method of changing the shape. However, in previous researches, only the channel cross-sectional shape has been changed. In this study, the flow patterns of vapor-liquid two-phase flow in a plate heat exchanger with straight and wavy mini-channel was visualized, and the effect of changing the shape in the flow direction and the prospects for improving the heat transfer characteristics of the heat exchanger were investigated. A visualization experiment showed that imbalance in the liquid film thickness in the annular flow region of the wavy mini-channel in the flow direction. The thickness of the liquid film in the wavy mini-channel was measured and it was found that the thickness of the liquid film in the thin sections was less than half of that in the straight mini-channel and that in the thicker sections it was about 1.4 times thicker than that in the straight mini-channel. Then the heat transfer coefficient of wavy channel was almost 1.53 times better than the straight one.

Keywords:Mini-channel, Heat transfer, Vapor-liquid two phase flow, Boiling

1. INTRODUCTION

Currently, global warming is becoming a problem on a global scale. The production and consumption of CFC which causes global warming was restricted by the Montreal Protocol in 1987 and the emission factor was fixed in the Kyoto Protocol in 1997. In addition, alternative CFC was restricted by the Kigali Revision of the Montreal Protocol in 2016, too. Under the circumstances, it is considered that the refrigerant used in the refrigerator and air conditioner shifts to natural refrigerant such as ammonia. However, it is desirable to minimize the amount of refrigerant in them for safety because ammonia is toxic. In addition, we can achieve not only safety but also heat exchangers can be smaller by reducing the amount of refrigerant in heat exchangers. Therefore, enhancing the heat transfer performance in heat exchangers is need.

The heat transfer performance in heat exchangers can be improved by using microchannels with a diameter of about 1 mm. The reason of this phenomena are the evaporation heat transfer which occurs by heat conduction through the liquid film (liquid film evaporation heat transfer) in the slug flow area because the smaller the tube diameter, the thinner the liquid film present on the tube wall in addition to nucleate boiling heat transfer and forced convective heat transfer which are the mechanism of boiling heat transfer in the conventional channels and since the tube diameter is small in the micro tube, the liquid film present near the tube wall becomes thinner and the densification the heat transfer area with respect to the flow path area is increased.

K. Enoki (2013) [1] conducted experiments on boiling heat transfer coefficient and pressure drop measurement for each mini-channels, which has circular, rectangular and triangular cross sections. R 410A was used as the refrigerant, and the flow direction were vertical upward, vertical falling and horizontal. It

* Corresponding author.
E-mail address: enoki.koji@uec.ac.jp.

has been found that the boiling heat transfer coefficient was good for both circular, rectangular and triangular mini-channels. The high heat transfer coefficient was maintained up to high quality and decreased rapidly after occurred dryout. However, it was reported that the local heat transfer coefficient was different depending on the cross section.

In this study, the vapor-liquid two-phase flow in a heat exchanger was visualized by changing the mini-channel shape in the flow direction from a straight to a wavy, and the effects on the flow patterns and whether it can be expected to improve the heat transfer characteristics were confirmed. In addition, the boiling heat transfer coefficient of a single mini-channel was experimentally examined to show how much better the boiling heat transfer coefficient of a wavy mini-channel is compared with that of a straight one.

2. EXPERIMENTAL SET-UP AND PRODURES

The fluid used in this study is HFE-7000. For calculating the physical property value, we used NIST's REFPROP ver9.1 [2].

2.1. Visualization of flow patterns of a heat exchanger with wavy mini-channels

Figure 1 presents the schematic diagram of the experimental set-up for visualization of flow patterns. The fluid leaving the tank was sufficiently cooled by the double-pipe heat exchanger and pumped out at a constant flow rate by the syringe pump. The fluid was sufficiently cooled again by the double-pipe heat exchanger and flowed into the Coriolis flowmeter to measured mass flow rate. After that, the fluid was heated to a predetermined vapor quality by the preheater and flowed into the test section. The refrigerant leaving the test section was cooled by the condenser and returned to the tank.

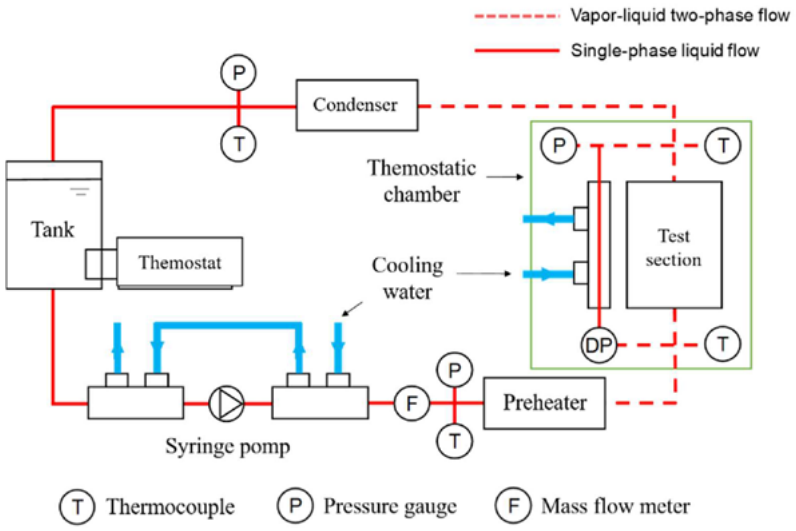


Fig. 1. Schematic diagram of experimental set-up for visualization

Two test sections were used in this study, one with a wavy and straight combined mini-channel and the other with only a straight mini-channel for comparison. The combined test section has wave-shaped in the upstream part and straight-shape in the downstream part channels, respectively. This combined test section is hereafter referred to simply as "wavy". Figure 2 shows a view of the wavy test section. The right figure of Fig. 2 shows the details of the test section when it is disassembled. As shown in these figures, the test section consisted of a glass for visualization, a metal plate made of stainless steel with a flow channel, a back plate with an inlet pipe, a back plate with an outlet pipe, and a copper plate, which were welded or bonded together. Flow channel plate is made of stainless steel in order to prevent corrosion even when ammonia is used as a refrigerant. The channels of the flow channel plate were created by etching. The visualization is achieved by mounting a glass in front of the flow channel plate and sealing it. The copper plate contains a cartridge

heater that directly heats the refrigerant flowing in the flow path uniformly by AC power. The refrigerant inlet is in the lower left corner and the outlet is in the upper center hole.

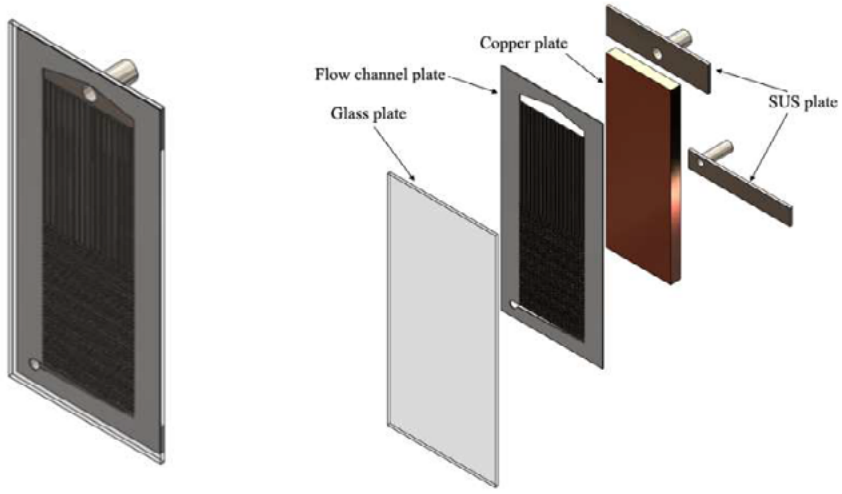


Fig. 2. Test section of wavy mini-channels

Figure 3 presents the schematic diagram of wavy mini-channels plate. Table 1 presents the specification of the wavy test section. The test unit processes 48 channels in a SUS304 plate. The flow path was structured such that the lower half was a wavy path with an amplitude of 0.4 mm and a wavelength of 4mm, and the upper half was a straight path. The right figure of Fig. 3 shows the details of the flow path of the test section. The width of the mini-channel was 1.49 mm and the width of the inlet of the mini-channel was 0.86 mm. The fluid flow was a vertical upward flow. The fluid flowed into the test section with an inlet quality of $x_{\text{in}} = 0.2$ and an outlet quality of $x_{\text{out}} = 0.9$. A high-speed camera was used to capture the flow of fluid in wavy paths. Red frames in Fig. 3 were the areas where videos were taken. The channel numbers are given from the inlet side and range from 1 to 48. The detailed locations of the red frames in Fig. 3 are, from left to right, channels 1 to 8 on the left side of the channel, 21 to 28 in the center of the channel, and 41 to 48 on the right side of the channel, and, from bottom to top, the inlet, 40 mm from the inlet, 132 mm from the inlet, and the outlet.

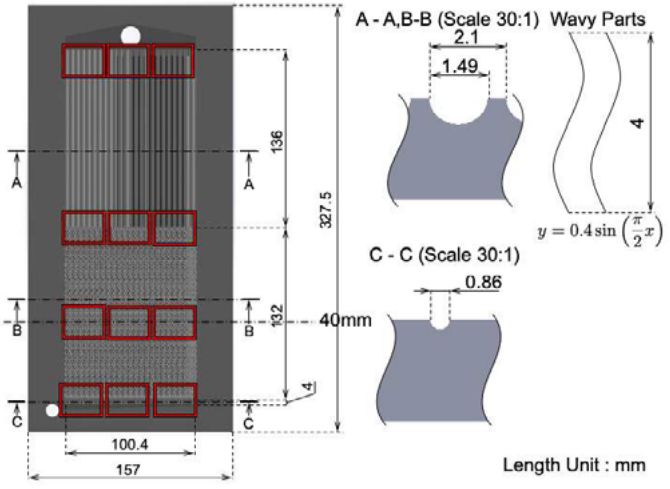


Fig. 3. Schematic diagram of wavy mini-channels plate

Table 1. Specification of wavy test section

	Flow path section	Choke section
Plate material	SUS316L	
Hydraulic diameter D[mm]	0.98	0.63
Flow area A[mm^2]	0.98	0.39
Wet perimeter l[mm]	4.02	2.46
Width d[mm]	1.49	0.86
Wavy amplitude a[mm]	0.4	
Wavelength of one wavy unit L[mm]	4	
The number of waves	33	1
Wavy line	$y = 0.4\sin(\frac{\pi x}{2})$	
The length of straight line [mm]	136	-
The length of wavy line [mm]	132	4
Number of flow paths	48	

2.2. Visualization of flow patterns of a heat exchanger with straight mini-channels

The visualization glass is installed in front of the flow channel plate, the heating method, the inlet and outlet ports, the direction of refrigerant flow, the shape of the inlet header, and shooting location are the same as for the wavy test section. The outlet header has a choke at the outlet end of the flow path to prevent backflow of the accumulated refrigerant. Figure 4 presents the schematic diagram of straight mini-channels plate. The right figure of Fig. 4 shows the details of the flow path of the test section. The width of the mini-channel was 1.59 mm and the width of the outlet of the mini-channel was 0.68 mm. Table 2 presents the specification of the straight test section

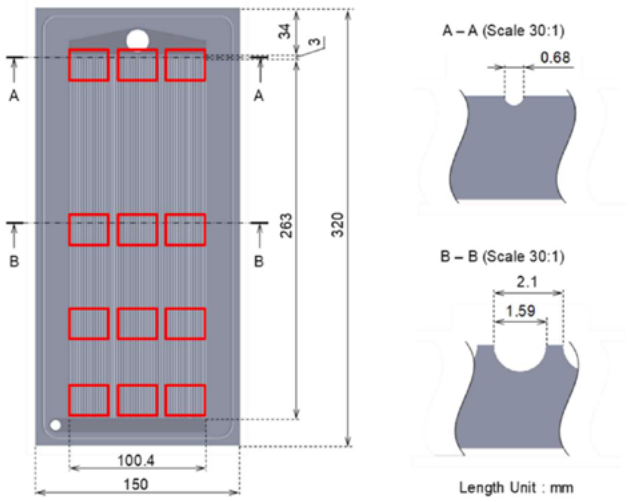


Fig. 4. Schematic diagram of straight mini-channels plate

Table 2. Specification of straight test section

	Flow path section	Choke section
Plate material	SUS316L	
Hydraulic diameter D[mm]	0.935	0.617
Flow area A[mm^2]	0.97	0.34
Wet perimeter l[mm]	4.14	2.22
Width d[mm]	1.61	0.69
Number of flow paths	48	

Table 3 presents the experimental conditions for the straight test section and the wavy test section.

Table 3. Experimental condition of test section

Refrigerant	HFE-7000
Saturation temperature [°C]	30
Absolute saturation pressure [MPa]	0.087
Mass flow rate M[kg/s]	0.002
Mass flux G [kg/(m^2 · s)]	40
Heat flux q [kW/m^2]	7.5
Latent heat Δh_v [kJ/kg]	135.5
Test section inlet quality x_{in}	0.2
Test section outlet quality x_{out}	0.9

The specific enthalpy of fluid mixing at the inlet and outlet of the test section was calculated based on the specific enthalpy at the inlet of the preheater, $h_{\text{PH in}}$. $h_{\text{PH in}}$ was determined from the pressure and temperature of the refrigerant in liquid single phase state measured at the inlet of the preheater. The specific enthalpy at the inlet of the test section, $h_{\text{TS in}}$, was calculated from the mass flow rate M, the electrical input at the preheater, Q_{PH}, and the heat gain from the inlet of the preheater to the inlet of the test section, Q_1, as shown in Equation (1). Furthermore, the specific enthalpy at the outlet of the test section, $h_{\text{TS out}}$, was calculated from the mass flow rate, M, the electrical input at the test section, Q_{TS}, and the heat gain from the inlet to the outlet of the test section, Q_2, as shown in Equation (2).

$$h_{\text{TS in}} = h_{\text{PH in}} + \frac{(Q_1 + Q_{\text{PH}}) \times 10^{-3}}{M} \tag{1}$$

$$h_{\text{TS out}} = h_{\text{TS in}} + \frac{(Q_2 + Q_{\text{TS}}) \times 10^{-3}}{M} \tag{2}$$

Using the values of Equations (1) and (2), the vapor quality x_{in} at the inlet of the test chamber and the vapor quality x_{out} at the outlet of the test chamber were calculated as shown in Equations (3) and (4) below. $h_{x=0}$ is the specific enthalpy of saturated liquid and Δh_v is the latent heat of evaporation of the refrigerant.

$$x_{\text{in}} = \frac{h_{\text{TSin}} - h_{x=0}}{\Delta h_v} \tag{3}$$

$$x_{\text{out}} = \frac{h_{\text{TSout}} - h_{x=0}}{\Delta h_v} \tag{4}$$

The quality errors at the inlet and outlet were calculated using the following equations (5) and (6).

$$\Delta x_{\text{in}} = \frac{(\Delta Q_1 + \Delta Q_{\text{PH}}) \times 10^{-3}}{M \times \Delta h_v} \tag{5}$$

$$\Delta x_{\text{out}} = \frac{(\Delta Q_2 + \Delta Q_{\text{TS}}) \times 10^{-3}}{M \times \Delta h_v} \tag{6}$$

The estimation errors for heat gain are $\Delta Q_1 = 0.00016\text{W}$ and $\Delta Q_2 = 0.00027\text{W}$, respectively. On the other hand, when we find the estimation error of each heater, we find that $\Delta Q_{\text{PH}} = 0.66\text{W}$ and $\Delta Q_{\text{TS}} = 1.5\text{W}$, which is large enough for the estimation error of heat gain. Therefore, the estimation error of each heater is dominant to the estimation error of quality. From the above, the quality errors at the inlet and outlet are calculated to be $\Delta x_{\text{in}} = 0.002$ and $\Delta x_{\text{out}} = 0.005$, respectively.

2.3. Measurements of boiling heat transfer coefficient

Figure 5 presents the schematic diagram of the experimental set-up for experimental investigation of boiling heat transfer coefficient in mini-channels. The fluid was pumped into the flow meter 1 and the flow rate was measured. Then, it branched in two directions, one goes to the test section and the other passes through the flow meter 2 and returned to the pump again. It was possible to adjust the flow rate of the fluid flowing to the test section accurately by adjusting the degree of opening of the valve before the preheater. The flow rate of fluid flowing to the test section was obtained by subtracting the value indicated by flow meter 2 from the value

indicated by flow meter 1. After that, the fluid heading for the test section was heated by the preheater. Afterward, the heat transfer coefficient was measured.

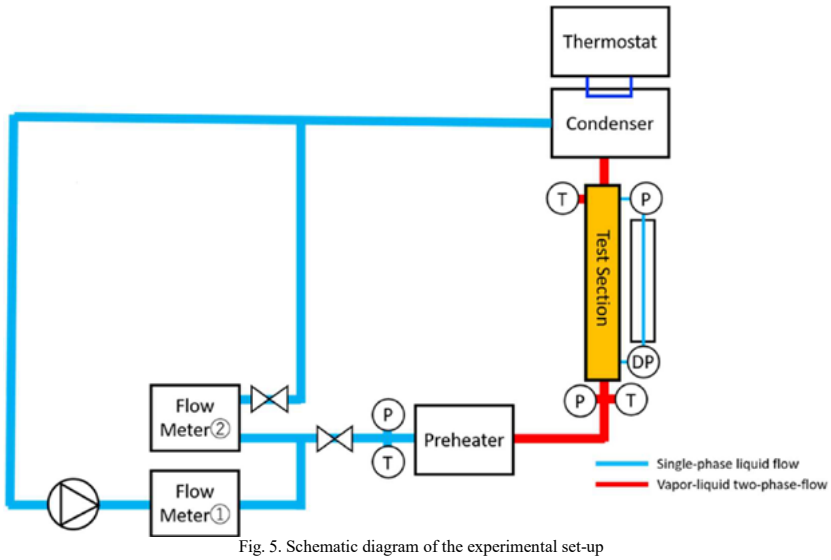


Fig. 5. Schematic diagram of the experimental set-up

Table 4 presents the specification of the mini-channels. The fluid was heated to a predetermined quality by the preheater and flowing into the test section. The temperature was measured at the test section inlet and outlet.

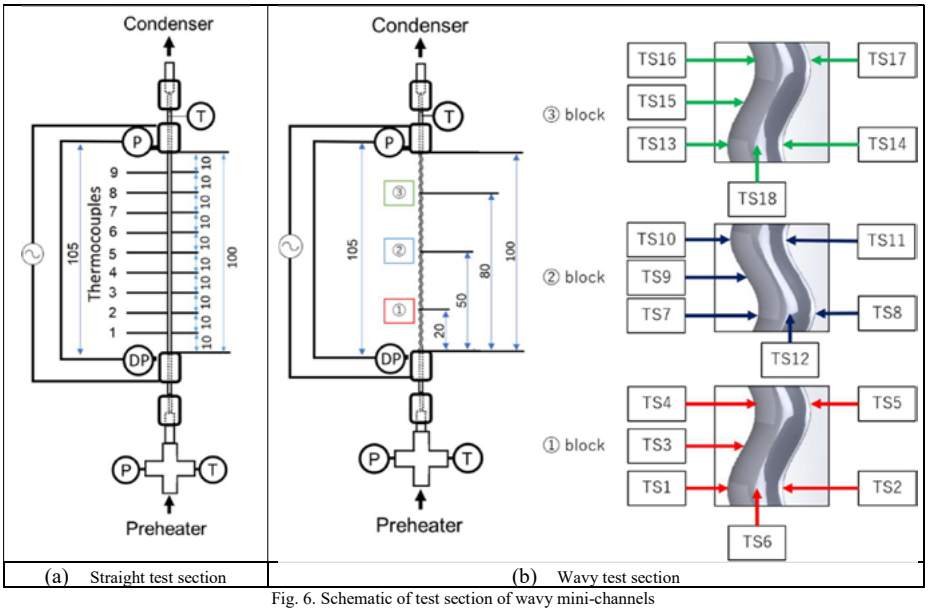
Table 4. Specification of the mini-channels

	Straight	Wavy
Material	SUS304	
Hydraulic diameter D[mm]	1.07	0.93
Flow area A[mm^2]	0.90	0.68
Differential pressure length [mm]	105	
Tube thick ness [mm]	0.29	
Thermal conductivity [W/(m · K)]	16.7	
Wave length L[mm]	-	4.0
Amplitude a[mm]	-	0.4

Figure 6 presents a schematic view of the test section of straight mini-channels and wavy mini-channels. The fluid was heated to a predetermined quality by the preheater and flowed into the test section. The test section was directly heated by AC power. Thermocouples were attached as shown in Fig. 6 in three areas of 20 mm, 50mm and 80 mm from below the wavy mini-channels and at nine locations 10 mm apart from the entrance to the exit of the straight mini-channels. Also, the test section was covered with a cylindrical heat insulating material and glass wool was packed inside to reduce the heat loss to the surroundings as much as possible. In the test section, experiments were conducted with constant heat flux, and the inlet quality of the test section was changed. Table5 presents the experimental conditions. Local heat transfer coefficient was calculated from

$$\alpha = \frac{q}{T_\mathrm{i} - T_\mathrm{b}} \tag{7}$$

T_i was the temperature of the inner wall of the mini-channel. Since the mini-channel was heated from an AC power, T_i was calculated from the heat conduction equation by using measured temperature of the outer wall, the thickness of the mini-channel used, heat flux and the thermal conductivity of SUS304 taking into account internal heat generation. T_b was the average temperature of fluid. It was calculated from the specific enthalpy and local pressure of the fluid at the location where the thermocouple was attached by using REFPROP.



(a) Straight test section (b) Wavy test section

Fig. 6. Schematic of test section of wavy mini-channels

Table 5. Experimental conditions of heat transfer measurement

Mass flux G [kg/(m^2 · s)]	40
Heat flux q [kW/m^2]	8
Quality x[−]	0 – 1
Saturation temperature[℃]	30

3. RESULTS AND DISCUSSION

3.1. Visualization of flow patterns in wavy mini-channels

Figure 7 shows the results of imaging of flow patterns at each location shown in Fig. 3 with a high-speed camera. In the inlet of the test section, slug flow was observed at channels of No.21 to No.28 and No.41 to No.48 and annular flow was observed at No.1 to No.8. In the area 40mm above the inlet of the test section, annular flow was observed at channels of No.1 to No.8 and No.41 to No.48 and slug flow was observed at No.21 to No.28. In other areas, annular flow was observed. It can be seen that the wavy area is filled with slug flow and annular flow. The annular flow has a high heat transfer rate in the tube forced convection boiling heat transfer. In the slug flow, liquid film evaporation heat transfer is generated by heat transfer through a thin liquid film in the mini-channels in addition to nucleate boiling heat transfer and forced convective heat transfer which are the mechanism of boiling heat transfer in the conventional channels. From this fact, it is considered the heat transfer performance of the wavy mini-channels is enhanced. Furthermore, flow disturbances were observed everywhere. Therefore, it is considered that the stretching and folding of the fluid elements by turbulence promotes fluid mixing and enhance heat transfer.

3.2. Visualization of flow patterns in straight mini-channels

Figure 8 shows the results of imaging the flow pattern of the straight test section at each of the locations shown in Fig. 4 with a high-speed camera. Annular flows were observed at the whole area of channels No.1 to No.8, slug flows in the inlet of the test section at channels No.21 to No.28 and No.41 to No.48, and annular flows in other areas. Back-flow was observed in channels No.45 to No.48, but it was only temporary.

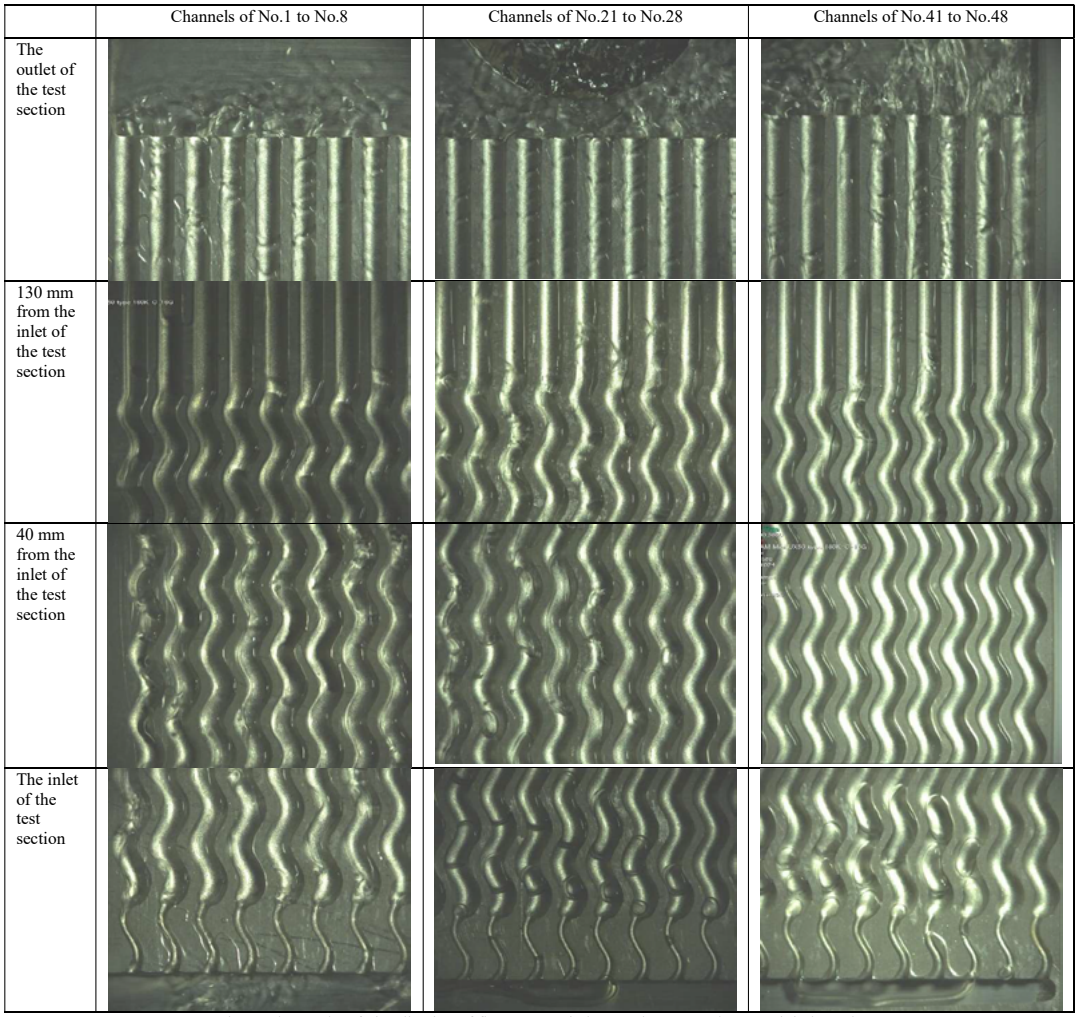


Fig. 7. The results of visualization of flow patterns in heat exchanger used wavy mini-channels

3.3. Effects of mini-channels shape change on the flow pattern and heat transfer coefficient

Enlarged images of the vapor-liquid two-phase flow in the straight test section and the wavy test section taken with a macro lens are shown in Figs. 9 and 10, respectively. The video images were taken at 132 mm from the channel entrance of channels No.21 to No.28 in the center of the test section. Figure 11 is the enlarged view of the red frame in Fig. 10. Figures 9 and 11 show that there is a clear bias in the thickness of the liquid film flowing through the channel wall in the annular channel region in the wavy channel compared to the straight channel, and that the liquid film is divided into thicker and thinner sections in the trough of the wavy mini-channel. In addition, it was found that the fluid is easily held in the trough of the wavy mini-channel and the liquid film is thick. Moreover, it turned out that thickness of liquid film is changing periodically as it became thicker and thinner in the points where it is thick. This phenomenon is considered to be due to the following mechanism. First, the liquid film grows and becomes thicker. After that, it breaks the surface tension of the channel wall and peels off as a droplet. Finally, the liquid film repeats the growth again. It can be seen that peeled droplets are believed to promote fluid mixing. On the other hand, the liquid film was very thin in other areas. Although liquid film evaporation heat transfer is originally observed in the

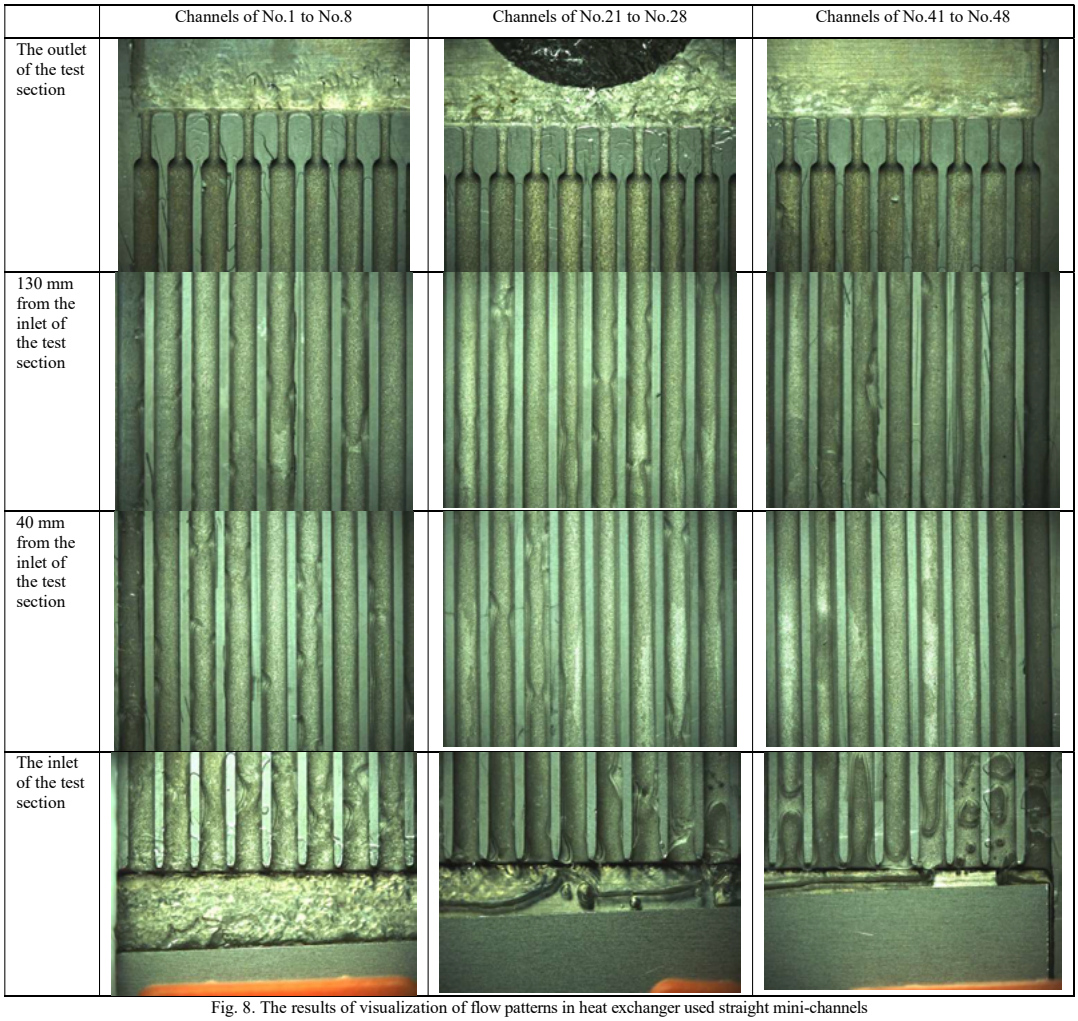


Fig. 8. The results of visualization of flow patterns in heat exchanger used straight mini-channels

slug flow area, since a very thin portion of the liquid film appears due to the thickness deviation of the liquid film, liquid film evaporation heat transfer is performed even in the annular flow area in wavy mini-channels. As a result, heat transfer performance is considered to be enhanced.

In order to estimate the thickness of the liquid film, measurements of the wall thickness of each channel were made using the video images. However, the thickness of the liquid film on the channel walls changed periodically in both straight and wavy channels. we measured the period of variation of the liquid film thickness at thicker points in the wave-shaped channel, and averaged the results of the measurement of the liquid film thickness within the period to obtain the average liquid film thickness as a parameter. In order to measure the period of the film thickness variation, images were taken at 132 mm from the channel entrance of the channel No.21 to No.28 (Fig. 8), where the film thickness variation was most clearly captured, by using a Photron FASTCAM Viewer 3. Table 6 shows the results of the measurement of the thickness variation period of the liquid film. The channel numbers are numbered 1 to 7, from left to right, for channels No.21 to No.28 in the center of the channel, as seen in the video taken at 132 mm from the channel entrance.

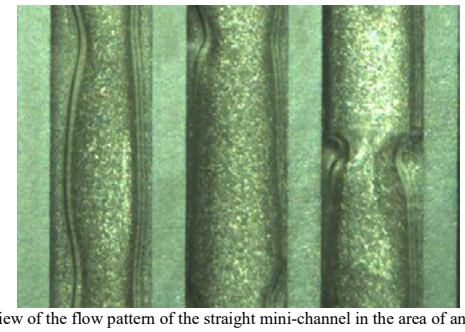


Fig. 9. View of the flow pattern of the straight mini-channel in the area of annular flow

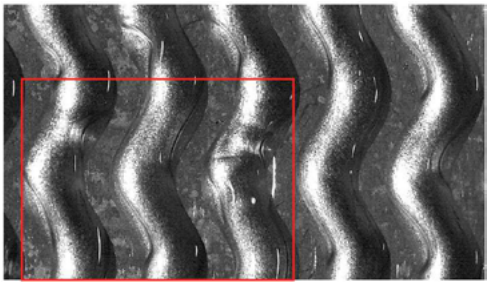


Fig. 10. View of the flow pattern of the wavy mini-channel in the area of annular flow

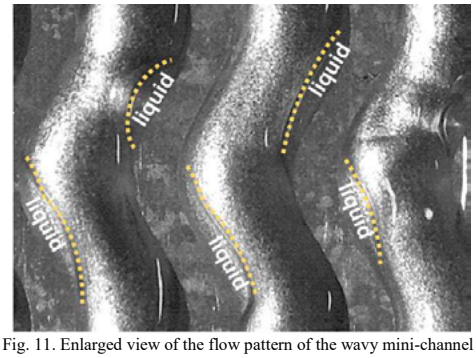


Fig. 11. Enlarged view of the flow pattern of the wavy mini-channel

Table 6. Fluctuation period of thickness of liquid film

Number of flow path	1	2	3	4	5	6	7
Fluctuation period of thickness of liquid film (frame, 1frame = 0.0005 s)	75.5 (0.038 s)	45.4 (0.023 s)	80.2 (0.040 s)	43.5 (0.022 s)	55.4 (0.028 s)	69.1 (0.035 s)	59.2 (0.030 s)

The average period of variation in the thickness of the liquid film was calculated by averaging the values in Table 6 to obtain 61.2. Therefore, the shooting speed used 60 frames out of 2000 fps as the approximate period of liquid film thickness variation, and measurements of 60 frames of liquid film thickness were made for both straight and wavy channels. Here, the period of liquid film thickness variation is 0.03 seconds. The wavy channel was divided into two sections, one where the film thickness was thicker and one where it was thinner, and the other where the film thickness was too thin to be measured, and the thickness of the wavy channel was measured for 60 frames. The area of the thickest liquid film in each frame was measured. The liquid film thicknesses were measured for 60 frames in the straight channel, the wavy channel where the film is thin, and the wavy channel where the film is thick, and averaged. The average liquid film thicknesses of the straight and wavy mini-channels are shown in Table 7. Table 7 shows that the liquid film thickness in

the wavy channel is about 1.4 times thicker than that in the straight mini-channel and less than half in the thin section.

Table 7. Average of thickness of liquid film

Straight	Wavy(thick parts)	Wavy(thin parts)
0.278mm	0.388mm	0.129mm

3.4. Boiling heat transfer coefficient in wavy mini-channels

Figure 12 shows that heat transfer coefficients at each position where thermocouples were attached. In addition, it is shown with heat transfer coefficients in straight mini-channels for comparison. As you can see from Fig. 12, the heat transfer coefficient at the mounting position of each thermocouple increases with increasing quality and it becomes maximum around the quality 0.45 and then drops. Therefore, it is considered that the dryout occurs at around the quality 0.45. In Fig. 12, the heat transfer coefficient is higher in the crest of the wavy mini-channels compared to the trough. From visualization experiments, it can be observed that the liquid film is thinner in the crest of the wavy mini-channels. These results suggest that the liquid film is thinner in the crest of the wavy mini-channels, which leads to liquid film evaporation heat transfer and thus improved heat transfer performance. The average heat transfer coefficients of the straight and wavy mini-channels before dryout are calculated as $\alpha = 1.73\mathrm{kW/(m^2 \cdot K)}$ for straight one and $\alpha = 2.65\mathrm{kW/(m^2 \cdot K)}$ for wavy one. Therefore, it can be seen that heat transfer coefficient of the wavy mini-chnnels was about 1.53 times better than that of straight one with the same cross section area of flow path.

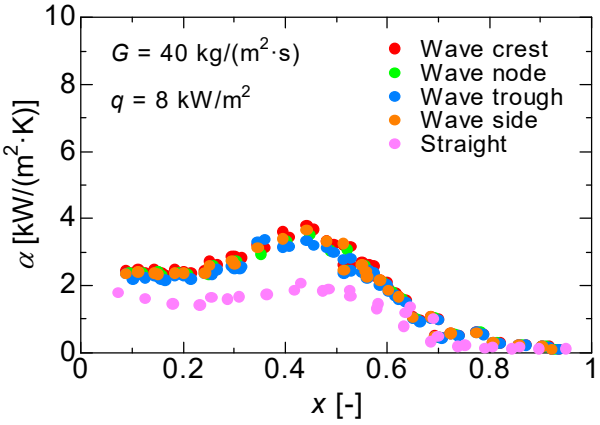


Fig. 12. Heat transfer coefficient at each thermocouple mounting position of the wavy mini-channel in $G = 40\ \mathrm{kg/(m^2 \cdot s)}$

4. CONCLUSIONS

In this study, the visualization of the flow pattern of vapor-liquid two phase flow in the wavy mini-channels and straight mini-channels were performed. In addition, in order to consider these, boiling heat transfer coefficient of wavy mini-channels and straight mini-channels were investigated experimentally. From the results of the experiment, we got the knowledge shown below.

(1) Compared to straight channels, there is a clear bias in the thickness of the liquid film flowing on the wall of the annular flow region in wavy channels. In addition, thickness of liquid film is changing periodically in the points where it is thick. As a result, heat transfer performance is enhanced by liquid film evaporation heat transfer not only in the slug flow region but also in the annular flow region. Furthermore, the disturbances observed may promote fluid mixing and contribute to improved heat transfer. The bias of the liquid film thickness in the wavy mini-channels is less than half of that in the straight mini-channels and about 1.4 times thicker in the thicker areas.

(2) Heat transfer coefficients in wavy mini-channels increase with increasing quality and it drop after becoming maximum. The heat transfer coefficient is improved in the crest where the liquid film in the wavy mini-channels is considered to be thin. In addition, heat transfer coefficients in wavy mini-channels before dryout show about 1.53 times better than that of straight mini-channels.

NOMENCLATURE

A	flow area	$[\mathrm{mm}^2]$
a	wavy amplitude	[mm]
D	hydraulic diameter	[mm]
d	Width	[mm]
G	mass flux	$[\mathrm{kg}/(\mathrm{m}^2 \cdot \mathrm{s})]$
Δh_v	latent heat	[kJ/kg]
$h_{x=0}$	the specific enthalpy of saturated liquid	[kJ/kg]
$h_{\mathrm{PH\ in}}$	the specific enthalpy at the inlet of the preheater	[kJ/kg]
$h_{\mathrm{TS\ in}}$	the specific enthalpy at the inlet of the test section	[kJ/kg]
$h_{\mathrm{TS\ out}}$	the specific enthalpy at the outlet of the test section	[kJ/kg]
M	mass flow rate	[kg/s]
L	wavelength of one wavy unit	[mm]
l	wet perimeter	[mm]
q	average heat flux	$[\mathrm{kW/m}^2]$
Q_1	the heat gain from the inlet of the preheater to the inlet of the test section	[W]
Q_2	the heat gain from the inlet to the outlet of the test section	[W]
ΔQ_1	The estimation errors for heat gain from the inlet of the preheater to the inlet of the test section	[W]
ΔQ_2	The estimation errors for heat gain from the inlet to the outlet of the test section	[W]
Q_{PH}	the electrical input at the preheater	[W]
Q_{TS}	the electrical input at the test section	[W]
ΔQ_{PH}	the estimation error of preheater	[W]
ΔQ_{TS}	the estimation error of test section	[W]
T_{i}	temperature of inner wall of the pipe	[℃]
T_{b}	average temperature of fluid	[℃]
x	quality	[−]
x_{in}	Test section inlet quality	[−]
x_{out}	Test section outlet quality	[−]
Δx_{in}	the quality errors at the inlet	[−]
Δx_{out}	the quality errors at the outlet	[−]

GREEK SYMBOLS

α	heat transfer coefficient	$[\mathrm{kW}/(\mathrm{m}^2 \cdot \mathrm{K})]$

References

[1] Koji ENOKI (2013): “Boiling Heat Transfer, Flow Patterns and Pressure Drop of the two-phase flow in small tubes”, Doctoral thesis UT51-2013-E770(In Japanese)

[2] Lemmon, E.W., Huber, M.L., McLinden, M.O. (2013): “NIST Reference Fluid Thermodynamic and Transport Properties – REFPROP Version 9.1”, NIST Standard Reference Database 23

13th IEA Heat Pump Conference
April 26-29, 2021 Jeju, Korea

Experimental investigation of local nucleate boiling heat transfer and mixing ratio on copper surface about mixture R 32 / R 1234ze(E)

Riku FUKUJU[a], Koji ENOKI[a*] and Kiyoshi SAITO[b*]

[a]Dept. of Mechanical and Intelligent System Engineering, The University of Electro-Communications, 1-5-1, Chofugaoka, Chofu, Tokyo, 182-8585, Japan

[b]Dept. of Applied Mechanics and Aerospace Engineering, Waseda University, 3-4-1, Okubo, Shinjuku-ku, Tokyo, 169-8555, Japan

Abstract

In this study, the heat transfer coefficients of R 32 and R 1234ze(E) were measured, respectively. In order to mixing affect, the heat transfer coefficient and mass ratio were measured and analyzed by changing the mixture mass ratio of the R 32 / R 1234ze(E) from 3 to 100 kW/m^2 heat flux. By attaching a thermocouple directly to the copper boiling surface, raw data were successfully measured without obtaining the surface temperature by a calculation formula. The mass fraction on the heating surface were also analyzed by gas chromatography. The above methods have made it possible to acquire data with high accuracy. The heat transfer coefficient was decreased for the zeotropic refrigerant mixtures compared to the pure refrigerants, specifically, the data of refrigerant mixture R 32 / R 1234ze(E) with a mass ratio of 0.2/0.8 showed the minimum value. The variation of the mass ratio near the heating surface that was not observed for the near-azeotropic refrigerant mixture occurred for the zeotropic refrigerant. In zeotropic mixtures, it was clear that the change in properties occurred in the boiling region.

Keywords: Nucleate Pool boiling, Local heat transfer coefficients, Mixture, Refrigerant, HFO

Introduction

1. Introduction

Currently, one of the measures to cope with global warming is the development of a refrigerant with a low GWP for use in refrigeration air conditioner. In addition, the Kigali amendment to the Montreal Protocol, agreed upon in 2016 and issued in 2019, restricted the production and consumption of HFC-based refrigerants. Therefore, development and use of natural refrigerants such as olefin-based low-GWP refrigerants and natural refrigerants using CO_2 and NH_3 as new alternative refrigerants have been promoted. However, due to flammability, toxicity, and reduced efficiency, some proposed new alternative refrigerants for use in refrigeration air conditioner units have not been determined at this stage[1]. New refrigerant mixtures of HFCs and olefin-based refrigerants are expected to be developed to solve this problem.

On the other hand, the phase change heat transfer equation is necessary for the optimal design of the heat exchanger of a refrigeration and air-conditioning equipment. There are various correlations, but they are limited due to their dependence on the diameter, the shape of the pipe and the type of refrigerant used. In actual phase change flow studies of existing refrigerant mixtures, boiling and condensation heat transfer and pressure drop in the tubes are obtained by changing the mixing ratio[2-9]. Pool boiling of refrigerant mixture has also

* Corresponding author.
E-mail address: enoki.koji@uec.ac.jp.

been studied from various viewpoints[10-13]. However, even if the mixing ratio of the system is known, the local properties where pressure drop and heat transfer occur remain unknown.

The purpose of this study is to measure the local physical properties by using an experimental apparatus of nucleate pool boiling heat transfer and to enable the calculation of local physical properties from the mixing ratios of the location where thermal physical phenomena occur. Ultimately, this method will enable us to treat complex refrigerant mixtures, which are not dependent on tube size or refrigerant, as a single refrigerant by simply using a conversion formula from system properties to local physical properties. In this study, as an initial step, the nucleate pool boiling heat transfer and phase of zeotropic mixture R 32 / R 1234ze(E) on a circular copper block were investigated and observed. Moreover, Gas chromatography was used to analyze the mass ratios of the boiling area of the refrigerant.

2. Experiment

2.1. Experimental apparatus and methods

A schematic diagram of the experimental apparatus used in this experiment is shown in Fig. 1. Refrigerants flowed through the port valves of System 2, passing through a solenoid valve, a check valve, a Coriolis flowmeter, and a needle valve, in that order, to the tank beyond valve 4. The Coriolis mass flowmeter, control system, and solenoid valve were synchronized, and the Coriolis mass flowmeter measured the mass flow rate, and when the mass flow rate reached the mass flow rate set by the control system, the solenoid valve automatically stopped the flow. Two thermostatic baths, one in the tank and the other in the test section, were used to transport the refrigerant using pressure fluctuations caused by temperature differences. The tanks were removable and weighed using digital measurements as the refrigerant was transported or recovered. Pressure sensors are installed in two locations to measure both in vapor and liquid. The mass flow rate of the lost refrigerant could be measured and confirmed by assembling a circuit to allow the refrigerant that was spilled when using gas chromatography to flow to the port valve in System 1. A vacuum pump was used to draw a vacuum throughout the entire apparatus before and after the experiment, and when the mixing mass ratio was changed, it was done outside the test section. After the experiment, refrigerants were disposed of in the refrigerant collection unit beyond valve 5.

Figures 2 and 3 show the test section of copper surface (diameter of 30 mm) and Copper block. Thermocouples were placed at seven locations: three on the copper surface, three in the copper block, and one in the liquid. Thermocouples in the copper block with metal grease were installed to measure the heat flux, and thermocouples on the copper surface were installed to measure the raw data directly, so it was expected to be measured with greater accuracy. Incidentally, all of the thermocouples used in this study were tested and were able to be measured with an accuracy of ±0.05°C.

Figure 4 shows a visualization of the nucleate pool boiling. The long bar in the center is a probe, which sucks up refrigerant and makes it possible to analyze the local mass ratio where boiling occurs. The distance between the probe tip and the copper surface is 6 mm. The wall superheat can be calculated from the saturation temperature measured by thermocouples in the liquid refrigerant and the wall temperature measured by thermocouples attached to the copper surface.

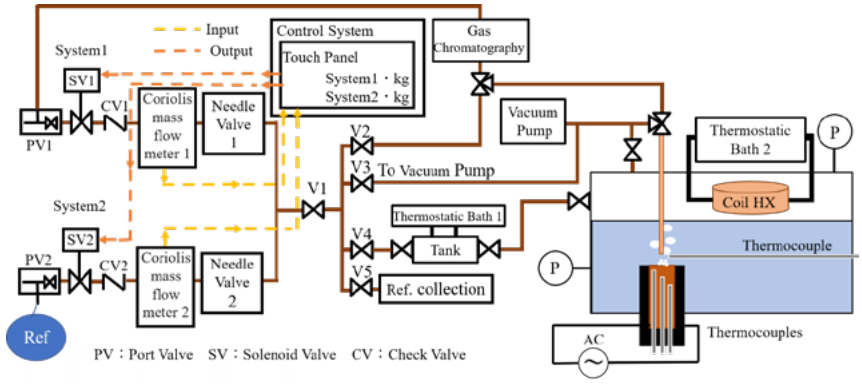


Fig. 1. Schematic diagram of experimental apparatus

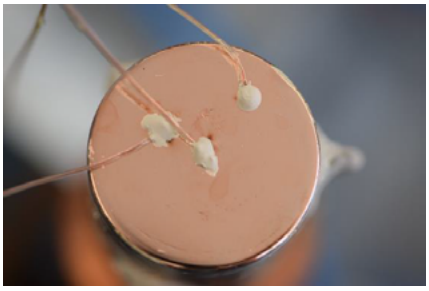


Fig. 2. Test section of copper surface

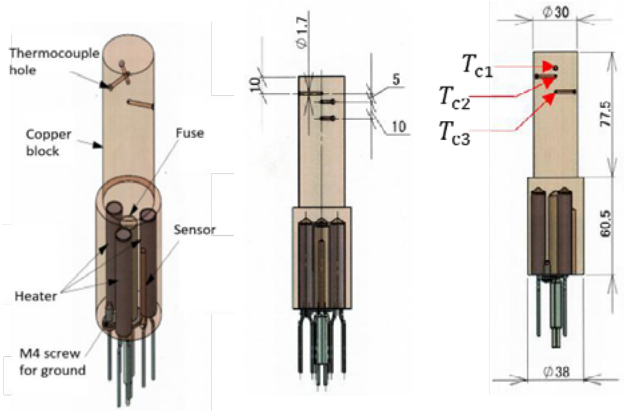


Fig. 3. Test section of copper block

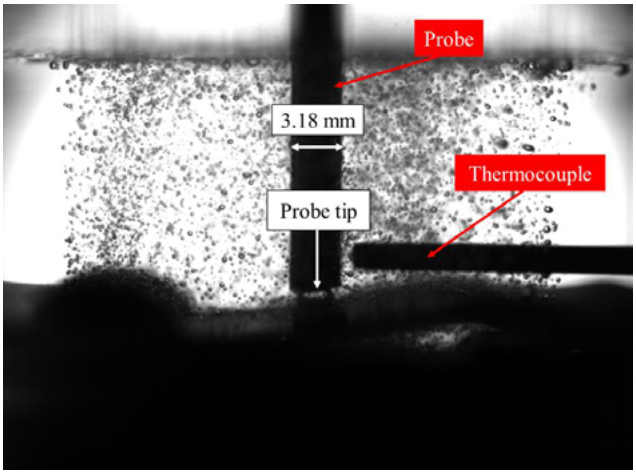


Fig. 4. Visualization of nucleate pool boiling (R 32 / R1234ze(E) (0.7/0.3), $q = 7$ kW/m^2)

2.2. Data reduction methods

The heat flux was calculated by Eq. (1).

$$q = \lambda \frac{dT}{dx} \tag{1}$$

where q and λ are the heat flux of the copper block [W/m^2] and the thermal conductivity of copper [W/mK], respectively. As for dT/dx, it is determined by the temperature gradient [K/m] calculated from the temperature T_{c1}, T_{c2} and T_{c3} measured by the first, second, and third thermocouples from the top inserted in the copper block and the displacement between each thermocouple, as shown in Fig. 5.

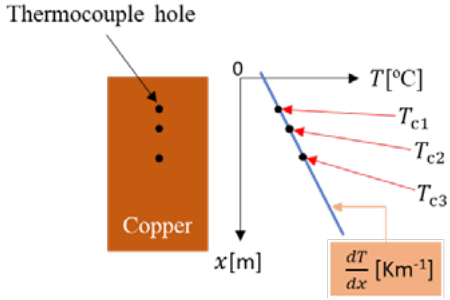


Fig. 5. How to determine heat flux

Using Equation (1), the local heat transfer coefficient is defined as follows:

$$\alpha = \frac{q}{(T_w - T_l)} \tag{2}$$

where α, T_w and T_l are local heat transfer coefficient of the copper surface [W/m^{2}K], the measured temperature of the thermocouple directly mounted on the copper surface [°C], and the temperature measured by the thermocouple in the liquid [°C], respectively. As described in section 2.1, raw data could be obtained by attaching the thermocouple directly to the copper surface, and therefore, more accurate measurements were expected.

When analyzing the local properties of a boiling region using gas chromatography, the mass ratio is calculated as follows:

$$W_{R\,32} = \frac{\frac{w_{R\,32}}{S_{R\,32}} S'_{R\,32}}{\frac{w_{R\,32}}{S_{R\,32}} S'_{R\,32} + \frac{w_{R\,1234ze(E)}}{S_{R\,1234ze(E)}} S'_{R\,1234ze(E)}} \tag{3}$$

$$W_{R\,1234ze(E)} = \frac{\frac{w_{R\,1234ze(E)}}{S_{R\,1234ze(E)}} S'_{R\,1234ze(E)}}{\frac{w_{R\,32}}{S_{R\,32}} S'_{R\,32} + \frac{w_{R\,1234ze(E)}}{S_{R\,1234ze(E)}} S'_{R\,1234ze(E)}} \tag{4}$$

where w and S are mass ratio and peak area determined by gas chromatography before boiling. W and S' are mass ratio and peak area determined by gas chromatography while boiling in optional heat flux. The peak area is automatically analyzed and shown by gas chromatography.

2.3. Investigation of soundness of the experimental equipment

In order to confirm the soundness of the experimental equipment used in this study, a comparison of the experimental data for refrigerant R 32 and R410A with the equation of Jung et al.[14] is shown in Fig. 6. The results were able to predict the experimental data within 8.2% mean deviation and 9.2% standard deviation. These results provide relatively accurate data that will enable reliable measurements of the heat transfer

coefficients for any unknown refrigerant from now on. All properties were obtained from REFPROP 10.0 when using the Jung et al.'s correlation.

Figure 7 shows the results of measuring the mass ratio of the R 32 component of R 410A for each heat flux. Since R 410A is a near-azeotropic refrigerant mixture, it was confirmed that the physical properties near the heat transfer surface didn't change during boiling. On the contrary, different mass ratios were revealed to cause changes in local physical properties.

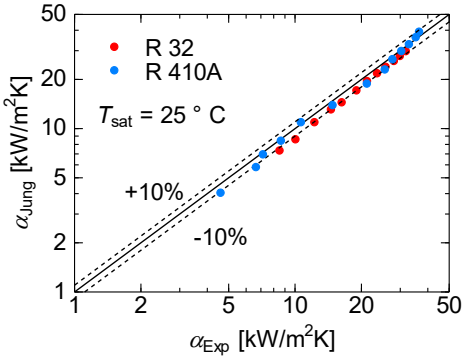


Fig. 6. Comparison of experimental values of R 32 and R 410A with Jung et al.'s correlation

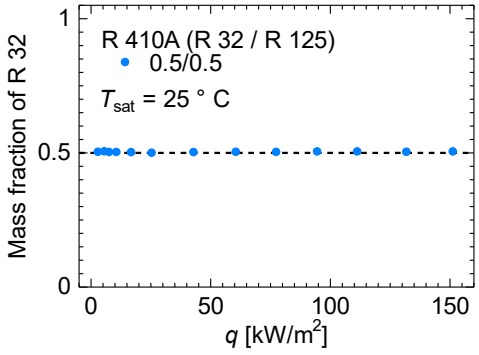


Fig. 7. Mass fraction of R 32 of R 410A

3. Results

In this study, local heat transfer coefficient measurements of pure refrigerants R 32 and R 1234ze(E) and local heat transfer coefficients and mass ratios of the refrigerant mixture R 32 / R 1234ze(E), varying the mixture mass ratio, were measured under the experimental conditions of saturation temperature of 25°C and heat flux of 3 to 100 kW/m^2.

3.1. Local heat transfer coefficients of each refrigerant

Figure 8 shows R 32, R 1234ze(E) and the refrigerant mixture R 32 / R1234ze(E) as heat flux on the horizontal axis and heat transfer coefficient on the vertical axis. As reported by other researchers, a feature of the zeotropic mixtures was found to be a decrease in the amount of increase in heat transfer coefficient decreased with increasing heat flux[10,11]. The reduction in heat transfer coefficient in this zeotropic mixture has been attributed to mass transfer resistance caused by interdiffusion due to the concentration gradient of the mixed refrigerant[2,3,6,7,8,12]. Moreover, the heat transfer coefficient of the nucleate pool boiling of R 32 /

R1234ze(E) was found to be the lowest at a mixing mass ratio of 0.2/0.8. The results are similar to the report that the evaporative heat transfer coefficient was at a minimum value for the mass ratios of refrigerant mixture R 32 / R 1234ze(E) of 0.15/0.85, 0.20/0.80, and 0.25/0.75 for quality 0.2, 0.5, and 0.8, respectively, as shown in the Kondo et al.'s flow experiments[3] and the evaporative heat transfer coefficient was at a minimum value for the mass ratios of refrigerant mixture R 32 / R 1234ze(E) of 0.25/0.75 as shown in the Lee et al.'s flow experiments[4]. The reason why the refrigerant mixture R 32 / R 1234ze(E) of 0.2/0.8 was the lowest heat transfer coefficient will be the subject of future research.

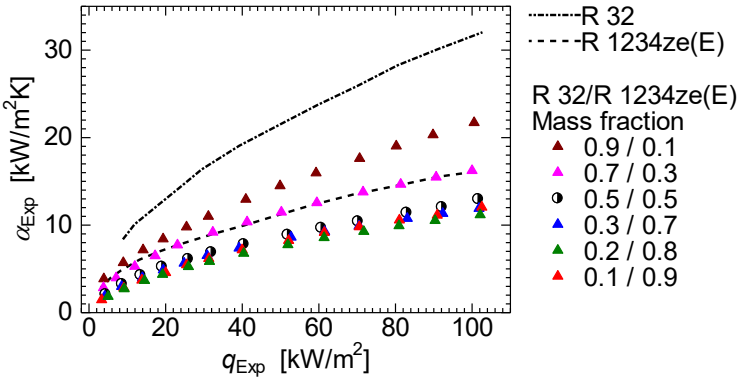


Fig. 8. Local heat transfer coefficients of R 32, R 1234ze(E) and R 32 / R 1234ze(E)

3.2. Mass fraction change of refrigerant mixture R 32 / R 1234ze(E)

Figure 9 shows the local mass fractions of nucleate pool boiling for R 32 and R 1234ze(E) during heat flux measurements for each mixture of R 32 / R 1234ze(E) with different mass ratios. The plot points represent the mean value of the mass ratio and the error bars indicate the range of concentrations that can be taken, i.e. the maximum and minimum values. When the mass ratio of the mixture was biased in favor of one of the refrigerants, there was relatively little variation, but when the mass ratio was close, significant variation was observed. In particular, for the refrigerant mixture R 32 / R1234ze(E) mass ratios of 0.5/0.5, there was an overall decrease in the mass ratio of R 32 and an increase in the mass ratio of R 1234ze(E). In addition, on the whole, in the case of a mass ratio of R 32 below 0.5, the local mass ratio of the boiling region tended to become decrease, and the mass ratio tended to become increase when the mass ratio was greater than 0.5. Comparing the results of Figs. 6 and 8, it was confirmed that the zeotropic refrigerant mixture caused a remarkable change in properties near the heat transfer surface. In addition to the mass transfer resistance, this change in physical properties may have a marked effect on the heat transfer coefficients of an azeotropic mixture.

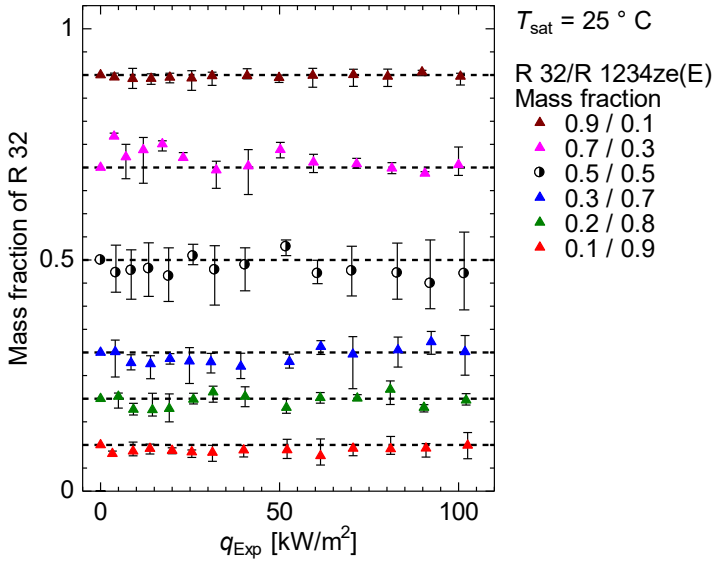


Fig. 9. Mass fraction of R 32 of R 32 / R 1234ze(E)

4. Conclusions

This study measured the pool boiling heat transfer coefficient for R 32, R 1234ze(E) and refrigerant mixture R 32 / R 1234ze(E) and the mass ratio near the heating copper surface for R 32 / R 1234ze(E) under experimental conditions of 25 °C saturation temperature and heat flux from 3 to 100 kW/m^2. Based on the results of this experiment, the following conclusions can be drawn.

1. For all refrigerants, the increase in heat transfer coefficient decreased as the heat flux increased, but for the zeotropic mixtures, the increase was significantly less. Especially, the heat transfer coefficient of the refrigerant mixture R 32 / R 1234ze(E) with a mass ratio of 0.2/0.8 was minimal.
2. In case of a mass ratio of 0.5/0.5 for the refrigerant mixture R 32 / R 1234ze(E), there was a large variation in the mass ratio near the heating surface and a noticeable decrease in the mass ratio of R 32.
3. The variation of the mass ratio near the heating surface that was not observed for the near-azeotropic refrigerant mixture occurred for the zeotropic refrigerant. In zeotropic mixtures, it was clear that the change in properties occurred in the boiling region.

Since there is little information on the local boiling properties of azeotropic refrigerant mixtures, more detailed investigation and further research are needed. We will develop our discussion and research based on these results and conclusions in the future.

Acknowledgements

This study was supported by the New Energy and Industrial Technology Development Organization (NEDO).

Nomenclature

dT/dx	Temperature gradient, K/m
q	heat flux, W/m^2
S	peak area determined by gas chromatography before boiling
S'	peak area determined by gas chromatography while boiling in optional heat flux
T_{c1}	temperatures measured at the first point from the top of the thermocouple inserted in the copper block, °C
T_{c2}	the temperatures measured at the second, °C
T_{c3}	the temperatures measured at the third, °C
T_l	liquid temperature, °C
T_w	wall temperature, °C
w	mass ratio before boiling
W	mass ratio while boiling in optional heat flux.
α	heat transfer coefficient, W/m^{2}K
λ	thermal conductivity, W/mK

References

[1] Ministry of Economy, Trade and Industry, https://www.meti.go.jp/index.html.
[2] Md. Anowar Hossain, Yoji Onaka, Hasan M.M. Afroz, Akio Miyara., 2012. "Heat transfer during evaporation of R1234ze(E), R32, R410A and a mixture of R1234ze(E) and R32 inside a horizontal smooth tube," International Journal of Refrigeration Vol. 36, Issue 2, p. 465-477.
[3] Chieko KONDO, Fumiya MISIMA, Shigeru KOYAMA., 2013 Condensation and Evaporation of Low GWP Refrigerant Mixture R 32/R 1234ze(E) in Horizontal Microfin tubes," Trans. of the JSRAE Vol. 30, No. 4, p. 401-411.
[4] DongChan Lee, Dongwoo Kim, Wonhee Cho, Yongchan Kim., 2019. " Evaporation heat transfer and pressure drop characteristics of R1234ze(E)/R32 as a function of composition ratio in a brazed plate heat exchanger," International Journal of Heat and Mass Transfer Vol. 140, p. 216-226.
[5] Daisuke Jige , Shogo Kikuchi , Naoki Mikajiri , Norihiro Inoue., 2020. "Flow boiling heat transfer of zeotropic mixture R1234yf/R32 inside a horizontal multiport tube," International Journal of Refrigeration Vol. 119, p. 390-400.
[6] Hasan M.M. Afroza, Akio Miyarab, Koutaro Tsubakib., 2008. "Heat transfer coefficients and pressure drops during in-tube condensation of CO2/DME mixture refrigerant," International Journal of Refrigeration Vol.31, p.1458–1466.
[7] Yoji Onaka, Akio Miyara, Koutaro Tsubaki., 2010. "Experimental study on evaporation heat transfer of CO2/DME mixture refrigerant in a horizontal smooth tube," International Journal of Refrigeration Vol. 33, p. 1277-1291.
[8] X. Zou, M.Q. Gong, G.F. Chen, Z.H. Sun, Y. Zhang, J.F. Wu., 2009. "Experimental study on saturated flow boiling heat transfer of R170/R290 mixtures in a horizontal tube," International Journal of Refrigeration Vol. 33, p. 371-380.
[9] Zhi-Qiang Yang, Gao-Fei Chen, Yan-Xing Zhao, Qi-Xiong Tang, Han-Wen Xue, Qing-Lu Song, Mao-Qiong Gong., 2018. "Experimental study on flow boiling heat transfer of a new azeotropic mixture of R1234ze(E)/R600a in a horizontal tube," International Journal of Refrigeration Vol. 93, p. 224-235.
[10] Sun Zhaohu, Gong Maoqiong, Li Zhijian, Wu Jianfeng,. 2007. "Nucleate pool boiling heat transfer coefficients of pure HFC134a, HC290, HC600a and their binary and ternary mixtures," International Journal of Heat and Mass Transfer Vol. 50, Issues 1-2, p. 94-104.
[11] Y.H. Zhao, Y.H. Diao, T. Takaharu., 2008. "Experimental investigation in nucleate pool boiling of binary refrigerant mixtures," Applied Thermal Engineering Vol. 28, Issues 2-3, p. 110-115.
[12] Dongsoo Jung, Kilhong Song, Kwangyong Ahn, Jongkon Kim., 2003. "Nucleate boiling heat transfer coefficients of mixtures containing HFC32, HFC125, and HFC134a," International Journal of Refrigeration Vol. 26, p.764–771.
[13] Jiaji He, Jinping Liu, Xiongwen Xu., 2016. "Analysis and experimental study of nucleation site densities in the boiling of mixed refrigerants," International Journal of Heat and Mass Transfer Vol.105, p.452-463.
[14] Dongsoo Jung, Youngil Kim, Younghwan Ko, Kilhong Song., 2003. "Nucleate boiling heat transfer coefficients of pure halogenated refrigerants," International Journal of Refrigeration Vol. 26, Issue 2, p. 240-248.



13th IEA Heat Pump Conference
April 26-29, 2021 Jeju, Korea

Load-Based Testing Methodology for Evaluating Advanced Heat Pump Control Design

Parveen Dhillon[a*], W. Travis Horton[a], James E. Braun[a]

[a]*Ray W. Herrick Laboratories, School of Mechanical Engineering, Purdue University, West Lafayette, 47907-2099, USA*

Abstract

Optimum control design has been an important aspect of improving the performance, efficiency and thermal comfort delivery of heat pump systems. Despite extensive research work on the development of advanced controls for heat pumps, most heat pump systems in the field still utilize simple controls such as PI (Proportional-Integral), cascaded PI, etc. One of the main reasons for this is the difficulty in assessing the actual improvement in energy performance and thermal comfort delivery of heat pumps with advanced controls. The current practice of performing extensive season-long field studies is time-consuming and requires significant resources to carry out. Also, the performance results of these field studies are limited to the test building type and local climate conditions. To overcome this problem, a load-based testing methodology has been developed to evaluate the performance of advanced heat pump control design for different building types and climate zones in a psychrometric test facility. This methodology provides a way for product developers to significantly accelerate the development of advanced control design and to obtain realistic performance assessments in a timely manner. In this paper, the load-based testing approach is demonstrated for performance assessment of two different control algorithms for a residential heat pump. In addition, the effect of equipment oversizing and undersizing on heat-pump performance is studied utilizing the test approach.

Keywords: Load-based Testing; Performance Evaluation; Control Design; Heat Pump

1. Introduction

In recent years, the increase in microprocessor computing power and decrease in hardware cost have facilitated an opportunity for implementing more advanced controls in heat pump and air-conditioning systems. Even though these improvements lead to more efficient system operation, only a very small fraction of residential air conditioners and heat pumps currently sold in the U.S. market utilize advanced high-efficiency controls [1]. One of the primary reasons for this is the difficulty in evaluating short-term and seasonal performance improvements with advanced controls in a timely and cost-effective manner. To address this issue, a load-based testing methodology has been developed, which allows qualitative and quantitative evaluations of equipment performance with different embedded control designs for representative buildings and climate conditions using tests performed in a laboratory facility. With this methodology, it is also possible to study how equipment performance varies with oversizing or undersizing for a building. The developed methodology can further be used as a basis for seasonal performance ratings of air-conditioning and heat-pumping equipment as presented in [2], [3] and [4].

The load-based testing methodology emulates the response of building sensible and latent loads to the equipment controls in a psychrometric test chamber by continuously updating the room temperature and humidity based on a virtual building model. The test unit thermostat naturally responds to this dynamic temperature variation and controls the equipment in response to a deviation from its setpoint. This method can

* Corresponding author.
E-mail address: dhillonparveen14@gmail.com

capture realistic performance of a heat pump in a psychrometric test chamber, similar to a field application. In this way, load-based testing can be implemented to quantify performance differences among different equipment control architectures in a lab-setup and also qualitatively study the dynamic performance and comfort delivery of the equipment. This testing methodology can be applied to both variable-speed as well as staged equipment.

The method is based on an approach presented by Hjortland & Braun [5] for performance characterization of fixed-speed and variable-speed unitary air-conditioning equipment. Patil *et. al.* [2] and Cheng *et. al.* [6] applied the load-based testing methodology to generate data for estimating seasonal performance of variable-speed residential heat pumping and air conditioning equipment. In the current paper, the load-based testing methodology is implemented to perform a qualitative and quantitative comparison of the dynamic performance of a variable-speed heat pump in cooling mode in terms of energy efficiency and comfort delivery. The impact of two different control modes is considered along with equipment undersizing and oversizing.

To capture the dynamic performance of equipment that is representative of field applications with this methodology, it is important to have a representative virtual building model and representative outdoor ambient conditions. Also, to allow for testing different size heat pumps, the virtual building model needs to be scalable with equipment rated capacity. In this study, the load-based testing methodology was implemented on a 5-ton residential heat pump with an appropriately scaled virtual building model. The study considered only cooling mode performance for typical mid-summer and peak-summer season days with representative daily outdoor temperature profiles.

2. Load-Based Testing Overview

The load-based testing methodology captures the holistic performance of an equipment including its thermostat and integrated controls in a test facility setup. Fig. 1 outlines the layout of the load-based test approach of a split-type heat pump system installed in two side-by-side psychrometric chambers.

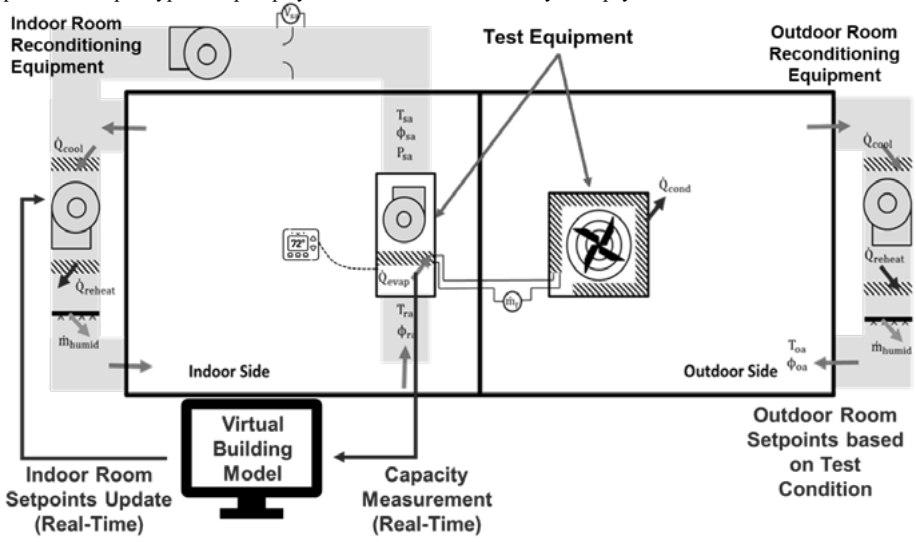


Fig. 1. Load-Based Testing Schematic of a Split-type Heat Pump System

As shown in Fig. 1, in this methodology, the equipment capacity is measured in real-time and fed into a virtual building model. The virtual building model estimates the building load based on the current indoor and outdoor conditions. Then, based on the difference in the equipment capacity and building load, the virtual building temperature and humidity are updated according to the virtual building thermal and moisture dynamics. The updated virtual building conditions are then provided as setpoints to the indoor psychrometric room reconditioning system. In this way, the response of a virtual building is emulated in the indoor-side test room. The outdoor test room conditions are varied according to a representative temperature profile according to climate and season.

In cooling mode tests, when the equipment sensible capacity is more than the sensible building load, the indoor room temperature decreases; whereas, the indoor room temperature increases when the capacity is lower than the load. Similarly, the indoor room humidity varies based on the virtual building latent load and the equipment latent capacity. The test unit thermostat senses this dynamic variation of indoor space temperature and humidity, and to maintain the indoor conditions to the thermostat setpoint, the equipment responds to this variation based on its integrated controls. This enables the load-based testing methodology to capture an overall dynamic performance of equipment that is representative of a field application.

The virtual building model can be defined based on the desired complexity of the representative building for the underlining experimental study. Hjortland & Braun [5] and Patil *et. al.* [2] described a virtual building model for a representative residential building that was employed for the experimental study presented here.

The virtual building model calculates the building sensible heat gain to the air or load scaled according to the equipment rated sensible capacity ($\dot{Q}_{cool,s,D}$) at design conditions as per the equation (1).

$$\dot{Q}_{load,s} = \frac{1}{F} \cdot \frac{\dot{Q}_{cool,s,D}}{\left(T_{OD,D} - T_{Bal,D}\right)} \cdot \left(T_{OD} - T_{Bal}\right) \tag{1}$$

where the building-load sizing factor (F) is used to scale the building load, based on the equipment sizing for a building. For example, for the case of F equal to 1.25 which makes $1/F$ 0.8 i.e. building load which the equipment meets is 80% of the load for which equipment is designed, so in this case, the equipment is 20% oversized. The effective balance point temperature (T_{Bal}) is updated according to equation (2) based on the current indoor temperature (T_{ID}) and the indoor target temperature ($T_{ID,SP}$) which is also the equipment thermostat temperature setpoint. This formulation accounts for the change in building load due to variations in the indoor temperature from its design conditions.

$$T_{Bal} = T_{Bal,D} + \left(T_{ID} - T_{ID,SP}\right) \tag{2}$$

The virtual building latent energy gain or load is calculated using a constant sensible heat ratio model for the representative building as per equation (3).

$$\dot{Q}_{load,l} = \dot{Q}_{load,s} \cdot \left(\frac{1}{SHR_{building}} - 1\right) \tag{3}$$

Then based on the virtual building loads and equipment measured capacities, the virtual building temperature and humidity ratio are updated for the next time step as per equation (4) and (5), which are supplied as the indoor test room setpoints that are controlled by the reconditioning system.

$$T_{ID}(t + \Delta t) = T_{ID}(t) + \Delta t \cdot \left(\frac{\dot{Q}_{load,s} - \dot{Q}_{cool,s}}{C_s}\right) \tag{4}$$

$$\omega_{ID}(t + \Delta t) = \omega_{ID}(t) + \Delta t \cdot \left(\frac{\dot{Q}_{load,l} - \dot{Q}_{cool,l}}{h_{fg} \cdot C_w}\right) \tag{5}$$

where the sensible (C_s) and moisture (C_w) capacitances for a representative residential building are scaled with the equipment capacities at design conditions using equation (6) and (7) respectively.

$$C_s[J/°\mathrm{F}] = \frac{\dot{Q}_{cool,s,D}[W] \cdot 150[s]}{\Delta T_{tstat,db}[°\mathrm{F}]} \tag{6}$$

$$C_w[kg] = \frac{\dot{Q}_{cool,D}[W]}{12.9[W/kg]} \tag{7}$$

Based on the equations (1)-(7), the virtual building model continuously controls the indoor test room conditions to emulate the response of a representative building to the equipment performance. The first step in

load-based testing is to measure the equipment rated sensible and latent capacity at design conditions and use them to scale the virtual building parameters. This measurement is done using a steady-state test with constant indoor and outdoor test room conditions and the equipment running at maximum capacity.

3. Experimental Method

For each test, the outdoor temperature is varied according to a typical daily temperature profile for the season considered. For a representative mid-summer day, the outdoor temperature is varied between 65°F (18.33°C) and 85°F (29.45°C). For a peak-summer day, the outdoor temperature is varied between 85°F (29.45°C) and 105°F (40.56°C). The representative hourly outdoor temperature profiles were generated based on Erbs *et. al.* [7] and Mitchell & Braun [8] as per equation (8).

$$T_{OD} = \left(T_{OD,max} - \frac{(T_{OD,max} - T_{OD,min})}{2}\right) + (T_{OD,max} - T_{OD,min}) \cdot [0.4632\, cos(\tau - 3.8051) + 0.0984\, cos(2\tau - 0.360) + 0.0168\, cos(3\tau - 0.822) + 0.0138 cos\,(4\tau - 3.513)] \quad (8)$$

where,

$$\tau = \frac{2\pi(2.4 \cdot t - 1)}{24}; t: time\ of\ day\ in\ hours \quad (9)$$

Equation (9) was modified to compress the complete daily temperature change from 24 hours to 10 hours to accelerate the testing. This is reasonable because the dynamic response of the equipment with its integrated controls is still orders of magnitude faster than the dynamic variation of the outdoor temperature. Fig. 2 shows the derived typical outdoor temperature profile for the emulated mid-summer and peak-summer days.

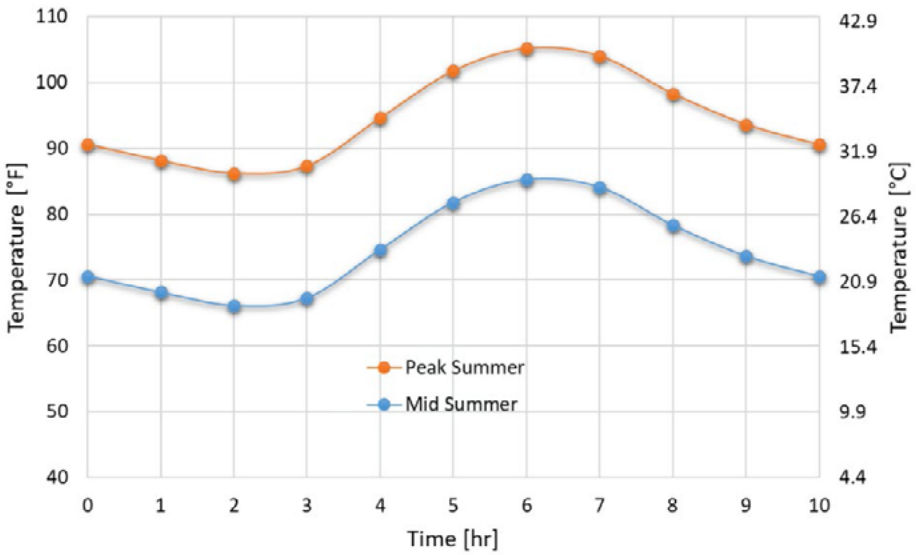


Fig. 2. Representative Outdoor Temperature Profile for Mid-Summer and Peak-Summer Day

The equipment was tested with two different control modes: A and B; three different equipment sizing scenarios: nominal, undersizing and oversizing; and for the two representative cooling season days: mid-summer and peak-summer. Table 1 outlines the test matrix for the experimental study conducted in this paper.

Table 1. Test Matrix for the Experimental Study of the Heat-Pump

Test	Cooling Season Day	Equipment Sizing	Control Mode
0	Baseline Steady-State Test at Design Conditions		
1	Peak-Summer	Nominal	A
3	Peak-Summer	Nominal	B
2	Mid-Summer	Nominal	A
4	Mid-Summer	Nominal	B
5	Mid-Summer	Oversize (20%)	A
6	Mid-Summer	Oversize (20%)	B
7	Peak-Summer	Oversize (20%)	B
8	Mid-Summer	Undersize (20%)	A
9	Mid-Summer	Undersize (20%)	B
10	Peak-Summer	Undersize (20%)	B

To scale the virtual building parameters for the heat-pump under investigation, first, rated capacity is measured through a baseline steady-state test conducted at the cooling design conditions (Table 2) using a thermostat setpoint such that the equipment providTable 7. Average of thickness of liquid film es maximum cooling capacity.

Table 2. Cooling Design Conditions

Indoor Conditions		Outdoor Conditions
Temperature	Relative Humidity	Temperature
75°F (23.8°C)	50%	95°F (35°C)

Based on the equipment performance at design conditions, the virtual building parameters were derived for the heat pump being studied as shown in Table 3.

Table 3. Virtual Building Parameters

Parameter	F			$\dot{Q}_{cool,s,D}$	$\dot{Q}_{cool,D}$	$T_{OD,D}$	$T_{Bal,D}$
	Nominal	Oversize (20%)	Undersize (20%)	W	W	°F (°C)	°F (°C)
Value	1	1.25	0.83	12850.6	15192.6	95 (35)	62 (16.6)
Parameter	$T_{ID,SP}$	$RH_{ID,SP}$	C_s	C_w	$\Delta T_{tstat,db}$	$SHR_{building}$	Δt
	°F (°C)	%	$J/°F\,(J/°C)$	kg	°F (°C)	-	second
Value	75(23.8)	50	1927596 (1070887)	1177.7	1 (0.56)	0.8	1

For each test, the first two hours were used as a warm-up period for the equipment. In these two hours, the outdoor temperature was kept constant to the 2nd hour temperature (Fig. 2); and indoor conditions were kept constant at target comfort conditions of $75°F\,(23.8°C)$ and 50% RH. Following this, the outdoor room temperature varied according to the defined temperature profile from the 2nd to 10th hour (Fig. 2). During these tests, the indoor temperature and humidity setpoints for the reconditioning system were updated continuously according to the virtual building model response, as outlined in section 2, utilizing the parameters from Table 3. In this way, the equipment dynamic performance was captured for an 8-hour test duration. The test unit performance results were analyzed only for this 8-hour duration when the outdoor temperature was varying. The results are presented in section 5.

In order to compare comfort delivery for the different strategies during cooling load-based tests, comfort violation limits were defined. Based on [9], a temperature limit of 2°F higher than the target indoor temperature setpoint, i.e. 77°F, was established. In addition, relative humidity of 10% higher than a target indoor relative humidity setpoint, i.e. 60%, was selected. The total time-duration that the heat-pump failed to maintain these limits was determined for temperature and humidity comfort individually and used as a measure of discomfort.

4. Test Setup Layout

The load-based testing was implemented at Purdue University on a split-type heat-pump system using two side-by-side psychrometric test chambers at the Ray W. Herrick Laboratories. Fig. 1 shows the layout of the system installation in the test facility, along with an outline for controlling the indoor and outdoor test room conditions during dynamic testing. Fig. 3 illustrates the schematic of the heat pump system along with the air, refrigerant, and power side measurements. The heat-pump was installed in the test rooms based on ASHRAE guidelines for performance measurement as outlined in [10], [11], [12], [13], [14], [15] and [16]. The indoor unit return and supply air temperatures were measured using a thermocouple grid, and humidities were measured using a chilled mirror dew point hygrometer. The indoor unit supply air volumetric airflow was measured using a nozzle box code-tester that was used to calculate the air-side sensible and latent capacity with the air-enthalpy method. To verify the air-side measurements, refrigerant side capacity was also measured. For this, refrigerant mass flow rate was measured using a Coriolis-effect based mass flow meter installed in the liquid line. In addition, pressure and temperature sensors were installed to measure the refrigerant side properties at different state points of the cycle as shown in Fig. 3. Furthermore, two power-meters were installed to measure the indoor and outdoor unit power consumption.

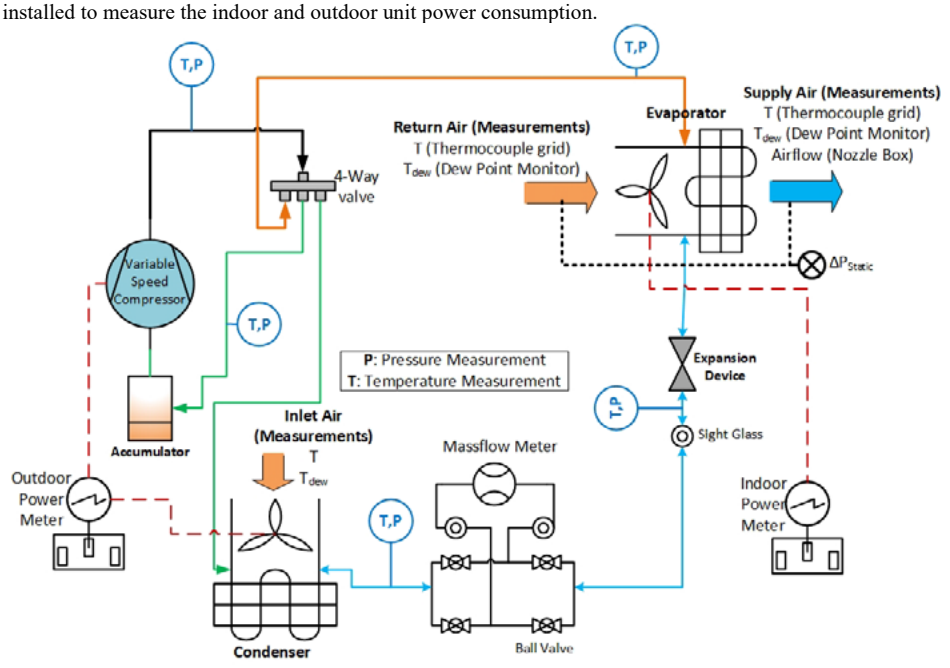


Fig. 3. Test Heat-Pump Schematic with the Air, Refrigerant, and Power Side Measurements

5. Results

Fig. 4 presents the performance of the heat pump for 8-hour dynamic test duration on a typical mid-summer day with nominal equipment sizing for control mode A. The upper subplot shows the equipment performance variation with time, including the virtual building load (sensible and latent), the heat-pump capacity (sensible and latent), and the equipment total power consumption. The lower subplot illustrates the virtual building and test rooms temperature and relative humidity variation for the test duration. In the lower subplot, the left vertical axis corresponds to the indoor virtual building (dotted line) and indoor test room (solid line) temperature and relative humidity; whereas, the right vertical axis corresponds to outdoor temperature variation.

As can be seen from Fig. 4, the virtual building outdoor temperature changed between 65°F and 85°F for this representative mid-summer day. When the heat-pump cycled on/off, the outdoor temperature fluctuated around the setpoint (Virtual Building ODT) which is due to the sudden changes in capacity requirement from

the test room reconditioning system. This could be overcome by fine-tuning the test room controller gains and updating architecture, but for this study, these modifications were not implemented due to time constraints.

The test unit thermostat was set at the target comfort conditions of 75°F (black dotted line); however, for this equipment, there is no provision to set a target humidity setpoint. Subsequently, the indoor temperature and humidity varied based on the interaction of the equipment thermostat controls with the virtual building load. When the building sensible load (red dotted line) is higher than the equipment sensible capacity (green solid line), the indoor temperature (blue solid line) increases; whereas, when the heat-pump sensible capacity is higher than the building sensible load, the indoor temperature decreases. Similarly, the indoor humidity varies based on the difference in the latent load (orange dotted line) and the latent capacity (sky-blue solid line).

In this test, the virtual building indoor temperature varied between 71°F and 76.4°F, and relative humidity varied between 49.7% to 64%. For moderate day, this variable-speed equipment cycled on and off throughout the day based on the thermostat interaction with the changing indoor temperature and demonstrated a behavior effectively similar to a single-stage system. As the outdoor temperature increased, correspondingly, the building load increased and to compensate for this higher load, the heat-pump run-time fraction for a cycle increased. The equipment was able to maintain the indoor temperature within comfort levels (<77°F) for the complete duration of the test; however, it failed to maintain the humidity within the comfort limit (<60%) for some duration around the 2nd hour and towards the end from the 7th hour onwards. Also, Fig. 4 reveals that the system maintained the indoor temperature below the thermostat setpoint for most of the time and the indoor temperature variation band was larger than ±1°F around the thermostat setpoint, which might be due to its inbuilt offset and dynamics. These results illustrate the ability of the test methodology to capture the dynamic interaction of the equipment, its controls, and the building load. On a side note, the building load does not follow the exact profile as of the outdoor temperature variation, because of the dependence of building load on indoor temperature deviations from its target design conditions.

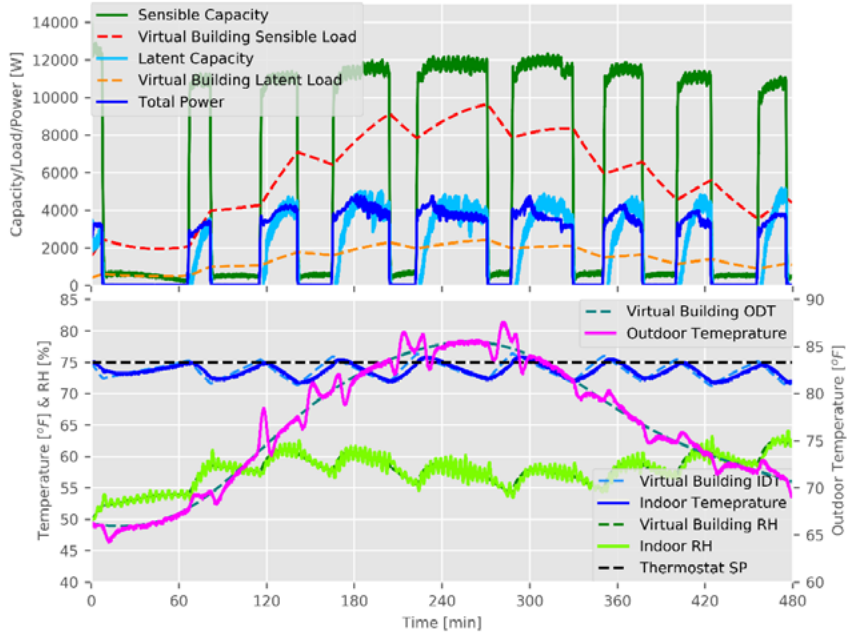


Fig. 4. Equipment Dynamic Performance on a Mid-summer Day with Nominal Equipment Sizing and Control Mode A

Fig. 5 presents the equipment performance for a peak-summer day with control mode A and nominal equipment sizing. Initially, when the ambient temperature was relatively low, the heat-pump cycled on/off and was able to maintain the indoor temperature around its setpoint; however, as the outdoor temperature increased, the equipment ran at full capacity and failed to compensate for the larger building load leading to indoor temperatures that rose above the comfort limits. However, the equipment was able to maintain the relative

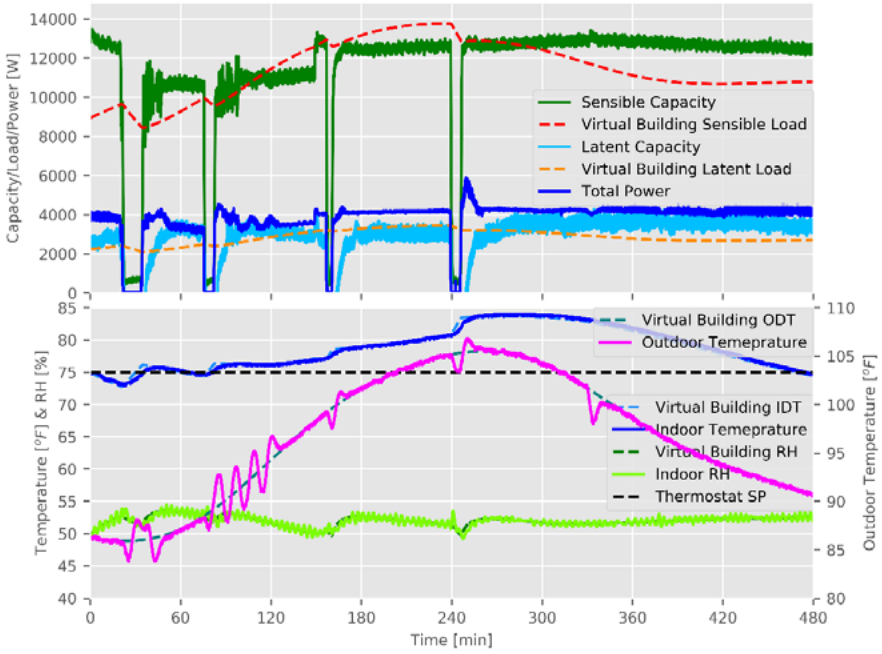


Fig. 5. Equipment Dynamic Performance on a Peak-summer Day with Nominal Equipment Sizing and Control Mode A

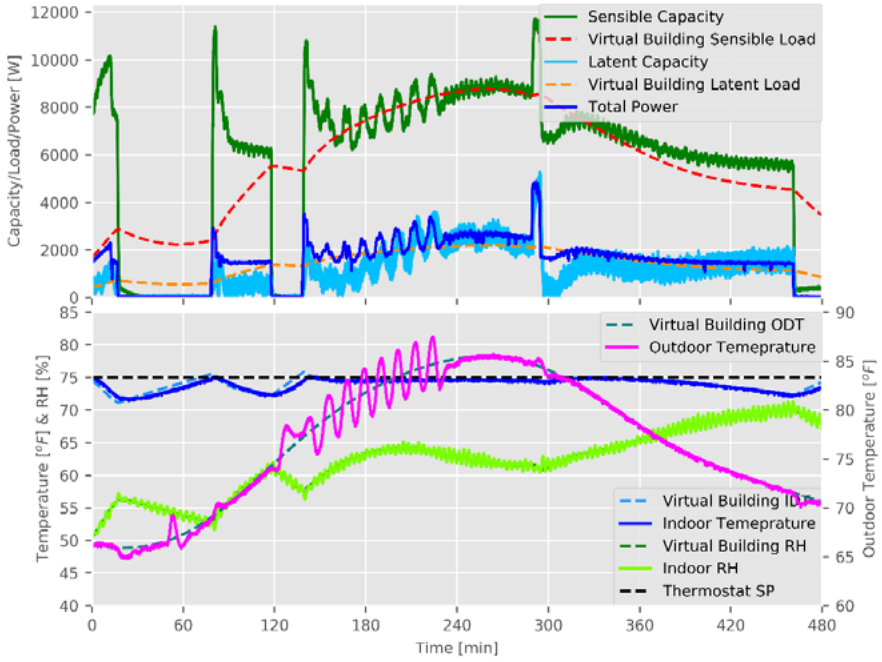


Fig. 6. Equipment Dynamic Performance on a Mid-summer Day with Nominal Equipment Sizing and Control Mode B

humidity within comfort limits, which can be attributed to a smaller sensible heat ratio of the evaporator coil at full compressor speed. These results illustrate the consequences of not properly sizing the equipment for the design conditions. The other interesting observation is that the equipment cycled off at some conditions even when the indoor temperature was well above the thermostat setpoint, which might be due to some inbuilt features in the equipment controls. These types of control issues and their impact on performance can be identified in the laboratory through load-based testing prior to deployment in the field.

The heat-pump performance was also evaluated with a 2nd controller design (control mode B). Fig. 6 shows the results of a test with control mode B for a mid-summer day and nominal equipment sizing. At the start, when the outdoor temperature was low i.e. the building load was low, the equipment cycled on/off similar to the case of control mode A (Fig. 4), although with lower power consumption and longer cycle duration compared to control mode A. Next, as the outdoor temperature increased the system ran continuously in variable speed mode rather than cycling on/off as with control mode A. Then the system cycled off again at low ambient temperature towards the end. The equipment was able to maintain the indoor temperature steadily around the thermostat setpoint instead of oscillating around the setpoint as occurred with control mode A (Fig. 4). However, in this control mode B, the heat-pump failed considerably to keep the indoor humidity within comfort levels compared to control mode A. These results illustrate the usefulness of the load-based test approach in comparing the dynamic performance and comfort delivery of a system with different controller designs.

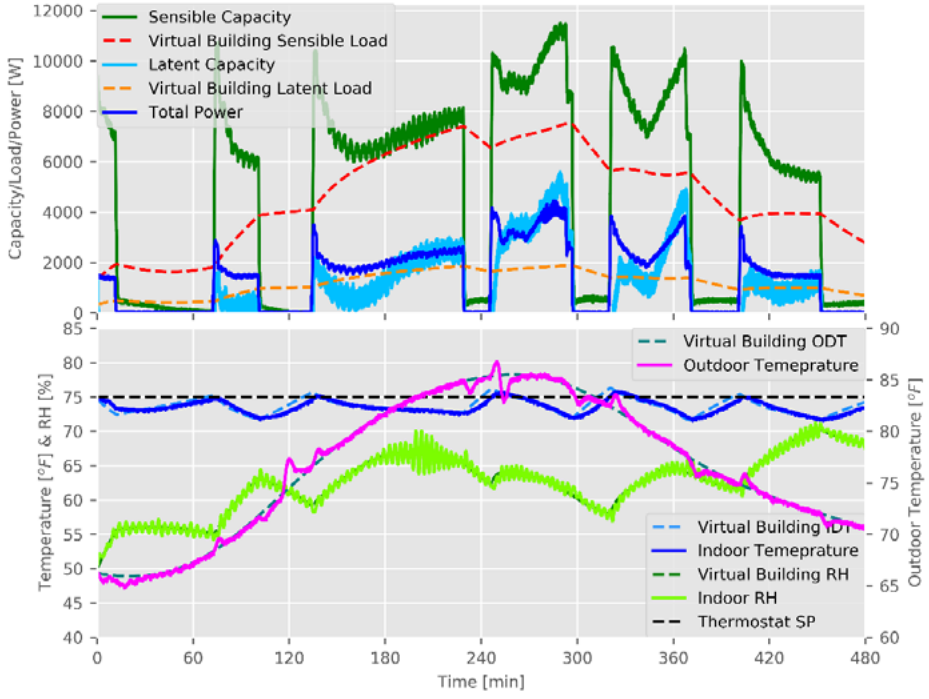


Fig. 7. Equipment Dynamic Performance on a Mid-summer Day with Equipment Oversizing and Control Mode B

Heat-pump performance was also evaluated for the case of equipment oversizing and undersizing. Fig. 7 and Fig. 8 illustrate the test results for the equipment oversizing and undersizing cases respectively, for a mid-summer day with control mode B. In the case of equipment oversizing (Fig. 7), where the building load was smaller compared to nominal sizing for the same ambient conditions, the equipment cycled on/off during the entire time, in contrast to the continuous operation in case of nominal sizing (Fig. 6). For equipment undersizing (Fig. 8), where building load was higher compared to nominal sizing, the heat-pump ran continuously for most of the time, similar to nominal sizing case (Fig. 6), but with higher power consumption to compensate for the larger building load. As observed earlier, when equipment is cycling on/off, as in case

of oversizing, the indoor temperature oscillations are relatively large around the thermostat setpoint, which can be uncomfortable for occupants; whereas, in the undersizing case with continuous equipment operation, the system was able to maintain indoor temperature more steadily around the setpoint. Nonetheless, with control mode B, the equipment was not able to provide humidity comfort for both the undersizing and oversizing cases.

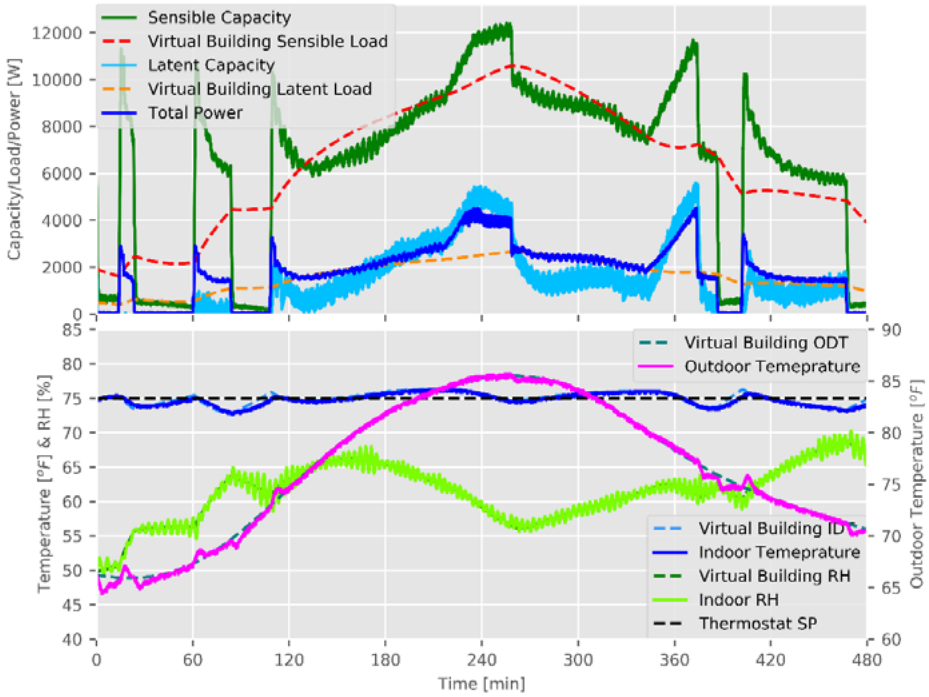


Fig. 8. Equipment Dynamic Performance on a Mid-summer Day with Equipment Undersizing and Control Mode B

Table 4 and Table 5 show overall performance results for the 10 different combination cases of the season (mid-summer & peak-summer), equipment sizing (nominal, oversize, & undersize) and control mode (A & B). Table 4 presents the integrated equipment capacity, building load, power consumption, and COP for the 8-hour dynamic load-based tests. For the same season and equipment sizing scenario, the integrated virtual building sensible and latent loads are comparable for both control modes. There is a slight difference, because with different control modes, the indoor temperature varies differently, which then propagates to the building load. The results show that as the ambient temperature increases in peak-summer season, the system average COP decreases. Furthermore, with the same ambient conditions and equipment sizing, the system performs more efficiently with control mode B. In addition, for mid-summer season, with control mode A, the equipment efficiency improves with oversizing and worsens with undersizing; whereas, the contrary happens with control mode B.

Table 5 summarizes the comfort delivery performance of the equipment for the different tests. It indicates the total number of hours, out of the 8-hour test duration, that the system is not able to maintain the indoor temperature and humidity within comforts limits for cooling, which were 77°F for temperature and 60% for relative humidity. Table 5 also shows the minimum and maximum virtual building temperature and relative humidity for each test. The system failed to maintain the temperature comfort for most of the peak-summer season tests. This was particularly extreme at high load periods with equipment undersizing. In the mid-summer season, even though the temperature comfort levels were mostly maintained, the humidity comfort was violated in both control mode A and B for all three equipment sizing scenarios. In addition, the humidity comfort violation duration with control mode B was more than twice the period in case of control mode A. So, although the control mode B is better from an energy consumption perspective, humidity comfort is sacrificed.

Table 4. Building Load, Cooling Rate, and Power Consumption Performance Results

Test	Season	Equipment Sizing	Control Mode	Virtual Building Sensible Load	Sensible Capacity	Virtual Building Latent Load	Latent Capacity	Power Consumption	System COP
				Integrated					Average
				kWh	kWh	kWh	kWh	kWh	-
1	Peak-Summer	Nominal	A	89.02	90.95	22.25	21.70	29.88	3.77
2	Peak-Summer	Nominal	B	91.66	93.43	22.91	21.35	29.34	3.91
3	Mid-Summer	Nominal	A	41.13	49.25	10.28	9.89	14.95	3.96
4	Mid-Summer	Nominal	B	40.35	44.17	10.09	8.30	11.40	4.60
5	Mid-Summer	Oversize (20%)	A	31.97	41.04	7.99	8.13	12.90	3.81
6	Mid-Summer	Oversize (20%)	B	32.51	38.47	8.13	6.09	10.54	4.23
7	Peak-Summer	Oversize (20%)	B	76.66	79.72	19.16	17.86	27.46	3.55
8	Mid-Summer	Undersize (20%)	A	42.90	52.77	10.73	10.88	15.86	4.01
9	Mid-Summer	Undersize (20%)	B	44.67	51.87	11.17	10.00	13.89	4.46
10	Peak-Summer	Undersize (20%)	B	97.66	92.97	24.41	20.09	29.38	3.85

Table 5. Comfort Delivery Performance Results

Test	Season	Equipment Sizing	Control Mode	Temperature Comfort Violation	Humidity Comfort Violation	Virtual Building Temperature		Virtual Building Relative Humidity	
				Total	Total	Min	Max	Min	Max
				Hour	Hour	°F	°F	%	%
1	Peak-Summer	Nominal	A	4.28	0.00	72.7	83.6	49.7	53.5
2	Peak-Summer	Nominal	B	3.64	0.00	73.3	81.6	49.8	59.9
3	Mid-Summer	Nominal	A	0.00	2.38	71.0	76.4	49.7	64.0
4	Mid-Summer	Nominal	B	0.00	6.36	71.1	75.8	49.8	70.1
5	Mid-Summer	Oversize (20%)	A	0.00	3.48	71.2	76.8	49.9	65.5
6	Mid-Summer	Oversize (20%)	B	0.00	6.86	71.1	76.3	49.8	71.5
7	Peak-Summer	Oversize (20%)	B	0.12	0.62	72.1	77.4	50.0	60.7
8	Mid-Summer	Undersize (20%)	A	0.19	2.43	71.4	77.6	49.4	65.8
9	Mid-Summer	Undersize (20%)	B	0.00	6.25	72.7	76.3	49.7	69.5
10	Peak-Summer	Undersize (20%)	B	5.45	0.00	75.0	86.2	49.2	57.1

6. Summary and Conclusions

This paper presents the application of a new load-based testing methodology for evaluating the dynamic performance of a residential heat-pump system under conditions that are similar to a field application. First, an overview of the approach was provided along with a representative residential virtual building mathematical model, followed by the experimental study method and the representative outdoor ambient conditions for this investigation. Testing of the heat-pump was limited to cooling mode and equipment dynamic performance was measured for various scenarios based on a combination of two different representative summer days, two different control modes, and three distinct equipment sizing situations. The results illustrate the benefits of load-based testing in assessing the qualitative and quantitative effect of different ambient conditions, control design, and equipment sizing on the equipment performance from efficiency as well as comfort perspective. For example, one of the control modes was observed to be more energy efficient but failed to maintain indoor humidity comfort levels. In this way, the methodology provides a way to evaluate realistic equipment dynamic performance in a test-facility environment much more quickly and at a much lower cost than would be possible

for field testing. The methodology can be readily used for different building types and climate locations of interest by updating the virtual building model and ambient conditions accordingly. This can be advantageous in accelerating the development and assessment of advanced controls, diagnostics, and other features.

7. Nomenclature

Variable	Description	Variable	Description
$\dot{Q}_{load,s}$	ng sensible load [W]	F	building load sizing factor [-]
$\dot{Q}_{cool,s,D}$	equipment design sensible capacity [W]	$T_{OD,D}$	the outdoor dry-bulb temperature at design condition [°C]
$T_{Bal,D}$	n balance point temperature [°C]	T_{OD}	outdoor dry-bulb temperature [°C]
T_{Bal}	effective balance point temperature [°C]	T_{ID}	virtual building indoor dry-bulb temperature [°C]
$T_{ID,SP}$	indoor temperature comfort condition (test unit thermostat setpoint) [°C]	$RH_{ID,SP}$	target indoor humidity comfort condition (test unit thermostat setpoint) [%]
$\dot{Q}_{load,l}$	ng latent load [W]	Δt	update time-step [s]
ω_{ID}	l building indoor humidity ratio $[kg_{water}/kg_{dryair}]$	h_{fg}	the heat of vaporization of water [J/kg]
$\dot{Q}_{cool,s}$	ment sensible cooling capacity [W]	$\dot{Q}_{cool,l}$	equipment latent cooling capacity [W]
C_s	l building sensible capacitance [J/°C]	C_w	virtual building moisture capacitance [kg]
$\Delta T_{tstat,db}$	ostat deadband [°C]	$\dot{Q}_{cool,D}$	equipment design total capacity [W]
RH	relative humidity [%]	$SHR_{building}$	building sensible heat ratio [-]
COP	coefficient of performance [-]	IDT	indoor temperature [°C or °F]

Acknowledgments

The authors would like to acknowledge the Herrick Lab's engineering technician - Frank Lee, research associate - Orkan Kurtulus, and graduate students - Vatsal Shah, Weigang Hou, and Jie Ma, for their help in the experiment work.

References

[1] ACEEE, "2019 Efficiency Programs : Promoting High- Efficiency Residential Air Conditioners and Heat Pumps," *ACEEE*, 2019.
[2] A. Patil, A. L. Hjortland, L. Cheng, P. Dhillon, J. E. Braun, and W. T. Horton, "Load-based Testing to Characterize the Performance of Variable-Speed Equipment," 2018, [Online]. Available: https://docs.lib.purdue.edu/iracc/2076.
[3] P. Dhillon, A. Patil, L. Cheng, J. E. Braun, and W. T. Horton, "Performance Evaluation of Heat Pump Systems Based on a Load-based Testing Methodology," 2018, [Online]. Available: https://docs.lib.purdue.edu/iracc/2077.
[4] CSA, *CSA EXP07:19 Load-based and climate-specific testing and rating procedures for heat pumps and air conditioners*. 2019.
[5] A. L. Hjortland and J. E. Braun, "Load-based testing methodology for fixed-speed and variable-speed unitary air conditioning equipment," *Sci. Technol. Built Environ.*, vol. 25, no. 2, pp. 233–244, 2019, doi: 10.1080/23744731.2018.1520564.
[6] L. Cheng, P. Dhillon, W. T. Horton, and J. E. Braun, "Automated laboratory load-based testing and performance rating of residential cooling equipment," *Int. J. Refrig.*, vol. 123, pp. 124–137, 2021, doi: 10.1016/j.ijrefrig.2020.11.016.
[7] D. G. Erbs, W. A. Beckman, and S. A. Klein, "Estimation of degree-days and ambient temperature bin data from monthly-average temperatures," *ASHRAE J.; (United States)*, 1983.
[8] J. W. Mitchell and J. E. Braun, *Principles of heating, ventilation, and air conditioning in buildings*. John Wiley & Sons, 2012.
[9] A. ASHRAE, "Standard 55-2017 Thermal environmental conditions for human occupancy," *ASHRAE Stand.*, 2017.
[10] ASHRAE, "ANSI/ASHRAE Standard 37-2009 (RA 2019). Methods of Testing for Rating Electrically Driven Unitary Air-Conditioning and Heat Pump Equipment." ASHRAE, 2019.
[11] ASHRAE, "ANSI/ASHRAE Standard 41.1-2013. Standard Method for Temperature Measurement." ASHRAE, 2013.
[12] ASHRAE, "ANSI/ASHRAE Standard 41.6-2014. Standard Method for Humidity Measurement." ASHRAE, 2014.
[13] ASHRAE, "ANSI/ASHRAE Standard 41.2-2018. Standard Methods for Air Velocity and Airflow Measurement." ASHRAE, 2018.
[14] ASHRAE, "ANSI/ASHRAE Standard 41.10-2013. Standard Methods for Refrigerant Mass Flow Measurement Using Flowmeters." ASHRAE, 2013.
[15] ASHRAE, "ANSI/ASHRAE Standard 41.3-2014. Standard Methods for Pressure Measurement." ASHRAE, 2014.
[16] ASHRAE, "ANSI/ASHRAE Standard 41.11-2014. Standard Methods for Power Measurement." ASHRAE, 2014.

13th IEA Heat Pump Conference
April 26-29, 2021 Jeju, Korea

Novel Cascade Solution of Ultra-temperature Industrial Heat Pump System With Multiple Functions

Xiaoning Chen*, Niansheng Han

Emerson Research and Solutions Center, No.35 Su Hong West Road, Suzhou, 215021, China

Abstract

Industrial Heat Pump (IHP) is widely leveraged to gain more economic benefits instead of boilers and electric heating. The process demands of high temperature above 80°C, such as chemical separation-rectification and lithium battery coating, are significantly increasing. Under such conditions, operating stability, system capability and efficiency are all technical difficulties. Therefore, to satisfy the industrial requirement and overcome the difficulties, this paper will provide an integrated cascade solution, including system design, component selection and control strategy, to obtain about 30kW heating capacity with 100°C ~ 120°C air stably. By method of simulation and prototyping test, enhanced vapor injection (EVI), heat recovery and valve cooling technology are well applied to guarantee high efficiency and system reliability, achieving an excellent applicability based on current component condition. In the meantime, not only ultra-temperature air function, space cooling function or medium cold source can be also acquired by evaporating side of MT circuit.

Keywords: Cascade; IHP; EVI; Ultra-temperature ;

1. Introduction

As is shown in Table 1, the heat source above 100 ℃ is in great demand in industry application, such as the coating process of Lithium battery, PCB board drying, rubber fluid making, etc. The medium is mainly hot wind and steam. Currently the heat source above 100℃ is usually achieved by electric heating, coal & gas burning. On the one hand, these methods consume a lot of energy and the waste heat is difficult to be recovered. On the other hand, the pollution is quite serious. Therefore, Heat pump system attracts a lot of attention due to its high efficiency and environmental friendliness and is now widely applied in many occasions.

However, there are still many challenges in IHP, such as high inlet temperature of expansion valve and low system efficiency. The required condensing temperature is higher than 100 ℃ in IHP. If the hot air temperature needs to be 125 ℃, the condensing temperature will reach up to 130~135 ℃. So the cascade system is a common system type for such high pressure ratio applications, which is shown in Fig. 1(a). Assume the system subcooling degree is 5℃, so the temperature before the throttle valve will be about 130 ℃. There are very few high temperature resistant EXVs in the market. One implementation is as shown in Fig. 1(b). The high-temperature (HT) cycle is enhanced vapor injection cycle which induces a higher efficiency and a lower liquid refrigerant temperature before EXV compared with non-injection cycle. The HT and LT pressure-enthalpy diagrams are shown in Fig. 1(c) and Fig. 1(d), respectively. Taking the condition of HT stage into calculation, the result of the saturation temperature of injection (SIT) is about 103 ℃. Assume that the heat exchange temperature difference between SIT and point b is 5 K, the liquid temperature before EXV is 108 ℃, which is still beyond most EXV product available range. This is a big challenge to the reliability of the EXV. Long-term operation at high temperatures may lead to demagnetization failure and bidirectional performance attenuation caused by non-metallic seal failure, so more solutions are necessary for ultra-temperature application.

* Corresponding author. Tel.: +86-187-17712-259.
E-mail address: chenxn0731@163.com.

Accordingly, in order to achieve air supply at 120°C stably and reliably, this paper presents an integrated solution of ultra-temperature IHP system with novel cascade structure. This solution can also recovery some special air condition function to take full advantage of heat source and to improve the system efficiency.

Table 1. Temperature proportion of required heat source [1]

Industry	<100 °C	100-150 °C	150-183 °C	>183 °C
Food and tobacco	2.5	62.5	16.6	18.4
Fiber	0.4	50.3	49.3	0.0
Wood	1.1	9.3	6.6	83.0
Paper pulp	0.0	85.9	4.1	0.0
Chemical	4.8	26.9	50.0	18.3
Rubber	0.0	26.3	53.4	20.4
Leatherware	0.0	100.0	0.0	0.0
Ceramics	0.0	85.6	14.4	0.0

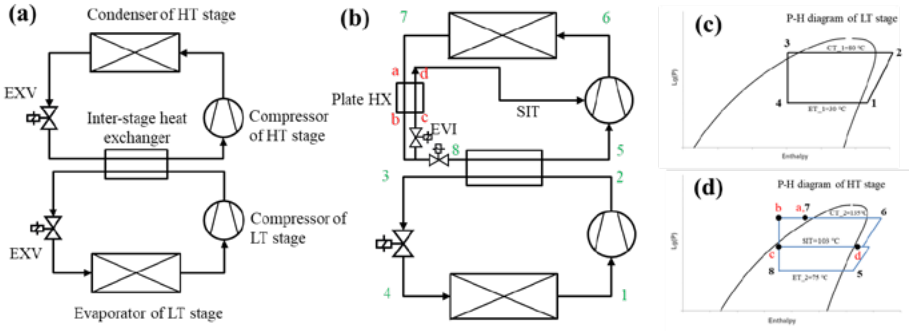


Fig.1 Ordinary Industrial Heat Pump
(a) Typical cascade system (b) cascade system with HT EVI (c) LT p-h diagram (d) HT p-h diagram

2. Solution and Prototyping

2.1. System Design

This novel cascade system is designed for two functions. One is to obtain stable hot air supply at 120°C, which applies EVI technology and valve inlet temperature cooling technology. The other function is designed to expand multiple capability of air conditioning, providing cold water at 7°C for space cooling.

Fig. 2 shows the layout of ultra-temperature industrial heat pump system. The system can be divided into three parts, LT cycle, HT cycle and hot air chamber. The LT cycle is a simple loop with R410A refrigerant. The compressor is variable speed model of Emerson ZWW050. The evaporator is plate heat exchanger (HX) and the design inlet water is air conditioning return water at 12°C. The HT cycle refrigerant is R245fa. Two EVI fix-speed compressors of high temperature heating compressor model are designed in parallel. This compressor model is developed by Emerson and specialized for high-temperature IHP application. With the enhanced design of motor cooling, lubrication system, and new high-temperature resistant materials, a special operation envelope of IHP compressor in Fig. 3 is achievable. Compared with conventional compressors, the evaporating and condensing temperature is significantly higher.

The designed condensing temperature of HT cycle is 125 °C. Hence, two-stage cooling structure of valve inlet temperature is designed. After the HT condenser, the refrigerant flows into two economizers, and then into the valve cooling plate heat exchanger, which path is shown by points (1 – 2 – 3). At this time, the fluid is divided into three branches. The main one (3 – 7 – 8 – 9) flows into HT EXV and condensing-evaporator with majority of refrigerant to guarantee enough heat exchange with LT cycle. The second one (3 – 5 – 6 – 9) is that the refrigerant passed through the evaporation side of the valve cooling plate heat exchanger after being throttled by EXV1, and then goes back to the accumulator. The third one (3 – 4 – 10/10') flows into two EVI EXVs (EXV2 and EXV3). Then after the evaporation side of two economizers, the refrigerant is injected into

two EVI compressors. With this two-stage valve inlet cooling and EVI structure, all the valve inlet temperature can be successfully controlled below 85 °C.

It is necessary that two parallel economizers connect two compressors, respectively. The main reason is EVI control logic related. When the compressor discharge temperature is below 140 °C, EVI EXV controls the injection superheat. If the compressor discharge temperature exceeds 140 °C, the EVI EXV will turn to expand opening to decrease the discharge temperature in higher priority although some liquid will be injected into compressor. In order to deal with this situation, two economizers can control two compressors, respectively. Once stepping into this logic only with one economizer, liquid has to be injected although one compressor's discharge temperature doesn't exceed limitation value. What's more, using one economizer may be not able to distribute liquid refrigerant evenly into two compressors, resulting that one compressor cannot obtain enough effects, while the other gets too much liquid.

Another water loop for heat recovery in hot air chamber is mainly designed for the pre-heating and pre-cooling function of inlet air (designed temperature at 27 °C) to improve the capability and efficiency. The re-cooling heat exchanger is just equipped for prototyping in Fig. 4 to ensure that the outlet air temperature is in safe operation. Fig. 4 also shows the internal structure of the prototyping and the designed temperatures in hot air chamber. The internal heat recovery loop can heat the inlet air up to 65 °C and cool the outlet air down to 83 °C. In the real field applications, this function can also be transferred into waste heat recovery of other heat source.

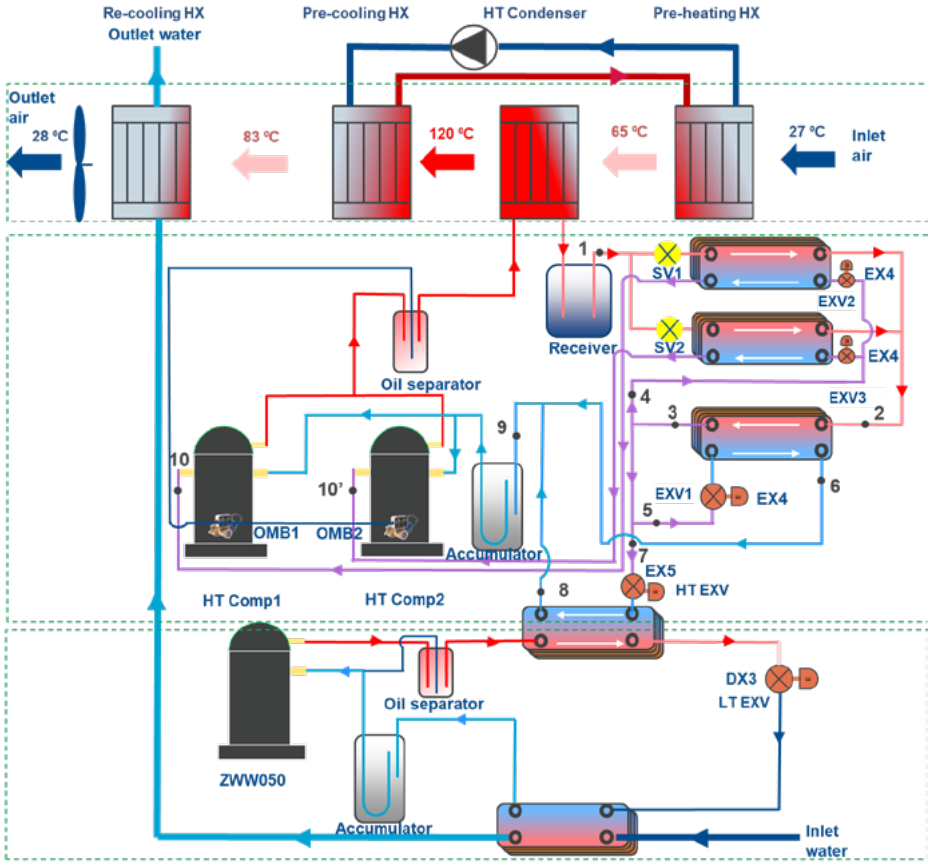


Fig. 2 Ultra-temperature Industrial Heat Pump System Layout

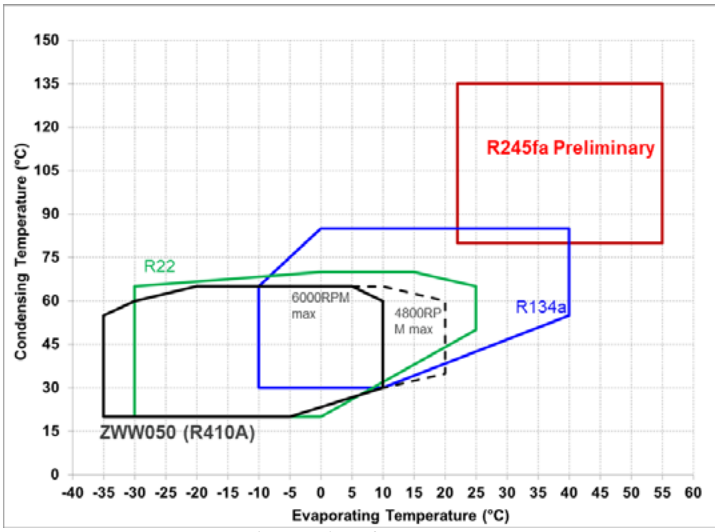


Fig. 3 Envelope of Compressors

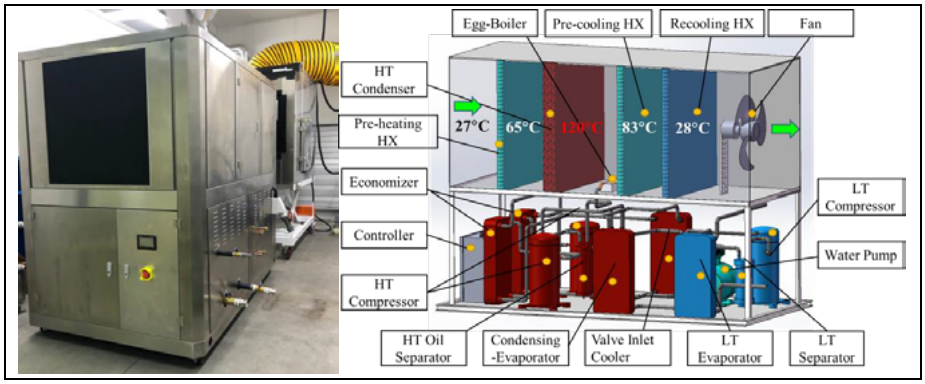


Fig. 4 Prototype and Internal Design

2.2. Control Method

It is a challenge for the reliability of control logic in such a system with multiple EXVs and variable speed compressor. There are five EXVs in this layout, LT EXV, HT EXV, EXV1, EXV2, EXV3. LT EXV is the throttling component of LT cycle, and the PID control target is the LT suction superheat at 6°C. HT EXV is the throttling valve of HT cycle with the PID control target of HT suction superheat at 8°C. EXV2 and EXV3 are the injection throttling valves with PID control target of the injection superheat at 10°C.Owing that there are four EXVs in parallel connection in HT stage, mutual interference will exist. To ensure stable system operation, EXV1 is selected to accommodate the disturbance caused by the other expansion valves because it mainly ensures cooling in front of the valve and has low control accuracy and speed requirements. Considering the cooling effect and the impact on the stability of the system operation, the opening of the cooler valve is limited, and the control method will adopt range control. The LT compressor speed is controlled by cascade adjustment. In order to avoid the delayed effect of the heat capacity of the heat recovery loop on the supply air temperature change, the outer loop PID controller with cascade control targets the HT condensing temperature, and outputs the set value of the low temperature condensing temperature. And the inner loop PID controller outputs the speed of LT compressor. Thus, the most difficult control problem is solved.

In addition, many system protection strategies are adopted, such as discharge temperature, pressure limitation, oil return, etc., are also taken into consideration.

A positive oil return loop with OMB is set to ensure the system oil balance. OMB is an oil management device to be equipped in the position of compressor oil sump. When the oil level is lower than standard level, the solenoid valve will be open to return the oil from oil separator under the action of pressure difference, until the oil level returns to normal. If the oil level lasts decreasing and exceed the upper limitation, alarm occurs, and the system will be shut down for protection. The control logic is achieved through programmable controller. And the electric control cabinet of prototyping is shown in Fig. 5.

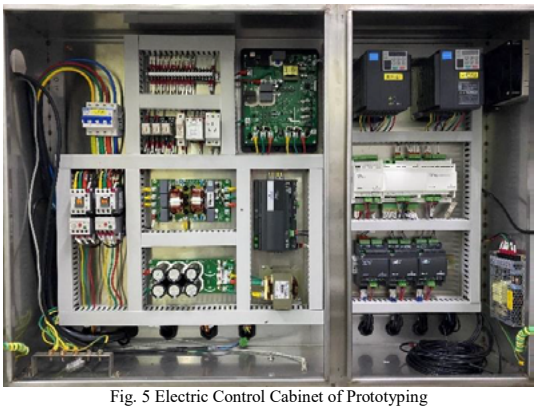


Fig. 5 Electric Control Cabinet of Prototyping

3. Test and Results Analysis

3.1. Test Conditions

Fig. 6 displays the system running envelop of the novel cascade IHP. Considering application environment and system reliability, the ambient temperature and water inlet temperature range are 15 ~ 30°C and 10 ~ 30 °C, respectively. If the water temperature is below 10°C, the risk of freezing will significantly increase. And if the water temperature is above 30 °C, LT evaporating temperature will exceed the upper limitation.

Accordingly, steady and transient performance tests were carried out with the prototyping mentioned above. And the test conditions are shown in Table 2. The rated condition is aiming to validate the IHP performance. The extreme conditions are mainly designed for system stability and reliability validation. All the steady state needs to be maintained over four hours.

3.2. Performance

Table 3 shows the comparison result of prototyping test validation and simulation in the rated condition. The feasibility of the concept can be seen that the test data and the simulation results match very well both in system performance and the operation parameters of LT stage and HT stage, respectively.

Focusing on the performance results, the hot air temperature perfectly exceeds 120°C in this rated condition, leading to enough capability of satisfying the demands of ultra-temperature application. The HT EXV inlet temperature is also successfully controlled below 85°C, which helps to guarantee the reliability of EXV under high temperature working environments. The multiple function of this IHP system is presented by the leaving water temperature. Although there exists a small difference between the simulation results, the leaving water temperature is still enough to carry part of cooling load. It means no energy will be wasted. Finally, the heating COP can reach up to 1.74, which will cause much benefit to replace boilers and electric heaters. Furthermore, taking cooling capacity of LT cycle for space cooling, the system total COP can even reach 2.83.

Table 2. Test Conditions

No.	Condition	Ambient Temperature	Water Inlet Temperature	Water Flow Rate	Target Air Temperature
		°C	°C	m3/h	°C
1	Rated Point	27	12	2	120
2		15	10	2	Above 100
3	Extreme Point	30	10	2	120
4		30	30	2	120

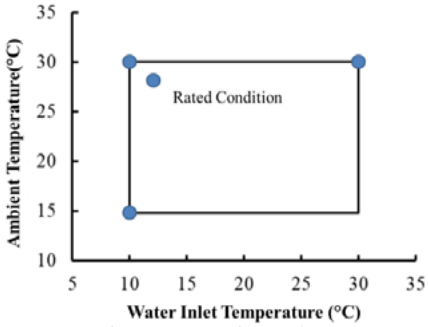


Fig. 6 System Running Envelop

Table 3. Comparisons between test validation and simulation design

Items		Test Validation Results	Design and Simulation Results
System Performance	Inlet Air Temperature	27 °C	27 °C
	Inlet Water Temperature	12 °C	12 °C
	Hot Air Temperature	121.6 °C	120 °C
	HT EXV Inlet Temperature	80.8 °C	70~85 °C
	Leaving Water Temperature	7.8 °C	7 °C
	Heating Capacity	29.7 kW	31.2 kW
	Total Compressor Power	17.1 kW	18.0 kW
	Heating COP	1.74	1.73
LT stage	Suction Saturation Temp.	2.6 °C	1.3 °C
	Discharge Saturation Temp.	54.7 °C	52.7 °C
	Suction Superheat	4.0 K	4.0 K
HT stage	Suction Saturation Temp.	49.7 °C	47.7 °C
	Injection Saturation Temp.	93.3 °C	86.2 °C
	Discharge Saturation Temp.	123.2 °C	124.8 °C
	Suction Superheat	11.0 K	11.0 K
	Injection Superheat	10.3 K	10.3 K

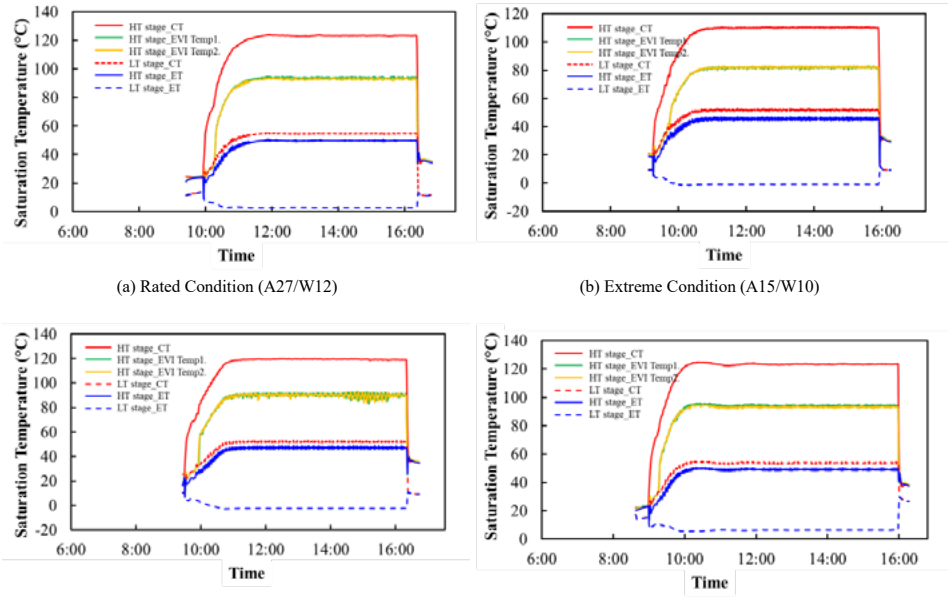
3.3. Transitional Behavior and Discussion

Fig. 7 displays an excellent result of the system dynamic characteristics. All the four conditions perform a stable running process from startup to steady operation. The hot air temperatures are 121.6°C, 103.2°C, 119.4°C and 120.2°C, respectively. In fact, No.3 condition is the worst condition for IHP and will rarely occur. Although the heating capacity has attenuation, the target air temperature is still higher than 100°C.

Compared with Fig. 7(c) and 7(d), when the water temperature decreases, it will take longer time to get to the steady state. When the water temperature is 10°C, the LT evaporating temperature is nearly below 0°C, increasing the freezing risk. And also, the capacity of LT stage is too small to induce a lower HT evaporating temperature.

The whole system is in interior relation and needs a balance adjustment control. For instance, if there are problems in the HT EXVs control method, the refrigerant distribution will cause big trouble. Once too little refrigerant flows into the condensing-evaporator, the LT condensing temperature will be too high duo to the lack of heat exchange. Or too much refrigerant flows into the condensing-evaporator, it means that too little fluid can be used to cool the valve inlet temperature.

Hence, the control logic is very crucial to obtain a good performance and reliability and has been solved in this study.



(a) Rated Condition (A27/W12)

(b) Extreme Condition (A15/W10)

(c) Extreme Condition (A30/W10)

(d) Extreme Condition (A30/W30)

Fig. 7 Test results of transient system performances

4. Conclusion

This study focuses on the performance and reliability of the novel cascade solution of ultra-temperature industrial heat pump. The EXV temperature resistance problem is solved by the design of economizer and valve inlet cooler, and the inlet temperature is controlled below 85°C. In this system, other technologies, such as OMB oil return, heat recovery loop and EVI technology, are also optimized to improve the efficiency and stability. In addition, the advanced control method is discussed and succeed to achieve the hot air temperature up to 120°C in an internal balanced state. In the future, the study on new refrigerant substitution can be developed.

Acknowledgements

We gratefully acknowledge the valuable cooperation of Prof. Chunlu Zhang and the members of his research group from Tongji University. Their developed system simulation software Greatlab plays a significant role in this study.

References

[1] Zhao L. Application And Development Of High Temperature Heat Pumps in China. Journal of Refrigeration, 2005, 2: 8-13. (in Chinese)

13th IEA Heat Pump Conference
April 26-29, 2021 Jeju, Korea

Electrochemical reaction and fluid flow analysis in PEMWE

Kyu Heon Rho[a], Dong Kyu Kim[a*]

[a]School of Mechanical Engineering, Chung-Ang Universaity, Seoul 06974, Korea

Abstract

In this study, a numerical model is developed to analyze the electrochemical reaction and fluid flow in a polymer electrolyte membrane water electrolyzer using OpenFOAM®. The activation overpotential distributions of hydrogen reduction reaction, and oxygen oxidation reaction and the current density distribution by electrochemical reaction are analyzed; Then, the volume fraction of oxygen in anode and hydrogen velocity in cathode are studied to verify their influences on the current density distribution and activation overpotentials. Where oxygen gas accumulates in the porous transport layer of anode, the local current density decreases sharply; The maximum and minimum local current density are 10,263 A/m^2 and 6,921 A/m^2 at operating current density of 10,000 A/m^2, respectively. Maldistribution of the overpotentials by electrochemical reaction are also observed by oxygen gas. This study contributes to the development of numerical analysis of polymer electrolyte membrane water electrolyte.

Keywords: Polymer electrolyte membrane water electrolyte; numerical analysis; electrochemical reaction analysis; two-phase flow analysis; interner behavior analysis

1. Introduction

With the rise of interest of green energy society, the interest of hydrogen was also rising. Currently, hydrogen is produced through by product hydrogen, so the price of hydrogen is 8,000 KRW/kg in Korea; and many researchers predict that the amount of by product hydrogen will be scarce when hydrogen energy becomes popular. Therefore, many researchers have interest on new technologies to produce hydrogen continuously, which is polymer electrolyte membrane water electrolyzer (PEMWE). PEMWE can produce the hydrogen at high current density, so it can produce the large amount of hydrogen, and produced hydrogen has a high purity of 99%. Therefore PEMWE is suitable to produce hydrogen to use in green energy society. However, PEMWE has disadvantage. The oxygen generated by the oxygen oxidation reaction (OOR) at the anode can decrease performance of PEMWE. When generated oxygen gas is accumulated in porous transport layer (PTL) in anode, oxygen gas disturbs the contact between catalyst and water, so active area for reaction also decrease. This phenomenon often occurs when PEMWE is operated at high current density. Therefore, it is necessary to smoothly remove the generated oxygen when PEMWE is operated at high current density.

In this study we developed the numerical model to analyze the two-phase flow and electrochemical reaction in PEMWE. The current density distribution and activation overpotentials in anode and cathode are analyzed. This study contributes to the development of numerical analysis of PEMWE.

2. Methodology

A PEMWE comprises end plate, current density, bipolar plate, gasket, and membrane electrode assembly (MEA); and MEA comprises the membrane, catalyst, and PTL. Water decomposition reaction occurs in PEMWE and this reaction is given by Eq. (1), which the standard voltage is 1.23V

* Corresponding author. Tel.: +82-02-820-5192 ;.
E-mail address: dkyukim@cau.ac.kr .

$$H_2O \quad \rightarrow \quad H_2 \quad + \quad \frac{1}{2}O_2 \tag{1}$$

The five serpentine flow field was analyzed to confirm the internal behavior in PEMWE, which shape is in Fig. 1, and geometric parameters are listed in Table 1.

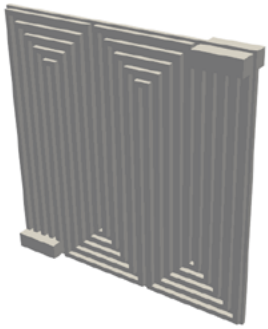


Fig. 1. Shape of the five serpentine flow field of PEMWE.

Table 1. Geometric parameters of PEMWE.

Parameter	Symbol	Value
Area of electrolyte	A_{cell}	25 cm^2
Area of inlet and outlet	$A_{in,out}$	27 mm^2
Membrane thickness	L_m	0.13 mm
PTL thickness at anode	L_A	0.36 mm
PTL thickness at cathode	L_C	0.20 mm
Chanel height	H_C	1 mm
Channel width	W_C	1 mm
Lib width	W_L	1 mm

2.1. Electrochemical model

The Nernst voltage(E^0) calculated by activities of reactant/product and the standard voltage of reaction (E_0), which can be expressed as [1]:

$$E^0 = E_0 - \frac{RT}{F} ln\left(\frac{\prod a_{product}}{\prod a_{reactant}}\right) \tag{2}$$

where F is Faraday's constant, T is temperature, and R is the gas constant. Activity of liquid is 1 and activity of gas is pressure of gas. The relation between activation overpotential (η) and current density (i) is expressed by Butler-Volmer equation, which equation is [2]:

$$i = i_0\left(e^{\frac{2\alpha F\eta}{RT}} - e^{\frac{2(1-\alpha)F\eta}{RT}}\right) \tag{3}$$

Where i_0 is the exchange current density, α is the transfer coefficients for the reaction.

2.2. Conservation equation

The mixture of liquid water and oxygen gas flow in anode, so two-phase flow model is applied in the anode. The continuity equation and momentum equation are expressed as [3,4]:

$$\begin{cases} \frac{\partial}{\partial t}\alpha_i\rho_i + \nabla\cdot(\alpha_i\rho_i U_i) = 0 \\ \nabla\cdot(\alpha_i\rho_i U_i U_i) = -\alpha_i\nabla P + \nabla\cdot\left(\alpha_i\mu_{eff}(\nabla\mu + (\nabla\mu)^T)\right) + \alpha_i\rho_i g + M_k \end{cases} \quad (4)$$

where α_i is volume fraction, ρ_i is density and U_i is velocity of species i. P is pressure of fluid, and μ_{eff} is the effective viscosity of fluid.

Only hydrogen gas is flow in cathode, so single-phase flow model is applied in the cathode. The continuity equation and momentum equation are express as [5]:

$$\begin{cases} \nabla\cdot(\rho U) = 0 \\ \nabla\cdot(\rho U U) = -\nabla P + \nabla\cdot(\mu\nabla U) \end{cases} \quad (5)$$

where ρ is density and U is velocity, and μ is viscosity of hydrogen, respectively. P is pressure of fluid.

2.3. Boundary and initial conditions

Boundary condition and initial condition is expressed as:

$$\begin{cases} U = \frac{Q}{A_{in}} \\ P_{out} = P_0 \\ T_{in} = T_0 \end{cases} \quad (6)$$

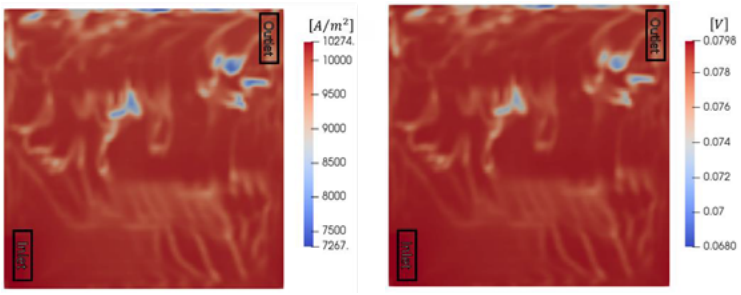
Where Q is the flow rate, P_0 is the outlet pressure, and T_0 is the inlet temperature (listed in Table 2). Simulation were conducted using OpenFOAM® (Open Field Operation and Manipulation).

Table 2. Boundary and initial condition of simulation.

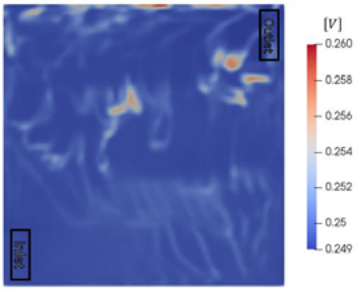
Parameter	Symbol	Value
Flow rate of water	Q	20 cm^3/min
Inlet temperature	T_0	80 ^{0}C
Outlet pressure	P_0	101,325 Pa

3. Result and discussion

Figure 2 presents the result of the electrochemical reaction in PEMWE. The current density was 10,000 A/m^2 and the flow rate was 20 cm^3/min. The maximum current density was 10,263 A/m^2 and the minimum current density was 6,921 A/m^2. The difference between maximum and minimum current density was 3,342 A/m^2. As a result, we conclude that maldistribution of current density distribution was observed. The maximum and minimum overpotential of anode reaction were 0.26 V and 0.24 V, respectively, and the maximum and minimum overpotential of cathode reaction were 0.068 V and 0.080 V, respectively. By these results we conclude that maldistribution of overpotential also occurred.



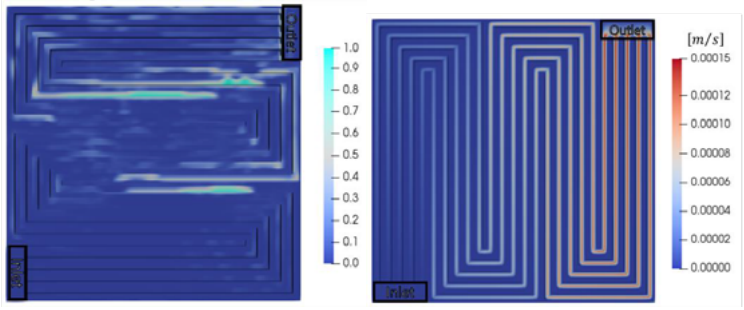
(a) (b)



(c)

Fig. 2. Electrochemical behaviors. The flow rate as 20 cm^3/min. (a) is current density distribution, (b) is overpotential of cathode reaction, and (c) is overpotential of anode reaction.

The volume fraction in anode and velocity of hydrogen are in Fig.3. The maximum volume fraction of oxygen was 0.99 in channel. When oxygen gas was accumulated in PTL, it disturbed the contact between catalyst and liquid water, so performance of PEMWE decreases. In anode, only hydrogen gas flow, so velocity of hydrogen increased continuously in channel. As a result, we conclude that oxygen gas was eliminated smoothly to increase performance of PEMWE.



(a) (b)

Fig. 3. Fluid flow distribution in PEMWE. (a) is volume fraction of oxygen in anode, and (b) is velocity of hydrogen in cathode.

4. Conclusion

In this study, we developed the numerical model for PEMWE; in this model, electrochemical reaction and fluid flows of mixture and single-phase gas in PEMWE. In cell, maldistributions of current density distribution and activation overpotential was observed; this maldistribution occurred by accumulated oxygen gas which was generated by water decomposition reaction. Therefore, to increase the performance of PEMWE, it is necessary to eliminate the oxygen gas in channel. We think that this study contributes to develop the numerical model of PEMWE.

Acknowledgements

This work was supported by Korea Institute of Energy Technology Evaluation and Planning (KETEP) grant funded by the Korea government (MOTIE) (NO. 20192050100060, Chemisorption heat pump system using electrochemical compressor); this work was supported by the Korea Institute of Energy Technology Evaluation and Planning(KETEP) and the Ministry of Trade, Industry & Energy(MOTIE) of the Republic of Korea (No. 20206810100030); and this work was supported by the National Fir Agency and the Korea Institute of Energy Technology Evaluation and Planning(KETEP) (No. 20008021).

References

[1] R. T. Nishida, S. B. Beale, and J. G. Pharoah, “Comprehensive computational fluid dynamics model of solid oxide fuel cell stacks,” Int. J. Hydrogen Energy, 2016, vol. 41, pp. 20592–20605.
[2] P. Choi, D. G. Bessarabov, and R. Datta, “A simple model for solid polymer electrolyte (SPE) water electrolysis,” in Solid State Ionics, 2004, vol. 175, pp. 535–539.
[3] P. Kwiatoń, D. Cekus, M. Miara, and I. Kubik-Maciąg, “Multiphase Modeling of Droplet Fall using Euler-Euler Approach,” Appl. Phys. Mech. Mater. Eng., 2020, vol. 138, pp. 276-279.
[4] W. Lou and M. Zhu, “Numerical simulation of gas and liquid two-phase flow in gas-stirred systems based on Euler-Euler approach,” Metall. Mater. Trans. B Process Metall. Mater. Process. Sci., 2013, vol. 44, pp. 1251–1263.
[5] S. B. Beale, H. W. Choi, J. G. Pharoah, H. K Roth, H. jasak, and D. H. Jeon, “Open-source computational model of a solid oxide fuel cell,” Comput. Phys. Commun., 2016, vol. 200, pp. 15–26.

13th IEA Heat Pump Conference
April 26-29, 2021 Jeju, Korea

Analysis of the operating characteristics of electrochemical hydrogen compressors through parametric study

Min soo Kim[a], Min sung Kim[a], Min kyu Jung[a], Jung chul Kim[b], Dong kyu Kim[a,*]

[a]Chung-Ang University, 84 Heukseok-ro, Seoul, 06974, Korea
[b]Korea Institute of Machinery&Materials, 156 Gajeongbuk-ro, Daejeon, 34103, Korea

Abstract

As the supply of hydrogen energy increases, the need for development of hydrogen storage technology is emerging. In the case of the existing mechanical hydrogen compressor, there are many problems such as low compression efficiency and high power consumption, huge volume and noise due to parts of the driving part, and high maintenance cost due to corrosion. As an alternative to this, an electrochemical hydrogen compressor that compresses hydrogen using an electrochemical reaction has been proposed. In this study, an analysis of the operating characteristics of an electrochemical hydrogen compressor was performed through a parametric study in consideration of the factors affecting the compression of the electrochemical hydrogen compressor. First, the performance change of the compressor due to the change of activation loss and resistance loss according to the change of current density was measured. Second, the performance change of the compressor due to the difference in potential energy according to the temperature change was measured. Finally, the performance change of the compressor due to the difference of inlet pressure was measured. Through this study, it is possible to understand the optimum driving conditions and efficiency of the electrochemical compressor. This study will serve as a guideline for introducing electrochemical compressors into the industry.

Keywords: Electrochemical compressor; Hydrogen; Polymer electrolyte membrane; Parametric study.

1. Introduction

Currently, the world is striving to realize an eco-friendly future globally [1]. They are striving to change the existing fossil fuel society to a hydrogen society and to use hydrogen as an energy source. In order to realize such a hydrogen society, a hydrogen compressor technology that compresses produced hydrogen and compresses transported hydrogen, stores it in a charging station is very important.

Existing hydrogen compressors are mostly mechanical, such as reciprocating piston and diaphragm. For example, the hydrogen compressor currently used in the Korean hydrogen charging station uses a diaphragm type compressor. In the case of a mechanical compressor, a large number of drives (cylinders) are required, and for this reason, the need for maintenance is large and noise and vibration are severe, so the life of the entire system is low. In addition, there is a risk of hydrogen contamination in the case of compressors using lubricating oil. An electrochemical compressor can be proposed as a way to overcome this [2].

In the case of an electrochemical compressor, the hydrogen purification and compression mechanism are unified, so the loss is small [3]. In addition, since there are no continuously moving parts such as pistons, energy consumption and maintenance costs are low, and there is no noise [4]. The study of the principle of electrochemical compressors was experimentally studied by S.A Grigoriev [5]. It is shown that a cell voltage of only 350 mV is required to obtain a current density of 1 A/cm^2. The polarization curve through modeling of the electrochemical compressor is shown in N.V Dale [6]. To account for real time losses the efficiency of electrochemical compressor is assumed to be 70% for current density of 0.7 A/cm^2. Studies on the performance of electrochemical compressors have been carried out, but mechanism analysis for the influencing factors has not been performed. It is necessary to grasp the mechanism of electrochemical compressors through parametric

* Corresponding author. Tel.: +82-02-820-5192.
E-mail address: dkyukim@cau.ac.kr.

studies of electrochemical compressors. In this research, a parameter study on an electrochemical compressor was carried out. An analysis of the performance of an electrochemical compressor according to current density, temperature and inlet pressure was performed.

2. Methodology

2.1. Principle of electrochemical compressor

Figure 1 shows the principle of electrochemical compressor. Hydrogen is oxidized to H^+ ions at the anode due to the potential difference. And it is reduced to hydrogen at the cathode after passing through the polymer electrolyte membrane. Hydrogen produced by proton reduction in an enclosed cathode space is compressed and discharged at high pressure. Table 1 describes the reactions that take place inside the electrochemical compressor.

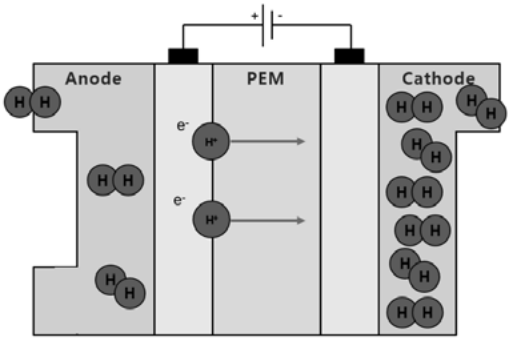


Fig. 1. Principle of electrochemical compressor

Table 1. Reactions in electrochemical compressor

Location	Expression
Anode	$H_2 \rightarrow 2H^+ + 2e^-$
Cathode	$2H^+ + 2e^- \rightarrow H_2$

The theoretical cell voltage of an electrochemical compressor is determined by the Nernst equation (1) [7].

$$E = \frac{RT}{2F} ln(\frac{P_c}{P_a}) \quad (1)$$

Here, R is the gas constant, T is the temperature of the cell, F is the Faraday constant, and P_a and P_c are the hydrogen partial pressures at the anode and cathode, respectively. For the total cell voltage, the resistance loss η_{ohm} and the activation loss η_{act} are included and are described as follows (2) [7].

$$V_{cell} = E + \eta_{ohm} + \eta_{act} \quad (2)$$

2.2. Experimental setup

The experiment was conducted with a single cell, and it was evaluated by mounting it on a test station. Hydrogen was controlled at a constant flow rate through mass flow constoller (MFC, Bronkhornst), humidified through bubbler (CNL), and supplied to the electrochemical compressor. The gas temperature was controlled using a line heater and a temperature controller (HX9, Hanyoungnux), and the gas temperature and pressure of the electrochemical compressor inlet and outlet were measured. The performance of the fuel cell was measured through power supply (EX20-240, ODA). The schematic of the electrochemical compressor experiment was shown in Figure 2.

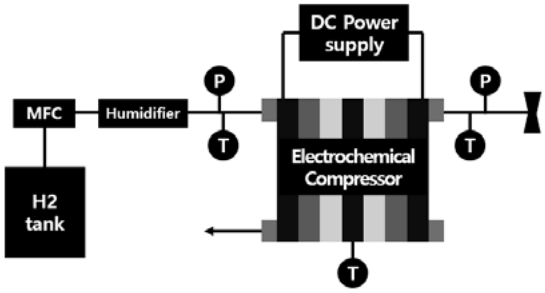


Fig. 2. Schematic of electrochemical compressor system

3. Result

3.1. Effect on current density on electrochemical compressor

Figure 3 shows the voltage change according to the pressure ratio on different current density. In order to reach the target pressure within a short time, it must be driven with a high current density. However, the voltage is lower at the same pressure when driven at a low current density. This means that the Nernst efficiency is high when driving with a low current density. This is because the ohmic loss and activation loss increase in proportion to the current. The total power consumption from 1 bar to 5.4 bar is 0.00632 Wh on 1 A/cm^2, 0.005 Wh on 0.7 A/cm^2, and 0.00359 Wh on 0.3 A/cm^2. When driving with a low current density, the total power consumption up to the target pressure can be reduced.

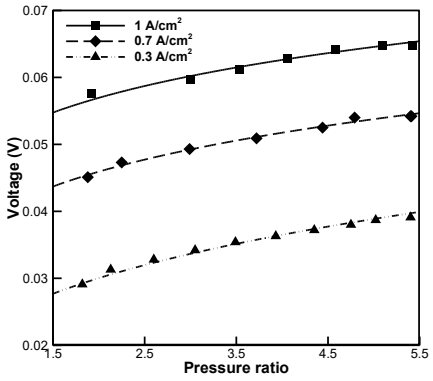


Fig. 3. Voltage change according to the pressure ratio on different current density

3.2. Performance analysis according to operating temperature

Figure 4 shows the voltage change according to the pressure ratio at different operating temperature. There is little difference in compression depending on temperature. However, when driven at a low temperature, the electrode potential of the battery is low, so the Nernst efficiency is high. The total power consumption from compression ratio 1.5 to compression ratio 5 is 0.00339 Wh at 70 ºC, 0.00330 Wh at 60 ºC, and 0.00318 Wh at 50 ºC. When operating at low temperatures, the total power consumption up to the target pressure can be reduced.

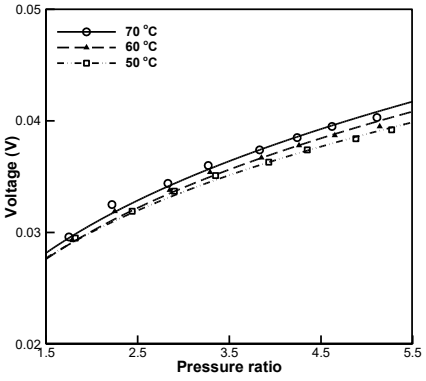


Fig. 4. Voltage change according to the pressure ratio at different operating temperature

3.3. Effect of inlet pressure on electrochemical compressor

Figure 5 shows the voltage change according to the pressure ratio on different inlet pressure. The higher the inlet pressure of the electrochemical compressor, the lower the compression ratio increase rate. This is because the number of H_2 passing from the anode to the cathode is determined according to the current density. Since the same amount of H_2 goes over, the lower the inlet pressure, the higher the increase rate of the compression ratio. The lower the inlet pressure, the lower the voltage at the same pressure ratio, so the Nernst efficiency is better.

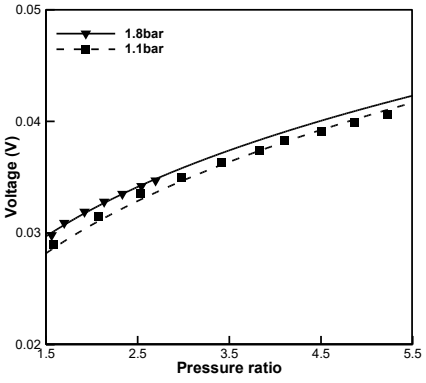


Fig. 5. Voltage change according to the pressure ratio on different inlet pressure

4. Conclusion

In this study, the performance of the electrochemical hydrogen compressor was analyzed through parametric studies that affect the compression of the electrochemical hydrogen compressor. For electrochemical compressors, the Nernst efficiency is good when operating at low current density, low temperature and low inlet pressure. This study will serve as a guideline for applying to industry by replacing the existing mechanical compressor with an electrochemical compressor.

Acknowledgements

This work was supported by Korea Institute of Energy Technology Evaluation and Planning (KETEP) grant funded by the Korea government (MOTIE) (NO. 20192050100060, Chemisorption heat pump system using electrochemical compressor); this work was supported by the Korea Institute of Energy Technology Evaluation and Planning(KETEP) and the Ministry of Trade, Industry & Energy(MOTIE) of the Republic of Korea (No. 20206810100030); and this work was supported by the National Fir Agency and the Korea Institute of Energy Technology Evaluation and Planning(KETEP) (No. 20008021).

References

[1] Kim MS, Song JH, Kim DK. Development of optimal conditioning method to improve economic efficiency of polymer electrolyte membrane (PEM) fuel cells. Energies 2020;13. https://doi.org/10.3390/en13112831.
[2] Sdanghi G, Dillet J, Didierjean S, Fierro V, Sdanghi G, Dillet J, et al. Operating heterogeneities in a PEM Electrochemical Hydrogen Compressor To cite this version : HAL Id : hal-02186747 2019.
[3] Rhandi M, Trégaro M, Druart F, Deseure J, Chatenet M. Electrochemical hydrogen compression and purification versus competing technologies: Part I. Pros and cons. Chinese J Catal 2020;41:756–69. https://doi.org/10.1016/S1872-2067(19)63404-2.
[4] Mackenzie BS, Bloomfield DP. Electrochemical hydrogen compressor. DOE Grant DE-FG02-05ER84220 to Analytic Power Corp. Final Report. 2006.
[5] Grigoriev SA, Shtatniy IG, Millet P, Porembsky VI, Fateev VN. Description and characterization of an electrochemical hydrogen compressor/concentrator based on solid polymer electrolyte technology. Int J Hydrogen Energy 2011;36:4148–55. https://doi.org/10.1016/j.ijhydene.2010.07.012.
[6] Dale N V, Mann MD, Salehfar H, Dhirde AM, Han T. Modeling and analysis of electrochemical hydrogen compression 2008.
[7] Bampaou M, Panopoulos KD, Papadopoulos AI, Seferlis P, Voutetakis S. An electrochemical hydrogen compression model. Chem Eng Trans 2018;70:1213–8. https://doi.org/10.3303/CET1870203.

13th IEA Heat Pump Conference
April 26-29, 2021 Jeju, Korea

"Experimental study of PEMFC conditioning methods"

Joohee Song[a], Minsoo Kim [a], Dongkyu Kim[a*]

School of Mechanical Engineering, Chung-Ang University, Seoul 06974, Korea

Abstract

The conditioning procedure of polymer electrolyte membrane fuel cell (PEMFC) requires to acquire its maximum performance and promote commercialization of fuel cell society. Depending on the conditioning method, this procedure terminates in various time. To analyze the effect and time required for conditioning, commonly used procedures involving constant current (0.25A/cm^2) and constant voltage (0.6V) and new method which suggested in this study were adopted to experiments and optimize most effective conditioning methods. The best performance was reached by new conditioning method called Cathode Oxygen Depletion (COD) during 2hours, but 4hours and 21hours for CC and CV, respectively. As that results, COD conditioning method proceeded remarkably fast, and most of the conditioning process was finished within just few hours. It could be concluded that the MEA activation procedure had a significant effect on the MEA durability and reduction hydrogen gas required for conditioning.

Keywords: Polymer electrolyte membrane fuel cell; Cathode oxygen depletion; conditioning

1. Introduction

The worldwide effort for the reduction of greenhouse gas emissions by fossil fuels has generated Eco-friendly devices which capable of replacing internal combustion engines. Among the commonly used Eco-friendly devices, the Polymer electrolyte membrane fuel cell (PEMFC) is highly demanded as zero-emission energy conversion devices. Typically, the PEMFC is used for portable power and transportation due to their compactness, simple-structure and sustainability. For an active electrochemical reaction of PEMFC, a part in which reaction gas, hydrogen ions and electrolyte can coexist is required. This part is called as triple-phase boundary (TPB), and it is important to secure TPB as much as possible during operating the fuel cell. The procedure so-called break-in/conditioning /activation is essential to acquire TPB expansion which described in Figure 1, leading to maximize PEMFC performance. However, using inappropriate conditioning methods can result in unnecessary hydrogen consumption and conditioning time. It is the main assignment to optimize effective conditioning method.

There are hypothetical theories usually mentioned during conditioning procedure are i) Conditioning expands passage of the reactants to reach the catalyst[1]. ii) Membrane of PEMFC is initially dry, hindering the cell performance until the membranes are hydrated during the conditioning[2]. iii) The continuous activity of hydrogen ions and electrons is secured by improving the ion conductivity. Most theories are lack of direct experimental support or concrete experimental validation A systematic investigation of conditioning and its theories about mechanism is still required[3].

The conditioning procedures are classified to two strategies: on-line and off-line conditioning methods. The traditional conditioning methods are as follows. On-line techniques explored include current control[4,5], potential control[7,8,], temperature control[9-11], hydrogen pumping[12], CO stripping[13], and air braking[14]. Off-line methods include electrochemical conditioning of the MEA and steaming or boiling the electrode[15]. In this study, we suggested state-of-the-art conditioning method called Cathode oxygen

* Corresponding author. Tel.: 82-02-820-519
E-mail address: dkyukim@cau.ac.kr

depletion (COD) that is controlled the air-supplying and shortened time to reach maximum MEA performance remarkably. To verify the effect of COD, the commonly used conditioning methods were chosen and compared each performance.

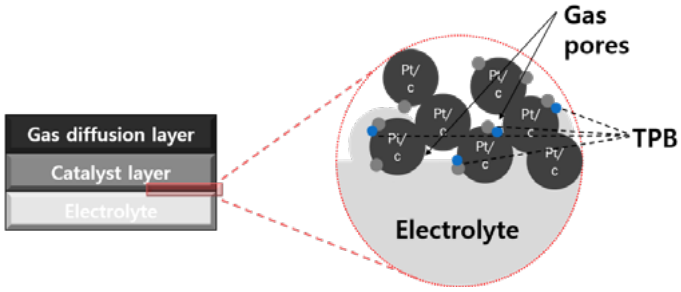


Fig. 1. Schematic of Triple-Phase Boundary (TPB)

2. Experimental

2.1 Description of Experiment equipment set-up

The PEMFC had an active area of 25cm^2. The entire conditioning methods were carried out using Vinatech Co. membrane-electrode-assembly. The Pt loading on the anode and cathode electrodes was 0.4mg/cm^2. The cell was assembled between two graphite plates with serpentine flow channel, current collectors coated with copper and fastened under constant pressure. After assembly, cell was connected to electrode load (PLZ664WA, Kikusui). The heating rods were used to maintain experiment operating temperature. Air and hydrogen gas were humidified and then controlled using mass flow controller (SEHWA Hightech). The flow rate of hydrogen and air were 100 and 200 mL/min, respectively. Experiment equipment diagram was described in Figure 2.

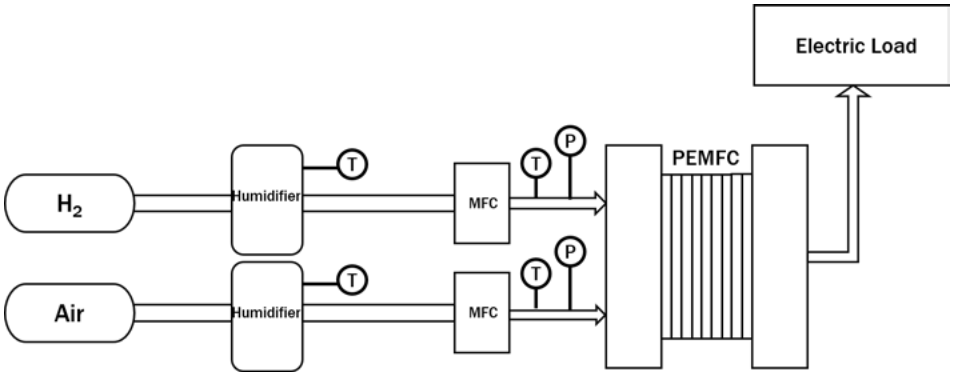


Fig. 2. Schematic of Experiment equipment

2.2 Performance measurement

The conditioned MEA performance was measured in galvanostatic mode and characterized by polarization curve. The applied conditions were maintained at 65℃ under relative humidity (RH) of 100%. For the polarization curve, the electric load was connected to PEMFC. The voltage from 0.9V to 0.1V was hold for 5 minutes at each voltage step. Power density was calculated from the current and applied voltage.

2.3 Conditioning procedures

The three kinds of conditioning methods were conducted in this study: Constant voltage, Constant current and Cathode Oxygen Depletion. Each method is explained below.

(a) Constant voltage. The cell is operated under constant voltage at 0.6V for 4h.
(b) Constant current. The cell is operated under constant current at 0.25A/cm^2 for 21h
(c) Cathode Oxygen Depletion. (i) Constant voltage Open circuit voltage (OCV) operation for 15~20s. (ii) Air supplied off and wait until voltage drops. (iii) Air supplied on and voltage maintains at 0.2V for 30s.

3. Results and discussion

3.1. Polarization curves of MEAs on conditioning methods

The comparison of Polarization curves after conditioning for 2h is shown in Figure 3(a). As can be seen, the OCV of COD, CV and CC has similar value due to experiment condition of temperature and gas partial pressure is equivalent. The current densities at 0.6V of COD, CV and CC are 1.0588 A/cm^2, 0.914A/cm^2 and 0.7632A/cm^2, respectively. We aimed that when the current density reaches above 1.0A/cm^2 at 0.6V, conditioning procedure terminates. According to the performance of COD achieves target value after 2h conditioning, activation using COD is sufficient only 2 hours. However, the performances of CV and CC do not reach aimed current density at 0.6V, it is difficult to finish conditioning within 2 hours.

Figure 3(b) describes the comparison of current density at 0.6V depending on conditioning time. It shows that a rapid performance increase within a short time using COD method. Also, the COD conditioning has its peak performance after 2 hours and maintains steady state as time passes. In case of CV, the performance achieves above 1.0A/cm^2 within 4hours and has steady state after 4hours. On the other hand, performance using CC increases slowly and the target performance does not reach over time.

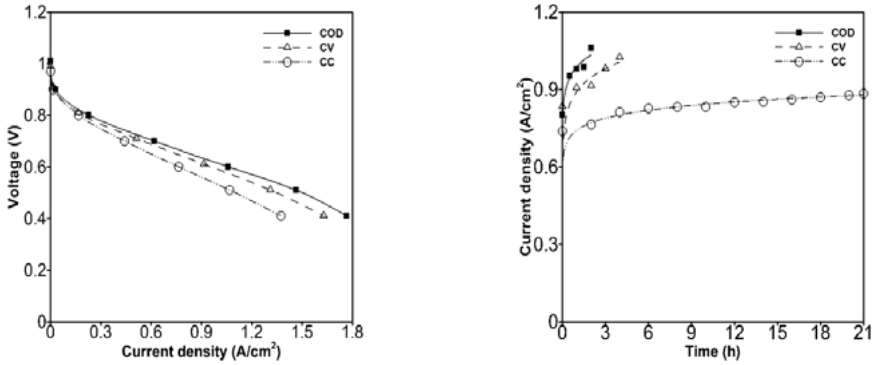


Fig. 3 (a) Polarization curve after 2h of conditioning procedures (b) Current density at 0.6V depending on conditioning time.

3.2. Final performance of conditioning by different procedures

Figure 4 presents the performance of all MEAs after finishing the conditioning procedures. The results show that current densities using COD, CV and CC are 2.062A/cm^2, 2.0308 A/cm^2 and 1.9256 A/cm^2, respectively. Using COD method can acquire highest performance of MEA within only 2hours. Because cod accelerates the catalyst penetration into membrane which is the component of TPB. Then, the MEA performance by CV method obtain second highest performance within 4hours. However, the performance CC has lowest performance and does not reach peak performance of MEA. This result indicates by the fact that amount of produced water in the MEA is insufficient, because it is operated at low current density; therefor the MEA can not be hydrated enough, leading to be unable to achieve aimed performance. Comparatively, investigation

of the conditioning cells shows that COD conditioning procedure is an effective method for conditioning and shorten conditioning time significantly.

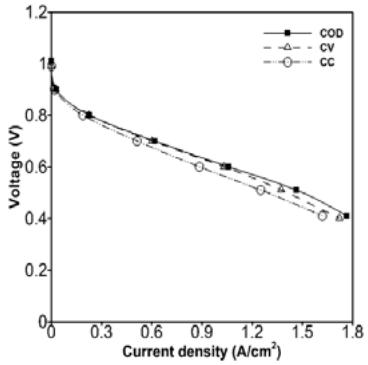


Fig. 4. Polarization curve after end of conditioning procedures

4. Conclusion

The performance of MEA subjected to a new conditioning method: Cathode Oxygen Depletion. Also, the effect of MEA using COD method by comparing commonly used conditioning methods, involving Constant current and Constant voltage. The time required to condition MEA using the COD procedure to reach maximum performance is 2 hours, comparing to 4 hours for CV and 21hours for CC. The results demonstrated that activating by COD conditioning is the most time-effective and secures economics of Fuel cell society.

Acknowledgements

This work was supported by Korea Institute of Energy Technology Evaluation and Planning (KETEP) grant funded by the Korea government (MOTIE) (NO. 20192050100060, Chemisorption heat pump system using electrochemical compressor); this work was supported by the Korea Institute of Energy Technology Evaluation and Planning(KETEP) and the Ministry of Trade, Industry & Energy(MOTIE) of the Republic of Korea (No. 20206810100030); and this work was supported by the National Fir Agency and the Korea Institute of Energy Technology Evaluation and Planning(KETEP) (No. 20008021).

References

[1] T. W. Lim, S. H. Kim, S. Y. Ahn, B. K. Hong, B. K. Ahn, US Patent, US 0129689 Al, 2010.
[2] R. Hallum, US Patent, US 6576356 B1, 2003
[3] X. Ren, M. S. Wilson, S. Gottesfeld, J. Electrochem. Soc.1996, 143, 112.
[4] W. Bi, Electrochem. Solid-State Lett. 10 (2007) B101–B104.
[5] J. Shan, X., Yan, X., Sun, Z., Hou, P., Qi, P. Ming, A fast activation method for a fuel cell stack, Chinese Patent, 201010010014.3 (2010).
[6] T.W. Lim, S.H. Kim, S.Y. Ahn, B.K. Hong, B.K. Ahn, System and method for activating fuel cell, US 2010/0129689 Al, 2010.
[7] F.-B. Weng, B.-S. Jou, A. Su, S.H. Chan, P.-H. Chi, J. Power Sources 171 (2007) 179–185.
[8] Z. Qi, A. Kaufman, J. Power Sources 111 (2002) 181–184.
[9] Z. Qi, A. Kaufman, J. Power Sources 114 (2003) 21–31.
[10] Z. Qi, A. Kaufman, Activation of electrochemical cells with catalyst electrodes, US Patent 6,805,983 (2004).
[11] C. He, Z. Qi, A. Kaufman, Electrochemical method to improve the performance of H2/air PEM fuel cells and direct methanol fuel cells, US Patent 6,730,424 (2004).
[12] Z. Xu, Z. Qi, J. Power Sources 156 (2006) 281–283.

[13] H.H. Voss, R.H. Barton, M. Sexsmith, M.J. Turchyn, Conditioning and MaintenanceMethods for Fuel Cells, Ballard Power Systems Inc., CA 2429598 A1, 2003.
[14] C. Eickes, P. Piela, J. Davey, P. Zelenay, J. Electrochem. Soc. 153 (2006) A171–A178.
[15] Z. Qi, A. Kaufman, J. Power Sources 109 (2002) 227–229.

13th IEA Heat Pump Conference
April 26-29, 2021 Jeju, Korea

Initial stage of Thermal Response Tests combined with transient numerical model – a foundation of short-term ground storage of cold for effective cooling of office buildings.

Kamil Kwiatkowski[a,*], Jakub Garbacik[a], Tomasz Walczak[a]

[a]Euros Energy, Macieja Rataja 4F, 05-850 Koprki, Poland

Abstract

The short-term storage of cold in borehole heat exchangers (BHE) is analysed to minimise the electricity consumption for air-conditioning in large commercial or office buildings in major cities. The cold is effectively produced during the night and stored in the ground. Next, during the day, the storage cold will be discharged with very low use of electricity by so-called free-cooling. Proper design of such short-term ground storage requires full knowledge of geological conditions provided locally by Thermal Response Test (TRT). The properties of rapid loading/unloading of BHE may come from the initial stage of TRT, when heat (cold) is locally transferred in transient, unsteady, non-equilibrium way. To handle such detail heat transfer phenomena a quick numerical model is designed and adjusted to interpret the TRT data. The solver, much quicker than detail Computational Fluid Dynamics (CFD) models, is validated with several TRT data. Finally, simulations of short-term cold storage in BHE is provided.

Keywords: BHE, Short-term storage, free-cooling, TRT, cold storage;

Introduction

According to the electricity demand forecast, in Poland limitations of energy supply in the coming years are to be expected. The problem of imbalance between supply and demand is even more visible when analysing the progress of daily electricity consumption where peaks in the day and valleys in the night can clearly be seen. The worst situation occurs in the summer when the capabilities of the transmission grid are limited by high temperatures, with simultaneous high demand for energy consumed by more and more popular cooling systems. This issue is critical for large commercial and office building in big cities, when the possibility of local electricity production with photovoltaic or wind-turbines is limited due to lack of space. Moreover, typical cooling demand of office or commercial buildings is high, exceeding the heat demand even by several times.

It is known that the efficiency of standard air-conditioning systems based on dry-coolers depend on the outside temperature. The higher the temperature outside, the worse the efficiency of the cooling system, and the increased consumption of electricity. Production of cold at night when the outside temperature is lower than in the daily demand peak, ensures that the system will still be working with higher efficiency than in the daily peak and relieving the network during the daylight peak. Moreover, usually cheaper tariffs of electricity are available at night, which amplify a measurable economic effect for the customer.

Favourable option is to produce cold during night and store it for day, mainly to discharge heat to borehole heat exchangers (BHE) in the form of e.g. vertical exchangers, normally used as a lower heat source of the heat pumps. Such a solution potentially gives excellent results (e.g. lowering condensing temperatures by more than 15 °C). The use of ground heat exchangers to power the ground with cold of plus temperature, can greatly improve the efficiency of cooling with the use of a heat pump (i.e. free cooling).

* Corresponding author. Tel.: +48 22 250 16 09;
E-mail address: kkwiatkowski@eurosenergy.com

The behaviour of BHE as a short-term storage for cold must therefore be known in order to make optimal decisions about the operation of the system and to estimate usable heat capacity of such a system in the short term. Unproper construction and size of the ground heat exchanger, or too much heat discharged into the ground can cause its heating increase of condensing temperature to an unprofitable value.

To address the challenge of designing the optimal ground heat exchangers for short-term storage of cold applicable for commercial or office buildings we improve and link well-established procedure of Thermal Response Test (TRT) with transient, non-equilibrium numerical modelling of heat transfer.

The TRT is valid and well-proved to correctly estimate the long-term thermal performance of the BHE, but it fails for short-term applications when dynamics loading/reloading are included. In standard approaches, the initial phase the TRT cannot be taken into account because non-equilibrium phenomena happened. Although the very first ten hours of the thermal response test provide the most valuable insight into the BHE loading in day-night time-scale, they are often neglected and removed from the analysis. Using these initial results of standard TRT to predict the efficiency of short-term energy storage requires a new, more complex approach when local phenomena inside the borehole itself have to be considered. In fact, solving transient, local and non-equilibrium heat transfer is essential for applications when a borehole heat exchanger is loaded and reloaded rapidly.

In the present work, we propose an extended procedure of analysing TRT data, based on transient numerical modelling focused on the short time phenomena. We describe the in-house model, validate it with the results of benchmark thermal response tests, and compare with detail Computational Fluid Dynamics solution from the OpenFOAM code. Sensitivity analysis proved that the model is capable of predicting the results of the thermal response tests, both in short-term and in long-term. Finally, we present the monthly simulations of thermal energy storage in a day-night cycle with various demands from the commercial or office buildings.

2. Thermal Response Tests

Results from three standard thermal response tests are used in this work. The benchmark TRT test comes from Vienna as a joint effort of Central European project called Geoplasma-CE. In this well-documented borehole three group of researchers conducted TRT and interpreted their results. The other thermal response tests have been performed in Warsaw, in Vistula River Valley and in Koprki, outside Warsaw where Euros Energy headquarter is. The TRT test were conducted with commercially available specialised devices GERT designed to conduct TRT by UBeG company.

The following table summarized the parameters of TRT tests that were used in this work.

Table 1. Parameters of the thermal response tests.

Location	Heat load [W]	Length [m]	Mass flow rate [kg/s]	Initial borehole temperature [°C]	BHE type	Fluid
Koprki	8590	100	0.44	10.9	1U 40x3	Water
Warsaw	8730	100	0.47	9.3	1U 40x3.7	Glycol
Vienna	5130	150	0.36	12.4	1U 40x3.7	Water

3. Numerical solver and modelling

Early mathematical and numerical approaches treat BHE as two separate regions, the inside of the borehole (fluid, pipe and grout) and the outside of the borehole (ground). One-dimensional (1D) models [1] and [2] describe temperature in the ground using an analytical function, where [3] a simplified finite difference model of heat conduction is presented. The thermal capacities of the fluid, pipe and grout are neglected to simplify the model. This operation is commonly known as the quasi-steady state. It means that heat transfer inside borehole is always considered as time-independent, or that the thermal equilibrium is reached. As a result, those models are appropriate for long-term simulations only. The doctoral thesis [1] states that for times lesser than $5{r_b}^2/\alpha_s$ models are inaccurate, where r_b means radius of borehole and α_s denotes thermal diffusivity of soil (ground).

In order to simulate the short-term heat pump workloads, a more complex model of the transient heat conduction in the inside of BHE must have been implemented during work on Heat Exchanger Numeric Solver (HENS). This model, based on the [4], is composed of two parts: the outside and the inside linked via borehole heat loading.

3.1. The outside part of the model HENS

The outside part of the BHE model is a 2D axisymmetric heat conduction with Neumann boundary condition at borehole wall and Dirichlet boundary condition at far-field boundary. The ground temperature is obtained by solving the energy equation in the cylindrical coordinate system:

$$\frac{1}{a_s}\frac{\partial T}{\partial t} = \frac{1}{r}\frac{\partial}{\partial r}\left(r\frac{\partial T}{\partial r}\right) + \frac{\partial^2 T}{\partial z^2} \tag{1}$$

Partial differential equation is transformed to algebraic linear system of equation using finite volume method discretization. Due to stability, time derivative is transformed using fully implicit method. As mentioned before, boundary condition at borehole wall and far-field radius are established upfront – Neumann type $\dot{T}\,[K/m]$ (where $\dot{T} = \dot{q}/(2\pi k_s)\,[K/m]$) and Dirichlet type $T_{ff}\,[K]$ respectively. Rest of boundary conditions are arbitrary. The far-field boundary radius can be estimated by Eskilson [1] assumption $r_f = 3\sqrt{a_s t_{max}}$.

The mesh cells size in vertical direction should be refined at top and bottom boundaries. Such operation improves stability and reduces computational error. In case of mesh in radial direction the smallest cell should be at borehole and its size may vary from $r_b/6$ to $r_b/3$. Mesh size may increase along radius.

3.2. The inside part of the model HENS

Inside part of the BHE model works as a modified MTRCM [5] model considering thermal resistances and capacities of all components/regions. There are 3 regions – fluid, pipe and grout. Moreover, the grout region is split into three sections. One corresponding to the section of grout between the pipes and two sections between each pipe and borehole. To be able to simulate transiency of heat conduction each grout sections can be divided by a specific number of segments.

The vertical heat conduction and fluid mass transfer were calculated using a finite difference method. Boundary conditions are as follows: BHE heat load [W] and borehole wall temperature [K].

The idea of modelling inside part of the BHE comes from Hellström [6], who presented a 2D quasi-steady-state model. He introduced dependencies of fluid, grout and borehole temperature as thermal resistances ("delta circuit").

The number of temperature data points in one layer of the model may vary depending on the grout segments division. The number of cells in the vertical direction is related to the outside part of the model.

3.3. Solving procedure

The simulation procedure include the following steps:

1) Preprocessing data:
   a) Input thermophysical, geometrical and simulation parameters.
   b) Create a mesh.
   c) Calculate the resistances and capacities of the inside part of the model.
   d) Create initial temperature fields.
   e) Create matrices for inside and outside part of the model.
   f) Create RHS vectors for inside and outside part of the model, based on initial conditions.
2) Solving loop:
   a) Solve an algebraic system of equations of the inside part of the model.
   b) Solve an algebraic system of equations of the outside part of the model.
   c) Retrieve borehole heat load $\dot{q}\,[W/m]$
   d) Retrieve borehole temperature $T_b\,[K]$.
   e) Update RHS vectors for both part using new temperature fields and heat load and borehole temperature.
   f) Save temperature fields.
   g) Update timestep.

3.4. Initial validation with the result of CFD

To validate the solver a series of analyses has been performed. The first one is a comparison with detail computational fluid dynamics (CFD) numerical model optimized to simulate BHE. The CFD model allows simulating 3D transient heat conduction. The main tool used to perform analyses is OpenFOAM's chtMutliRegionFoam solver. The momentum equation for the fluid is solved before heat transfer simulation using simpleFoam solver. The obtained fluid velocity field is transferred to the heat conduction model to reduce calculation time. The chtMultiRegionFoam solves energy equations for all regions simultaneously. Such CFD model gives results comparable to real-life TRT's. The main disadvantage is high demand for computational power which leads to long time simulation duration. The CFD mesh has over 2.4 million cells, HENS has around 2000 cells only. The calculation speedup is expected while using a simplified model.

To determine speedup, the same case has been performed using both models. It took over 4708 seconds on average to evaluate 3D simulation results and 29 seconds on average using HENS. So the speedup reaches around 162 times, as shown in Fig. 1. Moreover, the error between obtained results is lesser than ±0.3 [K].

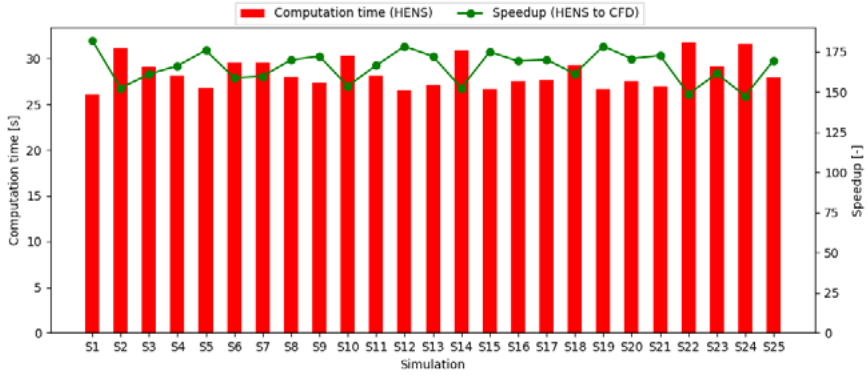


Fig. 1. Speedup of HENS solver, compare to the CDF solver in OpenFOAM.

4. Results - sensitivity analysis

4.1. Results from the TRT in Vienna, Austria

The reference thermal response test was carried on borehole heat exchanger located nearby Vienna City Centre area. This is a benchmark location to conduct TRT by various group, with well-determined geological parameters and properties od the borehole itself. The data from the TRT test is described in [7].
In Fig. 2 we summarised the results of the sensitivity analysis performed with different values of the thermal diffusivities of the ground (soil) and inject (cement). In this figure, and similar figures of the other TRT, the values of the temperature errors are presented. The errors are calculated as at each time step as a difference between the temperature directly measured during TRT and temperature computed with corresponding numerical simulation performed with HENS. We separately calculated errors based on temperature probed from the inlet and the outlet of the BHE.
The results with the minimum errors are presented in the centre sub-figure in Fig. 2. In the surrounding sub-figures errors are plotted for different values of thermal diffusivities of ground and cement, as specified in Table 2.

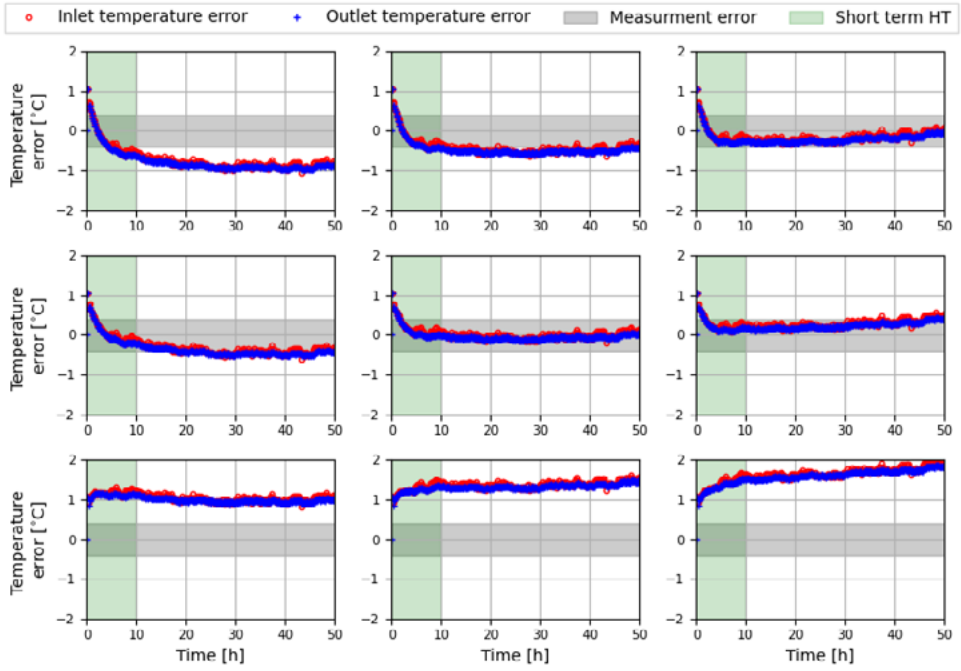


Fig. 2. Sensitivity analysis for the Vienna TRT. Each plot presents a temperature error plotted for the first 50 hours of TRT test, for the values of thermal diffusivity that corresponds to the layout in Table 2.

Table 2. The values of the thermal diffusivities of each subplots.

			Left column	Central Column	Right column
Upper row	α_s	$\left[\frac{m^2}{s}\right]$	$0.98 * 10^{-6}$	$1.09 * 10^{-6}$	$1.20 * 10^{-6}$
	α_c		$5.66 * 10^{-7}$	$5.66 * 10^{-7}$	$5.66 * 10^{-7}$
Middle row	α_s		$0.98 * 10^{-6}$	$1.09 * 10^{-6}$	$1.20 * 10^{-6}$
	α_c		$6.29 * 10^{-7}$	$6.29 * 10^{-7}$	$6.29 * 10^{-7}$
Lower row	α_s		$0.98 * 10^{-6}$	$1.09 * 10^{-6}$	$1.20 * 10^{-6}$
	α_c		$6.92 * 10^{-7}$	$6.92 * 10^{-7}$	$6.92 * 10^{-7}$

The initial temperature error converges to 0 in about 5 hours. It is worth to mention, that for this TRT the data was written every 10 minutes, so the exact time of the beginning of the test remains uncertain to this limit. That time shift may influence the temperature error values, especially when the temperature rises quickly. Such a situation occurs at the beginning of the TRT test. The overall behaviour of temperature error plots remains as stated before.

4.2. Results from the TRT in Warsaw, Poland

TRT test in Warsaw was carried on the Vistula River Shore area.

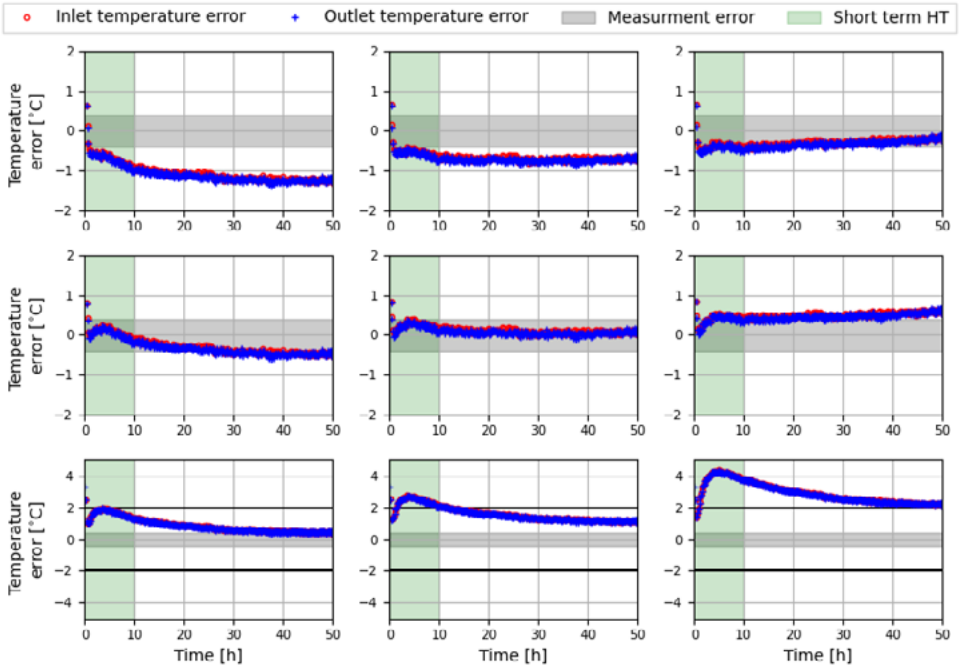


Fig. 3. Sensitivity analysis for the Warsaw TRT. Each plot presents a temperature error plotted for the first 50 hours of TRT test, for the values of thermal diffusivity that corresponds to the layout in Table 3. Note that the y-axis in the third row is expanded.

Table 3. The value of the thermal diffusivities of each subplots.

			Left column	Central Column	Right column
Upper row	α_s	$\left[\frac{m^2}{s}\right]$	$1{,}14 * 10^{-6}$	$1.27 * 10^{-6}$	$1.40 * 10^{-6}$
	α_c		$3.78 * 10^{-7}$	$3.78 * 10^{-7}$	$3.78 * 10^{-7}$
Middle row	α_s		$1{,}14 * 10^{-6}$	$1.27 * 10^{-6}$	$1.40 * 10^{-6}$
	α_c		$4.20 * 10^{-7}$	$4.20 * 10^{-7}$	$4.20 * 10^{-7}$
Lower row	α_s		$1{,}14 * 10^{-6}$	$1.27 * 10^{-6}$	$1.40 * 10^{-6}$
	α_c		$4.62 * 10^{-7}$	$4.62 * 10^{-7}$	$4.62 * 10^{-7}$

The result in lower right sub-plot is out of visible range. Despite different heat-carrying fluid, the behaviour of the results is similar.

4.3. Results from the TRT in Koprki, Poland

Next analysis presents the temperature influence of grout and soil thermal diffusivities on the accuracy of matching to TRT tests. The following figure shows the change in the differences between TRT and HENS inlet and outlet temperatures. The best matching result is shown in the centre subplot in Fig 4.

TRT test was carried on nearby the Euros Energy headquarters.

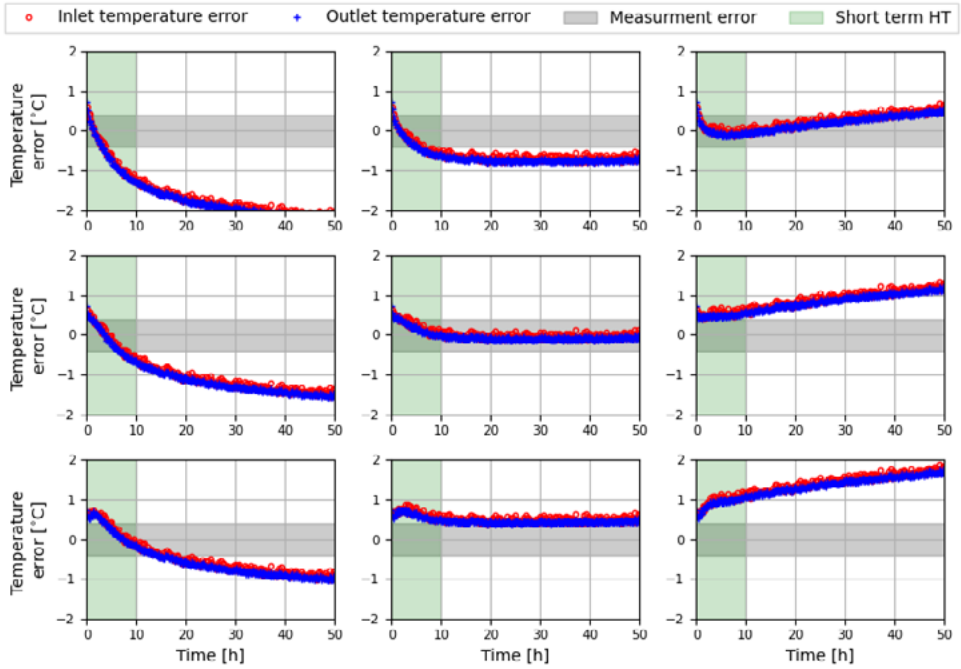


Fig. 4. Sensitivity analysis for the thermal response test in Koprki, nearby Warsaw. Each plot presents a temperature error plotted for the first 50 hours of TRT test, for the values of thermal diffusivity that corresponds to the layout in Table 4.

Table 4. The values of the thermal diffusivities of each subplots.

			Left column	Central Column	Right column
Upper row	α_s	$\left[\frac{m^2}{s}\right]$	$1.09 * 10^{-6}$	$1.21 * 10^{-6}$	$1.33 * 10^{-6}$
	α_c		$3.30 * 10^{-7}$	$3.30 * 10^{-7}$	$3.30 * 10^{-7}$
Middle row	α_s		$1.09 * 10^{-6}$	$1.21 * 10^{-6}$	$1.33 * 10^{-6}$
	α_c		$3.67 * 10^{-7}$	$3.67 * 10^{-7}$	$3.67 * 10^{-7}$
Lower row	α_s		$1.09 * 10^{-6}$	$1.21 * 10^{-6}$	$1.33 * 10^{-6}$
	α_c		$4.04 * 10^{-7}$	$4.04 * 10^{-7}$	$4.04 * 10^{-7}$

The results lead to the conclusion that soil thermal diffusivity determines the long term accuracy of temperature (the smaller the diffusivity value is the less heat is conducted through soil region and fluid temperature raise). Grout thermal diffusivity value specifies the rate of heat transfer in the short-term period.

5. Results – day/night cycles

Two four-weeks-long simulations present the simulated operation of the heat pump using different cycle schemes. Both tests are based on Koprki TRT parameters. The first one presents borehole heat load inversion every 12 hours. The second one shows a more complicated week-long cycle, during which there are 60 hours of heat delivery, 60 hours of heat extraction and 48 hours of idle.

5.1. Day cycle (12/12)

The 28 days of operation using 12/12 cycle plot presents high comparability of the results. Heat is delivered and extracted from a single BHE, with rate of 5 kW. During one cycle 60 KWh of energy is stored and restored out of the ground. There are no visible heat loss. An oscillating inlet temperature reaches 13.2 °C at peaks and

drops down to -9.2 °C. The lower plot visualizes the temporal values of coefficient of performance (COP). During the loading stage, when cold is stored in the BHE, the COP values drop from initial 8 to 5. The COP of cooling stage is divided into two components – the free-cooling part and regular cooling with heat pump. Free-cooling takes place when inlet temperature is smaller than 12 °C. The total cooling energy achieved by reusing cold stored in BHE reaches up to 43 kWh daily. The free-cooling COP is estimated by dividing total cooling energy by the electrical energy estimated to be used by fan coils and circulating pumps.

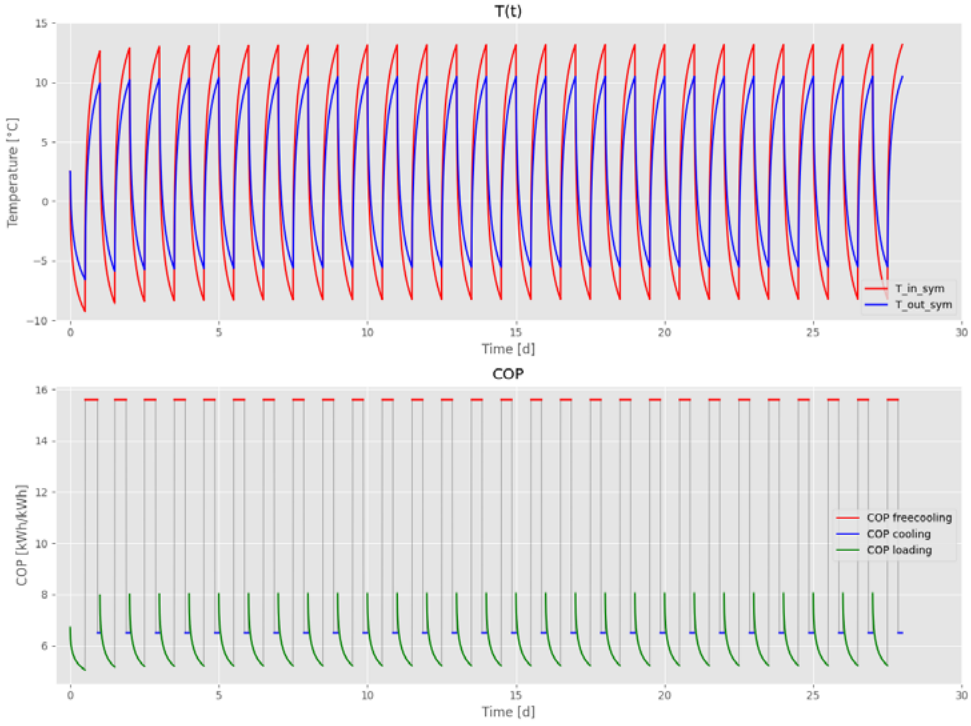


Fig. 5. Month simulation of the day/night cycle of loading and unloading the ground cold storage designed as a source of cooling of Euros Energy headquarter in Koprki.

5.2. Week cycle (12/9)

The second one shows a week-long cycle, during which there are 60 hours of heat delivery, 60 hours of heat extraction and 48 hours of idle. The details of cycle is specified in Table 5.

Table 5. Loading and unloading scheme. Notation: +Q states heat delivery; -Q states heat extraction; 0 states idle

	00^{00}-7^{00}	7^{00}-8^{00}	8^{00}-20^{00}	20^{00}-22^{00}	22^{00}-23^{59}
MON	+Q	0	-Q	0	+Q
TUE	+Q	0	-Q	0	+Q
WED	+Q	0	-Q	0	+Q
THU	+Q	0	-Q	0	+Q
FRI	+Q	0	-Q	0	
	00^{00}-7^{00}		7^{00}-19^{00}	19^{00}-23^{59}	
SAT	0		0	+Q	
SUN	+Q		0	+Q	

The week long cycle results plot presents that temperatures plots remain almost the same in case of comparing them week by week. The simulations starts on Friday at 20:00. During the weekdays inlet temperature at picks increases due to unbalanced heat energy supplied and received out of the BHE. The 12/9 cycle represents the

workload of a heat pump systems in an office building. The energy that is stored during nights and weekend can be retrieved during working hours at work days. Koprki's example presents 300 kWh of energy converted in BHE throughout one week. The COP of loading varies from 5.5 to 7.6. The free-cooling phase COP reaches 20.2, while conventional cooling phase coefficient of performance equals to 6.5.

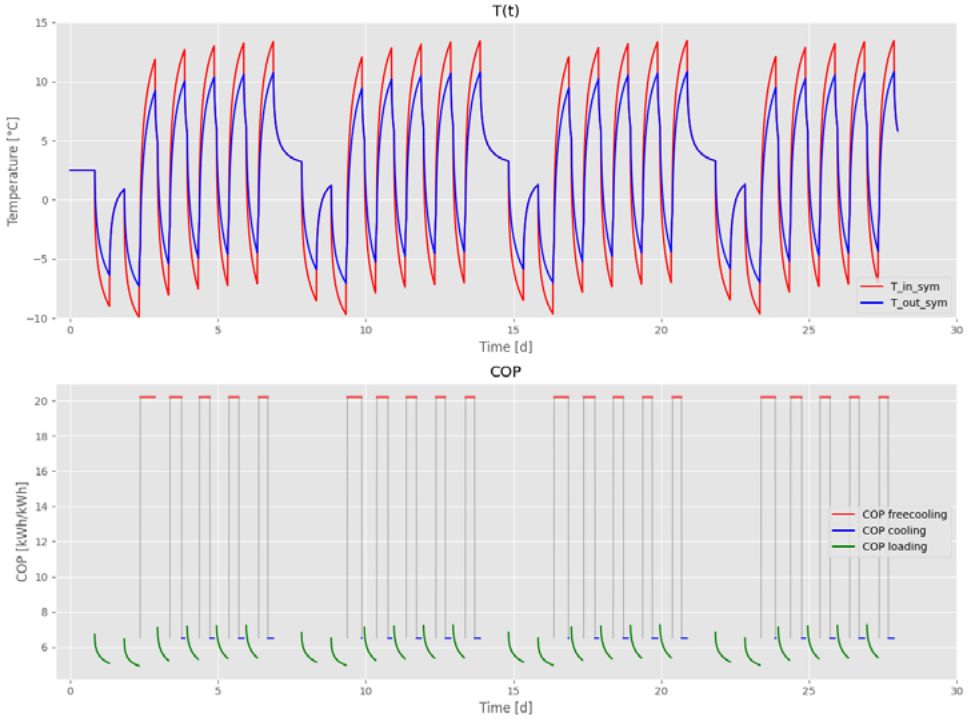


Fig. 6. Month simulation of the day/night cycle of loading and unloading the ground cold storage with weekends included.

6. Conclusions

The HENS model allows to solve complex heat conduction problem with relatively high accuracy. It is a great pre-processing tool to quickly evaluate the range of ground and soil thermophysical parameters. The correctness with three different TRT test proves that HENS can be highly applicable in research on heat pumps systems. Using HENS opens the possibility of investigation of long-term storage of heat or cold with defined workloads, including short-term cold storing with rapid loading/unloading. Moreover, a custom heat load may be specified. It allows to optimise cooling system for commercial of office buildings with specified energy tariff. Short-term heat storing takes place when the conditions are beneficial i.e. low energy tariff. Energy may be reused later to air condition buildings with free-cooling mode.

Nomenclature

r	Radius (m)	t	Time (s)
α	Thermal diffusivity (m^2/s)	Subscripts	
Q	Heat load (W)	b	Borehole
T	Temperature (K)	f	Fluid
q	Borehole heat load (W/m)	ff	Far-field
z	Depth (m)	g	Grout
k	Thermal conductivity (W/m/K)	s	Soil

Acknowledgements

This research was funded by NARODOWE CENTRUM BADAŃ I ROZWOJU grant number POIR.01.02.00-00-0355/16. We acknowledge GeoPLASMA-CE Project (https://portal.geoplasma-ce.eu/) for opportunity to use TRT data from Vienna and other locations. We thank Grzegorz Ryżyński and Mateusz Żeruń from Polish Geological Institute for their valuable geological insight and discussion.

References

[1] Eskilson P, *Thermal analysis of heat extraction boreholes* (Doctoral Thesis), Lund: Department of Mathematical Physics, University of Lund, 1987

[2] Carslaw HS, Jaeger J C, *Conduction of Heat in Solids*, Oxford: Oxford University Press,, 1947

[3] L. R. Ingersoll i H. J. Plass, „Theory of the ground pipe heat source for the heat pump," *Heating, Piping and Air conditioning 20,* pp. 119-122, 1948

[4] Biglarian H, Abbaspour H, Saidi HM, A numerical model for transient simulation of borehole heat exchangers, *Renewable Energy,* 2016

[5] Pasquier P, Marcotte D, Short-term simulation of ground heat exchanger with an improved TRCM, *Renewable Energy,* 2012, p. 92-99,

[6] Hellström G, Claesson J, Multipole method to calculate borehole thermal resistances in a borehole heat exchanger, *HVAC&R Research,* 2011 p. 895-911

[7] Götzl G, Fuchsluger M, Zschoke K, Janža M, Ryżyński G, .T3.5.2 calibration report based on the pilot activities for transfer of knowledge, Comparison and Validation report, Technical Report GEOPLASMA-CE, 2019

13th IEA Heat Pump Conference
April 26-29, 2021 Jeju, Korea

Diffusion barriers and strategies for heat pump systems with integrated storage and photovoltaic in Austrian 1-2 family dwellings: an explorative investigation for the IEA HPT Annex 55/ECES annex 34

Therese Guttmann[a], Thomas Schoberer[b], Caroline Haglund Stignor[c], Johann Emhofer[a]

[a]Austrian Institute of Technology, Gieffinggasse 2, 1210 Wien, Austria
[b] Forschung Burgenland GmbH, Department Energie-Umweltmanagement, Steinamangerstraße 21, 7423 Pinkafeld, Austria
[c] Research Institutes of Sweden, Box 857, 501 15, Sweden

Abstract

The Austrian building sector accounts for 16 percent of national CO_2 emissions. This makes it a key sector to decarbonize if long-term environmental targets are to be met. Relevant measures focus on the thermal-refurbishment of existing buildings and the phaseout of fossil-based technologies. The task specified by the Austrian government, involves replacing 600.000 oil heaters currently in use against renewable alternatives by 2035. This is the point of departure of this study. We investigate key barriers and solutions for the switch from fossil-based systems to c*omfort & climate boxes* (CCBs) in the Austrian 1-2 family housing segment. CCBs are integrated systems encompassing a heat pump, storage and integrated control. The study applies a two-step approach: First, 11 problem-centered stakeholder interviews are conducted and evaluated using quantitative content analysis. Next, a stakeholder survey is conducted to assess the subjective relevance of barriers identified in the interviews. Results yield 45 barriers clustered into 6 categories. We identify discrepancies in the relevance-perceptions between stakeholder groups, especially between researchers and key market actors. We advise realigning research agendas along market actors' perceptions, as these actors possess closeup insights about the market environment for CCBs.

Keywords: Heat pumps; innovation system; integrated storage; market barriers

1. Introduction

In line with the long-term goals of the European Parliament and Council, Austria has pledged to reach carbon-neutrality by 2050. These goals are to be met in part by national "effort-sharing": measures targeted at by increasing energy efficiency, the share of renewables in sectors not included in the European Emissions Trading Scheme (ETS). In 2017, the building sector accounted for over 16 % of total Austrian CO_2 emissions (excluding ETS sectors). Nearly a third of total energy consumption is used for space-heating, of which 17.6 % is provided using oil-based heaters and 28.2 % using natural gas [1]. Alternatives to these systems exist and are diffusing into the market at an accelerating pace, stimulated by falling technology prices and technical improvements, stronger environmental awareness and conducive policy shifts.

While the efficiency of heat pumps, thermal and electoral storage devices and solar PV systems is constantly improving, integrated systems that combine all or several of these individual technologies, are less common in Austria. Their integration, however, could valuably contribute to sectoral decarbonization. Integrated systems consisting of heat pumps and storage are an important technological option to accelerate the use of renewable energy for heating and cooling, in many countries worldwide. By combining heat pumps and storage, several issues may be tackled, such as: balancing and controlling electricity grid loads; capturing a larg(er) share of renewable (local/regional) input (i.e. solar thermal, solar PV); optimizing economics, CO_2-emissions, fuel use throughout time; providing optimal security of supply to buildings.

Commercial development of this type of solution is progressing very slowly in most countries, even in those who have relatively mature heat pump market. Therefore, the combined Annex HPT Annex 55/ECES Annex 34 (international collaboration project) was initiated in 2019 as a collaboration between two TCPs (Technology Collaboration Programmes) by IEA and the Mission Innovation initiative. This annex will aim at accelerating market diffusion of combined heat pump / storage packages including integrated control, a so called "Comfort and Climate Box", or "CCB". The work within the Annex is focused on systems that will be close to commercial realization, have a high quality and be adopted to their local market.

Aligned with the Annex goal, the aim of this study is to identify the factors hindering the diffusion of CCBs into the Austrian 1-2 family housing segment and to derive solutions for overcoming them. Findings may provide useful insights for industry strategy as well as targeted policy making on both a national and international level that could accelerate CCB diffusion.

The rest of this paper is structured as follows. Section 2 presents the technical CCB definition used. Section 3 introduces the conceptual framework used, as well as the key actors of the CCB system. Next, Section 4 explains the methodological design of the study. Section 5 presents research findings. Following a brief discussion in Section 6, we finish with conclusive remarks in Section 7.

2. CCB Definition

Contrary to the broader definition of CCBs used in the international IEA HPT Annex 55/ECES Annex 34 project, the data collection process of the present study mandates a more precise definition, as presented in Fig. 1.

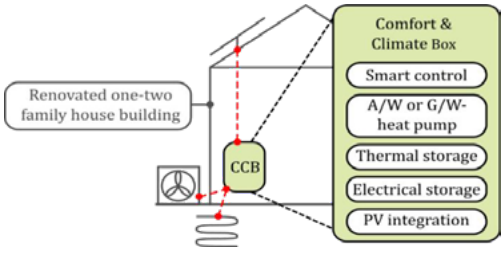


Fig. 1 Definition of the CCB for the present study

While heat pumps with integrated thermal storage are well-established in the Austrian market, their smart integration with PV systems and electrical storage is rather unknown. Ground- and air-source heat pumps with up to 10 kW heating power report rising yearly installation figures in Austria of +14.5% and +11.6 %, respectively [2]. Therefore, both systems are of great interest for this study. In line with the international annex definition, electrical and thermal storage as well as smart controls are included. Additionally, we include a PV system, as the increased installation of PV is a crucial measure specified by the Austrian government to reach climate goals [2]. Moreover, the combined use of PV and heat-pumps is associated with a higher proportion of own-consumption and lower electricity bills.

3. Technological innovation systems

The technological innovation system (TIS) provides a useful conceptual framework for our investigation of CCB diffusion in the Austrian 1-2 family housing segment. The central idea underlying TIS research is that technological innovation results from complex exchange of information and technologies between system actors [3]–[6]. Suurs et al. [3] describe a TIS in terms of its four principal components: its actors, institutions, technologies and their interrelations (networks). System *actors* include firms and non-firm organizations (such as interest groups, industry representatives, research organizations and authorities). *Institutions* refer to formal institutions (such as technical norms, laws and guidelines) as well as informal institutions (such as beliefs, habits and routines). Institutions play a pivotal part in the development of innovations, as they regulate actors' actions and the interactions between them, following Hekkert et al. [7]. The system *technology* refers to technical knowledge and skills, as well as technoeconomic factors such as costs and technical risks. Suurs et al. [3] stress that these technological factors are crucial for understanding feedback mechanisms between institutional and technological change.

The TIS framework focuses on a specific technology (or product) and is commonly applied to investigate what conditions foster or hinder the development of emergent technologies [7]. This makes the TIS framework ideal for the analysis of CCBs diffusion in the Austrian 1-2 family housing segment. Based on the expert knowledge about the research field within the research team – composed of applied researchers in the energy and buildings innovation nexus in Austria – a mapping of the system actors of the CCB TIS in Austria was conducted. The mapping is presented in Fig. *2* below. This mapping provided a useful basis for data collection and sampling decisions for the remainder of the research project.

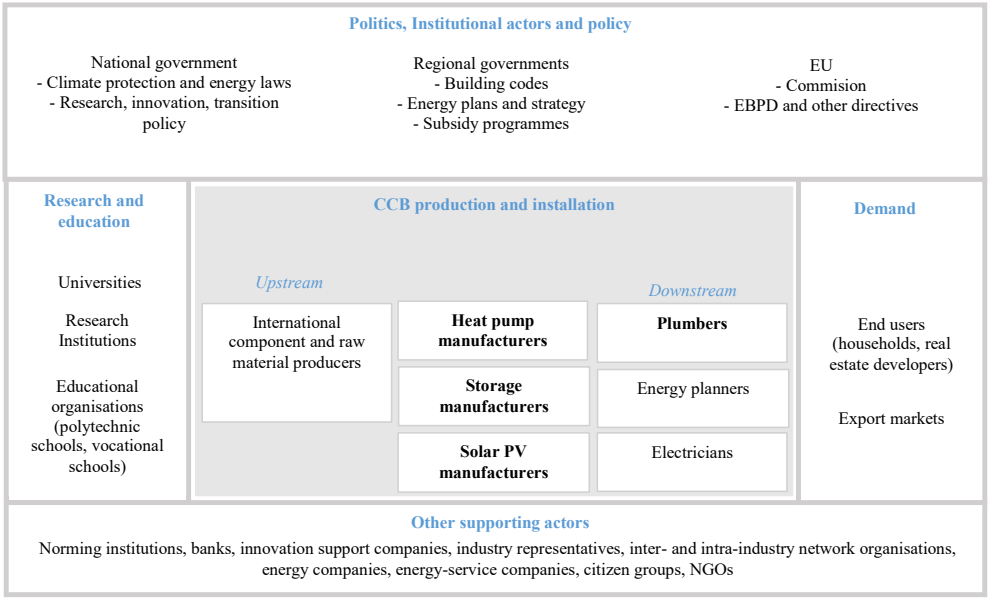


Fig. 2: Mapping of CCB innovation system actors - layout according to Hekkert et al. (2011) *[4]*. Key actors in bold.

A fruitful TIS does not develop overnight, but rather is formed with time during a complex build-up process [7]. A growing body of innovation system research has studied this buildup process by analyzing system functions (=key actions). This provided the starting point for the construction of our expert interview guidelines and provided support for our coding strategy in the data analysis section.

4. Methodology

This study adopts a mixed-method research (MMR) approach – an approach that combines at least one element of qualitative research with one element of quantitative research with the aim of increasing the depth of the investigation [8]. The benefits of mixed-methods research are increasingly recognized by the social science community, with authors such as Jungmann et al. (2015) [9] advocating for its wider application in multidisciplinary research domains such as that of innovation studies. The investigation is thus divided into two stages, as described in the following.

4.1. Expert interviews

In a first stage, 11 semi-structured expert interviews are conducted with key actors within the CCB TIS to identify potential barriers to CCB diffusion in Austrian 1-2 family housing segment. Expert interviews are an effective interviewing method commonly used in exploratory research to collect data about a specific field of interest. Following Meuser and Nagel (2004) [10], expert knowledge can be characterized as "specific knowledge in a particular field of action". While there is much ongoing debate about what constitutes an "expert", we adopt the broad definition of Bogner (2002) [11], where an expert is any actor who, due to his or

her current and past professional experiences, is in possession of a (institutionalized) competence to provide information on a specific topic.

Interviewees were selected using a theoretical sampling strategy [12] and snowballing (interviewees suggest further interview candidates). The aim was to include key actors relevant for the production and market diffusion of CCBs in Austria. The researcher teams' experience-based knowledge on the development and diffusion of other energy-innovations in the Austrian building sector, aided them in identifying these actors. The interview-sample thus included: 3 energy and building innovation researchers, 4 heat pump and storage technology producers, 1 plumber, 1 regional official responsible for regional energy-planning and 2 real estate developers. Focus was placed on regional diversification and on professional experience within the 1-2 family housing segment. Insights from a brief review on energy-innovation and TIS research provided the basis for the construction of the interview guidelines. Each interview was started with a brief introduction into the research project and technical overview of CCBs by the interviewer. The recorded interviews were transcribed, and a qualitative content analysis is conducted. In line with Mayring (2012) [13] the transcribed interviews were (1) openly coded, then (2) axially coded and finally (3) selectively coded to generate categories of barriers. The interviews and coding were conducted in German, then translated into English by the research team.

4.2. Survey

The target population for the survey were key industry actors involved in the development and diffusion of CCBs in Austria. Survey participants were provided with a concrete definition of a CCB prior to the survey (see section 2), then asked to rate the barriers collected during the expert interviews with respect to their relevance for the diffusion of CCBs in Austrian 1-2 family houses. In line with general opinion research, as reviewed by Marsden and Wright (2010) [14], a five-point Likert scale from 1 (irrelevant for CCB diffusion) to 5 (completely relevant for CCB diffusion) was selected for the survey. A pre-testing of the survey was conducted to ensure the questions and rating schemes were comprehensible by the target survey-participants.

The survey was initially disseminated to the participants of a workshop during the e-nova conference in November 2020 (https://www.fh-burgenland.at/news-termine/veranstaltungen/e-nova-2020/). The conference brings together researchers and interested professionals from the energy, buildings and environment domain across Austria, thus providing for a very valuable and informed survey participant sample (n=30). The survey was then further disseminated across the networks of the research team's institutional networks, yielding a total sample size of n=58.

Due to the limited sample size, we decided to limit the analysis to a descriptive statistical analysis. Given a sufficiently large and representative sample, a multivariate analysis will be presented in a follow-up paper.

5. Results

5.1. Expert interview findings

The expert interviews lasted between 30 and 50 minutes and were conducted between August and October 2020. All interview recordings were transcribed and deleted upon transcription. The anonymity of the interviewees was consistently safeguarded. The qualitative analysis yielded 45 barriers, clustered into 6 categories: Financial barriers (F), information barriers (I), regulatory and policy barriers (R), barriers related to subsidies (S), technical barriers (T) and stakeholder-specific resistance (W). See Table 1 below. Note that the table also includes the survey rating results (column *"Score A(R/M/P)"*, which will be discussed in section 5.2.

Table 1 Experts Interview results and score of the survey (A)ggregated value and (R)esearcher-, (M)anufacturer- and (P)lumber-specific. The 10 highest rated barriers are indicated with a bold style score.

Financial barriers		Score A (R/M/P)
CF1	Installation costs are too high for households	2.7 (2.5/2.7/2.7)
CF2	System costs are too high for households	2.9 (2.5/3.1/2.9)
CF3	The efficient use of CCBs requires extensive refurbishment efforts by households	3.3 (3.5/3.4/3.3)
CF4	Planning bureaus lack the financial incentive to plan CCBs	3.2 (3.4/3.5/2.9)
CF5	Energy consultancy costs are too high for households	2.3 (2.0/3.2/2.1)
CF6	Older households prefer systems with low upfront costs over systems with low operating costs	3.1 (3.4/3.0/3.1)
CF7	If the existing system is functional, households lack the financial incentive to switch to CCBs	3.6 (4.6/3.4/3.4)
Information barriers		
CI1	Better information on flammable refrigerants is required	3.5 (3.9/3.7/3.3)
CI2	**The general shortage of skilled workers reduces product and service quality in the construction market**	**4.0 (4.1/4.1/3.8)**
CI3	CCBs are generally unknown by plumbers	3.4 (3.4/3.9/3.0)
CI4	The comparison of combined products, like CCBs, with individual products, like heat pumps, is difficult	3.1 (3.8/3.7/2.0)
CI5	System labeling could help but is rarely used in practice	3.7 (3.6/3.8/3.8)
CI6	Information shortages among older households reduces propensity to switch to CCBs	3.7 (3.9/4.1/3.4)
CI7	There is no central CCB contact for households.	3.5 (4.0/3.7/2.9)
CI8	**There are diverging opinions on the usefulness of CCBs in un-renovated buildings**	**3.8 (3.9/3.9/3.4)**
Regulatory barriers		
CR1	Relevant technical international and national norms are unharmonized	3.2 (3.3/3.6/3.3)
CR2	**The regulation on maximal sound-emissions is unharmonized**	**3.8 (3.7/4.1/3.7)**
CR3	**Requirements for thermal refurbishment and withdrawal from fossil fuels are not strict enough**	**4.0 (4.1/3.9/4.2)**
CR4	The directive on refrigerants is outdated	3.1 (2.5/3.5/3.1)
CR5	There is no universal coefficient-of-efficiency for energy systems that considers storage-management	3.6 (3.9/3.6/3.6)
CR6	**National property law requires unanimous consent among the ownership community**	**4.2 (4.2/4.3/4.4)**
CR7	Uncertainty about future feed-in-tariffs reduce the incentive to switch to PV-coupled systems	3.3 (3.3/3.6/3.3)
Subsidy-related barriers		
CS1	**Subsidy schemes are not harmonized between federal states**	**3.9 (3.9/4.3/3.9)**
CS2	Subsidies for air-based heat pumps are insufficient	3.2 (3.1/3.9/2.9)
CS3	**Subsidies for ventilation systems are insufficient**	**3.7 (3.9/4.1/3.7)**
CS4	Subsidies for other CCB components (storage technologies, PV, etc.) are insufficient	3.5 (3.7/3.8/3.5)
CS5	Federal subsidies prioritize biomass-based systems	3.4 (3.3/4.4/2.8)
CS6	Subsidies for energy consultancy and supply of public energy consultancy services are insufficient	2.9 (3.1/3.5/2.6)
CS7	**The application process for relevant subsidies is complicated and lengthy**	**3.8 (4.2/4.4/3.4)**
Technical barriers		
CT1	Sound emissions are too high	3.3 (3.4/3.2/3.3)
CT2	There is limited space for indoor components	3.2 (3.2/4.1/2.5)
CT3	Without thermal refurbishment, system efficiency is limited	3.5 (3.7/3.7/3.8)
CT4	**If flammable refrigerants are used, this can cause difficulties for indoor installation**	**3.8 (3.7/4.1/3.5)**
CT5	CCBs are not flexible enough for their use in renovation cases (e.g. combinable with existing components)	3.1 (3.0/3.5/3.4)
CT6	If a ventilation system is included in the CCB, this can complicate the installation process	3.6 (3.6/4.4/3.3)
CT7	There is no universal communication protocol for energy systems	3.7 (3.8/4.3/3.2)
CT8	A CCB must be able to withstand power outages for extended time periods	2.3 (2.1/2.3/2.6)
Stakeholder-specific resistance		
CW1	The efficient use of CCBs requires behavioral adaptations by households	2.9 (2.6/3.6/2.8)
CW2	**Households prefer simple systems that require minimal adjustments to the building structure**	**4.0 (4.5/4.2/3.4)**
CW3	There is resistance against combined products by producers who do not produce these	3.2 (3.7/3.4/3.1)
CW4	There is resistance against combined products by plumbers, as the low required installation effort reduces their fees	2.7 (3.7/2.6/2.3)
CW5	There is resistance against combined products by housing companies, as they expect additional maintenance costs	3.1 (3.5/3.2/2.9)
CW6	Consultants and planers disregard CCBs, as they focus on systems that are eligible for subsidies	3.4 (3.2/3.7/3.5)
CW7	CCBs are only useful in passive-houses	1.9 (1.9/2.0/2.3)
CW8	Households that install complex energy systems tend to be demanding and require a lot of support	2.3 (2.1/2.9/2.4)

5.2. Survey findings

The close-ended survey was conducted using the online tool *Mentimeter* (https://www.mentimeter.com/) and was filled out by 58 individuals. The participants derived from different occupational groups from within the CCB TIS (as detailed in Section 3). Figure 1 shows the share of participants per occupational group. We find that 48 participants (83 %) were manufacturers (16 participants, 27 %), researchers (14 participants 24 %) or plumbers (18 participants, 31 %). We focus our analysis on the aggregate survey results and on occupational-group specific results of the aforementioned three groups only. The ten barriers with the highest mean rating across all occupational groups are indicated in bold in Table 1 above.

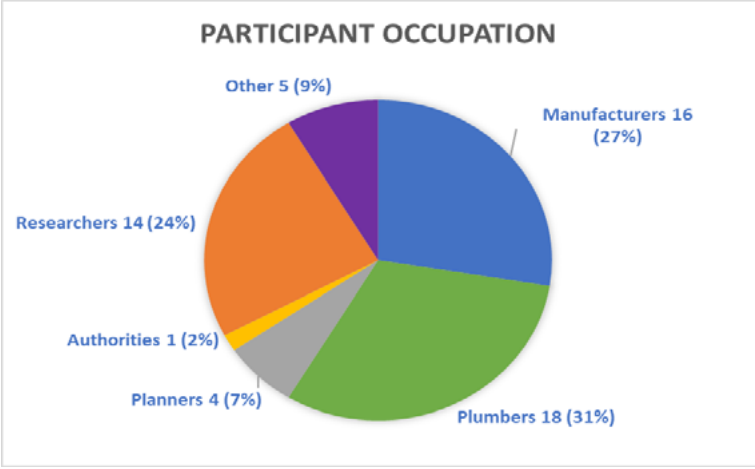


Fig. 3 Survey participants by occupational group

Notably, no financial barriers rank among the top 10 highest-rated barriers across occupational groups. In fact, the highest financial barrier (CF7) ranks 15th of 45. The top 10 highest-rated barriers are dominated by regulatory/policy-based barriers (CR6, CR3, CR2) and subsidy-based barriers (CS1, CS7, CS3).

The highest ranked barrier (CR6, score: 4.2) refers to the Austrian property laws (*Wohnungseigentumsgesetz* WEG2002). The law requires that any "unusual" changes to the building be unanimously agreed upon by the owner community. One abstention can block intentions to replace energy systems. This barrier is not relevant in a single-family house but becomes an issue in two- or multifamily houses. The second highest regulatory barrier for CCBs is CR3 (insufficiently strict requirements for thermal refurbishment and withdrawal from fossil fuels) with a score of 4.0. Without adequate regulatory pressure to reduce energy demand and emissions from buildings, demand growth for emerging renewable energy technologies like CCBs will be sluggish. The third regulatory barrier (CR2, score: 3.8) among the top 10 barriers, refers to unharmonized sound emission regulations across federal states in Austria. This requires and manufacturers to learn and monitor changes to different regulations when developing and installing CCBs all over Austria

Similarly, a lack of harmonization across subsidy-schemes between federal states (CS1, score 3.9) is rated a highly relevant barrier for CCB diffusion. Participants generally agree that complicated subsidy application processes and extensive waiting periods for subsidy-approval can hinder CCB diffusion (CS7, score 3.8). CS3 with a score of 3.7, refers to insufficient subsidies for ventilation systems. While not essential according to this study's CCB definition, several CCB currently on the market also include ventilation (see for example PKOM-4 from *Pichler Luft*). In several federal states, ventilation systems are not subsidized directly, but indirectly by means of subsidies for thermal refurbishments.

The fact that households prefer simple systems that require only minimal adjustments to the building structure (CW2, score 4.0) is rated as second highest overall CCB diffusion barrier. The installation of CCBs

can in fact involve extensive adjustments to the building structure – far more than just the replacement of one heating system for another. Therefore, solutions that can use as much as possible of the existing system should have advantages over others.

Two information/knowledge barriers are listed among the top 10 most relevant barriers: CI2 with a score of 4.0 addresses the general shortage of skilled workers in the CCB market. The need to plan and coordinate multiple CCB components require high-skilled work force. However, arguably many installation aspects could be simplified or standardized by manufacturers prior to installation. Diverging opinions on the usefulness of CCBs in unrenovated buildings (CI8, score 3.8) was also rated highly relevant.

Uncertainty among experts / consultants contribute to financial and technical uncertainty among decision-makers, thus reducing end-users' (household) willingness to invest and, similarly, plumbers' willingness to install CCBs. Finally, one technical barrier scores among the top 10 barriers. It refers to the difficulty of indoor installation of CCBs when flammable refrigerants are used (CT4, score 3.8). This is an issue for every new installed heat pump with a low GWP refrigerant and a high flammability. Some manufacturers solve this issue by placing all components that contain refrigerants in the outdoor unit. Others install additional safety measures to comply with the local guidelines and laws, or even reduce the amount of refrigerant in the system to fall below the minimum quantity for ignition.

The survey results disaggregated by occupational group yield interesting insights. Fig. 4 shows the barriers with mean researcher ratings greater than or equal to 4 (i.e. barriers rated "very relevant"). Researchers stress the relevance of household motivation: as long as the existing system is functional, there is little financial incentive to switch to new systems (CF7). With new oil-boilers living up to 20 years, this could mean that owners of homes newly outfitted with boilers within recent years, will lack the financial incentive to switch to new systems before the end of the 2030s. Researchers also stress the relevance of household preference for simple (non-invasive) system changes CW2, national property law unanimity clauses (CR6), complex and lengthy subsidy processes (CS7), lacking strictness of refurbishment strategy and regulations (CR3) and the lack of required skilled workers (CI2). Moreover, they stress that households in the 1-2 family housing segment have no central contact person for CCBS. In the multi-family residential building sector, this is the planer. Planning bureaus do not tend to operate in this 1-2 family segment. The current contact person for heating issues in this segment is the plumber. Plumbers are conventionally not trained to be able to perform complex technology-field overarching planning and coordinating.

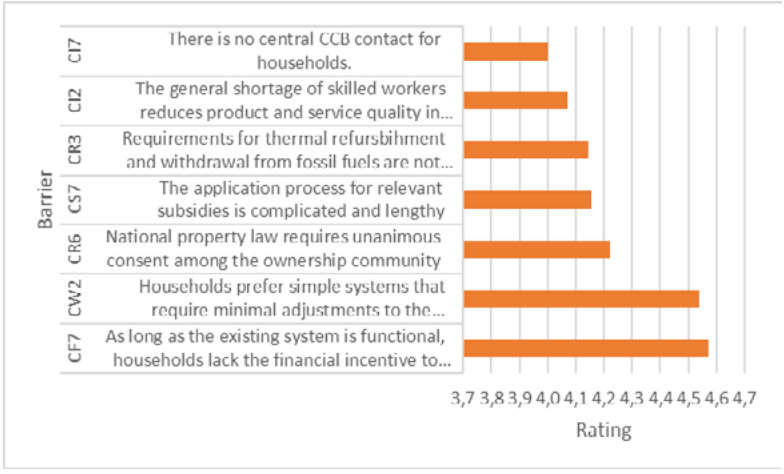


Fig. 4 Barriers rated 4 or higher by researchers

Thirteen barriers were rated greater than or equal to 4 in average by manufacturers, as seen in Fig. 5 We find a stronger perceived relevance of technical barriers and technology-oriented regulations among this occupational group. The surveyed manufacturers stress the relevance of CT6 (difficult retrofitting of CCBs with ventilation), CT7 (no standardized communication protocol), CT2 (limited space for indoor components)

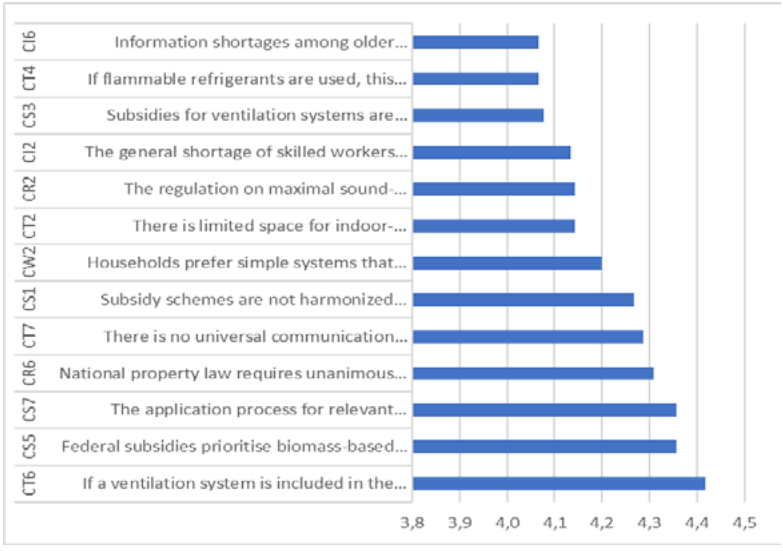


Fig. 5 Barriers rated 4 or higher by manufacturers

and CT4 (difficulty for indoor installation if flammable refrigerants are used). The focus on these technical/practical aspects by this group is unsurprising: They receive firsthand technical feedback from end-users and plumbers and can use this to improve product design, giving them a qualitative advantage over competitors.

Manufacturers consider the preferential treatment of biomass in federal subsidy schemes (CS5) a very relevant CCB barrier. Biomass is a strong competitor for heat pump-based systems in Austria, and very relevant for the 1-2 family house segment. Manufacturers also stress the generally complicated and lengthy subsidy application process (CS7) and their harmonization across federal states (CS1) that requires extensive bureaucratic efforts and reduces end-user incentives to apply for subsidies. They also stress the regulatory barriers CR6 (national property law, unanimity clause) and CR2 (unharmonized maximal sound emission regulation). Arguably, most of these regulatory and subsidy-based barriers refer to institutional phenomena that increase the *time* it takes to install CCBs. Thus, installation *speed* seems a crucial factor for CCB acceptance, according to manufacturers. Two information barriers are also rated highly: next to the issue of a general lack of skilled workers (CI2), manufacturers stress the limited access to relevant information among older generations. Of course, without awareness of innovative heating products and their benefits, households will not pursue them when engaging with their plumber.

Finally, two regulatory barriers were rated greater or equal to 4 by plumbers, as seen in Fig 6 below. CR6 (national property law unanimity clause) and CR3 (lacking strictness of refurbishment and withdrawal from fossil fuels). A closer look at the installers' survey results, yields a slightly larger variation in their rating behavior (standard deviation = 1.2 points), relative to researchers (= 1.12) and manufacturers (=1). This suggests a stronger heterogeneity of opinions among this occupational group and could explain its low count of highly relevant barriers. Exploring this further, however, exceeds the scope of this investigation.

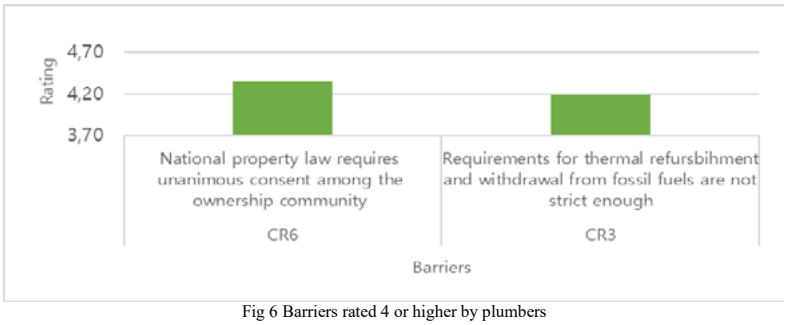


Fig 6 Barriers rated 4 or higher by plumbers

There are significant differences between the barrier-relevance perceptions of individual occupational groups. This is illustrated in the following figures (Fig. 7, Fig 8, Fig 9). The figures display those barriers with differences in ratings greater than 1 between two occupational groups.

Figure 7 displays those barriers for which the difference between the manufacturer rating and the researcher rating is greater 1. While researchers consider CW4 (resistance against combined products by plumbers, due to low installation effort, thus reduced revenues) a rather relevant CCB barrier (score: 3.7) manufacturers find it less of an issue (score 2.6). In fact, plumbers (score:2.3, cf. Fig 9 **오류! 참조 원본을 찾을 수 없습니다.**) consider it even less relevant. To understand this discrepancy, it would be interesting to further explore the channels through which CCBs reach end-users, and whether the installation of CCBs in fact reduce plumbers' revenues, thus disincentivizing their uptake into plumbers' service-portfolios. The knowledge gap between the researchers and the other two survey groups is worth uncovering, to better steer product development in the future. Next, we see manufacturers rating CS5 (biomass is prioritized in subsidies) higher than researchers. As manufacturers are directly involved in the market for heating technologies, while researchers are not, this result seems less surprising: heat-pump producers for example, directly compete with biomass-based heating technologies. Plumbers on the other hand, consider this less of a relevant barrier (score: 2.8). This might be an expression of end-users' non-monetary preferences, for example a preference for technical simplicity, or reliability. This raises the question of substitutability between renewable energy systems. Arguably, someone with a strong preference for heat-pumps, will not consider biomass-heating a reasonable substitute. In this case, a biomass-subsidy may then only affect his or her decision to invest in heat pumps weakly.

More of a surprise is the difference in CF7 (households lack financial incentive to switch to new systems if the old one is still functional), which was rated significantly higher by the researchers (4.6) than by the manufacturers (3.4). Plumbers (3.4) rate this barrier similarly to the manufacturers. They seem to believe, that households are not uninclined to switch away from a functioning system. As manufacturers and plumbers have more regular interaction with households, this insight could be of value to researchers developing systems that can compete against functioning systems, not just new systems. Finally, CF5 (high energy consultancy costs)

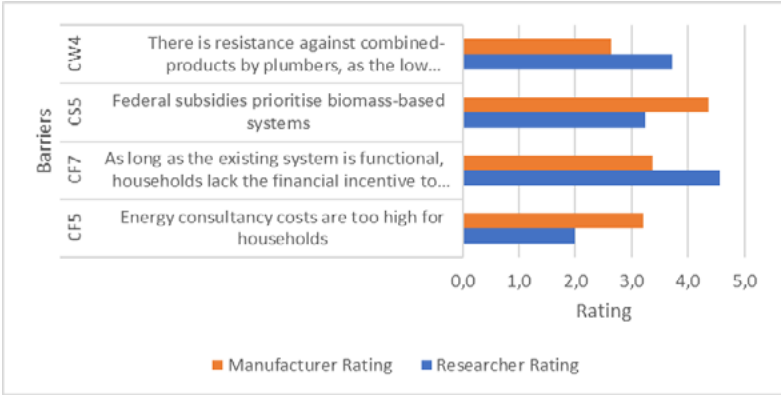


Fig. 7 Barriers with absolute difference in ratings greater than 1 – manufactures and researchers

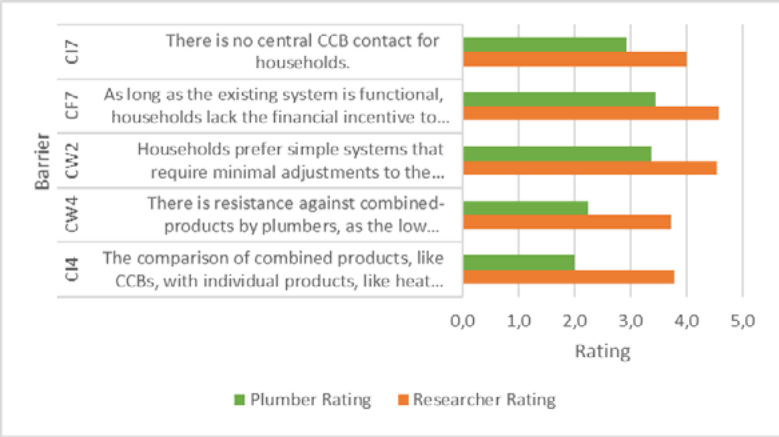


Fig 8 Barriers with absolute difference in ratings greater than 1 – plumbers and researchers

is rated rather irrelevant by researchers, while manufactures consider it relevant. Energy consultancy is a very heterogenous service and can range from a rudimentary consultancy provided (for free) by federal energy agents, to (costly) complex concept comparisons. These costs are often found lacking in technoeconomic studies of system alternatives.

Looking at Fig 8 we find that the largest rating differences between plumbers and researchers all refer to barriers perceived less relevant by plumbers. Like manufacturers, plumbers consider CW4 (plumber resistance against combined products) rather irrelevant for CCB diffusion, while researchers consider them very relevant. We also find that plumbers deem CI4 (difficulty of comparing combined systems) far less relevant than researchers (rating: 3.8) and manufacturers do (score 3.7., cf. Fig. 7 **오류! 참조 원본을 찾을 수 없습니다.**). One possible interpretation of this difference could be that the energy efficiency of the system is less important to plumbers than other points, such as reliability or simplicity of installation. Notably also, researchers seem to consider the fact that there is no central CCB contact for households (CI7) a more relevant barrier, while plumbers find it just relevant. Perhaps plumbers consider *themselves* the CCB contact for households. They may however be less informed about CCBs than researchers and might underestimate the extent to which CCB installation may differ from conventional heat pump installation processes.

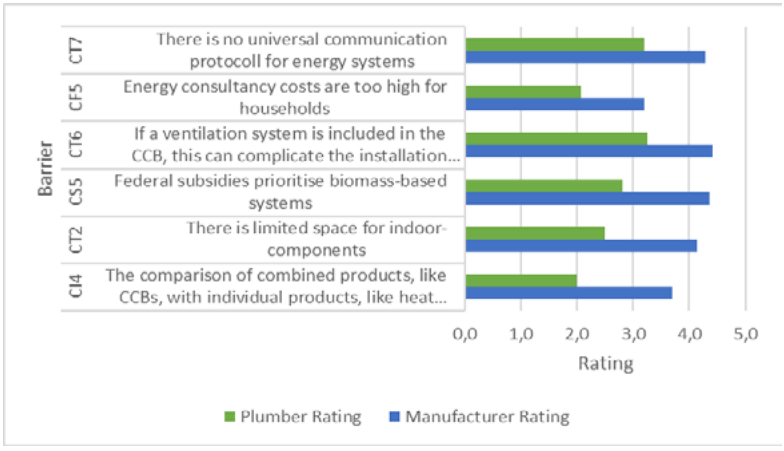


Fig 9 Barriers with absolute difference in ratings greater than 1 – plumbers and manufacturers

Similarly, as in Fig 8, we find that plumbers rate the relevance of six barriers lower than manufacturers. Differences largely concern technical barriers: CT7 (no universal communication protocol), CT6 (installation process if CCB it to contain a ventilation system) and CT2 (there is limited space for indoor components). Especially, the difference in CT2 ratings could be of great interest to manufacturers. Installers interact more

closely with the end-users, so this insight could be used by manufacturers to reconsider their product development strategy. The difference in CT7 could be explained by the fact that manufacturers tend to be specialized on specific components (e.g. heat pumps, or thermal storage technologies), thus integrating their component into a comfort climate box using components of other specialized producers will prove difficult given unharmonized protocols. This is an issue that installers may not feel as strongly, as they can simply go to those producers who provide complete CCBS (i.e. produce all components with harmonized protocols). The differences for CI4 (difficulty in comparing CCBs with individual products like heat pumps) and CS5 (biomass is prioritized by subsidies) were already discussed previously. Furthermore, the difference in rating of CI4 and CS5 could also stem from competition issues experienced by producers and felt less strongly by installers.

6. Discussion and Limitations

The selected methodology succeeded in generating interesting first insights into the dynamics of emerging energy-system in the Austrian 1-2 family building sector. Most importantly, it produced an extensive list of barriers blocking the diffusion of CCBs. Notably, we uncovered several potential knowledge gaps between occupational groups. Researchers could use these results to redirect their research to address practical barriers experienced by manufacturers and plumbers. Similarly, manufacturers and plumbers, two key actors in CCB diffusion, can use these findings to better align or synthesize product and service development to better reach the market.

However, the findings from the descriptive statistical analysis are limited. They do not allow for a deeper investigation of the *reasons* for rating-differences between occupational groups. Follow-up research should be conducted to further investigate these differences. Moreover, increasing the survey sample size to a representative size would allow for a more thorough multivariate analysis that could be of value to industry and research. Also including socioeconomic, geographic and company characteristics would prove interesting to understand differences in barrier-ratings. We also acknowledge the need to include the end-users into follow-up research and data collection. It would be interesting to discover whether supply-side perceptions of end-user energy-system adoption preferences are in line with actual household preferences.

Within the HPT Annex 55/ECES Annex 35, drivers and barriers for market diffusion for CCBs in all participating countries, from Europe, Asia and America, are investigated. The results from Austria will be compared to results from other countries, in order to map which barriers and drivers that are general for many countries and which are unique for Austria. As a next step, recommendations to important stakeholders/targets groups on both international and national level, to overcome the most important barriers, will be outlined, based upon the findings withing the Annex work.

7. Conclusion

CCBs are a promising, ecological alternative to fossil-based energy systems in the 1-2 family housing segment. Driving its development is the observation that demand for renewable energy technologies is obstructed by numerous barriers related to financial, technical, information-based, regulatory, subsidy-based factors and stakeholder-specific preference. This study contributes to the identification of these barriers and provides insights into their relevance from 3 key occupational groups involved in the development, innovation and diffusion of CCBs.

We find strong differences in the relevance-perception of barriers between researchers and the two key market actors for CCBs – manufacturers and plumbers. By aligning technology research with market actors' barrier perceptions, research can generate more problem-oriented solutions, thereby contributing to the acceleration of CCB diffusion in Austria. Diverging relevance-perceptions between the two key market actors, clearly presents a need for stronger industrial alignment. Manufacturers could benefit from adapting their product development strategies to the information supplied by plumbers about end-user preferences and technology-selection behavior. Household preference for simple systems requiring minimal adjustments to the building structure, call for CCBs that are largely integrable into the existing building and energy system. Moreover, as plumbers are (currently) the intermediary between manufacturers and the end-user, manufacturers could be advised to consider plumber needs and abilities in their product-development and marketing strategies. The current shortage of skilled labor, as well as the cross-technological nature of CCBs, call for the development of easy-to-install or standardized CCBs. Furthermore, small specialized components manufacturers (e.g. heat pump manufacturers, solar PV manufacturers), without the inhouse expertise or means

for producing all required components, could benefit from creating production consortia, to compete against large CCB producers.

As for policy and regulation, there is a unanimous call for the harmonization of building codes, subsidy schemes and norms. Moreover, calls for property law reforms and stricter obligations for thermal refurbishment are echoed by all surveyed system actors. Finally, policymakers are advised to focus on *actor-specific* barriers to develop truly effective measures.

Follow up research could yield more in-depth insights into CCB diffusion barriers as well as strategies for overcoming them, by extending the sample size and accounting for more system actors. Also, the inclusion of firm-level characteristics (e.g. firm size, segment-specific experience, networking behavior) could permit a more differentiated analysis of the results. We also advise to conduct a household-level investigation of heating-system preferences to augment this study's findings and generate fruitful insights for industry and research strategy.

8. Acknowledgements

The Austrian Research Promotion Agency (FFG) is gratefully acknowledged for funding this work under Grant No. 876733 and No. 871490. Furthermore, the authors would like to thank Christian Heschl (FH Burgenland), Andreas Heinz (TU Graz) and Fabian Ochs (Universität Innsbruck) from the Austrian IEA HPT Annex 55 team for discussions about CCB definitions and market barriers in the preparation phase of this study. Furthermore, we thank Christian Köfinger, Klemens Marx, Thomas Natiesta, Felix Hochwallner (all AIT) and Robert Kranner (FH Burgenland) for their help and support during the workshop at the e-nova conference

9. References

[1] Statistik Austria, 'Energiestatistik: MZ Energieeinsatz der Haushalte 2003-2018'. Jun. 11, 2019, Accessed: Dec. 12, 2020.
[2] P. Biermayr, 'Innovative Energietechnologien in Österreich. Marktentwicklung 2018', p. 253.
[3] R. A. A. Suurs, M. P. Hekkert, S. Kieboom, and R. E. H. M. Smits, 'Understanding the formative stage of technological innovation system development: The case of natural gas as an automotive fuel', *Energy Policy*, vol. 38, no. 1, pp. 419–431, Jan. 2010.
[4] M. Hekkert, S. Negro, G. Heimeriks, and R. Harmsen, 'Technological Innovation System Analysis', p. 16, Nov. 2011.
[5] A. Bergek, M. Hekkert, S. Jacobsson, J. Markard, B. Sandén, and B. Truffer, 'Technological innovation systems in contexts: Conceptualizing contextual structures and interaction dynamics', *Environ. Innov. Soc. Transit.*, vol. 16, pp. 51–64, Sep. 2015.
[6] A. Grubler *et al.*, 'Policies for the Energy Technology Innovation System (ETIS)', in *Global Energy Assessment (GEA)*, T. B. Johansson, N. Nakicenovic, A. Patwardhan, and L. Gomez-Echeverri, Eds. Cambridge: Cambridge University Press, 2012, pp. 1665–1744.
[7] M. P. Hekkert, R. A. A. Suurs, S. O. Negro, S. Kuhlmann, and R. E. H. M. Smits, 'Functions of innovation systems: A new approach for analysing technological change', *Technol. Forecast. Soc. Change*, vol. 74, no. 4, pp. 413–432, May 2007.
[8] C. Teddlie and A. Tashakkori, *Foundations of Mixed Methods Research: Integrating Quantitative and Qualitative Approaches in the Social and Behavioral Sciences*. SAGE, 2009.
[9] R. Jungmann, N. Baur, and D. Ametowobla, *Methods of Innovation Research: Qualitative, Quantitative and Mixed Methods Approaches*. 2015.
[10] M. Meuser and U. Nagel, 'ExpertInneninterview: Zur Rekonstruktion spezialisierten Sonderwissens', in *Handbuch Frauen- und Geschlechterforschung: Theorie, Methoden, Empirie*, R. Becker and B. Kortendiek, Eds. Wiesbaden: VS Verlag für Sozialwissenschaften, 2004, pp. 326–329.
[11] A. Bogner, Ed., *Das Experteninterview: Theorie, Methode, Anwendung*. Opladen: Leske + Budrich, 2002.
[12] B. G. Glaser and A. L. Strauss, *The discovery of grounded theory: Strategies for qualitative research*. New Brunswick: Aldine, 1967.
[13] P. Mayring, 'Qualitative Inhaltsanalyse', in *Handbuch Qualitative Forschung in der Psychologie*, G. Mey and K. Mruck, Eds. Wiesbaden: VS Verlag für Sozialwissenschaften, 2010, pp. 601–613.
[14] P. V. Marsden and J. D. Wright, Eds., *Handbook of survey research*, Second edition. Bingley, UK: Emerald, 2010.

13th IEA Heat Pump Conference
April 26-29, 2021 Jeju, Korea

Performance simulation of CO_2 transcritical cooling system with mechanical subcooling cycle using low GWP refrigerants

Sun-Ik NA, Gu Hwang KANG, Min Soo KIM* *

Department of Mechanical and Aerospace Engineering, Seoul National University, Seoul 08826, Republic of Korea

Abstract

The conventional automobile cooling systems using CO_2 as a refrigerant are hard to achieve proper cooling performance at hot summer season. In order to enhance the of CO_2 cooling systems, a mechanical subcooling cycle is proposed for application to vehicles with limited installation space. To analyze performance of the system, numerical models were built to predict the COP by changing the design parameters and heat exchanger arrangement. In addition, the maximum COP is determined by using an optimal method. The results show that the COP improves when applying the subcooling cycle, and the maximum COP is obtained based on the thermodynamic states at the outlets of the gas cooler and the sub-cooler.

Keywords: Low GWP; Carbon dioxide (CO_2); Mobile air-conditioning systme(MAC); Heat pump; Mechanical subcooling cycle

1. Introduction

In order to restrain global warming, F-gases with GWPs greater than 150 are prohibited that use it for vehicles by the mobile air conditioning system (MACs) Directive of EU. Also, the Kigali amendment to the Montreal Protocol and F-gas regulation of EU are required to cut the usage of the high GWP refrigerants. With these tightened environmental regulations, the development of the refrigerant cooling system using low GWP refrigerants become increasingly important.

The carbon dioxide (CO_2) have been attracted because its GWP is just 1. Also, the CO_2 boosted attention since the German Association of the Automotive Industry (VDA) officially announced that suitable air-conditioning systems for a future vehicle would apply CO_2 as a refrigerant in 2007. Since then, Kim *et al.* [1] deal with the effects of the operating parameters on the cooling performance for an automotive air conditioning system. A refrigeration system using CO_2 as a refrigerant, which is cheap and easily available, is a good choice if its performance is comparable to that of other systems. In this sense, a dedicated mechanical subcooling system is introduced in this study in an attempt to improve the performance of the CO_2 cooling system. The dedicated mechanical subcooling cycle in the CO_2 cooling system is an additional vapor compression cycle which uses a small charge amount of the low-GWP refrigerant. Thornton *et al.* [2] explored the optimum value of the subcooling evaporator temperature by developing a numerical model for an ideal subcooling cycle in consideration of supermarket applications. Khan and Zubair [3] presented that the performance of a system is related to the refrigerant saturation temperature of the sub-cooler and is enhanced as compared to a simple CO_2 cooling cycle. Despite the dedicated subcooling cycle has been studied, there are relatively few studies on automobile applications with it.

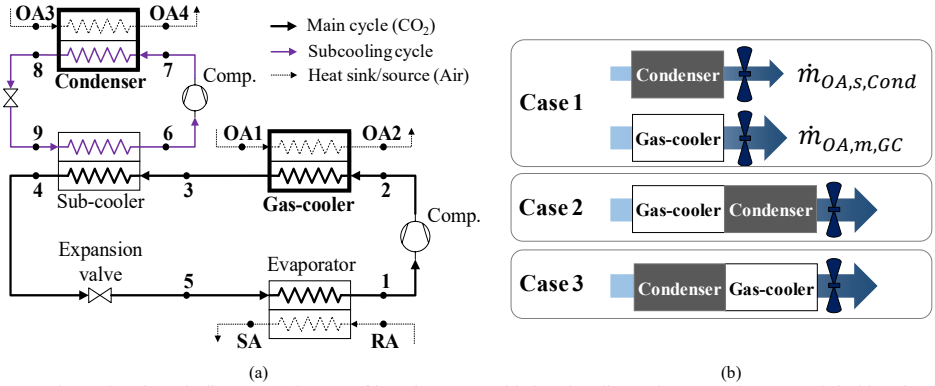
In this paper, in order to obtain the maximum performance of the mobile air conditioning system (MACs), the numerical model is built, and performance analysis is conducted using an optimal method. Also, the influence of the low GWP refrigerants such as R-290, R-600a, R-1270, R-32, R-1234yf, and R-1234ze(E) on the subcooling cycle is investigated. In addition to the above points, this paper investigates the impact of the install configuration of heat exchangers on system efficiency.

* Corresponding author. Tel.: +82 2 880 8362; fax: +82 2 880 6046.
E-mail address: minskim@snu.ac.kr (M. S. Kim) (Corresponding author).

2. System configuration and modeling

2.1. System configuration

The refrigeration system with mechanical subcooling consists of two as shown in Fig. 1(a). Each cycle uses a compressor, expansion valve, and heat exchangers. These two cycles are coupled with each other *via* a sub-cooler. The main cycle, as indicated by the bold line in Fig. 1(a), cools down the automotive cabin through heat exchange at the evaporator using CO_2. Meanwhile, the other cycle, named as the subcooling cycle, operates for the purpose of decreasing the quality of the CO_2 entering the evaporator of the main cycle by absorbing the heat at the sub-cooler.



(a) (b)

Fig. 1. The schematic diagram; (a) the CO_2 refrigeration system with the subcooling cycle. Two cycles are coupled with each other *via* a sub-cooler. (b) The layout cases according to the configuration of heat exchangers

For the refrigeration system using mechanical subcooling, it is necessary to install an additional condenser as compared to the conventional simple CO_2 cycle. This requirement is not a severe problem for a stationary system; however, for a vehicle, it should be considered that limited space is available for heat exchange with ambient air. Thus, the simulation cases were divided according to the heat exchanger configuration, as shown in Fig. 1(b). Case 1 is the case with two heat exchangers, the gas cooler of the main cycle and the condenser of the subcooling cycle, and they are located parallel with their faces to the outside of the vehicle, and the fans are operated separately. Meanwhile, in cases 2 and 3, the two heat exchangers are installed in a serial configuration, both cases have only one fan, and the air mass flow rate is the same through the two heat exchangers. Case 2 is that the gas cooler is located in front of the condenser of the subcooling cycle. Case 3 is that the gas cooler and the condenser are counterchanged compared with case 2.

2.2. System configuration

The energy balance equations for compressors and heat exchangers such as the gas cooler, sub-cooler, evaporator of the main cycle, and the condenser of the subcooling cycle are given in the following Eqs. (1)-(6):

$$\dot{W}_{m,Comp} = \dot{m}_{CO_2}(h_2 - h_1) = \dot{m}_{CO_2}(h_{2i} - h_1)\eta_{m,Comp} \quad (1)$$

$$\dot{W}_{s,Comp} = \dot{m}_s(h_7 - h_6) = \dot{m}_s(h_{7i} - h_6)\eta_{s,Comp} \quad (2)$$

$$\dot{Q}_{m,Evap} = \dot{m}_{CO_2}(h_1 - h_5) = \dot{m}_{RA}(h_{RA} - h_{SA}) \quad (3)$$

$$\dot{Q}_{m,GC} = \dot{m}_{CO_2}(h_2 - h_3) = \dot{m}_{OA,m,GC}(h_{OA2} - h_{OA1}) \quad (4)$$

$$\dot{Q}_{s,Cond} = \dot{m}_s(h_7 - h_8) = \dot{m}_{OA,s,Cond}(h_{OA4} - h_{OA3}) \quad (5)$$

$$\dot{Q}_{SC} = \dot{m}_{CO_2}(h_3 - h_4) = \dot{m}_s(h_6 - h_9) \quad (6)$$

$$COP_{c,AC} \equiv \frac{\dot{Q}_{m,Evap}}{\dot{W}_{m,Comp} + \dot{W}_{s,Comp}} \quad (7)$$

If the compressor performance is calculated by using a constant isentropic efficiency in Eqs. (1) and (2), the results might be different from actual situations because it considers only the inlet and outlet states of the compression process. The polytropic efficiency is known as it has the advantage of allowing real property effects to be included in a natural way because the polytropic efficiency calculates and integrates the work for

each differential step of the compression process. The polytropic efficiency can be translated analytically into an isentropic efficiency for a specific pressure ratio [4], as shown in Eq. (8).

$$\eta = \frac{W_{12,i}}{W_{12}} = \frac{\left(\frac{P_2}{P_1}\right)^{\left(\frac{k-1}{k}\right)}-1}{\left(\frac{P_2}{P_1}\right)^{\frac{1}{\eta_{PC}}\left(\frac{k-1}{k}\right)}-1} \quad (8)$$

The *UA* method is used in the model to obtain the results regarding the effect of varying the size of each heat exchanger. Because the *UA* values can represent the sizes of the heat exchangers [5-7].

All of the heat exchangers within the cycle were modeled to have countercurrent flow and were sliced into many segments so as to calculate the thermal properties of the fluid flowing inside. The *UA* values of a heat exchanger were calculated by summing the *UA* values of a segment as shown in the following Eqs. (9)-(12):

$$\sum_{k=0}^{n} UA_k = \sum_{k=0}^{n} \frac{\dot{Q}_k}{LMTD_k} \quad (9)$$

$$LMTD_k = \frac{\Delta T_k - \Delta T_{k+1}}{\ln(\Delta T_k / \Delta T_{k+1})} \quad (10)$$

$$\Delta T_k = T_{H,k} - T_{C,k} \quad (11)$$

$$\Delta T_{k+1} = T_{H,k+1} - T_{C,k+1} \quad (12)$$

In order to obtain the maximum COP, the generalized pattern search method, which is a direct search algorithm, was used in this paper. The direct search is a suitable method for solving non-linear optimization problems because it is not required any information about the gradient of the objective function. The simulation was performed through several iterations until the variables were converged within the error bound.

The simulation model was developed using the MATLAB program, and the thermal properties were loaded from the REFPROP database [8]. The operating condition and constraints were set up for calculating a reference result. In order to compare the calculation results under various conditions, the cooling load of the evaporator in the main cycle was kept at 5 kW. The equivalent thermal conductance of the gas cooler ($UA_{m,GC}$) and the evaporator ($UA_{m,Evap}$) were designed 500 W/K in the main cycle. In the subcooling cycle, the equivalent thermal conductance of the condenser ($UA_{s,Cond}$) and the sub-cooler (UA_{SC}) were sat as 100 W/K.

3. Performance analysis

3.1. Optimal operating conditions

According to the literature [9, 10], the cooling performance is depended on the thermal state of the CO_2 at the gas cooler outlet, i.e., state 3 in Fig. 1(a). To find the optimum operation condition, new variables are introduced as following Eqs. (13, 14).

$$\Delta T_{3-4} \equiv T_3 - T_4 \quad (13)$$

$$\Delta T_{3-OA1} \equiv T_3 - T_{OA1} \quad (14)$$

The CO_2 temperature difference between the inlet and outlet of the sub-cooler is defined as shown in Eq. (13). It is proportional relation with the heat capacity of the sub-cooler. And the temperature difference between the CO_2 and air at the gas cooler outlet (ΔT_{3-OA1}) is defined as Eq. (14). The CO_2 pressure of the gas cooler is mainly affected by ΔT_{3-OA1} and the equivalent thermal conductance of the gas cooler ($UA_{m,GC}$). To explore the influence of ΔT_{3-4} and ΔT_{3-OA1}, the simulation was conducted under the same condition except the values of ΔT_{3-4} and ΔT_{3-OA1}. As a result, the COP changed in a concave downward shape according to two variables of ΔT_{3-OA1} and ΔT_{3-4}, which means that the maximum point exists according to not only the temperature and pressure of the gas cooler outlet, but also the decreased temperature by the subcooling cycle.

3.2. Refrigerant for the subcooling cycle

To investigate the effect by the refrigerant type of the subcooling cycle, the model covers the refrigerants with not only natural refrigerants but also R-1234yf, R-1234ze(E), R-152a, and R-32 which are regarded as promising refrigerants. Fig. 2 displays the results of the simulation according to the ratio of the refrigerant flow rate (ϕ) which is defined as ratio of the subcooling cycle refrigerant mass flow rate ($\dot{m}_s$) to the CO_2 mass flow

rate in the main cycle($\dot{m}_m$), i.e., $\phi \equiv \dot{m}_s/\dot{m}_m$. The result reveals the reveal that the type of refrigerant in the subcooling does not show a significant difference. Even though the cases of R-600, R-601a, and R-610 were obtained higher efficiency, these refrigerants would be not recommended because the evaporating pressures are lower than an atmosphere. Even if there are minute leakage, air (non-condensation gas) and moisture can enter the system. Then injected non-condensation gas drops the cooling capacity and moisture cause corrosive and harmful to system components [11].

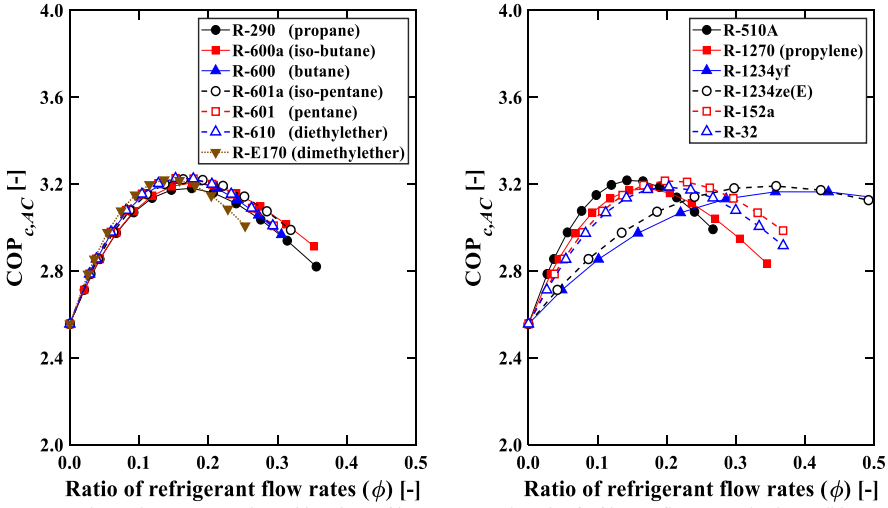


Fig. 2. The COP comparison with various refrigerants versus the ratio of refrigerant flow rate under the conditions. ($UA_{m,GC}$ = 500 kW/K, $UA_{s,Cond}$ = 100 kW/K, ΔT_{3-OA1} = 3°C)

While the optimum ratios of the refrigerant flow rate (ϕ_{opt}) of the hydrocarbon and R-32 were calculated similar values, the ϕ_{opt} of the R-1234yf and R-1234ze(E) were about twice. This result is obtained because the specific latent heat of vaporization of R-1234yf and R-1234ze(E) is roughly half with hydrocarbons'. In other words, the R-1234yf and R-1234ze(E) require a higher mass flow rate than hydrocarbons and R-32 to obtain the maximum COP.

3.3. Performance variation according to the heat exchanger configuration

In order to investigate the performance of the refrigeration system, the analysis was conducted by changing the configuration of heat exchangers. This analysis would be particularly necessary for automotive applications where the installation space for the mobile air conditioning system (MACs) is limited.

In case 1, the parallel configuration with two fans are applied with different capacities or operated at different revolution speeds. The air temperature of the gas cooler of the main and the condenser of the subcooling cycle is 35°C in both cases, i.e., $T_{OA1} = T_{OA3}$ =35°C. The air mass flow rate of the gas cooler in the main cycle, $\dot{m}_{OA,m,GC}$, is determined to reach the air temperature from 35 to 50°C in the gas cooler. Meanwhile, the air mass flow rate of the condenser in the subcooling cycle, $\dot{m}_{OA,s,Cond}$, is relatively calculated by the relative ratio of the air mass flow rate, as shown below in Eq. (15).

$$\psi \equiv \dot{m}_{OA,s,Cond}/\dot{m}_{OA,m,GC} \quad (15)$$

As a result, the COP was lower when it was placed in series than when it was placed in parallel. In case 2, the discharged air from the gas cooler is blowing into the subcooling cycle in order to form a higher condensation temperature than case 1, thereby increasing the pressure ratio of the subcooling cycle compressor and lowering the COP. In case 3, the air from the condenser of the subcooling cycle flows into the gas cooler of the main cycle. The increased air temperature of the gas cooler inlet leads to the raised pressure of the gas cooler and the reduced efficiency of the system. The results of case 3, in which the condenser of the subcooling cycle is arranged first, are not better than those of case 2. The first reason is that the performance is more sensitive to the pressure ratio of the main cycle due to the fact that the CO_2 refrigerant mass flow rate is greater

than the subcooling cycle refrigerant mass flow rate. Another reason is the thermodynamic property of the CO_2, as the thermodynamic state of the CO_2 gas cooler outlet exists above the CO_2 critical point. Near the critical point, the thermodynamic properties change drastically. For this reason, not even a slight difference from the optimum condition will affect the COP more sensitively.

The COP is improved when the air mass flow rate is high, but the power consumption of the fan should be considered for calculating the efficiency of the system. For this purpose, the system COP was newly defined as shown in Eq. (15) by adding the fan power consumption in the denominator.

$$COP_{c,sys} \equiv \frac{\dot{Q}_{m,Evap}}{\dot{W}_{m,Comp}+\dot{W}_{s,Comp}+\dot{W}_{Fan}} \tag{16}$$

The power consumption of a fan is strongly dependent on its specification and characteristics. Nevertheless, based on the fan laws [12], the power consumption of a fan is proportional to the cube of rotational speed when the density of the air and the diameters of the fans are constant, as shown in Eqs. (17)-(19):

$$\frac{\dot{W}_{Fan,\beta}}{\dot{W}_{Fan,\alpha}} = \left(\frac{D_{Fan,\beta}}{D_{Fan,\alpha}}\right)^5 \left(\frac{N_{Fan,\beta}}{N_{Fan,\alpha}}\right)^3 \left(\frac{\rho_{Fan,\beta}}{\rho_{Fan,\alpha}}\right) \tag{17}$$

$$\frac{\dot{V}_{Fan,\beta}}{\dot{V}_{Fan,\alpha}} = \left(\frac{D_{Fan,\beta}}{D_{Fan,\alpha}}\right)^3 \left(\frac{N_{Fan,\beta}}{N_{Fan,\alpha}}\right) \tag{18}$$

$$\frac{\dot{W}_{Fan,\beta}}{\dot{W}_{Fan,\alpha}} \cong \left(\frac{N_{Fan,\beta}}{N_{Fan,\alpha}}\right)^3 = \left(\frac{\dot{V}_{Fan,\beta}}{\dot{V}_{Fan,\alpha}}\right)^3 \cong \left(\frac{\dot{m}_{Fan,\beta}}{\dot{m}_{Fan,\alpha}}\right)^3 \tag{19}$$

In order to consider the fan power, a specific commercial radiator cooling fan was applied in the numerical model. It can blow about 0.89 kg/s by consuming 120 W at the 2,250 RPM. After considering the power consumption of fans, the system COPs are at their maximum points at a certain total air mass flow rate, as shown in Fig. 3. This result shows that fan power should be a design parameter of focus in the design of a MAC.

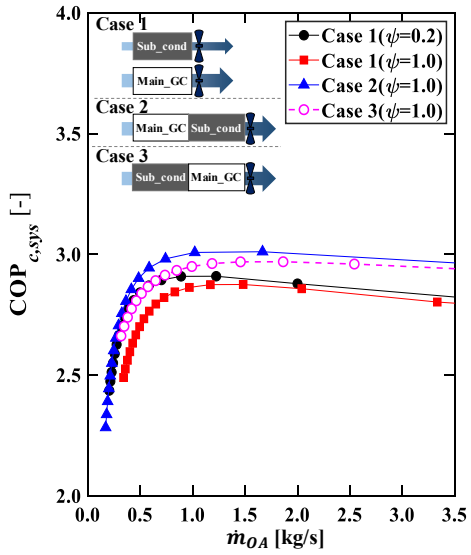


Fig. 3. The system performance ($COP_{c,sys}$) variation including the fan power consumption according to the total air mass flow rate. In contrast with $COP_{c,AC}$ which is calculated in Fig. 11, the $COP_{c,sys}$ is additionally considered energy consumption by the fan when obtaining the system efficiency. ($\dot{m}_{OA,m,GC}$).

4. Conclusions

This paper was conducted the thermodynamic analysis to investigate the performance of the CO_2 refrigeration system with the mechanical subcooling cycle using Low GWP refrigerants for a vehicle. The simulation was also conducted varied on the arrangement of the heat exchangers.

The results of this study show that the performance of CO_2 cooling system will be about 25% enhanced by using the subcooling cycle with the optimum operating condition. In order to obtain the optimum result, parameters such as mass flows of refrigerant, CO_2 temperatures and pressures at the gas cooler outlet and the sub-cooler outlet were variated. When the refrigerant mass flow rate in the subcooling cycle is optimum, the refrigerant type does not have a substantial effect on the performance. However, the systems using R-1234yf and R-1234ze(E) require a higher mass flow rate than hydrocarbons and R-32 to have the maximum COP. Because the specific latent heat of vaporization of R-1234yf and R-1234ze(E) is roughly half with hydrocarbons'.

Meanwhile, in order to implement the proposed mechanical subcooling system, heat exchangers would be additionally installed. If installation space is limited in a vehicle, design parameters and configuration should be considered about heat exchangers and fans. For this reason, performances were calculated according to heat exchanger arrangements. When two heat exchangers are installed serially, the gas cooler of the main cycle should be set to face outside in front of the condenser of the subcooling cycle in order to obtain higher COP. In addition, this study suggests that the power consumption of fans should be considered in the design of the mobile air conditioner system.

Acknowledgements

This research was supported by the R&D Center for reduction of Non-CO_2 Greenhouse gases (2017002430001) funded by the Korea Ministry of Environment (MOE) as the Global Top Environment R&D Program.

References

[1] Kim SC, Won JP, Kim MS. Effects of operating parameters on the performance of a CO2 air conditioning system for vehicles. Applied Thermal Engineering. 2009;29:2408-16.
[2] Thornton JW, Klein SA, Mitchell JW. Dedicated mechanical subcooling design strategies for supermarket applications. International Journal of Refrigeration. 1994;17:508-15.
[3] Khan Ju-R, Zubair SM. Design and rating of dedicated mechanical-subcooling vapour compression refrigeration systems. Proceedings of the Institution of Mechanical Engineers, Part A: Journal of Power and Energy. 2000;214:455-71.
[4] Razak AMY. 2 - Thermodynamics of gas turbine cycles. In: Razak AMY, editor. Industrial Gas Turbines: Woodhead Publishing; 2007. p. 13-59.
[5] Klein SA. Design considerations for refrigeration cycles. International Journal of Refrigeration. 1992;15:181-5.
[6] Bejan A, Vargas JVC, Sokolov M. Optimal allocation of a heat-exchanger inventory in heat driven refrigerators. International Journal of Heat and Mass Transfer. 1995;38:2997-3004.
[7] Chen L, Sun F, Wu C. Optimal allocation of heat-exchanger area for refrigeration and air-conditioning plants. Applied Energy. 2004;77:339-54.
[8] Lemmon EW, Bell IH, Huber ML, McLinden MO. NIST Standard Reference Database 23: Reference Fluid Thermodynamic and Transport Properties-REFPROP, Version 10.0, National Institute of Standards and Technology, Standard Reference Data Program, Gaithersburg. 2018.
[9] Cabello R, Sánchez D, Llopis R, Torrella E. Experimental evaluation of the energy efficiency of a CO2 refrigerating plant working in transcritical conditions. Applied Thermal Engineering. 2008;28:1596-604.
[10] Kim MS, Kang DH, Kim MS, Kim M. Investigation on the optimal control of gas cooler pressure for a CO2 refrigeration system with an internal heat exchanger. International Journal of Refrigeration. 2017;77:48-59.
[11] Ananthanarayanan PN. Basic Refrigeration and Air Conditioning: McGraw-Hill Education; 2005.
[12] Jorgensen R. Fan Engineering: An Engineer's Handbook on Fans and Their Applications; Howden Buffalo: Inc; 1999.

13th IEA Heat Pump Conference
April 26-29, 2021 Jeju, Korea

A study on the performance of heat pump by mixing ratio of isobutane/propane mixed refrigerants

Gu Hwang KANG, Sun-Ik NA, Min Soo KIM* *

Department of Mechanical Engineering, Seoul National University, Seoul 08826, Republic of Korea

Abstract

Natural refrigerants have global warming potential (GWP) and ozone depletion potential (ODP), but typical natural refrigerants have low COP, too. On the contrary, hydrocarbon refrigerants have high performance. In this study, using the characteristics of mixed refrigerants that can maintain a constant temperature difference during phase change, performance of the cycle according to the change in mixing ratio of isobutane and propane was calculated and measured. At outdoor temperature of 35℃ and indoor temperature 27℃, COP of the cycle was maximized at isobutane ratio is near 0.8.

Keywords: natural refrigerant; mixed refrigerant; isobutane; propane; COP

1. Introduction

As environmental problems such as global warming and the destruction of the ozone layer have emerged around the world, regulations on existing CFCs, HCFCs, and even HFCs refrigerants are being tightened. Therefore, research on heat pumps using natural refrigerants with low GWP and ODP is actively underway. There are many kinds of natural refrigerants, such as hydrocarbon, carbon dioxide, and water. Especially, isobutane shows low compressor work because of low compression ratio, and propane has a high cooling capacity. There are many studies on mixed refrigerant using isobutane and propane.

Nawaz *et al.* [1] studied water heaters using a mixed refrigerant of isobutane and propane, and Wu *et al.* [2] studied absorption heating cycles using natural refrigerants and low-GWP refrigerants mixtures. He *et al.* [3] calculated COP and cooling capacity of propane and isobutane mixed refrigerant with varying mixing ratios. Simulation was performed after fixing the cooling capacity, and the condensation temperature was 54.4℃, and the evaporation temperature was -23.3℃. Jung *et al.* [4] also conducted a study on the performance coefficient and the cooling capacity per unit volume due to changes in the mixing ratio of propane and isobutane. It fixed the cooling capacity at 130 W, fixed the secondary fluid inlet temperature is -15℃, and outlet temperature at -21℃. Chen *et al.* [5] conducted experimental studies on isobutane and propane mixed refrigerants, in which case only results were found when the propane ratio was 0.30 to 0.55 without conducting for the overall mixing ratio.

In this study, the performance of the heat pump according to the mixing ratio of the hydrocarbon refrigerant, isobutane and propane mixture is analyzed through a simulation and experimental study.

* Corresponding author. Tel.: +82-2-880-8362; fax: +82-2-880-4301.
E-mail address: minskim@snu.ac.kr.

2. Simulation result

2.1. Characteristics of mixed refrigerant

In the case of a single refrigerant, the temperature remains constant when fluid phase is changed, and there is a pinch point where the heat exchange rate decreases. Therefore, the heat exchange with secondary fluid is not uniform. However, in the case of mixed refrigerant, temperature gradients exist even when phase change occurs, which has the advantage of maintaining heat exchange with secondary fluid.

2.2. Simulation condition

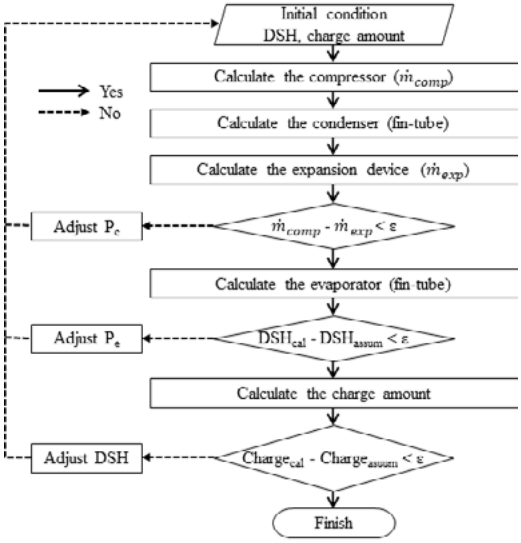


Fig. 1. Flow chart of simulation

The flow chart used of simulation is shows in Fig. 1. To maintain accuracy in the comparison between cycles, the degree of superheat was fixed at 5 K, and calculations were performed with the condenser pressure and evaporator pressure as variables to ensure the convergence of the cycles.

COP of cycles is calculated by equation (1) through compressor work and cooling capacity.

$$COP = \frac{Cooling\ capacity}{Compressor\ work} \tag{1}$$

In this simulation, reciprocating compressor model was used. Isentropic efficiency depends on pressure ratio, degree of superheat, etc., and isobutane and also have different isentropic efficiency in previous papers [6]. The enthalpy of compressor outlet can be calculated by equation (2)

$$h_{comp,out} = \frac{h_{comp,out,is} - h_{comp,in}}{\eta_{is}} + h_{comp,in} \tag{2}$$

The discharge mass flow rate of compressor, and compressor work are as shown in equation (3) and equation (4), respectively.

$$\dot{m}_{comp} = V_s \rho_{comp,in} Hz \left(1 - V_c \left(\frac{\rho_{comp,out}}{\rho_{comp,in}} - 1\right)\right) \tag{3}$$

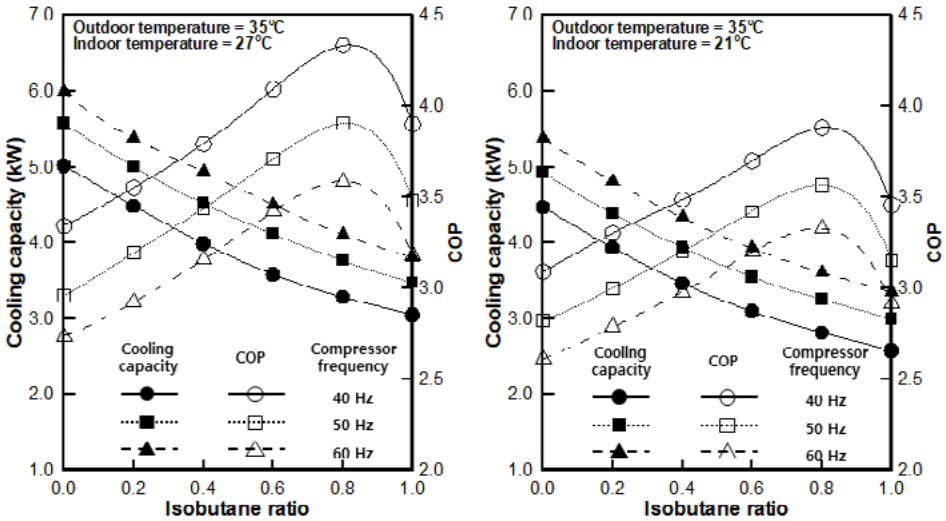
$$W_{comp} = \dot{m}_{comp}\left(h_{comp,out} - h_{comp,in}\right) \tag{4}$$

In this paper, simulation analysis of mixed refrigerants has been performed, and a corresponding heat transfer coefficient calculation expression is required. For mixed refrigerants, the heat transfer coefficient of condenser was calculated by referring model of Shah [7], and heat transfer coefficient of evaporator was calculated by referring model of Choi [8]. Heat transfer coefficient of Shah and Chis are represented in equation (5) and equation (6)

$$h_{tp,cond} = 0.023Re_{lo}^{0.8}Pr^{0.4}\left[(1-x)^{0.8} + \frac{3.8x^{0.76}(1-x)^{0.04}}{Pr_{cd}^{0.38}}\right]\frac{\lambda}{D} \tag{5}$$

$$h_{tp,eva} = E\left(0.023Re^{0.8}Pr^{0.4}\frac{\lambda}{D}\right) + SF_m\left(207\frac{k_l}{bd}\left(\frac{qbd}{k_l T_s}\right)^{0.674}\left(\frac{\rho_v}{\rho}\right)^{0.581}Pr^{0.533}\right) \tag{6}$$

Cycle calculation was performed using the above equations.



(a) 35℃/27℃ (b) 35℃/21℃

Fig. 2. Cooling capacity and optimal COP according to isobutane ratio

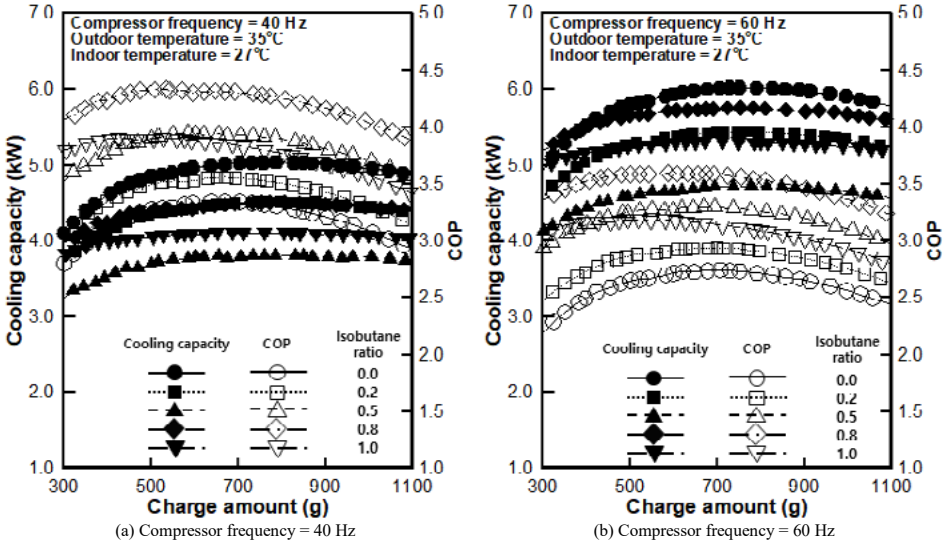
2.3. Simulation results

Simulation was performed on indoor temperature of 27℃, 21℃ under outdoor temperature of 35℃. The compressor frequency sets in the simulation are 50 Hz, 60 Hz, and 70 Hz. Fig. 2 is the cooling capacity and optimal COP according to the change of isobutane ratio at outdoor temperature is 35℃. Indoor temperature of (a) and (b) are 27℃ and 21℃, respectively. Isobutane ratio in x-axis is calculated by equation (7)

$$Isobutane\ ratio = \frac{m_{isobutane}}{m_{isobutane}+m_{propane}} \tag{7}$$

As isobutane ratio increases, cooling capacity decreases. This phenomenon due to the properties of isobutane and propane refrigerants. Propane refrigerant has better thermal properties that isobutane. However, isobutane has low compression ratio, so this leads low compressor work. Therefore, optimal COP exists between decreasing compressor work and increasing cooling capacity. Accordingly, as isobutane ratio increases, COP increases and decreases. The optimal isobutane ratio under all simulation compressor frequency and temperature conditions is approximately 0.8.

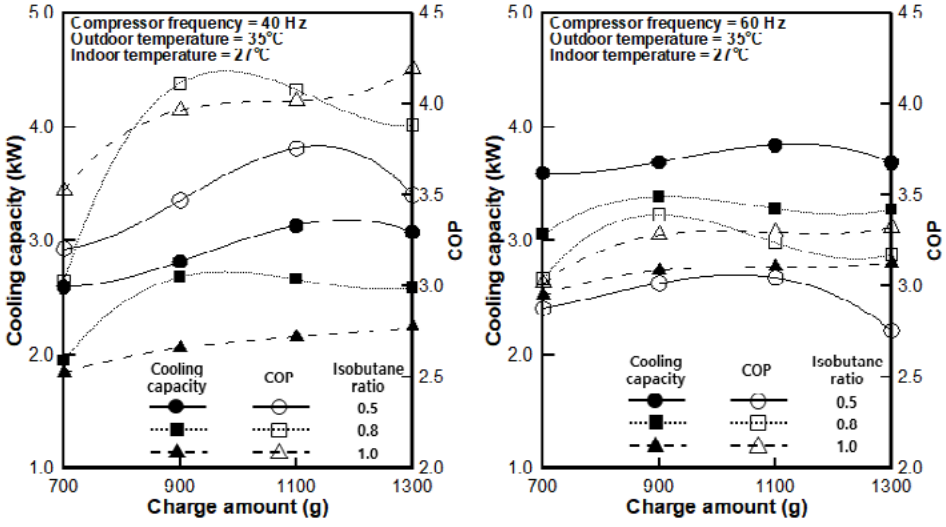
Calculation of the optimal amount of refrigerant according to the isobutane ratio was also carried out. The results can be seen in Fig. 3



(a) Compressor frequency = 40 Hz (b) Compressor frequency = 60 Hz

Fig. 3. Cooling capacity and COP according to refrigerant charge amount

Since isobutane and propane have different specific volume and the optimal refrigerant charge is present according to their respective isobutane ratio, calculation of the optimal refrigerant charge for each isobutane ratio is required to know the exact effect on the mixing ratio. As can be seen in Fig. 3, it can be seen that the optimum cooling capacity and the optimal refrigerant charge amount representing the optimal COP differ depending on the change in the isobutane ratio. This will be verified through further experiments.



(a) Compressor frequency = 40 Hz (b) Compressor frequency = 60 Hz

Fig. 4. Cooling capacity and COP according to the isobutane ratio and refrigerant charge amount

3. Experiment result

Based on the simulation results, experiments were conducted on the isobutane ratios of 0.5, 0.8, and 1.0, not on the overall mixing ratio. Furthermore, the simulation results showed that the optimal charge amount varies as the isobutane ratio changes, so the experiment was performed by varying the refrigerant volume. Outdoor temperature condition is 35℃, and indoor temperature condition is 27℃.

Fig. 4 shows experiment results. As the results of the simulations, the experiments also showed optimal COP near the isobutane ratio is 0.8. The cooling capacity also decreased as the isobutane ratio increased. In addition, experiment have identified the temperature distribution within the heat exchanger, shown in Fig. 8. As a result of the simulation, for single isobutane and propane refrigerants, the temperature remains constant before the superheated region, and the temperature glide occurs as the mixing takes place. The results of experiment have verified that the simulation results are close to reality.

4. Conclusions

In this study, a research was conducted on heat pump using mixed hydrocarbon refrigerants with very low GWP and zero ODP in preparation for continuously strengthened refrigerant regulations.

Simulation and experimental studies were conducted by mixing propane refrigerants with large cooling capacities and isobutane refrigerant with low compressor work. Simulation studies have shown that optimal COP near the isobutane ratio of 0.8 under various temperature conditions, and the temperature distribution inside the heat exchanger has also been calculated.

Simulation results were verified through experiment using a double-pipe heat exchanger, which allowed the optimal isobutane ratio of mixed refrigerants to be derived.

Acknowledgements

This research was supported by the R&D Center for reduction of Non-CO_2 Greenhouse gases (2017002430001) funded by the Korea Ministry of Environment (MOE) as the Global Top Environment R&D Program.

References

[1] Nawaz, K., Shen, B., Elatar, A., Baxter, V., Abdelaziz, O., 2017. R290 (propane) and R600a (isobutane) as natural refrigerants for residential heat pump water heaters. Applied Thermal Engineering 127, 870–883.. doi:10.1016/j.applthermaleng.2017.08.080

[2] Wu, W., Zhang, H., You, T., Li, X., 2017. Performance comparison of absorption heating cycles using various low-GWP and natural refrigerants. International Journal of Refrigeration 82, 56–70.. doi:10.1016/j.ijrefrig.2017.07.004

[3] He, M.-G., Song, X.-Z., Liu, H., Zhang, Y., 2014. Application of natural refrigerant propane and propane/isobutane in large capacity chest freezer. Applied Thermal Engineering 70, 732–736.. doi:10.1016/j.applthermaleng.2014.05.097

[4] Jung, D., Kim, C.-B., Song, K., Park, B., 2000. Testing of propane/isobutane mixture in domestic refrigerators. International Journal of Refrigeration 23, 517–527.. doi:10.1016/s0140-7007(99)00084-5

[5] Chen, Q., Yan, G., Yu, J., 2017. Performance analysis of an ejector enhanced refrigeration cycle with R290/R600a for application in domestic refrigerator/freezers. Applied Thermal Engineering 120, 581–592.. doi:10.1016/j.applthermaleng.2017.04.027

[6] Roskosch, D., Venzik, V., Atakan, B., 2017. Thermodynamic model for reciprocating compressors with the focus on fluid dependent efficiencies. International Journal of Refrigeration 84, 104–116.. doi:10.1016/j.ijrefrig.2017.08.011

[7] Shah, M.M., 1979. A general correlation for heat transfer during film condensation inside pipes. International Journal of Heat and Mass Transfer 22, 547–556.. doi:10.1016/0017-9310(79)90058-9

[8] Choi, T.Y., Kim, Y.J., Kim, M.S., Ro, S.T., 2000. Evaporation heat transfer of R-32, R-134a, R-32/134a, and R-32/125/134a inside a horizontal smooth tube. International Journal of Heat and Mass Transfer 43, 3651–3660.. doi:10.1016/s0017-9310(00)00005-3

13th IEA Heat Pump Conference
April 26-29, 2021 Jeju, Korea

Performance Test of Dense Membrane for Vaccum Membrane Dehumidification System

Jinwook Lee[1], Donik Ku[2], Sangmi Choi[3], Sanghun Jeong[2], Sujin Bae[1], Minsung Kim[1,2*]

[1]Department of Energy Systems Engineering, Chung-Ang University, 84 Heukseok-ro Dongjak-gu, Seoul 06974, Republic of Korea
[2]Department of Intelligent Energy and Industry, Chung-Ang University, 84 Heukseok-ro Dongjak-gu, Seoul 06974, Republic of Korea
[3]LG Electronics Inc., 84 Wanam-ro Seongsan-gu, Changwon-si, Gyeongsangnam-do 51554, Republic of Korea

Abstract

A membrane mass exchanger where water vapor is exchanged in a vacuum membrane dehumidification (VMD) system utilizes the vapor pressure difference between the permeate side and the feed side. However, differently from a typical moisture selective membrane, this membrane is located under pressure difference to accelerate the separation. Thus, a new approach to validate performance of the water vapor selective membrane is required. In order to quantitatively measure the effect of this phenomenon on the moisture permeability, an experimental system was setup to measure water vapor selectivity and permeance under the presence of absolute pressure difference before and after the membrane. So far, it is known that the performance of membrane is only a function of partial pressure of vapor. However, from the experiment, it is observed that selectivity and permeance are also changeable by absolute pressure difference due to the physical deformation caused by absolute pressure difference across the membrane.

Keywords: Permeance, Selectivity, Dense membrane, Dehumidification ;

1. Introduction

The energy consumption for air conditioning is constantly increasing. And dehumidification loads account for a large part of the cooling load. Therefore, many systems are currently being developed to replace the vapor compression cycle, and membrane heat pumps have been selected as one of the most feasible system [2].

As a key component of membrane heat pumps, studies have continued to improve membrane performance. Membrane dehumidification models for performance analysis are considered ideal models operated only by the vapor pressure difference, which is different from the actual phenomenon. This difference is expected to be attributed to the influence of absolute pressure on the selectivity of the membrane separation. Bui et al. [3] study shows that the COP of the membrane heat pump changes depending on the selectivity of the membrane applied to the system. Therefore, the exact COP value of the designed model can only be calculated by pre-checking the selectivity and permeability of the membrane to be used according to the operating pressure in the system configuration. However, the membrane characteristic values mentioned in various existing papers are often the result of no specified experimental conditions, or only simple diffusion model, which is different from the actual system's conditions. So, in this work, we construct conditions similar to real-systems and then experimentally calculate selectivity and permeability.

2. Background

2.1. Dense membrane

The major purpose of membrane-based vacuum dehumidification is to separate water vapor from the air without vapor-liquid phase change. Thus the type of membrane is gas-gas separation type one. Gas separation

* Corresponding author. Tel.: +82-2-820-5973 ; fax: +2-82-3280-5867.
E-mail address: minsungk@cau.ac.kr.

membrane can selectively separate substance and can separate mixture using chemical potential difference between membrane sides. It can be made using various materials such as metal, ceramic and liquid, and mainly uses polymers that are easy to form. It can be largely divided into porous and dense membrane, of which no physical porosity exists that allows a substance to pass through a membrane.

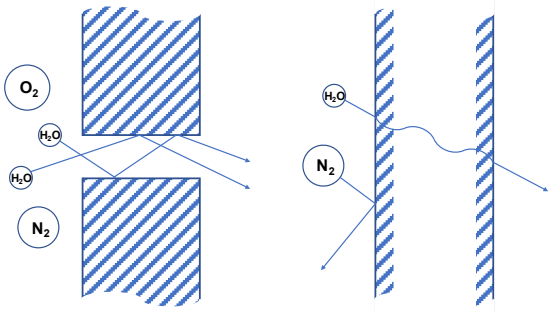


Fig. 1. Water vapor permeation in porous/dense membrane

In the case of dense membrane for water vapor separation, hydrophilic materials are usually bonded to hydrophobic polymer-based materials to form ion-nano channel in which water vapor molecules can move. Therefore, the solution-diffusion model can explain the movement of the substances, and steam vapor difference on both sides of the membrane acts as a driving force.

If you look at the previous analytical research data, it is often assumed that the selectivity is infinite using a dense membrane. However, in actual condition, the dense membrane also has a large but finite value. In this case, the design and operation of the system will be different, and not only steam but also air will pass through, so a method of periodically vacuuming should be devised.

2.2. Test method for water vapor permeability

The cup method measures the change in cup weight in an environment where water or desiccant filled cup is kept constant temperature and humidity [12]. If water is contained, the relative humidity inside the cup is assumed to be 100% and the amount of evaporated water is calculated. If desiccant is used, the water vapor mass is calculated through the vapor absorbed as 0% relative humidity. Although it is the most commonly used method, it has the disadvantage of creating a boundary layer according to the concentration of substance before and after the membrane. Accordingly, the measurement varies greatly depending on the distance from the water and desiccant to the membrane, so error analysis is essential. There are also disadvantages of not being able to add various experimental variables such as pressure changes.

To overcome these disadvantages, devices have been suggested that not only measure simply by gravimetric but also reflect various experimental conditions such as spring stiffness. A typical example is constant–volume variable–pressure method that permeates water vapor from feed side to the permeate side [13]. Depending on the amount of water vapor permeated in the device, the pressure on the permeate side changes, which allows the permeability to be calculated. However, in the case of gases mixed with other gases and water vapor, only the permeation of water vapor can be measured.

Therefore, this work uses experimental methods that combine different experimental methods.

3. Experiment

3.1. Experimental setup

As explained above, the experimental device was built based on the cup method and constant–volume variable–pressure method among the measurements described earlier. In the constant–volume variable–pressure method, the permeated water vapor is the cause of pressure rise, allowing the measurement of the permeability to be made through pressure change and time flow, but not the permeability of the additional substances. Considering this, the desiccant of cup method is applied to ensure that all permeated water vapor is absorbed into the absorbent, and the increase in pressure is the result of nitrogen. This allows for the calculation of permeability for both substances.

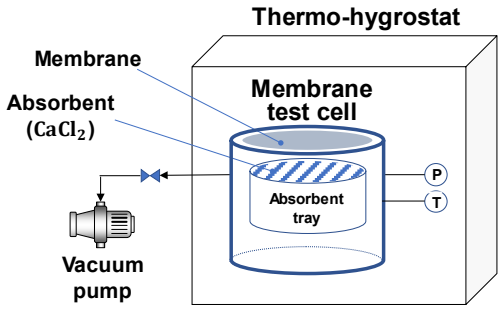


Fig. 2. Schematic diagram of test setup

The above figure represents the whole experimental device. The test cell has two tabs for the sensor, one for decompression or pressurization. In the experiment, the gas must pass through the membrane to enter the test cell, and the O-ring was installed in double to prevent leakage to the side of the membrane. The test cell was used in the experiment after checking its confidentiality through a pressure test in advance. In addition, a tray containing calcium chloride, was built in the test cell to keep the relative humidity at 0% and to measure the weight of the transmitted water vapor. During the experimental procedure, absolute pressure difference was generated before and after the membrane by vacuum pump or nitrogen tank, and the test cell was inserted into the thermo-hygrostat so that the experiment could be carried out at a constant temperature and humidity.

3.2. Membrane sample

The membrane used in this study was produced by dispersing silica particles, which are hydrophilic inorganic nanoparticles, to polyurethane, a hydrophobic material, and then joining them to polyamide supports. Membrane produced in this way is not over-spoiled by moisture, so its durability is complemented so that frequent replacement is not required.

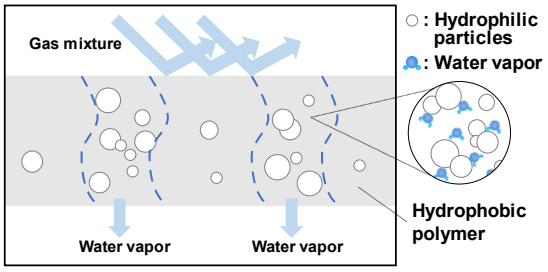


Fig. 3. Characteristic diagram of membrane sample used in experiment

The figure above shows the cross section of the membrane sample used. When hydrophilic particles are placed in the membrane as shown without being concentrated or too dispersed, ion-nano channels are created. In this case, water vapor inside the membrane moves in a molecular state by repeatedly adsorption and desorption to the hydrophilic particle surface.

3.3. Test condition and test

The experimental conditions were created close to the environment in which the actual system could be applied, considering the problems described earlier. It is arranged in the table below. The experiment was conducted in two main ways. The first is to compare two cells with nitrogen permeation set in opposite directions to see if nitrogen permeation affects water vapor permeability in a dense membrane. In addition, the experiment was conducted with the existing cup method, comparing the variation in the permeability with the occurrence of absolute pressure difference. Second, we measured the permeance and selectivity changes by changing humidity. The data from the measurements allow us to predict indicators in different humidity conditions with extrapolation.

Table 1. Experimental conditions for test setup

Variables	Value
Absorbent tray mass	70g - 100g
Distance from membrane to absorbent	5mm
Relative humidity	30% – 70%
Temperature	30℃
Test unit pressure (abs)	40kPa, 160kPa

3.4. Membrane performance unit

First, weight change of the absorbent tray, the area of the membrane through which the substance can be permeated in the cell, and the measurement time can be used to obtain the mass flux of water vapor.

$$J_{H_2O} = \frac{\Delta m_{CaCl_2}}{A_m \Delta t} \tag{1}$$

Since the above value does not consider the volume of the gas, the molar mass of H_2O is distributed to convert the mass of water vapor into mole. Since driving force of water vapor movement is vapor pressure difference, we separated steam pressure out of the mass flux to calculate the permeance. Since the steam pressure inside the cell is zero, the steam pressure difference can be calculated through the humidity of the chamber. In addition, multiplying the constants to fit the units allows the expression to be arranged as follows.

$$P_{H_2O} = \frac{\Delta m_{CaCl_2}}{M_{H_2O} p_v A_m \Delta t} \times \frac{10^{10}}{3.35} \tag{2}$$

The unit of GPU value obtained by the above formula is mol/m^2·s·Pa. The volume inside the cell is constant but the pressure continues to change, so the mass of permeated nitrogen can be calculated through the ideal gas equation. The slight change in volume due to compression of the O-ring, deformation of the membrane was ignored and the volume and pressure changes in the cell were calculated by the ideal gas equation. The mass flux of nitrogen obtained through this process is as follows.

$$J_{N_2} = \frac{\Delta m_{N_2}}{A_m \Delta t} = \frac{\Delta pV / R_{N_2} T}{A_m \Delta t} \tag{3}$$

R_{N_2} is the ideal gas constant of nitrogen. As with water vapor permeability calculations, the mass of nitrogen is divided into the molar mass of nitrogen. And in this experiment, the driving force of nitrogen is the absolute pressure difference excluding water vapor pressure, so the formula was calculated by dividing the formula by $(p_{atm} - p_v) - p$.

$$P_{N_2} = \frac{\Delta pV / R_{N_2} T}{M_{N_2}[(p_{atm} - p_v) - p] A_m \Delta t} \times \frac{10^{10}}{3.35} \tag{4}$$

The unit is mol/m^2·s·Pa, such as the water vapor permeance value. The selectivity of membrane is calculated by the permeance of water vapor and nitrogen calculated from the above equations.

$$\alpha = P_{H_2O} / P_{N_2} \tag{5}$$

Calculated from the data measured at intervals of five minutes using the above expression, the sum of the values and the values calculated at the beginning and end of the experiment were consistent with the error range. Therefore, it can be said that the assumptions included during the composition process of the expression are reasonable.

Table 3. Real-time measurement data of the representative Test A and test B

	Test 1		Test 2	
Time [hr]	p(abs) [kPa]	Absorbent mass [g]	p(abs) [kPa]	Absorbent mass [g]
0	42.22	77.31	41.98	79.92
12	58.78	-	57.36	-
24	69.02	-	67.68	-
36	76.76	-	75.19	-
48	82.48	80.60	80.97	83.21

4. Result and discussion

4.1. Measurement data

The experimental data were recorded using the LabVIEW program. For the weight of the absorbent tray, the cells were dismantled before and after the experiment and measured using the scale. The above table shows the representative case data that have been repeated under certain measurement conditions. After 48 hours of experimentation, both cells increased by about 40 kPa to measure the amount of nitrogen passed, and it can be confirmed that the weight of the absorbent tray has increased due to the permeation of water vapor.

Figure 4 shows the change in pressure within the cell over the measurement period. Since it was assumed that all the water vapor passed into the cell is absorbed by the absorbent, the cause of the increased pressure is the result of the permeation of nitrogen. The slope of the graph decreases over time, which can be interpreted as a weaker driving force as the absolute pressure difference decreases. Therefore, it was confirmed that the drive forces of nitrogen and air can work even in a dense membrane and that consideration is required.

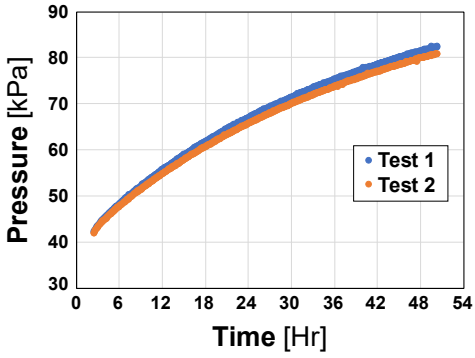


Fig. 4. Pressure variation in test cell

4.2. Calculation result

4.2.1. Effect of absolute pressure difference

This section presents the experimental results for checking the effects of absolute pressure difference in a water vapor permeability of dense membrane. At the start of the experiment, the absolute pressure difference before and after the membrane formed by pressurization or decompression is the same as 60 kPa, but both nitrogen and water vapor are brought into the cell for Test A, and Test B allows nitrogen to penetrate outward. The data measured under the same 50% relative humidity conditions are listed.

As nitrogen permeates, it can be confirmed that the cell pressure in Test A increases, and the pressure in Test B decreases. The above measurements were presented by converting them into performance factors. The data measured by the cup method are also listed for comparison. The relative humidity was measured at 70% for the cup method measurement.

The selectivity was not indicated for Test B because it was the ratio of the substance permeated in the same direction, nor was the test cup measurement recorded because it was not possible to measure the permeance of nitrogen. When looking at the data, we can see that the permeability of the water vapor was measured the highest at Test A with the same direction of permeation of nitrogen and water vapor. Depending on the direction in which nitrogen is permeated in the test cell, and partly confirmed that the presence of absolute pressure difference affects the permeability of water vapor.

Table 4. Real-time measurement data of the Test A and Test B which has opposite directions of nitrogen permeation

	Test A		Test B	
Time [hr]	p(abs) [kPa]	Absorbent mass [g]	p(abs) [kPa]	Absorbent mass [g]
0	42.25	89.19	162.46	75.78
12	58.24	-	153.40	-
24	68.95	-	144.95	-
36	76.58	-	138.03	-
48	82.43	92.38	132.22	77.76

Table 5. Membrane performance factor values of Test A, Test B and cup method

Performance factor	Test A	Test B	CUP
Permeance (H_2O) [GPU]	3.56×103	2.08×103	1.68×103
Permeance (N_2) [GPU]	4.40	2.52	-
Selectivity [-]	808.29	-	-

Among the membrane-based vacuum dehumidification systems introduced in the introduction, in the case of the W-MVD system, the membrane is mounted before and after the vacuum compressor, and each condition creates the direction of the pressure difference, such as Test A and Test B. The experimental results show different indicator values even for the same membrane sample and should be used to take this part into account during the analysis process.

4.2.2. Membrane performance according to relative humidity

This section describes the changes in permeability measured by varying relative humidity. The relative humidity was changed from 30% to 70% according to the conditions set earlier, and the error value due to membrane damage was removed during the experiment. After converting the measurements into performance factor, it was expressed as an average. Calculations showed that the permeance of both H_2O and N_2 increased as the relative humidity increased, but the permeance increase of H_2O was greater, so was the value of selectivity.

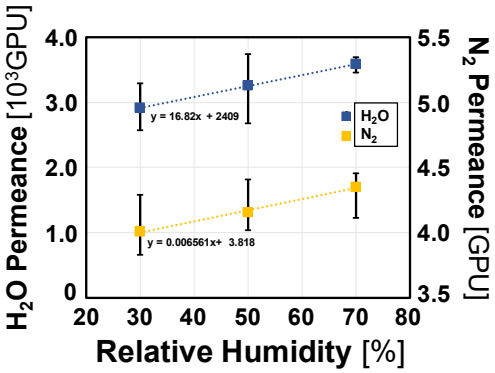


Fig. 5. Permeance variation of H_2O and N_2 according to relative humidity

The result of the calculation shows the data on the graph. The water vapor permeance formula used in this study is linearly proportional to changes in water vapor pressure, and data presented as actual averages can also be found to be close to linearity. The permeance of nitrogen also appears to be increasing like water vapor, which is interpreted as the effect of absolute pressure difference in the calculation formula has decreased as the water vapor pressure rises. Because both performance indicators exhibit linearity, the permeance of nitrogen and water vapor with changes in humidity was predicted through extrapolation. The trend line was calculated through the MATLAB curve fitting tool and the results were shown on the graph. Using this expression, the permeance and selectivity values for relative humidity of 0% were calculated, as shown in Table 1. The permeance value of H_2O is calculated as 2409 GPU and the permeance value of N_2 is 3.818 GPU and has a selectivity value of approximately 630.96. The following sections compare with data from existing studies.

4.3. Membrane performance factors comparison

The results of this experiment and analysis, and the conditions of the experiment were summarized in Table 6. Units were unified for comparison with the data previously investigated. Since permeance is an indicator calculated without considering membrane thickness, the measured membrane thickness average of 75 μm was multiplied by the result and converted to permeability.

Except for the test cases of the reverse direction and the cup method where selectivity data were unavailable, the remaining five results were placed on the Fig. 2 to compare with the data in the previous paper. From the results, water vapor permeability was high without considering experimental conditions. However, as the

selectivity is relatively low, additional device is required to prevent pressure rise of the compressor due to permeated N_2 if the corresponding membrane is used in the system configuration.

Table 6. Membrane factors data and condition in this paper

Test method	RH [%]	H_2O permeability [Barrer]	N_2 permeability [Barrer]	Selectivity [-]
Cup method	70	11390.51	-	-
Reverse permeation of N_2	50	15608.44	18.93	-
Test result	30	21821.67	30.08	725.56
	50	24425.44	31.16	783.81
	70	26868.04	32.04	838.47
Extrapolation	0	18067.5	28.64	630.96
	100	30682.5	33.56	914.37

5. Conclusion

In this study, experiments were conducted through simple experimental device to check the effect of absolute pressure difference on the performance of a dense membrane with water selective properties. There are several methods for measuring permeability and selectivity, but each threshold exists. Thus, in order to improve the shortcomings, a new experimental device was formed that fused the cup method with the constant-volume variable-pressure method.

The results of the cup method and reverse pressure gradient experiments show that there is an effect of absolute pressure difference on the movement of water vapor in a dense membrane, and it is concluded that consideration is necessary accordingly.

Nomenclature

A_m	area of membrane [m^2]	p_s	water saturation pressure [kPa]
b	width of masked edge [m]	p_v	water vapor pressure [kPa]
d	distance of absorbent from membrane [m]	Δp	pressure difference [kPa]
D	diffusion coefficient [-]	P_{H_2O}	water vapor permeance [mol/m^2sPa]
J_{H_2O}	mass flux of H_2O [g/m^2s]	P_{N_2}	nitrogen permeance [mol/m^2sPa]
J_{N_2}	mass flux of N_2 [g/m^2s]	R_{H_2O}	ideal gas constant of H_2O [kJ/kgK]
Δm_{CaCl_2}	mass variation of $CaCl_2$ [g]	R_{N_2}	ideal gas constant of N_2 [kJ/kgK]
Δm_{N_2}	mass variation of N_2 [g]	Δt	time variation [s]
M_{H_2O}	molar mass of H_2O [g/mol]	T	temperature [°C]
M_{N_2}	molar mass of N_2 [g/mol]	V	volume of cell [m^3]
p	pressure of test cell [kPa]	α	selectivity [-]
p_{atm}	atmospheric pressure [kPa]	δ	specimen thickness [m]

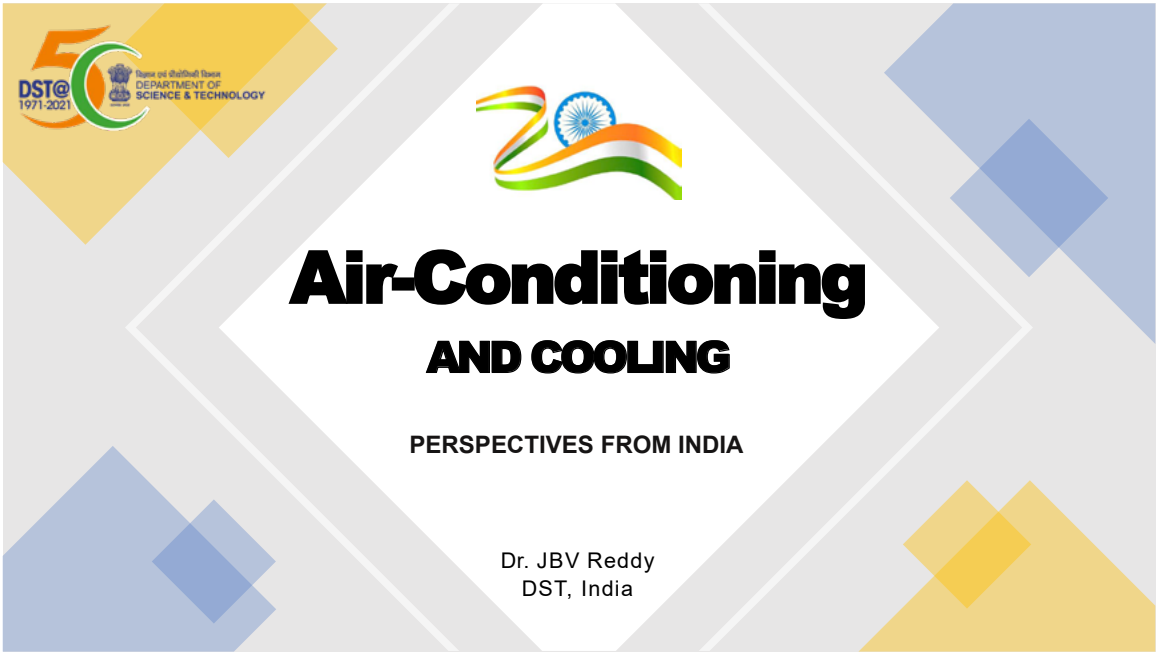
Acknowledgements

This research is jointly supported by National Research Foundation (NRF) (2019R1A2C1088694) funded by Ministry of Science and ICT, Korea Environmental Industry & Technology Institute (KEITI) (2020003060005) funded by Ministry of Environment, and Korea Institute of Energy Technology Evaluation and Planning (KETEP) (20192050100060, 20202020900290) funded by Ministry of Trade, Industry and Energy. Authors sincerely appreciate their supports.

References

[1] US DOE, Builing Technologies Office, Energy savings potential and RD&D opportunities for non-vapor-compression HVAC technologies, Office of Energy and Renewable Energy, March 2014.
[2] D.T. Bui, M. Kum Ja, J.M. Gordon, K.C. Ng, K.J. Chua, A thermodynamic perspective to study energy performance of vacuum-based membrane dehumidification, Energy 132 (2017) 106-115. http://dx.doi.org/10.1016/j.energy.2017.05.075
[3] ASTM International, Standard Test Methods for Water Vapor Transmission of Materials, E96/E96M
[4] S.A. Stern, P.J. Gareis, T.F. Sinclair, P.H. Mohr, Performance of a versatile variable-volume permeability cell. Comparison of gas permeability measurements by the variable-volume and variable-pressure methods, Journal of Applied Polymer Science 7 (1963) 2035-2051.

https://doi.org/10.1002/app.1963.070070607
[5] B.D. Freeman, Basis of permeability selectivity tradeoff relations in polymeric gas separation membranes, Macromolecules 32 (1999) 375-380. http://dx.doi.org/10.1021/ma9814548
[6] L.M. Robeson, The upper bound revisited, Journal of Membrane Science 320 (2008) 390–400. http://dx.doi.org/10.1016/j.memsci.2008.04.030
[7] R.W. Baker, J.G. Wijmans, Y. Huang, Permeability, permeance and selectivity: A preferred way of reporting pervaporation performance data, Journal of Membrane Science 348 (2010) 346–352. http://dx.doi.org/10.1016/j.memsci.2009.11.022
[8] Metz, S.J.; van de Ven, W.J.C.; Potreck, J.,; Mulder, M.H.V.; Wessling, M. Transport of water vapor and inert gas mixtures through highly selective and highly permeable polymer membranes, Journal of Membrane Science 251 (2005) 29–41. http://dx.doi.org/10.1016/j.memsci.2004.08.036
[9] R.S. Figliola, D.E. Beasley, Theory and Design for Mechanical Measurements, 6th ed; John Wiley & Sons: Hoboken, NJ, USA, 2015.


DST@
1971-2021
DEPARTMENT OF
SCIENCE & TECHNOLOGY
Air-Conditioning
AND COOLING
PERSPECTIVES FROM INDIA
Dr. JBV Reddy
DST, India

Global air conditioner stock, 1990-2050

By 2050,

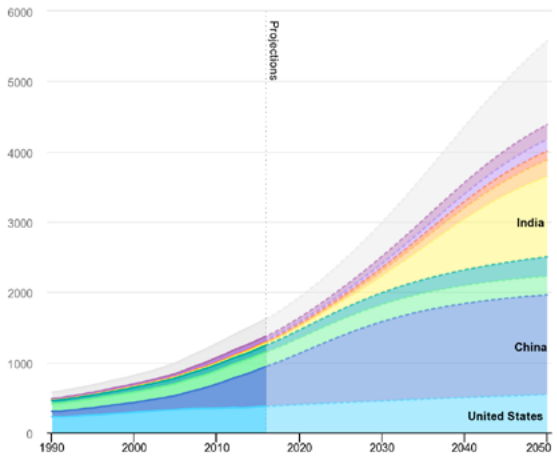
around 2/3 of the world's households

could have an air conditioner.

China, India and Indonesia

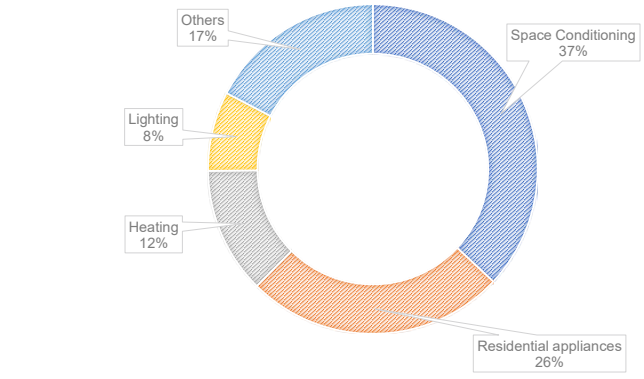
will together account for

half of the total number.



IEA, Global air conditioner stock, 1990-2050, IEA, Paris https://www.iea.org/data-and-statistics/charts/global-air-conditioner-stock-1990-2050

Global Electricity Energy Demand growth



Source: IEA 2018

Challenges in cooling: Indian Perspective

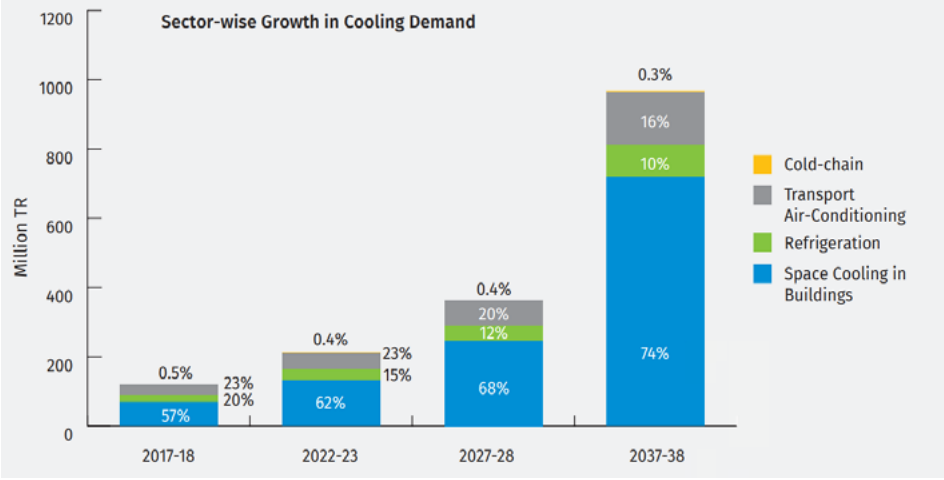


- **2.2x** Cooling energy demand of India to increase by 2027
- **57%** Indian energy demand for cooling comes from buildings
- **25 GW** new coal capacity can be avoided by energy efficiency in cooling
- **35%** India's commitment to reduce the carbon intensity by 2030[3]

Energy demand from fans and air coolers is higher than from ACs (currently)

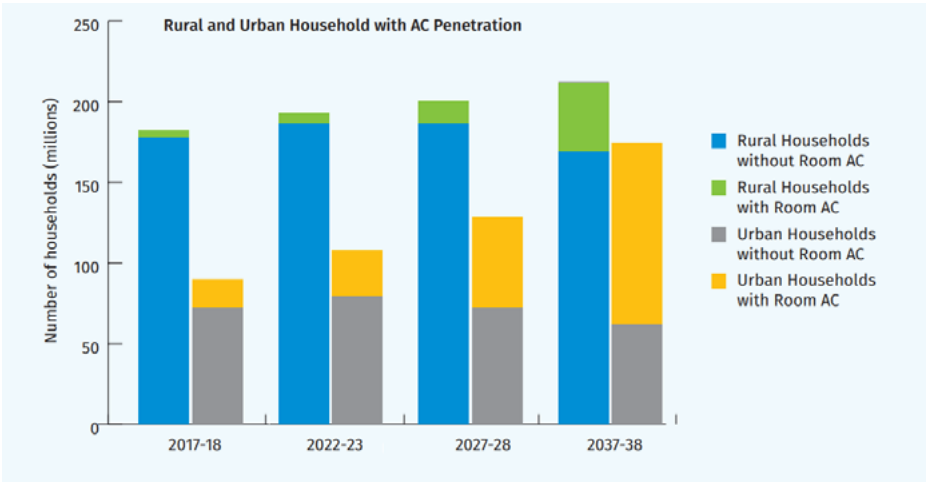
Source:Demand Analysis for Cooling by Sector in India in 2027,BEE, Ministry of power

Cooling demand growth projection



Source: ICAP report, 2019

Residential Cooling demand growth projection

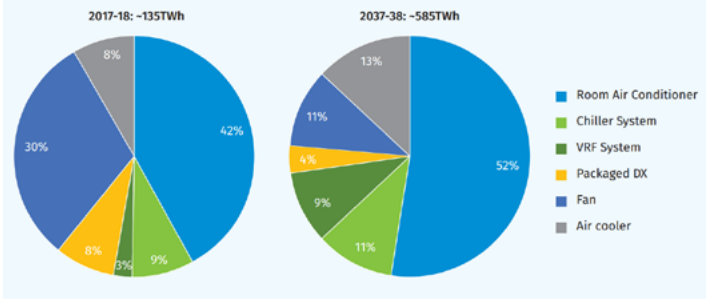


Source: ICAP report, 2019

Challenges in Heating and cooling

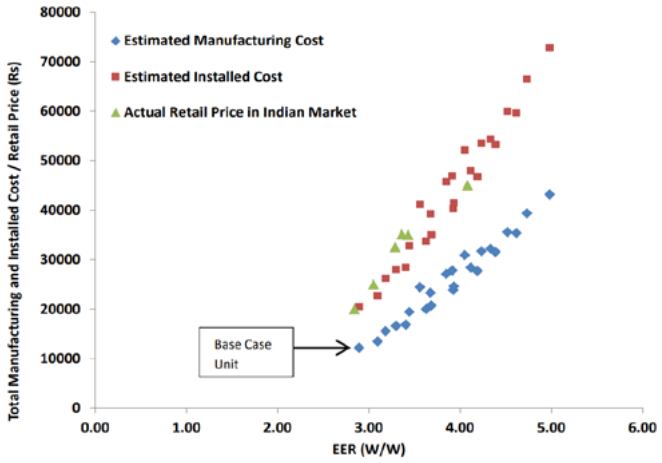
Space Cooling in Buildings

	2017	2027 (BAU)	2027 (Improved)	Saving Potential in 2027
Annual energy consumption (TWh)	126	281	233	17%
Total emissions ($mtCO_2e$)	124	284	224	21%



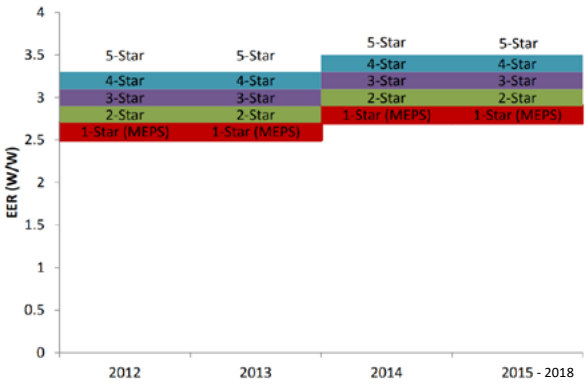
Source:Demand Analysis for Cooling by Sector in India in 2027,BEE, Ministry of power

Cost Vs Efficiency



Source: Increasing Efficiency of Room Air Conditioners in India: Opportunities and Challenges,LBNL

BEE - AC efficiency labelling



From 1st January 2021 to 31st December 2023

Indian Seasonal Energy Efficiency Ratio (kWh/kWh)		
Star level	Minimum	Maximum
1 star	3.3	3.49
2 star	3.5	3.79
3 star	3.8	4.39
4 star	4.4	4.99
5 star	5	

- 3 star ACs are most used on residential sectors[2]
- 1.5 TR is the most used

Source: Increasing Efficiency of Room Air Conditioners in India: Opportunities and Challenges,LBNL; Adaption of ATC standards by 2030[2]

India Cooling Action Plan

- The Indian plan (ICAP) was launched in March 2019 by the Ministry of Environment, Forests and Climate Change.
- ICAP provides a 20-year perspective and outlines actions needed to provide access to sustainable cooling.

1. Recognise "cooling and related areas" as a **thrust area** of research under national Science and Technology Programme
2. Reduce cooling energy requirements by 25%-40% **by 2037-38**
3. Reduce cooling demand across sectors by 20% - 25% **by 2037-38**
4. Reduce refrigerant demand by 25%-30% **by 2037-38**
5. Training and certification of 100,000 servicing sector technicians by **2022-23**.

Source: ICAP 2019

Policy guidelines towards thermal comfort

ECBC 2017
codes to maximise energy savings in large buildings

BEEP Guidelines for Energy-Efficient Residential Buildings
Comprehensive building design guide to achieve thermal comfort and reduce energy demand.



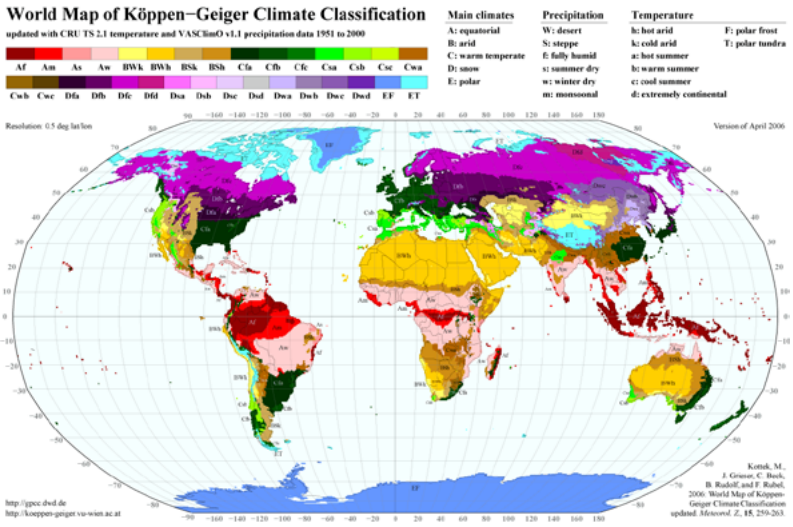
ECBC-R
Minimise heat transfer in residential buildings

CPWD General Specifications for HVAC Works 2017
recommended cooling demand densities (m2/TR)

NBC 2016
Building design code to ensure thermal comfort . Systems sized for not more than 26°C for cooling

ISHRAE
Handbooks on designing of HVAC

R&D Potential in India



- India embodies over 10 Koppen-Geiger climate zones
- Presents a natural **test bed of cooling-heating technologies**

DST's CLEAN ENERGY RESEARCH INITIATIVE



DST's Goal

- To bring R&D institutions, academia and industry on one platform to address industry relevant research problems



- DST is working very closely with industry, R&D Institutions and other government agencies to foster clean growth and low-carbon economic development

DST's Research Initiatives

01

Building Energy Efficiency

Energy Demand Reduction

Peak Demand Response

02

Smart Grids

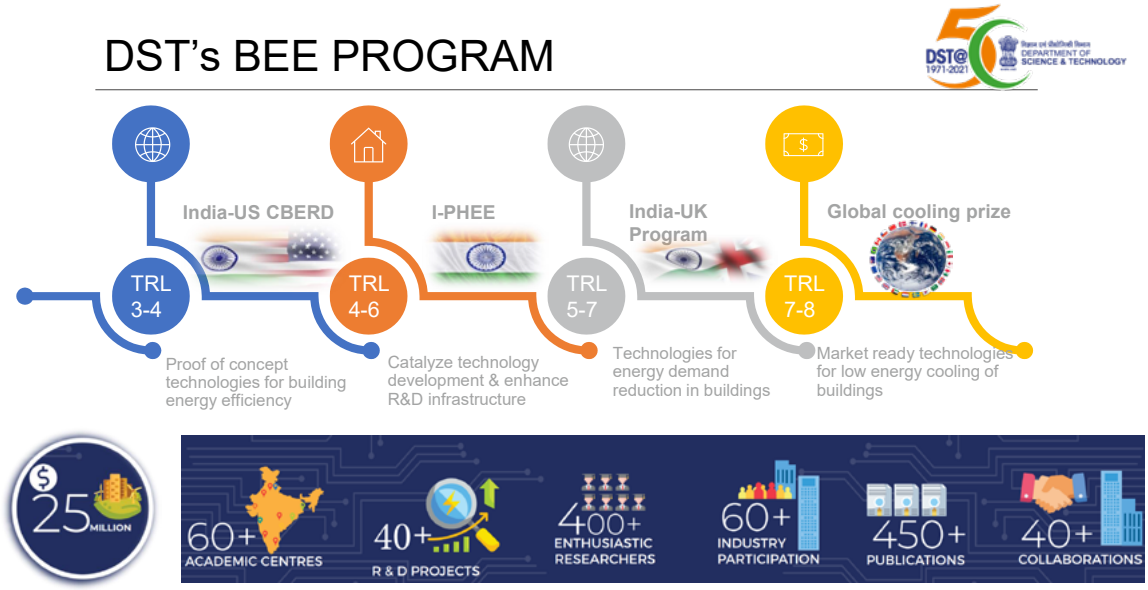
Resilient Grids
Demand Response



03

Mission Innovation

8 challenges on clean energy
IC1 and IC7 under this vector


DST's BEE PROGRAM
DST@50
1971-2021
DEPARTMENT OF SCIENCE & TECHNOLOGY
India-US CBERD
I-PHEE
India-UK Program
Global cooling prize
TRL 3-4
TRL 4-6
TRL 5-7
TRL 7-8
Proof of concept technologies for building energy efficiency
Catalyze technology development & enhance R&D infrastructure
Technologies for energy demand reduction in buildings
Market ready technologies for low energy cooling of buildings
$ 25 MILLION
60+ ACADEMIC CENTRES
40+ R & D PROJECTS
400+ ENTHUSIASTIC RESEARCHERS
60+ INDUSTRY PARTICIPATION
450+ PUBLICATIONS
40+ COLLABORATIONS

Thematic areas



Facilitating academic – industry collaboration and stakeholder engagement

Innovative Low-Carbon Building Materials
2/3rd reduction in embodied energy of buildings

Low-energy Heating and Cooling Technologies
1/3rd reduction in heating and cooling energy demand

ICT and Building Controls
1/5th reduction in building energy demand

Building Integration
Effective integration of energy efficient technologies

To demonstrate building energy demand reduction by ***1/3rd***

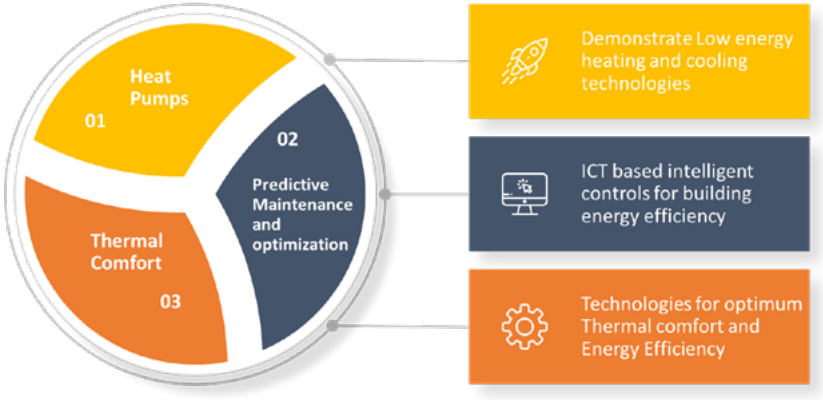

DST@
1971-2021
DEPARTMENT OF
SCIENCE & TECHNOLOGY
MI
MISSION
INNOVATION
accelerating the clean energy revolution
IC7: Affordable Heating and Cooling of Buildings

MISSION INNOVATION accelerating the clean energy revolution

IC7: Affordable Heating and Cooling of Buildings

DST@50 1971-2021 DEPARTMENT OF SCIENCE & TECHNOLOGY

Actively contributing to the R&D initiatives in the following fields

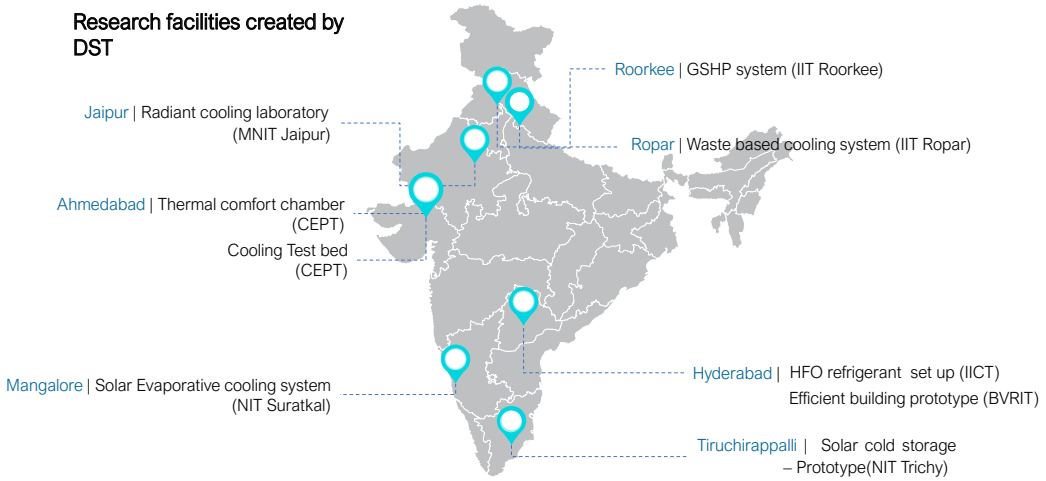


HVAC Activities Pursued by DST

Technologies	Type	Status
Ground source Heat pump	Full scale prototype - Building cooling	Developed
Solar powered Cold storage	Full scale prototype - Food storage	Developed
HFO-1234yf refrigerant	Refrigerant	In progress
Solar and Agri-waste based cooling system	Experimental Prototype	Developed
Methanol based Fuel cell system	Full scale prototype	Developed and demonstrated
Solar based Humidifier and dehumidifier	Experimental prototype	Developed
PCM based Thermal cold storage	Experimental prototype	Developed
Cooling using geothermal pile	Laboratory scale prototype	In progress
Low energy cooling test bed	Testing Facility	Developed

Research Facilities - Low Energy Heating and Cooling

Research facilities created by DST




Nurturing Startups


DST's STARTUP GALLERY
@
ACREX 2020, DELHI



DST's
STARTUP GALLERY @
Smart cities India 2021 Expo,
DELHI



Dr. JBV Reddy
Department of Science and Technology, India
jbvreddy@nic.in


IIF
IIR
INSTITUT INTERNATIONAL DU FROID
INTERNATIONAL INSTITUTE OF REFRIGERATION
THE LOW-GWP
REFRIGERANT CHALLENGE
IEA HP CONFERENCE
APRIL 27, 2021
Didier Coulomb
Director General

Plan

Introduction: IIR and low-GWP refrigerants

I. Environmental challenges and refrigerants

I. Required actions

Conclusion: Refrigerants and national strategies

Introduction: Who is the IIR?

Founded in 1908

Intergovernmental science and technology-based organisation

Dissemination and promotion of knowledge on all refrigeration technologies and uses



Key Domains Include…

- Food quality and safety from farm to consumer
- Comfort in homes and commercial buildings
- Health products and services
- Low-temperature technology and liquefied gas technology
- Energy efficiency
- Use of non-ozone depleting and low global warming refrigerants in a safe manner



- Databases
- Publications
- Conferences
- Working groups
- International, regional and national projects

….

a lot of information on refrigerants

I. Environmental challenges and refrigerants (1/2)

- The stratospheric ozone layer
  Montreal protocol
  Phase out of HCFCs

- Climate change
  - Refrigerating systems alone:
    - Energy 63% of the global warming impact of the systems
    - Refrigerants 37%
    - Total: 7.8% of global greenhouse gases emissions (IIR IN); increasing impact because of increasing refrigeration needs
  - Others: materials
  - Other issues: insulation, passive buildings…..

I. Environmental challenges and refrigerants (2/2)

- TFA
- Safety
- The Kigali amendment of the Montreal Protocol:
  Different schedules depending on the countries
  →Risks (traffic…), but same direction for all
- The Paris agreement
  International objectives but National Determined Contributions (NDCs) to be revised in 2021

II. Required actions (1/2)

- Research and development

  Few very new refrigerants possible (NIST study)

  → Low-GWP refrigerants will therefore continue to be used: natural refrigerants (ammonia, CO_2, hydrocarbons, water, air) + HFOs and mixtures

  → + Relatively low-GWP refrigerants (R32)

  + Intermediate refrigerants

  + Not-in-kind refrigeration systems (adsorption/absorption, solid-state technologies…)

  In any case, because of increasing constraints, many technological developments are underway and must continue.

II. Required actions (2/2)

- Immediate actions are however necessary:
  - Old equipment → Reduce leakages (containment, certification …)
    Intermediate refrigerants
  - New equipment → Existing low-GWP refrigerants (IIR INs…)
- Safety issues
  New international standards on flammability must be implemented in building codes, practice (IIR WG)
- Training on low-GWP refrigerants due to safety issues + energy efficiency issues and maintenance (Real Alternatives for Life…)
- Coordination between policies: renewable energies (solar refrigeration…), energy efficiency (Labelling, Ecodesign…)

Conclusion

- Growing refrigeration needs: air conditioning, cold chain for food and health products (vaccines…), heat pumps
  Refrigeration can be a tool for mitigating and adaptating to global warming
- International awareness: in 2019, United Nations declarations.
  Partnership with UNEP, ISA…
- Until now, actions were essentially focused on refrigerants. The energy issue is now at the top of the agenda: moving to a low-GWP refrigerant without a better energy efficiency, a new design… is not enough.
- The new challenges: including the refrigeration issue in the new NDCs to be presented in Glasgow.

  + helping developing countries to move.

New IIR website



IIFIIR.ORG

Now online!

IIFIIR.ORG 11


IIF
IIR
INSTITUT INTERNATIONAL DU FROID
INTERNATIONAL INSTITUTE OF REFRIGERATION
THANK YOU
QUESTIONS?

AUTHOR INDEX

AUTHORS INDEX

Author	Paper No.	Author	Paper No.
A. Phong Tran	340	Basil Anabtawi	206
Aaron Tam	283	Beat Wellig	271, 272
Abdelrahman Hassan	103	Beom Joon Lee	227, 240, 315
Abhishek Bandlore	016	Beom-Jun Kim	092, 093
Ahmad Abu-Heiba	206	Bernd Windholz	075
Ajay Prasad	014	Bernhard Adler	100
Akihiro Ichikawa	322	Biagio Lamanna	136
Akira Kobayashi	122	Bian Mengmeng	285
Akira Koyama	130	Bin Hu	135, 139
Alan S. Fung	123	Birgo Nitsch	178
Alisa Freyre	270	Bo Shen	204, 230
Amirali Rokn	123	Bo Zheng	031
Ammar M. Bahman	082	Bong Soo Choi	227
Ammi Amarnath	283	Bongsu Choi	315
Anderson Bortoletto	027	Brian Elmegaard	170
Andrea Frazzica	176, 181	Brigitte Blank-Landeshammer	192
Andreas Strehlow	178	Brigitte Gonzalez	050
Andreas Karageorgis	316	Byongguk Lim	321
Andreas Längauer	100	Byung Ha Kang	118
Andreas Lehr	272	Carlos Infante Ferreira	306, 307, 308, 309
Andreas Sporr	075	Carolina De Sousa Fraga	254, 255
Andrew Marina	156	Carolina Fraga	270, 273
Angeles Rivero Pacho	176	Caroline Haglund Stignor	131, 180, 183, 184, 352
Anna Ma	071	Carsten Wemhoener	162, 165, 167, 168
Annelies Vandermeulen	301	Cate Lyon	150, 151
Anton Soppelsa	281	Chan Ho Jeong	294
Anton Wemmers	156	Chan Ho Song	140
Antonino Bonanno	181	Chang Xu	248
Armin Hafner	141	Chaobin Dang	138
Arno Dentel	042, 162	Chen Yang	127
Ashish Chouhan	014	Chenghao Wei	286
Asier Martinez-Urrutia	103,104	Chenxi Ni	291
Aziz Mbaye	112, 310	Choongyeop Lee	312
Bamdad Bahar	014, 016, 017, 021, 023, 025, 026, 027, 054	Christian H. Kasess	192
Christian Kley	243	Dong Woo Hwang	262
Christian Köfinger	192	Donghyun Seo	312

Author	Paper No.	Author	Paper No.
Christian Rakusch	100	Dongkyu Kim	349, 350
Christian Sonner	203	Dongwon Han	260
Christian Vering	068, 069	Donik Ku	003, 355
Christiane Thomas	191, 229	Drew Turner	198, 329
Christina Betzold	042, 162	Eberhard Nicke	340
Christoph Höges	069	Eberhard Schlücker	239
Christoph Reichl	068, 088, 160, 192	Eckhard A. Groll	082, 102, 210, 311, 332
Christoph Thoma	134	Edo Wiemken	176
Chulwoo Roh	227, 240, 315	Edward J. Lucas	271, 272
Chun Yang	127	Eiji Hihara	138
Chunlu Zhang	101, 117, 127	Eirini Litina	268
Claus Madsen	170	Elliot Romano	273
Clemens Dankwerth	203	Emilio Navarro-Peris	079, 108
Constantin Zenz	067	Erasmus Damgaard Rothuizen	170
Cordin Arpagaus	059, 062, 216	Estefania Hervas-Blasco	079
Dae Bok Keon	262	Eun Seok Wang	227, 240
Daisuke Narumi	269, 286	Eun-Chul Kang	039
Daniel Colbourne	247	Euy-Joon Lee	039
Daniel Lange	241	Evgueniy Entchev	039
Daniel Steger	239	Fabian Ochs	066, 162, 175
Danny Günther	275	Fatih Meral	210, 311
David McAndrews	016	Felipe Trebilcock Kelly	103
Davide La Rosa	181	Felix Hochwallner	088
Davide Ziviani	082, 102, 332	Felix Linhardt	088
Di Wu	135	Feng Zhou	071
Didier Coulomb	357	Fleury De Oliveira Filho	254
Ding Lu	049	François Bessac	160
Dirk Müller	043, 068, 069, 074, 179	François Boudehenn	341
Dominic Zajonc	272	Franz Helminger	075, 097
Dominik Seliger	241	Franziska Bockelmann	008, 243
Dong Ho Kim	140	Frederic Amblard	222
Dong Kyu Kim	348	Frédéric Bless	062
Fu Yijun	285	Hidekazu Okamoto	213
Gabriel Zsembinszki	178	Hideki Tanaka	147
Gabyong Kim	124	Hideyuki Fujimoto	128
Gaétan Chardon	087	Hiroki Hayamizu	213
Gawon Lee	118	Hiroshi Nagai	122
George Hinopoulos	316	Hiroshi Nakayama	147, 148
George Hunter	055	Hiroyuki Yuki	163
Georgios Dermentzis	066	Hitoshi Akai	325

Author	Paper No.	Author	Paper No.
Gerrit Fueldner	176	Holger Waubke	192
Gerwin H.S. Drexler-Schmid	192	Hongbo Li	139
Fu Yijun	285	Hongfei Shu	127
Geun-Hyung Lee	342	Honghyun Cho	288
Gilbong Lee	227, 240, 315	Ho-Sang Ra	240, 315
Gregor P. Henze	281	Hua Liu	139
Gu Hwang Kang	353, 354	Hye-Jin Cho	090, 091
Gulsun Demirezen	123	Hyeongjoon Seo	321
Gumbae Choi	245	Hye-Won Dong	092, 095
Gunnar Harhausen	042	Hyoin Lee	022
Guoyuan Ma	013, 071	Hyung Joo Lee	294
Hae Eun Song	232	Hyung Won Choi	118
Haejun Lee	245	Hyungki Shin	227, 240, 315
Hai Trieu Phan	050, 341	Hyunjeong Lim	003
Haihong Huang	291	Ikurou Akada	344
Han Sol Jung	124	Inguk Hwang	245
Hanlong Wan	196	Ivan Bellanco	072
Hansol Lim	094, 095	Ivan Malenkovic	133, 134
Haotian Liu	332	Ivo Pothof	309
Harish Opradishta	023, 054	J.B.V. Reddy	356
Haruki Mitarai	344	Jacob Zergy	017, 021, 025, 026, 027
Hengyi Zhao	334, 335	Jae Chun Ryu	262
Henrik Hellgren	160, 184	Jae Dong Chung	086
Heunghee Bae	196	Jae Yeon Kim	113
Hidekazu Kainuma	122	Jae-Hee Lee	095
Jaehwan Shim	312	Jonas Klingebiel	068
Jaewan Joe	010	Jonathan Paul Ore	311
Jae-Weon Jeong	090, 091. 092, 093, 094, 095	Jong Jae Cho	227
Jaeyeon Kim	245	Jong Min Choi	258
Jakub Garbacik	351	Jongjae Cho	315
James E. Braun	346	Jong-Seok Lee	236
Jan A. Stampfli	271	Jongsoo Jeong	322
Jan Gerritsen	141	Jong-Taek Oh	336
Jan Richarz	179	Joohee Song	350
Jang Seok Lee	118	Jose Miguel Corberan	079, 108
Jason Woods	023	Joshua Hughes	111
Jaume Salom	072	Julien Hergott	341
Jea Wan Kim	113	Jun Hwang	321
Jeffrey Spitler	044, 045	Jens Gollasch	340
Hobyung Chae	282	Jerine Ahmed	283

Author	Paper No.	Author	Paper No.
Jessen Page	222	Jungchul Kim	349
Jessica Benson	131, 180	Junhyun Cho	240, 315
Ji Hwan Jeong	342	Junya Yamagishi	244
Jia-Hao Cheng	101, 117	Jürgen Fluch	241
Jiatong Jiang	139	Jussi Alpua	070
Jiazhen Ling	036, 109, 110	Jussi Hirvonen	164
Jihun Lim	003	Just Remmelts	308
Jihwan Jeong	022	Justin A. Weibel	332
Jin Woo Yoo	096, 140	Justin Tamasauskas	252
Jing Zhang	127	Kamil Kwiatkowski	351
Jintang Li	285	Karl Ochsner Sen.	098
Jinwook Lee	003, 355	Karl Ponweiser	241
Jinyoung Ko	091	Kashif Nawaz	204
Johann Emhofer	068, 088, 098, 178, 192, 352	Katsumi Hashimoto	130
Johannes Krämer	178	Katsunori Nagano	282, 325
Jóhannes Kristófersson	170	Katsuya Ueno	213
Johannes Oehler	340	Katsuyuki Osawa	122
John Clauß	165	Liang-Liang Shao	101, 117, 127
Kazuki Wajima	163	Libing Yang	039
Keiko Hosaka	122	Lieve Helsen	301
Kenji Ueda	163	Li-Hua Lin	092
Kenneth Hoffmann	141	Lindsay Sugden	150, 151
Khalid Ullah	123	Lingkun Liu	032
Ki Young Shin	262	Lingyan Yang	285
Kiyoshi Saito	250, 297, 322, 345	Lingzhe Wang	110
Klemens Marx	178	Lorenz P. Rast	271
Koichi Kitamura	250	Lovisa Axelsson	180
Koji Enoki	344, 345	Lucas Alvarez	108
Koji Takiguchi	250	Luisa F. Cabeza	178
Koji Tanifuji	325	Lukas Rominger	165, 167, 168
Koji Yamashita	122	Lingkun Liu	032
Kong Hoon Lee	140	Ma Ning	285
Konstantin Finkbeiner	179	Mahmood Thabaddor	214
Korbinian Kramer	224	Makoto Ito	138
Kosuke Bizen	250	Kwesi Mensah	258
Kousaku Nishida	344	Kyle R. Gluesenkamp	176, 201, 206, 209,
Kwang Ho Lee	258	Kwang-Seob Lee	039
Kwang-Seob Lee	039	Kyu Heon Rho	348
Jun Hyun Cho	227	Laura Maier	179
Jun Shishido	130, 325	Laure Itard	309

Author	Paper No.	Author	Paper No.
Laure Meljac	238, 247	Maoqiong Gong	049
Laurent Abbas	198	Mara Magni	175
Laurent Georges	165	Marcello Aprile	176
Lei Wang	071	Marek Miara	203, 275
Lei Yang	291	Mario Motta	176
Lena Schnabel	108, 203	Mark Golben	017, 021
Lennart Stania	082	Mark Stutman	023, 054
Leping Zhang	198, 329	Markus Lindahl	131, 183
Liang Shi	056	Markus Nürenberg	043, 068, 069, 074, 179
Markus Peter	008	Minjun Kim	288
Markus Zwiefler	239	Minkyu Jung	003, 349
Martin Forsen	238, 247	Minsoo Kim (Chung-Ang Univ.)	349, 350
Martin Kegel	252	Minsoo Kim (LG Electronics)	111
Martin Larsson	180	Minsu Park	047
Martin N. Johansson	004	Minsung Kim	003, 349, 355
Martti Kukkola	070	Mirza Popovac	067, 088
Masaaki Miura	147	Mitsuhiro Fukuta	128
Masaaki Motozawa	128	Mitsuhiro Ishikawa	325
Masafumi Hirota	148	Miwako Fujita	269, 286
Masafumi Katsuta	244	Moon Yong Park	086
Masanobu Sakai	163	Moonis Ally	230
Masanori Kobayashi	048	Muhamad Yulianto	297
Masashi Momota	331	Myung Sup Yoon	035, 236, 339
Masashiko Kumagai	331	Naiping Gao	334, 335
Massimo Cimmino	112	Naoki Kobayashi	163
Mathias Schlosser	008	Naoya Miyoshi	279
Mathilde Wirtz	341	Navin Kumar	206
Matt Golben	017	Neil J. Hewitt	104
Matthias Berthold	059	Ngoc Vi Cao	086
Matthias Rüetschi	270	Niansheng Han	347
Mauro Pipiciello	281	Nicholas P. Salts	210
Mehdi Rasti	342	Nicky Jason Cowan	253
Melanie Cop	229	Nicola Franzoi	066
Melissa Lapsa	010	Michael Wiesflecker	178
Malick Kane	310	Michael Lauermann	067, 075, 097, 098
Maneesh Avadhani	307	Michael Schmid	206
Man-Hoe Kim	314, 316	Mick Eschmann	059
Manju Oh	245	Miguel Ramirez Stefanou	103, 104
Manuel Prinzing	059	Min Kyeong Park	258
Manuel Verdnik	172	Min Soo Kim (SNU)	047, 096, 140, 353, 354

Author	Paper No.	Author	Paper No.
Ming Qu	056, 201	Robert E. Critoph	176
Mini Malhotra	010	Robert Langner	275
Omar Montero Dominguez	255	Roberto Fedrizzi	281
Ook Joong Kim	140	Roberto Fumagalli	160
Orkan Kurtulus	311	Rodrigo De Pablo	270
Oskar Räftegård	131, 180	Rohit Bhagwat	206
Paloma Albaladejo	108	Rohit Dhumane	110
Parveen Dhillon	346	Roland van Rooyen	307
Patrick J. Geoghegan	332	Roman Schwarz	168
Patrizia Norina Melograno	133	Ron Zevenhoven	004
Peng Gao	101	Rong Zhuang	031
Peng Shao	101	Roxanne Pieterse	150
Peter Schossig	133, 176, 203	Ryosuke Suemitsu	163
Peter Kremers	156	Sabrina Dusek	097
Peter Wimberger	088	Saeed Moghaddam	206
Philip Boudreaux	209	Saikee Oh	196
Philipp Mascherbauer	178	Samuel Boahen	258
Philipp Mehrfeld	043, 074	Samuel Dorman	021
Philipp Wagner	193	Sander Tensen	308
Pia Tiljander	180	Sangamesh Hosur	214
Pierre Hollmuller	254, 255, 270, 273	Sangchul Bae	244
Premanand Sivakumar	014	Sanghun Jeong	355
Quang Vu Pham	336	Sangmi Choi	003, 355
Quentin Blondel	050	Sara Beaini	283
R.Z. Wang	135, 139	Sarah Henn	179
Raimund Zitzenbacher	178	Sarah Kim	198
Ralph Herrmann	181	Seama Koohi-Fayegh	326
Ralph Kuster	059	Sebastiaan Knepper	309
Ramanunni Parakkal Menon	222	Seiichi Yamaguchi	322, 250, 297
Ramona Nosbers	229	Richard Rode	206
Raphael Agner	271	Riku Fukuju	345
Rene Rieberer	172, 193	Riley B. Barta	082, 102
Nicolas Tauveron	050	Rio Asakawa	244
Nicolas Voeltzel	050	Sergio Maria Capanelli	136
Nikhilkumar Shah	104	Shehryar Ishaque	314
Nobuhiro Takahashi	331	Shigeki Ishihara	122
Ola Gustafsson	131, 180, 183, 184	Sho Fukuda	279
Oliver Obst	210, 311	Shota Ikutaya	244
Oliver Ziegler	191	Shuxue Xu	013
Omar Abdelaziz	204	Sidharth Sanadhya	206

Author	Paper No.	Author	Paper No.
Signhild Gehlin	044, 045	Takaoki Suzuki	250, 297, 322
Sigrid Feyaerts	301	Takashi Inoue	331
Simon Braungardt	203	Takashi Kuwabara	130
Simon Buesser	167, 168	Takenobu Kaida	343
Simon Callegari	254, 255	Takeshi Kondo	282
Simon Smeding	156	Tanja Osterhage	179
Simon Spoelstra	156	Tao Cao	036, 196
Simone Buffa	281	Taoli Gu	016
Siyoung Choi	022	Tetsuo Otsuka	213
Sjors Wagenaar	306	Tetsusiro Iwatsubo	048
Soo Kwang Yang	232	Tetsuya Kobayashi	344
Soo-Jin Lee	094	Therese Guttmann	352
Soyeon Kim	003	Thibault Péan	072
Stefan Bertsch	059, 062, 216	Thomas Fleckl	088, 160
Stefan Flück	272	Thomas Nowak	267, 268
Stefan Löwe	181	Thomas Schoberer	352
Stephan Göbel	043	Thore Oltersdorf	160, 203
Stephanie Breton	252	Tiantian Wang	334, 335
Steven Metcalf	176	Tiejun Wang	291
Su Liu	090	Tilman Barz	178
Su-Il Park	342	Timo Methler	203
Sujin Bae	355	Tingwei Fan	334
Sun Ik Na	353, 354	Tomasz Walczak	351
Sung Bin Hong	096	Tommaso Toppi	176
Sung Je Lee	262	Tommy Walfridson	131, 180
Susanna Bordin	042	Torben Funder-Kristensen	329
Svein Ruud	183	Ximo Masip	079
Tor-Martin Tveit	004	Xingyu Liang	117, 127
Toshihiko Okuno	130	Toshihiko Ota	048
Selorm Kwaku Anka	258	Toshimasa Kato	122
Seok Ho Yoon	140	Toshio Otaka	145
Seong Hyuk Lee	294	Tsubasa Ito	148
Seong-Yong Cheon	090, 091	Tyler Shelly	102
Svend Pedersen	160	Tzu Wei Yeh	145
Tadahiko Ibamoto	331	Ullrich Hesse	191, 229
Tadao Watanabe	250	Urs Gumbel	134
Taesung Kim	113	Utsav Aryal	014
Takaharu Hasegawa	122	Valentin Salgado Fuentes	170
Takahiro Iwasaki	250	Valeria Palomba	181
Takao Katsura	282, 325	Van Baxter	010, 204

Author	Paper No.	Author	Paper No.
Veronika Wilk	075, 097, 241	Yong Hwan Eom	096
Vikrant Aute	036, 109, 110	Yong Tae Kang	118, 124
Viral K. Patel	206, 209	Yong-Kwon Kang	093, 094
W. Travis Horton	346	Yoong Chung	140
Wei Wei	285	Yoshie Togano	163
Wiebke Brix Markussen	170	Yoshihisa Sakamoto	122
William Monteleone	066	Yoshitaka Sakata	282
William Tomhon	021, 054	Young Chull Ahn	232
Wim Boydens	301	Young Jin Baik	227, 240, 315
Won Hee Kang	258	Young Soo Chang	260
Won Sik Yoon	035, 236, 339	Youngju Joo	321
Woo Su Lee	086	Young-Soo Lee	240
Xabier Peña	103	Youngsuk Nam	312
Xiang Cao	101, 127	Yu Liu	071
Xiangfei Liang	031, 032	Yueyue Shao	013
Xiaobing Liu	023, 056	Yueyue Wang	013
Xlaohui Yu	248	Yuichi Yashima	325
Xiaoning Chen	127, 347	Yuji Naka	147
Xiaoya Jia	071	Yu-Jia He	117
Yu-Jin Hwang	093	Zhanpeng Liu	334, 335
Yu-Jin Kim	039	Zheng Ge	297
Yuka Ogasawara	048	Zhenning Li	109
Yuki Shimizu	279	Zhihua Zhang	138
Yuki Terakado	244	Zhiping Zhang	139
Yunchan Shin	288	Zhiyao Yang (ORNL)	176, 246
Yunho Hwang	036, 196	Zhiyao Yang (Purdue Univ.)	201, 206
Yutaka Shoji	325		
Xuan Quang Duong	086		
Xuchao Ying	179		
Xudong Wang	055		
Xueqiang Dong	049		
Yanxing Zhao	049		
Yasushi Hasegawa	163, 279		
Yechan Yun	260		
Yeon Ho Kim	113		
Yeonghun Kim	288		
Yifeng Gao	334, 335		
Yin Bai	049		
Yiyuan Qiao	036		
Yoichi Miyaoka	250, 297, 322		

본 사업은 기획재정부의 복권기금 및 과학기술정보통신부의 과학기술진흥기금으로 추진되어 사회적 가치 실현과 국가과학기술 발전에 기여합니다.

This work was supported by the Korean Federation of Science and Technology Societies(KOFST) grant funded by the Korean government.